

ADVANCES IN MOLTEN SLAGS, FLUXES, AND SALTS:

Proceedings of



May 22–25, 2016

Seattle Grand Hyatt
Seattle, Washington, USA

Edited by:

**Ramana G. Reddy, Pinakin Chaubal,
P. Chris Pistorius, and Uday Pal**

**ADVANCES IN MOLTEN
SLAGS, FLUXES, AND SALTS:**

Proceedings of



ADVANCES IN MOLTEN SLAGS, FLUXES, AND SALTS:

Proceedings of



Sponsored by

Extraction & Processing Division and
Materials Processing and Manufacturing Division of
The Minerals, Metals & Materials Society (TMS)

Held

May 22–25, 2016
Seattle Grand Hyatt
Seattle, Washington, USA

Edited by

**Ramana G. Reddy
Pinakin Chaubal
P. Chris Pistorius
Uday Pal**

Editors

Ramana G. Reddy
Pinakin Chaubal

P. Chris Pistorius
Uday Pal

ISBN 978-3-319-48625-3
DOI 10.1007/978-3-319-48769-4

ISBN 978-3-319-48769-4 (eBook)

Chemistry and Materials Science: Professional

Copyright © 2016 by The Minerals, Metals & Materials Society
Published by Springer International Publishers, Switzerland, 2016
Reprint of the original edition published by John Wiley & Sons, Inc., 2016, 978-1-119-30876-8

This work is subject to copyright. All rights are reserved by the Publisher, whether the whole or part of the material is concerned, specifically the rights of translation, reprinting, reuse of illustrations, recitation, broadcasting, reproduction on microfilms or in any other physical way, and transmission or information storage and retrieval, electronic adaptation, computer software, or by similar or dissimilar methodology now known or hereafter developed.

The use of general descriptive names, registered names, trademarks, service marks, etc. in this publication does not imply, even in the absence of a specific statement, that such names are exempt from the relevant protective laws and regulations and therefore free for general use.

The publisher, the authors and the editors are safe to assume that the advice and information in this book are believed to be true and accurate at the date of publication. Neither the publisher nor the authors or the editors give a warranty, express or implied, with respect to the material contained herein or for any errors or omissions that may have been made.

Printed on acid-free paper

This Springer imprint is published by Springer Nature
The registered company is Springer International Publishing AG
The registered company address is: Gewerbestrasse 11, 6330 Cham, Switzerland

TABLE of CONTENTS

Advances in Molten Slags, Fluxes, and Salts: Proceedings of the 10th International Conference on Molten Slags, Fluxes and Salts

Preface	xxiii
Conference Organizing Committees	xxv
Proceedings Reviewers	xxix

Plenary Session

Waste to Value in Steelmaking	3
<i>Samane Maroufi, Irshad Mansuri, Paul O’Kane, Catherine Skidmore, Zheshi Jin, Andrea Fontana, Magdalena Zaharia, and Veena Sahajwalla</i>	
Current Status of Slag Design in Metallurgical Processes	17
<i>Dong Joon Min and Sung Mo Jung</i>	
Refractory Metals Recovery from Industrial Wastes	29
<i>Tran Van Long, Hironori Murase, Takahiro Miki, Yasushi Sasaki, and Mitsutaka Hino</i>	

Industrial Applications: Ferroalloys and Silicon

Softening and Melting of SiO ₂ , an Important Parameter for Reactions with Quartz in Si Production	43
<i>Eli Ringdalen and Merete Tangstad</i>	
High Temperature Corrosion Mechanisms of Refractories and Ferro-Alloy Slags	53
<i>Stefan Luidold, Christine Wenzl, Christoph Wagner, and Christoph Sagadin</i>	
Fundamental Investigation of Reduction and Dissolution Behavior of Manganese Ore at High Temperature	63
<i>Yusuke Fujii, Yoshie Nakai, Yu-ichi Uchida, Naoki Kikuchi, and Yuji Miki</i>	
An Investigation on the Formation of Molten Salt Containing Chromium Oxide during Roasting of Chromite Ore with Sodium and Potassium Hydroxides	71
<i>L. Escudero-Castejon, S. Sanchez-Segado, S. Parirenyatwa, and A. Jha</i>	

Effect of the CaO Addition in the Fusion Process of Nickeliferous Laterites for Ferronickel Production	79
<i>Sandra Diaz Bello, Oscar J. Restrepo, and Álvaro H. Forero P</i>	
Defining the Operating Regime and Methodology for the Furnace Method for the Production of Low Carbon Ferrochrome	87
<i>Heine Weitz and Andrie Garbers-Craig</i>	
Optimized Slag Design for Maximum Metal Recovery during the Pyrometallurgical Processing of Polymetallic Deep-Sea Nodules	97
<i>David Friedmann and Bernd Friedrich</i>	
Review of Liquidus Surface and Phase Equilibria in the TiO ₂ -SiO ₂ -Al ₂ O ₃ -MgO-CaO Slag System at PO ₂ Applicable in Fluxed Titaniferous Magnetite Smelting	105
<i>Xolisa Goso, Johannes Nell, and Jochen Petersen</i>	

Inclusions and Clean Steelmaking

Effect of Ladle Furnace Slag Composition in Si-Mn Killed Steel Transient Inclusion Changes	117
<i>Stephano P.T. Piva and P. Chris Pistorius</i>	
Reduction of Slag and Refractories by Aluminium in Steel and Inclusion Modification	127
<i>Haoyuan Mu, Bryan A. Webler, and Richard J. Fruehan</i>	
Reactivity of Selected Oxide Inclusions with CaO-Al ₂ O ₃ -SiO ₂ -(MgO) Slags	135
<i>B.J. Monaghan, H. Abdeyazdan, R.J. Longbottom, N. Dogan, M.A. Rhamdhani, and M.W. Chapman</i>	
A Study on Calcium Transfer from Slag to Steel and Its Effect on Modification of Alumina and Spinel Inclusions	145
<i>Deepoo Kumar and P. Chris Pistorius</i>	
Effect of Al ₂ O ₃ Content in Top Slag on Cleanness of Stainless Steel Fe-13Cr	155
<i>Qi Wang, Lijun Wang, and Kuochih Chou</i>	

Slag and Salt Structure

- Understanding of Cr-Containing Slags by Sulphide Capacity and Structural Study167
Lijun Wang and Kuo-chih Chou
- Structure Studies of Silicate Glasses by Raman Spectroscopy175
Chen Han, Mao Chen, Ron Rasch, Ying Yu, and Baojun Zhao
- Relation between Acoustic Properties and Structures on Molten Alkali Silicates183
Miyuki Hayashi

Use of Slags, Fluxes and Salts in Recycling

- Equilibria of Gold and Silver between Molten Copper and $\text{FeO}_x\text{-SiO}_2\text{-Al}_2\text{O}_3$ Slag in WEEE Smelting at 1300 °C193
Katri Avarmaa, Hugh O'Brien, and Pekka Taskinen
- Experimental Study on Smelting of Waste Smartphone PCBs Based on $\text{Al}_2\text{O}_3\text{-FeO}_x\text{-SiO}_2$ Slag System203
Youqi Fan, Yaowu Gu, Qiyong Shi, Songwen Xiao, and Fatian Jiang
- Recovery of Valuable Metals from Spent Lithium-Ion Batteries by Smelting Reduction Process Based on $\text{MnO-SiO}_2\text{-Al}_2\text{O}_3$ Slag System211
Ren Guoxing, Xiao Songwen, Xie Meiqiu, Pan Bing, Fan Youqi, Wang Fenggang, and Xia Xing

Crystallization/Freeze Linings

- In-Situ Observation of Rare Earth Containing Precipitated Phase Crystallization and Solidification of $\text{CaO-SiO}_2\text{-Nd}_2\text{O}_3$ and $\text{CaO-SiO}_2\text{-Nd}_2\text{O}_3\text{-P}_2\text{O}_5$ Melts221
Thu Hoai Le, Mayu Aketagawa, Annelies Malfliet, Bart Blanpain, and Muxing Guo
- In-Situ Studies on the Crystallization of $\text{CaO-SiO}_2\text{-CaF}_2\text{-CeO}_2$ System by a Confocal Laser Scanning Microscope229
Zengwu Zhao, Zhuang Ma, Fushun Zhang, Yongzhi Li, Yongli Jin, Xuefeng Zhan, and Baowei Li

Crystallization Kinetics of CaO-SiO ₂ -Al ₂ O ₃ -MgO Slags	237
<i>Shaghayegh Esfahani and Mansoor Barati</i>	
Freeze-Lining Formation from Fayalite-Based Slags	245
<i>Liugang Chen, Muxing Guo, Shuigen Huang, Peter Tom Jones, Bart Blanpain, and Annelies Malfliet</i>	

Mold Flux

Root Cause Analysis of Surface Defects in Coils Produced through Thin Slab Route	255
<i>Diptak Bhattacharya, Siddhartha Misra, Avinash Kumar, and Vinay V Mahashabde</i>	
Advanced Mold Flux Development for the Casting of High-Al Steels	263
<i>Dan Xiao, Wanlin Wang, Boxun Lu, and Xinwang Zhang</i>	
A Reaction Model to Simulate Composition Change of Mold Flux during Continuous Casting of High Al Steel	271
<i>Min-Su Kim and Youn-Bae Kang</i>	
Evaluation of Mold Flux for Continuous Casting of High-Aluminum Steel ...	279
<i>Wei Yan, Alexander McLean, Yindong Yang, Weiqing Chen, and Mansoor Barati</i>	
The Structure and the Crystallization Behaviour of the CaO-SiO ₂ -Al ₂ O ₃ -Based Mold Flux for High-Al Steels Casting	291
<i>Jinxing Gao, Guanghua Wen, Ting Huang, and Ping Tang</i>	
Fundamental Investigations for the Design of Fluorine Free Mold Powder Compositions	299
<i>Irmtraud Marschall, Xiao Yang, and Harald Harmuth</i>	
Cold-Finger Measurement of Heat Transfer through Solidified Mold Flux Layers	307
<i>Karina Lara Santos Assis and P. Chris Pistorius</i>	
Application of Cathodoluminescence in Analyzing Mold Flux Films	317
<i>Elizabeth Nolte, Jeffrey D. Smith, Michael Frazee, Neil Sutcliffe, and Ronald J. O'Malley</i>	
Effects of CaF ₂ on the Radiative Heat Transfer in Mould Fluxes for Continuous Steel Casting	327
<i>Masahiro Susa, Yuta Kono, Rie Endo, and Yoshinao Kobayashi</i>	

Effect of Na ₂ O on Crystallisation Behaviour and Heat Transfer of Fluorine-Free Mould Fluxes	335
<i>Jian Yang, Jianqiang Zhang, Yasushi Sasaki, Oleg Ostrovski, Chen Zhang, Dexiang Cai, and Yoshiaki Kashiwaya</i>	
Effect of Carbon Pickup on the Slab with Slag Pool Thickness in Ultra-Low Carbon Steel	343
<i>Min-Seok Park and Shin Yoo</i>	
Techniques for Controlling Heat Transfer in the Mould-Strand Gap in Order to Use Fluoride Free Mould Powder for Continuous Casting of Peritectic Steel Grades	349
<i>Adam Hunt and Bridget Stewart</i>	
Reduction of Iron Oxides in Mould Fluxes with Additions of CaSi ₂	357
<i>Min Wang, Rie Endo, Yoshinao Kobayashi, Zuoyong Dou, and Masahiro Susa</i>	

Physical Properties: Viscosity

Viscosity Measurement at the International Conferences on Molten Slags and Fluxes from 1980 to the Present	369
<i>Steven Wright and Wan-Yi Kim</i>	
A Structure-Based Viscosity Model and Database for Multicomponent Oxide Melts	397
<i>Guixuan Wu, Sören Seebold, Elena Zayhenskikh, Klaus Hack, and Michael Müller</i>	
Thermo-Physical-Chemical Properties of Blast Furnace Slag Bearing High TiO ₂	405
<i>Chenguang Bai, Zhiming Yan, Shengping Li, Pingsheng Lai, Chen Shan, Xuwei Lv, and Guibao Qiu</i>	
The Effect of TiO ₂ on the Liquidus Zone and Apparent Viscosity of SiO ₂ -CaO-8wt.%MgO-14wt.%Al ₂ O ₃ System	415
<i>Zhiming Yan, Xuwei Lv, Jie Zhang, and Jian Xu</i>	
Electrorheology of Ti-Bearing Slag with Different Composition of TiC at 1723 K	423
<i>Tao Jiang, Hongrui Yue, Xiangxin Xue, and Peining Duan</i>	

Study on Apparent Viscosity of Foaming Slag - Cold Model and High Temperature Experiments431
Johan Martinsson, Björn Glaser, and Du Sichen

Effect of Al₂O₃ and SiO₂ Addition on the Viscosity of BOF Slag439
Zhuangzhuang Liu, Lieven Pandelaers, Peter Tom Jones, Bart Blanpain, and Muxing Guo

Viscoelastic Properties of Calcium Silicate Based Mold Fluxes at 1623 K447
Seung-Ho Shin, Jung-Wook Cho, and Seon-Hyo Kim

Viscosity Property and Raman Spectroscopy of FeO-SiO₂-V₂O₃-TiO₂-Cr₂O₃ Slags455
Weijun Huang, Min Chen, Xiang Shen, Yu Shan, Meile He, and Nan Wang

Physical Properties: Thermal Properties and Electrical Conductivity

Techniques for Measuring Solubility and Electrical Conductivity in Molten Salts465
Shizhao Su, Thomas Villalon Jr., Uday Pal, and Adam Powell

A New Method for Apparent Thermal Conductivity Measurement of Mould Flux477
Mu Li, Rie Endo, Li Ju Wang, and Masahiro Susa

Controlling Heat Transfer through Mold Flux Film by Scattering Effects485
Dae-Woo Yoon, Jung-Wook Cho, and Seon-Hyo Kim

Diffusion Coefficients and Structural Parameters of Molten Slags493
Samane Maroufi, Shahriar Amini, Sharif Jahanshahi, and Oleg Ostrovski

The Cationic Effect on Properties and Structure of CaO-MgO-SiO₂ Melts501
Yong-Uk Han and Dong Joon Min

Effects of Structure on the Thermodynamic and Transport Properties of Na₂O-CaO-SiO₂-FeO-Fe₂O₃ Melts511
Lesley J. Beyers, Geoffrey A. Brooks, Bart Blanpain, and Frederik Verhaeghe

Thermal Conductivity of Borosilicate Melt519
*Tsuyoshi Nishi, Junpei Ojima, Yoshitaka Kuroda, Hiromichi Ohta,
Sohei Sukenaga, Hiroyuki Shibata, and Hidenori Kawashima*

Melting Point and Heat Capacity of $MgCl_2 + Mg$ Salts525
Yuxiang Peng and Ramana G. Reddy

Interfacial Phenomena

Does Interfacial Tension Play the Most Important Role in Slag-Metal
Reactions? An Important Aspect in Process Optimization535
Du Sichen and Jesse F. White

Control of Molten $CaO - Al_2O_3$ Oxide Jets with Focus on Thermophysical
Property Measurements and Some Limitations547
Luckman Muhmood, Mirco Wegener, Shouyi Sun, and Alex Deev

Slag Surface Tension Measurements with Constrained Sessile Drops557
Marc A. Duchesne and Robin W. Hughes

Interactions between Liquid $CaO-SiO_2$ Slags and Graphite Substrates565
Jesse F. White, Jaewoo Lee, Oscar Hessling, and Björn Glaser

Initial Wetting and Spreading Phenomena of Slags on Refractory
Ceramics573
Yongsug Chung, Tae Hee Yoon, and Kyuyong Lee

Modelling and Experimental Studies of Diffusivity of Sulfur and Its
Relevance in Observing Surface Oscillations at the Slag Metal Interface
through X-ray Imaging581
*Luckman Muhmood, Nurni N Viswanathan,
and Seshadri Seetharaman*

SPH Analysis of Interfacial Flow of the Two Immiscible Melts589
*Shungo Natsui, Ryota Nashimoto, Tatsuya Kikuchi,
and Ryosuke O. Suzuki*

Surface Properties of Molten Fluoride-Based Salts597
Thomas Villalón Jr., Shizhao Su, and Uday Pal

Foaming Index of $CaO -SiO_2 -FeO -MgO$ Slag System607
Youngjoo Park and Dong Joon Min

Modeling Slag and Salt Properties

Development of Slag Management System	619
<i>Kyei-Sing Kwong and James P. Bennett</i>	
Gaseous Fuel Production Using Waste Slags - Going beyond Heat Recovery	627
<i>Jinichiro Nakano, James Bennett, and Anna Nakano</i>	
Efficient Storage and Recall of Slag Thermochemical Properties for Use in Multiphysics Models	635
<i>Johannes H. Zietsman</i>	

Industrial Applications: Non-Ferrous

Production of Cobalt and Copper Alloys from Copper Slags via Reduction Smelting in DC Arc Furnace	647
<i>Onuralp Yücel</i>	
Slag Reduction Kinetics of Copper Slags from Primary Copper Production	657
<i>Boyd Davis, Trevor Lebel, Roberto Parada, and Roberto Parra</i>	
Fluxing Strategies for the Direct to Blister Smelting of High Silica and Low Iron Copper Concentrates	667
<i>Michael Somerville, Chunlin Chen, Gerardo R.F. Alvear F., and Stanko Nikolic</i>	
Behavior of Selenium in Copper Smelting Slag	677
<i>Bhavin Desai, Vilas Tathavadkar, Somnath Basu, and Kaushik Vakil</i>	
Selective Precipitation of Magnetite in Copper Slag by Controlled Molten Oxidation	687
<i>Yong Fan, Etsuro Shibata, Atsushi Iizuka, and Takashi Nakamura</i>	

Thermodynamics: Iron and Steel

Applications of ArcelorMittal Thermodynamic Computation Tools to Steel Production	697
<i>Jean Lehmann</i>	

Phase Equilibria Study of the CaO-“Fe ₂ O ₃ ”-SiO ₂ System in Air to Support Iron Sintering Process Optimisation	707
<i>Peter C. Hayes, Jiang Chen, and Evgueni Jak</i>	
Understanding Sulfide Capacity of Molten Aluminosilicates via Structural Information from ‘Raman’ and ‘NMR’ Spectroscopic Methodologies	715
<i>Joo Hyun Park</i>	
Thermodynamic Properties of the CaO-AlO _{1.5} -CeO _{1.5} System	7 23
<i>Ryo Kitano and Kazuki Morita</i>	
Distribution Behavior of Cr between CaO-SiO ₂ -Al ₂ O ₃ (-MgO) Slag and Fe-C-Cr (-Si/Al) Metal Phase	731
<i>Yanling Zhang, Xinlei Jia, Tuo Wu, Qiuhan Li, and Zhancheng Guo</i>	
Thermodynamics of ‘ESR’ Slag for Producing Nickel Alloys	745
<i>Jun-Gil Yang and Joo Hyun Park</i>	

Production Using Molten Salts

Recycling Titanium and Its Alloys by Utilizing Molten Salt	751
<i>Toru H. Okabe and Yu-ki Taninouchi</i>	
Electrochemical Upgrading of Iron-Rich Titanium Ores	761
<i>Farzin Fatollahi-Fard and Petrus Christiaan Pistorius</i>	
Investigations for the Recycle of Pyroprocessed Uranium	771
<i>B.R. Westphal, J.C. Price, E.E. Chambers, and M.N. Patterson</i>	
Zero-Direct-Carbon-Emission Aluminum Production by Solid Oxide Membrane-Based Electrolysis Process	781
<i>Shizhao Su, Uday Pal, and Xiaofei Guan</i>	
Alumina Concentration Gradients in Aluminium Reduction Cells	791
<i>Pascal Lavoie and Mark P. Taylor</i>	
Approach of the Molten Salt Chemistry for Aluminium Production: High Temperature NMR Measurements, Molecular Dynamics and DFT Calculations	799
<i>Kelly Machado, Didier Zanghi, Vincent Sarou-Kanian, Sylvian Cadars, Mario Burbano, Mathieu Salanne, and Catherine Bessada</i>	

Electrochemical Study of Cobalt in Urea and Choline Chloride807
Min Li, Zhongning Shi, Zhaowen Wang, and Ramana G. Reddy

The Current Efficiency for Aluminium Deposition from Molten Fluoride
Electrolytes with Dissolved Alumina817
Geir Martin Haarberg

Recycling and Reuse of Slag and Dust

Dissolution Mechanisms of Nutrient Elements from Steelmaking Slag into
Seawater829
*Hiroyuki Matsuura, Qian Zhou, Fuminori Katabe, Likun Zang,
Guohua Zhang, and Fumitaka Tsukihashi*

Effects of Three Types of Iron and Steel Slag on Fresh and Hardened
Properties of Ordinary Portland Cement837
*Seyed Vahid Hosseini, Shahnavaaz Eilbeigi,
and Mohammad Reza Nilforoushan*

Modification of BOF Slag for Cement Manufacturing847
*João B. Ferreira Neto, Catia Fredericci, João O.G. Faria,
Fabiano F. Chotoli, Tiago R. Ribeiro, Antônio Malynowskyj,
Andre N.L. Silva, Valdecir A. Quarcioni, and Andre A. Lotto*

Reaction between Synthesized Calcium Aluminates and Cr_2O_3 in Air
and CO_2 855
Shengqiang Song and Andrie Garbers-Craig

Immobilization of Hexavalent Chromium in Stainless Steelmaking Slag865
*Ryo Inoue, Yoshiya Sato, Yasushi Takasaki,
and Atsushi Shibayama*

Smelting Reduction of Bottom Ash in Presence of Liquid Steel Bath for
Recovery of Aluminium873
A.K. Mandal and O.P. Sinha

A Review of Slag Chemistry in Lead Recycling879
Doug Schriner, Patrick Taylor, and Joseph Grogan

Characterization and Recovery of Valuables from Waste Copper
Smelting Slag889
Sarfo Prince, Jamie Young, Guojun Ma, and Courtney Young

Development of Secondary Antimony Oxides from Metallurgical Slags for the Application in Plastic Products 899

Florian Binz and Bernd Friedrich

Improving the Dissolution of Phosphorus from $2\text{CaO}\cdot\text{SiO}_2\cdot 3\text{CaO}\cdot\text{P}_2\text{O}_5$ Solid Solution in Aqueous Solutions909

Chuan-ming Du, Xu Gao, Sun-joong Kim, Shigeru Ueda, and Shin-ya Kitamura

Thermodynamics: Non-Ferrous Production

Chromium Distribution between Liquid Slag and Matte Phases919

R Hurman Eric

Thermophysical Property Measurements of Molten Slag and Welding Flux by Aerodynamic Levitator929

Kenta Onodera, Airi Nakamura, Shinya Hakamada, Masahito Watanabe, and Florian Kargl

Solubility of CaO and Al_2O_3 in Metallic Copper Saturated Molten Phase937

Joseph Hamuyuni and Pekka Taskinen

Integrated Experimental and Modelling Research for Non-Ferrous Smelting and Recycling Systems947

Evgueni Jak, Taufiq Hidayat, Denis Shishin, Ata Fallah Mehrjardi, Jiang Chen, Sergei Decterov, and Peter Hayes

Experimental Study of Slag/Matte/Metal/Tridymite Four Phase Equilibria and Minor Elements Distribution in "Cu-Fe-Si-S-O" System by Quantitative Microanalysis Techniques961

Jeff (Jiang) Chen, Charlotte Allen, Peter C. Hayes, and Evgueni Jak

Experimental Determination of the Liquidus Surface (1473 K) in Cu-ZnO-SiO₂-O System at Various Oxygen Partial Pressures971

Longgong Xia, Zhihong Liu, and Pekka Antero Taskinen

Liquidus Measurement of Te-O-Na₂O-SiO₂ System between 1000 and 1200 °C in Equilibrium with Air979

Imam Santoso and Pekka Taskinen

Industrial Applications: Steel

- Kinetics of Phosphorus Mass Transfer and the Interfacial Oxygen Potential for Bloated Metal Droplets during Oxygen Steelmaking989
Kezhuan Gu, Neslihan Dogan, and Kenneth S. Coley
- Physical Modelling of the Effect of Slag and Top-Blowing on Mixing in the AOD Process999
Tim Haas, Ville-Valtteri Visuri, Aki Kärnä, Erik Isohookana, Petri Sulasalmi, Rauf Hürman Eriç, Herbert Pfeifer, and Timo Fabritius
- 3D CFD Modeling of the LMF System: Desulfurization Kinetics1009
Qing Cao, April Pitts, Daojie Zhang, Laurentiu Nastac, and Robert Williams
- Slag Formation – Thermodynamic and Kinetic Aspects and Mechanisms1017
Lauri Holappa and Yilmaz Kaçar
- Effects of Various Slag Systems on Metal/Slag Separation of CCA and Slag Composition on Desulfurization and Dephosphorization of Iron Nugget1025
Ji-Ook Park and Sung-Mo Jung
- Use of Al-killed Ladle Furnace Slag in Si-killed Steel Process to Reduce Lime Consumption, Improve Slag Fluidity1031
Narottam Behera, Ahmad Raddadi, Shahreer Ahmad, Neeraj Tewari, and Othman Zeghaibi

Refractories

- Influence of Physical Properties of Slag and Operational Parameters on Slag Splashing Process in an Oxygen Converter1043
Paula Maria Gomes Cunha Leão, Eliana Ferreira Rodrigues, Carlos Antonio da Silva, Itavahn Alves da Silva, and Varadarajan Seshadri
- Corrosion Mechanisms in Refractory Castables by Liquid Oxides1053
L. Tadeo Ibarra, A.M. Guzmán, D.I. Martínez, and G. Alan Castillo
- Viscous Behavior of Alumina and Titania in Amphoteric Slags and Their Influence on Refractory Corrosion1063
Frank Kaußen and Bernd Friedrich

Phase Chemistry Study of the Interactions between Slag and Refractory in Coppermaking Processes	1071
<i>Ata Fallah Mehrjardi, Peter C. Hayes, Turarbek Azekenov, Leonid Ushkov, and Evgueni Jak</i>	
The Study of Molten Liquid - Refractory Interactions – It Is All about the Phase(s)	1077
<i>Andrie Garbers-Craig</i>	
Effect of Slag Impregnation on Macroscopic Deformation of Bauxite-based Material	1093
<i>Antoine Coulon, Emmanuel De Bilbao, Rudy Michel, Marie-Laure Bouchetou, Séverine Brassamin, Camille Gazeau, Didier Zanghi, and Jacques Poirer</i>	
Corrosion Resistances of Cr-Free Refractories to Copper Smelting Slags	1101
<i>Mao Chen, Junhong Chen, and Baojun Zhao</i>	
Gasification Slag and the Mechanisms by Which Phosphorus Additions Reduce Slag Wear and Corrosion in High Cr ₂ O ₃ Refractories	1109
<i>James Bennett, Anna Nakano, Jinichiro Nakano, and Hugh Thomas</i>	

Additional Technical Papers

A High Temperature Double Knudsen Cell Mass Spectrometry Study of Gas Species Evolved from Coal-Petcoke Mixed Feedstock Slags	1119
<i>Jinichiro Nakano, Takashi Nagai, James Bennett, Anna Nakano, and Kazuki Morita</i>	
An Assessment of Slag Eye Formation Using Mathematical and Physical Modeling	1127
<i>Augusto Pereira de Sá, Filipe de Menezes Torres, Carlos Antonio da Silva, Itavahn Alves da Silva, and Varadarajan Seshadri</i>	
An Effect of Phosphorus Gas Generated in Slagging Gasifiers on Pt-Rh Sensor Degradation.....	1135
<i>Anna Nakano, Jinichiro Nakano, and James Bennett</i>	
An Experimental Study of Viscosity in FeO-SiO ₂ -V ₂ O ₃ -TiO ₂ System	1143
<i>Shiyuan Liu, Lijun Wang, and Kuo-chih Chou</i>	

Capturing and Condensation of SiO Gas from Industrial Si Furnace	1153
<i>Ksiazek Michal, Grådahl Svend, Rotevant, Eirik Andersen, and Wittgens Bernd</i>	
Corrosion Testing of Zirconia, Beryllia and Magnesia Ceramics in Molten Alkali Metal Carbonates at 900°C	1161
<i>Valery Kaplan and Igor Lubomirsky</i>	
Density, Viscosity, Vapor Pressure and Thermal Conductivity of MgCl ₂ + Mg Salts	1169
<i>Yuxiang Peng and Ramana G. Reddy</i>	
Development of “Slag-Remaining+Double-Slag” BOF Steelmaking Technology in Shougang Co.	1177
<i>Haibo Li, Yanchun Lu, Guosen Zhu, and Xinhua Wang</i>	
Effect of Basicity on Basic Oxygen Furnace (BOF) Slag Solidification Microstructure and Mineralogy	1185
<i>Chunwei Liu, Muxing Guo, Lieven Pandelaers, Bart Blanpain, and Shuigen Huang</i>	
Effect of Slag Prepared with Different Cooling Methods on Cleanliness of Bearing Steel GCr15	1191
<i>Dong-ping Zhan, Yang-peng Zhang, Lei Tang, Kun Fan, Zhou-hua Jiang, and Hui-shu Zhang</i>	
Effect of Zr Inhibitor on Corrosion of Haynes 230 and NS-163 Alloys in FLiNaK	1199
<i>Yuxiang Peng and Ramana G. Reddy</i>	
Experimental Study of Gas/Slag/Matte/Spinel Equilibria and Minor Elements Partitioning in the Cu-Fe-O-S-Si System	1207
<i>Taufiq Hidayat, Ata F Mehrjardi, Peter C Hayes, and Evgueni Jak</i>	
Experimental Study of Liquidus of the “FeO”-SiO ₂ -PbO Slags in Equilibrium with Air and with Metallic Lead	1221
<i>Maksym Shevchenko, Taufiq Hidayat, Peter C Hayes, and Evgueni Jak</i>	
Formation of Copper Sulfide Precipitate in Solid Iron	1229
<i>Kentaro Urata and Yoshinao Kobayashi</i>	

Integrated Heat Recovery and Material Recycling from Hot Slags: Toward Energy Saving and Emission Reduction	1237
<i>Yongqi Sun, Zuotai Zhang, and Seetharaman Sridhar</i>	
Interfacial Phenomena and Thermophysical Properties of Molten Steel and Oxides	1245
<i>Masahito Watanabe, Kenta Onodera, Shoya Ueno, Takao Tsukada, Toshihiro Tanaka, Haruka Tamaru, and Takehiko Ishikawa</i>	
Investigation of Molten Salt Phase Formation during Alkali Roasting of Titaniferous Minerals with Sodium and Potassium Hydroxide	1253
<i>S. Parirenyatwa, L. Escudero-Castejon, S. Sanchez-Segado, Y. Hara, and A. Jha</i>	
Precipitation Behavior of Titanium Bearing Blast Furnace Slag	1261
<i>Meilong Hu, Zhengfeng Qu, Xuewei Lv, and Yunhua Gan</i>	
Production of Ceramic Balls by High Temperature Atomization of Mine Wastes	1271
<i>Hyunsik Park, Minchul Ha, Dong-hyo Yang, Jeong-soo Sohn, and Joohyun Park</i>	
Properties of Bayer Red Mud Based Flux and Its Application in the Steelmaking Process	1277
<i>Yanling Zhang, Fengshan Li, and Ruimin Wang</i>	
Reduction Behavior of Assmang and Comilog Ore in the SiMn Process	1285
<i>Pyunghwa Peace Kim, Joakim Holtan, and Merete Tangstad</i>	
Regeneration of WC-Co Nanopowders via Sodiothermic Reduction in Molten Salts	1293
<i>Na Wang, Xue-Mei Liu, Li-Hua Chai, Jinyu Wu, and Xuyang Shen</i>	
Rheological Behavior of Fayalite Based Secondary Copper Smelter Slag in Iron Saturation	1301
<i>Huayue Shi, Liugang Chen, Annelies Malfliet, Tom Peter Jones, Bart Blanpain, and Muxing Guo</i>	
Silicon and Manganese Partition between Slag and Metal Phases and Their Activities Pertinent to Ferromanganese and Silicomanganese Production	1309
<i>Hakan Cengizler and R Hurman Eric</i>	

Stability of Fluorine-Free Mould Fluxes $\text{SiO}_2\text{-CaO-Al}_2\text{O}_3\text{-B}_2\text{O}_3\text{-Na}_2\text{O}$ for Steel Continuous Casting	1319
<i>Lin Wang, Jianqiang Zhang, Yasushi Sasaki, Oleg Ostrovski, Chen Zhang, and Dexiang Cai</i>	
Study of MnO Activity in $\text{CaO-SiO}_2\text{-MnO-Al}_2\text{O}_3\text{-MgO}$ Slags	1327
<i>Jun Tao, Dongdong Guo, Baijun Yan, and Longmei Wang</i>	
Study on Electrical Conductivity of $\text{CaO-SiO}_2\text{-Al}_2\text{O}_3\text{-FeO}_x$ Slags	1335
<i>Guo-Hua Zhang, Jun-Hao Liu, and Kuo-Chih Chou</i>	
The Distribution Rules of Element and Compound of Cobalt/Iron/Copper in the Converter Slag of Copper Smelting Process	1343
<i>Hongxu Li, Ke Du, Shi Sun, Jiaqi Fan, and Chao Li</i>	
The Management of Lead Concentrate Acquisition in “Trepca”	1351
<i>Ahmet Haxhiaj, Maoming Fan, and Bajram Haxhiaj</i>	
The Mineral Constitution and Leachability Characteristics of Dusts from Different Lead Smelting Furnace	1359
<i>Hongxu Li, Yang Xie, Chao Li, Zhaobo Liu, and Mengmeng Huang</i>	
The Wetting Behavior of CrMnNi Steel on Mg-PSZ as a Function of Phosphorous, Sulphur and Titanium Content	1371
<i>Tobias Dubberstein, Hans-Peter Heller, Claudia Wenzel, and Christos G. Aneziris</i>	
Thermodynamic Modelling of Liquid Slag-Matte-Metal Equilibria Applied to the Simulation of the Peirce-Smith Converter	1379
<i>Denis Shishin, Taufiq Hidayat, Sergei Decterov, and Evgueni Jak</i>	
Thermodynamics of the $2\text{CaO}\cdot\text{SiO}_2\text{-3CaO}\cdot\text{P}_2\text{O}_5$ Solid Solution at Steelmaking Temperature	1389
<i>Hiroyuki Matsuura, Ming Zhong, Xu Gao, and Fumitaka Tsukihashi</i>	
Understanding Phase Equilibria in Slags Containing Vanadium	1397
<i>Jinichiro Nakano, Marc Duchesne, James Bennett, Anna Nakano, Robin Hughes, and In-Ho Jung</i>	

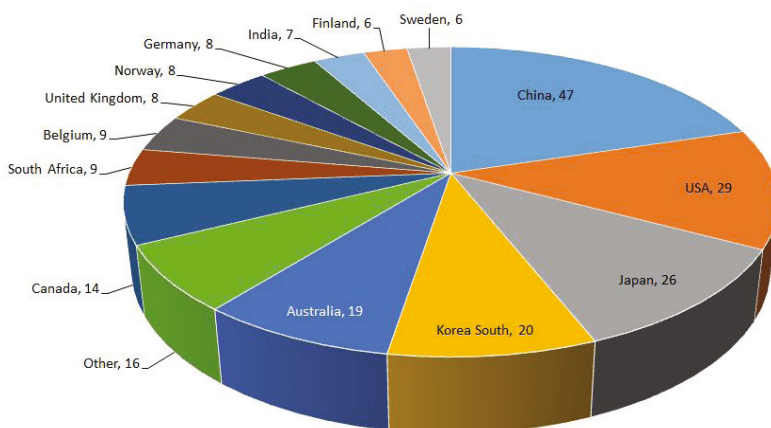
Vanadium Oxidation State Determination by X-ray Absorption Spectroscopy	1405
<i>Marc A. Duchesne, Jinichiro Nakano, Yongfeng Hu, Aimee MacLennan, Robin W. Hughes, James Bennett, and Anna Nakano</i>	
Author Index	1413
Subject Index	1419

PREFACE

The Tenth International Conference on Molten Slags, Fluxes and Salts (MOLTEN16) was held in Seattle, Washington, USA from May 22–25, 2016 and organized by TMS (The Minerals, Metals & Materials Society). The conference purpose was to provide an opportunity for scientists and engineers to share their new research findings, innovations, and industrial technological developments. The conference also aligns quite well with the TMS strategic goal to sustain and grow the core innovation in process engineering and to develop novel materials. The organizers are pleased to conclude that the set strategic goals were met and a very high-quality technical program with the participation of expert researchers in the field was held.

The conference was focused on ferrous and non-ferrous metallurgy where ionic melts, slags, fluxes, or salts play important roles in industrial growth and economy worldwide. Technical topics included are: thermodynamic properties and phase diagrams and kinetics of slags, fluxes, and salts; physical properties of slags, fluxes, and salts; structural studies of slags; interfacial and process phenomena involving foaming, bubble formation, and drainage; slag recycling, refractory erosion/corrosion, and freeze linings; and recycling and utilization of metallurgical slags and models and their applications in process improvement and optimization. These topics are of interest for not only traditional ferrous and non-ferrous metal industrial processes but also for new and upcoming technologies.

Advances in Molten Slags, Fluxes and Salts Oral and Poster Presentations



The program consisted of parallel sessions for all three days of technical programming. The conference included 185 oral presentations and 65 poster presentations. Plenary and invited talks in specialized topics were presented. Thirty nations participated in this conference. The distribution of submitted abstracts by nation is shown in the pie chart on the previous page.

We would like to thank all speakers and attendees for their valuable time in making presentations and actively participating in the symposium. We specially thank all the committee members and session chairs for their help in making this symposium successful.

We would like to express our sincere appreciation to the TMS leadership and staff for their support and dedication. All services in support of the conference, including but not limited to marketing, logistical management, timeline management, website design and development, web-based registration system, abstract collection, conference proceedings production and manufacturing provided by TMS staff is very much appreciated. We thank Louise Wallach, Senior Manager, Events, Education, and Exhibits for organizing the several social programs for all participants and their companions. We particularly thank Trudi Dunlap, Programming Manager, for her undivided attention to details in organizing the sessions and publication of conference proceedings.

Sincerely,

Ramana Reddy, Conference Chair
The University of Alabama

Pinakin Chaubal, Co-chair
ArcelorMittal USA, Global R&D

P. Chris Pistorius, Co-chair
Carnegie Mellon University

Uday Pal, Co-chair
Boston University

CONFERENCE ORGANIZING COMMITTEES

CONFERENCE ORGANIZERS

Ramana Reddy, Conference Chair, The University of Alabama, USA

Pinakin Chaubal, ArcelorMittal, USA

P. Chris Pistorius, Carnegie Mellon University, USA

Uday Pal, Boston University, USA

HONORARY ADVISORY COMMITTEE MEMBERS

Rob Boom, Delft University of Technology, Netherlands

Kuo-Chih Chou, University of Science and Technology of China, China

Richard J. Fruehan, Carnegie Mellon University, USA

Mitsutaka Hino, Kobe Steel Ltd., Japan

Lauri Holappa, Helsinki University of Technology, Finland

Hurman Eric, Wits University, South Africa

Sharif Jahanshahi, Metal-Logical Solutions, Australia

Ken C. Mills, Imperial College London, United Kingdom

Mario Sanchez, Universidad Andres Bello, Chile

Seshadri Seetharaman, KTH Royal Institute of Technology, Sweden

TECHNICAL ADVISORY COMMITTEE

Sunday Abraham,
SSAB Americas, USA

Antoine Allanore,
Massachusetts Institute of Technology,
USA

Chen Guang Bai,
Chongqing University, China

Wagner Viana Bielefeldt,
Federal University of Rio Grande do
Sul, Brazil

**André Luiz Vasconcellos
da Costa e Silva**,
Federal University Fluminense, Brazil

Neslihan Dogan,
McMaster University, Canada

Jonkion Font,
Codelco, Chile

Andrie Garbers-Craig,
University of Pretoria, South Africa

Bora Derin,
Istanbul Technical University, Turkey

Björn Glaser,
KTH Royal Institute of Technology,
Sweden

Animesh Jha,
University of Leeds, United Kingdom

Rodney Jones,
Mintek, South Africa

Sung-Mo Jung,
Postech, Korea

Venkat Kamavaram,
Oceanit, USA

Mirosław Karbowniczek,
AGH University of Science and
Technology, Poland

Pallava Kaushik,
ArcelorMittal, USA

Zi-Kui Liu,
Pennsylvania State University, USA

Siddhartha Misra,
Tata Steel, India

Kazuki Morita,
University of Tokyo, Japan

R.D. Morales,
Instituto Politécnico Nacional-ESIQIE,
Mexico

Jinichiro Nakano,
National Energy Technology
Laboratory Albany, USA

Neale R Neelameggham,
IND LLC, USA

Vaibhav V. Nikam,
ConocoPhillips Company, USA

Sutham Niyomwas,
Prince of Songkla University, Thailand

Viswanathan Nurni,
Indian Institute of Technology, India

Toru H. Okabe,
University of Tokyo, Japan

Ronald O'Malley,
Missouri University of Science and
Technology, USA

Rafael Padilla,
University of Concepción, Chile

Suresh Chandra Parida,
Bhabha Atomic Research Centre, India

Joo Hyun Park,
Hanyang University, Korea

Arthur D. Pelton,
École Polytechnique de Montréal,
Canada

Ray D. Peterson,
Real Alloy, USA

Eugene Pretorius,
Nucor, USA

Fernando Puchi,
Universidad Andres Bello, Chile

Eli Ringdalen,
Sintef, Norway

Gudrun Saevarsdottir,
Reykjavik University, Iceland

Mark E. Schlesinger,
Missouri University of Science and
Technology, USA

William Slye,
Vesuvius, USA

Merete Tangstad,
Norwegian University of Science and
Technology, Norway

Gabriella Tranell,
Norwegian University of Science and
Technology, Norway

Prabhat K. Tripathy,
Idaho National Laboratory, USA

Maurits Van Camp,
Umicore Research, Belgium

Somnath Basu,
Indian Institute of Technology, India

Cong Wang,
Northeastern University, China

Bryan Webler,
Carnegie Mellon University, USA

Onuralp Yucel,
Istanbul Technical University, Turkey

Jiayun Zhang,
University of Science and Technology
Beijing, China

Jieyu Zhang,
Shanghai University, China

Mingming Zhang,
ArcelorMittal, USA

Wen Hai Zhang,
Jiangxi University of Science and
Technology, China

Johan Zietsman,
University of Pretoria, South Africa

INTERNATIONAL ADVISORY COMMITTEE

Gerardo R.F. Alvear,
Xstrata Technology, Australia

N. Bharath Ballal,
Indian Institute of Technology, India

Mansoor Barati,
University of Toronto, Canada

Bo Björkman,
Luleå University of Technology,
Sweden

Bart Blanpain,
Katholieke Universiteit Leuven,
Belgium

Patrice Chartrand,
École Polytechnique de Montréal,
Canada

Ken Coley,
McMaster University, Canada

**André Luiz Vasconcellos
da Costa e Silva,**
Federal University Fluminense, Brazil

Rian Dippenaar,
University of Wollongong, Australia

Sichen Du,
KTH Royal Institute of Technology,
Sweden

I.J. Geldenhuys,
Mintek, South Africa

Zhancheng Guo,
University of Science and Technology
Beijing, China

Geir Martin Haarberg,
Norwegian University of Science and
Technology, Norway

- Peter Hayes,**
The University of Queensland,
Australia
- Juan Patricio Ibañez,**
Technical University Santa María,
Chile
- Evgueni Jak,**
The University of Queensland,
Australia
- Pär Jönsson,**
KTH Royal Institute of Technology,
Sweden
- In-Ho Jung,**
McGill University, Canada
- Shinya Kitamura,**
Tohoku University, Japan
- Florian Kongoli,**
Flogen Technologies Inc., Canada
- Jakob Lamut,**
University of Ljubljana, Slovenia
- Xionggang Lu,**
Shanghai Science and Technology
Institute, China
- Marcelo Breda Mourao,**
University of São Paulo, Brazil
- Joo Hyun Park,**
Hanyang University, Korea
- Veena Sahajwalla,**
University of New South Wales,
Australia
- Yasushi Sasaki,**
Pohang University of Science and
Technology, Korea
- Piotr Scheller,**
Freiberg University of Mining and
Technology, Germany
- Sridhar Seetharaman,**
University of Warwick, United
Kingdom
- Evgeniy Selivanov,**
Ural Division of the Russian Academy
of Sciences, Russia
- Volodymyr Shatokha,**
National Metallurgical Academy of
Ukraine, Ukraine
- H.Y. Sohn,**
University of Utah, USA
- Valentina Stolyarova,**
Saint Petersburg State University,
Russia
- Toshihiro Tanaka,**
Osaka University, Japan
- Pekka Taskinen,**
Aalto University, Finland
- Patrick Taylor,**
Colorado School of Mines, USA
- Xi-Dong Wang,**
Peking University, China
- Lifeng Zhang,**
University of Science and Technology
Beijing, China
- Živan Živković,**
University of Belgrade, Russia

PROCEEDINGS REVIEWERS

**André Luiz Vasconcellos
da Costa e Silva,**
Federal University Fluminense, Brazil

Andrie Garbers-Craig,
University of Pretoria, South Africa

Antoine Allanore,
Massachusetts Institute of Technology,
USA

Arthur D. Pelton,
École Polytechnique de Montréal,
Canada

Björn Glaser,
KTH Royal Institute of Technology,
Sweden

Bo Björkman,
Luleå University of Technology,
Sweden

Bryan Webler,
Carnegie Mellon University, USA

Chenguang Bai,
Chongqing University, China

Eli Ringdalen,
Sintef, Norway

Evgueni Jak,
The University of Queensland,
Australia

Gabriella Tranell,
Norwegian University of Science and
Technology, Norway

Geir Martin Haarberg,
Norwegian University of Science and
Technology, Norway

Gerardo R.F. Alvear,
Xstrata Technology, Australia

Gudrun Saevarsdottir,
Reykjavik University, Iceland

Guy Fredrickson,
Idaho National Laboratory

I.J. Geldenhuys,
Mintek, South Africa

In-Ho Jung,
McGill University, Canada

Jakob Lamut,
University of Ljubljana, Slovenia

Jinichiro Nakano,
National Energy Technology
Laboratory Albany, USA

Johan Zietsman,
University of Pretoria, South Africa

Jonkion Font,
Codelco, Chile

Joohyun Park,
Hanyang University, Korea

Judith Gomez,
National Renewable Energy
Laboratory, USA

Marcelo Breda Mourao,
University of São Paulo, Brazil

Mark E. Schlesinger,
Missouri University of Science and
Technology, USA

Maurits Van Camp,
Umicore Research, Belgium

Merete Tangstad,
Norwegian University of Science and
Technology, Norway

Mingming Zhang,
ArcelorMittal, USA

Mirosław Karbowniczek,
AGH University of Science and
Technology, Poland

N. Bharath Ballal,
Indian Institute of Technology, India

Neale R. Neelameggham,
IND LLC, USA

Neslihan Dogan,
McMaster University, Canada

Pallava Kaushik,
ArcelorMittal, USA

Patrick Taylor,
Colorado School of Mines, USA

Pekka Taskinen,
Aalto University, Finland

Peter Hayes,
The University of Queensland,
Australia

Prabhat K. Tripathy,
Idaho National Laboratory,

Ray D. Peterson,
Real Alloy, USA

Rian Dippenaar,
University of Wollongong, Australia

Siddhartha Misra,
Tata Steel, India

Somnath Basu,
Indian Institute of Technology, India

Sunday Abraham,
SSAB Americas, USA

Suresh Chandra Parida,
Bhabha Atomic Research Centre, India

Valentina Stolyarova,
Saint Petersburg State University,
Russia

Viswanathan Nurni,
Indian Institute of Technology, India

Wagner Viana Bielefeldt,
Federal University of Rio Grande do
Sul, Brazil

William Slye,
Vesuvius, USA

**ADVANCES IN MOLTEN
SLAGS, FLUXES, AND SALTS:**

Proceedings of



Plenary Session

WASTE TO VALUE IN STEELMAKING

Samane Maroufi, Irshad Mansuri, Paul O’Kane*, Catherine Skidmore*, Zheshi Jin*,
Andrea Fontana*, Magdalena Zaharia* and Veena Sahajwalla

SMaRT Centre, School of Materials Science and Engineering, the University of New South
Wales, Sydney, NSW 2052, Australia

*OneSteel, Rooty Hill, Sydney, NSW 2766, Australia

Abstract

The high temperature environment of steelmaking process, offers sustainable pathways for utilizing chemical reactions to re-purpose waste materials as resources. The use of waste polymeric materials in steelmaking is not only a solution for end-of-life products, which currently impose a serious burden on overstretched landfills but it also results in reduction of resource consumption and energy saving. This paper presents industrial plant results on the effect of the utilization of waste polymeric materials in steelmaking on coke and energy consumption.

The foaming slag phenomenon is an important criterion through which the effect of waste polymeric materials on EAF performance could be studied. The stability of foaming behaviour mainly depends upon physical properties of slag and also the size of gas bubbles which are generated during the process of reduction. The understanding of the relationship between these parameters and foaming is also presented in this paper.

1. Introduction

Due to the rise in the cost of raw materials worldwide and the world’s ever increasing appetite for steel, steel-making industries are currently under pressure to reduce their negative impact on environment. The steel industry accounts for 3-4 percent of greenhouse gas emissions worldwide and, on average, for a tonne steel to be produced about 1.7 tonnes of carbon dioxide are emitted [1].

At the same time, waste stockpiles ranging from polymeric materials to agricultural wastes are accumulating at a rapidly increasing rate because of the development of new technology and economic activity. A significant part of waste generated is plastic and used tyres which are not biodegradable and impose a significant and growing waste burden, with the additional complication of their potential to leach toxic chemicals into the environment. Of the approximately 20 million passenger tyres requiring disposal in Australia every year, only 23 % are recycled, 64% go to landfill and the remainder are dumped illegally [2]. In some states in Australia, tyres are now banned from landfill sites due to their toxicity. Worldwide, about 1.2 billion used tyres are thrown away annually and four billion or so waste tyres are currently in landfills and stockpiles, posing a risk to human health and the environment. Needless to mention that, such waste materials consist mainly of carbon and hydrogen; elements which are vital in the metallurgical industries due to their role as reductants/carburizers. These long chain hydrocarbons consist of highly volatile matter with generally low ash content. This gives steelmakers an opportunity to use waste streams to source free or low cost raw materials for production.

High temperature environment of steelmaking provides opportunity for a large scale recycling of waste materials without making fundamental changes to manufacturing processes. The waste materials can be re-purposed as resources through chemical reaction via sustainable pathways. The potential to implement such novel recycling solutions are not generally available to many other materials industries because they operate at relatively lower temperatures, which may not be suitable for triggering useful chemical transformations.

The trend of utilizing waste materials as resources in steelmaking industry not only decreases the consumption of depleting valuable resources but also could be considered as a novel recycling solution, which transforms problematic waste and reduces the cost of raw materials for the steelmaker.

OneSteel, an Australian-based steel manufacturer, has been actively developing innovative process technologies to utilize waste materials such as end-of-life tyres and post-consumer plastics as an alternative carbon unit in EAF steelmaking. In close co-operation with the SMaRT Centre, University of New South Wales (UNSW), OneSteel has developed and commercialized Polymer Injection Technology (PIT), which enables EAFs to inject blend of coke and rubber in place of coke, resulting in improved slag foaming and hence furnace efficiency.

OneSteel has been using PIT as a standard practice since 2008 at its Sydney Steel Mill (SSM) and Laverton Steel Mill (LSM) in more than 84,000 heats, consuming over 2.4 million recycled tyres in the process. PIT has been granted patent protection in most major industrial countries and it has been commercially implemented at UMC Metals, Thailand since May 2011, at SeAH Besteel, Korea since April 2014, at Celsa Group’s plant in Cardiff, UK since October 2014 and at Celsa Nordic in Norway since December 2015.

The benefits of using PIT, which were statistically proven during the commercial implementation trials on each site, are listed in **Table 1**. This innovation offered an excellent opportunity to improve furnace efficiency with a positive impact on the environment through energy savings and the transformation of waste streams into value added products.

Table 1 summary of the benefits of using PIT

Benefit Area	Reduction in Electrical consumption (KWh per billet tonne)	Reduction in inject carbon (kilograms per heat)	FeO % reduction in slag	Yield improvement
SSM	2.8 %	12.0%	3.0%	0.30%
LSM	2.4%	16.2%	2.5%	0.27%
USA Trial	1.7%	6.3%	2.4%	0.24%
Asia 1	5.1%	12.0%	2.0%	0.20%
Asia 2	3.8%	12.0%	-	-
Europe 1	1.6%	8.4%	1.5%	0.17%
Europe 2 Consteel	2.1%	7.2%	-	-

As it can be seen, the incorporation of PIT into OneSteel’s commercial has achieved 12.0 and 16.2 percent reduction in inject carbon in SSM and LSM, respectively. The incorporation of PIT

has also resulted in saving energy through reduction in electrical consumption which was reported 2.8 and 2.4 percent for SSM and LSM, respectively. The technology of waste polymer injection has also improved the yield of furnaces by about 0.3% and 0.27 % in SSM and LSM, respectively.

The incorporation of PIT also improves the foaminess of the slag, and therefore, furnace efficiency. The foaming slag phenomenon in electric arc furnace (EAF) is known to be an important feature which reduces the cost of energy, improves furnace efficiency and stability while reduces the sound, vibration and electrode consumption during the process of iron melting [3]. Thus an understanding the relationship between the physicochemical properties of slag and its foaming behavior is of great significance due to the considerable effect of slag on foaming phenomenon.

In a work reported by Ogawa et. al [4], the mechanism of slag foaming control with carbonaceous materials by experiments using a 1-tonne smelting reduction furnace was investigated. According to their report, from the X-ray fluoroscopic observation experiment, small and large gas CO bubbles, produced by the iron oxide reduction reactions, were both present in the foaming slag bath, and the large bubbles due to coalescence of small bubbles rose through the foam layer at a relatively high speed and resulted in restraining the foaming of slag.

The bubble growth and detachment mechanisms from the formation site have been studied. It is reported that, at the moment of detachment the main forces acting on the bubble are the buoyancy forces, the added mass force and the surface tension as reported by Loubiere et al. [5].

In present work three types of slag with different compositions were used to study their foaming behavior in reaction with metallurgical coke and coke-rubber and coke-plastic blends. This work is aimed to investigate the rate of gas generation and size of gas bubbles generated during the process of reduction with metallurgical coke and blends and their influence on the stability of slag foaming.

2. Materials and experimental set-up

The industrial slags from the industrial electric arc furnace were used for the experiments. The compositions of slags measured by XRF are shown in **Table 2**. The slags were crushed and sieved into different particle sizes. The particle size used for the experiments was $<150\ \mu\text{m}$. Metallurgical cokes and coke-rubber and coke-plastic blends were used as sources of carbon; the chemical compositions of the metallurgical coke and coke-rubber blend are shown in **Table 3**. For preparing coke-rubber/ coke-plastic blends, metallurgical coke and rubber/plastic were mixed and the blend was then crushed using a jaw crusher to increase the uniformity in particle size distribution. Both metallurgical coke and the prepared blend were then compacted without a binder in a steel die using a hydraulic pressure of 150 MPa. The prepared compacted blend was in cylindrical form in diameter of 20 mm and thickness 3-4 mm. About 0.07 gram of slag was placed on top of the blend which was located on an alumina stage. During the time of heating up, the assembly was held in the cold zone of the furnace in order to avoid any reaction that could take place at lower temperatures. Once the temperature reached the target temperature of 1550°C , the assembly was inserted into the hot zone of the furnace. The schematic diagram of the experimental set-up has been shown somewhere else [6].

The moment that slag started melting was marked the beginning of the contact time. Live in-situ phenomena in furnace were monitored using a high resolution camera. Computer processing software was used to determine the dynamic changes in slag volume from captured images. The slag volume changes which are attributed to formation, entrapment and release of gases were then quantified using the sessile-drop slag foaming software and V_t/V_0 versus reaction time was plotted. V_0 represents the initial volume of the slag droplet.

Table 2 Chemical composition of slags

	CaO	Fe ₂ O ₃	Al ₂ O ₃	SiO ₂	MgO	MnO
Slag #1	29.6	34.8	8.4	13	9.4	5.7
Slag #2	24.8	44.4	7.8	11.2	6.7	4.8
Slag#3	31.1	33.9	6.1	13.0	10.7	6.2

Table 3 Proximate analysis for all carbonaceous material samples

	Moisture	Ash	Volatile Matter	Fixed Carbon	Sulphur	Hydrogen
Metallurgical Coke #1	4.6	15.3	3.0	71.5	0.32	1.11
Metallurgical Coke #2	1.10	12.7	2.1	83.80	1.04	1.83
Metallurgical coke #3	0	14.2	3.0	82.8	0.3	1.28
PP/Coke #3	0	16.4	7.8	75.8	0.25	1.04
PU/Coke #3	0	18.3	8.8	72.9	0.27	1.73
Rubber/coke #1 blend 1	1	27.8	5.2	57.5	0.54	1.14
Rubber/coke #1 blend 2	0.9	22.3	5.5	55	0.59	1.4

3. Experimental results and discussions

The slag/carbon interaction is a dynamic process with respect to chemical reactions in which the composition of the slag is continually changing. The mechanism of the reaction between solid carbon and iron oxide present in the slag occurs via intermediate gas. CO gas produced in the initial stages of reaction between carbon and slag gets transported through the gas phase and reacts with FeO in slag to produce CO₂ and metallic iron. This CO₂ gets ferried back to carbon, where gasification of CO₂ to CO takes place via the Boudouard reaction.

The carbon available in the carbonaceous substrate starts to react with the FeO from the slag. CO and CO₂ gases are formed and the slag droplet is inflated. The rate of CO/CO₂ gases generation depends to a great extent on the chemistry of the carbon based material, volatile matter and ash content in addition to slag properties and process conditions such as temperature. Due to the evolution of the gases, bubbles of different dimensions are formed and then get entrapped in slag droplet for certain period of time which depends on gas bubble size and the physicochemical properties of the reacting slag. The rate of gas evolution is one of the main factors affecting the phenomenon of gas entrapment. If the rates are too high, then the increased gas velocity leads to lower level of slag foaming volumes.

3.1 Effect of the rate of gas generation on slag foaming

The rate of gas generation as a result of interaction between slag and carbonaceous materials plays a significant role in slag foaming phenomenon. Three types of metallurgical coke (coke #1, #2 and #3) and the blends of coke # 1 with rubber and coke #2 with two types of polymeric materials- Polypropylene (PP) and Polyurethane (PU) were used in this work to study the effect of the rate of gas generation on slag foaming.

Infrared off-gas analyser (IR) was used to analyse gas generated from the blank substrates of 100% coke #1 and coke #2. **Figure 1** shows the results obtained from analysing gas released during the process of heating coke #1 and coke #2 in argon at 1550 °C. It is seen clearly from **Figure 1**, in the case of coke #1, CO generated was almost double the value for coke #2 indicating that coke #1 had the capability of releasing higher amount of gas with high rate compared to coke #2. Given that the rate of gas generation in the case of coke #1 was much higher than coke #2, these cokes are expected to behave differently in terms of slag foaming phenomenon.

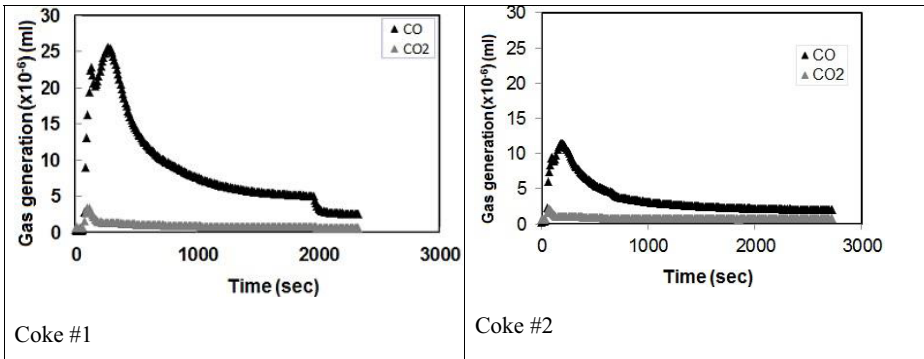


Figure 1: Gas generation from blank coke #1 and coke #2 in argon at 1550 °C as a function of time

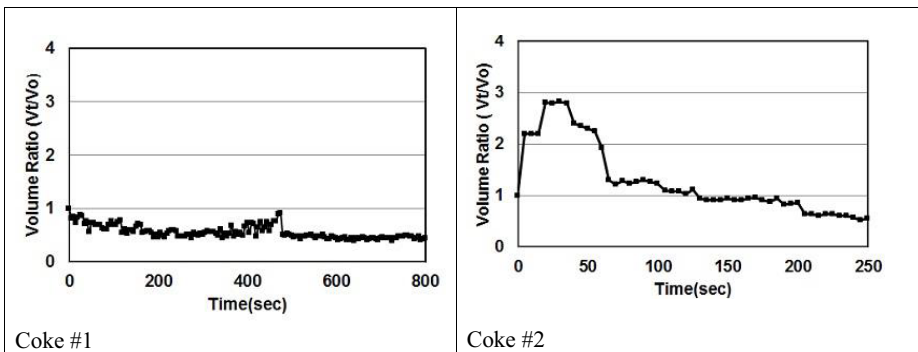


Figure 2: Slag foaming (volume ratio) results for coke #1 and coke #2 at 1550 °C as a function of time

Figure 2 illustrates the slag foaming results of slag #1 in reaction with coke #1 and 2 through V_t/V_0 variation versus reaction time. In the case of coke #2, in 25 seconds, V_t/V_0 ratio reached its highest value, after which it started decreasing. However in the case of coke #1, the volume of slag droplet decreased gradually over reaction time.

The poor foaming behaviour of coke #1 compared to coke #2 could be attributed to its high rate of gas generation. When the flow rate of gases evolved from the substrate is very high, a fast passage and escape through the slag occurs. Thus less gas remains entrapped in the slag, and a poor foaming behaviour is expected to be observed. On the other hand, very low gas flow rate also results in poor slag foaming due to the lack of generation of sufficient gas. Therefore it is important to control the rate of gas generation and keep that standing in the optimum range.

The reaction between slag #3 and coke #3 and blends of coke #3 with two types of polymeric materials- Polypropylene (PP) and Polyurethane (PU) at 1550 °C was also investigated. The slag foaming results for PP/Coke #3 and PU/Coke #3 compared to coke #3 are represented through the volume ratio (V_t/V_0) variation as a function of time in **Figure 3**.

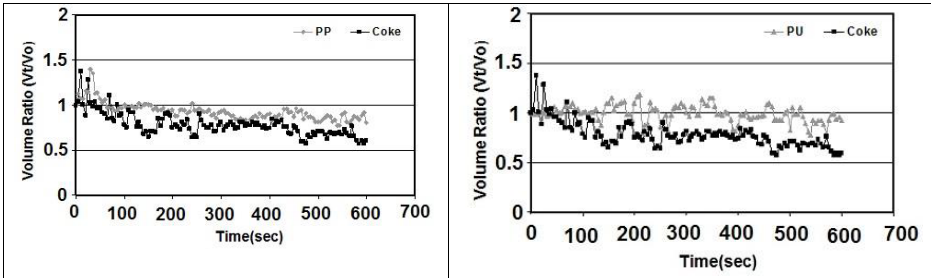


Figure 3: Slag foaming (volume ratio) results for PP/Coke #3 and PU/Coke #3 blends compared to coke #3 at 1550 °C as a function of time [7]

While the blend of polymer PU with coke #3 showed better slag foaming, slight improvement was observed in slag foaming of PP-coke blend at final stages of reaction. Rates of gas ($\text{CO}+\text{CO}_2$) generation during the reaction of slag and coke #3-plastic blends at 1550 °C are illustrated in **Figure 4**.

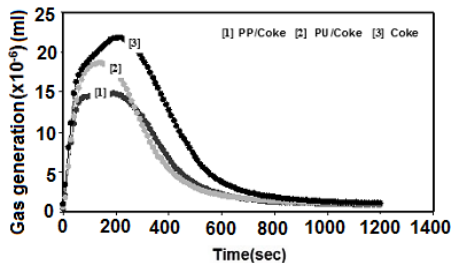


Figure 4: Gas generated ($\text{CO}+\text{CO}_2$) as a result of interaction of slag #3 with coke #3 and PP/coke #3, PU/coke #3 blends [7]

Coke #3 showed a higher rate of gas generation compared to the polymer containing blends. The rates of the gas generation decreased when the plastic containing blends were used. This is possibly due to the fact that some of the carbon and volatile matter in plastic/coke blends had been partially removed during the combustion in the DTF, and thus there was less carbon left in the char to react with liquid slag compared to the case of coke.

From this result it could be interpreted that very high and very low rate of gas generation results in a poor foaming behaviour. It can be seen from **Figure 4**, in the case of 100% coke #3 ([3] coke in **Figure 4**), the rate of gas generation was very high which resulted in a fast escaping of gas from the slag droplet and therefore a poor foaming behaviour was observed. On the other hand, gas generation for the case of PP-coke blend ([1] in **Figure 4**) was very low which had a negative effect on slag foaming. The improvement in foaming behaviour of PU-coke blend could be attributed to the rate of gas generation which was standing in optimum range ([2] in **Figure 4**).

The effect of gas generation from the interaction between rubber/coke #1 blends and slag #1 on foaming phenomenon was also studied. **Figure 5** illustrates the results of slag foaming for coke #1 and blends #1 and #2 through V_t/V_0 versus reaction time. Gas generated during the process of reduction of coke #1 and blends with slag #1 is also shown in **Figure 6**. The rate of gas generation increased when coke #1/rubber blends were used compared to coke #1 alone.

It can be observed in **Figure 5**, when the rubber proportion in the blend increased as in the case of Blend 2, the volume ratio decreased compared to Blend 1. It can be concluded that increasing rubber proportion in mixture improved slag foaming behaviour. However, this trend continued up to particular proportion of rubber, after that, increasing rubber proportion in the blend leads to a poor slag foaming performance as we see well in the case of blend [2], which is attributed to the higher gas flow rate from the coke/rubber blend (**Figure 6**). Therefore it is important to keep the balance between rubber and coke ratio in order to have the rate of gas generation at optimum levels.

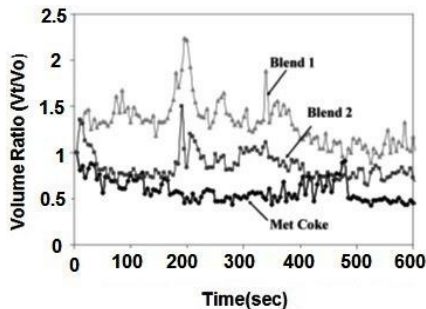


Figure 5: Carbon/slag interaction for metallurgical coke/slag and Blend 1, Blend 2/slag system at 1550 °C: volume ratio (V_t/V_0) as a function of time [6]

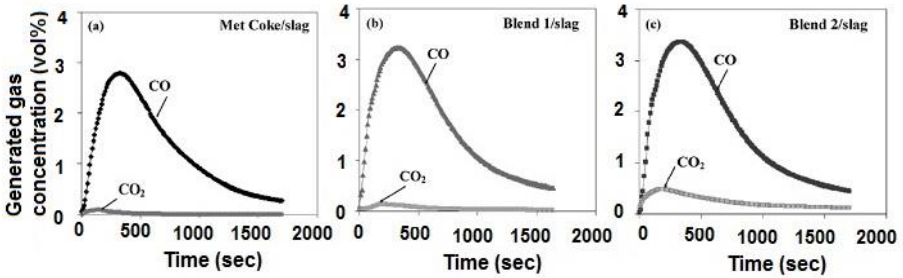


Figure 6: Gas generated as a result of the interaction of the slag with coke and rubber/coke blends [6]

3.2 Effect of bubble size on slag foaming

The experimental result on slag foaming for industrial slags #1 and #2 in reaction with 100% metallurgical coke #1 are represented through the volume ratio (V_t/V_0) versus reaction time (**Figure 7**). As it can be seen from **Figure 7**, when metallurgical coke was used the two slags showed different foaming behavior. In the case of slag #1, the volume of slag droplet decreased gradually over the reaction time, however when slag #2 was used, the volume of slag droplet increased to a high level in a short reaction time and then dropped quickly. Given that the same carbonaceous materials were used in both tests, the difference in foaming behavior could be attributed to the slags chemical composition.

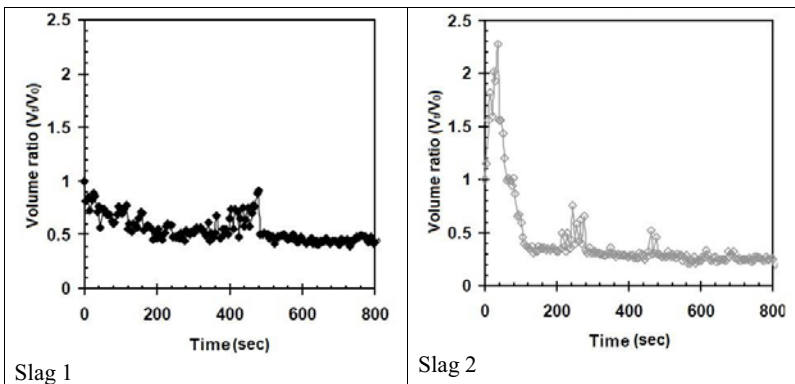


Figure 7 Slags volume ratio (V_t/V_0) in reaction with 100 % coke #1 at 1550 °C as a function of time

The effect of the two types of slag on the reduction and rate of gas generation could be clearly observed by the analysis of the gas released from the sample. **Figure 8** illustrates the variation in total gas generation due slag and coke interaction as a function of reaction time. The concentration of CO+CO₂ evolved in the case of slag #2 was slightly higher than that in slag #1 which could be attributed to high content of iron oxide in slag #2 and therefore high generation of gas. When the amount of iron oxide in the slag is high, the rate of reduction is expected to be greater as the reaction between the iron oxide and carbon is very fast. A high rate of reduction is accompanied by a high rate of gas generation. However, higher FeO content not only increases the rate of CO generation, but also lowers the viscosity of the slag, allowing the liquid slag of the foam bubbles to drain rapidly resulting in a less stable slag.

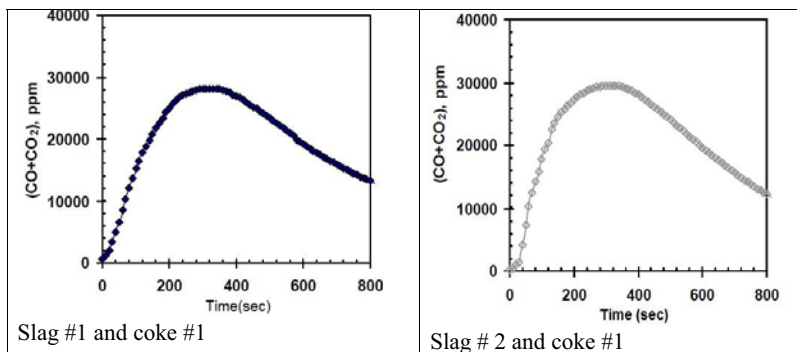


Figure 8 Variation in total gas generation due to reduction of slags with 100% coke at 1550 °C

The cross-sections of reduced slags were subjected to the optical microscopy in order to investigate size/number of distribution of gas bubbles entrapped within the slag droplet. **Figure 9** shows the optical microscopic images of the cross-sections of reduced slags #1 and #2 in reaction with 100% coke #1. In all optical microscopic images white area are metallic iron and dark black area are representative of gas bubble entrapped in slag droplet. As it can be seen from optical microscopic image of slag #2 reduced with 100 % MC #1 (**Figure 9**), large gas bubbles were formed after 60 second. However in the case of slag #1 with lower content of iron oxide, the size of gas was very small and number of gas bubbles was also limited. The variation in total gas generation also can prove that the rate of gas generation in Slag #2 was higher. However, the small size of gas bubbles in the case of slag #1 could be also attributed to slag physicochemical properties.

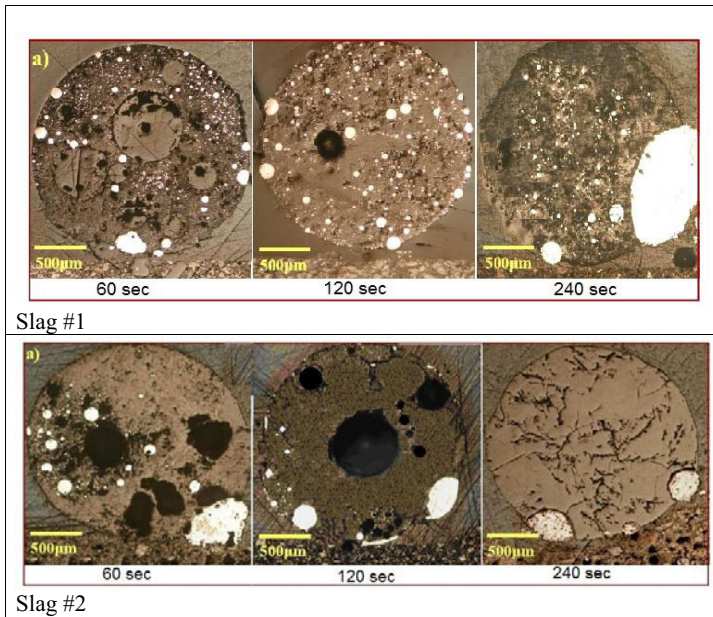


Figure 9 Optical microscopic images of slags reduced with 100 % coke #1 at 1550 °C

In present work coke #1-rubber blends were also used as sources of carbon in reaction with slag to study their influence on the size of gas bubbles formed during the process of reduction. When metallurgical coke replaced by rubber, the rate of gas generation is expected to be even higher due to the release of volatile matters along with the gases produced during the process of reduction. With increasing the proportion of rubber in the blend, the rate of gas generation increased. Changes of volume ratio (V_t/V_0) of slag droplets (#1 and #2) during the process of reaction with coke-rubber blends versus reaction time are shown in **Figures 10-A and 10-B**. The optical microscopic images of the cross-sections of reduced slags in reaction with coke-rubber blends are also illustrated in **Figure 11**.

When coke-rubber blend was used as a source of carbon in reaction with slag #1, the volume ratio of slag droplet increased to high level and stayed there for a relatively long period of time (**Figure 10-A**) which implies that not only the rate of gas generation increased, but also the generated gas bubbles remained entrapped in the slag droplet for a long time. As it can be seen in **Figure 11**, even with increasing the rate of gas generation in this slag, the size of gas bubbles were found to be small. In fact, distribution of large quantity of gas bubbles of small size was responsible for high level and stable foaming behavior of slag #1 in reaction with coke-rubber blend. It could be interpreted that both rate of gas generation and physiochemical properties of slag had influence on the size of gas bubbles and stability of the slag foaming.

In the case of slag #2, when coke-rubber blend was used as carbon resource the rate of gas generation increased compared to slag #1 (**Figure 8**) and the size of generated gas bubbles were large (**Figure 11**). However, such large gas bubbles escaped from the slag droplet in a short reaction time which resulted in destabilizing the foamy layer. It can be seen from **Figure 10-B** the volume of slag droplet soared to a high level in a very short reaction time and then dropped quickly.

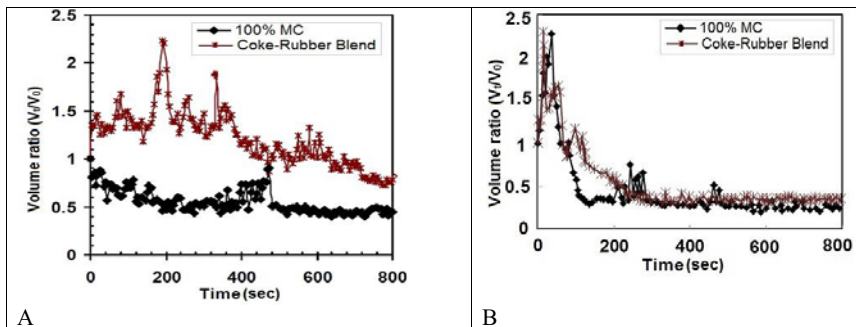


Figure 10 Volume ratios (V_t/V_0) in reaction with coke-rubber blend at 1550 °C (A) for slag #1 and (B) slag #2

It is reported in numerous literatures [8,9] that the size of gas bubbles formed during the process of reduction have influence on the stability of foamy layer. Depending upon the chemistry and surface tension of slag, the size of gas bubbles will change and based on the number and size of gas bubbles formed within the slag their entrapment extent could vary. Several authors correlated the surface tension of slags with the gas bubble diameter in the slag droplet. Ogawa's model [4] stated that with increasing surface tension, the critical bubble size increases.

Bubble bursting phenomena in gas/metal/slag systems was studied by Han and Holappa [10] and it was shown that with increasing surface tensions the mass ejection of gas bubbles increased. According to their work, large gas bubbles were travelling through the slag phase. When a shear flow propagates down the walls of the collapsing bubble cavity drawn by surface tension and a vertical motion occurs. Thus, with increasing surface tension the driving energy and wave speed will increase resulting in a more energetic system.

Many studies have been carried out in order to measure surface tension of different oxide systems. In present work, the slags could be assumed as pseudo- binary $\text{CaO-Fe}_2\text{O}_3$ system in which the effects of other oxides are negligible. The surface tension of $\text{CaO-Fe}_2\text{O}_3$ system has been measured in researches carried out by [11-15], however the results of all researchers are not consistent. According to the results reported by majority of reporters [11-14], slag in composition similar to slag#2 is expected to have higher surface tension.

The smaller size of gas bubbles formed in slag #1 could be attributed to its lower surface tension. With increasing the rate of gas generation due to the use of coke-rubber blends as source of carbon in reaction with such slag, the size of generated gas bubbles remained small which

implies that the physical property of the slag and its surface tension had a more significant influence on the size of gas bubbles than the rate of gas generation. The higher surface tension of slag #2 resulted in generation of larger gas bubbles which escaped from the slag droplet in a short time after being formed and therefore lead to a poor foaming behavior.

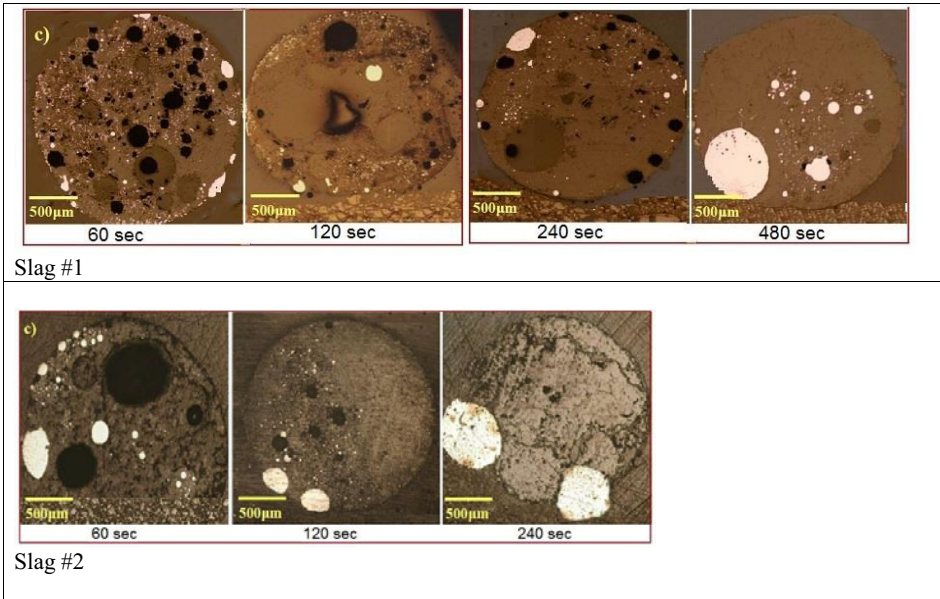


Figure 11 Optical microscopic images of slags reduced with coke-rubber blend at 1550 °C as a function of time

4. Conclusions

Three industrial slags and three metallurgical coke were used to investigate the effect of the rate of gas generation and physicochemical property of slags on foaming behaviour. Iron oxide content in slag #2 was higher compared to slag #1. The gas-entrapment phenomenon of slags in reaction with metallurgical coke and coke-rubber and coke-plastic blends were measured at temperature of 1550°C in a horizontal tube resistance furnace under argon, using the sessile drop approach.

- The rate of gas generation plays a significant role in slag foaming. Very high rate of gas generated during the process of reduction leads to a fast escape of gas from slag droplet and a poor foaming behaviour. Very low rate of gas generated has also negative effect on slag foaming. In order to improve the foaming behaviour of slag the rate of gas generation should be at optimum levels.

- Physicochemical properties of slag have significant effects on the size and distribution of gas bubbles generated due to interaction with slag and carbonaceous materials. Higher surface tension leads to poor foaming behaviour.
- When coke-rubber blend was used as a source of carbon in reaction with slags, the rate of gas generation increased due to removal of volatile matters along with gas produced from reduction. The height of foaming in slag #1 increased and it lasted for a longer period of time which was attributed to distribution of large quantity of gas bubbles of small size in slag droplet. Large gas bubbles formed in slag #2 resulted in poor foaming behavior. The large size of gas bubbles formed in slag #2 could be attributed to higher surface tension of the slag and also high gas generation due to higher content of iron oxide.
- For a slag to show a good foaming behavior it is crucial to have an optimum rate of gas generation with small size of gas bubbles.

REFERENCES

- [1] Climate Commission, Australia
- [2] <http://theconversion.edu.au/recycling-helps-tyred-out-rubber-hit-the-road-again-3982>, accessed Feb 2013
- [3] Schroeder, D. L.: Steel Times, 32 (2000), 368.
- [4] Ogawa, Y., Katayama, H., Hirata, H., Tokumitsu, N. and Yamauchi, M. "Slag Foaming in Smelting Reduction and Its Control with Carbonaceous Materials" ISIJ International (1992), Vol. 32(1), pp. 87-94.
- [5] Loubiere, K., Hebrard, G., Guiraud, P." *Dynamics of bubble growth and detachment from rigid and flexible orifices*" The Canadian Journal of Chemical Engineering (2003), Vol. (81), pp 499-507.
- [6] Zaharia, M., Sahajwalla, V., Khana, R., Koshy, P and O'Kane, P." Carbon/Slag Interactions between Coke/Rubber Blends and EAF Slag at 1550°C" ISIJ International (2009), Vol. 49 (10), pp. 1513-1521.
- [7] Kongkarat, S., Khanna, R., Koshy, P., O'kane, P and Sahajwalla, V." Recycling Waste Polymers in EAF Steelmaking: Influence of Polymer Composition on Carbon/Slag Interactions", ISIJ, 2012, 52 (3), 385-393.
- [8] Zhang, Y and R. J. Fruehan., Effect of the Bubble Size and Chemical Reactions on Slag Foaming, Metallurgical and Materials Transaction B, 26B, 1995, 803-812.
- [9] ITO, K and R. J. Fruehan., Study on the Foaming of CaO-SiO₂-FeO Slags: Part II. Dimensional Analysis and Foaming in Iron and Steelmaking Processes, Metallurgical and Materials Transaction B, 20B, 1989, 515-521.
- [10] Han, Z and Holappa, L., Bubble Bursting Phenomenon in Gas/Metal/Slag Systems", Results, Metallurgical and Materials Transaction B, 34B, (2003).
- [11] A. S. Abrodimov, E. G. Gavrin and V. I. Ereimeichenkov: Izv. VUZ Chernaya Metall., 1975, (8), 14 (English translation: B ISI 13897, Mar. 1976)
- [12] S. Sumita, K. Morinaga and T. Yangase: J. Jbn Ins. Met., 1983, 47, (2), 127
- [13] S. Sumita, K. Morinaga and T. Yangase: Trans. Jbn Ins. Met., 1983, 24, (1), 127
- [14] T. B. King: J. Soc. Glass Technol., 1951, 35, 241.

CURRENT STATUS OF SLAG DESIGN IN METALLURGICAL PROCESSES

Dong Joon Min* and Sung Mo Jung

Yonsei University; Yonsei-ro 50, Seodaemun-gu, Seoul, 03722, Republic of Korea

Keywords: Slag Designing, Viscosity, Structure

Abstract

Since the use of metallurgical slags is of great importance due to its versatile functions at high temperatures, comprehensive information is required to optimize the processes in iron and steelmaking processes. Primary silica-based slag composition can drastically deviate from expected norms by the significant amounts of additional constituents during processes. Accordingly, the comprehensive change in the slag composition and viscosity has a dramatic impact on the physico-chemical properties of the slags. In the current lecture, special focus will be put on the future technology relating the optimization of metallurgical slag composition and viscosity to cope with the situation with low quality of materials introduced into the metallurgical processes.

Introduction

Molten slags, considered as one of the most important materials in metallurgical processes, have been paid significant amount of interests for their physical properties. Among various physical properties of slags, the viscosity of blast furnace (BF) and basic oxygen steelmaking (BOS) slags were once reviewed by works of Sohn and Min[1], Kondratiev and Jak[2], Turkdogan and Bills[3], and Mills and Keene[4].

One of the early works on the viscosity of the molten slags was performed by Bockris and Lowe[5]. Saito *et al.*[6] measured the viscosity of BF type slags, and evaluate the effect of several compositions on the viscosity of the slags. Nakamoto *et al.*[7] also measured the viscosity of molten CaO-Al₂O₃-SiO₂-MgO system, and concluded that the viscosity lower than 6 poise at 1673 K is required for BF operation. Shankar *et al.*[8] investigated the effect of basicity and TiO₂ contents on the viscosity of CaO-Al₂O₃-SiO₂-MgO-TiO₂ slags. The effect of FeO, Fe₂O₃, and K₂O was also evaluated by the work of Sukenaga *et al.*[9]

Pioneering work of Mills and Keene³ are devoted for the elucidation of physical properties of highly basic slags. Seok *et al.*[10] discussed the viscosity of highly-basic slags, C/S varying from 1.4 to 3.76. The slag was considered to be in a solid-liquid coexisting region. and the effect of primary solid phase ratio was described by Einstein-Roscoe Equation. Lee *et al.*[11] also discussed the viscous behavior of dicalcium silicate-precipitated slags, and suggested the viscosity of the suspension as a function of the activity of solid dicalcium silicate.

Thermodynamic models have also been formulated to identify the molten slag structure. The earliest attempt was made by the work of Herasymenko[12], in which the two SiO₂ molecules were assumed to generate one Si atom, and one SiO₄⁴⁻ tetrahedron. Temkin[12] suggested that the entropy of mixing within the silicate melt was determined by the permutations among cation and anion sublattices, and that the activity of basic oxide is

simply expressed by the product of the activities of free cations and free oxygens. Later, Toop and Samis[14] discussed the quasi-chemical interactions between bridging (O^0), non-bridging (O^-), and free (O^{2-}) oxygens. Masson[15] proposed the polymer theory in which polymerization/depolymerization equilibria exist between silicate polymeric anions.

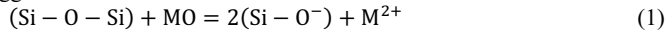
Theoretical attempts have also been made for the application of the structural analysis of metallurgical slags. Lee *et al*[11] investigated the viscosity of BF slag system for wider range of basicity, and evaluated the effect of basicity and FeO content on the BF slag viscosity using FT-IR(Fourier Transform - Infrared Spectroscopy) analysis. The work of Kim *et al*.[16] was also devoted for the elucidation of the effect of MgO and Al_2O_3 contents on the BF slags using FT-IR analysis. Several works[17],[18] were also performed to address the effect of alkaline oxides on the structure and viscosity of BF slags. In addition, the effect of TiO_2 on the BF slag viscosity was investigated by Park *et al*.[19], together with FT-IR analysis.

Spectroscopic analysis on the slag structure is contemporarily considered to require comprehensive utilization of various analyses such as Raman, XPS (X-Ray Photoelectron), and NMR (Nuclear Magnetic Resonance) spectroscopies. Various works are devoted for the establishment of the application of Raman spectroscopy[20-24]. Park *et al*.[19] applied the deconvolution of the Raman spectra using the Gaussian function, and semi-quantitatively assessed the structure of slags. Han *et al*.[25] calculated the equilibrium constant of structural relaxation using the deconvolution technique of Raman spectroscopy. Jung *et al*.[26] used XPS to distinguish bridging, non-bridging and free oxygen within the slag. Sohn *et al*.[27] also applied XPS for evaluation of the effect of TiO_2 on the viscosity of calcium silicate melts.

The current lecture aims to review the slag design for the optimum operation of metallurgical processes. Particularly, the viscous behavior of ironmaking [1],[4],[6-9],[16-18], steelmaking [3],[10], and non-ferrous metallurgy slags[28],[29] are critically reviewed.

Viscosity of blast furnace slags

Viscosity of blast furnace slags with several similar metallurgical slags can be described as a function of Vee ratio as shown in Fig. 1. General basicity of blast furnace slags lies in C/S of 0.6~1.2. Viscosity decreases with increasing basicity while the slope in the figure gradually decreases. In the operation temperature range of 1673 to 1823 K, the BF slags show viscosity less than 10 Poise, which is generally perceived as critical viscosity for slag tapping. The continuous decrease in viscosity with increasing basicity originates from the structural relaxation of the slag: As basic oxide is introduced into the melt, the aluminosilicate polyanions are depolymerized into the simpler ones. The general equation of structural depolymerization is suggested as below:



Further discussions on slag structure is made in the later of the present section.

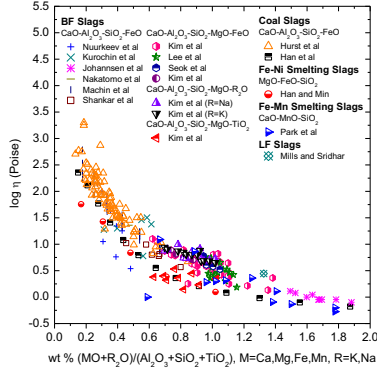


Fig. 1. Effect of basicity on the viscosity of metallurgical slags.

The effect of MgO content on viscosity and structure of the typical blast furnace slags is described in Fig. 2. As MgO content increases, viscosity of the slag gradually decreases until the curve reaches the local minima, generally at MgO content of 7 to 11 %, depending on the basicity and Al_2O_3 contents. Viscosity increases with increasing MgO content after the minima. The minima in viscosity coincide with the primary solidification phase transition composition from melilite to spinel. From FT-IR spectra, the structural relaxation is maximized at 7 % addition of MgO as well. The melt structure at 7 % addition of MgO shows the most remarkable SiO_4 -tetrahedra with $\text{NBO}/\text{Si} = 3+4$ bands (850 and 940 cm^{-1}).

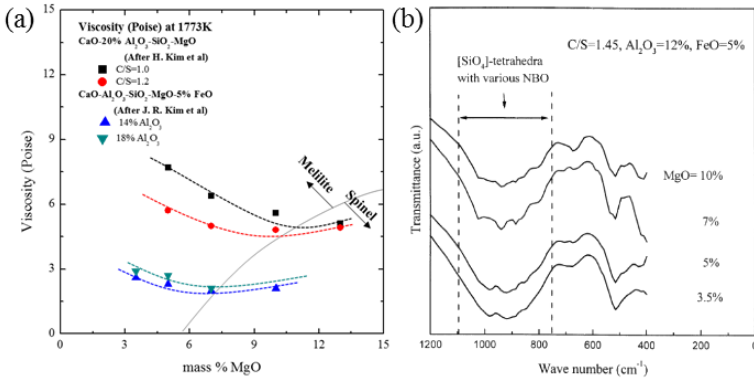


Fig. 2. (a) Effect of MgO addition on the viscosity of blast furnace slag, CaO- Al_2O_3 - SiO_2 -MgO-FeO system. (b) FT-IR spectra of CaO- SiO_2 -12% Al_2O_3 -MgO-5% FeO slags with C/S=1.45

Fig. 3 shows the effect of Al_2O_3 on the viscosity and structure of the blast furnace slags. As Al_2O_3 content increases, viscosity increases continuously. Hence Al_2O_3 behaves as a network former, and consists of AlO_4^{4-} tetrahedral anions. Such an acid behavior of Al_2O_3 is also shown in FT-IR spectra of CaO- SiO_2 - Al_2O_3 -5mass% MgO-5mass% FeO slags in Fig. 3(b). The major FT-IR bands of aluminosilicate structure are asymmetric stretching vibration of

AlO_4 -tetrahedra ($720\text{-}630\text{ cm}^{-1}$), AlO_6 -octahedra ($570\text{-}520\text{ cm}^{-1}$) and Si-O-Al bending (500 cm^{-1}). For blast furnace slag system of $\text{CaO-SiO}_2\text{-Al}_2\text{O}_3\text{-MgO-FeO}$, absorption of SiO_4 -tetrahedra band increases with increasing Al_2O_3 while that of AlO_6 -octahedra is negligible. Therefore, despite its amphoteric nature, Al_2O_3 behaves as an acid oxide and thus network former.

The effect of FeO , Na_2O , and K_2O on the viscosity of the blast furnace slag is expressed in Fig. 4. Increase in FeO and Na_2O content leads to the decrease in viscosity, meaning that both the oxides behave as a basic oxide over the compositions. The addition of K_2O , on the other hand, increases the viscosity of the slag, nevertheless K_2O is a strong basic oxide. The antithetic effect of Na_2O and K_2O addition is plausibly originated from the difference in capability of charge compensation with Al_2O_3 . Both oxides participate in charge compensation for Al^{3+} leading to formation of AlO_4^{4-} tetrahedron. Although Na^+ has smaller ionic radius (116 pm^{31}) than that of K_2O (152 pm), K_2O has an advantage in charge compensation: Na^+ , of which coordination number with oxygen is known to be 6 to 8³², has larger ionic radius than that of octahedral (65.49 pm) and cubic (115.73 pm) packing sites. K^+ , on the other hand, has coordination number of 6 to 12, can spontaneously be packed in close-packed site due to its smaller radius than close-packed site (158.71 pm). The addition of K_2O , therefore, increases the portion of tetrahedral aluminate units over octahedral units, increases the degree of polymerization of the melt. Such a polymerization increases viscosity as shown in Fig. 4(c). Further work is required for the elucidation of the effect of cations on the amphoteric behavior of Al_2O_3 .

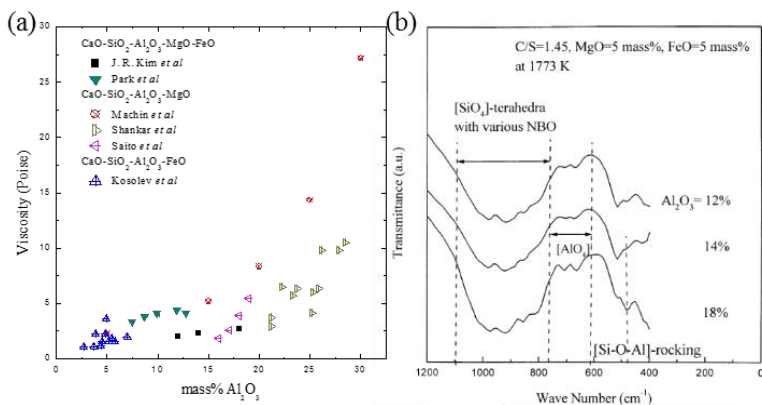


Fig. 3. (a) Effect of Al_2O_3 addition on the viscosity of blast furnace slag systems. (b) FT-IR spectra of $\text{CaO-SiO}_2\text{-Al}_2\text{O}_3\text{-5% MgO-5% FeO}$ slags with $\text{C/S}=1.45$

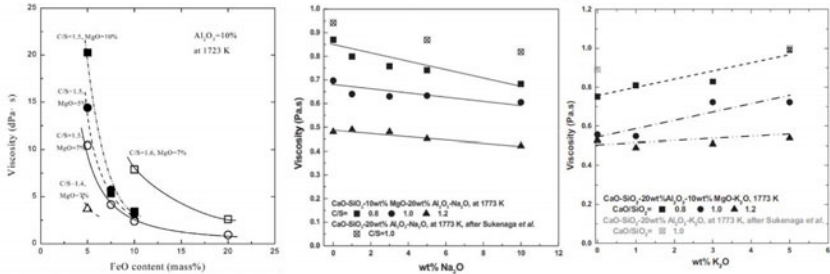


Fig. 4. Effect of (a) FeO, (b) Na₂O, and (c) K₂O content on the viscosity of blast furnace slag systems.

The temperature dependence of the slag viscosity is expressed in Fig. 5. The viscosity of slags rapidly increases as temperature decreases below the certain temperature. The temperature is considered a temperature at which solid phase ratio within the melt is considerable, and fluid starts to deviate from Newtonian flow: The temperature is defined by critical temperature.

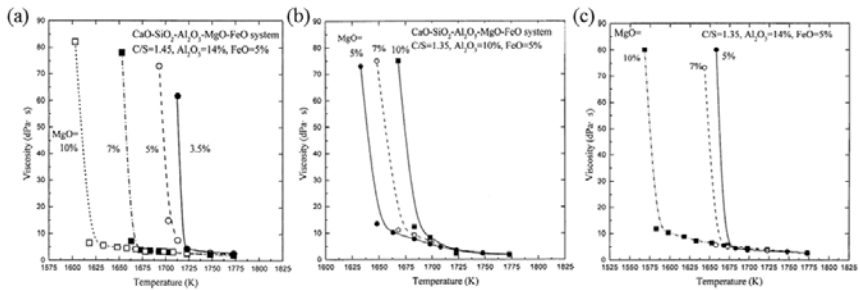


Fig. 5. Temperature dependence of viscosity of CaO-SiO₂-Al₂O₃-MgO- 5mass% FeO systems: (a) C/S=1.45, 14 mass% Al₂O₃ (b) C/S=1.35, 10 mass% Al₂O₃ (c) C/S=1.35, 14 mass% Al₂O₃

The critical temperature is distinguished from the break temperature, defined by the temperature of rapid increase in viscosity in super-cooled glasses. Critical temperature is obtained by crystallization within the melt. Temperature is maintained at each measurement leading to the crystallization of solid phases. Break temperature, on the other hand, is obtained from viscosity measurement with constant decrease in temperature, by which glass transition occurs, leading to glass transition within the melt. Han and Min[30] modified the Vogel-Fulcher-Tammann equation^{33,34} to express the temperature dependence of slag viscosity by Eq. (3).

$$\eta = \eta_0 \exp\left(-\frac{E_\eta}{R(T-T_{Cr})}\right) \quad (3)$$

where η is viscosity of pure liquid, η_0 is viscosity of the suspension, E_η is the activation energy of viscous flow, R is the gas constant, and T_{Cr} is empirically obtained critical temperature.

Hence, the critical temperature is also defined by the temperature at which the Arrhenian plot of viscosity initiates to deviate from linearity as shown in Fig. 6.

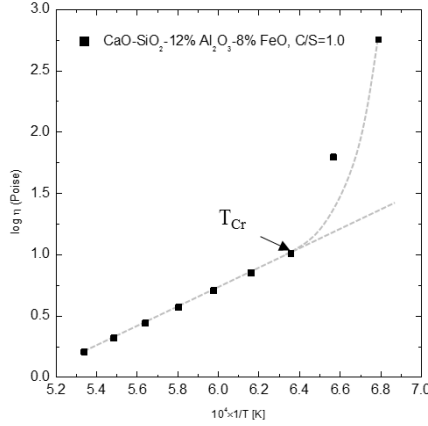
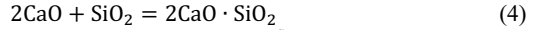


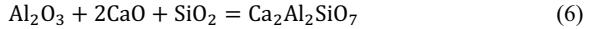
Fig. 6. Arrhenius plot of viscosity and determination of the critical temperature

Lee *et al.* [11] suggested the expectation of critical temperature using theoretical liquidus temperature. The theoretical liquidus temperature is calculated from Eqs. (4) and (5) as a temperature at which the activity of primary solidification phase, dicalcium silicate, reaches unity.



$$\Delta G_{\text{C}_2\text{S}}^0 = -126,400 - 5.02 \text{ [J/mol]}, K_{\text{C}_2\text{S}} = \frac{a_{2\text{CaO} \cdot \text{SiO}_2}}{a_{\text{CaO}}^2 a_{\text{SiO}_2}} \quad (5)$$

Expanding the work of Lee *et al.* [11], the theoretical liquidus temperatures for anorthite- and melilite-equilibrated liquids are calculated by Eqs. (6) to (9). Together with dicalcium-silicate equilibrated liquids, the relationship between theoretical liquidus temperatures and critical temperatures is expressed in Fig. 7. The activity of each component is calculated with the aid of FactsageTM 7.0 software.



$$\Delta G = -50305.83 + 9.33T \text{ [J/mol]}, K_{\text{C}_2\text{AS}} = \frac{a_{\text{Ca}_2\text{Al}_2\text{SiO}_7}}{a_{\text{CaO}}^2 a_{\text{Al}_2\text{O}_3} a_{\text{SiO}_2}} \quad (7)$$



$$\Delta G = -47997.55 + 7.34T \text{ [J/mol]}, K_{\text{C}_2\text{AS}_2} = \frac{a_{\text{CaAl}_2\text{Si}_2\text{O}_8}}{a_{\text{CaO}}^{1/2} \times a_{\text{Al}_2\text{O}_3}^{1/2} \times a_{\text{SiO}_2}} \quad (9)$$

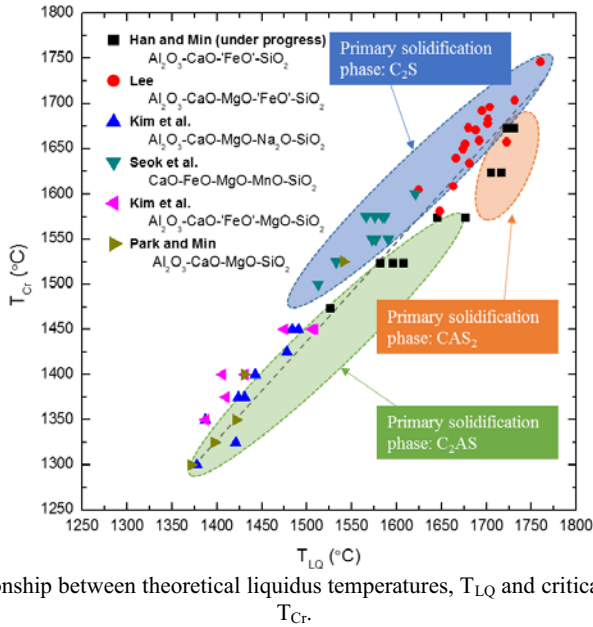


Fig. 7. Relationship between theoretical liquidus temperatures, T_{LQ} and critical temperatures, T_{Cr} .

Viscosity of highly basic slags

Although considerable amount of work has been devoted to address the viscosity of the blast furnace slags, the basicity is restricted for lower region. Mills and Keene[3] studied the viscosity of binary slags for wider range of basicity. Seok *et al.*[10] investigated the viscous behavior of the metallurgical slag system of CaO- SiO_2 -FeO- Al_2O_3 -MgO for wide range of C/S varying from 1.41 to 3.76. In higher C/S regions, the solidification is inevitable due to the extremely high melting temperature of solid dicalcium silicate phase. By adding a considerable amount of FeO, the dicalcium silicate-saturated compositions are restrictively derived for CaO- SiO_2 -8mass% MgO-FeO system at 1873 K, and expressed in Fig. 8. The slag viscosity increased from 1.4 to 5.1 poises with increasing basicity and FeO content. This shows that the slag basicity has a more significant effect on increasing slag viscosity since FeO plays a role in decreasing the slag viscosity. In addition, as the slag basicity increases, the slag composition might change to the liquid-solid coexisting region where solid phase has an effect on the increase in slag viscosity.

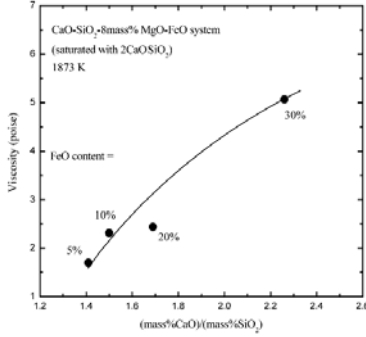


Fig. 8. Change in viscosity as a function of basicity and FeO content at 1873 K

In order to clarify the effect of slag basicity on viscosity, the viscosities of CaO-SiO₂-Al₂O₃-FeO-MgO slags were measured, and expressed as a function of slag basicity as shown in Fig. 9. Viscosity decreases with increasing basicity, as discussed in the previous section, until the C/S reaches 1.3. After minima, the dicalcium silicate initiates to precipitate, and the ratio of solid phase increases with increasing basicity. Such an effect of basicity cannot be explained by the effect of basic oxide on the depolymerization of silicate network, but by the effect of basic oxide on the formation of solid phase having higher melting temperature. It can be fully understood by a similar shape between the isotherms of composition and phase diagrams [35],[36]. Lee *et al.*[11] quantitatively modeled the viscosity in such a region as a function of the activity of dicalcium silicate by Eq. (10)

$$\log \eta = -2.7 + 0.55 \cdot \left[\frac{a_{2\text{CaO}\cdot\text{SiO}_2}}{a_{\text{Al}_2\text{O}_3} \cdot a_{\text{MgO}} \cdot a_{\text{FeO}}} - \left(\frac{1.6}{C/S} \right)^4 \right] \quad (10)$$

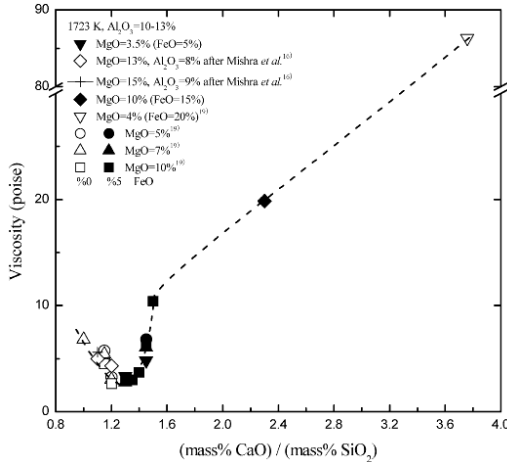


Fig. 9. Viscosities of CaO-SiO₂-FeO-MgO-Al₂O₃ slag systems as a function of basicity

In order to examine the effect of solid phase fraction on the viscosity below the melting temperatures, relative viscosity values with respect to that measured at 1873 K were plotted against the mass fraction of the solid phase. The fraction of the solid phase was calculated using FactSageTM software as shown in Fig. 10(a). An abrupt increase in relative viscosity occurred from mass fraction of solid phase of 17 to 25 %. This indicates that the slag viscosity in solid-liquid coexisting region linearly increases with increasing the mass fraction of the solid phases until it reaches a certain value. Therefore, it is necessary to evaluate the critical value of the abrupt increase in viscosity with solid phase fraction, meaning that the mechanism of fluid dynamics can be changed at the composition from Newtonian to non-Newtonian fluid.

Einstein-Roscoe equation could be applied for the viscosity evaluation of solid-liquid coexisting suspensions as shown in Eq. (11):

$$\eta = \eta_0(1 - \alpha f)^{-n} \quad (11)$$

where η , η_0 and f are the viscosity of liquid melt with solid particles, the viscosity without solid particles and volume fraction of solid particles, respectively. The constant α can be calculated by Einstein-Roscoe plot established in Fig. 10(b). From the inverse proportionality between the constant α and the maximum volume fraction of solid phase, f_{max} , the maximum volume fraction of solid phase was calculated to range from 0.26 to 0.36. Therefore, the volume of the solid phase less than 26 to 36 % in the entire slag system ensures the stable viscous behavior, namely Newtonian flow.

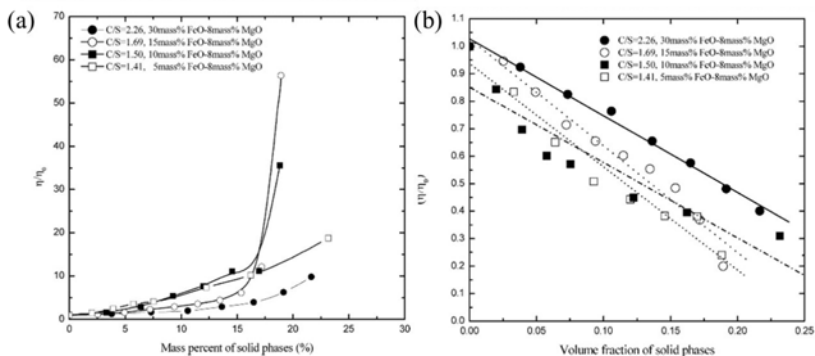


Fig. 10. (a) Dependence of the relative viscosity on the mass fraction of solid phases in CaO-SiO₂-MgO-FeO system. (b) Einstein-Roscoe relationship between relative viscosity and volume fraction of solid phases

Conclusions

The viscosity of several metallurgical slag systems was briefly reviewed in view of slag design. From the review, the following conclusions were obtained:

- (1) The viscosity of blast furnace slag decreases with increasing slag basicity. MgO and FeO behave as basic oxide, resulting in the decrease in the viscosity of the melt, while the addition of Al₂O₃ increases the viscosity of the melt.
- (2) The antithetic trend was observed for the effect of Na₂O/K₂O addition on the viscosity of the blast furnace slags. The difference in the behavior of two alkaline oxide are

originated from the difference in ionic radii and coordination number of each cation. Na₂O tends to depolymerize aluminosilicate structure as network modifier while K₂O tends to participate in charge compensation of aluminate so that ratio of AlO₄⁴⁻ tetrahedral unit increased.

- (3) The effect of basicity on the viscosity of highly basic oxide shows opposite trend with respect to blast furnace slags: Slag viscosity increases with increasing basicity, not by structural polymerization so much as the increase in solid phase fraction. The effect of solid phase fraction on the slag viscosity was well explained by Einstein-Roscoe equation, and critical fraction of the solid phase for Newtonian flow was suggested to be 26 to 36 %.

References

1. I. Sohn and D. J. Min, "A Review of the Relationship between Viscosity and the Structure of Calcium-Silicate-Based Slags in Ironmaking", *Steel Research International*, 83 (2012), 611-630
2. A. Kondratiev and E. Jak, "Review of experimental data and modeling of the viscosities of liquid slags in the Al₂O₃-CaO-FeO-SiO₂ system, *Metallurgical and Materials Transactions B*, 32 (2001), 1015-1025
3. K. C. Mills and J. Keene, "Physical Properties of BOS Slags", *International Materials Reviews*, 32 (1987), 1-120
4. E. T. Turkdogan and P. M. Bills, "A Critical Review of Viscosity of CaO-MgO-Al₂O₃-SiO₂ Melts", *British Ceramic Society Bulletin*, 39 (1960), 682-687
5. J. O'M Bockris and D. C. Lowe, "Viscosity and the Structure of Molten Silicates", *Proceedings of Royal Society A*, A226(1954), 423-435
6. N. Saito, N. Hori, K. Nakashima, and K. Mori, "Viscosity of Blast Furnace Type Slags", *Metallurgical and Materials Transactions B*, 34B (2003), 509-515
7. M. Nakamoto, T. Tanaka, J. Lee, and T. Usui, "Evaluation of Viscosity of Molten SiO₂-CaO-MgO-Al₂O₃ Slags in Blast Furnace Operation", *ISIJ International*, 44(2004) 2115-2119
8. A. Shankar, M. Gornerup, A. K. Lahiri, and S. Seetharaman, "Experimental Investigation of the Viscosities in CaO-SiO₂-MgO-Al₂O₃ and CaO-SiO₂-MgO-Al₂O₃-TiO₂ Slags", *Metallurgical and Materials Transactions B*, 38B(2007), 911-915
9. S. Sukenaga, Y. Gonda, S. Yoshimura, N. Saito, and K. Nakashima, "Viscosity Measurement of Calcium Ferrite Based Slags during Structural Relaxation Process", *ISIJ International*, 50 (2010), 195-199
10. S.-H. Seok, S.M. Jung, Y. S. Lee, and D. J. Min, "Viscosity of Highly Basic Slags", *ISIJ International*, 27 (2007), 1090-1096
11. Y. S. Lee, D. J. Min, S. M Jung, and S. H. Yi, "Influence of Basicity and FeO Content on Viscosity of Blast Furnace Type Slags Containing FeO", *ISIJ International*, 44 (2004), 1283-1290
- 12 P. Herasymenko and G. E. Speigy, "Ionic Theory of Slag-Metal Equilibria in Iron Smelting. I. Derivation of Fundamental Relations", *Journal of Iron and Steel Institution*, 166(1950) 169-183

- 13 M. Temkin, "Mixtures of Fused Salts as Ionic Solutions", *Acta Physicochimica URSS*, 20 (1945) 411-420
- 14 G. W. Toop and C. S. Samis, "Some New Ionic Concepts of Silicate Slags", *Canadian Metallurgy Quarterly*, 1(1962) 129-152
- 15 C. R. Masson, "An Approach to the Problem of Ionic Distribution in Liquid Silicates", *Proceedings of Royal Society A*, A287 (1965) 201-221
- 16 J. R. Kim, Y. S. Lee, D. J. Min, S. M. Jung, and Sang Ho Yi, "Influence of MgO and Al₂O₃ Contents on Viscosity of Blast Furnace Type Slags Containing FeO", *ISIJ International*, 44 (2004) 1291-1297
17. Kim, W. H. Kim, J. H. Park and D. J. Min, "A Study on the Effect of Na₂O on the Viscosity for Ironmaking Slags", *Steel Research International*, 81 (2010) 17-24
18. W. H. Kim, I. Sohn, and D. J. Min, "A Study on the Viscous Behaviour with K₂O Additions in the CaO-SiO₂-Al₂O₃-MgO-K₂O Quinary Slag System", *Steel Research International*, 81 (2010) 735-741
- 19, H. Park, J.-Y. Park, G. H. Kim, and I. Sohn, "Effect of TiO₂ on the Viscosity and Slag Structure in Blast Furnace Type Slags", *Steel Research International*, 83 (2012) 150-156
20. S. A. Brawer and W. B. White, "Raman Spectroscopic Investigation of the Structure of Silicate Glasses. I. The Binary Silicate Glasses", *Physical Review B*, 63 (1975) 2421-2432
- 21, B. O. Mysen, D. Virgo, P. Nackwerth, F. A. Seifert, and I. Kushiro, "The Structure of Silicate Melts: Implications for Chemical and Physical Properties of Natural Magma", *Reviews of Geophysics and Space Physics*, 20(1982) 353-383
22. B. O. Mysen, "Structure and Properties of Magmatic Liquids: From Haplobasalt to Haploandesite", *Geochimica Cosmochimica Acta*, 63(1999), 95-112
23. B. O. Mysen, "Physics and Chemistry of Silicate Glasses and Melts", *European Journal of Mineralogy* 15 (2003), 781-802
24. J. H. Park, "Composition-Structure-Property Relationships of CaO-MO-SiO₂ (M=Mg²⁺, Mn²⁺) Systems Derived from Micro-Raman Spectroscopy", *Journal of Non-Crystal Solids*. 358(2012), 3096-3102
25. Y.-U. Han, I. Sohn, and D. J. Min, "Cationic Effect on Phase Stability and Melt Structure in CaSiO₃-MgSiO₃ System", *Physical Review B*, under progress
26. E. J. Jung and D. J. Min, "Effect of Al₂O₃ and MgO on Interfacial Tension between Calcium Silicate-Based Melts and a Solid Steel Substrate", *Steel Research International*, 83 (2012) 705-711
27. I. Sohn, W. Wang, H. Matsuura, F. Tsukihashi, and D. J. Min, "Influence of TiO₂ on the Viscous Behavior of Calcium Silicate Melts Containing 17 mass% Al₂O₃ and 10 mass % MgO", *ISIJ International*, 52 (2012) 158-160
28. Y.-U. Han, W. W. Huh, and D. J. Min, "Correlation between High-Temperature Properties of Ferro-nickel Smelting Slag System, 'FeO'-MgO-SiO₂", under progress
29. J. H. Park, "Structure-Property Correlations of CaO-SiO₂-MnO Slag Derived from Raman Spectroscopy", *ISIJ International*, 52 (2012), 1627-1636

30. Y.-U. Han and D. J. Min, "Cationic Effect on Electrical Conductivity and Viscosity of Alkaline-earth Silicate Melts: Phenomenology", *Journal of American Ceramic Society*, 98 (2015), 2438-2444
31. R. D. Shannon, "Revised Effective Ionic Radii and Systematic Studies of Interatomic Distances in Halides and Chalcogenides", *Acta Crystallographica*, A32 (1976) 751-767
32. Y. Waseda and J. M. Toguri, *The Structure and Properties of Oxide Melts*, pp. 1-4 World Scientific Publishing, Singapore
33. G. S. Fulcher, "Analysis of Recent Measurement of the Viscosity of Glasses", *Journal of American Ceramic Society*, 8(1925), 339-355
34. G. S. Fulcher, "Analysis of Recent Measurement of the Viscosity of Glasses. II", *Journal of American Ceramic Society*, 8(1925), 789-794
35. S. Seetharaman and Du Sichen, "Viscosities of High Temperature Systems-A Modelling Approach", *ISIJ International*, 37 (1997), 109-118
36. L. S. Darken, "Thermodynamics of Binary Metallic Solutions", *Transactions of the Metallurgical Society of AIME*, 239(1967) 80-89

REFRACTORY METALS RECOVERY FROM INDUSTRIAL WASTES

Tran Van LONG¹, Hironori MURASE², Takahiro MIKI³, Yasushi SASAKI⁴ and Mitsutaka HINO⁵

¹Graduate student, Tohoku University; now MOIT; Vietnam

²Graduate student, Tohoku University; now Aichi Steel Co. Ltd.

³Department of Metallurgy, Graduate School of Engineering, Tohoku University

⁴Department of Metallurgy, Graduate School of Engineering, Tohoku University; now UNSW, Australia

⁵Professor Emeritus, Tohoku University

E-mail: mitsutaka.hino.a7@tohoku.ac.jp

Keywords: Recover, Molybdenum, Vanadium, Industrial Waste, Spent Lubricant, Combustion Ash, Orinoco Tar, Fe-Ni-V-C Quo-ternary Phase Diagram

Abstract

Refractory metals like Mo and V are alloyed in the special steels like heat-resisting, tool, ship and pipe steels for the improvement of their physical and mechanical properties. Most of refractory metals are refined as by-products in the other metals production processes. Recently, it becomes difficult to open new mines up for the environmental pollution issues, and as the results, it pays attention to recover them from industrial wastes as Mo and V resources instead of new mines development, because these wastes contain higher MoS₂ in spent lubricant, MoO₃ in oil refining catalysis and V₂O₅ in a domestic heavy oil combustion ash than the natural minerals containing them. In the present work, it was tried that these refractory metals was recovered as Fe-alloys because more than 80% of refractory metals are used as steel alloying elements and the energy consumption for reduction and production to Fe-alloys are less than that of pure refractory metals production.

At first, the recover principal of Fe-Mo alloy from spent lubricant, in which Mo existed as MoS₂, was experimentally established via their oxidizing roast and reduction processes at 1773K based on the knowledge of Cu process metallurgy. The spent lubricant mixed with CaCO₃, Fe₃O₄ and C was reduced in a C_{gr} crucible at 1773K. The mixed sample melted completely and separated into slag and metal phases.

In the second step, the recovery of Fe-V alloy from V₂O₅ in the combustion ash of Orinoco tar was tried. The ash mixed with CaO and C was reduced in a C_{gr} crucible at 1773K. The mixed sample melted completely and separated into slag and metal containing vanadium carbide. V was not almost observed in slag phase, and it meant that most of V in ash was recovered as vanadium carbides into the metal phase. The metal was Fe-Ni alloy. In the present work, Fe-Ni-V-C quo-ternary isothermal section phase diagram was experimentally assembled at 1773K.

As the result, 53.3mass%Fe-42.2mass%Mo-4.3mass%C alloy from spent lubricant and 37.4mass%Fe-46.4mass%Ni-12.3mass%Si-2.1mass%C alloy - V_xC_y mixture from Orinoco tar combustion ash by the reduction with carbonaceous materials were successfully recovered in the present work.

Introduction

Rare metals like molybdenum and vanadium are indispensable alloying elements as same as nickel and chromium to special steels such as high strength, high-speed tool, heat-resistant and stainless steels for improvement of their mechanical properties. These rare metals are supplied with raw materials from restricting countries in the world. Molybdenum is produced mainly in the United States, China and Chile, and vanadium is provided in large part from South Africa, China and Russia.

There is high risk to be unable for many industrial countries to import these metals when their prices are rising dramatically and the resource-producing countries invoke the export suppression system. And also, it becomes too hard to develop new mines because of the environmental issues on roasting process and wastewater treatment. It is an indispensable issue, therefore, to maintain these stable sources of supply for sustainable development of the multifunctional capability of steel.

The present authors[1-5] pay attention to their untouched resources and propose the fundamentals of these rare metals recovery from the resources. In concrete terms, the effective practical use of the slag discharged from cleaning furnace after matte-making process in copper production and the spent lubricant in chemical industry wastes as the sources of molybdenum and that of fired ash of oil-coke, Orinoco tar, oil sand and heavy oil as the source of vanadium are proposed. If the present proposal technologies are successfully realized, development of new mines does not required and it results in the depression of CO₂ generation.

Fundamentals of Proposal Rare Metal Recovery from Industrial Wastes

More than 80% of Mo and V production quantities is used as alloying elements, of which contents in steels are less than 1 mass%, for special steel production. Because of their low contents, it is quite difficult to recover Mo and V from these alloyed steels with the current technology.

It is practical to recover Mo and V as Fe-Mo and Fe-V alloys from industrial wastes, in which Mo and V are quite highly contained, from the viewpoints of lower energy consumption, economy and utility. The pyro-metallurgical process is applied from the same points of view in this paper.

Recovery of Molybdenum

Experimental demonstration for molybdenum recovery from industrial wastes

The present target material, which was used for the establishment of molybdenum recovery principal from industrial wastes, is slag after removal of matte carried in the cleaning furnace in Cu production process shown in **Fig. 1**.

The slag contains almost 40-45 mass% T.Fe, less than 10 mass% Fe₃O₄, 30 mass% SiO₂, 5 mass% (Al₂O₃ + CaO), 1 mass% Cu and 0.3 mass% Mo.

On the other hand, Mo ore in its mines contains about 0.6 mass% MoS₂ (0.36 mass% as metallic Mo). Namely, Mo content in the disposed cleaning furnace slag is comparable to high grade Mo ore. It means that a new Mo crude material can easily be procured from open-cut accumulated matte cleaning furnace slag without exploitation of new Mo mines.

The P_{S_2} - P_{O_2} diagram on M (M=Cu, Fe, Mo)-S-O system at 1 300 K is shown in **Fig. 2**. On the matte making condition, it is known from Fig.2 that Mo and Fe exist as oxides in the slag. Therefore, the location of present investigated slag in the cleaning furnace is indicated as an ellipse in Fig. 2.

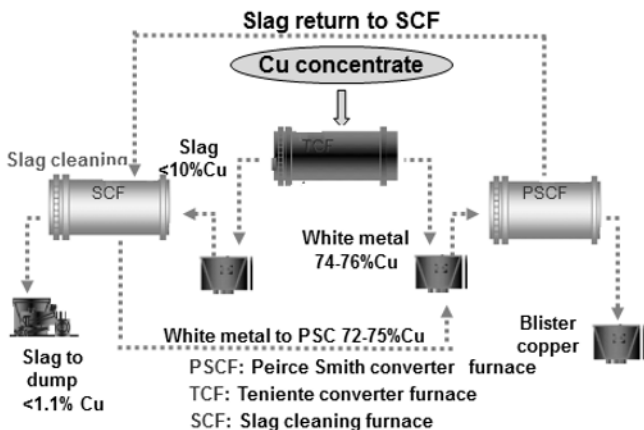


Fig.1 Copper production process

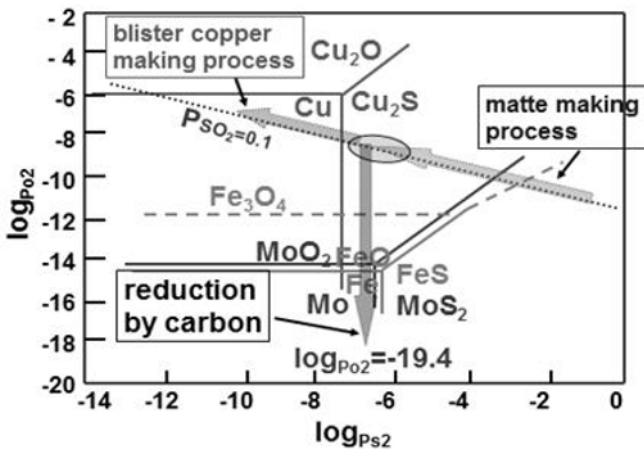


Fig.2 $\log P_{\text{O}_2}$ - $\log P_{\text{S}_2}$ diagram of Metal-S-O system at 1300K

If the cleaning furnace slag is reduced by carbon at high temperature, FeO and MoO₂ in the slag will be reduced and it results that Fe-Mo alloy will be produced as shown in Fig.2.

Molybdenum recovery from spent lubricant

About 20% of Mo produced in the world is used as catalysts and lubricants, in which Mo is existed as MoS₂ and MoO₃, in the chemical industry. These Mo carriers contain about 10-20 mass%

Mo. The recovery of Mo from these wastes is quite attractive as a stable Mo resource. Several recycling processes[6-10] of these waste carriers have been proposed on the basis of hydro-metallurgy and pyro-metallurgy. For the hydro-metallurgy methods, HNO₃ treatment and alkali leaching have been reported, where rigorous control technology of *pH*, solvent density and operation temperature is required and also the facilities of Mo solution tank have to be equipped. For the pyro-metallurgy methods, lime or caustic soda roasting and chlorination have been reported. But it makes large negative impacts on the environment caused by SO₂ and S₂Cl gas exhaust.

Therefore, a new Mo recovery technology as Fe-Mo alloy from the spent lubricant by carbon reduction with lime stone and iron oxide is proposed and demonstrated to avoid these environmental issues in the present authors' group. [5]

Recovery of Vanadium

Vanadium recovery from Orinoco tar

Vanadium natural ore doesn't exist, and it is produced as a by-product of other ores or recovered from to petroleum refining catalyst. Recently, crude oil, especially Orinoco tar, combustion ash is in the spotlight as V resource. It contains almost 20 mass% V₂O₅, 15 mass% NiO, 20 mass% Fe₂O₃, 15 mass% SiO₂, 10 mass% Al₂O₃, less than 5 mass% (CaO+MO+Na₂O+K₂O) and 5 mass% C, respectively. 1.2 trillion barrels reserves of Orinoco tar are found in 50,000km² northern region of Venezuela, where the recoverable reserves are 270 billion barrels. It will be possible to supply the tar for 700 years even if 60 million ton of the tar per year is exported.

Therefore, the vanadium recovery was examined from the combustion ash with CaO by carbon reduction in the present authors' group.[3]

Experiments

Experimental Methods

Molybdenum recovery from matte cleaning furnace slag

In a preparatory experiment for the possibility of Mo recovery from industrial wastes, Mo recovery from matte cleaning slag was tried. CaO and Al₂O₃ were added to Chilean matte cleaning furnace slag in order to decrease the melting temperature of the slag after reduction of Fe oxide and MoO₂ in the slag. The slag composition took aim at the eutectic composition of the slag system, which was 6.78 mass% Al₂O₃, 27.2 mass% CaO, 0.97 mass% Cu₂O, 34.64 mass% FeO, 6.26 mass% Fe₂O₃, 1.01 mass% FeS, 22.67 mass% SiO₂ and 0.3 mass% MoO₂. The Mo recovery from this slag with a carbon crucible as a reductant was done in Ar atmosphere at 1723, 1773 and 1823K using the vertical resistance furnace with LaCrO₃ heating elements as shown in **Fig.3**. The Al₂O₃ tube (O.D. 80 mm, I.D. 70 mm and the length of 1 000 mm) was held in the furnace. The bottom of the crucible is positioned to the center of the isothermal zone. The slag sample was pulled out from the furnace tube with a Mo wire after reduction, quenched by impinging He gas, cut and then delivered to the chemical analysis of Fe, Cu, Mo, Si, Al, Ca contents in both phases of slag and metal by inductively coupled plasma spectrometry (ICP) and C, S contents by combustion infrared detection method (LECO).

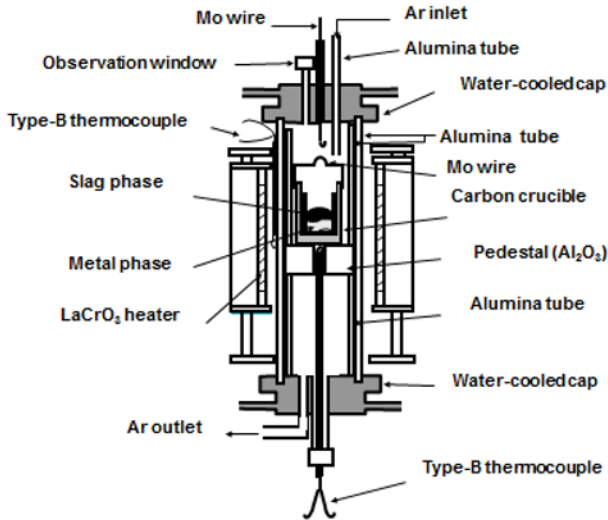


Fig.3 Schematic experimental apparatus

Molybdenum recovery from spent lubricant

The reduction of the spent lubricant was carried out in a MgO or a C_{gr} crucible at 1773K in Ar atmosphere for 2 hr using the same reacting system as shown in Fig. 3.

Fe oxide, lime stone and graphite were added to the spent lubricant, where Fe oxide acts as a medium of Mo, lime stone does as flux to gangue mineral in spent lubricant and graphite does as a reductant in the reduction process. The composition of the spent lubricant sample after addition of CaCO₃, Fe₃O₄ and C was 11.8 mass% SiO₂, 25.2 mass% Fe₃O₄, 26.0 mass% CaCO₃, 23.2 mass% MoS₂, 1.6 mass% Al₂O₃, 8.4 mass% C and others.

Vanadium recovery from Orinoco tar combustion ash

The combustion ash of the Orinoco tar, of which composition was 20.53 mass% V₂O₅, 13.18 mass% NiO, 18.62 mass% Fe₂O₃, 15.61 mass% SiO₂, 9.80 mass% Al₂O₃, 0.83 mass% CaO, 1.06 mass% MgO, 1.36 mass% (Na₂O+K₂O), 0.22 mass % S, 5.08 mass% C, and others, was used for recovery of vanadium in the present authors' group.³⁾ This ash was mixed with CaO and C powder, of which mixing ratio was 78.89 mass% ash, 7.00 mass% C and 14.11 mass% CaO, and compacted to a tablet shape. The compacted sample was put in a carbon crucible and heated to 1773K in Ar atmosphere. After holding for 3hr using the same reacting system as shown in Fig. 3, the sample was quenched, cut and analyzed chemically by SEM-EDS/WDS.

In the next stage, phase diagram experiment on Fe-V-C, Ni-V-C and Fe-Ni-V-C systems was carried out. Electrolysis Fe, Ni, and C powder were mixed and compacted to a tablet shape. The sample was put on V crumbs in an Al₂O₃ crucible. After holding for 3hr at 1773K, the sample was quenched, cut and observed with SEM-EDS/WDS.

Experimental Results

Molybdenum recovery from matte cleaning furnace slag

The experimental result is shown in Fig.4. After reduction of matte cleaning slag, the slag separated into two phases of Fe-C and slag. The formed slag was in liquid state over 1750K and all of Mo in the cleaning slag was participated into

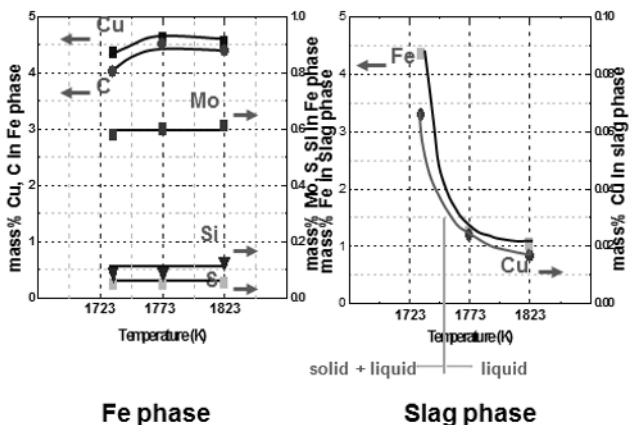


Fig.4 Experiment of Mo recovery from matte cleaning slag by C reduction.

Fe-C phase after C reduction. The Mo content was 0.65 mass%, but 4.3 mass% Cu and 0.05 mass% S dissolved also in Fe-C phase. Therefore, it makes clear that Cu must be removed from the obtained Fe-C-Mo alloy for practical use. Eventually, Fe-0.65mass%Mo-0.1mass%Cu-4.5mass%C alloy was obtained after Cu removal by FeS-Na₂S flux in a C_{gr} crucible at 1673K in Ar atmosphere.

This result proved that it was possible to remove Mo from the matte cleaning slag, *i.e.* industrial wastes, by C reduction.

Molybdenum recovery from spent lubricant

In case of reduction in a MgO crucible, Fe-37.43mass%Mo-0.09mass%C-6.70mass%S metal and 33.88mass%CaO - 51.98mass%SiO₂ - 2.07mass%Al₂O₃ slag phases were obtained. But the slag phase contained still 5.04mass%Mo. It means that the degree of reduction was insufficient, so it followed the reduction examination using a C_{gr} crucible. As the result, Fe-42.15mass%Mo-4.34mass%C - 2.33mass%S metal and 0.51mass%Mo containing 38.12mass%CaO-50.21 mass%SiO₂-1.68 mass% Al₂O₃ slag phases.

The Fe-C-Mo metal composition produced from these three kinds of reduction experiments was compared each other in Fig.5. The Mo contents are adequate high as raw materials for special steel production.

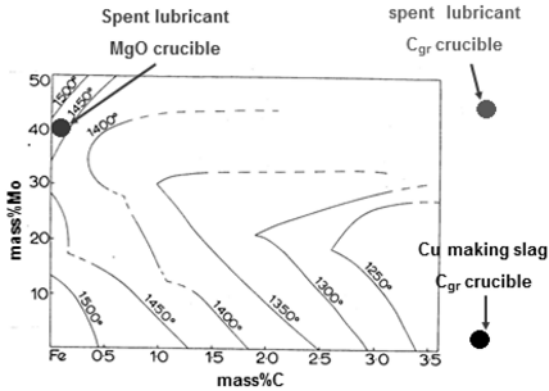


Fig.5 The Fe-C-Mo metal composition produced from industrial wastes

Vanadium recovery from Orinoco tar combustion ash

The mixed sample melted completely and separated to Fe-Ni-Si alloy, V_xC_y , and slag phases after carbothermic reduction as shown in Fig.6. V was not observed in slag phase, so that V in the combustion ash was completely recovered into metal and carbide phases. The composition of metal phase was 37.4 mass%Fe-46.4mass%Ni-12.3mass%Si-2.1mass%C-0.7mass%V, and that of carbide phase was 71.5mass%V-19.4mass%C-1.6 mass%Ti.

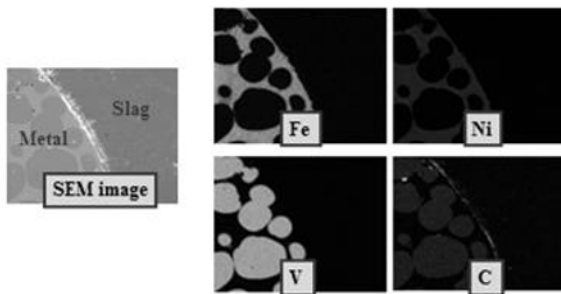


Fig.6 SEM result of Orinoco tar combustion ash after C reduction

Discussion

Mo Recovery Mechanism from Spent Lubricant

Quadruple mass spectroscopy (QMS), differential thermal analysis (DTA) and X-ray diffraction (XRD) were also applied to make clear the carbon reduction mechanism of the spent lubricant using its simulated samples. $CaCO_3$ - MoS_2 -C, $CaCO_3$ - MoS_2 - Fe_3O_4 -C and spent lubricant- $CaCO_3$ - Fe_3O_4 -C mixtures were synthesized to observe what kinds of gases and reactions happened during heating

process, and they provided for these experiments.

XRD analysis

The samples were heated up to given temperatures in Ar atmosphere at heating rate of 300K/hr, kept for 1hr, cooled down to room temperature at cooling rate of 300K/hr and supplied to XRD analysis. The identified phases by XRD analysis of these samples at each temperature are shown in **Table 1**.

Table 1 XRD results of sample mixtures after 1 hr retention at various temperatures

Temp(K)	CaCO ₃ -MoS ₂ -C mixtures	CaCO ₃ -MoS ₂ -Fe ₃ O ₄ -C mixtures	lubricant-CaCO ₃ -Fe ₃ O ₄ -C mixture
1073		MoS ₂ , C, CaMoO ₄ , CaS	
1173	CaO, MoS ₂ , CaS, C	CaS, CaMoO ₄ , Fe, Fe _{1.3} Mo ₅ S ₈ , C, Fe ₃ Mo ₃ C	CaO, C, SiO ₂ , MoS ₂ , Fe ₃ O ₄ , CaS, CaMoO ₄ , 2CaO·Al ₂ O ₃ ·SiO ₂
1273	Mo, CaS, CaO	CaS, CaMoO ₄ , Fe, C, Fe _{1.3} Mo ₅ S ₈ , Fe ₃ Mo ₃ C	Fe _{1.3} Mo ₅ S ₈ , C, Fe, CaS, SiO ₂ , 2CaO·Al ₂ O ₃ ·SiO ₂
1373	Mo, CaS, CaO		Fe _{1.3} Mo ₅ S ₈ , Fe, SiO ₂ , CaS, C, 2CaO·Al ₂ O ₃ ·SiO ₂
1473		CaS, Fe ₃ Mo ₃ C, C, Fe	Fe _{1.3} Mo ₅ S ₈ , Fe, CaS, C, SiO ₂ , 2CaO·Al ₂ O ₃ ·SiO ₂

Fe₃O₄ was remained at lower than 1173K, but Fe instead of Fe₃O₄ was observed at higher than 1273K. MoS₂ was existed at 1173K. However, Mo and Fe formed a sulfide compounds at higher than 1273K. In the case of CaCO₃-MoS₂-Fe₃O₄-C mixture, the carbide of Fe₃Mo₃C was observed, but it was not observed in case of spent lubricant-CaCO₃-Fe₃O₄-C mixture. The XRD analysis suggested that Al₂O₃, CaO and SiO₂ in the mixtures reacted each other even at 1173K and produced the stable gehlenite (Ca₂Al₂SiO₇).

QMS analysis

The evolved gases in the carbon reduction of spent lubricant-CaCO₃-Fe₃O₄-C mixture were measured in vacuum at heating rate of 300K/hr by using QMS. The results are shown in **Fig. 7**. CO₂ was observed at higher than 773K. The peak intensity increased with temperature and reached to the maximum at 973K, then quickly decreased with temperature. The produced CO started to increase at around 1173K. Beyond 1323K, most of the evolved gas was found to be CO. The species with the mass weights of 12, 14 and 16 were also observed. These species can be produced by the fragmentation of the gas molecules during the ionization process in the QMS detector. In the present study, the mass peak of 32 was found. It could be corresponded to S atom. However, its intensity was negligibly small compared with those of CO, CO₂ and H₂O gases. It simply means that S in MoS₂ was not gasified on the present experimental condition.

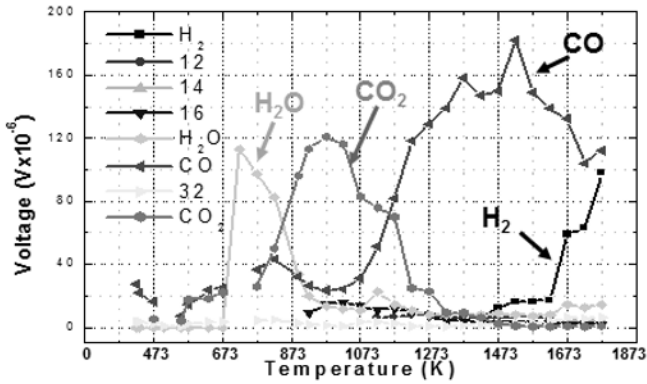


Fig.7 QMS result of spent lubricant-CaCO₃-Fe₃O₄-C

DTA analysis

The measurement of DTA of spent lubricant- CaCO₃-Fe₃O₄-C mixture was carried out in Ar atmosphere at heating rate of 10K/min. The results were shown in **Fig. 8**. A moderate endothermic peak at around 573K and a sharp endothermic peak at 1073K were observed. The previous peak corresponds

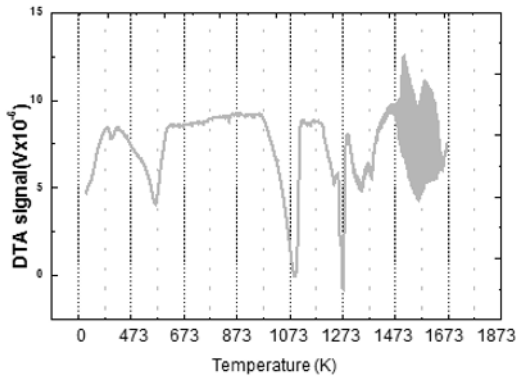


Fig.8 DTA curve of spent lubricant-CaCO₃-Fe₃O₄-C

to the dehydration reaction and the later dues to the CaCO₃ decomposition. At higher than 1200K, moderate endothermic curve, which is caused by carbon solution loss reaction, was found. The continuous intense endothermic-exothermic peaks were observed between 1473 and 1670K. It might be caused by direct and indirect reduction of Fe oxides by C and CO.

Carbothermic reduction mechanism of spent lubricant

The reduction mechanism of spent lubricant is deduced from the above-mentioned XRD,

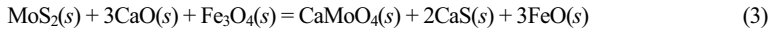
QMS and DTA analysis results as follows.

The dehydration reaction occurs at around 573K. CaCO_3 decomposes at 1073K.

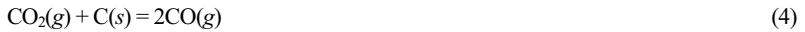


$$\Delta G_1^0 = 175930 - 150.69T \text{ (J)} \quad (2)$$

The formed CaO reacts with MoS_2 and Fe_3O_4 .



The evolved CO_2 gas reacts with C by the Boudouard reaction.



$$\Delta G_4^0 = 167230 - 172.2T \text{ (J)} \quad (5)$$

Fe_3O_4 is reduced to Fe by the produced CO.

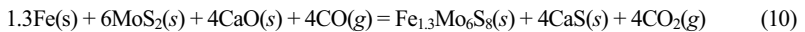


$$\Delta G_6^0 = 10610 - 17.80T \text{ (J)} \quad (7)$$



$$\Delta G_8^0 = -11570 + 23.0T \text{ (J)} \quad (9)$$

The produced CO and Fe will react with MoS_2 and CaO.



Fe_3O_4 is reduced by C in parallel with CO because C is mixed with spent lubricant.



$$\Delta G_{11}^0 = 182270 - 192.80T \text{ (J)} \quad (12)$$



$$\Delta G_{13}^0 = 154610 - 153.7T \text{ (J)} \quad (14)$$

Phase Diagram of Fe-Ni-V-C System

It has been reported that there are many kinds of compounds of vanadium oxides. But the phase diagram of Fe-Ni-V-C system has not yet been clear sufficiently. It was, therefore, tried to establish the phase diagram in the present authors' group.³⁾ Based on the result of the chemical composition analysis by WDS, the isothermal section of Fe-Ni-V-C system was drawn in **Figs. 9**.

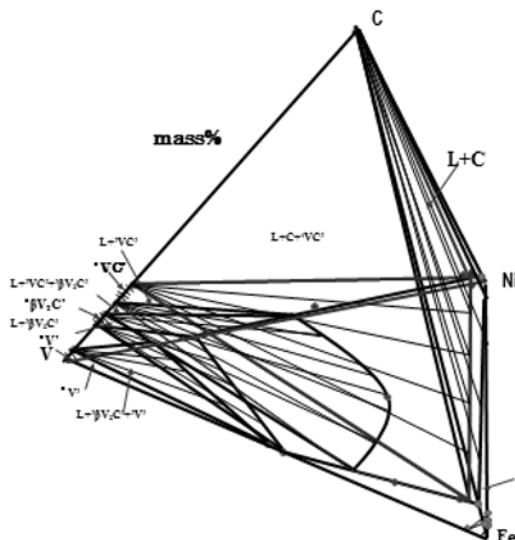


Fig.9 Iso-thermal section of Fe-Ni-V-C phase diagram at 1773K

The present experimental samples of which composition located in L+VC' area transferred into $\alpha(\text{FeV})$ and VC_x phases during cooling process. Similarly, the samples in L+VC'+ $\beta\text{V}_2\text{C}'$ area did into $\alpha(\text{FeV})$, VC_x and ' $\text{V}_2\text{C}'$ ' phases during cooling process. The samples in L+ $\beta\text{V}_2\text{C}'$ area did into $\alpha(\text{FeV})$ and ' $\text{V}_2\text{C}'$ ' phases during cooling process. These agree well with the result of Amara *et al.*[11] But the samples in L+V' area did into $\alpha(\text{FeV})$ and ' $\text{V}_2\text{C}'$ ' phases during cooling process. This disagrees with the result of Amara *et al.*[11]

Conclusions

Mo recovery as Fe–Mo alloys from Cu making slag has been investigated by taking into account that Mo is mainly used for the resource for Fe–Mo alloy. The Chilean Cu making slag with the addition of appropriate amounts of CaO and Al_2O_3 was reduced by C. As the result, MoO_2 in the slag was almost fully reduced and Fe–0.6mass%Mo–0.1mass%Cu–4.5mass%C alloy with low Cu content could be produced.

Based on the above-mentioned success of Mo recovery from Cu making slag, the feasibility of the recovery of Mo as a Fe–Mo alloy by applying the carbothermic reduction of the spent lubricant with the mixture of CaO and Fe_3O_4 and coke was confirmed in the present study. The reaction mechanism of the reduction of MoS_2 was also investigated and the formations of $\text{Fe}_3\text{Mo}_3\text{C}$ and

Fe_{1.3}Mo₆S₈ during the reduction of MoS₂ were confirmed. In the present reduction process, S in MoS₂ was not gasified and only CO and CO₂ gases were produced. On the present experimental condition, the MoS₂ in the spent lubricant is successfully recovered as Mo resource into Fe-42.1mass%Mo-4.3mass%C-2.3 mass%S alloy.

The spent Orinoco tar combustion ash reduction by C was also examined continuously in the present study. As the results, most of V in the ash could be recovered into 37.4mass%Fe-46.4mass%Ni-12.3mass%Si-2.1mass%C-0.7mass%V alloy and 71.5mass%V-19.4 mass%C-1.6 mass%Ti carbide. Fe-Ni-V-C quaternary isothermal section phase diagram was experimentally established at 1773K for the clarification of the present successful experimental reduction result.

References

1. Fernando PARADA, Roberto PARRA, Toshiki WATANABE, Mitsutaka HINO, Jose PALACIOS, Mario SANCHEZ, "Recovery of Iron-Molybdenum Alloy from Copper Slag", *Proc. of MOLTEN2009, VIII International Conference on Molten Slags, Fluxes and Salts*, 18-21 Jan., 2009, Santiago, Chile, (2009), 621-628.
2. Dusan BUSOLIC, Fernando PARADA, Roberto PARRA, Jose PALACIOS, Mitsutaka HINO, Felipe COX, Armando SANCHEZ, Mario SANCHEZ, "Recovery of Iron from Copper Flash Smelting Slags", *Proc. of MOLTEN2009, VIII International Conference on Molten Slags, Fluxes and Salts*, 18-21 Jan., 2009, Santiago, Chile, (2009), 12731280.
3. Hironori MURASE, Takahiro MIKI and Mitsutaka HINO, "Vanadium Recovery from Combustion Ash of Orinoco Tar in Venezuela", *Proc. of 9th Intern. Conf. on Molten Slags, Fluxes and Salts*, Organized by The Chinese Society for Metals, Beijing, China, 27-31 May, 2012, CD-ROM
4. Tran Van LONG, Jose PALACIOS, Mario SANCHEZ, Takahiro MIKI, Yasushi SASAKI and Mitsutaka HINO, " Recovery of Molybdenum from Copper Slags", *ISIJ Intern.*, **52**(2012), 1211-1216.
5. Tran Van LONG, Takahiro MIKI, Yasushi SASAKI and Mitsutaka HINO," Recovery of Molybdenum from Spent Lubricant", *ISIJ Intern.*, **52**(2012), 1217-1224.
6. K. H. Park, D. Mohapatra and B. Ramachandra Reddy, *J. Hazard Mater.*, **B138** (2006), 311.
7. T. N. Angelidis, E. Tourasanidis, E. Marinou and G. A. Stalidis, *Resour. Conserv. Recy.*, **13** (1995), 269.
8. T. Darjaa, T. H. Okabe, Y. Waseda and Y. Umetsu, *Shigen-to-Sozai*, **116** (2000), 203.
9. K. H. Park, B. Ramachandra Reddy, D. Mohapatra and C. W. Nam, *Int. J. Miner. Process.*, **80** (2006), 261.
10. B. B. Kar, B. V. R. Murthy and V. N. Misra, *Int. J. Miner. Process.*, **76** (2005), p. 143.
11. Sif Eddine Amara, Rafika Kesri, Nicole Valignat Sylvaine and Hamar-Thibault, *Mikrochim. Acta*, **114/115** (1994), 157.

ADVANCES IN MOLTEN SLAGS, FLUXES, AND SALTS:

Proceedings of



Industrial Applications: Ferroalloys and Silicon

SOFTENING AND MELTING OF SiO₂, AN IMPORTANT PARAMETER FOR REACTIONS WITH QUARTZ IN Si PRODUCTION

Eli Ringdalen¹, Merete Tangstad²

¹ SINTEF Materials and Chemistry, Alfred Getz Vei 2, N-7465 Trondheim, Norway

²Norwegian University of Science and Technology, Trondheim, Norway

Keywords: quartz, molten silica, silicon

Abstract

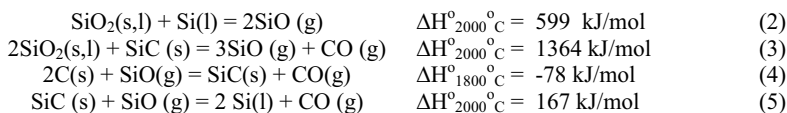
Quartz (SiO₂) is the main silicon source for production of metallurgical grade silicon in submerged arc furnaces. During heating in the furnace, quartz will first transform to other SiO₂ polymorphs, then soften and melt. Volume changes during heating and melting are expected to affect for the rate of reactions with SiO₂ and gas flow. Industrial quartz sources are investigated here with heating rates relevant for industrial furnaces. A method to study softening and melting of quartz at conditions relevant for Si-production was developed. Both volume expansion and melting properties vary considerably between quartz sources. Theoretical volume expansion is 22 % and melting temperature 1726 °C. Volume increase up to 40 %, softening temperatures in the range 1675 °C to 1800 °C, and melting temperatures in the range 1790 °C to 1900 °C were recorded.

Introduction

Metallurgical silicon (Si) and ferrosilicon (FeSi) are produced in submerged arc furnaces (SAF), where the two main raw materials are quartz and carbon reductants such as coke, coal, charcoal and woodchips. For FeSi production iron sources are added. Electrical energy, around 11-13 MWh/ton alloy for Si production, is another important input factor. The reduction of silica to Si takes place by the overall reaction (1). In industrial furnaces, the reactions take place in several steps as described by Schei et al. [1]



The raw materials are fed to the top of the charge mixture where the temperature is around 1000-1300 °C [2]. Quartz will descend further down and be heated at different rates varying both with operation and with distance from the electrodes. For Si furnaces a heating rate of 5.5 °C/min has been estimated [3] as normal for most of the quartz. Quartz will react by reaction (2) and (3) to form SiO that is further used to produce SiC by reaction (4) in the upper parts of the furnace and to produce Si by reaction (5) in the high temperature zone.



When descending in the furnace quartz will with increasing temperatures first change to other SiO₂ polymorphs, then soften and melt. Reaction mechanisms and reaction rates are expected to change with the change from liquid to solid phase. Formation of liquid SiO₂ might in addition affect furnace performance by reducing gas permeability and thereby reducing upward gas flow

and giving an uneven gas flow in the furnace. The highly viscous molten SiO_2 will also glue particles together and this may hinder an even flow of materials downwards in the furnace.

Changes in SiO_2 during heating.

Quartz will at $573\text{ }^\circ\text{C}$ (1 atm) change to β quartz by a fast and reconstructive transformation. The further transformation to tridymite described in the established SiO_2 phase diagram [4], is as discussed in [5], debated. Transformation to the high temperature polymorph β cristobalite which goes through an amorphous phase is slow. Quartz, amorphous silica and cristobalite have been found to occur together in quartz kept for relatively long time at temperatures at $1500\text{ }^\circ\text{C}$ to $1700\text{ }^\circ\text{C}$ [5,6,7]. The relative amounts vary between different quartz sources. The possibility for occurrence of unstable phases must thus be taken into account when melting of silica is discussed. Under equilibrium conditions, pure SiO_2 will melt at $1726\text{ }^\circ\text{C}$ by reaction (6). Cristobalite is the stable solid phase at this temperature. Content of common minor constituents in quartz, such as Na_2O , FeO , CaO and Al_2O_3 will change the rate of the solid state phase transformations [8] and the melting temperature. Liquid phase will then start to form at temperature below $1726\text{ }^\circ\text{C}$ and liquid and solid will coexists in a melting interval.



Quartz at $25\text{ }^\circ\text{C}$ has density of 2.65 g/cm^3 [10]. This will decrease slightly until β -quartz is formed at $573\text{ }^\circ\text{C}$, then increase slightly until tridymite or cristobalite is formed. Cristobalite at $25\text{ }^\circ\text{C}$ has density of 2.20 g/cm^3 [10] and a molar volume of $27.4 \text{ cm}^3/\text{mol}$ [11], and at $1726\text{ }^\circ\text{C}$ a molar volume of $27.6 \text{ cm}^3/\text{mol}$ [11] giving a density of 2.17 g/cm^3 . Liquid silica at $1400\text{ }^\circ\text{C}$ has a molar volume of $27.20 \text{ cm}^3/\text{mol}$ [12] representing a density of 2.20 g/cm^3 while its density at $1726\text{ }^\circ\text{C}$ is 2.08 g/cm^3 [13]. Amorphous silica is assumed to have a density between cristobalite and liquid silica. Due to this, the volume of quartz will increase with 17 % when it is transformed to cristobalite while melting at $1726\text{ }^\circ\text{C}$ will give a total volume increase of 22 %. Formation of an intermediate amorphous phase may increase the volume changes before melting. At lower temperatures, formation of β -quartz might cause some shrinkage.

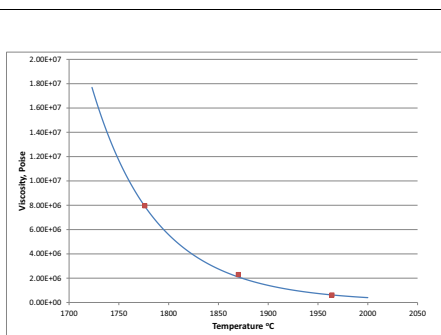


Figure 1 Viscosity of molten silica. Data from FactSage. Calculated by Halvor Dalaker and Kai Tang, Sintef.

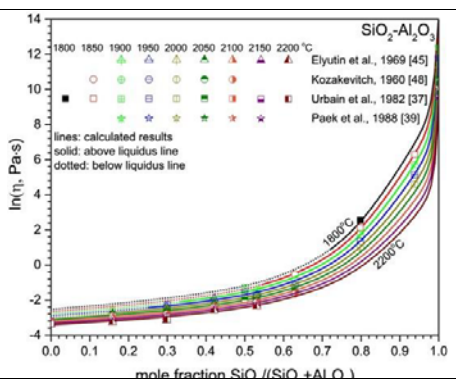


Figure 2 Viscosities in $\text{SiO}_2 - \text{Al}_2\text{O}_3$ melts¹⁴.

Liquid silica has a viscosity, around 2×10^7 Poise at the melting temperature and will then behave nearly as a solid. The viscosity will as shown in Figure 1 decrease rapidly with increasing temperature and be around 5×10^4 Poise at 2000 °C. Other constituents may affect the viscosity as seen in Figure 2 by the pronounced decrease with low Al₂O₃ contents. Reactions rates and how easily silica drain down in furnace is expected to increase with decreased viscosity.

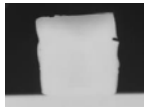
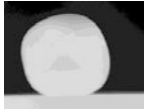
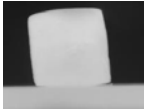

Investigations and Materials

Melting behaviour and temperatures were studied with two different methods with different scales, 10 mg samples and 0.5 kg samples. The investigations in smaller scale were done in a sessile drop apparatus by the method described earlier [4, 6, 5]. Results from these investigations are summarized and compared with the current work. The larger scale investigations are done by a new method simulating melting in industrial furnaces [15]. This method is still under development and only preliminary results are ready. For all the investigations, industrial quartz sources supplied by the Norwegian ferroalloy producers Elkem, FeSil and Eramet were used.

Melting Temperatures and Volume Expansion Investigations by Sessile Drop Apparatus

Cylinders of quartz with 4mm diameter and height were drilled from lump quartz samples. They were placed on an ISO88 graphite substrate and heated in CO first to 900 °C in about 3 min, then with the designated heating rate up to the final temperature. Images were recorded and analysed visually to determine temperature for *Softening* - when the shape of the sample has lost the sharp edges; *Final melting* - when the droplet is round, with no artefacts and the *Volume change*. The reported volumes are adjusted for the increased radius when the sample melts and change shape from cylindrical to round. Temperature for softening is determined by changes of the outer edge of the grain and temperature differences in the quartz particles are thus not taken into account. The samples changes gradually and it is difficult to give the exact temperatures and volumes with a good precision One test was run for each quartz source. Precision and uncertainty were not determined. Examples of mages are shown in Figure 3.

Figure 3 Recorded pictures of Qz 9 at softening and melting temperature from current investigation.

	5.5°C/min		10°C/min	
	Start melting	Complete melting	Start melting	Complete melting
Qz 9	 1720°C	 1825°C	 1680°C	 1790°C

In the investigations by Andersen [6], the samples were heated at 50 °C/min to 1500 °C, and further at 20°C/min to either 1500 °C or 1700 °C. In the investigations by Ringdalen [5] the samples were heated with 50 °C/min to 1500 °C, and further with 10 °C/min until final melting. In the current investigations, the samples were heated fast up to 1200 °C and further with either 10 °C/min or 5.5 °C/min up to melting. For quartz Qz 9 and Qz 27 both heating rates were used while for Qz 35 a quartz with high content of impurities, only 5.5 °C/min was used. One sample of Qz 27 was in addition heated with 5.5 °C/min up to 1700 °C and held at this temperature for 1 hour. Results from both earlier and current investigations are shown in Table 1. Volume change

from current investigations are shown in Figure 4. Results from earlier investigations are shown in Figure 5 for comparison.

Table 1 Softening and melting temperatures for quartz from current and earlier investigations. Quartz C-G from Andersen [6] . Qz1-Qz 11 from Ringdalen [5] . Marked with green from current investigation .

Quartz type	Softening °C	Melting °C	% Max vole expansion	°C for max vol expansion	Heating rate °C/min
C	1790		44	1700 (max temp)	20
D	1800		14	1700 (max temp)	20
E	1750		39	1700 (max temp)	20
G	1800		21	1700 (max temp)	20
Qz 1	1755	1900	28	1700	10
Qz2	1785	1900	23	1700	10
Qz 3	1790	1900	37	1800	10
Qz 4	1735	1880	20	1880	10
Qz 5	1800	1920	15	1850	10
Qz 6	1600	1880	18	1750	10
Qz 7	1800	1900	35	1800	10
Qz 8	1755	1830	10	1860	10
Qz 9	1775	1800	14	1700	10
Qz 10	1765	1910	32	1850	10
Qz 11	1770	1900	15	1750	10
Qz 9	1720	1825	28	1675	5.5
Qz 9	1680	1790	27	1625	10
Qz 27	1705	1820	18	1650	5.5
Qz 27	1710	1820	21	1700	5.5
Qz 27	1710	1820	16	1725	10
Qz 35	1675	1805	43	1650	5.5

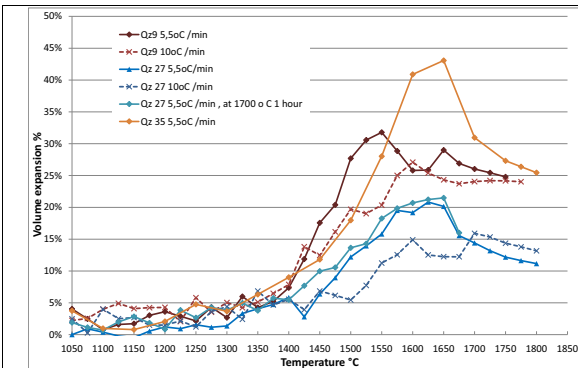


Figure 4 Volume expansion for Qz 9, Qz 27 and Qz 35 from current investigations.

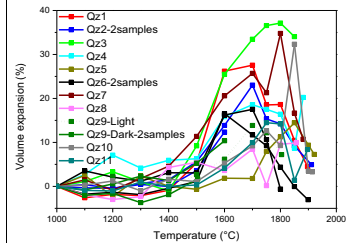


Figure 5 Change in volume with increasing temperature for Qz1-Qz 11. Results from Ringdalen [5].

Melting in Kilogram Scale Simulating Industrial Furnace

To better simulate softening and melting in industrial furnaces, a method for larger scale tests are now under development, started as a project work by Jusnes [15]. The test was done in graphite crucible, 40 cm high and with inner diameter of 11.5 cm heated in a 75 kW induction furnace. Commercial SiC 0-5 mm was used together with quartz 4.76 - 9.76 mm. A 5 cm thick layer of SiC was placed at the bottom of the crucible. Above this was a 10 cm thick layer of quartz mixed with SiC in the mol ratio 3:1 with a 5 cm thick layer of SiC for protection and insulation on top. Temperature at the top and the bottom of the quartz layer was measured with C-type thermocouples. The thermocouple at the bottom of the layer was used for furnace control. Heating of a graphite crucible in an induction furnace will give a higher temperature in the graphite bottom and a vertical temperature gradient in the crucible. Measured temperature at the top of the quartz layer was around 200 °C lower than at its bottom. A radial temperature gradient with a slightly higher temperature near the crucible walls is also expected

Quartz Qz 27 was used in the experiments. The crucible was heated with a rate of 40 °C/min up to 1000 °C and further by 5.5 °C/ min up to the predetermined temperature. After cooling, the crucible was filled with epoxy and cut in two halves. The cross section through the centre was scanned and the relative amounts of unreacted, softened and molten quartz were determined based on appearance by using Adobe Acrobat as analysing tool. Cross sections of crucibles heated to different temperatures are shown in Figure 6. The marked temperatures refer to the temperature at the bottom of the quartz layer in the centre of the crucible.

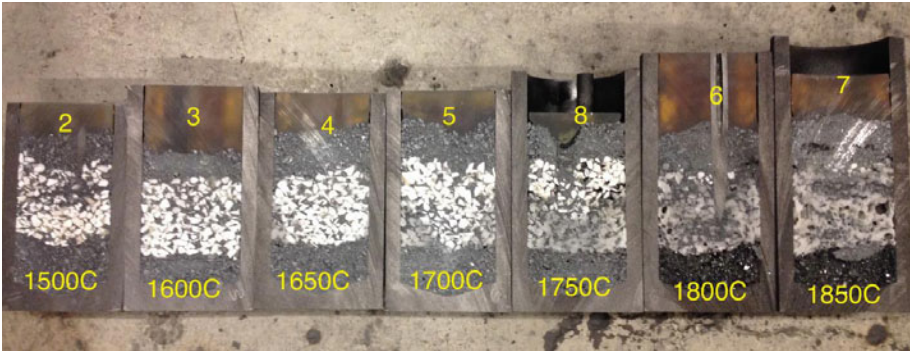


Figure 6 Cross sections of crucibles where quartz Qz 27 is heated to different temperatures. The marked temperature refers to the temperature at the bottom of the quartz layer in the centre of the crucible [15].

Examination of the crucibles at the point where the temperature is measured shows that below and at 1650 °C, the quartz has not started to soften or melt. It has not decrepitated during heating; only a slight cracking is observed. At 1700 °C, softening has just started while at 1750 °C, all quartz has softened and at 1800 °C it is molten and has started to react with SiC. The molten quartz has not drained down into the SiC below neither at 1800 °C or at 1850 °C.

Discussion

Both in the current and in earlier investigations several unexpected phenomena have been observed during heating and melting of quartz.

- Quartz was not fully molten until it reached a temperature well above the melting temperature of SiO₂ of 1726 °C
- Quartz had during heating a volume expansion up to 40 %, which is much higher than the expansion of 22% expected from the phase transformations.
- Different quartz sources show large differences in melting behaviour.

Melting temperatures

In earlier [5,6] and current experiments different quartz sources heated in mg scale in a sessile drop furnace started to soften between 1675 °C and 1800 °C, and were fully molten between 1790 °C and 1900 °C. One quartz Qz 27 was in addition tested with a new larger scale (kg) method. Softening temperature was 1710 °C in sessile drop and 1700-1750 °C in large scale while temperature for complete melting was 1820 °C in sessile drop and 1800 °C in large-scale experiments. These two methods then seem to give similar melting temperatures...

The high measured melting temperatures were assumed to be a result of too high heating rates to establish equilibrium. Melting properties were here studied by heating the same quartz source with two different heating rates, 10 °C/min and 5.5 °C/min in the sessile drop furnace. The highest heating rate gave as shown in Table 1, the highest melting temperature while it was no clear trend for softening temperature. When different quartz sources from current and earlier investigations are included, recorded softening and melting temperature increase with increasing heating rate as shown in Figure 7. The data represents only three different heating rates, several quartz sources and shows some overlap. The conclusion are thus so far regarded as indicative. Softening and melting temperatures vary between different quartz sources as seen in Table 1. There is no clear correlation between the observed softening temperatures and content of Al₂O₃ or alkalis in the quartz. Softening temperature decreases with increasing FeO content as shown in Figure 8 if the quartz with highest FeO content are omitted

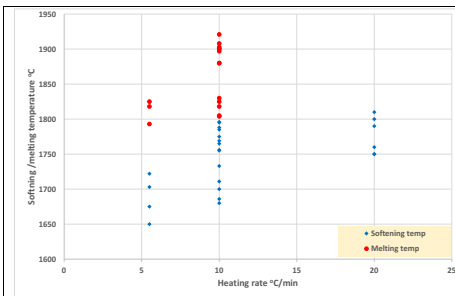


Figure 7 Correlation between softening and melting temperatures and heating rate.

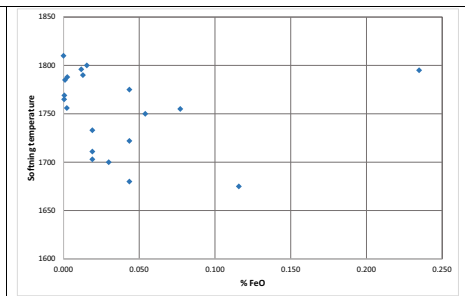


Figure 8 Softening temperature versus % FeO.

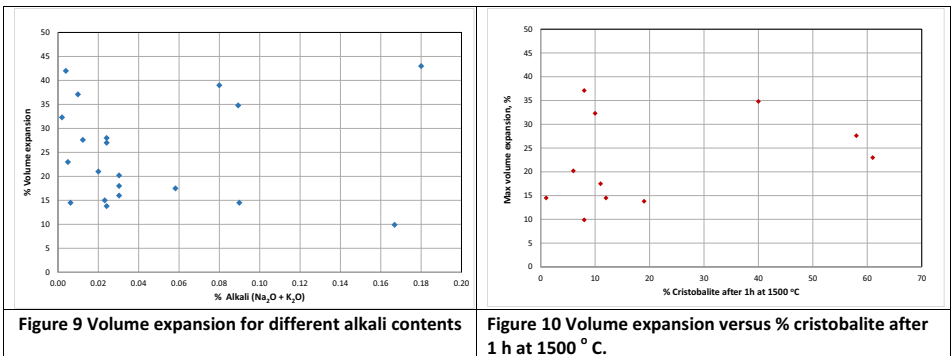
Contaminants are expected to give a lower softening temperature. The observed deviation from this might be a result of quartz and the phases with the contaminants not being in equilibrium. Mineralogy and texture of the quartz might thus affect melting properties. The observed higher than expected melting temperatures and their dependence of heating rate, indicate that either heating or melting of particle needs longer time to complete than available in the experiments.

The high softening temperature might result from either slow heat transfer from gas to solid quartz or that the phase transformation from solid to liquid is slow. It is not affected by heat transfer in the quartz since it is determined at the surface of the particle. But the observation so far is that quartz heated with rates relevant for industrial Si-furnaces, 5-20 °C/min, will not start to soften before the temperature reaches or is above 1700 °C and will not be fully molten until the temperature reaches 1800-1900 °C.

Volume expansion

When quartz is heated from room temperature to liquid silica at 1726 °C, its volume will theoretically increase with 22 %. Volume increase between 10 and 44 % was observed in the current and referred experiments in sessile drop apparatus. The volume expansions shown in Figure 5 and Figure 4, increased as expected rapidly around 1400 °C to 1500 °C when cristobalite formation takes place. At lower temperatures there are some shrinking due to formation of β quartz. The volumes reached their maximum around 1650 °C to 1800 °C and decreased with further temperature increase. Maximum volume expansions were reached at temperatures lower than the melting temperature. Increased heating rate, from 5.5 °C/min to 10 °C/min, gave a lower volume expansion as shown in Figure 4. The major differences in volume expansion are between different quartz sources independent of heating rate. Volume expansion for the two parallels of Qz 27 heated by 5.5 °C/min are close, indicating that the observed difference with heating rate is reliable. The decrease in volume at high temperatures has not been studied here. It might be caused by formation of SiO gas or by flow of partly molten phase into the substrate.

The observed volume expansions were not correlated with softening temperature or % Al₂O₃, % FeO, or % alkali. The large spread is illustrated by % alkali in Figure 9. Andersen [6] found highest cristobalite/quartz ratio in the quartz with highest volume expansion at 1700 °C. Ringdalen [5] determined amount of cristobalite after 1 hour at 1500 °C and volume expansion for different quartz sources. This indicates as shown in Figure 10 that maximum volume expansion increase with increasing amount of cristobalite confirming the findings of Andersen.



Volume expansion and cristobalite formation then seems to be affected by the same material property. To better understand the mechanism behind volume expansion in quartz, it will be

important to identify this property. In addition to phase transformations other parameters as cracking, water inclusions, OH-containing or other minerals, or chemical reactions might contribute to volume expansion. The correlation with FeO content may indicate the two last of these while the correlation with cristobalite formation may indicate cracking as a possible cause.

Industrial implications

Increased volume of quartz and clogging due to softening and melting of quartz may have a negative effect on furnace performance since they will decrease gas permeability. The importance of this depends on volume % of quartz in charge mixture, relative importance of other parameters that affects permeability, such as SiO condensation, and if permeability in the given case is a constraint for gas flow. Variation between different quartz sources in volume expansion and softening temperature may thus be of importance for furnace operation.

Reactions with quartz to produce SiO should preferably take place low down in the furnace in the high temperature zone. Reaction rate is expected to be higher for liquid than for solid quartz and to increase with decreasing viscosity. In industrial Si, furnaces where the expected heating rates are in the range 5-10 °C/min some quartz sources will not be fully molten until the temperature reaches 1900 °C. The liquid phase formed will at this temperature have considerably lower viscosity than liquid quartz at melting temperature of 1726 °C and more easily drain further down in the furnace. Melting at higher temperatures is based on this expected to be beneficial for furnace operation. Variation between different quartz sources in melting properties may thus be of importance for furnace operation.

Conclusions

A new method for investigations of melting properties in kg scale and for simulation of melting in industrial furnaces has been developed. The obtained results are comparable with measurements in mg scale in sessile drop furnace. Temperatures for softening and melting have been shown to vary considerably between different quartz sources. The investigated quartz sources were under these conditions not fully molten until well above the melting point for SiO₂ of 1726 °C. Some sources did not melt until 1900 °C. Softening and melting temperature both increased with increasing heating rate. During heating, volume of quartz increased with up to 40 %. This is higher than the volume expansion of 22 % due to phase transformations in SiO₂. Quartz source is the main parameter that affects volume expansion. The expansion is not directly correlated to content of any specific contaminant, but seems to vary with rate of cristobalite formation. Lower heating rate gave higher volume expansion.

In industrial operation low volume expansion and high softening and melting temperatures is expected to be preferable. The observed variation between different quartz sources for these parameters indicate that quartz source may affect furnace operation. The relative importance of quartz source compared to other parameters is not known.

Acknowledgements

Elkem, FeSil and Eramet have supplied quartz samples and data. The work is financed by Research Council of Norway, Elkem and Norwegian Metal producing Industry through the projects ReSiNa, ESiP and SFI Metal Production. They are all acknowledged.

References

- 1 A Schei A., J K Tuset J.K., and H. Tveit, *Production of High Silicon Alloys*, Tapir forlag, Trondheim, Norway, 1998, ISBN: 82-519-1317-9.
- 2 Ringdalen, E. and Tangstad, M: *Reaction Mechanisms in Carbothermic Production of Silicon, Study of Selected Reactions*, Proceedings of International Smelting Technology Symposium (Incorporating the 6th advances in sulphide smelting) held during TMS 2012, Editors: Jerome P Downey, Thomas P Battle, Jesse F White p. 195 – 204. ISBN 978-1-11829-116-0
- 3 Tveit Halvard, Elkem: Personal communication 2015
- 4 Kurt Aasly: Properties and behaviour of quartz for the silicon process. PhD thesis 2008:236, NTNU Trondheim, Norway 2008, ISBN 978-82-471-1163-5
- 5 Ringdalen E: Changes in quartz during heating and the possible effects on Si production; JOM (The Journal of the Minerals, Metals&Materials society (TMS) October 2014, ISSN 1047 -4838, DOI 10.1007/11837-014-1149-y
- 6 Andersen V: Investigation of thermal properties of quartz for the silicon industry under reducing atmosphere: Project work TMT 4500, NTNU, Norway, 2009
- 7 Kjelstadli M.E : Kinetics and Mechanism of Phase Transformation from Quartz to Cristobalite: Project work TMT 4500, NTNU, Trondheim, Norway, 2015
- 8 Breneman, R.C, Halloran, J.W: Kinetics of Cristobalite formation in Sintered Silica: Journal of American Ceramic Society, 1-7 (2014), DOI 10.1111/jace.12889
- 9 HSC 7.1
- 10 Pabst W, Gregorova E: Elastic properties of silica polymorphs, a review; Ceramics Silikáty 57 (3) 167-184 (2013).
- 11 Mao H, Sundman B, Wang Z, Saxena S.K: Volumetric properties and phase relations of silica- thermodynamic assessment: Journal of Alloys and Compounds 327 (2001) 253-262
- 12 V. Swamy, Surendra, Saxena: A thermodynamic assessment of silica phase diagram; JOURNAL OF GEOPHYSICAL RESEARCH, VOL. 99, NO. B6, PAGES 11,787-11,794, JUNE 10, 1994
- 13 Aksay I.A. Pask J.a., Davis r.f. : Densities of SiO₂-Al₂O₃ melts; Journal of the American Ceramic Society, Vol 62, no 7-8, p 332-336 (1979)
- 14 Guixuan Wu a, Elena Yazhenskikh, Klaus Hack, Erwin Wosch, Michael Muller: Viscosity model for oxide melts relevant to fuel slags. Part 1: Pure oxides and binary systems in the system SiO₂-Al₂O₃-CaO-MgO-Na₂O-K₂O; Fuel Processing Technology 137 (2015) 93-103
- 15 Jusnes, K F: Melting and Softening of Quartz; Project work TMT 4500, NTNU, Trondheim Norway, 2015,

HIGH TEMPERATURE CORROSION MECHANISMS OF REFRACTORIES AND FERRO-ALLOY SLAGS

Stefan Luidold¹, Christine Wenzl², Christoph Wagner², Christoph Sagadin¹

¹CD Laboratory for Extractive Metallurgy of Technological Metals; Franz-Josef-Strasse 18; Leoben, 8700, Austria

²RHI AG; Wienerbergstrasse 9; Vienna, 1100, Austria

Keywords: ferroalloys production, slag, refractories, corrosion, slag attack

Abstract

Refractory linings in pyrometallurgical furnaces are attacked by various process phases (e.g. metal, slag, gas). However, refractories are the barrier between these phases and the environment: refractory damages and consequent furnace failure can cause severe damages including potential danger for workers/operators. Hence, refractory corrosion and attack of molten phases require attention to study the mechanisms and effects on refractory performance and lifetime. This is of special importance in ferroalloys production, where temperatures are generally even higher than in base metal processes and the corrosion effects therefore more pronounced.

To understand the nature of the reactions involved in refractory corrosion, it is crucial to have an understanding of the chemical equilibria and the thermodynamics of the reactions.

The present work studies the high-temperature interactions between refractories and molten slags, comprising theoretical thermodynamic analysis (FactSageTM) and experimental work (hot-stage microscopy) to better understand the corrosion mechanisms and draw implications for improving the refractory performance and lifetime.

The results will provide a framework for investigating refractory corrosion processes and trigger research efforts in the area of thermodynamic applications, optimizations and simulations in high-temperature processes.

Introduction

Refractory performance is a decisive factor in high temperature furnace operations and hence requires continuous improvement to guarantee process efficiency and safety. The lining materials are chosen under the consideration of process phases involved (i.e. metal, slag, and gas) to minimize chemical attack and maximize furnace campaigns. Chemical attack and penetration by molten slags are important factors, the slag zone normally being the furnace area with highest refractory wear. Hence, numerous studies have been carried out to study slag corrosion phenomena in detail on lab scale ^[1, 2]. Due to the high process temperatures and slag chemistry involved in ferroalloys production, generally basic refractories with MgO as main component are used as furnace lining. A deeper theoretical understanding of high temperature refractory/slag interactions is required to optimize furnace linings.

The present work investigated typical FeNi smelting slag compositions (synthetic and industrial slags based on the system “FeO”-SiO₂-MgO^[3-7]) in contact with MgO refractory substrate, both on a theoretical (thermodynamic calculations using the software FactSageTM ^[8]) and practical (refractory/slag high temperature corrosion tests) basis.

Methodology

The practical corrosion tests were carried out using a hot stage microscope: cylinder-shaped slag samples of compacted powder were placed on the refractory substrate (14 x 14 x 2 mm) and heated up to process temperature, while continuously recording the sample shape. After the defined holding time the samples were cooled down to room temperature and prepared for mineralogical investigations and SEM/EDS (Scanning Electron Microscopy/Energy Dispersive X-ray Spectroscopy) analysis. The test conditions are summarized in table I.

Table I – Testing conditions (heating microscope)

Heating program	RT → 1650 °C, 10 K/min
Holding time	60 min at 1650 °C
Gas flow	200 ml/min, 1 bar
Gas	CO/CO ₂ mixture (60:40) - reducing conditions (p _{o2} at 1650 °C – 1.94 · 10 ⁻⁷ atm)
Imaging	CCD camera + analysis software starting at 600 °C every 60 seconds
RT room temperature;	

The thermodynamic calculations of the refractory/slag interactions were carried out with the software FactSage™. The results of the theoretical calculations were then compared to the practical findings.

The investigated slags, namely synthetically prepared and industrial slag from FeNi smelting operations, are based on the system SiO₂-Fe₂O₃-MgO. The compositions of the slags and the refractory substrate are shown in table II.

Table II – Chemical composition of slags and refractory substrate (including physical properties)

Chemical analysis	[wt.-%]										
	MgO	Cr ₂ O ₃	Al ₂ O ₃	Fe ₂ O ₃	CaO	SiO ₂	MnO	TiO ₂	Na ₂ O	SO ₃	K ₂ O
synthetical slag	20	-	-	30	-	50	-	-	-	-	-
industrial slag	25.7	1.48	5.54	10.6	2.31	53.2	0.42	0.10	0.12	0.18	0.30
refractory substrate			MgO	CaO	SiO ₂	Fe ₂ O ₃	Al ₂ O ₃	BD	AP	CTE	
			> 99.3	< 0.35	< 0.35	< 0.12	< 0.25	2.30	35	13	
BD bulk density [g/cm ³]; AP apparent porosity [%]; CTE coefficient of thermal expansion [10 ⁻⁶ /K]											

Practical corrosion tests – SEM/EDS analysis

Samples for mineralogical investigation were prepared and the respective contact areas, namely reaction zone refractory/slag, were investigated by SEM/EDS for studying the slag penetration into and chemical reaction with the refractory substrate. The EDS analyses given in the following were not obtained from a single spot but from a certain interaction volume (µm range) and offer a good qualitative statement of the chemical differences in the studied areas. The EDS mappings provide an overview of the elemental distributions in the investigated areas.

Refractory materials generally always consist of coarser crystals of the main phase (here: MgO) and a finer matrix phase. The latter is more susceptible to corrosion and chemical attack due to the finer particle size and higher porosity compared to the coarse grains.

A. SiO₂-MgO-FeO_x system (synthetic slag on refractory substrate)

The refractory/slag interface is shown in fig. 1. The slag infiltration depth amounts to about 0.30 mm. The EDS mappings of the main elements (Mg, Si, Fe, Al, Ca, O) and some spot analyses over the infiltration depth are shown in fig. 2 and 3, respectively in table III. It can be seen from the mappings that the Fe accumulated in the coarse grains, whereas the surrounding matrix is enriched in Si and also contains minor amounts of Al and Ca. O was detected over the whole area, which is due to the oxidic nature of the materials. Spots 1–3 represent the compositions at different depths in the slag layer on the refractory substrate. The analyses show an increasing MgO content in the slag towards the refractory substrate, namely from spot 1 to spot 3. Inside the MgO grain (spot 4), a certain amount of Fe was detected (as also shown in the mappings), while in spot 5 only minor amounts of Fe and Si were verified besides Mg. Spot 6 shows the original composition of a MgO grain without additional elements.

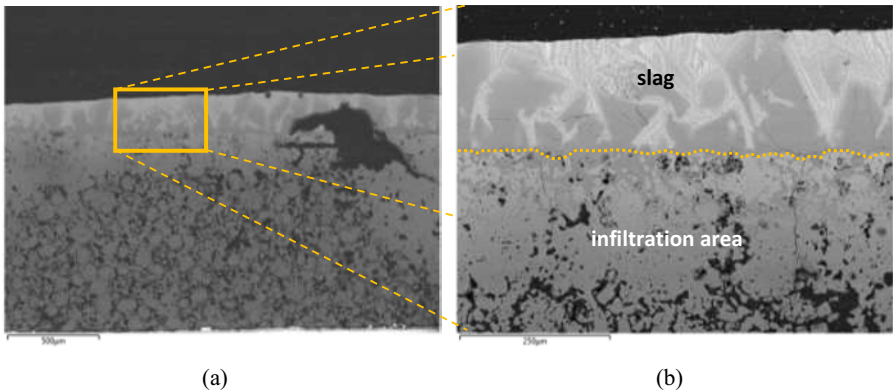
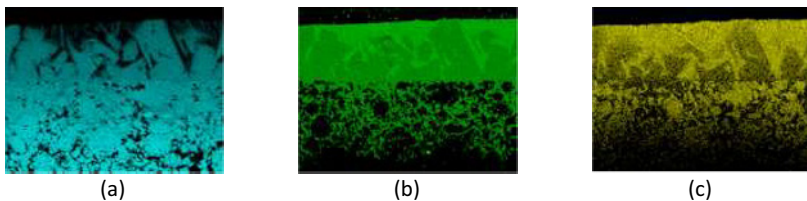


Fig. 1: SEM image of (a) interface between refractory material and molten slag; (b) marked area of beginning matrix infiltration



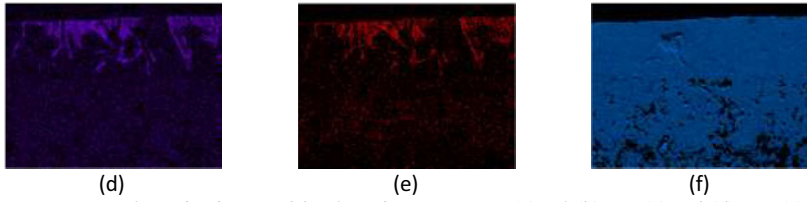


Fig. 2: EDS mapping of refractory/slag interface area, Mg (a), Si (b), Fe (c), Al (d), Ca (e), O (f)

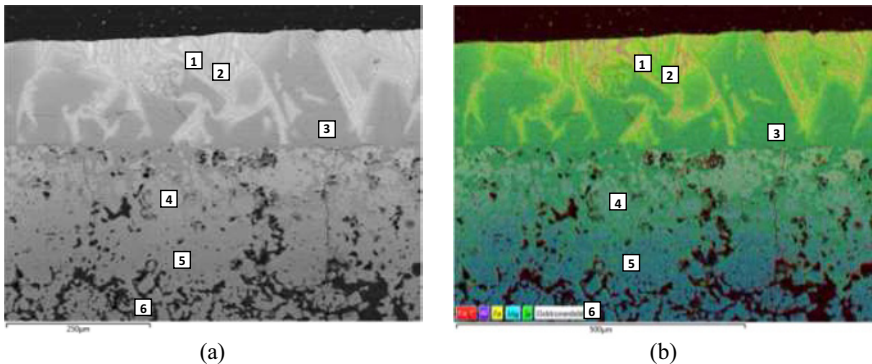


Fig. 3: Analyzed spots of refractory/slag interface area (spot 1–3 – slag, spot 4 and 5 – infiltrated area, spot 6 – coarse grain) (a) SEM-image (b) superposed corresponding illustration of areas of constant element concentration based on EDS

Table III – Elemental concentrations at analyzed spots (as described above)

Element [wt.-%]	EDX spot					
	1	2	3	4	5	6
Mg	1.2	19.0	27.5	46.5	50.9	56.3
Si	24.5	16.1	16.7	-	2.6	-
Fe	16.9	18.7	7.5	12.1	3.0	-
Al	5.2	-	-	-	-	-
Ca	2.4	-	-	-	-	-
O	49.8	46.2	48.4	41.4	43.6	43.7

The mineralogical investigations of the polished section showed that the brick microstructure is infiltrated with slag: the slag penetrated into the brick pores and mainly corroded the matrix fines. The coarse grains were also slightly corroded at the rims. The main reactions products include Mg silicates of type forsterite (Mg_2SiO_4). Additionally, due to a high iron oxide supply the MgO was highly enriched with Fe oxide. The latter resulted in a formation of low melting magnesia wuestite ($(Mg,Fe)O$). These findings indicate that SiO_2 plays a major role in refractory corrosion, attacking mainly the fines but also reacting with the MgO grains.

B. SiO₂-MgO-FeO_x-XX system (FeNi slag on refractory substrate)

The infiltrated refractory/slag interface area with an infiltration depth of about 0.40 mm can be seen in fig. 4. The FeNi slag was completely absorbed by the refractory substrate. EDS mappings (Fig. 5) and spot analyses (Fig. 6 and table IV) were performed in analogous way as described above for the synthetic slag.

Like for the synthetic slag, the coarse grains are enriched in Fe and the matrix fines are enriched in Si, the latter also containing minor amounts of Fe and Ca. The Si did not infiltrate into the coarse grains. The slag-surrounded coarse grains are composed of Mg, Fe and minor amounts of Al. Spot 7 represents the infiltrated slag and shows a higher Mg and lower Fe and Si content compared to the original slag composition. Spot 8 indicates the Fe-enrichment in a MgO grain, with additional low concentrations of Al and Cr. Spot 9 represents a MgO grain with minor amounts of Si.

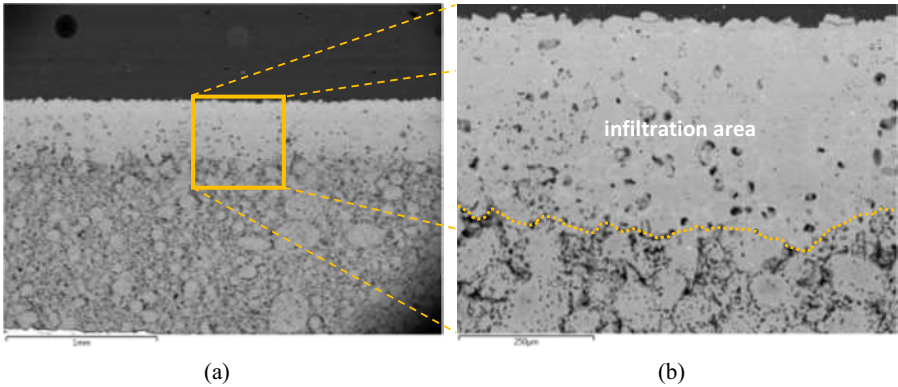


Fig. 4: SEM image of (a) infiltrated area between refractory material and molten slag; (b) marked area of matrix infiltration

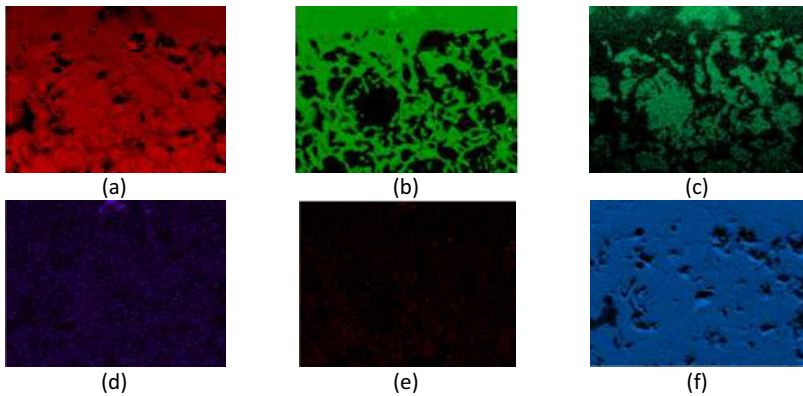


Fig. 5: EDS mapping of infiltrated area, Mg (a), Si (b), Fe (c), Al (d), Ca (e), O (f)

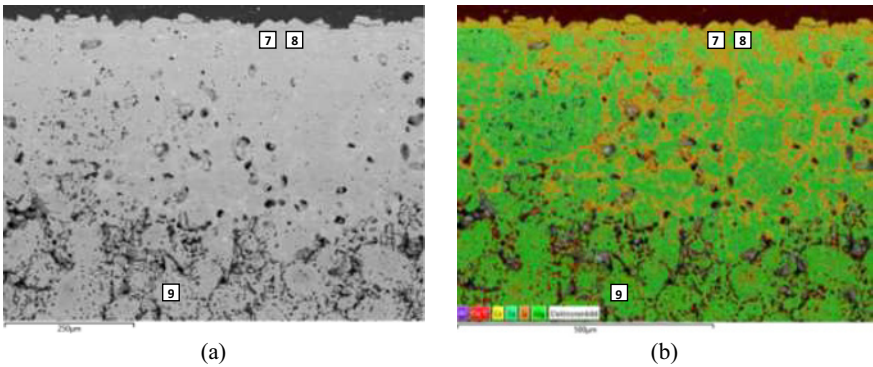


Fig. 6: Analyzed spots of interface area (spot 7 – slag, spot 8 – infiltrated area, spot 9 – coarse grain) (a) SEM image of infiltrated area (b) superposed corresponding illustration of areas of constant element concentration based on EDS

Table IV – Ratios of elements at different spots ranging from slag to MgO coarse grains analyzed by EDS.

Element [wt.-%]	EDX spot		
	7	8	9
Mg	31.9	49.0	57.6
Si	17.1	-	0.6
Fe	1.2	6.0	-
Al	-	1.2	-
Ca	0.6	-	-
O	49.2	42.0	41.9

The mineralogical investigations indicated slag penetration into the brick microstructure and subsequent corrosion of the matrix fines, as well as – to a minor extent – the rims of the MgO grains. The main reaction products include partly (Ca)-Mg-silicates of types monticellite (CaMgSiO_4) and forsterite (Mg_2SiO_4). Additionally due to a high iron oxide supply the MgO particles were highly enriched with Fe oxide. The latter resulted in a formation of low melting magnesia wuestite ($(\text{Mg,Fe})\text{O}$).

Based on these results, a similar corrosion mechanism as described above for the synthetic slag is suggested, namely mainly SiO_2 from the slag penetrating into the pores and corroding the matrix (and to a minor amount the MgO grains).

Thermodynamic calculations

Different thermodynamic calculation procedures have been applied and described to investigate refractory/slag interactions, which all have certain limitations.^[10, 11] The present study proposes a new representation of results, considering phase formation as a function of temperature and the ratio between refractory and slag. All calculations were performed for a constant oxygen partial

pressure with FactSage™ software. The present study investigated the following systems: SiO₂-MgO-FeO_x, SiO₂-MgO-FeO_x-X (with X = CaO, Al₂O₃, Cr₂O₃, MnO, TiO₂; each 5 wt.-%). The method is described for the ternary system SiO₂-MgO-FeO_x in the following and illustrated in Fig. 7. The new approach displays the resulting phases as a function of [MgO/(Fe₂O₃ + SiO₂)] for a constant [Fe₂O₃/(Fe₂O₃ + SiO₂)] ratio, which represents the varying refractory/slag portions, versus temperature. As the reaction of slag and refractory substrate proceeds, the composition of the liquid slag changes up to its saturation where the calculations results indicate that the refractory substrate should not be further chemically attacked by the slag. The newly formed phases that result from the refractory/slag reaction indicate corrosion.

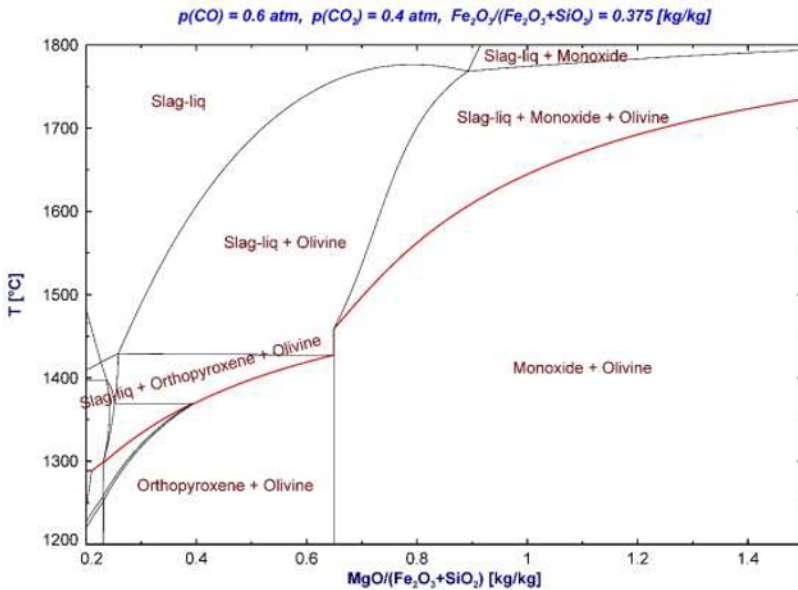


Fig. 7: Phase assemblage predicted by thermodynamic simulations for the corroded refractory substrate as a function of [MgO/(Fe₂O₃ + SiO₂)] ratio and temperature – system SiO₂-MgO-FeO_x

The following phase assemblages can be observed for this system at 1650 °C:

- [MgO/(Fe₂O₃ + SiO₂)] = ∞ : one phase / monoxide (MgO refractory substrate)
- 1.02 < [MgO/(Fe₂O₃ + SiO₂)] < ∞ : two phases / monoxide and olivine
- 0.76 < [MgO/(Fe₂O₃ + SiO₂)] < 1.02 : three phases / monoxide, olivine and slag
- 0.45 < [MgO/(Fe₂O₃ + SiO₂)] < 0.76 : two phases / olivine and slag
- 0 < [MgO/(Fe₂O₃ + SiO₂)] < 0.45: one phase / slag

According to the thermodynamic calculations, three species can be formed in the system SiO₂-MgO-FeO_x at 1650 °C, namely monoxide, olivine and slag. When the system is composed of two

solid phases and the slag, the amount of slag increases with decreasing $[\text{MgO}/(\text{Fe}_2\text{O}_3 + \text{SiO}_2)]$ ratio and the composition of the slag becomes constant in agreement with the phase rule of Gibbs. When the system comprises one solid and the slag, the composition varies. The liquid phase can be considered as the driving force behind the corrosion phenomenon. The reaction rate of the system can be correlated to the evolution of the slag phase (i.e., amount and composition).

The investigation of systems with further slag components as described above showed that these oxides do not significantly influence the range of first appearance of both the monoxide and a second solid phase besides liquid slag. The calculations for the industrial slag composition showed a more pronounced influence on the appearance of the phases (i.e., shift to higher $[\text{MgO}/(\text{Fe}_2\text{O}_3 + \text{SiO}_2)]$) and indicated that the industrial slag is able to dissolve larger amounts of refractory (MgO) before forming a solid phase at the refractory/slag contact zone and also before the monoxide becomes thermodynamically stable.

Results and discussion

The thermodynamic calculations of the slag/refractory interactions showed the formation of slag and solid phases, which can co-exist in different ratios in the system. When the system is composed of two solid phases and the slag, the amount of slag increases with decreasing $[\text{MgO}/(\text{Fe}_2\text{O}_3 + \text{SiO}_2)]$ ratio and the composition of the slag becomes constant. When the system is composed of one solid and the slag, the composition varies. Additional slag oxides were detected to have an influence on the appearance range of the phases, this effect being more pronounced for industrial slags containing multiple additional oxides.

The liquid phase is the driving force behind the corrosion phenomenon. The stability ranges of the refractory (monoxide) and the liquid slag as function of slag composition and temperature provide a first indication of the possible chemical attack of the slag and refractory corrosion. However, additional parameters have to be considered, for example wettability of refractory by slag, slag viscosity and reaction kinetics.

Conclusions

For understanding refractory corrosion by liquid slags, it is vital to investigate the microstructure of the involved materials and phases. The present study used a combined approach of practical and theoretical methods, namely hot-stage microscopy tests and thermodynamic calculations, to study the corrosion of MgO refractory substrates by synthetical and industrial FeNi smelting slags. The phases predicted by the thermodynamic calculations correspond very well with the experimental findings. Hence, the theoretic calculations are a suitable tool for predicting the sequence of phase transformations in equilibrium and are a valuable support for experimental work, including refractory selection and optimization.

Ongoing studies focus on applying the described methodology to different slag systems and refractory substrates, subsequent refractory material optimization and simulation of high-temperature processes.

Acknowledgements

The financial support by the Austrian Federal Ministry of Science, Research and Economy and the National Foundation for Research, Technology and Development is gratefully acknowledged.

References

- [1] W. Lee and S. Zhang, "Melt corrosion of oxide and oxide-carbon refractories", *Int Mater Rev*, 1999, 44 (3), pp. 77 - 104
- [2] D. Gregurek, A. Ressler, V. Reiter, A. Franzkowiak, A. Spanring and T. Prietl, "Refractory wear mechanisms in the nonferrous metal industry: testing and modelling results", *J Miner Metals Mater Soc*, 2013, 65 (11), pp. 1622 - 1630
- [3] N.L. Bowen and J.F. Schairer, "The System MgO-FeO-SiO₂", *Am. J. Sci.*, 1935, 29, pp. 151 - 217
- [4] S. Chen, E. Jak and P.C. Hayes, "Phase Equilibria in the Cristobalite, Tridymite and Pyroxene Primary Phase Fields in the MgO-"FeO"-SiO₂ System in Equilibrium with Metallic Iron", *ISIJ International*, 2005, 45, pp. 791 - 797
- [5] S. Chen, E. Jak and P.C. Hayes, "Phase Equilibria in the Olivine Primary Phase Field of the System MgO-"FeO"-SiO₂ in Equilibrium with Metallic Iron", *ISIJ International*, 2005, 45, pp. 1095 - 1100
- [6] E. Jak and P.C. Hayes, "Slag phase equilibria and viscosities in ferronickel smelting slags", *The Twelfth International Ferroalloys Congress*, 2010, Helsinki, Finland, pp. 631 - 639
- [7] C. M. Diaz, C.A. Landolt, A. Vahed, A.E.M. Warner and J.C. Taylor, "A Review of Nickel Pyrometallurgical Operation", *J. Met.*, 1988, 40, pp. 28 - 33
- [8] C.W. Bale, P. Chartrand, S.A. Degterov, G. Eriksson, K. Hack, R. Ben Mahfoud, J. Melancon, A.D. Pelton, S. Petersen, "FactSage thermochemical software and databases", *Calphad*, 2002, 26 (2), pp. 189 - 228
- [9] Slag Atlas, Edited by VDEh, Verein Deutscher Eisenhüttenleute, 2nd edition, 1995
- [10] J. Berjonneau, P. Pringent and J. Poirier, "The development of a thermodynamic model for Al₂O₃-MgO refractory castable corrosion by secondary metallurgy steel ladle slags", *Ceram. Int.*, 2009, 35 (2), pp. 623 - 635
- [11] A.P. Luz, A.G. Tomba Martinez, M.A.L. Braulio and V.C. Pandolfelli, "Thermodynamic evaluation of spinel containing refractory castables corrosion by secondary metallurgy slag", *Ceram. Int.*, 2011, 37, pp. 1191 - 1201

Fundamental Investigation of Reduction and Dissolution Behavior of Manganese Ore at High Temperature

Yusuke Fujii¹, Yoshie Nakai¹, Yu-ichi Uchida¹, Naoki Kikuchi¹ and Yuji Miki¹

¹Steelmaking Research Dept., Steel Research Laboratory, JFE Steel Corporation
Kokan-cho, Fukuyama City, Hiroshima, 721-8510, Japan

Keywords: Manganese ore, TG-DTA, melting point, X-ray diffraction

1. Abstract

The high temperature reduction behavior of manganese ore was investigated with the aim of utilizing ore as a more economical manganese source in the steelmaking process. The melting temperature and phase change behaviors of raw and sintered manganese ores were measured by high temperature X-ray diffraction and DTA in the temperature range from 303K to 1773K under atmospheric and vacuum conditions. The melting temperatures of the raw and sintered manganese ores were 1688K and 1732K, respectively. The main manganese compounds in the raw and sintered manganese ores were $\text{CaMn}_6\text{SiO}_{12}$ and MnO , Mn_3O_4 respectively. Under a vacuum (0.13kPa), both the raw and sintered manganese ores were reduced to MnO above 1473K, whereas under the atmospheric condition (101.3kPa), the manganese ores were reduced to Mn_3O_4 rather than MnO . The obtained results were discussed from a thermodynamic viewpoint.

2. Introduction

In recent years, manganese and phosphorus have been added to structural steel products as solute strengthening elements to improve the strength of the steel ¹⁾. In the steelmaking process, manganese alloy and metallic manganese are added during BOF tapping or in the secondary refining process ²⁾. Manganese ore is a more economical manganese source than manganese alloys such as ferromanganese and metallic manganese. In order to increase manganese ore usage in the steelmaking process, it is important to understand the decomposition and dissolution behaviors of manganese ore at high temperature. Many studies on techniques for high-temperature reduction and the gas reduction behavior of manganese ore have been reported ³⁻⁸⁾. Terayama et al. investigated the reduction behavior of manganese oxide. When manganese ore is heated with carbon, the manganese ore is thermally decomposed and reduced to the MnO phase at around 1200 K through interactions with CO and CO_2 ⁹⁻¹⁰⁾. Furthermore, when iron coexists with

manganese and $MnFe_2O_4$, a FeO-MnO type nonstoichiometric compound is generated at 1163K; that compound is reduced to metallic iron and MnO at 1273K, after which reduction of MnO proceeds¹¹). Kaneko et al.⁸⁾ investigated the change in oxygen content in manganese ore by using a 60kg sintering simulator. In their experiments, raw manganese ore was sintered from 1573K to 1673K, the oxygen content in the manganese ore decreased with chemical reduction from MnO_2 to Mn_3O_4 and then MnO. Kaneko et al.⁸⁾ also reported that the melting point of manganese ore containing 20% CaO is 100K lower than that of ore without CaO. However, the effect of the chemistry of manganese oxide in manganese ore on reduction and melting behavior has not been clarified.

In this work, the melting temperature and phase change behaviors of manganese ore were measured by high temperature X-ray diffraction and TG-DTA in the temperature range from 303K to 1773K under atmospheric and vacuum conditions.

2. Experimental Procedure

2.1. Manganese Ore

Table 1 shows the compositions of the manganese ores used in this study. A is a raw manganese ore and B is a sintered manganese ore. The oxygen content of the raw manganese ore is higher than that of the sintered manganese ore, since the oxygen in the raw manganese ore is removed in the sintering process.

2.2. High Temperature XRD Measurement

High temperature XRD measurements were performed to investigate the change of manganese compound during heating. Sample A was raw manganese ore, and sample B was sintered manganese ore. **Table 2** shows the experimental conditions for X-ray diffraction. Measurements were carried out under atmospheric and vacuum conditions (101.3kPa) at 303K, 1073K, 1473K and 1773K. The samples were heated at a fixed heating rate of 50K/min. X-ray diffraction was

Table 1 Chemical compositions of raw, sintered and heat-treated manganese ores and phases detected by X-ray analysis at room temperature (mass%)

Sample	Chemical Compound	T.Mn	T.Fe	SiO ₂	Al ₂ O ₃	CaO	MgO	P	S	T.O
A	Raw Mn ore	42.8	9.4	5.9	0.8	7.9	1.5	0.033	0.265	34.8
B	Sintered Mn ore	61.8	3.2	6.2	7.7	0.5	0.3	<0.005	0.017	27.8

Table 2 Experimental conditions
for X-ray diffraction

Radiation source	Cu
Voltage	45kV
Electric current	40mA
Degree(2θ)	10~60°
Pressure	Atmosphere (760Torr) Vacuum (1Torr)
Temperature	303K 1073K 1473K 1773K
Holding time	5min.

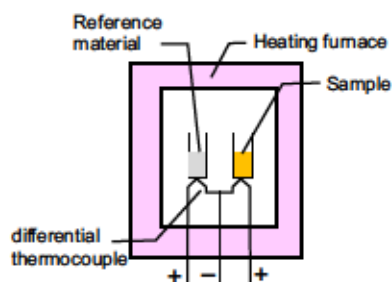


Figure 1 Schematic drawing of TG-DTA
measurement method

performed after holding for 5 minutes at each temperature. The obtained data were compared with those calculated by FactSage.

2.3. TG-DTA Measurements

TG-DTA measurements were used to investigate the effect of the chemistry of the manganese oxide in manganese ore on melting behavior. **Figure 1** shows a schematic drawing of the TG-DTA measurement method. Raw manganese ore and sintered manganese ore were used. The manganese ore samples were crushed and ground, and 0.1g was then placed in a platinum crucible. Both the sample and the reference material were then heated from 303K to 1923K at the heating rate of 10K/min in the Ar atmosphere.

3. Results and Discussion

3.1. Effect of Temperature and Oxygen Partial Pressure on Reduction Behavior of Manganese Ore

Figure 2 shows the results of the high temperature XRD measurement of A (raw manganese ore). At 303K, only $\text{CaMn}_6\text{SiO}_{12}$ was detected. Under the atmospheric condition, manganese oxide did not change until 1073K, and only Mn_3O_4 was identified at 1473K. At 1773K, the manganese ore is considered to melt, since only the platinum used as a substrate was detected. Under the vacuum condition, the manganese oxide in the manganese ore did not change until 1073K, and only MnO was detected at 1473K. **Figure 3** shows the results of the high temperature

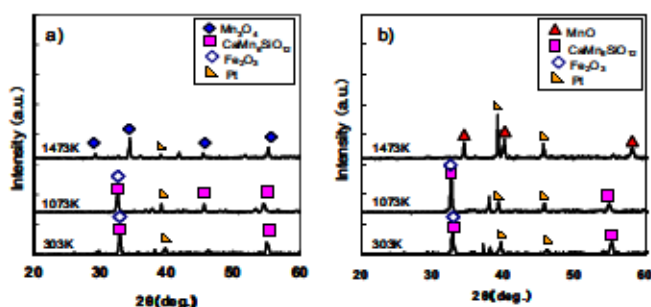


Figure 2 X-ray diffraction patterns of raw manganese ore at elevated temperature
a) atmospheric condition, b) vacuum condition

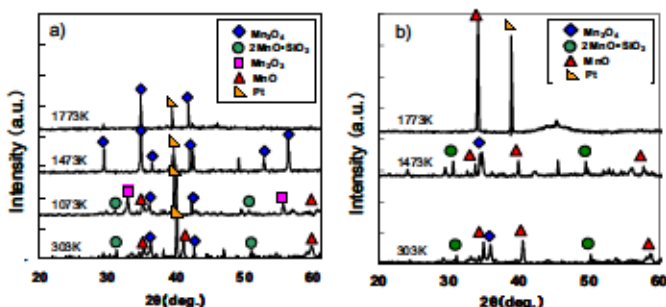


Figure 3 X-ray diffraction patterns of sintered manganese ore at elevated temperature
a) atmospheric condition, b) vacuum condition

XRD measurement of B (sintered manganese ore). $2\text{MnO} \cdot \text{SiO}_2$, Mn_3O_4 and MnO were identified at 303K. At 1073K, Mn_2O_3 was detected in addition to $2\text{MnO} \cdot \text{SiO}_2$ and Mn_3O_4 . Only Mn_3O_4 was identified at 1473K and 1773K. Under the vacuum condition, the manganese oxide in the manganese ore did not change until 1473K, and only MnO was identified at 1773K. The results obtained by high temperature XRD measurement were compared with the results calculated by FactSage. **Figure 4** shows the phase diagram of manganese oxidation calculated by Factsage. Manganese compounds change in the order of MnO_2 , Mn_2O_3 , Mn_3O_4 , MnO and liquid phase with increasing temperature. As shown in **Fig. 4**, the changes in the manganese oxide detected by high temperature X-ray diffraction roughly agreed with the FactSage calculation results in the case of ore B (sintered manganese ore). From these results, it is considered that the manganese ore can be defined as in an equilibrium condition during holding for 5 minutes at the specific temperature in the high temperature X-ray diffraction measurements. The results revealed

that both the raw ore and the sintered ore were reduced to MnO under the vacuum condition (0.13kPa) above 1473K. However, under the atmospheric condition (101.3kPa), both manganese ores were reduced to Mn₃O₄ rather than MnO.

3.2. Relationship Between Kind of Manganese Oxide in Manganese Ore and Reduction Behavior

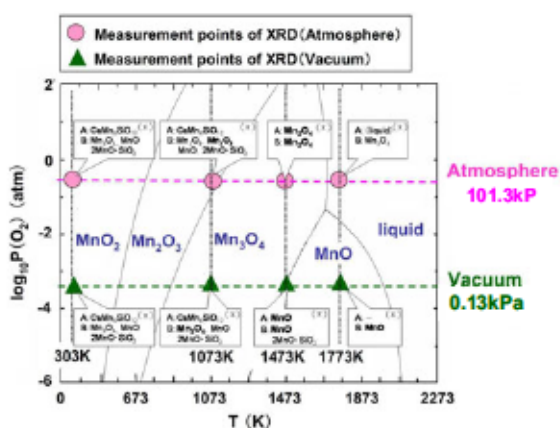


Figure 4 Phase stability diagram of Mn-O system

Based on the results of the high temperature X-ray diffraction measurements, the effect of the kind of manganese oxides in the ore on melting behavior was investigated. Figure 5 shows the results of TG-DTA measurements of the manganese ores. Weight decreased with increasing temperature. The weight decrease of the raw ore A was about 12mg while that of the sintered ore B was about 5mg. The amount of oxygen in the raw ore A is larger than that in the raw ore B. Therefore, the difference of the weight decrease between raw ore A and B is caused by the amount of release of oxygen during thermal decomposition of manganese compounds According to Fig.4, thermal decomposition of

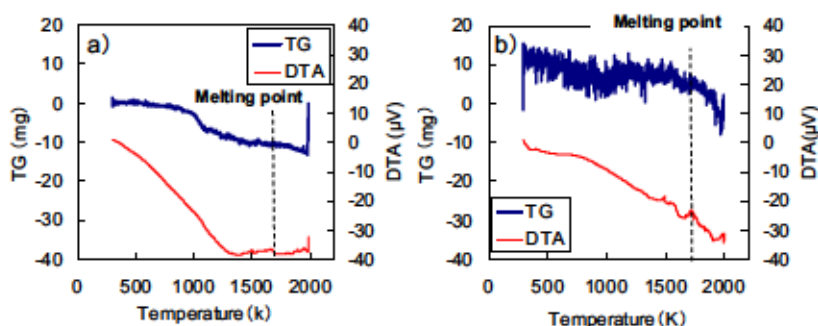


Figure 5 TG-DTA curves of manganese ore in Ar gas atmosphere, a) raw manganese ore, b) sintered manganese ore

CaMn₆SiO₁₂ and Mn₃O₄ generation take place at 1000K in the case of the raw ore A. In both cases of the raw ore A, and the sintered ore B, Mn₃O₄ decompose to MnO in the range between 1500 and 1650K. So, it is considered that the raw ore A, and the sintered ore B are reduced during heating in TG-DTA measurements. In the TG-DTA measurements, the largest peak during measurement was regarded as its melting points, although the amounts of solidus and liquidus ratio at the peak was unknown. The melting points obtained by TG-DTA of raw ore A and B were 1688 and 1732, respectively. Those melting points were compared with those calculated by FactSage. The Factsage calculation considered Mn₂O₃, Mn₃O₄ and MnO and SiO₂, Al₂O₃, CaO, Fe₂O₃, and MgO. In the FactSage calculations, melting points were regarded as a liquidus. **Figure 6** shows a comparison of the measured and calculated melting points of the manganese ores. The TG-DTA measurement results and thermodynamic calculation results were in good agreement. The Factsage calculation considered Mn₂O₃, Mn₃O₄ and MnO and SiO₂, Al₂O₃, CaO, Fe₂O₃, and MgO. In the FactSage calculations, melting points were regarded as a liquidus. In the case of ore B, the measured melting temperature obtained by TG-DTA was 100K higher than that of ore A. The difference in the melting points of A and B was thought to be due to minor elements. To confirm the effect of minor elements, the melting points were calculated for different ratios of Al₂O₃, CaO, Fe₂O₃, MgO, and SiO₂ by using FactSage. **Figure 7** shows the results of these calculations. It was found that the melting point increased with increasing contents of CaO and MgO and decreased with increasing Al₂O₃, Fe₂O₃ and SiO₂. The reason for the different melting points of A (raw manganese ore) and B (sintered manganese ore) was considered. **Figure 8** shows relationship between Mn₂O₃ / (Mn₂O₃+Mn₃O₄+MnO) and the calculated melting points when the ratio of Mn₃O₄ and MnO was constant at 0.29. The calculated melting point decreased when the ratio of Mn₂O₃ was increased in the range between Mn₂O₃=0 and 0.5. When the Mn₂O₃ ratio exceeded 0.5, the calculated melting point did not change greatly. The melting points of MnO, Mn₃O₄ and Mn₂O₃ were reported to be 2123K¹³), 1973K⁷) and 1853K¹³), respectively. Therefore, the ratio of Mn₂O₃, which has the lowest melting point among the three oxides, would have an influence on lowering the melting point. The difference between the two calculated lines in **Fig. 8** was regarded as the effect of chemical components other than the components of manganese oxide. In summary, it was found that the melting point of the raw manganese ore was lower than that of the sintered

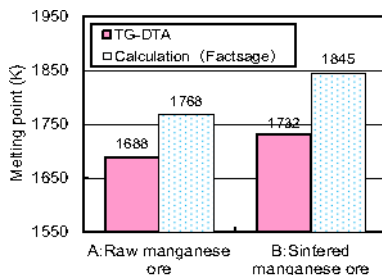


Figure 6 Melting point of manganese ore determined by DTA measurement

Figure 6 shows a comparison of the measured and calculated melting points of the manganese ores. The TG-DTA measurement results and thermodynamic calculation results were in good agreement. The Factsage calculation considered Mn₂O₃, Mn₃O₄ and MnO and SiO₂, Al₂O₃, CaO, Fe₂O₃, and MgO. In the FactSage calculations, melting points were regarded as a liquidus. In the case of ore B, the measured melting temperature obtained by TG-DTA was 100K higher than that of ore A. The difference in the melting points of A and B was thought to be due to minor elements. To confirm the effect of minor elements, the melting points were calculated for different ratios of Al₂O₃, CaO, Fe₂O₃, MgO, and SiO₂ by using FactSage. **Figure 7** shows the results of these calculations. It was found that the melting point increased with increasing contents of CaO and MgO and decreased with increasing Al₂O₃, Fe₂O₃ and SiO₂. The reason for the different melting points of A (raw manganese ore) and B (sintered manganese ore) was considered. **Figure 8** shows relationship between Mn₂O₃ / (Mn₂O₃+Mn₃O₄+MnO) and the calculated melting points when the ratio of Mn₃O₄ and MnO was constant at 0.29. The calculated melting point decreased when the ratio of Mn₂O₃ was increased in the range between Mn₂O₃=0 and 0.5. When the Mn₂O₃ ratio exceeded 0.5, the calculated melting point did not change greatly. The melting points of MnO, Mn₃O₄ and Mn₂O₃ were reported to be 2123K¹³), 1973K⁷) and 1853K¹³), respectively. Therefore, the ratio of Mn₂O₃, which has the lowest melting point among the three oxides, would have an influence on lowering the melting point. The difference between the two calculated lines in **Fig. 8** was regarded as the effect of chemical components other than the components of manganese oxide. In summary, it was found that the melting point of the raw manganese ore was lower than that of the sintered

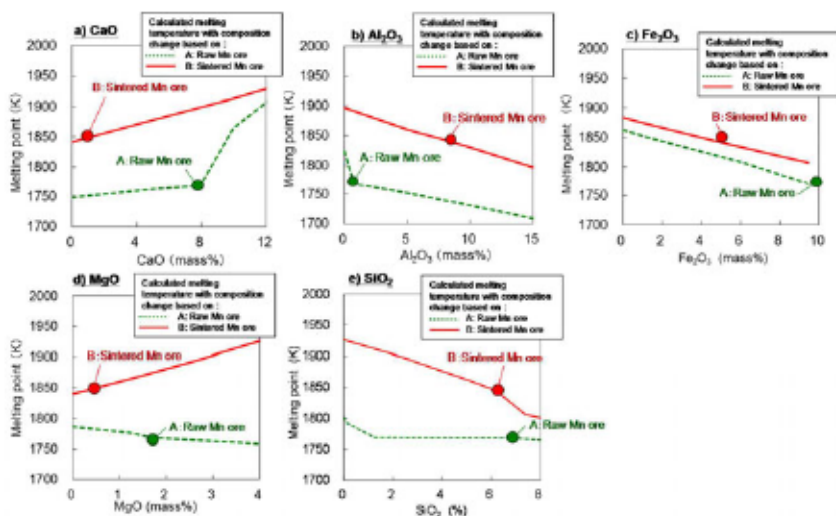


Figure 7 Effect of CaO, MgO, Al₂O₃, SiO₂ and Fe₂O₃ concentration on melting point of manganese ore

manganese ore due to the difference in the relative contents of the manganese oxides (i.e., ratio of Mn₂O₃) rather than the effect of differences in the contents of gangue components such as Al₂O₃, CaO, MgO, SiO₂ and Fe₂O₃.

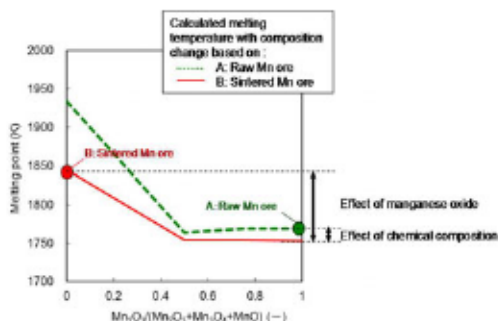


Figure 8 Effect of ratio of Mn₂O₃ to (Mn₂O₃+Mn₃O₄+MnO) on melting point of

4. Conclusion

The effects of temperature and oxygen partial pressure, as well as chemical composition, on the transformation and melting behavior of manganese ore were investigated using high temperature X-ray diffraction (XRD) and thermogravimetry-differential thermal analysis (TG-DTA) in order to obtain fundamental information on the pre-reduction process of manganese ore. The conclusions are summarized as follows.

- 1) The main manganese compound in the raw manganese ore used in this study was characterized as $\text{CaMn}_6\text{SiO}_{12}$ by XRD at room temperature, while the main Mn compounds in the sintered manganese ore were Mn_3O_4 and MnO . Under a vacuum condition, raw manganese ore and sintered manganese ore were reduced to MnO above 1473K. However, under atmospheric conditions (pressure: 101.3kPa), manganese ore was reduced to Mn_3O_4 rather than MnO at temperatures above 1073K. The results of high temperature XRD and the results of thermodynamic calculations were in good agreement.
- 2) The melting point of the raw manganese ore evaluated by TG-DTA was lower than that of the sintered manganese ore due to the difference in the relative contents of the manganese oxides in each ore rather than the effect of differences in the contents of gangue components such as Al_2O_3 , CaO , MgO , SiO_2 and Fe_2O_3 . It is considered that the higher melting temperature of the sintered manganese ore in comparison with the raw manganese ore is due to a higher content of Mn_2O_3 .

References

- 1) T. Fujita, K. Shibata, M. Yano: Design and Theory of Iron and Material, Maruzen, Tokyo, (1981), 9.
- 2) A.Tada, M. Nakato, Y. Uchida: Steelmaking Process, Educational Corporation of Iron and Steel, Hyogo, (2008), 56.
- 3) Y. Tabata, O. Terada, T. Hasegawa, Y. Kikuchi, Y. Kawai and Y. Muraki: *Tetsu-to-Hagané*, 79(1990), 1916.
- 4) T. Inaba, H. Takamoto, S. Tonomura, K. Endou, T. Tabuchi, K. Yonezawa: *Tetsu-to-Hagané*, 73 (1987), S1013.
- 5) M. Kimura, H. Matui, S. Itou, T. Saitou, T. Soezima, M. Kita: *Tetsu-to-Hagané*, 69 (1983), 1893.
- 6) T. Matsuo, S. Fukagawa and T. Ikeda: *Tetsu-to-Hagané*, 76(1990), 1831.
- 7) T. Kaneko and T. Matuzaki: *Tetsu-to-Hagané*, 79(1992), 473.
- 8) T. Kaneko, T. Matuzaki, T. Kugiyama, K. Ide, M. Kumakura and A. Kasama: *Tetsu-to-Hagané*, 79(1993), 941.
- 9) K. Terayama and T. Ishiguro: *Netsu Sokutei*, 18(1991), 164.
- 10) K. Terayama and M. Ikeda: *J. Japan Inst. Metals*, 45(1981), 901.
- 11) K. Terayama and M. Ikeda: *J. Japan Inst. Metals*, 47(1983), 729.
- 12) C.W. Bale, P. Chartrand, S.A. Deckerov, G. Eriksson, K. Hack, R.B. Mah-foud, J. Melancon, A.D. Pelton and S. Petersen: *Calphad Journal*, 62(2002), 189.
- 13) VEREIN, D.E. ED.: *Slag Atlas 2nd Ed.*, VERLAG STAHLISEN, (1995), 45.

AN INVESTIGATION ON THE FORMATION OF MOLTEN SALT CONTAINING CHROMIUM OXIDE DURING ROASTING OF CHROMITE ORE WITH SODIUM AND POTASSIUM HYDROXIDES

L. Escudero-Castejon, S. Sanchez-Segado, S. Parirenyatwa, A. Jha

Institute for Materials Research, School of Chemical and Process Engineering
Faculty of Engineering, University of Leeds
Leeds LS2 9JT

Keywords: chromite ore, oxidative roasting, molten salt phase, NaOH, KOH, chromium recovery

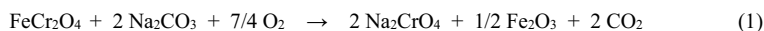
Abstract

The extraction of chromium from chromite ore is based on the oxidative alkali roasting of the mineral forming water-soluble alkali chromates. Previous investigations reported the formation of a molten $\text{Na}_2\text{CO}_3\text{-Na}_2\text{CrO}_4$ binary mixture during roasting of chromite with sodium carbonate. The physical properties of the $\text{Na}_2\text{CO}_3\text{-Na}_2\text{CrO}_4$ liquid phase, which are dependent on temperature, charge and gangue composition, play an important role in the oxidation reaction and may limit the chromium recovery by hindering the oxygen transport to the reaction interface.

This investigation focuses on the alkali roasting of chromite ore at 1000°C using NaOH and KOH, and subsequent water leaching. The influence of the alkali ratio on the chromium extraction yield is analysed, and the results obtained with both hydroxides are compared. The formation of molten salt phase under different roasting conditions and its effect on chromium recovery is studied by means of sample characterization and phase diagram analysis.

Introduction

Oxidative roasting of chromite ore with alkali salts is based on the oxidation of Cr^{3+} to Cr^{6+} and subsequent combination with the alkali to form water soluble chromates (Na_2CrO_4 , K_2CrO_4). During the traditional roasting process, chromite reacts with sodium carbonate to form sodium chromate following equation (1).



The roasted material is subsequently leached with hot water in order to selectively solubilise sodium chromate. The remaining chromite ore processing residue (COPR) mainly contains iron oxide, magnesium oxide and unreacted chromite. Around 15 wt.% of chromium in chromite is not converted to alkali chromate during the traditional alkali roasting process, as reported by previous investigations [1]. The landfilling of the COPR generated is an important source of hexavalent chromium, as the waste contains approximately 0.1 - 0.2 wt.% Cr^{6+} which remains entrapped after water leaching. Hexavalent chromium is highly hazardous to water, soil, flora

and fauna, and therefore, the environmental problem associated with waste disposal is the main drawback of the process [2].

Bearing this in mind, previous investigations have focused on the study of the thermodynamics and optimization of the process parameters in order to maximize chromium extraction and minimize waste generation [1, 3-5]. The parameters affecting the degree of extraction include chromite ore composition, roasting temperature and time, oxygen potential and the origin and quantity of gangue materials present in the ore. Another important factor which is known to have an important effect on the roasting reaction is the formation of a $\text{Na}_2\text{CrO}_4\text{-Na}_2\text{CO}_3$ molten phase. Previous findings on this topic are discussed below.

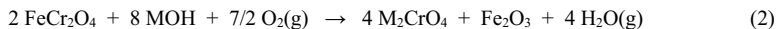
A. Previous investigations on the role of the liquid phase in the reaction mechanism

Tathavadkar et al. previously described the key role played by the binary $\text{Na}_2\text{CrO}_4\text{-Na}_2\text{CO}_3$ molten phase formed during alkali roasting of chromite ore with sodium carbonate [3]. The liquid phase mainly consists on the formation of an eutectic mixture at 928K between $\text{Na}_2\text{CO}_3\text{-Na}_2\text{CrO}_4$ with a 62.5 wt.% sodium chromate. They reported that the transport of gaseous compounds (O_2 and CO_2) during the oxidation reaction is hindered by the presence of the liquid layer surrounding the chromite particle, which leads to a reduction in the rate of sodium chromate formation [4]. At a fixed temperature, the decrease of the oxygen transport is more significant with increasing proportion of liquid phase in the reaction mixture. These authors pointed out the importance of the viscosity of the molten phase, as this is the property which mainly affects the thickness of the liquid layer and therefore its resistance to the transport of gaseous species. In the case of roasting with Na_2CO_3 , the viscosity of the $\text{Na}_2\text{CO}_3\text{-Na}_2\text{CrO}_4$ liquid was found to be highly dependent on the roasting temperature and the composition of the initial charge [3, 5].

The same researchers highlighted the significant effect that the ore composition and gangue materials have in the properties of the binary $\text{Na}_2\text{CrO}_4\text{-Na}_2\text{CO}_3$ liquid phase, which ultimately affects the extraction yield of chromium. Tathavadkar et al. reported that the presence of NaAlO_2 , NaFeO_2 and Na_2SiO_3 in the samples after roasting of chromite with Na_2CO_3 are able to change both the physical and chemical properties of the liquid phase [3].

The differences between the reaction mechanism with and without silica are significant and the yield of chromium strongly depends on the amount of silica present in the chromite ore [3]. It has been demonstrated that the presence of silica in a significant amount leads to the formation of sodium silicate compounds which increase the viscosity of the liquid phase hindering the oxygen diffusion. When sodium silicate is part of the liquid phase, sodium ferrite and aluminate tend to dissolve too, and the result is the formation of a liquid rich in alkali in which chromite dissolves completely, forming a complex $\text{Na-Cr-Fe-Al-Si-Mg-O}$ liquid at high temperature. The formation of sodium silicate drops the activity of sodium ions and disturbs the diffusion of Na^+ and Cr^{3+} towards the reaction zone where formation of sodium chromate takes place in the presence of O_2 gas. All this explains why the presence of silica in the ore has an important influence on the extraction efficiency of chromate, which is higher for ores with low silica content [5].

In this study, alkali hydroxides, namely NaOH and KOH, are used in the roasting of chromite ore as alkali source. The main reaction taking place is shown in equation (2), where M represents the alkali metal (Na or K).



The thermodynamic analysis of the possible reactions of the sodium/potassium hydroxides with the different elements present in the ore shows that besides the formation of alkali chromate, formation of alkali ferrite (NaFeO_2 , KFeO_2), alkali aluminate (NaAlO_2 , KAlO_2) and alkali silicate (Na_2SiO_3 , K_2SiO_3) is also possible when alkali is added in excess with respect to the stoichiometric ratio [6]. In this study, the reaction mechanism has been studied for the roasting of chromite with different ratios of NaOH/KOH. Relevant phase diagrams and equilibrium calculations were also computed with the aim of determining the different phases formed during roasting and their effect on the properties of the liquid phase, the rate of diffusion of oxygen to the reaction interface and, ultimately, the efficiency of the extraction of chromium.

Experimental work

The South African chromite ore used in this study had a particle size of 106 μm and the following chemical composition 48.80% Cr_2O_3 , 31.30% Fe_2O_3 , 7.03% MgO , 7.15% Al_2O_3 , 3.45% SiO_2 , 0.70% TiO_2 and 0.54% CaO . Sodium hydroxide (NaOH) and potassium hydroxide (KOH) of analytical grade were used for roasting chromite ore samples.

Samples composed of a mixture of chromite ore and sodium or potassium hydroxide were placed in an alumina crucible and roasted for 2 hours in a tube furnace in air atmosphere at a constant temperature of 1000°C. Samples were prepared by mixing thoroughly chromite ore with different ratios of the corresponding hydroxide. The Cr_2O_3 :hydroxide molar ratios tested in this study were 1:4, 1:6 and 1:8; which correspond to 100%, 150% and 200% the stoichiometric hydroxide amount needed to convert all Cr^{3+} contained in the ore to water soluble alkali chromates (Na_2CrO_4 and K_2CrO_4), respectively. Products of roasting were water leached for 2 hours at 60°C with the purpose of solubilising chromium as alkali chromate. Leached solutions were analysed by atomic absorption spectroscopy (AAS) while the solid residues obtained from the leaching step were characterised by X-ray powder diffraction (XRPD), scanning electron microscopy (SEM) and energy-dispersive X-ray spectroscopy (EDX).

Results and discussion

A. Phase diagrams and equilibrium calculations

The effect of the alkali ratio on the roasting reaction was studied by testing three different Cr_2O_3 :MOH molar ratios of 1:4, 1:6 and 1:8. A molten M_2CrO_4 -MOH phase (where M = Na or K) is expected to form and, therefore, the amount of alkali added will determine the volume of the liquid phase generated and its compositional properties, for governing the intergranular fluid flow in the chromite matrix.

It was mentioned before that the analysis of the Gibbs free energy of the roasting of chromite with NaOH/KOH indicated that NaOH and KOH can be consumed by alumina and silica to form alkali aluminates and alkali silicates [6]. This makes necessary to increase the amount of alkali above the stoichiometric, by taking into account the alumina and silica content of the ore. Iron oxide may also react with Na^+/K^+ to form $\text{NaFeO}_2/\text{KFeO}_2$, only if alkali is in excess.

Formation of alkali ferrites can be seen in Figure 1. The phase diagrams for the $\text{NaOH}-\text{Cr}_2\text{O}_3-\text{Fe}_2\text{O}_3-\text{Al}_2\text{O}_3-\text{O}_2$ and $\text{KOH}-\text{Cr}_2\text{O}_3-\text{Fe}_2\text{O}_3-\text{Al}_2\text{O}_3-\text{O}_2$ systems were calculated by using the FactSage 6.4 software. The diagrams indicate the phases coexisting in equilibrium at 1000°C in function of the partial pressure of oxygen, $P(\text{O}_2)$, and the activity of MOH. Both diagrams show the partial pressure of oxygen that may be needed to form the alkali chromates (M_2CrO_4), which decreases as the concentration of MOH increases; implying that, from a thermodynamic point of view, chromate formation will be enhanced by the presence of excess hydroxide. It should be noticed that NaFeO_2 can be seen in Figure 1a for certain conditions of $P(\text{O}_2)$ and NaOH activity, whereas KFeO_2 does not exist in Figure 1b under comparable conditions, as the thermodynamic data for this compound is not available in the software database. However, KFeO_2 is expected to form if there is excess KOH, since the reaction of formation of KFeO_2 by combination of Fe_2O_3 and KOH at 1000°C has a significant negative value of Gibbs energy equal to $\Delta G^\circ = -1129.88 \text{ kJ}$ per mol of Fe_2O_3 reacted (computed using HSC 5.1 software [7]) at 1000°C .

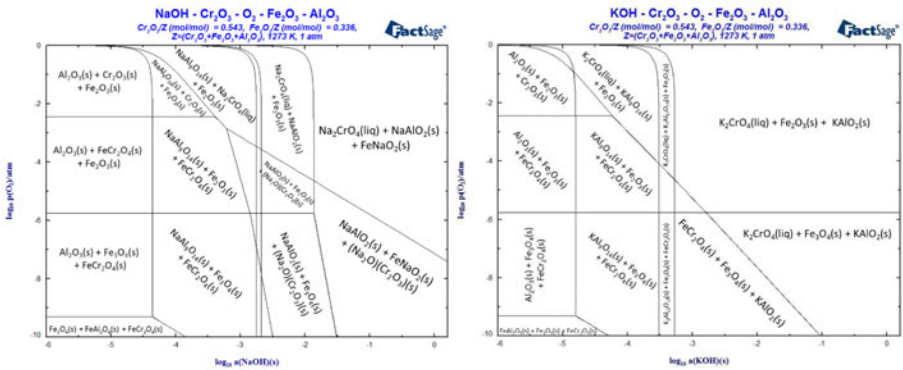


Figure 1. Phase diagrams of the a) $\text{Cr}_2\text{O}_3-\text{Fe}_2\text{O}_3-\text{Al}_2\text{O}_3-\text{NaOH}-\text{O}_2$ and b) $\text{Cr}_2\text{O}_3-\text{Fe}_2\text{O}_3-\text{Al}_2\text{O}_3-\text{KOH}-\text{O}_2$ systems. Computed using FactSage 6.4.

Phase equilibria conditions were also computed for the roasting of chromite and the three different alkali ratios tested experimentally by using FactSage 6.4 software. In Table I below, the moles of the different phases in equilibrium, after roasting 50g of chromite and the corresponding alkali amount at 1000°C , are compared. For calculation purposes it was assumed that there is excess of oxygen available.

Table I. Equilibrium data calculated for the roasting of 50g of chromite with three different ratios of NaOH/KOH (1:4, 1:6, 1:8) at 1000°C in air atmosphere.

Alkali	Cr ₂ O ₃ :MOH	Phases in equilibrium (moles)					
NaOH	1:4	Na ₂ CrO ₄ (liq) 0.31425	Fe ₂ O ₃ 0.09780	MgAl ₂ O ₄ 0.03368	Mg ₂ SiO ₄ 0.02643	NaAlSiO ₄ 0.00274	(MgO)(Cr ₂ O ₃) 0.00068
NaOH	1:6	Na ₂ CrO ₄ (liq) 0.31579	Fe ₂ O ₃ 0.01938	MgO 0.08722	FeNaO ₂ 0.15686	Na ₆ Si ₂ O ₇ 0.01458	NaAlO ₂ 0.07010
NaOH	1:8	Na ₂ CrO ₄ (liq) 0.31579	NaOH (liq) 0.24330	MgO 0.08722	FeNaO ₂ 0.19563	Na ₄ SiO ₄ 0.02917	NaAlO ₂ 0.07010
KOH	1:4	K ₂ CrO ₄ (liq) 0.31489	Fe ₂ O ₃ 0.09781	MgAl ₂ O ₄ 0.03432	MgSiO ₄ 0.02623	KAlSi ₂ O ₆ 0.00147	(MgO)(Cr ₂ O ₃) 0.00036
KOH	1:6	K ₂ CrO ₄ (liq) 0.31579	KOH (liq) 0.13960	MgO 0.08722	Fe ₂ O ₃ 0.09781	K ₂ SiO ₃ (liq) 0.02917	KAlO ₂ 0.07010
KOH	1:8	K ₂ CrO ₄ (liq) 0.31579	KOH (liq) 0.45520	MgO 0.08722	Fe ₂ O ₃ 0.09781	K ₂ SiO ₃ (liq) 0.02917	KAlO ₂ 0.07010

The comparison of equilibrium data in Table I and Figure 1 confirms that there may be need for having excess alkali in order to extract all Cr³⁺ in the form of water soluble chromate. When the stoichiometric amount of alkali is added a part of the chromium remains unreacted as MgCr₂O₄, since some alkali is consumed in the formation of alkali aluminosilicates (NaAlSiO₄, KAlSiO₄). When excess alkali is added, the magnesiochromite phase cannot be observed in the reaction product. Based on equilibrium calculations, the majority of Cr³⁺ is extracted as Na₂CrO₄ when the Cr₂O₃:NaOH molar ratio is 1:6, and therefore, a further increase of the amount of alkali in the charge does not necessarily mean an improvement of the chromium extraction yield. These observations were also found to be consistent with the KOH reaction of chromite ores.

Alumina forms MAISiO₄ and the unreacted alumina remains as MgAl₂O₄ for the stoichiometric alkali ratio, but when the alkali ratio is increased to Cr₂O₃:MOH = 1:6 it combines with Na⁺/K⁺ to form sodium or potassium aluminate. Oxides of iron and magnesium separate out by forming the respective phase (MgO, Fe₂O₃), however, iron may also react with excess alkali to form MFeO₂, as discussed before.

Table I also shows the state of the difference phases (solid and liquid), which indicates the expected composition of the molten salt phase. The liquid phase is mainly composed of M₂CrO₄ and MOH, however, as it can be seen in Table I, alkali silicates form when alkali is in excess (Cr₂O₃:MOH molar ratio of 1:6 and 1:8). Particularly, the K₂SiO₃ phase is present in the liquid as it melts below 1000°C (melting point of K₂SiO₃ = 976°C). The presence of silicates in the molten salt is expected to increase the viscosity of the liquid, and therefore, hinder the oxygen transport [3].

B. Reaction mechanism and effect of the alkali ratio

Using the equilibrium data in Figure 1 and Table I, the mechanism of the overall reaction may be analysed. In this context, the Cr_2O_3 -to-MOH ratio may affect the formation and properties of the molten phase. In Figure 2, the X-ray powder diffraction data for leached residues after roasting of chromite with NaOH/KOH are compared for different stoichiometric ratios of Cr_2O_3 :MOH. Leached residues contain the insoluble phases formed during roasting, while the alkali chromate and the rest of water soluble phases are extracted during leaching.

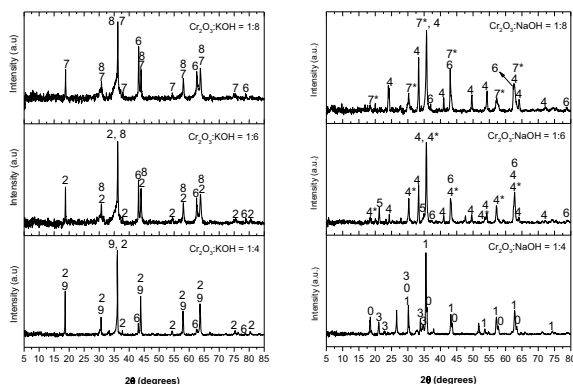


Figure 2. XRPD patterns of leached residues after roasting of chromite with different molar ratios of KOH and NaOH at 1000°C for 2 hours. (0. $\text{Mg}_{0.74}\text{Cr}_{0.96}\text{Fe}_{0.26}\text{Al}_{1.04}\text{O}_4$, 1. $\text{MgCr}_{0.2}\text{Fe}_{1.8}\text{O}_4$, 2. $\text{Mg}(\text{Fe}_{0.5}\text{Al}_{0.5})_2\text{O}_4$, 3. $\text{Na}_2\text{Mg}(\text{SiO}_4)$, 4. Fe_2O_3 (hematite, rhombohedral), 4*. Fe_2O_3 (cubic), 5. SiO_2 , 6. MgO , 7. MgFe_2O_4 , 7*. MgCr_2O_4 , 8. $\text{Fe}_{2.3}\text{Si}_{0.7}\text{O}_4$, 9. MgCrAlO_4)

Equilibrium data shown in Table I indicates that, for roasting of chromite with the stoichiometric Cr_2O_3 :alkali molar ratio, MgAl_2O_4 and MgCr_2O_4 spinel-type phases are in equilibrium. Experimental results demonstrate that these phases are present in the core of the partially-reacted particles and are found as complex Mg-Fe-Cr-Al-O spinel, which in fact corresponds to the initial composition of chromite ore which is depleted in Fe^{3+} species. The depletion of iron was observed in the backscattered SEM images by analysing elemental mappings of particles from water-leached residues after roasting with the stoichiometric alkali ratio. The results are presented in Figure 3 and Figure 4 for NaOH and KOH, respectively. In the XRPD patterns of the residue samples in Figure 2, $\text{Mg}_{0.74}\text{Cr}_{0.96}\text{Fe}_{0.26}\text{Al}_{1.04}\text{O}_4$ and $\text{MgCr}_{0.2}\text{Fe}_{1.8}\text{O}_4$ could be also identified when roasting with the stoichiometric amount of NaOH, and $\text{Mg}(\text{Fe}_{0.5}\text{Al}_{0.5})_2\text{O}_4$ and MgCrAlO_4 were present when roasting with KOH. Figure 3 and Figure 4 show that all remaining chromium is in form of partially-reacted chromite spinel, meaning that the water leaching step is highly efficient in terms of M_2CrO_4 extraction.

The edge of the particles, where chromite is in contact with oxygen, is richer in iron oxides. In agreement with the equilibrium data presented in Table I, Fe^{3+} seems to diffuse out first and remain at the edge of the partially reacted particles. This is evident in Figure 3, in which a rim of MgFe_2O_4 may be seen. In the microstructure, iron and magnesium may also phase separate depending on the alkali available [6]. Silica is mainly combined with Na^+ and Al^{3+} when roasting with NaOH (Figure 3), however, when roasting with KOH iron oxide is preferentially found as a complex K-Fe-silicate, which can clearly be seen in Figure 4.

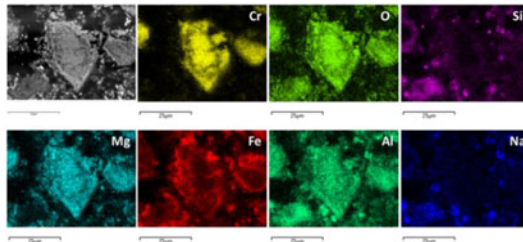


Figure 3. Backscattered SEM image and elemental mapping of a leached residue particle after roasting of chromite with NaOH ($\text{Cr}_2\text{O}_3:\text{NaOH} = 1:4$, $T = 1000^\circ\text{C}$ and $t = 2$ hours).

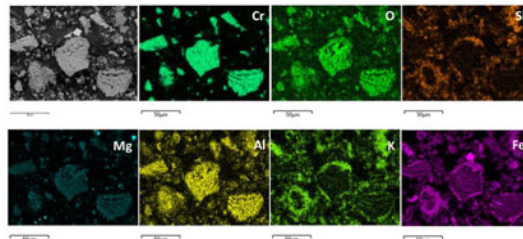


Figure 4. Backscattered SEM image and elemental mapping of a leached residue particle after roasting of chromite with KOH ($\text{Cr}_2\text{O}_3:\text{KOH} = 1:4$, $T = 1000^\circ\text{C}$ and $t = 2$ hours).

The concentration of chromium in the solutions obtained from the water leaching stage was analysed by AAS technique. The values of %Cr extraction for each experiment, shown in Figure 5, were calculated by the following formula: $\% \text{Cr extraction} = (\text{Cr}_{\text{in solution}} \cdot 100) / \text{Cr}_{\text{in chromite}}$.

Excess alkali is expected to increase the extraction yield of chromium as a result of the following: a) Equilibrium data in Table I shows the need for having higher $\text{Cr}_2\text{O}_3:\text{MOH}$ than the stoichiometric in order to fully decompose the chromite spinel phase; b) Excess alkali is necessary for neutralisation of alumina and silica and; c) Phases diagrams in Figure 1 show that as the MOH concentration in the charge increases, the $P(\text{O}_2)$ required to form M_2CrO_4 decreases. This is in agreement with the experimental values of %Cr extraction presented in Figure 5, being noticeable that the extraction of chromium is higher for a molar ratio of $\text{Cr}_2\text{O}_3:\text{MOH} = 1:6$ than

for 1:4. However, when the molar ratio is increased to 1:8, there is a slight decrease of the Cr extraction which may be explained by the fact that a higher amount of alkali in the charge increases the volume of molten salt phase. The liquid formed envelops the particles of chromite obstructing the diffusion of oxygen gas towards the reaction interface.

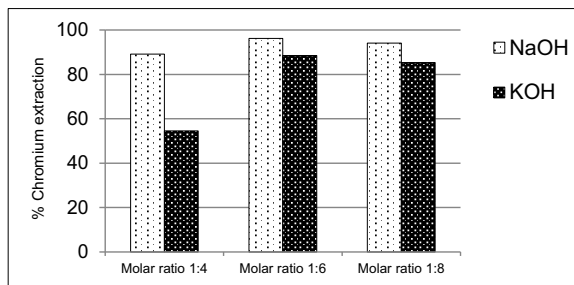


Figure 5. %Cr extraction after roasting of chromite at 1000°C with different Cr₂O₃:MOH ratios.

Conclusions

Phase diagrams for the MOH-Cr₂O₃-Fe₂O₃-Al₂O₃-O₂ systems (M=Na/K) were computed, showing the effect that the P(O₂) and the activity of the alkali compound have on the equilibrium phases formed. Equilibrium calculations were also performed for the roasting of chromite with different Cr₂O₃:MOH molar ratios (1:4, 1:6 and 1:8) for verifying the presence of the various phases formed and the expected composition of the molten phase. The reaction mechanism with different alkali ratios was discussed based on experimental results and thermodynamic data calculated, which are in good agreement. Excess alkali demonstrated to increase the extraction of chromium but it also generates a higher volume of molten phase, which may be responsible of a lower reaction rate as it represents an obstacle to the oxygen diffusion.

Acknowledgements

The authors acknowledge the financial support from the EPSRC standard grants (GR/T08074/01 and GR/L95977/01) and PhD studentships for research which were initiated in 1997 at the University of Leeds. AJ also acknowledges the support from the European Union's Marie Curie Fellowship grant number 331385 for Dr. Sanchez-Segado and from the NERC's Catalyst Grant reference NE/L002280/1.

References

1. Antony, M.P., et al., *Recovery of chromium from industrial wastes*, in *Environmental Issues and Waste Management in Energy and Mineral Production* Singhal Raj K. and Mehrotra Anil K., Editors. 2000, Balkema, Rotterdam. p. 751-755.
2. Nickens, K.P., S.R. Patierno, and S. Ceryak, *Chromium genotoxicity: a double-edged sword*. *Chemico-biological interactions*, 2010. **188**(2): p. 276-288.
3. Tathavadkar, V., A. Jha, and M. Antony, *The effect of salt-phase composition on the rate of soda-ash roasting of chromite ores*. *Metallurgical and Materials transactions B*, 2003. **34**(5): p. 555-563.
4. Tathavadkar, V., A. Jha, and M. Antony, *The soda-ash roasting of chromite minerals: Kinetics considerations*. *Metallurgical and Materials Transactions B*, 2001. **32**(4): p. 593-602.
5. Tathavadkar, V.D., *The process physical chemistry of extraction of sodium chromate from chromite ores*. 2001, Ph.D Thesis, Leeds University.
6. Parirenyatwa, S., et al., *Comparative study of alkali roasting and leaching of chromite ores and titaniferous minerals*. *Hydrometallurgy*, 2015.
7. Roine, A. and H. Outokumpu, *Chemistry for Windows: Chemical Reaction and Equilibrium Software with Extensive Thermodynamical Database, Version 5.1, User's Guide*. Outokumpu Research Oy, Finland, 2002.

EFFECT OF THE CaO ADDITION IN THE FUSION PROCESS OF NICKELIFEROUS LATERITES FOR FERRONICKEL PRODUCTION

Sandra Díaz Bello¹, Oscar J. Restrepo¹, Álvaro H. Forero P²

¹University National of Colombia, Kr 65 # 63-20 Bl 54, Medellín, Antioquia, Colombia

²University Pedagogic and Technologic of Colombia, Av. North km1. Tunja, Boyacá, Colombia

Keywords: CaO, ferronickel, nickeliferous laterites, smelting process, thermodynamic

Abstract

Ferronickel production process takes place in two basic stages. The first stage is calcination and preliminary reduction of minerals. These minerals contain significant amounts of iron, which must be partially reduced. The second stage is the final reduction and fusion process of the calcined product. This stage takes place at temperatures of 1600°C, in order to obtain ferronickel. The main objective is to treat nickeliferous laterites with the CaO addition, in order to decrease energy consumptions and the fusion temperature. The mineral composition was 1.78% nickel. The CaO additions were from 3% to 20%. The basicity indexes varied with respect to the CaO amount from 0.55 to 0.81. The fusion temperatures of mineral change between 1496.5 and 1462.9 °C. Metal recoveries (FeNi) change from 15.5 % to 19.3 %. It can be concluded that the addition of CaO is important to lower the melting points in obtaining ferronickel.

Introduction

Nickel is an essential alloying element in austenitic stainless steel and other special alloys. The drastic increase in production of such alloys over the last decade, mostly because of economic growth of Asian countries, particularly China, has resulted in a considerably increased demand for ferronickel [1]. Majority of the world's nickel is produced using pyrometallurgical techniques, the equipment and processes employed in such production encompass a variety of technologies [2]. One such technology is the RKEF system. RKEF smelting is widely used in ferronickel production to treat saprolite laterite ore. The RKEF process is a two-stage pyrometallurgical process that involves the calcination and the partial reduction of the saprolite ore in a rotary kiln, followed by high-temperature smelting in an electric arc furnace [3]. The current FeNi, Nickel Pig Iron (NPI) and Ni matte smelters operate with nickel laterite ore that meet fairly specific criteria in terms of their Ni grade, Fe/Ni, Ni/Co and SiO₂/MgO ratios [4].

Production of nickel from laterite ores has occurred for over 100 years beginning with processing of garnieritic ores from New Caledonia [5]. Nickel laterites are becoming more attractive for nickel production due to the depletion of high grade nickel sulfide ores [6], although, the recovery of Ni from laterites is difficult, due to, their complex mineralogy and the limited applicability of established technology [7].

In this work the effect of CaO addition was evaluated, in the smelting process of the nickeliferous laterites for the ferronickel production, of a sample with 1.78% content of Ni. It was done a thermodynamic analysis using the Factsage 7.0 software and it was obtained phase diagrams, with the variation of the CaO composition.

In order to optimize the process of ferronickel production and decrease the smelting point, it was added CaO. CaO is an oxide used in the laterites nickel processing. This oxide helps to increase the slag basicity index. With increasing basicity, the fusion characteristic temperatures decrease. It's revealed that the addition of an appropriate amount of CaO could lower the liquid temperature and increase the amount of metal [8] [9][10].

Materials and methods

Raw materials

It was used a Colombian mineral with content 1.78 % of Ni. The chemical analysis was obtained by X-Ray fluorescence and X- ray diffraction of. The XRF was performed using a team Philips brand FRX 2400. XRD was performed using a team PANalytical and reference X'pert, with Cu source K Alpha1 and wavelength of 1.5406A and a power of 1.8 kW (45 kV - 40 mA).

CaO used was dehydrated and it is commercial.

Experimental methods

Nickel ore was agglomerated in a hydraulic press using a pressure of 25 MPa. The granulometry used was of 150 microns. The samples obtained had a height of ½ inch with a weight of 5 g. The nickel ore was reduced to 1100°C during three hours. Coke was used as reducing agent.


A thermodynamic analysis using the 7.0  software was done and phase diagrams with the variation of the CaO composition was obtained. This variation was from 3% to 20% of CaO, with obtaining different smelting temperatures. Calcination product was smelting to 1600 °C in an electric furnace as show in the figure 1.



Figure 1. Electric furnace for the fusion process

Results and discussion

Characterization of mineral

The amount of nickel oxide, iron oxide and other oxides present was determined using the technique of X-ray fluorescence as shown in Table 1.

Table 1. Chemical composition of the mineral sample

Sample	Fe ₂ O ₃ %	%MgO (s)	%SiO ₂ (s)	%Al ₂ O ₃ (s)	NiO%	H ₂ O%
M2 (P2)	19.69	21.3	40.5	1.94	2.27	14.3

In Figure 2 X-ray diffraction, is showing the mineralogical composition of ore. In figure 2 is observed the presence of magnesium silicates as lizardite ($H_4Mg_3O_9Si_2$) and nepouite ($Ni_3Si_2O_5(OH)_4$), iron as Goethite ($Fe_2O_3.H_2O$) and silica content in the form of quartz (SiO_2), among others.

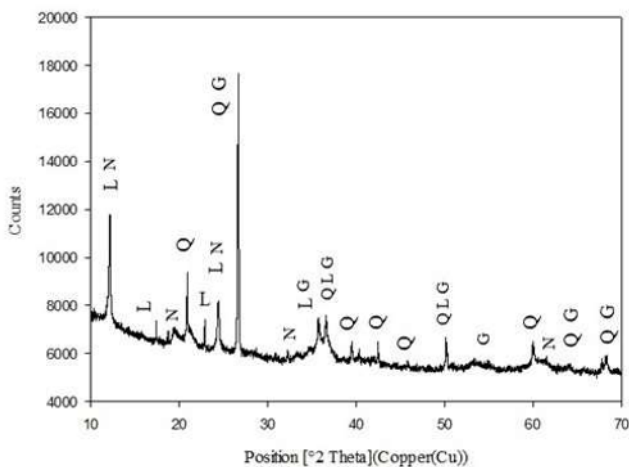


Figure 2. X-ray diffractogram of lateritic ore, L: Lizardite, N: Nepouite, Q: Quartz, G: Goethite

Thermodynamic analysis

The thermodynamic analysis was done using the XRF composition of the ore, obtaining a phase diagram, SiO₂-Al₂O₃-MgO system. This can be viewed in figure 3.

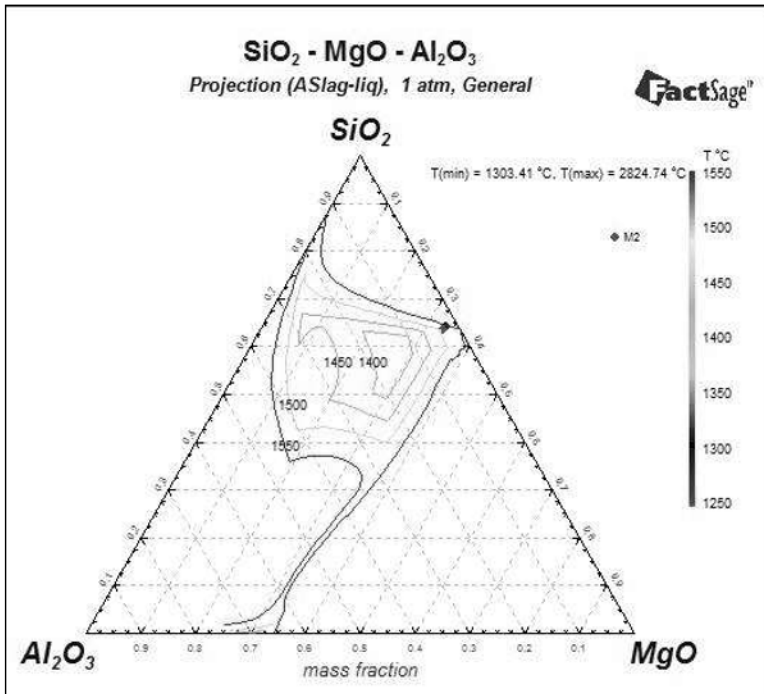


Figure 3. Phase diagram of mineral sample with initial composition, SiO₂-Al₂O₃-MgO system

In Figure 3 is shown the phase diagram of the SiO₂-Al₂O₃-MgO system. This diagram was done using initial composition of ore, without CaO addition.

The CaO addition was changed from 3 to 20% of CaO. This addition CaO was done in different percentages showed a change in the basicity index. These results are shown in table 2.

Table 2. Determination of basicity index with the CaO addition

% CaO	Basicity index	Liquidus temperature
0	0.50	1509
3	0.55	1487
6	0.59	1486
9	0.64	1489
12	0.68	1485
15	0.73	1477
20	0.80	1466

Table 2 show the increase of basicity index and decrease of the liquidus temperature. It is important in the low grade nickel ore fusion process, because it could to decrease the energy consumption and optimize the process.

For all percentages of CaO, corresponding phase diagrams were done. Figure 4 show the phase diagram with addition of 20% CaO.

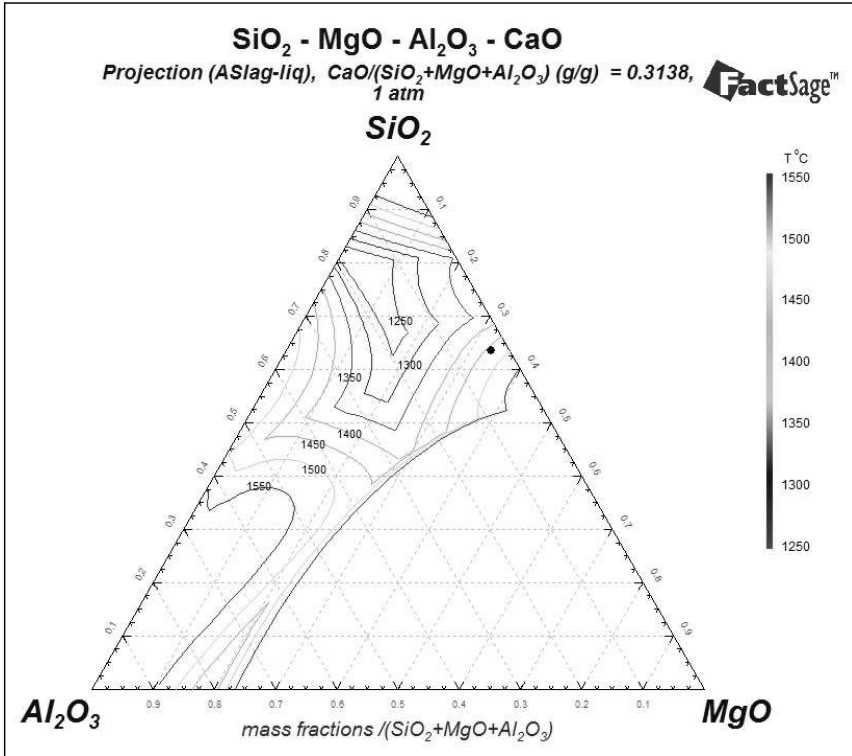


Figure 4. Phase diagram of mineral sample with CaO addition of 20%, SiO₂-Al₂O₃-MgO system

In Figure 4, where 20% of CaO was added, it can be seen that the liquidus temperature decreases significantly, down to 1466 C.

The metallization was studied experimentally with increasing CaO content. The metal recovery is shown in table 3. It can be seen that the metal recovery will increase with increasing CaO content.

Table 3. % Metal recovery

Sample	% CaO	% Metal recovery
1	3	15.5
2	6	13.5
3	9	19.3
4	12	18.7
5	15	20.3
6	20	19.3

In Table 3 is shown that with the CaO addition in 15% the metal recovery is 20.3 %. It is concluded that the CaO addition is important during the fusion process when it has low grade nickel ores.

The composition of ore is important because of its MgO and SiO₂ content. These compounds are refractories materials that increase the fusion temperature, and the CaO addition generate other compounds that help to the formation of mineralogical species in the slag, such as, diopside (CaMgSi₂O₆), akermanite (Ca₂MgSi₂O₇), rankinite (Ca₃Si₂O₇), which have smelting point of 1391°C, 1590°C, and 1410°C respectively.

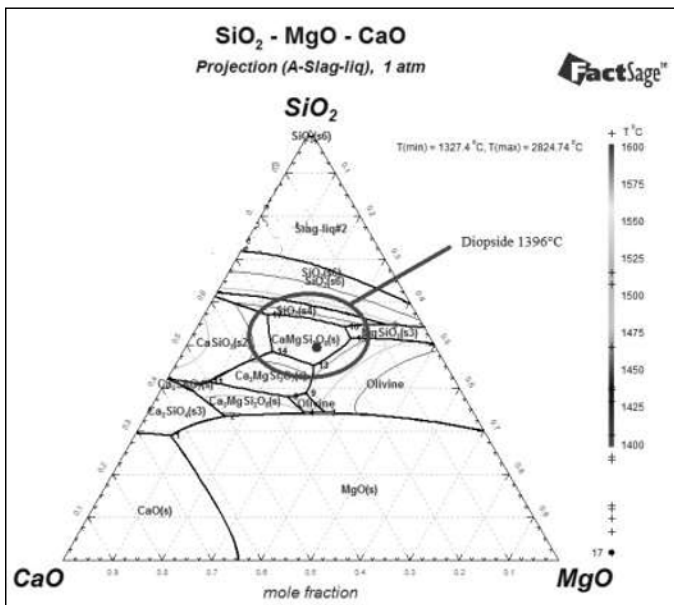


Figure 5. Phase diagram CaO-SiO₂-MgO system. Determination of composition by sample with 1.78% of Ni and the CaO addition of 20%.

In Figure 5 is shown the composition of samples with 1.78 % Ni with the CaO addition of 20%. The composition is located in the diopside zone. It is interesting because a suitable temperature for the fusion process is achieved. The temperature reached was 1396°C.

The metal recovery was quite similar from 9% to 20% CaO, and 9% may be preferred due to a lower total slag content.

Is very important the CaO addition because ferronickel at lower temperatures was obtained. This CaO addition can generate mineralogical species with lower smelting points. It can be an important factor in the fusion process, because this conditions help to decrease energy consumption.

The CaO addition is an important factor that affect the chemical composition of the ore, becoming in a great advantage for the fusion process, because this flux does all your functions and it doesn't interferes in the kinetic process of significant way

Conclusions

With the addition of 15% of CaO, good results in the metal recovery, with 20.3% of ferronickel was obtained. Although, with CaO addition of 20%, it was obtained greater amount of metal recovery, it can work with 9% of CaO, taking in account that the recovery is high, in order to do less expensive the fusion process.

The CaO addition, is important in the fusion process because, it helps to generate slag with mineralogical species with down smelting points such as, diopside ($\text{CaMgSi}_2\text{O}_6$), akermanite ($\text{Ca}_2\text{MgSi}_2\text{O}_7$), rankinite ($\text{Ca}_3\text{Si}_2\text{O}_7$), which have smelting point of 1391°C, 1590°C, and 1410°C respectively.

Calcium oxide is an excellent raw material, used in this process. This raw material is economically rentable and it helps to decrease the energy consumption, because helps decrease the fusion temperatures.

References

- [1] M. Y. Solar and S. Mostaghel, "Smelting of difficult laterite ores," *Miner. Process. Extr. Metall.*, vol. 124, no. 1, pp. 35–46, Mar. 2015.
- [2] C. M. Diaz, C. A. Landolt, A. Vahed, A. Warner, and J. C. Taylor, "A Review of Nickel Pyrometallurgical Operations," *J. Met.*, vol. 40, no. 9, pp. 28–33, 1988.
- [3] M. Rao, G. Li, T. Jiang, J. Luo, Y. Zhang, and X. Fan, "Carbothermic Reduction of Nickeliferous Laterite Ores for Nickel Pig Iron Production in China: A Review," *Jom*, vol. 65, no. 11, pp. 1573–1583, Sep. 2013.

- [4] A. Oxley and N. Barcza, "Hydro-pyro integration in the processing of nickel laterites," *Miner. Eng.*, 2013.
- [5] A. D. Dalvi, W. G. Bacon, R. C. Osborne, I. Limited, F. Boulevard, and S. Park, "The Past and the Future of Nickel Laterites," in *PDAC 2004 International Convention*, 2004, pp. 1–27.
- [6] A. Janwong, "The agglomeration of nickel laterite ore," The University of Utah, 2012.
- [7] K. Quast, J. N. Connor, W. Skinner, D. J. Robinson, and J. Addai-Mensah, "Preconcentration strategies in the processing of nickel laterite ores Part 1: Literature review," *Miner. Eng.*, pp. 1–8, Apr. 2015.
- [8] G. Li, Q. Zhi, M. Rao, Y. Zhang, W. Cai, and T. Jiang, "Effect of basicity on sintering behavior of saprolitic nickel laterite in air," *Powder Technol.*, vol. 249, pp. 212–219, Nov. 2013.
- [9] M. Liu, X. Lv, E. Guo, P. Chen, and Q. Yuan, "Novel Process of Ferronickel Nugget Production from Nickel Laterite by Semi-molten State Reduction," vol. 54, no. 8, pp. 1749–1754, 2014.
- [10] P. Chen, X. Lv, E. Guo, Q. Yuan, and M. Liu, "Preparation of ferronickel alloy nugget through," in *5th International Symposium on High-Temperature Metallurgical Processing*, 2014, pp. 41–50.

DEFINING THE OPERATING REGIME AND METHODOLOGY FOR THE FURNACE METHOD FOR THE PRODUCTION OF LOW CARBON FERROCHROME

Heine Weitz^{1,2}, Andrie Garbers-Craig¹

¹University of Pretoria, Lynnwood Road, Hatfield, South Africa

²OptiProc, 12 O'Hare Street, Highveld, Centurion, South Africa

Keywords: Low carbon ferrochrome, Furnace Method, Silicothermic reduction

Abstract

The Furnace Method for the production of low carbon ferrochrome has been found to offer significant savings in energy and raw material consumptions, compared to the Mixing Method processes. The operating conditions for the Furnace Method differ significantly from those of the Mixing Method processes. This paper describes the characterisation of the slag operating regime for the Furnace Method in order to minimise risks during implementation.

The slag liquidus temperature, as well as its chemical and thermal compatibility with different refractory systems was evaluated to identify the preferred fluxing agent, basicity ((CaO+MgO)/SiO₂) range and refractory system. A lime fluxed slag was found to provide the best combination of liquidus temperature and alloy product quality, while being compatible with a magnesia refractory at an operating temperature of 1750°C.

Slag chemistry variations throughout batches pose a risk to the integrity of the refractory lining. The impact that these variations have on the process chemistry was quantified in order to arrive at a feeding methodology for the process.

Introduction

Ferrochrome is one of the main raw materials used in the production of stainless steel (typically 10 and 20% Cr). An important benefit thereof is the increase in the steel corrosion and oxidation resistance [1]. Low carbon ferrochrome, required for the production of many steel types, cannot be produced directly by carbothermic reduction of chromite ore due to the amount of carbon that can go into solution with the metallic chromium and iron [2]. Most processes for producing low carbon ferrochrome from high carbon ferrochrome or charge chrome require very high process temperatures, result in high chromium losses or require uneconomically long reaction times [3]. Metallothermic production of low carbon ferrochrome is therefore preferred [4].

A number of metals that are produced in bulk can be used to reduce chromium from chromite ore. The stoichiometric consumption for the most notable ones is shown in Table 1, along with their cost per tonne of chromium metal produced. In practice, the consumptions may differ slightly, depending on the targeted chromium recovery.

From this data, it is evident that aluminium and silicon are economically the most viable options for use as metallothermic reductants. Of the two, only silicon (in the form of ferrochrome

silicide) can readily be produced on a smaller scale on site. This is likely the reason for the prevalence in its use.

Table 1: Metal consumption for Cr production

Metal	Consumption (t/t Cr)	Cost per tonne Cr* (US\$)
Aluminium	0.519	891
Magnesium	0.701	1 578
Manganese	1.585	2 877
Silicon**	0.405	704 - 1 069

* Prices from www.metalbulletin.com (15 August 2015).

** Calculated using 75% FeSi for the lower value and Si metal for the higher value.

Process Routes

Only two process routes (not considering the variations thereof) are considered to be commercially feasible for the production of LC FeCr, namely the Mixing Method and the Furnace Method. These have been described extensively in earlier works [1]. Of the two methods, the most commonly used process is the Mixing Method [4]. Both methods are illustrated in Figure 1. The process steps and furnace components indicated in blue are specific to the Mixing Method, while those in orange are used in the Furnace Method only. The remainder is common between the processes. Solid FeSiCr feed variations for both Methods are also possible (indicated with dotted line).

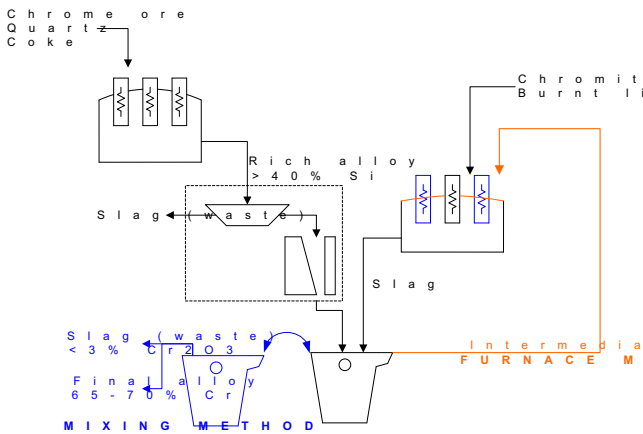
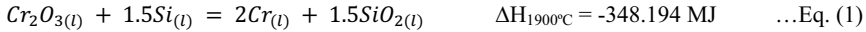


Figure 1: Mixing and Furnace Method processes

The Mixing Method

Processes that involve mixing of materials (cocktailing) in ladles will be referred to as the Mixing Method, in agreement with the work by Gasik [1]. The Mixing Method is a three-step process. FeSiCr is produced in a semi-open submerged arc furnace. Simultaneously, an ore-lime melt is produced in an open arc furnace. Lime is added to obtain a Cr₂O₃ content of approximately 27% [1, 5], where the liquidus temperature of the slag is 1831°C (FactSage 6.4).

The products from both of these steps are then mixed (cocktailed) in ladles to produce LC FeCr and a low Cr₂O₃ slag. Some Cr₂O₃ is retained to ensure that the Si content in the LC FeCr product is below 1.5%. The simplified reduction reactions are shown in Equations 1 and 2. The processes are exothermic, so the temperature in the ladle could be somewhat higher.



The Mixing Method has some distinct disadvantages, which include high energy losses due to the exothermic reactions during the ladle cocktailing step, high process temperatures that result in high refractory wear, as well as material losses due to spillage. In addition, the oxidising conditions in the ore-lime melt furnace, together with the high process temperature are conducive to the formation of Cr(VI) [6] and could result in the formation of up to 1% CrO₃ [1].

The Furnace Method

The Furnace Method is an alternative to the Mixing Method. In the Furnace Method, the FeSiCr is added directly to the ore-lime melt. The Liquid Feed Furnace Method (LFFM) was developed and patented by Mintek in South Africa [7], although not named as such. The reaction equations are similar to those of the Mixing Method. However, a lower operating temperature can be used, as discussed later.

High level mass and energy balances were developed for the Mixing and Furnace Methods, as well as their solid FeSiCr feed variations. In all cases, ore with a Cr₂O₃ content of 48.7% and FeSiCr with 40% Cr and 42% Si was used. The energy requirements are shown in Table 2. The Furnace Method, particularly the LFFM, offers a significant saving in the electrical energy requirement. This is due to the fact that the silicothermic reduction takes place inside the low carbon ferrochrome furnace, instead of in the ladles. The exothermic energy is therefore available for heating and melting of the ore-lime mixture.

Table 2: Smelting energy consumption for four process options

Process	Consumption * (kWh/t LC FeCr)	Ore-lime and LC FeCr furnace process temperature (°C)
Mixing Method (Perrin)	2254	1900
Mixing Method (Duplex, solid FeSiCr feed)	2326	1900
Solid Feed Furnace Method (SFFM)	1589	1750
Liquid Feed Furnace Method (LFFM)	1202	1750

* The energy consumption excludes that for the production of FeSiCr, which is common for all options.

Thermochemical Modelling Setup

At the time of writing there was no commercial installation producing low carbon ferrochrome using the LFFM. No information was therefore available relating to the operational parameters required to promote the product quality and recovery, nor for the refractory and slag systems that are the most appropriate for the process.

Thermochemical modelling was subsequently performed to evaluate different slag compositions and refractory materials to ascertain whether or not LC FeCr can be produced that is within specification, whether or not the process would be operable in terms of the slag liquidus temperature (and superheat), and to determine if the slag and refractory materials would be compatible at the selected process temperature. Modelling was done using FactSage 6.4.

The liquidus temperature of a 70% Cr LCFerCr product is approximately 1700°C. A slag superheat of between 50 and 200 degrees Celsius is generally required to achieve a balance between maintaining slag fluidity and refractory protection [8]. The operating temperature should therefore be in the region of 1750°C and the slag liquidus between 1550 and 1700°C.

Refractory systems were limited to magnesia and doloma (burnt dolomite, CaMgO₂), as they are readily available and low cost. Fluxes were limited to lime and doloma, again due to their availability and cost. The systems that were modelled are listed in Table 3. For the purposes of modelling, magnesia and lime were considered to be pure MgO and CaO respectively.

Table 3: Refractory and slag flux systems used in models.

System number	Refractory	Flux
1	Magnesia	Lime
2	Magnesia	Doloma
3	Doloma	Lime
4	Doloma	Doloma

The final slag basicity ((CaO+MgO)/SiO₂) for the Mixing Method processes ranges between 2.0 and 2.5. The natural basicity (no fluxes added) of the slag is 0.45. The basicity range used in the evaluation was between these two limits (0.45 to 2.5).

Thermochemical Modelling Results

Reaction Products

The alloy silicon content decreases with an increase in the slag basicity. The reason for this is that, as more flux is added, the activity of SiO₂ in the slag decreases. This promotes further reduction of the chromite with Si (to form SiO₂). Although a Si content of 1.5% is acceptable, 1.0% Si was chosen as the target at equilibrium, in order to compensate for process variability.

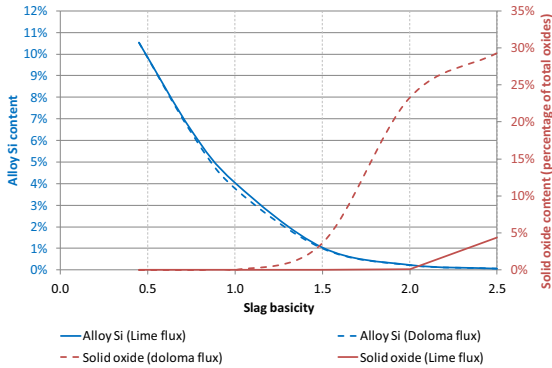


Figure 2: Alloy Si content and solid oxide content as a function of slag basicity (T = 1750°C)

For a lime fluxed slag, the targeted 1% Si is reached above a basicity of 1.5. Above a basicity of 2.0 a solid metal oxide (MO), consisting of mostly MgO (~95%) and Cr₂O₃ (~4%), starts forming. For a doloma fluxed system, the 1% Si is again reached above 1.5, but the solid MO already starts forming slightly above a slag basicity of 1.0. An operating basicity between 1.5 and 2.0 would therefore be preferable for a lime fluxed slag, considering the reaction products only. For a doloma fluxed slag, operating above a slag basicity of 1.5 may result in a high viscosity slag due to the presence of the solid MO phase. These results are shown in Figure 2.

Slag Liquidus Temperature

A plot of the slag liquidus temperature (Figure 3) shows both the lime and doloma fluxed slags to have liquidus temperatures within the required 1550 to 1700°C range between slag basicities of 1.68 to 1.90 and 1.07 to 1.23 respectively. Using a slag within these ranges would therefore ensure that the slag is fluid enough to be handled with ease, without having an excessively high superheat.

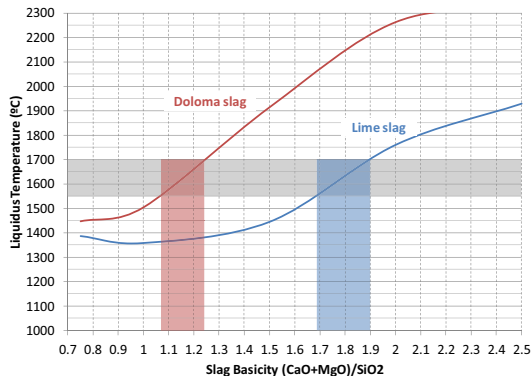


Figure 3: Slag liquidus temperatures for lime and doloma fluxed slags

Refractory-Slag Interaction

The commercial furnace will operate with a slag freeze lining on the refractory hot face. This is achieved by water cooling of the furnace shell. However, at times the freeze lining may be lost when it breaks off from the refractories due to thermal shock, or it may be worn away during periods of poor control. While the freeze lining is being re-established, the turbulence in the slag bath may cause the refractories to be exposed to slag with a temperature near the process temperature.

Modelling the interface between the slag and refractory is complex, as it is effectively a layer with a thickness of one molecule. This also does not take into consideration the effect of stirring, which continually replaces the slag on the interface with bulk slag. A more sensible way of modelling the potential refractory wear is by considering the maximum solubility of the refractory in the slag. The equilibrium slag products from the modelling were added (in new models) to 100 g of magnesia refractory. The liquid slag addition limit was chosen to be 100 g, as the mass of slag in contact with the refractory is not expected to exceed the mass of solid refractory at the refractory-slag interface.

The equilibrium amount of solid oxide material should be equal to or more than the 100 g of refractory that was initially added to the system. This indicates that the refractory is not absorbed into the slag and remains solid. For the systems with magnesia refractories (Systems 1 and 2), the solid MgO was also plotted. This is an important measure, as the total solid oxides can be high due to the precipitation of other oxides, even though the MgO from the refractory is being eroded by the slag. The results of the evaluation are shown in Figure 4.

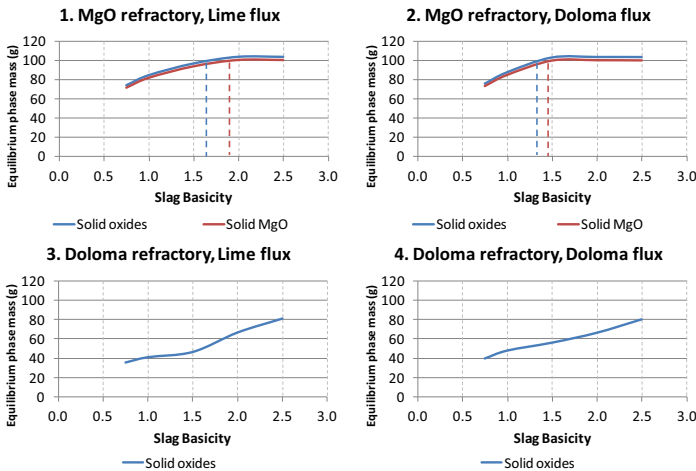


Figure 4: Solid oxides and solid MgO as a function of slag basicity for refractory slag systems at 1750°C (100 g initial refractory and 100 g slag added).

The curves in Figures 4.3 and 4.4 show that the equilibrium amount of solid oxides in the system never exceeds the 100 g of refractory that was added for slag in contact with a doloma refractory. In fact, it was found that approximately 14% of the refractory would have been taken into solution at the process temperature. Doloma refractory is therefore not suitable for use in this basicity range and temperature.

The results from Figures 4.1 and 4.2 were much more encouraging. For the lime fluxed slag, the total solid oxide and solid MgO contents exceed 100 g at basicities of 1.65 and 1.90 respectively. For the doloma fluxed slag these values are 1.35 and 1.48 respectively. Comparing these results to the liquidus temperatures plotted in Figure 3, one can see that the ranges overlap for the lime fluxed slag between 1.68 and 1.90, while there is no overlap for the doloma fluxed slag. Of the systems evaluated, the only suitable alternative is therefore a lime fluxed slag in contact with a magnesia refractory.

Operation

Although the furnace in the LFFM is operated on a continuous basis, the slag and alloy undergo distinct compositional changes with time, and is therefore classified as a semi-batch processes. As exothermic reactions take place in the LFFM LC FeCr furnace, control is somewhat more complex than for the Mixing Method processes. The control of the energy balance is therefore crucial for maintaining the integrity of the refractory lining. The feed ratio and power input are adjusted throughout the heat to maintain a constant energy balance and process temperature.

Deciding on when to feed the different raw materials in the LFFM process is probably the greatest challenge of the entire operation. Feeding all of the ore-lime mixture at the start of the batch will result in a slag with a high liquidus temperature, which will likely solidify in the furnace. However, feeding the FeSiCr at the start of the batch poses a severe risk to the refractory integrity.

FactSage models, with slag and alloy at equilibrium, show the magnesium metal content to be extremely high when gradually adding the ore-lime mixture to liquid FeSiCr (Figure 5). Although some of the Mg may originate from the slag, it is equally likely to come from the refractory. A balance therefore needs to be found between maintaining the integrity of the furnace refractory, while having a liquid slag.

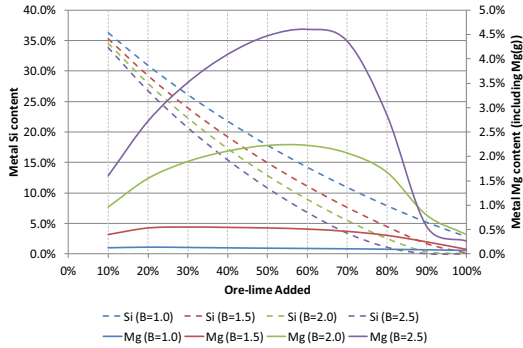


Figure 5: Metallic magnesium and silicon contents for basicities of 1.0 to 2.5 when adding ore-lime mixture to FeSiCr.

In practice, this requires a calculation of how much of the ore-lime mixture can be heated and melted by the exothermic energy from silicothermic reduction. This fraction of the ore-lime mixture should be fed at the end of the batch (after the FeSiCr), while the balance of the ore-lime mixture should be fed at the start of the batch. There should therefore be as much as possible of the ore-lime mixture in the furnace before feeding the FeSiCr. The Si would then preferentially react with the metal oxides from the ore, instead of the MgO in the refractory. Feeding the FeSiCr close to the centre of the furnace would be preferred to side feeding for two reasons. Firstly, contact between molten FeSiCr and the sidewall is limited and secondly, feeding close to the arc will improve reaction kinetics. Where the Mixing Method relies on the momentum imparted by the cocktailing process to ensure good contact between the reactants, the LFFM relies on the momentum from the electrical arc, as well as the large slag-metal interface in the furnace (relative to that of a ladle).

Conclusions

The Furnace Method, in particular the Liquid Feed Furnace Method, provides a saving in the electrical energy requirement when compared to the Mixing Method processes.

For both doloma and lime fluxed slags, the required alloy Si content (1%) is achieved above a slag basicity of 1.5. However, the doloma slag only has a liquidus temperature within the 1550 to 1700°C range between slag basicities of 1.07 and 1.23. Doloma fluxed slag is therefore not suitable for producing low carbon ferrochrome. A lime fluxed slag has a liquidus temperature within the required 1550 to 1700°C range for a slag basicity range of 1.68 and 1.90. The slag is also compatible with a magnesia lining between a slag basicity of 1.65 and 1.90. This system therefore has a suitable basicity range within which to operate.

Doloma refractories can also not be used for the production of low carbon ferrochrome at the required operating temperature, as approximately 14% of the refractory was found to be taken into solution at a process temperature of 1750°C.

Acknowledgements

The authors would like to thank the Department of Materials Science and Metallurgical Engineering's Centre for Pyrometallurgy at the University of Pretoria for providing the facilities and funding for this project.

References

- [1] M. Gasik, "Technology of chromium and its ferroalloys," in *Handbook of Ferroalloys - Theory and Technology*, M. Gasik, Ed. Oxford: Butterworth-Heinemann, 2013, pp. 267-316.
- [2] A.G.E. Robiette, *Electric smelting processes*. London: Charles Griffin & Company Limited, 1973.
- [3] P.J. Bhonde, A. M. Ghodgaonkar, and R. D. Angal, "Various techniques to produce low carbon ferrochrome," in *Proceedings of the Eleventh International Ferroalloy Conference*, New Delhi, 2007, pp. 85-90.
- [4] European IPPC Bureau, "Integrated pollution prevention and control (IPPC) reference document on best available technique in the non ferrous metals industry," Seville, 2001.
- [5] S. Ghose, J. K. Nanda, and B. B. Patel, "Duplex process for production of low carbon ferrochrome," in *Proceedings of the seminar on problems and prospects of ferro-alloy industry in India*, Jamsedpur, 1983, pp. 215-217.
- [6] J.P. Beukes, N.F. Dawson, and P.G Van Zyl, "Theoretical and practical aspects of Cr(VI) in the South African ferrochrome industry," *The Journal of the South African Institute of Mining and Metallurgy*, vol. 110, pp. 743-750, 2010.
- [7] H.L. Smith, G. M. Denton, and N. A. Barcza, "Ferrochromium production," 96/0877, 1996.
- [8] M.W. Kennedy, "Electric slag furnace dimensioning," , Orlando, 2012.

Optimized Slag Design for Maximum Metal Recovery during the Pyrometallurgical Processing of Polymetallic Deep-Sea Nodules

David Friedmann¹, Bernd Friedrich¹

¹RWTH Aachen University, IME Process Metallurgy and Metal Recycling
Intzestr. 3, 52072 Aachen, Germany

Keywords: Polymetallic Deep-Sea Nodules, Slag Design, Submerged Arc Furnace, Direct Slag Reduction, Thermo-chemical Modelling

Abstract

The steadily growing demand for critical metals and their price increase on the world market makes the mining of marine mineral resources in the not too distant future probable. Therefore, an enormous focus lays currently on the development of a viable process route to extract valuable metals from marine mineral resources such as polymetallic nodules. For a country with few natural resources like Germany, the industrial treatment of marine mineral resources could lead to a significantly decreased dependence on the global natural resource market. The focus during treatment of these nodules lies on the pyrometallurgical extraction of Ni, Cu and Co on one hand as well as the generation of a sellable ferromanganese and/or silicomanganese product on the other. All work is conducted in lab-scale SAF furnaces. The concept approach is zero-waste, which includes careful slag design, so that the produced slags adhere to environmental restrictions.

Introduction

The exploitation of manganese nodules from the deep sea has once again become a political and economic topic in recent years. Many countries have purchased exploration rights for territories in the equatorial pacific (“Clarion Clipperton Zone”; see Figure 1) south of Hawaii from the International Seabed Authority (ISA). The focus of the processing of these nodules lays on the extraction of the industrial metals nickel, copper and cobalt. The nodules would serve as an enormous reserve for these metals, since they are found in relative abundance in many areas in the world’s oceans. For example, nodules in the Clarion Clipperton Zone alone constitute an estimated reserve of up to 290 million tons of nickel and up to 60 million tons of cobalt. These estimated amounts currently surpass common land based reserves in mines for nickel, cobalt and manganese [1,2]. Additionally, other valuable metals such as Molybdenum and Vanadium are found in relatively high concentrations.

Much of the current research builds on findings and results from the 1970s [3–5]. Most researches only focus on hydrometallurgical approaches, since energy consumption to dry the 20 – 40% moisture-containing nodules is high. In the 1970s four processes emerged, which were considered viable to extract metal values from ocean nodules [3–6]:

- (1) Reductive ammonia leach [7,8]
- (2) High-pressure sulfuric acid leach [9]
- (3) Reduction and hydrochloric acid leach [10]
- (4) Reductive smelting and sulfuric acid leach [11]

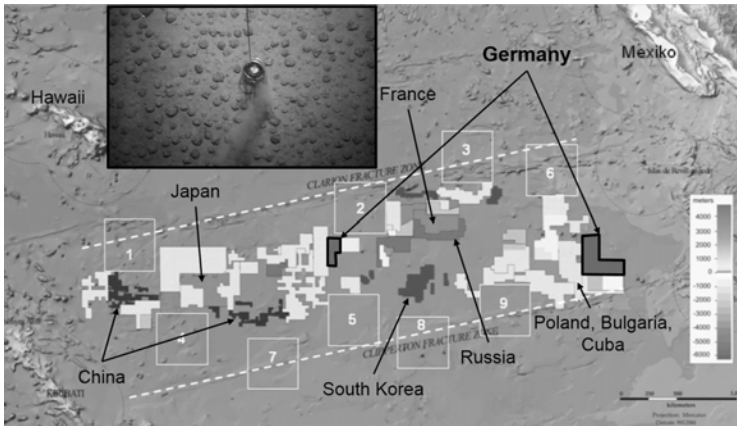


Figure 1. Deep-sea nodule exploration license areas to different countries in the Clarion Clipperton Zone in the Pacific and impression of nodules on the seabed at 4000-6000 m depth (top). [12]

The research presented in this paper solely focuses on pyrometallurgical processing methods and follows a similar processing route as presented by Sridhar et al. [11,11,13]. A simplified processing scheme is illustrated in Figure 2. The nodules are first dried and pre-reduced in a rotary kiln at 1000°C and charged in to an Electric Arc Furnace. The first reduction step reduces an FeNiCuCo alloy at 1400°C, which is further converted to remove the iron content. The MnO, FeO containing slag is further reduced to produce ferro-manganese. The converter slag may be used to adjust the FeO/MnO ratio in this step. Thus, creating a nearly zero-waste process, if the produced slags are suitable for further use.

More than 95% of the nickel, copper and cobalt are reduced into this metal phase. The alloy only constitutes 6 to 8.5% of the original dry nodule weight. Herein lies the first advantage of a pyrometallurgical processing option. The hydrometallurgical routes struggle with low concentrations of valuable metals in solution after leaching, resulting in complex solvent extraction processes needed to obtain solution suitable for electro winning. In the proposed pyrometallurgical option, the target metals are concentrated by a factor > 20 and may be sold to existing industries. The second main advantage of the pyro route is the production of a sellable manganese product. No hydrometallurgical options generate manganese, which however makes up nearly half of the nodules content (as oxide, moisture free). The chemical composition of nodules from the German license area is given in Table I.

Polymetallic nodules are composed of complex $Mn_xO_y \cdot SiO_2$ and $Fe_xO_y(OH)$ minerals with mineral particles below 1 μm [5]. Ni, Cu, Co and Mo are found in the manganese- or iron-oxide matrix. Therefore, beneficiation with classic techniques (density separation, floatation etc.) to generate a metal bearing concentrate, which could be directly used in existing industries, is not possible making direct metallurgical treatment necessary.

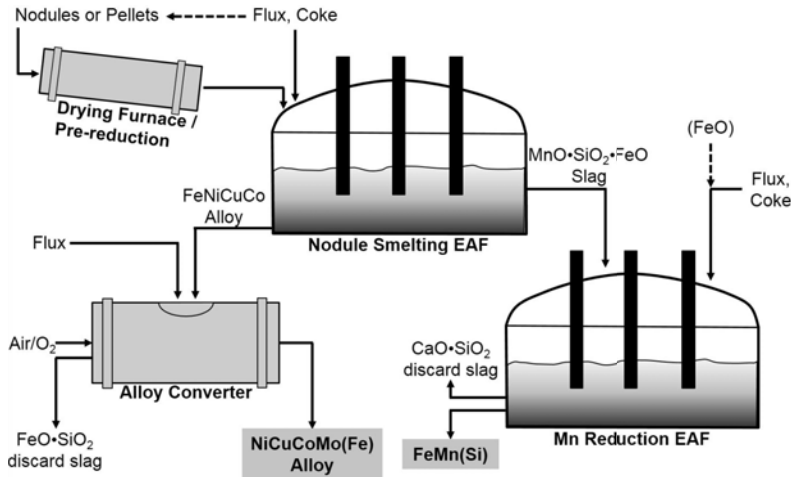


Figure 2. Simplified pyrometallurgical process for the extraction of metal values from polymetallic nodules

Thermo-chemical Models in FactSage™ 6.4

Thermodynamic models present a great advantage to research of the 1970s and allow the theoretic verification of process routes, which were developed in the past. FactSage™ is a complete thermochemical modelling program with many different applications e.g. phase diagram calculation, thermodynamic chemical reaction calculations, predominance as well as EpH modelling. The Equilib mode uses Gibbs free energy minimization calculations to simulate the reactions of different reactants to reach a state of chemical equilibrium and therefore allows the modelling of phase equilibria. It employs a vast variety of thermodynamic databases of pure substances and solutions. [14]

Table I. Average chemical composition of nodules from the German license area [wt.-%] (wet basis; ~ 20 wt.-% LOI as water)

Mn	Ni	Cu	Co	Mo	V	Fe	Si	Al	Mg	Ca	Zn
31	1.4	1.2	0.16	0.06	0.06	6.2	5.9	2.3	1.9	1.6	0.15
MnO	NiO	CuO	CoO	MoO ₃	V ₂ O ₅	FeO	SiO ₂	Al ₂ O ₃	MgO	CaO	ZnO
40.02	1.73	1.46	0.20	0.09	0.11	7.98	12.62	4.35	3.15	2.24	0.19

The FactSage™ models consider 15 elements as simple oxides (MnO, FeO, SiO₂, NiO, etc.). Trace elements (< 500 ppm) were not taken into account in the calculation to simplify the model. Figure 3 shows the relevant slag system for the first smelting step, a quasi-binary phase diagram of the main oxides is depicted.

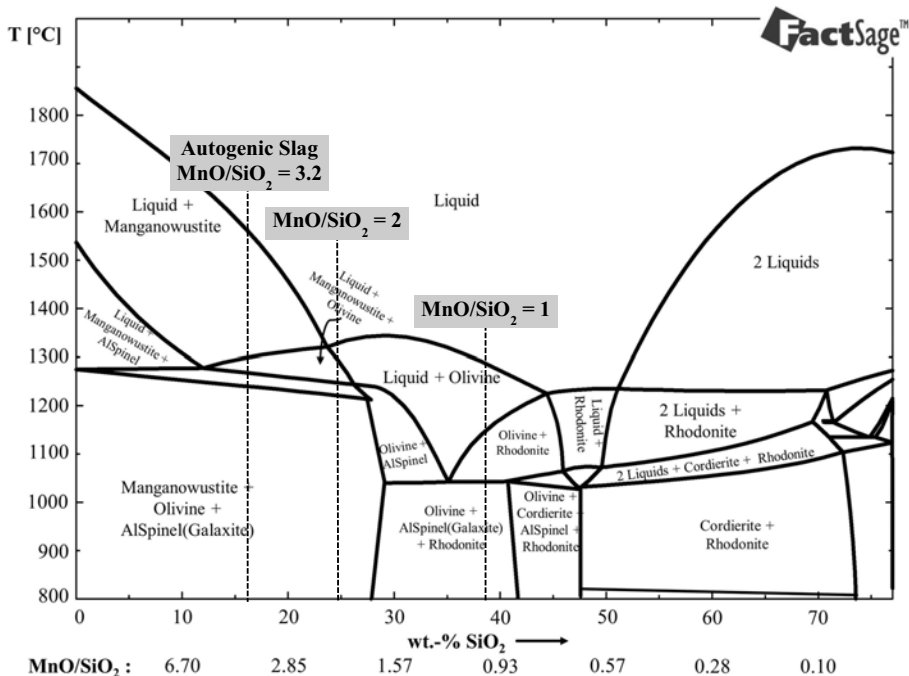


Figure 3. Quasi binary phase diagram of the five main oxides (MnO, SiO₂, FeO = 12 wt.-%, Al₂O₃ = 6 wt.-%, MgO = 5 wt.-%)

The x-axis shows the correlation of varying MnO/SiO₂ ratio and resulting equilibrium phases and the liquidus surface. The autogenic slag composition (compare Table I) is also indicated. The model predicts a liquidus temperature of approximately 1540°C, which was verified experimentally in DTA/TGA trials. In the first reduction step (see Figure 2) the main separation of valuable metals from the manganese stream is conducted. However, in a temperature range above 1500°C carbothermic reduction of MnO is significant. This results in high Mn concentrations in the first alloy and subsequently Mn loss for the FeMn reduction, which needs to be minimized.

Silica flux may be added to decrease the liquidus temperature of the slag to values below 1400°C. Different models were created in the “Equilib” mode of FactSage 6.4 to assess silica addition on the first reduction step. The addition of carbon as reductant was varied according to the percentage theoretically needed to reduce all NiO, CuO, CoO, MoO₃ and V₂O₅ up to the quadruple amount needed (~ 29g/kg oxides). The first model with no SiO₂ results in a metal phase with approximately 6.1 wt.-% Mn at 300% C addition. Here the reduction temperature was set at 1650°C (roughly 100°C above liquidus). In comparison, at a MnO/SiO₂ ratio of 1 reduction temperature may be reduced to 1400°C, which results in an Mn content in the alloy of ~2 wt.-%. The target metals Ni, Cu, Co, Mo are reduced with recoveries > 95% at MnO/SiO₂ of 1. Yet, with no flux addition Cu recovery is only about 84%, indicating potential metal loss to the slag. Vanadium is not reduced in this step, but remains in the slag at equilibrium composition. The reduction of iron may not be avoided thermodynamically, resulting in ~ 51 wt.-% in the alloy.

Similarly, the second reduction step of ferromanganese from the resulting slag was simulated and optimized using FactSage™ models. The ratio of $(\text{MnO}+\text{CaO})/\text{SiO}_2$ (i.e. basicity) was used to characterize the slag. Lime is used to form a calcium silica slag and thus minimize the co-reduction of Si, which is limited for most FeMn qualities to < 1.2 wt.-% [15,16]. Carbon additions were varied as well as the reduction temperature from 1500°C to 1800°C . As expected, Si co-reduction decreases with CaO additions and increases with the temperature. However, Mn reduction recoveries increase with the basicity of the initial slag mixture. Thus a trade-off between undesired Si reduction and maximized Mn recovery.

Experimental Evaluation

All experiments are conducted in a lab-scale DC electric arc furnace, which has a power supply of 50 kW and a melt capacity of 6 liters. The furnace has a water-cooled copper bottom-electrode and a 5 cm diameter graphite top-electrode. The first melting and reduction experiments were conducted in an alumina-chromia castable lining, which proved very stable against the slag and is suitable for temperatures up to 1800°C . The reduction of ferromanganese from the resulting slag was carried out in graphite crucibles.

For the first reduction experiments, nodules were ground (< 0.5 mm) and pelletized with different SiO_2 additions. The pellets were charged into the preheated lab EAF, during charging the furnace was run with an open arc. Once all pellets (~ 3 kg/trial) the graphite top-electrode was submerged into the liquid slag and held for 15 minutes (SAF operation). The solidified slags were broken up, mixed with varying CaO amounts, and charged once again into the preheated graphite crucible. For the reduction in SAF operation the electrode was submerged for 1.5 hours into the slag. During all trials, slag samples were taken in intervals and analyzed via XRF analysis.

Reduction of FeNiCuCo alloy

The alloy predicted in the models makes up approximately 7% of initial oxide input weight. Experimentally, metal weights of 5 to 8% of input weight were obtained, proving thermodynamic models. A phase distribution comparison between FactSage™ models and experimental results is given in Figure 4.

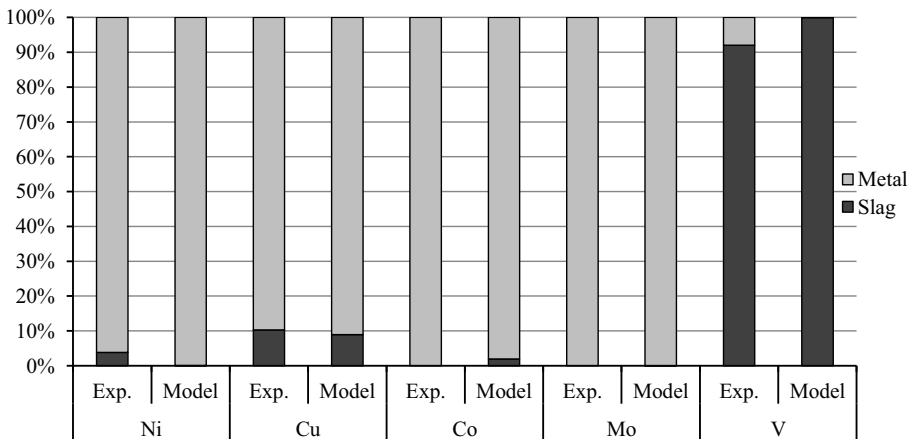


Figure 4. Phase distribution comparison of experimental values and model results ($\text{MnO}/\text{SiO}_2 = 1$, at a carbon addition of 200%)

The average metal composition of three different initial slag compositions is given in Table II. As may be seen Mn content in the alloy decreases dramatically when adjusting the MnO/SiO₂ ratio of the slag. Differences in smelting and reduction temperature were also observed and correspond well with liquidus data simulated in FactSage™. The tapping temperature for smelted nodules with no flux addition was between 1600 and 1650°C, whereas tapping temperatures with silica flux could be decreased to values between 1350 and 1450°C.

Table II. Comparison of alloy compositions after the first reduction step [wt.-%]

MnO/SiO ₂	Fe	Ni	Cu	Co	Mo	Mn
3.2	54.3	13.4	9.1	0.7	0.5	18.5
2	62.4	17.0	12.7	1.9	0.7	2.2
1	60.4	17.8	10.8	2.0	0.6	2.5

Reduction of FeMn from slag

For the reduction of ferromanganese a slag with 47.4 wt.-% MnO was generated from a larger trial series with an adjusted MnO/SiO₂ ratio of 2 in the first melting and reduction step. The full chemical analysis of the slag is given in Table III. A value for the basicity was established to describe the reduction step:

$$B = \frac{\%MnO + \%CaO}{\%SiO_2} \quad (1)$$

The autogenic slag possesses a basicity value of 1.63. This highlights the challenge for the FeMn reduction from this slag, when compared to standard manganese ores; whereas the Mn content of the slag is comparable to low-grade manganese ores ($B = 3 \dots 17$) [17], the basicity (i.e. silica content) of the slag is significantly higher (i.e. more acidic). Thereof arises the need for CaO flux to hold Si in the slag.

Table III. Chemical composition of slag for FeMn reduction [wt.-%]

MnO	SiO ₂	FeO	MgO	Al ₂ O ₃	TiO ₂	CaO	V ₂ O ₅	P ₂ O ₅
47.4	31.0	3.5	4.0	5.1	0.58	3.0	0.11	0.41

Due to limited supply of nodules and therefore limited amount of slag, initially four trials could be conducted. The results are illustrated in Figure 5. The basicity was increased (2.4, 2.6, 2.8 and 3.0) for this trial series. As can be seen from Figure 5 the lowest Mn content in the final slag may be achieved with the highest CaO additions.

The metal phases showed a manganese content of > 85 wt.-% in initial XRF analysis. However, analysis of carbon content is yet outstanding. Fe content in the alloy is ~ 8 wt.-%, which is inside requirements for FeMn. Yet, titanium as well as vanadium content in the reduced metal is problematic with contents ~ 1.3 wt.-% and 0.4 wt.-% respectively. The control of these metals will be subject to further studies. The phosphorous contents on the other hand was not significant and below 0.1 wt.-%. Reduction temperature during SAF operation varied between 1600 and 1800°C as was calculated in the simulations.

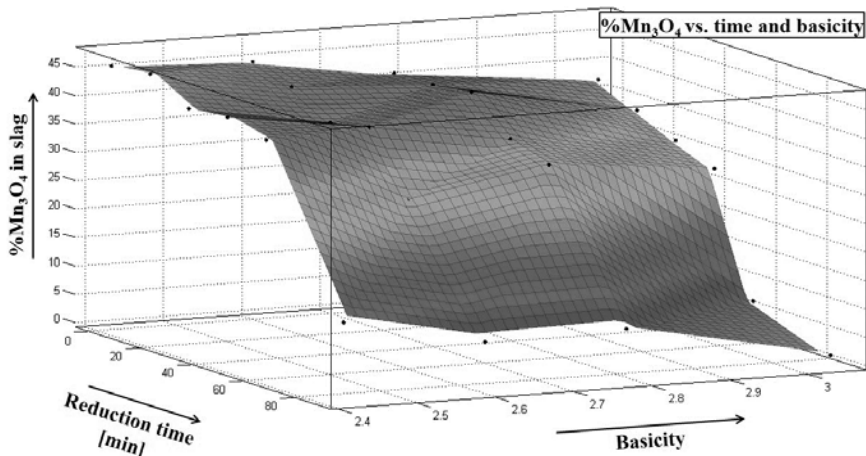


Figure 5. Correlation of Mn content in the slag during reduction versus time (in SAF operation) and basicity

Summary

The first experimental investigation into the described pyrometallurgical process for polymetallic deep-sea nodules were successful. The trials have so far proven the technical feasibility of the process developed mainly in the 1970s. Additionally, this study has shown that there are many advantages of thermodynamic modelling and that it may be used to verify metallurgical processes, which were developed in the past. The FactSage™ models allowed the calculation of the liquidus temperatures of the slag, which were close to experimental data, even though some simplifications had to be made in the models. The metal reduction was also successfully modelled in FactSage™ and the results could be proven in the experiments. Overall, it could be shown that by careful adjustment of the MnO/SiO₂ ratio it is possible to separate most of the manganese content of the nodules from metal values (i.e. Ni, Cu, Co). The use of an electric arc furnace to melt and separate the two phases has many advantages and could be easily adapted to an industrial scale.

The initial experiments on the reduction on ferromanganese from the slag produced in the first reduction step showed that the production of a sellable manganese product from deep-sea nodules is possible. However, further studies are needed to adjust the slag to produce FeMn that adheres to FeMn standards. The option of the production of SiMn as well as FeMn in a two-stage reduction step will also be investigated. Additionally, further studies on the entire process are planned in the future since the investigation of the conversion of the FeNiCuCo alloy is outstanding. Furthermore, a scale-up of the process from lab-scale is planned.

Overall, the advantages of the pyrometallurgical processing route compared to hydrometallurgical options are described and proven by the experimental trails. The valuable metals are easily separated and concentrated from the manganese stream. The advantage of the production of a manganese product from polymetallic deep-sea nodules are also outlined. However, the exploitation of these nodules remains a political topic, but could offer decreased dependency on raw material imports, which will be especially important for raw material import-dependent countries like Germany.

References

1. R. K. Jana, "Processing of Polymetallic Sea Nodules: An Overview," *The proceedings of the Third ISOPE Ocean Mining Symposium* (1999), 237–245.
2. J. Lehmköster, N. Gelpke, and M. Visbeck, *World Ocean Review 3* (www.worldoceanreview.com): *Resources of the sea - chances and risks* (Hamburg: maribus gGmbH, 2014).
3. P. Halbach, G. Friedrich, and U. von Stackelberg, *The Manganese Nodule Belt of the Pacific Ocean* (Stuttgart: Ferdinand Enke Verlag, 1988).
4. G. L. Hubred, "Manganese Nodule Extractive Metallurgy Review 1973 - 1978," *Marine Mining*, 1980, no. 3:191–212.
5. U.S. Bureau of Mines, "Pacific Manganese Nodules: Characterization and Processing (Bulletin 679)" (Bulletin 679, U.S. Bureau of Mines, 1985).
6. K. N. Han, and D. W. Fuerstenau, "Metallurgy and Processing of Marine Manganese Nodules," *Mineral Processing and Extractive Metallurgy Review: An International Journal*, 1983, Vol. 1:1–83.
7. J. C. Agarwal, and T. C. Wilder, *U.S. Patent 3788841: Recovery of metal values from manganese nodules*, 1974.
8. J. C. Agarwal, N. Beecher, and D. S. Davies, "Processing of ocean nodules: A technical and economic review," *Journal of Metals (JOM)*, 1976, Vol. 28 No. 4:24–31.
9. K. N. Han, and D. W. Fuerstenau, "Acid leaching of ocean manganese nodules at elevated temperatures," *International Journal of Mineral Processing*, 1975, no. 2:163–171.
10. P. H. Cardwell, and W. S. Kane, *U.S. Patent 3950486A: Method for separating metal constituents from ocean floor nodules*, 1976.
11. R. Sridhar, W. E. Jones, and J. S. Warner, "Extraction of copper, nickel, and cobalt from sea nodules," *Journal of Metals (JOM)*, 1976, Vol. 28 No. 4:32–37.
12. Federal Institute for Geosciences and Natural Resources, Manganese nodule exploration in the German license area. www.bgr.bund.de.
13. R. Sridhar, "Thermal Upgrading of Sea Nodules," *Journal of Metals (JOM)*, 1974 (12) (1974), 18–22.
14. C. W. Bale et al., "FactSage thermochemical software and databases," *Calphad*, 26 (2) (2002), 189–228.
15. ASTM International, *(A99-03) Standard Specification for Ferromanganese*, 2 pp. (accessed 25 June 2015).
16. DIN Deutsches Institut für Normung e.V., *(DIN 17564) Ferromanganese, Ferromanganese-Silicon and Manganese – Technical delivery conditions*, 6 pp., 2004 (accessed 29 January 2016).
17. F. Habashi, ed., *Handbook of Extractive Metallurgy* (Wiley VCH, 1997).

Acknowledgments

German Federal Institute for Geosciences and Natural Resources (BGR) for the supply of raw nodules and financial support.

REVIEW OF LIQUIDUS SURFACE AND PHASE EQUILIBRIA IN THE TiO₂-SiO₂-Al₂O₃-MgO-CaO SLAG SYSTEM AT PO₂ APPLICABLE IN FLUXED TITANIFEROUS MAGNETITE SMELTING

^{1,3}Xolisa Goso, ²Johannes Nell, ³Jochen Petersen

¹Mintek, 200 Malibongwe Drive, Private Bag X3015, Randburg, 2125, South Africa
XolisaG@mintek.co.za

²Hatch, Private Bag X20, Gallo Manor, 2052, South Africa

³University of Cape Town, Private Bag X3, Chemical Engineering Building, Rondebosch, 7701, South Africa

Keywords: Titanomagnetite slag, liquidus surface, phase equilibria, FactSage

Abstract

The current liquidus surface and phase equilibria established in air for fluxed titaniferous magnetite (titanomagnetite) slags conforming to a composition of 37.19% TiO₂, 19.69% SiO₂, 13.12% Al₂O₃, and 30.00% of various ratios of CaO+MgO were reviewed at applicable PO₂ using FactSage simulation and phase composition of a real plant titanomagnetite slag. The testwork included the incorporation into FactSage of a private MgTi₂O₅-Al₂TiO₅ pseudobrookite solution model. The results of the investigation showed that the liquidus surface and Ti³⁺/Ti⁴⁺ mass fraction ratio increased with decreasing the PO₂. At low PO₂, perovskite crystallizes as a primary phase at high CaO content. The spinel solution, i.e. (Mg)(Al,Ti)O₄, generally crystallizes as the primary phase at high MgO contents, though it is replaced by MgTi₂O₅-Al₂TiO₅ solution at PO₂ of 10⁻¹⁰ atm to 10⁻¹⁵ atm. An intermediate equilibrium phase diagram established at PO₂ of 10⁻¹⁶ atm is proposed. This phase diagram does not show the observed primary phase crystallization competition, however, the phase composition of a real titanomagnetite slag produced by Evraz Highveld Steel and Vanadium Corporation in South Africa does show primary phase crystallization competition between (Mg)(Al,Ti)₂O₄ and MgTi₂O₅-Al₂TiO₅. Smelting involving such slags is likely conducted around the transition PO₂, i.e. PO₂ of about 10⁻¹⁶ atm. Complex modelling with MgTi₂O₅, Al₂TiO₅ and Ti₃O₅ end members and experiments are underway to verify and update the intermediate phase diagram.

Introduction

Titanomagnetite is typically smelted in the presence of fluxes such as silica, dolomite and/or limestone, to produce a valuable high vanadium pig iron metal and a valueless TiO₂ (titania) bearing slag. The titanomagnetite slags conform to the TiO₂-SiO₂-Al₂O₃-MgO-CaO system and contain between 20 and 40% TiO₂ [1-3]. Several complex processes have been proposed for processing low-titania resources, including titanomagnetite slags, to marketable titania materials [4-7]. To date, these processes have not been implemented because they are not economically viable and produce insufficient TiO₂ grades to qualify as titania products [8]. A titanomagnetite slag with the right chemistry for subsequent TiO₂ recovery is desired.

Zhao et al [9] reviewed phase equilibria in the TiO₂-SiO₂-Al₂O₃-MgO-CaO system applicable to blast furnace ironmaking slag, i.e. <10% TiO₂, at carbon saturation, and found crystallization of

reduced titanium species (Ti^{3+}) in the pseudobrookite primary phase. Jochens et al [10] established an equilibrium phase diagram in an air atmosphere (referred to henceforth as “current phase diagram”) for titanomagnetite slags that conform to a composition: 19.69% SiO_2 , 13.12% Al_2O_3 , 37.19% TiO_2 and 30.00% of various ratios of $CaO+MgO$. This is shown in Figure 1. The composition is typical of a slag produced from dolomite-fluxed smelting of South Africa’s Bushveld Complex titanomagnetite. The primary phases in the phase diagram are perovskite ($CaTiO_3$) and a pseudobrookite solid solution ($MgTi_2O_5-Al_2TiO_5$) at high CaO and MgO , respectively [10]. As a consequence of the current phase diagram having been established in air, the presence of reduced titanium species such as Ti^{3+} reported by Zhao et al [9] are not included in the work of Jochens et al [10]. This is relevant since titanomagnetite slag is produced under very reducing conditions rather than in air.

The focus of the current study was thus to use FactSage thermochemical modelling software[11] to review the equilibrium phase diagram, produced by Jochens et al [10], at a range of PO_2 applicable to fluxed reductive smelting of titanomagnetite. This involved thermodynamic modeling for the development of a private $MgTi_2O_5-Al_2TiO_5$ solid solution database on FactSage, as well as the employment of the FactSage software to build on the work of Jochens et al [10] by implementing applicable PO_2 in the same slag compositions. The scope of work also included the examination of a real plant titanomagnetite slag composition.

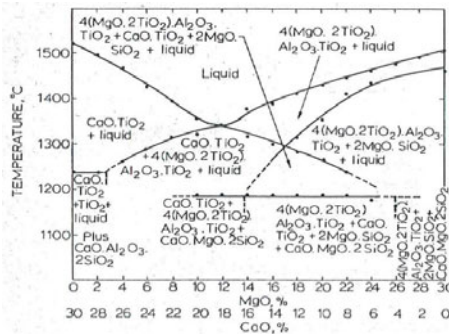


Figure 1: Equilibrium phase diagram in air for the slag system: $TiO_2 = 37.19\%$, $SiO_2 = 19.69\%$, and $Al_2O_3 = 13.12$, at varying proportions of CaO (30-0%) and MgO (0-30%)

Thermodynamic modelling

The latest version of FactSage (7.0) used in the current work contains data for all the essential compounds, including pseudobrookite-type compounds such as karrooite ($MgTi_2O_5$) and tialite (Al_2TiO_5). However, Al_2TiO_5 was not modelled as a component in the custom pseudobrookite solution. A private pseudobrookite solution database for $MgTi_2O_5-Al_2TiO_5$ therefore needed to be developed and subsequently incorporated into FactSage. In this first stage of the multi-stage study, although it is expected to be an important endmember under reducing conditions, Ti_3O_5 was not modelled as a component of the private $MgTi_2O_5-Al_2TiO_5$ solution.

In the development of the private MgTi₂O₅-Al₂TiO₅ solid solution database, regular or non-ideal mixing of the respective pseudobrookite-type compounds was adopted to describe the thermodynamic properties of the solid solution [12]. The MgTi₂O₅-Al₂TiO₅ solid solution is considered to be composed of cationic sublattices A and B, and an anionic (O²⁻) sublattice C. A random distribution of Mg²⁺, Ti⁴⁺ and Al³⁺ in the cationic sublattices at high temperatures is assumed [12-15]. The current modelling of MgTi₂O₅-Al₂TiO₅ followed a successful approach implemented by previous researchers in modelling related pseudobrookite-type solutions [16, 17]. The same model is adopted in which the MgTi₂O₅-Al₂TiO₅ solution is taken as (Mg_{1-x}Al_x³⁺)_A(Ti_{2-x}Al_x³⁺)_BO₅. (1-x) and x represent the overall mole fractions of MgTi₂O₅ and Al₂TiO₅, respectively. The MgTi₂O₅-Al₂TiO₅ solution is assumed to consist of four endmembers, namely: the real component MgTi₂O₅, and three pseudocomponents Al₃O₅⁻, AlTi₂O₅⁺, and MgAl₂O₅²⁻. The molar Gibbs energy of the solution is given by the following expression [16, 17]:

$$G = (1-x) \left(\frac{2-x}{2} \right) G_{MgTi_2O_5}^0 + x \left(\frac{x}{2} \right) G_{Al_3O_5^-}^0 + x \left(\frac{2-x}{2} \right) G_{AlTi_2O_5^+}^0 + (1-x) \left(\frac{x}{2} \right) G_{MgAl_2O_5^{2-}}^0 - T\Delta S^{ideal} + G^E \quad (1)$$

The thermodynamic properties of all compounds listed in Table 1 (from Pelton et al [17] and the FactSage compound database [11]) are considered to be the most reliable estimates of the true data. In equation (2), $G_{MgTi_2O_5}^0$ for the real component is obtained from Table 1.

Table 1. Thermodynamic properties of the reviewed compounds

$$H(Jmol^{-1}) = A + \int_{29815}^T C_p dT \quad S(Jmol^{-1}K^{-1}) = B + \int_{29815}^T (C_p / T) dT$$

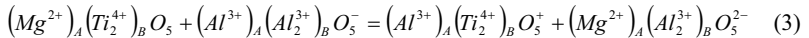
$$C_p(Jmol^{-1}K^{-1}) = a + b(10^{-3})T + c(10^5)T^{-2} + dT^{-1/2} + e(10^8)T^{-3}$$

	A = Enthalpy	B = Entropy	a	b	c	d	e
TiO ₂ (s) (298-2130 K)	-944750	50.460	77.838		-33.678		4.0294
Ti ₂ O ₃ (β) ^a (470-2115 K)	-1519375	80.529	169.96		16.096	-750.22	-15.655
MgO(s) (298-3098 K)	-601500	26.951	61.110		-6.2115	-296.20	0.0584
Al ₂ O ₃ (s) (1200-2327 K)	-1656864	52.300	-787.52	0.06588	2638.2		0.0007
MgTi ₂ O ₅ (s) (298-1930 K)	-2504887	137.34	232.58		-56.608	-755.50	5.8214
Al ₂ TiO ₅ (s) (298-2500 K)	-2577174	128.45	249.29		-48.061	-1350.1	5.1603

The combination of the pseudocomponents is such that the solid solution is always electrically neutral. The pure Al₂TiO₅ compound is thus assumed to be an ideal equimolar mixture of Al₃O₅⁻ and AlTi₂O₅⁺, as is demonstrated by the following expression [16, 17]:

$$G_{Al_2TiO_5}^0 = \frac{1}{2} \left(G_{Al_3O_5^-}^0 + G_{AlTi_2O_5^+}^0 \right) + 2RT \ln \left(\frac{1}{2} \right) \quad (2)$$

The value of $G_{Al_2TiO_5}^0$ is also obtained from Table 1. The Gibbs energies of the components and pseudocomponents of the solid solution are further related by the following exchange reaction:



$$\Delta G_{MgTi_2O_5-Al_2TiO_5} = a' + b'T = G_{AlTi_2O_5}^0 + G_{MgAl_2O_5}^0 - G_{MgTi_2O_5}^0 - G_{Al_2O_3}^0 \quad (4)$$

a' and b' are the adjustable empirical parameters of the model [16]. The standard Gibbs energy of one of the three pseudocomponents may be assigned an arbitrary value, followed by calculation of the other two from equations (2) and (4) and substitution into equation (1). The Gibbs energies of the four endmembers are then expressed in terms of the Gibbs energies of real components $MgTi_2O_5$ and Al_2TiO_5 [16, 17]. In equation (1), an additional excess Gibbs energy term, G^E , was included to account for solution non-ideality and is given as [17]:

$$G^E = c(1-x)(x)(2-x)/2 \quad (5)$$

where c is an empirical parameter. According to this expression, one binary interaction exists between Mg^{2+} and Al^{3+} on the A-sublattice when the B-sublattice is occupied by Ti^{4+} . The thermodynamic model information generated here was incorporated into the FactSage software in order to produce a private $MgTi_2O_5$ - Al_2TiO_5 solution database. To achieve this, the Gibbs energy expressions of the four respective endmembers and the G^E data were entered into the Gibbs energy minimization system (Compound Energy Formalism (CEF)) and the Redlich-Kister polynomial in FactSage to account for the ideal and the excess mixing respectively.

Methodology

The FactSage predictions were completed using the compositions and conditions that were used during the development of the current phase diagram. In this study, the PO_2 was varied between air or 0.21 atm (used by Jochens et al [10]) and 10^{-16} atm, a PO_2 deduced from the Ellingham diagram for the reduction of V_2O_3 to metallic V at a titanomagnetite smelting operational temperature of $1500^\circ C$ (an estimate, as the operational PO_2 is of course not exclusively driven by the PO_2 for V metallization). The modelling was conducted using the FactSage customary search databases, i.e. pure solids database FactPS and oxides database FToxid, as well as the private $MgTi_2O_5$ - Al_2TiO_5 solid solution database developed according to the above procedure. The phase equilibria and thermodynamic data relating to the titanomagnetite slags were plotted using the 'Phase Diagram' and 'Equilib' modules of the FactSage software.

The phase composition of a real plant titanomagnetite slag, viz. slag produced at Evraz Highveld Steel and Vanadium Corporation in South Africa (EHSV), was determined using Zeiss EVO@ MA15 scanning electron microscope (SEM) coupled with a Bruker energy dispersive spectroscopy (EDS). The phase composition of the real slag was then evaluated against the phase equilibria in the current and proposed equilibrium phase diagrams.

Results and discussions

The current equilibrium phase diagram, as well as the FactSage predictions, was selected to cover a range of titanomagnetite slag compositions that are likely to be achieved with fluxing with limestone, dolomite or magnesite. As the first task of the current work, FactSage was used to reproduce the current phase diagram shown in Figure 1 [10]. The simulated phase equilibria (Figure 2) show that the liquidus temperature of the slags change from $1540^\circ C$ at 30% CaO and 0% MgO to $1480^\circ C$ at 0% CaO and 30% MgO, passing through a minimum of $1305^\circ C$ at 20% CaO and 10% MgO. In terms of the liquidus surface, the current and simulated phase diagrams

are fairly comparable. In terms of the phase equilibria, it appears that at high CaO levels there is agreement that $\text{CaO}\cdot\text{TiO}_2$ is the primary phase. However there is a difference at higher MgO levels in that the FactSage simulation suggests that the primary phase is generally a titania spinel, a solid solution of $(\text{Mg})(\text{Al},\text{Ti})_2\text{O}_4$ and $(\text{MgAl}_2\text{O}_4\text{-MgTi}_2\text{O}_4)$, followed by Mg_2SiO_4 (or $\text{MgTi}_2\text{O}_5\text{-Al}_2\text{TiO}_5$ at 3%CaO and 27%MgO and above), with $\text{MgTi}_2\text{O}_5\text{-Al}_2\text{TiO}_5$ forming as a ternary phase. This is in contrast with the current phase diagram, which shows that the primary phase is a pseudobrookite-type solid solution with stoichiometry $4\text{MgTi}_2\text{O}_5\text{-Al}_2\text{TiO}_5$. Thus, with dolomite flux alone, $4\text{MgTi}_2\text{O}_5\text{-Al}_2\text{TiO}_5$ crystallizes as a primary phase, followed by forsterite (Mg_2SiO_4) with no prediction of the formation of the spinel. For the purpose of studying the effect of PO_2 on the titanomagnetite slag liquidus surface and phase equilibria, the simulated phase diagram was accepted as a true reflection of phase equilibria of fluxed titanomagnetite slags in air.

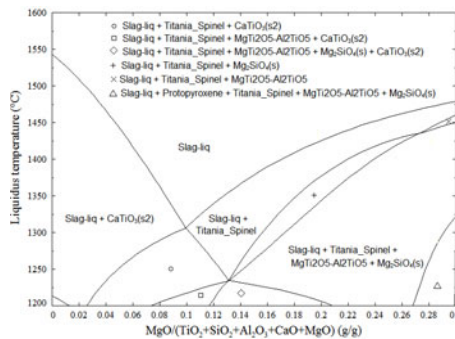


Figure 2: Simulated equilibrium phase diagram at $\text{PO}_2 = 0.21$ atm for the slag system: $\text{TiO}_2 = 37.19\%$, $\text{SiO}_2 = 19.69\%$, and $\text{Al}_2\text{O}_3 = 13.12$, at varying proportions of CaO (30-%0) and MgO (0-30%)

Effect of PO_2 on liquidus surface and phase equilibria

The effect of PO_2 on the liquidus surface of titanomagnetite slags was studied across the compositional range investigated by Jochens et al [10]. Figure 3 shows the liquidus temperatures plotted as a function of CaO/MgO ratio, i.e. MgO where $\text{CaO} = 30\text{-MgO}$, under varying PO_2 concentrations. It appears that the liquidus surface in the $\text{TiO}_2\text{-SiO}_2\text{-Al}_2\text{O}_3\text{-MgO-CaO}$ system with a composition comparable to a fluxed titanomagnetite slag increases with decreasing the PO_2 . This observation concurs with the findings of Nityanand et al [18] who studied the effect of TiO_2 additions and PO_2 on liquidus temperatures of some $\text{CaO-Al}_2\text{O}_3$ melts, and found that at low PO_2 and high TiO_2 contents there is a continuous increase of the liquidus temperatures.

The effect of PO_2 was investigated further on the dolomite-fluxed titanomagnetite slag composition, which falls in the spinel primary phase field and is currently operated by EHSV. Figure 4 shows the changes of liquidus temperatures as a function of PO_2 at fixed composition of the slag. It appears that the spinel generally crystallizes as a primary phase, except at PO_2 of between 10^{-10} and 10^{-15} atm where the primary phase is a pseudobrookite solution.

Oxidized titanium species, i.e. Ti^{4+} , are readily reduced to lower-oxidation-state titanium species when subjected to high temperature reducing conditions applicable to ironmaking processes [9]. The reduction of the Ti^{4+} has the potential of affecting the phase equilibria. In the present work, the effect of PO_2 on the phase equilibria was simulated by monitoring the reduction of titanium species. Figure 5 shows the Ti^{3+}/Ti^{4+} mass fraction ratio, i.e. the measure of the reduction of Ti species in the molten slag, plotted as a function of PO_2 in the range of 0.21 atm to 10^{-16} atm. The results predict an increase in Ti^{3+}/Ti^{4+} mass fraction ratio with decreasing PO_2 . This implies that by decreasing PO_2 to the range applicable in titanomagnetite smelting, the phase equilibria of the slag will diverge from the phase equilibria developed by Jochens et al [10].

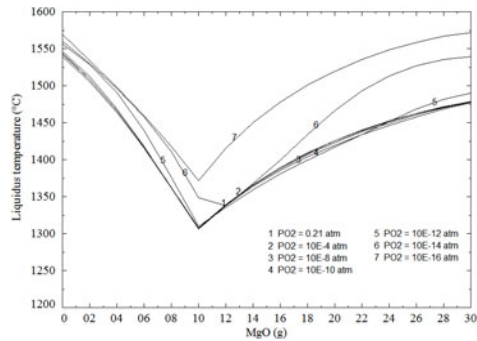


Figure 3: Effect of PO_2 on the liquidus surface of the titanomagnetite slag of the composition: $TiO_2 = 37.19$ g, $SiO_2 = 19.69$ g and $Al_2O_3 = 13.12$ g, with varying proportions of CaO (30-0 g) and MgO (0-30 g)

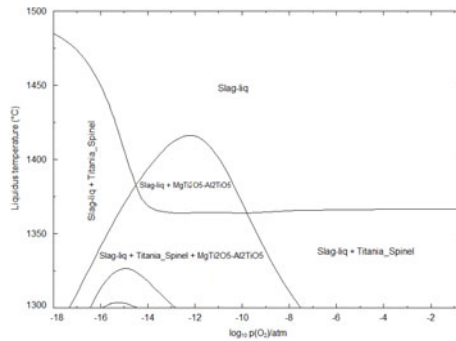


Figure 4: Effect of PO_2 on the liquidus surface and phase equilibria of the (dolomite) fluxed titanomagnetite slag with the composition: $TiO_2 = 37.19$ g, $SiO_2 = 19.69\%$, and $Al_2O_3 = 13.12\%$, $MgO = 14\%$ and $CaO = 16\%$

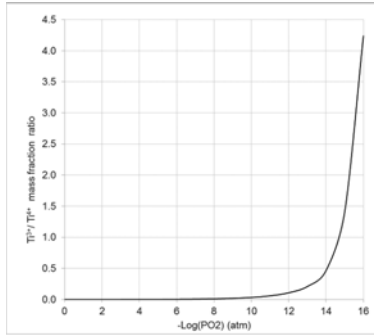


Figure 5: Effect of PO_2 on the titanium reduction in the fluxed titanomagnetite slag with the composition: $\text{TiO}_2 = 37.19$ g, $\text{SiO}_2 = 19.69\%$, and $\text{Al}_2\text{O}_3 = 13.12\%$, $\text{MgO} = 14\%$ and $\text{CaO} = 16\%$

Proposed equilibrium phase diagram for titanomagnetite slags

Figure 6 is proposed as a revised intermediate equilibrium phase diagram for predicting phase compositions of fluxed titanomagnetite slags that conform to a typical composition: 37.19% TiO_2 , 19.69% SiO_2 , 13.12% Al_2O_3 , and 30.00% of various ratios of $\text{CaO}+\text{MgO}$. The proposed equilibrium phase diagram shows that the liquidus surface of titanomagnetite slags varies around an average liquidus temperature of 1570°C in the composition range of 30% CaO and 0% MgO to 0% CaO and 30% MgO , passing through a minimum of 1370°C at 20% CaO and 10% MgO . It appears that at high CaO levels, the primary phase to crystallize is perovskite ($\text{CaO}\cdot\text{TiO}_2$), whereas at high MgO levels, the primary phase is a spinel solid solution, i.e. $(\text{Mg})(\text{Al},\text{Ti})\text{O}_4$. The proposed equilibrium phase diagram does not show the possible competition between primary phases, i.e. $(\text{Mg})(\text{Al},\text{Ti})\text{O}_4$ and $\text{MgTi}_2\text{O}_5\text{-Al}_2\text{TiO}_5$, that was observed previously. Modelling with Ti_3O_5 as a component of $\text{MgTi}_2\text{O}_5\text{-Al}_2\text{TiO}_5$ together with experimentation are required to verify and update the proposed liquidus surface and phase equilibria.

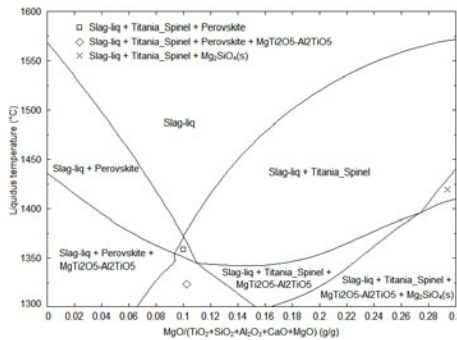


Figure 6: Proposed intermediate equilibrium phase diagram developed at PO_2 of 10^{-16} atm for the fluxed titanomagnetite slags that conform to the reviewed composition

Phase composition of a real plant titanomagnetite slag

The phase composition data of a real plant titanomagnetite slag using the dolomite-fluxed slag produced by EHSV as a case study were required to examine the ability of the proposed phase diagram to predict the phase compositions of fluxed titanomagnetite slags. The phase composition results of the EHSV titanomagnetite slag are shown in Figure 7. The intensities and shapes of the crystals of pseudobrookite ($\text{MgTi}_2\text{O}_5\text{-Al}_2\text{TiO}_5$) and spinel $[(\text{Mg})(\text{Al,Ti})\text{O}_4]$ phases in the real EHSV slag suggest that any of the two phases could have crystallized first directly from liquid phase. From this data, it is still not clear which of the two phases is a primary phase.

The real EHSV titanomagnetite slag is produced under reducing conditions, which are essential for vanadium metallization. According to Ellingham diagrams, the vanadium metallization PO_2 of about 10^{-16} atm at 1500°C is near to the transition for crystallization of the $(\text{Mg})(\text{Al,Ti})\text{O}_4$ and $\text{MgTi}_2\text{O}_5\text{-Al}_2\text{TiO}_5$ primary phases as shown in Figure 4. The EHSV phase composition concurs with the proposed phase diagram in Figure 6 in terms of spinel primary crystallization; however, the phase diagram does not predict the possibility of $\text{MgTi}_2\text{O}_5\text{-Al}_2\text{TiO}_5$ crystallizing first.

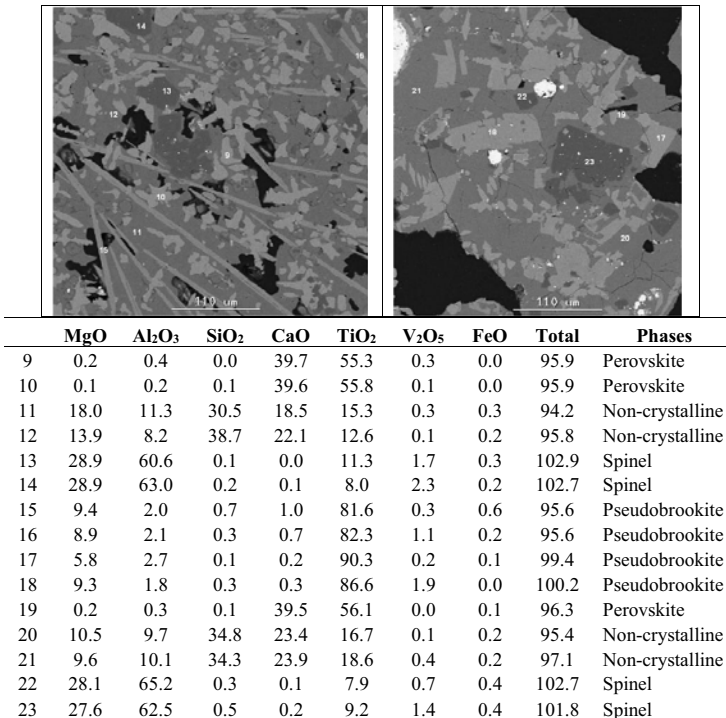


Figure 7: Typical backscattered electron images and EDS analysis results (mass%) of a titanomagnetite slag produced by EHSV

Conclusions

The following conclusions can be made:

- Liquidus temperature and Ti^{3+}/Ti^{4+} mass fraction ratio, i.e. the reduction of Ti species, of compositionally-matching titanomagnetite slags both increase with decreasing PO_2
- At higher MgO concentrations, the spinel generally crystallizes as the primary phase, whereas at PO_2 of between about 10^{-10} and 10^{-15} atm the primary phase may be a pseudobrookite-type solution.
- The proposed intermediate equilibrium phase diagram of titanomagnetite slags with the applicable chemical compositions is as shown in Figure 6.
- When dolomite-fluxed smelting is conducted at PO_2 of about 10^{-16} atm, the primary phase is either a spinel or a pseudobrookite. This scenario was observed experimentally in the phase composition of the titanomagnetite slag produced by EHSV.

More complex modelling with $MgTi_2O_5$, Al_2TiO_5 and Ti_3O_5 endmembers together with experimental measurements are underway to verify and update the intermediate phase diagram generated in the present work. The liquidus surface and phase equilibria at various TiO_2 grades should be investigated further to cover a wide range of titanomagnetite resources.

Acknowledgment

The authors wish to thank the following for their inputs: A.D. Pelton, M.W. Erwee and A. Corfield. Financial support of Mintek is greatly appreciated.

References

1. L. Zhang, L.N. Zhang, M.Y. Wang, T.P. Lou, Z.T. Sui, and J.S. Jang, "Effect of perovskite phase precipitation on viscosity of Ti-bearing blast furnace slag under the dynamic oxidation condition", *Journal of crystalline solids*, 352 (2006), 123-129.
2. B.F. Kelly, "Ironmaking at BHP New Zealand Steel Limited, Glenbrook, New Zealand", *Australasian Mining and Metallurgy, The Sir Maurice Mawby Memorial Volume*, 1 (1993), 348-353.
3. W.S. Steinberg, W. Geysler, and J. Nell, "The history and development of the pyrometallurgical processes at Evraz Highveld Steel and Vanadium", *Southern African Institute of Mining and Metallurgy* (2011), 63-76.
4. D.S. Van Vuuren, and G.T. Tshilombo, "Nitriding of ilmenite and high-grade slag fines", *Journal of the South African Institute of Mining and Metallurgy* (2011), 173-181.
5. J.H. Becker, "Recovery of titanium from titanium bearing materials". *United States Patent 7258847*, (2002), (Accessed on 2015-10-26).
6. O.A. Fouad, "Upgrading of a low – grade titanium slag by sulphation roasting technique to produce synthetic rutile", *Acta Metallurgical Slovaca*, 11(1) (2005), 14-24.
7. L. Zhang, L.N. Zhang, M.Y. Wang, G.Q. Li, and Z.T. Sui, "Recovery of titanium compounds from molten Ti-bearing blast furnace slag under the dynamic oxidation condition", *Minerals Engineering*, 20 (2007), 684-693.

-
8. P.C. Pistorius, "Titania slag smelting and calcination of crude zinc oxide: examples of processing under thermodynamic and kinetic constraints", *Proceedings of the second international slag valorization symposium, Leuven Belgium*, (2011), 263-270.
 9. B. Zhao, E. Jak, and P. Hayes "Phase equilibria studies in the slag system $\text{TiO}_2\text{-SiO}_2\text{-Al}_2\text{O}_3\text{-MgO-CaO}$ at carbon saturation", *Eighth International Conference on Molten Slags, Fluxes and Salts, Santiago, Chile*, (2009), 71-82.
 10. P.R. Jochens, G. Sommer, and D.D. Howat, "Preliminary equilibrium and non-equilibrium phase studies of titaniferous slags", *Journal of The iron and Steel Institute*, 207 (1969) 187-192.
 11. C.W. Bale, P. Chartrand, S.A. Degterov, G. Eriksson, K. Hack, R. Ben Mahfoud, J. Melancon, A.D. Pelton, and S. Petersen, "FactSage thermochemical software and databases", *Chalphanad*, 25 (2) (2002), 189-228.
 12. V. Buscaglia, G. Battilana, and M. Leoni, "Decomposition of $\text{Al}_2\text{TiO}_5\text{-MgTi}_2\text{O}_5$ solid solutions: a thermodynamic approach", *Journal of materials science*, 31 (1996), 5009-5016.
 13. D. Xirouchakis, A. Smirnov, K. Woody, D.H. Lindsley, and D.J. Andersen, "Thermodynamics and stability of pseudobrookite-type MgTi_2O_5 (karrooite)", *American mineralogist*, 87 (2002), 658-667.
 14. A. Navrotsky "Thermodynamics of formation of some compounds with pseudobrookite structure and of the $\text{FeTi}_3\text{O}_5\text{-Ti}_3\text{O}_5$ solid solution series", *American mineralogist*, 60 (1975), 249-256.
 15. T. Epicier, G. Thomas, H. Wohlfromm, and J.S. Moya, "High resolution electron microscopy study of the cationic disorder in Al_2TiO_5 ", *Journal of material research*, 6 (1) (1991), 138-145.
 16. G. Eriksson, A.D. Pelton, E. Woermann, and A. Ender, "Measurement and thermodynamic evaluation of phase equilibria in the Fe-Ti-O system", *Physical chemistry*, 100 (11) (1996), 1839-1849.
 17. A.D. Pelton, G. Eriksson, D. Krajewski, M. Gobbels, and E. Woermann "Measurement and thermodynamic evaluation of phase equilibria in the Mg-Ti-O system", *Zeitschrift fur physikalische chemie*, 207 (1998), 163-180.
 18. H. Nityanand, and H.A. Fine "The effect of TiO_2 additions and oxygen potential on liquidus temperatures of some Ca- Al_2O_3 melts", *Metallurgical and Materials Transactions B*, 14 (4) (1983) 685-692.

**ADVANCES IN MOLTEN
SLAGS, FLUXES, AND SALTS:**

Proceedings of



**Inclusions and
Clean Steelmaking**

EFFECT OF LADLE FURNACE SLAG COMPOSITION IN Si-Mn KILLED STEEL TRANSIENT INCLUSION CHANGES

Stephano P. T. Piva^{1,2}, P. Chris Pistorius¹

¹Center for Iron and Steelmaking Research
Department of Materials Science and Engineering
Carnegie Mellon University, Pittsburgh PA 15213, USA

²CAPES Foundation
Ministry of Education of Brazil
Brasília – DF 70040-020 - Brazil

Keywords: steelmaking, clean steel, non-metallic inclusions, steel-slag reactions, inclusion modification, kinetics

Abstract

This work investigates the effect of slag composition in steel-slag and steel-inclusion reaction kinetics in silicon-manganese killed steels by using FactSage macros to simulate and predict inclusion composition and morphology changes during ladle treatment. Two different conditions of ladle treatment were simulated in regard to alumina and silica content in a basic slag. The simulated changes in inclusion chemical composition and phases, as well as total oxygen and dissolved aluminum in steel were compared. One experimental trial was made to simulate ladle steel-slag and steel-inclusion reactions using an induction furnace to simulate deoxidation and slag addition. The average steel mass transfer coefficient for the experimental setup was calculated from the analyzed aluminium pick-up by steel. Average inclusion composition was measured using Scanning Electron Microscopy and Energy-Dispersive X-Ray Spectroscopy. The chemical compositions of the inclusions and the steel agreed with the FactSage macro simulations.

Introduction

The cleanliness of steel and its control have been the subject of several studies in the last decades, maintaining and developing a close relationship between universities and the steel industry. The presence of non-metallic inclusions in steel, their quantity, chemical composition and morphology are closely related to both upstream and downstream processability and to the properties of the final product [1]. The addition of Si and Mn at de-oxidation has been carried out due to the general benefits of their reaction products to the steelmaking processes: formation of low-temperature melting silicates, which can show high deformability during hot mechanical processing, reduction of nozzle clogging during continuous casting, and less expensive raw materials [2]. However, the formation of high melting point and low deformability inclusions containing calcium, aluminum and magnesium in steel wire rod production has been reported. Secondary refining practices such as desulfurizing require alumina-containing top slags, due to the necessity of high sulfide capacity and compatible liquidus temperature with the temperature

of molten steel. Recent efforts made by van Ende *et al.* [3], Piva *et al.* [4] and Harada *et al.* [5] explore computational thermodynamic software and its ability of executing iterative calculations to predict the kinetics of reactions in steelmaking reactors. These kinetic models typically assume rate-limiting steps such as mass transfer to the steel-slag and steel-inclusion interface. The application of these kinetic models can provide information on the influence of steel and slag chemistry on the controlling mechanisms for inclusion modification, the extent and timescale of these reactions.

The objective of this work is to experimentally assess the rate-limiting steps of the slag-based inclusion modification phenomena in Si-Mn killed steels and the effects of slag and steel chemistry on the chemical composition and morphology evolution of the non-metallic inclusions. Current literature does not present experimental assessment on the possible rate-determining steps for *Al*, *Ca* and *Mg* pick-up in *Si-Mn* killed steels. This work is testing the possibility of steel and slag mass transfer to their common interface as the rate-determining steps for inclusion modification.

Modeling of steel-slag reactions and inclusion composition changes

The kinetic model used to predict the effect of basic slags in Si-Mn killed steels inclusion modification is based on the surface renewal theory [6]. The amount of mass of phase transferred to the interface is given by equation (1), where ΔW_i is the transferred mass phase per timestep, k_i is the mass transfer coefficient, $A_{interface}$ is the interface area between the two liquid phases and ρ_i is the density of the phase.

The viscosity of steelmaking slags is expected to be around two orders of magnitude larger than the viscosity of steel at 1600°C [7], therefore, molecular diffusivity is expected to be two orders of magnitude smaller in slags than in steels. Thus, the slag mass transfer coefficient is expected to be 10 times smaller than the mass transfer coefficient in steel. In the model, the interfacial concentrations of species in steel and slag are calculated by the local equilibrium between the transferred masses of steel and slag (equation (1)). The bulk phases are assumed to be well-mixed, so the solute concentration changes at the interface eventually affect the compositions of the bulk phases (slag and steel).

$$\Delta W_{steel} = k_{steel} A_{interface} \rho_{steel} \Delta t \quad \Delta W_{slag} = k_{slag} A_{interface} \rho_{slag} \Delta t \quad (1)$$

Mass transfer coefficients for these reactions can be obtained in the literature for ladle furnaces, taking in account the stirring power of these systems. The mass transfer coefficient can also be back-calculated from the measured dissolved aluminum pick-up in the steel bath:

$$\frac{d[\%Al]}{dt} = -k_{Al} \frac{A_{interface} \rho_{steel}}{W_{steel}} * ([\%Al] - [\%Al]_{int}) \quad (2)$$

Nucleation and growth of inclusions are not considered as rate-determining steps for slag-based chemical composition modification, so it is assumed that the inclusion population will be in equilibrium with the composition of liquid steel (see Table I).

The inclusion modification by slag in Si-Mn killed steels was predicted using FactSage 6.4 macros, which communicate with Microsoft Excel to run iterative calculations.

- The inputs of the model are:

- Total mass, chemical composition, density and mass transfer coefficients for steel and slag;
 - $k_{steel} = 10k_{slag}$, where mass transfer coefficient for steel is calculated from the experimental results;
 - $\rho_{steel} = 6954 \text{ kg/m}^3$, $\rho_{slag} = 2500 \text{ kg/m}^3$
- Inclusion content and composition are given by equilibration in bulk steel;
- The reacting masses of slag and steel at the interface are controlled by mass transfer, given by equation (1).
- It is assumed that the bulk steel and slag phases are well-mixed, so the transferred elements from steel-slag reactions are added to the bulk phases for the next iteration of the model.
- Inclusion flotation is simulated in the steel-slag equilibration step, since the inclusions contained in the reacting steel fraction are transferred to slag.

The schematics of the model algorithm is shown in Fig. 1.

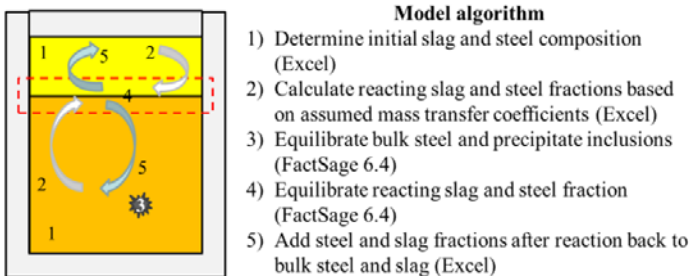


Figure 1 - Schematics of FactSage-Excel kinetic model algorithm

Results and discussions

The utilization of high alumina, basic slags is expected to promote aluminum pick-up in steel for the conditions simulated. The simulation results are shown in Figs. 2 and 3. It is expected from the simulations that increasing aluminum concentrations in the steel will severely reduce manganese silicate inclusions, forming solid phases such as corundum and magnesium spinel. At longer times, a lower rate of consumption of dissolved silicon by aluminum pick-up results in pick-up of magnesium and calcium from slag, causing the formation of Ca and Mg-containing higher melting temperature phases such as CM_2A_8 and CA_2 . The overall composition shown in Fig. 3 shows the rapid reduction of Mn and Si from inclusions and the increase in Al, Mg and Ca concentrations in the inclusions. As the steel composition approaches equilibrium with slag, the inclusion composition is expected to asymptotically approach the equilibrium slag composition. In contrast to the utilization of high alumina slags, it is shown that less basic, low alumina slags maintain the inclusions liquid for the whole simulated processing time. Aluminum, calcium, and magnesium pick-up is much less than for high alumina slags, reflecting the higher silica activity

(hence giving less-reducing conditions for a given silicon concentration in the steel). The presence of silicon and manganese in the inclusion seem to persist throughout the majority of the process, and it is expected that the inclusions will retain low melting points.

The decrease in inclusion content follows the same exponential decay as the total oxygen, which is attributed to flotation. Therefore, the oxygen decay is expected to follow similar kinetics to aluminum pick-up or desulfurization. The predicted decrease in total oxygen is shown in fig. 6. As expected, equilibrium aluminum content is higher for high alumina slags. The kinetics of oxygen removal do not change for the different cases. The time constant to approach 62.8% of equilibrium oxygen removal is approximately 500 s.

Although the total oxygen is predicted to be similar through ladle processing for both cases, the higher silica activity in the less basic (high-alumina) slag contributes to both less aluminum pickup and less pick-up of Mg and Ca by the steel. The alumina content in the silicates will depend on the extent of aluminum pick-up during processing. The predicted evolution of aluminum in molten steel is shown in Fig. 7.

Table Ia. Main parameters used in kinetic model: initial metal composition, contact area and mass transfer coefficients

T (K)	[%Mn]	[%Si]	[O] _{total} (ppm)	[S] (ppm)	Interfacial area [m ²]	Steel mass transfer coefficient [m/s]	Slag mass transfer coefficient [m/s]
1873	1.25	0.25	100	20	7.07	5.61×10^{-3} [8]	5.61×10^{-4}

Table Ib. Ladle processing conditions considered in the simulations

Mass of steel (t)	Mass of slag (t)	Argon flowrate (Nl min ⁻¹ t ⁻¹)	Ladle diameter (m)	Processing time (s)
150	1.7	14	3	3600

Table Ic. Initial slag composition (mass percentages)

Slag	(%CaO)	(%SiO ₂)	(%Al ₂ O ₃)	(%MgO)
High alumina	47	8	35	10
Low alumina	47	35	8	10

Laboratory experiments were performed, for comparison with model results [4]. In the experiments, radio-frequency induction heating (maximum power 10 kW) was used to melt 0.62 kg electrolytic iron in an MgO crucible (inner diameter 58 mm). The MgO crucible was contained within a graphite crucible which served as susceptor (heating element). After melting the iron, the melt contained approximately 400 ppm (by mass) of oxygen. The melt was deoxidized with silicomanganese and medium-carbon ferromanganese, to yield a Mn/Si mass ratio in the liquid metal of 5, with 0.25%wtSi. 182 grams of slag with similar composition as shown at Table Ib for high alumina was added after deoxidation. Steel samples were taken using a quartz tube of 4mm ID repeatedly within 5 minutes from each other. The inclusions in the sample were then analyzed using ASPEx Explorer Automated Feature Analysis using 10keV of beam energy, 48% spot size and 16mm working distance. Aluminum content was analyzed using ICP-OES. The results are briefly summarized in Figs. 8 and 9. The mass transfer coefficient for

steel was calculated from the analyzed aluminum with equation 3, then FactSage simulations using the calculated mass transfer coefficient were made. The simulation results agree with measured inclusion compositions, indicating that the assumption of steel-to-slag mass transfer limited inclusion modification. The approximate time constant for aluminum is calculated to be around 3400 s, which shows that the stirring conditions are much slower compared to a real ladle.

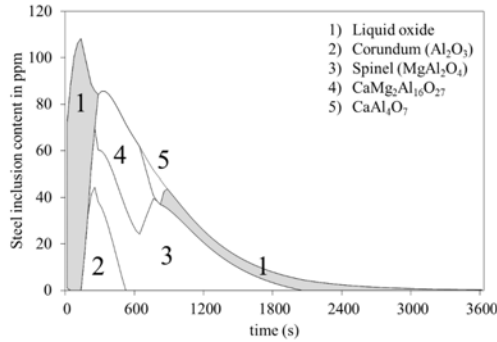


Figure 2 – FactSage macro simulation results showing transient inclusion phases for Si-Mn killed steels with basic, high alumina slags

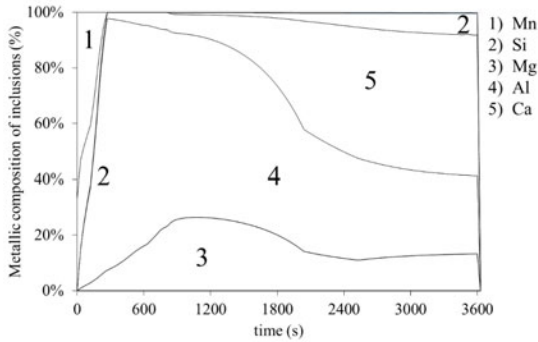


Figure 3 – Overall normalized cation composition of transient inclusions shown in Fig. 2

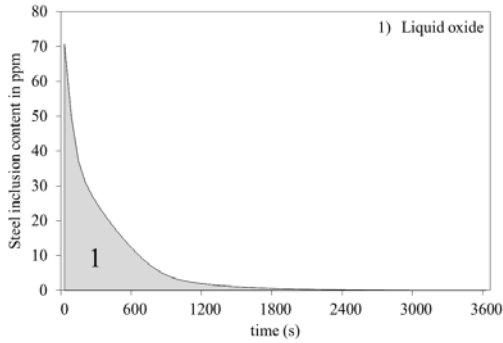


Figure 4 – FactSage macro simulation results showing transient inclusion phases for Si-Mn killed steels with less basic, low alumina slags

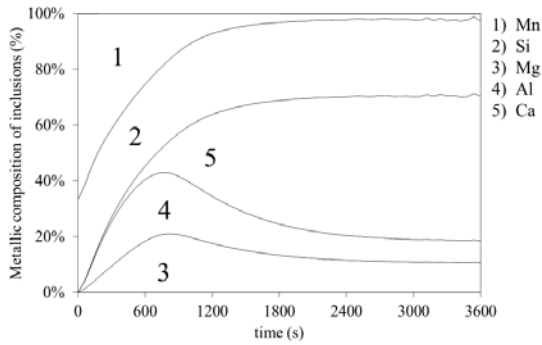


Figure 5 - Overall normalized cation composition of transient inclusions shown in Fig. 4

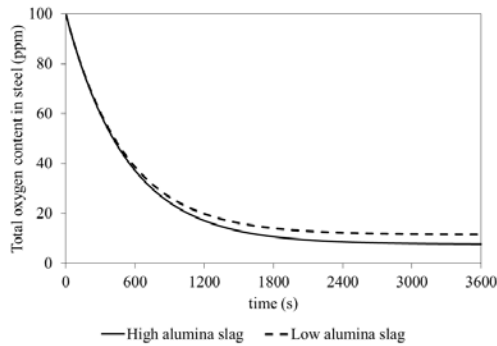


Figure 6 – Predicted evolution of total oxygen content in steel for both high and low alumina slags

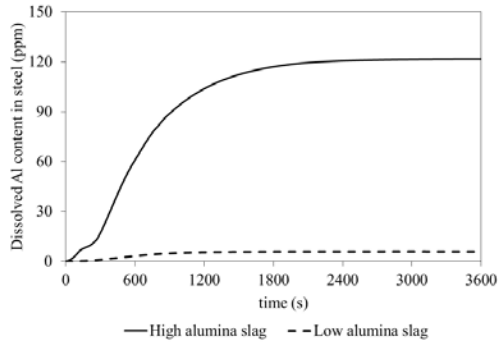


Figure 7 – Predicted evolution of dissolved aluminum in steel for both high and low alumina slags

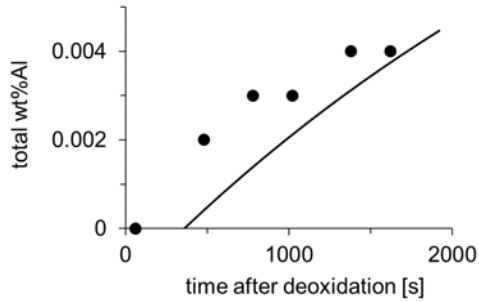


Figure 8. Measured aluminum content of steel from laboratory experiments (data points), compared with modeled behavior for $k_{steel} = 8 \times 10^{-6}$ m/s [4]

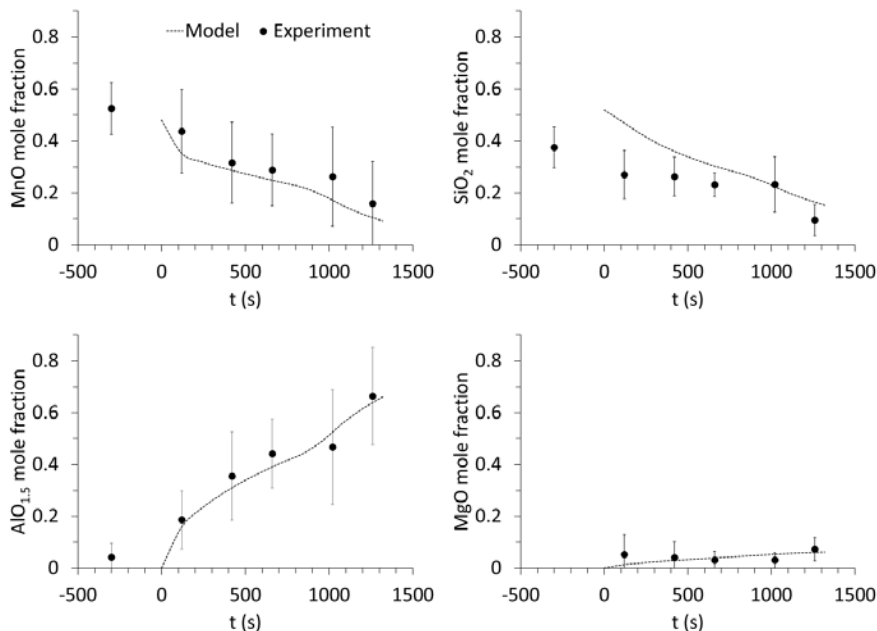


Figure 9. Change in inclusion composition with time: measured (data points) and modeled (broken lines). Error bars show sample standard deviation. Zero time is when the slag was added [4].

Conclusions

FactSage calculations show that steel-slag reactions can further modify inclusions and cause the formation of undesired solid phases inside the steel. The slag composition will change the transient inclusion phases. The pick-up of calcium and magnesium responds to changes in oxygen activity, caused by the rate of aluminum pick-up as well as changes in the Si-SiO₂ buffer.

Laboratory measurements and FactSage macro modeling show substantial changes in inclusion composition, from liquid manganese silicates to partially solid alumina-containing inclusions, as a result of steel-slag and steel-inclusions reactions.

Acknowledgement

Support of this work by the industrial members of the Center for Iron and Steelmaking Research is gratefully acknowledged.

The authors acknowledge use of the Materials Characterization Facility at Carnegie Mellon University supported by grant MCF-677785.

Financial support of Stephano P.T. Piva by CAPES under the process BEX 13379/13-5 – Doutorado Pleno/Ciência sem Fronteiras is gratefully acknowledged.

References

1. P. Kaushik, J. Lehmann, and M. Nadif, *Metall. Mater. Trans. B Process Metall. Mater. Process. Sci.* **43**, 710 (2012).
2. G. Bernard, P. V. Riboud, and G. Urbain, *Rev. Métallurgie - CIT* **78**, 421 (1981).
3. M. A. Van Ende, Y. M. Kim, M. K. Cho, J. Choi, and I. H. Jung, *Metall. Mater. Trans. B Process Metall. Mater. Process. Sci.* **42**, 477 (2011).
4. S.P.T. Piva, D. Kumar and P.C. Pistorius, in *Thermodynamic Applications, Optimizations, and Simulations in High-Temperature Processes: An EPD Symposium in Honor of Christopher W. Bale's 70th Birthday*, TMS 2016. Submitted to *Metallurgical and Materials Transactions B*.
5. A. Harada, N. Maruoka, H. Shibata, and S. Kitamura, *ISIJ Int.* **53**, 2110 (2013).
6. N. J. Themelis, *Transport and Chemical Rate Phenomena* (Gordon and Breach, 1995).
7. R. I. L. Guthrie, *Engineering in Process Metallurgy*, Second Edition (Oxford University Press, New York, 1992).
8. A. Ishii, M. Tate, T. Ebisawa, and K. Kawakami, *Iron Steelmak.* **35** (1983).

REDUCTION OF SLAG AND REFRACTORIES BY ALUMINIUM IN STEEL AND INCLUSION MODIFICATION

Haoyuan Mu¹, Bryan A. Webler¹, Richard J. Fruehan¹

¹Center for Iron and Steelmaking Research, Materials Science and Engineering Department, Carnegie Mellon University; 5000 Forbes Ave; Pittsburgh, PA, 15213, USA

Keywords: slag reduction, inclusion formation, mass transfer

Abstract

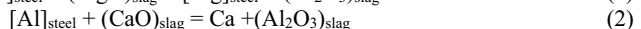
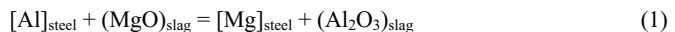
As Al contents in Advanced High Strength Steels (AHSS) increase, the possibility exists that Al will reduce CaO and MgO from slag or refractory. Excessive Ca or Mg transfer would form solid inclusions that can cause nozzle clogging. This study documents experimental observations of reduction of CaO and MgO from slag and refractory in steels containing 2, 0.5 and 0.1 wt% Al at 1600°C or 1700°C. Mg transfer was observed in all experiments, while Ca transfer was only noticed under certain conditions and less intense when comparing with Mg transfer. These observations were consistent with considering the rate of reaction to be controlled by Mg and Ca transfer from slag/crucible to liquid steel.

Introduction

Careful control of alloying elements plays a significant role in achieving multi-phase microstructure in steels. For example, the content of alloying elements of Al and/or Si in Transformation Induced Plasticity (TRIP) steels usually levels up to 2%. Si is added to prevent the formation of cementite, and Al is to substitute Si to improve the adhesion between steel surface and coating alloy.^[1] Highly alloyed production of AHSS in existing manufacturing lines demands fundamental knowledge of the reactions of the reactive alloying elements in the molten state and the products they form such as the non-metallic inclusions. This is particularly the case for high Al TRIP steels because of the high driving force for reduction of oxides in the slag and refractories at liquid steel refining temperatures.

In industry, unintended changes on inclusion chemistries have been observed in steels where Al was added only for deoxidation and have been proved as a result of CaO and MgO reduction by Al in steel. CaO reduction from slag and further formation of solid calcium aluminate inclusions have been reported by Story^[2] and Kaushik^[3], prospectively. In Pretorius's work, Al₂O₃ inclusions were modified to spinel (MgAl₂O₄) inclusions after MgO reduction^[4] or to liquid Al₂O₃-CaO-MgO phases if there were both CaO reduction and MgO reduction^[5].

Pickup of Mg and Ca and subsequent inclusion modification has also been studied on the laboratory scale.^[6,7] In both cases Al reduced Mg and Ca by the reactions



However, both industry and laboratory scale studies were conducted only in steels at a relatively low Al level (approx. 0.04 wt%). With the increasing application of high Al steels, this work

focuses on the reduction of slag and refractories by high Al steel (0.1wt% to 2wt%). Inclusion modification after the reduction is discussed from both thermodynamic and kinetic perspectives.

Experimental Approach

Laboratory experiments were conducted in which as steel samples were reacted with CaO, MgO double saturated slags and MgO crucibles in an induction furnace. Figure 1 shows a schematic of the experimental setup. The steel sample was contained in an MgO crucible, which in turn was surrounded by a graphite crucible. The graphite crucible acted as a susceptor to heat up and melt the steel sample. Two layers of Al₂O₃ insulating sheets were laid on MgO crucible top to reduce radiation loss and therefore controlled temperature gradient in liquid steel to about 25°C. The reaction chamber that contained the magnesia and graphite crucibles was a fused quartz tube with Al₂O₃ insulating paper wrapped inside. The guidance tube was designed for adding slag and taking samples. 3mm diameter quartz tubes were used to take liquid steel samples through the guidance tube. The temperature was measured by a R-type thermocouple from the top.

Master alloys described in Table I were previously examined and found to contain predominately Al₂O₃ inclusions. 500g high Al steel sample mixed by these two master alloys was prepared for each experiment. Pure Al₂O₃ and CaO powder were mixed at the ratio of CaO/Al₂O₃=1 and then pre-melted to serve as master slag. Pure CaO powder and MgO powder were later added into master slag to make slag CaO and MgO saturated. Table II lists the initial slag composition and Al content in steel for all experiments. Expt.1, Expt.2 and Expt.3 were conducted to compare the effect of Al content on MgO and CaO reduction, while Expt.4 were only associated with Expt.1 to investigate the effect of reaction temperature.

Steel was heated up by about 10°C/min under high purity argon flow at the rate of 300mL/min. When reaching 1600°C, alloy was held at this temperature for 30min for homogenization before taking the first steel samples. Slag was then added onto the surface of liquid alloy through guidance tube. Samples were taken at various points by inserting a quartz tube into the steel and evacuating with a pipette. Each steel sample was quenched in cold water after taking out from induction furnace. The sampling and slag addition plan for each experiment is giving in Figure 2.

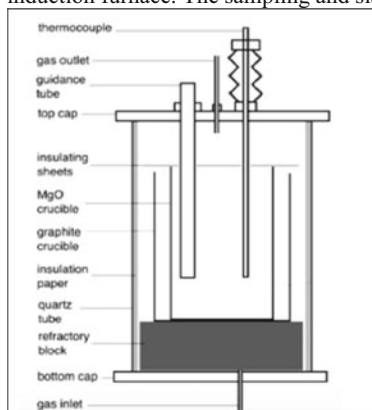


Figure 1. Schematic of the setup

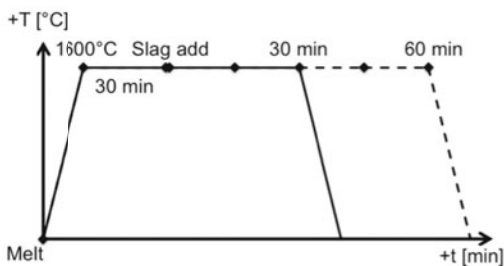


Figure 2. The temperature-time profile

Steel samples taken during experiments were then analyzed under scanning electron microscopy (SEM)/ energy-dispersive X-ray spectrometry (EDS), manually and automatically. Proportional inclusion ternary diagrams were plotted in mole fraction based on inclusion area. Total Al and Mg contents in steel for select experiments were measured by inductively coupled plasma mass spectrometry (ICP-MS). Select slag compositions were measured at the end of experiments by x-ray fluorescence (XRF) spectroscopy.

Table I. Master alloys served to make melts with different Al content

No.	Composition (in ppm unless otherwise stated)				Inclusions		
	C	Al (wt%)	S	Ca	Majority type	Number density (#/mm ²)	Area density (μm ² /mm ²)
Alloy 1	4	0.019	10	<1	Al ₂ O ₃	56	65
Alloy 2	8	2.027	10	<10	Al ₂ O ₃	28	115

Table II. Reaction temperature, slag composition and Al composition design of each experiment

No.	Reaction Temperature	Slag Composition	Designed Al Composition
Expt. 1	1600°C	CaO: 51wt% Al ₂ O ₃ : 39wt% MgO: 10wt%	2 wt%
Expt. 2			0.5 wt%
Expt. 3			0.1 wt%
Expt. 4	1700°C		2 wt%

Experimental Results

Figure 3 illustrates the change of steel composition with reaction time in Expt.1, Expt.2 and Expt.4. For all these experiments, Al level decreased continuously, while Mg content in steel increased. Total Ca was also measured but no detectable changes were observed.

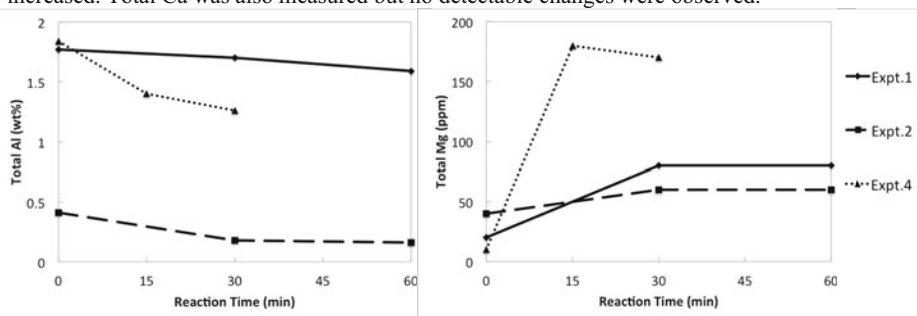


Figure 3. Steel composition in Expt.1, Expt.2 and Expt.4

The evolution of inclusion chemistry during the experiments is shown in Figure 4 to demonstrate the changes due to reduction of MgO from both slags and crucibles and the reduction of CaO from slags. In all experiments, inclusion chemistries showed to be stable after 30min reaction and therefore only samples in the first 30min were presented. It was observed in

every experiment that Mg modified initial Al_2O_3 inclusions into either $\text{MgO}\cdot\text{Al}_2\text{O}_3$ (spinel) or pure MgO , depending on steel chemistries. However, Ca transfer was only detected in 2wt%Al experiments, where complex $\text{CaO}\text{-Al}_2\text{O}_3\text{-MgO}$ inclusions were observed.

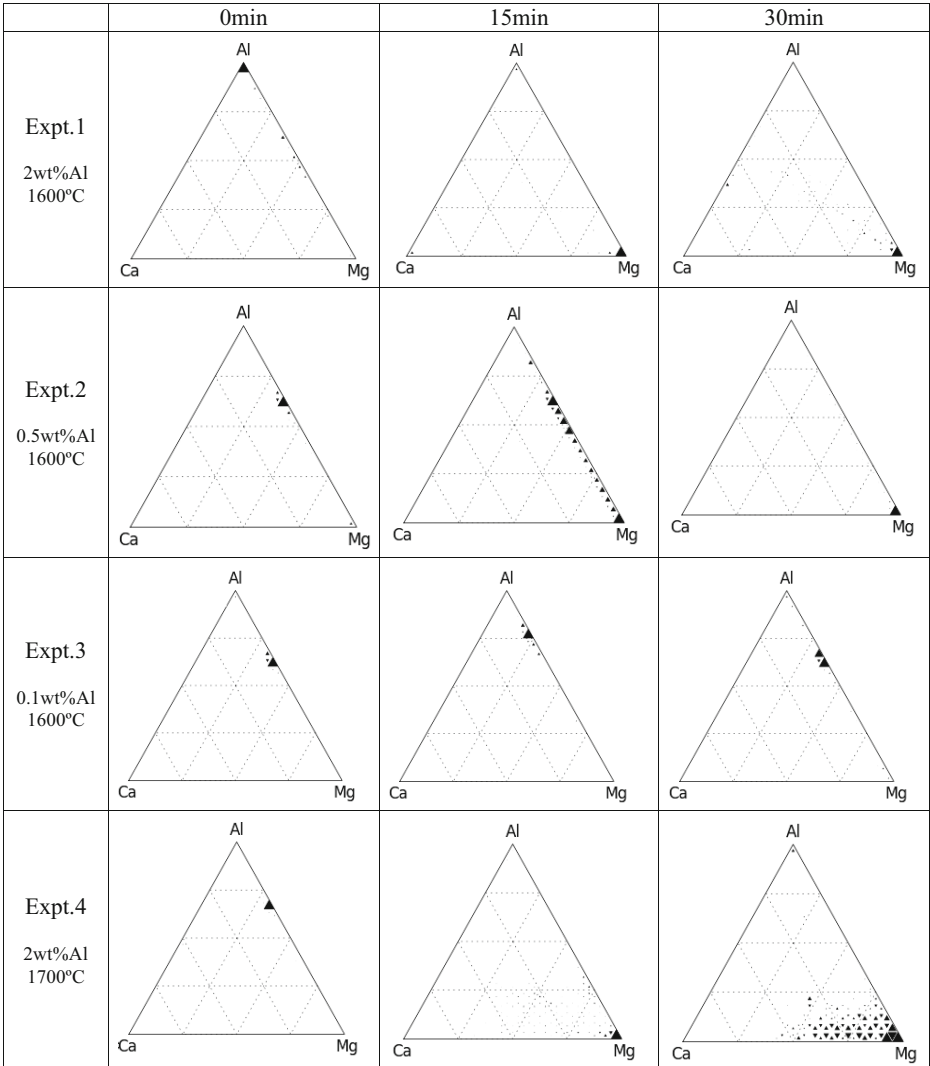


Figure 4. Inclusion chemistries in each experiment

Discussion

Inclusions in all experiments were changed by reactions between Al in the steel and oxides in the slag and crucible. Despite occasional reoxidation during sampling, the changes of inclusion chemistries and the general increase of total Mg content in steel indicates that there was some extent of slag and refractory reduction in every experiment. The reduction behaviors were highly related to Al contents in steel and reaction temperatures, while the whole process was consistent with rate control by mass transfer of elements in liquid steel at either the slag/steel or crucible/steel interface.

Effect of Al Content in Steel

Expt.1 to Expt.3 were three contrast experiments with different Al contents in steel. Upon addition of Mg-saturated slag to the 2 wt% Al alloy in Expt.1. A sufficient amount of Mg was transferred to stabilize MgO inclusions after 15 minutes. Ca appeared in the inclusions as well after 30 minutes steel-slag reaction. Figure 3 shows that decreased Al content corresponded to increased Mg in the metal during Expt.1. These observations were consistent with reduction of MgO from the slag and crucible along with CaO according to (1) and (2).

At an Al content of 0.5 wt% (Expt.2), Mg was found in inclusions but no Ca was detected. 15min after slag addition, Mg content in spinel inclusions increased as the triangles represent inclusions moved closer to Mg corner in the corresponding ternary diagram in Figure 4. After 30 minutes sufficient Mg was transferred to form MgO inclusions. Comparing with 2wt% Al experiment (Expt. 1), the gentler increase of Mg content in inclusions implies a delay of MgO reduction and Mg transfer in steel.

When content dropped to 0.1wt% (Expt.3), only spinel inclusions were observed and no Ca was detected. Reoxidation appeared to occur during slag addition, leading to an increase of Al content in inclusions in the 15min sample. But after 30min reaction, the spinel stoichiometry returned and was stable around afterward.

In short, less reduction of CaO and MgO occurred as Al content in steel decreased. CaO reduction by Al in steel was only observed as high as 2wt% Al level. The thermodynamic and kinetic analysis will be presented in following discussions.

Effect of Reaction Temperature

In steelmaking practice, the temperature at steel-slag interface can be much higher than 1600°C due to electric arcs among heating electrodes. Stronger reduction behaviors of both CaO and MgO were expected under locally higher temperature. Therefore, two experiments (Expt.1 and Expt.4) were designed with 2wt%Al steel in different temperatures to study the effect of reaction temperature on these reduction behaviors.

By comparing inclusion chemistry diagrams in Figure 4, Mg transfer appears similar in Expt.1 and Expt.4, as initial inclusions were all transferred into MgO inclusions in 15min after slag addition. The Al fade and the corresponding increase of Mg content in steel was much higher when reaction temperature increased from 1600°C to 1700°C. Figure 3 illustrates that there was more significant reduction of slags and crucibles in Expt.4 compared with Expt.1.

The increase of reaction temperature also showed faster Ca transfer from slag to steel. There were some amount of Ca-related inclusions detected as soon as 15min after slag addition in

Expt.4, while such inclusions was only observed in the 30min samples in Expt.1. After 30min reaction the average inclusion Ca content was higher than in Expt. 1. To summarize, both CaO and MgO reduction occurred more rapidly and to a greater extent at higher temperatures.

Kinetic Discussion

The above analyses indicate MgO and CaO reduction were enhanced with the increase of Al content and temperature. CaO reduction was only detected at 2 wt% Al while MgO reduction was observed at all Al levels. In addition, the Al and Mg concentration in steel showed large changes in the first 30min after slag addition but little change thereafter in Figure 3. All these suggest the rate of reduction is determined by mass transfer in the steel. Assuming the bulk steel is well-mixed, there are three mass transfer processes to be considered – from the steel/slag interface, from the steel/crucible interface, and at the steel/inclusion interfaces. The mass transfer fluxes for each step can be given by following equations.

$$\text{From steel/slag interface to bulk steel:} \quad J_i = k_i A_i (\%i^{int} - \%i^{bulk}) \quad (3)$$

$$\text{From bulk steel to steel/inclusion interface:} \quad J_i = k_i A_i (\%i^{bulk} - \%i^{int}) \quad (4)$$

In above equations, i represents either Ca or Mg; k_i is a mass transfer coefficient; A_i is an area for mass transfer; and $\pm(\%i^{int} - \%i^{bulk})$ represents the mass transfer driving force. The interface concentration of an element can be calculated from steel/slag equilibrium. However, the bulk concentration is a dynamic variable that controlled by both step (1) and step (2). Therefore, $k_i A_i$ is an easier and more rational variable to study the mass transfer of the whole process.

For mass transfer at steel-slag/crucible interface, area for Ca transfer is only steel-slag interface while area for Mg transfer is the total of steel-slag interface and steel-crucible interface. The values of k_{Mg} and k_{Ca} are expected to be similar under the same reaction temperature. There was no induction stirring in present experiments due to the usage of graphite crucibles. Natural convection currents were minimized since temperature gradient in induction furnace was controlled within 25°C by applying insulating sheets. The mass transfer coefficient for a slag/steel reaction was measured by a separate desulfurization experiment in the same setup. Desulfurization rates were controlled by mass transfer in the steel to the slag/steel interface, consistent with other work.^[8] The rate constant was found to be $8 \times 10^{-5} m/s$. This value was assumed to hold for both Mg and Ca at the slag/steel and steel/crucible interfaces.

In all experiments, the observed inclusions were generally around the size of 1 μm diameter. Assuming inclusions as spheres, the total inclusion surface area can be thereby estimated from the inclusion volume fraction (assumed equal to the measured area fraction) of each experiment, which was at least 30 ppm. Due to the lack of intentional stirring, the liquid steel flow can be assumed in the Stokes regime and the mass transfer coefficient is $k = D/R$, according to Brian and Hales work.^[9] D is the diffusion coefficient of the mass transfer element. The diffusivity of Si in liquid iron are approximately $4 \times 10^{-9} m^2/s$.^[10] Assuming this is similar to those Mg and Ca, k_{Mg} and k_{Ca} for mass transfer at steel-inclusion interface can be estimated as $8 \times 10^{-3} m/s$.

The kA values of each case are then calculated and listed in Table III. The value of kA for mass transfer to the inclusions is approximately two orders of magnitude larger than that of steel-slag/crucible interface for Mg and approximately three orders of magnitude larger for Ca (they are different because Ca is transferred only from the slag while Mg is transferred from the slag and the crucible). In other words, it is expected that Ca and Mg transfer from slag and crucible to bulk steel controls the overall mass transfer behavior.

Table III. Comparison of (kA) values at steel-slag/crucible interface and steel-inclusion interface

steel-slag & steel-crucible interfaces			
	k (m/s)	A (m ²)	kA (m ³ /s)
Mg	8×10^{-5}	1×10^{-2}	8×10^{-7}
Ca	8×10^{-5}	2×10^{-3}	1.6×10^{-7}
steel-inclusion interface			
	k (m/s)	A (m ²)	kA (m ³ /s)
Mg	8×10^{-3}	1.3×10^{-2}	1×10^{-4}
Ca	8×10^{-3}	1.3×10^{-2}	1×10^{-4}

Conclusions

The behavior of CaO and MgO reduction and subsequent inclusion changes were studied in Fe containing 0.1, 0.5, and 2 wt% Al. Laboratory experiments were conducted to evaluate the effects of Al content in metal and reaction temperature. The thermodynamics and kinetics of the reduction and inclusion formation were discussed and the following conclusions were obtained:

1. MgO and CaO reduction occurred in a 2 wt% Al alloy and inclusions evolved from Al₂O₃ to MgO to (Ca, Mg, Al)-containing inclusions. MgO reduction also occurred at 0.5 wt% to 0.1 wt% Al, but no Ca reduction was observed in either of these cases.
2. At 2 wt% Al and 1700°C, more Ca and Mg was transferred and rates were faster
3. By comparing the characterized kA value in mass transfer equations, Ca and Mg transfer from slag/crucible to bulk steel is the most likely controlling step for the overall slag/crucible reduction and inclusion formation behaviors.

References

- [1] T. L. Baum, R. J. Fruehan, and S. Sridhar, Metallurgical and Materials Transactions B, 2007, Vol 38B, pp. 287-297.
- [2] S. Story and R. Asfahani, Iron & Steel Technology, October 2013, pp. 86-99.
- [3] P. Kaushik and H. Yin, AIST Transactions, 2012, Vol.9, No.6, pp. 165-183.
- [4] E. Pretorius, H. Oltmann and T. Cash, Iron and Steel Technology, July 2010, pp. 31-44.
- [5] E. B. Pretorius, H. G. Oltmann, et al., AISTech Conference Proceedings (2013), pp.993-1026.
- [6] Z. Deng and M. Zhu, ISIJ International, Vol. 53 (2013), No. 3, pp. 450–458.
- [7] A. Harada, G. Miyano, N. Maruoka et al., Vol. 54 (2014), No. 10, pp. 2230–2238.
- [8] D. Roy, P.C. Pistorius, and R.J. Fruehan, Metall. & Mater. Trans. B, 2013, 44B, p. 1095-1104.
- [9] P.L.T.Brian, and H.B.Hales: AIChE J., 1969, Vol.15, No.3, pp.419-425.
- [10] R. J. Fruehan: The Making, Shaping and Treating of Steel (11th edition), pp.77, The AISE Steel Foundation, 1998.

REACTIVITY OF SELECTED OXIDE INCLUSIONS WITH CaO-Al₂O₃-SiO₂-(MgO) SLAGS

B. J. Monaghan¹, H. Abdeyazdan¹, R. J. Longbottom¹, N. Dogan², M. A. Rhamdhani³,
and M. W. Chapman⁴

¹ School of Mechanical, Materials and Mechatronics Engineering, University of Wollongong, Wollongong, NSW 2522, Australia

² McMaster University, Hamilton, ON, L8S 4L7, Canada

³ Swinburne University of Technology, Hawthorn, VIC 3122, Australia

⁴ BlueScope Ltd, Port Kembla, NSW 2505, Australia

Keywords: Slag wetting, spinel, calcium aluminate, alumina

Abstract

Inclusion content minimization is key in the production high quality steels. This is typically achieved through approaches ranging from preventing inclusion formation via process control to optimising process conditions to remove any inclusions that form. Inclusion removal from steel is generally through reaction with a slag. The inclusion transfers across the steel-slag interface to dissolve in the slag. This transfer process is primarily a dynamic interfacial tension/wetting driven process. In this study, the dynamic wetting (θ) of a range of slags in the CaO-Al₂O₃-SiO₂-(MgO) system on alumina (Al₂O₃), magnesia spinel (MgAl₂O₄) and calcium aluminate (CaO·Al₂O₃) substrates has been assessed using the sessile drop technique. The reactivity of selected inclusion phases was studied by evaluating the wetting results and characterizing the microstructure of the slag-inclusion interface. It was found the dependence of θ value on the composition was lower for the basic ladle type slags than the acid tundish type slags.

Introduction

The least understood component of inclusion removal in steelmaking is inclusion reactivity/separation with the slag [1]. The inclusion has to travel across the steel-slag interface to wet the slag. This is favored when contact angle (θ) for the steel-inclusion is greater than 90° (non-wetting) and when this contact angle is greater than θ for the inclusion-slag. While it is understood that inclusion-slag interfacial tension/wetting plays a critical role in inclusion removal, there are only limited wetting data for slags on typical inclusion phase types in literature. Choi and Lee [2] have developed a dynamic wetting model that has shown promise in predicting/representing wetting behavior of slag on alumina (Al₂O₃). The current authors have used/extended this approach and shown that it works well for basic type slags not only on alumina but also on magnesia spinel (MgAl₂O₄) and calcium aluminate (CaO·Al₂O₃) substrates [3,4].

In this study, the dynamic wetting (θ) of a range of slags in the CaO-Al₂O₃-SiO₂-(MgO) system on alumina (Al₂O₃), magnesia spinel (MgAl₂O₄) and calcium aluminate (CaO.Al₂O₃) substrates are presented and discussed with specific reference to their slag-substrate interactions. Specifically the focus of this paper is the microstructural characterization of the slag-substrate reactions. The phases chosen for study represent inclusions found in steel [5].

Experimental

A sessile drop furnace was used to characterize the wetting results with time at a temperature of 1500°C. The experiments were carried out under flowing argon and images of the slag spreading on the substrate were captured by a Sony 6.1 MP video camera. This is a standard technique and much of the detail of this technique has been presented elsewhere [4].

Video stills captured from the recordings were analyzed assuming a spherical cap and θ established from Equation 1.

$$\theta = 2 \times \tan^{-1} \frac{h}{a} \quad (1)$$

The symbols are as defined in the schematic shown in Figure 1 for a sphere of radius R.

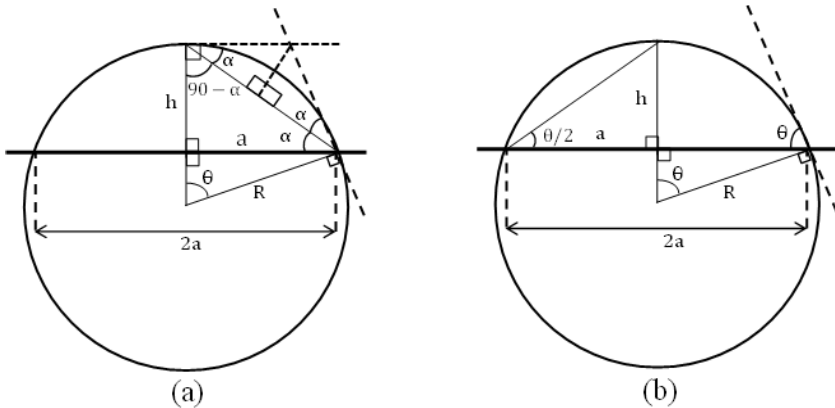


Figure 1 (a) and (b) showing a spherical cap schematic used in sessile drop analysis.

The slags used were prepared by mixing and fusing laboratory grade oxides CaO (CaCO₃), Al₂O₃, SiO₂ and MgO (where applicable) of appropriate proportions. The compositions are given in Table I. These were confirmed by XRF analysis. The alumina substrates were supplied by Rojan Advanced Ceramics, Western Australia. The MgAl₂O₄ and CaO.Al₂O₃ powders were prepared from high purity laboratory grade MgO, Al₂O₃ and CaCO₃ (> 99%) starting materials by reaction sintering and their phases confirmed by XRD. Full details of the materials preparation are given elsewhere [3,4].

Table I. Composition of slags used in mass%

Slag	Slag composition in mass%			Slag	Slag composition in mass%			
	CaO	Al ₂ O ₃	SiO ₂		CaO	Al ₂ O ₃	SiO ₂	MgO
T1	25.5	17.4	57.1	L1	41.8	42.7	9.2	6.3
T2	32.7	19.2	48.1	L2	46.3	37.1	9.8	6.8
T3	40.3	19.0	40.7	L3	50.9	32.9	9.5	6.7

Post experiment the slag-substrate couples were prepared for electro-optical analysis using standard techniques for scanning electron microscopy (SEM) and energy dispersive spectroscopy (EDS).

Results/Discussion

The θ was found to be a function of time, slag composition and substrate. Generally the θ of the slag-substrate couples decreased rapidly in the first 10s tending to a plateau value at ~30 to 70s for slag types on different substrates. The results for $\theta_{t=0}$ (initial) and θ_{plateau} (plateau) are given in Table II.

Table II. The initial and plateau θ of the T-type and L-type slags on different substrates at 1500°C

Slag	Substrate	$\theta_{t=0}$ (°)	θ_{plateau} (°)	Substrate	$\theta_{t=0}$ (°)	θ_{plateau} (°)
T1	Alumina	54.9	25.4	Calcium aluminate	32.2	10.4
T2		49.3	22.1		20.4	7.6
T3		46.0	20.2		19.6	5.6
L1		38.5	21.1		25.0	11.2
L2		30.2	21.8		23.0	10.2
L3		22.0	19.1		20.5	11.9
T1	Spinel	39.9	15.5			
T2		29.6	14.2			
T3		20.8	14.7			
L1		34.5	18.1			
L2		26.7	17.9			
L3		24.4	18.7			

The $\theta_{t=0}$ and θ_{plateau} values for alumina substrates are much higher than spinel and calcium aluminates regardless of slag types. The change of θ with time, slag and substrate may be a result of slag-substrate reactivity, the mechanism of slag-substrate reaction (kinetics), momentum/dampening effects resulting from slag addition to the substrate and perhaps liquid slag structure changing with changing slag composition as a result of reactivity. What is focused on in this paper is characterization of the reaction of the slag with the substrates.

A key challenge is condensing the information so that it is suitable for a conference publication but including enough information to ensure that the interface is fully characterized and representative of what is found. Selected analysis (detailed below) is given for the L3 slag on each substrate.

- A low magnification ($\times 100$) SEM micrograph from the center of the interface
- EDS mapping analysis of the elements contained from the $\times 100$ SEM image
- EDS area analysis of the phases identified in the $\times 100$ SEM micrograph
- A high magnification ($\times 500$) SEM image of the slag penetration/reaction layer
- EDS spot/area analysis of the phases identified in the penetration/reaction layer

Micrographs and EDS maps encompassing the above bullet points are given in Figures 2 to 4. EDS analysis for spot and area analysis shown on the micrographs are given in Table III.

Table III. EDS analysis of the phases identified in the L3-type slag-substrate interfaces

Substrate	Phase analyzed, analysis number and relevant figure		Composition in mass %			
			CaO	Al ₂ O ₃	SiO ₂	MgO
	L3 initial slag composition		50.9	32.9	9.5	6.7
Alumina	Crystalline slag (7), Figure 2		43.3	43.4	7.9	5.4
	Original substrate (8), Figure 2		0.0	93.3	4.1	2.6
	Penetration layer (9), Figure 2		9.3	84.9	3.2	2.6
Spinel	Crystalline slag (18), Figure 3		43.7	42.4	6.6	7.3
	Original substrate (19), Figure 3		0.5	72.3	2.8	24.4
	Penetration layer	Grey phase (20), Figure 3	0.2	69.9	2.4	27.5
		White phase (21), Figure 3	41.3	45.9	7.3	5.5
Calcium aluminate	Slag-substrate reaction area (32), Figure 4		44.3	47.2	4.0	4.5
	Original substrate (33), Figure 4		39.5	56.8	2.1	1.6
	Slag near interface	Grey phase (34), Figure 4	38.9	57.4	1.9	1.7
		Black phase (35), Figure 4	61.0	29.2	6.5	3.3
		Light phase (36), Figure 4	46.3	43.3	4.3	6.1

The area of analysis of the L3 slag-substrate micrographs is indicated in a schematic at the top of each micrograph.

Given the space limitations it is not possible to deal with all the slag-reaction couples using the same micrograph approach. To in part address this point a summary of interface reaction characteristics for the specific slag-substrate systems is given in Table IV

The characterization data (SEM, EDS, slag penetration/reaction of substrate, given in Figures 2 to 4 and Table III are indicative of a reactive system. This reaction likely explains much of the change of $\theta_{t=0}$ and $\theta_{plateau}$ shown in Table II.

From Table IV it can be seen that the reaction of the slag with the three substrate systems have resulted in significantly different slag-substrate interfaces. Examples of the different behaviours described in Table IV can be seen in Figures 2 to 4. Figure 2 shows a typical thin penetration layer; Figure 3 shows typical penetration of slag into the pores and grain boundaries; and Figure

4 shows reaction between the slag and substrate. The nature/specifics of the reaction interface for the systems studied with respect to substrates are briefly expanded on for all slag-substrate systems studied.

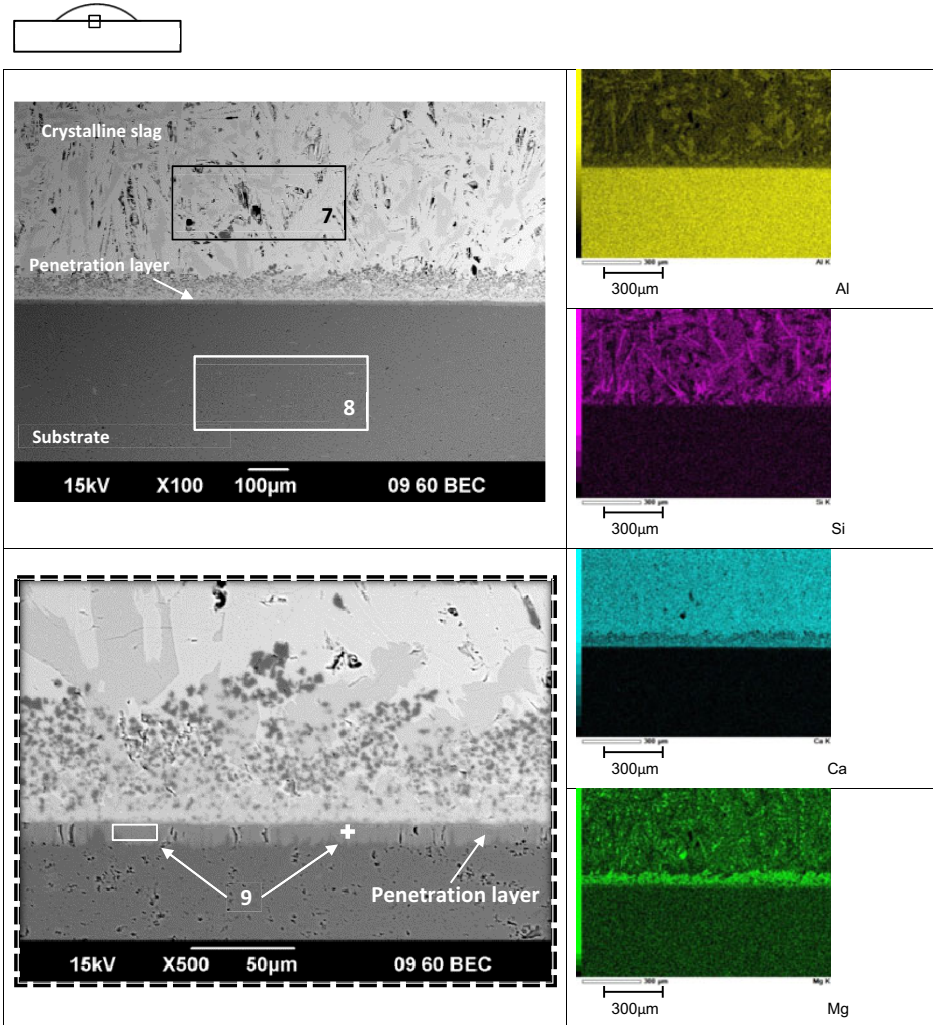


Figure 2. SEM backscattered images and EDS mapping from the center of the slag-substrate interface and EDS area/spot analysis of the identified phase(s) in the penetration layer of slag L3 on alumina substrate.

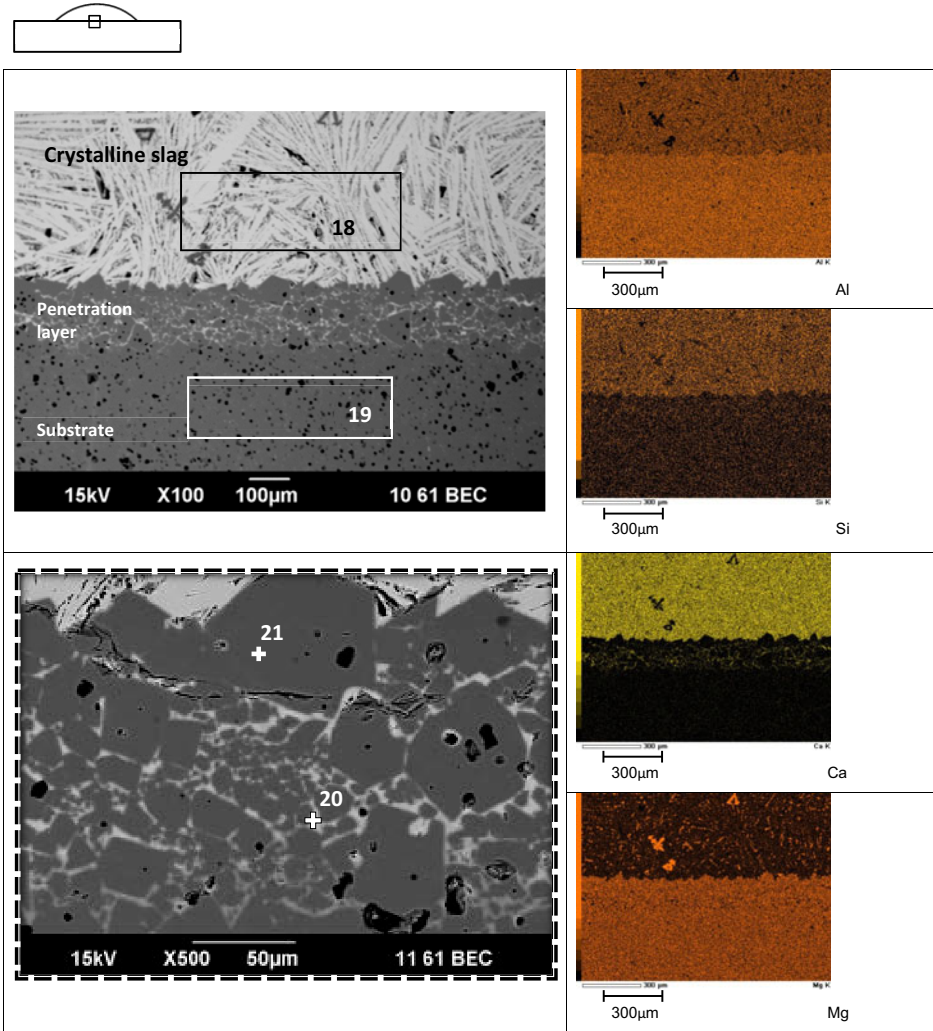


Figure 3. SEM backscattered images and EDS mapping from the center of the slag-substrate interface and EDS spot analysis of the identified phase(s) in the penetration layer of slag L3 on spinel substrate.

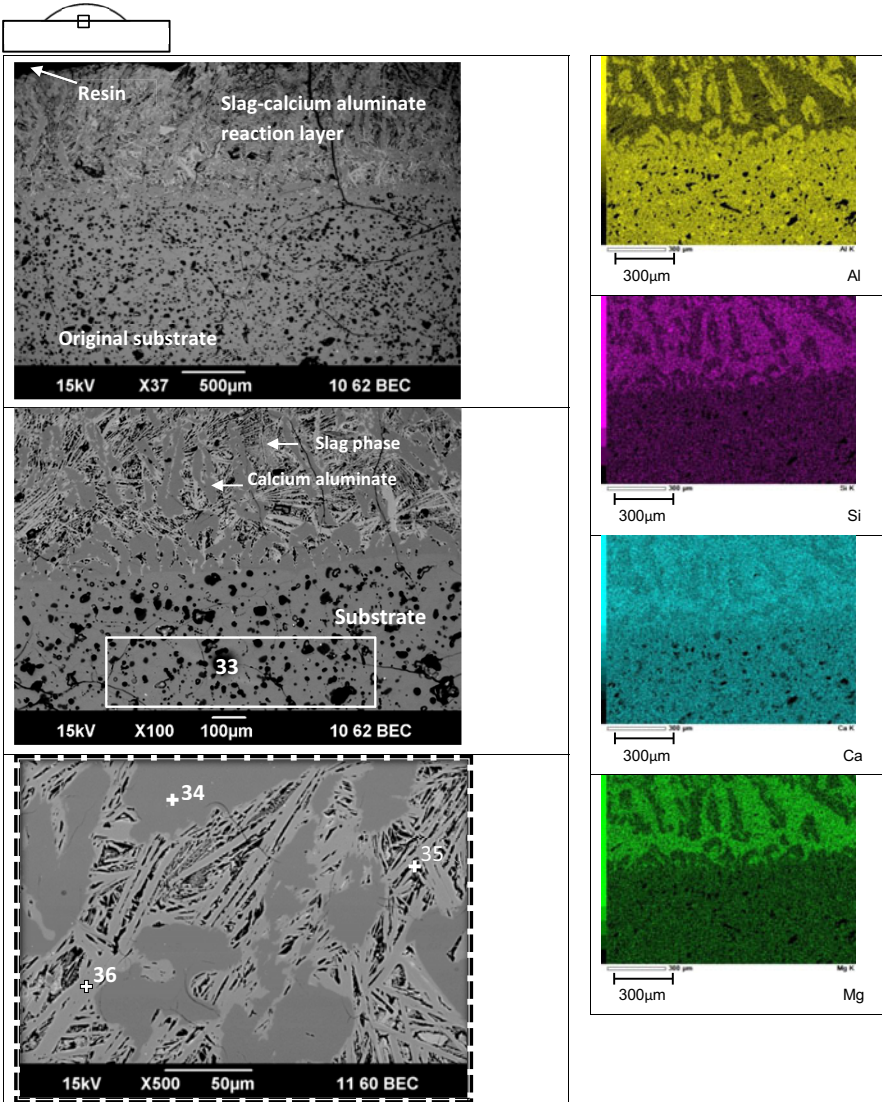


Figure 4. SEM backscattered images and EDS mapping from the center of the slag-substrate interface and EDS spot analysis of the identified phase(s) in the reaction area of slag L3 on calcium aluminate substrate.

Table IV. Summary of the nature of the reaction interface in the wetting systems studied

Slag	Substrate type		
	Alumina	Spinel	Calcium aluminate
L1	Slag penetration of substrate	Slag penetration of the substrate with no discernible product or intermediate phases	No obvious slag penetration of the substrate though substrate, surface appears to be breaking up
L2			
L3			
T1	Largely unmodified substrate surface with no discernible slag penetration of the substrate		
T2	Surface roughening of the substrate and slag penetration of the substrate, no discernible other phases formed in the penetration layer		
T3	Surface roughening of the substrate and slag penetration of the substrate, evidence of reaction products in the penetration layer		
			Difficult to assess due to experimental issues there may be slag penetration of the substrate but it was difficult to establish the original slag-substrate interface to assess.

Alumina

The characteristics of the reaction interface for the alumina substrate was dependent on slag type (L or T) and composition. For the L-type slags there was a thin penetration layer (~25µm thin) at slag-substrate interface. EDS analysis of this layer indicates the composition though primarily that of the substrate is slightly enriched by the slag oxide components. For T-type slags the interface appears largely unmodified by T1, but using T2 and T3 slags appear to cause roughening of the substrate. There is also evidence of slag penetration/reaction of the substrate for T2 and T3.

Spinel

For the spinel substrates there was a slag penetration/reaction layer has formed at the interface for both the L-type and T-type slags. The penetration is into the pores and along the grain boundaries of the substrate.

Calcium Aluminate

For the calcium aluminate substrate there was no simple reaction or obvious penetration layer similar to that of found for alumina and spinel. There was significant reaction of both slag types

(T and L) and the calcium aluminate substrate. For the L-type slags it would appear that there are pieces of the substrate breaking off into the slag. Experimental difficulties with T-type slags on the calcium aluminate substrate precluded meaningful comment.

The loss of slag volume associated with penetration or reaction (and its time dependence) of the slag-substrate systems would impact on the measured contact angle. This would be the case even if the penetrating slag was not reacting with the substrate. There are other reactions taking place though as the slag is not just penetrating the substrate (see Tables III showing EDS analysis of the penetrating slag and reacted substrates).

Though not discussed here the EDS data given in Table III and that measured but not shown for the other systems is broadly consistent with thermodynamic analysis of the slag-substrate systems [3].

Conclusions

The dynamic wetting (θ) of a range of slags in the CaO-Al₂O₃-SiO₂-(MgO) system on alumina (Al₂O₃), magnesia spinel (MgAl₂O₄) and calcium aluminate (CaO·Al₂O₃) substrates has been measured and the initial θ and plateau wetting values reported. It was found that over time that the wetting value decreased to a plateau value and that this was lower for the basic ladle type slags than the acid tundish type slags.

Detailed slag-substrate micrographic characterization was undertaken of the slag-substrate interface. All systems showed evidence of reaction/penetration of the slag into and with the substrate. This reaction is thought to be at least part explain why the θ value decreased with time. The different reaction behaviour observed for the different substrates may help explain the differences in θ between them, with the greater penetration/reaction corresponding with lower θ .

References

-
1. S. Seetharaman (Eds): *Fundamentals of Metallurgy*, (Cambridge: England, Woodhead Publishing in Materials, 2008), 23-25.
 2. J.Y. Choi and H.G. Lee: "Wetting of Solid Al₂O₃ with Molten CaO-Al₂O₃-SiO₂" *ISIJ international*, 43, (2003), 1348-55.
 3. H. Abdeyazdan, N. Dogan, M.A. Rhamdhani, M. Chapman, M., B.J. Monaghan, B. J., "Dynamic Wetting of CaO-Al₂O₃-SiO₂-MgO Liquid Oxide on MgAl₂O₄ Spinel," *Metallurgical and Materials Transactions B*, 46, (2015), 208-219.
 4. B.J. Monaghan, H. Abdeyazdan, N., Dogan, M.A., Rhamdhani, R.L. Longbottom, M. Chapman, "Effect of Slag Composition on Wettability of Oxide Inclusions," *ISIJ international*, 55, (2015), 1834-1840.
 5. B. Deo and R. Boom: *Fundamentals of Steelmaking Metallurgy*, (New York:USA, Prentice Hall International, 1993), 254-69.

A STUDY ON CALCIUM TRANSFER FROM SLAG TO STEEL AND ITS EFFECT ON MODIFICATION OF ALUMINA AND SPINEL INCLUSIONS

Deepoo Kumar, P. Chris Pistorius

Center for Iron and Steelmaking Research (CISR)
Materials Science and Engineering Department
Carnegie Mellon University
5000 Forbes Avenue, Wean Hall 3325, Pittsburgh, PA 15213

Keywords: Slag, Calcium transfer, Inclusion, Alumina, Spinel, Zirconia

Abstract

Aluminum deoxidized steel tends to form solid inclusions (alumina, spinel, partially modified calcium aluminates). These solid inclusions are known to present challenges during casting, cause slivers during mechanical working and act as crack initiation sites for mechanical failure. Calcium injection practice has been used by the industry to transform these solid inclusions into liquid inclusions for several decades. There has been a significant amount of study to understand the mechanism of calcium modification of alumina/spinel inclusions. However, there has been little attempt to understand calcium transfer from slag to steel to inclusions that may modify alumina inclusions. In this study, laboratory deoxidation experiments were conducted using an induction furnace, physically simulating a ladle furnace; samples were taken during these experiments to study the extent of calcium transfer through inclusion analysis. This study shows that in the presence of silicon, there can be significant amount of calcium transfer from slag. Also, as the rate of calcium transfer from slag is limited by mass transfer in steel and slag, it is difficult to modify a large concentration of inclusions. However, an appreciable extent of calcium transfer was found in the case of lower concentration of inclusions (less than 150 ppm area fraction).

Introduction

Aluminum killed steels have a tendency to undergo nozzle clogging during casting due to formation of solid inclusions like alumina, spinel or solid forms of calcium aluminates. The clogging results due to tendency of inclusions to deposit on nozzle walls followed by sintering as explained by Singh [1]. Calcium treatment is a common practice to modify solid alumina inclusions that was started in the late 1960s [2]. Earlier, it was thought that magnesium containing inclusions would not modify with calcium addition [3] [4]. However, recent studies show that modification of spinel inclusions into liquid Ca-Al-Mg-O inclusions can be achieved. Pretorius *et al.* [5] found that calcium modification of spinel inclusion is rather easier for LCAK steels with very low oxygen content. However, Yang *et al.* [6] have concluded from thermodynamic analysis of industrial data that spinel inclusions can be modified into liquid inclusions only if dissolved calcium content in alloy steel is at least 1 ppm.

Early studies on the modification mechanism of alumina inclusions were reported by Hilty *et al.* in 1975 [7], [8]. In 1980, they reported that alumina inclusions follow Ca-modification path as alumina \rightarrow $CA_6 \rightarrow CA_2 \rightarrow CA \rightarrow$ Liquid calcium aluminate (C: CaO, A: Al_2O_3) [4]. This mechanism is now well accepted in the literature. Ye *et al.* [9] and Han *et al.* [10] concluded that the rate of calcium modification is quite high for smaller inclusions ($<10 \mu m$) at the steelmaking temperature. Recent studies on calcium modification of alumina inclusions have been focused on the transfer of calcium to inclusions [11] [12]. Verma *et al.* [11][12] and Holappa *et al.* [13] pointed out the effect of sulfur content in steel on the calcium transfer mechanism from liquid steel to inclusions. Verma *et al.* [12] concluded that CaS and CaO form as intermediate products during calcium transfer to inclusions for high and low sulfur content respectively. However, CaO was not observed in the case of experiments with low sulfur due to very high rate of modification of smaller inclusions ($<10 \mu m$) [10]. In contrast to alumina inclusions, spinel inclusions start forming liquid phase immediately upon CaO pick-up [5]. Verma *et al.* [14] also concluded that modification of spinel inclusions occur via partial reduction of MgO followed by partial reduction of Al_2O_3 with formation of CaS as intermediate product. These intermediate modification products are summarized in the Figure 1. It should be noted that reduction of MgO from spinel inclusions increases the dissolved Mg concentration in steel that may cause re-appearance of spinels upon subsequent re-oxidation [6].

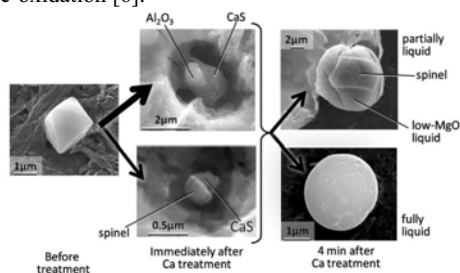


**Figure 1 Spinel modification route after calcium treatment in Al-killed steels [14].
With permission of Springer.**

Due to relatively high activity of CaO in typical secondary steelmaking slag and high activity of aluminum in steel, aluminum can reduce CaO at the steel-slag interface. This would result into dissolved calcium in steel [6]. The dissolved calcium may in turn react with alumina or spinel inclusions resulting in partial modification of these solid inclusions [5] [6]. Although calcium transfer from slag to steel to inclusions has been indirectly reported in the literature [5], [7], [15]; there has not been any systematic study to quantify the extent and rate of calcium transfer from slag to inclusions via steel. The present study focuses on developing a better understanding of mass transfer of calcium to inclusions. As part of this study, experiments were conducted in a laboratory induction furnace to estimate the extent of calcium transfer from slag to steel to inclusions.

Methodology

Experiments were conducted in an induction furnace to study the extent of calcium transfer from slag to steel. Calcium enrichment of alumina or spinel inclusions was used as an indication of this calcium transfer. The schematic of the setup is shown in Figure 2. The experiments were

conducted in an argon atmosphere in MgO crucibles (61 mm diameter) or yttria stabilized zirconia crucibles (31 mm diameter). 600 g (in MgO crucible) or 100g (in ZrO₂ crucible) of electrolytic iron containing 350 ppm of oxygen and 7 ppm of sulfur was melted and then deoxidized by adding aluminum at ~1600°C. Two compositions of slag were used for these experiments as shown in Table 1. The experiments are described in Table 2. Samples were taken at required intervals using fused-quartz tubes of 4 mm inner diameter and a suction tube. Tubes were flushed with argon before sampling to avoid any reoxidation due to entrapped air in the tube.

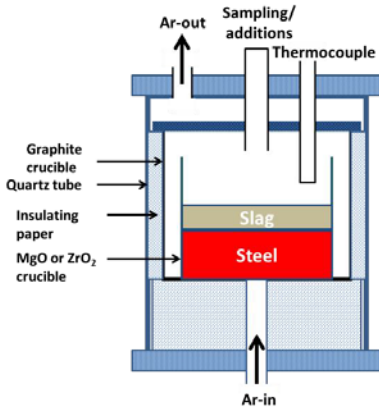


Figure 2 Schematic of induction furnace setup

Table 1 Slag compositions used for experiments

	Slag composition (wt%)			
	CaO	Al ₂ O ₃	MgO	SiO ₂
Slag-1	47.50	36.40	7.10	9.10
Slag-2	50.30	42.30	7.40	0

Table 2 Experiment summary

Exp. #	Crucible	Additions
1	MgO	Al (0.3%, t=0), slag-1 (200 g, t=11 min)
2	MgO	Al (0.3%, t=0), Fe-Si (1% Si), slag-1 (200 g, t=6min)
3	ZrO ₂	Al (0.15%, t=0), slag-2 (15 g, t=0)

Samples taken during these experiments were used to measure kinetic changes in inclusion composition and chemical composition of steel. Total oxygen concentration in steel was analyzed using LECO and Si, Al, Ca, and Mg in steel were analyzed using ICP at a third party laboratory. Compositions and concentrations of inclusions were measured automatically on polished sample sections using automatic feature analysis and energy-dispersive X-ray microanalysis available in an FEI/ASPEX scanning electron microscope. These analyses were conducted at 10 kV with 16-17 mm working distance and 40% spot size. Specific inclusions of interest were also analyzed at higher resolution in field-emission gun scanning electron microscopes. Some samples were electrochemically etched to reveal three-dimensional morphology of inclusions, especially clusters, using the method suggested by Tan & Pistorius [16].

Results and Discussion

In the first experiment, steel was deoxidized by adding 0.3 wt% of aluminum. Dissolved aluminum in steel reduced silica in slag which resulted into silicon pick-up in steel, as shown in Figure 3. A kinetic model was developed using the macro-feature available in the 'Equilib' module of FactSage 6.4 [17]. The mass transfer coefficient of steel (k_{steel}) to the slag-steel interface is the only unknown parameter in such a model assuming that k_{steel} is 10 times larger than k_{slag} . The experimental data (Al and Si content in steel with time) was used to find the product $k_{steel} \times A$ (A : slag-steel interfacial area) for mass transfer in steel, as the value of $k_{steel} \times A$ for which the

calculated composition fitted the experimental results. It should be noted here that it is not possible to measure k_{steel} independently because steel-slag interface may not be planar [18].

The fitted value of $k_{steel} \times A$ was equal to $1.3 \times 10^{-7} \text{ m}^3/\text{s}$ which is of the same order of the observed value in the past for a similar setup [19]. It is important to note here that the kinetic model over-predicts the concentration of dissolved calcium (3.0 ppm) in steel. This problem arises due to large uncertainty regarding calcium solubility in liquid steel as shown in Figure 4.

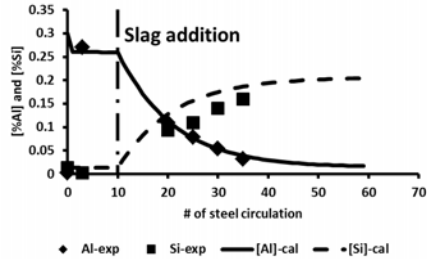


Figure 3 Experimental and calculated variation in total aluminum and silicon contents of steel

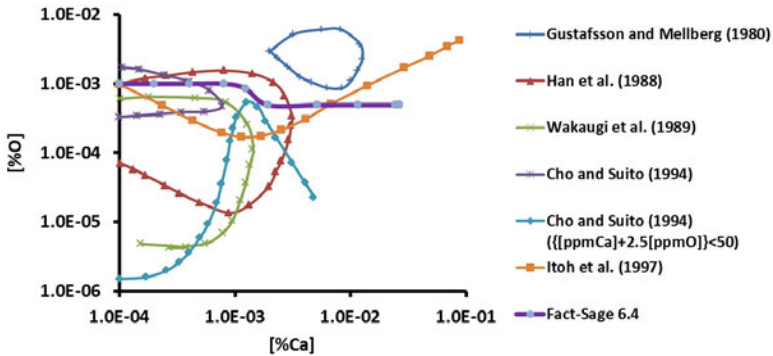


Figure 4 Reported relationships between dissolved oxygen and dissolved calcium in liquid steel at 1873 K. Redrawn after reference [20]

Inclusion analysis results of three samples taken during experiment 1 (in MgO crucible) are shown in Figure 5 (a, b and c) using proportionate symbol plots. In these plots, the area of each small dark triangle is proportional to the area fraction of inclusions present in sample with that composition. The results clearly show increasing magnesium content in inclusions with time. The sample taken before slag addition also shows significant magnesium content in inclusions (see Figure 5 (a)) which indicates magnesium pick-up from crucible as well. In samples taken at longer times, the average mole fraction of MgO in inclusions (~0.60) was higher than typical spinel phase. This large MgO concentration (higher than stoichiometric spinel) indicates partial transformation of spinel inclusions into MgO (resulting from Mg pick-up in steel from both slag and the crucible). The inclusion size and concentration did not change much among these samples. The average size of the inclusions was in the range of 3-4 μm and the corresponding oxygen content in inclusions was in the range of 110-160 ppm by mass.

It should be noted here that the induction furnace used for these experiments did not have any forced mechanical stirring mechanism like Ar-purging. In the absence of forced stirring, flotation

of inclusions, especially alumina clusters is expected to be slower due to their higher effective density [21]. These clusters also transform into spinel clusters as shown in Figure 6.

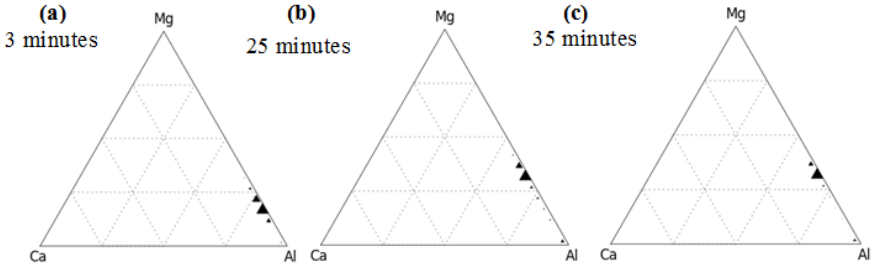


Figure 5 Inclusion composition in samples taken during Experiment 1 (steel with 0.3% Al initially; MgO crucible; Slag 1). Plotted as normalized mass fractions.

Calcium transfer from slag to inclusions via steel was not observed from the inclusion analyses of samples from experiment 1. It appears unlikely that there was no calcium transfer from slag to steel, as calcium containing inclusions have been reported in the past in steel samples taken before calcium treatment [5], [6], [15]. Possible reasons for the lack of measurable calcium transfer are a low rate of transfer (due to the low equilibrium calcium concentration and the large steel circulation time = ~30minutes as can be seen from Figure 3) and a relatively large concentration of inclusions in the steel.

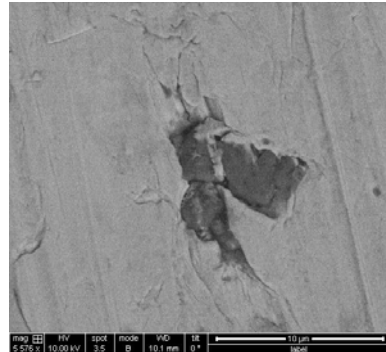


Figure 6 Alumina cluster transforming into spinel observed in the sample taken at $t=20$ min

Silicon (in steel) is known to increase calcium retention during calcium injection [22]. 1% Si was added after aluminum addition during experiment 2 to test the effect of silicon on calcium pick up from slag. Figure 7 (a, b and c) shows changes in inclusion composition with time. In this experiment, aluminum and slag were added at $t=0$ and $t=6$ minutes respectively. Similar to experiment 1, magnesium pick-up in steel was observed (from MgO-containing inclusions) in all samples. Pure MgO inclusions were also present in the sample taken 55 minutes after Al-deoxidation (see Figure 7 (c)). The presence of MgO inclusions has been reported in literature as well [14]. A spinel inclusion transforming into an MgO inclusion was observed in the final sample from experiment-2 (Figure 8). Figure 7 (c) clearly shows the presence of calcium containing inclusions that formed most likely due to calcium transfer from slag to steel. Calcium containing inclusions were present as both oxide and sulfide. The final oxygen content in steel due to detected inclusions was only 50-70 ppm, less than in experiment 1. It was probably due to

better flotation of some partially liquid inclusions. The average size of inclusions observed across samples in experiment 2 was in the range of 2-4 μm , smaller than in experiment 1.

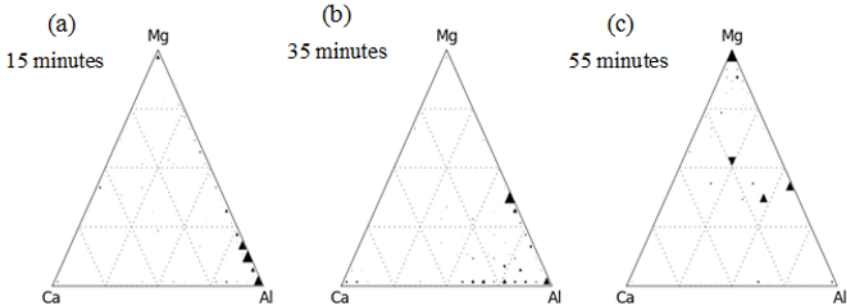


Figure 7 Time dependence of inclusion compositions during experiment 2 (steel with 1% Si and 0.15% Al initially; MgO crucible; slag 1). Plotted as normalized mass fraction.

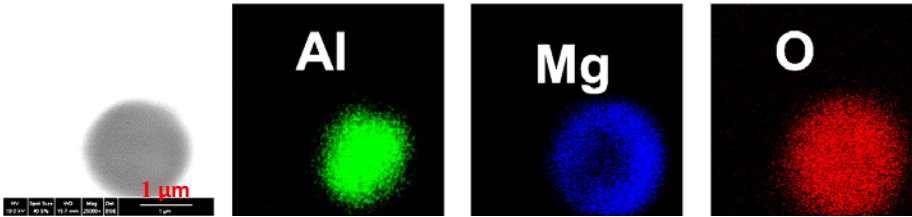


Figure 8 Partial transformation of spinel inclusion to MgO

Experiment 3 was conducted in a zirconia crucible to find the extent of magnesium transfer from slag and also to find the extent of calcium transfer while using a ZrO_2 crucible instead of a MgO crucible (For these experiments, the aluminum addition was 0.15% and the slag contained no SiO_2). The typical inclusions found in the samples taken after 20 minutes were of the following types: Al-Mg-O (Mg:Al = 0.5 by mass), Al-Mg-Zr-O, and Al-Mg-Zr-Ca-O. The average composition (wt %) of Al-Mg-Zr-O inclusions was 65% Al_2O_3 , 13% MgO, and 22% ZrO_2 ; there was significant transfer of magnesium from slag and zirconium from crucible. Hence, it can be concluded that the source of magnesium in experiment 1 was both MgO crucible (Figure 5(a)) and slag (Figure 5 (b and c)). A larger extent of magnesium transfer from slag to steel in comparison to calcium is likely due to the low equilibrium concentration of calcium in steel as compared to magnesium. A typical calcium containing inclusion is shown in Figure 9. These inclusions were rich in Al, Mg and Zr but lean in Ca (<5% by mass). Some CaS containing inclusions attached to oxide inclusions were also observed (see Figure 10). The steel produced in this experiment was very clean as the oxygen concentration in steel from analyzed inclusions was just 7 ppm. This may be due to two reasons: there was just 100 g of steel (in the smaller zirconia crucible) which means that the flotation distance for inclusions to reach to slag was smaller compared to other experiments; due to flotation of larger inclusions the average size of inclusions observed was just 1-2 μm . Secondly, due to the small diameter of the crucible (which precluded making additions after melting the steel), aluminum and slag were placed in the crucible with electrolytic iron at the beginning of the experiment. This is expected to have resulted into liquid

slag covering solid iron pieces before melting of the iron (as slag melts at a lower temperature than steel); such good mixing likely promoted inclusion removal.

Summary and Conclusions

The experiments conducted in this work aimed to understand the mechanism of calcium transfer to alumina/spinel inclusions in aluminum killed steel. Aluminum deoxidation experiments were conducted in an induction furnace in MgO and ZrO₂ crucibles to find the extent of calcium transfer from slag to inclusions via steel. The effect of silicon addition on calcium transfer was also analyzed by adding 1 wt% Si after Al-deoxidation. The extent of calcium transfer was analyzed with the help of automated inclusion analysis using SEM-ASPEX. The following conclusions can be drawn from this work:

1. Changes in aluminum and silicon content in steel can be used to calculate mass transfer coefficient in steel (k_{steel}) for steel-slag reaction with the help of a kinetic model using FactSage 6.4. In this case, $k_{steel} \times A = 1.3 \times 10^{-7} \text{ m}^3/\text{s}$.
2. The addition of 1% silicon can enhance calcium transfer from slag to steel and hence to inclusions. However, reduction of MgO may compete with CaO reduction and may limit calcium pick-up.
3. The steel with a large concentration of inclusions may not exhibit measurable calcium transfer from slag to inclusions due to the slower rate of calcium transfer from slag.
4. MgO crucible and MgO containing slag are significant source of magnesium transfer to steel for these experimental conditions.

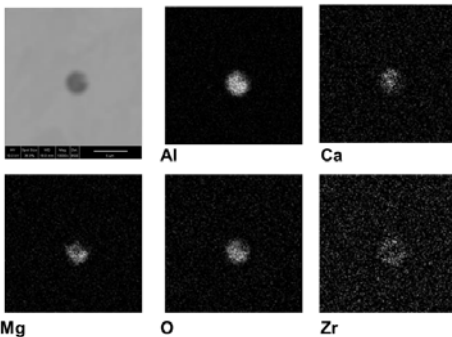


Figure 9 Calcium containing inclusion observed in experiment-3

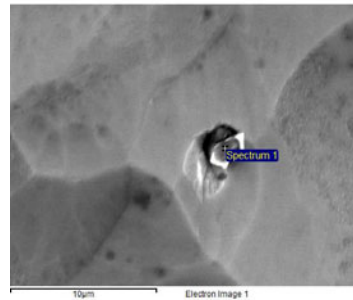


Figure 10 CaS-MgO inclusion observed in sample from experiment-3

Acknowledgement: Authors are grateful for the financial support as well as comments provided by the industry members of Center of Iron and Steelmaking research. Authors also acknowledge the use of Materials Characterization Facility at Carnegie Mellon University supported by grant MCF-677785.

References

- [1] S. N. Singh, "Mechanism of alumina buildup in tundish nozzles during continuous casting

- of aluminum-killed steels," *Metall. Trans.*, vol. 5, no. 10, pp. 2165–2178, 1974.
- [2] D. C. Hilty and V. T. Popp, "Improving the Influence of Calcium on Inclusion Control," in *Electric Furnace Proceedings*, 1969, pp. 52–66.
 - [3] G. J. W. Kor, "Calcium Treatment of Steel for Castability," in *First International Calcium Treatment Symposium*, 1988, pp. 39–44.
 - [4] G. M. Faulring, J. w. Farrel, and D. C. Hilty, "Steel flow through nozzles influence of calcium," *Iron Steelmak.*, vol. 7, no. 2, pp. 14–20, 1980.
 - [5] E. B. Pretorius, H. G. Oltmann, and T. Cash, "The effective modification of spinel inclusions by Ca treatment in LCAK steel," *Iron Steel Technol.*, vol. 7, no. 7, pp. 31–44, 2010.
 - [6] S. Yang, J. Li, Z. Wang, J. Li, and L. Lin, "Modification of MgO·Al₂O₃ spinel inclusions in Al-killed steel by Ca-treatment," *Int. J. Miner. Metall. Mater.*, vol. 18, no. 1, pp. 18–23, Mar. 2011.
 - [7] D. C. Hilty and J. W. Farrel, "Modification of inclusions by calcium-part I," *Iron Steelmak.*, vol. 2, no. 5, pp. 17–22, 1975.
 - [8] D. C. Hilty and J. W. Farrel, "Modification of inclusions by calcium-part II," *Iron Steelmak.*, vol. 2, no. 6, pp. 20–27, 1975.
 - [9] G. Ye, P. Jönsson, and T. Lund, "Thermodynamics and Kinetics of the Modification of Al₂O₃ Inclusions," *ISIJ Int.*, vol. 36, no. (suppl.), pp. S105–S108, 1996.
 - [10] Z. J. Han, L. Liu, M. Lind, and L. Holappa, "Mechanism and Kinetics of Transformation of Alumina Inclusions by Calcium Treatment," *Acta Met. Sin. (Eng. Lett.)*, vol. 19, no. 1, pp. 1–8, 2006.
 - [11] N. Verma, P. C. Pistorius, R. J. Fruehan, M. Potter, M. Lind, and S. Story, "Transient Inclusion Evolution During Modification of Alumina Inclusions by Calcium in Liquid Steel: Part I. Background, Experimental Techniques and Analysis Methods," *Metall. Mater. Trans. B*, vol. 42, no. 4, pp. 711–719, Apr. 2011.
 - [12] N. Verma, P. C. Pistorius, R. J. Fruehan, M. Potter, M. Lind, and S. R. Story, "Transient Inclusion Evolution During Modification of Alumina Inclusions by Calcium in Liquid Steel: Part II. Results and Discussion," *Metall. Mater. Trans. B*, vol. 42, no. 4, pp. 720–729, Apr. 2011.
 - [13] L. Holappa, M. Hämäläinen, M. Liukkonen, and M. Lind, "Thermodynamic examination of inclusion modification and precipitation from calcium treatment to solidified steel," *Ironmak. Steelmak.*, vol. 30, no. 2, pp. 111–115, 2003.
 - [14] N. Verma, P. C. Pistorius, R. J. Fruehan, M. S. Potter, H. G. Oltmann, and E. B. Pretorius, "Calcium Modification of Spinel Inclusions in Aluminum-Killed Steel: Reaction Steps," *Metall. Mater. Trans. B*, vol. 43, no. 4, pp. 830–840, Apr. 2012.
 - [15] E. B. Pretorius, H. G. Oltmann, and B. T. Scharf, "An Overview of Steel Cleanliness From an Industry Perspective," *AISTech 2013 Proc.*, pp. 993–1026, 2013.
 - [16] J. Tan and P. C. Pistorius, "Comparison of Three Approaches to Study Inclusions in Al-Si Deoxidized Steel and Al-killed Steel," *AISTech 2013 Proc.*, no. 412, pp. 1301–1311, 2013.
 - [17] C. W. Bale, E. Bélisle, P. Chartrand, S. A. Decterov, G. Eriksson, K. Hack, I. H. Jung, Y. B. Kang, J. Melançon, A. D. Pelton, and C. Robeling, "FactSage thermochemical software and databases-recent developments," *Calphad*, vol. 33, no. 2, pp. 295–311, 2009.
 - [18] S.-H. Kim and R. J. Fruehan, "Physical modeling of liquid/liquid mass transfer in a gas stirred ladle," *Metall. Trans. B*, vol. 18, no. 4, pp. 673–680, 1987.
 - [19] D. Roy, P. C. Pistorius, and R. J. Fruehan, "Effect of silicon on the desulfurization of Al-

killed steels: Part II. Experimental results and plant trials,” *Metall. Mater. Trans. B Process Metall. Mater. Process. Sci.*, vol. 44, no. 5, pp. 1095–1104, 2013.

- [20] M. Hino and K. Ito, Eds., *Thermodynamic Data for Steelmaking*. Sendai: Tohoku University Press, 2010.
- [21] Y. Miki, B. G. Thomas, A. Denissov, and Y. Shimada, “Model of Inclusion Removal during RH Degassing of Steel,” *Iron Steelmak.*, vol. 24, no. 8, pp. 31–38, 1997.
- [22] A. L. Gueussier, E. V. Vachery, J. L. Tranchant, and R. Szezesny, “In-ladle treatment using a new cored wire technique,” *Iron Steel Eng.*, vol. 60, no. 10, pp. 35–41, 1983.

Effect of Al_2O_3 Content in Top Slag on Cleanness of Stainless Steel Fe-13Cr

Qi Wang^{1,2}, Lijun Wang^{1,2*}, Kuochih CHOU^{1,2}

(1. State Key Laboratory of Advanced Metallurgy, University of Science and Technology Beijing, Beijing 100083, China.

2. Collaborative Innovation Center of Steel Technology, University of Science and Technology Beijing, Beijing 100083, China)

Keywords: stainless steel; non-metallic inclusions; refined slag.

Abstract

The evolution mechanisms of Al_2O_3 - SiO_2 system inclusion in 13Cr stainless steel with CaO - SiO_2 - Al_2O_3 top slag were investigated from thermodynamic, kinetic as well as experimental work.

From theoretical aspect: the stability diagrams of Ca-Si-Al-O and Mg-Al-O were obtained. From experimental aspect: Increasing Al_2O_3 content in slag would low slag melting temperature and the usage of CaF_2 . On the condition of relatively high Al_2O_3 in slag, the top slag would have a good kinetic condition. But excessive high Al_2O_3 in slag would increase total oxygen in stainless steel and cause a more complex series of slag-steel-inclusions reactions. Meanwhile, it is found that high basicity slag has good de-oxidation ability and it also accelerates the transition from high Al_2O_3 inclusions to low melt point CaO - Al_2O_3 - SiO_2 - MgO system inclusions. But excessive high basicity would have no effect on T.O and leads high content of [Al], [Mg] in liquid iron and which would promote the MgO - Al_2O_3 inclusions.

1 Introduction

The Fe-13Cr stainless steel is one important branch of the martensitic stainless steels. This kind of stainless steel, due to its high strength, high hardness and excellent corrosion resistance, is often used for pump shafts, screw bolts, and so on^[1]. The nonmetallic inclusions' size distribution, morphology and chemistry has significantly effect on the stainless steel quality. Though inclusions formed unavoidable in the stainless steel, hard and high melt point inclusions must be reduced.

In stainless steel making, liquid iron-chromium alloys are deoxidized with silicon in many cases, due to the harmful effect of Al_2O_3 and MgO - Al_2O_3 inclusions on corrosion-resisting property of the materials. The ferro-silicon, which is applied in silicon deoxidation, always contains small amount of aluminum as an impurity^[2]. SUZUKI^[3] calculates Cr13% silicon-aluminum complex deoxidation phase stability diagrams, and points out that Al_2O_3 - SiO_2 system inclusions could be easily formed in SiFe killed stainless steel even [Al] content is of quite low level. In fact, Al_2O_3 - SiO_2 system inclusions are also hard and have high melt temperature. But little attention has been paid on such kind of inclusions. Much research has aimed at improving the quality of different steel grades by optimizing the composition of top slags^{[4][5]}. Top slag plays important roles on transforming inclusion chemistry by slag-metal-inclusions reaction and also absorbing inclusions in refining process^[4]. Thus, it is pretty important to grasp the influence of top slag on the transformation of Al_2O_3 - SiO_2 system inclusion in Fe-13Cr stainless steel.

Two kinds of top slag are commonly used in steel production, one is CaO - SiO_2 - CaF_2 based

slag, and the other is CaO-Al₂O₃ based slag. CaO-SiO₂-CaF₂ based slag, due to its high basicity, has good deoxidation, good desulfurization and remove inclusions capacity [6][7]. However, high basicity slag has high melt temperature and low fluidity. So certain amount of CaF₂ is benefit to improve slag properties. However, addition of CaF₂ in top slag would enhance refractory erosion, meanwhile cause the environmental pollution. CaO-Al₂O₃ based top slag has a low oxidation potential, a low melting temperature, a low viscosity and it can improve steel cleanliness[8]. Although this CaO-Al₂O₃-based slag has excellent refining properties in both thermodynamics and kinetics, it hardly used in SiFe killed stainless steel. The reason is slag-steel reaction, high Al₂O₃ in slag cause more [Al] in liquid steel, which would promote Al₂O₃ and MgAl₂O₄ inclusions formation. The content of CaF₂ and Al₂O₃ in reported top slag are around 15% and 5% , respectively[9-12]. Few of study add further content of Al₂O₃ and reduce the usage of CaF₂ in CaO-SiO₂-based slag.

Therefore, in the current study, the CaO-SiO₂-Al₂O₃ based slag equilibrium between the Fe-13Cr stainless steel under SiFe(Al) deoxidation was investigated to understand the effect of basicity and Al₂O₃ contents on the composition of Al₂O₃-SiO₂ system inclusions.

2 Experiment

2.1 Materials

The stainless steel was prepared in a vacuum induction furnace and then cast into ingot under a protecting atmosphere. Table 1 shows the chemical composition of the experimental stainless steel.

Top slags were prepared by pure CaO, SiO₂, Al₂O₃, MgO and CaF₂, in which CaO was obtained by calcining CaCO₃ (Analytical grade) at 1373 K for 6 h, and the rest oxides were dried at 1273 K for 4h in a muffle furnace. The powders were mixed in an agate mortar and then ready for experiments. In the current study, 5 experiments followed the same procedure except for adjusting CaO, SiO₂, MgO, and Al₂O₃, as shown in Table 1. Experiment No.1, No.2 and No.3, had the same content of Al₂O₃ with different basicity in top slag. Experiment No.2, No.4 and No.5 had the same basicity with different content of Al₂O₃ in top slag. All Slags had the fixed content of MgO and CaF₂ to reduce disturbing factors.

Table 1 Chemical composition (wt %) of the stainless steel and synthetic slag

	C	Si	Mn	P	S	Cr	Ni	Al	Ca	Mg
Wt%	0.1159	0.557	0.3938	0.0187	0.0019	11.57	0.1195	0.004	0.0005	0.0005
No	CaO		SiO ₂	Al ₂ O ₃		MgO	CaF ₂			
1	0.44		0.24	0.16		0.1	0.05			
2	0.48		0.21	0.16		0.1	0.05			
3	0.49		0.19	0.16		0.1	0.05			
4	0.51		0.22	0.11		0.1	0.05			
5	0.44		0.19	0.21		0.1	0.05			

2.2 Experimental

In a typical run, 400g of Cr13 stainless steel were contained in an MgO crucible (ID of 50 mm, OD of 55 mm, and height of 115 mm) and placed in a vertical MoSi₂ resistance furnace. After the molten steel reached 1873K under high purity Ar atmosphere, 0.2g Fe₂O₃ was added to the

molten steel and then followed by 2.5gSiFe(73%Si,2%Al) addition to start deoxidation. 10minutes later, 70g synthetic slag was then added to the molten steel surface. The time when the slag addition completed was defined as the starting time (Time Zero). Thereafter, steel samples were taken at the times of 15, 30, 45, 60, 90minutes and quenched in water.

The concentrations of Ca, Mg and Al in the steel samples were measured by ICP-AAS or ICP-MS. The total oxygen were analyzed by Oxygen/Nitrogen determinator (TCH600). Inclusions were analyzed by SEM with EDS (FEI Quanta 250). Each sample was observed ten view field under 500X(0.034mm²), and random select 10 inclusions for composition comparison.

3 Results

3.1 Variation chemical composition in Steel

The variations of steel chemical compositions are shown in Figure.1. As shown in Figure 1a, the calcium contents in each heat were varied in the range of 0.0005~0.0015% ,during the reaction process. In addition, the content of [Ca] slightly increased with the increase of slag basicity and Al₂O₃ content. As shown in Fig1b, the content of [Al] in stainless steel is proportional to slag basicity and Al₂O₃ content. The content of [Al] in stainless steel also increase with the reaction time. The content of [Mg] in experiment is shown in Fig1c. From the No.3 experiment and No.5 experiment we can obtain that excessive high basicity and excessive high Al₂O₃ would case the content of [Mg] severe changes in stainless steel. The content of [Mg] in the rest experiment is stable.

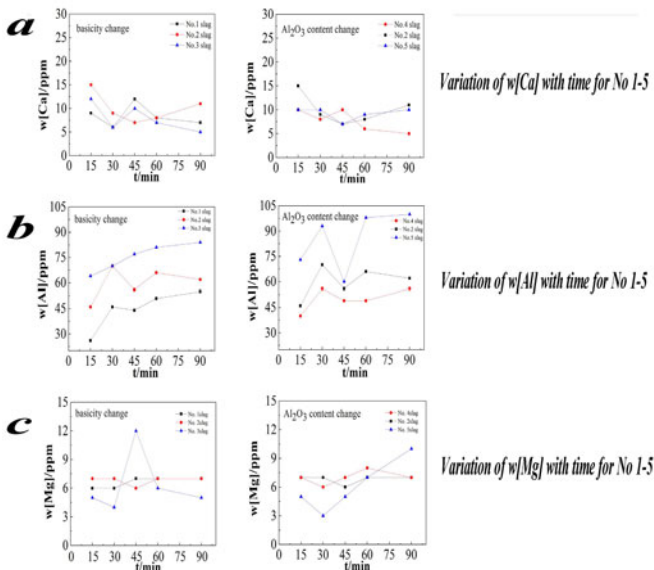


Figure 1. The evolution of [Ca], [Al] and [Mg] in experiment No.1-5

As shown in Figure 2a, the total oxygen content decreased as the increase of basicity, but when the slag basicity is over about 2.3, the total oxygen content will tend to be stable. High content of Al₂O₃ in top slag would lead high content of T.O in liquid iron.

The content of [Si] in experiment No.3 is shown in Figure 2b, which is used to characterize the variation of [Si] in all experiments. The content of [Si] had a quickly decrease for the direct deoxidation at the beginning of the reaction process and had a small change after 15min. The content of [Si] was 0.86% at the end of reaction process.

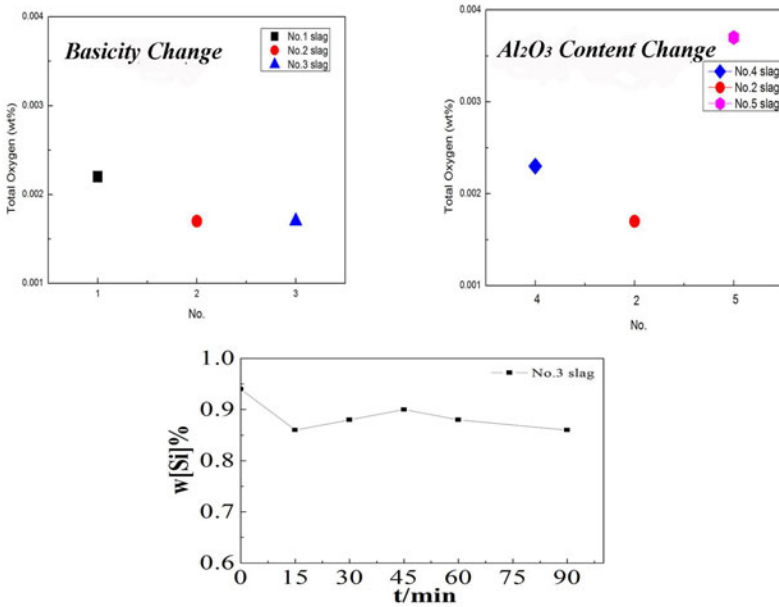


Figure 2. The content of T.O in experiment No.1-5 and the content evolution of [Si] in experiment No. 3

3.2 Variation of inclusions

The morphologies of inclusions in steel sample were observed by SEM and their chemical compositions were analyzed using EDS attached to SEM. The ferro-silicon, which was applied in experiment, contained 2% of aluminum as an impurity. Therefore, the silicon deoxidation changed to complex deoxidation of silicon and aluminum. The Al_2O_3 - SiO_2 system inclusion was observed after deoxidation in experiments. Some of these inclusions contained trace of CaO, MgO and MnO. These inclusions consist mainly of spherical or spheroidal shape. The composition mass ratios of Al_2O_3 and SiO_2 in these inclusions were around 3: 2.

Figure3 (a)-(e) give the variations of the inclusion compositions in different experiments. The Al_2O_3 - SiO_2 system inclusions serve as deoxidation product were observed in three experiments. In No.1 experiment, inclusions were SiO_2 - Al_2O_3 -CaO-based inclusion at 15min, and the average content of Al_2O_3 in inclusions increased to 60% at 30 - 60 min. However, inclusions after 90 min reaction were partly low melting temperature CaO- SiO_2 - Al_2O_3 -MgO-based inclusions although a few high- Al_2O_3 -based inclusions existed. In No.2 experiment, inclusions were high- Al_2O_3 -based inclusion at 15min and 30min. Inclusions after 45 min reaction, were mainly low melting temperature CaO- SiO_2 - Al_2O_3 -MgO-based inclusions. However, the average content of MgO in

inclusions was increased with reaction time and even pure MgO inclusions were observed. In No.3 experiment, two categories of inclusions were observed, viz MgO-Al₂O₃-based inclusions and Al₂O₃-SiO₂-CaO-MgO-based inclusions. MgO-Al₂O₃ based inclusions refer to high MgO-contained or even pure MgO inclusions. In No.4 experiment, two categories of inclusions were observed, one was SiO₂-CaO-Al₂O₃-MgO-based inclusions, and the other was high-Al₂O₃-based inclusion at 15min. There also were two categories of inclusions at 30min, low melting temperature CaO-SiO₂-Al₂O₃-MgO-based inclusions and high melting temperature MgO-Al₂O₃-based inclusions. The average content of MgO in inclusions was increased with time like experiment No.2. Inclusions were mainly low melting temperature CaO-SiO₂-Al₂O₃-MgO-based inclusions at 90min. In No.5 experiment the main part of inclusions at 15 min was high Al₂O₃ inclusion just like No.1 experiment. But MgAl₂O₄ wrapped by CaO-SiO₂-Al₂O₃-MgO-based inclusions were observed at 30 to 90min. Inclusions after 90 min reaction were partly low melting temperature CaO-SiO₂-Al₂O₃-MgO-based inclusions and a few high-MgO-based inclusions were appeared.

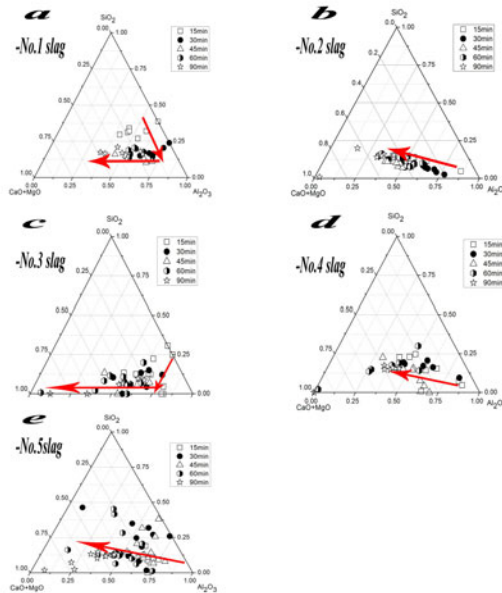


Figure 3. Composition evolution of typical inclusions observed in experiment No. 1-5.

From the Figure 3 we can obtain the inclusions evolution during the treatment. The first, Al₂O₃-SiO₂ system inclusions were generated after SiFe(Al) alloy added into liquid steel. The second, Al₂O₃-SiO₂ system inclusions change to high Al₂O₃ complex inclusions after the top slag added onto the liquid steel. The third, high Al₂O₃ complex inclusions change to low melting temperature CaO-SiO₂-Al₂O₃-MgO-based inclusions or MgO-Al₂O₃ system inclusions with reaction time. The fourth, two kinds of inclusions would change to high MgO complex inclusions, even pure MgO inclusions at the end of experiment.

4 Discussions

4.1 Formation Mechanism of CaO-SiO₂-Al₂O₃ system inclusions

Thermodynamic calculations were carried out to evaluate evolution of inclusions in Cr13 stainless steel. Formation of CaO-SiO₂-Al₂O₃ system inclusions was calculated.

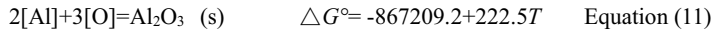
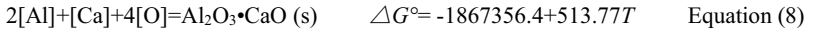
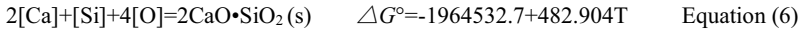
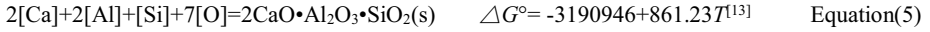


Table 2 Interaction coefficient used in calculation^[15]

<i>j</i>	Al	Si	Cr	C	Ni	O	Mn	S
e_{Si}^j	0.058	0.103	-0.021	0.18	-0.009	-0.119	0.0042	0.066
e_{Al}^j	0.043	0.056	0.012	0.091	-0.029	-1.98	0.035	0.035
e_{Mn}^j	-0.12	-0.088	0.047	-0.31	-0.012	-460		
e_{Ca}^j	-0.072	-0.097	0.02	-0.34	-0.044	-5600 ^[16]	-0.007	-140

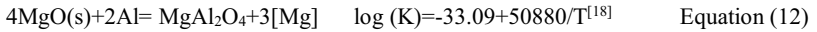
All relevant chemical equations and interaction coefficient are now known from present work and previous data listed in Table 2 and Equation 5-11 by other researchers; the rest of ΔG° was calculated by using FactSage6.4 software (Databases:FToxid, FactPS; Reaction module). The a_{Ca} , a_{Al} , a_{Si} and a_{O} represent Henrian activity of [Al],[Ca],[Si] and [O] based on infinitely dilute solution in liquid iron and $a_{2\text{CaO}\cdot\text{Al}_2\text{O}_3\cdot\text{SiO}_2}$ is Raoultian activity of $2\text{CaO}\cdot\text{Al}_2\text{O}_3\cdot\text{SiO}_2$ based on pure solid $2\text{CaO}\cdot\text{Al}_2\text{O}_3\cdot\text{SiO}_2$ and the activity of the product is unity, the same as in other equations. Assuming that local equilibrium between the inclusions and the molten steel is maintained. The phase stability diagrams are quantified by solving simultaneous equations based on the Gibbs principle of minimum free energy and mode of Wagner. The dissolved oxygen content was taken as 0.0001% when activity coefficients of aluminum and calcium were estimated. Figure.6a has shown the calculated stability diagram of Si-Ca-Al-O system in the Fe-13Cr stainless steel.

The liquid area in 1873K covered $2\text{CaO}\cdot\text{Al}_2\text{O}_3\cdot\text{SiO}_2$, $\text{Al}_2\text{O}_3\cdot\text{CaO}$ and $7\text{Al}_2\text{O}_3\cdot 12\text{CaO}$ is shown in Figure 4a. The Figure 4a show the content of [Ca], [Al] in 90min sample. As seen in Figure.6a, three relatively high basicity experiment date point located in liquid area, excessive high basicity experiment date point and excessive high Al₂O₃ content experiment located in solid area. This result indicate that high content of [Al] in molten steel is not helpful inclusions plastic. Besides, relatively high basicity top slag and enough reaction time could make inclusions plastic. The thermodynamic calculation shows a good agreement with experimental results. The range content of [Al] in SiFe deoxidation stainless steel is shown in Figure.6a, and in this area the low melt point inclusions is $2\text{CaO}\cdot\text{Al}_2\text{O}_3\cdot\text{SiO}_2$.

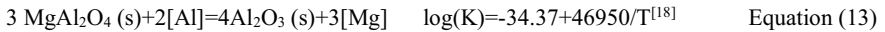
4.2 Formation Mechanism of Mg-Al-O system inclusions

Spinel inclusions are harmful to both the quality of products and the castability of the steel because of their high melting temperature and high hardness^[17]. Steelmakers have been always making great efforts to control the population of MgAl₂O₄ in stainless steel. A stability diagram for Mg-Al-O system can be calculated as shown in Figure 4b. It was established based on the Gibbs principle of minimum free energy and mode of Wagner. Here, the way how to calculate the diagram is explained.

The following reaction was considered to calculate the MgO/MgAl₂O₄ boundary.



To calculate the MgAl₂O₄/Al₂O₃ boundary, the following reaction was considered.



Fujii^[19] give the activity of MgO was taken as unity because of negligibly small solubility of Al₂O₃ into MgO while that of MgAl₂O₄ as 0.80 in MgO/MgAl₂O₄ boundary, the activity of MgAl₂O₄ was taken as 0.47 in MgAl₂O₄/Al₂O₃ boundary, while that of Al₂O₃ as unity because of negligibly small solubility of MgO into Al₂O₃.

Both high basicity and high Al₂O₃ content in slag can lead high content of [Al] and [Mg] in stainless steel. Therefore, it's not appropriate for high basicity slag add high content of Al₂O₃. The content of Al₂O₃ in slag and slag-steel reaction time are not the more, the better, but has a limitation.

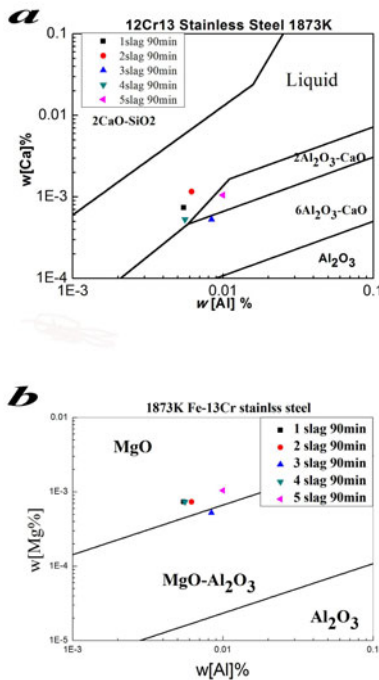


Figure 4. Effects of Al - Ca content Al - Mg content on the inclusion compositions for Fe-13Cr stainless steels at 1873K

5 Conclusions

Ladle treatment of Fe-13Cr stainless steel was simulated on a laboratory scale. The effects of slag chemistry on the steel and inclusions' compositions were discussed with thermodynamic considerations. The steel cleanliness in terms of factors for different types of slag are compared.

The main results are as follows:

1. Add right amount of Al_2O_3 in a relatively high basicity slag would reduce the usage of CaF_2 . Those Al_2O_3 in slag didn't lead $\text{MgO-Al}_2\text{O}_3$ formation in stainless steel.

2. Relatively high basicity slag has good deoxidation ability and it also accelerates the transition from high Al_2O_3 inclusions to low melt point $\text{CaO-Al}_2\text{O}_3\text{-SiO}_2\text{-MgO}$ system inclusions. High basicity slag also has a good effect on absorb inclusions. But excessive high basicity has no effect on T.O, but causes high content of [Al] in liquid iron which would promote the $\text{MgO-Al}_2\text{O}_3$ formation.

3. In the same basicity level, inclusions evolved to $\text{CaO-MgO-Al}_2\text{O}_3\text{-SiO}_2$ system instead of spinel inclusions with increasing Al_2O_3 content in top slag. However, when Al_2O_3 content reached 21% or higher, complex inclusion as Mg-Al-O system wrapped by $\text{CaO-MgO-Al}_2\text{O}_3\text{-SiO}_2$ inclusion was generated. Moreover, the relative higher Al_2O_3 content also increase the T.O in stainless steel and has a negative effect on absorb inclusions.

3. In SiFe(Al) alloy killed stainless steel, $\text{Al}_2\text{O}_3\text{-SiO}_2$ system inclusion formed at initial as expected, and then change to Ca-Mg-Al-Si-O complex inclusions characteristic with high Al_2O_3 composition, which composition was near to Al_2O_3 corner in $\text{Ca(Mg)O-SiO}_2\text{-Al}_2\text{O}_3$ diagram. The modification role of top slag on inclusions made the inclusion composition to relative lower melting point region. A proper reaction time is necessary to obtain low melting point inclusions, but long reaction time would lead to generate high-MgO inclusion.

Acknowledgement

The authors would like to express their appreciation to National Nature Science Foundation of China (No.51104013,51174022), a Fundamental Research Funds for the Central Universities (FRF-TP-14-109A2), Beijing Higher Education Young Elite Teacher Project (YETP0349) and China Postdoctoral Science Foundation (2014M560046).

References

- [1] R.Zhai, X.Cheng, Baosteel Technical Research,2009,01,56.
- [2]T. Fujisawa, M. Suzuki, Y. Wanibe and H. Sakao: Tetsu-to-Hagané,72 (1986), 218.
- [3]K. SUZUKI,M. HINO,ISIJ Int,2001,vol.41:813.
- [4]P. Yan,M. Guo:Metallurgical and Materials Transactions B,2013,44,1105.
- [5]W. Yang, X. Wang, L. Zhang,et al, Steel Res. Int., 2013, 84,473.
- [6] H. Suito, R.Inoue:ISIJ Int,1996,36,528.
- [7] P. K.Iwamasa, R. J. Fruehan: Metallurgical and Materials Transactions B,1997,28, 47.
- [8] B.Yoon,K.Heo,J.Kim,and H.Sohn:Ironmaking & Steelmaking,2002,29,214.
- [9]K. Mizuno, H. Todoroki, M. Noda, and T. Tohge: Iron Steelmak.,2001, vol. 28 (8), pp. 93 - 101.
- [10]J.W. Kim, S.K. Kim, D.S. Kim, Y.D. Lee, and P. Yang: ISIJ Int.,1996, vol. 36, pp. S140 - S43.
- [11]K. Sakata: ISIJ Int., 2006, vol. 46 (12), pp. 1795 - 99.
- [12]Y. Ehara, S. Yokoyama, and M. Kawakami: Tetsu-to-Hagane,2007, vol. 93 (7), pp. 475 - 82.

[13]H.Rein,J. Chipman,Transactions of the Metallurgical Society of AIME,1965,233(2),415.

[14] J.Schade, M.Burns,et al:Steel Technology International, 1993, 149.

[15]Steelmaking Data Sourcebook, The Japan Society for the Promotion of Science ,The 19th Committee on Steelmaking, Goldon Breach Science Pub, New York,(1988).

[16]M.Howard,et al:Metallurgical and Materials Transactions B, 1984,15,547.

[17]S.Yang,L.Zhang,Metallurgical and Materials Transactions B,2012,43,731.

[18]J.H.Park,H.Todoroki,ISIJ Int,2010,50,1333.

[19]K.Fujii,M.Hino,ISIJ Int,2000,40,1059.

**ADVANCES IN MOLTEN
SLAGS, FLUXES, AND SALTS:**

Proceedings of



**Slag and Salt
Structure**

UNDERSTANDING OF Cr-CONTAINING SLAGS BY SULPHIDE CAPACITY AND STRUCTURAL STUDY

Lijun Wang, Kuo-chih Chou

State Key Laboratory of Advanced Metallurgy, University of Science and Technology Beijing, Beijing 100083, PR China

Keywords: Sulphide capacity, Chromium-bearing slag, gas/slag equilibrium

Abstract

The sulphide capacities of $\text{CaO-MgO-Al}_2\text{O}_3\text{-SiO}_2\text{-Cr}_x$ slags with were measured by gas-slag equilibration method in the temperature range of 1823-1898K to reveal the effect of CrO_x on the sulphide capacities of slags. Both higher basicity and temperature enhanced sulphide capacities. The CrO_x additions in the range of 0-5 mass% increased the sulphide capacity, but, further increase of CrO_x contents to 7 % was found to lower the sulphide capacity. Utilizing the relationship for estimating the ratio of $\text{Cr}^{2+}/\text{Cr}^{3+}$ put forward by the present authors, the influence of Cr(II) on the sulphide capacities of the slags studied is discussed.

Introduction

Chromium-containing slags play a predominant role in production of stainless steel and high alloy steels. It is important to understand the chemistry of chromium-containing slags with special reference to the phase equilibria^[1-5], oxidation states of chromium in slag phase^[6-11] and distribution of Cr between the steel melt and slag phases^[6,12-14]. These studies provide invaluable information for the optimization of the processes for high alloy steels. However, experimental data on the properties of slags containing CrO_x are scarce in literature as the melting points of these slags are quite high. Drakaliysky et al. ^[15] reported sulfide capacities of $\text{CaO-MgO-SiO}_2\text{-Al}_2\text{O}_3$ slags containing small amounts of Cr_2O_3 . Their results indicate that adding 5 wt% Cr_2O_3 to a high-MgO(25 wt%) slag could cause a 4-fold decrease in sulfide capacities. Wang et al. ^[16] studied sulfide capacities of $\text{CaO-SiO}_2\text{-Cr}_x$ system in the temperature range 1823K - 1923K. These authors noticed that, when the SiO_2 content was fixed in the slag, the increasing content of CrO would initially decrease the sulfide capacity and increase it subsequently.

In the current study, experimental determinations of the sulphide capacities of chromium slags of 12 different compositions were carried out in the temperature range 1823K-1898K. $\text{CaO-MgO-Al}_2\text{O}_3\text{-SiO}_2$ was adopted as basic system and the chromium-oxide contents were varied.

Experimental work

The components after drying were mixed in required proportions and ground together in an agate mortar. The basicity, B, presented in Table 1 refers to the mass ratio of $(\text{CaO}+\text{MgO})/(\text{Al}_2\text{O}_3+\text{SiO}_2)$ and is valid for the entire manuscript. One gram of sample was used for each experimental run. The oxygen- and sulfur potentials of the $\text{CO-CO}_2\text{-SO}_2\text{-Ar}$ mixture, as estimated by Gibbs energy minimization program (FACT SAGE), were controlled by suitably adjusting the flow rates of the component gases. The gas flow rates were accurately controlled by Brukes mass-flow meters. A

horizontal furnace with MoSi₂ heating elements was used for the equilibration studies. In each run, the temperature was raised to the target temperature at the rate of 5K/min. During this process, purified argon gas with a flow rate of 200mL/min was kept flowing ensuring an inert atmosphere. When the temperature reached the targeted value, argon flow was replaced by the gas mixture according to the pre-set proportion. The gas-slag reaction took 6 hours to reach equilibration, as confirmed by the earlier work of the present authors^[16]. After 6 hours, the alumina sample holder was drawn quickly to the cold end of the reaction tube under argon gas. Ocular examination showed that the slag samples were glassy. The samples were subjected to chemical analysis. The combustion method using carbon/sulfur analyzer (Horiba, EMIA-820V, Japan) was used to determine the mass percentage of sulfur in each sample. Raman spectra were collected in a Raman spectrometer (Horiba, LabRAM HR Evolution, Japan) with a resolution of 0.67cm⁻¹.

Results and Discussion

3.1 Basicity dependence

The data obtained in the present work are listed in Table 1. In Fig.1, it can be seen clearly that, with increasing basicity, the sulphide capacity of the slag increases dramatically in the basicity range 0.7 – 0.8, irrespective of the chromium content. A similar trend was noticed even in the earlier work^[16]. It is generally known that, with increasing basicity, the availability of O²⁻ for the sulphur exchange reaction would increase facilitating the desulphurization process.

Table 1 Experimental sulphide capacities of CaO-MgO-Al₂O₃-SiO₂-CrO_x system

Sample No.	Basicity	mass%CrO _x	Temp./K	P _{O₂} × 10 ⁷	wt%S	Log ₁₀ C _S	Log ₁₀ ³ C _S
A1	0.67	0	1873	1.05	0.0217	-4.074	-5.41
A2	0.67	3	1873	1.05	0.0232	-4.045	-5.38
A3	0.67	5	1873	1.05	0.0256	-4.001	-5.33
A4	0.67	7	1873	1.05	0.0256	-4.002	-5.32
B1	0.82	0	1873	1.05	0.0501	-3.697	-5.02
B2	0.82	3	1873	1.05	0.0580	-3.610	-4.95
B3	0.82	5	1873	1.05	0.0818	-3.477	-4.80
B4	0.82	7	1873	1.05	0.0575	-3.583	-4.94
C1	1	0	1873	1.05	0.0719	-3.553	-4.88
C2	1	3	1873	1.05	0.0846	-3.482	-4.80
C3	1	5	1873	1.05	0.1001	-3.410	-4.72
C4	1	7	1873	1.05	0.0885	-3.463	-4.77
B1	0.82	0	1823	1.0544	0.0196	-3.987	-5.43
B2	0.82	3	1823	1.0544	0.0187	-4.007	-5.44
B3	0.82	5	1823	1.0544	0.0222	-3.932	-5.36
B4	0.82	7	1823	1.0544	0.0189	-4.002	-5.43
B1	0.82	0	1848	0.80523	0.0719	-3.720	-4.87
B2	0.82	3	1848	0.80523	0.0886	-3.630	-4.77
B3	0.82	5	1848	0.80523	0.0939	-3.604	-4.74
B4	0.82	7	1848	0.80523	0.0913	-3.617	-4.74

Sample No.	Basicity	mass%CrO _x	Temp./K	P _{O₂} × 10 ⁷	wt%S	Log ₁₀ C _S	Log ₁₀ 'C _S
B1	0.82	0	1898	0.84918	0.1393	-0.856	-4.58
B2	0.82	3	1898	0.84918	0.1696	-0.771	-4.48
B3	0.82	5	1898	0.84918	0.1829	-0.738	-4.45
B4	0.82	7	1898	0.84918	0.1729	-0.762	-4.47

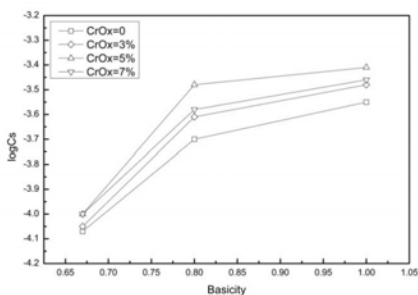


Figure 1 Basicity dependency of sulphide capacities on CaO-MgO-Al₂O₃-SiO₂-CrO_x at 1873K,

$$\log P_{O_2} = -7$$

3.2 Temperature dependence

The effect of temperature on the sulphide capacity of chromium-containing slags is shown in Fig.2. The trend that higher temperature leads to higher sulphide capacity is consistent with literature and is attributed to the sulphur-oxygen exchange reaction, which is a thermally activated process and is endothermic.

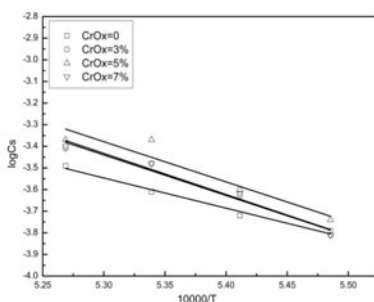


Figure 2 Dependence of log₁₀ C_S with reciprocal of temperature

The slope of the plot of log₁₀C_S as a function of 1/T is an Arrhenius-type of plot, the slope representing the enthalpy of the exchange reaction between oxygen in the slag and Sulphur in the gas phase. In the case of low basicity slags, it is well-known that the silicate chains are broken and oxygen ions are released for desulphurization. Thus, the slope of the above-mentioned plot is

expected to be small. The present results as well as the earlier work reveal that, at constant basicity, addition of CrO_x to the slag would increase the absolute value of slope of the $\log_{10}C_S$ vs $1/T$ lines, viz. desulphurization enthalpy. The contributions to the slope are from the desulphurization reaction, $\text{Cr}^{2+}\text{-Cr}^{3+}$ redox reaction as well as polymerization reaction.

On the basis of the earlier study^[17], slag systems containing CrO_x should actually be considered as consisting CrO and $\text{CrO}_{1.5}$. The ratio between the two Cr-containing species has been shown to be a function of basicity and temperature. This leads to a certain degree of non-linearity in the $\log_{10}C_S$ vs $1/T$ plots if CrO_x is treated as a single species.

3.3 Chromium oxides influence

The effect of chromium content on the sulphide capacity of the slag was not monotonous, which can be seen in Fig. 3. When the content of CrO_x increased from 0 to 5%, the sulphide capacity of slag increased gradually but when the chromium content reached 7%, C_S was found to decrease. In the present work, this effect is traced to the different valence of chromium ions. As reported by Wang and Seetharaman^[16], Cr^{2+} acts dominantly as a basic ion while Cr^{3+} would be more amphoteric. At low Cr contents and moderate basicities, the predominant species in a silicate melt would be CrO , which, in turn, would act as a basic oxide. Thus, increasing chromium content would increase the sulphide capacity. However, as the CrO_x content increases, the acid effect would be more predominant hindering the reaction between sulfur and oxygen ion.

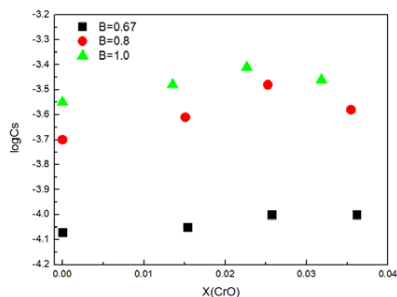


Figure 3 Effect of CrO on log C_S at 1873K, $\log P_{\text{O}_2} = -7$

In desulphuration process, the polymerization reaction involving different forms of oxygen in silicates is represented in Eqn.(1).

This reaction shows the charge balance required by the tetrahedral coordination of oxygen with silicon on the left-hand side of Eqn.(1) and the polymerization of two silicate units releasing a divalent oxygen ion. Although the effective refining agent is free oxygen ion, its amount is determined by the basicity of the slag or the degree of polymerization that would lead to the formation of free O^{2-} ions. Further, in a low basicity (metasilicate) environment, desulphurization reaction would be expected to lead continuously to the release of increased number free oxygen ions by the polymerization reaction.

The occurrence of reaction (1) in silicate systems containing transition metal cations is somewhat complicated by the presence of 3 d electrons. Apart from the variable valency exhibited by these cations, it has been shown in the earlier work^[18] that the electron distribution in the silicate matrix

is more even. From a thermodynamic point of view, the activity of O^- is raised. In the present discussion, the term “activity” is used to describe the thermodynamic situation and is not linked to any standard state. If O^{2-} can be replaced by S^{2-} continuously, the activity of O^{2-} is reduced, and consequently, the reaction of (1) will proceed further to the right side. This would, in turn, lead to an improvement of the desulphurization capacity. This effect is reflected in the trends shown by transition metal silicates with respect to molar sulphide capacities. With the same amount of silicon, the value of molar sulphide capacity of $MnO.SiO_2$ and $FeO.SiO_2$ have high values; viz. -4.18 at 1973 K^[19] for $MnSiO_2$, and -4.39 at 1773 K^[20] for $FeOSiO_2$ and ca -5 for $CrOSiO_2$ ^[16]. The value is close to that of $CaO.SiO_2$ (-5.4 at 1923K).

The ratio of Cr^{2+}/Cr^{3+} would fixed (1.728、1.437 and 1.199 at 1873K) when temperature, oxygen partial pressure and the slag chemical environment (basicity, 0.67, 0.82 and 1.0 respectively) are kept constant. According to the relationship presented in the earlier work by the present authors for the ratio Cr^{2+} / Cr^{3+} , divalent Cr would be the dominant valence state at 1873K and basicity < 1. Thus, in the present case, the enhancement of sulphide capacity could be regarded as the contribution of CrO.

Meanwhile, it can be noted that the amount of CrO and $CrO_{1.5}$ were both increasing with the continuous addition of CrO_x . In a study of the crystalline Cr_2O_3 , Tilley^[21] had suggested that trivalent chromium would prefer the octahedral position just as Al^{3+} . As reported by Irmann, Cr(III) would exist as $[CrO_2]^-$ in basic slag phase^[22]. It is known that Al^{3+} can fit into the Si polymeric chain but need to maintain charge balance. For Cr(III), such positive divalent ion could be Ca^{2+} , Mg^{2+} as well as Cr^{2+} . Assuming Cr^{2+} might act as charge compensator for Cr(III), it would cause a lessening of the effective amount of CrO involved in reaction (1). Thus, there will be a certain critical point at which more positive charge would be needed for the charge balance resulting in the lowering sulphide capacities in the system with 7% addition of CrO_x .

4.4 Raman spectrum for slag structure

Fig. 4 shows the deconvulsed Raman spectra for 3 different slag basicities. It is seen that, at basicity of 0.67, Q_2 is predominant in the whole slag. With more basic oxides(CaO and MgO) added, Q_2 and Q_3 both decreased while Q_0 and Q_1 both increased indicating depolymerization. According to Frantz and Mysen, the mole fractions of different structure units are proportional to the band areas in Raman spectra. Table 2 gave fitting results along with each band area. The average number of bridging oxygen of each sample is used to explain the contributions of each unit to depolymerization. Because $Q_0\sim Q_3$ could reveal the bridge oxygen in different Si-O structure, the average bridge oxygen content could be represented by Equation (1).

$$BO = 0 \times Q_0 + 1 \times Q_1 + 2 \times Q_2 + 3 \times Q_3 \quad (1)$$

Fig. 5 shows the relationship between basicity and average bridge oxygen in the slag. It can be seen that with increasing slag basicity, the average bridge oxygen decreases dramatically. It is well-known that a higher basicity would lead to a greater depolymerization degree in the slag, which could also be confirmed by the decreasing average bridge oxygen.

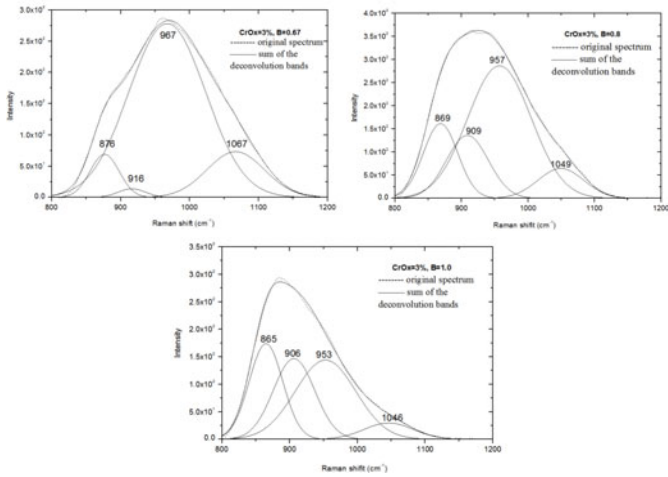


Figure 4 Effects of basicity on Raman Spectrum of CAMS-CrO_x(CrO_x=3%)

3.2 Effect of chromium oxide addition on structure

Fig. 5 shows the deconvolution results of Raman spectra of slags with different chromium contents. Generally, Q₂ is found to be predominant in the set composition ratio (B=0.8). When content of CrO_x increased to 5%, the amount of Q₂ decreased gradually and the amounts of Q₀ and Q₁ exhibited a corresponding increase. The present results lead to the conclusion that the depolymerization degree of the slag decreases with increase of Cr content upto 5%. Higher degree of depolymerization of the slag would increase the number of oxygen ion available for sulphur exchange with a consequent increase in the sulphide capacity.

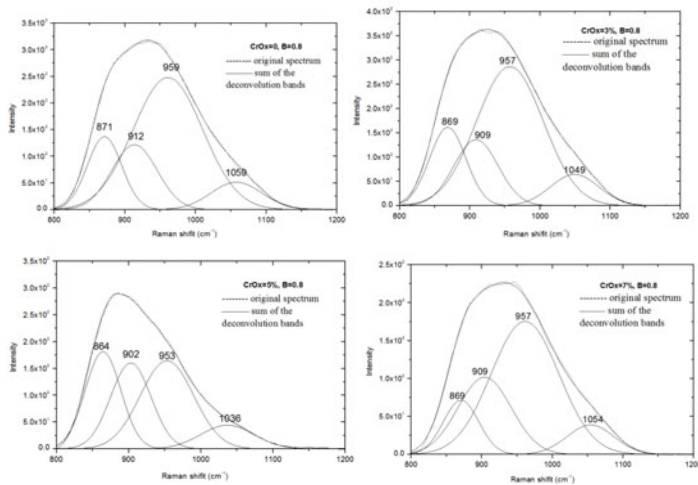


Figure 5 Effects of CrO_x on the Raman spectra of CAMS-CrO_x(B=0.8)

It is interesting to note that, when the content of CrO_x was increased to 7%, the fraction of Q_0 decreased but Q_1 was nearly the same. Comparing the sulphide capacities of slags with 7% CrO_x and 3% CrO_x , it can be inferred that both Q_0 and Q_1 had positive effects on the desulphurization of slag. This is in conformity with the results corresponding to different basicities.

Conclusion

Gas/slag equilibrium technique was used in the investigation of the effects of chromium oxides on the desulphurization process in the temperature range of 1823-1898K. It was found that the sulphide capacity of $\text{CaO-MgO-Al}_2\text{O}_3\text{-SiO}_2$ with the basicity from 0.67-1.0 can be enhanced by the addition of chromium oxide. By employing the formula of the $\text{Cr}^{2+}/\text{Cr}^{3+}$ ratio to evaluate the distribution of Cr(II) and Cr(III) in the slag phase, the contribution of CrO on desulphurization has been proposed. With relatively high content of CrO_x (7%), Cr(II) also will take a charge compensation role for Cr(III), which resulted in the lowering of sulphide capacity of the system.

Acknowledgement

The authors are grateful for the financial support for this work from National Nature Science Foundation of China (No.51104013, No. 51174022), China Postdoctoral Science Foundation (2014M560046), and Beijing Higher Education Young Elite Teacher Project (YETP0349), as well as the Fundamental Research Funds for the Central Universities (FRF-TP-14-109A2).

References

- [1] K. Morita, A. Inoue, N. Takayama and N. Sano: *ISIJ Int*, 1988, vol.74, pp.59-65.
- [2] F. P. Glasser and E. F. Osborn: *J. Am. Ceram. Soc.*, 1958, vol.41, pp.358-67
- [3] P. R. De Villers and A. Muan: *J. Am. Ceram. Soc.* 1992, vol 75, 6, pp.1333-1341.
- [4] S. Degterov and A. D. Pelton: *Journal of Phase Equilibria*, 1996, vol. 17, No.6, pp.476-487, pp. 488-494.
- [5] S. Degterov and A. D. Pelton: *Metall. Mater. Trans.*, 1997, vol.28B, pp.235-242.
- [6] Y. Xiao and L. Holappa: *ISIJ Int*, 1993, vol. 33, No.1, pp. 66-74.
- [7] K. Morita and N. Sano: *Steel Research Int.* 2005, vol.76, No.4, pp.279-283.
- [8] E.B.Pretorius, R. Snellgrove, and A. Muan: *J. Am. Ceram. Soc.*, 1992, vol.75.no.6, pp. 1378-1381.
- [9] M.G.Frohberg and K.Richter: *Arch. Eisenhüttenwes*,1968,vol. 39, pp.799-802.
- [10] A.J. Berry, H. S.C. O'Neill, D. R. Scott, G.J. Foran, and J.M.G. Shelley: *American Mineralogist*, 2006, vol.91, pp. 1901-1908.
- [11] B. Miric, A. Fajgelj, K. Lutar, M. Schara, and V. Kaucic: *J. Am. Ceram. Soc.*, 1992, vol. 75, n.8, pp. 2184-2188.
- [12] W.J.Rankin, A. K. Biswas: *Arch. Eisen hüttenwes.* 1979, Vol.50, pp.7-11.
- [13] K.Morita, M.Mori, M.Guo, T.Ikagawa, and N. Sano: *Steel Research Int.* 1999, Vol.70, pp.319-324.
- [14] W. Pei and O. Wijk: *Scandinavian Journal of Metallurgy*, 1994, Vol.23, pp.228-235.
- [15] E. Drakaliysky, N. S. Srinivasan and L. I. Staffansson: *Scand. J. Metall.*, 1991, vol. 20, pp. 251-55.
- [16] L. J.Wang and S. Seetharaman: *Metall. Mater. Trans. B*, 2010, vol. 41, pp. 367-73\
- [17] L. J. Wang and S. Seetharaman, *Metall. Mater. Trans. B*, 2010, vol. 41B, 946-54

- [18] L. Wang, M. Hayashi, K. C. Chou and S. Seetharaman: *Metall. Mater. Trans. B*, 2012, vol. 43, pp. 1338-43.
- [19] K. P. Abraham and F. D. Richardson: *J. Iron. Steel Inst.*, 1960, vol.196, pp.313.
- [20] C. J. B. Fincham and F. D. Richardson: *Proc. Roy. Soc. (London)*, 1954, A223, pp.40; *J. Iron Steel Inst.*, 1954, vol.178, pp.4.
- [21] Richard J. D. Tilly: *Crystals and crystal structures*, Wiley, 2006, pp.93.
- [22] F. Irmann: *J. Am. Chem. Soc.*, 1952, 74, pp.4767-4770.

STRUCTURE STUDIES OF SILICATE GLASSES BY RAMAN SPECTROSCOPY

Chen Han¹, Mao Chen¹, Ron Rasch¹, Ying Yu¹ and Baojun Zhao¹

¹The University of Queensland, Brisbane, Australia

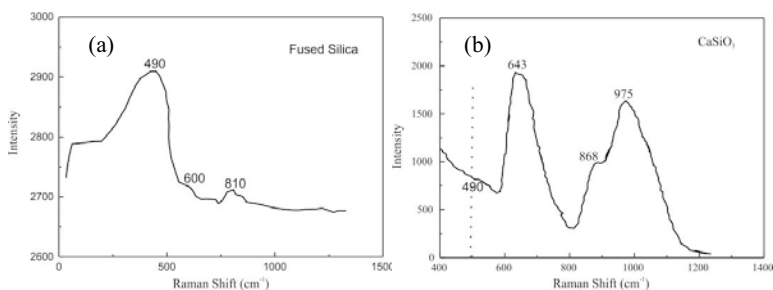
Keywords: SiO₂-CaO slag, Raman Spectrum, Degree of polymerization

Abstract

Silicate slags are widely used in many pyrometallurgical processes. The physiochemical properties of the slags, particularly viscosity, are closely related to their internal structures at operating conditions. To fundamentally investigate the correlation between slag structures and viscosities, the glassy samples in SiO₂-CaO, SiO₂-CaO-MgO and SiO₂-CaO-Al₂O₃ systems were prepared by directly quenching to water. The quenched slags that maintain structures at high temperature were analyzed quantitatively by Raman spectrometer. The appropriate conditions of Raman spectroscopy measurements have been evaluated to obtain a better spectra for quantitative analysis. The proportions of four types of Si with different coordination can be clearly revealed from the analyses of the Raman peaks. The viscosities of the slags are correlated with the changes of the characteristic peak positions and areas.

Introduction

Extensive studies on the structures of the SiO₂-CaO based melts have been performed using Raman spectroscopy. The intensity and shift of Raman bands with the silicate structural units were linked in the present study. The complex silicate melts are composed of different Si units, which can be clearly revealed from the analysis of the Raman bands [1]. From the Raman spectrum of pure silica (Figure 1a) [2], the bands at around 490 cm⁻¹, 600 cm⁻¹ and 800 cm⁻¹ are assigned to the vibrations of 4-fold, 3-fold ring and defected silicate structure respectively [3]. In the Raman spectrum of CaSiO₃ glass in Figure 1b [4], the diminished band at 490 cm⁻¹ and enlarged band at 643 cm⁻¹ indicate the degradation of 4 folded ring to 3 folded ring silicate structure. From the Raman spectra of Ca₂SiO₄ (Figure 1c) and Ca₃SiO₅ (Figure 1d), the dominant bands at 910 cm⁻¹ and 850 cm⁻¹ are defected silicate unit and the bands located 490 cm⁻¹ and 600 cm⁻¹ shrink and disappear.



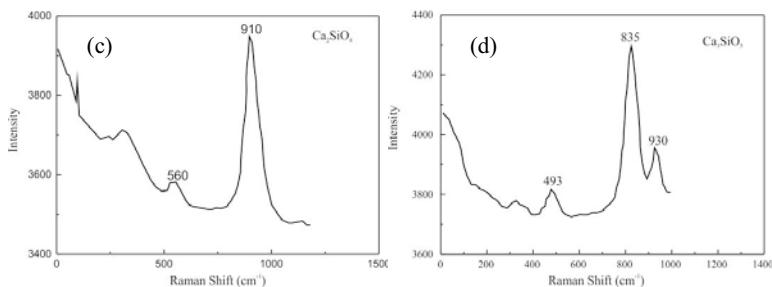


Figure 1. Raman spectrum of (a) fused pure silica [2], (b) CaSiO_3 [4], (c) Ca_2SiO_4 [5] and (d) Ca_3SiO_5 [6]

In present study, the quenched slag samples were analyzed by Raman spectrometer to investigate the degree of polymerization (DP) of SiO_2 -CaO based systems with additions of MgO or Al_2O_3 .

Methodology

The quenched slag samples were prepared for the SiO_2 -CaO, SiO_2 -CaO-MgO and SiO_2 -CaO- Al_2O_3 systems. Approximately 0.25g mixture was prepared by mixing the required chemicals with grinding. The details of equilibration experiments were described in the previous publication [7]. In brief, the sample in graphite crucible was equilibrated in Ar for 2 hours. After equilibration, the sample was instantly quenched into water to maintain its microstructure at high temperature. Raman spectroscopy and electron probe X-ray microanalysis (EPMA) were conducted for each sample and the results of EPMA are shown in Table I.

Table I: Experimental conditions and EPMA results

Chemical Systems	Temperature (°C)	EPMA Results (mol%)			
		SiO_2	CaO	Additive	CaO/ SiO_2
SiO_2 -CaO	1500	66.3	39.7	0	0.6
	1500	58.7	41.3	0	0.7
	1553	52.5	47.5	0	0.9
	1466	47.8	52.2	0	1.1
SiO_2 -CaO-MgO	1500	47.3	47.7	4.6 (MgO)	1.0
	1500	44.9	46.1	9 (MgO)	1.0
	1500	43	42.7	14.3 (MgO)	1.0
	1500	39.6	40.6	19.8 (MgO)	1.0
SiO_2 -CaO- Al_2O_3	1500	47.5	47.4	5.1 (Al_2O_3)	1.0
	1500	45	45.4	9.6 (Al_2O_3)	1.0
	1500	42.4	42.6	15 (Al_2O_3)	1.0

The quenched samples were mounted in epoxy resin and polished for Raman spectroscopy measurements (Ranishaw, Wotton-under-Edge, UK). The Raman spectra were recorded at room temperature in the frequency range of 100 - 1500 cm^{-1} using argon ion laser (514 nm).

With the studies of SiO₂-CaO glasses and silicate polymer theory, the major bands were assigned to different structural units, as shown in Table II [3]. The details of peak deconvultion were described in the literature [8] and utilized in the present study.

Table II. The descriptions of Raman bands (NBO/T=Non-bridging oxygen/total silicate)

Peak	Raman Shift (cm ⁻¹)	NBO/T	Polymer Theory
D1	480-500	NA	4-fold ring
D2	590-610	NA	3-fold ring
Q1	850-880	NBO/T=4	SiO ₄ with zero bridging oxygen
Q2	900-930	NBO/T=3	Si ₂ O ₇ with one bridging oxygen
Q3	950-980	NBO/T=2	Si ₂ O ₆ with 2 bridging oxygen
Q4	1040-1060	NBO/T=1	Si ₂ O ₅ with one bridging oxygen

Results and Discussions

Raman Spectrum Analyses

The addition of CaO into silica dramatically influences the structure of silicate melt. Figure 2 shows the Raman spectra for the SiO₂-CaO system with CaO/SiO₂ ranging from 0.6 to 1.1. As shown in Figure 2a, for each spectrum there are two major bands located in 580-680 cm⁻¹ and 800-1200 cm⁻¹ regions. The D1 band is not found in SiO₂-CaO, SiO₂-CaO-MgO and SiO₂-CaO-Al₂O₃ systems. The two bands were further deconvulted into 2 and 4 peaks respectively as shown in Figure 2. The D3 peak was reported from non-linear least squares minimization method [8], which may be defined as a kind of lower order silicate ring structural unit. The locations and area occupancies were summarized in Table III.

Table III. Peak shift and relative area fraction of each peak in SiO₂-CaO Raman spectrum

CaO/SiO ₂	D2	D3	Q1	Q2	Q3	Q4
	Peak Shift					
0.6	589.8	633.8	866.6	910.5	959.7	1061.6
0.9	624.3	667.0	864.7	913.2	963.1	1027.4
1.1	642.0	682.0	848.5	898.3	962.2	999.5
	Peak Area					
0.5	0.090	0.174	0.014	0.027	0.240	0.454
0.9	0.068	0.169	0.132	0.061	0.221	0.320
1.1	0.066	0.144	0.143	0.204	0.181	0.261

When the ratio of CaO/SiO₂ is increased from 0.6 to 1.1, the peaks D2 and D3 report 589.8 - 642 and 633.8 - 682 cm⁻¹ shifting respectively, which may be caused by the decrease of Si-O-Si bond angles [3].

It is assumed that the area of each peak is proportional to the concentration of structural unit. The area of each peak is plotted against CaO/SiO₂ ratio as shown in Figure 3. It is noticeable that Q4 are most abundant unit at CaO/SiO₂ ratio of 0.5. The area fractions of the D2, D3, Q3 and Q4 peaks continuously decrease, and the fractions of Q2 and Q1 increase with increasing CaO/SiO₂

ratio. This tendency qualitatively indicates that the silicate networks are depolymerized with addition of CaO.

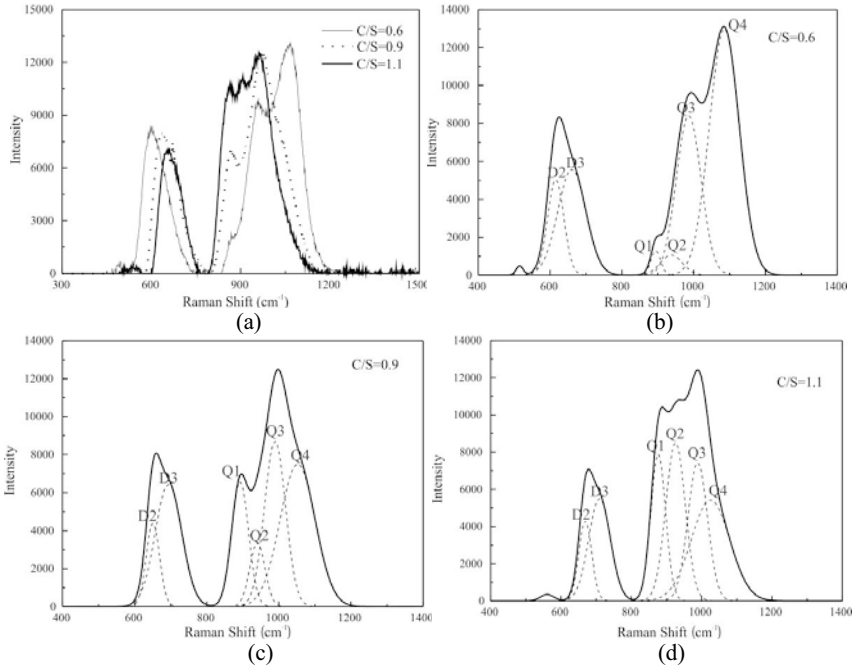


Figure 2. Raman spectra of SiO₂-CaO system at different CaO/SiO₂ molar ratios, (a) All (b) C/S=0.6, (c) C/S=0.9 and (d) C/S=1.1

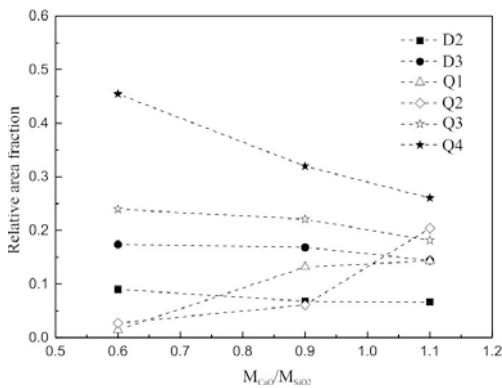


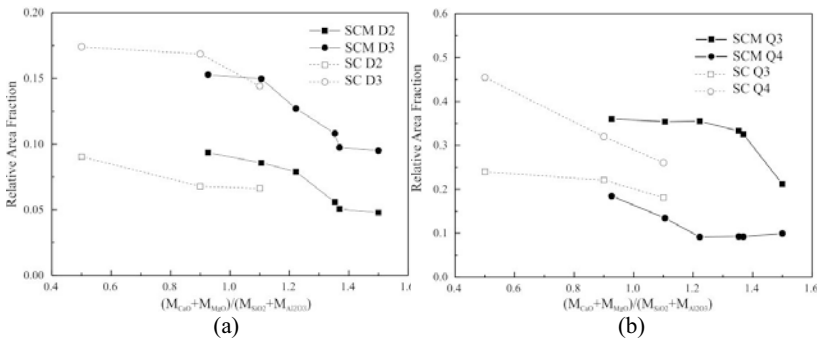
Figure 3. Abundance of structural units in the SiO₂-CaO system as a function of CaO/SiO₂ molar ratio

It is widely accepted that MgO performs as a network modifier similar to CaO [1]. At CaO/SiO₂ = 1, the Raman spectra of different MgO additions (5, 10, 15 and 20 mol%) are shown in Table IV. As the additions of MgO are increased from 5 to 20 mol%, the peaks D2 and D3 shift further from 635 to 658 cm⁻¹ and 680 to 697 cm⁻¹ respectively. However, the peaks Q1-Q4 do not have a clear shift trend with addition of MgO, which may be due to overlaps of the effects from Si-Ca and Si-Mg. From the area fraction trends, it still indicates the degradation of silicate network structure.

Table IV. Peak shift and relative area fraction of each peak in SiO₂-CaO-MgO Raman spectrum

CaO/SiO ₂	MgO mol%	D2	D3	Q1	Q2	Q3	Q4
Peak Shift							
1	5	635.3	680.1	860.7	903.2	965.0	1040.6
1	10	641.5	685.6	857.3	904.6	968.7	1061.4
1	15	655.1	696.2	853.1	895.4	960.8	1047.5
1	20	658.5	697.4	848.5	903.7	964.3	1026.4
Peak Area							
1	5	0.086	0.150	0.086	0.191	0.354	0.134
1	10	0.079	0.127	0.146	0.201	0.355	0.092
1	15	0.056	0.108	0.160	0.241	0.333	0.093
1	20	0.048	0.095	0.202	0.344	0.212	0.099

To further compare the depolymerization ability of CaO and MgO, the area of each peak is compared in the basicity ranges of 0.5 to 1.5. The molar ratio $(M_{CaO}+M_{MgO})/(M_{SiO_2}+M_{Al_2O_3})$ is used to describe the basicity in the present study. It can be seen from Figures 4 (a), (b) and (c), that the peaks D2, D3, Q3 and Q4 in both systems report a reducing trend with increasing basicity. In Figure 4c, the area fractions of peaks Q1 and Q2 increase with increasing basicity. In summary, within overlapping ranges of SiO₂-CaO and SiO₂-CaO-MgO systems, the comparisons report close area fractions in peak D2, D3 and Q1. The areas of peak Q2 and Q4 in the SiO₂-CaO system are larger than that in the SiO₂-CaO-MgO system. The degree of polymerization (DP) of two systems will be further discussed in the following section.



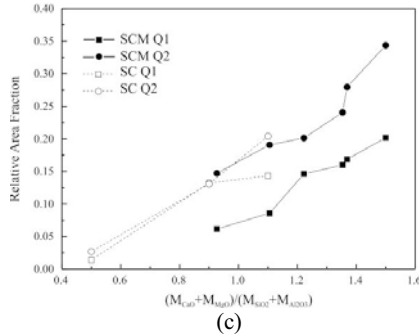


Figure 4: Area fraction of different peaks in the SiO₂-CaO and SiO₂-CaO-MgO systems as a function of basicity, (a) peak D2, D3; (b) peak Q3, Q4 and (c) peak Q1, Q2

The addition of Al₂O₃ was reported to enhance the polymerization of silicate melts [1]. Al₂O₃ will form [AlO₄]⁻ tetrahedral and connect with silicate network with charge balanced Ca²⁺. At CaO/SiO₂ = 1, Raman spectrum of the SiO₂-CaO-Al₂O₃ glass are presented in Table V.

Table V. Peak shift and relative area fraction of each peak in SiO₂-CaO-Al₂O₃ Raman spectrum

CaO/SiO ₂	Al ₂ O ₃ mol%	D2	D3	Q1	Q2	Q3	Q4
		Peak Shift					
1	5	570.7	679.9	864.1	895.2	945.8	1022.9
1	10	572.3	661.6	863.0	895.1	954.8	1037.9
1	15	551.8	657.2	874.7	913.4	966.3	1033.9
		Peak Area					
1	5	0.042	0.120	0.138	0.197	0.421	0.083
1	10	0.103	0.148	0.068	0.157	0.391	0.134
1	15	0.075	0.182	0.037	0.147	0.388	0.171

Due to the attachment of [AlO₄]⁻ unit onto silicate ring structure, the addition of Al₂O₃ shifts D2 and D3 peaks to the left, which indicates the increase of folded ring silicate structure. With the addition of Al₂O₃ content from 5 to 15 mol%, the area fractions of (Q1 + Q2) decrease, while the peak areas of (Q3 + Q4) increase. The tendencies of D2 and D3 assigned silicate ring structure are more complicated as the [AlO₄]⁻ may incorporate into silicate networks with charge compensated Ca²⁺.

Degree of polymerization

From Raman studies of the SiO₂-CaO, SiO₂-CaO-MgO and SiO₂-CaO-Al₂O₃ systems, the peaks can be classified into two groups. Peaks D2, D3, Q3 and Q4 are classified to be associated with polymerized silicate units, as their areas increase with increasing basicity. And peaks Q1 and Q2 are classified to be associated with depolymerized silicate units, because their areas decrease with increasing basicity.

In the present study, the area ratio of $(D2+D3+Q3+Q4)/(Q1+Q2)$ is used to represent the DP (degree of polymerization) index. The DP index is plotted against the basicity of the $\text{SiO}_2\text{-CaO}$, $\text{SiO}_2\text{-CaO-MgO}$ and $\text{SiO}_2\text{-CaO-Al}_2\text{O}_3$ systems. As shown in Figure 5, all three slag systems report decreasing trends while basicities increase. The degree of polymerization of the $\text{SiO}_2\text{-CaO}$ system is higher than that in the $\text{SiO}_2\text{-CaO-Al}_2\text{O}_3$ system at the same basicity, which may be due to the incorporation of the $[\text{AlO}_4]^-$ with Ca^{2+} in silicate network. At basicity 1.1, the substitution of Ca^{2+} by Mg^{2+} slightly increases the polymerization of silicate network.

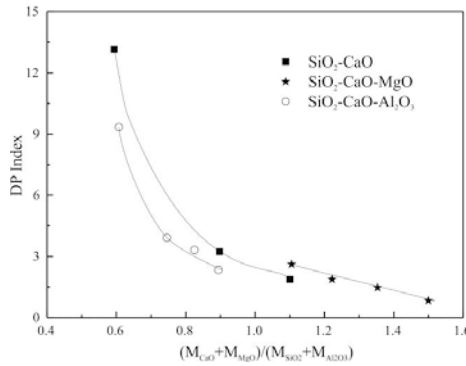


Figure 5. DP index agasin basicity for the $\text{SiO}_2\text{-CaO}$, $\text{SiO}_2\text{-CaO-MgO}$ and $\text{SiO}_2\text{-CaO-Al}_2\text{O}_3$ systems

Relationship with activation energies of slags

Arrhenius-type equation is widely used to determine the activation energy of slags. From the viscosity data in the $\text{SiO}_2\text{-CaO}$ [9], $\text{SiO}_2\text{-CaO-MgO}$ [10] and $\text{SiO}_2\text{-CaO-Al}_2\text{O}_3$ [11] systems, the activation energies can be determined and plotted against DP index. As shown in Figure 6, the activation energies clearly increase with increasing DP index. A polynomial equation can be drawn to describe the trend. Therefore, the DP index, which can be experimentally measured, can potentially be used to predict the activation energy of the silicate melts.

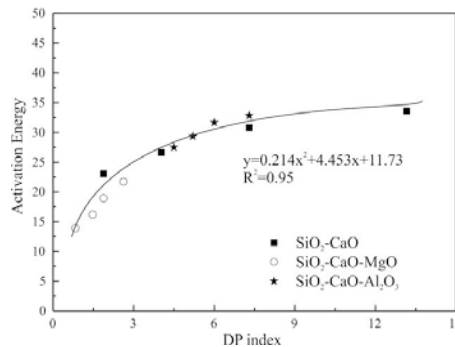


Figure 6. Correlation between activation energy and DP index of Raman spectrum

Conclusions

In the present study, the quenched slags in the SiO₂-CaO, SiO₂-CaO-MgO and SiO₂-CaO-Al₂O₃ systems were analyzed using Raman spectroscopy. The major bands located in 400-700 cm⁻¹ and 800-1200 cm⁻¹ were deconvoluted and assigned to folded rings and defect silicate units. It can be concluded that a high basicity will cause the bands at 400-700 cm⁻¹ shift to right and the bands at 800-1200 cm⁻¹ shift to left.

The peak areas of the Raman spectra can be quantitatively correlated to DP index. The DP index is proportional to the slag basicity and can be potentially used to predict the activation energy of the silicate melts.

References

1. Paul Mcmillan, "Structural studies of silicate glasses and melts applications and limitations of Raman spectroscopy", *American Mineralogist*, 69 (1984), 622-644.
2. Toshiharu Furukawa, et al, "Raman spectroscopic investigation of the structure of silicate glasses. III. Raman intensities and structural units in sodium silicate glasses", *The Journal of Chemical Physics*, 75(1981), 3226-3237.
3. F.L.Galeener, "Planar rings in glasses", *Solid state Communications*, 44 (1982), 1037-1040.
4. C.D.Yin, "Structural analysis of CaSiO₃ glass by X-Ray diffraction and Raman spectroscopy", *Journal of Non-Crystalline Solid*, 80 (1986), 167-174.
5. Corinne Remy, Bruno Reynard and Michel Madon, "Raman spectroscopic investigations of dicalcium silicate: polymorphs and high-temperature phase transformation", 80(1997), 413-423.
6. Hiroataka Fujimori, et al, " Vibrational spectra of Ca₃SiO₅: Ultraviolet laser Raman spectroscopy at high temperature", *Communications of the American Ceramic Society*, 88 (2005), 1995-1998.
7. Mao Chen and Baojun Zhao, "Phase equilibrium studies of "Cu₂O-SiO₂-Al₂O₃ system in equilibrium with metallic copper", *Journal of the American Ceramic Society*, 96 (2013), 3613-3636.
8. Kemmer G and Keller S, "Nonlinear least-squares data fitting in Excel spreadsheets", *Nature Protocols*, 5(2010), 267-281.
9. G.Urbain and Y.Bottinga, "Viscosity of liquid silica, silicates and alumino-silicates", *Geochimica et cosmochimica acta*, 46 (1982), 1061-1073.
10. T.Licko and V.Danek, "Viscosity and structure of melts in the system CaO-MgO-SiO₂", *Physics and Chemistry of Glasses*, 77 (1986), 22-26.
11. Tuneso. Saito and Yasuji Kawai, "On the viscosities of molten slags. I viscosities of CaO-SiO₂-Al₂O₃ slags", *The research institute of mineral dressing and metallurgy*, 1951, 492-501.

RELATION BETWEEN ACOUSTIC PROPERTIES AND STRUCTURES ON MOLTEN ALKALI SILICATES

Miyuki Hayashi¹

Tokyo Institute of Technology; 2-12-1 Ookayama, Meguro-ku, Tokyo 152-8552, Japan

Keywords: ultrasonic waves, molten alkali silicates, structural relaxation

Abstract

Temperature and frequency dependencies of velocities and absorption coefficients of ultrasonic waves were measured on molten 33(mol%)Na₂O-SiO₂ and 33(mol%)K₂O-SiO₂, and compositional dependencies of ultrasonic velocities were summarized using previous data on molten M₂O-SiO₂ (M = Li, Na and K) so as to elucidate the relation between acoustic properties and silicate network structures. The velocities and absorption coefficients of ultrasonic waves are identical irrespective of frequencies above ca. 1400 K for 33Na₂O-67SiO₂ and ca. 1500 K for 33K₂O-67SiO₂, respectively, while frequency dependencies appear below these temperatures. Frequency dependency stems from the structural relaxation of molten silicates. It has also been found that there is an identical linear relation between the ultrasonic velocities and the molar volumes for these alkali silicates. This indicates that the molar volume is one of the most significant factors affecting the ultrasonic velocity value instead of the ionicity of atomic bonding.

Introduction

Ultrasonic waves could be useful for refining processes. For example, size and distribution of nonmetallic inclusions in molten steel and thickness of refractory walls of blast furnace can be estimated using an ultrasonic inspection meter. Velocity and absorption coefficient of ultrasonic waves also have scientific interest because they are relevant to the thermodynamic, thermophysical and mechanical properties such as adiabatic compressibility, bulk and shear viscosities and elastic modulus. Ultrasonic waves propagate in materials as lattice vibration in analogy with thermal conduction. Mills has proposed that the thermal conductivities of molten silicates at their liquidus temperatures linearly decrease with increasing the ratio of the number of non-bridging oxygen atoms to that of tetrahedrally-coordinated atoms such as Si (denoted as NBO/T)¹. Nagata et al.² have reported that the ultrasonic velocities in the Na₂O-SiO₂ and PbO-SiO₂ systems at 1400 K decrease with decreasing silica contents, i.e., increasing NBO/T. As a consequence, it might be possible that ultrasonic velocities have the similar structural dependencies to thermal conductivities. However, the compositional dependency of ultrasonic velocities on molten silicates has not been intensively discussed from the viewpoint of the structures. One of the reasons that the compositional dependency has not been elucidated yet is that there are large discrepancies among reported ultrasonic velocities of molten silicates. Therefore, in this paper, previous data of ultrasonic velocities on molten silicates were reviewed at first, and then the compositional dependency of ultrasonic velocities of molten alkali silicates were discussed from structural viewpoint. As for the temperature dependency of acoustic properties, the ultrasonic velocity of molten silicates generally decreases with increasing

temperature. Although molten silicates exhibit so-called glass transition, there are very few reports with respect to the temperature dependency of acoustic properties of silicates around glass transition temperatures. Another aim of this paper is to measure the temperature dependencies of velocities and absorption coefficients of ultrasonic waves on molten alkali silicates so as to discuss the variation of acoustic properties with temperature around the glass transition temperature.

Experimental

The temperature and the frequency dependencies of velocities and absorption coefficients of ultrasonic waves have been measured on molten alkali silicates using the pulse transmission technique. Master glasses of (mol%) $33\text{M}_2\text{O}\cdot 67\text{SiO}_2$ ($\text{M} = \text{Na}$ and K) were prepared from reagent grade SiO_2 , Na_2CO_3 and K_2CO_3 powders. Powders were dried enough at elevated temperatures. Weighed mixtures of SiO_2 and carbonates were placed in platinum crucibles and melted in air for 20 min at temperatures around 1450°C . After being degassed, glassy samples were prepared by pouring the melts onto a copper plate and crushed to obtain the samples. Figure 1 shows the schematic diagram of experimental apparatus. The experimental setup consists of an alumina crucible (60 mm in outer diameter, 50 mm in inner diameter, and 50 mm in height) containing the sample and two buffer rods (30 mm in diameter and 265 mm in length) made of high-density polycrystalline alumina. The piezoelectric transducers of BaTiO_3 crystal for acoustic pulses with the catalog frequencies of 1, 5 and 10 MHz (Olympus, Models A114S-RB, A108S-RB and A111S-RB) were fixed to the ends of the rods in line.

A pulser-receiver (Panametrics-NDT, Model 5077PR) generated electrical signals (pulse voltage 400 V, pulse repetition rate 100 Hz), which were converted to longitudinal acoustic pulses by the lower transducer. The longitudinal acoustic pulses traveling through the liquid sample were converted to electrical signals by the upper transducer, which were detected and amplified by the same pulser-receiver, and displayed on an oscilloscope (Sony Tektronix, Model TDS520D).

After setting a sample in the furnace, the temperature was increased to the maximum measurement temperature and held at the temperature for 30 minutes. Subsequently, the sample was exposed to a vacuum for 30 minutes to remove air bubbles contained in the sample. After degassing, the vacuum pump was stopped and the air was introduced into the furnace. Measurements were carried out in air during the cooling cycle until the temperatures at which the samples were solidified and the upper rod could not be moved. At each measurement temperature, the distance between two ends of the rods was altered by changing the position of the upper rod, where the change in the distance (Δx) was measured by a cathetometer to an uncertainty of $10\ \mu\text{m}$. The transmission times were acquired for nine to ten different distances between two ends of the rods.

In order to obtain the velocity, c , and the absorption coefficient, α , from the analysis of acoustic pulse, the pulse may have to be taken as a superposition of waves with continuous frequencies instead of a single wave. Therefore, the values of c and α have been determined using Fourier transform. The detail of the analysis was described in elsewhere.³⁾

Temperature Dependencies of Acoustic Properties³⁾

Figures 2 and 3 show the temperature dependencies of the c and $\alpha\lambda$ values at 1.2, 3.6 and 6.0 MHz for $33\text{Na}_2\text{O}\cdot 67\text{SiO}_2$ and $33\text{K}_2\text{O}\cdot 67\text{SiO}_2$, respectively, where λ is the wavelength of ultrasonic waves. $\alpha\lambda$ means the absorption per wavelength. Figs. 2 and 3 also include previous data.^{4,5)} The liquidus temperatures of the samples are indicated by the dashed lines with 'L.T.'. The error bars represent the standard deviations of nine to ten c and α values measured by changing the position of the upper buffer rod nine to ten times. The measurements for $33\text{Na}_2\text{O}\cdot 67\text{SiO}_2$ and $33\text{K}_2\text{O}\cdot 67\text{SiO}_2$ were carried out until 898 K and 1113 K, respectively, which are around 200 K lower than the respective liquidus temperatures. It has been found that both samples are glassy after the experiments. It can be seen from Figs. 2 and 3 that the c and $\alpha\lambda$ values are identical irrespective of frequencies above ca. 1400 K for $33\text{Na}_2\text{O}\cdot 67\text{SiO}_2$ and ca. 1500 K for $33\text{K}_2\text{O}\cdot 67\text{SiO}_2$, respectively, while frequency dependency appears below these temperatures. Frequency dependency stems from the structural relaxation of molten silicates, which can be explained as follows: Molten silicates exhibit "glass transition", which corresponds to a kinetic barrier dividing the behavior of silicate melts into two types, liquid and glassy. Liquid behavior is the equilibrium response of a melt to an applied perturbation. Glassy behavior occurs when the timescale of the perturbation is too short for melt equilibrium, that is, when the time required for structural rearrangements is much longer than the timescale of our observations. The time- or frequency- dependent response of the structure and properties of a melt to a perturbation is termed "relaxation". Relaxation occurs around the glass transition temperature. It has been reported that the conventional "glass transition temperatures" obtained by thermal expansion measurement are 729 K for $33\text{Na}_2\text{O}\cdot 67\text{SiO}_2$ and 755 K for $33\text{K}_2\text{O}\cdot 67\text{SiO}_2$.⁶⁾ In ultrasonic studies, the observation timescale is microseconds instead of seconds for thermal expansion. Hence, the temperature around which the relaxation occurs is raised by several hundred degrees above the conventional glass transition temperatures.

It is found from Figs. 2 and 3 that the $\alpha\lambda$ value increases and then decreases with decreasing temperature. This can be explained as follows: For a liquid at high temperatures, the structure is in equilibrium and the response of a melt to acoustic pressure is instantaneous. Upon cooling of the liquid into the glass transition region, the response of a melt to acoustic pressure is delayed. The absorption of acoustic energy is associated with this delay between acoustic pressure and the medium response (density or volume change). As decreasing temperature, the delay becomes larger, and the absorption of acoustic energy becomes greater. However, when the temperature decreases further, the structure of the glass is becoming frozen and hardly responds to acoustic pressure, resulting in the less absorption of acoustic energy. Consequently, the peak temperature of the $\alpha\lambda$ versus T curve corresponds to the glass transition temperature for ultrasonic waves.

Figure 4 shows the reciprocal of glass transition temperature versus logarithm of the reciprocal of frequency, that is, logarithm of the observation time. Here, it is assumed that the observation time is 1 s for thermal expansion. It can be seen that there is an identical relation between glass transition temperatures and observation times for the different observation techniques of glass transition temperatures, as Webb has suggested.⁷⁾

Compositional Dependencies of Ultrasonic Velocities⁸⁾

Figures 5 through 7 show the reported ultrasonic velocities of the M_2O - SiO_2 systems ($M = Li, Na$ and K) at 1573 K as a function of the M_2O content. The velocity of the Li_2O - SiO_2 system increases from ca. $2700 \text{ m} \cdot \text{s}^{-1}$ to ca. $3200 \text{ m} \cdot \text{s}^{-1}$ with increasing the Li_2O content from 30 mol% to 60 mol% except for the data reported by Bloom and Bockris.⁹⁾ With respect to the discrepancy between the data by Bloom and Bockris and others, Baidov and Kunin¹⁰⁾ and Rivers and Carmichael¹¹⁾ have pointed out that the alumina buffer rods that Bloom and Bockris used may have been seriously corroded in the melts during the experiment. Corrosion of alumina buffer rods would increase the true wave path length in the melts, leading to an underestimate of the sound speed. The velocity of the Na_2O - SiO_2 system slightly increases from ca. $2500 \text{ m} \cdot \text{s}^{-1}$ to ca. $2700 \text{ m} \cdot \text{s}^{-1}$ with increasing the Na_2O content from 15 mol% to 60 mol% except for the data reported by Shiraishi et al.¹²⁾ The reason for the deviation in the results of Shiraishi et al. is not clear. On the other hand, the velocity of the K_2O - SiO_2 system decreases from ca. $2400 \text{ m} \cdot \text{s}^{-1}$ to ca. $1800 \text{ m} \cdot \text{s}^{-1}$ with an increase in the K_2O content from 20 mol% to 50 mol% except for the value obtained by Shiraishi et al.,¹²⁾ which is much higher than other data. They have used an ultrasonic frequency as large as 10 MHz while other researchers have used frequencies less than 4 MHz. As aforementioned, the ultrasonic velocity is generally independent of the frequency of waves, i.e., dispersionless. Dispersion means that the velocity varies with frequency. In fact, dispersion happens at very high frequencies (for example, with thermal phonons near the Brillouin zone boundaries) or for high viscous materials, in which part of the atomic movements cannot follow high frequencies of ultrasonics. In such an unrelaxed region, the velocity increases with an increase in the frequency. In fact, Bidov and Kunin¹⁰⁾ have measured the velocities at the frequencies of 1 and 4.7 MHz, and have observed the dispersion in the melts of K_2O - SiO_2 having viscosities of the order of magnitude $100 \text{ Pa} \cdot \text{s}$. Therefore, it is considered that 10 MHz is the frequency far above the relaxation region of the melt, and Shiraishi et al. have measured an unrelaxed ultrasonic velocity.

It is surprising that the ultrasonic velocities do not always decrease with decreasing silica contents, i.e., increasing NBO/T. Figure 8 shows the relation between the ultrasonic velocities at 1573 K and the molar volumes.⁸⁾ It can be found that there is an identical linear relation between the ultrasonic velocities and the molar volumes. This indicates that the molar volume is one of the most significant factors affecting the ultrasonic velocity value. The difference between thermal conductivity and ultrasonic velocity with respect to their dependencies on NBO/T can be explained as follows: Vibrational cycles of thermal phonons (GHz to THz) are shorter than the average times required for the cutting and bridging of Si-O-Si bonds due to the movement of metallic ions. As a result, conductive heat transfer occurs reflecting the ionicity (or covalency) of atomic bonding. On the other hand, vibrational cycles of acoustic waves are longer than the times for the rearrangement of silicate structures. Therefore, the transfers of acoustic waves may be hardly affected by the ionicity of atomic bonding.

Conclusions

Temperature and frequency dependencies of velocities and absorption coefficients of ultrasonic waves were measured on molten $33(\text{mol}\%)Na_2O$ - SiO_2 and $33(\text{mol}\%)K_2O$ - SiO_2 , and compositional dependencies of ultrasonic velocities were summarized on molten M_2O - SiO_2 ($M =$

Li, Na and K) so as to elucidate the relation between acoustic properties and silicate network structures. The following results were obtained:

- (1) The velocities and absorption coefficients of ultrasonic waves are identical irrespective of frequencies above ca. 1400 K for $33\text{Na}_2\text{O}\cdot 67\text{SiO}_2$ and ca. 1500 K for $33\text{K}_2\text{O}\cdot 67\text{SiO}_2$, respectively, while frequency dependency appears below these temperatures. Frequency dependency stems from the structural relaxation of molten silicates.
- (2) There is an identical linear relation between the ultrasonic velocities and the molar volumes for various alkali silicates. This indicates that the molar volume is one of the most significant factors affecting the ultrasonic velocity value.

References

- 1) K. C. Mills: Proc. 3rd Inter. Conf. on Metall. Slags and Fluxes, Inst. Metals, Glasfor, (1989), 229.
- 2) K. Nagata, K. Ohira, H. Yamada and K. S. Goto: *Met. Mat. Trans. B*, **18B** (1987), 549.
- 3) M. Hayashi, Y. Kitamura and K. Nagata: *ISIJ Int.*, **52** (2012), 1740.
- 4) J. O'M. Bockris and E. Kojonen: *J. Am. Chem. Soc.*, **82** (1960), 4493.
- 5) V. V. Baidov and L. L. Kunin: *Sov. Phys. Dokl.*, **13** (1968), 64.
- 6) T. Maehara, PhD thesis, Tokyo Institute of Technology (2005), 42.
- 7) S. L. Webb: *Chem. Geol.*, **96** (1992), 449.
- 8) M. Hayashi, Y. Matsuzono and K. Nagata: *ISIJ Int.*, **51** (2011), 689.
- 9) H. Bloom and J. O'M. Bockris: *J. Phys. Chem.*, **61** (1957) 515.
- 10) V. V. Baidov and L. L. Kunin, *Sov. Phys. Dokl.*, (English Translation) **13** (1968) 64.
- 11) M. L. Rivers and I. S. E. Carmichael, *J. Geophysical Research*, **92** (1987) 9247.
- 12) Y. Shiraishi, M. Yamashita, Y. Tokunaga and A. Tanaka, *Proc. 8th Inter. Conf. on Molten Slags, Fluxes and Salts*, Santiago, Chile, January, CD-ROM (2009).

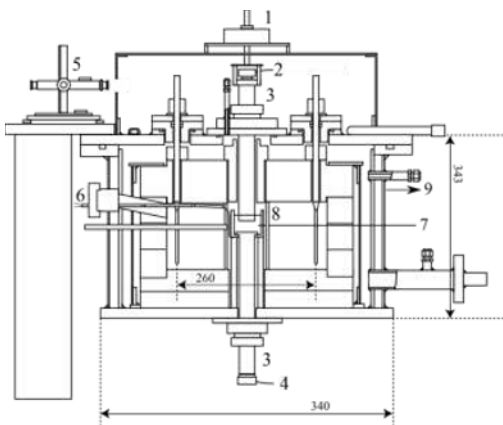


Fig.1 Schematic diagram of the experimental apparatus with actual dimensions (mm). 1. Induction motor, 2. Receiver, 3. Al_2O_3 rod, 4. Pulsar, 5. Cathetometer, 6. Thermocouple, 7. Sample, 8. Ceramics tube, 9. Vacuum pump.

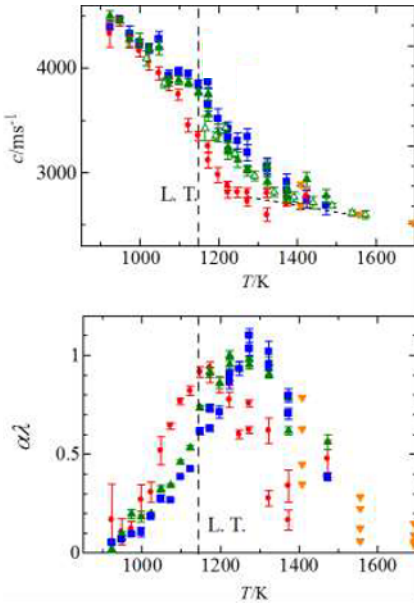


Fig.2 Temperature dependencies of the c and $\alpha\lambda$ values at various frequencies (\circ 1.2 MHz, \triangle 3.6MHz and \square 6.0MHz) for $33\text{Na}_2\text{O}\cdot 67\text{SiO}_2$. The dashed line after Bockris and Kojonen.⁴⁾

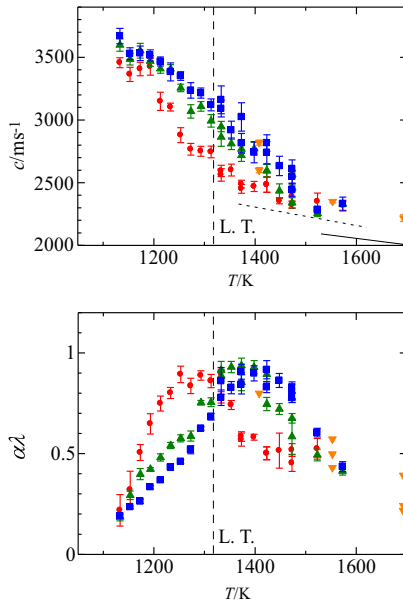


Fig.3 Temperature dependencies of the c and $\alpha\lambda$ values at various frequencies (\circ 1.2 MHz, \triangle 3.6MHz and \square 6.0MHz) for $33\text{K}_2\text{O}\cdot 67\text{SiO}_2$. The plain line after Baidov and Kunin⁵⁾ and the dashed line after Bockris and Kojonen⁴⁾.

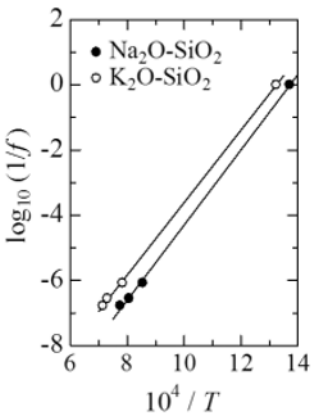


Fig.4 Reciprocal of glass transition temperature versus logarithm of the reciprocal of frequency, that is, logarithm of the observation time.

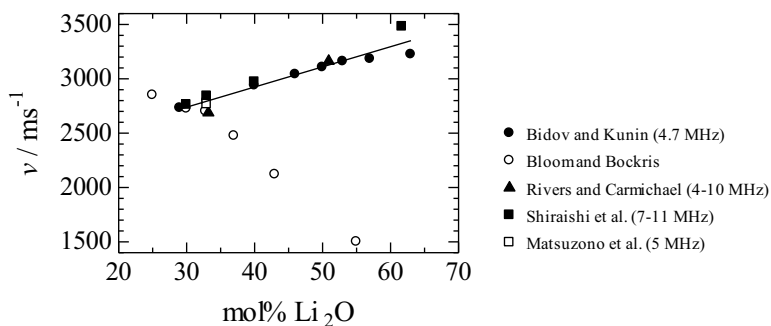


Fig.5 Velocities of the $\text{Li}_2\text{O-SiO}_2$ systems at 1573 K as a function of the Li_2O content (mol%).

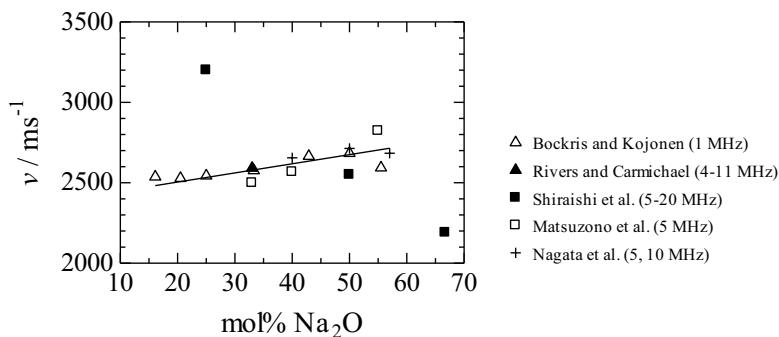


Fig.6 Velocities of the $\text{Na}_2\text{O-SiO}_2$ systems at 1573 K as a function of the Na_2O content (mol%).

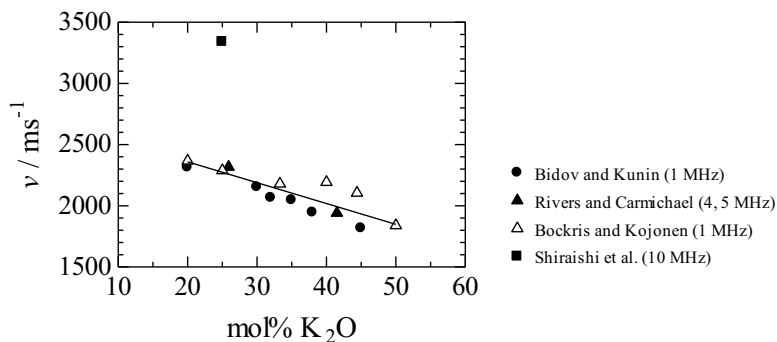


Fig.7 Velocities of the $\text{K}_2\text{O-SiO}_2$ systems at 1573 K as a function of the K_2O content (mol%).

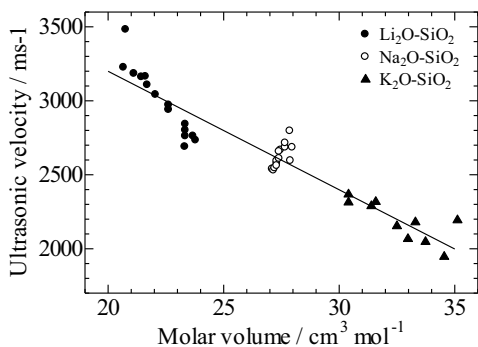


Fig.8 Velocities of the M₂O-SiO₂ systems (M = Li, Na and K) at 1573 K as a function of the M₂O content (mol%).

**ADVANCES IN MOLTEN
SLAGS, FLUXES, AND SALTS:**

Proceedings of



**Use of Slags, Fluxes
and Salts in Recycling**

EQUILIBRIA OF GOLD AND SILVER BETWEEN MOLTEN COPPER AND $\text{FeO}_x\text{-SiO}_2\text{-Al}_2\text{O}_3$ SLAG IN WEEE SMELTING AT 1300 °C

Katri Avarmaa¹, Hugh O'Brien², Pekka Taskinen¹

¹Aalto University School of Chemical Technology, Department of Materials Science and Engineering, Metallurgical Thermodynamics and Modeling Research Group; Vuorimiehentie 2K, PO Box 16200, FI-00076 Aalto, Finland

²Geological Survey of Finland; Betonimiehenkuja 4, 02150 Espoo, Finland.

Keywords: Distribution, Precious metal, Copper smelting, E-scrap, EPMA, LA-ICP-MS

Abstract

Waste Electrical and Electronic Equipment (WEEE) offers a significant resource for precious metals such as gold and silver. To maximize precious metal recoveries and sustainable use their behavior during WEEE smelting with copper as the collector metal needs to be characterized. This study experimentally determines the distributions of gold and silver between metallic copper and $\text{FeO}_x\text{-SiO}_2\text{-Al}_2\text{O}_3$ slag ($L^{\text{Cu/s}}[\text{Me}] = [\text{Me}]_{\text{Copper}}/[\text{Me}]_{\text{slag}}$) in alumina-saturation over the oxygen potential range of $10^{-5}\text{-}10^{-10}$ atm at 1300 °C. The experiments were conducted employing equilibration / quenching followed by major element analysis by Electron Probe Micro-Analysis (EPMA) and trace element analysis by Laser Ablation Inductively Coupled Mass Spectrometry (LA-ICP-MS) techniques. Our results show silver distribution increased exponentially from 30 to 1000 as a function of decreasing oxygen partial pressure. Gold distribution was 10^5 at $p_{\text{O}_2} = 10^{-5}$ atm and $>10^6$ at $p_{\text{O}_2} = 10^{-6}\text{-}10^{-10}$ atm.

Introduction

The most important industrial use of gold and silver is in electrical and electronic equipment (EEE). Their quantities in electronics vary widely depending on the e-product and also through time and location [1]. In much of today's sophisticated electronic equipment, including cell phones, computers and televisions, the precious metal amounts are considerable, even up to several thousands of ppm [2]. Thus, Waste Electrical and Electronic Equipment (WEEE) can be considered a high-potential resource for gold and silver. The recoveries of gold and silver from WEEE are favorably performed in the current copper-making circuits including copper converters and secondary copper smelters such as the Ausmelt furnace [1, 3].

The research concentrating on minor element behavior in WEEE smelting is a relatively new field of science, and no experimental study has been performed to investigate gold and silver distributions between copper and alumina-saturated $\text{SiO}_2\text{-FeO}_x\text{-Al}_2\text{O}_3$ slags. The presence of alumina refers to scrap-copper ie. copper raffinate, which contains significant amounts of aluminum after mechanical separation [4, 5]. Overall, the literature concerning silver and gold behavior in slags is surprisingly scarce and lacks an agreement in solubility and in the dissolution mechanisms. Silver distribution in the copper matte-slag system has been investigated recently with ambiguous results [6-10]. However, silver equilibria in copper-slag systems have been

examined only in few experimental studies [10-13] and thermodynamic assessments (also Au) [14-16] despite numerous silver solubility studies in basic binary slags [17-21]. Gold equilibria in matte-slag system have been also explored by us [6, 7] and Yamaguchi *et al.* [22, 23]. Results from previous studies suggest that gold solubility in iron-silicate slag is effectively zero [24-27], and this idea has been used to detect mechanical copper or copper matte entrainment in slag. Interestingly, these studies reported gold concentrations of 40-80 ppm [25], 80 ppm [24] and 0-800 ppm (50-400 ppm for most of the data points) [26] in slags. Additionally, only few other experimental studies about gold solubility in slags have been performed [12, 28, 29].

The purpose of the present study is to investigate the distribution behavior of gold and silver between molten copper and alumina-saturated iron-silicate slag in the partial pressure range of $p_{O_2} = 10^{-5}$ – 10^{-10} atm at $t = 1300$ °C. The initial alumina concentration in the slag was set to 20 wt% in order to simulate the presence of aluminum in WEEE.

Experimental Procedure

Sample preparation

The copper master alloy was prepared by melting copper cathode (Boliden Harjavalta, 99.999 %) with approximately 1 wt% of Ag (Alfa Aesar, 99.95 %) and Au (Alfa Aesar, 99.95 %) in an alumina crucible. The melting was performed at 1400 °C under 99 % Ar – 1 % H₂ gas atmosphere for 12 hours. The master alloy was analyzed by EPMA. The initial gold content was measured to be 0.58 ± 0.13 wt% and silver 0.72 ± 0.21 wt%.

The slag mixture was prepared from pure commercial powders of Fe₂O₃ (Alfa Aesar, 99.99 %), SiO₂ (Umicore, 99.99 %) and Al₂O₃ (Sigma-Aldrich, 99.99 %). The components were weighed out to an initial composition of 52 % of Fe₂O₃, 28 % of SiO₂ and 20% of Al₂O₃. The slag components were thoroughly ground and mixed in agate mortar to form a homogeneous slag powder blend.

Experimental apparatus and method

The equilibration experiments were performed in a vertical tube furnace (Lenton LTF 16/45/450) including silicon carbide heating elements and an alumina reaction tube (impervious recrystallized alumina, 45 mm OD and 38 mm ID). The controller unit of the furnace was a Eurotherm 3216 PID. The furnace temperature was measured with a calibrated S-type Pt / 90 % Pt – 10 % Rh thermocouple (Johnson-Matthey, UK, accuracy ± 3 °C) and the ambient room temperature with a Pt100 sensor (Platinum Resistance Thermometer; SKS Group, Finland). The Pt100 sensor and the S-type thermocouple were connected to a Keithley 2000 and 2010 multimeter – data loggers and the temperature measurement data were collected employing a NI LabVIEW temperature logging program. The experimental apparatus is illustrated schematically in Figure 1.

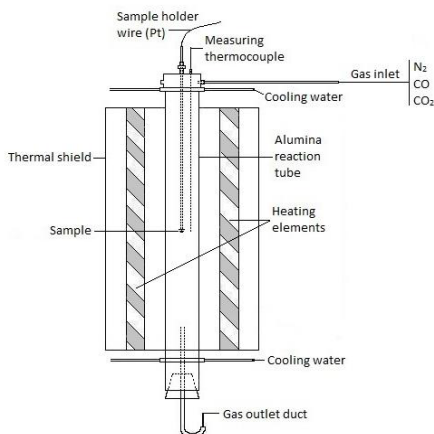


Figure 1. The experimental apparatus.

Three gases were connected to the inlet gas train: N₂ (purity ≥ 99.99 %), CO 4.7 (purity ≥ 99.997 %) and CO₂ 5.2 (purity ≥ 99.9992 %; all from AGA, Finland). N₂ were controlled by rotameter after each experiment as flushing gas, whereas the reagent gases of CO and CO₂ were controlled by mass-flow controllers (Aalborg DFC26, USA; accuracy ±1 % of full scale). CO-CO₂ mixtures were employed in order to control the oxygen partial pressure (pO₂) in the furnace at the experimental temperature (1300 °C). The equilibrium reaction considered for gas atmosphere is,



The equilibrium constant K for reaction (1) is,

$$K = \frac{p_{CO_2}}{p_{CO} \cdot p_{O_2}^{0.5}}. \quad (2)$$

The CO₂/CO ratios to produce the required oxygen partial pressures at 1300 °C were calculated using a K value of 71985.23 [31] and p_{O₂}^{0.5} of the target partial pressure. The calculated CO₂/CO ratios for each oxygen partial pressure are shown in Table I. The CO₂/CO ratio was set for a total gas flow of 300 ml/min.

Table I. Calculated CO₂/CO flow ratios at 1300 °C.

p _{O₂} (atm)	CO ₂ /CO ratio
1x10 ⁻⁵	227.64
1x10 ⁻⁶	71.99
1x10 ⁻⁷	22.76
1x10 ⁻⁸	7.20
1x10 ⁻⁹	2.28
1x10 ⁻¹⁰	0.72

The required experimental time was determined with a set of experiments 1 h, 2 h, 4 h, 8 h and 16 h. According to SEM-EDS results for the slag, aluminous spinels and copper on these test samples, equilibrium was reached in 8 h. However, to absolutely ensure full equilibrium, the run time for the experiments was set to 16 h. For each experiment, approximately 250 mg of copper master alloy and 250 mg of slag mixture were placed into an alumina crucible. Commercial alumina (Degussit AL23, >99.5 % Al₂O₃) crucibles with ID of 8mm, OD of 10mm and depth of 15mm supplied by Friatec NA, Germany were employed in the experiments. Two sets of experiments were executed. The alumina crucible was hooked to a platinum wire (0.5 mm diameter) in the bottom end of the reaction tube and introduced into the furnace. While the gas atmosphere was stabilized for 30–60 minutes, the sample was kept in the cold zone of the furnace, after which the sample was pulled into the hot zone of the furnace and equilibration initiated. As the equilibration time (16 h) was reached, the sample was released and quickly quenched in an ice-water mixture.

Specimen analysis

The specimens were prepared for microanalysis by cutting the sample into half, mounting the cross-sections in epoxy resin and employing traditional wet metallographic techniques to achieve polished sections. The analyses were performed with a Cameca SX100 EPMA with Wavelength Dispersive spectrometers (WDS) and an Excite193 nm ArF laser ablation system (Teledyne CETAC Technologies, Omaha, USA) with a Nu AttoM SC ICPMS (Nu Instruments Ltd., Wrexham, UK).

The EPMA analyses were performed on copper, slag and solid aluminous spinel. The EPMA analyzing conditions used were: accelerating voltage 20 kV and beam current 40 nA. The beam diameter varied depending on the analyzed phase, for copper 100 μ m, for spinel 1 μ m and for slag 10–100 μ m. The average elemental detection limits obtained are presented in Table II. The detection limits were not sufficient to define the precious metal concentrations in slag and in aluminous spinels reliably.

Table II. Elemental detection limits of EPMA (ppm).

O	Si	Cu	Al	Fe	Ag	Au
1315	223	239	240	230	402	1753

LA-ICP-MS analyses was performed to detect gold and silver concentrations in slag. 11 analysis spots were taken from each sample. The laser was run at a pulse frequency of 10 Hz and a pulse energy of 4 mJ at 40 % attenuation to produce a energy flux of 2.99 J/cm² on the sample surface with a 40 μ m spot size. Analyses were made using time resolved analysis (TRA), with each analysis consisting of 20 seconds of background measurement prior to switching the laser on for 60 seconds of signal measurement. Synthetic NIST SRM 612 glass (concentrations reported in Jochum *et al.* [32]) and ²⁹Si have been used, respectively, as external and internal standards for quantification along with the USGS reference glass BHVO-2G as an internal check on data quality. The measurements were performed over 12 elements (Mg, Al, Si, Ca, Fe, Co, Ni, Cu, Ag, Pt, Au, Pb) at low resolution ($\Delta M/M = 300$) using the fast scanning mode. Baseline reduction and quantification of the trace element data was performed using the Glitter software package (GEMOC Laser ICP-MS Total Trace Element Reduction; Macquarie University, Australia). The instrumental uncertainty of the LA-ICP-MS technique was ± 5 –10 %.

Results and discussion

Compositions of copper and slag

The experimental results, as calculated averages with standard deviations (1σ) for copper alloy and slag, are presented in Table III and Table IV, respectively.

Table III. EPMA results (wt-%) for copper alloy phase.

sample no.	pO ₂ (atm)	Cu	Ag	Au	O
F7	10 ⁻⁵	95.66±0.13	0.90±0.05	0.81±0.06	0.88±0.05
F19	10 ⁻⁵	94.99±0.17	1.02±0.04	1.06±0.11	1.07±0.12
F8	10 ⁻⁶	95.63±0.35	0.82±0.08	0.83±0.08	0.86±0.13
F25	10 ⁻⁶	96.09±0.11	0.95±0.08	0.82±0.07	0.59±0.08
F3	10 ⁻⁷	95.79±0.20	0.89±0.07	0.84±0.08	0.73±0.10
F21	10 ⁻⁷	96.05±0.17	0.94±0.10	0.81±0.08	0.77±0.05
F9	10 ⁻⁸	95.27±0.29	0.88±0.04	0.83±0.07	0.69±0.05
F26	10 ⁻⁸	96.05±0.11	0.93±0.07	0.82±0.06	0.65±0.07
F10	10 ⁻⁹	95.63±0.30	0.81±0.03	0.77±0.05	0.70±0.05
F27	10 ⁻⁹	96.04±0.12	0.90±0.05	0.85±0.07	0.63±0.05
F11	10 ⁻¹⁰	95.65±0.20	0.81±0.05	0.70±0.10	0.70±0.06
F18	10 ⁻¹⁰	95.36±0.12	0.94±0.05	0.83±0.05	0.72±0.06

Table IV. Slag analysis; EPMA results for main elements and LA-ICP-MS results for silver and gold. The number in brackets ⁰ refers to the number of analysis spots in which gold was observed above the detection limit and used to calculate the averages.

Sample no.	pO ₂ (atm)	EPMA (wt%)					LA-ICP-MS (ppm)	
		O	Si	Cu	Al	Fe	Ag	Au
F7	10 ⁻⁵	33.30±0.37	11.08±0.22	23.94±0.55	9.27±0.18	22.30±0.31	596.41±72.58	0.12±0.05
F19	10 ⁻⁵	34.22±0.18	11.88±0.23	22.18±0.61	9.58±0.09	22.02±0.26	624.92±47.50	0.05±0.01
F8	10 ⁻⁶	35.28±0.30	14.44±0.23	12.28±0.27	10.06±0.15	27.88±0.11	257.95±8.57	0.0066 ⁽⁵⁾
F25	10 ⁻⁶	37.19±0.53	15.26±0.43	10.14±0.50	9.64±0.21	27.70±0.35	269.25±31.92	0.0069 ⁽⁵⁾
F3	10 ⁻⁷	36.16±0.47	15.57±0.22	5.38±0.03	9.82±0.17	33.01±0.18	116.92±16.77	0.0065 ⁽²⁾
F21	10 ⁻⁷	37.91±0.44	15.72±0.10	5.02±0.13	10.50±0.07	30.80±0.28	116.91±10.69	0.0075 ⁽⁴⁾
F9	10 ⁻⁸	37.29±0.19	15.57±0.08	2.87±0.02	10.20±0.08	34.09±0.14	61.60±3.28	0.0066 ⁽²⁾
F26	10 ⁻⁸	38.62±0.22	15.07±0.12	2.52±0.05	9.51±0.08	34.22±0.14	44.11±6.34	0.0094 ⁽²⁾
F10	10 ⁻⁹	36.79±0.17	15.76±0.12	1.51±0.02	10.42±0.07	35.46±0.13	25.43±4.04	0.0073 ⁽²⁾
F27	10 ⁻⁹	37.10±0.17	16.21±0.07	1.42±0.01	10.47±0.06	34.73±0.16	24.49±0.67	0.0051 ⁽²⁾
F11	10 ⁻¹⁰	38.64±0.24	14.94±0.07	0.80±0.01	9.92±0.09	35.65±0.26	11.32±0.37	0.0070 ⁽⁵⁾
F18	10 ⁻¹⁰	39.39±0.11	15.28±0.08	0.70±0.03	9.79±0.12	34.78±0.12	12.24±0.22	n.d. ⁽⁰⁾

The concentrations of gold and silver in copper stayed constant as a function of oxygen partial pressure. Smaller amounts of silicon (0.01–0.5 wt%), iron (0.01–0.7 wt%) and aluminum (0.03–0.04 wt%) were also detected in the copper phase.

The slag composition is highly dependent on the oxygen partial pressure, as can be seen in Table IV. Gold solubility in slag was mainly below the detection limits. Only for the highest oxygen partial pressure was gold detected in all analysis spots within the detection limits of LA-ICP-MS method employed. In lower oxygen partial pressures, gold was detected at concentrations between 5 and 9 ppb, and the average concentrations were calculated from the observed values in 0–5 analysis spots (marked in brackets in Table IV). To be strictly statistically correct, gold should be marked as n.d. (not detected) for all samples but F7 and F19.

Distribution coefficients of precious metals between copper and slag

The distribution coefficients of precious metals Me between copper and slag phases was defined as:

$$L^{Cu/s}[Me] = \frac{[wt-\%Me]_{copper}}{(wt-\%Me)_{slag}}, \quad (3)$$

where Me refers to silver and gold. The ratio is determined from the EPMA and LA-ICP-MS analyses, see Tables III and IV. The uncertainties for the distribution coefficients were calculated from the equation:

$$\frac{\sigma L^{Cu/s}[Me]}{L^{Cu/s}[Me]} = \left(\frac{\sigma}{\bar{x}}\right)_{slag} + \left[\frac{\sigma}{\bar{x}}\right]_{copper}, \quad (4)$$

where σ and \bar{x} are the standard deviations and the (arithmetic) averages of Me respectively in slag () and copper [] phases.

The obtained distribution coefficients of silver with uncertainties as a function of oxygen partial pressure is presented in Figure 2. The (logarithmic) distribution coefficients increase linearly along with decreasing oxygen partial pressure with slope of 1/3.

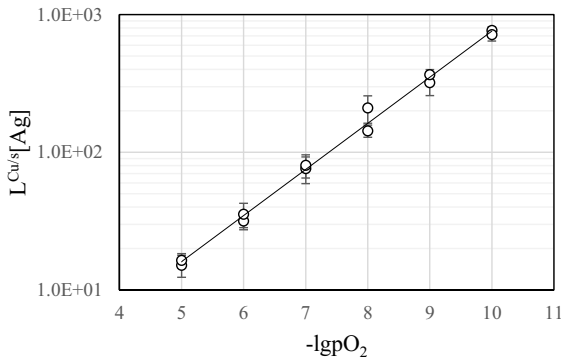


Figure 2. Distribution coefficients of silver between copper and FeO_x-SiO₂-Al₂O₃ slag at 1300 °C at a range of pO₂.

The observed solubility of gold in the slag was mainly below the elemental detection limit of out LA-ICP-MS method employed, being above the detection limit only in the highest pO_2 experiments. Figure 3 presents the distribution coefficient of gold between copper and slag as a function of oxygen partial pressure. The distribution coefficient of the detection limit (solid trend line) was calculated using the LA-ICP-MS detection limits of gold for the slag in the current measurements.

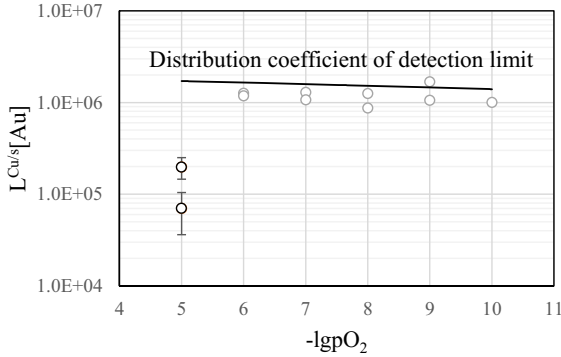


Figure 3. Distribution coefficients of gold between copper and $FeO_x-SiO_2-Al_2O_3$ slag at 1300 °C at a range of pO_2 .

The distribution coefficients of gold in the pO_2 range 10^{-6} to 10^{-10} are not reliable as they are calculated only from 2-5 analysis spot results. So, in reality the true distribution coefficients are greater than the distribution coefficient of the detection limit in the pO_2 range 10^{-6} – 10^{-10} atm, and hence, these values can be used as the minimum distribution coefficients of gold in this partial pressure range. It can be concluded that in $pO_2 = 10^{-5}$ atm the distribution coefficient for gold is around 10^5 and in the pO_2 range 10^{-6} – 10^{-10} atm, it is above 10^6 .

The distribution equilibria of minor element Me between metal and slag can be presented with the following equation [16, 19, 33]:



If the compositions of the phases and the activity coefficients of the species do not vary significantly, then equation (5) can be rewritten as:

$$Lg L^{Cu/s}[Me] = n/2lg pO_2 + lg C, \quad (6)$$

where C includes the activity coefficients, the equilibrium constant of equation (5) and the total number of moles in slag and copper. This thermodynamic approach can be used to define the oxidation state of the minor element in the slag. For silver, the slope of 1/3 (Figure 2) suggests a silver oxide form Ag_3O_2 . However, there is no known silver oxide of this form, so possibly silver exists in the slag as a combination of different Ag species. Most previous studies have suggested Ag^+ ions ($AgO_{0.5}$) [10, 13, 18, 19] and Ag^0 [11, 30] in slag. However, although Takeda [10]

suggested Ag^+ ions to be present in slags, some of his slopes were close to 1/3 as in our study. In general, the distribution coefficient of silver in our study for alumina-saturated iron-silicate slags was higher than in Takeda's study [10] for all investigated slags.

Without any proper dependency between the distribution coefficient of gold and oxygen partial pressure, gold can be considered to dissolve into the slag as metallic species (Au^0). In Swinbourne's research [28] a combination of several Au species in IS and CF slags were suggested. In general, all the previous experimental studies [19, 24-26, 28, 29] show a higher gold solubility in the slags. In Celmer's study [34] of gold distribution in nickel matte-slag system, $L^{m/s}[\text{Au}]$, a significant difference between alumina-saturated and silica-saturated iron-silicate slag was found. At high matte grade (70 % Ni) the $L^{m/s}[\text{Au}]$ was 6x higher in alumina-saturation compared to silica-saturation. The solubility, dissolution mechanism and form of precious metals in slag are dependent on the oxygen pressure, temperature, the equilibrium system and the slag composition, especially basicity [20, 28]. Thus, as no previous studies in this system at these conditions exist, information drawn from the previous studies should be considered relevant but not directly analogous and comparable to the results presented here.

Conclusions

With only limited information presently available on the precious metal behavior in copper-slag systems, this investigation provides valuable new insights and results in the field of WEEE smelting and the copper manufacturing technologies. The equilibrium distributions of gold and silver between copper and alumina-saturated $\text{FeO}_x\text{-SiO}_2\text{-Al}_2\text{O}_3$ slag were determined in the oxygen partial pressure range $10^{-5}\text{-}10^{-10}$ atm at 1300 °C. An advanced and very sensitive experimental method, equilibration-quenching-EPMA/LA-ICP-MS, was applied in this study. The silver distribution coefficient increased exponentially from 30 to 1000 as a function of decreasing oxygen partial pressure. The gold distribution $L^{\text{Cu/s}}[\text{Au}]$ is 10^5 at $p\text{O}_2 = 10^{-5}$ atm and 10^6 at a minimum for $p\text{O}_2 = 10^{-6}\text{-}10^{-10}$ atm. Further work, with higher doping levels and improved measurement parameters, should allow better definition of gold distribution at low $p\text{O}_2$ in these systems.

Acknowledgements

This research was financially supported by CLEEN Oy (Click Innovations OY), Kuusakoski Oy and Outotec as a part of ARVI project. The assistance of Lassi Pakkanen (GTK) in the EPMA analyses and Lassi Klemettinen in the LA-ICP-MS analyses is greatly appreciated.

References

- [1] J. Cui, L. Zhang, *Journal of Hazardous Materials*, 158 (2008), 228-256.
- [2] P. Chancerel, *Journal of Industrial Ecology*, 13 (2009), 791-810.
- [3] M.E. Schlesinger *et al.*, *Extractive Metallurgy of Copper* (5th edition, Oxford UK: Elsevier, 2011), 455.

- [4] M. Pizzol, M.S. Andersen, M. Thomsen, "Greening of Electronics" (Danish Ministry of the Environment, Environmental, Project No. 1416, 2012).
- [5] G. John *et al.*, "MTDATA and the Prediction of Phase Equilibria in Oxide Systems: Thirty Years of Industrial Collaboration", Submitted to *Metallurgical and Materials Transactions B*, 2016.
- [6] K. Avarmaa *et al.*, *Journal of Sustainable Metallurgy*, 1 (2015), 216-228.
- [7] K. Avarmaa, H. Johto, P. Taskinen, *Metallurgical and Materials Transactions B*, 47 (2014), 244-255.
- [8] G. Roghani, Y. Takeda, K. Itagaki, *Metallurgical and Materials Transactions B*, 31 (2000), 705-712.
- [9] G. Roghani, M. Hino, K. Itagaki, "Phase Equilibrium and Minor Element Distribution between Slag And Copper Matte under High Partial Pressures of SO₂", (Paper presented at the International Conference on Molten Slags, Fluxes and Salts, 1997), 693-703.
- [10] Y. Takeda, G. Roghani, "Distribution Equilibrium of Silver in Copper Smelting System", (Paper presented at the first International Conference on Processing Materials for Properties: Honolulu, USA, 7-10 Nov., 1993), 357-360.
- [11] F. Richardson, J. Billington, *Bull. Institution of Mining and Metallurgy*, 593 (1956), 273-297.
- [12] P. Mackey, G. McKerrow, P. Tarassoff, "Minor Elements in the Noranda Process", (Paper presented at the 104th AIME Annual Meeting, New York, 1975), 27.
- [13] Y. Takeda, *Transactions of the Japan Institute of Metals*, 24 (1983), 518-528.
- [14] M. Nagamori, P. Mackey, *Metallurgical Transactions B*, 9 (1978), 567-579.
- [15] K. Nakajima *et al.*, *Environmental Science and Technology*, 45 (2011), 4929-4936.
- [16] K. Nakajima *et al.*, *Materials Transactions*, 50 (2009), 453-460.
- [17] J.H. Park, D.J. Min, *Metallurgical and Materials Transactions B* 30 (1999), 689-694.
- [18] J.H. Park, D.J. Min, *Materials Transactions*, JIM, 41 (2000), 425-428.
- [19] D. Swinbourne, "Solubility of Precious Metals in Slags", (Paper presented at the European Metallurgical Conference, EMC 2005), 1, 223-235.
- [20] D. Swinbourne, X. You, *Transactions of the Institution of Mining and Metallurgy Section C-Mineral Processing and Extractive Metallurgy*, 108 (1999), C59-C65.

- [21] B. ZIOŁEK, W. Szklarski, A. Bogacz, *Archives of metallurgy*, 36 (1991), 395-408.
- [22] H.M. Henaio, K. Yamaguchi, S. Ueda, "Distribution of Precious Metals (Au, Pt, Pd, Rh and Ru) between Copper Matte and Iron-Silicate Slag at 1573 K", (Paper presented at the TMS Fall Extraction and Processing Division: Sohn International Symposium, San Diego, USA, 27-31 August 2006), 1, 723-729.
- [23] K. Yamaguchi, "Distribution of Precious Metals between Matte and Slag and Precious Metal Solubility in Slag", (Paper presented at the Copper 2010), 3, 1287-1295.
- [24] R. Altman, *Transactions of the Institution of Mining and Metallurgy*, 81 (1972), 163-175.
- [25] J. Taylor, J. Jeffes, *Transactions of the Institution of Mining and Metallurgy Section C-Mineral Processing and Extractive Metallurgy*, 84 (1975), C18-24.
- [26] J.M. Toguri, N.H. Santander, *Metallurgical Transactions*, 3 (1972), 586-588.
- [27] A. Geveci, T. Rosenqvist, *Transactions of the Institution of Mining and Metallurgy*, 82 (1973), 193-201.
- [28] D. Swinbourne, S. Yan, S. Salim, *Mineral Processing and Extractive Metallurgy*. 114 (2005), 23-29.
- [29] Y.S. Han, D.R. Swinbourne, J.H. Park, *Metallurgical and Materials Transactions B*, 46 (2015), 2449-2457.
- [30] M. Kashima, M. Eguchi, A. Yazawa, *Transactions of the Japan Institute of Metals*, 19 (1978), 152-158.
- [31] A. Roine, HSC Chemistry for Windows, vers. 6.12, Outotec Research, Pori. 2007.
- [32] K.P. Jochum *et al.*, *Geostandards and Geoanalytical Research*, 35 (2011), 397-429.
- [33] A. Yazawa, "Thermodynamic Interpretation on Oxidic Dissolution of Metal in Slag", (Paper presented at the Pyrometall. Complex Mater. Wastes, Aust. Asian Pac. Course Conf. Minerals, Metals and Material Society, Warrendale, 1994), 61-72.
- [34] R.S. Celmer, "Cobalt and Gold Distribution in Nickel-Copper Matte Smelting", (Paper presented at the Nickel Metallurgy, Symposium Proceedings 25th Annual Conference Metallurgy, Toronto, Canada 17-20 August 1986), 1, 147-163.

EXPERIMENTAL STUDY ON SMELTING OF WASTE SMARTPHONE PCBs BASED ON $\text{Al}_2\text{O}_3\text{-FeO}_x\text{-SiO}_2$ SLAG SYSTEM

Youqi Fan¹, Yaowu Gu¹, Qiyong Shi¹, Songwen Xiao², Fatian Jiang¹

¹School of Metallurgical Engineering, Anhui University of Technology, Ma'anshan, Anhui, 243002, PR China

²Changsha Research Institute of Mining & Metallurgy, Changsha, Hunan, 410012, PR China

Keywords: waste smartphone; PCBs; rare and precious metals; smelting

Abstract

Waste smartphone, as an important type of secondary resource has high content of rare and precious metals. The traditional mechanical process could easily lead to the dispersion and loss of precious metals. In this research, a smelting method using $\text{Al}_2\text{O}_3\text{-FeO}_x\text{-SiO}_2$ slag system is proposed to recover the valuable metals in smartphone PCBs. Based on the evaluation of liquidus projection calculated and plotted by Factsage software, reasonable smelting temperatures and slag composition ranges were selected, namely $1300^\circ\text{C}\text{-}1500^\circ\text{C}$, 10-15wt% Al_2O_3 , $\text{FeO} / \text{SiO}_2$ ratio of 0.8-1.5. Then several lab experiments were conducted, with Cu-Fe-Sn-Ni alloy obtained. The results show that distribution of valuable metals could be controlled by appropriate oxidation of iron. Rare metals primarily enrich in the alloy, and most of active metals like Fe, Al in slag as oxide. Recovery efficiencies of Cu, Ni, Sn, Au, Ag are more than 95wt%.

Introduction

Over the last five years, smartphones have rapidly replaced the traditional mobile phone many times over. Due to its high performance with numerous additional new applications, smartphone sales surpassed one billion units in 2014 [1]. And large quantity of smartphone has reached their end of life. Besides of the basic metals as in mobile phone[2] like copper, nickel, lead, bismuth, lithium and precious metals silver and gold, it entails a relatively high content of special (some critical) and precious metals[3], such as Cobalt, Gallium, Indium, Niobium, Tantalum, Tungsten, Platinum group metals and Rare earths. Thus, recovering such valuable metals is strongly required in terms of effective utilization of resources and environmental conservation. This research will focus on the recovery of printed circuit boards (PCBs) in smartphone.

Many processes have been developed to extract the valuable metals from PCBs. These are largely divided into mechanical, hydrometallurgical and pyrometallurgical processes[4]. In mechanical process, PCBs is usually shred to small pieces and grinded to particles in order to dissociate the organics from metallic components. Then physical separation methods are applied to obtain several concentrates, such as organics, iron and steel, light metals and copper-rich metals, which are sent to special plants for further treatments. This process has been widely adopted in China to recycle the metals of PCBs in traditional household appliances because of its simple equipment, lower cost. Hydrometallurgical process[5] treats materials in aqueous

solution using chemical reagents like acid, alkali and salt. Then the valuable metals are separated and purified. This process can produce high purity products, but it is suitable for postprocessing due to the large consumption of reagent and risk of waste water pollution. Furthermore, the PCBs generally need mechanical pretreatment. In the pyrometallurgical process[6-8], PCBs are smelted with fluxes after simple shredding. A molten bath is formed containing slag and “collector metal” like copper, nickel, lead etc., into which the precious metals dissolve and accumulate.

In either mechanical or hydrometallurgical processes, the precious metals easily disperse in the physical separation[9]. Among the above processes, the pyrometallurgical process is effective for extracting precious metals from smartphone PCBs[10-13]. Based on the chemical composition reported in literatures[14], copper is reasonable as a precious metals collector. And a difference Al₂O₃-FeOx-SiO₂ slag system is proposed. This study will focus on the chosen of suitable slag region and evaluation of smelting performance using this slag system.

Experimental

Raw materials

The waste smartphones were collected from recyclers by internet, including the main types of smartphone in the market, such as Samsung, iPhone, Huawei, etc. The phones were reserved for disassembly and removal of printed circuit boards (PCBs) (Fig.1), which were used in the following mechanical and smelting processing and recovery of valuable metals. Compared with the traditional mobile phone PCBs[15], it is much smaller in volume for smartphone PCBs and lots of components are integrated on the multilayer board. Outside the chips, there are some stainless steel shielding case. The chemical composition of PCBs was shown in Table 1.

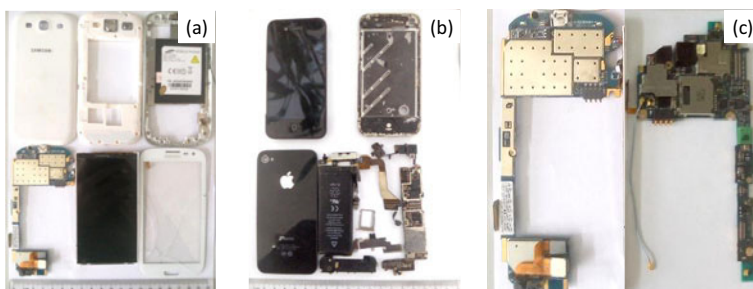


Fig.1 Smartphone disassembled

(a) Samsung GALAXY S3; (b) iPhone 4s; (c) PCBs in smartphone

Table 1 Chemical composition of PCBs used in this research

Element	Cu	Fe	Al	Sn	Ni	Ag	Au	SiO ₂	CaO
Content (wt%)	28.11	12.66	5.72	2.53	2.65	0.168	0.049	9.67	2.42

Experimental procedures

Fig.2 showed the summary flowchart of PCBs processing. Due to the varieties of shapes and metal quantities among different brands and models of smartphone, about 2 kilograms of PCBs were collected. A fine shredder was used together with a steel grate of small perforate size (20 mm). The small plates were then roasted at 700-800°C in order to partially oxidizing the metallic elements, like aluminum, iron, silicon and so on. A drum vibrating mill was applied to grind the residues in finer particles (particle size < 1mm). After that, the powder were divided into several samples by quartering method and each sample weighted 150g. One of them was sent for chemical composition analysis. The others was mixed with flux (Fe_2O_3 or SiO_2) according to the target slag composition. The mixtures was hold in corundum crucible and smelted for half hour at 1350~1550°C in nitrogen atmosphere. When the sample was cooling down to room temperature, alloy and slag samples could be obtained by broken the crucible (Fig.3).



Fig.2 The proposed flowchart of valuable metals recovery from waste smartphone PCBs



Fig.3 The photograph of smelting product of smartphone PCBs

Analysis

X-ray fluorescence (XRF) was used for quantification of the chemical compositions of solid samples. Scanning electron microscopy (SEM) and Energy Dispersive Spectrometer (EDS) were used for detailed composition and phase analysis of. Chemical analysis and inductively coupled plasma (ICP-OES) measurements were used to analyze the composition of alloy and slag.

Determination of Extraction Efficiency

In the present study, the extraction Efficiency of metals E_M were defined as:

$$E_M = \frac{A_M}{(A_M + S_M)} \times 100\% \quad (1)$$

where, E_M is the extraction ratio of M metal, A_M is the weight (g) of M metal concentrated into the molten metal phase (alloy phase), and S_M is the weight (g) of M metal remained in the slag phase.

Results and discussion

Choice of the slag system

To estimate the melting temperature of the PCBs used in this work, it is need to confirm the slag system by investigating the chemical composition in Table 1. Generally, aluminum, silicon and calcium are easily enter into slag as oxides in smelting. Iron may also partially or completely be oxidized under certain oxidizing atmosphere. So the main composition of slag is composed of aluminum oxide, ferrous oxide (ferric oxide), silicon dioxide and little calcium oxide, namely $Al_2O_3 - FeO_x - SiO_2$ slag system.

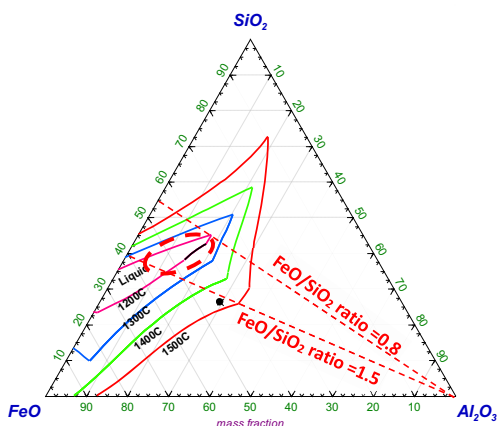


Fig.4 The isothermal liquidus lines of the $Al_2O_3 - FeO_x - SiO_2$ slag system ternary slag system (oxygen partial pressure 10^{-9} atm)

The isothermal liquidus lines (1200-1500 °C) of the ternary slag system consisting of three main slag components contained in the PCBs is shown in Fig. 4, which is calculated and plotted by the “phase diagram” module of Factsage 6.4. The oxygen partial pressure is set as 10^{-9} atm when the iron exists mainly as ferrous oxide. From Fig.4 it is revealed that the liquid phase area rapidly expands with the increase of temperature and the solubility of aluminum oxide can

reach 20wt% at 1300°C to 35wt% at 1500°C. The more of aluminum oxide in slag, the closer to “SiO₂” corner of liquid phase area. It is reasonable for controlling the smelting temperature at 1300-1500°C. Considering the high aluminum oxide content in PCBs, it is better to choose a slag composition with more Al₂O₃ solubility. So the displayed dashed-line oval region in this figure is the target slag composition region that will be used to calculate the input ratio of PCBs and fluxes.

The dot in the figure (29.4%Al₂O₃, 44.3%FeO, 26.3%SiO₂) represents the weight-percent composition based on the total mass of just the three main slag forming oxides contained in the PCBs used in this study, given all the iron existing in slag as ferrous oxide. Its melting temperature located between 1400-1500°C. The over content of aluminum oxide should be adjusted to the target region by adding some fluxes, especially at lower temperature.

Effect of pre-oxidizing roast and choice of alloy composition

In order to determine the effect of oxygen partial pressure on smelting, two contrast smelting experiments were designed before and after the pre-oxidizing roast of PCBs. Fig.5 showed the photographs of smelting products without pre-oxidizing roast. Although well separation of alloy and slag was obtained, immiscibility of Fe-rich phase and Cu-rich phase was observed in the alloy. Seen from the corresponding chemical compositions of alloy and slag in Table 2 and 3, the iron was partially oxidized into slag while considerable amount of it stayed in the alloy. It is revealed in Cu-Fe-Sn phase diagram of 1300°C (Fig.6) that the solubility of iron is less than 10wt% when tin content fall in 5-10wt% (oval region). Or the alloy will easily form two immiscible liquid, namely Cu-rich phase and Fe-rich phase. Consequently, it's necessary to oxidize more iron to ferrous oxide so as to avoid the immiscibility of alloy. In this research, a pre-oxidizing roast process was introduced before smelting.



Fig.5 Photographs of smelting products and the immiscibility of alloy without pre-oxidizing roast (smelting for 0.5h at 1350°C)

Table 2 Average chemical composition of the alloy

Element	Cu	Fe	Sn	Ni
Content / wt%	49.25	25.24	8.06	5.24

Table 3 Chemical composition of the slag

Element	FeO	SiO ₂	Al ₂ O ₃	CaO	Sn	Cu	Ni
Content / wt%	22.62	39.42	15.30	8.61	0.041	0.884	0.011

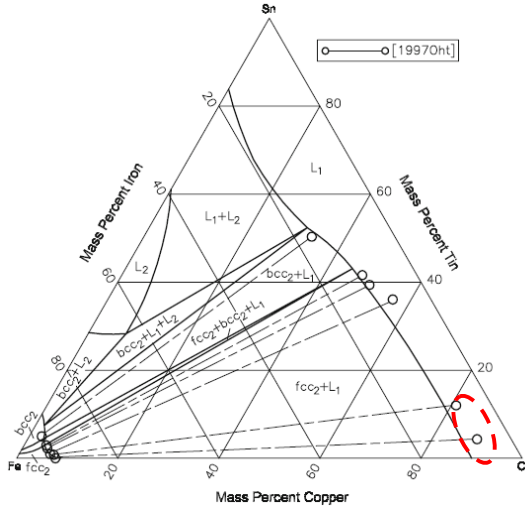


Fig.6 Cu-Fe-Sn computed isothermal section at 1300°C [16]

The effect of temperature and target Al₂O₃ content on recovery efficiency of valuable metals

Two smelting experiments A and B were carried out respectively at 1350°C and 1450°C for 0.5h using the pre-oxidized PCBs as raw material. The target Al₂O₃ content was set as 10-15wt%. The product compositions is shown in Table 4. As shown in Table 4, FeO, SiO₂, Al₂O₃ and CaO were the main components for obtained slags. FeO/SiO₂ ratio is 1.07 and 1.25, right located in the oval region of Fig.4. The alloy mainly composes of Cu, Ni and Sn, while the Fe content falls down to 1wt% by pre-oxidizing of PCBs.

The mineralogical structure of the slag A was characterized by SEM and EDS analysis (Fig.7). The result shows that slag A are primary composed of bar-shaped Olivine (2FeO·SiO₂) and compounds of CFAS. There are some square spinel of Al₂O₃·FeO_x and inclusion dot of alloy.

Table 4 Chemical composition of the alloy and slag

No.		Content (wt%)											
		FeO	SiO ₂	Al ₂ O ₃	CaO	Cu	Fe	Ni	Sn	Zn	Pb	Ag	Au
A	alloy	/	/	/	/	86.55	1.10	4.83	3.81	0.76	0.40	0.29	0.05
	slag	39.29	31.41	10.37	8.36	0.38	/	0.06	0.08	1.10	0.06	4ppm	1ppm
B	alloy	/	/	/	/	87.84	0.73	5.04	3.51	0.43	0.37	0.26	0.07
	slag	35.7	33.16	13.62	7.12	0.68	/	0.12	0.14	1.11	0.09	3ppm	1ppm

Note: “/” mean the composition not analyzed

As can be seen from Fig. 8, recovery efficiencies of Cu, Ni and Sn for A are all more than 95wt% while that of Zn and Pb are only 23wt% and 65wt% (the data may be lower if considering the vaporization). When smelting temperature raise to 1450 °C, the recovery efficiency decreases to some extent. It is obvious for Sn, Zn and Pb which may be due to the enhanced vaporization of them at higher temperature. But the change of temperature shows little effluence to precious metals Au and Ag, reaching 99.5wt% for both A and B.

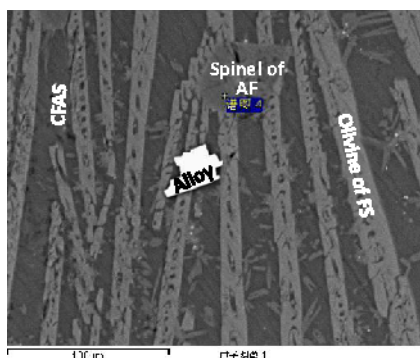


Fig.7 Mineralogical structure of the slag A
C-CaO; F-FeO_x; A-Al₂O₃; S-SiO₂

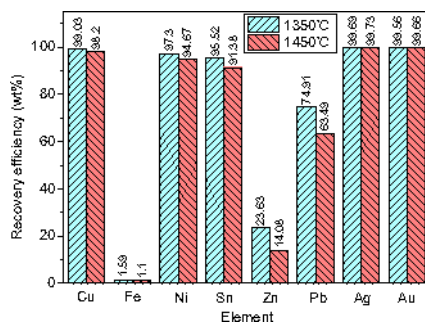


Fig.8 Recovery efficiency of valuable metals in smelting process

Conclusion

In this study, a smelting process is proposed to extract valuable metals contained in waste smartphone PCBs using Al₂O₃-FeO_x-SiO₂ slag system. Based on the evaluation of liquidus projection, suitable smelting conditions are selected, namely 1300 °C-1500 °C, 10-15wt% Al₂O₃, FeO / SiO₂ ratio of 0.8-1.5. by the contrast of the smelting performance, the iron content in alloy should be less than 10wt% to avoid immiscible liquid alloy, which can be realized with pre-oxidizing roast. Meantime, pre-oxidizing roast can also affect the metal distribution by appropriate oxidation of iron. In lab experiments, Cu-Sn-Ni-Fe alloy was obtained, in which most precious metals enriched. And almost all active metals like Fe, Al are oxidized and

concentrate in slag typically composed of 10-15wt%Al₂O₃, 35-40wt%FeO_x, 30-35wt%SiO₂, 7-9wt%CaO. At 1350°C, Recovery efficiencies of Cu, Ni, Sn are more than 95wt% as well as Au, Ag up to 99.5wt%.

In conclusion, the proposed process with Al₂O₃-FeO_x-SiO₂ slag system revealed an acceptable performance for smartphone PCBs recycling. The minor component in slag such as CaO, may further decrease the melting temperature and expand the liquid phase area. Thus this smelting process might be conducted in a lower temperature. Besides the metals concerned in this article, the distribution of other rare metals like In, Ga, Nd, and precious metals Pd, Pt are also worth of researching.

Acknowledgements

This work was supported by the National Natural Science Foundation of China (No. 51404004) and the SRTP projects (No. 201410360003), and the authors are very grateful to Analysis and Testing Centre of Anhui University of Technology and Changsha Research Institute of Mining & Metallurgy, for the sample examination and analysis.

References

- [1] Gartner: Smartphone Sales Surpassed One Billion Units in 2014, <http://www.gartner.com/newsroom/id/2996817>.
- [2] M.C. Vats, S.K. Singh. Assessment of gold and silver in assorted mobile phone printed circuit boards. *Waste Management*, 2015, 45: 280–288.
- [3] M. Buchert, A. Manhart, D. Bleher, et al. Recycling critical raw materials from waste electronic equipment. 2012, <http://www.oeko.de/oekodoc/1375/2012-010-en.pdf>.
- [4] J. Cui, L. Zhang. Metallurgical recovery of metals from electronic waste: A review. *Journal of Hazardous Materials*. 2008, 158(2–3): 228-256.
- [5] H.Yang, J. Liu, J.Yang. Leaching copper from shredded particles of waste printed circuit boards. *Journal of Hazardous Materials*, 2011, 187(1-3): 393-400.
- [6] A. Nolte. Metallurgical utilization of reusable products from the recycling industry in a secondary copper smelter, in: *Proceedings of the 1997 TMS Annual Meeting*, February 10, 1997 - February 13, 1997, Minerals, Metals & Materials Soc (TMS), Orlando, FL, USA, 1997: 377-400.
- [7] L. Theo. Integrated recycling of non-ferrous metals at Boliden Ltd. Ronnskar smelter, *IEEE International Symposium on Electronics & the Environment*, 1998: 42-47.
- [8] Annual Report 2013, Dowa Holdings Co., Ltd. http://www.dowa.co.jp/en/ir/library_annual.html.
- [9] C. Hageluken. Recycling of electronic scrap at Umicore's integrated metals smelter and refinery. *World of Metallurgy - ERZMETALL*, 2006, 59(3): 152-161.
- [10] B.S. Kim, J.C. Lee, S.P. Seo, et al. A Process for Extracting Precious Metals from Spent Printed Circuit Boards and Automobile Catalysts. *JOM*, 2004, 56(12): 55-58.
- [11] H.S. Kim, Y.B. Li, S.W. Lee. Effect of Slag Compositions on the Extraction of Metallic Components from the Used PCB. *Materials Science Forum* 2006, 510 – 511: 634-637.
- [12] A. Bernardes, I. Bohlinger, D. Rodriguez, et al. Recycling of printed circuit boards by melting with oxidizing/reducing top blowing process. *EPD Congress*, TMS 1997, pp363-375, USA.
- [13] B.S. Kim, J.C. Lee, J. Jeong, et al. A Novel Process for Extracting Precious Metals from Spent Mobile Phone PCBs and Automobile Catalysts. *Materials Transactions*. 2013, 54(6): 1045 - 1048
- [14] UNEP (2013). Metal Recycling: Opportunities, Limits, Infrastructure, <http://www.unep.org/resourcepanel/Publications/MetalRecycling/tabid/106143/Default.aspx>.
- [15] A.C. Kasper, G.B.T. Berselli, B.D. Freitas, et al. Printed wiring boards for mobile phones: Characterization and recycling of copper. *Waste Management*, 2011, 31: 2536–2545.
- [16] J. Miettinen. Thermodynamic Description of the Cu-Fe-Sn System at the Cu-Fe Side. *CALPHAD*, 2008, 32: 500-505.

RECOVERY OF VALUABLE METALS FROM SPENT LITHIUM-ION BATTERIES BY SMELTING REDUCTION PROCESS BASED ON MnO-SiO₂-Al₂O₃ SLAG SYSTEM

Ren Guoxing, Xiao Songwen*, Xie Meiqiu, Pan Bing, Fan Youqi, Wang Fenggang, Xia Xing

Changsha Research Institute of Mining & Metallurgy, Changsha 410012, Hunan, China

Keywords: spent lithium-ions battery, smelting reduction, MnO-SiO₂-Al₂O₃ slag, pyrolusite

Abstract

Plenty of valuable metals, such as cobalt, nickel, copper, manganese and lithium, are present in spent lithium-ion batteries. A novel smelting reduction process based on MnO-SiO₂-Al₂O₃ slag system for spent lithium ion batteries is developed, using pyrolusite ore as the major flux. And Co-Ni-Cu-Fe alloy and manganese-rich slag contained lithium are obtained. The results show that it is reasonable to control MnO/SiO₂ ratio in the range of 2.05-3.23 (w/w) and Al₂O₃ content in 19.23-26.32wt.%, while the MnO and Li₂O contents in the manganese-rich slag can reach 47.03 wt.% and 2.63 wt.%, respectively. In the following leaching experiments of the manganese-rich slag by sulphuric acid solution, the recovery efficiency of manganese and lithium can reach up to 79.86% and 94.85%, respectively. Compared with the conventional hydro-pyrometallurgical process of spent lithium-ion batteries, the present can preferably recover Mn and Li besides Co, Ni and Cu.

Introduction

With rapid market expansion of consumer electronics and electric vehicles, the consumption of lithium-ion batteries (LIBs) has been increased tremendously in recent years. At the same time, quantities of waste LIBs are generating worldwide, which could bring serious environmental issue. Spent LIBs contain plenty of valuable metals, such as cobalt, nickel, copper, manganese and lithium, as well as toxic ingredients [1-4]. Once discarding without proper treatment, both the environmental contamination and the waste of resource are inevitable. Therefore, developing advance technologies for spent LIBs recycling are of great significance.

The most common industrial processes for the recovery of valuable metals from LIBs are hydrometallurgy and pyrometallurgy methods[1]. Hydrometallurgical methods like Recupyl and Toxco processes are widely designed for specific type of batteries, which can't adapt to the diversity of real spent LIBs [3]. In contrast, various types of used battery, such as LIBs with Al shells, polymer LIBs, and nickel metal hydride batteries, can be treated by a pyrometallurgical based process, such as Val'Eas and Inmetco processes [2]. Additionally, the pyrometallurgical based also has the advantage of higher throughput. A selection of suitable slag system is one of key factors that influence the efficiency of pyrometallurgical process. Now, the smelting

reduction process of spent LIBs generally used the CaO-SiO₂-Al₂O₃ slag or FeO-CaO-SiO₂-Al₂O₃ slag system. However, the manganese and lithium can't be recovered effectively by conventional hydro-pyrometallurgical process which is based on above slag systems [3, 4].

The present study proposes a new smelting reduction method of spent LIBs based on MnO-SiO₂-Al₂O₃ slag system, in which the pyrolusite is used as the major slag former. After smelting, the Co, Ni and Cu from spent LIBs were concentrated into alloys, while the Mn and Li were enriched into slag phases. Effects of pyrolusite addition, SiO₂ addition, CaO addition, and smelting temperature on the recoveries of Co, Ni and Cu were explored in detail. And the leachability of the manganese-rich slag obtained was also investigated.

Materials and Methods

Materials

In this study, mixed spent LIBs which consist of LIBs with Al cans and polymer LIBs, were used as experimental materials. Table 1 presents the chemical composition of the LIBs. According to earlier study [3,4], the Al and C of spent LIBs exist as the form of metallic Al and graphite, respectively, which are used as reductant during the smelting process.

Table 1 chemical composition of LIBs used in this investigation.

Type	Co	Ni	Cu	Mn	Fe	Al	Li	C	others
Al-cans	16.0	2.0	8.0	0.0	0.0	33.0	2.0	15.0	23.9
polymer	2.0	3.0	10.0	21.0	0.1	13.0	2.0	25.0	25.9

Pyrolusite is used as the major slag former. Table 2 shows the chemical composition of the pyrolusite. According to the XRD pattern of the pyrolusite given in Fig.1, it was found that the pyrolusite mainly consists of quartz (SiO₂) and pyrolusite (MnO₂).

Table 2 chemical composition of the pyrolusite in this study

Elements	MnO ₂	Fe	P	Al ₂ O ₃	SiO ₂	CaO	MgO
contents/%	63.05	2.60	0.85	2.41	13.33	4.70	0.71

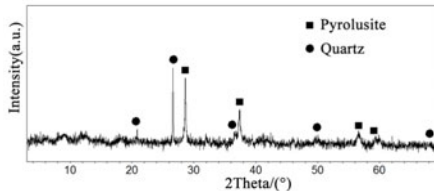


Fig. 1 XRD pattern of pyrolusite

Experimental

To investigate the feasibility of the new process, the experiments were conducted using the procedure shown in Fig. 2. Smelting process consists of two steps: (1) firstly, the polymer LIBs were roasted at 800°C for 2h in a muffle furnace to remove a partial carbon, and cooled in the furnace. The spent LIBs with Al cans were sheared into several small parts, and then mixed with the roasted polymer LIBs according to the mass ratios of LIBs with Al cans to the polymer LIBs=1:1. (2) Secondly, the mixed batteries, pyrolusite, and slag modifier (CaO and/or SiO₂) were together put into an alumina crucible with a cover after being thoroughly mixed. They were then melted at pre-determine temperature for 30 min in an electrical melting furnace (Box Type) with MoSi₂ alloy heating rods. After smelting, the specimens were cooled down naturally to ambient temperature (~25°C). The crucible was withdrawn from the furnace. Subsequently the alloy and slag were manually separated and ground for chemical analysis.

The manganese-rich slag obtained was firstly crushed, and ground to grain size <0.074 mm, then mixed with a determined amount of concentrated sulphuric acid (82 wt.%) corresponding to different acid to ore mass ratios. The obtained slurry was then heated at temperature 85°C for 60min in a loft drier. After heating, the slurry was then leached with water at room temperature. After 30 min the leached residues were filtered and dried for chemical analysis.

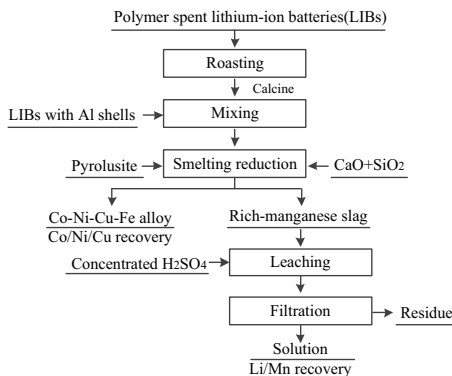


Fig. 2 Flow chart of Co, Ni, Cu, Mn and Li recovery from spent LIBs.

Results and Discussion

Effect of parameters on the smelting reduction process

Effect of pyrolusite addition Fig. 3 shows that the effect of pyrolusite addition on the recovery of valuable metals. It can be seen that pyrolusite addition did not obviously effect on the recoveries of Co, Ni and Cu, but had a significantly influence on the Mn recovery in alloy. Mn recovery decreased from 19.36% to 1.31% as the pyrolusite addition increased from 1.5 (w/w) to 2.8 (w/w). A part of Mn in the batteries and pyrolusite was reduced into the alloy, which can be explained by the reduction of manganese oxide according to the following reactions [5,6]:



From an economic point of view, the lower composition of slag maker means less energy composition, so the pyrolusite addition of 1.5 (w/w) is appropriate.

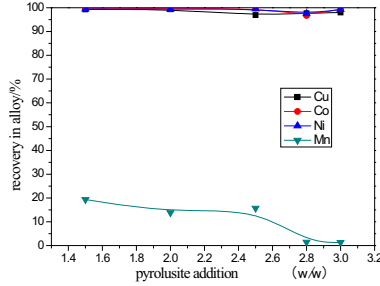


Fig. 3 Effect of pyrolusite addition on the recovery of valuable metals (SiO₂ addition 9.0%(w/w), CaO addition 2.0%(w/w), smelting temperature 1475 °C, smelting time 30min)

Effect of SiO₂ addition Fig. 4 shows that the effect of SiO₂ addition on the recovery of valuable metals. As verified in Fig. 4, the recoveries of Ni and Cu increased with the increasing of SiO₂ addition from 0% (w/w) to 6.0% (w/w), and remained constant after that. Co recovery was about 99% for the studied conditions. Mn recovery in alloy slightly increased until the SiO₂ addition below 4.0% (w/w). When the addition of SiO₂ exceeded 4.0% (w/w), the Mn recovery decreased obviously. The reason was probably that the activity of MnO from slag decreased with the increase of the SiO₂ addition, thus restraining the reductive ability of MnO and decreasing the manganese recovery [7]. The SiO₂ addition of 6% (w/w) was appropriate.

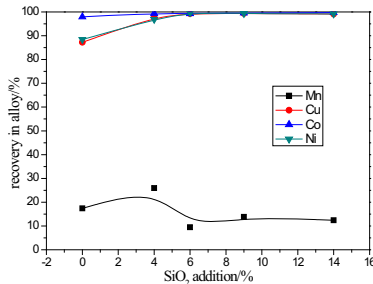


Fig. 4 Effect of SiO₂ addition on the recovery of valuable metals (pyrolusite addition 2.0(w/w), CaO addition 2.0% (w/w), smelting temperature 1475 °C, smelting time 30min)

Effect of CaO addition Fig. 5 shows that the effect of CaO addition on the recovery of valuable metals. From Fig. 5, the recoveries of Co, Ni and Cu increased until CaO addition reached

2.0% (w/w), where 99.85% of Co, 99.52% of Ni, and 98.03% of Cu were recovered. Further increasing of CaO addition presented no benefit to metal recoveries. Mn recovery in alloy increased from 2.07% to 11.33% with the increasing of the CaO addition from 0% (w/w) to 8.0% (w/w). This is attributed to the increase of activity of MnO from slags according to previous study[8]. The appropriate CaO addition was 2.0% (w/w).

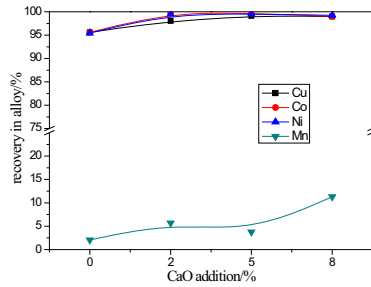


Fig. 5 Effect of CaO addition on the recovery of valuable metals (pyrolusite addition 2.0(w/w), SiO₂ addition 9.0%(w/w), smelting temperature 1475 °C, smelting time 30min)

Effect of smelting temperature Fig. 6 shows that the effect of smelting temperature on the recovery of valuable metals. It can be seen that the recoveries of valuable metals(Co, Ni and Cu) increased with the smelting temperature below 1475°C. When the smelting temperature exceeded 1475°C, the valuable metals recoveries kept nearly a constant. Therefore, the suitable smelting temperature was 1475°C.

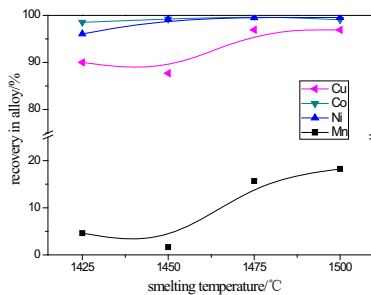


Fig. 6 Effect of smelting temperature on the recovery of valuable metals (pyrolusite addition 2.0 (w/w), SiO₂ addition 9.0% (w/w), CaO addition 2.0% (w/w), smelting time 30min)

From the results mentioned above, the optimum condition of the smelting reduction experiment was pyrolusite addition of 1.5(w/w), SiO₂ addition of 6.0%(w/w), CaO addition of 2.0% (w/w), smelting temperature 1475 °C, and smelting time of 30min. The results of the optimum condition test are shown in Table 3. As shown in Table 3, the recovery rates of Co, Ni, and Cu were 99.79%, 99.30%, and 99.30%, respectively. The contents of MnO and Li₂O in the slag obtained

were 47.03% and 2.63%, respectively. The major phases of the slag obtained were rich-calcium tephroite ((Mn,Ca)₂SiO₄) and galaxite (MnAl₂O₄) by the XRD analyze as shown in Fig. 7.

Table 3 experimental results under the optimum condition

item	Cu	Co	Ni	Fe	Mn	Li ₂ O
Recovery in alloy/%	99.30	99.79	99.30	/	19.13	/
Content in alloy/wt.%	21.78	24.43	5.05	10.85	30.13	/
Content in slag/wt.%	0.11	0.02	0.02	0.19	47.03*	2.63

*- content of MnO in slag

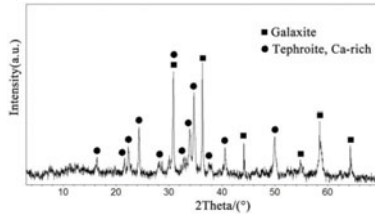


Fig. 7 XRD pattern of manganese-rich slag under the optimum condition

Table 4 results of slags vary different experimental conditions.

conditions	contents in slag obtained/%					Simplified slag	
	MnO	FeO	Al ₂ O ₃	SiO ₂	CaO	MnO/SiO ₂	Al ₂ O ₃
Pyrolysis addition							
1.5	42.74	0.25	22.18	19.35	8.81	2.21	26.32
2.0	46.83	0.18	20.98	18.86	6.95	2.48	24.21
2.5	46.87	0.11	18.35	21.20	7.76	2.21	21.23
2.8	48.47	0.38	18.97	15.00		3.23	23.01
3.0	48.96	0.34	16.44	20.11	7.35	2.43	19.23
SiO ₂ addition							
0.0	48.96	0.84	23.72	11.86	6.83	4.13	28.06
4.0	45.13	0.23	22.17	16.66	7.82	2.71	26.41
6.0	47.79	0.14	17.17	19.95		2.40	20.22
9.0	46.83	0.18	20.98	18.86	6.95	2.48	24.21
14.0	44.85	0.12	19.70	21.85	6.82	2.05	22.80
CaO addition							
0.0	49.47	0.48	17.65	19.35	5.81	2.56	20.41
2.0	46.87	0.11	18.35	21.2	7.76	2.21	21.23
5.0	46.24	0.15	18.78	19.59	9.97	2.36	22.20
8.0	43.56	0.12	19.30	19.19	12.5	2.27	23.52

Analysis of appropriate slag composition

Table 4 summarizes the results of slag compositions at different experimental conditions. It can be seen that MnO, SiO₂ and Al₂O₃ were the main compositions for obtained slags, so it is

feasible to describe the slag systems by the simplified ternary system MnO-SiO₂-Al₂O₃. Haccuria et al has proposed that this system would be employed for the smelting process [9]. However, the suitable composition of slags wasn't given. Assuming the compositions of the slag system is more suitable for the smelting reduction process of spent LIBs, when the recoveries of Co, Ni and Cu are up to 95%. Therefore, it can be concluded from Table 4 that the appropriate slag was MnO/SiO₂=2.05-3.23 (w/w), and 19.23-26.32wt.% Al₂O₃ content. Moreover, It's noted that the Al₂O₃ content in the manganese-rich slag is higher than that of slags for the Fe-Mn alloy production [10]. According to the results of Kim[11], the fluidity of these slags is very well under the temperature of 1475 °C, so that the slag-alloy separation may be very easy.

Leachability of manganese-rich slag

Lithium from spent LIBs is collected into CaO-(FeO)-SiO₂-Al₂O₃ slag during previous pyrometallurgical based process. However, the content of lithium in slags was less than 1.50 wt.% due to the high addition of slag maker, which can't be recovered by economical methods. By comparison, the lithium content in the manganese-rich slag was higher, up to 2.63 wt.% (see Table 3) in this study. This means that the extraction of lithium from the manganese-rich slag is more promising. In addition, most of manganese from spent LIBs and pyrolusite was enriched into the slag MnO-SiO₂-Al₂O₃. Besides the Mn containing manganese-rich slag existed as the form of MnO due to the lower oxygen partial pressure of the smelting process according to previous study [12]. This means that MnO₂ containing pyrolusite has been converted to acid-soluble MnO[13]. All of these are advantage to recover Li and Mn from the manganese-rich slag by the following leaching process.

In order to investigate the leachability of managanese-rich slag, further experiments were carried out under conditions of a sulfuric acid concentration of 82 wt. % with various acid to ore mass ratios, heating temperature of 85 °C, and heating time of 120 min. the results are depicted in Table 5. When the sulfuric acid addition exceeds 1.0 (w/w), the Mn and Li leaching efficiencies reached 79.86% and 94.85%, respectively. This means that the Li and Mn from spent LIBs can be effectively recovered by the new developed methods.

Table 5 results of the leachability of managanese-rich slag varying different sulfuric acid addition

Sulfuric acid addition/ (w/w)	Li leaching efficiency/%	Mn leaching efficiency/%
0.75	80.13	65.66
1.00	94.85	79.86
1.25	94.14	79.72
1.50	92.41	76.39

Conclusions

The present study proposed a new smelting reduction method of spent lithium-ion batteries based on MnO-SiO₂-Al₂O₃ slag system, in which the pyrolusite ore was used as the major slag former.

The Co-Ni-Cu-Fe alloy and lithium containing manganese-rich slag were obtained. The main results can be summarized as follows:

(1) Under conditions of the pyrolusite addition of 1.5 (w/w), SiO₂ addition of 6%(w/w), CaO addition of 2% (w/w), smelting temperature 1475°C, and smelting time of 30min. 99.79% Co, 99.30% Ni, and 99.30% Cu were recovered and the contents of MnO and Li₂O in the slag obtained were 47.03% and 2.63%, respectively. The major phases of the slag obtained were rich-calcium tephroite ((Mn,Ca)₂SiO₄) and galaxite (MnAl₂O₄).

(2) MnO-SiO₂-Al₂O₃ slag system for the smelting process was appropriate under the condition of about MnO/SiO₂=2.05-3.23 (w/w), and 19.23-26.32wt.% Al₂O₃ content.

(3) The lithium containing manganese-rich slag was leached in sulphuric acid media. The leaching efficiency of manganese and lithium reached 79.86% and 94.85%, respectively.

References

1. C. O. Vadenbo, "Prospective Environmental Assessment of Lithium recovery in battery recycling," (Semester Thesis, Natural and Social Science Interface, 2009), 19-38.
2. S. Al-Thyabat et al., "Adaptation of minerals processing operations for lithium-ion (LiBs) and nickel metal hydride (NiMH) batteries recycling: Critical review," *Miner. Eng.*, 45 (2013), 4-17.
3. Cheret et al., "Battery recycling" (European Patent, EP 1589121 B1).
4. T. Georgi-Maschler, et al., "Development of a recycling process for Li-ion batteries," *J. Power Sources*, 207(2012), 173-182.
5. J.H. Park, H.S. Song, and D.J. Min, "Reduction Behavior of EAF Slags Containing Cr₂O₃ Using Aluminum at 1793K," *ISIJ International*, 44(5)(2004), 790-794.
6. H. Sun, et al., "Reaction of manganese containing slag with carbon substrate," (Paper presented at The Twelfth International Ferroalloys Congress, Helsinki, Finland, 2010), 557-568.
7. İ.S. Çardaklı, N. Sevînc, and T. Öztürk. "Production of high carbon ferromanganese from a manganese ore located in Erzincan," *Turkish J. Eng. Env. Sci.*, 35(2011), 31-38.
8. T. Takagawa, et al., "Production of Mn-Fe Alloy from Slag Generated in Mn-removal Treatment of Molten Cast Iron," *ISIJ International*, 49(11)(2009), 1673-1677.
9. E. Haccuria, P. C. Hayes, and E. Jak, "Phase equilibria studies of the "MnO"-Al₂O₃-SiO₂ system in equilibrium with metallic alloy. Part 2: phase equilibria," *Int. J. Mater. Res. (formerly Z. Metallkd.)*, 106 (2015), 1-11.
10. L. Holappa and Y. Xiao, "Slags in ferroalloys production-review of present knowledge," *The Journal of the South African Institute of Mining and Metallurgy*, (2004), 429-438.
11. W. Y. Kim, et al., "modeling the viscosity of silicate melts containing manganese oxide," *J. Min. Metall. Sect. B-Metall.*, 49(3)B(2013), 323-337.
12. G. Roghani, E. Jak, and P. Hayes, "Phase Equilibrium Studies in the "MnO"-Al₂O₃-SiO₂ System," *Metall. Mater. Trans. B*, 33B (2002), 827-838.
13. Z. Cai, et al., "Co-recovery of manganese from low-grade pyrolusite and vanadium from stone coal using fluidized roasting coupling technology," *Hydrometallurgy*, 40-45(2013), 131-132.

**ADVANCES IN MOLTEN
SLAGS, FLUXES, AND SALTS:**

Proceedings of



**Crystallization/Freeze
Linings**

IN-SITU OBSERVATION OF RARE EARTH CONTAINING PRECIPITATED PHASE CRYSTALLIZATION AND SOLIDIFICATION OF CaO-SiO₂-Nd₂O₃ AND CaO-SiO₂-Nd₂O₃-P₂O₅ MELTS

Thu Hoai Le¹, Mayu Aketagawa^{1,2}, Annelies Malfliet¹, Bart Blanpain¹ and Muxing Guo¹

¹Department of Materials Engineering, KU Leuven, Kasteelpark Arenberg 44 bus 2450, B-3001 Leuven, Belgium

²Department of Materials Science, Tohoku University,

Aoba-yama 02, Sendai, 980-8579, Japan

Keywords: in-situ observation, phase precipitation, rare earths

Abstract

In order to optimize the recycling process, fundamental understanding of the rare earths distribution in the slag and the precipitation behavior of the REE containing compounds during slag solidification are of significant importance. In this work, “in-situ” observations of rare earth containing phase precipitation, and solidification behavior of the CaO-SiO₂-Nd₂O₃ and CaO-SiO₂-Nd₂O₃-P₂O₅ melts were performed using a confocal scanning laser microscope (CSLM) combined with an infrared imaging furnace heating (IIF). The compositions of the precipitates formed during cooling of those slags were examined using EPMA method. The addition of P₂O₅ was found to influence the precipitation behavior and to decrease the liquidus as well as the solidus temperatures of the slags.

Introduction

The rare earths or rare-earth elements (REEs) are key resources in the transition towards an environment-friendly, low-carbon sustainable economy. The unique magnetic, luminescent and electrochemical properties of these metallic elements allow them to play an often irreplaceable role in a wide range of applications. As the consumption of rare earth materials is rapidly increasing, their recycling has also attracted immense attention [1-6]. The present research focuses on the recycling of rare earths through the combination of pyrometallurgical and hydrometallurgical routes. In order to optimize the recycling process, fundamental understanding of the rare earths distribution in the slag and the precipitation behavior of the REE containing compounds during slag solidification are of significant importance. In our previous study, the phase diagram of the CaO-SiO₂-Nd₂O₃ system was constructed and two possible REE recycling schemes were proposed [7]. This work continues to study the precipitation and solidification behavior of this ternary slag through in-situ CLSM observation. Since rare earths have a high affinity to phosphate structures [8], the CSLM experiment was also carried out on the ternary system with an addition of P₂O₅.

Experimental

Based on the obtained phase diagram data and two possible REE recycling schemes proposed in our previous work [7], two slag compositions were chosen for the present study as shown in Table 1. Samples were prepared from high purity fine powders: CaO (obtained by calcination of

CaCO₃, 99.99%, Chempur, CAS no.: 471-34-1), SiO₂ (99.9%, Merck Millipore, CAS no.: 14808-60-7), Nd₂O₃ (99.99%, Chempur, CAS no.: 1313-97-9), and CaHPO₄ (98%, RPL, CAS no. 7757-93-9). For the quaternary CaO-SiO₂-Nd₂O₃-P₂O₅ system, 5 wt% P₂O₅ was added to the ternary sample. The CSLM-IIF [8] was used to observe in-situ the precipitation and solidification behavior of the selected slags, which were prepared according to the isothermal-quenching procedure at 1600 °C. The slag sample was put in a Pt-20%Rh crucible placed on a sample holder inside the CSLM heating chamber. The temperature calibration was performed using pure copper, nickel and palladium, separately, as references and the sample's temperature was observed to be 85 ± 5 °C lower than the measured temperature using the thermocouple. Before heating the sample, the CSLM chamber was evacuated and flushed with argon three times and then a constant Ar stream was maintained as 17 dm³/hour during the experiments. After being held at the desired temperature for 5 minutes, the slag was cooled to solidify temperature at a predefined cooling rate then quench to room temperature for later microscope analysis. The laser scanned images of this cooling process were captured and used for further investigation. The schematic of this experimental setup was shown in figure 1.

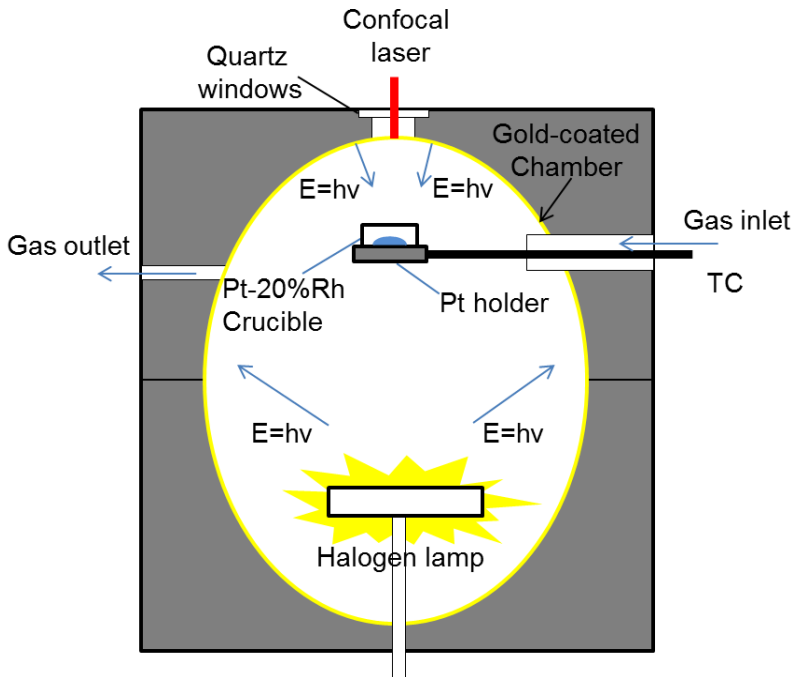


Figure 1: The experimental setup schematic

Table 1: Compositions of samples.

Sample	CaO, wt%	SiO ₂ , wt%	Nd ₂ O ₃ , wt%	P ₂ O ₅ , wt%
CNS	25.0	50.0	25.0	-
CNSP	23.8	47.5	23.8	5

For microstructure and phase composition analysis, the samples were mounted in resin, grinded, polished and coated with carbon. The samples are then analyzed by an electron probe micro-analyzer (EPMA, JEOL JXA-8530F) equipped with standardized wavelength dispersive spectroscopy (WDS) and operated at 15 kV-15 nA. A 16.9 wt% CaO - 12.1 wt% Al₂O₃-54.3 wt% SiO₂-16.7 wt% Nd₂O₃ glass was used as standard. The average accuracy of EPMA measurements on the main elements is ± 1 wt%.

Results and discussion

From the previous study [7], a possible REE recycling scheme could be based on either enriching the amorphous slag in REE by the precipitation of the SiO₂ and CaO.SiO₂ non-REE-containing solid phases or by precipitating the REE-rich solid phase from the liquid region. By collecting either of these precipitates from the slag, a REE-enriched product can be obtained, which could serve as a REE-rich input stream in a next step of the REE recycling process. In order to examine the possibilities, the solidification behavior of a 25%CaO-50%SiO₂-25%Nd₂O₃ slag is studied in this research. In order to investigate the influence of phosphorous, 5 wt% P₂O₅ was added to the ternary system by mixing CaHPO₄ in the slag.

The CSLM experiments were performed for these slags with a cooling rate of 20 °C/min. Since the slag was transparent before the precipitation of the first phase, the microstructure (i.e. grain boundaries) of the crucible bottom could be observed. By maintaining the focus of the microscope on the bottom of the crucible, the onsets of the precipitates were detected by the appearance, movement and growth of a new structure in the liquid. The CLSM images were continuously recorded during the experiments and the representative images are shown in Figures 2 and 3 for the CNS and CNSP slags, respectively. BSE images of the solidified slags are presented in figure 4. In figures 2 and 3, the first image represents the droplet sample in a complete liquid state at the indicated temperature. Circles, arrows are used to mark most visible precipitates, which appear as a brighter or darker color, depending on their positions. The figure 2 shows a top view of the precipitates growing in the ternary slag. At 1469 °C, two precipitates marked by circles A and B, could be clearly seen. These started to grow from heterogeneous nucleation sites at the bottom of crucible up to above 120 μ m in size (Figure 2b, c). They were observed to have dendritic structure with very long needle-like branches as the white phase shown in figure 4a. Figure 2d shows another type of precipitate that started to form at 1429 °C, which was transparent and its formation could only be confirmed by its movement within the liquid phase. As the temperature decreased, the newly formed precipitate grew, as indicated by the yellow arrow in figure 2e and f. For this slag, the compositional analysis shows the existence of two precipitated phases: Nd-rich needles and round-shaped SiO₂ particles (Figure 4a), which may be obtained by the heat treatment progress [10]. The results indicate that the Nd-rich phase is the phase observed in figure 2b while SiO₂ is the transparent phase that started to form at lower temperature, and show good agreement with our previous study [7].

When P₂O₅ was added to the slag, different precipitate morphologies were observed (Figure 3). In particular, as shown in figure 3b and c, the new irregular-shape precipitates prefer to form at the grain boundaries of the crucible. A BSE image of the samples indicates that the precipitate has a dendritic structure (Figure 4b). As the temperature decreased to 1223°C, the precipitate particle number increased but there was no significant increase in its size (Figure 3 d -3f). In addition, no other type of precipitate was further formed during the cooling of the slag, which is in good agreement with the compositional analysis (Figure 4b).

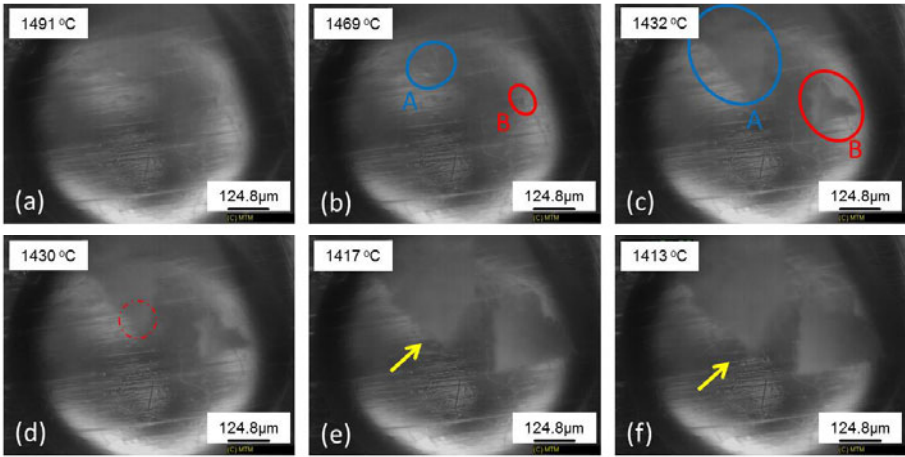


Figure 2: The CNS slag a cooling rate of 20 °C/min (a) transparent liquid slag (b) first precipitates appearing (c) first precipitates growing and moving (d) second type of precipitate forming in a dashed circle (e) second type of precipitate appearing (f) both types of precipitates growing and moving.

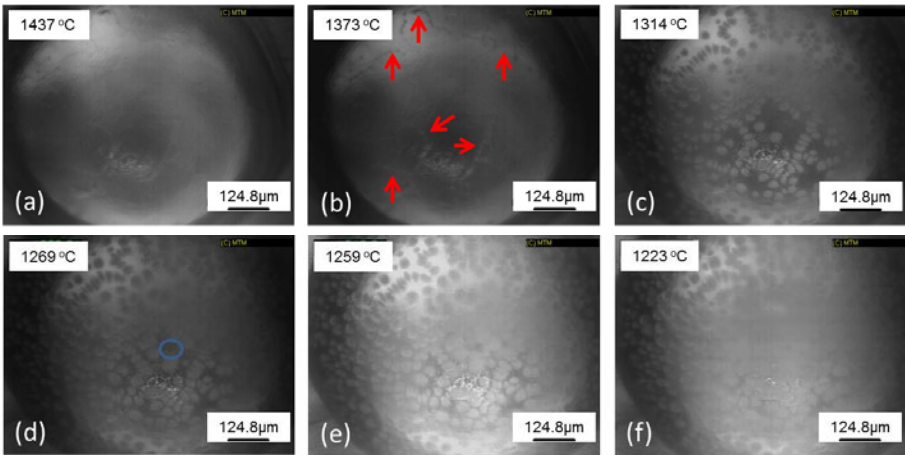


Figure 3: The CNSP slag at a cooling rate of 20 °C/min (a) transparent liquid slag (b) precipitate appearing (c) precipitate growing (d, e, f) precipitates increasing and growing.

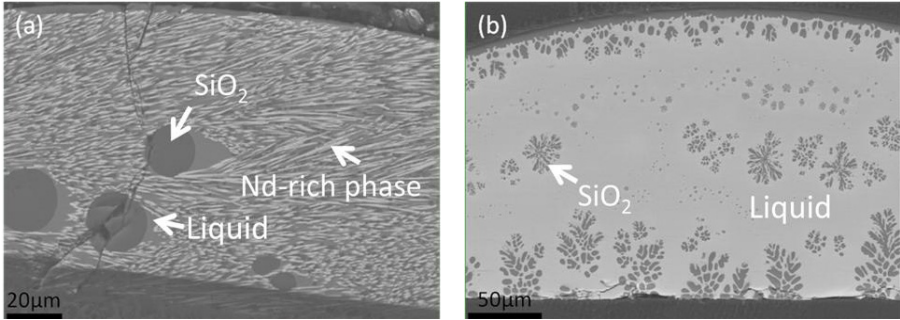


Figure 4: Back scattering electron (BSE) images of (a) 25%CaO-50%SiO₂-25%Nd₂O₃ and (b) 23.8%CaO-47.5%SiO₂-23.8%Nd₂O₃-5%P₂O₅ slags after the CSLM experiments. In Figure a, the needle-like white structure is a Nd-rich phase.

Figure 5 shows the on-set precipitation temperature (liquidus) and solidification complete temperature (solidus) as a function of time for the different samples. With the addition of 5% P₂O₅ and the cooling rate of 20 °C/min, the liquidus temperature and the solidus temperature decrease from 1484 to 1399°C and from 1284 to 1040°C, respectively.

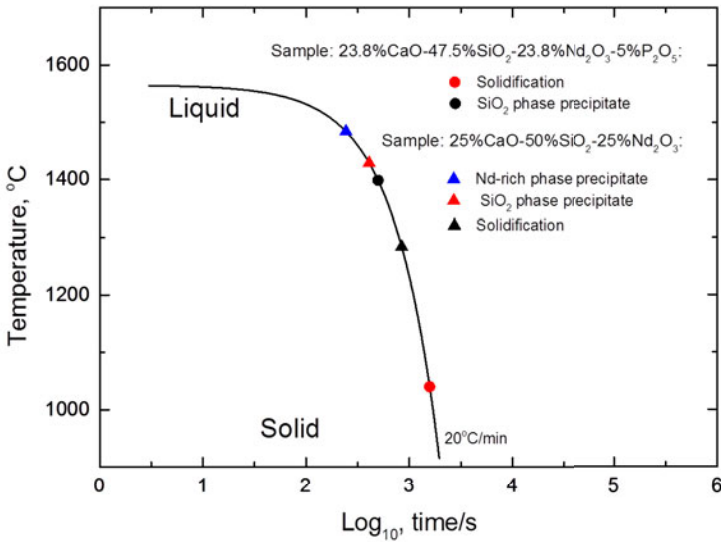


Figure 5: Precipitation and complete solidification temperatures with cooling rate at 20°C/min of 25%CaO-50%SiO₂-25%Nd₂O₃ and 23.8%CaO-47.5%SiO₂-23.8%Nd₂O₃-5%P₂O₅ slags.

As a follow-up of this preliminary study to evaluate the potential of recycling REE from the waste through either the precipitation of the none-REE-containing solid phase from the Liquid + SiO₂ region or the precipitation of the REE-rich ternary compound from the Liquid + Ca_{2+x}Nd_{8-x}(SiO₄)₆O_{2-0.5x} region, CSLM experiments and EPMA analysis will be done at different cooling rates and different compositions. These data are necessary to construct the CCT diagram, which is a practical tool for the REE recyclers to select appropriate slag compositions and cooling rates and to optimize the process.

Conclusion

Precipitation of the rare earth rich ternary compound were in-situ observed in 25%CaO-50%SiO₂-25%Nd₂O₃ system with a cooling rate of 20 °C/min. The addition of P₂O₅ influences the precipitation behavior and decreases the liquidus as well as the solidus temperatures of the slags. The results provide information on the selection of suitable flux materials for rare earth containing wastes recycling processes where slags are considered as the starting secondary raw materials, as an alternative to rare earth ores. The efficiency of REEs recovery and slag recycling can thus be enhanced by a properly engineered hot stage slag treatment process.

Acknowledgement

The authors acknowledge the support from the Hercules Foundation (project no. ZW09-09) in the use of the FEG-EPMA and from the GOA/13/008 project at the KU Leuven.

References

1. K. Binnemans, P. T. Jones, B. Blanpain, T. Van Gerven, Y. Yang, A. Walton, and M. Buchert, "Recycling of rare earths: a critical review", *J. Clean. Prod.*, 51, 1-22 (15 July 2013).
2. K. Binnemans, P. T. Jones, B. Blanpain, T. Van Gerven, and Y. Pontikes, "Towards zero-waste valorisation of rare-earth-containing industrial process residues: a critical review", *J. Clean. Prod.*, 99, 17-38 (15 July 2015).
3. S. Chu, "Critical materials strategy", U.S. Department of Energy, December 2011; http://energy.gov/sites/prod/files/DOE_CMS2011_FINAL_Full.pdf
4. R. J. Weber, and D. J. Reisman, "Rare earth element: A review of production, processing, recycling, and associated environmental issues", U.S. Environmental Protection Agency, August 2012; http://www.epa.gov/superfund/remedytech/tsp/download/2012_spring_meeting/fff_wed/4_weber-rare_earth_minerals.pdf.
5. L. T. Peiro, G. V. Mendez, and R. U. Ayres, "Rare and Critical Metals as By-products and the Implications for Future Supply", INSEAD Social Innovation Centre, 2011; <http://www.insead.edu/facultyresearch/research/doc.cfm?did=48916>
6. T.G. Goonan, 2011, "Rare earth elements—End use and recyclability", U.S. Geological Survey Scientific Investigations Report 5094, 2011; <http://pubs.usgs.gov/sir/2011/5094/>
7. T. H. Le, A. Malfliet, B. Blanpain, M. Guo, "Phase relations of the CaO-SiO₂-Nd₂O₃ system and the implication for the rare earths recycling", submitted.

8. T. Elwert, D. Goldmann, T. Schirmer, K. Strauß, "Affinity of rare earth elements to silico-phosphate phases in the system $\text{Al}_2\text{O}_3\text{-CaO-MgO-P}_2\text{O}_5\text{-SiO}_2$ ". *Chemie. Ing. Tech.*, 86, 840–847, (2014).
9. P. T. Jones et al., "Using confocal scanning laser microscopy for the in situ study of high-temperature behavior of complex ceramic materials", *J. Eur. Ceram. Soc.*, 27, 3497-3507, (2007).
10. G. Cerrato, B. Fubini, M. Baricco, C. Morterra, "Spectroscopic, structural and microcalorimetric study of stishovite, a non-pathogenic polymorph of SiO_2 ", *J Mater Chem*, 5, 1935–1941, (1995).

IN-SITU STUDIES ON THE CRYSTALLIZATION OF CaO-SiO₂-CaF₂-CeO₂ SYSTEM BY A CONFOCAL LASER SCANNING MICROSCOPE

Zengwu Zhao, Zhuang Ma, Fushun Zhang, Yongzhi Li, Yongli Jin, Xuefeng Zhang and Baowei Li

Key Laboratory of Integrated Exploitation of Bayan Obo Multi-Metal Resources, Inner Mongolia University of Science and Technology;
7 Arding Street; Baotou, Inner Mongolia, 014010, P.R. China

Keywords: Crystallization, *In-situ* CLSM observation, Rare earth, Slag solidification

Abstract

The recovery of rare earth elements from metallurgical slags containing rare earths is an important topic. The crystallization behavior of CaO-SiO₂-CaF₂-CeO₂ system with CeO₂ content range from 12 to 16 mass pct and a constant CaO/SiO₂ ratio of 1 has been examined by using a confocal laser scanning microscope (CLSM). Diagram of continuous cooling transformation and that of isothermal (time temperature) transformation for the slag have been constructed to characterize the solidification behavior of the slag with cooling rates between 3.125 and 100 K/minutes and temperature between 1373 and 1598 K. Depending on the CeO₂ content in the slag, the primary crystalline phase of CaO-SiO₂-CaF₂-CeO₂ system precipitates with elongated needle-like or short and rod-like crystals. The XRD analyses of crystalline phase of solidified slags confirm that the primary crystalline phase is a rare earth-rich phase Ca₂Ce₈O₂(SiO₄)₆, which contains no fluoride.

Introduction

Bayan Obo of China has the largest iron-rare earth-niobium deposit in the world, in which 71 elements and 170 minerals have been detected. Up to 1980s, it has been mined merely as an iron ore. Currently, to utilize the rare earth resources of the Bayan Obo ore, the concentrates of iron and rare earth are separated with applications of various mineral processing techniques, including low and high intensity magnetic separation, anti-flotation and flotation processes. However, only approximately 10 mass pct of rare earths can be recovered, while most of the rare earth minerals remain in the tailings and/or flow into blast furnace (BF) slags generated by using Bayan Obo ore. Since 1950s, effort has been attempted on recovering rare earth elements from the BF slags and tailings. Xu [1] found that the main rare earth containing phase in the BF slags and tailings is Cefluosil, i.e. 7[(Ca, Ce, Nd, La, Pr)₂SiO₄](F, O)₁₀, which precipitates as a rod-like crystal during cooling of the BF slag with 12.6 pct REO content. To recover rare earth from Bayan Obo tailings, Jiang et al. [2] proposed a reduction method and Ding et al. [3] a melting process respectively, for separating iron and rare earth of the melts generated in the processes. To efficiently separate rare earths from molten slags, it is significantly important to understand the crystallization behavior of rare earth phase during the slag solidification. By using a confocal laser scanning microscope with high temperature heating system (CLSM), this paper focuses on

the *in-situ* observation of the crystallization and solidification behavior of the CaO-SiO₂-CaF₂-CeO₂ system, which is relevant to the recovery of rare earth from Bayan Obo tailings and BF slag generated by using Bayan Obo ore.

Experimentals

A. Materials and Sample Preparation

The BF and the direct reduction slags generated by using Bayan Obo ore contain 13 to 39 mass pct CaO, 11 to 35 mass pct SiO₂, 3 to 18 mass pct REO, 10 to 36 mass pct CaF₂ and minor impurities, such as FeO, MgO, Al₂O₃ [1-4]. To mimic these slags, chemistry of the slag in the present CLSM test was designed as in table I

Table I The Chemical Composition of Experimentally Synthesized Slag (mass pct)

	CaO	SiO ₂	CeO ₂	CaF ₂
A	32	32	16	20
B	34	34	12	20

Synthetic slags were prepared from the chemical reagents, i.e. CaO (obtained by calcination of CaCO₃, 99.9%, analytically pure, Aladdin Industrial Corporation), SiO₂ (99.9%, analytically pure, Aladdin Industrial Corporation), CeO₂ (99%, analytically pure, Baotou Steel Rare-Earth Hi-Tech Co.) and CaF₂ (99.9%, analytically pure, Aladdin Industrial Corporation). These chemical powders were dried for 8 hours at 393 K under 0.08 MPa in a vacuum chamber and then weighed by using an analytical balance with 0.1 mg accuracy. The powders were mixed by an auto mixer (200 r/min) for 45 minutes to obtain a homogeneous sample. The mixture was further pressed to form a disc pellet with 6 mg weight for the following CLSM test.

B. Experimental set-up and Procedure

Firstly, samples were heated to 473 K at the heating rate of 200 K/min and maintained for 1 minute to evaporate water in materials, and then heated up to 1773 K at the heating rate of 200 K/min and held for 3 minutes to eliminate the bubbles and homogenize the melts. Figure 2(a) and (b) show the respective cooling history for investigating the continuous cooling transformation (CCT) and isothermal (time temperature) transformation (TTT) of the slags.

The crystallization and solidification behavior of rare earths-bearing slags was *in-situ* observed by using a CSLM equipped with an infrared furnace (VL2000DX; Lasertec Corporation, Yokohama, Japan). The present experimental set-up is schematically shown in Figure 1. Slag sample was put in a Pt crucible placed on a sample holder inside the CSLM heating chamber. Before heating the sample, the CSLM chamber was evacuated and flushed with argon gas (Ar > 99%) for three times and then a constant Ar stream (0.2L/min) was maintained during the experiments. The moisture and oxygen in argon gas were removed by a purifier.

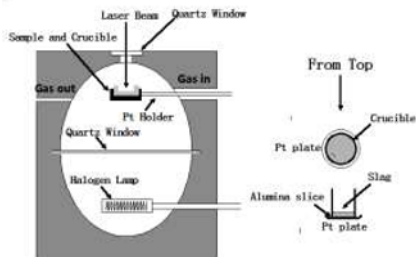


Figure 1. Schematic representation of CSLM experimental set-up.

The temperature calibration was conducted by using pure copper (melting point: 1356K) and pure nickel (melting point: 1726 K) as references. The heating and cooling processes were controlled. Firstly, samples were heated to 473 K at the heating rate of 200 K/min and maintained for 1 minute to evaporate water in materials, and then heated up to 1773 K at the heating rate of 200 K/min, the temperature was held for 3 minutes to eliminate the bubbles and homogenize the melts. Figure 2(a) and 2(b) show the respective cooling history for investigating the continuous cooling transformation (CCT) and isothermal transformation (TTT) of the slags. For the CCT study (Figure 2(a)), after the slag had melted and homogenized at 1773 K, it was cooled to 1623 K at the cooling rate of 500 K/min and held for 1 minute, then cooled to 1373 K at the various cooling rate ranged from 3.125 K/min to 100 K/min, followed by quenching the slag to room temperature. For the measurement of the TTT diagram, after the same heating process as that for CCT study, the slag sample was rapidly cooled at the cooling rate of 2000 K/s to the distinct temperatures ranged from 1373 K to 1598 K and maintained at the respective temperature for 5 minutes, followed by quenching the slag, as shown in Figure 2(b).

The crystallization and solidification of slag samples were *in-situ* observed and recorded. The obtained images were extracted from a series of CLSM video sequences at a rate of 5 frames per second. These images were used for further investigation, such as estimation of number, size and volume of the precipitates, determination of the on-set precipitation temperature for constructing the CCT and TTT diagram. Furthermore, the cooled samples were examined using scanning electron microscope (QUANTA 400, FEI) and X-ray diffraction (D8 ADVANCE, BRUKER).

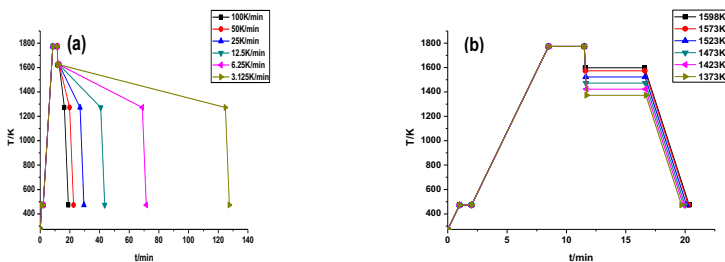


Figure 2. The thermal history of the CSLM test for (a) CCT and (b) TTT studies

Results and Discussion

A. Crystallization Process and Crystals Morphology of CaO-SiO₂-CaF₂-CeO₂ Slag

Since the molten slag was transparent, by maintaining the focus of the CLSM on the bottom of the crucible the on-sets of the crystallization were detected by the appearance and growth of a new phase in the slags. Figure 3 illustrates a representative melting and crystallization process of the slag A with 16 mass pct CeO₂ content. The slag started to sinter at around 1200 K (Figure 3(a)). The start of the melting was observed at around 1363 K with generation of a large number

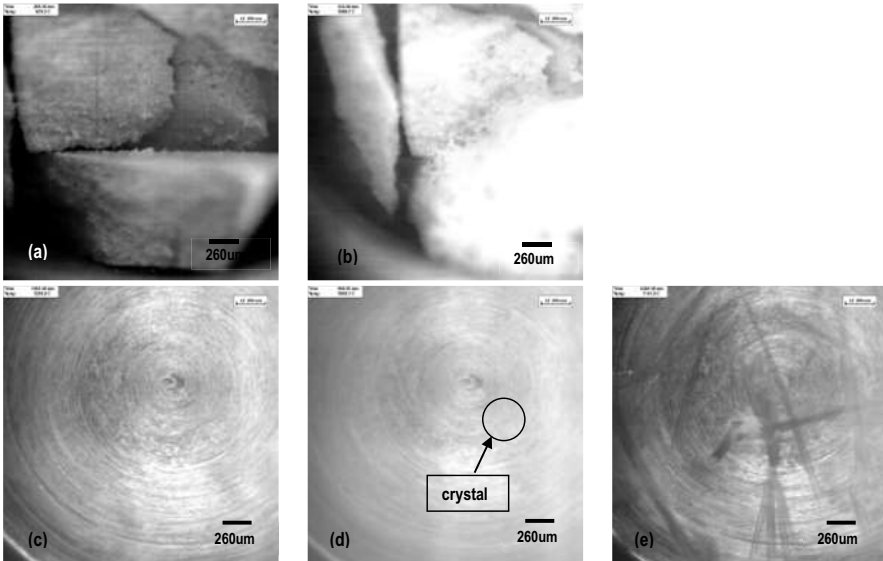


Figure 3. *In-situ* observation of melting and crystallization process for slag A using a CLSM. (a) beginning to sinter; (b) liquid appears; (c) transparent liquid slag; (d) on-set of a primary phase precipitation; (e) fast growth of the crystals

of gas bubbles (Figure 3(b)), and the slag became liquid at 1662 K, where the bottom of the crucible can be seen clearly as in Figure 3(c) due to the transparency of the liquid slag at high temperature. The sample was continuously heated up to 1773 K to ensure a fully liquid state. After holding for 3 minutes the slag was cooled down with a cooling rate of 6.25 K/min for *in-situ* observation of the solid phase precipitation. The primary phase with an elongated needle-like crystal precipitated at around 1445 K (Figure 3(d)) and the newly formed precipitate grew with further decreasing temperature (Figure 3(e)).

Figure 4 shows the representative CLSM images for the crystallization of slag B with 12 mass pct CeO₂ content at the cooling rate of 3.125 K/min. Compared to the crystallization of slag A, the following three crystallization characteristics were identified. Firstly, a multiple number of the crystals precipitated in the beginning of slag solidification (Figure 4(a)), whereas only a limited

number of crystals appeared in slag A at the initial crystallization stage (Figure 3(d)). Secondly, instead of the crystals with elongated needle-like shape in slag A (Figure 3(e)), the short and rod-like crystals were seen in slag B (Figure 4(b)). Thirdly, the rod-like crystals were aligned in parallel (Figure 4(b)). Comparing with the two kinds of crystals, it is obvious that the elongated needle-like crystals in slag A are much longer than the rod-like crystals in slag B.

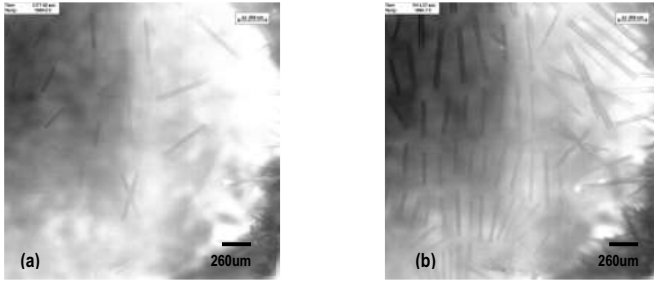


Figure 4. *In-situ* observations of the crystallization process for slag B using a CLSM. (a) a number of rod-like crystals precipitated in the beginning of slag cooling; (b) crystals grew and aligned in parallel.

B. Non-Isothermal and Isothermal Solidification Diagrams of 32 mass pct CaO - 32 mass pct SiO₂ - 20 mass pct CaF₂-16 mass pct CeO₂ Slag (Slag A)

To quantitatively understand slag solidification behavior, the on-set precipitation temperature as a function of time for sample A was plotted for the continuous cooling (CCT diagram in Figure 5(a)) and isothermal solidification (TTT diagram in Figure 5(b)) respectively. Due to the limitation of the CLSM resolution, the on-set precipitation temperature was defined as the temperature measured at the moment of the primary phase with 100 µm size. With increasing cooling rate from 3.125 to 100 K/min, the initial crystallization temperature decreased from 1460 to 1293 K (Figure 5(a)). For the isothermal solidification, on the other hand, the crystal incubation (or nucleation) time increased from 7.9 to 60.2 seconds as the isothermal solidification temperature increased from 1373 to 1598 K. These diagrams will provide a basis for selecting appropriate slag cooling rates and solidification temperature to optimize the recovery process of rare earth from Bayan Obo tailings and BF slag generated by using Bayan Obo ore.

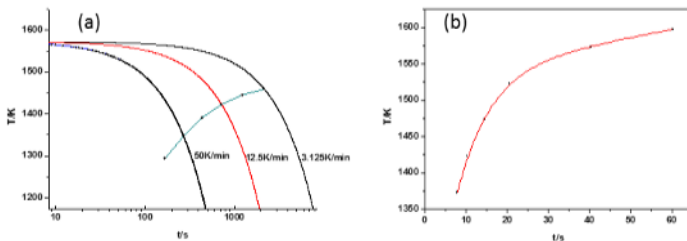


Figure 5. Continuous cooling and isothermal solidification behaviors of slag A. (a) CCT and (b) TTT diagrams

C. Analysis of Crystalline Phase of the Solidified Slags

In order to investigate the microstructure and phase composition of crystal, the samples after *in-situ* observation were examined for the isothermal experiments of Slag A and slag B at 1423K. Figure 6 (a) and (b), respectively, show morphology of the crystals on the slag A and slag B surface. The crystals in slag A are thick hexagonal prisms, while that of slag B are thin and tiny hexagonal prisms like the letter “H”. The “H”- like crystals were aligned in parallel, which is in an agreement with the *in-situ* CLSM observation (Fig. 4), while crystals on slag A surface is

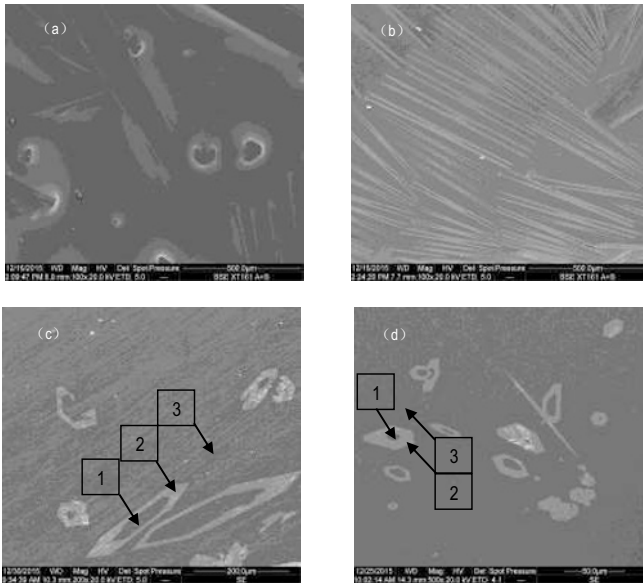


Figure 6. SEM photographs of the surface and polished surface. (a) surface of slag A, (b) surface of slag B, (c) cross section of slag A and (d) cross section of slag B

randomly directed. By cutting the slag sample perpendicular to the top slag surface, the crystals in both slag A and B show a hollow hexagonal prism shape (Figure 6(c) and (d)). However, the size of crystals in slag A is much bigger than that in slag B.

The phase compositions of crystals in slag A and B are analyzed by EDS as shown in table II. It is obvious that rare earths enriched in crystals of hexagonal prisms with hollow, while there are only 1 to 2 wt% rare earth in the slag matrix.

Table II. The Content of different locations by EDS (mole pct)

	Ca	Si	Ce	O	F
'1' of figure 6(c)	17.67	20.54	1.1	51.06	9.62
'2' of figure 6(c)	10.93	18.17	11.71	59.18	-
'3' of figure 6(c)	18.52	20.9	1.47	50.26	8.85
'1' of figure 6(d)	16.32	20.12	0.96	52.0	10.6
'2' of figure 6(d)	11.27	19.17	11.58	57.98	-
'3' of figure 6(d)	19.32	18.65	1.53	46.3	14.19

The primary crystalline phase observed in the CLSM test was identified with XRD analysis after high temperature experiment. 5 g of slag A sample were melted and then solidified with the same thermal history of the CLSM test. The obtained sample was characterized with X-Ray Diffraction and its characteristic pattern is shown in Figure 7. The primary crystalline phase was identified as a rare earth concentrated $\text{Ca}_2\text{Ce}_8\text{O}_2(\text{SiO}_4)_6$.

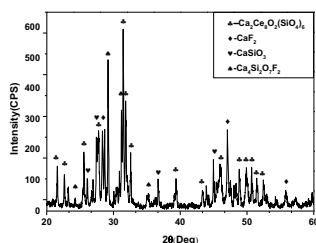


Figure 7. XRD patterns of the solidified slag A

Conclusion

The confocal scanning laser microscope (CSLM) was employed to study the crystallization behavior of $\text{CaO-SiO}_2\text{-CaF}_2\text{-CeO}_2$ slags with CeO_2 content ranged from 12 to 16 mass pct and a constant CaO/SiO_2 ratio of 1. CeO_2 content influences nucleation, growth and morphology of the primary crystals. With increasing CeO_2 content, shape of the primary precipitate changes from an elongated needle-like to a short and rod-like crystal. Furthermore, lowering CeO_2 content favors nucleation of the primary phase during solidification. The CCT and TTT curves for 32 mass pct CaO - 32 mass pct SiO_2 - 20 mass pct CaF_2 - 16 mass pct CeO_2 slag (Slag A) were determined to characterize the crystallization behavior of the slag with cooling rates between 3.125 and 100K/minutes and temperature between 1373 and 1598 K. The primary crystalline phase was identified as a rare earth concentrated $\text{Ca}_2\text{Ce}_8\text{O}_2(\text{SiO}_4)_6$.

Acknowledgment

The authors acknowledged the support from the National Natural Science Foundation of the Municipality of Inner Mongolia of China (Project No. 2012JQ02) and the National Natural Science Foundation of China (Project No. 51464040).

References

1. Xiuying Xu et al., "Study on the slow cooling crystallization and selection of Rare Earth from Baotou Blast Furnace Slag," *Rare Earth*, 3 (1980), 1-7.
2. Yinju Jiang et al., "Rare Earth Enrichment from Iron Concentrates of Main and East Orebodies of Baiyan Obo by Direct Reduction and Melting Separation Method," *Chinese Rare Earth*, 35 (3) (2014), 54-58.
3. Yingui Ding et al., "Innovative Methodology for Separating of Rare Earth and Iron from Bayan Obo Complex Iron Ore," *ISIJ International*, 52 (2012), 1772-1777.
4. Changzhen Wang and Yuanxin Zou, "Activity of La_2O_3 in liquid La_2O_3 - CaF_2 and La_2O_3 - CaF_2 - CaO - SiO_2 slags," *Acta Metallurgica Sinica*, 16 (2) (1980), 190-194.

CRYSTALLIZATION KINETICS OF CaO-SiO₂-Al₂O₃-MgO SLAGS

Shaghayegh Esfahani¹, Mansoor Barati²

^{1,2}Materials Science and Engineering, University of Toronto
184 College Street
Toronto, Canada M5S 3E4

Keywords: Crystallization kinetics, Nucleation, Growth, Activation energy, Avrami, Single Hot Thermocouple Technique (SHTT), Phase transformation

Abstract

Crystallization behavior of blast furnace slag is of great interest for generating value-added products from slag, such as cement feedstock, where the slag structure determines the material quality. Aided with a Hot Thermocouple Device, the kinetics of crystallization of CaO-SiO₂-Al₂O₃-MgO slags was determined. The rate of nucleation and growth of crystals were measured for a range of slag basicities, temperatures, and hold times.

Introduction

Blast furnace slags constitute over 50% of the total slag produced worldwide, amounting to 320 million tonnes per year. [1]. Blast furnace slags are most desired as feedstock for Portland cement production due to the large contents of silica and lime in these slags. For this application blast furnace slag has to be cooled rapidly to form an amorphous structure, as otherwise it will cause swelling of the concrete made from slag cement. Therefore, understanding of the crystallization behavior of BF slag is crucial with the purpose of controlling the cooling conditions or manipulating the slag composition so that the desired amorphous structure is achieved. Crystallization kinetics of mold fluxes has been previously studied by other researchers [1-7] due to their important role in steel continuous casting mold. However, similar investigations for metallurgical slags are limited [8-11]. In a recent study, [11] the transformation kinetics of a slag with composition close to the BF slags has been studied but to this date, a comprehensive study on the effect of composition on the rate and extent of crystallization is lacking.

Experimental Apparatus and Method

The kinetic study was carried out using the Single Hot Thermocouple Technique (SHTT). In this technique, a small piece of sample, is placed in tip of a type-B thermocouple (D=5mm) which is controlled by a thermocouple driver. The thermocouple acts as the heating element at the same time that it measures the temperature of the sample. This technique allows rapid heating/ cooling of the materials as well as *in-situ* observation of the crystallization kinetics. Also, higher accuracy of temperature measurement is possible due to the direct contact of the thermocouple with the sample.

Four CSAM slag samples with varying basicity ($C/S=CaO/SiO_2$) were prepared (Table 1). For each slag composition (wt %), 10 g of oxide powders were blended and melted in a graphite crucible ($D=4\text{cm}$, $h=4\text{cm}$) by heating the material to approximately 50°C above the slag liquidus temperature for 4 hours in an argon atmosphere. To avoid segregation during solidification, the molten slag was quenched in water, producing a glassy material from which small quantities were used for the crystallization study.

Table 1- Composition of the slag samples

Sample number	1	2	3	4
CaO	47	45	44	42
SiO ₂	33	35	36	38
Al ₂ O ₃	15	15	15	15
MgO	5	5	5	5
T _L (°C)*	1578	1444	1430	1396
C/S	1.4	1.3	1.2	1.1

* Liquidus temperature determined from FactSage™ calculations

The isothermal experiments were carried out by heating 3-5 mg of sample to 1600°C and holding it for 1 minute then cooling rapidly $70\text{-}75^\circ\text{C/s}$ to the target temperature. The transformation of glassy to crystalline slag was recorded until the sample was fully crystalline.

Isothermal Transformation Kinetics

Theoretical Treatment of Transformation

For quantifying the transformed volume fraction during isothermal transformation, the theoretical treatment was carried out through JMAK equation (1) [12-16].

$$X = 1 - \exp[-(kt)^n] \quad (1)$$

This expression describes the relationship between the transformed volume fraction and time as a sigmoidal curve. The coefficient K is a kinetic parameter which includes both nucleation and growth rates and Avrami exponent, n , can provide useful information on the mechanism of transformation.

Experimental Determination of Phase Change

Using image analysis techniques, the crystallized fraction of each slag was determined for 9-10 different isothermal temperatures ranging from $1100\text{-}1300^\circ\text{C}$ and repeated 3-4 times at each temperature. As an example, the crystallized fraction during isothermal transformation for slag sample with $C/S=1.2$ at 1200°C is shown in Figure 1. In these figures, the light regions are opaque crystals which form in the transparent amorphous slag matrix. The bright ring appearing in the middle of some of these figures is due to the additional light source used to increase the image resolution.

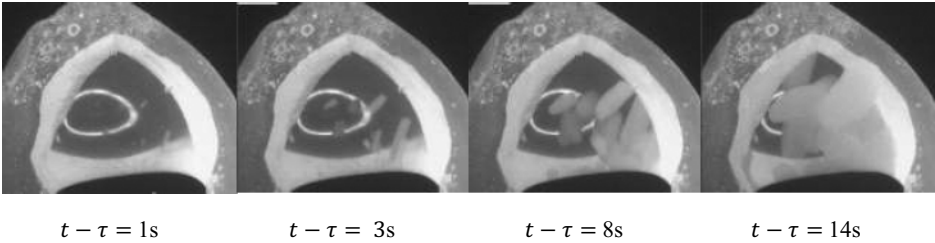


Figure 1- Crystallization of slag with C/S=1.2 at 1200°C isotherm (τ =incubation time).

Determination of the Avrami parameters

The crystallized fraction from the isothermal treatments were found to follow a sigmoidal form (Figure 2-a), described by the JMAK equation (1). In this figure it is observed that with the increase of temperature the crystallization is slower. This is due to the fact that nucleation is the dominant mechanism of crystallization and at higher temperatures there is less nucleation driving force thus lower kinetics. The mechanism of crystallization for all the slags has been discussed further in the following sections.

Constants n and Lnk could be obtained by plotting $Ln[-Ln(1 - X)]$ verses $Ln(t - \tau)$ (2) and Figure 2-b with values presented in Table 2.

$$Ln[-Ln(1 - X)] = nLn(k) + nLn(t - t_0) \quad (2)$$

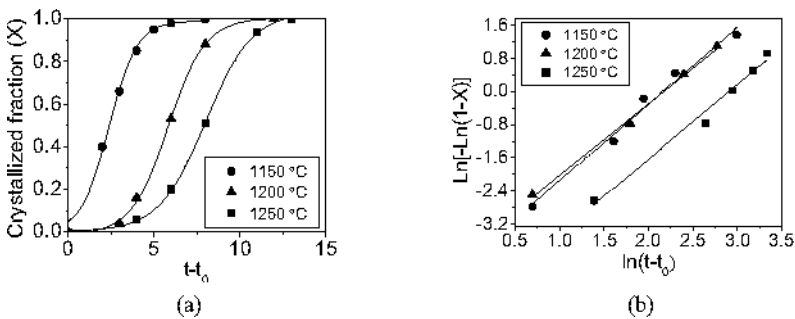


Figure 2- (a) Crystallized fraction as a function of time (b) JMAK plots for the slag with C/S=1.4.

Table 2- Avrami exponent (n) and Lnk

Temp (°C)	C/S=1.4		C/S=1.3		C/S=1.2		C/S=1.1	
	n	Lnk	n	Lnk	n	Lnk	n	Lnk
1100	–	–	1.9	-1.8	2.0	-1.8	–	–
1120	3.1	-0.8	1.4	-2.3	1.5	-1.9	–	–
1130	–	–	1.3	-2.6	1.6	-2.0	1.5	-5.4
1140	2.9	-1.1	1.3	-2.7	1.7	-2.1	1.5	-5.4
1150	2.7	-1.4	2.0	-2.8	1.9	-2.2	1.4	-4.9
1160	3.9	-1.3	1.4	-2.1	1.4	-2.3	2.0	-5.0
1170	3.1	-1.2	1.7	-2.0	1.8	-2.0	–	–
1180	2.8	-1.3	1.6	-2.0	1.9	-2.2	1.9	-4.7
1200	4.0	-1.9	1.7	-2.4	1.9	-2.2	2.2	-4.7
1250	3.8	-2.2	2.1	-3.0	1.7	-2.2	2.0	-5.1
1270	–	–	–	–	–	–	2.0	-5.3
1300	4.0	-2.6	1.6	-2.9	1.8	-2.9	–	–

Nucleation Rate

Depending on the nucleation mechanism, the nucleation rate may increase, decrease or remain constant with time. The dependence of nucleation rate on time was investigated by image analysis. The resulting nucleation rates for all slag compositions at $T= 1200^{\circ}\text{C}$ are presented in Figure 3. As seen, the slag with $C/S=1.4$ experiences a significant increase in the nucleation rate with time. On the other hand, for the slag with $C/S=1.2$ and 1.3 , the nucleation rate decreases with time. As the basicity is further decreased ($C/S=1.1$), the nucleation rate becomes close to zero.

Figure 4 shows Lnk versus $1/RT$ for various slags. As seen, at a constant temperature the rate constant increase with the increase of C/S . This is due to the oxide structure becoming depolymerized and the bonds weakened as the C/S increases resulting in lower viscosities. With the decrease of viscosity the ionic mobility increases and it becomes easier for the structure to rearrange and accommodate the changes induced by crystallization.

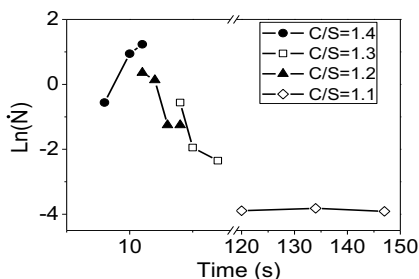


Figure 3- Change of nucleation rate with time for all slags at $T=1200^{\circ}\text{C}$.

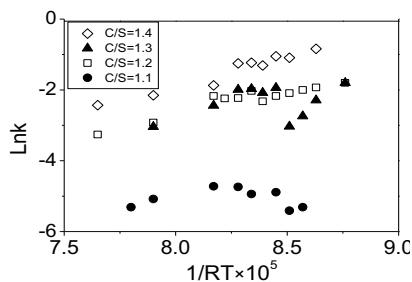


Figure 4- Lnk versus $1/RT$ for all slag compositions

Growth Rate

The growth rate can also be determined by measuring the thickness of the crystals at different times, using image analysis, as shown in Figure 5. For each slag, the measurements were made for three temperatures (1150°C, 1200°C, 1250°C) and the growth rate was measured until the crystal under study grows independently and before colliding with any neighboring crystals. The result of this analysis is presented in Figure 6. The slope of these curves which are all constant with time corresponds to the growth rate of individual crystals (i.e. constant growth rate), and are presented in Table 3.

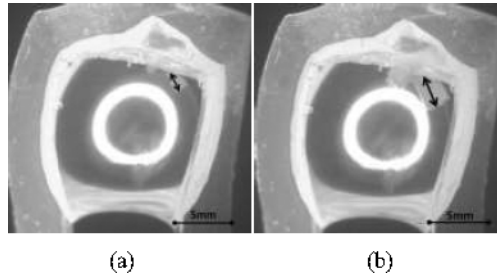


Figure 5- Growth rate measurement for sample with C/S=1.2 at T=1250°C (a) $t - \tau = 6s$ (b) $t - \tau = 9s$.

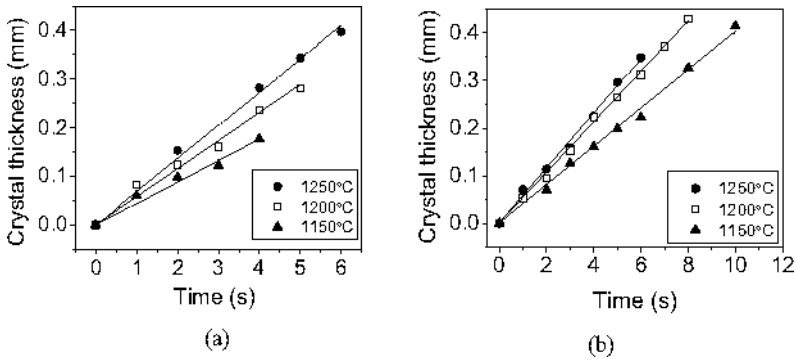


Figure 6- Crystal thickness versus time (a) C/S=1.4 (b) C/S=1.3.

Table 3- Crystal growth rate (mm/s) at different temperatures.

Basicity (C/S)	Growth rate (mm/s)		
	1250°C	1200°C	1150°C
1.4	68	58	44
1.3	58	53	40
1.2	38	32	29
1.1	10	8	4

The dependence of growth rate on time may provide some indications to the mechanism of growth. In most cases, linear dependence corresponds to interface-controlled growth whereas when growth is proportional to the square root of time, the growth can be considered to be diffusion-controlled. However, in the former case, it has been suggested that a constant growth rate does not always translate to interface-controlled growth [17-19] and for determining the mechanism of growth it is best to examine the morphology of the interface in atomic scale. In general, when faceted interface is observed, the rate-controlling step is the interface reaction. However, when the interface is rough and cellular, such as dendritic growth, the rate limiting mechanism for growth is diffusion [20]. In the case of the compositions in the current study, the morphology of the interface was not examined in near atomic scale but an observation through a microscope clearly shows that the interface is not faceted which confirms a dendritic growth (Figure 7).

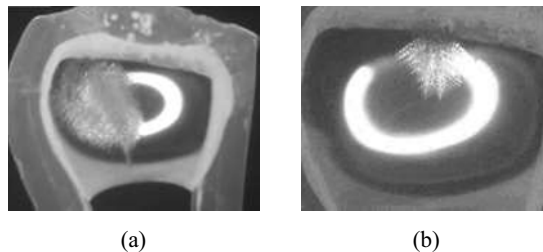


Figure 7- Fully dendritic interface morphology for sample with C/S=1.1 at a) T=1270°C b) 1250°C

Mechanism of Slag Crystallization

The n values obtained from experiments were compared with theoretical values to determine the crystallization mechanism pertaining to the slags of the present study. As discussed earlier, the growth for slags appear to involve a diffusion-controlled process. For slag with C/S=1.4, the nucleation rate is increasing, which according to the n values suggested by Christian [21], indicates that n must be above 2.5. This is in agreement with the measured value of $4.0 > n > 2.8$ presented in Table 2. However, for the slag with C/S=1.2 and C/S=1.3, the nucleation rate is

decreasing which would suggest n values between 1.5-2.5. This is also consistent with the measured values of n which falls within the same range as demonstrated in Table 2. For the sample with $C/S=1.1$ the nucleation rate is close to zero which again shows a match between the measured n values and the those suggested according to Christian [21] for temperatures below 1160°C ($n=1.5$). The only existing discrepancy is for sample with $C/S=1.1$ at temperatures above 1160°C which is attributed to the lower contrast between the matrix and the crystals which results in difficulty in defining the starting point of nucleation of this sample.

Conclusion

In this study, crystallization kinetics of synthetic CaO-SiO₂-Al₂O₃-MgO (CSAM) slags with different basicities were studied by Single Hot Thermocouple Technique (SHTT) during isothermal treatment. Kinetic parameters were obtained by analysis of images from *in-situ* observation of glassy to crystalline transformation. Also, the dependence of nucleation and growth rates of crystalline phases were quantified as a function of time, temperature, and slag basicity. Together with the observations of crystallization front, they facilitated establishing the dominant mechanisms of crystallization.

Acknowledgements

The funding for this research was provided by Natural Science and Engineering Council of Canada (NSERC) and Ontario Government through an Early Researcher Award and an Ontario Government Scholarship for Science and Technology (OGSST).

References

1. M. Barati and S. Esfahani, "Slag crystallization behavior pertaining to heat recovery" (Paper presented at the 6th International Congress on the Science and Technology of Steelmaking, Beijing, China, 2015).
2. Y. Kashiwaya, C. E. Cicutti, and A. W. Cramb, "Investigation of the crystallization of a continuous casting mold slag using the single hot thermocouple technique," *ISIJ International*, 38 (1998), 357-365.
3. Y. Kashiwaya, C. E. Cicutti, A. W. Cramb, and K. Ishii, "Development of double and single hot thermocouple technique for in situ observation and measurement of mold slag crystallization," *ISIJ International*, 38 (1998), 348-356.
4. J. L. Klug, R. Hagemann, N. C. Heck, A. C. F. Vilela, H. P. Heller, and P. R. Scheller, "Fluorine-free mould powders for slab casting: Crystallization control in the CaO-SiO₂-TiO₂-Na₂O-Al₂O₃ system," *Steel Research International*, 83 (2012), 1186-1193.
5. G.-H. Wen, H. Liu, and P. Tang, "CCT and TTT diagrams to characterize crystallization behavior of mold fluxes," *Journal of Iron and Steel Research, International*, 15 (2008) 32-37.
6. Z. T. Zhang et al. , "Observations of crystallization in mold slags with varying Al₂O₃/SiO₂ ratio," *Steel Research International*, 81 (2010), 516-528.
7. Y. G. Maldonado et al., "Kinetic study of the devitrification of mold powder slags," *Iron and Steel Technology*, 10 (2013), 65-75.
8. P. F. James, "Kinetics of crystal nucleation in silicate glasses," *Journal of Non-Crystalline Solids*, 73 (1985), 517-540.

9. P. Rocabois et al., "Crystallization kinetics of $\text{Al}_2\text{O}_3\text{-CaO-SiO}_2$ based oxide inclusions," (Paper presented at the 6th International Conference on Molten Slags, Fluxes and Salts, 12-17 June 2000, Netherlands, 2001) 98-109.
10. A. A. Francis, "Non-isothermal crystallization kinetics of a blast furnace slag glass," *Journal of the American Ceramic Society*, 88 (2005), 1859-1863.
11. Y. L. Qin, X. W. Lv, J. Zhang, J. L. Hao, and C. G. Bai, "Determination of optimum blast furnace slag cooling rate for slag recycling in cement manufacture," *Iron and Steelmaking*, 42- 5 (2015), 395-400.
12. M. Avrami, "Kinetics of phase change. I: General theory," *The Journal of Chemical Physics*, 7 (1939), 1103-1112.
13. M. Avrami, "Kinetics of phase change. II Transformation-time relations for random distribution of nuclei," *The Journal of Chemical Physics*, vol. 8 (1940), 212-224.
14. M. Avrami, "Granulation, phase change, and microstructure kinetics of phase change. III," *The Journal of Chemical Physics*, 9 (1941), 177-184.
15. W. A. Johnson and R. F. Mehl, "Reaction kinetics in processes of nucleation and growth," *American Institute of Mining and Metallurgical Engineers - Transactions*, 135 (1939) 416-442.
16. A. N. Kolmogorov, "A statistical theory for the recrystallization of metals," *Bull. Acad. Sci. URSS, Cl. Sci. Math. Nat.*, (1937), 355.
17. D. R. Uhlmann, *Glass: Current Issues* (Boston: Martinus Nijhoff Publishers), 1985.
18. H. R. Swift, "Some experiments on crystal growth and solution in glasses," *American Ceramic Society -- Journal*, 30 (1947), 165-169.
19. D. R. Uhlmann and G. W. Scherer, "Crystallization kinetics of $\text{Na}_2\text{O}\cdot 3\text{SiO}_2$," *Journal of Crystal Growth*, 29 (1975), 12-18.
20. R. J. Kirkpatrick, "Crystal growth from the melt: A review," *American Mineralogist* vol. 60 (1975), 798-814.
21. J. W. Christian, *The Theory of Transformations in Metals and Alloys* (Oxford: Pergamon, 1975).

FREEZE-LINING FORMATION FROM FAYALITE-BASED SLAGS

Liugang Chen*, Muxing Guo, Shuigen Huang, Peter Tom Jones, Bart Blanpain,
Annelies Malfliet

KU Leuven, Department of Materials Engineering
Kasteelpark Arenberg 44 bus 2450, 3001 Leuven, Belgium

Keywords: freeze-lining, fayalite slag, microstructure

Abstract

Formation of freeze-linings from aggressive process slags is used in industrial pyrometallurgical processes to protect the furnace wall. In this laboratory study, the formation of freeze-linings from fayalite-based ($\text{FeO-SiO}_2\text{-Al}_2\text{O}_3\text{-CaO}$) slags was investigated. This was performed with a gas-cooled probe at 1200 °C under protective atmosphere. The microstructure of the freeze-linings formed on the samples was characterized using scanning electron microscopy (SEM). The influence of cooling rate, slag agitation and slag composition on the freeze-lining formation was studied by varying the gas-flow rate, rotating the crucible and changing the CaO and Al_2O_3 contents in the fayalite-based slag, respectively. The results indicate that fayalite (Fe_2SiO_4) precipitated from the slag and grew into large columnar crystals along the heat gradient from the cooled probe to the bath slag. The thickness of the freeze-lining increased with increasing cooling rate, while an increase in the slag agitation and the CaO and Al_2O_3 contents in the slag decreased the thickness of the freeze-lining. These macroscopical observations are discussed with respect to the microstructural evolution in the formed freeze-lining samples.

Introduction

In conventional pyrometallurgical processes, refractory materials are commonly used to line furnaces/vessels. However, high smelting intensity, chemical corrosion by the slag and thermal stress in the refractories can drastically shorten the lifetime of furnace/vessel linings. To overcome these limitations of refractory integrity at high intensity operations, the use of freeze linings is common practice in smelting applications. A major advantage of the freeze-lining concept is that the freeze lining consists of solidified process material and, therefore, is self-regenerating and can resist aggressive process materials.

To apply the freeze-lining concept in a reactor, its formation and its stability have to be assured. A vast number of studies have been performed in recent years with respect to the freeze lining

behavior of pyrometallurgical processes – such as Zn fuming [1-4], continuous copper converting [5-8], and copper flash smelting [9,10] – and the influencing factors, *e.g.* temperature, cooling rate, slag composition, slag viscosity and other operation parameters. Slag properties found to affect the freeze-lining formation are the viscosity, the temperature stability range of the relevant phases, the microstructure of the formed phases (a closed structure or not, interlocking or not), the crystallization behavior, and the mass transfer of the slag. By changing these slag properties, the freeze lining formation rate can be influenced and the freeze lining stability can be controlled.

In this work, the formation of freeze-lining from fayalite-based slags was investigated by a gas-cooled probe technique at 1200 °C under protective atmosphere. The influence on the freeze-lining formation of cooling rate (gas flow rate), slag agitation (crucible rotation speed), and CaO and Al₂O₃ contents in the slag was also studied.

Experimental Procedure

Fayalite slag supplied by a copper producer was used in this work. The chemical composition of the slag is listed in Table 1. Minor elements, such as K, S, P, Cu, Mn, Pb, and Ni, are accounted as “others” in Table 1. CaO, calcined from CaCO₃ at 1000 °C for 24 h, and Al₂O₃ were added to change the CaO level in the slag to ~5 wt% and ~8 wt%, and Al₂O₃ to ~9 wt% (Table 1), respectively. The freeze-lining tests were called C1A5, C5A5, C8A5 and C7A9, according to the CaO and Al₂O₃ contents in the as-prepared slags.

Table 1: Chemical composition of the slag sample for freeze-lining tests (wt%).

Exp. no.	CaO	Al ₂ O ₃	FeO	SiO ₂	Na ₂ O	Cr ₂ O ₃	MgO	Others
C1A5	1.0	5.0	51.6	37.7	1.6	0.5	0.5	2.1
C5A5	4.7	4.7	49.6	36.3	1.5	0.5	0.5	2.0
C8A5	8.3	4.6	47.8	34.9	1.5	0.5	0.5	1.9
C7A9	7.0	8.9	44.5	32.5	1.4	0.4	0.4	1.8

The formation of freeze-lining from fayalite-based slags was investigated by a gas-cooled probe technique combining with rotating crucible. This method has been commonly used to investigate the formation and stability of freeze-lining in laboratory-scale [1-8]. The experimental apparatus for freeze-lining tests is illustrated in Figure 1a. Approximately 1000 g of the as-prepared fayalite slag was filled in an Al₂O₃ crucible (inside diameter = 80 mm; height = 100 mm). The Al₂O₃ crucible was fixed in another larger Al₂O₃ crucible (inside diameter = 100 mm; height = 100 mm) by MgO ramming materials (Figure 1a), and then heated in a vertical tube furnace (Thermo Aix, with SiC heating elements). Ar gas, which generally contains around 2 ppm O₂, was blown into the furnace at a flow rate of around 0.3 l/min to simulate a protective

atmosphere. The slag was heated to 1200 °C and kept at that temperature for 120 min to ensure the molten state. Subsequently, the gas-cooled probe was immersed in the molten slag for 120 min and the larger Al₂O₃ crucible with its contents was either stationary or rotated with a predetermined speed (as shown in Table 2). The cooling N₂ gas enters the probe through the inner tube and is released through the outer tube (Figure 1b) with a predetermined flow rate (Table 2). Afterwards, the gas-cooled probe with a frozen slag layer was removed from the molten slag and quenched in a water bath.

Table 2: Experimental parameters for freeze-lining tests at 1200 °C.

Exp. no.	Gas flow rate (l/h)	Crucible rotation speed (rpm)
C1A5	2400; 3000; 3500	0
	3500	5; 10; 20
C5A5	3500	5
C8A5	3500	5
C7A9	3500	5

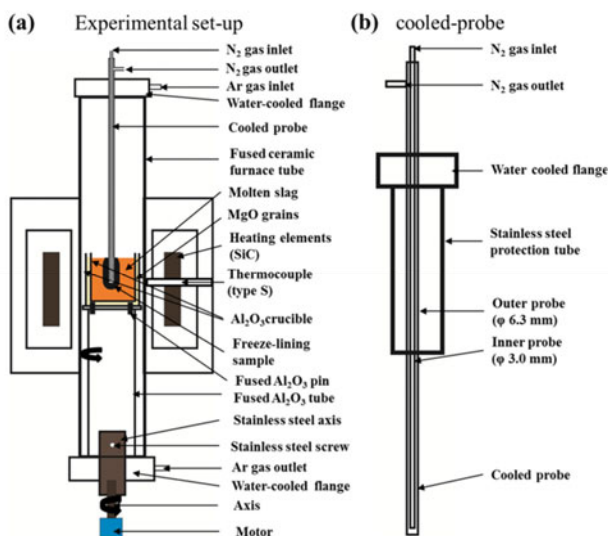


Figure 1. Schematic drawings of the set-up for (a) freeze-lining tests and (b) of the cooled-probe.

In order to avoid disintegration of the freeze-lining sample, the recovered frozen slag layer samples were firstly embedded in a low viscosity resin (Epofix) by vacuum impregnation, and then sliced with a diamond saw, 30 mm below the slag line. The embedded specimens were ground with silicon carbide grinding papers, polished with diamond paste, and carbon coated

for microstructural analyses. Microstructure images were obtained with a high resolution scanning electron microscope (SEM, Philips XL-30 FEG).

Results and Discussion

Figure 2 presents the influence of cooling-rate on the thickness and microstructure of the formed freeze-lining samples. The cooling rate was indicated as the flow rate of the N_2 gas in the cooled probe. The thickness of the frozen slag layer continuously increases from 4.6 mm, to 8.6 mm and to 10.5 mm, when the gas flow rate increases from 2400 l/h, to 3000 l/h and to 3500 l/h, respectively. In comparison, there was no frozen slag layer when the gas flow rate was lower than 1800 l/h (not shown here). This observation indicates that the freeze-lining formation is facilitated by increasing the cooling rate in the probe, because more heat is transferred by the larger gas flow rate.

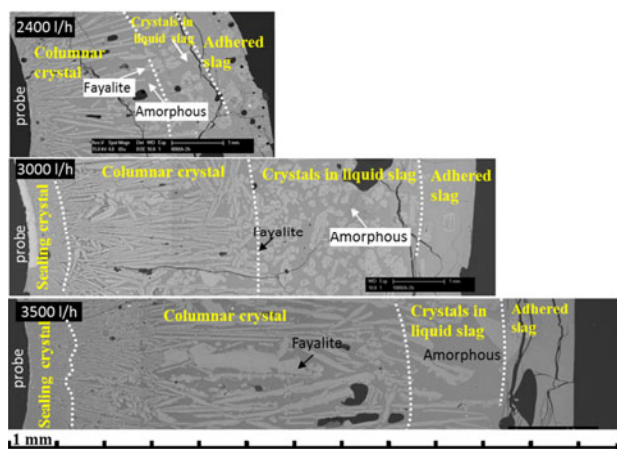


Figure 2. Influence of cooling rate (gas-flow rate) on the frozen slag layer formation, which is mainly composed of fayalite (Fe_2SiO_4) crystals and amorphous phases.

The microstructure of the frozen slag layer samples shows four zones, which are, from the surface of the probe towards the slag bath, respectively, a sealing crystal, a columnar crystal, a liquid slag with crystals and an adhered slag zone (Figure 2). The sealing crystal zone close to the cooled probe surface consists of dense, small fayalite grains. In the columnar crystal zone, fayalite precipitates grew into parallel columnar grains along the heat gradient from the probe to the slag bath. The thickness of this columnar crystal zone and the size of the columnar fayalite crystal continuously increases with increasing cooling rate. Close to the slag bath, large fayalite

grains with a diameter of over 200 μm were suspended in the liquid slag, forming the crystals in the liquid slag zone. The adhered slag zone is formed most likely due to the adhesion of the high viscosity slag upon removing the probe from the slag bath.

Figure 3 shows the microstructure of the freeze-lining samples formed from fayalite slags in tests with different crucible rotation speed. The thickness of the frozen slag layer decreased with the augmentation of crucible rotation speed. The thickness reduced from 10.5 mm at 0 rpm (3500 l/h in Figure 2), to 8.0 mm at 5 rpm, 7.0 mm at 10 rpm, down to 4.5 mm at 20 rpm. Simultaneously, the maximum thickness of the columnar crystal zone also decreased from 6.9 mm, to 5.8 mm, 3.7 mm and 2.6 mm with the rotation speed changes from 0 rpm to 5 rpm, 10 rpm and 20 rpm, respectively. This is probably because the increased slag agitation enhances convective heat transfer from the slag bath to the probe. Besides, the increased slag agitation can also increase the force on the columnar crystals, thereby breaking the large columnar fayalite crystals. In contrast, the thickness of the sealing crystal zone continuously increased from 0.9 mm, to 1.1 mm, up to 1.3 mm when increasing the rotation speed from 0 rpm, to 10 rpm and 20 rpm, respectively. The enhanced sealing crystal zone formation is probably due to the favored mass transfer from slag bath to the probe by the slag agitation, and the different temperature gradient in the frozen slag layer.

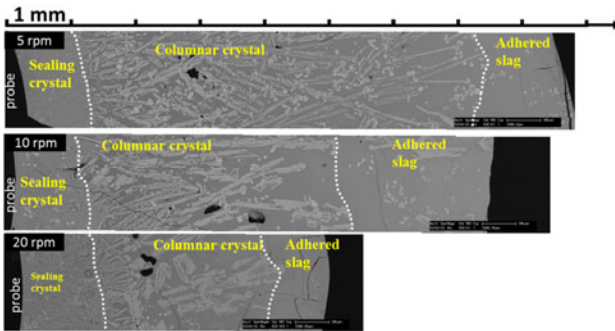


Figure 3. Influence of slag agitation (crucible rotation speed) on the frozen slag layer formation.

The influence of CaO and Al₂O₃ addition in fayalite slags on the freeze-lining formation is illustrated in Figure 4. The thickness of the frozen slag layer continuously decreased with increasing CaO and Al₂O₃ content in the slag. Specifically, the thicknesses are 8.0 mm, 5.3 mm, 4.6 mm and 3.7 mm for the slags containing 1 wt% CaO and 5 wt% Al₂O₃ (5 rpm, Figure 3), 5 wt% CaO and 5 wt% Al₂O₃ (C5A5), 8 wt% CaO and 5 wt% Al₂O₃ (C8A5), and 5 wt% CaO and 9 wt% Al₂O₃ (C5A9), respectively. This is probably because the addition of CaO and Al₂O₃ lowers the melting point of fayalite slags.

Note in Figure 4 for sample C8A9 that a zone containing low melting point anorthite ((Ca,Fe)Al₂Si₂O₈) grains instead of a columnar crystal zone was observed in the samples from the slags after adding both CaO and Al₂O₃. The (Ca,Fe)Al₂Si₂O₈ precipitates are interlocked with the fayalite crystals in this newly-formed zone. Although an interlocking structure in the frozen slag layer was formed, the thickness of the frozen slag layer was lowered by the addition of CaO and Al₂O₃ in fayalite slags.

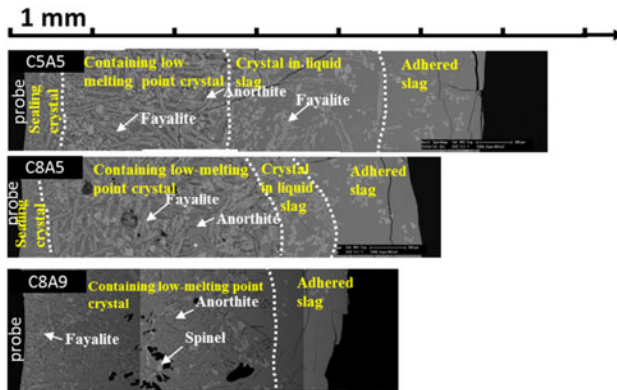


Figure 4. Influence of CaO and Al₂O₃ addition in fayalite slags on the frozen slag layer formation: Anorthite: (Ca,Fe)Al₂Si₂O₈; Spinel: FeAl₂O₄.

Conclusion

The formation of freeze-lining from fayalite-based slags was studied in laboratory-scale tests by gas-cooled probe technique at 1200 °C under a protective atmosphere. A sealing crystal zone, a columnar crystal zone, a crystal in liquid slag zone and an adhered slag zone were observed in the freeze-lining samples from slags with 1 wt% CaO and 5 wt% Al₂O₃. Fayalite precipitates formed a dense crystal zone close to the cooled-probe surface and grew into large columnar crystals along the temperature gradient from the probe to the bath slag. In comparison, a new zone containing low-melting point anorthite ((Ca,Fe)Al₂Si₂O₈) grains instead of a columnar crystal zone was formed with the addition of both CaO and Al₂O₃ into the slag. The anorthite grains are interlocked with the fayalite crystals in the frozen slag layer.

Both the thickness of the freeze-lining sample and of the columnar fayalite crystal zone increased when increasing the cooling rate (gas flow rate). The size of the fayalite columnar grains also augmented by the increased cooling rate. On the other hand, the thickness of the

freeze-lining sample and columnar crystal zone were reduced by slag agitation (crucible rotation), due to the increase of heat-transfer from the slag bath and the higher force on the fayalite columnar grains. The addition of CaO and Al₂O₃ reduced the thickness of the formed freeze lining, although a more stable interlocking structure formed in the frozen slag layer.

Acknowledgement

This work was performed with the financial support by the Agency for Innovation by Science and Technology (IWT, project no. 990348). The authors are grateful to the engineers of Metallo-Chimique for their close co-operation. The first author would like to thank the China Scholarship Council (CSC, Grant no. 20120704008) for providing scholarship studying in KU Leuven.

References

- [1] M. Campforts, K. Verscheure, E. Boydens, T. Van Rompaey, B. Blanpain, and P. Wollants, *On the microstructure of a freeze lining of an industrial nonferrous slag*. Metallurgical and Materials Transactions B, 2007. **38**(6): p. 841-851.
- [2] M. Campforts, B. Blanpain, and P. Wollants, *The importance of slag engineering in freeze-lining applications*. Metallurgical and Materials Transactions B. 2009. **40**(5): p. 643-55.
- [3] M. Campforts, E. Jak, B. Blanpain, and P. Wollants, *Freeze-lining formation of a synthetic lead slag: Part I. Microstructure formation*. Metallurgical and Materials Transactions B. 2009. **40**(5): p. 619-31.
- [4] M. Campforts, E. Jak, B. Blanpain, and P. Wollants, *Freeze-lining formation of a synthetic lead slag: Part II. Thermal history*. Metallurgical and Materials Transactions B. 2009. **40**(5): p. 632-42.
- [5] A. Fallah-Mehrjardi, P.C. Hayes and E. Jak, *Investigation of freeze-linings in copper-containing slag systems: Part I. Preliminary experiments*. Metallurgical and Materials Transactions B. 2013. **44**(3): p. 534-48.
- [6] A. Fallah-Mehrjardi, P.C. Hayes and E. Jak, *Investigation of freeze linings in copper-containing slag systems: Part II. Mechanism of the deposit stabilization*. Metallurgical and Materials Transactions B. 2013. **44**(3): p. 549-60.
- [7] A. Fallah-Mehrjardi, P.C. Hayes and E. Jak, *Investigation of freeze lining in copper-containing slag systems: part III. high-temperature experimental investigation of the effect of bath agitation*. Metallurgical and Materials Transactions B. 2013. **44**(6): p. 1337-51.
- [8] A. Fallah-Mehrjardi, J. Jansson, P. Taskinen, P.C. Hayes and E. Jak, *Investigation of the freeze-lining formed in an industrial copper converting calcium ferrite slag*. Metallurgical and Materials Transactions B. 2014. **45**(3): p. 864-74.
- [9] P. Taskinen, M. Kaskiala, P. Hietanen, K. Miettinen and A. Forsström, *Microstructure and formation kinetics of a freeze lining in an industrial copper FSF slag*. Mineral Processing and Extractive Metallurgy. 2011. **120**(3): p. 147-55.
- [10] P. Taskinen, M. Kaskiala, K. Miettinen and J. Jansson, *Freeze-lining formation and microstructure in a direct-to-blister flash smelting slag*. Journal for Manufacturing Science & Production. 2013. **13**(1-2): p. 77-83.

**ADVANCES IN MOLTEN
SLAGS, FLUXES, AND SALTS:**

Proceedings of



Mold Flux

ROOT CAUSE ANALYSIS OF SURFACE DEFECTS IN COILS PRODUCED THROUGH THIN SLAB ROUTE

Diptak Bhattacharya¹, Siddhartha Misra¹, Avinash Kumar¹, Vinay V Mahashabde¹
¹Product Technology- Flat Products, TATA Steel Ltd
 P.O. Bistupur, Jamshedpur, 831005, India

Keywords: Longitudinal Cracks, Heat Flux, Funnel Mold

Abstract

A metallurgical analysis of longitudinal cracks in a medium carbon grade of steel, produced through Thin Slab Casting and Rolling (TSCR) process is presented in this paper. Using characterization techniques, it was established that the defect originated from the funnel mold of thin slab caster. Temperature profiles of thermocouples in caster mold were employed to evaluate the heat transfer characteristics during primary solidification. The profiles helped to assess the performance of a standard mold flux used for casting this grade and hypothesize a possible mechanism of defect evolution. Slightly changed characteristics of the mold flux addressed the defect by promoting a stable and uniform heat transfer. This drastically lowered defect occurrence and rejections due to longitudinal cracks in this grade.

Introduction

Thin Slab Casting and Rolling (TSCR) is a cost effective and energy efficient route of hot rolled coil production.¹⁻²⁾ In this route, thin slabs of 55-70 mm thickness are cast at high speeds and directly charged into a soaking furnace followed by hot rolling into strips of required thickness. The product basket of LD3&TSCR unit of Tata Steel Jamshedpur ranges from low-C to med-C grades with varying levels of manganese, silicon and microalloying contents. The chemistries of the grades are carefully designed to avoid casting steels in the peritectic range. One of the major surface defects in hot rolled strips produced through TSCR facility of Tata Steel Jamshedpur is encountered in form of fine cracks in the rolling (longitudinal) direction of strips as shown in **Figure 1**. A medium carbon grade with composition as shown in **Table I** was observed to be most severely affected with this defect. A study was conducted to understand the root cause of the crack. This paper elucidates the analysis of the defect and highlights the measures adopted to cast such grades in thin slab casters with superior surface quality.

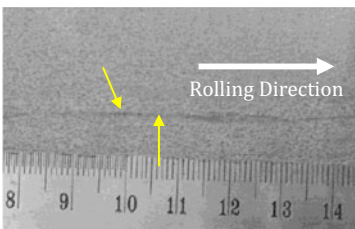


Figure 1: Longitudinal cracks on the surface of strips

Table I: Chemical composition of medium carbon grade affected with longitudinal cracks

C, %	Mn, %	Si, %	Al, %	S, %	P, %
0.25-0.3	1.5 max	0.2 max	0.05 max	0.01 max	0.02 max

2.0. Microscopic study of longitudinal cracks on strips

Optical microscopic images (Lieca, model: DMRX, Germany) of transverse samples from defect affected portion of HR strips are shown in **Figure 2**. The defect has an inclined crack appearance with a depth of about 80-200 microns. SEM observation in **Figure 3** indicates the presence of extraneous particles, identified by EDAX analysis to be iron-oxide scales, internal oxidation

products and entrapped mold slag particles as shown in **Table II**. The association of the defect with mold slag is a sign of the crack generating at the caster mold.

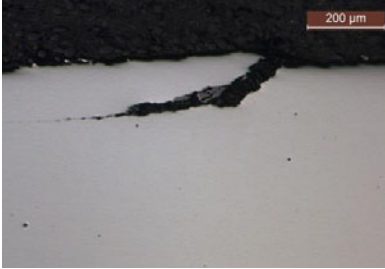


Figure 2: Optical microscopic images of longitudinal cracks

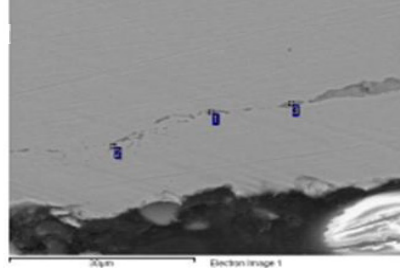


Figure 3: SEM-EDS observation at defect site

Table II: Composition of entrappings around obtained through EDAX

	O	Na	Al	Si	Ca	Mn	Fe
Mold Slag	26.28	1.04	0.26	8.65	22.84	1.99	38.09
Internal Oxidation	14.54			4.79		7.73	72.94
Scales	22.45						77.55

Table III: Casting parameters for 0.3 wt%C grade under study

Slab Thickness (mm)	60
Slab Width (mm)	1250-1350
Casting Speed(m/min)	4.0-4.5
Superheat (°C)	20-30
Cu plate thickness (mm)	17-27 (W); 17-13 (N)

3.0. Correlation of cracking with continuous casting process parameters

Cracks may originate in the primary shell formed in the continuous casting mold by stresses induced due to mechanical deformation or non-uniform solidification.³⁻⁴⁾ Thin slabs in TSCR facility of TATA Steel Jamshedpur are cast, following parameters displayed in **Table III**, using funnel shaped mold (SMS Semag design) with dimensions provided in **Figure 4**. As understood from **Figure 5**, depicting the location and distribution of cracks across the width of strips, maximum cracks are observed in the central 70% of the strip width corresponding to the mold funnel region. The mechanical stresses imposed on the solidifying shell as it transits from the funnel to the straight region of the mold have been a subject of study. The inflection points along the funnel curvature, act as stress raisers on the solidification front accentuating chances of hot tearing in shell. This may explain the major crack occurrence from the mold funnel region.⁵⁾

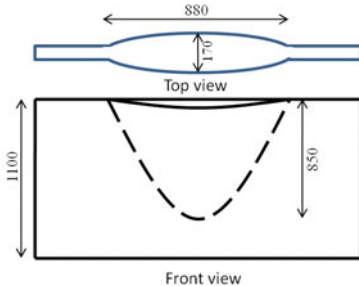


Figure 4: Schematic representation of funnel shaped thin slab mold (Dimension in mm)

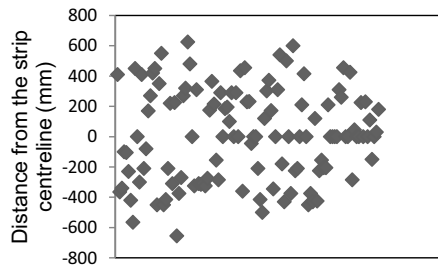


Figure 5: Distribution of crack locations across the strip surface

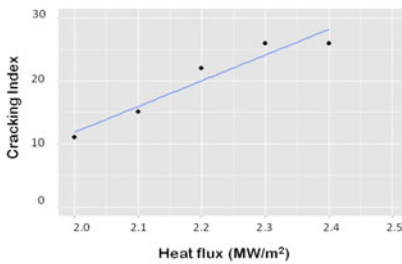


Figure 6: Relationship of cracking index with wide face heat flux (MW/m^2)

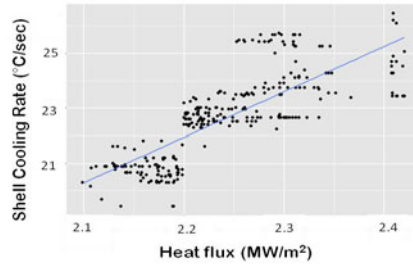


Figure 7: Correlation of broad face heat flux with shell cooling rate

The possibility of correlation between heat extraction rates through wide faces of mold and cracking intensity was explored. With the help of primary cooling water flow rate and water temperature difference between the inlet and outlet of mold, the overall heat flux of the broad faces was calculated as per the equation, $HF = m \times s \times \frac{(T_{diff})}{A}$, where HF is the Heat flux (MW/m^2); m is the mass flow rate (l/min) of water; $T_{diff} = T_{outlet} - T_{inlet}$ and A is the area of wide face. From an observation of over 1500 coils, a mapping of cracking index (Percentage of defective coils among total hot rolled coils) with heat extraction rates in mold is plotted and can be seen in **Figure 6**. For better understanding, the wide face heat flux is correlated with a calculated shell surface cooling rate as shown in **Figure 7**. It is established that milder the cooling rate of the shell, lower is the intensity of cracks on the strips. This grade being cast in a standard speed range of 4.0 – 4.5 m/min using a particular mold powder, the heat extraction rate is majorly governed by the mold plate thickness as depicted in **Figure 8**.

It is demonstrated in several literatures³⁻⁴⁾ that medium carbon steels (above 0.16 wt-% C) shrinks only by thermal contraction during solidification and the resultant surface tensile stresses are not always enough to generate cracks even at very high heat extraction rates. Therefore, the correlation with overall broad face heat flux may not alone explain crack evolution mechanism. Furthermore, since some cracks are also observed at regions away from geometrical influence of mold funnel, attributing cracks only to mechanical stresses may be inaccurate. Hence an attempt was made to understand the local heat transfer conditions with the help of thermocouples embedded in the mold, the arrangement of which is schematically represented in **Figure 9**. The typical temperature profiles observed from thermocouple columns located on the fix and loose side of mold (inside funnel) is shown in **Figure 10**. The fluctuations in the thermocouple temperature profile points to a lack of steady heat transfer across the wide face, even under normal casting conditions. The unsteady temperature profiles indicate fluctuations of shell surface temperature in the casting direction of the slab, with frequent hot and cold spot locations on the shell.

The thermocouple temperature fluctuations in defective (high severity cracks) coils are compared with reference coils which are found having low severity defect. The average temperature difference between thermocouples in first row with their nearest adjacent neighbors (Refer thermocouple locations in **Figure 9**) may be used to evaluate the evenness of shell temperature. When compared for the defective and reference coils, considerably steeper temperature gradients are observed both in longitudinal (T_1-T_2 , T_2-T_3 , ..., T_7-T_8) as well as transverse direction (T_1-T_9 , T_2-T_{10} ,, T_8-T_{16}) for slabs in the crack affected coils, as seen from **Figure 11 (a) and (b)**.

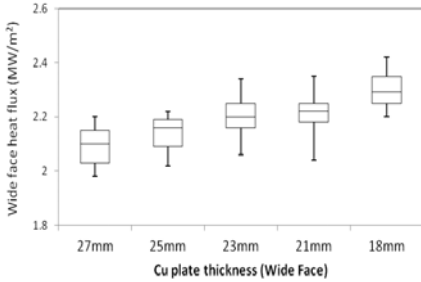


Figure 8: Effect of wide face copper plate thickness on heat extraction rate in mold

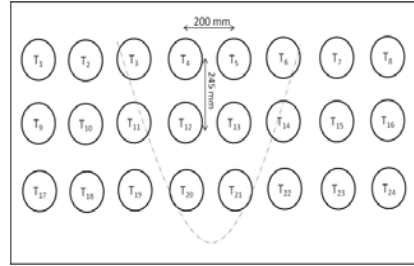


Figure 9: Thermocouple arrangement in slab caster mold

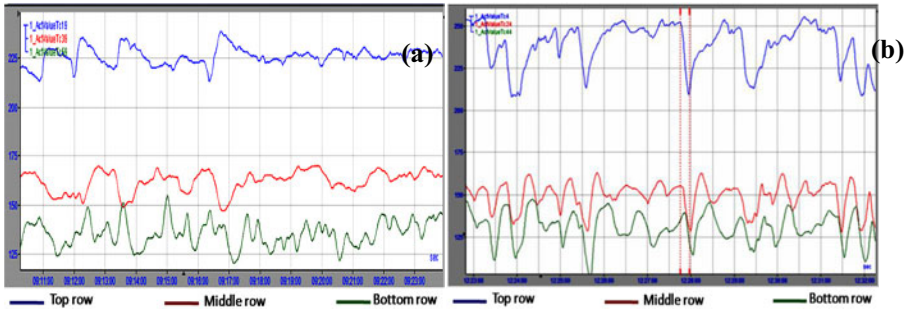


Figure 10: Temperature profile displayed by thermocouples in mold for defective coils Thermocouple location- (a) Fix side (b) Loose side

Furthermore, the effect of copper plate thickness on the observed fluctuations and concurrent cracking tendency is established from **Figure 12 (a) and (b)**. The differential temperature is a sign of variable heat transfer leading to non-uniform shrinkages across the shell that may cause surface cracks. A clear indication of a correlation of cracking intensity with unsteady heat transfer conditions is implied.

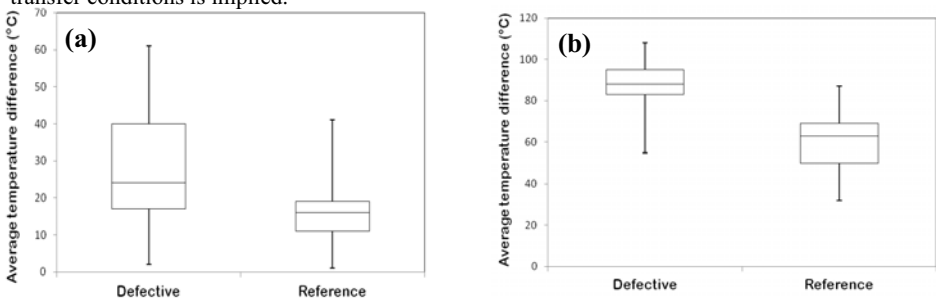


Figure 11: Comparison of average temperature difference between adjacent thermocouples in (a) top row (b) top row and middle row for different columns for defective and reference slabs

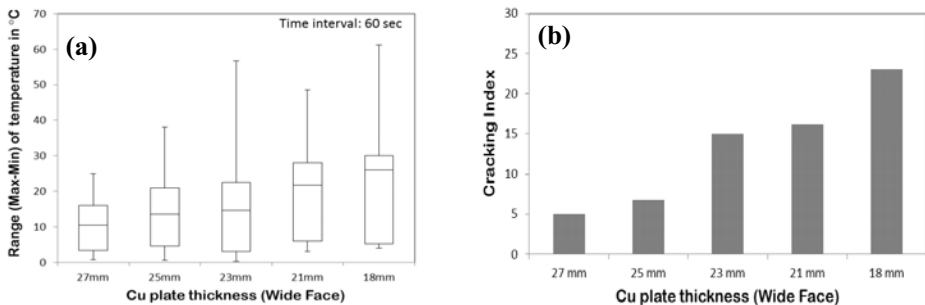


Figure 12: (a) Range of temperature fluctuations and (b) cracking intensity observed at different Cu plate thicknesses

4.0. Trials with modified mold powder

The main functions of mold powder in continuous casting are to provide uniform lubrication and control the heat transfer between the steel shell and mold wall. In order to provide sufficient strand lubrication, mold powders for high speed casting processes have lower viscosity as compared to conventional slab casting counterparts. Several literatures discuss the importance of stable and uniform heat transfer in early solidification stages to avoid formation of longitudinal facial cracks on the surface of slabs.^{1-4, 6)} In high speed casting processes, the major challenge is to control the horizontal heat transfer rate in mold and form a uniform shell. The use of mold powders with high basicity ($\text{CaO/SiO}_2 > 1$) helps to reduce the heat flux. However, use of such powders in high speed casting of crack sensitive grades is faced with the difficulties of increased mold-strand friction, as reported in literatures.⁶⁾ The uniformity of heat extraction across the surface of primary shell is also determined by the symmetry of mold slag infiltration during casting. In addition to mold level stability, a uniform slag infiltration is required to avoid occasional hot spots on the surface of the shell, which might lead to differential local shrinkages. Although mold fluxes of lower viscosity would exhibit superior infiltration behavior^{7,8)} a slag with very low viscosity may not always offer a uniform lubrication and heat transfer. It is reported that too low viscosity of mold powder may lead to non-uniformity in infiltration due to a highly fluid slag.^{6, 8)}

An effort was made to modify the characteristics of the existing powder to address the observed thermocouple fluctuations without much altering the basicity of the mold powder. Based on the hypothesized root cause of crack formation, it is believed that a modified mold powder characteristics may assist in reducing the crack occurrences, if it serves two purposes. First, the mold slag should reduce the overall heat transfer across the wide faces, promoting a mild cooling of the shell. Secondly, the slag should infiltrate uniformly and reduce chances of local variations in heat transfer and avoid creating frequent hot spots. The characteristics of a slightly modified powder supplied by M/s Metallurgica compared to standard powder are shown in **Table IV**. The viscosity of the modified powder (at 1300°C) was increased to 0.5 Poise in the modified powder and the solidification temperature (considered as Break temperature) was 10-15°C higher as compared to the standard powder as measured using the rotating cylinder method. The melting trajectory was recorded for the standard and modified powder using a hot stage microscope where the powder is pressed in form of a cylindrical sample and changes in the shape of the sample was monitored continuously while heat at constant rate. Shapes corresponding to




softening, melting and flowing temperatures are recorded for comparing the standard and modified powders as depicted in **Table V**.

Table IV: Characteristics of modified mold powder

	Standard Powder	Modified Powder
Bulk Density	0.55	0.56
Basicity (CaO/SiO ₂)	0.86	0.89
Viscosity (at 1300 °C)	0.25 Poise	0.5 Poise
Break Temperature (T _{br})	1045°C	1060°C

The corresponding strips of slabs cast using this powder are observed with much lowered instances of cracks. With the introduction of modified powder, the overall heat flux is lowered as seen from **Figure 13**. Furthermore, a more stable thermocouple temperature profile is observed as shown in **Figure 14**. A comparison of average temperature difference between adjacent thermocouples of first row (T1 – T2 , T2-T3 , ... ,T7-T8) for the standard and modified mold powder, depicted in **Figure 15(a)**, reveals significantly reduced local temperature gradients across the width direction of the shell, indicating uniform solidification. A reduction in the average temperature difference between the thermocouples of top and middle row (T1-T9, T2-T10... T8-T16) is observed from **Figure 15(b)**, also demonstrating the milder cooling effect of the modified powder and reduced solidification shrinkages.

Table V: Characteristic temperatures (°C) during hot stage microscopy of standard and modified mold powders (Heating rate: 10°C/sec)

			
	Deformation (Softening)	Hemisphere (Melting)	Flow
Standard Powder	867	885	937
Modified Powder	880	916	1003

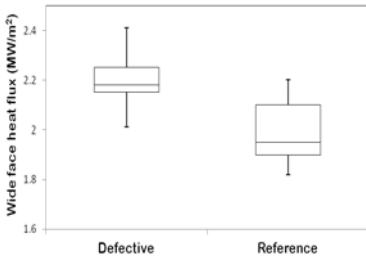


Figure 13: Comparison of wide face heat flux for standard and modified mold powder

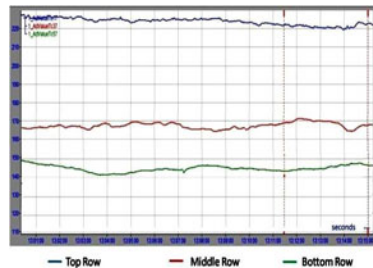


Figure 14: Typical thermocouple temperature profile while casting with modified mold flux

It is known that solidification in mold is accompanied by a shrinkage which may result in withdrawing the shell from the mold surface creating a gap. This may interrupt subsequent heat transfer. A smooth heat extraction may be continued if the mold slag infiltrates during the negative strip time of mold oscillation and uniformly fills up the entire space created between the shell and mold. The exact reason for anomalous heat transfer experienced with slags of very low viscosity is not very well understood. It may be hypothesized that a highly fluid slag may get

drained along the surface of the shell while infiltrating and may occasionally loose contact with the mold surface. It may not therefore provide a continuous channel for uninterrupted heat transfer between the shell and mold. In such situations, a powder with slightly higher viscosity may assist in reducing the anomalous heat transfer conditions by forming a thicker slag film. With the formation of a thicker slag film, a powder of higher viscosity would uniformly moderate heat transfer near the meniscus and promote the formation of a thinner shell, reducing shrinkage and resultant air gap. Secondly, it would promote more uniform heat transfer near the meniscus by offering a better connect of the shell with the mold surface for continuous heat transfer. This may be visualized with the help of a schematic diagram shown in **Figure 16**. The reduction in the thermocouple temperature fluctuation is indicative of better mold-strand support. The modified powder was found to have no deleterious effect on mold level stability and strand-mold friction. The observations of sticker alarms or breakouts were negligible as compared to the standard powder.

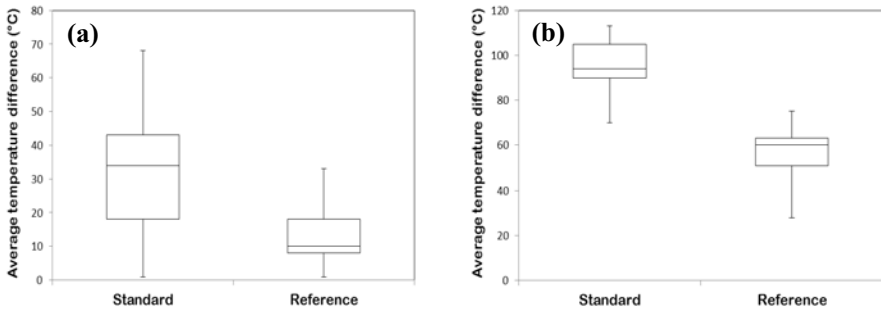


Figure 15: Comparison of average temperature difference between adjacent thermocouples in (a) top row (b) top row and middle row for different columns for standard and modified powder

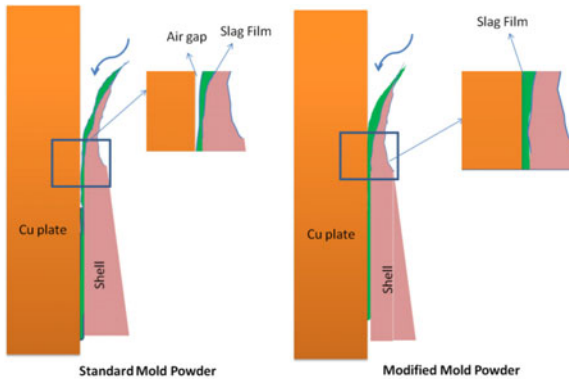


Figure 16: Schematic representation of hypothesized slag infiltration behaviour for standard and modified mold powders.

The viscosity of the powder needs to be optimized based on the steel composition being cast. In the present case, the standard mold powder did not reveal so severe abnormalities in heat transfer during casting of grades with higher carbon content. This observation may be explained by the

difference in solidification shrinkage at different carbon contents of steel. Since the shrinkage of 0.3 wt-% C steel is greater than steels with higher carbon levels, a larger mold-strand gap is expected to be created and it is believed that the flow characteristics of the standard mold powder is not suitable to evenly compensate this gap. The reduced temperature fluctuations and cracking with thicker mold copper plates, which would similarly induce a milder cooling of shell, may also support the hypothesis.

5.0. Conclusions

- 1) Optical and SEM-EDS microscopy indicates the origin of the defect from surface cracks generated on the slabs in the thin slab caster mold.
- 2) Longitudinal cracks are majorly observed in the strip portion corresponding to the funnel region of mold, indicating influence of mold geometry.
- 3) The cracking intensity is observed to increase at high heat extraction rates in mold. This primarily occurs while casting with older copper plates having low thicknesses.
- 3) Mold thermocouple temperature profile for defective strips is observed with fluctuations indicating temperature variations across the shell surface. The temperature patterns in defective coils points out to large gradient in the shell surface temperature both in the longitudinal and transverse direction. A lower temperature gradient is observed in reference coils with low severity defects.
- 4) A modification in the characteristics of mold slag was proposed to reduce overall heat flux and obtain a stable thermocouple temperature profile indicating more uniform heat transfer across the solidifying shell.
- 5) Very low viscosity of the standard powder was believed to cause the heat transfer anomaly. A slight optimization in the viscosity of the mold powder was able to reduce the cracks occurrences significantly.

5.0. Acknowledgements

The authors would like to acknowledge the support received from the operations team of LD3&TSCR. Special thanks to the technical team of M/s Metallurgicafor support.

6.0. References

- 1) C.I. Garcia, C. Torkaz, C. Graham: 'Physical metallurgy of high strength low alloy strip steel production using compact strip processing', *Iron making and Steelmaking*, Vol. 32(4), 2005, pp. 314-318.
- 2) M.Korchynsky: 'Strategic Importance of Thin Slab Casting Technology', *International Symposium on Thin-Slab Casting and Rolling*, Guangzhou, China, 2002.
- 3) Brimacombe, J. K., F. Weinberg, and E. B. Hawbolt. "Formation of longitudinal, midface cracks in continuously-cast slabs." *Metallurgical Transactions B* 10.2 (1979): 279-292.
- 4) Hiraki, Sei, et al. "Influence of mold heat fluxes on longitudinal surface cracks during high speed continuous casting of steel slab." *Steelmaking Conference*. Vol. 77. 1994.
- 5) Hibbeler, L. C., et al. "Longitudinal face crack prediction with thermo-mechanical models of thin slabs in funnel moulds." *la metallurgia italiana*2 (2009).
- 6) Sun, Yan-hui, et al. "Longitudinal surface cracks of thin slabs." *International Journal of Minerals, Metallurgy, and Materials* 17.2 (2010): 159-166.
- 7) Kromhout, J. A., et al. "Development of mould flux for high speed thin slab casting." *steel research international* 80.8 (2009): 575-581.
- 8) Konishi, J., et al. "Modeling the formation of longitudinal facial cracks during continuous casting of hypoperitectic steel." *Metallurgical and materials transactions B* 33.3 (2002): 413-423.

Advanced Mold Flux Development for the Casting of High-Al Steels

Dan Xiao^{1,2}, Wanlin Wang^{1,2*}, Boxun Lu¹ and Xinwang Zhang¹

¹School of Metallurgy and Environment, Central South University, Changsha, Hunan, 410083, China

²International Joint Research Center for Clean Metallurgy, Central South University, Changsha, 410083, China

Keywords: Melting, Heat transfer, Slag/steel reaction

Abstract

Mold flux plays key roles during the continuous casting process of molten steel, which accounts for the quality of final slabs. With the development of Advanced High Strength Steels (AHSS), certain amounts of Al have been added into steels that would introduce severe slag/metal interaction problems during process of continuous casting. In this article, through the studies of SHTT, IET and SEM, the melting range of mold flux was increased and the heat transfer rate was inhibited under the coordination effect of the combination of BaO and B₂O₃. It was found the case with BaO substituting for CaO to replace B₂O₃ shows the highest general heat transfer rate and lowest melting temperature. The results of slag/steel reaction experiments show that the degree of slag/steel reaction increases with the addition of C/A ratio. The latest developments for this new mold flux system were summarized with the aim to offer technical guidance for the design of new generation mold flux system for the casting of AHSS.

Introduction

In the continuous casting process, mold flux play an important roles to control heat transfer, lubricating the strand, protecting the molten steel from oxidation, providing insulation and absorbing inclusions between the steel and mold^{[1][2]}. With the development of advanced high strength steel (AHSS), aluminum as an alloy element was added into steels aims to improve features of special steel and reduce vehicle weight^[3]. However, the aluminum in the molten steel will react with the silica in the slag, which could causes the poor quality of slabs^[4], exacerbate mold flux properties such as melting and crystallization behavior^[5]. In order to solve these problems, intensive research has been conducted to optimize the composition of the traditional CaO-SiO₂ based mold flux with the fluxing agent as NaO, Li₂O^[6], or the ratio of CaO/Al₂O₃^[7]. However, it is difficult to optimize above mold fluxes system due to the pickup of alumina in the spent mold flux caused by the steel/slag reaction. Therefore the Non-reactive lime-alumina-based mold flux has been proposed recently, where the SiO₂ content was lowered down to 10-wt% to restrain the slag/steel reaction.

K E Blazek^[8] etc. have developed a series of CaO-Al₂O₃ based mold fluxes, in which C/A (CaO/Al₂O₃) ratio was set as 1 and the SiO₂ content was 10 percent. However, The result suggested that the slag/steel reaction for the CaO-Al₂O₃-based mold flux

was significantly reduced, but the consumption of the CaO-Al₂O₃-based mold flux was low. J W Cho et al^[3] researched a series of CaO-Al₂O₃ bases mold fluxes with the C/A ratio ranging from 1 to 3.3, compared with C/A ratio of 1, the result of the mold flux with C/A ratio of 3.3 indicated that slag/steel reaction was become severe, and it show an unstable heat transfer behavior. Therefore, it is essential to study the CaO-Al₂O₃ bases mold flux with C/A ratio of 2, as it can inhibit the Slag/steel reaction compared with C/A ratio of 3.3; meanwhile it tends to decrease the melting point compared with C/A ratio of 1 mold flux system. As an effective fluxing agent to lower the system melting temperature, the B₂O₃ is a strong glass former, and tends to inhibit the mold flux crystallization^{[9][10]}. However, B₂O₃ is a reducible oxide, and using of a large amount of B₂O₃ could lead to boron pickup in the steel^[8]. X. Yu^[11] and Y. Wang^[12] found that the substitution of BaO for CaO can also restrain the mold flux crystallization capability and lower the melting temperature. Therefore, it is possible to use the substitution of BaO for CaO to replace B₂O₃ to optimize the CaO-Al₂O₃ based mold flux system.

Consequently, the effect of the substitution of BaO for CaO to replace B₂O₃ on the melting and heat transfer behavior of CaO-Al₂O₃ based mold flux was conducted in this article, by using the Single hot thermocouple technology(SHTT) and infrared emitter technique(IET). Then scanning electron microscope(SEM) was applied to study the morphology of samples after the heat transfer test. Meanwhile, the reaction between the molten steel and CaO-Al₂O₃-based mold flux would be studied.

1. Experiment

1.1 Apparatus and Procedure

A. **Single Hot Thermocouple Technique.** The melting process were conducted by using Single hot thermocouple technology (SHTT) for the experiments, where the mold flux sample was mounted on a B type thermocouple and was heated from room temperature to 1500 °C at a rate of 15 K/S. The CCD camera was used to record the melting behavior.¹³ Figure 1 shows the thermal profiles for the experimental. The diagrams were constructed in line with the relationship between time and temperature.

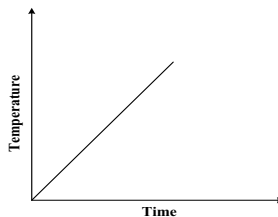


Figure 1: thermal profiles of SHTT tests

B. **Heat Transfer Simulator and Experimental Procedures.** Wang^[14] described the details of the Infrared Emitter Technique (IET), and its schematic was shown in figure 2. The experimental apparatus mainly includes four units: a power controller, an infrared radiant heater capable of emitting 2.0 MW/m² heat flux at the rate of 380

voltages, a data acquisition system, and a command-and-control unit. For the IET test, the heating profile was shown in Figure 3. First, the mold flux disk was placed on the top surface of the copper mold, then, it was subjected to the infrared radiation; meanwhile, the subsurface thermocouples measure the real-time responding temperatures. Therefore, the responding heat flux across the copper mold could be calculated through the measured temperature gradient inside the mold based on a 1D Inverse Heat Conduction Program.

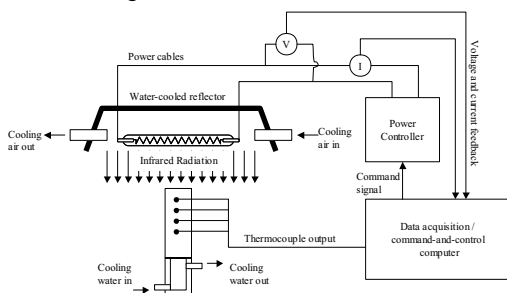


Figure 2: Schematic illustration of the infrared emitter

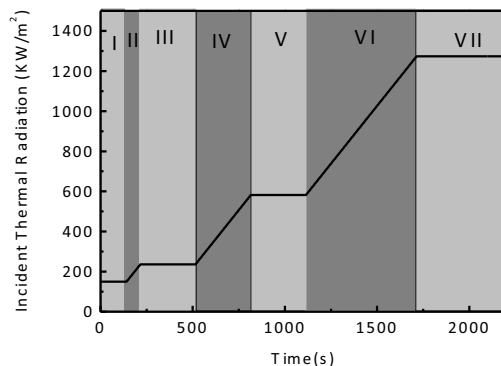


Figure 3: The heating profile for IET experiments

1.2 Preparations of Mold Flux Powder

The major chemical components of the designed samples is shown in Table 1, where Sample 1 and Samples 2, 3, 4 were designed with a fixed C/A ratio and varying with the combination of substitution of BaO for CaO and B₂O₃. Sample 5 and Sample 6 were obtained according to change the C/A ratio based on Sample 4. The raw materials for the preparation of above mold flux systems are pure chemical reagents CaCO₃, SiO₂, Al₂O₃, CaF₂, Li₂CO₃, B₂O₃ and BaCO₃.

The mold flux was melted at 1773K in a induction furnace for 300 second to eliminate bubbles and homogenize its chemical components, then they were quenched through pouring into cool water. After that, it was crushed and grinded to make the sample powers for SHTT test. For the IET test, the molten slag was first poured onto the top surface of a stainless steel plate, then a new cylindrical, tube-like copper mold

with the same diameter as the copper substrate in IET tests was used to cast the mold flux before it solidified on the steel. Then, the mold flux disks were polished to control its surface roughness and thickness. The polished samples were then placed on the top of the copper mold for heat transfer test.

Table 1 The Chemical Compositions of Slags (w%)

Num	C/A	CaO	SiO ₂	Al ₂ O ₃	Na ₂ O	F	Li ₂ O	B ₂ O ₃	BaO
Sample 1	2	37.33	9	18.67	10	9	6	10	0
Sample 2	2	37.00	9	20.00	10	9	6	6	3
Sample 3	2	34.33	9	20.67	10	9	6	4	7
Sample 4	2	34.00	9	22.00	10	9	6	0	10
Sample 5	1	23	9	33	10	9	6	0	10
Sample 6	3	39.5	9	16.5	10	9	6	0	10

2. Results and Discussion

2.1 Effect of Substitution of BaO for CaO to Replace B₂O₃ on the melting Behavior of Mold Flux System

In this article, the SHTT was employed to study the melting behavior of mold flux. Figure 4 shows the responding images during the melting period of the Sample 1, Sample 2, Sample 3 and Sample 4 when they were heated at a rate of 15 K/S. Table 2 lists the initial and complete melting temperature ranges, which could be found through the Figure 4. It could be observed that both the initial and complete melting temperature were increased with 3% addition of BaO to replace 4% B₂O₃, the melting temperature of Sample 2 is highest among all samples, and with the further addition of BaO to substitute CaO to replace B₂O₃, the melting temperature reduces; however, the melting temperature of Sample 3 is higher than Sample 1. It can be found that Sample 4 shows the lowest melting temperature through comparison of four Samples, which suggest that the mold flux that BaO totally substitute for B₂O₃ reduce the melting temperature of mold flux. The reason was that, the melting temperature of CaO is 2888K, the melting temperature of BaO is 2193K^[15], thus, using BaO to substitute CaO can reduce the melting temperature. Once the CaO was further reduced with the replacement of 10% BaO, the overall melting temperature was lowered to a largest degree. However, the reason for this kind of melting temperature reduction for above mold flux system, with the change of BaO and B₂O₃ content, is of great interest for the future study.

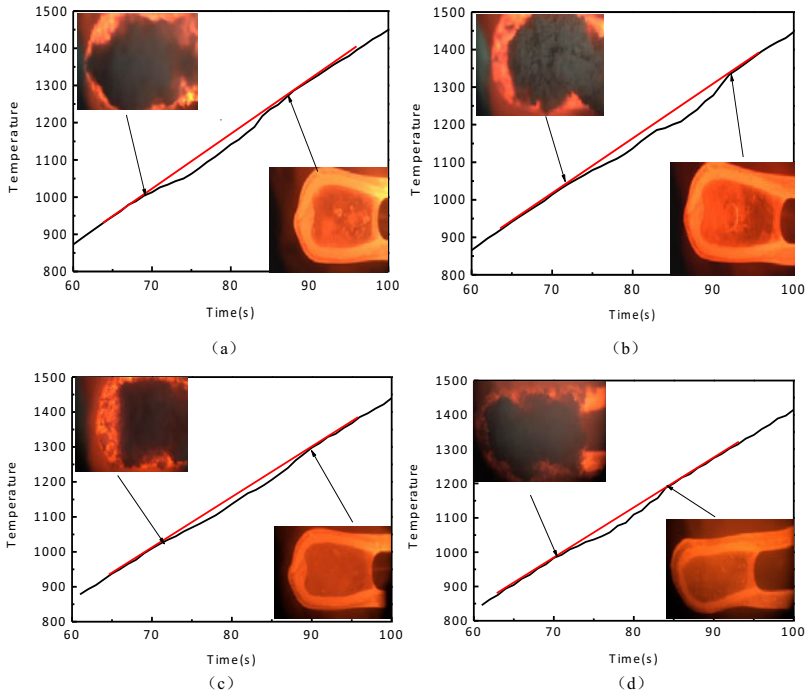


Figure 4-Melting behaviors for the four mold fluxes:(a) sample 1; (b)sample 2; (c)sample 3; (d)sample 4

Table 2. Melting ranges of four mold fluxes

Sample	1	2	3	4
$T_{initial}[K]$	1286(1013 C ^o)	1315(1042 C ^o)	1295(1022C ^o)	1237(964 C ^o)
$T_{complete}[K]$	1540(1267 C ^o)	1606(1333 C ^o)	1571(1298 C ^o)	1460(1187 C ^o)

2.2 Effect of BaO Substituted for CaO to Replace B₂O₃ on the Heat Transfer Rate of Mold Flux

Figure 5 shows the responding in-mold heat fluxes histories of Sample 4 as the represent for above four samples. There are eight stages appearing in the heat transfer histories of Sample 4. Stage I is a period in which the heat flux increase slowly, Stage II and IV is a period that the heat flux keeps a constant heating rate. Stage III is a period in which the heat flux increases linearly with the addition of thermal radiation. Then, in Stage V, the top surface temperature of the disk is getting higher and the crystallization is initiated at the disk top and penetrated into the bottom, where the picking rate of heat flux was lowered with the crystallization of mold flux. Stage VI is a time when the top flux disk was melted. Stage VII is a period in which the heat flux is further reduced with the further crystallization of mold disk. Finally, the heat flux become stable and the melting, crystallization layer was completed in Stage VIII.

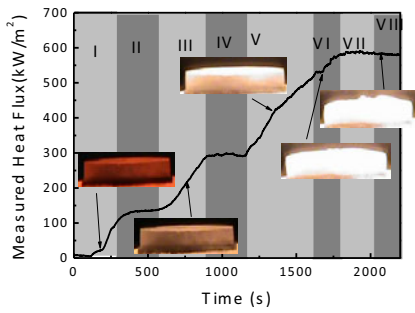


Figure 5-The measured heat flux history of Sample 4

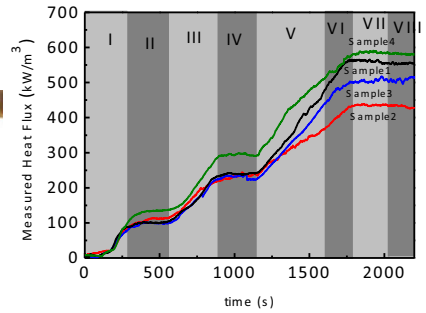


Figure 6-The measured heat flux histories for mold flux

The measured heat fluxes of Sample 1, Sample 2, Sample 3 and Sample 4 were combined together in Figure 6, it can be observed that the measured heat fluxes for each mold flux at steady state are around 582 KW/m² for Sample 4, 532 KW/m² for Sample 1, 505 KW/m² for Sample 3 and 433 KW/m² for Sample 2, respectively. It indicates that the heat flux at steady state increases when the 10% addition of the BaO to substitute CaO to replace B₂O₃, this may be due to the system has the lowest melting temperature region and the enhanced liquid layer will increase the general heat transfer behavior across the mold flux system. The heat flux for Sample 2 and 3 are lower than other two, as they were shown a stronger crystallization behavior as our previous study suggested, where the synergic effect of the combination of BaO and B₂O₃ tends to enhance the general crystallization tendency of the mold flux.^[7] Therefore, the heat transfer rate for Samples 2 and 3 are inhibited.

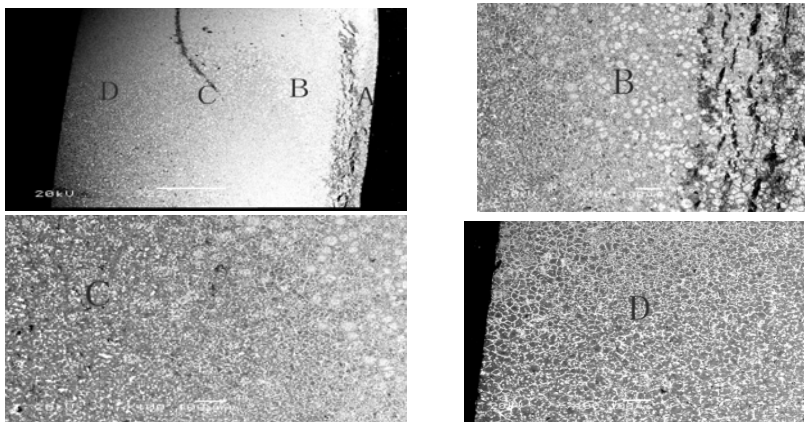


Figure 7-SEM result of the Sample 4 after heat transfer test

In order to observe the morphology of the Sample 4 after Heat transfer test, the SEM was adopted, as shown in Figure 7. It can be found that the Sample 4 was melted on the top area of A (right hand), and there is a large white crystalline phase in the area B,

C and D.

2.3 Effect of C/A ratio on degree of Slag/steel reaction

It is well known that aluminum in the steel is prone to react with SiO₂ in the continuous casting mold, as shown $3(\text{SiO}_2)+4[\text{Al}]=3[\text{Si}]+2(\text{Al}_2\text{O}_3)\dots(1)$. Figure 8 shows Al₂O₃ and SiO₂ composition change of Sample 4(C/A=2), Sample 5(C/A=1) and Sample 6(C/A=3) during the continuous casting of 20Mn23AlV. Table 3 shows the main composition change of three Samples. For the Sample 5, Sample 4 and Sample 6, the CaO content nearly kept constant, and the Al₂O₃ content increased about 4.96%, 5.71% and 7.26% while the SiO₂ content declined about 4.48%, 5.09%, and 6.16%. It indicates that the degree of Slag/Steel reaction increases with the addition of C/A ratio. The reason is that the Al₂O₃ content in mold flux decreases with the addition of C/A ratio, and then the Equation 1 is prone to be further processed, so the degree of reaction was increased.

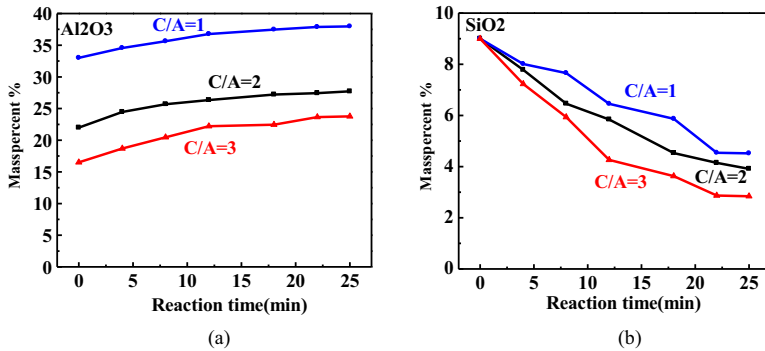


Figure 8: Al₂O₃ and SiO₂ composition change of Sample 4, Sample 5 and Sample 6

Table 3: The main composition change of Sample 4, Sample 5 and Sample 6

Num		CaO	Al ₂ O ₃	SiO ₂
Sample 5	C/A=1	23	33	9
	Final slag	21.95	37.961	4.52
			+4.96	-4.48
Sample 4	C/A=2	34	22	9
	Final slag	33.65	27.71	3.91
			+5.71	-5.09
Sample 6	C/A=3	39.5	16.5	9
	Final slag	38.47	23.76	2.84
			+7.26	-6.16

3. Conclusions

In this article, SHTT and IET were adopted to investigate the effect of the substitution of BaO for CaO to replace B₂O₃ on the melting and heat flux behavior for the lime-alumina based non-reactive mold flux system. Meanwhile, the effect of C/A ratio on the degree of Slag/steel reaction was also been conducted. The main conclusions are summarized as follows:

- (1) The results of melting tests indicated that the melting range of mold flux was increased under the coordination effect of the combination of BaO and B₂O₃. The mold flux with the full replacement of BaO to for B₂O₃ shows the lowest melting temperature.
- (2) The results of the IET tests indicated that the steady state heat flux of mold flux was reduced under the coordination effect of the combination of BaO and B₂O₃. The mold flux with the full replacement o BaO for B₂O₃ shows the highest steady state heat flux rate.
- (3) The results of slag/steel reaction experiments show that the degree of slag/steel reaction increases with the addition of C/A ratio.

References:

-
- [1] K.C. Mills and A.B. Fox: *ISIJ Int.*, 2003, vol. 43, p. 1479.
 - [2] W.L. Wang and A.W. Cramb: *ISIJ Int.*, 45(2005), 1864.
 - [3] J. W. Cho, K. Blazek, M. Frazee, and Hongbin Yin: *ISIJ Int.*, 2013, vol. 53(1), pp. 62-70.
 - [4] W. Wang, K. Blazek and A. Cramb: *Metall. Mater. Trans. B*, 2008, vol. 39 (B), pp. 66-74.
 - [5] T. Omoto, T. Suzuki, and H. Ogata: *Shinagawa Technical Report.*, 2007, vol. 50, pp. 57-61.
 - [6] B. Lu, K. Chen, W. Wang, and B. Jiang: *Metal. Mater. Trans. B*, 2014, vol. 45, pp. 1496-1509.
 - [7] D. Xiao, W. Wang, and B. Lu: *Metall. Mater. Trans. B*, 2015, vol. 46, pp. 873-881.
 - [8] K. Blazek, Hongbin Yin, G. Skoczylas, M. McClymonds and M. Frazee: *Iron Steel Technol.*, 2011, vol. 8(3), pp. 231-240.
 - [9] B. Lu, W.Wang, J. Li, H. Zhao, and D. Huang: *Metall. Mater. Trans. B*, 2013, vol. 44B, pp.365-77.
 - [10] L. Zhou, W. Wang, J. Wei, and B. Lu: *ISIJ Int.*, 2013, vol. 53, pp. 665-672.
 - [11] X. Yu: Ph. D. Dissertation, Chongqing University, Chongqing, China, 2011.
 - [12] Y. Wang, F. Dong, B. Wang: *Special steel*, 2007, vol. 28(2), pp.22-23.
 - [13] Y. Kashiwaya, K. Ishii: *ISSTech 2003 Conference Proc., Iron and Steel Society*, Indianapolis, IN, U.S.A., 1021.
 - [14] W. Wang and A.W. Cramb: *ISIJ Int.*, 2005, vol. 45 (12), pp. 1864-70.
 - [15] Kubasohewskj O, Alcock: *Metallurgical Thermochemistry*, 1979, 272-275.

A REACTION MODEL TO SIMULATE COMPOSITION CHANGE OF MOLD FLUX DURING CONTINUOUS CASTING OF HIGH Al STEEL

Min-Su Kim¹, and Youn-Bae Kang¹

¹Graduate Institute of Ferrous Technology, Pohang University of Science and Technology, Pohang, Rep. of Korea

Keywords: High Al steel, Multi-component kinetic model, Continuous casting

Abstract

In order to find countermeasures against degradation of mold flux properties in high Al steel continuous casting, it is important to understand the reaction between Al-containing steel and CaO-SiO₂-based molten flux. In the present authors' research group, the reaction rate and mechanism governing the reaction have been experimentally investigated. Based on those observed mechanism, a slag-metal reaction model was developed in order to interpret the reaction and to predict similar reactions between high Al steel and mold flux used for continuous casting process. The model considers both thermodynamic and kinetic information, as well as rate-controlling step observed in the authors' previous investigation. Thermodynamic information for chemical reaction was interpreted by ChemApp coupled with FactSage thermodynamic database. This is connected to mass flux equations for all relevant components in the system. Flux viscosity change and its effect on the mass flux are also taken into account. The reaction model developed in the present study showed good reproduction of the experimental data. Some possible applications are also shown.

Introduction

During continuous casting of high Al steel grades, drastic composition changes in the mold flux occur such as Al₂O₃ accumulation and loss of SiO₂ [1]. It leads to increase of flux melting temperature and change of the crystalline phase from cuspidine (3CaO·2SiO₂·CaF₂) to calcium aluminate. Therefore, estimation of composition changes in mold flux during steel-flux reactions is very important in order to predict mold flux performance. From this practical point of view, development of a multi-component kinetic model is of importance to predict composition evolutions in the conventional mold flux and to design a new mold flux composition.

For accurate prediction of composition changes in the liquid steel and flux, a kinetic model should be developed based on the reaction mechanism of the steel-flux system. From the previous experimental investigations done by the present authors [2 - 4], the reaction mechanism between high Al steels and CaO-SiO₂-type fluxes have been intensively investigated. Some important conclusions are summarized here:

- At low Al concentration ($[\%Al]_0 \leq 1.8$), the Al₂O₃ formation reaction with SiO₂ reduction is mainly controlled by mass transfer of Al in liquid steel.
- At high Al concentration ($[\%Al]_0 \geq 4.8$), the rate controlling step changes into the mass transfer in the flux phase but retardation degree of the reaction rate depends on the type of aluminate formed in the vicinity of the steel-flux interface.

- When initial MgO content in the flux was low, CaAl_4O_7 layer was formed near the steel-flux interface at high Al concentration ($[\%Al]_0 = 5.2$), resulting retardation of mass transfer in liquid flux. When initial MgO content in the flux was high, however, Al_2O_3 accumulation in the flux occurred rapidly at high Al concentration ($[\%Al]_0 = 5.2$) with formation of many numbers of MgAl_2O_4 particles in the liquid flux.

Compared to a typical slag-metal system, mass transport phenomena in the liquid flux is quite complex in the high Al steel and CaO-SiO₂-type mold flux system. During the reaction, chemical composition of the flux keeps varying. This changes physico-chemical properties of the flux, and consequently affect kinetic aspect. The existing kinetic models [5 - 7] for prediction of Al₂O₃ accumulation in the flux, however, do not explicitly consider the mass transfer in slag or flux phase in terms of viscosity changes and aluminate formation. Also, some of those [6, 7] are based on a simple steel-slag system such as Fe-Al and CaO-SiO₂-Al₂O₃ system. In the present study, a multi-component kinetic model was developed based on the reaction mechanism elucidated by the present authors [2-4] in order to describe steel-flux reactions in high Al steel and CaO-SiO₂-type flux system.

Development of a new multi-component kinetic model

Fig 1 shows the basic concepts and the calculation procedure of the present kinetic model. Each phase is assumed to have a reaction layer in order to perform equilibrium calculation between the reaction layers under local equilibrium assumption at the steel-flux interface. Once concentrations in each reaction layer was obtained from equilibrium calculations, then mass transfer in each phase was calculated by using flux equations. For the mass transfer in the liquid flux, the calculated mass flux was distributed into the flux boundary layer and the flux bulk layer. The concentration in the flux boundary layer was utilized in order to calculate flux viscosity which alters the mass transfer coefficients in the liquid flux. This concept is similar to an approaches as long as the reaction zones were defined for the equilibrium calculations [5] or mass flux equations of various moving species were employed [6,7]. However, the present approach is distinguished from the previous approaches [5-7] that 1) actual reaction mechanism is taken into account, 2) varying chemical composition of the flux during the reaction is taken into account in the evaluation of mass transport coefficient, 3) experimentally determined mass transport coefficient [2] was used. The details for each calculation module will be followed with some assumptions and equations.

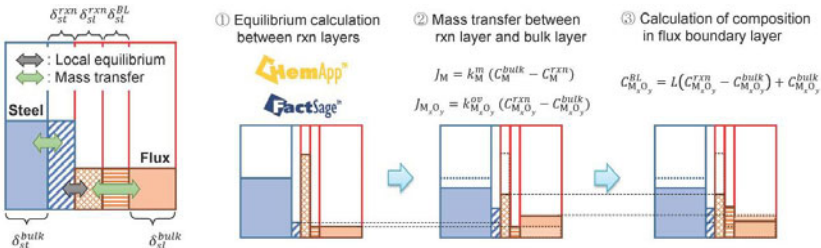


Figure 1. Model concept and calculation sequence of the present multi-component kinetic model

Equilibrium calculations

In the present kinetic model, two independent equilibrium calculations were performed for 1) steel-flux reaction at the interface, and 2) aluminate formation in the flux boundary layer. It was assumed that chemical reactions between steel and flux only occur between steel reaction layer and flux reaction layer. In the flux boundary layer, formation of $MgAl_2O_4$, $CaAl_2O_4$, and $CaAl_4O_7$ in liquid flux is considered in equilibrium calculation and those calcium aluminates are assumed to be additional resistances of mass transfer in the liquid flux. Thermodynamic calculation was conducted by ChemApp [8]. Thermodynamic database required for the calculation was extracted from commercial database in FactSage [9, 10].

Mass transfer in liquid steel

Flux density of an element M in the liquid steel was calculated by using a simple flux equation:

$$J_M = k_M^m (C_M^{bulk} - C_M^{rxn}) \quad (1)$$

where k_M^m , C_M^{bulk} , and C_M^{rxn} are mass transfer coefficient of the element M in liquid steel, concentration of the M in steel bulk layer, and concentration of the M in steel reaction layer, respectively. k_M^m was calculated from the mass transfer coefficient of Al experimentally determined in the previous study [3] by considering diffusivity of Al and M in liquid steel:

$$k_M^m = k_{Al}^m \frac{D_M^{st}}{D_{Al}^{st}} \quad (2)$$

Mass transfer in liquid flux

Similar to the flux density equation in liquid steel, the flux equation for the components in liquid flux could be written by using the number of moles of a component M_xO_y , as:

$$J_{M_xO_y} = k_{M_xO_y}^{ov} (C_{M_xO_y}^{rxn} - C_{M_xO_y}^{bulk}) \quad (3)$$

where $k_{M_xO_y}^{ov}$, $C_{M_xO_y}^{bulk}$, and $C_{M_xO_y}^{rxn}$ are overall mass transfer coefficient of the component M_xO_y in liquid flux, concentration of the M_xO_y in flux bulk layer, and concentration of the M_xO_y in flux reaction layer, respectively. From the previous kinetic investigation in the high Al steel and CaO-SiO₂-type flux system [4], it was found that formation of calcium aluminate layers near the steel-flux interface interfered mass transfer in liquid flux. Therefore, formation and growth of calcium aluminates and its effect on the overall reaction rate are considered in $k_{M_xO_y}^{ov}$ to describe drastic changes in mass transfer phenomena in liquid flux:

$$\frac{1}{k_{M_xO_y}^{ov}} = \frac{1}{k_{M_xO_y}^{CAx}} + \frac{1}{k_{M_xO_y}^s} \quad (4)$$

where $k_{M_xO_y}^{CAx}$ and $k_{M_xO_y}^s$ indicate virtual mass transfer coefficient of the component M_xO_y through calcium aluminate layer and that in the liquid flux, respectively. Based on the amount of calcium aluminates from the equilibrium calculation in the flux boundary layer, thickness of the calcium aluminate layer was calculated. $k_{M_xO_y}^{CAx}$ is defined to be inversely proportional to the thickness of the calcium aluminate layer, resulting decrease in mass flux with increase in the thickness of the calcium aluminate layer.

In order to consider the effect of flux viscosity change during the steel-flux reaction on mass transfer in the liquid flux, $k_{M_xO_y}^s$ is defined as a function of flux viscosity by using the following relationship between diffusivity and viscosity:

$$k_{M_xO_y}^s = k_{M_xO_y}^{s,0} \frac{\mu_0^{sl}}{\mu^{sl}} \quad (5)$$

where μ^{sl} , μ_0^{sl} , and $k_{M_xO_y}^{s,0}$ are flux viscosity in the flux boundary layer at the current timestep, initial flux viscosity in the flux boundary layer, and the mass transfer coefficient of M_xO_y when the flux viscosity in the boundary layer was μ_0^{sl} , respectively. Similar to k_M^m , $k_{M_xO_y}^{s,0}$ is obtained from optimized initial mass transfer coefficient of $k_{Al_2O_3}^{s,0}$ by using the diffusivity of M_xO_y and Al_2O_3 .

Flux composition and viscosity in the flux boundary layer

Once the amount of component M_xO_y to be transferred from the flux reaction layer to the flux bulk layer was calculated, it was distributed into the flux boundary layer and the flux bulk layer in order to obtain the composition in the flux boundary layer. For the simplicity, it was assumed that the concentration in the flux boundary layer can be set to a value between the concentration in the flux reaction layer and that in the flux bulk layer. Once the compositions in the flux boundary layer was obtained, then flux viscosity was calculated and utilized for modification of mass transfer coefficients in liquid flux.

Results and discussion

Calculation results compared with experimental data

Calculation results at various initial steel and flux compositions are compared with the experimental data obtained in the previous studies [2, 4], and a few examples are show in Fig. 2. Even though some discrepancies between the calculation results and the experimental data were observed in the flux compositions, most of the concentration changes in liquid steel and flux are well-predicted from the present kinetic model.

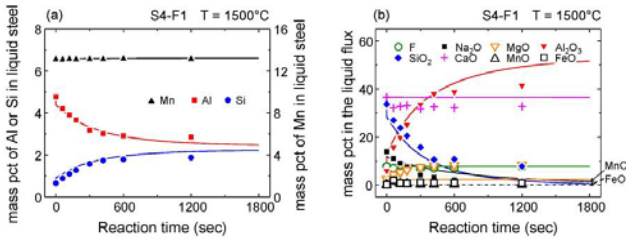


Figure 2. Calculated composition evolutions (solid lines) in (a) liquid steel and (b) liquid flux under 4.8 mass pct of $[\%Al]_0$ condition with experimental data[4] (solid and open symbols)

Depending on the initial Al concentration in liquid steel, the effect of flux viscosity change on the overall reaction rate shows considerable differences as can be seen in Fig. 3. When initial Al concentration in the liquid steel was low, the composition evolutions in liquid flux were almost similar regardless of consideration of flux viscosity for the calculation of mass transfer coefficients in liquid flux, indicating steel phase mass transfer control. At high Al condition, however, the present kinetic model predicted faster Al_2O_3 accumulation in the liquid flux when changes of mass transfer coefficients with respect to flux viscosity was not considered, which shows dominant mass transfer in flux phase. Therefore, it can be concluded that the present kinetic model is compatible with the reaction mechanism experimentally elucidated in the previous studies.

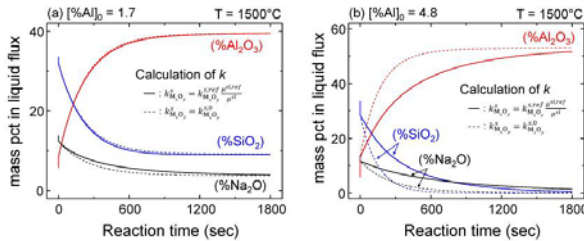


Figure 3. Calculated composition evolutions of Al_2O_3 , SiO_2 , and Na_2O in liquid flux at (a) low Al concentration ($[\%Al]_0 = 1.7$) and (b) high Al concentration ($[\%Al]_0 = 4.8$) with different calculation methods for mass transfer coefficients in liquid flux.

Application of the present kinetic model to continuous casting process

Based on the multi-component kinetic model developed in the present study, development of a continuous casting model was possible by simple modifications of the present kinetic model such as adding incoming and outgoing flux in the flux bulk layer, and constant concentration in the steel bulk layer. In order to check the accuracy of the present continuous casting model, several calculations based on the casting parameter from literatures [6, 11] were compared with the pilot casting data available from the same literatures, showing good prediction on the composition changes in the mold flux. In addition to that, mold flux viscosity change, one of the important

mold flux properties for successful casting, could be calculated using the composition changes obtained from the present continuous casting model.

Conclusion

A new multi-component kinetic model for high Al steel and CaO-SiO₂-type flux system was developed based on the reaction mechanism experimentally elucidated in the previous investigations [2, 3, 4]. The present kinetic model consists of a reaction layer in each phase and a boundary layer in the liquid flux, which enables simple calculations of local equilibrium calculation and flux density equation separately. Multi-component equilibrium calculation was performed by ChemApp [8] with thermodynamic database from FactSage [8, 9]. Also, flux viscosity changes and formation of calcium aluminate layer in the boundary layer are considered in the model for better description of mass transfer in the liquid flux. Generally, the calculation results are in good agreement with the experimental data obtained in the present study. Rate controlling step transition from mass transfer of Al in liquid steel to mass transfer in liquid flux was successfully predicted as initial Al concentration in liquid steel increased. Application of the present kinetic model also shows good calculation results compared with pilot casting data available from literature [6, 11].

References

- [1] K. Blazek, H. Yin, G. Skoczylas, M. McClymonds, M. Frazee, Evaluation of lime-silica and lime-alumina mold powders developed for casting high aluminum TRIP steel grades, in: 7th ECCS, Dusseldorf, 2011, pp. 1–10.
- [2] M.-S. Kim, S.-W. Lee, J.-W. Cho, M.-S. Park, H.-G. Lee, Y.-B. Kang, A reaction between high Mn-high Al steel and CaO-SiO₂-type molten mold flux: Part I. Composition evolution in molten mold flux, *Metall. Mater. Trans. B* 44 (2) (2013) 299–308.
- [3] Y.-B. Kang, M.-S. Kim, S.-W. Lee, J.-W. Cho, M.-S. Park, H.-G. Lee, A reaction between high Mn-high Al steel and CaO-SiO₂-type molten mold flux: Part II. Reaction mechanism, interface morphology, and Al₂O₃ accumulation in molten mold flux, *Metall. Mater. Trans. B* 44 (2) (2013) 309–316.
- [4] M.-S. Kim, Reaction mechanism and kinetic analysis of chemical reactions between high Mn-high Al steel and CaO-SiO₂-type mold flux, Ph.D. thesis, Pohang University of Science and Technology, Pohang, Rep. of Korea (2016).
- [5] M.-A. Van Ende, I.-H. Jung, Development of a thermodynamic database for mold flux and application to the continuous casting process, *ISIJ Int.* 54 (3) (2014) 489–495.
- [6] Q. Wang, S. Qiu, P. Zhao, Kinetic analysis of alumina change in mold slag for high aluminum steel during continuous casting, *Metall. Mater. Trans. B* 43 (2) (2011) 424–430.

- [7] J. Park, S. Sridhar, R. J. Fruehan, Ladle and continuous casting process models for reduction of SiO₂ in SiO₂-Al₂O₃-CaO slags by Al in Fe-Al(-Si) melts, *Metall. Mater. Trans. B* 46 (2014) 109–118.
- [8] S. Peterson, K. Hack, The thermochemistry library ChemApp and its applications, *Int. J. Mat. Res.* 98 (10) (2007) 935–945.
- [9] C. Bale, P. Chartrand, S. Degterov, G. Eriksson, K. Hack, R. Mahfoud, J. Melançon, A. Pelton, S. Peterson, FactSage thermochemical software and databases, *Calphad* 26 (2) (2002) 189–228.
- [10] C. Bale, E. Bélisle, P. Chartrand, S. Decterov, G. Eriksson, K. Hack, I.-H. Jung, Y.-B. Kang, J. Melançon, A. Pelton, C. Robelin, S. Petersen, FactSage thermochemical software and databases – recent developments, *Calphad* 33 (2) (2009) 295–311.
- [11] J.-W. Cho, K. Blazek, M. Frazee, H. Yin, J.-H. Park, Assessment of CaO-Al₂O₃ based mold flux system for high aluminum TRIP casting, *ISIJ Int.* 53 (1) (2013) 62–70.

EVALUATION OF MOLD FLUX FOR CONTINUOUS CASTING OF HIGH-ALUMINUM STEEL

Wei Yan^{1,2}, Alexander McLean¹, Yindong Yang¹, Weiqing Chen² and Mansoor Barati¹

¹ Department of Materials Science and Engineering, University of Toronto, Ontario, Canada M5S 3E4

² State Key Laboratory of Advanced Metallurgy, University of Science and Technology, Beijing 100083, China

Keywords: mold flux, high-aluminum steel, CaO-Al₂O₃-based, viscosity, crystallization, fluoride-free

Abstract

Study of mold fluxes for continuous casting of high-aluminum steel has attracted increasing attention due to severe reaction between aluminum in liquid steel and silica in the flux which results in changes in composition, properties and performance of the flux and adversely affects slab quality. This research began with sampling during the casting process of high-Al nonmagnetic steel 20Mn23AlV to evaluate potential problems. A mold flux was developed in which SiO₂ was partially replaced with Al₂O₃. Different compositions including CaO/Al₂O₃, fluoride-free and low-fluoride lime-alumina-based fluxes were evaluated with respect to their influence on flux viscosity, crystallization and subsequent effects on steel quality. It was concluded that mold flux with CaO/Al₂O₃ ratio in the range 1.1 to 1.6 and characterized by low viscosity, low initial crystallization temperature and good heat transfer properties was appropriate for casting of high-aluminum steel. A viscosity model with high reliability in predicting the viscosity of mold flux containing high Al₂O₃ was also established.

Introduction

Application of conventional CaO-SiO₂-based mold flux to the continuous casting of high-aluminum, nonmagnetic steel 20Mn23AlV (1.5~2.5 Al in mass pct.) results in substantial increase of Al₂O₃ and decrease of SiO₂ in the molten flux due to severe slag/metal reaction, followed by issues such as massive formation of slag rims, poor lubrication, uneven heat transfer, sticking breakouts and poor surface quality. Lubrication and uniform heat transfer, probably the most important functions of a mold flux, are directly affected by the viscosity and crystallization behavior of the flux. It is particularly important to maintain good lubrication and uniform heat transfer in order to obtain good surface quality and castability. A number of studies^[1,2] have been performed with conventional CaO-SiO₂-based mold flux in attempts to obtain appropriate lubrication and crystallization properties during casting of high-Al steels. However, the significant change in Al₂O₃ and SiO₂ contents in the slag is still the main reason for unstable lubrication and excessive crystallization which in turn provides an incentive for the development of less-reactive mold flux.

To solve the aforementioned problems CaO-Al₂O₃ mold flux with a low content of the reactive component SiO₂ has been proposed and evaluated for the casting of high-Al steels.^[1,3] A principal step in the design of a less-reactive mold flux is the determination of an optimal CaO/Al₂O₃ ratio, by examining the effects of compositional change on the mold flux properties. Studies^[1,4,5] have described the application of CaO-Al₂O₃-based mold flux. However they focused on the crystallization of mold flux with only limited changes in the CaO/Al₂O₃ ratios

at the same time as the contents of other components, such as Na_2O , Li_2O , CaF_2 and B_2O_3 . It was therefore difficult to evaluate the specific effect of $\text{CaO}/\text{Al}_2\text{O}_3$ ratios on mold flux performance. Moreover, the flux compositions did not simultaneously meet the coupled requirements for good crystallization and lubrication. Thus there is a need for a systematic study of the effect of a wide range of $\text{CaO}/\text{Al}_2\text{O}_3$ ratios on the viscosity and crystallization behavior of $\text{CaO}-\text{Al}_2\text{O}_3$ -based mold flux in order to establish optimal $\text{CaO}/\text{Al}_2\text{O}_3$ ratios which will fulfil the dual requirements for good crystallization and lubrication properties.

With conventional $\text{CaO}-\text{SiO}_2$ -based mold flux, although CaF_2 causes corrosion of equipment, SEN erosion and environmental pollution as well as health hazards, it is still added to control crystallization by forming the primary crystalline phase cuspidine and also to serve as a fluxing agent to decrease the solidus/liquidus temperatures and improve lubrication. Currently, almost all $\text{CaO}-\text{Al}_2\text{O}_3$ -based mold fluxes are designed with additions of 10% to 20% CaF_2 . However, cuspidine may be difficult to form in $\text{CaO}-\text{Al}_2\text{O}_3$ -based mold flux due to the low SiO_2 content. Several studies have been conducted to develop fluoride-free or low-fluoride mold flux by substituting CaF_2 with TiO_2 , Na_2O or B_2O_3 .^[6-8] in $\text{CaO}-\text{SiO}_2$ -based mold flux for plain carbon steel. Very few studies on low-fluoride or fluoride-free $\text{CaO}-\text{Al}_2\text{O}_3$ -based mold flux have been reported. One study from Lu^[9] focused on a very limited decrease of F in $\text{CaO}-\text{Al}_2\text{O}_3$ -based mold flux but did not discuss the effect of a large decrease in fluoride content on heat transfer, crystallization and phase compositions, and did not discuss fluoride-free, $\text{CaO}-\text{Al}_2\text{O}_3$ -based mold flux for high-Al steel. In the current study the replacement of CaF_2 with B_2O_3 in $\text{CaO}-\text{Al}_2\text{O}_3$ -based mold flux will be systemically investigated and in particular the viscosity properties as well as the crystallization behavior, in order to develop fluoride-free or low-fluoride $\text{CaO}-\text{Al}_2\text{O}_3$ -based mold flux for the casting of high-Al non-magnetic steel which requires good lubrication and weak crystallization.

Sampling during production operations

High-Al non-magnetic steel 20Mn23AlV studied in the current work was produced using a vertical continuous caster. During casting a large number of slag rims were formed around the meniscus. Samples of molten mold flux and slag rims were taken during casting process to examine changes in compositions and properties. Sampling was carried out about every 10min after the start of casting and all samples air cooled to room temperature. The original mold fluxes and the spent mold flux samples were subjected to chemical analysis, examination of melting temperature and evaluation of crystalline phases. It can be seen from **Figure 1(a)** that the $\text{Al}_2\text{O}_3/\text{SiO}_2$ mass ratio of molten fluxes has increased from 0.2 to ca. 1.2 after approximately 15min of casting due to rapid reaction between Al and SiO_2 . Greater increases of the $\text{Al}_2\text{O}_3/\text{SiO}_2$ mass ratio from 0.2 to ca. 1.7 was found in the slag rims. These changes in chemical composition of mold fluxes during continuous casting can introduce a series of severe consequences such as rapid increase in melting temperature, as shown in **Figure 1(b)**, and precipitation of the high-melting point phase gehlenite $\text{Ca}_2\text{Al}_2\text{SiO}_7$ (melting point 1596°C), as shown in **Figure 1(c)**, which in turn adversely affects lubrication and crystallization, and ultimately the casting process and surface quality of the cast slabs. Therefore, improvement in mold flux for high-Al non-magnetic steel should focus on suppression of deterioration of the above properties.

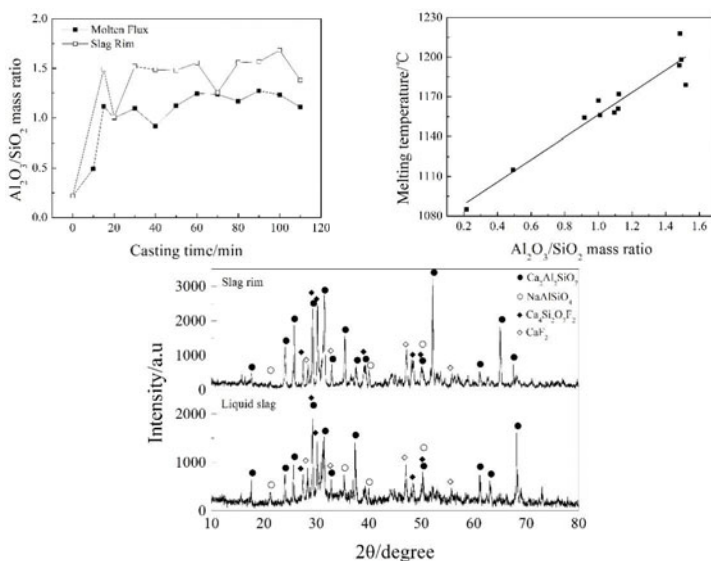


Fig. 1 Changes in (a) composition, (b) melting temperature and (c) crystalline phase of mold flux during continuous casting of 20Mn23AlV

Evaluation of CaO-Al₂O₃-based mold flux

3.1. Experimental

The chemical compositions of the experimental fluxes are: various CaO/Al₂O₃ 0.6–3.2, constant SiO₂ 5%, Na₂O 10%, CaF₂ 20% and B₂O₃ 10%. All samples were synthesized using reagent-grade chemicals CaO, SiO₂, Al₂O₃, CaF₂ and B₂O₃, with Na₂CO₃ used as the source for Na₂O. CaF₂ is generally added to serve primarily as a fluxing agent to control viscosity and solidification temperature in CaO-Al₂O₃-based mold flux. The synthetic fluxes were pre-melted in a graphite crucible at 1350°C for 0.5h under Ar (99.99% purity) and then quenched in water. The water-quenched fluxes were dried at 120°C for 4h and crushed into powder with particle size less than 75µm and then used for the following experiments.

3.1.1. Viscosity Measurements Viscosity was measured utilizing the rotational cylinder method. A schematic diagram of the apparatus and dimensions of the graphite crucible and Mo bob are shown in Fig. 2. MoSi₂ bars were used as the heating elements for the furnace and a Pt-Rh/Pt thermocouple was employed to determine the furnace temperature.

The viscometer was calibrated with standard oil. The furnace was heated at a rate of 15°C/min to the required temperature with Argon as a protective atmosphere. A graphite crucible (80mm in height and 40mm in inner diameter) containing 130g pre-melted mold flux was placed in the furnace and held at constant temperature for 30min to achieve thermal equilibrium. The depth of the liquid flux was approximately 40mm. The Mo bob was immersed into the flux to a depth of about 10mm from the bottom of the crucible and rotated at a constant speed of 200rpm to homogenize the liquid flux. After holding at constant temperature for 30min, the flux was cooled at a rate of 5°C/min. Meanwhile, viscosities and corresponding temperature were recorded automatically. The measurements were stopped when the viscosity increased sharply.

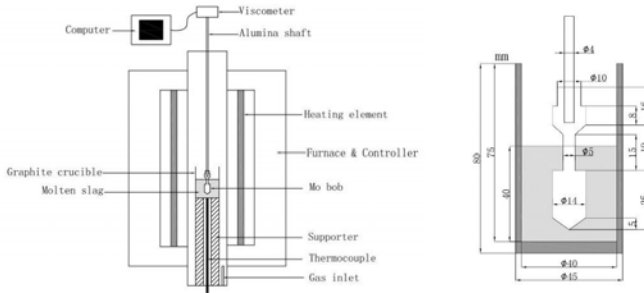


Fig. 2 Schematic diagram of the viscosity apparatus

3.1.2. CCT and TTT Tests To investigate the crystallization behavior of the fluxes, continuous cooling transformation (CCT) and time temperature transformation (TTT) diagrams were constructed using the single hot thermocouple technique (SHTT). A flux sample of about 10mg was mixed with alcohol, mounted on the tip of a B-type thermocouple and heated directly. The temperature was continuously monitored while the crystallization process was recorded by collecting images every second using a CCD camera. **Figure 3** shows the thermal cycles for construction of the CCT and TTT diagrams. The thermocouple was heated at a rate of $30^{\circ}\text{C}/\text{s}$ to 1500°C , and the flux sample held at this temperature for 1min to eliminate bubbles and allow homogenization of composition and temperature. The sample was then cooled continuously to 900°C at different cooling rates to construct the CCT diagram by recording the start time and start crystallization temperature at various cooling rates. To construct the TTT diagram, the sample was rapidly cooled at a cooling rate of about $80^{\circ}\text{C}/\text{s}$ to various isothermal temperatures while recording the start time and the end time of crystallization. During CCT and TTT tests, 5% and 95% volume fraction of crystallization were defined as the start and the end of crystallization, respectively. The volume fraction of crystallization was determined using image analysis software.

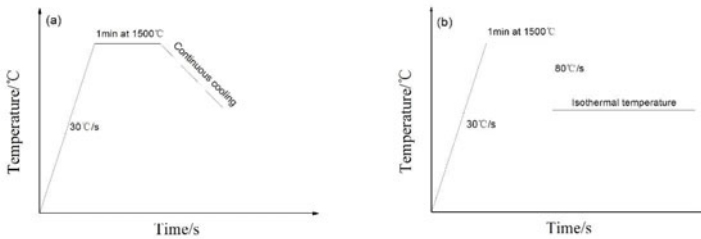


Fig. 3 Thermal cycles for (a) CCT and (b) TTT tests

3.2. Viscosity and Structural Characteristics

Fig. 4(a) shows the change in flux viscosity as a function of $\text{CaO}/\text{Al}_2\text{O}_3$ ratio in the temperature range from $1125\sim 1325^{\circ}\text{C}$. At temperatures above 1270°C the viscosity first rapidly decreases and then gradually becomes stable. However, at temperatures less than 1270°C , the viscosity first decreases and then increases. These changes in viscosity are closely related with the network structure characteristics of the melt at higher temperature and solid particles that are precipitated at lower temperature.

It is known that Al_2O_3 is an amphoteric oxide and that the behavior as an acidic oxide (network former) or basic oxide (network modifier), depends on the basicity of the melt.^[10] For all fluxes tested in the current study, the mole fractions of the basic oxides CaO and Na_2O are far higher than that of Al_2O_3 , and therefore Al_2O_3 functions as an acidic oxide to form $[\text{AlO}_4]^{5-}$ -tetrahedra or is incorporated into the silicon-oxygen network structure when sufficient charge compensation is available through the presence of basic oxides. As shown in **Fig. 4(b)**, this behaviour has been confirmed using FTIR spectra for mold flux quenched from 1350°C , which show the band for $[\text{AlO}_4]^{5-}$ -tetrahedral structural units near 650 cm^{-1} and Si-O-Al bending at about 500 cm^{-1} .^[11] At higher temperatures, with decrease in the CaO/ Al_2O_3 ratio, more Al_2O_3 is involved in the formation of aluminate or alumino-silicate network structures to increase the degree of polymerization which in turn increases the viscosity. With increasing CaO/ Al_2O_3 ratio, more free oxygen ions (O^{2-}) are available to promote depolymerization, reducing the extent of the alumino-silicate network structure, and hence decreasing the viscosity. The FTIR spectra also show that with increase in the CaO/ Al_2O_3 ratio, the center of the $[\text{AlO}_4]^{5-}$ -tetrahedral structural units shifts toward lower wave-numbers and the band width decreases, which is consistent with a decrease in the degree of polymerization.

At lower temperatures, precipitation of solid particles with high melting points begin to have a dominant role in controlling viscosity, so the viscosity increase.

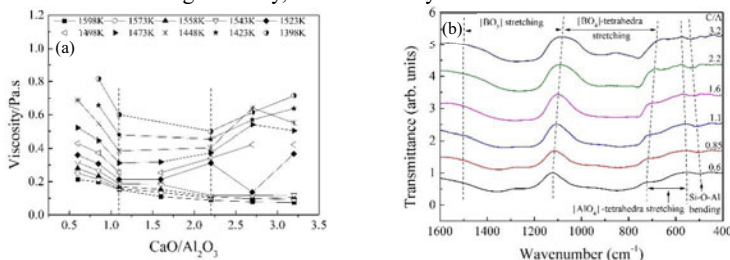


Fig. 4 Effect of CaO/ Al_2O_3 ratio on (a) viscosity and (b) FTIR spectra of fluxes

3.3. Crystallization Behaviour

Fig. 5(a) shows the relationship between the CaO/ Al_2O_3 ratio and the initial crystallization temperature at a fixed cooling rate of 0.5°C/s . The initial crystallization temperature first decreases from 1204°C to 1050°C with increase in CaO/ Al_2O_3 ratio from 0.6 to 1.6, and then increases to 1138°C and 1422°C when the ratio increases to 2.2 and 3.2, respectively. This demonstrates that an increase in the CaO/ Al_2O_3 ratio over a wide range from 0.6 to 3.2 first weakens and then enhances the tendency for crystallization.

Fig. 5(b) compares the incubation time for initial crystallization at different holding temperatures and CaO/ Al_2O_3 ratios. It can be observed that mold flux with a CaO/ Al_2O_3 ratio of 3.2 begins to crystallize almost immediately even at higher temperatures, followed by mold fluxes with CaO/ Al_2O_3 ratios of 0.6, 2.2, 1.1 and 1.6, respectively. The same phenomenon is observed with respect to the incubation time in the higher temperature zone. A high crystallization temperature and short incubation time suggest a strong crystallization ability, which is consistent with the results obtained from the CCT tests.

From the above study, mold flux with a CaO/ Al_2O_3 ratio in the range 1.1~1.6 has a low viscosity and a relatively weak tendency for crystallization. These conditions will enhance the

infiltration of the liquid flux into the gap between the steel shell and the copper mold, improve lubrication, promote heat transfer and consequently enhance the formation of a thick steel shell with fine grains and high strength thus decreasing the possibility of a liquid steel breakout. This is particularly significant for the casting of high-aluminum, non-magnetic steel 20Mn23AlV, which is prone to form a coarse columnar structure at low cooling rates thus decreasing the strength of the initial steel shell and leading to cracks and potential breakouts.

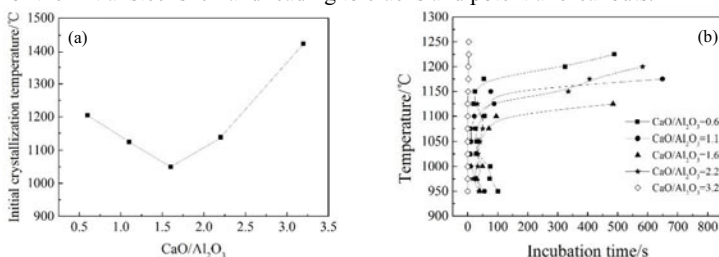


Fig. 5 Effect of CaO/Al₂O₃ ratio on (a) initial crystallization temperature at a cooling rate of 0.5°C/s and (b) incubation time for crystallization at different holding temperatures

Evaluation of B₂O₃ as a replacement for CaF₂ in CaO-Al₂O₃-based mold flux

To evaluate the feasibility of development of fluoride-free or low-fluoride CaO-Al₂O₃-based mold flux from the perspectives of viscosity and crystallization properties, the chemical compositions of the mold fluxes were designed by replacing CaF₂ with B₂O₃ as listed in Table 1. The experimental methods were same as those described in the section 3.1.

Table 1 Chemical composition of the experimental mold fluxes (in mass percent)

CaO	SiO ₂	Al ₂ O ₃	Na ₂ O	CaF ₂	B ₂ O ₃
28.8		26.2		20	10
32.5		29.5		13	10
36.1	5	32.9	10	6	10
39.3		35.7		0	10
36.7		33.3		0	15
34.0		31.0		0	20

4.1. Viscosity characteristic

As shown in Fig. 6(a), increases of CaF₂ and temperature decrease the viscosity of CaO-Al₂O₃-based mold flux. The viscosity of molten flux at high temperature is related to the structure. The effect of CaF₂ on viscosity is due to its effect on the structure and melting temperatures of the mold flux. Study^[12] has indicated that CaF₂ decomposes into Ca²⁺ and F⁻ in a similar way to CaO Eq. (1). The F⁻ ion then plays a similar role to that of free oxygen O²⁻ ions and depolymerizes the complicated aluminate network structures [AlO₄]⁵⁻ into [AlF₆]³⁻ and [AlO₆]⁹⁻ according to Eqs. (2) and (3)^[13]. FTIR study also indicated this reaction can depolymerize aluminate network structures and accordingly decrease the polymerization degree of molten flux, and the viscosity eventually decreases. Moreover, CaF₂ also decreases viscosity by decreasing the melting temperature since viscosity is a function of temperature. The combined effects of depolymerization of network structures and decrease in melting temperatures caused by CaF₂ result in a decrease in viscosity.



In order to examine whether B_2O_3 can duplicate the effect of CaF_2 on viscosity of $\text{CaO-Al}_2\text{O}_3$ -based mold flux, the effect of B_2O_3 was also studied with and without CaF_2 addition. **Fig. 6(b)** shows addition of B_2O_3 has a similar effect to CaF_2 in decreasing the viscosity, especially at low temperatures. As mentioned above, the viscosity of a melt is related to its structure. Addition of B_2O_3 depolymerizes the 3-D $[\text{BO}_4]^{5-}$ into 2-D $[\text{BO}_3]^{3-}$ structure, meanwhile, bridging oxygen O^0 transforms into non-bridging oxygen O^- during depolymerization. Moreover, addition of B_2O_3 can reduce Al-O stretching vibration of $[\text{AlO}_4]^{5-}$ tetrahedral structures^[11]. These changes from complicated structures to relatively simple structures caused by addition of B_2O_3 are responsible for a decrease in viscosity.

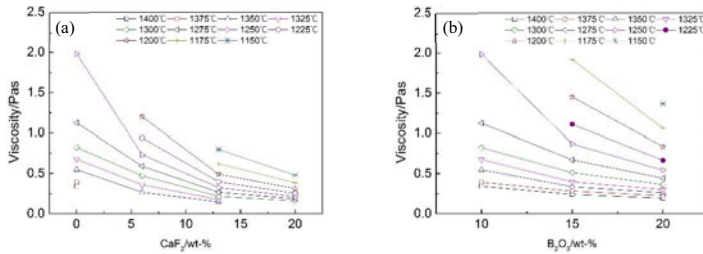


Fig. 6 Effect of (a) CaF_2 and (b) B_2O_3 on viscosity of $\text{CaO-Al}_2\text{O}_3$ -based mold flux

4.2. Crystallization behavior

The initial crystallization temperature as a function of CaF_2 at the fixed cooling rate of 0.5°C/s is plotted in **Figure 7(a)**. Decrease of CaF_2 from 20% to 13%, 6% and 0 increases the initial crystallization temperature from 1125°C to 1138°C , 1150°C and 1177°C , respectively. This result indicates that decrease in CaF_2 content enhances crystallization of $\text{CaO-Al}_2\text{O}_3$ -based mold flux, which is the opposite effect to that observed with conventional CaO-SiO_2 -based mold flux. This may be because addition of CaF_2 promotes precipitation of cuspidine in CaO-SiO_2 -based mold flux. **Figure 7(b)** shows the relationship between initial crystallization temperature and B_2O_3 . A similar effect of B_2O_3 to CaF_2 on the initial crystallization temperature can be observed. Increase in B_2O_3 content from 10% to 15% and 20% decreases the crystallization temperature from 1177°C to 1136°C and 1109°C respectively. This change suggests that addition of B_2O_3 restrains crystallization of $\text{CaO-Al}_2\text{O}_3$ -based mold flux. It also indicates that the equivalent amount of B_2O_3 has almost a twofold effect compared to that of CaF_2 on the initial crystallization temperature of $\text{CaO-Al}_2\text{O}_3$ -based mold flux. This phenomenon may be because B_2O_3 serves as a network former to strengthen the glassy ability of mold flux.

Fig. 8(a) summarizes the incubation times at different holding temperatures for $\text{CaO-Al}_2\text{O}_3$ -based mold flux with different amounts of CaF_2 . It is evident that within the high and middle temperature zones, the incubation time increases with increasing CaF_2 content. This means crystallization of $\text{CaO-Al}_2\text{O}_3$ -based mold flux within the high and middle temperature zones is retarded by higher CaF_2 contents. It is also confirmed once again that decrease of CaF_2 promotes crystallization of $\text{CaO-Al}_2\text{O}_3$ -based mold flux. This conclusion is consistent with the

CCT results. The relationships between incubation time and holding temperature for the different B_2O_3 concentrations are summarized in **Fig. 8(b)**. Mold flux with 10%, 15% and 20% B_2O_3 initiate crystallization at 1225°C, 1200°C and 1150°C, respectively. The incubation time at 1150°C is prolonged significantly from 34s to 50s and then 606s with increase of B_2O_3 from 10% to 15% and 20%. These findings are consistent with the behavior of B_2O_3 as a network forming oxide.

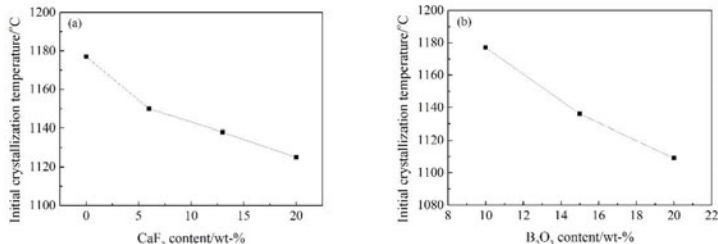


Fig. 7 Effect of (a) CaF_2 and (b) B_2O_3 on the initial crystallization temperature at a cooling rate of 0.5°C/s

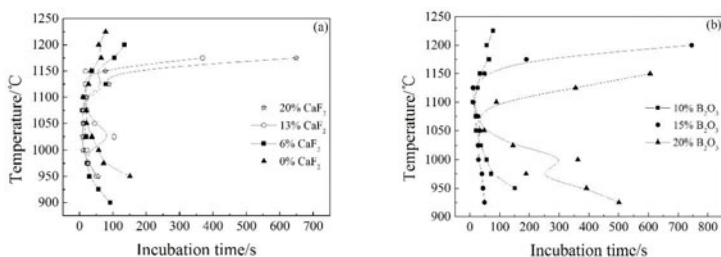


Fig. 8 Effect of (a) CaF_2 and (b) B_2O_3 on incubation time for crystallization

From the perspectives of viscosity and crystallization, it has been shown that B_2O_3 can be used to replace CaF_2 for the generation of $CaO-Al_2O_3$ -based mold flux with free, or very low, CaF_2 content.

Viscosity model for mold flux with high Al_2O_3 content

Viscosity is an important property of mold flux, but its measurement requires much time and high cost. Thus there is no doubt that a viscosity model with high accuracy is of considerable benefit for evaluation of mold flux behaviour. Several researchers^[14-17] have obtained semi-empirical or empirical viscosity models based on different slag compositions and experimental results, but the Al_2O_3 content in these models is always less than 10%. There is therefore considerable limitation in predicting the viscosity of mold fluxes with high Al_2O_3 contents such as those in the present study with 30% Al_2O_3 . **Fig. 9** shows the comparison of experimental and calculated viscosities of mold flux with high Al_2O_3 . The calculated viscosities using the Riboud^[14], Urban^[15] and RIST^[16] models show large deviations from the experimental results. However the NPL^[17] viscosity model, based on optical basicity shows a relatively better prediction. The present study has modified the NPL model based on the Weymann-Frenkel equation and optical basicity to improve accuracy in the prediction of viscosity of mold fluxes containing high concentrations of Al_2O_3 .

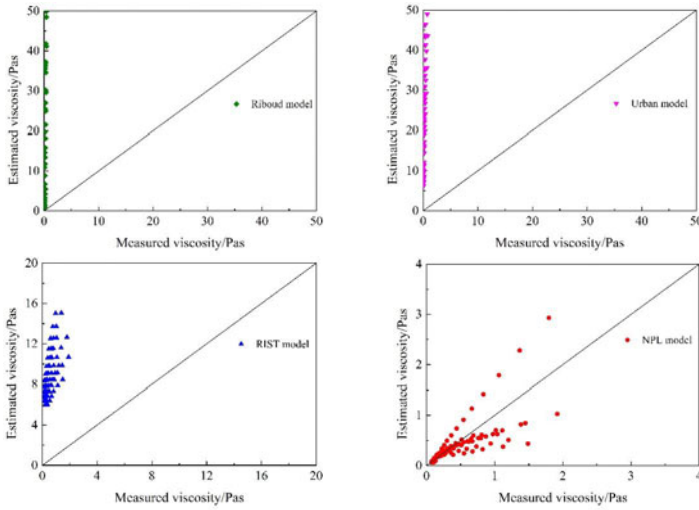


Fig. 9 Comparison between measured viscosities and those predicted by different models

Weymann-Frenkel equation Eq. (4) describes the correlation between viscosity and temperature.

$$\ln \frac{\eta}{T} = \ln A + \frac{1000B}{T} \quad (4)$$

The correlation between parameters $\ln A$ and B can be seen from **Fig. 10(a)** based on Eq. (4) and experimental viscosity of the mold fluxes shown in **Table 1**. It can be seen that the relationship between $\ln A$ and B shows good linearity and can be represented by the following equation:

$$\ln A = -0.4327B - 13.053 \quad (R^2 = 0.9791) \quad (5)$$

The corrected optical basicity expression proposed by Shankar^[18], Eq. (6), was used to establish a model based on the view that Al_2O_3 behaves as an acidic oxide when the molar ratio of basic oxides to Al_2O_3 is greater than unity. The optical basicity A of molten flux can be calculated from a knowledge of the flux composition and the optical basicity value of each oxide^[17]. The correlation between B and A shown in **Fig. 10(b)** corresponds to the following relationship Eq. (7).

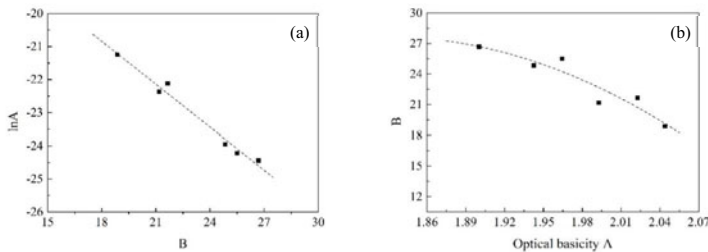


Fig. 10 (a) Correlation between $\ln A$ and B , and (b) Correlation between B and optical basicity A

$$\Lambda = \frac{\frac{\sum (X_B n_B A_B + \dots)}{\sum (X_B n_B + \dots)}}{\frac{\sum (X_A n_A A_A + \dots)}{\sum (X_A n_A + \dots)}} \quad (6)$$

$$B = -180.67A^2 + 659.88A - 574.85 \quad (R^2 = 0.8911) \quad (7)$$

Fig. 11 (a) shows a comparison between the measured viscosity of the fluxes listed in **Table 1** and the values calculated using the present model as well as previous models. **Fig. 11 (b)** provides a comparison between the measured viscosity of the fluxes (the compositions listed in **section 3.1**) and the values calculated with the present model. It should be noted that Eqs. (5) and (7) were obtained based on the viscosity of the fluxes shown in **Table 1**. However, the viscosities of fluxes listed in **section 3.1** were not used for establishment of the viscosity model. It is evident that there is good agreement between the proposed model and the measured data for the fluxes listed in both **section 3.1** and **Table 2** despite the fact that model parameters were not derived based on the experimental results for the fluxes listed in **section 3.1**.

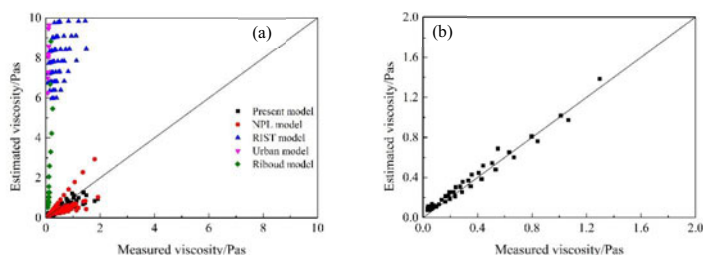


Fig. 11 Comparison between the measured and calculated viscosities of fluxes listed in (a) Table 2 and (b) section 3.1

Conclusions

- (1) Sampling from the mold during continuous casting of high-Al non-magnetic steels shows slag/metal reactions have resulted in significant increase in the $\text{Al}_2\text{O}_3/\text{SiO}_2$ ratio in mold flux from 0.25 to ca. 1.5. This increases the melting temperature of fluxes from 1080°C to greater than 1200°C and promotes precipitation of the high-melting point compound gehlenite.
- (2) Mold fluxes with $\text{CaO}/\text{Al}_2\text{O}_3$ ratios in the range 1.1~1.6 have a low viscosity and a relatively weak tendency for crystallization, both of which are good conditions for casting high-Al nonmagnetic steel 20Mn23AlV.
- (3) It was found that B_2O_3 played a similar role to CaF_2 in changing the viscosity and crystallization of $\text{CaO}-\text{Al}_2\text{O}_3$ -based mold flux. From the perspectives of viscosity and crystallization, it has been shown that B_2O_3 can be used to replace CaF_2 for the generation of $\text{CaO}-\text{Al}_2\text{O}_3$ -based mold flux with free, or very low, CaF_2 content.
- (4) Based on the concept of optical basicity, a model with high reliability was established to predict the viscosity of mold fluxes containing high concentrations of Al_2O_3 .

References

1. K. Blazek et al, "Development and evaluation of lime alumina-based mold powders for casting high-aluminum TRIP steel grades," *AIST Trans.*, 8(2011), 232-240.
2. H. S. Park, H. Kim, and I. Sohn, "Influence of CaF_2 and Li_2O on the viscous behavior of

- calcium silicate melts containing 12 wt pct Na₂O,” *Metall. Mater. Trans. B*, 42(2011), 324-330.
3. S. Street, K. James, and N. Minor, “Production of high aluminum steel slabs,” *Iron Steel Tech.*, 7(2008), 38-49.
 4. J. W. Cho et al, “Assessment of CaO-Al₂O₃ based mold flux system for high aluminum TRIP casting,” *ISIJ Int.*, 53(2013), 62-70.
 5. C. B. Shi et al, “Crystallization characteristics of CaO-Al₂O₃-based mold flux and their effects on in-mold performance during high-aluminum TRIP steels continuous casting,” *Metall. Mater. Trans. B*, 45(2014), 1081-1097.
 6. S. Y. Choi, D. H. Lee, and D. W. Shin, “Properties of F-free glass system as a mold flux: viscosity, thermal conductivity and crystallization behavior,” *J. Non-Cryst. Solids*, 345&346(2004), 157-160.
 7. S. P. He, Q. Wang, and D. Xie, “Solidification and crystallization properties of CaO-SiO₂-Na₂O based mold fluxes,” *Int. J. Min. Met. Mater.*, 16(2009), 261-264.
 8. H. Nakada and K. Nagata, “Crystallization of CaO-SiO₂-TiO₂ slag as a candidate for fluorine free mold flux,” *ISIJ Int.*, 46(2006), 441-449.
 9. B. X. Lu and W. L. Wang, “Effects of fluorine and BaO on the crystallization behavior of lime-alumina-based mold flux for casting high-Al steels,” *Metall. Mater. Trans. B*, 46(2015), 852-862.
 10. G. H. Zhang, Q. G. Xue, and K. C. Chou, “Study on relation between viscosity and electrical conductivity of aluminosilicate melts,” *Ironmaking Steelmaking*, 38(2011), 149-154.
 11. G. H. Kim and I. Sohn, “Role of B₂O₃ on the viscosity and structure in the CaO-Al₂O₃-Na₂O based system,” *Metall. Mater. Trans. B*, 45(2014), 86-95.
 12. T. Schulz et al, “Structurally based assessment of the influence of fluorides on the characteristics of continuous casting powder slags,” *Metall. Mater. Trans. B*, 44(2013), 317-327.
 13. J. H. Park, D. J. Min, and H. S. Song, “Structural investigation of CaO-Al₂O₃ and CaO-Al₂O₃-CaF₂ slags via Fourier transform infrared spectra,” *ISIJ Int.*, 42(2002), 38-43.
 14. P. V. Riboud et al, “Improvement of continuous casting powders,” *Fachberichte Hüttenpraxis Metallweiterverarbeitung*, 19(1981), 859-869.
 15. J. Muller, J. H. Zietsman, and P. C. Pistorius, “Modeling of manganese ferroalloy slag properties and flow during tapping,” *Metall. Mater. Trans. B*, 46(2015), 2639-2651.
 16. I. R. Lee et al, “Development of mould powder for high speed continuous casting,” *Conf. on Continuous Casting of Steel in Developing Countries*, Beijing, 1993.
 17. K. C. Mills and S. Sridhar, “Viscosities of ironmaking and steelmaking slags,” *Ironmaking Steelmaking*, 26(1999), 262-268.
 18. A. Shankar et al., “Estimation of viscosity for blast furnace type slags,” *Ironmaking Steelmaking*, 34(2007), 477-481.

THE STRUCTURE AND THE CRYSTALLIZATION BEHAVIOUR OF THE CaO-SiO₂-Al₂O₃-BASED MOLD FLUX FOR HIGH-AL STEELS CASTING

Jinxing Gao, Guanghua Wen, Ting Huang, Ping Tang

School of Materials Science and Engineering, Chongqing University, China.

E-mail: gaojinxing@cqu.edu.cn,400044.

Keywords: Structure, Crystallization behavior, High-Al steel, Mold flux

Abstract

The reaction between [Al] and SiO₂ sharply converted the original CaO-SiO₂-based flux into CaO-SiO₂-Al₂O₃-based flux during the continuous casting of high-Al steels, promoting the crystallization and deteriorating the mold lubrication. Therefore, study on the structure and crystallization behavior of CaO-SiO₂-based and CaO-SiO₂-Al₂O₃-based flux is important to solve this problem. The structure and crystallization behavior were investigated by Raman spectra and the single hot thermocouple technique. The results show that the [AlO₄]⁵⁻ entered the silicate network (CaO-SiO₂-based) and the melt converted into the aluminosilicates structure (CaO-SiO₂-Al₂O₃-based), the formation of Al-O-Al linkages and Si-O-Al linkages increased the instability of network structure. From the time temperature transformation diagrams, the strong crystallization tendency and the variety of crystals are mainly the properties of slag film in the CaO-SiO₂-Al₂O₃-based flux. Hence, the improvement of the structural stability and suppression the crystallization tendency of the CaO-SiO₂-Al₂O₃-based flux are key to design a high-Al steel mold flux.

Introduction

Recently, advanced high-strength steels have drawn much attention owing to their enhanced strength and formability^[1-3]. These new grades of steel are characterized by a high Al content that improves the mechanical properties and produces lighter steel products^[2]. However, alloying elements, such as Al, react with CaO-SiO₂-based mold flux, thus converting the original CaO-SiO₂-based flux into a CaO-SiO₂-Al₂O₃-based flux^[4]. The structure and crystallization behavior change with this conversion of the mold flux, resulting in partially solidified steel shell that sticks because of decreased lubrication. Hence, it is important to study the structure and crystallization behavior of the mold flux during this conversion.

Intensive efforts have been carried out to study the mold flux for high-Al steels casting, and most of them are concentrated on the CaO-SiO₂-Al₂O₃-based mold flux^[5-7]. KIM et al.^[4] studied the viscosity trend of the mold flux as the SiO₂ was gradually replaced with Al₂O₃ and reported that the viscosity increased with the increase in the Al₂O₃ content. Cho et al.^[5] found that the viscosity increased because the mold flux replaced the SiO₂ with Al₂O₃ that was prone to crystallization, thus deteriorating the mold lubrication. Wang et al.^[6] studied the effects of Na₂O and Li₂O on the crystallization property of CaO-SiO₂-Al₂O₃-based mold flux and found that CaO-SiO₂-Al₂O₃-based mold flux had a shorter crystallization incubation time and a strong ability to crystallize. Moreover, Wang also reported that 2CaO·Al₂O₃·SiO₂ was the main crystal phase in the CaO-SiO₂-Al₂O₃-based mold flux. Gao et al.^[7] studied the solidification and crystallization behavior of the CaO-SiO₂-Al₂O₃-based mold flux and found that the strong crystallization tendency and the variety of crystals are mainly the properties of the CaO-SiO₂-Al₂O₃-based mold flux. Moreover, Gao also reported that the slag structure

could be changed by adjusting the composition of the mold flux, thus varying the crystallization behavior of the mold flux. Although many researchers found that the CaO-SiO₂-Al₂O₃-based mold flux was prone to crystallization and deteriorated the mold lubrication, the reason has not been reported. Hence, the structure and crystallization behavior of the mold flux with the progress of the slag–steel reaction was studied, and the growth mechanism of the crystallization in the CaO-SiO₂-Al₂O₃-based mold flux was elucidated. This will help to design a high-Al steel mold flux.

In this study, the structural characteristics of a molten slag were studied using Raman spectroscopy. The changes in the crystallization behavior during the conversion from CaO-SiO₂-based flux to CaO-SiO₂-Al₂O₃-based flux were analyzed by the single hot thermocouple technique (SHTT) and the characteristics of crystals were studied by scanning electron microscopy (SEM) and X-ray energy-dispersive spectroscopy (EDS). This can be used to determine the reason of strong crystallization tendency in the CaO-SiO₂-Al₂O₃-based mold flux and design a high-Al steel mold flux.

Materials and methods

To study the changes in the structure and crystallization behavior during the conversion from CaO-SiO₂-based mold flux into the CaO-SiO₂-Al₂O₃-based mold flux, samples SA-2 (8% reacted SiO₂) and SA-3 (Spent flux, 16% reacted SiO₂) were designed based on SA-1 (Base flux) sample from the CaO-SiO₂-based mold flux. The contents of SiO₂ and Al₂O₃ changed due to the slag–steel reaction, whereas the contents of other compositions remained the same. The samples were prepared using pure chemical reagents; Na₂CO₃ and Li₂CO₃ were used to replace Na₂O and Li₂O, respectively. 100 g of each slag sample was placed in a platinum crucible and heated to 1673 K (1400 °C) using a silicon-molybdenum furnace for 30 min to ensure that the slag melted uniformly. Then, the slag samples were removed and poured into a water-cooled steel plate for quenching. The quenched slag samples were removed, and samples with a size of <0.72 μm were prepared for further studies.

Table 1 Chemical compositions of mold fluxes (wt.%)

Sample	CaO	SiO ₂	Al ₂ O ₃	Na ₂ O	Li ₂ O	CaF ₂	MgO	Total
SA-1	29.3	36.7	2.6	10.3	1.9	16.1	3.2	100.0
SA-2	29.0	28.3	11.7	10.2	1.9	15.9	3.1	100.0
SA-3	28.7	20.0	20.6	10.1	1.9	15.7	3.1	100.0

A LabRAM HR Evolution micro-Raman spectrometer (HORIBA, Japan) was used to study the slag structure. A solid laser with a wavelength of 532 nm and a power of 100 mW was used as the light source. The measurement threshold of the equipment was as low as 10 cm⁻¹, and the spectra in the range 200–1600 cm⁻¹ were used to study the slag structure. The crystallization behavior was studied through SHTT, and the crystallization characteristics were studied using CCT and TTT curves. The method to construct CCT and TTT curves has been described in previous reports [7]. Because the amount of samples obtained through the TTT experiment was relatively small (~10mg), their crystallized phases could not be directly identified using X-ray diffraction (XRD). Therefore, in this paper, after the TTT experiments, the samples were used for the SEM-EDS analysis. By stopping the TTT experiment, the slag sample was rapidly cooled down at a rate of ~150K/s to room temperature. The microstructural aspects of the slags at a high temperature may be preserved in the quenched samples. Finally, the crystal types under different temperature conditions were obtained. The samples for SEM-EDS analyses were prepared as follows: The samples were mounted, grinded, polished, and spray-coated with gold on the surface to enhance the electrical conductivity of the mold fluxes.

Results and discussion

A. Structure of molten slag

The Raman spectra of the experimental slag samples are shown in **Figure 1a**. The characteristic peaks of each sample mainly appeared within three regions, namely, the low-frequency region ($400\text{--}600\text{ cm}^{-1}$), intermediate-frequency region ($600\text{--}800\text{ cm}^{-1}$), and high-frequency region ($800\text{--}1200\text{ cm}^{-1}$). The peaks around 550 cm^{-1} , 680 cm^{-1} , and $800\text{--}1200\text{ cm}^{-1}$ were characteristic of Al–O–Al bonding, bending vibration of Si–O–Si, and stretching vibration of (Si, Al)–O[−], respectively [8–11]. The characteristic peaks within the high-frequency region should be fitted according to Gaussian function because the peaks within this region can be attributed to the (Si, Al)–O[−] stretching vibrations in various microstructural units [11]. The typical deconvolution of the Raman spectra is shown in **Figure 1b**. After the deconvolution analysis, the peak positions and areas of the slag samples obtained are listed in **Table 2**. The integrated area of the individual deconvoluted peaks provides a semi quantitative evaluation of the amount of the Q_n units [8]. The Raman spectra of SA-2 and SA-3 are significantly different from SA-1. SA-1 sample exhibited a typical network structure of silicate melts, mainly composed of Q₀, Q₁, Q₂, and a small amount of Q₃ structural units. After the slag–steel reaction, both the contents of Al₂O₃ in the slag samples SA-2 and SA-3 increased gradually, whereas the contents of SiO₂ gradually decreased, clearly changing the network structure of the mold flux. The new characteristic peaks at $\sim 550\text{ cm}^{-1}$, 790 cm^{-1} and 830 cm^{-1} can be attributed to Al–O–Al bonding, [AlO₄]^{5−}, and Si–O–Al bonding [8]. This indicates that as the slag–steel reaction progressed, the Al³⁺ ions were absorbed into the silicate structure, mainly acting as the network formers in the CaO–SiO₂–Al₂O₃-based mold flux. With the decrease in the content of SiO₂, the number of network formers also decreased. Thus, the excessive network breakers led to the slag mainly composed of smaller structural units such as Q₀, Q₁, and Q₂. Moreover, the area of the characteristic peak corresponding to the Si–O–Si bending vibration also decreased significantly, and the polymerization degree of the silicate network decreased. Hence, a certain amount of Al entered into the network structure, acting as the network former. According to the changes of characteristic peaks' areas, SA-1 had a silicate network structure, mainly consisting of Q₂. SA-2 had an aluminosilicate network structure, mainly consisting of Q₀, and a small amount of Al acts as the network former. However, for SA-3, the network structure mainly consists of Q₁; moreover, a large amount of Al was absorbed into the silicate structure participated in the formation of an aluminosilicate network structure.

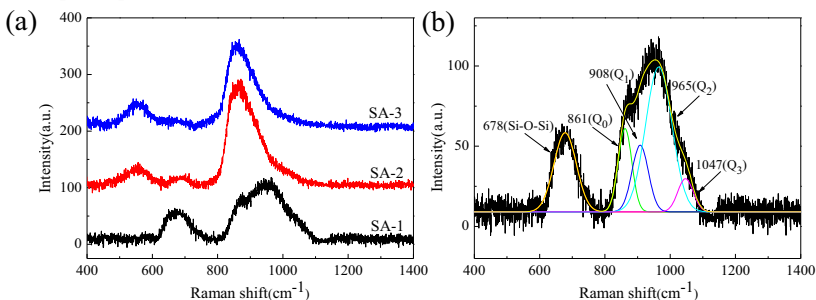


Figure 1. Raman spectra for mold flux (a) Effect of slag–steel reaction on the structure (b) Typical deconvolution of the Raman spectra

Table 2 Peak analysis of Raman in the mold flux

Raman shift (cm^{-1})			Peak area ratio (%)			Raman bands
SA-1	SA-2	SA-3	SA-1	SA-2	SA-3	
	555	554		10.8	16.1	Symmetric Al-O-Al stretching vibration
678	681	665	21.3	4.7	3.4	Bending Si-O vibration of $[\text{SiO}_3]^{2-}$
	791	790		0.3	2.9	Symmetric stretching Al-O ⁻ of $[\text{AlO}_4]^{5-}$
	839	839		3.3	14.4	Symmetric Si-O-Al stretching
861	859	868	13.6	40.2	11.5	Symmetric stretching Si-O ⁻ of Q_0
908	910	890	13.2	24.4	33.0	Symmetric stretching Si-O ⁻ of Q_1
965	970	953	45.8	16.3	18.7	Symmetric stretching Si-O ⁻ of Q_2
1047			6.2			Symmetric stretching Si-O ⁻ of Q_3

B. Effect of slag-steel reaction on the crystallization behavior of molten slag

The crystallization behaviors of the mold flux are shown in **Figure 2**. As shown in **Figure 2a**, the crystallization temperatures of all the samples decreased with continuous cooling rate increase. The main reason is because the nucleation and growth rate of crystals are the functions of the viscosity and the degree of undercooling. As the viscosity increases quickly under the higher cooling rate, the diffusion of the solute in the slag decreased, reducing the crystallization rate of the mold flux. Therefore, it requires a stronger driving force to initiate the mold flux nucleation. Moreover, under the same cooling conditions, the crystallization temperature characteristics of the mold flux were significantly different. A lower crystallization temperature and lower critical cooling rate indicate that SA-1 had relatively poor crystallization ability. As the slag-steel reaction progressed, the crystallization temperature and the critical cooling rate first increased and then decreased, indicating the presence of a relatively strong crystalline region during the conversion from the original CaO-SiO₂-based mold flux to the CaO-SiO₂-Al₂O₃-based mold flux. Most of the studies [6, 7, 12] mainly focused on the original CaO-SiO₂-based mold flux and the CaO-SiO₂-Al₂O₃-based mold flux after the reaction. However, the mold flux easily entered the relatively strong crystalline region during the conversion from the original CaO-SiO₂-based mold flux to the CaO-SiO₂-Al₂O₃-based mold flux, which may be one of the reasons why the mold flux easily formed the coarse slag on the steel liquid surface during the high-Al steel casting [12].

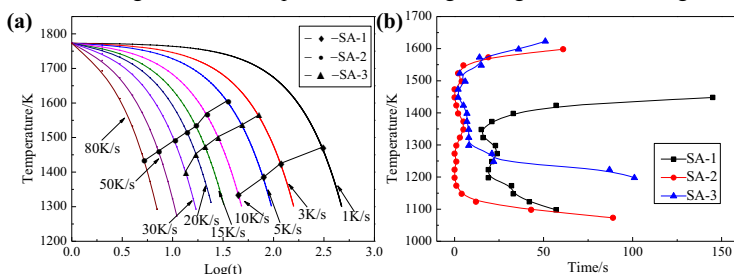


Figure 2. Crystallization behaviors of mold flux: a) CCT diagrams and b) TTT diagrams

Figures 2b and **3** show the TTT curves of the mold flux. The difference in the crystallization ranges of the samples was obvious. The crystallization temperature zone of SA-1 was in the range 1173–1373 K (900–1100 °C), and its crystallization incubation time was relatively longer. But the crystallization temperature zones of SA-2 and SA-3 were mainly within 1173–1523 K (900–1250 °C), indicating that the crystal phases of these slag samples changed by changing the slag system. Based on the crystal incubation time, it is concluded that the crystallization inclinations of SA-2 and SA-3 were obviously stronger than

that of SA-1. This indicates that after the steel–slag reaction, the lower SiO₂ content decreased the amount of network formers for molten slag, thus decreasing the degree of polymerization of the slag. Although a part of Al₂O₃ entered the silicate network as the network formers and formed the aluminosilicate structure, the slag was still easy to crystallize. This indicates that the stability of the formed aluminosilicate structure was not as good as that of the silicate structure. Therefore, at proper temperatures, the mold flux with an aluminosilicate structure first easily changed from the disordered structure to an ordered structure and then crystallized.

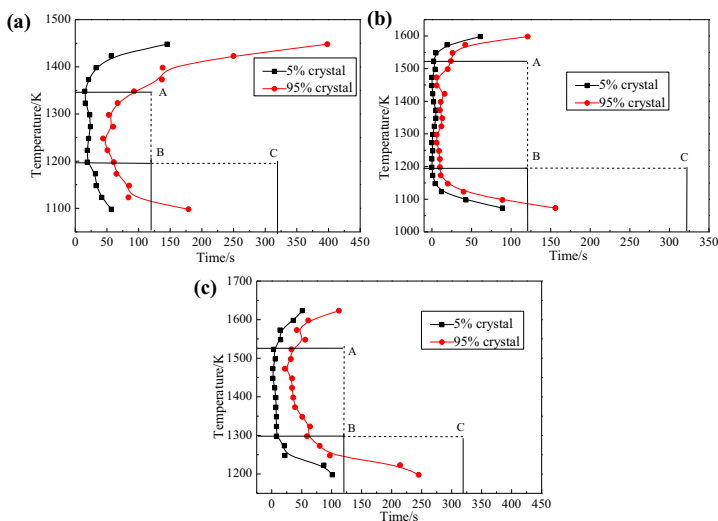


Figure 3. TTT diagrams of mold flux: a) SA-1, b) SA-2, and c) SA-3

C. Change in the crystal phases in the mold flux

The crystal morphologies and compositions of the slag samples after the TTT experiments were analyzed using SEM-EDS. The analyzing points are shown in **Figure 3**, where point A represents the crystal phases of the slag samples kept at a high temperature for 120 s, point B represents the crystal phases of the slag samples kept at a low temperature for 120 s. The temperature was different at different positions in the mold; some crystals formed in the high-temperature region moved to the low-temperature region because of the vibration of the mold. Thus, point C shows the crystal variation during the conversion from the crystals obtained after 120 s preservation at a high temperature to those at a low temperature for 200 s. **Figures 4–6** show the SEM images of the samples obtained at different temperatures. The crystal compositions of the different morphologies in the SEM were analyzed by EDS, and the results are listed in **Table 3**. Apparent differences were observed in the crystal morphologies and compositions between the samples obtained under different conditions. The main elements comprising the crystals were Ca, Si, and O. Therefore, the ratio, $X_{\text{CaO}}/X_{\text{SiO}_2}$, in the crystal was used to determine the crystal type in the slag sample (the existence of Au can be attributed to the spray-coating of gold). Moreover, small amounts of Al, Mg or Na elements were observed in crystals. As the slag–steel reaction progressed, the content of SiO₂ gradually decreased, thus increasing the ratio of $X_{\text{CaO}}/X_{\text{SiO}_2}$. The CaO·SiO₂ and 3CaO·2SiO₂ in SA-1 sample were converted to 2CaO·SiO₂, 3CaO·2SiO₂, and 2CaO·Al₂O₃·SiO₂ in SA-2 sample, whereas the main crystalline phases in SA-3 were 2CaO·SiO₂ and 2CaO·Al₂O₃·SiO₂. The crystallization of 2CaO·SiO₂ in SA-2 and SA-3

extended the crystallization temperature region on the TTT curve into the high-temperature region and formed crystals within the high-temperature region. This inevitably resulted in a thinner liquid slag layer between the mold and the steel shell, deteriorating the mold lubrication. Moreover, a comparison of **Figures A and C** shown for all the samples show that both the morphologies and compositions of crystals were significantly different. This indicates that the crystals crystallized at high temperatures (**Figure A**) would undergo crystal phase transition when they were kept at low temperatures (**Figure C**). Furthermore, after adding a small amount of other elements (Mg or Na) in the crystals of the same type, the morphologies changed significantly, as shown in SA-1 (A) and SA-3 (C).

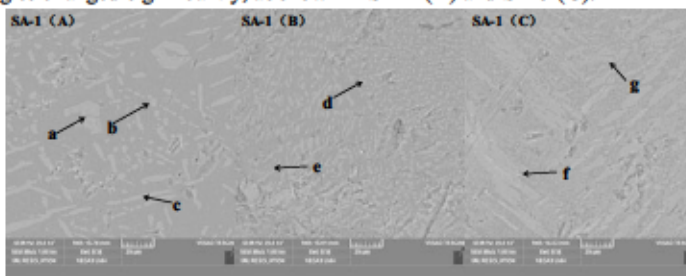


Figure 4. SEM of SA-1

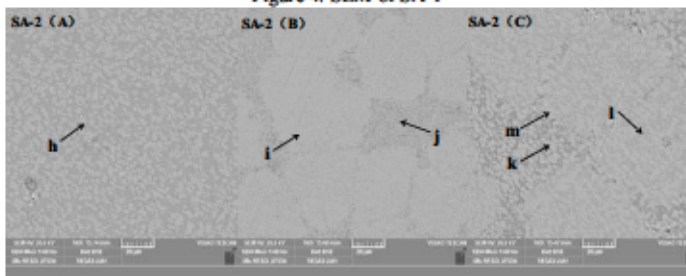


Figure 5. SEM of SA-2

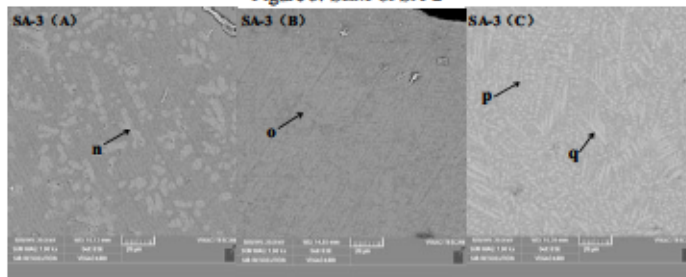


Figure 6. SEM of SA-3

According to the above analysis, the polymerization degree of the silicate network structure in the base slag, SA-1, was higher. Therefore, only small amounts of $3\text{CaO}\cdot 2\text{SiO}_2$ (Q_1) and $\text{CaO}\cdot \text{SiO}_2$ (Q_2) were formed rather than $2\text{CaO}\cdot \text{SiO}_2$ (Q_0). A relatively longer crystallization incubation time was required for the formation of $\text{CaO}\cdot \text{SiO}_2$; thus, it was more difficult to crystallize. As the slag–steel reaction progressed, the content of SiO_2 in SA-2 and SA-3 decreased, thus decreasing the polymerization degree of the silicate network. The main crystal phases in the slag were $2\text{CaO}\cdot \text{SiO}_2$ and a small amount of $3\text{CaO}\cdot 2\text{SiO}_2$. Although a large amount of Al_2O_3 was generated during the slag–steel reaction, only a part of AlO_4 was

absorbed on the silicate structure. This AlO_4 was unable to stabilize the silicate structure (connected to SiO_4 to form a three-dimensional polymerized network structure) and inhibited the crystallization of $2\text{CaO}\cdot\text{SiO}_2$ in the mold flux. Only a small amount of AlO_4 connected with SiO_4 and formed the Al-O-Si linkages, but this helped the formation of $2\text{CaO}\cdot\text{Al}_2\text{O}_3\cdot\text{SiO}_2$. Combined with the variation in the crystallization incubation time, after the silicate structure (SA-1) converted into the aluminosilicate structure (SA-2), the stability of the slag structure significantly decreased. Hence, the slag was prone to undergo structural rearrangements followed by crystallization. During the development of the CaO-SiO₂-based mold flux for high-Al steel casting, Al_2O_3 should replace SiO_2 as the network former in the slag to compensate the insufficient network former because of the consumption of SiO_2 during the slag-steel reaction. The CaO-SiO₂- Al_2O_3 -based mold flux after the slag-steel reaction also need the formed AlO_4 repair the network structure that connected the island-shaped SiO_4 into the three-dimensional polymerized network structure to inhibit the crystallization of the molten slag and provided the mold lubrication. Therefore, the key in developing the CaO-SiO₂-based mold flux for high-Al steel casting was the inhibition of its crystallization by adjusting the compositions of the mold flux to promote the participation of more AlO_4 in the mold flux after the reaction in repairing the network structure.

Table 3. EDS point analyses of mold flux for samples

Serial numbers	Weight percentage of elements (wt%)							$X_{\text{CaO}}/X_{\text{SiO}_2}$	Crystal phase
	O	Si	Ca	Al	Mg	Na	Au		
a	34.70	17.69	34.45		6.92		6.24	1.36	$3\text{CaO}\cdot 2\text{SiO}_2$
b	37.55	18.16	32.66		3.17	1.81	6.65	1.26	$3\text{CaO}\cdot 2\text{SiO}_2$
c	36.39	17.52	36.49		2.62		6.98	1.46	$3\text{CaO}\cdot 2\text{SiO}_2$
d	40.31	18.97	29.56	1.32	2.15	2.61	5.08	1.09	$\text{CaO}\cdot\text{SiO}_2$
e	39.52	17.17	30.80	1.12	5.30		6.09	1.26	$3\text{CaO}\cdot 2\text{SiO}_2$
f	34.98	16.88	35.57		5.68		6.89	1.48	$3\text{CaO}\cdot 2\text{SiO}_2$
g	33.44	20.04	32.44		3.52	3.33	7.23	1.13	$\text{CaO}\cdot\text{SiO}_2$
h	37.72	16.05	38.92	1.40			5.91	1.70	$2\text{CaO}\cdot\text{SiO}_2$
i	35.96	15.21	32.36	7.29	2.25		6.93	1.49	$2\text{CaO}\cdot\text{Al}_2\text{O}_3\cdot\text{SiO}_2$
j	38.62	14.55	28.91	3.34	2.65	5.05	6.88	1.39	$3\text{CaO}\cdot 2\text{SiO}_2$
k	34.88	16.36	30.83	4.13	2.57	4.59	6.64	1.32	$3\text{CaO}\cdot 2\text{SiO}_2$
l	37.07	13.18	29.12	12.10	1.87		6.66	1.55	$2\text{CaO}\cdot\text{Al}_2\text{O}_3\cdot\text{SiO}_2$
m	37.12	14.87	36.26	2.36	2.94		6.45	1.71	$2\text{CaO}\cdot\text{SiO}_2$
n	34.95	15.74	37.40				11.91	1.66	$2\text{CaO}\cdot\text{SiO}_2$
o	32.51	11.46	30.72	11.62	2.04		11.65	1.88	$2\text{CaO}\cdot\text{Al}_2\text{O}_3\cdot\text{SiO}_2$
p	36.14	13.51	38.29	5.20			6.86	1.98	$2\text{CaO}\cdot\text{SiO}_2$
q	33.94	15.27	40.53	2.76			7.50	1.86	$2\text{CaO}\cdot\text{SiO}_2$

Conclusion

During the high-Al steel casting, the original CaO-SiO₂-based mold flux converted to the CaO-SiO₂- Al_2O_3 -based mold flux with the progress in the slag-steel reaction, and the molten slag structure changed from the original silicate structure to the aluminosilicate structure. The contents of Q_2 and Q_3 significantly decreased, the polymerization degree of the

network structure decreased, the crystallization incubation time was shortened, and the crystalline phases were converted from $3\text{CaO}\cdot 2\text{SiO}_2$ and $\text{CaO}\cdot \text{SiO}_2$ to $2\text{CaO}\cdot \text{SiO}_2$ and $2\text{CaO}\cdot \text{Al}_2\text{O}_3\cdot \text{SiO}_2$ during this conversion. Moreover, the crystallization inclination significantly increased. Although a certain amount of AlO_4 participated in the formation of the network structure, the instability of the aluminosilicate structure cannot inhibit the crystallization of $2\text{CaO}\cdot \text{SiO}_2$ which increased the crystallization property, thus decreasing the lubrication. Therefore, the key in developing the $\text{CaO}\cdot \text{SiO}_2$ -based mold flux for high-Al steel casting was to inhibit the crystallization of $\text{CaO}\cdot \text{SiO}_2\text{-Al}_2\text{O}_3$ -based mold flux by adjusting the compositions of the mold flux to promote more AlO_4 participate in repairing the network structure.

Acknowledgement

This study was supported by the National Natural Science of China (Grant Nos. 51274260 and 51574050)

References

- [1] Street S, James K, Minor N, Roelant A, Tremp J. "Production of High-Aluminum Steel Slabs" [J]. *Iron & Steel technology*, 2008; 5(7): 38-49.
- [2] Grassel O, Kruger L, Frommeyer G, Meyer L W. "High strength Fe-Mn-(Al,Si) TRIP/TWIP steels development-properties-application"[J]. *International journal of plasticity*, 2000; 16: 1391-1409.
- [3] Turteltaub S, Suiker A S J. "Transformation-induced plasticity in ferrous alloys"[J]. *Journal of the mechanics and physics of solids*, 2005; 53: 1747-1788.
- [4] Kim G H, Sohn I. "Effect of Al_2O_3 on the viscosity and structure of calcium silicate-based melts containing Na_2O and CaF_2 "[J]. *Journal of Non-Crystalline solids*, 2012; 358: 1530-1537.
- [5] Cho J W, Blazek K, Frazee M, Yin H. "Assessment of $\text{CaO}\text{-Al}_2\text{O}_3$ Based Mold Flux System for High Aluminum TRIP Casting"[J]. *ISIJ International*, 2013;53 (1): 62-70.
- [6] Lu B, Chen K, Wang W, Jiang B. "Effects of Li_2O and Na_2O on the Crystallization Behavior of Lime-Alumina-Based Mold Flux for Casting High-Al Steels"[J]. *Metall and Materi Trans B*, 2012; 43B: 424-430.
- [7] Gao J X, Wen G H, Sun Q H, Tang P, Liu Q. "The Influence of Na_2O on the Solidification and Crystallization Behavior of $\text{CaO}\text{-SiO}_2\text{-Al}_2\text{O}_3$ -Based Mold Flux"[J]. *Metall and Materi Trans B*, 2015; 46B: 1850-1859.
- [8] Kim G H, Kim C S, Sohn I. "Viscous Behavior of Alumina Rich Calcium-Silicate Based Mould Fluxes and Its Correlation to the Melt Structure"[J]. *ISIJ International*, 2013; 53: 170-176.
- [9] Kim T S, Park J H. "Structure-Viscosity Relationship of Low-silica Calcium Aluminosilicate Melts"[J]. *ISIJ International*, 2014; 54: 2031-2038.
- [10] McMillana P, Pirioub B, Navrotskya A. "A Raman spectroscopic study of glasses along the joins silica-calcium aluminate, silica-sodium aluminate, and silica-potassium aluminate"[J]. *Geochimica et Cosmochimica Acta*, 1982; 46 (11): 2021-2037.
- [11] Neuville D R, Cormier L, Massiot D. "Al coordination and speciation in calcium aluminosilicate glasses: Effects of composition determined by ^{27}Al MQ-MAS NMR and Raman spectroscopy"[J]. *Chemical Geology*, 2006;229: 173-185.
- [12] Fu X J, Wen G H, Liu Q, Tang P, Li J Z, Li W. "Development and Evaluation of $\text{CaO}\text{-SiO}_2$ Based Mould Fluxes for Casting High Aluminum TRIP Steel"[J]. *Steel research international*, 2015;86(2): 110-120.

Fundamental investigations for the design of fluorine free mold powder compositions

Irmtraud Marschall^{1,2}, Xiao Yang³, Harald Harmuth¹

¹Montanuniversitaet Leoben, Chair of Ceramics; Peter-Tunnerstraße 5; Leoben, 8700, Austria

²K1-MET GmbH; Stahlstraße 14; Linz, 4020, Austria

³Zhengzhou University, School of Materials Science and Engineering;
Kexue Road 100; Zhengzhou, 450001, China

Keywords: mold powder, fluorine free, crystallization

Abstract

The influence of the CaO/SiO₂ ratio on flux viscosity at 1300°C, break temperature and crystallization was investigated.

The thermo-chemical software FactSage was used for the calculation of the viscosity, the equilibrium phase content and the liquidus temperature. Based on these results, two sample series with 8.8 wt% TiO₂, 5 wt% B₂O₃ and CaO/SiO₂ ratios from 0.8-1.2 were manufactured. Series M1 contained Li₂O which was replaced by a higher content of Na₂O for F-free mixtures in series M2. The viscosity and break temperature were determined through rotational viscometry, the crystallization temperature and crystalline fraction by a so called Furnace Crystallization Test, a macro style differential thermal analysis which enables a mineralogical investigation of the samples afterwards.

The experiments exhibited that the break temperature, the liquidus temperature and the crystalline fraction rose with increasing C/S ratio while the viscosity decreased for both sequences.

Introduction

Commercial mold powders are synthetic slags that usually contain SiO₂, CaO, Na₂O, CaF₂, C, etc. [1,2,3]. Fluorine is an essential component to decrease liquidus temperature and viscosity of the mold slag, and it further promotes the crystallization of the slag film through the formation of cuspidine [1,4,5]. However, fluorine is undesirable concerning health and environmental issues. Fluorine emissions may bring about corrosion and the acidification of cooling water [6]. Thus the investigation of mold powders without fluorine has become a research area of interest.

It is noted that flux components as B₂O₃, TiO₂, Li₂O and Na₂O are, to some extent, alternatives to fluorine on decreasing melting point and viscosity [7,8,9,10].

In this study the influence of the CaO/SiO₂ (C/S) ratio on flux viscosity at 1300 °C, break temperature and crystallization of laboratory slags, situated in the CaO-SiO₂-Al₂O₃-Na₂O-B₂O₃-system was investigated.

Experimental

Chemical Composition

The thermo-chemical software FactSage was used for the calculation of the viscosity, the equilibrium phase content, and the liquidus temperature. From these calculations two series of samples with chemical compositions given in Table I followed.

Table I. Chemical composition (mass%) of the samples investigated

	CaO/SiO ₂	CaO+SiO ₂	TiO ₂	Na ₂ O	B ₂ O ₃	MgO	Al ₂ O ₃	Li ₂ O	FeO
M1	0.8-1.2	68	8.8	8.0	5.0	4.5	3.5	1.2	1.0
M2	0.8-1.2	68	8.8	9.2	5.0	4.5	3.5	-	1.0

Sample Preparation

The mixtures were made from purified oxides and carbonates (reagent grades with at least $\geq 98\%$ purity). CaCO₃, Na₂CO₃ and Li₂CO₃ were added to provide CaO, Na₂O, Li₂O respectively and Fe₂O₃ was added as a source of FeO. For decarburization the samples were annealed within ceramic containers in a high temperature chamber furnace at 700 °C for 12 hours. Subsequently the samples were melted in covered platinum crucibles at 1400 °C in a preheated chamber furnace for 15 min, afterwards poured into a steel mold and quenched to room temperature with cold water to obtain glassy pieces. Finally the samples were ground into powder and split up for the consecutive tests.

Inclined Plane Test

Determining the ribbon length of a viscous fluid after pouring on an inclined plane is a relatively simple, practical rheometric test [11]. Slags with lower viscosities will produce a longer ribbon, if the samples' solidification temperatures are equal or in the same range. Thus, the Inclined Plane Test was used in this study to roughly evaluate the viscosities of fluxes at 1300 °C. 15 g of a sample were put into a platinum crucible and liquefied at 1490°C in a high temperature chamber furnace for 15 min. Then the platinum crucible with the molten slag was removed and quickly inserted into a cylinder-shaped container. The mold slag was poured out immediately to let the slag flow down the plane and cool at ambient temperature, whereas the temperature of the slag upon impinging was controlled by a thermocouple and averaged 1300 °C. Finally the length of solidified specimen was measured.



Figure 1. The device for the Inclined Plane Test.

Rotational Viscometry

The dynamic viscosities and the break temperatures of the sample fluxes were evaluated with a commercial high temperature rotational viscometer. The crucible as well as the rotor were made of platinum. 27 g of the sample were heated within 30 min to 1400 °C and measured at a cooling rate of 10 °C/min. During the experiment the furnace chamber was purged with argon.

Furnace Crystallization Test

The Furnace Crystallization Test (FCT) is a sort of a big scale differential thermal analysis and was performed in a high temperature chamber furnace as shown in Figure 2. A sample weight of 27 g was put in one platinum crucible and the equal mass of alumina was used as a reference material in a second crucible. The crucibles were heated up to 1350 °C and held for 15 min to ensure that the powders became completely liquid and then the furnace was allowed to cool to room temperature at a cooling rate of 10 °C/min. The temperatures of the F-free mold powder and the alumina were measured with type S thermocouples and recorded via a data logger at intervals of 30 s.



Figure 2. Set up of the Furnace Crystallization Test.

After this procedure, the crucible was turned upside down to retrieve the solidified specimen, which was cut across the platinum wire into two pieces. One half was crushed into powder and analyzed by X-ray diffraction (XRD), the other part was polished for reflected light microscopy and scanning electron microscopy (SEM) investigations.

Simultaneous Thermal Analysis

Simultaneous thermal analysis (STA) measurements were carried out in order to determine the liquidus temperature and the crystallization temperature of the specimens. 80 mg mixture were put into a platinum crucible together with a platinum loop with a diameter of 2 mm to enhance crystallization. The crucible was covered with a platinum lid during the measurement process. The measurement was performed with a heating rate of 20 °C/min and a cooling rate of 10 °C/min, the sample chamber was purged with nitrogen.

Results and Discussion

Viscosity

The results of the rotational viscometry at 1300°C are given in Figure 3a; they are somewhat lower than those predicted by FactSage with the data available at the beginning of 2015. The ribbon length from inclined plane test as function of basicity (C/S) is shown in Figure 3b. As

expected, both methods exhibit that the viscosities of the fluxes at 1300°C decrease with the increase of basicity and mixtures with Li₂O have lower viscosities than mixtures without Li₂O. CaO, Na₂O and Li₂O all act as network modifiers within the silicate structure. In M2 1.2mass% Na₂O are replaced by 1.2 mass% Li₂O. Due to the lower molecular weight of Li the molar amount of Li₂O is more than double of the Na₂O reduction and thus increases the available network modifiers. Due to the viscosity decrease with rising C/S ratio only the samples with basicities ranging up to 1.1 remain glassy during the Inclined Plane Test. Mixtures with C/S of 1.2 have a higher crystallization tendency, and the cooling rate was too low to prevent the samples from crystallizing at the surface.

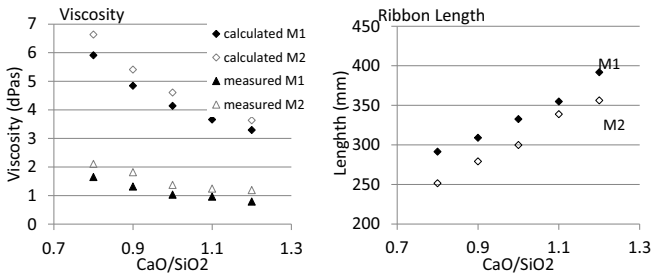


Figure 3. Viscosity at 1300°C (a) and the ribbon lengths (b) of different F-free mixtures after Inclined Plane Test in dependency of basicity (C/S).

Solidification

Solidified samples after the Furnace Crystallization Test are pictured in Fig. 4. The black parts of the specimen are glassy while the yellow ones contain crystal phases. For mixtures with C/S of 0.8 crystal phases formed only along the platinum wire. For a ratio of 0.9 this crystalline mass slightly increased. With a value of 1.0 it could be observed that the interface of the samples became yellow, which indicated that a lot of crystals were formed around the surface, but still a large amount of glass phase existed inside the samples. For C/S of 1.1, just small amounts of glass phase appeared in the middle of the samples and no glass phase could be observed with C/S=1.2. Therefore, it can be concluded that the tendency for crystallization increases with increasing slag basicity. Due to the fact that the amount of crystals within samples of series M1 and M2 and a basicity of 0.8, 0.9 and 1.0 was that small, no crystal phase could be precisely identified through XRD. In Figure 5 XRD patterns of series M2 are given. For C/S of 1.1 and 1.2 combeite (NaCaSiO₄), perovskite (CaTiO₃), nepheline ((Na,K)AlSiO₄) and a calcium borate silicate (Ca₁₁B₂Si₄O₂₂) could be determined in both series.

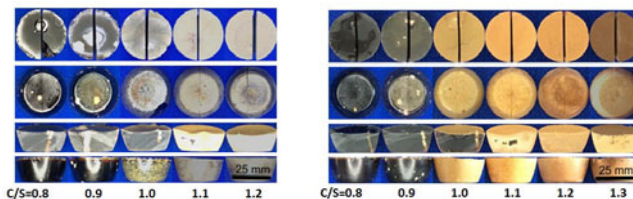


Figure 4. Samples after FCT test M1 left, M2 right.

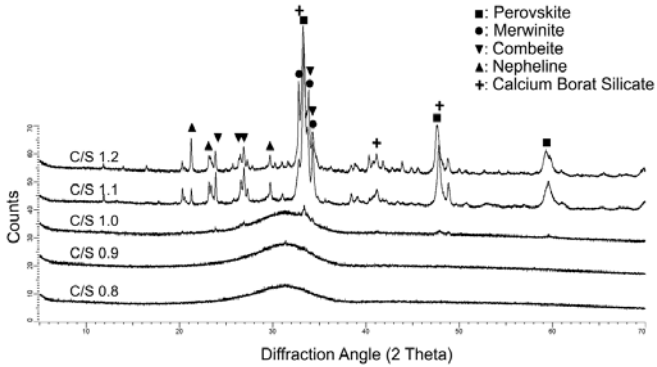


Figure 5. X-ray diffraction spectra of series M2 after Furnace Crystallization Test.

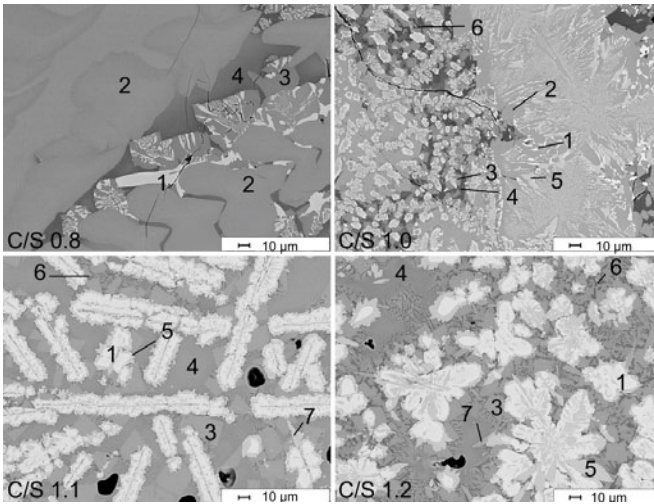


Figure 6. Back scattered electron images of series M2 after FCT. Phases: perovskite (CaTiO_3) (1), wollastonite (CaSiO_3) (2), combeite (NaCaSiO_4) (3), amorphous phase (4), calcium borate silicate $\text{Ca}_{11}\text{B}_2\text{Si}_4\text{O}_{22}$ (5), nepheline (Na,K)AlSiO_4) (6) and merwinite ($\text{Ca}_3\text{MgSi}_2\text{O}_8$)(7).

Microstructure

As mentioned before, with M1 and M2 C/S 0.8, 0.9 and 1.0 some crystals appeared in the thermocouple area since heterogeneous nucleation occurred at the platinum wires. In both series for C/S of 0.8 and 0.9 wollastonite (CaSiO_3) was formed first and became the main crystalline phase, followed by perovskite, the brightest phase visible in Fig 6. Finally trigonal combeite

crystallized. For samples with a C/S ratio of 1.0 perovskite became the first phase to form and $\text{Ca}_{11}\text{B}_2\text{Si}_4\text{O}_{22}$ and nepheline were formed additionally.

Raising the C/S ratio to 1.1 led to a drastic change in the crystal formation. In Fig.6 perovskite is now visible as large dendroid crystals surrounded by merwinite and $\text{Ca}_{11}\text{B}_2\text{Si}_4\text{O}_{22}$. Moreover $\text{Ca}_{11}\text{B}_2\text{Si}_4\text{O}_{22}$ became the main crystalline phase, combeite and some nepheline formed additionally. Large merwinite crystals grew in contact with the platinum wire. Wollastonite could not be observed any more. Finally, raising the C/S ratio to 1.2, perovskite and $\text{Ca}_{11}\text{B}_2\text{Si}_4\text{O}_{22}$ increased their size, as can be seen from Figure 8. Again combeite appeared around the perovskite and $\text{Ca}_{11}\text{B}_2\text{Si}_4\text{O}_{22}$ is framed by nepheline and merwinite.

The increase of the crystalline portion and the crystal size is caused by the function of CaO as a network modifier, which weakens the glass structure. On the other hand lower viscosities promote diffusion processes and therefore crystal growth. Since the amount of TiO_2 is $> 6.7\%$, perovskite was always present in line with Xin [10].

Melting and Solidification

As can be seen from Fig. 7 the impact of the C/S ratio on the liquidus temperatures, as measured by STA exceeds the FactSage prediction (which was not performed with a database optimized for the boron containing compositions). Furthermore, in accordance with [12] substitution of Na_2O for LiO_2 led to an increase of the liquidus temperature.

To determine the crystallization temperatures, the FCT and STA were applied and their results compared in Fig.7. The FCT results display only a slight increase of the crystallization temperature with rising C/S ratio, whereas the STA temperature values are lower for C/S of 0.8 to 1.0 and much higher for C/S above 1.0. The reason for this discrepancy is the characteristic of each method. Whereas with the FCT the thermocouple, which promotes crystallization, is inserted into the sample, the thermocouple of the STA is located under the crucible. In the first case only a small area around the thermocouple is measured, where crystals always form first, while with the STA the whole sample mass may contribute to the measurement. STA measurements represent a higher undercooling thus leading to lower results. If crystallization occurs in the bulk volume, temperature results of both methods are similar. On the other hand, due to the higher sensitivity of the STA device very small peaks of first crystallization, most likely from perovskite, which are not the main peaks, could be detected. These peaks are not visible in the FCT curves. The lower viscosity and therefore faster diffusion processes in the liquid of the samples with LiO_2 may also be the reason why the crystallization temperatures of M1 were higher than those of M2.

Fig. 8a displays selected curves from which it can also be deduced that more than one crystal phase has formed during the viscosity measurement in some cases, especially with the samples of C/S ratio of 1.1 and 1.2. But in these two cases the crystallization of the first precipitating phase had an insignificant impact on the viscosity curve progression. This was the reason why for Fig. 8b not the first but the break temperatures with the most distinguished rise in viscosity, so to say the main break temperatures, were chosen. From this it follows that, in accordance with the crystallization temperatures, the samples with Li_2O show the higher break temperatures and that the main break temperature will rise with increasing C/S ratio as long as the main break temperature is the first break temperature.

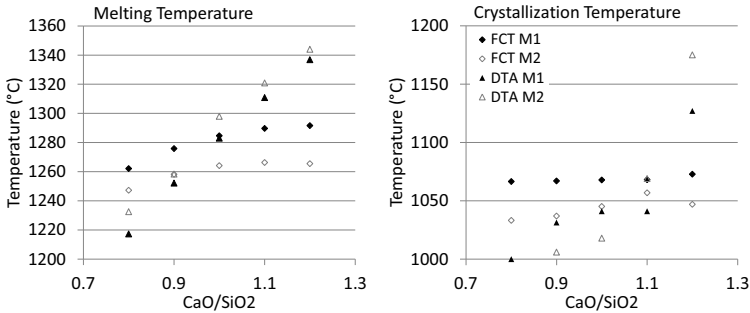


Figure 7. Melting (a) and b) Crystallization temperatures (b) received from STA and Furnace Crystallization Test.

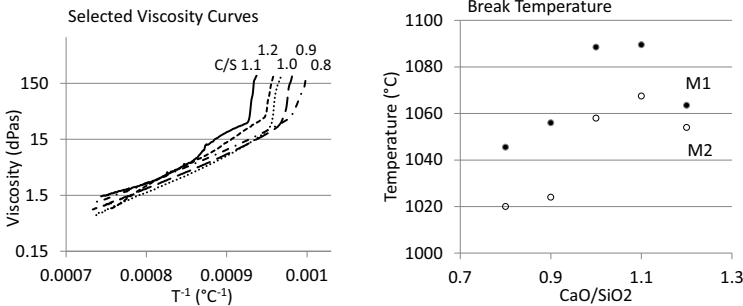


Figure 8. Selected viscosity curves of M1 (a) and main break temperatures (b).

Conclusion

From this work can be concluded that a rise of the C/S ratio leads to an increase of the melting and crystallization temperatures. Furthermore the amount of crystal portion formed can be controlled by the CaO/SiO₂ ratio. Especially the amount, the shape and the size of perovskite correlate positively with the CaO/SiO₂ ratio. For a C/S ratio of 1.0 to 1.2 perovskite supports heterogeneous nucleation of other phases. Additional crystalline phases form dependent on the CaO/SiO₂ ratio. LiO₂ enhances crystallization due to its action as a network modifier.

Acknowledgement

The research program of the “metallurgical competence center” (K1-MET) is supported within the Austrian program for competence centers COMET (Competence Center for Excellent Technologies) with funds of the Federal Ministry for Transport, Innovation and Technology, the Federal Ministry of Economy, the province of Upper Austria and Styria, the Styrian Business Promotion Agency, the Tyrol and the Tyrolian Future Foundation. Moreover this work was supported by the industrial partners voestalpine Stahl GmbH and RHI AG.

References

1. J.A. Kromhout, "Mold powders for high speed continuous casting of steel" (PH.D. thesis, Delft University of Technology, 2011)
2. J.A. Bothma, P.C. Pistorius, "Heat transfer through mould flux with titanium oxide additions," *Ironmaking & Steelmaking*, 34 (6) (2007), 513-520.
3. K.C. Mills, A.B. Fox, Z. Li, et al., "Performance and properties of mould fluxes," *Ironmaking & steelmaking*, 32 (1) (2005), 26-34.
4. Y. Meng et al., "Mould slag property measurements to characterize CC mould-shell gap phenomena," *Canadian Metallurgical Quarterly*, 45 (1) (2006), 79-94.
5. J.H. Park, D.J. Min, H.S. Song, "The effect of CaF₂ on the viscosities and structures of CaO-SiO₂-(MgO)-CaF₂ slags," *Metallurgical and Materials Transactions B*, 33 (5) (2002), 723-729
6. J.L. Klug, et al., "Fluorine-Free Mould Powders for Billet Casting Technological Parameters and Industrial Tests," *Steel research international*, 83 (8) (2012), 791-799.
7. E. Benavidez, L. Santini, M. Valentini and E. Brandaleze, "Influence of different oxides on the viscosity of fluorine-free mold fluxes," *Procedia Material Science*, 1 (2012), 389-396.
8. Z. Zuotai, G. Wen, Y. Zhang, "Crystallization behavior of F-free fluxes," *International Journal of Minerals, Metallurgy, and Materials*, 18 (2) (2011), 150-158.
9. S.Y. Choi, D.H. Lee, D.W. Shin, et al., "Properties of F-free glass system as a mold flux: viscosity, thermal conductivity and crystallization behavior," *Journal of non-crystalline solids*, 345 (2004), 157-160
10. Q. Xin, G. H. Wen, P. Tang. „Investigation on heat transfer performance of fluorine-free and titanium-bearing mold fluxe," *Journal of Non-Crystalline Solids*, 352 (52) (2008) 5444-5452
11. P. Coussot, S. Boyer, "Determination of yield stress fluid behaviour from inclined plane test," *Rheologica acta*, 34 (6) (1995), 534-543
12. D. Janke, T. Schulz T., M. Tonelli et al., "Improvement of casting fluxes and slags by minimisation of environment: polluting and corrosive constituents (fluorine, alkali components)" EUR 20645, (2003) 1-137

COLD-FINGER MEASUREMENT OF HEAT TRANSFER THROUGH SOLIDIFIED MOLD FLUX LAYERS

Karina Lara Santos Assis¹, P. Chris Pistorius¹

¹Center for Iron and Steelmaking Research, Department of Materials Science & Engineering, Carnegie Mellon University; 5000 Forbes Avenue; Pittsburgh, PA, 15213, U.S.A.

Keywords: Mold flux, Continuous Casting, Heat Transfer, Cold Finger

Abstract

The thermal resistance between the cast strand and the copper mold in continuous casting is dominated by the conduction resistance through the partially solidified mold flux layer and the contact resistance between the solidified mold flux and the mold. In the cold-finger approach, a freeze layer of mold flux is grown on a water-cooled probe immersed in molten flux. In principle, the thickness of the solid layer and the steady-state heat flux can be used to estimate conductivity and contact resistance. Lower-basicity fluxes generally give somewhat lower heat fluxes under these conditions and result in formation of glassy films. Glassy films are generally significantly thinner than crystalline films, because of the higher thermal conductivity of crystalline films. A potential approach to estimate thermal conductivity and contact resistance from transient changes in solid film thickness and heat flux is outlined.

Introduction

Of the multiple roles that mold flux performs in the continuous caster mold, control of heat transfer is possibly the least understood. In part, this is due to the significant experimental difficulty of measuring the heat flux through a controlled thickness (of the order of millimeters thick) of mold flux, under conditions relevant to caster molds. Heat fluxes in casters range from around 1 MW/m² for slab casters, to 4 MW/m² for thin-slab casters, and the typical temperature difference across the thickness of the mold flux is around 1000°C. Current mold flux compositions are also unstable at temperature, tending to lose fluorides by evaporation. The mold flux consists of multiple phases: liquid next to the strand surface, often glassy solid next to the mold, fully or partially crystalline in between, and with gas bubbles captured within the flux layer and at the flux-mold interface.

Given this difficult and complex combination, it is not surprising that there is disagreement regarding the main factors which control heat transfer: whether radiative heat transfer through the flux is significant compared with conduction, and whether conduction or the interfacial resistance (between mold flux and mold) is the main resistance to heat transfer.

As examples of the apparently contradictory results reported in the literature, Yamauchi *et al.* [1] stated that the interfacial resistance (affected by roughness of the mold flux film at its interface with the mold) is the main factor controlling heat transfer, whereas Tsutsumi *et al.* [2] found the conduction resistance to be larger, at least for films in the practically important thickness range

of thicker than 0.5 mm, and Kromhout *et al.* [3] concluded that surface roughness and interfacial resistance are of lesser importance. Of course, some of this lack of agreement may reflect differences in the mold fluxes which were studied, but there does appear to be a gap in the fundamental knowledge of what controls heat transfer, and how this can be measured.

Cold-finger measurements [4] have been used to study solidification of mold flux under more realistic casting conditions, and correlate its thermal properties with morphology and composition. In this method, a water-cooled copper probe is immersed in molten mold flux with a controlled flux temperature. The temperature differential of the cooling water is used to determine the heat transfer rate at the cold face of the copper probe; under steady-state conditions, the heat transfer rate is the same at the hot and cold faces of the copper probe, and at the hot face of the solidified mold flux layer.

For heat transfer across mold flux, the boundary conditions in cold-finger measurements differ in important ways from those in continuous casters, as illustrated schematically in Figure 1. The main difference is that the total thickness of the mold flux layer is around 1 mm in continuous casters, whereas in the cold-finger measurements the solid film thickness is unconstrained; the solid film grows until steady-state heat transfer is attained.

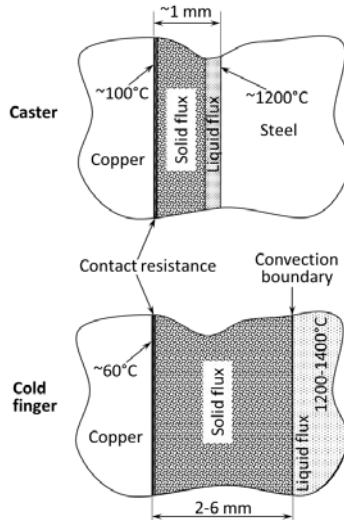


Figure 1. Schematic of the main differences in boundary conditions for heat transfer across the mold flux in the continuous caster (upper drawing) and in cold-finger measurements (lower drawing).

At steady state, the heat transfer rate across the solidified film is equal to the rate of convective heat transfer between the liquid flux and solid layer. Analysis of a range of mold flux compositions (spanning the range of basicities of industrially used fluxes) indicated that the temperature at the solid-liquid interface is close to the solidus temperature [5], similar to what

was concluded by Fallah-Mehrjardi et al. [6]. This means that the steady-state heat transfer rate is given by Equation (1):

$$q = h_{\text{flux}}(T_{\text{bulk}} - T_{\text{solidus}}) \quad (1)$$

where q is the heat flux (W/m^2), h_{flux} ($\text{W}/\text{m}^2\text{K}$) is the convective heat transfer coefficient between the solid and liquid mold flux, T_{bulk} (K) is the (controlled) temperature of the liquid mold flux, and T_{solidus} (K) is the solidus temperature of the mold flux.

As shown by Equation (1), the steady-state heat flux contains no direct information on the thermal conductivity of the solid mold flux layer, nor the contact resistance between the solid mold flux layer and the copper probe. These values, which are the ones of importance to heat transfer in the continuous caster mold, can be extracted from cold-finger measurements, but this requires additional analysis of the results. The directly measured heat transfer rate in cold-finger measurements is not useful in itself for comparing heat transfer between different mold fluxes. In this paper, results of a simple one-dimensional heat transfer model is used to illustrate the principles of the methods which can be used to obtain the thermal resistance of solid mold flux layers from cold-finger measurements.

Heat transfer model

The expected response of the cold-finger measurement to changes in the heat transfer conditions was predicted with a simple transient, finite difference, one-dimensional purely heat transfer model; the main features of the model are shown in Figure 2. This was a pure explicit finite-difference heat-transfer model. The temperature at the liquid-solid interface was taken to be the melting point (solidus temperature) of the mold flux; the position of the solid-liquid interface was tracked explicitly.

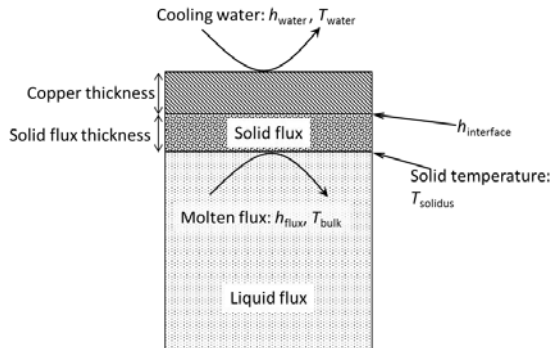


Figure 2. Main elements of 1D transient model of cold-finger measurement.

The default conditions assumed in the calculations are given in Table I. The initial conditions were taken to be those when the cold finger is first immersed into the molten mold flux, i.e. cold copper (at the temperature of the cooling water) with zero thickness of solidified flux.

Results and discussion

Typical results are shown in Figures 3 and 4. The change with time of the calculated heat flux at the cold face of the copper has the same shape as that measured experimentally [4,7,8], namely an increase to a peak value, with a subsequent decrease to a steady-state value. The initial increase in heat flux results from the thermal inertia of the copper layer between the cooling water and the mold flux; the heat flux at the interface between the copper probe and the mold flux is highest at time zero and decreases over time to approach steady state. Figure 3 illustrates that the steady-state heat flux is proportional to the convective heat transfer coefficient between the molten flux and solid layer (see also Equation [1]); the interfacial resistance (between the probe and the solid flux layer) and the thermal conductivity of the solid layer have no effect on the steady-state heat transfer rate but do affect the peak rate somewhat (Figure 4).

Because the thermal resistances (conduction and interfacial resistances) of the solidified mold flux do not affect the steady-state heat flux, additional measurements are required to obtain these resistances. Based on the relationship in Equation (2), the steady-state thickness of the solid flux film is a useful measurement:

$$L_{\text{solid}} = k_{\text{solid}}[(T_{\text{solidus}} - T_{\text{water}})/q - L_{\text{Cu}}/k_{\text{Cu}} - 1/h_{\text{water}} - R_{\text{int}}] \quad (2)$$

where k_{solid} is the thermal conductivity of the solid flux layer, T_{solidus} the solidus temperature of the mold flux, T_{water} the cooling water temperature, q the steady-state heat flux, L_{Cu} the thickness of the copper probe and k_{Cu} is thermal conductivity, h_{water} the convective heat transfer coefficient between the cooling water and the copper probe, and $R_{\text{int}}=1/h_{\text{int}}$ the contact resistance between the solid flux film and the copper probe.

Table I. Default conditions for 1D cold-finger model calculations

Copper					
k_{Cu} (W/mK)	c (J/kgK)	ρ (kg/m ³)	L_{Cu} (m)	T_i (°C)	
400	385	8960	0.005	25	

Mold flux					
k_{solid} (W/mK)	ΔH_f (kJ/kg)	ρ (kg/m ³)	T_f (°C)	T_{bulk} (°C)	h_{flux} (W/m ² K)
1	559	2500	1200	1500	1500

Interface	Cooling water	
h_{int} (W/m ² K)	T_w (°C)	h_{water} (W/m ² K)
1000	25	20000

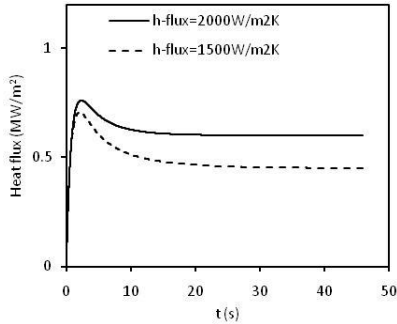


Figure 3. Calculated effect of the heat transfer coefficient between solid and liquid flux on the measured heat flux at the cold face of the copper probe.

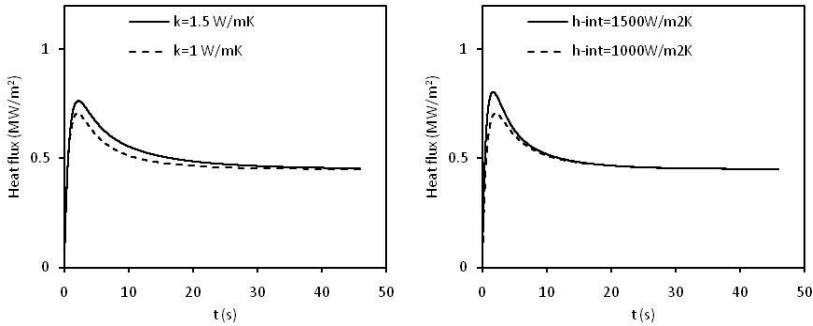


Figure 4. Predicted effects of differences in the thermal conductivity of the solidified flux (left) and interfacial resistance (right) on the measured heat flux.

Equation (2) shows that, for a given set of measurements of steady-state heat flux and solid film thickness, different pairs of values of interfacial resistance and thermal conductivity of solid can fit the results; it is not possible to find interfacial resistance and thermal conductivity from a single steady-state measurement.

However, one possible approach is to perform measurements at different bulk temperatures. The solid layer is thinner for higher bulk liquid flux temperatures; the change in solid-layer thickness with temperature depends on the balance between conduction and interfacial resistances; see Figure 5.

This predicted effect of bulk temperature on solid-layer thickness was tested experimentally using two mold fluxes, with higher and lower basicity; compositions are given in Table II. Details of the measurement approach are given elsewhere [5,7]. The solid layers formed from the higher-basicity mold flux were largely crystalline (with cuspidine the major phase) whereas the

lower-basicity mold flux formed glassy solid layers. Measured film thicknesses are given in Figure 6, with fitted thermal properties listed in Table III.

Table II. Compositions (mass percentages) of mold fluxes used to illustrate effect of bulk temperature on cold-finger measurements

	CaO	CaF ₂	SiO ₂	Li ₂ O	Na ₂ O	MgO	Al ₂ O ₃	Fe ₂ O ₃	MnO
Higher B	33.1	24.5	30	5.4	0.9	0.5	3.4	2.1	0
Lower B	15	20.5	38.7	0	17.5	1.3	3.3	0	3.1

Table III. Fitted values for Figure 6.

	\dot{h}_{flux} (W/m ² K)	k_{solid} (W/mK)	R_{int} (m ² K/W)
Higher B	1500	2.8	6×10^{-4}
Lower B	1400	1	3×10^{-4}

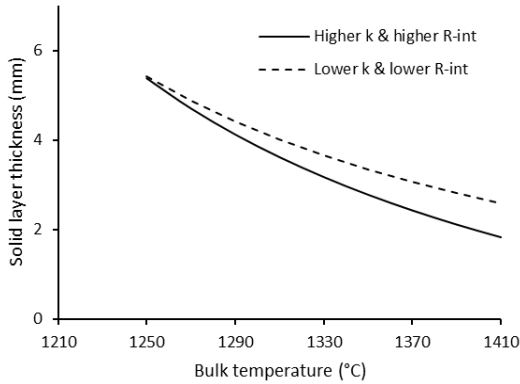


Figure 5. Illustration of the principle behind using different bulk temperatures to evaluate the film conductivity (k_{solid}) and interfacial resistance (R_{int}): the change in steady-state solid film thickness with bulk temperature depends on the balance of k_{solid} and R_{int} (calculated $k_{\text{solid}}=2.8$ W/mK and $R_{\text{int}}=0.6 \times 10^{-3}$ m²K/W, or $k_{\text{solid}}=3.5$ W/mK and $R_{\text{int}}=1 \times 10^{-3}$ m²K/W; $h_{\text{flux}}=1500$ W/m²K; $T_{\text{solidus}}=1000^\circ\text{C}$; other values as in Table I).

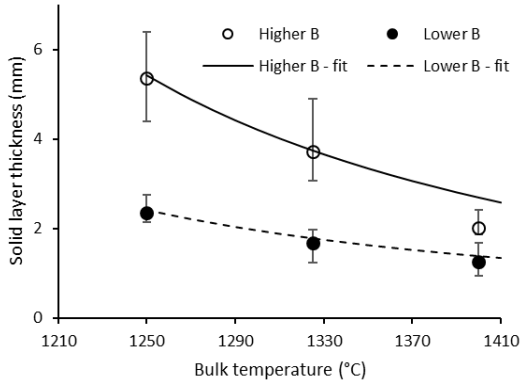


Figure 6. Measured solid layer thickness (data points) with fitted relationships (lines; see Table III), for higher- and lower-basicity mold fluxes tested at 1250°C, 1325°C and 1400°C.

In choosing the thermal properties to fit the experimental results (Figure 6 and Table III), the assumption is that the effective thermal conductivity and interfacial resistance do not depend on the bulk temperature of the liquid mold flux. It seems reasonable to assume that the effective thermal conductivity is the same, since the temperature range across the solid layer is similar in all cases (this range is from the solidus temperature to the much lower temperature adjacent to the copper probe). However, roughness measurements of the surface of the solid film which had been adjacent to the probe showed that the interface was rougher for crystalline (higher-basicity) solid films formed at higher temperatures [5]. The rougher interface is expected to result in a higher interfacial resistance, which is why the measured thickness for the highest bulk temperature in Figure 6 falls significantly below the fitted line, for the crystalline (higher-basicity) mold flux.

The dependence of interfacial roughness on the bulk liquid temperature likely results from the rate at which the film grows. For a higher liquid temperature, the film grows more slowly, and the interface is rougher. This effect of the bulk temperature invalidates the assumptions which underpin this approach, and another method is needed to estimate the solid-film thermal conductivity and interfacial resistance. A promising approach is to use the transient heat flux and change in solid-film thickness as the system approaches steady state. Equation (2) shows that different combinations of solid-film thermal conductivity (k_{solid}) and interfacial resistance (R_{int}) could fit the measured steady-state heat flux and solid film thickness, for a single bulk liquid temperature. However, for such a set of steady-state measurements, Equation (2) defines a fixed relationship between k_{solid} and R_{int} ; for different pairs of values of k_{solid} and R_{int} which fit this relationship, the transient changes in measured heat flux (especially the peak heat flux) and solid layer thickness can be quite different. An example of this effect is shown in Figure 7.

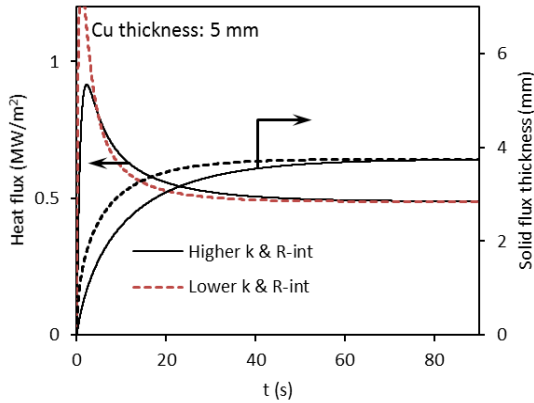


Figure 7. Principle of using measured transient heat transfer at one liquid-flux temperature to fit the solid-layer thermal conductivity and interfacial resistance: combinations of k_{solid} and R_{int} which yield the same steady-state thickness (for the given heat flux) give very different peak heat flux values, and different film growth rates. Values plotted for 1325°C bulk temperature, $k_{\text{solid}}=3$ W/mK or 2 W/mK, and $R_{\text{int}}=6.9\times 10^{-4}$ m²K/W or 0.62×10^{-4} m²K/W.

The results of Wen *et al.* [8] illustrate just such a relationship. In that work, mold fluxes with the same overall composition were prepared using different raw materials; the choice of raw material affected the crystallization behavior. As expected from the relationships presented here, the measured steady-state heat flux was the same for mold fluxes prepared with different raw materials [8] – this is expected, because the steady-state heat flux is controlled by liquid-flux heat transfer. However, the *peak* (transient) heat flux was lower for more-crystalline films (of the same composition) [8]; again as expected, since more-crystalline films would tend to have a higher thermal conductivity and a higher interfacial resistance – resulting (as shown in Figure 6) in a lower peak heat flux.

Conclusions

The cold-finger method is useful in yielding heat fluxes and solid-film microstructures which are similar to those encountered in industrial continuous casters, as shown in previous work [7]. The heat flux measured with the cold finger does not give direct information on the thermal resistances of the solidified mold flux. However, measuring the steady-state heat-flux and the steady-state thickness of the solid film constrains the values of the solid-film thermal conductivity and the interfacial resistance to one functional relationship. Using this relationship together with the transient changes in measured heat flux should allow reliable determination of the solid-film properties.

Acknowledgements

Support of this work by the industrial members of the Center for Iron and Steelmaking Research is gratefully acknowledged.

References

1. A. Yamauchi, K. Sorimachi and T. Yamauchi, "Effect of solidus temperature and crystalline phase of mould flux on heat transfer in continuous casting mould," *Ironmaking and Steelmaking*, 29 (2002), 203-207.
2. K. Tsutsumi, T. Nagasaka and M. Hino: "Surface roughness of solidified mold flux in continuous casting process." *ISIJ International*, 39 (1999), 1150-1159.
3. J.A. Kromhout, C. Liebske, S. Melzer, A.A. Kamperman and R. Boom, "Mould powder investigations for high speed casting," *Ironmaking and Steelmaking*, 36 (2009), 291-299.
4. H.G. Ryu, Z.T. Zhang, J.W. Cho, G.H. Wen and S. Sridhar, "Crystallization behaviors of slags through a heat-flux simulator," *ISIJ International*, 50 (2010), 1142-1150.
5. K. Lara Santos Assis, "Heat transfer through mold fluxes: a new approach to measure thermal properties of slags: (Ph.D. thesis, Carnegie Mellon University, 2016).
6. A. Fallah-Mehrjardi, P.C. Hayes and E. Jak: "Investigation of freeze linings in copper-containing slag systems: Part II. Mechanism of the deposit stabilization." *Metallurgical and Materials Transactions B*, 44 (2013), 549-560.
7. K.L.S. Assis and P.C. Pistorius, "Analyses of Phase Formation and Its Effect on the Thermal Resistance of Mold Flux," *AISTech 2013 Proceedings*, May 6-9, 2013, Pittsburgh, PA, USA, pp. 1451-1459.
8. G.H. Wen, X.B. Zhu, P. Tang, B. Yang and X. Yu, "Influence of raw material type on heat transfer and structure of mould slag," *ISIJ International*, 51 (2011), 1028-1032.

APPLICATION OF CATHODOLUMINESCENCE IN ANALYZING MOLD FLUX FILMS

Elizabeth Nolte¹, Jeffrey D. Smith¹, Michael Frazee², Neil Sutcliffe², Ronald J. O'Malley¹

¹Missouri University of Science and Technology
238 McNutt Hall, 1400 N. Bishop Ave., Rolla, MO, 65401, USA

²Nucor Steel Gallatin
4831 US Highway 42 West, Ghent, KY, 41045, USA

Keywords: Mold Flux, Continuous Casting, Cathodoluminescence

Abstract

Mold fluxes are used in continuous casting of steel to control heat transfer from the steel shell to the copper mold based on their structure and properties. Structures observed in mold flux film samples extracted from conventional and thin slab continuous casters at the end of a cast were examined using cathodoluminescence (CL) imaging in conjunction with XRD and SEM/EDS analysis. Glassy and crystalline structures in the flux films varied greatly depending on sampling location in the mold, distance from the mold wall and the mold flux being examined. Temperature data collected from thermocouple arrays in a thin slab funnel mold indicated saw-tooth temperature fluctuations in the lower area of the funnel region, presumably due to cyclic fracture and regrowth of the mold flux crystalline layer in that region of the mold. The temperature observations correlate well with the structures observed in the flux film samples from the region. CL microscopy clearly distinguishes glassy regions from regions with devitrified and dendritic crystal growth, as well as continuous and fractured crystallite layers and cuspidine and nepheline phases that are present. The technique also highlights small variations in Mn oxide content in the glassy region of the flux that results from exchange reactions with the steel, making flow lines in the previously liquid portion of the flux film clearly visible. The benefits of applying cathodoluminescence imaging to the analysis of mold flux films in continuous casting are discussed.

Introduction

Mold flux is critical for regulating mold heat flow and controlling slab surface quality in the continuous casting process [1,2,3]. The crystalline structure that forms in the mold flux film in the mold gap region of the continuous caster plays a significant role in the performance of a mold powder for a given steel grade and caster (Figure 1). Mold powders are often selected based on their viscosity and primary crystallization temperature even though the crystallite phases and morphologies that are observed in the mold gap generally do not form by the primary crystallization path [4]. The crystalline layers that are observed in the mold gap have been found to form by devitrification of the super-cooled glass layer that remains in contact with the caster mold well beyond the residence time of the steel shell [4,5]. The phases and structures formed by

devitrification have a strong influence on the mold thermal behavior through their influence on the crystalline layer's resistance to shear and fracture in the mold gap. Crystalline film fracture and reformation appears to be a primary cause of periodic temperature and heat transfer fluctuations in the mold [4]. Techniques such as: DSC [6-8], DTA [9-11], SHTT [6,12-14], and DHTT [14], can be used to characterize mold flux. However, these techniques rely on simulating only a small portion of the mold environment. Cathodoluminescence (CL) analysis has been a standard technique for geological materials for 30 years, but in the last 20 years has been developed as an effective method to observe refractory corrosion. [15] This paper will discuss the application of cathodoluminescence analysis to the investigation of crystallization behavior for industrial flux films, in conjunction with XRD and SEM.

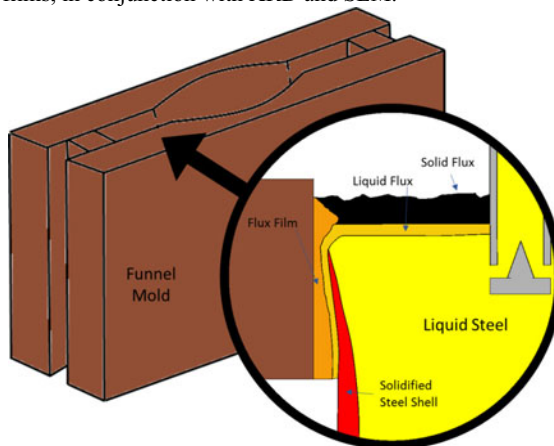


Figure 1: Schematic of the funnel mold and the cross section of the mold.

Experimental Procedure

Flux film samples were extracted from the funnel mold of a thin slab caster at the end of a cast. The flux composition, as reported by the supplier, is recorded in Table I.

Table I. Composition of mold flux in wt% (R=Na, K, Li).

Basicity	MgO	Al ₂ O ₃	Σ R ₂ O	F
0.8	2.6	5.9	16.5	8.6

Specimens were analyzed using powder x-ray diffraction (XRD) on a PANalytical X'Pert Pro Multi-Purpose Diffractometer with a Cu K α x-ray source. Specimens were mounted in epoxy and polished to a 0.1 μ m finish. Crystallite structures were analyzed using cathodoluminescence (CL) microscopy (model 8200 MK II) and SEM/EDS using an ASPEX-PICA 1020.

Results and Discussion

Many of the flux film samples exhibited a crystalline layer on the mold wall side of the film as reported elsewhere [5,24,25]. Samples obtained from lower in the funnel also exhibited fractures

in the crystallite film, and areas that were almost fully glassy. Figure 2 shows the variation in the flux film appearance as the sample location progressed lower into the funnel.

Figures 2 (a) and (b) are primarily crystalline with very little glass infiltration except along a large crack in (b). Figures 2 (c) and (d) are glassy and show longitudinal striations across the face. This structure is believed to result from crystalline layer fracturing and re-filling with glass. This behavior is consistent with thermal data collected from an instrumented funnel mold, where temperature was monitored at several locations both within and outside of the funnel region. Large saw tooth shaped fluctuations in temperature ($\pm 45^{\circ}\text{C}$) were evident within the high-stress funnel region (Figure 3a). The rapid temperature decrease is associated with crystal fracture and removal, while the rapid temperature increase is associated with glass infiltration in the fractured region. The slow drop in temperature is associated with aging and crystallization of the glass. Outside of the funnel region, smaller ($\pm 10^{\circ}\text{C}$) temperature fluctuations were evident (Figure 3b).

CL imaging proved to be a valuable method for identifying crystalline phases and structure in polished flux film samples. Figure 4 shows a cross section of a flux film from lower in the funnel area. The yellow and bright orange regions are crystalline and the light orange regions are glassy. The crystalline layer on the mold side of the flux film is fractured. The flow lines in the glassy region suggest that glass flowed and infiltrated the fracture region. The structures in the CL image support the theory of crystalline fracture and backfilling with glassy material by the mechanism proposed in Figure 5.

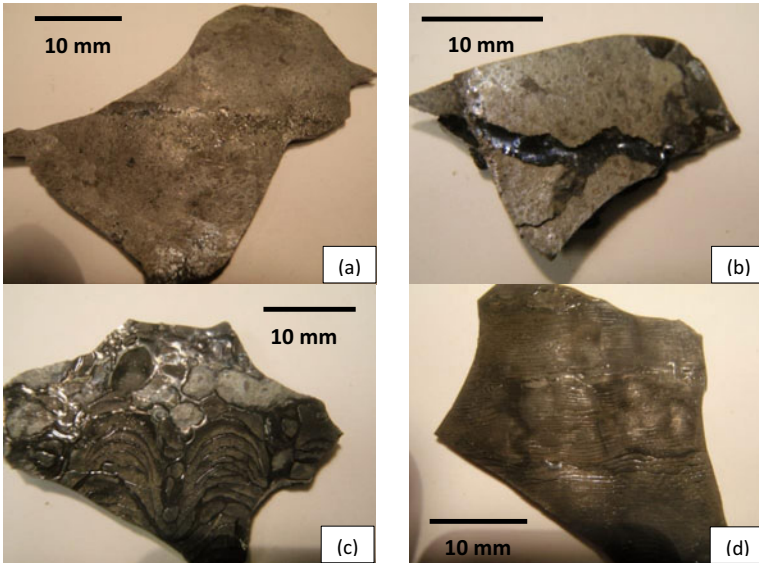


Figure 2: Flux film samples from upper funnel area (a) to lower funnel area (d) - Mold side.

The variation in shades in the darker orange region opposite the mold highlights the flow lines in the glassy region of the flux film that was fluid during casting. The color variations are directly

related to variations in manganese oxide content in the flux that was picked up during casting from interaction of the mold flux with the molten steel. Figure 6 documents this pickup. These variations in manganese oxide level were also documented using SEM/EDS analysis.

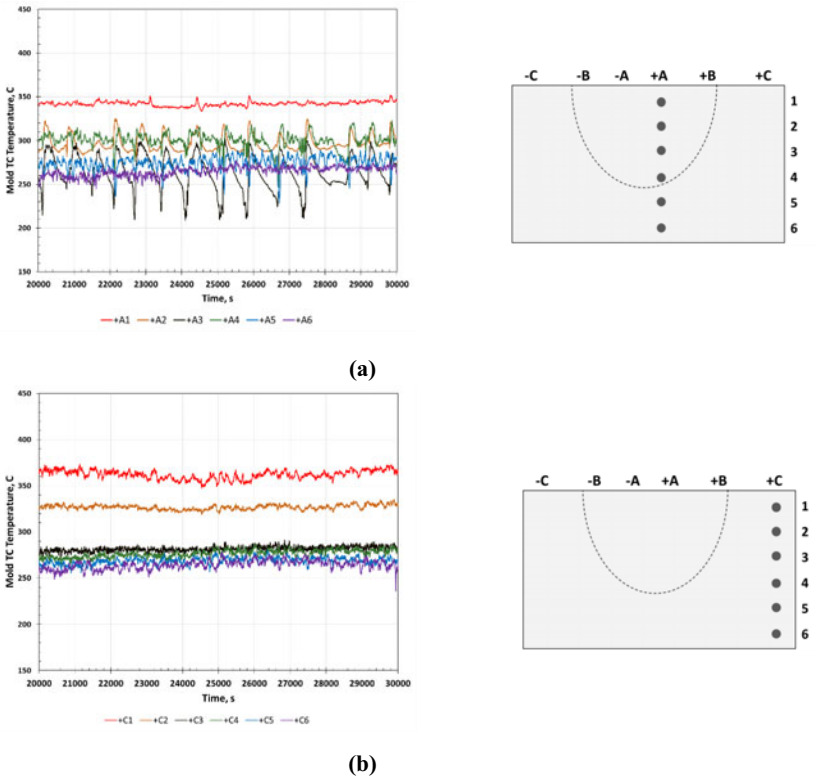


Figure 3: Inside the funnel area (a) exhibits saw tooth behavior, where temperature fluctuates on a semi-regular basis with respect to time. Outside the funnel area (b), temperature fluctuations are mild ($\pm 10^{\circ}\text{C}$). Corresponding diagrams indicate thermocouple locations in the funnel mold.

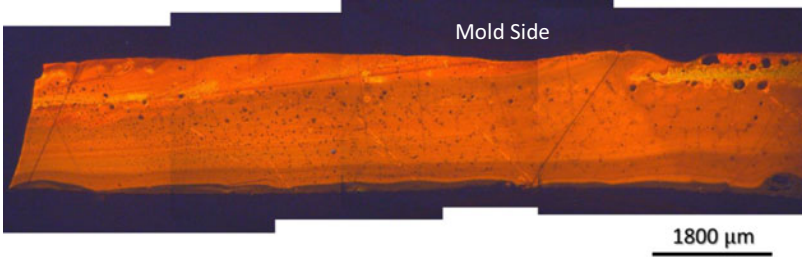


Figure 4: CL image of flux film sample – lower funnel region.

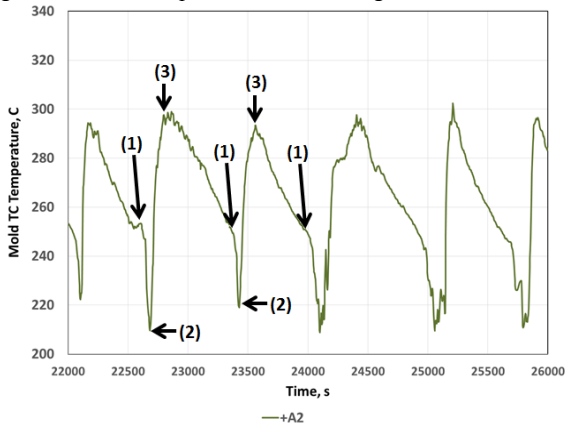


Figure 5: Proposed origin of saw tooth temperature fluctuations: (1) fracture of flux crystalline film, (1→2) withdraw of flux crystalline film, (2) air gap, (2→3) inflow of glass, (3) complete glass infiltration, (3→1) aging and crystallization of glass.

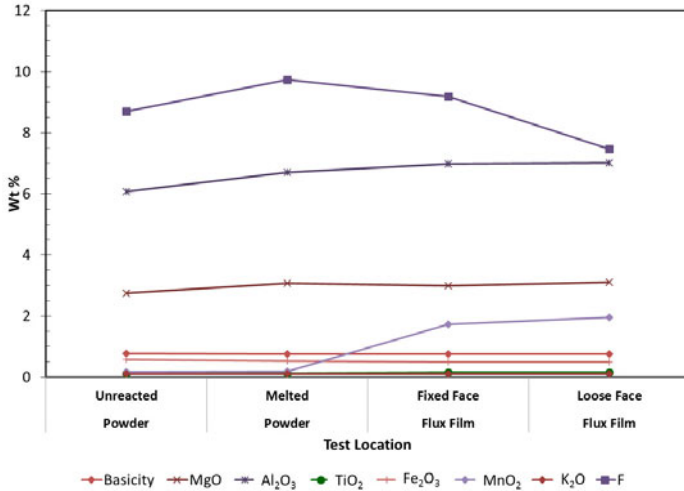


Figure 6: Flux film chemical analysis indicating manganese oxide pickup in mold flux.

XRD analysis of the flux films shows both the cuspidine and the nepheline phases are present in the flux film. The presence of nepheline in the crystalline layer suggests that this layer formed by devitrification of a super-cooled glass and not by primary crystallization [1, 9]. Devitrification follows a cooling path achieved by cooling faster than the critical cooling rate, avoiding crystallization, and isothermally holding at a temperature. In flux films, nepheline can only be formed through devitrification [9]. Its presence suggests that a super-cooled glass layer that remains in contact with the caster mold well beyond the residence time of the steel shell [1]. The distribution of cuspidine and nepheline in the crystalline layer can be seen more clearly in the CL image in Figure 7 (a), cuspidine being yellow and nepheline being brown. These phases were also confirmed by SEM EDS analysis, Figure 7 (b).

CL images best show the morphology and crystallites present. The cuspidine (yellow-orange) appears to co-crystallize with nepheline (dark orange) along the mold face. The crystal structures in the flux film change based on distance from the mold wall. Along the mold wall both cuspidine and nepheline have crystallized as small equiaxed crystals. As the temperature increases with distance away from the mold wall, the nepheline crystals do not appear to form as readily and the cuspidine crystal concentration increases. This forms a dense crystalline layer approximately 200 μ m from the mold wall. EDS confirmed the compositions of the crystals. In Figure 6 (b) the orange region indicates nepheline, yellow is cuspidine and purple is the bulk glass where the Ca to Si ratio is approximately 1:1.

Although the nepheline and cuspidine phases can both be distinguished in the SEM image, it is much easier to visualize the crystallization of cuspidine and nepheline using CL analysis. In addition, small variations in manganese oxide content in the glass can be easily observed.

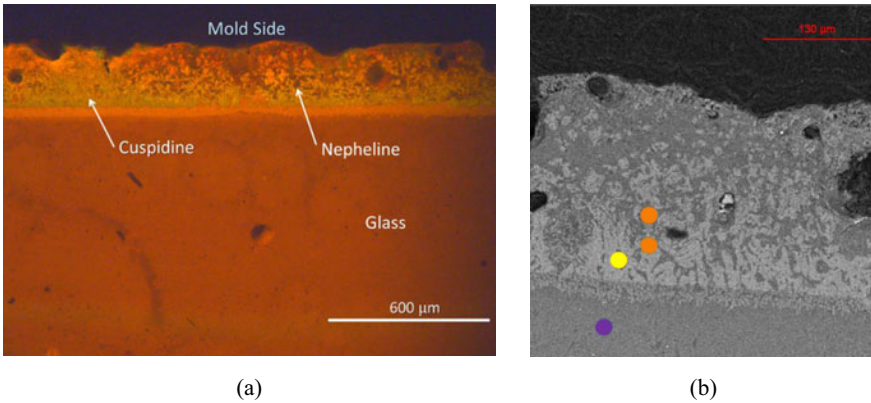


Figure 7: CL image (a) and SEM image (b) of the crystal growth along the mold wall. In (b) orange is nepheline, yellow is cuspidine, and purple indicates the bulk glassy region.

Conclusions

Flux films have widely varying structures based on distance from the mold wall and position in the mold. Information on these structures can be obtained by carefully extracting flux films at the end of a cast sequence and analyzing their microstructure. Cathodoluminescence imaging allows different structures to be observed more readily than by SEM analysis. This technique makes variations in the content of transition metal oxides in the flux film readily visible. Flux film structures can also vary significantly within a funnel mold. Flux film samples from high stress regions in the funnel area are observed to have fracture and glass re-infiltration marks that match the saw tooth temperature behavior in these regions. The following specific conclusions are made based on these experiments:

1. Large fluctuations in temperature on the mold side of the flux film are observed in the funnel region. In addition, glassy striations are observed on the mold face side of the flux film suggesting that the flux film repeatedly fractures, dropping the mold temperature sharply on initial withdrawal of the crystalline layer and then increasing temperature sharply when new glass infiltrates the fractured region. Following infiltration, the mold temperature then drops slowly as the re-infiltrated glass ages and crystallizes. This mechanism explains the observed periodic saw tooth mold temperature behavior.
2. Cathodoluminescence is a useful tool for studying flux films. It provides high resolution at low magnification, so phases can be easily distinguished optically and other small details can be observed that may have been missed using other techniques. It provides better visualization the distribution and type of crystal structures than SEM analysis and can also be used to observe small variation in composition in the bulk glass regions. Therefore, use of CL in analyzing flux films is recommended.

References

1. K.C. Mills, "Mold Fluxes for Continuous Casting and Their effect on Product Quality", McLean Symposium, Proc., ISS, Toronto, Canada, 1998, pp. 195-201.
2. K. Ichikawa, A. Morita, Y. Kawabe, "Behavior of Powder Slag Film and Influence of Powder Slag Film on Mold Heat Transfer Rate", Shinagawa Technical Report, Vol. 36, pp. 99-107, 1993.
3. K. Watanabe, M. Suzuki, K. Murakami, H. Kondo, A. Miyamoto, and T. Shiomi, "The Effect of Mold Powder Crystallization on Heat Transfer in Continuous Casting Mold", NKK Technical Review, No. 77, 1997, pp. 20-26.
4. R.J. O'Malley, "Observations of Various Steady State and Dynamic Thermal Behaviors in a Continuous Casting Mold", Proc. 82nd Steelmaking Conf., ISS, Chicago, IL, March 21-24, 1999.
5. Y. Meng and B.G. Thomas, "Simulation of Microstructure and Behavior of Interfacial Mold Slag Layer in Continuous Casting of Steel", *ISIJ Int.*, 46, 2006, pp. 660-669.
6. Y. G. Maldonado et al., "Estimation of Time-Temperature-Transformation Diagrams of Mold Powder Slags from Thermo-analysis of Non-isothermal Crystallization," *Met. And Mat. Trans. B*, (2014).
7. M.-D. Seo, C.-B. Shi, J.-W. Cho, and S.-H. Kim, "Crystallization Behaviors of CaO-SiO₂-Al₂O₃-Na₂O-CaF₂-(Li₂O-B₂O₃) Mold Fluxes," (n.d.).
8. M.-D. Seo, C.-B. Shi, H. Wang, J.-W. Cho, and S.-H. Kim, "Non-isothermal melt crystallization of cuspidine in CaO-SiO₂-CaF₂ based glasses," *J. Non. Cryst. Solids*, 412 58-65 (2015).
9. Y.G. Maldonado, F.A. Acosta, A.H. Castillejos, and B.G. Thomas, "Kinetic Study of the Devitrification of Mold Powder Slags," *AISTech*, 11 (2012).
10. R. Carli and C. Righi, "Mould flux crystallization : A kinetic study," *VII Int. Conf. Molten Slags Fluxes Salts*, [Mm] 821-826 (2004).
11. Z. Wang et al., "Crystallization Kinetics and Structure of Mold Fluxes with SiO₂ Being Substituted for Casting of Titanium Stabilized Stainless Steel," *Met. And Mat. Trans. B*, 44 606-612 (2013).
12. J. Li et al., "A Kinetic Study of the Effect of Na₂O on the Crystallization Behavior of Mold Fluxes for Casting Medium Carbon Steel," *ISIJ Int.*, 52 [12] 2220-2225 (2012).
13. B. Jiang et al., "A Kinetic Study of the Effect of ZrO₂ and CaO/Al₂O₃ Ratios on the Crystallization Behavior of a CaO- Al₂O₃-Based Slag System," *Met. And Mat. Trans. B*, 45 1057-1067 (2014).
14. Y. Kashiwaya, C.E. Cicutti, A.W. Cramb, and K. Ishii, "Development of Double and Single Hot Thermocouple Technique for in Situ Observation and Measurement of Mold Slag Crystallization.," *ISIJ Int.*, 38 [4] 348-356 (1998).
15. M. Karakus and R. E. Moore, "Cathodoluminescence (CL) Microscopy Application to Refractories and Slags", *Journal of Minerals & Materials Characterization & Engineering*, Vol. 1, No. 1, 2002, pp. 11-29.
16. R.B. Tuttle, K.D. Peaslee and J.D. Smith, "Interaction of Molten Ultra Low Carbon Steel with Carbide and Nitride Refractory Materials", *Refractories Applications Transactions*, 3 [1] 101-108 (2007).

17. L. Trueba, K.D. Peaslee, J.D. Smith and M. Karakus, "Effect of Nozzle Base Material on the Rate of Clogging during the Continuous Casting of Aluminium-killed Steels," *Steel Research International*, **77** [1] 37-47 (2006).
18. S. Ramachandran, K.D. Peaslee and J.D. Smith, "Thermochemistry of Steel-Refractory Interactions in Continuous Casting Nozzles," *ISS Transactions*, September 2003, 55-63 (2003).
19. M. Karakus, J.D. Smith and K.D. Peaslee, "Study of Non-Metallic Inclusions in Continuously Cast Steel Using Cathodoluminescence Microscopy," 38th Annual Meeting of the St. Louis Section of the American Ceramic Society, Chesterfield, MO, 201-212 (2002).
20. M. Karakus, J.D. Smith and R.E. Moore, "Cathodoluminescence Mineralogy of used MgO-C Bricks in Basic Oxygen Furnaces," *Veitsch-Radex Rundschau*, **1** 24-32 (2000).
21. J.D. Smith, K.D. Peaslee, M. Karakus and L. Trueba, "Study of Continuous Casting Nozzle Clogging Using Cathodoluminescence Microscopy," *Advances in Refractories for the Metallurgical Industries III*, eds. C. Allaire and M. Riguad, 187-200 (1999).
22. J.D. Smith, K.D. Peaslee, M. Karakus and H. Ruiz, "Post Mortem Analysis of Foundry EAF Refractories," 53rd Technical and Operating Conference, Steel Founders' Society of America, Chicago, IL, (1999).
23. M. Karakus, J.D. Smith, and R.E. Moore, "Mineralogy of the Carbon Containing Steelmaking Refractories," *UNITECR '97*, New Orleans, LA, 2745-754 (1997).
24. R.J. O'Malley and J. Neal, "An Examination of Mold Flux Film Structures and Mold gap Behavior Using Mold Thermal Monitoring and Petrographic Analysis at Armco's Mansfield Operations", *METEC Congress 99*, Dusseldorf, Vol. 1, 1999, pp.188-195.
25. W. Yan, W. Q. Chen, C. Lippold, H. G. Zheng, "Structure and performance characteristics of mold flux films for continuous casting of special alloy steels", *La Metallurgia Italiana* - n. 11-12/2013, pp. 35-42.
26. Y. Kashiwaya, C. Cicutti, A. Cramb, "Crystallization Behavior of Mold Slags", *ISS Steelmaking Conference Proc.*, Vol. 81, pp. 185-191, 1998.
27. Grieveson, P., Bagha, S., Machingawuta, N., Liddell, K. and Mills, K.C. 1988: 'Physical properties of casting powders: Part 2 Mineralogical constitution of slags formed by powders', *Ironmaking and Steelmaking Vol.15 No.4*, pp. 181-186.

EFFECTS OF CaF_2 ON THE RADIATIVE HEAT TRANSFER IN MOULD FLUXES FOR CONTINUOUS STEEL CASTING

¹Masahiro Susa, ¹Yuta Kono, ¹Rie Endo and ²Yoshinao Kobayashi

¹Department of Metallurgy and Ceramics Science, Tokyo Institute of Technology

²Research Laboratory for Nuclear Reactors, Tokyo Institute of Technology
2-12-1, Ookayama, Meguro-ku, Tokyo 152-8552, JAPAN

Keywords: continuous casting, mould flux, calcium fluoride, radiative heat transfer

Abstract

Effects of CaF_2 additions to mould fluxes have been investigated from the perspective of radiative heat transfer reduction to design mould flux for mild cooling. Glassy and crystallised mould flux samples were prepared so that the basicity of CaO/SiO_2 was 1 and the Fe_2O_3 concentration was 1mass%, whereas the concentration of fluorine ranged between 2 and 14mass%. The samples were analysed by SEM-EDS and XRD. The apparent reflectivities and transmissivities were measured using two types of spectrophotometer with an integrating sphere. The replacement of CaO by CaF_2 gives no effect on the optical characteristics of the glassy samples, not leading to radiative heat transfer reduction. In contrast, the replacement affects the optical characteristics of the crystallised samples and also the radiative heat transfer, which appear due to changes in the crystalline phases produced and the degree of crystallinity rather than the interaction between iron and fluoride ions.

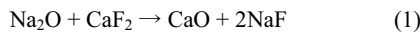
Introduction

In the continuous casting of steel, mild cooling is an effective technique to minimise surface defects such as longitudinal cracking, especially for medium-carbon (MC) peritectic steel grades. In practice, mild cooling is attained by crystallisation of the film. So far there have been two mechanisms of mild cooling proposed: (a) conductive heat transfer reduction due to the air gap at the interface between the film and the mould [1-4] and (b) radiative heat transfer reduction due to the increase in the reflectivity of the film [5]. More recently, Hanao *et al* have suggested that further reduction in radiative heat flux is required for high speed continuous casting because higher casting speed provides thinner air gaps [6].

Against the above background, the authors have made several studies from the viewpoint of radiative heat transfer reduction [7-10]. The magnitude of radiative heat flux depends on the optical characteristics of mould flux and thus the apparent reflectivity and transmissivity have been measured using a type of practical mould flux as base sample with systematic variations in the degree of crystallinity (the fraction of cuspidine) and the concentration of iron oxides. Approximated calculation of radiative heat flux using the optical characteristics data has suggested that crystallised mould fluxes with no iron oxides can reduce radiative heat transfer more efficiently as a result of increased reflectivity and decreased absorptivity [7]. In actuality, however, it is very difficult to prepare iron oxide-free mould flux because it exists as impurity in raw materials. As Wang *et al* have suggested [9], even if iron oxide free mould flux were

prepared, the molten flux would pick up some iron oxides during the coexistence with molten steel in the mould. Thus they have proposed to add reducing agents into mould flux powders. In contrast, Kobayashi *et al* have proposed to decrease Fe^{2+} ions by controlling the basicity of CaO/SiO₂ because FeO is known to absorb main radiation from molten steel in the near infrared region [10]. However, there is a concern that the increase in the basicity would affect other physical properties of the mould flux.

On the other hand, the practical mould flux commonly contains CaF₂ as major component. This compound is indispensable to form cuspidine and, at the same time, is known to decrease the melting temperature of mould flux. In addition, it has been pointed out that the following reaction can occur where CaF₂ is added to molten silicate containing Na₂O [11-13]:



This means that replacement of CaO by CaF₂ does not change the ratio of CaO/SiO₂ but may affect the optical property of the mould flux. In addition, there is a possibility of different crystalline phases forming, which would also affect the optical characteristics. However, there have been no studies from these perspectives. Consequently, the present work aims to investigate effects of CaF₂ on the optical characteristics of mould fluxes with systematic replacement of CaO by CaF₂ to find conditions suitable for radiative heat transfer reduction.

Experimental

Sample preparation

Table 1 gives the chemical compositions in mass% of five samples prepared for the present work, where CaO includes CaO originating from CaF₂ according to Eq.(1). In all the samples the ratio CaO:SiO₂:Al₂O₃:Na₂O is approximately kept as 1:1:0.01:0.33 on a mass basis while the concentration of fluorine is varied in the range 2 – 14mass%. All the samples also contain 1mass% Fe₂O₃. The samples are identified by the fluorine concentration, *e.g.*, 2mass%F is sample 2F as shown in Table 1.

Table 1 Chemical compositions of samples (in mass%)

Sample	CaO	SiO ₂	Al ₂ O ₃	Na ₂ O	F	Fe ₂ O ₃	T.CaO/Si
2F	39.97	39.97	3.98	13.02	2	1	1
5F	38.74	38.74	3.86	12.62	5	1	1
8.3F	37.38	37.38	3.72	12.18	8.34	1	1
11F	36.30	36.30	3.61	11.82	11	1	1
14F	35.07	35.07	3.49	11.43	14	1	1

The samples were prepared from reagent grade SiO₂, Al₂O₃, Na₂CO₃, CaF₂, Fe₂O₃ and CaO powders. Weighed mixtures of these powders were melted in platinum crucibles in air at 1673 K for 10 min, and the melts were poured into brass moulds at room temperature to obtain glassy samples ~ 5 mm thick. These samples are named ‘as-quenched samples’ and denoted as 2F_q *etc.* Some of as-quenched samples were heat-treated at a temperature of 933 K for 30 min for crystallisation. The heat-treated samples are named ‘annealed samples’ and denoted as 2F_a *etc.*

Characterisations and measurements

X-ray diffraction (XRD) analysis using a cobalt target was applied to identify the crystal phases present in the samples. A scanning electron microscope with an energy dispersion spectrometer (SEM-EDS) was applied to observe microstructures and to analyse the chemical compositions of the phases. SEM images were also used to evaluate the degree of crystallinity. The apparent

reflectivity (R) and transmissivity (T) were measured at room temperature using a UV spectrophotometer and a Fourier-transform infrared (FT-IR) spectrophotometer, both having integrating spheres.

Results

Sample Characterisation

Table 2 summarises the phases observed in each sample. Sample $2F_q$ contained un-melted grains of CaF_2 but the most parts were glassy. Samples $5F_q$, $8.3F_q$ and $11F_q$ were glassy and coloured green. In contrast, sample $14F_q$ was coloured greenish white and crystallised just after being quenched. After heat treatment for crystallisation, samples $8.3F_a$ and $11F_a$ were crystallised and coloured milky white, and sample $14F_a$ also became milky white and more crystallised; there were little changes in

samples $2F_a$ and $5F_a$. In the present work, for convenience, samples $5F_q$, $8.3F_q$ and $11F_q$ fall into ‘glassy samples,’ and samples $14F_q$, $8.3F_a$, $11F_a$ and $14F_a$ into ‘crystallised samples’.

Figure 1 shows XRD profiles for crystallised samples $8.3F_a$, $11F_a$, $14F_a$ and $14F_q$. It can be seen from this figure that samples $8.3F_a$ and $11F_a$ contain only a cuspidine phase as crystalline phase, whereas sample $14F_q$ contains only a CaF_2 phase; in addition, sample $14F_a$ contains both.

Figure 2 shows SEM images for the crystallised samples. Crystalline grains in samples $8.3F_a$ and $11F_a$ are cuspidine, and “flower-like” crystalline grains in sample $14F_q$ are CaF_2 . Both crystalline grains are seen in sample $14F_a$. These SEM images have been digitized to evaluate the degree of

Table 2 Phases observed in samples

%F	2	5	8.3	11	14
	$2F_q$	$5F_q$	$8.3F_q$	$11F_q$	$14F_q$
as-quenched	glassy + CaF_2 (un-melted)	glassy	glassy	glassy	glassy + CaF_2
	$2F_a$	$5F_a$	$8.3F_a$	$11F_a$	$14F_a$
annealed	glassy + CaF_2 (un-melted)	glassy	glassy + cuspidine	glassy + cuspidine	glassy + CaF_2 + cuspidine

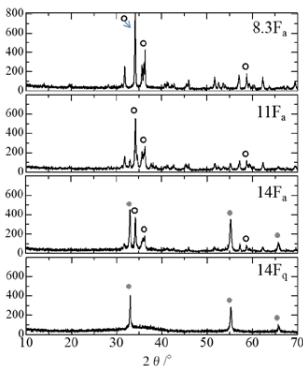


Figure 1 XRD profiles for samples containing crystalline phases, ○: cuspidine, ●: CaF_2 (Co K α radiation)

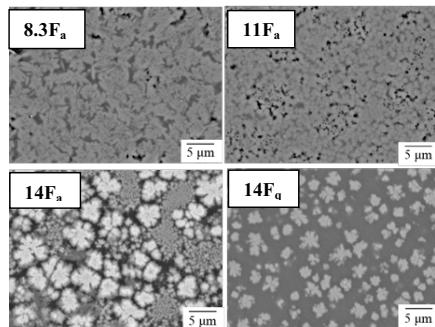


Figure 2 SEM images of samples containing crystalline phases

crystallinity from the area fraction, resulting in 73% for 8.3F_a, 71% for 11F_a, 56% for 14F_a and 27% for 14F_q on a volume basis. In addition, SEM-EDS results have suggested that iron ions tend to be concentrated into the glassy phase rather than into cuspidine and CaF₂ phases for samples 8.3F_a, 11F_a, 14F_a and 14F_q.

Optical characteristics

Figures 3(a), (b) and (c) show the apparent reflectivities, transmissivities and absorptivities of the as-quenched samples. It can be seen that there are gaps between the corresponding spectra above and below 2600 nm in wavelength because the measurements were made by two types of spectrophotometer. The reflectivities of silicate glasses are generally about 5% and thus the spectra below 2600 nm are quantitatively more reliable, which will be used for calculation of radiative heat flux. It can be seen from the figures that all the as-quenched samples commonly exhibit strong absorptions (i) below 500 nm, (ii) around 1000 nm, (iii) around 3000 nm, (iv) above 4500 nm and (v) above 10000 nm [14-16]. At wavelengths higher than 4500 nm all the samples show roughly zero transmissivity and almost the same values in reflectivity and absorptivity. At wavelengths lower than 2600 nm sample 14_q has the highest reflectivity and the lowest transmissivity in the as-quenched samples, which is because this sample was partly crystallised to form CaF₂ even in as-quenched condition. In addition, sample 2F_q contained un-melted CaF₂ particles.

Hence focus on the absorptivity spectra for the glassy samples. Figure 3(c) has also shown that there is no distinct movement of the absorption edge below 500 nm. On the contrary, Hayashi *et al* have studied the relationship between basicity and the absorption edge in Fe₂O₃-CaO-SiO₂ and Fe₂O₃-Na₂O-SiO₂ glasses and found that this absorption edge shifts to higher wavelengths with increasing basicity. [17] Thus, the replacement of CaO by CaF₂ in the present work does not affect the basicity.

Next focus on the absorption around 1000 nm for samples 5F_q, 8.3F_q and 11F_q. This absorption peak wavelength as well as its absorptivity value does not depend upon the fluorine concentration very strongly. Generally, Fe²⁺ ions take six oxide ions as ligands in silicates, which causes strong absorption around 1000 nm due to the d-d transition. If the replacement of CaO by CaF₂ changed oxide ions as ligands to fluoride ions, the magnitude of absorptivity would depend upon the fluorine concentration and the absorption peak wavelength might also be moved due to the change in ligand field strength. However, there are no such signs in Figure 3(c). Accordingly, it is assumed that fluoride ions are not bound to iron ions. This supposition is

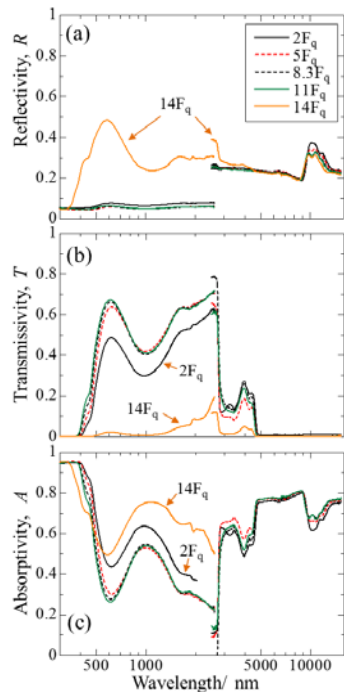


Figure 3 (a) reflectivity, (b) transmissivity and (c) absorptivity for as-quenched samples

consistent with the finding that iron ions tend to be concentrated into the glassy phase rather than the fluoride phases. In addition, Iwamoto *et al* have also studied chemical states of Fe^{3+} in $x\text{CaF}_2-(1-x)\text{CaO} \cdot \text{SiO}_2$ glass ($0 \leq x \leq 0.3$) using electron spin resonance spectroscopy and suggested that $\text{Fe}^{3+} - \text{O} - \text{Fe}^{3+}$ bonds are formed more easily than $\text{Fe}^{3+} - \text{F} - \text{Fe}^{3+}$ bonds [18], which also supports the above supposition.

Figures 4(a), (b) and (c) show the apparent reflectivities, transmissivities and absorptivities of the annealed samples. It can be seen that for the crystallised samples, especially 8.3F_a and 11F_a, the reflectivities are increased greatly and the transmissivities become roughly zero compared with those before heat treatment. This would be due to enhanced scattering by crystalline grains. At wavelengths lower than 2600 nm the crystallised samples have various values of the optical characteristics, whereas at higher wavelengths all the samples show roughly zero transmissivity and almost the same values in reflectivity and absorptivity.

Discussion

The total radiative heat flux across the mould flux film has been calculated using the optical characteristics in the present work on the basis of the model in the previous report [8]. This model assumes that the mould flux film consists of molten phase and solid phase layers, and the radiative heat flux (I) which may reach the mould across the the mould flux film is derived as

$$I = [\text{radiative energy transmitted through solid flux}] + [\text{radiative energy absorbed by solid flux}] - [\text{radiative energy absorbed by steel shell}]$$

Figure 5 shows the total calculated radiative heat flux (I_{Total}) as a function of the fluorine concentration for the as-quenched samples, where it is assumed that the present system reaches a steady state and that the interface temperature between steel and molten flux is 1800 K and that between molten and solid fluxes is 1400 K [8]. The total calculated radiative heat flux for glassy samples 5F_q, 8.3F_q and 11F_q is about $3.20 \times 10^5 \text{ Wm}^{-2}$ and does not depend

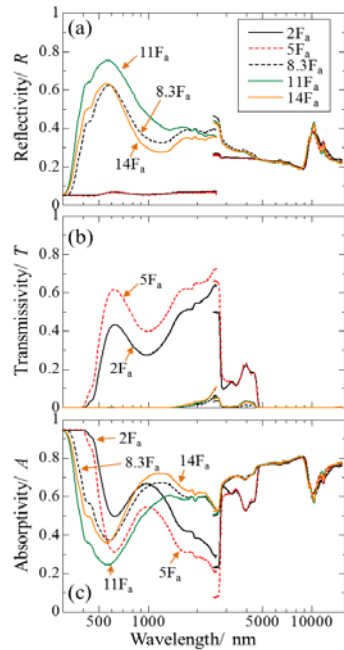


Figure 4 (a) reflectivity, (b) transmissivity and (c) absorptivity of annealed samples

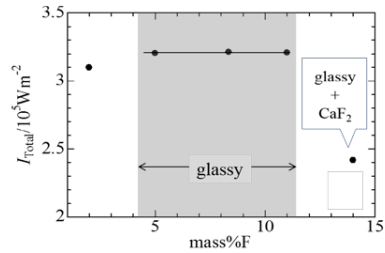


Figure 5 Total calculated radiative heat flux (I_{Total}) as function of fluorine concentration for as-quenched samples (See the text about the boundary conditions)

on the fluorine concentration. This corresponds to the experimental finding that there are no distinct differences in the optical characteristics of these samples, as shown in Figure 3. In contrast, samples 2F_q and 14F_q exhibit smaller values of I_{Total} because these two samples contained un-melted and precipitated CaF₂ grains. Thus, additions of CaF₂ do not affect the total radiative heat flux for glassy samples directly but indirectly affects *via* the presence of crystalline grains depending on the additive level.

Figure 6 shows the total calculated radiative heat flux (I_{Total}) as a function of the fluorine concentration for annealed samples 8.3F_a, 11F_a and 14F_a. The heat flux value ranges from 2.2×10^5 to 2.3×10^5 Wm⁻² and shows a slight increase with increasing fluorine concentration. Comparison between Figures 5 and 6 indicates that the value for sample 14F_a is smaller than that for sample 14F_q. These two samples have the same fluorine concentration but different degrees of crystallinity. Accordingly, it is likely that the slight increase in the total calculated radiative heat flux in Figure 6 would be due to the degree of crystallinity rather than the fluorine concentration itself.

Figure 7 shows the total calculated radiative heat flux (I_{Total}) as a function of the degree of crystallinity for samples 8.3F_a, 11F_a, 14F_a and 14F_q in comparison with the data reported for mould fluxes with and without 1mass% iron oxides [8], where the diameter of cuspidine grains is given for information. The data obtained in the present work seem to fall on a single straight line, irrespective of the type of crystalline phase produced, and the reported data for mould fluxes containing 1mass% iron oxides also fall down near the line. Accordingly, it is an important factor to increase the degree of crystallinity to reduce the total radiative heat flux.

Now consider the main factor to reduce the total radiative heat flux by crystallisation. Comparison between Figures 3 and 4 indicates that crystallisation of samples 8.3F_a, 11F_a, 14F_a causes the reflectivity to increase and the transmissivity to decrease to a large extent: the reflectivity and the transmissivity are complementary; in contrast, the change in absorptivity is not significant. Namely, it is likely that produced crystalline grains increase scattering of light at the interface between grains and the matrix, leading to the increase of reflectivity and the decrease of transmissivity. Accordingly, it is relevant to consider how to increase the reflectivity

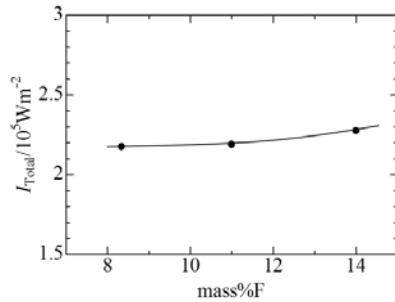


Figure 6 Total calculated radiative heat flux (I_{Total}) as function of fluorine concentration for annealed samples

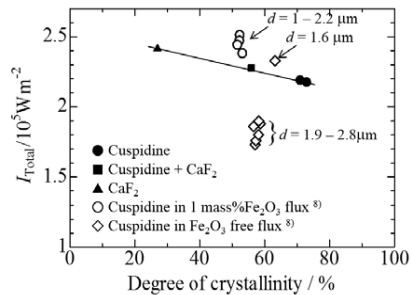


Figure 7 Total calculated radiative heat flux as function of degree of crystallinity, where d represents the average diameter of cuspidine grains

to reduce radiative heat transfer. This discussion is possible on the basis of Eq.(2) which expresses the reflectivity.

$$R = [(n_1 - n_2)^2 + (k_1 - k_2)^2] / [(n_1 + n_2)^2 + (k_1 + k_2)^2] \quad (2)$$

where n and k are the refractive index and the extinction coefficient and the subscripts 1 and 2 represent two media such as grains and the matrix.

The value of refractive index has been reported to be 1.590-1.602 (589 nm) for cuspidine by Larsen and Berman [19], 1.4338 (589 nm) and 1.429 (633 nm) for CaF₂ by Malitson [20] and Firoz *et al* [21], respectively, and 1.57-1.60 (589 nm) for mould flux by Susa *et al* [22]. Assuming $n_{\text{cuspidine}} = 1.60$, $n_{\text{CaF}_2} = 1.43$ and $n_{\text{matrix}} = 1.58$ and that the extinction coefficients are negligible, the value of R has been derived as 4.0×10^{-5} for cuspidine and 2.5×10^{-3} for CaF₂. These values are for single reflection at the interface and thereby are not in agreement with the values of R_a in Figure 4 for the crystallised samples, in which multiple reflections occur at the interface. Nevertheless, it would be true that CaF₂ grains scatter light more efficiently than cuspidine. Hence the difference between refractive indices is a crucial factor. On the contrary, Figure 7 has shown that cuspidine is more useful for radiative heat transfer reduction, which would be because these samples containing cuspidine have higher degree of crystallinity. Consequently, in order to further reduce radiative heat transfer, it would be required to design mould flux so as to have higher degree of crystallinity as well as greater difference between refractive indices of crystalline grains and the matrix.

Conclusions

- 1) The replacement of CaO by CaF₂ gives no effect on the optical characteristics of the glassy samples, not leading to radiative heat transfer reduction. In addition, it is supposed that fluoride ions do not exist adjacent to iron ions, which tend to be concentrated into the glassy phase rather than into CaF₂ and cuspidine.
- 2) The replacement of CaO by CaF₂ affects the optical characteristics of the crystallised samples and also the radiative heat transfer; however, this effect would be due to the changes in crystalline phases produced and the degree of crystallinity.
- 3) To further reduce the radiative heat transfer by controlling the optical characteristics, it would be important to increase the degree of crystallinity of mould flux as well as to enhance the difference between refractive indices of crystalline grains and the matrix.

Acknowledgement

Parts of this paper have been reprinted from the article '*Tetsu-to-Hagané*, **100**(2014), 571-580', by permission of the Iron and Steel Institute of Japan.

References

- 1) A. Yamauchi, K. Sorimachi, T. Sakuraya and T. Fujii, "Heat Transfer between Mold and Strand through Mold Flux Film in Continuous Casting of Steel," *ISIJ Int.*, **33** (1993), 140-147.
- 2) K. Watanabe, M. Suzuki, K. Murakami, H. Kondo, A. Miyamoto and T. Shiomi, "The Effect of Crystallization of Mould Powder on the Heat Transfer in Continuous Casting Mould" *Tetsu-to-Hagané*, **83** (1997), 115-119.
- 3) J. W. Cho, T. Emi, H. Shibata and M. Suzuki, "Heat Transfer across Mold Flux Film in Mold during Initial Solidification in Continuous Casting of Steel," *ISIJ Int.*, **38** (1998), 834-842.

- 4) K. Tsutsumi, T. Nagasaka and M. Hino, "Surface Roughness of Solidified Mold Flux in Continuous Casting," *ISIJ Int.*, **39** (1999), 1150-1159.
- 5) H. Nakada, M. Susa, Y. Seko, M. Hayashi and K. Nagata, "Mechanism of Heat Transfer Reduction by Crystallization of Mold Flux for Continuous Casting," *ISIJ Int.*, **48** (2008), 446-453.
- 6) M. Hanao, M. Kawamoto and A. Yamanaka, "Influence of Mold Flux on Initial Solidification of Hypo-Peritectic Steel in a Continuous Casting Mold," *ISIJ Int.*, **52** (2012), 1310-1319.
- 7) M. Susa, A. Kushimoto, H. Toyota, M. Hayashi, R. Endo and Y. Kobayashi, "Effects of Both Crystallisation and Iron Oxides on the Radiative Heat Transfer in Mould Fluxes," *ISIJ Int.*, **49** (2009), 1722-1729.
- 8) M. Susa, A. Kushimoto, R. Endo and Y. Kobayashi, "Controllability of Radiative Heat Flux across Mould Flux Films by Cuspidine Grain Size," *ISIJ Int.*, **51** (2011), 1587-1596.
- 9) M. Wang, Y. Kobayashi, R. Endo and M. Susa, "Formation Kinetics of Iron Oxide in Mould Flux during Continuous Casting," *ISIJ Int.*, **53** (2013), 56-61.
- 10) Y. Kobayashi, R. Maehashi, R. Endo and M. Susa, "Effects of Valence Control of Iron Ions on Radiative Heat Transfer in Mould Flux," *ISIJ Int.*, **53** (2013), 1725-1731.
- 11) K. C. Mills, "Physical Properties of Casting Powders: Part 1 Scheme to Represent Chemical Compositions of Powders," *Ironmaking Steelmaking*, **15** (1988), 175-180.
- 12) M. Hanao, M. Kawamoto and A. Yamanaka, "Influence of Mold Flux on Initial Solidification of Hypo-Peritectic Steel in a Continuous Casting Mold," *ISIJ Int.*, **52** (2012), 1310-1319.
- 13) M. Hayashi, T. Watanabe, K. Nagata and S. Hayashi, "Coordination Environment of Fluorine in the CaO-SiO₂-CaF₂ Glasses Bearing Na₂O A Solid-state 19F MAS NMR Study," *ISIJ Int.*, **44** (2004), 1527-1533.
- 14) M. Susa, K. Nagata and K. C. Mills, "Absorption Coefficients and Refractive Indices of Synthetic Glassy Slags Containing Transition Metal Oxides," *Ironmaking Steelmaking*, **20** (1993), 372-378.
- 15) M. Radhakrishnan, "Potential Constants of Some XY₄ Type Molecules and Ions," *Z. Physik. Chem. Neue Folge*, **41**(1964), 201-204.
- 16) H. Toyuki, "Effect of Na₂O on the Nature of Si-O Bonds in Na₂O-SiO₂ Glasses," *Yogyo-Kyokai-Shi*, **85** (1977), 554-558.
- 17) M. Hayashi, M. Susa, T. Oki and K. Nagata, "Shift of the Absorption Edge for the Charge Transfer Band in Slags Containing Iron Oxides," *ISIJ Int.*, **37** (1997), 126-133.
- 18) N. Iwamoto, Y. Makino and S. Kasahara, "State of Fe³⁺ ion and Fe³⁺-F⁻ Interaction in Calcium Fluorosilicate Glasses," *J. Non-Cryst. Solids*, **55** (1983), 113-124.
- 19) E.S. Larsen and H. Berman: *The Microscopical Determination of Nonopaque Minerals*, 2nd ed., Washington D.C.U.S. Geological Survey, (1934), 109.
- 20) I. H. Malitson, "A Redetermination of Some Optical Properties of Calcium Fluoride," *Appl. Opt.*, **2** (1963), 1103-1107.
- 21) S. H. Firoz, T. Sakamaki, R. K. Endo, M. Susa, "Refractive Index Measurements of CaF₂ Single Crystal and Melt by Ellipsometry," *High Temp.- High Pressures*, **37** (2008), 163-173.
- 22) M. Susa, K. C. Mills, M. J. Richardson, R. Taylor and D. Stewart, "Thermal Properties of Slag Films Taken from Continuous Casting Mould," *Ironmaking Steelmaking*, **21** (1994), 279-286.

EFFECT OF Na₂O ON CRYSTALLISATION BEHAVIOUR AND HEAT TRANSFER OF FLUORINE-FREE MOULD FLUXES

Jian Yang¹, Jianqiang Zhang¹, Yasushi Sasaki¹, Oleg Ostrovski¹, Chen Zhang², Dexiang Cai², Yoshiaki Kashiwaya³

¹ School of Materials Science and Engineering, University of New South Wales; Kensington; NSW, 2052, Australia

² Baosteel Group Corporation Research Institute; Shanghai, 201900, China

³ Department of Energy Science and Technology, Kyoto University, Yoshida Honmachi, Sakyo-ku; Kyoto, 606-8501, Japan

Keywords: Na₂O, crystallisation behaviour, heat transfer, DHTT, fluorine-free mould fluxes.

Abstract

Most of the commercial mould fluxes contain fluorides which bring about serious environmental problems. The major challenge in the application of fluorine-free mould fluxes is to control the heat transfer from the strand to copper mould which is closely related to crystallisation behaviour. In this study, the effects of Na₂O on the crystallisation behaviour and heat transfer of CaO-SiO₂-Na₂O-B₂O₃-TiO₂-Al₂O₃-MgO-Li₂O mould fluxes were investigated using single/double hot thermocouple technique (SHTT/DHTT) and infrared emitter technique (IET), respectively. Continuous cooling transformation (CCT) and time-temperature transformation (TTT) diagrams constructed using SHTT showed that the increase of Na₂O concentration led to higher critical cooling rate and shorter incubation time. The crystallisation behaviour in a thermal gradient was examined using DHTT. The heat flux measured by IET showed that the increase of Na₂O concentration decreased the heat flux when Na₂O was lower than 9 mass% but the further increase of Na₂O raised the heat flux. The relationship between flux crystallisation and heat transfer was also discussed.

Introduction

Mould fluxes serve essential roles in continuous casting of steel, such as lubrication, heat transfer control, thermal insulation, inclusion entrapment, etc.^[1]. Uneven heat withdrawal across the continuous casting mould is likely to cause cracking defects on the surface of steel products, especially, in the case of the peritectic steel casting which undergoes the δ-Fe to γ-Fe transformation during solidification with 4% volumetric shrinkage. In practice, mould fluxes with high crystallisation tendency are favoured in the casting of cracking-sensitive steel since the thick crystalline flux layer formed between strand and copper mould suppresses radiative heat transfer^[2]. Radiation is scattered by grain boundaries; its transfer is impeded by pores, cracks and air gaps formed as a consequence of the formation of crystalline flux layer. Currently, most of commercial mould fluxes contain fluorides, *e.g.* CaF₂, NaF, etc., to ameliorate lubricity of liquid flux layer and control heat transfer rate across the crystalline flux layer through the precipitation of cuspidine (Ca₄Si₂O₇F₂)^[3]. However, pollutive emission of fluorides during casting operation causes environmental concern and corrosion of the cooling system of casters^[1]. Therefore, the

development of fluorine-free mould fluxes has become a focus of research in steelmaking in recent years.

Among potential substitutes for cuspidine in fluorine-free fluxes are $\text{Ca}_{11}\text{Si}_4\text{B}_2\text{O}_{22}$ ^[4-6], $\text{Ca}_2\text{Si}_3\text{Na}_2\text{O}_9$ ^[7], CaSiTiO_5 ^[8], and other compounds. Na_2O has been proved to be an important component that significantly affects the performance of fluorine-containing mould fluxes^[4, 9]. It is considered to be an essential component for the fluorine-free mould fluxes. In this study, the influence of Na_2O on the crystallisation behaviour and heat transfer of $\text{CaO-SiO}_2\text{-Na}_2\text{O-B}_2\text{O}_3$ based fluorine-free mould fluxes is investigated using hot thermocouple technique (HTT) and infrared emitter technique (IET), respectively. The aim of this study is to build a deeper understanding of the role of Na_2O in fluorine-free flux system and pave the way for the design of eco-friendly mould fluxes.

Experimental

2.1 Sample preparation

In present study, the fluorine-free mould fluxes were prepared by melting pre-mixed reagent grade CaCO_3 , SiO_2 , Al_2O_3 , B_2O_3 , Na_2CO_3 , TiO_2 , MgO and Li_2CO_3 at 1400°C for 20 min. The melted fluxes were quenched onto a copper plate and then ground into powders. Measured chemical composition of the prepared fluorine-free fluxes is listed in Table I. Typical chemical compositions of two fluorine-containing industrial mould fluxes for low-carbon (LC) steel and medium-carbon (MC) steel casting are also listed in this table.

Table I Chemical composition of mould fluxes with different Na_2O concentration (mass%).

Sample	CaO	SiO_2	Al_2O_3	B_2O_3	Na_2O	TiO_2	MgO	Li_2O	F
1	40.8	37.3	3.6	6.3	5.0	4.2	2.2	1.0	0
2	39.5	35.7	3.6	6.7	7.2	4.2	2.1	1.1	0
3	38.3	34.7	3.7	6.8	8.7	4.2	2.3	1.1	0
4	37.8	34.2	3.6	6.7	11.0	4.3	2.2	1.0	0
LC ^[10]	34.5	37.5	3.0	-	12.5	-	2.5	0.5	8.5
MC	43.5	30	3.8	-	6	-	-	-	10

2.2 A study of crystallisation behaviour of fluxes

The crystallisation behaviour of mould fluxes was investigated by single hot thermocouple technique (SHTT) and double hot thermocouple technique (DHTT) developed by Kashiwaya *et al.*^[11, 12]. The schematic setup of the HTT was described elsewhere^[10-12]. SHTT simulated the high cooling rate that mould fluxes encounter in the infiltration process^[11]. The mould flux sample (*ca.* 10 mg) was mounted on the tip of B-type thermocouple, and heated or cooled in accordance with the programmed temperature profiles. The crystallisation process was in-situ observed and recorded by a video camera. The CCT and TTT diagrams were constructed using SHTT in continuous cooling and isothermal experiments whose temperature profiles are given in Figures 1(a) and 1(b), respectively. In the continuous cooling experiments, a sample was first heated up to 1500°C and held for 3 min to homogenise composition. Then, it was cooled down to 800°C with different pre-set cooling rates. The time and temperature at which the crystallinity of

mould fluxes reached 0.5 vol% were used to construct CCT diagrams^[12]. In isothermal experiments, the mould fluxes were rapidly quenched to different pre-set temperatures after high temperature homogenisation and held isothermally at the target temperatures. The times at which crystallinity of mould fluxes reached 0.5 vol% and 99 vol% were used for the construction of TTT diagrams. The precipitated phases at 900°C and 1000°C were analysed using X-ray diffraction (XRD).

Crystallisation evolution of mould fluxes in a simulated thermal field was investigated in DHTT experiments, of which the temperature profile is shown in Figure 1(c). A liquid flux film with a length of 1.5 mm was created between two thermocouples when both of the thermocouples were heated to 1500°C. After holding at 1500°C for 3 min, one thermocouple (CH-1) was quenched to 600°C, whilst the other thermocouple (CH-2) was kept at 1500°C. Considering the decreasing cooling rate when the temperature of CH-1 was approaching 600°C, a start time in the DHTT experiment was defined when the tangent to the initial cooling path was intersected by the isothermal temperature line^[6].

2.3 Infrared emitter technique

The heat flux measurements were carried out using infrared emitter technique (IET) developed at Carnegie Mellon University. The schematic layout of IET was presented in previous papers^[13, 14]. A polished flux disk with a thickness of 4 mm was placed on the brass base in which four thermocouples were embedded to record temperatures. Infrared radiation was emitted from the heating lamp to the flux disk. The radiation intensity was adjusted by the applied voltage. The power profile of IET is presented in Figure 1(d). The system emitted thermal radiation up to 1.6 MW/m², which is close to the radiation emitted from the steel strand in continuous casting. The responding temperatures recorded by the thermocouples were converted to heat flux for the evaluation of radiative heat transfer. The calculated heat flux across different mould flux films was compared with that across industrial flux disks.

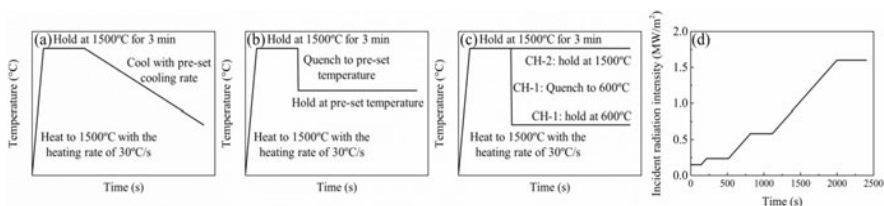


Figure 1 Schematic temperature profiles in (a) continuous cooling experiments; (b) isothermal experiments; (c) DHTT experiments; and power profile in (d) IET tests.

Results and discussion

3.1 Effect of Na₂O on crystallisation behaviour of mould fluxes

The CCT diagrams of mould fluxes with Na₂O content varying from 5 to 11 mass% are shown in Figure 2. Three parallel measurements were carried out for the determination of crystallisation temperatures at each cooling rate. For all fluxes, the crystallisation temperature at which the

crystallinity reached 0.5 vol% decreased with increasing cooling rate; for example, the crystallisation temperature of Sample 1 decreased from 1095 to 923°C as cooling rate raised from 0.1°C/s to 1°C/s. The critical cooling rate, above which crystallisation was not observed, raised from 1°C/s to, 2, 20 and 30°C/s when Na₂O content increased from 5 mass% to 7, 9 and 11 mass%, respectively. The crystallisation temperature averaged out from three measurements at each cooling rate also increased with increasing Na₂O content. At a fixed cooling rate of 1°C/s, the crystallisation temperature increased from 923°C when Na₂O content was 5 mass% to 1264°C when Na₂O increased to 11 mass%.

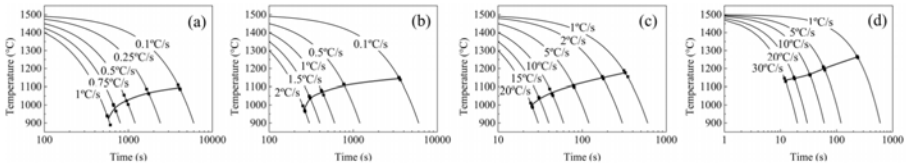


Figure 2 CCT diagrams of mould fluxes: (a) Sample 1: Na₂O = 5 mass%; (b) Sample 2: Na₂O = 7 mass%; (c) Sample 3: Na₂O = 9 mass%; (d) Sample 4: Na₂O = 11 mass%.

TTT diagrams of mould fluxes with Na₂O content ranging from 5 to 11 mass% are given in Figure 3. Part of the end of crystallisation curve of Sample 1 is not given in Figure 3(a) since the crystals became translucent when temperature was higher than 1000°C, which made it impossible to determine the crystallised area when crystallisation proceeded. The shortest incubation time decreased and highest crystallisation temperature increased with increasing Na₂O content in fluxes, from 190 s and 1100°C for fluxes with 5 mass% Na₂O, to 47 s and 1125°C for 7 mass% Na₂O, to 1 s and 1150°C for 9 mass% Na₂O, and to almost 0 s and 1300°C for 11 mass% Na₂O.

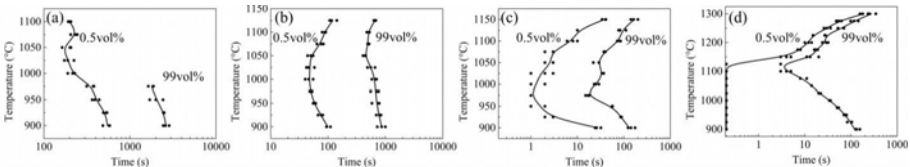


Figure 3 TTT diagrams of mould fluxes: (a) Sample 1: Na₂O = 5 mass%; (b) Sample 2: Na₂O = 7 mass%; (c) Sample 3: Na₂O = 9 mass%; (d) Sample 4: Na₂O = 11 mass%.

Figures 2 and 3 demonstrate that the addition of Na₂O enhanced crystallisation tendency of mould fluxes, especially when Na₂O content was higher than 9 mass%. The addition of Na₂O tends to break Si-O bonds in the SiO₄⁴⁻ tetrahedral network, forming non-bridging oxygens (NBOs) as a network modifier. As the mobility of ions is promoted in such depolymerised silicate melts, it reduces the initial viscosity of flux melts and consequently the kinetic barrier for nucleation and crystal growth. Therefore, the increase of Na₂O raised the critical cooling rate and shortened the incubation time in continuous cooling and isothermal experiments. The role of Na₂O as a network modifier in the fluorine-free mould fluxes is similar to that in the fluorine-containing mould fluxes^[4]. The maximal cooling rate in the meniscus zone in the industrial casting is expected to be 20 °C/s; therefore Samples 3 and 4 are expected to crystallise directly

from the molten state. It makes them favourable in casting cracking-sensitive steel which requires heat transfer suppression once strand starts solidification.

Precipitated phases of mould fluxes treated at 900°C and 1000°C were determined by XRD as shown in Figure 4. CaSiO₃ was the dominant phase in the mould fluxes with 5 mass% Na₂O at 900°C (Figure 4(a)). Minor precipitates of Ca₁₁Si₄B₂O₂₂, Ca₂MgSi₂O₇, and CaTiO₃ were also found in the XRD patterns. The precipitation of CaSiO₃ gradually diminished as Na₂O increased and vanished when Na₂O content reached 11 mass%, whilst the precipitation of Ca₁₁Si₄B₂O₂₂, Ca₂MgSi₂O₇, CaTiO₃ was promoted. Both Ca₁₁Si₄B₂O₂₂ and Ca₂MgSi₂O₇ became the dominant phases when Na₂O content was 11 mass%. Ca₂Si₃Na₂O₉ was also detectable when the Na₂O content was higher than 9 mass%.

The phase composition of mould fluxes treated at 1000°C is shown in Figure 4(b). CaSiO₃ also dominated the precipitates in the mould fluxes with low concentration of Na₂O. The variations of Ca₁₁Si₄B₂O₂₂, CaTiO₃ and Ca₂Si₃Na₂O₉ with the increase of Na₂O were similar to the cases at 900°C. However, Ca₂MgSi₂O₇ was absent in all the samples treated at 1000°C and Ca₂Si₃Na₂O₉ was only detected in Sample 4.

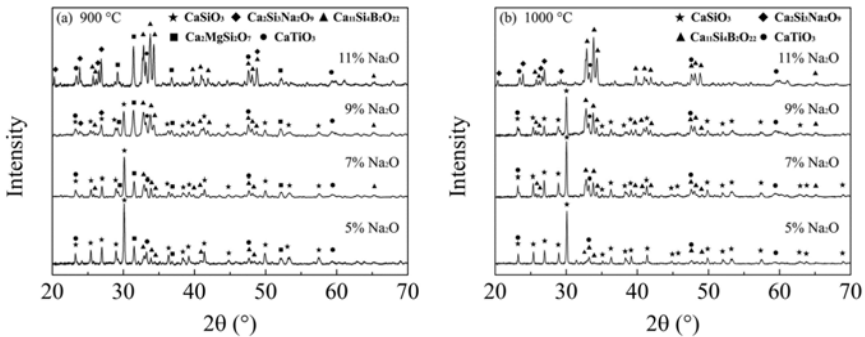


Figure 4 XRD patterns of mould fluxes with varied Na₂O contents at (a) 900°C and (b) 1000°C.

The crystallinity evolution of mould fluxes under a temperature gradient of 1500°C to 600°C is shown in Figure 5. The crystallisation behaviour of Sample 1 (Na₂O = 5 mass%) is indicated in Figures 5(a1) to 5(a4). Small spherical crystals were formed between 900 s to 1200 s and gradually developed into a clear crystalline layer. Sample 2 started crystallisation much earlier than Sample 1 as a number of nuclei were developed in the middle of flux film as shown in Figure 5(b1). Crystals grew rapidly and formed a distinct crystalline layer after 600 s. Sample 3 started crystallisation once CH-1 reached isothermal stage. Crystals started to precipitate before 10 s and propagated to low temperature area at a fast growth rate. Crystallisation reached a relatively stable state with a thick crystalline layer before 300 s. Crystallisation of Sample 4 occurred even before it reached the isothermal stage. But unlike the small primarily precipitated crystals in other Samples, the crystals formed in Sample 4 appeared in large equiaxed morphology with high mobility as shown in Figure 5(d1). Crystals grew to low temperature side promptly. Some of the equiaxed crystals formed in the liquid layer or the weak part of the

crystalline layer torn apart from the crystalline layer were driven to the high temperature region by Marangoni convection flow easily in this sample and finally melted.

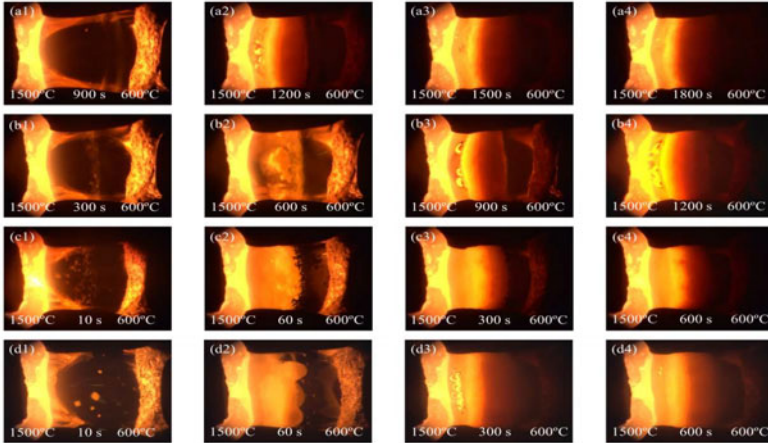


Figure 5 Crystallisation of mould fluxes in the DHTT experiments: (a1) to (a4): Sample 1 at 900 s, 1200 s, 1500 s and 1800 s; (b1) to (b4): Sample 2 at 300 s, 600 s, 900 s and 1200 s; (c1) to (c4): Sample 3 at 10 s, 60 s, 300 s and 600 s; (d1) to (d4): Sample 4 at 10s, 60 s, 300 s and 600 s.

3.2 Effect of Na_2O on the heat transfer of mould fluxes

The calculated heat flux through the mould flux disks is given in Figure 6. As the incident radiation increased in accordance with Figure 1(d), the responding heat flux increased accordingly. As seen in Figure 6(a), the average responding heat flux at the incident radiation of 1.6 MW/m^2 dropped from 743 kW/m^2 , to 677 and 595 kW/m^2 with increasing Na_2O content from 5 to 9 mass%, but a further increase of Na_2O increased the heat transfer rate to 641 kW/m^2 . Sample 3 (9 mass% Na_2O) was closest to the fluoride-containing industrial mould fluxes under the same incident radiation intensity as shown in Figure 6(b).

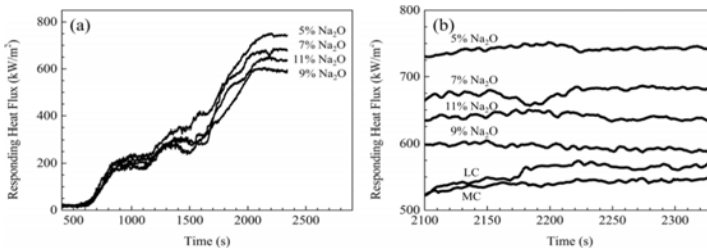


Figure 6 (a) Heat flux of mould fluxes; (b) Comparison of the heat flux of fluoride-free mould fluxes and industrial fluxes under the incident radiation of 1.6 MW/m^2 .

Generally speaking, the increase of crystallisation tendency restrains heat transfer across mould fluxes^[2, 15, 16]. The heat flux was expected to decrease with the addition of Na₂O since crystallisation tendency of mould fluxes increased. Indeed, the heat flux decreased with increasing content of Na₂O from 5 to 9 mass%, but a further increase in the Na₂O slightly increased the heat flux across flux disk. This phenomenon may result from the morphology of crystals. The promotion of crystallisation became less significant when Na₂O ≥ 9 mass%. But large equiaxed crystals that emerged in the vicinity of the liquid/crystalline interface of Sample 4 with 11 mass% Na₂O had a relatively high mobility (Figure 5(d1)) and were easily driven by Marangoni flow. Therefore, the newly-formed crystals could hardly grow from crystalline layer close to the liquid side, which made the formation of stable crystalline layer difficult in the initial solidification. As shown in Figure 7, the fraction of crystalline layer of Sample 4 was slightly lower than Sample 3 in the first a few minutes as stable growth of crystalline phase in Sample 4 was impeded by the convection flow compared with Sample 3. Such crystallisation behaviour can explain the increase in the heat flux when Na₂O content increased from 9 to 11 mass%.

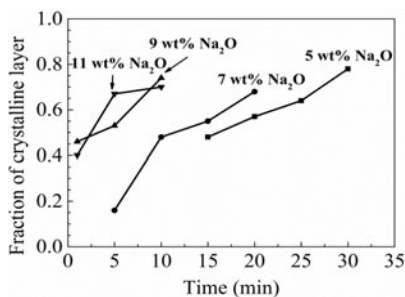


Figure 7 Fraction of crystalline layer as a function of time in the DHTT experiments.

Conclusions

The crystallisation behaviour and heat transfer of mould fluxes of the CaO-SiO₂-Na₂O-B₂O₃-TiO₂-Al₂O₃-MgO-Li₂O system with different Na₂O content were investigated using SHTT, DHTT, XRD, and IET. The major findings of this study are summarised below:

- (1) CCT and TTT diagrams showed that the increase of Na₂O content raised the critical cooling rate and shortened the incubation time of mould fluxes, suggesting an increasing crystallisation tendency;
- (2) XRD results indicated that with the increasing amount of Na₂O, the dominant phase changed from CaSiO₃ to Ca₁₁Si₄B₂O₂₂. Ca₂MgSi₂O₇ was a major phase in the mould fluxes with high Na₂O content at 900°C but it was not observed at 1000°C;
- (3) According to the heat flux measured by IET, Sample 3 had the lowest responding heat flux of 595 kW/m², which is closest to the industrial fluorine-containing fluxes.

Acknowledgement

Financial support by Baosteel through the Baosteel-Australia Joint Research Centre, Abel Metal Services, and Australian Research Council (ARC Linkage Project LP130100773) is gratefully acknowledged.

References

1. A. Fox, K. Mills, D. Lever, C. Bezerra, C. Valadares, I. Unamuno, J. Laraudogoitia and J. Gisby, "Development of fluoride-free fluxes for billet casting," *ISIJ Int.*, 45 (7) (2005), 1051-1058.
2. H. Nakada, M. Susa, Y. Seko, M. Hayashi and K. Nagata, "Mechanism of heat transfer reduction by crystallization of mold flux for continuous casting," *ISIJ Int.*, 48 (4) (2008), 446-453.
3. T. Watanabe, H. Fukuyama and K. Nagata, "Stability of Cuspidine ($3\text{CaO} \cdot 2\text{SiO}_2 \cdot \text{CaF}_2$) and Phase Relations in the $\text{CaO-SiO}_2\text{-CaF}_2$ System," *ISIJ Int.*, 42 (5) (2002), 489-497.
4. J. Wei, W. Wang, L. Zhou, D. Huang, H. Zhao and F. Ma, "Effect of Na_2O and B_2O_3 on the Crystallization Behavior of Low Fluorine Mold Fluxes for Casting Medium Carbon Steels," *Metall. Mater. Trans. B*, (2013), 1-10.
5. L. Zhou, W. Wang, J. Wei and K. Zhou, "Melting and Heat Transfer Behavior of Fluorine-Free Mold Fluxes for Casting Medium Carbon Steels," *ISIJ Int.*, 55 (4) (2015), 821-829.
6. J. Yang, J. Zhang, Y. Sasaki, O. Ostrovski, C. Zhang, D. Cai and Y. Kashiwaya, "In-situ Study of Crystallisation Behaviour of $\text{CaO-SiO}_2\text{-Na}_2\text{O-B}_2\text{O}_3\text{-TiO}_2\text{-Al}_2\text{O}_3\text{-MgO-Li}_2\text{O}$ Fluorine-free Mould Fluxes with Different CaO/SiO_2 Ratios," *ISIJ Int.*, 56 (4) (2016), 574-583.
7. N. Takahira, M. Hanao and Y. Tsukaguchi, "Viscosity and Solidification Temperature of $\text{SiO}_2\text{-CaO-Na}_2\text{O}$ Melts for Fluorine Free Mould Flux," *ISIJ Int.*, 53 (5) (2013), 818-822.
8. H. Nakada and K. Nagata, "Crystallization of $\text{CaO-SiO}_2\text{-TiO}_2$ slag as a candidate for fluorine free mold flux," *ISIJ Int.*, 46 (3) (2006), 441-449.
9. M. Hayashi, T. Watanabe, H. Nakada and K. Nagata, "Effect of Na_2O on crystallization of mould fluxes for continuous casting of steel," *ISIJ Int.*, 46 (12) (2006), 1805-1809.
10. J. Yang, Y. Cui, L. Wang, Y. Sasaki, J. Zhang, O. Ostrovski and Y. Kashiwaya, "In - Situ Study of Crystallization Behavior of a Mold Flux Using Single and Double Hot Thermocouple Technique," *Steel Res. Int.*, 86 (6) (2015), 636-643.
11. Y. Kashiwaya, C. E. Cicutti, A. W. Cramb and K. Ishii, "Development of double and single hot thermocouple technique for in situ observation and measurement of mold slag crystallization," *ISIJ Int.*, 38 (4) (1998), 348-356.
12. Y. Kashiwaya, C. E. Cicutti and A. W. Cramb, "An investigation of the crystallization of a continuous casting mold slag using the single hot thermocouple technique," *ISIJ Int.*, 38 (4) (1998), 357-365.
13. K. Gu, W. Wang, L. Zhou, F. Ma and D. Huang, "The Effect of Basicity on the Radiative Heat Transfer and Interfacial Thermal Resistance in Continuous Casting," *Metall. Mater. Trans. B*, 43 (4) (2012), 937-945.
14. W. Wang, K. Gu, L. Zhou, F. Ma, I. Sohn, D. J. Min, H. Matsuura and F. Tsukihashi, "Radiative Heat Transfer Behavior of Mold Fluxes for Casting Low and Medium Carbon Steels," *ISIJ Int.*, 51 (11) (2011), 1838-1845.
15. A. W. Cramb, "The Solidification Behavior of Slags: Phenomena Related to Mold Slags," *ISIJ Int.*, 54 (12) (2014), 2665-2671.
16. M. Kawamoto, Y. Tsukaguchi, N. Nishida, T. Kanazawa and S. Hiraki, "Improvement of the initial stage of solidification by using mild cooling mold powder," *ISIJ Int.*, 37 (2) (1997), 134-139.

EFFECT OF CARBON PICKUP ON THE SLAB WITH SLAG POOL THICKNESS IN ULTRA-LOW CARBON STEEL

Min-Seok Park¹, Shin Yoo²

¹POSCO Technical Research Laboratories 8, Pokposarang-gil,
Gwangyang-si, Jeollanam-do, 57807, Republic of Korea

²Thermo-Fluid and Process Research Group, Technical Research Laboratories, POSCO,
6261, Donghaean-ro, Nam-gu, Pohang-si, Gyeongbuk, 37859, Republic of Korea

Keywords: Carbon pickup, Ultra-low carbon steel, Slag pool thickness, Slag rim

Abstract

Carbon is easily picked up on the slab surface from the mold flux in the ultra low carbon steel (ULCS). We were trying to find ways to prevent the C-pickup in ULCS. Naturally, we were interested in the C-pickup with slag pool thickness. When the slag pool thickness was increased up to about 30mm, C-pickup on the slab was dramatically decreased and the deviation in the width direction of the C-pickup was also decreased. However, even if the slag pool thickness was thicker, C-pickup was increased when slag bear was formed. More details will be discussed in the paper.

Introduction

Carbon-pickup (C-pickup) on the slab surface is one of major surface quality issues in the ultra low carbon steel (ULCS) causing a black band in the hot rolling. Study on the C-pickup has been in progress since the 1980's^[1] and the main mechanism of C-pickup for ULCS is well known to be due to contact with unmelted mold flux or enriched carbon layer of mold flux during the continuous casting^[1-5]. The best way to avoid the C-pickup on the surface of as-cast slab does not use a free carbon which is an important factor for controlling the melting rate of the mold flux. Because the use of carbon in the mold flux is inevitable, it has suggested ways to minimize C-pickup. By adding MnO₂ in the mold flux as an oxidizing agent, casting trials showed 50% reduction in C-pickup compared with the case of MnO₂-free mold flux^[3]. On the other hand, recarburization of a solidified shell was reduced by replacing carbon to Si₃N₄ in the mold flux^[4-5]. In other words, it is possible to reduce recarburization of the shell by using less carbon or increasing the thickness of slag pool. In addition, recarburization of the shell was reported to occur within 2mm from the surface of as-cast slab. In this study, an examination on how the recarburization of the shell occurs at ULCS in the conventional powder casting is presented, then comparison of the recarburization of a shell of new casting method having a thick slag pool thickness with that of a conventional method is considered.

Experimental

To analyze the C-pickup effect on the slab surface, ULCS casting through two strand caster using, not only a molten slag, but also a conventional powder at the same time in Gwangyang

Steelworks, POSCO. Molten slag was prepared from the outside of the mold and it is freely adjustable thickness of the slag pool. The apparatus using the LNG gas was used as a melting device for melting mold flux. Casting conditions and Mold flux specification are listed below.

Table 1. Casting conditions for experiments

Steel grade (carbon content)	Slab size	Casting speed
0.001~0.002%	1800mm x 250mm	1.2m/min

Table 2. Mold flux specification

	C free	basicity	application
Flux A	2.5	0.89	Conventional powder method
Flux B	16	0.89	molten mold flux feeding method

Flux B was applied to the new molten mold flux feeding method. After the casting, chips were made by every 1mm depth from the surface of slab for the carbon analysis. Chips were collected in pairs in all positions as shown in Fig.1. Especially, chips were sampled at the same depth from the center of the slab symmetrically. Carbon analysis was characterized by LECO CSLS600 carbon/sulfur determinator.

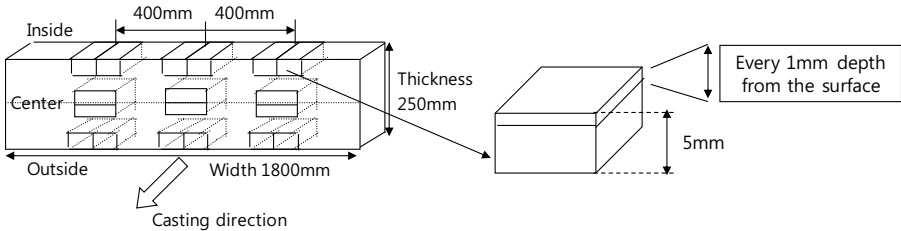


Figure 1. Chip manufacturing schematic.

Results and discussions

There are two ways to reduce the recarburization of the shell as mentioned above. One is to reduce the amount of carbon in the mold flux, and the other is to increase the thickness of slag pool, and the latter method is applied to reduce the recarburization of the shell in this study. Since molten mold flux is continuously fed into the mold it can freely adjust the thickness of slag pool. To increase the slag pool thickness, the new molten mold flux feeding technology is used. In order to compare the C-pickup of the shell between the conventional powder casting and the new molten mold flux casting, a ULCS containing 0.001% carbon was cast in Gwangyang Steelworks POSCO. The two strand commercial caster, which had a 250ton ladle, was used for the casting trials. The conventional powder casting and the new molten mold flux casting were cast in the same heat for direct comparison of C-pickup. The thickness of slag pool was approximately 10mm for a conventional powder casting and it was about 30mm thick enough for the new molten mold flux casting.

Figure 2 shows the carbon content on the inside slab surface (a), the center (b), and the outside slab surface (c) when the conventional powder casting is applied. Figure 2(b) indicates a segregation of carbon at the center. A bulk value of carbon can be determined except for the value of 1mm depth from the center. The bulk value of carbon for as-cast slab is 0.001%. Figure 2(a) and Figure 2(c) show carbon pickup on the surface of as-cast slab. The maximum C-pickup occurred at the 1mm deep from the surface. The depth is deeper as the amount of C-pickup was smaller. Interestingly, C-pickup occurred even at 5mm depth from the surface of as-cast slab. In addition, the amount of C-pickup was different in the width direction. In the case of conventional powder casting with slag pool of 10mm thick, C-pickup takes place non-uniformly depending on the thickness and the depth.

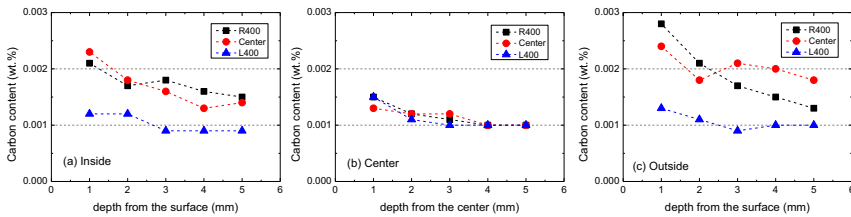


Figure 2. C-pickup on a surface of as-cast slab in the conventional powder casting at the same trial heat.

Figure 3 shows the carbon content of the inside surface (a), the center (b), and the outside surface (c) of as-cast slab when the new molten mold flux casting is applied. Figure 3(b) indicates a segregation of carbon at the center as shown in Figure 2(b). The bulk value of carbon for as-cast slab is 0.00096%. Surprisingly, C-pickup did not occur in the new molten mold flux casting. The small C-pickup occurred only 1mm depth from the surface. 1.4ppm C-pickup occurred at R400 in inside surface. In the new method with slag pool of 30mm thick, C-pickup rarely happens on the shell. The slag rim on the mold wall was not observed in both strands. From this casting trial, it is observed that C-pickup can be minimized by maintaining a sufficient slag pool with 30mm thick.

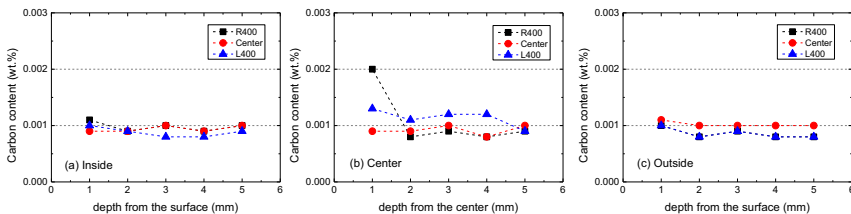


Figure 3. C-pickup on a surface of as-cast slab in the new molten mold flux casting at the same trial heat

Figure 4 shows carbon content in different molten mold flux feeding trial. Bulk carbon is 0.0018% as shown in Figure 4(b). Despite the thick slag pool thickness, maximum C-pickup occurs 7ppm at L400 in outside surface. Nevertheless, C-pickup of shell is still less than that of

the conventional powder casting. In this molten mold flux feeding trial, slag rim on mold wall was generated. Recarburization of the shell is thought to be the cause of slag rim generation.

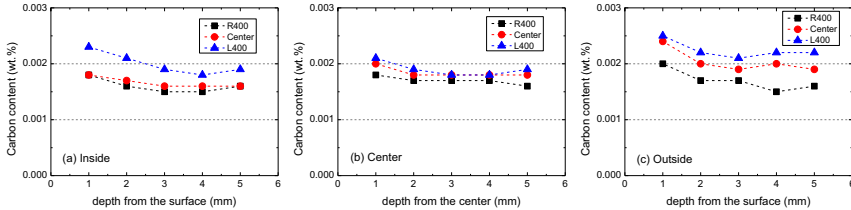


Figure 4. C-pickup of a surface of as-cast slab in another new molten mold flux casting trial

Figure 5 shows slag rim formed in the test trial. The arrow tip indicates the surface of mold wall as shown in Figure 5(a). The size of slag rim is 15mm thick and 40mm long. Slag rim are composed of molten slag, unmelted powder, and carbon black. EDS image shows the granular type of materials trapped in the slag rim. EDS analysis also showed the same results as shown in Figure 5(b).

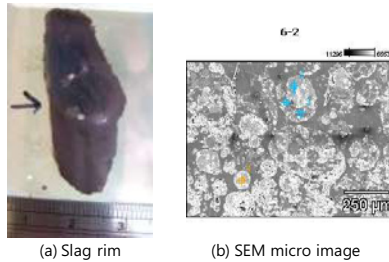


Figure 5. Optical microscopic image (a) and electron microscopic image of slag rim

Conclusion

In the case of conventional powder casting with slag pool of 10mm thick, C-pickup takes place non-uniformly depending on the thickness and the depth. C-pickup occurred even at 5mm depth from the surface. On the other hand, when the slag pool thickness was increased up to about 30mm, C-pickup rarely happens on the shell. However, C-pickup occurred a little at the 1mm deep from the surface when the slag rim is formed.

Acknowledgement

This work was supported by POSCO through the PosLAB R&D program.

References

[1] H. Nagano and N. Masuo, “Mechanism of Carburization by Mold Flux in Continuous Casting Steel”, CAMP-ISIJ, vol. 2, 1989, p.259

- [2] K. Yamasaki et al., "Carburization by Mold Powder in Continuous Casting Steel", *CAMP-ISIJ*, vol. 3, 1990, p.181
- [3] S. Terada, S. Kaneko, T. Ishikawa, and Y. Yoshida: Development of Mold Fluxes for Ultra-Low-Carbon Steels, *I&SM*, September 1991 pp. 41-44.
- [4] C. Lefebvre, J. P. Radot, J. N. Pontoire, and Y. Roux: *La Revue de Metallurgie-CIT*, Avril 1997, PP. 489-496.
- [5] P. Valentin, C. Bruch, K. Harste, H. Lachmund, M. Hecht, and J. Potschke: Carbon Pickup in Continuous Casting Processes, 2003, vol.74, No.3, PP. 139-146.

TECHNIQUES FOR CONTROLLING HEAT TRANSFER IN THE MOULD-STRAND GAP IN ORDER TO USE FLUORIDE FREE MOULD POWDER FOR CONTINUOUS CASTING OF PERITECTIC STEEL GRADES

Adam Hunt¹, Bridget Stewart^{1,2}

¹Teesside University, Middlesbrough, TS1 3BA, UK

²Materials Processing Institute, Middlesbrough, TS6 6US, UK

Keywords: Continuous Casting, Fluoride Free Mould Powder, Heat Transfer

Abstract

When casting peritectic steel grades, control of heat transfer from the steel shell is critical for minimising surface defects. Cuspidine ($3\text{CaO}\cdot 2\text{SiO}_2\cdot \text{CaF}_2$) is the preferred crystal phase to control horizontal heat flux, due to its high crystallisation temperature and low incubation time. However, the presence of fluoride creates environmental and operational problems. Research into fluoride-free mould powder for peritectic steel grades has still to yield a fully effective substitute.

This research has investigated whether horizontal heat flux in the mould can be controlled by manipulating the interface between the copper mould plate and the slag film. Calculations estimate that the removal of fluoride will decrease the total thermal resistance between the mould and strand by 28%. Results show that interfacial thermal resistance can be increased by the techniques developed, with one technique meeting and exceeding the requirements to replace fluoride in terms of thermal resistance needs for peritectic steel grades.

Introduction

When casting steel grades in the peritectic range it is critical to control the horizontal heat flux from the steel shell in order to minimise longitudinal crack defects. In practice, horizontal heat flux in the upper mould is controlled by the properties of the mould flux; the key property being mould flux crystallinity [1-4]. In order to produce the desired crystallinity, fluoride is added to the mould powder composition to precipitate cuspidine ($3\text{CaO}\cdot 2\text{SiO}_2\cdot \text{CaF}_2$). Unfortunately, this creates environmental and operational problems due to evaporation of volatile compounds and leaching of fluoride into secondary cooling water.

Previous research into fluoride free mould powder for peritectic steel grades has highlighted the potential of TiO_2 crystal phases in terms of a crystallisation temperature that matches cuspidine [5-7]. However, the use of TiO_2 comes with operational problems from the formation of high melting point compounds such as TiN and TiC in the slag pool that inhibit the infiltration of liquid slag into the mould strand gap [8]. The use of other mould powder components, such as CaO and Na_2O , to replace fluoride have also encountered issues due to a lower crystallisation temperature than cuspidine [9, 10].

An aim of this work was to assess whether heat flux can be controlled by directly manipulating the mould flux film and the interfacial gap. This arose from the idea that heat flux could be controlled by deliberately introducing porosity into the mould-strand gap [11] and would allow for the use of mould powders with low or even zero fluoride content. It has

been calculated by the author that the removal of fluoride from a mould flux would decrease the total thermal resistance from strand to mould by $0.38 \text{ m}^2\cdot\text{K}\cdot\text{kW}^{-1}$ [12]. A successful technique must therefore increase thermal resistance by a similar amount for application with fluoride free mould powder casting.

It is thought that the required increase in thermal resistance could be achieved by use of coatings between the copper mould plate and the mould flux film [13]. The selected coatings would decompose under exposure to heat from the molten flux and create a thermal barrier of porosity in the interfacial gap. This paper looks at the effect of magnesium carbonate and waterglass based coatings on interfacial thermal resistance using laboratory scale equipment.

Experimental

Equipment

In order to test the thermal performance of the various coatings, a steady state thermal conductivity device was used and can be seen in Figure 1. By assuming a constant temperature gradient through each material, as in Figure 2, it is possible to calculate the interfacial thermal resistance, R_{int} .

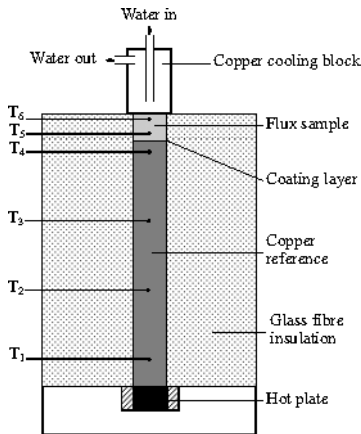


Figure 1. Schematic of thermal conductivity device

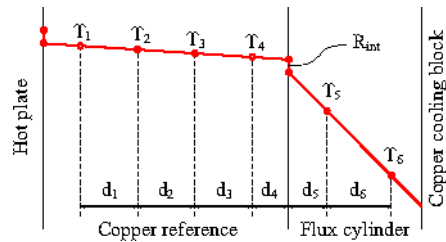


Figure 2. Schematic of temperature gradient

Sample preparation

All mould flux samples used to measure interfacial thermal resistance were prepared directly into the thermal conductivity device. This was to give a comparable interfacial thermal resistance to mould flux quenched on the surface of a continuous casting mould during operation.

To create the desired coating, a given volume of coating solution was evenly spread over the upper surface of the copper and left for a minimum of 12 hours to dry. The different coating solutions and volumes used can be seen in Table I. Waterglass ($\text{Na}_2\text{SiO}_3 \cdot n\text{H}_2\text{O}$) was selected for its intumescent properties and magnesium carbonate (MgCO_3) was selected for its low decomposition temperature ($350 \text{ }^\circ\text{C}$) compared with other carbonates. Lithium carbonate

(Li₂CO₃) and calcium carbonate (CaCO₃) were also trialled at a preliminary stage, but showed poor gas evolution when exposed to molten mould flux.

Table I. List of coating solutions used during investigation

Solution	Concentration	Gas Evolved	Test 1	Test 2	Test 3	Test 4	Test 5
Na ₂ SiO ₃ (aq)	724 g/l	H ₂ O	0.1 ml	0.2 ml	0.3 ml	0.35 ml	0.4 ml
MgCO ₃ (aq)	120 g/l	CO ₂	0.1 ml	0.2 ml	0.3 ml	-	-

For the investigation, a glassy mould flux was used as this would best mimic a low fluoride or fluoride free mould powder. To prepare a sample in the device the mould powder was first decarburised in a furnace at 700 °C for 18 hours. 25 g of decarburised mould powder was then fused in a platinum crucible in a furnace for 10 minutes at 1300 °C. The molten mould flux was poured directly into the sample holder lined with heat resistant mica paper, with thermocouples set at defined distances. The sample was then allowed to cool slowly within the device.

Experimental method

To give maximum heat flux through the thermal conductivity device, a small amount of thermal paste was applied on the top of the cooled sample, giving a good contact with the cooling block. The weight of the cooling block also applies a constant pressure on the mould flux.

To create the temperature gradient required for measuring thermal resistance, the hot plate was firstly set to 160 °C. The cooling water was turned on and the temperature from all thermocouples was allowed to settle before recording the temperatures at steady state. Steady state temperatures were recorded at increments of 60 °C up to 700 °C. After the full temperature program, the equipment was left to cool before removing the sample and measuring the thermocouple distances with a vernier calliper. Equations 1 to 3 were used to calculate thermal resistance between copper and mould flux:

R_{int} = Interfacial thermal resistance (m².K.kW⁻¹)
 ΔT_{int} = Temperature change across interface (°C)
 q = heat flux (W.m⁻²)
 T_i = Temperature of thermocouple (°C)
 d = distance (m)
 k = thermal conductivity (W.m⁻¹.K⁻¹)

$$R_{int} = \frac{\Delta T_{int}}{q} \quad (1)$$

$$\Delta T_{int} = \left(T_4 - \frac{qd_4}{k_{(Cu)}} \right) - \left(T_5 + \frac{qd_5}{k_{(flux)}} \right) \quad (2)$$

$$q = k_{(Cu)} \frac{(T_3 - T_4)}{d_3} \quad (3)$$

Before proceeding with the next test, the copper reference within the device was cleaned of excess oxide and the surfaces polished to maintain a constant roughness.

Results

For all samples it was observed that gas was given off from the coating when pouring the molten flux into the sample holder. In most cases the gases escaped before the viscosity of the sample became high enough to retain the gas. Microscopy images of the coatings after a full

test cycle can be seen in Figures 3 and 4. Figures 5a-e show the cross section of the waterglass coatings and mould flux set in resin. In these figures, the interface of the mould flux is highlighted in red.

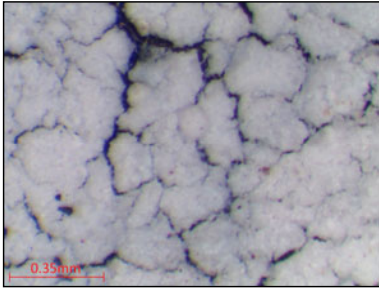


Figure 3. Image of magnesium carbonate coating

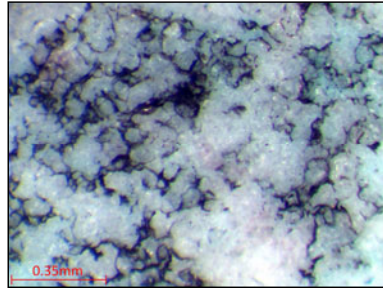
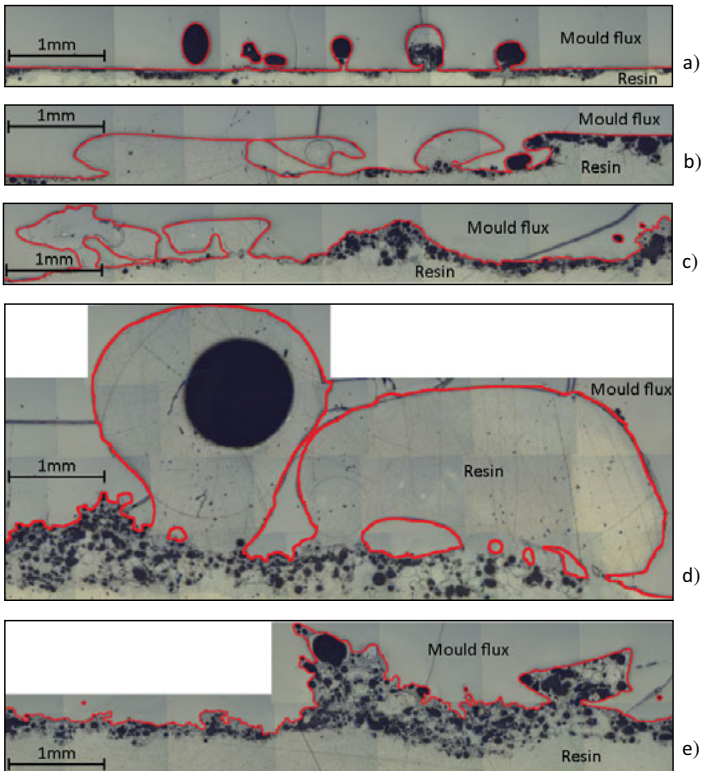


Figure 4. Image of waterglass coating



Figures 5a-e. Cross section images showing influence of waterglass coating on mould flux. a) 0.1 ml waterglass; b) 0.2 ml waterglass; c) 0.3 ml waterglass; d) 0.35 ml waterglass; e) 0.4 ml waterglass;

The thermal resistance results for the magnesium carbonate coatings can be seen in Figure 6. The thermal resistance results for the waterglass coatings can be seen in Figure 7.

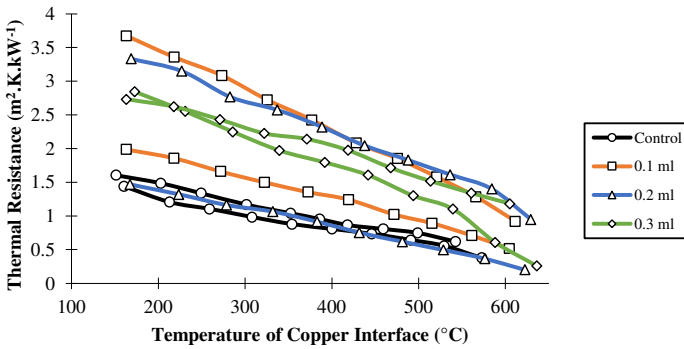


Figure 6. Thermal resistance of magnesium carbonate coatings

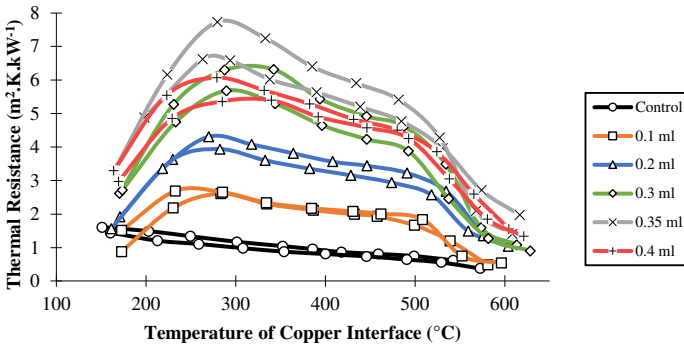


Figure 7. Thermal resistance of waterglass coatings

Discussion

Magnesium carbonate coating

The main observation of the optical microscopy images of the magnesium carbonate coatings is that they appear with cracks exposing mould flux in between. The cracks in the coating are formed during the drying process and transfer over to the mould flux surface. These cracks would create an air gap between the copper and mould flux surfaces that would increase the interfacial thermal resistance.

From Figure 6 it can be seen that all volumes of magnesium carbonate coating have produced an increase in thermal resistance. However, it is unclear from the results if there is a relationship between the amount of magnesium carbonate used and thermal resistance. It could be stated that for all volumes of magnesium carbonate coatings investigated, a consistent increase in thermal resistance is seen. This increase is double that of the control sample at any given temperature. This may be due to the magnesium carbonate coating producing a similar surface roughness for all volumes, but since the evolved gas cannot be retained, the increase in coating gave an insignificant increase in interfacial distance.

Effect of heat on waterglass coatings

From Figure 7 it can be seen that the addition of a waterglass coating to the copper face produced an increase in the thermal resistance. The variation in thermal resistance through the temperature range can be explained by the response of the waterglass coating to heat. Up to 280 °C, the waterglass coating shows intumescent properties and expands due to the evaporation of chemically bonded H₂O, creating a foam. A peak in thermal resistance is seen between 280 °C and 320 °C. From 320 °C up to 480 °C the thermal resistance enters a region of reduction with a similar gradient seen in the control sample. This linear reduction of thermal resistance in the control sample is attributed to the increase in convection in the air gap between the copper and the mould flux. It is proposed that during this period the waterglass foam is mechanically stable. The last phase occurs above 500 °C, where a sharp reduction in thermal resistance is seen. X-ray diffraction analysis of waterglass shows that β -Na₂Si₂O₅ crystallises at 400 °C [14]. This correlates well with the reduction in thermal resistance, since the average coating temperature will be about 100 °C less than the copper interface at 500 °C due to the temperature gradient. Crystallisation may lead to mechanical weakening of the foam and subsequent collapse of the interfacial gap. During industrial application, it is therefore important that the average coating temperature does not exceed 400 °C. At the end of this final stage, all volumes of foam coatings reach a similar value of thermal resistance. The three stages explained above are illustrated in figure 8.

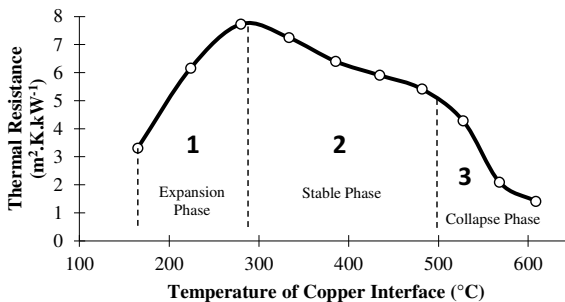


Figure 8. Phases of development of waterglass coating

Relationship between amount of waterglass and thermal resistance

As seen in Figure 7, up to 0.35 ml of waterglass increases the maximum thermal resistance, at which point a decrease is seen when the amount of waterglass is increased to 0.4 ml. This can be explained by analysis of the cross section images in figures 5a-e. The size of pores retained in the mould flux increases to a maximum at 0.35 ml of waterglass. However, the large pores are not seen when 0.4 ml of waterglass is used. When 0.4 ml of waterglass is used, the large volume of gas evolved when the molten flux comes into contact with the coating, may cause the pores to become so big that they float out before being retained. An increase in the amount of waterglass over 0.35 ml therefore has a detrimental effect on thermal resistance.

It can also be said that as the amount of waterglass increases, the variability in pore size increases. This may explain why there is a greater spread of results between comparable samples as the amount of waterglass increases.

Comparison with industrial values

The values of interfacial thermal resistance obtained by a previous parallel plate experimental setup were between 0.5 and 1.0 $\text{m}^2\cdot\text{K}\cdot\text{kW}^{-1}$ [15]. The control samples tested in this investigation gave slightly higher results, between 0.5 and 1.5 $\text{m}^2\cdot\text{K}\cdot\text{kW}^{-1}$. This may be due to less pressure being applied by the cooling block, that allows a larger interfacial gap to appear.

Previous observations of industrial mould flux film samples have, however, estimated that interfacial thermal resistance is between 0.1 and 0.2 $\text{m}^2\cdot\text{K}\cdot\text{kW}^{-1}$ [16]. This was attributed to the greater force applied by the ferro-static pressure in the mould that decreases the interfacial gap. The performance of the coatings in the current investigation should therefore be used as a comparative measure rather than a directly transferrable result.

The author has previously estimated that the removal of fluoride from a peritectic mould powder composition will decrease the total thermal resistance from the steel shell to the copper mould by 0.38 $\text{m}^2\cdot\text{K}\cdot\text{kW}^{-1}$ [12]. Comparatively, this is around two and a half times the interfacial thermal resistance seen from industrial mould flux film samples [16]. Looking at the results from the current investigation, it could be said that the use of 0.2 ml waterglass and above would give this level of increase in thermal resistance. However, using the same comparative measure for the magnesium carbonate coating, an increase of only 0.15 $\text{m}^2\cdot\text{K}\cdot\text{kW}^{-1}$ was achieved, which is not suitable for fluoride free mould powder casting.

Further Work

To look at the effect of ferro-static pressure and investigate the durability of the foam coating under casting conditions, two larger scale investigations will take place. This includes a copper finger experiment, where a water cooled copper finger is submerged into molten flux, measuring the heat removed. The other experiment will be a pilot plant trial using a 7 tonne continuous caster at the Materials Processing Institute, Middlesbrough.

Conclusion

Irrespective of amount used, the effect of magnesium carbonate coatings produced an average increase in interfacial thermal resistance relative to 0.15 $\text{m}^2\cdot\text{K}\cdot\text{kW}^{-1}$ under casting conditions.

The exposure of the waterglass coatings to molten mould flux produced porosity in the solidified mould flux surface and created a foam that increased the distance of the mould flux from the copper surface. This increased the interfacial thermal resistance, with a peak at 0.35 ml of waterglass. Expansion of the coating took place between 150 °C and 280 °C. A stable region is seen up to 500 °C after which a sharp decrease in interfacial thermal resistance is seen. This sharp decrease has been attributed to the weakening of the foam structure.

When comparing the values from the current investigation with industrial results it is estimated that the waterglass coating could provide enough increase in interfacial thermal resistance to replace fluoride in the mould powder.

Acknowledgements

The authors would like to thank EPSRC and Tata Steel for funding the PhD studentship for Mr. Adam Hunt under which this work was completed, the Materials Processing Institute for

providing facilities, and Prof. Ken Mills (Imperial College), Prof. Simon Hodgson and Dr Paul Shelton (Teesside University), Dr. Arghya Dey (Tata Steel) and Mr. Alan Sholes and Dr. Ian Whiteside (Materials Processing Institute) for the valuable discussions and support.

References

1. Susa M, Kushimoto A, Toyota H, Hayashi M, Endo R, Kobayashi Y. Effects of both crystallisation and iron oxides on the radiative heat transfer in mould fluxes, *ISIJ International*. 2009;49(11):1722-9.
2. Nakada H, Susa M, Seko Y, Hayashi M, Nagata K. Mechanism of heat transfer reduction by crystallisation of mold flux for continuous casting, *ISIJ International*. 2008;48(4):446-53.
3. Ozawa S, Susa M, Goto T, Endo R, Mills K. Lattice and radiation conductivities for mould fluxes from the perspective of degree of crystallinity, *ISIJ International*. 2006;46(3):413-9.
4. Hayashi M, Abdul Abas R, Seetharaman S. Effect of crystallinity on thermal diffusivities of mould fluxes for the continuous casting of steel, *ISIJ International*. 2004;44(4):691-7.
5. Qi X, Wen G, Tang P. Investigation on heat transfer performance of fluoride-free and titanium-bearing mold fluxes, *Journal of Non-Crystalline Solids*. 2008;354(52-54):5444-52.
6. Wen G, Seetharaman S, Tang P, Qi X, Liu Y. Development of fluoride-free mold powders for peritectic steel slab casting, *ISIJ International*. 2007;47(8):117-1125.
7. Nakada H, Nagata K. Crystallization of CaO–SiO₂–TiO₂ slag as a candidate for fluorine free mold flux, *ISIJ International*. 2006;46(3):441-9.
8. Wang Q, Lu Y, He S, Mills K, Li Z. Formation of TiN and Ti(C,N) in TiO₂ containing, fluoride free, mould fluxes at high temperature, *Ironmaking and Steelmaking*. 2011;38(4):297-301.
9. Takahira N, Hanao M, Tsukaguchi Y. Viscosity and solidification temperature of SiO₂-CaO-Na₂O melts for fluorine free mould flux, *ISIJ International*. 2013;53(5):818-22.
10. He S, Wang Q, Xie D, Xu C, Li Z, Mills K. Solidification and crystallization of CaO-SiO₂-Na₂O based mold fluxes, *International Journal of Minerals, Metallurgy and Materials*. 2009;16(3):261-4.
11. Stewart B. Control of horizontal heat flux in a continuous casting mould by the deliberate introduction of porosity into the mould-strand gap, *Internal Report*, Tata Steel. 2013.
12. Hunt A. Measurement of interfacial thermal resistance between copper and mould flux using current thermal conductivity device, *Internal Report*, Teesside University. 2015.
13. Stewart B, Hunt A, inventors; Flexible control of heat transfer during continuous casting by deliberately introducing porosity into the mould-strand gap, *Patent Pending*. 2016 .
14. Subasri R, Näfe H. Phase evolution on heat treatment of sodium silicate water glass, *Journal of Non-Crystalline Solids*. 2008;354(10):896-900.
15. Yamauchi A, Sorimachi K, Sakuraya T, Fujii T. Heat transfer between mold and strand through mold flux film in continuous casting of steel, *ISIJ International*. 1993;33(1):140-7.
16. Hanao M, Kawamoto M. Flux film in the mold of high speed continuous casting, *ISIJ International*. 2008;48(2):180-5.

REDUCTION OF IRON OXIDES IN MOULD FLUXES WITH ADDITIONS OF CaSi₂

Min Wang^{1,2}, Rie Endo¹, Yoshinao Kobayashi¹, Zuoyong Dou² and Masahiro Susa¹

¹ Tokyo Institute of Technology;

2-12-1, Ookayama, Meguro-ku, Tokyo, 152-8552, Japan

² Institute of Materials, China Academy of Engineering Physics;
No. 9, Huafengxincun, Jiagyong, Sichuan, 621908, China

Keywords: Mould flux, Iron oxide, Reduction, Calcium silicide.

Abstract

Iron oxides in mould fluxes enhance heat extraction from the molten steel to the mould due to energy absorption by d-d transitions of Fe²⁺ and re-emission. Thus, the existence of iron oxides is against mild cooling of molten steel. In this study, mould flux powders containing *ca* 2 mass% Fe₂O₃ were mixed with sufficient amounts of CaSi₂. The mixtures were contained in alumina crucibles and melted at 1673 K in Ar-H₂ atmosphere. The melts were poured into brass moulds to obtain glassy samples 5 mm thick. The Fe₂O₃ concentration was analysed by a scanning electron microscope with an energy dispersive spectrometer. The concentration decreased from *ca* 1.71 mass% to 0.49 mass% within 5 min and then settled down. Mass transfer of Fe₂O₃ is supposed to be the rate-controlling step at high temperature. The mass transfer coefficient has been calculated to be $1.8 \times 10^{-3} \text{ cm} \cdot \text{s}^{-1}$, which seems reasonable. Since crystallisation of mould flux enhance heat reflection from the molten steel to reduce heat transfer, crystallisation kinetics of mould fluxes has been investigated using the Avrami equation, which suggests that additions of reducing agents such as CaSi₂ suppress the crystallisation process. In addition, CaSi₂ additions result in a dramatic decrease in the total radiative heat flux across mould fluxes in glassy state and would be effective for mild cooling of molten steel.

Introduction

Continuous casting requires mild cooling of molten steel to prevent longitudinal surface cracking. The cooling rate of the steel can be controlled using mould flux which has an influence on the heat transfer from the steel shell to the casting mould. The heat transfer takes place mainly through two mechanisms, namely, conduction and radiation, which could be both reduced by crystallisation of mould flux[1-3]. The addition of iron oxides enhances the radiative heat transfer across the mould flux film due to corresponding changes in optical properties including reflectivities, transmissivity and absorptivities[4,5]. It is necessary to reduce iron oxides in mould flux to give it suitable optical properties for production of steel slabs with good surface quality.

In a previous study mould fluxes it was found that oxygen dissolved in molten iron is the primary oxygen source leading to the dissolution of iron oxides in mould flux, and suggested that additions of reducing agents would be efficient methods of reducing iron oxide concentrations in the final flux materials[6]. Previous studies on the reduction of iron oxides from slags at high temperatures have that carbon in the form of coke or graphite can reduce the iron oxide to

several mass percent in slags[7-9]. These studies have succeeded in providing a good understanding of the kinetics of iron oxide reduction by carbon and the control of foaming phenomena by addition of carbonaceous materials for iron smelting. Carbon particles are commonly mixed with mould flux powders to prevent oxidation of the steel surface. However, these particles are not able to easily dissolve into mould flux baths and are maintained as solids, which have much lower reduction rate of iron oxide than solute carbon[8]. The carbon reduction usually results in the formation of gaseous carbon monoxide and carbon dioxide which would form gas bubbles in mould fluxes. Thus, carbon does not seem to be a suitable reducing source for iron oxides.

Against this background, this study reconsiders reducing agents other than carbon materials for the reduction of iron oxides in mould flux and chooses calcium silicide. Calcium silicide is being used in mould flux to maintain the steel temperature by the exothermic reaction with iron oxides. Although Tsukaguchi *et al*[10,11] have studied exothermic powder containing CaSi and FeO, they have mainly focused on heat of calcium silicide combustion instead of iron oxide reduction. Consequently, this study aims to investigate the reducibility of calcium silicide for the reduction of iron oxides in mould flux at a low concentration level, and to evaluate the crystallisation and radiative heat transfer characteristics of the reduced fluxes.

Experimental

A synthetic mould flux (base mould flux) was employed with the nominal composition (in mass%): $\text{Al}_2\text{O}_3+\text{MgO}=3.23$, $\text{Na}_2\text{O}+\text{F}=19.6$, $\text{Fe}_2\text{O}_3=2.0$, and the basicity $\text{T.CaO}/\text{SiO}_2=1.0$, **Table 1** gives the respective reducing conditions of Exps. 1-3.

Table 1. Summary of experimental conditions

	Mould flux	Reducing agent		Ambient gas	Temperature / K	Holding time / s
		Sort	Mass%			
Exp. 1	Base mould flux	-	-	Ar-H ₂	1673	300
Exp. 2		CaSi ₂	3.1	Ar, Ar-H ₂	1673	240, 600, 1200
Exp. 3		$\Phi \sim 300\mu\text{m}$	1.0, 2.0, 3.1	Ar-H ₂	1673	1800

In Exp. 1, base mould fluxes in powders were used without reducing agent and melted at 1673 K in a platinum crucible in Ar-H₂ gas mixture. In Exps. 2-3, mould flux was used after sufficiently mixing with CaSi₂ and the mixture was melted at 1673 K in an alumina crucibles for reducing reaction within a desired holding time. At the end of each experiment, the melt was rapidly poured into a brass mould to obtain a glassy sample 5 mm thick. Parts of glassy samples were annealed above their crystallisation temperatures determined by DSC: the detailed annealing conditions are shown in **Table 2**.

Table 2. Annealing conditions

Sample	Reducing condition	Temperature / K	Holding time / s
Anneal-1	Exp. 1-0 %, Ar-H ₂ , 5 min	950	1800
Anneal-2	Exp. 3-1.0% CaSi ₂ , Ar-H ₂ , 30 min		
Anneal-3	Exp. 2-2.0% CaSi ₂ , Ar, 30 min	973	1800
Anneal-4-1	Exp. 2-3.1% CaSi ₂ , Ar, 20 min		
Anneal-4-2	Exp. 2-3.1% CaSi ₂ , Ar, 20 min	973	5400

The surface morphologies and the compositions of each of the samples were analysed by SEM-EDS after Au coating and the valence of iron ion was analysed by XPS. The phases present in the annealed samples were determined by XRD using Co K_{α} radiation. The apparent reflectivity (R_a) and transmissivity (T_a) were measured for glassy samples at room temperature using a spectrophotometer with an integrating sphere covering the wavelength range 300-2600 nm.

Results

The base mould flux in the glassy state appears yellowish green due to strong spectral absorption caused by ferric iron ion Fe^{3+} at wavelengths below 500 nm[4,12]. The reduced samples are generally in black colour and opaque, possibly due to strong absorption by dispersion of metallic particles in the samples. Metallic particles were found above the inner wall of alumina crucibles and seemed to be rich in iron, which agglomerated and separated from the molten mould flux due to the significant density difference between iron ($7.25 \text{ g}\cdot\text{cm}^{-3}$)[13] and mould flux ($2.40 \text{ g}\cdot\text{cm}^{-3}$)[14].

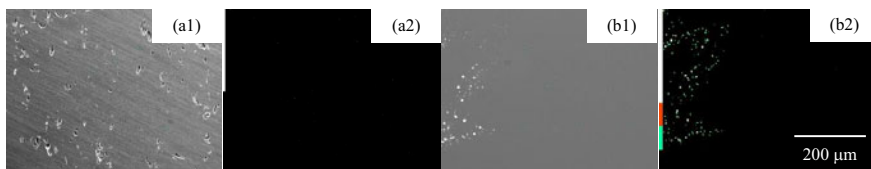


Figure 1. SEM and EDS mapping images of Fe for samples: (a) base mould flux in Exp. 1, and (b) a sample reduced by $CaSi_2$ in Exp. 2.

Figures 1(a)-(b) show SEM images and corresponding EDS mapping images of Fe for representative samples before and after reduction: (a) base mould flux, and (b) after $CaSi_2$ reduction. There is no sign corresponding to iron particles in the base mould flux, whereas iron rich particles in green colour are clearly observed in the sample with enough additions of $CaSi_2$ as shown in Fig. 1(b2). Corresponding EDS point analysis further proves low iron concentration areas in mould flux matrix and high iron concentration areas in iron rich particles. In addition, XPS profiles of Fe in the reduced sample have identified peaks at the binding energy around 707 and 711 eV corresponding to atomic Fe and Fe^{3+} ion[15]. The peak of atomic Fe agrees with the finding of iron rich particles by SEM-EDS. Thus, the concentration of iron oxide in the mould flux matrix has been calculated assuming that all iron oxide exists in the form of Fe_2O_3 . The Fe_2O_3 concentration is *ca* 1.71 mass% in the base mould flux.

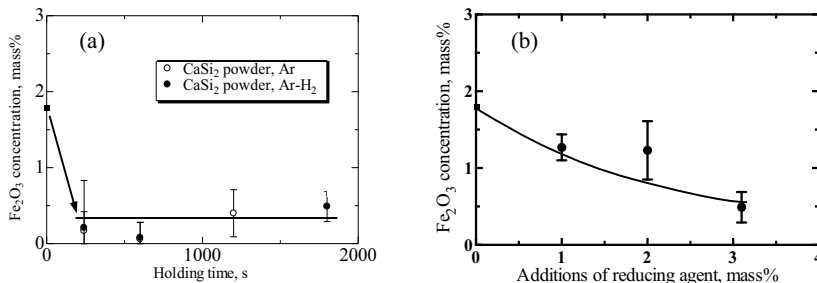


Figure 2. Fe_2O_3 concentration change with (a) holding time, and (b) $CaSi_2$ additions.

Figure 2(a) shows Fe_2O_3 concentration changes in mould fluxes by CaSi_2 reduction with holding time in Ar and Ar- H_2 atmosphere, respectively. Mould flux weighing 14 g empirically requires 2-3 min for complete melting. The reduction of iron oxide proceeds soon after melting of mould flux. There is almost no concentration dependence on atmosphere, which suggests that there is no influence of H_2 in atmosphere on iron oxide reduction. **Figure 2(b)** shows the iron oxide concentration change with CaSi_2 additions. The Fe_2O_3 concentration decreases to 0.49 mass% with additions of 3.1 mass% CaSi_2 .

After annealing under the conditions described in Table 2, the base mould flux became milky white due to strong surface scattering. In contrast, the colour of reduced samples remains black with an almost imperceptible change. Small appearance differences of reduced samples before and after annealing give an indication of crystallisation. **Figures 3(a)** and **(b)** show SEM images of annealed samples corresponding to Anneal-4-1 and Anneal-4-2 conditions in Table 2. Crystallisation of grains in pale colour could be distinguished by inhomogeneous distribution in the observation field. Crystallisation is enhanced while the grains grow up with increasing holding time. **Figure 3(c)** shows a typical XRD profile of Anneal-4-2 sample. The identified peaks of cuspidine ($\text{Ca}_4\text{Si}_2\text{O}_7\text{F}_2$) is recognized as the crystalline phase.

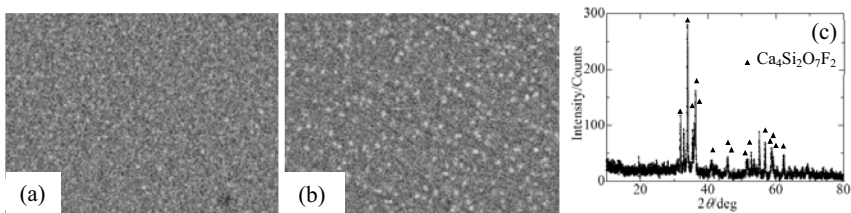


Figure 3. SEM images of (a) Anneal-4-1, and (b) Anneal-4-2 with (c) XRD profile for Anneal-4-2.

Figures 4(a), **(b)** and **(c)** show apparent transmissivities (T_a), reflectivities (R_a) and absorptivities (A_a) of glassy samples with and without CaSi_2 additions, respectively. For the base sample, the values of R_a remain at a low level over all wavelengths, while the values of A_a have absorption peaks below 500 nm and around 1000 nm due to ferric and ferrous iron ions. For the CaSi_2 reduced sample, there are low values of both R_a and T_a and high values of A_a probably due to the absorptions of metallic iron particles formed as a result of the reduction of Fe_2O_3 from the melt.

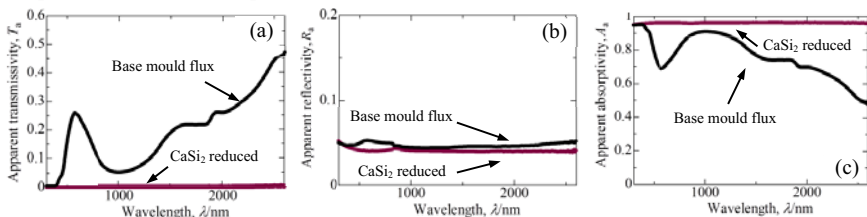


Figure 4. (a) Apparent transmissivities, (b) reflectivities and (c) absorptivities of samples.

Discussion

The reduction of Fe_2O_3 by CaSi_2 is assumed to follow Eq. (1):

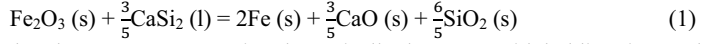


Figure 2(a) has shown that the Fe_2O_3 concentration dramatically decreases with holding time and maintains constant after about 300 s. For high temperature redox reactions, the chemical reaction rate is commonly higher than the diffusion rate at high temperature. Therefore, mass transfer of Fe_2O_3 in the boundary layer is assumed to be the rate controlling step. The diffusion flux of Fe_2O_3 ($J_{\text{Fe}_2\text{O}_3}$) can be expressed by Eq. (2) following Fick's law.

$$J_{\text{Fe}_2\text{O}_3} = -\frac{D}{\delta} \cdot (C_{\text{Fe}_2\text{O}_3} - C_{\text{Fe}_2\text{O}_3}^*) = -k \cdot (C_{\text{Fe}_2\text{O}_3} - C_{\text{Fe}_2\text{O}_3}^*) \quad (2)$$

where δ is the boundary layer thickness, D is the diffusion coefficient of Fe_2O_3 in mould flux, k is the mass transfer coefficient of Fe_2O_3 across the boundary layer, $C_{\text{Fe}_2\text{O}_3}^*$ is the equilibrium concentration of Fe_2O_3 and $C_{\text{Fe}_2\text{O}_3}$ is the Fe_2O_3 concentration in mould flux. In addition, $J_{\text{Fe}_2\text{O}_3}$ through the boundary layer per unit time can be expressed by Eq. (3) as well.

$$J_{\text{Fe}_2\text{O}_3} = \frac{V}{A} \cdot \frac{dC_{\text{Fe}_2\text{O}_3}}{dt} \quad (3)$$

where V is the volume of mould flux, A is the interfacial area and t is the holding time. By substituting Eq. (2) into Eq. (3) and integrating, the following equation can be derived and used to calculate the value of k .

$$\frac{V}{A} \cdot \ln(C_{\text{Fe}_2\text{O}_3} - C_{\text{Fe}_2\text{O}_3}^*) = -k \cdot t + \frac{V}{A} \cdot \ln(C_{\text{Fe}_2\text{O}_3}^0 - C_{\text{Fe}_2\text{O}_3}^*) \quad (4)$$

where $C_{\text{Fe}_2\text{O}_3}^0$ is the initial concentration of Fe_2O_3 in mould flux. Values of $C_{\text{Fe}_2\text{O}_3}$ and $C_{\text{Fe}_2\text{O}_3}^0$ in molar concentration have been derived from the mass fraction obtained by EDS analyses, molar mass and relevant densities ($2.46 + 0.018 \times [C_{\text{Fe}_2\text{O}_3} \text{ in mass\%}] \text{ g/cm}^3$ for mould fluxes containing Fe_2O_3 around 1700 K[16], the value of $C_{\text{Fe}_2\text{O}_3}^*$ at equilibrium is very low and assumed to be zero, the value of V has been calculated to be *ca* 12 cm^3 and the value of A has been estimated to be *ca* 36 cm^2 . As a result, the value of k has been derived to be $1.8 \times 10^{-3} \text{ cm} \cdot \text{s}^{-1}$. This value for iron oxide reduction is much larger than the value for iron oxide formation[9] possibly due to larger interfacial areas for the reduction in powder mixture. In addition, it is suggested that iron oxide formation can be sufficiently suppressed by CaSi_2 within 600 s, which is as short as the estimated dwelling time of molten mould flux in continuous casting[9].

The crystallisation of mould flux has been investigated using the DSC profiles and the Avrami equation as follows:

$$\ln\{-\ln(1-x)\} = n \ln t + \ln K \quad (5)$$

where x is the relative degree of crystallinity, K is the crystallisation rate constant, t is the crystallisation time and n is the Avrami index[17-19]. At a start of crystallisation peak in the DSC profile, the time t is valued zero. While the time continuing, a corresponding value of x is calculated as the ratio of an instantaneous area over the whole area of the crystallisation peak in the DSC profile. The Avrami equation is a classic model applicable to explain crystallisation kinetics of materials including metal, ceramics and polymer on the assumptions: (i) nucleation occurs randomly and homogeneously in the entire untransformed portion of the material, (ii) growth occurs at the same rate in all directions, and (iii) the growth rate keeps constant.

Table 3 gives parameters of crystallisation kinetics including r , n , K , K_j and R^2 calculated using DSC curves, where r is the cooling rate of DSC analysis, K_j is the corrected constant of crystallisation rate satisfying the relationship $\ln K_j = \ln K / r$, and R is the correlation coefficient of the approximate curve. The value of R^2 entirely exceeds 0.95, which suggests that the Avrami equation is substantially applicable to explain the crystallisation kinetics of mould fluxes. Besides the sample reduced by CaSi_2 in this study, three other samples made previously have been compared[20-22]: the sample reduced by Si, base mould flux with *ca* 1.0 mass% Fe_2O_3 and

Fe₂O₃ free mould flux, respectively. The values of n for all four kinds of mould fluxes are around 3.0 in an agreement with Xie *et al*'s study[18,19], which indicates that cuspidine precipitates in the way of heterogeneous nucleation and has a 3-dimensional growth. The highest value of K_j for Fe₂O₃ free mould flux indicates a most rapid process of crystallisation. Crystallisation of mould flux is suppressed by the presence of iron oxide and reducing agents instead of enhancing the nucleation rate of cuspidine.

Table 3. Kinetics parameters of crystallisation on the basis of Avrami equation

	$r, ^\circ\text{C}\cdot\text{min}^{-1}$	n	K	K_j	R^2
CaSi ₂ reduced	10	2.8	0.0073	0.6114	0.9574
Si reduced ²⁰⁾	10	3.0	0.0160	0.6613	0.9971
Base mould flux ²¹⁾	10	3.2	0.0127	0.6462	0.9564
Fe ₂ O ₃ free mould flux ²²⁾	10	2.8	0.1373	0.8199	0.9712

The radiative heat flux across the reduced sample has been estimated by the following the optical process model previously established[20]. The key equation in the optical process model developed from the net radiation method is Eq. (6) for calculation of spectral radiative heat flux across the mould flux layer I_R :

$$I_R = \frac{\varepsilon_2}{1-\varepsilon_2} \left(\frac{N}{D} - E_{2-} \right) \quad (6)$$

$$\text{where } N = [\varepsilon_4 E_{4-} + (1 - \varepsilon_4)(\varepsilon_3 E_{3+} + R_a^* \varepsilon_3 E_{3-} + T_a^* \varepsilon_2 E_{2+})][1 - (1 - \varepsilon_1)R_a] \\ + (1 - \varepsilon_4)T_a[\varepsilon_1 E_{1+} + (1 - \varepsilon_1)(\varepsilon_2 E_{2-} + R_a^* \varepsilon_2 E_{2+} + T_a^* \varepsilon_3 E_{3-})] \quad (7)$$

$$D = 1 - (2 - \varepsilon_1 - \varepsilon_4)R_a + (1 - \varepsilon_1)(1 - \varepsilon_4)(R_a^2 - T_a^2) \quad (8)$$

$$\text{and } E_j = 3.742 \times 10^{-16} n^2 \lambda^{-5} \left[\exp\left(\frac{1.439 \times 10^{-2}}{\lambda T_j}\right) - 1 \right]^{-1} \quad (9)$$

where E_j is the blackbody radiation energy emitted at interface j , subscript “+” means the direction of the energy from the shell to the mould while “-” means the reverse direction, λ is the wavelength, n is the refractive index of materials refracting radiation, ε_1 (T_1) and ε_4 (T_4) are the respective emissivities (temperatures) of the shell and the mould, ε_2 (T_2) and ε_3 (T_3) are the respective emissivities (temperatures) of the solid flux at interfaces in contact with the liquid flux and the air gap layer, R_a and T_a are the respective apparent reflectivity and transmissivity of the solid flux, and R_a^* and T_a^* are the apparent reflectivity and transmissivity for radiation emitted within solid flux, respectively. Parameters involved take the following values: interfacial temperatures $T_1 = 1800$ K, $T_2 = 1400$ K, $T_3 = 500$ K, $T_4 = 400$ K, and the thickness of solid flux layer $d_f = 5.0$ mm. The total radiative heat flux ($I_{\text{Total R}}$) has been derived by integrating Eq. (6) for all wavelengths (0.3-10.0 μm in this study). The values of $I_{\text{Total R}}$ is *ca.* 9.05×10^4 and 464 $\text{W}\cdot\text{m}^{-2}$ for the base sample and the sample reduced by CaSi₂, respectively. Additions of CaSi₂ cause a decrease up to three orders of magnitude in radiative heat flux due to a large decrease in apparent transmissivities and an increase in apparent absorptivities as shown in Fig. 4. Although the crystallisation kinetics is slowed down, additions of CaSi₂ could cause a dramatic decrease in the total radiative heat flux across the glassy mould flux, which would be effective to realize mild cooling in actual continuous casting of steel.

Conclusions

Iron oxides in mould fluxes have been reduced by calcium silicide. Some of the reduced samples have been annealed for crystallisation.

- The average Fe_2O_3 concentration progressively decreases from *ca* 1.71 mass% to 0.49 mass% in mould fluxes with additions of CaSi_2 within 1.8 ks at a temperature of 1673 K.
- The apparent reaction rate constant for the reduction of iron oxide by CaSi_2 has been derived as the magnitude of $10^{-3} \text{ cm}\cdot\text{s}^{-1}$, which is much larger than for iron oxide formation: the addition of CaSi_2 is efficient to keep the iron oxide concentration at a low level.
- Crystallisation kinetics of mould fluxes has been investigated using the DSC profiles and the Avrami equation to suggest that crystallisation of mould flux is suppressed by the presence of iron oxide and CaSi_2 instead of enhancing the nucleation rate of cuspidine.
- Additions of CaSi_2 result in a dramatic decrease in the total radiative heat flux of mould fluxes in glassy state due to effects of metallic iron particles formed in the final flux materials and would be effective to realise mild cooling in actual continuous casting of steel.

References

1. K. Tsutsumi, T. Nagasaka and M. Hino, "Surface Roughness of Solidified Mold Flux in Continuous Casting Process," *ISIJ Int.*, 39 (1999), 1150-1159.
2. H. Nakada, M. Susa, Y. Seko, M. Hayashi and K. Nagata, "Mechanism of Heat Transfer Reduction by Crystallization of Mold Flux for Continuous Casting," *ISIJ Int.*, 48 (2008), 446-453.
3. M. Hanao, M. Kawamoto and A. Yamanaka, "Influence of Mold Flux on Initial Solidification of Hypo-Peritectic Steel in a Continuous Casting Mold," *ISIJ Int.*, 52 (2012), 1310-1319.
4. M. Susa, A. Kushimoto, H. Toyota, M. Hayashi, R. Endo and Y. Kobayashi, "Effects of both crystallisation and iron oxides on the radiative heat transfer in mould fluxes," *ISIJ Int.*, 49 (2009) 1722-1729.
5. Y. Kobayashi, R. Maehashi, R. Endo and M. Susa, "Effects of Valence Control of Iron Ions on Radiative Heat Transfer in Mould Flux," *ISIJ Int.*, 53 (2013) 1725-1731.
6. M. Wang, Y. Kobayashi, R. Endo and M. Susa, "Formation Kinetics of Iron Oxide in Mould Flux during Continuous Casting," *ISIJ Int.*, 53 (2013) 56-61.
7. H. Katayama, M. Matsuo, M. Yamauchi, M. Michitaka, T. Kawamura and T. Ibaraki, "Mechanism of Iron Oxide Reduction and Heat Transfer Smelting Reduction Process with a Thick Layer of Slag," *ISIJ Int.*, 32 (1992) 95-101.
8. P.K. Paramguru, H.S. Ray and P. Basu, "Some Kinetic Aspects of Reduction of FeO in Molten Slags by Solute Carbon," *ISIJ Int.*, 37 (1997) 756-761.

9. A.K. Jouhari, R.K. Galgali, P. Chattopadhyay, R.C. Gupta and H.S. Ray, "Kinetics of Iron Oxide Reduction in Molten Slag," *Scand. J. Metall.*, 30 (2001) 14-20.
10. Y. Tsukaguchi and M. Kawamoto: "Exothermic Mold Fluxes for Slab Casting in Sumitomo Metals" (Paper presented at the Proc. of 11th China-Japan Symp. on Iron and Steel Tech., Beijing, 2007), 154.
11. Y. Tsukaguchi, S. Ura, A. Shiraishi, Y. Hitomi, T. Nagahata, "Development of Slab Casting Technology for High Carbon Steel" (Paper presented at the Proc. of 76th Steelmaking Conf., Warrendale, PA, 1993), 397.
12. M. Susa, K. Nagata and K. C. Mills, "Absorption Coefficients and Refractive Indices of Synthetic Glassy Slags Containing Transition Metal Oxides," *Ironmaking Steelmaking*, 20 (1993) 372-378.
13. J. E. Jensen, W. A. Tuttle, R. B. Stewart, H. Brechna and A. G. Prodel: *BROOKHAVEN NATIONAL LABORATORY SELECTED CRYOGENIC DATA NOTEBOOK, VOLUME II* (Washington, D. C.: AUI 1980), XIV-E-2.
14. Verein Deutscher Eisenhüttenleute, *SLAG ATLAS 2nd ed.* (Düsseldorf: Verlag Stahleisen 1995), 316.
15. J. Chastain and R.K. King, Jr., *Handbook of X-ray Photoelectron Spectroscopy* (Chigasaki: ULVAC-PHI, Inc. 1995), 81.
16. Verein Deutscher Eisenhüttenleute, *SLAG ATLAS 2nd ed.* (Düsseldorf: Verlag Stahleisen 1995), 344.
17. M. Avrami, "Kinetics of Phase Change. II: Transformation-Time Relations for Random Distribution of Nuclei," *J. Chem. Phys.*, 8 (1940), 212-224.
18. B. Xie, Y. Lei, F. Qi and J. Diao, "Effects of MnO on non-isothermal crystallisation kinetics of mould fluxes using DSC curves" (Paper presented at the Technical Seminar of CC Mold Flux and Quality Control, Beijing, 2009), 72-84.
19. Y. Lei, B. Xie, F. Qi and J. Diao, "Effects of MnO on Crystallisation Kinetic Characteristics of Mould Fluxes," *the Chinese Journal of Process Engineering*, 8 (2008), 185.
20. M. Wang, R. Endo, Y. Kobayashi, Y. Susa and M. Susa, "Radiative Heat Transfer Reduction across Mould Fluxes with Silicon Additions as Reducing Agent for Continuous Casting of Steel," *Taikabutsu Overseas*, 36 (2016).
21. R. Maehashi, "Effects of Valence Control of Iron Ions on Radiative Heat Transfer in Mould Flux" (in Japanese, bachelor thesis, Tokyo Institute of Technology, 2012).

22. A. Kushimoto, "Effect of Cuspidine Grain Sizes on Radiative Heat Transfer in Mould Fluxes" (in Japanese, master thesis, Tokyo Institute of Technology, 2011).

**ADVANCES IN MOLTEN
SLAGS, FLUXES, AND SALTS:**

Proceedings of



**Physical Properties:
Viscosity**

Viscosity Measurement at the International Conferences on Molten Slags and Fluxes from 1980 to the Present

Steven Wright¹, Wan-Yi Kim²

¹CSIRO Minerals Resources, Bayview Ave, Clayton, Vic 3169, Australia

²Steelmaking Research Group, Technical Research Laboratory, POSCO, Korea

Keywords: Viscosity, fluidity, homogeneous, slag, silicate, reference, Newtonian, Bingham

Abstract

Many papers have been presented, and the sessions well attended, on the viscosity measurements of silicate and calcium ferrite based slag systems since this conference series inception in 1980 in Halifax. Over the years, the emphasis has been spent on developing reliable measurement techniques of pure liquids, trustworthy datasets, extending the slag systems and the number of components in the liquids, understanding the behaviour of amphoteric oxides, and extending measurements to two phase systems.

This paper reviews the viscosity measurement papers presented at Halifax through to Beijing, with the view to showing how the understanding and practise of viscosity measurement has changed, along with our understanding of the nature of the liquids being measured and ultimately mathematically modelled. Much of the development can be attributed to Professor Ken Mills, and this review attempts to pay tribute to his outstanding contribution to the field.

Introduction

Determination of the effects of temperature and chemistry on the viscosity of high temperature melts has always been a challenging area of research. Viscosity measurement usually requires knowledge of the melt phase diagram, or at least the composition range being studied. There is no single viscosity measurement method that can measure the entire range of viscosity of high temperature liquids. The viscosity of the liquid can vary over several orders of magnitude or by only a few percent with temperature depending upon the composition. Bouyancy and reactions between the container and melt-measuring material can limit what can be used experimentally. The melt composition may change with time and temperature. Temperature differentials between the furnace wall and the melt and thermal gradients along the furnace wall can increase measurement uncertainty. Thermal expansion may also increase uncertainties. The measurement technique requires calibration, usually with at least one material of known viscosity. The experimental method can also have significant uncertainties, due to geometric flow considerations, or the difficulties of the measurement, as with the rotational viscometer.

The viscosity papers at the affectionately dubbed “Slag” conferences have reflected the desire to innovate and improve the accuracy of measurements and to link the measurements to a greater understanding of the melt structure. Much of the recent improvements can be attributed to the energy and drive and collaborative approach of Professor Ken Mills to develop a suitable high temperature reference melt in the applicable viscosity range for metallurgical slags and refine the measurement approach to improve accuracy.

This paper looks back at all the viscosity papers presented at these meetings, but is not intended to be a critical review of each paper, but the aim is to examine the key findings and forecast possible future areas of viscosity research.

The Papers

1980

At the first meeting in Halifax (International Symposium on Metallurgical Slags, 1980) papers with data on viscosity measurements were presented mainly in two sessions with both reviews of previously published data and new measurements (Table I) presented during the meeting*. The viscosity data (at the time) on slags produced in copper smelting was reviewed by Mackey (1980). Viscosity data on industrial slag from a reverberatory furnace operated by Noranda (Peacey and Pelletier, 1980) was also presented in a paper regarding production of mineral wool, but no details on how the measurements were performed were given.

Viscosity measurements using a counterbalanced sphere method on ternary lead silicate melts were presented (Ouchi and Kato, 1980). The method relies on determining the velocity of a sphere as it descends in the melt. The velocity of the falling sphere can be adjusted by changing the mass on the counterbalance. A platinum-rhodium crucible was used to contain the melt and the measurement sphere was platinum. The viscometer was calibrated with standard oils. The study showed that when the temperature was kept constant, and the silica mole fraction remained constant, the viscosity increased by up to 15% when alkali earth oxides were partially substituted lead for up to a mole fraction of 0.05. Lime had the greatest increase, with the behaviour of MgO and BaO slightly less. Substitution of PbO with NiO or CoO up to a mole fraction of 0.05 resulted in a very small or almost no change in viscosity.

The effect of magnesia addition on the viscosity of Na₂O-SiO₂ slags by a rotating cylinder method was reported by Kawahara *et al.*, (1980). In melts with a high silica content (Na₂O/SiO₂ = 1/4), the addition of MgO overall decreased the viscosity for additions up to 30 mole%. As the silica content decreased, (Na₂O/SiO₂ ratio increased), MgO addition did not appear to decrease the viscosity significantly, and at Na₂O/SiO₂ ratio of 1 or 1.5 the viscosity did not change for MgO contents of up to 20 mole%. The authors also investigated the impact of substituting CaO with NiO for CaO-SiO₂ slags at constant silica content. Substitution of CaO with NiO reduced the viscosity.

The viscosity of slags with potential for application as mould fluxes in continuous steel casting was measured using the rotating cylinder approach with Mo components and using an Ar atmosphere (McCauley and Apelian, 1980). Twenty different compositions were studied in the Al₂O₃-CaF₂-CaO-Na₂O-SiO₂ system, with the Al₂O₃ content being kept constant, and the other components varied. The silica content had the greatest effect on viscosity, which decreased as the CaO/SiO₂ ratio was increased. Na₂O and CaF₂ also decreased the viscosity as their concentration was increased. The viscosity was dependent on the ratio of network forming ions to anions in the slag, and the several empirical models were applied to the data, with most giving a reasonable fit based on melt composition.

*A presentation by Toguri and Wang on the "Viscosity of Molten slags" was listed in the symposium program, but no paper appeared in the proceedings.

Table I Systems for which new viscosity data were presented at the first conference (Halifax).

System	Method	Material	Temperature range (°C)	Reference
Al ₂ O ₃ -CaO-FeO-MgO-SiO ₂	N/A	N/A	1150-1500	Peacey & Pelletier, 1980
BaO-PbO-SiO ₂ CaO-PbO-SiO ₂ CoO-PbO-SiO ₂ MgO-PbO-SiO ₂ NiO-PbO-SiO ₂ PbO-SiO ₂	Counter-balanced sphere	Pt/Rh Pt	1000-1200	Ouchi & Kato, 1980
MgO-Na ₂ O-SiO ₂ CaO-NiO-SiO ₂	Rotating cylinder		-1550	Kawahara <i>et al.</i> , 1980
Al ₂ O ₃ -CaF ₂ -CaO-Na ₂ O-SiO ₂	Rotating cylinder	Mo	1400	McCauley & Apelian, 1980

N/A No information given.

1984

The second meeting was held at Lake Tahoe (Proceedings of the Second International Symposium on Metallurgical Slags and Fluxes, 1984) and the viscosity papers are given in Table II. Viscosity measurements of slags produced in steelmaking were presented (Drissen *et al.*, 1984; Nichols *et al.*, 1984; McCauley and Apelian, 1984; Yanagase *et al.*, 1984) as well as viscosity measurements on synthetic coal slags (Vorres *et al.*, 1984). These measurements all used the rotating cylinder method.

The measurements on steelmaking slag (Drissen *et al.*, 1984) used Pt-20%Rh components and were performed in air. This would have minimised loss of Fe from the slag to the crucible and bob. The bob was calibrated using standard oils. A range of composition was studied in the CaO-Fe₂O₃-MgO-SiO₂ system. Measurements examined the effect of basicity (CaO+MgO)/SiO₂ and total iron, expressed as Fe₂O₃, as well as temperature. For melts with a constant molar basicity ratio, (x_{CaO}+x_{MgO})/x_{SiO₂}, substitution of CaO with MgO increased the viscosity slightly, irrespective of the Fe content of the slag. When the basicity was kept constant and Fe₂O₃ is added to the slag, the viscosity decreased.

The coal slag viscosity studies were performed at low oxygen potentials or in air (Vorres *et al.*, 1984). For the low oxygen potential conditions, Mo components were used, and a H₂-CO₂-N₂ or H₂-CO₂-Ar gas mixture was used to established the oxygen partial pressure. For viscosity measurements of coal slags in air, Pt components were used. Twenty compositions in the Al₂O₃-CaO-FeO_x-MgO-SiO₂ system were studied. The key findings for fully liquid slags were:

- There was a linear relationship between $\ln \mu$ and $1/T$.
- Increasing the silica content of the slag increased the viscosity
- At fixed silica content, increasing Al₂O₃ increased viscosity
- The effect of oxygen potential on viscosity increased as the iron oxide content increased.
- A rapid change in viscosity during measurements in the lower temperature range of the study was most likely due to the formation of solid phases.

Isothermal measurements on the Al₂O₃-CaF₂-CaO system were also presented (Yanagase *et al.*, 1984). The measurements were performed using the rotating cylinder method using Pt

components. The behaviours of CaO and CaF₂ in the liquid melt with respect to viscosity were very similar and decreased viscosity. Alumina exhibited amphoteric behaviour; for melts with the CaO/Al₂O₃ >1, alumina forms complex ions and the viscosity increases. At CaO/Al₂O₃ <1, the behaviour of Al₂O₃ was similar to CaO, and the iso-viscosity lines were parallel to the lines of constant CaF₂ composition.

The viscosity of mould slags that could be used in a bottom filled ingot process was presented by Nichols *et al.* (1984). The slags were contained in a graphite crucible under an argon atmosphere and a Mo spindle was used to measure the viscosity. The viscosities of ten compositions in the Al₂O₃-CaF₂-CaO-FeO-K₂O-MgO-Na₂O-SiO₂ (+ impurities) system were measured. The log of the measured viscosity was linear with respect to 1/T for all the compositions studied. The viscosity increased as the silica content increased, and the authors found that the Y parameter (Kingery *et al.*, 1976) combined with the mole fraction of silica gave an excellent correlation between the network properties of the slag and the viscosity. The correlation was of the form:

$$\log \eta_{1500^\circ\text{C}} = 7.368 + 2.068 \cdot x_{\text{SiO}_2} + 1.985 \cdot Y$$

Where Y was:

$$Y = 8 - (2 \cdot (x_{\text{FeO}} + x_{\text{CaO}} + x_{\text{Na}_2\text{O}} + x_{\text{K}_2\text{O}} + 2 \cdot x_{\text{CaF}_2} + 2 \cdot x_{\text{SiO}_2} + 3 \cdot x_{\text{Al}_2\text{O}_3})) / (x_{\text{SiO}_2} + 2 \cdot x_{\text{Al}_2\text{O}_3})$$

The regression coefficient was $r^2=0.974$,

The temperature dependence of viscosity of the mould fluxes presented at the first conference and subsequently published in a journal of the conference proceedings (McCauley and Apelian, 1980; McCauley and Apelian, 1981) was examined with respect to several models. The Clausius-Clapeyron equation was found to give the best fit across a broad range of liquids including slags, liquid metals, molten salts and organic liquids.

$$\eta = e^{(a + \frac{b}{T} + c \cdot \ln T)}$$

An indirect approach correlating measured viscosity with slag fluidity, measured the string length per gram of slag formed by tipping hot slag onto an inclined steel launder (Chen *et al.*, 1884). A slag from an industrial slag cleaning furnace was fluxed with SiO₂ or Al₂O₃ or CaO, to vary the slag chemistry. The slag viscosity was also measured using a rotating cylinder method using Mo components under an argon atmosphere. The slag fluidity (as measured by the string length) was inversely proportional to the viscosity.

Table II New viscosity measurements presented at the 2nd conference (Lake Tahoe).

System	Method	Material	Temperature range (°C)	Reference
CaO-FeO _x -MgO-SiO ₂	Rotating cylinder	Pt-20%Rh	1310-1600	Drissen <i>et al.</i> , 1984
Al ₂ O ₃ -CaF ₂ -CaO-FeO-K ₂ O-MgO-Na ₂ O-SiO ₂	Rotating cylinder	Mo	1200 -1500	Nichols <i>et al.</i> , 1984
Al ₂ O ₃ -CaO-FeO _x -SiO ₂	Rotating cylinder	Mo	1200	Chen <i>et al.</i> , 1984
Al ₂ O ₃ -CaF ₂ -CaO	Rotating cylinder	Pt	1450-1580	Yanagase <i>et al.</i> , 1984
Al ₂ O ₃ -CaO-FeO _x -MgO-SiO ₂	Rotating cylinder	Mo or Pt	1250-1450	Vorres <i>et al.</i> , 1984
Al ₂ O ₃ -CaF ₂ -CaO-Na ₂ O-SiO ₂	Rotating cylinder	Mo	1400	McCauley & Apelian, 1984

1989

At Glasgow, where the third Conference was held (3rd International Conference on Metallurgical Slags and Fluxes, 1989), two papers were presented on viscosity measurements (Table III). Measurements on the B₂O₃-Na₂O-SiO₂ system (Shiraishi and Ogawa, 1989) were on solid glasses and fully liquid melts using two measurement techniques for both phase types; namely parallel plate and rotating cylinder. The measured viscosity ranged from 4.4 x 10² Pa s to 0.76 Pa s. The measurements on the liquid slag showed that for melts with Na₂O/B₂O₃ >1, B₂O₃ was amphoteric and a network former. However at these ratios, if the SiO₂ content was high, B₂O₃ was a network modifier or breaker. At Na₂O/B₂O₃ < 1, B₂O₃ behaves as a network breaker, irrespective of the SiO₂ concentration. The second paper on borate melts (Iida *et al.*, 1989) used a custom built oscillating plate viscometer, and the measurements on pure B₂O₃ were in good accord with published data. For binary B₂O₃-PbO melts, addition of PbO decreased the viscosity. The measured viscosity of liquid melts ranged between 1000 Pa s for B₂O₃ at 873 K and 0.003 Pa s for liquid PbO at 1273K. There was again good agreement with the published data across the B₂O₃-PbO composition range.

Table III Systems where new viscosity measurements were presented at the 3rd conference (Glasgow).

System	Method	Material	Temperature range (°)	Reference
B ₂ O ₃ -Na ₂ O-SiO ₂	Parallel plate		527-677	Shiraishi and Ogawa, 1989
	Rotating cylinder	Pt-6%Rh	827-1127	
B ₂ O ₃ B ₂ O ₃ -PbO	Oscillating plate	S. Steel Pt	527-1127	Iida <i>et al.</i> , 1989

1992

At the Sendai meeting (Molten Slags and Fluxes, 92), Professor Ken Mills presented a plenary lecture and paper on the relationship between physical properties of slags (viscosity, electrical conductivity, self diffusion coefficients and thermal expansion coefficients) with the structure of the silicate network in the slag (Mills, 92). A slag consists of a 3-dimensional network of interconnected SiO₄⁴⁻ tetrahedra which are joined by bridging oxygens (O⁰). These linked tetrahedral are de-coupled by non-bridging oxygen (O⁻) which come from the oxygen of other cations in the slag (eg, Ca²⁺, Mg²⁺, Na²⁺, etc.). Cations with smaller radius (*r*) and higher valence (*z*), favour depolymerisation of the silicate units to SiO₄⁴⁻ tetrahedra. This tendency can be ranked by the parameter *z/r*². High valence state cations (M³⁺, M⁴⁺, M⁵⁺) can also form tetrahedra and be network formers, so the structure of the slag can be thought of as the total number of tetrahedra bridged by oxygen, however local charge balance considerations must be accommodated by having other cations nearby. Cations such as Fe³⁺ can also have four(IV) or six (VI) co-ordination so can be a network former or breaker depending upon the concentration and Fe³⁺/(Fe²⁺+Fe³⁺) ratio. The principles on defining the structural units are explained in detail in the paper.

The ratio of number of non-bridging oxygen (NBO) over the number of bridging oxygen (T) atoms (NBO/T) was correlated to the variation of slag physical properties with composition. The main findings with respect to viscosity behaviour were:

- The degree of depolymerisation is the primary factor affecting the viscosity of a fully liquid slag, and the cation a “second order” effect.

- The NBO/T ratio is probably superior to optical basicity (Λ_{corr}) as a measure of depolymerisation for silicates, while the latter has broader application to other melt types.
- For aluminosilicate melts, cations involved in charge balancing do not contribute to depolymerising the melt.

The variation of the activation energy of viscous flow with depolymerisation of the melt using the NBO/T ratio did not yield a satisfactory correlation. The NBO/T ratio does not account for different M-O bond lengths when cations other than Si form tetrahedra.

Professor Ramana Reddy, co-chair of the 1992 conference presented a structurally based model to describe the viscosity behaviour with composition and temperature for borate slags using the concept of oxygen bridging between boron atoms to form polymers along with non-bridging oxygen to break up the network (Reddy *et al.*, 1992). The viscosity behaviour of $\text{Na}_2\text{O-B}_2\text{O}_3$ melts was described and compared with the literature.

The papers presenting new viscosity at the meeting are given in Table IV. Professor Mills presented on his findings of a round robin study to develop a Standard Reference Material for viscosity measurements at high temperatures (Broadbent *et al.*, 1992). This development was driven by the need for a suitable reference slag which had a viscosity in the range of most metallurgical slags, and could be used in atmospheres ranging from reducing, neutral or oxidising. A large quantity of slag with a target composition of 19.46% Li_2O_3 -14.06 % Al_2O_3 and 63.8 % SiO_2 was prepared and homogenised. A measurement study over two round robins was then performed by 13 organisations using a variety of measurement techniques and container/contact materials. The results of the first round of measurements from 11 laboratories showed that there was appreciable scatter in the value of the measured viscosity, equivalent to a temperature variation of ± 80 K. The slopes of the temperature dependence of $\ln \mu$ plotted against $1/T$ for most of the measurement sets were similar. The key result from the first round robin measurements was a set of protocols to reduce variation and uncertainty. The key requirements were:

- Drying of the sample at 110°C overnight prior to measurement.
- Use of Mo or Pt components to contain/contact the slag.
- Calibration of thermocouples with a traceable standard thermocouple.
- The melt position optimised for the isothermal region of the furnace.
- The temperature difference between the melt and the furnace determined.
- Upper measurement temperature restricted to 1400°C.
- A neutral or reducing atmosphere to be used in the working tube.
- Calibrated with at least two standard oils with viscosity in the range of 0.1 to 1 Pa s.
- Post chemical analysis of the slag.

In the 2nd round of measurements, 13 laboratories participated; the measurement scatter was reduced, but still significant at ± 55 K. When the results were grouped into container/contact material type, the group of measurements using Mo components had the least scatter (± 10 K) while the group using graphite components had the greatest scatter. The variation of the measurements with Pt components lay somewhere in between, with some laboratories measuring the same values as reported for Mo components.

The study concluded that the SRM was suitable as a reference material, and recommended values of the temperature dependent viscosity of the liquid SRM slag with an estimated uncertainty of ± 10 K were quoted.

Iida and Tanaka (1992) presented oscillating plate viscometer measurements on the SRM using the protocols outlined previously. The oscillating plate method is suitable for measuring slag viscosity, but the end effect of the plate increases with increasing plate thickness and increasing liquid viscosity, affecting the calculated viscosity. The true viscosity was calculated using the empirical relationship between the viscosity and the damping factor using a second order term for the damping factor. Measurements on the SRM were in good accord with the recommended values. Sasahara *et al.*, (1992) presented an abstract on a viscometer based on the Iida oscillating plate viscometer and described viscosity measurements on the CaO-FeO-SiO₂ system with CaCl₂ or CaF₂ flux addition. They reported that addition of the fluxes reduced the viscosity by similar amounts[†].

The viscosity of 35 synthetic slags for potential use in continuous casting as mould powders was measured using a rotating spindle viscometer (Kim *et al.*, 1992). Graphite crucible and spindle were used and the effect of slag composition was examined by varying; Li₂O, Al₂O₃, B₂O₃, MgO, Na₂O, F and CaO/SiO₂ ratio to a base slag containing 6% Al₂O₃, 35% CaO, 3% Li₂O, 0.6% Fe₂O₃, 5% MgO, 11% Na₂O, 38% SiO₂. Addition of CaO, F, Li₂O, Na₂O, and MgO each decreased the viscosity and the activation energy for viscous flow, addition of Al₂O₃ increased the viscosity and the activation energy, while B₂O₃ addition decreased the viscosity but increased activation energy. The authors reported that from the results of the study a mould powder for high speed casting had been developed which has optimum conditions and a lower F content, by adding a small amount of Li₂O and B₂O₃ to the basic mould flux.

Table IV Viscosity measurements presented at the 4th conference (Sendai).

System	Method	Material	Temperature range(°C)	Reference
Al ₂ O ₃ -Li ₂ O- SiO ₂ *	Various	Various	1100-1400	Broadbent <i>et al.</i> , 1992
Al ₂ O ₃ -Li ₂ O- SiO ₂ *	Oscillating plate		1100-1400	Iida & Tanaka, 1992
Al ₂ O ₃ -CaO-Li ₂ O-Fe ₂ O ₃ -MgO-Na ₂ O- SiO ₂ .	Rotating cylinder	Graphite		Kim <i>et al.</i> , 1992

*Standard Reference <1% impurity oxides

1997

The next symposium was held in Sydney (Molten Slags, Fluxes and Salts '97, 1997) and the papers that presented new viscosity data are presented in Table V.

The simple test for measuring viscosities which was presented at the 2nd Slag conference (Mills, 1984) was extended to a round robin study involving 6 laboratories using reference slags (Mills *et al.*, 1997). The method was based on an inclined plate technique and correlated the string length to the known viscosity. The viscosity of Al₂O₃-CaO-CaF₂-Na₂O-SiO₂ (+ impurities) slags and the SRM slag (Broadbent *et al.*, 1992) was measured at NPL or Metallurgica using the rotating cylinder method with Mo or Pt components respectively. The authors claimed that viscosities predicted by a correlation of the reciprocal of the string

[†] No viscosity measurements were detailed in the abstract presented.

length were within $\pm 15\%$ of the real value. A key factor was to ensure that the melt was at least 100°C higher in temperature than the solidus temperature. Several other viscosity measurement papers also presented data where there had been prior calibration of the hot system using the SRM slag and the protocols for viscosity measurement (Broadbent *et al.*, 1992; Hurst *et al.*, 1997; Ji *et al.*, 1997; Wright *et al.*, 1997). Measurements on mould flux slag were also presented by Sorimachi (1997) using the rotating cylinder viscometer with graphite components.

Wright presented a paper on viscosity measurements of lead slags in which lime was substituted for some of the lead oxide (Wright *et al.*, 1997). The measurements were performed using the protocols developed for the SRM (Mills *et al.*, 1991; Broadbent *et al.*, 1992) and Pt-Rh components were used in an air atmosphere. The equipment was calibrated using a sample of SRM and the agreement between the measurements and the recommended SRM values was within the quoted experimental uncertainties. The key finding was that both CaO and PbO are network breakers, with PbO being more effective than CaO, as the viscosity of CaO-PbO-SiO₂ melts was greater than PbO-SiO₂ melts at a constant silica content. At the low concentration of CaO added to the melt, CaO was thought not to change the liquid structure, so the difference in viscosity was attributed to the differences in the interaction strengths of the cations (Pb, Ca) and the oxygen containing anions.

Three papers on the viscosity of borosilicate melts were presented (Nakashima *et al.*, 1997; Reddy *et al.*, 1997; Shiraishi *et al.*, 1997), with one study measuring the viscosity of solid glasses and the fully liquid melt using a viscometer developed to study both states (Shiraishi *et al.*, 1997). The results on B₂O₃ and Na₂O-SiO₂ glasses and melts were in good accord with the literature.

The viscosity of the pseudo four component Al₂O₃-CaO-FeO_x-SiO₂ system was measured in air (Hara *et al.*, 1997) and reducing conditions where the Fe³⁺/Fe²⁺ ratio was 0.1 (Hurst *et al.*, 1997). Hara *et al.*, measured the viscosity of slags at a constant CaO/SiO₂ ratio and temperature, and varied the Al₂O₃ and Fe₂O₃ contents between 0 and 50%. The viscosity increased as the alumina content increased to 40%. For example at 1500°C , the slag containing 25% CaO, 25% SiO₂ and 10% Al₂O₃ and 40% Fe₂O₃ had a viscosity of 0.8 Pa s. The slag with the same lime and silica contents and containing 40% Al₂O₃ and 10% Fe₂O₃ had a viscosity of 9 Pa s. The authors concluded that at CaO/SiO₂ = 1, alumina is an amphoteric oxide and acted as a network former. The Hurst *et al.* study focused on measuring the viscosity of low iron coal ash slags and modelling the viscosity behaviour. When the viscosity data were plotted on a ternary Al₂O₃-CaO-SiO₂ diagram, in the region where the Al₂O₃/SiO₂ ratio was between 0.25 and 0.95, the iso-viscosity lines ran parallel to the lines of constant lime composition, so Al₂O₃ was acting as a network former. A modified Urbain model (Urbain *et al.*, 1981) was fitted to their data for Al₂O₃-CaO-FeO_x-SiO₂ slags containing less than 5% FeO and had satisfactory fits over the limited composition range studied.

Ji *et al.* (1997) made measurements on a number of key systems in order to develop a viscosity model for the CaO-FeO_x-MnO-SiO₂ system. They used iron components to measure viscosity and calibrated the viscometer system using a reference slag (Mills *et al.*, 1991; Broadbent *et al.*, 1992). There was generally good agreement with other studies for the systems studied which included the CaO-FeO_x-SiO₂, CaO-MnO-SiO₂ and CaO-FeO_x-MnO-SiO₂. The viscosity model developed gave a good representation of the data. Several other viscosity modelling studies were reported at the conference: correlating viscosity with

chemical composition (Hurst *et al.*, 1997) optical basicity and basicity index (Seshadri *et al.*, 1997; Iida *et al.*, 1997) and a structural model (Zhang and Jahanshahi 1997).

Table V New viscosity measurements presented at the 5th conference (Sydney).

System	Method	Material	Temperature range	Reference
Al ₂ O ₃ -Li ₂ O-SiO ₂ * CaO-PbO-SiO ₂	Rotating cylinder	Pt-Rh	1100-1400°C	Wright <i>et al.</i> , 1997
Al ₂ O ₃ -Li ₂ O-SiO ₂ *	Rotating cylinder	Mo Pt	1200-1400°C	Mills <i>et al.</i> , 1997
B ₂ O ₃ -BaO-SiO ₂ B ₂ O ₃ -CaO-SiO ₂ B ₂ O ₃ -K ₂ O-SiO ₂ B ₂ O ₃ -Na ₂ O-SiO ₂	Rotating cylinder	Pt-20%Rh	1000-1550°C 1100-1550°C 800-1150°C 840-1180°C	Nakashima <i>et al.</i> , 1997
B ₂ O ₃ -Na ₂ O-SiO ₂	Rotating cylinder	N/A	677-1050°C	Reddy <i>et al.</i> , 1997
B ₂ O ₃ -Na ₂ O-SiO ₂ Na ₂ O-SiO ₂	Indentation Parallel plate Rotating plate	S. Steel	200-1200°C	Shiraishi <i>et al.</i> , 1997
Al ₂ O ₃ -CaO-Fe ₂ O ₃ - SiO ₂	Counter-balanced sphere	Pt &Pt- 20%Rh	1400-1623°C	Hara <i>et al.</i> , 1997
Al ₂ O ₃ -Li ₂ O-SiO ₂ * Al ₂ O ₃ -CaO-FeO-SiO ₂	Rotating cylinder	Mo	1000-1300°C 1450-1500°C	Hurst <i>et al.</i> , 1997
Al ₂ O ₃ -Li ₂ O-SiO ₂ * CaO-Fe ₂ O ₃ -SiO ₂ Fe ₂ O ₃ -MgO-SiO ₂ Fe ₂ O ₃ -MnO-SiO ₂ CaO-MnO-SiO ₂ CaO-Fe ₂ O ₃ -MnO-SiO ₂	Rotating cylinder	Fe	1000-1300°C 1150-1480°C 1335-1480°C 1250-1480°C 1300-1480°C 1300-1480°C	Ji <i>et al.</i> , 1997
Al ₂ O ₃ -CaO-F-Na ₂ O-SiO ₂	Rotating cylinder	Graphite		Sorimachi, 1997

*SRM with <1% impurity oxides. See Broadbent *et al.*,1992 for full details.

N/A

2000

Helsinki and Stockholm were the venue cities for the sixth conference in the series, referred to as Molten 2000 (SIXTH International Conference on Molten Slags, Fluxes and Salts, 2000) and the viscosity measurements are summarised in Table VI. At this conference viscosity measurements by Hurst and co-workers on the Al₂O₃-CaO-FeO_x-SiO₂ system which had been presented at the Sydney meeting (Hurst *et al.*, 1997) were extended to higher iron oxide contents of up to 15 % (Hurst *et al.*, 2000). At 1450°C, some of the high iron oxide slags exhibited non-Newtonian behaviour, which may have been due to the presence of solid phases in the melt. For the slags in which the measurements were Newtonian, at 10 to 15% FeO levels in the slag, the iso-viscosity lines were parallel to the lines of constant CaO content when plotted on a pseudo three component Al₂O₃-CaO-SiO₂ diagram. The viscosity measurements were used to develop a fluxing practise for coal gasifiers. In a similar manner, the viscosity of blast furnace type slags containing FeO was measured using a rotating cylinder viscometer with iron components (Sugiyama, 2000) and the measured data were fitted to an empirical viscosity model. This model was then used in a mathematical model of the lower region of the blast furnace to develop a picture of the flowing characteristic of the liquid inside the blast furnace.

Two papers relevant to the viscosity of non-ferrous smelting slags were presented at the conference. The viscosity of magnesia containing iron silicate slags of relevance to nickel matte smelting was presented by Ducret and Rankin (2000) using iron components. They found that the viscosity decreased significantly as the Fe/SiO₂ ratio was increased in the range 1.3 to 2.00. The addition of low levels of CaO or MgO lowered the viscosity. Above a certain concentration, the addition MgO increased the viscosity. The MgO content at which the viscosity began to increase decreased with increased CaO content. Viscosity measurements on industrial Mistubishi slags measured by the rotating cylinder method using a magnesia crucible and spindle were presented by Hasegawa and Tanaka (2000). They reported an empirical equation for estimating slag viscosities from the slag composition and temperature, derived by using viscosity modulus $k_v = (\text{FeO}+\text{CaO}+\text{MgO})/(\text{Al}_2\text{O}_3+\text{SiO}_2)$ fitted to an Arrhenius-type equation.

Also relevant to non-ferrous smelting was the study by Zhang and Reddy (2000) on the viscosity of industrial lead slags with high lead oxide contents. A rotating cylinder viscometer with graphite components was used. The magnitude of the measurements were similar to literature values[‡].

The viscosity measured as a slag transitions from glassy to molten state was reported by Shiraishi *et al.* (2000). Boron oxide rich B₂O₃-K₂O-SiO₂ slags were studied using a viscometer capable of two different measurement techniques, a penetration method and a rotating cylinder (crucible). The measured values agreed well with previous measurements on both the glassy and molten states.

The effect of solid particles on the viscosity of liquid slags was presented by Wright *et al.* (2000). The viscosity of a calcium ferrite slag containing Fe₃O₄ particles up to a volume fraction of 0.1 was measured and compared with a previous study of the viscosity of a blast furnace type slag containing spinel particles (Wright *et al.*, 2000). The viscosity of both slag/solid particle mixtures increased as the volume fraction of particles increased. The mixtures all showed apparent “Bingham” behaviour; that is; the viscosity decreased as the shear rate increased.

Several papers on modelling the viscosity of silicate melts was presented (Bjorkvall *et al.*, 2000; Mogutnov *et al.*, 2000; Wang *et al.*, 2000; Zhang and Jahanshahi, 2000) mainly using a structural approach. Mills reported on the results of a “Round robin” study comparing viscosity model predictions with experimental data (Mills *et al.*, 2000). The findings were that the bulk of the experimental viscosity-temperature-composition data held in the databases are probably subject to uncertainties of ± 20%. The estimated accuracy of viscosities for mould fluxes using the models (in terms of the global Δ values) are modified Iida (25%), Riboud (30%), Gupta (35%), NPL(37%). The Zhang, KTH and modified Iida models all performed well (Δ ~20%) for slag systems without fluorides (Gupta and Santra, 1994; Gupta *et al.*, 1998; Iida *et al.*, 1989; Iida *et al.* 2000; Mills and Sridhar, 1999; Riboud and Larrecq, 1979; Seetharaman *et al.*, 1999; Zhang and Jahanshahi, 1998).

[‡]The buoyancy of the lighter bob in dense lead slags is likely to lead to higher measurement uncertainty due to displacement or wobble and possible generation of gas bubbles due to reduction of lead in the slag, compared to using a metal bob of Mo or Pt-Rh alloy.

Table VI Systems with new viscosity data presented at the 6th meeting (Stockholm and Helsinki).

System	Method	Material	Temperature range (°C)	Reference
Al ₂ O ₃ -Li ₂ O-SiO ₂ * Al ₂ O ₃ -CaO-FeO-SiO ₂	Rotating cylinder	Mo	1000-1300 1450-1500	Hurst <i>et al.</i> , 2000
Al ₂ O ₃ -CaO-FeO _x -MgO-SiO ₂ Al ₂ O ₃ -CaO- MgO-SiO ₂	Rotating cylinder	Fe Graphite	1350-1500 1400-1600	Sugiyama, 2000.
CaO-FeO-Fe ₂ O ₃ -MgO-SiO ₂	Rotating cylinder	Fe	1200-1400	Ducret & Rankin, 2000.
Al ₂ O ₃ -CaO-Cu ₂ O-FeO _x - MgO-SiO ₂ -ZnO	Rotating cylinder	MgO	1150-1250	Hasegawa & Tanaka, 2000.
Al ₂ O ₃ -CaO-Cu ₂ O-FeO _x - MgO-NiO-PbO-S-SiO ₂ -ZnO	Rotating cylinder	Graphite	1050-1300	Zhang & Reddy, 2000
CaO-FeO _x ⁺ Al ₂ O ₃ -CaO-MgO-SiO ₂ [#]	Rotating cylinder	Pt-Rh	1280 1373	Wright <i>et al.</i> , 2000
B ₂ O ₃ -K ₂ O-SiO ₂	Penetration Rotating cylinder	N/A	200-1000	Shiraishi <i>et al.</i> , 2000

*SRM with <1% impurity oxides. See Broadbent *et al.*, 1992 for full details.

⁺Fe₃O₄ particles added to slag

[#]MgO.Al₂O₃ particles added to slag

N/A Not available

2004

The seventh meeting was held in Capetown in 2004, and many of the presentations were focussed on the smelting processes operating in South Africa including ferro-alloy production, the Pt industry and titania industries (Table VII). The viscosity of industrial slags relevant to the South African platinum industry containing solid chrome spinel particles was reported by Somerville and co-workers (2004). Non-Newtonian behaviour at low temperatures was observed for some of the slags and this was attributed to the presence of dispersed of spinel particles, and in some cases a second Olivine or Pyroxene solid phase. Eric (2004) presented a review paper of physical property measurements including viscosity of homogeneous Al₂O₃-CaO-FeO-MgO-SiO₂ slags covering a broad range of composition and relevant to South African platinum industry. A keynote paper on the viscosities of slags was presented by Seetharaman *et al.*, (2004). He noted that there are only a few high temperature viscosity measurement techniques, with the rotating cylinder viscometer the most used experimentally. The main sources of experimental error can be grouped into:

- Instrumental
- Materials factors
- Hydrodynamics.

Readers can refer to the paper for details of the arising uncertainties. A key message was that any one, or a combination of, these factors can lead to significant errors and corresponding misinterpretation of measured data. Repeatability on different instruments at different shear rates would reduce uncertainties significantly. Uncertainties can also be reduced with calibration using certified oils and high temperature melts. Seetharaman *et al.*, also found that with a well calibrated system, when metal spindles and crucibles were used, there was little difference between the measured values, irrespective of whether the material was platinum 30% rhodium, molybdenum, ARMCO iron or nickel. Variations in reported viscosity values for laboratories using good practice on Newtonian melts are less than 10%.

The authors thought that measurements of surface viscosity, two phase mixtures and dynamic viscosity should be extended. Surface viscosities (shear and dilatational or Marangoni), are needed to fully describe and comprehend interfacial phenomena; however the high temperature challenges are great; the kinetics of surface changes has to be understood, as well as the chemistry of the equilibrium surface. Low temperature methods may not be applicable at high temperature and the technique needs development. Viscosity measurements on dispersed two phase mixtures are needed since most smelting processes have mixed liquid phases (eg, metal droplets dispersed in a slag) or the slag is saturated with a primary phase. There has been some experimental progress with these measurements. Dynamic viscosity measurement would be useful in following changes in structure due to chemical reactions,(eg redox reactions), or dissolution of an oxide.

The effect of TiO_2 on the viscosity of Al_2O_3 -CaO-MgO-SiO₂-TiO₂ slags was investigated using a rotating cylinder viscometer under reducing conditions and Mo bob (Xie *et al.*, 2004). The viscosity increased with reduction time due to the formation of solid TiC with an accompanying change in oxidation state of the slag, with TiO being formed in the slag. In non-reduced slags, addition of TiO_2 caused a slight reduction in viscosity, but in reduced slags, the viscosity increased. The authors argued that although the solids had an impact on increasing the viscosity, the size of the increase was greater than expected for a few percent of solids, and that the formation of TiO in the slag must be the major reason for the higher viscosity.

Viscosities of quasi-ternary CaO-SiO₂-CrO_x melts in contact with metallic chromium were measured by the rotating cylinder method up to 1750°C (Forsbacka and Hollapa, 2004) using a Mo bob and crucible. The slag compositions were in the range of 20–55 wt% SiO₂, 10–45 wt% CaO and 10–60 wt% CrO_x, with the amounts of CrO and Cr₂O₃ estimated from equilibrium measurements (Xiao, 1993). The viscosity for slags of fixed basicity decreased as the CrO_x content of the slag increased.

Viscosity measurements on the CaO-Cu₂O-CuO-MgO-SiO₂ system containing ~ 63 wt% SiO₂ were carried out using the rotating cylinder technique with Pt-Rh bob and crucible in air were reported (Wright, 2004). Initial measurements were on CaO-SiO₂ slag to which incremental additions of Cu_xO-MgO-SiO₂ slag with the same silica mole fraction were made. The viscosity-temperature relationship was measured for slags with ‘Cu₂O’ contents between 0.02 and 10.0 wt%. The viscosity of the slag containing 10 wt% Cu_xO was nearly 4.5 times smaller than the binary CaO-SiO₂ slag. As the silica mole fraction (x_{SiO_2}) was constant (0.61±0.01), Cu_xO acted as a network breaker and appeared to have a stronger effect on lowering the viscosity than FeO or MnO has on a molar basis. Wright also presented work on the effect of $\text{Fe}^{3+}/\text{Fe}^{2+}$ ratio on the viscosity of FeO_x-SiO₂ melts under controlled oxygen potentials with CO₂/CO gas mixtures (Wright and Zhang, 2004). In order to keep the slag composition and the $\text{Fe}^{3+}/\text{Fe}^{2+}$ ratio constant, the CO₂/CO ratio was kept constant as the temperature was varied. Increasing the Fe^{3+} content had little effect on viscosity for slags with a silica mole fraction of 0.31. At higher silica contents, increasing the Fe^{3+} content brought a small decrease in the viscosity.

Park and co-workers (2004) measured viscosity of Al_2O_3 -CaF₂-CaO-MgO-SiO₂ melts and subsystems with the rotating cylinder technique with Pt-Rh bob and crucible. They related the changes in viscosity to the changes in the silicate polymer network measured by IR spectra on the quenched glassy slags. Fluorine addition depolymerised the melt and alumina showed amphoteric behaviour in the aluminosilicate melts which was correlated to the effect of

[AlO₄]⁻ tetrahedra and [AlO₆]³⁻ octahedra, on the stability of silicate polyanions by taking the activity coefficients of slag components into account.

The viscosities of Al₂O₃-CaO-FeO-MgO-SiO₂ slags containing 10 to 13% alumina and 5 to 10 percent magnesia at basicity ratios of 1.15 to 1.6 with varying iron oxide content were measured using the rotating cylinder approach with an iron bob and Pt-10% Rh crucible (Lee *et al.*, 2004). Viscosity decreased with increasing FeO content at a fixed basicity of slag. At constant iron oxide content, viscosity decreased with increasing slag basicity up to 1.3, and increased as slag basicity increased from 1.3 to 1.5. The viscosity at low FeO (<7.5 %) exhibited a minimum value when the MgO content was varied. The authors considered that depolymerization of silicate network at CaO/SiO₂ ≤ 1.3 decreased the viscosity and at higher basicity, a primary solid phase increased the viscosity.

The ideal properties of mould fluxes for thin slab casting was discussed and viscosity measurements for three industrial fluxes presented (Kromhout *et al.*, 2004). Although viscosity is important, melting behaviour and addition of fine carbon to expedite melting is critical to the performance of the flux.

Measurements on molten salts (Na₂O, ZnCl₂) using a novel gliding cylinder method, which is a combination of the falling or counterbalanced sphere method and a moving capillary method, gave reliable low viscosity measurements with values in agreement with other literature values. (Shiraishi and Sakurai, 2004). A key outcome of this technique should be the development of a wide range viscometer: capable of measurements between 100 Pas and 0.05 Pa s at high temperature.

Several papers were on modelling the viscosity behaviour of melts, either using empirical fits to the data or underlying principles around the structure of the melt (Forsbacka and Holappa; 2004; Hurst *et al.*, 2004; Jia 2004; Kondratiev and Jak; 2004; Zhang and Jahanshahi, 2004)

Table VII Systems with new viscosity measurements at the VII international slag conference (Capetown).

System	Method	Materials	Temperature range (°C)	Paper
CrO _x -CaO-SiO ₂	Rotating cylinder	Mo	1450-1750	Forsbacka & Holappa, 2004
Al ₂ O ₃ -CaO-FeO _x -MgO-SiO ₂	-	-		Eric,2004
Al ₂ O ₃ -CaO-FeO _x -MgO-SiO ₂	Rotating cylinder	Pt-Rh		Lee <i>et al.</i> , 2004.
Al ₂ O ₃ -CaF ₂ -CaO-MgO-SiO ₂ CaF ₂ -CaO-MgO-SiO ₂ CaF ₂ -CaO-SiO ₂	Rotating cylinder	Pt-Rh	1300-1600	Park <i>et al.</i> , 2004
NaNO ₃ ZnCl ₂	Gliding cylinder*	Fe	300-380	Shiraishi & Sakurai, 2004
Al ₂ O ₃ -CaO-CrO _x -FeO _x -MgO-MnO-NiO-SiO ₂	Rotating cylinder	Mo	1350-1550	Somerville <i>et al.</i> , 2004
CaO-Cu _x O-MgO-SiO ₂	Rotating cylinder	Pt-Rh	1393-1580	Wright, 2004
FeO _x -SiO ₂	Rotating cylinder	Pt-Rh	1200-1300	Wright & Zhang, 2004.
Al ₂ O ₃ -CaO-MgO-SiO ₂ -TiO ₂	Rotating cylinder	Mo	1393-1512	Xie., 2004
Al ₂ O ₃ -CaO-F-MgO-Na ₂ O-SiO ₂	Rotating cylinder	N/A	1300	Kromhout <i>et al.</i> , 2004

*See text for explanation

2009

The 2009 meeting was at Santiago, Chile in January (Molten 2009, 2009), with plenty of interest in viscosity measurement and modelling (Table VIII). Wang *et al.*, (2009) presented data for the $\text{Al}_2\text{O}_3\text{-CaO-MgO-SiO}_2\text{-TiO}_2$ system where titania was varied from 20 to 40 wt% at constant Al_2O_3 , MgO and CaO/SiO₂ ratio. The viscosity was determined as the slag cooled from 1550°C at 2 °C per minute[§].

The effect of alkali oxides (K_2O , Li_2O and Na_2O) and alkali earth oxide (BaO and MgO) on the viscosities of $\text{CaO-SiO}_2\text{-Al}_2\text{O}_3$ slags was also reported at Molten 2009 (Sukenaga *et al.*, 2009) where the rotating cylinder technique with a Pt-Rh bob and crucible was used. For slags containing 20% Al_2O_3 , and at basicities (CaO/SiO₂) of 0.67, 1.00 or 1.22, addition of Li_2O or Na_2O up to 30 wt% decreased the melt viscosity, with Li_2O more effective than Na_2O , while addition of K_2O up to 15% increased the viscosity. At a basicity of 0.67, addition of MgO or BaO decreased the viscosity, with MgO more effective than BaO, and at the higher basicities, MgO addition decreased viscosity, while BaO increased the viscosity. At a constant MgO content, the effect of MgO on reducing viscosity decreased as the basicity increased and, for constant BaO, the impact shifted from decreasing viscosity to increasing viscosity as the basicity increased from 0.67 to 1.22. The authors presented a structural analysis based on ²⁷Al MAS-NMR spectra which indicated that the amount of Al^{3+} in tetrahedral coordination ($\text{Al}^{3+}(4)$), which behaved as a network-former, was increased with addition of R_2O , but was independent of the alkali oxide.

The effect of high alumina content on viscosity in the $\text{Al}_2\text{O}_3\text{-CaO-MgO-SiO}_2$ system and the effect of Na_2O addition on the viscosity of synthetic blast furnace slags containing 20% Al_2O_3 and 10% MgO, and basicities of 0.8, 1 and 1.2 was presented in two papers at the conference (Kim *et al.*, 2009; Kim *et al.*, 2009a). When measuring viscosity, the rotating cylinder technique with Pt-Rh crucible and spindle were used and measurements were made at thermal equilibrium, Composition changes were checked with chemical analysis. Addition of Na_2O decreased the viscosity at a constant CaO/SiO₂ ratio, with the effect decreasing as the basicity increased from 0.8 to 1.2 in the $\text{Al}_2\text{O}_3\text{-CaO-MgO-Na}_2\text{O-SiO}_2$ system. The authors concluded that alumina behaved as an amphoteric oxide in both the $\text{CaO-SiO}_2\text{-Al}_2\text{O}_3$ and $\text{Al}_2\text{O}_3\text{-CaO-MgO-SiO}_2$ systems. This was confirmed by measuring viscosity and FT-IR spectra and thermodynamically demonstrated from the excess stability function proposed by Darken (Darken, 1967) as a function of the alumina content.

The viscosity of CaO-FeO-SiO_2 slags, with and without alumina and/or copper oxide was measured using magnesia components (Cabrera *et al.*, 2009). The authors also used a ramping temperature approach, where the furnace was cooled at a rate of 4 degrees per minute. The measurement uncertainties of this approach would be higher than other studies^{§,**}.

[§]It is very likely that thermal equilibrium was not attained and the viscosity was lower than that at thermal equilibrium at the same temperature.

^{**}The density difference between the slag and the measuring spindle will be relatively small compared to using a metallic spindle, so that uncertainties due to displacement or wobble will be greater. Magnesia will react with the slag, forming magnesia-ferrite or magnesia wustite on the crucible and bob surfaces depending upon the oxygen partial pressure (Fukayama *et al.*, 1997; Kaur *et al.*, 2011) changing the slag chemistry at the interface and the texture of the spindle surface.

Matsuzono *et al.* (2009) studied the effect of Na₂O on the viscosity of synthetic mould flux slags (CaF₂-CaO-Na₂O-SiO₂). The viscosity was measured using a rotating cylinder viscometer using iron components. The viscosity decreased with increasing Na₂O/CaO ratio at a constant SiO₂ content. This was thought to be from the breaking of the electrostatic bonding of Ca²⁺ by the substitution of one Ca²⁺ ion with two Na⁺ ions.

Kromhout *et al.* (2009) reported on the viscosity of several commercial mould fluxes being used in trials for development of thin slab casting. The measurements were performed using an oscillating plate viscometer and under a cooling rate of 2°C/m.

The Al₂O₃-CaO-CrO_x-MgO-SiO₂ system was studied systematically with measurements and modelling by Hollapa and Forsbacka (2009) continuing on from the results presented at the previous meeting (Hollapa and Forsbacka, 2004) and the doctoral study by Forsbacka (2007). The viscosity measurements were made with either Mo or Cr metal components and under neutral or fixed oxygen partial pressure. Both CrO and Cr₂O₃ had basic network modifying character with CrO having a slightly stronger effect.

Table VIII Summary of the viscosity measurements presented at Molten 2009 (Santiago).

System	Method	Material	Temperature range (°C)	Paper
Al ₂ O ₃ -CaO-MgO-SiO ₂ -TiO ₂	Rotating cylinder	Mo	1393-1512	Wang <i>et al.</i> , 2009
Al ₂ O ₃ -CaO-FeO _x -SiO ₂ Al ₂ O ₃ -CaO-Cu ₂ O-FeO _x - SiO ₂ CaO-FeO _x -SiO ₂	Rotating cylinder	MgO	1180-1370	Cabrera <i>et al.</i> , 2009
Al ₂ O ₃ -CaO-CrO _x Al ₂ O ₃ -CaO-MgO-SiO ₂ Al ₂ O ₃ -CrO _x -MgO-SiO ₂ CaO-SiO ₂ CaO-MgO-SiO ₂ CrO _x -CaO-SiO ₂ CrO _x -CaO-MgO-SiO ₂ CrO _x -MgO-SiO ₂ MgO-SiO ₂	Rotating cylinder	Mo	1450-1700	Hollapa and Forsbacka, 2009
CaO-Na ₂ O-SiO ₂ CaF ₂ -CaO-Na ₂ O-SiO ₂	Fe	Fe	1277-1477	Matsuzono <i>et al.</i> , 2009
Al ₂ O ₃ -CaO-K ₂ O-SiO ₂ Al ₂ O ₃ -CaO-Li ₂ O-SiO ₂ Al ₂ O ₃ -CaO-Na ₂ O-SiO ₂ Al ₂ O ₃ -BaO-CaO-SiO ₂ Al ₂ O ₃ -CaO-MgO-SiO ₂	Pt-20%Rh	Pt-20%Rh	1400-1600	Sukenaga <i>et al.</i> , 2009
CaO-K ₂ O-SiO ₂ CaO-FeO _x -PbO-SiO ₂ -ZnO Al ₂ O ₃ -CaO-FeO _x -MgO-SiO ₂	Rotating cylinder	Mo Pt/Al ₂ O ₃ Pt-10%Rh	1100-1400 800-1000 1300-1330	Zhao <i>et al.</i> , 2009
Al ₂ O ₃ -CaO-FeO _x -MgO-SiO ₂	Rotating cylinder	Pt-10%Rh	1200-1300	Zhao <i>et al.</i> , 2009a
Al ₂ O ₃ -CaO-MgO-SiO ₂ Al ₂ O ₃ -CaO-MgO-Na ₂ O-SiO ₂	Rotating cylinder	Pt-10%Rh	1273-1500	Kim <i>et al.</i> , 2009
Al ₂ O ₃ -CaO-MgO-SiO ₂	Rotating cylinder	Pt-10%Rh	1500-1550	Kim <i>et al.</i> , 2009a
Al ₂ O ₃ -CaO-F-MgO-Na ₂ O-SiO ₂	Oscillating plate	N/A	1300	Kromhout <i>et al.</i> , 2009

The viscosity of three types of synthetic slags relevant to industrial processes were reported by Zhao *et al.* (2009) using viscosity bobs suited to the slag being measured. For a standard glass, a platinum spindle was used, for a K_2O - CaO - SiO_2 slag, molybdenum crucible and spindle in an argon atmosphere; for a synthetic high lead slag in the Al_2O_3 - CaO - FeO_x - MgO - PbO - SiO_2 - ZnO system, alumina components were used in an air atmosphere, and for a copper smelting slags in the Al_2O_3 - CaO - FeO - Fe_2O_3 - MgO - SiO_2 system, Pt-Rh components under a controlled CO_2/CO ratio were used to ensure that the slag was at equilibrium. The same team also presented further measurements on the Al_2O_3 - CaO - FeO - Fe_2O_3 - MgO - SiO_2 under controlled oxygen partial pressure (Zhao *et al.*, 2009a). The effect of oxygen potential and the Fe^{2+}/Fe^{3+} ratio on the viscosity of fully liquid slag was small at the oxygen partial pressure range studied.

The modelling papers continued the theme of linking viscosity and melt structure (Decterov *et al.*, 2009; Jak, 2009; Robelin *et al.*, 2009; Shu *et al.*, 2009; Wang *et al.*, 2009) although novel approaches such as the use of neural networks continue to be applied (Hanao *et al.*, 2009).

2012

At Molten 2012, which was held in Beijing, several papers were presented describing new viscosity measurements at high temperatures (Table IX). Of interest in estimating high temperature measurement uncertainties, Wu *et al.* (2012) carried out a detailed study using standard oils on the measurement uncertainties introduced by fixed shafts, flexible shafts, non vertically hanging bobs, and wobble from long and bent shafts that might occur in high temperature experiments. They found that uncertainties were minimised by using flexible couplings between the viscometer and the bob shaft, which also reduced uncertainties introduced by the bob not being parallel to the crucible. The uncertainties were between 4 and 6% and were independent of the shear rate. When the bob was not aligned vertically with the crucible, the uncertainties increased as the alignment worsened and became larger on the higher viscosity oil. When flexible couplings were used, the side motion or angular displacement of the bob was the same regardless of the oil viscosity and the alignment of the bob. When longer shafts were used, the measurement uncertainties decreased as the viscosity of the oil used increased. The uncertainties decreased as the rotation speed increased as the bob tended to centralise. In low viscosity oils, uncertainties were greater if the bob was not vertical, and in high viscosity oils, the bob angle had little impact on the uncertainty. Side movements decreased as the viscosity of the oil increased. The uncertainties expected for a rotational dynamics component of the bob in the liquid of a typical rotating cylinder viscometer hanging in a furnace therefore is 4-5%, providing the bob is rotating smoothly in the liquid and the viscosity is high enough to dampen angular or side motion. In calculating the overall uncertainties, other uncertainties must be considered, such as, wall effects between the crucible and bob, the standard oil uncertainty and at high temperatures, the thermal expansion of the bob, temperature measurement uncertainties etc.

The effects of possible combinations of container and measuring spindle on the viscosity of coal ash slags was presented by Zhu *et al.* (2012). For one coal ash slag which was nearly saturated with alumina, the post measurement analysis showed no significant dissolution of alumina (crucible or spindle) or zirconia (crucible) into the slag. For this slag which contained 18% FeO_x , when iron containers and spindles were used in inert atmospheres, the viscosity values were larger than those measured using Al_2O_3 spindles. Reactions between the iron oxide and metallic iron changed the spindle surface morphology, roughening the surface and forming a significant volume of solid iron particles which would affect the

viscosity near the bob surface. For the other coal ash slag studied, only alumina spindles were used, and these were attacked by the slag. The viscosity results were interpreted in terms of formation of a dispersed solid primary phase in the slag.

Sukenaga *et al.* (2012) showed for R_2O - FeO_x - SiO_2 melts, where R was either K, Na or Li, and the FeO_x content was 10% and using Pt-Rh alloy components, the viscosity decreased as the Fe^{2+} content increased, consistent with studies on FeO_x - SiO_2 melts. For melts with constant silica content and Fe^{2+}/Fe^{3+} ratio, Li_2O was greatest at depolymerising the network, followed by Na_2O , and least effective was K_2O . A similar trend, with Na_2O lowering viscosity more than K_2O was observed in synthetic blast furnace type slags (Kim and Moon, 2012). Na_2O reduced the viscosity of melts containing 20% Al_2O_3 and 10% MgO at CaO/SiO_2 ratios between 0.8 and 1.2, whereas K_2O addition had no effect on viscosity at $CaO/SiO_2 = 1.2$, and increased the viscosity at lower basicity. In high alumina slags, addition of K_2O induces Al_2O_3 to behave as an acidic oxide and stabilises the bridging oxygen linking the $[AlO_4]^-$ tetrahedral. Thus, K_2O would appear to preferentially interact with the $[AlO_4]^-$ tetrahedra more than the $[SiO_4]^-$ tetrahedra.

The viscosity of selected compositions of the Al_2O_3 - Cu_2O - SiO_2 system at Cu saturation was measured for slags with high copper contents (Chen *et al.*, 2012) using alumina crucible and bob. There are few viscosity data for high copper slags, and these data should be useful for viscosity model refinement, especially for predicting the viscosity of copper converting slags.

Several authors studied the effects of solid phases on the viscosity assuming a homogeneous mixture of two phases, one being the slag, the other a saturating primary phase (Bronsch *et al.*, 2012; Migas *et al.*, 2012). In these studies, a thermodynamic model which predicts the proportion of liquid phase and solid phase and the chemistry of both phases was used to calculate the volume fraction of particles in the melt. The authors used experimental viscosity measurements, the volume fraction of solid particles and the predicted viscosity of the pure liquid at the temperature to determine the parameters of the Einstein-Roscoe equation :

$$\eta = \eta_0 \cdot (1 - a \cdot f)^{-n}$$

where η is the viscosity of the two phase mixture, η_0 is the viscosity of the pure liquid slag, f is the volume fraction of particles, a and n are constants. For identical sized spherical particles a and n have values of 1.35 and 2.5, respectively. The reciprocal of the a value in the physical sense refers to the maximum concentration of particles in the slag at which the viscosity becomes infinite^{††}.

The viscosity measurements on Al_2O_3 - CaO - MgO - SiO_2 slags (Migas *et al.*, 2012) show Newtonian behaviour for fully liquid slags and shear thinning behaviour for solid liquid mixtures, consistent with the earlier work on liquid plus solid mixtures, where solid MgO - Al_2O_3 particles were added to a melt at or very near to MgO - Al_2O_3 saturation (Wright *et al.*, 2000). The viscosity behaviour with respect to shear rate suggests that particles were dispersed in the melt, rather than settling or adhering to the crucible or to the bob, as Newtonian behaviour would still be observed if that were the case.

^{††}It should be recognised that physical effects such as supercooling, which may hinder phase formation at temperatures just below the liquidus and the uncertainties of both the experimental viscosity measurement and the thermodynamic model predictions when combined will give a total uncertainty of far greater than 20%, (Mills *et al.*, 2000; Suzuki and Jak, 2012), so optimized the values of "a and n" in this case will have little real meaning.

Viscosities and liquidus temperature data for Chinese blast furnace slags and synthetic slag of similar composition except for the minor elements of S, Ti and Fe, were presented by Zhao *et al.*, (2012). The liquidus temperatures of the synthetic slags are 40-50 °C higher than the corresponding industrial slags implying that the minor components in the blast furnace slag decreased the liquidus temperature. The viscosities of the industrial slags were between 0.3 and 0.4 Pa s at 1500°C. The viscosities of the synthetic slags were 30% higher than the corresponding industrial slags. As has been observed many times, silica had the greatest impact on viscosity, then other network formers and this difference may be attributable to a slightly higher SiO₂+Al₂O₃ content in the synthetic slag (0.7 wt% difference), and the possible impact of sulphur in depolymerising the silicate network in the industrial slags. Viscosity measurements of blast furnace slags and development of a neural network model was also presented by Wang *et al.* (2012). Physical property measurements including viscosity of slags with varying CaF₂ content in the Al₂O₃-CaF₂-CaO-SiO₂ system with relevance to reducing power usage in an electric arc furnace and F losses to the atmosphere were also presented (Wang, Li *et al.*, 2012). A suitable slag with lower liquidus and a lower CaF₂ content was recommended.

Muhmood *et al.*, (2012) presented a paper on dynamic interfacial tension measurements and the determination of interfacial viscosity with observations at the slag-metal interface during dynamic mass transfer. During an experiment a surface active element (S or O) was introduced and oscillations were observed at the slag/metal interface. These oscillations were analysed to extract information including the interfacial velocity and interfacial dilatational modulus. The variation in the dilatational modulus was due to the non-uniform distribution of surface active elements at the interface and also to the varying surface pressure. A methodology was put forward for estimating the interfacial shear viscosity. The authors believed that these measurements and estimations were the first of their kind.

Table IX Systems studied where new viscosity measurements were presented at Molten 2012 (Beijing).

System	Method	Material	Temperature range (°C)	Paper
CaO-SiO ₂ (+primary phase)	Rotating cylinder	Pt-30%Rh	1538-1600	Bronsch <i>et al.</i> , 2012
Al ₂ O ₃ -Cu _x O-SiO ₂ Cu _x O	Rotating cylinder	Al ₂ O ₃	1200-1300 1240-1305	Chen <i>et al.</i> , 2012
Al ₂ O ₃ -CaO-MgO-SiO ₂ Al ₂ O ₃ -CaO-K ₂ O-MgO-SiO ₂ Al ₂ O ₃ -CaO-MgO-Na ₂ O-SiO ₂	Rotating cylinder	Pt-10%Rh	1500	Kim & Min, 2012
Al ₂ O ₃ -CaO-MgO-SiO ₂ (+primary phase)	Rotating cylinder	Graphite	1310-1400	Migas <i>et al.</i> , 2012
FeO _x -K ₂ O-SiO ₂ FeO _x -Li ₂ O-SiO ₂ FeO _x -Na ₂ O-SiO ₂	Rotating cylinder	Pt-20%Rh	1500	Sukenaga <i>et al.</i> , 2012
Al ₂ O ₃ -CaF ₂ -CaO-SiO ₂	-	-	1325-1500	Wang <i>et al.</i> , 2012
Al ₂ O ₃ -CaO-FeO _x -MgO-SiO ₂	Rotating cylinder	Mo	1390-1480	Wang, Zhao <i>et al.</i> , 2012
Al ₂ O ₃ -CaO CaO-SiO ₂ CaO-SiO ₂ -TiO ₂ Al ₂ O ₃ -CaO-Na ₂ O-SiO ₂ -TiO ₂	Rotating cylinder	Mo	1350-1550 1350-1600 1240-1600 1140-1400	Wu <i>et al.</i> , 2012
Al ₂ O ₃ -CaO-FeO _x -MgO-SiO ₂ Al ₂ O ₃ -CaO-FeO _x -MgO-MnO-S-SiO ₂ -TiO ₂	Rotating cylinder	Mo	1410-1600	Zhao <i>et al.</i> , 2012
Al ₂ O ₃ -CaO-FeO _x -K ₂ O-MgO-Na ₂ O-SiO ₂	Rotating cylinder	ZrO ₂ /Fe Fe Al ₂ O ₃ ZrO ₂ /Al ₂ O ₃	1300-1500	Zhu <i>et al.</i> , 2012

A common feature of the viscosity models published at Molten 2012 are that they attempt to describe the viscosity data flowing from the underlying structure of the silicate melt (Guo *et al.*, 2012; Lian *et al.*, 2012; Mills *et al.*, 2012; Suzuki and Jak, 2012; Zhang and Chou, 2012). Several approaches have been used to either simply correlate the structure to the composition of the melt (Lian *et al.*, 2012, Mills *et al.*, 2012) or calculate a structural parameter from a thermodynamic model that uses structure as its basis and then fit the viscosity data to the calculated structural parameters (Suzuki and Jak, 2012; Zhang and Chou, 2012). Guo *et al.* (2012) developed a viscosity model for the Al_2O_3 -CaO-MgO-SiO₂ system in which the model formulation is correlated to the structure and the mobility of an ion relative to pure SiO₂. As there are no measurements of the mobility of an ion relative to SiO₂, the model relies heavily on correlating the measured viscosity with a calculated structure based on melt composition.

Trends and the future

The rotating cylinder viscometer is the dominant viscometry approach used for measuring the viscosity of high temperature silicate melts, and since the work to develop a high temperature reference silicate slag by Mills and others (Broadbent *et al.*, 1992), the protocols recommended from the work have generally been adopted, especially the use of inert metal spindles and containers, and post measurement chemical analysis of the slag to confirm the composition. Many publications have described laboratory viscometers where the atmosphere is controlled to protect reactive metals (Fe, Mo) from oxidation or an oxygen potential is maintained to study the effects of transition metal oxidation state ratio in the slag on the viscosity.

The protocols for viscosity measurement should be further refined. Even if the composition of the melt studied has not changed from post chemical analysis, and there is minimal solubility of the crucible or spindle in the slag, a realistic appraisal of changes to the measuring spindle surface should be reported in the results.

Innovation in high temperature viscometry is essential, as many high temperature melts have viscosities lower than the current rotating cylinder viscometers can measure accurately. The viscosity of silica-free systems, such as calcium ferrite based melts are at the limit of the rotating spindle viscometer. To measure low viscosity melts with a rotating cylinder viscometer, generally a much larger spindle is required than typically used. Larger spindles have greater mass, may cost more to manufacture and be too heavy for the fine viscometer torque-measuring components and increase measurement errors. Alignment errors by rotating a heavy mass may be exacerbated. Although the demand may be less than for measurements on silicate based melts, there will be a need for accurate high temperature low viscosity techniques based on other approaches.

The implications that a liquid slag may not be homogeneous and may contain a second solid phase and the impact that has on the viscous properties of slag are much better understood. The rapid increase in viscosity for a melt measured at temperatures below its liquidus is now understood to be due to the formation of a solid phase melt. However it is also generally recognised that these measurements may not represent the “real viscosity” of the two phase melt, as there are too many unknowns in the measurement approach, including the need to have an accurate understanding of the phase diagram of the melt system. The effect of particle size and morphology of the solid particles are important variables that are not well understood. Researchers are identifying more model systems and approaches to demonstrate and measure the viscosity of high temperature two phase mixtures which exhibit non-Newtonian behaviour. These systems can be studied with greater accuracy in establishing the

relationship between the solid fraction and viscosity than the traditional viscosity/temperature relationship at temperatures below the slag liquidus.

Our understanding of the structure of the silicate network and how it is depolymerised by other oxides is key to further development of models that link chemistry and viscosity. Therefore experimental techniques that can elucidate high temperature structure play a vital role. Well designed dynamic viscosity measurements may also aid in developing understanding, especially if the silica content can be maintained at a constant level, for example changing the $\text{Fe}^{3+}/\text{Fe}^{2+}$ ratio in iron oxide containing slags. Dynamic experiments in which the changes in bulk chemistry, viscosity and structure can be measured simultaneously may help improve understanding of structural changes in the melt and the impact on the viscosity, and the relative ability of oxides to depolymerise the melt.

Determining interfacial viscosities from dynamic interfacial measurements for high temperature systems is a new area of research and requires development of reliable measurement techniques.

Concluding Remarks.

There has always been much interest in the viscous behaviour of molten silicate slags at this series of meetings, and the sessions on viscosity were always well attended. Measurements on most of the industrially relevant slags for ferrous and non-ferrous metal production have been presented over the series of conferences, with consistent themes of improving process properties, ranking the viscous behaviour of oxides in melts, and developing a mathematical description of the behaviour. Measurements on many synthetic analogues of industrial slags and accompanying broadening of the composition range have also been presented.

Viscosity measurement and modelling will always be responsive to the needs of industry, and especially the steel industry. For example, the impact of declining ore grades and increasing Al_2O_3 content in iron ores will drive research to look to fluxing and operational strategies that try to minimise flux addition and maintain the viscosity in the current range, so that the blast furnace operation is not negatively impacted and the pozzolanic qualities of quenched slag are maintained. Measurements will be needed to confirm the predicted strategies. Similarly for non-ferrous smelting, declining ore grades along with increased impurity elements could be a driver for re-designing slag and processing conditions.

Many of the real advances over the period of the last nine conferences can be attributed to the energy and collaborative spirit of Professor Ken Mills, bringing industry, research laboratories and academics together to improve the quality of physical properties measurement. This should be a lasting legacy of a very distinguished career.

Acknowledgements

Wright would like to acknowledge that the preparation of this manuscript was supported by CSIRO Mineral Resources, and was undertaken in the Resources, Community and Environment Program. Kim would like to acknowledge the support of POSCO. The authors would also like to acknowledge the contributions to the manuscript of Prof Piotr Scheller, Director of the Institute for Iron and Steel Technology, Technical University of Freiberg and Dr John Rankin, CSIRO fellow.

References

- Bjorkvall J, Sichen D, Seetharaman S, 2000., "A model description of the thermochemical and thermophysical properties of multicomponent slags", CDROM, *Proceedings of the Sixth International Conference on Molten Slags, Fluxes and Salts*, KTH, Stockholm.
- Broadbent CP, Franken M, Gould D and Mills KC, 1992, "Standard reference material (SRM) for high temperature viscosity measurement", pp. 439-443, *Proceedings of the 4th International Conference on Molten Slags and Fluxes (Molten Slags & Fluxes '92)*, Sendai, Japan, ISIJ, Tokyo.
- Bronsch AM, Duchesne MA, Masset PJ and Schmetterer C, 2012, "Prediction and measurement of the coal slag viscosity including the influence of solid particle fractions", CDROM, *Molten 12, Ninth International Conference on Molten Slags, Fluxes and Salts*, Chinese Society for Metals, Beijing.
- Cabrera J, Riveros G and Warczok A, 2009, "Viscosity of alumina-olivine slags", CDROM, *Molten 2009, Proceedings of the VIII International Conference on Molten Slags, Fluxes and Salts*, Gecamin, Santiago, Chile.
- Chen M, Zhao B and Jak E, 2012, "Viscosity measurements of high "Cu₂O" containing slags in the "Cu₂O"-SiO₂-Al₂O₃ system in equilibrium with metallic Cu", CDROM, *Molten 12, Ninth International Conference on Molten Slags, Fluxes and Salts*, Chinese Society for Metals, Beijing.
- Chen WJ, Partelpoeg E, Davenport WG and Toguri JM, 1984, "An industrial slag fluidity test", pp. 779-787, *Proceedings of the Second International Symposium on Metallurgical Slags and Fluxes*, Lake Tahoe, Nevada, 1984, Metallurgical Society of AIME, New York.
- Chou K-C, Zhang G-H, Chen Z-Y and Wang L, 2012, "Calculation of physicochemical properties in molten melts", CDROM, *Molten 12, Ninth International Conference on Molten Slags, Fluxes and Salts*, Chinese Society for Metals, Beijing.
- Darken LS, 1967, "Thermodynamics of binary metallic solution". *Trans. TMS-AIME*, Vol. 239, pp. 80-89.
- Decterov S, Grundy N and Pelton A, 2009, "A model and database for the viscosity of molten slags", CDROM, *Molten 2009, Proceedings of the VIII International Conference on Molten Slags, Fluxes and Salts*, Gecamin, Santiago, Chile.
- Drissen P, Engell H-J and Janke D, 1984, "Viscosity of steelmaking slags at elevated temperatures", pp. 583-592, *Proceedings of the Second International Symposium on Metallurgical Slags and Fluxes*, Lake Tahoe, Nevada, 1984, Metallurgical Society of AIME, New York.
- Ducret AC and Rankin WJ, 2000. "Liquidus Temperatures and Viscosities of FeO-Fe₂O₃-SiO₂-CaO-MgO Slags at Compositions Relevant to Nickel Matte Smelting", CDROM, *Proceedings of the Sixth International Conference on Molten Slags, Fluxes and Salts*, KTH Stockholm.
- Eric RH, "Slag properties and design issues pertinent to matte smelting Electric furnaces", pp. 531-541, *VII International Conference on Molten Slags, Fluxes and Salts*, The South African Institute of Mining and Metallurgy, Johannesburg.
- Forsbacka L, 2007, *Experimental Study and Modelling of Viscosity of Chromium Containing Slags*, Dr. Tech. Thesis, Helsinki University of Technology, TKK-MT-196, 64, pp. 5, App.
- Forsbacka L and Holappa L, 2004, "Viscosity of SiO₂-CaO-CrOx Slags in Contact with Metallic Chromium and Application of the Iida Model", pp. 129-136, *VII International Conference on Molten Slags, Fluxes and Salts*, The South African Institute of Mining and Metallurgy, Johannesburg.
- Fukuyama H, Donald JR and Toguri JM, 1997, *Journal of the American Ceramic Society*, vol.80(9), "Wetting behavior between fayalite-type slags and solid magnesia", pp.2229-2236.
- Guo J, Cheng S and Zhao H, 2012, "A model for estimating viscosity of molten silicate slag based on slag structure theory", CDROM, *Molten 12, Ninth International Conference on Molten Slags, Fluxes and Salts*, Chinese Society for Metals, Beijing.
- Gupta VK and Santra A K, 1994, *Steel India*, vol. 17 (2), "Viscosity-composition relationships for continuous casting mould fluxes", pp.74-78.
- Gupta VK, Sinha SP and Raj B, 1998, *Steel India*, vol. 21(1), "A model for describing viscosity-composition relationship for continuous casting mould fluxes", pp. 22-29.

- Hanao M, Kawamoto M, Nakamoto M and Tanaka T, 2009, "Estimation of physical properties of molten mold flux by neural network computation", CDROM, *Molten 2009, Proceedings of the VIII International Conference on Molten Slags, Fluxes and Salts*, Gecamin, Santiago, Chile.
- Hara S, Inoue K, Tanaka T, 1997, "Viscosity of molten slags containing iron oxide and alumina", pp. 515-517, *Proceedings of the 5th International Conference on Molten Slag, Fluxes and Salts*, ISS, Sydney.
- Hasegawa N and Tanaka F, 2000. "Viscosity of the copper smelting slag in the Mitsubishi Process", CDROM, *Proceedings of the Sixth International Conference on Molten Slags, Fluxes and Salts*, KTH Stockholm.
- Holappa L and Forsbacka L, 2009, "Experimental study and modelling of viscosity of chromium containing slags", CDROM, *Molten 2009, Proceedings of the VIII International Conference on Molten Slags, Fluxes and Salts*, Gecamin, Santiago, Chile.
- Hurst HJ, Novak F and Patterson JH, 1997, Viscosity models for fluxed Australian bituminous coal ashes, pp. 873-876, *Proceedings of the 5th International Conference on Molten Slag, Fluxes and Salts*, ISS, Sydney.
- Hurst HJ, Patterson JH and Quintanar A, 2000. "Viscosities of Fluxed Australian Coal Ash Slags Containing 10-15 wt% FeO", CDROM, *Proceedings of the Sixth International Conference on Molten Slags, Fluxes and Salts*, KTH, Stockholm.
- Iida T, Morita Z, and Rokutanda T, 1989, "Determination of viscosity of B₂O₃, PbO and binary B₂O₃-PbO melts using an oscillating plate viscometer", pp. 195-198, *3rd International Conference on Metallurgical Slags and Fluxes*, The Institute of Metals, 1989, London
- Iida T, Sakai H, Kawashima T and Kurihara Y, 1997, "An equation for the viscosity of molten multicomponent fluxes and slags", pp. 877-879, *Proceedings of the 5th International Conference on Molten Slag, Fluxes and Salts*, ISS, Sydney.
- Iida T, Sakai H, Kita Y, Murakami K and Iida T, 2000, *High Temperature Materials and Processes*, Vol.19 (3-4), "Equation for estimating viscosities of industrial mold fluxes", pp.153-164.
- Iida T and Tanaka T, 1992, "Characteristics of a new oscillating plate viscometer", pp. 444-449, *Proceedings of the 4th International Conference on Molten Slags and Fluxes (Molten Slags & Fluxes '92)*, Sendai, Japan, ISIJ, Tokyo.
- International Symposium on Metallurgical Slags*, 1980, Canadian Institute of Mining and Metallurgy.
- Jak E, 2009, "Viscosity model for slags in the Al₂O₃-CaO-FeO- K₂O-Na₂O-MgO-SiO₂ system", CDROM, *Molten 2009, Proceedings of the VIII International Conference on Molten Slags, Fluxes and Salts*, Gecamin, Santiago, Chile.
- Ji F, Sichen D and Seetharaman S, 1997, "Experimental studies of the viscosities of multicomponent slags", pp. 519-533, *Proceedings of the 5th International Conference on Molten Slag, Fluxes and Salts*, ISS, Sydney.
- Jia J-Y, Bai C-G, Qiu G-B, Chen D-F and Xu Y, 2004. "Calculation models on the viscosity of CaO-SiO₂-TiO₂ slag system", pp.137-139, *VII International Conference on Molten Slags, Fluxes and Salts*, The South African Institute of Mining and Metallurgy, Johannesburg.
- Kaur R, Swinbourne D, Wadsley, M and Nexhip C, 2011, *Metallurgical and Materials Transactions*, Vol.42(3), "Comparison of ferrous calcium silicate slag and calcium ferrite slag Interactions with magnesia-chrome refractories", pp.451-459.
- Kawahara M, Morinaga K-J and Yanagase T, 1980, "Behaviour of MgO and NiO in molten slags", Session 7, *International Symposium on Metallurgical Slags*, 1980, Halifax, Nova Scotia, Canada, Canadian Institute of Mining and Metallurgy.
- Kim H, Lee YS and Min DJ, 2009, "Experimental determination of the effect of Na₂O on the viscosity of molten slag", CDROM, *Molten 2009, Proceedings of the VIII International Conference on Molten Slags, Fluxes and Salts*, Gecamin, Santiago, Chile.
- Kim H, Min DJ, Lee YS and Park J-H, 2009, "The viscous behaviour of high Al₂O₃ containing blast furnace type slags", CDROM, *Molten 2009, Proceedings of the VIII International Conference on Molten Slags, Fluxes and Salts*, Gecamin, Santiago, Chile.
- Kim JW, Choi J, Kwon OD, Lee IR Shin YK and Park JS., 1992, "Viscous characteristics of synthetic mold powder for high speed continuous casting, pp. 468-473, *Proceedings of the 4th International Conference on Molten Slags and Fluxes (Molten Slags & Fluxes '92)*, Sendai, Japan, ISIJ, Tokyo.

- Kim WH and Moon DJ, 2012, "Effect of alkaline/alkaline earth oxides on the viscous behaviour of iron-making slag system", CDROM, *Molten 12, Ninth International Conference on Molten Slags, Fluxes and Salts*, Chinese Society for Metals, Beijing.
- Kingery WD, Bowen HK and Uhlmann DR, 1976, *Introduction to Ceramics*, pp. 102-105, 757-759, 2nd ed., Wiley and Sons, New York.
- Kondratiev A and Jak E, 2004. "Quasi-chemical viscosity model for fully liquid slags in the $\text{Al}_2\text{O}_3\text{-CaO-FeO-SiO}_2$ system", pp.141-149, *VII International Conference on Molten Slags, Fluxes and Salts*, The South African Institute of Mining and Metallurgy, Johannesburg.
- Kromhout J, Boom R, Kawamoto M and Hanao M, 2009, "Development of Mould flux for high speed thin slab casting", CDROM, *Molten 2009, Proceedings of the VIII International Conference on Molten Slags, Fluxes and Salts*, Gecamin, Santiago, Chile.
- Kromhout JA., Kamperman AA, Kick M and Trouw J, 2004, "Mold powder selection for thin slab casting", pp. 731-736, *VII International Conference on Molten Slags, Fluxes and Salts*, The South African Institute of Mining and Metallurgy, Johannesburg.
- Lee YS, Kim JR, Yi, SH and Min, DJ, 2004. "Viscous behaviour of $\text{CaO-SiO}_2\text{-Al}_2\text{O}_3\text{-MgO-FeO}$ slag", pp. 225-230, *VII International Conference on Molten Slags, Fluxes and Salts*, The South African Institute of Mining and Metallurgy, Johannesburg.
- Lian S-S, Wu TC, Zhang G and Lu MR, 2012, "Estimate of the surface tension and the viscosity of the slag in the magnesium injection process", CDROM, *Molten 12, Ninth International Conference on Molten Slags, Fluxes and Salts*, Chinese Society for Metals, Beijing.
- Mackey PJ, 1980, "The Physical chemistry of copper smelting slags – a review", Session 5, *International Symposium on Metallurgical Slags*, 1980, Halifax, Nova Scotia, Canada, Canadian Institute of Mining and Metallurgy.
- Matsuzono Y, Watanabe T, Hayashi M, Nagata K, Matsushita T and Seethraman S, 2009, "The effect of Na_2O on the viscosity of mould flux", CDROM, *Molten 2009, Proceedings of the VIII International Conference on Molten Slags, Fluxes and Salts*, Gecamin, Santiago, Chile.
- McCauley WL and Apelian D, 1980, "Viscosity characterisation of continuous casting mold fluxes", Session 7, *International Symposium on Metallurgical Slags*, 1980, Halifax, Nova Scotia, Canada, Canadian Institute of Mining and Metallurgy.
- McCauley WL and Apelian D, 1981, *Canadian Metallurgical Quarterly*, Vol. 20, "Viscosity characterisation of continuous casting mold fluxes", pp.247-262.
- McCauley WL and Apelian D, 1984, "Temperature dependence on the viscosity of liquids", pp. 925-947, *Proceedings of the Second International Symposium on Metallurgical Slags and Fluxes*, Lake Tahoe, Nevada, 1984, Metallurgical Society of AIME, New York.
- Migas P, Korolczuk-Hejnak M and Karbowniczek M, 2012, "Rheological Analysis Of Blast Furnace Synthetic Slag Admixtures Of Al_2O_3 ", CDROM, *Molten 12, Ninth International Conference on Molten Slags, Fluxes and Salts*, Chinese Society for Metals, Beijing.
- Mills KC, 1992, "Influence of structure on the physico-chemical properties of slags", pp. 1- 7, *Proceedings of the 4th International Conference on Molten Slags and Fluxes (Molten Slags & Fluxes '92)*, Sendai, Japan, ISIJ, Tokyo.
- Mills KC, Chapman L, Fox AB and Sridhar S, 2000, "Round robin project on the estimation of slag viscosities", CDROM, *Proceedings of the Sixth International Conference on Molten Slags, Fluxes and Salts*, KTH, Stockholm.
- Mills KC, Franken M, Machingawuta N, Green P, Broadbent C, Urbain G, Scheel R, Hocesior J and Pontoire JN, 1991, "Commision Report on Standard Reference Material (SRM) for High Temperature Viscosity Measurements", *NPL Report DMM(A) 30*, 1991, NPL, Teddington, UK.
- Mills KC, Haladi M, Lorz HP, Kinder A, Pomfret R and Walker B, 1997, "A simple test for the viscosity measurement of slag viscosities", pp. 535- 542, *Proceedings of the 5th International Conference on Molten Slag, Fluxes and Salts*, ISS, Sydney.
- Mills KC and Sridhar S, 1999, *Iron and Steelmaking*, Vol. 26, "Viscosities of ironmaking and steelmaking slags," pp. 262-268.

- Mills KC, Yuan L, Li Z, Chou K-C and Zhang G, 2012, "The factors affecting the thermophysical properties of slags and glasses", CDROM, *Molten 12, Ninth International Conference on Molten Slags, Fluxes and Salts*, Chinese Society for Metals, Beijing.
- Mogutnov BM, Zaitsev AI, Shelkova NE and AD Litvina, 2000, "Associated solution approach to description of structure and properties of Molten slags", CDROM, *Proceedings of the Sixth International Conference on Molten Slags, Fluxes and Salts*, KTH, Stockholm.
- Muhmood L, Viswanathan N N and Seetharaman S, 2012, "Concepts and Measurement of Velocities and Viscosities at the Slag-Metal Interface", CDROM, *Molten 12, Ninth International Conference on Molten Slags, Fluxes and Salts*, Chinese Society for Metals, Beijing.
- Nakano T, Kishi T, Koyama K, Komai T and Naitoh S, 1984. *Transactions of ISIJ*, vol. 24, Mold powder technology for continuous casting of aluminium killed steel, pp. 950-956.
- Nakashima K, Kawagoe T, Ookado T and Mori, K, 1997, "Viscosity of binary and ternary borosilicate melts", pp. 215-221, *Proceedings of the 5th International Conference on Molten Slag, Fluxes and Salts*, ISS, Sydney.
- Nichols MW, Lingras AP and Apelian D, 1984, "Viscosity characteristics of commercial fluxes for bottom poured ingots", pp. 235-251, *Proceedings of the Second International Symposium on Metallurgical Slags and Fluxes*, Lake Tahoe, Nevada, 1984, Metallurgical Society of AIME, New York.
- Ninth International Conference on 'Molten slags, fluxes and Salts (Molten 12)*, 2012, CDROM, The Chinese Society for Metals, Beijing.
- Ouchi Y and Kato N, 1980, "Viscosities of ternary lead silicate melts and activities of PbO in these melts", Session 7, *International Symposium on Metallurgical Slags*, 1980, Halifax, Nova Scotia, Canada, Canadian Institute of Mining and Metallurgy.
- Park JH, Kim DS, Lee YD, Song HS and Min DJ, 2004, "The viscosities and structures of calcium silicate slags containing MgO, CaF₂, and Al₂O₃", pp. 157-164, *VII International Conference on Molten Slags, Fluxes and Salts*, The South African Institute of Mining and Metallurgy, Johannesburg.
- Peacey JG and Pelletier A, 1980, "Mineral wool production from copper reverberatory slag", Session 6, *International Symposium on Metallurgical Slags*, 1980, Halifax, Nova Scotia, Canada, Canadian Institute of Mining and Metallurgy.
- Proceedings of the Second International Symposium on Metallurgical Slags and Fluxes*, 1984, Metallurgical Society of AIME, New York.
- Proceedings of the 4th International Conference on Molten Slags and Fluxes (Molten Slags & Fluxes '92)*, 1992, ISIJ, Tokyo.
- Proceedings of the 5th International Conference on Molten Slags, Fluxes and Salts '97*, 1997, Sydney, Australia, ISS, Warrendale.
- Proceedings of the Sixth International Conference on Molten Slags, Fluxes and Salts*, 2000, CDROM, KTH, Stockholm.
- Proceedings of the VIII International Conference on 'Molten slags, fluxes and Salts (Molten 2009)*, 2009, Santiago, Chile, Editors: M Sanchez, R Paira, G Riveros and C Diaz, CDROM, GECAMIN, Santiago.
- Reddy RG, Yen JY and Shrivastava S, 1992, "Viscosity of Na₂O-B₂O₃ melts", pp. 450-455, *Proceedings of the 4th International Conference on Molten Slags and Fluxes (Molten Slags & Fluxes '92)*, Sendai, Japan, ISIJ, Tokyo.
- Reddy RG, Yen JY and Zhang, Z, 1997, "Viscosities of Na₂O-SiO₂-B₂O₃ melts", pp. 203-213, *Proceedings of the 5th International Conference on Molten Slag, Fluxes and Salts*, ISS, Sydney.
- Riboud P and Larrecq M, 1979, "Lubrication and heat transfer in a continuous casting mould", *NOH - BOS Conference*, AIME, Detroit.
- Robelin C, Pelton A, Chartrand P and Eriksson G, 2009, "Models for the thermodynamic properties, density and viscosity of molten Salts", CDROM, *Molten 2009, Proceedings of the VIII International Conference on Molten Slags, Fluxes and Salts*, Gecamin, Santiago, Chile.
- Sasahara S., Inaba S. and Tomita M., 1992, "New oscillating plate viscometer for instantaneous measurement of viscosity of molten slag", p. 456, *Proceedings of the 4th International Conference on Molten Slags and Fluxes (Molten Slags & Fluxes '92)*, Sendai, Japan, ISIJ, Tokyo.

Seetharaman S, Mukai K and Sichen D, 2004, "Viscosities of slags- an overview", pp. 31-41, *VII International Conference on Molten Slags, Fluxes and Salts*, The South African Institute of Mining and Metallurgy, Johannesburg.

Seetharaman S, Sichen D, and Zhang JY, 1999, *Journal of Metals*, vol. 51(8), "The computer-based study of multicomponent slag viscosities", pp. 38-40.

Seshadri V, Silva CA, Silva IA and von Kruger FL, 1997, "Evaluation of correlations for viscosity of blast furnace type slag as a function of composition and optical basicity", pp. 543-546, *Proceedings of the 5th International Conference on Molten Slag, Fluxes and Salts*, ISS, Sydney.

VII International Conference on Molten Slags, Fluxes and Salts, 2004, Capetown, South Africa, Book & CDROM, SAIMM, Johannesburg.

Shiraishi Y, Nagasaki S and Yamashiro M, 1997, "Development of ultrawide range viscometer and it's application to boro-silicate glasses and melts", pp. 223-229, *Proceedings of the 5th International Conference on Molten Slag, Fluxes and Salts*, ISS, Sydney.

Shiraishi Y, Nagasaki S and Yamashiro M, 2000, "Viscosity of potassium boro-silicate system in glassy and molten states", CDROM, *Proceedings of the Sixth International Conference on Molten Slag, Fluxes and Salts*, KTH Stockholm.

Shiraishi Y and Ogawa H, 1989, "Viscosity of Na₂O-B₂O₃-SiO₂ system in glassy and molten states", pp. 190-194, *3rd International Conference on Metallurgical Slags and Fluxes*, The Institute of Metals, 1989, London.

Shiraishi Y and Sakurai Y, 2004. "Gliding cylinder method for the viscosity measurement of molten Salts, slags and glasses", pp. 215-218 *VII International Conference on Molten Slags, Fluxes and Salts*, The South African Institute of Mining and Metallurgy, Johannesburg.

Shu Q, Zhang J and Huang J., 2009, "Estimation of viscosities of high temperature silicate melts", CDROM, *Molten 2009, Proceedings of the VIII International Conference on Molten Slags, Fluxes and Salts*, Gecamin, Santiago, Chile.

Somerville M, Wright S, Sun S, and Jahanshahi S, 2004. "Liquidus temperature and viscosity of melter slags", pp. 219-224, *VII International Conference on Molten Slags Fluxes and Salts*, The South African Institute of Mining and Metallurgy, Johannesburg.

Sorimachi K, 1997, "Visco-elastic behaviour of mold flux for continuous casting of steel", pp. 781-785, *Proceedings of the 5th International Conference on Molten Slag, Fluxes and Salts*, ISS, Sydney.

Sugiyama T, 2000. "Measurement of BF slag viscosity and application to the in-furnace simulation", CDROM, *Proceedings of the Sixth International Conference on Molten Slags, Fluxes and Salts*, KTH Stockholm.

Sukenaga S, Ohsugi T, Inatomi Y, Gonda Y, Watanabe T, Saito N and Nakashima K, 2012, "Effect of Oxidation State of Iron Ions on the Viscosity of Silicate Melt", CDROM, *Molten 12, Ninth International Conference on Molten Slags, Fluxes and Salts*, Chinese Society for Metals, Beijing.

Sukenaga S, Yamaoka Y, Saito N and Nakashima K, 2009, "Viscosity and structure of quaternary amuminosilicate melts", CDROM, *Molten 2009, Proceedings of the VIII International Conference on Molten Slags, Fluxes and Salts*, Gecamin, Santiago, Chile.

Suzuki M and Jak E, 2012, "Revision of quasi-chemical viscosity model for viscosity estimation of molten multi-component oxide slag", CDROM, *Molten 12, Ninth International Conference on Molten Slags, Fluxes and Salts*, Chinese Society for Metals, Beijing.

3rd International Conference on Metallurgical Slags and Fluxes, 1989, The Institute of Metals, London.

Toguri JM and Wang SS, 1980, "Viscosities of molten slags", Session 7, *International Symposium on Metallurgical Slags*, 1980, Halifax, Nova Scotia, Canada, Canadian Institute of Mining and Metallurgy.

Urbain G, Cambiet F, Deletter M and Anseau MR, 1981, *Transactions of the British Ceramic Society*, vol. 80, "Viscosity of silicate melts", pp. 139-141.

Vorres KS, Greenberg S and Poeppel RB, 1984, "The viscosity of sythnetic coal slags as a function of composition, temperature and oxygen partial pressure", pp. 949- 957, *Proceedings of the Second International Symposium on Metallurgical Slags and Fluxes*, Lake Tahoe, Nevada, 1984, Metallurgical Society of AIME, New York.

- Wang L, Seetharaman S and Chou K-C, 2009, "Physicochemical properties of ternary slag systems - a modelling approach.", CDROM, *Molten 2009, Proceedings of the VIII International Conference on Molten Slags, Fluxes and Salts*, Gecamin, Santiago, Chile.
- Wang R, Guo M, Zhang M and Wang X, 2009, "Viscosity measurements and estimation of high TiO₂ containing blast furnace slags", CDROM, *Molten 2009, Proceedings of the VIII International Conference on Molten Slags, Fluxes and Salts*, Gecamin, Santiago, Chile.
- Wang X, Li W, Bao H, Zhen Q, 2000. "Estimation of Viscosity with New Thermodynamic Geometric Model", CDROM, *Proceedings of the Sixth International Conference on Molten Slags, Fluxes and Salts*, KTH, Stockholm.
- Wang X, Li Y, Yan C, Ma B and Zeng J, 2012, "The physical properties of CaF₂-CaO-Al₂O₃-SiO₂ slag system for ESR of 12Cr", CDROM, *Molten 12, Ninth International Conference on Molten Slags, Fluxes and Salts*, Chinese Society for Metals, Beijing.
- Wang X, Zhao D , Wang R , Hou L and Liao J, 2012, "Fundamental Research and Applications of Blast Furnace Slag", CDROM, *Molten 12, Ninth International Conference on Molten Slags, Fluxes and Salts*, Chinese Society for Metals, Beijing.
- Wright S, 2004. "Viscosity Of CaO-Cu_xO-MgO-SiO₂ Slags", pp. 151-155, *VII International Conference on Molten Slags, Fluxes and Salts*, The South African Institute of Mining and Metallurgy, Johannesburg.
- Wright S and Zhang L, 2004. "The influence of Fe³⁺/Fe²⁺ ratio on the viscosity of iron silicate slags", pp.231-236, *VII International Conference on Molten Slags, Fluxes and Salts*, The South African Institute of Mining and Metallurgy, Johannesburg.
- Wright S, Zhang L and Jahanshahi S, 1997, "The effect of CaO on the viscosity of PbO-SiO₂ melts", pp. 231-240, *Proceedings of the 5th International Conference on Molten Slag, Fluxes and Salts*, ISS, Sydney.
- Wright S, Zhang L, Sun S and Jahanshahi S, 2000. "Viscosity of calcium ferrite and calcium aluminosilicate slags containing spinel particles", CDROM, *Proceedings of the Sixth International Conference on Molten Slags, Fluxes and Salts*, KTH Stockholm.
- Wright S, Zhang L, Sun S and Jahanshahi S, 2000, *Metallurgical and Materials Transactions B*, vol. 31, "Viscosity of a CaO-MgO-Al₂O₃-SiO₂ melt containing spinel particles at 1646 K", pp. 97-104.
- Wu L, Heller P, Bi X and Scheller PR, 2012, "Accuracy of viscosity measurement using rotation viscometer", CDROM, *Molten 12, Ninth International Conference on Molten Slags, Fluxes and Salts*, Chinese Society for Metals, Beijing.
- Xiao Y, 1993." Thermodynamic study on CrO_x containing slags". *Acta Polytechnica Scandinavica, Chemical Technology and Metallurgy Series*, no. 210. 1993.
- Xie D, Mao Y and Zhu, Y, 2004. "Viscosity and flow behaviour of TiO₂-containing blast furnace slags under reducing conditions", pp. 43-50, *VII International Conference on Molten Slags, Fluxes and Salts*, The South African Institute of Mining and Metallurgy, Johannesburg.
- Yanagase T, Morinaga K, Ohta Y and Aiura T., 1984, "Physical properties of CaO-Al₂O₃-CaF₂ melts", pp. 995-1004, *Proceedings of the Second International Symposium on Metallurgical Slags and Fluxes*, Lake Tahoe, Nevada, 1984, Metallurgical Society of AIME, New York.
- Zhang G-H and Chou K-C, 2012, " Modeling the viscosities of alumino-silicate melts", CDROM, *Molten 12, Ninth International Conference on Molten Slags, Fluxes and Salts*, Chinese Society for Metals, Beijing.
- Zhang L and Jahanshahi S, 1997, "Modelling viscosity of silicate melts, pp. 861-871, *Proceedings of the 5th International Conference on Molten Slag, Fluxes and Salts*, ISS, Sydney.
- Zhang L and Jahanshahi S, 1998, *Metallurgical Transactions B*, vol. 29(1), "Review and modelling of viscosity of silicate melts. Part 1. Viscosity of binary and ternary silicates containing CaO, MgO, and MnO ", pp. 177-186.
- Zhang L and JahanshahiS, 2000. "Modelling Viscosity of Alumina-containing Silicate Melts" CDROM, *Proceedings of the Sixth International Conference on Molten Slags Fluxes and Salts*, KTH, Stockholm.
- Zhang L and Jahanshahi S, 2004. "Modelling viscosity of TiO_x containing silicate melts", pp. 51-56, *VII International Conference on Molten Slags, Fluxes and Salts*, The South African Institute of Mining and Metallurgy, Johannesburg.

Zhang Z and Reddy RG, 2000. "Viscosities of lead slags", CDROM, *Proceedings of the Sixth International Conference on Molten Slags, Fluxes and Salts*, KTH Stockholm.

Zhao B, Jak E and Hayes P, 2009, "High temperature viscosity measurements for slags at controlled oxygen potential", CDROM, *Molten 2009, Proceedings of the VIII International Conference on Molten Slags, Fluxes and Salts*, Gecamin, Santiago, Chile.

Zhao B, Jak E, Hayes P, Font J and Moyano A, 2009, "Viscosity and Electrical conductivity of copper slag at controlled oxygen potential", CDROM, *Molten 2009, Proceedings of the VIII International Conference on Molten Slags, Fluxes and Salts*, Gecamin, Santiago, Chile.

Zhao B, Zhang D, Zhao Z, Jak E and Hayes P, 2012, "Liquidus temperatures and viscosities of Shougang iron blast furnace slags", CDROM, *Molten 12, Ninth International Conference on Molten Slags, Fluxes and Salts*, Chinese Society for Metals, Beijing.

Zhu J, Kaneko TK, Mu H, Bennett JP and Sridhar S, 2102, "Effects of Measurement Materials and Oxygen Partial Pressure on Synthetic Coal Slag Viscosity Values", CDROM, *Molten 12, Ninth International Conference on Molten Slags, Fluxes and Salts*, Chinese Society for Metals, Beijing.

A STRUCTURE-BASED VISCOSITY MODEL AND DATABASE FOR MULTICOMPONENT OXIDE MELTS

Guixuan Wu¹, Sören Seebold¹, Elena Zayhenskikh¹, Klaus Hack², and Michael Müller¹

¹Institute of Energy and Climate Research (IEK-2), Forschungszentrum Jülich GmbH, Wilhelm-Johnen-Straße, 52425 Jülich, Germany.

²GTT Technologies, Kaiserstraße 100, 52134 Herzogenrath, Germany.

Keywords: Molten slag, Thermodynamic modelling, Viscosity, Structure, Model

Abstract

Based on the thermodynamic associate species model, a new viscosity model and database are currently being developed for the fully liquid system SiO₂-Al₂O₃-CaO-MgO-Na₂O-K₂O-FeO-Fe₂O₃-P₂O₅ and its subsystems in the Newtonian range. The modified Arrhenius model, employed in this database, is a structure-based viscosity model, in which the associate species link the viscosity to the internal structure of melts. Both the temperature- and composition-induced structural changes of melts are then described by a set of monomeric associate species in combination with the critical clusters induced by self- and inter-polymerization. The viscosity, therefore, is well described over the whole range of compositions and a broad range of temperatures by using only one set of model parameters, which have clear physico-chemical meaning. Moreover, the model is self-consistent, meaning the extension of viscosities from lower order systems to higher order systems is valid, and vice versa.

Introduction

The knowledge of viscosity as a function of temperature and composition has important practical applications to a variety of industrial processes, such as soldering, fusion casting of ceramic materials, metallurgical processes, glass production, and coal combustion and gasification. By way of example, slag viscosity is identified as a significant process variable for metallurgical smelting and refining and also plays a key role in determining the optimum continuous casting conditions [1, 2]. In the field of glass, glass viscosity is regarded as an important parameter for all stages of the manufacturing process. Successful melting and fining require viscosities below 20 Pa·s, whereas other processes such as blowing, pressing, drawing, and rolling require viscosities in the range from 10² to 10⁶ Pa·s [3]. Accurate viscosity control improves the performance and efficiency of these processes, and for this purpose, viscosity-temperature-composition relationships are needed. Extensive viscosity measurements have been made, but it is not practicable to provide data for all possible combinations of temperatures and compositions encountered in practice. Moreover, measuring viscosity is not only time consuming but also expensive. These factors result in an obvious demand for viscosity models, by which viscosities are rapidly calculated from temperature and composition. Due to complicated nonlinear relationships between viscosity and composition, many early viscosity models such as the Lakatos model [4], Urbain model [5] and Riboud model [6] are only valid in a limited range of compositions. A new model is therefore developed to predict the viscosity of molten slags over

the whole range of compositions. The methodology is outlined using the system $\text{SiO}_2\text{-Al}_2\text{O}_3\text{-CaO-Na}_2\text{O}$.

The viscosity model

The viscosity as a function of temperature and composition essentially depends on the structure. A comprehensive description of structural dependence is therefore required for the development of a new viscosity model. The idea of the current model is to link the viscosity to the associate species distribution obtained from the thermodynamic modified associate species model [7], which has been successfully applied to describe the Gibbs energy of oxide melts. Due to the common structural basis of viscosity and Gibbs energy [8], the associate species in turn are assumed to be the common structural units. To effectively describe the structural dependence of viscosity, each associate species is transformed to a monomeric associate species (i.e. a discrete structural unit expressed with the formula that contains only one reference atom, marked in bold, in Table I). The monomeric associate species are defined as basic structural units, some of which can produce larger structural units (i.e. clusters) through self- and inter-polymerization, which cause a higher degree of roughness at atomic scale. Such increased roughness leads to an increased viscosity. This is because the nature of melt viscosity is an internal fluid friction. It is noted that the self- and inter-polymerization are taken into account only for silica and silicon-aluminium based ternary associate species such as $\text{CaSi}_2\text{Al}_2\text{O}_8$. Such ternary associate species contain the Al^{3+} -based quasi-tetrahedra, which can further self-polymerize and inter-polymerize with the silica tetrahedra. Only when the size of a resulting cluster reaches a critical value [9], does the viscosity increase significantly. For the self-polymerization, in the current model only two critical silica clusters are employed, while for each ternary associate species involved only one critical cluster is employed. For the inter-polymerization, only one critical cluster is incorporated into the model.

Table I. Associate species and structural units employed for the system $\text{SiO}_2\text{-Al}_2\text{O}_3\text{-CaO}$

Compounds	Associate species	Structural units
SiO_2	Si_2O_4	SiO₂
Al_2O_3	Al_2O_3	AlO_{1.5}
CaO	Ca_2O_2	CaO
$\text{Al}_6\text{Si}_2\text{O}_{13}$	$\frac{1}{4}\text{Al}_6\text{Si}_2\text{O}_{13}$	Al₃SiO_{6.5}
CaSiO_3	CaSiO_3	CaSiO₃
Ca_2SiO_4	$\frac{2}{3}\text{Ca}_2\text{SiO}_4$	Ca₂SiO₄
CaAl_2O_4	$\frac{2}{3}\text{CaAl}_2\text{O}_4$	Ca_{0.5}AlO₂
$\text{CaSi}_2\text{Al}_2\text{O}_8$	$\frac{2}{5}\text{CaSi}_2\text{Al}_2\text{O}_8$	Ca_{0.5}SiAlO₄

Each resulting structural unit has a relative contribution to viscosity, which can be described by the Arrhenius model. Consequently, the total viscosity of melts can be calculated by a linear combination of such relative contributions, given in Eq. (1).

$$\ln \eta = \ln \eta_{\text{ideal}} + \ln \eta_{\text{excess}} \\ = (\sum_i X_i \cdot \ln \eta_i) + (\ln \eta_{\text{self-pol.}} + \ln \eta_{\text{inter-pol.}}) \quad (1)$$

where: $\ln \eta_i = A_i + B_i/T$,

$$\ln \eta_{\text{self-pol.}} = \sum_j (A_{(\text{SiO}_2)_{n_j}} + B_{(\text{SiO}_2)_{n_j}}/T) \cdot (X_{\text{SiO}_2}^{n_j}) \\ + \sum_k (A_{(\text{Si-Al})_k} + B_{(\text{Si-Al})_k}/T) \cdot (X_{(\text{Si-Al})_k}^{n_k}),$$

$$\ln \eta_{\text{inter-pol.}} = \sum_m (A_{(\text{Si-Al})_m} + B_{(\text{Si-Al})_m}/T) \cdot (X_{(\text{Si-Al})_m} \cdot X_{\text{SiO}_2}^{n_m}),$$

$j = 1, 2$.

$k = 1, 2, 3 \dots$

$m = 1, 2, 3 \dots$

$(\text{Si} - \text{Al})_m$ and $(\text{Si} - \text{Al})_k$: the silicon-aluminium based ternary associate species.

η_{ideal} and η_{excess} are the ideal viscosity and the excess viscosity respectively; X_i is the mole fraction of the monomeric associate species i ; η_i is the viscosity contribution from the monomeric associate species i ; $\eta_{\text{self-pol.}}$ is the excess viscosity resulting from the critical self-polymerizations; $\eta_{\text{inter-pol.}}$ is the excess viscosity resulting from the critical inter-polymerizations; n_j , n_k , and n_m are the integer coefficients that relate to a particular degree of polymerization; A_i and B_i are the temperature- and composition-independent constants, respectively, for the ideal viscosity; $A_{(\text{SiO}_2)_{n_j}}$, $A_{(\text{Si-Al})_k}$, and $A_{(\text{Si-Al})_m}$ are the temperature-independent constants for the excess viscosity; $B_{(\text{SiO}_2)_{n_j}}$, $B_{(\text{Si-Al})_k}$, and $B_{(\text{Si-Al})_m}$ are the composition-independent constants for the excess viscosity; T is the absolute temperature; $X_{\text{SiO}_2}^{n_j}$, $X_{(\text{Si-Al})_k}^{n_k}$, and $(X_{(\text{Si-Al})_m} \cdot X_{\text{SiO}_2}^{n_m})$ are the weighting factors indicating relative contribution of each associate species involved to the excess viscosity. The weighting factor is derived from the mole fraction of the critical clusters. In view of chemical equilibrium, for example, there is a dynamic equilibrium between the monomeric associate species SiO_2 and the critical silica cluster $(\text{SiO}_2)_{n_j}$, as shown in Eq. (2).



The mole fraction of the critical silica cluster, therefore, can be calculated by the mole fraction of the monomeric associate species SiO_2 , as shown in Eq. (3).

$$X_{(\text{SiO}_2)_{n_j}} = K_{n_j} \cdot X_{\text{SiO}_2}^{n_j} \quad (3)$$

where: $X_{(\text{SiO}_2)_{n_j}}$ is the mole fraction of the critical silica cluster $(\text{SiO}_2)_{n_j}$; K_{n_j} is an equilibrium constant for a particular degree of polymerization. Here, the mole fraction in place of activity is used to calculate the mole fraction of the critical silica cluster. To simplify the equation to estimate the excess viscosity, the equilibrium constant K_{n_j} is implicitly incorporated into the model parameters $A_{(\text{SiO}_2)_{n_j}}$ and $B_{(\text{SiO}_2)_{n_j}}$. It should be noted that a possible dependence of K_{n_j} on temperature is ignored.

Results and discussion

Pure oxides

Figure 1 shows the calculated viscosities for pure oxides SiO_2 and Al_2O_3 are in good agreement with the experimental data [10-15] and the viscosity decreases with increasing temperature. The temperature-induced structural change for the pure oxides Al_2O_3 , CaO , and MgO is described using only the monomeric associate species. In contrast, the temperature-induced structural change for the SiO_2 is described by the coexisting monomeric associate species SiO_2 and two common critical silica clusters $(\text{SiO}_2)_6$ and $(\text{SiO}_2)_{109}$, which are obtained by fitting experimental data for both pure molten silica and the relevant SiO_2 -based binary systems.

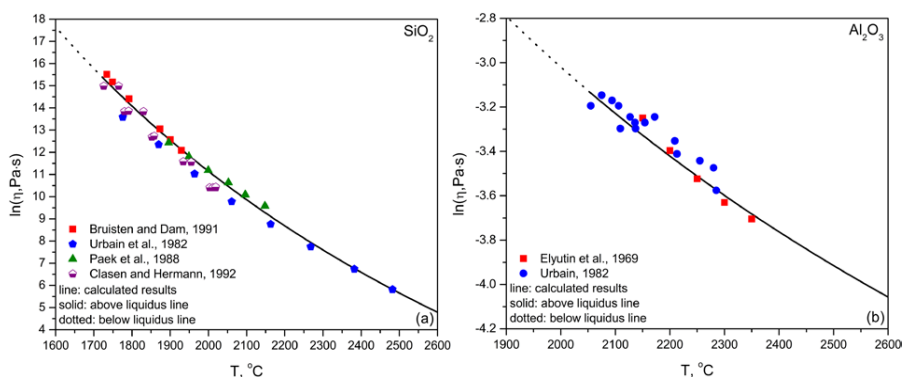


Figure 1. Model performance for pure oxides (a) SiO_2 and (b) Al_2O_3

It is noted that the viscosity of SiO_2 is much greater than that of Al_2O_3 . In a pure silica melt, the basic structural units (silica tetrahedra) can interconnect with each other and thereby produce various large structural units such as chain structures, ring structures, and network structures, which can cause a significant increase in viscosity. A pure alumina melt does not have such structural features.

Binary systems

The viscosity of molten silica decreases significantly when a small amount of network modifiers such as Al_2O_3 and Na_2O is added into a pure silica melt, as shown in Figure 2. This is the so-called lubricant effect reported by Avramov et al. [16], in which the network modifiers play the role of lubricants allowing silica clusters to glide more easily past each other. This challenging viscosity behavior can be described by the current model. For the description of the composition-induced structural change in the system SiO_2 - Al_2O_3 , the binary associate species $\text{Al}_6\text{Si}_2\text{O}_{13}$ is used in addition to the monomeric associate species for the pure oxides and two common critical silica clusters $(\text{SiO}_2)_6$ and $(\text{SiO}_2)_{109}$. Then, the calculated viscosities at temperatures from 1800 $^\circ\text{C}$ to 2000 $^\circ\text{C}$ sufficiently agree with the experimental data [11, 12, 14, 17]. In contrast, the structural change in the system SiO_2 - Na_2O is more complex and three binary associate species Na_4SiO_4 , Na_2SiO_3 , and $\text{Na}_2\text{Si}_2\text{O}_5$ are therefore employed. The experimental data [18-22] are

consequently well reproduced with the current model. In addition to the lubricant effect, another dramatic drop in viscosity (the so called weak lubricant effect due to the possible ring structures [23]) occurs in somewhere in the middle (see Figure 2(b)), which is also well predicted.

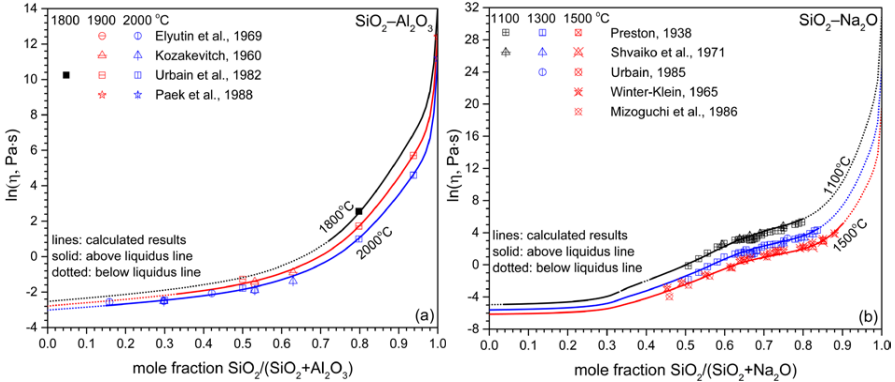


Figure 2. Model performance for the binary systems (a) $\text{SiO}_2\text{-Al}_2\text{O}_3$ and (b) $\text{SiO}_2\text{-Na}_2\text{O}$

Moreover, the viscosity extension from the binary system $\text{SiO}_2\text{-Al}_2\text{O}_3$ and $\text{SiO}_2\text{-Na}_2\text{O}$ to the pure SiO_2 is valid. In contrast, the viscosity values extrapolated from different SiO_2 -based binary systems to the pure SiO_2 are different in the model of Zhang and Jahanshahi [24]. This indicates the current model is self-consistent.

Multicomponent systems

The viscosity of the system $\text{SiO}_2\text{-CaO-Na}_2\text{O}$ is extrapolated from the corresponding lower order systems $\text{SiO}_2\text{-CaO}$ and $\text{SiO}_2\text{-Na}_2\text{O}$, where the ternary associate species $\text{Na}_2\text{Si}_6\text{Ca}_3\text{O}_{16}$ is employed. As shown in Figure 3(a), the calculated viscosities agree well with the experimental data [25-27]. For a constant SiO_2 content of 0.75 mole fraction, the viscosity increases when replacing Na_2O with CaO at temperatures from 1100 °C to 1300 °C. This indicates that Na_2O has a greater ability to decrease the viscosity than CaO in the system $\text{SiO}_2\text{-CaO-Na}_2\text{O}$. When the model is extended to the system $\text{SiO}_2\text{-Al}_2\text{O}_3\text{-CaO}$, the ternary associate species $\text{CaSi}_2\text{Al}_2\text{O}_8$ is introduced to describe the Al^{3+} -induced structural change. The monomeric associate species Al_2O_3 , $\text{Al}_6\text{Si}_2\text{O}_{13}$, and CaAl_2O_4 for the pure oxides and binary systems are also included. The associate species Al_2O_3 and $\text{Al}_6\text{Si}_2\text{O}_{13}$ behave as network modifiers, whereas the associate species CaAl_2O_4 and $\text{CaSi}_2\text{Al}_2\text{O}_8$ behave as network formers, which are employed to describe the charge compensation effect. Figure 3(b) shows that the viscosity maximum for the system $\text{SiO}_2\text{-Al}_2\text{O}_3\text{-CaO}$ is well described by the current model for a constant SiO_2 content of 0.5 mole fraction at temperatures from 1600 °C to 2000 °C. Using the current model, the calculated viscosities are in good agreement with experimental data [11, 17]. It is noted that the position of the viscosity maximum is slightly shifted towards the Al_2O_3 -rich side with increasing temperature. The viscosity maximum tends to be less pronounced due to lower stability of the Al^{3+} -based quasi-tetrahedral structures. Moreover, increased separation of the viscosity isotherms occurs when approaching the fully charge-compensated composition. Similarly, the

ternary associate species NaSiAlO_4 , and $\text{NaSi}_3\text{AlO}_8$ are employed to describe the Al^{3+} -induced structural change in the system $\text{SiO}_2\text{-Al}_2\text{O}_3\text{-Na}_2\text{O}$, the experimental data [28-32] are then reproduced well with the current model, as shown in Figure 3(c).

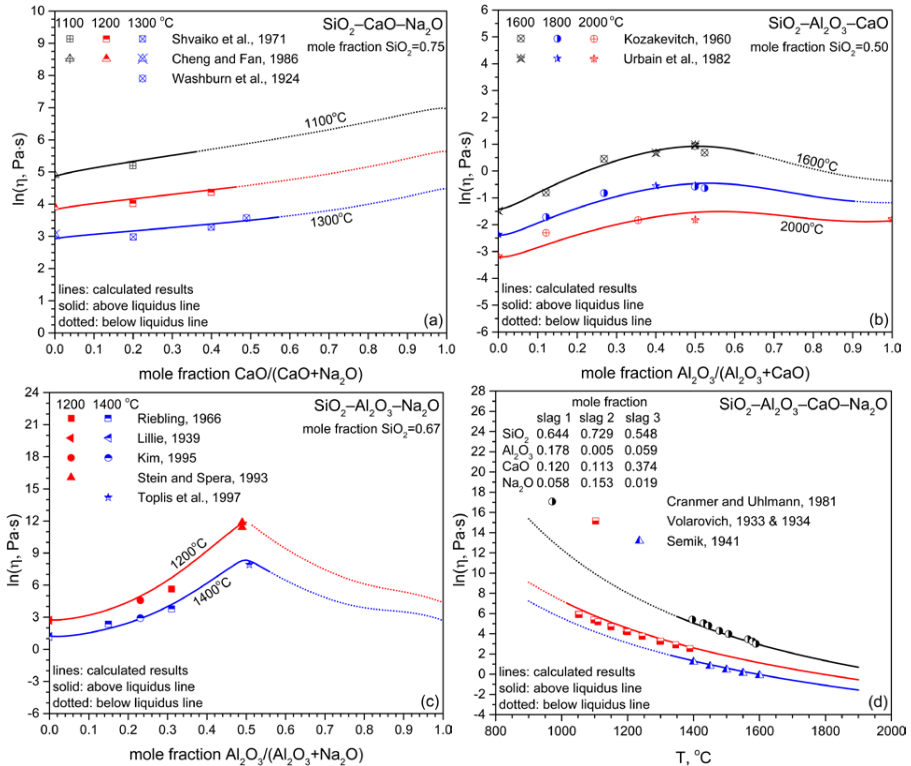


Figure 3. Model performance for the systems (a) $\text{SiO}_2\text{-CaO-Na}_2\text{O}$, (b) $\text{SiO}_2\text{-Al}_2\text{O}_3\text{-CaO}$, (c) $\text{SiO}_2\text{-Al}_2\text{O}_3\text{-Na}_2\text{O}$ and (d) $\text{SiO}_2\text{-Al}_2\text{O}_3\text{-CaO-Na}_2\text{O}$

When the model is extended to the system $\text{SiO}_2\text{-Al}_2\text{O}_3\text{-CaO-Na}_2\text{O}$, no additional associate species and model parameters are employed. The calculated viscosities still agree well with the experimental data [33-36], as shown in Figure 3(d). It is noted that the viscosities of the three slags follow the sequence: slag 1 > slag 2 > slag 3, which is consistent with the sequence of the sum of the SiO_2 and Al_2O_3 contents although the amount of the charge compensators for Al^{3+} might be not enough for slag 1. Due to the charge compensation effect, Al_2O_3 behaves as a network former and the effective concentration of SiO_2 is increased, both of which lead to an increase in viscosity.

Conclusion

A new structure-based model, designated as the modified Arrhenius model, has been developed to describe the viscosity of multicomponent oxide melts. In the new model, the structural dependence of the viscosity is successfully described by using the associate species distribution and the critical clusters derived from the associate species. The new model provides a reliable prediction over the whole range of compositions and a broad range of temperatures using only one set of model parameters, all having clear physico-chemical meaning. The challenging viscosity behaviors such as the lubricant effect and charge compensation effect are well captured. Moreover, the model is self-consistent. The model parameters have been assessed for the system $\text{SiO}_2\text{-Al}_2\text{O}_3\text{-CaO-MgO-Na}_2\text{O-K}_2\text{O-FeO-Fe}_2\text{O}_3$ and further relevant oxides such as P_2O_5 are currently being assessed and incorporated.

Acknowledgments

The work described in this article has been performed in the framework of the HotVeGas Project supported by Bundesministerium für Wirtschaft und Technologie (FKZ 0327773) and the HVIGasTech Project supported by the Helmholtz Association of German Research Centers (VH-VI-429).

References

1. K.C. Mills and S. Sridhar, "Viscosities of ironmaking and steelmaking slags," *Ironmaking & Steelmaking*, 26 (1999) 262-268.
2. A. Kondratiev et al., "Predicting Slag Viscosities in Metallurgical Systems," *JOM*, 54 (2002) 41-45.
3. http://www.schott.com/epackaging/chinese/download/schott-brochure-technical-glasses_english.pdf.
4. T. Lakatos et al., "Viscosity-temperature relations in the glass system $\text{SiO}_2\text{-Al}_2\text{O}_3\text{-Na}_2\text{O-K}_2\text{O-CaO-MgO}$ in the composition range of technical glasses," *Glass Tech.*, 13 (1972) 88-95.
5. G. Urbain et al., "Viscosity of Silicate Melts," *Trans. J. Br. Ceram. Soc.*, 80 (1981) 139-141.
6. P.V. Riboud et al., "Improvement of continuous casting powders," *Fachber. Huttenprax. Metallweiterverarb.*, 19 (1981) 859-869.
7. E. Yazhenskikh et al., "Critical thermodynamic evaluation of oxide systems relevant to fuel ashes and slags. Part 1: Alkali oxide-silica systems," *Calphad*, 30 (2006) 270-276.
8. R.E. Aune et al., "Viscosities and Gibbs Energies-On a Common Structural Base," *High Temp. Mater. Processes (London)*, 22 (2003) 369-378.
9. A.N. Grundy et al., "A model to calculate the viscosity of silicate melts Part I: Viscosity of binary $\text{SiO}_2\text{-MeO}_x$ systems (Me=Na, K, Ca, Mg, Al)," *Int. J. Mater. Res.*, 99 (2008) 1185-1194.
10. P.M. Bruisten and H.B.B. Dam, "Viscosity measurement of quartz glass" (*Proc. 1st Intern. Conf. Fundamentals of Glass Manufacturing Process, Sheffield, 1991*), 18-21.
11. G. Urbain et al., "Viscosity of liquid silica, silicates and alumino-silicates," *Geochim. Cosmochim. Acta*, 46 (1982) 1061-1072.
12. U.C. Paek et al., "Determination of the viscosity of high silica glasses during fibre drawing," *Glass Technol.*, 29 (1988) 263-266.
13. R. Clasen and W. Hermann, "Differences in properties of natural and synthetic silica glass on the basis of impurity levels" (*Boll. Soc. Espan. Ceram. Vidrio - Proc. XVI Intern. Congr. on Glass, Madrid, 1992*), 233-238.

14. V.P. Elyutin et al., "Measurements of viscosity of aluminium oxide," *Zh. Fiz. Khim.*, 43 (1969) 579-583.
15. G. Urbain, "Viscosite de l'alumine liquide," *Rev. Int. Hautes Temp. Refract.*, Fr., 19 (1982) 55-57.
16. I. Avramov et al., "Effect of chemical composition on viscosity of oxide glasses," *J. Non-Cryst. Solids*, 324 (2003) 29-35.
17. P. Kozakevitch, "Viscosite et elements structuraux des alumino-silicates fondus: leitiers CaO-Al₂O₃-SiO₂ entre 1600 et 2000 °C," *Rev. Metall. Paris*, 57 (1960) 149-160.
18. E. Preston, "The Viscosity of the Soda-Silica Glasses at High Temperatures and its Bearing on their Constitution," *J. Soc. Glass Technol.*, 22 (1938) 45-81.
19. T.P. Shvaiko-Shvaikovskaya et al., "The viscosity of glasses in the Na₂O-SiO₂ system in a molten state," *Neorg. Mater.*, 7 (1971) 143-147.
20. G. Urbain, "Viscosité de Liquides Silice-Alumine-Oxydes Na et K. Mesures et Estimations," *Rev. Int. Hautes Temp. Refract.*, Fr., 22 (1985) 39-45.
21. A. Winter-Klein, "Structure and physical properties of glass" (*Stekloobraznoe Sostoyanie, Moskva-Leningrad, 1965*), 45-54.
22. K. Mizoguchi et al., "Viscosity measurements of the molten MeO(Me=Ca, Mg, Na)-SiO₂-Ge₂O₃ silicate system," *J. Japan Inst. Metals*, 50 (1986) 76-82.
23. W.-Y. Kim et al., "A model to calculate the viscosity of silicate melts Part III: Modification for melts containing alkali oxides," *Int. J. Mater. Res.*, 103 (2012) 313-328.
24. L. Zhang and S. Jahanshahi, "Review and Modeling of Viscosity of Silicate Melts: Part I. Viscosity of Binary and Ternary Silicates Containing CaO, MgO, and MnO," *Metall. Mater. Trans. B*, 29 (1998) 177-186.
25. T.P. Shvaiko-Shvaikovskaya et al., "The viscosity of glasses in the Na₂O-CaO-SiO₂ system within a wide temperature range," *Neorg. Mater.*, 7 (1971) 713.
26. J.-J. Cheng and M.-X. Fan, "The effect of fluorine ions and hydroxyl groups on some properties of silicate glasses" (*Collect. Pap. XIVth Intern. Congr. on Glass, 1986*), 225-232.
27. E.W. Washburn et al., "The viscosities and surface tensions of the soda-lime-silica glasses at high temperatures," *Univ. Ill. Bull.*, 21 (1924) 33-48.
28. E.F. Riebling, "Structure of sodium aluminosilicate melts containing at least 50 mole % SiO₂ at 1500°C," *J. Chem. Phys.*, 44 (1966) 2857-2865.
29. H.R. Lillie, "High-temperature viscosities of soda-silica glasses," *J. Am. Ceram. Soc.*, 22 (1939) 367-374.
30. K.D. Kim, "Viscosity in mixed-alkali alumino-silicate glass melts" (*Proc. XVIIth Intern. Congr. on Glass, Beijing, 1995*), 747-752.
31. D.J. Stein and F.J. Spera, "Experimental rheometry of melts and supercooled liquids in the system NaAlSiO₄-SiO₂: implications for structure and dynamics," *Am. Mineral.*, 78 (1993) 710-723.
32. M.J. Toplis et al., "Viscosity, fragility, and configurational entropy of melts along the join SiO₂-NaAlSiO₄," *Am. Mineral.*, 82 (1997) 979-990.
33. D. Cranmer and D.R. Uhlmann, "Viscosities in the system albite-anorthite," *J. Geophys. Res.*, 86 (1981) 7951-7956.
34. M.P. Volarovich, "Investigation of viscosity and plasticity of molten slags and rocks," *Zh. Fiz. Khim.*, 4 (1933) 807-814.
35. M.P. Volarovich, "Investigation of viscosity of melted rocks," *Dokl. Akad. Nauk SSSR*, 1 (1934) 561-563.
36. I.P. Semik, "On the viscosity of blast-furnace slags" (*Soveshchanie po Vyazkosti Zhidkosti i Kolloidnykh Rastvorov, Moskva, 1941*), 257-269.

THERMO-PHYSICAL-CHEMICAL PROPERTIES OF BLAST FURNACE SLAG BEARING HIGH TiO₂

Chenguang Bai, Zhiming Yan, Shengping Li, Pingsheng Lai, Chen Shan, Xuewei Lv, Guibao Qiu,

School of Materials Science and Engineering, Chongqing University, China.

E-mail:baichenguangcd@163.com, 400044

Keywords: Thermo-Physical-Chemical Properties, High TiO₂, BF slag.

Abstract

Cost issues and decrease of high grade raw materials has sparked interest in the use of other potential sources of iron bearing materials once regarded as uneconomical. China is rich in mineral resources of titanium, After decades of basic research and industrial production practice, a complete set of blast furnace-converter smelting process has been successful developed to produce steel and vanadium/titanium products. This paper begins with an introduction to the sever defects of blast furnace process and focuses on elucidating the effect of TiO₂ on the thermo-physical-chemical properties of blast furnace slag including viscosity, surface properties, foaming performance and formation and regulation mechanism of TiCN. Using molecular dynamics simulation and spectroscopy techniques, the viscous behavior and the structure of the slag system were correlated. Models were used and compared with experimental data.

Introduction

There is a lot of vanadium-titanium magnetite (VTM) in Panxi region, China, in which the proven VTM reserves is approximately 10 billion tons. The VTM is a very complex ore containing Ti, V, Co, Ni, Sc et al. besides Fe,^[1] and the phase of Ti exists in ilmenite (FeTiO₃), titanomagnetite (Fe₃O₄·Fe₂TiO₄), ulvite (Fe₂TiO₄) and pseudobrookite (Fe₂TiO₅). After decades of basic research and industrial production practice, a complete set of blast furnace-converter smelting process has been successful developed to produce steel and vanadium/titanium products. Although it has high production efficiency and large scale, the blast furnace-con- verter smelting process has many severe defects, especially in blast furnace process to reduce the VTM ore. In the blast furnace process, most of the iron and part of vanadium can be reduced into the hot metal, however, almost all of the titanium enters into the slag in phase formation of perovskite and titanaugite, Ti-rich diopside, forming the high titanium slag with the content of TiO₂ varying from 22 to 25wt%,^[2-3] which results in the foaming behavior, the increase of melting temperature and viscosity of slag,^[3] as well as the difficult separation of slag-iron.^[4-5] Therefore, the fundamental research for thermo-physical-chemical properties of blast furnace slag bearing high TiO₂ is quite essential.

Thermo-Physical-Chemical Properties

Effect of TiO₂ on the Viscosity and Structure

In the BF process, the viscosity of slag containing TiO₂ is an important parameter that influences the gas permeability, the ability to tap the slag from the reactor, the efficiency of separation of slag from metal, the extent of slag foaming, etc. The viscosity of the BF slag has a wide range, depending on the temperature and slag composition. Viscosity measurements for the CaO-SiO₂-Al₂O₃-MgO-TiO₂ slag system were conducted by Ohno and Ross^[5], Sohn et al.^[6], Park et al.^[7], and author under neutral atmosphere. **Figure 1** demonstrates the effect of TiO₂ additions within a broad compositional range on the quaternary and quinary calcium-alumino-silicate slag systems. The viscosity was observed to decrease with higher concentrations of TiO₂ at a fixed (wt% CaO)/(wt% SiO₂) ratio and Al₂O₃ content at 1773 K, suggesting that TiO₂ is a network-modifying oxide. As a network-modifying oxide, TiO₂ is expected to depolymerize the slag network structure, which has subsequently been verified by using FTIR and Raman spectroscopy.^[8] The FTIR results at a constant CaO/SiO₂ ratio of 1.1 are presented in **Figure 2a** and support the role of TiO₂ as a basic oxide and a network modifier. FTIR spectra of silicate slags are typically focused within the wavenumber region between 1200 and 400cm⁻¹.^[9-11] This region represents the symmetric stretching vibration bands of the [SiO₄]-tetrahedra, the symmetric stretching vibrations of the [AlO₄]⁻ tetrahedra, and the symmetric Si-O bending vibration bands, etc. The vibration band between the wavenumbers of 1200 and 800 cm⁻¹ is the [SiO₄]⁻ tetrahedra symmetric stretching vibration band, which are well known to be the convoluted band of the NBO/Si transmission troughs from Q0 to Q3. This characteristic stretching vibration band for the large silicate network structures becomes less pronounced and the depth of the convoluted band becomes shallower with TiO₂ additions.

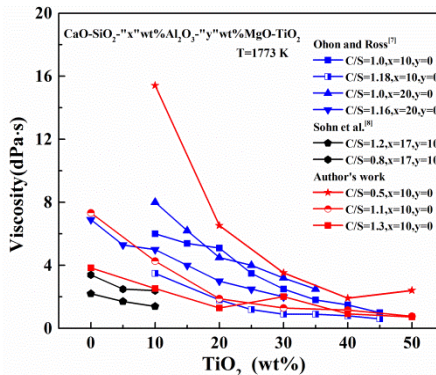


Figure 1. Effect of TiO₂ on the viscosity at various (wt%CaO)/(wt%SiO₂) ratios at 1773 K.

The as-quenched slag structure was also studied using Raman spectroscopy (**Figure 2b**). The characteristic band of silicate structure to semi-qualitatively identify the complex slag structure showed that several [SiO₄]⁻ tetrahedral peaks with symmetric stretching vibrations pertaining of NBO/Si=1,2,3,4 from 850-1100 cm⁻¹ and asymmetric stretching vibrations of NBO/Si=0 near 1040 and 1170cm⁻¹^[12]. Ti-O-Ti stretching vibrations are observed near

830 cm^{-1} [[13]]. The lower wavenumber shift with increasing TiO_2 content might cause by two factors. One possible reason is that TiO_2 increase results the decrease of SiO_2 . Another possible reason is that further support the role of TiO_2 as a basic oxide and a network modifier to depolymerize the structure resulting the NBO/Si=3 and 4 become more and more.

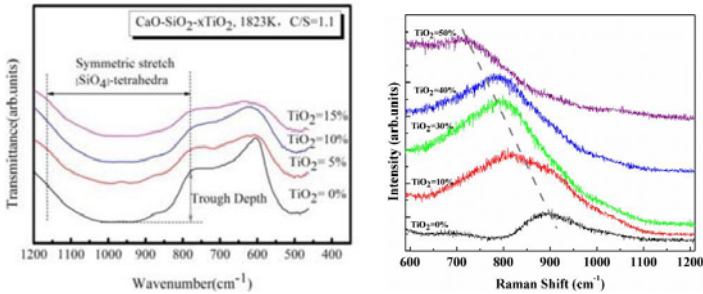


Figure 2. Structural analysis of $\text{CaO-SiO}_2\text{-TiO}_2$ slags as a function of TiO_2 content using (a) FTIR spectroscopy and (b) Raman spectroscopy.

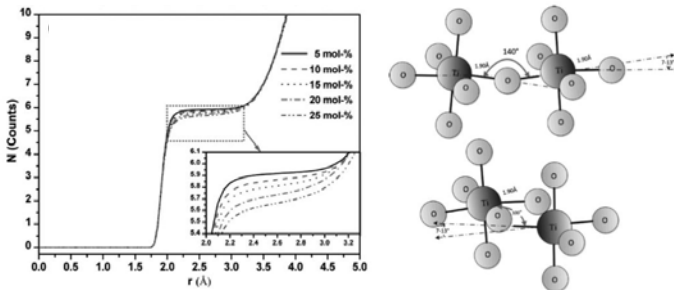


Figure 3. The CNs of the atomic pair Ti-O (a) and the angles of Ti-O-Ti (b)

The molecular dynamics (MD) simulation is an excellent tool for studying the microstructure with classical dynamics, which was generally used in numerous fields these years. Owing to the difficulty in high temperature experiments the molecular dynamics simulation is also applied into research of the metallurgical melt. The structure of the ternary system $\text{CaO-SiO}_2\text{-TiO}_2$ was simulated investigated by molecular dynamics technology with variation of TiO_2 contents under a fixed basicity^[14]. The majority of Ti^{4+} is coordinated by 6 O atoms but the 4-coordinated Ti^{4+} barely present within this system. CN is a key parameter to present the structure of the short-range ordering. The CN Si-O almost equals to 4 and has a little variation from 4.12 to 4.03 with varying mole fraction of TiO_2 , while the CN Ti-O decreases from 5.83 to 5.52 as the mole fraction of TiO_2 varies from 0 to 25%. Two $[\text{TiO}_6]$ octahedrons are connected by two ways with the angles of Ti-O-Ti equaling to 100° and 140° shown in **Figure 3a**. The distribution of the angles of Ti-O-Ti has an obvious variation with the TiO_2 (**Figure 3b**) additions. When the TiO_2 fraction is small the angle of 140° is the main

connectivity angle, the percentage of angle of 140° decreases with TiO_2 increasing and it reaches the minimum of 17% for 10% TiO_2 addition.

The viscosity of BF high-titanium slag will not curdle in the oxidation atmosphere or neutral atmosphere. Titaniferous slag has a characteristics of non-Newtonian fluid. The reduction extent of titanium dioxide plays an important role in the process of the slag's bodying, and the apparent viscosity will increase because of the increase of titanium carbide and titanium nitride generated by the deep reductions, especially when the concentration of titanium carbide and titanium nitride exceeds six percent, the slag viscosity will increase sharply (**Figure 4b**); It was also found that the scattered state of titanium carbide and titanium nitride played an important part in the increase of viscosity, in the case of same content, the greater the extent of scatter is, the higher the viscosity becomes, vice versa, the situations of reaction kinetics and scatter have a great effect to the scattered state. It was found that the free running temperature is generally high, which is eighty to one hundred degree higher than the common BF slag. The main cause is the existence of titanium carbide and titanium nitride which has a high smelting point in slag and the out phase point can be easily provided for uniform nucleation in the process of crystallization of slag, which can meet the need to reduce the degree of superheat.^[15]

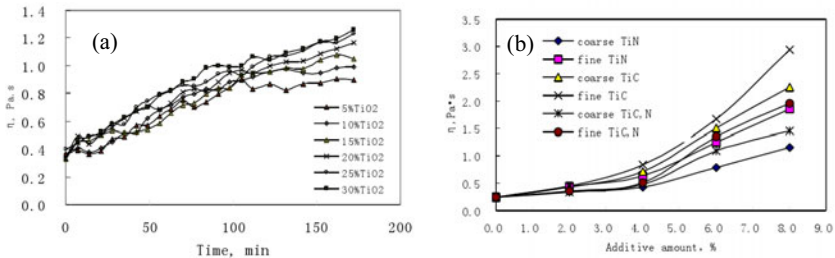


Figure 4. The relationship between of viscosity vs time under 1783 K(a) and viscosity vs additive amount of different size of TiC, TiN at 1623 K(b)

Effect of TiO_2 on the Surface Tension

The surface tension of molten slag is a key parameter in industrial process at high temperature for controlling the various surface and interfacial phenomena^[16-18] in ironmaking and steelmaking process. Although a large number of experimental surface tension data has been reported for silicate melts^[19-20], it is not possible to find appropriate data on the surface tension of molten slag bearing TiO_2 because of the limited availability of these data, resulting in a difficulty not only for studying the interfacial phenomena between slag and hot metal but also for the slag foaming in the blast furnace. Therefore, to fully understand the physical and chemical aspects of the blast furnace slag bearing TiO_2 , the contribution arising from surface properties cannot be overlooked. Besides, knowledge of the dependence of surface tension on liquid composition might provide useful insight into liquid structure.

A prediction model derived by Tanaka et al^[21], for the equation of the surface tension of ionic mixtures was applied to the 5-component molten slag in the $\text{SiO}_2\text{-CaO-MgO-}$

Al₂O₃-TiO₂ system based on the Butler's equation^[22].

Firstly, the surface tension of one sample of slag was measured and substituted in Butler's equation as a known quantity. Then the mole fractions of SiO₂, CaO, Al₂O₃ and MgO at the surface were obtained because the surface tensions for pure SiO₂, CaO, Al₂O₃ and MgO were also known quantities. Thereby, the mole fraction of TiO₂ at the surface was got because the sum of the mole fractions of TiO₂, SiO₂, CaO, Al₂O₃ and MgO principally equals to 100%. Finally, the surface tension for pure TiO₂ at 1673 K was achieved by the aid of the surface tension of the slag at 1673 K. At the moment, the surface tension of the samples were calculated. **Figure 5** shows the relation between TiO₂ mass fraction and the surface tension of the molten slag. The surface tension decreases along with the addition of TiO₂, proving that TiO₂ plays a role as a surface active agent in the 5-component slag. Moreover, there is a comparison between the calculated results and the experimental values, showing that the evaluated values are in a good agreement with the experimental results.

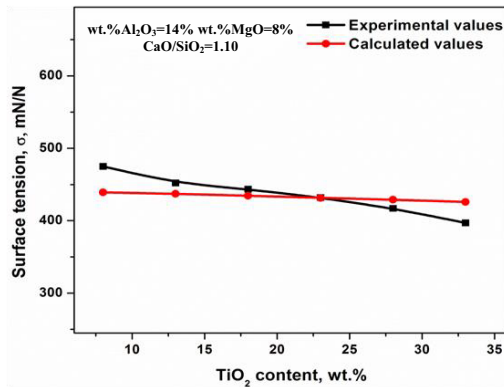


Figure 5. Effect of TiO₂ content on the surface tension of the 5-component slag

It is well known to us that the two principal parameters which influence the surface tension of liquid metal or alloys are the melt composition and temperature. As for the molten slag, the melt's structure may play an equally important role in the determination of the surface tension of the slag. The influence of the melt's structure on the surface tension of the slag along with the compositional variation will be discussed.

It is generally recognized that there are three kinds of ions existing in the slag melts: cations (Ca²⁺, Mg²⁺ and Ti⁴⁺ in this study), simple anions (O²⁻) and complicated units (Q¹, Q², Q³, Q⁴ for Si and Al). *NBO/T*, a measure for the degree of the polymerization of the slag was proposed by Mills et al.^[23], which is defined as following: *NBO/T* = number of non-bridging oxygen / tetragonally-bonded oxygen. As a basic oxide, TiO₂ can promote the depolymerization of the slag structure, and *NBO/T* will increase. In other words, the much more complicated units, such as Qⁿ(Si) and Qⁿ(Al) (Here n=3, 4), will turn into Qⁿ(Si) and Qⁿ(Al) (Here n=1, 2). Furthermore, the complicated units, Q¹ and Q² for Si and Al, have a much smaller moment than that of the simple anion, O²⁻, resulting in that Q¹ and Q² will be excluded outside to the surface layer. As a result, the number of the complicated units will

increase, while the number of free oxygen will reduce. As a consequence, the surface tension of the melt will drop down because of the decrease of the total ion moment at the surface.

Under high temperature reducing conditions, TiO_2 will be over-reduced and high-melting –point heterogeneous particles TiC , TiN and $Ti(C, N)$ will generate. The formation of solid particles can also lead to the decrease of slag surface tension. **Figure 6** shows the relation between TiC and TiN mass fraction and the surface tension of the molten slag. With the increase of TiC and TiN , the slag surface tension shows a downward trend. Proving that TiC and TiN are surfactants. At the same time, TiN has greater influence to surface tension than TiC .

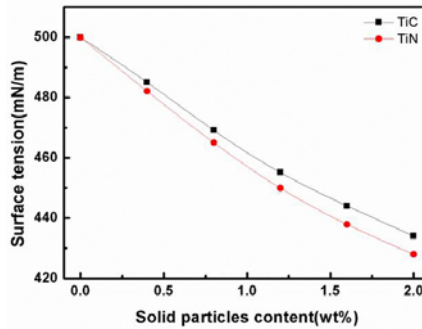


Figure 6. Relationship between surface of slag and mass fraction of TiC and TiN

Slag Foaming Phenomenon

Implementation of smelting with high V-Ti-magnetite proportion or full V-Ti-magnetite smelting will lead to the increase of TiO_2 in slag by more than 25% or 30%, generating serious problem of foaming in the furnace. Forming of foaming slag depends on two conditions: gas and properties of slag, in which, surface tension takes a great place in foam generation stage and viscosity takes a great place in foam stabilization stage, which play important roles to slag foaming. Comparing to normal BF slag, TiO_2 in high Ti-bearing BF slag will be over-reduced and high-melting point heterogeneous particles TiC , TiN and $Ti(C, N)$ will generate leading to great changes of the slag properties. So foaming slag is closely related with heterogeneous particles generated.

Based on the definition of foaming index (Σ) created by Fruehan^[24,25] :

$$\Sigma = C \frac{\mu}{\sqrt{\rho\sigma}}$$

Giving the relationship between foaming index (Σ) and the physicochemical properties (density ρ , viscosity μ , surface tension σ). Where, the constant C is unsure. In Ti-bearing slag, the change law of C was obtained by calculation is shown in **Figure 7**.

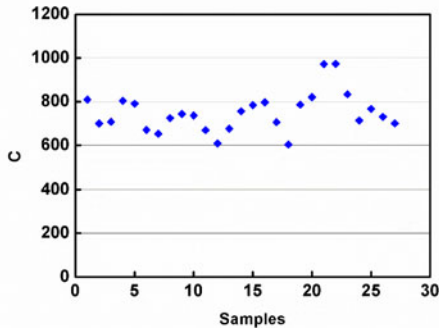


Figure 7. C Value Change in Foaming Index Formula

So, except in rare cases, the value of C in the foaming formula is between 600~800. Thus foaming formula of Ti-bearing BF slag was obtained:

$$\Sigma = (600 - 800) \frac{\mu}{\sqrt{\rho\sigma}} \dots\dots\dots (1)$$

In addition, the mathematical expression of relationship between foaming index and mole fraction of the compositions of the slag was obtained by stepwise method. In the regression process, the regression relation expression was fitted between mole fraction relations of the slag $\frac{X_{CaO}+X_{MgO}+X_{TiO_2}}{X_{Al_2O_3} * X_{SiO_2}}$, $\frac{X_{CaO}+X_{MgO}+X_{TiO_2}}{X_{Al_2O_3}+X_{SiO_2}}$, $\frac{X_{CaO}+X_{MgO}}{X_{Al_2O_3}+X_{SiO_2}+X_{TiO_2}}$, $\frac{X_{CaO}+X_{MgO}}{X_{Al_2O_3} * X_{SiO_2}}$, $\frac{X_{CaO}}{X_{SiO_2}}$ acting as its composition feature and foaming index of the slag. Their correlation coefficient are: 0.91520, 0.91657, 0.92575, 0.92519 and 0.94501 separately. The expression was as follow.

$$\Sigma = -6.25 - 3.12 \left(\frac{X_{CaO}}{X_{SiO_2}} \right) + 127.34X_{Al_2O_3} + 3.42X_{MgO} + 3.39X_{TiO_2} + 97.49X_{Ti_2O_3} + 785.73X_{TiC} + 384.74X_{TiN} - 72.79X_{MnO} - 84.98X_{CaF_2} \dots\dots\dots (2)$$

Which can be used to forecast and compare foaming performance of slag in a certain range of composition.

In room temperature, simulation experiments of slag foaming were performed based on the solution of glycerol and distilled water, and factors of foaming caused by blowing and from reaction. And the conclusions obtained are as follows [26]. Under the condition of external gas source, the lower viscosity has a promotion on foaming phenomenon, while higher viscosity will inhibit this phenomenon. With the increase of particle concentration, the foaming phenomenon was strengthened firstly and then weakened. Among the factors of slag foaming, solid particles holds a leading post, viscosity and surface tension take the second place; Under the condition of endogenous gas source, with increasing the viscosity of the solution, the foam height is reduced. Higher viscosity will give rise to more difficulty in eliminating foaming and longer time for defoaming. However, the influence of solid particle content on foaming exhibits a similar pattern with that observed under the condition of external gas source .

Formation of TiCN and Regulation Mechanism

The utilization of vanadium-bearing titanomagnetite in blast furnace process remained as a worldwide problem until the 1970s in the last century. It was found that the main problems occurred during the process were all somehow related to a high melting point phase which was produced from over-reduced titanium oxide. That is the TiC_xN_y . As mentioned before, these problems include slag foaming, large viscosity of slag, difficulty of iron-slag separation and low efficient desulfuration. As a solution, certain amount of common iron ores was added to the raw materials to relieve those problems to some extent. However, this approach became a limitation for the multipurpose utilization of the vanadium-bearing titanomagnetite. Moreover, with the increase of common iron ores' price, the production cost of the process is getting higher. Therefore, it is a critical point to restrain the formation of $Ti(CN)$ in blast furnace.

The results of thermodynamic calculation indicate that when TiC_xN_y was produced in slag-coke reaction, it is likely to occur in the softening zone which corresponds to the experimental result of blast furnace dissection. For another, under the current condition of raw material in Panzhihua Steel Ltd.(black point in **Figure 8**). The formation of TiC_xN_y would theoretically begin at about 15530 K. The restriction of formation of TiC_xN_y in blast furnace could be achieved by increasing the systematic pressure or oxygen enrichment. Another approach is to adjust the slag composition by decreasing the content of titanium dioxide and alumina in the slag or increasing the slag basicity and the content of magnesium oxide in the slag. However, the decrease of titanium dioxide content in the slag was not appreciated.

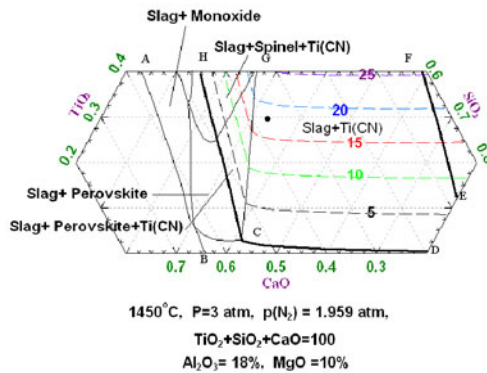


Figure 8. Effect of composition of slag on the final TiCN content in slag^[24]

In experimental study, the composition of TiC_xN_y produced in the slag-iron reaction was recognized as $TiC_{0.67}N_{0.33}$ and the content of $TiC_{0.67}N_{0.33}$ would increase with the increasing of temperature. These observations match the results calculated with FactSage very well. The potential measures to prevent TiC_xN_y from being produced in the slag-iron reaction were similar with those in the slag-coke reaction. It was found that the lower down of nitrogen partial pressure could efficiently prevent the formation of TiC_xN_y . Furthermore, the prevention means could also be either increasing the slag basicity and the content of

magnesium oxide or decreasing the content of alumina in the slag.^[27]

Acknowledgement

This study was supported by the National Natural Science of China(Grant No.51374263)

References

1. L. Zhang, L. Zhang, M. Wang, G. Li and Z. Sui: "Recovery of titanium compounds from molten Ti-bearing blast furnace slag under the dynamic oxidation condition" *Miner. Eng.*, 20 (2007), 684.
2. L. Zhang, L. N. Zhang, M. Y. Wang, G. Q. Li and Z. T. Sui: *ISIJ Int.*, 46 (2006), 458.
3. A. Shankar, M. Görnerup, A. Lahiri and S. Seetharaman: "Experimental investigation of the viscosities in CaO-SiO₂-MgO-Al₂O₃ and CaO-SiO₂-MgO-Al₂O₃-TiO₂ slags" *Metall. Trans. B*, 38 (2007), 911.
4. G. Handfield and G. Charette: "Viscosity and structure of industrial high TiO₂ slags" *Can. Metall. Q.*, 10 (1971), 235.
5. A. Ohno, H.U. Ross: "Reduction of titania by methane-hydrogen-argon gas mixture" *Can. Metall. Q.* 1963, 2,259.
6. I. Sohn, W. Wang, H. Matsuura, F. Tsukihashi, D.J. Min: "Influence of TiO₂ on the Viscous Behavior of Calcium Silicate Melts Containing 17 mass% Al₂O₃ and 10 mass% MgO" *ISIJ Int.* 2012, 52(1),158.
7. H.Park, J.-Y. Park, G.H. Kim, I. Sohn: "Effect of TiO₂ on the Viscosity and Slag Structure in Blast Furnace Type Slags", *Steel Res. Int.* 2012, 83(2),150.
8. Long, Wang, Wen Liang - ying, and Bai Chenguang. "FTIR and Raman Spectroscopic Investigation on the Structure of CaO - SiO₂ - TiO₂ Ternary Slags." *Characterization of Minerals, Metals, and Materials* 2014: 1-10.
9. H. Kim, W. H. Kim, I. Sohn, D. J. Min: "The Effect of MgO on the Viscosity of the CaO-SiO₂-20wt%Al₂O₃-MgO Slag System" *Steel Res. Int.*2010, 81, 261.
10. S. M. Han, J. G. Park, I. Sohn: "Surface kinetics of nitrogen dissolution and its correlation to the slag structure in the CaO—SiO₂, CaO—Al₂O₃, and CaO—SiO₂—Al₂O₃ slag system" *J.Non-Cryst. Solids* 2010, 357, 2868.
11. S. Agathopoulos, D. U. Tulyaganov, J. M. G. Ventura. "Structural analysis and devitrification of glasses based on the CaO MgO SiO₂ system with B₂O₃, Na₂O, CaF₂ and P₂O₅ additions": *J. Non-Cryst. Solids* 2006, 352, 322.
12. Sohn I, Min DJ. "A Review of the Relationship between Viscosity and the Structure of Calcium-Silicate-Based Slags in Ironmaking". *steel research international*, 2012;83:611-30.
13. MYseN BRO, Virgo D, "Scarfe CM. Relations between the anionic structure and viscosity of silicate melts—a Raman spectroscopic study". *Am Mineral*, 1980;65:690-710.
14. Shengfu ZHANG, Xi ZHANG, Chenguang BAI, Liangying WEN, and Xuewei LV." Effect of TiO₂ Content on the Structure of CaO-SiO₂-TiO₂ System by Molecular Dynamics Simulation" *ISIJ International*,2013,53,pp: 1131-1137
15. Bai Chenguang, "study on Some Physical Chemistry Problems of Blast Furnace Slag - Bearing Titania"[D] 2003, Chongqing University, China.
16. Mukai K. Wetting and Marangoni "Effect in Iron and Steelmaking Processes". *ISIJ international*, 1992, 32(1): 19-25.
17. Minaev Y A. "Thermodynamics of surface phenomena in liquid metal at phase boundaries". *Metallurgist*, 2006, 50(3-4): 168-175.
18. Siddiqi N, Bhoi B, Paramguru R K, et al. "Slag-graphite wettability and reaction kinetics Part 1

- Kinetics and mechanism of molten FeO reduction reaction". *Ironmaking & steelmaking*, 2000, 27(5): 367-372.
19. Skupien D, Gaskell D R. "The surface tensions and foaming behavior of melts in the system CaO-FeO-SiO₂". *Metallurgical and Materials Transactions B*, 2000, 31(5): 921-925.
20. Kingery W D. "Surface tension of some liquid oxides and their temperature coefficients". *Journal of the American Ceramic Society*, 1959, 42(1): 6-10.
21. Tanaka T, Kitamura T, Back I A. "Evaluation of surface tension of molten ionic mixtures"[J]. *ISIJ international*, 2006, 46(3): 400-406.
22. Butler J A V. "The thermodynamics of the surfaces of solutions"[C]//*Proc. R. Soc. A*. 1932, 135(827): 348.
23. K. C. Mills: "Proc. of Int. Conf. of Southern African Pyrometallurgy," Cradle of Humankind, *South Africa*, (2011).
24. Ito, K.; Fruehan, R. J. "Study on the Foaming of CaO-SiO₂-FeO Slags: Part I. Foaming Parameters and Experimental Results". *Metallurgical Transactions B-Process Metallurgy* **1989**, 20, 509-514.
25. Ito, K.; Fruehan, R. J. "Study on the Foaming of CaO-SiO₂-FeO Slags: Part II. Dimensional Analysis and Foaming in Iron and Steelmaking Processes." *Metallurgical Transactions B-Process Metallurgy* **1989**, 20, 515-521.
26. Xu, Z. "Research on the Foaming Phenomenon in Blast Furnace Process Treating Vanadium Titanium Magnetite." Chongqing, 2015.
27. Deng Qingyu, "Research on the Formation of TiCN and Regulation Mechanism in Blast Furnace Process Treating Vanadic Titanomagnetite"[D]. 2012, Chongqing University, China.

THE EFFECT OF TiO₂ ON THE LIQUIDUS ZONE AND APPARENT VISCOSITY OF SiO₂-CaO-8wt.%MgO-14wt.%Al₂O₃ SYSTEM

Zhiming Yan, Xuewei Lv, Jie Zhang, Jian Xu

School of Materials Science and Engineering, Chongqing University, China

E-mail: lvxuewei@163.com,400044

Keywords: Viscosity, Titanium, Liquidus zone

Abstract

TiO₂ has been approved as a viscosity-decreasing agent in blast furnace slag under inert atmosphere both by experimental and structure calculation. However, the validity of the above conclusion in a much bigger zone in CaO-SiO₂-Al₂O₃-MgO phase diagram has not approved. The viscosity of slag dependent on the TiO₂ content and basicity were measured in the present work. It was found that the viscosity and viscous activation energy decrease with increasing TiO₂ content and basicity at a reasonable range, indicating TiO₂ behaved as a viscosity-decreasing agent by depolymerizing the silicate network structure when its less than 50wt. %. The liquidity of the slag can be improved when TiO₂ content less than 50wt. % and basicity from 0.5 to 1.1. The free running temperature increase at TiO₂ content from 10wt.% to 30wt. %. The results of calculation does not agree well with the experimental values at a high basicity of 1.3 with TiO₂ content from 20wt.% to 30wt.% and the lower basicity of 0.5 with TiO₂ content more than 50wt.%.

Introduction

Cost issues and decrease of high grade raw materials has sparked the interest in using of other sources (such as vanadium-titanium magnetizes (VTM))of iron bearing materials which were regarded as uneconomical before. In the blast furnace process of using VTM, most of the iron and part of vanadium can be reduced into the hot metal. However, almost all of the titania enters into the slag in phase formation of perovskite and titanite, Ti-rich diopside, forming the high titania slag with the content of TiO₂ varying from 22 to 25wt.%^[1]. Therefore, the work for the influence of TiO₂ on the viscosity of slag has been continued.

Figure 1 demonstrates the effect of TiO₂ additions within a broad compositional range on the quaternary and quinary calcium-alumina-silicate slag systems under inert atmosphere. Ohno and Ross^[2], Park et al.^[3], Liao et al.^[4], and Sohn et al.^[5] revealed that TiO₂ acts as a basic oxide resulting in the depolymerization of the slag with higher concentrations of TiO₂ at a fixed (wt.% CaO)/(wt.% SiO₂) ratio and Al₂O₃ content at 1773 K(1500 °C). The viscosity experiments conducted by Saito et al.^[6] indicated that TiO₂ decreases the viscosity in quaternary CaO-SiO₂-Al₂O₃-TiO₂ slag system. Shankar et al.^[7] found that TiO₂ up to 2wt.% lower the viscosity in CaO-SiO₂-MgO-Al₂O₃. Handfield et al.^[8] described the industrial slag with high TiO₂ are very fluid melts once completely molten. However, Ohno and Ross^[2], and Qiu et al.^[9] reported that TiO₂ can increase the viscosity of the CaO-SiO₂-Al₂O₃-TiO₂-(MgO) slag under reducing atmosphere indicating that it could be caused by the formation of solid particles of TiC and the

polymerization of orthosilicate ions. Xie et al.^[10] indicated that slag thickening occurred under prolonged reduction when a considerable amount of both TiO₂(3~7wt.%) and TiC (1~3wt.%) was formed, particularly in acidic slag.

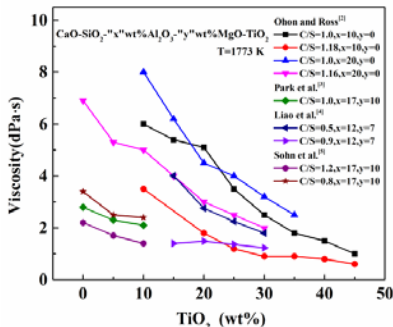


Figure 1. Effect of TiO₂ on the viscosity of CaO–SiO₂–Al₂O₃–MgO based slag at various (wt.% CaO)/(wt.% SiO₂) ratio at 1773 K(1500°C)

TiO₂ has been approved as a viscosity-decreasing agent in blast furnace slag under inert atmosphere both by experimental and structure calculation. However, the validity of the above conclusion in a much bigger zone in CaO–SiO₂–Al₂O₃–MgO phase diagram has not approved.. Therefore, the object of this work is to approve the validity of the conclusion that TiO₂ decrease the viscosity of the slag. In other words, the maximum content of TiO₂ as a viscosity reducer should be given.

Experimental

The rotating cylinder method was used to measure the viscosity in present work. The schematic figure of the experimental apparatus is shown in **Figure 2**. A rotating viscometer(Brookfield, model LVDV-II+ Pro, Middleboro, MA) installed in the furnace was connected with a computer to record the value of the torque from the rotation of the spindle. The heater of the furnace is made of MoSi₂. The slag sample was loaded in the molybdenum(Mo) crucible which was put into a corundum crucible, with a graphite crucible in the out layer for removing the left oxygen in the furnace. The rotating bob was made of Mo. The viscometer was regularly calibrated before the experiment using three standard silicone oils of known viscosities(0.96, 4.92 and 9.80 dPa·s) at 298 K(25°C) .

The slag for the viscosity measurement was synthetic slag, which were synthesized with the known chemical composition slag from the analysis pure grade reagent. the analysis pure grade reagent were first claimed at 1273 K(1000°C) in a muffle furnace to remove all the impurities such as carbonate, hydroxide and moisture, and then weighed. The weighted chemicals (CaO, SiO₂, Al₂O₃, MgO and TiO₂) were thoroughly and pressed into cylindrical pellets before used in the experiments. About 200g sample was used in the Mo crucible, which gave a slag bath of at least 40mm deep contained in crucibles.

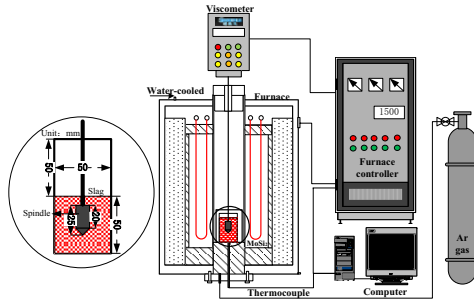


Figure 2. Schematic experimental setup for the viscosity measurement

The liquid region of the CaO-SiO₂-14wt. %Al₂O₃-8wt. %MgO-TiO₂ slag system at 1723K (1450°C) was calculated by FactSage to help design the experimental scheme. The chemical compositions of the slag investigated in the present study are presented in **Table 1**. The slag used for the viscosity measurement was synthetic slag obtained from analytically pure reagents of a known composition. The reagents were first calcined at 1273 K(1000°C) in a muffle furnace to remove all of their impurities, such as carbonate, hydroxide, and moisture. The pretreated powders were combined according to the desired proportions and then mixed homogeneously in a mixer for 30 min.

Table 1. Chemical compositions of the studied slag.

No.	Al ₂ O ₃	MgO	TiO ₂	CaO	R= CaO(wt.%)/SiO ₂ (wt.%):	
					SiO ₂	R
A1	14.00	8.00	0.00	44.09	33.91	1.30
A2	14.00	8.00	10.00	38.43	29.57	1.30
A3	14.00	8.00	20.00	32.78	25.22	1.30
A4	14.00	8.00	30.00	27.13	20.87	1.30
A5	14.00	8.00	40.00	21.48	16.52	1.30
A6	14.00	8.00	50.00	15.83	12.17	1.30
B1	14.00	8.00	0.00	40.86	37.14	1.10
B2	14.00	8.00	10.00	35.62	32.38	1.10
B3	14.00	8.00	20.00	30.38	27.62	1.10
B4	14.00	8.00	30.00	25.14	22.86	1.10
B5	14.00	8.00	40.00	19.90	18.10	1.10
B6	14.00	8.00	50.00	14.67	13.33	1.10
C1	14.00	8.00	0.00	26.00	52.00	0.50
C2	14.00	8.00	10.00	22.67	45.33	0.50
C3	14.00	8.00	20.00	19.33	38.67	0.50
C4	14.00	8.00	30.00	16.00	32.00	0.50
C5	14.00	8.00	40.00	12.67	25.33	0.50
C6	14.00	8.00	50.00	9.33	18.67	0.50

The mixed powders were heated to 1798 K(1525°C) and held for 3h to homogenize the slag. The bob was lowered and the upper surface of the bob was inserted 5 mm deep into the slag

layer. The spindle was carefully adjusted to ensure that it was placed on the central axis line of the crucible because experimental errors can be easily caused by slight deviations of the spindle from the central axis. Argon was blown into the furnace chamber at a constant gas flow rate of 1.5 L/min to avoid oxidation of the molybdenum crucible and spindle. After the slag was held at 1798 K(1525°C) for 3 h, the spindle began to rotate at a fixed speed of 12 rpm. The viscosity was recorded after the reading had stabilized at the desired temperature. Measurements were carried out at every 25 K(°C) from 1798 K(1525°C) to 1673 K(1400°C). The equilibration time for viscosity measurements was 30 min., and viscosity measurements are reported as the average value of data collected 2 min after the 30 min. thermal equilibrium was achieved. The standard errors of viscosity were found to be less than ± 0.02 dPa·s. When the measurement was finished, the slag was reheated to 1773 K(1500°C). Then the viscosity was measured again at 10 seconds intervals with decreasing the temperature continuously at a rate of 2 K(°C)/min, as a result, the viscosity-temperature curves were got. After completing the viscosity measurements, slag samples were reheated to 1773 K(1500°C) and quenched on a water-cooled copper plate, the quenched samples were used to check the slag structure using XRD and Raman spectroscopy(Lab RAMHR Evolution; HORIBA Scientific, France).

Results and Discussion

A. Effect of TiO₂ on viscosity

Figure 3 represents the influence of TiO₂ on the viscosity with varying basicity. TiO₂ reduced the viscosity, especially for the slag with lower basicity at 0.5, which conforms with the previous research, supporting that TiO₂ is a network-modifying oxide. As a network-modifying oxide, TiO₂ is expected to depolymerize the slag network structure. When basicity was increased to 1.3, the viscosity first decrease by adding TiO₂, however, it will increase when TiO₂ content reach to 20-30wt.%, the reason for the viscosity increasing is the formation of perovskite near the liquids line as shown in **Figure 4**. With increasing of basicity, the amount of perovskite is increase and the precipitation temperature of the perovskite become higher. However, the results of calculation does not relate well with the experimental values. At a high basicity of 1.3 with TiO₂ content from 20wt.% to 30wt.%, the liquid phase line of TiO₂ content near 20wt.% should move to the place where the TiO₂ content near 30wt.%. At the basicity of 0.5, the TiO₂ content more than 50wt.% would locate out the liquid phase region.

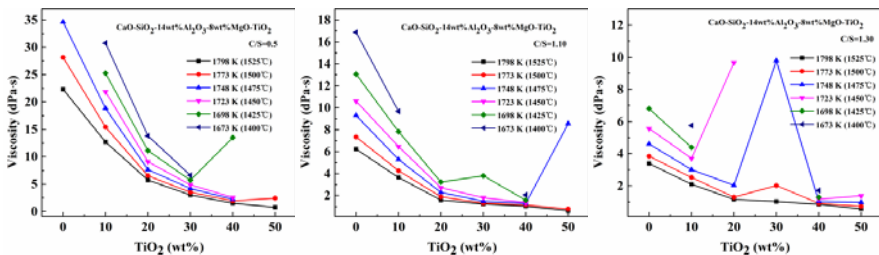


Figure 3. Effect of TiO₂ on the viscosity with varying basicity

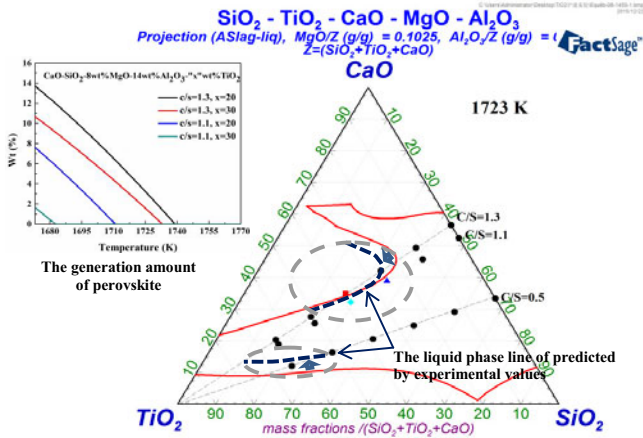


Figure 4. Liquid region of the slag system calculated from FactSage at 1723K (1450°C) and modification with experimental values

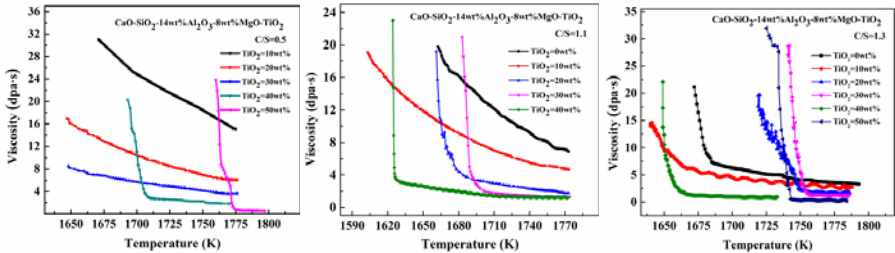


Figure 5. Effect of TiO₂ on the viscosity-temperature curves of the slag

B. Free running temperature and viscous activation energy

The sensitivity of viscosity with temperature (thermal stability) is used to describe the viscosity variation with temperature. The so-called short slag means that its viscosity change occurs in a narrow interval of temperature and bad thermal stability than the long slag does. **Figure 5** shows the effect of TiO₂ on the viscosity-temperature curves of the slag with varying basicity. It could be found that with basicity at 1.1, the viscosity changed dramatically at TiO₂ from 20wt.% at a certain temperature, but the change at 40wt.% with basicity at 0.5. The critical point correct well with the precipitation temperature of the perovskite. Therefore, the free running temperature which means the critical point of the curves could be got by drawing a tangent line of the slopes is -1 on the curve. It is evident from **Figure 6** that the free running temperature increase with TiO₂ from 10wt. % to 30wt.%, which means that poor viscosity

thermal stability with TiO₂ content increasing caused by the precipitation. However, the free running temperature decrease at TiO₂ content of 40wt.%.

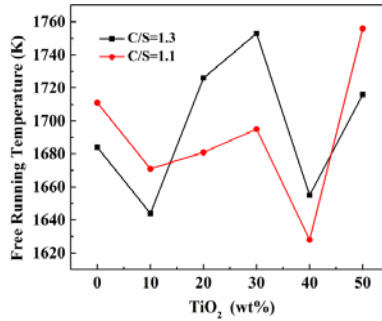


Figure 6. Effect of TiO₂ on the free running temperature of the slag

The viscosity data can be described by an Arrhenius equation over the entire temperature region in this study.

$$\eta = \eta_0 \exp\left(\frac{E_\eta}{RT}\right) \quad (1)$$

where η_0 , E_η , R, and T are a constant, the apparent activation energy of viscous flow, the universal gas constant, and the absolute temperature, respectively. Variations of E_η can reveal the change of frictional resistance for viscous flow and suggest a change in the structure of the molten slag or more directly a change in the cohesive flow units forming the slag structure. The viscous activation energy is get and plot in the **Figure 7**. The change of viscosity and viscous energy show the same regularity indicating that the main factor is the same as impact viscosity and viscous activation energy.

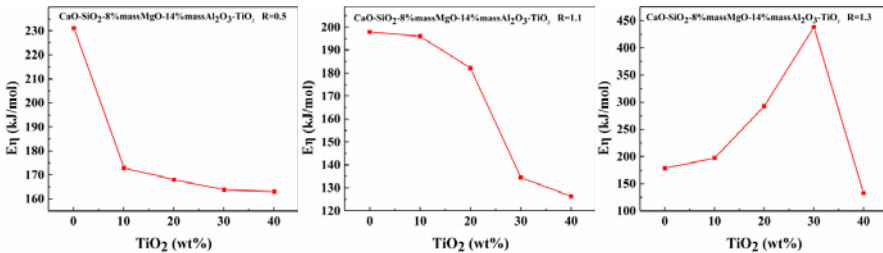


Figure 7. Effect of TiO₂ on the apparent activation energy of the slag

C. Effect of basicity on viscosity

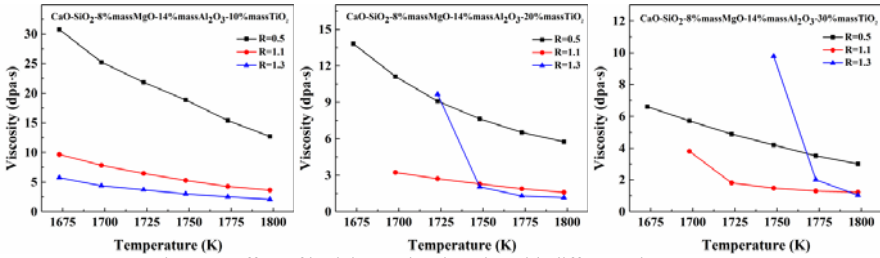


Figure 8. Effect of basicity on the viscosity with different TiO₂ content

The influence of basicity on the viscosity with TiO₂ from 10wt.% to 30wt.% are showing in **Figure 8**. It is obvious that the lower the basicity, the higher the viscosity. CaO is a well-known typical basic oxide that can modify the melt structure effectively. The addition of CaO can result in a large-scale depolymerization with lower basicity. It indicates that the size of the silicate flow unit becomes smaller with increasing content of basic oxides, resulting in decreasing slag viscosity. However, the increase of CaO will result in precipitation of perovskite. Therefore, to get appropriate viscosity with high TiO₂ content, the maximum of basicity must be less than 1.3.

Conclusions

In present work, viscosity of the quinary system CaO-SiO₂-MgO-Al₂O₃-TiO₂ were experimentally measured. The conclusions are summarized as follows:

1. The increasing of TiO₂ additions and basicity lowered the viscosity by affecting the silicate network structure, where the complex silicate sheets were depolymerized into simpler silicate structures.
2. TiO₂ content less than 50wt. % and basicity from 0.5 to 1.1 could get a good liquidity melt. The slag shows the short slag feature at high TiO₂ content with high basicity and shows the long slag feature at low basicity.
3. The results of calculation does not agree well with the experimental values at a high basicity of 1.3 with TiO₂ content from 20wt.% to 30wt.% and the lower basicity of 0.5 with TiO₂ content more than 50wt.%.

Acknowledgement

This study was supported by the National Natural Science of China(Grant No.51374263).

References

1. Zhang Z, Wen G, Tang P, Sridhar S. "The Influence of $\text{Al}_2\text{O}_3/\text{SiO}_2$ Ratio on the Viscosity of Mold Fluxes"[J]. *ISIJ International*, 2008;48:739-46.
2. Ohno A, Ross H. "Optimum slag composition for the blast-furnace smelting of titaniferous ores"[J]. *Canadian Metallurgical Quarterly*, 1963;2:259-79.
3. Park H, Park J-Y, Kim GH, Sohn I. "Effect of TiO_2 on the Viscosity and Slag Structure in Blast Furnace Type Slag"[J]. *Steel Research International*, 2012;83:150-6.
4. Liao J, Li J, Wang X, Zhang Z. "Influence of TiO_2 and Basicity on Viscosity of Ti Bearing Slag"[J]. *Ironmaking & Steelmaking*, 2012;39:133-9.
5. Sohn I, Wang W, Matsuura H, Tsukihashi F, Min DJ. "Influence of TiO_2 on the Viscous Behavior of Calcium Silicate Melts Containing 17 mass% Al_2O_3 and 10 mass% MgO "[J]. *ISIJ international*, 2012;52:158-60.
6. Saito N, Hori N, Nakashima K, Mori K. "Viscosity of Blast Furnace Type Slag"[J]. *Metall and Materi Trans B*, 2003;34:509-16.
7. Shankar A, Görnerup M, Lahiri AK, Seetharaman S. "Experimental Investigation of the Viscosities in $\text{CaO-SiO}_2\text{-MgO-Al}_2\text{O}_3$ and $\text{CaO-SiO}_2\text{-MgO-Al}_2\text{O}_3\text{-TiO}_2$ Slag"[J]. *Metall and Materi Trans B*, 2007;38:911-5.
8. Handfield G, Charette G. "Viscosity and structure of industrial high TiO_2 slag"[J]. *Canadian Metallurgical Quarterly*, 1971;10:235-43.
9. Qiu G, Shiwei Ma, Qingyu Deng, Xuwei Lv, Hua Wang. "Study on the formation of Ti(C,N) between blast furnace hot metal and slag bearing high TiO_2 "[J]. *Metallurgia International*, 2012;17:94-6.
10. Xie D, Mao Y, Zhu Y. "Viscosity And Flow Behaviour of TiO_2 -containing Blast Furnace Slag Under Reducing Conditions". *The South African Institute of Mining and Metallurgy*, [J] 2004. p. 28.

ELECTRORHEOLOGY OF Ti-BEARING SLAG WITH DIFFERENT COMPOSITION OF TiC AT 1723K

Tao Jiang^{1,2}, Hongrui Yue¹, Xiangxin Xue^{1,2}, and Peining Duan^{1,2}

¹School of Metallurgy, Northeastern University, Shenyang 110819, China

²Liaoning Key Laboratory of Metallurgical Resources Recycling Science; Engineering and
Technology Research Center for Boron Resource Comprehensive Development and
Application of Liaoning Province; Liaoning Key Laboratory for Ecological Comprehensive
Utilization of Boron Resources and Materials, Shenyang 110819, China

Keywords: Electrorheology, Fluid type, Ti-bearing slag, TiC.

Abstract

Electrorheology of Ti-bearing slag was investigated by a reconstructive equipment at 1723K. The slag samples were based on slag of Panzhihua Steel and the viscosity was measured with different composition of TiC. The constitutive equations which simulated the Herschel-Bulkley model were established by the relationship between shear rate and shear stress of slag, thus the fluid type was confirmed under the condition of different electric field intensity. The result was that the slag sample containing TiC had an obvious phenomenon of electrorheology, the increase of electric field intensity gave rise to the increase of viscosity and shear stress. It can be extracted from the constitutive equations of 4% TiC slag that the fluid type converted into a Bingham fluid with application of the electric field.

Introduction

Electrorheology (ER) is a typical property of kinds of non-Newtonian fluids. The ER behavior, a rapid and reversible response on application of a direct or alternating electric field, has been the object of a number of studies^[1,2]. In an ER fluid, the solid particles are randomly distributed within a non-conducting liquid. However, when an electric field is applied, the solid particles start to create highly organized structures due to the electric field. At this moment the viscosity and shear stress change rapidly. ER response is controlled not only by the magnitude and characteristics of the applied electric field but also by a wide range of properties of the slag system itself, such as the dielectric constant, the particle conductivity, and the volume fraction of particles. The rapid and reversible property of ER fluid is not limited to the study for academic researches, at the same time it has lots opportunity for application in industry, such as electrical clutches, locks, valves and shock absorbers^[3-5].

Numerous studies have been conducted in the past to investigate the viscosity of slag containing TiC. As found by D. Xie^[6], the viscosity showed a rapid increase with the appearance of TiC. The relationship between torque and shear rate was investigated by Y.L. Zhen^[7]. The conclusion was that 2wt% TiC slag can be considered as a Newtonian fluid for the slight viscosity change with the shear rate. The result of fluid type in our previous study^[8] was that the 8wt% TiC slag, as a liquid dispersed with solid phase, behaved as a non-Newtonian fluid. In another hand, an obvious ER response had been observed for kinds of liquids dispersed with TiC, such as epoxy^[9]. So it is reasonable and necessary to investigate the behavior of Ti-bearing slag containing TiC with the application of an electric field.

Experimental

Synthetic slag samples (Table 1) based on the chemical composition of on-site slag from Panzhihua steel (Table 2) were prepared from chemical reagents such as CaO, SiO₂, MgO, Al₂O₃, TiO₂ and TiC. The grain size of TiC is in range of 3.18-33.43 μ m and its mean grain size is 14.1 μ m (Figure 1). The mixtures of CaO, SiO₂, MgO, Al₂O₃, TiO₂ and TiC were packed into a Mo crucible and pre-melted in an electric resistant furnace under an Ar gas atmosphere at 1773 K for 20 min to ensure uniformity of the compositions.

Table 1. Experimental composition of slag examples, wt%.

No.	CaO	SiO ₂	MgO	Al ₂ O ₃	TiC	TiO ₂	∑TiO ₂	CaO/SiO ₂
a	30.03	27.30	8.00	14.00	4.00	16.67	22.00	1.10
b	30.75	27.95	8.00	14.00	8.00	11.33	22.00	1.10

Table 2. Chemical composition of BF slag from Panzhihua Steel, wt%.

CaO	SiO ₂	MgO	Al ₂ O ₃	TiO ₂
27.0	24.3	8.3	14.4	22.3

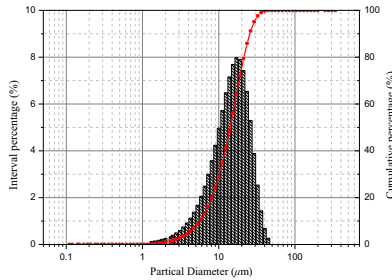


Figure 1. Grain size distribution of TiC powder.

The rheology of slag samples within an electric field was investigated using a reconstructive equipment^[10] which consisted of a Brookfield DV-III rheometer, a high-temperature resistance furnace, a direct current (DC) electrical source and data acquisition systems (Figure 2). The crucible, filled with 140g slag was placed in the resistance furnace, heated up to 1773K at the rate of 5K·min⁻¹ and kept there for 60 min. After the melting and reacting sufficiently, the slag was cooled to 1723K at the rate of 3K·min⁻¹ and kept there for 30 min before the measurement. The procedure of rheological measurement was shown in Figure 3.

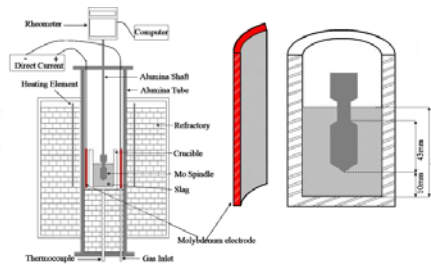


Figure 2. Schematic diagram of the experimental apparatus.

The Herschel-Bulkley fluid (Formula 1) is a generalized model of a non-Newtonian fluid, in which the strain experienced by the fluid is related to the stress in a complicated, non-linear way^[11].

$$\tau = \tau_y + kD^n \quad (1)$$

Where τ is shear stress, Pa; τ_y is yield stress, Pa; k is viscosity factor; D is shear rate, s^{-1} ; n is flow index. The fluid is considered to be a Newtonian fluid^[12] when $\tau_y = 0$ and $n = 1$, a dilatant fluid when $\tau_y = 0$ and $n > 1$, a pseudo plastic fluid when $\tau_y = 0$ and $n < 1$, a Bingham fluid when $\tau_y \neq 0$ and $n = 1$, a plastic pseudo plastic fluid when $\tau_y \neq 0$ and $n < 1$, and a plastic expansion fluid when $\tau_y \neq 0$ and $n > 1$. Both the process of data fitting and error analysis were noted by our previous paper^[8].

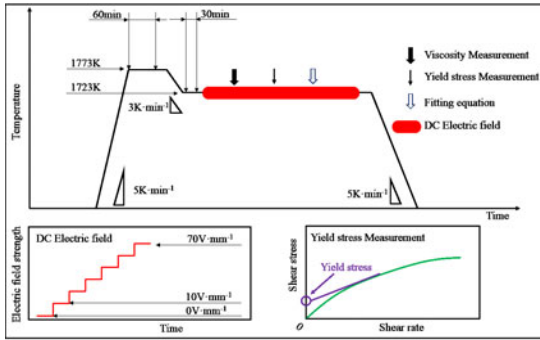


Figure 3. Temperature-time schedule of the experiment.

Results and discussion

As illustrated in Figure 4, a considerable influence of electric field on the flow behavior of Ti-bearing slag containing TiC slag has been found. As the slag is applied for the maximum electric field intensity $70V \cdot mm^{-1}$, the viscosity of 8% TiC slag is approximately 40 percent higher than that in absence of an electric field. And a 10 percent increasing for 4% TiC slag, although kind of tiny, is greater than the error mentioned above. Perovskite, the first-crystallized phase in a $29.3CaO-26.7SiO_2-14Al_2O_3-8MgO-22TiO_2$ slag, starts to be crystallized once the temperature below $1709K$ ^[13]. So the increasing of viscosity could be attributed to the influence of TiC totally which should be the unique solid phase in the slag at $1723K$. In the slag system, a three-dimensional network structure is formed with the core of TiC particle, for kinds of polymer matrix^[14], the agglomerates alike the three-dimensional network structure in Ti-bearing slag are present even at low composition of TiC. So the conclusion, extracted from the paper^[14] mention above that values of dielectric permittivity increase with TiC content, since the composites become more conductive, their heterogeneity raises, charges accumulate at the interfaces of the system and thus interfacial polarization enhances, may be a reference for the conclusion in the present paper.

The shear rate dependence of the shear stress of slag sample (a) is shown in Figure 5. The shear stress in presence of the electric field is greater than the value without any electric field over the entire range of shear rates. When the curve of $0V \cdot mm^{-1}$ is extrapolated to Y axis, the

curve passes the origin, and at the same time the slope keeps at a same value mostly, so the fluid type of the sample (a) without any electric field could be considered as a Newtonian fluid based on the Newton's Law of Viscosity. For the electric field intensity $70\text{V}\cdot\text{mm}^{-1}$, curve of slag turns into a non-zero axial line once the electric field is applied. Polarization of disperse phase TiC particles gives rise to the establishment of field-induced structure^[15], and then the extrapolate value of shear stress at zero shear rate, known as yield point, is observed in slag system. At a very low shear rate, the shear forces are unable to destroy the field-induced structure. Meanwhile, the resistance to flow is much greater than in the absence of an electric field. Hence, the fluid type should be a non-Newtonian fluid once the electric field is applied in consideration of the slope fluctuates slightly as well.

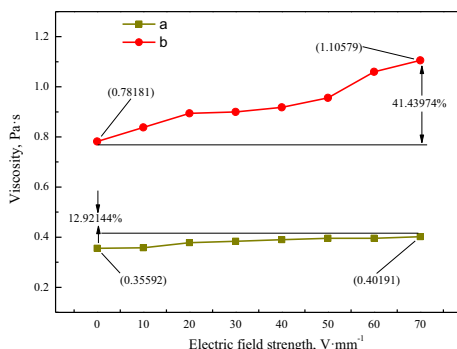


Figure 4. Plots of viscosity of slag samples with electric field applying.

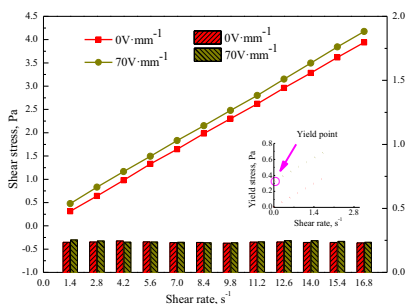


Figure 5. Rheological curves of sample (a).

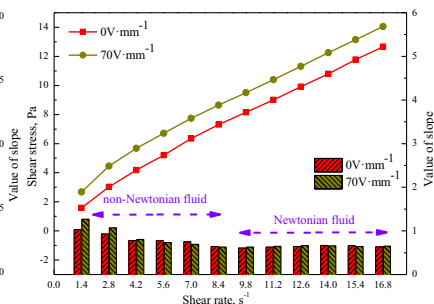


Figure 6. Rheological curves of sample (b).

The relationship between shear rate and shear stress of sample (b) is depicted in Figure 6. A typical non-Newtonian fluid behavior, shear thinning^[16,17], is observed in the slag system. The slopes are decreasing with the shear rates both in the absence and presence of the electric field. Once the shear rate is beyond 9.8s^{-1} , the shear stresses decrease hardly and the slag performs as a Newtonian fluid. The decrease range of slope value under the application of an electric field is greater than in absence of an electric field, it is obviously that the application

of electric field is a promotion for the establishment of three-dimensional network structure in Ti-bearing slag due to the formation of field-induced structure. After the yield point is reached, the shear stress maintains a plateau level and, as a consequence, the viscosity shows decrease as a function of shear rate. Due to the non-zeroaxial propriety and shear thinning behavior of the rheological curves, a similar conclusion^[18] could be extracted from Figure 6 is that when an electric field is applied, the apparent viscosity and the shear stress increase and the flow curves become slightly pseudoplastic.

The results of constitutive equations are shown in Table 3. Coefficient indexes (R^2) of these established equations are all greater than 0.99 to ensure a good fitness between each equation founded and result measured. The conclusion similar with existed research^[19,20] could be obtained for 4% TiC slag that without an electric field, the slag behaves as a Newtonian fluid, however, once applying the electric field on slag system, the particles in this system polarize and align parallel to the field vector, thus, the slag behaves as a Bingham fluid. For the 8% TiC slag, the slag performs as a plastic pseudo plastic fluid which possesses yield stress and shear thinning behavior both in the absence and presence of the electric field. The absolute values of k and τ_y , which mean the viscosity factor and yield stress respectively, increase as the response for the electric field application.

Table 3. Constitutive equations of slag sample (a) and (b)

TiC	Electric field	Constitutive equations	Fluid type	R^2
4	$0V \cdot mm^{-1}$	$\tau=0.4018D^{1.0000}$	Newtonian	0.9994
	$70V \cdot mm^{-1}$	$\tau=0.3592+0.5357D^{1.0000}$	Bingham	0.9991
8	$0V \cdot mm^{-1}$	$\tau=1.8683+0.6883D^{0.9098}$	Plastic pseudo plastic	0.9974
	$70V \cdot mm^{-1}$	$\tau=2.3175+0.9388D^{0.8755}$	Plastic pseudo plastic	0.9968

Conclusions

An obviously ER response is observed in Ti-bearing slag containing TiC, once the electric field is applied, both the viscosity and shear stress increase with the electric field, and the enhancement of 8% TiC slag is greater than 4% TiC slag.

The fluid type of 4% TiC slag converts from a Newtonian fluid to a Bingham fluid with the application of the electric field, at same time, the flow resistance is greater than in absence of the electric field due to the appearance of yield stress. It is already a non-Newtonian fluid even without any external impact for the 8% TiC slag. And as a plastic pseudo plastic fluid, which possesses the shear thinning behavior, the shear stress decreases with the increasing of shear rate among the electric field.

Acknowledgements

This work was financially supported by the National Science Foundation of China (Nos. 51174051 and 51090383).

References

1. T. Plachy, M. Sedlacik, V. Pavlinek, M. Trchová, Z. Morávková, and J. Stejskal, "Carbonization of aniline oligomers to electrically polarizable particles and their use in electrorheology," *Chem. Eng. J.*, 256(2014), 398-406.
2. Y. Hirose, Y. Ostubo, "Electrorheology of suspensions of poly(ethylene glycol)/poly(vinyl acetate) blend particles," *Colloids Surf., A*, 414(2012), 486-491.
3. K. Shin, D. Kim, J.C. Cho, H.S. Lim, J.W. Kim, and K.D. Suh, "Monodisperse conducting colloidal dipoles with symmetric dimer structure for enhancing electrorheology properties," *J. Colloid Interface Sci.*, 374(2012), 18-24.
4. J.B. Yin, Y.J. Shui, R.T. Chang, and X.P. Zhao, "Graphene-supported carbonaceous dielectric sheets and their electrorheology," *Carbon*, 50(2012), 5247-5255.
5. M.M. Ramos-Tejada, M.J. Espin, R. Perea, and A.V. Delgado, "Electrorheology of suspensions of elongated goethite particles," *J. Non-Newtonian Fluid Mech.*, 159(2009), 34-40.
6. D. Xie, Y. Mao, and Y. Zhu, "Viscosity and flow behaviour of TiO₂-containing blast furnace slags under reducing conditions," (Paper presented at the *VII Int. Conf. on Molten Slags Fluxes and Salts*, the South African Mining and Metallurgy, Cape Town, South Africa, 2004), 43.
7. Y.L. Zhen, G.H. Zhang, and K.C. Chou, "Viscosity of CaO-MgO-Al₂O₃-SiO₂-TiO₂ Melts Containing TiC Particles," *Metall. Mater. Trans. B*, 46B(2015), 155-161.
8. T. Jiang, D.M. Liao, M. Zhou, Q.Y. Zhang, H.R. Yue, S.T. Yang, P.N. Duan, and X.X. Xue, "Rheological behavior and constitutive equations of heterogeneous titanium-bearing molten slag," *Int. J. Miner. Metall. Mater.*, 22(2015), 804-810.
9. Y. Wang, F. Luo, W.C. Zhou, and D.M. Zhu, "Dielectric and electromagnetic wave absorbing properties of TiC/epoxy composites in the GHz range," *Ceram. Int.*, 40(2014), 10749-10754.
10. T. Jiang, H.R. Yue, X.X. Xue, P.N. Duan, and Q.Y. Zhang, CN. Patent, CN.201520798586.0, 2015-10-14.
11. H.S. Tang, D.M. Kalyon, "Estimation of the parameters of Herschel-Bulkley fluid under wall slip using a combination of capillary and squeeze flow viscometers," *Rheol. Acta.*,

43(2004), 80-88.

12. R.Z. Liu, K. Wu, Y. Zhao, and M.F. Jiang, "Measurement of Rheologic Characteristics of Melts," *J. Northeast. Univ. Nat. Sci.*, 25(2004), 570-573.
13. G.B. Qiu, L. Chen, J.Y. Zhu, X.W. Lv, and C.G. Bai, "Effect of Cr₂O₃ Addition on Viscosity and Structure of Ti-bearing Blast Furnace Slag," *ISIJ Int.*, 55(2015), 1367-1376.
14. C.G. Raptis, A. Patsidis, and G.C. Psarras, "Electrical response and functionality of polymer matrix-titanium carbide composites," *Express Polymer Letters*, 4(2010), 234-243.
15. J.K.G. Dhont, and K. Kang, "Electric-field-induced polarization of the layer of condensed ions on cylindrical colloids," *Eur. Phys. J. E*, 34(2011), 1-19.
16. C.R. Lin, W.J. Chen, "The links-nodes-blobs model for shear-thinning-yield-stress fluids," *Colloid. Polym. Sci.*, 277(1999), 1019-1025.
17. Y. Satio, H. Ogura, and Y. Otsubo, "Rheological Behavior of Silica Suspensions in Aqueous Solutions of Associating Polymer," *Colloid. Polym. Sci.*, 286(2008), 1537-1544.
18. A. Lengálová, V. Pavlínek, P. Sába, J. Stejskal, and O. Quadrat, "Electrorheology of polyaniline-coated inorganic particles in silicone oil," *J. Colloid Interface Sci.*, 258(2013), 174-178.
19. D.J. Klingenberg, C.F. Zukoski, "Studies on the steady shear behavior of electrorheological suspensions," *Langmuir*, 6(1990), 15-24.
20. J. W. Goodwin, G. M. Markham, and B. Vincent, "Studies on Model Electrorheological Fluids," *J. Phys. Chem. B*, 101(1997), 1961-1967.

STUDY ON APPARENT VISCOSITY OF FOAMING SLAG - COLD MODEL AND HIGH TEMPERATURE EXPERIMENTS

Johan Martinsson, Björn Glaser, Du Sichen

KTH Royal Institute of Technology, Stockholm, Sweden

Emulsion, apparent viscosity, foaming slag, BOF

Abstract

The apparent viscosities of foaming silicon oil and foaming slag was measured. In both studies, the rotating cylinder method was used for the measurements. Additionally, the movement of particles in foaming silicon oil and the behavior of pig iron droplets in foaming slag was investigated. An increase of the apparent viscosity compared to the dynamic viscosity could be observed. The apparent viscosities decreased with increasing rotation speed of the spindle. The moving particles in the foaming silicon oil gave reasonable information regarding the behavior of particles and droplets in foam. This information are needed to get a better understanding of the behavior of iron droplets in foaming slag. After high temperature experiments, the pig iron droplets were collected and analyzed. Conclusions were made regarding mass transfer between foaming slag and iron droplets.

Introduction

Foaming slag has been a topic for many researchers because of its crucial role in industrial processes such as LD-converters and electric arc furnaces (EAC). Still, there are many unknowns and uncertainties in the processes. Due to the extreme conditions in these processes, it is very hard to study the foaming slag efficiently while running. Therefore the understanding of the matter is far from complete.

Discussions are still ongoing about whether the reactions in the processes take place in the interface between the steel droplets and the foaming slag or at the interface between the steel bath and the slag. In LD-converters, the decarburization and dephosphorisation processes are the most important reactions which were studied by many researchers [1-9]. The foaming slag is a complex matter consisting of gas, liquid and even solid phases as mentioned by many [6, 9, 10].

Due to the complexity of the process and the complex nature of the slag foam, it is very difficult to adapt modeling tools due to the challenging verification of the results. Also, the mathematical models used are usually made for Newtonian fluids, while literature has reported that foams are non-Newtonian [11]. Every on-line model used in industry would benefit from a better understanding of the slag foaming behavior. Improved models would lead to a better control of the processes.

The purpose of the present work is to carry out laboratory-scale experiments in order to improve the knowledge of the slag foaming behavior and its influence on moving particles and droplets. Starting with cold model measurements where silicone oil and argon gas was used to measure the

apparent viscosity of silicon oil foam. The measured values were compared with the given dynamic viscosity of the silicon oil. A second experimental approach was introduced to study the resistance time of droplets and particles in silicon oil foam.

A high temperature experimental setup was employed to confirm if the cold model observations are similar to the high temperature measurements with slag. A major study focus was whether the structures obtained in foaming slag and foaming silicone oil are similar. The high temperature apparent viscosity measurements on foaming slag were based on LD-converter slag consisting of CaO-SiO₂-FeO. The dynamic viscosity of slag was measured as a reference. The foaming slag was generated by the reaction of pig iron and graphite powder with converter slag.

Experimental

Cold Model Experimental Procedure

Figure 1 schematically shows the setup used to simulate the foaming slag at room temperature. A transparent Plexiglas cylinder (inner diameter: 93 mm and height: 280 mm) was used as a vessel. A silica filter with pore size 10-16 μm was mounted inside. Under the filter a gas chamber was created. The silicon oil was stored above the filter. The argon was introduced from the bottom of the gas chamber and uniformly passed through the filter into the silicone oil. Foam made of silicon oil was generated. The silica filter was mounted 100 mm above the bottom.

Silicone oils with dynamic viscosities of 0.1 Pa·s and 0.2 Pa·s were used. Both with a density of 980 kg m⁻³. In order to control the gas flow rate, a Bronkhorst mass flow meter (model F-201CV-1K0-AAAD-33-V, calibrated for 1 ln/min⁻¹ Ar, 2 bar (g)/0 bar (g) at 293 K) and a Bronkhorst High-Tech B.V.E -7000 flow-buss controller were used. For the viscosity measurements a viscometer Brookfield LVDV-II+Pro using the Rotating Spindle Technique was mounted above the vessel. As measurement spindle a Brookfield standard spindle of model LV2 was used with a cylindrical bob diameter of 18.6 mm and a height of 6.7 mm. All parameters needed for the viscosity measurements with this type of spindle are given by standard controlling software of the viscometer provided by the company Brookfield.

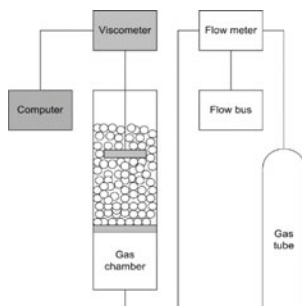


Figure 1. Cold model experimental setup.

The foam height above the silica filter was kept at 150 mm. Since different gas flow rates created foams with different relative foaming heights ($\Delta h/h_0$), different amounts of silicone oil were used to keep a constant foam height. The viscosity measurements were started when the foam of silicone oil had become stable.

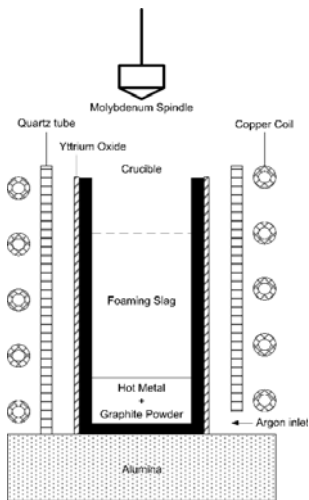


Figure 2. High temperature experimental setup.

In order to record the movement and path of particles and droplets, a high speed camera and a regular camera were mounted close to the vessel. The particles and droplets were dropped from 20 mm above into the stabilized foam made of silicon oil. The falling time were measured with a stop watch and the resulting velocity was calculated. For the study, pig iron and silica gel particles and liquid metal (Ga-In-Sn) and liquid sodium polytungstate (SPT) droplets were used. At least ten tests with each of the particles and droplets carried out in order to confirm the reproducibility of the results.

High Temperature Experimental Procedure

In the high temperature experiments, graphite crucibles were used with an inner diameter of 30 mm, wall and bottom thickness of 10 mm and a total height of 140 mm. All crucibles were painted on the outside with yttrium oxide paint to reduce oxidation during experiment. In order to generate foaming slag, 7 g of hot metal (3.9 mass% carbon), 1 g of graphite powder and 67 g slag was put into the crucible. The slag composition was based on LD-converter slag which usually consists CaO(43 mass%)-SiO₂(32 mass%)-FeO(25 mass%).

The FeO was produced by mixing Fe₂O₃ and iron powder. The mixture was heated to 1123 K and kept there for approximately 70 hours. The obtained sintered FeO was crushed into smaller pieces and mixed with CaO (calcined for 10 hours at 1173 K) and an already pre-melted slag consisting of 54 mass% CaO and 46 mass% SiO₂ for the final slag composition.

The high temperature experiments were carried out in an open air setup using an induction furnace equipped with a water cooled copper coil, a schematically drawing of the setup is given in Figure 2.

For temperature measurement and experimental control, an infrared temperature sensor of model thermometer CTM-1SF75-C3 was used. Regular thermocouples are not suitable for these kind of applications because of the influencing effect of the magnetic field induced by the induction furnace on the temperature measurements [12]. The IR-sensor was calibrated with a pyrometer of model Raytek Thermoalert ET. Since the magnetic field is changing from the middle part of the coil to the upper and bottom part, the crucible temperature can be unstable. The authors of the present manuscript are aware of it. Since the purpose of the experiment was to find trends and not to report absolute values of the slag foam or slag viscosity, a temperature difference of 50 K was considered acceptable.

As a reference value, the dynamic viscosity of slag was measured. In comparison to the slag foam measurements, painted molybdenum crucibles were used. To avoid any gas formation and thus slag foam generation, no graphite powder or hot metal was put into the crucible. The molybdenum crucible was protected by continuously flushed argon gas in a quartz tube (Figure 2) in order to reduce oxidation during experiment.

A viscometer of model Brookfield RVDV-II+Pro was used for the high temperature slag foam measurements, while a viscometer of model Brookfield LVDV-II+Pro was used for the liquid slag. The viscometer Brookfield LVDV-II+Pro is more suitable for considerable lower viscosities as measured in slag. As spindle, a nonstandard spindle made of molybdenum was used. The spindle was designed as a cylinder with a conical tip to be able to introduce the spindle easily into the slag. The cylindrical part of the spindle was 15 mm in diameter and 7 mm in height. The conical part had a height of 4 mm. Due to the missing parameters in the controlling software of the viscometers for non-standard spindles, only the torque could be measured. The viscosities, μ , were calculated with equation (1),

$$\mu = \frac{100}{RPM} \times TK \times SMC \times Torque \quad (1)$$

where RPM is the revolutions per minute, TK is the torque constant, the SMC is the Spindle Multiplier constant, which was calculated using silicone oil as reference.

Results

Cold Model Experiments

It can be seen in Figure 3 that the silicone oil foam has a homogeneous structure with spherical bubbles and a size distribution of 1-2 mm. The gas volume fraction is approximately 0.7 (depending on gas flow rate) and the liquid phase occurs only as a thin film between the bubbles.

The results from the apparent viscosity measurements show that the silicone oil foam is a shear thinning non-Newtonian fluid. This finding is in accordance with literature [11]. The apparent viscosity of the foam is higher than the dynamic viscosity for pure silicone oil. In the low rotation speed region, the apparent viscosity is up to five times higher as in pure silicon oil, as given in Figure 4 a) and 4 b). Figure 4 a) shows the measured apparent viscosities in silicone oil foam. For these measurements a silicon oil with a dynamic viscosity of 0.1 Pa·s was used. The measured apparent viscosities in silicon oil foam vary from 0.3 to 0.47 Pa·s depending on the rotation speed of the spindle. The apparent viscosity also seem to vary with different gas flow rates, a higher viscosity with decreasing gas flow rates can be observed. Figure 4 b) shows similar behavior for a silicon oil with a dynamic viscosity of 0.2 Pa·s.



Figure 3. Silicone oil foam.

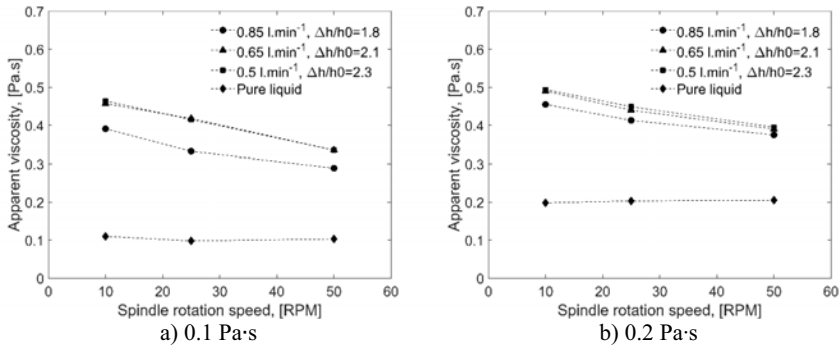


Figure 4. The apparent viscosity of silicon oil foam as a function of spindle rotation speed.

The falling time, residence time, of the particles and droplets in silicon oil foam can be seen in Figure 5. The heavier and larger particles destroyed the silicon oil foam, making smaller bubbles collide and turned into bigger ones, and fell fast down towards the bottom of the vessel. For lighter and smaller particles and droplets, the paths were decided by the resistance of the foam bubbles which pushed the particles and droplets aside as they fell, prolonging the residence time. It can be observed that the velocity of these particles and droplets are much lower than expected.

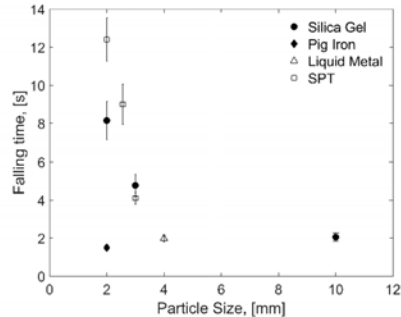


Figure 5. Particle/ droplet residence time in silicon oil foam as a function of particle size.

High Temperature Experiments

The trends shown for the cold model viscosity measurements are confirmed to be similar at high temperatures. The slag foam shows a similar shear-thinning non-Newtonian behavior. With increasing rotation rate (shear rate) the viscosity is lower and the measured apparent viscosity in slag foam is much higher comparing to the pure slag. The results are shown in Figure 7.

Keep in mind that the measured values of the apparent viscosity are only valid for the present setup. With different temperatures, different spindles, the results can change. But as mentioned earlier, the purpose of the study is not to report accurate values, but to find trends. The results form a good basis for discussion.

Foaming slag samples were quenched, mounted into pellets and cut into discs. Two samples can be seen in Figure 6. Unlike the silicone oil foam, the structure of foaming slag seem to be heterogeneous with irregular shaped gas phase and a bigger size distribution of 0.1 - 4 mm.

Discussion

As mentioned above, the smaller and lighter particles and droplets do not destroy the foam. These light particles/droplets have considerably longer residence time than expected. One reason of the longer residence time is that the path is not straight, the particles moving in both vertical and horizontal directions through the foam in between the bubbles. Another more important reason for the longer residence time is the much higher apparent viscosity in the oil foam. In view of the low velocities of the moving particles, the viscosities obtained using lower rotation speed of the spindle would be more relevant. The apparent viscosity is five times higher than the dynamic viscosity of the silicone oil, which leads to much lower velocity of the falling particles/droplets and consequently much longer residence time.

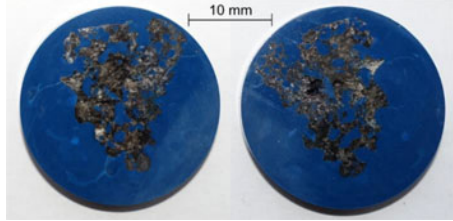


Figure 6. Structure of slag foam after quenching.

As discussed in connection with Figure 4, the silicone oil foam does not show a behavior of Newtonian flow. Instead a shear thinning behavior is observed. Similarly, the slag foam also shows a non-Newtonian shear thinning behavior, (Fig.7). Non-Newtonian fluids are difficult to predict, since it depends on the experimental setup and conditions. For example, the results may differ with the type of spindle as well as vessel. Despite of the nature of the non-Newtonian flow, the results shown in Figures 4 and Figure 7 still indicate evidently that the dynamic viscosity of the liquid (for both oil and slag) plays much less important role in determining the apparent viscosity of the foam and therefore the movement of the particles in the foam.

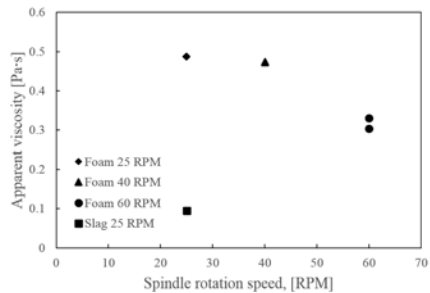


Figure 7. Apparent viscosity of foaming slag as a function of spindle rotation speed.

The apparent viscosity is not proportional to the dynamic viscosity. A comparison of the apparent viscosities of the two different silicone oils (Fig. 4) reveals that the apparent viscosity of the foam using 0.2 Pa·s oil is only 10-20% higher than the foam formed by the silicone oil of 0.1 Pa·s. The fact that the apparent viscosities are not proportional to their dynamic viscosities indicates that there is a common factor affecting the viscosity of the foam.

As discussed in detail in the literature [13]; the energy needed to deform an interface between the liquid and gas is higher than the energy needed to deform the bulk liquid. This finding is in fact in good agreement with the literature [11]. A semi-quantitative calculation is made in the previous work [14]. Assuming no volume change, when a sphere with radius of 1 mm is compressed into a spheroid with height $c = 0.7$ mm, the deformation leads to an increase in surface area of 6.4%, and consequently an increase of 6.4% in surface energy. The silicone oil used has a surface tension of

$2.1 \cdot 10^{-2} \text{ J} \cdot \text{m}^{-2}$. For a spherical bubble with dimension $r = 1 \text{ mm}$, the surface energy change due to deformation would be of $1.02 \cdot 10^{-7} \text{ J}$, since the movement of a particle would involve approximately the deformation of six bubbles (in minimum) at the same time. The work against the viscous force needed to move the particle through the pure liquid was found to be approximately 20% of the surface energy change for deformation of the bubbles. This semi quantitative calculation explains well the experimental result that the apparent viscosity of a foam is about 4-5 times bigger than the dynamic viscosity of the liquid. The calculation indicated evidently that it was the change of the surface energy that plays a very profound role in determining the apparent viscosity in comparison with the viscous energy of the liquid. This calculation could even explain why there is only a 10-20 % increase in apparent viscosity when using silicone oil with a 100 % higher dynamic viscosity shown in Figure 4 a) and b).

As revealed by Fig. 7, even in a foaming slag, the dynamic viscosity of the pure slag plays a much smaller role in determining the apparent viscosity of the foam. It is expected that the surface tension of the slag is still dominating in this context. On the other hand, the simple estimation made above for foaming silicone oil would suggest a much higher apparent viscosity of a slag foam in comparison with the experimental results shown in Fig.7, since the surface tension of slag is substantially higher than silicon oil [15, 16]. A careful comparison of the structures of the two types of foams would help the understanding of this difference.

As shown in Figure 3, the silicone oil foam has a homogeneous structure with spherical bubbles and a size distribution of 1-2 mm. The gas volume fraction is approximately 0.7. It is important to point out that the liquid phase occurs only in the thin film surrounding the bubbles. The thin liquid film is not seen in the slag foam. Small liquid “bulks” are present all over the foam along with the gas bubbles. In other words, the gas is not separated by liquid films. The bubbles distribute in the liquid phase creating a two phase mixture, but not a bubble structure. A careful microscopic examination reveals that the bubble size in the slag foam ranges from 0.1 mm to 4 mm. This is in strong contrast with the silicone foam, where all the bubbles are in the range between 1 - 2 mm. The ratio of the gas volume over the total volume of the slag foam ($V_{\text{gas}}/V_{\text{tot}}$) is estimated to be approximately 0.35 by using point counting [17], which is only 50% of the ratio in silicon oil foam. The lower ($V_{\text{gas}}/V_{\text{tot}}$) of the slag foam along with the existence of the small liquid “bulks” would suggest that the role of surface energy change due to the movement of any particle in the foam would be less profound comparing to the silicone oil foam.

Conclusions

The present results reveals confidently that the surface tension has much bigger impact on the apparent viscosity and therefore on the movement of particles in the foam in comparison with the dynamic viscous energy. The required surface energy change could slow down the particle movement greatly in a foaming slag. Therefore the use of the dynamic viscosity to estimate the residence time of a particle is seriously questioned. The difference in foam structure between silicone oil and slag indicates that while the cold model study using silicone oil is very useful, the conclusion obtained should be used with certain precaution when applied to slag system.

Acknowledgements

The research leading to these results has received funding from the European Union's Research Fund for Coal and Steel (RFCS) research program under grant agreement no. RFSR-CT-2014-00005.

References

1. Cicutti, C., et al., *Analysis of slag foaming during the operation of an industrial converter*. Latin American applied research, 2002. **32**(3): p. 237-240.
2. Deo, B., et al., *Characterization of slag-metal droplet-gas emulsion in oxygen steelmaking converters*. ISIJ international, 1996. **36**(6): p. 658-666.
3. Martín, M., M. Rendueles, and M. Díaz, *Emulsion Analysis in a Gas/Liquid/Liquid Reactor With Top Blowing*. The Canadian Journal of Chemical Engineering, 2004. **82**(2): p. 249-255.
4. Jung, S.-M. and R.J. Fruehan, *Foaming characteristics of BOF slags*. ISIJ international, 2000. **40**(4): p. 348-355.
5. Meyer, H., et al., *Slag-metal emulsions and their importance in BOF steelmaking*. J METALS, 1968. **20**(7): p. 35-42.
6. Ito, K. and R.J. Fruehan, *Study on the foaming of CaO-SiO₂-FeO slags: Part II. Dimensional analysis and foaming in iron and steelmaking processes*. Metallurgical Transactions B, 1989. **20**(4): p. 515-521.
7. Luomala, M.J., et al., *Splashing and Spitting Behaviour in the Combined Blown Steelmaking Converter*. ISIJ International, 2002. **42**(9): p. 944-949.
8. Ek, M., *A study of some aspects of gas-slag-metal interactions: Towards dynamic process model and control*. 2012.
9. Brämning, M., *An Operational View on Foaming and Slopping Control in Top-blown BOS Vessels*. 2015.
10. Ito, K. and R.J. Fruehan, *Study on the foaming of CaO-SiO₂-FeO slags: Part I. Foaming parameters and experimental results*. Metallurgical Transactions B, 1989. **20**(4): p. 509-514.
11. Cohen-Addad, S., R. Höhler, and O. Pitois, *Flow in foams and flowing foams*. Annual Review of Fluid Mechanics, 2013. **45**(1): p. 241.
12. Smalcerz, A. and R. Przylucki, *Impact of Electromagnetic Field upon Temperature Measurement of Induction Heated Charges*. International Journal of Thermophysics, 2013. **34**(4): p. 667-679.
13. Miller, C.A. and P. Neogi, *Interfacial phenomena: equilibrium and dynamic effects*. Vol. 139. 2007: CRC Press.
14. Martinsson, J. and D. Sichen, *Study on Apparent Viscosity of Foam and Droplet Movement Using a Cold Model*. steel research international, 2015.
15. Moretto, H.-H., M. Schulze, and G. Wagner, *Silicones*, in *Ullmann's Encyclopedia of Industrial Chemistry*. 2000, Wiley-VCH Verlag GmbH & Co. KGaA.
16. Eisenhüttenleute, V.D. and V.D.E.A.f.M. Grundlagen, *Schlackenatlas*. 2nd ed. 1995: Verlag Stahleisen.
17. Vander Voort, G.F., *Metallography, principles and practice*. 1984: ASM International.

Effect of Al_2O_3 and SiO_2 Addition on the Viscosity of BOF Slag

Zhuangzhuang Liu, Lieven Pandelaers, Peter Tom Jones, Bart Blanpain, Muxing Guo

KU Leuven Department of Materials Engineering, Kasteelpark Arenberg 44, 3001 Leuven, Belgium

Keywords: BOF slag, Viscosity, Hot stage slag engineering, Solid particles

Abstract

The effect of solid phases and SiO_2 and Al_2O_3 additions on the viscosity of BOF slag was measured with a rotational viscometer in the temperature range of 1500°C-1700°C. Various viscosity models for completely liquid slag were evaluated and parameters in the Einstein-Roscoe equation were optimized to estimate the influence of the solid phases on the BOF slag viscosity.

Introduction

One of the important by-products of the oxygen converter process is basic oxygen furnace (BOF) slag. With the booming of steelmaking industry, a vast amount of BOF slag is produced^[1]. However, the recycling of BOF slag is a significant challenge for steelmaking industry. The traditional application of BOF slag as aggregate in road construction is limited because of the presence of free CaO and MgO, which leads to a long term volume expansion, resulting in rapid deterioration of the road or cement. Several treatments have been developed in order to stabilize BOF slag, amongst which a hot stage slag engineering that has been applied commercially to both stabilize BOF slag and achieve high value products^[2]. In this process additives (SiO_2 , Al_2O_3 , etc.) are introduced to stabilize the free CaO and MgO and to modify the mineralogy to facilitate subsequent use in building products^[3]. However, the current hot stage slag engineering practice does not work for slags with a low liquid fraction or a high viscosity. Viscosity is a crucial parameter for the slag treatment practice due to its influence on the flow properties of the slag, dissolution speed of additives, mass and heat transfer through the slag and the sedimentation of metallic iron particles (or droplets) to the bottom of slag pot. The injection of additives during the hot stage treatment process can be hampered and blocked due to the high viscosity of the slag. Therefore, it is essential to obtain specific knowledge of BOF slag viscosity and to understand how the additives affect the viscosity of the slag system. In the present study, the viscosity of a typical BOF slag has been measured and the effect of SiO_2 and Al_2O_3 addition on the slag viscosity has been investigated. The Einstein-Roscoe equation with optimized parameters combined with the FactSage viscosity model was used in prediction of the BOF slag viscosity.

Experimental

Materials and sample preparation

Industrial BOF slag samples were obtained from a steel plant having a typical composition as shown in Table 1. The basicity (CaO/SiO_2) of the investigated BOF slag is in the range of 3.5–4.6.

Table 1. Chemical composition of BOF slag sample (XRF, wt %)

Sample	CaO	T.Fe	SiO ₂	MnO	MgO	Al ₂ O ₃	SiO ₂ /CaO
BOF	42-55	14-20	12-18	0.0-8.0	0.0-5.0	0.0-3.0	3.5-4.6

Dried reagent grade SiO₂ and Al₂O₃ powders were used as additions in this study. Different quantities of both additions were mixed with original BOF slag powders for viscosity measurement.

Viscosity measurement

Viscosity measurement of the samples was conducted with a rotational viscometer (Ravenfield Model FG MkIV viscometer; Ravenfield Designs Ltd, Heywood, UK). The viscometer consists of a rotating outer cylinder (crucible) and fixed inner column (spindle) that measures the torque. The outer cylinder rotating viscometer is of higher precision than the inner column rotating viscometer due to the static axis and non-friction loss for torque measurement. The measurement was carried out under Ar (99.999 mol %) atmosphere. The details of the set-up and dimensions of the crucible and spindle can be found elsewhere^[4].

The viscometer was calibrated with standard oil at room temperature before each measurement. 50 gram of slag sample was milled into powders to guarantee its homogeneity. About 5 gram of the slag sample was loaded in the crucible, heated up to the temperature of interest and held for 30 minutes for homogenization. Afterwards, the spindle was lowered down into the molten slag and the crucible was rotated at a speed of 200 rpm. The torque was registered and converted to viscosity according to the Ravenfield software. Viscosity of samples was measured at the following temperatures: 1500°C, 1550°C, 1600°C, 1650°C and 1700°C.

Results and discussion

Viscosity of original BOF slag

The measured viscosity of the original BOF as a function of temperature is shown in Figure 1. It is observed that the BOF slag viscosity gradually increases from 36.7 mPa · s to 171.3 mPa · s as temperature decreases from 1650°C to 1500°C. Due to the high basicity, solids are frequently present in the BOF slag, e.g. undissolved CaO, MgO, etc.^[5] According to the FactSage (version 6.4, FactPs and FToxid are selected as database) calculations, solid CaO is present in the temperature range from 1550°C to 1700°C. The volume fraction of solid phases (free CaO) and liquid phases were determined by FactSage and Mill's density model^[6], respectively. Figure 1 shows that the investigated BOF slag contains 6.4 vol% solids even at 1650°C. The volume fraction of solids gradually increases as temperature decreases.

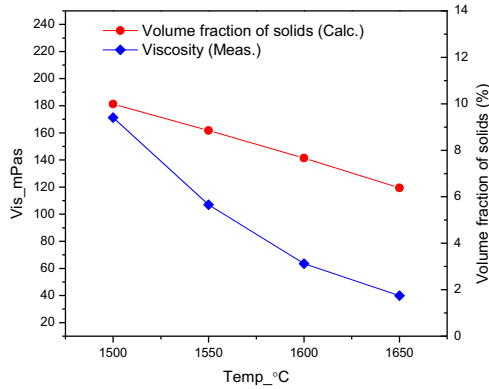


Figure 1. Experimental viscosity and calculated volume fraction of solids of BOF slag sample as a function of temperature

Effect of Al₂O₃ and SiO₂ on BOF slag viscosity

In order to investigate the effect of SiO₂ and Al₂O₃ additions on BOF slag viscosity, different quantities of SiO₂ and Al₂O₃ were added to the original BOF slag. Figure 2.a) shows the correlation between the measured BOF slag viscosity and the Al₂O₃ addition amount. It is observed that the viscosity decreases slightly up to 5 wt% Al₂O₃ addition, with further Al₂O₃ addition leading to a viscosity increase. This can be interpreted by the combined contribution of solid and liquid phases to the viscosity of the solid-containing slag. Viscosity of a solid-liquid mixture is determined by two factors: the volume fraction of solids and the viscosity of the liquid phase. As shown in Figure 2.b), the solid fraction decreases with increasing Al₂O₃ content. This explains the Al₂O₃ effect at 5 wt% addition (Fig.2a)). It suggests that the effect of solid phases on viscosity is a dominant factor for the original BOF slag. However, once the slag becomes fully liquid (e.g. 11 wt% and 15 wt% Al₂O₃ addition), Al³⁺ can partially substitute Si⁴⁺ in the silicate network, due to the charge compensation effect in highly basic slag, thereby acting as network former and increasing viscosity^[7]. The result implies that in order to decrease the viscosity of the present BOF slag the addition of Al₂O₃ should be below 11 wt%.

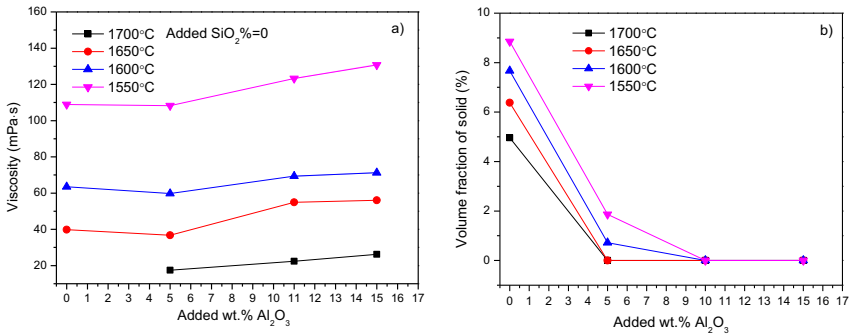


Figure 2. a) Dependence of BOF slag viscosity on added Al₂O₃
b) Correlation between volume fraction of solids in BOF slag with added Al₂O₃

The effect of SiO₂ addition on BOF slag viscosity after 5 wt% Al₂O₃ addition is shown in Figure 3.a). It is found that the viscosity decreases after addition of 1 wt% SiO₂, but increases gradually for higher SiO₂ additions. This can be understood by comparison with the calculated volume fraction of solid phases (Figure 3.b)): the addition of up to 3 wt% SiO₂ removes all solid phases. As the SiO₂ content increases in the highly basic slag, more bridging oxygen atoms are provided to the slag due to the formation of silicate dimers, trimers and even longer chains, rings and a three-dimensional network, resulting in a viscosity increase^[8].

Although no solids are expected to be present at 1650°C and 1700°C according to the calculations, the viscosity measurements (Figure 3.a)) suggest that some solid phases still exist at these temperatures, which can be deduced from the viscosity decrease from 0 wt% SiO₂ to 1 wt% SiO₂ addition at these temperatures. The discrepancy between calculations and experiments is due to the presence of other minor elements (e.g. TiO₂, V₂O₅, Cr₂O₃, MoO₃, S, etc.) which have not been accounted for in the solid fraction calculation. It can be concluded from the experimental results in Figure 3.a) that even a small amount of SiO₂ addition, such as 1 wt% SiO₂ can decrease BOF slag viscosity after 5 wt% Al₂O₃ addition.

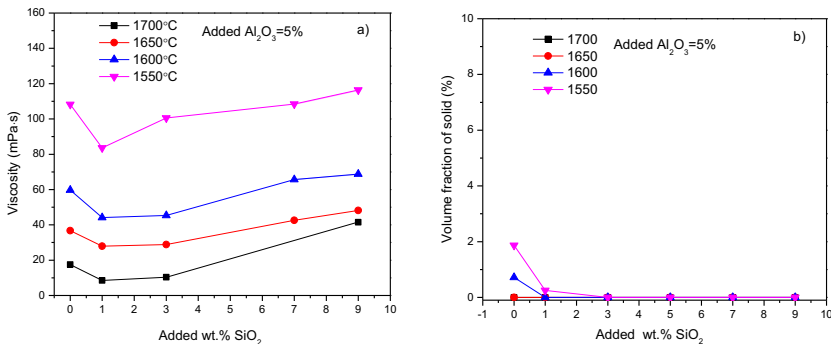


Figure 3. a) Dependence of BOF slag viscosity on added SiO₂
b) Correlation between volume fraction of solids in BOF slag with added SiO₂

Viscosity modelling

There is considerable literature on the prediction of silicate melt viscosity. This includes the well-known Urbain^[9], Riboud^[10], Iida^[11], quasi-chemical^[12] and modified quasi-chemical (MQC) models^{[13][14][15]}, which have been applied for different slag systems at distinct composition ranges. However, these viscosity models are only valid for homogeneous Newtonian liquids and cannot correctly predict the viscosity when solid phases are present. To account for the presence of solid particles, the Einstein-Roscoe equation^[16] is commonly used.

$$\eta_R = \frac{\eta_s}{\eta_l} = \left(1 - \frac{\Phi_s}{\Phi_m}\right)^{-B} \quad (1)$$

where η_R is the relative viscosity; Φ_s is the volume fraction of solids; η_s and η_l are the viscosity of the suspension (mixture of solid and liquid phases) and the remaining liquid, respectively; Φ_m is the maximum packing fraction of solids, B is a shape factor representing the effect of the solids' shape on viscosity. Limited studies have been reported to apply the Einstein-Roscoe equation in estimating the viscosity of metallurgical slag and there is no consensus yet on the parameters in this equation. Additionally, the viscosity model applied in predicting the viscosity of the liquid phase in BOF slags can have an enormous influence on the accuracy of the Einstein-Roscoe model. Therefore, a number of models for fully liquid slag were evaluated by comparing the calculated results with the measured viscosity of completely liquid slag (according to calculation, only completely liquid slags at corresponding temperatures were used for the comparison). The errors on the estimated viscosity for different models were summarized in Table 2.

Table 2. Errors of viscosity models in estimating liquid slag viscosity

Models	$\Delta/\%$
MQC ^{[13][14][15]}	29.10
Utigard-Warczok ^[17]	30.35
S2 ^[18]	34.36
Optical basicity ^[19]	39.39
T-shift ^[20]	41.01
Iida ^[21]	41.32
Riboud ^[10]	44.65
MLL ^[22]	56.05
Urbain ^[23]	153.94

The error Δ is adopted in the present study to evaluate the performance of different models for predicting slag viscosity:

$$\Delta\% = \sum \frac{\delta n\%}{N} \quad (3)$$

$$\delta n\% = 100 \frac{(\eta_{meas} - \eta_{calc})}{\eta_{meas}} \quad (4)$$

where N is the number of data points, η_{meas} and η_{calc} indicates the measured and calculated viscosity, respectively.

Among the nine viscosity models, FactSage (MQC) gives a relatively accurate prediction, which can be used to predict the viscosity of the liquid phase in BOF slag. Mills^[22] commented that the uncertainty in high temperature viscosity measurement is about 20%, due to the changes in slag composition and systematic errors of different types of apparatus. Hence, it is acceptable to calculate the viscosity of the liquid phase in BOF slags using the FactSage viscosity model. Combining the FactSage viscosity model with the Einstein-Roscoe equation, the relative viscosity of the solid-containing slag is plotted against the volume fraction (<0.11) of solid phases in Figure 4. The solid curve represents the prediction of the Einstein-Roscoe model with optimized parameters (Equation (2)).

$$\eta_s = \eta_l \left(1 - \frac{\Phi_s}{0.13}\right)^{-1} \quad (2)$$

The optimized parameters were obtained by minimizing the sum of squared differences between the predicted and experimental values. The Φ_m obtained in the present study indicates that the relative viscosity approaches infinity as the solid volume fraction increases up to 0.13. The shape factor B in this study (B=1) is smaller than the theoretical value obtained by Einstein, which takes the value of 2.5 for uniform spheres. Also in literature, other attempts to identify the value of Φ_m and B have been made. Kondratiev^[24] has investigated the viscosities of the partly crystallized slags in the $\text{Al}_2\text{O}_3\text{-CaO-“FeO”-SiO}_2$ system and found that the calculated viscosity by using the Einstein-Roscoe equation with $\Phi_m=0.49$ and $B=1.29$ yields good agreement with experimental results. Wright^[25] measured the viscous properties of a $\text{CaO-MgO-Al}_2\text{O}_3\text{-SiO}_2$ slag with different amounts and sizes of MgAl_2O_4 spinel particles and concluded that the measured viscosity fitted well with the Einstein-Roscoe equation with $\Phi_m=0.24, 0.30,$ and 0.28 and $B=1.28, 2.36,$ and 2.24 for fine, medium, and coarse particles, respectively. Seok et al^[26] studied the effect of solid crystals on the viscosity of $\text{CaO-SiO}_2\text{-FeO-MgO-Al}_2\text{O}_3$ slags at 1773 K and concluded that the maximum packing fraction ranged from 0.26 to 0.36. This overview illustrates that as both parameters are influenced by the size, shape and distribution of the solid phases, different slag systems yield different B and Φ_m values. Further study is needed to investigate systematically the effect of amount, size, shape and distribution of solid phases on the viscosity of solids-containing slag.

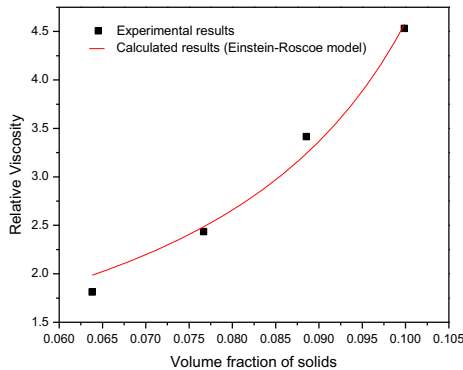


Figure 4. Relative viscosity of BOF slag as a function of solid fraction

Conclusions

The viscosity of industrial BOF slag with different Al_2O_3 and SiO_2 additions was measured by using a rotational viscometer. The effect of Al_2O_3 and SiO_2 additions on the volume fraction and viscosity of BOF slag has been discussed. Various viscosity models have been evaluated by comparing with the experimental results. The following conclusions were obtained:

- (1) BOF slag studied in this work contains solid phases even at high temperature (1700°C).
- (2) Al_2O_3 and SiO_2 can decrease the viscosity as long as they lead to a decrease in the fraction of solid phases, but increase the viscosity of the fully liquid slag by network forming.
- (3) The Factsage viscosity model has the smallest error amongst the 9 evaluated viscosity models (Factsage, Utigard-Warczok, S2, Optical basicity, T-shift, Iida, Riboud, MLL, Urbain) in estimating the viscosity of fully liquid BOF slag after addition of $\text{Al}_2\text{O}_3/\text{SiO}_2$.
- (4) Combining the Factsage viscosity model for liquid phase viscosity with the Einstein-Roscoe equation (optimized parameters: $\Phi_m = 0.13$, $B=1$) allows to predict solid-containing BOF slag viscosity.

Acknowledgements

The authors acknowledge the support from IWT grant 140514. Zhuangzhuang Liu would like to thank the China Scholarship Council for providing scholarships and Professor Jungwook Cho (Pohang University of Science and Technology) and Dr SeungHo Shin (Pohang University of Science and Technology) for valuable guidance with respect to the viscosity measurements.

References

-
- [1] R.M. Santos, D. Ling, A. Sarvaramini, et al., Stabilization of basic oxygen furnace slag by hot-stage carbonation treatment. *Chemical Engineering Journal*, Vol. 203, 2012, pp. 239–250.
 - [2] M. Kühn et al., Treatment of Liquid Steel Slags. 2nd European Slag Conference, Düsseldorf, Germany, 2000, pp. 123-135.
 - [3] Y. Pontikes, L. Kriskova, X. Wang, et al. Additions of industrial residues for hot stage engineering of stainless steel slags. *Proceedings of 2nd International Slag Valorisation Symposium*, Belgium, 2011, pp. 313-326.
 - [4] S.H. Shin, J.W. Cho and S.H. Kim, Shear thinning behavior of calcium silicate-based mold fluxes at 1623 K, *J. Am. Ceram. Soc.*, Vol.97, 2014, 3263–3269.
 - [5] A.M. Bronsch, M A. Duchesne, P J. Masset et al. Prediction and measurement of the coal slag viscosity including the influence of solid particle fractions. *Ninth International Conference on Molten Slags, Fluxes and Salts*. 2012.
 - [6] K.C. Mills and B.J. Keene, Physical properties of BOS slags. *International Materials Review*. Vol.32, 1987, pp.1-120.

- [7] A. Grundy, I. Jung, A.D. Pelton, et al., model to calculate the viscosity of silicate melts. *International Journal of Materials Research*, 2008, Vol. 99, pp. 1194-1209.
- [8] A. Grundy, H. Liu, I. Jung, et al., A model to calculate the viscosity of silicate melts. *International Journal of Materials Research*, 2008, Vol. 99, pp. 1185-1194.
- [9] G. Urbain, Y. Bottinga, and P. Richet. Viscosity of liquid silica, silicates and alumina-silicates, Vol.46, 1982, pp.1061-1072.
- [10] P.V. Riboud,, Y. Roux, L.D. Lucas, et al., Improvement of continuous casting powders. *Fachberichte Hüttenpraxis Metallweiterverarbeitung*, Vol. 19, 1981, pp. 859-869.
- [11] T. Iida, H. Sakai, Y. Kita. et al., Equation for estimating viscosities of industrial mold fluxes. *High Temperature Materials and Processes*. 2000, Vol.19, pp. 153–164.
- [12] A. Kondratiev, E. Jak. A quasi-chemical viscosity model for fully liquid slags in the Al_2O_3 - CaO - FeO - SiO_2 system. *Metallurgical and Materials Transactions B*. Vol.36, 2005, pp 623-638.
- [13] W. Kim, A.D. Pelton, S. A. Decterov. A model to calculate the viscosity of silicate melts. *International Journal of Materials Research*, 2012 Vol. 103, pp.313-328.
- [14] E. Brosh, A. D. Pelton, S. A. Decterov. A model to calculate the viscosity of silicate melts. *International Journal of Materials Research*, 2013, Vol. 103, pp.494-501.
- [15] E. Brosh, A. D. Pelton, S. A. Decterov. A model to calculate the viscosity of silicate melts. *International Journal of Materials Research*.2013, Vol. 103, pp.537-550.
- [16] R. Roscoe. The viscosity of suspensions of rigid spheres. *Br. J. Appl. Phys.* Vol.3, 1952, pp.267-269.
- [17] T.A. Utigard, A. Warczok. Density and viscosity of copper/nickel sulphide smelting and converting slags. *Proceedings of COPPER*, 1995.
- [18] S. Vargas, F.J. Frandsen, K. Dam-Johansen. Rheological properties of high temperature melts of coal ashes and other silicates. *Prog Energy Combust Sci.* Vol.27, 2001, pp. 237–429.
- [19] K.C Mills, and S. Sridhar, Viscosities of ironmaking and steelmaking slags. *Ironmaking and Steelmaking*, Vol. 26, 1999, pp. 262-268.
- [20] G. J. Browning, G. W Bryant, J. Hurst, et al., An empirical method for the prediction of coal ash slag viscosity. *Energy Fuels*, Vol.17, 2003, pp. 731-737.
- [21] L. Forsbacka, L. Holappa, T. Iida, et al. Experimental study of viscosities of selected CaO - MgO - Al_2O_3 - SiO_2 slags and application of the Iida model. *Scandinavian Journal of Metallurgy*, Vol. 32, 2003, pp. 273-280.
- [22] K.C. Mills. *The Estimation of Slag Properties*. Southern African Pyrometallurgy, 2011.
- [23] G. Urbain, Viscosity estimation of slags. *Steel Research*, Vol. 58, 1987, pp. 111–116.
- [24] A. Kondratiev and E. Jak. Modeling of viscosities of the partly crystallized slags in the Al_2O_3 - CaO - FeO - SiO_2 system. *Metallurgical and Materials Transactions B*, Vol. 32, 2001, pp. 1027-1032.
- [25] S. Wright, L. Zhang, S. Sun et al., Viscosity of a CaO - MgO - Al_2O_3 - SiO_2 melt containing spinel particles at 1646K. *Metallurgical and Materials Transactions B*, Vol 31, 2000, pp. 97-104.
- [26] S. Seok, S. Jung, Y. Lee et al., Viscosity of highly basic slags. *ISIJ International*, Vol. 47, 2007, pp. 1090–1096.

Viscoelastic Properties of Calcium Silicate Based Mold Fluxes at 1623K

Seung-Ho Shin^{1*}, Jung-Wook Cho², Seon-Hyo Kim¹

¹ Department of Materials Science and Engineering, Pohang University of Science and Technology, Pohang 37673, Republic of Korea

² Graduate Institute of Ferrous Technology, Pohang University of Science and Technology, Pohang, 37673, Republic of Korea

Keywords: shear thinning, mold flux, continuous casting, dynamic viscosity measurement

Abstract

CaO-SiO₂-CaF₂ based flux in a continuous steel caster has to show dual viscous functions to minimize slab defects - high viscosity enough to avoid flux entrainment at mold top surface and low viscosity enough to maximize lubrication capability at oscillated mold wall region. Liquid flux could show a shear thinning behavior when its viscosity decreases with increasing shear rates. Flux viscosity was measured by a rotational type viscometer as a function of shear rates. Raman and XPS analysis were employed to understand structural changes of flux for correlating with shear thinning behavior. The present work has focused on developing an optimum mold flux system with strong shear thinning behavior. The strong shear thinning behavior appropriate for dual viscous functions could be achieved by incorporating borate or silicon nitride into the flux. The flux compositions with a strong shear thinning behavior will be presented from the viewpoint of clean slab production.

Introduction

Due to the need for sound slab surface quality and higher productivity, the continuous casting of steel has adopted for a long time. During the casting process, the liquid flux encounters contradictory situation because it has to show dual viscous functions to minimize slab surface defects- high viscosity enough to avoid entrainments of mold flux at the mold top surface where shear rate is approximately between 10 and 40 reciprocal seconds and low viscosity enough to maximize lubrication capability at mold wall region where shear rate equals to 100 to 1000 reciprocal seconds.

Such dual viscous functions of the flux melts could easily be achieved by enhancing shear thinning behavior. The previous researches have suggested two different ways to enhance shear thinning behavior of the flux melts: one is incorporation of borate into glass network system and the other is incorporation of silicon nitride into the same system. Interestingly, it had been found that each associative additive works for enhancing shear thinning behavior with a completely opposite manner. When borate is added to the system, viscosity decreased at higher

shear rates without a significant change in viscosity at lower shear rates. On the other hands, silicon nitride incorporates into silicate network system and increases viscosity at lower shear rate without a significant viscosity change at higher shear rates.

Despite considerable progress in understanding associate additives' role to enhance shear thinning property for the academic purpose and application to continuous casting process for the industrial purpose, the researches regarding dynamic viscosity measurement profile of the flux melts and development of flux melts' chemical composition applicable to the steel industry still remain elusive.

Here we report the strongest shear thinning behavior of CaO-SiO₂-CaF₂ based melts ever that is successfully achieved by modifying melts' structure with a simultaneous incorporation of two associative additives: borate and silicon nitride. Also, our dynamic viscosity measurements confirm amount of storage modulus (elastic property) and loss modulus (viscose property) of each mold flux sample. In doing so, it is feasible to understand about role of associative additive by comparing each modulus from the standpoint of rheological study.

Experimental Technique

Sample preparation For the glass melts preparation, the reagent-grade chemicals including CaCO₃, SiO₂, CaF₂, Al₂O₃, MgO and Na₂CO₃ were melted in a pt crucible at 1573K for half an hour to complete homogeneous state of mixtures. Subsequently, the prepared melts were quenched by applying glass melts into a cold water cooled steel plate. The prepared glass melts have basicity (CaO/SiO₂ ratio) of 0.94 and used for the precursor of glass melts with associative additive. For the preparation glass melts with associative additives, each additive: reagent grade borate and silicon nitride were added to the precursor with an appropriate amount and melted for half an hour to achieve homogeneous state and followed by quenching process on a cold steel plate. Before conducting viscosity measurement, all prepared samples were pre-melted to achieve chemically stable state. In doing so, it is feasible to avoid a significant chemical composition change before and after the viscosity measurement.

Rheological measurement Rheological study was carried out on rotational type rheometer equipped with high temperature furnace (Ravenfield Modle FG MkIV; Ravenfield Designs Ltd, Heywood, UK) under controlled oxygen fugacity. The schematic drawings, specific dimensions and procedures performed are described in ref 5-7. Rheological measurement consists of classic viscosity measurement and dynamic viscosity measurement. For the former, the viscosity was measured with a planned stepwise shear rate history. The latter measures viscosity with a continuous shear rate history and followed by its analysis with deformation zone estimation. Fig1. below represents shear rate history for each rheological measurement.

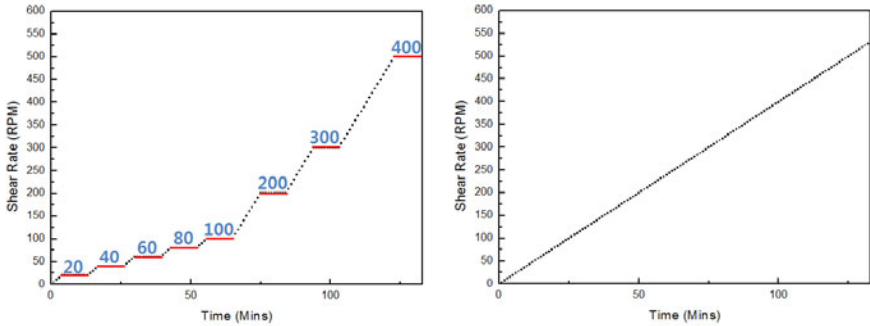


Fig1. (a) shear rate history during classic viscosity measurement. Once the viscometer reaches target temperature, the spindle begins to rotate at each target shear rate (from 20 to 400 rpm) for 10 minutes to collect approximately thousands of viscosity data points which will eventually be averaged. (b) shear rate history during dynamic viscosity measurement. The viscosity measured continuously at each shear rate points. This means that a special care needs to be taken to complete the experiment due to the insufficient data point to confirm the viscosity at each shear rate.

Results and Discussion

Figure2 reveals viscosity measurement of glass liquid flux by increasing shear rates at 1623K. For the accurate and precise measurement of viscosity, the test for associative additive effect has been conducted with a planned stepwise shear rate history.

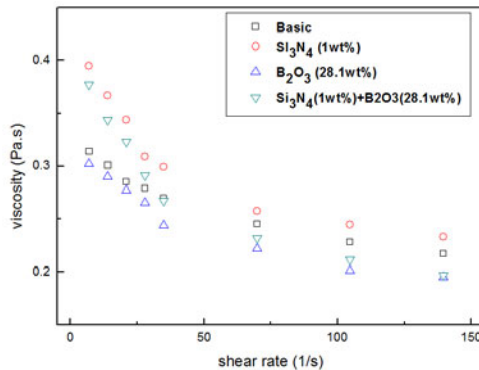


Fig2. Effect of associative additive on shear thinning behavior of liquid flux

It is notable that the effect of each associative additive is clearly different from one another. Borate is effective in decreasing viscosity at higher shear rates without significant viscosity

changes at lower shear rates. On the other hands, silicon nitride enhances shear thinning behavior by increasing viscosity at lower shear rate without a significant change at higher shear rates. In particular, it is interestingly discovered that a simultaneous addition of both associative additives, indeed, leads to the strongest shear thinning behavior ever by taking advantages of both additives. In order to quantify shear thinning degree, a power law model is used within specific ranges of shear rates. The Oswald De Waele's power law model could be used to mathematically express the power law region of a flow curve as follows:

$$\eta = K(\dot{\gamma})^{n-1}$$

where K is consistency and n is flow behavior index.

The flow behavior index, n, is dimensionless number which relates the closeness to Newtonian flow. When amount of $0 < n < 1$, the fluid is called shear thinning and when $n > 1$, the fluid is recognized as shear thickening in natures. That is, the range of power law changes from 0 for extremely shear thinning fluids to 1 for Newtonian fluids. According to the results, the strongest shear thinning behavior of liquid flux has been achieved when 28.1 wt percent of borate and 1 wt percent of silicon nitride are simultaneously incorporated with a flow behavior index of 0.77. Compared to the flow behavior index of basic sample (0.87), this dimensionless flow behavior index is low and increases opportunity to use this concept to actual continuous casting process of steel. Especially, the experimental evidence suggests that simultaneous incorporation of borate and silicon nitride could increase the viscosity at lower shear rates and decrease the viscosity at higher shear rates at the same time which is perfect condition to reduce the melt's entrainment and maximize lubrication capability of continuous casting process.

In dynamic viscosity measurement exhibited in Fig3, the storage modulus is higher at the absence or present of low shear rate, thus the molecules behave more like a rigid solid structure. However, loss modulus is higher than storage modulus at higher shear rates, therefore the material adapt a liquid like structure. The crossover point of modulus curves, $G' = G''$ provides important information about structural difference among 4 different types of mold flux melts' molecules. Interestingly, the crossover point for each glass melt is different due to the role of associative additive. In comparison of the crossover points for each sample, silicon nitride addition increases elasticity of liquid flux and shift crossover point to the right. This is presumably because a small amount of silicon nitride is effectively incorporated into the melt's network system by taking advantage of its bonding superiority resulting in an appropriate polymerization and complexity level which generates a partial increase on viscosity at lower shear rates without a remarkable change of viscosity at higher shear rates. On the other hands, borate addition decreases elasticity of mold flux and moves the crossover point to the left compared to the basic sample. Substitution between tetrahedral silicate network and triangular borate with lower bonding energy may be a plausible explanation of such behavior. As previously discussed, a relatively large number of borate addition (28.1wt%) causes an increase

on polymerization degree and replacement from silicate network to weaker borate bonds. Thus, elasticity of material decreases and reaches crossover point at lower shear rates than basic sample.

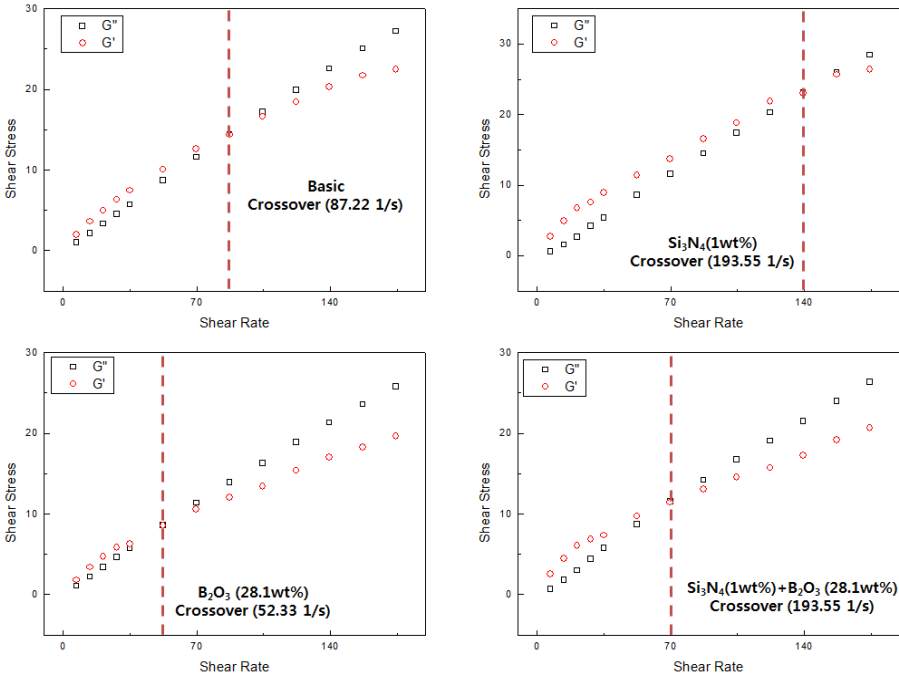


Fig3. Elastic (G'') and viscous (G') modulus as a function of imposed shear rate history. The figures are drawn by the results of dynamic viscosity measurement profile and analysis of deformation zone estimation. The increasing level of shear rates causes a transition from a solid-like to a viscous-like structure. The results clearly indicate that role of each associative additive is opposite to one another.

This result strongly supports mechanism to enhance shear thinning property with borate. According to the previous study, 28.1 wt % of borate addition results in viscosity decrease at higher shear rates without a significant change of viscosity at lower shear rate. The liquid flux with 28.1wt percent of borate additives have a relatively high level of polymerization degree caused by 3 dimensional borate incorporation, as a result, it caused no significant changes in viscosity at lower shear rate. However, at the same time, a relatively low level of elasticity is induced by B-O substitution with lower bonding energy, resulting in a viscosity decrease at higher shear rates. Consequently, the strong shear thinning property achieved by borate is not caused by strong elasticity like the way silicon nitride did but by an appropriate level of

polymerization together with low level of elasticity. To get deeper insight into the origin of the strongest shear thinning behavior of mold flux with simultaneous incorporation of borate and silicon nitride additive, we have conducted dynamic viscosity measurement and observed that the crossover point is placed between glass melt without any associative additives and with silicon nitride additives. This could indicate that the stronger elasticity induced by silicon nitride and softer structure generated by borate substitution are achieved at the same time and leads to a perfect structure to exhibit the strongest shear thinning behavior.

Conclusion and Summary

Enhancing shear thinning behavior of liquid flux is desirable for continuous casting process of steel. The role of associative additives which modify shear thinning behavior was studied in this work with a dynamic viscosity measurement. From the experimental results, it can be concluded that

1. Incorporation of 28.1 wt percent borate additive leads to decrease on viscosity at higher shear rate without significant change at lower shear rate with a flow behavior index of 0.841. The basic sample without any associative additive has a flow behavior index of 0.874. Dynamic viscosity measurement confirms that borate incorporation causes loosely linked structure by moving crossover point, $G' = G''$, toward left hand side. Such behavior implies that borate addition results in a weak liquid like structure compared to the one without borate additive.
2. Incorporation of 1 wt percent of silicon nitride causes increase on viscosity at lower shear rate without significant change at higher shear rate with a flow behavior index of 0.812. Dynamic viscosity measurement indicates that silicon nitride incorporation causes more stiff structure by shifting crossover point, $G' = G''$, toward right hand side. This behavior means that silicon nitride addition leads to a rigid solid like structure compared to the one without silicon nitride additive.
3. Simultaneous incorporation of 28.1 wt percent borate and 1 wt percent silicon nitride is the most effective way to generate shear thinning behavior of liquid flux because simultaneous incorporation increases viscosity at lower shear rate and decreases viscosity at higher shear rate at the same time. The flow behavior index of liquid flux with simultaneous incorporation is found to be 0.772 which is the strongest shear thinning behavior ever.

References

1. S.H. Shin, J.W. Cho and S.H. Kim, *J. Am. Cer. Soc.*, 2014, vol.97, pp. 3263-3269.
2. T.Matsushita, Y.Sasaki, M.Gornerup and S. Stteharaman, *ISIJ int.*, 2006, vol.46, pp. 1258-1253.

3. Sorimachi, S. Sakai and T. Fujii, *Tetsu-to-Hagane*, 1995, vol.81, pp. 1144-1149.
4. K. Tsutsumi, K. Watanabe, S. Makoto, N. Masayuki, H. Satoru, S. Takayuki and O. Tomoaki, *CAMP-ISIJ*, 2006, vol.19, pp. 94.
5. K. Watanabe, K. Tsutsumi, M. Suzuki, H. Fujita, S. Hatori, T. Suzuki and T. Omoto, *ISIJ int*, 2012, vol.54, pp.865-871.
6. R. Bruckner and Y. Yuanzheng, *Journal of Non-Crystalline Solids*, 1994, vol 175, pp.118-128
7. D.B. Dingwell and S.L. Webb, *Physics and Chemistry of Minerals*, 1989, vol 16, pp.508-516
8. G.A. Dobрева and J. Schmelzer, *Journal of Materials Science*, 1993, vol 28, pp.890-900
9. R. Bruckner and Y. Yuanzheng, *Glass Science and Technology*, 1994, vol 67C, pp.620-623
10. J. Deubener and R. Bruckner, *Journal of Non-Crystalline Solids*, 1997, vol 209, pp.96-111
11. B.G. Thomas, *Continuous casting The Encyclopedia of Materials and Technology*, Elsevier Science Ltd., Oxford, 2001.
12. K.C. Mills and A.B. Fox, *ISIJ int*, 2003, vol.43, pp.1479-1486.
13. K.Okazawa, M. Yamane and Y. Fukuda, *Tetsu-to-Hagane*, 2003, vol.89, pp.629.
14. K. Watanabe, K. Tsutsumi, M. Suzuki, M. Nakada and T. Shiomi, *ISIJ Int*, 2009, vol.49, pp.1611.
15. E. Chiellini, M. Giordano and D. Leporini, *Structure and Transport Properties in Organized Polymeric Materials*, World Scientific, Singapore, 1997.
16. S.G. Advani and E. M. Sozer, *Process Modeling in Composites Manufacturing*, CRC press Oxon, 2002.

VISCOSITY PROPERTY AND RAMAN SPECTROSCOPY OF FeO-SiO₂-V₂O₃-TiO₂-Cr₂O₃ SLAGS

Weijun Huang, Min Chen, Xiang Shen, Yu Shan, Meile He, Nan Wang

School of materials and metallurgy, Northeastern University, Shenyang, 110004, China

Keywords: Vanadium slag, Viscosity, Raman spectroscopy, Polymerization degree, Structure

Abstract

The viscosity and structure characteristics of FeO-SiO₂-V₂O₃-TiO₂-Cr₂O₃ systems as the main composition of V-slag were investigated with different Cr₂O₃ and TiO₂ contents using the rotating cylinder method and Raman. The results showed that the viscosity was below 3.5 Pa·s at 1540 K, and the polymerization degree of the silicate structure was lower than the main monomer structure (Q⁰) in FeO-SiO₂-V₂O₃ system. With the induction of Cr₂O₃ to FeO-SiO₂-V₂O₃ system, the viscosity obviously increased (3.5 Pa·s at 1770 K), with the polymerization degree of molten structures enhanced drastically as formation of a chain structure (Q²) and the O-Cr-O band) and a sheet structure (Q³). With the further induction of TiO₂ to the FeO-SiO₂-V₂O₃-Cr₂O₃ system, the viscosity was 3.5 Pa·s at 1630 K, and the polymerization degree became weaker as the forms of discrete Si-O-Ti and Ti-O-Ti decrease to Q³ in a sheet structure.

Introduction

It is well known that vanadium-titanium magnetite (VTM) is a characteristic resource in China, and the main route for the extraction of vanadium is by oxidizing the vanadium-bearing hot metal in converter to form vanadium-bearing slag and semi-steel [1]. Since the blowing smelting time is merely 3 to 5 minutes, the thermodynamics and the dynamics conditions for oxidizing vanadium in hot metal are very important during the blowing smelting process [1,2]. With the gradual consumption of high quality VTM, the low-grade bearing chromium VTM has caused much attention and is beginning to be utilized in recent years. However, during the vanadium-extraction process, the viscosity of the slag increases after the chromium in the hot metal is oxidized to Cr₂O₃ and dissolves into the slag. Thus, the dynamics condition for vanadium-extraction becomes worse, and the yield ratio of vanadium is decreased [1,2]. Though the viscosity of Cr₂O₃-bearing slag would decrease with increasing of the temperature, the oxidation of vanadium would be suppressed according to the selective oxidation theory, and thus the practical blowing smelting temperature is usually controlled below 1653K [1,2]. Therefore, the viscosity and structure of the vanadium slag system with different content of Cr₂O₃ and TiO₂ were investigated using the rotating cylinder method and Raman spectra, respectively. The purpose of this study is to provide the structure information of vanadium slag and its relationship with the viscosity of Cr₂O₃-bearing vanadium slag, and to provide theoretic basis for optimizing the vanadium-extraction process.

Raw Materials and Procedures

Reagent grade powders of Cr₂O₃ (>99.50 mass%), V₂O₃ (>99.50 mass%), FeC₂O₄ (>99.50 mass%), TiO₂ (>99.50 mass%), and high purity SiO₂ (>99.99 mass%) were used as raw

materials. These five kind powders were dried at 473 K for 4 hours in a drying oven to remove moisture, and then were well mixed in ball mill in the required proportion according to the actual components of Cr₂O₃-bearing vanadium slag as shown in Table I (with external addition of TiO₂ and Cr₂O₃ in the samples). Then the mixed powders were pressed into tablet samples and heated at 1823K for 2h in a MgO-stabilized zirconia crucible (with 95 mass% ZrO₂ and 5 mass% MgO stabilizer, 2273K operating temperature, and 99.9 mass% purity) to prepare pre-melted slag under CO/CO₂ gas flowing atmosphere. After heating, the sample was rapidly taken out from the furnace and quenched by water to avoid the oxidation of elements during the cooling process. According to oxygen-potential diagram of the elements [3], the rank of the stability of various oxides in the slag was TiO₂>SiO₂>V₂O₃>Cr₂O₃>FeO, which indicated that FeO was the most unstable oxide in the FeO-SiO₂-V₂O₃-TiO₂-Cr₂O₃ system slag. In order to protect FeO from oxidation, the oxygen partial pressure was ensured 10⁻³ Pa by changing the composition of CO/CO₂ according to Reaction (1) [3]. In addition, during the heat process, the sample was held at 873 K for 2 h to decarburize FeC₂O₄.

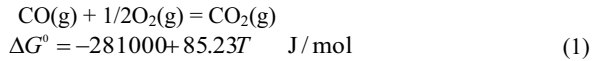


Table I. Typical chemical composition of the studied slag systems for synthetic (with external addition of TiO₂ and Cr₂O₃), mass%

Sample No.	FeO	SiO ₂	V ₂ O ₃	TiO ₂	Cr ₂ O ₃
1	52.12	28.59	19.29	0.00	0.00
2	52.12	28.59	19.29	0.00	6.00
3	52.12	28.59	19.29	13.00	6.00
4	52.12	28.59	19.29	13.00	10.00

After completion of the pre-melting process, 150 g of the pre-melted sample was put into a zirconia crucible and heated in a rotatory viscometer under the oxygen partial pressure of 10⁻³ Pa. When the temperature reached the target temperature, it was maintained for more than 30 min to ensure that the molten slag was homogenized. Subsequently, the molybdenum bob was immersed in liquid slag for 10 mm and rotated at a fixed speed of 180 r/min, and the viscosity was measured at different temperatures (with temperature step of 5 K) during temperature dropping process [4]. In order to verify the effects of Cr₂O₃ and TiO₂ on the structure characteristics of the FeO-SiO₂-V₂O₃-TiO₂-Cr₂O₃ system slag, 8 g of the pre-melted slag was placed in a zirconia crucible (inner diameter 15 mm, height 30 mm) for the molten state in a resistance furnace at approximately 1823 K for 4 hours under the oxygen partial pressure of 10⁻³ Pa. High temperature melts were also quenched in water to form the glasses. In addition, the phase compositions of the samples were examined by X-ray diffraction, and the structural properties were analyzed by Raman spectroscopy using an excitation wavelength of 633 nm with the laser power of 2 mw at room temperature. And the spectra of Raman were fitted by assuming Gaussian line shapes for the peaks of different structural units.

Results and Discussion

Viscosity Property of FeO-SiO₂-V₂O₃-TiO₂-Cr₂O₃ System Slags

Figure 1 shows the viscosity changes of the samples at varying temperatures with different contents of Cr_2O_3 and TiO_2 . It is observed that the viscosity of all the samples first decreased rapidly and then decreased gradually with increasing of temperature, and it finally was closed to a constant value. However, the constant value was different for different samples. It was about 0.7 Pa·s for sample 1 at temperature above 1650 K, but it was about 3.0 Pa·s for sample 2 at temperature above 1800 K, about 1.4 Pa·s for sample 3 at temperature above 1700 K, and about 3.4 Pa·s for sample 4 at temperature above 1810 K, respectively. The critical temperatures for the viscosity decreasing to 3.5 Pa·s were 1534 K, 1767 K, 1624K and 1803K for sample 1, sample 2, sample 3, and sample 4 respectively, which indicates that the viscosity of the samples increased significantly with increasing the Cr_2O_3 content, but decreased with introduction of TiO_2 .

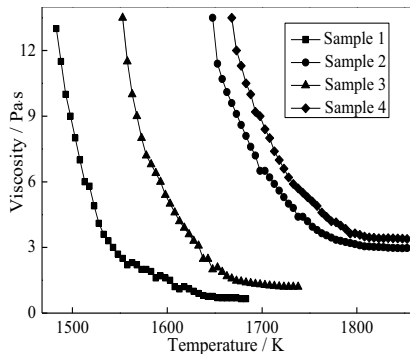


Figure 1. The viscosity of the vanadium slag with various content of Cr_2O_3 and TiO_2 at given temperatures

Raman Spectroscopy and Phase compositions

All original spectra for glassy samples with different contents of Cr_2O_3 and TiO_2 are shown in Figure 2. It is observed that the dominant peaks of the Raman spectra for the $\text{FeO-SiO}_2\text{-V}_2\text{O}_3$ system slag were at about 600-1000 cm^{-1} . With the introduction of 6 mass% Cr_2O_3 into this system, new strong Raman bands appeared at about 252, 550-800, and 1300 cm^{-1} , while the bands at about 70-113, 379, and 750-1050 cm^{-1} of the Raman spectra became weaker, especially for the relative intensity of the main bands at 750-1050 cm^{-1} which was down to about 50%. With the introduction of 6 mass% Cr_2O_3 and 13 mass% TiO_2 into the $\text{FeO-SiO}_2\text{-V}_2\text{O}_3$ system, the relative intensity of the bands at about 180-320, 800-1050, and 1300 cm^{-1} of the Raman spectra became weaker. In addition, with further increase of Cr_2O_3 , the Raman bands near 970 and 1300 cm^{-1} became stronger.

Figure 3 shows the XRD patterns of the quenched samples with different Cr_2O_3 and TiO_2 contents. For the sample without Cr_2O_3 and TiO_2 addition, the crystalline phases was not detected (sample 1), which indicated that the $\text{FeO-SiO}_2\text{-V}_2\text{O}_3$ system slag melted completely and did not form any spinel. For the sample with addition of Cr_2O_3 , new stronger peaks of the spinel (FeCr_2O_4) appeared (sample 2), while the intensity of the peaks became weaker with the introduction of 13 mass% TiO_2 (sample 3). Furthermore, the peak intensity of the spinel became stronger with further increase of the Cr_2O_3 addition (sample 4).

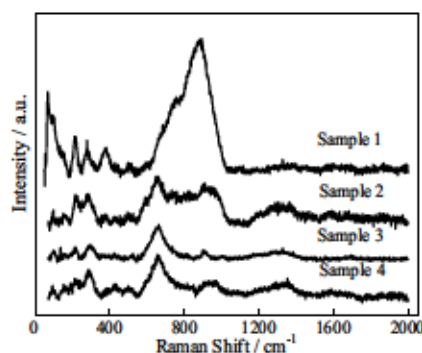


Figure 2. Original Raman spectra for quenched samples with different contents of Cr_2O_3 and TiO_2 at room temperature

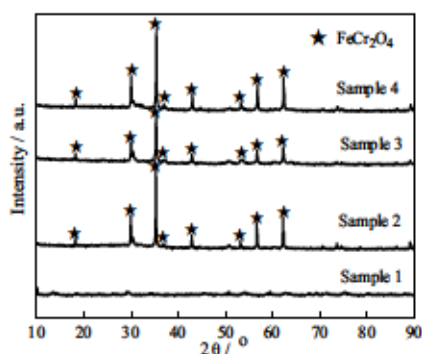


Figure 3. XRD pattern of the quenched sample

Discussion

According to previous research results, the different Raman bands are related to the different structure units. The main band at about $830\text{-}1060\text{ cm}^{-1}$ corresponds to the silicate sites for the Q^0 , Q^1 , Q^2 , and Q^3 structure units (superscripts 0, 1, 2, and 3 are the numbers of bridging oxygen per SiO_4 tetrahedral) [5]. The bands at about $600\text{-}750\text{ cm}^{-1}$ are attributed to the structural units of titanium in the melts, but $830\text{-}850\text{ cm}^{-1}$ are attributed to Ti^{4+} which is substituted for Si^{4+} in tetrahedron to form Ti-O-Si structure units [5]. The bands at about $690\text{-}710$ and $730\text{-}750\text{ cm}^{-1}$ are assigned to the structural units of vanadium and chromium in melts, respectively [6-10]. As the structural behavior of irons is different in the different slag system, the present work investigated the structural behavior of various ions in $\text{FeO-SiO}_2\text{-V}_2\text{O}_3\text{-Cr}_2\text{O}_3\text{-TiO}_2$ system.

The chemical bonds between oxygen and vanadium in V_2O_3 -bearing slag are divided into three types [6,7]: (1) threefold coordinated oxygen O_3 belonging to the chains at about 698 cm^{-1} ; (2) twofold coordinated oxygen O_2 constituting bridges between two chains at about 524 cm^{-1} ; (3) apex oxygen O_1 belonging to the short V-O bond at about 992 cm^{-1} . The band at about 698 cm^{-1} was assigned to the stretching of the V-O₂-V bond; the second vibrational mode at 524 cm^{-1} was

assigned to the stretching vibration of the V-O₃ bond [6,7]. In addition, the third type at 992 cm⁻¹ was assigned to the stretching vibration mode of the short V-O₁ bond [6,7]. In the present work, the first and second types were employed to interpret Figure 2, and it is worth to notice that the first type is the main existing form of V³⁺ in the melt. The peak located at about 698 cm⁻¹ was considered to be attributed to the mode involving the bond stretching vibration localized within the V-O-V bridges, and forming ‘rails’ of ladders to increase the polymerization degree of the melt [6,7]. However, the combined capacity of Si⁴⁺ and O²⁻ is stronger than V³⁺ and O²⁻ [6,7], which meant a larger number of V₂O₃ entered the silicate network to enhance slightly the polymerization degree of melts.

With the introduction of Cr₂O₃ into the slag, Raman spectra was changed greatly. In the first case, the presence of a shoulder at about 745 cm⁻¹ was considered due to the symmetric stretching vibration of Cr-O-Cr [8-10]. In the lower wavenumber region, a band at about 439 cm⁻¹ was observed and assigned to be the antisymmetric stretching modes of Cr-O-Cr [8-10]. The plenty of the Cr-O-Cr bonds were consequence of the constraints imposed by their membership of a ring structure, which included Cr-O-Cr, V-O-V, and Si-O-Si bonds [8-10]. Meanwhile, Dines’s revealed that SiO₂ could stabilize the supported Cr³⁺ in tetrahedral coordination to enhance the ring structure [8-10]. The band at 258 cm⁻¹ observed for this slag could probably be attributed to the bending/deformation modes of the [Cr³⁺O₆] units in the structure. In the second series, the spectrum of pure FeCr₂O₄ shows well-defined peaks at about 1030, 737, 677, 516, 595, 495, and 250 cm⁻¹ [8-10], so the results are consistent with the XRD analysis.

Three possible models for the structural role of titanium, suggested in previous reports on the structure of Ti-bearing glasses, were considered: (1) Ti⁴⁺ substitutes for Si⁴⁺ in tetrahedral coordination in the structural units in melts; (2) Ti⁴⁺ forms TiO₂-like clusters with Ti⁴⁺ in tetrahedral coordination; (3) Ti⁴⁺ as a network modifier possibly occurs in five-fold or six-fold coordination [5]. As can be seen from Figure 2 (sample 3-4), the second and third models could be employed to interpret the results. It means that Ti⁴⁺ as a network modifier could possibly occur in five-fold or six-fold coordination, which would significantly decrease the polymerization degree of silicates. Meanwhile, a small number of Ti⁴⁺ formed TiO₂-like clusters with Ti⁴⁺ in tetrahedral coordination. As the first model stated, Ti⁴⁺ is substituted for Si⁴⁺ in tetrahedral coordination in structural units of the glassy slag, so the polymerization degree of the silicates should be significantly enhanced according to Li’s study [5]. Accordingly, the first model could not consistently predict the present results, as listed in Table III. The second and the third models are most appropriate to describe the role of titanium in structure. The relative intensity of the Raman bands of spinel (FeCr₂O₄) became weaker, while the band at about 670 cm⁻¹ of the Raman spectra for Cr-O-Cr, Si-O-Si, and Ti-O-Ti became stronger with the introduction of TiO₂ in the slag. According to Dines’s study, the crystallization ability of the SiO₂-TiO₂ system decreases with an increase of TiO₂ [8]. Another reason for this could be increased numbers of discrete Si-O-Ti and Ti-O-Ti structural units, which would hamper the crystallization of FeCr₂O₄ as main crystallization product of slag [9].

The bands at 830-1000 cm⁻¹ could correspond to the silicate sites for the Q⁰, Q¹, Q², and Q³ structure units [5]. Considering that the molar fractions of different structure units are related to the band areas, all samples were deconvolved using the Gauss-Deconvolution method by assuming contribution from the structural units of Qⁿ with the minimum correlation coefficient $r^2 \geq 0.99$ to study the effect of different components. As the scattering coefficient of Qⁿ is different in the Raman spectra, the mole fraction of the silicate structure units can be calculated according to the following equation:

$$x_n = \theta_n \cdot A_n \quad (2)$$

where x_n is the mole fraction of the silicate structure units, A_n is the area fraction of each structural unit. θ_n listed in the Table II is the scattering coefficient of Q^n [5]. The number of non-bridging oxygen ($n(\text{NOB}/\text{T})$) in the silicate slag could be calculated by the following equation:

$$n\left(\frac{\text{NOB}}{\text{T}}\right) = \sum x_n \cdot (4 - n) \quad (3)$$

The best-fit simulations are shown in Figure 4 (a)-(d) by the Gauss-Deconvolution method. The summary of the deconvolution and calculation results is listed in Table III.

Table II. Coefficient of scattering of Q^n

Q^n	Q^0	Q^1	Q^2	Q^3
θ_n	1	0.514	0.242	0.09

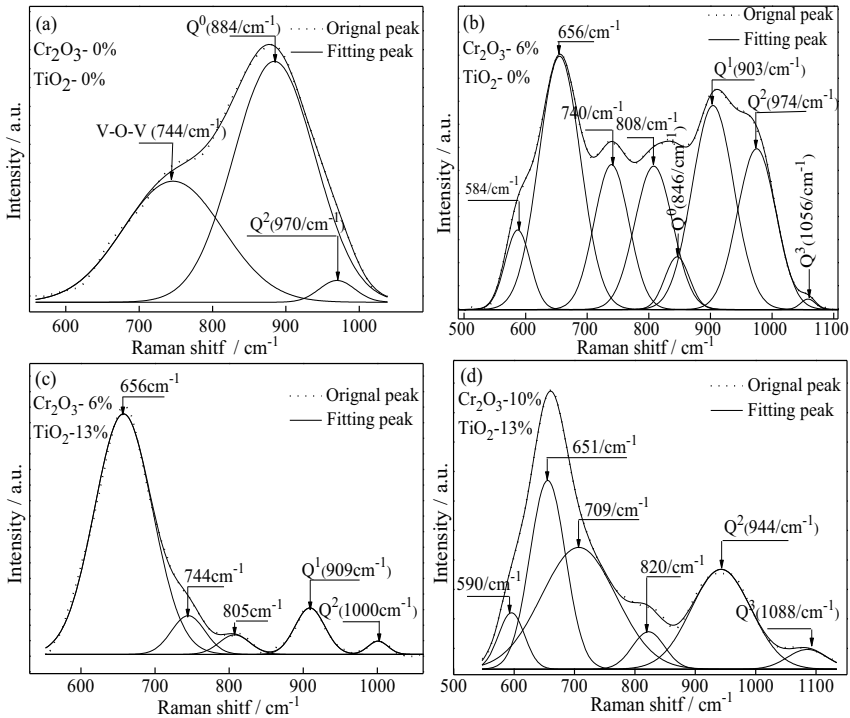


Figure 4. Deconvolved results of Raman spectra for samples with different Cr_2O_3 and TiO_2 contents

Table III. Deconvolved results of Raman spectra for FeO-SiO₂-V₂O₃-TiO₂-Cr₂O₃ slag

Sample number	Q ⁰ / %	Q ¹ / %	Q ² / %	Q ³ / %	n(NOBT)
1	96.21	0.00	3.79	0.00	3.87
2	7.99	52.72	38.34	0.95	2.70
3	0.00	84.00	16.00	0.00	2.84
4	0.00	0.00	88.43	11.57	1.88

Table III shows that the number of non-bridging oxygen rapidly decreased while the content of Cr₂O₃ increased from 0 to 10% in the slags, which could be explained by the Cr₂O₃ playing the role of network formation to increase the polymerization degree of the silicate slag. This result meant that the majority of Cr³⁺ formed the bands of Cr-O-Cr with Cr³⁺ in tetrahedral coordination and changed the polymerization degree of the silicates. In addition, Table 3 also shows that the number of non-bridging oxygen slightly increased as the content of TiO₂ increased from 0 to 13% in mass, indicating that the polymerization degree of silicates became weaker due to the decrease of Q³ in the sheet structure unit and Q² in the chain structure as well as the increase of Q¹, O-Ti-O, and Si-O-Si in the monomer structure. Thus, it could be conclude that the addition of TiO₂ broke up the 3-dimensional networks formed by Si and O, which was consistent with the conclusion proposed by Park's work [5].

Correlation between the structural information and physicochemical properties of vanadium slag could naturally be expected. Many researchers have reported that the viscosity and melting temperature of vanadium slag increased with an increase of w(Cr₂O₃) and decreased with an increase of w(TiO₂) [8-10]. According to the present structural study, the polymerization degree increased drastically with Cr₂O₃ introduction because of the formation of Cr-O-Cr in chain structures. The plenty of high melting point of solid spinel (FeCr₂O₄, with melting temperature about 2273 K) formed in molten slag would increase the viscosity and melting temperature of vanadium slag. On the contrary, the polymerization degree became weaker with an increase of TiO₂ due to a decrease of Si₂O₅²⁻ as a sheet structure and an increased number of discrete Si-O-Ti as well as Ti-O-Ti structural units, which would hamper the crystallization of FeCr₂O₄ as the main crystallization product of the melts, and thus the melting temperature and viscosity of the vanadium slag could be decreased.

Conclusions

The viscosity and the structure of FeO-SiO₂-V₂O₃-TiO₂-Cr₂O₃ system slag with varied Cr₂O₃ and TiO₂ contents were investigated by the rotating cylinder method and Raman spectroscopy, respectively. Based on the above results, the following conclusions have been drawn:

(1) The viscosity of the FeO-SiO₂-V₂O₃ system slag was decreased to 3.5 Pa·s at temperatures above 1450 K. With the introduction of 6 mass% Cr₂O₃ into the FeO-SiO₂-V₂O₃ system, the viscosity increased rapidly and was decreased to 3.5 Pa·s until temperature higher than 1770 K. With the introduction of 13 mass% TiO₂ into the FeO-SiO₂-V₂O₃-Cr₂O₃ system, the viscosity decreased and reached to 3.5 Pa·s at a low temperatures of 1630 K. But the viscosity increases again after increase of the Cr₂O₃ to 10 mass% in the FeO-SiO₂-V₂O₃-Cr₂O₃-TiO₂, and the viscosity was decreased to 3.5 Pa·s until temperature higher than 1803 K.

(2) V^{3+} mainly existed in the form of V-O-V as a chain structure in the FeO-SiO₂-V₂O₃ system, which slightly enhanced the polymerization degree of molten slag. Part of the chromium existed in the form of solid spinel (FeCr₂O₄), and most of the others existed in the bond of Cr-O-Cr to form network structures, which enhanced the polymerization degree of molten slag. Ti⁴⁺ mainly existed in the form of discrete Si-O-Ti and Ti-O-Ti and it decreased Q³ in sheet structures which hampered the crystallization of FeCr₂O₄ in molten slag and decreased the polymerization degree of the FeO-SiO₂-V₂O₃-Cr₂O₃-TiO₂ system.

(3) The polymerization degree of silicate structures was lower in the FeO-SiO₂-V₂O₃ system, which existed mainly as a monomer structure (Q⁰). With the introduction of 6 mass% Cr₂O₃ into the FeO-SiO₂-V₂O₃ system, the polymerization degree of the silicate structure was enhanced significantly due to the formation of Q² in a chain structure and Q³ in a sheet structure. With the introduction of 13 mass% TiO₂ into the FeO-SiO₂-V₂O₃-Cr₂O₃ system, Q² and Q³ decreased in the silicate structure, and the polymerization degree of the silicate structure became weaker, which could decrease viscosity of the FeO-SiO₂-V₂O₃-Cr₂O₃-TiO₂ system slag.

Acknowledgment

The authors gratefully acknowledge the National Natural Science Foundation of China (No. 51174049, 51174052, 51374057, 51374062) which has made this research possible.

REFERENCES

- [1] X. Zhang et al., "Nucleation and Growth Kinetics of Spinel Crystals in Vanadium Slag," *Ironmaking & steelmaking*, 39 (2) (2012), 147-154.
- [2] H. X. Fang, H. Y. Li, and B. Xie, "Effective Chromium Extraction from Chromium-containing Vanadium slag by Sodium Roasting and Water Leaching," *ISIJ International*, 52 (11) (2012), 1958-1965.
- [3] D. X. Huang, *Vanadium Extraction and Steelmaking* (Beijing, NY: Metallurgical Industry Press, 2000), 52-98.
- [4] K. C. Mills, L. Yuan, and R. T. Jones, "Estimating the Physical Properties of Slags," *The Journal of the Southern African Institute of Mining and Metallurgy*, 2011, no. 111: 649-658.
- [5] J. L. Li, Q. F. Shu, and K. Chou, "Structural Study of Glassy CaO-SiO₂-CaF₂-TiO₂ Slags by Raman Spectroscopy and MAS-NMR," *ISIJ International*, 54 (4) (2014), 721-727.
- [6] L. Whittaker, J. M. Velazquez, and S. Banerjee, "A VO-seeded Approach for the Growth of Star-shaped VO₂ and V₂O₅ Nanocrystals: Facile Synthesis, Structural Characterization, and Elucidation of Electronic Structure," *The Royal Society of Chemistry*, 2011, no. 13: 5328-5336.
- [7] X. B. Chen et al., "Raman Analyses of Co-phasing and Hysteresis Behaviors in V₂O₅ Thin Film," *Journal of Raman Spectroscopy*, 2012, no. 43:2025-2028.
- [8] T. Itoh, T. Nagaska, and M. Hino, "Phase Equilibria between SiO₂ and Iron-chromite Spinel Structure Solid Solution, and Deoxidation of Liquid Fe-Cr Alloy with Silicon," *ISIJ International*, 42 (1) 2002, 33-37.
- [9] J. Yang et al, "Transition of Synthetic Chromium Oxide Gel to Crystalline Chromium Oxide: a Hot-stage Raman Spectroscopic Study," *Journal of Raman Spectroscopy*, 2011, no. 42: 1069-1074.
- [10] T. J. Dines and S. Inglis, "Raman Spectroscopic Study of Supported Chromium (VI) Oxide Catalysts," *Physical Chemistry Chemical Physics*, 2003, no. 5: 1320-1328.

**ADVANCES IN MOLTEN
SLAGS, FLUXES, AND SALTS:**

Proceedings of



**Physical Properties:
Thermal Properties
and Electrical
Conductivity**

TECHNIQUES FOR MEASURING SOLUBILITY AND ELECTRICAL CONDUCTIVITY IN MOLTEN SALTS

Shizhao Su¹, Thomas Villalon Jr.¹, Uday Pal*^{1,2}, Adam Powell³

¹ Division of Materials Science and Engineering, Boston University, Brookline, MA, 02446

² Department of Mechanical Engineering, Boston University, Boston, MA, 02215

³ Infinium Inc., Natick, MA, 01760

Keywords: oxy-fluoride molten salt, alumina solubility, zirconia solubility, conductivity

Abstract

Eutectic MgF₂-CaF₂ based salt containing YF₃, CaO and Al₂O₃ additions were used in this study. The electrical conductivity was measured as a function of temperature by a calibration-free co-axial electrode setup. The materials selection and setup design were optimized to accurately measure the electrical conductivity of the highly conductive molten salts (>1 S/cm). The solubility and diffusion behavior of alumina and zirconia in the molten salts were investigated by drawing and holding the molten salt for different lengths of time within capillary tubes made of alumina and zirconia, respectively. After the time-dependent high temperature holds, the samples were cooled and the solubility of the solute within the molten salt was determined using scanning electron microscopy, energy-dispersive X-ray spectroscopy analysis and wavelength-dispersive X-ray spectroscopy analysis.

Introduction

Molten fluoride salt has been widely used as coolant and fuel in the molten salt nuclear reactors[1] and used as molten flux for electrolytic metals production[2]–[4]. Particularly, molten fluoride salt has been used to produce several energy-intensive metals, such as Mg, Ti, Ta, Yb and Si, directly from their oxides using solid oxide membrane (SOM) based electrolysis[5]–[13]. The SOM electrolysis process features the utilization of an oxygen-ion-conducting membrane, typically made of yttria-stabilized zirconia (YSZ), for directly electrolyzing desired metal oxides dissolved in the pre-selected molten fluoride flux, producing pure metal at the cathode and oxygen as a byproduct at an inert anode[7]. The SOM process is a low-cost, energy-efficient and low emission process compared to other metal extraction technologies[14]. It is crucial to engineer the molten oxy-fluoride flux composition based on its physio-chemical properties for successful operation of the SOM electrolysis process. Due to the high melting point and the complicated nature of the molten oxy-fluoride flux systems, the available information on physio-chemical properties of such molten salts are very limited. In this paper, the quaternary molten oxy-fluoride salt MgF₂-CaF₂-CaO-YF₃ was studied. The aluminum oxide solubility of the molten salt was measured. The zirconia solubility and the electrical conductivity of the molten salt with desired amount of aluminum oxide addition were measured. The temperature dependence of the molten salt electrical conductivity was also investigated. These physio-chemical property measurements will be helpful for modeling and designing of electrolytic metal extraction processes such as the SOM process.

Experimental

A. Alumina Capillary Tube Sampling Setup

Figure 1 shows the schematic of the alumina capillary tube sampling setup. The setup consists of a graphite crucible that was heated to 1200°C in forming gas (95% Argon-5% H_2) to ensure an inert atmosphere. 300g of powdered flux (45wt% MgF_2 –55 wt% CaF_2 containing 6wt% CaO and 4wt% YF_3) was placed inside the crucible and heated to the desired temperature. Three alumina tubes (0.318cm i.d., 0.635cm o.d., 91.44cm length) were inserted into the molten flux. Each alumina tube was connected with a 3-way pipette bulb at the top of the tube. The pipette bulb was gently squeezed to create a negative pressure compared with the atmosphere. When releasing the pipette bulb, molten flux was drawn into the alumina tube. The alumina tube was subsequently lifted out of the furnace and quenched to room temperature. The alumina tubes were then sectioned into 2 inches pieces with quenched flux inside.

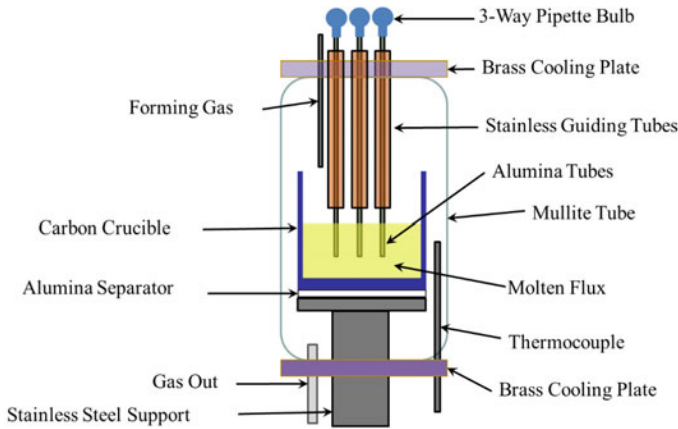


Figure 1: Experiment setup of capillary tube sampling

B. Alumina Solubility Measurement Setup

The alumina solubility of the molten flux was measured by holding the alumina capillary tube at 1200°C with flux inside for sufficient time so that the flux was saturated with alumina; alumina diffuses from the alumina tube. Figure 2 shows the schematic of the two-end-cap setup for sealing the alumina capillary tube. Two stainless steel (SS-304) end caps were placed on both ends of the alumina capillary tube. A shallow divot was drilled on each end cap to accommodate the alumina capillary tube. Once the end caps were placed on the alumina tube, two stainless steel support rods were welded between the top and bottom end caps to ensure both caps stay in place during the experiment. The assembly was then placed in a tube furnace and heated to 1200°C in a forming gas atmosphere and held for 24 hours. The assembly was then quickly removed from the furnace and quenched to room temperature. After disassembling the setup, the capillary tube was sectioned by a precision diamond saw. The capillary tube sample was mounted in epoxy and polished. The cross-section of the capillary tube with flux inside was then characterized by scanning electron

microscopy (SEM), energy-dispersive X-ray spectroscopy (EDS) and wavelength-dispersive X-ray spectroscopy (WDS).

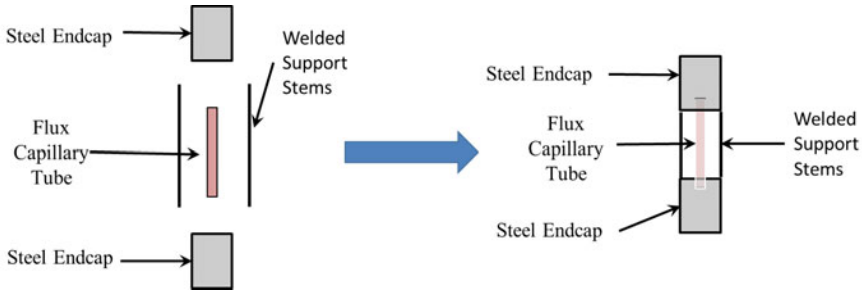


Figure 2: Two end caps design for alumina solubility measurement

C. Zirconia Solubility Measurement Setup

The zirconia tube was more sensitive to thermal shock compared with the alumina tube. When drawing capillary tube sample using the method illustrated earlier in part A, the zirconia tube often failed under thermal shock and broke. Thus an alternative approach shown in Figure 3 was used as the setup for the zirconia solubility measurement. A graphite crucible was made such that the capillary tube could be inserted in the crucible and fit tightly. 5g of flux powder (45 wt% MgF_2 – 55 wt% CaF_2 containing 6wt% CaO , 3wt% of Al_2O_3 and 4wt% YF_3) was solvent mixed and subsequently dried. Then the flux was pre-melted and crushed several times to ensure homogeneity. After the capillary tube was inserted in the graphite crucible, flux powder was filled in the capillary tube. The crucible was then sealed on top with a graphite cap and graphite paste. The assembly was then placed in a tube furnace and heated to 1200°C in a forming gas atmosphere and held for 24 hour before quenching it to room temperature. The capillary tube was easily removed after cooling since both zirconia and the flux did not wet graphite. The zirconia capillary tube was sectioned by a precision diamond saw, mounted in epoxy and polished. The cross-section of the capillary tube with flux inside was then characterized by SEM and EDS.

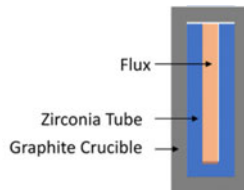


Figure 3: Graphite crucible setup for zirconia solubility measurement

D. Molten Salt Conductivity Experiment Setup

The electrical conductivity of the molten salt was determined by a high-accuracy-height-differential measurement technique using a concentric coaxial two electrodes cell and measuring the impedance spectra of the molten salt as a function of immersion depth[15]–[18]. Figure 4

shows the schematic of the electrical conductivity measurement setup. The setup consists of a graphite crucible that was heated to the operating temperature between 1060°C and 1250°C. Forming gas (95% Argon - 5% H₂) was purged in the reaction chamber at a rate of 1000cm³/min during the experiment to ensure an inert atmosphere. 500g of pre-mixed powdered flux (45wt% MgF₂ – 55wt% CaF₂ containing 6wt% CaO, 3wt% Al₂O₃ and 4wt% YF₃) was used as the source to create the molten salt inside the crucible. Three threaded molybdenum rods with 0.318cm diameter served as the electrode current collectors. The concentric electrodes were made of low carbon steel (C1018). The inner electrode had a diameter of 0.635cm. The outer electrode had an inner diameter of 3.175cm and an outer diameter of 5.715cm. The two tapped holes on the outer electrodes were 5.080cm apart. The molybdenum rods were threaded into the concentric steel electrodes to maintain good uniform contact during the measurement. An alumina spacer with a 0.635cm thickness and three 0.318cm openings were placed on top of the steel electrodes to level the electrodes and ensure concentricity of the electrodes.

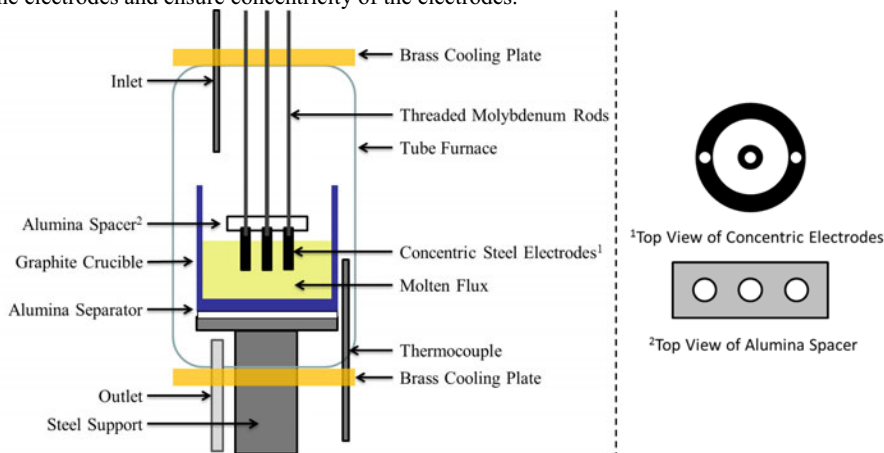


Figure 4: Experiment setup of the electrical conductivity measurement

E. Electrochemical Measurements

Electrochemical impedance spectroscopy (EIS) scans were performed between the molybdenum rod connected with the outer electrode and the molybdenum rod connected with the inner electrode using a Princeton Applied research 263A potentiostat and a Solartron 1250 frequency response analyzer. The EIS scans were from 20000 to 1 Hz with 20mV amplitude. The total ohmic resistance of the cell (R_{cell}) was obtained from the value of the high-frequency intercept on the real axis of the Nyquist plot [19], [20]. The total resistance consists of the lead wire resistance (R_{leads}), the electrodes resistance ($R_{electrodes}$) and the liquid flux resistance (R_{liq})

$$R_{cell} = R_{leads} + R_{electrodes} + R_{liq} \quad (1)$$

The lead wire resistance (R_{leads}) and the electrodes resistance ($R_{electrodes}$) were measured prior to the conductivity measurement. The concentric electrodes were inserted in a steel stand and

electrically shorted. The setup was then heated to the desired temperature and the resistance of the electrodes was measured by performing an EIS scan between the two molybdenum rods. The liquid flux resistance (R_{liq}) contains radial and fringe parts. The fringe component of the resistance does not change with respect to the immersion length and can be cancelled out by taking multiple measurements with different immersion depths.

$$\frac{1}{R_{liq}} = \frac{1}{R_{liq}^{radial}} + \frac{1}{R_{liq}^{fringe}} \quad (2)$$

Differentiate equation (2),

$$\frac{d[1/R_{liq}]}{dz} = \frac{d[1/R_{liq}^{radial}]}{dz} \quad (3)$$

For the coaxial electrodes geometry, the conductivity is related to the radial component of the resistance as follows,

$$\frac{1}{R_{liq}^{radial}} = \kappa \left(\frac{2\pi z}{\ln(b/a)} \right) \quad (4)$$

Where b is the inner radius of the outer electrode, a is the outer radius of the inner electrode, z is the relative immersion depth. Combining equation (3) and equation (4) gives the relation between the electrical conductivity as a function of liquid flux resistance and the immersion depth

$$\kappa = \left(\frac{\ln(b/a)}{2\pi} \right) \frac{d[1/R_{liq}^{radial}]}{dz} \quad (5)$$

The R_{liq} was calculated by subtracting the lead-wire resistance (R_{leads}) and the electrodes resistance ($R_{electrodes}$) from the cell resistance (R_{cell}). The linear regression of the inverse of the liquid flux resistance and the immersion depth was used to calculate the electrical conductivity of the flux based on equation (5). The accuracy of this measurement technique was benchmarked by measuring the conductivity of cryolite (Na_3AlF_6) at 1000°C and comparing it with the literature value.

F. Chemicals and Materials

Magnesium fluoride hydrate ($MgF_2 \cdot xH_2O$, min. 87% MgF_2), calcium fluoride (99.5%), calcium oxide (reagent grade), aluminum oxide (99%), yttrium (III) fluoride (99.9%) were supplied by Alfa Aesar (Ward Hill, MA). Cryolite was supplied by Pyro Chem Source (Hayward, MN). The powders were dried for 4 hours at 400°C to remove moisture and crystallized water. Then the powders were dry mixed in a ball mill overnight according to the flux stoichiometry. The molybdenum rods were supplied by Eagle Alloys Corporation (Talbot, TN). The C1018 steel and stainless steel were supplied by McMaster-Carr (Princeton, NJ). The alumina tubes were supplied by CoorsTek (Golden, CO). The zirconia tube (6 mol% Y_2O_3) was supplied by McDanel (Beaver Falls, PA).

Results

A. Alumina Solubility Measurement

The composition of the flux before high temperature hold was determined by EDS quantitative spot analysis with a Zeiss Supra 55VP Field Emission SEM. The EDS analysis uses internal standards for quantitative analysis. The internal standards are installed through the EDAX genesis software supplied by the manufacturer. The results are shown in Table I. It is confirmed that before the high temperature hold, there is no alumina in the flux.

Table I: Initial elemental composition of the flux

Elements	O	F	Mg	Al	Y	Ca
Atomic %	1.70	59.89	17.83	0.00	1.15	19.43

Figure 5 shows the SEM image of the cross-section of the flux in the alumina capillary tube. Three phases were identified from the high magnification images. The composition of each phase was measured by taking a WDS spot analysis with a JEOL-JXA-8200 Superprobe. The results are shown in Table II. Phase 1 (bright) is calcium rich, phase 2 (dark) is magnesium rich, and phase 3 (gray) is a eutectic Mg-Ca-F phase with aluminum in it.

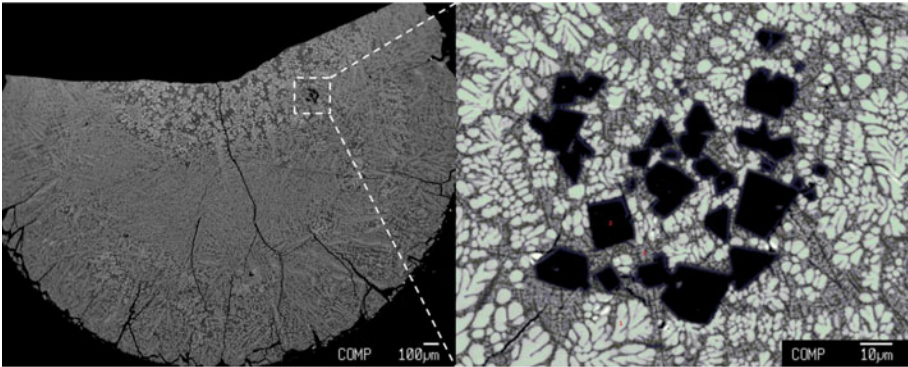


Figure 5: SEM image of the flux cross-section of the alumina solubility sample

Table II: Elemental analysis of difference phases in the alumina capillary tube sample

	Elements	O	F	Mg	Al	Y	Ca
Phase 1 (Bright)	Atomic %	0.23	67.69	1.4	0.01	1.01	29.37
Phase 2 (Dark)	Atomic %	5.97	62.89	27.74	1	0.11	2.29
Phase 3 (Gray)	Atomic %	9.67	59.08	14.84	1.97	0.58	13.86

The alumina solubility of the flux was measured by taking 5 WDS radial line scans starting from the center of the flux to the interface between the flux and the alumina tube, each containing ten $30\mu\text{m} \times 30\mu\text{m}$ spots. The average elemental composition of the flux is shown in Table III. Attributing all the aluminum to Al_2O_3 , the Al_2O_3 solubility is calculated to be 3.16wt%.

Table III: Average elemental composition of the flux sample saturated with alumina

Elements	O	F	Mg	Al	Y	Ca
Atomic %	14.50	57.21	10.35	1.43	0.64	15.87

Similar experiments performed with 40 hours hold showed similar alumina solubility (3.52wt%), indicating that the flux is saturated with alumina within 24 hours.

B. Zirconia Solubility Measurement

Figure 6 shows the SEM image of the cross-section of the flux inside the zirconia capillary tube. Three phases were identified from the SEM image, and the composition of the phases were measured by EDS quantitative spot analysis. The results are shown in Table IV. Phase 1 (bright) is calcium rich; phase 2 (gray) is eutectic Mg-Ca-F; phase 3 (dark) is mainly MgAlO₂.

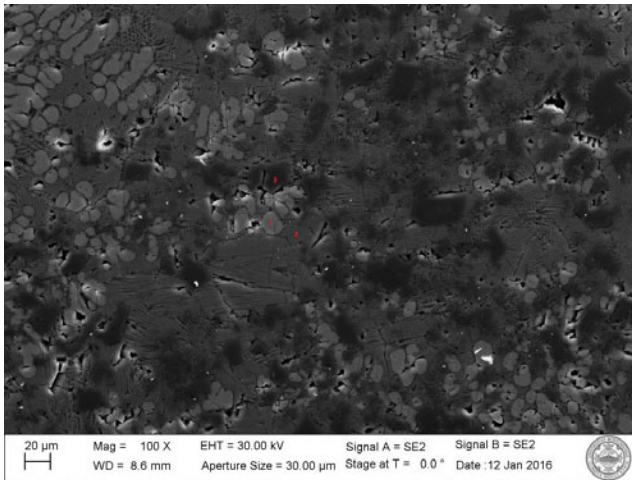


Figure 6: SEM image of the flux cross-section of the zirconia solubility sample

Table IV: Elemental analysis of difference phases in the zirconia capillary tube sample

	Elements	O	F	Mg	Al	Y	Ca	Zr
Phase 1 (Bright)	Atomic %	2.40	59.45	3.50	0.38	1.05	33.12	0.37
Phase 2 (Dark)	Atomic %	3.47	57.81	20.50	0.22	0.53	17.42	0.06
Phase 3 (Gray)	Atomic %	46.95	0.25	17.78	34.36	0.13	0.46	0.08

The zirconia solubility of the flux was measured by taking a quantitative EDS analysis on a large area of flux cross-section (2.25mm x 3.01mm). The average elemental composition of the flux is shown in Table V. The zirconium content is below the detection limit of the EDS and it was confirmed that the zirconia solubility of the flux is less than 0.4wt%. There is negligible zirconia dissolved in the molten flux.

Table V: Average elemental composition of the flux sample saturated with zirconia

	Elements	O	F	Mg	Al	Y	Ca	Zr
Phase 1 (Bright)	Atomic %	9.21	55.34	15.40	2.70	0.55	16.72	0.08

The zirconia tube was also analyzed after the solubility experiment with EDS line scan as shown in Figure 7. Each line represents the normalized concentration of its corresponding element. It is shown that there is no zirconium or yttrium depletion from the yttria-stabilized zirconia into the flux. The flux also did not attack the zirconia. It is confirmed that the zirconia is chemically compatible with this particular molten flux composition. Previous research has shown that the zirconia membrane degradation is the limiting factor for SOM cell lifetime[21], [22]. The fact that the zirconia membrane is compatible with this molten flux composition suggested that it is potentially suitable for the SOM electrolysis process.

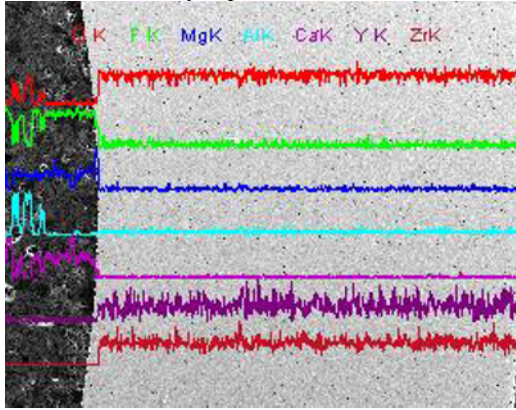


Figure 7: EDS line scan of the zirconia tube after the molten salt solubility experiment

C. Molten Flux Conductivity Measurements

The lead wire resistance plus the electrodes resistance of the coaxial concentric cell was measured from 1000°C to 1250°C. The resistances have a linear relationship with temperature:

$$R_{leads} + R_{electrodes} = 8.5 * 10^{-5}(T(^{\circ}C) - 1000) + 0.015 (\Omega) \quad (6)$$

The conductivity benchmark experiment was performed with cryolite at (Na_3AlF_6) at 1000°C. The immersion depth of the electrodes were from 0.635cm ~ 3.810cm with a 0.317cm interval in order to get rid of surface and bottom fringe effects. The inverse of the impedance was plotted as a function of immersion depth as shown in Figure 8. The electrical conductivity of the cryolite was calculated to be 2.59 ± 0.19 (S/cm) from equation (5) using the slope from the linear fit in Figure 8. Taking into account the inaccuracy of the electrode resistance measurement ($\pm 2m\Omega$), the conductivity value is within the error limit of the literature value (2.80S/cm) [23].

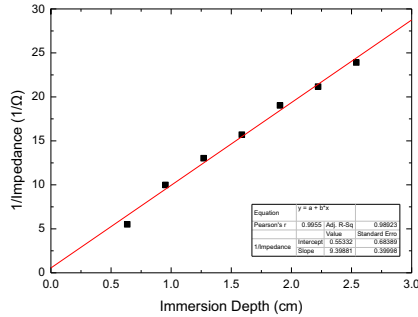


Figure 8: Linear fit of the inverse of impedance vs. immersion depth for cryolite

The electrical conductivity of 45wt% MgF_2 – 55wt% CaF_2 containing 6wt% CaO , 3wt% Al_2O_3 and 4wt% YF_3 was measured from 1060°C to 1250°C. It is widely accepted that the temperature dependence of the electrical conductivity of molten salt can be expressed by the Arrhenius equation as

$$\kappa = Ae^{-E_a/RT} \quad (7)$$

Or

$$\ln \kappa = \ln A - E_a/RT \quad (8)$$

Where κ is the electrical conductivity, A is the pre-exponent factor, E_a is the activation energy, R is the gas constant (8.314J/(mol·K)), and T is the absolute temperature. Figure 9 shows the change of electrical conductivity as a function of temperature. It can be seen that the electrical conductivity increased from 2.01S/cm at 1060°C to 7.16S/cm at 1200°C. As the temperature increases, ion mobility is higher, which results in the increase of the electrical conductivity. Moreover, the temperature dependence of electrical conductivity obeys the Arrhenius law very well (activation energy E_a is 48.92kJ/mol) indicating that the conduction mechanism remains the same within the investigated temperature interval. The high conductivity of this molten salt also suggests that the flux will not contribute significantly to the ohmic polarization of the electrolytic cell. Thus it is an ideal flux candidate for the electrolytic metal extraction processes.

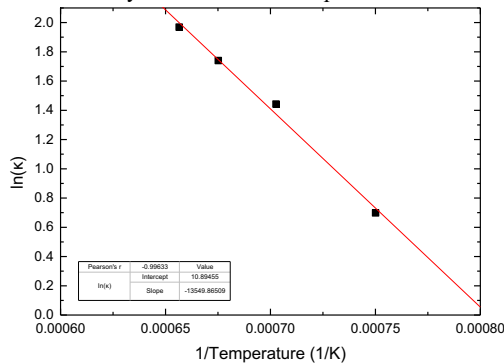


Figure 9: Arrhenius fitting of molten salt conductivity as a function of temperature

Conclusions

The alumina solubility of quaternary molten oxy-fluoride salt $\text{MgF}_2\text{-CaF}_2\text{-CaO-YF}_3$ was measured using capillary tube method. The alumina solubility was measured to be 3.17wt% at 1200°C for 24 hours. The zirconia solubility and the electrical conductivity of the quaternary molten oxy-fluoride with 3wt% alumina was measured. It was shown that the zirconia has negligible solubility in such flux composition, and the zirconia is thus chemically compatible with the flux. The electrical conductivity of the flux was high, and increases with increasing temperature. The electrical conductivity also follows the Arrhenius relationship with respect to temperature. All of these physio-chemical properties suggested that such flux composition can be potentially used in electrolytic metals extraction processes such as the SOM process.

Acknowledgements

This project was financially supported by the Department of Energy (DOE) through arpa-e REMOTE program. The authors would like to thank Matthew Mirek for assisting with performing some of the experiments.

References

- [1] G. Locatelli, M. Mancini, and N. Todeschini, "Generation IV nuclear reactors: Current status and future prospects," *Energy Policy*, vol. 61, pp. 1503–1520, 2013.
- [2] H. Zhu, "Rare Earth Metal Production by Molten Salt Electrolysis," in *Encyclopedia of Applied Electrochemistry*, G. Kreysa, K. Ota, and R. F. Savinell, Eds. New York, NY: Springer New York, 2014, pp. 1765–1772.
- [3] K. Maeda, K. Yasuda, T. Nohira, R. Hagiwara, and T. Homma, "Silicon Electrodeposition in Water-Soluble KF-KCl Molten Salt: Investigations on the Reduction of Si(IV) Ions," *J. Electrochem. Soc.*, vol. 162, no. 9, pp. D444–D448, Jun. 2015.
- [4] R. Lumley, Ed., *Fundamentals of Aluminium Metallurgy*. Woodhead Publishing Limited, 2011.
- [5] U. B. Pal, D. E. Woolley, and G. B. Kenney, "Emerging SOM technology for the green synthesis of metals from oxides," *JOM*, vol. 53, no. 10, pp. 32–35, Oct. 2001.
- [6] A. Krishnan, U. B. Pal, and X. G. Lu, "Solid oxide membrane process for magnesium production directly from magnesium oxide," *Metall. Mater. Trans. B*, vol. 36, no. 4, pp. 463–473, Aug. 2005.
- [7] X. Guan, U. B. Pal, S. Gopalan, and A. C. Powell, "LSM ($\text{La}_{0.8}\text{Sr}_{0.2}\text{MnO}_3$)-Inconel Inert Anode Current Collector for Solid Oxide Membrane (SOM) Electrolysis," *J. Electrochem. Soc.*, vol. 160, no. 11, pp. F1179–F1186, Sep. 2013.
- [8] E. S. Gratz, X. Guan, J. D. Milshtein, U. B. Pal, and A. C. Powell, "Mitigating Electronic Current in Molten Flux for the Magnesium SOM Process," *Metall. Mater. Trans. B*, vol. 45, no. 4, pp. 1325–1336, Aug. 2014.
- [9] X. Guan, U. B. Pal, and A. C. Powell, "Energy-Efficient and Environmentally Friendly

Solid Oxide Membrane Electrolysis Process for Magnesium Oxide Reduction: Experiment and Modeling,” *Metall. Mater. Trans. E*, vol. 1, no. 2, pp. 132–144, Jun. 2014.

- [10] M. Suput, R. Delucas, S. Pati, G. Ye, U. Pal, and A. C. Powell IV, “Solid oxide membrane technology for environmentally sound production of titanium,” *Miner. Process. Extr. Metall.*, vol. 117, no. 2, pp. 118–122, Jun. 2008.
- [11] A. Krishnan, X. G. Lu, and U. B. Pal, “Solid Oxide Membrane (SOM) technology for environmentally sound production of tantalum metal and alloys from their oxide sources,” *Scand. J. Metall.*, vol. 34, no. 5, pp. 293–301, 2005.
- [12] Y. Jiang, J. Xu, X. Guan, U. B. Pal, and S. N. Basu, “Production of Silicon by Solid Oxide Membrane-Based Electrolysis Process,” *MRS Proc.*, vol. 1493, pp. MRSF12–1493–E19–89, Jan. 2013.
- [13] X. Guan, S. Su, U. B. Pal, and A. C. Powell, “Periodic Shorting of SOM Cell to Remove Soluble Magnesium in Molten Flux and Improve Faradaic Efficiency,” *Metall. Mater. Trans. B*, vol. 45, no. 6, pp. 2138–2144, Dec. 2014.
- [14] U. B. Pal and A. C. Powell, “The use of solid-oxide-membrane technology for electrometallurgy,” *JOM*, vol. 59, no. 5, pp. 44–49, May 2007.
- [15] C. J. Macdonald, “Calibration-Free Electrical Conductivity Measurements For Highly Conductive Slags,” Boston University, 2000.
- [16] S. L. Schiefelbein, N. a. Fried, K. G. Rhoads, and D. R. Sadoway, “A high-accuracy, calibration-free technique for measuring the electrical conductivity of liquids,” *Rev. Sci. Instrum.*, vol. 69, no. 9, p. 3308, 1998.
- [17] S. L. Schiefelbein and D. R. Sadoway, “A high-accuracy, calibration-free technique for measuring the electrical conductivity of molten oxides,” *Metall. Mater. Trans. B*, vol. 28, no. 6, pp. 1141–1149, Dec. 1997.
- [18] U. B. Pal, “Determining physio-chemical properties of slags by electrical measurements,” *JOM*, vol. 54, no. 11, pp. 57–61, Nov. 2002.
- [19] K. R. Cooper and M. Smith, “Electrical test methods for on-line fuel cell ohmic resistance measurement,” *J. Power Sources*, vol. 160, no. 2, pp. 1088–1095, 2006.
- [20] S. C. Britten and U. B. Pal, “Solid-state amperometric sensor for the In-situ monitoring of slag composition and transport properties,” *Metall. Mater. Trans. B*, vol. 31, no. 4, pp. 733–753, 2000.
- [21] E. S. Gratz, J. D. Milshtein, and U. B. Pal, “Determining Yttria-Stabilized Zirconia (YSZ) Stability in Molten Oxy-Fluoride Flux for the Production of Magnesium with the SOM Process,” *J. Am. Ceram. Soc.*, vol. 96, no. 32300, pp. 3279–3285, Jun. 2013.
- [22] J. Xu, B. Lo, Y. Jiang, U. Pal, and S. Basu, “Stability of yttria stabilized zirconia in molten oxy-fluorite flux for the production of silicon with the solid oxide membrane process,” *J. Eur. Ceram. Soc.*, vol. 34, no. 15, pp. 3887–3896, Dec. 2014.
- [23] J. D. Edwards, C. S. Taylor, L. A. Cosgrove, and A. S. Russell, “Electrical Conductivity and Density of Molten Cryolite with Additives,” *J. Electrochem. Soc.*, vol. 100, no. 11, p. 508, 1953.

A NEW METHOD FOR APPARENT THERMAL CONDUCTIVITY MEASUREMENT OF MOULD FLUX

Mu Li¹, Rie Endo¹, Li Ju Wang² and Masahiro Susa¹

¹Department of Metallurgy and Ceramics Science, Tokyo Institute of Technology, Ookayama, Meguro-ku, Tokyo, 152-8552 Japan

²School of Mechanical and Materials Engineering, Washington State University, Pullman, WA, 99164, USA

Keywords: quasi-steady state hot plate method, mould flux, thermal conductivity, silica glass.

Abstract

A new quasi-steady state hot plate method has been proposed to measure heat flux across a sheet sample such as mould flux film, finally to determine its apparent thermal conductivity *via* Fourier's equation. The heat flux across the sheet sample is derived from the volume change caused by melting of ice utilizing a modified Bunsen Ice Calorimeter. This measurement method was applied to Ni-base super alloy (Inconel 600), alumina and PTFE (Teflon) with known thermal conductivity values to confirm the reliability of this new method. The experimental thermal conductivity values obtained were in good agreement with the respective reported values. Measurements were also conducted on sheet silica glasses which sized $20 \times 20 \times 0.5 \text{ mm}^3$ and $20 \times 20 \times 1.0 \text{ mm}^3$, and produced a value of $1.34 \pm 0.03 \text{ Wm}^{-1}\text{K}^{-1}$ at 293 K – 303 K under a temperature gradient of 20 Kmm^{-1} , which value is reasonable compared with the reported one. In addition, a process simulation has been applied to confirm the applicability of the present method to mould flux used in continuous casting under a steep temperature gradient at high temperature.

Introduction

In the continuous casting, various factors affect the surface quality of slab, including cooling conditions [1] and physical properties [2] of mould powders that are placed on the surface of molten steel in the mould. The heat transfer mechanism from the shell to the mould is very complicated [3] but the heat flux is dominated by the properties of solid mould flux film. Thus, in order to obtain qualified steel, it is necessary to evaluate the conductive heat transmission between the steel and the mould.

There are some researches focusing on the thermal conductivity of mould fluxes [4, 5], Yamauchi *et al.* [4] reported the values at temperature range between 573 K – 1073 K, Ozawa *et al.* [5] measured the thermal conductivity from 773 K to 1053 K. Both the data are almost at the same order of magnitude, however, the thermal conductivity has not been yet evaluated under steep temperature gradients close to the actual operation.

Bunsen [6] has reported an ice-calorimeter that can determine a quantity of heat transferred to an ice/water mixture by measuring the volume change of the mixture due to melting of ice. Jessup [7] has applied this technique to obtain a heat quantity of the magnitude of 160 J with a precision of about 0.05%, and also succeeded in measuring the heat quantity change associated with chemical reaction using a Bunsen Ice Calorimeter. More recently a quasi-steady state hot plate method has been established utilizing the principle of Bunsen Ice Calorimeter to measure the apparent thermal conductivity of oxide scale on steel under steep temperature gradients. [8] Thus, it is possible to apply this method to a mould flux film to determine its apparent thermal conductivity using the temperature gradient in the mould flux on the basis of Fourier's law.

Consequently, the present work aims to determine the apparent thermal conductivity of a silica plate as a model of mould flux film using the quasi-steady state hot plate method.

Experimental

Principle of Quasi-steady State Hot Plate Method

Figure 1 shows a schematic diagram of the heat flux measurement apparatus developed for the quasi-steady state hot plate method utilizing the principle of a Bunsen Ice Calorimeter. A vertical barrel container (calorimeter) that was filled with an ice/water mixture inside was placed in an ice box to reduce the effect of surrounding conditions. Ice was made by an ice-making machine from distilled water, and crushed into small pieces sized around $10 \times 10 \times 10 \text{ mm}^3$. The container was hermetically sealed with a copper lid, which had 77 fins 50 mm long at the downside to promote the heat transmission from the sample to the ice/water mixture. In addition, there was a stirrer placed at the bottom of the container to keep the temperature more uniform. The sheet sample was placed upon the copper lid. Two aluminum metal blocks sized $20 \times 20 \times 10 \text{ mm}^3$ weighing *ca.* 11 g were positioned on the sample: the lower was used to accommodate a thermocouple and the upper was used as a heat source. In principle, heat transmits from the heat source to the ice/water mixture across the sample and melts parts of ice; thereby the volume of the mixture changes. The volume change was detected by a laser displacement meter as the liquid height decrease in the pipe that was connected to the container.

The liquid height change provides the number of moles of melted ice, $\Delta n_{\text{H}_2\text{O}}$, as follows:

$$\Delta n_{\text{H}_2\text{O}} = \frac{\pi r^2 \cdot \Delta h}{M_{\text{H}_2\text{O}}} \left(\frac{1}{\rho_{\text{water}}} - \frac{1}{\rho_{\text{ice}}} \right) \quad (1)$$

where r is the radius of the pipe, ρ is the density of each substance, h is the liquid height and $M_{\text{H}_2\text{O}}$ is the molar mass of water. The number of moles of melted ice, in turn, provides the heat deposited to the ice/water mixture. Thus, the heat flux (q_{ice}) across the sample is derived from the derivative of the liquid height with respect to time as follows:

$$q_{\text{ice}} = \frac{\Delta_{\text{trs}} H_{\text{H}_2\text{O}} \pi r^2 \cdot \rho_{\text{ice}} \cdot \rho_{\text{water}}}{A \cdot M_{\text{H}_2\text{O}} \cdot (\rho_{\text{ice}} - \rho_{\text{water}})} \cdot \frac{dh}{dt} \quad (2)$$

where A is the surface area of the sample across which area heat transmits and $\Delta_{\text{trs}} H_{\text{H}_2\text{O}}$ is the enthalpy for fusion of ice at 273.15 K.

As shown in Figure 1, a sheathed K-type thermocouple was positioned inside the aluminium block 1.3 mm away from its bottom surface and a platinum thermometry resistance element was placed at the lower surface of the copper lid to monitor temperatures T_{up} and T_{down} , respectively. Using Fourier's law, the relationship between the temperature difference and the heat flux (q_{temp}) can be given as follows:

$$q_{\text{temp}} = \left(\frac{T_{\text{up}} - T_{\text{down}}}{x_{\text{sample}} / k_{\text{sample}} + R} \right) \quad (3)$$

where x is the thickness and k is the thermal conductivity of a sample and the term R is the heat resistance factor that contributes from parts other than the sample.

It has been confirmed that this heat-transfer system reaches a quasi-steady state in a time as short as 20 s. As a consequence, the term q_{temp} can be replaced by q_{ice} . Now consider measurements of heat fluxes for two same samples with different thicknesses. The heat resistance factor is originated from the aluminum block, the two interfaces and the copper plate, and thus values of R should be the same with each other as long as the samples have the same surface roughness. Finally the thermal conductivity of the sample can be derived by the following equation:

$$\left(\frac{1}{q_{\text{ice1}}} - \frac{1}{q_{\text{ice2}}} \right)^{-1} = k_{\text{sample}} \cdot \frac{T_{\text{up}} - T_{\text{down}}}{x_{\text{sample1}} - x_{\text{sample2}}} \quad (4)$$

Samples and Measurements

To confirm the reliability of this new quasi-state hot plate method and to validate the applicability to mould flux, Ni-based super alloy (Inconel 600), alumina and PTFE (Teflon) with know thermal conductivity values were employed as samples; [9] silica glass sheets were also measured because SiO_2 is a major component of mould flux [4]. Two samples with different thicknesses were prepared: $20 \times 20 \times 0.5 \text{ mm}^3$ and $20 \times 20 \times 0.1 \text{ mm}^3$ for Inconel; $20 \times 20 \times 0.5 \text{ mm}^3$ and $20 \times 20 \times 0.2 \text{ mm}^3$ for alumina and Teflon; $20 \times 20 \times 1.0 \text{ mm}^3$ and $20 \times 20 \times 0.5 \text{ mm}^3$ for silica glass. The surface

roughness was measured by a laser microscope at ten different places for each sample.

In experiment, silver paste or heat conductive grease was applied to both surfaces of a sample to reduce interfacial heat resistance, then the sample was placed upon the copper lid, and finally the heat source heated at 873 K was placed upon the sample at 100 s after the sample setting-up. The liquid height in the pipe was measured by a laser displacement meter where a plastic disc was placed on the water surface to make laser reflection stronger.

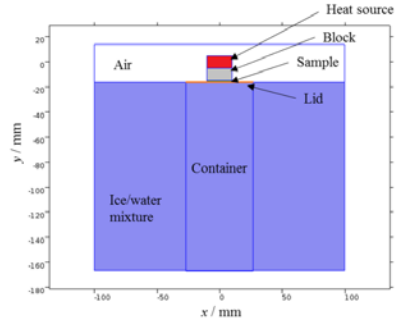
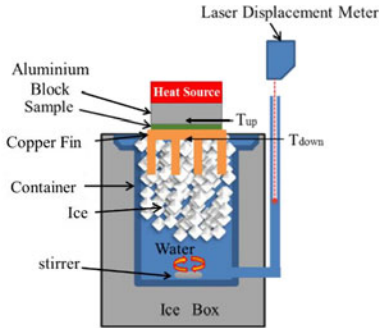


Figure 1. Schematic diagram of measurement apparatus. Figure 2. Conceptual diagram of simulation geometry.

Applicability to Mould Flux Film

In order to examine the applicability of the measurement to mould flux film, a two-dimensional model is used with COMSOL simulation software, as shown in Figure 2. The top rectangle is a heat source $20 \times 10 \text{ mm}^2$, the next rectangle is a block $20 \times 10 \text{ mm}^2$, which is placed between the heat source and the mould flux film to accommodate a thermocouple. The top two rectangles are made of aluminum. The next thin layer is a mould flux film $20 \times 0.5 \text{ mm}^2$, and the assumed composition of the mould flux film is shown in Table 1, which composition is typical of practical mould flux used in the continuous casting of steel. [4] The thermal conductivity value of this mould flux is $1.11 \text{ Wm}^{-1}\text{K}^{-1}$ at 573 K. [4] The bottom rectangle is a container $54 \times 150 \text{ mm}^2$, which is filled with an ice/water mixture. The container is sealed with a lid $54 \times 1 \text{ mm}^2$, which is made of copper. It should be noted that there are no fins and stirrer provided in this simulation system. The thermophysical properties of the materials except mould flux used were obtained from the COMSOL Multiphysics Material Library. [10] The whole system is governed by transient heat transport in each part is described by the following equation.

$$d_z \rho C_p \frac{\partial T}{\partial t} + d_z \rho C_p \mathbf{u} \cdot \nabla T + \nabla \cdot \mathbf{q} = d_z Q + q_0 + d_z Q_{\text{ted}} \quad (5)$$

where d_z , ρ , C_p , T , \mathbf{u} and Q denote the distance in z direction, density, specific heat,

temperature, fluid velocity and heat with respect to each part, respectively. In the simulation system, well-insulation, no fins and stirrer are considered so that convection and radiation are negligible in this system. Therefore, the heat flux q is derived from the following:

$$q = -d_z k \nabla T \quad (6)$$

The initial temperature of the heat source is set at 873.15 K, whereas the other parts are set at 273.15 K; the top boundary is in contact with air at 298.15 K. The boundary condition in the bottom contacted with the ice/water mixture is set at 273.15 K.

Table 1 Chemical compositions of the mould flux (wt.%) [4]

SiO ₂	CaO	Al ₂ O ₃	Na ₂ O	F	C-free
34.4	33.0	6.1	13.4	8.1	2.9

Results and Discussion

Thermal Conductivity of Silica Glass

Figure 3 shows the temperature changes (T_{up} and T_{down}) with time obtained in experiments for silica glass samples. It can be seen that T_{up} values increase significantly and rapidly just after the heat source is placed and then start to decrease after reaching the maxima. The maximum of T_{up} for the thinner sample is higher than that for the thicker sample, which is because the thicker sample has larger thermal resistance. It is also noted that T_{down} is not kept at 273.15 K, which might affect the thermal conductivity value. However, the increase in T_{down} is less than 10 K.

Figure 4 shows the liquid height change with time obtained for the glass samples. It can be seen that the liquid height decreases slowly before the heat source is placed but drastically immediately after the heat source is placed and then slowly again.

Figure 5 compares values of q_{ice} determined from the liquid height decrease *via* Eq. (2) for the glass samples. The values of q_{ice} increase quickly at about 100 s, namely, just after the heat source is placed, and then decrease after reaching the maxima. There can be seen a difference between the values of q_{ice} for the two samples with different thicknesses.

The results by a laser scanning microscope indicate that the same material samples with different thicknesses have almost the same average roughness values. Thus, Figure 6 is obtained on the basis of Eq. (4), showing the relation between the heat flux and the temperature difference for glass, using q_{ice} data having the same value of ($T_{up} - T_{down}$) in Figure 5. It is considered that before the calculation region the sample is just heated up by the heat source and the system has not yet reached a quasi-steady state. On the other hand, after the calculation region the temperature difference is too small for analysis. There can be seen a linear portion in Figure 6, which

corresponds to the data within the calculation region. The slope of the linearity provides the thermal conductivity of glass, and the intercept might be due to the heat loss but is small enough to be neglected. Table 2 gives the experimental values derived for the four kinds of sample with their standard deviations, along with the respective reported values. [9] The experimental scatter of thermal conductivity values is less than 5%, and all the experimental values are in good agreement with the reported values. Consequently, this apparatus can be applied to sheet samples with thermal conductivity ranging between $0.25 \text{ Wm}^{-1}\text{K}^{-1}$ and $30 \text{ Wm}^{-1}\text{K}^{-1}$.

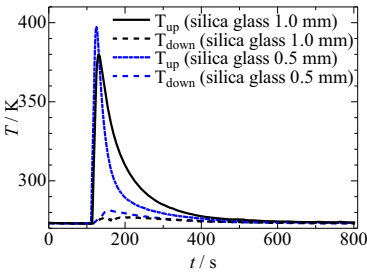


Figure 3. Change with time in temperatures for silica.

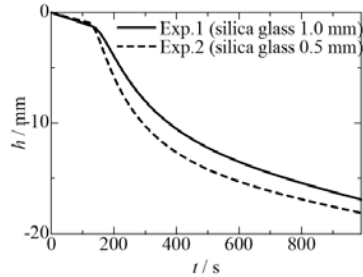


Figure 4. Change with time in liquid height for silica.

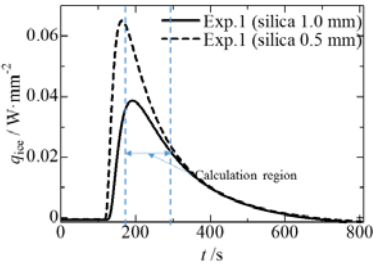


Figure 5. Comparison between heat flux changes with time for silica.

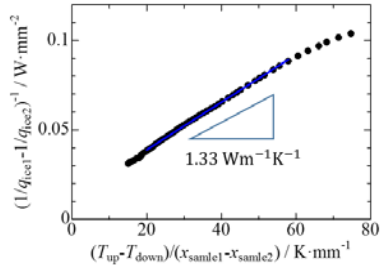


Figure 6. Plots based upon Eq.(5) for silica.

Table 2 Experimental thermal conductivities in comparison with reported data

	Literature Data ($\text{Wm}^{-1}\text{K}^{-1}$) [9]	Experimental Data ($\text{Wm}^{-1}\text{K}^{-1}$)
Inconel	14.8	14.7 ± 0.4
Alumina	23-30	24.8 ± 0.7
Teflon	0.25	0.313 ± 0.04
Silica	1.38	1.34 ± 0.03

Applicability of the present method to thermal conductivity measurements of oxide scales

Figure 7 shows the heat flux changes in the block and the mixture (q_{block} and q_{ice}) with time,

where the negative sign means that heat flows downwards. The numerical results predict that heat is mainly transferred from the heat source to the ice/water mixture across the sample and q_{block} equals q_{ice} in 20 s, indicating that the system approaches a quasi-steady state in 20 s. Figure 8 shows temperatures of T_{up} and T_{down} as a function of time. It can be seen that T_{up} and T_{down} increase first and reach the maxima and then start to decrease. These tendencies are the same as obtained in the present work. However, it should be noted that the maximum of T_{up} is 550 K when the calculation time region starts, and the steepest temperature gradient is only 160 Kmm^{-1} . A heat source with higher temperature should be applied if the temperature gradient close to that in the actual mould flux is required. It should also be noted that T_{down} increases by about 140 K, which is greater than the increase of T_{down} obtained for the present work. Thus, another key factor to apply the present method to mould flux at higher temperatures is to control the temperature of the ice/water mixture as close to 273.15 K as possible by optimizing the fin design. In addition, as mentioned above, the simulation system provides no fins, the use of which would be of help to improve this situation.

According to the above, it has been confirmed that the present method can be applied to mould flux film. However, there is a key factor to prepare mould flux films with different thicknesses in the range 0.5 – 1.0 mm and with the same surface roughness; and the measurement system should be improved in the following aspects: (i) the increase in the initial temperature of heat source, (ii) the use of high heat capacity material as heat source and (iii) the increase in the mass of heat source.

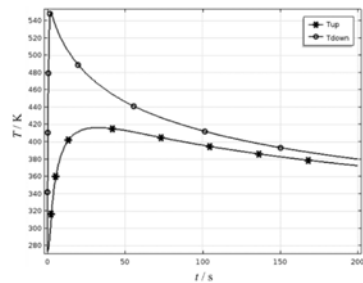
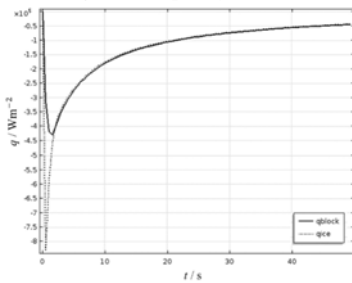


Figure 7. Change with time in heat flux in 0 ~50 s. Figure 8 Change with time in temperatures of T_{up} and T_{down}

Conclusions

A new quasi-steady state hot plate method has been developed and the procedure to derive the thermal conductivity has also been established for future measurements of apparent thermal conductivities of mould flux film.

The method proposed has been applied to sheet samples of Inconel, alumina, Teflon, and silica glass, and the thermal conductivity values have been obtained as $14.7 \pm 0.4 \text{ Wm}^{-1}\text{K}^{-1}$ for Inconel

at 281 K – 287 K, $24.8 \pm 0.7 \text{ Wm}^{-1}\text{K}^{-1}$ for alumina at 281 K – 287 K, $0.313 \pm 0.004 \text{ Wm}^{-1}\text{K}^{-1}$ for Teflon at 286 K - 412 K, and $1.34 \pm 0.03 \text{ Wm}^{-1}\text{K}^{-1}$ for glass at 293 K – 303 K under a temperature gradient of 20 Kmm^{-1} , which results are in good agreement with the respective reported values. Simulation study has also been made to discuss the applicability of the present method to mould flux film at higher temperature under a steeper temperature gradient and concludes that the method would be applicable to the mould flux.

ACKNOWLEDGEMENTS

Parts of this paper have been reprinted from the article ‘*ISIJ Int.*, **56** (2016), p366-p375’, by permission of the Iron and Steel Institute of Japan.

REFERENCES

1. K. Nakai, T. Sakasita, M. Hashio, M. Kawasaki, K. Nakajima and Y. Sugitani, “Effect of Mild Cooling in Mould upon Solidified Sheel Formation of Continuously Cast Slab,” *Tetsu-to-Hagane*, **73** (1987), 498.
2. K. Kinoshita, H. Kitaoka and T. Emi, “Influence of Casting Conditions on the Solidificaion of Steel Melt in Continuous Casting Mold,” *Tetsu-to-Hagane*, **67** (1981), 93.
3. H. Nakada, M. Susa, Y. Seko, M. Hayashi and K. Nagata, “Mechanism of Heat Transfer Reduction by Crystallization of Mold Flux for Continuous Casting,” *ISIJ Int.*, **48** (2008), 446.
4. A. Yamauchi, K. Sorimachi, T. Sakuraya and T. Fujii, “Heat Transfer between Mold and Strand through Mold Flux Film in Continuous Casting of Steel,” *ISIJ Int.*, **33** (1993), 140.
5. S. Ozawa, M. Susa, T. Goto, R. Endo and K. C. Mills, “Lattice and Radiation Conductivities for Mould Fluxes From the Perspective of Degree of Crystallinity,” *ISIJ Int.*, **46** (2006), 413.
6. R. Bunsen, “Calorimetric Researches,” *Phil. Mag.*, **41** (1871), 161.
7. R. S. Jessup, “A New Bunsen-Type Calorimeter,” *J.Res. Nat. Bur. Stand.*, **55** (1955), 317.
8. M. Li, R. Endo, L. Wang, L. Li and M. Susa, “A New Method for Apparent Thermal Conductivity Determination for Sheet Samples Utilizing Principle of Bunsen Ice Calorimeter,” *ISIJ Int.*, **56** (2016), 366.
9. Japan Society of Thermophysical Properties: *Thermophysical Properties Handbook* (Tokyo, NY: Yokendo, 2008), 210.
10. COMSOL AB: *COMSOL Multiphysics Modelling Guide Version 3.5a* (Stockholm, NY: COMSOL AB, 2007).

Controlling Heat Transfer through Mold Flux Film by Scattering Effects

Dae-Woo Yoon¹, Jung-Wook Cho², Seon-Hyo Kim¹

¹POSTECH(Department of Materials Science and Engineering)
77 Cheongam-Ro; Pohang, Gyeonbuk, 37673, Republic of Korea

²GIFT(Graduate Institute of Ferrous Technology)
77 Cheongam-Ro; Pohang, Gyeonbuk, 37673, Republic of Korea

Keywords: Extinction coefficient, Infrared emitter technique, Radiative heat transfer, Scattering

Abstract

Regulating thermal behavior between the solidifying shell and a mold is one of primary roles of the mold flux film during continuous casting of steel. This is particularly important as excessive heat flux through slag film will induce surface defects on cast steel. This study focuses on controlling radiative heat transfer through liquid slag film by utilizing finely dispersed metallic particles in commercial CaO-SiO₂-CaF₂-Na₂O based mold flux system. In order to investigate the scattering effect on heat transfer during industrial casting processes, the extinction coefficient of various mold fluxes was measured using an FT-IR and a UV-visible spectrometer. Also, series of IET (Infrared Emitter Technique) tests were conducted in order to simulate mold heat transfer during commercial casting processes. Finally, it is found that the Mie scattering effect due to metallic particles will reduce the overall heat flux density through mold slag film by 10% or more.

Introduction

Mold flux acts as a lubricant after infiltrating into the gap between steel shell and copper mold to prevent the sticking of solidifying shell on continuous casting mold. In the casting mold wall after infiltration, mold flux exists as the slag film with two layers: molten glassy layer next to steel shell, and solid layer of partially crystallized glass adjacent to copper mold. Each flux film layer affects heat transfer through mold flux film by providing thermal resistances which consist of both the conduction and radiation.¹ Many previous studies suggested that mold heat transfer during continuous casting process will be governed by radiative thermal resistance across molten glassy layer, thermal conduction through solid layer.^{2,3}, and air gap at the interface between copper mold and solid flux film layer.^{4,5} Among them, radiative heat transfer is supposed to be dominant especially at initial stage of solidification near meniscus, where the surface defects such as longitudinal crack and break-out can be easily occurred due to excessive heat flux from molten steel to mold. Therefore, it is highly necessary to suppress the excessive thermal radiation by controlling the optical properties of molten glassy film layer to achieve the sound surface quality of cast steel products.

Several attempts have been made to measure the extinction coefficient which governs radiative heat transfer through mold flux film. For example, it is reported that extinction coefficient is markedly dependent on the contents of transition metal oxide in slag system.⁶ However, there has

not been systematic investigation on thermal radiative heat transfer considering both the absorption and scattering behavior of molten glassy flux film. In this study, for the comprehensive understanding of thermal radiation through molten glassy film layer, absorption and scattering coefficients have been investigated using an FT-IR and a UV-visible spectroscopy. Especially, contribution of metallic particles on scattering behavior was discussed based on Mie scattering theory. In addition, for evaluation of the overall heat transfer through mold flux film, an infrared emitter has been employed in this research. By infrared emitter technique, the mold fluxes with different extinction coefficient have been tested in order to clarify the effect of controlling thermal radiation on overall heat flux density during commercial continuous casting process.

Experimental

1. Sample preparation

Boron oxide containing mold fluxes were chosen for investigation of optical properties as shown in Table 1. Each mold flux was melted in the graphite crucible using a muffle furnace at 1653K, and then quenched in a copper mold, annealed at 700K for 1 hour to relieve thermal stress. . These glassy specimens were slice and polished into a thin disk type of 13mm in diameter and 10-20mm in thickness. The chemical composition of mold fluxes are shown in Table I.

Table I. Chemical composition of mold fluxes (wt. %)

Sample	SiO ₂	CaO	MgO	Al ₂ O ₃	Fe ₂ O ₃	Na ₂ O	F	B ₂ O ₃	Basicity
B6	37.9	36.4	0.9	4.5	0.3	6.8	6.7	6.5	0.96
B9	37.0	36.1	1.0	4.3	0.4	6.3	5.6	9.3	0.98
B11	35.6	35.8	0.9	4.2	0.3	6.0	5.8	11.4	1.0
B15	34.3	34.0	1.0	4.0	0.3	5.7	5.5	15.2	1.0
B28	30.1	30.2	1.0	3.2	0.2	5.2	2.0	28.1	1.0

2. Determining extinction coefficient

Extinction coefficient, E , of mold fluxes was investigated using Fourier transformation infrared spectroscopy and ultra violet/visible spectrometer in the range of 0.5-5 μ m. As the radiation energy passes through the specimen, its intensity is decreased by absorption or scattering phenomenon which can be estimated by extinction coefficients. As the reflectivity of glassy film of mold flux is known to be only 1-3 percent, ¹⁾ the dissipation of thermal radiation through a glass medium can be expressed by simple Lambert-Beer's law, equation (1).

$$\frac{I_T}{I_0} = \exp\{-(\alpha + s)l\} \quad (1)$$

where I_0 is the incident beam of light, I_T is transmitted infrared intensity, α is absorption coefficient, s is scattering coefficient, and l is the thickness of the specimen. The extinction coefficient is simply the sum of absorption and scattering coefficients..

3. Measuring particels on matrix

In order to investigate the effects of particle properties such as constituent, morphology and size

on extinction coefficients of mold fluxes, an automatic scanning electron microscopy has been employed. By SEM technique, each sample were analyzed in the area of $25.0 \times 10^{-6} \text{ m}^2$ and particles were detected on back scatter electron mode image using automatic threshold of the image grey level. All of sample matrix were quantified for Si, Ca, Na, Al, Mg, Fe, O with recording during measurements.

4. Infrared emitter technique

Infrared emitter technique (IET) has been applied to measure thermal properties of mold fluxes under controlled conditions. The experiment was accomplished in following step: First, the halogen lamp of IET irradiates the surface of copper mold which is covered by solidified disk type(diameter:40mm, thickness:5mm) of glassy mold flux; after that heat flux across flux film was measured by the calculating temperature gradient of different position in subsurface copper mold. Simultaneously, video recording has been carried out to monitor the morphological change of mold fluxes by melting, solidification, and crystallization.

Results and Discussion

1. Thermal absorption behavior

According to the investigation by Kusabiraki and Shiraishi et al.^{7,8}, the extinction coefficient of solidified glassy mold fluxes will not yield significant error of demonstrate the radiative heat transfer across molten mold flux in the mold. Thus, in this study, extinction coefficients of mold fluxes have been measured at room temperature using solid glassy specimen. Extinction coefficients of commercial glassy mold fluxes in near infrared region are reported to be below 1000 m^{-1} .⁹ However, two mold fluxes with 6.5% and 9.3% of B_2O_3 show distinctly larger extinction coefficients than others and reported commercial fluxes as shown in figure 1. The sharp peak is appeared in the $3.8\text{-}4.1 \mu\text{m}$ due to the ring stretch of cyclic meta-borate ion.¹⁰ The average extinction coefficient of borate contained mold fluxes increase until nearly 10wt. % of borate addition, and then decreases with more than 10 wt. % of boron oxide addition. This complicated behavior of extinction would arise from the scattering effects due to particles on sample matrix, which will be discussed in following section.

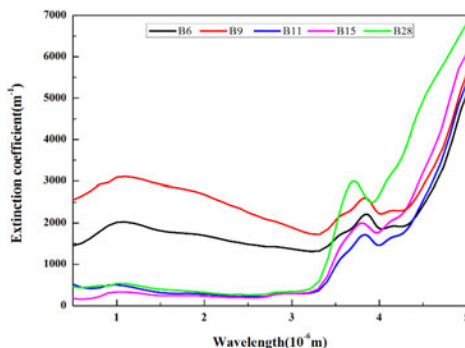


Figure 1. Extinction coefficient of B_2O_3 contained mold flux as function of wavelength.

Also, this drastic change of extinction coefficient according to amounts of boron oxide could explain with variation of particle density and molar structure by each borate glassy sample.

2. Scattering phenomenon for mold fluxes

According to investigation of SEM-EDS analysis, spherical particles were detected and identified as metallic iron by reduction reaction of ferric oxide with carbon crucible during melting process. It is found that both the average particle size (B6: 0.769, B9: 0.779, B11:0.344, B28: 0.371/ μm) and number of particle (B6: 336, B9: 427, B11: 35, B28: 89) are closely concerned with averaged extinction coefficients (B6: 1,841, B9: 2,695, B11:861, B28:1,127/ m^{-1}) of glassy fluxes. These results show that the number of spherical metallic particles are intensively related to extinction coefficient by scattering effects. In this respect, it is necessary to extract the contribution of scattering effects on extinction coefficients. B3 flux which shows the minimum number of metallic particle has been chosen for reference. It is assumed that scattering behavior through reference flux can be ignored. Then, the scattering coefficient of other fluxes can be derived by the difference of extinction coefficient with reference flux, as shown in figure 2.

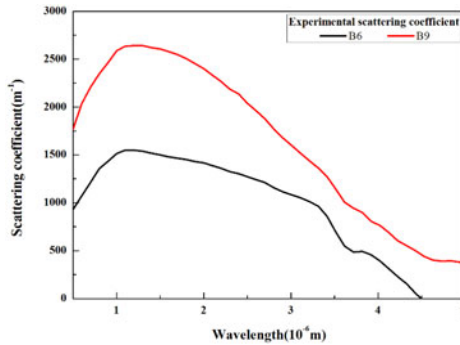


Figure 2. Experimental scattering coefficient of B6 and B9 fluxes.

It can be seen that mold fluxes which contain boron oxide below 10 wt. % have distinct scattering behavior due to many tiny metallic particles in the glassy matrix. In order to figure out this phenomenon, it is essential to apply the scattering effect on the basis of scattering theory. For this reason, Mie theory is chosen for clarifying scattering effect in this study. This theory could well explain the scattering behavior when the particle size is similar to the incident light wavelength.¹¹ In Mie theory, the scattering coefficient could confirmed with size parameter(x) and relative refractive index of medium and spherical particle.

$$x = \frac{2\pi r n_{med}}{\lambda} \quad (2)$$

where r is the radius of particle, n_{med} is refractivity of medium and λ is the incident beam wavelength. And, the scattering coefficient (μ) is defined as

$$\mu_s = \rho_s \cdot \sigma_s \quad (3)$$

where ρ_s is number density of particles, σ_s is scattering cross section. Numerical values of σ_s were calculated using the subroutine $BHME$.¹² This code and comparable ones are readily available

online.¹³ In this study, scattering coefficients of boron oxide containing mold fluxes were calculated by above procedure with compensating size parameters. Previous studies showed that larger asymmetry parameter will bring the lack of enhancement of backscattering behavior, which is not suitable for this study but only for geometric optics.^{14,15} Therefore, theoretical scattering coefficients is calculated by controlled range of size parameter which intentionally related to wavelength and particle size as shown in figure 3. However, there are slightly difference between experimental and theoretical data. It is assumed that particle number distribution of glassy flux matrix is incorrect because the metallic particles would be detached from glassy matrix during etching. Adding to this, automatic SEM technique has some detective limitation to identify the fine or dark. Based on Mie scattering theory, the origin of increased extinction coefficient can be logically explained as dispersed metallic particles in glassy matrix.

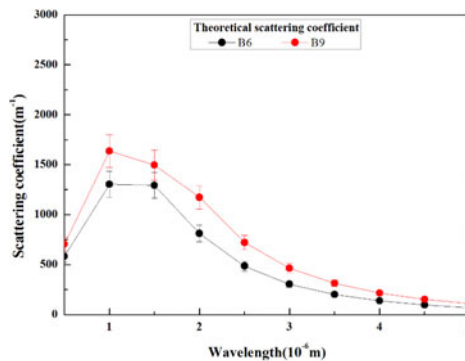


Figure 3. Scattering coefficients calculated by Mie theory as function of wavelength.

3. Demonstrating of overall heat transfer through mold flux film by using IET

During the tests using an infrared emitter technique, the mold flux film would be exposed to the thermal circumstance close to the industrial continuous casting mold.

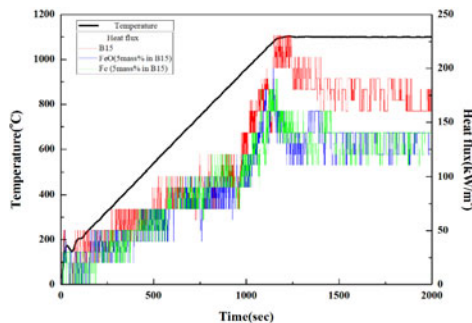


Figure 4. The measured heat flux history for different mold fluxes .

In order to confirm the scattering effect without changing absorption behaviors on total heat flux through mold slag film, 5 wt. % of metallic iron particles were added in mold flux with 15 wt. % of boron oxide. Also, iron oxide was put into slag for clarifying the extinction coefficient which is comprised of absorption and scattering coefficient. As can be seen in figure 4, it could be observed that the measured average heat flux for each mold flux at steady state(1500-2000second) are around 174(flux-B15), 134(B15 with 5wt. % of FeO), and 130(B15 with 5wt. % of metallic Fe) kW/m², respectively. The difference of heat transfer rate arises from scattering effect of iron particles by addition of FeO and metallic iron in the sample. It is worthy to note that the increase of scattering coefficients will not bring any fatal effects on friction in a casting mold while any other countermeasures to enhance the degree of crystallinity will significantly disturb the lubrication. Therefore, it is highly desirable to modify mold flux system by using scattering factors has been enhanced to reduce heat flux from steel shell to copper mold.

Conclusion

Comprehensive understanding of heat transfer through mold flux film is attained by considering the thermal radiative absorption into glass phase for commercial CaO-SiO₂-Na₂O based mold fluxes.

- (1) Metallic particles in mold flux increase extinction coefficient which affect radiative thermal conductivity and shows a marked increase in the radiative heat controlling region from 1 to 5 μm .
- (2) Scattering effects could be useful to control heat transfer rate by growth of extinction coefficient due to reduction reaction of iron oxide with carbon in mold flux system.
- (3) Selection of proper flux component for casting steel should be intensively dependent on thermal performance as slow cooling which can be effectively achieved by scattering coefficient in mold flux without bad lubrication.

References

1. J.W. Cho, T. Emi, H. Shibata, M. Suzuki, "Radiative heat transfer through mold flux film during initial solidification in continuous casting of steel," *ISIJ International*, 38 (1998), 268.
2. H. Shibata, K. Kondo, M. Suzuki, T. Emi, "Thermal resistance between solidifying steel shell and continuous casting mold with intervening flux film," *ISIJ International*, 36 (1996), 179.
3. K. Watanabe, M. Suzuki, K. Murakami, H. Kondo, A. Miyamoto, T. Shiomi, "The effect of crystallization of mold powder on the heat transfer in continuous casting mold," *Tetsu-to-Hagane*, 83 (1997), 115.
4. S. Ohmiya, K.H. Tacke, K. Schwerdtfeger, "Heat transfer through layers of casting fluxes," *Ironmaking Steelmaking*, 10 (1983), 24.
5. J.W. Cho, T. Emi, H. Shibata, M. Suzuki, "Thermal resistance at the interface between mold flux film and mold for continuous casting of steels," *ISIJ International*, 38 (1998), 440.
6. M. Susa, K. Nagata, K.C. Mills, "Absorption coefficients and refractive indices of synthetic glassy slags containing transition metal oxides," *Ironmaking Steelmaking*, 20 (1993), 372.

7. K. Kusabiraki, Y. Shiraishi, "Infrared-emission spectra of molten alkaline metal silicates," *Jap. Inst. Met.* 45 (1981), 250.
8. K. Kusabiraki and Y. Shiraishi, "On the Infrared-emission spectra of the molten Na₂O-Al₂O₃-SiO₂ system," *Jpn. Inst. Met.* 45 (1981), 888.
9. D.W. Yoon, J.W. Cho, S.H. Kim, "Assessment of heat transfer through mold slag film considering radiative absorption behavior of mold fluxes," *Metals and Materials international*, 21 (2015), 580-587.
10. I.C. Hisatsune and N.H. Suarez, "Infrared spectra of metaborate monomer and trimer ions," *Inorganic Chemistry* 3 (1964), 171.
11. G. Mie, "Beiträge zur Optik trüber Medien, speziell kolloidaler Metallösungen," *Ann. Phys.*, 25 (1908), 377-445.
12. Craig F. Bohren and Donald R. Huffman, *Absorption and Scattering of Light by Small Particles* (New York, Wiley, 1983), 477-482.
13. For example, <http://omlc.ogi.edu/software/mie/> has links to several sites, including the URL, <http://omlc.ogi.edu/calc/mie-calc.html>, where calculations can be done interactively online
14. S. Asano, M. Sato, "Light scattering by randomly oriented spheroidal particles," *Appl. Opt.* 19 (1980), 962-974.
15. M.I. Cabrera, O.M. Alfano, A.E. Cassano, "Absorption and scattering coefficients of titanium dioxide particulate suspensions in water," *J. Phys. Chem.* 100 (1996), 20043-20050.

DIFFUSION COEFFICIENTS AND STRUCTURAL PARAMETERS OF MOLTEN SLAGS

Samane Maroufi¹, Shahriar Amini², Sharif Jahanshahi¹, and Oleg Ostrovski¹

¹ School of Materials Science and Engineering, the University of New South Wales, Sydney, NSW 2052, Australia

² Flow Technology Department, SINTEF Materials and Chemistry, Norway

Abstract

This paper presents the results of two experimental studies on diffusion of SiO₂ in “silicomanganese” (SiO₂-MnO-CaO-Al₂O₃-MgO) slag and CaO in calcium aluminosilicate slag. The diffusivity of SiO₂ was measured in the temperature range of 1400-1550 °C; while the diffusivity of CaO was determined at 1430-1600°C. The effects of additives on the chemical diffusivities of SiO₂ and CaO were also examined. Addition of CaO and MnO to the silicomanganese slag increased silica diffusivity, while addition of SiO₂ and Al₂O₃ slowed it down. Addition of TiO₂ and MnO_x to the aluminosilicate slag increased the diffusivity of CaO, while the addition of SiO₂ had a negative effect on the diffusivity of CaO. Analysis of diffusivity in relation to the structure of silicate melts demonstrated a good correlation between diffusion coefficients of SiO₂ and CaO and NBO/T (non-bridging oxygen per tetrahedrally coordinated atom).

1 Introduction

Many pyrometallurgical processes include dissolution of solid oxides (e.g. fluxes and refractories) into molten slag, which could affect the metallurgical performance rate of the whole process. Silicomanganese (SiMn) alloy production and secondary steel making are two examples of pyrometallurgical processes in which oxides dissolution into molten slag plays a significant role.

In the production of SiMn alloy, quartz is dissolved into the molten slag, from which silica is reduced to the metallic phase. The presence of undissolved lumpy silica in the reaction zone of the furnace was observed, while the concentration of silica in SiMn slag (35-45 wt. %) was found to be much lower than the silica-saturation value [1]. This is an indication that dissolution of silica into molten slag is slow and can contribute to the process rate control.

In steelmaking, during the production of aluminium killed steels, the removal of residual alumina and silicate inclusions in liquid steel is carried out using lime based (calcium alumina-silicate) slag. Rapid and complete dissolution of lime into such slag is of considerable importance. Different fluxes are added in order to promote dissolution of lime into the slag. The addition of fluxes and additives to the slag results in changing its structure and accordingly diffusion phenomenon.

The diffusion of silicon and calcium oxides in different melts has been investigated by a number of researchers [2-8]. Dolan and Johnston [2] studied diffusion behavior of Mn, Fe, Ca and Si in molten silicate slag (Al₂O₃, SiO₂, CaO) over the temperature range of 1400-1600°C using the

semi-infinite capillary method. They found a relationship between “molecular structure” of melts and diffusivity. A decrease in the average size of the silicate anions as a result of depolymerisation resulted in the increasing diffusivity of all species. Feichtinger et al. [4] investigated the dissolution behaviour of well-shaped spherical SiO₂ particles in a number of CaO-Al₂O₃-SiO₂ slags at 1450°C using high-temperature confocal scanning laser microscopy and thermodynamic/kinetic analyses. The rate of silica dissolution was determined from the measurements of the change in the diameter of the spherical SiO₂ particles. Their results showed that the rate of dissolution of silica decreased with increasing slag viscosity.

Keller and Schwerdtfeger [5] also measured the tracer diffusivity of Si in CaO-SiO₂ melts at 1600°C using the capillary technique. In their work, Si isotope was produced by neutron bombardment in a nuclear reactor. According to their results, the diffusivity of Si decreased with increasing silica content.

Dissolution of lime over the temperature range 1450-1600°C in calcium silicate based slags was measured by Matsushima et al.[6] using a rotating disk technique. In their experiments, slags contained about 20 wt % Al₂O₃ or FeO_x and CaO/SiO₂ ratio was constant at one. According to their experimental data in slags containing FeO_x the dissolution rate was several times higher. The influence of different additives (CaF₂, CaCl₂, Al₂O₃, and B₂O₃) on the dissolution of lime in calcium-iron silicate slags (40 wt. % FeO_x with CaO/SiO₂ ratio of 1) at temperatures in the range of 1300°C-1400°C was examined by Hamano et al.[7]. CaO diffusivity in iron-silicate slag was examined by Hara et al. [8] over a temperature range of 1270-1450°C. They showed that self-diffusivity of Ca45 increased with addition of CaO.

The present work was aimed at extending the current understanding of the relationship between the structure of SiMn industrial slag and calcium aluminosilicate slag and diffusion of silica and lime in such slags. The diffusion coefficient of silica in silicomanganese slag under argon and the diffusivity of CaO in calcium aluminosilicate in air were measured using a rotating rod technique. The influence of different additives on the diffusivity was also investigated. Experimental data on diffusivity were analysed in relation to the structure of the oxide melts.

2 Experimental

The dissolution rate and diffusivity of silica were measured in the industrial SiMn slag supplied by Tasmanian Electro Metallurgical Company (TEMCO). The slag was crushed using ring mill and then kept in oven at 150°C overnight to remove moisture. The dissolution rate and diffusivity of CaO were measured in the synthetic steel ladle (calcium aluminosilicate) slag which was prepared from fine reagent grade chemicals of high purity and dried at 120°C for at least 12 hours; the slag composition was close to the composition of the steelmaking ladle slag. The calcium aluminosilicate slag was made in a 15 KW, 450 KHz induction furnace at 1500°C in air. The industrial SiMn slag and synthetic calcium aluminosilicate slag were analyzed by XRF analysis; the results are shown in **Table 1**.

Table 1: Chemical composition of industrial SiMn slag and synthetic calcium aluminosilicate slag

Component, wt. %	K ₂ O	MgO	MnO	CaO	Al ₂ O ₃	SiO ₂	Fe ₂ O ₃
SiMn slag	2.7	5.5	15.3	19.2	12.4	44.9	-
Calcium aluminosilicate slag	0.01	0.04	-	48.8	42.2	7.8	0.2

In the measurement of the dissolution rate of SiO₂ in SiMn slag, fused quartz rods (20 mm diameter and 200 mm long, tolerances of ±1.5%), with a purity of >99% supplied by Technical Glass Products, Inc. USA were used as specimens in the rotation experiments. About 130 g of crushed slag was contained in a Mo crucible (30 mm OD, 60 mm high).

A lime crucible (20 mm diameter and 30 mm height) was used as the rotating samples in measurements of the CaO dissolution rate in calcium aluminosilicate melt. About 60 g of slag was contained in a Pt-10% Rh crucible (40 mm diameter and 44 mm height). Crucibles containing samples were placed on a platform on an alumina tube. Temperature was measured by a type-R thermocouple. Experimental set-up and the procedure followed has been presented elsewhere [9,10].

3 Experimental results and discussions

3.1 Dissolution rate and diffusivity

To investigate the effects of rotation speeds of samples on their dissolution rates, experiments were carried out with rotation speeds ranging from 40 to 100 revolutions per minute (RPM) in the measurements of the dissolution rate of silica and 30-150 RPM in the measurements of the dissolution rate of CaO. The following equation was applied to calculate the dissolution rate of quartz and CaO in molten slag [10]:

$$rate = \frac{slope * W}{100 * A * 60} \quad (1)$$

where *slope* (wt. %./min) is the slope of silica or CaO concentration curve versus reaction time, which was obtained by fitting a straight line through the experimental concentration data. *W* (g) is the mass of slag and *A* (cm²) is the total area of silica rod and lime crucible in contact with molten slag. Both silica rod and lime crucible were considered as consisting of a disk at the bottom and cylindrical wall. The cylinder height was assumed to be the depth of immersion of the rod into molten slag. Consequently total area was assumed to be the area of disk and cylinder in contact with slag. The diffusivities of silica in SiMn slag and CaO in calcium aluminosilicate slag were calculated from experimental data on the dissolution rate.

Levich-Cochran [11] and Kosaka et al. [12] correlations were used to describe mass transfer from disk and cylinder sides of specimen, respectively. The following equation was derived for the total mass transfer based on the mass flux from disk and cylinder sides of quartz rod and lime crucible:

$$k_{total} = \frac{r}{r + 2h} 0.621D^{2/3} \omega^{1/2} \left(\frac{\rho}{\mu}\right)^{1/6} + \frac{2h}{r + 2h} 0.055D^{2/3} r^{1/2} \omega^{3/4} \left(\frac{\rho}{\mu}\right)^{5/12} \quad (2)$$

where ω (rad/s) is angular velocity of the disk ($V = \omega.r$), *r* is the radius of the silica rod and lime crucible and *h* is the length of specimen immersed in the slag; ρ , μ and *D* are slag density, viscosity and diffusivity. The total mass transfer coefficient was calculated using the experimental data on the rate of dissolution, according to the following equation:

$$k_{total} = \frac{rate}{(C_s - C_b) \cdot \rho_{slag}} \quad (3)$$

where; C_s and C_b are concentrations of $\text{SiO}_2 / \text{CaO}$ (wt. %) at specimen-slag interface and in bulk slag, respectively. Slag density ρ_{slag} was estimated by a model proposed by Mills and Keene [13]. Chemical diffusivity was calculated using Equations (2) and (3).

In the case in which the rate of dissolution is controlled by mass transfer in molten slag, the dissolution rate of disk is expected to increase linearly with the square root of rotation speed [14] and dissolution rate of cylinder is proportional to the power of 3/4 of rotation speed [15]. **Figure 1** shows CaO and SiO_2 dissolution rates plotted vs the square root and the power of 3/4 of rotation speed at the temperatures of 1430°C and 1600°C for CaO and 1500°C for SiO_2 . This implies that under experimental conditions in this work, mass transfer in the liquid phase controls the dissolution rates of silica and CaO.

It is worth noting that due to the difference in physical properties of SiMn and calcium aluminosilicate slags (viscosity in particular), different ranges of the rotation speeds and temperatures were selected for each case. The effects of temperature and slag chemical composition were studied at the rotation speed of 60 and 90 RPM for the SiO_2 and CaO dissolution, respectively. The uncertainties in estimation of the diffusivity of silica and CaO were about ± 36 and 33%, respectively; which were deduced from uncertainties in calculation of the slope of SiO_2/CaO concentration data, weight of molten slag, contact area between the specimen and slag and dissolution rate data.

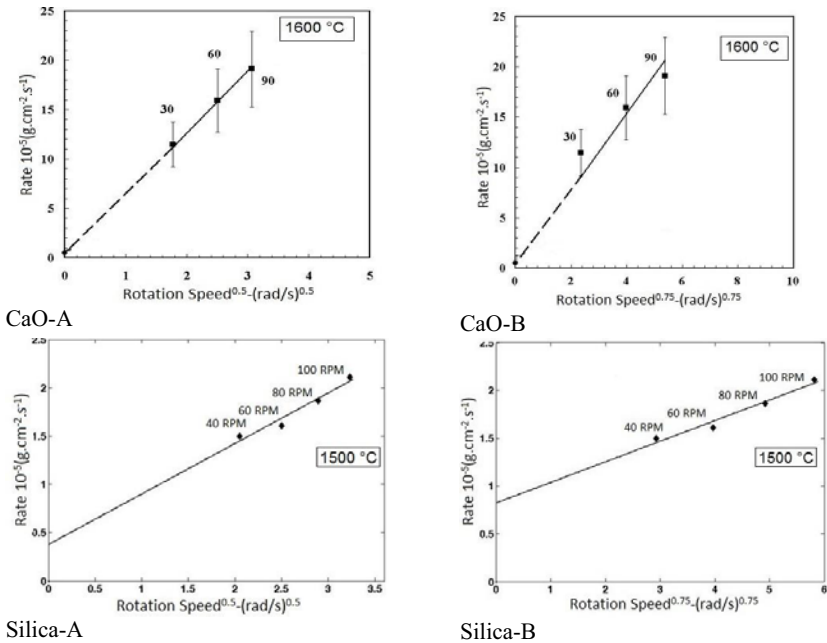


Figure 1. Dependence of the dissolution rate of CaO and SiO_2 in calcium aluminosilicate and SiMn slags on the rotation speed; A: in the power 0.5, and B: in the power 0.75.

In the study of the influence of slag chemical composition on the dissolution rate and diffusivity of SiO₂ and CaO, different oxides were added to the master slags. The dissolution rates and diffusivities of SiO₂ and CaO over the temperature ranges of 1430-1600°C for CaO and 1450-1550°C for SiO₂ are listed in **Table 2**. The addition of MnO, and TiO₂ to calcium aluminosilicate slag significantly increased the effective diffusivity of CaO, while the addition of SiO₂ slowed down the diffusivity of CaO.

The SiO₂ dissolution rate and diffusivity increased with increasing temperature, and additions of MnO and CaO. Addition of Al₂O₃ and SiO₂ decreased the dissolution rate and diffusivity of silica.

Table 2 Dissolution rate and diffusivity of CaO in the calcium aluminosilicate slag and SiO₂ in silicomanganese slag.

CaO

Slag	Temperature °C	Dissolution rate (gr.cm ⁻² .s ⁻¹)	Diffusivity (cm ² /s)
Master slag	1430	5.03×10^{-5}	9.20×10^{-6}
	1500	6.37×10^{-5}	1.32×10^{-5}
	1550	8.83×10^{-5}	1.9×10^{-5}
	1600	1.27×10^{-4}	3.07×10^{-5}
Master slag+5% MnO _x	1430	9.55×10^{-5}	3.54×10^{-5}
	1500	1.40×10^{-4}	4.28×10^{-5}
	1550	1.66×10^{-4}	5.01×10^{-5}
	1600	2.17×10^{-4}	6.82×10^{-5}
Master slag+5% TiO ₂	1430	7.96×10^{-5}	1.38×10^{-5}
	1500	1.21×10^{-4}	2.37×10^{-5}
	1550	1.34×10^{-4}	2.49×10^{-5}
Master slag+5% SiO ₂	1500	6.61×10^{-5}	8.77×10^{-6}
	1600	1.01×10^{-4}	1.51×10^{-5}

SiO₂

Slag	Temperature °C	Dissolution rate (gr.cm ⁻² .s ⁻¹)	Diffusivity (cm ² /s)
Master slag	1450	1.1×10^{-5}	8.2×10^{-7}
	1500	1.6×10^{-5}	8.4×10^{-7}
	1550	2.5×10^{-5}	1.2×10^{-6}
Master slag+10% Al ₂ O ₃	1450	4.4×10^{-6}	9.4×10^{-8}
	1500	8.1×10^{-6}	1.9×10^{-7}
Master slag+10% CaO	1550	1.8×10^{-5}	4.9×10^{-7}
	1450	2.2×10^{-5}	8.4×10^{-7}
	1500	2.9×10^{-5}	1.1×10^{-6}
Master slag+10% SiO ₂	1550	4.3×10^{-5}	1.3×10^{-6}
	1450	2.7×10^{-6}	1.5×10^{-7}
	1500	5.9×10^{-6}	3.9×10^{-7}
Master slag+10% MnO	1550	1.2×10^{-5}	6.4×10^{-7}
	1450	1.8×10^{-5}	7.3×10^{-7}
	1500	2.4×10^{-5}	9.5×10^{-7}
	1550	3.3×10^{-5}	1.3×10^{-6}

Diffusivity of SiO₂ in slag containing 54.6 wt. % SiO₂, 34.1 wt. % CaO, and 10.6 wt. % Al₂O₃ measured by Feichtinger et al. [4] was found to have a magnitude of 10⁻⁷ cm²/s, which is in a good agreement with the present study on diffusivity of SiO₂ in the industrial SiMn slag with addition of 10 wt. % CaO at 1450°C. The diffusivity of SiO₂ in the SiMn slag with addition of CaO at 1450 °C is in a good accord with data [16] on self-diffusivity of Si in slag containing 21 wt. % Al₂O₃-39% CaO-40% SiO₂ at 1430°C. It should be mentioned that self-diffusivity is a measure of random movement of atoms in the melt while the diffusion of SiO₂ in the present work is the chemical diffusivity. Therefore chemical diffusivity is expected to be higher than self-diffusivity. However, slag in the measurements of self-diffusivity of Si contained higher CaO content.

Keller et al. [5], in the study of the self-diffusivity of Ca45 in the CaO-SiO₂ melts in the temperature range of 1500 to 1700°C showed that diffusivity of calcium was decreased by the increasing silica content of the slag from 0.448 to 0.634 (mole fraction). This is in an agreement

with results obtained in the present work. Self-diffusivity of Ca45 determined in [5] is lower compared to the present results. This difference could be explained by substantial difference in the silica content of slags, and methods of diffusivity measurements. Slag examined in [5] had higher silica content than in the present work; it should be also noted that self diffusivity is lower than chemical diffusivity.

3.2 Slag structure and diffusivity

Silicate melts are characterised by large silicate anions with their size increasing with increasing silica content (slag polymerization). Silicate anions form a network structure in which nearly all oxygen atoms act as bridges between two silicon atoms [17]. However, addition of basic oxides such as CaO, MnO and MgO to silicate melts breaks down the silicate network with formation of non-bridging oxygen ions. Such oxygen ions are bonded to both network modifying metal cations (Ca^{2+} , Mn^{2+}) and tetrahedrally coordinated cations (Si^{+4}) in the silicate network [18].

The effect of Al_2O_3 on physical and transport properties of the slag at a given silica content depends upon the ratio of alumina to metal cations such as Ca^{2+} , Mn^{2+} , K^+ (R =alumina/metal oxide) [19-23]. Cation Al^{3+} can form tetrahedra AlO_4^{5-} , however, to fit to the silicate network, a charge compensation is needed to provide the electrical charge of the tetrahedral unit 4- as in the silica unit SiO_4^{4-} . In the slag studied in the present work, the number of charge compensators is higher than the number of AlO_4^{5-} tetrahedra ($R < 1$). Alumina acts as a network former causing increase of the slag viscosity and slowing silica diffusion.

Calcium aluminosilicate slag studied in this paper was basic; in this slag, the SiO_4^{4-} anions were mostly in the form of non-chained anions. It is reported in [24, 25] that bond strength between ionic species should influence the structure of aluminic melts. At the given aluminate content, the variation in diffusivity of CaO can be attributed to the difference in the strength of M^{2+} -oxygen ion interaction, i.e., the stronger the interaction between the atoms in the melt, the more difficult the movement of atoms and slower diffusion.

Mills [26] demonstrated that depolymerisation of the melt is the primary factor affecting physical properties of silicate slag including diffusivity. The degree of depolymerisation of the melt can be characterised by the number of non-bridging oxygens per tetrahedrally-coordinated atom (NBO/T). Values of NBO, T and NBO/T ratio were calculated using the following equations which were suggested in [31]:

$$Y_{NBO} = \sum [2x(\text{CaO}) + x(\text{MgO}) + x(\text{FeO}) + x(\text{MnO}) + x(\text{Na}_2\text{O}) + x(\text{K}_2\text{O})] + 6(1-f)x(\text{Fe}_2\text{O}_3) - 2x(\text{Al}_2\text{O}_3) - 2fx(\text{Fe}_2\text{O}_3) \quad (4)$$

$$x_T = \sum x(\text{SiO}_2) + 2x(\text{Al}_2\text{O}_3) + 2fx(\text{Fe}_2\text{O}_3) + x(\text{TiO}_2) + 2x(\text{P}_2\text{O}_5) \quad (5)$$

$$(NBO/T) = \left(\frac{Y_{NBO}}{x_T} \right) \quad (6)$$

where $x(i)$ is a mole fraction of oxide I, and $f = \text{Fe}^{3+}(\text{IV}) / (\text{Fe}^{3+}(\text{IV}) + \text{Fe}^{3+}(\text{VI}))$,

Plots in **Figure 2** show a good correlation between $\log_{10} D$ and the NBO/T ratio for both calcia and silica at temperatures in the ranges of 1430-1600°C and 1450-1550°C. Diffusivity of CaO and SiO₂ increases with increasing degree of depolymerisation of silicomanganese and calcium aluminosilicate slags. It is worth noting that at a given value of NBO/T, the diffusivity of CaO is about two orders of magnitude higher than the diffusivity of SiO₂. Such a large difference was also observed in the self-diffusivity of relatively small cations (e.g. Ca²⁺) and large silicate anions (SiO₄⁴⁻, Si₂O₇⁶⁻, Si₃O₁₀⁸⁻ etc). The differences in size of ionic species and their interactions with neighboring ions are thought to be responsible for their relative ease of movement and hence diffusion in the melt.

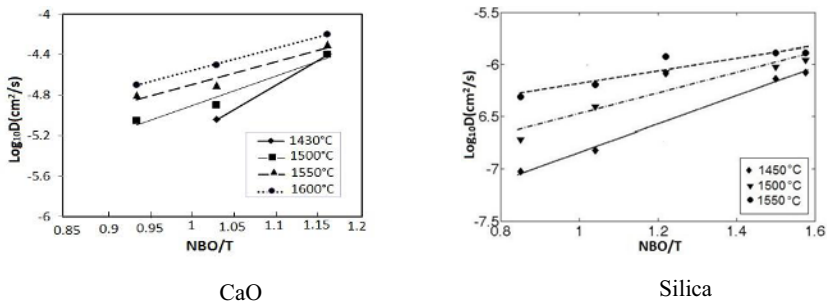


Figure 2. Diffusion coefficients of CaO and SiO₂ as functions of the NBO/T ratio

4 Conclusions

Diffusivity of silica in SiMn slag at temperatures of 1450, 1500 and 1550°C was in the range of 8.2×10^{-7} – 1.2×10^{-6} cm²/s which increased with addition 10 wt. % CaO and MnO. Addition of SiO₂ and Al₂O₃ to the slag resulted in the lowering the diffusivity of silica to 4.9×10^{-7} cm²/s and 6.9×10^{-7} cm²/s, respectively at 1550°C.

The increase in the diffusivity of silica in SiMn slag with addition of CaO and MnO was attributed to the melt depolymerisation. Additions of SiO₂ and Al₂O₃ to the slag slowed down the diffusion of SiO₂ in the slag, and strongly increased slag viscosity. Expansion of a network of SiO₄⁴⁻ tetrahedra, which also incorporated AlO₄⁵⁻, slowed the movement of anions leading to a slower diffusion of SiO₂ in slag.

Addition of MnO_x and TiO₂ to the calcium aluminosilicate slag at 1550°C increased the diffusion coefficient of CaO from 1.9×10^{-5} to 5.1×10^{-5} cm²/s and 2.49×10^{-5} cm²/s, respectively. The addition of SiO₂ decreased the diffusivity of CaO in slag to 2.02×10^{-5} cm²/s. This trend was attributed to the difference in the strength of M-O bonds. The slower movement of atoms in the environment with stronger M-O bonds results in the lowering diffusivity.

Diffusivity of calcia and silica correlated well with the NBO/T ratio, which characterises the degree of the slag depolymerisation.

5 References

1. Ostrovski. O and Swinbourne. D. *Steel Res. Int.*, 2013, 84 (7), pp 680-686.
2. Dolan. M. D and Johnstone. R.F. *Metall. Mater. Trans. B.*, 2004, 35 B, pp675-684.
3. Liang. Y; Richter. F. M; Davis. A.M and Watson. E.B. *Geochim. Cosmochin. Ac.*, 1996, 60(22), pp 4353-4367.
4. Feichitinger. S; Michelic. S. K; Kang. Y and Bernhard, C., *J. Am. Ceram. Soc.*, 2014, 97(1), pp316-325.
5. Keller. H and Schwerdtfeger. K. *Met. Trans. B.*,1979, 10B, pp 551-554.
6. Matsushima. M; Yadoomaru. S; Mori, K and Kawai, Y: *Trans. Iron Steel Inst. Jpn.*, 1977, vol. 17, pp. 442-49.
7. Hamano, T; Horibe, M and Ito, K. *Trans. Iron Steel Inst. Jpn.*, 2004, vol. 44, pp. 263-67.
8. Hara, S; Akao, K and Ogino, K. *Tetsu-to-Hagane'*, 1989, vol. 75, pp. 1891-96.
9. Maroufi,S; Ciezki,G; Jahanshahi, S; Shouyi, S and Ostrovski, O. Dissolution rate and diffusivity of silica in SiMn slag, *Metall. Mater. Trans. B.*2015,46, pp 101.
10. Amini. S.H; Brungs. M. P; Jahanshahi. S and Ostrovski. O. *Metall. Mater. Trans. B.*, 2006, 37B, pp 773-780.
11. Cochran. W. L. *Proceedings of the Cambridge Philosophical Society*,1934, 30, pp 365-374.
12. Kosaka. M and Minowa. S. *Tetsu.To. Hagane* 1966, 52(12), pp 22-36.
13. Mills. K. C and Keene, B., *J. International Materials reviews*, 1987, 32 (1-2), 1-120.
14. Levich. V. G. *Physiochemical Hydrodynamics*, Prentice-Hall, New York, NY, 1962, p. 69.
15. Eisenberg. C. W and Tobias. W. *Chemical Engineering Progress Symp. Series*, 1995, 51, 25-29
16. Zhang. L; Sun. S and Jahanshahi. S. *Journal of Phase Equilibria and Diffusion*, 2007, 28 (1), 121-129.
17. Mysen, B. O. *Structure and Properties of Silicate Melts*. Elsevier, Amsterdam. 1988.
18. *Slag Atlas*, 2nd Edition 03, Edited by Verein Deutscher Eisenhüttenleute, 541-556, 1995.
19. Urbain. G; Cambier. F; Deletter. M; Anseau. M.R. *Brit., Ceram. Trans J*, 1981, 80, 139-141.
20. Zhang. L and Jahanshahi. S. *Scand. J. Metall.*, 2001, 30, 364-369.
21. Park. J. H; Min. D. J and Song. H. S. *Metall. Mater. Trans. B.*, 2004, 35 B, 269-275.
22. Zhang. L; Sun, S and Jahanshahi. S., *J. non-Cryst Solids*, 2001, pp 24-29.
23. L. Zhang and S. Jahanshahi: *Metall. Mater. Trans. B*, 1998, vol. 29B, pp. 177-86.
24. L. Zhang and S. Jahanshahi: *Metall. Mater. Trans. B*, 1998, vol. 29B, pp. 187-95.
25. Johnston, R. F; Stark, R. A and J. Taylor: *Ironmaking and Steelmaking*, 1974, vol. 1, pp. 220-27.
26. Mills. K., *ISIJ International*, 1993, 33(1), 148-155.

THE CATIONIC EFFECT ON PROPERTIES AND STRUCTURE OF CaO-MgO-SiO₂ MELTS

Yong-Uk Han and Dong Joon Min

Yonsei University; Yonsei-ro 50, Seodaemun-gu, Seoul, 03722, Republic of Korea

Keywords: Electrical Conductivity, Viscosity, Slag Structure, Stability

Abstract

A study on the effect of cation species on the viscosity and electrical conductivity of CaO-MgO-SiO₂ system is carried out. Rotating cylindrical and two-plate method is used for viscosity and electrical conductivity measurements, respectively. Raman spectroscopy is also carried out to understand the structure of the slags. Experimental results indicated that the cationic effect on viscosity and ionic conductivity is governed by classical Anderson-Stuart theory: The dominance of electrostatic interaction on steric hindrance is confirmed for depolymerized melts (NBO/T=2.0). For polymerized melts (NBO/T=0), however, the major cationic effect on transport properties are examined to be a strain field distortion energy. The viscosity and ionic electrical conductivity are in strong correlation and assumed as the structure-dependent property. The structure of polymerized melts is also affected by the transition in primary solidification phase: Abnormal changes in properties and structure are observed at diopside congruent composition. Such a change at the congruent composition is assured by the entropy calculation and the stability function, ψ

Introduction

Structure-composition-property relationship of silicate glasses and melts has long been of vast interest from geology, glass science, and metallurgy. Plenty of studies are devoted to elucidation of silicate melt structures with the aid of spectroscopic structural analysis including FT-IR[1],[2], Raman[3]-[7], and MAS-NMR[8]-[11] analysis. The effect of ionic distribution of silicate polymeric anion on properties of such melts were well reviewed by several pioneering works[5]-[7]. To the best of our knowledge, the effect of cations, however, has not been organized.

Mysen[6] once suggested the application of topological entropy as a measurement of the deviation of cations from random mixing. Topological entropy, calculated by subtracting random mixing entropy of Qⁿ species from configurational entropy[12], indicates that the cation is unevenly distributed throughout the silicate melts. Although the idea of Mysen provides a glimpse into the cationic effect in molten silicates, the effect is only considered by the ionization potential, z/r^2 . Several works defies the z/r^2 hierarchy in which the opposite trend in physical properties is experimentally observed.

The innovative aspect of present study is that it provides comprehensive understanding on the cationic effect on structure and property of molten silicate system, CaO-MgO-SiO₂. To distinguish structural effect from ionic nature of cations, discussion on the fully polymerized melts (SiO₂-saturated compositions) is performed. The classical Anderson-Stuart theory[13] is successfully applied for the explanation of the antithetic cationic effect on properties in polymerized and depolymerized melts. For polymerized melts, the effect of the transition in primary solidification phase is also discussed for its effect on properties and melt structure.

Experimental procedure

Reagent-grade MgO and SiO₂ powders are used. CaO was obtained by calcining reagent-grade CaCO₃ at 1273K for 10 hours. 100mg of powders are mixed and melted in a Pt crucible at 1873 K under high purity Ar atmosphere. To minimize segregation during the quenching procedure, a small amount of sample is melted in a halogen lamp installed high temperature confocal-laser microscope (Lasertec LV2000DX-SVF17SP). After a homogenized melt is obtained, He-quenching is applied to sustain initial cooling rates of 3000K/min. Fully-polymerized silica-saturated compositions (blue circles in Fig 1 (a)) are chosen as a control group for the ionic interactions and CaSiO₃-MgSiO₃ compositions (green diamonds in Fig 1 (a)) are chosen to exclude the effect of the basicity on the properties.

The electrical conductivities of the melts were measured in a Pt–Rh crucible (ϕ 54 mm, length 65 mm). A pair of Pt-10Rh electrodes (10 × 40 × 1 mm) in contact with a Pt-Rh wire (ϕ 1 mm, length 1 m) was calibrated using a 1.0 N KCl aqueous solution and the cell factor was determined. A Wheatstone bridge was established to measure the electrical resistance between electrodes. The alternating current was made using a 500 mV electrical potential with a frequency of 1 kHz. A Keithley 2182A nanovoltmeter was used to measure the resistance in the Wheatstone bridge circuit. The validity of the measurements was confirmed by measuring CaO–CaCl₂ and CaO–CaF₂ molten salts.

The rotating cylinder method was applied in the viscosity measurements (Fig. 1). A Brookfield digital viscometer (RVDV-II+, Middleboro, MA) with a full-scale torque of 7.187×10^{-4} N·m was used. To avoid slag contamination and eccentricity during the rotation, triple-joint Pt–Rh spindles were linked to the viscometer. The whole measuring system was calibrated using Brookfield standard oils with viscosities of 0.474, 0.967, 4.85, 9.25, and 49.8 dPa·s at room temperature.

A Pt–Rh crucible was placed in the mullite reaction tube and heated up to 1923 K under an Ar atmosphere of 99.9999% purity. The electrodes and viscometer were inserted into the melts at 1923 K and the temperature was decreased in 50 K increments. A stabilizing interval of 20 min was carried out before every measurement.

The Raman spectra of the samples were investigated at room temperature in the range of 100–1900 cm⁻¹. An Ar excitation laser was used with a wavelength of 514.532 nm at 2 mW for 300 s. A HORIBA Jobin Yvon Raman spectroscopy (LabRam Aramis) was employed. Quantitative peak deconvolution was carried out following the procedure described by Mysen et al.⁶. Peakfit™ was applied to fit a Gaussian function in the range of 800–1200 cm⁻¹ within a $\pm 0.5\%$ error limit.

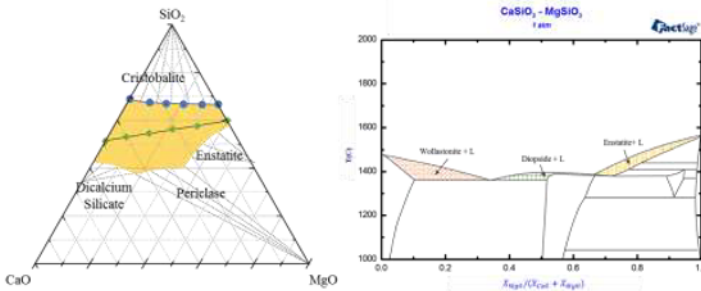


Fig. 1. (a) The experimental compositions and phase diagram of CaO-MgO-SiO₂
(b) Pseudo-binary phase diagram for CaSiO₃-MgSiO₃

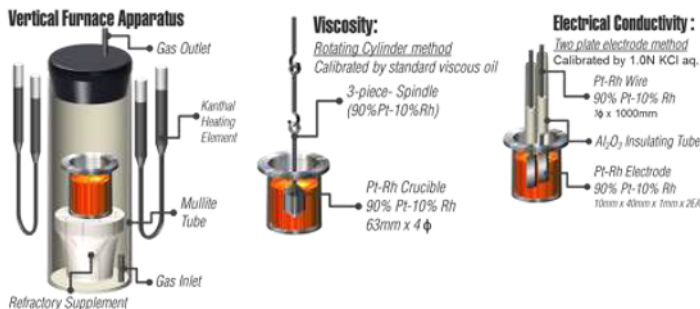


Fig. 2. Experimental apparatus for viscosity and electrical conductivity measurements

Results and Discussion

1. Cationic Effect on Electrical Conductivity and Viscosity in Polymerized and Depolymerized Melts

The effect of the cationic exchange on electrical conductivity and viscosity of the polymerized ($\text{CaO-MgO-SiO}_2^{\text{satd}}$, $\text{NBO}/\text{T}=0$) and depolymerized (CaO-MgO-0.5-SiO_2 , $\text{NBO}/\text{T}=2.0$) melts are described in Fig 3. (a) and (b), respectively. An antithetic trend on the cationic effect is observed for the sets: For polymerized melts, electrical conductivity increases and viscosity decreases with Ca to Mg substitution. For depolymerized melts, however, electrical conductivity decreases and viscosity increases with the substitution.

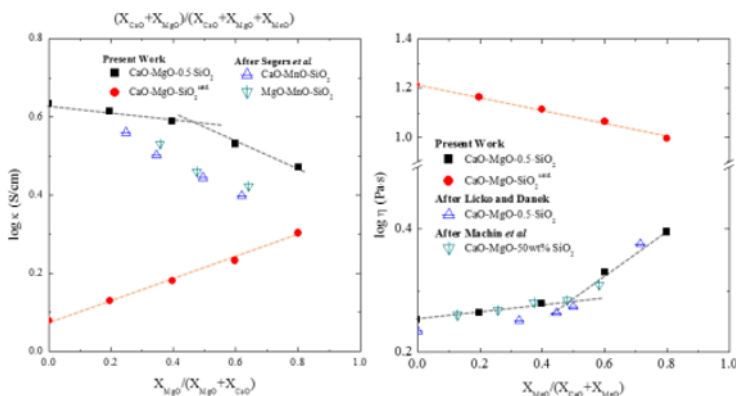


Fig 3. The effect of cationic substitution on (a) electrical conductivity and (b) viscosity for polymerized and depolymerized melts

To remedy this major discrepancy, Anderson-Stuart theory[13] is revisited for opposite dependence on the cationic radius. In the theory, the cationic radius has different effect on ionic interaction energy in strain field distortion energy as Eq (1):

$$E_a = \frac{\beta z z_O e^2}{\varepsilon(R+R_O)} + 4\pi G R_D (R - R_D)^2 \quad (1)$$

z, z_O and R, R_O are the valences and ionic radii of the mobile ion and stationary oxygens, respectively; e is the electronic charge, and R_D is the effective radius of the doorway. β , the Madelung constant, is the liquid lattice parameter, and G is the shear modulus. ε is the dielectric permittivity of the melt. It is notable that the effect of cationic radius, R , is opposite for two energy barriers. The electrostatic interaction energy, the former term, decreases with increasing cationic radius while the strain field distortion energy, the latter term, increases.

To ensure the difference in the effect of cationic radius on two activation energies, the apparent activation energy is calculated by the Arrhenian relationship from the temperature dependence of viscosity and electrical conductivity. The strain field distortion energy on the other hand, is calculated following McElfresh's suggestion[13]. Radius of doorway passage for ion migration is taken to be 0.6 atomic unit from Norton's approximation[13] and shear modulus of 3.05×10^{11} dyne/cm² is quoted from work of Anderson and Stuart. The calculated activation energies are described in Fig. 4.

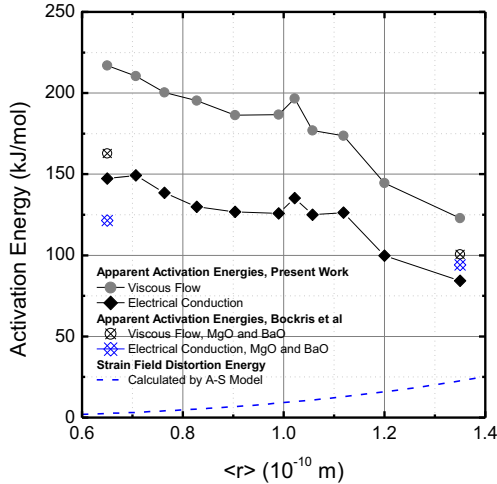


Fig. 4. Apparent activation energy and strain field distortion energy of CaO-MgO-SiO₂ system as a function of the arithmetic average cationic radius, $\langle r \rangle$.

From the activation energy discussion, the electrostatic interaction energy, the subtraction of strain field distortion energy from apparent activation energy, is larger enough than strain field energy to take the strain field distortion energy to be negligible. As the cationic radius increases, the activation energy for the ionic migration consistently decreases allowing the ionic migration easier. Thus the electrical conductivity is enhanced and viscosity is decreased by enhanced ionic transfer. In fully-polymerized melts, in which silicate flow units are fully polymerized and electrochemically neutral, however, electrostatic interaction energy is assumed to lack hence the overall ionic migration is dependent only on the strain field distortion energy. Therefore, the ionic migration is easier for the cation of the smaller radius. Although the postulation successfully explains the antithetic trend of the cationic radius, the absence of electrostatic energy is yet to proven.

To prove the absence of ionic interaction in fully-polymerized melts, the Walden plot¹⁶⁻¹⁸ is exploited. From Nernst-Einstein equation, Harris¹⁹ modified the relationship between electrical conductivity and viscosity of ionic melt as following equation:

$$\eta^t \times \sigma = (\text{Constant}) \quad (2)$$

Angell *et al.*[16]-[18] discussed on the slope of logarithmic plot of Walden's equation as an index of the intensity of ionic interaction: For ideal ionic solution, in which electrochemical neutrality is satisfied without electrostatic interaction, slope of the logarithmic Walden plot is unity.

The logarithmic Walden plot is established in Fig. 5. The Walden plot of depolymerized melts lies on the typical plots of alkaline-earth silicate of which slopes range of 0.65 to 0.8. The Walden plot of polymerized melts, however, is nearly unity, meaning the silica-saturated melts be an ideal ionic melts and the silicate units be the electrochemically neutral solvent.

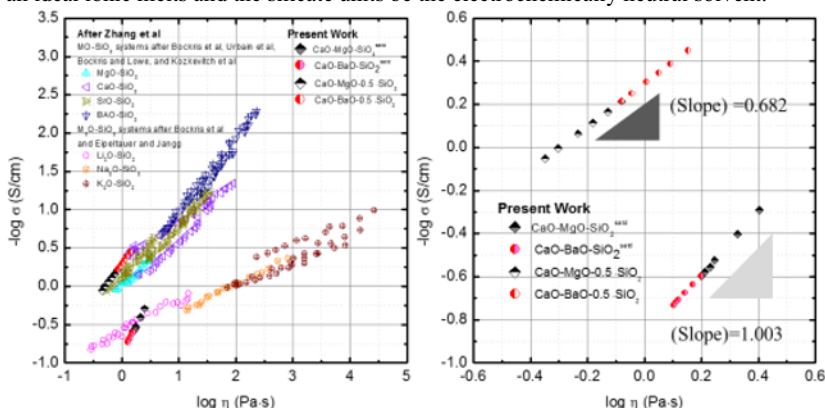


Fig 5. Walden plot of (a) several alkali and alkaline-earth silicate melts including the results of present works (b) the results of present work only for convenience.

2. The Effect of the Transition in Primary Solid Phase on the Melt Properties and Structure

Further discussion lies on the elucidation of abrupt change in electrical conductivity and viscosity of the melt at the 50% of Ca to Mg substitution. (See Fig. 3 (a) and (b).) Together with the pseudo-binary phase diagram depicted in Fig 1 (b), the abrupt change in properties occurs at the vicinity of the diopside congruent composition.

The Raman spectra of CaSiO_3 - MgSiO_3 melts are described in Fig. 6 (a). Notable changes in the Raman spectra by Mg^{2+} for Ca^{2+} substitution does not occur only at the high-frequency regions, but also at the low- and mid-range frequencies.

In the low-frequency range around 340cm^{-1} and 380cm^{-1} , the peaks shifts toward to lower wavenumbers with higher MgO. Such a blue shift of wollastonite characteristic peak with increasing MgO composition infers the decrease in local crystallinity of wollastonite for cationic substitution: A Ca^{2+} ion of 114 pm of radius has coordination numbers of 7 to 9. Hence, Ca^{2+} is located in a cubic packing site with oxygen. The maximum radius of cation in cubic site of Si-O is 115.73 pm. A Mg^{2+} ion, on the other hand, has coordinate number of 6, occupying an octahedral packing with oxygen. The ionic radius of Mg^{2+} is 86 pm, which is larger than that of geometric maximum radius of cation in octahedral site of 65.49 pm. Therefore, Mg^{2+} in

silicate necessarily leads local distortion of Si-O lattice. The increase in Si-O vibrational frequency with Ca^{2+} to Mg^{2+} substitution in Raman spectra is plausibly caused by such an energetic destabilization of Si-O bond. After the Mg^{2+} substitution for Ca^{2+} exceeds the congruent point ($x=50$), the low frequency peaks disappears

620 cm^{-1} and 720 cm^{-1} bands are regarded to be the bending motion of oxygen bonds in the Si-O-Si bonding and Si-O stretching, respectively. Combining the information from the high-frequency regions, the decrease in the 720 cm^{-1} peaks indicate a polymerization of the melt by Ca^{2+} to Mg^{2+} substitution, which corresponds well with previously measured viscosity values. Description of the high-frequency $800\text{--}1200\text{ cm}^{-1}$ bands is well categorized by several researchers including Brawer[20], Mysen *et al.*[21], and McMillan *et al.*[22].

Deconvolution using a Gaussian function is employed to quantitatively assess the high-frequency Q^n . The result of the deconvolution is expressed in Figure 6 (b). Notably, the main structural units of silicate melts is determined to be Q^2 , Q^3 , and Q^0 (in order of abundance). Virgo *et al.* [23] concluded equilibria of these structural units as following:

$$3Q^2 = 2Q^3 + Q^0 \quad (3)$$

It is notable that the population of each Q^n species abruptly changes at the diopside congruent point. Q^2 increases whereas Q^3 and Q^0 decreases, indicating a polymerization of the melt. The change in slope of the Q^2 , Q^3 , and Q^0 is in the ratio of 3:2:1, supporting the equilibria expressed in eq. (3). The equilibrium constants in eq (3) can be calculated and correlated to the degree of depolymerization as Mysen suggested⁶.

$$K = \frac{[Q^3]^2[Q^0]}{[Q^2]^3} \quad (4)$$

Degree of depolymerization, $\ln K$ decreases abruptly after the diopside congruent point implying polymerization of the melt.

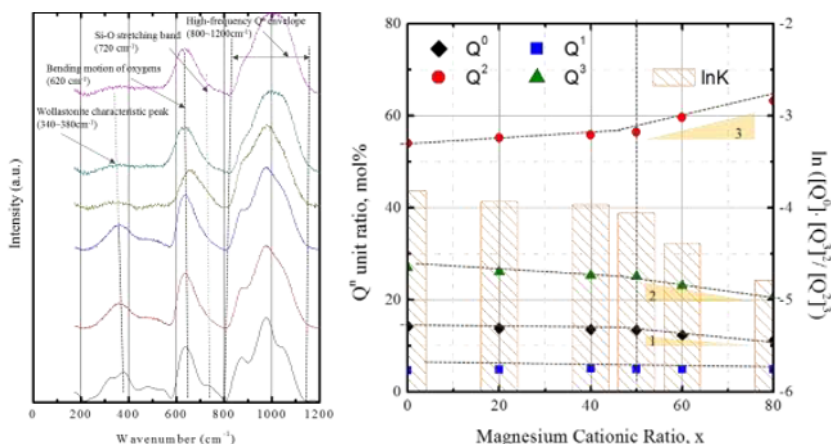


Fig. 6. (a) Raman spectra of $\text{CaSiO}_3\text{-MgSiO}_3$ melts (b) Fig. 7 Q^n unit population and calculated $\ln K$ in $(100-x)\text{CaSiO}_3\text{-}x\text{MgSiO}_3$ melts. It is notable that the slope of Q^0 change is 1/3 of that of Q^2 and half of that of Q^3 , corresponding with results of Virgo *et al.*[23,24]

The abrupt change in melt dynamic measurements of stability function, liquid fragility, and configurational and topological entropies are organized in Fig. 8[24]. Liquid fragility and entropies are acquired from the temperature dependence of viscosity whereas the stability function is calculated as Eq (5):

$$\psi = \begin{bmatrix} 1 + X_2 \frac{\partial \ln \gamma_2}{\partial X_2} & \cdots & X_n \frac{\partial \ln \gamma_2}{\partial X_n} \\ \vdots & \ddots & \vdots \\ X_2 \frac{\partial \ln \gamma_n}{\partial X_2} & \cdots & 1 + X_n \frac{\partial \ln \gamma_n}{\partial X_n} \end{bmatrix} \quad (5)$$

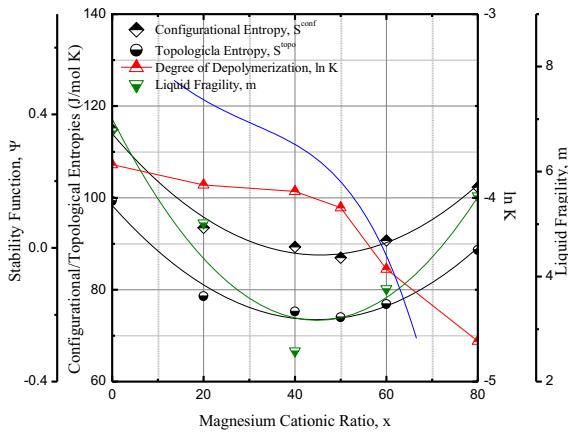


Fig. 7. Configurational and topological entropies, degree of depolymerization, liquid fragility, and stability function of CaSiO₃-MgSiO₃ melts at 1873K [24]

Conclusions

In this work is performed the mutual measurement of the electrical conductivity and viscosity of CaO-MgO-SiO₂ melts combined with Raman spectroscopic analysis to elucidate the cationic effect on the properties and structure of the melt. From the findings, followings are concluded:

(1) The effect of the cationic radius on the electrical conductivity and viscosity shows the antithetic trend in polymerized and depolymerized melts. In depolymerized melts, the electrostatic interaction energy dominates the strain field distortion energy leaving larger ions easier to migrate. In polymerized melts, however, the overall activation energy of ionic migration is solely dependent of strain field distortion energy thus the smaller ions are easier to move. Such a postulation is assured by the application of Walden plot.

(2) Structure and properties in depolymerized melts are concluded to be dependent of phase equilibria. The structural change at the congruent composition is confirmed by deconvolution of Raman spectra. The stability function is suggested to expect such a change from calcium silicate to magnesium silicate melt.

References

1. J. H. Park, D. J. Min, and H. S. Song, "FT-IR Spectroscopic Study on Structure of CaO-SiO₂ and CaO-SiO₂-CaF₂ Slags", *ISIJ International*, 42 (2002), 344-351
2. H. Kim, W. H. Kim, I. Sohn and D. J. Min, "The Effect of MgO on Viscosity of the CaO-SiO₂-20 wt%Al₂O₃-MgO Slag System", *Steel Research International*, 81 (2010), 261-264
3. S. A. Braver and W. B. White, "Raman Spectroscopic Investigation of the Structure of Silicate Glasses. I. The Binary Silicate Glasses", *Journal of Chemical Physics*, 63 [6], 2421-32 (1975)
4. B. O. Mysen, D. Virgo, P. Nackwerth, F. A. Seifert, and I. Kushiro, "The Structure of Silicate Melts: Implications for Chemical and Physical Properties of Natural Magma", *Reviews in Geophysics and Space Physics*, 20 (1982), 353-383
5. B. O. Mysen, "Structure and Properties of Magmatic Liquids: From Haplobasalt to Haploandesite", *Geochimica et Cosmochimica Acta*, 63 (1999), 95-112
6. B. O. Mysen, "Physics and Chemistry of Silicate Glasses and Melts", *European Journal of Mineralogy* 15 (2003), 781-802
7. J. H. Park, "Composition-Structure-Property Relationships of CaO-MO-SiO₂ (M=Mg²⁺, Mn²⁺) Systems Derived from Micro-Raman Spectroscopy", *Journal of Non-Crystalline Solids*, 358 (2012), 3096-102
8. C. M. Schramm, B. H. W. S. DeJong, and V. F. Parziale, "²⁹Si Magic Angle Spinning NMR Study of Local Silicon Environments in-amorphous and Crystalline Lithium Silicates", *Journal of American Chemical Society*, 108 (1984), 4396-4402
9. H. Maekawa, T. Hasegawa, K. Kawamura, and T. Yokokawa, "The Structural Groups of Alkali Silicate Glasses Determined from ²⁹Si MAS-NMR", *Journal of Non-Crystalline Solids* 108 (1984), 54-64
10. J. B. Murdoch, J. F. Stebbins, and I. S. E. Carmichael, "High-resolution ²⁹Si NMR Study of Alkaline Earth Aluminosilicate Glasses", *Journal of Non-Crystalline Solids*, 124 (1985), 194-206
11. J. F. Stebbins, "Identification of Multiple Structural Species in Silicate Glasses by ²⁹Si NMR", *Nature*, 330 (1987), 465-467
12. P. Richet, "Viscosity and Configurational Entropy of Silicate Melts". *Geochimica et Cosmochimica Acta*, 48(1982) 471-483
13. O. L. Anderson and D. A. Stuart, "Calculation of Activation Energy of Ionic Conductivity in Silica Glasses by Classical Methods", *Journal of American Ceramic Society*, 37 (1954), 573-580
14. D. K. McElfresh and D. G. Howitt, "Activation Enthalpy for Diffusion in Glass", *Journal of American Ceramic Society*, 69 (1986) C237-238
15. F. J. Norton, "Helium Diffusion through Glass", *Journal of American Ceramic Society*, 36(1953) 90-96
16. W. Xu, E. I. Cooper, and C. A. Angell, "Ionic Liquids: Ion Mobilities, Glass Temperatures, and Fragilities", *Journal of Physical Chemistry B*, 107 (2003), 6170-6178

17. W. Xu and C. A. Angell, "Solvent-free Electrolytes with Aqueous Solution-like Conductivities", *Science*, 302 (2002) 422-425
18. M. Yoshizawa, W. Xu, and C. A. Angell, "Ionic Liquids by Proton Transfer: Vapor Pressure, Conductivity, and the Relevance of ΔpK_a from Aqueous Solutions", *Journal of American Chemical Society*, 125 (2003), 15411-15419
19. K. R. Harris, "Relations between the Fractional Stokes-Einstein and Nernst-Einstein Equations and Velocity Correlation Coefficient in Ionic Liquids and Molten Salts", *Journal of Physical Chemistry B*, 114(2010) 9572-9577
20. S. A. Brawer, "Theory of the Vibrational Spectra of Some Network and Molecular Glasses", *Phys. Rev. B.*, B11 3173-94 (1975)
21. B. O. Mysen, D. Virgo, and C. M. Scarfe, "Relations between the Anionic Structure and Viscosity fo Silicate Melts-a Raman Spectroscopic Study", *American Mineralogist*, 65 (1980), 690-710
22. P. McMillan, "A Raman Spectroscopic Study of Glasses in the System CaO-MgO-SiO₂", *American Mineralogist*, 69(1984), 645-59
23. Virgo, B. O. Mysen, and I. Kushiro, "Anionic Constitution of 1-atmoaphere Silicate Melts: Implications for the Structure of Igneous Melts", *Science*, 208(1980), 1371-1373
24. Y.-U. Han, and D. J. Min, Under progress

EFFECTS OF STRUCTURE ON THE THERMODYNAMIC AND TRANSPORT PROPERTIES OF $\text{Na}_2\text{O-CaO-SiO}_2\text{-FeO-Fe}_2\text{O}_3$ MELTS

Lesley J. Beyers¹, Geoffrey A. Brooks², Bart Blanpain¹, and Frederik Verhaeghe^{1,3}

¹ KU Leuven, Department of Materials Engineering; Kasteelpark Arenberg 44 bus 2450, B-3001 Leuven, Belgium.

² Swinburne University of Technology, Faculty of Science, Engineering and Technology; John Street, Hawthorn, Victoria, 3122, Australia.

³ Umicore, Precious Metals Refining; Adolf Greinerstraat 14, B-2660 Hoboken (Antwerp), Belgium.

Keywords: Iron oxide melts, structural species, viscosity, oxidation thermodynamics

Abstract

Iron oxide slags play a critical role in both ferrous and non-ferrous metallurgical processes. The relative abundance of FeO and Fe₂O₃ will determine the slag oxidation potential and influence transport properties, which makes an accurate prediction of their proportions crucial to process operations. The nature of the iron oxide structures in the liquid slag has been a long standing issue, which is in part related to the variety of structural species that can be formulated to accommodate the observed property changes. In this study, spectroscopic data is used to clarify the dual structural behaviour of both ferric and ferrous iron oxide. The identified oxide structures are shown to have characteristic effects on the thermodynamic properties and viscosity of Na₂O-CaO-SiO₂-FeO-Fe₂O₃ melts. These insights into the structural behaviour of iron oxide and its composition dependence can also improve the mathematical modelling of these properties.

Introduction

Iron oxide slags are abundantly used in ferrous and non-ferrous extractive metallurgy and play a critical role in the control of these processes. Besides FeO and Fe₂O₃, a slag typically contains CaO, SiO₂, MgO, Al₂O₃ and a range of oxides in minor concentrations. These oxides are often classified in terms of "acids" and "bases", based on the effect their addition has on various thermodynamic and physical properties of the slag. Acidic oxides (e.g. SiO₂) form strong covalent bonds with oxygen and are classified as network-forming oxides because of their ability to form a polymer structure in the melt. Basic oxides (e.g. Na₂O and CaO) readily dissociate upon dissolution to donate their oxide anion to the melt (an acid-base reaction) and are network-modifying oxides i.e. they will interact with the silicate network and effectively disrupt the otherwise continuous network. Oxides such as Al₂O₃ and Fe₂O₃ (and for the purpose of this discussion also FeO) fall in the centre of this acid-base range and are classified as amphoteric oxides as their behaviour as an acid or a base will depend on the composition of the melt.

The behaviour of ferrous (Fe^{2+}) and ferric (Fe^{3+}) iron oxide in the slag of interest is not always straightforward. The possibility of ferrous and ferric to coexist under a variety of conditions [1] makes that the properties of iron oxide-containing melts exhibit a complex dependence on the composition. Combined with the already difficult experimental conditions, this created the situation that aspects of the structure and physical properties of iron-containing liquid oxides have not been fully explored. Based on an extensive review of the structure and properties of iron-containing melts relevant to petrological processes, Mysen and Richet [1] classified ferric iron as a weak analogue to aluminium and mainly a network-forming oxide.

Due to their different affinity for oxygen, the oxygen coordination of acidic and basic oxides will typically differ. The basic structural unit for the acidic oxide SiO_2 is a tetrahedral coordination with oxygen. Basic oxides have a weaker bond with oxygen and will typically have a higher (octahedral) oxygen coordination [1–3]. The typical amphoteric oxides Al^{3+} and Fe^{3+} can have both a tetrahedral ($\text{Al}^{3+}(\text{IV})$) and octahedral ($\text{Al}^{3+}(\text{VI})$) coordination.¹ The existence of $\text{Al}^{3+}(\text{IV})$ and $\text{Fe}^{3+}(\text{IV})$ as $[\text{AlO}_2]^-$ and $[\text{FeO}_2]^-$ anions requires its remaining charge to be compensated by another cation. The ability to charge balance such an anion is often correlated with the cation field strength, which identifies alkali cations (low Z/r^2) as very effective for this purpose [1, 2] and recent thermodynamic modelling accounts for the possible formation of NaFeO_2 clusters in the melt [4, 5], analogous to the (previously implemented) NaAlO_2 [6]. In cases where insufficient alkali cations are present to act as a charge-balancing cation, part of the amphoteric oxides typically take up a higher oxygen coordination.

The formation of ferric anions as part of the melt structure in the presence of only alkaline earth cations is less evident, but has often been deduced from observed variations of the physical properties [7–9] and experimentally confirmed with Mössbauer spectroscopy on metallurgical slags [10, 11]. Such different structural arrangements of the iron oxides will have an effect on various thermodynamic and physical properties, with the largest effect typically expected for the viscosity. However, Mills and Keene [12] concluded from the data of Seki and Oeters [9] that “ $\text{Fe}_2\text{O}_3/\text{FeO}$ does not have an appreciable effect on the viscosity” and suggested that its behaviour is more like a network modifier. This view and the one of Mysen and Richet [1] on the behaviour of ferric iron in silicate melts cannot be more contrasting and originates from the predominant conditions in petrology (fully oxidised) and ferrous metallurgy (iron saturation). In steelmaking, the iron saturation condition will not prevent the existence of ferric iron, though it will keep its contents and any specific influence low, making its specific behaviour less relevant. However, in the more oxidising conditions in non-ferrous metallurgical processes the structural behaviour of the iron oxides will become important and have an effect on the evolution of various thermodynamic and physical properties between the conditions of iron saturation and equilibration in air.

¹Our use of IV and VI to indicate tetrahedral and octahedral oxygen coordination by no means implies that only these two coordinations can exist. It simply follows current conventions and is indicative of the fact that the low oxygen coordination will tend to approach four, while the other will be a higher oxygen coordination, for the oxides considered here.

In this paper the CaO-SiO₂-FeO-Fe₂O₃ system is used as case example of pyrometallurgical slag. The Na₂O-SiO₂-FeO-Fe₂O₃ is used for comparison and as a starting point, as some of its physical property variations and structural features are more prominent and more extensively characterised due to its importance for petrological processes.

Thermodynamics of the Iron Oxidation Reaction

The relative abundance of FeO and Fe₂O₃ in a slag can be expressed by the iron redox ratio Fe³⁺/Fe²⁺, which will have a fixed value for a given set of conditions. The interpretation of the effect of any variable condition is sensitive to the formulation of the iron oxidation equation, which in this work is formulated as



Alternative formulations include the use of Fe₂O₃ and wüstite [13]. The equilibrium condition of this reaction is given by

$$K = \exp\left(-\frac{\Delta G^\circ}{RT}\right) = \frac{a_{\text{FeO}_{1.5}}}{a_{\text{FeO}}}\left(\frac{1}{P_{\text{O}_2}}\right)^{1/4} \quad (2)$$

$$\log\left(\frac{\text{Fe}^{3+}}{\text{Fe}^{2+}}\right) \equiv \log\left(\frac{X_{\text{FeO}_{1.5}}}{X_{\text{FeO}}}\right) = \frac{1}{4}\log P_{\text{O}_2} + \log K - \log\left(\frac{\gamma_{\text{FeO}_{1.5}}}{\gamma_{\text{FeO}}}\right) \quad (3)$$

For an ideal system the redox equilibrium would be independent of the composition of the melt. However, even for simple systems this assumption of ideal behaviour does not hold [14] and the activity coefficient ratio needs to be accounted for.

The ratio of the activity coefficients is the term that is typically difficult to capture in terms of melt composition, which led to the development of a wide variety of models. Bowker et al. [10] deduced that the effect of both temperature and oxygen partial pressure on this ratio is limited. On the other hand, the effect of the composition is significant, especially on $\gamma_{\text{FeO}_{1.5}}$ [15], consistent with the primary focus of a number of empirical models proposed for complex natural melts [13, 16–18]. These models are all based on a linear formulation for the ratio of the activity coefficients

$$\log\left(\frac{\gamma_{\text{FeO}_{1.5}}}{\gamma_{\text{FeO}}}\right) = \sum_i a_i X_i \quad (4)$$

This linear formulation puts restrictions on their applicability range and gives an apparent enthalpy of the oxidation reaction (Eq. 1) that is dependent on the data set, or equivalently, gives different enthalpies for each composition class [18]. A more fruitful approach is to use more realistic variables, resembling the structure of the melt (see e.g. Mysen [19]), but this requires more accurate knowledge on the structural behaviour of the iron oxides.

Structural Characteristics of Iron Oxides

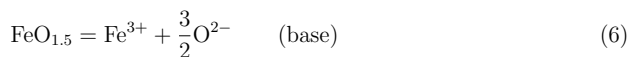
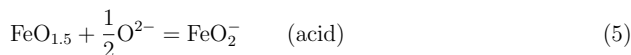
^{57}Fe Mössbauer spectroscopy is a typical method to investigate the local structure around iron cations in silicate melts [1, 10]. The characterisation of the spectra in terms of the isotropic shift (IS) and quadruple splitting (QS) is used to distinguish between different oxidation states and oxygen coordination. While there is a general agreement that the spectroscopic results indicate the presence of $\text{Fe}^{3+}(\text{IV})$, $\text{Fe}^{3+}(\text{VI})$ and $\text{Fe}^{2+}(\text{VI})$, the existence of $\text{Fe}^{2+}(\text{IV})$ in silicate melts is still controversial [1, 10, 20]. However, the bulk of the compositions evaluated by Mysen and Richet [1] constitute oxidised magmatic melts and a second ferrous iron coordination $\text{Fe}^{2+}(\text{IV})$ in these melts is likely not present in sufficient quantities to be detected.

The higher cation field strength of CaO is indicative of its reduced ability to stabilize Fe^{3+} in tetrahedral coordination [1] and both $\text{Fe}^{3+}(\text{IV})$ and $\text{Fe}^{3+}(\text{VI})$ are typically present in the $\text{CaO-SiO}_2\text{-FeO-Fe}_2\text{O}_3$ system [10, 11, 21, 22]. This is consistent with the view that Na_2O is more effective in stabilising the ferric iron anions and leading to an increase in the iron oxidation state compared to a (charge-)equivalent amount of CaO.

Evidence for the existence of $\text{Fe}^{2+}(\text{IV})$ has been obtained from X-ray spectroscopy under reducing conditions [23–25]. However, some X-ray techniques cannot strictly distinguish between a tetrahedral site and a distorted octahedral site e.g. a highly-distorted site might yield similar EXAFS results. In contrast, Mössbauer spectroscopy would yield a shift in the spectra [23] and the asymmetry of the Fe^{2+} Mössbauer peak can indicate the presence of two distinctive sites for ferrous iron cations [20]. Further indirect evidence for the existence of $\text{Fe}^{2+}(\text{IV})$ are recent density measurements in the CaO-FeO-SiO_2 system [26].

The Amphoteric Character of Iron Oxides

Regardless of the particular behaviour of FeO and the compositions to which its expected acidic behaviour might apply, it is important to consider the amphoteric character of ferric iron in the thermodynamic modelling of slags. The acid and basic dissolution reaction of ferric iron can be represented by [27]



Each reaction will dominate in a specific composition range. An example is the variation of the iron redox ratio as a function of a single compositional parameter (optical basicity), shows opposing trends in basic and acidic slags [28].

While a distinction is made between the possible tetrahedral and octahedral coordination (sub-lattices) of ferrous and ferric iron oxide in thermodynamic modelling of the spinel

structure [29], no such explicit distinction (or analogously, the possibility of $[\text{CaFeO}_2]^+$ clusters) is included for the liquid state. However, the optimised parameters do indicate a strong second-nearest-neighbour pairing of Ca^{2+} and Fe^{3+} [29].

Oxidation Effect on Melt Viscosity

A number of slag viscosity models do not take into account a (possibly very) different behaviour of Fe^{2+} and Fe^{3+} in terms of their effect on the viscosity [30] and adhere to the idea that ferric iron does not influence the viscosity of *steelmaking* slags [3]. As argued above, from a structural point-of-view, such assumptions are not generally valid and it will be illustrated here that an effect of Fe^{3+} (IV) is discernible in the viscosity.

The effect of the iron oxidation state on the (natural logarithm of the) viscosity of various iron oxide melts with alkali and alkaline earth oxides are illustrated in Figure 1. It demonstrates that also alkaline earth oxide systems exhibit a viscosity increase. Two compositions from Seki and Oeters [9] (their samples 8 and 18) have also been included, but due to the limited range no conclusion can be drawn concerning any effect of the oxidation state of the slag on the melt viscosity in the $\text{CaO-SiO}_2\text{-FeO-Fe}_2\text{O}_3$ system. However, among the alkali and alkaline earth oxides displayed in the graph, CaO has the highest cation field strength. Therefore, the stabilisation of Fe^{3+} (IV) and subsequent oxidation effect on the viscosity (if any) is expected to be the smallest in this system.

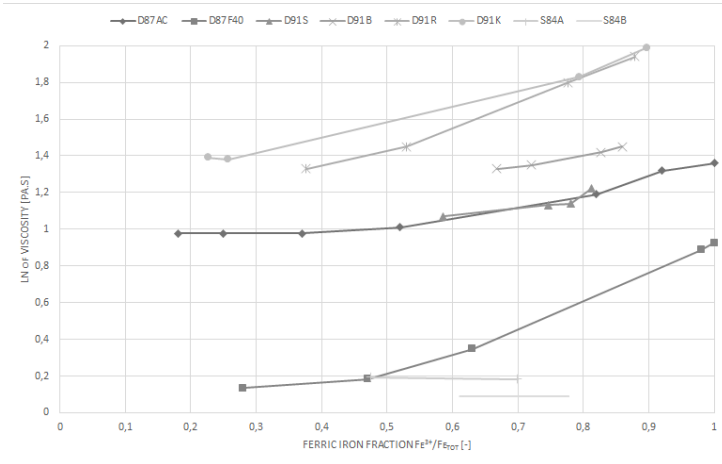


Figure 1: Increase in melt viscosity as a function of the fraction $\text{Fe}^{3+}/\text{Fe}_{\text{Tot}}$ for the systems $\text{Na}_2\text{O-SiO}_2\text{-FeO-Fe}_2\text{O}_3$ (D87AC;F40)[31], $\text{SrO-SiO}_2\text{-FeO-Fe}_2\text{O}_3$ (D91S)[32], $\text{BaO-SiO}_2\text{-FeO-Fe}_2\text{O}_3$ (D91B)[32], $\text{Rb}_2\text{O-SiO}_2\text{-FeO-Fe}_2\text{O}_3$ (D91R)[32], $\text{K}_2\text{O-SiO}_2\text{-FeO-Fe}_2\text{O}_3$ (D91K)[32] and $\text{CaO-SiO}_2\text{-FeO-Fe}_2\text{O}_3$ (S84A;B)[9].

Similarly to the structural considerations, petrological viscosity models [33] have incorporated the strong effect of a charge-balanced $\text{Fe}^{3+}(\text{IV})$, but have left out the much weaker effect of ferrous iron and $\text{Fe}^{3+}(\text{VI})$ based on the limited relevance to their compositions of interest. This again points out the contrasting view and conditions in the two fields. A more nuanced solution has recently emerged; the possibility of NaFeO_4 clusters in the melt, and therefore their effect on viscosity, has been taken into account in viscosity modelling linked to the Modified Quasi-Chemical (thermodynamic) Model [34].

Conclusions

An evaluation of structural information on iron oxide coordination in slag revealed that for compositions relevant to the metallurgical industries a high and a low oxygen coordination can exist for both Fe^{3+} and Fe^{2+} under conditions more oxidising than iron saturation. It is suggested that these structural changes are at the origin of non-linear terms in thermodynamics modelling of such melts. Moreover, the significant effect of the oxidation state of the slag on its viscosity is illustrated, but the results also show that the effect might be limited in the absence of an oxide more basic than CaO .

Acknowledgements

Financial support for this work and a research visit at Swinburne University of Technology (LJB) was provided by Umicore and the Flemish Government, through the agency for Innovation by Science and Technology (IWT) (IWT-project no. 130306).

References

- [1] B. O. Mysen and P. Richet, *Silicate Glasses and Melts: Properties and Structure*. Developments in Geochemistry 10, Elsevier, 2005.
- [2] Y. Waseda and J. M. Toguri, *The Structure and Properties of Oxide Melts: Application of Basic Science to Metallurgical Processing*. World Scientific, 1998.
- [3] K. C. Mills, "The Influence of Structure on the Physico-chemical Properties of Slags," *ISIJ International*, vol. 33, no. 1, pp. 148–155, 1993.
- [4] E. Moosavi-Khoonsari and I.-H. Jung, "Critical Evaluation and Thermodynamic Optimization of the Na_2O - FeO - Fe_2O_3 - SiO_2 System," *Metallurgical and Materials Transactions B*, vol. 47B, pp. 291–308, 2016.
- [5] E. Moosavi-Khoonsari and I.-H. Jung, "Critical Evaluation and Thermodynamic Optimization of the Na_2O - FeO - Fe_2O_3 System," *Metallurgical and Materials Transactions B*, vol. 47B, pp. 576–594, 2016.
- [6] P. Chartrand and A. D. Pelton, "Modeling the charge compensation effect in silica-rich Na_2O - K_2O - Al_2O_3 - SiO_2 melts," *Calphad*, vol. 23, no. 2, pp. 219–230, 1999.

- [7] J. Chipman and L.-C. Chang, "The Ionic Nature of Metallurgical Slags. Simple Oxide Systems," *Transactions of the Metallurgical Society of AIME*, vol. 185, pp. 191–197, 1949.
- [8] Y. E. Lee and D. R. Gaskell, "The Densities and Structures of Melts in the System CaO-FeO-SiO₂," *Metallurgical Transactions*, vol. 5, pp. 853–860, 1974.
- [9] K. Seki and F. Oeters, "Viscosity Measurements on Liquid Sags in the System CaO-FeO-Fe₂O₃-SiO₂," *Transactions ISIJ*, vol. 24, pp. 445–454, 1984.
- [10] J. C. Bowker, C. H. P. Lupis, and P. A. Flinn, "Structural studies of slags by Mössbauer spectroscopy," *Canadian Metallurgical Quarterly*, vol. 20, no. 1, pp. 69–78, 1981.
- [11] L. Pargamin, C. H. P. Lupis, and P. A. Flinn, "Mössbauer Analysis of the Distribution of Iron Cations in Silicate Slags," *Metallurgical Transactions*, vol. 3, pp. 2093–2105, 1972.
- [12] K. C. Mills and B. J. Keene, "Physical properties of BOS slags," *International Materials Reviews*, vol. 32, no. 1-2, pp. 1–120, 1987.
- [13] V. C. Kress and I. S. E. Carmichael, "Stoichiometry of the iron oxidation reaction in silicate melts," *American Mineralogist*, vol. 73, pp. 1267–1274, 1988.
- [14] J. W. Matousek, "Equilibrium Oxygen Pressures of Iron Silicate Slags," *Metallurgical and Materials Transactions B*, vol. 25B, pp. 463–465, 1994.
- [15] P. Kurka, J. Kupčák, and J. Leško, "Influence of the basicity on the redox equilibrium in the CaO-FeO-Fe₂O₃-SiO₂ system," *Chemical Papers*, vol. 43, no. 5, pp. 633–641, 1989.
- [16] K. D. Jayasuriya, H. St.C. O'Neill, A. J. Berry, and S. J. Campbell, "A Mössbauer study of the oxidation state of Fe in silicate melts," *American Mineralogist*, vol. 89, pp. 1597–1609, 2004.
- [17] A. Kilinc, I. S. E. Carmichael, M. L. Rivers, and R. O. Sack, "The Ferric-Ferrous Ratio of Natural Silicate Liquids Equilibrated in Air," *Contributions to Mineralogy and Petrology*, vol. 83, pp. 136–140, 1983.
- [18] G. S. Nikolaev, A. A. Borisov, and A. A. Ariskin, "Calculation of the Ferric-Ferrous Ratio in Magmatic Melts: Testing and Additional Calibration of Empirical Equations for Various Magmatic Series," *Geochemistry International*, vol. 34, no. 8, pp. 641–649, 1996.
- [19] B. O. Mysen, "Magmatic silicate melts: Relations between bulk composition, structure and properties," in *Magmatic Processes: Physicochemical Principles* (B. O. Mysen, ed.), pp. 375–399, Pennsylvania: The Geochemical Society, 1987.
- [20] H. V. Alberto, J. L. Pinto da Cunha, B. O. Mysen, J. M. Gil, and N. Ayres de Campos, "Analysis of Mössbauer spectra of silicate glasses using a two-dimensional Gaussian distribution of hyperfine parameters," *Journal of Non-Crystalline Solids*, vol. 194, pp. 49–57, 1996.

- [21] D. B. Dingwell and M. Brearley, "Melt densities in the CaO-FeO-Fe₂O₃-SiO₂ system and the compositional dependence of the partial molar volume of ferric iron in silicate melts," *Geochimica et Cosmochimica Acta*, vol. 52, pp. 2815–2825, 1988.
- [22] B. O. Mysen, F. Seifert, and D. Virgo, "Structure and redox equilibria of iron-bearing silicate melts," *American Mineralogist*, vol. 65, pp. 867–884, 1980.
- [23] G. A. Waychunas, G. E. Brown Jr., C. W. Ponader, and W. E. Jackson, "Evidence from X-ray absorption for network-forming Fe²⁺ in molten silicates," *Nature*, vol. 332, pp. 251–253, 1988.
- [24] W. E. Jackson, J. Mustre de Leon, G. E. Brown Jr., G. A. Waychunas, S. D. Conradson, and J.-M. Combes, "High-Temperature XAS Study of Fe₂SiO₄ Liquid: Reduced Coordination of Ferrous Iron," *Science*, vol. 262, pp. 229–233, 1993.
- [25] Y. Waseda and J. M. Toguri, "The Structure of the Molten FeO-SiO₂ System," *Metallurgical Transactions B*, vol. 9B, pp. 595–601, 1978.
- [26] X. Guo, R. A. Lange, and Y. Ai, "The density and compressibility of CaO-FeO-SiO₂ liquids at one bar: Evidence for four-coordinated Fe²⁺ in the CaFeO₂ component," *Geochimica et Cosmochimica Acta*, vol. 120, pp. 206–219, 2013.
- [27] D. G. Fraser, "Activities of trace elements in silicate melts," *Geochimica et Cosmochimica Acta*, vol. 39, pp. 1525–1530, 1975.
- [28] A. McLean, Y. D. Yang, I. D. Sommerville, Y. Uchida, and M. Iwase, "The Science and Technology of Slags for Iron and Steelmaking," *High Temperature Materials and Processes*, vol. 20, no. 3-4, pp. 185–193, 2001.
- [29] T. Hidayat, D. Shishin, S. A. Decterov, and E. Jak, "Thermodynamic Optimization of the Ca-Fe-O System," *Metallurgical and Materials Transactions B*, vol. 47B, pp. 256–281, 2016.
- [30] L. Zhang and S. Jahanshahi, "Review and Modeling of Viscosity of Silicate Melts: Part II. Viscosity of Melts Containing Iron Oxide in the CaO-MgO-MnO-FeO-Fe₂O₃-SiO₂ System," *Metallurgical and Materials Transactions B*, vol. 29B, pp. 187–195, 1998.
- [31] D. B. Dingwell and D. Virgo, "The effect of oxidation state on the viscosity of melts in the system Na₂O-FeO-Fe₂O₃-SiO₂," *Geochimica et Cosmochimica Acta*, vol. 51, pp. 195–205, 1987.
- [32] D. B. Dingwell, "Redox viscometry of some Fe-bearing silicate melts," *American Mineralogist*, vol. 76, pp. 1560–1562, 1991.
- [33] D. Giordano, J. K. Russell, and D. B. Dingwell, "Viscosity of magmatic liquids: A model," *Earth and Planetary Science Letters*, vol. 271, pp. 123–134, 2008.
- [34] M. Suzuki and E. Jak, "Development of a Quasi-chemical Viscosity Model for Fully Liquid Slags in the Al₂O₃-CaO-FeO-MgO-SiO₂ System: The Revised Model to Incorporate Ferric Oxide," *ISIJ International*, vol. 54, no. 10, pp. 2134–2143, 2014.

THERMAL CONDUCTIVITY OF BOROSILICATE MELT

Tsuyoshi NISHI¹, Junpei OJIMA¹, Yoshitaka KURODA¹, Hiromichi OHTA¹,
Sohei SUKENAGA², Hiroyuki SHIBATA², Hidenori KAWASHIMA³

¹Ibaraki University (Department of Materials Science and Engineering);
4-12-1 Nakanarusawa, Hitachi, Ibaraki, 316-8511, Japan

²Tohoku University (Institute of Multidisciplinary Research for Advanced Materials);
2-1-1 Katahira, Sendai, Miyagi, 980-8577, Japan

³IHI Corporation (Nuclear Fuel Cycle Project Dept.);
1 Shin-nakahara-cho, Isogo-ku, Yokohama, 235-8501, Japan

Keywords: Borosilicate Melt, Front-heating Front-detecting Laser Flash Method,
Thermal Effusivity, Thermal Conductivity

Abstract

Borosilicate glass is used in mixture of high-level radioactive waste (HLW) generated by nuclear spent fuel. Thermophysical property data of borosilicate melts in molten state during processing of HLW were studied to investigate a possibility of a simpler and flexible process for immobilisation of high level wastes. Especially, these data are indispensable information to optimize the process of the temperature distribution in the glass melting furnace. In this study, the thermal effusivity of B_2O_3 -CaO-SiO₂ melt was measured using a front heating-front detection laser flash method. The thermal conductivity was evaluated by combining the measured thermal effusivity data with specific heat capacity and density. In these results, the thermal conductivity of CaO-B₂O₃-SiO₂ melt was increased with temperature.

Introduction

The long-term hazards of radioactive waste arising from nuclear energy production are a topic of serious discussion and a matter of public concern. High-level radioactive wastes (HLW) produced by a spent fuel reprocessing containing fission products and actinides must be immobilized in highly durable solid matrices. Borosilicate glass is a candidate materials for the immobilization of HLW due to its good glass-forming ability, chemical durability, radiation stability, and so on [1]. In these backgrounds, it is important to clarify the thermal conductivities of borosilicate melts as the indispensable basic information to optimize the process of the temperature distribution in the glass melting furnace. Recently, Hasegawa et al. measured the thermal conductivities of silicate melts for Al₂O₃-CaO-Na₂O-SiO₂ [2]. However, there are few experimental data for the thermal conductivities of silicate melts due to the experimental difficulty.

In this study, the authors prepared borosilicate glass sample of B₂O₃-CaO-SiO₂. Thermal effusivity of the borosilicate melt was measured by the front heating-front detection laser flash method. The thermal conductivity was evaluated by combining the present thermal effusivity data with specific heat capacity and density. Furthermore, the temperature and concentration dependences of the thermal conductivity were evaluated from the experiment results.

Experimental

A. Principle of Thermal Conductivity Measurement

A schematic diagram of the platinum crucible employed in this work is shown in Fig. 1. A single laser pulse was flashed on the bottom of the platinum crucible containing borosilicate melt sample, and the rate of temperature decay at the same surface after pulse heating was measured by an infrared detector. From information of the rate, the thermal conductivities of the melt sample were determined. In the time region immediately after pulse heating, conductive heat transfer is dominant because the temperature gradient in the melt samples in the vicinity of bottom is steep. The effect of radiative heat flow from the bottom surface of the crucible on the temperature response is relatively insignificant compared with conductive heat flux driven by the gradient [3]. It is also noted that measurement in a short initial time region is preferable to avoid the onset of convection in the liquid layer. The upper part of the crucible was open so that bubbles could be released from this side. Theoretical temperature decay was determined under the following conditions:

- (a) The system is kept in thermal equilibrium before laser irradiation.
- (b) The heat flow is one dimensional.
- (c) The melt layer is semi-infinite.

The temperature decay $T_d(t)$ can be given by

$$T_d(t) = T_0 \exp(-h^2 t) \operatorname{erfc}(h\sqrt{t}) \quad [1]$$

$$h = \frac{b_s}{\rho_d C_d l_d} \quad [2]$$

where T_0 , C_d , ρ_d , ρ_s , and l_d are the maximum temperature rise of the temperature response, the specific heat capacity, density, the thermal effusivity, and the thickness of platinum plate, respectively. The subscripts d and s indicate the platinum and the sample, respectively. Here, time t is defined as the elapsed time after irradiating a laser pulse. The values of T_0 and h in Eq. [1] can be estimated by least-square fitting of the measured temperature decay to theoretical temperature response. The thermal diffusivity value of the sample liquid α_s is easily obtained from the following simple equation with respect to thermal effusivity b_s :

$$b_s = \sqrt{\alpha_s \rho_s C_s} \quad [3]$$

The thermal conductivity is also obtained from the following relation (Eq. [4]).

$$\lambda_s = \alpha_s \rho_s C_s \quad [4]$$

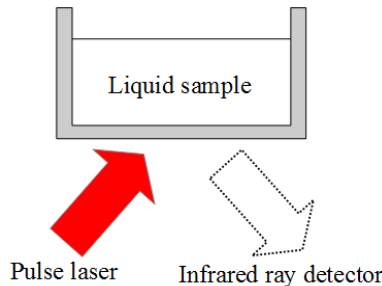


Fig. 1 Schematic diagram of the cell of front-heating front-detection initial method.

B. Materials of borosilicate

The materials used in current work were B_2O_3 , SiO_2 , and $CaCO_3$ manufactured by Kanto Chemical (Tokyo, Japan). The purities of the used materials were more than 99.9 mass% for B_2O_3 , SiO_2 , and CaO , respectively. The synthetic borosilicate samples were then prepared by mixing in desired quantities of powders of each chemical. The mixed samples were calcined in order to decompose carbonate or any hydroxide present, and then they were melted at 150 K higher than its liquidus for 60 minutes in a platinum crucible by muffle furnace [4]. The molten sample was quenched at room temperature and crashed into small pieces in order to introduce into a platinum crucible to facilitate the subsequent melting in the heating chamber of the laser-flash apparatus. Chemical composition of B_2O_3 -CaO- SiO_2 was 20mol% B_2O_3 -30mol%CaO-50mol% SiO_2 .

C. Apparatus of Thermal Conductivity Measurement

Fig. 2 shows the apparatus has been described elsewhere in detail about the method [5]. The essential point is shown in this article. The platinum crucible filled with melt as shown in Fig. 1 was placed on an alumina pedestal. The platinum crucible was 0.2 mm thick, 5 mm deep, and 20 mm in diameter. In order to avoid the effect of the steady-state convection, thin sample was located in the center of the heater. The thickness of the melt sample was 2 to 3 mm. The crucible was put into a heating chamber with kanthal super heating elements. The bottom surface of the crucible was flashed by a Nd-glass laser 10 J, 1060 nm emission wavelength. The InSb infrared detector, 1.2 to 5.5 mm effective wavelengths, was focused onto the bottom surface of the crucible. A charge-coupled device image sensor monitored the sample liquid through the quartz window on

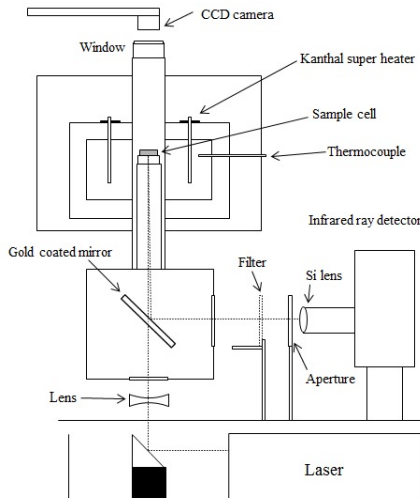


Fig. 2 Schematic diagram of the front-heating front-detection laser flash apparatus.

the top of the chamber. A high-speed electronic circuit system was employed to measure the rapid temperature decay by heat transfer to the melt sample immediately after pulse irradiation. The initial time region of temperature decay was used to avoid the effect of radiative heat transfer of the melts. The use of the initial time region can also avoid the effect of the transient convection occurred by the heating of the melt sample in the vicinity of the bottom of the cell of the laser pulse [3]. Since the measurement was just over in an instant, which was approximately 12 ms, before the transient convection occurred, the effect of the transient convection can be avoided.

All data were measured under atmospheric conditions. The overall errors of thermal conductivity measured by this apparatus has been estimated less than $\pm 6\%$ [5].

D. Procedure

The borosilicate melt samples were thermally equilibrated at each measurement temperature before the data acquisition. The detail information of procedure is mentioned in Ref. [6]. Ten sets of temperature response curves were measured and accumulated to obtain one temperature curve in order to reduce noise ratio to signal. The temperature of the bottom surface of the crucible instantaneously increases by irradiation of a laser pulse and decreases depending on thermal conductivity of the sample. The values of h were obtained by fitting Eq. [1] to the measured temperature response curves. The solid line denotes the values derived from Eq. [1] by fitting the equation to the measured temperature response. Then the thermal conductivity values were estimated from Eq. [2]. The values of specific heat capacities and densities of platinum are estimated in the temperature range investigated from reference data [7]. These data are also extended to a higher temperature by using a linear extrapolation as a function of temperature.

The specific heat capacity and density of the 20mol%B₂O₃-30mol%CaO-50mol%SiO₂ sample are 1.02x10³ Jkg⁻¹K⁻¹ and 2.79x10³ kgm⁻³, respectively. The specific heat capacities were evaluated from the Neumann-Kopp's law. The densities were measured using Archimedes' principle at room temperature in glassy state.

Results and discussion

The thermal conductivities of the 20mol%B₂O₃-30mol%CaO-50mol%SiO₂ melt sample together with those of R₂O(R=Li, Na, K)-CaO-SiO₂ melt samples [8] are shown in Fig. 3. The thermal conduction of silicate melts depend on the bridging oxygen consisted of the SiO₄ tetrahedral network. In the case of R₂O-CaO-SiO₂ melt samples, the ion of R⁺ acts as network modifier. On the other hand, in the case of the B₂O₃-CaO-SiO₂ melt sample, the ion of B³⁺ acts as network former. The thermal conductivity of the B₂O₃-CaO-SiO₂ melt sample is higher than those of R₂O-CaO-SiO₂ melt samples since the silicate network frame could be path of heat conduction. Recently, Y. Kim et al. measured the thermal conductivities of B₂O₃, B₂O₃-SiO₂, and Na₂O-B₂O₃-SiO₂ melts by the Hot-wire method [9,10]. The thermal conductivities of the 20mol%B₂O₃-30mol%CaO-50mol%SiO₂ melt sample are higher than those of the B₂O₃, B₂O₃-SiO₂, and Na₂O-B₂O₃-SiO₂ melts. It can be presumed that 30mol%CaO promote the increase the thermal conductivity. It was also found that the obtained thermal conductivity increased with temperature. Although the positive temperature dependency would need more investigation in future, it might be noted that the characteristic of borosilicate malts is slightly different from that of other silicate melts.

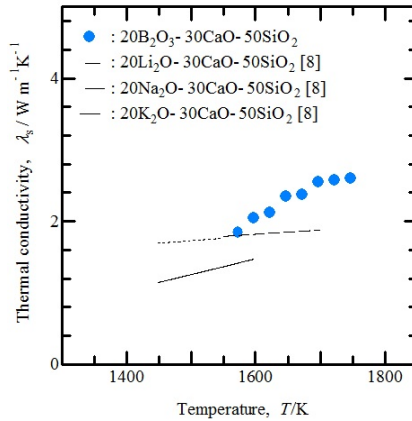


Fig. 3 Thermal conductivity of B₂O₃-CaO-SiO₂ melt sample together with those of R₂O(R=Li, Na, K)-CaO-SiO₂ melt samples.

Acknowledgement

This work was carried out as a part of the basic research programs for the next generation vitrification technology supported by the Ministry of Economy, Trade and Industry. The authors (H.O. and T.N.) is grateful for the financial support from the Cooperative Research Program of “Network Joint Research Center for Materials and Devices”, Institute of Multidisciplinary Research for Advanced Materials, Tohoku University. H. Sato of Ibaraki Univ. and T. Uno of PASONA Co. Ltd. were appreciate for their kind support.

References

1. H. Li, L. Wu, D. Xu, X. Wang, Y. Teng, Y. Li, “Structure and chemical durability of barium borosilicate glass-ceramics containing zirconolite and titanite crystalline phases,” *Journal of Nuclear Materials*, 466 (2015), 484-490.
2. H. Hasegawa, T. Kowatari, Y. Shiroki, H. Shibata, H. Ohta, Y. Waseda, “Thermal conductivity measurements of some synthetic Al₂O₃-CaO-SiO₂ slags by means of a front-heating and front-detection laser-flash method,” *Metallurgical and Materials Transactions B*, 43 (2012) 1405-1412.
3. H. Ohta, H. Shibata, and T. Kasamoto, “Estimation of Heat Transfer of A Front-heating Front-detection Laser Flash Method Measuring Thermal Conductivity for Silicate Melts at High Temperatures,” *ISIJ International*, 46 (2006) 434-440.
4. E.M. Levin et al., *Phase Diagrams for Ceramists, vol. 1*. (Westerville, OH, American Ceramic Society, 1964), 219-221.
5. H. Shibata, A. Suzuki, and H. Ohta, “Measurement of thermal transport properties for molten silicate glasses at high temperatures by means of a novel laser flash technique,” *Material*

- Transaction*. 46 (2005), 1877-1881.
6. H. Ohta, H. Shibata, A. Suzuki, and Y. Waseda, "Novel laser flash technique to measure thermal effusivity of highly viscous liquids at high temperature," *Review of Scientific Instrument*, 72 (2001) 1899-1903.
 7. Japan Society of Thermophysical Properties, *Thermophysical Properties Handbook, 1st ed.*, (Tokyo, Japan Society of Thermophysical Properties, Yonendo, 1990), 24 (in Japanese).
 8. J.Ojima, H.Hasegawa, Y.Shiroki, T.Inose, H.Shibata, S.Sukenaga, H.Ohta, "Thermal conductivity of borosilicate melts," *Proc.34th Jpn.Symp.Thermophys. Prop.*, Toyama (2013), A323 (in Japanese).
 9. Y. Kim, Y. Yanaba, K. Morita, "The Effect of Borate and Silicate Structure on Thermal Conductivity in the Molten Na₂O-B₂O₃-SiO₂ System," *Journal of Non-Crystalline Solids*, 415 (2015) 1-8.
 10. Y. Kim, K. Morita, "Thermal Conductivity of Molten B₂O₃, B₂O₃-SiO₂, Na₂O-B₂O₃, and Na₂O-SiO₂ Systems," *Journal of the American Ceramic Society*, 98 (2015) 1588-1595.

MELTING POINT AND HEAT CAPACITY OF $MgCl_2 + Mg$ SALTS

Yuxiang Peng, and Ramana G. Reddy

Department of Metallurgical and Materials Engineering,
The University of Alabama, Tuscaloosa, AL 35487, U.S.A

Keywords: Magnesium salts, $Mg + MgCl_2$ salts, heat capacity, and melting point

Abstract

$MgCl_2$ -containing salt is one of the candidates for the solar thermal energy storage applications. To protect the structural alloy from corrosion, the addition of Mg to salt as a corrosion inhibitor is considered. Melting point, heat capacity, enthalpy, entropy and Gibbs energy of $MgCl_2$ with different amount of Mg are studied in this paper. Depression of melting point is calculated using a derivation of Raoul-Van't Hoff formula. The $MgCl_2$ rich phase diagram is constructed. The $MgCl_2$ with a small amount of Mg addition shows no significant effect on melting point of the salt mixture. Moreover, it can be a candidate as heat transferring fluid for $MgCl_2$ in solar thermal energy storage applications.

Introduction

From the reports of Oak Ridge National Lab (ORNL), molten salts are used in the nuclear industry started with Aircraft Reactor Experiment (ARE) in 1949. Even the heat capacity of carbonate and nitrate salts are higher [1, 2], for the high-temperature service, the initial consideration of the molten salt is fluoride salt even in the later program, Molten Salt Reactor Experiment for the nuclear application [3, 4]. At the same time of ARE, chloride salts were studied in Brookhaven National Laboratory including the investigation of corrosion of structural materials [5]. Nowadays, molten salts have been not only used in the nuclear application but also considered as a candidate for thermal energy storage media in solar energy applications [6]. Although fluoride salts show better thermal properties compared with chloride salts, chloride salts are less corrosive to the structural alloys. At 850°C for 500hrs corrosion experiment, the corrosion rate of 800H alloy is 11mg/cm² in KCl-MgCl₂. However, the corrosion rate is more than 20mg/cm² in FLiNaK [4]. Moreover, as $MgCl_2$ -containing salt presents less expensive than LiCl-containing salt [3], KCl-MgCl₂ has been used for the secondary process in nuclear applications [7]. However, individual salt like $MgCl_2$ is much cheaper than binary salt KCl-MgCl₂. Moreover, they both show the similar heat capacity, viscosity, and thermal conductivity [3]. Thus, $MgCl_2$ molten salt could be the candidate as thermal energy storage media. And Heine [8] has studied $MgCl_2$ molten salt at 760°C to find a proper heat storage material. However, corrosion problem still exists. Addition of inhibitor like Zr [9] and Y [10] to FLiNaK molten salt showed good ability in protecting alloys from further corrosion. Therefore, the addition of active metal in $MgCl_2$ may be a useful method of retarding corrosion. Mg is always selected as one of the proper inhibitors for numerous alloys corrosion in the severe environment [11]. Hence, it could be also considered as a proper inhibitor in protecting or retarding alloys corrosion in $MgCl_2$ molten salt. Reaction (1) is taking place as Mg is added into the $MgCl_2$, showing the mechanism of Mg in protecting alloys, which exerts a continuous interest in the investigation of Mg as an inhibitor in the molten salt.



Many studies have shown that the corrosion of alloys can be inhibited when Mg is added to the molten salts at high temperatures. However, less attention has been paid to the effect on melting point and heat capacity of $MgCl_2$ after adding Mg inhibitor. Before choosing Mg as the proper

inhibitor in $MgCl_2$, the effect on thermal properties of molten salt has to be taken into account [12]. Therefore, the investigation of change in the thermal properties of $MgCl_2$ molten salt with the addition of Mg inhibitor is of not only practical but also theoretical interest. The present work attempts to establish the suitability of Mg as an inhibitor for the alloys corrosion in $MgCl_2$ molten salt. From this point of view, melting point, heat capacity, enthalpy, entropy, and Gibbs energy after adding different amounts of Mg in $MgCl_2$ molten salt are studied in this article.

1. Calculations

Thermal properties of the mixture ($MgCl_2$ with different mole% Mg) are predicted using the mixing rule, which requires thermal properties of $MgCl_2$ and Mg. However, the melting point is calculated from the derivation of van't Hoff-Raoult formula shown in equation (2):

$$\frac{d \ln K_{eq}}{dT} = \frac{\Delta H^\theta}{RT^2} \quad (2)$$

where K_{eq} is equilibrium constant, ΔH is standard enthalpy change in kJ/mol , T is the temperature in K and R is universal gas constant.

1.1. Melting point calculation

An ideal solute has no effect on the enthalpy of the solution because the enthalpy of mixing is zero. A change in entropy arises due to the introduction of small amount of disordered solute in the pure solvent. As a result, the physical properties, such as the melting point, of the solution is expected to change. For a given solution, the increase in disorderness is independent of the solutes type, i.e., only the number of the solute particles not the chemical properties of solute effects the melting point [13].

Van't Hoff-Raoult formula of equation (2) is used to determine the effect of solute on melting point of solution (ignoring physical properties of solute) since the equilibrium constant is a function of the temperature. The van't Hoff-Raoult formula can be rearranged to give equation (3):

$$\frac{d \ln K_{eq}}{d \frac{1}{T}} = - \frac{\Delta H^\theta}{R} \quad (3)$$

Integration of equation (3) on temperature gives equation (4):

$$\ln \left(\frac{K_2}{K_1} \right) = \frac{-\Delta H^\theta}{R} \left(\frac{1}{T_2} - \frac{1}{T_1} \right) \quad (4)$$

The change in melting point of $MgCl_2$ is observed with the addition of Mg, thus, K is equilibrium constant of the $MgCl_2$ solution. For the pure solvent of $MgCl_2$, K_1 is equal to 1, and T_1 is melting point of pure $MgCl_2$, which is 987.15 K. The equilibrium constant K_2 is equal to the activity of $MgCl_2$ in the $MgCl_2$ -Mg solution, which is given as:

$$K_2 = a_2 = x_{mgcl_2} * \gamma \quad (5)$$

where x_{mgcl_2} is the concentration of $MgCl_2$, and γ is the activity coefficient of $MgCl_2$. As the concentration of Mg is very small in the solution, γ is assumed to be 1 (from Raoult's Law). Thus, the equilibrium constant is assumed to be equal to the concentration of $MgCl_2$. At melting point, ΔH^θ is considered to be the enthalpy of fusion, which is 43100 J/mol for $MgCl_2$ [14].

$$T_2 = T_1 - \Delta T_{dep} \quad (6)$$

where ΔT_{dep} is the depressed melting temperature, T_1 is initial melting point of pure compound (it is written as T_m in equation (7)), T_2 is the melting point of solution after adding solute.

Therefore, by substituting equation (6) in the equation (4), we can obtain the formula (7):

$$\Delta T_{dep} = \frac{\Delta T_m^2 * \ln(K_2) * R}{-\Delta H_{fus}} / \left(1 + \frac{\ln(K_2) * R}{-\Delta H_{fus}} \right) \quad (7)$$

T_m is melting point of pure compound, ΔH_{fus} is the heat of fusion, K_2 is the activity of $MgCl_2$ in the $MgCl_2$ -Mg solution.

The maximum concentration of Mg in the solution for the liquid monotectic point is 0.2 mol% of Mg [15], thus all parameters are known for the calculation of ΔT_{dep} .

1.2. Calculation for heat capacity of mixture

By ignoring the contribution from the slight amount of Mg solute in $MgCl_2$ on properties, the mixture is assumed as two separate compounds. Hence, the simple mixing rule of equation (8) is used to predict the heat capacity, enthalpy, density and other thermal properties of the $MgCl_2$ -Mg system.

$$P_{mix}^n = P_1^n * x_1 + P_2^n * x_2 \quad (8)$$

where P is thermal properties of materials and x is mole fraction for each compound, and n is taken as 1 for all the properties calculation.

Heat capacity varies with the temperature and the standard enthalpy and entropy at 298.15 K of $MgCl_2$ and Mg required for the calculations are obtained from the database of thermodynamic modeling software. Using the equations (9-11) and mixing rule of equation (8) with n equal to 1, enthalpy, entropy and Gibbs energy varying with temperature (298.15 - 1273.15 K) is calculated for the $MgCl_2$ -Mg system.

$$\Delta H = \int_{T_1}^{T_2} C_p dT \quad (9)$$

$$\Delta S = \int_{T_1}^{T_2} \frac{C_p}{T} dT \quad (10)$$

$$\Delta G = \Delta H - T * \Delta S \quad (11)$$

The heat capacity data for the $MgCl_2$ and Mg in the temperature range of 298.15-1273.15K are obtained from thermodynamic modeling. The fitting equations are listed in Equation. (12-15).

$$C_p \text{ of } MgCl_2(s): 76.651 + 9.984 * 10^{-3} * T - 6.439 * 10^5 * T^{-2} - 0.006 * 10^{-6} * T^2$$

Temperature range: 298-987K (12)

$$C_p \text{ of } MgCl_2(l): 88.141 + 0.002 * 10^{-3} * T + 59.212 * 10^5 * T^{-2}$$

Temperature range: 987-2900K (13)

$$C_p \text{ of } Mg(s): 28.455 - 6.447 * 10^{-3} * T - 2.481 * 10^5 * T^{-2} + 11.932 * 10^{-6} * T^2$$

Temperature range: 923-987K (14)

$$C_p \text{ of } Mg(l): 34.3$$

Temperature range: 923-1361K (15)

2. Results and discussion

2.1. Effect of Mg on melting temperature

The van't Hoff-Raoult formula is evaluated by calculating the melting point depression of other chloride salts and comparing them with actual melting point depression of $MgCl_2$ -Mg system. The experimental data of melting point, the heat of fusion of pure salts, and the monotectic points of different chloride salt-metal systems are obtained from literature [15, 16]. The calculations are performed using derivation from van't Hoff-Raoult formula (6), and the detail results are shown in Table 1.

Table 1 Depression of melting point of several chloride salts compared with experimental data

Salt system	ΔH_{fus} (J/mol)	Melting point (K)	Monotectic point (conc. of salt)	coefficient γ	Depression(K)		Reference
					Calc.	Expt.	
NaCl-Na	28160	1074.15	0.979	1	7.23	7	[11]
KCl-K	26530	1044.65	0.895	1	37.94	20	[11]
BaCl ₂ -Ba	15850	1235.15	0.85	1	130.1	72	[11]

The prediction of depression for NaCl-Na system is comparable to the experimental values of the chloride salts. However, assuming coefficient to be one is only available when the solution follows Roul't's law as the concentration of metal in salt is slight enough. As the concentration of the respected metal is too much in the solution (K is 0.105 and Ba is 0.15), the contribution of coefficient will be significant to the depression of melting point. The comparable depression of melting point is calculated using different coefficient to verify the reasonable coefficient in a real solution. Furthermore, the corresponding depression on the coefficients are listed in Table 2.

Table 2 Comparable depression of several chloride salts with respected coefficient

Salt system	ΔH_{fus} (J/mol)	Melting point (K)	Monotectic point (conc. of salt)	coefficient	Depression (K)		Reference
					Calc.	Expt.	
NaCl-Na	28160	1074.15	0.979	1	7.23	7	[3]
KCl-K	26530	1044.65	0.895	1.05	20.7	20	[3]
BaCl ₂ -Ba	15850	1235.15	0.85	1.07	71.1	72	[3]

Evidently, the coefficients are close to unity (1 - 1.07) for both the systems, which is reasonable for all real solid solutions. However, as a liquid monotectic point of Mg in MgCl₂ is 0.002 [15], the presence of trace amount of Mg in the solution indicates that MgCl₂-Mg mixture follows Roul't's law. In which case, the coefficient is assumed to be 1 for all the melting point depression calculations. When 0.002 mole Mg (liquid monotectic point) is added into 1 mole MgCl₂, melting point depression of 0.38 K is obtained for the system. Additionally, the slight decrease in melting point with Mg addition to MgCl₂ is reasonable.

As the mole fraction of Mg in MgCl₂ increases to 0.009, the melting temperature also increases to 800 °C [15]. For simplification, linear increase or decrease of melting point with increasing amount of Mg is assumed. Thus, the partial phase diagrams of the MgCl₂-Mg system is constructed in Figure 1 & 2. From Figure 1 & 2, the slight depression with addition Mg solute to the MgCl₂ salt shows a negligible effect on thermal properties of the system.

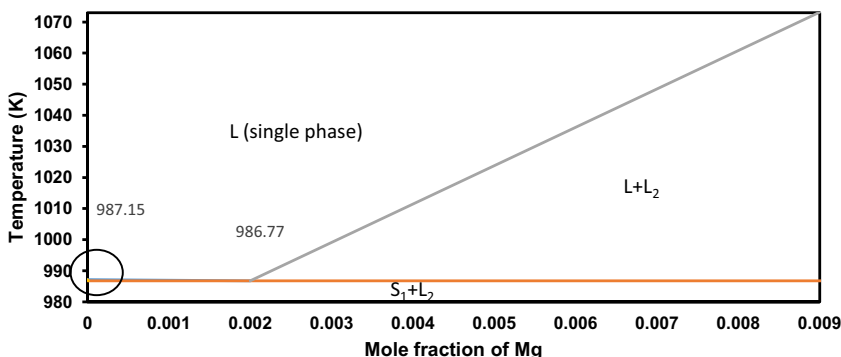


Figure 1 Partial phase diagram of MgCl₂-Mg, S₁ is solid of MgCl₂, L₂ is liquid of Mg and L is liquid consolute by MgCl₂ and Mg

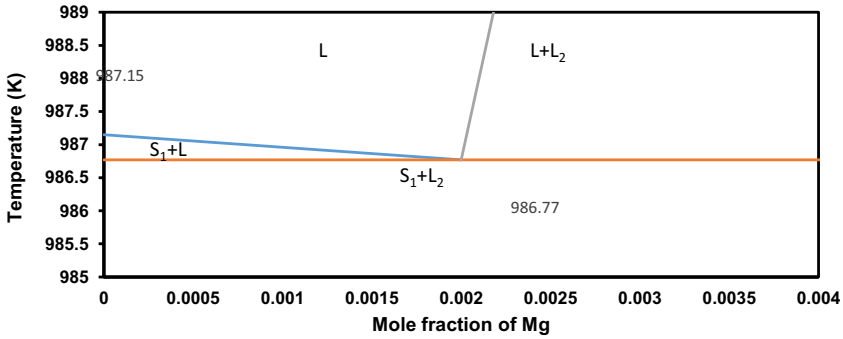


Figure 2 Partial phase diagram of MgCl_2 -Mg with 0.004 x-axis scale, S_1 is solid of MgCl_2 , L_2 is liquid of Mg and L is liquid con-solution of MgCl_2 and Mg

2.2. Effect of Mg on heat capacity and respected enthalpy, entropy and Gibbs energy

By using mixing rule, the heat capacity of MgCl_2 without and with different amount of Mg is shown in Figure 3 calculated with the linear mixing rule.

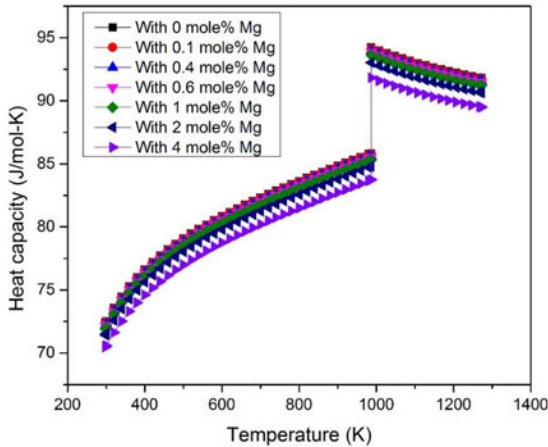


Figure 3 Heat capacity of MgCl_2 without and with different amount of Mg

As heat capacity of Mg is lower than that of MgCl_2 in the temperature range, the addition of Mg to MgCl_2 slightly decreases the heat capacity of MgCl_2 . In addition, the solution is melted to a liquid phase after 987K. As shown in equation (13) and (15), increased temperature results in the decrease of the heat capacity of the mixture. One essential criterion of heat storage media is high heat capacity, and a tolerable decline in the heat capacity at high temperatures do not worsen the chances of the mixture as media for the heat storage applications.

As discussed previously in equations (9) to (15), the integration of function containing the heat capacity term gives both change in enthalpy and entropy for a particular temperature range.

Therefore, known the standard enthalpy and entropy at 987K, enthalpy and entropy of the mixture at different temperatures are calculated and shown in Figure 4 & 5.

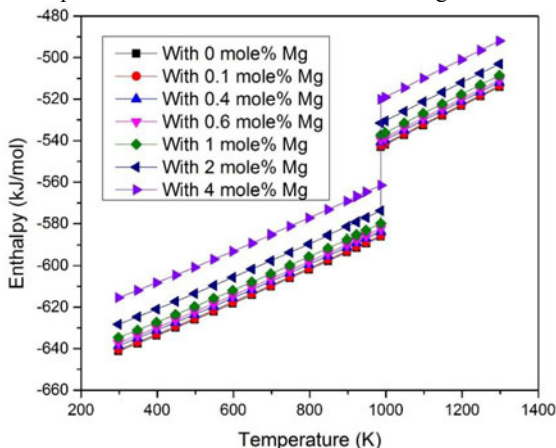


Figure 4 Enthalpy of MgCl_2 without and with different amount of Mg

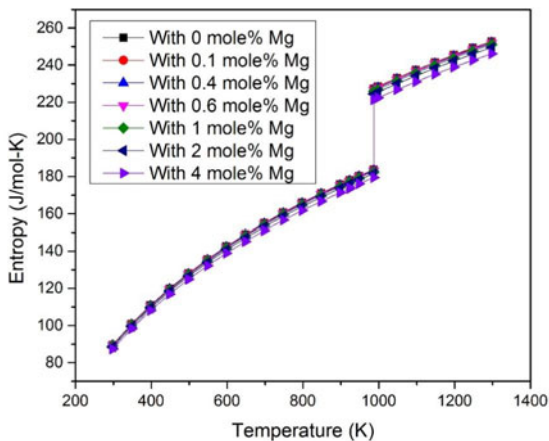


Figure 5 Entropy of MgCl_2 without and with different amount of Mg

As shown in Figure 4, the change in enthalpy of the mixture and pure MgCl_2 increases with the rise in temperature. Similarly, a significant increment in a change in the enthalpy is also observed with more amounts of Mg added to MgCl_2 salt. As shown in Figure 5, the change in the entropy shows a similar increase with the increase in the temperature. However, a slight decrease in the change in entropy of the salts is observed with the increase in the content of Mg in the MgCl_2 salts. As shown in Figure 6, by knowing the changes in the enthalpy and entropy, the change in Gibbs energy for the mixtures are calculated at different temperatures. The change in

the Gibbs energy of the mixture increases with the amount of Mg added to $MgCl_2$ salt, and the negative values of the change in Gibbs energy indicate that the systems are stable at higher temperatures.

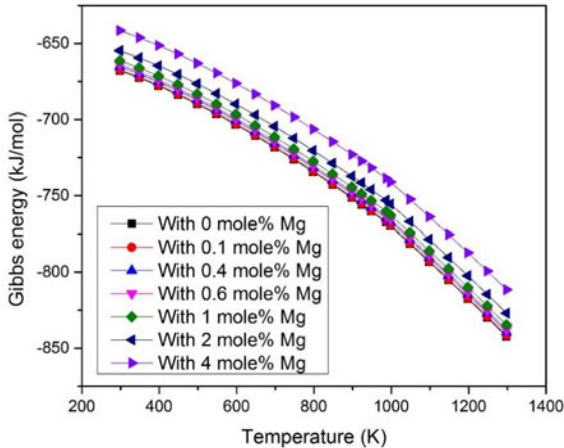


Figure 6 Gibbs energy of $MgCl_2$ without and with different amount of Mg

3. Conclusions

The melting point of the mixture of $MgCl_2$ and Mg slightly decreases while compared to the pure $MgCl_2$ salt. That is concluded from the calculation derived from van't Hoff-Raoult formula, and the decrease in melting temperature is 0.38 K at 0.2 mol% of Mg addition to the $MgCl_2$ salt.

The calculations on heat capacity, entropy, enthalpy and Gibbs energy reveal that Mg solute does not worsen the stability of $MgCl_2$ salt or deteriorate the candidate of $MgCl_2$ -Mg as heat storage media.

References

- [1] Y. Takahashi, R. Sakamoto, M.Kamimoto, Heat Capacities and Latent Heat of $LiNO_3$, $NaNO_3$ & KNO_3 , International Journal of Thermophysics, Vol. 9, 1998. pp. 1081-1090.
- [2] Araki, N., et al. "Measurement of thermophysical properties of molten salts: mixtures of alkaline carbonate salts." International journal of thermophysics Vol. 9, 1988. pp. 1071-1080.
- [3] Williams, D. F., Assessment of candidate molten salt coolants for the NGNP/NHI Heat-Transfer Loop, ORNL/TM-2006/69, 2006. pp. 1-44.
- [4] Sridharan, Kumar, et al. Liquid Salts as Media for Process Heat Transfer from VHTR's: Forced Convective Channel Flow Thermal Hydraulics, Materials, and Coating. No. DOE/ID14826. University of Wisconsin, Madison, 2012.
- [5] Susskind, H., et al. Corrosion Studies for a Fused Salt-Liquid Metal Extraction Process for the Liquid Metal Fuel Reactor. No. BNL-585. Brookhaven National Lab., Upton, NY, 1960.
- [6] Forsberg, Charles W., Per F. Peterson, and Haihua Zhao. "High-temperature liquid-fluoride-salt closed-Brayton-cycle solar power towers." Journal of Solar Energy Engineering Vol. 129.2, 2007. pp. 141-146.

- [7] Sohal, Manohar S., et al. "Engineering database of liquid salt thermophysical and thermochemical properties." Idaho National Laboratory, Idaho Falls, 2010.
- [8] Heine, D., F. Heess, and D. Steiner. "Investigation of latent heat storage materials in the medium and high temperature range." NASA STI/Recon Technical Report N 83: 16933, 1982.
- [9] Sellers, R. S., et al. "Materials corrosion in molten LiF-NaF-KF eutectic salt under different reduction-oxidation conditions." Proc. Int. Conf. Advances in Nuclear Power Plants. Vol. 12, 2012. pp. 12189.
- [10] Li, Xiao-li, et al. "High-temperature corrosion behavior of Ni-16Mo-7Cr-4Fe superalloy containing yttrium in molten LiF-NaF-KF salt." Journal of Nuclear Materials, Vol. 464, 2015. pp. 342-345.
- [11] J.A. Lane, H.G. MacPherson, F. Moslan (Eds.), Fluid Fuel Reactors, Addison-Wesley, 1958
- [12] Arenas, M. A., A. Conde, and J. J. De Damborenea. "Cerium: a suitable green corrosion inhibitor for tinplate." Corrosion Science Vol. 44, 2002. pp. 511-520.
- [13] Atkins, Peter, and Julio De Paula. Elements of physical chemistry. Oxford University Press, 2012.
- [14] Chase, Malcolm W., et al. JANAF thermochemical tables, 1975 supplement. Journal of physical and chemical reference data Vol. 4.1, 1975. pp. 1-176.
- [15] Bredig, M. A. Mixtures of metals with molten salts. No. ORNL-3391. Oak Ridge National Lab., Tenn., 1963.
- [16] Bredig, M. A., J. W. Johnson, and Wm T. Smith Jr. "Miscibility of Liquid Metals with Salts. I. The Sodium-Sodium Halide Systems¹." Journal of the American Chemical Society Vol. 77.2, 1955. pp. 307-312.

**ADVANCES IN MOLTEN
SLAGS, FLUXES, AND SALTS:**

Proceedings of



**Interfacial
Phenomena**

DOES INTERFACIAL TENSION PLAY THE MOST IMPORTANT ROLE IN SLAG-METAL REACTIONS? AN IMPORTANT ASPECT IN PROCESS OPTIMIZATION

Du Sichen¹ and Jesse F. White²

¹Royal Institute of Technology (KTH), Stockholm, Sweden

²Elkem AS, Technology, Kristiansand, Norway

Keywords: Interface, heterogeneous reaction, interfacial phenomena, Gibbs energy

Abstract

In view of the nature of heterogeneous reaction of many materials processes, great attention has been paid to the reaction interfaces. Very often, the interfacial tension is given the foremost importance in the study of interfaces in general and slag-metal reactions in particular. As an example, the dependence of entrainment of ladle slag into liquid steel on interfacial tension has been the topic of many researchers.

In the present work, the interface between liquid silicon and CaO-SiO₂ slag and the interfacial reaction between silicon and graphite were studied experimentally to gain an insight into the impacts of chemical driving force and interfacial tension on the interfacial phenomena. The results strongly suggested that the chemical driving force could play dominating role in determining the interface, while the interfacial tension would only become important when the slag and metal were reaching equilibrium. Based on the experimental findings, the kinetics of the slag-metal reaction was discussed. Also, the possibility of the entrainment of ladle slag as a source of nonmetallic inclusions was evaluated. The present study would like to draw researchers' attention regarding the important role of Gibbs energy of the reaction at the interface in the interfacial phenomena and therefore getting an improved understanding of the reaction process.

Introduction

Slag-metal reactions and gas-metal reactions hold the key to successful steelmaking. The former plays also great role in silicon refining. Two-film and surface renewal models had been very popular in describing slag-metal reactions, before the computer became really available to researchers. However, they could only be applied to specific reactors under specific operating conditions, based on which the mass transfer coefficients are optimized. The lack of understanding of the slag/metal interface and the assumption of uniform concentration in the bulk are the foremost factors making the models unrealistic.

It is commonly accepted that most chemical reactions reach thermodynamic equilibrium locally at steelmaking temperatures. To the knowledge of the present authors, the models describing the slag-metal reactions have all made this assumption.^[1-4] While the models trying to simulate the

slag-metal interface^[2-4] have shown good potential of simulating slag-metal interface, the real physical behavior of the slag-metal interface still need very careful study.

Both the formation of inclusions by slag entrainment and inclusion separation to the slag have been discussed by many researchers. A number of publications have been devoted to the separation of inclusion removal to the top slag. The model developed at an early stage assumed that all inclusions reaching the interface between the steel and the slag would be separated from the steel.^[5-7] Realizing the importance of interfacial energy and liquid metal film in the removal of inclusions to the slag, researchers have developed models taking these factors into consideration.^[8-11] However, in all the modelling approaches, no chemical potential differences between the two phases have been taken into account.

In connection with silicon refining, a number of studies have investigated the wettability and reaction of liquid silicon with different substrates, including graphite and vitreous carbon^[12-17] The open porosity of the graphite, surface roughness, and not the least, contact time have all been documented to greatly influence the “dynamic wetting” of liquid silicon on graphite. Although the variation of the contact angle with time has been well known, in process modelling and process optimization the importance has always been given to the interfacial energy. The present work focuses on a discussion regarding whether the chemical driving force has been overlooked when studying the interface and whether the interfacial energy has been given too much importance. The discussion is based on the experimental results obtained under well-defined experimental conditions.

Experimental

Two types of experiments were conducted, namely (1) interfacial reaction between slag and silicon metal, and (2) the wetting behavior of liquid silicon on carbon substrates.

Interfacial reaction between slag and silicon

The mixing crucibles and impellers were made of Mersen 2020 graphite. The impeller was 45 mm high and 15 mm wide. The mixing crucible was fabricated by boring four 18-mm diameter holes into a graphite blank in such a manner as to create an internal volume with a quatrefoil profile. The resulting four vertical protrusions acted as baffles to prevent bulk rotation of the melt and consequent generate vortex. A schematic diagram of the setup is provided in Fig. 1, with the details of the crucible arrangement shown in (b). A description of the setup can be found in a previous publication.^[18] A stirring motor was used to drive a graphite impeller that stirred the melt. The stirring motor and support tube were fastened to a motorized belt drive that allowed the vertical movement of the crucible assembly in and out of the hot zone of the furnace. To seal the moving mechanical components, radial shaft seals were used between the impeller shaft and support tube, and between the support tube and the cooling chamber.

CaO–SiO₂ slags, designated Slag A B, and C were prepared prior to the experiments by fusing high-purity fused silica and calcium oxide in a graphite crucible. The silicon was polycrystalline, semiconductor-grade purity. Boron was added either to the slag phase (in the form of SiB₆) or to the metal phase (in the form of H₃BO₃) at an initial concentration of approximately 436 ppm. In preparation for each heat, 40 grams of silicon chips were placed in the bottom of the mixing crucible, and 40 grams of slag constituents were placed on the top. After placing the mixing

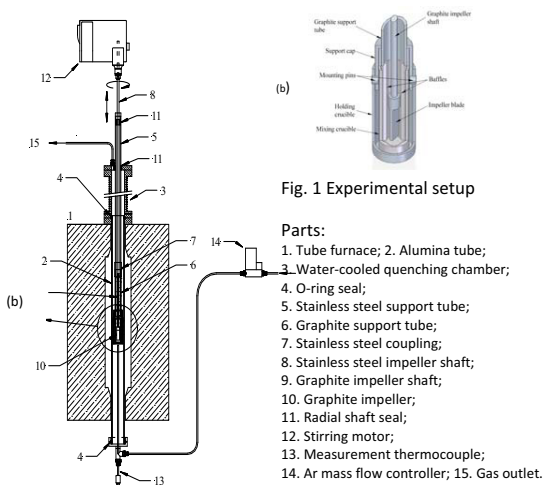


Fig. 1 Experimental setup

minimize thermal shock to the alumina reaction tube. The crucible assembly was then lowered into final position in the hot zone of the furnace. When the impeller was in position (10 mm above the bottom of the mixing crucible), the stirring motor was engaged (zero-time $t = 0$).

At the end of an experiment, the crucible assembly was rapidly retracted out of the furnace into the water-cooled quenching chamber by raising the stainless steel support tube with the motorized belt drive. A high flow of argon gas was immediately initiated to expedite quenching of the samples. Photographs and micrographs were taken of the crucible cross-sections.

Interfacial phenomena between liquid silicon and carbon substrates

The experimental apparatus was a high-temperature sessile drop apparatus as depicted in Fig. 2. A detailed description can be found in a previous paper.^[19] The main component of the setup was a horizontal tube furnace and an alumina reaction tube (70 mm inner diameter). The reaction tube was sealed with O-rings on its ends by an internally water-cooled quenching chamber on one end, and the other end had a water-cooled aluminum cap with a sealed quartz glass window. The reaction gas entered on the window end and exited the quenching chamber. A carriage made of graphite held the specimen in the hot zone of the furnace. The carriage was threaded onto a water-cooled pushrod (sealed with a packing). The pushrod was fastened to a motorized screw drive that enabled the precise positioning and movement of the specimen to reproducibly control heating rates. The measurement thermocouple was a Type C (W / W-5 % Re), and was mounted axially in the pushrod and carriage, with the tip inside the carriage body positioned directly under the substrate. A gas train prepared the



Fig. 2 Experimental setup for contact angle measurements

reaction gas mixture when needed. High-purity argon gas was metered using a Bronkhorst mass flow meter ($\pm 0.5\%$ accuracy).

In preparation for each experiment, the silicon piece and the graphite substrate were first cleaned with ethanol and then placed on the carriage. The carriage was positioned in the quenching chamber, and the whole system was then sealed. The reaction tube was evacuated with a vacuum pump and back-filled with argon. To start the run, a flow of reaction gas and the furnace control sequence were initiated. The flow rate of the inlet gas was fixed at 0.02 l min^{-1} . The temperature was ramped up to 1703 K ($1430\text{ }^\circ\text{C}$) at 2 degrees per minute. The variation of the sample was followed by video recording.

At the end of each experiment, the carriage was rapidly withdrawn from the furnace into the water-cooled quenching chamber by activating the mechanical drive. In some of the tests the specimens were quenched shortly after melting started, while in other tests the silicon was given time to completely wet the graphite substrate so that dynamic changes in infiltration could be observed. Still images were extracted from the video files.

Results

Interfacial reaction between slag and silicon

Figure 3 and Figures 4 show photographs of the crucible cross-sections for the heats where boron was added to the slag phase or metal phase, respectively. Note that mixing was stopped prior to quenching, and that the mixing conditions were kept constant in all the experiments. At short reaction times of $t = 30$ seconds and $t = 60$ seconds, (Figure 3(a) and (b), Figure 4(a) and (b), it can be seen with the naked eye that the interfacial boundary between the metal phase and slag phase is markedly irregular, and that there are countless small yet visible metal droplets entrained in the slag phase. By 300 seconds of reaction time (Fig. 3d and Fig. 4d), the interface is smooth, and the slag phase color has transformed from grey to green. To show this aspect



a) Heat 7, 30s b) Heat 8, 90s c) Heat 24, 180s d) Heat 6, 300s

Fig. 3 Changes in characteristics of slag–metal interface, slag phase doped with boron



a) Heat 16, 30s b) Heat 17, 90s c) Heat 23, 180s d) Heat 11, 300s

Fig. 4 Changes in characteristics of slag–metal interface, metal phase doped with

clearer, Fig. 5(a) and 5(b) show LOM micrographs at $50\times$ magnification of the bulk slag phase at $t = 30\text{ s}$ and $t = 300\text{ s}$. At 30 seconds reaction time, metal is finely dispersed in the slag phase as

irregularly formed droplets of varying size, indicating thereby that the interfacial area is very large at this stage. In contrast, under the same mixing conditions at $t = 300$ s (Fig. 5b), the slag phase is nearly devoid of metal droplets. Higher magnification (500x) reveals that only very tiny metal droplets less than 5 micrometers in diameter are left in the slag phase.

Fig. 6 shows the change in boron concentration with increasing reaction time for the slag being doped with boron or the metal phase being doped with boron. In the case of boron addition into the metal phase, the concentration decreased exponentially and leveled out by about 300 seconds. When boron was added to the slag phase, the concentration in the metal phase increased and leveled out. Since the total amount of boron was added to the system was equal in each case, these two curves converge at 300 seconds. The converging of the curves indicates strongly that slag and metal have almost reached equilibrium after 300 seconds.

Fig. 7 shows the variation of calcium concentration in the metal phase as a function of reaction time and mixing speed (rpm). The calcium concentration in the silicon increases with time as CaO in the slag is reduced. It is readily apparent that a stirring speed greater than 100 rpm does not appear to increase the rate of calcium transfer. With stirring, by 600 seconds the calcium concentration in the slag reaches around 0.5 mass %Ca. Note that the variation of the concentration is very small after 300 s, within the experimental uncertainties.

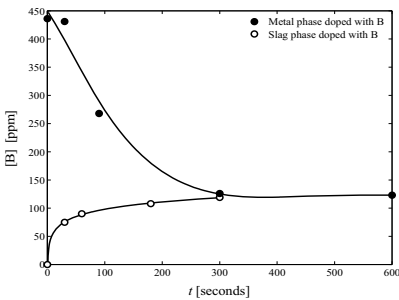


Fig. 6 Boron concentration as a function of time

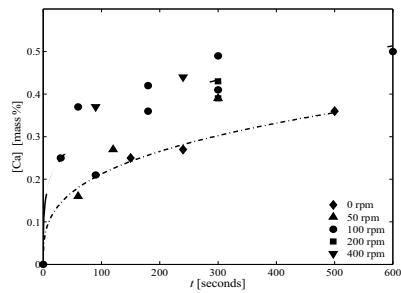
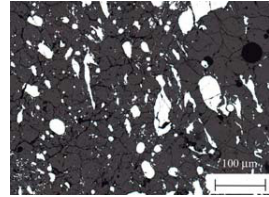
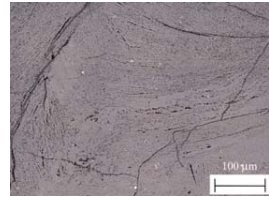


Fig. 7 Ca concentration as a function of time



a) Heat 7, $t = 30$ s, 50 \times



b) Heat 11, $t = 300$ s, 50 \times

Fig. 5 Optical micrographs of the slag phase

Interfacial phenomena between liquid silicon and carbon substrates

The starting time, $t = 0$ (designated t_0) was assigned to when the silicon was completely molten. It took only a few minutes for the molten silicon to completely spread and infiltrate the graphite. In this case, the substrate actually fractured during infiltration due to internal stresses as also described by Israel *et al.*^[20] It should be mentioned that the “contact angle” observed in a non-

equilibrium system is not a fundamental property but a reaction of the system and its tendency to go towards equilibrium. Hence, the term “apparent contact angle” is used in the current study for all further discussions.

The change in apparent contact angle as a function of time for the three different graphite grades at rapid heating rate are presented in Fig. 8. In every one of these runs, the specimen was pushed at the same velocity (corresponding to a rate of temperature increase calculated to be 6.6 K/s) into the hot zone of the furnace at 1703 K (1430 °C). It is evident that there are clear differences in the dynamic wetting behavior of these graphite grades. For all of the graphite grades tested, the apparent contact angle decreased linearly with time until approaching equilibrium, corroborating the observation of Israel *et al.*^[20]. Silicon melting on Grade A in Test SD1 started out at a high apparent contact angle and did not attain an equilibrium contact angle until after over 250 seconds; this is expected since this is an isostatically pressed, dense graphite grade with low open porosity. The initial apparent contact angle for Grade C, surprisingly, was quite similar to Grade A grade despite having the highest open porosity since it is an extruded graphite quality. Melting on Grade B (the vibration molded quality), in contrast, started at a low apparent contact angle and was completely wetted in just under 150 seconds, although the initial rate of spreading differed.

Discussion

Importance of Gibbs energy change.

The variation of the contact angle between two phases that are not in equilibrium is well reported and documented.^[12-17] The present discussion would not focus on this variation, since this kind of variation is inevitable. It is essential to have an in-depth understanding of the dynamic nature of wetting behavior in order to make this type of measurement useful for the development and optimization of any materials process. Note that the situation described by Young’s law is only valid for systems in thermodynamic equilibrium. In a system under non-

equilibrium conditions, the interfacial tension between liquid silicon and graphite, $\gamma_{Si/C}$, varies with time. Unfortunately, $\gamma_{Si/C}$ is not measurable in reality. Exactly as in the case that the activity of a component cannot be defined and measured in a non-equilibrium system, the interfacial tension $\gamma_{Si/C}$ term cannot be defined and measured in this system since molten silicon and carbon cannot exist in thermodynamic equilibrium. Actually, the variation of the apparent contact angle is not only a result of the change in $\gamma_{Si/C}$, but also due to the change in the total Gibbs energy between the two states:

$$\Delta G_{Tot} = \Delta G_{Reaction} + \gamma \cdot A \quad [1]$$

where $\Delta G_{Reaction}$ is the Gibbs energy of the reaction to form silicon carbide by graphite and liquid Si, and $\gamma \cdot A$ is the interfacial energy term. Hence, a scientific consideration of the dynamic variation in this system (see Fig. 8) should really be based on Eq. [1]. For this reason, the observed contact angle should strictly be called an “apparent contact angle”.

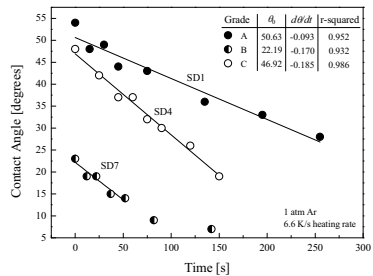
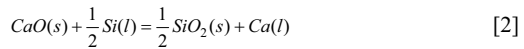


Fig. 8. The contact angle of Si(l) on different graphite substrates as a function of time.

It is expected that the mechanism and rate of the reaction are directly related to the experimental conditions, e.g. in the present case, the type of substrate and the heating history. The variation of the apparent contact angle is in fact a measure of the reaction rate. In order to properly utilize this type of measurement in a proper scientific manner for process optimization, a good understanding of the reaction mechanism including the effects of the substrate properties and the heating history is required. The apparent contact angle or the apparent interfacial energy between a liquid and either solid or another liquid would, no doubt, vary with time if the two phases in contact are not in equilibrium. The variation rate may be high or low depending on the system. One must be careful when using the value of apparent interfacial energy reported in the literature, since the value is system dependent.

The above discussion does also apply to the system of slag-metal reactions. Note that the interfacial tension between silicon and slag at the initial stages of the experiments (corresponding to Fig 3a, b and Fig.4a, b) cannot be measured as a physical property. Only at the final stage, when the two phases have reached equilibrium, the interfacial tension can be determined. The authors would like to draw people's attention that the system in Fig. 3a (Fig. 4a) is not the same as the system shown in Fig.3d (Fig.4d), since the compositions of both phases have changed. It emphasizes again that one should be careful when using the value of interfacial energy reported in the literature. To explain the observation that slag-metal system rapidly generates a very large interfacial area that decreases with reaction time (see Figs. 3-5), the overall driving force, viz. the total change in the Gibbs energy of the system between the initial and the final states is also described by eq. [1]. Considering the chemical reaction involved, the Gibbs energy term $\Delta G_{\text{Reaction}}$ is related to the following reaction,



with

$$\Delta G_2 = \Delta G_2^0 + RT \ln Q \quad [3]$$

Hence, eq. [1] can be rewritten as

$$\Delta G_{\text{Tot}} = \Delta G_2 + \gamma \cdot A \quad [1']$$

As pointed out in a previous section, the apparent interfacial tension that is observed indeed depends on the total ΔG_{Tot} and not only on γ .

At the initial stages of the process, the two phases are far from equilibrium with respect to calcium, i.e. ΔG_2 is very negative, and therefore it is the dominating term in Eq. [1']. The extremely low apparent interfacial tension would result in a large interfacial area between slag and silicon, facilitating emulsion formation. As the two phases approach chemical equilibrium (ΔG_2 approaches zero), the second term, $\gamma \cdot A$ in Eq. [1'] becomes increasingly important. To reach the minimum Gibbs energy level, the system would prefer a minimum interfacial area at the latter stage of the process, which explains the drastic decrease in the interfacial area as equilibrium is approached.

Mechanical agitation inputs kinetic energy into the system and therefore facilitating the break-up and dispersion of metal droplets into the slag phase. At this point where the ΔG_2 has almost reached zero, with 100 rpm mixing speed, there is not enough energy imparted to the melt to

maintain the slag-metal emulsion, and the metal phase re-coalesces. It is strongly felt that a process optimization concerning the slag-metal interfacial phenomena would be unrealistic when the chemical potential is excluded in the consideration and only the interfacial tension is highlighted. In metallurgical and material processes, chemical reactions always take place at the interface, e.g. in the present case: slag-silicon or silicon-graphite. Overlooking of the chemical reaction and too much emphasis on interfacial tension would mislead the modelling and optimization of the process.

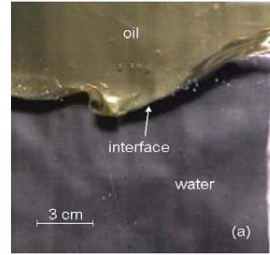


Fig.9 Detachment of emulsified droplet in an oil-water model (Reproduced from Ref.[21])

Although the variation of the contact angle with time has been well known, in process modelling and process optimization the foremost importance has always been given to the interfacial energy. In the consideration of the interfacial phenomena, the Gibbs energy term in eq.[1] is very often overlooked. As seen in the case of both slag-metal reaction and silicon-graphite reaction, the apparent interfacial energy is in fact a function of the kinetic conditions. While the contact angle (interfacial energy) could be somehow followed dynamically, the contribution of the Gibbs energy term can very often be dominating in the dynamically followed apparent interfacial energy. This dominating behavior has been evidently seen in the initial stages (before 90 s) of the slag-metal reaction.

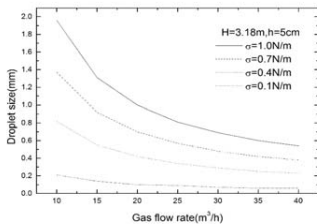


Fig. 10 Model predictions for droplet sizes at different conditions (Reproduced from Ref. [22])

came to the conclusion that the momentum of interfacial shear was not significant for emulsification of oil but it is rather triggered by Kelvin-Helmholtz instability when two stratified fluids are in relative motion. One important fact is that the phenomenon illustrated in the above figure is evidence for the formation of slag droplets. On the other hand, the size of the droplets formed in this manner has so far been at the millimeter scale. No evidence has so far been reported for the formation of slag droplets less than 20-30 μm , which are the potential source of inclusions. To form certain amount of inclusions in this size range and even smaller would need a considerably large amount of energy.

No real quantitative model has so far been developed to describe the slag-metal emulsification. A simple model based on energy balance was suggested by Wu in his PhD thesis.^[22] As seen in Fig. 10, interfacial tension has a great impact on droplet size. The influence of gas flow rate on droplet size is obvious when interfacial tension between slag and liquid metal is big. Otherwise, the effect is weak. It is seen that droplets smaller than 50 μm can only form when the interfacial

As a matter of fact, in the case of study of both slag entrainment into liquid steel forming inclusions and inclusion separation to the slag phase, almost all the models have neglected the Gibbs energy term in eq. [1].

Possibility of slag entrainment into liquid steel

Formation of inclusion by slag entrainment has been discussed by many researchers. The mechanism of droplet formation is illustrated in Fig. 9, which is reproduced from the publication by Krishnapisharody and Irons^[21]. The authors

tension is low, e.g. 0.1 N/m. On the other hand, droplets formed with higher interfacial tensions, e.g. 0.7 N/m are usually bigger than 0.2 mm, which would float up easily. These bigger droplets would not form inclusions.

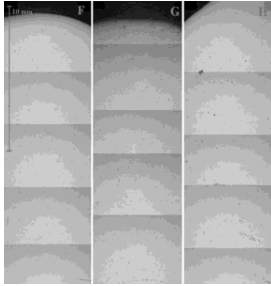


Fig.12 Series of photomicrographs taken from the three samples

Note that as discussed earlier in the present work, the slag-metal reaction at the initial stages of the ladle treatment would dramatically lower the apparent interfacial tension between slag and metal. It could be lower than 0.1 N/m, though the equilibrium interfacial tension is usually between 0.5 and 1 N/m. The variation of apparent interfacial tension along the process would offer us an opportunity for process optimization regarding inclusion entrainment and inclusion removal.

To verify the results from the laboratory study, three samples of slag-metal interface taken around the open-eye in the gas stirred ladle at Uddeholm Tooling (currently Uddeholm AB) were investigated to evaluate the presence

of slag entrainment in the steel.^[23-25]

Fig. 11 illustrates this aspect clearly. Fig.11a presents a photograph of an opened sample showing slag-metal interface in the case of gas-stirring mode, while Fig. 11b presents the LOM photograph of the steel sample in contact with the slag (magnification – 50 X). The results strongly suggest further systematic study is needed for an in-depth understanding of slag-metal interface in the ladle treatment.

Fig.12 presents series of photomicrographs taken from the three samples, respectively. While the first picture in each series shows the surface of the steel in contact with slag, the lowest picture shows the steel part about 20 mm from the slag-metal interface. Note that almost all the dot spots are pores. No visible amount of slag is observed in any of the three samples. The results are in very good accordance with the semi empirical model suggested by Wu in his PhD thesis.^[22]

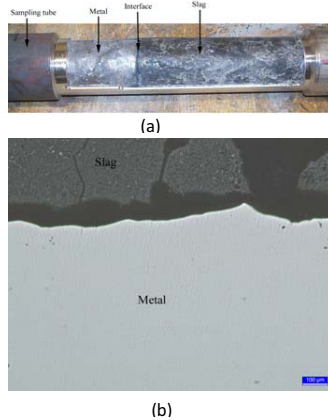


Fig.11 (a) slag-metal interface in the case of gas-stirring mode,^[23] (b) LOM photograph of the steel sample in contact with the slag^[25]

Note that these sample were taken when the slag was almost in equilibrium with the liquid metal. The situation could be very different when the top slag has just been added to ladle (the slag and steel are far from equilibrium at this stage). In this stage, the Gibbs energy term in eq.[1] might play great role in determining the slag-metal interface, the entrainment of slag and even the removal of inclusions. It is strongly felt that an optimization of the ladle process considering the

function of Gibbs energy term in eq.[1] in determining the slag-metal interface would be essential with respect to slag-metal reaction and steel cleanness. The present work would function as a starting point to initiate a discussion about the importance of Gibbs energy change in determining the behavior of interface. It is hoped that this discussion would lead to better process models.

Conclusion

The interface between liquid silicon and CaO-SiO₂ slag and the interfacial reaction between silicon and graphite were studied experimentally. The results revealed evidently that the chemical driving force could play dominating role in determining the interface, while the interfacial tension would only become important when the slag and metal were reaching equilibrium.

In the case where the two phases are not in thermodynamic equilibrium, it is impossible to measure the interfacial tension. This is similar as the situation where equilibrium chemical potential cannot be determined in a non-equilibrium system. The apparent interfacial tension measured is in fact a kinetic parameter that depends greatly on the experimental conditions, but not a physical property of the system. The measured values cannot be used to other experimental conditions.

The possibility of the entrainment of ladle slag as a source of nonmetallic inclusions was also evaluated on the basis of the above findings. The present study would like to draw researchers' attention regarding the important role of Gibbs energy of the reaction in the interfacial phenomena. The study would also raise a question whether the interfacial tension determined at equilibrium condition can be applied to a non-equilibrium system.

References:

1. P. Jönsson, G. Ye and L. Jonsson, Int. Conference, MSMM'96, June 11-13, **1996**, Beijing, China, proceedings, 309.
2. L. Jonsson, Du Sichen and P. Jönsson, ISIJ International **1998**, 38, 260.
3. H. Liu, Z-Y. Qi, and M-G. Xu, Steel Research Int., **2011**, 82, 440.
4. P. Sulasalmi, A. Kärnä, T. Fabritius and J. Savolainen, ISIJ International, **2009**, 49, 1661.
5. S. Linder, Scand. J. Metal., **1974**, 3, 137.
6. Y. Miki and B. G. Thomas, Metal. Mater. Trans. B, **1999**, 30B, 639.
7. M. Hallberg, P. G. Jonsson, T. L. I. Jonsson and R. Eriksson, Scand. J. Metal., **2005**, 34, 41.
8. K. Nakajima and K. Okamura, Proc. of 4th Int. Conf. on Molten Slags and Fluxes, ISIJ, Tokyo, **1992**, 505.
9. J. Strandh, K. Nakajima, R. Eriksson and P. Jonsson, ISIJ Int., **2005**, 45, 1597.
10. G. Shannon, L. White, S. Sridhar, Materials Science and Engineering, **2008**, A 495, 310.
11. J. Strandh, K. Nakajima, R. Eriksson and P. Jonsson, ISIJ International, **2005**, 45, 1838.
12. B. R. Bathey, G. F. Hurley, and H. E. Bates: *J. Mater. Sci.* 1980, vol. 15, pp. 2192-2196.
13. J-G. Li, and H. Hausner: *Scripta Metall. et Mater.*, 1995, vol. 32, pp. 377-382.
14. A. Ciftja, T. A. Engh, and M. Tangstad: *Metall. Mater. Trans. A*, 2010, vol. 41A, pp. 3183-3195.
15. Z. Yuan, W. L. Huang, and K. Mukai: *Appl. Phys. A*, 2004, vol. 78, pp. 617-622.
16. O. Dezellus, S. Jaques, F. Hodaj, and N. Eustathopoulos: *J. Mater. Sci.*, 2005, vol. 40, pp. 2307-2311.

17. P. J. Yunes Rubio, L. Hong, N. Saha-Chaudhury, R. Bush, and V. Sahajwalla: *ISIJ Int.*, 2006, vol. 46, pp. 1570–1576.
18. Jesse F. White and Du Sichen: *Metall. and Materials Trans. B*, 2014, vol.45B, pp.96-105
19. Jesse F. White, Luyao Ma, Karl Forwald1, and Du Sichen: *Metall. and Materials Trans. B*, DOI. 10.1007/s11663-013-9947-0. 2014, Volume 45B, pp. 150-160
20. 10. R. Israel, R. Voytovych, P. Protsenko, B. Drevet, D. Camel, and N. Eustathopoulos: *J. Mater. Sci.*, 2010, vol. 45, pp. 2210–2217.
21. K. Krishnapisharody, G. Irons, G., Proc. ICS 2008 - 4th Int. Conf. Science & Technology of Steelmaking, Oct. 6-8, **2008**. Gifu, Japan, 367
22. L-S. Wu, Doctoral Thesis “Study on some phenomena of slag in steelmaking process”, ISBN 978-91-7415-955-4, **2011**, Department of Materials Science and Engineering, KTH, Stockholm, Sweden
23. K. Beskow, P. Dayal, J. Björkvall, M. Nzotta and Du Sichen, *Ironmaking and Steelmaking*, **2006**, 33, 74.
24. P. Dayal, K. Beskow, J. Björkvall and Du Sichen, *Ironmaking and Steelmaking*, **2006**, 33, 454.
25. M. Thunman, S. Eckert, O. Hennig, J. Björkvall, and Du Sichen: *Steel Research International*, 2007, vol. 78, pp.849-856.

CONTROL OF MOLTEN CaO – Al₂O₃ OXIDE JETS WITH FOCUS ON THERMOPHYSICAL PROPERTY MEASUREMENTS AND SOME LIMITATIONS

Luckman Muhmood^a, Mirco Wegener^b, Shouyi Sun^c and Alex Deev^c

^a K J Somaiya College of Engineering, Vidyavihar, Mumbai, India

^b SOPAT GmbH, Berlin, Germany

^c CSIRO Melebourne, Australia

ABSTRACT

A unique cross tube furnace was designed to focus on the study, development and control of molten oxide jets. The cross alumina tube along with a high speed camera arrangement facilitated observations of jet formation and break up at temperatures 1550 - 1700 °C. The slag flow rate was controlled with the help of a nozzle-plunger system along with suitable back pressure of argon. Various phenomena like drop formation and pinch off, drop oscillation and jet breakup was observed. Surface tension of calcia-alumina slags with composition close to its eutectic was studied using dynamic methods like oscillating jet as well as elliptical jet technique. The values were observed to be comparable with existing literature as well as independent sessile drop measurements. The current paper discusses the jet technique for surface tension measurements as well as other dynamic phenomena involved during jet formation. It also discusses the effect of phenomena like wetting on the jet method.

INTRODUCTION

Heat recovery from industrial wastes have been a significant topic of interest especially in context of carbon credits. Among industrial wastes, metallurgical slags are the bulk in terms of volume and hence have come under predominant focus. Slags have lower thermal conductivity hence in order to extract heat the area needs to be large in comparison to volume¹. The popular configuration for heat recovery from slag demands the formation of fine drops. All methods of heat extraction involve the formation of jets and subsequent breakup of jets into drops²⁻⁸. It is critical to observe and study the phenomena of jet breakup into drops as it can indicate to methods by which various thermophysical properties could be measured. The Rayleigh jet indicates the combined effect of viscosity and surface tension of the fluid while drop formation and free fall oscillation could give properties like density and viscosity.

Property measurements at high temperature is challenging for the fact that material interactions are difficult to control. Another limitation is the sophisticated level of equipment and measuring methods involved in it. Owing to this as well as other factors like initial purity of materials and atmosphere used, the scatters of values obtained at the same property measured across various laboratories prevail. Viscosity is probably the only property of slag for which a detailed standardization procedure was devised⁹. However nothing significant was devised for other properties like surface tension, density etc.

This paper discusses the observation of various phenomena like jet break up, drop formation and oscillation. Properties like surface tension and viscosity have been measured from these phenomena. Also parallel experiments on surface tension using the sessile drop technique was carried out for lower temperatures. The effect of substrate material on wetting is briefly discussed.

EXPERIMENTAL

In order to observe various phenomena occurring at high temperature as well as having a control over the flow of slag, a cross tube furnace was designed. A plunger-nozzle system made of graphite was used as the crucible. It also had the provision of applying back pressure to the slag for achieving higher flow rates. The horizontal section of the cross tube had the provision of observing the inside of the furnace via a quartz window. The slag jet formed was recorded using a high speed camera. Further details of the set up are mentioned in earlier publications^{10,11}. The set up was capable of heating slag up to a temperature of 2023 K and temperature uniformity of the jet was achieved by having 3 split furnaces stacked over another. The detailed description of the furnace is available in earlier publications from the authors (ref).

OBSERVED PHENOMENA

DROP GROWTH AND PINCH OFF

a) Drop weight method

The drop growth, pinch off and oscillation was observed at high temperatures using a high speed camera. The drops were grown slowly. This avoided the effects of hydrodynamics on the contours of the drop. The drop weight method involves the detachment of a drop when the weight of the drop is no longer balanced by the surface tension. Since the detachment involves a portion of the drop being attached to the capillary tip, a drop weight correction factor needs to be incorporated in the force balance equation. The weight of 30 drops were taken for finding the weight and various version of the Harkings and Brown drop weight correction factor was used¹². A comparison of the effect of various drop weight correction factors on surface tension is given in Figure 1. It is seen that apart from clift all other correction factors yield similar surface tension values.

a) Pendant drop method

The pendant drop method involves the slow growth of a drop and holding at a point at which the surface tension value just balances the weight of the drop. Due to the dynamics of the system it was very difficult to hold the drop for a long period. A dynamic pendant drop method was used which was later analysed using the selected plane method. In this method only two planes are of interest d_s and d_e which is the shown in Figure 2 (a). Based on the

Bidwell et al. ¹⁴, the values for surface tension as the drop grows is shown in Figure 2 (b). The start and end values are high due to the fact that they are drop formation and pinch off regions. The middle points are relatively horizontal and an average value was used for reporting the surface tension. A point to be noted is that the errors are relatively high owing to the fact that the method takes only two dimensions into consideration for the calculation. A refinement to the process could be plotting the contour and using it for surface tension estimation.

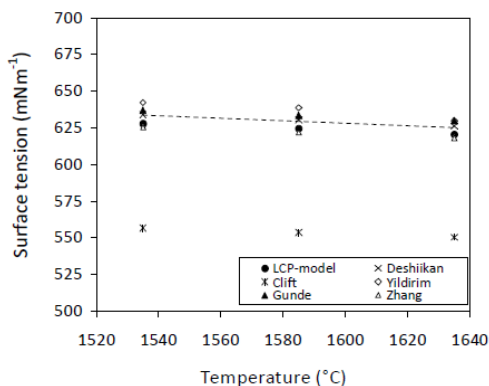


Figure 1: Comparison of surface tension values for various drop correction factors ¹³.

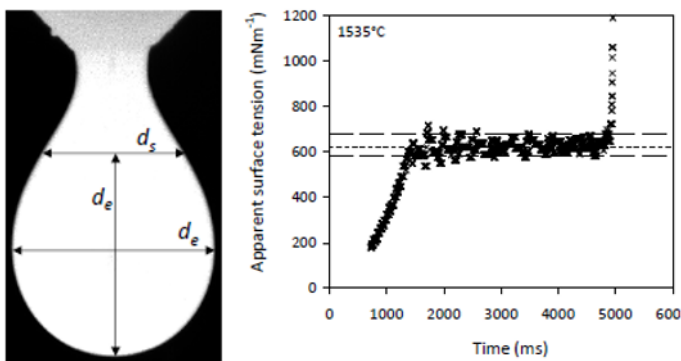


Figure 2: Pendant drop profile of the molten calcia-alumina slag with the planes of interest (left). Surface tension values obtained from different image between two consecutive drop formation and pinch off (right) ¹⁴.

JET FORMATION AND BREAK UP

a) Circular Jets

A jet was initiated with the help of argon pressure above the molten slag inside the crucible as well as the plunger movement. This jet emanates from a circular nozzle and instabilities grow in the axial direction as a function of time and space creating necks and swells along the axis. A finite number of images from a recorded sequence were loaded in an image analysis software and the contour of the jet was plotted as a function of axial distance till the point where the jet disintegrates to form drops. The generalized equation for the jet radius as a function of time and distance is given as :

$$r(z, t) = R_0 + \epsilon_0 e^{\alpha t} \cos(kz) \quad [1]$$

R_0 is the initial radius of the jet, ϵ_0 is the amplitude of the initial disturbance, α is the growth factor and k is the wave number. Figure 3 (top) shows the profile of the jet with and without the cosine term, the variation in the jet profile is shown in the middle figure. The logarithmic difference between the maximum radius minus the initial radius of the jet divided by the initial disturbance was plotted as a function of time in the Figure 3 (bottom). The slope of this graph gives the growth factor α . Once this known, using the relation between surface tension, viscosity, growth rate and wave length ¹⁵

$$\sigma = 2\rho R_0^3 \frac{\alpha^2 + \alpha \frac{3\mu}{\rho R_0^2} (kR_0)^2}{(kR_0)^2 - (kR_0)^4} \quad [2]$$

The density was calculated from the drop volume method by noting the weight against a fixed number of drops collected. The viscosity was calculated from the Urbain model for the slag composition ¹⁶. Substituting these values in the above equation the surface tension was calculated as a function of time.

a) Elliptical Jets

An elliptical nozzle was fabricated through which the molten slag jet was generated. A standing wave jet is generated. Figure 4 shows the standing wave jet being generated from the elliptical nozzle. The figure also shows the cross section of the nozzle used. Using the equation generated by Masutani and Stenstrom ¹⁷, which is a modified Bohrs model ¹⁸, the surface tension for the liquid could be linked with measurable quantities as shown in equation 3.

$$\sigma = K \frac{4\rho Q^2 \left(1 + \frac{37}{24} \left(\frac{b}{r}\right)^2\right)}{6r\lambda^2 + 10\pi^2 r^3} \quad [3]$$

Here Q is the volumetric flow rate and λ is the wavelength.

The stream radius r is given by the equation

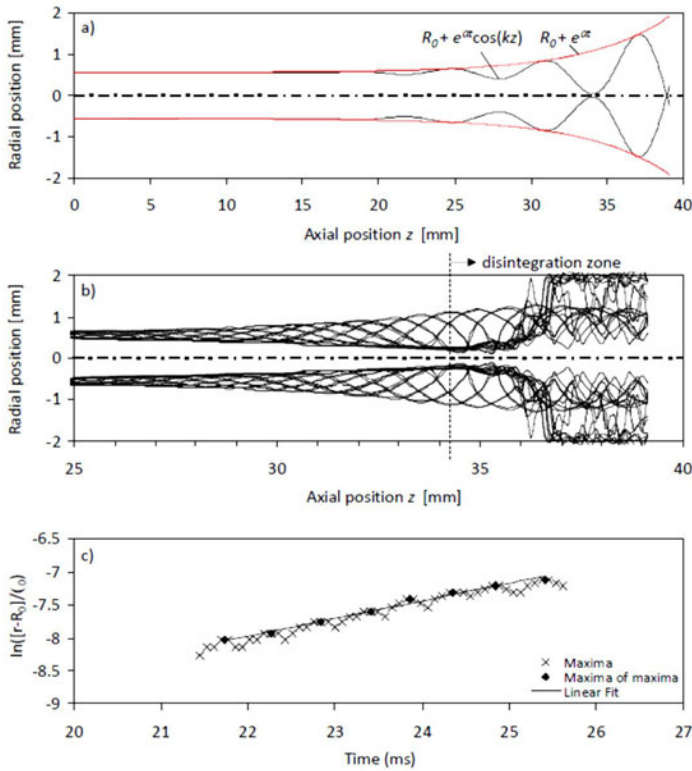


Figure 3: Jet profile according to equation 1 (top). Actual jet profile extracted from recorded images (middle). Determination of instability growth rate and initial disturbance of the jet. The slope of the line through the maxima gives the growth rate ¹³.

$$r = \frac{r_{max} + r_{min}}{2} \left[1 + \frac{1}{6} \left(\frac{b}{r} \right)^2 \right] \quad [4]$$

The correction factor which takes in to account the effect of viscosity is given by the equation

$$K = 1 + 2 \left(\frac{\mu \lambda}{\pi \rho U r^2} \right)^3 + 3 \left(\frac{\mu \lambda}{\pi \rho U r^2} \right)^2 + \dots \quad [5]$$

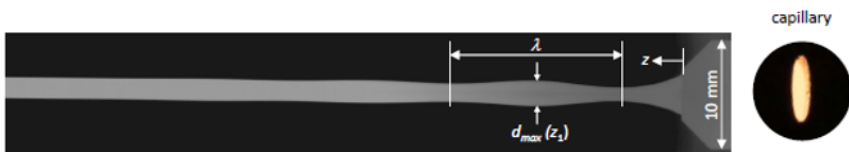


Figure 4: Standing wave produced by elliptical jet. The cross section of the capillary used is shown on the right.¹³

STATIC MEASUREMENTS - SESSILE DROP STUDY

The major limitation of using jet technique for dynamic surface tension measurement was that the slag required a minimum superheat for it to form a jet. The melting point of 49 CaO-51 Al₂O₃ was estimated through independent observation to be around 1673 K¹⁹. It is not possible to operate the jet at this temperature. The operating temperature for this technique was between 1800-1973 K. Hence sessile drop experiments were carried out separately to find the surface tension of the slag between the temperature range 1700- 1773 K.

RESULTS

Comparison of the surface tension values using the abovementioned static and dynamic techniques are compiled in Table I. It can be seen for the pendant drop technique the value obtained was significantly lower than that of the drop weight method. This is attributed to the fact that only four points on the drop are used in selected plane method. The temperature dependence on the surface tension for the calcia-alumina slag used was obtained by fitting the values obtained from the sessile drop, drop weight and the oscillating jet (circular and elliptical) method. The temperature dependency coefficient obtained is 0.13 mN/K, which is similar to that obtained by Zielinski and Sikora²⁰ as well as Dou et al²¹ (0.14 and 0.13 mN/K respectively).

Table I – Surface tension values of 49 CaO – 51 Al₂O₃ given by various methods.

Temperature	Surface Tension (mN/m)				
	Sessile Drop Method	Drop Weight Method	Pendant Drop Method	Circular Jet Method	Elliptical Jet Method
1705	654.4	-	-	-	-
1728	654.8	-	-	-	-
1745	650.1	-	-	-	-
1773	647.6	-	-	-	-
1808	-	638	-	-	-
1858	-	632	-	-	-
1908	-	625	-	-	-
1808	-	-	625	-	-
1858	-	-	600	-	-
1908	-	-	590	-	-
1933	-	-	-	624	-
1973	-	-	-	-	626

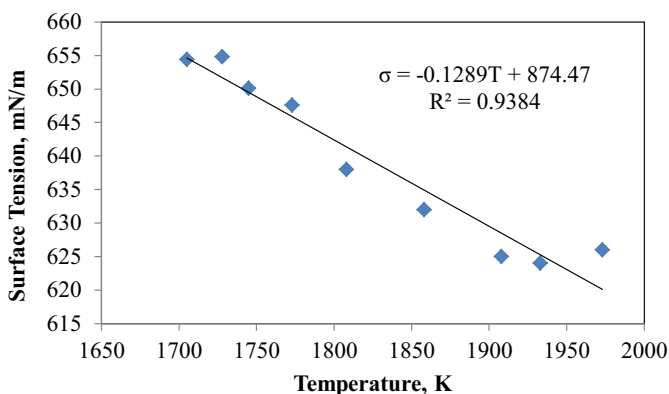


Figure 5: Surface tension variation with temperature compiled from data using 4 methods (sessile drop, drop weight, circular jet and elliptical jet methods).

Another property that can be studied is the wetting of the slag with the substrate material. The material of construction for nozzle using the jet technique prefers that the slag should be non-wetting in nature. The contact angle between the slag and graphite varied between 148 – 156 degrees as a function of temperature. In order to study the dynamic effect of surfactants, the slag composition was changed. B₂O₃ was preferred as the surfactant as its surface tension is quite low and is stable at high temperatures. However graphite in this case cannot be used as the constructional material as it could produce carbon monoxide hence reducing the surfactant. Molybdenum was chosen for making the nozzle, plunger as well as crucible. The wetting of the slag against molybdenum is shown in Figure 6. The contact angle of the slag containing 21% B₂O₃ with molybdenum is less than 10 degrees which indicates that the slag is wetting. The oscillating jet method was performed on this slag with molybdenum as the capillary material. The slag was observed to wet the tip and creep upwards resulting in a preferred orientation of the jet.

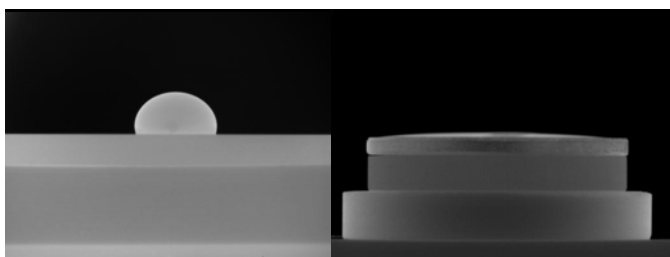


Figure 6: CaO-Al₂O₃- 21% B₂O₃ slag on graphite (left) and molybdenum (right)

CONCLUSION

Surface tension of 49 CaO – 51 Al₂O₃ slag was measured using various techniques. Apart from pendant drop method, surface tension values and its variation with temperature showed a similar trend. Dynamic methods like oscillating jet method for measuring surface tension were successfully tested. The slag should be non-wetting for accurate results using dynamic jet methods.

REFERENCES

1. Slag Atlas, Verein Deutscher Eisenhüttenleute, 1995.
2. C. Nexhip, R. Davidson, T. Norgate, S. Sanetsis, B. Washington, Dry Granulation of Slags for Producing Cement Binder, in: Proceedings of Green Processing 2004 Conference, 10-12 May 2004, Fremantle, Australia.
3. D. Xie, S. Jahanshahi, T. Norgate, Dry granulation to provide a sustainable option for slag treatment, in: Proceedings of Sustainable Mining Conference, 17-19 August 2010, Kalgoorlie, Western Australia.
4. M. Yoshinaga, K. Fujii, T. Shigematsu, T. Nakata, Dry granulation and solidification of molten blast furnace slag, *T. Iron Steel I. Jpn.* 22 (11) (1982) 823-829.
5. Y. Kashiwaya, Y. In-Nami, T. Akiyama, Development of a rotary cylinder atomizing method of slag for the production of amorphous slag particles, *ISIJ Int.* 50 (9) (2010) 1245-1251.
6. Y. Kashiwaya, Y. In-Nami, T. Akiyama, Mechanism of the formation of slag particles by the rotary cylinder atomization, *ISIJ Int.* 50 (9) (2010) 1252-1258.
7. J. Liu, Q. Yu, Q. Qin, System for recovering waste heat from high temperature molten blast furnace slag, in: Proceedings of TMS Annual Meeting, 27.02. - 03.03.2011, San Diego, CA.
8. S. J. Pickering, N. Hay, T. F. Roylance, G. H. Thomas, New process for dry granulation and heat recovery from molten blast-furnace slag, *Ironmak. Steelmak.* 12 (1) (1985) 14-21.
9. C P Broadbent, M Franken, D Gould and K C Mills, Standard reference material for viscosity measurements, 4th International Conference on Metallurgical Slags and Fluxes, Sendai, Japan.
10. Mirco Wegener, Luckman Muhmood, Shouyi Sun and Alex V Deev, A novel high temperature experimental setup to study the dynamics interfacial phenomena in slags, *Industrial and Engineering Chemistry Research*, 52 (46), pp. 16444-16456, 2013.
11. Mirco Wegener, Luckman Muhmood, Shouyi Sun and Alex V Deev, "Formation and breakup of molten oxide jets", *Chemical Engineering Science*, 105, pp. 143-154, 2014.
12. W.D Harkins and F E Brown, Determination of surface tension (free surface energy) and the weight of falling drops ; The surface tension of water and benzene by capillary height method, *The Journal of American Chemical Society*, 41 (4), 1919, 499-524.
13. Mirco Wegener, Luckman Muhmood, Shouyi Sun and Alex V Deev, Surface tension measurements of Calcia-Alumina slags – A comparison of dynamic methods, *Metallurgical and Materials Transactions B*, 8, 2015
14. R. M. Bidwell, J. L. Duran, G. L. Hubbard, Tables for the determination of the surface tensions of liquid metals by the pendant drop method, University of California, Los Alamos, New Mexico, (1964).
15. J Eggers and V E Villermaux, Physics of liquid jets, *Reports on progress in Physics*, 3 , 2008, 036601.

16. G. Urbain, Viscosity of silicate melts, *Rev. Hautes Tempér. Réfract.* 20 (1983) 135-139.
17. G Masutani and M K Stenstrom, A review of surface tension measuring techniques, surfactants, and their implications on oxygen transfer in waste water treatment plants, Water resources program, School of Engineering and Applied Science, University of California, Los Angeles (1984).
18. N Bohr, Determination of the surface tension of water by the method of jet vibration, *Philosophical Transaction of the royal Society of London. Series A, Containing paper of a mathematical and physical character*, 209 (1909) 281-317.
19. Luckman Muhmood, Mirco Wegener, Alex Deev and Shouyi Sun, private communications.
20. M Zielinski and B Sikora, Surface tension of the calcium oxide – alumina system with addition of silica, iron (III) oxide, calcium fluoride, sodium oxide, *Prace Instytutu Metallurgii Zelaza* 29 (3-4), 1977, 229-232.
21. Dou Z, Zhang A, Yao J, Jiang X, Niu L and He J: *The Chinese Journal of Process Engineering*, 9 (1), (2009), pp. 246-249.

SLAG SURFACE TENSION MEASUREMENTS WITH CONSTRAINED SESSILE DROPS

Marc A. Duchesne, Robin W. Hughes

Natural Resources Canada, CanmetENERGY; 1 Haanel Drive; Ottawa, ON K1A 1M1 Canada

Keywords: Slag, Surface tension, Density, Constrained sessile drop

Abstract

Physical properties of slag are critical in the design and operation of refining technologies and slagging energy systems. The surface tension of slag impacts phenomena such as granulation, foaming, removal of solid inclusions, erosion of refractory and fouling. In this study, slag sessile drops formed on graphite, alumina and molybdenum substrates were compared. Use of graphite resulted in the largest contact angles, a desirable trait for surface tension measurements, but also led to reactions with the slag. Alumina and molybdenum were less reactive, but resulted in contact angles too small for measurements. When sessile drops were constrained by small substrate diameters to increase the apparent contact angle, surface tension measurements could be achieved with alumina and molybdenum substrates. The surface tension of coal slag was measured at up to 1600 °C in oxidizing and reducing gas atmospheres.

Introduction

Physical properties of slag, such as viscosity, density, surface tension, heat conductivity and heat capacity, are important for mineral processing, metal processing, slagging combustion and slagging gasification. The surface tension of slag impacts phenomena such as granulation, foaming, removal of solid inclusions, erosion of refractory and fouling [1–4]. There are several techniques to determine the surface tension of slags, such as maximum bubble pressure, sessile drop, pendant drop, and levitating drop techniques [5]. With sessile drops, the accuracy of surface tension measurements is greater when the contact angle (θ in Figure 1a) is large and the drop volume is large [5]. Unfortunately, the contact angle of slag on most materials able to contain slag at high temperatures (e.g., molybdenum, platinum and alumina) is relatively low [6]. Some researchers have achieved a high contact angle with slag on graphite. However, graphite may only be used in reducing gas atmospheres and can react with slag [6,7]. To produce slag sessile drops with larger apparent contact angles (θ_A), the substrate can be sized as a circular disc with a sharp edge so that the slag drop is unable to spread to its equilibrium contact angle (Figure 1b).

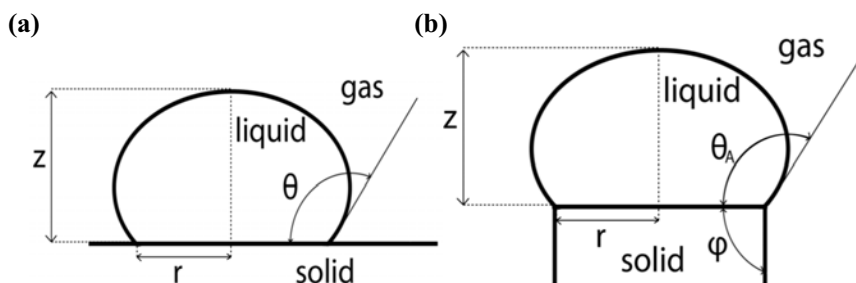


Figure 1. (a) Conventional and (b) constrained sessile drop contours.

Materials and Methods

For measurements with the tensiometer, all samples were placed on a molybdenum ($\geq 99.95\%$, Marketch International), alumina (99.5% , Ortech Inc.) or graphite (grade ET-10, Morgan Advanced ceramics) disc-shaped substrate with a diameter of 8, 13 or 25.4 mm. The coal ash considered in this study is derived from a Saskatchewan, Canada lignite. Real ash was prepared following ASTM D5142. The composition of the ash was determined by X-ray fluorescence following ASTM D4326 (Table I). A synthetic version of the ash (Table I) was prepared by mixing laboratory or analytical grade SiO_2 , Al_2O_3 , Fe_2O_3 , TiO_2 , CaO , MgO , Na_2O , V_2O_5 and/or NiO in a Turbula shaker-mixer for 12 h. Sulphur was not included in the synthetic ashes as it is expected to devolatilize during surface tension measurements. For placement of powder samples, including iron oxide and ash samples, 6 mm pellets were formed by pressing 0.1-0.4 g of powder using a hydraulic press with 15 kN force held for 30 s. Ash pellets were melted in the tensiometer furnace to form slag.

Table I. Composition of real and synthetic coal ash (wt.%)

	Real coal ash	Synthetic coal ash
SiO ₂	37.59	45.4
Al ₂ O ₃	16.61	20.0
Fe ₂ O ₃	5.54	6.7
TiO ₂	0.69	0.8
P ₂ O ₅	0.41	-
CaO	13.16	15.9
MgO	2.93	3.5
SO ₃	14.10	-
Na ₂ O	6.36	7.7
K ₂ O	0.28	-
BaO	0.471	-
SrO	0.356	-
MnO	0.025	-
CuO	0.008	-
Loss on fusion	1.45	-

For surface tension measurements, a Dataphysics OCA 15 LHT tensiometer with an HTFC 1700 furnace was used. A ceramic tube, with water-cooled flanges on either end, passes horizontally through the furnace (Figure 2). Samples on substrates were placed in this tube, near the furnace center. One water-cooled flange was attached to a plate with a port for a type B thermocouple that measured the sample temperature and recorded it at 2 s intervals. The other water-cooled flange was attached to a window providing a visual line of sight for a CCD camera. As was done by Melchior et al. [8], an infrared cutoff filter was used to reduce blurriness, and a polarizing filter was used to reduce reflections. SCA20 software, also supplied by Dataphysics, was used to control the furnace and record video captured by the CCD camera. A flow of ~250 ml/min of either air or 4 vol.% hydrogen in argon, here forth referred to as Ar/H₂, was used to produce oxidizing or reducing conditions, respectively. At the beginning of each experiment, the furnace was heated at a rate of 10-15 °C/min until a temperature of about 100 °C below the melting point of the sample. The heating rate was then set to 5 °C/min for the remainder of the experiment. Unless specified otherwise, measurements were completed during heating of the samples. To reduce blurriness, the camera iris had to be progressively closed as the temperature and sample brightness increased. A 0.255 cm gauge block was used to determine the size of pixels in recorded images at various zoom levels. Video files recorded with SCA20 software were exported as AVI type files. VirtualDub 1.10.4, a free video processing program [9], was used to convert the AVI file to a series of bitmap images. These images were then processed by a purchased program named ADSA to determine the sample's surface tension as a function of temperature [10,11].

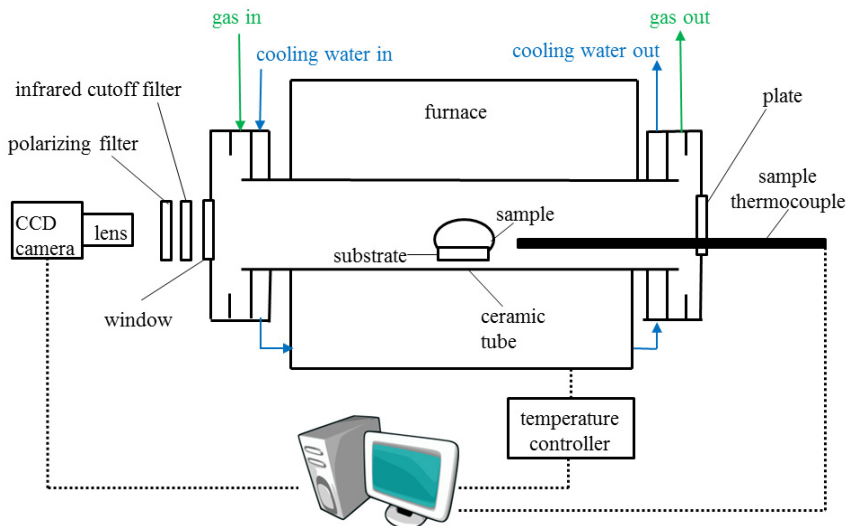


Figure 2. Schematic of the tensiometer system.

Results and Discussion

Contact angle and reactivity

The contact angle of synthetic coal ash on various substrate materials as a function of temperature is shown in Figure 3. When applying the sessile drop method to determine surface tension, elevated contact angles are desired for the best accuracy [5]. From Figure 3, it is obvious why graphite substrates were used in previous studies [6,8,12] instead of alumina or molybdenum substrates for slag surface tension measurements as the contact angle is much greater with graphite. However, there are disadvantages of using graphite. Slag usually reacts with graphite, forming bubbles in the slag drop [6,7]. The inset in Figure 3 shows the coal slag drop on graphite at 1585 °C. As observed previously [8,12], bubbling accompanied by expansions and collapses of the drop was most intense above 1500 °C. This explains the scatter of contact angle values in Figure 3. Another disadvantage of using graphite is that it cannot be used in air as it readily oxidizes. The synthetic coal slag on molybdenum and alumina substrates did not present the bubbling observed with graphite. However, the contact angles were too low to obtain accurate surface tension values. This justifies the use of the constrained sessile drop method that limits spreading of liquids. A higher contact angle is still preferred for the constrained sessile drop method, as it limits the potential for spillage over the substrate edge. Use of a molybdenum substrate resulted in a slightly higher contact angle than use of an alumina substrate (Figure 3). Contact angles were too low to be measured on alumina above 1400 °C.

Molybdenum cannot be used in air as it readily oxidizes, while alumina can be used in both air and Ar/H₂ [13].

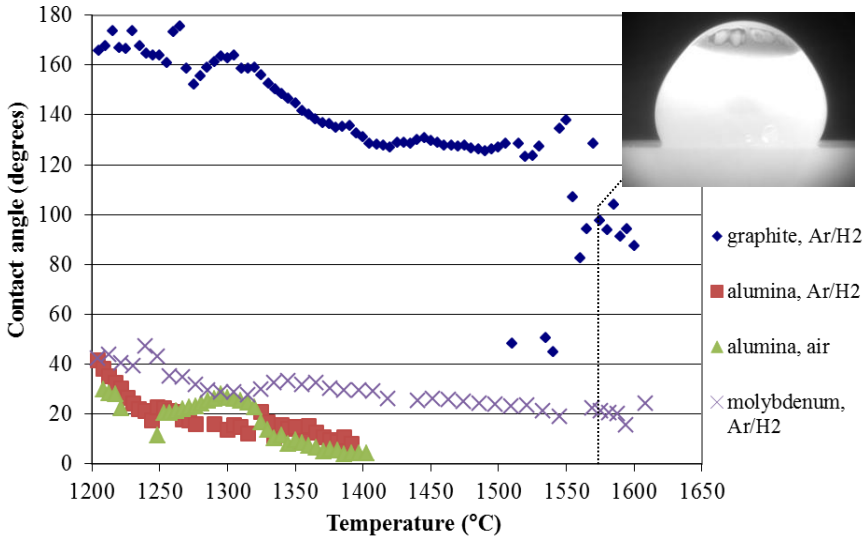


Figure 3. Contact angle of synthetic coal slag as a function of temperature on various substrate materials and in various gas atmospheres. The top right inset shows the slag drop on graphite at 1585 °C.

Substrate diameter for constrained sessile drops

Figure 4 shows measured surface tension values of synthetic coal slag on various substrates and in various gas atmospheres. Sessile drops on 25 mm substrates were conventional (unconstrained) drops. Sessile drops on 13 and 8 mm substrates were constrained. With 25 mm substrates, values could be obtained for the entire temperature range of interest on molybdenum, but not on alumina. This is presumably due to the lower contact angles on alumina making it difficult for the ADSA software to extract a drop profile. For all substrate material and gas composition combinations tested, density and surface tension values with 8 mm substrates are more consistent than with 13 or 25 mm substrates. The constrained sessile drops provide an improvement in precision over the unconstrained drops, and the smaller constrained drops provide an improvement in precision over the larger constrained drops. This mirrors Hoorfar and Neumann's statement that the range of drop shapes that are acceptable for surface tension measurements is greater with smaller substrate diameters [10]. Furthermore, the use of constrained sessile drops allows for measurements with materials that interact less with slag than graphite, and a material (alumina) that is suitable for oxidizing and reducing gas environments.

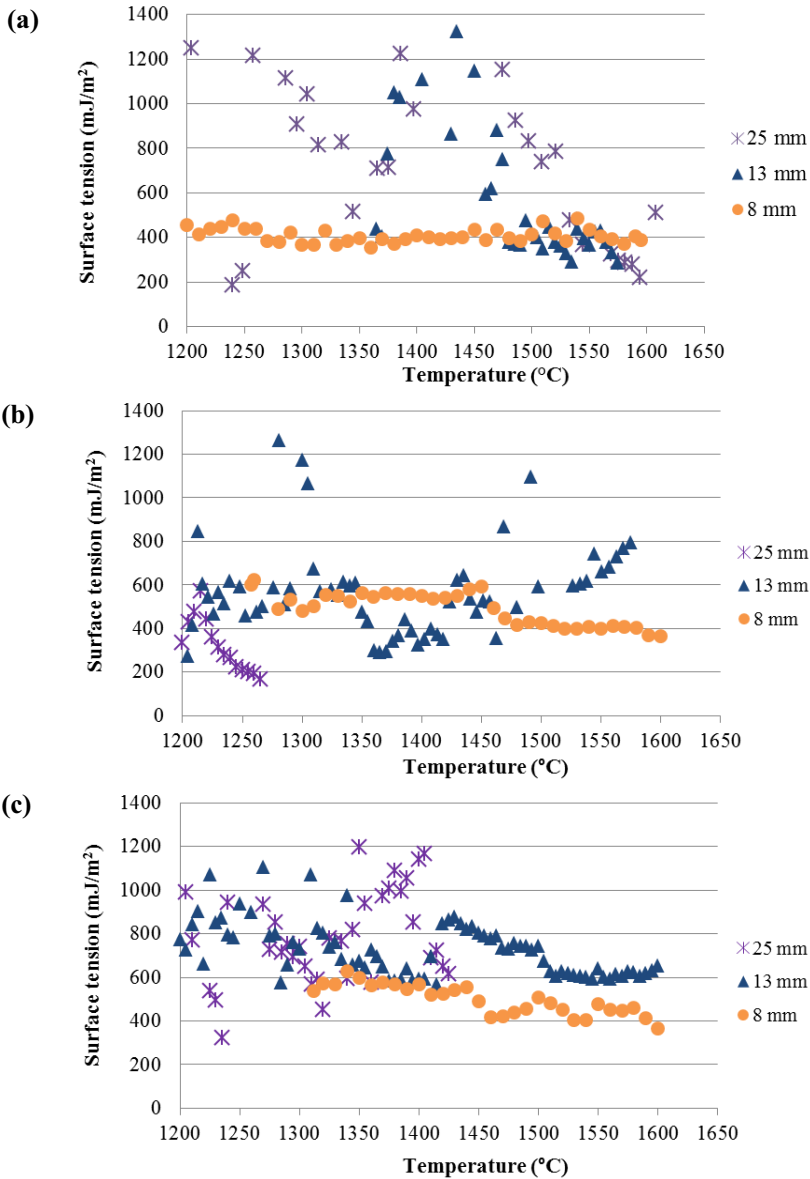


Figure 4. Surface tension of synthetic coal slag measured on 25, 13 and 8 mm substrates of: (a) molybdenum in Ar/H₂; b) alumina in Ar/H₂; c) alumina in air.

Surface tension of coal slag

For synthetic coal slag surface tension measurements on 8 mm molybdenum with Ar/H₂, on 8 mm alumina in Ar/H₂ and on 8 mm alumina in air, values fall within the range of 360-630 mJ/m² for the temperature range of 1200-1600 °C (Figure 4). Surface tension values on alumina substrates are ~550 mJ/m² below 1450 °C, and ~440 mJ/m² above 1450 °C. With the molybdenum substrate, surface tension values are ~420 mJ/m² for the entire temperature range tested. The surface tension of melted real ash, i.e., real slag, on molybdenum in Ar/H₂ is compared to synthetic slag in Figure 5. All surface tension values fall within the range of 450 mJ/m² ± 20%. As was found in another study by Horstenkamp and Müller [14], use of synthetic slag yields similar results as the use of real slag for surface tension measurements.

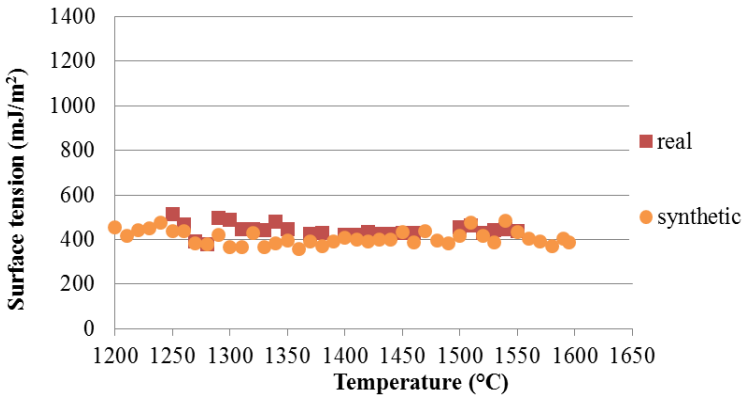


Figure 5. Surface tension of real and synthetic coal slag measured on 8 mm substrates of molybdenum in Ar/H₂.

Conclusion

Slag contact angles on graphite substrates are higher than on molybdenum or alumina substrates, which is favorable for surface tension measurements. However, unlike with the molybdenum and alumina substrates, there was strong interaction between the slag and graphite substrate. Alumina substrates have the advantage of being stable in both reducing and oxidizing environments, while graphite and molybdenum are only stable in reducing environments. The use of constrained sessile drops is justified by potentially improving measurement accuracy with substrates that avoid interaction issues, but provide low contact angles. Comparing results with non-constraining (25 mm) and constraining (13 and 8 mm) substrates, the constrained sessile drops provide an improvement in precision over the unconstrained drops, and the smaller constrained drops provide an improvement in precision over the larger constrained drops. Based on measurements with a molybdenum substrate, the surface tension of synthetic coal slag in reducing conditions is ~420 mJ/m² for the temperature range of 1200-1600 °C. Measurements with alumina substrates, in both oxidizing and reducing conditions yielded similar results above 1450 °C, but higher surface tension was observed at lower temperatures. Measurements with real coal slag yielded similar results to measurements with synthetic coal slag.

Acknowledgements

This work was supported by the Government of Canada's Program of Energy Research and Development, ecoENERGY Innovation Initiative, and Natural Sciences and Engineering Research Council of Canada. Desiree Gravelle, Imman Jami and Brandon Fitchett experimental activities during co-op work terms with Natural Resources Canada.

References

- [1] Walsh PM, Sarofim AF, Beer JM. Fouling of convection heat exchangers by lignitic coal ash. *Energy Fuels* 1992;6:709–15. doi:10.1021/ef00036a004.
- [2] Ni J, Yu G, Guo Q, Zhou Z, Wang F. Submodel for Predicting Slag Deposition Formation in Slagging Gasification Systems. *Energy Fuels* 2011;25:1004–9. doi:10.1021/ef101696a.
- [3] Kaneko TK, Zhu J, Howell N, Rozelle P, Sridhar S. The effects of gasification feedstock chemistries on the infiltration of slag into the porous high chromia refractory and their reaction products. *Fuel* 2014;115:248–63. doi:10.1016/j.fuel.2013.06.052.
- [4] Mills KC, Hondros ED, Li Z. Interfacial phenomena in high temperature processes. *J Mater Sci* 2005;40:2403–9. doi:10.1007/s10853-005-1966-z.
- [5] Verein Deutscher Eisenhüttenleute, editor. *Slag Atlas*. 2. ed. Düsseldorf: Verl. Stahleisen; 2008.
- [6] Shen P, Fujii H, Nogi K. Wettability of some refractory materials by molten SiO₂–MnO–TiO₂–FeOx slag. *Mater Chem Phys* 2009;114:681–6. doi:10.1016/j.matchemphys.2008.10.021.
- [7] Raask E. *Mineral Impurities in Coal Combustion: Behavior, Problems, and Remedial Measures*. Taylor & Francis; 1985.
- [8] Melchior T, Pütz G, Müller M. Surface Tension Measurements of Coal Ash Slags under Reducing Conditions at Atmospheric Pressure. *Energy Fuels* 2009;23:4540–6. doi:10.1021/ef900449v.
- [9] Anonymous. VirtualDub v1.10.4 n.d. virtualdub.org (accessed January 20, 2016).
- [10] Hoorfar M, W. Neumann A. Recent progress in Axisymmetric Drop Shape Analysis (ADSA). *Adv Colloid Interface Sci* 2006;121:25–49. doi:10.1016/j.cis.2006.06.001.
- [11] Saad SMI, Neumann AW. Total Gaussian curvature, drop shapes and the range of applicability of drop shape techniques. *Adv Colloid Interface Sci* 2014;204:1–14. doi:10.1016/j.cis.2013.12.001.
- [12] Melchior T, Bläsing M, Pütz G, Müller M. Surface tension measurements of coal ash slags under reducing conditions at elevated pressures. *Fuel* 2011;90:280–7. doi:10.1016/j.fuel.2010.07.051.
- [13] Vargas S, Frandsen FJ, Dam-Johansen K. Rheological properties of high-temperature melts of coal ashes and other silicates. *Prog Energy Combust Sci* 2001;27:237–429. doi:10.1016/S0360-1285(00)00023-X.
- [14] Horstenkamp A, Mueller M. Measurement of surface tension of coal slags. *Proc. 31st Annu. Int. Pittsburgh Coal Conf., Pittsburgh, United States: 2014.*

© *Her Majesty the Queen in Right of Canada as represented by the Minister of Natural Resources, 2016.*

INTERACTIONS BETWEEN LIQUID CaO–SiO₂ SLAGS AND GRAPHITE SUBSTRATES

Jesse F. White, Jaewoo Lee, Oscar Hessling, Björn Glaser

KTH Royal Institute of Technology, Stockholm, Sweden

Keywords: Slag melting, SiO₂, graphite, dynamic wetting, infiltration

Abstract

In this study, the spreading and infiltration behavior of slag in contact with different grades of graphite was investigated. The wetting and infiltration of slag into graphite were found to be highly material dependent. Temperature and silica content of the slag also have a major influence on how slag spreads and infiltrates: The higher the temperature and silica content, the greater the slag infiltration, and the faster the rate of spreading. Reactions that generate gaseous products occurred during spreading of slag on graphite as evidenced by the observation of bubble formation. Silicon infiltrated into the graphite substrates much deeper than the slag phase, indicating gas-phase transport of silicon-bearing vapor species. Complete wetting of the interface and reduction of silica in the slag near the interface may lead to passivation by formation of a solid, CaO-rich layer.

Introduction

Graphite is an exceptional refractory material, and is used extensively in the smelting, melting, refining, and crystallization of silicon as well as in other non-ferrous systems where carbon solubility is limited. Besides high refractoriness, at low oxygen potential graphite is chemically stable, has high resistance to thermal shock, high thermal conductivity, and is a soft material that is easily machinable to almost any shape or form. In actuality, commercially available synthetic graphites are not simple materials – there are a panoply of graphite grades on the market from numerous suppliers, and the manufacturing processes and production recipes can be quite diverse. As such, the thermophysical properties as well as the chemical reactivity of these different graphite grades can widely vary.

There are many studies of silicon infiltration and spreading on graphite, as outlined in a previous publication [1]. Some have investigated the wetting of carbon substrates with FeO-containing liquid slags of varying compositions; these studies were related to ironmaking processes where the focus was on examining the reduction of iron oxide from the slag phase [2,3,4,5,6,7,8]. In a similar study, the wettability of silicon carbide by CaO–SiO₂ slags was investigated by Safarian and Tangstad [9]. Heo, Lee, and Chung made similar measurements on graphite and MgO–C [10]. All of these studies employed high-temperature sessile drop apparatuses to measure the change in apparent contact angle of a molten slag droplet on a substrate over time, followed by scanning electron microscopy (SEM) of the specimens to analyze the reaction interfaces.

There are some industrial processes which contain both a liquid metallic phase and a slag phase in contact with a graphite refractory, such as during slag refining of silicon. Graphite readily reacts with silicon to form SiC, and the kinetics of this reaction dictates the manner in which silicon

interacts with different types of graphite grades [1]. Similarly, liquid slag does not merely mechanically coat a graphite substrate, but reacts chemically with the carbon substrate. The wetting of the substrate is dynamic in the sense that the system is not in chemical equilibrium, so the “apparent” contact angle changes with time as the reactions take place. The objective of the current study was to explore the melting behavior of liquid slag in contact with graphite from a fundamental perspective to better understand the reactions involved, and to determine to what extent this phenomenon can be fully exploited.

Experimental

A high-temperature sessile drop system was used in this investigation, which is illustrated in Figure 1. A horizontal Entech electrical tube furnace with Kanthal Super heating elements and an alumina reaction tube (70 mm inner diameter) was used. On one end of the tube, an internally water-cooled quenching chamber sealed the tube with a viton o-ring; the opposite end of the tube was sealed in a similar fashion with a water-cooled aluminum cap with a sealed quartz glass window. The specimen was placed on a graphite carriage that transported the specimen in and out of the hot zone of the furnace. A water-cooled pushrod, sealed with a shaft packing, was connected to the graphite carriage, which in turn was fastened to a screw drive that enabled the precise positioning and movement of the specimen to reproducibly control heating and cooling rates.

A Eurotherm controller was used to set and maintain the target furnace temperature, with an even temperature zone was defined as ± 2 K from the target temperature. A control thermocouple was a Type B (Pt–6% Rh / Pt–30% Rh) thermocouple (mounted in the wall of the furnace), which was positioned in the hot zone of the furnace outside of the reaction tube. A measurement thermocouple was a Type C (W / W–5% Re), 1 % accuracy, and was mounted axially in the pushrod and carriage, with the tip inside the carriage body positioned directly under the substrate.

High-purity argon gas was metered using a Bronkhorst mass flow meter (± 0.5 % accuracy). The reaction gas entered on the window end, passed through the tube, and exited out of the quenching chamber.

A Leica V-LUX3 digital camera with full HD video (1920×1080) capability at 30 fps was mounted with a view into the quartz glass window on the end of the furnace opposite the quenching chamber. Video recording was initiated when the specimen began to melt.

Materials Preparation

Two binary CaO–SiO₂ master slags were prepared prior to the experiments by fusing high-purity fused silica and calcium oxide, which in turn was prepared by calcining precipitated calcium hydroxide, in a graphite crucible and subsequently granulated in water. There was a wide difference in the compositions of the slags, 46 and 63 mass pct. SiO₂. The 46 mass percent SiO₂ slag was near the first eutectic composition with a melting point of 1623 K. The second slag was near the second eutectic composition at a much higher silica content of 63 mass percent.

Graphite qualities were chosen based on industrial relevance. Substrate disks were milled out of three different grades of graphite, and as can be seen in Table I and Figure 2, there is large disparity in the physical characteristics of these graphite grades. The substrates were 38 mm in diameter,

and 8 mm thick. Prior to the runs, the disks were heated at 393 K (120 °C) for at least 2 hours to remove any adsorbed water on the surfaces.

Table I. Characteristics of the Graphite Substrates Used in this Study

Graphite Grade	Manufacturing Method	Bulk Density	C.T.E. [$10^{-6}/K$]	Max. Grain Size	Open Porosity [%]
A	Isostatically pressed	1.77	4.3	15 μm	11
B	Vibration molded	1.73	2.2 /2.5	0.8 mm	15
C	Extruded	1.70	2.1/3.1	0.8 mm	17

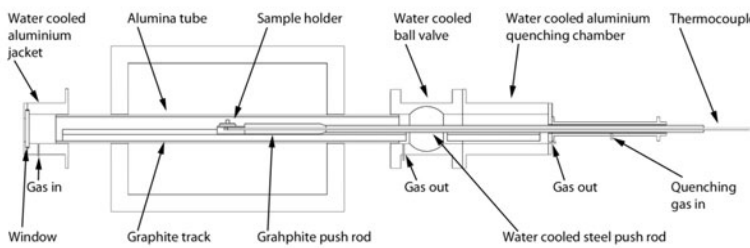


Figure 1. Schematic of the experimental setup.

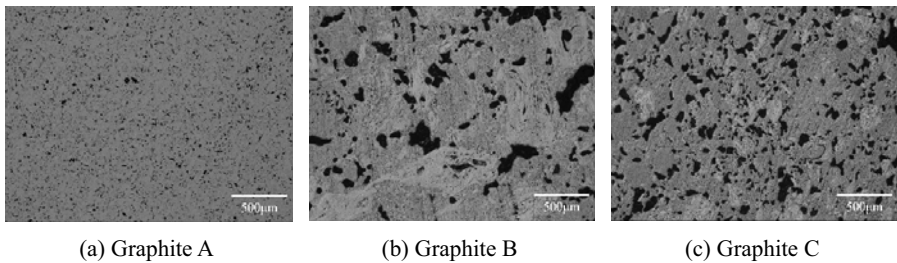


Figure 2. Optical micrographs of surfaces of graphite substrates at 50 \times magnification.

Experimental Procedure

In preparation for each experiment, granulated slag was pressed into 10 mm diameter pellets. The graphite substrate was cleaned with ethanol, and after drying placed on the carriage. The slag pellet was positioned on top of the graphite substrate and the system was sealed with the carriage positioned in the quenching chamber. The reaction tube was evacuated with a vacuum pump for 30 minutes, and back-filled with argon. To commence the run, the flow of reaction gas started at 0.05 l/min, while the furnace control sequence was initiated to ramp the temperature up to 1823 K (1550 °C) or 1873 K (1600 °C) at 2 degrees per minute. Video recording with the digital camera

was started as soon as the melting temperature of the slag was exceeded. After 30 minutes of video recording, the rest of the experiment was photographed at 5 minute intervals.

At the end of each run, the carriage was rapidly extracted from the furnace into the water-cooled quenching chamber by activating the mechanical screw drive. After quenching, the specimens were taken out of the furnace and prepared for scanning electron microscopy (SEM) analysis and electron dispersive spectroscopy (EDS) using a Hitachi S-3700N coupled with a Bruker XFlash Detector 4010. Still images were extracted from the video files, and from these the rate of spreading of slag (apparent contact angle) on the graphite substrate was quantified.

Results

Table II outlines the conditions of the experiments that were conducted and the duration of each experiment.

Table II. Experimental Conditions

Test no.	Slag composition [mass pct. SiO ₂]	Graphite Substrate	Temperature [K]	Duration [min]
SG13	46	A	1823	150
SG2	46	A	1873	120
SG11	46	B	1823	140
SG1	46	B	1873	150
SG7	46	C	1823	120
SG8	46	C	1873	60
SG15	46	C	1873	210
SG17	63	A	1823	160
SG14	63	A	1873	60
SG12	63	B	1823	25
SG16	63	B	1873	60
SG19	63	C	1823	210
SG18	63	C	1873	60

Wetting

Figure 3 is comprised of snapshots taken at time intervals during Run no. SG11 showing the reaction and dynamic wetting of Graphite B with 46 pct. SiO₂ slag at 1823 K. After approximately 1 minute, the slag pellet fused ($t = 0$) and formed a droplet on the graphite substrate as seen in (a). As molten slag was drawn into the pores by capillary action, the height of the droplet and apparent contact angle decreased dramatically (within 20 minutes), shown in (b). After this initial infiltration, the apparent contact angle decreased slightly until bubble formation started occurring (c). Eventually, bubble formation attenuated and the droplet continued spreading, reaching a maximum by 140 minutes.

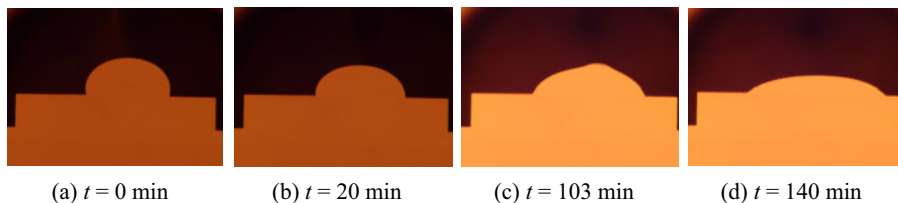


Figure 3. The spreading of 46 pct. SiO₂ slag on Graphite B at 1823 K.

The apparent contact angle as a function of time for the two slag compositions on each graphite substrate were recorded. Figure 5 shows the apparent contact angle on the three graphite grades at 1873 K for both slag types. In Figure 5(a), the spreading behavior of 46 pct. SiO₂ slag is seen to be quite different on the various graphite materials. The apparent contact angle of the slags on Graphite A changes very rapidly, almost linearly.

For the high-silica (63 pct. SiO₂) slag, the spreading behavior is quite different than for the 46 pct. SiO₂ slag, as seen in Figure 5(b): The apparent contact angles change much more rapidly on all graphite grades. In fact, for Graphite B, the apparent contact angle is low from the very start of the run.

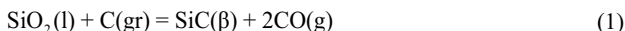
Infiltration

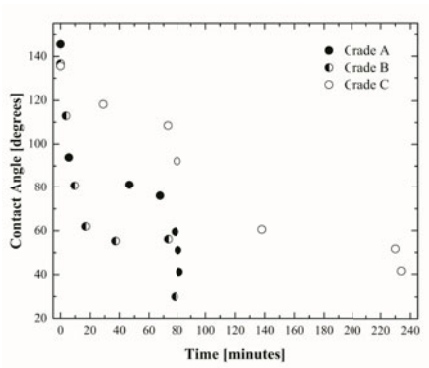
As seen in Figure 2, the internal structures of the different graphite grades are quite different. The isostatically pressed graphite quality Graphite A has by far the finest and most homogeneous internal structure, exhibiting small, evenly sized and spaced pores. This is in contrast to Graphite B, which is a vibration-molded quality that has large, irregularly shaped pores of widely varying size and distribution. Graphite C, the extruded quality, has the highest open porosity (see Table I), yet has smaller and more evenly distributed pores than Graphite B.

To examine the extent of infiltration, scanning electron microscopy (SEM) and electron dispersive spectroscopy (EDS) mapping were conducted for the elements oxygen, calcium, and silicon. It should first be noted that it does not appear that any SiO₂ and CaO present as ash constituents are visible in the EDS mapping. Figure 6 shows infiltration of 63 pct. SiO₂ slag at 1873 K into Graphite A. The spatial association of O, Ca is clear, but with deeper Si infiltration compared to O or Ca. Infiltration is deeper with the slag with high silica content.

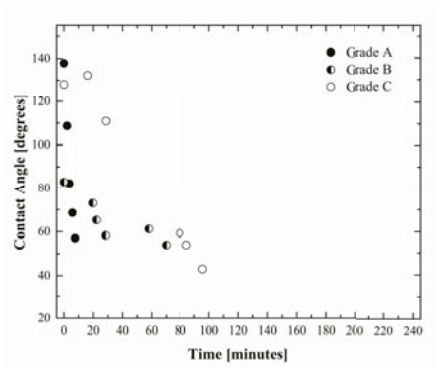
Discussion

The Si–C–O system is rather complex with many possible reactions. At 1873 K, silica can be reduced in the presence of carbon. However, SiC can readily form under these conditions as well. It is conceivable that silica will directly react with graphite to form silicon carbide according to:



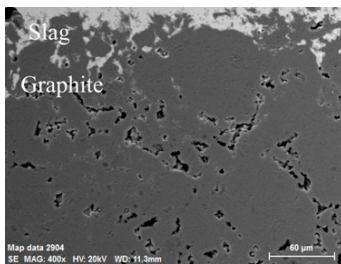


(a) 46 pct. SiO₂ slag

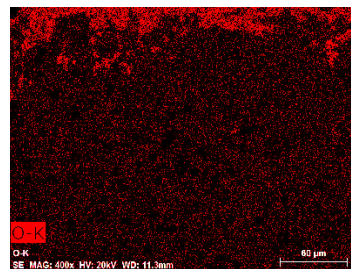


(b) 63 pct. SiO₂ slag

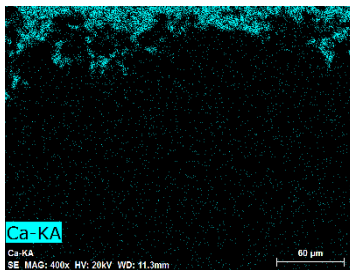
Figure 5. Apparent contact angle as a function of time of on the different graphites at 1873 K.



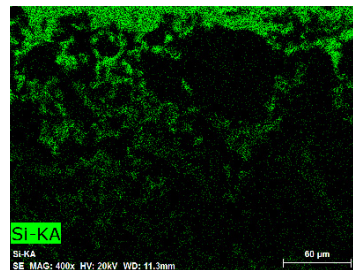
(a) SEM micrograph



(b) Depth of O infiltration



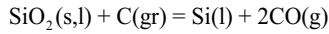
(c) Depth of Ca infiltration



(d) Depth of Si infiltration

Figure 6. SEM micrograph and EDS mapping showing extent of infiltration of 63 pct. SiO₂ slag into Graphite A at 1873 K.

The reaction



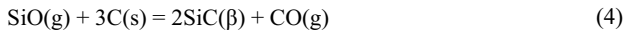
is not considered valid for the reason that Si and C cannot coexist in thermodynamic equilibrium due to the formation of SiC [1,11]. Moreover, silica is known to partially reduce to form silicon monoxide vapor. Fundamentally, this reaction can be written as:



With the oxygen potential being controlled by the reaction:



Evidence was presented in a previous publication that silicon-bearing vapor species can react with graphite to form silicon carbide [1]. Silicon monoxide, for example, can react directly with carbon to form SiC according to:



Although SiO(g) is the dominant vapor species in terms of partial pressure, there are actually many other silicon-bearing vapor species [1,12]. The total effective vapor pressure in the Si–C–O system is considerable, and increases exponentially with increasing temperature [1].

Wetting and Infiltration

There is wide disparity in the spreading behavior of 46 pct. SiO₂ slag on the different graphite grades. The increase in spreading rate of slags on the graphite substrates with higher temperature is likely attributed to the increased reaction kinetics of Eq. (1).

For the high-silica (63 pct. SiO₂) slag, the spreading behavior is different than for the 46 pct. SiO₂ slag; the apparent contact angles change much more rapidly on all graphite grades. Thus it is evident that the slag composition plays an important role in wetting. Since the silica in this case is in solution, its activity is dependent on concentration. Thus, it is expected that a higher silica activity in the slag will yield a greater driving force for the reaction shown in Eq. (1) to take place; this is in line with observations made by Sahajwalla, Mehta, and Khanna [2,8]. The 63 pct. SiO₂ slag at 1873 K is very close to the liquid–cristobalite phase boundary, i.e. the silica activity is near unity for this slag composition.

The extent of infiltration also appears to increase at higher temperature, and is greatly influenced by silica content. Infiltration depths of O, Ca, and Si are greater with the 63 pct. SiO₂ slag. Liquid slag itself is able to penetrate the open pores in the graphite substrate near the interface, the extent of which is indicated by the depth of Ca and O infiltration. The wide disparity in infiltration in the graphite grades can be attributed to open porosity, pore morphology, and reactivity of the graphite. Additionally, a higher total effective vapor pressure of silicon could enhance silicon infiltration.

Conclusions

Wetting of graphite by CaO–SiO₂ slag has been found to be quite complex. Some salient conclusions can be drawn from the current study:

1. The wetting and infiltration behavior of slag with graphite is highly material dependent. Synthetic graphites are not simple materials: the graphite recipe, grain size, open porosity, pore distribution, reactivity, and manufacturing method all come into play.
2. Temperature and silica activity of the slag have a major influence on how slag spreads and infiltrates. The higher the temperature and silica content, the greater the slag infiltration, and the faster the rate of spreading.
3. Reactions that generate gaseous products occurred during spreading of slag on graphite as evidenced by the observation of bubble formation, with the exception of Graphite C. Silicon infiltrated into the graphite substrates much deeper than the slag phase, indicating gas-phase transport of silicon-bearing vapor species.
4. Reduction of silica in the slag near the interface may lead to passivation by formation of a solid CaO-rich layer, halting the reaction at the interface and infiltration by forming a diffusion barrier, effectively passivating the interface.

An immediate industrial application of this knowledge is “slag washing” of graphite refractory can be an effective way of passivation to extend the lifespan of the refractory. How amenable a particular graphite is to passivation is not straightforward just judging by grain size and open porosity. For this application good wetting is preferred, with adequate penetration and stable passive layer formation to “seal” the graphite.

Acknowledgements

The authors would like to thank Elkem AS and the Norwegian Research Council (project no. 235159) for their financial support.

References

1. J. F. White, L. Ma, K. Forwald, and D. Sichen, *Metallurgical and Materials Transactions B*, 45B (2013), vol. 45, 150–160.
2. A. S. Mehta and V. Sahajwalla, *Scandinavian Journal of Metallurgy*, 29 (2000), 17–29.
3. N. Siddiqi, B. Bhoi, R. K. Paramguru, V. Sahajwalla, and O. Ostrovski, *Ironmaking and Steelmaking*, 27 (2000), 367–372.
4. S. L. Teasdale and P. C. Hayes, *ISIJ International*, 45 (2005), 634–641.
5. B. Bhoi and H. S. Ray, *IE(I) Journal-MM*, 89 (2008), 3–8.
6. P. Migas and M. Karbowiczek, *Archives of Metallurgy and Materials*, 55 (2010), 1147–1157.
7. P. Shen, H. Fujii, and K. Nogi, *Materials Chemistry and Physics*, 114 (2009), 681–686.
8. V. Sahajwalla, A. S. Mehta, and R. Khanna, *Metallurgical and Materials Transactions B*, 35B (2004), 75–83.
9. J. Safarian and M. Tangstad, *Metallurgical and Materials Transactions B*, 40B (2009), 920–928.
10. S-H. Heo, K. Lee, and Y. Chung, *Transactions Nonferrous Met. Soc. China*, 22 (2012), s870–s875.
11. Anders Schei, Jon. Kristian. Tuset, and Halvard Tveit, *Production of High Silicon Alloys*, (Trondheim: Tapir Forlag, 1998), 340.
12. T. Rosenkvist and J. K. Tuset, *Metallurgical Transactions B*, 18B (1987), 471–477.

INITIAL WETTING AND SPREADING PHENOMENA OF SLAGS ON REFRACTORY CERAMICS

¹Yongsug Chung, ²Tae Hee Yoon and ³Kyuyong Lee

¹Professor and ²Graduate Student, Department of Advanced Materials Engineering

³Professor, Department of Consilience

Korea Polytechnic University, Siheung-si, Gyunggi-do, 15073, Korea (ROK)

Keywords: Wettability, Spreading rate, Refractory ceramics, Slag, Reactive wetting

Abstract

Wetting angle and spreading rate between slags and refractory ceramics such as Al₂O₃, MgO, MgO-C or SiC have been recently determined by using dispensed drop technic with a high speed camera. Intrinsic value of wetting angle and the effect of reactions on wetting and spreading are reviewed and discussed. Role of carbide or graphite in refractories are also reviewed when these were in contact with reducible slags. Driving force for spreading and a spreading model (non-reactive viscous model) are discussed.

Introduction

It is important to know wetting and spreading phenomena between slags and refractories. This knowledge provides a better understanding of inclusion removal of refractory ceramics where they are indigenously or exogenously formed during steelmaking, and of penetration behavior of slags into refractories which causes degradation [1, 2].

The penetration behavior is considerably affected by wetting and spreading of liquid slag on refractory material as shown in Eq. (1) [2].

$$h = (r \sigma \cos\theta / 2\eta)^{1/2} \quad (1)$$

where h is depth of penetration, r is radius of pore of refractory, σ is surface tension of slag, θ is wetting angle between slag and refractory, η is viscosity of slag, and t is time.

Although the values of surface tension and viscosity of slag can be easily found, the contact angles cannot be obtained in open literatures due to difficulty of the measurement. The conventional sessile drop technic has some limitation to obtain an intrinsic angle since a reaction can be occurred while temperature elevates.

Several successful measurements have been carried out by using the dispensed drop technic. [3, 4] Recently, the dispensed drop technic with a high speed camera provided intrinsic values both of wetting angle and spreading rate for the system between slags and Al₂O₃, MgO, MgO-C or SiC [5-8] In those studies, reactive wetting was quantitatively considered [5, 6, 8].

Wettability is divided into two categories: non-reactive wetting and reactive wetting. In non-reactive wetting, mass transfer through the solid/liquid interface is very limited and the wetting is mostly driven by the physical forces such as inertial, gravitational, and viscous

force. In reactive wetting, wettability is strongly influenced by the reaction at the solid/liquid interface such as diffusion and the formation of intermediate compounds or bubbles at the interface.

In most non-reactive wetting, spreading of droplet is either inertial force dominant spreading or viscous force dominant spreading. In inertial spreading for low viscosity liquid, local equilibrium is rapidly established at the triple line, thus the contact angle approaches the equilibrium angle immediately. Then, spreading is controlled by inertial force due to the Laplace pressure difference caused by the curvature difference between the bulk and the region near the triple line. On the other hand, viscous spreading is controlled by viscous friction inside the droplet and the dissipation of energy at the triple line of the droplet. The driving force in this case is the change in the surface and the interfacial energy of the system caused by the displacement of the triple line [9, 10].

In this paper, wetting phenomena between slags and refractory ceramics such as Al_2O_3 , MgO , MgO-C or SiC are reviewed and the intrinsic contact angles are discussed based on a comparison of the similar systems; oxide ceramics and C containing ceramics. Spreading phenomena by De Gennes's non-reactive model are also reviewed for systems between oxide ceramics and slags [11].

Experimental Methods

The slag and substrate were separately heated and the molten liquid droplet of slag was dispensed onto the substrate by the push bar, so droplet was contacted with substrate in isothermal condition (Fig.1). The distance between crucible and solid substrate was carefully set to 1cm for each run to maintain consistent droplet shape. A high speed camera was used to capture the images of the initial wetting and spreading behaviors.

The chamber was sealed and evacuated to 2.0×10^{-2} tor using a rotary vacuum pump and filled with 99.999wt% Ar gas. This process was repeated more than three times. Then the chamber was heated up to 1600°C at the rate of $10^\circ\text{C}/\text{min}$. When the droplet contacts the substrate, the high speed camera was used to capture the initial contact angle at 1000~1500 frame/s.

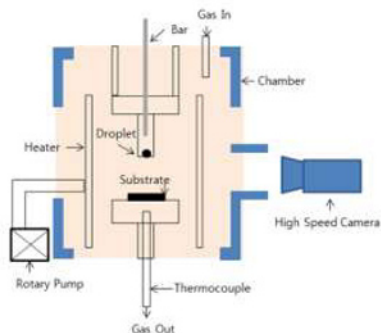


Fig. 1 Schematics of experimental apparatus of dispensed drop technic

Results and Discussion

1. Intrinsic wetting angle between slags and oxide ceramics

Most popular oxide refractory ceramics used for steelmaking are mainly composed with Al_2O_3 or MgO . An intrinsic value of wetting angle is not easy to obtain due to a reaction between two solid-liquid oxides. Dissolution of refractory component into slag occurs in most cases. Therefore, in order to remove the dissolution effect, a saturation condition is required. Kim et al. [5] measured wetting angle between single crystal Al_2O_3 and $\text{CaO-Al}_2\text{O}_3$ binary slag at saturated and non-saturated condition at 1550°C as can be seen in Fig. 2. The compositions of Al_2O_3 were 57.9 wt% at saturated condition and 42.8 wt% at non-saturated condition, respectively. The apparent wetting angle rapidly decreases to almost 20° within 1 second. From 0 to 3 seconds, the apparent contact angle of the two kinds of slag is similar. After 3 s, the apparent contact angle of the saturated slag slowly reaches to 17° . In contrast, that of the non-saturated slag slowly decreases to the angle less than 17° . The lower value for the non-saturated slag was induced by a crater formation at the substrate due to dissolution during the spreading as can be seen in Fig. 3 (b).

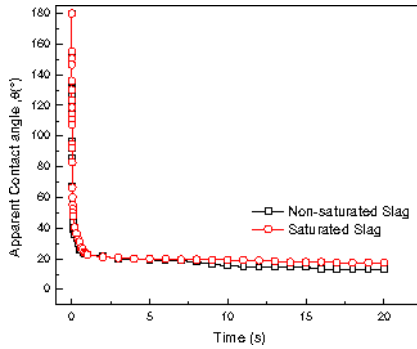


Fig. 2 Apparent wetting angles between two kinds of slag droplet and Al_2O_3 single crystal at 1550°C [5]

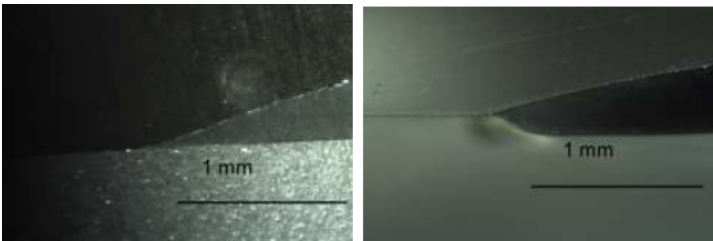


Fig. 3 Stereoscopic microscope image of cross section. (a) Saturated slag and Al_2O_3 substrate. (b) Non-saturated slag and Al_2O_3 substrate. [5]

Similar study has been carried out for the system MgO and CaO-SiO₂ (50: 50 in weight) slag, of which condition was non-saturated. Park et al. [6] determined wetting angle between MgO and CaO-SiO₂ slag by using single crystal and poly crystal of MgO at 1600°C. As can be seen in Fig. 4(a), the wetting angle of single crystal rapidly decreased to the equilibrium angle (about 5°) within 0.5 seconds which is much lower and faster than the one of Al₂O₃. They found 7% increase of MgO content in the slag after quenching but did not find any formation of the crater so that the interface remained to be flat after spreading.

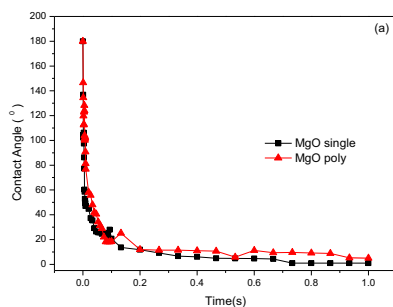
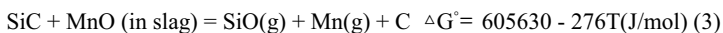


Fig. 4 Initial wetting angles of slag droplet on MgO single and poly crystal substrates at 1600°C.[6]

2. Reactive wetting between slags and C containing refractory ceramics.

Carbon is used for refractory as carbide or graphite. Silicon carbide is of great technological interest because of its good mechanical properties, high thermal conductivity, and good thermal shock resistance. MgO-C is also widely used due to its excellent chemical corrosion resistance, thermal resistance and mechanical properties. However, refractories containing C can be reacted with reducible slag components such as FeO, MnO and possibly SiO₂ at steelmaking temperature.

Recently, wetting angle has been measured with various CaO-SiO₂-MnO slags [8]. Figure 5 shows the changes of contact angle at C/S = 0.8, in which the contact angle rapidly decreases with time, reaches 30 degrees within 1 second, and slowly decreases to 20 degrees in 20 seconds. While this overall tendency is observed in both cases of two different MnO contents (about 12.5% vs 37.9%), a significant variation of contact angle occurs at 8 seconds in the case of 37.9% MnO. This abrupt change in contact angle reflects the bubble formation at the interface. Based on thermodynamic consideration, the bubble formation reactions can be suggested as follows [12]:



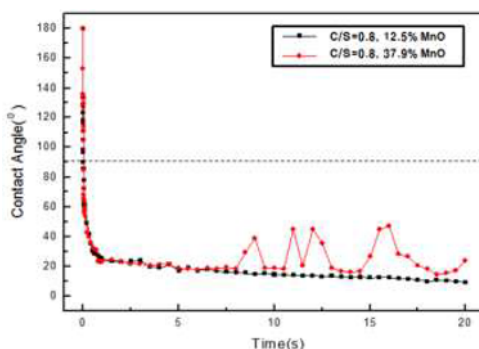


Fig. 5 Apparent wetting angles of slags on SiC substrates at 1550°C at different MnO content[8]

Graphite plays an important role in chemical corrosion where it provides poor wettability to slags. Figure 6 clearly shows the changes of wetting angles of CaO-55%SiO₂ slags in contact with different content of carbon in MgO-C. The initial contact angles were 115° for the pure graphite, 92° for MgO-17%C and 40° for MgO-4%C, showing that the contact angle increased with increasing carbon content in MgO-C. A slight decrease in the wetting angle of MgO-17%C as time passes can be understood from the following reactions [7]:



In this case, we did not find bubble formation which was found in SiC case. The reason could be either because the slag was in poor contact with MgO-17%C, or because the reactions proceeded very slowly.

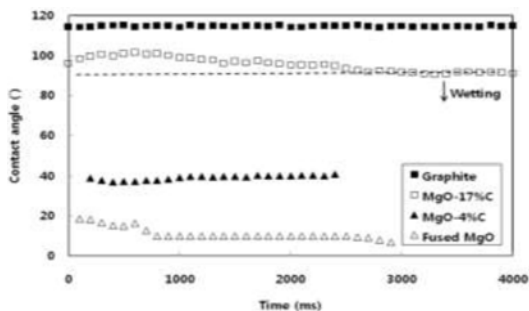


Fig. 6 Apparent wetting angles between CaO-SiO₂ slag and MgO-C substrates at 1600°C [7]

Values of the initial contact angle and the observed reactions are summarized in Table 1.

Table 1. Initial contact angles between slags and refractory ceramics

	Al ₂ O ₃ (1550°C)	MgO (1600°C)	SiC (1550°C)	C (1600°C)	MgO- 17%C (1600°C)	MgO- 4%C (1600°C)	Reaction remarks
CaO- 57.9%Al ₂ O ₃	20	-	-	-	-	-	-
CaO-42.8% Al ₂ O ₃	17	-	-	-	-	-	Dissolution [Crater formation]
CaO-50% SiO ₂	-	<5	-	-	-	-	Dissolution [No Crater formation]
CaO-SiO ₂ - 12.5%MnO (C/S=0.8)	-	-	20	-	-	-	-
CaO-SiO ₂ - 37.9%MnO (C/S=0.8)	-	-	20 ~ 40	-	-	-	Bubble Formation
CaO-55% SiO ₂	-	-	-	115	92	40	-

3. Driving force for spreading between slags and oxide ceramics

Slags and oxide refractory ceramics promptly wet each other. Spreading nature can be discussed in this case. When $\theta \ll 90^\circ$, the ratio of inertial force to viscous force is given by

$$\frac{f_{in}}{f_v} = 0.0024 \frac{\rho \sigma_{LV}}{\eta^2} \theta^5 R, \quad (7)$$

where f_{in} is the inertial force, f_v is the viscous force, ρ is the density, σ_{LV} is the liquid/vapor surface tension, η is the viscosity, θ is the contact angle, and R is the droplet radius[13]. The ratio can be used as a measure to determine which effect is dominant in the spreading. As shown in Fig. 7, the viscous force is dominant over the inertial force throughout the spreading for both systems. [5, 6]

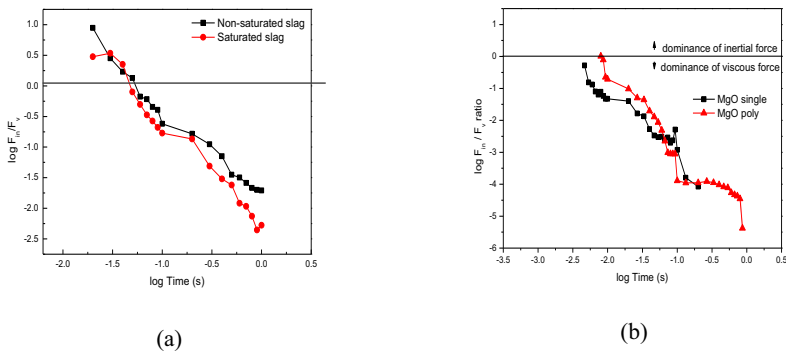


Fig. 7 The ratio of inertial to viscous force for Al₂O₃/CaO- Al₂O₃(a) and for MgO/CaO-SiO₂(b).

4. Non-reactive viscous model for spreading rate.

As previously mentioned, viscous force was dominant during the early stage of the spreading. And, variation of wetting angle and spreading radius with time for the saturated slag with alumina (there was no reaction) was not significantly different from the ones for the non-saturated slag (there was a dissolution reaction). De Gennes’s non-reactive model can be applied to the spreading of the slag droplets [9]. The non-reactive viscous equation is given by

$$U = \frac{\sigma_{LV}}{3K\eta} \tan\theta(t)(\cos\theta_F - \cos\theta(t)) \quad (8)$$

$$U = \frac{\sigma_{LV}}{6\eta K} \theta(\theta^2 - \theta_F^2) \quad (9)$$

This equation is valid for $\theta < 90^\circ$. For $\theta < 45^\circ$, the $\tan \theta$ is replaced by θ and the $\cos \theta$ by $(1 - \theta^2/2)$ as a good approximation so the Eq. (8) becomes Eq. (9). U is spreading rate, σ_{LV} is the liquid/vapor surface tension (J/m^2), η is the viscosity ($Pa \cdot s$), θ is the contact angle, θ_F is the final contact angle at 20 s ($\theta_F^S = 17^\circ, \theta_F^{NS} = 13^\circ$), and $K(\ln | \frac{x_{max}}{x_{min}} |, x \approx$ radius of droplet) is 10.

The experimental spreading rate evaluated by droplet radius and the theoretical value calculated by De Gennes’s equation are compared. Fig. 8 shows the experimentally obtained spreading rate and theoretical spreading rate against contact angle for $Al_2O_3/CaO- Al_2O_3$ system (a) and for $MgO/CaO-SiO_2$ (b). The experimental values are in good agreement with the theoretical values. It means that although dissolution occurs during spreading, wettability between oxide slags and solid oxides are strong so that spreading behavior appears to be a non-reactive system.

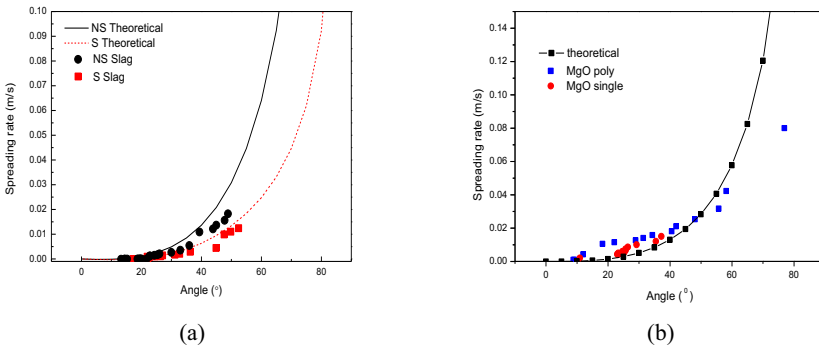


Fig. 8 Measured and theoretical spreading rate for $Al_2O_3/CaO- Al_2O_3$ (a) and for $MgO/CaO-SiO_2$ (b) based on non-reactive viscous spreading model[5,6]

Conclusions

1) Initial contact angle between CaO-Al₂O₃ slag and Al₂O₃ at dissolutive condition resulted in 3° lower than the one (20°) at saturated condition due to a crater formation during spreading of the slag. Initial contact angle between CaO-SiO₂ slag and MgO rapidly decreased to the equilibrium angle (about 5°) within 0.5 seconds which is much lower and faster than the one of Al₂O₃.

2) SiC in refractory reacted with reducible slags during spreading and created a bubble and C in MgO provided poor wettability against slags as its content increased.

3) Viscous spreading was dominant for wettings between CaO-SiO₂/MgO and CaO-Al₂O₃/Al₂O₃. In both systems, experimentally obtained spreading rate agrees with the calculated value using the viscous model, which suggests that the initial spreading can be regarded as non-reactive wetting controlled by viscous friction.

References

1. S.H. Lee, Tse, K.W. Yi, P. Misra, V. Chevrier, C. Orrling, S. Sridhar and A.W. Cramb: *J. Non-Crystalline Solids.*, 2001, vol. 282, pp. 41-48.
2. L. Teng: *Treatise on Process Metallurgy*, vol.2, Elsevier, Oxford, 2014, p.284
3. Ja-Yong CHOI and Hae-Geon LEE: *ISIJ Int.*, 2003, vol. 43, no. 9, pp. 1348-1355.
4. H. Abdeyazdan, N. Dogan, M. A. Rhamdhani, M.W.Chapman, and B. J. Monaghan: *Metallurgical and Materials Transactions B*, 2015, vol. 46B, no. 2, pp. 208-219
5. S. Kim, K. Lee and Y. Chung: *Metallurgical and Materials Transactions B*, 2016, 10.1007/s11663-016-0587-z
6. J. Park, K. Lee, J. PAK and Y. Chung: *ISIJ Int.*, 2014, vol., 54, pp. 2059-2063.
7. S. H. Heo, K. Lee, Y. Chung: *Transactions of Nonferrous Metals Society of China*, 2012 vol. 22, pp. 870-875.
8. J. Park, J. Jeon, K. Lee, J.H. Park and Y. Chung: *Metallurgical and Materials Transactions B*, 2016, to be published.
9. Eustathopoulos N, Nicholas M G, Drevet B. *Pergamon Materials Series*, 3rd, Pergamon: An imprint of Elsevier Science, 1999.
10. J. Park, K. Lee and Y. Chung: *proceedings of ICS 2015*, 2015, Beijing, China
11. De Gennes. *Reviews of modern physics*, 1985, 57 (3), pp. 827-863.
12. J.H. Park, J.G. Park, D.J Min, Y.E. Lee and Y.-B. Kang: *J. Eur. Ceram. Soc.*, 2010, vol. 30(15), pp. 3181–86
13. L. H. Hocking and D. A. Rivers: *Journal of Fluid Mechanics*, 1982, vol. 121 pp. 425-442.

MODELLING AND EXPERIMENTAL STUDIES OF DIFFUSIVITY OF SULFUR AND ITS RELEVANCE IN OBSERVING SURFACE OSCILLATIONS AT THE SLAG METAL INTERFACE THROUGH X-RAY IMAGING

Luckman Muhmood^a, Nurni N Viswanathan^b, Seshadri Seetharaman^c

^a K J Somaiya College of Engineering, Vidyavihar, Mumbai, India

^b Indian Institute of Technology Bombay, India

^c Royal Institute of Technology Stockholm, Sweden

ABSTRACT

A generic model was conceived for predicting the diffusion coefficient of species in slag. The diffusion coefficient of sulfur in CaO-Al₂O₃-SiO₂ slag with low silica was measured using a combinational technique of the generic model and experiments. The uniqueness of the experiments was in the method of collecting samples. Another milestone was that the diffusion coefficient of sulfur in the slag was obtained through the sulfur levels in the metal (silver). Later the order of magnitude of the diffusion coefficient of sulfur in slag was used to estimate the time required for sulfur to reach the slag-metal interface of an iron drop immersed in CaO-Al₂O₃-FeO-SiO₂ slag. This estimated time for arrival of sulfur at the interface was comparable to the actual observation. The current paper describes the challenges in measuring the diffusion coefficient of sulfur. It also describes the time estimates calculated based on the X-ray image for sulfur to reach the slag-metal interface.

INTRODUCTION

System dynamics pertaining to any process is difficult to assimilate due to its complexity. The perfect understanding of any process is usually carried out by dissecting it into sub processes and apart from understanding these individual processes, the knowledge of the linkage between them also becomes critical. On a lab scale, significant studies have been made regarding processes/ phenomena involving the slag-metal interface like sulfur, phosphorous or oxygen transport¹⁻⁴. In most of these studies, there are extensive interactions at the slag-metal interface owing to which there is significant shape change of the drop(s). In the current study we look into the sulfur transport from the gaseous media to the metal via a slag phase. This involves dissociation of the sulfur dioxide gas used to sulfur gas, electrochemical reaction at the gas-slag interface by virtue of which it enters the slag as sulfur ions, its transport through the slag media, electrochemical reaction at the slag-metal interface

where the sulfur ions are converted to sulfur atoms and finally transport of sulfur atoms in the metal media.

The aim of the study is to find the effect of sulfur on interfacial tension at the slag-metal interface. In the sub processes explained earlier, the rate determining step for sulfur to reach the slag-metal interface is the transport of sulfur through the slag and metal phases. In order to capture the dynamic effect of sulfur on the profile of the slag metal interface, the time required for the sulfur to reach the interface is of extreme importance.

As sulfur is in its ionic state in slag, its transport through slag would be a result of making and breaking of bonds and hence it should be slower in comparison to its transport in the metallic phase (where it prevails as an atom). This is reflected in the values obtained by various researchers for the diffusion of species in the metal as well as slag phases. As a rule of thumb, the transport of species in the ionic state is two orders of magnitude slower than the same species in its atomic configuration.

The paper describe in brief the experimentation required for calculating the diffusion coefficient of sulfur in slag as well as its help in x ray recording events occurring at the slag – metal interface due to the presence of sulfur.

SULFUR DIFFUSION COEFFICIENT IN SLAG – METHODOLOGY

Traditional experiments to determine the diffusivity of species in slag involves rapid quenching after sufficient equilibration time between the specie “rich” slag and the slag undergoing analysis ^{5,6}. The concentration profile of the specie as a function of time and distance is indicative of the diffusivity. This method may not be accurate enough as rapid quenching could induce convective currents hence disturbing the actual readings. In this regard it was decided to go for *insitu* measurements of species in slag. The focus was given on sulfur diffusivity as this value would help in determining the time taken for sulfur to travel through a fixed slag height, enabling X-ray videography of the process.

The diffusivity of sulfur was determined using a unique combination of modelling and experiments. The prime assumption was that the concentration of sulfur in the metal phase is uniform. This depends on the coefficient of diffusivity in the metal with respect to slag. Two conditions of the model were considered; the first with the assumption that sulfur concentration was uniform in the metal and the second in which the diffusivity in both the metal and slag phase were considered. Comparison between these two conditions gives the error of the estimation of diffusivity using this approach.

In the model, real time parameters like partition ratio, sulphide capacity, density were used ⁷⁻⁹. The only unknown was the diffusivity of sulfur in slag. This was assumed to have the order of magnitude of $10^{-6}\text{cm}^2/\text{s}$ which is typical for slags. The concentration profile of sulfur as a function of time was generated using the model and was later compared with actual sampling concentrations taken through experiments. This value was later refined so that the concentration points experimentally determined were closely located on the curve obtained

by the model. Further details on the model are available in previously published works by the authors¹⁰.

EXPERIMENTAL HURDLES

The experimental evaluation of the sulfur diffusivity posed many challenges. The prime challenge was the crucible design. Since the methodology was to collect *insitu* samples of metal without disturbing the slag layer, the design and fabrication of the crucible was complicated. In the final design, it consisted of a central tube with holes at the bottom and this tube was surrounded by another crucible. Figure 1 shows the crucible design. The metal and the slag were loaded in the annular region at a height well-above the height of the holes in the central tube. Once the metal was melted, it would fill the central chamber through which sampling was facilitated. Both the annular region as well as the central chamber were purged with argon. Armco iron was chosen as the crucible material to hold both the metal phase and the slag.

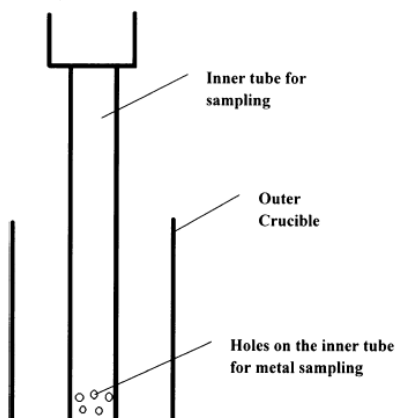


Figure 1: Schematic of the crucible design used for diffusivity measurements.

Once the material for the crucible was finalized, the next critical component to be decided was the metal. The metal should have low solubility for iron and vice versa. Since the maximum operational temperature was limited to about 50 degrees lower than the melting point of iron, a low melting metal was required. Silver was chosen as the metal. The solubility of Ag in Fe could be neglected.

Both sulfur as well as oxygen have a good tendency to dissolve in iron; hence the partial pressures of these needs to be controlled stringently. Using a gaseous combination proved impossible to meet these partial pressure requirements. After a thorough study, it was decided to use CaS as the source for sulfur. Since the density of CaS is lower than the metal and the slag, it would float on the slag surface providing a constant source for sulfur. At the temperature of interest CaS is solid.

The experimental set up showing the furnace, crucible along with other arrangements is shown in Figure 2. During the heating stage of the metal the sulfur source was kept away from the slag surface. Once the desired temperature is reached, the sulfur source was lowered down to have contact with the slag surface. This was taken as the zero time for the sulfur diffusion process. Samples are then taken at random time frames; they were then sent for sulfur analysis to NILAB AB and the concentration profiles are plotted. A detailed description of the set up as well as experimental procedure is given elsewhere ¹¹.

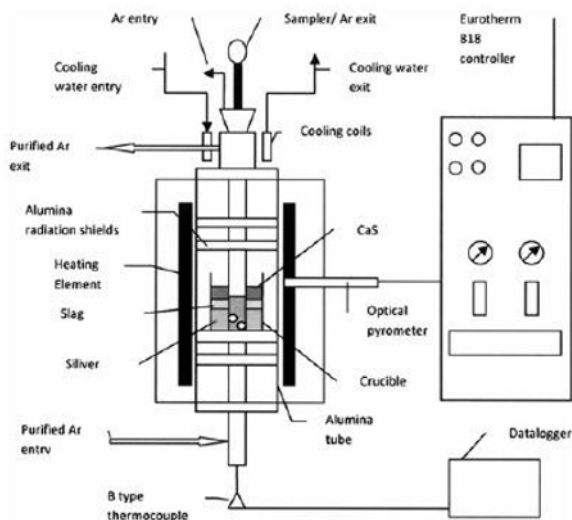


Figure 2: Layout of the furnace, crucible and other related connections ¹¹

RESULTS

The composition of the slag used is 51.5% CaO- 9.6% SiO₂- 38.9% Al₂O₃. As mentioned in earlier section, the concentration of sulfur was measured in silver samples taken at various time intervals. The concentration profile using the model was also obtained ¹¹. Sulfur concentration variation with time is shown in Table 1. The slag density and partition ratio at the slag metal interface was measured separately.^{9,10,11} The only unknown in the model was the diffusion coefficient of sulfur in slag. This term in the model was later fine-tuned to obtain a better agreement with the experimental results. Figures 3 show the concentration of sulfur in the metal as per the model curve and the experimental points at temperature 1723 K. The order of magnitude was similar to that obtained by earlier researchers ⁵.

Table I. Sulfur concentration in silver metal during the diffusion experiments repeated at 1723 K. Sampling time is from the time CaS was introduced into the system.

Sampling time (seconds)	Concentration of sulfur in silver metal (ppm)	
	First trial	Second trial
18600	9.7	-
20100	16	15.6
21600	20.2	19.9

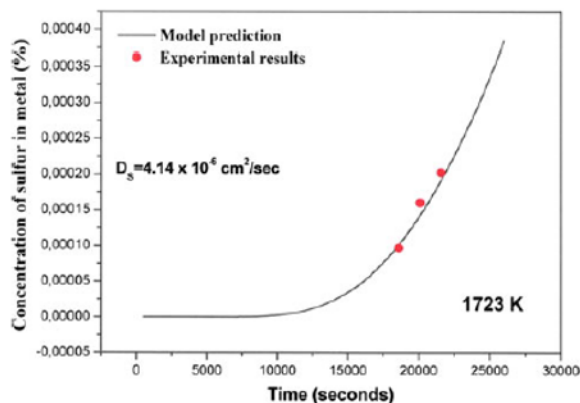


Figure 3: Concentration profile of sulfur in metal as a function of time; experimental (dots) and models values (curve) ¹¹.

X-RAY CAPTURE AND CALCULATIONS

An independent experiment to study the effect of sulfur at the slag-metal interface was conducted. This involves the sulfur to be introduced in to the furnace in its gaseous form later dissolving in slag and slowly diffusing through the slag till it reaches the slag –metal interface. The slag-gas interface was a concave surface while the slag-metal interface was convex in nature. This leads to varying distances for the sulfur to travel till it reaches the slag-metal interface from the gas media. Since sulfur is a surfactant for the metal phase, as soon as it reaches the slag-metal interface, the interfacial tension decreases locally. This leads to the interface oscillations which could be observed using an X-ray set up in its video mode. Since there is a limitation in the minutes of video recording, it is required to know the approximate time at which the sulfur would reach the interface. From the X-ray image, it is possible to measure the thickness of the slag layer and hence, if one knows the diffusion coefficient, it is possible to estimate the time taken to reach the slag-metal interface. Figure 4(a) and (b) show the schematic of the process described as well as an X-ray image of the metal drop surrounded by slag ¹².

In order to avoid change in slag composition during melting, the slag was saturated with Al_2O_3 . The composition of the slag was taken as 22.9% CaO - 51.4% Al_2O_3 - 18% SiO_2 - 5% FeO .

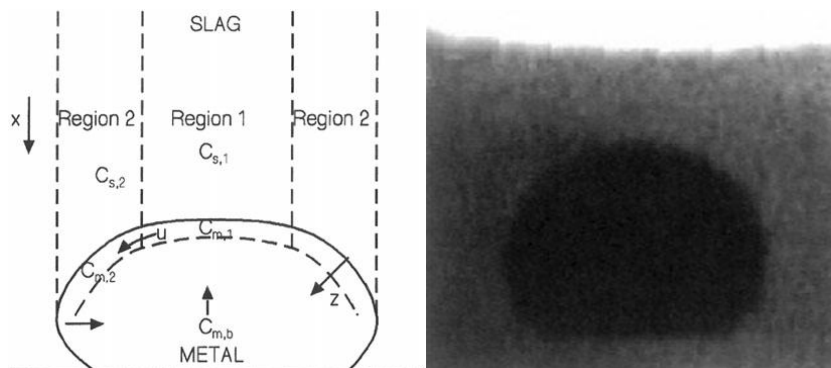


Figure 4: (a) Schematic of sulfur movement from slag phase to metal phase. X-ray image of the sessile drop of iron surrounded by $\text{CaO-Al}_2\text{O}_3$ - FeO-SiO_2 slag at 1823K. The drop height was measured to be 5.16 mm and width was 9.03 mm respectively.

The slag layer height above the slag-metal interface was calculated to be approximately 2.23mm. Earlier, the diffusion coefficient of sulfur in $\text{CaO-Al}_2\text{O}_3$ - SiO_2 slag at 1723 K was evaluated to be $4.14 \times 10^{-6} \text{ cm}^2/\text{s}$. Assuming a similar order of magnitude of sulfur diffusion coefficient in the slag, the time taken for sulfur to travel this slag thickness and reach the slag-metal interface was estimated as 453 seconds. Figure 5 shows that the change in contact angle which is indicative of drop oscillations start roughly at 400 seconds. This is in line with the value predicted by earlier calculations.

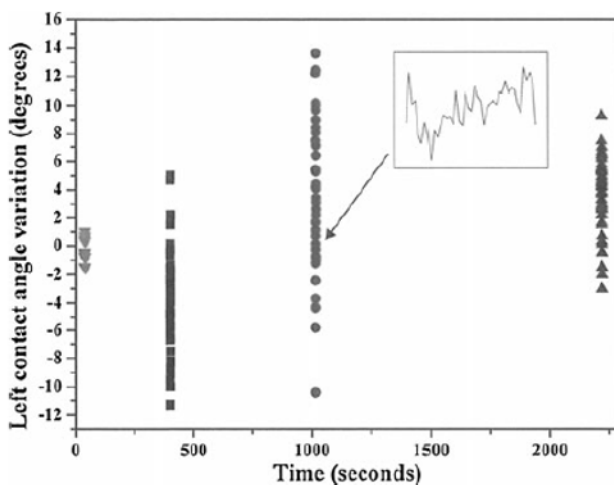


Figure 5: Contact angle variation with respect to time from sulfur introduction into the system
12.

CONCLUSION

Diffusion coefficient of sulfur in CaO-Al₂O₃- SiO₂ slag was evaluated using a combination of modelling and experimentation. The value of the diffusivity of sulfur in slag was the only unknown in the model. The model was later refined by a comparison between the concentration profile of sulfur and time both experimentally and as per the model. The order of magnitude of the value obtained was similar to that reported by others. This value was later used to record the surface velocity of sulfur at the slag-metal interface via X-ray videography observed by interfacial oscillations due to sulfur concentration variation at the slag-metal interface.

REFERENCES

1. Kozakevitch P, Urbain G and Sage M: *Revue de Metallurgie*, L11 (2), 1955, pp. 161-172.
2. Ooi H, Nozaki T and Yoshu Y: *Tetsu-to-Hagane*, 58, 1972, pp. 830-841.
3. Riboud P.V and Lucas L.D: *Can. Met. Qtrly.*, 20(2), 1981, pp. 199-208.
4. Chung Y and Cramb A.W: *Metall. Trans. B*, 31, 2000, pp. 957-971.
5. T. Saitô and Y. Kawai: *Japan J. Inst. Metals*, 1953, vol. 17, pp. 434.
6. G. Derge, W.O. Philbrook and K.M. Goldman: *Trans. AIME*, 1950, vol.188, pp. 1111-1119.
7. Y. Taniguchi, L. Wang, N. Sano, S. Seetharaman. *Met. and Mat. Trans. B*, Available online, 2012, DOI: 10.1007/s11663-011-9621-3.
8. P. Kozakevitch: *Rev. Metallurg.*, 1960, vol.57, pp. 149-160.
9. L. Muhmood and S. Seetharaman: *Met. and Mat. Trans. B*, 2010, vol. 41B, pp.833-840.
10. L. Muhmood, N. N Viswanathan, S Seetharaman . *Met. and Mat. Trans. B*, Vol 42(2), 2011, p. 460-470.
11. L. Muhmood, N. N Viswanathan, M. Iwase, S Seetharaman . *Met. and Mat. Trans. B*, Vol 42(2), 2011, p. 274.
12. Muhmood L, Viswanathan N.N and Seetharaman S: *Met. Mater. Trans. B*, 42, 2011, pp. 460-470.

SPH Analysis of Interfacial Flow of the Two Immiscible Melts

Shungo Natsui, Ryota Nashimoto, Tatsuya Kikuchi, and Ryosuke O. Suzuki

Hokkaido University;
Kita 13 Nishi 8, Kita-ku; Sapporo, 060-8628 Japan

Keywords: molten metal-slag, gas-liquid-liquid system, SPH, multi-phase flow

Abstract

The transient behavior of the immiscible two liquids interface, which is initiated by the rising gas bubble was investigated using Smoothed Particle Hydrodynamics (SPH) model. This developed numerical method is using fully Lagrangian particle-based model, which can track the movement of both the gas and the liquid phase directly. Numerical simulations have been performed for different conditions corresponding to different values of $E\ddot{o}$ number, and the predicted topological changes as well as the theoretical pressure and interfacial shape of bubbles are validated. In the case of immiscible two liquids, the column of a lower liquid phase penetrating into the upper liquid phase influences interface area, whose shape strongly depends on the wake flow pattern of a bubble. Thus, the dynamic balance between the buoyancy and the liquid-liquid interfacial tension determines an interface area. Under higher surface tension condition, such as molten metal-slag system, the liquid-liquid interface shape is greatly influenced by the fluctuation of a bubble. Then, non-linearly changed interface shape can be observed, indicating that this shape becomes easily unstable by slight change of the curvature.

Introduction

In the high-temperature metallurgical processes, the molten metal-slag interface plays an important role in increasing the efficiency of the refining process. Given the immiscibility of these two liquids typically involved, stirring is usually achieved by a flow of gas, i.e. the gas injected into a steelmaking converter accelerates the decarburization reaction by increasing molten metal-slag interface area. An effective method for increasing the interfacial area between the molten metal and slag phases is to emulsify the lower metal phase into the upper slag phase as “metal droplets” [1, 2]. The behavior of gas bubbles when they are passed through the molten metal-slag interface is intimately associated with the overall reaction rate. Unfortunately, droplets of a molten metal are usually suspended in the slag phase; a phenomenon referred to as “mechanical slag loss”. This “slag loss” should be reduced for resource saving, thus the control of the shape of liquid-liquid interface has been strongly required over the past decades. However, despite of its importance, the behavior of interfacial boundary between the metal and the slag has not been well understood. It is still difficult to accurately predict from the limited experimental data alone the actual molten metal-slag interface behavior at the temperature higher than 1773 K in steelmaking process. Direct observation of the dynamic behavior of a molten metal-slag boundary has been also difficult due to an extremely limited observation domain [3]; i.e., the behavior of a three-dimensional bubble cannot be clarified from two-dimensional image analysis. Reiter et al. [4,5] performed a non-dimensional analysis by using the entrainment phenomena observed in a cold scale model (water-oil-nitrogen system etc.) and quantitatively relate mass transfer to physical

entrainment; however, the liquid-liquid interfacial shape in this case was estimated by local rotational symmetry approximation, and the accuracy of this procedure was not described in details. The behavior at the gas-liquid-liquid interface depends greatly on the physical properties of the fluid such as density, viscosity, and interfacial tension. Thus, the accurate prediction of a transient liquid-liquid interface behavior is not possible by using cold model, because the physical properties of a high temperature fluid are often very different from those at room temperature.

Recently, three-dimensional fluid simulation has received considerable attention. It was used to analyze the above mentioned problem in the chemical industry. In order to describe the dispersed phase movement, the most instinctive approach is mesh-free particle simulation method, such as the Smoothed Particle Hydrodynamics (SPH) method [6-8]. The SPH method is one of fully-Lagrangian approaches which does not use grids, and discretizes fluid by moving particles, and numerical diffusion does not exist even for the dispersed phase. It involves no interface reconstruction steps, and an applied algorithm is very simple if a fully explicit procedure is used. Recently, SPH has been often applied for the description of dynamics of multiple-fluid flows by using improved interfacial representation [9-11]. We first attempt to observe the gas-liquid-liquid interfaces behavior using low-melting point metal and salt. Then, detailed analysis of three-dimensional simulations of a gas bubble penetrating through the interface of two immiscible liquids is carried out in order to predict the influence of various physical properties on the above-mentioned refining efficiency.

Observation of Interface Behavior between Sn and LiCl-KCl Due to Rising Gas Bubble

Experimental setup

To understand the dynamic behavior of a liquid-liquid-gas interface, direct optical observation of an interfacial flow in a wide domain is necessary. However, for example, the physical properties of water ($\rho = 997 \text{ kg/m}^3$, $\sigma = 7.2 \times 10^{-2} \text{ N/m}$) and oil ($\rho = 935 \text{ kg/m}^3$, $\sigma = 2.0 \times 10^{-2} \text{ N/m}$) phases are too different for comparison with Fe ($\rho \cong 7000 \text{ kg/m}^3$, $\sigma \cong 1.0 \text{ N/m}$) and slag ($\rho \cong 3000 \text{ kg/m}^3$, $\sigma \cong 0.4 \text{ N/m}$) systems. The two immiscible melts of a low-melting-point metal and molten salt system are particularly interesting. A molten salt is clear and chemically stable, and it is possible to design the values of the physical properties. In this study, a LiCl-KCl eutectic melt (LiCl:KCl = 59:41 mol%, m.p. = 625 K), which is widely used for electrolysis, is employed as the "slag phase". Molten Sn is used as the "metal phase" because its density is close to that of liquid Fe and Cu. The advantage of this system is the widely available thermodynamic data and thermal stability in a wide temperature range (650–900 K). To simulate the various interfacial flow modes, we focus on the temperature dependence of the physical properties. This attempt is made to clarify the sensitivity of the interfacial flow to changes in the physical properties (especially density and surface tension; viscosity changes can be ignored). A borosilicate glass crucible 100 mm in diameter and 250 mm in height was employed. The gas injection nozzle was also made of borosilicate glass; its outer diameter and thickness are 6.0 and 1.0 mm, respectively. Sn shot (1,500 g) with a purity of 99.9 mass% was placed in the crucible. Approximately 520 g of eutectic salts (LiCl: >99 mass%, KCl: >99.5 mass%, Wako Chemical Co.) were mixed and placed on the Sn. The electric resistance furnace was designed to observe phenomena in the interior directly. The interface temperature was measured with a K-type thermocouple with a glass protection tube. The salt was dehydrated in vacuum at 573 K or lower temperature. After one night, it was continuously heated to the desired melt temperature in an

argon gas atmosphere. After the materials melted completely, Ar (>99.999%) gas was then blown through the glass pipe into the molten Sn at a desired gas flow rate using a mass flow controller (MQV9500, Azbil). Changes in the interface were recorded at a rate of 500–1000 frames per second and a resolution of 1024×1024 pixels using a high-speed video camera (Fastcam SA3 model, Photron Co., Ltd.).

Results and discussion

Fig. 1 shows the behavior of the interface between molten Sn and the LiCl–KCl eutectic melt as a single Ar gas bubble rose. The interface temperature conditions were obtained from the values directly displayed on the digital multimeter. At 885.8 K (case 1), a single bubble reached the Sn–salt interface at $t = 0.06$ s. Then a “metal dome” appeared; i.e., the rising bubble started to modify the interface shape by pulling the Sn phase upward through the interface. At $t = 0.12$ s, this dome was ruptured, and the gas bubble started to penetrate the upper salt phase. After full penetration, the bubble rose up through the salt phase. The liquid–liquid interface was unsteady even after $t = 0.30$ s. At a lower temperature, the behaviors of the bubble were very different from those in case 1. At 729.3 K (case 2), a single bubble started to spring back when it reached the Sn–salt interface ($t = 0.12$ s). The reason could be that, because of the lack of buoyancy force, a gas bubble cannot break through the Sn–salt interface with only one impact. At $t = 0.18$ s, the dome held the bubbles on the metal phase, and it ruptured at $t = 0.30$ s, after which bubbles penetrated the slag phase. The process in case 2 is summarized as follows: first, a bubble is lifted by buoyancy, and it springs back owing to interfacial tension after striking the interface once; then the dome breaks.

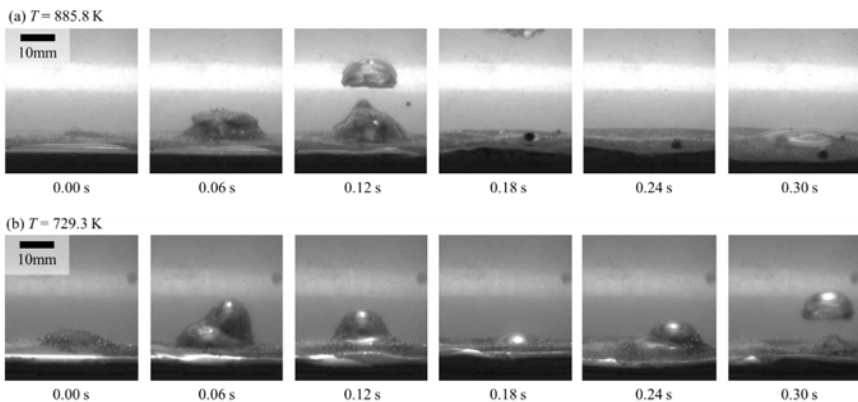


Fig. 1. Observed behavior of single Ar gas bubble rising through liquid Sn–molten salt interface at various temperatures. Flow rate of Ar gas is controlled at 0.067 ml/s to generate an isometric single bubble. Each snapshot shows representative behavior in their temperature range.

The dependence of the detention time of the bubble in the Sn phase on the temperature is summarized in Fig. 2. The behavior described above as case 1 mainly appears only for $T > 785$ K. For $T < 785$ K, cases 2 could appear at every temperature. However, the detention time was long, in particular at $710 < T < 780$ K. At the $700 < T < 800$ K, the fluctuation range becomes relatively large. The Sn film stability would be contributed greatly on this fluctuation of bubble detention time. From the Grace's diagram [12], a rising single bubble in molten Sn is in “wobbling” state. Due to its instability, the frequency of metal-salt interfacial fluctuation is not constant. Therefore, the error bar of detention time must be extended in interfacial tension dominant condition. On the other hand, in water-oil system, we see that the rising bubble starts to modify the water/oil interface by pulling the water phase upwards through the oil/water interface. The behavior at the gas-liquid-liquid interface depends greatly on the physical properties of the fluid especially density and interfacial tension.

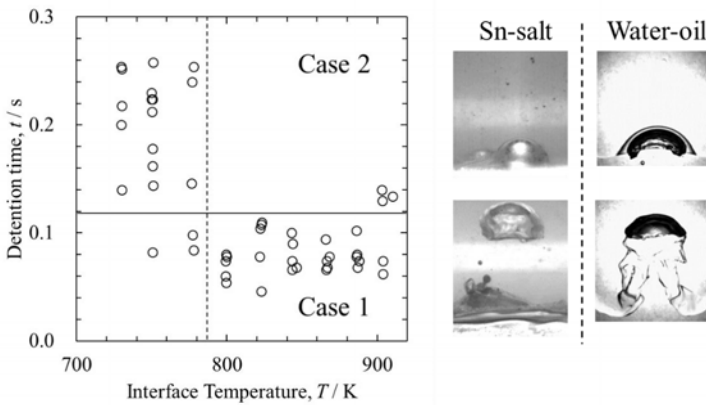


Fig. 2. Temperature dependence of detention time of single Ar bubble in liquid Sn.

SPH Numerical Simulation

In this section we present SPH equations obtained from discretization of the Navier-Stokes equation governing a multiphase flow. We first describe the numerical scheme used in the present work, then modeling of the surface tension and interfacial tension is presented.

SPH basic scheme and multiple fluid flow modeling

In fully Lagrangian particle-based simulation, gas, liquid and solid phases are represented by a number of particles, which exhibit properties of each phase such as the composition, mass, and density. The basic idea of the SPH method is to introduce kernel function for flow quantities in such a way that fluid dynamics is represented by a set of particle evolution equations [7]. The governing equations for incompressible viscous flow are composed of the Navier–Stokes equation:

$$\rho \frac{D\mathbf{u}}{Dt} = -\nabla p + \mu \nabla^2 \mathbf{u} + \rho \mathbf{g} + \mathbf{F}_s \quad (1)$$

where \mathbf{u} is the velocity, t is the time, p is the pressure, μ is the viscosity, \mathbf{g} is the gravity, and \mathbf{F}_s is the surface tension, respectively. Here, the density approximation:

$$\langle \rho \rangle_i = m_i \sum_{j \neq i} W_{ij} \quad (2)$$

This is very important in the SPH method since density basically determines particles distribution and the smoothing length evolution. In this approach, the density field is represented only by the spatial distribution of neighboring particles. Unless the number of particles changes, a total mass of the system is preserved. The right-hand side of Eq. (1) consists of the pressure gradient term, viscous term, gravity term, and surface tension term. Using the technique mentioned above, each term is discretized [13]. It is feasible to use an equation of state for the model the incompressible flow in this explicit scheme. In such a case, Tait's equation of state is applied in most circumstances [14].

$$\langle p \rangle_i = \frac{c_i^2 \rho_0}{\gamma} \left\{ \left(\frac{\rho_i}{\rho_0} \right)^\gamma - 1 \right\} \quad (3)$$

where γ is adiabatic exponent, equal to $\gamma = 7.0$ for the liquid and $\gamma = 1.4$ for the gas (Hashimoto et al, 2007), ρ_0 is the reference density, and c is the sound speed, respectively. We have decided to use the Interparticle Potential (IP) approach to simulate numerically the surface tension. One advantage of this method is that complex calculations are not necessary because this model gives the surface tension between particles using the same algorithm as that used in the molecular dynamics. The particle-particle interaction force \mathbf{F}_s is localized on the fluid interface by applying it to the fluid elements in the transition region of the interface. The surface tension is then converted into a force per unit volume using the relation. The interfacial tension between the two immiscible liquids A and B, σ_{AB} , is expressed as [15]:

$$\sigma_{AB} = \sigma_A + \sigma_B - 2\sqrt{\sigma_A \sigma_B} \quad (4)$$

where σ_A and σ_B are the surface tension coefficients of liquid A and B, respectively. The dynamics of the dispersed molten metal droplets in the slag phase may play a dominant role during the refining process and may contribute to the pressure oscillations. Therefore, neglecting the pressure fluctuation in impact flows may result in an incorrect approximation, particularly in predicting the short-time pressure characteristics. The pressure p_i is calculated from Tait's equation as a function of local density ρ_i , thus the smooth density field of a bulk phase gives continuous pressure distribution. Colagrossi and Landrini [16] introduced a density re-initialization procedure, called Moving-Least-Square (MLS) method, which improves the mass-area-density consistency and filters out small-scale pressure oscillations. MLS method is the most widely used 1st order consistent gradient approximation which allows to smooth pressure and its first derivative values are obtained by use of this method in homogenous bulk phase [17]. In this study, Least Square Interplant with Constraint condition (CLS) method is introduced, which gives more accurate approximation around sampling points than MLS method.

Results and discussion

In Fig. 3 and Fig. 4 we compared the three-dimensional interface changes for each k_d , and in Fig. 5 we compared the changes in the interfacial area of the liquid-liquid interface in time. Here, the liquid physical properties used are based on liquid water (A) and liquid oil (B), and the absolute values of ρ_l, μ_l, σ_l were multiplied by parameter k respectively, i.e. the densities of both liquids A and B are simultaneously given as $\rho_{l,A}^* = k_d \rho_{l,A}, \rho_{l,B}^* = k_d \rho_{l,B}$. Because our interest is in the influence of liquid properties on the liquid-liquid interface area, we simulate gas-liquid-liquid system using the developed model. The main advantage of this approach is its instant prediction of the liquid-liquid interface area ψ from its initial condition ψ_0 and the surface judgment function ξ .

$$\left\langle \frac{\psi}{\psi_0} \right\rangle^t \sim \sum_i \xi_i^t / \sum_i \xi_{i,0} \quad (5)$$

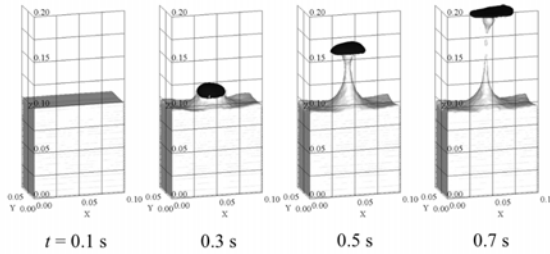


Fig. 3. Calculated snapshots of single gas bubble rising through the interface of a liquid phase A and B. In these simulation results, light grey interfaces are liquid phase A, black interfaces are gas phase, respectively. In order to help show the change of 3-dimensional interface, the liquid phase B is not displayed.

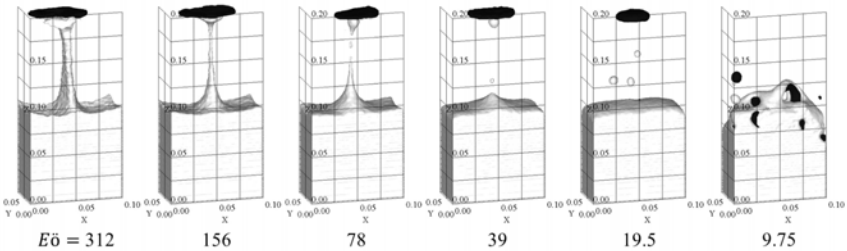


Fig. 4. Calculated snapshots of single gas bubble rising through the interface of a liquid phase A and B with various liquid density ratio. Liquid density is set as $\rho^* = k_d \rho_l$ in each case.

The flow fields of three phases are successfully calculated without unphysical mixing. In the case of $k_d = 1$, the rising bubble breaks the liquid-liquid interface at $t = 0.3$ s, and starts to change the interface shape by pulling the liquid A upwards. The “column” of liquid A is generated

below the bubble ($t = 0.5$ s), and penetrates fully into the upper liquid B layer before it finally collapses ($t = 0.7$ s). Thicker column is generated with increasing k_d , whereas it is broken easily with decreased k_d except for $E\ddot{o} = g\Delta\rho D^2/\sigma = 9.75$. Because of the lack of buoyancy, the gas bubble which cannot break through the liquid-liquid interface, disperses and penetrates into upper phase along a wall side. The column growth depends on the bubble wake flow pattern. Thus, the dynamical balance between buoyancy force and liquid-liquid interfacial tension can determine the thickness of a column. The ψ is significantly increased with subsequent growth of the column after $t = 0.3$ s, thus higher k_d increases ψ . On one hand, the interfacial area is stabilized after bubble's penetration in time dependent on k_d . On the other hand, for $E\ddot{o} = 9.75$, dispersed bubbles stir liquid-liquid interface drastically despite of weak buoyancy. Although wettability of a solid wall is completely ignored in this study, it might also influence the liquid-liquid interface shape.

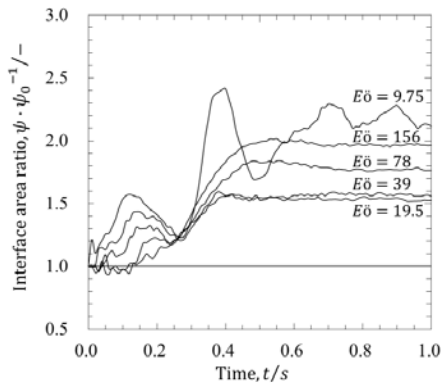


Fig. 5. Comparison of the transient liquid-liquid interface area calculated for different value of the liquid density ratio k_d .

Conclusions

The gas-liquid-liquid multi-phase flow was simulated using the SPH based multi-phase incompressible flow model, in which the gas phase and the liquid phase are directly discretized as particles. The advantage of this simulation model is a direct calculation in both of dispersed phase and continuous phase seamlessly. By applying this model to a gas-liquid-liquid system, the change of the liquid-liquid interface shape in time was demonstrated. Thereby this model estimates transient behavior of interface area by predicting the changes of liquid-liquid interface shape.

The column of lower liquid penetrating upper liquid phase influences interface area drastically. The column growth depends on the bubble wake flow pattern. The dynamical balance between buoyancy and liquid-liquid interfacial tension determines the column's thickness. Significant increase of interface area can be seen under convection dominant (higher density and lower surface tension) conditions. However, for higher surface tension conditions such as one can encounters in molten metal-slag system, the liquid-liquid interface shape is greatly influenced by the fluctuation of a bubble. Then, non-linear changes of the interface shape can be seen, which mean that the slight change of curvature will affect the direction of the action of interfacial tension.

References

1. Song, D. Y., Maruoka, N., Maeyama, T., Shibata, H., and Kitamura, S. Y., "Influence of Bottom Bubbling Condition on Metal Emulsion Formation in Lead-Salt System", *ISIJ int.*, 50(11), (2010), 1539-1545.
2. Song, D. Y., N. Maruoka, G. S. Gupta, H. Shibata, S. Y. Kitamura, and S. Kamble, "Modeling of Ascending/Descending Velocity of Metal Droplet Emulsified in Pb-Salt System", *Metall. Mater. Trans. B*, 43(4), (2012), 973-983.
3. Han, Z. and L. Holappa, "Mechanisms of Iron Entrainment into Slag due to Rising Gas Bubbles", *ISIJ int.*, 43, (2003), 292-297.
4. Reiter, G. and K. Schwerdtfeger, "Observations of Physical Phenomena Occurring during passage of bubbles through Liquid/Liquid interfaces", *ISIJ int.*, 32, (1992), 50-56.
5. Reiter, G. and K. Schwerdtfeger, "Characteristics of Entrainment at Liquid/Liquid Interfaces due to Rising Bubbles", *ISIJ int.*, 32, (1992), 57-65.
6. Lucy, L. B., "A numerical approach to the testing of the fission hypothesis", *Astronomic. J.*, 82, (1977), 1013-1024.
7. Monaghan, J. J., "An introduction to SPH", *Comput. Phys. Commun.*, 48, (1988), 89-96.
8. Harting, J., S. Frijters, M. Ramaoli, M. Robinson, D.E. Wolf, S. Luding, "Recent advances in the simulation of particle-laden flows", *EPJ-Special Topics*, 223, (2014), 2253-2267.
9. Ren, B., C. Li, X. Yan, M. C. Lin, J. Bonet, and S. M. Hu, "Multiple-Fluid SPH Simulation Using a Mixture Model", *ACM Trans. Graph. (TOG)*, 33(5), (2014), 171.
10. Cleary, P. W., "Prediction of coupled particle and fluid flows using DEM and SPH", *Minerals Eng.*, 73, (2015), 85-99.
11. Grenier, N., D. Le Touzé, A. Colagrossi, M. Antuono, and G. Colicchio, "Viscous bubbly flows simulation with an interface SPH model", *Ocean Eng.*, 69, (2013), 88-102.
12. Grace, J. R., "Shapes and velocities of bubbles rising in infinite liquids", *Trans. Inst. Chem. Eng.*, 51, (1973), 116-120.
13. Liu, G. R. and M. B. Liu, *Smoothed Particle Hydrodynamics (a meshfree particle method)*, (World Scientific Publishing Co., 2003), 118-137.
14. Monaghan, J. J., "Simulating free surface flows with SPH", *J. Comput. Phys.*, 110, (1994), 399-406.
15. Fowkes, F. M., "Attractive Forces at Interfaces", *Ind. Eng. Chem.*, 56(12), (1964), 40.
16. Colagrossi, A., and M. Landrini, "Numerical simulation of interfacial flows by smoothed particle hydrodynamics", *J. Comput. Phys.*, 191, (2003), 448-475.
17. Lancaster, P., and K. Salkauskas, "Surfaces Generated by Moving Least Squares Methods", *Math. Comput.*, 37, (1981), 141-158.

SURFACE PROPERTIES OF MOLTEN FLUORIDE-BASED SALTS

Thomas Villalón Jr.¹, Shizhao Su¹, Uday Pal*^{1, 2}

¹Division of Materials Science and Engineering, Boston University, Brookline, MA 02446

²Department of Mechanical Engineering, Boston University, Boston, MA 02215

Keywords: Surface Tension, Molten Fluoride Salts, Sessile Drop, Maximum Bubble Pressure

Abstract

Two techniques were used to determine the surface characteristics of a molten fluoride-based salt. The maximum bubble pressure method was used to measure the surface tension of the molten salt. Regulated Ar-2%H₂(g) was passed through a steel tube into a molten salt at high temperature. The surface tension of the gas-liquid interface was calculated by measuring the maximum pressure within the tube using a pressure transducer. Contact angles between the flux and solid interfaces were measured by imaging droplets of the molten flux on various surfaces using a camera with a high shutter speed. The camera took images of the high temperature sessile droplet on a solid surface through an optically clear pane. This image was processed through multiple software packages to determine the contact angle and surface tension between the solid-liquid interfaces. The surface properties measured were used to optimize the salt for electrolytic metals production processes.

Introduction

In order to design an efficient electrolysis process for metals production, an electrolytic cell must use materials that have optimal surface tension characteristics. This is a key requirement at electrodes where wetting between liquids and solids provides low contact and charge transfer resistances. In addition, the surface tension of the flux is a key physical property that also influences the fluid behavior and its interactions with the gas phase when bubbling is used to stir the flux. To characterize the surface tension behavior of molten flux, two different types of experiments were conducted: a). maximum bubble pressure experiment and b). sessile drop experiment. The former helps determine gas-liquid surface tension by blowing gas through a liquid [1]. The latter finds an equilibrium condition between gas-solid-liquid interfaces by observing the characteristics of a molten drop with respect to the surface it lies on and the gas surrounding it [1-2]. However, these experiments, although simple in theory, can become very complex when attempted under high temperature conditions. In order to properly acquire the data, materials must be selected that do not interact and affect the experiment while being cost effective and safe. The nature of high temperature experiments quickly limits the range of materials that can be used over 1000°C. To cope with these high temperatures, many experimental components were replaced with either steel or ceramic counterparts. Additionally, all experiments were designed to work in a reducing environment to prevent oxidation from altering the surfaces from their original condition. Running these experiments several times, the goal was to validate the effectiveness of these techniques in high temperature conditions in addition to acquiring data that would help characterize the materials for use in an electrolytic cell.

Experimental

A. Maximum Bubble Pressure Setup

Figure 1 shows the schematic of a maximum bubble pressure setup. The setup consists of mild steel crucible holding the molten salt that was heated to 1200°C. The steel crucible was selected because it is inert when exposed to a eutectic magnesium fluoride-calcium fluoride based molten salt while not introducing any impurities to the salt. This crucible was held in forming gas environment (98% argon-2% hydrogen gas by volume) to create a slightly reducing environment. The forming gas flowrate was 100 mL/min. 400 grams of powdered flux (45 wt% MgF_2 – 55 wt% CaF_2 containing 6 wt% CaO , 3wt% Al_2O_3 and 4 wt% YF_3) was placed inside the crucible which was heated to the desired temperature for the measurement. To find the maximum bubble pressure, a 1/8" inner diameter, 1/4" outer diameter stainless steel tube was immersed into the flux at differing heights below the surface of the flux. In line with the steel tube there was a pressure transducer and a source of the forming gas. The pressure transducer measured the bubble pressure when the gas line was opened and the gas was allowed to flow into the molten salt.

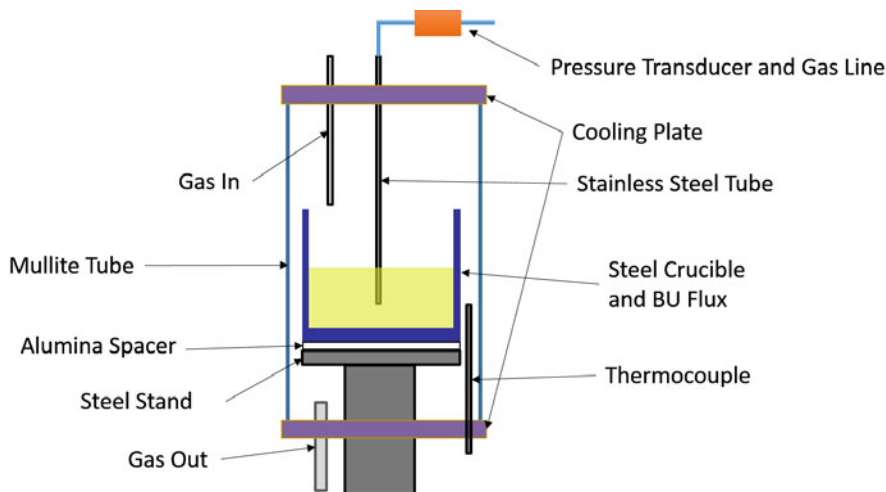


Figure 1: Maximum Bubble Pressure Setup

Procedure: Prior to the experiment, the powders were dried, massed into stoichiometric quantities, and dry mixed in a ball mill overnight. Then, the powders were put into the steel crucible and the unit was heated to the desired temperature. Once at temperature, the stainless steel tube was placed near the surface of the flux. A port was then opened, and the stainless steel tube was used to find the surface of the flux. This was accomplished by finding a location where the pressure was zero and just below the pressure spiked due to the liquid creating a back pressure. The stainless steel tube was immersed 1/8" below the surface of the flux and allowed to equilibrate. Once at equilibrium, the gas line was cracked open as little as possible to allow gas through at a very slow rate. The intent was to permit the least amount of gas through and observe the pressure changes

and record the peak pressure. To aid with this procedure, the pressure transducer signal was recorded in a laptop and the pressure was actively monitored. Once this was done, the stainless steel tube was lowered another 1/8" and the process was repeated.

B. Maximum Bubble Pressure Chemicals, Materials, and Electronics

Calcium fluoride (99.5%), magnesium fluoride (99.5%), calcium oxide (reagent grade), yttrium (III) fluoride (99.9%), and aluminum oxide (99.5%) were supplied by Alfa Aesar (Ward Hill, MA). The stainless steel tube and mild steel crucible were made from steel tubes and round supplied by McMaster-Carr (Robbinsville, NJ). The pressure transducer was a High Speed USB Output Pressure Transducer, rated for 0 to 5 PSIG (gauge PSI). It was acquired from OMEGA Engineering, Inc. (Stamford, Connecticut).

C. Surface Tension Characteristics of a Gas-Liquid Interface

The gas-liquid surface tension was characterized between the flux and the forming gas by passing the forming gas through the flux at varying heights. By viewing the system as having hydrostatic and surface tension components, $\gamma_{g/l}$ can be calculated based on the following two equations:

$$P_{max} = P_{st} + P_{hydro} = \frac{2\gamma_{g/l}}{r_{eff}} + \rho gh \quad (1)$$

$$r_{eff} = \sqrt{r^2(1 + 2\alpha_{stainless}\Delta T)} \quad (2)$$

Here, P_{max} is the total pressure recorded by the pressure transducer. It is made of two separate components. The first component is the differential pressure created by the surface tension interaction between the liquid salt and the forming gas inside the bubble, P_{st} . P_{st} has two variables: $\gamma_{g/l}$, the gas-liquid surface tension, and r_{eff} , the effective radius of the tube that is used for gas flow. The second component of the first equation, P_{hydro} , is the hydrostatic pressure in the system. This is composed of three values: ρ , the density of the flux, g , the acceleration due to gravity, and h , the height of the flux column. The second equation is used to compensate for the thermal expansion that occurs in the stainless steel tube when immersed at high temperatures for prolonged periods. The thermally expanded radius, r_{eff} , has three associated variables: r , the initial radius of the tube, $\alpha_{stainless}$, the coefficient of thermal expansion, and ΔT , the change in temperature from the start of the experiment.

D. Post Experiment Data Analysis

The data from the pressure transducer was recorded and exported by a software package supplied by OMEGA. This data was then analyzed in Microsoft Excel and sampled to find where bubble peaks occurred. Selecting an area of pressure peaks, an average value for peak pressure is acquired for every height. These values are then plotted to see the trend of pressure as a function of submersion depth.

E. High Temperature Sessile Drop Setup

Figure 2 shows the schematic for a high temperature sessile drop setup. The setup revolves around using a horizontal tube furnace heated to 1200°C. The sample is held in a horizontal alumina tube (3/4" inner diameter, 1" outer diameter) that is capped on both ends to create a slightly reducing environment. This is accomplished by purging forming gas (98% argon-2% hydrogen gas) into the

sealed tube. To hold the sample, an open top stainless steel crucible was made that holds 40 grams of silver. On top of the silver, a sample of the cathode substrate material was placed. For this particular experiment, the cathode material selected was titanium diboride. The design of the crucible serves two purposes. The first is to use the silver as a self-leveling mechanism in the event that the cathode material and salt sample are not perfectly vertical. The second is to catch any molten salt that might overflow the surface of the cathode material within the silver bath. On top of the cathode material, a sample of homogenized molten salt (45 wt% MgF_2 – 55 wt% CaF_2 containing 6 wt% CaO , 3 wt% Al_2O_3 and 4 wt% YF_3) was equilibrated, approximately weighing 0.1 grams. This sample was made by solvent mixing the powders overnight, melting the powders, and then crushing the resulting salt block. The melting and powder crushing procedure was repeated up to three times to ensure homogeneity. At one end of the alumina tube, the end cap must be transparent to see the sample inside the furnace. For this particular experiment, an assembly was made that used two aluminum disks, a quartz viewing port, sealing gaskets, and tensioning screws.

Procedure: A camera is then placed collinearly with the sample, inside the alumina tube, by using a scissor lift. The distance of the camera from the sample is adjusted along with focusing the lens prior to starting the experiment. To ensure that no distortion effects occur during the experiment, both the tube and the camera are made level and test images are taken to create a 2D image of the cathode material and salt sample. Prior to the experiment, the end cap was taken off and cleaned with ethanol. A picture was then taken of the sample to ensure optical clarity and final assembly collinearity. As the experiment progressed, the camera's shutter speed was progressively decreased as the luminosity of the furnace kept increasing. At 1200°C , the camera was using a shutter speed of $1/4000^{\text{th}}$ of a second. Five images were taken over the span of 15 minutes after permitting the system to equilibrate at 1200°C for over an hour.

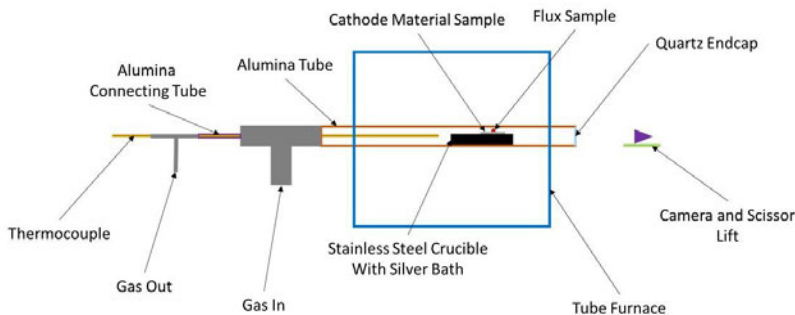


Figure 2: High Temperature Sessile Drop Setup

F. High Temperature Sessile Drop Chemicals, Materials, and Electronics

Calcium fluoride (99.5%), magnesium fluoride (99.5%), calcium oxide (reagent grade), yttrium (III) fluoride (99.9%), aluminum oxide (99.5%), and silver castings were supplied by Alfa Aesar (Ward Hill, MA). The stainless steel tube, stainless steel round, aluminum round, gasket seals,

socket cap hex screws, and quartz endcap were supplied by McMaster-Carr (Robbinsville, NJ). The camera used in the experiment was a Nikon D610 with a 24-85 mm VR lens acquired from Adorama (New York City, NY). The grease used to help make the seals airtight was DOW Corning high vacuum grease, supplied by DOW Chemicals. To support the camera, an 8" x 8" scissor lift was procured from Amazon. The furnace used to run this operation was a Barnstead Thermolyne 21110 Horizontal Tube Furnace. The titanium diboride was provided by Infinium, Inc. (Natick, MA) and machined via wire-cut electrical discharge machining into a square shape.

G. Sessile Drop Characteristics for a Molten Salt and Solid Substrate

Given the three phase equilibrated system of cathode material, molten salt, and the gas, the contact angle (θ) can be used to relate all three surface tensions. This is shown in Equation 3.

$$\cos\theta = \frac{\gamma_{g/s} - \gamma_{l/s}}{\gamma_{g/l}} \quad (3)$$

Using the contact angle acquired and the previously calculated $\gamma_{g/l}$, (gas-liquid surface tension) the $\gamma_{l/s}$ (liquid-solid surface tension) can be found if a literature value for $\gamma_{g/s}$ (gas-solid surface tension) exists. By analyzing the contact angle, an assessment of the wettability between the liquid and the solid can be determined.

H. Image Post Processing and Data Analysis

After the pictures were taken, they were imported into Adobe Lightroom and modified to create a high level of contrast between the sessile drop and the background. The images were then converted into black and white, maintaining a high level of contrast. The images were subsequently imported into ImageJ. Contact angles for each image were then found by running the images through the DropSnake plugin.

Results

A. Maximum Bubble Pressure Results

Figure 3 shows an example of the data produced when the tube was submerged half an inch into the molten salt. Note the repeating increasing pressure followed by a sudden drop. This cyclical behavior is indicative of bubbles forming and subsequently escaping.

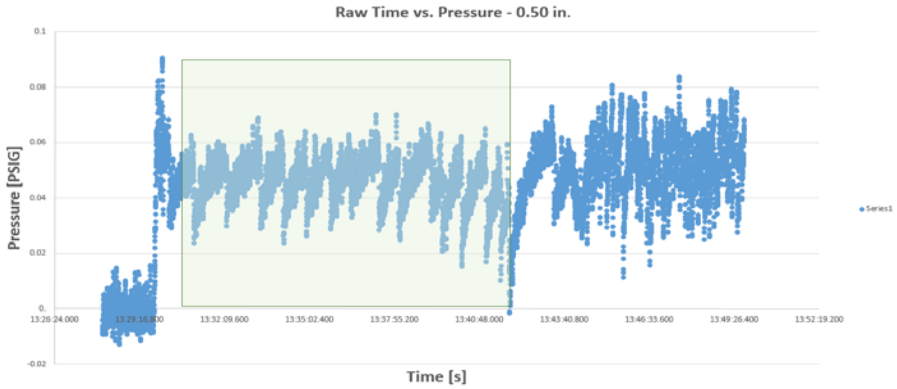


Figure 3: Maximum Bubble Pressure Raw Data - 0.50" Depth

Figure 4 shows a plot of peak pressure values per bubble event within the region highlighted in green.

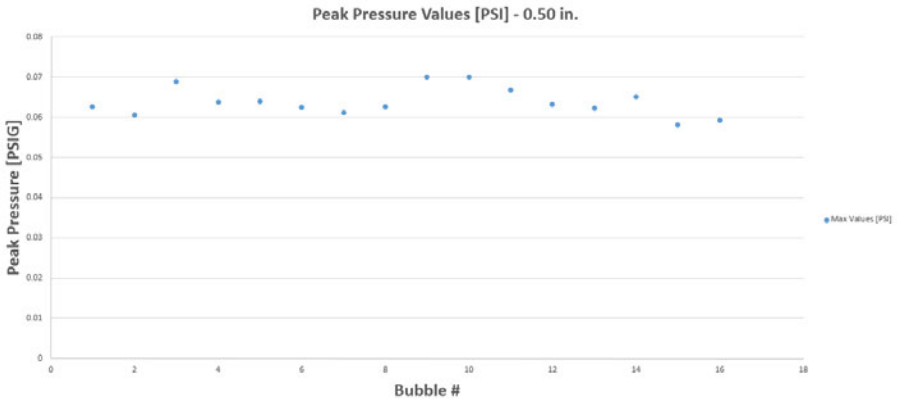


Figure 4: Peak Pressure Values - 0.50" Depth

Using the values from the 0.50", 0.75", and 1.00" submersion depths, a plot can be made comparing immersion depth and peak pressure. This plot then provides a slope and a y-intercept as seen in Figure 5. Data is provided in Table I.

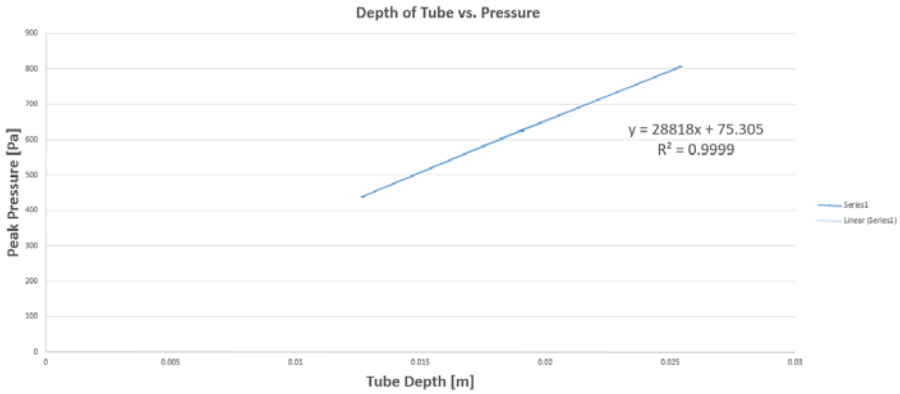


Figure 5: Tube Submersion Depth vs. Average Peak Pressure

Table I: Tube Depth vs. Average Peak Pressure Data Values

Tube Depth [in]	Tube Depth [m]	Peak Gauge Pressure [PSI]	Peak Gauge Pressure [Pa]
0.50	0.0127	0.0638	440.23
0.75	0.01905	0.0909	626.42
1.00	0.0254	0.1170	806.22

Extrapolating the plot to the y-intercept gives a value of 75.305 pascals. This indicates that at zero hydrostatic pressure the total pressure, exerted only by the surface tension, is 73.305 pascals. Applying the condition of zero hydrostatic pressure to Equation 1, Equation 4 is created.

$$\gamma_{g/l} = \frac{P_{max} r_{eff}}{2} \quad (4)$$

Using equation 4, the y-intercept pressure, and the effective tube outer radius, the surface tension of the gas-liquid interface is calculated to be 121.95 mN/m. Applying statistical analysis, the standard deviation for this system is 9.29 mN/m. Thus, the surface tension of the gas-molten salt interface is 121.95 ± 9.29 mN/m. The relatively low surface tension value of our fluoride salt is similar to that of cryolite-based melts [3] and could be attributed to the lower melting point ($\sim 970^\circ\text{C}$) as measured by differential thermal analysis as seen in Figure 6.

Sample: Al flux 9 test 1
Size: 0.0650 mg
Method: AI

DSC-TGA

File: C:\Aluminum\MCAC_9_02252014.001
Operator: SS
Run Date: 25-Feb-2014 22:07
Instrument: SDT Q600 V8.3 Build 101

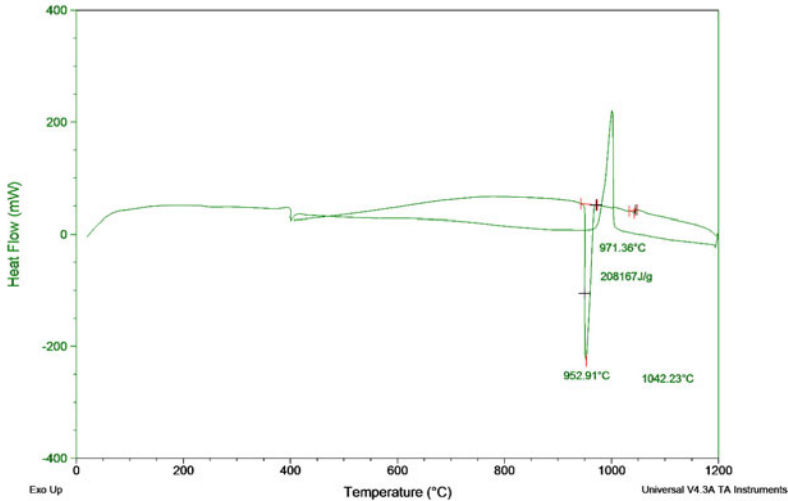


Figure 6: Differential Scanning Calorimetry Data of the BU Salt (45 wt% MgF_2 – 55 wt% CaF_2 containing 6 wt% CaO , 3wt% Al_2O_3 and 4 wt% YF_3)

Further analysis of the salt also shows that the flux has very low volatility $0.171 \mu g/cm^2*s$ indicating that the composition will not change during electrolysis. It is to be also noted that the low surface tension value of the flux would allow efficient gas-stirring of the melt.

In addition to the surface tension, analyzing the slope of the submersion depth vs. maximum bubble pressure plot in Figure 5 provides data that can be used to calculate the density of the flux. Equating the slope to the second term of Equation 1, specifically $\rho*g$, a density of $2.94 g/cm^3$ is found for the salt.

B. High Temperature Sessile Drop Results

Taking the images and processing them, contact angles were found over the course of 15 minutes. Each image was taken over a three minute interval. These images can be seen with contact angles in Figure 7 with data values supplied in Table II.

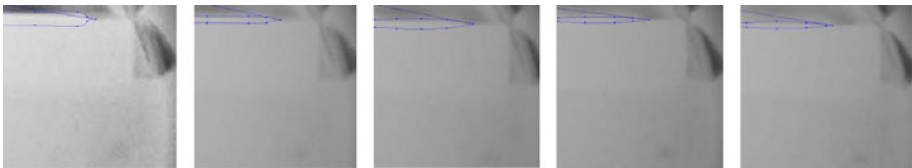


Figure 7: Contact Angle of Flux Samples

Table II: Contact Angle Data for Flux Samples

Sample	Contact Angle [Degrees]
1	8.473
2	11.697
3	10.739
4	7.022
5	8.839
Average	9.354
Standard Deviation	1.357

The images analysis show that the contact angle is $9.354^{\circ} \pm 1.357^{\circ}$. From the contact angle measurement, it can be concluded that the flux does wet the titanium diboride cathode substrate quite well. This is beneficial in two regards. It would lower both the charge transfer and contact resistances at the electrodes.

Conclusions

Two types of experiments were conducted, showing the ability to characterize surface behavior via a maximum bubble pressure measurement and sessile drop observation. The former experiment found that a molten fluoride salt, under an environment of Ar-2% $H_2(g)$ at $1200^{\circ}C$, has a gas-liquid surface tension of 121.95 ± 9.29 mN/m which is similar to that of cryolite-based salts. Additionally, data analysis of the plot indicates that the salt's density is 2.94 g/cm³. The second experiment noted that a molten fluoride salt, placed on a titanium diboride substrate and exposed to the same gas environment, produces a contact angle value of $9.354^{\circ} \pm 1.357^{\circ}$ which indicates good wetting between the cathode substrate and the molten salt. Both values show promise for the salt and titanium diboride to be used in an electrolytic cell.

Acknowledgements

This project was financially supported by the Department of Energy (DOE) through ARPA-E REMOTE program. The authors would like to thank Matthew Mirek for assisting with the preparation and execution of these experiments.

References

- [1] Adamson, Arthur W., and Alice P. Gast. *Physical Chemistry of Surfaces*. New York: Wiley, 1997. Print.
- [2] Zisman, W. A. "Relation of the Equilibrium Contact Angle to Liquid and Solid Constitution." *Advances in Chemistry Contact Angle, Wettability, and Adhesion* (1964): 1-51. Web.
- [3] Fernandez, R., and T. Østvold. "Surface Tension and Density of Molten Fluorides and Fluoride Mixtures Containing Cryolite." *Acta Chem. Scand. Acta Chemica Scandinavica* 43 (1989): 151-59. Web.

FOAMING INDEX OF CaO-SiO₂-FeO-MgO SLAG SYSTEM

Youngjoo Park¹, Dong Joon Min¹

¹Yonsei University; Yonsei-ro 50 Seodaemun-gu; Seoul, 03722, Republic of Korea

Keywords: Foaming Index, Viscosity, Surface Tension, Dimensional Analysis, EAF Slag System

Abstract

A study on the effect of FeO and MgO content on foaming index in EAF slag system was carried out. The height of the slag foam was measured by electric probe maintaining steady state in gas formation and escape. Foaming index, which is the measurement of gas capturing potential of the slag, is calculated from the foam height and gas flow rate. Viscosity and surface tension, which are the key properties for the foaming index, are calculated by Urbain's model and additive method, respectively. Dimensional analysis also performed to determine the dominance of properties and resulted that the important factor was a ratio between viscosity and surface tension. The effect of each component on the viscosity, surface tension and foaming index of the slag is evaluated to be in strong relationship.

Introduction

The foaming behavior of the metallurgical slags has frequently been observed for steelmaking operation such as EAF and BOF process. Optimizing the amount of the slag foam is crucial technique for the steelmaking process since the foaming could be either a beneficial factor for the process efficiency or a substantially dangerous factor by the slag slopping. In modern electric arc furnace process, an adequate slag foaming enhances the energy efficiency due to the lower heat transfer through the slag layer, higher post combustion ratio and arc efficiency. Despite these advantages of the slag foaming, it is hard to maintaining the foam layer due to the fluctuation of the operation condition. Therefore, understanding the fundamental features of the slag foaming is important to stabilize the foam in the electric arc furnace process.

Early studies about the foaming phenomena were conducted by Bikerman [1, 2] in aqueous solution. Bikerman has established the expression of foaminess as a definite physical property of each liquid, which is independent of the apparatus used and of the amount of material employed in measuring. The foaming index is expressed as the ratio of the height of the foam layer over the superficial gas velocity in steady state of gas forming and escaping. Furthermore, the physical factors for foam-stabilizing have been investigated and several stabilizing mechanism were suggested based on the viscosity and the surface tension of the liquid material. Ito and Fruehan [3, 4] applied the foaming index to high temperature CaO-SiO₂-FeO ternary slag system. They concluded that the foaming behavior of the high temperature slag in real situation was expressed better by foaming index than foam life time which is based on the observation in static experimental condition. The dimensional analysis technique was also performed to the experimental results for quantify the effect of each factor. The foaming index was proportional to the viscosity and was inversely proportional to the half of the surface tension and the density. In their investigation, the viscosity was concerned as a resistance to drainage of the liquid film due to the gravity and the surface tension was related to the surface-elastic property. Jiang and

Fruehan [5] investigated the foaming index of the bath smelting slag which has high basicity and have reported the similar dimensional analysis result to Ito and Fruehan.

The foaming index of MgO saturated slag has been reported by Kim *et al.* [6] and Jung and Fruehan [7]. Kim *et al.* has reported the increasing foaming index by FeO content in MgO saturated slag and this result was explained by the viscosity change based on the network forming behavior of Fe^{3+} ion in slag melt. On the other hand, Jung and Fruehan have reported the decreasing foaming index in $\text{CaO-SiO}_2\text{-FeO-MgO}_{\text{Satd.}}$ system and the viscosity of the experimental composition was calculated by Modified Urbain's Model. While the dependency of the foaming index on physical factors in $\text{CaO-SiO}_2\text{-FeO}$ system is well reported, there is a distinct difference of composition dependency when the system contains both FeO and MgO. This shows that the factors to determine the foaming index and their relative importance in such system are not clearly known.

Thus, the objective of the present study is to clarify the effect of the MgO and the foaming behavior of MgO saturated slag.

Experimental

A diagram of the experimental apparatus is shown in Figure 1. A vertical resistance furnace with MoSi_3 heating element was applied to foam height measurement. The slag sample was prepared by mixing of each oxide reagent. CaO was prepared by calcining reagent grade CaCO_3 at 1273K, 6 hours. The slag weighed approximately 150 grams which corresponded to a slag depth of about 40 mm for a crucible diameter of 44 mm.

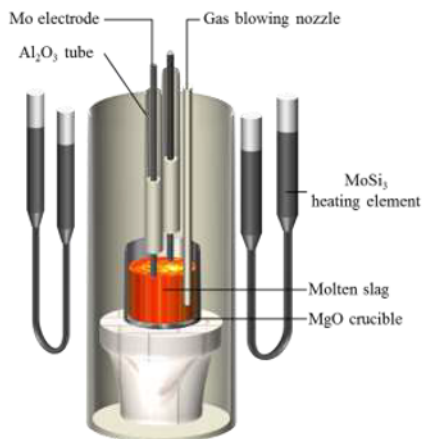


Figure 1. Experimental apparatus for foam height measurement.

The experiments were conducted at 1773K. After the sample was melted, the argon gas was introduced into the molten slag through an iron or Al_2O_3 tube (2 mm I.D., 4 mm O.D.) which was placed 5 mm above the bottom of the crucible. When the foam formation reached a steady state which was confirmed with preliminary test, the height of the total slag was measured by

detecting the top surface position using a Molybdenum electric probe. The foaming index (Σ) was calculated as Equation (1) proposed by Bikerman

$$\Sigma(s) = \frac{\Delta h \text{ (cm)}}{V_g^s \text{ (cm/s)}} \quad (1)$$

where Δh is the height of the foam layer (cm) and V_g^s is the superficial gas velocity (cm/s) which is determined the ratio of the volumetric gas flow rate over the cross-sectional area of the crucible.

The dissolution of the crucible materials into the slag during the experiments was inevitable. Therefore the duration for the experiments was set as short as possible. The experiments were carried out in 30 minutes after the slag was melted and the amount of dissolution of the crucible materials was 2–6 weight percent in the slag. For the slag system which contains Al_2O_3 or MgO , the crucible that is made of the same material was used to minimize the change of the slag chemistry and Al_2O_3 crucible was used for $\text{CaO-SiO}_2\text{-FeO}$ slag system. In all cases, the slag chemistry change due to the dissolution of the crucible material is assumed to be negligible.

Results and Discussion

1. Foaming Index of $\text{CaO-SiO}_2\text{-MgO}$ System

The experimental result about foaming index of $\text{CaO-SiO}_2\text{-MgO}$ ternary system is shown as a function of MgO concentration in Figure 2. The concentration of MgO is varied up to saturate concentration in CaO-SiO_2 base slag. The saturate concentration of MgO at 1773K is about 23 wt% and 8 wt% in (wt% CaO)/(wt% SiO_2)=1.0 and 1.25, respectively. These compositions show a good agreement to the liquidus line of $\text{CaO-SiO}_2\text{-MgO}$ phase diagram.

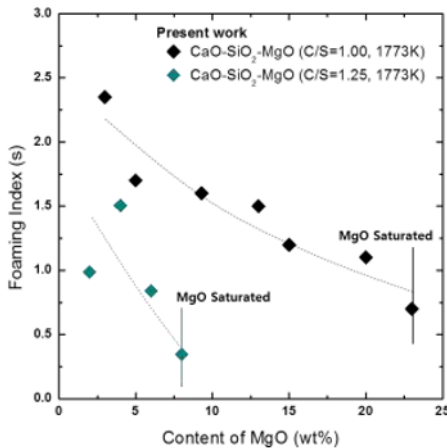


Figure 2. Foaming index of $\text{CaO-SiO}_2\text{-MgO}$ slag system as a function of MgO concentration.

The foaming index of CaO-SiO₂-MgO ternary system is decreased with increasing MgO concentration at a fixed CaO/SiO₂ ratio. This result could be explained mainly by the viscosity change since the change of the surface tension is not much compared to the total value as shown by partial molar surface tension reported by Mills [8]. The effect of MgO on the viscosity in CaO-SiO₂-MgO or CaO-SiO₂-Al₂O₃-MgO system is well reported by Licko and Danek [9] and Kim *et al.* [10]. The experimental result of Licko and Danek shows that the viscosity is decreased by increasing MgO at 1773K. Kim *et al.* explained the viscosity change in point of the network modifying effect of MgO applying the structural analyzing technique for the molten slag.

Hence in present slag system, the lower viscosity of higher MgO containing slag causes the lower foaming index. It is also noted that the slag which has higher (wt% CaO)/(wt% SiO₂) ratio shows lower foaming index since the viscosity is lower due to the depolymerization of silicate structure by basic slag, i.e. CaO.

2. Foaming Index of CaO-SiO₂-FeO-MgO System

The experimental result for CaO-SiO₂-FeO and CaO-SiO₂-FeO-MgO_{Satd.} system is shown as a function of FeO concentration in Figure 3. The foaming index of CaO-SiO₂-FeO system is decreased with increasing FeO concentration up to 20 wt% FeO as reported earlier by several authors [6, 7]. Again, it is believed that the lower foaming index is caused by the lower viscosity as reported by Kim *et al.* [6] while there is a minor contribution from the surface tension effect as mentioned above.

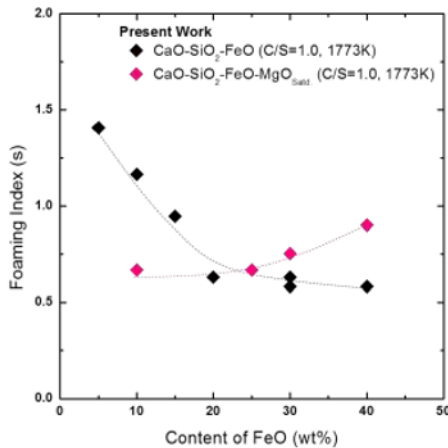


Figure 3. Foaming index of CaO-SiO₂-FeO and CaO-SiO₂-FeO-MgO_{Satd.} slag system as a function of MgO concentration.

On the other hand, the foaming index of CaO-SiO₂-FeO with MgO saturated slag is increasing with FeO concentration. The opposite trend is obtained probably due to the change of Fe³⁺/Fe²⁺ ratio occurred by increasing basicity with MgO saturation. Fe³⁺/Fe²⁺ ratio could affect foaming index as following.

The experimental result of Sumita *et al.* [11] suggests that the Fe^{3+}/Fe^{2+} ratio does not have an appreciable effect on the viscosity of the slag. This result is corroborated by the work of Seki and Oeters [12], who found little difference in the viscosity values when using different partial oxygen pressure values. No substantial change of FeO dependency within different MgO concentration is also reported by Seok *et al.* [13]. Therefore the viscosity of CaO-SiO₂-FeO-MgO slag would be decreased by higher FeO or MgO and this relationship between the viscosity and the foaming index is conflict with the explaining in above section. Thus, the increasing foaming index with FeO concentration should be explained by the effect of the surface tension.

In contrast to other cases, the surface active element could drastically decrease the surface tension of the slag. It is generally known that the Fe^{3+} ion in ionic melt is surface active element [8]. Most of the conditions for the partial oxygen pressure and the slag basicity of aforementioned and present foaming index measurement were in Fe^{2+} predominant region. Thus FeO is assumed to stoichiometric compound that the entire Fe ion in melt has same valence of 2. The assumption typically works for many slag engineering problems but there is a probability that the effect of surface tension on the foaming index is underestimated in some case since even the small amount of the Fe^{3+} ion could affect surface tension value substantially.

The values for the viscosity and the calculated surface tension by additive method of CaO-SiO₂-Fe_xO-MgO system are shown in Figure 4. If we assume that iron oxide is stoichiometric compound and Fe ions are totally Fe^{2+} , the viscosity is decreased and the surface tension is increased in all cases. This tendency corresponds to the decreasing foaming index. Otherwise if the Fe^{3+} ion is taken into account with the corresponding Fe^{3+}/Fe^{2+} ratio reported by Yang and Belton [14], the change of the surface tension with the MgO turn around in certain iron oxide concentration as shown in Figure 4, (b).

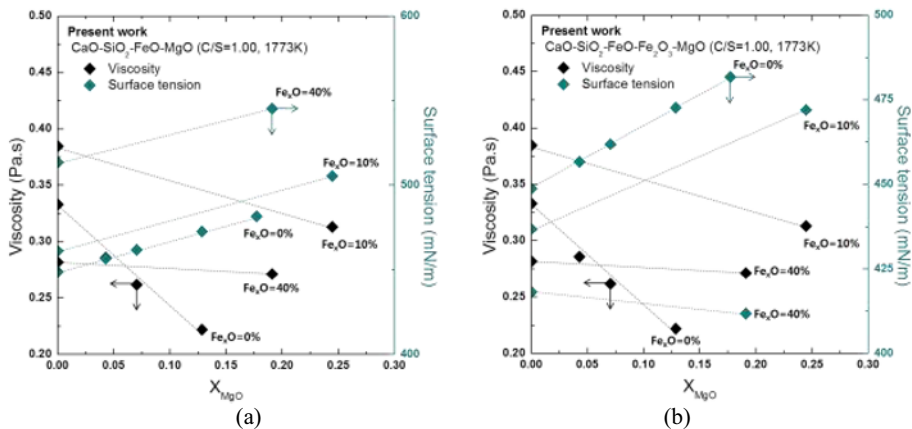


Figure 4. Calculated viscosity and surface tension values in case of (a) FeO with totally Fe^{2+} , (b) Fe^{3+} is taken into account.

Due to this contribution of Fe^{3+} ions, the effect of MgO on the foaming index of FeO containing slag has various composition dependencies as shown in Figure 5. The systems that the foaming index is increased with X_{MgO} in Figure 5 have relatively high basicity (0.74~0.76 in

optical basicity scale) and FeO concentration (30~40 wt%). On the other hand, the other systems in Figure 5 have relatively low basicity (0.68~0.69 in optical basicity scale) and low FeO concentration (up to 10 wt%). It is clear that the Fe^{3+}/Fe^{2+} ratio affects the foaming index above certain critical value. Thus to clarify the effect of MgO in such slag system, it is needed to quantify the Fe^{3+}/Fe^{2+} ratio and investigate the effect of the surface tension on the foaming index in much detail.

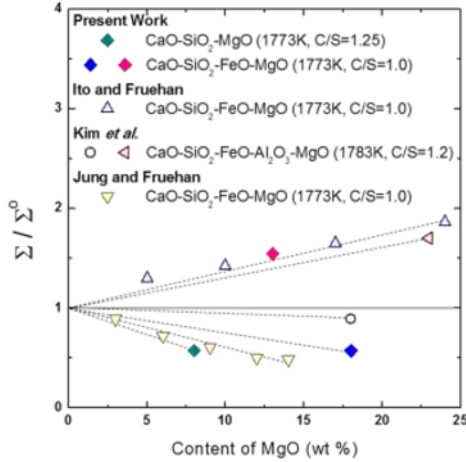


Figure 5. Various MgO dependencies of the foaming index in FeO containing case.

3. Dimensional Analysis

Foaming index is known to a function of viscosity, surface tension of the liquid. But property-foaming index correlation is not clearly derived yet, and no pertinent equation with wide range of consistency is proposed. Fruehan group [4, 5] applied the dimensional analysis technique to correlate the slag property and the foaming index mathematically. The foaming index is postulated as a function of the viscosity, the surface tension, the density and the gravitational constant and following dimensional groups are set according to Buckingham's Pi Theorem.

$$\pi_1 = \frac{\Sigma g \eta}{\sigma} \quad (2)$$

$$\pi_2 = \frac{\rho \sigma^3}{\eta^4 g} \quad (3)$$

where Σ is the foaming index (s), g is the gravitational constant (m/s), η is the viscosity (Pa·s), ρ is the density (kg/m^3), and σ is the surface tension (N/m).

The relationship between two dimensional groups is derived from each slag property and the result of $\log \pi_1$ vs $\log \pi_2$ plot is shown in Figure 6. The slopes of CaO-SiO₂-FeO and CaO-SiO₂-MgO system are same as -2.17 and this result corresponds to the contribution of each factor as Equation (4)

$$\Sigma = C \sqrt{\frac{\eta^{1.68}}{\sigma^{0.76} \rho^{0.92}}} \quad (4)$$

where C is the constant depends on the slag system and determined empirically. This result indicates that we could postulate the Fe ions in slag as totally Fe^{2+} up to (wt% CaO)/(wt% SiO_2) ratio is 1.0 without other basic oxide.

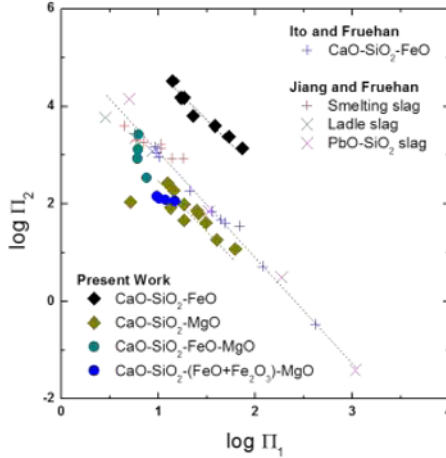


Figure 6. Dimensional analysis result for various slag system.

On the other hand, the dimensional analysis result of CaO-SiO₂-FeO-MgO system has almost vertical slope. This is due to the underestimated surface tension effect by Fe^{3+} as mentioned above. If we take into account the $\text{Fe}^{3+}/\text{Fe}^{2+}$ ratio in the molten slag and recalculate the slag properties, the result of dimensional analysis has consistency with other slag system. This result indicates that Equation (4) is still holds for CaO-SiO₂-FeO-MgO within wide range of composition.

Conclusions

The effect of MgO on the foaming index for CaO-SiO₂-MgO and CaO-SiO₂-FeO-MgO system is investigated. The dimensional analysis was applied using experimental results and calculated slag properties to correlate the foaming index and the foam stabilizing factors. The remarkable conclusions are as following:

(1) The foaming index of CaO-SiO₂-MgO ternary system is decreased with increasing MgO concentration at a fixed basicity and temperature. It could be explained as the viscosity effect in point of modified network structure by MgO. The change of surface tension as MgO addition has relatively little effect compared to change of viscosity since MgO has similar partial molar surface tension to that of CaO.

(2) In case of FeO containing slag, the addition of MgO either increases or decreases the foaming index. This result is due to the effect of surface active by Fe^{3+} ions in molten slag. The basicity of the slag could be increased by MgO addition and hence $\text{Fe}^{3+}/\text{Fe}^{2+}$ ratio is increased, the foaming index could increase beyond the critical $\text{Fe}^{3+}/\text{Fe}^{2+}$ ratio since the surface tension decreases substantially.

(3) By revising the surface tension value as take into account the $\text{Fe}^{3+}/\text{Fe}^{2+}$ ratio, the result of the dimensional analysis for CaO-SiO₂-FeO-MgO system shows consistency with other system. It indicates that the balance of the viscosity and the surface tension has consistent effects on foaming phenomena for those slag systems.

References

1. J.J.Bikerman, "The Unit of Foaminess," *Transactions of the Faraday Society*, 34 (1938), 634-638.
2. J.J.Bikerman, "Foams and Emulsions," *Industrial and Engineering Chemistry*, 57 (1) (1965), 56-62.
3. K.Ito and R.J.Fruehan, "Study on the Foaming of CaO-SiO₂-FeO Slags: Part I. Foaming Parameters and Experimental Results," *Metallurgical transactions B*, 20 (4) (1989), 509-514.
4. K.Ito and R.J.Fruehan, "Study on the Foaming of CaO-SiO₂-FeO Slags: Part II. Dimensional Analysis and Foaming in Iron and Steelmaking Processes," *Metallurgical Transactions B*, 20 (4) (1989), 515-521.
5. R.Jiang and R.J.Fruehan, "Slag Foaming in Bath Smelting," *Metallurgical Transactions B*, 22 (4) (1991), 481-489.
6. H.S.Kim, D.J.Min, and J.H.Park, "Foaming Behavior of CaO-SiO₂-FeO-MgO_{satd}-X (X=Al₂O₃-MnO, P₂O₅ and CaF₂) Slags at High Temperatures," *ISIJ International*, 41 (4) (2001), 317-324.
7. S.M.Jung and R.J.Fruehan, "Foaming Characteristics of BOF Slags," *ISIJ International*, 40 (4) (2000), 348-355.
8. K.C.Mills and B.J.Keene, "Physical Properties of BOS Slags," *International Materials Reviews*, 32 (1) (1987), 1-120.
9. T.Licko and V.Danek, "Viscosity and Structure of Melts in the System CaO-MgO-SiO₂," *Physics and Chemistry of Glasses*, 27 (1) (1986), 22-26.
10. H.Kim *et al.*, "The Effect of MgO on the Viscosity of the CaO-SiO₂-20wt%Al₂O₃-MgO Slag System," *Steel Research International*, 81 (4) (2010), 261-264
11. S.Sumita *et al.*, "Viscosity of Slag Melts Containing Fe₂O₃," *Journal of the Japan Institute of Metals*, 44 (1) (1980), 94-99.

12. K.Seki and F.Oeters, "Viscosity Measurements on Liquid Slags in the System CaO-FeO-Fe₂O₃-SiO₂," *Transactions of the Iron Steel Institute of Japan*, 24 (6) (1984), 445-454.
13. S.H.Seok *et al.*, "Viscosity of Highly Basic Slags," *ISIJ International*, 47 (8) (2007), 1090-1096.
14. L.Yang and G.R.Belton, "Iron Redox Equilibria in CaO-Al₂O₃-SiO₂ and MgO-CaO-Al₂O₃-SiO₂ Slags," *Metallurgical and Materials Transactions B* 29 (4) (1998), 837-845.

**ADVANCES IN MOLTEN
SLAGS, FLUXES, AND SALTS:**

Proceedings of



**Modeling Slag
and Salt Properties**

Development of Slag Management System

Kyei-Sing Kwong¹, James P. Bennett¹

¹National Energy Technology Laboratory, US DOE
1450 SW. Queen Ave. Albany, OR 97321 USA

Keywords: Slag Management, Coal Slag Viscosity, Gasification

Abstract

Degradation of refractory liners is one of the key factors limiting the service life of entrained flow slagging gasifiers, which is caused primarily by refractory/slag interactions. Slag originates from impurities in the carbon feedstock, typically coal and/or petcoke, which melt and coalesce during gasification, flowing over the refractory liner in the gasifier and interacting with it. Slagging gasifier operators attempt to minimize refractory degradation by controlling slag viscosity (and interactions) through the gasification process temperature. A computer model utilizing empirical and neural network calculations was developed to predict T_{100} , T_{250} , fluid temperature, and liquidus temperature of slag compositions based on chemistry and a newly developed “similarity index”. Development of the model and its application in designing slags to minimize refractory degradation will be discussed.

Introduction

Gasification is a process of converting carbonaceous materials, water and oxygen into steam, carbon monoxide, hydrogen, carbon dioxide and methane in a high pressure and high temperature reaction vessel (gasifier). Non-volatile mineral impurities in the carbon feedstock are liquefied at gasification temperatures, forming corrosive slags. The slag attacks refractory linings used to insulate and protect the steel pressure vessel from the harsh operating conditions present in a gasifier. Slagging gasifiers are typically operated between about 1300 and 1550 °C and at pressures of 2.75 MPa (400 psi) or higher, with a mass flow rate of molten slag often exceeding 10 tons/hour [1, 2]. The slag composition and the gasifier operating temperature are significant factors affecting the refractory lining performance. The gasifier operating temperature can be optimized using the slag liquidus temperature, ash fusion temperature, and viscosity characteristics of the ash. The optimized operating temperature should be high enough to allow slag flow out the gasifier yet low enough to minimize refractory corrosion. Refractory service life can be improved if the operating temperature is lower than the slag liquidus temperature. Slag liquidus temperature, ash fusion temperature, and viscosity characteristics of the ash are dependent on the slag composition.

Typically, more than 90 % of the mineral component of a coal ash slag contains oxides of silicon, aluminum, iron, and calcium. Minor constituents such as magnesium, potassium, sodium, titanium, and sulfur account for about 8 % of the mineral component; while trace constituents such as arsenic, cadmium, lead, mercury, and selenium, when combined make up less than 1 %

of the total composition. Table I summarizes the average, maximum, and minimum oxide content of coal slags in the NETL slag management tool set's viscosity database in weight percent. The NETL slag management tool set will be discussed later.

Table I. The composition range of slag constituents in the NETL slag management tool-set database in weight percent.

Weight %	SiO ₂	Al ₂ O ₃	FeO	CaO	MgO	Na ₂ O	K ₂ O	MnO	TiO ₂	P ₂ O ₅	SO ₃
Average	42	23	11	15	4	1	1	0	1	0	1
Maximum	68	37	35	40	20	10	4	0.8	20	3	18
Minimum	19	10	1	1	0	0	0	0	0	0	0
Standard deviation	8	5	7	9	4	2	1	0.2	1.3	0.6	2

The fluidity of coal slags has a close relationship with the properties: T₁₀₀, T₂₅₀, T_{cv}, ash fusion fluid temperature and liquidus temperature. Coal slags consist primarily of a silicate network, where each silicon atom is tightly bonded to 4 oxygen atoms. Cations such as Na⁺, Ca²⁺, Mg²⁺, Fe²⁺ and K⁺ tend to depolymerize the silicate networks by forming non-bridging oxygen (NBO), O⁻, and free oxygen O²⁻. The degree of de-polymerization of coal slags can be characterized by the ratio of NBO to the number of tetrahedral-coordinated atoms (T), expressed as NBO/T [3]. In general, a higher index value means a lower viscosity coal slag.

Per Lux and Flood's definition of acid-base properties for oxides melts, the high quantity of silica or silicon oxide present in coal ash slags makes them acidic [4]. Basic oxides such as Na₂O, CaO, MgO, K₂O and FeO tend to react with silica, leading to lowered melting temperature and thinner (low viscosity) slags. Therefore, the ratio of the total amount of basic oxides to the amount of SiO₂ is an important index for both liquidus temperature and slag viscosity.

Al₂O₃, an amphoteric (i.e. a compound that can act as an acid or base), is also an important oxide in coal ash slags. Phase diagrams (CaO-SiO₂-Al₂O₃, MgO-SiO₂-Al₂O₃ and FeO-SiO₂, Al₂O₃) indicate that the ratio of SiO₂/Al₂O₃ is also an important factor affecting slag liquidus temperatures. Slags containing principally Al₂O₃ and low basic oxide quantities tend to form mullite as their primary phase (first phase to precipitate from the melt during cooling), creating a slag of a high liquidus temperature. High Al₂O₃ and FeO content in a slag promote the formation of a spinel primary phase (FeAl₂O₄). Lower Al₂O₃ content with high CaO leads to the formation of slags with anorthite as their primary phase, resulting in slags with a low liquidus temperature. In general, the best slags for gasification of coal should have a high liquidus temperature and low T₁₀₀; moreover, the temperature difference between the two should be large enough to allow for easy control of the viscosity during gasification process.

Coal slags may contain solids phases at a gasifier's operating temperature that do not melt or have time to melt during their residence in the gasifier. The presence of those solids in the gasifier slag affects the fluidity of the slag during gasification. In general, increasing the solid content of a slag increases its apparent viscosity. The liquidus temperature, a function of the slag composition, determines whether solids are present at the operating temperature.

Viscosity is the measure of the internal friction of a fluid during flow. The ease by which a molten coal ash slag flows from an entrained flow gasifier is directly related to slag viscosity. Molten slag viscosity can be measured by many ways, with a rotating spindle being commonly used. Slag can exhibit Newtonian or non-Newtonian flow behavior, with the viscosity of a Newtonian fluid being independent of spindle's shear rate. The viscosity of non-Newtonian fluids change as a function of shear rate and time; therefore, viscosity measurements of a typical non-Newtonian fluid can be considered accurate only when these experimental parameters are accounted for and reported. Depending on a coal slag's composition and test temperature, coal slags typically behave as Newtonian fluids at high temperature and undergo a transition to non-Newtonian flow when solid content is high in it as solid phases precipitate at the lower end of the gasifier operating temperature range (generally, below T_{cv}).

Ash fusion testing is based on the position a pyramidal ash cone sample bending (deforming) due to increasing liquid content with increasing temperature in either an oxidizing or reducing atmosphere. The sample deformation measured during ash fusing testing is reported as four temperatures: initial deformation, softening, hemispherical and fluid temperatures. The major drawback associated with the ash fusion testing is the reliance on visual observation and operator subjectivity, leading to reproducibility issues between different laboratories.

Modeling Procedures

Figure 1 shows the modeling procedure followed in this study. First, slag viscosity and slag fusion temperatures data was collected and assembled into a database. The NETL slag viscosity database contains 262 records from sources published in the open literature, while the slag fluid temperature database (ash fusion information) containing around 2000 records from the USGS CoalQual database [5]. These slag constituents were used as the starting point for calculating corresponding liquidus temperatures through FactSage™ (version 6.4) thermodynamic calculations [6]. Results from these calculations were collected into a database of liquidus temperatures. The viscosity database was used to evaluate the performance of six empirical models and the FactSage™ slag viscosity module. In addition, viscosity, fluid temperature, and liquidus temperature databases were used to build similarity and neural network models.

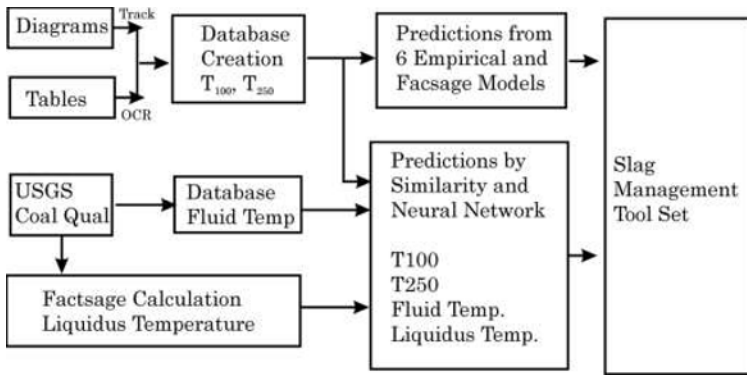


Figure 1. A flow chart representing the modeling procedures used in this study to suggest an optimal gasifier operating temperature range.

A slag management tool set was developed to suggest a gasifier’s operating temperature from the prediction result for T_{100} , T_{250} , fluid, and liquidus temperatures determined by the NETL models (similarity and neural network). This tool set allows users to review referenced records in similarity modeling and to verify the model’s prediction. This tool set also allows advanced users to select, modify, or input these values if users prefer a value different from the predicted one. The slag management tool set is not a black box - it allows users to review the reference records, provides detailed information about each model’s predicted performance, explains some of the terminology used in calculations, adopts to a specific users’ database, and allows advanced users to adjust predictions. This paper focuses on the performance of empirical and NETL similarity models on coal slag viscosity. NETL similarity models will be discussed later.

Viscosity models

Many empirical viscosity models have been published in the open literature, with each based on their own experimental data and regression analysis. Quite often, users use an empirical model without fully understanding its limitations and performance. Many of these empirical models are generally not amenable to extrapolation outside the range of the original experimental data. Coal slags have a wide range of compositions containing different solids and solid quantities, depending on their chemistry, temperature, the oxygen partial pressure of the gasifier, and the residence time in the gasifier (short residence times do not allow system equilibrium to be achieved in a system). Because of the way literature models were developed, it is unlikely that a single model will yield good predictions for every coal slag. Several empirical models were selected for inclusion in the viscosity model being developed based on their ability to predict coal slag properties; which were the following: Browning, Urbain, Kalmanovitch, silica ratio, Riboud, and Watt-Fereday [7, 8]. An experimental slag viscosity database was created using charts or tables published in the literature or in reports. A computer program was written to track

data curves in a chart and convert them to digital format. The predicted slag viscosities of these empirical models were then compared with the slag viscosity database created using published information.

FactSage™ has a viscosity module which directly relates slag chemistry viscosity to the structure of the melt, and the structure in turn is calculated from the thermodynamic description of the melt using the Modified Quasichemical Model [9]. The FactSage™ model requires very few optimized parameters to fit the experimental data for pure oxides and selected binary and ternary systems. The viscosities of multicomponent melts and glasses are then predicted by the model within experimental error limits without using any additional parameters [9].

Similarity models as developed and used by NELT do not use mathematic regression methods, instead being based on a large database, with predictions made based on data from similar sample chemistries in the database. A figure-of-merit based on chemical composition, silica ratio, optical basicity and NBOT was adopted to define similarity between reference and target samples. Using this approach, predicted performance was improved over an earlier approach based solely on a slag's chemical composition. Given the experimental uncertainty and errors during slag viscosity measurements, a "regional" group fit within a reasonable temperature range is adopted rather than the "best" fit. A regional group fit means that three similar referenced samples from the database were selected for making comparison within a range of 50 °C from a predicted slag chemistry, then the best regional group fit samples were used to yield temperature predictions for specific viscosities (such as T₁₀₀ and T₂₅₀). The prediction performance was improved using this approach versus a simple look-up of the "best" individual fit values.

Gasifier users need an accurate and reliable model to predict viscosity and temperature relationships for different slag compositions. It is, however, impossible to know which models are reliable without extensive testing. In addition, the size of a database or datasets is closely related to the prediction performance of a model. High-temperature viscosity measurements are both time and resource intensive, with a large investment required in order to build a reasonably sized database.

The performance index of models

In order to know which model perform best, an error index term was developed to define the model's accuracy in °C.

$$Error = \frac{\sum_{v=50}^{v=500} |T_{Exp} - T_{Model}|}{N}$$

Where:

N = Number of calculate times

T = Temperature (°C) at 50 to 500 P with a step increment of 50 P (P: poise)

Exp = Experiment value
 Model = Prediction value
 V = Constant viscosity

The number of calculations was used in determining the model error because each record may not cover the whole slag’s viscosity range from 50 to 500 P. Note that the calculated error term is for only a set of viscosity-temperature record from a slag. The slag viscosity database has 262 records (each record contains information for a slag); therefore, the distribution of prediction error for the 262 slags predicted by models can be calculated and normalized. The above performance index is designed for industry users so they may understand the average of error prediction for a specific temperature.

Results and Discussions

Coal slag viscosity

Table II shows the results of prediction for six empirical and FactSage’s modified quasichemical models. This table indicates variability between the predictions of the different models, and that the silica ratio and Kalmanovitch models perform better than other models. The table also illustrates the need for models with improved predictions of slag flow behavior than those that exist in the literature.

Table II. The prediction error distribution of viscosity and temperature for six empirical and FactSage™ models (in percentage)

Error (°C)	Browning	Urbain	Kalmanovitch	Silica Ratio	Riboud	Watt-Fereday	FactSage™
0-40	35.88	6.87	45.04	52.29	3.05	12.98	26.56
40-80	21.76	24.43	22.52	20.99	10.69	31.68	18.36
80-120	18.70	32.44	13.36	11.45	32.44	24.05	20.31
>120	23.66	36.26	19.08	15.27	53.82	31.30	34.77

The Similarity Model Developed by NETL

Three similarity modeling versions were developed to predict slag viscosity based on the assumption that similar slags should have similar physical properties, including viscosity. Note that the definition of “similar slags” affects the accuracy of a slag viscosity prediction. Also note that most slags contain at least 10 oxides, making the definition of a “similar slag” complex and subjective. The development of a model was a self-study process from trial results based on multiple dataset calculation using a target sample selected from one of 262 slag viscosity curves. The calculations generated using the target sample was treated as experimental data, and the other 261 data set records treated as reference samples in a database or knowledge base to make

a prediction for the target sample. Using this approach, the accuracy of each trial can be computed by the above performance index after multiply calculations. Table III lists prediction made using the four similarity approaches.

Four similarity modeling approaches are discussed concisely as follows:

- 1) Find similar slag, and then predict temperature at various viscosities from a known calculated knowledge base.
- 2) Rank the temperature at a specific constant viscosity, then determine the best fit regions using three consecutive samples to predict the temperature at a specific constant viscosity.
- 3) Rank the temperature at a specific constant viscosity from a group of three consecutive similar slags, then determine best fit region for predicting the temperature at specific constant viscosity
- 3+) More similarity indexes were used and the definition of “region” was modified by a temperature range (three samples within 50 °C), not a group of three consecutive samples.

Table III The prediction error distribution of viscosity and temperature for NETL similarity models (in percentage)

Error (°C)	Version 1	Version 2	Version 3	Version 3 ⁺
0-40	48.24	47.66	58.78	66.1
40-80	23.14	27.73	22.52	16
80-120	16.08	11.33	8.02	9.5
>120	12.55	13.28	10.69	8.4

Comparing Table III and II, it is evident that version 3⁺ of the similarity model developed by NETL can yield improved accuracy predictions of coal slag viscosity. Currently, this slag management system is being implanted and evaluated at a commercial gasifier user.

Conclusions

A viscosity database was assembled from literature data which contains 262 records and used to compare and evaluate six empirical models from the literature against a modified quasichemical model. Similarity and neural network models were developed to improve performance predictions of viscosity versus temperature based on slag composition. Results indicated that similarity and neural network models could yield improved viscosity versus temperature predictions than empirical models or the modified quasichemical model. Coal ash fluid temperature and liquidus temperature databases were also collected and used to predict fluid and liquidus temperature by similarity and neural network models. This slag management model was developed with a goal of improving the service life of refractory lining in gasifiers and to improve control of the gasification processes through improved predictions of T₁₀₀, T₂₅₀, fluid temperature, and liquidus temperature.

References

1. Kwong, K.-S., et al., Wear mechanisms of chromia refractories in slagging gasifiers. *International Journal of Applied Ceramic Technology*, 2007. 4(6): p. 503-513.
2. Bennett, J.P., K-S. Kwong, A.V. Petty, C. Powell, H. Thomas, and R. Krabbe; "Field Trial Results of NETL'S Phosphate Modified High Chrome Oxide Refractory Material for Slagging Gasifiers", GTC 2007 Conference; San Francisco, CA; Oct 14-17, 2007; published in on-line meeting proceedings.
3. Stahleisen, V., Verein Deutscher Eisenhüttenleute (R.F.A) *Salg Atlas* 2nd Edition. 1995. 616 pages, Verlag Stahleisen mbH.
4. Moretti, R., Polymerisation, basicity, oxidation state and their role in ionic modelling of silicate melts. *Annals of Geophysics*, 2005. 48(4-5): p. 583-608.
5. Bragg, L.J., et al., U.S. Geological Survey coal quality (COALQUAL) database; version 2.0, in Analytical data, sample locations, and descriptive information, analytical methods and sampling techniques, database perspective, and bibliographic references for selected U.S. coal samples. 1998, U.S. Geological Survey: Denver, Colorado.
6. Bale, C., et al., FactSage™ thermochemical software and databases. *Calphad-Computer Coupling of Phase Diagrams and Thermochemistry*, 2002. 26(2): p. 189-228.
7. Kinaev, N., A review of mineral matter issues in coal gasification. A report from Cooperative Research Centre for Coal in Sustainable Development (Australia). Pushlshed by Pullenvale, Qld: QCAT Technology Transfer Centre, 2006
8. Van Dyk J. C., et al., Viscosity prediction of slag composition of gasified coal utilized Factsage equilibrium modeling, *Fuel*, 2009, 88(1): P67-74
9. Decterov, S.A., et al., Modeling the viscosity of aluminosilicate melts, in *Computation in Modern Science and Engineering*. 2007, AIP: Corfu, Greece. p. 404-407.

DISCLAIMER: This report was prepared as an account of work sponsored by an agency of the United States Government. Neither the United States Government nor any agency thereof, nor any of their employees, makes any warranty, express or implied, or assumes any legal liability or responsibility for the accuracy, completeness, or usefulness of any information, apparatus, product, or process disclosed, or represents that its use would not infringe privately owned rights. Reference herein to any specific commercial product, process, or service by trade name, trademark, manufacturer, or otherwise does not necessarily constitute or imply its endorsement, recommendation, or favoring by the United States Government or any agency thereof. The views and opinions of authors expressed herein do not necessarily state or reflect those of the United States Government or any agency thereof.

GASEOUS FUEL PRODUCTION USING WASTE SLAGS - GOING BEYOND HEAT RECOVERY

Jinichiro Nakano^{1,2}, James Bennett¹, Anna Nakano¹

¹ U.S. Department of Energy National Energy Technology Laboratory; 1450 Queen Ave.; Albany, OR 97321, USA

² AECOM; P.O. Box 1959; Albany, OR 97321, USA

Keywords: Slag Utilization, Iron and Steelmaking, Gasification, CO₂, CO, H₂O, H₂

Abstract

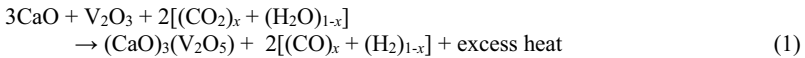
Large quantities of carbon dioxide gas and slag are generated as waste byproducts through iron & steelmaking and slagging gasification processes, using carbon feedstock to produce metal, electric power, and/or chemicals. The increasing use of petroleum coke in the modern gasification industry has changed slag chemistry – causing it to become rich in vanadium (III) oxide. When the vanadium rich gasification slag is interacted with metallurgical slag targeting a specific slag chemistry and temperature; calcium orthovanadate forms, changing vanadium valence from 3+ to 5+. This valence change involves oxygen removal from the surrounding environment. The reaction is highly exothermic, which is more than enough to break bonding in carbon dioxide and water molecules and to still have excess thermal energy. In this work, generation of carbon monoxide from carbon dioxide was investigated using synthetic slag mixtures containing vanadium. Results indicated rapid CO₂→CO conversion occurred at temperatures below those at which metallurgical slag is typically tapped out of furnaces in industries.

Introduction

Carbon feedstock such as coal and petroleum coke (petcoke) is used in metallurgy (mainly iron & steelmaking) and slagging gasification (including the integrated gasification combined cycle (IGCC)) processes to produce metal, and power and/or chemicals, respectively. In these manufacturing processes, large quantities of gas (rich in CO₂) and molten slag as waste byproducts are generated. Slag is generated from non-volatile components in feedstock, additives, and/or metal ore impurities. As an example, in primary steelmaking, 1.5 tons of CO₂ is emitted for every ton of iron produced, while additional 0.9 tons of CO₂ per ton of steel produced is produced from subsequent steelmaking processes [1]. Reportedly, approximately 0.5 billion tons of slag is annually generated by metallurgical industries worldwide (2011) [2], with less than 65 wt.% utilized for recovering valuable elements [3]. In the gasification industry, a 500 megawatts thermal slagging gasifier operating at a 35% efficiency would need 3,800 tons of petcoke carbon feedstock per day, producing approximately 38 – 118 tons/day of slag (the high end ash percent from [4]). Gasifiers generating 174 gigawatts thermal are being constructed or are planned in the world from 2016 to 2019 in the world [5], including Jamnagar Gasification Plant in India with 9.8 gigawatts thermal syngas output (100% petcoke feed) [6]. With the existing plants worldwide, gasifiers generating a total of 310 gigawatts thermal will be in

operation by 2019 [5], generating up to 9 – 27 million tons petcoke slag annually, depending on the petcoke usage worldwide.

Iron & steelmaking slags are typically rich in calcium oxide, while gasification petcoke slags are rich in vanadium oxide. Literature data [2, 7-11] are summarized in Figure 1, where up to 60 wt.% CaO in steelmaking slag and up to 75 wt.% V₂O₅ in petcoke ash are reported. Note that vanadium content is often reported as V₂O₅ but typically exists as V₂O₃ in iron & steelmaking and gasification slags. Due to strong chemical affinity of calcium oxide for vanadium oxide under certain conditions, the presence of calcium influences the valence of vanadium, changing it from 3+ to 5+ and forming calcium orthovanadate (3CaO·V₂O₅). The vanadate formation occurs by removing oxygen from surrounding process gases in the system. If the formation occurs in a gas mixture of CO₂ and H₂O, the following fundamental reaction is expected:



The formation of the calcium vanadate is highly exothermic, causing the breakdown of carbon dioxide and/or water molecules into carbon monoxide and/or hydrogen. The reactions leave an appreciable amount of excess thermal energy in the form of heat. Product heat associated with the overall reaction ranges from -163 kJ to -104 kJ per mole of calcium vanadate at 1300 °C [12], depending on *x* (*x* = 0 – 1). In the present study, a synthetic slag mixture determined based on calcium rich metallurgical slag and vanadium rich petcoke slag was investigated in-situ for potential CO and/or H₂ gas production from waste streams (slag + CO₂ and/or H₂O).

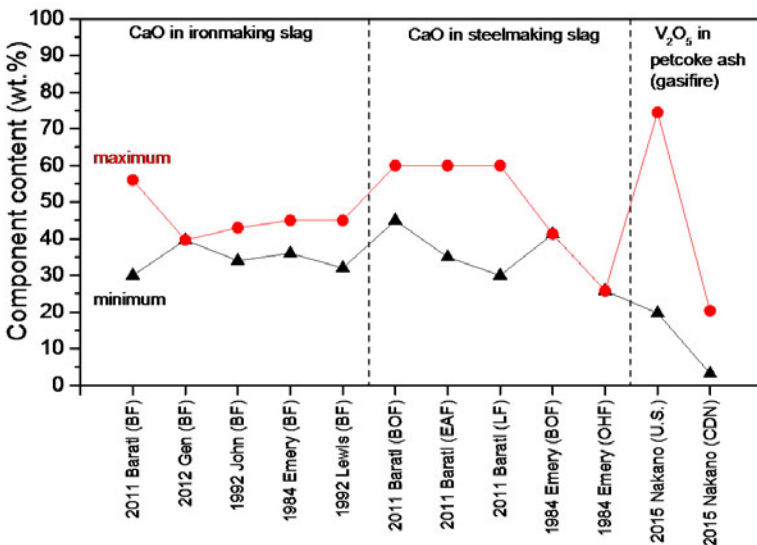


Figure 1. Industrial sources of calcium oxide and vanadium oxide [2, 7-11]. Note vanadium content is frequently reported as V₂O₅ but typically exists as V₂O₃ in

iron & steelmaking and gasification slags. (BF = blast furnace, BOF = basic oxygen furnace, EAF = electric arc furnace, LF = ladle furnace, OHF = open hearth furnace, U.S. = United States, CDN = Canada).

Experimental

The slag composition used in the study was based on mixing a metallurgical slag (Ca-rich) and gasification petcoke ash (V-rich). The composition was determined by using a series of thermodynamic evaluations to maximize the $\text{CO}_2 \rightarrow \text{CO}$ (or $\text{H}_2\text{O} \rightarrow \text{H}_2$) gas conversion and to sustain slag melting. A synthetic slag composition of $8.2\text{Al}_2\text{O}_3$ - 24.7CaO - $8.2\text{Fe}_2\text{O}_3$ - 1.6SiO_2 - $57.3\text{V}_2\text{O}_5$ (by weight %) was mixed and placed in a high density alumina crucible. The mixture was heated from room temperature to $1500\text{ }^\circ\text{C}$ at $2.5\text{ }^\circ\text{C}/\text{min}$ in a closed alumina tube resistance furnace. The atmosphere in the tube was saturated with CO_2 by carbon powder in the sealed air during the heating stage. The electromotive force (ε) of an yttria-stabilized zirconia oxygen sensor ($\text{SIRO}_2^\text{®}$) inside the furnace tube was continuously monitored and used to indicate oxygen partial pressure, which was located immediately above the slag sample. An experimental error of the oxygen sensor was reported to be less than ± 0.2 on a log scale at temperatures between 1000 and $1500\text{ }^\circ\text{C}$ for $10^{-10} - 10^0\text{ atm}$ [13]. Concentrations of CO and CO_2 in the furnace tube were determined by thermodynamic computational software, FactSage 6.4, with FactPS and FToxid databases [14] using the empirical oxygen potentials (converted from ε). In the computations mentioned above, V_2O_5 solubility in the slag was assumed to be negligible due to a lack of such data. Creation of a thermodynamic database for slag containing vanadium is currently underway [7, 15]. Each test was conducted twice for reproducibility. Separate ε measurements without the slag under the same conditions were also employed as a reference on oxygen levels during the heating test.

Results and Discussion

The ε values for the atmosphere during the test without the slag stayed relatively constant during heating. The averaged value of the oxygen partial pressure (without the slag) was converted from ε to be $5 \times 10^{-2}\text{ atm}$ at temperatures between 1100 and $1500\text{ }^\circ\text{C}$. The obtained oxygen pressure agrees with a theoretical value of $2 \times 10^{-2}\text{ atm}$ as calculated by FastSage.

Changes in ε for the CO_2 saturated atmosphere in the reaction tube are presented in Figure 2 as first and third derivatives with respect to time ($d\varepsilon/dt$ and $d^3\varepsilon/dt^3$). Rapid increases in $d\varepsilon/dt$ initiated at approximately 55 min into test 1 and 58 min into test 2 when furnace temperature exceeded $1400\text{ }^\circ\text{C}$. These increases correspond to sudden drops in the oxygen partial pressure caused by interactions between CaO and V_2O_5 (in the slag) with oxygen (originating from the surrounding CO_2). CO was generated by stripping oxygen from CO_2 during the formation of calcium vanadate. During heating, the $\text{CO}_2 \rightarrow \text{CO}$ conversion began and occurred rapidly at approximately $1426\text{ }^\circ\text{C}$ in both tests, with the majority of the reaction completed within 5 min (assuming positive peaks of $d^3\varepsilon/dt^3$, the highest rates of the reaction acceleration, dictate the beginning and ending of the majority of the reaction.) It is still not certain whether the reaction time would be shortened if it occurred at higher temperatures because 5 min of reaction time counted time periods needed to increase temperature during continuous heating in the tests. A

minimal decrease in the oxygen partial pressure (*i.e.*, a minimal increase in ε) was observed after the peak which corresponded to the rapid conversion. As heating progressed, the oxygen partial pressure (determined from the ε) approached asymptotes around $\sim 10^{-10}$ atm, indicating a CO_2 conversion rate at 97%.

Calcium vanadate ($(\text{CaO})_3\text{V}_2\text{O}_5$) was confirmed using the scanning electron microscope with X-ray energy dispersive spectroscopy (FEI Inspect F and Oxford INCA WAVE) and X-ray diffraction analysis (Rigaku Ultima IV) on the quenched slag as presented in Figure 3. The formation of fine calcium vanadate particles was noted throughout the slag. The presence of $(\text{CaO})_3\text{V}_2\text{O}_5$ implies the correlation of the CO generation to the vanadate formation with a valence change from V^{3+} to V^{5+} .

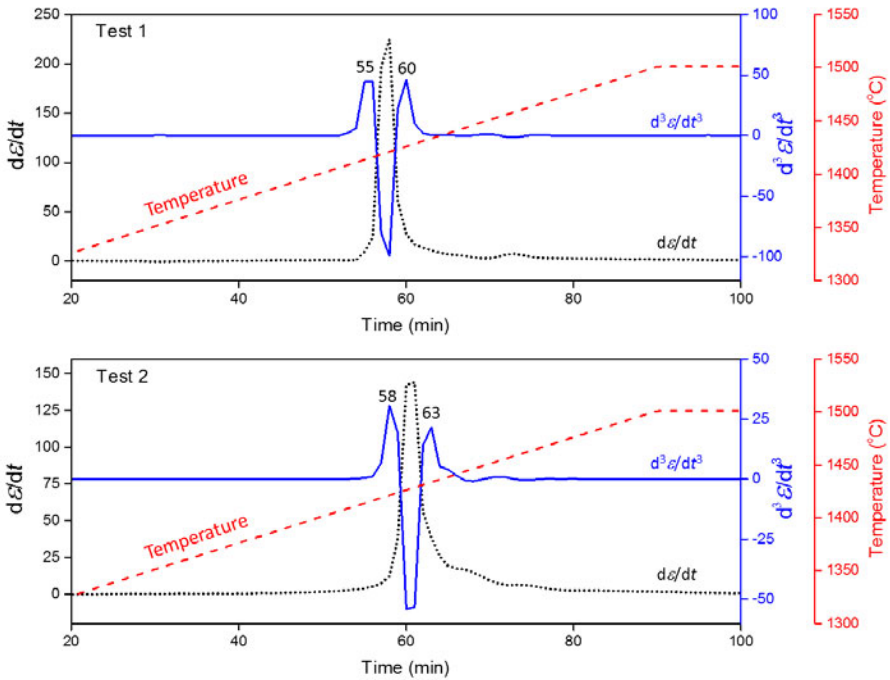


Figure 2. $d\varepsilon/dt$ and $d^3\varepsilon/dt^3$ of tests 1 and 2 from in-situ measurements showing the occurrence of rapid CO_2 conversions during heating when it reached around 1426 °C.

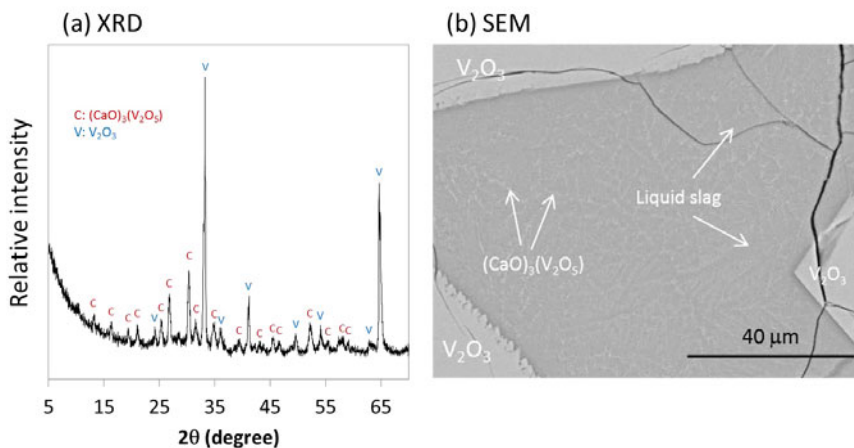


Figure 3. (a) X-ray diffraction patterns showing the presence of the calcium vanadate and (b) SEM backscattered micrograph of the quenched slag sample showing its morphology.

Computational thermodynamic simulations (using FactSage) suggest that, if the same slag methodology is applied to water or steam instead of carbon dioxide, H_2 would be generated following reaction (1). In this case, an oxygen atom is removed from a H_2O molecule over a reaction of CaO and V_2O_3 to form a thermodynamically more stable phase $(\text{CaO})_3(\text{V}_2\text{O}_5)$, leaving H_2 as a byproduct. Theoretically, up to 1 ton of H_2 gas would be produced from the reaction of water with slag containing 4.2 tons of V_2O_3 . Because H_2 is generated from the highly exothermic reaction, the H_2 conversion rate is expected to be significantly greater than that from the traditional thermal dissociation (heat recovery) routes where heat is supplied by extraction from the discharged slag in iron and steelmaking.

Testing to evaluate the “practicality” of the process is ongoing. Process parameters, slag chemistry, and configurations are being studied to optimize the production of heat and conversion of waste streams (CO_2 and slag) into syngas (H_2 and CO).

Conclusion

A synthetic slag mixture of a specific composition based on iron & steelmaking and gasification slags was heated in the presence of CO_2 to a range of industrial slag tapping temperatures. In the controlled atmosphere studies, 97% of CO_2 was converted to CO in approximately 5 min of reaction time over the formation of calcium orthovanadate. Thermodynamic computations predicted that H_2 would be generated from H_2O using the same mixed slag approach. The results suggest a potential approach to help reduce current CO_2 loads to the environment while commercially benefitting the industries.

Acknowledgement

This technical effort was performed in support of the National Energy Technology Laboratory's ongoing research under the RES contract DE-FE0004000. This research was supported in part by an appointment to the National Energy Technology Laboratory Research Participation Program, sponsored by the U.S. Department of Energy and administered by the Oak Ridge Institute for Science and Education.

Disclaimer: "This report was prepared as an account of work sponsored by an agency of the United States Government. Neither the United States Government nor any agency thereof, nor any of their employees, makes any warranty, express or implied, or assumes any legal liability or responsibility for the accuracy, completeness, or usefulness of any information, apparatus, product, or process disclosed, or represents that its use would not infringe privately owned rights. Reference herein to any specific commercial product, process, or service by trade name, trademark, manufacturer, or otherwise does not necessarily constitute or imply its endorsement, recommendation, or favoring by the United States Government or any agency thereof. The views and opinions of authors expressed herein do not necessarily state or reflect those of the United States Government or any agency thereof."

References

1. R.J. Fruehan, "Research on Sustainable Steelmaking," *Metall Mater Trans B*, 40(2) (2009), 123-133.
2. M. Barati, S. Esfahani and T.A. Utigard, "Energy recovery from high temperature slags," *Energy*, 36(9) (2011), 5440-5449.
3. A. Semykina, et al., "Kinetics of Oxidation of Divalent Iron to Trivalent State in Liquid FeO-CaO-SiO₂ Slags," *Metall Mater Trans B*, 41(6) (2010), 1230-1239.
4. M.A. Duchesne and R.W. Hughes, "Partitioning of inorganic elements in pilot-scale and demonstration-scale entrained-flow gasifiers," *Fuel*, 127 (2014), 219-227.
5. *U.S. Department of Energy National Energy Technology Laboratory. Gasifipedia*. 2015.
6. *Gasification Technology Council. World Gasification Database*.
7. J. Nakano, et al., "Thermodynamic effects of calcium and iron oxides on crystal phase formation in synthetic gasifier slags containing from 0 to 27 wt.% V₂O₃," *Fuel* (doi:10.1016/j.fuel.2014.11.008), (2014)
8. L. Gan, et al., "A Differential Scanning Calorimetry Method for Construction of Continuous Cooling Transformation Diagram of Blast Furnace Slag," *Metall Mater Trans B*, 43(3) (2012), 460-467.
9. *Mineral Aggregate Conservation Reuse and Recycling*, in *Report for Aggregate and Petroleum Resources Section, Ontario Ministry of Natural Resources prepared by John Emery Geotechnical Engineering Limited*. 1992.
10. J. Emery, "Steel slag utilization in asphalt mixes," *National Slag Association MF186-1*, (1984), 1-11.
11. D.W. Lewis, "Properties and uses of iron and steel slags," *National Slag Association MF182-6*, (1992), 1-11.
12. J. Nakano and J. Bennett, "CO₂ and H₂O gas conversion into CO and H₂ using highly exothermic reactions induced by mixed industrial slags," *Int J Hydrogen Energy*, 39(10) (2014), 4954-4958.

13. R.A. Mendybaev, et al., "Measurement of oxygen fugacities under reducing conditions: Non-Nernstian behavior of Y_2O_3 -doped zirconia oxygen sensors," *Geochim Cosmochim Acta*, 62(18) (1998), 3131-3139.
14. C.W. Bale, et al., "FactSage thermochemical software and databases - recent developments," *Calphad*, 33(2) (2009), 295-311.
15. J. Nakano, et al., "Phase Equilibria in Synthetic Coal-Petcoke Slags (SiO_2 - Al_2O_3 - FeO - CaO - V_2O_5) under Simulated Gasification Conditions," *Energ Fuel*, 25(7) (2011), 3298-3306.

EFFICIENT STORAGE AND RECALL OF SLAG THERMOCHEMICAL PROPERTIES FOR USE IN MULTIPHYSICS MODELS

Johannes H. Zietsman¹

¹Department of Materials Science and Metallurgical Engineering, University of Pretoria, South Africa

Keywords: phase diagram, multiphysics model, interpolate

Abstract

High temperature thermochemical equilibrium calculations are computationally expensive, taking several milliseconds to complete for simple systems on existing computer hardware. Integrating such calculations into a multiphysics model to describe thermochemical behavior in addition to fluid flow and heat transfer, may result in a model that cannot be solved with the available computing resources.

This problem can be solved by pre-calculating, storing, recalling and interpolating the required thermochemical data. If recall and interpolation can be done quickly, the time required to obtain results can potentially be reduced by several orders of magnitude. Some researchers have implemented this approach on systems with small numbers of components. Pyrometallurgical processes, however, involve many system components, including, for example, Al-C-Ca-Cr-Fe-Mg-Mn-N-O-Si-Ti in significant amounts.

An approach is demonstrated for binary and ternary slag systems using the Al₂O₃-CaO-SiO₂ system as example. The results are compared with ChemApp calculations.

Introduction

Pyrometallurgical processes are complex systems involving combinations of various physical phenomena. This can include heat transfer, mass transfer, multi-phase fluid flow, electromagnetics, chemical reactions and phase changes.

Multiphysics modelling techniques such as the finite element method (FEM), the finite volume method (FVM) and the discrete element method (DEM) have been used for decades to combine mathematical formulations of these different phenomena into computation models to describe high-temperature processes.

FEM models that describe heat transfer and mechanical deformation [5], computational fluid dynamics models (CFD, usually implemented with FVM) that describe heat transfer, fluid flow and electromagnetics [10], and DEM models that describe the behaviour of complex particulate systems [7] are no longer a novelty.

Notably, one very important phenomenon has been mostly omitted, sometimes incorporated in a simplified manner, and on rare occasions integrated into multiphysics models of pyrometallurgical processes. This is thermochemistry.

Thermochemistry is central to most high-temperature processes, since the objective is usually to concentrate valuable elements or substances into a specific phase by solid state reduction, smelting, converting, roasting, etc. High temperatures cause atoms and molecules to be highly mobile, enhancing transport and reaction kinetics, and creating a strong drive to thermochemical equilibrium. This is why equilibrium calculations are so useful in describing these processes. Having thermochemistry available in a multiphysics framework would provide valuable insight into process behaviour and mechanisms.

The reasons why thermochemistry, and more specifically equilibrium calculations, rarely features in multiphysics models of pyrometallurgical processes are quite simple. Firstly, equilibrium calculations on systems with a realistic number of components are computationally expensive. Secondly, integration into multiphysics models would mean repeating these calculations tens of thousands to millions of times per iteration of the multiphysics solver. The resulting computational cost makes such an endeavor infeasible given existing computing hardware.

This paper describes the first steps of an initiative that we have undertaken to integrate thermochemical equilibrium calculations into multiphysics models of high-temperature processes. It focuses on the nature of these calculations and how they can be accelerated to make integration feasible. The continuum modeling aspects are not addressed in this document. Because of the importance of oxide systems in most pyrometallurgical processes, and because of the complexity of these systems, we decided to use a collection of commonly found oxides (Al_2O_3 , CaO , and SiO_2) as the subject of this first investigation.

Purpose

The purpose of this work is to develop a software component that makes fast thermochemical calculations available for use in multiphysics models. Figure 1 provides an overview of the main components of the envisaged system.

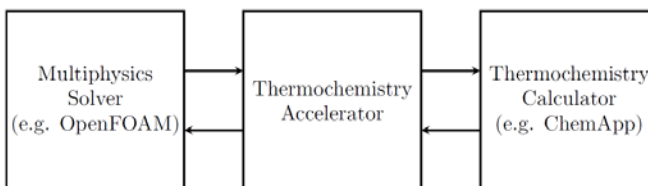


Figure 1. Overview of the components required to integrate thermochemical calculations into multiphysics models.

In our case the multiphysics component is an OpenFOAM solver application. Because of the data available in FactSage [1] and the ease of performing thermochemical calculations through the ChemApp API [4], we use ChemApp as our thermochemistry calculation component.

An accelerator is required that can act as an intermediary between OpenFOAM and ChemApp, making thermochemical calculations fast enough to make multiphysics-thermochemistry integration viable.

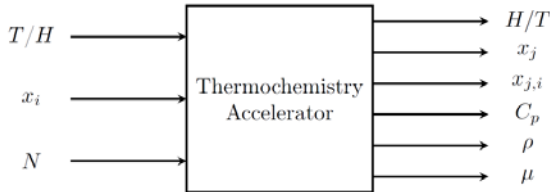


Figure 2. Overview of the thermochemistry accelerator component.

Figure 2 shows the inputs and outputs of the accelerator. It takes as inputs either temperature or enthalpy, a list of mole fractions to describe the system composition, and the total number of moles of system components in the system.

The results produced are enthalpy or temperature, a list of phase fractions, a list of system component mole fractions for each phase, and the system heat capacity, density and viscosity.

Previous Work

The concept of integrating thermochemical equilibrium calculations into multiphysics models is certainly not a new idea. Several authors have reported on such models to describe the casting of aluminum alloys.

Ten Cate et al. [11] confirmed that direct coupling of the casting simulation and equilibrium calculations will yield an infeasible simulation. They reviewed the continuum modeling part of the problem, and proposed methods for incorporating the thermochemistry of multi-element alloys. The main method presented involved a database of pre-calculated thermochemical property values on uniform grids and piecewise discontinuous polynomials to capture temperature dependence and reduce the amount of data that needs to be stored. With this method the data for a 4-component system would be approximately 5GB in size. [11]

These researchers also proposed that a hierarchical representation on sparse grids can be used to describe the continuous variation of enthalpy with composition and temperature. They suggested that the lever rule can be used to determine system phase fractions for binary systems, but that this would require capturing the phase boundaries. [11]

Phase boundaries, which are c -dimensional hyper-surfaces for a system with c components, can be captured either explicitly by using a multi-dimensional splines or an unstructured n -simplex grid, or implicitly using a number of smooth, local basis functions and level set methods. [11]

Finally, Ten Cate et al. [11] proposed local caching of calculated thermochemical properties in the multiphysics model cells, and recalculation only when the state of a cell has changed by more than a certain threshold value. This can reduce the computational load significantly.

Zhao et al. [13] studied the solidification of ternary Al-Cu-Si alloys by combining a continuum model with thermochemistry. Three different methods were used to incorporate the thermochemical equilibrium calculations, namely direct coupling with the Thermo-Calc TQ6 interface, as well as a mapping technique and regression functions to store and recall thermochemical property values. Similar mapping techniques were also used by Doré, Combeau, and Rappaz [2] and Du, Eskin, and Katgerman [3].

The investigators found that direct coupling has a significantly higher computational cost compared with the other two methods, but comparable accuracy. Mapping calculates in 1.7% and regression functions in 1.1% of the time required by direct coupling. Such techniques can therefore speed up calculations between 50 and 100 times, which is significant. [13]

Marin [6] presented an approach to model coupled problems involving multiphysics and thermochemistry. This involved the development of a Gibbs free energy minimisation routine and integrating it into the COMSOL multiphysics software. Results of simple tests on a hypothetical non-ideal binary system was presented. Given what was reported by Ten Cate et al. [11] and Zhao et al. [13] this approach would become infeasible for a realistic number of system components.

Qiu et al. [9] captured phase boundaries by univariate and multivariate polynomials. They also described phase fractions and phase composition using such polynomials. The coefficients of the polynomials were determined by interpolation as a function of temperature. They applied this technique to a ternary system, and then extended it to a limited region of a quaternary system.

Approach

At this stage of the work, we have made the following decisions about the accelerator implementation:

- Use a geometric representation of the thermochemical system to perform calculations.
- Use principles from thermochemical theory to simplify and accelerate calculations, and minimize the dimensionality of data that must be calculated and stored to capture the geometric representation.
- Implement the first prototype accelerator in Python to reduce complexity and development time.

Geometric Representation

Phase diagrams are commonly used to describe thermochemical systems. They are useful for demonstrating changes that occur with varying temperature and composition. X-Y diagrams are used for binary systems, while Gibbs triangle diagrams are used for ternary systems. The same diagrams can also be used for sections through higher-order systems (pseudo-binaries and pseudo-ternaries).

In addition to describing behavior of a thermochemical system, a phase diagram can also be viewed as a geometrical system, consisting of phase regions and phase region boundaries. Figure 3 shows an example of a binary system.

Phase regions are areas on the diagram where the combination of stable phases remains constant. These regions are separated from each other by phase region boundaries. In the $\text{Al}_2\text{O}_3\text{-CaO}$ binary system the phase regions are represented by a set of 16 2D areas, some of which are barely visible, separated by 1D boundaries (curves and straight lines).

The entire diagram is captured simply and accurately by a set of lines and polynomials that are used to calculate phase quantities and phase compositions for the entire system. Properties like heat capacity and enthalpy are captured by additional curve fits based on the phase region boundary curves and lines. In essence, once the system's phase boundaries are captured geometrically, most of the thermochemical behavior of the system can be described.

The same principles apply to higher-order systems (ternary, quaternary, n-component), with the dimensionality of the phase regions and boundaries increasing with the number of system components. A ternary system will therefore consist of 3D volume regions separated by 2D surface boundaries, and a five-component system will have 5D hyper-volume regions separated by 4D hyper-surface boundaries. Multivariate polynomials are used to describe phase boundaries of ternary and higher-order systems.

Thermochemistry Theory

The Gibbs phase rule and the lever rule, both taken from thermochemistry theory, can be used to reduce the complexity of the accelerator implementation, and improve its speed.

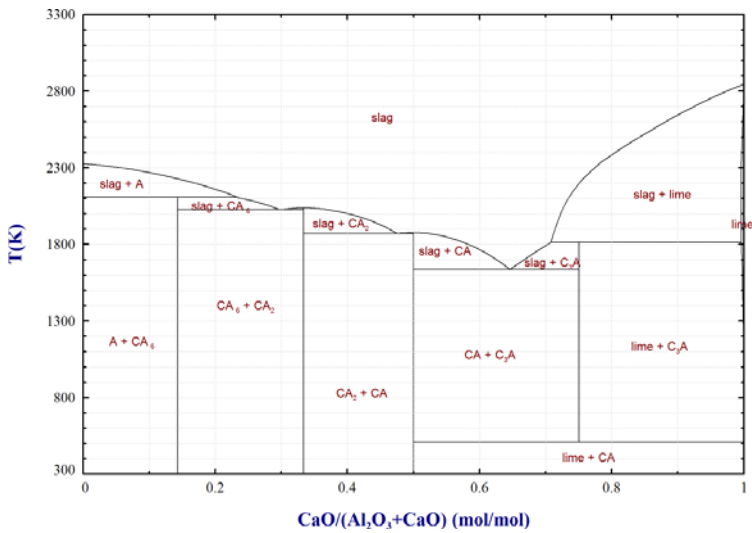
The Gibbs Phase Rule

The phase rule (Equation 1) and the number of components in the phases present at equilibrium can be used to classify phase regions and determine the characteristics of a region's boundaries. Because pyrometallurgical processes are generally operated at or close to atmospheric pressure, and because we are dealing only with condensed phases at the moment, pressure can be kept constant. We can therefore work with the altered phase rule in Equation 2.

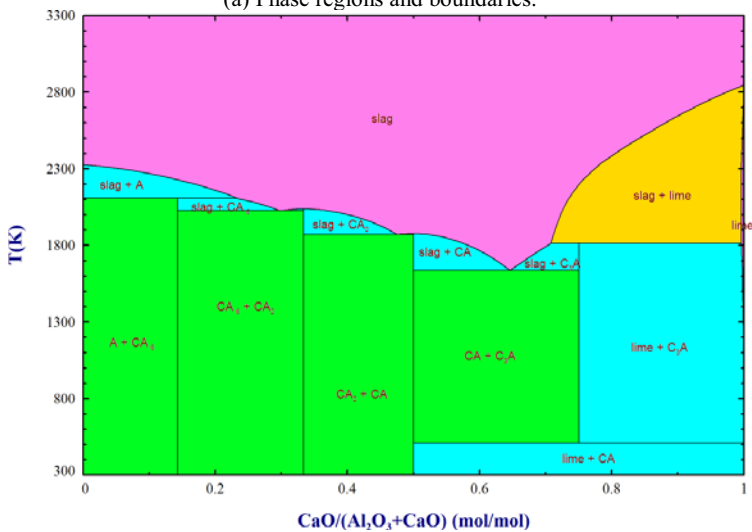
$$f = c - p + 2 \quad (1)$$

$$f' = c - p + 1 \quad (2)$$

The phase rule specifies the maximum number of phases that can exist at equilibrium for a given number of system components. Using the structure of the phase rule, the phase regions of the binary system in Figure 3 are classified into four categories. This is shown in Figure 3b. Table 1 presents the characteristics of the phases and boundaries of each region category. This classification is used to develop algorithms to extract the geometric representation, and do thermochemical calculations based upon this representation.



(a) Phase regions and boundaries.



(b) Phase regions categories. (green: $f'_{2,2,11}$, cyan: $f'_{2,2,12}$, yellow: $f'_{2,2,22}$, pink: $f'_{2,1,2}$)

Figure 3. Binary phase diagram of the Al_2O_3 - CaO system. ($A=\text{Al}_2\text{O}_3$, $\text{CA}_6=\text{CaAl}_{12}\text{O}_{19}$, $\text{CA}_2=\text{CaAl}_4\text{O}_7$, $\text{CA}=\text{CaAl}_2\text{O}_4$, $\text{C}_2\text{A}=\text{Ca}_2\text{Al}_2\text{O}_5$)

Table 1. Phase region categories for binary systems. (Notation of $f_{c,p,pc}^r$: c = number of system components, p = number of phases present at equilibrium, pc = number of components in each phase)

Category	f^r	c	p	Phases	Boundaries
$f_{2,2,11}^r$	1	2	2	2 pure substances	2 vertical lines 2 horizontal lines
$f_{2,2,12}^r$	1	2	2	1 pure substance 1 solution	1 vertical line 1 to 2 horizontal lines 1 curve
$f_{2,2,22}^r$	1	2	2	2 solutions	2 curves 1 horizontal line
$f_{2,1,2}^r$	2	2	1	1 solution	1 or more curves 0 or more straight lines

For example, the slag+CA region is classified as $f_{2,2,12}^r$. The subscript notation indicates that the system has two components, and the region has two stable phases. The last part of the subscript indicates that the one phase is pure and has effectively a single component, and the second phase is a solution with two components. This is valuable information, since it is now known that the pure substance will create a vertical straight line boundary that can be captured and used very simply. The second phase is a solution, and a polynomial is used to capture its boundary.

The Lever Rule

The lever rule is a well-known technique for calculating the phase fractions of a 2-component system from a binary phase diagram at constant temperature. The method can, in fact, be used for any 2-phase region, regardless of the number of system components.

This last statement is significant, since it reduces the dimensionality of all 2-phase regions by 1, regardless of the number of system components (c). Moreover, lever rule calculations on tie-lines in 2-phase regions can be extended to equivalent phase fraction calculations on tie-triangles in 3-phase regions, and tie-simplexes [12] in regions with arbitrary numbers of phases. The dimensionality of all phase regions, except for single-phase ones, can therefore be reduced by one. Rather than having to store a mesh of points in a c -dimensional hyper-volume, we only need to store p ($c-1$)-dimensional hyper-surfaces per phase region. This reduces the storage space and memory required by the accelerator significantly.

In many cases the dimensionality of the phase region boundary hyper-surfaces is lower than ($c-1$). This is determined by the number of components in the phase in question. A pure substance, for example, is represented by a constant composition line that does not change as a function of temperature, since it effectively has a single component. A 2-component solution is described by a 2D surface, a 3-component solution by a 3D surface, etc.

In the case of $f^r=1$ regions, the boundaries are described by curves rather than surfaces. This is due to the fact that at constant temperature the number of degrees of freedom becomes zero, and the phase compositions are all constant within the region. There is then no need to store higher-

dimensional surfaces. p (number of phases) parametric curves that describe the composition of each phase as a function of temperature are all that are required.

Implementation

Python [8] was used to develop the first accelerator prototypes, since it contains a number of useful libraries (numpy, scipy), and because ChemApp could be accessed from within Python. The nature of the language and the available infrastructure makes rapid prototyping possible.

Python does have one serious drawback, namely its execution speed. It is estimated that, depending on the exact nature of the algorithm, an equivalent Fortran implementation can be 10 to 1000 times faster than a Python implementation.

At the initial stage of the project, algorithm prototyping was considered more important than execution speed. The final algorithms will be translated to Fortran to derive maximum benefit from the accelerator.

The implementation has two parts. The first part constructs a geometric representation of a binary or ternary system. It is referred to as the geometric constructor, or "Gcon". The second part uses the geometric representation to calculate thermochemical data upon request. It is referred to as the geometric calculator, or "Gcalc".

Results

ChemApp Calculations

ChemApp was used to perform equilibrium calculations on 6 binary systems, 4 ternary systems and one quaternary system. The components that were used included Al_2O_3 , CaO, MgO, and SiO_2 . A standard set of calculations were done at 1% intervals from 0% to 100% along all composition axes, and at 50K intervals from 1300K to 2300K along the temperature axis. The results are presented in Figure 4.

It is clear that calculation duration increases exponentially with the number of system components. This increase is one reason why it is infeasible to integrate thermochemical calculations of realistic systems directly into a multiphysics model.

Al_2O_3 -CaO Binary

A geometric representation of the Al_2O_3 -CaO system was created semi-automatically. The Gcon component is not yet able to perform reliably without human intervention. This is the reason why results are reported for only this one binary system.

The Gcalc component was used to perform the standard set of equilibrium calculations for this binary system to calculate phase quantities and phase compositions. The average calculation duration was 0.063 ms, as opposed to 2.710 ms in the case of ChemApp. That is more than 20 times faster.

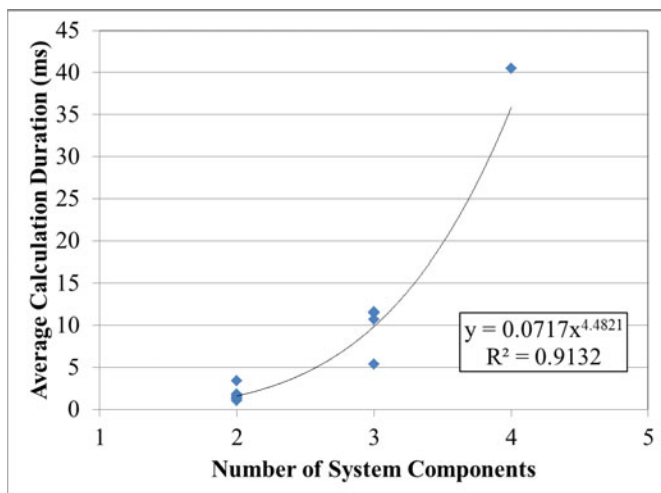


Figure 4. Duration of ChemApp equilibrium calculations on an Intel i7 3840QM 2.8 GHz CPU.

Agreement between Gcalc and ChemApp results were virtually exact. Most of the two-phase regions contain only pure substances, making it possible to obtain exact results. In the case of regions containing solutions (lime and slag), boundaries were fitted with polynomials that made errors of no more than 10^{-6} mole fraction and 3×10^{-4} °C. Given the inherent uncertainty in modelling high-temperature processes, this level of accuracy is more than adequate.

The geometric representation was stored in a text file in JSON (JavaScript Object Notation) format. The file size is 16 kB.

Al₂O₃-CaO-SiO₂ Ternary

The same procedure was followed for the Al₂O₃-CaO-SiO₂ system. In this case, the average Gcalc calculation duration was 0.768 ms, and the ChemApp duration was 11.458 ms, which is almost 15 times faster.

In terms of accuracy, agreement was again almost exact, with errors for solutions boundaries in the same range as for the binary system.

The size of the JSON file for the ternary system is 260 kB. This is significantly larger than for the binary system. With some further development, storage efficiency will be improved.

Conclusions

Geometric representations were generated of two thermochemical systems, Al₂O₃-CaO and Al₂O₃-CaO-SiO₂. These representations were used to calculate phase quantities and phase

compositions to compare speed of calculation with the speed at which ChemApp performs the same calculations. The geometric approach were able to perform the calculations between 15 and 20 times faster than ChemApp. It is expected that this acceleration will increase by 10 to 1000 times when the algorithms are translated to Fortran. This will provide acceleration between 150 and 20 000 times compared to ChemApp.

If higher order systems of practical interest can be accelerated to the same extent as the binary and ternary systems investigated here, integration of thermochemistry into multiphysics models will become feasible for the investigation of pyrometallurgical processes.

References

1. C.W. Bale et al. "FactSage thermochemical software and databases - recent developments". In: CALPHAD 33 (2013), pp. 295–311.
2. X. Doré, H. Combeau, and M. Rappaz. "Modelling of microsegregation in ternary alloys: Application to the solidification of Al-Mg-Si". In: Acta Materialia 48 (2000), pp. 3951–3962.
3. Q. Du, D.G. Eskin, and L. Katgerman. "Modeling Macrosegregation during Direct-Chill Casting of Multicomponent Aluminum Alloys". In: Metallurgical and Materials Transactions A 38A (2007), pp. 180–189.
4. GTT-Technologies. ChemApp. 2016. url: <http://gtt.mch.rwth-aachen.de/gttweb/chemapp> (visited on 02/01/2016).
5. J. Konishi et al. "Modeling the formation of longitudinal facial cracks during continuous casting of hypoperitectic steel". In: Metallurgical and Materials Transactions B 33.3 (2002), pp. 413–423.
6. T. Marin. "Coupled thermodynamic and multiphysics modelling in pyrometallurgical process simulation". In: The Conference of Metallurgists 2015. (Montreal, Canada). 2015, pp. 1–15.
7. T. Mitra and H. Saxen. "Simulation of burden distribution and charging in an ironmaking blast furnace". In: IFAC Proceedings Volumes 48.17 (2015), pp. 183–188.
8. Python Software Foundation. Python 3.3.6 Documentation. 2016. url: <https://docs.python.org/3.3/> (visited on 02/01/2016).
9. K. Qiu et al. "Polynomial regression and interpolation of thermodynamic data in Al-Si-Mg-Fe system". In: Computer Coupling of Phase Diagrams and Thermochemistry 48 (2015), pp. 175–183.
10. Q.G. Reynolds. "Interaction of dust with the DC plasma arc - A computational modelling investigation". In: Journal of the Southern African Institute of Mining and Metallurgy 115.5 (2015), pp. 395–407.
11. A. Ten Cate et al. "Modeling and simulation of phase-transitions in multicomponent aluminum alloy casting". In: Proceedings of the Sixty-third European Study Group Mathematics with Industry. (Enschede, The Netherlands). 2008, pp. 117–139.

**ADVANCES IN MOLTEN
SLAGS, FLUXES, AND SALTS:**

Proceedings of



**Industrial Applications:
Non-Ferrous**

PRODUCTION OF COBALT AND COPPER ALLOYS FROM COPPER SLAGS VIA REDUCTION SMELTING IN DC ARC FURNACE

Onuralp Yücel

Metallurgical and Materials Engineering Department, Faculty of Chemical and Metallurgical Engineering, Istanbul Technical University, Maslak, Istanbul, 34469, Turkey

Keywords: Arc Furnace, Copper Slag, Cobalt, Copper

Abstract

In the present work, the effects of amount of coke, reduction temperature and furnace types on copper slag smelting in a dc arc furnace were studied. Optimum coke amount was found to be 10% of the slag weight in an open-top furnace for a 1 hour reduction time in the temperature between 1703 K and 1753 K. Similar conditions in a closed-top furnace resulted in higher cobalt and copper contents of the metallic matte, recoveries and reduction rates, as compared with the open-top furnace. In the covered system, for cobalt and copper, recoveries reach 95.7% and 90%, concentrations were 2.38% and 3.51% respectively, and reduction rate constants were found to be $1.7 \times 10^{-3} \cdot s^{-1}$. For both furnaces, higher reduction temperatures yielded higher reduction rates but lower cobalt, copper and sulfur content in the metallic matte. The specific conductivity of the slag was also estimated by using furnace geometric factor given in the literature as an empirical formula and by using furnace resistance measured during smelting of the copper slag with or without different additives.

Introduction

Copper slags usually contain non-ferrous metals such as copper, cobalt, nickel, zinc depending on the distribution properties of these metals between slag and matte. After the reduction of copper slag by addition of coke, cobalt, copper and other non-ferrous metals, iron can be collected in a metallic matte phase. One of the production sources of cobalt, a highly strategic metal, is the copper smelting slag from processing of cobalt containing copper ores and concentrates [1-10].

An approximate amount of 2 million tons of copper slag has been lying on the northern part of Turkey-Küre dating from Genevian times. This slag contains 0.4% Co and 0.82% Cu. Many researches on the recovery of cobalt from Küre slags have been carried out by a hydrometallurgical treatment of Co-Cu-Fe containing matte, which can be obtained by the carbothermal reduction of copper slag in an arc furnace [11-13]. The main study comprises reduction smelting of ancient Küre slag in a dc arc furnace to collect Co, Cu, and S in a metallic matte, granulation of the metallic matte and reduced discarded slag with pressurised water separately, and leaching of matte granules in H₂SO₄ solution. Granulated slag was also tested as grit material. Cobalt can be recovered from leach solution by gas-precipitation, calcination, leaching, chemical-precipitation or crystallization, calcination, leaching, electrolysis techniques. The present paper focuses on the optimization the process parameters affecting the enrichment of cobalt and copper in metallic matte in a dc arc furnace.

Experimental Procedure

The chemical composition of Küre copper slag, which is used as initial material for this study is given in Table I. The chemical analysis of coke used as a reductant is given in Table II. The average particle size of copper slag and coke is 2-4 mm and 1-3 mm respectively. 99% purity CaO was obtained by calcination of CaCO₃ at 1273 K whereas Al₂O₃ has the purity of 99%.

Table I. Chemical Composition of Ancient Küre Copper Slag (wt.%)

Co	Cu	Zn	Fe	S	SiO ₂	Al ₂ O ₃	CaO	MgO
0.40	0.82	0.15	47.80	1.50	26.10	6.80	0.70	1.00

Table II. Chemical Composition of Coke (wt.%)

C _{fix}	Volatile	Ash
78.50	3.60	17.90

Slag smelting was carried out in two different kinds of dc arc furnaces each having crucibles powered with 270 kVA each. One of the furnaces was 36 cm in diameter, 80 cm in height with 150 kg charging capacity and had open-top-design [14]. The other furnace was 30 cm in diameter and 45 cm in height with a capacity of 50 kg and of close-top-cover design [11]. Both furnaces were lined with magnesia for this investigation. The details of electrothermic process can be found elsewhere [15]. The voltage, current and temperature were measured and recorded using a computer. During the smelting of the charge, temperature measurements for both metal and slag were carried out with a Pt-Pt10Rh submerged thermocouple in every 10 minutes, whereas tapping temperatures were measured with a help of an optical pyrometer. To determine the reaction rate, a titanium rod of 2.5 cm in diameter was used for sample collection from the liquid slag at predetermined time intervals.

Varying amounts of copper slag and coke were mixed in a rotary mixer for a period of half-hour. For each batch, 25 kg of these mixture was fed to the open arc furnace which had been preheated to 1300 K. In the open top furnace, both the effect of the amount of reductant and fluxing materials on recovery, and the reaction rate were studied. In the closed-top furnace, the effect of reduction time and reduction temperature on the concentration of cobalt, copper and sulfur in the slag were investigated, as well as increase in concentration of the same elements in the metallic matte by adding controlled amounts of reductant to the charge. Furnace temperature, a function of power applied to the furnace, was fixed by adjusting the energy consumed. Cobalt and copper concentration in the slag and metal were determined using an atomic absorption technique (Perkin Elmer 1100B) and sulfur concentrations were determined using a wet chemical method.

Results and Discussion

Effects of Reductant Addition

In the first group of experiments using the open-top furnace, the effect of different amounts (2.5-12.5 weight percent of slag) of coke additions to charge, on cobalt and copper concentrations in metallic matte, and their recoveries, were studied. The temperature and time were maintained constant at 1703-1753 K and 1 hour respectively.

It was observed that the reduction recovery of cobalt to metallic matte was increased to about 90% with 10% of coke addition. However, further increase in coke had no further effect on the recovery of cobalt (Figure 1).

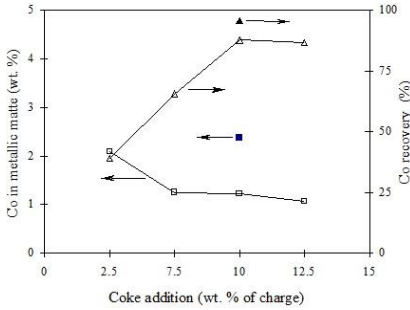


Figure 1. Cobalt concentration and cobalt recovery in metallic matte versus coke addition at 1703-1753 K for 1 hour for open- and closed-top furnaces (□, △: open-top furnace, ■, ▲: closed-top furnace).

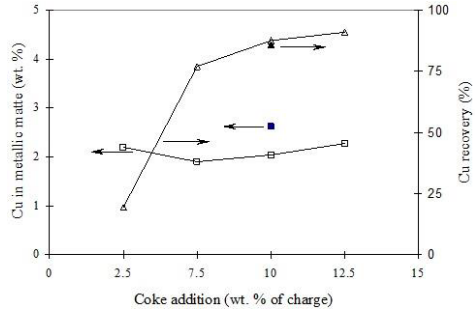


Figure 2. Copper concentration and copper recovery in metallic matte versus coke addition at 1703-1753 K for 1 hour for open- and closed-top furnace (□, △: open-top furnace, ■, ▲: closed-top furnace).

Figure 1 also shows for a 2.5% coke addition, the cobalt concentration is 2.2%, and the cobalt content of the metallic matte declines with further coke addition in an open-top furnace. This is due to weight increase of metallic matte as a result of further iron reduction. For the smelting experiments with the closed-top furnace at 10% coke addition, the cobalt recovery and cobalt concentration reached 95.7% and 2.38%, respectively. Both cobalt recovery and concentration were higher in the closed-top furnace experiments under the same conditions. Figure 2 shows the copper concentration and recovery in metallic matte versus coke addition. For 7.5% coke addition in the open-top furnace, copper recovery from the slag was about 80%, increasing to about 90% for 12.5% coke addition. The copper concentration of the metallic matte did not vary with the amount of coke addition but remained constant at about 2% whereas this value was 2.6% in the closed-top furnace. The experimental results indicate that coke addition beyond 10% does not appreciably influence the recovery of cobalt and copper (Figure 1 and Figure 2). By increasing the amount of coke from 2.5% to 7.5%, the Co content decreased from 2% to 1.5% in metallic matte; this is due to the increasing amount of iron in the matte in open-top furnace. Under these circumstances, an increase in the Cu content of metallic matte indicates that copper has similar reduction behavior as iron. Although reduction recoveries obtained from both closed-top and open-top furnace experiments with 10% coke addition were similar, an increase was observed in Co and Cu contents of metallic matte due to the geometrical factors of the closed-top furnace.

The Effects of Reduction Time and Temperature

Reduction rates of Co and Cu in both furnaces with 10% coke addition, were obtained by measuring Co and Cu concentrations in the slag as a function of time, keeping the temperature

constant. The reduction rates were determined at several temperatures. Rate constant of Co and Cu can be calculated using the following equations.

$$\frac{W_{Me,t} - W_{Me,\infty}}{W_{Me,0} - W_{Me,\infty}} = \frac{\Delta W_{Me,t}}{\Delta W_{Me,0}} \quad (1)$$

$$\frac{\Delta W_{Me,t}}{\Delta W_{Me,0}} = e^{-k.t} \quad (2)$$

Where $W_{Me,0}$, $W_{Me,t}$ and $W_{Me,\infty}$ are mass contents of component Me at the beginning, at time t and infinity, respectively whereas k is the reduction rate constant. These values were determined from the reduction curves using Arrhenius Equation (2) [17].

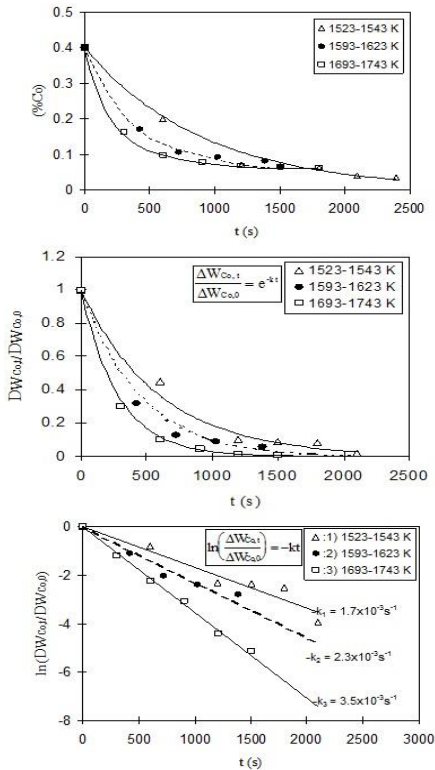


Figure 3. (a) The effect of temperature and time on concentration of cobalt in slag in closed-top furnace. (b), (c) Determination of rate constants, k_{Co} , of cobalt reduction from reduction curves in (a).

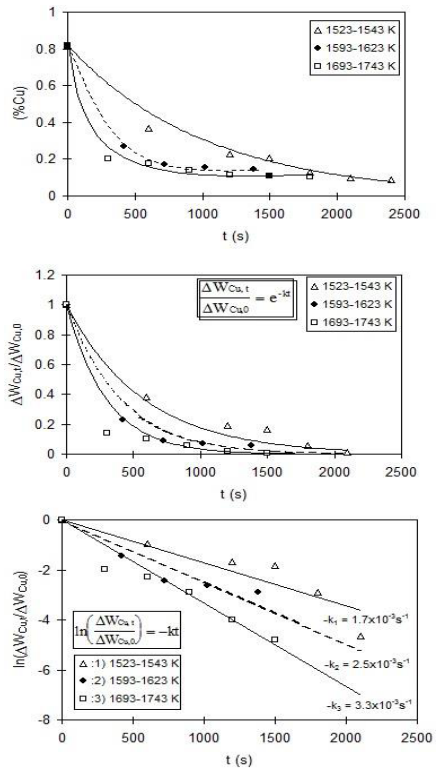


Figure 4. (a) The effect of temperature and time on concentration of copper in slag in closed-top-furnace.(b), (c) Determination of rate constants, k_{Cu} , of copper reduction curves in (a).

Figure 3a and Figure 4a shows the results obtained for cobalt and copper contents in slag as a function of reduction time and temperature for closed-top-furnace. Reduction rate constants (k_{Co} , k_{Cu}), determined from $Me\% - t$, $(\Delta W_{Me,t} / \Delta W_{Me,O}) - t$ and $\ln(\Delta W_{Me,t} / \Delta W_{Me,O}) - t$ variations. Reduction curves for different temperatures, which were obtained by assuming the final slag concentration as at infinity are given in Figure 3b and Figure 4b. Reduction rate constants of cobalt and copper calculated by using equation (2) for different temperatures are given in Figure 3c and 4c. These results show that with an increase in reduction temperature the reduction rate increases. Similar calculation method was used for determine the reduction rate constants of cobalt and copper in open-top furnace and reduction rate constants obtained for different temperatures in both types of furnaces are shown in Table III, for different addition ratios and process durations in Table IV.

Table III. Calculated k Values for Different Temperatures

Run	Slag T, K	-k (10^{-3} /s)		Metallic Matte, %			Matte T, K
		Co	Cu	Co	Cu	S	
1*	1523-1573	0.90	1.60	1.56	2.51	2.88	1538
3*	1603-1633	1.30	1.70	1.38	2.38	2.83	1863
2*	1703-1755	1.50	1.50	1.22	2.04	2.49	1923
117**	1523-1543	1.70	1.70	2.38	3.51	2.89	1558
116**	1593-1623	2.30	2.50	1.89	3.12	2.83	1571
118**	1693-1743	3.50	3.30	1.76	2.62	2.71	1829

*Open-top furnace, **Covered-top furnace.

Table IV. Calculated k Values for Different Addition Ratios and Process Durations

Run	Additions, %	Metallic Matte, %			End Slag, %			-k (10^{-3} /s)		Duration, sec.	Recovery, %	
		Co	Cu	S	Co	Cu	S	Co	Cu		Co	Cu
5*	2.50 Coke	2.09	2.20	-	0.10	0.12	-	0.60	0.80	3600	39.5	20.3
9*	7.50 Coke	1.25	1.90	2.22	0.09	0.11	1.17	0.90	0.90	3600	65.5	77.0
2*	10.00 Coke	1.22	2.04	2.49	0.09	0.10	1.15	1.10	0.90	3600	87.6	87.6
15*	12.50 Coke	1.06	2.27	-	0.03	0.14	-	2.00	1.30	3000	86.6	91.0
2*	10 Coke, 2 CaO	1.43	2.41	2.89	0.10	0.10	1.01	-	-	3600	86.7	89.2
3*	10 Coke, 4 CaO	1.38	2.38	2.83	0.09	0.10	1.07	1.00	1.40	3600	93.5	92.0
4*	10 Coke, 6 CaO	1.17	2.05	3.03	0.04	0.10	0.96	1.00	1.60	3600	95.7	90.7
36*	10 Coke, 5 Al ₂ O ₃	1.10	1.61	1.89	0.05	0.11	0.58	1.50	1.60	2400	92.5	87.8
38*	10 Coke, 10 Al ₂ O ₃	1.06	1.90	2.09	0.05	0.11	0.56	1.70	1.70	2400	88.5	85.7
40*	10 Coke, 15 Al ₂ O ₃	1.08	1.70	2.19	0.06	0.10	0.48	1.90	1.40	2400	79.9	86.5
41*	10 Coke, 20 Al ₂ O ₃	1.05	1.59	2.46	0.06	0.10	0.56	-	-	2400	73.1	67.5
119**	6 Coke	2.12	2.24	3.02	0.06	0.13	-	0.90	0.90	3600	49.9	70.9
111**	10 Coke	2.31	3.12	2.90	0.06	0.11	1.01	2.30	2.50	1500	95.7	86.0

*Open-top furnace, **Covered-top furnace, (-) Not analyzed.

Electrical Characteristics of Copper Slags

The electric resistance between two electrodes in slag resistance furnace (SRF) is important factor for furnace design and performance [18-20] and can be defined as following equation.

$$R = \frac{f_g}{\sigma} = \frac{cm^{-1}}{\Omega^{-1}.cm^{-1}} \quad (3)$$

where R: furnace resistance, f_g : geometric factor, and σ : slag electrical conductivity. The furnace geometric factor, being linearly proportional to (R), is a function of diameter of the electrode (d), the depth of immersion (h), electrode spacing (s) and the depth of slag layer (H).

$$f_g = f(d, h, s, H) \quad (4)$$

According to the calculations of Nielsen on salt solutions [19, 21], the furnace geometrical factor of a system is described in Equation 5 as an empirical formula and it can be applied to such an arc furnace system shown in Figure 5.

$$f_g = \frac{0,3034}{d} \times \frac{[(H-h)/d]^{0,45}}{(h/d)^{0,24}} \quad (5)$$

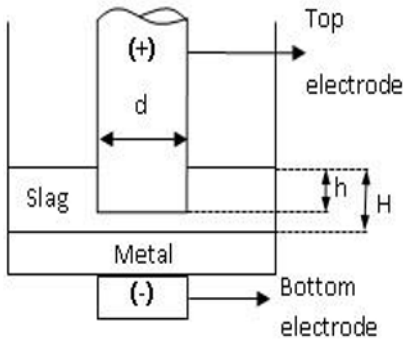


Figure 5. Schematic diagram of a direct current slag resistance furnace (DC-SRF).

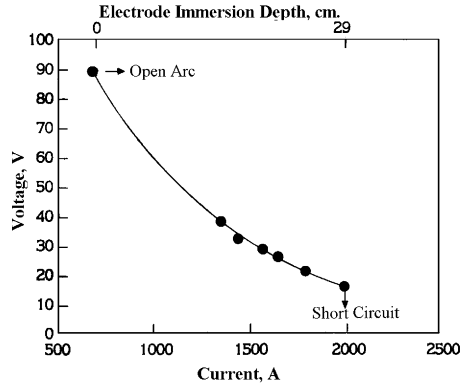


Figure 6. The relationship between current-voltage variations and the distance between the electrodes.

The geometric factor and the specific conductivity of the slags were calculated using Equations (3) and (5), respectively. Electrical values measured during smelting of 120 kg of slag without additives and the calculated values were given in Table V. In this experiments (Run: 106), no metallic or matte phase were observed in the crucibles. The slag temperatures were measured as ~1440 °C. Mean specific conductivity of the slags was calculated as 1.848 $\Omega^{-1}.cm^{-1}$. The relationship between current-voltage variations and the distance between the electrodes were plotted in Figure 6. As can be seen, when the distance between electrodes is zero, the short-

circuit occurs at 15 V and 2000 A. The power applied to the furnace is kept constant at 60 kW using a potentiometer. Moving the electrode upwards increases the voltage and decreases the current. At the surface of the slag layer, the voltage reaches its maximum and the current reaches its minimum values.

Table V. The Measured and Calculated Electrical Values of Küre Slag (Run: 106, d: 10 cm)

H, cm	H, cm	V	A	R, Ω	f_{e} , cm ⁻¹	σ , Ω ⁻¹ cm ⁻¹	σ_{mean} , Ω ⁻¹ cm ⁻¹
measured	measured	measured	measured	measured	calculated	calculated	calculated
29	29	15.0	2000	0.0075	-	-	1.848
29	24	20.0	1800	0.0111	0.0180	1.622	
29	19	25.0	1650	0.0154	0.0260	1.689	
29	14	27.5	1575	0.0175	0.0336	1.919	
29	9	32.0	1450	0.0220	0.0425	1.932	
29	4	37.5	1360	0.0275	0.0571	2.076	
29	0	90.0	700	0.0190	-	-	

The measured and calculated electrical values of the ancient Küre slag with additives were given in Table VI. Since metallic phases were obtained in the bottom of the crucibles in each experiments, in addition to electrodes and conjunction cables, effect of metallic phase were also neglected in the calculations because of their high electrical conductivities.

Table VI. The Measured and Calculated Electrical Values of Küre Slag with additives (d: 10 cm)

Run	Additives	Slag Composition, %				h cm	H cm	f_{e} cm ⁻¹	R Ω	σ Ω ⁻¹ cm ⁻¹	T °C
		SiO ₂	FeO	Al ₂ O ₃	CaO						
35	10 coke	38.28	42.03	8.69	1.46	5.00	9.50	0.0250	0.0321	0.78	1250
105	10 coke	32.73	46.28	7.50	1.37	11.00	23.40	0.0326	0.0403	1.16	1320
110	10 coke	32.73	46.28	7.50	1.37	12.57	21.65	0.0270	0.0250	1.08	1327
22	10 coke	36.10	44.18	8.23	1.45	6.20	9.50	0.0340	0.0290	1.17	1388
10	10 coke, 2 CaO	42.20	28.67	8.77	1.60	1.10	9.50	0.0476	0.0321	1.48	1443
11	10 coke, 4 CaO	41.75	28.31	9.00	6.09	2.70	9.50	0.0350	0.0250	1.40	1421
12	10 coke, 6 CaO	39.11	31.58	9.06	8.69	2.14	9.50	0.0385	0.0250	1.54	1470
36	10 coke, 5 Al ₂ O ₃	42.67	30.81	18.91	1.60	3.80	10.50	0.0320	0.0860	1.12	1399
41	10 coke, 20 Al ₂ O ₃	34.50	25.36	34.75	0.29	5.10	11.50	0.0292	0.0250	1.17	1315

The relationship between slag temperature and conductivity were also plotted in Figure 7. As can be seen, increasing temperature also increases the specific conductivity of the slag.

In Figure 8, the results of the entire study were compared to those of previous published data. It can be seen that electrical conductivity of the slags that we obtained with/without additives are strongly similar to those of fayalite-based slags.

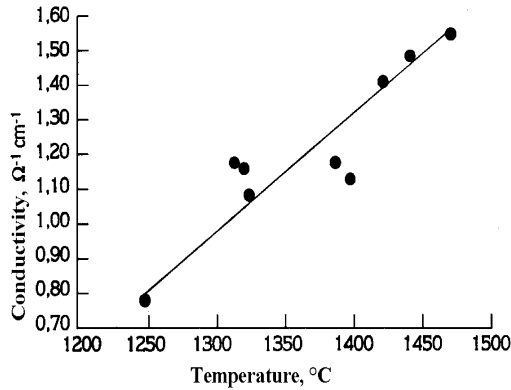


Figure 7. The temperature vs slag conductivity diagram of the copper slags.

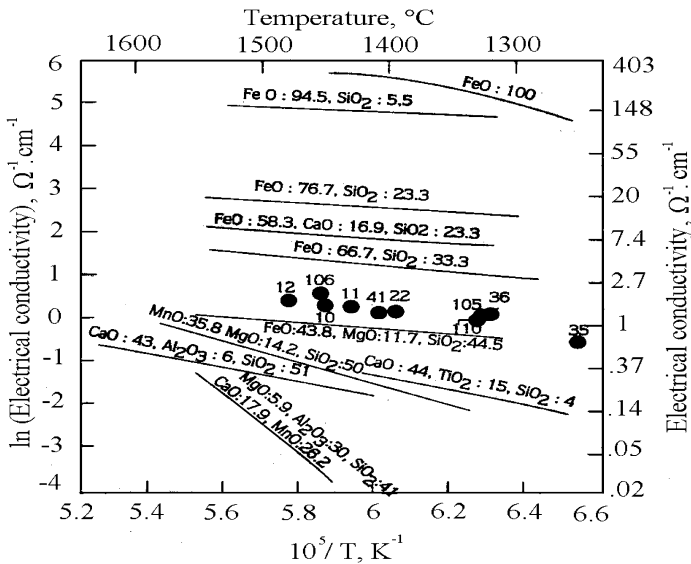


Figure 8. The variation of electrical conductivity of different slags with temperature.

Conclusions

Carbothermal reduction process carried out in a dc arc furnace to recover metals from the ancient Küre copper slag by adding 10% coke resulted in 95% cobalt recovery and 90% copper recovery and 2.38% cobalt concentration and 3.51% copper concentration at 1523-1543 K. An increase in the amount of coke resulted with increase in the reduction recoveries of Co and Cu in open-top design. However the concentrations of Co and Cu in the metallic matte decreases due to excess

reduction of iron. In this process optimum coke amount, which does not cause excess iron reduction, is found as 10% charge weight. At the same coke content, higher Co and Cu recoveries and concentrations were obtained in closed-top furnace.

It is possible to determine reduction rates for cobalt and copper by using Arrhenius equation at different reduction temperatures. Increase in reduction rate by increasing temperature seems to be positive at first. However, low cobalt, copper and sulfur content was observed in metallic matte phase, which obtained by higher reduction rates. This may be due to higher cobalt and copper distribution ratio between metallic matte and slag at lower reduction temperatures. Therefore, to recover cobalt by hydrometallurgical treatment from alloy produced by the carbothermal reduction must be carried out at the lowest temperature in which alloy is melted, in other words lower reduction rates must be preferred in the reduction stage.

Even at low temperature, in a closed-top furnace, the formation of foamy slag was observed because of reduced heat losses which allow reduction gases for longer times in the furnace. The most important effect for increasing the reduction rates is to keep the heat, which is necessary for endothermic reduction reactions, longer within the system by using cover and producing foam. Therefore, when compared to other systems, the time to reach equilibrium is shorter with covered furnaces because high reduction rates can be obtained at lower temperatures.

The disadvantage of high reduction temperature, high reduction rate and open-top design is decreasing sulfur content for the purpose of leaching of metallic matte. Although an increase in reduction temperature decreases sulfur content of the metallic matte, the main reason for sulfur loss in metallic matte is oxidation of metal bath by increased stirring rate caused by increased reduction rate. Since the foam contains CO gas in the closed-top furnace, oxidation of sulfur is prevented and the metallic matte produced in the closed-top furnace will have higher sulfur content which is suitable concentration for further treatment such as leaching.

The electrical resistance values of the molten ancient Küre copper slags were also measured during smelting conditions with or without additives in a DC electric arc furnace. The specific conductivities of the slags were calculated using empirical formula known as "furnace geometric factor". Mean specific conductivity of the slag was determined as $1,85 \Omega^{-1} \cdot \text{cm}^{-1}$ at 1440°C . Addition of coke, Al_2O_3 and CaO resulted to change in specific conductivity between 0.78 and $1.56 \Omega^{-1} \cdot \text{cm}^{-1}$ at temperatures of 1250 to 1470°C . The specific conductivity of the slag tends to increase with increasing temperature.

References

1. R. M. Whyte et al., *Advances in Extractive Metallurgy* (London: IMM, 1977), 57-68.
2. J. W. Matousek, *CIM Bulletin*, 75 (1982) 121-127.
3. W. R. N. Snelgrove, J. C. Taylor, *Canadian Metallurgical Quarterly*, 20 (2) (1981) 231-240.
4. J. M. Floyd, P. J. Mackey, *Extraction Metallurgy* (London: IMM, 1981), 345-371.
5. S. C. Barnett, *Mining Magazine*, 140 (1979) 408-417.
6. H. Hensgen, O. Yücel, W. Wuth, G. Wei, *Trans. of the Institution of Mining and Metallurgy, Sec. C. Mineral Processing and Extractive Metallurgy*, (1989) C 111-116.

7. B. S. Terry, C. L. Harris, *Trans. of the Institution of Mining and Metallurgy, Sec. C. Mineral Processing and Extractive Metallurgy*, 104 (1995) C 81-91.
8. B. S. Terry, C. L. Harris, *Trans. of the Institution of Mining and Metallurgy, Sec. C. Mineral Processing and Extractive Metallurgy*, 104 (1995) C 92-101.
9. O. Addemir, *Erzmetall*, 39 (2) (1984) 74-80.
10. T. J. Rodney, Recovery of Cobalt, *Cobalt News*, 2 (1998) 3-8.
11. O. Yücel, O. Addemir, A. Tekin, S. Nizamoğlu, *Mineral Processing and Extractive Metallurgy Review*, 10 (1992) 99-107.
12. E. Açma, *Canadian Metallurgical Quarterly*, 36 (1) (1997) 25-29.
13. O. Yücel, *Journal of Engineering and Environmental Sciences*, 21 (1997) 335-341.
14. O. Yücel, O. Addemir, A. Tekin, INFACON 6, Proc. of the 6th International Ferroalloys Congress, Cape Town, Johannesburg, SAIMM, 1 (1992) 285-289.
15. K. C. Tasyurek, M. Alkan, O. Yucel, "Development of Nickel Boron Alloys for Brazing Materials", TMS 2013, Proc. of the TMS Annual Meeting, 3-7 March 2013, San Antonio, USA.
16. B. O. Mysen, *Structure and Properties of Silicate Melts, Developments of Geochemistry 4* (Elsevier Science, 1988), 84-91.
17. D. B. Spalding and N. H. Afgan, *Heat and Mass Transfer in Metallurgical Systems* (Washington: Hemisphere Publishing Corp., 1981), 271-280.
18. R. M. Westcott, N. J. Themelis, "An Experimental Slag Resistance Furnace", Proc. of EPD Congress, TMS 1994, 789-801.
19. Q. Jiao, N. J. Themelis, *Metallurgical Trans. B*, 19 B (1988) 133-140.
20. Q. Jiao, N. J. Themelis, *Metallurgical Trans. B*, 22 B (1991) 183-192.
21. R. C. Urquhart et al. "The Smelting of Copper-Nickel Concentrates in an Electric Furnace," *Extractive Metallurgy of Copper*, ed. J. C. Yannopoulos and J. C. Agarwall (Bristol: The Metallurgical Society of AIME, 1964), 275-295.

SLAG REDUCTION KINETICS OF COPPER SLAGS FROM PRIMARY COPPER PRODUCTION

Boyd Davis¹, Trevor Lebel¹, Roberto Parada², Roberto Parra³

¹Kingston Process Metallurgy; 759 Progress Avenue; Kingston, Ontario, K7M 6N6, Canada

²Anglo American Chagres Smelter; Pedro de Valdivia 291; Santiago, Chile

³Metallurgical Department - University of Concepción; Edmundo Larenas 285; Concepción, Chile

Keywords: Copper Slags, Reduction, Slag cleaning

Abstract

In the classical pyrometallurgical route for copper production from sulphide concentrates, the treatment of slags aims to recover copper through the coalescence of copper metal and copper sulphide particles. To assist with this settling process, a reductant is added to the slag to reduce the spinel precipitated phases (magnetite) in order to diminish the viscosity of the slag. While the impact on viscosity is typically the majority of reports in the literature, there is also the potential to reduce Cu_2O and Cu_2S dissolved in the slag. This can result in improved settling and increased recovery of copper.

An experimental study on the reduction kinetic of industrial slags was done to evaluate the intrinsic rate of reduction of those types of copper slags by methane. The results are compared with the available literature on the rate of reduction for these types of reactions, showing that copper reduction is one the order of magnitude higher than the reduction of FeO , which is the key step of the smelting reduction processes developed in the '80s.

Introduction

The recovery of Cu is a key parameter that impacts on the performance, and therefore, on the business of a smelter. Independent of the technologies used for the smelting and converting steps, all smelters treat their slags so that they are discarded with less than 1% Cu. The recovery process, called slag cleaning, is typically based on the coalescence and settling of copper and copper sulfides particles dispersed in the slag. This is achieved by decreasing its viscosity by increasing the bath temperature and reducing the iron spinel solid phases (commonly known as "magnetite") that increase the apparent viscosity of the slag. The process is usually called a reduction process because of the use of reductant as fuel for temperature control and magnetite reduction. Typically, the reduction does not extend to the reduction of copper, and soluble copper (mainly as oxide) is lost in the slag at concentrations at or above 0.5%.

An alternative to slag cleaning as discussed above is the slow cooling/flotation process where there is some settling of copper and copper sulphide particles followed by the slow cooling of the slag in beds or ladles. The slow cooling promotes precipitation of the particles from solution and the slag can then be milled to recover the copper through flotation. The use of slag

cleaning combined with slow cooling and flotation as an alternative to treat copper slags is more costly but leaves Cu in tailings typically about or below 0.4% - a level not possible from slag cleaning alone. Nevertheless, a detailed evaluation must be done considering the energy cost related to grinding, the use of water, and the availability of tailing dumps. At the same time, the retreatment of the Cu concentrate produced in the mill will displace fresh concentrate, which ultimately results in a reduction of the throughput.

The standard pyrometallurgical process for slag treatment, either in electric or tilting furnaces, could be improved by increasing the recovery of a major fraction of the dissolved Cu in the slag. Despite the evidence that most of the copper lost in discard slag is in the form of dissolved copper [1, 2], reduction of the slag to elemental copper has seen limited research, although there are reasons to suggest that this process could lead to practical recovery of copper from slags.

The work presented here is intended to give proof of principle that is possible to reduce the Cu content of the primary Cu slag with extended reduction. This experimental study used methane as the reductant and the evaluation was done by characterization of the reduced slag and on line gas analysis from the reduction experimental process to determine the rate of reduction of a mix of flash smelting and converter slags (Peirce Smith).

Physicochemical Background

Thermodynamic considerations

The Cu dissolved in the slag is as Cu^+ corresponding to Cu_2O and Cu_2S . The concentration of Cu_2O is significantly more than that of Cu_2S and therefore, the discussion centres around Cu_2O . The reduction will proceed by a competition between the dissolved Cu_2O and the iron oxides in the slag: solid spinel phases (represented by Fe_3O_4 , magnetite), Fe_2O_3 and FeO ; the last two ones as part of the liquid slag.

The reduction of magnetite is thermodynamically more favourable than for Cu_2O . There are three stages of the reduction, each overlapping slightly with the others. In the first stage, solid Fe_3O_4 and dissolved Fe_2O_3 are reduced to FeO dissolved in the slag. As the Fe_3O_4 becomes exhausted, the reduction of Cu_2O takes over in the second phase. As the concentration of dissolved copper species drops, FeO in the slag will be reduced to iron in the third phase (with still ongoing Cu_2O reduction). The equilibrium that represents this last condition is written by the following reaction.



The expression that quantifies the limit at which the reduction of Cu_2O is overtaken by the reduction of FeO is the following:

$$\frac{\Delta G_{(1)}^o(T)}{RT} < \ln(a_{\text{Fe}}) + \ln(a_{\text{Cu}_2\text{O}}) - \ln(a_{\text{FeO}}) - 2\ln(a_{\text{Cu}}) \quad (1)$$

From this relation, the diagram in Figure 1 is obtained with $a_{\text{Cu}} = 1$ (the metallic Cu reduced will form a new phase) and by using the Factsage® software and databases for the initial

conditions of a mixture of 80 wt% flash smelting slag and 20% converter slag according to the compositions shown in Table 1. The FeO activity in the slag varies with temperature only slightly (0.42 to 0.44). This diagram can be interpreted by starting at $a(\text{Cu}_2\text{O})$ close to 1 (where the activity of Fe in Cu is 1×10^{-4}) and moving up the line to the left as the Cu_2O is reduced from the slag. For example, for an activity of 0.01 Cu_2O in the slag, the equilibrium Fe in the Cu would be less than 1% (a_{Fe} in Cu = 0.01). This indicates that while the precipitated copper will have some iron contained in it, if the reduction is done with good control it may be possible to avoid significant precipitation of iron in copper, and certainly avoid iron solid particles in the slag. The phase diagram in Figure 2 shows that there is about 10% Fe than can be dissolved in copper before and iron rich copper alloy precipitation.

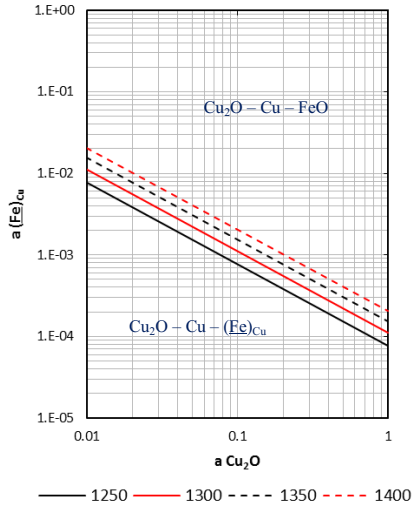


Figure 1. Stability diagram for the reduction of FeO to Fe dissolved in Cu from 1250°C to 1400 °C for a composition of 80% of flash smelting slag and 20% of converter slags.

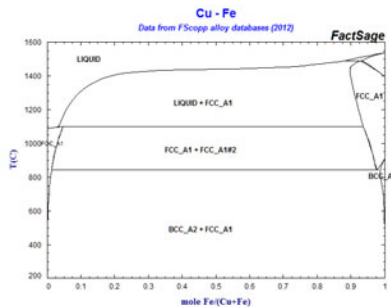


Figure 2. Cu - Fe phase diagram from Factsage® database.

Reduction mechanism

The reduction of oxides from melts has been widely studied in the field of iron production. Figure 3a [3] is a good summary of the measured rate of reduction of FeO with different reductants in different types of slags. In most of the cases, it was shown that the reduction follows a first order reduction with FeO content in the slag. The equivalent information for the reduction of Cu_2O from slags is scarce. A good summary was done in a Masters thesis from the Helsinki University of Technology [4] where a simulation of the co-reduction of Cu^+ and Fe^{+3} is developed from the literature review for slags with 1.5 wt% of Cu_2O and 11% wt% of Fe_2O_3 (Figure 3b) using graphite as reductant. Unfortunately, this simulation does not mention the size of the solid reductant.

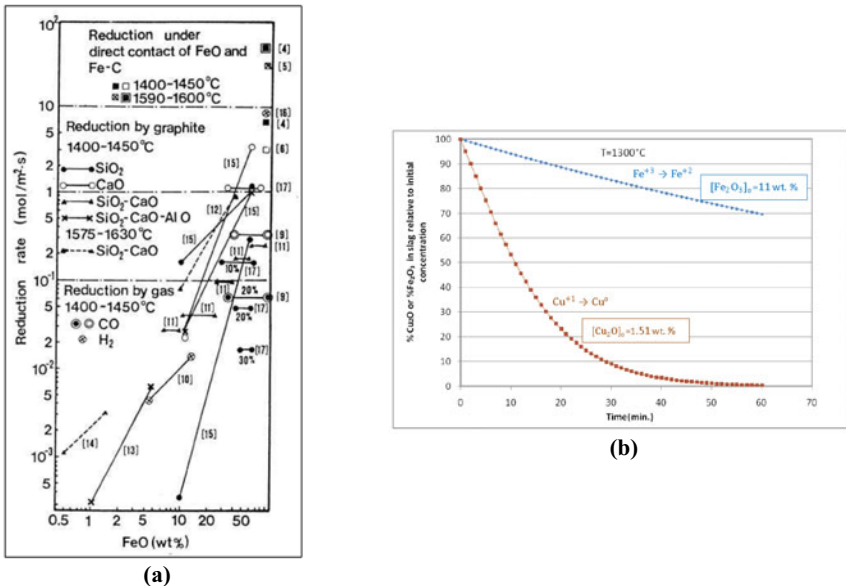


Figure 3. Comparative kinetic information for the reduction of FeO and Cu_2O . (a) Rate of reduction of FeO by different reductants, slags and temperature [3]. (b) Simulation of the kinetic of reduction of Cu_2O to Cu and Fe_2O_3 to FeO [4].

A study using graphite as reductant [5] reports that the reduction of Cu_2O to Cu in a fayalite slag is about 1 to 10 moles $\text{Cu}_2\text{O} \times \text{m}^{-2} \times \text{s}^{-1}$, that is around $1 \text{ ton} \times \text{m}^{-2} \times \text{hr}^{-1}$. This result is almost one order of magnitude higher than the reduction of FeO in similar conditions. It was shown that the rate of reduction is first order with respect to Cu_2O concentration in the bath with a constant of $4 \times 10^{-3} \text{ s}^{-1}$. The same study shows that for CO as reductant and similar slag characteristics the reaction is first order with CO partial pressure with rates of 0.5 moles $\text{O}_2 \times \text{m}^{-2} \times \text{s}^{-1}$. In both cases the rate of reduction is at least one order of magnitude higher than the one for FeO. Those studies were done with slags at high Cu content (more than 10 wt% of Cu at the beginning), so they represent only a reference to compare with the study reported here where the content of Cu is below 2%.

Experimental Study

Characterization of the slags

The slag used from this study was taken from the Chagres Smelter, north of Santiago, Chile. The analysis reported does not consider the sulphides trapped in the slag. The blend used for the experiments was 80% flash smelting slag and 20% converter slag.

Table 1: Characterization of slags.

Constituent	Flash	Converter	Flash normalized	CPS normalized
Fe ₃ O ₄		13.57%		13.42%
Fe ₂ O ₃	8.39%		8.32%	
FeO	49.77%	52.97%	49.38%	51.74%
Cu ₂ O	1.31%	3.31%	1.30%	2.94%
SiO ₂	29.61%	30.90%	29.38%	30.56%
Al ₂ O ₃	6.40%	0.35%	6.35%	0.35%
CaO	1.90%	0.30%	1.89%	0.30%
MgO	1.10%	0.20%	1.09%	0.20%
Na ₂ O	2.20%	0.30%	2.18%	0.30%
ZnO	0.10%	0.20%	0.10%	0.20%
	100.78	101.11	100.00%	100.00%

Methane reduction set up

The set-up for the reduction is shown in Figure 4. The on line IR gas analyzer allows for tracking of the CO_(g) and CO_{2(g)} content in the gas during reduction. The experimental conditions of the inlet gas were such that the reducing gas flow was always far in excess to ensure that there was no control by mass transfer in the gas phase. For each mole of C that reacts (and forms CO_(g) or CO_{2(g)}) two moles of H_{2(g)} are produced, which in turn will reduce the reactive oxides from the slag. The calculation of the H₂O_(g) formation allows an online determination of the total amount of oxygen released from the bath (CO + CO₂ is analysed), and this corresponds to the reduction of Cu₂O and Fe₂O₃ or Fe₃O₄.

The experimental set-up was complemented by a sound recording system to follow the breaking of bubbles on the surface, which gives a count of the number of bubbles over a certain time. The gas flow injected into the system and the off gas composition, allowed for a mass balance to estimate the outflow from the reactor. Knowing, for a period of time, the number of bubbles breaking on the surface and assuming uniform size and shape, the area of bubbles can be calculated, and so on the associated total area, which is assumed for the calculations as the reactive area. Although this approach assumes that the bubble shape and size are uniform during ascent, it allows an estimation of the order of magnitude of interfacial area, (the coalescence of two bubbles of the same size will result in a loss of 1/3 of the area of the initial two bubbles). An example of the signal and its treatment is shown in Figure 5.

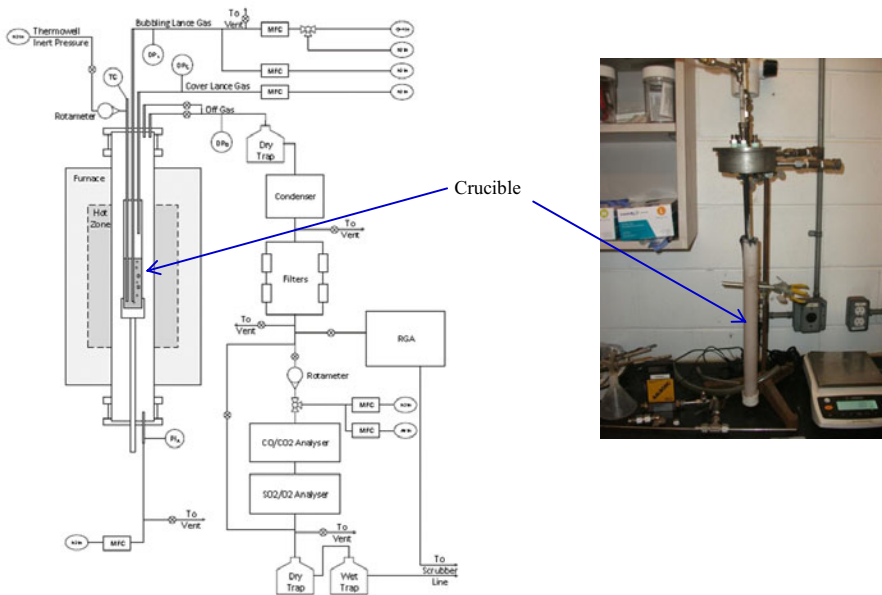


Figure 4. Set-up for reduction study.

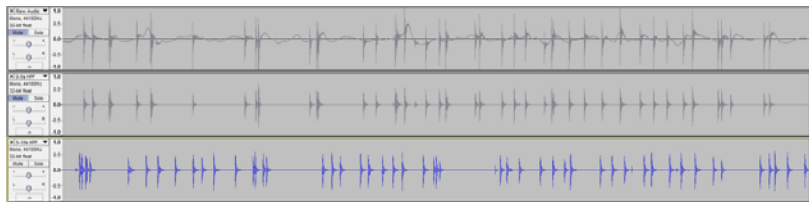


Figure 5. Audio signal of the bubbling produced during the $\text{CH}_4(\text{g})$ reduction allowing the quantification of number of bubbles. Each pulse in the blue line represents a bubble.

Results

Methane reduction

The dynamic mass balance allows for a measurement of the oxygen released from the bath and thus provides for a calculation of the slag composition. In a first part, a parallel reduction process was considered producing FeO from the reduction of precipitated and dissolved Fe^{+3} compounds (solid Fe_3O_4 and dissolved Fe_2O_3) and Cu from Cu_2O . Once those reactions were modelled, some experiments were extended to push the reduction to reduce FeO to Fe. Figure 5 illustrates this type of calculation for experience N°3 (Table 2).

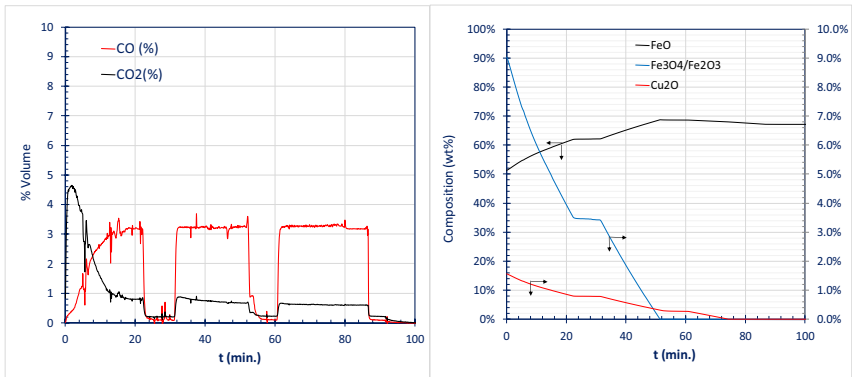


Figure 5. Gas composition of out gases and slag composition estimated from the mass balance using this composition (Test 3 in Table 2).

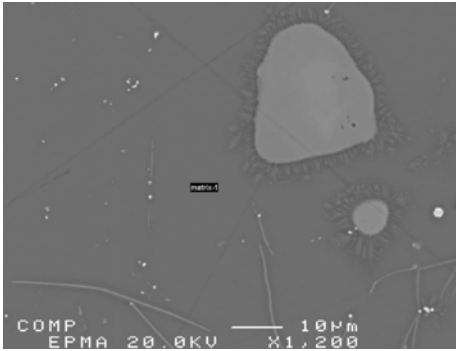
Table 2: Results for rate of reduction.

Test	Slag	CH _{4(g)} (ml/min)	N _{2(g)} (ml/min)*	dnO/dt (mol/min)	Bubbles area in 1 min. (mm ²)	Specific rate of reduction (mol O×m ⁻² ×s ⁻¹)
1	FSF - CPS	120	80	2.00×10 ⁻²	9386	3.55×10 ⁻²
2	FSF - CPS	220	80	1.50×10 ⁻²	11818	2.12×10 ⁻²
3	FSF – CPS + CaO	120	80	1.50×10 ⁻²	9386	2.66×10 ⁻²
4	FSF - CPS	60	60	9.00×10 ⁻³	6724	2.23×10 ⁻²
5	FSF - CPS	60	60	7.00×10 ⁻³	6724	1.74×10 ⁻²
6	FSF - CPS	60	60	7.00×10 ⁻³	6724	1.74×10 ⁻²

(*): N_{2(g)} has used to ensure a neutral atmosphere during the eating and melting of the slag. The lance has also a design where the CH_{4(g)} was injected shrouded by N_{2(g)}.

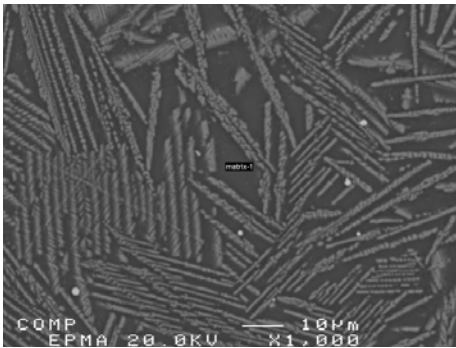
Microstructural characterization of solidified phases after reduction.

The reduced slags were analysed using electron microprobe to establish the microstructural characteristics of the oxides phases in the slag and also the metal produced. It can be concluded that the reduction of the slag effectively permits a virtually complete reduction of Cu₂O. Likewise, it can be seen that as the Cu₂O becomes exhausted, the metal is enriched with Fe at a non-negligible level. The following figures show those results.



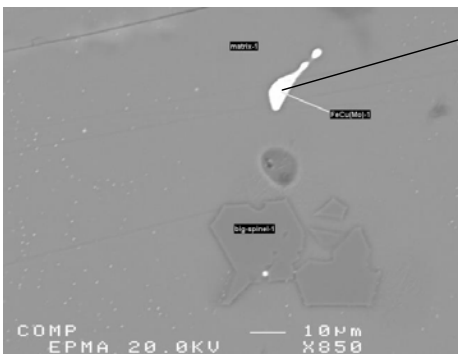
Na₂O	0.135	0.187	0.193
MgO	0.206	0.148	0.211
K₂O	0.367	0.375	0.390
Cu₂O	0.183	0.213	0.200
SiO₂	37.66	37.60	37.58
Al₂O₃	17.49	17.35	17.59
CaO	0.225	0.241	0.249
FeO	43.61	43.90	44.01
Total	100.08	100.20	100.60

Figure 6. Matrix composition for test N° 5 (Table 2).



Na₂O	1.427
MgO	0.175
K₂O	1.354
Cu₂O	0.081
SiO₂	52.28
Al₂O₃	20.59
CaO	3.087
FeO	20.06
Total	99.63

Figure 7. Matrix composition for test N° 3 (Table 2).



S	Cu	Fe	Total
0.015	8.330	91.04	99.53
0.000	8.860	89.90	99.66
0.034	8.980	89.80	100.37

Na₂O	1.002	1.002	0.977
MgO	0.881	0.873	0.931
K₂O	1.236	1.210	1.260
Cu₂O	0.079	0.110	0.123
SiO₂	37.04	37.15	37.16
Al₂O₃	18.69	18.74	18.93
CaO	1.610	1.605	1.628
FeO	38.87	38.79	38.54
Total	100.21	100.37	100.35

Figure 8. Matrix and metal composition for extended reduction, test N° 2 (Table 2).

Conclusion

The reduction rates measured in this study were in the order of $0.02 \text{ mol O} \times \text{m}^{-2} \times \text{s}^{-1}$, higher than those reported for FeO. This result is aligned with the comparative data for reduction rates between Cu_2O and FeO reported in the literature. As for gaseous reduction of FeO (H_2 and CO), the rate of reduction of Cu_2O with CH_4 is comparatively low compared to the one obtained with graphite: 0.02 v/s 1 to $10 \text{ mol O} \times \text{m}^{-2} \times \text{s}^{-1}$.

In the case of slag with higher content of Cu_2O , the rate of reduction with CO appears to be far superior to that obtained with CH_4 (0.5 v/s $0.02 \text{ mol O} \times \text{m}^{-2} \times \text{s}^{-1}$), however it is also reported that the rate of reduction is 1st order with Cu_2O concentration in the slag, (possible control by mass transfer in the slag), which explains very well that having slag with as low contents of Cu as used in this study the rate must be lower.

The process conceptualized from this experimental study should consider that the use of the reductant in a first stage is determined by a co-reduction of Cu_2O and Fe_2O_3 / Fe_3O_4 . The reduction can be extended to achieve a complete reduction of Cu_2O , leaving a slag with Cu_2O as low of 0.15 wt%.

In the perspective of a complete reduction, beyond the Cu_2O limit, one can conclude that there is no intrinsic physical chemistry limitation to produce pig iron and copper. In this case the remaining oxides of the slag could be fluxes in a similar way that the operation of a blast furnace does, obtaining a co-product available to be used as component of Portland cement. It should be noted that the operating temperature must be controlled at a higher level that guarantees to be in 100% liquid area of the Fe-Cu phase diagram, to prevent the formation of metallic Fe solid accretions.

References

1. The Physical Chemistry of Copper Smelting Slags and Copper losses at Paipote Smelter. Part. II: Sampling and Mineralogical characterization, N. Cardona, P. Coursol, J.C. Vargas and R. Parra. Can. Met. Quart., Vol 50, N°4, December 2011, pp 330 – 340.
2. Nubia Cardona, Aporta al estudio fisicoquímico de las pérdidas de Cobre en escorias de procesos de producción primaria de cobre. Doctorate Thesis, Univesity of Concepción, August 2011.
3. Masanori Tokuda & Saburo Kobayashi, Process Technology Conference Proceedings, ISIJ, 1988, pp 3-11.
4. Fiseha Tesfaye Firdu, Kinetics of Copper Reduction from Molten Slags, Master of Science Engineering Thesis, Helsinki University of Technology, August 2009.
5. “Direct Reduction of Copper-Iron-Silicon Melts”, R. Parra, M Allibert & I Wilkomirsky, 4th Internation Conference Copper 99, TMS, Phoenix, Arizona, USA, October 10-13, 1999.

FLUXING STRATEGIES FOR THE DIRECT TO BLISTER SMELTING OF HIGH SILICA AND LOW IRON COPPER CONCENTRATES

Michael Somerville¹, Chunlin Chen¹, Gerardo R. F. Alvear F.², Stanko Nikolic³

¹CSIRO Mineral Resources; Private Bag 10, Clayton South, Vic, 3169, Australia

²Glencore Technology; Level 10, 160 Ann Street, Brisbane, QLD, 4000, Australia

³Formerly Glencore Technology, presently Tenova Pyromet, Level 10, 140 Ann Street, Brisbane, QLD, 4000, Australia

Keywords: single-stage copper making, concentrates, blister copper, TSL smelting, MPE

ABSTRACT

Copper concentrates which have high silica but low iron contents are difficult to smelt using conventional two stage smelting processes. Direct to blister smelting is possible using either iron oxide fluxes to produce a fayalite type slag or silica and lime fluxes to produce a lime-silica-iron oxide slag. The benefits of lime and silica fluxing option, have been quantified using both thermodynamic modelling and a campaign of pilot scale TSL (Sirosmelt) direct to blister smelting.

Direct to blister smelting simulations were made with the MPE thermodynamic package. The simulation results predicted that the copper losses to slag would be 7.9, 20.4 and 7.0% of input copper for the un-fluxed, iron oxide flux and the lime and silica fluxing scenario respectively. The slag make per unit of copper was 1.4 for the un-fluxed system, 2.4 for the iron oxide flux and 1.9 for the lime and silica fluxed systems.

A series of pilot scale direct to blister smelting tests were conducted on the lime and silica fluxing system. The copper content of slag varied between 7 and 10% and increased slightly with excess oxygen in the system (smelting ratio). The slag make per unit of input copper varied between 1.5 and 2.4 which was in reasonable agreement with the calculated predictions. Copper losses to slag were mostly between 22 and 26% which is higher than predicted, due to the presence of entrained copper prills in the slag

INTRODUCTION

A new type of copper concentrate, containing low levels of iron and high silica content, is expected to come into production in the next 20 years [1]. These types of concentrates are not suitable for conventional matte smelting or single stage direct-to-blister smelting using a fayalite based slag, due to a low iron or pyrite content. Iron oxide could be used to flux the high silica containing concentrates but will result in high rates of slag production and increased copper losses to the slag. An alternative fluxing strategy using lime with small amounts of silica has been proposed.

There are three copper smelters operations that operate direct to blister processes [2]. All three use flash furnaces and include: the Glowgow copper smelter in Poland, the Olympic Dam smelter in Australia and the Chingola smelter in Zambia. The direct to blister route is generally restricted to concentrates which have chalcocite (Cu_2S) and bornite (Cu_5FeS_4) as primary minerals and relatively small amounts of pyrite (FeS_2), chalcopyrite (CuFeS_2) and silica (SiO_2). Subsequently the concentrates have low iron and relatively high copper contents. Table 1 shows the composition of concentrates and Table 2 shows the composition of the slag used for the three operations.

Table 1: Composition of concentrates used in direct to blister copper smelting processes

Operation	Concentrate composition (wt %)						
	Cu	Fe	S	SiO_2	Al_2O_3	CaO	MgO
Olympic Dam	44	20	25	5	-	-	-
Glogow	28	2.7	9.3	20	5.2	7.3	3.9
Chingola	39	8	19	18	10	2	2

Table 2: Composition of slag used in direct to blister copper smelting operations [2]

	Slag composition (wt %)						
	Cu	Fe	SiO_2	CaO	MgO	Al_2O_3	Fe/ SiO_2
Olympic Dam	25	33	18	0	0	3.5	1.83
Glogow	14.4	6	31	14	6	9	0.19
Chingola	19.5	22.5	25.7	5.9	2.5	3.9	0.88

The Glogow smelter operates without additional fluxing, [2-4]. Although the slag make is high at about 2.5 t/t of copper, the total copper losses are controlled to about 28% of input copper. The Olympic Dam smelter uses silica as a flux and the resulting slag can be described by the Cu_2O - FeO_x - SiO_2 system with a small amount of alumina [2, 4]. Slag production is about 1.4 t/t of copper and copper losses are 34% of input copper. The Chingola concentrate contains low levels of iron and sulphur but high amounts of silica compared to conventional concentrates [2, 5]. A lime flux is used which helps dissolve the high alumina and magnesia content of the concentrate and also decreases the dissolved copper content of the slag. Slag production is between 1.4 and 1.6 t/t of copper. Copper losses are between 28 and 43% of input copper.

Taskinen [6-7] explained the benefits of adding a small amount of lime to an iron silicate slag system in direct to blister smelting. Pure iron silicate slag systems are not thermodynamically stable in direct to blister smelting conditions and additives are required to increase the solubility of magnetite and olivine and to reduce the solubility of copper. Lime additions of 5-15% to the iron silicate system can expand the molten slag range to include the stability range of blister copper containing less than 1 % sulphur. This modified slag composition can increase the solubility of magnesia and alumina from gangue minerals in the concentrate.

Most direct to blister copper smelting slags contain both silica and lime components, the exception is Olympic Dam where a slag from the SiO_2 - FeO_x - Cu_2O system is used. The present work also advocates the use of slags in the silica-iron oxide-lime system to process concentrates which have high silica but low iron oxide contents. The benefits include lower dissolved copper content, less copper losses in slag and low viscosity slags.

THERMODYNAMIC MODELLING

In the design of fluxing strategies for single stage smelting of high silica low iron copper concentrates to blister copper, the thermodynamic properties of copper solubility, solid phase stability and viscosity need to be considered. In particular consideration should be given to minimizing slag volume to avoid additional fuel and minimizing copper losses to slag.

Figure 1 shows a calculated pseudo-ternary phase diagram of the $\text{SiO}_2\text{-CaO-FeO}_x + (\text{Al}_2\text{O}_3+\text{MgO}+\text{Cu}_2\text{O})$ system. This diagram was calculated using the MPE thermodynamic package [8]. A liquid region is predicted at 1200°C which is approximately triangular in shape. The liquid region extends close to the $\text{SiO}_2\text{-FeO}_x$ border at about 35% SiO_2 . The center region of the diagram at about 45% SiO_2 and 15% CaO is in the middle of the liquid region at 1200°C .

When smelting a high silica concentrate containing chalcopyrite (CuFeS_2) and bornite (Cu_5FeS_4), the molten concentrates, with no fluxing will produce a slag with a composition close to 42 % SiO_2 and 1.5 % CaO which is marked by 'A' in Figure 1. When fluxing with iron oxide (Fe_2O_3) the slag composition moves to the composition marked 'B' in Figure 1. The alternative fluxing with limestone and silica will see the slag composition shift from the initial position to point 'C'.

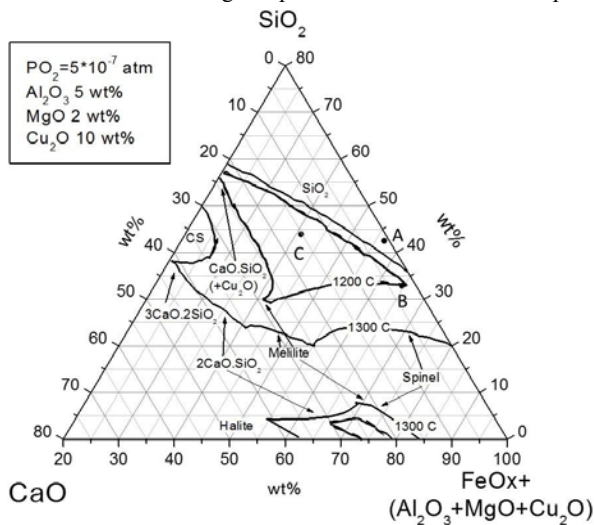


Figure 1: Pseudo ternary phase diagram of the $\text{SiO}_2\text{-CaO-FeO}_x + (\text{Al}_2\text{O}_3+\text{MgO}+\text{Cu}_2\text{O})$ system showing the un-fluxed slag composition and the two fluxing alternatives.

The results of the MPE calculations for smelting 100 kg/h of the concentrates to these three areas are shown in Tables 3 and 4 which contain the composition of the slags for each fluxing scenario and the mass of each stream, respectively.

Table 3 shows that the un-fluxed system will produce a silica saturated slag that will have a liquidus temperature and viscosity too high for practical use. The first fluxing option will produce an operable slag with a liquidus temperature close to 1200°C and a copper content of 9.7% (as Cu₂O). The viscosity of slag from the first fluxing scenario was calculated from MPE and found to be 0.14 Pa.S at 1250°C. In comparison the lime and silica fluxing option produced a slag with a calculated viscosity of 1.6 Pa.S at 1250°C with about 4.2 % dissolved copper (as Cu₂O). The higher viscosity for the second fluxing option is due to the higher silica content of the slag.

Table 4 shows that when comparing the mass of slag and blister copper produced from the smelting of 100 kg of concentrates using lime and silica fluxing has a lower slag make and greater blister copper mass. In this case the lower copper content of slag has restricted the copper losses and hence the amount of blister copper is increased.

Table 3: Composition and viscosity of slags produced in direct to blister copper smelting

Fluxing system	Slag composition (wt %)							Viscosity (Pa.S)
	SiO ₂	CaO	FeO	Fe ₂ O ₃	Cu ₂ O	MgO	Al ₂ O ₃	
Un-fluxed	39.6	2.0	26.5	10.1	6.6	2.0	13.1	SiO ₂ sat.
Fe ₂ O ₃	33.0	1.2	32.8	14.6	9.7	1.2	7.5	0.14
CaCO ₃ and SiO ₂	43.6	15.0	18.1	8.17	4.2	1.5	9.4	1.61

Table 4: Masses of materials used in direct to blister copper smelting with different fluxing.

Fluxing system	Input streams (kg)				Output streams (kg)		
	Cons	Fe ₂ O ₃ flux	SiO ₂ flux	CaCO ₃ flux	Slag	Blister copper	Gas (m ³)
Un-fluxed	100	0	0	0	45.4	32.0	51.6
Fe ₂ O ₃	100	22.6	0	0	79.2	27.6	50.0
CaCO ₃ and SiO ₂	100	0	1.7	15.4	63.4	32.4	55.0

PILOT SCALE TESTWORK

The operation of the mixed silica and lime fluxing strategy was tested in a series of pilot scale smelting tests. Solid materials used in the direct-to-blister smelting included: high silica -low iron copper concentrates (concentrate-1), a more conventional copper concentrate (concentrate-2) quartz and limestone flux. The composition of these materials is shown in Table 5.

The Siros melt pilot plant at CSIRO laboratories at Clayton Australia was used for the smelting testwork. The plant consists of four main components and include: a feed delivery system, a smelting vessel and lance control equipment, a gas and fume removal and treatment system and a process control and data logging system. Together these components form the Siros melt pilot plant which is illustrated schematically in Figure 2. Sulphide materials were rolled into pellets of 5-10 cm. These pellets and fluxes were fed to the furnace via a belt and vibratory feeder. Heat was generated by the submerged combustion of natural gas with oxygen enriched gases which was injected into the slag bath through a stainless steel lance.

Table 5: Composition of materials used in the smelting experiments

Material	Composition (Wt %)								
	Fe	Cu	S	SiO ₂	CaO	MgO	Al ₂ O ₃	Na ₂ O	K ₂ O
Concentrates -1	11.2	33.6	17.4	20.4	0.78	0.85	5.46	0.88	1.74
Concentrates -2	25	20.8	22.6	20.2	1.92	2.08	3.78	0.054	0.18
Limestone	1.17	0.02	0.01	6.06	48.4	0.43	1.55	0.15	0.141
Quartz	0	0	0	99.9	<0.01	0.03	0.02	0.03	<0.005
Matte	4.78	68.5	20.0	1.41	0.18	0.10	0.38	0.14	0.02

During smelting samples of slag and blister copper were collected at regular intervals using a steel dip rod and a steel cup on a long steel rod respectively. The smelting progress was monitored through the analysis of these slag and copper samples.

Seven direct-to-blister pilot scale smelting tests were conducted in the smelting campaign. All the tests involved the continuous feeding of concentrates, fluxes to a molten slag bath while injecting gases through a Siros melt lance. The target temperature for the smelting tests was 1250°C.

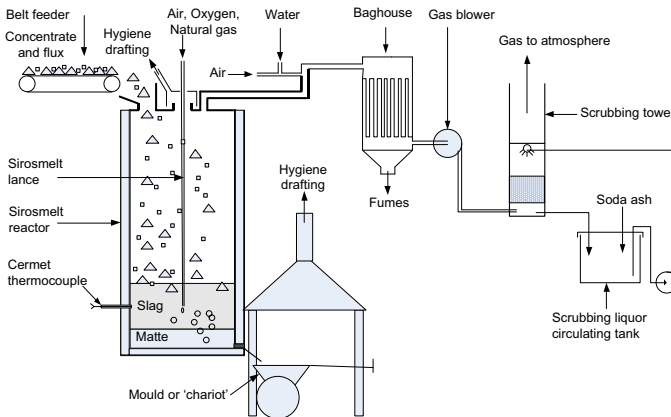


Figure 2: Schematic diagram of the Siros melt plant and ancillary equipment

STEADY STATE

The aim of the pilot plant smelting tests was to reach a steady state while producing blister copper containing about 1% sulphur. The approach to steady state can be illustrated using the

slag composition for Test 3 (Figure 3). The initial slag samples have slightly elevated copper levels at about 11 and 10% respectively. After 120 minutes the copper levels remain fairly constant at an average of 8.5%. The CaO/SiO₂ and Fe/SiO₂ ratios remained constant through the three hour test. The steady state silica, lime and iron content of the slag was 39, 17 and 16% respectively. The slag was very fluid at the operating temperature of 1250°C. A stable foam was observed during the tests did not cause any operational difficulties.

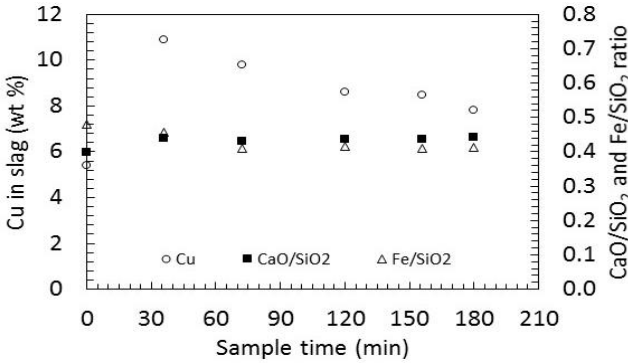


Figure 3: Slag composition during direct to blister smelting Test 3

SMELTING RATIO AND SMELTING CONDITIONS

The key operating parameter in oxidative smelting systems is the oxygen to concentrate ratio. This is expressed as the amount of oxygen (Nm³/h) which is available to smelt a unit of concentrates (kg/h), and is termed the “smelting ratio”. The amount of oxygen available for smelting was calculated using equation 1.

$$\text{Smelting oxygen} = \text{oxygen flow} + 0.21 \times \text{air flow} - 2.04 \times \text{natural gas flow} \quad [1]$$

For each Sirosmelt test the gas flows (oxygen, air and natural gas) were logged and the total amount of each gas injected to the slag bath was calculated and are shown in Table 6, along with the calculated smelting ratio. High smelting ratios indicate more oxidising conditions and would be consistent with higher copper contents in slag and lower sulphur contents of blister copper.

Table 6: The amount of injected gases, smelting oxygen and smelting ratio for the Sirosmelt tests

Test No	Total natural gas (Nm ³)	Total air (Nm ³)	Total oxygen (Nm ³)	Smelting oxygen (Nm ³)	Total feed (kg)	Smelting ratio (Nm ³ /kg)
1	19.77	229.6	4.28	12.18	80	0.152
2	21.77	176.7	22.78	15.48	95	0.163
3	29.05	204.5	41.15	24.84	150	0.166
4	26.01	155.6	42.09	21.72	130	0.167

5	23.12	177.2	46.58	24.82 ¹	140	0.177
6	19.17	148.1	31.53	23.53	130	0.181
7	20.87	157.8	32.92	23.48	130	0.181

Figure 4 shows a graph of the copper content of slag plotted against the smelting ratio for the Siros melt tests. The general trend is a slight increase in the copper content of slag as the smelting ratio increases. The copper content of slags are generally higher than calculated (3.7%). This difference could be explained by entrained copper prills in the direct-to-blister slags.

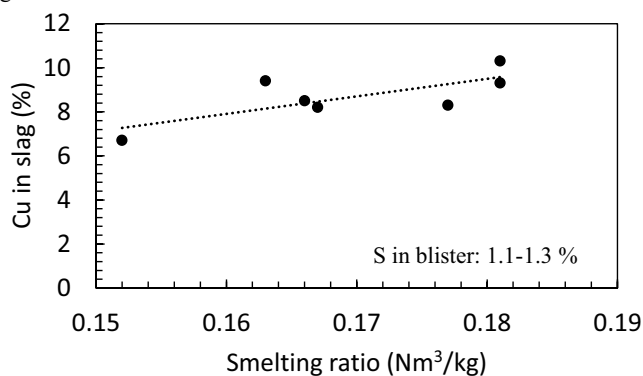


Figure 4: Graph of copper content of tapped slag plotted against the smelting ratio

DEPARTMENT OF COPPER

During copper smelting, copper can deport to the slag or blister phases. Copper department to the fume has not been considered. Table 7 shows the input and output copper flows for the smelting tests. The amount of copper in the output streams (slag and blister copper) was calculated from the steady state composition of the slag and copper and the recovered mass of the streams.

Table 7 shows that the copper losses to slag varied between 22 and 42 as a percentage of input copper. Most of the results were between 22 and 26 %. Outliers occurred in Tests 2 and 7. In Test 7 the amount of copper in slag was much higher than the other tests. This was because at the end of the last test the furnace was thoroughly cleaned out with all the slag and accretions removed. This increased the amount of slag recovered and hence the amount of copper in the slag. In Test 2 the amount of blister copper recovered was much lower than in the other test. Overall the copper lost to slag is higher than predicted in the thermodynamic modelling. The net amount of slag produced per unit of copper contained in concentrates varied between 1.5 and 2.4 with an average value of 2.1. This is close to the expected ratio predicted from the smelting simulations of 1.9.

¹ In Test 5, 8.4 kg of crushed coal was added which consumed 11.8 m³ of oxygen. This oxygen was removed from the calculated smelting oxygen (36.62 Nm³).

Table 7: Copper balance during direct to blister copper smelting

Test No.	Cu in starting slag + copper (kg)	Cu in cons (kg)	Total Cu in (kg)	Cu in slag (kg)	Cu in blister (kg)	Total Cu out (kg)	Cu in slag (%)
1	2.4	26.9	29.3	6.8	21.6	27.8	23
2	3.4	31.9	35.3	17.2	14.8	32.0	42
3	3.0	50.4	53.4	13.6	29.4	43.0	25
4	12.2	43.7	55.9	13.3	29.5	42.8	24
5	12.2	47.0	59.2	15.4	38.2	53.6	26
6	10.0	53.0	63.0	13.7	32.2	45.9	22
7	10.9	64.0	74.9	29.1	30.7	59.8	39

CONCLUSIONS

Copper concentrates containing high amounts of silica and relatively small amounts of iron can be smelted directly to blister copper using iron oxide to form a traditional fayalite (FeO-30% SiO₂-10% Cu₂O) type slag or fluxed with silica and lime to form a 15 % Ca-44% SiO₂-FeO_x-4.2% Cu₂O slag. The benefits of the lime and silica fluxing include: lower dissolved copper content, less slag make and lower copper losses to slag. These benefits have been demonstrated in a thermodynamic modelling exercise using the MPE thermodynamic package and through a pilot scale direct to blister smelting campaign using the TSL Sirosmelt reactor at CSIRO in Clayton, Australia.

ACKNOWLEDGEMENTS

The authors wish to acknowledge the efforts of Jason Donnelly, Dylan Marley and Tom Austin from CSIRO and Alistair Burrows from Glencore Technology in the operation of the Sirosmelt pilot plant during the smelting work described in this paper. The support of the CSIRO Mineral Resources analytical laboratory is the analysis of slag and copper samples generated in the project are warmly acknowledged. Financial support for the project was supplied by Xstrata Technology, now Glencore Technology, and CSIRO Minerals Down Under Flagship.

REFERENCES

1. A Burrows, Private communication, Glencore Technology, 2015
2. M Schlesinger, et al., *Extractive metallurgy of copper – Chapter 10*, Elsevier, 2011, 179-189.
3. Z Smieszek, S Sedzik, W Grabowski, S Musial and S Sobierajski, “Glowgow 2 copper smelter- seven years of operational experience”, (Paper presented at *Extraction Metallurgy '85 Conference*, London UK, IMM, 9-12 September 1985), 1049-1056.
4. P Taskinen and I Kojo, “Fluxing options in the direct-to-blister copper smelting,” (Paper presented at Molten 2009 Conference, Santiago Chile, 2009), 1139-151.

5. H M Chikashi, "Influence of slag composition on reduction control and operations of the slag-cleaning furnace at KCM Zambia", (Paper presented at Southern Africa Pyrometallurgy 2011, Johannesburg SA, SAIMM, 6-9 March 2011), 185-198.
6. P Taskinen, "Direct-to blister smelting of copper concentrates: The fluxing chemistry," (Paper present at the Seetharaman seminar –Materials processing towards properties, MSE Department of ITM School of KTH, Sigtuna Sweden, 14-15 June 2010), 110-120
7. P Taskinen, "Direct-to-blister smelting of copper concentrates: the slag fluxing chemistry," *Mineral Processing and Extractive Metallurgy*, 120 (4), (2011), 240-246.
8. L Zhang, S Jahanshahi, S Sun, C Chen, B Biourke, S Wright and M Somerville, "CSIRO's multiphase reaction models and their industrial applications", *JOM*, 54, (2002), 51-56.

BEHAVIOR OF SELENIUM IN COPPER SMELTING SLAG

Bhavin Desai^{a,*}, Vilas Tathavadkar^a, Somnath Basu^b, Kaushik Vakil³

Email: bhavin.desai@adityabirla.com

^aAditya Birla Science and Technology Company Limited, Navi Mumbai, India

^bIndian Institute of Technology, Powai, Mumbai, India

³Hindalco Birla Copper, Dahej, Gujarat, India

Keywords: selenium dioxide, entrapped matte, slag

Abstract

Selenium is a value added by-product of copper process. The lower recovery of selenium from the copper process is attributed to the high loss of selenium in the discarded slag. Knowledge of selenium behavior in slag is very important in the control of the selenium loss. The samples of slag and matte were collected from the smelter exit before their separation. The experiments involving slag-matte separation were performed at 1250° C for 4 hours of soaking time under inert atmosphere in a vertical tubular furnace with the addition of selenium dioxide in different proportions. The association of selenium in various phases of the slag was determined using electron microscopic analysis. The selenium was found to be replacing the sulfur of the entrapped matte phase in slag. With an increase in selenium content, the size of entrapped matte phase decreased, thus causing high loss of copper in slag.

1. INTRODUCTION

Copper concentrates, the primary source of commercial selenium, are well known to be sulfide concentrates. Copper concentrates usually contain a number of elements such as selenium (Se), Tellurium (Te), Gold (Au), Silver (Ag), Platinum (Pt) etc. The recovery of these elements in copper smelting processes is often a key to the overall economics of the process. The selenium concentration in copper concentrates is low enough, less than 500 ppm. This selenium is a valuable by-product in the smelting of copper concentrates. Selenium is recovered as a by-product during processing of electrolytic copper refinery slimes for gold and silver. The low recovery of selenium in copper process is attributed to the selenium loss in discard smelting slag after the slag-matte separation. Since the distribution behavior of selenium between matte and slag during the pyro-metallurgical treatments of copper sulfide concentrates affects the recovery

of selenium and the revenues gained from by-products, the investigation of selenium dissolution mechanism in slag and matte system is necessary to achieve the desirable control of selenium.

A number of investigations have been carried out for the distribution of selenium between slag and metallic copper under converting conditions [1-6]. However, only few investigations reported the distribution of selenium between matte and slag system. Elizabeth et. al. [7] considered iron silicate slag and matte of the matte grade 40 to 60% at 1250 °C, which is irrelevant at present for the matte grade above 60%. Also, the matte becomes ionic above 60% of matte grade. The distribution of Se is therefore expected to be different at higher matte grades. Choi et. al. [8] and Sinha et. al. [9] considered iron silicate slag and nickel-copper-iron matte at 1250 °C and proposed the reduction of FeO in slag by gaseous Se to form FeSe as the mechanism of selenium dissolution in matte. Under oxidizing conditions during copper smelting, the reduction of FeO by Se is unlikely, as the former is thermodynamically more stable. Besides, there is no sufficient information available to substantiate the hypothesis of Se dissolution in slag as FeSe. Moreover, the data of the sulfide matte system, which is the interest of present investigation, were not mentioned. Furthermore, there is a scarcity of published thermodynamic data to study the selenium distribution between matte & slag. In the present work, the distribution of selenium between slag and matte has been studied and the mechanism of selenium dissolution in slag and matte has been established.

2. EXPERIMENTAL

The representative sample, which is the mixture of molten slag and matte, from smelter outlet (base sample), was collected for investigation. In the process, the molten slag-matte mixture is separated owing to their density difference in the Settler. The slag from the settler is discarded off, whereas the matte is further treated in the convertor. The molten mixture of matte and slag sample collected from smelter outlet was allowed to cool in air at the collection site. The sample was then crushed to a uniform size < 75 µm. The pellets (height ~ 8 mm & dia ~ 25 mm) of the samples were prepared using molasses at 35 KN force. Pellets were placed inside the alumina crucible (height ~ 40 mm & inner diameter ~ 28 mm). The crucible was placed over the base of the furnace as shown in Figure 1. The entire assembly was inserted inside the alumina reaction tube of a vertical tube furnace using movable tube support. The furnace was flushed with nitrogen gas before the experiment. Nitrogen flow ~ 3 lpm was maintained during the experiment. The sample was heated at 1250 °C. The crucible was kept into the hot zone of the furnace, a region 5-cm long over which the temperature variation was ± 2 K. The temperature was measured by R-type (Pt/Pt-13% Rh) thermocouples. One thermocouple was located just above the crucible and other at the bottom. After the heating, the sample was cooled slowly by nitrogen inside the furnace. The slag and matte phases were then removed from the crucible and weighed.

Slag being oxides of various elements, the selenium dioxide in powder form (>99.9% purity, 100 mesh size) was added to the 30 gm of the base sample. The 5 sets of samples (pellets) were prepared with addition of selenium dioxide powder to the sample i.e. 0%, 0.1%, 0.5%, 1.0%, and 5.0% by weight. '0%' indicates there is no addition of selenium in the sample. However, the original sample contained ~500 ppm of selenium. All the experiments were conducted in alumina crucible at 1250 °C under nitrogen atmosphere and at four hours of soaking time. The

sample were cooled under nitrogen atmosphere. After the experiments, the samples were weighed and separated by physical means before finely ground for chemical analysis. Samples were analyzed for selenium by inductively coupled plasma (ICP) techniques following acid digestion. The bulk compositions of slag and matte samples were determined by titration and gravimetric methods.

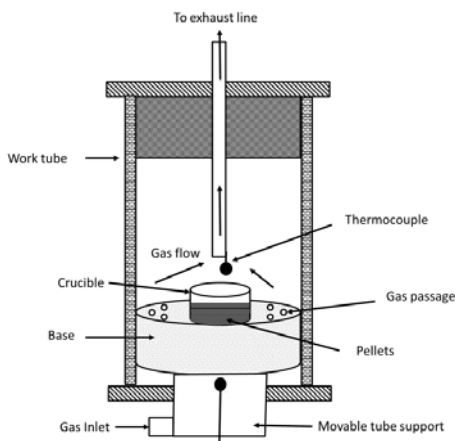


Figure 1. Schematic diagram of experimental set up (vertical tube furnace)

3. RESULTS & DISCUSSION

3.1 Phase separation

The quantity of slag and matte separated after the experiments is shown in Figure 2. The slag to matte ratio reduces marginally up to 1.0% SeO_2 addition and significantly at 5.0% SeO_2 addition. This can be explained from the quantity of matte separated. The quantity matte separated increases steadily with an addition of SeO_2 . Figure 3 shows the variation in selenium content of slag and matte with selenium dioxide addition. The selenium content of slag and matte increased with selenium dioxide addition. However, the selenium deportation to matte is much higher than to slag at 1250 °C. It shows higher affinity of selenium for matte. This could be the reason for the increase in matte quantity with selenium addition. The chemical analysis of matte is shown in Figure 4. The copper, iron and sulfur content (in wt. %) of matte decreased with SeO_2 addition. The chemical analysis of matte thus confirms the association of selenium with matte.

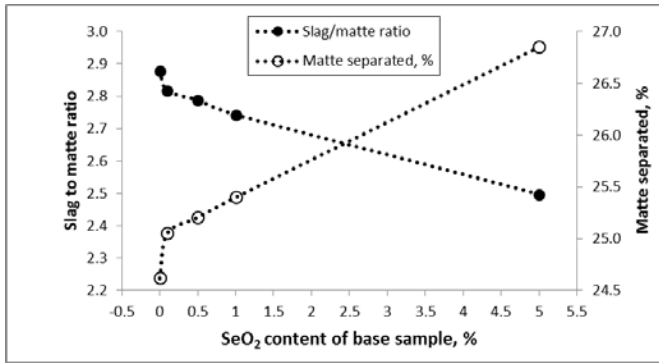


Figure 2. Variation of slag to matte ratio and matte quantity with selenium dioxide addition at 1250 °C.

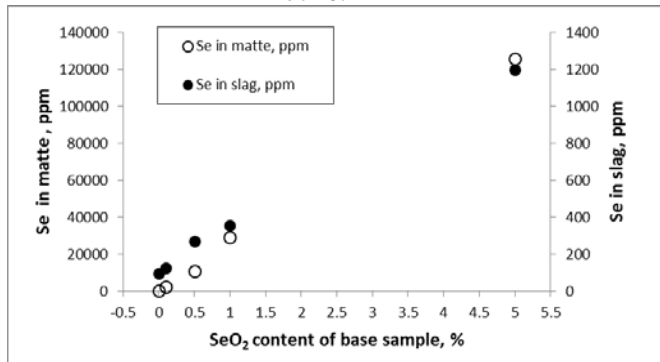


Figure 3. Variation of selenium content of slag and matte with selenium dioxide addition at 1250 °C.

3.2 Se dissolution in slag and matte

X-ray diffraction (XRD- Bruker D8 Advance) analysis was carried out at 2- θ from 5 to 80 with CuK α (1.54 \AA) radiation. The XRD analysis of matte samples is shown in Figure 6. Bornite (Cu₅FeS₄) was identified as the major phase of matte, followed by chalcocite (Cu₂S), magnetite (Fe₃O₄), metallic copper (Cu) etc. The selenium Cu₂Se (copper selenide) was found in matte phase at higher content of selenium. Cu₂Se phase could not be detected by X-ray diffraction in matte containing selenium less than 5%. The main peak of bornite phase is at 2 θ =47°. But with selenium content in matte at & above 2.2%, the shift in the pick of bornite phase observed to the left side. This shifted pick is expected to be Cu₅FeS_{4-x}Se_x. The intensity of the chalcocite pick at

$2\theta=33^\circ$ decreases with an increase in selenium content in matte. The selenium is believed to have replaced the sulfur of matte. The slag was found to contain mainly in fayalite phase.

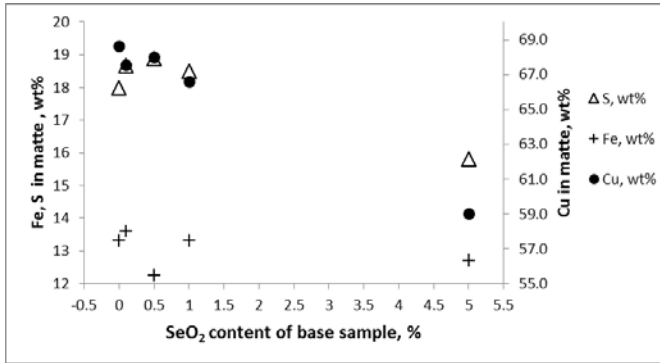


Figure 4. Variation of copper, iron and sulfur (wt. %) in matte with selenium dioxide addition at 1250 °C.

The slag and matte samples were analyzed by scanning electron microscope (Hitachi, S-4800, type-1). Microstructures of the nitrogen cooled slags and matte and compositions of the phases present in the samples were determined using an energy dispersive spectroscopy (EDS/EDX) (Horiba Software used: Enca). An accelerating voltage of 20 KV and a probe current of 10 nA were used. The average accuracy of the measurements was estimated to be within 1 weight percent.

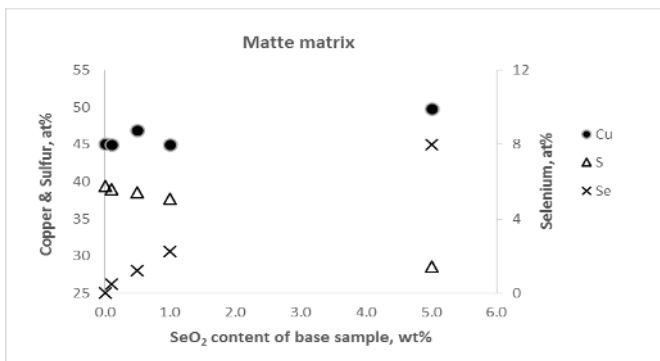


Figure 5. Variation of copper, sulfur and selenium (at. %) of EDX area scans on matte matrix with selenium dioxide addition at 1250 °C. Each result is an average of ten analyses.

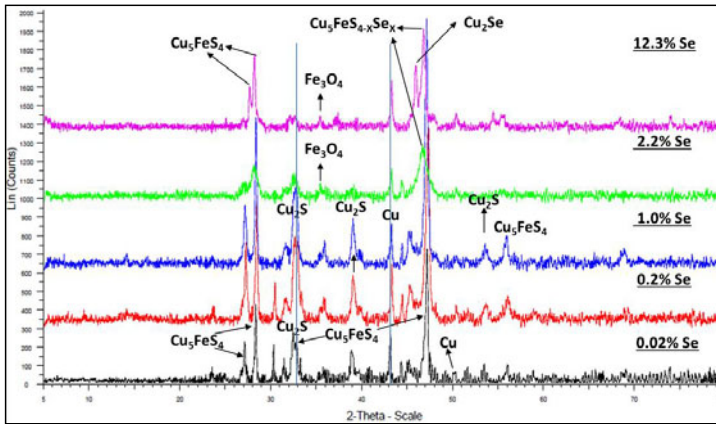
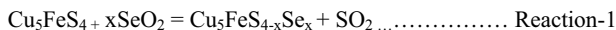


Figure 6. X-ray diffraction patterns of matte at different selenium content

The results of electron microprobe analysis of matte and slag samples are shown in Figure 7(a) and 7(b), respectively. All the matte samples consist of predominantly three phases (1) Bornite phase (Cu_5FeS_4), which is in dark grey. Bornite phase is the main matte matrix, (2) Metallic copper (Cu), which is in light grey. (3) Magnetite (Fe_3O_4), which is in black. The trace metals such as arsenic, antimony and lead are concentrated in the metallic Cu only. The Cu, S and Se content (in atomic %) of EDX scans of matte matrix is shown in Figure 5. The selenium content of matte matrix of matte samples was plotted against copper and sulfur content. Each point on the graph is an average of ten analyses. Selenium was not detected in matte samples separated from the base sample. Selenium was detected in a matte sample separated from the base sample with 0.1%, 0.5%, 1.0% and 5.0% SeO_2 addition. Selenium was detected in the matte matrix (bornite phase) only of the matte sample. The selenium content of the matte matrix increased with selenium dioxide addition. It is also observed that the sulfur content of matte matrix decreased proportionately with increasing selenium content. However, the copper content of the matte matrix was unchanged with SeO_2 addition. Selenium was not detected in metallic copper, as it is evident from table 1. Selenium was not detected also in the magnetite phase of the matte (analysis not shown). It is therefore inferred that the sulfur of the matte (Cu_5FeS_4) is substituted by selenium according to reaction-1.



The substitution of matte sulfur by selenium can be explained from their crystal ionic radii size, which is nearly similar for sulfur and selenium. The bulk chemical analysis of matte as shown in Figure 4 further corroborates the fact that sulfur of the matte samples was substituted by selenium, thus changing the matte from Cu_5FeS_4 to $\text{Cu}_5\text{FeS}_{4-x}\text{Se}_x$. It was calculated from the Se mass balance that nearly 5 to 10% of Se added to the base sample was vaporized to gas phase. Se was not detected in the gas stream during the experiments. The amount of Se vaporized was thus calculated based on the Se mass imbalance by subtracting the Se quantity in matte and slag from the known quantity of Se added in the base sample.

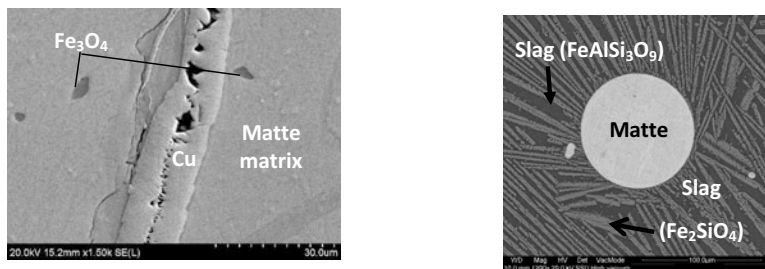


Figure 7. BSE images of (a) matte separated (b) slag separated from base sample

The results of electron microprobe analysis of slag samples are shown in Figure 7(b). All the slag samples consist of predominantly three phases (1) Matte phase, which is white color and entrapped in slag matrix, (2) Slag matrix (Fe_2SiO_4), which is in light grey. (3) Slag matrix ($\text{FeAlSi}_3\text{O}_9$), which is in dark grey color. The compositions of entrapped matte phase in slag, as shown in table 2, show the presence of selenium in samples with 0.1% or more selenium dioxide addition. As the selenium content of entrapped matte increased, the sulfur content decreased proportionately, while iron and copper content did not show much variation. As expected, the selenium dissolution in entrapped matte particles was similar to that in matte matrix (Figure 5). The initial copper content of the starting slag was 0.9 wt. %.

Table 1. Compositions of the metallic copper phase in the matte samples determined by SEM-EDAX (indicated in Figure 7(a)). Each result is an average of ten analyses.

Se addition in base sample, Wt.%	Cu (at. %)	Fe (at. %)	S (at. %)	O (at. %)	Se (at. %)
0.0%	92	1.6	0.7	5.6	0
0.1%	99	0.0	1.1	0.0	0
0.5%	94	0.6	0.0	5.0	0
1.0%	95	0.0	0.5	4.2	0
5.0%	94	1.3	0.0	4.5	0

Table 2. Compositions of the phase indicated by Matte particles in the slag samples (Figure 7(b)) determined by SEM-EDX. Each result is an average of ten analyses.

Se addition in base sample, Wt.%	Cu (at. %)	Fe (at. %)	S (at. %)	Se (at. %)
0	37	14	43	0.0
0.1	52	9	38	0.6
0.5	50	8	36	1.3
1	49	10	37	1.8
5	50	9	31	6.4

Table 3. Compositions of the phase indicated by Fe_2SiO_4 [$\text{FeAlSi}_3\text{O}_9$] in the slag samples (Figure 8(b)) determined by SEM-EDX. Each result is an average of ten analyses.

SeO2 addition in base sample, wt%	O (at.%)	Mg (at.%)	Al (at.%)	Si (at.%)	S (at.%)	K (at.%)	Ca (at.%)	Ti (at.%)	Fe (at.%)
0.0%	63 [66]	1 [0]	0 [6]	14 [18]	0 [0]	0 [1]	0 [2]	0 [0]	22 [5]
0.1%	41 [44]	2 [0]	3 [12]	22 [28]	0 [1]	0 [1]	1 [5]	0 [0]	30 [10]
0.5%	44 [46]	0 [0]	8 [12]	24 [27]	0 [1]	1 [1]	3 [5]	0 [0]	16 [8]
1.0%	44 [45]	2 [0]	4 [12]	20 [28]	0 [1]	1 [1]	1 [5]	0 [0]	28 [8]
5.0%	44 [48]	2 [1]	4 [10]	22 [27]	0 [0]	1 [1]	1 [5]	0 [0]	26 [7]

The compositions of slag matrix as determined by SEM-EDX are shown in table 3. The slag matrix, which is light grey in Figure 7(b), is fayalite ($\sim\text{Fe}_2\text{SiO}_4$) phase as it is evident from its compositions in table 3. Similarly, the slag matrix, which is in dark grey in Figure 8(b), is $\sim\text{FeAlSi}_3\text{O}_9$ phase (table 3). Alumina crucible was used during the experiments and thus the dissolution of alumina to some extent was also observed while removing the slag from the crucible. The dissolved alumina reported to the slag and caused formation of alumina rich phase (table 3). However, the selenium could not be detected in slag matrix (table 3). The selenium was detected only in the matte phase entrapped in slag (table 2). Thus the selenium dissolution in slag as SeO_2 , the slag being oxides of Si, Fe, Al etc, is ruled out. As the selenium is associated with copper rich matte phase in slag, the recovery of selenium from slag can thus be increased by improving settling of entrapped matte particles from slag.

4. CONCLUSIONS

The mechanism of selenium dissolution in slag and matte has been established in present investigation. It is observed that the selenium is dissolved in the matte by substitution of sulfur.

The selenium dissolution was observed only in the matte matrix (phase containing sulfur) of the matte phase. The selenium does not dissolve in slag. The selenium is lost to slag in the form of entrapped matte particles (physical inclusions), which are not able to settle through the slag layer. Selenium dissolution in slag by any other mechanisms is thus ruled out and thus the recovery of selenium from slag can be increased by improving settling of entrapped matte particles from slag.

5. ACKNOWLEDGEMENT

Authors are thankful to Hindalco Birla Copper Ltd. for providing samples for experimental investigations. Authors wish to express their gratitude to the analytical team of Aditya Birla Science & Technology Pvt. Co. Ltd for providing analytical support in this study.

6. REFERENCES

1. Nagamori M. and Mackey P. J., "Distribution Equilibria of Sn, Se and Te between FeO-Fe₂O₃-SiO₂-Al₂O₃-CuO_{0.5} Slag and Metallic Copper", *Metallurgical Transaction B*, 8B, (1), (1977), pp. 39-46.
2. Nagamori M, P.J.Mackey, "Thermodynamics of Copper Matte Converting: Part II. Distribution of Au, Ag, Pb, Zn, Ni, Se, Te, Bi, Sb and As between Copper, Matte and Slag in the Noranda Process", *Metallurgical Transaction B*, 9B (1978) 567.
3. Nagamori, M., Chaubal, P.C., "Thermodynamics of Copper Matte Converting: Part III. Steady-State Volatilization of Au, Ag, Pb, Zn, Ni, Se, Te, Bi, Sb AND As from Slag, Matte, and Metallic Copper", *Metallurgical Transactions B*, 13B, (1982), 319-329
4. S.S. Wang, N.H. Santander, and J.M. Toguri, "The solubility of nickel and cobalt in iron silicate slags", *Metallurgical Transactions B*, 5, (1974), 261-65.
5. L. Fang and D.C. Lynch, "Evaluation of the behavior of selenium in silicate slag", *Metallurgical Transactions B*, 18B, (1987), 181-87.
6. Johnston M. D., S. Jahanshahi, and F. J. Lincoln, "Thermodynamics of Selenium and Tellurium in Calcium Ferrite Slag", *Metallurgical Transactions B*, 38B, 2007, 433
7. Elizabeth A., L. L. Oden, P. E. Sanker, and R. L. Fulton, "Minor Element Interactions in Copper Matte Smelting", *Bureau of Mines Report of Investigations*, United States Department of The Interior, 1984.
8. N. Choi and W.D. CHO, "Distribution Behavior of Cobalt, Selenium and Tellurium between Nickel-Copper-Iron Matte and Silica-Saturated Iron Silicate Slag", *Metallurgical Transactions B*, 28B (1997) 429.
9. S.N. Sinha and M. Nagamori, "Activities of CoS and FeS in copper mattes and the behavior of cobalt in copper smelting", *Metallurgical Transactions B*, 13B, 1982, 461-70.

SELECTIVE PRECIPITATION OF MAGNETITE IN COPPER SLAG BY CONTROLLED MOLTEN OXIDATION

Yong Fan¹, Etsuro Shibata², Atsushi Iizuka², and Takashi Nakamura²

¹Graduate School of Environmental Studies, Tohoku University
6-6-20 Aramaki-Aza-Aoba, Aoba-ku, Sendai, 980-8579, Japan;

²Institute of Multidisciplinary Research for Advanced Materials (IMRAM), Tohoku University
2-1-1 Katahira, Aobaku, Sendai 980-8577, Japan

Keywords: Molten oxidation, Magnetite precipitation, Copper Slag.

Abstract

Molten oxidation is a sustainable process for direct precipitation of magnetite from melt copper smelter slag because it involves zero or less energy input due to the exothermic reaction and free reducing carbon addition. During molten oxidation, magnetite precipitation occurred preferentially because of its intensive ferromagnetism and large crystal size, which enables downstream magnetic separation. Previous milligram-scale experiments conducted using an infrared furnace show that magnetite could be precipitated, while precipitation of hematite was limited under an atmosphere of 1 vol% oxygen. In this study, gram-scale experiments were conducted using an electric furnace to verify larger-scale molten oxidation at 1 vol% oxygen.

Introduction

Copper slag, a solid waste product of copper smelting operations, is dumped in huge quantities around the world. It is estimated that approximately 30–40 million tons of copper slag, mainly smelting slag, is produced worldwide every year^[1,2]. The most common and effective method of recycling copper slag is using it in cement production as an additive. However, in developed markets such as North America, Western Europe, and Japan, overcapacity in the cement industry has become increasingly serious, thereby increasing the necessity for alternative recycling processes. Asia's share of worldwide copper smelter output jumped from 27% to 56% in the last 10 years. Thus, reconsideration of the practice of dumping slag is a pressing issue for Asia. In addition, the tightening of environmental regulations provides further motivation to recycle slag^[3,4].

Copper smelting slag, an amorphous granulated material, results from quick solidification. Generated as industrial solid waste from matte smelting, it mainly contains iron silicates [(Fe, Al,

Ca, Mg)_xSiO_y] melted by smelting the copper concentrate and silica flux. Iron concentrations are nearly 40% by mass in the slag. Utilization of this secondary resource is under widespread consideration: recovering the iron content would effectively decrease the volume of dumped slag. The recovered high iron-bearing product could then be reused for iron or steel production^[5].

Proposal

Figure 1 depicts our proposed molten oxidation process for the precipitation of magnetite based on directly blowing an oxidizing gas onto the molten copper smelting slag. During this process, most nonmagnetic iron-containing components (iron silicate or fayalite) are designed to be transformed into magnetite, which would permit selective recovery of iron-bearing and non-iron-bearing slag constituents for specific purposes. The solid residue, mainly silica, would be suitable for future use as flux for a copper smelter or in the production of ceramic materials.

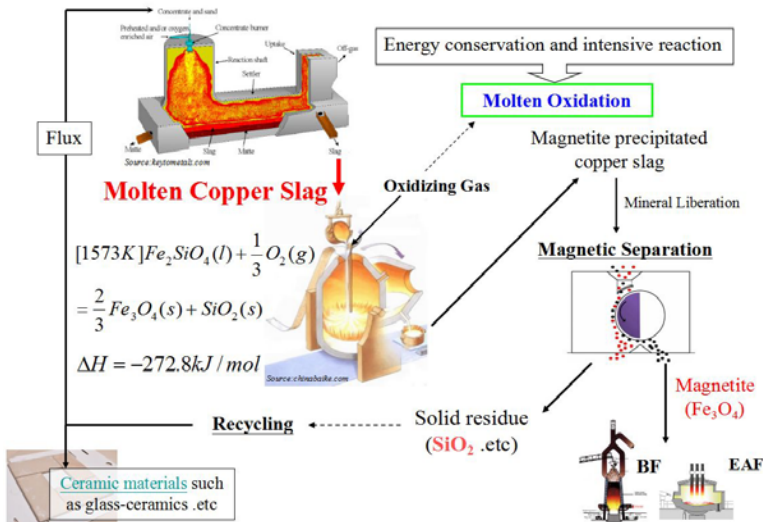


Fig.1 Proposed process flow for recycling molten copper slag.

In a recently published study^[6], a simulation of our proposal, i.e., directly blowing oxidizing gas onto molten slag for magnetite precipitation, was implemented using an infrared furnace. The crystallization behaviors were studied, which showed a trade-off relationship between magnetite and hematite. It was found that a lower oxygen partial pressure was beneficial for the precipitation of magnetite. In particular, the use of 1 vol% oxygen resulted in selective oxidation for magnetite precipitation.

In the above milligram-scale experiments, magnetite could be precipitated from the molten slag during molten oxidation using 1 vol% oxygen. In the present study, gram-scale experiments will be performed using an electric furnace. It was designed that the magnetite precipitated copper slag would be used in the downstream magnetite liberation and separation.

Experimental

The schematic of the experimental apparatus is shown in figure 2. The gas system was assembled to simulate the conditions of our proposal for studying magnetite precipitation. In this study, Ar gas was used during the heating and cooling processes to ensure that copper slag was in the original state.

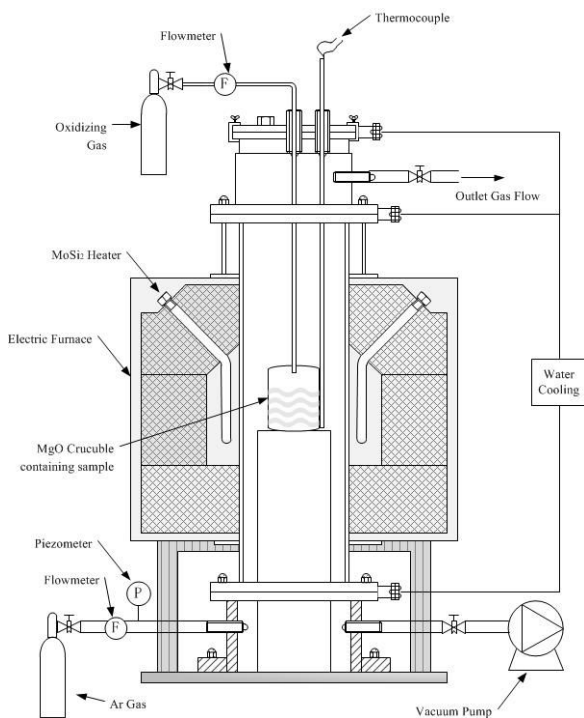


Fig.2 Schematic of the experimental apparatus.

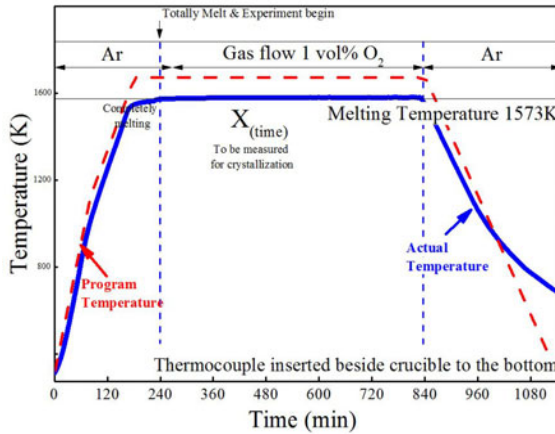


Fig.3 Experimental procedures of molten oxidation.

Molten oxidation was performed using the following procedures as shown in figure 3. First, the copper slag sample (100 g of original copper slag in a magnesia crucible) was melted at 1573 K under Ar gas. Then, the temperature of the molten sample was stabilized at the melting temperature to ensure uniform melting. Subsequently, gas flow comprising 1 vol% oxygen was initiated into the furnace and to the sample surface at 5 L/min to begin the crystallization, as shown in figure 4. After heat treatment for a certain duration, the sample was cooled under Ar gas to room temperature.

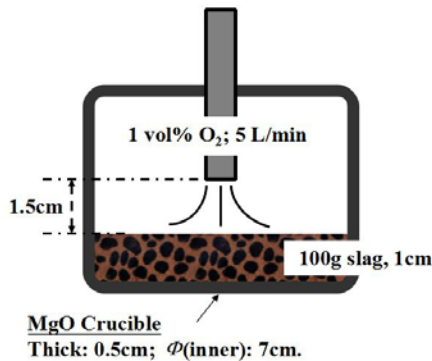


Fig.4 Top blowing parameters of molten oxidation in an electric furnace.

The magnetite content was measured by X-ray diffraction (XRD; D2 PHASER, 30 kV, 10 mA, Cu-K α , Bruker, Germany) using the internal standard method for semi-quantitative analysis. Typical samples obtained by the different treatment conditions were characterized using a laser microscope (OLS4100, Olympus, Japan).

Results and Discussion

Gram-scale experiments in the electric furnace show almost the same phenomenon as the milligram-scale experiments performed in the infrared furnace. The use of 1 vol% oxygen resulted in selective oxidation, resulting in magnetite precipitation and limiting hematite.

Hundred grams of melted copper slag in the crucible was approximately 1 cm in height. The blowing of oxidizing gas on top would cause a variation in the magnetite content throughout the molten slag because of chemical diffusion. Considering this, samples from the top and bottom parts of the magnetite-precipitated copper slag were extracted and subjected individually to XRD analysis to determine their magnetite content. The results are shown in Figure 5.

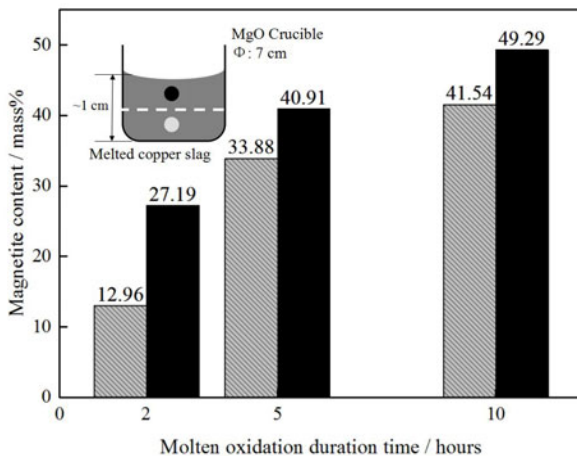


Fig.5 Variation of the magnetite content in copper slag during molten oxidation under an atmosphere of 1 vol% oxygen.

It was observed that as the oxidation time increased, the magnetite content increased from the original 7.5 mass% to approximately 40–50 mass% after 10 h of molten oxidation in a 1 vol% oxygen atmosphere. During this process, the iron in the slag matrix is hypothesized to be

oxidized into magnetite. In particular, because of the selective oxidation ability of 1 vol% oxygen, oxidation of hematite was limited and the main precipitated iron oxide was magnetite, as shown in the XRD patterns (Figure 6).

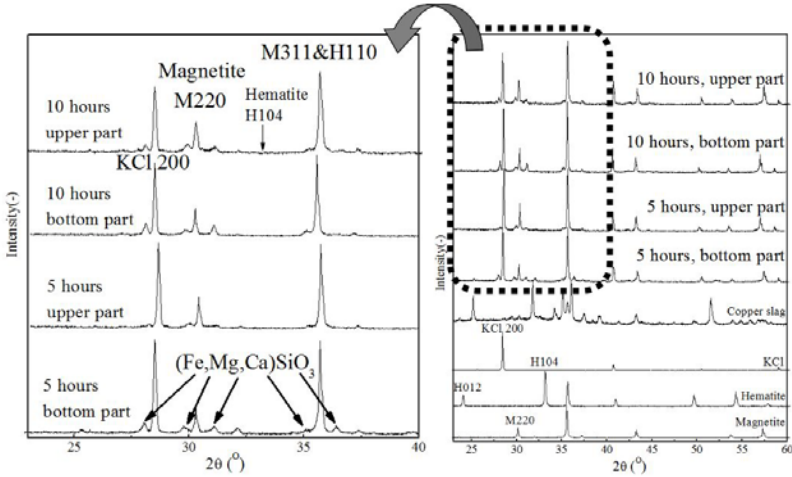


Fig.6 Typical examples of XRD patterns of copper slag after molten oxidation.

Moreover, the use of the magnesia crucible might cause magnesium dissolution into the slag during molten oxidation. It was found that the magnesia content increased to approximately 7 mass%. The rise of magnesium content would contribute to a new phase of (Fe, Mg, Ca)SiO₃ in the slag and this is indicated by small peaks in the XRD patterns. Because magnesia dissolution was impossible to avoid using the current experimental conditions, the discussion takes into account this condition.

After molten oxidation, the crucible containing the copper slag with precipitated magnetite was cut and a cross-section of the sample was fixed in resin and polished for micro-analysis of the crystal morphology using the laser scanning microscope. The microscope images of the copper slag after molten oxidation in a 1 vol% oxygen atmosphere for 5 h are presented below.

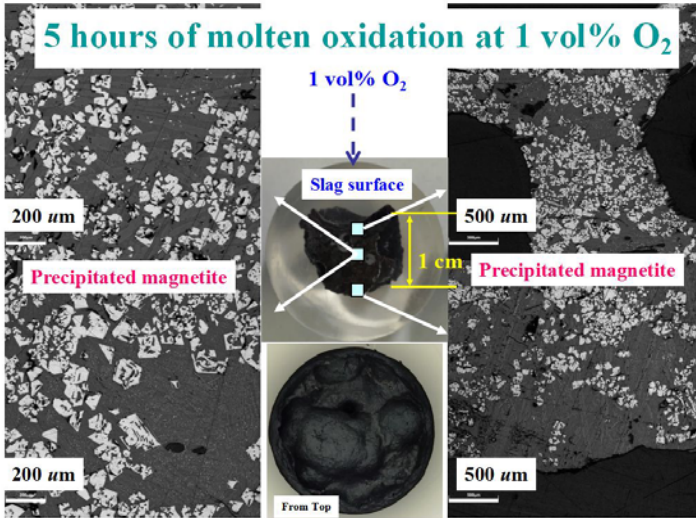


Fig.7 Typical laser microscope images of copper slag after molten oxidation in 1 vol% oxygen atmosphere for 5 h.

The cross-section of slag samples produced characteristic crystal structures. It can be seen that square-like crystals, larger than approximately 50 μm , occupied the majority of the sample, and are magnetite. There were some other characteristic tower- or needle-like structures. These crystals are hypothesized to be a type of transformation structure between magnetite and hematite examined in the previous study.

Conclusions

In this study, gram-scale experiments were performed using an electric furnace under 1 vol% oxygen atmosphere. At this condition, the iron in the slag matrix was selectively oxidized into magnetite, and oxidation of hematite was limited. Magnetite crystals, larger than approximately 50 μm , occupied the majority of the sample.

References

1. M. E. Schilesinger et al., *Extractive Metallurgy of Copper* (Great Britain: Elsevier. 2011).
2. British Geological Survey, *World Mineral Production 2008–12*. (Keyworth. Nottingham: British Geological Survey, 2013).
3. International Copper Study Group, *World Copper Factbook 2013* (Lisbon, Portugal: ICSG.

2013).

4. Y. Fan et al., “Review on iron recovery and cleaning of copper slag,” *Journal of MMIJ*, 5 (2013), 177–184.

5. Y. Fan et al., “Crystallization behaviors of copper smelter slag studied using Time-Temperature-Transformation diagram,” *Material Transaction*, 55 (6) (2014), 958–963.

6. Y. Fan et al., “Crystallization Behavior of Copper Smelter Slag during Molten Oxidation,” *Metallurgical and Materials Transactions B*, 46 (5) (2015), 2158–2164.

**ADVANCES IN MOLTEN
SLAGS, FLUXES, AND SALTS:**

Proceedings of



**Thermodynamics:
Iron and Steel**

APPLICATIONS OF ARCELORMITTAL THERMODYNAMIC COMPUTATION TOOLS TO STEEL PRODUCTION

Jean Lehmann¹

¹ArcelorMittal Global R&D Maizières BP 30320 57 283 Maizières les, Metz Cedex, France

Keywords: Slag, metal, inclusions, sulfur, phosphorus, viscosities

Abstract

CEQCSI is an ArcelorMittal in-house built thermodynamic equilibrium calculation software which is used both at high temperatures typically for slag-metal reactions but also at “low” temperatures to study solid phase transformations and precipitation in solid steel. It has been built to accommodate different thermodynamic models for slag (the Cell model, the Generalized Central Atom model - product of a collaboration between ArcelorMittal Global R&D Maizières and CSIRO Melbourne), for steel (sublattice model, Wagner Interaction Parameter Formalism) as well as for oxide, sulfide, carbide... solid solutions. Examples of application concern Si, Mn, S slag-metal equilibrium in Blast-Furnace, P partition in BOF slags, slag-metal equilibrium for flat and long products in ladle... Apart from data relating to mass transfer between different phases at equilibrium, CEQCSI proposes several estimates for slag viscosities with among them one delivered by a new model based on the Generalized Central Atom thermodynamic model for slags. CEQCSI conception allows also handling some kinetic problems such as desulfurization in ladle or slag/metal reaction in mold.

Introduction

In recent years, the steelmaking industry has benefited from the development of mathematical models able to reproduce the main chemical reactions occurring at the different stages of the steel production. At ArcelorMittal, the CEQCSI software (Chemical EQUilibrium Calculations for the Steel Industry) has been developed to that purpose. It includes models of the different phases involved in these reactions: liquid and solid metal, slag, inclusions, precipitates... For slags, one option is to use the Generalized Central Atom (GCA) model developed in the framework of a 7-year collaboration between ArcelorMittal Global R&D Maizières and CSIRO Melbourne. In a first part of this paper, the theoretical principles on which the GCA model is built will be briefly reminded and a new viscosity model using the slag description provided by the GCA model will be presented. Two applications to hot metal and to liquid steel will illustrate the practical use of CEQCSI even if the software is not limited to these high temperatures and can be applied to solidification as well as to steel transformation and precipitation at lower temperatures.

Even for processes when the equilibrium state cannot be reached, the thermodynamic models provide the background for more appropriate kinetic approaches. Thus, CEQCSI is used for the development of kinetic models of slag/metal reaction for steel desulfurization in ladle and, more

recently, for slag/metal reaction in CC mold. The latter model, still in development, beneficiaries from the recent progress obtained in the evaluation of mass transfer coefficients.

The Generalized Central Atom for Metallurgical Slags

The Generalized Central Atom model, based on the quasichemical approach, has been developed through a collaborative research project between the CSIRO Mineral Resources Flagship and ArcelorMittal Global R&D Maizieres. Its database covers now the P_2O_5 - SiO_2 - TiO_x - CrO_x - Al_2O_3 - FeO_x - MnO - MgO - CaO - Na_2O - K_2O - S - CaF_2 system. It is based on the same principals as the so-called "Cell model" developed by H. Gaye and co-authors [1] but provides a better description of the short range order phenomenon.

GCA unifies in the same formalism the Cell model and the Central Atom model originally proposed by Lupis and Elliott [2] for solid steel and very similar to the "surrounded atoms model" developed at about the same period at the LTPCM [3,4]. In the GCA model, the structure is also described in terms of cells composed of a central atom surrounded by a shell of its nearest neighbors but also by a shell of its second-nearest neighbors. The central atom can be either an anion or a cation. In a system with m components with t substitutional elements, a cell is noted as:



Similarly to the Cell model, two kinds of parameters are considered in the GCA model, namely formation and interaction energy parameter. The formation energy of the cell is noted $\phi_{\{i\},\{j\}}^J$ where J represents the central atom and {i} and {j} presents the whole set of cations and anions present on the first- and second-nearest neighbors shells. For the sake of simplicity, the formation energy term is assumed to be the sum of the contributions of the two shells:

$$\phi_{\{i\},\{j\}}^J = \phi_{\{i\}}^J + \phi_{\{j\}}^J \quad (2)$$

To reduce the number of parameters, different assumptions can be formulated to describe the energy variation for the central atom according to the composition of the chemical neighborhood. For the formation energy, the following expression has been chosen:

$$\phi_{\{i\}}^J = \sum_{k=1}^t i_k \phi_{kk}^J + \frac{1}{2} \sum_{\substack{k,l=1 \\ k \neq l}}^t i_k i_l \phi_{kl}^J \quad (3)$$

This formula shows that the model accepts ternary parameters as for example ϕ_{SiCa}^{Al} . A simple dependence on temperature and a linear dependence on composition have been introduced.

The more precise description of Short Range Ordering (SRO) phenomenon as well as the added flexibility in the definition of the parameters solves the problem of the inaccuracy of the Cell model for silica-rich compositions of alumina bearing slags [5].

Recently, a modification has been done to better fit the systems containing both Al_2O_3 and Na_2O . Similarly to what has been implemented in the MQM model [6], an atom-like species $NaAl^{4+}$ has been introduced and this modification improves a lot the description of the SiO_2 -rich part of the SiO_2 - Al_2O_3 - Na_2O system (Figure 1).

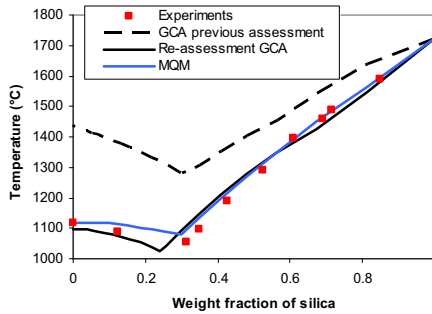


Figure 1. Comparison between liquidus temperature measurements along the joint silica-albite and calculations performed with the initial GCA model, the revised GCA model and the MQM model [6]

As an example of the predictions delivered by the model, Figure 2 compares, for a very large bunch of experimental works collected in the literature, calculated and experimental values of P activity. Given the uncertainties affecting thermodynamic measurements in these systems, the agreement is believed to be fairly satisfactory.

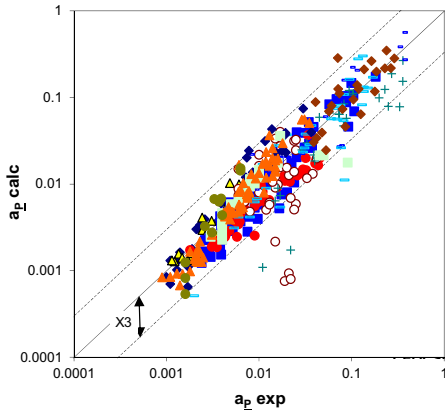


Figure 2. Comparison between P activity (ref state: 1 wt% diluted solution in liquid steel) calculated with GCA and experimental values [7-20].

The GCA Model for Slag Viscosity

Besides “old” slag viscosity models as Urbain’s model [21] for ladle slags or Riboud’s model [22] for mold slag, CEQCSI now proposes to the users a new viscosity model based on the description in terms of cells of the slag structure provided by the GCA thermodynamic model. The formalism is the one proposed by Kondratiev et al. [23]:

$$\mu = \frac{2RT}{\Delta E_v} \frac{(2\pi m_{SU} kT)^{1/2}}{v_{SU}^{2/3}} \cdot \exp\left(\frac{E_a}{RT}\right) \quad (4)$$

where μ is the viscosity, k the Boltzmann constant, ΔE_v the energy of vaporization, E_a the activation energy, m_{SU} and v_{SU} the weight and volume of the structure units (atom or molecule in simple liquids), T the temperature (K) and R the perfect gas constant. ΔE_v and E_a are expressed as polynomials function of the cell numbers (or exponential polynomials in case of Na_2O -bearing systems). The coefficients of these polynomials are assessed against the experimental data.

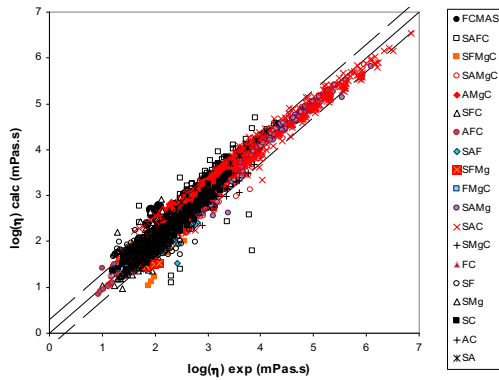


Figure 3. Comparison between experimental and calculated values of slag viscosities belonging to the SiO_2 - Al_2O_3 - FeO_x - MnO - MgO - CaO system. S= SiO_2 , A= Al_2O_3 , Mn= MnO , Mg= MgO , C= CaO , Fe= FeO_x

A global view of the results is given in Figure 3 for the system SiO_2 - Al_2O_3 - FeO_x - MnO - MgO - CaO .

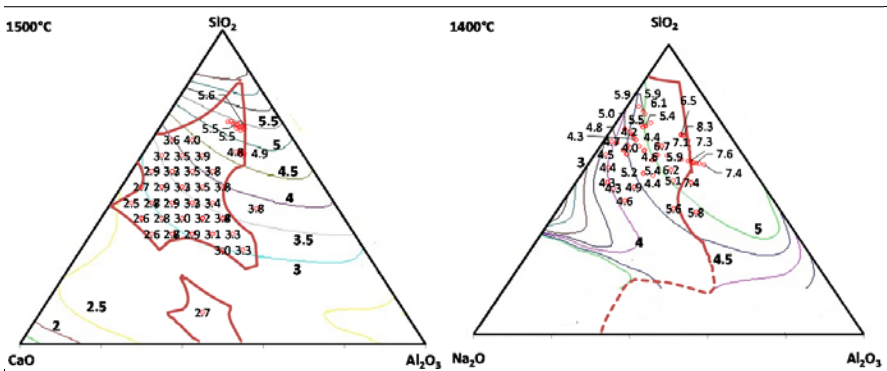


Figure 4. Iso-viscosity values - $\log(mPas.s)$ - in the ternary SiO_2 - Al_2O_3 - CaO at $1500^\circ C$ and in the ternary SiO_2 - Al_2O_3 - Na_2O at $1400^\circ C$. Isotherms (red heavy lines) have been calculated with the GCA model. Red points represent experimental data [24-44].

Figure 4 provides another way to look at the results. On the same ternary diagrams, values of experimental determinations are plotted along iso-viscosity lines for two chemical systems of prime importance for the steelmaker: $\text{Al}_2\text{O}_3\text{-CaO-SiO}_2$ for secondary metallurgy slags and $\text{Al}_2\text{O}_3\text{-Na}_2\text{O-SiO}_2$ for mold slags.

Equilibrium

Ceqcsi is built in such a way to allow easy calculations of various quantities of prime importance for hot metal or steel production operations: slag liquidus temperatures, slag physical state, slag/metal equilibrium conditions (through, for instance, the comparison of the oxygen activities given by the different couples oxide/deoxidizer), effect of alloy additions on inclusions, etc...

Figure 5 is an example concerning Blast Furnace slags. It shows that substituting MgO to CaO could favor K capture by the slag without hampering the desulfurization.

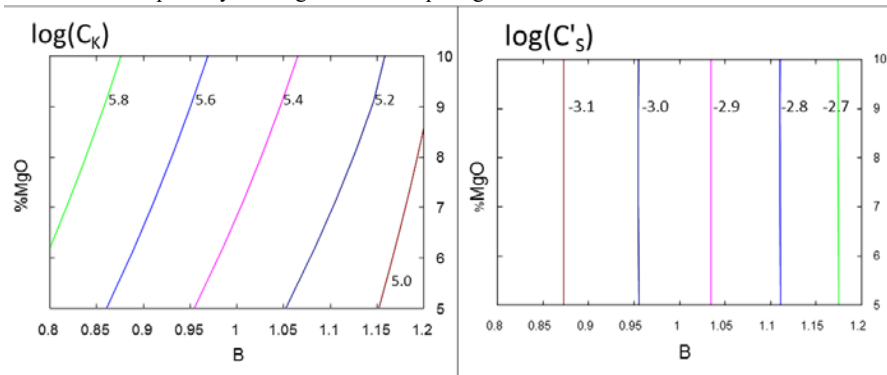


Figure 5. Isovalues of the logarithms of the potassium (left) and sulfide capacity (right) as function of the MgO contents (wt%) and of the basicity

$B = (\text{wt}\% \text{CaO} + \text{wt}\% \text{MgO}) / (\text{wt}\% \text{SiO}_2 + \text{wt}\% \text{Al}_2\text{O}_3)$ of slags containing 2 wt% Al_2O_3 and 0.1 wt% K_2O calculated at 1550°C with the GCA model.

Figure 6 concerns Basic Oxygen Furnace operations. CEQCSI has been used to simulate the effect of increasing additions of MgO in BOF slag. It can be seen that these additions have an effect on the physical state of the slag (small additions push the slag outside the primary phase domain of C_2S and, for additions larger than 6 kg, inside the primary phase domain of magnesio-wüstite – see figure caption for details) and on the P equilibrium partition ratio which decreases noticeably when the slag is completely liquid.

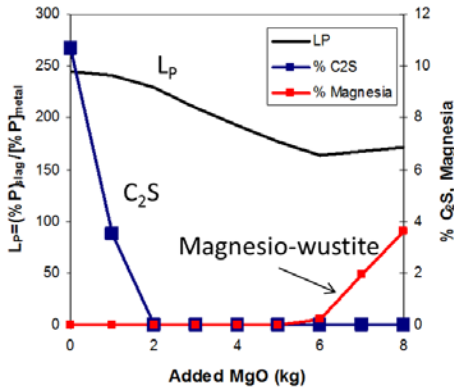


Figure 6. Effect of MgO additions on P partition ratio and percentages of dicalcium silicate (C_2S) and of magnesio-wüstite. Initially 70 kg of slag of the following composition 0.5% P_2O_5 – 18% SiO_2 – 1% Al_2O_3 – 30% FeO – 2% MgO and 48.5% CaO at 1650°C is brought to equilibrium at 1650°C with 1 tonne of a steel containing 0.08%Mn – 0.008%P – 0.03%C – 700 ppm O.

Kinetics

CEQCSI formalism allows easy handling of some kinetic problems as for instance complex oxides inclusions precipitation during steel solidification [45], carbo-nitrides precipitation in austenite [46] or ladle desulfurization [47] assuming either complete equilibrium at phase interface or including models for interfacial reactions.

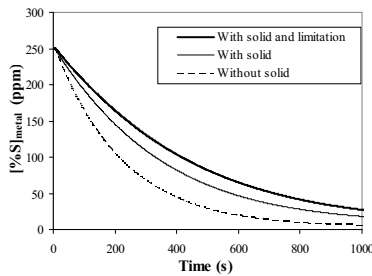


Figure 7. Calculated evolution with time of the metal sulfur content at 1600°C. Dotted line: "metastable" slag w/o solids; light line: slag partly crystallized; heavy line: partly crystallized slag with a slag/metal interface area reduced proportionally to the percentage of solids.

Figure 7 is an example of the latter modeling which considers all possible reactions between slag and metal and not only the S transfer. Diffusion in slag and metal are taken into account and reaction can occur with a top slag and with slag droplets whose size, number and residence time can be chosen (in accordance with experimental results or with CFD calculations). The effect of the presence of solid phases is clearly shown: a partial crystallization of the slag hampers the desulfurization process and this phenomenon is exacerbated if the slag/metal interface area is

assumed to be reduced proportionally to the percentage of crystallized oxides.

One of the key-components of these kinetic models are the mass transfer coefficients and research at ArcelorMittal is presently focused on deriving precise values for them [48]. First application will concern reactions between mold flux and steel in CC mold. Figure 8 presents the result of a preliminary calculation and consists in mimicking some results obtained by P. Chaubal et al. for free machining steel [49]. The enrichment of the slag in MnO is consistent with the industrial observations. One of the advantages of the method under development when compared to [49] is the possibility to use more sophisticated thermodynamic models for slag and steel, which could be necessary in particular for new steel grades.

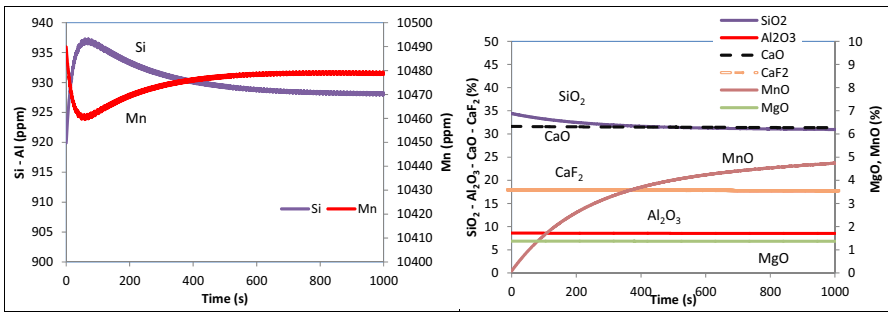


Figure 8. Calculated evolution of steel and slag composition in CC mold for a free machining steel.

Conclusion and Future Work

CEQCSI is continuously improved to better fit the needs of the steel industry. For instance, the new generation of steel grades motivates presently a research project on the improvement of the thermodynamic mixing models for the steel phases. If the interest of Li_2O and B_2O_3 additions in mold slags is confirmed, an extension of the thermodynamic GCA model as well as of the GCA viscosity model will certainly be contemplated.

Kinetic modeling requires a coupled development between CFD and CEQCSI. Two steps are envisaged for the model of slag/metal reaction in mold presented in the paper: a full coupling where thermodynamics (and possibly chemical kinetics) is used “locally” in each cell defined for CFD and a “lighter” version suitable for quick and easy calculations where simplifications will be done based on results derived from the CFD calculations as for instance a partition of the vessel in perfectly mixed zones. Examples of such approaches can already be found in the literature [50,51].

References

1. H. Gaye, J. Lehmann, T. Matsumiya, W. Yamada, “A statistical thermodynamics model of slags: applications to systems containing S, F, P_2O_5 and Cr oxides”, 4th International Conference on Molten Slags and Fluxes. Sendai, Japan: ISIJ; 1992.

2. C.H.P. Lupis and J.F. Elliott, "Prediction of enthalpy and entropy interaction coefficients by the « central atoms » theory", *Acta Met.*, 15 (1967), 265-276.
3. J.C. Mathieu, F. Durand and E. Bonnier, "L'atome entouré, entité de base d'un modèle quasi-chimique de solution binaire, I. Traitement général", *J. Chim. Phys.*, 62 (1965), 1289-1296.
4. B. Pascal, J.C. Mathieu, P. Hicter, P. Desré and E. Bonnier, "L'atome entouré, entité de base d'un modèle quasi-chimique de solution binaire, VII. Traitement général d'une solution interstitielle", *J. Chim. Phys.*, 68 (1971) 774-781.
5. L. Zhang, J. Lehmann, "Application of the generalized central atom model to oxide slags", *Molten 2009*, Santiago, Chile (2009) 403-411.
6. P. Chartrand, A.D. Pelton, "Modeling the charge compensation effect in silica-rich Na₂O-K₂O-Al₂O₃-SiO₂ melts", *Calphad*, 23 (1999), 219-230.
7. H. Ishii and R.J. Fruehan, *Iron Steelmaker*, 24 (1984), 47-54.
8. R. Nagabayashi, M. Hino and S. Ban-ya, "Solubilities of CaO, MgO, SiO₂ and 2CaO·SiO₂, and Ferric-Ferrous Equilibrium in Fe₂O-(CaO+MgO)-(SiO₂+P₂O₅) Phosphate Slags", *Tetsu-to-Hagane*, 74 (1988), 1577-1584.
9. H. Suito, R. Inoue and M. Takeda, "Phosphorus distribution between liquid iron and MgO saturated slags of the system CaO-MgO-FeO_x-SiO₂", *Trans ISIJ*, 21 (1981), 250-259.
10. H. Suito and R. Inoue, "Effect of Calcium Fluoride on Phosphorus Distribution between MgO Saturated Slags of the System CaO-MgO-FeO_x-SiO₂ and Liquid Iron", *Trans ISIJ*, 22 (1982), 869-877.
11. R. Selin, *Scandinavian Journal of Metallurgy*, 20 (1991), 279-299.
12. S. Jahanshahi and G.R. Belton: Fifth Int. Iron and Steel Congress: Process Technology Proc. Vol.6, Washington DC, (1986), ISS, 641-651.
13. K. Kunisada and H. Iwai, "Effects of CaO, MnO, and Al₂O₃ on phosphorus distribution between liquid iron and Na₂O-MgO-Fe₂O-SiO₂ slags", *Trans ISIJ*, 27 (1987), 332-339.
14. G.J.W.Kor: *Met. Trans.*, 8B (1977), 107-113.
15. T.B. Winkler and J. Chipman, *Trans. AIME*, 167 (1946), 111-133.
16. H. Suito and R. Inoue, "Thermodynamic assessment of manganese distribution in hot metal and steel", *Trans ISIJ*, 35 (1995), 266-271.
17. T. Usui, K. Yamada, Y. Kawal, S. Inoue, H. Hiroaki and Y. Nimura, "Experiment of Phosphorus and Oxygen Distribution between CaO-SiO₂-MgO-FeO Slag and Liquid Steel and Estimation of Phosphorus Content at End Point of Top and Bottom Blowing Converter", *Tetsu-to-Hagane*, 77 (1991), 1641-1648.
18. E. Schurmann and H. Fischer, *Steel Research*, 62 (1991), 303-313.
19. H. Suito and R. Inoue, "Effects of Na₂O and BaO additions on phosphorus distribution between CaO-MgO-Fe₂O-SiO₂ slags and liquid iron" *Trans ISIJ*, 24 (1984), 47-53.
20. C.M. Lee and R.J. Fruehan, *Ironmaking and Steelmaking*, 32 (2005), 503-508.
21. G. Urbain, F. Cambier, M. Deletter and M.R. Anseau, "Viscosity of Silicate Melts". *Transactions and Journal of the British Ceramic Society*, 80 (1981), 139-141.
22. P.V. Riboud, Y. Roux, L.D. Lucas and H. Gaye, "Improvement of Continuous Casting Powders", *Fachberichte Hüttenpraxis Metallweiterverarbeitung*, 19 (1981), 859-869.
23. A. Kondratiev, P.C. Hayes, E. Jak, "Development of a Quasi-chemical Viscosity Model for Fully Liquid Slags in the Al₂O₃-CaO-FeO'-MgO-SiO₂ System. Part 1. Description of the

Model and Its Application to the MgO, MgO–SiO₂, Al₂O₃–MgO and CaO–MgO Sub-systems”, *ISIJ International*, 46 (2006), 359-367.

24. G. Urbain, “Mesures des viscosités de laitiers synthétiques du système FeO SiO₂ TiO₂”, *Comptes Rendus Hebdomadaires des Séances de l'Académie Des Sciences*, 232 (1951), 330-332.

25. G. Urbain, “Viscosité de l'alumine liquide”, *Revue Internationale des Hautes Températures et des Réfractaires*, 19 (1982), 55-57.

26. J.S. Machin, T.B. Yee, “Viscosity studies of system CaO-MgO-Al₂O₃-SiO₂. 2. CaO-Al₂O₃-SiO₂”, *J. Am. Ceram. Soc.*, 31 (1948), 200-204.

27. J.S. Machin, T.B. Yee, D.L., Hanna, “Viscosity of system CaO-MgO-Al₂O₃-SiO₂. 3. 35 45 and 50% SiO₂”, *J. Am. Ceram. Soc.*, 35 (1952), 322-325.

28. M.J. Toplis, D.B. Dingwell, “Shear viscosities of CaO-Al₂O₃-SiO₂ and MgO-Al₂O₃-SiO₂ liquids: Implications for the structural role of aluminium and the degree of polymerisation of synthetic and natural aluminosilicate melts”, *Geochimica et Cosmochimica Acta*, 68 (2004), 5169-5188.

29. P. Kozakevich, “Viscosité et éléments structuraux des aluminosilicates fondus : Laitiers CaO-Al₂O₃-SiO₂ entre 1600 et 2100°C”, *Revue de Métallurgie*, (1960), 149-160.

30. I.I. Gul'tyai, “Effect of alumina on the viscosity of calcium oxide-magnesium oxide-silica slags”. *Izvestia Akademii Nauk SSSR. Otdelenie Tehniceskih Nauk. Metallurgia*, 5 (1962), 28-38.

31. C.M. Scarfe, D.J. Cronin, J.T. Wenzel, D.A. Kauffman, “Viscosity temperature relationships at 1 atm in the system diopside-anorthite”, *Am. Miner.*, 68 (1983), 1083-1088.

32. T. Kou, K. Mizoguchi and Y. Suginothara, *Nippon Kinzoku Gakkaishi*, (1978), 775-781

33. K. Kim and S. Lee, “Viscosity Behavior and Mixed Alkali Effect of Alkali Aluminosilicate Glass Melts”, *Journal of the Ceramic Society of Japan*, 105 (1997), 827-832.

34. N'Dala I., et al., “Viscosity of Liquid Feldspars. Part I: Viscosity Measurements”, *Br. Ceram. Trans. J.*, 83 (1984), 105-107.

35. M.J. Toplis, D.B. Dingwell and T. Lence, “Peraluminous viscosity maxima in Na₂O-Al₂O₃-SiO₂ liquids: The role of triclusters in tectosilicate melts”, *Geochimica et Cosmochimica Acta*, 61 (1997), 2605-2612.

36. D.J. Stein, F.J. Spera “Experimental rheometry of melts and supercooled liquids in the system NaAlSi₃O₈-SiO₂: Implications for structure and dynamics”, *American Mineralogist*, 78 (1993), 710-723.

37. E.F. Riebling, “Structure of Sodium Aluminosilicate Melts Containing at Least 50 mole % SiO₂ at 1500°C”. *The Journal of Chemical Physics*, 44 (1966), 2857-2865.

38. D.B. Dingwell, “Viscosity-temperature relationships in the system Na₂Si₂O₅-Na₄Al₂O₅”. *Geochimica et Cosmochimica Acta*, 50 (1986), 1261-1265.

39. S. English, “The Effect of Composition on the Viscosity of Glasses. Part II”, *Journal of the Society of Glass Technology*, 8 (1924), 205-251.

40. I. Kushiro, “Viscosity and structural changes of albite (NaAlSi₃O₈) melt at high pressures”, *Earth and Planetary Science Letters*, 41 (1978), 87-90.

41. G. Gehlhoff and Z. Thomas, Leipzig : s.n., *Z. Techn. Phys.*, 7 (1926), 260-278.

42. S. Kozu, K. Kani, *Proc. Imp. Acad. Jpn.*, 11 (1939), 383-.

43. D.R. Neuville et Richet P. "Viscosité et entropie des silicates fondus". *Rivista della Staz. Sper. Vetro*, 6 (1990), 213-221.
44. K. Hunold and R. Brückner, "Chemische Diffusion von Na- and Al-Ionen in Natrium-Alumosilicatschmelzen". *Glastechn. Ber.*, 53 (1980), 207-219.
45. J. Lehmann, P. Rocabois, H. Gaye, "Kinetic model of non-metallic inclusions precipitation during steel solidification", *Journal of Non-Crystalline Solids*, 282 (2001), 61-71.
46. J. Lehmann, N. Bontems, M. Simonnet, P. Gardin and L. Zhang, "Thermodynamics, Precipitation Kinetics, Coupled Models development: Three Main Axes of Research in Physical Chemistry at ArcelorMittal Global Maizières Process", *Steel Research International*, 81 (2010), 772-776.
47. J. Lehmann, In-Ho Jung and L. Zhang, "Slag models: none is perfect but how useful they are!", ICS 2012, Dresden, Oct. 1-3
48. L. D. O. Campos, P. Gardin, S. Vincent, JP. Catagirone, "Physical modeling of turbulent multiphase flow in a continuous casting steel mold", *Computational Methods in Multiphase Flow VIII* 89 (2015) 439-450.
49. P. Chaubal and R. Bommaraju, « Development and Use of a Model to Predict In-Mold Slag Composition during the Continuous Casting of Steel, 1992 Steelmaking Conference Proceedings, 665-675.
50. M-A. Van Ende, Y-M. Kim, M-K. Cho, J. Choi and In-Ho Jung, "A kinetic model for the Ruhrstahl Heraeus (RH) Degassing process", *Metall. Mater. Trans. B*, 42 (2011), 477-489.
51. P. Scheller, Q. Shu, "Inclusion Development in Steel During Ladle Metallurgical Treatment - A Process Simulation Model – Part: Industrial Validation", *Steel Research International*, 85 (2014), 1310-1316.

PHASE EQUILIBRIA STUDY OF THE CaO-“Fe₂O₃”-SiO₂ SYSTEM IN AIR TO SUPPORT IRON SINTERING PROCESS OPTIMISATION

Peter C. Hayes¹, Jiang Chen¹, Evgueni Jak¹

PYROSEARCH, Pyrometallurgy Research Laboratory, School of Chemical Engineering, The University of Queensland, Brisbane, Queensland, 4072, Australia

Keywords: Phase equilibria, liquidus, slags, CaO-“Fe₂O₃”-SiO₂

Abstract

Phase equilibria studies of the CaO-Fe₂O₃-SiO₂ system in air from 1200°C to 1260°C have been carried out at Fe-rich region with particular focus on the phase chemistry of Silico-Ferrite of Calcium (SFC) phase and associated equilibria. The measurements have been made possible through the use of a modified experimental technique involving high temperature equilibration, rapid quenching followed by electron probe X-ray micro analysis (EPMA). The compositions and temperatures determining the limits of the primary phase field of the SFC phase have been determined for the first time. Isothermal sections for 1220°C, 1240°C, 1255°C and 1260°C have been measured and the liquidus in the SFC primary phase field has also been determined.

Introduction

The system CaO-FeO-Fe₂O₃-SiO₂ forms the basis for the description of the chemical behaviour of slags encountered in a wide range of metallurgical ferrous and non-ferrous processing systems. One of the important features of the system is that the phases present and the phase equilibria are dependent on not only bulk composition and temperature but also on the effective oxygen partial pressure of the system. At the one extreme, at low oxygen partial pressures, the system is limited by equilibrium with metallic iron; even under these conditions the iron species in the liquid oxide phase are present in both ferrous, Fe²⁺ and ferric, Fe³⁺ states [1]. The proportions of ferric iron in these slags increase with increasing oxygen partial pressure and decreasing temperature [2].

The CaO-FeO_x-SiO₂ system (see Figure 1) [3, 4] can be characterised by two low melting temperature regions; one at relatively high silica concentrations, the other at low silica concentrations approaching the CaO-FeO_x pseudo-binary join. Most experimental studies of the system have been undertaken to define the phase assemblages formed and the liquidus in the silica-rich region of the phase diagram. This silica-rich region is of direct relevance to steelmaking and non-ferrous, fayalitic smelting slags. The low-silica region is of interest to non-ferrous, “calcium ferrite” converter slags and ironmaking.

It is the iron-rich, low-silica corner of the system that is of particular interest to ironmaking practice. The majority of iron ore fines used in primary metal production are agglomerated into

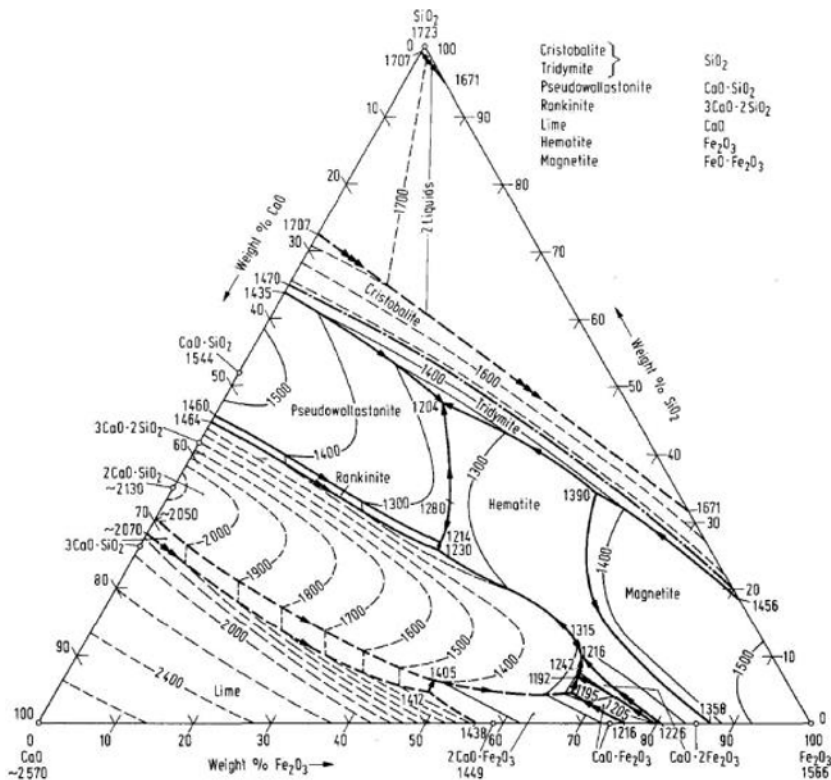


Figure 1. SiO₂-Fe₂O₃-CaO ternary phase diagram in air [3], [4].

porous, reactive but physically strong, lump material for feed into the iron blast furnace using the Dwight Lloyd moving grate sintering process [5]. The feed to the process consists of typically, iron ore fines and return sinter fines, limestone and dolomite flux, and fine coke. As the charge progresses through the process air is drawn through the porous bed and the charge is heated through combustion of the coke in the bed. The charge then experiences a range of temperatures and gas conditions as the combustion and the heat fronts progress through the bed.

The production of high quality iron ore sinter is an important factor in achieving high productivity, and high thermal and chemical efficiencies in modern blast furnace practice. Control of sinter microstructure is the key factor in attaining optimum physical and chemical properties. Research reports and literature available to date [6] have suggested the formation of a particular phases namely Silico-Ferrite of Calcium (SFC) and/or Silico-Ferrite of Calcium and Aluminium (SFCA) during the sinter making play a dominate role in determining the sinter microstructure, and the metallurgical properties of iron ore sinter, such as, reducibility, mechanical strength and soften temperature. There is strong experimental and anecdotal evidence to suggest that SFC and SFCA are formed through crystallisation from the liquid phase,

however, inspection of the liquidus surfaces for the CaO-Fe₂O₃-SiO₂ system in air, see Figure 1 [1, 2] shows no primary phase field for these compounds. Iron-rich, low-silica corner of the diagram consists of primary phase field of magnetite, Fe₃O₄; hematite, Fe₂O₃; calcium oxide, CaO; calcium di-ferrite, CaO.2Fe₂O₃; monocalcium ferrite, CaO.Fe₂O₃; di-calcium ferrite, 2CaO.Fe₂O₃. The lack of experimental data also means that current thermodynamic databases do not include the SFC and SFCA phases.

The SFC phase has been found [7] to be stable of the system CaO-Fe₂O₃-SiO₂ in air; and its crystal structure reported has been confirmed [8] by X-ray powder diffraction studies. Isothermal phase equilibria studies [9] for temperatures in the range at 1240°C to 1270°C have been undertaken for the iron-rich corner of the phase diagram. In this study it was found that the SFC phase was stable up to 1252°C in air and to melt incongruently at higher temperature to form hematite and liquid. The compositional range of SFC was measured by electron probe microanalysis and reported to be between 3.9wt% and 6.8wt% SiO₂. The experiments involved the equilibration of (3.5g) pellitised, synthetic chemical mixtures supported by Pt foil in air and quenching into water. The samples were then examined using optical microscopy, EPMA and XRD analysis. Using this technique it was not possible to measure the compositions of the coexisting solid and liquid phases. The results have provided a valuable initial guide to the phases present in the sub-system CaO-FeO-Fe₂O₃-SiO₂ in the composition ranges of interest to iron ore sintering, however, the compositions of all the phases observed were not reported. It was clear that using this technique it was not possible to retain the liquid present at temperature as a glass phase on cooling to room temperature in these low-SiO₂ liquids; this meant it was not possible to accurately determine the liquidus surface in the high-iron region of the system or the conjugate phase relations between solid and liquid solutions.

The aim of present study is to accurately determine the slag liquidus compositions and the solid/liquid phases that coexist at equilibrium with focus on the SFC primary phase field. Particular efforts have been put on addressing the issue of quenching high-fluidity, low-SiO₂ liquid.

Experimental

Over a number of years experimental procedures for phase equilibrium measurements have been developed by the Pyrometallurgy Research Laboratory (PYROSEARCH) at the University of Queensland [10]. The technique involves high temperature equilibration of a synthetic oxide sample in a controlled gas atmosphere. The sample is then rapidly quenched so that the phase assemblage present at high temperature remains unaltered. The quenched sample is mounted in epoxy resin, polished for metallographic examination and microanalysis, and the compositions of the crystalline solid phases are measured by electron probe X-ray microanalysis (EPMA) with wavelength dispersive detectors (WDD).

Preparation of oxide mixtures

The starting mixtures were made from CaO (99.98 wt% purity), Fe₂O₃ (99.98 wt% purity), SiO₂ (99.98 wt% purity). Mixtures of selected bulk compositions were prepared by weighing the high

purity powders, mixing them thoroughly using an agate mortar and pestle then compacted to produce a pellet weighing around 0.2 gram.

To ensure that the specimen could be cooled rapidly following equilibration the pellet was supported initially on a platinum wire formed into a spiral shape (see Figure 2a). During equilibration, the sample became partially molten and flowed into the gaps between the spirals and was held onto the wire by the surface tension (See Figure 2b). In this way on quenching the sample the liquid slag phase was the first phase to come in direct contact with the quenching medium (water). This results in very high quenching rate and minimizes the extent of crystallisation of the liquid during the quenching process. It was found that platinum, under the conditions investigated, did not dissolve in or contaminate the slag samples.

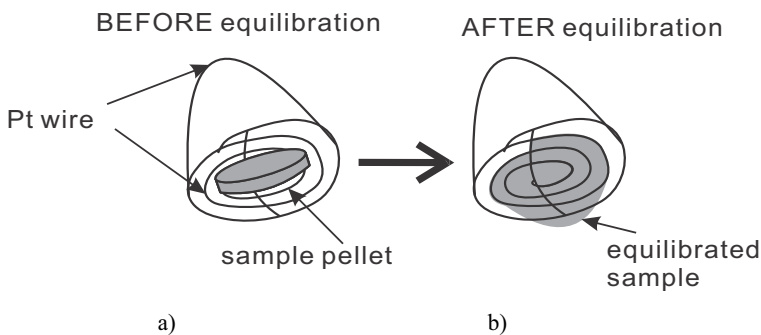


Figure 2 Sample a) before and b) after equilibration

High temperature equilibration technique

All equilibration experiments were conducted in a vertical impervious re-crystallized alumina, reaction tube in electrical resistance-heated furnaces. The sample was introduced from the bottom of the vertical tube furnace and suspended by a sample holder constructed using Pt wire. The experiment commenced by raising the sample into the uniform temperature hot zone of the furnace. After the equilibration, the specimen was rapidly quenched by dropping it directly into the iced water. The samples were mounted in epoxy resin, polished using conventional metallographic polishing techniques and carbon coated for subsequent electron probe X-ray micro-analysis (EPMA).

To monitor the actual temperature of the sample, a working thermocouple of 6-30 wt% Rh/Pt was placed in a re-crystallised alumina thermocouple sheath immediately adjacent to the sample. It is estimated that the overall absolute temperature accuracy of the experiment is within 5°C.

Analysis technique and selection of measurement points

The rapid quenching technique successfully retains phase assemblages present at the equilibration temperatures. The compositions of various phases were measured using JEOL

8200L EPMA with wavelength dispersive detectors (JEOL is a trademark of Japan Electron Optics Ltd., Tokyo). A 15-kV accelerating voltage and 15 nA probe current were selected for the micro-analyzer operation. The standards (Charles M. Taylor, Stanford, CA) used in the EPMA measurements were as follows: wollastonite (CaSiO_3) for Ca and Si, hematite (Fe_2O_3) for Fe. The Duncumb–Philibert correction based on atomic number, absorption, and fluorescence (ZAF correction, supplied by JEOL) was applied. The accuracy of compositions measured was expected to be within 1wt%. Only the Me-cations concentrations were measured with EPMA; the corresponding oxidation states were assigned.

As mentioned previously, due to the high fluidity of low SiO_2 liquid, it is impossible to obtain well-quenched liquid phase across the whole sample even when the open support method was used. Mounted samples were examined carefully under the electron microscope at high magnifications and well quenched areas were selected when carrying out the EPMA measurement for the liquid phase. Following example is given. A micrograph of a sample containing hematite-SFC-liquid three phase equilibrium phase assemblage is shown in Figure 3. It consists of large crystalline hematite and SFC grains surrounded by a liquid phase. Within the liquid phase and at the interface of liquid and solids, clusters of fine needle-shaped microcrystalline phases were observed; these phases were believed to have precipitated out of the liquid during quenching (e.g. region A). It is generally found that better quenching was obtained at the edges of the sample where direct contact with quenching media was expected. Measurement of the liquid composition should then be carried out on the well quenched areas, such as B, rather than those of type A, where there is the presence of microcrystalline precipitates. The direct observation of the phase assemblage makes it possible to distinguish phases that were present at the equilibration temperature. In this sense the present technique is superior to the use of XRD, although the latter can provide useful information on the crystal structures and confirm the individual phases present. The cracks in the sample have formed after cooling as evidenced by the continuity of the crack position across the phase boundaries between solid and (liquid) glass phases, and the solid/solid interface boundaries.

The following phases have been identified in the range of compositions investigated: liquid (L), silicoferrite of calcium solid solution (SFC); hematite, H, (Fe_2O_3); dicalcium silicate, C_2S , ($2\text{CaO}\cdot\text{SiO}_2$); calcium diferrite, CF_2 , ($\text{CaO}\cdot 2\text{Fe}_2\text{O}_3$) and calcium monoferrite, CF, ($\text{CaO}\cdot\text{Fe}_2\text{O}_3$).

Liquidus between 1200°C to 1260°C

The liquidus of the iron-rich corner of the $\text{CaO}\text{-Fe}_2\text{O}_3\text{-SiO}_2$ system in air deduced from the results of the present investigation is shown in Figure 4. The eutectic and peritectic temperatures on the $\text{CaO}\text{-“Fe}_2\text{O}_3”$ binary system in air were taken from previously studies by Liu et al. [11]. The CF and CF_2 phases melt incongruently and form a binary eutectic at 1205°C. This eutectic reaction extends into SiO_2 -containing system and a peritectic reaction involving C_2S , CF and CF_2 phases occurs at 1192°C and approximately 4.2wt% SiO_2 . The eutectic liquidus temperature continues to decrease with increasing silica concentration; at 1192°C and 4.4wt% SiO_2 the eutectic reaction is between C_2S and CF_2 . The temperature continues to decrease until the ternary eutectic point involving $\text{C}_2\text{S}\text{-CF}_2\text{-SFC}$ is reached at 1185°C and 6wt% SiO_2 .

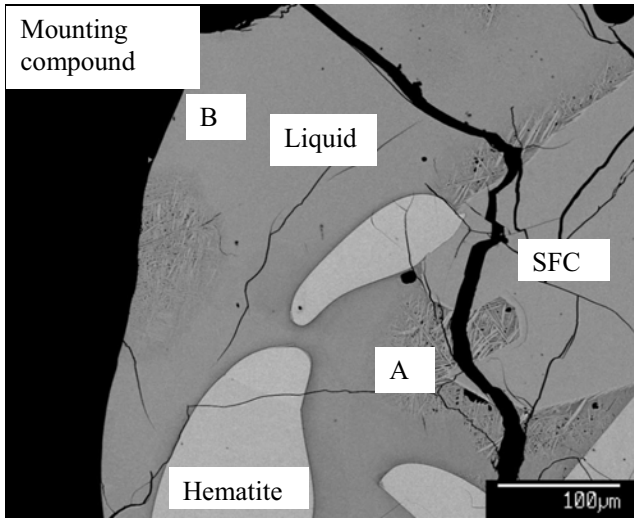


Figure 3 Example of microstructures observed (in backscattered electron mode) in the CaO- Fe_2O_3 - SiO_2 system in air at 1240°C showing the hematite-liquid-SFC phases in equilibrium.

The primary phase field of the SFC solid solution (labelled as “S”) was found to exist in a narrow range of compositions between 4-8.5 wt% SiO_2 . The SFC field is bounded by the primary phase fields of hematite (labelled as “H”), calcium di-ferrite (labelled as “ CF_2 ”) and di-calcium silicate (labelled as “ C_2S ”). The points abcd on Figure 4 mark the limits of the SFC primary phase field. The point a) marks the coexistence of the SFC- CF_2 -H phases; point b) marks the coexistence of the C_2S - CF_2 -SFC phases; at point c) the phases C_2S -SFC-H are present and at point d) SFC and H. Point d) represents the maximum temperature at which SFC can exist; above this temperature only liquid and hematite are present. The dashed lines marking the particular temperatures indicate the estimated positions of these isotherms.

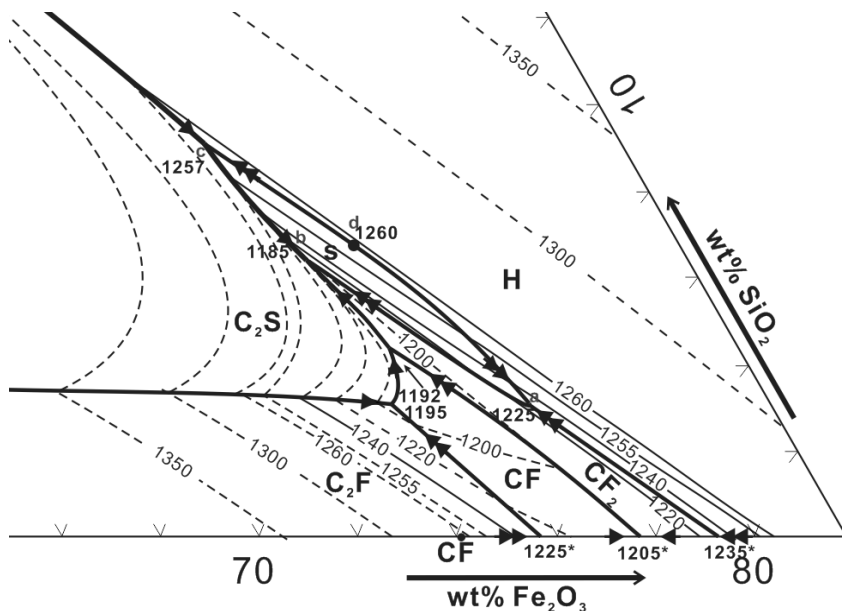


Figure 4. Estimated liquidus of CaO-Fe₂O₃-SiO₂ system in air including the SFC primary phase field based on the results of the present study and binary data reported by [11]. Legend: H = Hematite (Fe₂O₃), SFC = SFC solid solution, L = Liquid, C₂S = Dicalcium silicate (2CaO.SiO₂), C₂F = Di-calcium ferrite (2CaO. Fe₂O₃), CF = Calcium monoferrite (CaO.Fe₂O₃) and CF₂ = Calcium diferrite (CaO.2Fe₂O₃). Temperatures in °C.

Liquidus

The liquidus obtained in the present study for the CaO-Fe₂O₃-SiO₂ system, shown in Figure 4, differs from that of Phillips and Muan [3], which has been the accepted diagram for this system to date. The SFC phase did not appear on the previous versions of the liquidus. The present study provides information on the limits of the SFC primary phase field. This information is essential to identify the compositions and temperatures in which this phase will form from the liquid.

The narrow region over which the SFC phase can be formed helps to explain why the presence of this SFC primary phase field was not recognised in the earlier investigations.

Summary

Phase equilibria in the CaO-“Fe₂O₃”-SiO₂ ternary system in air have been determined between 1200°C to 1260°C with the focus on identifying the limits of stability of the SFC phase. Particular attention has been paid to minimizing the experimental uncertainties including:

- Developing special experimental techniques to address the challenges in quenching the low-SiO₂, high-fluidity liquid encountered in iron-rich compositions.
- Confirmation of attainment of equilibrium

- Area selection for composition measurement using EPMA.

The major findings and results of the present study are summarised as follows

- Isothermal sections in the CaO-Fe₂O₃-SiO₂ system in air have been constructed for 1220°C, 1240°C, 1255°C and 1260°C.
- The primary phase field of SFC and the liquidus between 1200°C to 1260°C of CaO-“Fe₂O₃”-SiO₂ system at Fe-rich side have been determined and constructed for the first time.
- The SFC solid solution was found to be stable below 1255°C in air and melt incongruently to form hematite and liquid above this temperature.
- The substitution mechanism of SFC solid solution was found to be in good agreement with the reaction $Si^{4+} + Ca^{2+} = 2Fe^{3+}$
- The SFC primary phase field was found to exist over a narrow range of compositions bounded by the primary phase fields of hematite (Fe₂O₃), dicalcium silicate (2CaO.SiO₂) and calcium diferrite (CaO.2Fe₂O₃).

Acknowledgements

This research was supported financially by the Baosteel Australia Joint Research Centre (BAJC). The authors wish to thank the members of the Baosteel Ironmaking Institute for their support and collaboration; in particular Director, Xiaoming Mao and Mr Qi Wei.

Thanks also to

- Suping Huang for the careful work in preparation of samples and assisting with the sample preparation and experiments.
- the Centre for Microscopy and Microanalysis, The University of Queensland, for the provision of electron microscope facilities and to the staff of the Centre for their support in maintaining these facilities.

References

1. A. Muan and E.F Osborn, Phase Equilibria among Steelmaking, Addison-Wesley, Reading, Mass., USA, 1965.
2. M. Timucen and A.E. Morris, Metall. Trans., 1970, vol.1(11), pp.3193-3201.
3. B. Phillips and A. Muan, J. Amer. Ceram. Soc., 1959, vol.42, pp.413-423.
4. Slag Atlas, StahlEisen, 2nd Ed., 1999.
5. P.R. Dawson, J. Ostwald and K.M. Hayes, BHP Tech. Bulletin, 1983, vol. 27, pp. 47-51.
6. M.I. Powcenby and J. M. Clout, Trans IMM C, 2003, vol.112, pp.C44-C51.
7. K. Inoue and T.Ikeda, Tetsu te Hagane, 1982, vol.68, pp.2190-2199.
8. J.D.G. Hamilton, B.F. Hoskins, W.G. Mumme, W.G. Borbridge and M.A. Montegue, N. Jb. Miner. Abh. 1989, vol.161, pp.1-26.
9. M.I. Powcenby, J. M. Clout and J.F. Fisher-White, Trans IMM C, 1998, vol.107, pp.C1-10.
10. E. Jak and P.C. Hayes, Trans IMM-C, 2008, vol.117(1), pp.1-117.
11. X. Liu, Experimental phase equilibria studies in oxide systems for copper smelting slags, MPhil Thesis, 2013, The University of Queensland, Australia.

UNDERSTANDING SULFIDE CAPACITY OF MOLTEN ALUMINOSILICATES VIA STRUCTURAL INFORMATION FROM ‘RAMAN’ AND ‘NMR’ SPECTROSCOPIC METHODOLOGIES

Joo Hyun PARK*

Department of Materials Engineering, Hanyang University, Ansan 426-791, Korea

* Contact ; basicity@hanyang.ac.kr

Keywords: Sulfide capacity, Aluminosilicate melts, Structure, Raman, NMR spectroscopy

Abstract

The effect of Ca-Mn substitution on the sulfide capacity of the MnO-CaO-SiO₂ (-Al₂O₃-MgO) melts were explained from the Raman scattering data, from which the structure information for the network modifying role and sulfur stabilizing role of Ca²⁺ and Mn²⁺ ions were obtained. The effect of Ce₂O₃ on the sulfide capacity of the MnO-SiO₂-Al₂O₃-Ce₂O₃ melts were understood based on the structure data, from which the charge compensating role of Ce³⁺ and the amphoteric behavior of alumina were obtained. Employing the structure analysis, the thermochemical properties such as capacity of the oxide melts with no thermodynamic data can be understood in terms of ‘composition-structure-property’ relationship.

Introduction

Desulfurization (de-S) has been emphasized over several decades in iron- and steelmaking processes, because sulfur is harmful to the mechanical properties of steel products. Additionally, the de-S of Mn (ferro-)alloys and high Mn steels is an important issue, due to the introduction of AHSS such as TRIP and TWIP aided steels that were recently developed to contain Mn up to about 30% [1]. Thus, Even though many researchers have investigated the sulfide capacities of molten slags, there are a few experimental data regarding high MnO-containing aluminosilicate melts. Moreover, there is still room for further understanding in regard of the influence of Ca-Mn substitution on the sulfur dissolution mechanism in (alumino-)silicate melts.

On the other hand, the addition of rare earth elements such as Ce, etc. in molten steel has been known to improve the high temperature oxidation resistance of stainless steels [2]. We recently found that the CeO_x-containing aluminosilicate inclusions are formed in melting and refining processes of Ce-containing steels [3,4], during which the sulfur in molten steel can be dissolved into the CeO_x-containing oxides. Thus, the thermodynamic information of the sulfide absorption ability, i.e. sulfide capacity of the CeO_x-containing aluminosilicate system is also necessitated. Unfortunately, however, there is no experimental and thermodynamic data for this oxide system.

Therefore, in the present paper, the influence of molten oxide composition on the sulfide capacity of the MnO- and CeO_x-containing aluminosilicate melts will be discussed in terms of composition-structure-property relationship by employing the micro-Raman and NMR spectroscopic methodologies for structure analysis.

Experimental procedure

A super-kanthal vertical electric resistance furnace was used for the equilibration between the MnO-CaO-SiO₂ (-Al₂O₃-MgO) slags and gas phase at 1873 K. The temperature

was controlled within ± 2 K using an installed B-type thermocouple and a PID controller. The slag samples were prepared using reagent-grade chemicals. The slag sample of 1.2 g was maintained in a Pt crucible which was held in the porous alumina holder under the CO-CO₂-SO₂-Ar gas mixture for 8 hours. A constant flow rate of 400 ml/min was maintained during the equilibration of the slag with gas mixture at the experimental temperature. Each gas was passed through the purification system to remove the impurities. The oxygen and sulfur partial pressures were $p(\text{O}_2)=2.8 \times 10^{-7}$ and $p(\text{S}_2)=4.7 \times 10^{-3}$ atm, respectively. A schematic diagram of the experimental apparatus is given elsewhere [5-7].

After equilibration, the sample was quickly drawn from the furnace and then quenched by dipping it into brine. The quenched samples were crushed to $<100 \mu\text{m}$ using stainless and agate mortars for chemical analysis. The content of sulfur and each component in the slag were determined by combustion analyzer and XRF spectroscopy, respectively. The activity of each component in slag phase was calculated by commercial thermochemical computing program, FactSage™7.0 with “FToxid” database.

The sulfide capacity of the MnO-SiO₂-Al₂O₃-CeO_x system at 1873 K was measured by similar procedure under the same gas potentials as mentioned above. In order to confirm the predominant oxidation state of Ce under the present experimental conditions, the XPS analyzer was employed with a reference to the binding energy of Ce³⁺ and Ce⁴⁺. The details of the preparation of glass samples and the experimental procedure of Raman and NMR spectra analysis are given elsewhere [8,9].

Results and Discussion

Composition-Structure-Capacity relationship of the MnO-CaO-SiO₂ (-Al₂O₃-MgO) melt

The iso-sulfide capacity of the MnO-CaO-SiO₂ and the MnO-CaO-SiO₂-20%Al₂O₃-5%MgO slags at 1873 K is shown in Figure 1. The capacity contours commonly seem to rotate clockwise from the MnO-free side to the MnO-rich corner in both systems [5-7]. Thus, the sulfide capacity increases by increasing the MnO/CaO ratio at a fixed silica content which is greater than about 30%, whereas it decreases by increasing the MnO/CaO ratio at silica content lower than about 30%.

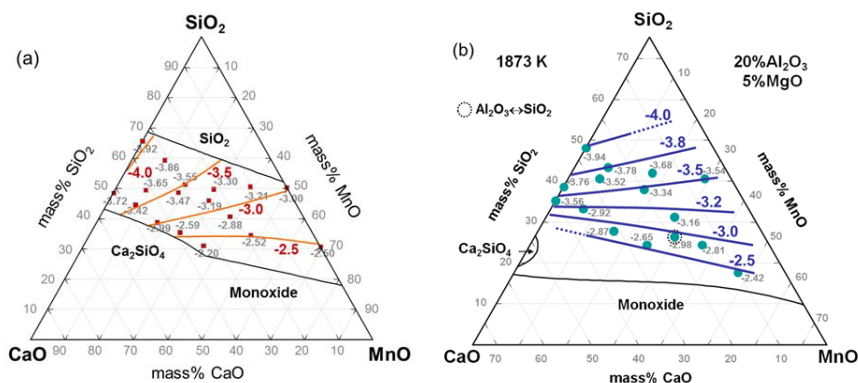


Figure 1. Sulfide capacity contours in the MnO-CaO-SiO₂ (-Al₂O₃-MgO) slags at 1873 K.

The CaO which has more ionic bond character, i.e. 79% based on the Pauling's equation

[10], dominantly contributes to the depolymerization of silicates than the MnO (ionic bond character 63%) does. Hence, the large amount of Ca^{2+} is electrically balanced with two non-bringing oxygen (NBO) ions, indicating that the Mn^{2+} is relatively free from the role of network modifier and mainly participate into the de-S reaction in high silica region.

However, in the relatively low silica region, viz. less than about 30% SiO_2 , the amount of Ca^{2+} balancing with NBO is reduced and thus free Ca^{2+} and Mn^{2+} competitively react with the S^{2-} ions, resulting in the dominant contribution of $\text{Ca}^{2+} \leftrightarrow \text{S}^{2-}$ attraction which is greater than $\text{Mn}^{2+} \leftrightarrow \text{S}^{2-}$ attraction in terms of the stability of each sulfide determined from the Gibbs free energy of the formation of CaS and MnS at 1873 K [11]. This indicates that the contribution of Ca^{2+} to the stabilization of S^{2-} ions would be larger than that of Mn^{2+} in the relatively low silica region.

The Raman spectra of the MnO-CaO-50% SiO_2 system is shown in Figure 2(a) in order to understand the structural change as MnO substitutes for CaO at a fixed silica content. The main silicate envelope is definitely resolved to Q^0 ($860(\pm 5)$ cm^{-1} for SiO_4 -monomer) and Q^2 ($960(\pm 5)$ cm^{-1} for SiO_3 -chain) bands in the calcium silicate binary system, while there is a broad asymmetric band between 800 and 1150 cm^{-1} at $\text{Mn}/(\text{Mn}+\text{Ca}) \sim 0.8$ [5-7]. Even though it is not easy to find a conclusive variation of Raman spectra with one's eye as MnO substitutes for CaO, a broadening of Raman band qualitatively suggests that the substitution of CaO by MnO made a stronger perturbation and hence a more depolymerized configuration of local environment of Q-species in high MnO melts at a fixed silica content.

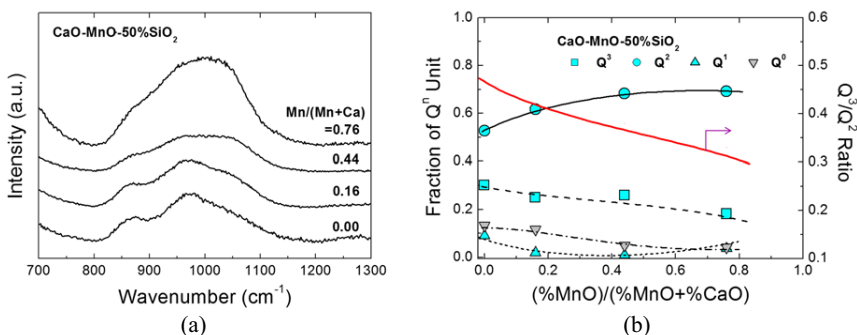
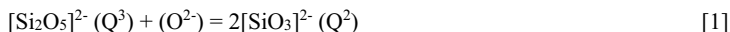


Figure 2. (a) Raman spectra and (b) fraction of structural unit of MnO-CaO-50% SiO_2 system.

The relative fractions of the silicate anionic units obtained from Gaussian deconvolution of Raman bands shown in Figure 2(a) are also plotted against the MnO/(MnO+CaO) ratio in Figure 2(b). The fraction of Q^2 (SiO_3 -chain) unit increases and that of Q^3 (Si_2O_5 -sheet) unit decreases with increasing MnO/(MnO+CaO) ratio [5-7]. The fractions of Q^0 (SiO_4 -monomer) and Q^1 (Si_2O_7 -dimer) units slightly decrease but not significant. Therefore, the Q^3/Q^2 ratio, viz. degree of polymerization decreases by increasing the MnO/(MnO+CaO) ratio based on the following equation:



The network-modifying role of Ca^{2+} and Mn^{2+} in this composition range can be discussed as follows. From an analysis of McMillan [12], doubly-charged M^{2+} of large ionic radius, i.e. small ionization potential ($=Z/r^2$) should preferentially occupy the more open, coupled Q^3 ($=\text{Si-O}$)₂ sites, while smaller M^{2+} with larger ionization potential will favor the

higher charge concentration offered by the Q^2 ($=Si-2O^-$) sites. This is schematically expressed in Figure 3. Because the ionization potential of Ca^{2+} ($Z/r^2=2$) is lower than that of Mn^{2+} ($Z/r^2=2.4\sim 3.0$ according to electron spin) [13], the Ca^{2+} is charge balanced with two open O^- ions due to its large size of $[CaO_6]$ cage, whereas the Mn^{2+} is balanced with two adjacent corner-shared O^- ions due to its small size of $[MnO_6]$ cage as shown in Figure 3 [5-7].

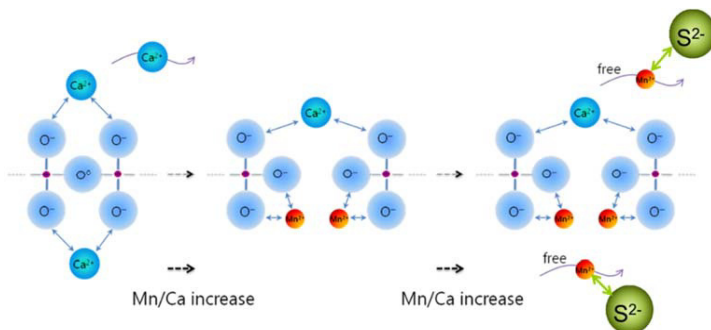


Figure 3. Structure modification by network-breaking role of Ca^{2+} and Mn^{2+} in silicate melts.

Composition-Structure-Capacity relationship of the $MnO-SiO_2-Al_2O_3-Ce_2O_3$ melt

The effect of Ce_2O_3 on the sulfide capacity of the $MnO-SiO_2-Al_2O_3-Ce_2O_3$ system ($X_{MnO}/X_{SiO_2} = M/S = 0.28, 0.85, 2.54$) at 1873 K is shown in Figure 4. It is very interesting that the influence of Ce_2O_3 on the sulfide capacity exhibits a different tendency according to the M/S ratio [14]. The sulfide capacity of the oxide melts with highly basic composition, i.e. $M/S=2.54$, decreases with increasing content of Ce_2O_3 to approx. 4 mol%, beyond which the sulfide capacity increases by increasing the Ce_2O_3 content. The sulfide capacity continuously decreases as the Ce_2O_3 is added to the Mn-aluminosilicate melts in the less basic system, i.e. $M/S=0.85$, whereas it is hardly affected by Ce_2O_3 in the relatively acidic (high silica) composition, i.e. $M/S=0.28$.

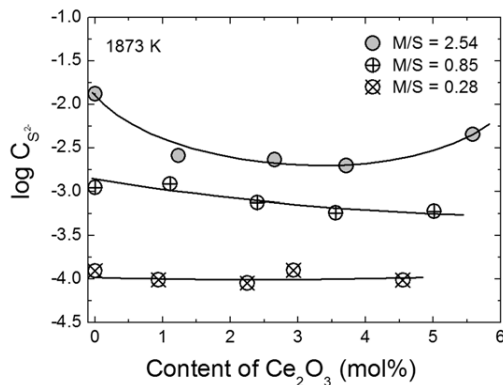


Figure 4. Effect of Ce_2O_3 on sulfide capacity of $MnO-SiO_2-Al_2O_3-Ce_2O_3$ system at 1873 K.

In order to thermodynamically understand these complicated phenomena, both the activity coefficient of MnS (or Ce₂O₃S) and the activity of MnO (or Ce₂O₃) should be evaluated. However, unfortunately, because none of thermodynamic data (activity of each component, phase equilibria, etc.) of the MnO-SiO₂-Al₂O₃-Ce₂O₃ system is available in the literature, the Raman spectroscopic analysis for the influence of Ce₂O₃ on the structure of Mn-aluminosilicate system was employed in the present study to reveal the composition-structure-property relationship.

The Raman spectra of the MnO-SiO₂-Al₂O₃-Ce₂O₃ systems (M/S=2.54 and 0.85) are shown in Figure 5 in order to understand the relationship between the structural change and the variation of sulfide capacity of the oxide melts. It is commonly found that the Raman band for the Si-O asymmetric stretching vibration between 800 and 1150 cm⁻¹ very slightly shifts to the lower wavenumbers by increasing the content of Ce₂O₃, indicating that there is no considerable change in the environment of silicate units by the incorporation of Ce³⁺ ions [14].

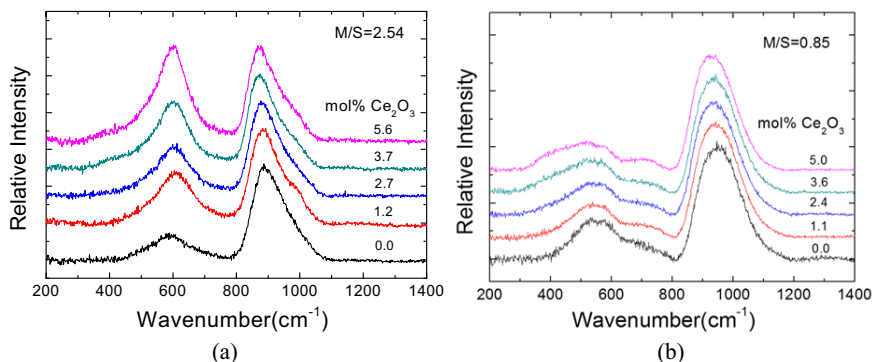
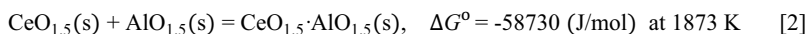


Figure 5. Raman scattering of MnO-SiO₂-Al₂O₃-Ce₂O₃ system at different Ce₂O₃ contents.

In the Raman spectra of the M/S=2.54 system shown in Figure 5(a), there is a significant increase in the relative intensity of the scattering band at about 600 cm⁻¹ with increasing content of Ce₂O₃. It is considered that the increase in the relative intensity of Raman band at 600 cm⁻¹ is due to the [AlO₆]-unit as mentioned by Okuno et al. [15], because of the strong attraction between Al₂O₃ and Ce₂O₃ in the present system. However, this tendency was not observed in the less basic melts, viz. M/S=0.85 system as shown in Figure 5(b).

Lin et al. [16] suggested that the Ce³⁺ conducts a role of charge compensator or network modifier rather than network former because Ce³⁺ ion ($r=1.01\text{\AA}$) has a radius close to that of Ca²⁺ ($r=1.0\text{\AA}$), which is too large to be a (tetrahedrally coordinated) network former like [SiO₄] or [AlO₄] units. Wu and Pelton reported the strong affinity between Ce₂O₃ and Al₂O₃ in the Ce₂O₃-Al₂O₃ system [17]. Morita et al. [18,19] found that the addition of Ce₂O₃ to the CaO-Al₂O₃ system decreases the activity coefficient of Al₂O₃ in the melts because of the strong attraction between Ce₂O₃ and Al₂O₃ based on the following reaction.



Before adding Ce₂O₃, the concentration of [AlO₆]-unit in the less basic (M/S≤0.85) systems are larger than that in the highly basic (M/S=2.54) system as shown in Figure 5.

Thus, Ce^{3+} ions added in the less basic melts instantly interact with large amounts of (pre-existing) $[AlO_6]$ -units to form more stable $[(Al,Ce)O_6]$ -unit as schematically shown in Figure 6(a). Therefore, the structure of aluminosilicate melts was not significantly disturbed by addition of Ce_2O_3 , resulting in the insensitive dependency of sulfide capacity of the melts on the content of Ce_2O_3 as shown in Figure 4 [14].

On the other hand, in the highly basic system ($M/S=2.54$), relatively large amounts of (pre-existing) $[(Al,Mn_{0.5})O_4]$ -units should be converted to the $[(Al,Ce)O_6]$ -unit with consumption of free oxygen by addition of Ce^{3+} ions, resulting in a decreases in sulfide capacity. However, the sulfide capacity increases by addition of Ce_2O_3 greater than about 4mol% (Figure 4) because the excess Ce^{3+} and free Mn^{2+} cations contribute to the stabilization of S^{2-} ions as schematically shown in Figure 6(b). This tendency was not observed in the less basic systems because the cations (Ce^{3+} and Mn^{2+}) are still not free from a charge compensating role with large amounts of silicate anions within the present experimental compositions [14].

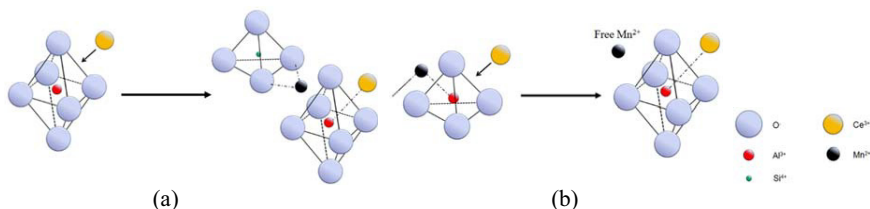


Figure 6. Structural changes of (a) less basic and (b) highly basic melts by Ce_2O_3 addition.

Conclusions

The influence of molten oxide composition on the sulfide capacity of the aluminosilicate melts containing MnO and/or Ce_2O_3 was discussed in terms of ‘composition-structure-property’ relationship by employing the micro-Raman spectroscopy for structure analysis.

For the sulfide capacity of the MnO-CaO-SiO₂ (-Al₂O₃-MgO) melts at 1873 K, because CaO dominantly contributes to the depolymerization of silicates than MnO does, the large amount of Ca^{2+} is electrically balanced with two NBO, indicating that the Mn^{2+} is relatively free from the role of network modifier and mainly participate into the de-S reaction in high silica region. However, in the relatively low silica region, the amount of Ca^{2+} balancing with NBO is reduced and thus free Ca^{2+} and Mn^{2+} competitively react with the S^{2-} ions, resulting in the dominant contribution of $Ca^{2+} \leftrightarrow S^{2-}$ attraction which is greater than that of $Mn^{2+} \leftrightarrow S^{2-}$ pair. This indicates that the contribution of Ca^{2+} to the stabilization of S^{2-} ions would be larger than that of Mn^{2+} in the relatively low silica region.

For the sulfide capacity of the MnO-SiO₂-Al₂O₃- Ce_2O_3 melts at 1873 K, because the concentration of $[AlO_6]$ -unit in the high silica systems are larger than that in the lower silica system, Ce^{3+} ions added in the former instantly interact with large amounts of $[AlO_6]$ -units to form more stable $[(Al,Ce)O_6]$ -unit. Hence, the structure of aluminosilicate melts was not significantly disturbed by addition of Ce_2O_3 , resulting in the insensitive dependency of sulfide capacity of the melts on the content of Ce_2O_3 . However, in the lower silica region, the relatively large amounts of $[(Al,Mn_{0.5})O_4]$ -units should be converted to the $[(Al,Ce)O_6]$ -unit with consumption of free oxygen by addition of Ce^{3+} ions, resulting in a decreases in sulfide capacity. The sulfide capacity increases by addition of Ce_2O_3 greater than about 4mol% because the excess Ce^{3+} and free Mn^{2+} cations contribute to the stabilization of S^{2-} ions. This

tendency was not observed in the high silica systems because the cations (Ce^{3+} and Mn^{2+}) are still not free from a charge balancing role with large amounts of silicate anions.

References

1. K.T. Park et al., "Stacking fault energy and plastic deformation of fully austenitic high manganese steels," *Materials Science & Engineering A*, 527 (2010), 3651-61.
2. S.T. Kim et al., "Effects of rare earth metals addition on the resistance to pitting corrosion of super duplex stainless steel - Part 1," *Corrosion Science*, 52 (2010), 1897-1904.
3. S.K. Kwon, Y.M. Kong and J.H. Park, "Effect of Al deoxidation on the formation behavior of inclusions in Ce-added stainless steel melt" *Metals & Materials International*, 20 (2014), 959-66.
4. S.K. Kwon, J.S. Park and J.H. Park, "Influence of Refractory-Steel Interfacial Reaction on the Formation Behavior of Inclusion in Ce-containing Stainless Steel Melt," *ISIJ International*, 55 (2015), 2589-96.
5. G.H. Park, Y.B. Kang and J.H. Park, "Sulfide capacity of the CaO-SiO₂-MnO slag at 1873 K," *ISIJ International*, 51 (2011), 1375-82.
6. J.H. Park and G.H. Park, "Sulfide capacity of the CaO-SiO₂-MnO-Al₂O₃-MgO slags at 1873 K," *ISIJ International*, 52 (2012), 764-69.
7. J.H. Park, "Competitive Dissolution Mechanism of Sulphur in Ca-Mn-Silicate Melts: Structural View," *Steel Research International*, 84 (2013), 664-69.
8. J.H. Park, "Composition-structure-property relationships of CaO-MO-SiO₂ (M=Mg²⁺, Mn²⁺) systems derived from micro-Raman spectroscopy," *Journal of Non-Crystalline Solids*, 358 (2012), 3096-3102.
9. J.H. Park, "Structure-Property Correlations of CaO-SiO₂-MnO Slag derived from Raman Spectroscopy," *ISIJ International*, 52 (2012), 1627-36.
10. L. Pauling, *The Nature of Chemical Bond and the Structure of Molecules and Crystals*, 3rd ed. (Cornell University Press, NY, 1960), 97-102.
11. Y.B. Kang and J.H. Park, "On the dissolution behavior of sulfur in ternary silicate slags," *Metallurgical & Materials Transactions B*, 42B (2011), 1211-17.
12. P. McMillan, "A Raman spectroscopic study of glasses in the system CaO-MgO-SiO₂," *American Mineralogists*, 69 (1984), 645-59.
13. R.D. Shannon, "Revised Effective Ionic Radii and Systematic Studies of Interatomic Distances in Halides and Chalcogenides," *Acta Crystallographica A*, 32A (1976), 751-67.
14. S.J. Jeong, T.S. Kim and J.H. Park, "Sulfide capacity and structure analysis of MnO-SiO₂-Al₂O₃-Ce₂O₃ system," *ISIJ International*, 56 (2016), to be published.
15. M. Okuno et al., "Structure of SiO₂-Al₂O₃ glasses: Combined X-ray diffraction, IR and Raman studies," *Journal of Non-Crystalline Solids*, 351 (2005), 1032-38.
16. S.L. Lin, C.S. Hwang and J.F. Lee, "Structure and Properties of CeO₂-Al₂O₃-SiO₂ Glasses," *Japanese Journal of Applied Physics*, 35 (1996), 3975-83.
17. P. Wu and A.D. Pelton, "Coupled thermodynamic-phase diagram assessment of the rare earth oxide-aluminium oxide binary systems," *Journal of Alloys & Compounds*, 179 (1992), 259-87.
18. S. Ueda, K. Morita and N. Sano, "Activity of AlO_{1.5} for the CaO-AlO_{1.5}-CeO_{1.5} System at 1773 K," *ISIJ International*, 38 (1998), 1292-96.
19. R. Kitano, M. Ishii and K. Morita, "Phase Equilibria and Activities of AlO_{1.5} for the CaO-AlO_{1.5}-CeO_{1.5} System at 1823 and 1873 K," (Paper presented at the Asia Steel International Conference, Tokyo, Japan, October, 2015), 40.

THERMODYNAMIC PROPERTIES OF THE CaO- $\text{AlO}_{1.5}$ - $\text{CeO}_{1.5}$ SYSTEM

Ryo Kitano, Kazuki Morita

Department of Materials Engineering, The University of Tokyo
7-3-1 Hongo, Bunkyo-ku, Tokyo 113-8656, Japan

Keywords: Rare-earth element, Calcium oxide, Aluminum oxide, Cerium oxide, Steel, Complex deoxidation, Phase relations, Activity

Abstract

Rare earth (RE) elements are expected to be effective deoxidizing agents in steelmaking because of their strong affinity for oxygen. Deoxidation products would be composed of the CaO- $\text{AlO}_{1.5}$ - REO_x system with the existence of secondary refining fluxes and/or in case of complex deoxidation with Ca and Al. This study focuses on Cerium (Ce), which is one of the main components in the misch metal alloys. The phase relations for the CaO- $\text{AlO}_{1.5}$ - $\text{CeO}_{1.5}$ system have been investigated at 1823 K and 1873 K by chemical equilibration technique also by clarifying the existence of ternary intermediate compounds, $\text{CaO}\cdot\text{AlO}_{1.5}\cdot\text{CeO}_{1.5}$ and $\text{CaO}\cdot 3\text{AlO}_{1.5}\cdot\text{CeO}_{1.5}$. Also, by clarifying the activity of $\text{AlO}_{1.5}$ of the present system, Al-Ce complex deoxidation behavior is discussed.

1. Introduction

Rare earth elements have higher affinity for oxygen and sulfur, and are evaluated to be suitable for the complex deoxidation and desulfurization of steels with Al co-addition [1, 2]. Furthermore, the oxide inclusions containing such elements are known to be finely dispersed and expected to improve the property of steels by hardening the inclusions [3]. The behavior of such inclusions during the steel refining processes, however, are not well assessed, hence thermodynamic properties of rare earth oxide bearing systems, such as the CaO- $\text{AlO}_{1.5}$ - REO_x system, are desired to be evaluated

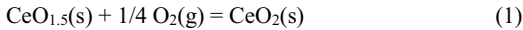
After the rare earth crisis in Japan in 2010, recycling and alternative materials were developed which made the excess supply of light rare earth metals leading to considerable falling in their prices. For this reason, it would be important to pioneer the way of their utilization. Furthermore, utilization of misch metal is considered to be realistic due to the difficulty in extraction and/or separation of respective pure elements.

In the present study, by focusing Ce as a representative light rare earth element, phase relations for the CaO- $\text{AlO}_{1.5}$ - $\text{CeO}_{1.5}$ system as well as some thermodynamic consideration at steelmaking temperatures have been investigated.

2. Experimentals

2.1 Consideration of Experimental Atmosphere

A cerium oxide exists as either trivalent (Ce^{3+}) or tetravalent (Ce^{4+}) depending on the ambient oxygen potential. Since $\text{CeO}_{1.5}$ dominantly exists at the condition of steel deoxidation, oxygen partial pressure of the present experiment was controlled so that the Ce^{3+} was stable in the oxide system. The oxygen partial pressure which allows coexistence of $\text{CeO}_{1.5}$ and CeO_2 is determined by Eq.1 and its Gibbs energy of reaction, ΔG°_1 , is expressed by Eq.2 [4].



$$\Delta G^{\circ}_1 = -192,000 + 67.9T \quad (\text{J/mol}) \quad (2)$$

The equilibrium oxygen partial pressures are obtained as 1.70×10^{-3} Pa and 6.55×10^{-3} Pa at 1823 K and 1873 K, respectively. Accordingly, Ar gas atmosphere with graphite crucible was employed in the experiment for phase relation determination, while the activity measurement of $\text{AlO}_{1.5}$ in the system was conducted in the atmosphere of CO-Ar gas with graphite crucible.

2.2 Evaluation of Ternary Compounds

Unknown ternary compounds newly confirmed in the present measurement were investigated by comparing the X-ray diffraction (XRD) data with those of similar compounds in the CaO- $\text{AlO}_{1.5}$ - $\text{LaO}_{1.5}$ system reported in respect to composition and crystal structure. Regarding the CaO- $\text{AlO}_{1.5}$ - $\text{LaO}_{1.5}$ system, two ternary compounds, $\text{CaO} \cdot \text{AlO}_{1.5} \cdot \text{LaO}_{1.5}$ and $\text{CaO} \cdot 3\text{AlO}_{1.5} \cdot \text{LaO}_{1.5}$, are reported to exist. [5, 6] About 0.5 g of chemicals were weighed and mixed so that the composition might become $\text{CaO}:\text{AlO}_{1.5}:\text{CeO}_{1.5} = 1:1:1$ and $1:3:1$, and were kept at 1873 K in a graphite crucible in Ar atmosphere for 20 hours. Then the samples were quenched and subjected to XRD analysis for comparison with those of the CaO- $\text{AlO}_{1.5}$ - $\text{LaO}_{1.5}$ system.

2.3 Phase Relations for the CaO- $\text{AlO}_{1.5}$ - $\text{CeO}_{1.5}$ System

A constituent CaO was prepared by calcination of CaCO_3 in air at 1273 K for 24 hours, while reagent grade of CeO_2 was used for $\text{CeO}_{1.5}$ without pretreatment assuming that reduction occurred during the experiment. Other saturating compounds were prepared by sintering at 1873 K for 20 hours after being compressed at 200 MPa for 3 min.

Figure 1 shows the cross section of the experimental apparatus used in the present study. The furnace was equipped with MoSi_2 heating elements and PID controller for the accurate temperature control within ± 1 K. About 0.5 g of initial molten oxide samples were prepared by weighing and mixing each chemical to designed molten compositions, then followed by equilibration with 0.5 g of saturating oxide compounds in a reducing atmosphere at 1823 K or 1873 K for 16 hours. When molten oxides are saturated with two compounds, both compounds were grounded to powder and mixed to be calcined after the compression. In case of CaO saturation, a chunk of a commercially available fused material was used due to instability of sintered CaO during the experiment. During the experiment, 150-200 mL/min of Ar gas (or Ar + CO gas) was flown onto the sample to keep the inside of the reaction tube (60 x 52 x 1000 mm)

to be a reducing atmosphere. After the equilibrium experiment, the sample was withdrawn from the furnace and the molten oxide phase was separated from the saturation solid phase and then subjected to chemical analysis using ICP-AES.

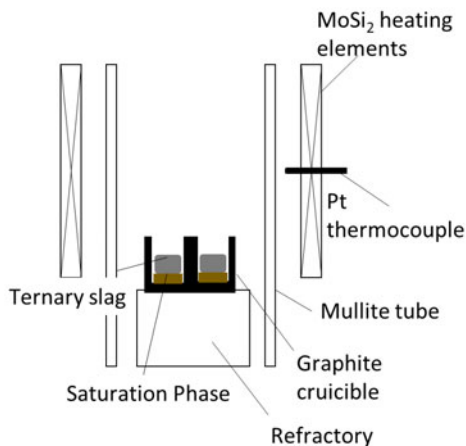


Fig.1 Cross section of the experimental apparatus.

2.4 Activity of $\text{AlO}_{1.5}$ in the $\text{CaO}\text{-AlO}_{1.5}\text{-CeO}_{1.5}$ System at 1873 K

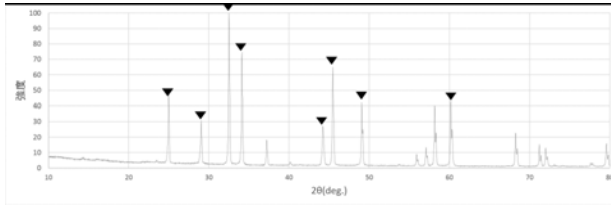
The apparatus and reagents were the same as those for the phase equilibria experiment. In this experiment, 1.0 g of the oxide mixture and 1.5 g of Cu were placed in a graphite crucible and kept in the furnace for 25 h, which was determined by the equilibrating experiment. Ar and CO mixed gas ($\text{Ar}:\text{CO} = 1:9$, $P_{\text{O}_2} = 2.51 \times 10^{-11}$ Pa) were introduced into the furnace with a gas lance, which was located more than 100 mm away from the sample. After 25 h, the Cu was removed and cleaned with HCl for 4 h to remove the flux, and then, 0.5 g Cu was dissolved in HNO_3 and analyzed using ICP emission spectrometry.

3. Results and Discussion

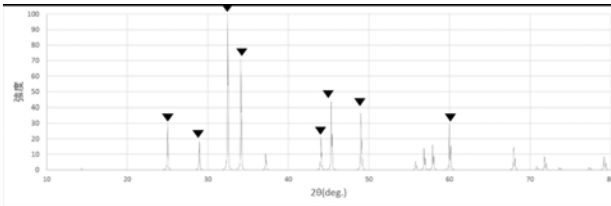
3.1 Evaluation of Ternary Compounds

In the preceding report by Ueda *et al.* [1], two ternary compounds were not clarified in terms of structure, which were confirmed prior to the measurement of phase relations. The XRD patterns of the sintered samples of $\text{CaO}:\text{AlO}_{1.5}:\text{CeO}_{1.5} = 1:1:1$ and $1:3:1$ were compared with those of $\text{CaO}\cdot\text{AlO}_{1.5}\cdot\text{LaO}_{1.5}$ and $\text{CaO}\cdot 3\text{AlO}_{1.5}\cdot\text{LaO}_{1.5}$ as shown in Fig.2. From the fact that each peak of the sample ((a) and (c)) corresponded to that of the $\text{LaO}_{1.5}$ bearing compounds ((b) and (d)), both of the sintered oxides were considered to be the compounds, $\text{CaO}\cdot\text{AlO}_{1.5}\cdot\text{CeO}_{1.5}$ and $\text{CaO}\cdot 3\text{AlO}_{1.5}\cdot\text{CeO}_{1.5}$, respectively. In Fig.2 (c), some peaks cannot be identified, which are considered to be those of $\text{AlO}_{1.5}\cdot\text{CeO}_{1.5}$ shown in Fig.2 (e). Although ionic radii of Ce^{3+} and La^{3+}

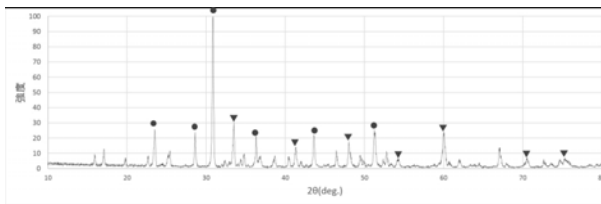
are almost identical, each peak of both ternary compounds appears to be shifted slightly toward smaller angles compared with that of $\text{LaO}_{1.5}$ containing compounds, indicating the compounds with $\text{CeO}_{1.5}$ would have larger lattice constant.



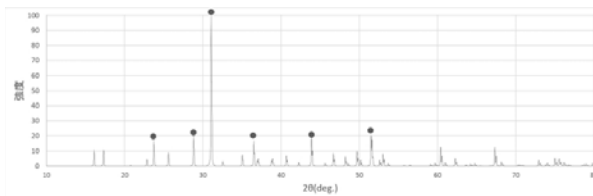
(a) $\text{CaO}:\text{AlO}_{1.5}:\text{CeO}_{1.5} = 1:1:1$



(b) $\text{CaO}\cdot\text{AlO}_{1.5}\cdot\text{LaO}_{1.5}$ [7]



(c) $\text{CaO}:\text{AlO}_{1.5}:\text{CeO}_{1.5} = 1:3:1$



(d) $\text{CaO}\cdot 3\text{AlO}_{1.5}\cdot\text{LaO}_{1.5}$ [7]

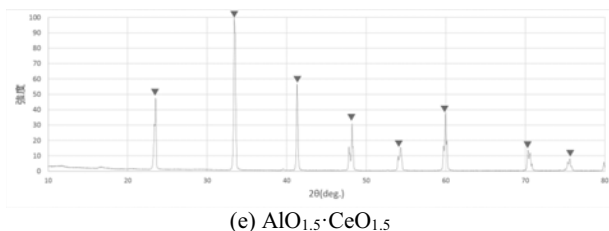
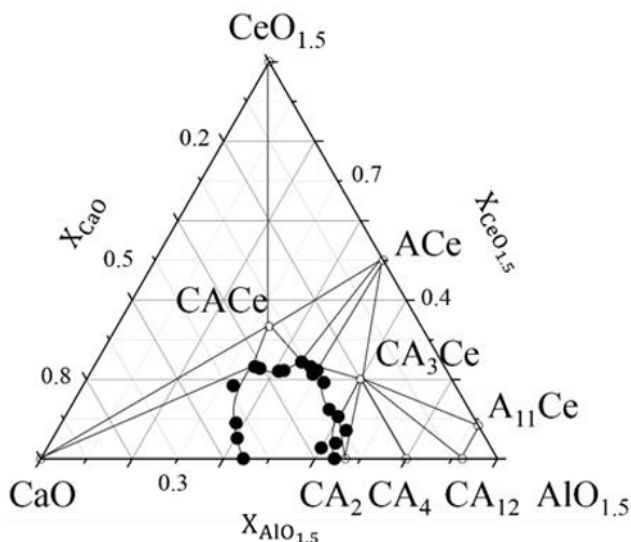


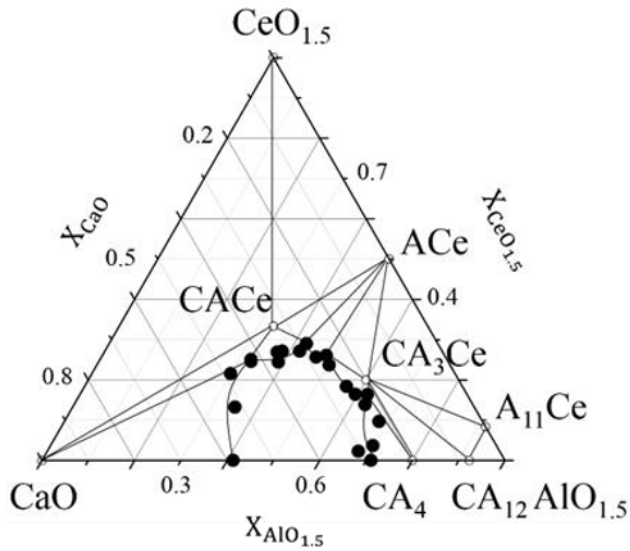
Fig.2 X-ray diffraction patterns of the sintered samples, (a) $\text{CaO}:\text{AlO}_{1.5}:\text{CeO}_{1.5} = 1:1:1$, (c) $\text{CaO}:\text{AlO}_{1.5}:\text{CeO}_{1.5} = 1:3:1$, (e) $\text{AlO}_{1.5} \cdot \text{CeO}_{1.5}$, and those of calculated $\text{LaO}_{1.5}$ bearing compounds, (b) $\text{CaO} \cdot \text{AlO}_{1.5} \cdot \text{LaO}_{1.5}$, (d) $\text{CaO} \cdot 3\text{AlO}_{1.5} \cdot \text{LaO}_{1.5}$.

3.2 Phase Relations for the $\text{CaO}-\text{AlO}_{1.5}-\text{CeO}_{1.5}$ System

Liquidus compositions for the $\text{CaO}-\text{AlO}_{1.5}-\text{CeO}_{1.5}$ system at 1823 K and 1873 K are plotted in Figs.3 (a) and (b), respectively, together with liquidus curves. The shape of liquid region is similar to that at 1773 K [1], and the area was confirmed to increase with temperature. At 1873 K, $\text{CaO} \cdot 2\text{AlO}_{1.5}$ disappeared which was one of the solid in equilibrium with the liquid phase at 1823 K, while $\text{CaO} \cdot 4\text{AlO}_{1.5}$ existed as a saturating solid instead. Although the temperature dependence of CaO saturated composition was found to be small, that of other compounds, such as $\text{CaO} \cdot \text{AlO}_{1.5} \cdot \text{CeO}_{1.5}$, $\text{AlO}_{1.5} \cdot \text{CeO}_{1.5}$, $\text{CaO} \cdot 3\text{AlO}_{1.5} \cdot \text{CeO}_{1.5}$ and $\text{CaO} \cdot 2\text{AlO}_{1.5}$ ($\text{CaO} \cdot 4\text{AlO}_{1.5}$) was considerably large.



(a) 1823 K



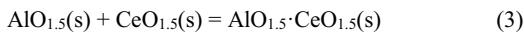
(b) 1873 K

Fig.3 Phase relations for the CaO-AlO_{1.5}-CeO_{1.5} system at (a) 1823 K and (b) 1873 K.

Regarding the oxidation state of Ce, it was confirmed to exist as trivalent (Ce³⁺) in the molten oxide by the XAFS analysis of the quenched samples. Furthermore, other compositions without the liquid phase were examined to verify the three phase regions (Gibbs triangles) surrounded by three tie lines, which were also drawn in the isothermal sections as Figs.3 (a) and (b).

3.3 Activity of AlO_{1.5} in the CaO-AlO_{1.5}-CeO_{1.5} System at 1873 K

After equilibrating Cu with the CaO-AlO_{1.5} melt saturated with CaO under a controlled oxygen partial pressure ($P_{O_2} = 2.51 \times 10^{-11}$ Pa), X_{Al} in Cu was 2.02×10^{-3} . The concentrations of Al in Cu after 25 hours and 40 hours were found to be identical. Since the activity of AlO_{1.5} ($a_{AlO_{1.5}}$) in the present oxide melt was reported to be 0.076 at 1873 K [8], activity coefficient of Al(l) in molten Cu (γ_{Al} in Cu^o) at infinite solution was calculated to be 1.81×10^{-2} . Since X_{Al} in Cu did not exceed 0.01 for any sample in the activity measurement, γ_{Al} in Cu^o was used in the derivation of $a_{AlO_{1.5}}$. The isoactivity curves of AlO_{1.5} in the CaO-AlO_{1.5}-CeO_{1.5} melts are drawn in Fig.4. As $X_{CeO_{1.5}}/X_{CaO}$ increased, $a_{AlO_{1.5}}$ was shown to decrease. The activity of CeO_{1.5} for the melts saturated with AlO_{1.5}-CeO_{1.5} was calculated from Eq.4 based on the reaction of Eq.3 [4].



$$\Delta G^{\circ}_3 = -40,000 + 10 T \quad (J/mol) \quad (4)$$

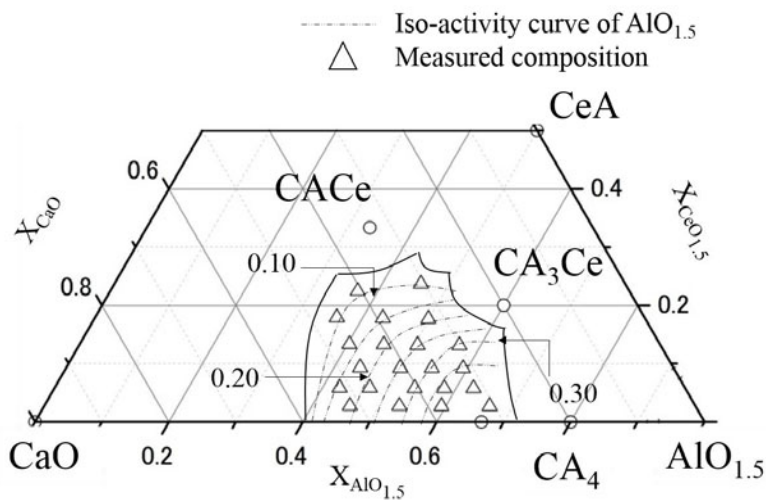


Fig.4 Isoactivity curves of $\text{AlO}_{1.5}$ in the $\text{CaO-AlO}_{1.5}\text{-CeO}_{1.5}$ melts at 1873 K.

From Eq.4 and $a_{\text{AlO}_{1.5}}$ being 0.10, $a_{\text{CeO}_{1.5}}$ could be calculated to be 0.22 [4]. With these values and assuming that the interaction between Al and Ce and Ca content were negligible, the deoxidization equilibria between Al, Ce, and O in molten iron could be estimated with the reported interaction parameters [9] as shown in Fig.5 with the coexistence of ACe and CA_3Ce .

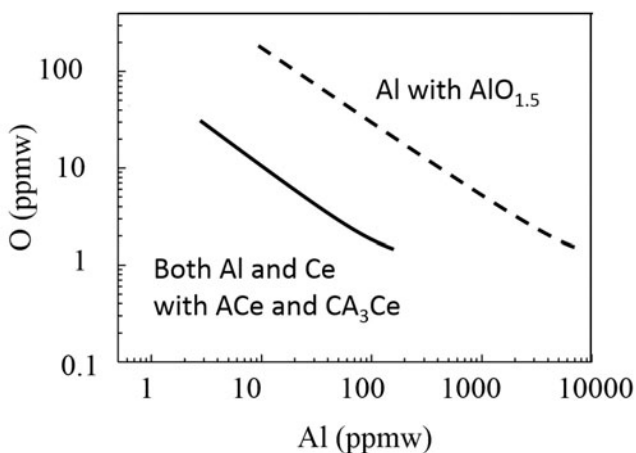


Fig.5 An example of Ce addition effect on Al deoxidation at 1873 K.

When only Al is used for the deoxidizing agent ($a_{\text{AlO}_{1.5}} = 1$), 1800 ppm of Al must be added to the molten iron to make the oxygen concentration 5 ppm [10], while only 160 ppm of Al and 1.2 ppm of Ce are needed to obtain the same oxygen concentration in case of complex deoxidation both by Al and Ce. This effect is also enhanced by the decrease in the activity coefficient of $\text{AlO}_{1.5}$ with existence of $\text{CeO}_{1.5}$.

4. Conclusions

The phase relations for the $\text{CaO-AlO}_{1.5}\text{-CeO}_{1.5}$ system at 1823 K and 1873 K as well as the existence of ternary solid compounds, $\text{CaO}\cdot\text{AlO}_{1.5}\cdot\text{CeO}_{1.5}$ and $\text{CaO}\cdot 3\text{AlO}_{1.5}\cdot\text{CeO}_{1.5}$. Also, by clarifying the activity of $\text{AlO}_{1.5}$ of the present system, Al-Ce complex deoxidation behavior was evaluated and it was confirmed that Ce could decrease the usage of Al for making ultra-low oxygen steel.

References

- [1] S. Ueda *et al.*, “Activities of $\text{AlO}_{1.5}$ for the $\text{CaO-AlO}_{1.5}\text{-CeO}_{1.5}$ Systems at 1773 K”, *ISIJ International*, 38 (1998), 1292-1296.
- [2] H. Ono *et al.*, “Influence of Neodymium on the Deoxidation and Desulfurization Equilibria of Liquid Iron in the Fe-Nd-O-S(-Al) System at 1873K”, *ISIJ International*, 49 (2009), 1656-1660.
- [3] S. K. Paul *et al.*, “Effect of Rare Earth Additions on the Inclusions and Properties of a Ca-Al Deoxidized Steel”, *Metallurgical Transactions B*, 13B (1982), 185-192.
- [4] I. Barin *et al.*, *Thermochemical Properties of Inorganic Substances* (Weinheim, Germany: Verlagsgesellschaft mbH, 1977), Part I: 383, 384, Part II: 1093.
- [5] L. S. Vorotilova and L. V. Dmitrieva, “NMR of ^{27}Al in Mixed Rare Earth Aluminates CaLnAlO_4 (Ln= La, Pr, Eu, Y)”, *Soviet Physics, Crystallography*, 34 (1989), 623-624.
- [6] E. V. Antipov and A. V. Luzikova, “Zur Kristallstruktur von $\text{CaLaAl}_3\text{O}_7$ und $\text{CaLaGa}_3-x\text{Al}_x\text{O}_7$ ($x = 0,66$)”, *Zeitschrift für Anorganische und Allgemeine Chemie*, 619 (1993), 889-892.
- [7] K. Momma and F. Izumi, “VESTA 3 for Three-dimensional Visualization of Crystal, Volumetric and Morphology Data”, *Journal of Applied Crystallography*, 44 (2011), 1272-1276.
- [8] R. Rein and J. Chipman, “Activities in the Liquid Solution. $\text{SiO}_2\text{-CaO-MgO-Al}_2\text{O}_3$ at 1600 °C”, *Transactions of the Metallurgical Society of AIME*, 233 (1965), 415-425.
- [9] M. Hino and K. Ito, *Thermodynamic Data for Steelmaking* (Sendai, Japan: Tohoku University Press, 2010), 259-264.
- [10] Y. Kang *et al.*, “Aluminum Deoxidation Equilibrium of Molten Iron–Aluminum Alloy with Wide Aluminum Composition Range at 1873 K”, *ISIJ International*, 49 (2009), 1483-1489.

DISTRIBUTION BEHAVIOR OF Cr BETWEEN CaO-SiO₂-Al₂O₃ (-MgO) SLAG AND Fe-C-Cr (-Si/Al) METAL PHASE

Yanling Zhang Xinlei Jia Tuo Wu Qiuhan Li Zhancheng Guo

State Key Laboratory of Advanced Metallurgy, University of Science & Technology Beijing,
Xueyuan Road 30, Haidian District, Beijing 100083, China

Keywords: distribution ratio, chromium, slag, metal melt

Abstract

Cr is an important alloying element for metal materials. Thermodynamic behaviors of Cr in metal and slag phase are basic knowledge for enhancing its yield ratio in pyrometallurgy process. In this research, laboratory experiments on distribution ratios of Cr between slag (CaO-SiO₂-Al₂O₃sat-CrOx, CaO-SiO₂-MgOsat-CrOx, and CaO-SiO₂-Al₂O₃-MgOsat-CrOx) and Fe-C(-Si/Al)-Cr metal phase were carried out under 1500°C-1600°C by using gas-slag-metal equilibrium method. The effects of influencing factors such as slag compositions, temperature, and metal melt compositions were examined. The results suggested that the distribution ratio of chromium between slag and metal phase increased with increasing the carbon and silicon contents in metal phase; Aluminum can reduce some silicon oxides into silicon in metal melt, which further promote the reduction of chromium oxides into metal phase. And the basicity, along with Al₂O₃ content in slag also gave important influence on L_{Cr}.

Introduction

Cr is an important alloying element for high quality steel materials. A nearly equilibrium state between Cr-bearing slag and metal phases is involved in many pyrometallurgy processes such as production of ferrochromium alloys and that of stainless steel. Therefore, thermodynamic behaviors of Cr in metal and slag phases are great important basic knowledge for enhancing its yield ratio in such processes. Much previous research concerning the reduction of pure Cr₂O₃ or Cr₂O₃ in a complicated system by using carbon,^[1,2] ferrosilicon,^[3] aluminum,^[3,4] an Fe-C melt,^[5] or an Fe-C-Si^[6] melt has been carried out. Most of these studies focused on the reduction mechanism of Cr₂O₃ and have kinetically promoted the yield of Cr. Thermodynamically, the yield ratio of Cr tends to be determined by the distribution ratio of Cr between the acquired metal melt and the residual slag. That strongly depends on the thermodynamic behaviors of Cr in metal melt and that of CrO_x in residual slag. Previous research has been conducted on the activity information of Cr in iron^[7] or a typical stainless steel melt such as AISI 304^[8]. The interaction

parameters of Cr with other elements such as $e_{Cr}^S, e_{Cr}^{Al}, e_C^{Cr}, e_{Ni}^{Cr}$ according to Wagner's formalism have been studied. Pretorius *et al.*^[9], Xiao^[10], Teng *et al.*^[11], and Wang^[12] have studied the thermodynamic behaviors of chromium oxides in slag systems including their oxides state and activity information. However, all of the above research gives little information about the distribution of Cr between metal melt and slag phases.

In this research, laboratory experiments on distribution ratios of Cr between slag (CaO-SiO₂-Al₂O₃sat-CrOx, CaO-SiO₂-MgOsat-CrOx, and CaO-SiO₂-Al₂O₃-MgOsat-CrOx) and Fe-C(-Si/Al)-Cr metal phase were carried out under 1500 °C-1600 °C by using gas-slag-metal equilibrium method. The effects of influencing factors such as slag compositions, temperature, and metal compositions were examined. The results gave useful information on promoting reduction of chromium from slag into metal melt.

1. Experimental

1.1 Materials

Chemical reagents such as CaO, SiO₂, MgO, Al₂O₃ and Cr₂O₃ were used to make molten slag, and iron powder, graphite, ferrosilicon, and Al powder were applied to form metal melt. The purity of the raw materials are analytical reagent(AR). Argon gas with purity of 99.999% was used as the inert atmosphere. CaO powders was heated at 1273K for 6 hours to decompose the hydroxides and carbonates that might have been formed. SiO₂, MgO, Al₂O₃ and Cr₂O₃ powders were dried at 433 K for 6 hours in order to remove the moisture. Fine powders of the oxides were weighed carefully and mixed together to obtain the target slag composition (total mass of each mixture was 8 g). The iron, graphite, Si and Al powders were mixed to obtain the target metal composition(total mass of each mixture was 10 g). The two compositions were ground thoroughly in porcelain mortar, and then cylindrical compacts (diameter = 10 mm) were pressured under pressure of 20 MPa for 2 min and put into the experimental crucible (ID=25 mm and height=33 mm). When using alumina crucible or magnesia crucible, the corresponding slag is the alumina saturated slag or magnesia saturated slag. The experimental schedules are shown in Table 1 and Table 2. Only the number of B1-B5 used the alumina crucible, and the rest are magnesia crucible.

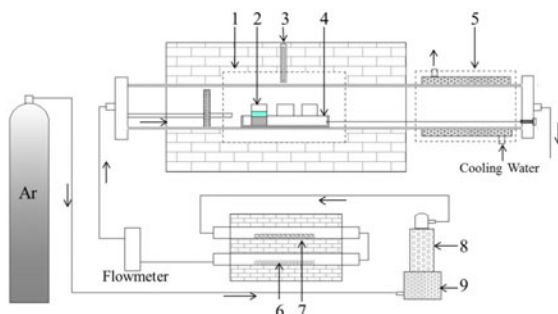
Table 1 Experimental schedule 1

No	Composition of metal (%)				Composition of slag(%)	%CaO/ %SiO ₂	Reaction time (hour)
	Fe	C	Si	Al			
A1	97	3			CaO-SiO ₂ -MgO-3%Cr ₂ O ₃	1.1	3
A2	97	3			CaO-SiO ₂ -MgO-3%Cr ₂ O ₃	1.1	6
A3	97	3			CaO-SiO ₂ -MgO-3%Cr ₂ O ₃	1.1	8
A4	97	3			CaO-SiO ₂ -MgO-3%Cr ₂ O ₃	1.1	10
A5	97	3			CaO-SiO ₂ -MgO-3%Cr ₂ O ₃	1.1	15
A6	100				CaO-SiO ₂ -MgO-3%Cr ₂ O ₃	1.1	10
A7	99	1			CaO-SiO ₂ -MgO-3%Cr ₂ O ₃	1.1	10
A8	98	2			CaO-SiO ₂ -MgO-3%Cr ₂ O ₃	1.1	10
A9	96	3	1		CaO-SiO ₂ -MgO-3%Cr ₂ O ₃	1.1	10
A10	95	3	2		CaO-SiO ₂ -MgO-3%Cr ₂ O ₃	1.1	10
A11	94	3	3		CaO-SiO ₂ -MgO-3%Cr ₂ O ₃	1.1	10
A12	96	3		1	CaO-SiO ₂ -MgO-3%Cr ₂ O ₃	1.1	10
A13	95	3		2	CaO-SiO ₂ -MgO-3%Cr ₂ O ₃	1.1	10
A14	94	3		3	CaO-SiO ₂ -MgO-3%Cr ₂ O ₃	1.1	10

Table 1 Experimental schedule 2

No	Composition of metal (%)		Composition of slag	%CaO/ %SiO ₂
	Fe	C		
B1	97	3	CaO-SiO ₂ -Al ₂ O ₃ -3%Cr ₂ O ₃	0.8
B2	97	3	CaO-SiO ₂ -Al ₂ O ₃ -3%Cr ₂ O ₃	1
B3	97	3	CaO-SiO ₂ -Al ₂ O ₃ -3%Cr ₂ O ₃	1.1
B4	97	3	CaO-SiO ₂ -Al ₂ O ₃ -3%Cr ₂ O ₃	1.2
B5	97	3	CaO-SiO ₂ -Al ₂ O ₃ -3%Cr ₂ O ₃	1.3
B6	97	3	CaO-SiO ₂ -MgO-3%Cr ₂ O ₃	0.8
B7	97	3	CaO-SiO ₂ -MgO-3%Cr ₂ O ₃	1
B8	97	3	CaO-SiO ₂ -MgO-3%Cr ₂ O ₃	1.1
B9	97	3	CaO-SiO ₂ -MgO-3%Cr ₂ O ₃	1.2
B10	97	3	CaO-SiO ₂ -MgO-3%Cr ₂ O ₃	1.3
B11	97	3	CaO-SiO ₂ -10%Al ₂ O ₃ -MgO-3%Cr ₂ O ₃	0.8
B12	97	3	CaO-SiO ₂ -10%Al ₂ O ₃ -MgO-3%Cr ₂ O ₃	1
B13	97	3	CaO-SiO ₂ -10%Al ₂ O ₃ -MgO-3%Cr ₂ O ₃	1.1
B14	97	3	CaO-SiO ₂ -10%Al ₂ O ₃ -MgO-3%Cr ₂ O ₃	1.2
B15	97	3	CaO-SiO ₂ -10%Al ₂ O ₃ -MgO-3%Cr ₂ O ₃	1.3
B16	97	3	CaO-SiO ₂ -6%Al ₂ O ₃ -MgO-3%Cr ₂ O ₃	1.1
B17	97	3	CaO-SiO ₂ -8%Al ₂ O ₃ -MgO-3%Cr ₂ O ₃	1.1
B18	97	3	CaO-SiO ₂ -12%Al ₂ O ₃ -MgO-3%Cr ₂ O ₃	1.1
B19	97	3	CaO-SiO ₂ -14%Al ₂ O ₃ -MgO-3%Cr ₂ O ₃	1.1

1.2 Apparatus and procedure



1-Heating zone 2-Crucible 3-Thermocouple 4-Porcelain boat 5-Cooling zone
6-Magnesium chips 7-Copper sheet 8-Molecular sieve 9-Allochromic silicagel

Figure 1. Schematic illustration of the experimental apparatus

Figure 1 shows the schematic arrangement of the furnace. The experiment system includes a high temperature furnace and a gas cleaning plant. The furnace was equipped with MoSi_2 heating elements and controlled by a PID controller with a Pt-30%Rh/Pt-6%Rh thermocouple as the sensor, which was calibrated before using. The ends of the reaction tube were kept at 193 K by a water-cooling system where filled with circulating water. In view of the extremely high inert atmosphere involved in the equilibration, it was necessary to purify the gases before introducing into the reaction tube. A gas cleaning system was used in the present experiment. Columns of molecular sieve and silica gel were used to remove the H_2O in the gas. The residual O_2 in the argon gas was removed by passing it through copper turnings and magnesium chips both at 773 K. The experimental crucibles containing the samples were positioned inside an alumina holder.

In a typical experiment, argon gas was passed through the furnace tube at a high rate to drive out the air before heating. When the target temperature was reached, the alumina holder was pushed into the furnace and placed in the even-temperature zone under argon gas at a flow rate of $200 \text{ ml} \cdot \text{min}^{-1}$ and keep it stable during the experiment. After the equilibration time, the alumina holder with the experimental crucibles was quickly pulled by the molybdenum wire to the cooling zone under production of argon gas and the samples were quenched. Samples were then taken out from experimental crucibles and weighted.

1.3 Analysis

The chemical composition of the metal was analyzed by chemical analysis(C: GB/T 20133-2006; Cr: NACIS/C H 008:2013; Si: NACIS/C H 013:2013) and that slag was ground and analyzed by X- ray fluorescence spectrometer.

The metallization ratio (η_{Cr}) and distribution ratio (L_{Cr}) between metal and slag of

chromium is given by (1) and (2), respectively.

$$\eta_{Cr} = \frac{\varphi_{Cr} \cdot m}{m_0} \times 100\% \quad (1)$$

$$L_{Cr} = \frac{[\%Cr]}{(\%Cr)} \quad (2)$$

where m is the mass of the metal and m_0 is the mass of the total chromium; φ_{Cr} and $[\%Cr]$ is the mass fraction of Cr in the metal; $(\%Cr)$ is the mass fraction of Cr in the slag.

2. Results and Discussion

2.1 Equilibrium time

Before the actual measurements were started, it was necessary to determine the soaking duration in order to ensure the attainment of the equilibrium between the metal phase and slag phase. The relationship between content of Cr in the metal phase and slag phase as function of soaking time, obtained in these trials, is plotted in Figure 2. When the soaking time is more than 3 hours, the content of Cr in the metal can be seen in the figure to be constant. In the present work, an equilibration time of 10 hours was chosen for all the experiments.

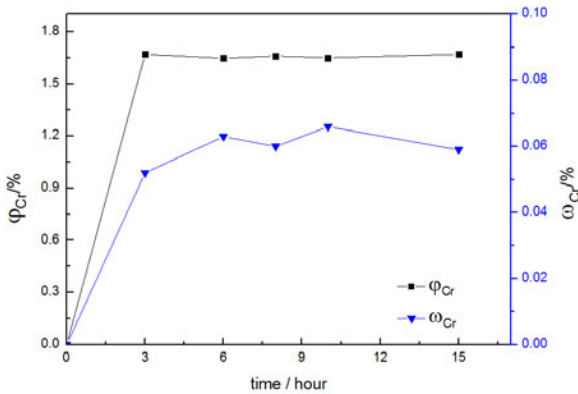


Figure 2. Effect of time on Cr content in the metal (φ_{Cr}) and that in slag (ω_{Cr})

2.2 Relationship between metallization ratio (η_{Cr}) and distribution ratio (L_{Cr})

The metallization ratio of chromium indicates the mass proportion of chromium in metal melt phase. The distribution ratio of chromium is the ratio of chromium content in the metal phase to that in slag phase. There is a deep connection between them. The following relationship

(6) about η_{Cr} and L_{Cr} can be obtained by comparing the equations (3-5). Figure 3 shows the metallization rate of Cr (η_{Cr}) as functions of distribution ratio (L_{Cr}). It can be seen in this figure that η_{Cr} and L_{Cr} have obvious function relationship, which is consistent well with the results of our formula. This result proves the reliability of the experimental data. The metallization ratio increases with the increase of the distribution ratio. When the distribution ratio becomes large enough, the metallization rate is much closer to 1, which suggested that almost all of chromium element have been reduced into metal phase.

$$L_{Cr} = \frac{[\%Cr]}{(\%Cr)} = \frac{\frac{m_{Cr(m)}}{m_m}}{\frac{m_{Cr(s)}}{m_s}} = \frac{m_{Cr(m)} \cdot m_s}{m_{Cr(s)} \cdot m_m} \quad (3)$$

$$\eta_{Cr} = \frac{m_{Cr(m)}}{m_{Cr}} = \frac{m_{Cr(m)}}{m_{Cr(m)} + m_{Cr(s)}} \quad (4)$$

$$\frac{L_{Cr}}{\eta_{Cr}} = \frac{m_s}{m_m} \cdot \frac{m_{Cr(s)} + m_{Cr(m)}}{m_{Cr(s)}} = \frac{m_s}{m_m} + \frac{m_s}{m_{Cr(s)}} \cdot \frac{m_{Cr(m)}}{m_m} = \frac{m_s}{m_m} + L_{Cr} \quad (5)$$

$$\eta_{Cr} = \frac{L_{Cr}}{L_{Cr} + \frac{m_s}{m_m}} = \frac{1}{1 + \frac{A}{L_{Cr}}}, \text{ where } A = \frac{m_s}{m_m} \quad (6)$$

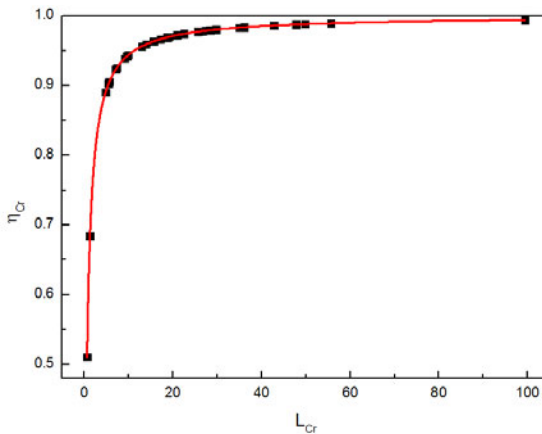


Figure 3. The metallization rate of Cr as functions of distribution ratio

Temperature is one of the key parameters that influence the distribution ratio of chromium between metal and slag. Figure 4 shows the effect of temperature on L_{Cr} in

CaO-SiO₂-MgO-CrOx and CaO-SiO₂-MgO-Al₂O₃-CrOx slag. The distribution ratio L_{Cr} increase slightly with increasing temperature. The Cr-containing slag belongs to high melting slag, the higher the temperature is, the better is the fluidity of slag, high temperature is conducive to the reduction and migration of chromium. The reduction reaction of chromium is endothermic reaction, so increasing the temperature will increase the distribution ratio of chromium between metal and slag. The experimental results show that the distribution ratio of CaO-SiO₂-MgO-CrOx slag is greatly influenced by temperature, there is no obvious metal phase and slag phase formation at 1450°C, and the slag can't be melted. It is found that the distribution ratio of two slag system is close with increasing temperature, which shows that the effect of composition of slag on the distribution of chromium decreases with the increase of temperature.

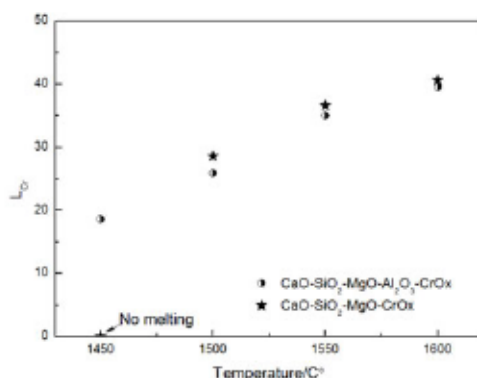


Figure 4. Effect of temperature on L_{Cr}

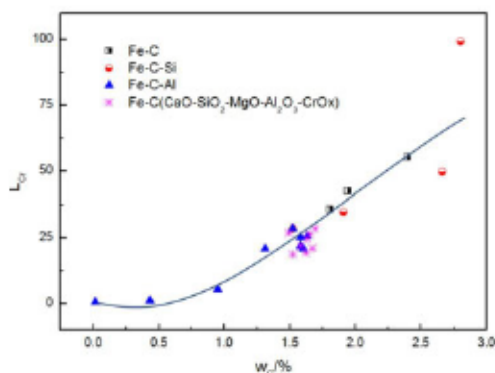


Figure 5. Effect of carbon content in the metal on L_{Cr}

2.3 Effect of metal components on L_{Cr}

2.3.1 Effect of carbon content in the metal on L_{Cr}

Figure 5 shows effect of the final carbon content in the metal on L_{Cr} . It is seen that there is an increasing tendency for L_{Cr} with increasing carbon content in metal. With the initial metal composition changing, the carbon content in the metal phase equilibrium is different. The impact of carbon content in the metal is mainly divided into two aspects: (1) the chromium oxide in the slag was reduced to metal chromium by carbon, and the reducing atmosphere of the system is ensured; (2) carbon can reduce the activity of chromium in metal. Ohtani^[13] indicated that the activity coefficient of chromium in the metal decreases with increasing carbon content of metal. The lower activity of chromium in metal is, more difficult is the chromium to be oxidized to the slag phase. The distribution ratio of chromium between metal and slag can be increased by enhancing the carbon content in the metal and the trend is consistent with the results of Pan^[14], the chromium content in slag decrease with increasing carbon content in metal. The higher chromium content in the metal phase, the effect is more significant.

2.3.2 Effect of silicon content in the metal on L_{Cr}

In order to examine the silicon content in metal phase on distribution ratio of Cr between slag and metal phase, during experiments some ferrosilicon powder was added into the initial Fe-3%C melts. After experiments, the effects of initial silicon content ($w_{[Si]}^0$) in metal phase on the carbon content ($w_{[C]}$) in final metal phase and that of silicon content ($w_{[Si]}$) in final metal phase on L_{Cr} (b) are shown in Figure 6(a) and (b), respectively. As evident in the figure, the final contents of carbon and silicon increase as the initial silicon content in the metal increased from 0 to 3. As a strong reducing agent, a part of silicon replaced some carbon reacting with chrome oxide to form SiO_2 . Figure 6(b) shows the distribution ratio L_{Cr} increases slightly with increasing silica content of metal and the trend is consistent well with the results of Nakasuga^[15].

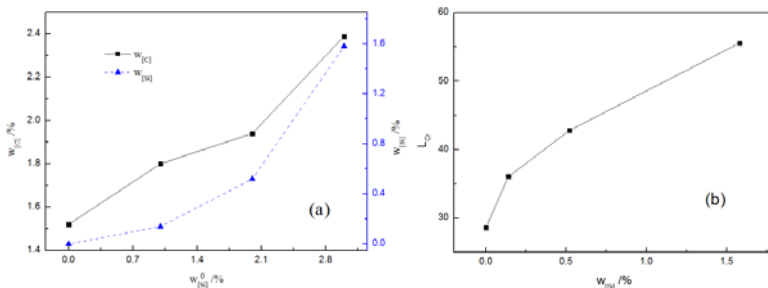


Figure 6. Effects of initial silicon content in metal phase on the carbon content of ending metal phase (a) and that of silicon content in final metal phase on L_{Cr} (b)

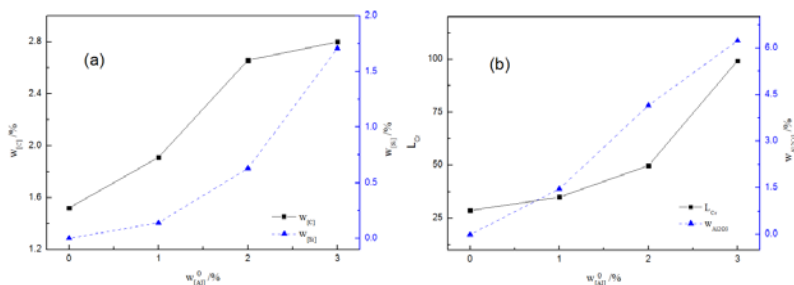


Figure. 7 Effects of initial aluminum content in metal phase on the carbon and silicon contents in final metal phase (a) and that on L_{Cr} (b)

2.3.3 Effect of initial aluminum content in the metal on L_{Cr}

Similarly, in order to examine the aluminum content in metal phase on distribution ratio of Cr between slag and metal phase, some Al powder was added into the initial Fe-3%C melts during experiments. After experiments, the effect of initial aluminum content ($w_{[Al]}^0$) in metal phase on the carbon and silicon contents in final metal phase and that on L_{Cr} (b) are shown in Figure 7(a) and (b), respectively. However, after analysis of the final products, there is no detection of aluminum elements in the final metal, while Al_2O_3 was observed in the final slag. This suggested that the aluminum in the present melt can't be stable, and nearly all the aluminum is gradually oxidized to form Al_2O_3 and transferred to the slag phase. It can be seen in Figure 7(a) that the final contents of carbon and silicon increase as the initial aluminum content in the metal is increased from 0 to 3. It indicates that SiO_2 in the slag can be reduced to silicon and entered to the metal phase by aluminum. The results of Nakasuga^[15] obtained the same conclusion. We know that the presence of carbon and silicon in the metal contribute to improve the distribution ratio of chromium between metal and slag from previous section. In the Figure 7(b), the Al_2O_3 content in the slag increase slightly with increasing initial aluminum content in the metal. The formation of Al_2O_3 changed CaO-SiO₂-MgO-CrOx slag to CaO-SiO₂-MgO- Al_2O_3 -CrOx slag, reduced the slag melting point and improved the fluidity of slag and is benefit to chromium element transferred to the metal phase from slag phase.

Through Figure 7 we can see that when the initial content of Al and Si in the metal is same, the two elements can greatly improve the equilibrium distribution ratio of chromium. Under the same initial content, when the initial content is low, the impact of the two elements is similar, with the increase of the initial content, the effect of Al on L_{Cr} is more obvious. From the last section, we know that aluminum in metal could't stably exist under the condition of present experiment and reduced a slight amount of SiO_2 to Si, the product, Si, is with strong reducibility, which can further reduce chrome oxide into metal melt. The equilibrium carbon content in metal when adding Al is higher than when adding Si in (Figure 8), which is conductive to improve L_{Cr} . When the initial slag doesn't contain Al_2O_3 , the generation of Al_2O_3 can decrease the melting

point of the slag and improve the liquidity of slag. The promotion of distribution ratio by Al is greater than Si in CaO-SiO₂-MgO-CrOx slag.

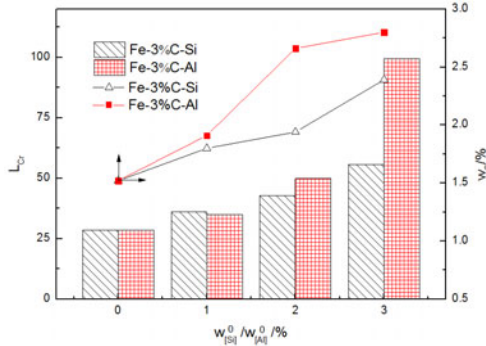


Figure 8. Effect of initial Si ($w_{[Si]}^0$) and Al ($w_{[Al]}^0$) content on L_{Cr}

2.4 Effect of slag components on L_{Cr}

2.4.1 Effect of slag basicity(%CaO/%SiO₂) on L_{Cr}

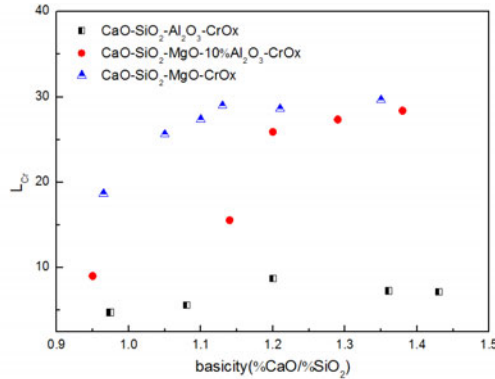


Figure 9. Effect of slag basicity on L_{Cr}

Slag basicity has a strong influence on the distribution behavior of chromium between metal and slag. Figure 9 shows the equilibrium distribution ratio of chromium in CaO-SiO₂-Al₂O₃-CrOx slag, CaO-SiO₂-MgO-CrOx slag and CaO-SiO₂-MgO-10%Al₂O₃-CrOx slag as a function of slag basicity. It is seen that L_{Cr} increase with increasing basicity of three slags. The result are in agreement with reported by Henao^[16]. They added CaO to FeOx-MgO-SiO₂ slag and found that the chromium oxide content in the slag decreases with

increasing CaO content. The distribution ratio changed little with the increase of %CaO/%SiO₂ in CaO-SiO₂-Al₂O₃-CrOx slag. Because of high content in slag and amphoteric oxide of Al₂O₃, the influence of %CaO/%SiO₂ on the distribution behavior of chromium in CaO-SiO₂-Al₂O₃-CrOx slag is small. It can be seen that the distribution ratio of Cr in CaO-SiO₂-Al₂O₃ slag is relatively small under the same basicity range in Figure 9. Compared with other slag systems, the effect of basicity on L_{Cr} in CaO-SiO₂-MgO-10%Al₂O₃-CrOx slag system is greater.

2.4.2 Effect of Al₂O₃ content in slag on L_{Cr}

Figure 10 shows the effect of Al₂O₃ content in CaO-SiO₂-MgO-Al₂O₃-CrOx slag on distribution ratio of chromium between metal and slag. It seems that the Al₂O₃ content serves a dual influence: to increase L_{Cr} with lower Al₂O₃ content while with higher Al₂O₃ content may decrease L_{Cr}. The liquidity of the slag is significantly improved while the slag melting point is low since the Al₂O₃ content in the slag is low. Nakasuga^[15] found that Al₂O₃ in the slag can make the liquid phase in the slag earlier generate and improve the reduction rate of chromium oxide. The increase of Al₂O₃ content will increase the viscosity of the slag, which is not conducive to the reduction of chromium oxide and separation liquid metal from slag. By adding Al₂O₃ to slag, Hena^[16] found that the chromium content in the slag increased obviously with the increase of the Al₂O₃ content and the distribution ratio of chromium was reduced when the content of Al₂O₃ was more than 10%.

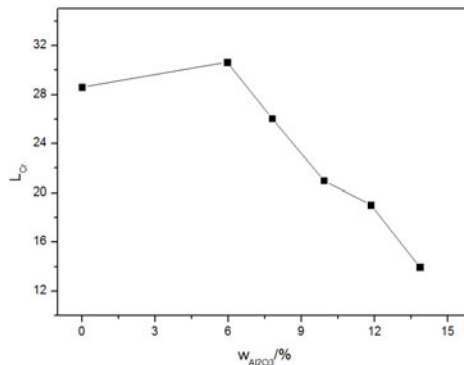


Figure 10 Effect of Al₂O₃ content in slag on L_{Cr}

Conclusions

Based on the above research, the results could be concluded as the follows.

(1) The distribution ratio of chromium between CaO-SiO₂-Al₂O₃ (-MgO) slag and Fe-C-Cr (-Si/Al) metal phase increased with increasing the carbon and silicon content in metal phase. Under this experiment situations, aluminum can't be stable in metal phase, while it can reduce

some silicon oxides into silicon in metal melt, which further promote the reduction of chromium oxides into metal phase..

(2) The distribution ratio L_{Cr} increased with increasing basicity of slag in the three kinds of slags involved in this research. Al_2O_3 content in slag also gave important influence on L_{Cr} , and two high Al_2O_3 tends to decrease the distribution ratio L_{Cr} .

Acknowledgements

The authors would like to appreciate the National Natural Science Foundation of China (No. 51474021) for their financial support.

References

- [1] T. Mori, J. Yang, and M. Kuwabara, "Mechanism of carbothermic reduction of chromium oxide," *ISIJ Int.*, 47 (10) (2007), 1387-1393.
- [2] B. Peng, et al., "Reduction process of Cr_2O_3 /carbon pellets," *J. Cent. South Univ. Sci. Technol.*, 36 (4) (2005), 571-575.
- [3] E. Shibata, S. Egawa, and T. Nakamura, "Reduction behavior of chromium oxide in molten slag using aluminum, ferrosilicon and graphite," *ISIJ Int.*, 42 (6) (2002), 609-613.
- [4] O. M. Cintho, C. D. L. Parra, and J. D. T. Capocchi, "Kinetics of the non-isothermal reduction of Cr_2O_3 with aluminum," *ISIJ Int.*, 44 (5) (2004), 781-784.
- [5] R. J. Fruehan, "Rate of reduction of Cr_2O_3 by carbon and carbon dissolved in liquid iron alloys," *Metal.&Trans. B*, 8 (2) (1977), 429-433.
- [6] T. Nakasuga, et al., "Reduction rate of Cr_2O_3 in a solid powder state and in CaO-SiO₂-Al₂O₃-CaF₂ slags by Fe-C-Si melts," *ISIJ Int.*, 41(9) (2001), 937-944.
- [7] J. H. Park, D. J. Min, C. H. Rhee, "Activities of chromium in molten Fe-Cr-C Alloy," *ISIJ Int.*, 38 (12) (1998), 1287-1291.
- [8] A. M. Azad, O. M. Sreedharan, J. B. Gnanamoorthy, "Direct measurement of thermodynamic activities of metals in an AISI 304 stainless steel by calcium fluoride EMF technique," *J. Nucl. Mater.*, 151 (3) (1988), 301-305.
- [9] E. B. Pretorius, A. Muan, "Activity-composition relations of chromium oxide in silicate melts at 1500°C under strongly reducing conditions," *J. Am. Ceram. Soc.*, 75 (6) (1992), 1364-1377.
- [10] Y. Xiao, M. A. Reuter, and L. Holappa, "Oxidation state and activities of chromium oxides in CaO-SiO₂-CrO_x slag system," *Metall. Mater. Trans. B*, 33 (4) (2002), 595-603.
- [11] L. Teng, et al., "Retention, Recovery and recycling of metal values from high alloyed steel slags," *Arch. Metall. Mater.*, 55(4)(2010), 1097-1104.
- [12] L. J. Wang, S. Seetharaman, "Experimental studies on the oxidation state of chromium oxides in slag systems," *Metall. Mater. Trans. B*, 41(5)(2010), 946-954.
- [13] M. Ohtani, "On the activities of Cr and C in molten Fe-C-Cr alloys," *Tohoku University*, 1956(8), 337-351.

- [14] X. Pan, R. H. Eric, "Chromium distribution between slag and non-carbon saturated metal phases under changing partial pressure of carbon monoxide," *Journal of The South African Institute of Mining and Metallurgy*, 104(10) (2004), 583-587.
- [15] T. NAKASUGA, et al., "Reduction Rate of Cr_2O_3 in a Solid Powder State and in $\text{CaO-SiO}_2\text{-Al}_2\text{O}_3\text{-CaF}_2$ Slags by Fe-C-Si Melts," *ISIJ Int.*, 41 (9) (2004), 937-944.
- [16] H. M. Henao, M. Hino, K. Itagaki, "Distribution of Ni, Cr, Mn, Co and Cu between Fe-Ni alloy and $\text{FeO}_x\text{-MgO-SiO}_2$ base slags," *Materials Transactions*, 42 (9) (2001), 1959-1966.

THERMODYNAMICS OF 'ESR' SLAG FOR PRODUCING NICKEL ALLOYS

Jun-Gil YANG, Joo Hyun PARK*

Department of Materials Engineering, Hanyang University, Ansan 426-791, Korea

*Contact: basicity@hanyang.ac.kr

Keywords: Ni-base alloys, ESR (Electro-Slag Remelting) process, Electrode, Ingot

Abstract

Ni-base alloys have been used for steam turbine in power plant that operates at temperatures higher than 873 K due to their high strength and superior heat resistance. Commercially, nickel alloys are generally produced by ESR (Electro-Slag Remelting) process with high cleanliness. During the ESR process, however, several alloying elements such as Ti and Al react with molten slag ($2\text{Ti} + \text{Al}_2\text{O}_3 = 2\text{Al} + \text{Ti}_2\text{O}_3$), resulting in a different composition between electrode and solidified ingot. Therefore, in the present study, we investigated the equilibrium between $\text{CaO-Al}_2\text{O}_3\text{-CaF}_2\text{-TiO}_x$ type ESR slag and Ni-Ti-Al(-C) alloys at 1773 K to minimize the change in the alloy composition during ESR process.

Introduction

Ni-base superalloys are widely used in power plants that operate at temperatures higher than 873 K with the properties of superior resistance to corrosion.^[1] Thus, the Electro-Slag Remelting (ESR) is employed as a secondary refining process for the production of ultra-clean Ni alloys.^[1] However, the easily oxidative elements in an electrode such as Al and Ti react with $\{\text{O}_2\}$ in air as well as with molten slag during ESR process, resulting in a difference in the composition between electrode and solidified ingot.

Many researchers reported that the contents of [Al] and [Ti] in the solidified ingot are strongly dependent on the slag composition, which means that a reaction between molten slag and alloy droplets should be thoroughly considered for maintaining the composition of electrode.^[2-6] Consequently, the objective of the present study is to provide an appropriate information in regard of slag design for producing Ni-Al-Ti(-C) alloys during ESR process.

Experimental procedure

Thermochemical equilibrium experiments were carried out using a super kanthal electric furnace with a MoSi_2 heating element. A schematic diagram of the experimental apparatus is shown in Figure 1. The Ni-Al-Ti(-C) alloy and the $\text{CaO-Al}_2\text{O}_3\text{-CaF}_2\text{-TiO}_x$ slag were loaded in a graphite crucible placed in a graphite holder for 8 hours at 1773 K. The oxygen partial pressure was fixed to 1×10^{-16} atm. The Al and Ti contents in the alloy samples were analyzed by ICP and the equilibrium composition of the slag was analyzed with an XRF analysis.

Results and Discussion

Titanium is known to be present in the form of Ti^{4+} , Ti^{3+} , and Ti^{2+} in molten slag according to oxygen partial pressure of the system at a given slag composition.^[7,8] To confirm the stable ionic species of titanium under the present metal-slag equilibrium experiments, the quenched slag samples were analyzed by XPS. The representative result of

the XPS analysis is shown in Figure 2, wherein each titanium oxide is given at the binding energy of each species.^[8] From the result shown in Figure 2, it is confirmed that titanium is mainly stable as Ti^{3+} (Ti_2O_3) in molten slag under the present experimental conditions.

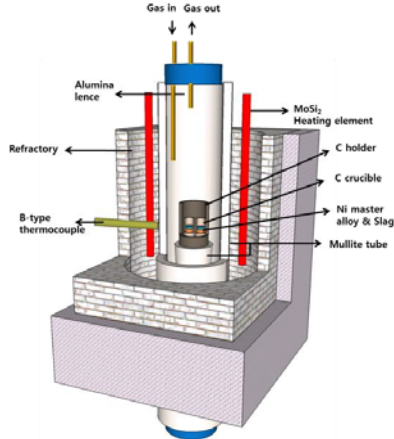


Figure 1. Schematic diagram of the experimental apparatus.

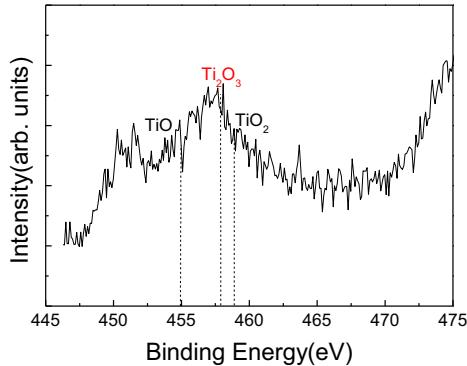
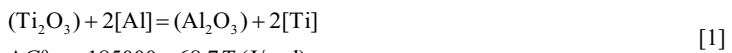


Figure 2. X-ray Photoelectron Spectroscopy (XPS) spectra of the quenched slag.

Slag-metal equilibrium reaction can be described by Eq. [1], and the equilibrium constant (K) of Eq. [1] is expressed by Eq. [2].^[9]



$$\Delta G^{\circ} = -185000 + 68.7T \text{ (J/mol)}$$

$$\frac{a_{Ti_2O_3}}{a_{Al_2O_3}} = \frac{1}{K_{(l)}} \cdot \frac{a_{Ti}^2}{a_{Al}^2} \quad [2]$$

From Eq. [2], the relationship between the metal and slag activity ratio can be obtained at

1773 K. The activity ratio of Ti and Al in metal phase was calculated by FactSageTM7.0,^[10] from which the slag activity ratio at a given slag composition can be deduced using Eq. [2]. Consequently, the relationship between the activity and composition ratio of Ti_2O_3 and Al_2O_3 in molten slag in equilibrium with Ni-Al-Ti- C_{sat} alloys can be represented by a linear function as shown in Figure 3.

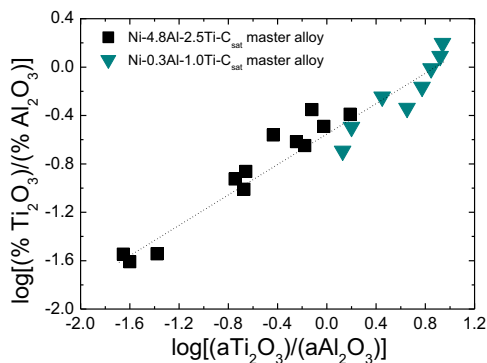


Figure 3. Composition-Activity relationship of Ti_2O_3 and Al_2O_3 in molten slag at 1773 K.

Therefore, it is expected that Ni alloys with various $[Al]/[Ti]$ ratios ($=0.3$ to 2.0) can be produced without the changes in the composition during the ESR process by designing the slag system based on the linear function given in Figure 3. That is, the initial content of Al_2O_3 and Ti_2O_3 in the ESR slag can be deduced from the present results.

The influence of temperature on the activity-composition relationship of Ti_2O_3 and Al_2O_3 in the slag in equilibrium with the Ni-Al-Ti- C_{sat} alloys is shown in Figure 4. The exchange reaction given in Eq. [1] is exothermic, indicating that the reaction proceeds backward, viz. the oxidation of Ti is more predominantly occurred than that of Al as temperature increases. The measured results are in good accordance to the thermodynamic considerations. Hence, the temperature-composition-activity relationship measured in the present study can be a good guidance for producing Ni-Al-Ti- C_{sat} alloys via ESR process.

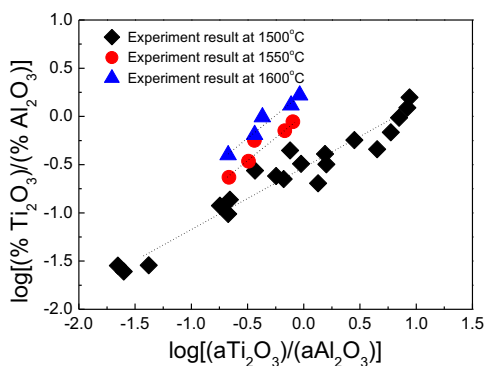


Figure 4. The activity-composition relationship at different temperature.

Conclusions

The equilibrium reaction between Ni-base alloys and CaO-Al₂O₃-CaF₂-TiO_x slag was investigated at temperatures ranging from 1773 to 1873 K, and oxygen partial pressure $p(\text{O}_2)=1\times 10^{-16}$ atm to optimize slag composition to prevent the composition changes in the easily oxidative elements such as [Al] and [Ti] in the alloy during the ESR process. It is expected that Ni-base alloys with various [Ti]/[Al] ratios in the electrode can be produced by maintaining the original composition during ESR process. A temperature dependency of the activity-composition relationship of the Ni-base alloys and the CaO-Al₂O₃-CaF₂-TiO_x slag was also investigated.

References

1. R.C. Reed: *The Superalloys: Fundamentals and Applications*, Cambridge University Press, Cambridge, 2006, pp. 217-29.
2. C.Y. Chen, G.W. Wang and Y.M. Hu: *China Steel Technical Report*, (2013), pp. 7-12.
3. G. Pateisky, H. Biele and H.J. Fleischer: *J. Vac. Sci. Technol.*, 9 (1972), pp. 1318-21.
4. M. Okamura et al.: Proc. 10th Int. Forging Conf. (IFC), Sept. 1985, Sheffield, pp. 7.1-6
5. M. Okamura, M. Maeda and K. Hirose: Proc. 6th Int. Iron & Steel Cong. (IISC), Nagoya, 3 (1990), pp. 715-22.
6. M. Okamura et al.: Proc. 7th Int. Conf. Vac. Metall. (ICVM), 1982, Tokyo, pp. 1511-18.
7. S.M. Jung and R.J. Fruehan : *ISIJ Int.*, 41 (2001), pp. 1447-53.
8. J.A. Rotole et al.: *J. Vac. Sci. Technol.*, 19 (2001), pp. 1176-81
9. E.T. Turkdogan: *Physical Chemistry of High Temperature Technology*, Academic Press, New York, 1980, pp. 1-24.
10. FactSage, www.factsage.com.

**ADVANCES IN MOLTEN
SLAGS, FLUXES, AND SALTS:**

Proceedings of



**Production Using
Molten Salts**

RECYCLING TITANIUM AND ITS ALLOYS BY UTILIZING MOLTEN SALT

Toru H. Okabe and Yu-ki Taninouchi

Institute of Industrial Science,
The University of Tokyo,
4-6-1 Komaba, Meguro-ku, Tokyo 153-8505, JAPAN

Keywords: Titanium, Recycling, Oxygen removal, Deoxidation, Titanium scrap

Abstract

It is commonly believed that the deoxidation of titanium (Ti), or the direct removal of oxygen (O) dissolved in metallic Ti, is practically impossible when magnesium (Mg) is used as the deoxidizing agent. In recent years, it has been experimentally demonstrated that O dissolved in Ti can be directly removed using $MgCl_2$ molten salt electrolysis. By the electrochemical deoxidation technique, Ti wires containing 0.12 mass% O were deoxidized to less than 0.02 mass% O. In some cases, the concentration of O in the Ti wires was reduced to the level of 0.01 mass% O, which cannot be attained using the current Kroll process. The possible application of this deoxidation technique to practical industrial recycling processes is also discussed.

Introduction

The recycling of Ti and its alloys has become an important issue in recent years [1, 2] as the demand for Ti and its alloys in the aerospace industry is increasing, and large amounts of Ti scrap are generated from the fabrication of Ti and Ti alloy products. Figure 1 shows a representative situation of the generation of Ti scrap in the aerospace industry [3]. The volume of scrap generated is far greater than that of fabricated Ti products. Some of the scrap is heavily contaminated with O, which is a major impurity in Ti and its alloys.

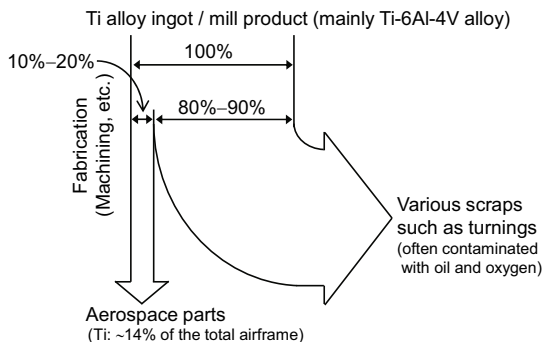


Figure 1. Representative situation of scrap generation of Ti alloys from the aerospace industry. The volume of scrap generated is far greater than that of fabricated Ti products [3].

Commercial Ti and Ti alloys contain approximately 0.1 mass% O (1000 mass ppm) as a major impurity. Contamination of the product by O must be avoided, as the presence of O deteriorates the mechanical properties of metals. Table I shows the ASTM grades and acceptable impurity concentrations in Ti and Ti-V-Al alloy [4]. In manufacturing commercially pure Ti of ASTM Grade 1, low-O Ti feed such as high-purity Ti sponge (0.03–0.1 mass% O) produced by the Kroll process [5] is used. Using large amounts of scrap metal to produce low-O Ti is hindered by the high O level in Ti scrap, which typically exceeds 0.1 mass%. Ti and its alloys containing more than 0.4 mass% O cannot be recycled into Ti alloys, and these metals are mainly used in cascade recycling as additive elements for materials such as steel and Al [3].

Table I. Grades and impurity concentrations of pure Ti and Ti alloy [4].

Specification		Concentration of element i , C_i (mass%)						
		C	H	O	N	Fe	Al	V
Pure Ti	ASTM Gr. 1	≤0.08	≤0.015	≤ 0.18	≤0.03	≤0.2	–	–
	ASTM Gr. 2	≤0.08	≤0.015	≤ 0.25	≤0.03	≤0.3	–	–
	ASTM Gr. 3	≤0.08	≤0.015	≤ 0.35	≤0.05	≤0.3	–	–
	ASTM Gr. 4	≤0.08	≤0.015	≤ 0.40	≤0.05	≤0.5	–	–
Ti-Al-V alloy	ASTM Gr. 5	≤0.08	≤0.015	≤ 0.20	≤0.05	≤0.40	5.5– 6.75	3.5– 4.5
	ASTM Gr. 23	≤0.08	≤0.0125	≤ 0.13	≤0.03	≤0.25	5.5– 6.5	3.5– 4.5

Removal of O directly from Ti and Ti alloys, and reducing the level of O to below 0.1 mass% (1000 mass ppm), are quite difficult because O dissolves in Ti to form an interstitial solid solution, and Ti has an extremely strong affinity for O [6, 7].

Table II lists some effective methods for the direct removal of O from Ti [8–29]. As listed in Table II, the deoxidation of solid Ti by reaction with chemically active calcium (Ca) in the temperature range of 1273 to 1473 K has been examined. Okabe *et al.* successfully produced Ti containing less than 50 mass ppm O with a high residual resistivity ratio (RRR > 120) by using Ca and CaCl₂ as deoxidant and flux, respectively [20, 21]. Ca metal is thought to be the most effective deoxidation agent because it has an extremely strong affinity for O and very low solubility in solid Ti. In the Ca-halide flux deoxidation process shown in Table II, the CaCl₂ flux contains the deoxidation agent Ca and facilitates the reaction by diluting the reaction product CaO, thus decreasing the activity of the by-product. However, the purity of flux and the initial O content of the Ti are subject to limits, as the ultimate limit of deoxidation depends on the amounts of both O present as an impurity in the CaCl₂ flux and CaO produced during deoxidation.

An effective technique for preparing O-free Ti by electrochemical deoxidation using CaCl₂ molten salt was developed in 1993 [23]. Removal of O²⁻ (present as CaO in the flux) and production of Ca deoxidant by using electrochemical techniques improves the deoxidation limit of the Ca-halide flux deoxidation process. Under certain conditions, Ti containing less than 0.001 mass% (10 mass ppm) O has been successfully produced by the electrochemical deoxidation technique.

Table II. Examples of deoxidation process for Ti or its alloys [8–28].
For more detailed information, see recent reference [29].

Method	Reference	Merit (deoxidation limit)	Demerit
Deoxidation by M/MO _x eq. (e.g., DOSS process, M = Ca)	Ono and Miyazaki [8] Fisher [9–12] Okabe et al. [13–16] Oh et al. [17, 18] Roh et al. [19]	Ti powder can be deoxidized. Ca deoxidant (~500 ppm O)	Low capability of deoxidation
Calcium halide flux deoxidation	Okabe et al. [20–22]	High capability of deoxidation (~50 ppm O)	Not suitable for removing large amounts of O; leaching of molten salt bath is needed
Electrochemical deoxidation	Okabe et al. [23, 24] Nakamura et al. [25] Hirota et al. [26] Chen et al. [27] Taninouchi et al. [28]	Ultrahigh capability of deoxidation CaCl ₂ bath (<10 ppm O) MgCl ₂ bath (<100 ppm O)	Long processing time

In addition to the deoxidation processes listed in Table II, various methods were investigated in the past. For example, Hashimoto *et al.* proposed a method for the deoxidation of Ti during electrowinning by using molten fluoride baths [30–32], but contamination of Ti by O or carbon (C) is unavoidable when using this method. In 2001, Chen *et al.* developed a novel process, called the FFC process, for producing Ti directly from TiO₂ immersed in CaCl₂ molten salt by using electrochemical methods [33–35]. They succeeded in obtaining low-O Ti by using this process. Ono and Suzuki developed a new Ti reduction process that utilizes electrochemically produced Ca reductant in CaCl₂ molten salt [36–38]. To obtain low-O Ti, a highly reducing atmosphere is required. For this reason, molten CaCl₂ with high metallic Ca activity is employed as the reaction medium in many cases. Other recent developments in deoxidation techniques for Ti and its alloys are reviewed in a recent article [29].

In the past, deoxidation of Ti by using magnesium (Mg) as the deoxidizing agent had been believed to be almost impossible. This is because the deoxidation limit of a Ti-O solid solution by Mg under MgO saturation is approximately 2.5 mass% (25000 mass ppm) at 1273 K. Considering this high O level under Mg/MgO equilibrium, lowering the deoxidation limit to a level of 100 mass ppm is believed to be difficult from a practical perspective.

However, if deoxidation of Ti by using a MgCl₂ medium becomes feasible, the reduction and electrolysis facilities of the conventional Kroll process [5] could be utilized. Therefore, developing an effective deoxidation process for Ti and its alloys by using molten MgCl₂ may significantly enhance the recovery rate for Ti scrap and the production of low-O Ti.

Principle

Because the principle of electrochemical deoxidation of Ti has been reported in detail previously [7, 23, 29], the deoxidation process is only briefly outlined here. By the following overall reaction, a solid Ti-O solution is deoxidized by Mg:

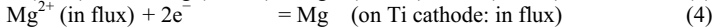
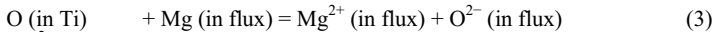


The equilibrium concentration of O in Ti depends thermodynamically on temperature T based on the following equation:

$$[\text{mass\% O}] = (a_{\text{MgO}} / a_{\text{Mg}})(1 / f_{\text{O}}) \exp(\Delta G^{\circ}_{(1)} / RT) \quad (2)$$

where $\Delta G^{\circ}_{(1)}$ is the standard Gibbs energy change associated with the deoxidation reaction described by Equation (1); a_{MgO} and a_{Mg} are the activities of MgO and Mg, respectively; and f_{O} is the activity coefficient of O in solid Ti. The equilibrium concentration of O under an Mg/MgO equilibrium is approximately 2.5 mass% at 1273 K [7, 13, 39]. This shows that it is thermodynamically difficult to directly reduce the level of O in Ti to below 1 mass% by using Mg deoxidant when the activity of MgO (a_{MgO}) is high. In contrast to the Mg system, the equilibrium concentration of O in Ti under Ca/CaO equilibrium at 1273 K is approximately 0.05 mass% [7, 13, 29].

The electrochemical deoxidation process using molten MgCl_2 as flux examined in this study is expressed by the following reactions. A schematic of the electrochemical deoxidation of Ti in molten MgCl_2 is shown in Figure 2.



or

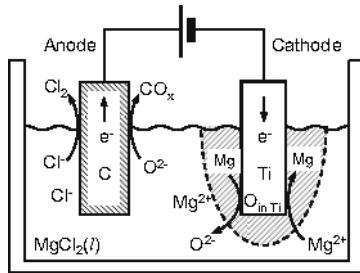
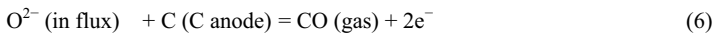
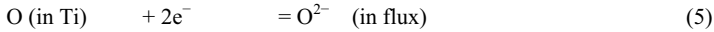


Figure 2. Schematic illustration of electrochemical deoxidation in MgCl_2 molten salt. Electrolysis is achieved using Ti as the cathode and C as the anode. A detailed explanation of the electrochemical deoxidation is given in the references [7, 23, 28, 29].

On the basis of the thermodynamic calculation [7, 13, 39], when a_{MgO} is decreased to the level of 10^{-2} in the presence of metallic Mg at 1200 K, the chemical potential of O_2 (p_{O_2}) in the system is decreased to approximately 10^{-45} atm, and Ti containing approximately 0.018 mass% (180 mass ppm) O can be obtained [29]. In other words, when Ti is deoxidized to commercial O levels for high-grade Ti (0.05 mass% O, or 500 mass ppm) by using Mg as a reductant, a_{MgO} at 1200 K must be decreased to approximately 0.025.

Experimental procedure

Figure 3 shows the schematic illustration of a typical experimental apparatus [28, 29]. Detailed information of the experimental apparatus used for the electrochemical deoxidation of Ti in MgCl_2 is provided in the references [28, 29]; only an outline is provided here. Ti samples in the form of small pieces and wires with different O concentrations and configurations were used as the starting material. The flux was reagent-grade anhydrous MgCl_2 (>97.0%) in flake form, dried at 523 K for more than 43 ks (12 h).

The dehydrated MgCl_2 flux (approximately 1000 g) was contained in a Ti or mild steel crucible (~200 mm in height, 89 mm I.D.) and set in a gas-tight stainless steel chamber. The Ti cathode consisted of several strands of Ti wire (~40 mm in length and 1.0 mm in diameter) or Ti rod (~35 mm in length and 3.0 mm in diameter). This cathode and a high-purity graphite anode (99.9%, ~35 mm in length, and 3 or 6 mm in diameter) was prepared and inserted into the chamber through the gas-tight chamber head.

Deoxidation experiments were performed by applying voltages between 0 and 3.1 V between the electrodes, which were separated by a distance of ~30 mm. In most cases, the deoxidation of the Ti cathode was carried out by applying voltages exceeding 2.6 V at 1173 K for longer than 54 ks (15 h). The electrochemical properties of the molten salt were measured by cyclic voltammetry (CV) before and after the deoxidation experiments.

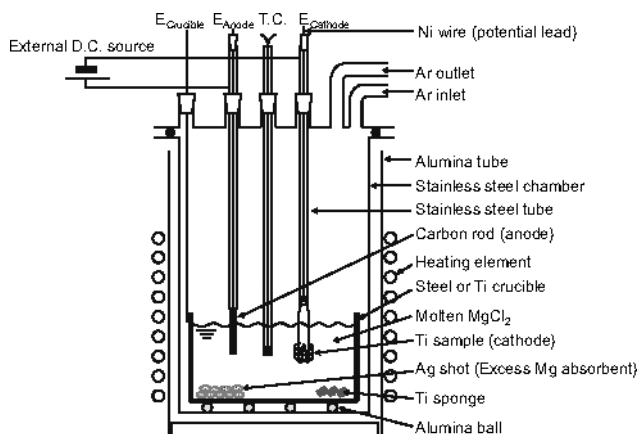


Figure 3. Typical experimental apparatus for electrochemical deoxidation [28, 29].

After the deoxidation experiment, the electrodes were removed from the molten MgCl_2 , and the cell was cooled in a stream of Ar gas. In some cases, only the Ti cathode was pulled out from the molten salt and replaced after cooling for the next experimental run. The salt that adhered to the surface of the Ti electrode was removed by leaching. The concentrations of O and nitrogen (N) in the Ti samples were analyzed by the inert gas fusion technique.

Results and Discussion

By applying a voltage of around 3 V between the electrodes, the chemical potential of metallic Mg (a_{Mg}) in MgCl_2 on the surface of the Ti cathode was increased to a value approaching 1, and the Ti samples were deoxidized by the electrochemically produced Mg. The resulting O species, present mainly as O^{2-} dissolved in the molten MgCl_2 , reacted at the C anode to form CO (or CO_2) gas, which was removed from the molten salt system.

After electrochemical deoxidation at 1173 K for 86 ks, Ti wires 1.0 mm in diameter and containing 0.084 mass% (840 mass ppm) O were deoxidized to 0.009 mass% (90 mass ppm) (Exp. D13 shown in Table III, [28]). When a Ti rod of 3.0 mm in diameter containing 0.12 mass% (1200 mass ppm) O was deoxidized at 1173 K for 86 ks, Ti with 0.027 mass% (270 mass ppm) O was obtained (Exp. D15 shown in Table III, [28]). The concentration of N in the sample was increased from 10–40 to 40–440 mass ppm after deoxidation.

In Table III, some representative analytical results for O and N levels in Ti before and after deoxidation are listed, as well as results from previous studies [13, 14, 16, 21, 25, 26, 28]. The analytical values below 0.01 mass% (100 mass ppm) listed in the table include some uncertainty because gas analysis of Ti samples below 0.01 mass% (100 mass ppm) is difficult. However, notably, Ti with an O level of approximately 0.01 mass% (100 mass ppm) was obtained using Mg as the deoxidant when the electrochemical technique was used.

Figure 4 shows the new Ti recycling process proposed in this study. Oxides attached to the Ti scrap are removed by molten salt rinsing and/or pre-electrolysis, and then the O dissolved in the Ti scrap is directly removed by molten salt electrolysis in MgCl_2 . By employing the oxide removal process prior to the electrochemical deoxidation process, the disadvantage of oxide accumulation in molten MgCl_2 can be avoided, and effective deoxidation directly from scrap becomes feasible.

Based on the process shown in Figure 4, various recycling technologies for recycling Ti scrap can be developed. For example, Figure 5 shows a new concept of the recycling process for Ti scrap by using electrochemical deoxidation in molten MgCl_2 followed by the removal of MgCl_2 by vacuum distillation or some other method. The electrochemical cell for MgCl_2 electrolysis used in the conventional Kroll process can also be utilized in the process shown in Figure 5.

As Ti production increases, scrap treatment becomes increasingly important. In particular, recycling of Ti scrap heavily contaminated with O will be particularly significant. In the future, the direct removal technique of O proposed in this study may be applied for recycling Ti scrap.

Table III. Representative results for Ti deoxidation by using various solid-state deoxidation techniques [13, 14, 16, 21, 25, 26, 28].

Method [Ⓜ]	O (mass ppm)		N [Ⓝ] (mass ppm)		Note and references (Exp. #)
	Init.	After deox.	Init.	After deox.	
Ca-CaO	430 → 1430 →	460 470	20 → 100 →	340 470	1273 K, 86 ks, [13] (Eq-3)
Y-Y ₂ O ₃	200 → 1100 →	120 150, 170	n.a. n.a.		1231 K, 260 ks, [14] (#2U)
Y-Y ₂ O ₃	210 → 950 →	90 100, 220	10 → 20 →	(30) (50)	1213 K, 551 ks, [16] (#U)
Y-Y ₂ O ₃	670 → 210 → 950 → 670 →	80, 100 40, 080 160, 160 030, 240	30 → 10 → 20 → 30 →	(60) (50) (120) (80)	1173 K, 518 ks, [16] (#T)
Ca-Y-Y ₂ O ₃	210 → 950 → 670 →	130 60, 090 60, 090	10 → 20 → 30 →	(40) (50) (120)	1173 K, 604 ks, [16] (#W)
Ca-CaCl ₂	130 → 130 →	16 17	10 → 10 →	41 34	1273 K, 90 ks, [21] (#17B1), RRR _{4.2} ⁺ = 98, Hv [§] = 85
Ca-CaCl ₂	130 → 130 →	35 22	10 → 10 →	49 45	1373 K, 40 ks, [21] (#19B1), RRR _{4.2} ⁺ = 95, Hv [§] = 92
Ca-CaCl ₂	150 →	62	10 →	86	1273 K, 86 ks, [21] (#3C), RRR _{4.2} ⁺ = 122, Hv [§] = 82
Electrochem. (CaCl ₂)*	900 → 1400 →	< 10 < 10	40 → 20 →	20 20	1223 K, 22 ks, [23] (#49), Contaminated by C
Electrochem. (CaCl ₂)*	110 → 900 →	10 20	< 10 → 30 →	< 10 50	1223 K, 27 ks, [25] (#69), C: 20→30, 50→80 ppm RRR _{4.2} ⁺ = 155, Hv [§] = 64
Electrochem. (CaCl ₂)*	210 →	40, 050	10 →	10	1189 K, 36 ks, [26] (#12) (O in Gd: 2100 → 10, 50 ppm, O in Tb: 2600 → 20, 20 ppm, O in Dy: 2300 → 20, 30 ppm O in Er: 2800 → 40, 40 ppm, O in Y: 11200 → 340, 380 ppm)
Electrochem. (MgCl₂)*	110 → 900 → 840 → 1200 →	100 60 90 270	< 10 → 30 → 20 → 40 →	40 70 440 260	1173 K, 86 ks, [25] (#75), C: 20→50, 50→120 ppm 1173 K, 86 ks, [28] (D13_150121^a) 1173 K, 86 ks, [28] (D15_150123^b)

Ⓜ : “M-MOx”: deoxidation by metal / metal oxide; “Ca-CaCl₂”: calcium-halide flux deoxidation; “Electrochem.”: electrochemical deoxidation.

* : Salt in parentheses shows molten salt used for electrochemical deoxidation.

& : Values in parentheses include uncertainties.

+ : Residual resistivity ratio, $\rho_{298} / \rho_{4.2}$, determined by measurement at 298 and 4.2 K.

§ : Vickers micro hardness (kgf/mm²), measured using a 500-g load at room temperature.

n.a. : Not analyzed or not reported.

a : Ti wire (ϕ 1.0 mm) was used. O and N contents were determined by KOBELCO Research Institute, Inc.

b : Ti rod (ϕ 3.0 mm) was used. O and N contents were determined by KOBELCO Research Institute, Inc.

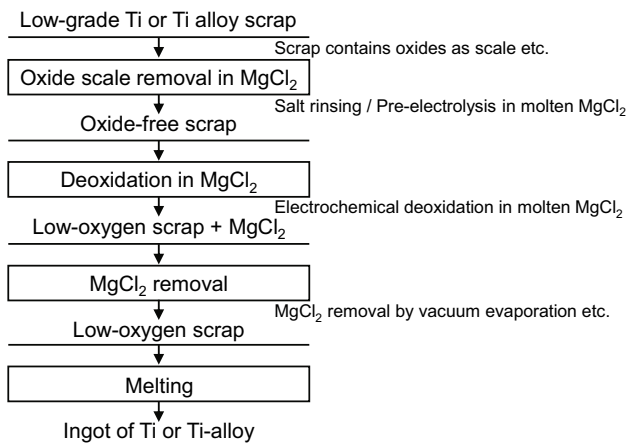


Figure 4. Ti recycling process proposed in this study. Oxide in the Ti scrap is removed by salt rinsing and pre-electrolysis, and then the O dissolved in the Ti scrap is directly removed by molten salt electrolysis in $MgCl_2$.

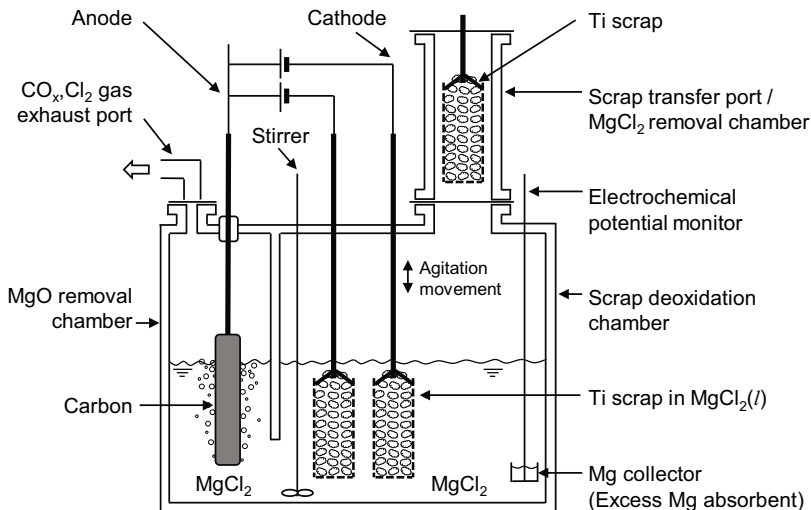


Figure 5. New concept of industrial application of the Ti recycling process based on $MgCl_2$ electrolysis. This process is feasible by applying existing $MgCl_2$ electrolysis technologies for use in Ti smelters based on the Kroll process.

Conclusions

The removal of O from Ti by using an electrochemical technique in molten MgCl_2 was examined at temperatures of ~ 1173 K. The activity of Mg increased and that of MgO decreased near the Ti cathode surface when voltages were applied between Ti and C electrodes immersed in molten MgCl_2 . These activity changes facilitated the deoxidation of a Ti cathode in Ti samples. A Ti sample containing approximately 1000 mass ppm O was deoxidized to less than 200 mass ppm by applying 3.1 V between the Ti and C electrodes for 86 ks. In some cases, the concentration of O in Ti was decreased to below 100 mass ppm, which cannot be accomplished using the conventional Kroll process. The application of this deoxidation technique to industrial recycling processes may become practical in the future.

Acknowledgements

The authors are grateful to Professor Masafumi Maeda and Professor Kazuki Morita of The University of Tokyo, and to Dr. Tetsushi Deura and Messrs. Daisuke Matsuwaka and Fumiaki Kudo of Kobe Steel, Ltd., for their sample analysis. The authors thank Mr. Yuki Hamanaka, Dr. Katsuhiro Nose, and Mr. Hisao Kimura for their valuable suggestions and technical assistance. This research was partly funded by a Grant-in-Aid for the Next Generation of World-Leading Researchers (NEXT Program) for the Research Project for Development of Environmentally Sound Recycling Technology of Rare Metals (NEXT Program #GR019), and a Grant-in-Aid for Scientific Research (S) (KAKENHI Grant #26220910) by JSPS.

References

1. T. G. Goonan, "Titanium Recycling in the United States in 2004," *Flow Studies for Recycling Metal Commodities in the United States*, ed. S. F. Sibley, (U.S. Geological Survey Circular 1196, 2010), Y1–Y16.
2. B. Rotmann, C. Lochbichler, and B. Friedrich, "Challenges in Titanium Recycling: Do We Need a New Specification for Secondary Alloys?," *Proceedings of EMC 2011* (2011).
3. T. H. Okabe and K. Nose, eds., *The Latest Technological Trend of Rare Metals* (Tokyo, Japan: CMC Publishing Co. Ltd., 2012), 95–107 and 117–127. (in Japanese)
4. American Society for Testing and Materials, *Standard Specification for Titanium and Titanium Alloy Strip, Sheet, and Plate*, (ASTM International, West Conshohocken, PA, 2006), B265-06b.
5. W. Kroll, "The Production of Ductile Titanium," *Trans. Electrochem. Soc.*, 78 (1940), 35–47.
6. T. B. Massalski et al., eds., *Binary Alloy Phase Diagrams, 2nd ed., vol. 3*, (ASM International, Materials Park, OH, United States of America, 1990), 2924–2927.
7. T. H. Okabe, K. T. Jacob, and Y. Waseda, "Removal of Oxygen in Reactive Metals," *Purification Process and Characterization of Ultra High Purity Metals*, ed. Y. Waseda and M. Isshiki (Springer, Berlin, 2001), 3–37.
8. K. Ono and S. Miyazaki, "Study on the Limit of Deoxidation of Titanium and the Reduction of Titanium Dioxide by Saturated Calcium Vapors," *J. Japan Inst. Metals*, 49(10) (1985), 871–875. (in Japanese)
9. R. L. Fisher, "Deoxidation of Titanium and Similar Metals Using a Deoxidant in a Molten Metal Carrier," US Patent No. 4923531A, 1990. (UK Patent No. GB 2224749A, 1989)
10. R. L. Fisher, "Deoxidation of a Refractory Metal," US Patent No. 5022935, 1991.
11. R. L. Fisher and S. R. Seagle, "Removal of Oxide Layers from Titanium Castings Using an Alkaline Earth Deoxidizing Agent," US Patent No. 5211775 A, 1993.
12. R. L. Fisher and S. R. Seagle, "DOSS, An Industrial Process for Removing Oxygen From Titanium Turnings Scrap," *Proc. Titanium '92, Science and Technology*, vol. 3, ed. F. H. Froes and I. Caplan, (TMS, Warrendale, PA, U.S.A., 1993), 2265–2272.

13. T. H. Okabe, R. O. Suzuki, T. Oishi, and K. Ono, "Thermodynamic Properties of Dilute Titanium-Oxygen Solid Solution in Beta Phase," *Mater. Trans., JIM*, 32(5) (1991), 485–488.
14. T. H. Okabe et al., "Thermodynamic Properties of Oxygen in Yttrium Solid Solution," *Met. Trans. B*, 27(5) (1996), 841–847.
15. T. H. Okabe et al., "Thermodynamic Properties of Oxygen in Ln-O (Ln=La, Pr, Nd) Solid Solutions and Their Deoxidation by Molten Salt Electrolysis," *Shigen-to-Sozai (J. Min. Mater. Process. Inst. Jpn.)*, 114(11) (1998), 813–818.
16. T. H. Okabe et al., "Thermodynamic Properties of Oxygen in RE-O (RE=Gd, Tb, Dy, Er) Solid Solutions," *J. Alloys Compd.*, 279 (1998), 184–191.
17. J.-M. Oh et al., "Preparation Method of Ti Powder with Oxygen Concentration of <1000 ppm Using Ca," *Powder Metallurgy*, 55(5) (2012), 402–404.
18. J.-M. Oh et al., "Preparation of Low Oxygen Content Alloy Powder from Ti Binary Alloy Scrap by Hydrogen-Dehydrogenation and Deoxidation Process," *J. Alloys Compd.*, 593 (2014), 61–66.
19. K.-M. Roh et al., "Comparison of Deoxidation Capability for Preparation of Low Oxygen Content Powder from TiNi Alloy Scraps," *Powder Technology*, 253 (2014), 266–269.
20. T. H. Okabe et al., "Preparation of Extra Low Oxygen Titanium by Calcium-Halide Flux Deoxidation," *Tetsu-to-Hagane (J. Iron Steel Inst. Jpn.)*, 77(1) (1991), 93–99. (in Japanese)
21. T. H. Okabe, T. Oishi, and K. Ono, "Preparation and Characterization of Extra-Low-Oxygen Titanium," *J. Alloys Compd.*, 184 (1992), 43–56.
22. T. H. Okabe, T. Oishi, and K. Ono, "Deoxidation of Titanium Aluminide by Ca-Al Alloy under Controlled Aluminum Activity," *Met. Trans. B*, 23(5) (1992), 583–590.
23. T. H. Okabe et al., "Electrochemical Deoxidation of Titanium," *Met. Trans. B*, 24(3) (1993), 449–455.
24. T. H. Okabe et al., "Electrochemical Deoxidation of Yttrium-Oxygen Solid Solution," *J. Alloys Compd.*, 237 (1996), 150–154.
25. M. Nakamura et al., "Electrochemical Deoxidation of Titanium," *Proc. Int. Symp. Molten Salt Chem. Tech.*, (1993), 529–540.
26. K. Hirota et al., "Electrochemical Deoxidation of RE-O (RE=Gd, Tb, Dy, Er) Solid Solution," *J. Alloys Compd.*, 282 (1999), 101–108.
27. G. Z. Chen, D. J. Fray, and T. W. Farthing, "Cathodic Deoxidation of the Alpha Case on Titanium and Alloys in Molten Calcium Chloride," *Met. Trans. B*, 32(6) (2001), 1041–1052.
28. Y. Taninouchi, Y. Hamanaka, and T. H. Okabe, "Electrochemical Deoxidation of Titanium Using Molten Magnesium Chloride," (in preparation).
29. T. H. Okabe, Y. Hamanaka, and Y. Taninouchi, "Direct Oxygen Removal Technique for Recycling Titanium Using Molten MgCl₂ Salt," *Faraday Discussions* (in print).
30. Y. Hashimoto, K. Uriya, and R. Kono, "Electro-Winning of Titanium Metal from Its Oxide by Fused Salt Electrolysis at Temperatures above the Melting Point of the Metal," *Denki Kagaku*, 39(6) (1971), 516–522. (in Japanese)
31. Y. Hashimoto, "Influences of Fluoride Salt Baths on Fused-Salt Electrodeposition of Titanium Metal from TiO₂," *Denki Kagaku*, 39(12) (1971), 938–943. (in Japanese)
32. Y. Hashimoto, "Electro-Winning of Titanium from TiO₂ or CaTiO₃ in CaF₂-MgF₂ Molten Salt Bath," *Denki Kagaku*, 40(1) (1972), 39–44. (in Japanese)
33. G. Z. Chen, D. J. Fray, and T. W. Farthing, "Direct Electrochemical Reduction of Titanium Dioxide to Titanium in Molten Calcium Chloride," *Nature*, 407(6802) (2000), 361–364.
34. G. Z. Chen, D. J. Fray, and T. W. Farthing, "Removal of Oxygen from Metal Oxides and Solid Solutions by Electrolysis in a Fused Salt," US Patent No. 2004/0159559 A1, 2004.
35. D. J. Fray, "Emerging Molten Salt Technologies for Metals Production," *JOM*, 53(10) (2001), 26–31.
36. K. Ono and R. O. Suzuki, "A New Concept for Producing Ti Sponge: Calciothermic Reduction," *JOM*, 54(2) (2002), 59–61.
37. R. O. Suzuki and S. Inoue, "Calciothermic Reduction of Titanium Oxide in Molten CaCl₂," *Met. Trans. B*, 34(3) (2003), 277–285.
38. R. O. Suzuki, "Direct Reduction Process for Titanium Oxide in Molten Salt," *JOM*, 59(1) (2007), 68–71.
39. I. Barin, *Thermochemical Data of Pure Substances*, 3rd ed. (VCH Verlagsgesellschaft mbH, Weinheim, Germany, 1995).

Electrochemical Upgrading of Iron-Rich Titanium Ores

Farzin Fatollahi-Fard¹ and Petrus Christiaan Pistorius¹

¹Materials Science and Engineering, Carnegie Mellon University
5000 Forbes Avenue, Pittsburgh, PA 15213

Keywords: Titanium, Synthetic Rutile, Ilmenite, Molten Salt

Abstract

The production of synthetic rutile using a novel electrochemical process using a molten salt electrolyte is described. The product produced by this process is of similar quality and composition to existing synthetic rutile materials, which are used as a feedstock to many titanium and pigment production processes. The mechanism that underlies this process is the solubility of iron(III) oxide in chloride salts, which can then be reduced electrochemically, producing metallic iron, and leaving behind synthetic rutile. The effect of electrolyte composition is also investigated.

Introduction

Both the Kroll process for making titanium metal and pigment production from titanium require titanium (IV) chloride (TiCl₄) as a feedstock. The process of chlorination is very sensitive to impurities in the titanium concentrate, so natural and synthetic rutile can be used due to their low impurity content. However, synthetic rutile itself is produced from titanium mineral concentrates that are often high in iron, such as ilmenite (ideal formula FeTiO₃) [1].

In order to produce titanium of low enough iron to be considered synthetic rutile, the material needs to be “upgraded”. One such process is the Becher process, which involves carbothermal reduction of ilmenite to reduce the iron to metallic form, described in reaction (1). This is then followed up with a leach in a dilute ammonium chloride solution in oxygenated water, which results in the dissolution and re-precipitation of the iron as an oxide away from the titanium concentrate. This leaves behind a porous synthetic rutile material.



In the 1970's, Pollard and Stewart proposed a novel method of iron removal from titaniferous concentrates using a molten salt process [2, 3, 4]. Their process involved immersing the concentrate into molten sodium chloride in conjunction with hydrogen chloride, carbon, and with a nitrogen and carbon monoxide atmosphere. Pollard and Stewart suggested that the hydrogen chloride was the driving mechanism for the dissolution of the iron oxide.

Our recreation of Pollard and Stewart's methods showed that when using an iron(III) oxide bearing titanium mineral sand, hydrogen chloride and carbon monoxide was not necessary, implying that another mechanism was driving dissolution [5]. We determined that the dissolution of the iron was due to a low—but nonzero—solubility of iron(III) oxide in both molten sodium chloride and a sodium chloride–potassium chloride eutectic mixture, giving a concentration of dissolved iron oxide of up

to 43 molar ppm after dissolution for 24 hours. When iron(III) oxide is dissolved in molten salt in the presence of a carbon, it precipitates out as metallic iron, keeping the amount of dissolved iron oxide in solution low, providing a constant driving force for dissolution despite having a very low solubility limit. The actual reaction can be written as a typical iron reduction reaction, as expressed in reaction (2).



In theory, any mechanism which could remove iron(III) oxide from solution would maintain this driving force for dissolution. We believe that if the correct electrochemical potential is applied (by the Nernst equation, the potential of reaction (2) is 0.18 volts at 850 °C, for standard conditions), the iron can be plated out, providing the same driving force for dissolution as a chemical reductant. If this is the case, the resulting synthetic rutile can be removed from the salt after the process is complete, and will be ready for use after a simple water wash. This approach of electrochemical removal of dissolved iron oxide was tested in the work presented here.

Methods

The titanium concentrate used in these experiments was a pseudorutile mineral sand, whose composition is listed in Table I. This mineral sand is a mixture of pseudorutile ($\text{Fe}_2\text{Ti}_3\text{O}_9$) [6], natural rutile, and small amounts of ilmenite (FeTiO_3). In all cases, the materials were ground for 2 minutes using a “ring and puck” type tungsten carbide grinder (SPEX SamplePrep ShatterBox 8530).

For the electrolyte used in these experiments we used either pure sodium chloride (Fisher Chemical, >99.0%) or a eutectic mixture of 50.6 molar percent sodium chloride with 49.4 molar % potassium chloride (Fisher Chemical, >99.0%). For all experiments, the electrolyte was contained in a high-purity alumina crucible (Coorstek, 99.8%) with an inside diameter of approximately 6.65 centimeters (2.625 inches). The amount of electrolyte used was the amount necessary to make a 3 centimeter deep pool of molten salt (this was determined by the density of molten salts given by Janz et al. [7]). We used a Gamry Reference 3000 potentiostat to both control the cell voltage and current, as well as collect voltage and current data.

Characterization of the samples was carried out by x-ray diffraction (XRD) using a PANalytical X'Pert Pro x-ray diffractometer. When unknown phases were encountered in the x-ray diffraction pattern, these were identified by QualX2 software [8]. Imaging was performed by an Aspex Explorer, Phillips XL30, or FEI Quanta 600 scanning electron microscope (SEM). Phase identification and composition maps were obtained by energy-dispersive spectroscopy (EDS) on the SEM. Bulk compositions were determined using PANalytical MiniPal4 x-ray fluorescence spectrometer (XRF).

Electrochemical Reactor Design

The reactor is placed into a normal vertical tube furnace. All reactor components are made of 316/316L stainless steel unless otherwise specified. The main reactor tube is an NPT size 3 (3.5 inch OD) unthreaded pipe (schedule 10), with a 3.5 inch disk and flange attachment welded to the

bottom and top, respectively. The reactor is held in place in the furnace by a flange that is bolted to a frame above the furnace. The reactor cap is placed over the flange and the entire flange assembly is bolted together, holding the reactor tube, flange, and reactor cap firmly bolted to the furnace's frame. There is a 1/8 inch thick Viton gasket providing a gastight seal between the reactor tube and the reactor cap.

The reactor cap contains 6 ports. There are two 7/8 inch Swagelok fittings, which are the main anode and cathode ports for the reactor. There are also four 1/4 inch Swagelok fittings, which are for the gas inlet, gas outlet, reference electrode, and the thermocouple tube. The thermocouple tube can also be replaced by a pressure gauge, or the port could be used as an in-situ electrolyte sampling port, if necessary (these options are mutually exclusive).

The main electrodes are 1/4 inch diameter stainless steel rods with threaded ends, inserted into high-temperature silicone stoppers. The stoppers are the correct size to plug up the 7/8 inch Swagelok fittings on the electrode ports, while also being an electrically insulating barrier between the rods and the reactor cap. We currently have 3 options for the threaded ends: 1/2 inch diameter high-purity graphite rods, metal strips (304 stainless steel or Grade 2 titanium), and the graphite anode basket. The metal strips have a 1/4 inch hole and an L-bend, and are held in place by bolts. The graphite rods are put on via 1/4 inch to 1/2 inch threaded adapters. The anode basket can be attached to the electrode rod by Kanthal wire.

Molten silver chloride reference electrode: For the reference electrode in our system, we have selected a silver-silver chloride reference electrode, due to the fact that silver only has a single (+1) valance state. However, the temperature at which our reactor operates is above the melting point of silver chloride. Therefore, unlike a typical aqueous salt system where a silver-silver chloride reference would be used, we cannot have a solid film of silver chloride on silver. However, as silver chloride is soluble in the chloride salts we use as electrolytes, we can still utilize this as a reference.

The literature shows a few examples of silver chloride solutions being used as a reference electrode [9, 10]. In the case of our system, reactions (3) and (4) are used to define the electrode potential relative to chlorine evolution. We can then use the Nernst equation to find the potentials of this reaction, taking into account the activity of dissolved silver chloride. As a first-order approximation, the molar concentration of the salt is taken to be equal to its thermodynamic activity, with a constant activity coefficient (reasonable for dilute solutions). Figure 1 is a plot of potential as a function of silver chloride activity.



The silver chloride electrode uses 1 millimeter diameter silver wire (Alfa Aesar, 99.95%), a 1/4 inch outside diameter alumina tube (Coorstek, 99.8%), alumina insulation material (ZIRCAR alumina felt type RS-3000), and hardener (ZRCI AL-HARD Rigidizer). A small piece of the alumina insulation was dipped in the hardener and put into one end of the alumina tube. Drying this produced an alumina tube with a porous plug on one end. The molten chloride salts we use wet alumina very well, and percolate through the porous plug to provide a small pool in contact

with the silver wire. The potentiostat, operating in galvanostatic mode, can dissolved silver into the small electrolyte pool (producing silver chloride), providing an effective reference. For our experiments, we passed 50 mA for 300 seconds in order to produce a local concentration of 4 molar % AgCl. At the end of the experiment, the silver chloride can be recycled by passing the opposite current for the same amount of time.

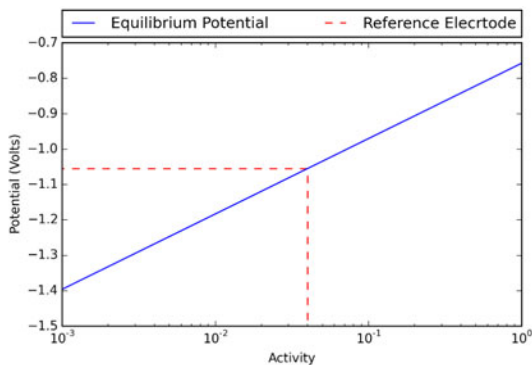


Figure 1. Plot of Ag/AgCl potential (relative to chlorine evolution) as a function of AgCl activity ($T = 800\text{ }^{\circ}\text{C}$). 4% concentration (used in all experiments) is shown as red dotted line.

Experimental Procedure and Characterization

In the first experiment, the pseudorutile mineral sand was immersed in the salt in a small (~2 cm diameter) alumina crucible (Coorstek, 99.8%) in a eutectic NaCl-KCl electrolyte at $850\text{ }^{\circ}\text{C}$. The material was allowed to sit for 24 hours for the iron oxide to dissolve into the electrolyte. Afterwards, a stainless steel working electrode and a graphite rod counter electrode were inserted. The potentiostat was set to potentiostatic mode applying a voltage of -0.5 volts for 24 hours, to plate the dissolved iron from solution. After this, the electrodes were removed and the resulting titanium concentrate collected during the dissolution of the salt in water. Washing involved putting the crucible containing the salt into a 1 liter beaker of boiling water. The collected mineral sand was further washed with clean water using a Soxhlet extractor.

In the second experiment, the electrolyte was pure sodium chloride at $900\text{ }^{\circ}\text{C}$. The mineral sand was placed in a graphite basket and affixed to an electrode rod. The basket was placed in into the molten salt and allowed to remain for 24 hours. Afterwards, a stainless steel electrode was inserted as a working electrode, and the graphite basket itself was used as the counter electrode. The potentiostat was set to potentiostatic mode to apply -0.5 volts for 3.75 hours. After this, the reference electrode was recycled and regenerated (since it was found that loss of silver chloride from the reference electrode occurred, affecting its voltage). This electrochemical regime was repeated two more times, for a total run time of 12 hours, after which the basket is removed, and the contents of the reactor cooled to room temperature. The salt in the graphite basket was then dissolved with water and its contents placed in the Soxhlet extractor for washing.

Results

Electrochemical Leaching in NaCl-KCl Electrolyte

Due to difficulties in the removal of the titanium concentrate from the solidified salt, only 0.2 grams was recovered, insufficient for XRF measurements. The material was subjected to x-ray diffraction, yielding the XRD pattern shown in Figure 2. QualX2 identified the compounds present as rutile, ilmenite, and $\text{KTi}_8\text{O}_{16}$.

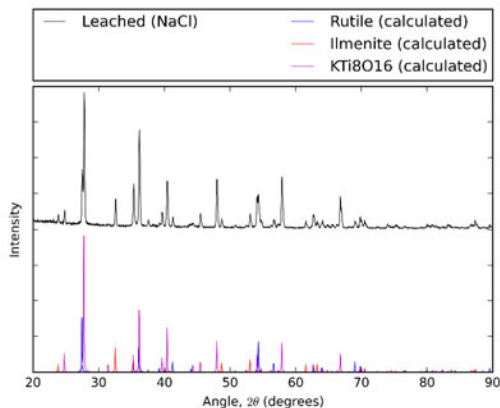


Figure 2. X-ray diffraction pattern of the pseudorutile concentrated after electrochemical leaching in NaCl-KCl electrolyte (top) and the calculated patterns of rutile, ilmenite, and $\text{KTi}_8\text{O}_{16}$ (bottom)

SEM was performed on the bulk material mounted on a stub, as well as a mounted and polished sample. Secondary electron imaging of the sample on the stub (Figure 3), showing a very needle-like structure. Backscattered electron imaging of the mounted section (Figure 4(a)) shows slight variations in contrast, indicating minor differences in composition. EDS measurements suggest that these brighter spots contain potassium. We also performed SEM on the working electrode, where we expected iron deposition. We did observe clusters formed on the surface of the electrode, and EDS confirmed these to be iron. However, as well as an increase in iron, we observed bright spots in the backscattered image. EDS analysis showed these spots to be silver.

Electrochemical Leaching in NaCl Electrolyte

Due to the minor adjustments in the procedure (use of the anode basket, to allow for easy removal), most of the pseudorutile was recovered. After magnetic separation (to remove any potential metallic iron formation due to the use of a carbon crucible), the material was subjected to XRD (Figure 5) and was also analyzed by XRF (composition listed in Table I).

The sample was analyzed by SEM, shown in Figure 6. We observed small mostly spherical particles, with some irregularly shaped particles, similar to the ground pseudorutile starting material. Backscatter imaging showed particles that were mostly uniform in contrast, with some small particles being brighter. The EDS map in Figure 6 shows that the dark particles (the majority of the material) was titanium oxide, with small amounts (<5 wt. %) of iron. The small bright particles had iron contents approaching 50 weight %, implying they were ilmenite particles.

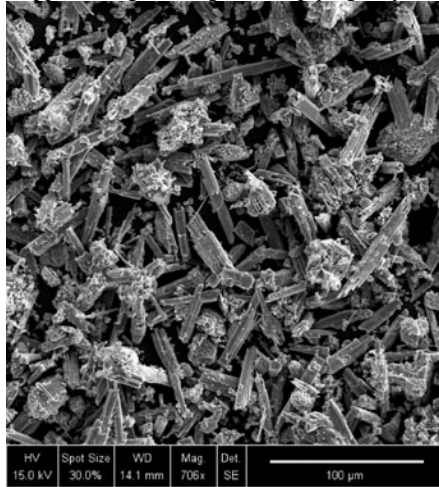


Figure 3. Secondary electron image of the NaCl-KCl leached pseudorutile

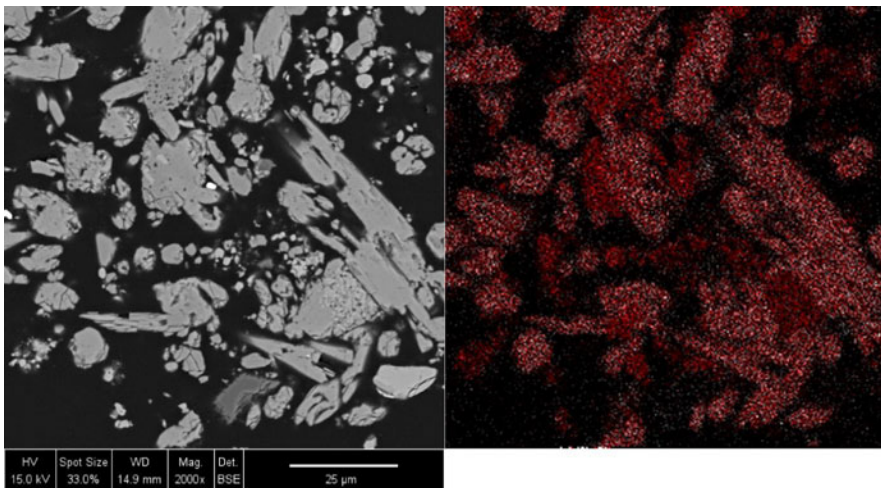


Figure 4. (Left) Backscattered electron image of NaCl-KCl leached pseudorutile (polished section), (Right) EDS map showing titanium (red) and potassium (white)

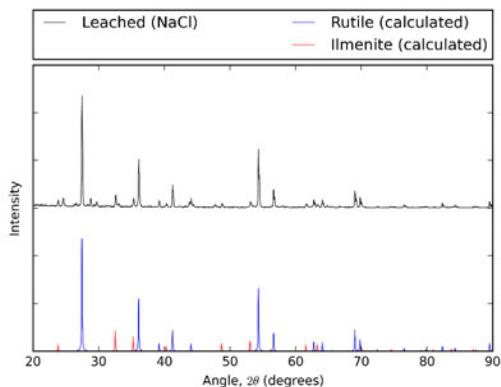


Figure 5. X-ray diffraction pattern of the pseudorutile concentrate after electrochemical leaching in NaCl electrolyte (top) and the calculated patterns of rutile and ilmenite (bottom)

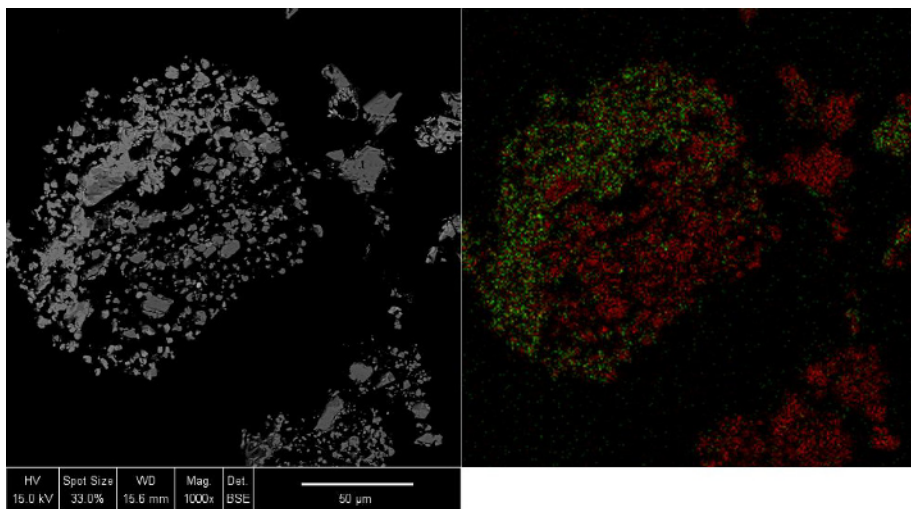


Figure 6. (Left) Backscattered electron image of NaCl leached pseudorutile (polished section), (Right) EDS map showing titanium (red) and iron (green)

Table I. Compositions of pseudorutile mineral sand and the NaCl leached sample in wt%

Compound	Pseudorutile	Leached (NaCl)
TiO ₂	80.5	88.0
Fe ₂ O ₃	15.9	8.0
Al ₂ O ₃	0.3	0.4
CaO	0.2	0.1
Cr ₂ O ₃	0.4	1.2
MgO	<0.1	<0.1
MnO	0.9	0.3
SiO ₂	1.6	1.5
ZrO ₂	0.2	0.4

Discussion

In the case of the leaching in NaCl-KCl eutectic molten salt, the emergence of the KTi₈O₁₆ compound was surprising. However, upon the discovery of the silver on the working electrode, this led us to a theory as to what occurred. During the 24 hour potentiostatic run, the silver in the reference electrode pool diffused across the porous plug, and was plated on to the working electrode. Due to the drop in the silver concentration, the reference drifted (towards more negative potentials), allowing the potential to reach the point where electrolyte decomposition could occur. Potassium chloride will decompose at a higher potential relative to sodium chloride, and potassium is miscible in potassium chloride [11]. The free potassium could then reduce the TiO₂ directly, to form KTi₈O₁₆.

The lessons from the NaCl-KCl experiment led us to make changes, such as changing the electrolyte to pure sodium chloride, and recycling and regenerating the reference electrode to prevent the potential from drifting. While this did not prevent silver chloride loss from the reference electrode, it would reset the potential to the correct value every few hours, to avert decomposition of the electrolyte. Given the lack of sodium seen in EDS, it is safe to assume this worked.

From the XRF results, we can see that the TiO₂ content has not reached the threshold of 95% to be considered a synthetic rutile. However, from the XRD pattern, we can see that there is still ilmenite present. This is a holdover from the pseudorutile ore itself, which contains some amount of ilmenite. Since the ilmenite is expected to contain iron(II) oxide, the iron oxide is not expected to dissolve in our molten salts. If the ore was ilmenite free, or if the ore was roasted in air at a temperature sufficient to oxidize the iron(II) oxide to iron(III) oxide, then we believe we could reach the concentration levels necessary for the mineral sand to reach rutile levels of purity after electrochemical leaching.

Conclusion

We have shown that using the inherent solubility of iron(III) oxide in molten sodium and potassium chlorides, we can use an electrochemical process to purify titanium ores. Although we did not reach the purity levels necessary to achieve the 95 weight % TiO₂ threshold of natural and synthetic

rutile materials, some minor modifications to the procedure (i.e. an oxidizing roast before leaching) could allow this to occur.

References

1. G. Auer et al., "Pigments, Inorganic, 2. White Pigments," *Ullmann's Encyclopedia of Industrial Chemistry*, (2012), 257-291.
2. D. F. Stewart and L. J. Pollard, "Process of Beneficiating Titaniferous Ores in the Presence of Hydrogen Chloride," (Patent, US 3854929, 1974).
3. D. F. Stewart and L. J. Pollard, "Process for Producing Metallic Iron Concentrates and Titanium Oxide Concentrates from Titaniferous Ores," (Patent, US 3816099, 1974).
4. L. J. Pollard and D. F. Stewart, "Beneficiation of the Non-Ferrous Metal Values of Oxide-Containing Materials," (Patent, US 4047934, 1977).
5. F. Fatollahi-Fard and P. C. Pistorius, "Upgrading of Iron-Rich Titanium Minerals Using a Molten Salt Process," *7th International Symposium on High Temperature Metallurgical Processing*, TMS 2016, In Press.
6. I. E. Grey and J. A. Watts, "Mineralogical Nomenclature: Pseudorutile Revalidated and Neotype Given," *Mineralogical Magazine*, 58 (393) (1994), 597-600.
7. G. J. Janz et al., "Molten salts: Volume 4, part 2, chlorides and mixtures—electrical conductance, density, viscosity, and surface tension data," *Journal of Physical and Chemical Reference Data*, 4 (4) (1975), 871-1178.
8. A. Altomare et al., "QUALX2.0: a qualitative phase analysis software using the freely available database POW COD," *Journal of Applied Crystallography*, 48 (2) (2015), 598-603.
9. S. Flengas and T. Ingraham, "Voltaic Cells in Fused Salts: Part I. The Silver-silver Chloride, Cobalt-cobaltous Chloride System," *Canadian Journal of Chemistry*, 35 (10) (1957), 1139-1149.
10. J. Guion et al., "Thermodynamic Treatment and Electromotive Force Measurement of the Ternary Molten Salt Systems Silver Chloride-Sodium Chloride-Potassium Chloride and Silver Chloride-Sodium Chloride-Cesium Chloride," *Journal of Physical Chemistry*, 72 (6) (1968), 2086-2095.
11. J. W. Johnson and M. A. Bredig, "Miscibility of Metals with Salts in the Molten State. III. The Potassium-Potassium Halide Systems," *Journal of Physical Chemistry*, 62 (5) (1958), 604-607.

INVESTIGATIONS FOR THE RECYCLE OF PYROPROCESSED URANIUM

B.R. Westphal, J.C. Price, E.E. Chambers, and M.N. Patterson

P.O. Box 1625
Idaho Falls, ID 83415

Keywords: Pyroprocessing, Uranium Recycle

Abstract

Given the renewed interest in uranium from the pyroprocessing of used nuclear fuel in a molten salt system, the two biggest hurdles for marketing the uranium are radiation levels and transuranic content. A radiation level as low as possible is desired so that handling operations can be performed directly with the uranium. The transuranic content of the uranium will affect the subsequent waste streams generated and, thus also should be minimized. Although the pyroprocessing technology was originally developed without regard to radiation and transuranic levels, adaptations to the process have been considered. Process conditions have been varied during the distillation and casting cycles of the process with increasing temperature showing the largest effect on the reduction of radiation levels. Transuranic levels can be reduced significantly by incorporating a pre-step in the salt distillation operation to remove a majority of the salt prior to distillation.

Introduction

During the last twenty years, several nuclear entities have shown various interest levels in the uranium products from the pyroprocessing of used metallic nuclear fuel at the Fuel Conditioning Facility (FCF). The used nuclear fuel originates from the core or driver regions of the retired Experimental Breeder Reactor II (EBR-II) and Fast Flux Test Facility (FFTF) and is highly enriched (~60% U-235) with moderate burnup (~10 atom%). Inevitably, the two biggest hurdles for marketing the uranium products are radiation levels and transuranic (viz. plutonium) content. Since most of the operations by other entities would not be remotely handled as in FCF, a radiation level as low as possible is desired so that these entities can handle the recycled uranium directly. The transuranic content will affect the subsequent waste streams generated by the entities during the processing of the uranium products and, thus also should be minimized. It should be noted that pyroprocessing technology was originally designed and developed to be performed remotely and without regard to radiation and plutonium levels [1-3]. Thus, retrofitting the process to market uranium presents challenges not anticipated with the original technology. This paper reports on the experimental research in FCF to reduce the radiation and plutonium levels such that the uranium products may be more attractive for other nuclear entities.

Equipment

Two unit operations of the pyroprocess have been targeted to reduce the radiation levels and transuranic content by varying the process conditions; the distillation and casting operations. Distillation is performed on electrorefined dendritic material to remove salt from metallic uranium and consolidate the uranium. The casting operation down-blends the fissile content of the uranium and allows sampling of the molten uranium product for chemical analyses. Both operations are performed in a hot cell environment where all tasks are performed remotely with electro-mechanical manipulators.

Figure 1 shows a layout of the distillation equipment, or cathode processor, including splatter shield, process crucible, radiation shield, condenser, and receiver crucible. The furnace region of the cathode processor is heated by a passively cooled induction coil that susceptes to the graphite furnace liner which, in turn, heats the graphite process crucible by radiation. The process crucible is either coated with a slurry of zirconia (ZrO_2) and dried or has a ceramic liner of zirconia cast into the graphite crucible. A vacuum system is connected to the condenser region and consists of mechanical pumps that are connected to the vessel through an assembly of piping, manifolds, and valves. Distillate material is transferred to the condenser region from the process crucible in the vapor phase and collected in the receiver crucible.

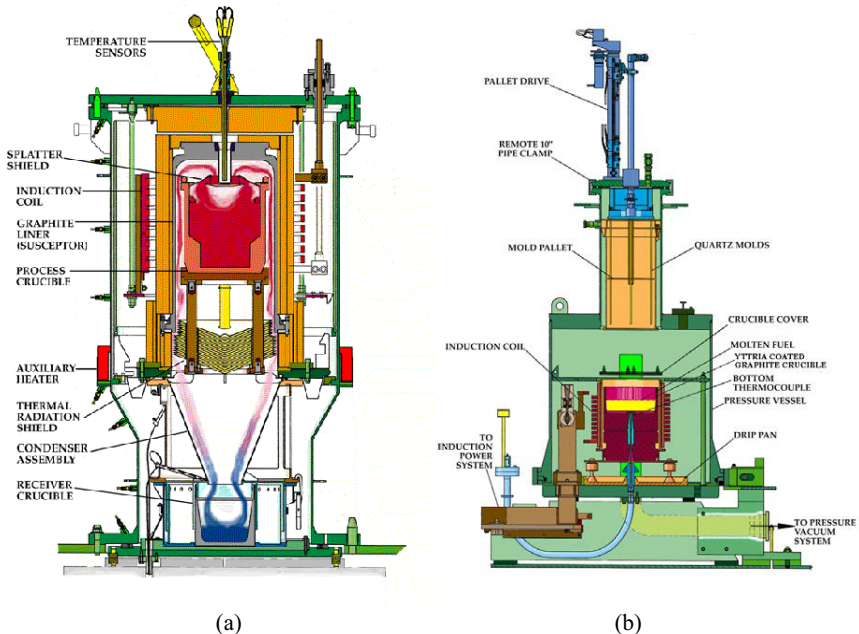


Figure 1. Schematics of cathode processor (a) and casting furnace (b)

Testing with irradiated materials in the cathode processor commenced in August 1996 with a batch of enriched dendrites from the Mk-IV electrorefiner [4]. Enriched batch sizes in the cathode processor are less than 20 kg with an approximate salt fraction of 20 wt.%. As designed, the cathode processor is capable of temperatures as high as 1673 K and pressures less than 10 Pa. For typical distillations, it is only heated to 1473 K at less than 100 Pa to achieve sufficient separation of distillate from the uranium ingots. A more thorough description of the cathode processor equipment and operations is given elsewhere [5].

Also shown in Figure 1 is a schematic of the casting equipment, an inductively-heated furnace capable of melting and casting uranium ingots. A graphite crucible coated with yttria contains the molten uranium from which samples are taken via an evacuation/pressurization cycle. The vacuum capability is instrumental in casting molten metal into quartz molds (0.43 cm inside diameter by 41 cm length). Following a system evacuation, the molds are submerged into the melt and the system is repressurized rapidly to fill the molds. The solidified metal is removed from the molds, sectioned (0.64 cm length), and sent to the analytical laboratory for chemical analyses.

More than 100 heats of the casting furnace have been performed to down-blend, sample, and produce uranium products (20 cm diameter by approximately 8 cm height) ranging in size from 15-50 kg [6]. Additional depleted uranium is utilized for the down-blending to take the enrichment to less than 20% U-235. The casting furnace is capable of temperatures as high as 1873 K and vacuums to less than 100 Pa. The uranium products, once characterized by chemical analyses, are being placed in interim storage awaiting final disposition.

Following the dissolution of the solidified metal sections in nitric acid in the analytical laboratory, two different techniques are utilized for the determination of chemical compositions; inductively-coupled plasma mass spectroscopy (ICP-MS) and gamma-ray spectroscopy. The equipment for these techniques has been modified for use with radioactive solutions to limit personnel exposure by their operation in a shielded glovebox and monitoring of the transmission by a spectrometer located exterior to the box.

Radiation Readings of Uranium Products

There are two methods for measuring the radiation readings from uranium products produced during the treatment of used EBR-II and FFTF fuel; ingot form and pin form. The ingot form measurements are made at several positions on the storage container with the uranium products. Typically the measurements, in R/hr, from the bottom of the storage container on contact are used for comparison purposes. This measurement is through 0.95 cm steel plate and usually is performed on the ingot's top surface. The pin form measurements are performed in the analytical laboratory directly on sectioned pin pieces before dissolution for chemical analyses. Shown in Table I are the ingot and pin form data for the three processing campaigns of the driver fuel to date (U-10Zr is a binary uranium-zirconium fuel and U-5Fs is a uranium-fissium alloy where fissium includes Mo, Ru, Rh, Pd, and Zr).

Table I. Radiation readings (R/hr/kg) of driver uranium products

Fuel Form	EBR-II U-10Zr	FFTF U-10Zr	EBR-II U-5Fs
Ingot	0.2 (5)	0.1 (15)	0.1 (3)
Pin	1.0 (14)	1.8 (24)	0.5 (3)

The first value is the radiation reading and the second value in parentheses is the number of units averaged for the data. The data for the ingot form have been adjusted for the 0.95 cm plate and the slag layer on the top of the ingot so that a direct comparison with the pin form is possible [7]. As seen from the data, the ingot form radiation readings are much lower, presumably due to the self-shielding effects in the ingot form.

The primary contribution to the radiation level is gamma-based Cs-137 which oxidizes to the electrorefiner salts as cesium chloride [7]. Although the distillation step of pyroprocessing removes the majority (>99%) of the salt from uranium, a residual quantity remains that can either react with the oxide-based crucible components to form stable cesium compounds (e.g. Cs_xU_yO_z) or remain as undistilled cesium chloride. In both instances, the cesium can preferentially accumulate on the surface of uranium products, both ingots and pins, based on the differential cooling characteristics of the products.

Shown in Table II are specific radiation measurements of uranium product batches (FF for FFTF and FS for fissium) with their associated maximum temperatures at the cathode processor (CP) and casting furnace (CF). For consistency, only radiation readings from the bottom of the storage container on contact (~2.54 cm) are reported in Table II. Radiation readings were only taken following the casting step for the FFTF batches while the fissium batches had measurements taken on both the cathode processor and casting ingots. In general, increasing the maximum temperature at the cathode processor reduced the radiation readings of the casting ingots. Conversely, no significant effect has been seen to date in increasing the temperatures at the casting furnace.

Also included in Table II is the quantity of Cs-137 found from sampling during the casting operation. Since the sampling of uranium ingots is performed during the casting cycle, the amount of Cs-137 detected represents a bulk or homogeneous quantity and may not represent that associated with the top surface of the ingot. Despite the bulk versus surface concern, the amount of Cs-137 in the casting ingots appears to be correlated with the radiation measurements, see Figure 2. Possible sources of errors in the Cs-137 data include analytical, sampling, and cross-contamination from reusable casting crucibles or other casting equipment components. The most significant error in the radiation reading data derives from the measurement location; the reading is a function of the inverse of distance squared.

Table II. Radiation readings and other data from uranium ingots

Batch	CP Maximum Temperature (K)	CP Ingot Radiation Reading (R/hr @ 2.54 cm)	CF Maximum Temperature (K)	CF Ingot Radiation Reading (R/hr @ 2.54 cm)	Cs-137 in U Product Ingot (ppb)
FF001	1473	Not Measured	1661	28.5	62
FF002	1473	Not Measured	1625	16.7	2
FF003	1473	Not Measured	1625	10.0	50
FF004	1473	Not Measured	1585	19.0	43
FF005	1623	Not Measured	1589	3.0	15
FF006	1623	Not Measured	1586	4.6	9
FF007	1473	Not Measured	1584	1.4	13
FF008	1473	Not Measured	1586	0.9	9
FF009	1623	Not Measured	1586	1.5	6
FF010	1623	Not Measured	1586	0.7	7
FF011	1473	Not Measured	1588	21.0	40
FF012	1473	Not Measured	1829	24.0	11
FF013	1623	Not Measured	1585	0.5	9
FF014	1623	Not Measured	1589	4.2	5
FF015	1623	Not Measured	1584	2.7	6
FS001	1503	10.7	1833	7.1	16
FS002	1623	11.4	1823	11.5	23
FS003	1473	59.6	1823	34.4	260

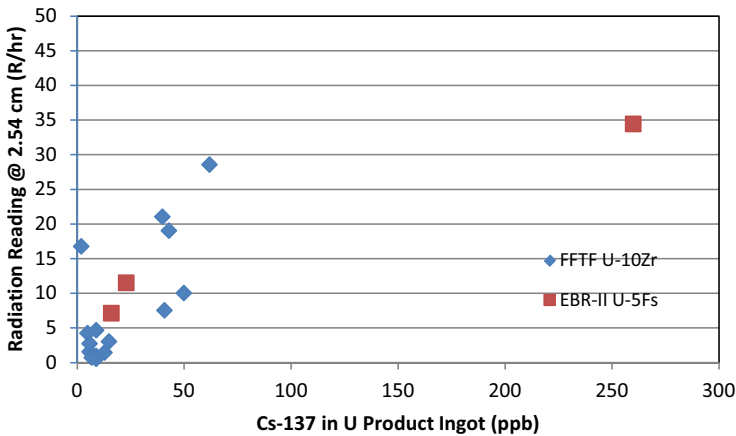
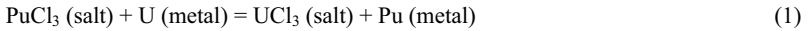


Figure 2. Radiation readings versus Cs-137 in FFTF and EBR-II uranium products

Plutonium Content of Uranium Products

The two most recent campaigns of processing driver uranium products in FCF include the FFTF fuel as well as the EBR-II U-5Fs fuel. The plutonium content for these campaigns is shown in Figure 3. In general, the plutonium levels of the uranium products averages about 100 ppm with one ingot as high as 200 ppm. Plutonium in the ingots is a result of the reaction of plutonium chloride with uranium metal in the cathode processor according to the following reaction [8]:



Thermodynamically, this reaction would be driven to the left although the conditions in the cathode processor favor the reaction to the right given the distillation of salt away from metal. Thus, plutonium metal is left as an impurity on the uranium products.

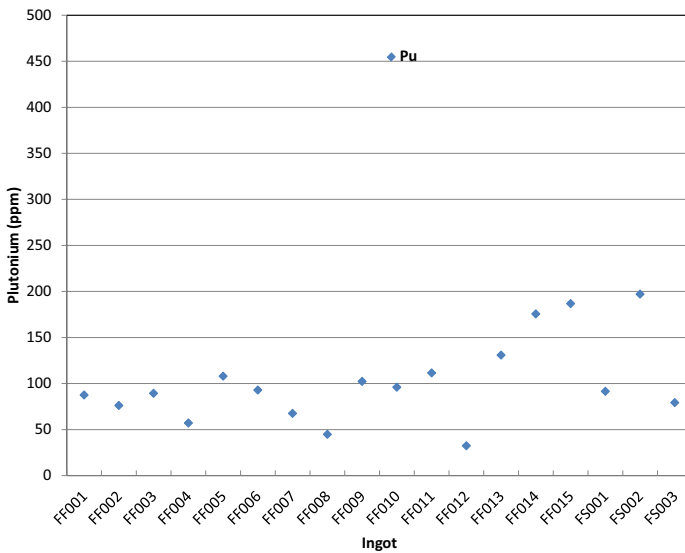


Figure 3. Plutonium levels for FFTF and EBR-II U-5Fs uranium products

Although external entities have not specified an acceptable transuranic (TRU) content, levels as low as 10-20 ppm have been implied based on anticipated process scenarios and subsequent waste stream requirements. Recognizing that approximately 75% of the TRU elements in the uranium product are plutonium, a plutonium value of 15 ppm is targeted as a requirement for the product specification. Additional contributing TRU elements would be neptunium (Np-237) and americium (Am-241). Given the current level of plutonium in the uranium products, a reduction by a factor of approximately seven would be required to meet this specification.

Since the plutonium in the uranium products originates from the salt, a scoping set of experiments was performed in FCF to remove a fraction of the salt prior to distillation and observe the effects on plutonium contamination. An additional benefit of salt removal may be a reduction in the cesium levels of the uranium products and hence, the radiation levels, since cesium is present as a distillable chloride species. The basis for the pre-distillation salt removal tests has been demonstrated previously [9]. Although the investigation was with salt only and not dendritic material, salt removals of 73% at 773 K and 94% at 873 K were realized.

Two tests were performed with dendritic material loaded into a screened bucket in the FCF cathode processor to demonstrate the feasibility of salt draining. The screen material was 100 mesh welded to the bottom of the bucket supported by a plate with 0.64 cm diameter holes. Following each test, the consolidated dendrites were removed from the bucket and loaded into a normal cathode processor crucible for distillation of the remaining salt.

For the first test, approximately 7.3 kg of dendritic material from the Mk-IV electrorefiner was loaded into the bucket and heated to 873, 973, and 1073 K for 1 hour during three separate salt draining heats in the cathode processor. In between the heats, weight measurements were taken on the bucket to assess the amount of salt draining. The bucket was placed on a graphite ring which resided on the graphite crucible stand in the lower region of the cathode processor coil. Shown in Figure 4 are photographs of the bucket prior to the 873 K run and following the 1073 K run. Note the consolidation of the dendrites between the three runs. For the three runs, 428 g, 51 g, and 90 g of salt were removed per run, respectively. An additional 373 g of salt was removed during a final distillation run to 1473 K in a separate crucible for a total of 942 g of salt. Thus, the amount of salt removed by salt draining was approximately 44% by weight of the total.



(a)



(b)

Figure 4. Photographs of first salt draining test before 873 K (a) and after 1073 K (b)

For the second test, approximately 7.2 kg of dendritic material from the Mk-IV electrorefiner was loaded into a new second bucket and heated to 1073 K for 1 hour in the cathode processor. After the run, a weight measurement was taken on the bucket to assess the amount of salt

draining. For this test, the bucket was placed inside a graphite crucible which placed the bucket in the upper region of the cathode processor coil. The consolidation of the dendrites was noted as similar to the previous test. For the run, 581 g of salt was removed from the bucket and collected in the bottom of the graphite crucible. An additional 750 g of salt was removed during the final distillation run in a separate crucible for a total of 1331 g of salt. Thus, salt draining removed approximately 60% of the total salt. Although the casting operations for the two salt draining tests have not yet been performed, it is anticipated that with a reduction of salt between 44-60% that the plutonium levels would be reduced similarly. Future salt draining tests will extend the hold times and maximize dendrite/screen contact area in an effort to improve salt removal.

Conclusions

- Based on the radiation readings taken on the casting ingots, increasing the cathode processing operating temperature resulted in reduced radiation levels.
- Although testing to reduce the radiation levels of uranium products continues, adjustment of the cathode processor operating conditions has had more of an effect than on the casting conditions.
- Radiation readings of uranium products in their storage containers appear to be dependent on the bulk Cs-137 levels in the product ingots.
- Salt removals as high as 60% by a draining operation should result in a significant improvement in the transuranic levels of the uranium products.

Acknowledgements

The authors would like to acknowledge the Fuel Conditioning Facility operations personnel for their contributions and the Analytical Laboratory staff for chemical services. This work was supported by the U.S. Department of Energy, Office of Nuclear Energy, Science, and Technology, under DOE-NE Idaho Operations Office Contract DE-AC07-05ID14517.

References

- [1] Y.I. Chang, "The Integral Fast Reactor," *Nucl. Tech.*, 88 (1990), 129-138.
- [2] C.E. Till and Y.I. Chang, *Plentiful Energy – The Story of the Integral Fast Reactor* (Charleston, SC: CreateSpace, 2012).
- [3] R.W. Benedict and H.F. McFarlane, "EBR-II Spent Fuel Demonstration Project Status," *Radwaste*, 5, 23 (1998).
- [4] S.X. Li et al., "Electrorefining Experience for Pyrochemical Processing of Spent EBR-II Driver Fuel," *Proc. GLOBAL 2005* (Tsukuba, Japan: AESJ, 2005), 487.
- [5] B.R. Westphal et al., "On the Development of a Distillation Process for the Electrometallurgical Treatment of Irradiated Spent Nuclear Fuel," *Nucl. Eng. Tech.*, 40 (2008), 163-173.

- [6] B.R. Westphal et al., "Zirconium Determination by Cooling Curve Analysis during the Pyroprocessing of Used Nuclear Fuel," *J. Nucl. Mat.*, 457 (2015), 241-245.
- [7] B.R. Westphal et al., "Radiation Measurements of Uranium Ingots from the Electrometallurgical Treatment of Spent Fuel" (Report ANL-NT-188, Argonne National Laboratory Report, 2001).
- [8] B.R. Westphal et al., "Transformation of Uranium Products from the Pyrometallurgical Processing of Used Nuclear Fuel," *Proc. Pu Futures-The Science 2010* (Keystone, CO: ANS, 2010), 352-353.
- [9] K.M. Park et al., "The Solid-Liquid Separation Characteristics of Pure LiCl-KCl Eutectic Salt using Different Types of Crucibles," *J. Radioanal. Nucl. Chem.*, 295 (2013), 1187-1193.

ZERO-DIRECT-CARBON-EMISSION ALUMINUM PRODUCTION BY SOLID OXIDE MEMBRANE-BASED ELECTROLYSIS PROCESS

Shizhao Su¹, Uday Pal^{*1,2}, Xiaofei Guan^{1,2}

¹Division of Materials Science and Engineering, Boston University, Brookline, MA 02446

²Department of Mechanical Engineering, Boston University, Boston, MA 02215

Keywords: Solid oxide membrane; Yttria stabilized zirconia; Aluminum production

Abstract

A zero-direct-carbon-emission solid oxide membrane (SOM) electrolysis process was designed and developed to produce high purity aluminum metal. An inert anode assembly containing liquid silver in a one-end-closed YSZ (yttria-stabilized zirconia) membrane tube and LSM ($\text{La}_{0.8}\text{Sr}_{0.2}\text{MnO}_{3-\delta}$)-Inconel inert anode current collector was immersed in an alumina containing molten fluoride flux. A proof-of-concept electrolysis experiment was performed to confirm the aluminum production by depositing liquid aluminum directly on a TiB_2 cathode. An improved setup employing liquid aluminum cathode was subsequently used to produce high purity aluminum using the SOM electrolysis process. The membrane stability was confirmed using scanning electron microscopy and energy-dispersive X-ray spectroscopy. High purity aluminum (>99wt%) was produced and collected after the electrolysis.

Introduction

Aluminum is the third most abundant element in the earth's crust, and the most abundant metallic element. It is an essential material in modern manufacturing. It is known for its low density, high strength, corrosion resistance and high electrical and thermal conductivities. It has been the second largest used industrial metal for the past fifty years. Demand for aluminum production is increasing in recent years, mainly due to the substitution of aluminum in the transportation sector and other lightweight structural applications[1].

The production process of aluminum was invented in 1886 by Charles Martin Hall and Paul L.T. Héroult (i.e. the Hall-Héroult process) by electrolyzing a cryolite-alumina melt. While the Hall-Héroult process has been significantly improved during the past 100 years, resulting in cheaper aluminum and lesser energy consumption, the current energy consumption in primary aluminum production is still 13kWh/kg of aluminum while the theoretical minimum energy requirement of the process is 5.99kWh/kg[2]. The anode effects of the process results in perfluorocarbon emissions that has a global warming potential 6500 – 9200 times that of CO_2 . Use of graphite anode in the current process also causes 1.52kg CO_2 emission per kg of Al produced (excluding CO_2 emission introduced by electricity consumption) [2]. The market potential of aluminum and the environmental impact of the current aluminum production process justify research and development of alternative electrolytic processes for aluminum production that can both reduce the cost and eliminate adverse environment impacts.

Solid oxide membrane (SOM) electrolysis is a novel metals extraction technique that is being developed for the production of several energy-intensive metals, such as Mg, Ti, Ta, Yb and Si[3]–[11]. The SOM electrolysis process features the utilization of an oxygen-ion-conducting membrane, typically made of yttria-stabilized zirconia (YSZ), for directly electrolyzing metal oxides. The desired metal oxide is dissolved in a pre-selected non-consumable molten flux. The YSZ membrane separates an inert anode from the molten flux and a cathode. When applied DC potential between the anode and the cathode exceeds the dissociation potential of the desired metal oxide, the metal is reduced at the cathode and oxygen ions migrate through the YSZ membrane and are oxidized at the anode. A novel LSM ($\text{La}_{0.8}\text{Sr}_{0.2}\text{MnO}_{3-\delta}$)-Inconel inert anode current collector and liquid silver anode are used in SOM electrolysis process for oxygen evolution[5]. Thus, the process also produces pure oxygen gas as a value-added byproduct[7].

In this paper, a novel laboratory-scale process for aluminum production using SOM based electrolysis is presented. Aluminum oxide dissolved in a pre-selected molten fluoride flux, which is chemically compatible with the YSZ membrane, was reduced in a SOM cell at 1200°C. By employing the YSZ membrane based inert-anode assembly, this process produces and collects pure aluminum and oxygen separately. By removing the carbon anode and its manufacture, the direct emission of CO₂ and other greenhouse gases are eliminated. The process enables the use of an insulated, corrosion-free lined steel vessel without frozen salt ledge and thus significantly reduces the heat loss and increases the energy efficiency. The electrochemistry of the process was monitored. The aluminum that was produced in the process was characterized by scanning electron microscope (SEM) and energy-dispersive X-ray spectroscopy (EDS). The YSZ membrane stability during the electrolysis was also studied in order to provide insights for long term aluminum production.

Experimental

A. SOM Electrolysis Setup

Figure 1 shows the schematic of a SOM electrolysis setup. The setup consists of a grade 304 stainless steel (SS-304) crucible that was heated to 1200°C in forming gas (95% Argon-5% H_2) to ensure an inert atmosphere. Inside the crucible, 450g of powdered flux (45 wt% MgF_2 – 55 wt% CaF_2 containing CaO, Al_2O_3 and YF_3) was used to form the molten electrolyte. 45 wt% MgF_2 – 55 wt% CaF_2 is a eutectic composition having a melting temperature of 974°C[12]. YF_3 was added to prevent yttrium depletion from the YSZ membrane and increase the membrane stability[13], [14]. A one-end-closed 6 mol% YSZ membrane tube separated the flux from 44g of liquid silver enclosed inside the YSZ tube. An LSM-Inconel inert anode current collector was disposed in the YSZ tube and was submerged in the liquid silver anode. The structure of the anode assembly is described in previous research where it was successfully used in Mg-SOM electrolysis cell[5], [7]. An Al_2O_3 dielectric tube served as a cathode separator as well as a source of Al_2O_3 . Because liquid aluminum is less dense than the molten flux, the aluminum produced in the electrolysis would float on top of the molten flux and be confined within the dielectric tube. This prevents the aluminum from spreading on the surface of the flux and shorting the cell. The Al_2O_3 dielectric tube was inserted in a stainless steel support welded to the bottom of the stainless steel crucible. The stainless steel support had multiple opening at the side to allow flux to go through the support and contact with the cathode. The powdered flux was pre-melted in the stainless steel crucible with the

Al_2O_3 tube inserted in the stainless steel support prior to the electrolysis. 2.30g of aluminum shots were added through the Al_2O_3 tube to form a liquid aluminum pool when melted. The liquid aluminum pool served as the cathode. The cathode current collector consisted of a stainless steel crucible welded to a stainless steel rod. The crucible contained a layer of liquid silver that formed a liquid contact with a piece of TiB_2 , which is a conductive ceramic that wets but does not alloy with liquid aluminum pool. The liquid silver layer ensured that the contact resistance between the stainless steel crucible and the TiB_2 piece was minimized. A boron nitride cover supported by an alumina pin was tightly fit on the TiB_2 bar to prevent aluminum from climbing up the TiB_2 bar. During the electrolysis, the TiB_2 cathode current collector was inserted in the liquid aluminum but stayed above the molten flux (see the detailed cathode design in Figure 1). Two stainless steel reference electrodes were inserted in the molten flux to monitor the electrochemical behavior of the flux during the electrolysis. The two reference electrodes were electrically isolated by two alumina tubes. One of the alumina tubes also served as a gas stirring tube. To facilitate chemical homogeneity in the molten flux during the experiment, forming gas was passed through the stirring tube at $20 \text{ cm}^3/\text{min}$. Forming gas was also purged in the reaction chamber at a rate of $1000 \text{ cm}^3/\text{min}$ during the experiment to ensure the SOM cell was in an inert environment.

A proof-of-concept electrolysis experiment using a slightly different setup was performed in order to demonstrate the feasibility of producing aluminum by SOM electrolysis. The proof-of-concept electrolysis setup had no aluminum shots added in the cathode alumina dielectric tube prior to the electrolysis. The alumina was reduced directly at the TiB_2 cathode, which was inserted in the molten flux. Such an experimental setup confirmed that all the aluminum collected near the cathode was produced due to the dissociation of aluminum oxide.

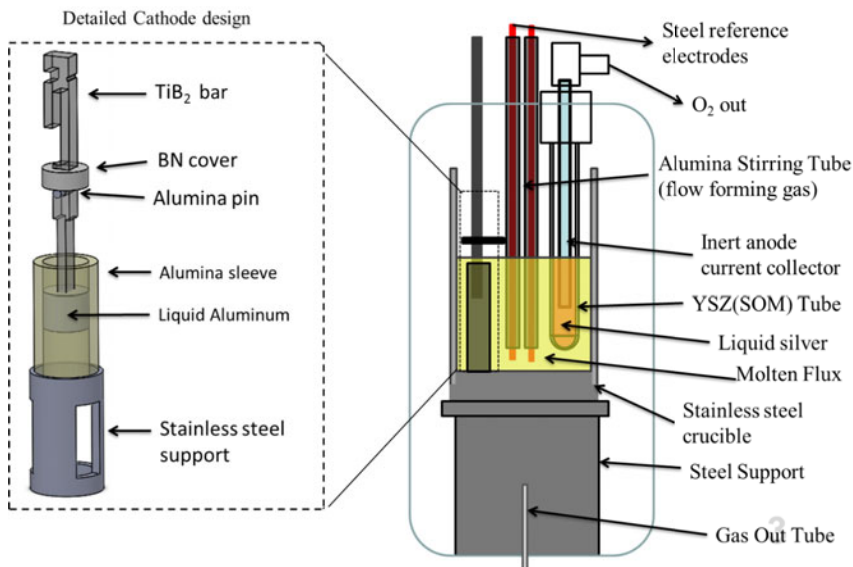


Figure 1: Experiment setup of SOM electrolysis

B. Chemicals and Materials

Magnesium fluoride hydrate ($\text{MgF}_2 \cdot x\text{H}_2\text{O}$, min. 87% MgF_2), calcium fluoride (99.5%), calcium oxide (reagent grade), aluminum oxide (99%), yttrium (III) fluoride (99.9%) and aluminum shots (99.5%) were supplied by Alfa Aesar (Ward Hill, MA). The powders were dried for 4 hours at 400°C to remove moisture and crystallized water. The powders were dry mixed in a ball mill overnight according to the flux stoichiometry. The closed one end YSZ tube (6 mol% Y_2O_3 , 1.90cm o.d., 1.27cm i.d., 60.96cm length) was supplied by McDanel (Beaver Falls, PA). The alumina stirring tubes and the cathode alumina sleeve were supplied by CoorsTek (Golden, CO). The forming gas was supplied by Airgas (Billerica, MA). The boron nitride cover was machined from a boron nitride plate supplied by Saint-Gobain (Malvern, PA). The titanium diboride was provided by Infinium Inc. (Natick, MA) and machined by wire-cut electrical discharge machining (EDM) to the desired shape.

C. Electrochemical Characterization of Electrolysis Process

The electrochemical characterization of the SOM cell was performed between the LSM-Inconel inert anode current collector and the stainless steel rod cathode current collector. When an applied DC potential exceeded the dissociation potential of Al_2O_3 , Al was produced at the cathode, and O_2 evolved at the liquid silver anode. The overall cell reaction is shown as



Potentiodynamic scans (5 mV/s) were performed to determine the dissociation potential of Al_2O_3 and to identify impurity cations dissociation. The potentiodynamic scans were performed using a Solartron SI 1280B electrochemical measurement system. Electrolysis runs were performed by applying a constant DC potential which exceeds the dissociation potential of Al_2O_3 between the cathode and the anode. The electrolysis runs were performed using an Agilent Technologies N5743A power source. The anode exit gas (oxygen) during the electrolysis passed through a FMA-4305 digital flow meter (OMEGA Engineering) that measures its flow rate.

The electronic transference number of the flux was measured using the two stainless steel reference electrodes. Previous work has shown that the dissolution of metallic species in the fluoride flux decreases the SOM electrolysis current efficiency and provides a pathway for the applied potential to reduce the ZrO_2 at the outer surface of the YSZ membrane[15], [16]. It is therefore important to monitor the electronic current by measuring the electronic transference number during the electrolysis. The electronic and ionic resistances of the flux can be modeled by two resistors in parallel. Therefore, the relationship between the total ohmic resistance ($R_{T(\text{flux})}$), the ohmic electronic resistance ($R_{e(\text{flux})}$), and the ohmic ionic resistance ($R_{i(\text{flux})}$) of the flux can be expressed by the relation

$$\frac{1}{R_{T(\text{flux})}} = \frac{1}{R_{e(\text{flux})}} + \frac{1}{R_{i(\text{flux})}} \quad (2)$$

Electrochemical impedance spectroscopy (EIS) scans were performed between the two reference electrodes to determine $R_{T(\text{flux})}$. The EIS scans were performed using a Princeton Applied research 263A potentiostat and a Solartron 1250 frequency response analyzer. The EIS scans were from

20000 to 1 Hz with 20mV amplitude. $R_{T(\text{flux})}$ was obtained from the value of the high-frequency intercept on the real axis of the Nyquist plot [17], [18]. The ohmic electronic resistance, $R_{e(\text{flux})}$, was determined by performing a potentiostatic hold between the two reference electrodes with a constant small electric potential ($\sim 0.1\text{V}$). $R_{e(\text{flux})}$ was calculated by dividing the applied potential by the measured current. $R_{i(\text{flux})}$ was calculated from $R_{T(\text{flux})}$ and $R_{e(\text{flux})}$ according to Eq.(2). In the flux system, the electronic transference number $t_{e(\text{flux})}$ is the ratio of the electronic conductivity to the total conductivity as shown in Eq. (3), where σ_e is the electronic conductivity, and σ_{tot} is the total conductivity.

$$t_{e(\text{flux})} = \frac{\sigma_{e(\text{flux})}}{\sigma_{(\text{tot})}} \quad (3)$$

The electronic conductivity is proportional to the inverse of electronic resistance, and the ionic conductivity is proportional to the inverse of ionic resistance; the cell constant does not change during the experiment, therefore the electronic transference number $t_{e(\text{flux})}$ can be calculated using the following equations [19]:

$$t_{e(\text{flux})} = \frac{\frac{1}{R_{e(\text{flux})}}}{\frac{1}{R_{e(\text{flux})}} + \frac{1}{R_{i(\text{flux})}}} \quad (4)$$

$$t_{e(\text{flux})} = \frac{R_{i(\text{flux})}}{R_{e(\text{flux})} + R_{i(\text{flux})}} \quad (5)$$

D. Post-experimental Characterization

After the SOM electrolysis experiment, the setup was disassembled for detailed analysis. A piece of flux sample near the cathode containing the aluminum product and a piece of YSZ membrane were mounted in epoxy, polished, spray coated with carbon, and then characterized using a Zeiss supra 55VP field emission SEM. The purity of the aluminum was measured by EDS quantitative spectra analysis. The yttrium and zirconium content in the YSZ membrane were measured by EDS line scan to assess membrane stability after the electrolysis.

Results

A. Proof-of-concept Electrolysis Results

The proof-of-concept electrolysis was performed with an applied DC potential of 2.75V between the liquid silver anode and the TiB_2 cathode for 24 hours. The electrolysis was stopped and the current-potential relationship is characterized by a potentiodynamic scan between the anode and the cathode shown in Figure 2. The negative current seen in the potentiodynamic scan prior to alumina dissociation is due to reverse reaction of the electrolysis process. This is because the cathodic chamber after electrolysis has a lower O_2 chemical potential (due to the presence of aluminum) compared with the anodic chamber (O_2 environment). Thus the negative current prior to alumina dissociation is due to high aluminum activity at the cathode. The only dissociation potential identified from the potentiodynamic scan was at 2.10V which appears to correspond to the Nernst potential (2.08V) for the reaction $\text{Al}_2\text{O}_3 = 2\text{Al(l)} + 3/2\text{O}_2(\text{g})$ at 1200°C. This indicates that all impurity cations were dissociated during the first electrolysis. The leakage electronic

current before alumina dissociation was negligible, indicating that the flux was primarily ionic. Subsequently, electrolysis with an applied potential of 2.75V for 3 hours were performed.

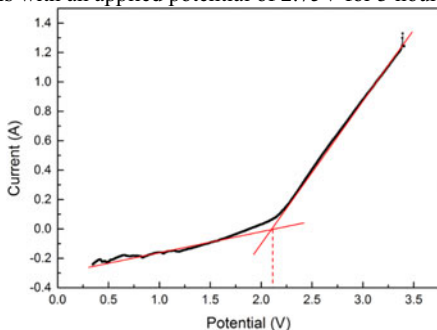


Figure 2: Potentiodynamic scan (5mV/s) after 1st electrolysis

After SOM electrolysis, aluminum was found inside the cathode alumina sleeve as shown in Figure 3. EDS quantitative analysis showed that the product was primarily Al-Mg alloy with 94wt% Al. MgO activity in the flux is due to the presence of Mg^{2+} and O^{2-} , and its reduction results in the observed Mg in the aluminum produced.

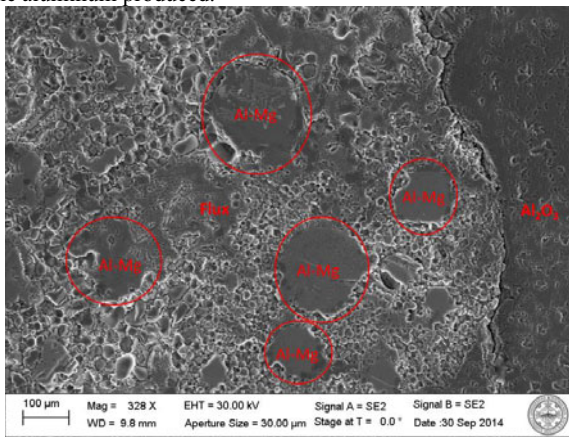


Figure 3: SEM image of aluminum metal produced in the proof-of-concept electrolysis

Figure 4 shows the SEM image and the EDS line scan of the YSZ membrane after the electrolysis. It is shown from the line scan that the flux did not attack the YSZ membrane during the electrolysis. The yttrium and zirconium content was uniform along the YSZ membrane. The ratio of yttrium and zirconium was similar to as received YSZ membrane. It is confirmed that the YSZ membrane was chemically and electrochemically stable after 28 hours of electrolysis.

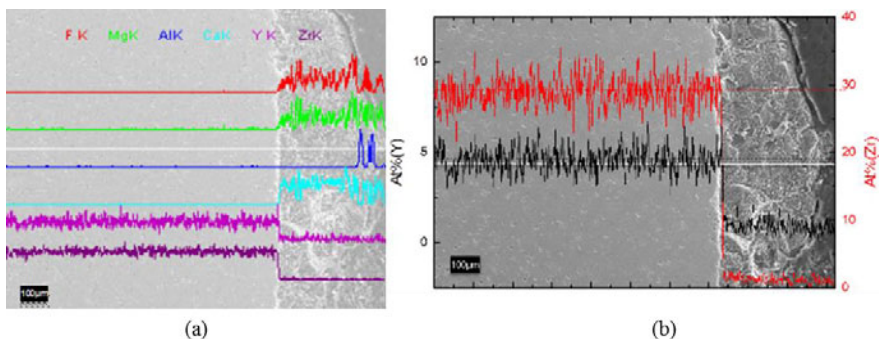


Figure 4: SEM image and EDS line scan of YSZ membrane after electrolysis. (a) Element analysis of EDS line scan. (b) Quantitative element analysis of atomic percentage of Y and Zr

B. Electrochemical Characterization of the Electrolysis Process

The SOM electrolysis was performed with the experimental setup shown in Figure 1 employing the liquid aluminum cathode. A PDS was conducted between the inert anode current collector and the stainless steel current collector prior to the electrolysis, and the current-potential relationship is shown in Figure 5. The dissociation potential of the impurity oxides and Al_2O_3 were identified to be approximately 1.5V and 2.1V, respectively. The leakage current caused by the dissociation of impurity oxides was approximately 0.1A. A pre-electrolysis at the potential of 2V (less than the dissociation potential of Al_2O_3) was performed to dissociate the impurity oxides and reduce the leakage current. After 1 hour of pre-electrolysis, another PDS was conducted between the inert anode current collector and the stainless steel current collector. The current-potential relationship is also shown in Figure 5. The dissociation potential of Al_2O_3 was identified to be approximately 2.1V. Negligible leakage current indicates that there was no electronic current passing through the flux.

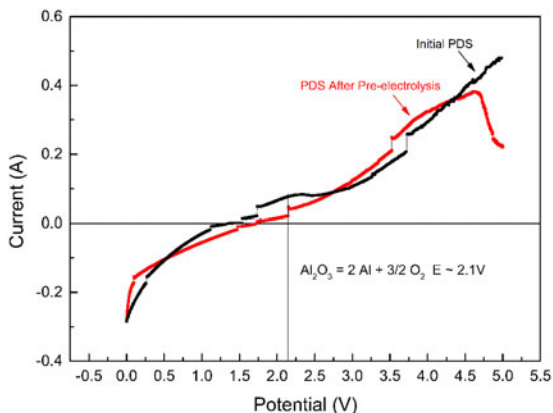


Figure 5: Potentiodynamic scans (5mV/s) showing the current-potential relationship before pre-electrolysis and after pre-electrolysis

C. SOM Electrolysis

After pre-electrolysis hold and scans, the setup was subjected to three electrolytic holds. The first electrolysis was performed at 3.5V for 2 hours; the second at 4V for 0.5 hours, and the third at 4.3V for 22 hours (see Figure 6). Total charge passed through the cell was 31254.75C, corresponding to production of 2.91g of aluminum assuming 100% current efficiency.

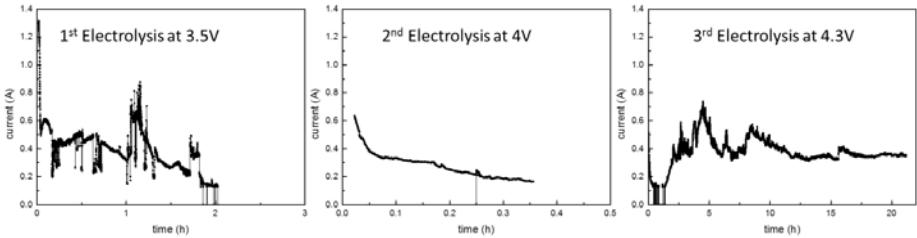


Figure 6: Current-time relationship of the three SOM electrolysis

D. Electronic Transference Number of the Flux

Before the first electrolysis, and immediately after the pre-electrolysis and 1st electrolysis, the electronic transference number using the stainless steel reference electrodes were measured. Table I shows the measured resistances and the electronic transference number of the flux. It is seen that the electronic transference number was low and did not increase during electrolysis. This indicates that the flux was primarily ionic during electrolysis, and the electronic conductivity of the flux did not change due to dissolution of the metal.

Table I: The Measured Resistances and the Electronic Transference Number of the Flux

Measurement	$R_{T(\text{flux})}$ (Ω)	$R_{e(\text{flux})}$ (Ω)	$R_{i(\text{flux})}$ (Ω)	$t_{e(\text{flux})}$
Initial	0.780	18.186	0.815	0.043
After pre-electrolysis	0.320	11.120	0.329	0.029
After 1 st electrolysis	0.284	16.046	0.289	0.018

E. Post-experimental Characterization

The furnace was cooled after the SOM electrolysis experiment, and the setup was disassembled. The aluminum was mounted in epoxy, polished and characterized with EDS. Figure 7 shows the cross-section of the aluminum produced during electrolysis and the EDS spectra of the cross-section. Quantitative analysis of the EDS spectra shows the purity of Al was >99wt% with less than 1wt% Mg impurity. The liquid aluminum cathode is always in contact with the alumina dielectric tube, therefore the alumina activity at the cathode interface is high. This is expected to lower the cathodic polarization, and MgO reduction. Employing the liquid aluminum cathode also allows any Mg metal reduced during electrolysis to evaporate from the surface of the liquid aluminum. Thus the amount Mg impurity in the Al product was significantly reduced. However, the Mg that evaporated from the cathode was small and could have oxidized, making its detection difficult after electrolysis.

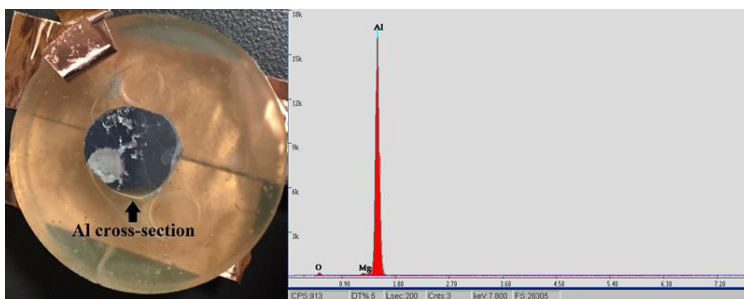


Figure 7: The cross-section of the Al collected near the cathode (left) and its EDS spectra (right)

Conclusions

Aluminum has been produced by electrolyzing aluminum oxide dissolved in pre-selected molten fluoride flux using SOM electrolysis process. The flux system (eutectic $\text{MgF}_2 - \text{CaF}_2$ containing CaO , Al_2O_3 and YF_3) was used in the electrolysis process at 1200°C . The dissociation potential of aluminum oxide was identified to be around 2.1V. The production of aluminum was confirmed by a proof-of-concept electrolysis experiment. The YSZ membrane was stable after the electrolysis. By employing a liquid aluminum cathode, the aluminum produced in the process was with high purity ($>99\text{wt}\%$). The electronic transference number of the flux remained small and did not increase during electrolysis indicating no metal dissolution occurred in the flux.

Acknowledgements

This project was financially supported by the Department of Energy (DOE) through ARPA-E REMOTE program. The authors would like to thank Alexander Kithes, Thomas Villalon Jr. and Matthew Mirek for assisting with performing some of the experiments and Dr. Adam Powell of Infinium Inc., Natick MA, for helpful discussions.

References

- [1] "Global Nonferrous Metal Industry Overview." [Online]. Available: <http://www.statista.com/statistics/242777/aluminum-demand-and-supply-growth-rates/>.
- [2] "US energy requirements for aluminum production," *U.S. Dep. Energy EERE Rep.*, 2007.
- [3] U. B. Pal, D. E. Woolley, and G. B. Kenney, "Emerging SOM technology for the green synthesis of metals from oxides," *JOM*, vol. 53, no. 10, pp. 32–35, Oct. 2001.
- [4] A. Krishnan, U. B. Pal, and X. G. Lu, "Solid oxide membrane process for magnesium production directly from magnesium oxide," *Metall. Mater. Trans. B*, vol. 36, no. 4, pp. 463–473, Aug. 2005.
- [5] X. Guan, U. B. Pal, S. Gopalan, and a. C. Powell, "LSM ($\text{La}_{0.8}\text{Sr}_{0.2}\text{MnO}_3$ -)-Inconel Inert Anode Current Collector for Solid Oxide Membrane (SOM) Electrolysis," *J. Electrochem. Soc.*, vol. 160, no. 11, pp. F1179–F1186, Sep. 2013.

- [6] E. S. Gratz, X. Guan, J. D. Milshtein, U. B. Pal, and A. C. Powell, "Mitigating Electronic Current in Molten Flux for the Magnesium SOM Process," *Metall. Mater. Trans. B*, vol. 45, no. 4, pp. 1325–1336, Aug. 2014.
- [7] X. Guan, U. B. Pal, and A. C. Powell, "Energy-Efficient and Environmentally Friendly Solid Oxide Membrane Electrolysis Process for Magnesium Oxide Reduction: Experiment and Modeling," *Metall. Mater. Trans. E*, vol. 1, no. 2, pp. 132–144, Jun. 2014.
- [8] M. Suput, R. Delucas, S. Pati, G. Ye, U. Pal, and A. C. Powell IV, "Solid oxide membrane technology for environmentally sound production of titanium," *Miner. Process. Extr. Metall.*, vol. 117, no. 2, pp. 118–122, Jun. 2008.
- [9] A. Krishnan, X. G. Lu, and U. B. Pal, "Solid Oxide Membrane (SOM) technology for environmentally sound production of tantalum metal and alloys from their oxide sources," *Scand. J. Metall.*, vol. 34, no. 5, pp. 293–301, 2005.
- [10] Y. Jiang, J. Xu, X. Guan, U. B. Pal, and S. N. Basu, "Production of Silicon by Solid Oxide Membrane-Based Electrolysis Process," *MRS Proc.*, vol. 1493, pp. MRSF12–1493–E19–89, Jan. 2013.
- [11] X. Guan, S. Su, U. B. Pal, and A. C. Powell, "Periodic Shorting of SOM Cell to Remove Soluble Magnesium in Molten Flux and Improve Faradaic Efficiency," *Metall. Mater. Trans. B*, vol. 45, no. 6, pp. 2138–2144, Dec. 2014.
- [12] P. Chartrand and A. D. Pelton, "Thermodynamic evaluation and optimization of the LiF-NaF-KF-MgF₂-CaF₂ system using the modified quasi-chemical model," *Metall. Mater. Trans. A*, vol. 32, no. 6, pp. 1385–1396, Jun. 2001.
- [13] E. S. Gratz, J. D. Milshtein, and U. B. Pal, "Determining Ytria-Stabilized Zirconia (YSZ) Stability in Molten Oxy-Fluoride Flux for the Production of Magnesium with the SOM Process," *J. Am. Ceram. Soc.*, vol. 96, no. 32300, pp. 3279–3285, Jun. 2013.
- [14] J. Xu, B. Lo, Y. Jiang, U. Pal, and S. Basu, "Stability of yttria stabilized zirconia in molten oxy-fluorite flux for the production of silicon with the solid oxide membrane process," *J. Eur. Ceram. Soc.*, vol. 34, no. 15, pp. 3887–3896, Dec. 2014.
- [15] E. Gratz, S. Pati, J. Milshtein, A. Powell, and U. Pal, "Effect of Electronic Current on the Solid Oxide Membrane (SOM) Process for Magnesium Production," in *Electrometallurgy 2012*, John Wiley & Sons, Inc., 2012, pp. 111–118.
- [16] X. Guan, P. a. Zink, U. B. Pal, and A. C. Powell, "Recycling of Magnesium Alloy Employing Refining and Solid Oxide Membrane (SOM) Electrolysis," *Metall. Mater. Trans. B*, vol. 44, no. 2, pp. 261–271, Apr. 2013.
- [17] K. R. Cooper and M. Smith, "Electrical test methods for on-line fuel cell ohmic resistance measurement," *J. Power Sources*, vol. 160, no. 2, pp. 1088–1095, 2006.
- [18] S. C. Britten and U. B. Pal, "Solid-state amperometric sensor for the In-situ monitoring of slag composition and transport properties," *Metall. Mater. Trans. B*, vol. 31, no. 4, pp. 733–753, 2000.
- [19] A. V. Virkar, "Theoretical analysis of the role of interfaces in transport through oxygen ion and electron conducting membranes," *J. Power Sources*, vol. 147, no. 1–2, pp. 8–31, 2005.

ALUMINA CONCENTRATION GRADIENTS IN ALUMINIUM REDUCTION CELLS

Pascal Lavoie¹, Mark P. Taylor¹

¹The University of Auckland, Private Bag 92019, Auckland New Zealand

Keywords: Alumina, Concentration, Aluminium, Reduction, Electrolysis

Abstract

The length of aluminium electrolysis cells have constantly increased over the last decades. The drive to increase productivity resulted in the need to feed and dissolve more alumina in less electrolyte. There is mounting evidence that these two trends are pushing the electrolysis cells above their capability to maintain alumina concentration, through time and space, at levels preventing both conventional and non-propagating anode effects. Alumina concentration gradient measurements were performed within large industrial cells and showed that large gradients occurred between locations in cells.

Introduction

Aluminium is produced industrially by electrolytic reduction of alumina dissolved in a cryolite-based molten salt. The alumina concentration must be replenished as aluminium is produced to prevent reduction of other species present in the electrolyte. Failure to replenish and distribute dissolved alumina throughout the electrolysis cell results in an Anode Effect (AE), a phenomenon where other bath species are electrolyzed instead of alumina when polarisation increases local potential above other species decomposition potential.

Aluminium reduction cells production is proportional to their operating amperage, which has constantly increased over decades with each design iterations. This is generally done in conjunction with lengthening of the cells. For example, Kaiser's P69, a cell design from the 1970s, operated at 160kA contained 18 anodes and is less than 9 meters long. Comparatively, a modern 300-500kA design can have up to 48 anodes over a cell length of 18 meters.

Alumina is replenished in modern designs using point feeders in small batches of 1.0 to 5.0 kg [1]. As the cell length is increased, more point feeders are used. However, where 3 point feeders were used in the 1980s in cells operating between 180 to 220 kA, recent designs have up to 6 feeders at over 500kA. The specific electrolyte mass available for dissolution has also decreased significantly, passing from 30 kg/kA to 12 kg/kA [2]. The length of cells coupled with lower electrolyte available for dissolution can therefore lead to lack of alumina concentration control, both in space and time.

This paper will present an alumina concentration gradient measurement campaign in a modern large cell design. A discussion on factors affecting the gradients observed, their impact on process performance and actions required to control the gradients is also presented.

Background

Concentration gradient in aluminum cells was numerically simulated by Feng et. al. Their findings suggest that dissolved alumina is distributed reasonably fast locally but can take an order of magnitude longer to equalise throughout the cell [3]. Feng et al. also found that dissolved alumina is distributed mostly through turbulent bath flow [4] whilst von Kaenel et al. predicted a small impact from magnetohydrodynamics-induced flow in the electrolyte [5]. Inferring from physical modelling, Walker et al. found that the number and placement of point feeders can be optimized to control dissolution and distribution spatially around each point feeder but concluded that acceptable concentration gradients should exist, even if only one point feeder would be operational (out of 2) [1]. These studies were carried out in simulations of relatively small cells – less than 200kA.

However, even following these guidelines, concentration gradients appear to be difficult to control in large cells, inducing operational issues such as local anode effects. Moxnes et al. found that adjusting the feed rates depending on electrolyte velocity at each of the 5 point feeding locations of a large cell led to improved cell performance, possibly because of better concentration control throughout the cell [6].

Recently, several observations challenging findings from numerical simulations were made in large cells, where sudden increases in resistance have often been observed [7, 8]. These are Anode Effects occurring at a much lower voltage than traditionally accepted. The mechanisms of these localised, non-propagating anode effects has been investigated by Wong et al. [8]. Essentially, the alumina concentration under a very limited number of anodes is low enough to trigger local anode effect. The Anode Effect does not propagate as the rest of the cell has sufficient alumina concentration and in larger cells, the higher number of anodes connected in parallel, can better share the additional current preventing excessive overvoltage that would propagate the Anode Effect.

A measurement campaign was undertaken to measure alumina concentration across several locations in large reduction cells in order to verify this hypothesis; to assess whether localised zones with low alumina concentration were present and attempt to understand the causes.

Measuring Concentration Gradient

A modern aluminium reduction cell technology operated at multiple locations was selected for this study. The cell is greater than 18m long, has 48 anodes and 6 point feeders. Since implementation of the technology the cells have experienced a very high anode effect frequency, mostly low voltage non-propagating anodes effects of short durations that self-terminate.

The purpose of this campaign was to measure the alumina concentration gradient throughout the cell during all phases of the feed cycle. Feed cycles are necessary to control alumina concentration in a desirable window. In the present case, the feeding strategy consists in cycling between 3 feed phases:

1. Nominal feed, a fixed time feed rate close to the theoretical demand.
2. Underfeed, a feed rate lower than theoretical demand resulting in gradual decrease of the alumina concentration. Underfeed continues until a pre-determined increased in cell resistance is achieved.
3. Overfeed, a fixed time phase where the feed rate is higher than theoretical demand, aiming at replenishing the concentration to a fixed point.

Similar to a previous study by Kvande et al. [9], electrolyte samples were obtained periodically by simultaneously flash freezing electrolyte on steel rods at 12 locations around the cell, as shown on Figure 1. The sampling frequency was designed to capture the start of each feed phase, with a few more samples taken during the phase depending on its length.

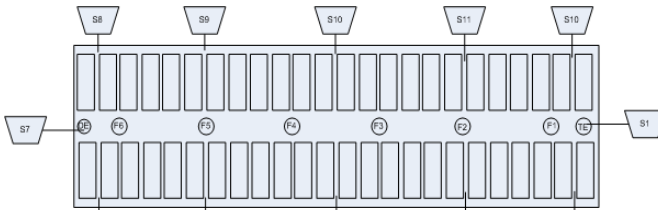


Figure 1. Alumina concentration sampling locations

Each sample was analysed on-site by XRD using a Panalytical Cubix Pro with standard calibration procedure, analysing alumina by scanning intensity peaks at 2θ angles of 35.1 and 45.0. Select random split samples were also returned to the University of Auckland and analysed with a LECO R_O416DR oxygen analyser for validation. As shown on Figure 2, the split samples showed good correlation, although the XRD tended to underestimate the concentration by 0.24%.

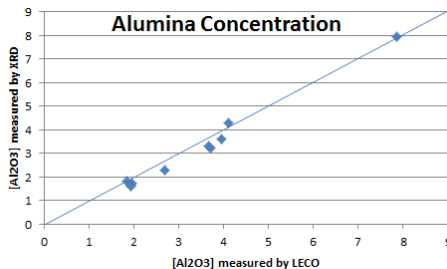


Figure 2. Comparison of alumina concentration of split samples measured by XRD and LECO oxygen analyzer

Electrolyte temperature measurement was also carried out in one of the feeder hole using a Type-K thermocouple paired with a portable data logger Omegaette HH306 at a measurement frequency of 1 Hz.

Results and Discussion

Figure 3 displays the average alumina concentration during the feed cycles in two cells. Concentration (wt. %) is showed in blue on the left axis while the time between feed is showed in red on the right axis. Mass balance calculations showed that the increase in alumina concentration during the overfeed period should be 0.31% for cell A and 0.58% for cell B. However, the average concentration only increased by 0.11% and 0.39% respectively. This clearly demonstrates that the alumina fed to the cell is not being completely dissolved during the overfeed phase.

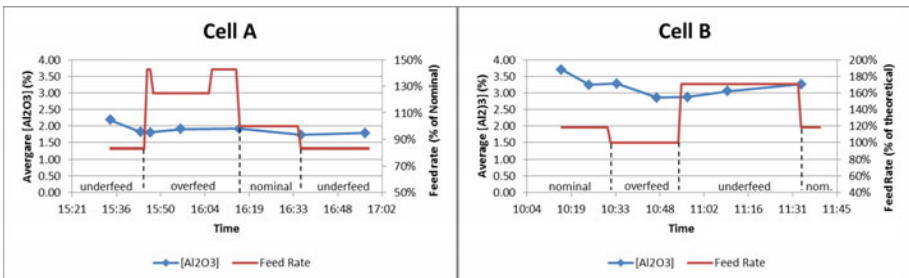


Figure 3. Average alumina concentrations through different feed phases on two cells.

The thermal response to feed recorded in a feeder hole of cell B is shown on Figure 4. As can be seen, the local electrolyte temperature goes through a deep depression as the alumina dose is delivered to the electrolyte but recovers quickly. This should result in a rapid dissolution, at least for this feeder location. However, this was not the case. Examining the concentration evolution at specific locations on Figure 5 reveals two critical issues. Firstly, the concentration varies largely depending on the location. Secondly, the concentration gradient varies temporally with only specific positions experiencing significant increase in concentration during the overfeed period. The trend is that the concentration gradient increases during overfeed, while the underfeed period tends to equalises the concentration throughout the cell. It appears the alumina is only dissolved in parts of the cell during overfeed and then is distributed slowly to parts of the cell where alumina fed could not be dissolved. This is consistent to the conclusions of Feng et al., who predicted rapid local mixing but much slower global distribution.

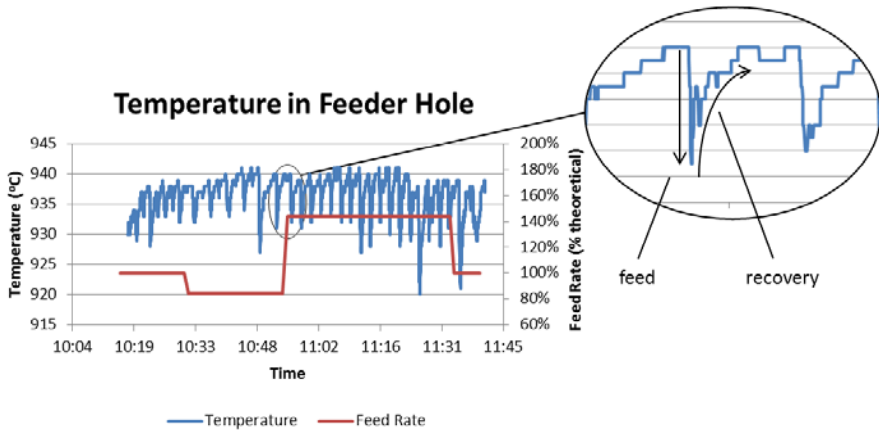


Figure 4 Thermal response in a feeder hole of Cell B. Clear depressions in temperature are observed directly after the alumina feed mass is delivered to the electrolyte. The depressions are followed by a relatively quick recovery.

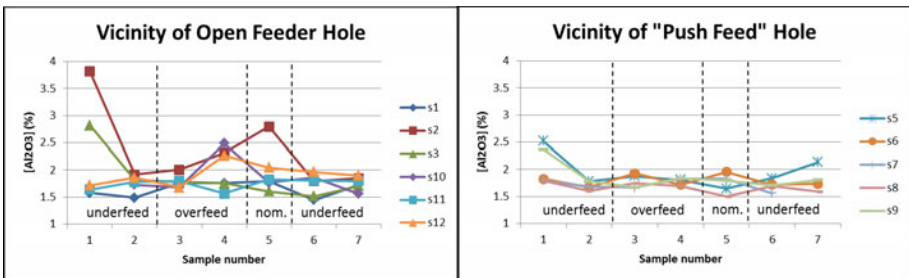


Figure 5. Local alumina concentration temporal variation. The variation is significantly larger at the sampling locations close to the open feeder hole (left). The locations close to a feeder hole operating a “push feed” (right) stay relatively low in alumina concentration, especially during the overfeed phase where a significant increase is expected.

Another interesting observation was that the concentration evolution around a primary feeder that operated open seems to follow the metal flow pattern under the electrolyte in that part of the cell (Figure 6). Although the turbulent bath flow could still be a driver for mixing [Feng LM10], this suggests that metal pad flow could also play a significant part in distributing the dissolved alumina spatially.

Cell A at Sample Time 1

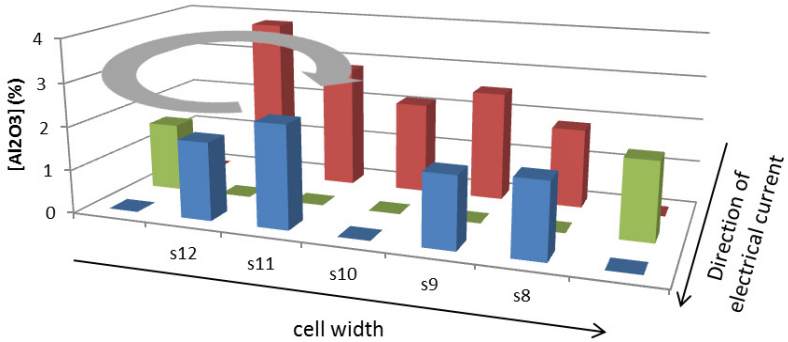


Figure 6. Concentration at end of overfeed and metal pad flow pattern around the open feeder hole (grey circular arrow). The direction of electrical current denotes cell to cell current flow in the bus bar. Current flow in the cell itself is vertical between the anode beam (all anodes in parallel) and the metal pad, which is the cathode.

Generally, the following observations were made and are discussed below:

- Contrary to findings of numerical simulations, there are significant alumina concentration gradients throughout the cell.
- The gradients vary temporally, with different feed phases.
- The gradient increases during overfeed period, possibly in areas where dissolution conditions are more favourable either because of open feeder holes, higher local superheat or higher turbulent bath flow. The effect of the open feeder hole was observed and seemed to be a significant driver, although the other factors were not measured during this study.
- The gradient decreases during underfeed as the alumina is being distributed more widely through turbulent bath flow, but also metal pad circulation.

Concentration gradients increase during overfeed and decrease during underfeed. The quantum of increase during overfeed is only a fraction of what it should be but is as expected in some locations. This is highlighted by the fact that zones with low concentration remained low during the trial. It suggests that some feeder locations experience difficulty either in delivery of the alumina to the hole, or with dissolution.

The condition of each feeder hole during the experiment appeared to have a significant impact. The zones adjacent to the open feeder holes were the ones with highest increase of concentration during overfeed whilst the zones adjacent to feeders operating a “push feed” were the ones staying lean. Superposing the metal pad circulation patterns to the concentration also lead to an interesting observation. It appears that the concentration decreased as the sampling point position

got further from the feeder hole, following the metal pad circulation pattern. This departs from Feng's model predictions but confirm von Kaenel's simulations.

It seems that maintaining open feeder hole is the best way to achieve adequate dissolution. In order to avoid Anode Effects, including low voltage, non-propagating AEs, the bulk concentration must be high enough to ensure alumina has time to be distributed throughout the cell, especially towards the end of underfeed and the start of overfeed.

Conclusions and Future Work

Concentration gradient were found to be significant, enough to cause localized effects such as low voltage, non-propagating anode effects.

The feeder hole conditions appear to influence the concentration and gradients evolution significantly.

The metal pad circulation also appears to influence the concentration gradient.

This suggests that feeder location and control of the hole condition are important to proper dissolution and dispersion control. Since the feeder hole conditions were not continuously monitored throughout the experiment but only at the beginning, repeating the experiment with continuous monitoring of the feeder hole should confirm the findings.

Acknowledgement

The authors would like to acknowledge the precious work of LMRC team members that helped carry out the sampling campaign: David Wong, Yashuang Gao, Jenny Hung as well as Zhou Dongfang, Liu Wei, Liu Ming, Fu Yong, Tang Xinzhong and Yin Xiaobao. Reece Oosterbeek for Leco analysis and support from David Cotton is also acknowledged.

References

1. M.L. Walker et al., Design considerations for selecting the number of point feeders in modern reduction cells. *Light Metals*, 1995, 363-370.
2. Martin Forté et al., Arvida Aluminum Smelter–AP60 Technological Center, Start-Up Performance and Development of the Technology. *Light Metals*, 2015, 495-498.
3. Yuqing Feng, Mark A. Cooksey, and M. Philip Schwarz. Development of Whole Cell CFD Model of Bath Flow and Alumina Mixing. *Proceedings of the 9th Australasian Aluminium Smelting Technology Conference and Workshops*, Terrigal, Australia, 2007.
4. Yuqing Feng, Mark A. Cooksey, and M. Philip Schwarz. CFD modelling of alumina mixing in aluminium reduction cells. *Light Metals*, 2011, 543-548.
5. René von Kaenel et al., Impact of Magnetohydrodynamic and Bubbles Driving Forces on the Alumina Concentration in the Bath of an Hall-Héroult Cell. *Light Metals*, 2013, 585-590.
6. Bjørn Moxnes et al., Improved cell operation by redistribution of the alumina feeding. *Light Metals*, 2009, 461-466.
7. David S. Wong, and Jerry Marks. Continuous PFC Emissions Measured on Individual 400kA Cells. *Light Metals*, 2013, 865-870.

8. David S. Wong, Alton Tabereaux, and Pascal Lavoie. Anode Effect Phenomena during Conventional AEs, Low Voltage Propagating AEs & Non-Propagating AEs. *Light Metals* 2014, 529-534.
9. Halvor Kvande et al., Pseudo Resistance Curves for Aluminium Cell Control-Alumina Dissolution and Cell Dynamics. *Light Metals*, 1997, 403-409.

APPROACH OF THE MOLTEN SALT CHEMISTRY FOR ALUMINIUM PRODUCTION: HIGH TEMPERATURE NMR MEASUREMENTS, MOLECULAR DYNAMICS AND DFT CALCULATIONS

Kelly Machado¹, Didier Zanghi¹, Vincent Sarou-Kanian¹, Sylvian Cadars², Mario Burbano³,
Mathieu Salanne³, Catherine Bessada¹

¹CEMHTI (Conditions Extrême Matériaux Haute Température et Irradiation) CNRS, Université Orléans;

1D Avenue de la Recherche Scientifique CS90055; Orléans, 45071, France

²IMN (Institut des Matériaux Jean Rouxel) CNRS, Université de Nantes;

2 Rue de la Houssinière BP32229; Nantes, 44322, France

³UPMC (University Pierre et Marie Curie), PHENIX CNRS;

4 place Jussieu, Paris, 75005, France

Keywords: NaF-AlF₃; high temperature NMR; chemical shifts, anionic species; molecular dynamic; functional theory of density (DFT); Polarizable Ion Model (PIM).

Abstract

In aluminum production, the electrolyte is a molten fluorides mixture typically around 1000°C. In order to have a better understanding of the industrial process, it is necessary to have a model which will describe the molten salts on a wide range of compositions and temperatures, to accurately cover all the combinations that may be encountered in an operating electrolysis vessel. The aim of this study is to describe the speciation in the electrolyte in terms of anionic species in the bulk materials far from electrodes. To determine the speciation in situ at high temperature in the absence of an electrical field, we develop an original approach combining experimental methods such as Nuclear Magnetic Resonance spectroscopy (NMR) at high temperature with Molecular Dynamics (MD) simulation coupled with first principle calculations based on Density Functional Theory (DFT). This approach allows the calculation of NMR parameters and the comparison with the experimental ones. It will provide an additional validation and constraint of the model used for MD. We test this approach on the model NaF-AlF₃ system.

Introduction

In Hall-Héroult electrolytic process used for aluminum production, the industrial electrolyte is mainly composed of a mixture of NaF, AlF₃ and Al₂O₃ for an operating temperature around 1000°C [1]. Due to its industrial interest, several studies have been made in order to improve the process, in particular around the electrolyte composition in order to lower the temperature and thus to minimize the operating costs. An important point necessary to improve the process is to know the structure of the molten salt used as an electrolyte.

Under the high temperature conditions, these electrolytes are corrosive and difficult to handle, making any experimental measurement particularly challenging. In situ Raman [4] or NMR [2,3] spectroscopies at high temperature in NaF-AlF₃ melts have succeeded in identifying and quantifying the anions present in the electrolyte, *i.e.* free F⁻, as well as different aluminum-

bearing fluorinated species, AlF_6^{3-} , AlF_5^{2-} , AlF_4^- . Some questions still remain, however, regarding their nature, the evolution of their relative amounts with temperature and their lifetime. To further extend our understanding of such systems, it is necessary to develop in parallel numeric tools that are capable of simulating the liquid phase. To fulfill these objectives, we propose to focus on the description of the speciation in NaF-AlF_3 melts, using an original approach combining in situ NMR measurements at high temperature with simulation by molecular dynamics (MD) coupled with "first principle" calculations of NMR chemical shifts at the density functional level of theory (DFT). For molecular dynamics simulations we use the Ion Polarizable Model (PIM) which was initially developed by Madden and Wilson [5, 6]. This force field, specifically designed for the description of ionic liquids, is based on an interatomic potential containing four interactions: the electrostatic interaction between two formal charges, the overlap repulsion component, the dispersion component and the polarization, with parameters typically obtained by force-fitting to ab initio electronic structure calculations. The result of MD simulations gives the ion trajectories of each ion along the simulation time, which may then be analyzed to calculate several important macroscopic and molecular-level properties such as viscosity, conductivity, the radial distribution functions of each atomic pair and the coordination states of the aluminum.

The interatomic potential is ultimately validated with a combination of MD and DFT calculation to obtain the NMR chemical shifts of each nucleus in the NaF-AlF_3 system at a given temperature. The calculated parameters are thus compared with the experimental values and allow us to go further in the description of such melts.

The NMR measurements were done using the laser heating NMR setup developed in Orleans in the system NaF-AlF_3 , for each nucleus (^{23}Na , ^{19}F and ^{27}Al) at different temperatures and compositions. In these melts, at high temperature, the spectrum obtained for all the observed nuclei, is a single, narrow line, characterized by its position: the chemical shift. Because of the rapid exchange existing between the different local environments around the observed nucleus, the chemical shift measured is the average of the chemical shifts of each individual anionic species, weighted by their respective atomic fraction.

Some computational simulations have been published for some compositions in the NaF-AlF_3 system corresponding to the cryolite (Na_3AlF_6), chiolite ($\text{Na}_5\text{Al}_3\text{F}_{14}$) and NaAlF_4 [7, 8]. In this work, the challenge was to build an interatomic potential valid for a wide range of NaF-AlF_3 compositions at high temperature.

Experimental

NMR experiments

Different NaF-AlF_3 compositions have been prepared with 0 to 50 mol% of AlF_3 . The different mixtures were introduced in a glove box, in a high purity boron nitride crucible tightly closed by a screw cap. The NMR experiments were carried out using a Bruker DSX 400 NMR spectrometer operating at 9.4T. The laser heating NMR setup has been described in details in previous publications [2, 9, 10]. Two CO_2 laser ($\lambda = 10.6\mu\text{m}$, 250 W) heat directly the top and the bottom of the crucible and allow heating up to 1500°C . The crucibles are protected from oxidation at high temperature by a continuous argon flow. The electronics and the radio frequency coil are cooled by an air flow at room temperature and protected by a zirconia thermal shield. The chemical shifts of all nuclei (^{27}Al , ^{23}Na , ^{19}F) are referenced to 1M aqueous solutions

Al(NO₃)₃, NaCl, CFCl₃, respectively. The spectra acquisition starts 5 minutes after reaching the desired temperature to insure thermal equilibrium and the three nuclei are observed sequentially.

Molecular Dynamics

Molecular dynamics is based on the resolution of the equation of motion for each particle interacting with its neighbors. It is therefore necessary to know the forces involved in the system to integrate this equation over time. We use the polarizable ion model [5, 6] (PIM) where the interatomic potential (V^{Total}) is a pairwise sum of four interactions: charge, dispersion, repulsion and polarization.

$$V^{\text{Total}} = V^{\text{charge}} + V^{\text{dispersion}} + V^{\text{repulsion}} + V^{\text{polarisation}} \quad (1)$$

The parameters involved in such interaction potential were obtained by force matching with *ab initio* calculations. These calculations were performed using a plane wave electronic structure code, the Vienna Ab initio simulation package (VASP) and projector augmented wave (PAW-PBE) pseudopotential was used. The target function involves the forces and dipoles of each ion, along with the stress of each configuration. Several cubic boxes were prepared representing the full range compositions up to 50 mol% of AlF₃ in the NaF-AlF₃ system.

MD simulations were performed for a cubic box of length approximately of 15.4 Å with nearly 200 atoms. For all simulations, the systems were equilibrated constant temperature and fixed pressure at 0 GPa (NPT ensemble) and the lengths of the cubic box were obtained. The Nosé-Hoover thermostat algorithm was used [11]. Atoms trajectories were obtained at constant temperature and volume (NVT ensemble) for 1ns. Then a statistical analysis of the given trajectories provides access to different physical properties.

Functional theory of density

Density functional theory (DFT) is a computational quantum mechanical method used to investigate the electronic structure of a system. To calculate the NMR chemical shifts, using DFT calculations, snapshots of the MD simulations are extracted at different times (sufficiently far apart to avoid correlation), and used without further optimization to calculate electronic properties with the CASTEP code [12, 13], which is based on DFT with a plane-wave basis set and pseudopotentials. The generalized gradient approximation (GGA) was used with the exchange-correlation functional of Perdew, Burke and Ernzerhof (PBE), a cutoff energy of 610 eV and a 1×1×1 Monkhorst-Pack [14] grid of k-points (yielding NMR shielding converged within 1 ppm or less). Chemical shift are referenced on the basis of series of calculations conducted on simple crystalline systems [15].

Results

Simulations and NMR experience were done 20°C above the melting point for the different NaF-AlF₃ compositions. Molecular dynamics reproduce the ionic motion for the system NaF-AlF₃ making it possible to identify, quantify, and track the different ionic species present: AlF₆³⁻, AlF₅²⁻, AlF₄⁻ and free F⁻, (figure 1).

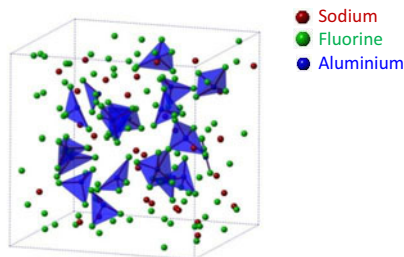


Figure 1 - Simulation cell with the atomic model for NaF-AlF₃ mixture derived from molecular dynamics at 1305K. (Blue areas: AlF₆³⁻, AlF₅²⁻ or AlF₄⁻)

The chemical shifts evolution of ²³Na, ¹⁹F and ²⁷Al were measured by NMR and calculated with CASTEP for all configurations (up to 50 mol% of AlF₃). In figure 2 we reported the experimental and calculated chemical shifts for all three nuclei as open and: the empty markers are measured experimentally and the full markers are the calculated chemical shifts.

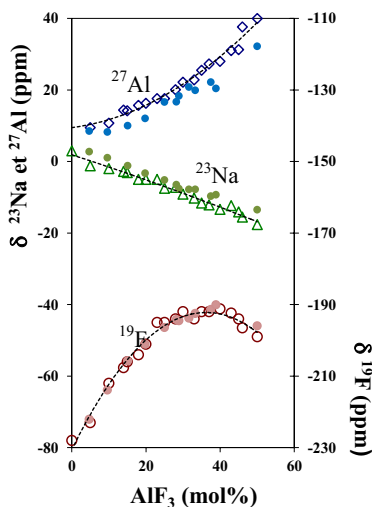


Figure 2 - Comparison of calculated (full markers) and experimental [3] (empty markers) NMR chemical shifts vs AlF₃ content at liquid temperature.

For ²³Na, ¹⁹F and ²⁷Al nuclei, not only the trends but also the absolute values of the calculated average chemical shifts are in excellent agreement with the experimental values measured at high temperature. Given the extreme sensitivity of NMR chemical shifts to both the fine details of the local structure around atoms [16] and to the speciation in molten salts [2,3] these results are a solid proof that the force field used to describe inter-atomic interactions in the classical MD

simulations. Such a validation is all the more valuable that very few physico-chemical parameters can be reliably measured under such extreme temperature and corrosive conditions.

The ^{19}F chemical shift in molten NaF, measured in the melt at $995\text{ }^\circ\text{C}$ is -232 ± 5 ppm and can be associated to free F $^-$. As AlF_3 is added to NaF, the contribution of free fluorine decreases due to the formation of anionic complexes AlF_x^{3-x} , the relative amounts of which appear to be accurately reproduced by the calculation, as well as their evolution as a function of composition.

Molecular dynamics provides detailed information on the structure, dynamic and thermodynamic properties of the melts. And the validation of the inter-atomic potential for the system NaF- AlF_3 now allows us to conduct more extensive dynamic studies with systems containing larger numbers of atoms, from which important macroscopic properties such as conductivity and viscosity can be evaluated. To improve the electrolyte used in aluminum production is important to have a detailed understanding of chemical and physical phenomena occurring in these melts.

Because inter-atomic models are pair-wise interactions, this validation on the binary NaF- AlF_3 system was also a prerequisite to then explore more complex compositions, and in particular those involving Al_2O_3 , the Al precursor in the electrochemical syntheses of aluminum.

Conclusion

The main idea of this work is to build a polarizable interaction potential that reproduce the structure of the molten mixtures of the binary NaF- AlF_3 at high temperature in a wide range of composition (0 – 50 mol. %). In challenging high-temperature and corrosive conditions, where reliable experimental data are particularly challenging to obtain, the comparison of experimental NMR results with data obtained from the combination of MD and DFT simulations provides an essential and particularly solid approach for the evaluation of the ionic potential of atomic interactions used in our simulations. Now the force field can be transferred to more complex systems. Analyzing the radial distribution function, the coordination number of aluminum ions was also calculated from MD simulation and confirms the presence of the ionic complex AlF_6^{3-} , AlF_5^{2-} , AlF_4^- and of free F $^-$.

An important point of this study is to describe the speciation in the electrolyte to obtain input data for modeling electrokinetic transport phenomena during the process of aluminum production. The corrosion behavior and the interactions between the molten electrolyte and the anode are not completely understood. These models should identify forward, the species present on the surface of the electrode and to better understand the mechanisms of corrosion observed on the anodes.

Acknowledgments

This study was financially supported by the ANR MIMINELA project of the French National Agency of Research. For the MD and DFT calculations, we thank the “Centre de Calcul Scientifique en Région Centre” (CCSC, Orléans, France).

References

1. J.Thonstadt et al., *Aluminium Electrolysis Fundamentals of the Hall Héroult Process* (Aluminium-Verlag: Marketing Kommunikation GmbH, 3rd edition, 2001).

2. V.Lacassagne, C.Bessada, P.Florian, S.Bouvet, B.Ollivier, J.P.Coutures, D.Massiot, 'Structure of High-Temperature NaF-AlF₃-Al₂O₃ Melts: A Multinuclear NMR study', *J. Phys. Chem. B*, 106 (2002), 1862-1868.
3. I.Nuta, E.Véron, G.Matzen, C.Bessada, 'High Temperature NMR Study of Aluminum Metal Influence on Speciation in Molten NaF-AlF₃ Fluorides', *Inorg. Chem*, 50 (8) (2011), 3304 – 3312.
4. E.Robert, V.Lacassagne, C.Bessada, D.Massiot, B.Gilbert, J.P.Coutures, 'Study of NaF-AlF₃ Melts by High-Temperature ²⁷Al NMR Spectroscopy: Comparison with Results from Raman Spectroscopy', *Inorg. Chem*, 38 (1999), 214-217.
5. P.Madden, M.Wilson, "'Covalent' effects in 'ionic' systems", *Chem. Soc. Rev*, 25 (1996), 339-350.
6. F. Hutchinson, M. Wilson, P.A. Madden, 'A unified description of MCl₃ systems with a polarizable ion simulation model', *Molecular Phys*, 99 (2001), 811.
7. Z. Akdeniz and P. A. Madden, 'Raman Spectra of Ionic Liquids: A Simulation Study of AlF₃ and Its Mixtures with NaF', *J. Phys. Chem. B*, 110 (13) (2006), 6683–6691.
8. S. Cikit, Z. Akdeniz, and P. A. Madden, 'Structure and Raman Spectra in Cryolitic Melts: Simulations with an ab Initio Interaction Potential', *J. Phys. Chem. B*, 118 (4) (2014), 1064–1070.
9. D. Massiot, C. Bessada, P. Echegut., J.P. Coutures, *Solid State Ionics*, 37 (1990), 223-229.
10. A. L. Rollet, V. Sarou-Kanian, C. Bessada, 'Self-diffusion coefficients measurement at high temperature by PFG NMR', *Comptes Rendus Chimie*, 13 (2010), 399-404.
11. S. Nosé, 'A unified formulation of the constant temperature molecular dynamics methods', *J. Chem. Phys.*, 81 (1) (1984), 511–519.
12. M.D.Segall, P.J.D.Lindan, M.J.Probert, C.J.Pickard, P.J.Hasnip, S.J.Clark, M.C.Payne, *J. Phys.: Condens. Matter*, 14 (2002), 2717-2744.
13. S. J. Clark, M. D. Segall, C. J. Pickard, P. J. Hasnip, M. J. Probert, K. Refson, M. C. Payne, *Zeitschrift fuer Kristallographie*, 220 (5-6) (2005) , 567-570.
14. H. J. Monkhorst and J. D. Pack, *Phys. Rev. B*, 1976, 13, 5188–5192.
15. A. Sadoc, M. Biswal, M. Body, C. Legein, F. Boucher, D. Massiot and F. Fayon, "NMR parameters in column 13 metal fluoride compounds (AlF₃, GaF₃, InF₃ and TlF) from first principle calculations", *Solid State Nuclear Magnetic Resonance*, 59-60 (2014), 1–7.

16. C. Bonhomme, C. Gervais, F. Babonneau, C. Coelho, F. Pourpoint, T. Azais, S. E. Ashbrook, J. M. Griffin, J. R. Yates, F. Mauri and C. J. Pickard, "First-principles calculation of NMR parameters using the gauge including projector augmented wave method: a chemist's point of view", *Chemical Reviews*, 112 (2012), 5733–5779.

ELECTROCHEMICAL STUDY OF COBALT IN UREA AND CHOLINE CHLORIDE

Min Li,^{a,b} Zhongning Shi,^a Zhaowen Wang,^a and Ramana G. Reddy^{b,z}

^a*School of Materials and Metallurgy, Northeastern University, Shenyang 110819, China*

^b*Department of Metallurgical and Materials Engineering, The University of Alabama, Tuscaloosa, Alabama 35487, USA*

^zCorresponding author, E-mail: rreddy@eng.ua.edu

Abstract

The nucleation mechanism of Co(II) in urea-choline chloride-CoCl₂ melt at 373 K was studied using chronoamperometry. Chronoamperometry experiments confirm that the electrodeposition of cobalt on tungsten electrode is governed by three-dimensional (3D) progressive nucleation and diffusion-controlled growth mechanisms. The average diffusion coefficient of Co(II) in the melt at 373 K is $1.1 \times 10^{-6} \text{ cm}^2 \text{ s}^{-1}$, which is in good agreement with the estimated value obtained from cyclic voltammetry data. Characterization of the Co electrodeposit using scanning electron microscope (SEM), energy-dispersive spectroscopy (EDS), and X-ray diffraction (XRD) techniques indicate that the electrodeposit obtained at -0.75 V and 373 K contain dense and compact surface formed from pure cobalt metal.

Introduction

Cobalt is a hard magnetic material and cobalt-based alloys show excellent magnetic properties, adequate mechanical durability and good corrosion resistance that are needed for high-performance magnetic recording applications.¹⁻⁴ The electrodeposition of cobalt and cobalt alloys from aqueous solutions is difficult because of narrow electrochemical window of water, which further results in low current efficiencies and poor quality deposits due to hydrogen embrittlement.

Ionic liquids (ILs) have been substituting aqueous electrolytes for electrodeposition of metals and semiconductors because of advantages such as wide electrochemical window, negligible vapor pressure, good electrical conductivity and no hydrogen gas evolution.^{5,6} First generation ILs or chloroaluminate-based ILs have been used for electrodeposition of cobalt and cobalt alloys because of their adjustable Lewis acidity or basicity.⁷⁻⁹ Reddy et al. have extensively studied the electrodeposition of aluminum and aluminum alloys from chloroaluminate ILs.¹⁰⁻¹³ But, the hygroscopic nature of chloroaluminate systems limits their wide-spread applicability and therefore, air and water-stable ILs or second generation ILs have attracted the attention of researchers in various fields. However, the transition metal halides have low solubility in second generation ILs because of weak Lewis base nature of the anions.^{14,15} The eutectic mixture of urea and choline chloride (2:1 molar ratio) is considered in the present study due to high solubility of metal halides and low cost of the IL.^{5,16,17} Hydrogen bonding interactions between urea and chloride ions resulted in the formation of deep eutectic mixture that exhibit useful electrolyte properties; low freezing point of 12 °C and wide electrochemical window of ~ 2.5 V.¹⁶ Recently, urea-choline chloride mixture have been used as alternative solvents for electrodeposition of several metals.¹⁸⁻²⁴

The electrodeposition of cobalt has been carried out in several ILs. Srivastava et al.²⁵ compared the structure and properties of cobalt coatings obtained from both ionic liquid and aqueous electrolytes. The Co coating deposited from the ionic liquid displayed fine, equiaxial crystallite morphology, while Co coating obtained from aqueous electrolyte showed acicular flake type morphology. In addition, the equiaxial crystallite morphology of Co coating obtained from IL showed relatively higher microhardness in comparison to Co coating deposited from aqueous electrolyte. Chen et al.²⁶ studied the electrodeposition of cobalt on nickel electrode from 40-60 mol % zinc chloride-1-ethyl-3-methylimidazolium chloride ionic liquid containing cobalt (II) ions at 353 K. The cobalt deposition occurred via 3D instantaneous nucleation followed by diffusion-controlled growth process of the nuclei. An et al.²⁷ reported the electrodeposition behavior of cobalt in ZnCl₂-EMIC-CoCl₂ ionic liquid. A high-pure cobalt coating was obtained at cathodic potential of 100 mV (vs. Zn/Zn²⁺) and at current density of 85 μAcm⁻². Also, the authors indicated that the electrodeposition of cobalt metal proceeds through diffusion-controlled growth process. Katayama et al.²⁸ investigated the effect of temperature and additives on electrodeposition of cobalt from IL containing imide functional group. The deposition over potential was reduced with the increase in reaction temperature and also with the addition of acetone to the IL. Electrochemical deposition of lead from lead oxide²⁹ and zinc from zinc oxide^{30, 31} in 2:1 urea/choline chloride ionic liquid. Recently, our research group has studied the electrodeposition of cobalt from BMIMBF₄ IL.³² Although, several investigations have been made on electrodeposition of cobalt in different ILs, very limited information is available on nucleation mechanism of cobalt ions in urea and choline chloride.³³

In the current study, chronoamperometry technique was used to study the electrochemical behavior of cobalt in eutectic mixture of urea and choline chloride. The electrodeposit was characterized using scanning electron microscope (SEM), energy dispersive spectroscopy (EDS), and X-ray diffraction (XRD) methods.

Experimental

All the chemicals, CoCl₂ (Alfa Aesar, >99.7%), urea (Alfa Aesar, >99.3%) and ChCl [HOC₂H₄N(CH₃)₃Cl] (Alfa Aesar, >98%), were dried under vacuum for more than 10 h at 393 K prior to the start of experiments. The deep eutectic solvent was prepared by stirring the mixture of urea and choline chloride (2:1 molar ratio) at 373 K until a homogeneous colorless liquid was formed. The eutectic composition is 46.2 wt% urea and 53.8 wt% choline chloride and eutectic temperature of the IL melt is 12 °C.

The electrochemical measurements were performed by an EG&G PARC model 273A Potentiostat / Galvanostat under an Ar atmosphere. The working electrode, the counter electrode and the quasi-reference electrode used for chronoamperometry studies were tungsten (99.9%, 0.157 cm²), platinum and silver respectively. The electrodes were polished with increasing finer grades of emery paper, rinsed with distilled water and completely dried in air before obtaining electrochemical measurements.

The electrodeposition experiments were carried out using three-electrode system, under Ar atmosphere, with copper sheet (0.5 cm²) as working electrode.³³ The as-deposited Co sample was washed with anhydrous ethanol, to remove any IL adhered on to the cathode surface. The phase and structure of the Co sample was determined using X-ray diffraction (XRD, Philips APD 3720, Netherlands) and surface morphology of the electrodeposit was examined using scanning electron microscope (SEM, JEOL 7000, Japan). The composition

of the deposit was analyzed using energy dispersive spectroscopy (EDS) detector attached to the SEM.

Results and Discussion

Chronoamperometry.— To study the mechanism of the cobalt nucleation and growth process, chronoamperometric experiments were performed using urea-choline chloride electrolyte containing $0.05 \text{ mol} \cdot \text{L}^{-1} \text{ CoCl}_2$. The potential was increased from a value where no Co(II) reduction takes place to a sufficiently negative value that initiates the nucleation and growth of Co particles, immediately after the short induction times. Typical current–time transient curves of the experiments are shown in Figure 1. All the transients exhibits classical characteristics of nucleation process, i.e., after a sharp decay of the electrode double layer charging current, an increase in the faradaic current was observed due to nucleation and growth of Co nuclei. The cathodic current reaches to a peak current maximum, i_m , as the discrete diffusion zones of individual growing crystallites begin to overlap at time, t_m . All the current transients decay slowly after t_m , and overlaps with one another to form a common curve at longer intervals of time. The current decay, resulted from diffusion-controlled process, is a function of $t^{-1/2}$ and is given by Cottrell equation as follows:³⁴

$$I = nFAD^{1/2}C(\pi t)^{-1/2} \quad [1]$$

where I is the current passing through electrolyte in A, n is the number of transferred electron, F is the Faraday constant, 96485 C mol^{-1} , A is the electrode area in cm^2 , C is the bulk concentration in mol cm^{-3} , t is the time in s and D is the diffusion coefficient of electro-active species in $\text{cm}^2 \text{ s}^{-1}$. As shown in Figure 2, the plot of I vs. $t^{-1/2}$ gives a straight line. From Eq. [1] and using the slopes of the straight lines of I vs. $t^{-1/2}$, the diffusion coefficient of Co(II) ions in urea-choline chloride lies between $1.7 \times 10^{-6} \text{ cm}^2 \text{ s}^{-1}$ and $0.6 \times 10^{-6} \text{ cm}^2 \text{ s}^{-1}$ and the values are listed in Table I. The average value of diffusion coefficient of Co(II) ions is calculated to be $1.1 \times 10^{-6} \text{ cm}^2 \text{ s}^{-1}$ and is in good agreement with the estimated value obtained from cyclic voltammetry.³⁵ The diffusion coefficients of Co(II) ions in various ILs are listed in Table II. The different values of diffusion coefficient for Co(II) ions is possibly because of the effect of change in temperature and molten salt system.

In general, electrodeposition of metals on foreign substrate involves 3D nucleation process followed by hemispherical growth of developing nuclei. Scharifker et al.^{36,37} described the nucleation and growth mechanism of metal nuclei by using two models; instantaneous and progressive nucleation models. The instantaneous model refers to a process in which a fixed number of nucleation sites are all activated at same time after the potential step, while the progressive model describes a process in which the nucleation sites are gradually activated as the chronoamperometric experiment proceeds. To identify the nucleation and growth mechanism governing electrodeposition of cobalt, the data from the chronoamperometric experiments are compared with the theoretical dimensionless $(i/i_m)^2$ vs. (t/t_m) curves, predicted by Scharifker and co-workers for 3D instantaneous (Eq. [2]) and progressive (Eq. [3]) nucleation processes:^{38,39}

$$\left(\frac{i}{i_m}\right)^2 = 1.9542 \left(\frac{t_m}{t}\right) \left(1 - \exp\left[-1.2564 \left(\frac{t}{t_m}\right)\right]\right)^2 \quad [2]$$

$$\left(\frac{i}{i_m}\right)^2 = 1.2254\left(\frac{t_m}{t}\right)\left[1 - \exp\left[-2.3367\left(\frac{t}{t_m}\right)^2\right]\right]^2 \quad [3]$$

The experimental and theoretical plots are shown in Figure 3. A close agreement of the experimental data with the theoretical curves defined by Eq. [3], indicates that the reduction of Co (II) ions to Co on tungsten cathode involves a 3D progressive nucleation and growth mechanism mediated by diffusion-controlled process.

Electrodeposition and characterization of cobalt.— Electrodeposition of cobalt was performed on copper (0.5 cm²) substrate using urea-choline chloride containing 0.05 mol·L⁻¹ CoCl₂ at constant potential of -0.75 V and at 373 K. After electrolysis, the deposited Co sample was rinsed thoroughly with ethanol, completely dried and then examined using SEM, EDS and XRD techniques.

The SEM micrograph of the electrodeposited Co sample at -0.75 V and at 373 K is shown in Figure 4. The surface morphology shows that the deposit consists of flat and compact surface with the nodular structures. EDS spectrum of the Co sample is shown in Figure 5. EDS analysis indicate that the electrodeposit contain pure cobalt, with no trace of other impurities such as trapped Cl atoms from the ionic liquid. Figure 6 shows that the XRD pattern of as-deposited Co sample. All peaks of the XRD pattern are assigned to Co element and no diffraction peaks of cobalt oxide are observed. Therefore, the electrodeposited sample primarily consists of pure Co metal.

Conclusions

An electrochemical study was conducted on reduction of Co(II) ions from deep eutectic mixture of urea and choline chloride(2:1 molar ratio) containing 0.05 mol·L⁻¹ CoCl₂ at 373 K. Chronoamperometric experiments show that the electrodeposition of cobalt involves a 3D progressive nucleation and growth process. From Cottrell equation, the average diffusion coefficient of Co(II) ions in the melt was calculated to be 1.1 × 10⁻⁶ cm² s⁻¹ at 373 K, which is in good agreement with the estimated value from cyclic voltammetry. A dense and compact electrodeposit of cobalt was obtained under the experimental conditions. EDS and XRD results show that the electrodeposit is pure cobalt metal.

Acknowledgments

The author (Min Li) is thankful for the award of scholarship by China Scholarship Council (CSC) to pursue current study as a visiting student at United States of America. The authors also acknowledge the financial support from National Science Foundation Grant No. DMR-1310072, ACIPCO and The University of Alabama for conducting the research work.

References

1. W. Kockelmann, W. Schafer, J. K. Yakinthos, and P. A. Kotsanidis, *J. Magn. Magn. Mater.*, **177**, 792 (1998).
2. Y. Xiao, J.-H. Xu, and K. V. Rao, *J. Appl. Phys.*, **79**, 6267 (1996).
3. H.-P. D. Shieh and M. H. Kryder, *J. Appl. Phys.*, **61**, 1108 (1987).
4. C.-J. Lin, J. C. Suit, and R. H. Geiss, *J. Appl. Phys.*, **63**, 3835 (1988).
5. A. P. Abbott, K. S. Ryder, and U. Konig, *Trans. Inst. Met. Finish*, **86**, 196 (2008).
6. S. Z. E. Abedin and F. Endres, *ChemPhysChem*, **7**, 58 (2006).
7. R. T. Carlin, P. C. Trulove, and H. C. D. Long, *J. Electrochem. Soc.*, **143**, 2747 (1996).
8. R. T. Carlin, H. C. D. Long, J. Fuller, and P. C. Trulove, *J. Electrochem. Soc.*, **145**, 1598 (1998).
9. J. A. Mitchell, W. R. Pitner, C. L. Hussey, and G. R. Stafford, *J. Electrochem. Soc.*, **143**, 3448 (1996).
10. V. Kamavaram, D. Mantha, and R. G. Reddy, *Electrochim. Acta*, **50**, 3286 (2005).
11. D. Pradhan, D. Mantha, and R. G. Reddy, *Electrochim. Acta*, **54**, 6661 (2009).
12. D. Pradhan and R. G. Reddy, *Electrochim. Acta*, **54**, 1874 (2009).
13. D. Pradhan and R. G. Reddy, *Metall. Mater. Trans. B*, **43B**, 519 (2012).
14. P.-Y. Chen and I.-W. Sun, *Electrochim. Acta*, **45**, 441 (1999).
15. P.-Y. Chen and I.-W. Sun, *Electrochim. Acta*, **45**, 3163 (2000).
16. A. P. Abbott, G. Capper, D. L. Davies, R. K. Rasheed, and V. Tambyrajah, *Chem. Commun.*, 70 (2003).
17. A. P. Abbott, K. E. Ttaib, K. S. Ryder, and E. L. Smith, *Trans. Inst. Met. Finish*, **86**, 234 (2008).
18. T. Tsuda, L. Boyd, S. Kuwabata, and C. L. Hussey, *ECS Trans.*, **16**, 529 (2009).
19. H. Y. Yang, X. W. Guo, X. B. Chen, S. H. Wang, G. H. Wu, W. J. Ding, and N. Birbilis, *Electrochim. Acta*, **63**, 131 (2012).
20. M. Polzler, A. H. Whitehead, and B. Gollas, *ECS Trans.*, **25**, 43 (2010).
21. A. P. Abbott, J. C. Barron, and K. S. Ryder, *Trans. Inst. Met. Finish*, **87**, 201 (2009).
22. A. P. Abbott, J. C. Barron, G. Frisch, K. S. Ryder, and A. F. Silva, *Electrochim. Acta*, **56**, 5272 (2011).
23. A. P. Abbott, G. Capper, K. J. Mckenzie, and K. S. Ryder, *J. Electroanal. Chem.*, **599**, 288 (2007).
24. A. Florea, L. Anicai, S. Costovici, F. Golgovici, and T. Visan, *Surf. Interface Anal.*, **42**, 1271 (2010).
25. M. Srivastava, G. Yoganandan, and V. K. W. Grips, *Surf. Eng.*, **28**, 424 (2012).
26. P.-Y. Chen and I.-W. Sun, *Electrochim. Acta*, **46**, 1169 (2001).
27. M. Z. An, P. X. Yang, C. N. Su, N. Atshushi, and T. Tooru, *Chin. J. Chem.*, **26**, 1219 (2008).
28. Y. Katayama, R. Fukui, and T. Miura, *J. Electrochem. Soc.*, **154**, D534 (2007).
29. H. Yang and R. G. Reddy, *Journal of The Electrochemical Society*, Vol. 161(10) pp. D586-D592, (2014).
30. H. Yang, and R.G. Reddy, *Electrochimica Acta*, Vol. 147, pp. 513-519, (2014).
31. H. Yang and R. G. Reddy, *Electrochimica Acta*, Vol. 178, pp. 617-623, (2015).
32. M. Li, Z. W. Wang, and R. G. Reddy, in *Materials Processing Fundamentals*, J. Yurko, L. F. Zhang, A. Allamore, C. Wang, J. S. Spangenberg, R. E. Kirchain, J. P. Downey, and L. D. May, Editors, EPD Congress, p. 241, TMS, San Diego, CA (2014).

33. M. Li, Z. Wang and R. G. Reddy, "Cobalt Electrodeposition using Urea and Choline Chloride", *Electrochimica Acta*, Vol. 123, pp. 325-331, (2014).
34. A. J. Bard and R. L. Faulkner, *Electrochemical methods fundamentals and applications* [M]. Y. S. Shao, K. Y. Zhu, X. D. Dong, B. L. Zhang, transl. Beijing: Chemical Industry Press, (2008) (in Chinese).
35. M. Li, Z. W. Wang, and R. G. Reddy, *Electrochim. Acta*, **123**, 325 (2014).
36. G. Gunawardena, G. Hills, I. Montenegro, and B. Scharifker, *J. Electroanal Chem*, **138**, 225 (1982).
37. B. Scharifker and G. Hills, *Electrochim. Acta*, **28**, 879 (1983).
38. Q. Q. Yang, K. R. Qiu, D. R. Zhu, and L. C. Sa, *Electrochemistry*, **1**, 274 (1995).
39. C. W. Xu, W. J. Pan, D. S. Yuan, Y. X. Tong, and G. K. Liu, *T. Nonferr. Metal. Soc.*, **12**, 1007 (2002).
40. R. Fukui, Y. Katayama, and T. Miura, *Electrochim. Acta*, **56**, 1190 (2011).

Table I. Diffusion coefficient of Co(II) at different potentials

Potential (V)	D (cm ² s ⁻¹)
-0.74	1.7×10^{-6}
-0.76	1.1×10^{-6}
-0.78	1.0×10^{-6}
-0.80	0.9×10^{-6}
-0.85	0.6×10^{-6}
Average	1.1×10^{-6}

Table II. Comparison of diffusion coefficient of Co(II) in various ILs.

System	Temperature (K)	Method	D (cm ² s ⁻¹)	Reference
CoCl ₂ -urea-choline chloride	373	chronoamperometry	1.1×10^{-6}	This work
CoCl ₂ -urea-choline chloride	373	cyclic voltammetry	1.7×10^{-6}	35
CoCl ₂ -AlCl ₃ -EMIC	295	chronoamperometry	4.4×10^{-7}	8
CoCl ₂ in urea-NaBr-KBr	373	cyclic voltammetry	2.5×10^{-6}	38
CoCl ₂ -urea-NaBr-acetamide	353	cyclic voltammetry	2.8×10^{-7}	39
Co(TFSA) ₂ -BMPTFSA	300	chronoamperometry	7.2×10^{-8}	40

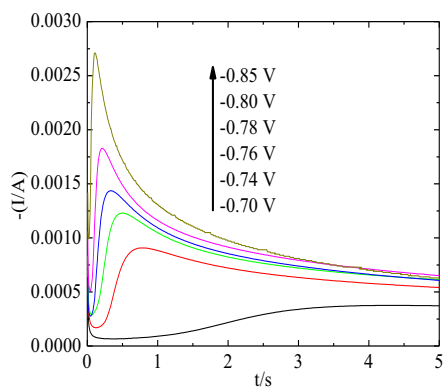


Figure 1. Current-time transients of chronoamperometric experiments for mixture of urea and choline chloride containing $0.05 \text{ mol}\cdot\text{L}^{-1} \text{ CoCl}_2$ on tungsten electrode at 373 K.

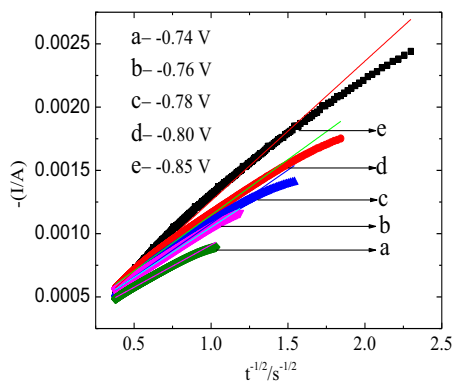


Figure 2. Variation of current (I) with time ($t^{-1/2}$) for decreasing portion of current-time transients in Figure 1 during electrodeposition of cobalt on tungsten electrode at 373 K.

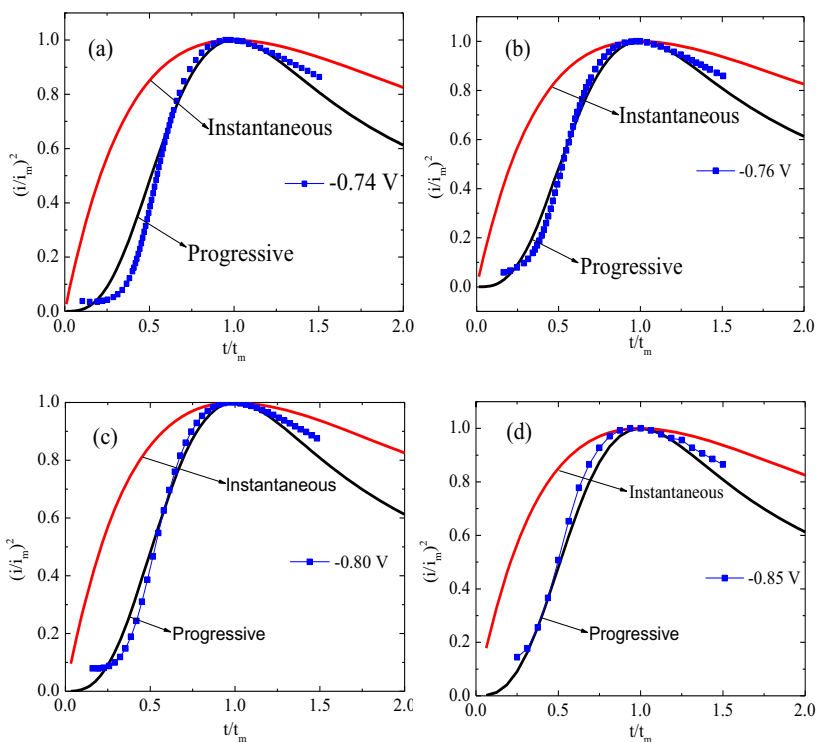


Figure 3. Comparison of the dimensionless current-time transients of chronoamperometric experiments for mixture of urea and choline chloride containing $0.05 \text{ mol}\cdot\text{L}^{-1}$ CoCl_2 on tungsten electrode with the theoretical models of 3D nucleation process at (a) -0.74 V , (b) -0.76 V , (c) -0.80 V and (d) -0.85 V .

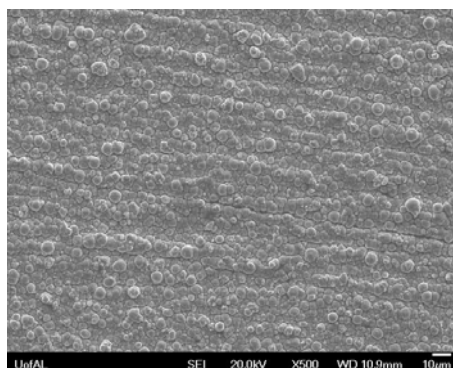


Figure 4. SEM micrograph of the cobalt electrodeposit obtained from mixture of urea and choline chloride containing $0.05 \text{ mol}\cdot\text{L}^{-1}$ CoCl_2 on copper substrate at -0.75V and at 373 K .

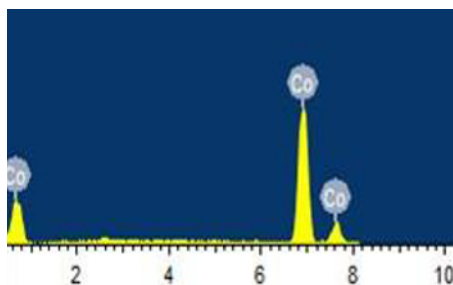


Figure 5. EDS spectrum of the cobalt electrodeposit obtained from mixture of urea and choline chloride containing $0.05 \text{ mol}\cdot\text{L}^{-1}$ CoCl_2 on copper substrate at -0.75V and at 373 K .

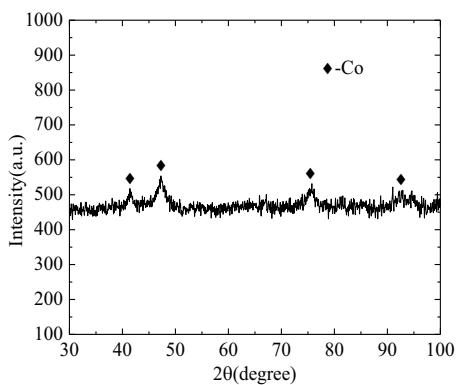


Figure 6. XRD pattern of the cobalt electrodeposit obtained from mixture of urea and choline chloride containing $0.05 \text{ mol}\cdot\text{L}^{-1}$ CoCl_2 on copper substrate at -0.75V and at 373 K .

The Current Efficiency for Aluminium Deposition from Molten Fluoride Electrolytes with Dissolved Alumina

Geir Martin Haarberg

Norwegian University of Science and Technology (NTNU), Trondheim, Norway,

Keywords: Aluminium electrolysis, Current efficiency, Impurities

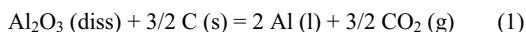
Abstract

Controlled laboratory experiments were carried out to determine the current efficiency for aluminium deposition from fluoride electrolytes containing dissolved alumina. Electrolysis was performed at constant current density, and the amount of deposited aluminium was determined. Effects of temperature, cathodic current density, electrolyte composition and the presence of dissolved impurities were studied. The loss in current efficiency is strongly linked to the solubility of dissolved aluminium. The rate of the so called back reaction between dissolved aluminium and CO₂ depends on the diffusion of dissolved aluminium near the cathode. Both dissolved aluminium and dissolved alkali metals must be considered. Impurities with several oxidation states, such as phosphorus, cause a loss in current efficiency by undergoing cyclic red/ox reactions at the electrodes. The results are of interest for the industrial process of producing aluminium.

Introduction

More than 50 million tonnes of aluminium is produced annually by the Hall-Heroult process. Alumina is dissolved in a molten fluoride electrolyte based on cryolite (Na₃AlF₆) and containing some AlF₃ as well as CaF₂ [1]. Modern cells are operating at ~ 955 - 965 °C. The current efficiency with respect to aluminium can be as high as 96 % and the corresponding energy consumption may be ~13 kWh/kg Al and higher in cells running at ~ 300 kA or higher. The basic principles of the original process remain unchanged, but significant technological developments have taken place. The main improvements have been related to environmental issues and controlling the high induced magnetic fields allowing for increasing the size of the cells. The productivity of the process can be increased by increasing the current in existing cells, and such efforts have been implemented in industrial cells in recent years. Another possibility is to increase the current density. The cathodic current density is typically in the range from 0.7 – 0.8 A/cm² in modern industrial cells.

The current efficiency with respect to aluminium can be as high as 96 % in modern cells. The primary cell reaction is:



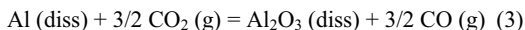
The loss in current efficiency for aluminium deposition is strongly linked to the fact that aluminium is soluble in the electrolyte. Metal solubility is a general phenomenon in molten salts [2]. In molten cryolite based electrolytes dissolved Na must be considered in addition to

dissolved Al [1]. A small but significant activity of sodium is established at the metal/electrolyte interface due to the following equilibrium:



It is known that the subvalent species AlF_2^- is formed as well as dissolved Na. Excess electrons from sodium are responsible for a small contribution to electronic conductivity [1], which may set the upper limit for the attainable current efficiency. Solubility studies have been carried out in laboratory experiments, and the metal solubility is generally in the order of ~ 0.05 wt% Al in electrolytes used in industrial cells. The solubility decreases by increasing content of AlF_3 and decreasing temperature. The most reliable metal solubility data have been published by Ødegård et al. and Wang et al. [3,4].

The so-called back reaction between dissolved metals (Al and Na) and the anode product is responsible for the major loss in current efficiency:



The rate of the back reaction is determined by diffusion of dissolved metals (Al and Na) through the diffusion layer near the cathode. The rate of the diffusion of dissolved metals depends on the total metal solubility and the diffusion layer thickness. The presence of small amounts of CaF_2 , LiF and MgF_2 is known to be beneficial for the current efficiency [1]. It is likely that the total metal solubility is reduced upon these additions.

Sterten studied the mechanism for the loss in current efficiency for aluminium deposition in the industrial process [5]. Sterten and Solli and coworkers presented experimental results and model calculations for the current efficiency based on laboratory studies [6-8]. The effects of cathodic current density, electrolyte impurities and electrolyte composition were included in their investigations. Realistic values for the current efficiency were obtained. The variation of the current efficiency with respect to current density, electrolyte composition and temperature was found to be closely linked to the concentration of dissolved metal. Fig. 1 shows results from laboratory experiments for the current efficiency versus the current density [6].

It has been established that the back reaction takes place outside the diffusion layer next to the cathode/electrolyte interface. The rate of the back reaction is independent of current density, so the current efficiency with respect to Al should increase by increased current density. However, transport phenomena in the electrolyte in the cathode diffusion layer lead to a more complex relationship between loss in current efficiency and cathodic current density [1]. The rate of the back reaction can be expressed as follows:

$$v_B = k' (dc/dx) = k' (c^0/\delta) \quad (4)$$

where k' is a constant including the diffusion coefficient, c^0 is the saturation concentration of dissolved metal at the cathode-electrolyte interface and δ is the diffusion layer thickness. Li et al. [9] recently presented a revised model for calculating the current efficiency based on local variations in cathodic current density related to the three-phase flow of electrolyte at the cathode

interface. The average current efficiency for a typical 300 kA cell at 960 °C and CR=2.3 was estimated to be 95.0 %.

Impurities enter the electrolyte mainly from the consumable carbon anode and aluminium oxide. Important impurity elements are iron, silicon, phosphorus and sulfur. Metallic impurities more noble than aluminium, such as iron and silicon, codeposit at the cathode. The main effect of such impurities is contamination of the metal. Other impurities such as phosphorus undergo cyclic redox reactions at the electrodes, so that the loss in current efficiency may be significant. In modern industrial cells more impurities end up in the produced metal due to the efficient recycling of impurities within the process, mainly by secondary alumina used in dry scrubbers. Studies of the behaviour and impact of impurities have been published [10-12].

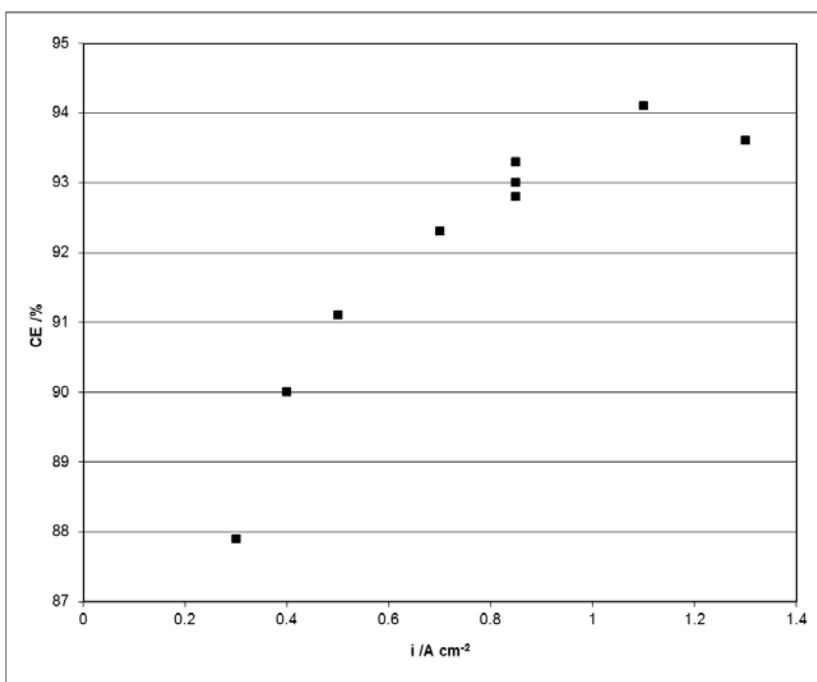


Figure 1. Current efficiency for aluminium deposition as a function of the cathodic current density in molten NaF-AlF₃(CR=2.5)-CaF₂(5 wt%)-Al₂O₃(sat) at 980 °C and 0.85 A/cm². Replotted data [6].

Experimental

A sketch of the laboratory cell used to determine the current efficiency by galvanostatic

electrolysis is shown in Fig. 2. The cell was similar to that used by Sterten and Solli [5-8]. The current efficiency was calculated from Faraday's law by weighing the amount of aluminium deposited during electrolysis. The electrolysis cell was placed in a closed furnace with dry argon atmosphere. A graphite crucible with a sintered alumina lining served as the container for the molten electrolyte. A steel plate was placed at the bottom of the crucible acting as the cathode to ensure that the liquid Al was well wetted. A graphite anode was immersed about 4 cm into the electrolyte and placed about 4 cm above the steel cathode. The influence of cathodic current density, electrolyte additions of LiF and KF, and additions of impurities of AlPO_4 and Na_2SO_4 was studied in separate experiments. The electrolyte was saturated with respect to alumina. Standard experimental conditions were molten $\text{Na}_3\text{AlF}_6\text{-Al}_2\text{O}_3$ (sat) with excess AlF_3 corresponding to a molar ratio of NaF/AlF_3 of 2.5 and 5 wt% CaF_2 at 980 °C and a constant current density of 0.85 A/cm^2 . The possible loss of phosphorus and sulphur due to chemical reactions between the added compounds and the electrolyte was also examined by analyses of electrolyte samples taken as a function of time after the additions of impurities.

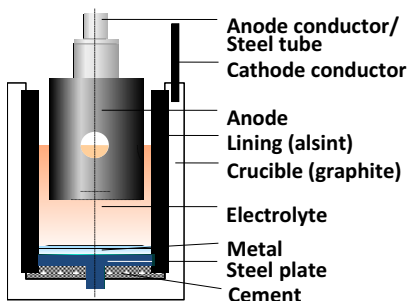


Figure 2. Sketch of the experimental cell for determining the current efficiency for aluminium deposition during electrolysis.

Results and discussion

Current efficiencies for aluminium deposition ranging from ~89-96 % were obtained. Good agreement with literature data [6] was found in pure molten $\text{NaF-AlF}_3(\text{CR}=2.5)\text{-CaF}_2(5 \text{ wt}\%)\text{-Al}_2\text{O}_3$ (sat), where the current efficiency at 0.85 A/cm^2 and 980 °C was determined to be ~ 91 - 93 %.

Fig. 3 shows current efficiency versus cathodic current density from 0.85 - 1.50 A/cm^2 . The current efficiency was found to increase by increasing cathodic current density. This is in accordance with theory, since the main reason for loss in current efficiency is the back reaction between the electrolysis products. Literature data shown in Fig. 1 indicate that there is a maximum CE at ~1.1 A/cm^2 . However, the present results show that there is an increase in CE

up to at least 1.5 A/cm^2 , the increase being less than linear with current density at high current densities. This is likely to be due to the fact that the transport phenomena at the cathode boundary layer cause a higher metal solubility, thus giving a slightly increased rate of the back reaction at increasing current density. However, the main reason for increased current efficiency at high current densities is the fact that the rate of the back reaction is almost independent of the current density. The presented laboratory results for the current efficiency may not be directly applicable to industrial operation. Industrial cells have some constraints with respect to the design which is largely given by the energy and heat balance. An increase of the current density may not be feasible because it will imply a decrease of the interpolar distance in order to reduce the heat production. The results from laboratory experiments at very high current density may be inaccurate due to the intensive anodic gas evolution which may cause increased electrolyte convection and affect the diffusion layer thickness. In industrial cells it is important to maintain a frozen layer of solid cryolite at the side walls to protect the side lining. The interpolar distance is adjusted so that the heat production due to the ohmic voltage drop in the electrolyte is not too high or too low. Therefore the convection at the cathode/electrolyte interphase, which is due to the anodic gas evolution, cannot be controlled in industrial cells.

Figure 4 shows results from determining the current efficiency for aluminium during electrolysis at 1.5 A/cm^2 as a function of the electrolyte composition. A similar trend was obtained by Sterten et al. [7] at 0.85 A/cm^2 . Increasing amounts of AlF_3 cause decreasing metal solubility.

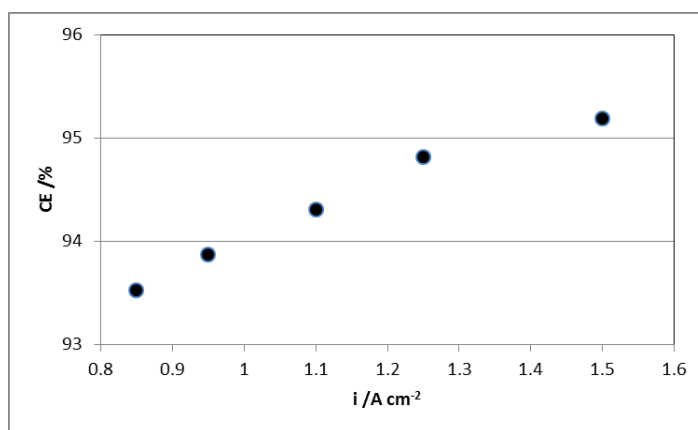


Figure 3. Current efficiency for aluminium deposition as a function of the content of phosphorus in the electrolyte after additions of Na_2SO_4 . Molten $\text{NaF-AlF}_3(\text{CR}=2.5)\text{-CaF}_2(5 \text{ wt\%})\text{-Al}_2\text{O}_3(\text{sat})$ at $980 \text{ }^\circ\text{C}$ and 0.85 A/cm^2 .

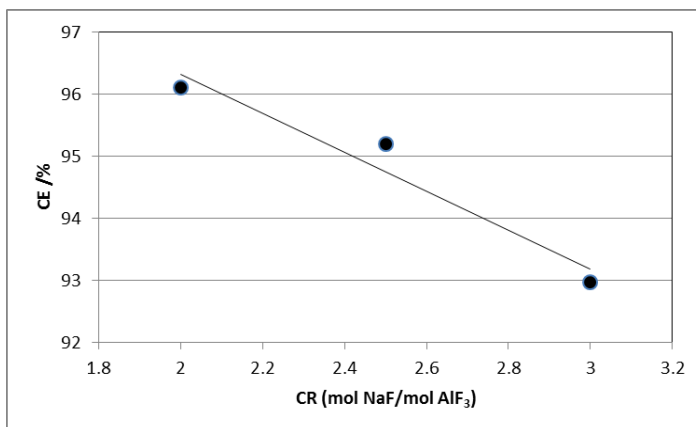


Figure 4. Current efficiency for aluminium deposition as a function of the electrolyte composition (NaF/AlF₃ molar ratio) in molten NaF-AlF₃-CaF₂(5 wt%)-Al₂O₃(sat) at 980 °C and 1.5 A/cm².

The effect of LiF additions up to 5 wt% gave a small but significant increase of the current efficiency, as shown in Fig. 5. This agrees with literature, where Dewing [13] and Tabereaux et al. [14] reported that the loss in current efficiency in industrial cells was found to increase somewhat with increasing LiF content. However, theoretical considerations may suggest that the current efficiency should not depend on relatively small additions of LiF. Additions of LiF in industrial cells may lead to other changes of the electrolysis operation, so that industrial data for the current efficiency may not be reliable. At very high contents of LiF (10 wt%) the current efficiency was drastically reduced.

Fig. 6 shows the effect of additions of KF on the current efficiency. Adding 1 wt% of KF caused a small increase of the current efficiency. At higher contents of KF the current efficiency was found to decrease significantly. This is probably due to dissolution of potassium, which may lead to an increase in the total metal solubility. KF is not a common additive as it is regarded not to be beneficial for the electrolysis process. However, in some cases KF is present as an impurity in the alumina.

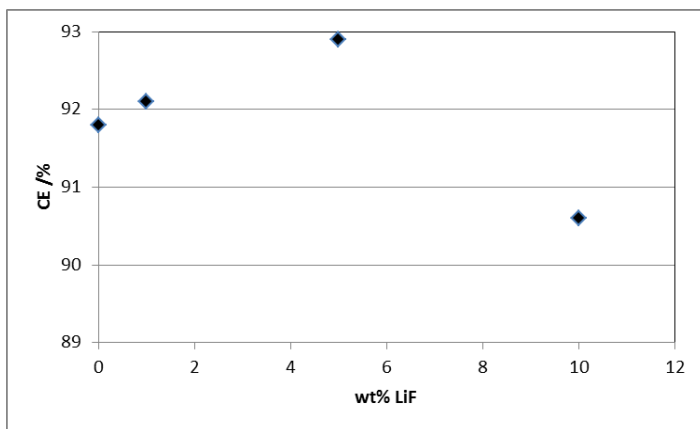


Figure 5. Current efficiency for aluminium deposition as a function of additions of LiF to the electrolyte of molten NaF-AlF₃-CaF₂(5 wt%)-Al₂O₃(sat) at 980 °C and 0.85 A/cm².

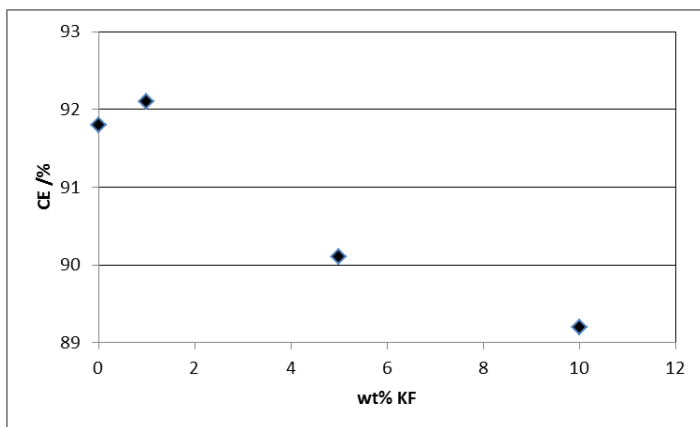


Figure 6. Current efficiency for aluminium deposition as a function of additions of KF to the electrolyte of molten NaF-AlF₃-CaF₂(5 wt%)-Al₂O₃(sat) at 980 °C and 0.85 A/cm².

After additions of both phosphate and sulfate to the electrolyte it was found that the contents of dissolved phosphorus and sulfur in the electrolyte were decreased due to chemical reactions and possible evaporation in experiments without electrolysis. Especially the content of sulfur was rapidly reduced. In current efficiency experiments the loss of phosphorus and sulfur was compensated for by regular additions of the compounds during electrolysis. The effects of the presence of dissolved AlPO₄ and Na₂SO₄ on the current efficiency are shown in Fig. 7.

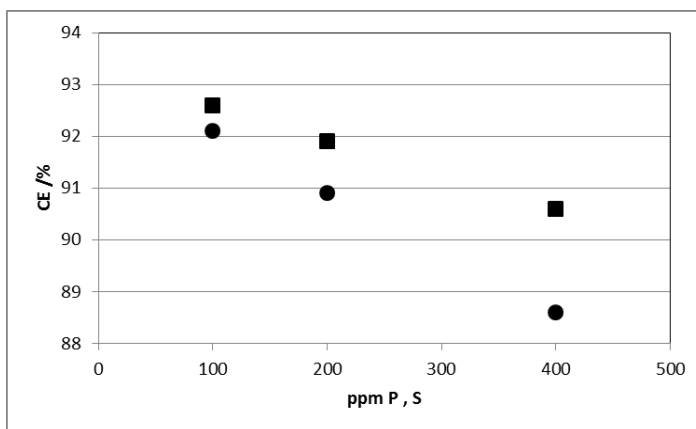


Figure 7. Current efficiency for aluminium deposition as a function of the content of phosphorus and sulfur in the electrolyte after additions of AlPO_4 (squares) and Na_2SO_4 (circles). Molten $\text{NaF-AlF}_3(\text{CR}=2.5)\text{-CaF}_2(5 \text{ wt}\%)\text{-Al}_2\text{O}_3(\text{sat})$ at 980°C and 0.85 A/cm^2 .

The effect of phosphorus on reducing the current efficiency was similar to reported results [6, 15], and the main mechanism is the cyclic redox reactions of dissolved phosphorus species at the electrodes. The effect of sulfur on the current efficiency has not been widely studied. However, it was shown by Pietrzyk and Thonstad [16] that large amounts of sulfur in the anode caused a significant decrease of the current efficiency. The results in Fig. 7 show that dissolved sulfate has a more negative effect on decreasing the current efficiency than dissolved phosphate. Large amounts of sulfate were added during the experiment, and it is believed that dissolved sulfur species are reduced at the cathode while chemical reactions to form SO_2 also take place.

Conclusions

Laboratory experiments were carried out to determine the current efficiency for aluminium deposition. The variation of the current efficiency with changes in cathodic current density and electrolyte composition was found to reflect the changes in the metal solubility. The current efficiency with respect to aluminium was found to increase by increasing the cathodic current density in the range from $0.85 - 1.5 \text{ A/cm}^2$ during galvanostatic electrolysis in molten cryolite based electrolytes. The current efficiency was found to increase by increasing the content of AlF_3 in the electrolyte. Moderate additions of LiF caused a small increase in current efficiency, but high LiF (10 wt%) had an opposite effect. Additions of KF caused a steady decrease of the current efficiency. Both additions of phosphate and sulfate to the electrolyte caused a significant reduction in the current efficiency, mainly due to cyclic redox reactions at the electrodes.

Acknowledgments

Valuable contributions from Dr. Rauan Meirbekova and Dr. Peng Cui are gratefully acknowledged.

The Norwegian research council and Hydro are acknowledged for support.

References

1. J. Thonstad, P. Fellner, G.M. Haarberg, J. Hives, H. Kvande, and Å. Sterten, "Aluminium Electrolysis. Fundamentals of the Hall-Heroult Process", 353 pages, Aluminium-Verlag, Düsseldorf, 2001.
2. M.A. Bredig, in "Molten Salt Chemistry", M. Blander, ed., Interscience, New York, 1964, p. 367.
3. R. Ødegård, Å. Sterten, and J. Thonstad, "Solubility of aluminium in cryolitic melts", *Light Metals 1987*, The Metals Materials and Minerals Society, 389 - 398.
4. X. Wang, R.D. Peterson, and N.E. Richards, "Dissolved metals in cryolitic melts", *Light Metals 1991*, The Metals Materials and Minerals Society, 323 - 330.
5. Å. Sterten, *J. Appl. Electrochem.*, "Current efficiency in aluminium reduction cells", 18 (1988), 473-483.
6. Å. Sterten, P.A. Solli, and E. Skybakmoen, "Influence of electrolyte impurities on current efficiency in aluminium electrolysis cells", 28 (1998), 781-789.
7. Solli, P.A., T. Haarberg, T. Eggen, E. Skybakmoen, and A. Sterten, "Laboratory study of current efficiency in cryolitic melts", *Light Metals 1994*, The Metals Materials and Minerals Society, 195-203.
8. Å. Sterten and P.A. Solli, "An electrochemical current efficiency model for aluminium electrolysis cells", *J. Appl. Electrochem.*, 26 (1996), 187-193.
9. J. Li, Y. Xu, H. Zhang, and Y. Lai, "An inhomogeneous three-phase model for the flow in aluminium reduction cells", *Int. J. Multiphase Flow*, 37(1) (2011), 46-54.
10. K. Grjotheim and K. Matiasovsky, *Aluminium*, 59 (1983), 687.
11. H. Grini Johansen, J. Thonstad, and Å. Sterten, *Light Metals 1977*, 253 - 261.
12. G.M. Haarberg and P. Cui, "Mass transfer reactions near the cathode during aluminium electrolysis", *Light Metals 2014*, The Metals Materials and Minerals Society, 747 - 752.
13. E.W. Dewing, *Metallurgical Transactions B*, 22B (1991), 177.
14. A.T. Tabereaux, T.A. Alcorn, and L. Trembley, *Light Metals 1993*, The Metals Materials and Minerals Society, p. 221.
15. E.W. Thisted, "Electrochemical properties of Phosphorus Compounds in Fluoride Melts cells", Ph.D. dissertation, Norwegian University of Science and Technology, Trondheim, Norway (2003).
16. S. Pietrzyk and J. Thonstad, "Influence of the Sulphur content in the carbon anodes in aluminium electrolysis- a laboratory study", *Light Metals 2012*, The Metals Materials and Minerals Society, 659.

**ADVANCES IN MOLTEN
SLAGS, FLUXES, AND SALTS:**

Proceedings of



**Recycling and Reuse
of Slag and Dust**

DISSOLUTION MECHANISMS OF NUTRIENT ELEMENTS FROM STEELMAKING SLAG INTO SEAWATER

Hiroyuki Matsuura¹, Qian Zhou¹, Fuminori Katabe¹, Likun Zang^{1,2}, Guohua Zhang^{1,3}
and Fumitaka Tsukihashi¹

1 Graduate School of Frontier Sciences, The University of Tokyo;
5-1-5 Kashiwanoha, Kashiwa, Chiba 277-8561, Japan

2 School of Chemistry and Biological Engineering,
University of Science and Technology Beijing;

30 Xue Yuan Road, Haidian District, Beijing 100083, China

3 State Key Laboratory of Advanced Metallurgy, University of Science and Technology Beijing;
30 Xue Yuan Road, Haidian District, Beijing 100083, China

Keywords: Steelmaking slag, Recycling, Sea Desertification, Environment Rehabilitation

Abstract

Steelmaking slag is one of major by-products from steelmaking process and its efficient recycling is essential to establish the environmentally-friendly steelmaking industry. Recently steelmaking slag has been recognized as an effective supplier of nutrient elements to recover the ocean environment from sea desertification. It is believed that the efficient dissolution of iron ion is critical to rehabilitate the damaged sea coast, while the solubility of iron ion in seawater is much below the required concentration. Therefore, the simultaneous addition of humic acids to steelmaking slag is necessary to produce the stable chelated iron ion in seawater. In the present paper, the effect of natural substances containing humic acids or a chemical organic acid on the dissolution behavior of nutrient elements from steelmaking slag was studied and the dissolution mechanisms of steelmaking slag into seawater were discussed.

Introduction

The sea desertification has extended along Japanese coast with the gradual destruction of the coastal ecological system year by year. Among various causes such as the increase of seawater temperature or the ingestion by herbivorous animals such as sea urchin, the lack of nutrient elements in seawater especially iron is considered as one of the most important factors of barren ground[1], since iron is indispensable for the chlorophyll synthesis and the respiration of various seaweeds as a micronutrient. Considering various oxides such as FeO, SiO₂, and CaO as constituents, steelmaking slag is one of the prominent candidates as a source of iron. It has been confirmed that steelmaking slag buried in the coast exhibits the significant enhancement effect on the growth of marine photoplankton or the recovery of the disappeared seaweed beds[2]. However, the solubility of iron in oxic seawater is extremely small at the normal pH range[3] and the dissolution of iron from steelmaking slag is significantly little. Simultaneous supply of organic acid acting as chelating agent is one of solutions to stabilize the dissolved iron in seawater and increase its solubility.

In the present study, the effect of organic acid on the dissolution of various elements from steelmaking slag into seawater was studied by (1) the addition of gluconic acid into seawater and

(2) mixing steelmaking slag with dredged soil. Laboratory scale shaking experiments have been conducted to investigate the dissolution behavior of elements and the change of pH and ORP. The dissolution mechanisms have been discussed from experimental results and calculated solubility diagrams.

Experimental

Materials

Two synthesized slags (S-1: 30.0mass%FeO-33.8%CaO-33.7%SiO₂-2.5%P₂O₅, S-2: 30.0%FeO-45.0%CaO-22.5%SiO₂-2.5%P₂O₅) with a particle size under 150 μm were used. Slags were prepared by melting a mixture of produced CaO and FeO, and reagent grade SiO₂ and Ca₃(PO₄)₂·xH₂O at 1723 K for 50 min in Ar stream of 1 L/min, and quenching on a steel plate by jetting Ar gas. Slag S-1 was completely melted while slag S-2 was partly melted.

The phases of slags were characterized by high-powder X-ray diffraction (XRD: M18XHF, Mac Science, Japan) with a CuKα radiation source at 40 kV and 200 mA over a range between 20 and 80 degrees. Figure 1 shows XRD patterns of synthesized slags. XRD patterns revealed that slag S-1 was composed of CaO·FeO·SiO₂ phase, and slag S-2 was composed of 2CaO·SiO₂ phase and FeO phase. The phases detected by XRD analysis were consistent to those as predicted by the CaO-SiO₂-FeO_x ternary system.

The artificial seawater was prepared by dissolving an artificial seawater raw material ("Aquamarine" supplied by BizScience company, Japan) into distilled water and adjusting pH to around 8.20 by adding NaOH solution. Its composition is shown in Table I. The 0.12, 0.25 and 0.50 g/L gluconic acid-seawater solution was prepared in advance before each experiment. Firstly, pH of 50% gluconic acid (analytical reagent grade, Wako Pure Chemical Industries, Ltd., from 47.0 to 53.0 mass%, density: 1.24 g/cm³) was adjusted to 8.3 by NaOH solution. And then this gluconic acid was diluted 100 times by seawater to prepare the solution with 6.2 g/L and pH of 7.74. Subsequently, 0.12, 0.25 or 0.50 g/L gluconic acid-seawater solution was obtained and their final pH values were 7.60, 7.47 and 7.45, respectively.

The dredged soil used in the present shaking experiments was collected from an inner harbor in west Japan and the ratio of water to dried soil is 3.4. The dried dredged soil is mainly composed of crystalline SiO₂ and NaCl phases.

Table I. Chemical composition of artificial seawater

Constituent	Concentration (mg/L)
NaCl	24534
MgCl ₂ ·6H ₂ O	11112
Na ₂ SO ₄	4094
CaCl ₂ ·2H ₂ O	1535
KCl	694.5
NaHCO ₃	201
KBr	101
SrCl ₂ ·6H ₂ O	43
H ₃ BO ₃	27
NaF	3

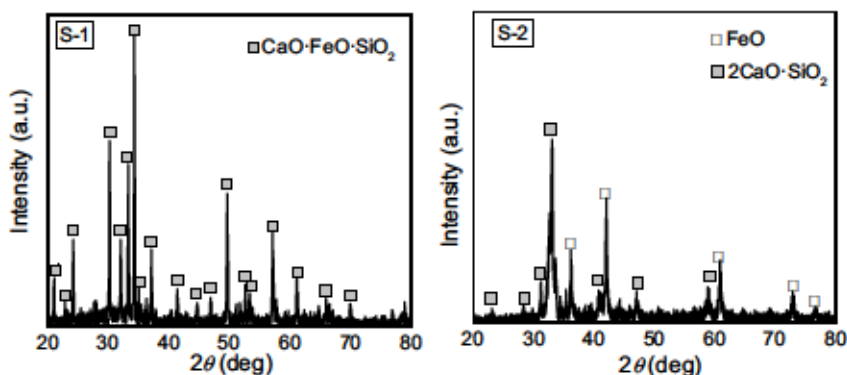


Figure 1. XRD patterns of synthesized slags S-1 and S-2.

Shaking procedure

One gram of slag was added into 100 mL of artificial seawater-gluconic acid solution in a 250 mL of polyethylene bottle and then shaken by a shaking machine with the oscillation speed of 160 cycles/min and the amplitude of 20 ± 5 mm at room temperature. The shaking time was varied from 1 to 96 h. At the same time, the shaking experiment of 100 mL seawater without any solid sample was also conducted as a reference.

After shaking, pH and oxidation-reduction potential (ORP) of the shaking solution were measured immediately by a pH meter (IM-55G with GST 5731C probe, DKK-TOA Corp.) and an ORP meter (HM-25R with PS-5111C probe, DKK-TOA Corp.). Subsequently, the solution was filtrated with a $0.45 \mu\text{m}$ Millipore membrane filter. Concentrations of Ca, Mg, Si and Fe were measured by an inductively-coupled plasma optical emission spectrometry (ICP-OES, Seiko Instruments Inc., SPS7800 Plasma Spectrometer) and concentration of P by the molybdenum blue spectrometry.

Measurement of the dissolution behavior of slag-soil mixture was conducted in the following manner. Firstly, from 0 to 3 g of slags were mixed with 8 g of dredged soil in a 250 mL polyethylene bottle and then it was cured for 24 h inside a fume cupboard. The prepared mixture was put into 100 mL seawater and mixed well. The following procedure was the same as the previous case. The concentration of Fe was examined by the 1,10-phenanthroline spectrometric method instead ICP-OES due to its low concentration.

Results and Discussion

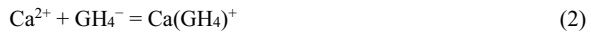
Addition of gluconic acid[4,5]

Figure 2 shows the dissolution behaviors of Ca from slags S-1 and S-2 into seawater with various concentrations of gluconic acid. Concentration of Ca increased with increasing both of the shaking time and concentration of gluconic acid, while it was much larger in the case of slag S-2 than that with slag S-1. After 96 h shaking, concentration of Ca changed from 394 to 417 mg/L

for slag S-1 and from 604 to 828 mg/L for slag S-2. For slag S-1, concentration of Ca in seawater with gluconic acid was larger than that without gluconic acid, while those with 0.25 and 0.50 g/L gluconic acid were similar. Since the dissolved amount of Ca from slag S-1 was small, Ca dissolution behavior was largely influenced by other elements contained in seawater. In the case of slag S-2, the increment of Ca concentration was followed by concentration of gluconic acid. The dissolution of Ca from slag into seawater is expressed by reaction (1).



Dissolution of CaO is enhanced by the complexation reaction between Ca and gluconic acid such as reaction (2). Hence, pH increased with increasing concentration of gluconic acid for slag S-1.



where GH_4^- is the symbolic form of gluconate ion.

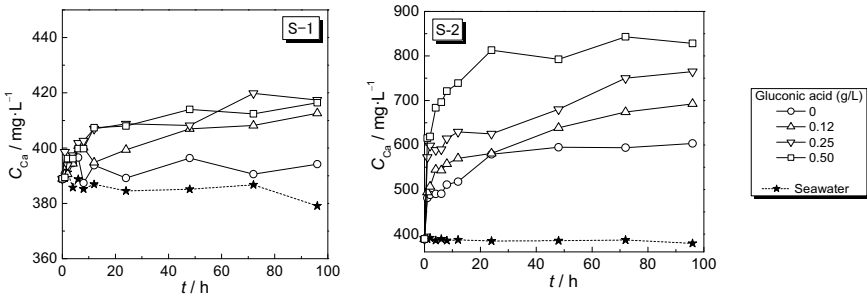
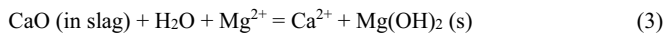


Figure 2. Dissolution behaviors of Ca from slags S-1 and S-2 into seawater with various concentrations of gluconic acid.

Even the significant dissolution of Ca from slag S-2 by adding gluconic acid, pH was still constant around 10.1, which is attributed to the precipitation of Mg^{2+} contained in the original artificial seawater. Figure 3 shows concentration change of Mg in seawater during shaking of slags S-1 and S-2 with seawater containing various concentrations of gluconic acid.

With slag S-1, concentration of Mg changed in a small range between 1172 and 1217 mg/L, which is close to that of seawater. With slag S-2, concentration of Mg decreased with increasing both the shaking time and concentration of gluconic acid. The smallest concentration of Mg was 918 mg/L after shaking 96 h with 0.50 g/L gluconic acid.

Magnesium hydroxide has relatively lower solubility compared with calcium hydroxide and thus Mg^{2+} in the seawater precipitates as $\text{Mg}(\text{OH})_2$ by the substitution reaction (3) when pH reaches to a certain extent. Hence, concentration change of Mg shows an opposite trend to that of Ca for slag S-2.



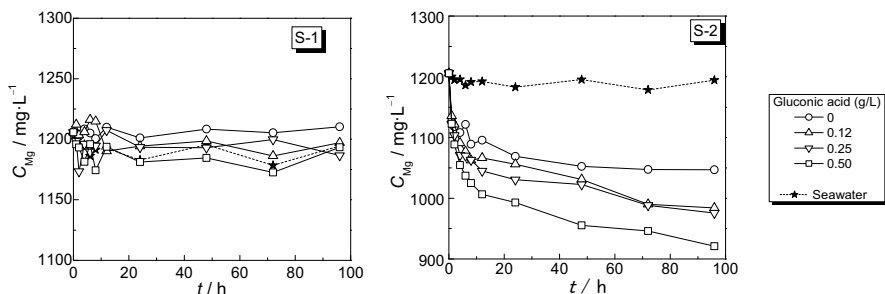


Figure 3. Concentration change of Mg in seawater during shaking of slags S-1 and S-2 with seawater containing various concentrations of gluconic acid.

The dissolution behaviors of Fe from slags into seawater containing gluconic acid are shown in Fig. 4. The soluble Fe was not detected in the seawater without gluconic acid for both slags S-1 and S-2. The CaO/SiO₂ ratio of slag determines the dissolution behaviors of Fe from slags into seawater. In the case of slag S-1, the dissolution of Fe increased with increasing the shaking time as well as concentration of gluconic acid. In the case of slag S-2, concentration of Fe decreased quickly before 12 hours and then further decreased gradually with the shaking time.

The ORP fluctuated in the initial shaking period and that for shaking with slags was smaller than that for shaking of seawater. At the same time, the ORP in the case of shaking with slag S-2 was much smaller than that with slag S-1. Increase in concentration of gluconic acid decreased the ORP. The measured soluble Fe concentration in seawater with gluconic acid was much larger than that predicted by the potential-pH diagram of iron-water system.

From the solubility diagram of Fe in seawater[6], soluble Fe during shaking of slag S-1 is in equilibrium with FeO and Fe(OH)₂ phases but its concentration was larger than the equilibrium values. The soluble Fe species is considered to be Fe²⁺. On the contrary, the soluble Fe during shaking of slag S-2 is in equilibrium with Fe(OH)₃ phase but its concentration was also larger than the equilibrium value, and the soluble Fe species would be Fe(OH)₄⁻. These excess portion is attributed to the formation of iron-gluconate complexes.

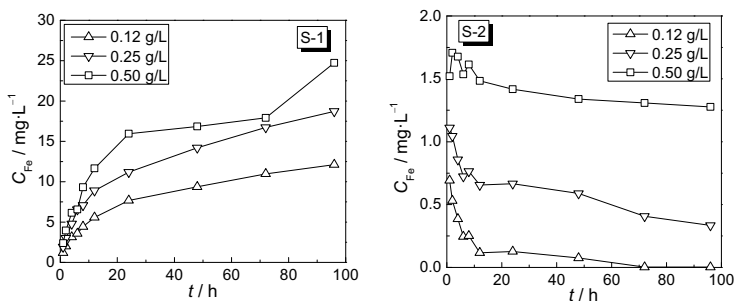


Figure 4. Dissolution behaviors of Fe from slags S-1 and S-2 into seawater with various concentrations of gluconic acid.

Mixing of slag and soil[7]

The pH values showed the incubation period before 12 h and then gradually decreased until stabilized between 24 h and 96 h in the case of slag S-1. The pH values of the slag – dredged soil mixture changed between those of seawater only and of seawater shaken with dredged soil. After 96 h, the pH value was 8.26 for seawater, 7.80, 7.72, 7.72 or 7.53 for the mixture of 3, 2, 1 or 0.5 g slag with 8 g dredged soil, or 6.62 for dredged soil, respectively. The values decreased with decreasing the amount of slag in the mixture.

The dissolution of Ca occurred in two stages. An incubation period was observed at the first stage until 12 h with increasing of Ca concentration by about 50 mg/L and after 24 h it increased suddenly by about 180 mg/L. The slag amount in the mixture did not show the obvious effect on the dissolution behavior of Ca. Even though Ca dissolution from the mixture was observed, the pH values of the seawater after shaking were still smaller than that of the original seawater. This is attributed to the buffering effect of the dredged soil on the pH change of seawater.

In the case of slag S-2, the pH values increased immediately after starting the shaking of seawater with the mixture and after that values were relatively stable. After 96 h, the pH value was 10.4, 10.0, 9.4 or 9.1 for the mixture of 3, 2, 1 or 0.5 g slag with 8 g dredged soil, respectively, which decreased with decreasing the amount of slag.

The Ca concentration increased greatly with increasing the shaking time and also the amount of slag in the mixture. After 96 h, the Ca concentration was 911, 1415, 2365 or 2437 mg/L for the mixture of 0.5, 1, 2 or 3 g slag with 8 g dredged soil, respectively. The significant dissolution of Ca from the S-2 slag and soil mixture is not only due to its larger CaO/SiO₂ ratio than S-1 slag but also due to the possible complexation reactions with organic acids contained in the dredged soil.

Figure 5 shows the dissolution behavior of Si from the mixture of slag and dredged soil. The concentration of Si in seawater with dredged soil is a little larger than that of the original seawater. In the case of the S-1 slag and dredged soil mixture, the dissolution of Si showed an incubation period of 12 h followed by the significant increase in Si concentration from 24 h to 96 h regardless the amount of slag. In the case of the S-2 slag and dredged soil mixture, the concentration of Si was relatively large in the beginning and then it decreases to minimum. Subsequently, the Si concentration gradually increased with the shaking time. Though the influence of the slag amount on it was obscure, the Si concentration in the seawater with the mixture was generally larger than that with dredged soil only or that of the original seawater.

From the solubility diagram of Si, the soluble Si from dredged soil only was equilibrated with H₄SiO₄ phase and its form is H₄SiO₄⁰. The dissolution of the S-1 slag and dredged soil mixture resulted in the formation of H₂SiO₃ and H₄SiO₄ and thus the Si concentration was in the range between two solubility lines. The soluble Si from the S-2 slag and dredged soil mixture was mainly in equilibrium with H₄SiO₄ phase and its forms are H₄SiO₄⁰ or H₃SiO₄⁻.

All of the ORP values during shaking with the slag and dredged soil mixture were lower than that of seawater and in the stable condition of solid Fe₂O₃ phase on the potential – pH diagram for the iron-water system. It forecasts that the soluble Fe in the shaking solution is in equilibrium with the solid Fe₂O₃ phase which is extremely low.

It has been confirmed that the low ORP for the dredged soil case can promote the dissolution of Fe[8]. The dissolution behavior of Fe from the mixture of the S-1 or S-2 slag and dredged soil is shown in Fig. 6. The soluble Fe in the original artificial seawater and in some shaking solutions

was not detected. During shaking, the concentration of Fe showed maximum at 12 h for the S-1 slag and dredged soil mixture and at 24 h for the S-2 slag and dredged soil mixture and varied from several to 132 $\mu\text{g/L}$. Furthermore, the influence of the slag amount on the Fe concentration was ambiguous.

From the solubility diagram of Fe, the soluble Fe in the case of the S-1 slag and dredged soil mixture or dredged soil only was close to the solubility of the $\text{Fe}(\text{OH})_3$ phase and thus its form is $\text{Fe}(\text{OH})_3^0$, while that in the case of the S-2 slag and dredged soil mixture was close to that of the FeO , $\text{Fe}(\text{OH})_2$ or $\text{Fe}(\text{OH})_3$ phase with the form of Fe^{2+} or $\text{Fe}(\text{OH})_3^0$.

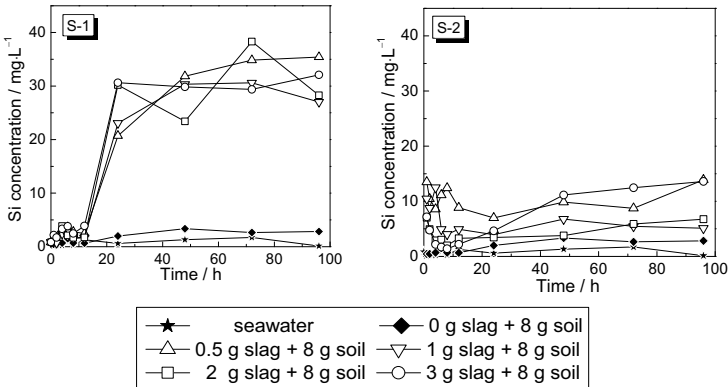


Figure 5. Dissolution behaviors of Si from slags S-1 and S-2 mixed with dredged soil into seawater.

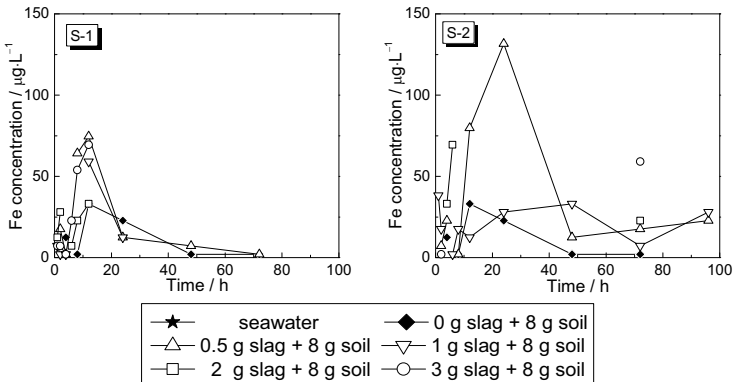


Figure 6. Dissolution behaviors of Fe from slags S-1 and S-2 mixed with dredged soil into seawater.

Conclusions

The dissolution behavior of major elements contained in steelmaking slag into seawater was studied by shaking the synthesized slag with artificial seawater containing gluconic acid or the mixture of slag and dredged soil with seawater.

Iron dissolved effectively by adding gluconic acid into seawater because of the formation of iron and gluconic acid complex which is stable in seawater. Dissolution of Ca was also greatly enhanced by gluconic acid.

Mixing dredged soil to slag significantly increased the dissolved concentration of Si in seawater. Iron also dissolved slightly more by mixing slag and soil together. However, the effect of soil on the dissolution behavior of iron was extremely complex due to the various simultaneous phenomena.

References

1. M. Yamamoto et al., "Recovery from Barren Ground by Supplying Slug and Humic Substances," *J. Jpn. Inst. Energy*, 85 (12) (2006), 971-978.
2. K. Sugie and A. Taniguchi, "Continuous Supply of Bioavailable Iron for Marine Diatoms from Steelmaking Slag," *ISIJ Int.*, 51 (3) (2011), 513-520.
3. K. Kuma et al., "Photo-Reduction of Fe(III) by Dissolved Organic Substances and Existence of Fe(II) in Seawater during Spring Blooms," *Mar. Chem.*, 37 (1-2) (1992), 15-27.
4. X. Zhang et al., "Influence of Gluconic Acid on Dissolution of Si, P and Fe from Steelmaking Slag with Different Composition into Seawater," *ISIJ Int.*, 54 (6) (2014), 1443-1449.
5. X. Zhang, H. Matsuura and F. Tsukihashi, "Enhancement of the Dissolution of Nutrient Elements from Steelmaking Slag into Seawater by Gluconic Acid," *J. Sustain. Metall.*, 1 (2) (2015), 134-143.
6. X. Zhang, H. Matsuura and F. Tsukihashi, "Dissolution Mechanism of Various Elements into Seawater for Recycling of Steelmaking Slag," *ISIJ Int.*, 52 (5) (2012), 928-933.
7. X. Zhang, H. Matsuura and F. Tsukihashi, "Dissolution Mechanisms of Steelmaking Slag-Dredged Soil Mixture into Seawater," *J. Sustain. Metall.*, DOI 10.1007/s40831-015-0040-6.
8. A. Hayashi et al., "Effects of the Seaweed Bed Construction Using the Mixture of Steelmaking Slag and Dredged Soil on the Growth of Seaweeds," *ISIJ Int.*, 51 (11) (2011), 1919-1928.

EFFECTS OF THREE TYPES OF IRON AND STEEL SLAG ON FRESH AND HARDENED PROPERTIES OF ORDINARY PORTLAND CEMENT

Seyed Vahid Hosseini¹, Shahnavaz Eilbeigi², Mohammad Reza Nilforoushan¹

¹Faculty of Materials Science and Engineering, Shahrekord University
Rahbar Boulevard, Shahrekord, Chaharmahal Bakhtiari Province, Post Code: 8815915655, Iran

²MSc. Mechanical Engineering, University of Texas at Arlington (UTA)
720 N cascades, Fort Worth, TX, Post Code: 76137, USA

Keywords: BOF-slag, EAF-slag, GBF-slag, Cement, Slurry, Paste, Mortar

Abstract

Slag is a by-product of different metal extraction and refining processes. This paper reports the results of an experimental study on replacing part of ordinary Portland cement (OPC) with iron and steel slags. In Iranian iron and steel plants, slags are generated at three different stages of processing; Basic Oxygen Furnace (BOF), Electrical Arc Furnace (EAF) and Granulated Blast Furnace (GBF) are the slags used in this study. In this respect, some mixtures were made with 10%, 20% and 30 wt% of each slag replaced in ordinary Portland cement. For this study, the effects of slag additions in cement was determined by measuring of electrical conductivity and pH of slurry, setting time of paste and mechanical strength of mortar at various ages. According to the results, 10% EAF or BOF slag can safely replace part of OPC in mortars.

Introduction

Recently, utilization of waste materials in other industries has been attracted by researchers. However, most industrial slags are being used without taking full advantage of their properties or disposed rather than used. In Iranian iron and steel plants, slags are generated at three different stages of processing and in view of that categorized as:

- i. Granulated blast-furnace slag (GBFS) is a glassy granular material of the manufacture of pig iron from iron ore, limestone and coke. The liquid slag is rapidly cooled by quenching to get an almost completely amorphous material. Up to now, the use of GBFS in cement and concrete technology has been extensively discussed [1-3].
- ii. Electric arc furnace slag (EAFS) is essentially based on addition of burned lime, dolomite [$\text{Ca.Mg}(\text{CO}_3)_2$] and etc. together with steel scraps in electrical arc furnace under high voltages. After separating from molten metal, the liquid slag cooled by a combination of spraying water and air. The water quenched electric arc furnace slag has a physical appearance which is partly granular and partly flaky. In the type of air cooled, high Fe-oxide content coupled with the highly crystalline nature of the slag are proposed to be the reasons for its chemical inactivity during the process of hydration in the presence of clinker or lime. Hence the EAFS is used mainly as aggregates for landfills and roads [4-6].
- iii. Basic oxygen furnace slag (BOFS) produced in the process of conversion pig iron to steel in a basic oxygen furnace. The principle of the basic oxygen furnace is to blow oxygen and neutral gas into the furnace to decrease carbon contents. Moreover,

during the conversion of pig iron, lime and dolomite are added in the converter. Lime is used to fix the silicon and phosphorous contained in pig iron and dolomite is added to protect the refractory brick. At the end of the conversion, BOF slag is separated from steel because of their different specific gravities and then cooled slowly in the air with water spraying [7-9].

There are some reasons for trying to apply the utilization of slags in the manufacturing of cement or, alternatively, as cement replacement materials in concrete. One good reason is the decrease of a significant amount of slag being sent to landfill each year. Other reasons are the potential for reducing energy consumption and carbon dioxide emissions within the cement industry, and to save natural resources [1, 8-9].

In addition to the above reasons, replacement of clinker by slags had another advantages such as low heat of hydration, high sulfate and acid resistance, better workability, and good ultimate strength and durability [10]. There are two different approaches for the incorporation of iron and steel slags in cement production. The first one involves the use of slag, mixed with limestone and clay, as raw material feed to the cement kiln [2]. This may be a solution to the disposal problem but there is not any energy benefit, (because of the slag must be clinkered) or economic benefit (one low-cost material is substituted for another). A more attractive approach is the utilization of iron and steel slags in the production of special cements [8, 11-15].

In this study, we introduce experimental results: mechanical properties of hardened cement pastes and morphology of product obtained by X-ray diffraction, Scanning electron microscopy under different conditions. In order to have a clear description of the amount of slag that can safely replaces OPC in mortar by improving its properties.

Materials and methods

Raw materials

The slags are produced by Esfahan Steel Company. One kilogram of each batch was taken for experiments randomly and mixed completely. The mixed Batches were dried, crashed and milled by various mills such as ball and fast mills, in order to make a powder which pass the #200 sieve ($<75 \mu\text{m}$). The chemical composition of slags and OPC used in this study was determined by X-ray fluorescence and the results are listed in Table 1. X-ray diffraction patterns of raw materials are shown in Fig. 1.

Characterization and testing procedures

The mineralogical structure of materials was analyzed by X-Ray diffraction. The apparatus was Bruker D8 Advance with nickel-filtered $\text{CuK}\alpha_1$ radiation ($\lambda=1.5406 \text{ \AA}$). The effects of slag additions on the rheological properties of slurries were investigated by the measurement of pouring time of slurry through a 5 mm orifice in the standard funnel. The values of electrical conductivity and pH of Slurries were measured in situ using Consort C933 multi-parameters portable.

The setting times of the pastes were determined by the Vicat apparatus. A needle of a known weight and area was used in this method [16, 17]. Two distinct stages of setting were recorded in the laboratory for pastes: the initial set (time of commencement of the setting) and the end, or final, set. The mechanical strength measurements of mortars were performed on a Baldwin

machine in a load control regime with a loading rate of 2 MPa/min. Three specimens were made and tested for each data point. The specimens were tested at 3, 7, 28 and 90 days after casting. Scanning electron microscopy (SEM) observation were done by Leo 435-VP, operating at EHT=20 kV.

The slags were replaced by part of cement based on the design shown in table 2. For each blended of slag and cement, dry powder was mixed in the ball mill for 10 minutes to get a uniform composition.

Table I. Chemical composition of raw materials

Mineral	OPC	BOFS	EAFS	GBFS
SiO ₂	21.7	10.2	13.9	36.4
CaO	63.5	56.1	49.1	38.0
Al ₂ O ₃	5.9	2.1	2.3	8.3
MgO	1.8	1.5	7.7	9.5
Fe _(total)	3.1	20.5	17.1	1.9
MnO	-	2.6	6.3	1.0
V ₂ O ₅	-	2.2	2.1	0.1
P ₂ O ₅	-	1.2	0.5	-
TiO ₂	0.6	2.1	-	4.3
K ₂ O	0.7	0.4	-	0.3
L.O.I	2.7	1.1	1.0	0.2
<i>Specific gravity (g/cm³)</i>	3.15	3.47	3.28	2.74

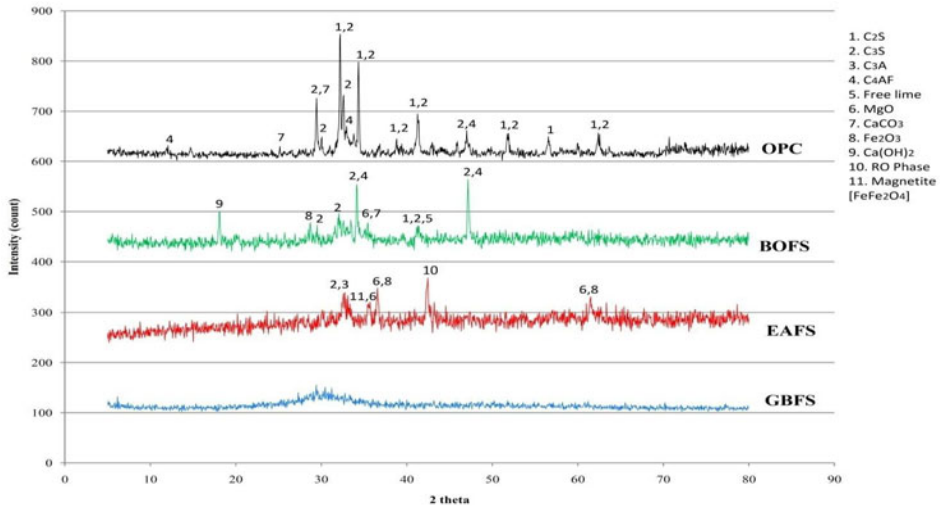


Figure 1. X-ray diffraction patterns of materials

Table II. Mix proportions of blends (wt %)

Mixture name	OPC (%)	BOFS (%)	EAFS (%)	GBFS (%)
Ref	100	-	-	-
BOF10	90	10	-	-
BOF20	80	20	-	-
BOF30	70	30	-	-
EAF10	90	-	10	-
EAF20	80	-	20	-
EAF30	70	-	30	-
GBF10	90	-	-	10
GBF20	80	-	-	20
GBF30	70	-	-	30

Results and Discussion

Slurry

Rheological properties

The batch of slurry was considered 50 grams powder together with water to cementitious materials ratio (w/cm) equal to 0.5. The blend was mixed in a rotary mixer for 5 minutes in order to get uniform slurry. Based on these results (Table 3), by increasing amounts of BOFS, the pouring time increased while GBFS and EAFS acted in the reverse manner. This may be due to the higher basic composition of BOFS which release Ca ions right after mixing with water, compared to the other slags. It has been mentioned as follows by other researchers, when cement mixed with water, due to hydration reactions, calcium (Ca) and hydroxyl (OH) ions go into solution within the first 10 min. The degree of hydration describes the process of hydration, and directly is related to the fraction of the hydration products or porous structure in a hydration system in cement based materials [18-20].

pH

The pH of the slurry plays an important role in the hydration process and in determining the nature of C-S-H. It was reported that C-S-H does not form in a solution with a pH below 9.5 [16]. In order to have a rough estimation of slag hydration, the pH of slurries made with different slag additions were measured at 10 and 60 minutes of hydration, respectively. The results are shown in table 3. According to the results, the alkalinity of all slags is closely the same.

Electrical-Conductivity

Electrical conductivity process occurs mainly due to ion transport through the pore solution in a cement-based system and it is an important parameter to study the hydration process of cement pastes at early stages. The variation of conductivity as a function of time can indeed reflect on internal changes of the pore solution of cement paste with time. On the other hand, electrical conductivity of cement slurries decreased with time [21]. The conductivity of various mixtures of slag and OPC were measured. Based on the results, by replacement of slag as part of OPC, the electrical conductivity of slurries decreased, this may be the case for increase in the setting time

of the pastes. Results of electrical conductivity of slurries are shown in table 3. Due to specimen of Ref at time of 60 min had been set, their values of pH and EC could not be measurable.

Table III. Values of measured pouring time (Sec), pH and electrical conductivity (mS/c) of slurries

Mixture Name	Pouring time (Sec)	pH		EC*	
		10 min	60 min	10 min	60 min
Ref	7.15	12.97	-	10.02	-
BOF10	8.29	12.71	12.90	9.06	9.54
BOF20	9.03	12.20	12.92	8.21	9.01
BOF30	11.67	12.28	12.96	7.65	8.60
EAF10	5.82	12.79	12.80	9.96	10.02
EAF20	5.07	12.77	12.75	9.33	9.32
EAF30	4.86	12.78	12.64	8.90	8.93
GBF10	6.78	12.74	12.85	9.29	9.72
GBF20	6.33	12.72	12.80	8.56	8.86
GBF30	5.97	12.68	12.76	7.93	7.80

*Electro-conductivity (mS/c)

Paste and mortar

Setting behavior of the pastes

The initial and final setting time of the pastes was evaluated and the results are graphically presented in figures (2, 3 & 4). Based on the results, the initial and final setting time of blended cement paste both increased which was depended on the amount and kind of slag used in the blended cement. This may initially be due to the reduction in the amount of C₃A but finally due to the reduction in the Ca ion releasing from the cement part of the pastes which effects on the crystals growth in the during final setting of the pastes.

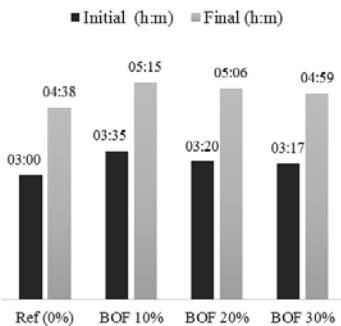


Figure 2. Setting time of blended cement pastes with BOFS

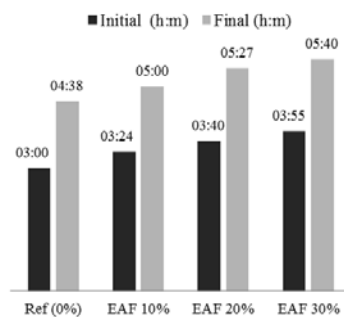


Figure 3. Setting time of blended cement pastes with EAFs

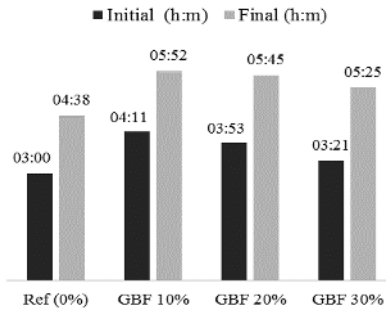


Figure 4. Setting time of blended cement pastes with GBFS

Mechanical properties of mortars

Both flexural and compressive strength of mortars was measured as per Iranian standard ISIRI393 [22]. Mortars prisms (Dimensions 40×40×160 mm) and cubes (Dimensions 50×50×50 mm) were made with cement, sand and water (1:3:0.5) for flexural and compressive strength, respectively, which were first cured in accordance with the standard until ages 3, 7, 28 and 90 days. According to the results, additions of slag at early ages have negative effects on the mechanical properties of blended cements but it recovers at longer times. Based on these results EAFS and BOFS may safely replaces up to 15% of OPC but GBFS decreases mechanical properties of cement at early ages and it does not recovers even up to 90 days of hydration. Results are shown in Table 4.

Table IV. Mechanical strengths of mortars made containing slags at different ages of curing

Sample Name	Mechanical Strength (MPa)							
	3 days		7 days		28 days		90 days	
	Flexural	Compressive	Flexural	Compressive	Flexural	Compressive	Flexural	Compressive
Ref	2.7	21.28	2.9	36.91	4.0	43.29	5.4	51.20
BOF10	2.5	18.03	2.8	30.22	3.5	40.70	4.9	47.56
BOF20	2.4	14.92	2.7	21.54	3.2	37.91	4.7	44.95
BOF30	2.1	11.63	2.4	18.00	3.0	34.32	3.9	40.37
EAF10	2.4	19.54	2.7	31.97	3.8	41.22	5.2	50.21
EAF20	1.9	16.93	2.4	28.03	3.4	39.75	4.4	48.91
EAF30	2.1	12.73	2.3	22.80	3.1	36.44	3.7	46.29
GBF10	2.4	20.01	2.9	34.46	3.6	42.82	4.9	51.32
GBF20	2.2	17.22	2.6	30.50	3.2	39.63	3.9	49.08
GBF30	1.8	14.98	2.2	20.19	2.6	34.22	2.9	41.76

Microstructural investigations of the hardened cement pastes

Microstructure of cement pastes after 7 and 90 days of hydration was investigated by scanning electron microscopy (SEM) to have a clear understanding of the effect of various slags on the hydration products of hardened cement pastes. The electron micrographs are shown in figures 5-8. Microstructure of OPC shows a dense texture composed of tobermorite (CSH) and plates of $\text{Ca}(\text{OH})_2$. By replacement of 30% BOFS with cement (Fig. 6), the paste becomes porous due to the formation of lumps of $\text{Ca}(\text{OH})_2$ after 7 days which turns to plates after 90 days and needle like crystals of ettringite $[\text{Ca}_6\text{Al}_2(\text{SO}_4)_3(\text{OH})_{12}\cdot 26\text{H}_2\text{O}]$. Fig. 6 compared to Fig. 7, reveals due to the presence of less lime in the composition of EAFS, the needle like crystals of ettringite and platy crystals of calcium hydroxide are well formed after 7 days but at 90 days, there is not much difference between hydration products of BOFS and EAFS. By looking at Fig. 8 from the hardened paste of GBFS, it seems that needle crystals of ettringite has formed after 7 day of hydration but, after 90 days, the crystals in the paste becomes lumpy covered with ill platy crystal of tobermorite $[\text{Ca}_5\text{Si}_6\text{O}_{16}(\text{OH})_2]$. When the results of micro-structural studies are compared with mechanical strength in table 4, the pore mechanical strength of GBFS is interpretable. Due to the micro cracks and bigger crystal size that leads to less mechanical strength.

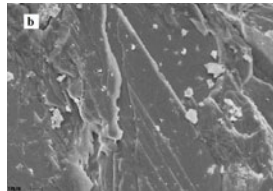
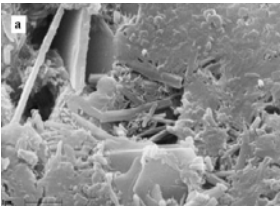


Figure 5. SEM Images of reference sample at: a) 7 & b) 90 (days)

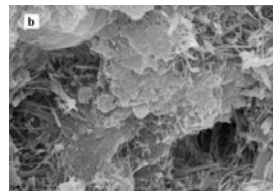
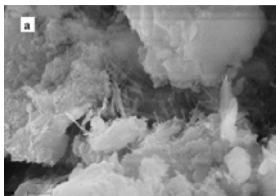


Figure 6. SEM Images of BOF30 sample at: a) 7 & b) 90 (days)

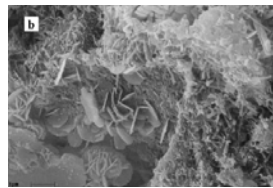
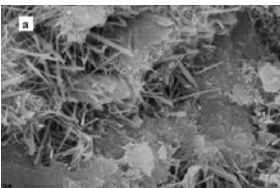


Figure 7. SEM Images of EAF30 sample at: a) 7 & b) 90 (days)

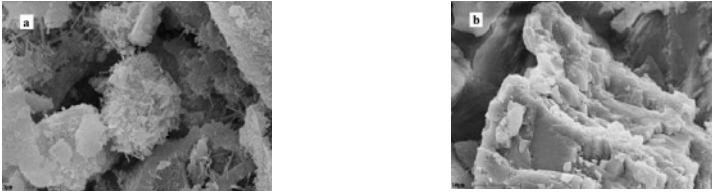


Figure 8. SEM Images of GBF30 sample at: a) 7 & b) 90 (days)

Hydration products

For study of the hydration products, pieces of pastes with ages of 3, 7, 28 and 90 days were left in acetone and ether solution in order to stop their hydration. In order to have a clear understanding of the hydrated phases which formed during hydration of cement and slag the X-Ray diffraction pattern of the pastes after 28 days was taken. It seems from the pattern that shown in fig. 9, the pastes with 30% of EAFS or BOFS has stronger peaks of $\text{Ca}(\text{OH})_2$ and tobermorite compared to GBFS. These phases are the most important phases that contribute to the mechanical properties of the paste. Besides, $\text{Ca}_6\text{Fe}_2(\text{SO}_4)_3 \cdot 32\text{H}_2\text{O}$, FeO and $\text{FeO}(\text{OH})$ and $\text{Ca}_6\text{Fe}_2(\text{SO}_4)_3 \cdot 32\text{H}_2\text{O}$ are also identified in samples.

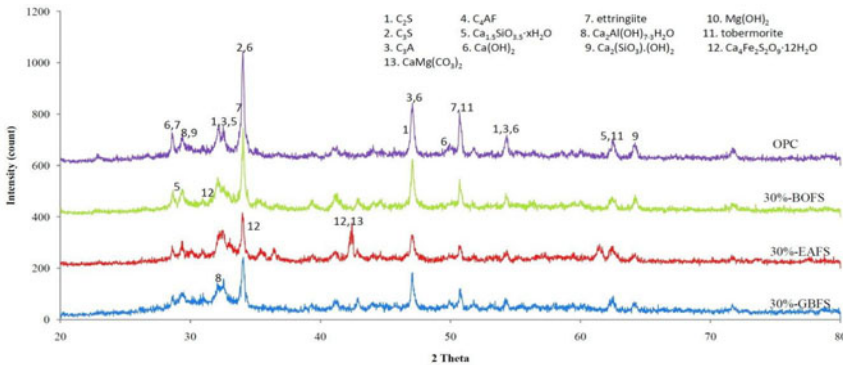


Figure 9. X-ray diffraction of reference and blended cements, hydrated at 28 days

Conclusions

In this study, the effects of additions various types of iron and steel slags on fresh and hardened properties of OPC were investigated by measuring rheological properties, pH, electrical conductivity of slurries and Setting behavior, Mechanical properties of the pastes and mortars. The following conclusions may be drawn from the obtained experimental data:

- X-ray diffraction showed that the main minerals present in BOF slag mostly like the one in OPC. The activity of BOF slag in cement-based mortars was evaluated and the results show that BOF slag has a poor hydraulic activity at younger ages, but it becomes

activated after 7 days of hydration. The compressive strength of the blended pastes was similar to OPC at 90 days. This means that it has a good hydraulic activity and can safely replace part of OPC in blended concretes.

- EAFS has similar behavior to BOFS due to its similarity to their chemical composition but additions of GBFS does not improve the properties of mortars which may be due to its lower amounts of lime in its chemical composition.
- The pH of the mixing solution is expected to have a significant effect on the nature of C-S-H by affecting the chemistry of the pore solutions. A high pH in the pore fluids may help the formation of C-S-H of a low C/S ratio and/or a different physical distribution because of the solubility of silica.
- As it is a well-known fact, the hydration process in cement paste results in the formation of C-S-H, calcium CH, ettringite and other compounds. During hydration, the capillary pores in hardening cement paste are gradually filled up with hydration products and the solid phases form a rigid microstructure with increasing strength.
- SEM observations showed microstructure of pastes become more compact with passing time from 7 to 90 days for all of samples. Moreover, in reference sample we saw there are some crystalline phases greater than cements containing slag.

References

- [1] B. Samet, and M. Chabouni, "Characterization of the Tunisian blast-furnace slag and its application in the formulation of cement," *Cement and Concrete Research*, 34 (2004), 1153-1159.
- [2] A. Monshi, and M.K. Asgarani, "Producing Portland cement from iron and steel slags and limestone," *Cement and Concrete Research*, 29 (1999), 1373-1377.
- [3] S. Song, and Jennings, H.M, "Pore solution chemistry of alkali-activated ground granulated blast-furnace slag," *Cement and Concrete Research*, 29(1999), 159-170.
- [4] M.P. Luxan, et al. "Characteristic of the slags produced in the fusion of scrap steel by electric arc furnace," *Cement and Concrete Research*, 30 (2000), 517-519.
- [5] M.F. Rojas, and M.I. Sanchez de Rojas, "Chemical assessment of the electric arc furnace slag as a construction material," *Cement and Concrete Research*, 34 (2004), 1881-1888.
- [6] L. Muhmood, et al. "Cementitious and pozzolanic behavior of electric arc furnace steel slags," *Cement and Concrete Research*, 39 (2009), 102-109.
- [7] P.Y. Mahieux, et al. "Utilization of weathered basic oxygen furnace slag in the production of hydraulic road binders," *Construction and Building Materials*, 23 (2009), 742-747.
- [8] A.S. Reddy, et al. "Utilization of basic oxygen furnace (BOF) slag in the production of a hydraulic cement binder," *International Journal of Mineral Processing*, (2006), 98-105.
- [9] E. Belhadj, et al. "Characterization and activation of Basic Oxygen Furnace slag," *Cement and Concrete Composites*, 34 (2012), 34-40.
- [10] F. Sajedi, "Mechanical activation of cement-slag mortars," *Construction and Building Materials*, 26 (2012), 41-48.
- [11] A. Altun, and I. Yilmaz, "Study on steel furnace slags with high MgO as additive in Portland cement," *Cement and Concrete Research*, 32(2002), 1247-1249.
- [12] H. Motz, and J. Geiseler, "Products of steel slags and opportunity to save natural resources," *Waste Management*, 21 (2001), 285-293.
- [13] W. Xuequan, et al. "Study on steel slag and fly ash composite Portland cement," *Cement and Concrete Research*, 29 (1999), 1103-1106.
- [14] L. Dongxue, et al. "Durability study of steel slag cement," *Cement and Concrete Research*, 27 (1997), 983-987.
- [15] C. Shi, and S. Hu, "Cementitious properties of ladle slag fines under autoclave curing condition," *Cement and Concrete Research*, 33 (2003), 1851-1856.
- [16] Iranian Standard, ISIRI 392: Cement – "Determine the time of setting of hydraulic cement by vacate needle- Test methods," Revised, (2009), 17.
- [17] ASTM C191-08, "Standard Test Methods for Time of Setting of Hydraulic Cement by Vicat Needle,"

- [18] K.R. Backe, et al. "Characterizing curing cement slurries by electrical conductivity," *SPE Drilling & Completion*, (2001), 201-207.
- [19] N. Schwarz, et al. "Electrical conductivity based characterization of plain and coarse glass powder modified cement pastes," *Cement and Concrete Composites*, 29 (2007), 656-666.
- [20] X. Wei, and Z. Li, "Early hydration process of Portland cement paste by electrical measurement," *Journal of Materials in Civil Engineering*, 18 (2006), 99-105.
- [21] I.B. Topcu, et al. "Electrical conductivity of setting cement paste with different mineral admixtures," *Construction and Building Materials*, 28 (2012), 414-420.
- [22] Iranian Standard, ISIRI 393: "Cement – Determination of flexural and compressive strengths- Test methods," 2nd Revision, (1996).

MODIFICATION OF BOF SLAG FOR CEMENT MANUFACTURING

João B. Ferreira Neto¹, Catia Fredericci¹, João O. G. Faria¹, Fabiano F. Chotoli¹, Tiago R. Ribeiro¹, Antônio Malynowskyj¹, Andre N. L. Silva¹, Valdecir A. Quarcioni¹, Andre A. Lotto¹

¹Institute for Technological Research (IPT), 532 Av. Prof. Almeida Prado, São Paulo – SP, 05508-901, Brazil

Keywords: Steel Slag, Cement Slag, Pyrometallurgy

Abstract

The use of metallurgical slags in cement manufacturing depends on the phases that compose such slags, which are affected by changes in slag chemical composition as well as by cooling rates adopted during solidification. Two different slags were produced in a pilot scale metallurgical reactor by mixing additives into 300 kg of re-melted BOF slag followed by natural cooling or by adding of steel balls to it. Quantitative XRD, SEM and Raman analysis of slag samples revealed the relationship among cooling conditions and crystalline phases.

The modified slags had CaO/SiO₂ between 1.8 and 2.0 which is lower than the 3.8 for Steelmaking slag. This reduced basicity resulted in the presence of di-calcium silicates (C₂S) in higher amounts than in the Steelmaking slag. These di-calcium silicates were part composed of β-C₂S and part of Bridgite when slag solidified slowly or α'-C₂S when slag was cooled faster by the addition of steel balls.

Cement samples were produced by mixing 25% of treated steelmaking slag with 75% of Portland cement, resulting in expansion lower than 0,1% in the autoclave tests and compressive strength higher than 42 MPa after 28 days. The process indicates potential to be applied as a steelmaking slag treatment.

Introduction

The construction industry in Brazil has grown more than 5%/y, whereas the crude steel production has been steady at approximately 32 millions of tons in the last 10 years, and there is no expectation of growth. Therefore, a shortage of blast furnace slag is happening and the cement industry needs to find alternatives. Steelmaking slag could be an alternative in cement mineral admixture, as a substitute for blast furnace slag [1-4]. However, the use of steelmaking slag directly in cement admixture is not allowed because of expansion during hydration, caused by free CaO and MgO and Mg-rich wustite (RO phase) [5,6]. A pyrometallurgical process has been investigated to promote the modification of the chemical composition of molten steel slag to make it more appropriate for cement manufacturing. The hydraulic activity of slags is affected by the chemical composition, glass content and their combination [7]. Highly basic slags (CaO+MgO/SiO₂+Al₂O₃ = 1.5) are mainly crystalline [7] and a glassy structure forms in acidic slags containing sufficient Al₂O₃. In addition, the development of glassy phase or crystalline, and crystal size, depends on cooling conditions [8].

Methodology

The purpose of the experiments conducted in the present work was to study the effect of cooling rate and chemical composition on slag crystallization. Modified slags were produced in a metallurgical reactor [9] by adding modifying agents to 300 kg of BOF molten Steel Slag (SS) supplied by a Steelmaking Company in Brazil. The modifying agent used in this work was rich in SiO₂.

Table I shows the chemical composition of BOF steel slag (SS) and of two modified steel slags (SS-M11 and SS-M12) determined by X-ray fluorescence (XRF).

The experiments were aimed at obtaining crystalline slags, especially Ca₂SiO₄ (C₂S) formation.

Table I. Chemical compositions and basicity (%CaO/%SiO₂) of Steel Slag (SS) and modified slags (wt%).

Samples	Fe ₂ O ₃	FeO	Fe ^o	CaO	SiO ₂	Al ₂ O ₃	MgO	TiO ₂	MnO	P ₂ O ₅	CaO ^(*)	CaO/SiO ₂
SS	13.6	18.3	0.2	38.1	9.9	1.7	8.6	0.3	4.4	1.3	5.7	3.9
SS-M11	2.5	21.8	0.3	36.2	19.9	2.8	11.2	0.3	4.4	1.4	0.3	1.8
SS-M12	6.9	21.3	0.2	36.4	18.5	1.6	10.3	0.3	4.4	1.4	0.2	2.0

FeO: ASTM E 246-10 - Determination of Iron by Dichromate Titrimetry. Fe^o: XU, Z et al[10], Fe³⁺ (%) = Fe, FRX (%) Fe²⁺ (%) - Fe^o(%) CaO free.

After chemical modification, slag SS-M12 was cooled by steel balls, using the technique developed and patented by the company Paul Wurth, which has authorized the Institute for Technological Research (IPT), based on a cooperation agreement, to perform tests using such cooling conditions. The principle of cooling by steel balls is described in the patent [11] and in the literature [12]. Slag SS-M11 was naturally cooled in the same reactor in which the modification occurred, to evaluate the effect of cooling conditions on the slag crystallization.

After cooling, steel balls were separated from the slag by magnetic separation. The slags were milled and homogenized to obtain samples suitable for characterization. The mineralogical characterization was performed by XRD analysis with Rietveld quantification method. Additionally, Raman spectroscopy (WiTec alpha 300R, λ=532 nm) was used to microscopically identify the phases and also validate the XRD analysis. Finally, samples were examined in SEM with EDS analysis in order to evaluate the chemical composition of phases.

The hydration heat of modified slags was determined by mixing 50 g of slag into 20 g of 20% NaOH aqueous solution. The generated heat was measured for 72 hours.

Chemically modified steel slags were ground to a particle size less than 0.075 mm and mixed with Ordinary Portland Cement (OPC) resulting in Portland Slag Cements samples (PSC) in a proportion of 25 wt%/75 wt% (modified slag/Portland cement), named PSC-M11 and PSC-M12. Cement manufactured with steelmaking (PSC-SS) was also prepared using the same ratio (25% slag/75% Portland cement), for comparison.

Compressive strength, according to Brazilian Standard NBR 11578 (analogous to European Standards EN 197-1, ISO EN 196-1 and ISO EN 196-3) and volume soundness (slag expansion), according to autoclave expansion test (standard ASTM C), were performed in PSC samples.

Results and Discussion

Table II presents the mineralogical phases of slag samples, determined by X-ray diffraction (XRD), adopting the Rietveld methodology for quantification.

Table II. Mineralogical phases (%) of Steel Slag and modified slags determined by XRD (Rietveld). NF = not found.

Phases		SS	SS-M11	SS-M12
C ₂ S	2CaO.SiO ₂	35.6	58.6	56.3
Brownmillerite	2CaO.(Al,Fe) ₂ O ₃	38.7		
RO	FeO, MgO, MnO, CaO	21.5	29.4	31.3
Lime	CaO	4.2	NF	NF
Merwinite	3CaO.MgO.2SiO ₂	NF	4.5	NF
Melilite	2CaO.MgO.2SiO ₂	NF	NF	3.1
	+ 2CaO.Al ₂ O ₃ .SiO ₂			
Diopsita	CaO.MgO.SiO ₂	NF	NF	5.1
Gehlenite	2CaO.Al ₂ O ₃ .SiO ₂	NF	4.2	NF
Others	-	NF	1.3	4.2
Amorphous	-	NF	0	0

As shown in Table II, the steel slag (SS) is mostly crystalline, because this type of slag has high basicity ($\text{CaO/SiO}_2 = 3.8$) and a high content of iron oxides, which may act as nuclei for crystallization [13]. The crystalline phases are those typically observed in steelmaking slags [14,15,4,8]: brownmillerite ($\text{Ca}_2(\text{Fe,Al})_2\text{O}_5$), larnite (Ca_2SiO_4), RO phase (solid solution among FeO, MnO, MgO and CaO) and lime. The free lime content (5.7 wt% in Table I), is too high to prevent volume soundness. The chemical composition of the RO phase determined through EDS analysis at different points of microstructure of Steel Slag, revealed a high MgO/FeO molar ratio (0.81), which is, together with free MgO and CaO, a limitation for the utilization of steelmaking slag in cement. Qian et al. [6] reported that a higher MgO/FeO ratio in the RO phase increases potential reactivity with water, affecting the expansion of the material. According to their results, when the RO phase is a Mg-rich wustite it has the potential to react with water to produce brucite ($\text{Mg}(\text{OH})_2$).

As shown in Table I, a significant fraction of Fe^{3+} content in the slags SS-M11 and SS-M12 was reduced, causing an increasing of Fe^{2+} compared to the SS slag. Most of Fe^{2+} was incorporated in the RO phase causing a decrease in the MgO/FeO ratio, preventing volume soundness. The chemical composition determined by EDS analysis in several points of RO phase, revealed lower MgO/FeO ratios than in the Steel Slag (SS). This ratio was 0.50 and 0.47 for SS-M11 and SS-M12 respectively. This is an indication of Mg-poor wustite formation, which presents less potential to react with water and consequent expansion, according to Qian et al [6]. Slag SS-M11 was naturally cooled in the metallurgical reactor where the modification process occurred, whereas SS-M12 was cooled by steel balls.

The identification and quantification of C_2S by Rietveld method requires a deeper analysis as this phase has polymorphs. Figure 1 presents the diffractograms of samples SS-M11 and SS-M12, showing the main crystalline phases. The XRD patterns of α' - C_2S and Bredigite (7CaO.MgO.4SiO_2) according to JCPDS cards numbers 33-3003 and 36-0399, respectively, are very similar and it is difficult to conclude whether the samples contain C_2S as the alpha

polymorph or Bredigite. For SS-M12 slag the peak close to $2\theta=33^\circ$ is significantly smaller than for SS-M11, which is an indication that the α' -C₂S or Bredigite is present in less quantity in the slag that was cooled faster (SS-M12). Beta polymorph (β -C₂S) was identified in both slags by the JCPDS card number 33-0302.

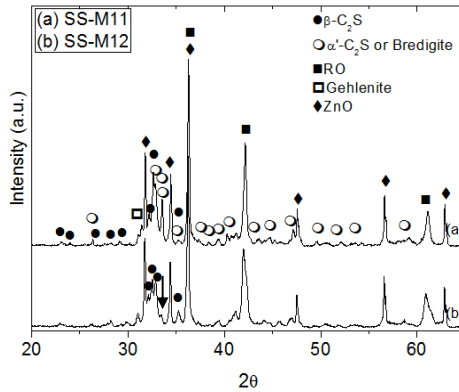


Figure 1. XRD patterns of samples (a) SS-M11 e (b) SS-M12

Figure 2 shows examples of the microstructure of SS-M11 and SS-M12, and Table III presents the chemical composition measured by EDS of some indicated points.

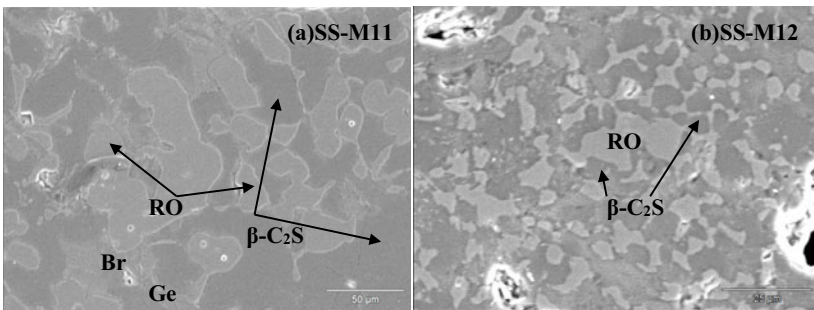


Figure 2. Microstructures of modified slag SS-M11 (naturally cooled) and SS-M12 (cooled by steel balls). Ge=Gehlenite, possible Br=Bredigite.

Table III – Chemical composition determined by EDS in the points indicated in Figure 2.

Points	MgO	Al ₂ O ₃	SiO ₂	CaO	TiO ₂	MnO	FeO
Possible Br-SS-M11	2.56	0.0	33.4	61.2	0.0	0.9	2.0
RO-SS-M11	18.4	0.0	1.5	0.9	0.0	11.8	67.5
Ge-SS-M11	0.0	23.6	19.0	44.6	4.0	1.0	7.6
β -C ₂ S-SS-M11	0.0	0.0	31.9	66.7	0.0	0.0	1.3
RO-SS-M12	20.2	0.0	0.0	0.7	0.0	11.7	67.4

β -C ₂ S-SS-M12	0.3	0.0	32.2	66.3	0.0	0.0	1.2
----------------------------------	-----	-----	------	------	-----	-----	-----

Raman spectroscopy analyses were performed in the same points indicated in Figures 2a and 2b. These analyses give further information for validation of XRD data and for differentiate C₂S polymorphs. Figure 3 shows the micrograph obtained by SEM and by optical microscopy (coupled to the Raman spectrograph) of the same region in SS-M11 slag.

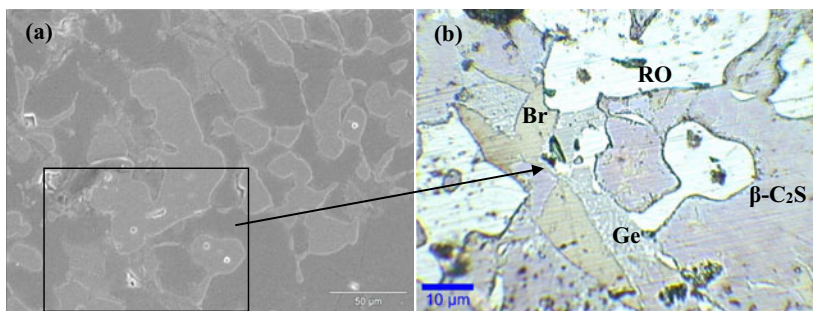


Figure 3. (a) Microstructures of modified slag SS-M11 (naturally cooled): (a) by SEM and (b) by optical microscope acoppled to Raman spectrograph.

Figure 4 shows the Raman spectra of the phases presented in Figure 3 for SS-M11 slag. Figure 4a shows the typical peaks of Gehlenite: 240, 303, 626, 665 and 914 cm^{-1} [16], while the spectra of RO phase (Figure 4b) do not present any peak, possible due to the effect of fluorescence in phases with high amount of iron. Figure 4c presents the main Raman wavebands of the β -C₂S phase showing the peak at 856 cm^{-1} of the highest intensity [17]. The last Raman spectra (Figure 4d) could not be properly identified as it was found only one peak of high intensity at 890 cm^{-1} . This peak is dislocated 34 cm^{-1} in relation to the highest intensity peak of β -C₂S (Figure 4c) showing this phase is not a β -C₂S. Bensted [18] reported the spectra of α' -C₂S and attributed the main peaks of this phase at 828, 864 and 892 cm^{-1} all with high intensity, which differ from the spectra in Figure 4d. Unfortunately, the Raman spectra of Bredigite was not find in literature. Although further studies are necessary to conclude that the pattern presented in Figure 4d could be from Bredigite, the EDS analysis indicates high amount of Mg (around 2.5 wt% of MgO) in this phase. Bredigite is a magnesium calcium silicate with stoichiometric composition of 58.3 CaO, 6.0 MgO, and 35.7 SiO₂ (wt%), but Mg²⁺ can be substituted by other divalent cations in its structure such as Fe²⁺ and Mn²⁺.

The same study of EDS and Raman spectroscopy was carried out for the sample SS-M12 and the MgO content in the calcium silicates was smaller than 0.5 wt% which is inconsistent with the possible presence of Bredigite.

The presence of a higher intensity peak in $2\theta=33.5^\circ$ in the XRD and the presence of MgO in some calcium silicate particles are evidences of the presence of Bredigite in slag SS-M11. For slag SS-M12, the XRD pattern of Bredigite is found but the MgO content in the phase is very low. This is a possible indication of the presence of α' -C₂S instead of Bredigite. Therefore, part of the calcium silicates in slag SS-M11 and SS-M12 are in the form of β -C₂S. The remaining is probably Bredigite for slag SS-M11 and α' -C₂S for slag SS-M12.

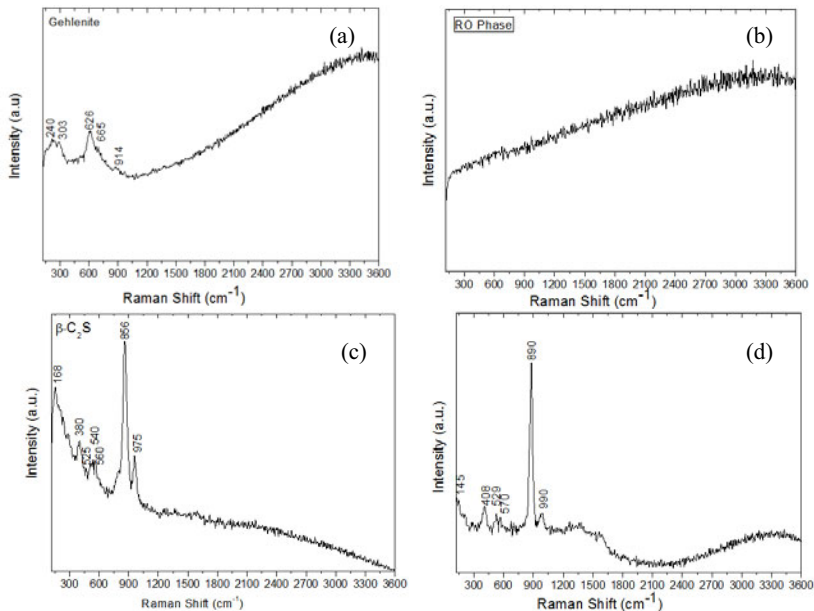


Figure 4. Raman spectra of the phases indicated in figure 3.

The problem with Bredigite is that this phase shows low hydraulic reactivity when compared to β -C₂S and α -C₂S [19]. This would make the slag less proper to the use in cement manufacturing. The hydration heat measured in NaOH aqueous solution is twice as high for SS-M12 as for SS-M11, as shown in Table IV. This difference can be caused by the difference in the mineral composition as discussed above and also by the C₂S crystal size. The increase in cooling rate, by the presence of steel balls in slag SS-M12, caused a decrease of C₂S crystals size, as shown in Figure 2.

Table IV. Heat generated in 72 h, for samples SS-M11 and SS-M12

	SS	PSC-M11	PSC-M12
Total Hydration Heat(J/g)	ND	35	70

Table V presents the results for expansion determined according to autoclave test and compressive strength in ages of 3, 7, 28 and 91 days for cement samples produced with 75% of ordinary Cement and 25% of Steel Slag (PCS-SS) and with 75% of ordinary Cement and 25% modified slags of (PCS-M11 and PSC-M12).

Cement samples produced by adding modified slags presented expansions 5 times lower than that determined for cement sample produced by adding steel slag without any modification. An increase of compressive strength in cement sample produced by adding SS-M12 slag was observed in comparison to PSC-M11. This is probably caused by a higher reactivity due to the presence of smaller C₂S crystals and the absence of Bredigite formation. PCS-M12 sample has

also higher compressive strength than PCS-SS. This slag represents an improvement in volume soundness behavior and in development of compressive strength.

Table V. Expansion in autoclave and compressive strength in 3, 7, 28 and 91 days of cements samples produced with 25% of slag and 75% of ordinary cement.

	PCS-SS	PSC-M11	PSC-M12
Autoclave expansion (%)	0.44	0.07	0.08
R 3d (MPa)	27.0	29.4	29.8
R 7d (MPa)	34.1	34.0	35.4
R 28d (MPa)	41.1	40.7	42.4
R 91d (MPa)	N/D	42.1	43.9

N/D: Not determined.

Conclusions

The main conclusions can be summarized as follows:

The partial reduction of Fe^{3+} to Fe^{2+} and a lowering in basicity from 3.9 to the range from 1.8 to 2.0 stabilized C_2S and RO, with low MgO/FeO ratio, as the main crystalline phases of modified slags.

XRD, SEM-EDS and Raman spectroscopy analyses showed that the calcium silicate was part in the form of β - C_2S for modified slags. The remaining part was possibly in the form of Bredigite for the slag cooled naturally and in the form of α' - C_2S for the slag cooled by steel balls.

The total hydration heat of the sample cooled by steel ball is twice as high as that of the sample cooled slowly, possible due the finer grain of β - C_2S and the absence of Bredigite formation during solidification.

Cement samples produced by adding 25% of modified slag specially that cooled by steel balls, resulted in an increasing of 1,3 MPa (3,16%) of compressive strengths at 28 days compared with cement sample produced by adding Steel Slag. In addition, Steel Slag caused significant expansion in cement sample, whereas cements, produced by adding modified slags, presented values five times lower of volume soundness.

Acknowledgements

The authors acknowledge the financial support from InterCement and Embrapii.

References

1. Belhadj E, Diliberto C, Lecomte A (2012) Characterization and activation of Basic Oxygen Furnace slag. *Cement and Concrete* 34, 34-40.
2. Faraone N, Tonello G, Furlani E, Maschio S (2009) Steelmaking slag as aggregate for mortars: Effects of particle dimension on compression strength. *Chemosphere* 77, 1152-1156.
3. Li JX, Yu QJ, Wei JX, Zhang TS (2011) Structural characteristics and hydration kinetics of modified steel slag. *Cement and Concrete* 41, 324-329.
4. Tossavainen M, Engstrom F, Yang Q, Menad N, Larsson ML, Bjorkman B (2007) Characteristic of steel slag under different cooling conditions. *Waste Management* 27, 1335-1344.

5. Kriskova L, Pontikes Y, Pandelaers L, Cizer O, Jones PT, van Balen K, Blanpain B (2013) Effect of High Cooling Rates on the Mineralogy and Hydraulic Properties of Stainless Steel Slags. *Metallurgical and Materials Transaction B* 44, 1173-1184.
6. Qian GR; Sun DD; Tay JH; Lai ZY (2002) Hydrothermal reaction and autoclave stability of Mg bearing RO phase in steel slag – *British Ceramic Transactions* 101, 4, 159-164.
7. Mostafa NY, El-Hemaly SAS, Al-Wakeel EI, El-Korashy SA, Brown PW (2001) Characterization and evaluation of hydraulic activity of water-cooled slag and air-cooled slag. *Cement and Concrete Research* 31, 899-904.
8. Gautier M, Poirier J, Bodenan F, Franceschini G, Véron E (2013) Basic oxygen furnace (BOF) slag cooling: Laboratory characteristics and prediction calculations. *International Journal of Mineral Processing* 123, 94–101.
9. Ferreira Neto JB, Ribeiro TR, Lotto AA, Quarcioni VA, Chotoli FF (2014) Sistema de Modificação de Escória, Patent application BR 10 2014 023505 1.
10. Xu Z, Hwang J, Greenlund R, Huang X, Luo L, Anshuetz S (2003) Quantitative Determination of Metallic Iron Content in Steel-Making Slag”. *Journal of Minerals and Materials Characterization and Engineering* 2, 65-70.
11. Solvi M, Greiveldinger B, Hoffmann M, Friederici C, Michels D (2012) Granulation of metallurgical slag. WO2012/0836 A1, pp 1–15.
12. Kappes H, Michels D (2015) Dry slag granulation and energy recovery. In: *Proceedings of the fourth international slag valorization symposium*. Leuven, pp 39–52.
13. Jung SS, Sohn II (2013) Effect of FeO Concentration on the Crystallization of High-Temperature CaO-Al₂O₃-MgO-FeO Melts. *Journal American Ceramic Society* 96, 4, 1309-1316.
14. Shi CJ (2004) Steel Slag – Its Production, Processing, Characteristics and Cementitious Properties. *Journal of Materials in Civil Engineering* 16, 230-236.
15. Ferreira Neto, J. B.; Faria, J. O. G. ; Fredericci, C.; Chotoli, F. F.; Silva, A. L. N.; Ferraro, B. B.; Ribeiro, T. R. ; Malynowskyj, A.; Quarcioni, V. A. ; Lotto, A. A. . Modification of molten steelmaking slag for cement application. *International Slag Valorisation Symposium Zero Waste*, 4, 2015, Leuven. *Proceedings*, 2015. p. 1-7.
- [16]Sharma,S.K.; Simons,B.; Yoder, H.S. Raman study of anorthite, calcium Tschermank’s Pyroxene, and gehlenite in crystalline and glassy state – *Am. Mineral.*, 68, 1983, 113-1125.
- [17]Remy, C.; Reynard, B.; Madom, M. Raman spectroscopy investigation of dicalcium silicate: polymorphs and high-tempearyures phase transformation – *J.Am.Ceram. Soc.*, 80, 2, 1997, 413-423.
- [18]Bensted, J. – Uses of Rman spectroscopy in cement chemistry - *J.Am.Ceram. Soc.*, 59, 3-4, 1976, 140-143.
- [19] Kriskova, L.; Pontikes, Y.; Pandelaers, L.; Cizer, Ö.; Jones, P.T.; van Balen, K.; Blanpain, B – Effect of high cooling rates on mineralogy and hydraulic properties of stainless steel slags – *Metallurgical and Materials Transactions B*, 44B, 2013, 1173-1184.

REACTION BETWEEN SYNTHESIZED CALCIUM ALUMINATES AND Cr_2O_3 IN AIR AND CO_2

Shengqiang Song and Andrie Garbers-Craig

Centre for Pyrometallurgy, Department of Materials Science & Metallurgical Engineering,
University of Pretoria, Pretoria, 0002, South Africa

Keywords: Cr_2O_3 -containing castables, Calcium alumina cement, $\text{Ca}_4\text{Al}_6\text{CrO}_{16}$, $\text{Ca}_6\text{Al}_4\text{Cr}_2\text{O}_{15}$, Cr(VI)

Abstract

Cr(VI) formation in low cement Cr_2O_3 -containing refractory castables was examined by reacting pre-synthesized calcium aluminate phases (C_3A , C_{12}A_7 , CA and CA_2) with Cr_2O_3 at 1300°C . In order to investigate the effect of oxygen partial pressure on Cr(VI) formation, experiments were conducted in both air and in a CO_2 atmosphere. XRD results indicated that the Cr(VI)-containing phase $\text{Ca}_4\text{Al}_6\text{CrO}_{16}$ formed in all the examined samples in air, while a Cr(III)-containing phase $\text{Ca}_6\text{Al}_4\text{Cr}_2\text{O}_{15}$ formed in samples ($\text{C}_3\text{A}+\text{Cr}_2\text{O}_3$) and ($\text{C}_{12}\text{A}_7+\text{Cr}_2\text{O}_3$) in CO_2 . Cr(VI) in the samples was extracted according to the TRGS 613 standard method, and then quantified using the diphenylcarbazide spectrophotometric method. The amount of water soluble Cr(VI) exceeded the allowable EPA U.S. limit of 5 mg/l only in samples ($\text{CA}+\text{Cr}_2\text{O}_3$) and ($\text{CA}_2+\text{Cr}_2\text{O}_3$) in air.

Introduction

Refractory materials that contain chromium (III) oxide are known to have excellent corrosion resistance and thermal shock resistance, and are therefore widely used in pyrometallurgical processes [1, 2]. The Cr(III) in chromium-containing refractories, can however be oxidized to hexavalent chromium [2-4]. Cr(VI) is known to be highly soluble in water and toxic, which poses a serious threat to the human environment [5, 6]. In the past decades, chromium-free refractories have rapidly been developed and successfully applied [7-9]. However, there are no alternatives with the same superior slag corrosion resistance. Consequently Cr_2O_3 -containing refractories are still being used in waste melting furnaces, gasification furnaces and glass tank furnaces [10-12].

It is thermodynamically favourable to oxidise Cr_2O_3 to Cr(VI) in the presence of K_2O , Na_2O , and CaO between 25°C and 792°C in air (see Figure 1) [13]. Nishino and Sakurai investigated the reactions between synthesized CaO -bearing compounds and Cr_2O_3 [14]. They found that $\text{CaO}\cdot\text{SiO}_2$ and $\text{CaO}\cdot 2\text{Al}_2\text{O}_3$, regarded as acidic compounds, do not react with Cr_2O_3 . In contrast, basic compounds such as $3\text{CaO}\cdot\text{SiO}_2$, $2\text{CaO}\cdot\text{SiO}_2$, $\text{CaO}\cdot\text{Al}_2\text{O}_3$ and $3\text{CaO}\cdot 5\text{Al}_2\text{O}_3$, react with Cr_2O_3 to produce CaCrO_4 . Lee and Nassaralla [15, 16] reported that the contribution of CaO from calcium silicate slag, calcium aluminate slag, or calcium aluminate silicate slag, can lead to the formation of Cr(VI) when these slags come in contact with magnesia-chrome refractories.

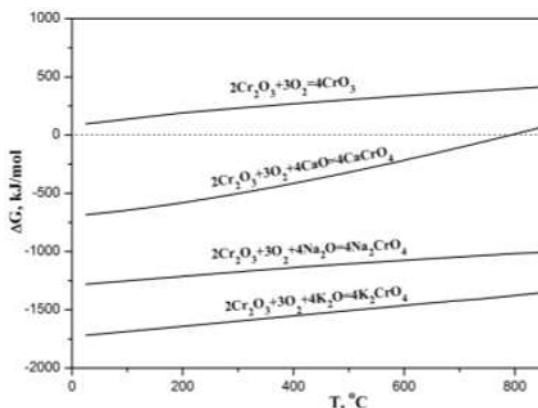


Figure 1. Stability diagram for the formation of Cr(VI)-containing phases from Cr_2O_3 and oxygen [13]

In recent years the most significant trend in refractories has been the increased use of castables [17, 18]. Calcium alumina cements are used as hydraulic binders in refractory castables as they are fast setting and provide high green mechanical strength [17]. Calcium aluminate cements mainly consist of the phases CA ($\text{CaO} \cdot \text{Al}_2\text{O}_3$), C_{12}A_7 ($12\text{CaO} \cdot 7\text{Al}_2\text{O}_3$), C_3A ($3\text{CaO} \cdot \text{Al}_2\text{O}_3$) and CA_2 ($\text{CaO} \cdot 2\text{Al}_2\text{O}_3$). It is of great interest to investigate the reaction between these phases and Cr_2O_3 in order to examine the possibility of Cr(VI) formation in low cement, Cr_2O_3 -containing castables.

Experimental

Synthesis of pure calcium aluminates

Pure C_3A , C_{12}A_7 , CA and CA_2 were produced by sintering stoichiometric amounts of CaCO_3 and Al_2O_3 . The mixtures were pressed into pellets, 20 mm in diameter. Each sample was placed on platinum foil. C_3A and C_{12}A_7 were sintered twice at 1300°C , each time for 8 h, while CA and CA_2 were sintered twice at 1450°C . The samples were ground and repressed into pellets after the first sinter procedure. XRD patterns of the synthesized C_3A , C_{12}A_7 , CA, and CA_2 were subsequently compared with the standard PDF cards (see Figure 2). This confirmed that pure C_3A , C_{12}A_7 , CA, and CA_2 were successfully synthesized in the present experiments.

Reaction between calcium aluminates and Cr_2O_3

In order to investigate the effect of oxygen partial pressure on Cr(VI) formation, experiments were conducted in both air and in pure CO_2 . The synthesized calcium aluminates (C_3A , C_{12}A_7 , CA, and CA_2 , respectively) were each mixed with 4 mass% Cr_2O_3 , pressed into pellets (10mm in diameter), and then fired twice at 1300°C for 24 hours in air and in CO_2 (see Table I).

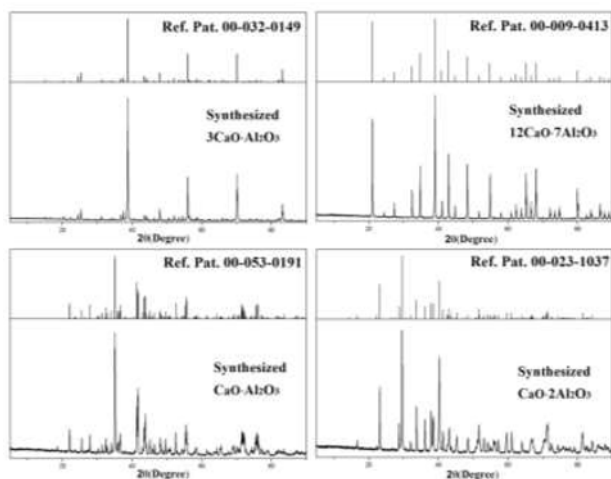


Figure 2. XRD patterns of synthesized C_3A , $C_{12}A_7$, CA and CA_2

Table I. Experimental parameters

No.	Composition, wt%	Atmosphere	Temperature
S1	96% C_3A +4% Cr_2O_3	Air	1300°C
S2	96% $C_{12}A_7$ +4% Cr_2O_3	Air	1300°C
S3	96%CA+4% Cr_2O_3	Air	1300°C
S4	96% CA_2 +4% Cr_2O_3	Air	1300°C
S5	96% C_3A +4% Cr_2O_3	CO_2	1300°C
S6	96% $C_{12}A_7$ +4% Cr_2O_3	CO_2	1300°C
S7	96%CA+4% Cr_2O_3	CO_2	1300°C
S8	96% CA_2 +4% Cr_2O_3	CO_2	1300°C

The samples were reacted in a SiC-heated vertical tube furnace, controlled with a Rex-P96 controller equipped with a type-S (Pt-10%Rh / Pt) thermocouple. Each pellet was suspended from a Pt-20%Rh spiral in the hot zone. The CO_2 (>99%) was further purified by passing it through a gas cleaning system of copper filings, kept at 300°C, to remove any residual O_2 .

Analysis of the reacted samples

The reacted samples were analysed by XRD using a PANalytical X'Pert Pro powder diffractometer with X'Celerator detector and with $Co\ K\alpha$ X-radiation.

The leachability of water soluble Cr (VI) in the reacted samples was evaluated according to the TRGS 613 standard method [19]. The milled sample (0.5000 g) was suspended in 10 ml of distilled water and vigorously stirred for 15 minutes with a magnetic stirrer (stirrer bar 20 mm, 300 rpm). At the end of stirring, the pH was determined using a CRISON Basic20 pH-Meter, and the solution filtered through a 0.45 μm membrane filter. The Cr (VI) content in the leachate was determined with the 1,5-diphenylcarbazide method. A Perkin Elmer Lambda 750S UV spectrometer, using WinUV software, was used for the absorbance measurements.

Results and discussion

XRD analysis

Samples of different colours were produced (see Figure 3). It is known that chromium (VI)-containing $\text{CaO-Al}_2\text{O}_3\text{-Cr}_2\text{O}_3$ -based phases are yellow in colour, while chromium (III) - containing $\text{CaO-Al}_2\text{O}_3\text{-Cr}_2\text{O}_3$ -based phases are dark green. Samples S2 and S3 turned yellow on firing, especially sample S3. It can therefore be deduced that in air Cr_2O_3 has reacted with C_{12}A_7 and CA to form Cr(VI) in samples S2 and S3.

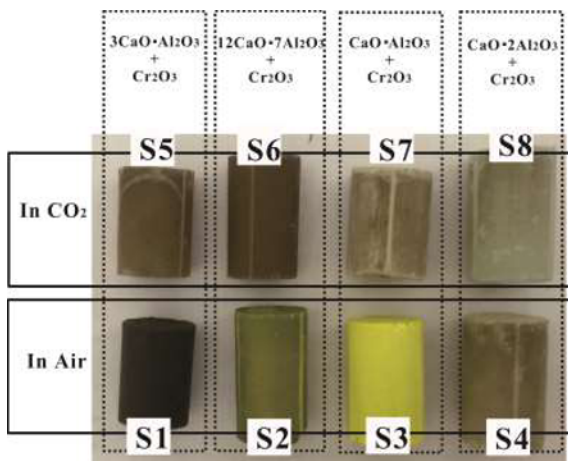


Figure 3. Samples after reacted in CO_2 and air

X-ray diffraction (XRD) analysis of the reacted samples S1-S4 in air confirmed that a Cr(VI)-containing phase, $\text{Ca}_4\text{Al}_6\text{CrO}_{16}$ (hauyne), formed in all four samples (see Figure 4). The XRD peaks of the $\text{Ca}_4\text{Al}_6\text{CrO}_{16}$ phase in samples S2 and S3 are strong, while those in samples S1 and S4 are weak.

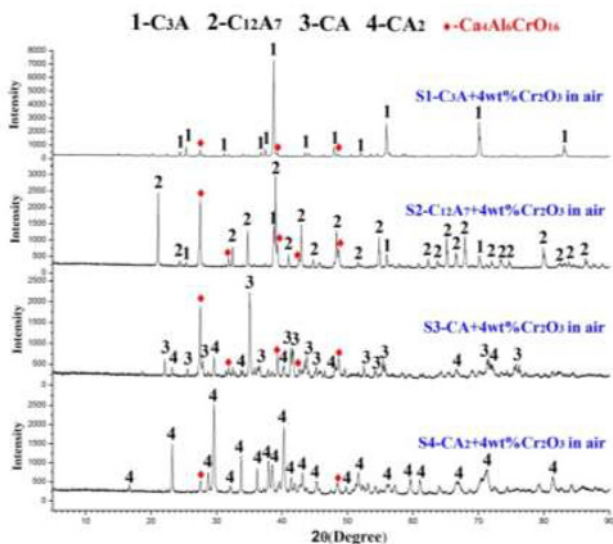
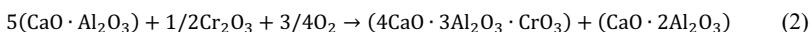
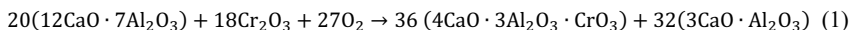


Figure 4. XRD patterns of samples S1-S4 in air

C₃A formed, in addition to Ca₄Al₆CrO₁₆ (4CaO·3Al₂O₃·CrO₃), in sample S2, while CA₂ formed together with Ca₄Al₆CrO₁₆ in sample S3. Hence, the following reactions can be proposed, Eq.(1) - Eq.(2):



Quantitative XRD analysis by the Rietveld method (Autoquan Program) confirmed high concentrations (>24 mass%) of Ca₄Al₆CrO₁₆ in samples S2 and S3, while only 7.7% and 4.2% in samples S1 and S4, respectively (see Table II). The presence of high concentrations of the Cr(VI)-containing phase Ca₄Al₆CrO₁₆ can explain the yellow colour of samples S2 and S3.

Table II. Phase contents quantified by Autoquan program (mass%)

Sample	Phase Composition				
	C ₃ A	C ₁₂ A ₇	CA	CA ₂	Ca ₄ Al ₆ CrO ₁₆
S1	92.31±0.90	-	-	-	7.69±0.90
S2	15.17±0.48	58.04±0.75	-	-	26.79±0.78
S3	-	-	55.25±0.69	20.31±0.78	24.44±0.54
S4	-	-	-	95.80±0.42	4.20±0.42

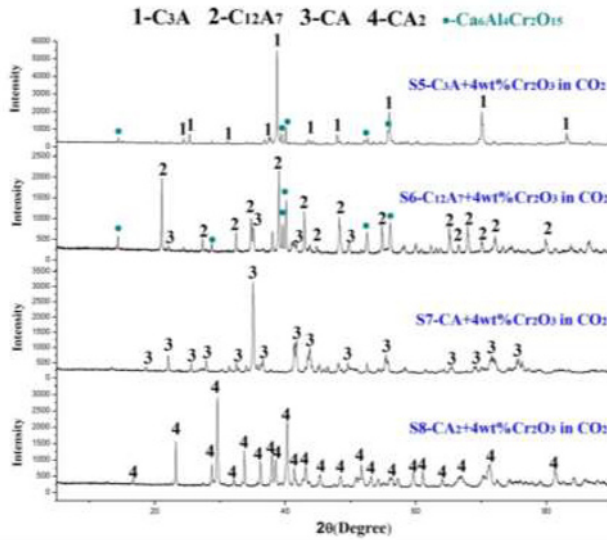
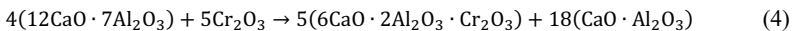
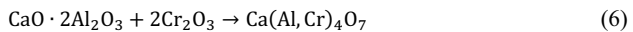
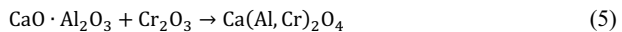


Figure 5. XRD patterns of samples S5-S8 in CO₂

The X-ray diffraction (XRD) patterns of the reacted samples S5-S8 in CO₂ are presented in Figure 5. A new phase Ca₆Al₄Cr₂O₁₅, of which the valence of chromium is +3, formed in samples S5 and S6. CA is another new phase that formed in sample S6. For samples S5 and S6, the proposed reactions can be expressed by Eq.(3) - Eq.(4):



The XRD patterns of samples S7 (CA + 4% Cr₂O₃) and S8 (CA₂ + 4% Cr₂O₃) remained unchanged. The Cr₂O₃ presumably went into solid solution with the CA or CA₂, thereby forming Ca(Al,Cr)₂O₄ and Ca(Al,Cr)₄O₇ according to equations (5) - (6). Chromium exists in the +3 oxidation state in these solid solutions.



Leach tests

The filtrate solutions obtained from samples S1-S8 were different in colour (see Figure 6). The solutions of samples S3 and S4 were very yellow, which implied that the solutions should contain significant amounts of Cr(VI). The Cr(VI) concentrations of samples S3 and S4 were 146.92 mg/l and 131.91 mg/l, respectively (see Table III). Both of them far exceeded the

allowable EPA U.S. limit of 5 mg/l (see Figure 7) [20]. Trace amounts of Cr(VI), 1.94 mg/l and 2.26 mg/l, were detected in the leach solutions of samples S7 and S8, respectively. The Cr(VI) concentrations in samples S1, S2, S5, and S6 were below the detection limit of 0.01 mg/l.

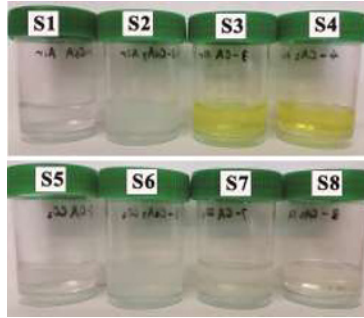


Figure 6. Filtrate solutions obtained from samples S1-S8

Table III. Leach test results

Sample	S1	S2	S3	S4	S5	S6	S7	S8
pH	11.48	11.45	11.13	10.80	11.70	11.47	11.50	9.79
Cr(VI), mg/l	<0.01	<0.01	146.92	131.91	<0.01	<0.01	1.94	2.26

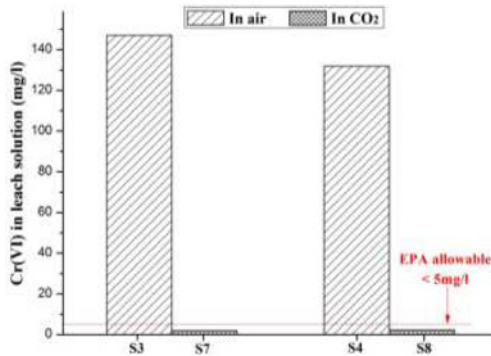


Figure 7. Cr(VI) concentrations in leach solutions from samples S3, S4, S7 and S8

The leach solutions of all samples were basic, with pH values ranging between 11.70 and 9.79 (see Table III). The pH slightly decreased from 11.48 to 10.80 in samples S1-S4, and from 11.70 to 9.79 in samples S5-S8. During the leaching process, the C_3A , $C_{12}A_7$, CA and CA_2 phases presumably dissolved in water as Ca^{2+} and $Al(OH)^{4+}$, which lead to a rise in pH [21]. The hydration speed of these phases decrease as follows: $C_3A > C_{12}A_7 > CA > CA_2$ [18, 22]. This can

explain why the pH of the leach solutions slightly decreased from sample S1 to sample S4, and from sample S5 to sample S8.

XRD results confirmed that the Cr(VI)-containing phase $\text{Ca}_4\text{Al}_6\text{CrO}_{16}$ exists in samples S1-S4. However, the presence of hydrated C_3A , C_{12}A_7 and CA phases has a strong influence on the leachability of Cr(VI) [13]. The co-existing hydrated phases encapsulate the Cr(VI) by forming Cr(VI) analogue phases $3\text{CaO}\cdot\text{Al}_2\text{O}_3\cdot\text{CaCrO}_4\cdot n\text{H}_2\text{O}$. The C_3A phase in sample S1 and phases C_3A and C_{12}A_7 in sample S2 quickly encapsulated the Cr(VI), whereby no Cr(VI) (below the limit of 0.01 mg/l) could be leached. As the hydration process of CA_2 is slow [23], the amount of Cr(VI) leached from sample S4 was high (131.91 mg/l), even though the sample only contains 4.2% $\text{Ca}_4\text{Al}_6\text{CrO}_{16}$.

Compared to the high concentrations of Cr(VI) that leached from samples S3 and S4 (146.92 mg/l and 131.91 mg/l), trace amounts of Cr(VI) leached from samples S7 and S8 (1.94 mg/l and 2.26 mg/l). This indicates that less Cr(VI) formed in CO_2 than that in air, which agrees with the XRD results.

Conclusions

- (1) In air calcium aluminates C_3A , C_{12}A_7 , CA and CA_2 react with Cr_2O_3 to form the Cr(VI)-containing compound $\text{Ca}_4\text{Al}_6\text{CrO}_{16}$, while in CO_2 , C_3A and C_{12}A_7 react with Cr_2O_3 to form $\text{Ca}_6\text{Al}_4\text{Cr}_2\text{O}_{15}$, where chromium exists in the 3+ oxidation state.
- (2) The amounts of water soluble Cr(VI) that leached from samples (CA+ Cr_2O_3) and (CA_2 + Cr_2O_3) that were reacted in air significantly exceeded the allowable EPA U.S. limit. When reacting these samples in CO_2 however, the amounts of Cr(VI) that leached were below the EPA U.S. limit.
- (3) The hydrated phases of C_3A and C_{12}A_7 encapsulate Cr(VI) and significantly reduce its leachability at high pH (11.5 – 11.7).

Acknowledgments

The authors wish to thank Kerneos for cooperation and financial support.

References

- [1] A. Yamaguchi, "Utility and problems of chrome-containing refractories," *Journal of the Technical Association of Refractories*, 26 (2) (2006), 96-99.
- [2] D.J. Bray, "Toxicity of chromium compounds formed in refractories," *American Ceramic Society Bulletin*, 64 (7) (1985), 1012-1016.
- [3] V.A. Sokolov, "Problem of hexavalent chromium in the production of fusion-cast chromium-containing refractories," *Refract. Ind. Ceram.*, 53 (2) (2012), 112-114.
- [4] M. Nyoka and A.M. Garbers-Craig, "Formation of hexavalent chromium in chromite and chromic oxide containing refractory materials" (Paper presented at the UNITECR 2011, Kyoto, Japan, 30 Oct. 2011).

- [5] A.D. Dayan and A.J. Paine, "Mechanisms of chromium toxicity, carcinogenicity and allergenicity: Review of the literature from 1985 to 2000," *Hum. Exp. Toxicol.*, 20 (9) (2001), 439-451.
- [6] H. Oliveira, "Chromium as an environmental pollutant: insights on induced plant toxicity," *Journal of Botany*, 2012 (2012), 1-8.
- [7] R. Lodha, C. Oprea, T. Troczynski, et al, "Sintering studies on magnesia-rich chromium-free spinel-bonded basic refractories," *Industrial Ceramics*, 31 (3) (2011), 223-228.
- [8] M. Muller, K. Hilpert, and L. Singheiser, "Corrosion behaviour of chromium-free ceramics for liquid slag removal in Pressurized Pulverized Coal Combustion," *J. European Ceram. Soc.*, 29 (13) (2009), 2721-2726.
- [9] S. Ghanbarnezhad, A. Nemati, and M. Bavand-Vandchali, "New development of spinel bonded chrome-free basic brick," *Journal of Chemical Engineering and Materials Science*, 4 (1) (2013), 7-12.
- [10] S. Mizuhara, T. Urabe, and A. Yamaguchi, "Fundamental study on the formation mechanism of hexavalent chromium compounds from refractories including chromium trioxide for waste melting furnace," *Journal of the Japan Society of Material Cycles and Waste Management*, 21 (5) (2010), 170-177.
- [11] P.A. Bingham, A.J. Connelly, N.C. Hyatt, et al., "Corrosion of glass contact refractories for the vitrification of radioactive wastes: a review," *International Materials Reviews*, 56 (4) (2011), 226-242.
- [12] Y. Qian and H. Ren, "The Application and Forground of Refractories with chomite," *Journal of Luoyang Technology College*, 17 (5) (2007), 6-9.
- [13] S. Song and A.M. Garbers-Craig, "Formation, leachability and encapsulation of hexavalent chromium in the Al_2O_3 -CaO- Fe_2O_3 - Cr_2O_3 system," *J. European Ceram. Soc.*, (2016), doi:10.1016/j.jeurceramsoc.2015.1012.1036.
- [14] T. NISHINO and T. SAKURAL, "On the reaction between CaO-bearing compound and Cr_2O_3 ," *J. Ceram. Assoc. Japan.*, 75 (9) (1967), 259-264.
- [15] Y. Lee and C.L. Nassaralla, "Minimization of hexavalent chromium in magnesite-chrome refractory," *Metall. Mater. Trans. B*, 28 (5) (1997), 855-859.
- [16] Y. Lee and C.L. Nassaralla, "Formation of hexavalent chromium by reaction between slag and magnesite-chrome refractory," *Metall. Mater. Trans. B*, 29 (2) (1998), 405-410.
- [17] A.P.d. Luz, M.A.L. Braulio, and V.C. Pandolfelli, *Refractory Castable Engineering*, (Germany, Goller Verlag GmbH: Baden-Baden, 2015).
- [18] W.E. Lee, W. Vieira, and S. Zhang, "Castable refractory concretes," *International Materials Reviews*, 46 (3) (2001), 145-167.
- [19] TRGS 613, "The Technical Rules for Hazardous Substance" (2002).
- [20] Cr(VI) Policy and Guidance:
https://clu-in.org/contaminantfocus/default.focus/sec/chromium_VI/cat/Policy_and_Guidance/.
- [21] H.F.W. Taylor, *Cement Chemistry. 2nd ed.*, (London, Thomas Telford, 1997).
- [22] N. Ukrainczyk, "Kinetic modeling of calcium aluminate cement hydration," *Chemical Engineering Science*, 65 (20) (2010), 5605-5614.
- [23] S.R. Klaus, J. Neubauer, and F. Goetz-Neunhoeffer, "Hydration kinetics of CA_2 and CA -Investigations performed on a synthetic calcium aluminate cement," *Cem. Concr. Res.*, 43 (2013), 62-69.

IMMOBILIZATION OF HEXAVALENT CHROMIUM IN STAINLESS STEELMAKING SLAG

Ryo Inoue¹, Yoshiya Sato², Yasushi Takasaki¹, Atsushi Shibayama¹

¹Faculty of International Resource Sciences, Akita University;
1-1, Tegatagakuen-machi; Akita, Akita 010-8502, Japan

²Materials Eco-Refining Co., Ltd.; Iwaki, Fukushima 971-8101, Japan
Formerly, Graduate School of Engineering and Resource Science, Akita University

Keywords: Elution, Immobilization, Hexavalent chromium, Stainless steelmaking slag

Abstract

Chromium is an essential element which contributes to our life activity. However, since the hexavalent chromium causes health damage, its content in water is strictly limited below 0.05 mg/L as the aqueous and soil environment standard values in Japan. The development of high-efficient stabilization method of the steelmaking slags containing chromium is urgent in order to utilize the slags to civil engineering works. In present work, the elution behavior of chromium from stainless steelmaking slags was clarified. Then, a principle of prevention of hexavalent chromium formation and chromium immobilization by the hydrate formation was discussed.

Introduction

Chromium is known as a life activity indispensable element which contributes to glucose metabolism and control of serum cholesterol [1]. However, it was reported that the hexavalent chromium (Cr(VI)) causes health damages such as contact dermatitis, nasal septum hole, lung cancer and paranasal sinus cancer [2]. Therefore, its content in water is strictly limited below 0.05 mg/L after the elution test of Notification No.46 of Environment Agency as the aqueous and soil environment standard values in Japan.

Since the solubility of Cr(VI) oxide in aqueous solution is extremely high, though the ionic species of Cr(VI) changes depending on chromium concentration in solution and pH [3], the Cr(VI) oxide in slag is considered to be easily dissolved in solution. In the research concerning chromium elution characteristic from steelmaking slag, the Cr (VI) amount eluted from the slag heated in air was remarkably high compared with that heated in reducing atmosphere, and was varied with heating temperature [4]. Therefore, it is worried that trivalent chromium (Cr(III)) in the slag changes to Cr(VI) during refining and cooling periods in steelmaking process. The Cr(III) and Cr(VI) oxides in oxidizing slags exhausted by stainless steelmaking process could be removed by carbon in rotary kilns and/or electric furnace. At the steel works which don't have those reducing equipments, the slags are conveyed in the special disposal place. The development of high-efficient stabilization method of the slags containing chromium is urgent in order to utilize the slags to civil engineering works.

In present work, the mineral phases in chromium-containing slags were identified, and the formation mechanism of hexavalent chromium was discussed. From the viewpoint of stable

hydrate formation, the hexavalent chromium immobilization was investigated for the purpose of the technological development of environment protection.

Experimental

Identification of Mineral Phases in Stainless Steelmaking Slag

The cross sectioned plane of each stainless steelmaking slag, which was sampled in steel plant, and synthesized slag was mirror-polished using dry abrasive papers. The mineral phases on the plane were identified using SEM-EDS and XRD. The chemical compositions of those slags were determined by ICP-AES after alkali-fusion.

Sample Preparation for Elution Test

The synthesized slag was prepared by melting the mixture of CaCO_3 , SiO_2 , FeO , Al_2O_3 , Cr_2O_3 and MgO reagents and pure iron at 1873K in MgO crucible under Ar flowing. The iron melt contributed to control the oxygen potential of system to that of Fe/FeO equilibrium. After holding for 30min at 1873K, the slag was cooled to 1073K at a rate of 150K/h under air, and quenched into water. The slag was crushed and classified to less than 0.1mm by sieves.

In order to synthesize MgCr_2O_4 and CaCr_2O_4 compounds, the mixture of MgO and Cr_2O_3 reagents ($\text{MgO/Cr}_2\text{O}_3$ molar ratio = 1) and that of CaCO_3 and Cr_2O_3 reagents ($\text{CaO/Cr}_2\text{O}_3$ molar ratio = 1), respectively, were heated at 1873K for 12h under air, and quenched by He gas blowing.

Formation of Cr(VI) Oxide in MgCr_2O_4 during Heating and Cooling

The mixture of MgO and Cr_2O_3 reagents ($\text{MgO/Cr}_2\text{O}_3$ molar ratio = 1.1, 10 mg) was heated to 1673K, and cooled at a rate of 2K/min under air in a thermal gravimetric analyzer. From the variation of sample weight with temperature, the oxidation behavior of Cr(III) to Cr(VI) was observed.

Procedure of Elution Test

Fifty grams of slag sample was charged in a polyethylene bottle along with 500mL of distiller water, and shaken 200 times/min according to the revised method [5] of Notification No.46 of Environment Agency [6]. For the immobilization of Cr(VI) ion dissolved from slag, an appropriate amount of secondary refining slag (grain size < 0.1mm) and gypsum reagent was also charged in the bottle. For a complete immobilization of Cr(VI) and Cr(III) in slag, the slag was mixed with secondary refining slag and gypsum reagent, and pressed to a cylindrical shape. This pressed sample was hydrothermally treated at 393K for 3h using an autoclave, and crushed to less than 0.1mm.

Five grams of MgCr_2O_4 or CaCr_2O_4 compound was shaken 200 times/min in 500mL of distiller water. In order to investigate the effect of pH value on MgCr_2O_4 dissolution, the pH value of water was maintained to 12.0 by the addition of only a few drops of 1w/v% NaOH solution every 6h. The solution was sampled by whole pipette after respective time. After suction filtration with a membrane filter, quantitative analysis of Cr(VI) and total Cr (= Cr(III) + Cr(VI)) in filtrate was

carried out using Flow Injection method (JIS-K-0170-7). Other elements dissolved from solid sample into solution were analyzed using ICP-AES or ICP-MS.

Results and Discussion

Mineral Phases in Stainless Steelmaking Slag

The chemical composition of stainless steelmaking slag are listed in Table 1. The mineral phases of CaO-SiO₂-Al₂O₃ system and those containing Cr oxide are also shown in Table 1, where the order of area fraction of mineral phases is LL>L>M>S>s. Since MgO-Cr₂O₃ compounds are identified and any compounds of CaO-Cr₂O₃ system are not observed, it is noted that Cr₂O₃ combined with MgO in these slag composition range.

Table 1. Chemical composition and major mineral phases of stainless steelmaking slags (No.1-4) and synthesized slag (S), and secondary refining slag (SR)

Sample No.		1	2	3	4	S	SR
Chemical composition	(mass%CaO)/(mass%SiO ₂)	2.03	2.18	2.99	5.18	3.01	2.75
	(mass% Al ₂ O ₃)	1.9	7.6	6.8	13.9	18.2	6.8
	(mass% T.Fe)	0.5	28.0	7.1	15.0	4.9	1.4
	(mass% T.Cr)	0.4	9.7	2.6	0.8	3.4	0
Mineral phase	3CaO·SiO ₂						M
	2CaO·SiO ₂	LL	S	L	L	L	M
	12CaO·7Al ₂ O ₃						S
	2CaO·SiO ₂ ·Al ₂ O ₃		L	M	M	M	L
	2CaO·8MgO·2SiO ₂		L				
	MgCr ₂ O ₄	s					
	Mg(Fe,Cr) ₂ O ₄		M	S	s	S	
Ca ₄ Al ₆ CrO ₁₆	s						

Area fraction : LL > L > M > S > s.

Dissolution of Cr(VI) and Cr(III) from Cr-containing Mineral Phase

In the elution test with synthesized MgCr₂O₄ or CaCr₂O₄ compound, the variation of Cr(VI) and Cr(III) contents in solution with shaking time are shown in Figure 1. In this figure, the pH value of the solution with MgCr₂O₄ and CaCr₂O₄ becomes voluntarily to be 7 and 11, respectively. Since the Cr(VI) and Cr(III) contents dissolved from CaCr₂O₄ are higher than those from MgCr₂O₄, it is expected that the solubility of CaCr₂O₄ is higher in solution and Cr(VI) generates more easily during heating under air, compared with MgCr₂O₄. It was reported that MgCrO₄ is unstable and easily decomposed to MgCr₂O₄, while CaCrO₄ is stable below 1373K [7]. It was also noted that CaCrO₄ can be easily produced by heating of CaO and Cr₂O₃ mixture, while MgCrO₄ formation requires the oxygen pressure more than 12atm at 693K [8]. The reason for an existence of CrO₃ in

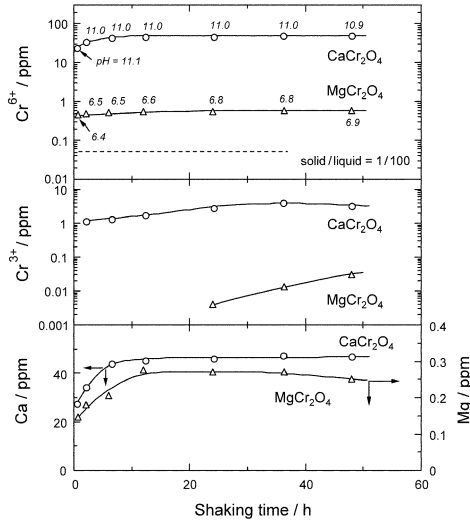


Figure 1. Variation of Cr(VI), Cr(III) and Ca (Mg) contents in solution with shaking time after the elution test of synthesized CaCr_2O_4 or MgCr_2O_4 compound.

MgCr_2O_4 , as shown in Figure 1, might be explained by the formation of $\text{MgO-Cr}_2\text{O}_3\text{-CrO}_3$ solid solution, in which the activity of CrO_3 is very low.

The results for MgCr_2O_4 dissolution at $\text{pH}=12.0$, which is normally obtained in elution test using high basicity slag, are shown in Figure 2. From the comparison with the data at $\text{pH}=6.4\text{-}6.9$, which is same as those shown in Figure 1, it is said that Cr(VI) content in solution is not affected by pH value of solution, while Cr(III) and Mg content decrease with increasing pH value. The generation of Cr(VI) oxide in MgCr_2O_4 during heating under air is considered to be indispensable.

Formation of Cr(VI) Oxide in MgCr_2O_4

The weight change of the mixture of MgO and Cr_2O_3 ($\text{MgO}/\text{Cr}_2\text{O}_3$ molar ratio = 1.1, 10mg) during heating and cooling is shown in Figure 3. during heating due to the evaporation of adsorbed H_2O in reagents and decomposition of $\text{Mg}(\text{OH})_2$ on MgO surface. Nishio [7] reported that a small amount of Cr_2O_3 evaporated above 1073K. Therefore, it is predicted that the decrement of above 1073K is caused by Cr_2O_3 evaporation. In the sample quenched at 1673K, only MgCr_2O_4 phase was identified by XRD. The mineral phases containing Cr(VI) such as MgCrO_4 and CrO_3 were not detected, probably because the amounts of those Cr(VI) phases were very small. On the other hand, an increase in sample weight is found below 1400K in Figure 3. This increment is presumably because Cr_2O_3 in MgCr_2O_4 are oxidized to CrO_3 . It is presumed that CrO_3 begins to form in MgCr_2O_4 around 1400K during cooling according to Equation (1).

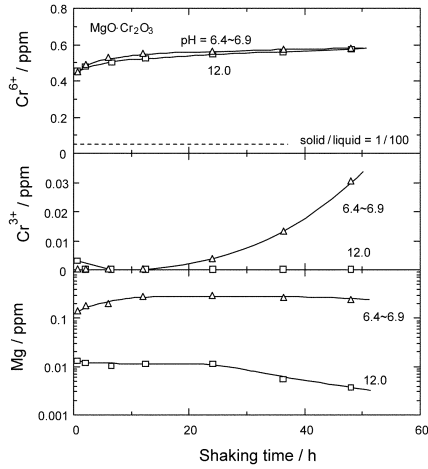


Figure 2. Variation of Cr(VI), Cr(III) and Mg contents with shaking time after the elution test of MgCr_2O_4 compound as a function of pH value.

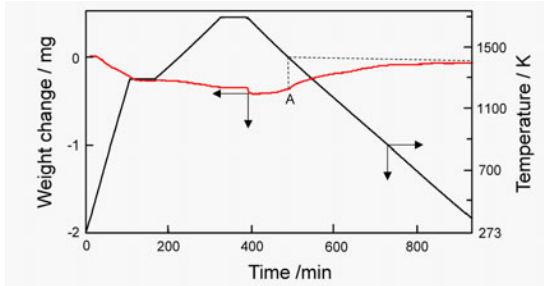
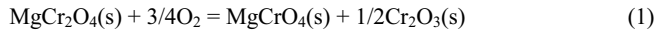
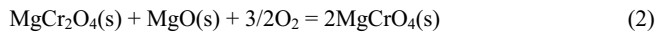


Figure 3. Weight change of the mixture of MgO and Cr_2O_3 during heating and cooling under air.



When an excess MgO , which is called “free MgO “, is present in slag, the formation of CrO_3 might be accelerated following Equation (2).



To minimize Cr(VI) formation, slag should be cooled rapidly from 1400K, or cooled in inert atmosphere.

Dissolution of Cr(VI) and Cr(III) from Slag

In the elution test using the synthesized slag S listed in Table 1, the variation of total Cr and Cr(VI) content in solution with shaking time was obtained. The results are shown in Figure 4 (● marks). Both contents of total Cr and Cr(VI) in solution are higher than 0.05ppm, which is the aqueous and soil environment standard values in Japan. The reason for the decrease in both contents after 6h shaking might be the formation of CaO-SiO₂-H₂O (C-S-H) gel in solution. The details will be explained in next section.

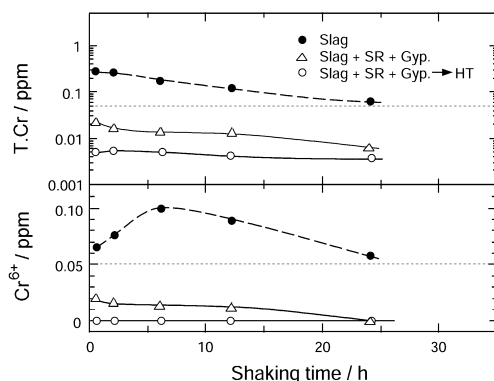


Figure 4. Variation of total Cr and Cr(VI) contents in solution dissolved from synthesized slag (●), the mixture of slag, secondary refining slag and gypsum (Δ), and hydrothermally treated mixture of slag, secondary refining slag and gypsum (○).

Immobilization of Cr(VI) and Cr(III)

It was reported in the research field of hydration of cementitious materials that harmful elements could be absorbed in C-S-H gel, (tricalcium)-Aluminate Ferrite-tri(sulfate, hydroxide, etc.)-(hydrate)-phase (AFt phase), and (tricalcium)-Aluminate Ferrite-mono(sulfate, hydroxide, etc.)-(hydrate)-phase (AFm phase) [9]. Fluorine ion dissolved from steelmaking slags was immobilized by the addition of calcium aluminate and calcium silicate [10]. The addition of Gypsum along with CaO-SiO₂ compound or secondary refining slag, whose major mineral phases were 2CaO·SiO₂, 3CaO·SiO₂ and 2CaO·SiO₂·Al₂O₃, significantly immobilized fluorine ion by the formation of C-S-H-SO₄²⁻ gel [8]. After a hydrothermal treatment of the mixture of steelmaking slag, gypsum and secondary refining slag, fluorine in slag became insoluble [11].

Following these investigations, gypsum reagent and secondary refining slag SR listed in Table 1 were mixed with synthesized slag S in mass ratio = 0.6:1.4:3.0. The results obtained by the elution test using this mixture are shown in Figure 4 (Δ marks). It is favorable that the contents of both total Cr and Cr(VI) were lower than 0.05ppm. The reason for this phenomena is expected as a formation of C-S-H-SO₄²⁻ gel.

The effect of hydrothermal treatment on the dissolution of Cr(VI) and Cr(III) from the mixture of slag, gypsum reagent and secondary refining slag are also plotted in Figure 4 by \circ marks. It is found that Cr(VI) in slag is completely immobilized, and Cr(III) in slag becomes stable. From this tendency, it is suggested that the stable hydrate containing Cr(VI) and Cr(III) can be constructed during hydrothermal treatment using gypsum and calcium silicate.

Conclusions

For the utilization of stainless steelmaking slags to civil engineering works, the formation and immobilization mechanisms of hexavalent chromium was discussed. The conclusions are summarized as follows.

- 1) The major mineral phases containing chromium were MgCr_2O_4 and $\text{Mg}(\text{Cr},\text{Fe})_2\text{O}_4$ in stainless steelmaking slags used in this work.
- 2) The generation of Cr(VI) oxide in MgCr_2O_4 and CaCr_2O_4 compounds during heating under air is considered to be indispensable.
- 3) The amounts of Cr(III) and Cr(VI) dissolved from MgCr_2O_4 were smaller than those from CaCr_2O_4 .
- 4) Since the formation of CrO_3 in MgCr_2O_4 started at around 1400K during cooling, slag should be cooled rapidly from 1400K, or cooled in inert atmosphere in order to minimize Cr(VI) formation.
- 5) The addition of gypsum and secondary refining slag reduced the contents of Cr(III) and Cr(VI) in solution due to the formation of C-S-H SO_4^{2-} gel.
- 6) The dissolution of Cr(VI) and Cr(III) from slag were prevented by hydrothermal treatment using gypsum and calcium silicate.

References

1. Kei-ichiro Fuwa, *Life and Heavy Metals* (Tokyo: Kodansha Ltd., 1981), 52.
2. Ministry of Land, Infrastructure, Transport and Tourism, ed., *Water information System* (Tokyo), <http://www1.river.go.jp/100304.html>.
3. Marcel Pourbaix et al., ed., *Atlas D'Equilibres Electrochimiques* (Paris: Gauthier-Villars & C, Editeur-Imprimeur-Libraire, 1963), 458.
4. Hirotaka Hatada, "Chemical state and Dissolution Characteristics of Cr in Steel-making Slag", *Bulletin of the Advanced Materials Processing Building, IMRAM, Tohoku University*, 63(1 and 2) (2007), 27-33.
5. Hideaki Suito and Ryo Inoue, "Behavior of Fluorine dissolution from Hot Metal Pretreatment Slag", *Tetsu-to-Hagané*, 88(6) (2002), 340-346.
6. Ministry of the Environment, ed., *Environmental Quality Standards for Groundwater Pollution* (Tokyo), <http://www.env.go.jp/en/water/gw/gwp.html>.
7. Tadashi Nishino, "Anion Exchange Reactions, CO_3^{2-} - CrO_4^{2-} and CO_3^{2-} - SO_4^{2-} ", *Gypsum & lime*, 149 (1977), 188-192.
8. Joseph William Mellor, *A Comprehensive Treatise on Inorganic and Theoretical Chemistry*, vol.XI (London: Longmans, Green and Co. Ltd.), 274.

9. Hongye He and Hideaki Suito, "Immobilization of Hexavalent Chromium in Aqueous Solution through the Formation of $3\text{CaO}\cdot(\text{Al,Fe})_2\text{O}_3\cdot\text{Ca}(\text{OH})_2\cdot x\text{H}_2\text{O}$ Phase, Ettringite and C-S-H gel", *ISIJ International*, 42(2) (2002), 139-145.
10. Ryo Inoue and Hideaki Suito, "Immobilization of Fluorine Dissolved from Hot Metal Pretreatment Slag", *Tetsu-to-Hagané*, 88(6) (2002), 347-353.
11. Ryo Inoue and Hideaki Suito, "Influence of Gypsum Addition and Hydrothermal Treatment on Dissolution Behavior of Fluorine in Hot Metal Pretreatment Slags", *ISIJ International*, 42(8) (2002), 930-937.

SMELTING REDUCTION OF BOTTOM ASH IN PRESENCE OF LIQUID STEEL BATH FOR RECOVERY OF ALUMINIUM

A.K. Mandal* and O.P. Sinha

Department of Metallurgical Engineering

IIT(BHU), Varanasi, India

* Corresponding author: arup9180@yahoo.co.in

Abstract

For the recovery of aluminium from industrial waste bottom ash, a new concept was developed for smelting reduction in presence of metal solvent bath. Nitrogen plasma arc was generated by passing current and nitrogen gas through a hollow graphite electrode. Nitrogen plasma generated heat for reduction as well as melting under inert atmosphere inside the furnace. Pellets containing 50%bottom ash, 50% iron slime and charcoal were fed in the plasma zone above the liquid steel bath which was acted as for the absorption of reduced metals after reduction of oxides present in the wastes. Due to the immediate absorption of aluminium in the liquid steel bath after subsequent reduction from waste, vaporization loss of aluminium metal got minimized. The percent recovery of aluminium were determined in case of different exposure time, types of arcing and plasma gas etc. Maximum recovery of aluminium was recovered upto 21% with 30 minute exposure of pellets containing 50% bottom ash and 50% iron slime. It was observed that aluminum, could be recovered effectively from the wastes.

KEYWORDS: Industrial wastes, Smelting reduction, Aluminium recovery, Recovery of metals

Introduction

Recycling of industrial wastes is gaining popularity due to their adverse impact on environment day by day. Value added materials recovery from the wastes could be a right choice of recycling [1]. Countries having shortage of bauxite ore for production of aluminum, trying to recover aluminium from coal combustion residues as a replacement of bauxite ore [2]. The commercial technology for aluminum production includes production of alumina from bauxite and smelting reduction of alumina to aluminum. Carbothermic reduction of alumina is only the alternative economical method for aluminum or alumino-alloy production. It could be replace 'Hall-Heroult' process, due to advantages like simplicity of the process, lower cost and raw materials requirement. This process also reduce energy consumption, capital costs and CO₂ emissions. It has no fluoride emission and decrease overall operating costs by 25–30% [3-5].

In 2010, Wang *et al.* (2010) produced a high aluminum alloy at 2573–2773K (2300-2500°C) by an electric arc furnace reducing bauxite flotation tailings. They observed aluminium silicon alloy formation at high temperature ~ 2073K (1800°C) temperature [6].

Like bauxite floating tailings, bottom ash, produced from coal burning thermal power plants has also major constituencies are silica, alumina. The major crystalline phases presents in bottom ash are mullite and with varying contents of unburnt carbon. With the diminishing of bauxite resources as well as the increase in alumina demand, the profitable industrial utilization of coal bottom ash in alumina recovery has attracted

extensive attentions. Mullite phase having strong aluminosilicate bonding requires more energy to break [7].

Pickles *et al*, 1990 was melted fly ash by argon plasma in an extended arc flash reactor (EAFR) and recovered Silicon and iron was successfully [8]. Due to high temperature he could not recover aluminium which became vaporized.

In the present work, an effort was made to recover aluminum from the smelting reduction of bottom ash under nitrogen plasma arc condition. Carbothermic reduction was done in a neutral atmosphere of nitrogen in presence of solvent metal bath.

Experimental

Materials

The bottom ash was collected from the thermal power plant of DPL, Durgapur, India having pulverized coal combustion facility boiler. The mild steel scrap and wood char was used for liquid steel bath and as a reducing agent. The analysis of raw material used is mentioned in Table 1. Pulverized charcoal of (-0.5mm) was used with bottom ash in stoichiometric ratio of required carbon content for reduction of oxides. Mixture of 50% slime and 50% bottom ash and charcoal powder was sent to a disk type pelletizer (diameter 760 mm, rim height 120 mm, disk angle 45°, r.p.m. 20) for making pellets. Addition of 5% bentonite was done for increasing pelletizing efficiency and providing green strength of the pellets. Green pellets were dried at 383K (110°C) for 4 hours for moisture removal as well as getting adequate strength for further processing.

Table I: Raw materials analysis (weight %)

Bottom ash		Wood char		Iron slime		Mild steel scrap	
SiO ₂	70.04	V.M	33.72	SiO ₂	31.36	C	0.04
Al ₂ O ₃	22.05	Ash	5.80	Al ₂ O ₃	24.11	Si	0.10
Fe ₂ O ₃	2.49	F.C	60.48	Fe ₂ O ₃	42.09	Mn	0.80
MgO	1.18			CaO	0.0147	S	0.03
CaO	0.76			P ₂ O ₅	1.48	P	0.04

Equipment

The plasma arc furnace was fabricated indigenously having 0.08 m diameter and 0.10 m deep chamber of magnesite lining with embedded graphite block at the bottom as described in our previous work [9]. Graphite block was drilled to make crucible inside the chamber for melting. A single phase AC current giving 30kVA power, was supplied to the unit for arc generation. The generation of plasma was done by passing nitrogen through the hollow graphite electrode to near arc zone. After various trial, the nitrogen gas flow rate was fixed to 6.67×10^{-5} m³/s during charging of pellets to get smoother arc. During the preparation of melting steel bath, solid electrode was used to save the ionizing gas.

Melting procedure

With the help of solid electrode, 1 kg steel scrap was melted first. Solid rod was replaced by hollow one after preparing complete liquid steel bath for starting of plasma. Addition of pellets at the plasma zone gradually through hopper fitted above the furnace was done to reduce the pellets. After complete dissolution of pellets, sample was taken out in different time intervals for composition analysis.

Results and Discussion

Effect of Exposure time

Metal composition of different exposure time as well as slag produced after 80 minutes exposure time is given in Table 2. Only 10 grams of slag was produced after final exposure time (i.e. 80 minutes). Effect of exposure time on recovery of aluminium in plasma arc environment is shown in Figure 1.

Table 2: Composition metal sample after smelting reduction (wt.%)

Exposure time (minute)	Metal Composition						Slag composition
Exposure time	10	20	30	40	50	80	
Si	2.00	1.98	1.83	1.74	1.71	1.72	11.68
Al	0.081	0.121	0.193	0.145	0.125	0.064	33.74
Fe	95.30	95.50	95.70	95.80	95.90	96.10	1.530
P	0.118	0.140	0.106	0.103	0.102	0.108	3.860
Ti	0.079	0.072	0.06	0.060	0.060	0.052	0.436
S	0.050	0.045	0.030	0.030	0.030	0.029	0.198
Mn	0.487	0.489	0.501	0.521	0.541	0.487	0.158
C	1.61	1.58	1.54	1.46	1.43	1.36	0

From the figure it is evident that, increasing the exposure time initially recovery increases than gradually decreases. This is due to increasing exposure time, the reduction of alumina to aluminium increases and goes to the liquid steel bath. Over exposure time aluminium got vaporized, therefore reduced recovery level.

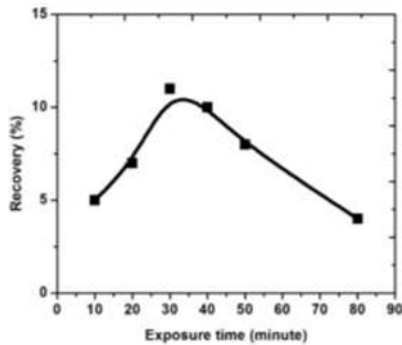


Figure 1: Effect of exposure time on recovery of aluminium

Effect of Plasma type

To know the effect of plasma, on recovery of aluminium one heat was done by sending no plasma gas (i.e. nitrogen through the electrode. For the same exposure time (30 minute) the recovery of aluminium in case of plasma arc shows more than non-plasma arc melt. In plasma arc, the heat generation is more than normal arc, resulting more recovery of aluminium metals which reduced from alumina at very high temperature (Figure 2).

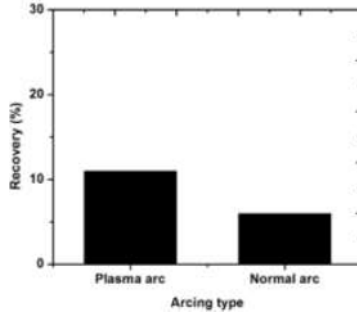


Figure 2: Effect of plasma gas on recovery of aluminium

Effect of arc condition

To show the effect of arc condition one heat was done by charging total pellets in one time so that the arc got submerged by the pellets completely and same exposure time was given (i.e. 30 minutes). In case of submerged arc, more heat generates and metals are not exposed in the atmosphere directly which protects the aluminium from oxidation, resulting more recovery (Figure 3).

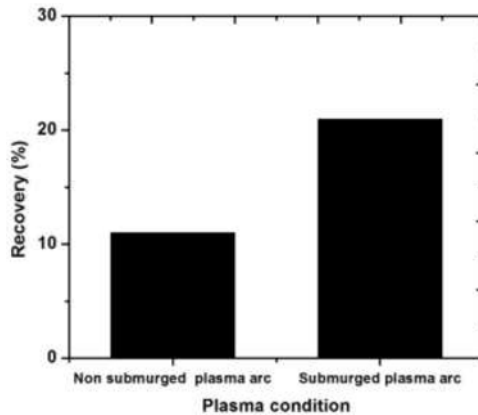


Figure 3: Effect of arc condition on recovery of aluminium

Conclusions

From the present feasibility study it is proved that, smelting reduction of Bottom Ash is effective alternative for multi-metallic component recovery. The plasma smelting in presence of liquid steel bath can recover metals having lower melting points such as aluminium, although reduction of alumina occurred at such tremendous high temperature. Plasma arc creates the furnace environment inert, which decreases the oxidation loss of metals. When arc became totally submerged by pellets, recovery yield increases. Recovery of Al increases with increasing time then decreases.

References

1. A. Rai, A. K. Mandal, K.K. Singh and T. R. Mankhand, "Preparation and Characterization of Lime Activated Unfired Bricks Made With Industrial Wastes," *International Journal of Waste Resources*, 3(2013), 40-46
2. G. Bai, W. Teng, X. Wang, J-g. Qin, P. Xu and P.Li, "Alkali desilicated coal fly ash as substitute of bauxite in lime-soda sintering process for aluminum production," *Trans Nonferr Met Soc China*,20(2010),169-175
3. M.J. Bruno, "Aluminium carbothermic technology comparison to Hall–Herault technology.In: Crepeau, P.N. (Ed.), *Light Metals 2003*. TMS (The Minerals, Metals & Materials Society), 395–400
4. Y. Sayad-Yaghoubi, "Carbothermic production of aluminium," Patent WO2007012123,(2007), p.19.
5. H. Myklebust and P. Runde, "Greenhouse gas emissions from aluminum carbothermic technology compared to Hall–Heroult technology"*Light Metals.*, pp. 519-522. TMS (2005)
6. Y.Wang, N. Feng, J. You and J. Peng, "Method for producing coarse aluminum–silicon alloy from bauxite flotation tailings by carbothermal reduction Patent" CN 101632958 A(2010).
7. A.K. Mandal and O.P. Sinha: *Proceeding of International Conference On Multifunctional Materials, Structures and Applications*, pp. 22-24, Mc Graw Hill, New Delhi,(2014)
8. C. A. Pickles , A. McLean , C. B. Alcock and R. N. Nikolic, "Plasma Recovery of Metal Values From Fly Ash," *Canadian Metallurgical Quarterly*, 29(1990), 193-200.
9. A.K. Mandal, O.P. Sinha, "Recovery of Multi-Metallic Components from Bottom Ash by Smelting Reduction Under Plasma Environment,"*Met. Trans. B.*,47(2016), 19-22.

A REVIEW OF SLAG CHEMISTRY IN LEAD RECYCLING

Doug Schriener¹, Patrick Taylor¹, Joseph Grogan²

¹Colorado School of Mines; 1500 Illinois St.; Golden, CO, 80401, USA

²Gopher Resource; 685 Yankee Doodle Rd.; Eagan, MN, 55121, USA

Keywords: Lead Recycling, Blast Furnace, Slag Chemistry

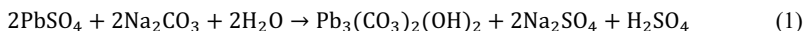
Abstract

A critical review of the technical literature on slag chemistry in lead recycling is presented. Laboratory methods used to improve our understanding of these systems is described. Ongoing investigations in the Kroll Institute for Extractive Metallurgy are presented.

Introduction

In 2015, about 86% of smelted North American lead came from secondary sources (1,800,000 short tons). Of that, 95% came from spent lead-acid batteries. The other 14% of production came from smelting of primary lead (290,000 st). No primary smelting occurred in the United States, although lead concentrates are still produced. Compared to 1980, the percentage of secondary output has increased from 50% and the proportion from batteries has risen from 70% [1]. Given the importance of lead battery recycling to the US lead supply this paper presents a review of lead slag chemistry and behavior, past experimental methods to study lead slags, and recent advances at the Kroll Institute for Extractive Metallurgy.

A description of the lead battery recycling process shown in Figure 1 is required. The contents of a lead-acid battery are the sulfuric acid and lead sulfate battery paste, the metallic and oxidic lead grid parts, the plastic battery casings, and the silica separators. Although the methods have changed over the years and vary from plant to plant, the batteries must initially be broken and separated. Acid is recovered and sold, casings are melted and extruded into new plastics, and separators are fluxed in the furnaces and the grid parts are fed to the reverberatory furnace. Historically the paste was also directly fed to the reverb, where it would form a matte phase, but due to concerns with sulfur dioxide generation, the paste material is now desulfurized. This is commonly done with soda ash and leads to a marketable sodium sulfate product. The lead continues to the furnace as a carbonate:



In the reverb, lead is reduced, while impurities like antimony, arsenic, and tin are slagged. Dross can form when lead sulfide crystallizes out of the cooling bullion. The reverb process leaves much lead oxide in the slag, so it is then sent to a blast furnace for reduction. The lead products are then impurity-free “soft” lead and impurity-containing “hard” lead.

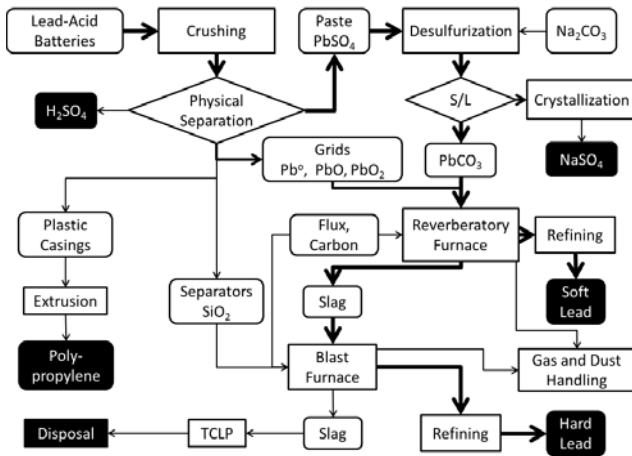


Figure 1. The Lead-acid Battery Recycling Process.

Historical Blast Furnace Slags

Operation of a Lead Blast Furnace

The first smelting metallurgists brought the blast furnace to the western US from Germany [2]. An objection to early reverb furnaces was considerable valuable metallurgical losses to smoke. Blast furnace baghouses are able to retain this value. Thus, the blast furnace came into use.

A lead blast furnace operates at a lower temperature and with a lower coke requirement than an iron blast furnace [3]. They are generally rectangular with tuyeres along the long side. Magnesite brick typically composes the crucible lining. Because the conditions are not strongly reducing, iron oxide is maintained in the slag. Scrap iron will reduce the lead according to:



There can be up to four products from the lead blast. The crude lead bullion contains the lead. Sulfur, if desulfurization is not used, will create a matte that will attract the copper. Antimony and arsenic in excess may react with iron to form a speiss, which will contain cobalt and nickel. Lead and antimony can both be reduced by iron:



Any less-noble impurities will slag out, but because the change in free energy about 900°C is only slightly negative, substantial lead oxide will also be contained in the slag. With no desulfurization (historical practice), CaO-FeO-SiO₂ slag will melt around 1200°C and the lead at

330°C. When modern desulfurization occurs, the sodium content creates a $\text{Na}_2\text{O-FeO-SiO}_2$ slag. Both are corrosive and are contained in the lower part of the hearth with water cooled steel plates onto which the slag solidifies and forms a lining. It should be removed as quickly as possible because it can only cool and create operational troubles.

Changes in Slag Characteristics Caused by Additives

The effects of many additives to slags have been determined qualitatively through years of practice [4]. Keeping the slag easy to handle without containing too much lead has always been and continues to be the smelter's biggest struggle. While the thermodynamic and metallurgy of lead systems hasn't changed over the last hundred or so years, the constraints to the metallurgists have. Conversion to lead carbonate has a significant change in the chemistry of the final slag and leads to little to no matte production. While desulfurization decreases lead losses, the slags can contain enough to not pass the TCLP. A similar result can be achieved with modern addition of barite.

Lime rejects lead sulfide from the slag and reduces it to metallic lead. Replacing lime with barite gives a lower temperature and more-fluid slag. Barite also mitigates difficulties with magnesia and zinc oxide. However, modern practice would stray from adding more barite to the system, because when it ends up in the slag it can lead to failure of the TCLP. Barium produces a deep green flame over the slag and matte, a stony appearance, and a large amount of matte.

Too much alkaline earths or too much zinc can "freeze" a blast furnace [2]. A low silica high-lime slag is a dangerous sign that the furnace is about to freeze. Magnesia will produce a stony slag that fuses hard, raises the formation temperature, and makes the slag "pasty."

A slag that is curdy, short, brittle, rapidly cooling, and does not leave a string on the bar has too much lime. Low silica a high iron or lime slags will not fuse but instead become curdy. These slags break short, do not make strings, produce round drops, fall quickly, form a heavy shell, quickly chill matte boxes, are bad for the tuyeres, tap hard, and are prone to freezing up the furnace.

When lime is substituted by alumina, the formation temperature of the slag is raised. But when alumina replaces silica, the temperature is lowered. This is due to alumina's amphoteric nature in slags. A 'lazy' slag with an oily stream contains a "safe" amount of silica. Low silica and high magnesia and zinc cause a curdy, fast-cooling slag. The shell spits as the slag in the pot darkens in color. Alumina increases the viscosity of the slag and makes it stringy and wavy.

Iron and manganese raise the formation temperature, but reduce lead and other sulfides and prevent lead oxide from combining with silica. Iron slags zinc oxide. Zinc will be signified by white smoke and volcanoes on top of the cooling slag exhibiting a yellow (sulfur-like) coat.

Potash and soda produce tough slags with high amount of lead. High copper will cause more lead to be contained in the matte. A high copper matte can be a valuable product; either re-smelted or sold.

Wrinkly, fish-scale-like liquid slags will produce a thick brittle shell and freeze up the furnace. A slag with a warty surface and inclusions of unfused particles into the underside of the shell is produced when fines sink through the furnace.

Characterization of Lead Slags

Beyke characterized slags from three secondary operations: (A) one using a reverb then blast furnace, (B) one using only a blast furnace, and (C) one using a reverb and blast furnace after desulfurizing the feed [5]. Nominal slag compositions were 15-30 wt% CaO, 25 to 25% FeO, and 30-35% SiO₂, with minor concentrations of 1-3 wt% Pb, 2-4% S, and 1-8% Na. The mattes were 25-25 wt% Pb, 35-45% Fe, and up to 25% S.

Slag A contained silicates of calcium and iron as the major phases, magnetite, and metallic lead. SEM images showed that the lead was not found as a silicate, but as entrained metallic particles. The associated matte contained pyrrhotite and magnetite with spheres of metallic lead often rimmed with galena.

Similar dominant phases were found for slag B, except that the metallic lead particles were larger (25 μm up from lows of 2-3 μm). They also contained subparticles containing other elements: antimony, calcium, and chlorine (from casings). The matte was more complex, with iron oxides and sulfides growing around galena unassociated with metallic lead.

The desulfurization process resulted in no matte to accompany the third slag, which contained approximately 3% S – in the same region as slags A and B. Phase identification was difficult because of the amorphous, glassy quality of the slag. In this slag, the lead particles were embedded in iron oxides, sulfides, and sulfates.

Slags in the Laboratory

Jak and Hayes summarized many types of experiments that are performed in order to study various characteristics of slags [6]. A common theme among these experiments is that laboratory-based binary or ternary phase systems can only be at best an approximation of their industrial counterparts. These diagrams are much easier to represent using two- and three-dimensional diagrams.

When designing these experiments, material selection and sample preparation must be done carefully in order to obtain equilibrium (and not metastable) phases at the desired conditions. Containment of experiments and their products must be carried out with solubility, nobility, and reactivity of those materials and products in mind. This can often limit the materials and atmospheres available for experiments.

Table I. Methods and Suitability for Study of Oxide Systems. From [6].

Methods	Suitability for oxide systems
STATIC METHODS	
Electrochemical	Thermodynamic props (e.g. a_i , ΔG , ΔS)
Vapour Pressure	Knudsen – low metal vapour pressure, non-aggressive slags
	Reactive gas equilibration – low metal vapour pressure – PO_2 control
	Isopeistic equilibria - high metal vapour pressure
X-Ray powder Diffraction (XRD)	Phase detection/identification; Extensive solid solutions – lattice parameters at temperatures
Hot stage microscopy	Liquidus of low vapour pressure systems, transparent liquids
Calorimetry	Enthalpies, ΔH
	- of formation
	- of solution
	- of phase transition
Equilibration/quench/analysis techniques	Liquidus of high viscosity liquids (e.g. high silica slags); solid state phase equilibria
DYNAMIC METHODS	
Thermogravimetric Analysis (TGA)	Gas/solid; Gas/liquid reactions
Differential Thermal Analysis (DTA)	Rapid phase transitions (m.p. of congruently melting compounds)
	Liquidus/solidus of low viscosity liquids

Part of that design can be done using computer simulation methods. These new computer modelling techniques combined with critical examination of previous data can bring to light inconsistencies and inaccuracies with even the most highly-regarded of data sets. Software which analyze multiphase equilibrium systems with databases include Thermo-Calc, FACT, ChemSage, MTDATA, and GEMINI2. Solution models and data assessment has been performed by SGTE (Scientific Group Thermodata Europe). FACTSage and ChemApp combine thermodynamic databases in a more user friendly experience, while Thermo-Calc and DICTRA combine thermodynamic databases with kinetic models. The Flood- Grjotheim model and the above packages were discussed by Gaye and Lehmann [7].

According to Jak and Hayes, electron probe X-ray microanalysis (EPMA) is the preferred technique for phase identification and measurement, with XRD as a complimentary method. Energy-Dispersive Spectrometry (EDS) is not suitable for accurate phase determination, but Wavelength Dispersive Detectors (WDD) may be used for accurate chemical analysis.

Experimental Methods for Lead Slag Characterization

Battle and Hager studied the viscosity of lead slags using a rotational viscometer [8]. Their setup used an alumina crucible and a quartz reaction vessel and operated between 1150 and 1350 °C in

a nitrogen environment. They also performed partitioning experiments, cautioning against the use of their data outside the composition ranges specified.

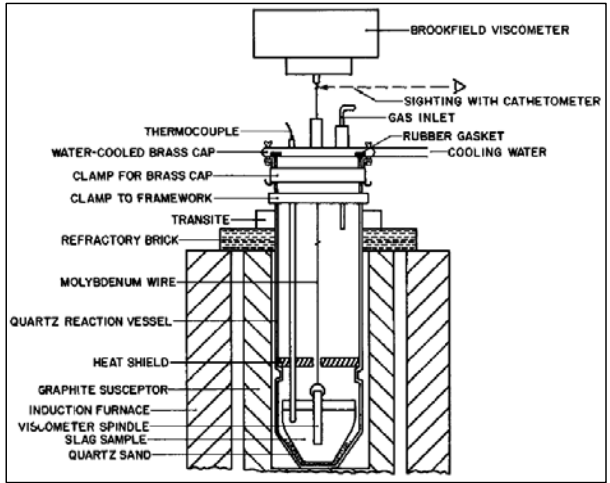


Figure 2. Experimental Setup Used by Battle and Hager, [8].

Reddy and Zhang also created and studied lead slags with a viscometer, this time employing a graphite crucible and argon environment from 1050-1300 °C [9].

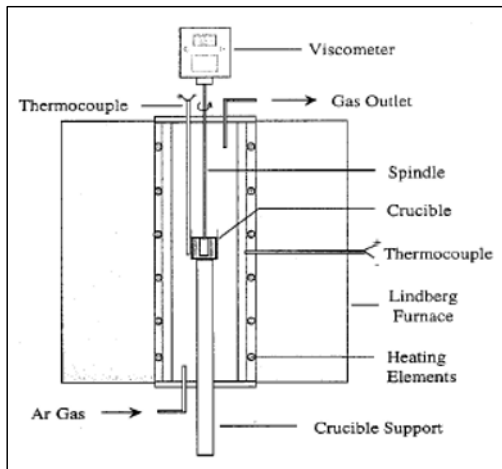


Figure 3. Experimental Setup Used By Reddy and Zhang, [9].

Their work focused not only on the temperature dependence of viscosity, but on the composition dependence, particularly the effect of similar actors whose characteristics may be lost when grouped simply as “chain breakers” and “chain modifiers” [10].

An Archimedeian spindle can be used to calculate the density of these slags at molten temperatures. The weight change of the immersed spindle (designed to minimize surface effects) relates to the exerted on the spindle, from which the density can be calculated. Such a design was used when examining the vitrification of iron phosphate containing radioactive wastes [11].

Fisher and Bennington examined the partitioning behavior of minor elements [12]. Minor element (silver, cadmium, zinc, and cobalt) distributions were found to be insensitive to changes in calcium ferrite slag composition over the ranges examined in that study. The composition did affect melting and fluidity characteristics, however. The calcium ferrite slags held <1wt% lead, which was much better than the 6% in iron silicate slags.

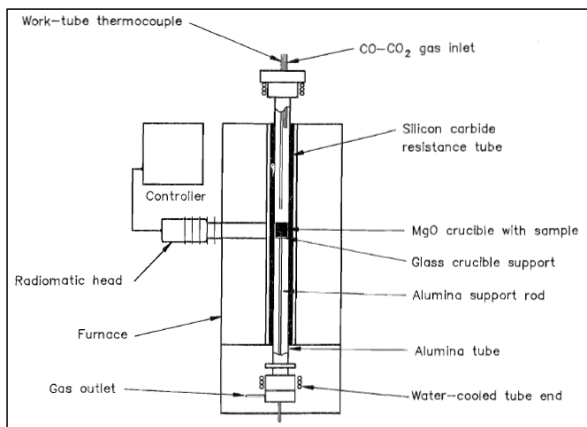


Figure 4. Experimental Setup Used By Fisher and Bennington, [12].

Hollitt measured Lead oxide activities in conventional and direct smelting slags at 1200°C [13]. Much higher coefficients than previously reported were obtained and were attributed to interactions between iron and lead oxides. The authors stated that the most suitable methods for measuring the activities of PbO are those using a stabilized zirconia solid electrolyte. Assuming ideal solution behavior of the silicates allowed for significant interactions between dissolved oxides. Gas-phase PbO vapour equilibrium was considered in the experimental setup. While the slags were 2.3 wt% Pb, the dissolved lead was only 0.64 wt%, with the rest being prills of metallic lead.

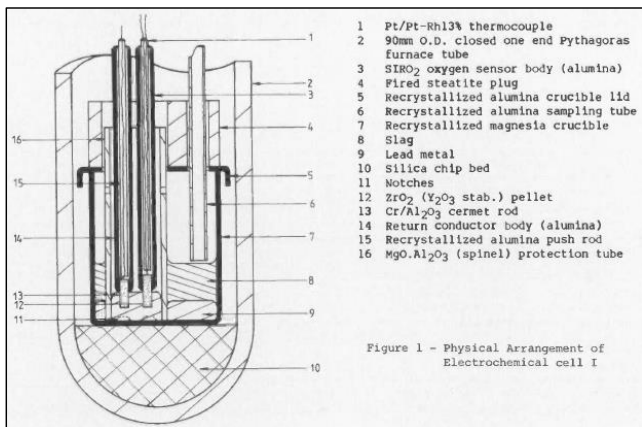


Figure 5. Experimental Setup Used By Hollitt, [13].

Environmental Concerns of Slag Constituents

As was discussed earlier, constraints for operation of a blast furnace and disposal of waste generated are different in the modern era as composed to those of a hundred years ago. In the United States, the Environmental Protection Agency sets the regulatory limits for certain toxic elements and compounds [14].

Table II. TCLP Inorganic Elements

Contaminant	Regulatory Level (mg/L)
Arsenic	5.0
Barium	100.0
Cadmium	1.0
Chromium	5.0
Lead	5.0
Mercury	0.2
Selenium	1.0
Silver	5.0

The Toxicity Characteristic Leaching Procedure (TCLP) is the standard determinant for toxic elements that slags must pass to be disposed of in landfills. It involves a buffered or non-buffered acetic acid leach, depending on sample composition [15]. However, alternatives have been put forward because industrial wastes are not typically disposed of in common landfills. One such, the Synthetic Precipitation Leaching Procedure was developed to simulate acid rain using a combination of nitric and sulfuric acid. [16]

Slags of the CaO-FeO-SiO₂ system have been tested to determine the behavior of such toxic elements [17]. Slags were constructed and doped with arsenic, antimony, cadmium, chromium, and zinc, and leached according to the TCLP. When slow-cooled slags were analyzed, they were found to be crystalline with toxic elements distributed among the lower melting point phases. The cadmium was found to volatilize during the melt. According to that research, arsenic and antimony are best contained in basic slags while zinc and chromium are stabilized in acidic melts.

Ongoing investigations at the Kroll Institute for Extractive Metallurgy

The Kroll Institute for Extractive Metallurgy is researching the fundamental characteristics of Na₂O-FeO-SiO₂ slags. The testwork being performed consists of high-temperature viscosity and density measurements; partitioning of species between metal, slag, and vapor phases; and leachability of elements according to the TCLP.

References

- [1] P. B. Queneau, R. Leiby, and R. Robinson, "Recycling Lead and Zinc in the United States," *World of Metallurgy - ERZMETALL*, 2015.
- [2] M. W. Iles, *Lead-Smelting*. New York: John Wiley & Sons, 1902.
- [3] T. Rosenquist, *Principles of Extractive Metallurgy*. USA: McGraw-Hill, Inc., 1974.
- [4] R. W. Ruddle, "Difficulties Encountered in Smelting in the Lead Blast Furnace," Institution of Mining and Metallurgy, 1957.
- [5] C. J. Beyke, "Characterization study of secondary lead blast furnace slags and mattes," in *Process Mineralogy XIII: Applications to Beneficiation Problems, Pyrometallurgical Products, Advanced Mineralogical Techniques, Precious Metals, Environmental Concerns, Ceramic Materials, Hydrometallurgy, and Minerals Exploration*, R. D. Hagni, Ed. The Minerals, Metals & Materials Society, 1995.
- [6] E. Jak and P. C. Hayes, "Phase Equilibria Determination in Complex Slag Systems," presented at the VII International Conference on Molten Slags, Fluxes, and Salts, 2004.
- [7] H. Gaye and J. Lehmann, "Modelling and prediction of reactions involving metals, slags and fluxes," presented at the VII International Conference on Molten Slags Fluxes and Salts. The South African Institute of Mining and Metallurgy, 2004.
- [8] T. P. Battle and J. P. Hager, "Viscosities and activities in lead-smelting slags," *Metall. Trans. B*, vol. 21B, 1990.
- [9] R. G. Reddy and Z. Zhang, "Viscosity Measurements of Lead Slags," in *Recycling of Metals and Engineered Materials*, D. L. Stewart, S. R. Stephens, and J. C. Daley, Eds. The Minerals, Metals & Materials Society, 2000.
- [10] Z. Zhang and R. G. Reddy, "Viscosities Of Lead Silicate Slags," presented at the SME Annual Meeting, 2001.
- [11] W. Huang, "Laboratory Research for High Temperature Waste Vitrification," University of Idaho, 2000.
- [12] G. T. Fisher II and K. O. Bennington, "Solubility of Lead and Distribution of Minor Elements Between Bullion and Calcium Ferrite Slag at 1,250°C," 9369, 1991.

- [13] M. J. Hollitt, "Measurement and Prediction of PbO Activities in Industrial Lead Smelting Slags," presented at the Melbourne Branch Symposium on "Extractive Metallurgy," 1984.
- [14] "Part 261--Identification and Listing of Hazardous Waste," in *Code of Federal Regulations Title 40: Protection of Environment*, US Environmental Protection Agency, 2011.
- [15] "EPA Test Method 1311 - TCLP, Toxicity Characteristic Leaching Procedure." 1992.
- [16] A. E. Lewis and A. Hugo, "Characterization and batch testing of a secondary lead slag," *J. South Afr. Inst. Min. Metall.*, 2000.
- [17] S. Jahanshahi, F. R. A. Jorgensen, F. J. Moyle, and L. Zhang, "The Safe Disposal Of Toxic Elements In Slags," in *Pyrometallurgy for Complex Materials & Wastes*, M. Nilmani, T. Lehner, and W. J. Rankin, Eds. The Minerals, Metals & Materials Society, 1994.

CHARACTERIZATION AND RECOVERY OF VALUABLES FROM WASTE COPPER SMELTING SLAG

Sarfo Prince¹, Jamie Young¹, Guojun Ma^{1,2}, Courtney Young¹

¹ Department of Metallurgical and Materials Engineering, Montana Tech of the University of Montana, Butte, MT, USA, 59701

² The State Key Laboratory of Refractories and Metallurgy, Wuhan University of Science and Technology, Wuhan, China, 430081

Keywords: slag; recovery; characterization; carbothermal; reduction

Abstract

Silicate slags produced from smelting copper concentrates contains valuables such as Cu and Fe as well as heavy metals such as Pb and As which are considered hazardous. In this paper, various slags were characterized with several techniques: SEM-MLA, XRD, TG-DTA and ICP-MS. A recovery process was developed to separate the valuables from the silicates thereby producing value-added products and simultaneously reducing environmental concerns. Results show that the major phases in air-cooled slag are fayalite and magnetite whereas the water-cooled slag is amorphous. Thermodynamic calculations and carbothermal reduction experiments indicate that most of Cu and Fe can be recovered from both types using minor amounts of lime and alumina and treating at 1350°C (1623K) or higher for 30 min. The secondary slag can be recycled to the glass and/or ceramic industries.

1. Introduction

Over the years, a large amount of slag has been produced because of the increased demand for copper. About 80% of the world's copper is produced from sulfide ores by concentrating, smelting and refining [1,2]. During copper smelting, two liquid phases are formed, namely a copper-rich matte and a slag [3]. It is estimated that, for a ton of copper produced, 2.2 to 3 tons of slag is generated [2-5]. These molten copper slags are dumped near the smelter site and is either allowed to cool slowly under air forming a dense, hard crystalline product or granulated with water resulting in a glassy, amorphous material.

Copper smelted slag typically contains about 1% copper (Cu) and 40% iron (Fe) with the balance being significant amounts of silica (SiO₂) and minor amounts of other elements (e.g., zinc, Zn; molybdenum, Mo; lead, Pb; and arsenic, As). Some of these minor elements can be deleterious to the environment. Notwithstanding this negative aspect, the copper slag does contain valuables which can be recovered by recycling the slag, hence mitigating its negative impact by producing economic benefits and returning the affected site to its near-natural setting after the slag is removed.

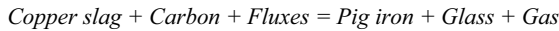
Metal recovery from the copper slag in this study was performed at a high temperature with graphite as a reducing agent and some fluxes to adjust the slag properties. Based on their thermodynamic stability, the carbothermal reduction is able to produce a Cu and Fe rich alloy as a pig iron as well as a secondary slag herein referred to as glass for simplicity purposes.

2. Thermodynamic calculations

In this study, theoretical thermodynamic calculations of chemical reactions, binary alloy phase diagrams of Cu-Fe-C-Si-Mo-As systems and CaO-SiO₂-Al₂O₃ ternary phase diagrams were considered thoroughly using a typical slag composition.

2.1. Selection of slag forming system

Based on the pyrometallurgical principles, the overall reduction reaction of waste copper slag by carbon can be illustrated simply by the following equation:



In order to improve the productivity of metal, fluxes such as CaO, Al₂O₃, and Na₂O, are usually added in the system. In the reduction process, the oxides (and sulfides) of Fe and Cu would be reduced to form pig iron. Other oxides of Mo, P and As would also be reduced and dissolved into the pig iron along with small amounts of silica. Carbon is typically saturated in the molten iron-based alloy, while zinc and lead oxides in waste slag would be vaporized.

Fig. 1 shows that the phase diagrams of Fe-Cu, Fe-Mo, Fe-Si, Fe-P, and Fe-As, as well as Cu content variation with temperature in Fe-Cu-C system [6-10]. It indicates that ~10% copper can be dissolved into the liquid phase at 1573K (Fig. 1a), while the solubility of copper increases with decreasing of carbon content and temperature increase (Fig. 1b). Silicon and molten iron at high temperature are miscible (Fig. 1d) but silicon can decrease the solubility of carbon in molten iron [3]. Phosphorous exists in the pig iron in the forms of Fe₂P and Fe₃P (Fig. 1e). Arsenic has similar behavior with that of phosphorus (Fig. 1f) and would be completely reduced and dissolved in the pig iron [11].

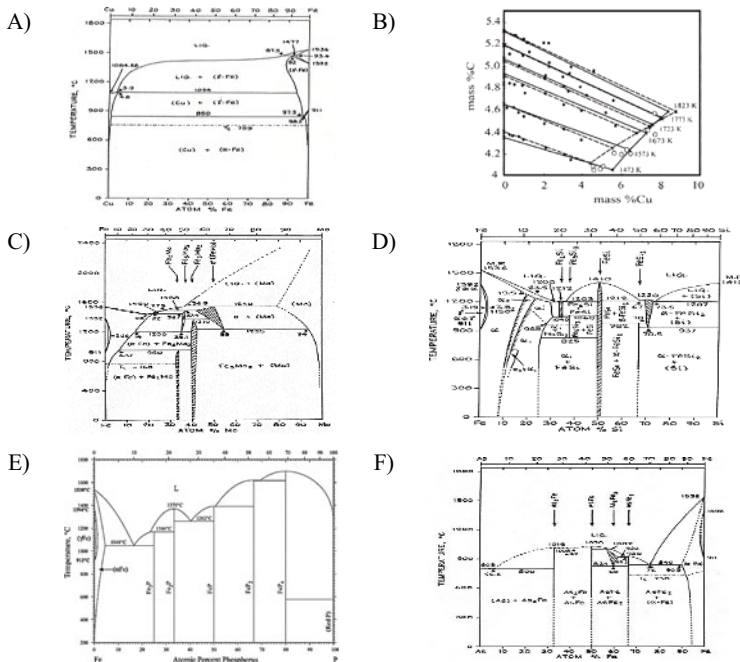


Fig. 1 Phase diagrams of alloys [6-10] (a) Cu-Fe; (b) Effects of T and C content on Cu content; (c) Fe-Mo; (d) Fe-Si; (e) Fe-P; and (f) Fe-As.

Considering the overall slag forming system and reaction temperature, CaO, SiO₂ and Al₂O₃ are the major components in the waste slag so only the iron oxides would be reduced. After modifying the chemical composition of the slag, their approximate positions of various slags present in the CaO-SiO₂-Al₂O₃ phase diagram are shown in Fig. 2 [12]. The chemical composition of the original copper slag sample is plotted in Fig. 2 along with that of a typical Blast Furnace (BF) ironmaking slag.

It can be seen from Fig. 2 that there are two areas with low melting points less than 1573K, i.e., Slag I after reduction and Slag II after reduction (marked areas). The advantages for this targeted slag composition are mainly due to its lower melting point (the lowest melting point is ~1443K) and possibly higher silicon in pig iron which is essential for its fluidity. However, in the area for Slag I after reduction, since the final slag phase has a lower basicity (B) (%CaO/%SiO₂= 0.4-0.5 at ~25% CaO, ~60% SiO₂ and ~15% Al₂O₃), the desulphurization ratio of the slag would be reduced and could also seriously corrode the refractory lining of the smelting furnace. Therefore, it is also suggested that Slag II after reduction be examined as a second targeted final slag area. This has a basicity of ~1.0-1.2 and a composition of ~40% CaO, ~40% SiO₂ and ~20% Al₂O₃ [12]. This might be good for impurities removal from the pig iron. Moreover, because the alumina content in Slag II is higher than that of Slag I, a higher strength slag could result assuming that property is important to have.

Moreover, Maweja et al. suggested that a good viscosity of less than 5 poise of the slag would be easy to separate the slag and molten metal [13]. According to the viscosity diagram of CaO-SiO₂-Al₂O₃ at 1673K (Fig. 3), it is possible to obtain the Slag II composition after reduction.

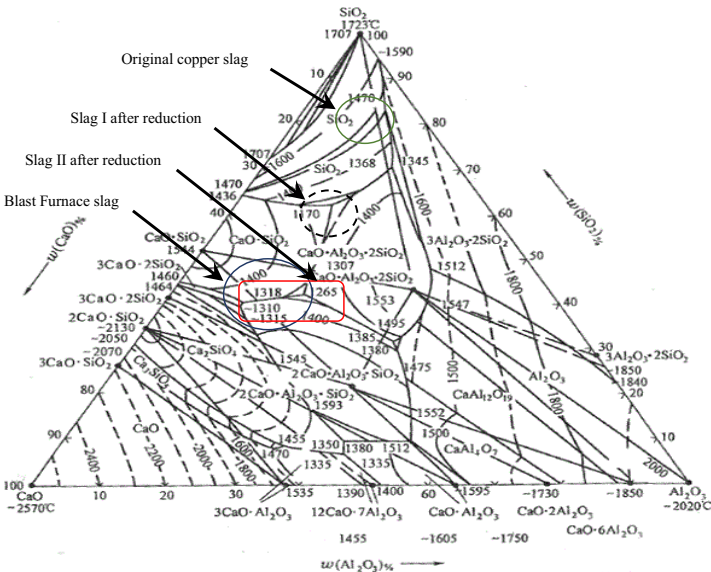


Fig. 2 Phase diagram of CaO-SiO₂-Al₂O₃ [12].

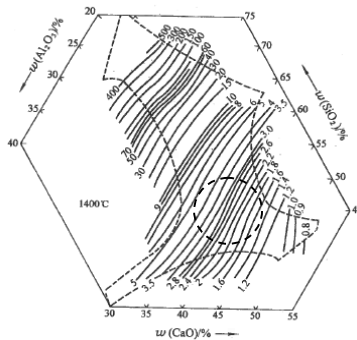


Fig. 3 Viscosity diagram of CaO-SiO₂-Al₂O₃ at 1673K (Poise) [13].

2.2. Chemical reactions in the reduction system

The chemical composition of the copper slag is very complex and it mainly exists as oxides or sulfides in the slag [5,14]. Many chemical reactions would occur in the reduction systems, such as the direct and indirect reduction of oxides or silicates (see Table 1) as well as the reduction of oxides by molten iron. Table 1 shows that most of the major oxides (except silica) in the slag can be directly reduced by carbon, only iron oxides can be reduced indirectly with carbon monoxide. Moreover, the on-set temperatures of these chemical reactions would decrease when the fluxes are added in the reduction system. The reduction temperature can be set as >1623K after considering the possibility of reduction reactions, melting point and viscosity of the final slag.

3. Materials and methods

3.1. Materials

In this study, copper slags from the inactive Anaconda Copper Company smelter in Anaconda, Montana and the active Freeport McMoRan smelter in Miami were used. Samples obtained from both sites had size distributions ranging from .015 to .323 inches.

3.2. Methods

3.2.1. Chemical characterization

Elemental compositions of the slags were measured by the Montana Bureau of Mining and Geology (MBMG) using inductively coupled plasma mass spectrometry (ICP-MS) after lithium tetraborate fusion and acid digestion with 5% hydrochloric acid. Results are shown in Table 2 as oxide or element in weight percent.

3.2.2. Mineralogical characterization

The slags were analyzed by X-ray diffraction (XRD), scanning electron microscopy (SEM), and thermogravimetric and differential thermal analysis (TG-DTA)

3.2.3. XRD

X-ray diffraction (XRD) was carried out with a Rigaku Ultima IV X-ray Diffractometer using Cu-K α radiation at 40kV and 40mA. Results were analyzed using Rigaku PDXL software (Fig. 4 is presented and discussed later).

Table 1 Major chemical reactions in the carbothermal reduction system [15].

No.	Chemical reaction	$\Delta G^\circ(\text{J/mol})$	On-set T(K)
1	$\text{Cu}_2\text{O}_{(l)} + \text{C}_{(s)} = 2\text{Cu}_{(l)} + \text{CO}_{(g)}$	9410-122.31T	76.9
2	$\text{Fe}_3\text{O}_{4(s)} + \text{C}_{(s)} = \text{FeO}_{(s)} + \text{CO}_{(g)}$	207510-217.62T	953.5
3	$1/2\text{MoO}_{2(l)} + \text{C}_{(s)} = \text{Mo}_{(l)} + \text{CO}_{(g)}$	161120-173T	931.3
4	$\text{ZnO}_{(l)} + \text{C}_{(s)} = \text{Zn}_{(l)} + \text{CO}_{(g)}$	231902-187.55T	1236.5
5	$\text{PbO}_{(l)} + \text{C}_{(s)} = \text{Pb}_{(l)} + \text{CO}_{(g)}$	73520-158.79T	463.0
6	$\text{FeO}_{(l)} + \text{C}_{(s)} = \text{Fe}_{(l)} + \text{CO}_{(g)}$	141740-140T	1012.4
7	$\text{SiO}_{2(s)} + 2\text{C}_{(s)} = \text{Si}_{(s)} + 2\text{CO}_{(g)}$	675889-363.71T	1858.3
8	$2\text{FeO-SiO}_{2(s)} + \text{C}_{(s)} = \text{Fe}_{(s)} + \text{SiO}_{2(s)} + \text{CO}_{(g)}$	354140-341.59T	1036.7
9	$\text{Cu}_2\text{O}_{(l)} + \text{CO}_{(g)} = 2\text{Cu}_{(l)} + \text{CO}_{2(g)}$	-161380+52.24T	3089.2
10	$\text{Fe}_3\text{O}_{4(s)} + \text{CO}_{(g)} = \text{FeO}_{(s)} + \text{CO}_{2(g)}$	35380-40.16T	881.0
11	$1/2\text{MoO}_{2(l)} + \text{CO}_{(g)} = \text{Mo}_{(l)} + \text{CO}_{2(g)}$	9670+1.55T	-
12	$\text{ZnO}_{(l)} + \text{CO}_{(g)} = \text{Zn}_{(l)} + \text{CO}_{2(g)}$	61112-13T	4700
13	$\text{PbO}_{(l)} + \text{CO}_{(g)} = \text{Pb}_{(l)} + \text{CO}_{2(g)}$	-97270+15.76T	6172.0
14	$\text{FeO}_{(l)} + \text{CO}_{(g)} = \text{Fe}_{(l)} + \text{CO}_{2(g)}$	-24910+31.6T	788.3
15	$1/2\text{SiO}_{2(s)} + \text{CO}_{(g)} = \text{Si}_{(l)} + \text{CO}_{2(g)}$	194021-15.07T	12874.7
16	$1/2(2\text{FeO-SiO}_{2(l)}) + \text{CO}_{(g)} = \text{Fe}_{(l)} + \text{SiO}_{2(s)} + \text{CO}_{2(g)}$	-20890+32.34T	645.9
17	$2\text{C}_{(s)} + \text{O}_{2(g)} = 2\text{CO}_{(g)}$	-221840-178.01T	-
18	$\text{C}_{(s)} + \text{CO}_{2(g)} = 2\text{CO}_{(g)}$	170790-174.55T	-
19	$1/2(2\text{FeO-SiO}_{2(l)}) + \text{C}_{(s)} + 1/2\text{CaO}_{(s)} = \text{Fe}_{(l)} + 1/2\text{CaO-SiO}_{2(l)} + \text{CO}_{(g)}$	43345-72.36T	599.0
20	$1/2(2\text{FeO-SiO}_{2(l)}) + \text{CO}_{(g)} + \text{CaO}_{(s)} = \text{Fe}_{(l)} + 1/2\text{CaO-SiO}_{2(l)} + \text{CO}_{2(g)}$	-84100+29.83T	2819.3
21	$1/4\text{Fe}_3\text{O}_{4(s)} + 3/8\text{SiO}_{2(s)} + 3/4\text{CaO}_{(s)} + \text{C}_{(s)} = 3/4\text{Fe}_{(l)} + 3/8(2\text{CaO-SiO}_{2(l)}) + \text{CO}_{(g)}$	118000-168.015T	702.3
22	$1/4\text{Fe}_3\text{O}_{4(s)} + 3/8\text{SiO}_{2(s)} + 3/4\text{CaO}_{(s)} + \text{CO}_{(g)} = 3/4\text{Fe}_{(l)} + 3/8(2\text{CaO-SiO}_{2(l)}) + \text{CO}_{2(g)}$	-52790+6.535T	8078.0

Table 2. Oxide and elemental composition of Anaconda and Freeport slags (wt. %).

Oxides/ elements	SiO ₂	Al ₂ O ₃	Fe ₂ O ₃	CaO	MgO	Na ₂ O	K ₂ O	Cu	As	Mo	Zn	Pb
Anaconda %	34.61	5.48	43.93	6.65	0.33	1.39	1.36	0.50	0.28	-	1.77	0.16
Freeport %	28.07	3.01	59.64	2.76	0.53	1.43	1.21	0.68	-	0.53	0.33	-

3.2.4. SEM-EDS-MLA

The scanning electron microscope was a LEO 1430 VP with a tungsten filament, coupled with an EDAX Genesis XM 4 Energy Dispersive Spectrometer (EDS) and Mineral Liberation Analysis (MLA) software to convert the results into mineralogical percentages. Slag samples were mounted as grains in EpoFix resin and hardener using 1-inch diameter molds. Resulting pucks were cut with diamond saw and remounted in fresh resin/hardener with cross-sections as the exposed face in order to minimize orientation effects due to density differences of locked particles. This face was then polished using alumina paste, coated with carbon, and analyzed by SEM-EDS-MLA (Fig. 's 5 and 6 are presented and discussed later).

3.2.5. TG-DTA

Non-isothermal oxidation of the slag samples was carried out using TA Instruments SDT Q600 simultaneous thermal analysis (STA) with thermogravimetric (TG) and differential thermal analysis (DTA) capabilities. Argon gas and corundum crucibles were used at atmospheric pressure from room temperature to 1300°C under dynamic conditions at heating rates of 20°C/min and gas flow rates of 10 ml/min (Fig. 's 7 and 8 are presented and discussed later).

3.2.6. Carbothermal reduction

Based on thermodynamic calculations as well as chemical and mineralogical characterization, carbothermal reduction experiments were performed using a Sentro Tech furnace with Eurotherm 2404 controller. For the Anaconda slag experiments, 30g of ground slag was mixed with 3.627g of graphite, 2.829g of calcium oxide, and 1.353g of alumina. For the Freeport slag experiments, 30g of ground slag was mixed with 3.627g of graphite, 8.925g of calcium oxide, and 3.966g of alumina. These amounts were determined from thermodynamic and mass-balance considerations of the reactions listed in Table 1. Mixtures were placed in alumina crucibles and heated to 1400°C at 5°C/min. Samples were left at the targeted temperature for 30 minutes. Cooling to room temperature at approximately 2°C/min was performed in the furnace (Fig. 's 9 and 10 are presented and discussed later). The heating and cooling rates were chosen for safety reasons (i.e., prevents boiling and shattering, respectively) which prevented damage to the furnace and extended the life of the WC heating elements. The reaction time was considered the minimum time needed for the tests to work. Many of these variables will be examined via statistical experimental design in a subsequent study [15].

4. Results and discussions

4.1. Chemical composition

As can be seen from the ICP-MS results in Table 2, the slag samples from Anaconda and Freeport are made up of significant amount of SiO₂, Fe₂O₃ and Cu. However, the Zn-content in Anaconda slag is more than that of the Freeport slag, while the Freeport slag contains more Mo.

4.1.1 XRD analysis

XRD powder diffraction patterns for the slag samples are shown in Fig. 4. Anaconda slag is absent of any definitive pattern thereby suggesting it is amorphous. By comparison, Freeport slag exhibits a strong pattern not only indicating it is crystalline but an analysis of the 2θ values between 25 and 40 indicates two major phases are present: magnetite and fayalite. The amorphous feature of the Anaconda slag further suggests it must have been water quenched such that fast cooling rates did not allow crystalline phases to develop. On the other hand, Freeport slag exhibits crystalline features because it solidified slowly as would occur with air-cooling.

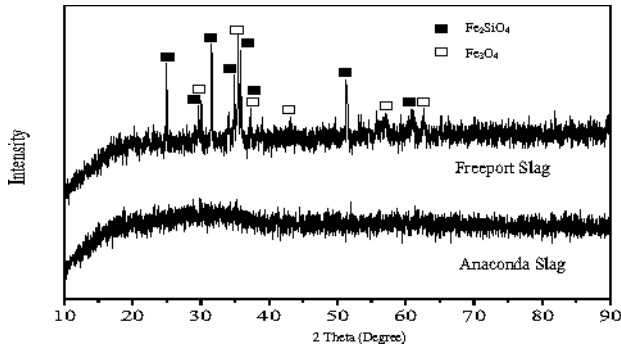


Fig. 4 XRD result of the copper slags.

4.1.2. Microscopy analysis

SEM-EDS-MLA was needed to determine the chemical compositions of all phases in each slag particularly the amorphous features in Anaconda slag and the minor phases not detected in Freeport slag. Several particulate samples of each slag were randomly selected and presumably representative, each measuring at least 3-mm in shortest dimension, and mounted in the epoxy pucks. After polishing the pucks with a series of grit papers and ultimately 0.05- μm alumina powder, all exposed surfaces were examined. Example back-scatter-electron (BSE) images and EDS elemental determinations from spot analyses are shown in Fig.'s 5 and 6. Typically, bright inclusions are Cu, Fe and Pb sulfides, gray areas are Fe oxides and silicates, and dark gray masses are Al and Ca silicates, often incorporated with Fe. Mineral Liberation Analyzer (MLA) was then used to determine the chemical compositions from the EDS signals.

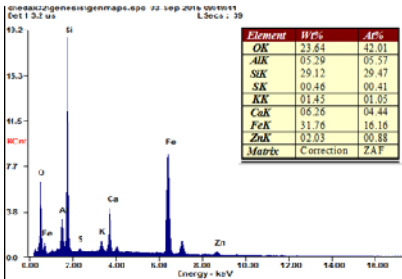
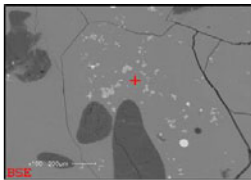


Fig. 5 SEM/EDS results of Anaconda slag.

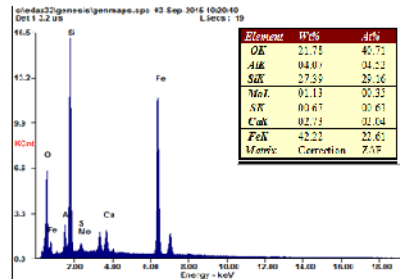
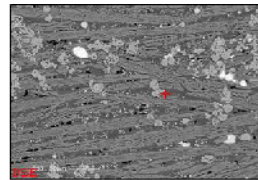


Fig. 6 SEM/EDS results of Freeport slag.

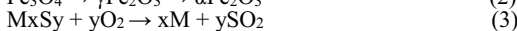
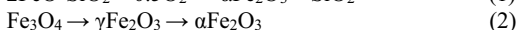
Results presented in Table 3 are overall averages expressed as minerals in weight percent. Interestingly, the major phases are $\text{Fe}_{1.2}\text{Ca}_{0.5}\text{Al}_{0.3}\text{SiO}_4$ and Fe_2SiO_4 (fayalite) with Anaconda slag measuring 71.8 and 27.47% and Freeport slag having reverse percentages at 22.90 and 60.56%, respectively. Freeport slag also has more magnetite (11.41%) than the Anaconda slag (0.05%). Surprisingly, the non-water quenched Freeport slag contained more hydrated minerals (biotite, 0.02%; muscovite, 0.03%) than the Anaconda slag (muscovite, 0.01%). Conichalcite [$\text{CaCu}(\text{AsO}_4)(\text{OH})$] was found in both slags but in negligible amounts.

Table 3. Chemical/mineral compositions of Anaconda and Freeport slags (wt %).

Mineral	Formula	Anaconda	Freeport
(FeCa)SiO	$\text{Fe}_{1.2}\text{Ca}_{0.5}\text{Al}_{0.3}\text{SiO}_4$	71.80	22.90
Al ₂ O ₃	Al_2O_3	0.00	0.03
Albite	$\text{NaAlSi}_3\text{O}_8$	0.00	0.01
Biotite	$\text{K}(\text{Mg},\text{Fe})_3(\text{AlSi}_3\text{O}_{10})(\text{OH})_2$	0.00	0.02
Bornite	Cu_5FeS_4	0.20	0.29
Calcite	CaCO_3	0.00	0.00
Chalcocite	Cu_2S	0.06	0.68
Conichalcite	$\text{CaCu}(\text{AsO}_4)(\text{OH})$	0.00	0.00
Fayalite	Fe_2SiO_4	27.47	60.56
FeO	Fe_3O_4	0.05	11.41
Galena	PbS	0.00	0.00
Ilmenite	FeTiO_3	0.00	0.01
Iron	Fe	0.02	0.20
Muscovite	$\text{KAl}_2(\text{AlSi}_3\text{O}_{10})(\text{OH})_2$	0.01	0.03
Plagioclase	$(\text{Na},\text{Ca})(\text{Al},\text{Si})_4\text{O}_8$	0.01	0.00
Pyrite	FeS_2	0.00	0.00
Pyroxene	$\text{CaMgSi}_2\text{O}_6$	0.00	0.00
Pyrrhotite	FeS	0.00	0.24
Quartz	SiO_2	0.18	0.05
Quartz FeAlCa	$\text{Fe}_{1.4}\text{Ca}_{0.5}\text{AlSi}_5\text{O}_7$	0.18	3.56
Total		100.00	100.00

4.1.3. TG-DTA

The thermogravimetric and differential thermal analysis (TG-DTA) results are shown in Fig. 7 and 8 and indicate that the waste slags gain weight (~7%) due to oxidation of fayalite to hematite and silica (~750°C) as well as transformation of magnetite to hematite (~400°C) as indicated below with Eq. 1 and Eq. 2 [16]. The weight loss of Anaconda slag below 100°C is attributed to the moisture in the slag. It is also noted that a weight loss near 400°C in the Freeport slag possibly resulting from the dehydration of biotite and muscovite. Moreover, the plateaus of the curves at 950-1050°C concur with the oxidation of sulfides as illustrated in Eq. (3).



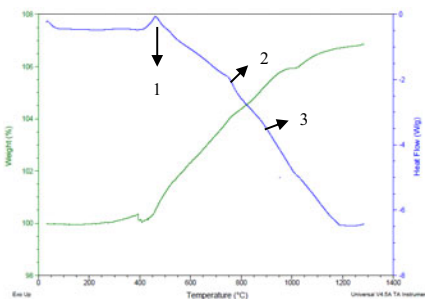


Figure 7. TG-DTA of Freeport slag.

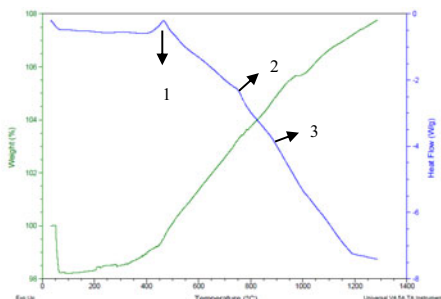


Figure 8. TG-DTA of Anaconda slag.

4.1.4. Carbothermal reduction

Duplicate carbothermal reduction experiments were conducted for each slag. All results confirmed that the final products was pig iron and glass which were separated by breaking with a hammer. After weighing the products, 89.1 and 99.6% of metal was reduced for Anaconda slag (see Fig. 9) and 99.9 and 93.1% of metal was reduced for Freeport slag (see Fig. 10). Resulting products can be recycled to the steel, glass and ceramic industries.

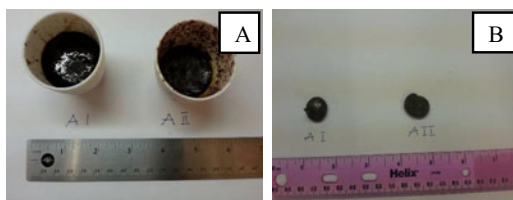


Figure 9: (A) product formed from Anaconda slag after the reduction test, (B) metal recovered from the Anaconda slag.

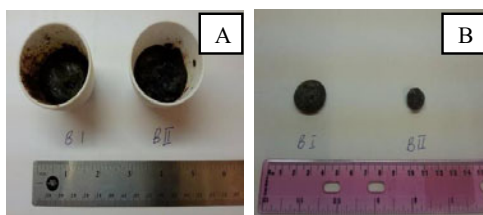


Figure 10: (A) product formed from the Freeport slag after the reduction test, and (B) metal recovered from the Freeport slag.

5. Conclusions

According to the thermodynamic calculations and the analysis of phase diagrams of alloys and oxides, it is possible to reduce waste copper slag with graphite into pig iron and glass. Most of

Cu and Fe can be recovered from both types using minor amounts of lime and alumina and treating at 1400°C or higher for 30 min. The residual slags are similar with the ironmaking slag and therefore can be recycled to the glass and/or ceramic industry.

6. Acknowledgements

The authors gratefully acknowledge the support from the China Scholarship Council (CSC) for Dr. Guojun Ma and his visit to Montana Tech, USA. Thanks are also extended to Mr. Gary Wyss of the Center for Advanced Mineral & Metallurgical Processing (CAMP) for analytical work and to Dr. Rod James for his contributions to the research and manuscript.

7. References

- [1] E. Heimlich, et al. World Copper Factbook, (International Copper Study Group, Lisbon, Portugal, 2010) p. 53.
- [2] Y. Fan, E Shibata, A. Iizuka and T. Nakamura: Crystallization Behaviors of Copper Smelter Slag Studied Using Time-Temperature-Transformation Diagram, (The Mining and Processing Institute of Japan, 2014) p. 958-963.
- [3] S. Gyurov, Y. Kostova, G. Klitcheva and A. Ilinkina. Thermal decomposition of pyrometallurgical copper slag by oxidation in synthetic air (Waste Management and Research, 2010) p. 1-8.
- [4] B. Das, B. K. Mishra, S. Angadi, S. K. Pradhan, S. Prakash, and J. Mohanty. Characterization and recovery of copper values from discarded slag, (Institute of Minerals and Materials Technology, Council of Scientific Research, Bhubaneswar, India) p. 561- 567.
- [5] C. Gonzalez, R. Parra, A. Klenovcanova, I. Imris, M. Sanchez. Reduction of Chilean copper slags: a waste management project. Scandinavian Journal of Metallurgy, 2005, 34:143–149.
- [6] SGTE-SGTE Alloy Phase Diagrams. http://www.crct.polymlt.ca/fact/documentation/SGTE/SGTE_Figs.htm
- [7] M. Turchanin, and P. Agraval. Thermodynamics of liquid alloys, and stable and metastable phase equilibria in the copper-iron system, Powder Metall. Met. Ceram. 2001, 40(7–8):337–353.
- [8] D. Busolic, F. Parada, R. Parra, M. Sanchez, J. Palacios, M. Hino. Recovery of iron from copper flash smelting slags. Mineral Processing and Extractive Metallurgy (Trans. Inst. Min. Metall. C), 2011, 120(1): 32-36.
- [9] J.A. Burgo, “The Manufacture of Pig Iron in the Blast Furnace”, The Making, Shaping, and Treating of Steel, 11th edition, Ironmaking Volume, D.H. Wakelin, ed., AISE Steel Foundation, Pittsburgh, 1999, pp. 756-757.
- [10] W.G. Moffatt. The Handbook of Binary Phase Diagrams, 1987, vol.1, 4.
- [11] X. Huang, Principles of ferrous metallurgy, Beijing: Metallurgical Industry Press, 2008.
- [12] K. Mawejaa, T. Mukongo, I. Mutombo. Cleaning of a copper matte smelting slag from a water-jacket furnace by direct reduction of heavy metals, Journal of Hazardous Materials, 2009, 164:856–862.
- [13] P K. Gbor, V. Mokri, C Q. Jia. Characterization of smelter slags. J. ENVIRON. SCI. HEALTH, 2000, A35(2):147-167.
- [14] R J. Hwang. Lime roast and leach of sulfuric acid treated copper reverberatory slag. Master Dissertation, Montana College of Minerals Science and Technology, Butte, Montana, 1975.
- [15] P. Sarfo, G. Ma, A. Das, C. Young. Carbothermal reduction of copper smelter slags for recycling into pig iron and glass. Submitted: Minerals Engineering, 2016.
- [16] B. Gorai, R.K. Jana, Premchand, Characteristics and utilisation of copper slag: a review. Resources, Conservation and Recycling, 2003, 39:299-313.

DEVELOPMENT OF SECONDARY ANTIMONY OXIDES FROM METALLURGICAL SLAGS FOR THE APPLICATION IN PLASTIC PRODUCTS

Florian Binz¹, Bernd Friedrich¹

¹IME - Institute of Process Metallurgy and Metal Recycling, RWTH Aachen University
Intzestraße 3, 52056 Aachen, Germany

Keywords: Antimony, Antimony white, Fuming, Modelling

Abstract

Bottom-up process design is performed for an antimony white fuming approach from antimony-rich lead refining residues. Thermochemical modelling is used to evaluate process boundaries regarding temperature and slag composition allowing the fuming of qualified antimony white from mentioned residues. Fuming boundaries indicate that state of the art drosses are not suitable for fuming qualified antimony white. Slag conditioning by antimony enrichment of the slag has to be carried out in advance. Carbothermic reduction of lead oxide from named oxides is simulated and evaluated in lab scale to achieve optimal slag enrichment while avoiding antimony losses to the metal phase.

Introduction

The use of antimony as flame retardant in plastic products nowadays plays a major role in the antimony processing industry with antimony trioxide accounting for over 70 % of today's worldwide antimony consumption [1]. Forecasts estimate further growth of around 4 % per year regarding the Antimony Trioxide demand. Currently China holds a nearly monopolistic market position for primary antimony from which the trioxide is produced by oxidizing smelting. As the Chinese strictly control export rates, they apply strong pressure to the market leading to an uncertain situation regarding the antimony price as well as the availability of antimony for the growing demand of western industrial nations. [2] Therefore the European Union – for the second time – listed antimony as one of the critical raw materials in 2014 due to its high supply risk and economic importance [3]. Mobilization of new – especially secondary – Antimony sources therefore seems inevitable for the future oriented industry. Despite the tensed situation on the market a significant stream of antimony in the form of complex oxidic slags, originating from softening of primary or secondary lead bullion, is left unused in western industrial nations. Antimony rich drosses from industrial lead refining usually contain ~ 30 Wt.% of antimony and ~ 60 Wt.% of lead in oxide form. These residues have been reduced to hard lead alloys in the past which were used in lead-acid-battery grids. As the antimony contents in the grids were reduced from ~12 Wt.% to less than 2 Wt.% in the past, application of antimony in lead-antimony alloys are of small importance. [1] The mentioned developments in the antimony market lead to a government funded research project, carried out at IME. Aim of the project is to develop a process for antimony trioxide winning directly from described oxidic residues. The product has to meet the strict regulations of the plastic industry to be applicable in this sector. In case of success, the project provides an innovative reworking route for aforementioned lead

refining residues while allowing western industrial nations to partially cover the demand for antimony trioxide from internal sources. The innovative process is based on a fuming approach. To evaluate boundaries for the antimony trioxide fuming from antimony rich drosses, extensive thermochemical modelling is carried out. After determination of slag composition requirements the requirements are addressed by slag conditioning. Carbothermic reduction of named drosses is investigated by thermochemical simulation software and carried out in lab scale to determine optimal parameters.

Process boundaries

Antimony trioxide volatilizes easily at temperatures above 600 °C. This property is used in different industrial applications such as roasting of sulfidic antimony ores where the antimony is separated as trioxide via the off gas due to its high vapor pressure. Production of high purity antimony trioxide from high grade antimony metal is considered state of the art. Antimony is melted to around 1000 °C in a suitable furnace whilst air is blown above the surface. Oxidized and volatilized compounds are carried to the offgas system, quenched and collected in a bag filter or cyclone. [4] Product of the oxidation blowing process is high grade antimony trioxide which has to meet different requirements depending on customers. International antimony association specifies antimony trioxide properties as shown in Table 1 [5].

Table 1. Specifications for antimony trioxide by International Antimony Association [5]

Physical form	powder
Particle size	0.2 – 44 µm
Sb ₂ O ₃ content	> 98.0 Wt.%
PbO content	< 0.25 Wt.%
As ₂ O ₃ content	< 0.1 Wt.%
Other impurities	< 1.75 Wt.%

Lead- and Arsenic oxides are considered most critical condensate impurities as they influence product properties of antimony white and both are often accompanied with antimony. Arsenic oxide will inevitable enter the product due to its high vapor pressure. Therefore arsenic contents in the feed charge have to be controlled. Lead oxide vapor pressure is considerably lower but with lead enrichment in the metal bath it may also enter the gas phase in undesired amounts. Therefore bath composition has to be monitored carefully. [4] Opposing to the oxidation blowing process mentioned innovative approach aims to fume antimony white from antimony rich drosses originating from lead softening. These drosses are complex oxides consisting of PbO, Sb₂O₃, As₂O₃ and other accompanying oxides. Exact composition heavily depends on lead bullion and softening parameters. Although lead oxide tends to volatilize at higher temperatures than antimony trioxide it is expected to form the major impurity in the product due to the high contents in the drosses. A vapor pressure calculation is executed to determine the maximum allowed PbO content in the slags for a direct fuming process. A similar method has recently been used by Liu et al. [6] who calculated the maximum allowed Pb and As contents in antimony metal for an oxidation blowing process using condensate composition standards to determine a boundary for the vapor pressure relations between antimony and lead as well as antimony and arsenic. The authors used the Chinese antimony white standards to determine minimum allowed

mole ratios in the product which must not be lower than 1353 for Sb/As respectively 955 for Sb/Pb in case of Chinese grade 1 antimony white. Using the Clausius Clapeyron equation, Liu [6] stated that vapor pressure ratios p_{Sb}/p_{As} and p_{Sb}/p_{Pb} must not undercut these ratios as mole ratios in the condensate are equal to the vapor pressure ratio of mentioned elements. However the authors did not take activities into account when calculating the partial pressures as they describe the Sb rich side of the system Pb-As-Sb. This work adopts the basic principle and applies it to the PbO-Sb₂O₃ System as the aim is to fume antimony white from oxidic slags. Only the relations between lead- and antimony oxide are taken into consideration as the As₂O₃ content in the slags is expected to completely volatilize due to its high vapor pressure.

Product mole fraction is calculated by equation 1 according to the International Antimony Association standards from Table 1.

$$x_{\left(\frac{Sb_2O_3}{PbO}\right)} = \frac{c_{\min}(Sb_2O_3)}{c_{\max}(PbO)} \quad (1)$$

With x : product mole fraction, c_{\min} : minimal molar Sb₂O₃ product concentration, c_{\max} : maximum molar PbO product concentration. The calculation yields a product mole ratio Sb₂O₃/PbO of 300. In order to obtain a suitable product, vapor pressure ratio of Sb₂O₃ to PbO must not be lower than this. Partial pressures of substances in solutions can be calculated by the equation [5]

$$p_i = a_i * p_i^0 \quad (2)$$

With p_i : partial pressure of substance I, a_i : activity of substance i in the solution, p_i^0 : pressure of the pure substance i. Vapor pressures of pure PbO and Sb₂O₃ are calculated for a temperature of 656 °C to 1100 °C according to literature. [7] Activities in the binary system are taken into account and allow partial pressure calculation. Vapor pressures are set in to relationship by the equation

$$f = \frac{p_{Sb_2O_3}}{p_{PbO}} \quad (3)$$

With f : vapor pressure ratio, $p_{Sb_2O_3}$: partial pressure of antimony trioxide, p_{PbO} : partial pressure of lead oxide. Result of the vapor pressure ratio calculation is shown in Figure 1. Calculation shows that temperature control is a crucial factor for the desired process. An increase in temperature from 700 to 900 °C favors volatilization of higher lead oxide amounts hence reducing the vapor pressure ratio. At 700 °C the critical boundary ratio of 300 is reached for antimony trioxide contents in the slag higher than 38 Wt.%. This content boundary moves towards higher required Sb₂O₃ contents with increasing temperature. Desired product can be fumed from slags containing more than 49 Wt.% Sb₂O₃ at 800 °C respectively 65 Wt.% Sb₂O₃ at 900 °C according to the calculation. It can also be seen that temperatures higher than 900 °C are not suitable for the process as selectivity would decrease further.

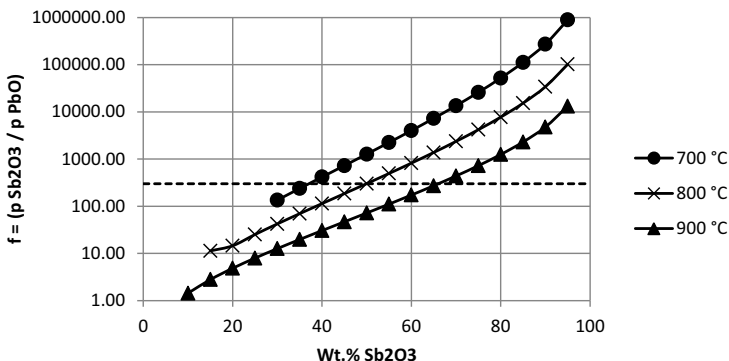
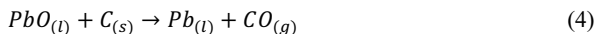


Figure 1. Calculated vapor pressure ratios as function of temperature and composition compared to the product mole ratio ($x = 300$)

Conditioning of antimony rich drosses for antimony white fuming

As mentioned above, industrial Sb-bearing drosses contain about 30 to 35 Wt.% Sb_2O_3 and are not suitable for a direct fuming process under previously described hypothesis. Carbothermic reduction of the drosses is identified as most practical method for dross enrichment. Sb_2O_3 contents around 70 Wt.% in the dross phase are set as target for fuming. The method has previously been described by Foerster et al. [9] in their United States Patent. The authors used drosses containing approximately 70 Wt.% PbO and 30 Wt.% Sb_2O_3 and found that an addition of 3 Wt.% coke at reduction temperatures of 840-870 °C yields a slag phase containing 60 to 65 Wt.% Sb_2O_3 and a metal phase containing not more than 5 Wt.% antimony.

To validate temperatures and coke addition, thermochemical modelling of the reduction process was executed using FactSage™ 6.4. Named software does not feature a solution model for the binary PbO- Sb_2O_3 system. As activities are crucial for accurate modelling of reduction processes, a custom solution database is created in association with GTT-Technologies based on thermochemical data published by Kopyto et al. [8] A stoichiometric coke factor is introduced based on the reaction



to allow description of coke addition for varying PbO contents in slags. Slag reduction is simulated for a hypothetical binary slag containing 30 Wt.% Sb_2O_3 and 70 Wt.% PbO under varying coke addition according to equation 4. Fuming of Sb_2O_3 and PbO is suppressed in the calculation to exclusively describe reduction behavior. Figure 2 shows calculated reduction behavior according to the simulation at 800°C. It can be seen that up to coke factors of 0.4 exclusive reduction of PbO takes place with remaining slag reaching Sb_2O_3 content of 68 Wt.%. Further coke addition promotes simultaneous reduction of both oxides. However PbO reduction is still dominant with slag reaching 87 Wt.% Sb_2O_3 at coke factor 0.6. Metal phase reaches 87 Wt.% Pb under these conditions. Coke additions larger than 0.6 result in higher antimony losses

to metal phase without further enrichment of slags and are therefore not suitable for desired process.

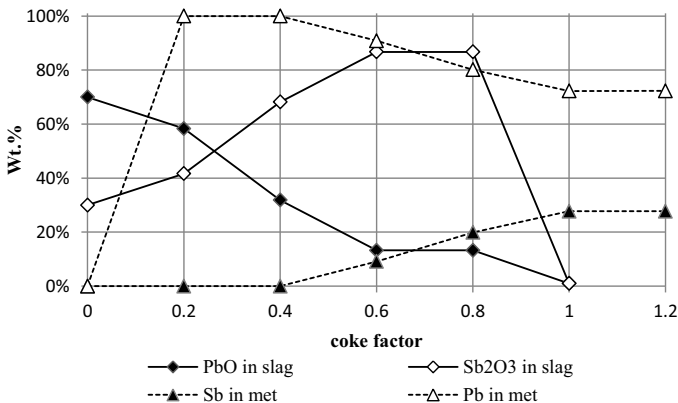


Figure 2. Calculated reduction behavior of binary slag containing 30 Wt.% Sb₂O₃ and 70 Wt.% PbO at 800 °C

Experimental

Reduction trials are carried out in a resistance heated furnace with a maximum power of 14 kW. The furnace chamber measures 200 mm in height, 270 mm in width and 450 mm in depth. Automatic furnace control allows exact temperature setting as well as realization of temperature profiles. A steel muffle is placed in the furnace chamber and purged with 3 l/min Ar to prevent oxidation and coke losses. Three alumina crucibles per trial are placed in the muffle. Figure 3 shows a schematic representation of the trial setup. 300 g of industrial antimony dross (composition see Table 2) is mixed and milled with desired amount of petrol coke. The mixture is fed into the alumina crucibles and placed in the muffle. Furnace is heated to the desired temperature with a heating rate of 300 °C/h. After desired temperature is reached, the melt is held for 60 minutes before the muffle is taken out of the furnace. Argon flow is kept until the slag has cooled below 300 °C.

Table 2. Composition of Antimony dross used for reduction trials (XRF analysis)

Compound	Concentration [Wt.%]
PbO	62.81
Sb ₂ O ₃	35.79
ZnO	0.89
SnO ₂	0.24
As ₂ O ₃	0.09

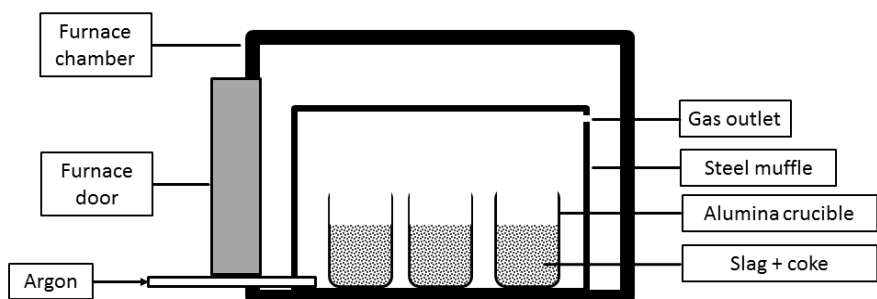


Figure 3. Schematic setup used for slag reduction trials

Reduction trials are carried out at 700 °C, 800°C and 900 °C for stoichiometric coke additions of 0.4 to 1.2 according to reaction 6 resulting in 15 parameter sets. Every parameter set is run three times. Therefore total number of trials is 45. Slag and metal phases are separated and weighed. The slag is milled to < 90 μm and analyzed by XRF spectroscopy. Slag samples are also analyzed by SEM/EDX. Metal phases are remelted for homogenization in a laboratory scale induction furnace using a clay graphite crucible. Remelted metal phases are casted into a mould, trimmed and analyzed by spark emission spectroscopy.

Results and Discussion

Figure 4 shows experimental reduction behavior of industrial antimony dross as function of coke addition at 800°C. Opposing to the calculation no exclusive PbO reduction is achieved up to coke factor of 0.4 as metal phase reaches 4.5 Wt-% Sb at this point. However PbO reduction is dominant and slag enrichment is successful by reaching 75 Wt.% Sb_2O_3 at coke addition of 0.6. Compared to the calculated model, antimony trioxide content at this point is 12 Wt.% lower. As mentioned before partial Sb_2O_3 reduction is one factor which hinders slag enrichment. Furthermore fuming of Sb_2O_3 from slag phase can take place in during experiments thus lowering antimony trioxide content in slags compared to the model. Coke additions larger than 0.6 do not yield higher enrichment grades of antimony trioxide but promote antimony losses to the metal phase. However it can be assumed that higher reduction grades temporary are achieved during the trial. As increased Sb_2O_3 content raises activity of Sb_2O_3 and therefore antimony trioxide partial pressure, fuming is promoted in this case. This temporary state can not be detected by analysis as the gas phase can leave the system during trials. Complete reduction at coke factors of 1.0 or higher is not taking place opposing to the model prediction.

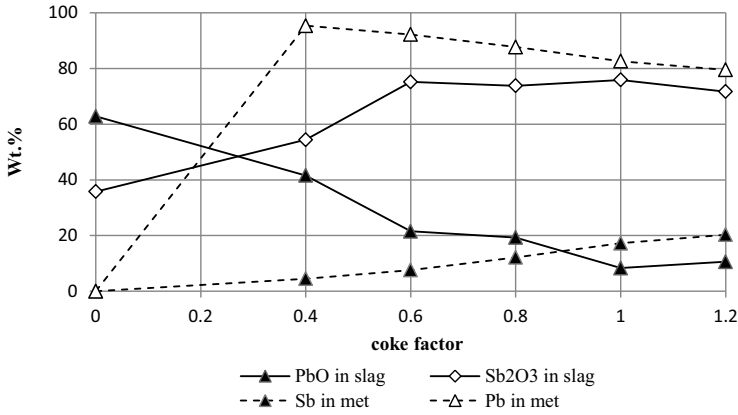


Figure 4. Experimental reduction behavior of antimony rich dross under varying coke addition at 800 °C

Figure 5 shows all measured antimony contents in slag phase. It can be seen that enrichment rates as high as predicted from calculation can not be reached. Maximum Sb₂O₃ content for all trials is not higher than 78 Wt.%. Temperature has no significant influence on reduction grade according to slag analysis, however it can again be assumed that larger amounts of antimony trioxide have evaporated during the trial at higher temperatures.

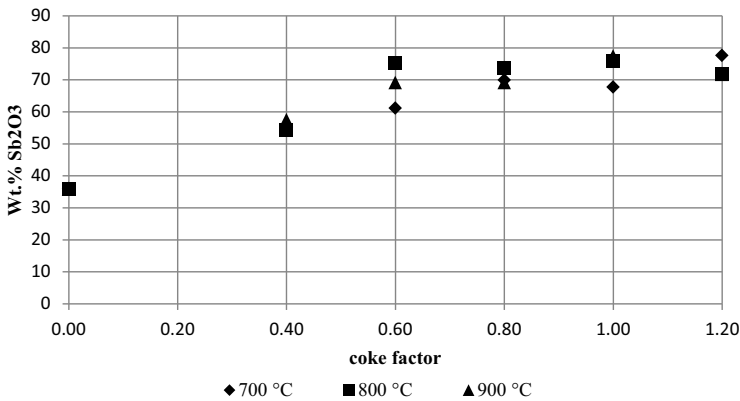


Figure 5. Temperature dependency of antimony trioxide enrichment under varying coke addition

Reduction with a stoichiometric factor of 0.6 at 800 °C is considered as optimal operating condition yielding a slag containing 75.2 Wt.% Sb₂O₃ with high lead yield and low antimony

loss to the metal phase. Temperatures lower than 800 °C hinder slag and metal phase separation due to increased viscosity.

Summary

A new pyrometallurgical process is currently being developed for antimony white production from antimony rich lead refining residues by direct fuming. Mentioned residues contain about 30 Wt.% Sb_2O_3 and 60 Wt.% PbO as well as oxides of arsenic, tin and other elements. Antimony white products for the application in plastic industry have to meet strict requirements regarding lead and arsenic contents. Due to the large PbO contents in residues originating from state of the art lead refineries, PbO is identified as most problematic compound for a fuming process. Extensive thermochemical modelling is carried out in the framework of bottom up process design to testify requirements for the feed material of such process. Vapor pressures of antimony trioxide and lead oxide are calculated under consideration of their activities in hypothetical slag compositions and different fuming temperatures. Calculation reveals that state of the art drosses are not suitable for fuming of qualified antimony white. Sb_2O_3 contents in named slags need to be raised to around 70 Wt.% for direct fuming. Carbothermic reduction is simulated using FactSage 6.4™ to confirm this enrichment possibility. A series of trials is conducted to prove principle of antimony enrichment in dross by carbothermic reduction where drosses containing up to 78 Wt.% Sb_2O_3 are achieved. Optimal reduction parameters are identified in regards to the trial results. As conditioning of the drosses is successful, future work will focus on optimizing fuming parameters.

Acknowledgements

The project upon which this publication is based is funded by the German Federal Ministry of Education and Research (BMBF) under project number 03X3592. This publication reflects the views of the authors only.

References

1. C G. Anderson, “The metallurgy of antimony“ *Chem. Erde*, 72 (4) (2012), 3-8.
2. Roskill Information Services Ltd, “Study of the antimony market” (Report 2011).
3. European Commission, “Report on Critical raw materials for the EU 2014”, (Report <http://ec.europa.eu/enterprise/policies/raw-materials/files/docs/>, 2015).
4. Zhao Tian-cong, *The Metallurgy of Antimony*, 1st ed., (Changsha, China; Central South University of Technology Press, 1988)
5. International Antimony Association, Diantimony Trioxide Specifications, http://www.antimony.com/en/detail_diantimony-trioxide_33.aspx (19.05.2015)
6. W. Liu, T. Yang, D. Zhang, L. Chen, Y. Liu, “ A New Pyrometallurgical Process for Producing Antimony White from By-Product of Lead Smelting” *JOM* 66 (9) (2014), 1694-1700.

7. C. L. Yaws, *Handbook of Vapor Pressure Vol. 4: Inorganic Compounds and Elements*, 1st ed., (Houston, TX; Gulf Publishing Company, 1995)

8. M. Kopyto, W. Przybyło, B. Onderka, K. Fitzner, "Thermodynamic properties of Sb₂O₃-SiO₂ and PbO-Sb₂O₃-SiO₂ liquid solutions" *Arch. Metall. Mater.*, 54 (3) (2009), 811-821.

9. G.S. Foerster, H.A. Stuhler, "Production of lead and purified antimony oxide" US Patent 4,194,904, (New York, NY 1980).

IMPROVING THE DISSOLUTION OF PHOSPHORUS FROM $2\text{CaO}\cdot\text{SiO}_2\text{-}3\text{CaO}\cdot\text{P}_2\text{O}_5$ SOLID SOLUTION IN AQUEOUS SOLUTIONS

Chuan-ming Du¹, Xu Gao², Sun-joong Kim², Shigeru Ueda², Shin-ya Kitamura²

¹Graduate School of Engineering, Tohoku University; Katahira 2-1-1, Aoba-ku; Sendai; 980-8577; Japan

²Institute of Multidisciplinary Research for Advanced Materials, Tohoku University; Katahira 2-1-1, Aoba-ku; Sendai; 980-8577; Japan

Keywords: Phosphorus recovery; $\text{C}_2\text{S-C}_3\text{P}$ solid solution; Steelmaking slag; Na_2SiO_3 modification; Leaching

Abstract

Steelmaking slag is a potential P resource in Japan, because the P quantity in it is almost equal to that in imported phosphate ores. P_2O_5 is mainly concentrated in the $2\text{CaO}\cdot\text{SiO}_2\text{-}3\text{CaO}\cdot\text{P}_2\text{O}_5$ solid solution in slag. It has been clarified that P can be selectively leached out from $\text{C}_2\text{S-C}_3\text{P}$ rather than the matrix phase of slag. To recover P from slag, its dissolution ratio from $\text{C}_2\text{S-C}_3\text{P}$ should be increased. In this study, the effects of leaching agent and Na_2SiO_3 modification on the dissolution of the $\text{C}_2\text{S-C}_3\text{P}$ solid solution and slag in aqueous solutions have been investigated. $\text{H}_3\text{C}_6\text{H}_5\text{O}_7$ is beneficial for P dissolution from $\text{C}_2\text{S-C}_3\text{P}$ in aqueous solutions because of the formation of the $\text{CaC}_6\text{H}_5\text{O}_7^-$ complex, which can suppress phosphate precipitation. The P-rich phase is changed from the original $\text{C}_2\text{S-C}_3\text{P}$ to $\text{C}_2\text{S-C}_2\text{NP}$ with higher water solubility by Na_2SiO_3 modification, which facilitates P dissolution. At $\text{pH}=5$, 85.7% of P from the modified $\text{C}_2\text{S-C}_3\text{P}$ can be dissolved in the $\text{H}_3\text{C}_6\text{H}_5\text{O}_7$ solution. The selective leaching of P from the $\text{CaO-SiO}_2\text{-Fe}_2\text{O}_3$ system slag can be achieved by Na_2SiO_3 modification and leaching in the $\text{H}_3\text{C}_6\text{H}_5\text{O}_7$ solution at $\text{pH}=5$. The P dissolution ratio reaches 78.4%, and only 19.7% of Fe is dissolved.

Introduction

Phosphorus is an essential agricultural nutrient and the demand for it increases as the increase in the world population. To secure supplies of P, it is necessary to consider the quantity and availability of P resources that are untapped, because the high-grade natural P resource is decreasing and Japan has no domestic natural resources^[1]. Based on the statistical data for the material flow of P in Japan^[1], as shown in Figure 1, steelmaking slag is considered as a potential P resource, because the P quantity in it is almost equal to that in imported phosphate ore. Therefore, the efficient recovery of P from steelmaking slag is of great importance.

It is known that steelmaking slag generally consists of two phases^[2, 3]. One is the dicalcium silicate ($2\text{CaO}\cdot\text{SiO}_2$) which can react with the dephosphorization product of $3\text{CaO}\cdot\text{P}_2\text{O}_5$ to form the $2\text{CaO}\cdot\text{SiO}_2\text{-}3\text{CaO}\cdot\text{P}_2\text{O}_5$ ($\text{C}_2\text{S-C}_3\text{P}$) solid solution; the other is the liquid phase consisting of the $\text{CaO-SiO}_2\text{-Fe}_2\text{O}_3$ system which is rich in Fe. There is a high distribution ratio of P between the $\text{C}_2\text{S-C}_3\text{P}$ solid solution and liquid phase^[4], indicating that P is mainly concentrated in the $\text{C}_2\text{S-C}_3\text{P}$ solid solution in steelmaking slag. With the increase in P content in the hot metal because of the use of low-grade iron ores, P_2O_5 content in the steelmaking slag increases. Shimauchi *et al.*

[5] confirmed that a higher distribution ratio of P could be obtained when the P_2O_5 content in slag was very high. Therefore, the efficient recovery of P from slag depends on how the P-rich C_2S-C_3P solid solution is treated. Various methods have been adopted to recover P by separating C_2S-C_3P from slag, including magnetic separation, floating C_2S-C_3P solid solution, and the capillary phenomenon [6-8].

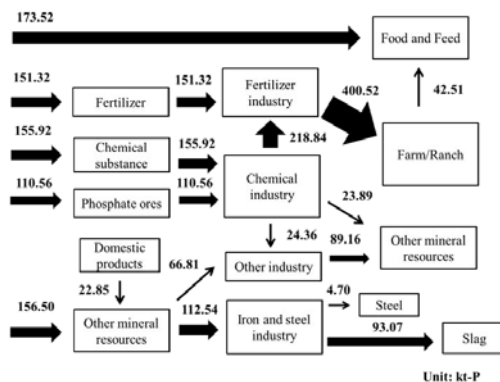


Figure 1. Domestic material flows of P in Japan (kt-P) [1]

Compared with above treatments, leaching method has an advantage in recovering P from slag, because the obtained soluble P is convenient for the production of phosphate fertilizer. Teratoko *et al.* [9] investigated the dissolution behavior of C_2S-C_3P and that of the matrix phase in aqueous solutions and clarified the possibility of selective leaching of P from C_2S-C_3P rather than from the matrix phase of slag. It was found that the dissolution ratio of P from C_2S-C_3P was not sufficiently high in the nitric acid solution (HNO_3) at pH=7 because of the precipitation of hydroxyapatite (HAP) and had no relationship with the C_3P content in solid solution. It is considered that the higher Ca^{2+} concentration and lower solubility of C_2S-C_3P leads to the lower P dissolution ratio.

If most of the P from the C_2S-C_3P solid solution can be leached, the dissolved P in aqueous solutions can be used to produce phosphate fertilizer, and the undissolved Fe-rich matrix phase can be recycled in the steelmaking process. In order to increase P dissolution, it is necessary to eliminate the Ca^{2+} ions in the aqueous solution and improve the solubility of C_2S-C_3P itself. Therefore, use of citric acid ($H_3C_6H_5O_7$) as a leaching agent and the modification of C_2S-C_3P by adding Na_2SiO_3 at high temperatures were proposed. In this study, the effects of leaching agents and Na_2SiO_3 modification on P dissolution from C_2S-C_3P in aqueous solutions were first investigated. Based on the obtained optimum condition, the dissolution behavior of $CaO-SiO_2-Fe_2O_3$ system slag in aqueous solutions was also studied.

Experimental Method

Synthesis and Modification of C_2S-C_3P Solid Solution

First, calcined CaO and reagent-grade SiO₂ were mixed at a molar ratio of 2:1, pressed into tablets and heated at 1773 K for 48 h under air atmosphere to synthesize 2CaO·SiO₂. Then, the synthesized 2CaO·SiO₂ powder was fully mixed with the Ca₃(PO₄)₂ at a target mass ratio, pressed into tablets and heated at 1773 K for 48 h under air atmosphere to synthesize the C₂S-C₃P solid solution. The crystalline was confirmed by X-ray diffraction analysis (XRD). For the Na₂SiO₃ modification procedure, about 20 mass% of Na₂SiO₃ powder was added into the synthesized C₂S-C₃P powder to make the molar ratio of Na₂O and P₂O₅ 1:1. The mixture was pressed into tablets and heated at 1773 K for 2 h in air. To compare the dissolution behavior of P, the P₂O₅ content in C₂S-C₃P samples with and without modification was fixed as 20 mass%. The composition of C₂S-C₃P samples is shown in Table I.

Table I. Composition of the C₂S-C₃P samples with and without Na₂SiO₃ modification (mass%)

	CaO	SiO ₂	P ₂ O ₅	Na ₂ SiO ₃
C ₂ S-C ₃ P	60.4	19.6	20.0	0
Modified C ₂ S-C ₃ P	47.5	12.8	20.0	19.7

Synthesis of Slag

To prepare the CaO-SiO₂-Fe₂O₃ system slag, reagent-grade CaCO₃, SiO₂, Ca₃(PO)₄, Fe₂O₃, and MgO were used and fully mixed. Meanwhile, 8 mass% Na₂SiO₃ powder was added to modify the slag and make the molar ratio of Na₂O and P₂O₅ about 1:1. The mixture was placed in a Pt crucible, heated to 1823 K in air and kept at this temperature for 1 h to form a homogeneous liquid phase. Then, it was cooled to 1623 K at a rate of 3 K/min to precipitate C₂S-C₃P solid solution. Finally, the crucible was taken out of the furnace and cooled in air. The heat treatment pattern is shown in Figure 2. The composition of the original slag and modified slag is shown in Table II. The synthesized C₂S-C₃P solid solution with Na₂SiO₃ modification and slag were observed and investigated by electron probe microanalyses (EPMA).

Table II. Composition of the original and modified CaO-SiO₂-Fe₂O₃ slag (mass%)

	CaO	SiO ₂	Fe ₂ O ₃	P ₂ O ₅	MgO	Na ₂ O
Original slag	37.0	23.0	29.0	8.0	3.0	0
Modified slag	34.3	24.9	26.8	7.4	2.8	3.8

Leaching Experiments

The obtained C₂S-C₃P samples and modified slag were ground into particles of size less than 53 μm. One gram of sample was added to 400 mL of deionized water. The temperature of the aqueous solution was kept constant at 298 K using an isothermal water bath and a rotating stirrer. To maintain the pH at a constant value, a pH meter was attached to this system, and acid was automatically added by a PC control system. The experimental apparatus is shown in Figure 3. About 5 ml of aqueous solution was sampled at adequate intervals for 120 min and filtered using a syringe filter (< 0.45 μm). The concentration of each element in the sampled aqueous solution was analyzed using inductively coupled plasma emission spectroscopy (ICP-AES). In this study, five sets of leaching experiments were conducted, as shown in Table III.

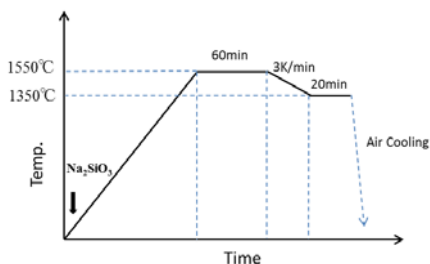


Figure 2. Experimental condition for synthesizing slag

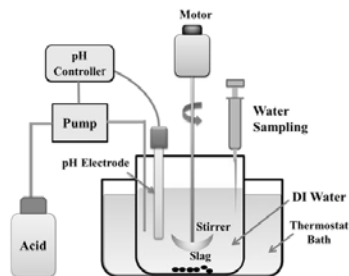


Figure 3. Experimental method for leaching

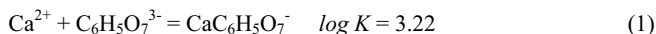
Table III. Leaching experiments

Sample Acid	C ₂ S-C ₃ P	Modified C ₂ S-C ₃ P	Modified Slag
HNO ₃	pH=7	-	-
H ₃ C ₆ H ₅ O ₇	pH=7	pH=5,7	pH=5

Experimental Results

Effect of Leaching Agents on the C₂S-C₃P Dissolution ^[10]

To investigate the effect of leaching agents, unmodified C₂S-C₃P was leached in the HNO₃ and H₃C₆H₅O₇ solutions, respectively. Figure 4 shows the change in Ca and P concentrations in each leaching agent. In the HNO₃ solution, with the continuous increase in Ca concentration, the dissolved P was not stable and started to decrease after 20 min. Because Ca and P concentrations in aqueous solutions are controlled by the solubility product of HAP ^[11], the higher Ca concentration results in phosphate precipitation. In the H₃C₆H₅O₇ solution, Ca concentration was as high as that in the HNO₃ solution, but the P concentration increased continuously and reached 41.4 mg/L. The reason is that C₆H₅O₇³⁻ can combine with Ca²⁺ to form CaC₆H₅O₇⁻ complex in aqueous solutions, as shown in equation (1) ^[12], which results in lower free Ca²⁺ concentration and restrains the precipitation of HAP.



The dissolution ratio of each element was calculated using equation (2) and is shown in Figure 5, where R_M is the dissolution ratio of element M, C_M is the M concentration (mg/L), V is the volume of the aqueous solutions (L), and m_M is the original mass of element M in 1 g of sample (mg). It shows that only a small fraction of P is dissolved in the HNO₃ solution. However, the P dissolution ratio in the H₃C₆H₅O₇ solution significantly increases reaching 17.7%. Therefore, H₃C₆H₅O₇ is more efficient than HNO₃ at extracting P from C₂S-C₃P in aqueous solutions.

$$R_M = (C_M \cdot V) / m_M \quad (2)$$

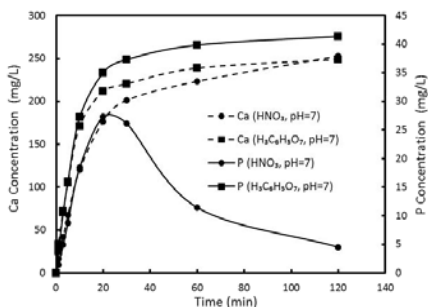


Figure 4. Change in the Ca and P concentrations in each leaching agent

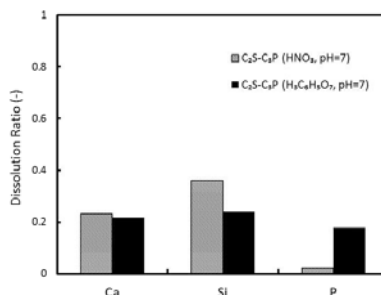


Figure 5. Dissolution ratio of each element from the C_2S-C_3P

Dissolution Behavior of the Modified C_2S-C_3P [10]

To further improve P dissolution, Na_2SiO_3 modification was proposed to change the solubility of C_2S-C_3P itself. First, the effect of Na_2SiO_3 modification on the C_2S-C_3P composition was examined. The modified C_2S-C_3P solid solution consists of two phases, as shown in Figure 6 and Table IV. One phase corresponds to the C_2S-C_3P solid solution containing Na_2O , the other one is the newly formed $CaO \cdot SiO_2$. Compared to the composition before modification, the SiO_2 and P_2O_5 content changed very little, but the CaO content decreased. This showed that added Na_2O could be introduced into the C_2S-C_3P structure to substitute for CaO . The reaction between the C_2S-C_3P and Na_2SiO_3 at high temperatures can be described by equation (3). Because of the Na_2SiO_3 modification, the P-rich phase changes from the original C_2S-C_3P to C_2S-C_2NP .

Table IV. Composition of the modified C_2S-C_3P

Sample	CaO	SiO_2	P_2O_5	Na_2O
Modified	49.9	15.5	25.7	8.9
C_2S-C_3P	41.1	45.9	4.9	8.1

Then, the dissolution behavior of modified C_2S-C_3P in the $H_3C_6H_5O_7$ solution at $pH=7$ was investigated. As shown in Figure 7, the P concentration in the $H_3C_6H_5O_7$ solution reached 56.2 mg/L, which was higher than that of the unmodified C_2S-C_3P . This is considered to be because of the transformation from C_2S-C_3P to C_2S-C_2NP with higher water solubility [13]. As shown in Figure 8, the dissolution ratio of P from the modified C_2S-C_3P increased to 24.6%, indicating that Na_2SiO_3 modification facilitates P dissolution.

To reach the optimum leaching conditions, the dissolution behavior of modified C_2S-C_3P in the $H_3C_6H_5O_7$ solution at $pH=5$ was also investigated. With decreasing pH, the dissolution of modified C_2S-C_3P was improved significantly. The P concentration in the $H_3C_6H_5O_7$ solution increased to 178.2 mg/L. The dissolution ratios of Ca and P were 90.3% and 85.7%, respectively, indicating that most of the modified C_2S-C_3P could be dissolved at this condition. Therefore, Na_2SiO_3 modification and decreasing pH was beneficial for C_2S-C_3P dissolution in the $H_3C_6H_5O_7$ solution.

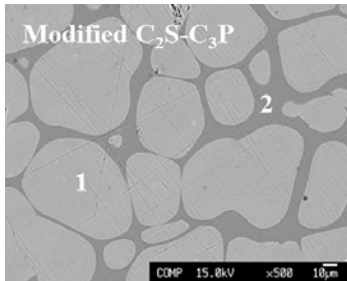


Figure 6. EPMA image of the modified C_2S-C_3P sample

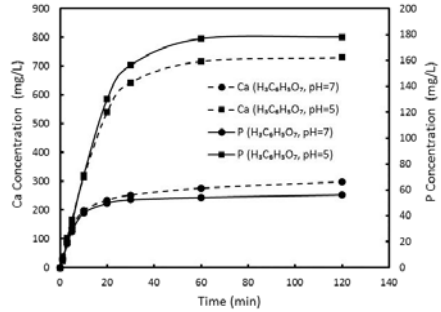


Figure 7. Change in the Ca and P concentrations in the $H_3C_6H_5O_7$ solution

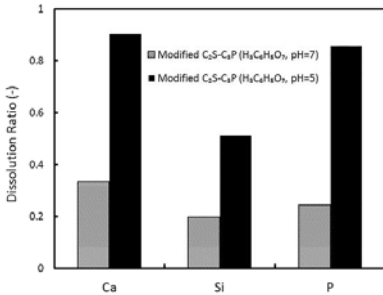


Figure 8. Dissolution ratio of each element from the modified C_2S-C_3P

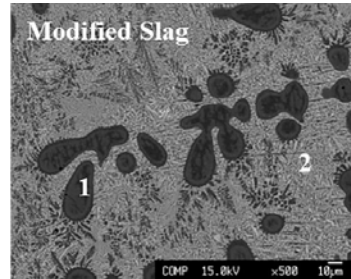


Figure 9. EPMA image of the modified $CaO-SiO_2-Fe_2O_3$ slag

Dissolution Behavior of the Modified Slag

Based on the obtained results for C_2S-C_3P , it is necessary to modify the slag by adding Na_2SiO_3 and use $H_3C_6H_5O_7$ as a leaching agent to improve P dissolution from slag. First, the effect of Na_2SiO_3 modification on slag composition was investigated. The modified slag consists of two phases, as shown in Figure 9 and Table V. The black phase is the precipitated C_2S-C_2P solid solution containing Na_2O (C_2S-C_2NP); the grey phase is the $CaO-SiO_2-Fe_2O_3$ matrix phase with little P. The Na_2O and P_2O_5 content in the C_2S-C_3P solid solution were higher than that in the matrix phase, indicating that they were mainly concentrated in C_2S-C_3P . It is believed that the Na_2O can combine with P_2O_5 to form C_2S-C_2NP solid solution.

Table V. Composition of the modified $CaO-SiO_2-Fe_2O_3$ system slag

Sample	CaO	SiO_2	P_2O_5	Na_2O	Fe_2O_3	MgO	
Modified Slag	1	43.9	14.1	32.0	7.4	1.4	1.2
	2	26.0	30.4	2.3	3.2	34.3	3.8

Then, the dissolution behavior of modified slag in the $\text{H}_3\text{C}_6\text{H}_5\text{O}_7$ solution at $\text{pH}=5$ was investigated, as shown in Figure 10. In the beginning, the slag dissolution was fast because of low ion concentrations in aqueous solutions, and the concentrations of each element were rapidly increasing. The P and Fe concentrations reached 63.4 mg/L and 92.5 mg/L, respectively. According to equation (2), the dissolution ratio of each element from the modified slag in the $\text{H}_3\text{C}_6\text{H}_5\text{O}_7$ solution was calculated and is shown in Figure 11. Most of the Ca, Si, and P were dissolved in the $\text{H}_3\text{C}_6\text{H}_5\text{O}_7$ solution, except for Fe. The P dissolution ratio reached 78.4%, but the Fe dissolution ratio was only 19.7%, indicating that P-rich $\text{C}_2\text{S}-\text{C}_2\text{NP}$ solid solution was easier to be dissolved than the Fe-rich matrix phase in aqueous solutions. Therefore, the selective leaching of P from steelmaking slag and higher P dissolution ratio can be achieved by using $\text{H}_3\text{C}_6\text{H}_5\text{O}_7$ as a leaching agent, with Na_2SiO_3 modification at $\text{pH}=5$.

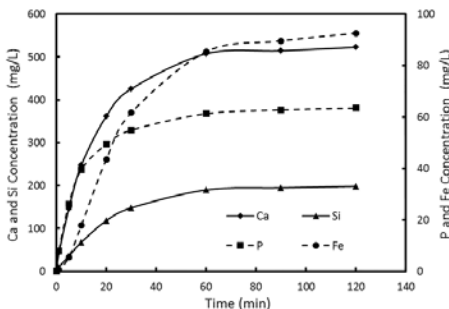


Figure 10. Change in the concentrations of each element in the $\text{H}_3\text{C}_6\text{H}_5\text{O}_7$ solution at $\text{pH}=5$

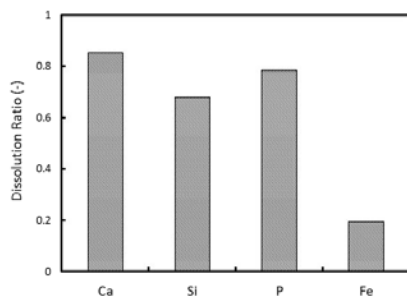


Figure 11. Dissolution ratio of each element from the modified slag

Conclusions

In order to improve P dissolution from the $\text{C}_2\text{S}-\text{C}_3\text{P}$ solid solution in aqueous solutions, the effects of leaching agents and Na_2SiO_3 modification were investigated. The obtained results are summarized as follows:

- (1) $\text{H}_3\text{C}_6\text{H}_5\text{O}_7$ is beneficial for P dissolution from $\text{C}_2\text{S}-\text{C}_3\text{P}$ solid solution in aqueous solution because of the formation of the $\text{CaC}_6\text{H}_5\text{O}_7^-$ complex which can suppress the precipitation of HAP.
- (2) The P-rich phase was changed from the original $\text{C}_2\text{S}-\text{C}_3\text{P}$ to $\text{C}_2\text{S}-\text{C}_2\text{NP}$ with higher water solubility by Na_2SiO_3 modification, which results in a higher P dissolution ratio. At $\text{pH}=5$, 85.7% of P from the modified $\text{C}_2\text{S}-\text{C}_3\text{P}$ can be dissolved in the $\text{H}_3\text{C}_6\text{H}_5\text{O}_7$ solution.
- (3) The selective leaching of P from steelmaking slag can be achieved by Na_2SiO_3 modification and leaching in the $\text{H}_3\text{C}_6\text{H}_5\text{O}_7$ solution at $\text{pH}=5$. The P dissolution ratio reached 78.4%, and only 19.7% of Fe was dissolved.

References

1. K. Matsubae-Yokoyama, H. Kubo, K. Nakajima and T. Nagasaka, "A Material Flow Analysis of Phosphorus in Japan," *J. Ind. Ecol.*, 13(2009), 687-705.

2. J. Diao et al., "Recovery of Phosphorus from Dephosphorization Slag Produced by Duplex High Phosphorus Hot Metal Refining," *ISIJ Int.*, 52 (2012), 955-959.
3. T. Futatsuka et al., "Dissolution Behavior of Nutrition Elements from Steelmaking Slag into Seawater," *ISIJ Int.*, 44 (2004), 753-761.
4. K. Ito, M. Yanagisawa and N. Sano, "Phosphorus Distribution between Solid $2\text{CaO}\cdot\text{SiO}_2$ and Molten $\text{CaO}\cdot\text{SiO}_2\text{-FeO}\cdot\text{Fe}_2\text{O}_3$ Slags," *Tetsu-to-Hagané*, 68 (1982), 342-344.
5. K. Shimauchi, S. Kitamura and H. Shibata, "Distribution of P_2O_5 between Solid Dicalcium Silicate and Liquid Phases in $\text{CaO}\cdot\text{SiO}_2\text{-Fe}_2\text{O}_3$ System," *ISIJ Int.*, 49 (2009), 505-511.
6. H. Kubo, K. Matsubae-Yokoyama and T. Nagasaka, "Magnetic Separation of Phosphorus Enriched Phase from Multiphase Dephosphorization Slag," *ISIJ Int.*, 50 (2010), 59-64.
7. H. Ono et al., "Removal of Phosphorus from LD Converter Slag by Floating of Dicalcium Silicate during Solidification," *Tetsu-to-Hagané*, 66 (1980), 1317-1326.
8. T. Miki and S. Kaneko, "Separation of FeO and P_2O_5 from Steelmaking Slag Utilizing Capillary Action," *ISIJ Int.*, 55 (2015), 142-148.
9. T. Teratoko, N. Maruoka, H. Shibata and S. Kitamura, "Dissolution Behavior of Dicalcium Silicate and Tricalcium Phosphate Solid Solution and other Phases of Steelmaking Slag in an Aqueous Solution," *High Temp. Mater. Proc.*, 31 (2012), 329-338.
10. C. M. Du, X. Gao, S. J. Kim, S. Ueda and S. Kitamura, "Effects of Acid and Na_2SiO_3 Modification on the Dissolution Behavior of $2\text{CaO}\cdot\text{SiO}_2\text{-3CaO}\cdot\text{P}_2\text{O}_5$ Solid Solution in Aqueous Solutions" (*ISIJ Int.*, 2015).
11. M. Bohner, J. Lemaitre and T. A. Ring, "Kinetics of Dissolution of β -Tricalcium Phosphate," *J. Colloid Interface Sci.*, 190 (1997), 37-48.
12. J. Muus and H. Lebel, "On Complex Calcium Citrate," *Mat. Fys. Medd. Dan Vid. Selsk.*, 13 (1936), 1-17.
13. R. P. Gunawardane and F. P. Glasser, "Reaction of chlorapatite, $\text{Ca}_5(\text{PO}_4)_3(\text{Cl}, \text{F})$ with sodium carbonate and silica," *J. Mater. Sci.*, 14 (1979), 2797-2810.

**ADVANCES IN MOLTEN
SLAGS, FLUXES, AND SALTS:**

Proceedings of



**Thermodynamics:
Non-Ferrous
Production**

CHROMIUM DISTRIBUTION BETWEEN LIQUID SLAG AND MATTE PHASES

R Hurman Eric

School of Chemical and Metallurgical Engineering
University of the Witwatersrand, Private Bag 3, WITS 2050 Johannesburg, South Africa

Keywords: Chromium, partition/distribution, slag, matte,

Abstract

The distribution of chromium between liquid silicate slags and copper-iron-nickel matte phases encountered in electric smelting of PGM containing South African sulphide concentrates were experimentally studied under controlled partial pressures of oxygen and sulphur. The reported experiments were conducted under silica saturation through the use of silica crucibles. Seven representative slag compositions were equilibrated with a typical sulphur deficient matte containing 18% Ni, 11% Cu, 42% Fe and 29% S. The slag constituents varied in the following ranges: SiO₂: 42-58%, Al₂O₃: 3.5-9.0%, Fe₂O₃: 13-21%, MgO: 15.6-25%, CaO: 2-15%, Cr₂O₃: 0.2-3.5%. The slag and matte samples were synthetically prepared from pure components. The chromium content of the two phases was analysed chemically. According to the present available results of this ongoing research it was found that the partition of chromium to the matte phase decreased with an increase in the partial pressures of both oxygen and sulphur where the value of the distribution coefficient of chromium between the matte and the slag phase varied from as low as 0.07 to as high as 5.5.

Introduction

The copper-nickel and PGM (Platinum Group Metals) bearing sulphide concentrates produced in South Africa are smelted in electric furnaces. The slags obtained in the smelting of these low grade concentrates have relatively high MgO contents, which as a consequence of their high electrical resistivity renders them suitable for sufficient heat generation needed for the smelting process. The other main slag constituents are SiO₂, FeO, Al₂O₃ and CaO. Originally the electric furnace smelters were designed to utilize the sulphide concentrates derived from the Marentsky Reef of the Bushveld Complex, which contained insignificant amounts of chromium oxide in the ore body resulting in very low concentrations of chromium in the slags mentioned above. As the reserves of the Marentsky Reef decreased, the smelters started to utilize another reef known as UG2, which contained similar PGM and Cu, Ni contents but was richer in chromium oxides. In fact the tailing stream of the concentration process for the UG2 reef is significantly rich in chromite and is actually used as a fine sized chromite concentrate in ferrochromium smelters using DC open arc furnaces. The relatively high chromite content of the UG2 sulphide concentrate employed in PGM smelters results in slags with much higher chromium contents. Thus chromium is regarded as an element of high significance in the smelting of these sulphide concentrates especially from the UG2 Reef because its presence is deleterious to the process. The solubility of chromium oxide in the typical PGM smelting slags at smelting temperatures of

around 1300°C normally utilized is low and hence remains as solid oxide. The slag becomes a solid-liquid mixture with increased effective viscosity which will cause potential problems of settling of matte droplets through the slag, decreased mass transfer between slag and matte as well as flow and tapping problems. Solid chromium oxide also has a higher density than the slag and the matte and will tend to settle at the hearth of the furnace eventually decreasing the working volume and hence the smelting capacity of the furnace.

In general sulphide smelting slags are either saturated or are close to saturation with respect to both silica and magnetite and hence the oxygen potential in the system is near FeO-Fe₃O₄ equilibrium at the temperatures employed. The solid chromium oxide can react with solid magnetite (if exists due to saturation) and form spinels with densities intermediate between that of the slag and the matte and can form false bottoms at the slag-matte interface. This will stop slag-matte interactions and reactions at these locations and affect negatively the smelting operation.

The solubility of chromium in these slags at the given temperatures can only be increased by operating under more reducing lower oxygen potentials where Cr³⁺ is reduced to Cr²⁺ (CrO in molecular notation). While operating under more reducing conditions enhances the solubility of chromium in the slag and hence decreasing the magnitude of potential problems, there will be the possibility of increased transfer of chromium into the matte, which could significantly complicate the downstream processes of recovering Cu, Ni and PGMs. Another way to increase the solubility of chromium in the current slags is to increase temperature of operation. At higher temperatures the viscosity of the matte phase decreases considerably and tends to penetrate into any cracks or porosities of the refractories of the hearth region which can cause severe operational problems. At present the South African smelters use both of these approaches; decreasing the oxygen potential by creating more reducing conditions through charging some carbonaceous materials and increasing temperatures up to 1500°C by increasing the power. Thus the partitioning of chromium between liquid silicate slags and liquid sulphide matte phases is obviously of importance in the processing of these ores.

There is extremely limited information in literature on slag-matte equilibrium and distribution of chromium between these phases under controlled conditions pertinent to the PGM smelting conditions mentioned above although numerous studies can be seen most of which fail to ensure correct equilibrium conditions and correct gas composition control. The partition of transition elements in a basic silicate melt with sulphide phases has been examined by Al'mukhamedov and Medvedev¹, and they determined a partition coefficient of chromium of 1.9 to 2.0 between the sulphide and silicate phases. However, the experiments were done in an induction furnace with helium gas in the presence of carbon, indicating that, for their system, the partial pressures of oxygen and sulphur were indeterminate. Some preliminary work was done at the Council for Mineral Technology (Mintek) of South Africa². This work involved the use of UG2 concentrate in contact with carbon and mixtures hydrogen and carbon dioxide gas. It was found that chromium partitions strongly into the matte phase under reducing conditions and that the distribution coefficient of chromium in the matte and the slag phases gradually decreases with an increase in the partial pressure of oxygen. However these experiments were performed under non-equilibrium conditions, since sulphur was escaping from the system throughout the runs. These tests were supplemented by experiments performed at 1450°C under controlled partial pressures of sulphur and oxygen at sulphide saturation using synthetic mixtures of oxides and four natural rock types approximating the slag compositions². The samples in the form of pellets were fixed to platinum loops and due to sulphide saturation and adjusted conditions only a very

small amount of sulphide melt was formed. Thus the partitioning of the chromium was determined by electron microprobe. The use of platinum wire loops to hold the samples resulted in iron loss to the platinum (which was compensated based on an approximate calculation procedure) and the studied system was somewhat far from actual metal slag interactions in the PGM smelting processes. Nevertheless the partition results although highly variable indicated that the chromium in sulphide melts increased with a decrease in the partial pressure of oxygen.

Experimental Procedure

Starting Materials

A total of seven slag samples were prepared from reagent grade powdered oxides; SiO₂, Al₂O₃, Fe₂O₃, MgO, CaO and Cr₂O₃, three of which approximating UG2 (designated as U) slags and three representing Marentsky (designated as M) slags. The main difference between the two types of slags is their Cr₂O₃ concentration. While the chromium oxide concentration of Marentsky slags is less than 0.5%, the UG2 slags usually contain over 2.5% Cr₂O₃ reaching up to 3.5%. The slag designated as 9UM can be considered to represent the case where the two ores are blended. The pure oxides were first dried in an oven at 105°C followed by mixing in the appropriate proportions in an agate mortar under a liquid blanket of acetone until all the acetone vaporized and again being bone dried in an oven. The powder mixtures were then pressed into disk shaped pellets followed by sintering and homogenization by heating to 1200°C for 12 hours in a muffle furnace. After cooling they were kept in closed bottles inside a desiccator. The initial slag compositions are summarized in Table I. The Cr to Fe ratio of the slags varied in the range 0.015 to 0.2 and their basicity were in the range 0.376 to 0.729. The basicity was defined as:

$$B = (\text{CaO}\% + \text{MgO}\%) / \text{SiO}_2\% \quad (1)$$

The PGM smelting matte compositions do not vary much; Ni concentration is in the 16% to 18% range, Cu concentration in the 9% to 11% range, Fe concentration in the 38% to 42% range and S concentration in the 26% to 28% range. Thus only one single matte sample was prepared from pure electrolytic grade Ni, Cu and Fe and triple distilled pure sulphur. The metallic powders and sulphur powder were carefully weighed and mixed and were then put in quartz tubes of 20mm in diameter which were first filled with argon gas and then evacuated by a mechanical-diffusion pump couple and sealed under vacuum by a hydrogen torch. The quartz sample tubes were heated to 1200°C to homogenize the composition and form the matte phase. After homogenization quartz tubes were carefully broken and the sulphide matte samples were recovered and kept in desiccators.

Equilibration Procedure

A gas-tight vertical molybdenum resistance furnace has been assembled and employed for the study of slag-matte equilibrium. Molybdenum wires were protected from oxidation by the use of ammonia gas, which cracks into hydrogen and nitrogen at high temperatures. Actual sample temperatures in the furnace were measured with a Pt-6 %Rh/Pt-30%Rh (B-type) thermocouple. In the slag-matte distribution experiments performed at 1450°C quartz crucibles were used

saturation of the slag with respect to silica similar to actual industrial conditions. The slag to matte mass ratio was kept constant at 1.5 while the total sample mass was 10 grams.

No	SiO ₂	Al ₂ O ₃	Fe ₂ O ₃	MgO	CaO	Cr ₂ O ₃	Basicity	Cr/Fe
1M	42.00	6.00	21.00	15.60	15.0	0.40	0.729	0.019
5U	49.0	3.50	17.00	25.00	2.00	3.50	0.551	0.201
7U	50.50	9.00	13.00	20.00	5.00	2.50	0.495	0.188
8U	51.25	5.50	16.25	17.50	7.50	2.00	0.488	0.120
9UM	52.00	6.50	15.25	16.25	8.50	1.50	0.476	0.096
15M	58.00	7.00	13.00	18.50	3.30	0.20	0.376	0.015
12M	54.20	7.50	15.00	20.00	3.0	0.3	0.424	0.020

Table I. Initial slag sample compositions

M- Marentsky type, U: UG2 type, UM blend of UG2 and Marentsky, All composition values are in mass %

The appropriate fixed partial pressures of oxygen and sulphur were achieved by mixing CO, CO₂ and SO₂ gases. A manometer type of gas mixing apparatus employing calibrated capillary flowmeters was used to mix the three gases in the correct volume proportions. The calibration of the capillary flowmeters was done by the bubble-flowmeter technique where special care was taken to ensure that the soap solution was saturated especially in the calibration of the SO₂ capillary flowmeter. The P_{O₂} calibration was tested by the use of iron-wustite reaction at 1303°C and a value of logP_{O₂} (atm) = -10.79 was recorded as comparison to the theoretical value of -10.72. The current experimental value is also in very good agreement with previous data^{2,3}. The P_{S₂} calibration was tested by the use of pressed pellets of ruthenium and tests the presence of ruthenium sulphide by microscopic techniques. At 1127°C, the equilibrium between ruthenium and ruthenium sulphide was found to be at logP_{S₂} (atm) = -2.56, compared to the theoretical calculated value of -2.35.

The quartz crucibles containing the samples were introduced to the furnace from the bottom and the furnace tube was immediately sealed through the use of brass flanges while the sample is still at the bottom flange area. The reaction tube of the furnace was flushed for about 15 minutes with spectrographically pure argon before the actual gas atmosphere was employed. After the actual gas mixture was turned on the sample was raised to the hot zone by the use of a quartz rod and pedestal and equilibrated for 24 hours and then fast quenched by speedy extraction through the bottom brass flange and immersion into ice water. The slag and matte samples separated into two distinct liquid layers which were mostly preserved during quenching and solidification. Slag and matte were recovered by breaking the quartz crucible, the reaction between the quartz crucible and the slag was not extensive. Both samples were analyzed for their chromium content by the ICP technique. Duplicate analyses were performed on each sample.

Experimental Results and Discussion

It was observed that in spite of all the care and precautions taken to ensure adequate equilibration and homogenization of the samples some variation in the partition values of chromium occurred. In certain instances, the discrepancy between the chromium contents of the phases and the starting materials is possibly due to the formation of varying amounts of chromium containing spinels at the slag matte interface and also due to some inconsistencies in the chemical analysis procedure employed. Another potential source of error is the inhomogeneous nature of some of the sulphide melts, which may show exsolution of an oxide phase² possibly during quenching although this is thought to be occurring rarely. It must however be mentioned that this is an ongoing research and the results presented here are preliminary and initial in character. Nevertheless the results indicate strong tendencies of partition values of chromium with respect to partial pressure of oxygen and sulphur. The available results are collected in Table II and are illustrated in Figures 1 and 2. As can be seen the partition/distribution ratio of chromium defined as:

$$P_{Cr} = (\text{Mass percent of Cr in the matte}) / (\text{Mass percent of Cr in the slag}) \quad (2)$$

increases very rapidly with decreasing partial pressure of oxygen even when the sulphur partial pressure is decreasing for all types of slags at 1450°C. The change of partition ratio of chromium with changing partial pressure of sulphur will definitely require further investigation. Chromium prefers to dissolve in the sulphide matte phase under reducing conditions. This is a result of increased proportions of chromium existing as CrO in the silicate slag and, as a consequence, more chromium partitions into the sulphide matte phase, which is similar to the behavior of iron². It is apparent that the oxygen potential in the system is the more dominant parameter in determining the behavior of chromium.

The plotted partition ratios of chromium for each slag displayed linear relationships and the regression equations had very high correlation coefficients as shown below in equations (3) to (9) as a function of the partial pressure of oxygen and in equations (10) to (16) as a function of the partial pressure of sulphur.

$$P_{Cr} = -1.292 \log P_{O_2} - 10.900 \quad (1M, r^2 = 0.992) \quad (3)$$

$$P_{Cr} = -2.524 \log P_{O_2} - 2.129 \quad (5U, r^2 = 0.981)$$

(4)

Table II. Experimental Results

Sample No	log P _{O₂}	log P _{S₂}	Cr in slag (mass %)	Cr in matte (mass %)	P _{cr} =(Cr)M/(Cr)S
1M B=0.729 Cr/Fe=0.019	-8.5	-1.2	0.410	0.030	0.07
	-9.0	-1.4	0.357	0.251	0.70
	-9.5	-1.7	0.107	0.161	1.50
	-10.0	-2.1	0.205	0.390	1.90
	-10.5	-2.5	0.193	0.521	2.70
5U B= 0.551 Cr/Fe=0.201	-8.5	-1.2	1.360	0.150	0.11
	-9.0	-1.4	2.431	3.841	1.58
	-9.5	-1.7	2.481	6.962	2.81
	-10.0	-2.1	2.321	8.113	3.50
	-10.5	-2.5	1.706	9.315	5.46
7U B= 0.495 Cr/Fe=0.188	-8.5	-1.2	1.650	0.660	0.40
	-9.0	-1.4	2.853	3.538	1.24
	-9.5	-1.7	2.113	3.783	1.79
	-10.0	-2.1	2.051	5.107	2.49
	-10.5	-2.5	2.021	6.559	3.24
9UM B= 0.476 Cr/Fe=0.096	-8.5	-1.2	0.827	0.612	0.74
	-9.0	-1.4	0.648	0.713	1.10
	-9.5	-1.7	0.713	1.062	1.49
	-10.0	-2.1	0.476	0.881	1.85
	-10.5	-2.5	0.373	0.880	2.36
15M B= 0.376 Cr/Fe=0.015	-8.5	-1.2	0.071	0.035	0.44
	-9.0	-1.4	0.084	0.110	1.31
	-9.5	-1.7	0.056	0.112	2.00
	-10.0	-2.1	0.064	0.166	2.59
	-10.5	-2.5	0.053	0.178	3.36
8U B= 0.488 Cr/Fe=0.120	-9.5	-2.6	0.0993	0.685	0.69
	-10.0	-3.0	1.286	1.980	1.54
	-10.5	-3.5	0.623	1.320	2.12
12M B= 0.424 Cr/Fe=0.0.20	-9.5	-2.6	0.144	0.151	1.09
	-10.0	-3.0	0.076	0.1401	1.84
	-10.5	-3.5	0.071	0.183	2.57

$$P_{Cr} = -1.386 \log P_{O_2} - 11.335 \quad (7U, r^2 = 0.9967) \quad (5)$$

$$P_{Cr} = -0.798 \log P_{O_2} - 6.073 \quad (9UM, r^2 = 0.995) \quad (6)$$

$$P_{Cr} = -1.424 \log P_{O_2} - 11.588 \quad (15M, r^2 = 0.996) \quad (7)$$

$$P_{Cr} = -1.430 \log P_{O_2} - 12.850 \quad (8U, r^2 = 0.988) \quad (8)$$

$$P_{Cr} = -1.481 \log P_{O_2} - 12.967 \quad (12M, r^2 = 0.999) \quad (9)$$

$$P_{Cr} = -1.918 \log P_{S_2} - 2.041 \quad (1M, r^2 = 0.969) \quad (10)$$

$$P_{Cr} = -3.757 \log P_{S_2} - 3.995 \quad (5U, r^2 = 0.963) \quad (11)$$

$$P_{Cr} = -2.062 \log P_{S_2} - 1.836 \quad (7U, r^2 = 0.977) \quad (12)$$

$$P_{Cr} = -1.196 \log P_{S_2} - 0.620 \quad (9UM, r^2 = 0.990) \quad (13)$$

$$P_{Cr} = -2.081 \log P_{S_2} - 0.176 \quad (15M, r^2 = 0.971) \quad (14)$$

$$P_{Cr} = -1.571 \log P_{S_2} - 3.316 \quad (8U, r^2 = 0.971) \quad (15)$$

$$P_{Cr} = -1.637 \log P_{S_2} - 3.137 \quad (12M, r^2 = 0.995) \quad (16)$$

The findings of this work are in reasonably good agreement with the work done by De Villiers and Kleyenstuber²; both studies indicate that the distribution of chromium to the liquid sulphide phase is more favorable under lower oxygen partial pressures and that linear relationships are observed between the partition ratio of chromium and partial pressure of oxygen. Despite also varying the sulphur partial pressure no clear tendency were observed in their study². The range of the partition ratio of chromium in their work was narrower changing from about 0.27 to 3.16 but also their sulphur partial pressure range was narrower. It must again be emphasized that their work is not a true slag matte equilibrium; and the authors² themselves expressed that there was also doubts that equilibrium may not have been fully reached.

The partition ratio of chromium can, in principle, be related to the following chemical exchange reaction:



$$K = (P_{O_2} / P_{S_2})^{1/2} (a_{CrS} / a_{CrO}) \quad (18)$$

Due to limited data on Standard Gibbs Free Energy of formation of CrO and CrS and lack of data on activities and activity coefficients of both CrO and CrS at low concentrations in the slag and

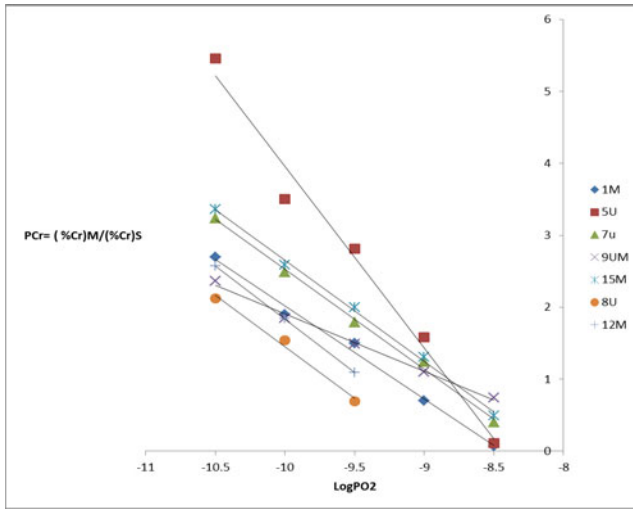


Figure 1. The variation of the partition ratio of chromium with the partial pressure of oxygen.

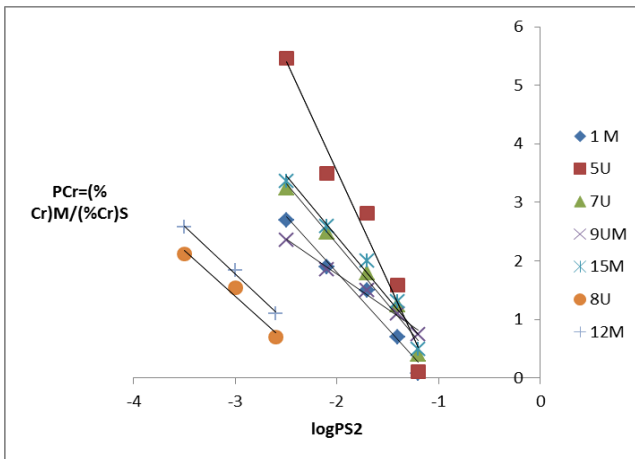


Figure 2. The variation of the partition ratio of chromium with the partial pressure of Sulphur.

matte compositions used in this study, this approach was not pursued. However equation 18 clearly indicates that at a given temperature when the equilibrium constant is fixed, the partition ratio of chromium, here the activity ratio of CrS to CrO, will increase by decreasing partial pressure of oxygen qualitatively in accord with the findings of this work.

Conclusions

The partitioning/distribution ratios of chromium between silicate slags and sulphide mattes encountered in electric smelting of PGM containing Cu-Ni concentrates of South Africa have been studied at 1450°C under silica saturation and under controlled partial pressures of oxygen and sulphur. The available results of this ongoing research presented here are somewhat variable but definitely show a strong trend of increasing the chromium content in the oxide slag phase with an increase in the partial pressure of oxygen while the partial pressure of sulphur also increases. The partition coefficients determined changed from a low value of 0.07 to a high value of 5.5.

References

1. Al' Mukhamedov, A. I., and Medvedev, A.Y. An experimental investigation of the interaction of a basic silicate melt with sulphur containing phases. *Geochem. Int.*, Vol.16, no.1. 1980. pp 6-16.
2. De Villiers, J.P.R., and Kleyenstuber, A.S.E. The partitioning of chromium between sulphide and silicate melts at controlled partial pressures of oxygen and sulphur. Mintek Report, No. M139D, 1984.
3. Huebner, J.S. Oxygen fugacity values of furnace gas mixtures. *Am. Mineral.*, Vol.60. 1975. pp. 815-823.

Thermophysical Property Measurements of Molten Slag and Welding Flux by Aerodynamic Levitator

Kenta Onodera¹, Airi Nakamura¹, Shinya Hakamada¹, Masahito Watanabe¹ and Florian Kargl²

¹Department of Physics, Gakushuin University
1-5-1 Mejiro, Toshima, Tokyo, 171-8588, Japan

²Deutsches Zentrum für Luft- und Raumfahrt (DLR),
51170 Köln Raumfahrt (DRL), 51170, Germany,

Keywords: Molten slag, Welding flux, Density, Viscosity, Levitation

Abstract

Molten slag and welding flux are important materials for steel processing. Due to lack of durable refractory materials, there is limited publication data on the thermophysical properties of these slags. Therefore, in this study, we measured density and viscosity of CaO-Al₂O₃-SiO₂ slag and welding flux using Aerodynamic Levitation (ADL) with CO₂-laser heating in which can be achieve containerless and non-contacting conditions for measurements. For density measurements, in order to obtain correct shape of the droplet we used high-speed camera with the extended He-Ne laser to project the shadow image without the influence of the self-luminescence at the high temperature. For viscosity measurement, we also have a unique vibration method; it caused oscillation in a sample by letting gas for levitation vibrate by an acoustic speaker. Using these techniques, we succeeded to measure systematically density and viscosity of molten oxides system.

Introduction

Thermophysical properties of molten oxides are very important in manufacturing process control of iron and steel making, smelting, refining, casting and welding¹. Molten oxide as slags and fluxes (usually silicates and aluminates) are used in all steps of iron and steelmaking. The slags provide protection of the molten metal surface from the atmosphere, absorption of impurities during casting and refining, lubrication between the mold and metal strand during continuous casting, and refining of the molten metal through slag/metal reactions at the interface. For these processes control, high-temperature thermophysical data of molten oxides needed for computer modeling of processes, development of scientific/technical understanding of processes, and improved process control and product quality. However, molten oxide system have very wide range of components, thus, there is a considerable demand for mathematical models that will predict properties based on chemical composition and temperature. For this purpose, we must directly and precisely measure thermophysical properties of the several key components of molten oxide. However, precise measurements of thermophysical properties of high-temperature molten oxide is very difficult, because of its high temperature conditions and high chemical reactivity. Therefore, previous measurements have been limited to temperature around 1800K. To achieve measurements over 1800K, we must use container-less approach, but we cannot use the electromagnetic levitation²) due to low electrical conductivity of the molten oxides. The

electrostatic levitation (ESL)³⁾ technique is possible applicable for molten oxide levitation. However since the ESL needs ultra high vacuum conditions to avoid electric spark at the electrode, we cannot apply the ESL technique to measure the thermophysical properties from the reason of compositional change in the vacuum conditions. From these reasons we must select the aerodynamic levitation (ADL) technique⁴⁾ for molten oxide levitation and thermophysical properties measurements. For measurement of thermophysical properties, density, surface tension and viscosity, using the aerodynamic levitation, we improved the unit of nozzle for gas jet flowing to the samples. If we use the conventional aerodynamic levitation nozzle, we cannot observe the shape of molten samples by hiding in the nozzle. The density of the molten sample by levitation method is obtained by dividing the mass by the volume. The volume of levitated molten sample obtained from the shape of the droplet using the images from the side view due to the modification by gravity and gas jet flow. Therefore we improved the conical nozzle shape to enable the observation of levitated droplet shape from the side view. We designed the nozzle shape by the computer-assisted design (CAD) using the numerical fluid dynamics simulations. Using the improved conical shape of the nozzle unit we succeeded to observe the droplet shape over the three quarter of the full shape. Moreover, for surface tension and viscosity measurements we need to measure the surface oscillation of levitated droplet, therefore we must develop the generation system for the surface oscillation of liquid droplet into the ADL system. To generate the surface oscillation of levitated droplet by ADL technique, Langstaff *et al*⁵⁾ applied the acoustic oscillation system using sound speakers. We combined the improved conical nozzle system and the acoustic oscillation system into the ADL system for measurements of density and viscosity of molten oxides. We report our measurement results of molten oxides, CaO-SiO₂-Al₂O₃ system and welding fluxes, using this new ADL system.

Aerodynamic levitation (ADL) system for measurement of density and viscosity of molten oxides

Aerodynamic levitation (ADL) technique is fundamentally simple floating method of the samples by the gas-jet flow from conical nozzles, and achieves the containerless conditions to keep sample position. In the ADL technique, we newly applied the acoustic oscillation system to generate the surface oscillation of levitated droplets. Figure 1 shows the schematic figure of our ADL system for thermophysical properties measurement of molten oxides. Spherical shaped solid oxide samples with about 2 mm in diameter were levitated by the gas-jet flow from the conical nozzle, and then solid samples were melted under the containerless conditions by CO₂ laser irradiation. For the thermophysical property measurements, we applied two CO₂ laser irradiation to the samples from the top and the bottom in order to reduce the temperature gradient in samples. The sample temperature was measured by the monochromatic pyrometer with wavelength of nm.

The droplet shape from the side view shown as shown in Figure 2 was observed by the high-speed camera as the shadow image by the back light illumination with 200mW He-Ne laser and with the beam shape modification system to make parallel beam. Using the static shape of levitated droplet of molten oxides without the surface oscillation, we obtained the volume of molten oxides with the assumption of symmetrical ellipsoid shape, and then we obtained the density using the average mass of samples measured before and after the experiments. For the viscosity measurements, we newly applied the acoustic oscillation system into the gas flow path

for the gas jet. Two sound speakers with phase matching were set in the small chamber inserted into gas flow path, then the single wave length signal input into two speakers. By the acoustic oscillation system the levitation gas-jet flow from the conical nozzle has single wavelength oscillation, as a result the droplet oscillates with the same frequency as the input signal. The oscillation generates the surface oscillation as shown in Figure 3. From the surface oscillation damping time constant t_0 , we obtain viscosity η of droplet samples from following equation⁶⁾;

$$\eta = \frac{3M}{20\pi R} t_0 \quad (1)$$

where M, R , are sample mass and radius respectively.

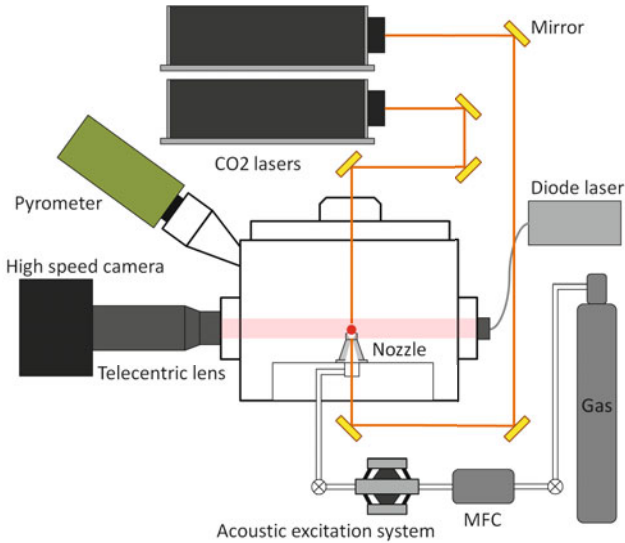


Figure 1 Schematic diagram of aerodynamic levitation system combine with acoustic oscillation generators.

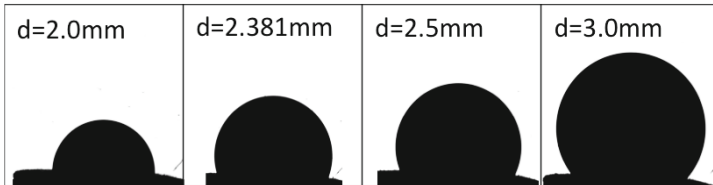


Figure 2 Shadow image of oxide droplet by ADL from the side view. Revealing over the half shape of sample from the top of nozzle in the case of over the diameter of 2.381mm.

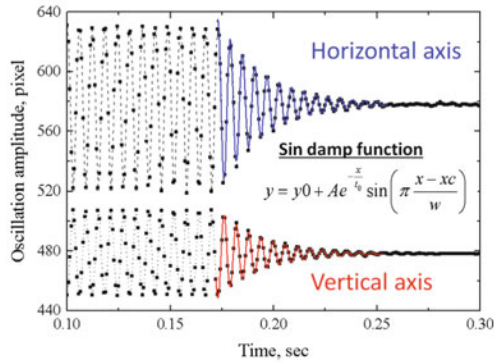


Figure 3 Surface oscillation data from the time variation of horizontal and vertical axis length of levitated oxide droplet. Damping time obtained from the time at stopping oscillation generation by acoustic speakers.

Preparation of Oxide samples, slag and welding flux, for ADL

For slag sample, we selected ternary oxide system of $\text{CaO-Al}_2\text{O}_3\text{-SiO}_2$, which were based on $\text{CaO-Al}_2\text{O}_3$ with small additions of SiO_2 . To make the samples for ADL experiments, we prepared following procedures. At first, powder oxides of CaO , Al_2O_3 , and SiO_2 with purity of 99.9% were annealed in N_2 gas flow conditions at 1200K and 1hour for reducing moistures in the powders. Then these powders were measured weight for adjusting the compositions and there were melted for making spherical shaped samples with diameter of 1.5-2.5mm by CO_2 laser on the chill Cu plate. Also for welding flux sample, we prepared same procedures. All oxide samples compositions are listed in Table 1 and Table2. In table 2, the names of flux are IL (ILmenite), RT(Rutile Type), LT(Lime Titania) and LH(Low Hydrogen). These names are classified by welding conditions and welding purposes. We also used the sample of G300 oxide. The G300 oxide is used in the commercial welding rod. We used in measurements the G300 samples peeled off from the welding rod. T_m is liquids-line temperature calculated by CALPHD.

Table 1 Slag oxide sample composition (wt%)

	CaO	Al ₂ O ₃	SiO ₂	T _m [K]
CAS-1	50	40	10	1681
CAS-2	55	35	10	1639
CAS-3	60	30	10	1773
CAS-4	50	30	14	1665

Table 2 Welding flux oxide compositions (wt%)

	SiO ₂	Al ₂ O ₃	CaO	MgO	Mn ₃ O	TiO ₂	Fe ₂ O ₃	T _m [K]
IL flux	25.9		5.8		20.4	19.2	28.8	
RT flux	24.0		2.6		9.0	64.4		
LT flux	21.9		12.2		21.0	44.8		
LH flux	16.7	7.6	57.8		3.2	14.7		

Measurement results of density by ADL

Using ADL technique combined with the acoustic oscillation method, we obtained density and viscosity of molten oxides. Figure 4 shows the results of density measurements of slag oxide sample CaO-Al₂O₃-SiO₂ systems. We obtained the density data of all samples in the temperature range from 800K to over 2200K. These density data of molten oxides of CaO-Al₂O₃-SiO₂ system at high temperature could be first time obtained. At low temperature regions, our measured data is good agreement with published data. Published density data of CAS-1 is $2.75 \times 10^3 \text{ kg/m}^3$ at $1480^\circ\text{C}^{7)}$, and that of CAS-2 is $2.73 \times 10^3 \text{ kg/m}^3$ at $1600^\circ\text{C}^{7)}$. Using ADL system for a containerless technique, we could obtain the density data at high temperature over 2000K without published data. These density data obtained by free cooling in the dried air conditions by laser power-off at the highest temperature. Therefore, all oxides changed from supercooled liquid to solid with the amorphous structure. After solidification, we confirmed that all samples had amorphous structure by x-ray diffraction. Therefore, these density data shown in Figure 4 include the liquid state and the solid state with amorphous structure. In Figure 4, for CAS-1 and CAS-4 slope of density change with temperature changed at around 1500K. We attributed that this temperature was transition temperature from the supercooled liquid to the amorphous solid, but we found the transition temperature was at an even lower temperature around 800K by the differential thermal analysis (DTA). Therefore, for CAS-1 and CAS-4 slope change of density with temperature around 1500K should be another reasons. Possible reason is deformation of droplet by gas-jet flow with the change of sample viscosity at the temperature. Future experiments, we should be clarified the slope change reasons. From present results, we found characteristic nature of CaO-Al₂O₃-SiO₂ system density. In the Figure 4, solid and dashed line shows previous results of molten CaAl₂O₄. Comparing the CaAl₂O₄ density^{3,5)}, the density of CaO-Al₂O₃-SiO₂ system relatively small. This means that, SiO₂ addition expands molten CaO-Al₂O₃ system volume⁸⁾. From the structure viewpoint, expansion of volume by addition of SiO₂ means making large free volume space in liquids. We try to clarify the hypothesis by scattering experiments. Combining our new density measurements technique with structure analysis, x-ray and neutron scattering, should be powerful tool for understanding molten oxide properties for the future.

Figure 5 is density measurements results of molten oxides for the welding flux. From the results, we found that density of molten oxides for the welding flux is larger than molten oxide for slag. Welding flux oxides includes Fe and Ti atoms, so mass is larger than the slag oxide. However, temperature dependence of these densities almost the same slope with the temperature changes. This means that, SiO₂-CaO system makes mainly atomic coordinate structure in the liquid, and Fe₂O₃ and TiO₂ does not strongly effect on the formation of the atomic coordinate

structure. Based on the present results, a future project will be planned to study the atomic coordinate structure by scattering experiment in the future. In that experiment, these density data many useful for structure analysis.

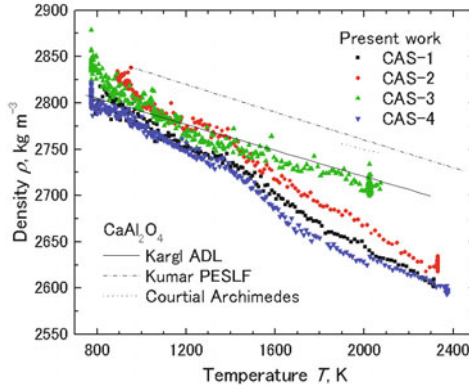


Figure 4 Temperature dependence of density of molten slag oxides by ADL. Line data is molten CaAl_2O_4 density.

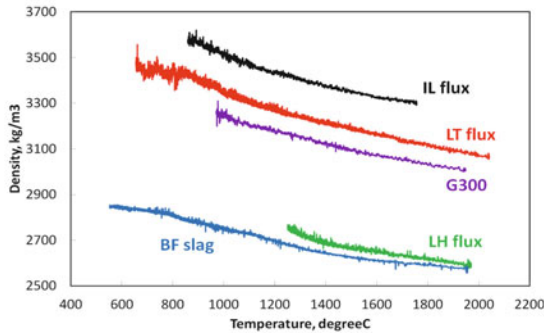


Figure 5 Temperature dependence of density of molten oxides used for welding flux.

Measurement results of viscosity of molten oxides by ADL with acoustic oscillation system

Results of viscosity measurements by ADL with acoustic oscillation system for molten oxide of slag and welding flux are shown in Figure 6 and 7. Figure 6 shows the results of slag oxides. CAS-1 to 4 are listed in Table 1, and CAS-1 to 4 are same compositions of CAS with small amount of Fe for checking about the absorption of laser wave length. Comparing CAS with CASF, there are no differences, and consequently we confirmed the reproducibility of the measurement technique. Present viscosity measurements using ADL system with CO_2 laser heating achieved easily high temperature of slag samples, the previous measurement data using containers is in the lower temperature regions around 1500°C . For the case of CAS-1 to 4, the

viscosity at 1500 °C reported from 0.2 to 0.5 Pa·s⁷⁾. Our measurements did not cover the temperature, but extrapolating of measured data to the low temperature regions the viscosity value agrees with the published data range. From the temperature dependence of viscosity of slag oxides, all viscosity data were well fitted by Arrhenius type equations. From Arrhenius plotting of viscosity with inverse temperature, CAS-3 shows different tendency with other compositions. In density data shown in Figure 4, CAS-3 show difference with other compositions. The relationship between viscosity and density⁹⁾ is being studied future.

Figure 7 shows the result of viscosity measurement of molten oxide for welding fluxes. Comparing the viscosity of welding flux oxides with slag oxides, the viscosity of welding flux oxides is smaller than that of slag oxides. Since welding flux is used with moving Arc, it must move with Arc, low viscosity is required. Our data confirmed that the properties of the flux were within required range for welding applications. The viscosity of LH-flux is relatively larger than the other fluxes. LH-flux contains 7.6wt% of Al₂O₃. This shows that Al₂O₃ increase viscosity of molten oxides for welding flux. Moreover, from the results, IL-flux, RT-flux, LT-flux and G300 shows similar viscosity values. Since G300 sample is commercial products, we did not know the details compositions. From the viscosity data, tendency of temperature dependence of viscosity, we expect that G300 composition similar with RT-flux composition. However, density of G300 is smaller than RT-flux. The real composition of G300 is different with RT-flux.

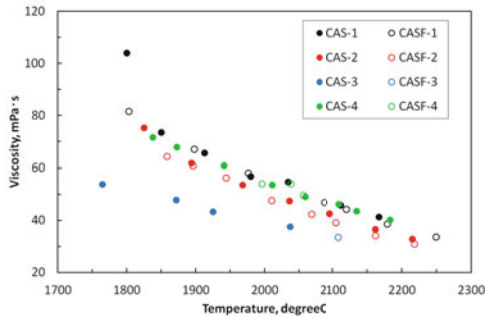


Figure 6 Temperature dependence of viscosity of molten oxide for slag of CaO-Al₂O₃-SiO₂ system.

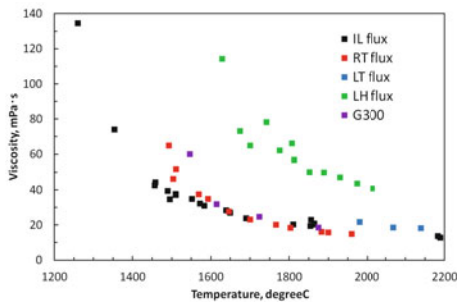


Figure 7 Temperature dependence of viscosity of molten oxide for welding fluxes.

Conclusion

Using Aerodynamic Levitation (ADL) system, we succeeded to measure density and viscosity of molten oxides for slags and welding fluxes. We obtained density and viscosity of several compositions of molten oxides at the high temperature regions without published data. Density at low temperature regions, present data was good agreement with the published data. However, for the viscosity, temperature region in our measurement is higher than the previous measurements, therefore our obtained data could not directly compare to the published data. These data showed characteristic feature of molten oxide for requirement properties according to the application of industrial processes. However, we have not yet evaluated the accuracy of this measurement system. This is reason from the deformation of molten oxide droplet shape from the ellipsoidal with axisymmetric to the vertical axis by the gas-jet flow. We have not understood the deformation reason and mechanism not yet, but for evaluating accuracy of the measurement system we must clarify the deformation droplet in future.

Acknowledgment

This work was funded by Japan Astronautical and Exploration Agency (JAXA) and KAKENHI No. 24360316.

References

- ¹⁾ E.T. Turkdogan, "Physicochemical Properties of Molten Slags and Glasses" (London: The Metals Society, 1983).
- ²⁾ I. Egry, "Containerless processing for thermophysical property measurements of liquid metals: review and outlook", *High Temp.-High Press.*, 40 (2011) 203-214..
- ³⁾ M. V. Kumar, J. T. Okada, T. Ishikawa, P. -F. Paradis and Y. Watanabe, "Density measurement of glass and liquid CaAl_2O_4 using a pressurized electrostatic levitator" *Meas. Sci. Tech.*, 25 (2014) 085301.
- ⁴⁾ A. Mizuno, J. Tamura, S. Kohara, M. Watanabe, "Comparative study on structural variations during containerless solidification processes of Fe-B and Fe-C eutectic alloys", *ISIJ International*, 52 (2012), 770–773.
- ⁵⁾ D. Langstaff, M. Gunn, G. N. Greaves, A. Marsing, and F. Kargl, "Aerodynamic levitator furnace for measuring thermophysical properties of refractory liquids", *Rev. Sci. Instrum. Methods*, 84 (2013) 124901.
- ⁶⁾ H. Lamb, "Hydrodynamics", 6th ed. (Cambridge University Press, Cambridge, 1932), 473–639.
- ⁷⁾ Data listed in the "SLAG ATRAS, 2nd Ed., Ed. By VDEh, (Verlag Stahleisen GmbH, 1995)".
- ⁸⁾ P. Courtial and D. B. Dingwell, "Nonlinear composition dependence of molar volume of melts in the $\text{CaO-Al}_2\text{O}_3\text{-SiO}_2$ system", *Geochim. Cosmochim. Acta*, 59 (1995) 3685.
- ⁹⁾ T. Iida, H. Sakai, Y. Kita and K. Murakami, "Equation for Estimating Viscosities of Industrial Mold Fluxes" *High Temp. Mater. and Process.*, 19 (2000), 153.

Solubility of CaO and Al₂O₃ in Metallic Copper Saturated Molten Phase

Joseph Hamuyuni, Pekka Taskinen

Aalto University School of Chemical Technology, Department of Materials Science and Engineering, Metallurgical Thermodynamics and Modeling Research Group, Vuorimiehentie 2K, PO Box 16200, FI-00076 Aalto, Finland

Keywords: Phase diagram, copper smelting, Cu₂O, CaO, Al₂O₃

Abstract

Solubilities of CaO and Al₂O₃ in copper rich molten oxide phases have wide industrial applications in various copper smelting and refining operations producing copper matte or blister copper. However, experimentally determined solubility data on these simple systems are still scarce even after a long spell of industrial copper making. In this experimental study, these solubilities have been quantified by a static equilibration technique at 1250 °C in an inert atmosphere of purified argon gas. The compositions of condensed molten phases and all solids in equilibrium have been analyzed and quantified using Electron Probe Micro-Analyzer (EPMA).

Introduction

The Cu-O-Al₂O₃-CaO system is an important sub system of copper making slag [1,2]. This is because fundamental slag properties of viscosity, surface tension and density are all affected by CaO, Al₂O₃ content of slag [1]. Additions of CaO, Al₂O₃ increases surface tension and slag density while CaO additions also decreases the slag viscosity [1]. Accurate thermodynamic and equilibria data of this system therefore enhances capabilities of predicting slag behavior in smelting and converting processes [3,4,5,6]. Accurate description of simple systems (sub systems) leads to improved estimation of phase equilibria of multicomponent systems.

In the copper smelting process, Cu is introduced from feed materials while Al₂O₃ and CaO are mainly contained in flux. Due to very high oxidation nature of the process, copper is introduced in the slag phase. Most smelting furnaces utilizes fluxing as a tool for achieving optimal operating conditions, i.e. high yields at both low energy consumption and minimal refractory corrosion. Good knowledge of slag chemistry is therefore necessary for process control. With the application of multicomponent phase equilibria, thermodynamics has been used as a valuable tool in estimation of temperature, pressure and composition ranges in which phases of interest in processes are stable. However, composition of molten phase cannot be estimated solely from first principle calculations. As such, experimental data carefully obtained is mandatory for simple systems (binaries and ternaries) if accurate information is to be acquired for simulation of multicomponent systems [6].

The sub-systems Cu-O [7,8], Cu-O-CaO [4,5,9,10], and Cu-O-Al₂O₃ [11,12,13,14] have been investigated before despite gaps in liquidus data. The system Cu-O-Al₂O₃-CaO in air has also been recently studied in Hamuyuni et al.[6]. In their study they investigated the triple points' equilibria in the temperature range 1150 to 1400 °C, employing the static equilibration technique in oxidizing conditions (air). Based on this recent study, the starting compositions for this study (in inert atmosphere of purified argon gas) have been estimated.

This paper presents experimental phase equilibria results in the system Cu-O-Al₂O₃-CaO at copper saturation and temperature of 1250 °C. The equilibration and rapid quenching technique and followed by EPMA has been employed.

Method

Sample Preparation

We employed high purity powders as well as self-prepared cuprite (Cu₂O) in the study, see Table 1. The cuprite was prepared from A-grade copper cathode by oxidation.

Table 1 Purities and sources of materials used in the present study

Chemical	Source	Mass fraction purity
Copper pellets	Boliden Harjavalta Oy (Finland)	0.99996
Calcium oxide	Sigma-Aldrich (Germany)	0.999
Aluminium oxide	Sigma-Aldrich (Germany)	0.9999

Self-made cuprite was acquired by oxidizing pure cathode copper in air at 1050 °C for 120 hours in a Lenton muffle furnace (Type; UAF 16/10) and quenching in air. Using EDS the purity of cuprite was estimated to be 99.99 wt %. CaO and Al₂O₃ when needed in right proportions were calcined, pelletized (1 g pellets) and synthesized to acquire primary phases, see in table 2.

Table 2 Conditions for synthesizing primary phases for the experiments

Batch number	CaO/(CaO+Al ₂ O ₃) (wt %)	Synthesizing Temperature (°C)	Synthesizing time (hours)
1	0.8	1500	8
2	0.55	1365	8
3	0.42	1365	8
4	0.29	1575	5
5	0.15	1600	5

Palletization of powders to enhance reaction was done at 30 MPa before synthesized at target temperatures. About 14 mm diameter and 3mm thick pellets were obtained. During synthesization, heating and cooling rates were maintained at 4 °C per minute. Sample amount for equilibration experiments were small (0.2 g), in order to facilitate both fast equilibrium plus good quenching at the end of equilibration experiments. Platinum envelope (for holding sample) and wire (for suspension) have been used for the purpose of preserving the purity of the system.

Experimental Apparatus and Procedure

A Lenton vertical electrical resistance tube furnace (type; LTF- 16/450) (previously employed in Hamuyuni et al. [6]) of 35-mm inner diameter alumina work tube, see Figure 1, was employed in this study. Temperature measurement was achieved with a calibrated S-type thermocouple (Johnson-Matthey Noble Metals, UK). The thermocouple was connected to a Keithley 2010 DMM multimeter, and cold junction compensation was performed by a PT100 resistance thermometer

(SKS-Group, Finland, tolerance class B 1/10), connected to a Keithley 2000 DMM multimeter. Employing this calibrated thermocouple, temperature profiles were acquired in order to map the 'hot zone' length of the furnace.

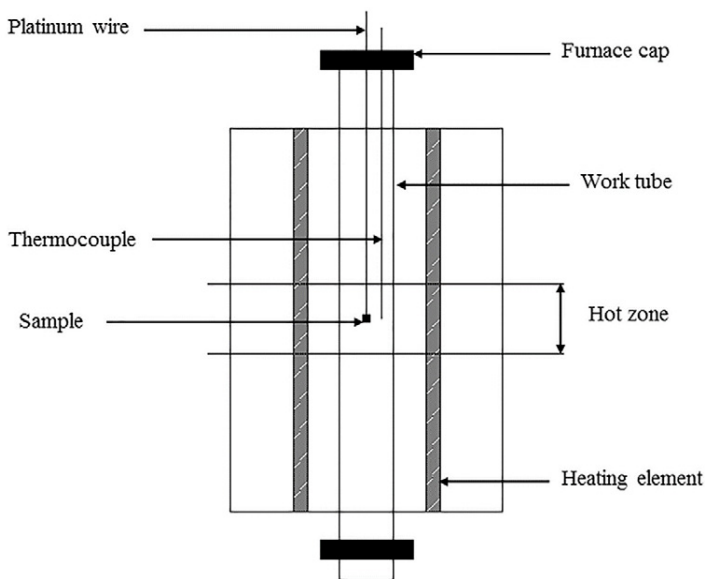


Figure 1 Schematic vertical section of the experimental furnace.

Samples were introduced into the furnace's hot zone supported by platinum wire, and were pulled from the bottom of the furnace's work tube. Purified argon gas was employed in creating an inert atmosphere. Therefore argon gas was flushed for 30 minutes before the sample was brought in hot zone, so as to remove residual oxygen or any gas in the tube. Equilibria investigated in this system contains two solids in equilibrium with two liquids (4 phases). Thus for this system (using 4 components) fixing the temperature brings the system to univariant. Five (5) univariant points in the dimension space of interest in the system have been chosen and experimentally studied. Their 4- phase equilibria as numbered and referred to in this study is seen in Table 3.

Table 3 The four-phase equilibria studied in this work

Experiment number	Corresponding four- phase equilibria
1	Liquid ₁ + Liquid ₂ + Halite + C ₃ A
2	Liquid ₁ + Liquid ₂ + C ₃ A + C ₁₂ A ₇
3	Liquid ₁ + Liquid ₂ + C ₁₂ A ₇ + CA
4	Liquid ₁ + Liquid ₂ + CA + CA ₂
5	Liquid ₁ + Liquid ₂ + CA ₂ + CA ₆

In Table 3, the notation Liquid₁ and Liquid₂ are the molten oxide and molten metal alloy respectively.

At the end of equilibration time, the flask of cold water (0 °C) was placed at the bottom of the work tube. The specimen was then released so that it quenched in the quenching media. Samples were dried and imbedded in epoxy resin. Because of the hygroscopic nature of CaO, all specimens were prepared with non-water- based lubricants. For this reason, Propylene glycol (Sigma Aldrich, Germany) was employed for fine polishing. All specimens were carbon-coated by means of a Leica EM SCD050 Coater (supplied by Leica Mikrosysteme GmbH, Wien, Austria.), before EPMA analyses.

Specimen Analysis

The composition of homogenous phases were measured using Electron Probe Micro-Analyzer (EPMA). Cross sections of samples were employed to get a representative composition across the entire specimen. A CAMECA SX100 (Cameca SAS, France) equipment with five wavelength dispersive spectrometers (WDS) and a probe current of 40 nA was employed for EPMA. The beam diameter was kept between 1-10 μm. In certain cases where precipitates were observed, care was taken when selecting the beam diameter. An accelerating voltage of 15 kV was employed. Standards employed for analysis were Al as K α (almandine), Cu as K α (chalcopyrite), O K α (hematite) and Ca as K α (Diopside), all of which are natural minerals. All standards were acquired from Astimex Scientific ltd. The PAP matrix correction procedure [15], supplied by the equipment manufacture, was used for raw data correction. Elemental detection limits for EPMA results were: Cu; 0.07, Ca; 0.02, Al; 0.02, O; 0.14 wt %.

Results and Discussions

Results of the four phase equilibria from this study can be understood well from the tetrahedron and represented by the tie-tetrahedron in Figure 2. The five primary phase compositions for corresponding univariant equilibria investigated in this study represents fixed CaO, Al₂O₃ ratios i.e. (CaO/(CaO+Al₂O₃)), are numbered 1-5 along the CaO-Al₂O₃ binary joint of the tetrahedron. All the experimental points in the study fall thus inside the Cu-Cu₂O-CaO-Al₂O₃ dimension space of the tetrahedron and their equilibria as such may not be accurately represented by a classical isothermal section. Though the oxygen pressure is fixed in all 4 phase equilibria, its value is not known.

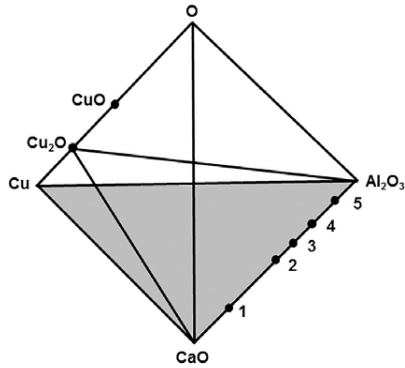


Figure 2 Schematic of the quaternary system from which the univariant equilibria was derived

The phase compositions for the univariant points as measured by EPMA are depicted in Table 4, and representing five phase regions at 1250 °C for the system Cu-O-CaO-Al₂O₃ at copper saturation. Each point represents 10 independent measured values from different locations of the same phase with a standard deviation not exceeding 1 wt %. The uncertainty of the measurements of temperature (T), elemental composition of phases, are depicted in the table as footnotes. In the table, elemental compositions of the phases quantified have been given. For comparison purposes, these elemental compositions have been recalculated to oxides, except for copper and oxygen.

Table 4 Experimentally determined compositions of liquid and solid phases for the system Cu-O-CaO-Al₂O₃ at Cu saturation equilibrated at univariant conditions. *

Sample Number	CaO/(CaO+Al ₂ O ₃)	Phase	EPMA (wt %)*				Recalculated Composition (wt %)			
			Cu	Ca	Al	O	Cu	CaO	Al ₂ O ₃	O
1	0.8	Liquid oxide	75.16 ±0.29	9.10 ±0.12	0.20 ±0.03	14.51 ±0.85	75.94	12.87	0.38	10.81
		Halite	0.26 ±0.16	56.72 ±0.19	0.17 ±0.02	41.00 ±1.27	0.26	80.86	0.33	18.55
		C ₃ A	0.16 ±0.02	42.60 ±0.31	18.67 ±0.63	38.36 ±0.95	0.16	59.73	35.35	4.76
2	0.55	Liquid oxide	78.39 ±0.65	6.76 ±0.08	0.22 ±0.08	13.58 ±0.74	79.22	9.56	0.42	10.80
		C ₃ A	1.32 ±0.02	42.27 ±0.12	18.45 ±0.23	37.62 ±0.29	1.32	59.35	34.98	4.35
		C ₁₂ A ₇	1.27 ±0.08	32.56 ±0.30	25.46 ±0.23	40.28 ±0.34	1.28	45.75	48.31	4.66
3	0.42	Liquid oxide	74.44 ±0.85	8.73 ±0.22	0.73 ±0.06	14.99 ±0.14	75.28	12.35	1.39	10.98
		C ₁₂ A ₇	1.72 ±0.05	32.39 ±0.31	25.32 ±0.40	40.50 ±0.46	1.72	45.35	47.87	5.05
		CA	0.79 ±0.09	24.26 ±0.08	32.12 ±0.12	42.52 ±0.12	0.79	34.05	60.88	4.28
4	0.29	Liquid oxide	86.34 ±0.65	0.28 ±0.02	0.34 ±0.09	13.30 ±0.33	86.12	0.39	0.64	12.85

		CA	1.03 ±0.07	24.38 ±0.58	32.13 ±0.27	42.28 ±0.34				
		CA ₂	0.71 ±0.03	15.18 ±0.16	39.39 ±0.36	44.49 ±0.27	0.71	21.29	74.60	3.40
5	0.15	Liquid oxide	87.51 ±0.90	0.09 ±0.01	0.05 ±0.03	11.54 ±0.29	88.22	0.13	0.10	11.55
		CA ₂	1.71 ±0.18	14.74 ±0.12	38.62 ±0.33	44.50 ±0.26	1.72	20.71	73.28	4.28
		CA ₆	1.64 ±0.04	5.84 ±0.05	46.15 ±0.14	46.26 ±0.16	1.64	8.18	87.29	2.88

*Standard uncertainty $u(T) = 2\text{ }^\circ\text{C}$, $u(x) = 0.5\text{ wt } \%$.

From Table 4, the solubility of CaO in liquid phase for univariant 1-3 vary within a narrow range of composition i.e., between 9.56 and 12.87 wt %. For 4 and 5, the solubility is negligible at < 0.5 wt %. Al₂O₃ solubility in the liquid phase on the other hand is low for the entire number of invariant equilibria investigated in the study with the highest composition at 1.39 wt %. The solubilities observed in this study are fairly consistent with those of the ternary system in air [6]. Liquidus experimental results have been projected on the Cu₂O-CaO-Al₂O₃ plane and are depicted in figure 3.

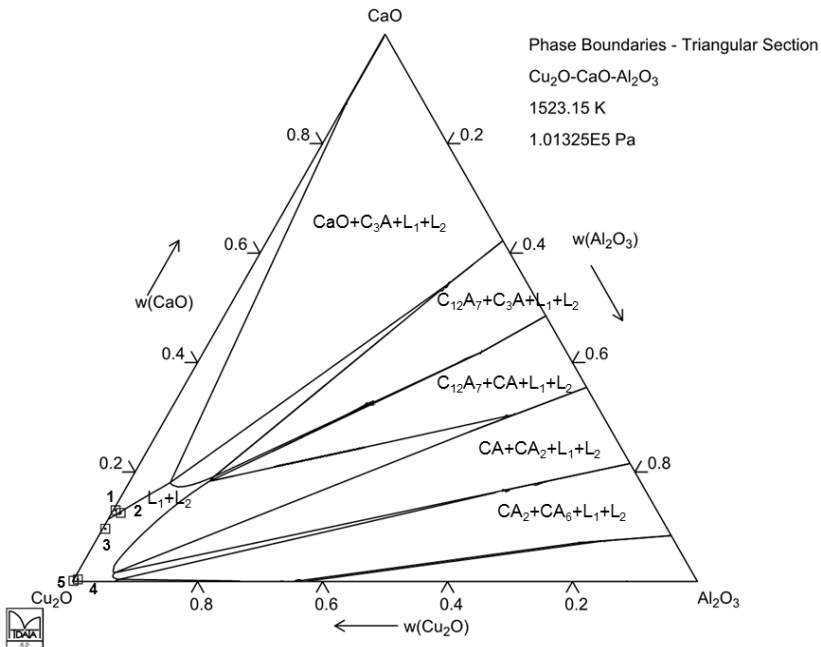


Figure 3 Experimental points projected on the Cu₂O-CaO-Al₂O₃ ternary plane. The numbers represents corresponding univariant points, the phase boundaries were calculated using MTOX database.

From Figure 3, the difference between the experimental results and MTOX can be observed. Especially the concentration of Al_2O_3 in the liquid oxide phase has the largest difference in composition.

Copper was found to be soluble in all solid phases but to varying degrees. This is depicted in Figure 4. In the figure, the number attached to each phase represents the corresponding four-phase region of Table 3. In both CA_6 and CA_2 , copper was found to dissolve more than in the other aluminates with solubilities between 1.64 and 1.72 wt % copper. The C_3A and C_{12}A_7 in univariant 2 as well as CA when in equilibria with CA_2 also have high solubilities of copper with copper content exceeding 1 wt % in all three phases. Halite (CaO) and C_3A when in equilibrium with Halite have negligible copper solubilities.

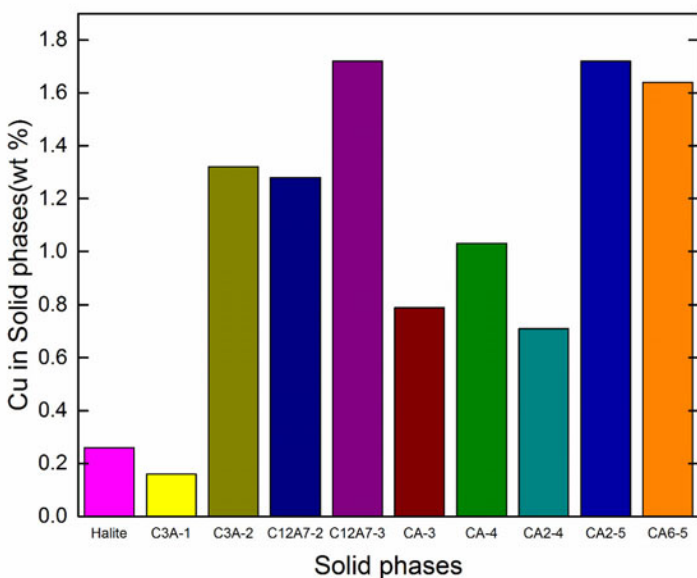


Figure 4 Solubilities of copper in halite (CaO) and calcium aluminate phases in the four-phase equilibria of Table 3 with molten metallic copper and an oxide melt.

Four phase equilibria for the 5 univariants points investigated in this study are depicted in Figure 5 using backscattered images of 4 homogenous phases in equilibrium at fixed temperature of 1250 °C. In all the micrographs in the figure, the brighter matrices are the liquid phases L_1 and L_2 representing oxide liquid and liquid copper respectively. Univariant point 3 with similar phenomena as point 2 has not been included.

In Figure 5b, small precipitates of Cu_2O were observed on quenched samples. Selecting of areas for analysis therefore had to be carefully done so that this phenomena does not interfere with measured values. C_3A is the most hygroscopic of the calcium aluminates and can be observed by the breaking down of the phase in Figure 5a and b.

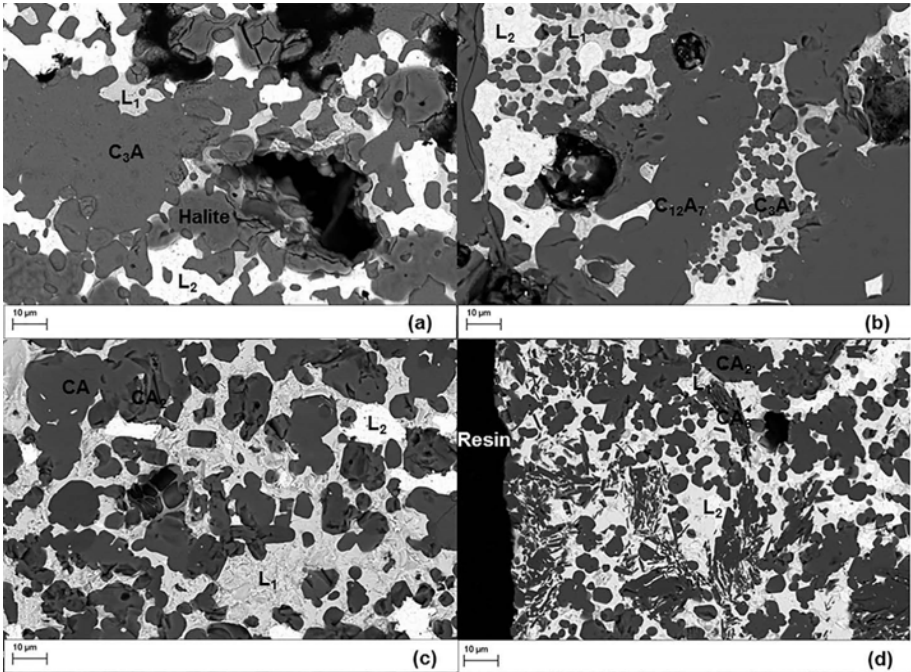


Figure 5 Backscattered scanning electron micrographs of quenched samples, equilibrated in copper saturation at 1250 °C: (a) univariant #1, (b) univariant #2, (c) univariant #4, (d) univariant #5, from Table 3

Conclusions

Solubilities of CaO and Al₂O₃ in copper rich molten oxide phases have been investigated in the system Cu-O-Al₂O₃-CaO. In the investigation, the high temperature equilibration followed by fast quenching technique has been employed. Experiments were conducted in an inert atmosphere of purified argon gas at 1250 °C. The compositions of condensed molten phases and all solids in equilibrium have been analyzed by Electron Probe Micro-Analyzer (EPMA).

Five (5) four phase univariant equilibria systematically chosen to represent the system have been used in the study. For the univariant equilibria investigated at this temperature, CaO in liquid phase studied varies between 0.13 and 12.87 while Al₂O₃ is negligible at ≤1.39 wt %. C₁₂A₇ when in equilibrium with CA and CA₂ when in equilibrium with CA₆ have the highest copper solubilities between 1.64 and 1.72 wt % copper.

Acknowledgements

This research was financially supported by Association of Finnish Steel and Metal Producers and Systems Integrated Metal Processes (SIMP) project of FIMECC.

References

1. H. G. Kim and H.Y. Sohn, Effects of CaO, Al₂O₃, and MgO Additions on the Copper Solubility, Ferric/Ferrous Ratio, and Minor-Element Behavior of Iron-Silicate Slags, *Metallurgical and Materials Transactions B*, 29 (3) (1998) 583-590.
2. A. Malfliet, S. Lotfian, L. Scheunis, V. Petkov, L. Pandelaers, P.T. Jones, B. Blanpain. Degradation mechanisms and use of refractory linings in copper production processes: A critical review. *Journal of the European Ceramic Society*, 34 (3) (2014) 849–876.
3. S. Nikolic, P. C. Hayes, and E. Jak, Phase Equilibria in Ferrous Calcium Silicate Slags: Part III. Copper-Saturated Slag at 1250 °C and 1300 °C at an Oxygen Partial Pressure of 10⁻⁶ atm, *Metallurgical and Materials Transactions B*, 39 (2) (2008) 200-209.
4. J. Hamuyuni, N. Hellstén, G. Akdogan, & P. Taskinen, Experimental determination of the liquidus of the binary system Cu₂O-CaO in air from 1050 to 1500 °C. *The Journal of Chemical Thermodynamics*, 7 (2014) 112 - 115.
5. J. Hamuyuni, N. Hellstén, G. Akdogan, & P. Taskinen, The Liquidus in Cu-O-CaO System at Metallic Copper Saturation up to 1698 K. *Journal of the American Ceramic Society*, 98 (1) (2015) 320-323.
6. J. Hamuyuni, P. Taskinen, Experimental phase equilibria of the system Cu–O–CaO–Al₂O₃ in air, *Journal of the European Ceramic Society* 36 (2016) 847–855.
7. D. Shishin & S. A. Decterov, Critical assessment and thermodynamic modeling of the Cu–O and Cu–O–S systems. *Calphad*, 38 (2012) 59 - 70.
8. B. Hallstedt, D. Risold, & L. J. Gauckler. Thermodynamic Assessment of the Cu-O System. *Journal of Phase equilibria*, 15 (1994) 483-499.
9. A. M. Gadalla, & J. White. Equilibrium relationships in the system CuO-Cu₂O-CaO. *Transactions of the British Ceramic Society*, 65 (1966) 181-190.
10. C. F. Tsang, J. K. Meen, & D. Elthon, Phase Equilibria of the Calcium Oxide-Copper Oxide System in Oxygen at 1 atm. *Journal of the American Ceramic Society*, 78 (1995) 1863-1868.
11. S. K. Misra, & A. C., Chaklader. The system Copper oxide-Alumina. *Journal of the American Ceramic Society*, 46 (1963) 509.
12. A. M. Gadalla, & J. White, Equilibrium relationships in the system CuO-Cu₂O-Al₂O₃. *Journal of the British Ceramic Society*, 63 (1964) 39 - 62.
13. B. Hallstedt., Assessment of the CaO-Al₂O₃ System. *Journal of the American ceramic society*, 73 (1990) 15 - 23.
14. G. Eriksson, & A. D. Pelton, Critical Evaluation and Optimization of the Thermodynamic Properties and Phase Diagrams of the CaO-Al₂O₃, Al₂O₃-SiO₂, and CaO-Al₂O₃-SiO₂ Systems. *Metallurgical and Materials Transactions B*, 24 (1993) 807 - 816.
15. J.L. Pouchou F., Pichoir, Basic Expression of PAP Computation for Quantitative EPMA, in 11th International Congress on X-ray Optics and Microanalysis (ICXOM), in: J.D. Brown, R.H. Packwood (Eds.), ICXOM-11, Ontario, Canada, 1987.

INTEGRATED EXPERIMENTAL AND MODELLING RESEARCH FOR NON-FERROUS SMELTING AND RECYCLING SYSTEMS

Evgueni Jak¹, Taufiq Hidayat¹, Denis Shishin¹, Ata Fallah Mehrjardi¹, Jiang Chen¹, Sergei Decterov², Peter Hayes¹

¹ PYROSEARCH, Pyrometallurgy Research Laboratory, School of Chemical Engineering, The University of Queensland, Brisbane, Queensland, 4072, Australia

² CRCT, Ecole Polytechnique de Montreal, Canada

Abstract

The chemistries of industrial pyrometallurgical non-ferrous smelting and recycling processes are becoming increasingly complex. Optimisation of process conditions, charge composition, temperature, oxygen partial pressure, and partitioning of minor elements between phases and different process streams require accurate description of phase equilibria and thermodynamics which are the focus of the present research. The experiments involve high temperature equilibration in controlled gas atmospheres, rapid quenching and direct measurement of equilibrium phase compositions with quantitative microanalytical techniques including electron probe X-ray microanalysis and Laser Ablation ICP-MS. The thermodynamic modelling is undertaken using computer package FactSage with the quasi-chemical model for the liquid slag phase and other advanced models. Experimental and modelling studies are combined into an integrated research program focused on the major elements Cu-Pb-Fe-O-Si-S system, slagging Al, Ca, Mg and other minor elements. The ongoing development of the research methodologies has resulted in significant advances in research capabilities. Examples of applications are given.

Keywords: copper and lead smelting, recycling, slag, phase equilibria, thermodynamic modelling, liquidus, minor elements distribution.

1. Introduction

Economic and environmental issues require optimisation of the metallurgical primary and recycling operations that in turn needs accurate and reliable information on high temperature chemistry of increasingly complex slag/matte/metal systems. The lack of data and reliable models exists due to difficulties in high temperature experiments and thermodynamic modelling. Recent advances in analytical techniques, experimental methodologies, computer power and thermodynamic modelling theory provide new opportunities in this field. Present paper i) outlines recent progress by the authors and ii) gives examples of the integrated experimental and thermodynamic modelling research on the high temperature slag/matte/metal system with major elements Cu-Pb-Fe-O-Si-S, slagging elements Al, Ca, Mg and other minor elements such as As, Ag, Au, Sb, Sn, Bi and Zn. This research program is undertaken to support smelting and recycling production of copper, lead and other non-ferrous metals.

2. Research Tools

2.1. Experimental Methodology

The equilibration/quenching/EPMA experimental approach that is being continuously developed

and applied to the increasingly complex systems is briefly explained with reference to Figure 1 [1]. An artificial oxide mixture prepared from the analytically pure powders, pre-sintered solids or pre-melted master slags to obtain after equilibration a predetermined bulk composition X with two or more phases, is placed in a crucible, a thin foil or on a substrate made of a primary phase, then suspended on a wire to be equilibrated at controlled temperatures and gas atmospheres (maintained by mixture of pure gases such as CO, CO₂, H₂, Ar, SO₂ etc) or inside sealed ampoules. Predictions with preliminary thermodynamic models using FactSage package [2] are used to plan experiments. The furnace temperature is controlled to achieve overall accuracy within 5 K or better. The gas atmosphere is controlled to the actual accuracy of P_{O₂} better than ± 0.1 Log (P_{O₂}) units (~±0.02 LogP_{O₂} can be achieved with special measures). The samples are quenched into iced water or salt solution so that the liquid phases are converted to glass or fine microcrystalline material, and the solid crystals existed at the temperature are frozen in place thus representing equilibrium phases existed at the temperature (see example of final microstructure in Figure 1). The sections are prepared, resulting microstructures are examined with optical and then Scanning Electron Microscopy (SEM) and the compositions of the phases (glass, microcrystalline and solids) are then measured using an electron probe X-ray microanalyser (EPMA) with Wavelength Dispersive Detectors (WDD) with accuracy within 1 wt % or better. Laser Ablation ICP-MS microanalysis technique is used for minor elements at low (ppm and ppb) concentrations with spatial resolution of ~30-50µm.

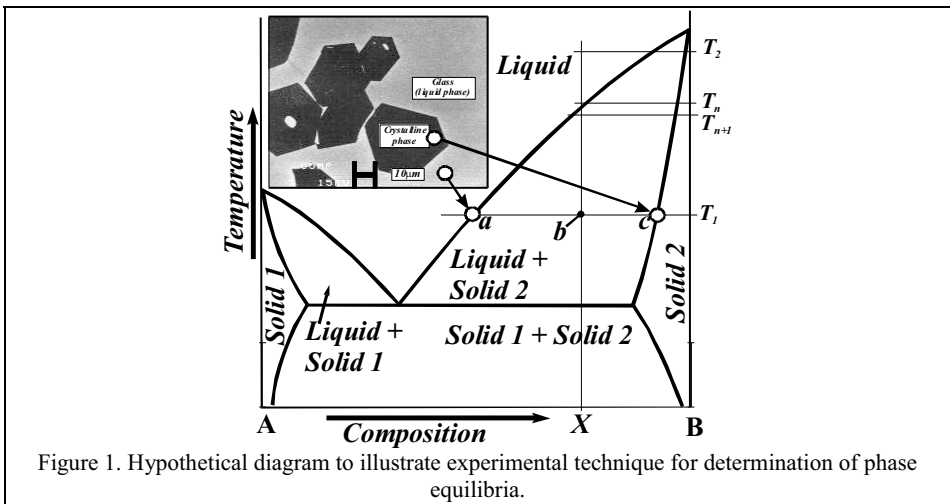


Figure 1. Hypothetical diagram to illustrate experimental technique for determination of phase equilibria.

The key advantage of this approach is that the accuracy of results are independent from the changes of bulk composition during the experiment (provided the achievement of equilibrium between phases is confirmed) since the compositions of phases are measured after rather than before the experiment thus eliminating uncertainties due to interaction with the containment material (crucible, substrate), vaporisation of some elements during equilibration, uncertainties in the initial mixture composition and the changes in phase compositions due to the gas / metal / matte / slag / solid(s) interactions. The small size (down to a several micron film) and direct exposure to gas and quenching media of the liquid slag /matte / metal phases equilibrated on

solid substrates enhances achievement of a) equilibrium of condensed phases with the gas phase as well as b) high quenching rates, thus extending the applications to the systems where these factors are the limitations for research. The compositions of all liquid and solid solution phases at equilibrium are measured directly providing data for further thermodynamic modelling. The achievement of equilibrium and other factors affecting uncertainties can be directly investigated from microstructural analysis and compositional profiles at micro ($\sim <20\mu\text{m}$) and macro ($\sim >20\mu\text{m}$) scale measured with EPMA or other microanalysis techniques. The key tests to ensure the achievement of equilibrium include:

1. Changing the equilibration time to confirm that no further changes take place with time.
 2. Confirming the chemical homogeneity of phases and samples.
 3. Approaching equilibrium from different directions.
 4. Analysing possible reactions taking place during equilibration.
- Available analytical techniques including SEM imaging and EPMA analysis of the compositional gradients across the phases used in the present study are particularly effective for the analysis of possible signs of incomplete reaction pathways during equilibration. None of the separate tests on their own can be taken as the final prove of the achievement of equilibria and the systematic and simultaneous application of all four tests is essential.

The equilibration / quenching / microanalysis approach to phase equilibrium determination has greatly extended the range of metallurgical systems that can be characterised. Experimental methodology is described in more details in previous publications [1, 3]. Examples of the application of this experimental approach can be found in a number of publications for various chemical systems, and a summary of earlier publications relevant to different chemical systems is given in Jak [3].

2.2. Thermodynamic modelling

Thermodynamic databases are developed through thermodynamic optimization that involves selection of proper thermodynamic models for all phases in a system, critical simultaneous evaluation of all available thermodynamic and phase equilibrium data and optimization of thermodynamic model parameters to obtain one self-consistent set best reproducing all experimental data as functions of temperature and composition.

In the thermodynamic "optimization" of a system, all available thermodynamic and phase equilibrium data for the system are evaluated simultaneously to obtain one set of model equations for the Gibbs energies of all phases as functions of temperature and composition. From these equations, the thermodynamic properties and the phase diagrams can be back-calculated. Thermodynamic property data, such as activity data, can aid in the evaluation of the phase diagram, and phase diagram measurements can be used to deduce thermodynamic properties. Discrepancies in the available data can be identified during the development of the model. These discrepancies can then be resolved through new experimental studies that, if possible, are undertaken in areas essential for further thermodynamic optimizations. Multicomponent data, if available, are used to derive and test low-order (binary and ternary) model parameters, and if multicomponent data for a system are lacking, the low-order parameters are extrapolated. In this way, the thermodynamic databases are developed and all the data are rendered self-consistent and consistent with thermodynamic principles. FactSage computer system [2] has been used by the authors for the thermodynamic

modelling. The molten slag phase is modelled by the Modified Quasichemical Model [4] in which short-range-ordering is taken into account. Oxide solid solutions are described with a polynomial model or with the Compound Energy Formalism [5].

2.3. Integrated thermodynamic database development using modelling and experimental studies

The integrated combination of experimental and thermodynamic modelling studies carried out in parallel is an important factor in the present study to ensure high productivity and quality of research outcomes. The initial thermodynamic assessment is used a) to evaluate existing experimental data, b) to identify areas of importance for experimental research, c) to focus new experimental work to resolve discrepancies of previous or acquire new data, and d) to assist in detailed planning of the individual experiments in complex systems. There is usually a lack of experimental information to test model predictions in the multi-component slags and therefore multi-component databases are frequently developed on the basis of only binary and ternary data thus effectively extrapolating the low order binary and ternary parameters into a multi-component area without test. The present experimental program, in addition to the work on the binary and ternary systems, specifically focuses on multi-component systems in the composition and oxygen partial pressure ranges close to the important industrial slags. The thermodynamic model then is checked and corrected to agree with those multi-component measurements in the vicinity of the industrial slags. This is an important feature of the present study – the optimisation is performed in a number of cycles from binary and ternary to the multi-component systems and back so that binaries and ternaries are reoptimized to reach agreement also with the extensive data set in the multi-component area. Summary of the examples of the integrated experimental and thermodynamic modelling approach can be found in Jak [3].

3. Overview of results relevant to the non-ferrous smelting and recycling systems.

3.1. Example of experimental study in the Cu-Fe-O-S-Si system

The Cu-Fe-O-S-Si system is essential to copper and many other non-ferrous smelting and recycling processes. Present study on this system used experimental and overall integrated approach outlined above. Reactions taking place during equilibration between gas/slag/matte/solids phases are complex and substantial development of experimental methodology was required to achieve high reliability of results. Experiments were undertaken on tridymite or spinel substrates at fixed temperature and gas atmosphere with P_{O_2} and P_{SO_2} controlled by CO/CO₂/SO₂ gas mixtures. The smallest set of graphs but sufficient to describe measured compositions of all phases included i) P_{O_2} , and S in matte and ii) “FeO”, S and Cu in slag, all plotted as functions of Cu in matte (oxygen concentrations in matte and slag were not measured in this study). Pure oxide, sulfide and metal powders were mixed in carefully planned proportions to obtain slag and matte starting compositions based on the assumption of relatively fast equilibration achieved between condensed phases. Initial starting phase compositions and proportions of oxide, sulfide and metal powders were predicted with FactSage with preliminary database. The microstructures of the preliminary short experiments were carefully analyzed, compositions of slag and matte phases were plotted in graphs and compared to predicted, composition gradients at micro and macro scales were measured in all phases across samples and

presented on the selected set of graphs. The trends of the compositional changes across phases and across samples were analyzed and this way key reactions taking place during equilibration were identified. The classification of phase microstructures was developed and introduced based on relative locations of phases. Figures 2 and 3 present example of non-equilibrium preliminary experiment in the Cu-Fe-O-S-Si system undertaken at 1200°C, $P_{\text{SO}_2}=0.25$ atm and $P_{\text{O}_2}=10^{-8.6}$ atm. The microstructure of this sample presented in Figure 2 illustrates different morphologies of matte dependent on relative locations to the gas and slag phase.

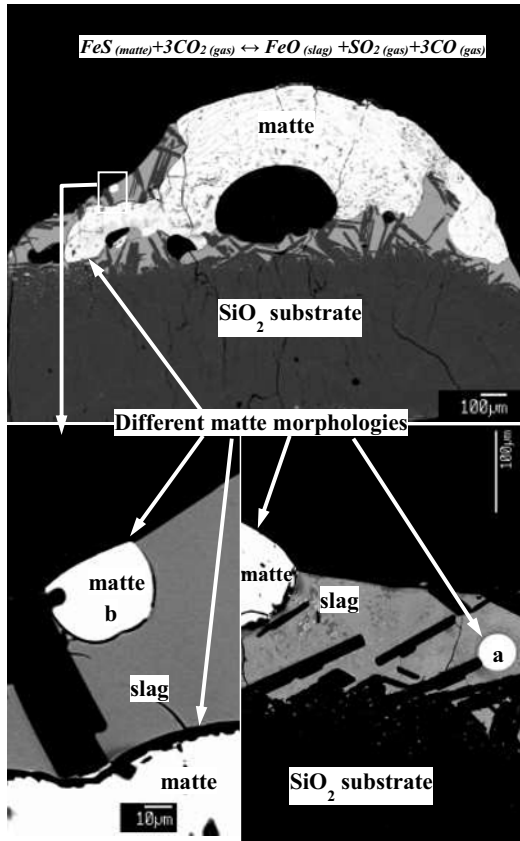


Figure 2. Example of microstructure from non-equilibrium preliminary experiment in the Cu-Fe-O-S-Si system undertaken at 1200°C, $P_{\text{SO}_2}=0.25$ atm and $P_{\text{O}_2}=10^{-8.6}$ atm.

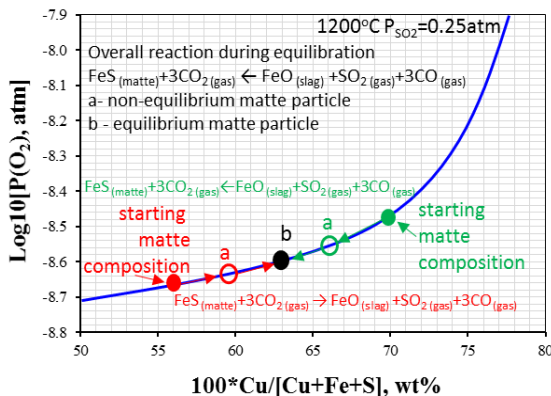


Figure 3. Schematic with oxygen partial pressure vs matte grade in the Cu-Fe-O-S-Si system at 1200°C and $P_{SO_2}=0.25$ atm showing change of the matte and slag compositions in non-equilibrium samples during equilibration at fixed oxygen partial pressure $10^{-8.6}$ atm due to the mass exchange reaction $FeS_{(matte)}+3CO_{2(gas)} \leftrightarrow FeO_{(slag)}+SO_{2(gas)}+3CO_{(gas)}$.

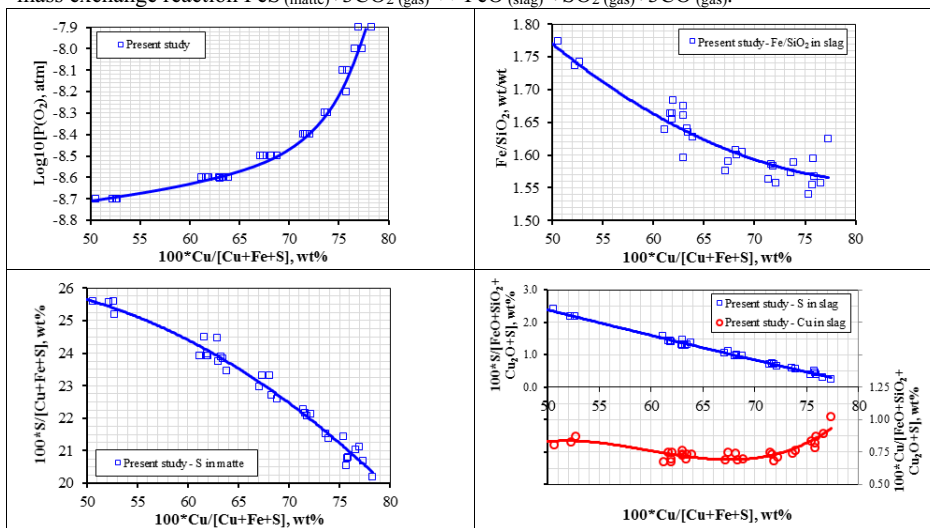


Figure 4. Set of graphs describing phase equilibria in the Cu-Fe-O-S-Si system between gas/slag/matte/tridymite at $T=1200^\circ C$ and $P_{SO_2}=0.25$ atm.

The key overall mass exchange reaction between gas, slag and matte in this series of experiments was identified as $FeS_{(matte)}+3CO_{2(gas)} \leftrightarrow FeO_{(slag)}+SO_{2(gas)}+3CO_{(gas)}$ (1) (a number of other elemental reactions also have to be considered). The matte particle “a” completely surrounded by slag (see Figure 2) is blocked from the gas by the slag layer, and therefore the overall mass

exchange reaction (1) requires a number of additional steps including gas-slag, diffusion of reactants and products through the slag phase and slag-matte reactions, so that the rate of the overall reaction (1) would be slow and the composition of the “a”-matte particle will be close to the initial matte composition and far from equilibrium (see schematic in Figure 3). The matte particle “b” on the surface of the slag is exposed to the gas, the overall reaction (1) would therefore progress fast, and the composition of the matte particle “b” would be close and eventually equal to the equilibrium matte composition – this is confirmed by longer experiments with starting matte composition located on both sides from but close to the final equilibrium point (see Figure 3). Identification of the key reactions was used to introduce a number of other experimental modifications such as substrate shape, initial mixture preparation (e.g. different proportions of metal/sulfide/oxide powders), master slag, master matte and other. Independent tests by other researchers were used in this study.

Figure 4 presents results for the equilibria between gas/slag/matte/tridymite phases in the Cu-Fe-O-S-Si system at $T=1200^{\circ}\text{C}$ and $P_{\text{SO}_2}=0.25$ atm obtained in this study using approaches outlined above.

Ranges of temperatures 1200-1300°C, SO_2 partial pressures 0.1-0.6 atm, matte grades 50-80wt%Cu, slag compositions from equilibria with tridymite to spinel, liquid phase assemblages (slag/matte, slag/metal and slag/matte/metal) are being investigated in the Cu-Fe-O-S-Si system with addition of Ca, Al, Mg as part of the overall research program. These experiments continue systematic characterization of the high-temperature chemistry of copper, lead and other non-ferrous smelting and recycling systems; summary of previous research is given in [3], more recent experimental work is published in [6-12].

3.2. Thermodynamic modelling results and integrated approach

A series of studies focused on phase equilibria and thermodynamics of the chemical systems important to the Cu pyrometallurgical production have been undertaken over recent years using the integrated experimental and thermodynamic modelling approach resulting in the development of thermodynamic database for copper-containing systems; the summary of previous studies is given in [3], more recent results are published in [13-22].

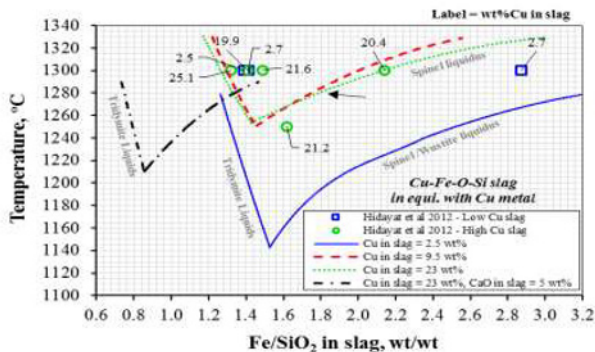


Figure 5. Comparison of the experimental data and thermodynamic model predictions in the Cu-Fe-O-Si system in equilibrium with metallic copper at fixed copper oxide concentrations in slag

and prediction of the effect of CaO addition on liquidus and solidus in the Ca-Cu-Fe-O-Si system in equilibrium with metallic copper.

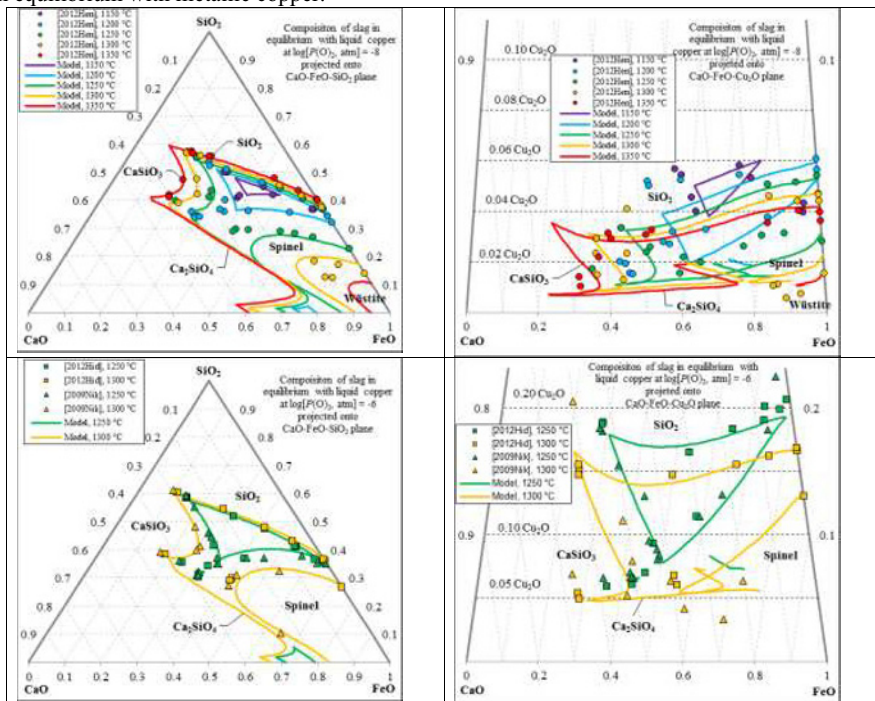


Figure 6. Comparison of the experimental data and thermodynamic model predictions in the Ca-Cu-Fe-O-Si system in equilibrium with metallic copper and gas at fixed oxygen partial pressures of 10^{-8} and 10^{-6} atm.

Figure 5 illustrates an example of comparison of thermodynamic model predictions with the experimental results on the Cu-Fe-O-Si system in equilibrium with metallic Cu at conditions relevant to the direct to blister production [6]. Figure 6 provides an example of study on multi-component system Ca-Cu-Fe-O-Si system in equilibrium with metallic Cu [6, 13]. Good agreement between experimental data and FactSage predictions with the new thermodynamic database is demonstrated in these figures.

Integrated research program on the development of multi-component thermodynamic database ranges from a) the work on low order (binary and ternary) systems that are particularly important foundation for thermodynamic modelling to b) the investigations of the multi-component systems close to the industrial slags – the latter are used directly in industrial practice as well as provide an essential test for the development of the multi-component thermodynamic model.

Example of the application of thermodynamic database along with the FactSage package is given in Figure 5 that gives predicted effect of fluxing with CaO to reduce liquidus and solidus in the slag relevant to the direct-to-blister copper smelting. Predictions show that although addition of CaO results in the significant decrease of the solidus temperatures, the shift of the spinel liquidus to the lower Fe/SiO₂ range indicates at a possible need to increase addition of SiO₂ flux. The thermodynamic model can now be used to evaluate the optimum combination of temperature, flux additions and other thermochemical parameters to reach required operational criteria.

4. Characterization of minor elements distribution coefficients – application of the EPMA / Laser Ablation ICP-MS microanalysis

Present research program is further extended to characterize distribution coefficients of minor elements such as As, Pb, Zn, Sn, Sb, Bi, Au, Ag between slag, matte and metal phases in the non-ferrous system Cu-Fe-O-S-Si with addition of minor slagging elements Al, Ca, Mg. The distribution coefficients for some elements (e.g. Ag, Au) are far from 1:1 resulting in very low concentrations in some phases. The limitation of the research in this direction is the minimum detection limit and spatial resolution of the available quantitative microanalysis techniques. EPMA cannot routinely provide required accuracy at elemental concentration of ppm (parts per million) level. The laser ablation inductively coupled plasma mass spectrometry (LA-ICP-MS) microanalysis technique provides the necessary low minimum detection limits [11]. Present research program is extended to develop a combined EPMA / LA-ICP-MS methodology to measure concentrations of elements in slag, matte and metal phases down to ppb levels [11]. Figure 7 demonstrates recent results [11] on the distribution coefficients of Ag and Au between slag and metal (wt% Me in slag / wt% Me in metal, where Me=Ag or Au) vs matte grade in the sample with slag/matte/metal/tridymite 4 phases in equilibrium at 1200°C in the Cu-Fe-O-Si system with addition of Ag and Au minor elements.

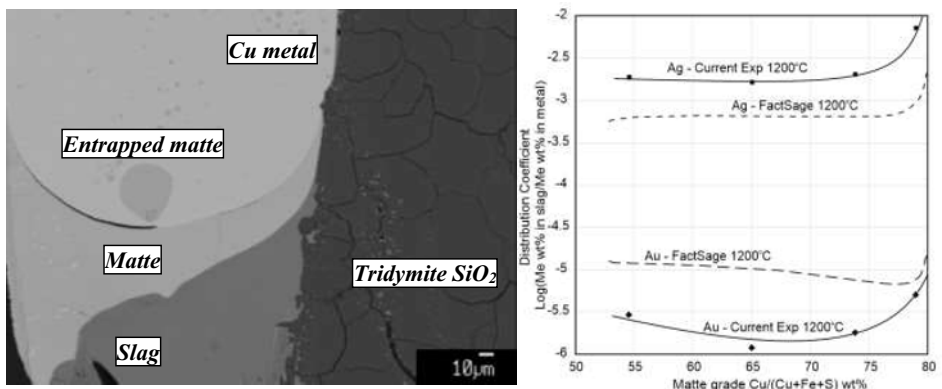


Figure 7. a) Microstructure of and b) distribution coefficients of Ag and Au between slag and metal vs matte grade wt% Cu/[Cu+Fe+S] in the sample with slag/matte/metal/tridymite 4 phases in equilibrium at 1200°C in the system Cu-Fe-O-Si with addition of Ag and Au minor elements [11].

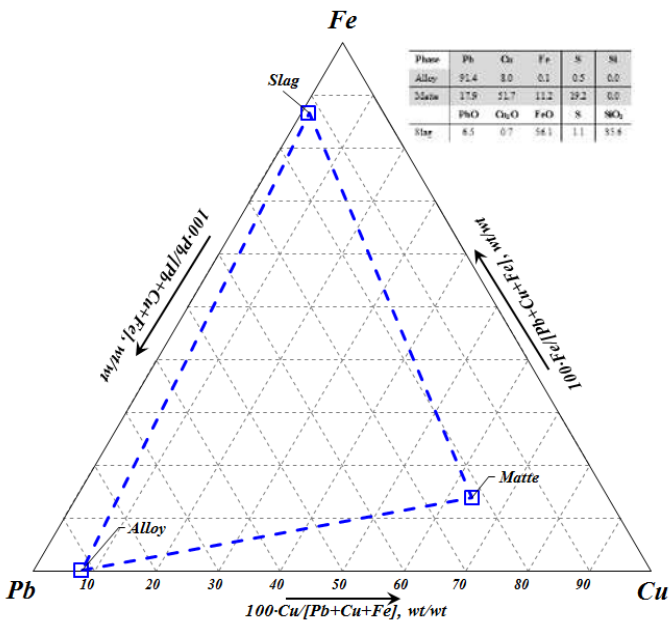
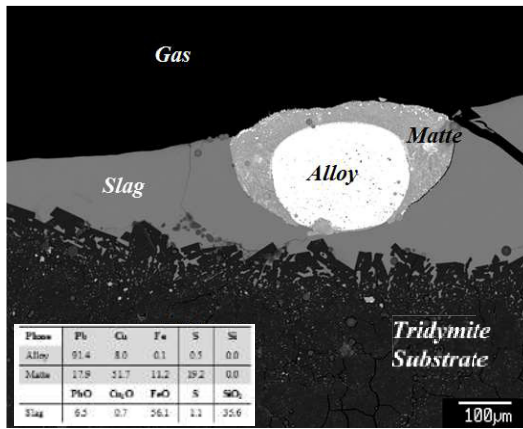


Figure 8. Back-scattered image of microstructure (top) and projection of phase compositions in the slag/matte/alloy/tridymite sample in the Cu-Fe-O-Pb-S-Si system equilibrated in the SiO₂ ampoule at T=1250°C for 18h.

5. Further research on the Pb-Cu-Zn-S-containing systems

The research has recently been extended to characterize the Pb-Cu-Zn-S-containing systems. Previous research on the Pb-Zn-containing systems was undertaken on the oxide-only systems $\text{PbO-ZnO-FeO-Fe}_2\text{O}_3\text{-CaO-SiO}_2$ with addition of Al_2O_3 and MgO in two extreme conditions – in air and in equilibrium with metallic iron. Thermodynamic database for the Pb-Zn-O-containing slag developed nearly two decades ago [23] used models available at that time. Many improvements in experimental and modelling techniques have been made and are being implemented now to characterize the thermo-chemistry of the Pb-Cu-Zn-S-containing slag / matte / metal / speiss systems of particular importance to non-ferrous and recycling systems.

Figure 8 presents the microstructure and projection of phase compositions in the sample in the Cu-Fe-O-Pb-S-Si system equilibrated in the SiO_2 ampoule at $T=1250^\circ\text{C}$ with complex slag, matte and metal alloy phases in equilibrium. These experiments provide important data on the tridymite liquidus of the complex slag as well as on the characterization of these complex systems and partitioning of Pb, Cu, Fe and S between phases. Results of these experiments are critical for further development of the thermodynamic database.

6. Conclusions

Advanced experimental and thermodynamic modelling techniques are continuously developed to characterize the thermochemistry of complex non-ferrous smelting and recycling systems. There is an opportunity now to use these powerful outcomes to improve metallurgical operations. The combination of several related research and development activities is believed to be the most efficient and promising approach that should include:

- a) continuous laboratory-based fundamental and applied experimental research,
- b) theoretical modelling integrated with experimental research,
- c) plant tests and experiments, and
- d) systematic implementation program combining collaborative efforts of technologists and researchers.

7. Acknowledgements

The authors would like to thank Australian Research Council Linkage program, Altonorte Glencore, Atlantic Copper, Aurubis, BHP Billiton Olympic Dam Operation, Kazzinc Glencore, Nyrstar, PASAR Glencore, Outotec (Espoo and Melbourne), Anglo American Platinum, and Umicore for the financial and technical support.

8. References

1. Jak E., Lee H.G. and Hayes P.C., "Improved methodologies for the determination of high temperature phase equilibria", Korean IMM J, 1995, vol.1, pp. 1-8.
2. Bale, C. W.; Chartrand, P.; Decterov, S. A.; Eriksson, G.; Hack, K.; Mahfoud, R. B.; Melançon, J.; Pelton, A. D.; Petersen, S. CALPHAD; FactSage, Ecole Polytechnique, Montréal. 2002 <http://www.factsage.com/>, 2002.

3. E.Jak, "Integrated experimental and thermodynamic modelling research methodology for copper and other metallurgical slags", Keynote Invited Lecture, MOLTEN 12, The 9th int. conf. on molten slags, fluxes and salts, Beijing, China, May 2012, paper w77.
4. Pelton, A.D., Decterov, S.A., Eriksson, G., Robelin, C., and Dessureault, Y.(2000). The Modified Quasichemical Model. I—Binary Solutions. Metall. Mater. Trans. B, vol. 31B. pp. 651–659; *ibid* vol. 32A. pp. 1355-1360; *ibid* vol. 32A, 1397-1407.
5. Hillert, M., Jansson, B., and Sundman, B.(1988). Application of the Compound-Energy Model to Oxide Systems. Z. Metallkd., vol. 79, no. 2. pp. 81–87.
6. T. Hidayat: "Equilibria Study of Complex Silicate-based Slag in the Copper Production", Ph.D. thesis, The University of Queensland, 2013.
7. T.Hidayat, D.Shishin, S.Decterov, and E.Jak, "Experimental Study and Thermodynamic Re-evaluation of the FeO-Fe₂O₃-SiO₂ system", Met. Trans. B, submitted May 1, 2013, Accepted, Jan 2014, Paper #: E-TP-13-344-B.
8. T.Hidayat, D.Shishin, S.Decterov, P.Hayes and E.Jak, "Integrated Experimental And Modelling Research on Copper-Making Slags", Conference of Metallurgists, Canadian Institute of Metallurgy, Bill Davenport Honorary Symposium, Vancouver, Canada, 2014.
9. E. Jak, T. Hidayat, D. Shishin, P. Hayes, "Recent Advances in Research for Non-ferrous Smelting and Recycling", in Proceedings of EMC 2015, Dusseldorf, Germany.
10. T. Hidayat, A. Fallah Mehrjardi, P. Hayes, E. Jak, "Experimental study of slag/matte/spinel equilibria and minor elements partitioning in the Cu-Fe-O-S-Si system", Molten 2016, 10th International Conference on Molten Slags, Fluxes and Salts, May 2016, Seattle, Washington, USA.
11. J. Chen, C. Allen, P. Hayes, E. Jak, "Experimental Study of Slag/Matte/Metal/Tridymite Four Phase Equilibria and Minor Elements Distribution in "Cu-Fe-Si-S-O" System by Quantitative Microanalysis Techniques", Molten 2016, 10th International Conference on Molten Slags, Fluxes and Salts, May 2016, Seattle, Washington, USA.
12. M. Shevchenko, T. Hidayat, P. Hayes, E. Jak, "Liquidus of "FeO"-SiO₂-PbO slags in equilibrium with air and with metallic lead", Molten 2016, 10th International Conference on Molten Slags, Fluxes and Salts, May 2016, Seattle, Washington, USA.
13. D. Shishin: "Development of a thermodynamic database for copper smelting and converting", Ph. D. thesis, Ecole Polytechnique of Montreal, 2013.
14. D. Shishin, T. Hidayat, E. Jak, S. A. Decterov, "Critical assessment and thermodynamic modeling of the Cu-Fe-O system", CALPHAD: Computer Coupling of Phase Diagrams and Thermochemistry 41 (2013) 160–179.
15. T.Hidayat and E.Jak, "Thermodynamic modelling of the "Cu₂O"-SiO₂, "Cu₂O"-CaO, and "Cu₂O"-CaO-SiO₂ systems in equilibrium with metallic copper", International Journal of Materials Research (formerly: Zeitschrift fuer Metallkunde), , Vol. 105, 2014, pp. 249–257.
16. T. Hidayat, D. Shishin, E.Jak and S.A. Decterov, "Thermodynamic Re-evaluation of the Fe-O System", CALPHAD: Computer Coupling of Phase Diagrams and Thermochemistry, Vol.48, March 2015, Pages 131–144.
17. D. Shishin, E. Jak, S. A. Decterov, "Critical assessment and thermodynamic modelling of the Fe–O–S system", J. Phase Equilib. & Diff., June 2015, Volume 36, Issue 3, pp 224-240
18. D. Shishin, E. Jak, S. A. Decterov, "Thermodynamic assessment and database for the Cu–Fe–O–S system", Calphad, Volume 50, September 2015, pp. 144–160.

19. T.Hidayat, D.Shishin, S.Decterov, and E.Jak, "Critical Thermodynamic Evaluation and Optimization of the CaO-FeO-Fe₂O₃-SiO₂ System", Met. Trans, submitted May 19, 2013, Paper #: E-TP-13-369-B, accepted Nov 2013.
20. D. Shishin, V. Prostakova, E. Jak, and S. Decterov, "Critical Assessment and Thermodynamic Modeling of the Al-Fe-O System", Metall Mater Trans B, 47(1), 2016, pp. 397-424.
21. T.Hidayat, D.Shishin, S.Decterov, and E.Jak, "Thermodynamic Optimization of the Ca-Fe-O System", Metallurgical and Materials Transactions B, February 2016, Volume 47, Issue 1, pp 256-281
22. D. Shishin, T. Hidayat, S. Decterov, E. Jak, "Thermodynamic modelling of liquid slag-matte-metal equilibria applied to the simulation of the Pierce-Smith converter", Molten 2016, 10th International Conference on Molten Slags, Fluxes and Salts, May 2016, Seattle, Washington, USA.
23. Jak E., Decterov S., Hayes P.C., Pelton A.D., "Thermodynamic modelling of the system PbO-ZnO-FeO-Fe₂O₃-CaO-SiO₂ for zinc/lead smelting", *Proceedings of the Fifth International Symposium on Metallurgical Slags and Fluxes*, Iron and Steel Society, AIME, Sydney, publ. Iron and Steel Society, Warrendale, PA, 1997, pp. 621-628.

Experimental Study of Slag/Matte/Metal/Tridymite Four Phase Equilibria and Minor Elements Distribution in "Cu-Fe-Si-S-O" System by Quantitative Microanalysis Techniques

Jeff (Jiang) Chen¹, Charlotte Allen², Peter C. Hayes¹, Evgueni Jak¹

¹PYROSEARCH, School of Chemical Engineering, The University of Queensland, Brisbane, Australia

²Central Analytical Research Facility, Institute for Future Environments, Queensland University of Technology, Brisbane, Australia

Keywords: phase equilibria, trace elements, quantitative microanalysis

Abstract

Laboratory studies have been carried out to determine the slag/matte/metal/tridymite four condensed-phase equilibria in the "Cu-Fe-Si-S-O" system and the minor element distributions between the equilibrated phases at 1200°C. A combined quantitative microanalysis technique including electron probe X-ray microanalysis (EPMA) and laser ablation inductively coupled plasma mass spectrometry (LA-ICP-MS) has been developed to accurately characterize the equilibrated system for both major and minor elements. Analysis precision, estimated accuracy and current limitations are discussed. The resulting elemental distributions are plotted against matte grade and compared to FactSage predictions. It was found that the experimental results for major elements are in good agreement with FactSage predictions. The simultaneous distributions of Ag and Au between slag, matte and metal phases are reported for the first time.

Introduction

Current copper production via pyrometallurgical process involves: a smelting process in which copper sulfide concentrate is smelted to produce copper-rich matte and fayalite or calcium ferrite slag; and a converting stage in which copper matte is converted to copper metal. In order to optimize and improve present industrial practice for copper production, extensive laboratory scale studies have been carried out to obtain the fundamental data on phase equilibria, thermodynamic and physicochemical properties of complex multi-component slag/matte/metal systems. However, there are significant difficulties in conducting high temperature experiments and quantitatively analyzing samples using conventional experimental and analysis techniques. These difficulties arise from the fact that the samples contain many phases at micro-scale with presence of trace elements at concentration of ppm (part per million, or 0.0001wt%) levels. As a result, there are significant knowledge gaps and discrepancies in the existing scientific data for these systems.

This project is part of an integrated research program that combines both experimental and thermodynamic modelling studies to characterize the complex multi-component oxide/sulfide/metal systems at high temperature, of interest to pyrometallurgical production of copper. The specific aim of the present study is to

1. develop experimental and analytical methodology to characterize phase equilibria of the slag/matte/metal/tridymite systems;

2. determine the equilibrium distribution coefficients of minor elements between four condensed phases, slag/matte/metal/tridymite.

The experimental conditions in the present study are in some cases not directly relevant to the current industrial conditions for copper making, however, the fundamental data generated from this study is vital for the construction of a self-consistent thermodynamic database to model and to subsequently optimise industrial processes.

Experimental

Experimental technique for high temperature phase equilibria

The experimental technique used in present study was based on the technique previously developed at PYROSEARCH [1-2]. It involves the preparation of a chemical mixture sample of predetermined composition. The sample mixture is equilibrated at a fixed temperature. On rapid cooling the liquid phases convert to glass so that the phase assemblage that exists at high temperature is "frozen in". The compositions of the solid and liquid phases are then measured using microanalysis techniques.

In this system, the equilibrium is determined by the presence of the four condensed phases. The procedure used follows the sequence outlined below.

a. Determination of initial bulk composition

An estimation of the initial bulk composition of the mixture is carried by FactSage 6.2 [3] calculation at the temperature of interest. The initial chemical components used were Cu_2O , Cu, Cu_2S , Fe, FeO, FeS and SiO_2 . The criteria for composition selection in this case are

1. All slag, matte and copper metal three phases are present at equilibrium with tridymite;
2. Matte grade is within the composition range interest;
3. The proportion of slag, matte and copper metal is close to 50, 25 and 25wt% respectively.

High purity chemicals of Cu_2O , Cu, Cu_2S , Fe, FeO, FeS and SiO_2 were mixed at the selected ratios; Small amounts (<1wt%) of the minor elements of interest (e.g. Au and Ag) were doped into the mixture. The prepared chemical mixture of total weight approximately 0.3g was added into a silica ampoule before it was evacuated and sealed.

b. Equilibration

The sample mixture in the silica ampoule was equilibrated at 1200°C for 6 to 24 hours in a vertical tube furnace.

c. Quenching

Rapid quenching rate is crucial to ensure a quality sample for following microanalysis. Both the matte and copper metal require much faster quenching rates than slag in order to produce homogeneous phases for analysis. The much larger thermo-mass of silica ampoule (8-9g) compared to the actual sample (0.3g) would result in a decrease in cooling rate, which is undesirable.

In the quenching procedure previously used samples are dropped directly into a container that contains large amount of cold water. In present study, modification has been made to this by

placing a hard ceramic brick at the bottom of the container. The container then was filled with water to a height just about 20mm above the top level of the brick. During quenching, the silica ampoule dropped under gravity onto the brick and was found to disintegrate on impact so that sample inside the ampoule could be in direct contact with water almost instantaneously. Reducing the amount of water reduced the buffering effect and ensured the disintegration of the ampoule. Photos of samples before and after equilibration are shown in Figure 1

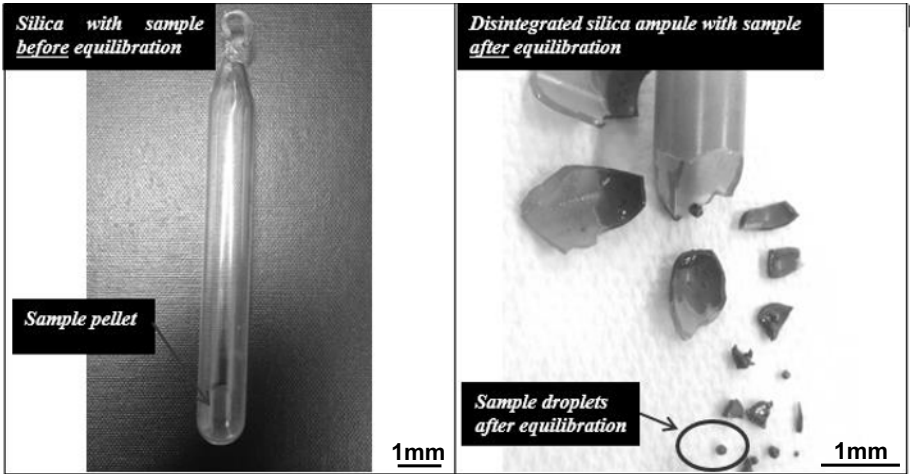


Figure 1 Photos of samples before and after equilibration

Development of analysis technique

EPMA

Electron Probe X-ray Microanalysis (EPMA) is a powerful microanalysis technique and has been increasingly used to quantitatively determine the composition of metallurgical samples including oxides, sulfides and metals. At PYROSEARCH efforts have been made to ensure accurate measurements by EPMA based on the understanding of its capability and limitation at fundamental level. The following issues were taken into account.

1. Identify and minimize background/peak interferences

The probability of background/peak interferences during EPMA measurement increases proportionally with increase of number of elements in the sample for analysis. Efforts have been made, and accurate background positions of each element have been determined for the measurement, to avoid/minimize the background/peak interferences.

2. Reduce minimum detection limit (MDL)

EPMA is generally used for quantification of elements with concentration greater than 1wt% with good accuracy and precision. However, complications arise when the concentrations of the elements of interest are below 1wt%. The concentration of an element below its limit of detection

cannot be measured with confidence. As part of the development of analysis technique, current procedure has been modified to enable the measurement of some of the minor elements of interest. An example is shown in Figure 2. It can be seen, according to current analysis procedure with 10 second counting time on background, the MDL of Ag is close to 1400ppm, by increasing background counting time during the measurement to 300 seconds, the MDL is decreased down to close 200ppm.

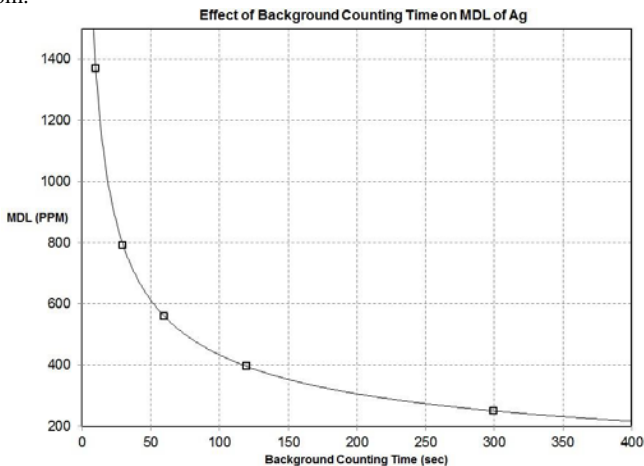


Figure 2 Relationship between MDL of EPMA measurement on Ag and background counting time on JEOL 8200 superprobe (probe current: 15nA, acceleration voltage: 15Kev, probe size: 0, X-ray measured: Ag $L\alpha$)

3. Reduce the effect of boundary secondary X-Ray fluorescence

Uncertainties in measurement as a result of secondary X-Ray fluorescence can occur when EPMA measurements are undertaken on material close to phase boundaries. Excited high energy X-Rays of a particular element in one phase can travel through to another phase and excite low energy X-Rays of another element and therefore influence the observed concentration. This effect can introduce significant error to the measurement results, especially when there is a significant concentration difference of an element in the two adjacent phases (e.g. Fe concentration in copper metal measured close to the interface with slag phase could be systematically higher than actual). In the present study this effect has been evaluated by simulation software CalcZAF and action has been taken during actual EPMA measurement to minimize its effect on the measurement results (i.e. taking measurements at a distance from phase boundary where the effect of boundary secondary X-Ray fluorescence is negligible).

Laser Ablation - Inductively Coupled Plasma Mass Spectrometry (LA-ICPMS)

In present study, Laser Ablation - Inductively Coupled Plasma Mass Spectrometry (LA-ICPMS) has been used to quantitatively determine the concentration of trace/ultra-trace elements in the phases presented at equilibrium.

The technique begins with a laser beam focused on the sample surface to generate fine particles – a process known as Laser Ablation. The ablated particles are then transported to the secondary excitation source of the ICP-MS instrument for ionization of the sampled mass. The excited ions in the plasma torch are subsequently introduced to a mass spectrometer detector for both elemental and isotopic analysis.

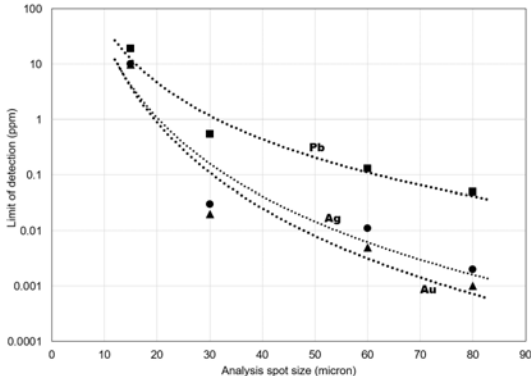


Figure 3 Relationship between analysis spatial resolution and limit of detection using LA-ICP-MS determined in present study

LA-ICP-MS can generally analyze an area of 20-100 μm on the sample and provide an ultra-highly sensitive chemical analysis with limits of detection for many elements down to the ppb (parts per billion) level without much sample preparation work. The relationship between analysis spot size and detection limits for the minor elements of interests have been determined in the present study and an example is shown in Figure 3. Uncertainties in the measurement results generally come from mass interference (e.g. Cu⁶⁵ and Zn⁶⁵) and elemental fractionation occurred during laser-sample interaction. Figures 4a-b show examples of the crater left in a slag phase(4a) and a matte phase(4b) after laser ablation process. More significant melting effect observed in matte phase induced by laser generally leads to more elemental fractionation therefore makes accurate measurement more difficult. Efforts have been made to evaluate these uncertainties and introduce appropriate correction procedures to ensure the accuracy of the measurements.

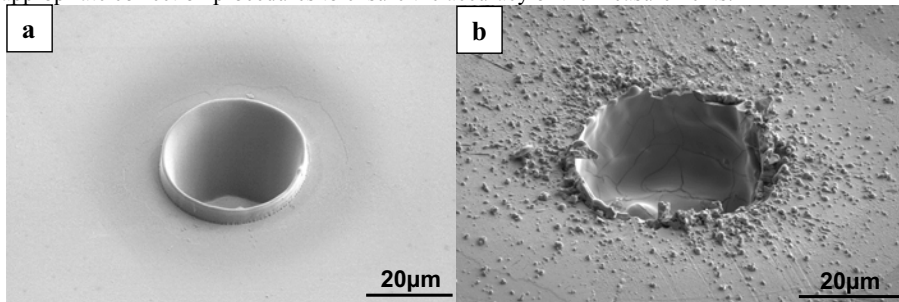


Figure 4a-b SEM micrographs of a crater left in a a) slag sample and in b) a matte phase after laser ablation process.

Results

Microstructures of equilibrated sample

Typical micrographs of samples from slag/matte/metal/tridymite experiments at 1200°C taken using scanning electron microscope with backscattered electron detector (SEM-BSE) are shown in Figures 5a-c. Three types of microstructures after equilibration have been identified.

TYPE I Metal-matte-slag 3 phases all in contact with each other

This type of microstructure is typically seen as Figure 5a. The spherical metal phase is seen surrounded partially by the matte phase and the rest by the slag phase. A slag/matte/metal 3 phase adjacent point can be observed. It is expected best equilibrium state is achieved with this microstructure. This microstructure is not commonly observed across the sample.

TYPE II Metal encapsulated by matte phase in contact with slag

This type of microstructure is typically seen as Figure 5b. The spherical metal phase is seen fully surrounded by the matte phase; while the matte phase is in good contact with the slag phase, it blocks the direct contact between metal and slag phase. This microstructure is more commonly observed across the sample.

TYPE III Individual metal or matte particles suspended in slag phase

Another type of microstructure which is more commonly observed in the sample consists of individual metal or matte particles that are suspended in the slag, which are shown in Figure 5c. There is no direct contact between matte and metal phases. Analysis on this type of microstructure should be avoided since equilibrium is unlikely to be achieved in this case.

In addition to the three typical microstructures described above, it is commonly observed that the matte phase contains some entrapped metal particles, this is probably due to the low interfacial tension between matte and metal phase that leads to a poor separation between the two phases. The metal phase may also contain some fine pores which might be formed when S is released during the quenching process.

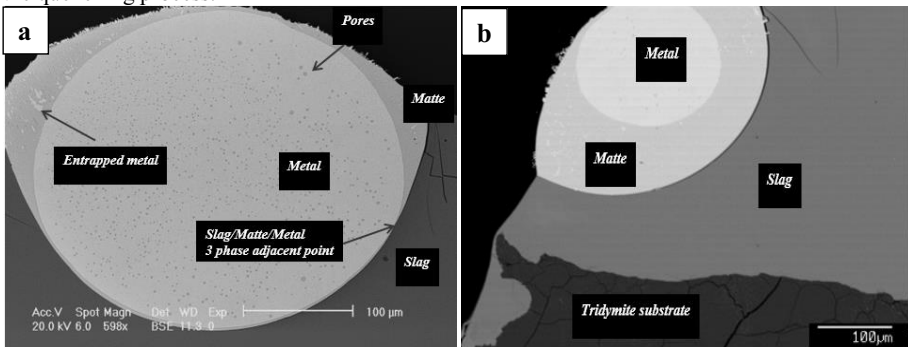


Figure 5a-b Typical Microstructures observed in slag/matte/metal/tridymite four phase equilibrium samples.

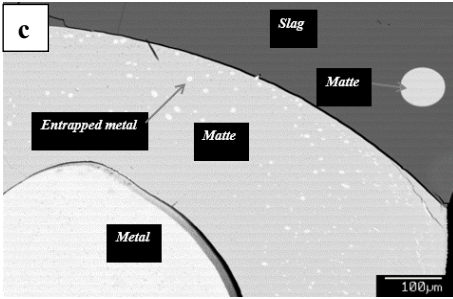


Figure 5c Typical Microstructures observed in slag/matte/metal/tridymite four phase equilibrium samples.

Slag/matte/metal/tridymite four condensed phase equilibria at 1200°C

The experimental results obtained in present study together with available literature data of the 4-condensed-phase Slag/Matte/Metal/Tridymite equilibria at 1200°C are given plotted against matte grade in Figure 6a-c together with FactSage predictions. It can be seen, the relationship between Cu concentration in the slag phase and matte grade is in good agreement with results obtained by Shimpo et al. [5] as well as the FactSage prediction; the measured S concentrations in the matte phase also agree well with the predicted values and reported data; S dissolved in Cu metal phase was found to be lower than predictions for about 0.2wt%;

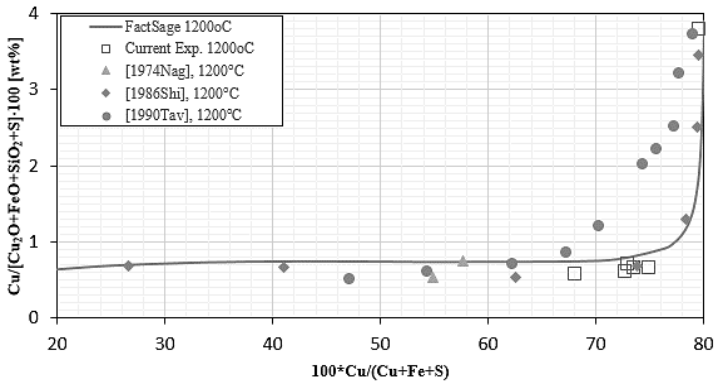


Figure 6a Concentration of Cu in slag wt% vs matte grade Cu/(Cu+Fe+S) wt% [4-6]

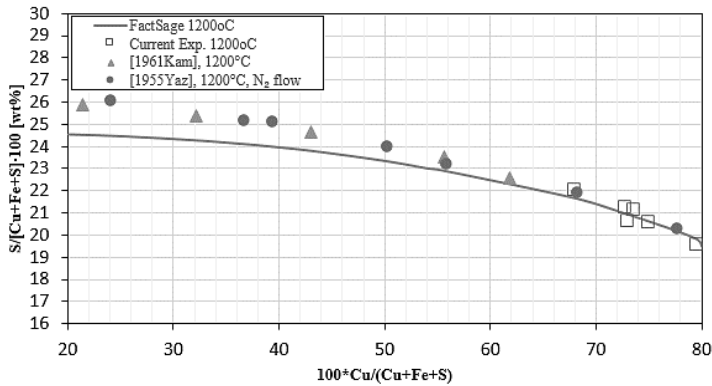


Figure 6b Concentration of S in matte wt% vs matte grade Cu/(Cu+Fe+S) wt% [7-8]

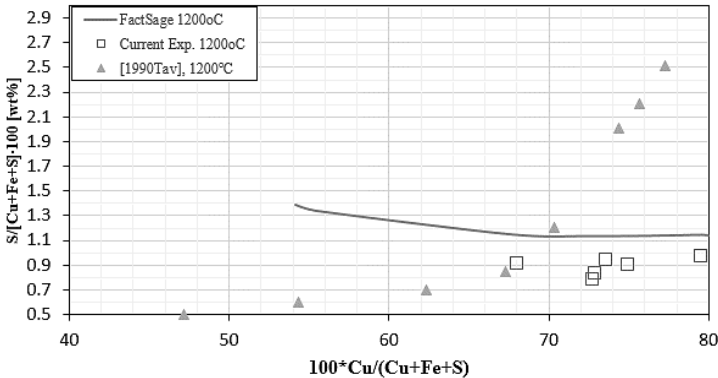


Figure 6c Concentration of S in Cu metal wt% vs matte grade Cu/(Cu+Fe+S) wt% [6]

Distribution of Ag and Au in slag/matte/metal/tridymite four condensed phase equilibria at 1200°C

The distribution coefficients of Au and Ag between slag and Cu metal at equilibrium have been determined for the first time by present study. The results together with FactSage predictions are plotted against matte grade in Figures 7a-b. Significant differences were found between predicted and experimentally determined values.

It can be seen from the results, the experimentally determined distribution coefficients of Au between slag and metal are about half order of magnitude lower than predicted values; in contrast, the distribution coefficients of Ag between slag and metal are found to be half order of magnitude higher than predicted values. The discrepancies between FactSage predictions and experimental results are expected due to the fact that no data on the distribution coefficients for both Au and Ag at four-phase equilibrium condition were available and FactSage database has not been optimized for this system.

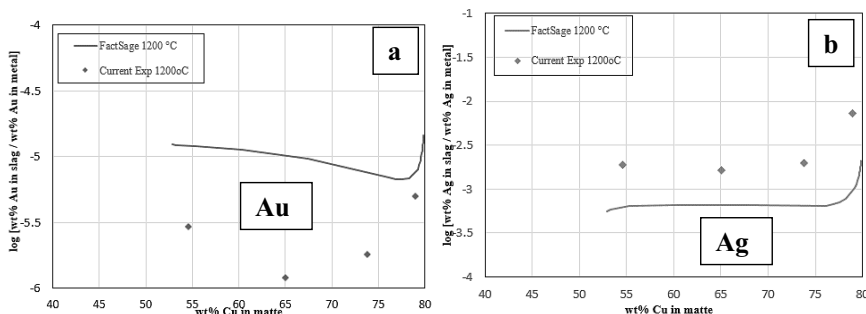


Figure 7 a: Distribution coefficients of Au between slag and metal vs matte grade wt %Cu/[Cu+Fe+S]; b: Distribution coefficients of Ag between slag and metal vs matte grade wt %Cu/[Cu+Fe+S];

Summary

Experimental and analysis techniques have been successfully developed for characterization of slag/matte/metal/tridymite four condensed phase equilibria in Cu-Fe-O-S-Si system and for the determination of minor elements distribution in the phases at equilibrium.

The phase equilibria results obtained in present study for major elements are found to be in good agreement with FactSage predictions for the range of conditions investigated. The distribution coefficients of Au and Ag between slag and Cu metal at slag/matte/metal/tridymite four condensed phase equilibria at 1200°C were reported for the first time.

The previously available data and the new experimental data for the system will be critically evaluated and used to optimize the current FactSage database for copper making applications.

Acknowledgement

The authors would like to thank Australian Research Council Linkage program, Altonorte Glencore, Atlantic Copper, Aurubis, BHP Billiton Olympic Dam Operation, Kazzinc Glencore, PASAR Glencore, Outotec Oy (Espoo), Anglo American Platinum, and Umicore for the financial and technical support.

References

- [1] Jak, E., Liu, N., Lee, H. G., & Hayes, P. C, "The Application of phase equilibria studies to describe behaviour of lead smelting slags." *6th AusIMM Extractive Metallurgy Conference*. Vol. 94. No. 4. Australasian Institute of Mining and Metallurgy, 1994, vol. 94, No. 4, pp. 261-268
- [2] E. Jak, "Integrated experimental and thermodynamic modelling research methodology for metallurgical slags with examples in the copper production field." In *Proceedings of IX International Conference on Molten Slags, Fluxes and Salts*, Beijing, 2012 paper 77.

- [3] C.W. Bale, A.D. Pelton and W.T. Thompson: "Facility for the Analysis of Chemical Thermodynamics" (FACT), Ecole Polytechnique, Montreal, Canada, 1996
- [4] F. J. Tavera and E. Bedolla, "Distribution of copper, sulfur, oxygen and minor elements between silica-saturated slag, matte and copper - experimental measurements," *Int. J. Miner. Process.*, 1990, vol. 29, pp. 289-309
- [5] R. Shimpo, S. Goto, O. Ogawa, and I. Asakura, "A study on the equilibrium between copper matte and slag," *Can. Metall. Q.*, 1986, vol. 25, pp. 113-121
- [6] M. Nagamori, "Metal loss to slag: Part I. Sulfidic and oxidic dissolution of copper in fayalite slag from low grade matte," *Metall. Trans. B*, 1974, vol. 5B, pp. 531-538
- [7] M. Kameda and A. Yazawa, "The oxygen content of copper mattes," in *Physical Chemistry of Process Metallurgy, part 2*, 1961, vol. 8, pp. 963-988
- [8] A. Yazawa and M. Kameda, "Fundamental studies on copper smelting. IV. Solubility of FeO in copper matte from SiO₂-saturated FeO-SiO₂ Slag," *The Technology Reports of the Tohoku Univ.*, 1955, vol. 19, pp. 251-261

EXPERIMENTAL DETERMINATION OF THE LIQUIDUS SURFACE (1473 K) IN Cu-ZnO-SiO₂-O SYSTEM AT VARIOUS OXYGEN PARTIAL PRESSURES

Longgong Xia^{1,2,*}; Zhihong Liu²; Pekka Antero Taskinen^{1,2}

¹ Aalto University, School of Chemical Technology, Metallurgical Thermodynamics and Modeling Research Group, Espoo, 02150, Finland

² Central South University, School of Metallurgy and Environment, Changsha, Hunan, 410083, China

Keywords: Phase diagram; MTDATA; MTOX; EPMA; Copper

Abstract

Thermodynamic information of the Cu-ZnO-SiO₂-O system has significant importance for high temperature industries. By employing the equilibration/quenching/EPMA technique, phase relation and liquidus surface of the Cu-ZnO-SiO₂-O system at 1473 K has been systematically studied at various oxygen partial pressures (pure argon and 0.21 atm). No ternary compound was found. A pseudo-ternary phase diagram (Cu₂O-ZnO-SiO₂) was used to represent the liquidus of Cu-ZnO-SiO₂-O system in equilibrium with air ($P_{O_2} = 0.21$ atm). Two univariant equilibria (SiO₂ + Zn₂SiO₄ + Oxide liquid, and Zn₂SiO₄ + ZnO + Oxide liquid) were found in the experiments. The phase equilibria of the Cu-ZnO-SiO₂-O system in equilibrium with copper has also been studied at a fixed mole ratio between SiO₂ and SiO₂ + ZnO. With increasing SiO₂ content in initial pellets, the concentration of Cu in liquid oxide phase decreases rapidly. Solubility data of Cu in solid phases of Zn₂SiO₄, ZnO and SiO₂ is also reported.

Introduction

The Cu-ZnO-SiO₂-O system is widely used in pyrometallurgical processes [1-3], ceramics and advanced materials [4-7]. However, thermodynamic information and direct phase diagram measurements about this system are poor in literature. Evident discrepancies in extrapolated phase diagrams [8, 9] inspired the present experimental study.

In previous studies [8-10], the ZnO-SiO₂, Cu-O-ZnO and Cu-O-SiO₂ subsystems have been systematically studied. Willemite (Zn₂SiO₄, melting congruently at 1785 ± 2 K) has been determined to be the only compound. In binary ZnO-SiO₂ system, there were two eutectic points, which are occurring at 1715 ± 2 K with 0.52 ± 0.01 mole fraction of ZnO, and at 1770 ± 2 K with 0.71 ± 0.01 mole fraction of ZnO, respectively. The liquidus temperatures agreed well with the work of Hansson et al. [11]. The Cu-O-ZnO system has one simple eutectic point with two primary phase fields of cuprite (Cu₂O) and wurtzite (ZnO). The eutectic points of the system were determined to be 1371 ± 2 K and 0.10 ± 0.01 mole fraction of ZnO in air, and 1481 ± 2 K and 0.03 ± 0.01 mole fraction of ZnO, 0.63 ± 0.01 mole fraction of Cu at copper saturation. In Cu-O-SiO₂ system, one simple eutectic reaction with two primary phases of cuprite (Cu₂O) and silica (SiO₂) was found. The eutectic point was determined to be 1336 ± 2 K and 0.23 ± 0.01 mole fraction of SiO₂ in air ($P_{O_2}=0.21$ atm), which was consistent with the data reported by Hidayat et al. [12]. The eutectic point was found to be 1456 ± 2 K and 0.08 ± 0.01 mole fraction of SiO₂, 0.60 ± 0.01 mole fraction of Cu, when the system was in equilibrium with metallic copper.

In the present study, the phase equilibria of Cu-ZnO-SiO₂-O system in various oxygen partial pressures ($P_{O_2}=0.21$ atm, and in argon) are investigated using the equilibration/quenching/EPMA technique [13] at 1473 K. Both the chemical composition of liquidus (i.e. the liquid phase) and the compositions of the solid phases present in equilibrium are determined by EPMA, which greatly increases the accuracy and productivity of phase equilibrium research.

Experiments

Starting materials

High-purity Cu cathode (0.99996, Boliden Harjavalta, Finland), Cu powder (0.9996, Alfa Aesar, Germany), ZnO powder (0.9999, Alfa Aesar, Germany) and SiO₂ powder (0.9999, Umicore, Belgium) were employed as starting materials. Cu₂O was prepared by oxidizing the copper cathode in air at 1298 K for 120 h. The composition of the oxide was determined by EPMA. Only Cu (0.8882 mass fraction) and O (0.1118 mass fraction) were detected, and the purity of the 'Cu₂O' was derived to be 0.9999 (mass fraction). Purified argon gas (0.99999, volume fraction, AGA, Finland) was used as flushing gases in the experiments with metallic copper saturation. Platinum wire and foil (0.9999, Johnson-Matthey Nobel Metals, UK), which were inert in experimental conditions of this study, were used as the suspending and holding wrap to preserve the purity of the system. In the equilibrium experiments, 0.2 g powder in desired proportions was mixed thoroughly in an agate mortar, and pelletized to 5 MPa in a 5 mm-diameter pressing tool.

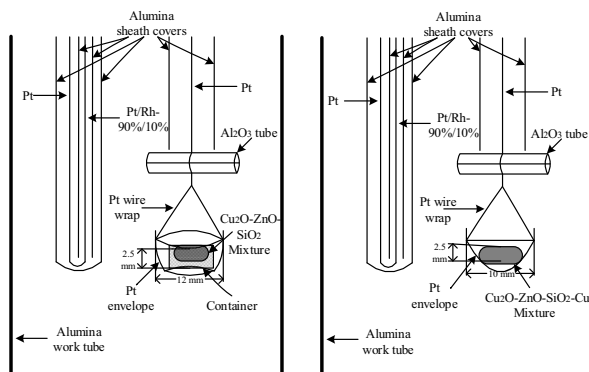


Fig. 1. Schematics of the specimen, container and suspension techniques.

For the experiments in equilibrium with air, the pellet was placed in a suitable container (quartz crucible (0.9998, OM Lasilaite Oy, Finland), ZnO substrate, or Zn₂SiO₄ substrate [8-10]) and equilibrated in a Pt envelope. Specimen hooked to a platinum wire (\varnothing 0.5 mm) was kept in the hot zone at the target temperature for the required equilibration time (Fig. 1 left). Experiments with metallic copper saturation were conducted without any substrates. Pellets were placed directly in Pt envelope, and equilibrated at target temperature for certain period of time, as shown in Fig. 1 right.

Experimental apparatus and procedure

The equilibrium experiments were carried out in a vertical tube furnace (LTF 16/--/450, Lenton, UK) with electrical resistance of silicon carbide heating elements, and the schematic vertical section of the furnace and auxiliaries have been presented in previous studies [8-10].

Experiments equilibrated with air were conducted with the bottom and the top of the reaction tube opened to the ambient atmosphere ($P_{O_2}=0.21$ atm). For metallic copper saturated experiments, an inert high-purity argon gas was continuously fed through the gas tight system. The specimen was introduced into the working tube by a platinum wire, and hanged at the bottom. The working tube was sealed with a rubber plug after the specimen was inserted. The specimen was pulled up to the hot zone after 30 min's flushing with argon. Once, the equilibration time was reached, the specimen was released rapidly and quenched into an ice-cold water bath (273 K). Afterward it was dried and mounted in epoxy resin. A polished cross section of the mounted specimen was prepared using the conventional metallographic grinding and polishing techniques.

Two sets of experiments were conducted to optimize the equilibration time. The equilibria was determined by measuring the compositions of the liquid phases at different equilibration times. The results indicated that homogenous phase can be achieved within 8 h in air, and 4 h in argon.

Analysis

Samples were carbon-coated with a Leica EM SCD050 Coater (supplied by Leica Mikrosysteme GmbH, Vienna, Austria). The microstructure was examined by a LEO 1450 (Carl Zeiss Microscopy GmbH, Jena, Germany) scanning electron microscope. The compositions of the equilibrated phases were measured by an Electron-Probe X-ray Microanalyser (CAMECA SX100, Cameca SAS, France). An accelerating voltage of 15 kV, beam current of 40 nA, and spot size of 1-100 μm (diameter) were utilized in the analysis. The standards used in the measurements were natural minerals (quartz for Si: $K\alpha$; metallic copper for Cu: $K\alpha$; sphalerite for Zn: $K\alpha$; hematite for O: $K\alpha$). The raw measurement results were corrected using the PAP on-line matrix correction program [14], supplied by the equipment manufacturer. The detection limit of the EPMA analyzes is 0.01 wt%.

Results and discussions

According to experimental and thermodynamic studies of the Cu-O system [15, 16], cuprite (Cu_2O) is the stable phase of copper oxide rather than tenorite (CuO) in air at temperatures above 1299 ± 2 K. The melting point of Cu_2O in equilibrium with air has been determined to be 1396 ± 2 K. However, the melting temperature of cuprite (Cu_2O) in equilibrium with metallic copper (Cu) has been reported to be 1496 ± 2 K, based on thermodynamic evaluations [15, 16].

In the present study, Cu, O, ZnO and SiO_2 are considered as system components, as shown in Fig. 2. According to the Gibbs phase rule in isobaric conditions ($F = C - (P+B) + 2$, where F is the number of degrees of freedom that can be varied independently, P is the number of phases, B is the number of global constraints, and C is the number of components.), when the system is in equilibrium with air ($P = 1$ atm, $P_{O_2} = 0.21$ atm), B equals to 2, O, Cu, ZnO and SiO_2 are considered as components, the equation can be derived to be $F = 4 - P$. When temperature is fixed, and the liquid oxide equilibrates with two solid phases ($\text{SiO}_2 + \text{Zn}_2\text{SiO}_4$ or $\text{Zn}_2\text{SiO}_4 + \text{ZnO}$), F equals to 0, and the system is completely defined, and it is called the univariant equilibria under the boundary conditions of present study. The light grey section in Fig. 2 represents the equilibria in air. However when the system is in equilibrium with metallic copper, the oxygen partial pressure is not fixed. The system needs one more global constraint to fully define the system. The mole ration between SiO_2 and $(\text{SiO}_2 + \text{ZnO})$ in the

initial pellet was fixed as constant values ($\frac{SiO_2}{SiO_2+ZnO} = 0, 0.25, 0.5, 0.75$ and 1) to maintain zero degree of freedom in the system, shown as the dark grey plane in Fig. 2.

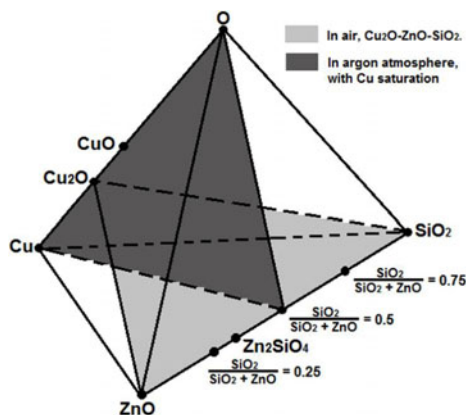


Fig. 2. The sections from quaternary Cu–ZnO–SiO₂–O system, studied in the present study.

Cu–ZnO–SiO₂–O in equilibrium with air

The well equilibrated (equilibrium time, 12h) and quenched samples were analyzed by EPMA. At least 10 independent measurement points from each phase were analyzed to quantify its accuracy, and those points came from different parts of the sample. The obtained EPMA results of the Cu₂O–ZnO–SiO₂ system in equilibrium with air are listed in Table 1. For a better understanding and comparison, the chemical compositions have been recalculated based on the measured elements (Cu, Zn and Si), and Cu₂O, ZnO, SiO₂ are considered as the components for presentation purposes only. The overall standard deviation of EPMA has been calculated from all the measurement points, and given as footnote below the table.

Table 1. Phase compositions for the Cu–ZnO–SiO₂–O system in equilibrium with air*.

N o.	Phase**	EPMA (wt %) **				Recalculated (mol %)		
		O	Si	Cu	Zn	Cu ₂ O	ZnO	SiO ₂
ZnO primary-phase field								
1	L	11.75±0.01	0.00	82.84± 0.04	5.41±0.04	88.74	11.26	0.00
	ZnO	19.40±0.02	0.00	2.71±0.18	77.89±0.16	1.76	98.24	0.00
Univariant equilibria: Liquid Oxide + Zn ₂ SiO ₄ + ZnO								
2	L	16.53±0.13	1.96±0.04	72.07±0.16	9.44±0.16	72.55	18.48	8.96
	Zn ₂ SiO ₄	29.38±0.26	13.01±0.08	2.08±0.14	55.53±0.17	1.23	63.91	34.86
	ZnO	21.15±0.13	0.14±0.04	1.08±0.16	77.63±0.16	0.71	98.89	0.40
Univariant equilibria: Liquid Oxide + Zn ₂ SiO ₄ + SiO ₂								
3	L	29.13±0.13	15.25±0.04	32.99±0.35	22.63±0.04	22.60	30.13	47.27
	Zn ₂ SiO ₄	29.82±0.15	12.66±0.03	2.71±0.06	54.81±0.03	1.63	63.97	34.40
	SiO ₂	53.37±0.34	45.19±0.15	0.75±0.13	0.69±0.08	0.37	0.66	98.98
SiO ₂ primary-phase field								
4	L	24.69±0.11	6.43±0.15	68.88±0.27	0.00	70.32	0.00	29.68
	SiO ₂	52.84±0.05	46.15±0.07	1.01±0.13	0.00	0.48	0.00	99.52

* Temperature 1473 K, $\mu(T) = \pm 2$ K; $P=1$ atm, $\mu(P) = \pm 5$ %; $P_{O_2}=0.21$ atm, $\mu(P_{O_2}) = \pm 3$ %;

** L: Liquid Oxide phase; Standard deviation: $\sigma(EPMA) = 0.10$.

There are two univariant equilibrium (liquid oxide + SiO_2 + Zn_2SiO_4 + gas, and liquid oxide + Zn_2SiO_4 + ZnO + gas) in the system. Cu_2O has small solubility in the terminal solid phase of SiO_2 , less than 0.50 at.%. Zn_2SiO_4 can dissolve 1.63 at.% Cu_2O at 1473 K, and Cu_2O shows smaller solubility in ZnO than in Zn_2SiO_4 . The results of the present study have been compared with the phase diagram calculated by MTDATA (version 5.10) [17] software with Mtox 8.1 database [18]. The comparison is depicted graphically in Fig. 3.

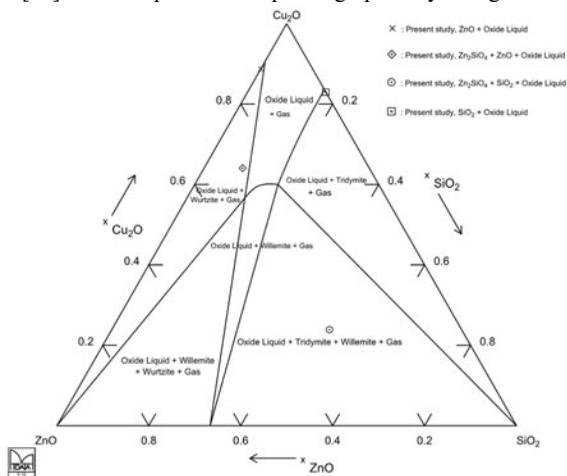


Fig. 3. Cu_2O - ZnO - SiO_2 isopleth of the quaternary Cu - ZnO - SiO_2 - O system ($P_{\text{O}_2}=0.21$ atm), calculated by MTDATA and Mtox database, with the experimental points superimposed.

The experimental point (\square , #04 in Table 1) agrees well with the calculation, which is consistent with the previous study [10]. Once ZnO was introduced into the system, the consistence between the calculated diagram and the experimental data becomes poor, because of the shortage of experimental data in the previous assessments of the ZnO - SiO_2 and Cu - O - ZnO subsystems [8, 9].

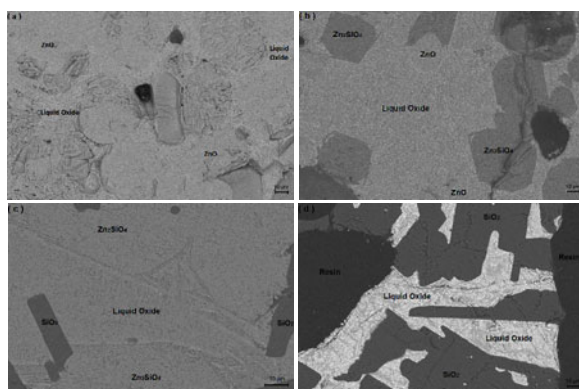


Fig. 4. Backscattered images of samples from Cu - ZnO - SiO_2 - O system in equilibrium with air: (a) #01 in Table 1; (b) #02 in Table 1; (c) #03 in Table 1; (d) #04 in Table 1.

There is one solid phase (ZnO or SiO₂) in equilibrium with the molten phase in Fig. 4 (a) and (d). The microstructures of samples equilibrated at the univariant equilibria are presented in Fig. 4 (b) and (c). Solid Zn₂SiO₄, ZnO and liquid oxide are in equilibrium with each other in Fig. 4 (b). Solid Zn₂SiO₄, SiO₂ and liquid oxide coexist with each other in Fig. 4 (c).

Cu-ZnO-SiO₂-O in equilibrium with metallic copper

Chemical compositions of the phases in equilibrium with metallic copper were carefully analyzed with EPMA. The obtained results are collected in Table 2. For a better understanding and comparison, Cu, O, ZnO, SiO₂ are considered as the components in the recalculation for presentation purposes. Overall standard deviation of EPMA has been calculated from all the measurement points, and given below the table.

Table 2. Experimentally determined phase compositions for the Cu-ZnO-SiO₂-O system (metallic copper saturation, in argon)*.

N o.	Phase**	EPMA (wt %) **				Recalculated (mol %)			
		O	Si	Cu	Zn	Cu	ZnO	SiO ₂	O
$\frac{SiO_2}{SiO_2+ZnO} = 0$									
1	Cu ₂ O	12.03±0.19	0.00	87.97±0.20	0.00	64.88	0.00	0.00	35.12
	ZnO	21.49±0.08	0.00	2.11±0.05	76.40±0.07	2.33	84.59	0.00	13.08
$\frac{SiO_2}{SiO_2+ZnO} = 0.25$									
2	L	14.33±0.08	1.29±0.01	76.71±0.01	7.67±0.08	58.69	5.70	2.23	33.38
	Zn ₂ SiO ₄	30.18±0.07	13.38±0.07	1.25±0.02	55.19±0.15	1.38	59.04	33.34	6.24
	ZnO	21.36±0.09	1.62±0.15	1.70±0.21	75.32±0.45	2.05	88.32	4.43	5.20
$\frac{SiO_2}{SiO_2+ZnO} = 0.5$									
3	L	28.10±0.20	14.45±0.10	37.10±0.35	20.35±0.08	31.94	17.12	28.04	22.90
	Zn ₂ SiO ₄	30.00±0.03	12.72±0.04	1.69±0.03	55.59±0.05	1.81	58.87	31.38	7.94
	SiO ₂	52.96±0.12	44.89±0.11	1.07±0.16	1.08±0.07	1.08	1.00	92.42	5.50
$\frac{SiO_2}{SiO_2+ZnO} = 0.75$									
4	L	28.08±0.16	16.04±0.13	35.12±0.11	20.76±0.13	31.82	18.28	32.87	17.03
	Zn ₂ SiO ₄	29.27±0.07	13.40±0.13	2.27±0.03	55.06±0.21	2.57	60.66	34.39	2.38
	SiO ₂	53.03±0.10	45.64±0.05	0.72±0.11	0.61±0.04	0.67	0.55	95.56	3.22
$\frac{SiO_2}{SiO_2+ZnO} = 1$									
5	L	16.20±0.11	5.48±0.07	78.32±0.14	0.00	59.86	0.00	9.44	30.70
	SiO ₂	52.92±0.01	46.11±0.01	0.97±0.01	0.00	0.89	0.00	97.71	1.40

* Temperature 1473 K, $\mu(T) = \pm 2$ K; $P=1$ atm, $\mu(P) = \pm 5$ %; Equilibration time 8h.

** L: Liquid Oxide phase; Standard deviation: $\sigma(EPMA) = 0.12$.

The lowest temperature for the co-existence of liquid oxide with liquid copper in the Cu-O-ZnO system has been reported to be 1451 K [9], which agrees well with the results (#01, Table 2) in present study. When SiO₂ was introduced into the system (#02, #03, #04 in Table 2), four phases can be detected. Willemite (Zn₂SiO₄) is the only compound, which exists in this system, and it can dissolve up to 2.57 at. % Cu at the experimental conditions of present study. Cu shows lower solubility in tridymite (SiO₂) than in wurtzite (ZnO). Liquid copper (Cu), cuprite (Cu₂O) and tridymite (SiO₂) were in equilibrium with each other in the wurtzite (ZnO) free experiment (#05, in Table 3).

The microstructures of the samples in equilibrium with metallic copper are shown in Fig. 5. The co-existence of metallic copper (Cu), wurtzite (ZnO) and cuprite (Cu₂O) in Fig. 5(a) (#01 in Table 2) indicates that 1473K was not sufficient for the formation of liquid oxide

phase. There are three phases in equilibrium with metallic copper in Fig. 5(b), (c) and (d). With increasing of the amount of SiO₂ in the initial pellet, the samples varies from wurtzite (ZnO) and willemite (Zn₂SiO₄) saturation to tridymite (SiO₂) and willemite (Zn₂SiO₄) saturation. The sample in Fig. 5(f) has one homogenous liquid oxide phase in equilibrium with tridymite (SiO₂) and metallic copper (Cu).

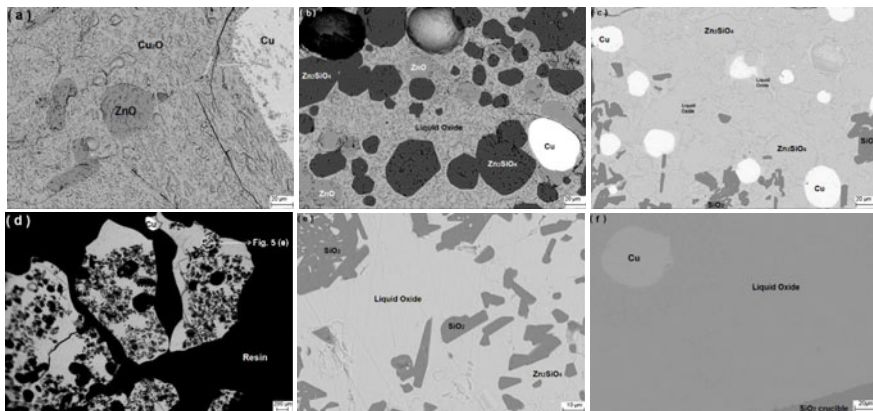


Fig. 5. Backscattered images of the samples in equilibrium with Cu: (a) #01 in Table 2; (b) #02 in Table 2; (c) #03 in Table 2; (d) & (e) #04 in Table 2; and (f) #05 in Table 2.

Conclusion

The phase relationships of the Cu-ZnO-SiO₂-O system for a range of oxygen partial pressures were derived from direct measurements obtained in equilibrium with air ($P_{O_2} = 0.21$ atm) and argon ($P_{O_2} \approx 10^{-5}$ atm) respectively. Willemite (Zn₂SiO₄) is the only compound, which has been found in the experiments. There are four solid primary phases (Cu₂O, SiO₂, Zn₂SiO₄, and ZnO) and two univariant equilibria (liquid oxide + SiO₂ + Zn₂SiO₄ + gas, and liquid oxide + Zn₂SiO₄ + ZnO + gas) at 1473K, when the system was in equilibrium with air ($P_{O_2} = 0.21$ atm). The locations of the univariant equilibria and the liquidus of the system have been quantified, as well as the solubility of Cu₂O in the solid phases. The experimental results have been compared with the phase diagram calculated by MTDATA software and Mtox database, the difference is significant. The system needs a re-assessment.

The phase equilibria of the Cu-ZnO-SiO₂-O system in equilibrium with metallic copper has also been studied at fixed ratios of $\frac{SiO_2}{SiO_2+ZnO}$. The liquid oxide phase in equilibrium with wurtzite (ZnO) and willemite (Zn₂SiO₄) can take much more Cu than the one in equilibrium with tridymite (SiO₂) and willemite (Zn₂SiO₄). For tridymite (SiO₂) and willemite (Zn₂SiO₄) saturated experiments, the concentration of Cu is very stable. Willemite (Zn₂SiO₄) can take up to 2.57 at. % Cu at the experimental conditions in present study. Cu shows lower solubility in tridymite (SiO₂) than in wurtzite (ZnO). The new experimental data will be used for improving the thermodynamic description of the system.

Acknowledgments

The research was supported by Association of Finnish Steel and Metal Producers, and Systems Integrated Metal Processes (SIMP) program by FIMECC and Tekes. One of the author acknowledges the support from CIMO Fellowship Programme TM-15-9810.

References

1. Fathi Habashi, Handbook of Extractive Metallurgy, Volume 2, Heidelberg, Germany, WILEY-VCH (1997).
2. M. E. Schlesinger et al., Extractive Metallurgy of Copper, 5th edition, Elsevier Science Ltd, Oxford (UK), ISBN 978-0-08-096789-9 (2011).
3. J. M. Floyd and W. E. Short, "Ausmelt technology for secondary zinc recovery," Sixth international recycling conference held by the International Lead and Zinc Study Group: Recycling lead and zinc into the 21 Century, Madrid, Spain, 18-23 June, 207-218 (1995).
4. N. H. Nguyen, J. B. Lim, J. H. Paik and J. H. Kim. "Effects of Zn/Si Ratio on the Microstructure and Microwave Dielectric Properties of Zn₂SiO₄ ceramics," J. Am. Ceram. Soc., 90 (2007), 3127-3130.
5. J. Zou, Q. Zhang, H. Yang and H. Sun, "A New System of Low Temperature Sintering ZnO-SiO₂ Dielectric Ceramics," Jpn. J. Appl. Phys., 45 (5A) (2006), 4143-45.
6. G. Gao, S. Reibstein, M. Peng and L. Wondraczek, "Tunable dual-mode photoluminescence from nanocrystalline Eu-doped Li₂ZnSiO₄ glass ceramic phosphors," J. Mater. Chem., 21 (2011), 3156-61.
7. Y. H. Kim, D. K. Lee, H. G. Cha, C. W. Kim, Y. C. Kang and Y. S. Kang, "Preparation and Characterization of the Antibacterial Cu nanoparticle Formed on the Surface of SiO₂ Nanoparticles," J. Phys. Chem. B, 110 (49) (2006), 24923-24928.
8. L. Xia, Z. Liu and P. A. Taskinen, "Experimental determination of the liquidus temperatures of the binary (SiO₂-ZnO) system in equilibrium with air," J. Euro. Ceram. Soc., 35 (2015), 4005-10.
9. L. Xia, Z. Liu and P. A. Taskinen, "Phase equilibria study of Cu-O-ZnO system at various oxygen partial pressures," Ceram. Int. 42 (2016) 5418-5426.
10. L. Xia, Z. Liu and P. A. Taskinen, "Equilibrium study of the Cu-O-SiO₂ system at various oxygen partial pressures," (Submitted for publication).
11. R. Hansson, B. J. Zhao, P. C. Hayes and E. Jak, "A Reinvestigation of Phase Equilibria in the System Al₂O₃-SiO₂-ZnO," Metall. Mater. Trans. B, 36B (2) (2005), 187-193.
12. T. Hidayat, H. M. Henao, P. C. Hayes and E. Jak, "Phase Equilibrium Studies of Cu-O-Si Systems in Equilibrium with air and Metallic Copper and Cu-Me-O-Si Systems (Me = Ca, Mg, Al, and Fe) in Equilibrium with Metallic Copper," Metall. Mater. Trans. B, 42 (1) (2012), 1290-1299.
13. E. Jak and P. C. Hayes, "Phase equilibria determination in complex slag systems," Trans. Inst. Min Metall. C, 117 (1) (2008), 1-17.
14. J. L. Pouchou and F. Pichoir, "Basic Expression of "PAP" Computation for Quantitative EPMA, in 11th International Congress on X-ray Optics and Microanalysis (ICXOM)", Ontario, Canada, Edited by Brown JD and Packwood RH. ICXOM-11, (1987).
15. L. Schramm, G. Behr, W. Loser and K. Wetzig, Thermodynamic reassessment of the Cu-O phase diagram, J. Phase Equilib. Diff., 26 (6) (2005), 605-612.
16. M. T. Clavaguera-Mora, J. L. Touron, J. Rodriguez-Viejo and N. Clavaguera, Thermodynamic description of the Cu-O system, J. Alloys Compd. 377 (1-2) (2004), 8-16.
17. MTDATA ver. 5. 10. 2011, NPL, Teddington, U.K., (2011). (www.npl.co.uk/science-technology/mathematics-modelling-and-simulation/mtdata/).
18. MTOX. Release Notes for Version 7.0 of Mtox Database, National Physical Laboratory, Teddington, UK, (2011).

LIQUIDUS MEASUREMENT OF Te-O-Na₂O-SiO₂ SYSTEM BETWEEN 1000 AND 1200 °C IN EQUILIBRIUM WITH AIR

Imam Santoso^{*,*}, Pekka Taskinen^{*}

^{*}Aalto University, School of Chemical Technology, Metallurgical Thermodynamic and Modelling Research Group, Espoo, 02150, Finland

[†]Institut Teknologi Bandung, Department of Metallurgical Engineering, Bandung 40135, Indonesia

Keywords: Thermodynamics; Slag; Solubility, Tellurium, Melting point

Abstract

Thermodynamic properties of Te-O-Na₂O-SiO₂ system at high temperatures are essential for improving the metallurgical processes especially for smelting the anode slime which contains tellurium compounds. However, the literatures review of previous investigation, showed that there are no liquidus data reported for this system. In the present study the experimental data were obtained by equilibrating the high purity of oxide mixtures at selected temperature, followed by rapid quenching of the equilibrated samples in cold water and compositional analysis using electron probe X-ray microanalyzer. Phase characteristic and the liquidus in the Te-O-Na₂O-SiO₂ system have been investigated at silica saturation between 1000 and 1200 °C in equilibrium with air. New data sets of the liquidus in the Te-O-Na₂O-SiO₂ system have been generated and evaluated.

1. Introduction

Although the Te-O-Na₂O-SiO₂ system is important for metallurgical industries, the experimental phase equilibria study of this system is very limited. Tellurium is mostly produced as a byproduct of copper industries. During electrorefining of copper, the tellurium is separated from copper cathode forming anode slime with other valuable element such as Ag, Au, Se and Pt. The anode slime is then processed by pyrometallurgical route in reverberatory or top-blowing rotary furnace using Dore Smelting process in which oxygen is injected¹. Sodium carbonate and silica are added as flux forming with sodium borate a slag to which the most of the tellurium will distribute. The soda will increase the fluidity of the slag so that the loss of precious metal due to slag entrainment can be minimized. When the targeted purity of metal is achieved, the slag is skimmed off. The slag is then treated to recover tellurium².

Studies of thermodynamic property of tellurium have been done by some authors^{3,4,5} dealing with removal of tellurium as minor element from the metal to slag. Kojo et al.³ and Alvear et al.⁵ showed that the distribution of tellurium between slag and molten copper was affected by the partial pressure of oxygen in the system. The distribution ratio was reported to decrease to a minimum value and then increase when the oxygen partial pressure increases. The majority of tellurium distribute to the slag during the anode slime smelting at the final oxidation stage⁵.

The binary liquidus in the TeO₂-Na₂O system was investigated by Troitskii et al.⁶ at TeO₂ using a heating curve technique. The reported liquidus temperature is between 732 and 458 °C ranging

from pure TeO_2 to 83.3 mol% of TeO_2 in the liquid phase. The minimum liquidus temperatures at $\text{Na}_2\text{Te}_4\text{O}_9$ and Na_2TeO_3 saturation were reported at 413 °C at 28 mol% Na_2O and at 420 °C at 38 mol% Na_2O , respectively. Kavaklıoğlu et al.⁷ also determined liquidus of the TeO_2 - Na_2O system at TeO_2 saturation using a DTA technique. The reported liquidus result was in a close agreement with that reported by Troitskii et al⁶.

In the binary SiO_2 - Na_2O system, the liquidus line was determined using melting and quenching technique by Morey and Bowen⁸. The samples prepared from SiO_2 and Na_2CO_3 mixtures were melted to form a glass. The chemical composition of the quenched glass was analyzed by dissolving to HF and measured as Na_2SiF_6 . The liquid and solid phases in the quenched sample were examined using optical microscope. At silica saturation, the liquidus temperatures were reported to decrease from melting temperature of pure silica to 793 °C at the eutectic point between silica and $\text{Na}_2\text{Si}_2\text{O}_5$ at 35 mol% Na_2SiO_3 . The lowest liquidus temperature at Na_2SiO_3 saturation was reported at 840°C at the eutectic point between Na_2SiO_3 and $\text{Na}_2\text{Si}_2\text{O}_5$ at 62.5 mol% Na_2SiO_3 . The liquidus line in the SiO_2 - Na_2O system was also investigate by Kracek⁹ employing the same methodology as Morey and Bowen⁸ used. The reported liquidus at SiO_2 , Na_2SiO_3 and $\text{Na}_2\text{Si}_2\text{O}_5$ saturations was at a good agreement with the data reported by Morey and Bowen⁸. Another liquidus line was reported at Na_4SiO_4 saturation and in eutectic at 1022 °C with Na_4SiO_4 and Na_2SiO_3 at 43.1 wt% SiO_2 . Study by Mochida et al.¹⁰ indicated that the solubility of tellurium oxide in the ternary TeO_2 - Na_2O - SiO_2 glasses could reach up to 24.9 mol%.

However, our literature research showed that the ternary liquidus data of the slags containing tellurium and sodium oxides at or close to silica saturation were not available. This data is vital for the process optimization. The key metallurgical properties of a slag, e.g. fluidity, separation from metal and capacity to remove impurities from the metal, are related to its phase relations. In present the study new experimental data of the liquidus in the TeO_2 - Na_2O - SiO_2 system were determined at silica saturation between 1000 and 1200 °C at oxygen partial pressure, P_{O_2} , 0.21 atm and over a wide range TeO_2 concentrations relevant to the industrial operations of the Dore smelting process.

2. Experimental Technique

The methodology employed included equilibrating the samples at selected temperatures, quenching the samples in iced cold water and analyzing them using electron probe micro analyzer (EPMA)¹¹. By using this technique equilibrium properties of liquid and solid phases stable at high temperature can be retained to room temperature, by dropping to a cold quenching medium. At high temperature, sodium evaporates easily¹². This means that the initial bulk compositions can change when the samples were heated to high temperature. The volatilization of sodium in the samples during equilibration does affect the proportions of the liquid and solid phases, however, by employing this methodology, it will not affect the final equilibrium compositions of the phases.

2.1 Sample Preparation

The samples were prepared by mixing high purity SiO_2 , Na_2CO_3 and TeO_2 as presented in Table 1. The chemicals were mixed in an agate mortar using pestle. The initial compositions were selected so that at equilibrium, ternary liquid and solid SiO_2 phases would exist. The 0.25 g mixtures were pressed under 5 MPa pressure to form a pellet with diameter 9 mm. The pellets were placed in a container. To avoid contamination from supporting materials, SiO_2 glass was

selected as the container to ensure silica saturation in the sample. The design of the container is presented in Figure 1.

Table 1. Purity of starting materials.

Chemical	Supplier	Purity (wt%)
Na_2CO_3	Alfa Aesar	99.5
SiO_2	Umicore	99.9
TeO_2	Sigma Aldrich	99.995
$\text{Na}_2\text{O}\cdot\text{SiO}_2$	Alfa Aesar	96.04 %, bal CO_2

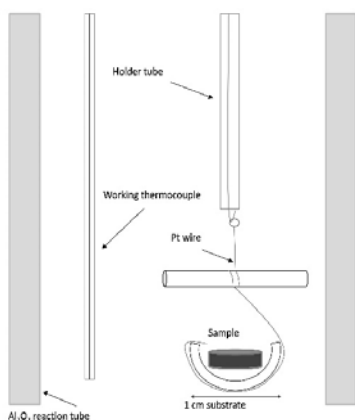


Figure 1. Sample holder arrangement.

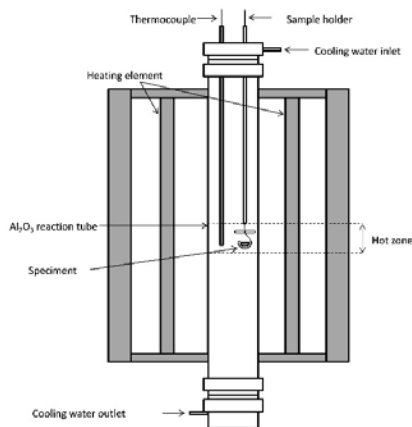


Figure 2. Schematic arrangement of the furnace.

2.3 Furnace Specification and Control

A vertical reaction tube was employed to equilibrate the samples. The samples were raised using platinum wire to hot zone inside the vertical tube made of impervious recrystallized alumina with 30 mm inner diameter. The furnace was heated using silicon carbide (SiC) heating elements. The top of the furnace contained two holes for thermocouple and holder wire insertions. The top and the bottom of the furnace were open to the atmosphere. The schematic arrangement of the furnace is presented in Figure 2. The hot zone temperature inside the furnace was measured using S type thermocouple made from calibrated platinum-10 wt% rhodium and the platinum wires. These thermo-elements were supplied and certified by Johnson-Matthey, UK. and calibrated against melting point of palladium and copper in air. The thermocouple was placed next to the sample. The temperatures were record continuously by connecting the thermocouple to the monitoring system which is NI LabVIEW and Keithley 2010 (OH, USA) data logging programs. The accuracy of the temperature measurement is ± 2 K.

2.4 Equilibration Attainment

To ensure that equilibrium was achieved, the examinations were undertaken (1) by equilibrating the sample at different holding time. Preliminary experiments were conducted to determine equilibration time. The samples were equilibrated at 3, 5 and 12 hours at 1000°C. The result indicated that the time needed to reach equilibrium is 5 hours. (2) by approaching the equilibrium point from different directions by using different starting chemicals. Besides SiO₂, TeO₂ and Na₂CO₃ mixtures, the equilibration of the sample was also tested using SiO₂, TeO₂ and Na₂O.SiO₂ mixtures. The final equilibrium composition remained the same when different starting materials were used. (3) by examining chemical homogeneity of the sample using EPMA at different location of the samples. The chemical composition assessment indicated that the compositional homogeneity was observed in all liquid phases of the well quenched samples.

2.5 Sample Quenching

To preserve the high temperatures properties to room temperatures, after equilibrium time was reached, the sample was dropped to quenching medium by pulling upward the platinum wire that hold the sample. Ice cooled water was selected as the quenching medium. When dropping the sample to iced cooled water, the solid phase was unchanged whereas the liquid phases was transformed to a glassy or microcrystalline phases. There was no difficulty to obtain a glassy phase from the sample. The quenched sample was dried by flushing with hot air and mounted in an epoxy resin. The samples were then polished using a dry polishing method. The samples were kept in a desiccator with silica gel to protect soda from absorbing CO₂ and H₂O from the air and sent for EPMA analysis immediately after polishing. A typical microstructure of the quenched phase assembly was presented in Figure 3.

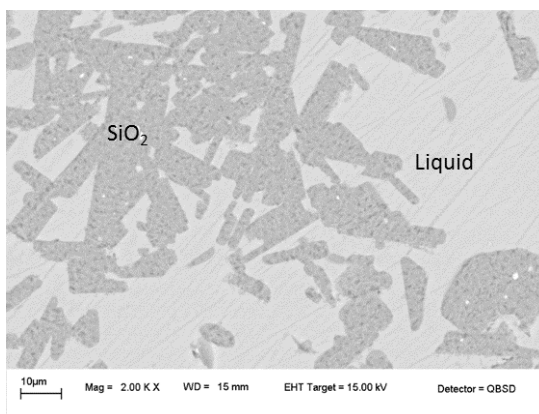


Figure 3. A backscattered electron image of the Te-O-Na₂O-SiO₂ system at silica saturation quenched from 1200°C in air.

2.6 Chemical Analysis

The chemical compositions of the phases were examined by using EPMA, CAMECA SX100 (Cameca SAS, France) at the Geological Survey of Finland (GTK). The appropriate beam intensity of EPMA must be determined to avoid the depletion of sodium in the sample. The optimum condition for beam current and diameter during analysis were 6 nA and 50 μm , respectively. Selected standards for silica, sodium and tellurium were Si Ka (quartz), Na Ka (tugtupite) and Te La (Sb-telluride), respectively, supplied by Astimex Standards Ltd., Toronto, Canada. Atomic number, absorption, and fluorescence (ZAF) corrections were employed. The total accuracy of the EPMA analysis was within 1 wt%. The uncertainty of EPMA analysis is reported as standard deviation taken from the analyzed 10 points in each sample.

Table 2. The chemical analysis of the liquid phases obtained in this study.

Temperature °C	Liquidus composition (wt%)		
	SiO ₂	TeO ₂	Na ₂ O
1000	75.13 ± 1	11.5 ± 0.45	13.37 ± 0.95
1000	77.75 ± 0.47	7.13 ± 0.11	15.11 ± 0.52
1000	70.89 ± 0.53	14.1 ± 0.29	15.1 ± 0.5
1000	75.17 ± 0.4	9.35 ± 0.32	15.49 ± 0.4
1000	65.54 ± 0.29	22.44 ± 0.26	12.02 ± 0.26
1000	80.82 ± 0.46	0	19.18 ± 0.46
1100	78.56 ± 0.3	6.62 ± 0.22	14.82 ± 0.38
1100	77.13 ± 0.4	8.861 ± 0.37	14.27 ± 0.42
1100	73.31 ± 0.28	7.6 ± 0.24	15.09 ± 0.33
1100	80.80 ± 0.32	0.72 ± 0.14	18.47 ± 0.29
1100	74.57 ± 0.6	11.84 ± 0.6	13.59 ± 0.39
1200	82.45 ± 0.38	0.23 ± 0.05	17.06 ± 0.4
1200	74.34 ± 0.49	14.3 ± 0.26	11.37 ± 0.45
1200	76.73 ± 0.46	10.13 ± 0.28	13.34 ± 0.43
1200	80.61 ± 0.19	4.68 ± 0.28	14.71 ± 0.3
1200	82.49 ± 0.24	0.02	17.49 ± 0.23
1200	83.61 ± 0.69	0	16.39 ± 0.69

3 Result and Discussion

The chemical compositions of the quenched liquid phases at silica saturation between 1000 and 1200 °C measured by EPMA are provided in Table 2 along with the estimated standard deviation. The projection of the isothermal sections of the system between 1000 and 1200 °C at silica saturation in equilibrium with air can be seen in Figure 4. The liquidus temperatures at selected SiO₂/Na₂O or SiO₂/TeO₂ ratios (w/w) in the liquid phase are presented in Figure 5, to describe the influence of TeO₂ or Na₂O to SiO₂ saturation the temperatures of the liquid oxide phase.

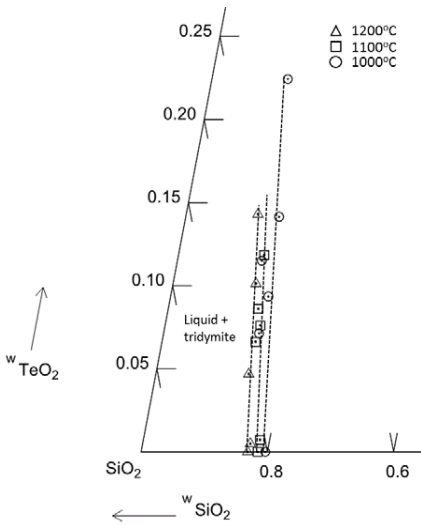


Figure 4 A projection of isothermal sections of Te-O-Na₂O-SiO₂ system at silica saturation from 1000 to 1200 °C.

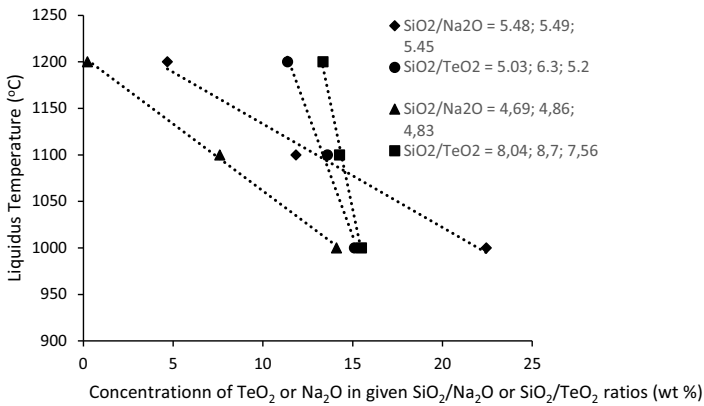


Figure 5 The experimental liquidus temperatures at different concentration of TeO_2 or Na_2O at given $\text{SiO}_2/\text{Na}_2\text{O}$ or $\text{SiO}_2/\text{TeO}_2$ ratios (w/w) in the liquid slag.

Figure 4 shows that between 1000 and 1200 °C at silica saturation and at silica rich side, the liquidus temperatures are sensitive to the Na₂O concentration in the slag. It also shows that the effect of Na₂O on the liquidus temperature is greater than that of TeO₂, since the slope of the line at given SiO₂/TeO₂ ratio is much bigger than that at given SiO₂/Na₂O ratio, as indicated in Figure 5. It shows that at silica saturation and at fixed SiO₂/TeO₂ ratio in liquid phase around 5, liquidus temperature drops from 1200 to 1000 °C when Na₂O concentration in the melt increases only from 11.37 to 15.11 wt %. On the other hand, at SiO₂/Na₂O ratio in liquid phase around 5.5, the decrease in the liquidus temperature from 1200 to 1000 °C is resulted from the increase in the TeO₂ concentration in the liquid phase from 4.68 to 22.24 wt %. This value of temperature difference also remains unchanged when TeO₂ concentration in the melt increases from 0.23 to 14.1 wt % at the SiO₂/Na₂O ratio in liquid phase of around 8. It indicates that ternary liquidus surface at silica saturation at silica rich side only gradually decrease towards the TeO₂ corner.

This ternary liquidus data also suggests that in the pseudobinary binary SiO₂-TeO₂ system, eutectic should exist in the tellurium rich side. At silica saturation below 1000°C, the SiO₂-Na₂O melts would thus dissolve large amounts of TeO₂.

In industrial practice, the data obtained from present study can indicate the effect of the changing variations of slag composition on the key operating parameter i.e. temperature during the smelting process. The result shows that at silica saturations, the tellurium oxide concentration in the silica rich slag will not significantly affect the melting point of the slag. However, adding of the sodium oxide can reduce greatly the temperature liquidus of the slag.

4 Conclusion

The liquidus temperatures and compositions of Te-O-Na₂O-SiO₂ system between 1000 and 1200 °C in equilibrium with air have been investigated experimentally. The samples could be quenched to the homogeneous glassy phases. The results indicate that at silica saturation within this temperature range, the liquidus temperature is affected greatly by sodium oxide. At silica saturation and on this silica rich side, on the other hand, tellurium oxide will not significantly affect the liquidus temperatures. At fixed SiO₂/TeO₂ or SiO₂/Na₂O ratios in the liquid phase, the liquidus temperature decreases from 1200 to 1000 °C when TeO₂ or SiO₂ concentrations increase from 11.37 to 15.11 wt % or from 0.23 to 14.1 wt%. The information can be used to assess the phase diagram of the TeO₂-Na₂O-SiO₂ system useful for industrial applications and to improve the expressions for thermodynamic database containing tellurium oxide.

5 Acknowledgements

The author wish to thank to the LPDP scholarship from Indonesian Government and a project of the SIMP program of Finland by Fimecc Oy and Tekes. EPMA measurements by Mr. Lassi Pakkanen at GTK are also greatly acknowledged.

6 References

1. J. Hait, R. K. Jana, and S. K. Sanyal, "Processing Of Copper Electrowinning Anode Slime: a Review," *Mineral Processing and Extractive Metallurgy*, 118 (4) (2009), 240-252.
2. W. C. Cooper, "The Treatment of Copper Refinery Anode Slimes," *JOM*, 42 (8) (1990), 45-49.
3. I. V. Kojó, P.A. Taskinen, and K.R. Lilius, "Thermodynamics Of Removing Selenium And Tellurium From Liquid Copper By Sodium Carbonate Slags," *Metallurgical and Materials Transactions B*, 16 (1) (1985), 171-172.
4. G.R. Alvear, T. Kanai, H. Fukuyama, T. Fujisawa, and C.Yamauchi, "Thermodynamic Considerations for Elimination of Te and Se from Molten Copper by Using Na₂CO₃ Slag," *Materials Transactions, JIM*, 35 (8) (1994), 508-515.
5. D. R. Swinbourne, G. G. Barbante, and A. Sheeran, "Tellurium Distribution in Copper Anode Slimes Smelting," *Metallurgical and Materials Transactions B*, 29 (3) (1998), 555-562.
6. B. Troitskii, A. Yakhkind, and N. Martyshchenko, "NS Martyshche Nko," *Neorg. Mater.*, 3 (1967), 741-743.
7. K.B. Kavaklıođlu, S. Aydin, M. Çelikkilek, and A.E. Ersundu, "The TeO₂-Na₂O System: Thermal Behavior, Structural Properties, and Phase Equilibria," *International Journal of Applied Glass Science*, 6 (4) (2015), 406-418.
8. G. W. Morey and N. L. Bowen, "The Binary System Sodium Metasilicate-Silica," *The Journal of Physical Chemistry*, 28 (11) (1924), 1167-1179.
9. F. C. Kracek, "The System Sodium Oxide-Silica," *The Journal of Physical Chemistry*, 34 (7) (1930), 1583-1598.
10. N. Mochida, K. Takahashi, and S. Shibusawa, "The Behavior of Te⁴⁺ Ion in Na₂O-TeO₂-SiO₂ Glasses," *Journal of Ceramic Society Japan*, 88 (10) (1980), 583-588.
11. E. Jak, and P. C. Hayes, "Phase Equilibria Determination In Complex Slag Systems," *In the International Conference on Molten Slags Fluxes and Salts, The South African Institute of Mining and Metallurgy*, 2004.
12. H. V. Limpt, R. Beerkens and O. Verheijen, "Models and Experiments for Sodium Evaporation from Sodium-Containing Silicate Melts," *Journal of American Ceramic Society*, 89 (11) (2006), 3446-3455.

**ADVANCES IN MOLTEN
SLAGS, FLUXES, AND SALTS:**

Proceedings of



**Industrial Applications:
Steel**

KINETICS OF PHOSPHORUS MASS TRANSFER AND THE INTERFACIAL OXYGEN POTENTIAL FOR BLOATED METAL DROPLETS DURING OXYGEN STEELMAKING

Kezhuan Gu¹, Neslihan Dogan¹ and Kenneth S. Coley¹

¹McMaster Steel Research Centre
Department of Materials Science and Engineering
McMaster University
1280 Main Street West, Hamilton, Ontario, Canada, L8S 4L7
Phone: 905-525-9140 x24503
Email: coleyk@mcmaster.ca

Keywords: BOF, Reaction Kinetics, Dephosphorization, Mass transfer, Metal Droplets, Interfacial Oxygen Potential

Abstract

Knowledge of oxygen potential is crucial for better understanding of fundamentals of refining reactions kinetics within droplets during oxygen steelmaking. In this study, the changes in the phosphorus content of droplets were measured with time using X-ray fluoroscopy technique at 1853K. Specifically, the effects of sulfur content on dephosphorization kinetics of droplets were investigated during periods of intense decarburization. The experimental results showed that the droplets with low sulfur contents (0.007wt%, 0.011wt%) exhibit a lower minimum phosphorus level and an earlier and more significant reversion compared to those with high sulfur contents. The authors suggest that dephosphorisation rate and maximum partition are favored at lower CO evolution rates as well as lower amount of CO gas generation which result in a higher interfacial oxygen potential between slag and bloated droplets. Equating the rate of CO evolution with that of FeO mass transport allowed mass transfer coefficient of FeO to be calculated, which show that FeO mass transport in dense slag is faster than it is in foaming slag.

Introduction

Several researchers have studied aspects of droplet behavior relevant to steelmaking including, decarburization [1-6], droplet generation [7-16], size distribution [17-18] and residence time [19]. Other workers have developed models [20-23] and conducted plant trials [24-28], which consider the role of droplets in the overall steelmaking process. Previous work in the authors' laboratory [19] introduced the Bloated Droplet model, which has since been employed in an overall BOF model [20-21]. Convincing experimental evidence for bloated droplets has been reported by several researchers [5,6,29]. The current paper presents research on the interplay between dephosphorization and decarburization in bloated droplets. Dephosphorization of steel and hot metal has been studied extensively, important details relevant to the current work can be found in the following publications [30-33]. The importance of the interfacial oxygen potential is demonstrated by considering Equations 1, and 2. Equation 1 is written for rate is control by mass transport in the metal; subscripts b and i represent the bulk metal and the interface respectively,

k_m is the mass transfer coefficient for phosphorus, W_m is the mass of metal, A is the area of the slag-metal interface and ρ_m is the density of the metal. It is clear that $[\%P]_i$ has a strong influence on the driving force for dephosphorization. Similar equations may be written for mass transport in the slag and for mixed control.

$$-\frac{d[\%P]}{dt} = \frac{A}{W_m} k_m \rho_m ([\%P]_b - [\%P]_i) \quad (1)$$

L_p , the partition coefficient for phosphorus is given by Equation 2, where $(\%P)$ represents phosphorus in the slag and $[\%P]$ represents phosphorus in the metal. The subscripts e and i indicate equilibrium and interface respectively, $C_{PO_4^{3-}}$ is the phosphate capacity of the slag,

$$L_p = \frac{(\%P)_e}{[\%P]_e} = \frac{(\%P)_i}{[\%P]_i} = \frac{C_{PO_4^{3-}} P_{O_2}^{5/4} f_P M_P}{K_P M_{PO_4^{3-}}} \quad (2)$$

f_P is the activity coefficient for phosphorus in the metal M_P and $M_{PO_4^{3-}}$ are the molar mass of phosphorus and phosphate respectively, K_P is the equilibrium constant for the dissolution of phosphorus gas in steel and P_{O_2} is the partial pressure of oxygen, in this case at the slag metal interface. This last term is critical in determining the phosphorus partition at the interface. Researchers are divided on the reaction which controls the oxygen partial pressure. Wei et al [34] showed that the interfacial oxygen partial pressure varied between that in equilibrium with carbon in the metal and that in equilibrium with FeO in the slag. Monaghan et al [31] found that, the oxygen potential was controlled by iron oxide in the slag at low stirring whereas Wei et al found that high stirring rates favoured control by carbon in the metal. Wei proposed that the interfacial oxygen potential was set by the balance of supply by FeO in the slag and consumption by carbon in the metal. By encouraging CO nucleation, high stirring rates favour lower interfacial oxygen potentials. Gu et al [35] demonstrated that the foregoing analysis could be applied to dephosphorisation of bloated droplets. Previous work in the authors' laboratory [6] showed that CO nucleation is strongly affected by sulphur. Gu et al [35] used this observation, to determine the dephosphorization rate as a function of CO evolution rate. The current work is aimed at quantifying the relationship between CO evolution during droplet swelling and the interfacial oxygen potential which drives dephosphorization.

Experimental Procedure

The experimental setup and procedure have been described elsewhere [35]. All experiments employed a vertical tube furnace equipped with, X-ray imaging to observe swelling of droplets, and a pressure transducer to measure gas evolution. 25g of slag prepared by mixing of reagent grade Al_2O_3 , CaO, SiO_2 and FeO was placed in a 45 mm diameter alumina crucible and held at temperature for one hour. An iron droplet containing 2.62%C, 0.088% P, ~ 50ppm oxygen and sulphur between 0.007% and 0.021% [36] was then added to the slag. Samples were quenched at different reaction times and taken for chemical analysis using Inductively Coupled Plasma. The slag composition for all experiments was 35wt% SiO_2 , 32wt%CaO, 17wt% Al_2O_3 and 16wt%FeO.

Results

The change of phosphorous and droplet size as a function of time and droplet sulfur content is

shown in Figure 1. Figure 2(a) shows that CO generation rate goes through a maximum at about 0.017wt%S which is higher than the 0.011 wt%S previously reported by the authors [37]. This discrepancy is believed to be related to a change in the technique for making the droplets and a more detailed explanation is currently under investigation by the authors. Inspection of Figure 2(b) shows the total amount of CO generated increases with increasing droplet sulfur content although the amount of gas produced by 0.021wt%S droplets is only slightly higher than for 0.017wt%S. It is also noteworthy that in Figure 2(b) the duration of peak gas generation is 12s, 13s, 12s and 23s corresponding to droplets with 0.007wt%S, 0.011wt%S, 0.017wt%S and 0.021 wt%S, respectively. An elongated period of peak gas generation lowers the interfacial oxygen potential but increases the residence time. Comparing gas generation during the incubation period for all conditions reveals similar initial decarburization rates, around 8.0E-6 mole/s.

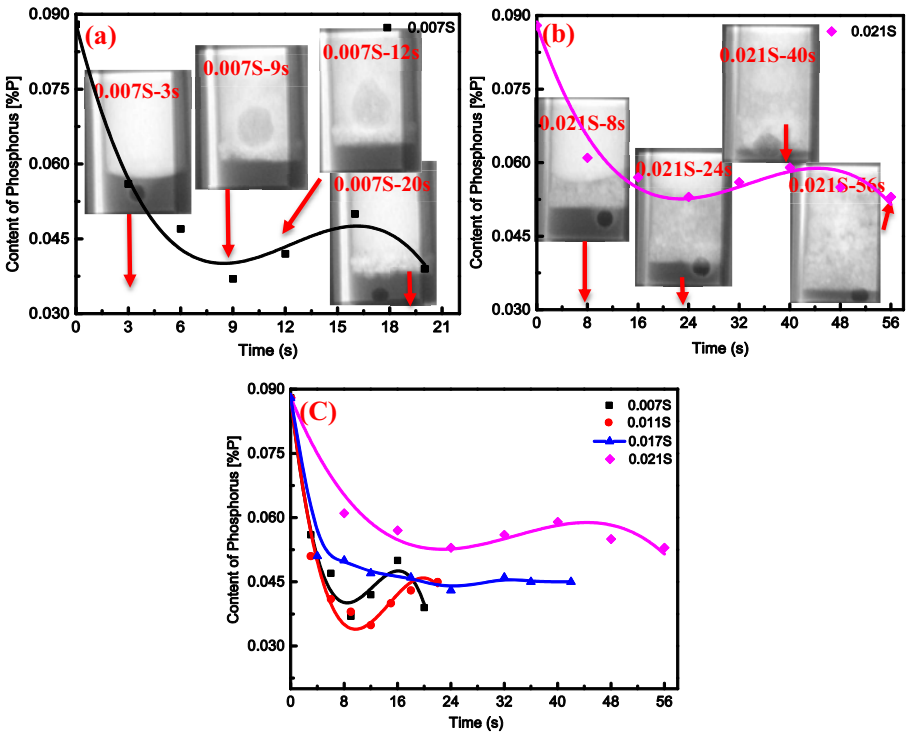


Figure 1: Plot of dephosphorization as a function of time and droplet sulfur content at 1853K: (a) 0.007wt%S; (b) 0.021wt%S and (C) all conditions.

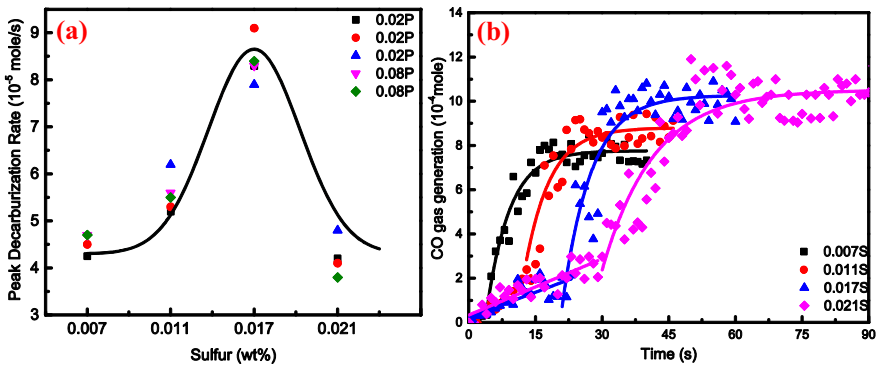


Figure 2: (a) CO evolution rate as a function of metal sulfur content at 1853K and (b) CO gas generation with time.

Comparing the data in Figure 1 with that in Figure 2 for droplets with sulfur less than 0.021, the phosphorus content at the reversion point is seen to increase with increasing CO evolution rate which is consistent with the authors' previous work [35]. However, the phosphorus concentration at the reversion point for 0.021wt%S droplets is much higher than 0.007wt%S droplets although they have a similar peak CO generation rate, and is higher compared to 0.017wt%S droplet which has the highest CO generation rate.

Inspection of the recorded X-ray videos reveals the time at which droplets float out of the dense slag as summarized in Figure 3(a). As the metal sulfur content increases, the time for droplets to float out of the dense slag increases to approximately 32 seconds for the 0.021 wt%S case. Figure 3(b) presents behaviors of droplets with different sulfur contents where droplets can be grouped according to behavior; those with lower sulfur contents (0.007wt%S and 0.011wt%S) have shorter incubation times and show similar behavior with regard to surface area change and dephosphorisation. For droplets with 0.017wt%S, they have the largest maximum surface area due to its' highest CO generation rate. Droplets with 0.021 wt%S have longest incubation time and despite the fact that they show similar decarburization rates to the droplets with 0.07wt%S the peak surface area is considerably lower. Defining the residence time as the time where droplet surface area is more than twice its original area, the peak width of each curve in Figure 3(b) is equivalent to residence time in the foam. Therefore, the residence times are approximately 11s, 14s, 16s and 22s for droplets with 0.007wt%S, 0.011wt%S, 0.017 wt%S and 0.021 wt%S, respectively. Comparing results in Figure 1 with those in Figures 2 and 3, it is seen that the phosphorus content at the reversion point increases with increasing total amount of gas generation. The peak CO generation rate goes through a maximum with respect to sulfur which was suggested in previous work to be caused by the interplay between increasing rates of bubble nucleation and decreasing rates of growth with increasing sulfur [35]. Each of the two groups of droplets exhibit two distinct behaviors with respect to dephosphorization. The lower sulfur droplets exhibit a lower minimum phosphorus level and an earlier and more significant reversion. This behavior can be understood by considering the incubation time and the residence time in the foamy slag relative to the time for dephosphorisation. The low sulfur droplets

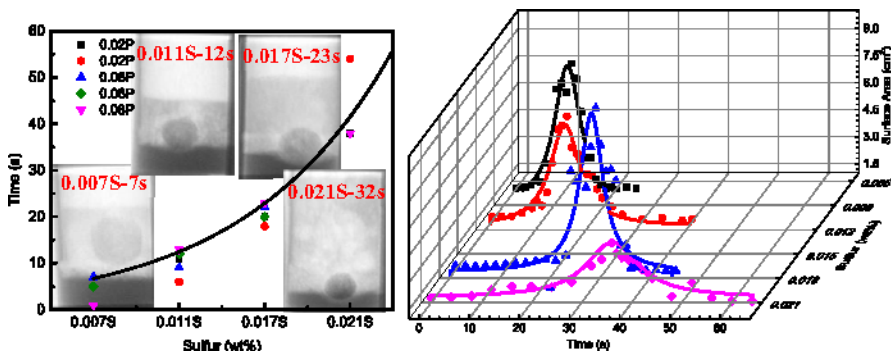


Figure 3: (a) Time needed for different droplets rise out of the dense slag and (b) Typical behavior of droplets with different metal sulfur content.

dephosphorized primarily in the dense slag and entered the foam shortly before reversion took place. The high sulfur droplets went through reversion before the droplet entered the foam. In the case of the low sulfur droplets approximately one third of the dephosphorisation occurred after the droplet entered the foam. The foam which is a much lower liquid slag volume than the dense slag will be quickly reduced driving phosphorous back into the metal. The high sulfur droplets do not swell and enter the foam until after reversion occurs. In this case the dephosphorization is slower probably because of a combination of a lower level of stirring in the metal and surface poisoning due to sulfur, the phosphorous that has been removed from the metal reverts to the slag when the carbon reaction accelerates leading to a lower oxygen potential at the slag-metal interface.

Figure 4(a) shows the volume of foaming slag as a function of time; the maximum volume is similar for all experiments at around 50 cm^3 , five times higher than original dense slag (10 cm^3). The rate of volume increase is tied to decarburization rate. The void fractions for different foaming slags are calculated and summarized in Figure 4(b). Here, void fraction for the whole residence time where droplets rest in foaming slag is calculated. As you can see, the average void fractions of 0.007%wtS and 0.011%wtS are 0.921 and 0.916 which is higher compared with 0.809 and 0.821 for 0.017wt%S and 0.021wt%S, respectively. The authors cannot offer an explanation for this observation but are investigating this phenomenon as part of ongoing research.

Discussion

The results presented above, show that dephosphorisation rate and maximum partition are favored at lower CO evolution rates as well as lower amount of CO gas generation which result

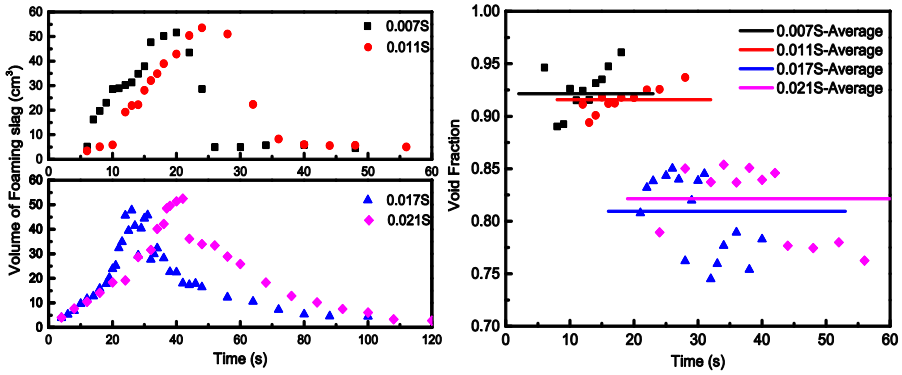


Figure 4: (a) The volume of foaming slag as a function of time and (b) Void fractions of foaming slag during droplet residence time in the foam

in a higher interfacial oxygen potential. These observations are consistent with the mechanism proposed by Wei et al [34] that the oxygen potential at the slag-metal interface is controlled by competition between oxygen supply from the slag and oxygen consumption by reaction with carbon in the metal, represented in this case by CO evolution rate. Based on this concept one can determine a dynamic interfacial oxygen potential by equating the rates of supply and consumption as shown in Equation 3.

$$k_{FeO}(C_{FeO}^b - C_{FeO}^i) = \frac{1}{A} \frac{dn_{CO}}{dt} \quad (3)$$

Here, $\frac{dn_{CO}}{dt}$ is the CO generation rate (mol/s), C_{FeO} is the concentration of FeO, A is the surface area of the droplet, k_{FeO} is the mass transfer coefficient for FeO in the slag and superscripts b and i indicate bulk and interfacial values respectively. If C_{FeO}^i is expressed as activity of oxygen and the equation rearranged and C_{FeO}^b expressed as a function of the initial value C_{FeO}^o and the amount reduced, one obtains:

$$P_O^i = \left[\frac{\gamma_{FeO} K_{Fe}}{C^* a_{Fe}^i K_O} \left(C_{FeO}^o - \frac{1}{V_{dS}} \int \frac{dn_{CO}}{dt} dt - \frac{1}{A k_{FeO}} \frac{dn_{CO}}{dt} \right) \right]^2 \quad (4)$$

Where K_{Fe} and K_O are the equilibrium constants for FeO dissociation and oxygen dissolution in iron γ_{FeO} is the activity coefficient for FeO in the slag, C is the overall molar density of the slag, C_{FeO}^o is molar concentration of FeO in the slag and V_{dS} is the volume of dense slag. Although the CO evolution rate has been shown the dependence on CO nucleation, the authors are yet to develop a model which includes the bubble growth effect, therefore in the current work $\frac{dn_{CO}}{dt}$ has been determined empirically using pressure transducer data. From Figure 1 it is known that droplets experience phosphorus reversion in the foaming slag but obtain driving force to dephosphorize again when sinking back into the dense slag. This manifests that foam slag and dense slag have different mass transfer coefficient of FeO due to the difference of density.

Therefore, Equation 4 was modified to calculate the interfacial oxygen potential between foaming slag and bloating metal droplets when take the foaming slag into consideration:

$$P_O^i = \left[\frac{\gamma_{FeO} k_{FeO}}{C^* a_{Fe}^i K_O} \left(C_{FeO}^o - \frac{1}{V_{dS}} \int_0^{t_f} \frac{dn_{CO}}{dt} dt - \frac{1}{V_{fS}} \int_{t_f}^t \frac{dn_{CO}}{dt} dt - \frac{1}{A k_{FeO}} \frac{dn_{CO}}{dt} \right) \right]^2 \quad (5)$$

Where V_{fS} is the volume of foaming slag and t_f represents the time when droplets enter the foaming slag.

If one assumes dense slag and foaming slag have different mass transfer coefficient of FeO and which do not change with time; it is possible to determine the mass transfer coefficient of FeO for different slag based on a technique presented in a recent publication by the authors [35]. The minimum points in Figure 1 are of particular interest because the forward and backward reaction rates for dephosphorisation are equal but decarburization and FeO reduction continue. Therefore, one can assume the system is in equilibrium with regard to phosphorus and that bulk concentrations may be used to calculate L_p for the interface. If the phosphate capacity of the slag is known, it is then possible to calculate the interfacial oxygen potential from Equation 2. Substituting into Equation 4 and 5 allows k_{FeO} to be calculated. From Table I, we can see that

Table I – Calculated Interfacial Oxygen Potential and Mass Transfer Coefficient of FeO

Droplets	S	$P_{O_2}^i$ based on minimum [P]e	k_{FeO} (cm/s) of dense slag	k_{FeO} (cm/s) of foam slag
1	0.007	2.51E-12		0.0013
2	0.011	2.34E-12		0.0018
3	0.017	1.56E-12	0.0055	
4	0.021	9.65E-13	0.0044	

the calculated mass transfer coefficient of FeO in the dense slag is higher than that in the foaming slag. This result is to be expected if one considers the pathway for mass transfer to be through the liquid the cross sectional area of the path is dramatically reduced by the presence of bubbles. In the case of 0.017wt%S and 0.021wt%S, droplets sit between dense slag and foaming slag at the early step of phosphorus reversion. But for the simplicity of calculation, we assume that they sit inside dense slag at the period of phosphorus reversion.

Comparing k_{FeO} in foaming slag with k_{FeO} in dense slag, the magnitude of difference between the two is only moderate rather than vast as expected. The reason is that in foaming slag with intensive voids, the mass transfer will be hindered due to the limits of the transport pathway. However for droplets in dense slag without too much voids, we still will not expect a high mass transfer coefficient of FeO due to the formation of gas halo around droplets. The gas halo formed at the outside layer will block the mass transfer inside dense slag by acting as a barrier layer. In order to study the kinetics of dephosphorization, Equation 1 for mass transport control in the metal phase is integrated and expressed in Equation 6. In this case, the surface area A in

$$\ln \left[\frac{[\%P]_b - [\%P]_e}{[\%P]_o - [\%P]_e} \right] \left(\frac{[\%P]_o - [\%P]_e}{[\%P]_o} \right) \left(\frac{W_m}{\rho_m A} \right) = -k_m t \quad (6)$$

Setting $C = \frac{[\%P]_b - [\%P]_e}{[\%P]_o - [\%P]_e}$ and $B = \left(\frac{[\%P]_o - [\%P]_e}{[\%P]_o} \right) \left(\frac{W_m}{\rho_m A} \right)$ Equation 6 becomes $B \ln C = kt$

As A in Equation 6 changes with time, a time averaged area must be used [36]. The data presented in Figure 1 are re-plotted in Figure 5 according to Equation 6. Differences in droplet chemistry do not allow a definitive conclusion that the mass transfer in metal phase is the rate-determining step. However, when the data are normalized for driving force, the mass transfer coefficient is very similar at the initial dephosphorization period for droplets with sulfur less than 0.021. But for droplets with 0.017wt%S, Figure 5 shows a lower mass transfer coefficient after about 4 seconds, probably due to a gas halo formed around droplets as shown in X-ray photos. The authors believe that at higher sulfur levels bubbles mainly form at the outer layer of droplets (external decarburization) at the beginning, leading to a lower rate of surface renewal and lower mass transfer coefficients. For this to be the case, the rate must be controlled by mass transport in the metal. Work is ongoing in the authors' laboratory to elucidate the true rate determining step.

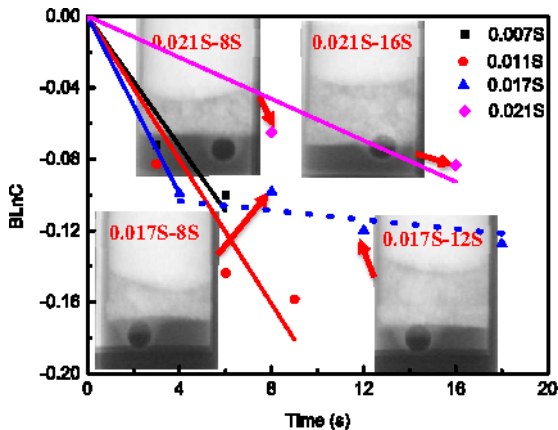


Figure 5: First order rate plot for dephosphorization as a function of metal sulfur content at 1853K

Conclusions

1. During dephosphorization of bloated liquid iron-carbon droplets the interfacial oxygen potential is controlled by the competition between supply of oxygen by iron oxide in the slag and consumption by formation of CO in the metal.
2. The phosphorus partition decreases with the increasing of metal sulfur content due to the increasing of total amount of CO gas, which lowers the interfacial oxygen potential.
3. Equating the rate of CO evolution with that of FeO mass transport allowed mass transfer coefficient of FeO to be calculated, which show that FeO mass transport in dense slag is faster than it is in foaming slag.

4. Internal decarburization offers a higher mass transfer coefficient due to the faster surface renewal rate, leading to a higher dephosphorization rate.

References

1. E.W. Mulholland, G.S.F. Hazeldean, and M.W. Davies, "Visualization Of Slag-Metal Reactions By X-Ray Fluoroscopy: Decarburization In Basic Oxygen Steelmaking," *Journal of The Iron and Steel Institute*, Vol. 211, September 1973, 632-639.
2. T. Gare and G.S.F. Hazeldean, "Basic Oxygen Steelmaking: Decarburization of Binary Fe-C Droplets and Ternary Fe-C-X Droplets in Ferruginous Slags," *Ironmaking and Steelmaking*, 1981, No. 4, 169-181.
3. H. Gaye and P.V. Riboud, "Oxidation Kinetics of Iron Alloy Drops in Oxidizing Slags," *Metallurgical Transactions B*, Vol. 8B, 1977, No. 9, 409-415.
4. D.J. Min and R.J. Fruehan, "Rate Of Reduction Of FeO In Slag By Fe-C Drops," *Metall. Trans. B*, 1992, vol. 23B, pp. 29-37.
5. C.L. Molloseau and R.J. Fruehan, "The Reaction Behavior of Fe-C-S Droplets In CaO-SiO₂-MgO-FeO Slags," *Metall. Trans. B*, vol. 33B, 2002, pp. 335-344.
6. E. Chen And K. S. Coley, "Kinetic Study of Droplet Swelling in BOF Steelmaking," *Ironmaking And Steelmaking: Volume 37(7) October 2010*, Pages 541-545
7. R.C. Urquhart and W.G. Davenport, "Foams and Dmulsions in Oxygen Steelmaking" *Can. Metall. Quarterly*, Vol. 12, No. 4, 1973, pp. 507-516.
8. N. Standish and Q.L. He, *ISIJ Int.*, Vol. 29, No. 6, 1989, pp. 455-461.
9. Q.L. He and N. Standish, "A model study of droplet generation in the BOF steelmaking" *ISIJ Int.*, Vol. 30, No. 4, 1990, pp. 305-309.
10. Q.L. He and N. Standish, "A model study of residence time of metal droplets in the slag in BOF steelmaking" *ISIJ Int.*, Vol. 30, No. 5, 1990, pp. 356-361.
11. G. Turner and S. Jahanshahi, *Trans. ISIJ*, Vol. 27, 1987, pp. 734-739.
12. S.C. Koria and K.W. Lange, *Ironmaking and Steelmaking*, Vol. 10, No. 4, 1983, pp. 160-168.
13. S.C. Koria and K.W. Lange, "A new approach to investigate the drop size distribution in basic oxygen steelmaking", *Metall. Trans.*, Vol. 15B, 1984, pp. 109-116.
14. S.C. Koria and K.W. Lange, "Estimation of drop sizes in impinging jet steelmaking processes", *Ironmaking and Steelmaking*, Vol. 13, No. 5, 1986, pp. 236-240.
15. Subagyo, G.A. Brooks, K.S. Coley, and G.A. Irons, "Generation of droplets in slag metal emulsion through top gas blowing", *ISIJ Int.*, Vol. 43, No. 7, 2003, pp. 983-989.
16. Subagyo, G.A. Brooks, and K. Coley, "Interfacial area in top blown oxygen steelmaking", *Steelmaking Conference Proceedings, ISS, Warrendale Pa.*, Vol. 85, 2002 pp. 749-762
17. Subagyo, G.A. Brooks, and K. Coley, "Residence time of metal droplets in slag metal gas emulsions through top gas blowing", *Canadian Metallurgical Quarterly*, Vol 44 [1], 2005, pp119-129
18. J. Schoop, W. Resch, and G. Mahn, *Ironmaking and Steelmaking*, Vol. 2, 1978, pp. 72-79.
19. G. A. Brooks, Y. Pan, Subagyo and K. S. Coley "Modeling of Trajectory and residence time of metal droplets in slag metal gas emulsions in oxygen steelmaking", *Metall and Mater Trans B*, Vol 36B, 2005, pp 525-535.
20. N. Dogan, G. A. Brooks And M. A. Rhamdhani, "Comprehensive Model of Oxygen Steelmaking Part I: Model Development and Validation," *ISIJ International*, 2011, Vol. 51, No. 7, pp. 1086-1092

21. N. Dogan, G. A. Brooks And M. A. Rhamdhani, "Comprehensive Model of Oxygen Steelmaking Part 2: Application of Bloated Droplet Theory for Decarburization in Emulsion Zone," *ISIJ International*, 2011, Vol. 51, No. 7, pp. 1093–1101.
22. C. Kattenbelt and B. Roffel, "Dynamic Modeling of the Main Blow in Basic Oxygen Steelmaking Using Measured Step Responses," *Metall and Mater Trans B*, 2008, vol 39B, pp764-769
23. R. sarkar, P Gupta, Somnath Basu, and Bharath Ballal, "Dynamic Modeling of LD Converter Steelmaking: Reaction" Modeling Using Gibbs' Free Energy Minimization", *Metallurgical and Materials Transactions B*, Published On-line Jan 2015
24. C. Cicutti, M. Valdez, T. Perez, R. Donayo and J. Petroni, "Analysis of Slag Foaming During the Operation of an Industrial Converter," *Latin Am.Appl. Res.*, 32 (2002), 237.
25. D.J. Price, "L.D.Steelmaking: Significance of the emulsion in carbon removal", *Process Engineering of Pyrometallurgy*, Edited by M.J. Jones, The Institution of Mining and Metallurgy, London, UK, 1974, pp. 8-15.
26. B. Trentini, *Trans. Met. Soc. AIME*, Vol. 242, 1968, pp. 2377-2388.
27. P. Kozakevitch, "Foams and Emulsions in Steelmaking", *JOM*, Vol. 22, No. 7, 1969, pp. 57-68.
28. A. Chatterjee, N.O. Lindfors, and J.A. Wester, *Ironmaking and Steelmaking*, Vol. 3, No. 1, 1976, pp. 21-32.
29. Pomeroy M., Chen, E., Coley, K. S. and Brown, G., "Kinetic Study of Droplet Swelling in BOF Steelmaking" *Proceedings of The 6th European Oxygen Steelmaking Conference*, Stockholm Sweden, September 7-9th (2011), 141-151 38
30. S. Basu, A.-K. Lahiri and S. Seetharaman, Distribution of phosphorus and oxygen between liquid steel and basic oxygen steelmaking slag *Revue de Métallurgie / Volume 106 / Issue 01 / January 2009*, pp 21-26
31. B.J. Monaghan, R.J. Pomfret, and K.S. Coley, "The Kinetics of Dephosphorization of Carbon-Saturated Iron Using an Oxidizing Slag", *Metall and Mater Trans B*, 29B (1998), 111-118.
32. P. Wei, M. Sano, M. Hirasawa, and K. Mori, "Kinetics Of Phosphorus Transfer Between Iron-Oxide Containing Slag And Molten Iron Of High-Carbon Concentration Under Ar-O2 Atmosphere", *ISIJ.Int.*, 33 (1993), 479-87.
33. Christopher P. Manning and Richard J. Fruehan, "The Rate of Phosphorus Reaction between Liquid Iron and Slag", *Metallurgical And Materials Transactions B*, Volume 44B, February 2013, pp37-44.
34. P. Wei, M. Ohya, M. Sano, and K. Mori, "Estimation Of Slag Metal Interfacial Oxygen Potential In Phosphorus Reaction Between Fe(T)O Containing Slag And Molten Iron Of High-Carbon Concentration" *ISIJ. Int.*, 33 (1993), 847-54.
35. K. Gu, B. Jamieson, N. Dogan and K. S. Coley, "Kinetics of Dephosphorisation and the Interfacial Oxygen Potential for Bloated Metal Droplets During Oxygen Steelmaking", 2015 AISTech Conference Proceedings.
36. M.A.Rhamdhani, G.A.Brooks and K.S. Coley, "The Kinetics of Dephosphorization of Carbon-Saturated Iron Using an Oxidizing Slag", *Metall and Mater Trans B*, 36B (2005), 219-227.
37. E Chen and K.S. Coley, *Ironmaking and Steelmaking: Volume 37(7) October 2010*, 541-545.

PHYSICAL MODELLING OF THE EFFECT OF SLAG AND TOP-BLOWING ON MIXING IN THE AOD PROCESS

Tim Haas^{1,2}, Ville-Valtteri Visuri¹, Aki Kärnä¹, Erik Isohookana¹, Petri Sulasalmi¹, Rauf Hürman Eriç³, Herbert Pfeifer² and Timo Fabritius¹

¹ Process Metallurgy Group, University of Oulu,
PO Box 4300, FI-90014 University of Oulu, Finland.

² Department of Industrial Furnaces and Heat Engineering, RWTH Aachen University,
Kopernikusstraße 10, D-52074 Aachen, Germany.

³ Department of Materials Science and Engineering, Aalto University,
PO Box 16200, FI-00076 Aalto, Finland.

Keywords: AOD, mixing time, slag, top-blowing

Abstract

The argon-oxygen decarburization (AOD) process is the most common process for refining stainless steel. High blowing rates and the resulting efficient mixing of the steel bath are characteristic of the AOD process. In this work, a 1:9-scale physical model was used to study mixing in a 150 t AOD vessel. Water, air and rapeseed oil were used to represent steel, argon and slag, respectively, while the dynamic similarity with the actual converter was maintained using the modified Froude number and the momentum number. Employing sulfuric acid as a tracer, the mixing times were determined on the basis of pH measurements according to the 97.5% criterion. The gas blowing rate and slag-steel volume ratio were varied in order to study their effect on the mixing time. The effect of top-blowing was also investigated. The results suggest that mixing time decreases as the modified Froude number of the tuyères increases and that the presence of a slag layer increases the mixing time. Furthermore, top-blowing was found to increase the mixing time both with and without the slag layer.

Introduction

The argon-oxygen decarburization (AOD) process is nowadays the most common process for refining stainless steel. Tuyères, which are mounted along the sidewall of the vessel, are used to inject O₂-N₂ and O₂-Ar gas mixtures. Modern vessels are often equipped with a top lance in order to expedite decarburization in the high-carbon region. The advantage of the process is that the high gas injection rates provide violent stirring and thus good preconditions for a high decarburization rate, while the gradual dilution of the gas mixture prevents the excessive oxidation of valuable alloying elements.

Mixing in the AOD process has been the subject of numerous physical modelling studies, which have focused mostly on the effect of tuyères and their arrangement on the mixing time [1, 2, 3]. During the process, the viscosity of the slag varies as its composition changes due to chemical reactions. However, the effect of slag on the mixing has received relatively little attention, especially in connection with combined top- and side-blowing. Therefore, the aim of this work was to study the effect of a slag layer, top-blowing and the modified Froude number on the

mixing time for both the reduction stage and the combined top- and side-blowing decarburization stage.

Materials and Methods

Experimental Setup

The experiments were performed in an acrylic glass model of a 150 t AOD converter. The employed physical model was built to geometric similarity with the actual converter in a 1:9 ratio and features seven tuyères along the sidewall of the vessel. Owing to its similar kinematic viscosity, water was used to represent the liquid steel bath, while rapeseed oil was used to simulate the slag phase. The water was deionized to avoid reactions between impurities and added acid. Pressurized air was used to represent the argon-oxygen mixtures used in the AOD process. Table I shows the employed physical properties and parameters.

Table I. Employed properties and parameters.

Parameter	Unit	Converter	Model 1:9
<i>Vessel properties</i>			
Vessel diameter	mm	4,122	473
Bath height	mm	2,400	295
<i>Tuyère properties</i>			
Number of tuyères	–	7	7
Exit diameter	mm	10–14	2
Gas flow rate	Nm ³ /min	60–140	0.14–0.56
Modified Froude number	–	750–11,750	750–11,750
<i>Top lance properties</i>			
Number of nozzles	–	3	3
Exit diameter	mm	33.9	3
Nozzle inclination angle	°	11	11
Lance height	m	1.8	0.28
Gas flow rate	Nm ³ /min	110	0.25
Modified Froude number	–	4.26	4.20
Momentum number	–	0.153	0.157
Blowing number	–	–	0.059
<i>Steel/water phase properties</i>			
Density	kg/m ³	7,000	988
Kinematic viscosity	m ² /s	6.8×10 ⁻⁷ (1700 °C)	10.4×10 ⁻⁷ (20 °C)
<i>Slag/oil phase properties</i>			
Density	kg/m ³	2,990	899
Kinematic viscosity (reduction)	m ² /s	3.3×10 ⁻⁵	5.67×10 ⁻⁵
Kinematic viscosity (decarburization)	m ² /s	3.3×10 ⁻⁴	5.67×10 ⁻⁵

Dynamic Similarity Criteria

The gas flow rate through the tuyères was calculated by using the modified Froude number $N_{Fr,t}$, which represents the ratio of the aerodynamic force to the gravitational force [1, 2, 3]:

$$N_{Fr,t} = \frac{u_t^2 \rho_g}{g d_t \rho_l} \quad , \quad (1)$$

where u_t is the gas velocity at the tuyère exit (m/s), ρ_g is the density of the gas (kg/m³), g is the gravitational acceleration (m/s²), d_t is the exit diameter of the tuyère (m) and ρ_l is the density of the liquid phase (kg/m³). In order to obtain dynamic similarity of top lance blowing, four kinds of forces need to be considered: the gravitational force, the aerodynamic force, the inertial force and the viscous force [5]. In the literature, different criteria have been used to determine the lance gas flow rate and the lance height in the model. Often, the modified Froude number is also used [5, 6, 7, 8]. In the literature, lance height [5, 8], cavity depth [7] and lance nozzle diameter [6] have been employed as the characteristic length. In this work, the nozzle exit diameter was used as the characteristic length. The gas velocity at the bath surface u_x , which is used to calculate the modified Froude number, is usually calculated by the following approximation formula [9, 10]:

$$u_x = \frac{0.97 u_e}{0.07 \frac{H}{r_n} + 0.29} \quad , \quad (2)$$

where u_e is the gas velocity at lance exit (m/s), H is the lance height (m) and r_n is the radius of the lance nozzle (m). In this work, initial experiments were conducted to study whether this formula is appropriate to predict the gas velocity. Another similarity criteria for top lance blowing is the momentum number Mo , which is the ratio between jet momentum and displaced bath inertia [5]:

$$Mo = \frac{0.7854 \times 10^5 d_n^2 N p_a \left(1.27 \frac{p_a}{p_0} - 1\right)}{\rho_l g H^3} \quad , \quad (3)$$

where d_n is the diameter of the lance nozzle (m), N is the number of nozzles in the lance, p_a is the atmospheric pressure (bar) and p_0 is the supply pressure (bar). Subagyo et al. [11] identified the blowing number as the similarity criteria. The blowing number N_B represents the ratio of inertia force to surface tension force:

$$N_B = \frac{\rho_g u_g^2}{2 \sqrt{\rho_l \sigma g}} \quad \text{where} \quad u_g = \eta u_x \quad , \quad (4)$$

where u_g is the critical gas velocity (m/s), σ is the surface tension (N/m) and u_x is the axial velocity of the gas jet at the bath surface. Originally, η was treated as a constant [11]. However, Alam et al. have shown that η is a function of the lance height [12] and the nozzle inclination angle [13]. The value of η differs approximately 300% between lance heights of 250 mm and 900 mm [12]. However, no values or equations are available for a lance height over 900 mm, and for this reason the blowing number could not be calculated accurately for the actual AOD converter. With the these considerations in mind, the gas flow rate through the top lance as well

as the lance height were calculated by using both the modified Froude number and the momentum number, but not the blowing number. In the calculations, the employed three-hole lance was treated as a single-hole lance. This is reasonable as the effects of three-hole top-blowing become negligible at sufficient lance heights. For sake of simplicity, the influence of the slag layer was also neglected. Additional experiments were conducted in order to determine the gas velocity u_x at the surface of the bath. Therefore, a pitot tube was placed underneath the lance and connected to a manometer. The lance height varied between 2 cm and 30 cm, while the gas flow rate varied from 0.03 Nm/min to 0.275 Nm/min. For each lance height H and volume flow rate, ten gas velocity measurements were conducted and the average of these values was calculated. Based on the experiments it was found that Eq. 2 over-predicts the gas velocity considerably. However, Eq. 7 showed reasonably good accordance with the experimental data:

$$\frac{u_x}{u_e} = c \left(\frac{H}{d_n} \right)^{-0.92}, \quad (7)$$

where u_e is the gas exit velocity, c is the lance factor and d_n is the lance nozzle diameter. The exponent -0.92 was found to be the best fitting one. However, it should be noted that c is not constant; it is a function of the volume flow rate through the lance. Based on linear regression, the lance factor c was found to vary between 2.84 and 3.18. The predicted and measured gas jet velocities are shown in Figure 1.

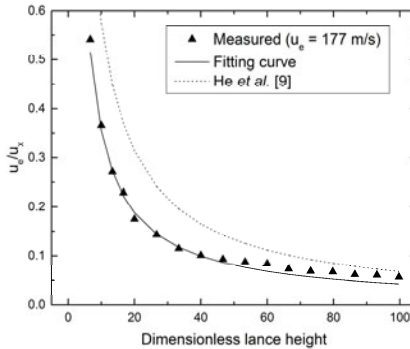


Figure 1. Predicted vs. measured dimensionless gas jet velocity.

Mixing Time Measurements

The experimental set-up of the mixing time measurements is illustrated in Figure 2. The drop in pH was measured with a pH meter using a sampling rate of 20 measurements per second. Ten milliliters of concentrated sulfuric acid (98%) was injected in one go with a pipette 60 seconds after the measurements started. Afterwards, the pH was measured for a further 240 seconds. Due to the decreasing temperature, the pH decreased slightly after the pH drop in some experiments. Therefore, a temperature-compensating criterion was developed to identify the mixing time. The pH values of the last 180 seconds were taken to calculate a line of best fit. This line was

extrapolated backwards, and the function value of $t = 60$ s was used as a reference level for the employed 97.5% criterion. As a result, the yield of the experiments could be increased significantly and the variation in the results could be decreased.

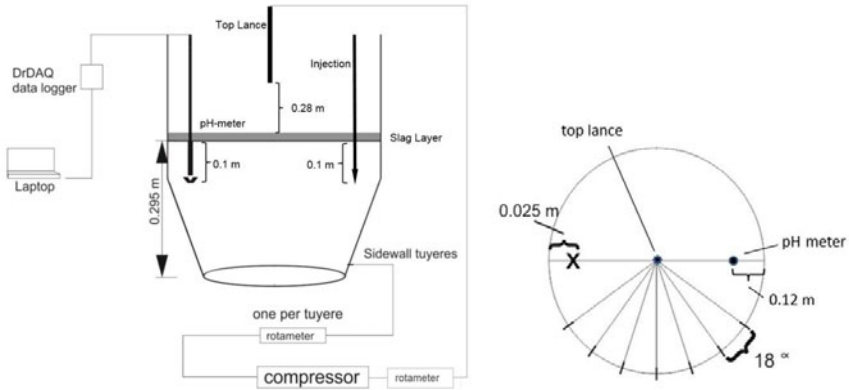


Figure 2. Experimental setup.

For every data point, the number of required experiments was calculated using the following equation [14]:

$$n \geq \left(\frac{s z_{\alpha/2}}{E} \right)^2, \quad (6)$$

where s is the standard deviation of the mixing times (s), $z_{\alpha/2}$ is the confidence interval factor and E is the mixing time error (s). The error E was set to one-third of the mixing time. The confidence level was chosen to be 95% and, therefore, $z_{\alpha/2}$ was 1.96.

Results

Mixing Time Measurements (Reduction Stage)

In the first set of experiments, the effect of top slag on the mixing time in the reduction stage was studied without oil, with 2.9 l of oil and with 5.8 l; these values correspond to water-to-oil volume ratios of 0.1 and 0.2, respectively. The flow rates through a single tuyère were 20 l/min, 50 l/min and 80 l/min, which correspond to modified Froude numbers of 750, 4,750 and 11,750, respectively. Table II shows the results for average mixing time as well as the absolute and relative standard deviations. The standard deviations of the measured mixing times were found to be higher when the oil phase was used to represent the top slag.

Table II: Results for mixing time (reduction stage).

Parameter	Series A			Series B			Series C		
Oil volume [l]	0			2.9			5.8		
Volume ratio	0			0.1			0.2		
$N_{Fr,t}$	750	4750	11750	750	4750	11750	750	4750	11750
Average mix. time [s]	16.60	14.94	11.40	29.10	17.88	10.55	29.57	19.00	11.20
Standard deviation [s]	2.29	5.89	2.44	15.19	9.76	4.68	6.04	6.79	4.14
Relative std. dev.	0.14	0.39	0.21	0.52	0.54	0.44	0.20	0.36	0.37
Number of samples	5	9	5	10	12	10	7	6	5
Required samples	1	6	2	10	11	7	2	5	5

As shown in Figure 3, the mixing time decreased as the modified Froude number increased. The mixing time was found to increase along with the slag-steel ratio. However, the effect is different for different modified Froude numbers. While the effect of the steel-slag ratio is relatively high at the smallest modified Froude numbers, it is almost negligible at the highest modified Froude number. Due to the violent stirring, the employed oil layer emulsified into the water bath to a large extent.

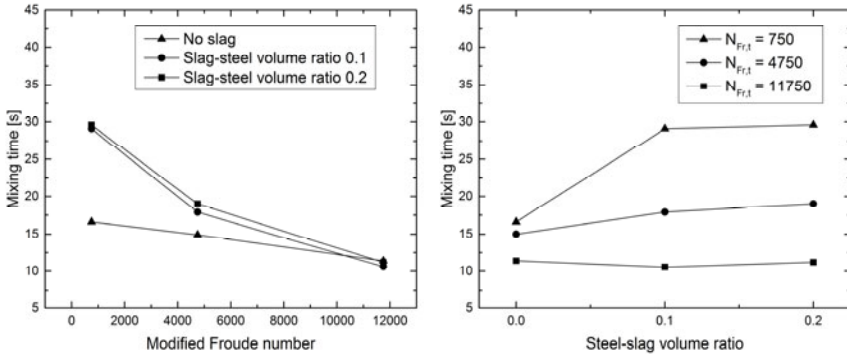


Figure 3. Mixing time vs. modified Froude number (left) and vs. slag-steel ratio (right).

Different types of equations were tested to identify a mixing time equation that depends only on dimensionless process parameters. At first, a simple linear equation was tested:

$$\tau = \underbrace{\varphi}_{\text{Constant}} - \underbrace{v N_{Fr,t}}_{\text{Tuyere blowing}} + \underbrace{y R_{sl}}_{\text{Slag-steel volume ratio}}, \quad (9)$$

where φ , v and y are fitting parameters, while R_{sl} is the slag-steel volume ratio. The experimental results showed that the effect of slag is smaller at higher modified Froude numbers. Thus, slightly better accuracy was obtained by adding a cross-correlation term with fitting parameter k :

$$\tau = \underbrace{\varphi}_{\text{Constant}} - \underbrace{vN_{Fr,t}}_{\text{Tuyere blowing}} + \underbrace{yR_{sl}}_{\text{Slag-steel volume ratio}} + \underbrace{kR_{sl}N_{Fr,t}}_{\text{Tuyere-slag cross correlation}} \quad (10)$$

The fitting parameters were determined by using the sum of the least squares method, and their values are shown in Table III.

Table III: Parameters of the mixing time equation for reduction stage.

Parameter	φ	v	y	k	R^2
Value with linear equation	22.1	0.00123	28.0	–	0.8
Value with cross-correlation	18.8	0.00067	60.6	-0.00565	0.89

Mixing Time Measurements (Decarburization Stage)

In the second set of experiments, the physical model was fitted with a three-hole top lance in order to study the mixing behavior during the combined top- and side-blowing decarburization stage. The modified Froude numbers of the sidewall tuyères were again chosen to be 750, 4,750 and 11,750. The effect of a slag layer was studied using 2.9 l of rapeseed oil, which corresponds to a steel-slag volume ratio of 0.1. The experiments were conducted without lance or slag (Series A), with lance but without slag (Series B), and with both lance and slag (Series C). The results of these experiments are shown in Table IV .

Table IV: Results for mixing time (decarburization stage).

Parameter	Series A			Series B			Series C		
$N_{Fr,l}$	0			4.2			4.2		
Slag volume [l]	0			0			2.9		
Volume ratio	0			0			0.1		
$N_{Fr,t}$	750	4750	11750	750	4750	11750	750	4750	11750
Average mix time [s]	16.60	14.94	11.40	24.17	15.10	14.70	39.50	21.40	12.00
Standard deviation [s]	2.29	5.89	2.44	8.76	3.53	1.72	6.19	3.84	2.35
Relative std. dev.	0.14	0.39	0.21	0.36	0.23	0.12	0.16	0.18	0.20
Number of samples	5	9	5	6	5	5	5	5	5
Required samples	1	6	2	5	2	1	1	2	2

Figure 4 shows the mixing time during the decarburization stage for the experiments conducted without slag as well as the experiments conducted with a slag phase. The results indicate that the presence of top slag increases the mixing time, although this effect decreases as the modified Froude number of the tuyères increases. In addition, it was found that top-blowing increases the mixing time. This result is in accordance with the experiments conducted by Wei et al. [3], who suggested that mixing is caused primarily by side-blowing, while top-blowing disturbs the flow pattern of the main vortex. The effect decreases slightly with increasing gas flow rates through the tuyères.

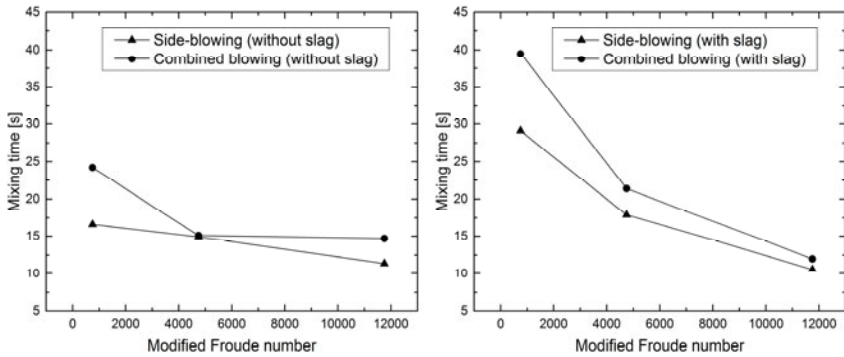


Figure 4. Mixing time vs. modified Froude number without (left) and with slag phase (right).

Again, a mixing time equation was developed by using the least squares method:

$$\tau = \underbrace{\varphi}_{\text{Constant}} - \underbrace{vN_{Fr,t}}_{\text{Tuyere blowing}} + \underbrace{yR_{sl}}_{\text{Slag-steel volume ratio}} + \underbrace{kR_{sl}N_{Fr,t}}_{\text{Tuyere-slag cross correlation}} + \underbrace{tN_{Fr,l}}_{\text{Lance blowing}} + \underbrace{wN_{Fr,t}N_{Fr,l}}_{\text{Lance-slag cross correlation}}, \quad (11)$$

where t and w are fitting parameters. The values of the fitting parameters are given in Table V. It should be noted that the number of data points might not be sufficient to deduct the coherence between the investigated process values and the mixing time correctly.

Table V. Parameters of the mixing time equation for decarburization stage.

Parameter	φ	v	y	k	t	w	R^2
Value	17.5	0.00057	104.3	-0.0095	2.48	-0.00023	0.92

Discussion

Wuppermann et al. [1] studied the mixing time in a 1:4 water model of a 120 t AOD converter and found that the mixing time decreases as the modified Froude number increases and that there is an ideal bath height-to-diameter ratio of between 0.7 and 0.75. Ternstedt et al. [2] investigated the effect of volume flow rate through the tuyères, bath height and vessel diameter during side-blowing in two models using potassium chloride as a tracer. The results of their experiments suggest that the influence of the bath height is almost negligible and that the mixing time decreases as the volume flow rate increases and with decreasing bath diameter. Wei et al. [3] examined the influence of the angle between the side-blowing tuyères, the number of tuyères and the gas flow rate for both side- and top-blowing in a 1:3 model of a 120 t AOD converter. Their experiments showed that the mixing time decreased when the tuyère angle was increased from 18° to 22° and when the number of tuyères was decreased from seven to six. Moreover, the mixing time was found to increase with increasing top-blowing rate. In an earlier study, Wei et al. [4] employed a 1:3 model of an 18 t AOD converter and found that rotating jets decreased the mixing time. Table VI concludes the effect of all the parameters investigated so far on the mixing time within an AOD converter.

Table VI: Overview of the effect of certain parameters on the mixing time.

Parameter	Effect on mixing time	Reference
Modified Froude number (tuyères)	Decreasing	[1, 2, 3], this work
Height-to-diameter ratio of bath	Increasing*	[1, 2]
Angle between tuyères	Decreasing	[3]
Number of tuyères	Increasing	[3]
Top-blowing	Increasing	[3], this work
Rotating jets	Decreasing	[4]
Slag/oil layer	Increasing	this work
Top-blowing with slag/oil layer	Increasing	this work

* The ideal bath height-to-diameter ratio was between 0.7 and 0.75.

There are certain points that need to be considered when interpreting the results. The viscosity of the AOD slag changes significantly during the process as solid phases might occur due to changing composition. Therefore, the viscosity values given in Table I should be understood as a snapshot in time and the identified equation describes merely one period during the process each time. Based on numerical simulations of an AOD vessel, Odenthal et al. [15] found that the damping effect of the top slag increases with increasing viscosity, which suggests that the mixing time would also increase. In addition, it should be noted that the steel–slag interfacial tension is considerably higher than that of oil and water and, therefore, the model exhibits more aggressive emulsification behavior than was expected to occur in an actual AOD vessel. In fact, it might be possible that the increasing mixing time is the result of an increasing effective viscosity and not of damping effects. In future work, it might be sensible to employ food coloring instead of sulfuric acid as a tracer, as suggested by Wuppermann et al. [1], as the standard deviation of their measurements was much lower than in this work. Nevertheless, it remains uncertain whether the color of the rapeseed oil would affect the reliability of this measurement method.

Conclusions

The aim of this study was to investigate the effect of different process parameters on the mixing time in an AOD converter. The mixing time measurements were conducted with a 1:9-scale water model of a 150 t AOD converter using concentrated sulfuric acid as a tracer. Rapeseed oil was used to represent the top slag phase. The experiments permit the following conclusions:

- (1) In the reduction stage as well as in the decarburization stage, the mixing time decreases as the modified Froude number of the tuyères increases.
- (2) Top-blowing increases the mixing time, which is believed to be due to the disturbance of the main vortex caused by side-blowing.
- (3) The presence of a slag layer increases the mixing time, but the increment is not linear with the amount of slag used. The effect decreases as the modified Froude number increases. In the case of combined blowing, the presence of a slag layer increases the mixing time further.

Finally, mixing time equations were proposed for the reduction stage and the decarburization stage; the correlation factors for these equations were 0.89 and 0.92, respectively.

References

1. C. Wuppermann et al., "A novel approach to determine the mixing time in a water model of an AOD Converter," *ISIJ Int.*, 52 (2012), 1817-1823.
2. P. Ternstedt et al., "Mixing time in a side-blown converter," *ISIJ Int.*, 50 (2010), 663-667.
3. J.-H. Wei et al., "Physical modeling study on combined side and top blowing AOD refining process of stainless steel: Fluid Mixing Characteristics in Bath," *ISIJ Int.*, 50 (2010), 26-34.
4. J.-H. Wei et al., "Water modeling study of fluid flow and mixing in an AOD bath with rotating gas jets," *Iron Steelmaker*, 28 (2001), 59-67.
5. S. C. Koria and K. W. Lange, "A new approach to investigate the drop size distribution in basic oxygen steelmaking," *Metall. Trans. B*, 15 (1984), 109-116.
6. R. C. Urquhart and W. G. Davenport, "Foams and emulsions in oxygen steelmaking," *Can. Metall. Quart.*, 12 (1973), 507-516.
7. W. Kleppe and F. Oeters, "Modellversuche über das Abreißen von Flüssigkeitstropfen beim Aufblasen eines Gasstrahles auf eine Flüssigkeitsoberfläche," *Arch. Eisenhüttenwes.*, 47 (1976), 271-275.
8. T. M. Fabritius et al., "Combined blowing with three-hole lance in a sidewall blowing converter," *Steel Res.*, 72 (2001), 237-244.
9. B. Sabah and G. Brooks, "Splash Distribution in Oxygen Steelmaking," *Metall. Mater. Trans B*, 46 (2014), 863-672.
10. Q. L. He and N. Standish, "A Model Study of Droplet Generation in the BOF Steelmaking," *ISIJ Int.*, 30 (1990), 305-309.
11. Subagyo et al., "Generation of droplets in slag-metal emulsions through top gas blowing," *ISIJ Int.*, 43 (2003), 983-989.
12. M. Alam et al., "A Computational Fluid Dynamics Model of Shrouded Supersonic Jet Impingement on a Water Surface," *ISIJ Int.*, 52 (2012), 1026-1035.
13. M. Alam et al., "Inclined Jetting and Splashing in Electric Arc Furnace Steelmaking," *ISIJ Int.*, 51 (2011), 1439-1447.
14. D. C. Montgomery and G. C. Runger, *Applied Statistics and Probability for Engineers* (John Wiley & Sons, Inc., 2003), 252
15. H.-J. Odenthal et al., "Simulation of Fluid Flow and Oscillation of the Argon Oxygen Decarburization (AOD) Process," *Metall. Mater. Trans B*, 41 (2010), 396-413.

3D CFD Modeling of the LMF System: Desulfurization Kinetics

Qing Cao¹, April Pitts^{1,2}, Daojie Zhang¹, Laurentiu Nastac¹, and Robert Williams²

¹The University of Alabama, Department of Metallurgical and Materials Engineering,
Box 870202, Tuscaloosa, AL, 35487, USA, email: lnastac@eng.ua.edu

²Nucor Tuscaloosa, Tuscaloosa, AL, 35401, USA

Keywords: 3D CFD Modeling; Ladle Metallurgical Furnace; Fluid Flow Characteristics; Desulfurization Kinetics.

Abstract

A fully transient 3D CFD modeling approach capable of predicting the three phase (gas, slag and steel) fluid flow characteristics and behavior of the slag/steel interface in the argon gas bottom stirred ladle with two off-centered porous plugs (Ladle Metallurgical Furnace or LMF) has been recently developed. The model predicts reasonably well the fluid flow characteristics in the LMF system and the observed size of the slag eyes for both the high-stirring and low-stirring conditions. A desulfurization reaction kinetics model considering metal/slag interface characteristics is developed in conjunction with the CFD modeling approach. The model is applied in this study to determine the effects of processing time, and gas flow rate on the efficiency of desulfurization in the studied LMF system.

Introduction

The ladle metallurgical furnace (LMF) is responsible for alloy additions, steel temperature control, desulphurization, deoxidation, and inclusion removal in steelmaking process. Inert gas stirring is needed to transport the steel to the slag/steel interface where most reactions occur. To understand the mechanisms of various phenomena inside the ladle, a large amount of work was conducted on various aspects of gas-metal-slag interactions.

First, in order to investigate the three-phase fluid flow behavior, many models for predicting gas stirring in LMF have been developed [1-4]. Lou *et al.* [5] established a gas and liquid two-phase flow model based on the Euler-Euler approach and investigated the influences of the interphase force including turbulent dispersion force, drag force, and lift force. By taking the slag phase into account, Jonsson *et al.* [6] used a two-dimensional three-phase model to investigate the effect of viscosity on ladle-refining. Later, Cloete *et al.* [7] developed a mathematical model by employing the Lagrangian discrete phase model (DPM) to describe the bubble plume and the Eulerian multiphase volume of fluid (VOF) model for tracking the free surface of the melt. Li *et al.* [8] used the VOF method to simulate the transient three-phase flow and the effects of gas injection on the behaviors of slag layer. Although significant number of models have been developed, it is still not

clear which model can accurately predict the effect of gas stirring and other operating parameters on the three phase flow and interaction behavior.

The second major feature of an LMF system is the sulfur removal capability. Owing to the increasing demand for low-sulfur steel, slag-metal reactions and desulfurization efficiency under different conditions have also been widely studied. In 1998, Jonsson et al. [9] developed a sulfur refining model by coupling thermodynamic reactions of slag/metal and fluid flow. The model showed that desulfurization rate mainly depends on the transfer rate of sulfur from the metal to the slag/steel interface. Lou et al. [10] proposed a computation fluid dynamics-simultaneous reaction model (CFD-SRM) coupled model to describe the desulfurization behavior in a gas-stirred ladle. The simultaneous slag/metal reaction rates at the interface were calculated by SRM, and then they were added into the CFD source terms to calculate the transport and distribution of each component in the liquid steel. However, it's well known that liquid metal may become entrapped in the slag phase and form metal droplets depending on gas blowing number. The generated droplets enhance the rates of heat transfer and chemical reactions. Sample analysis results in [11] showed that the total interfacial area between the steel droplets and the slag was 3-14 times larger than the projected flat interfacial area between the steel and the slag. Wang et al. [12] developed a numerical model for dephosphorization including reaction at the bath metal-slag interface and the droplet metal-slag interface. Their results showed that the dephosphorization rate at the interface between the droplet metal and the slag is about two orders of magnitude faster than that at the bath metal-slag interface.

The objective of the present work is to develop a fully transient 3D CFD modeling approach in the argon gas bottom stirred ladle with two off-centered porous plugs. This model can predict the three phase (gas, slag, and steel) flows and behavior of the slag/steel interface. Then the model is coupled with a desulfurization kinetics submodel to predict the sulfur removal rate. The effects of key processing parameters including Ar flow rate, processing time and interface area on the three phase flows and desulfurization behavior were also studied in detail.

Model Description

Assumptions

In the present study, the desulphurization is made by a slag containing 30 mass% Al_2O_3 , 55 mass% CaO , 7.5 mass% MgO and 7.5 mass% SiO_2 . The initial concentration of the dissolved oxygen in the liquid steel is 0.02 mass%. The mathematical model for three-phase fluid flow and kinetic reaction in LMF systems is based on the following assumptions:

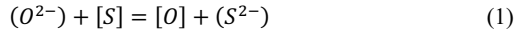
- The dissolved elements are uniformly distributed in the steel at the start of the calculation.
- The concentrations of slag components are assumed to be homogeneous due to the small thickness of slag layer compared with liquid steel.
- The walls in the ladle are assumed to be smooth and non-slip. All the computations were done at 1800K.
- The free surface of the slag/air interface is frictionless. An allowance is made for the escape of gas bubbles at the interface.

CFD model

The CFD model consists of a multiphase VOF-Level Set explicit model in conjunction with momentum, energy, and species transfer models as well as the k-epsilon realizable turbulence model with standard wall functions in ANSYS Fluent [13]. A detailed description of the complete VOF model can be found in [14].

Reaction Model

Based on the slag-metal reaction, the desulfurization process in the ladle can be expressed by the following reaction:



where () indicates the species in the slag, and [] represents species in the liquid steel bath [15].

The reaction rate is controlled by the mass transfer of elements in the steel from bulk to the slag/steel interface, since the concentrations of these species in the bulk steel are much lower than the compound of these species in the slag. The kinetics of the reaction at both the bath metal/slag and the droplet metal/slag interfaces are considered. The details of the reaction kinetics of these reactions can be found in [8]. The kinetics model of the droplet formation is described in [16]. The droplet size can be related to the turbulent energy and surface tension. Since the available interfacial area of the droplets is very large, the metal droplets can significantly increase the desulfurization rate in the ladle [12].

At the slag-metal interface, the overall desulfurization reaction rate S_s (the change in the concentration of sulfur in steel) can be written as:

$$S_s = R_k \rho_l k_{eff,S} \frac{A}{V} \left\{ [wt\%S] - \frac{(wt\%S)}{L_s} \right\} \quad (2)$$

where the (wt%S) indicates the mass fraction of sulfur in slag phase, [wt%S] is the local mass fraction of S in liquid steel, ρ_l is the density of liquid steel. $k_{eff,i}$ characterizes the overall mass transfer coefficient of element i. R_k is the modification coefficient related to the droplet metal/slag interface reaction [12] and is determined to be ~70 via experimental measurements at Nucor. L_s is the distribution ratio of element S between slag and metal phases at equilibrium:

$$L_s = \frac{(wt\%S)^*}{[wt\%S]^*} \quad (3)$$

The equilibrium concentrations of sulfur in steel and slag phases, $[wt\%S]^*$ and $(wt\%S)^*$, can be calculated using Factsage (SlagA and Fe-liquid model) [15, 17].

The overall mass transfer coefficient of element i can be calculated as

$$k_{eff,i} = \frac{k_{m,i} k_{s,i} L_i \rho_S}{k_{s,i} L_i \rho_S + \rho_m k_{m,i}} \quad (4)$$

where $k_{m,i}$, $k_{s,i}$ are the mass transfer coefficient of species i in liquid steel and slag, respectively. The mass transfer coefficients could be calculated through the Komogorov theory of isotropic turbulence as follows:

$$k_{m,i} = cD_{m,i}^{0.5} \left(\frac{\epsilon_l}{\nu} \right)^{0.25} \quad (5)$$

$$k_{s,i} = cD_{s,i}^{0.5} \left(\frac{\epsilon_l}{\nu} \right)^{0.25} \quad (6)$$

where c is a constant and is 0.4 for this work [18]. $D_{m,i}$ and $D_{s,i}$ are diffusion coefficients of species i in liquid steel and slag, respectively. In the current model, the diffusion coefficients of species in liquid steel are assigned to $7.0 \times 10^{-9} \text{ m}^2/\text{s}$ [10]. The diffusivity of species in slag are generally two orders of magnitude lower than that of steel species. As shown in the equation, the mass transfer coefficient is proportional to the square root of the diffusion coefficient. Thus, the relations between k_s and k_m can be obtained as follows:

$$k_{s,i} = 0.1k_{m,i} \quad (7)$$

By the Eqs. (2) through (7), the desulfurization reaction kinetics can be calculated.

Numerical Procedure

The geometry of the LMF is shown in Figure 1. It has two off-centered plugs (diameter 92 mm). The initial thickness of the slag layer is 150 mm, and depth of the steel is 3.35 m. Two argon flow rates were used: $0.0281 \text{ m}^3/\text{s}$ and $0.11238 \text{ m}^3/\text{s}$. The thermo-physical properties of the steel, slag and argon at 1800K are presented in Table I.

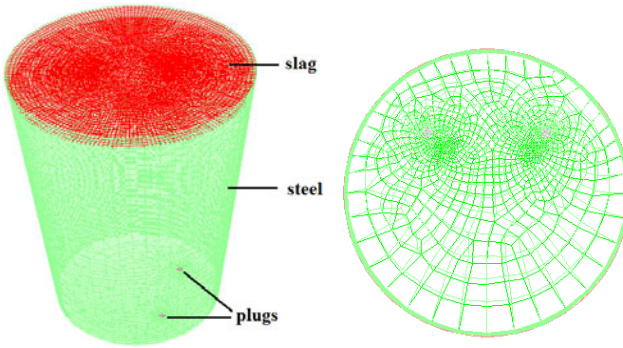


Figure 1. Meshed geometry of the LMF system.

Initially, the slag layer rests on top of the steel bath, and no argon blows through the porous plugs. The inlet velocity of argon gas is calculated as [8]:

$$V_{in} = \frac{Q_L}{A} = \left(\frac{p_S T_L}{p_L T_S} \right) \frac{Q_S}{A} \quad (8)$$

where subscript L means ladle operating condition, and S is standard condition. T_S and T_L are solidus and liquidus temperature, respectively. A is plug area, and Q_S is argon gas flow rate at standard condition.

Table I. Thermo-physical properties of materials at 1800K

Steel		Slag		Argon	
Density, kg/m ³	Viscosity, kg/(m·s)	Density, kg/m ³	Viscosity, kg/(m·s)	Density, kg/m ³	Viscosity, kg/(m·s)
7020	0.006	3500	0.03	0.568	2.125×10^{-5}

Results and Discussion

Figures 2 and 3 show the volume fraction profile for the Ar in the plug cross section and for the slag phase at free surface, respectively. And it can be seen that the mixing is very strong along the Ar path and become weaker further from it (as displayed in Fig. 2). As it can be seen from these figures, the mixing of the phases under high gas stirring rate is significantly stronger compared with the low flow rate case. Also, Figs. 3 show the size of the open slag eye for the low and high flow rates, respectively. The size of slag eyes increases with the gas flow rate, which is in reasonable agreement with our experimental observations and previous publications [8, 10].

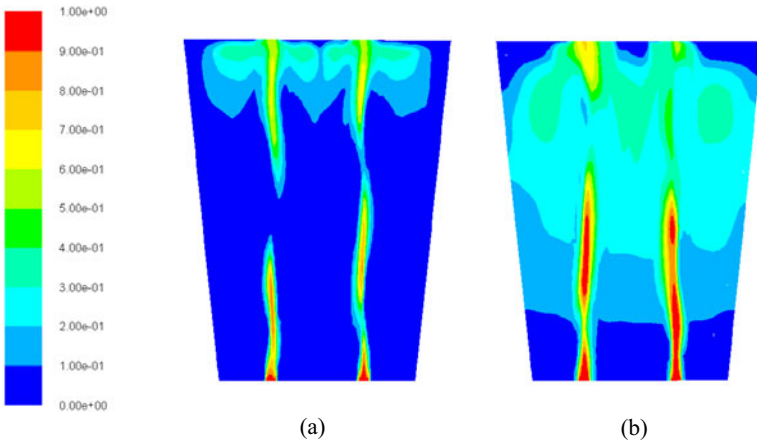


Figure 2. Volume fraction profile for the Ar phase at 100s: (a) low flow rate case, (b) high flow rate case.

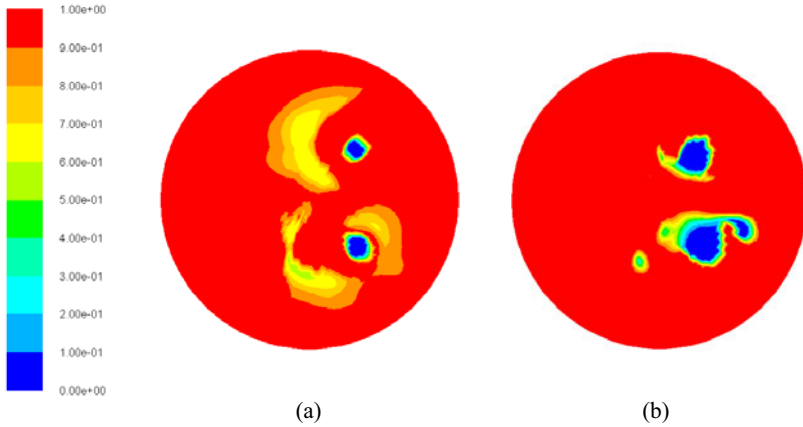


Figure 3. Volume fraction profile for the slag phase at 100s: (a) low flow rate case, (b) high flow rate case.

Figures 4a, 4b, 5a, and 5b show the S mass fraction profile in the steel phase at 100s and 200s for the low and high flow rate cases. The S content is very high in the bubbly plume zone, and then it is transferred upward to center of slag eyes by upping steel flow. At the steel surface the S content gradually decreases due to the desulfurization reaction, and the S concentration is lowest at the side wall where the liquid steel leaves the slag/metal interface. Then, it would increase again inside the ladle because the species would be further mixed. As a result, sulfur is removed with time, as shown in Fig. 6.

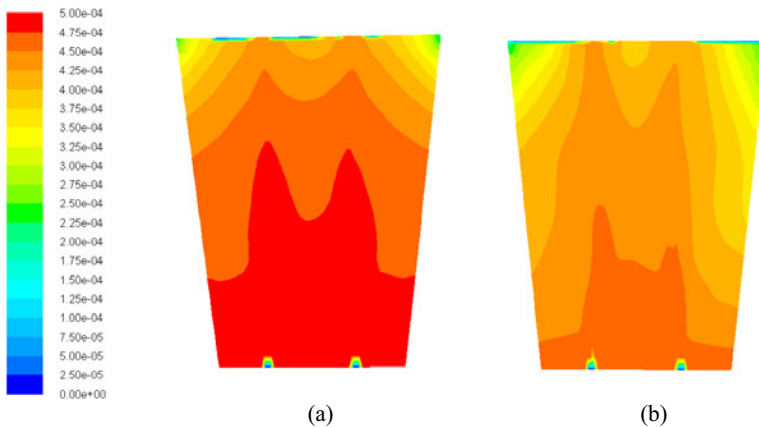


Figure 4. Mass fraction profile of sulfur in the steel phase at 100s: (a) low flow rate case, (b) high flow rate case.

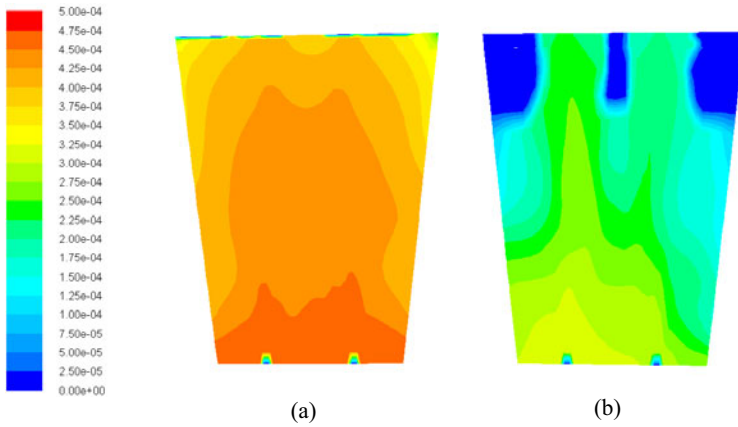


Figure 5. Mass fraction profile of sulfur in the steel phase at 200s: (a) low flow rate case, (b) high flow rate case.

Figures 4-6 display that the desulfurization efficiency under high Ar flow rate is much higher than that under low Ar flow rate. Lou et al. [10] have got similar results in their previous research. The improved desulfurization efficiency is attributed to the higher mixing rate and stronger interaction between steel and slag phases under high Ar flow rate. The enhanced turbulence degree and emulsification improves the species mass transfer rate as well as the desulfurization rate [10].

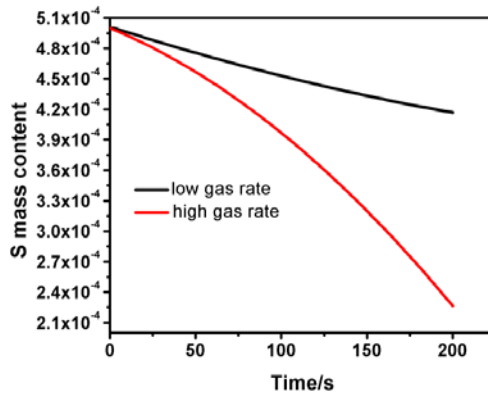


Figure 6. Mass fraction of sulfur in the steel phase with time.

Conclusions and Future Work

A fully transient 3D CFD modeling approach capable of predicting the fluid flow, solute transport and desulfurization kinetics in the LMF was developed. The model can be used to predict the three-phase fluid flow, the behavior of the metal/slag interface as well as the sulfur removal during the Ar stirring process. The reaction kinetics model for sulfur removal will soon be validated against experimental measurements of sulfur content at different times in the LMF. Also, the model will further be refined by accurately considering the droplet metal/slag interface reaction.

References

- [1] D. Guo and G.A. Irons, "Modeling of Gas-Liquid Reactions in Ladle Metallurgy: Part II. Numerical Simulation," *Metallur. and Mater. Trans. B*, 31B (12) (2000), 1458-1464.
- [2] P. Sulasalmi, A. Kärnä, T. Fabritius, and J. Savolainen, "CFD Model for Emulsification of Slag into the Steel," *ISIJ International*, 49 (11) (2009), 1661-1667.
- [3] S.T. Johansen and F. Boysan, "Fluid Dynamics in Bubble Stirred Ladles: Part II. Mathematical Modeling," *Metallur. and Mater. Trans. B*, 19B (10) (1988), 755-764.
- [4] E. Ramström, "Mass transfer and slag-metal reaction in ladle refining-a CFD approach" (Licentiate Thesis, Royal Institute of Technology, 2009), 1-31.
- [5] W.T. Lou and M.Y. Zhu, "Numerical Simulation of Gas and Liquid Two-Phase Flow in Gas-Stirred Systems Based on Euler-Euler Approach," *Metallur. and Mater. Trans. B*, 44B (10) (2013), 1251-1263.
- [6] P.G. Jonsson, L. Jonsson and D. Sichen, "Viscosities of LF Slags and Their Impact on Ladle Refining," *ISIJ Intern.* 37 (5) (1997), 484-491.
- [7] S. W. P. Cloete, J. J. Eksteen and S. M. Bradshaw, "A mathematical modelling study of fluid flow and mixing in full-scale gas-stirred ladles," *Pro. Comput. Fluid Dy.*, 9 (6-7) (2009), 345-356.
- [8] B. K. Li, H. Yin, C. Q. Zhou, and F. Tsukihashi, "Modeling of Three-phase Flows and Behavior of Slag/Steel Interface in an Argon Gas Stirred Ladle," *ISIJ Intern.*, 48 (12) (2008), 1704-1711.
- [9] L. Jonsson, D. Sichen and P. Jönsson, "A new approach to model sulphur refining in a gas-stirred ladle - A coupled CFD and thermodynamic model," *ISIJ Int.*, 38 (3) (1998), 260-267.
- [10] W.T. Lou and M.Y. Zhu, "Numerical Simulation of Desulfurization Behavior in Gas-Stirred Systems Based on Computation Fluid Dynamics-Simultaneous Reaction Model (CFD-SRM) Coupled Model," *Metallur. and Mater. Trans. B*, 45B (10) (2014), 1706-1721.
- [11] J. Ekengard, A.M.T. Andersson and P.G. Jönsson, "Distribution of metal droplets in top slags during ladle treatment," *Ironmaking and Steelmaking*, 35 (8) (2008), 575-588.
- [12] A.R. Wang, W. Liu, J.S. Li and S.F. Yang, "Numerical Model of Dephosphorization Reaction Kinetics in Top Blown Converter Coupled with Flow Field," (Paper from MS&T 2015, Columbus, Ohio, USA, October 2015), 1023-1031.
- [13] Fluent 6.3: User's Guide Manual Fluent Inc. and Ansys's Fluent, (2006), <http://ansys.com/>.
- [14] M.V. Annaland, N.G. Deen and J.A.M. Kuipers, "Numerical simulation of gas bubbles behaviour using a three-dimensional volume of fluid method," *Chem. Eng. Sci.* 60 (11) (2005), 2999-3011.
- [15] D. Roy, P.C. Pistorius, and R.J. Fruehan, "Effect of Silicon on the Desulfurization of Al-Killed Steels: Part I. Mathematical Model," *Metallur. and Mater. Trans. B*, 44B (10) (2013), 1086-1094.
- [16] B. Deo and R. Boom. *Fundamentals of Steelmaking Metallurgy*, London, UK, Prentice Hall Intern. 1993.
- [17] C.W. Bale, P. Chartrand, S.A. Degterov, et.al, "FactSage thermochemical software and databases," *Calphad*, 26 (2) (2002), 189-228.
- [18] P.G. Jönsson and L.T.I. Jonsson, "The Use of Fundamental Process Models in Studying Ladle Refining Operations," *ISIJ Intern.*, 41 (11) (2001), 1289-1302.

SLAG FORMATION – THERMODYNAMIC AND KINETIC ASPECTS AND MECHANISMS

Lauri Holappa¹, Yilmaz Kaçar²

¹Aalto University, Materials Science and Engineering
PO Box 16200; Espoo FI-00076 Finland

²Erdemir Iron&Steel Works Co, Research & Development
PO Box 67330; Ereğli Turkey

Keywords: Slag formation, Fluxes, Thermodynamics, Kinetics, Mechanisms, BOF, LF

Abstract

Slags have a central role in pyro-metallurgical processes. They bind impurity compounds and absorb reaction products like oxides and sulfides. Functional slags are made by adding lime, magnesia, fluorspar, bauxite, calcium aluminate or other compounds into the reactor vessel where they form the slag together with the targeted reaction products. Additionally, refractory materials of the vessel tend to dissolve into the slag and thus influence its properties.

Slag formation is extremely essential in rapid processes, to ensure sufficient time for desired purifying reactions and to avoid harmful reactions with the refractory materials. Slag formation is a complex series of numerous phenomena. In this contribution, thermodynamic constraints, kinetic aspects and mechanisms in slag formation and in adjustment of properties were reviewed. Slag formation and conditioning in steel converter process and in secondary metallurgy aiming for improved desulfurization and steel cleanliness, were examined and discussed as examples.

Introduction

In basic oxygen converter (BOF) hot metal silicon is first oxidized forming SiO₂. It is an acid oxide and tends to react with basic lining materials (MgO and CaO). In order to avoid lining wear the formed silica should directly bind in slag. At the very beginning of the blow there is, however, no real slag available but only solid lime or dolomitic lime containing some MgO. Rapid slag formation is desirable in order to bind SiO₂ with the added lime and to form slag. However, it is a well-known problem that the slag formation is retarded by the formation of solid silicate layer (Ca₂SiO₄) between the added lime lumps and SiO₂ formed from oxidation of [Si] in hot metal. To promote slag formation fluxing materials like CaF₂ were added. Another way was to utilize the fluxing effect of “FeO” in the slag. FeO originates from either oxidation of iron from hot metal surface when using “soft” oxygen blow or from iron oxide additions (sinter, iron ore, dust) in the O₂ blow beginning. These phenomena were well-known already during the second decade of the emerging LD/BOF process in 1960s [1-4]. Even the influence of lime quality on slag formation was established. Lime quality includes its composition (CaO, SiO₂, S, CO₂, H₂O) and “reactivity” which are dependent on the mineralogy and composition of limestone as well as on the burning process (shaft furnace vs rotary kiln) and temperature. Lime is typically burnt at 1100-1200 °C. At low temperature, mechanically “soft” reactive lime is produced whereas at high temperature the product is “hard” and less reactive. In hard burnt lime the carbonate CaCO₃ is fully decomposed

to CO_2 and CaO lumps or grains, which are denser, more sintered and crystalline and have less porosity and smaller surface area than soft burnt lime, respectively. Although the role of lime quality was recognized, it was difficult to verify in an industrial process. Testing methods based on dissolution rate into water were used to control the lime reactivity [5,6]. They were able to express the “burning degree” for pure lime but were not relevant for any complex lime products. Already in late 1960s Obst et al [7] proposed “special lime products”, e.g. lime-iron oxide briquettes to speed up slag formation. In the late 70s - early 80s a comprehensive project was carried out by the Scandinavian Ironmasters Society (Jernkontoret) as an aim to develop special lime products for steel making processes. Numerous different lime-based products doped with other oxides and compounds (Fe_2O_3 , MnO , B_2O_3 , TiO_2 , Al_2O_3 , CaF_2) were prepared and tested by using a sessile drop technique by melting a slag sample on a lime product cylinder in a furnace equipped with a camera [8]. The effect of different additions on lime dissolution were stated and measured. Later in this contribution, selected results of these studies have been represented.

Thermodynamic constraints of slag formation

A classical way to illustrate the slag formation event is to draw a “slag path” in the ternary slag diagram $\text{CaO-SiO}_2\text{-FeO}$. In Figure 1, the left arrow represents a “hard” blow with low “FeO” content in the slag. It passes the first CaSiO_3 “nose” but meets the second Ca_2SiO_4 “nose” at 1500-1700 °C, which then inhibits lime dissolution. On the other hand, along the “FeO”-rich path (right) slag formation can proceed freely as the Ca_2SiO_4 “ridge” comes up only to 1600 °C which temperature is easily exceeded towards the blow end.

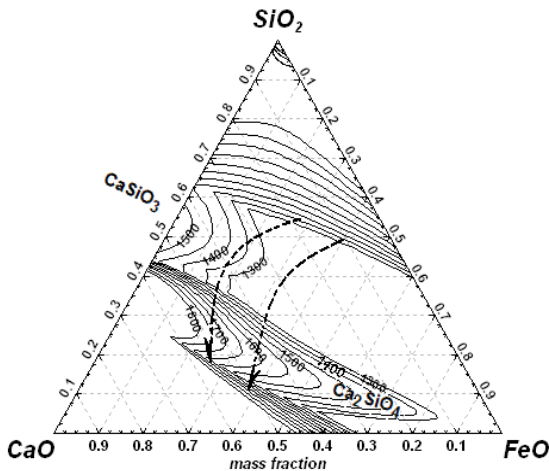


Figure 1. Typical slag paths during BOF blow presented in ternary diagram of main slag constituents. During the oxygen blow the slag temperature rises from 1300 °C to 1700 °C [9].

Principally, another way to promote slag formation is to add compounds, which “flux” the silicate nose by shifting the Ca_2SiO_4 isotherms towards the CaO-SiO_2 axis. In the next figure the influence

of selected compounds on the liquidus line in the $\text{Ca}_2\text{SiO}_4 - \text{M}_x(\text{O},\text{F})_y$ systems can be seen. The calculations were done by using the FactSage 7.0 Package with FToxide database.

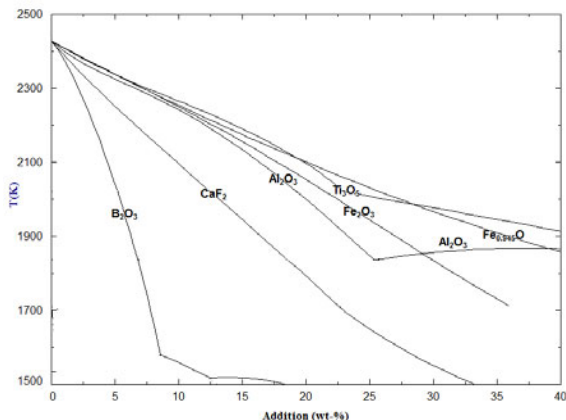


Figure 2. Influence of different additions on liquidus line in $\text{Ca}_2\text{SiO}_4 - \text{M}_x(\text{O},\text{F})_y$ -system.

Iron oxides ($\text{Fe}_{0.945}\text{O}$, Fe_2O_3) can be used as references to describe the fluxing effect. Ti-oxide is in the same category, Al_2O_3 little stronger, CaF_2 much stronger and boron oxide the strongest. Of these fluorspar CaF_2 is commonly used. B_2O_3 , as colemanite (calcium borate hydroxide) mineral was already tested in 1970s [7, 8]. It was an efficient flux but had one significant drawback: even a small amount of B_2O_3 -bearing converter slag carried over into the ladle can result in little boron pick-up into steel as [B]. Boron has an extremely strong hardening effect in steel. That might be very dangerous in many steel grades. Hence, colemanite did not become any common flux in BOF. In addition to the liquidus temperature the width of the solid-liquid region and the position of solidus line in relation to the pure phase is essential. They were not drawn in the figure. For oxide additions the solidus is close to the y-axis, whereas for CaF_2 the solid-liquid region is narrower

Experimental investigations

As discussed earlier, slag formation is conventionally tried to promote by adding fluxing components into the primary slag to dissolve the solid silicate or to prevent its formation. Another possibility might be to modify the lime itself by increasing its “self-fluxing” properties. The idea was studied in laboratory scale by a modified sessile drop method. Burnt lime and lime-mixtures (3g) were pressed ($P=2000 \text{ kg/cm}^2$) to flat cylinders which were used as substrates ($A=3\text{cm}^2$). Premelted slag (20%CaO-30%FeO-50%SiO₂) simulating the primary BOF slag was weighed 200mg and pressed to small cylinder ($A=0.25\text{cm}^2$) and located on the lime substrate (Figure 3). Each specimen was heated in purified Ar atmosphere at 1350 °C for 3min. Then the specimen was cooled down, CaO content in the slag analyzed and the penetration zone investigated in detail. The effect of different additions on lime dissolution are shown in Figure 3. The powerful effect of CaF_2 and B_2O_3 is clearly seen. In Figure 4, the experimental course is demonstrated via specimens of pure lime and lime + BOF dust (82% Fe-oxides, 12 %CaO). We see that dust addition strongly increases slag spreading and penetration into lime as well as lime dissolution itself.

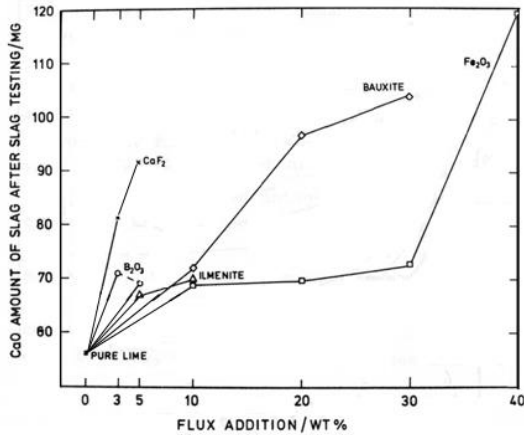


Figure 3. Effect of different additions in lime on its dissolution into slag in a laboratory test [8].

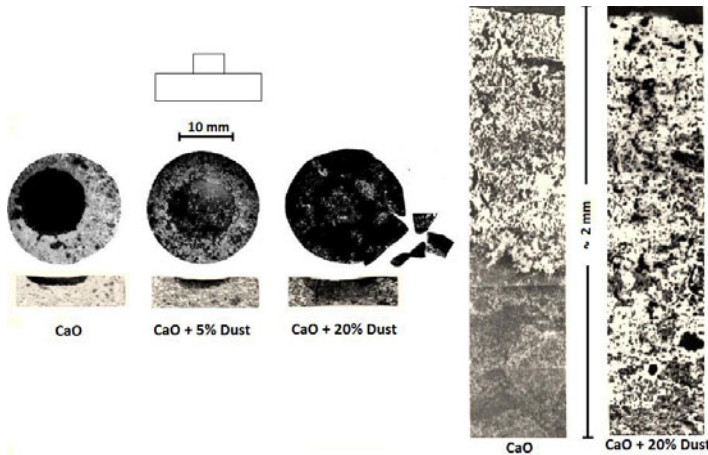


Figure 4. Left from the top: schematic layout of substrate and slag sample, next three specimens after sessile drop test - outlook from above; then cross-section of the specimens on the bottom. Right: optical micrographs of two specimens - cross sections downward from the top surface. Lime and mixtures burnt at 1100 °C; sessile drop experiments at 1350 °C/3 min/ Ar atmosphere.

Somewhat similar research was done in industrial scale too. Burnt lime and iron oxide (25%) were mixed and cold-pressed to briquettes, which were then used in 55 tons BOF. The results were promising showing better dephosphorization and iron yield and less slopping [10]. Briquettes were however, too weak causing extra dust formation in the LD converter. Implementation in large scale would require investments in lime production facilities. Recently, interest in this kind of ferruginous lime products seems to be waken again [11].

Slags in Ladle Metallurgy

Generally, slags in ladle metallurgical processes are designed to maximize their refining capacity, which includes optimized chemical composition as well as physical properties. In clean steel process slags should not contain high amounts of unstable reducible oxides (FeO, MnO), they should protect against the influence of air atmosphere and minimize heat losses. Additionally, secondary steelmaking slags should not be corrosive against the ladle furnace refractory. Ladle furnace slags originate from different sources i.e. carry-over slag from converter, lime and other flux additions, deoxidation and desulfurization products, residual ladle slag of the previous heat and refractory oxides from the lining wear. Furnace slag carry-over results in higher deoxidizer consumption. It reduces alloy recovery and is largely responsible for the fade of aluminum. Slag's high FeO content has adverse effects on desulfurization, steel cleanliness, ladle process time and refractory wear. Many developments have been achieved to prevent slag carry-over such as tap hole plugs, slide gate mechanisms, thermal camera systems etc. However, these techniques can minimize the slag carry over not entirely eliminate. A wide variety of fluxes is available today as slag conditioners along with lime, bauxite, calcium aluminate, Al dross, dolomitic lime, CaC₂, CaF₂ etc. Spent refractory materials can be used for this purpose such as alumina and MgO based refractories. Aluminum dross is a by-product of aluminum production and is used as a slag conditioner in steelmaking process. Its main components are metallic aluminum and aluminum oxide (> 90%) plus additional oxides, SiO₂, CaO and MgO. Thus it works also as slag reductant/deoxidizer like metallic Al. For the same purpose even CaC₂, SiC and carbon have been used, but they contain carbon, which can influence the steel composition. Reduction of reducible oxides (FeO, MnO) is crucial for desulfurization and steel cleanliness.

Some industrial trials are reported here to compare the deoxidation efficiency of Al dross and Al granules for slag reduction of low C, low Si (0.030% max.), Al killed steel grade in 120 tons ladles. Ingot Al was added for primary deoxidation at the 70% of ladle filling according to blow-end [O]. During tapping, 600 kg lime was added to each ladle. Slag samples were taken from ladle furnace after 3 min of heating without any addition at 1600 °C steel temperature. According to FeO+MnO level Al dross and Al granules were added on the slag to give the same amount of metallic Al. Additions were made in the same slag and process conditions. For this purpose, five trials were made at 4, 8, 12, 16 and 20% of initial FeO+MnO level by using 40, 80, 120, 160, 200 kg of Al dross. Slag samples were taken after 3 min of heating without any addition. Five trials were made at the same initial FeO+MnO levels by using 20, 40, 60, 78, 98 kg of Al granules, respectively.

Table 1. Physical and chemical properties of Al Dross and Al Granules

Material	Chemical Composition						Physical Properties		
	%CaO	%Al ₂ O ₃	%SiO ₂	%MgO	%Other	%Al _{metallic}	-5 mm (%)	5-30 mm (%)	+30 mm (%)
Al Dross	1.9	44.6	4.4	1.2	1.2	46.7	10.0	86.2	4.8
Al Granules	-	-	-	-	4.3	95.7	5.3	93.5	1.2

Figure 5 shows that Al dross is more efficient for ladle slag deoxidation resulting in final FeO+MnO contents, which are only half of those by Al granules. Al dross seemed to have spread more evenly throughout the slag and to stay longer time due to its slag-like physical properties.

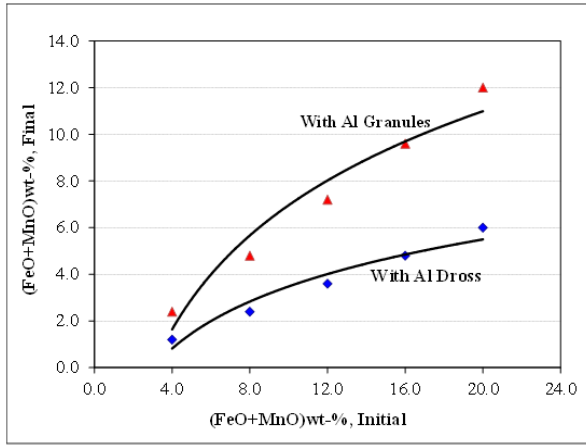


Figure 5. Comparison of slag deoxidation efficiency with Al dross and Al granules

As a result, it makes better slag deoxidation without significant Al pick-up into the steel. On the other hand, even though lower amount of Al granulates is used, some Al can go into the steel during addition resulting in increased [Al] content in the steel.

For efficient desulfurization in ladle furnace FeO and MnO should be low. The other slag composition (CaO, Al₂O₃, SiO₂, MgO) should be kept in a suitable range to obtain a liquid and homogeneous ladle slag with high basicity and reasonable viscosity. The crucial physico-chemical criteria include high sulfide capacity of the slag, low oxygen activity in the steel, sufficient temperature and intensive stirring to assist sulfur transport in the bulk steel and its transfer to the slag. In the next example the effect of slag reduction on sulfur partition ratio was studied with LC, Al killed steel grade in similar process conditions at 1600°C (Figure 6).

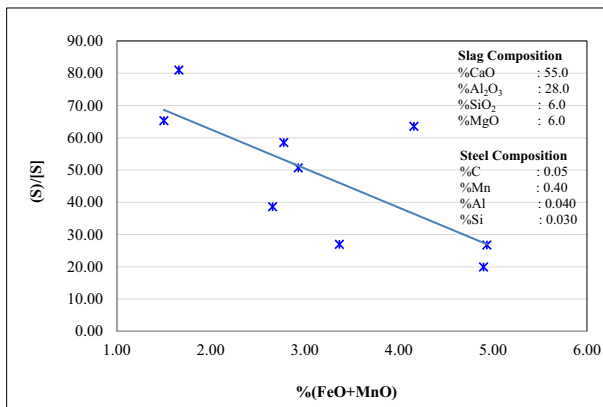


Figure 6. Effect of (FeO+MnO) in slag on sulfur partition ratio in LF treatment.

The same stirring practice was used in the trials, 3 minutes of lance stirring and 20 minutes of Ar bottom soft stirring (180 Nl/min) was applied. During the trials, CaO, Al₂O₃, SiO₂ and MgO were controlled by lime and calcined bauxite additions and Al granules were used as slag deoxidizer in the ladle furnace. Steel and slag samples were taken to determine the sulfur partition ratio. The results showed how sulfur partition ratio increased proportionally to the decreased content of reducible oxides (Figure 6). Best desulfurization is achieved with CaO-saturated, low FeO+MnO (< 2%) slags. Low a_[O] in the steel is attained by Al-deoxidation and sufficient prevailing Al-content in the steel, respectively.

Discussion

The recent developments throughout the iron and steelmaking route have changed the role of slag in converter process. Earlier even desulfurization was an aim in BOF, nowadays it is first done for hot metal and finally in ladle furnaces. Dephosphorization is possible for hot metal as well, which practice was developed and widely applied in Japan [12]. Elsewhere it is less common as low-P ores are more common for iron production. Then deP in BOF is still quite important and fast slag formation and strict mastery of slag properties are essential parts of the holistic process control. As blast furnaces are running nowadays producing lower Si and Mn contents in hot metal, the slag amounts in converter process are significantly smaller than some decades ago. This makes slag steering maybe easier but at the same time more critical.

One extra important aspect is dust formation in BOF process. Dust is formed 2% or even more of the amount of steel. One origin is “Direct” dusting of slag additions, whereas the other source is the hot metal iron/steel bath via mechanisms like vaporization and ejections. The restraining role of slag should cover essentially both these origins. Soft-burnt reactive lime is suffering from mechanical weakness and abundant dust formation whereas hard-burnt lime can be metallurgically less effective. “Blended” lime products made by burning e.g. mixture of limestone and iron oxide (dust, concentrate, mill scale) would produce ideal combination of high reactivity and mechanical strength. Even recycled materials like highly basic ladle slags are potential constituents of slag formers and conditioners.

The management of slag formation and conditioning in ladle metallurgy has based on the knowledge of thermodynamic and physical properties of slags (phase diagrams, activities, capacities, viscosity). That knowledge is then applied to substantiate the practical data of relations between process parameters and metallurgical results. Frankly speaking, slag formation in ladle furnace has not been any common topic for research because it is not a critical stage owing to relatively high temperature, arc-assisted melting and moderate time available for the operation. As discussed afore, slag deoxidation seems to be a more critical and time-demanding phase. It is a necessary pioneering event for successful deoxidation and desulfurization. An “ideal” slag reduction + conditioning process and subsequent deoxidation + desulfurisation process might be the following: 1) addition of reductant based on material balance calculation, 2) intensive gas rinsing under Ar atmosphere in order to avoid air contact, 3) moderate rinsing for desulfurization, 4) final soft rinsing to promote separation of slag droplets and removal of oxide inclusions for clean steel.

Conclusions

Slag formation in steel converter process as well as formation and conditioning in secondary metallurgy were examined and discussed. The following conclusions can be drawn:

- Slag formation in converter process is promoted by high iron oxide content achieved by oxidizing iron or by oxide addition into slag. Of other fluxes, fluorspar is commonly used whereas boron oxide (colemanite) has not become common due to the risk of getting reduced boron into steel.
- Prefabricated lime + iron oxide mixture with “self-fluxing” properties could be a potential slag forming agent or ingredient. Mechanically strong, reactive slag forming agent would decrease dust formation from BOF. Recycled slag, dust etc. are potential raw materials too.
- Slag deoxidation has a crucial role on desulfurisation and deoxidation in ladle metallurgy. Amount of reducible oxides (FeO+MnO) should be reduced to 2% or below.
- Al dross and Al granules were tested as slag deoxidisers. Al dross can be distributed more evenly in ladle slag and it influences longer time due to its slag-like physical properties. So, it was stated to be more effective than Al granules as slag deoxidiser. Al dross also works as a slag modifier due to high alumina content.

References

1. G. König, H. Rellermeier, K.-H. Obst; ”Vorgänge bei der Auflösung von Hart- und Weichbrandkalk in Schlacken aus dem Sauerstoffaufblas-Konverter”. *Stahl und Eisen*, 87. (1967), 1071-1077
2. F. Oeters, R. Scheel; “Untersuchungen zur Kalkauflösung in CaO-FeO-SiO₂- Schlacken”, *Arch. Eisenhüttenwesen*, 45, 9 (1974), 575-580
3. L.E.K. Holappa, P.A. Kostamo; “Development of Blowing Practice in the Koverhar LD Plant”, *Scandinavian Journal of Metallurgy* 3(1974), 56-60.
4. K.-H. Obst, J. Stradtman, W. Ullrich, G. König; “Present Status and Technical Advances of Steelworks Lime for Basic Oxygen Furnaces in Germany. The reaction parameters of Lime”, *ASTM STP 472*, ASTM (1970), 173-192.
5. L.A. Leonard; “Influence of lime quality on oxygen steelmaking” *JISI*, 4(1970), 324-328
6. L.C. Anderson, J. Vernon; “The quality and production of lime for basic oxygen steelmaking”. *JISI* 208, 4(1970), 329-335
7. K.-H. Obst, J. Stradtman, G. Trömel; “Reducing the blowing time in the LD process by the use of special lime products”. *Journal Iron Steel Inst.* 1970, 198, 450-455.
8. L.E.K. Holappa, H. Ylönen, L. Kari, M. Häikiö, “Improving Lime Dissolution in Slag”, *Jernkontorets project 297/77*, Report D321 (1980), 69 pp.
9. H. Jalkanen, L. Holappa; “Converter steelmaking” in; Seetharaman, S. (Ed.), *Treatise on Process Metallurgy*, Vol.3: Industrial Processes, Part A; Holappa, L., (Ed.), Elsevier Ltd 2014, 223-270.
10. L. Holappa; Glimmers of research in metallurgy. *Scandinavian Journal of Metallurgy*. 2005. 34, 66-78.
11. M.S. Lee, P.V. Barr; Ferruginous lime as a flux in primary steelmaking. *Trans. Inst. Min. Metall.* 2001. 110. 3, 144-148.
12. S. Kitamura; “Hot Metal Pretreatment” in; Seetharaman, S. (Ed.), *Treatise on Process Metallurgy*, Vol.3: Industrial Processes, Part A; Holappa, L., (Ed.), Elsevier Ltd 2014, 177-221.

EFFECTS OF VARIOUS SLAG SYSTEMS ON METAL/SLAG SEPARATION OF CCA AND SLAG COMPOSITION ON DESULFURIZATION AND DEPHOSPHORIZATION OF IRON NUGGET

Ji-Ook PARK¹ and Sung-Mo JUNG²

¹Ironmaking Research Group, POSLAB, POSCO; Pohang, 790-300 Korea

²Graduate Institute of Ferrous Technology (GIFT), Pohang University of Science and Technology (POSTECH), Cheongam-ro 77; Pohang 790-784, Korea

Keywords: carbon composite agglomerate, desulfurization, dephosphorization, metal-slag separation

Abstract

The reduction experiment of iron ore containing high Alumina content with petroleum coke was carried out in the temperature range of 1673 to 1773K by changing the slag composition. The sulfur and phosphorous content in the reduced iron nugget were measured to investigate the desulfurization and dephosphorization behavior during the reduction. The mineralogy of iron ore and additives to the carbon composite agglomerate (CCA) highly influenced on not only the reduction itself but also the melting, carburization, metal-slag separation, desulfurization and dephosphorization. High basicity of slag retarded the melting of CCA and the metal-slag separation, but enhanced sulfur and phosphorous removal degrees in the separated metal.

Introduction

Low grade irons containing high magnetite and alumina content had not been considered as main sources for conventional iron making process before the depletion of high grade lump ores became a significant issue. In particular, the low grade iron ores cannot be used for blast furnace iron making process by several problems.[1,2] Some iron making processes such as MIDREX, HYL III and rotary kiln have abilities to adopt low grade ores to produce direct reduced iron for electric arc furnace (EAF) operation. But, reducing iron ore of high alumina content is still a challenge even the processed.[3]

Compared to blast furnace process, the process for direct reduced iron can adopt the slag composition in the generous range. The usage of high basicity slag for the reduction of carbon composite iron containing high alumina content was proposed in RHF process.[4] The effect of high basicity slag with high alumina content on the CCA reduction and the metal-slag separation was also investigated.[4,5] It has been known that the high basicity of slag has an advantage to remove sulfur and phosphorous in the reduced iron.[6]

In this study, high basicity slag was adopted to reduce the high alumina containing CCA to investigate the melting, carburization, desulfurization and dephosphorization behaviors in the experiment carried out in the temperature range of 1673K to 1773K.

Sample preparation

As a representative high alumina iron ore, the limonitic laterite iron ore of high alumina and low silica was used. For the reducing carbon source, a petroleum coke of low ash was adopted. The iron ore and the coke were crushed and sieved into powders in the size range of 100~150 μ m. Their chemical composition are shown in the **Tables 1** and **2**, respectively.

Table 1. Chemical composition of limonitic laterite ore used in the present study (mass%).

	T.Fe	Fe ²⁺	M.Fe	SiO ₂	Al ₂ O ₃	Ni	P	S
Limonitic Laterite	42.52	0.42	-	5.11	7.80	1.5	0.03	1.58

Table 2. Chemical composition of petroleum coke used in the lab scale test.

Proximate analysis (mass%)				Ultimate analysis (mass%)				
VM	FC	Ash	IM	C	H	N	S	O
10.97	87.7	0.06	0.68	87.25	3.70	1.03	5.73	2.29

The iron ore mainly contains Al₂O₃ and SiO₂ which would form Al₂O₃-SiO₂ based slag which might have high melting temperature. To control the melting temperature, specific amounts of CaO and SiO₂ were added into the iron ore so that the expected final slag compositions would have low melting temperatures in the CaO-SiO₂-Al₂O₃ slag system. The coke adopted in the experiment contains high sulfur content and low ash content. The high sulfur content in the coke increased the total sulfur content in the CCA and the total sulfur content was used as the initial value to measure desulfurization degree in the iron nugget after the reduction experiment. By adjusting the total basicity and fixing C/O ratio, 4 kinds of CCAs with different mixing condition were prepared for the experiment as shown in **Table 3**.

Table 3. Mixing conditions of the pellets with various slag systems.

	Ore (g)	Petro coke (g)	CaO (g)	SiO ₂ (g)	Al ₂ O ₃ (g)
CCA_origin	3.0	0.47	-	-	-
CCA_A	3.0	0.47	0.36	0.81	-
CCA_B	3.0	0.47	0.47	0.32	-
CCA_C	3.0	0.47	0.18	0.02	-
CCA_D	3.0	0.47	1.21	-	0.73

The slag melting behaviors of the expected chemical compositions induced by the mixing conditions were predicted based on FactSage data base in **Table 4**. [7]

Table 4. Slag liquefying temperatures of samples

	Liquid formation starting temperature (K)	Fully liquefied temperature (K)
CCA_origin	1870	-
CCA_A	1460	1535
CCA_B	1532	1580
CCA_C	1668	1687
CCA_D	1603	1691

In short, CCA_A and CCA_B have lower melting temperatures than CCA_C and CCA_D due to their own chemical compositions.

Experimental Procedure

5g of the each CCA was put into a graphite crucible and heated up to the target temperature in the range of 1673K to 1773K in the air and held for 5, 10, 15 and 20 minutes to observe the melting and reduction behaviors for the given time at the given temperature. After the reaction, the sample was quenched by high purity Argon gas to reduce the change for the further reaction during the cooling. The carbon, sulfur and phosphorus contents in the iron nugget which was separated from the slag were analyzed to analyze the carburization, desulfurization and dephosphorization degree in the reduction process. The slag composition also was analyzed by X-ray fluorescence spectrometry.

Metal-Slag Separation with Different Slag Composition

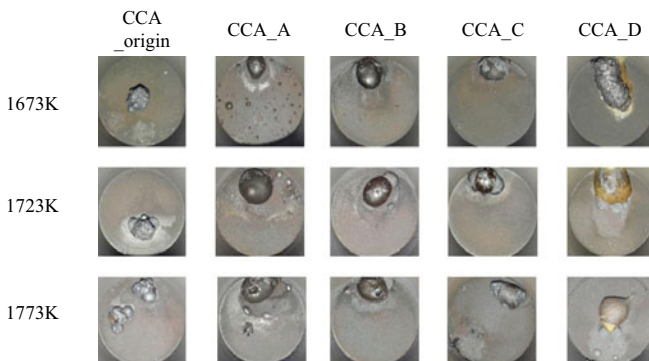


Fig.1. Images of CCAs of different slag compositions with different reaction temperatures

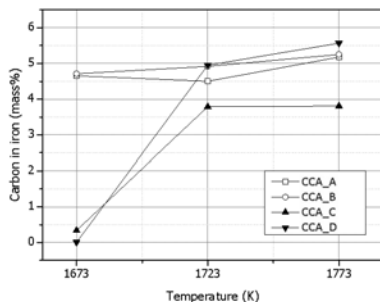


Fig.2. Effect of temperature and slag composition on the carbon content in iron nugget

Figure 1 shows the images of CCAs after the reductions at the given temperatures. Compared to the CCA without additives, the other CCAs showed relatively promoted metal-slag separation behaviors at any temperature. But, at low temperature (1673K), CCA_C and CCA_D showed relatively poor metal-slag separation which might be induced by their high slag melting temperatures as shown in **Table 4**. In detail, the CaO-Al₂O₃ based slag has a high melting temperature than the CaO-SiO₂ based slag, so the direct contact between carbon and reduced iron is retarded by the less liquefied slag.[5] **Figure 2** shows the carbon content change in the iron nuggets depending on the reaction temperatures and slag compositions. As expected from the metal-slag separation behaviors, the carbon content in the iron nuggets obtained from CCA_C and CCA_D at 1673K were particularly lower than those of the other cases. It shows that the metal-slag separation behavior is nicely correlated with the carburization degree of the iron nugget.[5]

During the reduction of CCA and the carburization of iron nugget, an intermediate iron oxide, namely FeO, can be formed. Because of the SiO₂ additions to CCA_A, B and C, they had chance to allow the formation of fayalite (2FeO·SiO₂) which has a low melting temperature of 1483K. [8] To clarify the effect of FeO on the metal-slag separation, the metal-slag separations of the CCAs for given reaction times at 1723K were observed as in **fig.3**. And the FeO contents in the separated slags were measured as in **fig.4**. CCA_D showed the poor metal-slag separation until 10 minutes and it might be induced by the rapid decrease of FeO content.

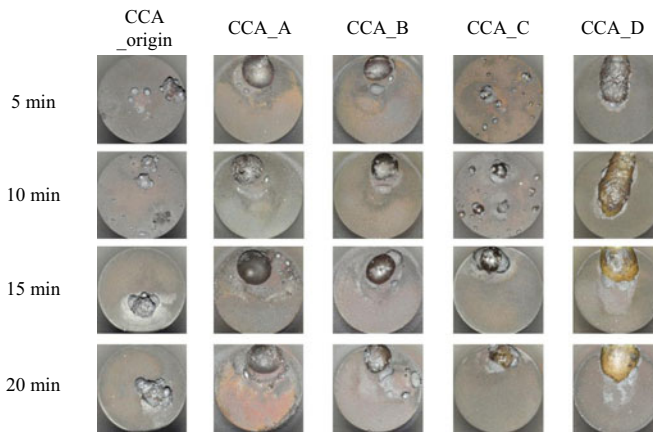


Fig.3. Images of CCAs of different slag compositions with different reaction times at 1723K

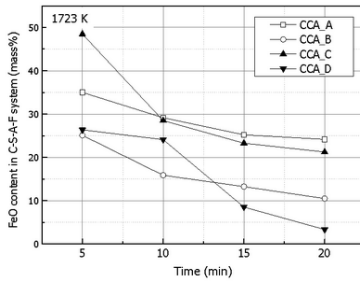


Fig.4. FeO content of separated slags with different reaction times at 1723K.

Desulfurization and Dephosphorization Behaviors in CCA Reduction

The sulfur content in the iron nugget separated from the slag was analyzed. The iron nugget without additives (from CCA_origin) shows the highest sulfur content among the reduced iron nuggets in **fig.5**. Interestingly, the lowest sulfur content was obtained from the iron nugget separated from the CCA_D which has the highest CaO content, i.e, the highest basicity. This results corresponds the well-known fact that the high basicity induces the high desulfurization degree

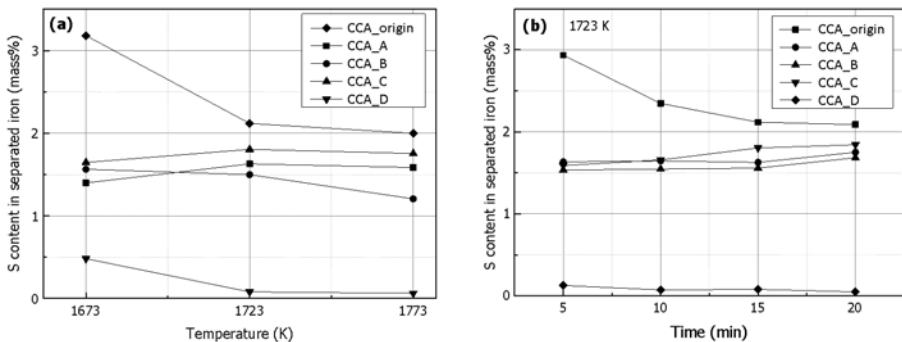


Fig.5. Sulfur content in separated iron nugget at given reaction temperatures and times

In terms of the phosphorus content, similar to the sulfur content, the high basicity induced the effective dephosphorization degree in the iron nugget as shown in **fig.6**. In detail, the phosphorus removal degrees of CCA_B and CCA_D reach at 80%~90%. The degree is much higher than that of any conventional process.[9]

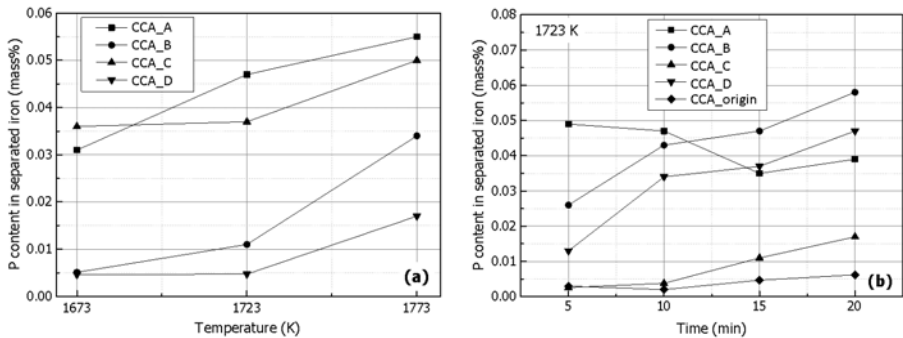


Fig.6. Sulfur content in separated iron nugget at given reaction temperatures and times

Conclusions

From the experimental results, the following conclusions were obtained:

- (1) Iron nugget separated from slag was successfully produced by direct reduction of high alumina containing iron ore with coke of high sulfur and ash.
- (2) The high basicity of slag retarded the metal-slag separation due to the high melting temperature, but, the desulfurization degree is much higher than the other slag compositions.
- (3) More than 80% of the initial phosphorus could be removed from the iron nugget by reducing the high basicity CCA at 1723K.

References

1. L. Lu, R. J. Holmes and J. R. Manuel "Effects of Alumina on Sintering Performance of Hematite Iron Ores," *ISIJ Int.*, 47 (2007), 349-358.
2. A. Cores, A. Babich, M. Muñiz, S. Ferreira and J. Mochon, "The Influence of Different Iron Ores Mixtures Composition on the Quality of Sinter," *ISIJ Int.*, 50 (2010), 1089-1098.
3. S. Inaba, "Advanced Approach to Intelligent Ironmaking Processes. Overview of New Direct Reduced Iron Technology," *Tetsu-to-Hagane*, 87 (2001), 221.
4. J. O. Park and S. -M. Jung "Effect of Slag Composition on Reaction Kinetics of Carbon Composite Agglomerate in the Temperature Range of 1273 K to 1573 K (1000 °C to 1300 °C)," *Metall. Mater. Trans. B.*, (2015), 46B, 1207- 1217.
5. J. O. Park, I. -H. Jeong, S. -M. Jung and Y. Sasaki, "Metal-slag Separation Behaviors of Pellets Consisted of Iron, Graphite and CaO–Al₂O₃ Based Slag Powders," *ISIJ Int.*, 54 (2014), 1530-1538.
6. N. Sano, W. -K. Lu, P. V. Riboud and M. Maeda: *Advanced Physical Chemistry for Process Metallurgy*, Academic Press, San Diego, CA, USA, (1997), 51.
7. C.W. Bale, E. Bélisle, P. Chartrand, S.A. Decterov, G. Eriksson, K. Hack, I.-H. Jung, Y.-B. Kang, J. Melançon, A.D. Pelton, C. Robelin, S. Petersen, "FactSage Thermochemical Software and Databases - Recent Developments," *Calphad*, 33 (2009), 295.
8. A. K. Viswas, *Principles of Blast Furnace Ironmaking* (SBA Pub., Calcutta, India, 1981), 108, 227.
9. K. Ohno, private communication, Kyushu University, 2014.

USE OF Al-KILLED LADLE FURNACE SLAG IN Si-KILLED STEEL PROCESS TO REDUCE LIME CONSUMPTION, IMPROVE SLAG FLUIDITY

Narottam Behera¹, Ahmad Raddadi², Shahreer Ahmad³, Neeraj Tewari⁴, Othman Zeghaibi⁵

^{1,4,5} SABIC Metal SBU, Jubal Industrial City 31961, Saudi Arabia

^{2,3} SABIC Technology Center, Jubal Industrial City 31961, Saudi Arabia

Keywords: Ladle slag¹, Calcium Aluminate flux², slag fluidity³

Abstract

Slag is a by-product formed in most metallurgical process. During the steelmaking process a large amount of slag is produced, which becomes a source of waste, which in many instances is land filled. Such areas filled with waste materials have become a significant source of pollution. Slag recycling is then becoming important in recent years. Recycling can be an efficient option to reduce such waste. Fluorspar (Calcium Fluoride) is generally used to help fluidize the slag; however, Fluorspar has a corrosive effect on the ladle refractory and is environmentally harmful. Alternatively, Calcium Aluminate synthetic slag is very effective in making the slag more fluid, but it is costly. The slag generated in Al-killed treatment at ladle can provide a material with advantages over Calcium aluminate synthetic slags and Fluorspar, by being low-cost, noncorrosive, and less environmentally harmful. Plant trials conducted at Hadeed indicate that Al-killed ladle slags coming from its Flat Product Ladle Furnace process could be used in place of Calcium Fluoride/ Bauxite/Calcium Aluminate fluxes for the production of Si- killed steel grades, thus reducing Lime consumption, reducing waste and improving desulphurization levels.

Introduction

Slag is a by-product formed in many metallurgical processes. In the iron and steelmaking industry, there are three main types of slag. The first type is the Blast furnace slag, which is predominantly used for the production of cement throughout the world. The second type is Steelmaking slag generated from BOF or EAF. Steelmaking slag has a high FeO content, which limits its application in the cement industry. Steelmaking slag is then used after proper processing, in construction (as aggregate material), for water filtration (as filtering media), and finally, for land filling. The third type of slag is Ladle Furnace (LF) slag, which is generated during the secondary steelmaking in the Ladle Furnace process. After completion of the primary steelmaking operations through Electric Arc Furnace (EAF), the liquid steel is tapped in the ladle. The tapped steel has an oxygen content between 500 and 1000ppm, depending on grade and operations conditions. During tapping, de oxidants and fluxes are added to reduce the oxygen level in the steel. The oxidation products and added fluxes, plus the slag carried over from furnace during tapping form the ladle slag. The treatment of liquid steel in the ladle is usually done by deoxidation with Ferro-Manganese, Ferrosilicon, Silico-Manganese, and Aluminum, depending on the final steel quality to be produced. In Al-killed steel making process, the steel is deoxidized with Aluminum in order to reduce the Oxygen content to a minimum, so that no reaction occur between Carbon and Oxygen during the steel solidification in the casting . Final dissolved Oxygen levels between 1 to 4 ppm are achieved in the product, which is commonly rolled into flat products. In Si-killed steel making process, steel is deoxidized with Ferrosilicon and Silico Manganese, which can reduce the Oxygen level down to 20 to 50 ppm.[1]

The slag formed during tapping is very important for the further processing of the steel and plays the following roles: [2]

- Improve thermal efficiency (the ladle slag covers the arc during ladle processing to reduce arc flaring);
- Improve desulfurization (Slag saturated with CaO with optimum basicity);
- Improve steel cleanness (Slag absorb inclusion from steel);
- Improve refractory life (Slag saturated with refractory oxide- MgO).

Different fluxing additions influence the slag properties during secondary metallurgy, such as Calcium Aluminates, Fluorspar (CaF₂) and Bauxite. Fluxing agents reduce the melting point and the viscosity of basic steel slag[3]. At the same time, these fluxing agents reduce unstable oxides (FeO + MnO) coming from the EAF carryover slag, which, if not reduced, would significantly reduce the desulphurization capacity of the slag [4]. Fluorspar has traditionally been the most commonly used fluxing agent for Lime. However, its corrosive effect on ladle refractories, as well as its reaction with Carbon and Silicon to produce environmentally and physically harmful Carbon tetrafluoride and Silicon tetrafluoride, has led to its elimination from many processes and to a search for a replacement flux that could be used in the ladle refining of steel.[3] The production of these harmful compounds also causes the fluorine in the slag to evaporate in the gaseous form and there by depletes the slag from this fluidizing substance. Alumina on the other hand, is very stable. When fluid, it can combine with CaO from Lime to form Calcium Aluminate, which has a melting point of around 1400°C. Additionally, slag fluidity is essential in modern steelmaking to promote absorption of nonmetallic inclusions from the steel bath, since inclusions can cause clogging at caster and result in production losses. Nonmetallic inclusions also cause surface defects in the final rolled steel, making lower quality steel[3]. Calcium Aluminate is very effective as slag fluxing and is usable as a desulfurizing agent. However, it is very expensive. Lower cost substitutes include the use of a byproduct from Ladle Furnace Al-killed steel production, which is a slag consisting of a large percentage of CaO (50%) and Al₂O₃ (30%), along with MgO.

Plant Trial

The Saudi Iron and Steel Company (Hadeed), located in Jubail, Kingdom of Saudi Arabia, has three steelmaking facilities, being Steel Plant Long Product-I (SPLP-I), Steel Plant Flat Product (SPFP) and Steel Plant Long Product-II (SPLP-II). Generally, the steel plant flat product produce Al-killed steel and long product produce Si-killed steel. There are two types of ladle furnace slag in Hadeed processes: the first one is higher in silica and a byproduct of the production of Silicon killed steel, and the second is higher in Alumina content and a byproduct of the production of Aluminum killed steel. Table-1 shows the typical composition of LF slag at Hadeed steel plant flat product.

Table-1 Typical slag composition for Al-Killed steel grades

%CaO	%MgO	%Al ₂ O ₃	%SiO ₂	%FeO	%MnO
50	9	35	3.6	1.2	0.5

Cast steel slag pots are used to collect ladle slag after end of casting. Prior to collection, 2 to 3 tons of EAF (30% FeO) cold slag was added to the bottom of the slag pot to prevent slag sticking to the slag pot walls. After casting completed, the remaining slag-metal in the ladle is poured into a slag pot. Slag pot carriers then transported the pot to the slag yard. The material in the slag pot is comprised of EAF slag (with 30% FeO) at the bottom, ladle slag (with 1-2% FeO) at the top,

besides some steel still remaining in the ladle by the end of casting. To avoid mixing of EAF slag and Al-killed ladle slag, the top liquid slag was dumped at one location and the bottom solid portion in a separate location. After the slag was cooled for 3- 4 days, it was bagged for use in Si-Killed steel making process. The plant trial was conducted in a Ladle Furnace with the capacity of 150 t. Regularly 700 kg of Lime is added during EAF tapping. A trial was conducted for several heats using Al-Killed ladle slag addition during tapping in Si-killed steel. 250 kg of Al-Killed ladle slag was added to the ladle bottom before tapping, to reduce the Lime addition during tapping to 500kg. Table-2 below shows the additions made for these trials heats:

Table-2 Tapping additions for trial heats

Tapping Addition	Quantity	%Mn	%Si	%C	%CaO
Si-Mn	10 kg/t	68-78%	16-20%	2-2.5%	
Fe-Mn	1.2 kg/t	75-78%		6-7%	
Fe-Si	2 kg/t		75%		
Lime	3.5kg/t				90%

Results and Discussion

Metal and slag samples were collected for the trial heats. Complete characterization was performed. The slag samples chemical composition were investigated using X-Ray Fluorescence Analysis (XRF) and Carbon Analyzer (LECO). Additionally, the different phases identified were investigated using Scanning Electron Microscopy (SEM), coupled with Energy Dispersive Spectroscopy (EDX). The steel samples for the trial heats collected and the results obtained are given in Table-3 below:

Table-3 Chemical compositions of steel samples for the trial heats

Heat No	%C	%Si	%Mn	%S	%P	%Al	%N
Heat-1	0.20	0.22	0.85	0.017	0.012	0.0015	0.0075
Heat-2	0.17	0.15	0.79	0.011	0.008	0.0007	0.0036
Heat-3	0.19	0.22	0.78	0.015	0.015	0.0017	0.0045
Heat-4	0.18	0.23	0.78	0.014	0.011	0.0012	0.0058
Heat-5	0.17	0.22	0.76	0.016	0.012	0.0011	0.0042
Average	1.82	0.208	0.79	0.0146	0.0116	0.0012	0.00512

The average chemical composition of steel samples for the several normal heats for the same grade of steel is shown in table -4

Table-4 Average chemical compositions of steel samples for several normal heats

Heat No	%C	%Si	%Mn	%S	%P	%Al	%N
Average	1.88	0.211	0.81	0.0148	0.012	0.0011	0.00492

The ladle slag samples for the trial heats are collected and the results obtained are given in Table-5 below:

Table-5 Chemical compositions of ladle slags for the trial heats

Heat No	FeO	CaO	SiO ₂	Al ₂ O ₃	MgO	MnO	S
Heat-1	2.30	50.04	28.81	8.01	7.82	2.36	0.059
Heat-2	2.43	51.23	28.53	7.39	7.28	2.37	0.100
Heat-3	1.17	43.22	31.96	7.05	9.76	5.67	0.04
Heat-4	1.64	51.6	28.66	6.78	8.07	2.40	0.080
Heat-5	1.23	48.83	28.00	8.35	8.76	3.19	0.059
Average	1.75	48.99	29.19	7.52	8.34	3.2	0.067

The average chemical composition of ladle slag for the several normal heats for the same grade of steel is shown in table -6

Table-6 Average chemical compositions of ladle slags for several normal heats

Heat No	FeO	CaO	SiO ₂	Al ₂ O ₃	MgO	MnO	S
Average	1.8	50.6	30.17	4.97	7.78	3.88	0.057

The ladle slag composition shown in Table-5 for the trial heats shows the average Al₂O₃ is 7.52%, whereas ladle slag composition shown in Table-6 for the normal heats the average Al₂O₃ is 4.97%

The parameters influence on desulphurization degree are Sulfur partition, Basicity (B₂), content of easily reducible oxides (ERO), proportion of CaO /Al₂O₃ and Mannesmann's index(MM) [5]

Sulfur partition between slag and metal (L_s) = (S %) / [S%]

(S%) - Sulfur weight percent in the slag

[S%] - Sulfur weight percent in the steel

Mannesmann index, which characterizes the ability of slag to purify steel from Sulphur and non-metallic oxide inclusions and which is defined according to formula $M = (CaO/SiO_2)/(Al_2O_3)$

Slag Basicity: $B_2 = (CaO)/(SiO_2)$

Easily reducible oxides (ERO) = (FeO) + (MnO)

Calcium-aluminum ratio C/A = (CaO) / Al₂O₃

Table-7 Slag parameters for normal and trial heats

Slag Parameters	L _s	B ₂	MM	C/A	ERO
Average of Trial Heats	4.59	1.57	0.23	6.55	4.95
Average of Normal Heats	3.85	1.67	0.34	10.23	5.74

Comparison of slag parameter such as Sulfur partition (L_s), Basicity (B₂), Mannesmann index (MM), C/A ratio, easily reducible oxides (ERO) for the trial and normal heats are shown in Table-7. The normal heats having lower sulfur partition and higher Basicity (B₂), Mannesmann index (MM), C/A ratio, easily reducible oxides (ERO) compare to trial heats.

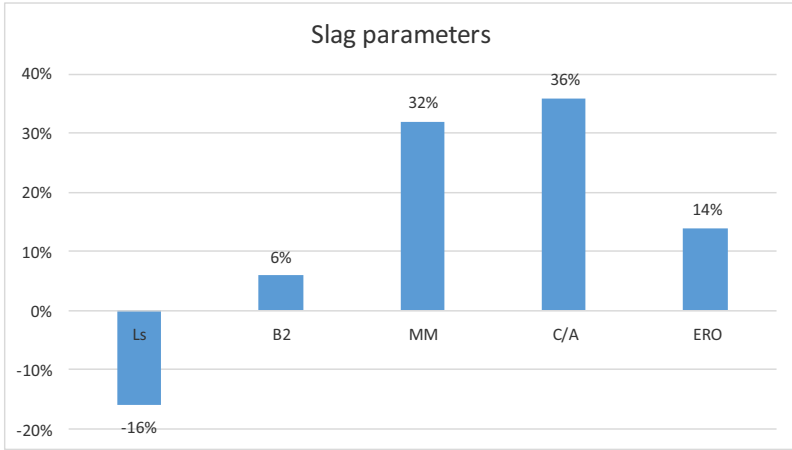


Figure-1 Comparison of Slag parameters for trial and normal heats

The normal heats have 16% lower Sulfur partition (Ls), 6% higher Basicity (B2), 32% higher in Mannesmann index (MM), 36% higher C/A ratio and 14% higher in easily reducible oxides (ERO) than the trial heats.

SEM analysis of ladle slags

Ladle slag samples from trial and normal heats were analyzed in an SEM, coupled with energy dispersive X-Ray (EDX) for chemical composition determination. The samples were mounted and polished for SEM analysis to identify the different phases. To avoid charging of the samples during analysis, the samples were coated with gold on a sputter for 30 seconds.[6] Based on the SEM analysis, shown in Figure-2, the two distinctive phases (A1 and A2) were found in the trial heats slag. Figure-3 shows two distinctive phases (A1 and A2) found in the normal heats slag samples

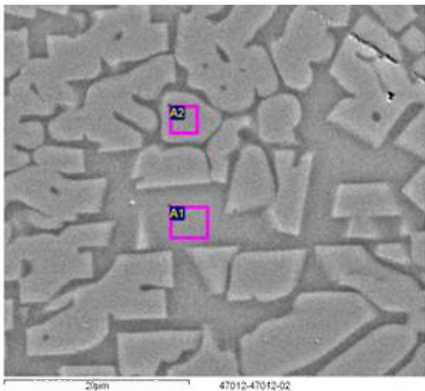


Figure-2 SEM analysis for Trial heat slag

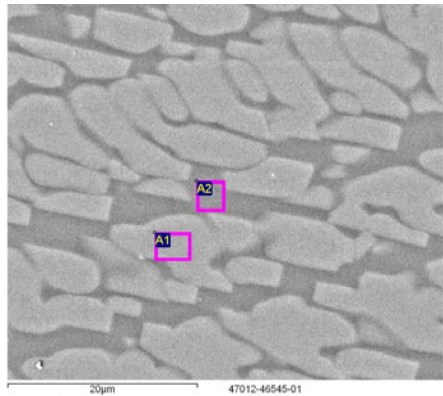


Figure-3 SEM analysis for normal heat slag

Table-8 EDX analysis of trial heat ladle slag

Spectrum	O	Mg	Al	Si	Ca	Mn	Fe
A1	43.85	1.63	12.34	13.48	23.7	3.13	1.87
A2	42.29	6.24	0.96	16.84	32.48	0.85	0.35

EDX analysis results of trial heat ladle slag shown in Table-8 A1 having Ca (23.7%), Al (12.34%), and Si (13.48%). Whereas A2 having Ca (32.48%), Si (16.84%) and Mg (6.24%).

Table-9 EDX analysis of Normal heat ladle slag

Spectrum	O	Mg	Al	Si	Ca	Mn	Fe
A1	42.9	6.8	0.09	17.2	32.5	1.12	0.6
A2	43.87	7.6	4.38	17.6	18.84	6.71	1.9

EDX analysis results of normal heat ladle slag shown in Table-9. A2 having Al (4.38%), Ca (18.84 %), Si (17.6%) and Mg (7.6%). Whereas A1 having Ca (18.84%), Si (17.6%) and Mg (6.8%).

EDX analysis result shows trial heat slag in Table-8 having phase with higher alumina compare with normal heat slag shown in Table-9.

Inclusions analysis

A scanning electron microscope (SEM) with automated feature analysis was utilized to evaluate the inclusions in lollypop samples after ladle processing, for the trial and normal heats. The SEM inclusion analysis was performed using a Quanta 200SEM, coupled with Oxford energy dispersive X-ray (EDX), with inclusion classifier (INCAF 250). In this mode, predefined areas were scanned and every inclusion larger than 1µm was detected and quantified [7]. The location of each inclusion, size, area, composition, and its classification was recorded. Each inclusion was classified based on its composition. An area of 30mm², containing 122 scan fields, were analyzed in each sample, at a magnification of 500X. The elements monitored during the SEM analysis included Manganese, Aluminum, Silicon, Sulfur, Calcium, and Magnesium.

The inclusion analysis shows in Table- 10 give the complete picture of number of inclusion present, type of inclusion present and area of inclusions for the normal heat samples.

Table-10 Inclusion statistics of Normal heats

Total Inclusions	SiO ₂	Mn-Si-Al	Mn-Si	MnS	% Area
1780	9	432	121	1212	0.055

The inclusion found in normal heat samples shown in Table -10 having total inclusion 1780 numbers, SiO₂ inclusions 9 numbers, Mn-Si-Al inclusions 432 numbers, Mn-Si inclusions 121 numbers, MnS inclusions 1212 numbers and percentage area of inclusions 0.055%.

The majority of inclusion shown in Table-10 are sulphide inclusions (MnS). MnS of type-1 is formed in semi- killed steel, where the oxygen content of the liquid steel is high (20 to 50ppm) and Sulphur solubility low, resulting in a precipitation of sulphide is parallel to the de oxidation process and Sulphur and oxygen are precipitated at the same time from the liquid steel. The resulting inclusions are either a results of primary precipitation of both sulphide and oxides from the liquid steel in duplex or Sulphur and oxygen rich silicate melt is formed. The duplex

inclusions of sulphide and silicate, the silicate phase deforms more readily than the sulphide phase. The duplex MnS inclusions with oxides are not as plastically deformed as monophasic sulphide inclusions. [8]. Generally, sulphur improves machinability in steel. However, the presence of sulphur also produces deleterious effects on some service properties such as forgeability, ductility, toughness, weldability and corrosion resistance. It is known that solid solubility of sulphur in iron (Fe-S system) at temperatures below 769°C is very low. [8]

Ternary plot shown in figure 4 uses the composition of inclusions after LF process. Each dot in ternary plot represents one inclusion regardless of the size

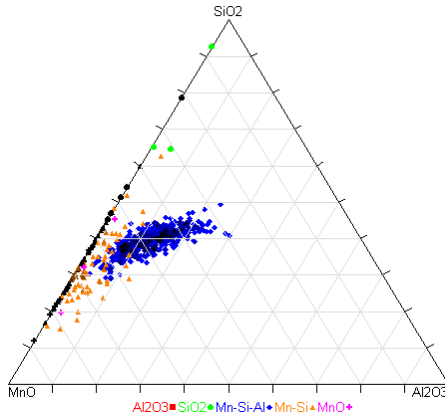


Figure -4 Ternary plot of inclusion LF out sample for one of the normal heat

The Phases observed in MnO-SiO₂-Al₂O₃ system are Cristobalite and Tridymite(SiO₂), Mullite(3Al₂O₃.2SiO₂), Corundum(Al₂O₃), Rhodonite (MnO.SiO₂), Tephroite(2 MnO.SiO₂), Spessartite(3MnO.Al₂O₃.3SiO₂), Mn-cordierite(2Mn.2Al₂O₃.5SiO₂) [8]

The inclusion analysis result in Figure-4 shows inclusions present in MnO-SiO₂-Al₂O₃ system are mostly Spessartite(3MnO.Al₂O₃.3SiO₂), Mn-Cordierite (2Mn.2Al₂O₃.5SiO₂), Tephroite (2 MnO.SiO₂) and few Cristobalite (SiO₂). Corundum (Al₂O₃) and Cristobalite (SiO₂) are the solid inclusions can cause clogging at caster also causes surface defects in the final rolled steel

The inclusion analysis shows in Table- 11 give the complete picture of number of inclusion present, type of inclusion presents and area of inclusions for the trial heat samples.

Table-11 Inclusion statistics of Trial heats

Total Inclusions	Mn-Si-Al	Mn-Si	MnS	% Area
1099	411	30	658	0.027

The inclusion found in trial heat samples shown in Table -11 having total inclusion 1099 numbers, Mn-Si-Al inclusions 411 numbers, Mn-Si inclusions 30 numbers, MnS inclusions 658 numbers and percentage area of inclusions 0.027%.

The count of total inclusions and total area of inclusion of trial heats having lower than the normal heats as shown in Table-11.

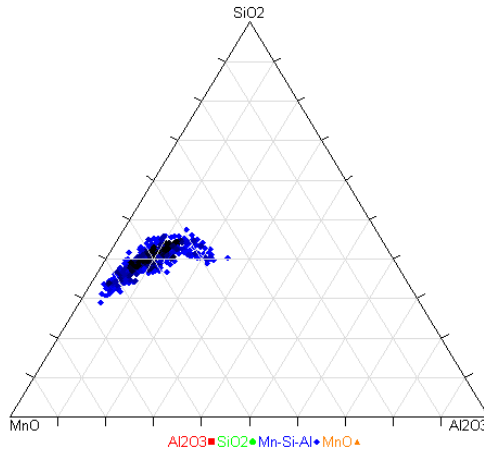


Figure -5 Inclusion analysis for LF out sample for one of the Trial heat

The inclusion analysis result in Figure-5 shows inclusions present in MnO-SiO₂-Al₂O₃ system are mostly Spessartite(3MnO.Al₂O₃.3SiO₂.) Tephroite (2 MnO.SiO₂), which are liquid inclusions in steel making and casting temperature.

Conclusions

Plant trial results showed that:

1. Ladle slag from Al- killed steel process could be used in Si- Killed steel process without adversely affecting its operation or steel chemistry.
2. Lime consumption reduced by 1.5kg/ton (30-40%), while still having potential to be increased further.
3. Trial heats slag having 16% higher Sulfur partition ratio (Ls) ,6% lower Basicity (B1), 32% lower in Mannesmann index (MM) and 36% lower C/A ratio and 14% lower in easily reducible oxides (ERO) compared to normal heats, which indicates more fluid slag, with higher desulphurization capacity .
4. SEM-EDX analysis confirm two different phases one with higher Al (12.34%) compare with the normal heat having Al (4.38%)
5. Inclusion analysis of ladle sample for trial heats having lower inclusion and liquid inclusions compared to normal heats, indicating cleaner steel.

Acknowledgments

The authors are grateful to Hadeed and SABIC management. The authors also would like to thank Hadeed slag handling department, Sabic Metal analytical laboratory for their support and Mr. Renato Brandao for helping plant trial and reviewing the paper.

References

- [1] E. T. Turkdogan, *Fundamentals of steel making*, (London Institute of Materials, 1996).
- [2] Z. Weisło, A. Michaliszyn, A. Baka “Role of slag in the steel refining process in the ladle”, *Journal of achievements in materials and manufacturing engineering*, 55(2012) 390-395.
- [3] Adrian Gavanescu, “Refining of steel by using synthetic slag. Annals of Faculty engineering Hunedoara. International Journal of Engineering, Romania.
- [4] P.L. Cavallatti, C. Mapelli, F. Memoli, M. Pustorino “Recycling of white slag” (Paper presented at AIM-Federacciai-VDEh Joint meeting, Seminar on Metallurgical Fundamentals, Dalmine , 15 September 2007)
- [5] L. Socha, J. Bazan, K. Gryc , P. Machovcak , A. Opler , A. Trefil , P. Styrnal , J. Melecky “Evaluation of Slag regime in ladle during utilization of briquetted synthetic slag in VHM”, *International Scientific journal* ,57 (2012),80-87.
- [6] Narottam Behera, Shahreer Ahmad, Carlos Pinheiro, “Characterization of Ladle furnace slag and its utilization in steel making” (METEC & 2nd ESTAD, 15-19 June 2015, Dusseldorf, Germany).
- [7] P.C. Pistorious, D. Tang and M.E. Ferreira. “Consistency in automated inclusion micro analysis” (9th International conference on clean steel, 8-10 September, 2015, Budapest, Hungary).
- [8] Roland Kiessling and Nils Lange, *Non-Metallic Inclusions in Steel*, (London Institute of Materials, 1978).

ADVANCES IN MOLTEN SLAGS, FLUXES, AND SALTS:

Proceedings of



Refractories

INFLUENCE OF PHYSICAL PROPERTIES OF SLAG AND OPERATIONAL PARAMETERS ON SLAG SPLASHING PROCESS IN AN OXYGEN CONVERTOR

Paula Maria Gomes Cunha Leão¹Eliana Ferreira Rodrigues¹Carlos Antonio da Silva¹Itavahn Alves da Silva¹Varadarajan Seshadri²

¹Universidade Federal de Ouro Preto, Minas Gerais, Brazil ² Universidade Federal de Minas Gerais , Minas Gerais, Brazil

Keywords: basic oxygen Furnace; slag splashing, mathematical modeling

Abstract

A mathematical model using Fluent 14.0 was implemented in order to describe the flow of Nitrogen and slag under transient and isothermal conditions in the slag splashing process for the improvement of refractory life. The influence of parameters affecting this process and the consequent effects on refractory linings has been investigated applying the model. For a given blow pattern, the influence of parameters such as temperature, density, viscosity and interfacial tension of the fluids involved have been discussed. The results are compared with projection data available in the literature.

Introduction

The wear causes of refractory lining of an oxygen converter result from a combination of thermal, chemical and mechanical phenomena occurring inside the reactor. The thermal effects are linked to temperature fluctuations and thermal shock, while the degradation of the linings can be caused by chemical interactions between the refractory, slag and the gases in the converter. Those of mechanical origin are associated with erosion due to scrap charging, liquid movement between refractory surface and the metal, oxygen blowing and effect of gas movement at high temperatures in the vicinity of the refractory lining. Through wear profile monitoring technique of the refractory lining by laser beam, it is possible to obtain a map of the lining wear profile in each region of the converter.. The regions where the liquid steel flows out of the convertor after each blow and zone of impact due to scrap charging are the most susceptible to degradation. With this knowledge, one can establish a suitable repair strategy for the worn out regions to extend the campaign life of the linings of the reactor. Maintenance and repair techniques of refractory lining include coating with slag. This is done through slag splashing or gunning refractory material towards the damaged lining. The slag splashing process is characterized by projecting chemically reconditioned molten slag in the convertor through nitrogen blowing through a lance ,on the hot surface of the convertor lining(1,2) Many factors affect this projection of slag such as converter dimensions, nitrogen blowing rate, height, tilt and shape of nitrogen lance, temperature, composition and volume of slag. The duration of this practice is 1 to 4 minutes and it is possible to maintain the lining for 10,000 converter runs or more. The influence of parameters such as trajectory and size distribution of droplets on the slag splashing process has been evaluated(3). There is an optimum height of lance and optimal nitrogen flow so that the projection rate of slag droplets and the thickness of the slag layer on the refractory lining can be optimized (4).As the critical gas flow for ejection of the droplets is independent of lance height, the main contributing factor for increased generation of slag droplets is likely to be,

change in the surface area of the cavity formed in the impact zone of gas and slag (5). The generation of drops (Figure 1) by splashing is possible in different ways like generation of individual or discrete drops or swarm of drops characterized by production of several drops of various sizes (6). The increase in the gas blowing velocity or reduction of height of the lance for gas blowing may cause reduction in the amount of ejected drops of slag (7,8). This can be attributed to the increased depth of the cavity generated by the gas jet due to increased dynamic pressure of the gaseous jet. These can also cause oscillation and vorticity of the slag. This work on CFD simulation of slag splashing has the objective of evaluating the influence of physical parameters such as slag density and viscosity of slag on projection in the inside walls of the converter.

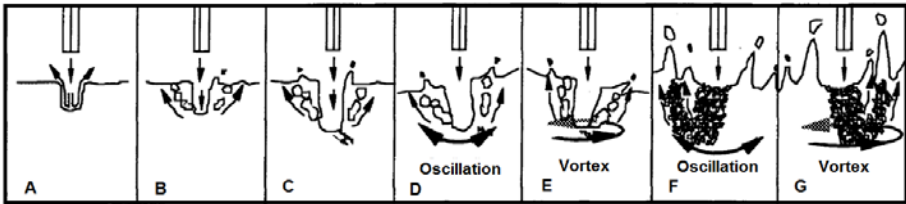


Figure 1 - Characteristics of liquid phase interaction with a vertical gas jet (8)

Methodology

The motion of slag and gas has been described with the aid of Navier-Stokes equations, the $\kappa - \epsilon$ turbulence model along with the volume fraction formulation -VOF (for tracking the position of the interface between nitrogen and slag). Where there is presence of more than one fluid phase, the VOF formulation is used to express the interactions between the gas and slag. For the incompressible and Newtonian fluid flow the equation of Momentum Conservation can be given as:

$$\rho \left(\frac{\partial \vec{u}}{\partial t} + \vec{u} \cdot \nabla \vec{u} \right) = -\nabla p + \mu_{eff} \nabla^2 \vec{u} + \rho \vec{g} + F \quad (1)$$

where: ρ = fluid density, \vec{u} = velocity vector, t = time, g = gravity, p = pressure, μ_{eff} = effective viscosity of the fluid and F are the other forces. There is a balance between the inertial (Fi), interfacial ($F\gamma$), and gravitational forces (Fg) when the droplet breakaway occurs [1,15],

$$Fi = F\gamma + Fg \quad (2)$$

The droplet diameter (d) derived from the balance of forces of (2) is given by:

$$d = \frac{3U^2}{8g} \left(1 - \left(1 - \frac{128\gamma g}{3\rho U^4} \right) \right) \quad (3)$$

where U is the magnitude of the jet velocity at the impact point and γ is the surface tension. The computation involves the $\kappa - \epsilon$ model with the following equations for conservation of turbulent kinetic energy and rate of dissipation of turbulent kinetic energy, respectively:

$$\rho \frac{\partial K}{\partial t} + \rho v_j \frac{\partial K}{\partial x_j} = \frac{\partial}{\partial x_j} \left(\frac{\mu_t}{\sigma_K} \frac{\partial K}{\partial x_j} \right) + \mu_t \frac{\partial v_i}{\partial x_i} \left(\frac{\partial v_i}{\partial x_j} + \frac{\partial v_j}{\partial x_i} \right) - \rho \epsilon \quad (4)$$

$$\rho \frac{\partial \varepsilon}{\partial t} + \rho \mathbf{v}_j \frac{\partial \varepsilon}{\partial x_j} = \frac{\partial}{\partial x_j} \left(\frac{\mu_t}{\sigma_\varepsilon} \frac{\partial \varepsilon}{\partial x_j} \right) + C_1 \mu_t \frac{\varepsilon}{K} \frac{\partial v_j}{\partial x_i} \left(\frac{\partial v_i}{\partial x_j} + \frac{\partial v_j}{\partial x_i} \right) - C_2 \frac{\varepsilon}{K} \rho \varepsilon \quad (5)$$

Where: K = kinetic energy of turbulence, ε = the rate of dissipation of kinetic energy of turbulence; \mathbf{v}_j = velocity component; μ_t = turbulent viscosity; \mathbf{x}_j = coordinate distance; C_1 and C_2 = model constants. The effective viscosity is the sum of molecular (μ_0) and turbulent (μ_t) viscosities :

$$\mu_{eff} = \mu_0 + \mu_t \quad \text{and} \quad \mu_t = \frac{\rho C_\mu K^2}{\varepsilon} \quad (6)$$

Where: K = kinetic energy of turbulence, ε = the rate of dissipation kinetic energy of turbulence; C_μ = constant; ρ = fluid density. The location of the liquid slag /nitrogen interface is determined by the volume fraction VOF formulation, and the continuity equation for a couple of phases is represented by:

$$\frac{\partial}{\partial t} (r_\alpha \rho_\alpha) + \nabla \cdot (r_\alpha \rho_\alpha \mathbf{U}_\alpha) = 0 \quad (7)$$

where: r = the fraction by volume; ρ = density; \mathbf{U} = velocity ; α = a given phase, gas or slag. Also the sum of volume fractions is unitary, ie:

$$\sum_\alpha r_\alpha = 1 \quad (8)$$

In order to reduce the computational effort, one $\frac{1}{4}$ of a three-dimensional isothermal converter was considered. The Navier-Stokes equations, turbulence model equations and VOF model equations were numerically solved using by means of Ansys software – FLUENT. The segregated algorithm (pressure based) was used with the implicit scheme linearization. In order to obtain a solution more accurate the Second-order Upwind scheme was employed in the discretization of the governing equations. PRESTO algorithm was used for the interpolation of the pressure values on the faces of the cells using the equation of motion and PISO algorithm to obtain pressure-velocity coupling. A tetrahedral mesh composed of 627 535 cells was used for this purpose. The maximum processing time for all the simulations was 2 seconds with a timestep of 1×10^{-5} seconds. For this analysis the nitrogen jet speed was taken as $520 \text{ m} \cdot \text{s}^{-1}$ which is injected downwards through a one hole nozzle with a diameter of 0.064 m. A lance height of 1m above the slag bath and a molten slag depth of 1 m were assumed. Slag kinematic viscosities were varied as 16, 23, 40, 200 e $400 \times 10^{-6} \text{ m}^2 \cdot \text{s}^{-1}$ in the computations. The surface tension value amounted to $1.54 \text{ N} \cdot \text{m}^{-1}$. Slag densities of 2500 and $3490 \text{ kg} \cdot \text{m}^{-3}$ were considered. Non slipping conditions were assumed at slag walls interfaces. Boundary conditions for k and ε at the inlet nozzle is calculated from [11]: $k = 0.01 U_{gas}^2$ and $\varepsilon = 2 k^{1.5} / D_n$, where U_{gas} and D_n are the inlet nominal velocity and the nozzle diameter respectively.

Results and discussion

The results as given by Figures 2 and 3 show erratic behavior in respect of droplets trajectories as suggested by an uneven deposition on the walls. This is probably associated with transient and unstable behavior at the impact zone of the gas jet on the slag. This type of behavior was also observed by other researchers (9,10,11). Figure 2 shows the effect of the density of the slag on the projection. Greater the density of the slag lower is the projection rate. Lower viscosity of the

slag leads to increasing depth of penetration of the gas jet and higher projection (9). However, more fluid slag tends to run down the wall of the converter, resulting in a fine coating layer on the surface of the refractory. The quality of projection (height, number of projected drops and thickness of the coating layer) is strongly affected by the viscosity of the slag. High viscosity values lead to lower projection rate, which would also require higher temperatures and flow rates of nitrogen. So good efficiency of repair requires optimization of composition and temperature of the slag and other parameters affecting the process of slag splashing. From an operational point of view, the covering of the upper side walls of the converter (regions of the trunnions and the upper cone) can be improved by increasing the nitrogen blowing rate and the reduction of the slag density. For the operating conditions investigated, the results obtained show that the slag is unevenly projected (Figure 3) and increasing the viscosity of the slag decreases the projection rate. This behavior is expected, as can be seen in Figure 4. Studies on slag splashing with a physical model have been made(9). Their results show the influence of the blowing pattern (slag lance height, blow rate from the bottom, the top blowing rate), lance nozzle geometry, the degree of filling of the reactor by residual slag, and the physical properties of the slag on slag projection rate.

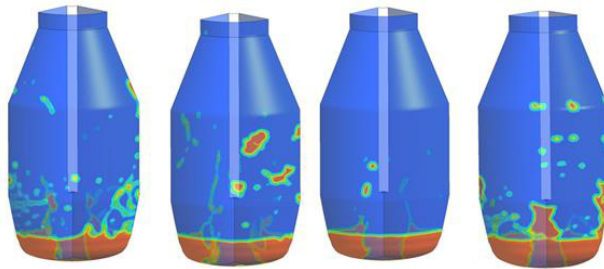


Figure 2 - Projection against the wall using a slag of viscosity of 0.058 Nsm^{-2} and density of a) 3490 kg.m^{-3} b) 2500 kg.m^{-3} (left) and using a slag of viscosity of 1 N.sm^{-2} and density of c) 3490 kg.m^{-3} and d) 2500 kg.m^{-3} (Right); lance to slag distance of 1 m , gas velocity of 520 m/s ; according to results of CFD simulation.



Figure 3: Fraction of slag covering the wall of the converter in time of 2 seconds in the case of kinematic viscosities of (a) $23 \times 10^{-6} \text{ m}^2 \cdot \text{s}^{-1}$; (b) $40 \times 10^{-6} \text{ m}^2 \cdot \text{s}^{-1}$; (left) (c) $200 \times 10^{-6} \text{ m}^2 \cdot \text{s}^{-1}$ and d) $400 \times 10^{-6} \text{ m}^2 \cdot \text{s}^{-1}$ (Right); lance to slag distance of 1 m , gas velocity of 520 m/s ; according to CFD simulation

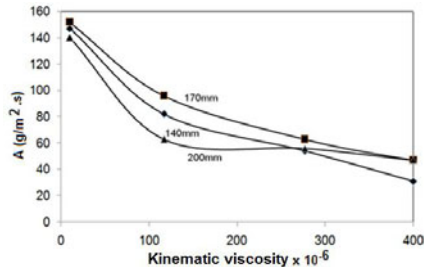


Fig. 4 - Effect of kinematic viscosity on slag projection rate, for lance height of 140mm, 170mm and 200mm (9)

From the analysis of the experimental results , using physical modeling, (9) the following equation was obtained for the rate of projection of slag A ($\text{g} / \text{m}^2\text{s}$) as a function of lance height h (in mm) and the kinematic viscosity of the slag ν ($10^{-6}\text{m}^2 / \text{s}$) :

$$A = - 0.6 - 0.286\nu + 1.42h - 0.00371h^2 + 0.000572\nu^2 - 0.000953\nu h \quad (R^2 = 0,82) \quad (7)$$

For a given viscosity of the slag, there is a optimum lance height when the slag projection rate is maximum. Table 1 shows the specific flow rate of slag as a function of the distance to the slag layer and the slag viscosity as per CFD simulation in this work. The flow is greater in the lower region of the converter (slag line) compared with the area of the sleeve and the upper region. This result is consistent with the results of other researchers (9). According to the present work on CFD simulation of slag splashing, the slag line region receives 66.8% of the projected mass, the sleeve receives 29.2% and the upper cone about 3%. It can be noted also that the increase of the viscosity of the slag decreases the projection rate of the slag line region.

Table 1: Slag mass flow in transverse planes of the converter values $\text{kg}.\text{m}^{-2}.\text{s}^{-1}$; initial lance to slag distance of 1m; gas velocity of 520 m/s; according to CFD simulation

Slag viscosity	Distance from slag layer	
	1m	2m
0.1 N.s.m ⁻²	0.0621 $\text{kgm}^{-2}\text{s}^{-1}$	0.0008 $\text{kgm}^{-2}\text{s}^{-1}$
1 N.s.m ⁻²	0.0552 $\text{kgm}^{-2}\text{s}^{-1}$	0.0008 $\text{kgm}^{-2}\text{s}^{-1}$

The area of the inner surface of the investigated converter is $126,6\text{m}^2$. According to this work, (Figure 5 (a)), the rate of deposition for a slag with viscosity of $23 \times 10^{-6}\text{m}^2 / \text{s}$ is close to $1.30\text{m}^2/\text{s}$. Thus the time required to coat the refractory lining of the reactor would be 93s (1.55 min.). To this duration of this process one should also add a fraction of $\frac{1}{4}$ to $\frac{1}{2}$ as an incubation period (9). The coating time of the converter could be considered greater than 2min. This is consistent with operational practice (1), which ranges from 2 to 4 minutes. The model presented in this work enables also to evaluate the quantitative effects of increasing kinematic viscosities on decreasing the area of the coating, as shown in Figure 5 (b) However others have suggested that decreasing the viscosity of the slag, while facilitating the projection to higher levels inside the reactor, results in the thinning of the coating layer, which is detrimental to the repair of the refractory .

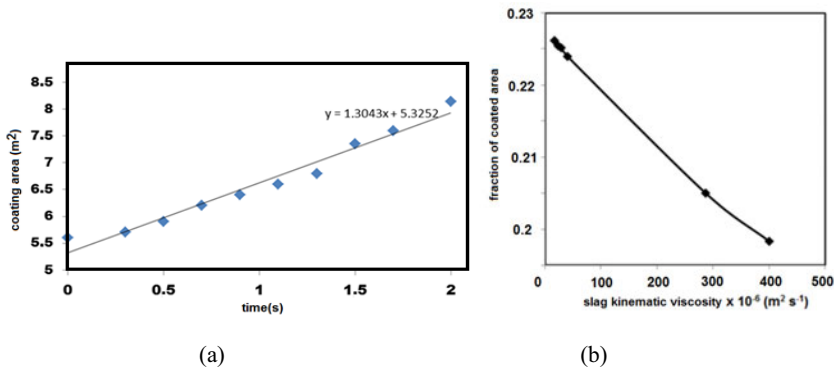


Figure 5 – (a) Variation of the covering area of the walls of the converter by slag (for kinematic viscosity of slag equal to $23 \times 10^{-6} \text{ m}^2/\text{s}$; initial lance to slag distance of 1m; gas velocity of 520m/s) with time computed from CFD modeling (b) Effect of the viscosity of slag on the coated area fraction; initial lance to slag distance of 1m; fractional area initially covered by slag ~ 0.198 ; gas velocity of 520m/s .

This behavior has also been observed by other researchers. Accordingly there is need to adjust the viscosity of the slag by adding fluxes or other raw materials(9,10). From physical modeling results it was concluded that only 46.8% of the amount of slag is effectively used for coating the refractory (9). Taking this as a reference, and a 340 ton steel converter with 40 tons of refining slag, about 18.7 tons of this slag would be used for the repair. However, it is also reported that the amount of slag actually used for the purpose is around 14 tons (1). To simplify, assuming that the thickness of the coating is uniform and the area of the refractory lining of the converter 126.6 m^2 , the amount of adhered slag would be about $147.70 \text{ kg} / \text{m}^2$. However the results of this mathematical modeling showed the heterogeneous nature of the projection of slag drops and, consequently, the non-spatial uniformity of the coating. The quality of droplets ejection (number, size) depends on the instability of the cavity formed by the impact the gas jet with the slag (3,9,13). Results for simulation of temperature profile inside the furnace refractory as well as the internal atmosphere as given by CFX are shown in Figure 6. Refractory thermophysical data for this simulation are given on Table 2; a heat flow of $12,000 \text{ W}/\text{m}^2$ has assumed in the simulations

Table 2: Refractory thermophysical data for thermal profile simulation

Property	Refractory 1	Refractory 2	Refractory 3	Refractory 4	Steel casing	Lance
$k [\text{w} \cdot \text{m}^{-1} \cdot \text{K}^{-1}]$	5.2	18.84	12.21	5.2	41.87	5.2
$\rho [\text{kg} \cdot \text{m}^{-3}]$	3100	2820	2950	2950	7800	2950
$c [\text{J} \cdot \text{kg}^{-1} \cdot \text{K}^{-1}]$	1.046	1.046	1.129	1.129	0.487	1.129

Slag coating is given as a combination of droplets ejection and their adhesion to the refractory. The latter is influenced by the temperature. A wide temperature distribution is apparent and the same is expected from physical properties. It is possible to observe the formation of cavities resulting from the projection of slag, confirming similar conclusions from other authors like Mills et al. (1). The simulated results obtained in the present work are fairly consistent with those provided by other authors, and this also includes data obtained from experimental results. Hence the described procedure is a reliable and efficient tool which can help to obtain better results in the steel industry. Additionally the simulated results can help to clarify the refractory material behavior and provide an insight into the refractory damage process. The likelihood of efficient droplet projection is influenced by dimensionless numbers such as Weber (We) and the moment (Mn). Higher values of these lead to higher rate of projection (1) :

$$We = \frac{\rho_{gas} U_{gas}^2}{\sqrt{\sigma g \rho_{slag}}} \quad Mn = \frac{\rho_{gas} A_{orif} U_{gas}^2}{\rho_{slag} g h_{cav}^3} \quad (8)$$

Where ρ_{slag} , ρ_{gas} , A_{orif} , U_{gas} , σ , g , h_{cav} are the specific mass of slag and gas; area of the gas injection orifices; velocity of the gas jet, interfacial tension, acceleration due gravity and depth of the cavity generated by the jet of nitrogen, respectively. The above dimensionless numbers enable to quantify the (negative) effects of increasing viscosity and density of slag. These negative effects can be counterbalanced by adopting a standard nitrogen blowing pattern with optimum height and geometry of the nozzle and gas flow (1,5,9). With this, one can provide additional moment forces, improving the formation of small dense slag droplets, favoring the coating of the upper regions of the converter. However, as shown by this simulation the quality and uniformity of the coating can be an issue. The thermal profile of the converter is transient and heterogeneous as shown in Figure 6. Slag coating is given as a combination of droplets ejection and their adhesion to the refractory and the latter is influenced by the temperature. The dimensionless numbers (We, Mn) given above have a decisive influence on the generation and projection of drops of slag. That is to say the physical properties of slag (viscosity, surface tension and density), and the rate of solidification of the slag coating are affected by temperature. Therefore, it is important to further investigate the effects of the thermal profile in the converter on the characteristics of instability of the impact area of the jet of nitrogen and the area covered by slag. This has been planned as a future work. With this the effect of temperature profile in the converter on the projection height and the adhesion rate of drops of slag can be investigated. The impact region of the nitrogen jet has low temperature (blue and green regions in Figure 6) as nitrogen is blown at normal ambient temperature the gas gets heated up later.

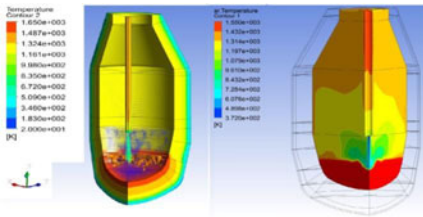


Figure 6. CFD Simulation results

of temperature distribution inside the converter slag during the projection operation (to reduce the computational effort, $\frac{1}{4}$ of a three-dimensional isothermal converter was considered for simulation)

Conclusions

The efficiency of the slag splashing process requires optimization of blow pattern variables such as gas flow rate and lance to slag distance as well as slag properties dictated by its composition. However this simulation weighs the importance of physical properties like viscosity, density. The projection rate increases with decreasing viscosity of the slag and with decreasing density. These observations are in agreement with the findings in the actual slag splashing process adopted in the industry. The CFD simulation results would be of help in optimizing the variables mentioned above in the industrial slag splashing process for repair of refractories. Models such as the one developed in this work are useful to industry since actual data regarding physical properties and operational parameters are mostly unknown. This model stresses the importance of these properties for better efficiency of the slag splashing process.

Acknowledgements

The Scientific program of UFOP, Gorceix Foundation, Fapemig, Capes and CNPQ of Brasil.

References

- 1 K.C Mills et al., A Review of Slag Splashing, ISIJ International, Vol. 45, No. 5, 2005, 619-633.
2. M.I.J Strelbisky and J. Manning, J - Current slag splashing practices in selected, http://www.tallman-bronze.com/articles/article_2/article-slag.htm,
3. S. Sabah and G. Brooks, Splashing in Oxygen Steelmakin "ISIJ International, Vol. 54, No.4, 2014 . 836–844.
- 4.P. Koopmans and al. Primary Steelmaking: Consistent BOS performance. "Technical Steel Research, EUR2081, 2003", 1-136
- 5.M. Alam et al., A Computational Fluid Dynamics Model of Shrouded Supersonic Jet Impingement on a Water Surface. ISIJ International, Vol. 52 (2012), No. 6, 1026–1035
6. Q. L. He and N. Standish, Model study of droplet generation in the BOF steelmaking. ISIJ International, vol. 30, no. 4, 1990, 305-309.
7. N.A Molloy, Impinging jet flow in a two-phase system. The basic flow pattern, .Journal of Iron Steel Inst, vol. 208, no. 10, 1970, 943-950.
8. T. Kumagai, and M. Iguchi, Instability phenomena at bath surface induced by top lance gas injection, ISIJ International, vol. 41, 2001, , 52-55.
9. C. J. Liu, Y.X. Zhu and M.F. Iang - Physical modelling of slag splashing in converter, Ironmaking and Steelmaking. vol. 30 No. 1, 2003, 36-42
10. M.A. Barron, D.Y. Medina, and I. Hilerio, CFD Analysis of Influence of Slag Viscosity on the Splashing Process in an Oxygen Steelmaking Converter, Modeling and Numerical Simulation of Material Science, 3, 2013, 90-93
11. M.A. Barron et al., Influence of the Slag Density on the Splashing Process in a Steelmaking Converter, ISRN Metallurgy, 2014, 1-7
12. H. J. Odenthal, U. Falkenreck and J. Schlüter, CFD simulation of multiphase melt flows in Steelmaking converters, European Conference on Computational Fluid Dynamics ECCOMAS CFD 2006, 1-21
13. Subagyo et al. Generation of droplets in slag-metal emulsions through top gas blowing, (ISIJ International, vol. 43, no. 7, 2003, 983-989.
14. S. Koria and K. Lang, A new approach to investigate the drop size distribution in basic oxygen steelmaking. Metallurgical Transactions B, vol. 15, no. 1, 1984, 109-116.

15. P. C. Mahapatra, S. Majumdar, R. Shrinivas et al., "Understanding slag splashing technology in BOF,"SEAIISI Quarterly,vol.29,no. 4, 2000, 54-60

CORROSION MECHANISMS IN REFRACTORY CASTABLES BY LIQUID OXIDES

L. Tadeo Ibarra¹, A.M. Guzmán¹, D.I. Martínez¹, G. Alan Castillo¹

¹Faculty of Mechanical and Electrical Engineering, Autonomous University of Nuevo León, Pedro de Alba S/N, Cd. Universitaria, San Nicolás de los Garza, Nuevo León 66451, Mexico

Abstract

Corrosion in refractories in a commercial furnace is a very complex phenomenon which involves chemical and physical wear. In this work three refractory castables (A, B and C) are being characterized and studied to compare their properties and determine their corrosion mechanisms in the presence of slag obtained from a steel furnace. The chemical composition of the slag consists mainly of CaO, SiO₂, alumina and Fe₂O₃. Using a heating microscope, it was determined that the slag starts to melt around 1350 °C. The chemical composition of the castables consist mainly of alumina (86%, 90% and 92% respectively) with a variation in material A which contains 5.8% MgO. Prismatic bars were made and sintered at 1400 C to run the hot modulus of rupture at 1000 C. A non-destructive technique was used to investigate the Young's modulus of the specimens before and after sintering.

The corrosion tests were performed at 1400 C in cubic crucibles (8x8 cm) with 50 g of slag.

The investigated castable samples exhibited low values of Young's Modulus and HMOR. The corrosion tests showed a high impact on the castables integrity, which can be seen in the multiple cracks and spalling formed after the test.

1. Introduction

Refractory materials are an important class of ceramics that are utilized in large quantities and are important components of the equipment used in the production, refining, and handling of metals and glasses, for constructing heat-treating furnaces, and for other high-temperatures processing equipment.^[1, 2] Charles A. Schacht^[3] defines refractories as materials which are supposed to be resistant to high temperatures and are exposed to different degrees of mechanical stress and strain, thermal stress and strain, corrosion from solids, liquids and gases, gas diffusion, and mechanical abrasion at various temperatures. In alumino-silicate castables systems, calcium aluminate cements are still the principal bonding agents. Nevertheless when CaO is present in the refractory composition it reduces refractory properties of materials consisting of Al₂O₃-SiO₂ and Al₂O₃-MgO systems. In some studies made by M. R. Ismael et. al. ^[4] colloidal silica is used as bonding agent and it has been reported that it improves mechanical resistance compared with materials containing calcium aluminate cements. They also present an important increase in mechanical resistance at elevated temperatures (750-1500°C) due to possible formation of mullite. During curing and drying is in the matrix where the highest amount of porosity is produced, due to the decomposition of the hydrates and liberation of water. To prevent explosion sometimes organic fibers are added to allow the exit of water at higher velocity.^[5]

In alumina and alumina-silicate based refractory castables, microsilica has become a common ingredient. That is because microsilica is known for its positive effect on the flowability of the material, the decreasing of its porosity and the formation of mullite at very high temperatures. In addition, microsilica has the ability to react and form strong

bonds at both relatively low and high temperatures. Nevertheless, it has been shown that at temperatures above 1000 °C the silica containing castables softens and loose strength probably caused by transfer of lime from the cement of the castable. It can be solved by maintaining the microsilica addition above a certain limit (it has been shown in literature that the adequate microsilica content is lower than 3% in LCC^[6]) and lower the cement content.

Corrosion resistance is one of the most important features of refractory castables, since they are commonly exposed to molten liquid oxides. It is caused by mechanisms such as dissolution in contact with liquid, penetration of the vapor or liquid in the pores, etc.^[3]

The corrosion process can be defined according to literature as an interaction (which involves phenomena of dissolution and precipitation of new crystalline compounds) between a solid phase and a fluid phase that has a negative effect to either of the phases.^[7,8] This process also leads to the degradation of the material surfaces or grain boundaries, as a consequence of chemical attack by a corroding fluid, and to a decrease in the strength of the structure.

Corrosion by liquid oxides is one of the most severe modes of degradations which limit the lifetime of the refractory linings. In lining materials in contact with slag during ladle refining of steel is usually described in three major categories: dissolution, penetration and erosion. In literature it is mentioned that microstructures of corroded refractories have the following features to be considered before interpreting them:

- They are multi-component and heterogeneous ceramics.
- The microscopic observations are carried at room temperature and there are certain vitreous phases existing at very high temperatures and they evolve once the material starts to cool.^[7]

Shaowei Zhang, et. al.^[9] studied the dissolution of commercial white fused and tabular Al₂O₃ grains into a model silicate slag. They found that unsaturated slags, with respect to Al₂O₃ dissolved both types of alumina at 1450°C and 1600°C. Some layers, such as CA₆ and hercynitic spinel were found at the Al₂O₃/slag interfaces. Compared with the CA₆ layers the spinel layers were not continuous, and they had no significant effect on the dissolution process, although their formation at temperature might have increased the slag viscosity in the boundary layer and helped decrease slag penetration.

Salah A. Abo-El-Enein et. al.^[10] performed a research work in which bauxite-based and kaolin-based refractory castables were carefully prepared with a binder mixture of 80% alumina and MA-spinel either preformed or in situ. The XRD patterns showed that a corundum phase and a mullite phase is formed in all of the bauxite-based castable samples. In general, the investigated castable samples showed a somewhat decrease in penetration by the molten slag and a light increase in corrosion as the spinel content increases.

2. Experimental

Three commercial refractory castables (A, B, C) were selected with the purpose of studying their properties and to determine their corrosion mechanisms under the influence of slag from a foundry.

2.1 Production of samples

Using the ball-in-hand test it was determined that the required amount of water the castables needed was 4.5 wt%. The specimens were fabricated according to the following procedure:

- The material is weighed including the correct amount of water.

- The mixer was turned on with a paddle attachment for 30 seconds to homogenize the mixture.
- After that time 80% of the water is added to the mixture and then it gets mixed for 5 minutes at medium velocity.
- The remaining water is added, and everything gets fold in for 2 minutes.
- The mixture was casted in the molds with a vibration time of 2 minutes
- The molds were left to cure for 24 hours and then to dry for 1 hour at 110°C.
- The specimens were sintered at 1400°C with a dwell time of 4 hours.

2.2 Characterization of concretes before mixing

The castable and slag composition was determined using the X Ray Fluorescence technique.

2.3 Characterization of concretes after sintering

The Young's Modulus was obtained at low and high temperatures with a non-destructive technique called Resonant Frequency and Damping Analysis (RFDA).^[11-14] After that procedure the Modulus of Rupture at high temperatures was tested at a temperature of 1000°C.

2.4 Corrosion test

For the test, small cubic bricks (8x8x8cm) were produced for each material and a hole with a diameter of 40 mm was drilled in the center. Afterwards, it was filled with 50 g of slag.

The corrosion test was held at a temperature of 1400°C with a dwell time of 4 hours.

3. Results and discussion

3.1 Chemical composition

The chemical composition of the three castables and the slag is showed in Tables I and II. Castables B and C have a very similar chemical composition. Castable A contains a slightly different composition with an addition of MgO.

Table I. Chemical composition of castables.

	A	B	C
Component	Percentage	Percentage	Percentage
SiO ₂	5,07	6,42	5,76
Al ₂ O ₃	86,96	91,31	91,86
Fe ₂ O ₃	0,15	0,11	0,11
CaO	1,39	1,39	1,50
MgO	5,85	0,00	0,00
Na ₂ O	0,41	0,59	0,56
ZrO ₂	0,17	0,19	0,21
Total	100,00	100,00	100,00

Table II. Chemical composition of Slag.

Component	Percentage
SiO ₂	9,08
Al ₂ O ₃	2,52
Fe ₂ O ₃	7,93
TiO ₂	1,00
CaO	58,76
MgO	4,28
K ₂ O	0,14
Na ₂ O	0,06
MnO	0,20
P ₂ O ₅	0,08
ZrO ₂	0,01
SO ₃	14,48
F	1,41
Cl	0,03
SrO	0,02
Total	100,00

3.2 XRD Results

As can be seen in Figure 1, In all samples Corundum, Ca, and Beta Alumina was found. In the castable A, which contains MgO, the spinel phase is present. No phases containing silica were found with this technique. The following hypothesis can be made: the SiO₂ does not react with the Al₂O₃, and stays in the sample as tridymite or cristoballite, it could be possible that the amount is so small, that the peak on the diffractogram can not be seen.

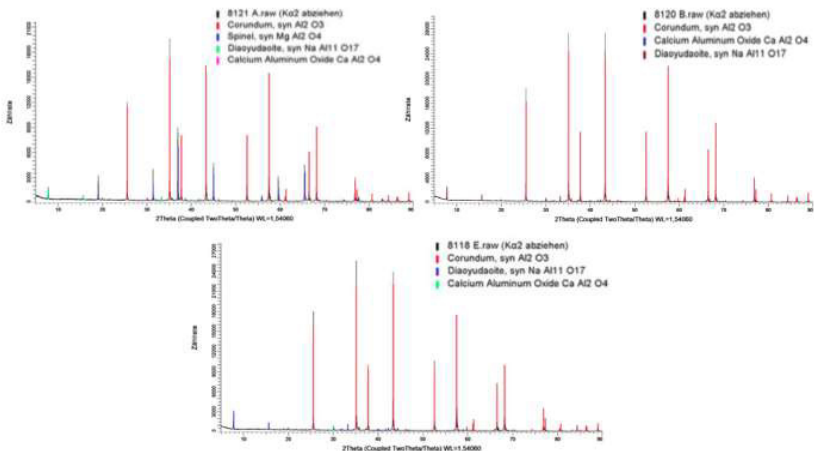


Figure 1. XRD diagrams of castable A (upper left corner), B (upper right corner) and C.

3.3 HMOR and RFDA results

Table III. HMOR and RFDA Results

	Dried at 110 °C	Sintered at 1400 °C	1000 °C
Material	Young's Modulus (GPa)	Young's Modulus (GPa)	HMOR (Mpa)
A	62.075	135.88	15.452
B	54.086	134.484	17.366
C	51.59	102.05	13.782

3.4 Corrosion test

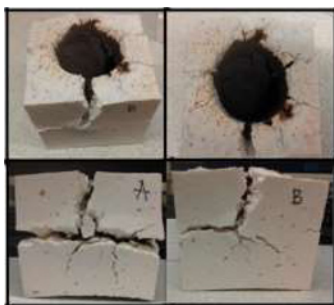
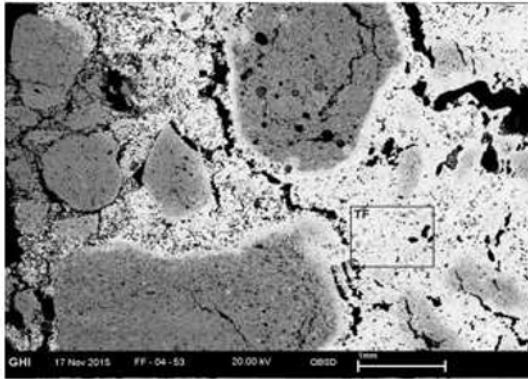


Figure 2. Specimens after corrosion test .



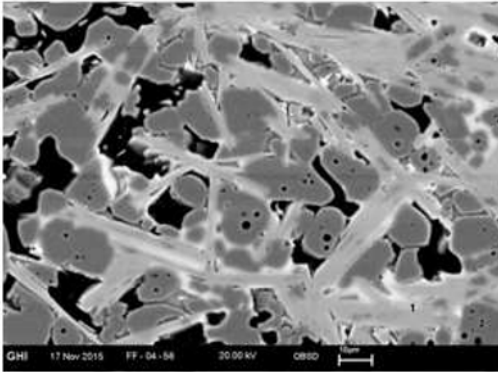
Figure 3. Corroded specimen

At the bottom of the refractories (Fig. 3), it can be observed that the phenomenon called flux line erosion occurred during the test. The high level of spalling observed in the castables may have occurred due to the difference of thermal expansion coefficient between the components formed in the slag and the original material.



TF	
Component	Wt. %
Al ₂ O ₃	51,2
SiO ₂	13,27
CaO	26,25
TiO ₂	0,64
Fe ₂ O ₃	8,63
Total	100

Figure 4. SEM image of castable A and composition of matrix after test.



1	
Component	Wt. %
Na ₂ O	1,32
Al ₂ O ₃	79,29
SiO ₂	4,49
CaO	11,71
TiO ₂	0,22
Fe ₂ O ₃	2,97
Total	100

Figure 5. SEM image of interface between aggregates and dissolved matrix of castable A.

By determining the composition of the crystals in point 1 it was proved that they consisted of a glassy phase and CA₆ with an impurity of iron oxide. It was possible to identify a complete dissolution of the refractory matrix and some micro-cracks in the aggregates. It can also be observed a superficial dissolution of the aggregates that may have been stopped by the formation of calcium hexaluminate, since in the literature it has been mentioned that the formation of CA₆ layers can stop the slag from infiltrating the material.

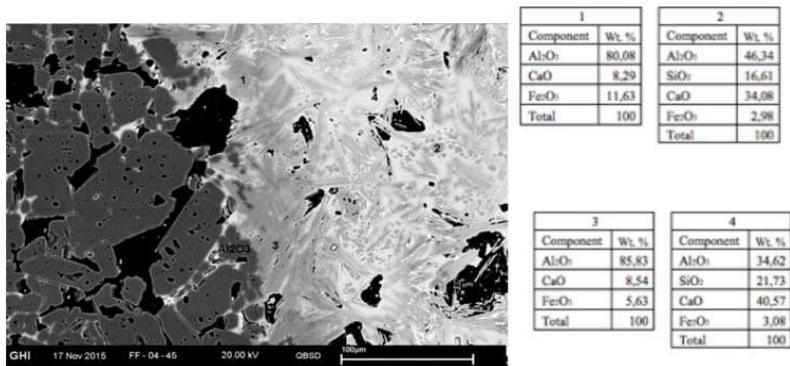


Figure 6. SEM image of interface between dissolved matrix and aggregates of castable B.

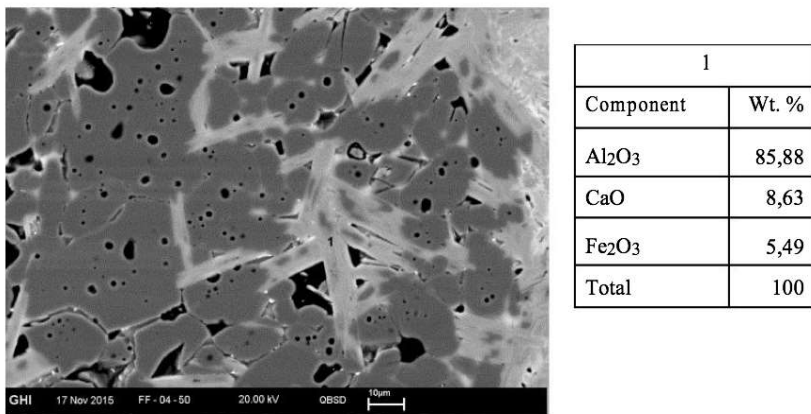


Figure 7. SEM image of castable C

In castables B and C it was observed the same behavior as in castable A, regarding the formation of a glassy phase and calcium hexaluminate. The SEM images also show the precipitation of a phase that could be ghlenite.

3.5 Mechanism of corrosion-erosion wear

1. As mentioned in literature [7] four main regions were found in the refractory: the slag zone, the precipitation zone, the penetration zone and the refractory zone. The slag infiltrates the castables through the pores and cracks formed right after sintering dissolving the matrix producing a liquid solution, which can be defined as homogenous, rich in silica, calcia and alumina.

2. During cooling, due to the difference of thermal expansion coefficient between the slag-matrix solution and the undamaged refractory, several cracks and spalling are formed causing the destruction of the crucibles.
3. During cooling, as said in literature [7] the precipitation zone is formed by a succession of monomineral layers (calcium hexaaluminate) of crystals surrounded by glass. Ca_6 precipitates from the slag-matrix solution preventing further penetration of the slag according to literature.

4. Conclusions

Even when all materials showed low values of Young's moduli and HMOR, materials A and B showed better mechanical properties at high temperatures than material C. In the case of castable A it could be due to the presence of preformed spinel in the mixture. The post-mortem analysis of the specimens that were submitted to the corrosion test showed that their behavior was very similar in the three cases. All of them were completely destroyed with a high amount of spalling which could be caused by the difference of thermal expansion coefficient between the slag and the refractories. It is suggested that the slag penetrated the castable through the pores and cracks formed during cooling right after sintering, dissolving the matrix and infiltrated to the aggregates with micro-cracks. The SEM analysis in all three cases showed the formation of calcium hexaluminate and a glassy phase rich in alumina, silica and calcia. Which lead us to infer that there was a liquid solution at 1400 °C.

5. Acknowledgements

Special thanks to the people at the GHI Institute in RWTH Aachen, Germany for their support and providing all the equipment to perform the tests.

6. References

1. Donald R. Askeland, Pradeep P. Fulay, Wendelin J. Wright. (2010). *The Science and Engineering of Materials*. USA: Cengage Learning.
2. Mendoza Bedoya, José Luis. *Evolución tecnológica de concretos refractarios Parte I-Sistema CaO-Al₂O₃-SiO₂*. (Saltillo, Coahuila, México, 2004)
3. Charles A. Schacht. *Refractories Handbook*. (USA: Marcel Dekker, Inc. 2004)
4. M. R. Ismael, F. A. O. Valenzuela, L. A. Polito, V. C. Pandolfelli. Thermo-mechanical properties fo colloidal silica-containing castable. Universidade Federal de S. Carlos 2007
5. Mendoza Bedoya, José Luis. *Evolución tecnológica de concretos refractarios Parte I-Sistema CaO-Al₂O₃-SiO₂*. Saltillo, Coahuila, México.
6. E. A. Firoozjaei, A. Saidi, A. Monshi, P. Koshy. *The effect of microsilica and refractory cement content on the properties of andalusite based Low Cement Castables used in aluminum casthouse*. (Ceramica 56, 2010)
7. J. Poirier, et. Al. *Analysis and interpretation of refractory microstructures in studies of corrosion mechanisms by liquid oxides*. (Journal of the European Ceramic Society, 2008). 1557-1568.
8. S. Jansson, V. Brabie, L. Bohlin. *Corrosion mechanism and kinetic behaviour of refractory materials in contact with CaO-Al₂O₃-MgO-SiO₂ slags*. (VII International Conference on Molten Slags Fluxes and Salts, 2004)
9. Shaowei Zhang, Hamid Reza Rezaie, Hossain Sarpoolaky, William Edward Lee..

- (2000). *Alumina Dissolution into Silicate Slag*. *Journal of American Ceramic Society*, 83. 897-903.
10. Salah A. Abo-El.Enein, Morsy M. Abou-Sekkina, Nagy M. Khalil, Osama A. Shalma. (2010). Microstructure and refractory properties of spinel containing castables.. *Ceramics International* 36. 1711-1717.
11. E. Dahlem, et. Al. *Resonant frequency and damping analysis technique as a tool to investigate elastic moduli by the microstructure alteration of refractories at elevated temperature*. University of Leoben (Austria), GEMH-ENSCI (France).
12. Christian Manhart, Harald Harmuth. (N/A). *Resonant frequency and damping analysis of refractories with and without reduced brittleness*. Materials Center Leoben Forschung GmbH, Dept. Mineral Resources and Petroleum Engineering (Austria).
13. Thorsten Tonnesen, Rainer Telle. *Impact of thermal shock and related microstructural changes on elastic properties of refractories by non-destructive impulse excitation*.. RWTH Aachen University (Aachen, Germany).
14. A.H.A. Pereira, et. al. *Study of the Young's modulus and damping changes in a refractory castable due to thermal shock damage*. GEMM (Brazil), RWTH Aachen (Germany), ATCP Physical Engineering Ltda. (Brazil).

VISCOUS BEHAVIOR OF ALUMINA AND TITANIA IN AMPHOTERIC SLAGS AND THEIR INFLUENCE ON REFRACTORY CORROSION

Frank Kaußen¹, Bernd Friedrich¹

¹IME Department of Process Metallurgy and Metal Recycling, RWTH Aachen University
Intzestraße 3, 52056 Aachen, Germany

Keywords: Amphoteric slags, thermodynamic calculation, viscosity calculation, refractory corrosion

Abstract

Recovering iron from bauxite residue (red mud) by carbothermic reduction creates, depending on the composition of bauxite, slag phases with high amounts of alumina and titania which are commonly known as amphoteric slag components. In this case the prediction of slag properties and even the calculation of basicity are very difficult since the slag consists of about 50 wt.-% amphoteric components. As a consequence the correct choice of refractory materials has to be taken into consideration as well. In this study synthetic slags similar to the compositions which occur during the reductive smelting of bauxite residue are mixed and melted. By the addition of CaO and Na₂O and SiO₂ the basicity is constantly adjusted to 1 [(CaO+Na₂O)/SiO₂] to monitor the influence of the addition of amphoteric compounds regarding the viscosity and refractory corrosion. In advance thermodynamic calculations concerning the liquidus temperature and viscosity of the examined slag are done by the software FactSage (vers. 6.4). The molten slags are qualitatively examined regarding the viscosity and later on exposed to three different types of refractory materials (MgO, Al₂O₃, mullite) in order to observe the refractory corrosion and infiltration behavior.

Introduction

Most commonly pyrometallurgically treated raw materials, minerals and ores are selected regarding their content of targeted metal and their gangue which will contribute to the composition of slag phase later on. Silica is a major compound of many minerals and therefore most widely spread are silica based slags like calcium silicate slag in ferrous metallurgy or fayalite slags in non-ferrous metallurgy. But in case of aluminum production, the hydro-metallurgical Bayer process is used with its special requirements of aluminum hydroxide rich and low silica containing feedstock. As a result the content of acidic acting silica is very low depending on the origin of the ore. Tropical bauxites which are preferred due to their low silica content and high content of easy digestible Al(OH)₃ phases usually contain less than 5 wt.-% SiO₂. In contrast karst bauxites from i.e. Europe, US or Australia contain up to 10 wt.-% SiO₂. [1] The typical range of composition for bauxite ores is given in Table . [2–4] After the Bayer process and the extraction of aluminum hydroxide, the bauxite residue varies in its composition which is also shown in Table . Today's common practice is the disposal of bauxite residue due to its high alkaline content. But the high amount of iron oxide offers potential for the production of iron.

Table I. Range of compositions of bauxite and the intermediates bauxite residue and slag after iron reduction

in wt.-%	Al ₂ O ₃	Fe ₂ O ₃	SiO ₂	TiO ₂	CaO	Na ₂ O
Bauxite	40-60	10-20	2-10	1-3 (up to 10)	< 2	n.a.
Bauxite Residue	10-20	30-60	5-15	5-20	5-12	5-10
After Iron Reduction	30-50	0-1	20-30	10-30	10-15	5-10

With the intention to use bauxite residue as raw material for winning of iron via carbothermic smelting, two problems arise: What is actually the basicity of the generated slag and which refractory material can be used to treat this slag?

Usually basicity is an empiric indicator defined according to equation 1 as the ratio of network depolymerizing basic oxides like alkaline and divalent alkaline metal oxide (Na₂O, CaO, MgO, etc.) and network forming acidic oxides like SiO₂ or P₂O₅. [5]

$$B = \frac{\sum_{i=1}^n x_i(\text{basic oxides})}{\sum_{i=1}^n x_i(\text{acidic oxides})} \quad (1)$$

x_i : wt.-% of oxide component

Background is the structure of molten slags. Silica tends to polymerization and forms three-dimensional networks of corner linked tetrahedral units by bridging oxygens between the silicon cations. Basic oxides dissociate into metal cations and oxygen anions. Thus the addition of basic oxides provides free oxygen to the network which can be integrated in the structure by breaking the Si-O-Si bonds of the bridging oxygen and creating Si-O and O-Si endings of now non-bridging oxygens. As a result the degree of polymerization of the network decreases and the ratio of depolymerizing and polymerizing components is a rough indicator for the degree of polymerization in the liquid slag which strongly affects the viscosity of the melt. [6–8]

Table 1 also gives the expected slag composition after the carbothermic reduction of bauxite residue. The calculation of B according to equation 1 gives values of 0.75-1, a slightly acidic or even neutral slag after the iron reduction. But the acidic and basic oxides constitute to just 50 % of the overall slag composition. The remaining 50 % are alumina and titania which must not be neglected. These oxides are amphoteric oxides which means that they can either act as acidic or as basic oxides depending on the concentration of free oxygen, thus depending on the basicity of the matrix.

The acidic behavior of alumina is commonly explained by its ability to form tetrahedral units of [AlO₄]⁵⁻ polyanions which fit perfectly in the network of [SiO₄]⁴⁻ tetrahedrons. In order to compensate the charge balance in case of fivefold negatively charged alumino tetrahedrons, dissociated basic metal cations position themselves in proximity to the alumino tetrahedrons. But with increasing aluminum addition the network becomes instable and aluminum arranges in a sixfold octahedral structure which disturbs the network, breaks the network and reduces the viscosity. [6,9,10]

The effect of titania addition is commonly described as network modifying influence in calcium silicate slags. The amount of O²⁻ -ions is increased with increasing titania addition and as a consequence the viscosity generally lowered. But at higher titania amounts of more than 10 wt.-% the effect becomes less significant. In alumina bearing calcium silicate slags titania addition affects the depolymerization of the silica network without changing the aluminate order. [6, 11-12]

In literature many different authors made attempts to calculate the viscosity of several slag systems. One of the most famous viscosity models was created by Urbain and uses the Weymann

relationship (equation 2) and was made for ternary systems SiO₂-Al₂O₃-MO with MgO, CaO or MnO as basic oxide MO. The examined range of concentration (in weight %) is roughly 30-60 % SiO₂, 10-40% Al₂O₃, 7-40% CaO that means rather high silica containing slags:

$$\eta = A_W \cdot T \cdot e^{\left(\frac{E_W}{RT}\right)} \quad (2)$$

Thereby all oxides are divided into three groups: network former (Si⁴⁺, Ge⁴⁺, P⁵⁺), modifier (Na⁺, K⁺, Ca²⁺, Mg²⁺, Fe²⁺, Cr³⁺, Ti⁴⁺) und and amphoteric (Al³⁺, Fe³⁺) and the basicity B is calculated as follows:

$$\ln(A_W) = -m \cdot B - n \quad (3)$$

$$E_W = 1000 \cdot B \quad (4)$$

$$B = B_0 + B_1 \cdot X + B_2 \cdot X^2 + B_3 \cdot X^3 \quad (5)$$

$$B_i = a_i + b_i \cdot \beta + c_i \cdot \beta^2, \quad i = 0, 1, 2, 3 \quad (6)$$

$$\beta = \frac{\sum_{i=1}^n x_i(\text{modifier})}{\sum_{i=1}^n x_i(\text{modifier}) + \sum_{i=1}^n x_i(\text{amphoteric})} \quad (7)$$

X: molefraction of network former; x_i: mole fraction of component i; a_i, b_i, c_i are empirical constants

Kondratiev [13] adapted this model to the SiO₂-Al₂O₃-FeO-CaO system of coal ashes and calculated new parameters a_i, b_i, c_i and adapts the range of composition to 40-60 % SiO₂, 20-40 % Al₂O₃, 0-25 % CaO, 0-40 % FeO (as substitution for CaO), which means a silicon aluminate slag and is comparable to the red mud composition.

Another viscosity model was developed by Riboud and tailored for continuous casting powders of the SiO₂-Al₂O₃-CaO-CaF₂-Na₂O system. But it was found out that it works also well for other slags systems due to the similar character of MnO, MgO and FeO to CaO but it fails in cases like CaO-Fe₂O₃-SiO₂ and Fe_nO-MnO-SiO₂ [14]. Thereby the slag components are divided into five groups: SiO₂-group (SiO₂+P₂O₅+TiO₂+ZrO₂), CaO-group (CaO+MgO+FeO), Na₂O-group (Na₂O+K₂O), CaF₂ and Al₂O₃, which is treated as an acidic component. The studied range of slag compositions is 30-50 % SiO₂, 7-45 % CaO, 0-12 % Al₂O₃, 0-22 % Na₂O, 0-18 % CaF₂.

Another famous model is made by Iida [15] and later been adapted by Xu [16] to the CaO-Al₂O₃-MgO-system. The range of compositions varies from 35-50 % SiO₂, 10-20 % Al₂O₃ and 25-50 % CaO (1-20 % MgO, respectively)

Calculations with FactSage

In order to represent the red mud slag system after the reduction of iron as good as possible the basic requirements are a fixed basicity of 1 created by the main constituents SiO₂, CaO and Na₂O with the ratio of 2:1:1. Then the addition of alumina and titania is calculated in the appropriate phase diagrams to understand the process temperature (affected by the liquidus temperature of the system) and the phases which precipitate at first. It was find out that an alumina content of more than 60 wt.-% will set the liquidus temperature to values higher than 1600 °C which is not

useful for experimental verification and later on in the process. Therefore the addition of alumina is in this study limited to 50 wt.-% of the mixture. In case of the quaternary system $\text{TiO}_2\text{-SiO}_2\text{-CaO-Na}_2\text{O}$ the liquidus temperature is moderate up to 70 wt.-% titania content. But a miscibility gap occurs at about 45 wt.-% titania and the considered range is therefore limited to 30 wt.-% TiO_2 content.

The calculated viscosities for both systems are shown in figure 1. FactSage© predicts in case of alumina addition a significant increase of the viscosity up to 30 wt.-% Al_2O_3 . At higher alumina concentrations, the viscosity decreases again. In case of rising titania content, the viscosity continuously decreases, indicating that FactSage© treats titania as a basic, depolymerizing compound. It is remarkable that the viscosity is independent from the calculated liquidus temperature and thus independently treated from the superheat of the melt, explicitly shown by the plotted slag liquidus temperature in the viscosity diagrams of figure 1.

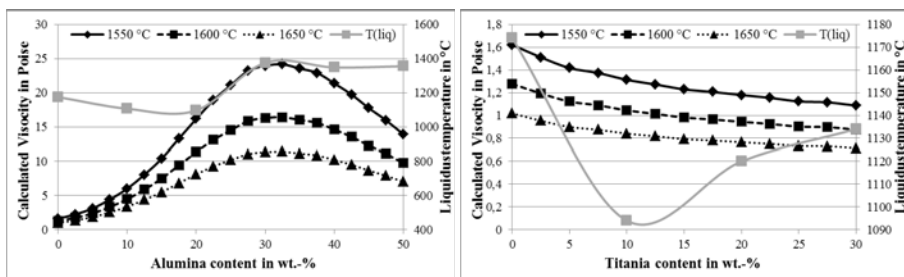


Figure 1. With FactSage© calculated course of viscosity dependent on the alumina content (left) and the titania content (right) of a $\text{CaO-Na}_2\text{O-SiO}_2$ slag (wt.- ratio 50/25/25) at different temperatures

For comparison also the introduced viscosity models are applied on the slag system at a temperature of 1550 °C and the results are shown in figure 2. Urbain's, Ribout's and Iida's models are created for slags with considerable higher silica contents and therefore the predicted viscosities are generally far too low. Only Kondratiev's modified model from Urbain predicts almost the same course of viscosity with increasing alumina content. The case of titania is more difficult since many models do not tolerate titania (Kondratiev) or only in low contents of $\ll 5$ wt.-% (Riboud, Iida). Thus only the Urbain's model, which is valid up to ~ 10 wt.-% TiO_2 , gives the right tendency of decreasing viscosity with increasing titania content.

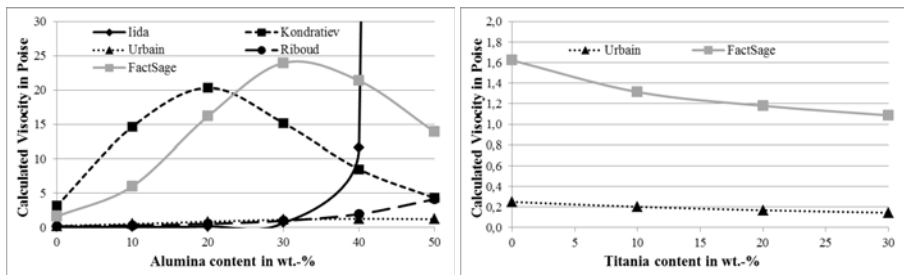


Figure 2. Calculated viscosities dependent on the alumina content (left) and the titania content (right) of a $\text{CaO-Na}_2\text{O-SiO}_2$ slag (wt.- ratio 50/25/25) using different viscosity models

Experimental studies

In order to confirm the tendency and test the basicity experiments with synthetic slag mixtures experiments have been conducted in an induction furnace, which is shown in figure 3. An aluminum crucible or graphite crucible with chromium corundum ramming mass inlet and an operation volume of 400 ml is used. The temperature is controlled by a type B thermocouple in an alumina sheath. For viscosity measurements a graphite shaft of 12 mm diameter and a flattened tip of 40 mm length is used. The revolutions per minute in idle mode are optically (contactless) measured. After melting of the blended raw material powders (purity Na_2CO_3 , TiO_2 , Al_2O_3 , $\text{CaO} > 99.5\%$) the tip of the shaft is completely introduced in the melt and the decrease of the rotational speed due to the friction in the melt is recorded. The induction furnace is shut off for the duration of the measurement. After the viscosity measurement, four different types of refractory bricks [pure alumina, pure electro-fused alumina, mullite (71 wt.-% Al_2O_3 , 27 wt.-% SiO_2) and pure MgO] are inserted in the melt for 60 min as shown in figure 3 (right side). The furnace is poured with argon during all experiments.

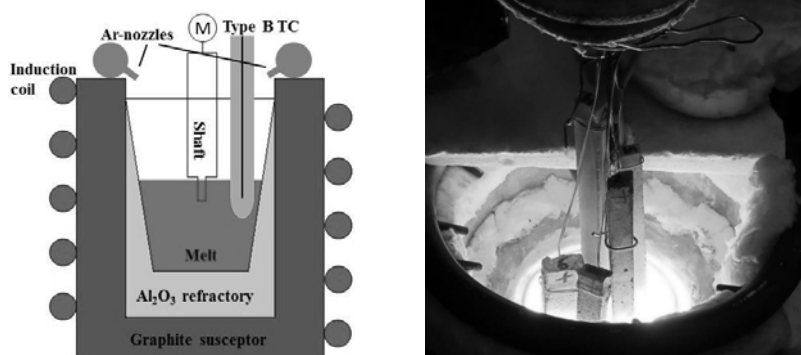


Figure 3. Experimental setup schematic for viscosity measurement (left) and picture of refractory test (right)

The induction furnace is switched on for this holding time and the induced bath convection leads to an increased refractory stress. All experiments are conducted at 1600 °C. The examined slag compositions and measured declines in rotation speed are shown in table 2.

Table II. Slag composition of experiments and decrease of rotation speed during dipping in melt (Δ rpm)

in wt.-%	Al_2O_3	SiO_2	CaO	Na_2O	Δ rpm
1	0	50	25	25	20
2	10	45	22,5	22,5	24
3	20	40	20	20	26
4	30	35	17,5	17,5	30
5	40	30	15	15	n.a.

It becomes obvious that the assumption of an increase in viscosity with higher amounts of alumina can be verified by the experiments. Although the viscosity apparatus is not calibrated, the qualitative evidence of the acidic and thus network forming acting of alumina in calcium sodium silicate slags of basicity of 1 can be provided.

The attack on the tested refractories is moderate. The MgO brick is completely infiltrated, partly in combination with a substantial loss of physical strength, but it is not dissolved. Thus it can be assumed that the basicity of the slag is neutral till slightly basic. All alumina bricks are infiltrated. The sintered alumina brick is even partly dissolved but the electro-fused alumina brick is though slightly infiltrated still rigid and without any superficial erosion. It is surprising to see, that the cheapest brick, the Al₂O₃/SiO₂ brick, still perform satisfactory. After 60 min the brick is slightly dissolved at its edges but only slightly infiltrated.

Conclusion

It has been shown that the addition of alumina to neutral (basicity=1) CaO-Na₂O-SiO₂ slags, as they appear in reductive smelting processes of red mud, increases the viscosity up to a Al₂O₃ content of about 30 wt.-%. Beside FactSage© even the viscosity model from Kondratiev suggests a similar course of slag viscosity with increasing alumina content. At higher contents of > 60 wt.-% the liquidus temperature increases dramatically due to the formation of corundum. The effect of titania is not experimentally verified yet but literature and all viscosity models show clearly a decrease of viscosity in case of rising titania concentrations, assigning titania a role as network modifier which depolymerizes the silicate structures.

Especially electro-fused corundum withstands this slag system. But even low cost mullite brick erodes slowly. The magnesia brick was infiltrated but not dissolved, indicating that the slag has a neutral till slightly basic character.

References

1. M. Authier-Martin et al., "The Mineralogy of Bauxite for Producing Smelter-Grade Alumina," *Journal of Metals* (2001), 36–40.
2. Luigi Piga, Fausto Pochetti, and Luisa Stoppa, "Recovering metals from red mud generated during alumina production," *JOM*, 45 (11) (1993), 54–59.
3. Karoly Solymar et al., "Characteristics and Separability of Red Mud," *Light Metals 1992* (1992), 209–223.
4. International Aluminium Institute, Bauxite residue management – Best practice. http://aluminium.org.au/literature_175772/Bauxite_Residue_Management_-_Best_Practice_%28IAI%29 (accessed 22 January 2016).
5. M. Allibert, *Slag atlas* (Düsseldorf: Verlag Stahleisen, 1995).
6. Il Sohn, and Dong J. Min, "A Review of the Relationship between Viscosity and the Structure of Calcium-Silicate-Based Slags in Ironmaking," *steel research international*, 83 (7) (2012), 611–630.
7. S. Seetharaman, "Viscosities of slags—an overview," *The South African Institute of Mining and Metallurgy*, 2004, VII International Conference on Molten Slags Fluxes and Salts:31–42.

8. P. J. Mackey, "The Physical Chemistry of Copper Smelting Slags - A Review," *Canadian Metallurgical Quarterly*, 21 (3) (1982), 221–260.
9. Joo H. Park, Dong J. Min, and Hyo S. Song, "Amphoteric behavior of alumina in viscous flow and structure of CaO-SiO₂ (-MgO)-Al₂O₃ slags," *Metallurgical and Materials Transactions B*, 35 (2) (2004), 269–275.
10. Georges Urbain, "Viscosity Estimation of Slags," *steel research international*, 58 (3) (1987), 111–116.
11. Hyunsik Park et al., "Effect of TiO₂ on the Viscosity and Slag Structure in Blast Furnace Type Slags," *steel research international*, 83 (2) (2012), 150–156.
12. J. L. Liao et al., "Influence of TiO₂ and basicity on viscosity of Ti bearing slag," *Ironmaking & Steelmaking*, 39 (2) (2012), 133–139.
13. Alex Kondratiev, and Jak Evgueni, "Predicting coal ash flow characteristics (viscosity model for the Al₂O₃-CaO-FeO-SiO₂ system)," *Fuel*, 80 (2001), 1989–2000.
14. S. Sridhar, "Estimation models for molten slag and alloy viscosities," *JOM*, 54 (11) (2002), 46–50.
15. Takamichi Iida et al., "An Equation for Accurate Prediction of the Viscosities of Blast Furnace Type Slags from Chemical Composition," *ISIJ International*, 40 (Suppl) (2000), S110-S114.
16. J-F Xu et al., "Experimental measurements and modelling of viscosity in CaO-Al₂O₃-MgO slag system," *Ironmaking & Steelmaking*, 38 (5) (2011), 329–337.

PHASE CHEMISTRY STUDY OF THE INTERACTIONS BETWEEN SLAG AND REFRACTORY IN COPPERMAKING PROCESSES

Ata Fallah Mehrjardi¹, Peter C. Hayes¹, Turarbek Azekenov², Leonid Ushkov², Evgueni Jak¹

¹PYROSEARCH, Pyrometallurgy Research Laboratory, School of Chemical Engineering, The University of Queensland, Brisbane, Queensland, 4072, Australia.

²KAZZINC, Glencore, Kazakhstan

Keywords: refractory, hot face, Phase chemistry, slag, copper

Abstract

The molten oxides (slag), matte and metal charges during smelting, converting and refining stages of the pyrometallurgical coppermaking processes are contained in refractory-lined vessels. The refractory materials are selected so as to provide resistance to corrosion by molten phases and thermal insulation to minimize heat losses while maintaining the charge in a molten state. However, high process temperature, highly agitated and chemically aggressive melts in furnaces can result in rapid degradation of the refractory and premature shutdown of the reactor for relining; imposing additional costs on processes in the form of planned and unplanned maintenance.

The focus of the present study is on detailed characterization of the phase chemistry and slag interactions with refractories. The rate of reactions between refractories and liquids depends on the phase equilibria. Post-mortem analysis of the spent brick from Isa smelter was followed by isothermal finger laboratory test under controlled conditions. Electron probe X-ray microanalysis (EPMA) is used to measure the compositions of the phases across the samples. This information is linked to the phase equilibria. Thermodynamic modelling is carried out by FactSage to assist in interpretation of the results.

Phase analysis of used refractory and laboratory tests for Isa smelter indicate formation of a protective spinel layer on the hot face slowing refractory dissolution.

Introduction

Most pyrometallurgical coppermaking processes involve smelting and converting stages. Isa and flash smelters are primarily used for the smelting stage, forming two different liquid phases i.e. copper matte and slag. The ISASMELT reactor is primarily used for lead and copper-containing materials [1]. The furnace consists of a top submerged lance (TSL), and a refractory-lined vessels in the shape of a vertical cylinder. Refractory materials are selected so as to provide (1) high resistance to abrasion effects due to the strong bath convection, corrosion and chemical attacks by the low viscosity slag phase and (2) thermal insulation to minimize heat losses to the surroundings. However, high process temperature and highly agitated bath in both ISA and Pierce-Smith furnaces may give rise to rapid degradation of the refractory and premature shutdown of the reactor for relining; imposing additional costs on processes in the form of planned and unplanned maintenance [2].

The rate of refractory degradation is a function of several variables such as liquid bath temperature, chemical composition on of the liquid bath, liquid properties (density, viscosity, and diffusivity) and degree of bath agitation. The infiltration of the liquid slag/matte phases into the brick occurs through the in-the matrix-brick pores acting as channels speed up the chemical degradation of the brick [3, 4]. Therefore, firstly minimization of porosity in the prefabricated brick is of significance to decrease infiltration depth of low viscosity liquid into refractory. Secondly, formation of a protective solid phase layer on the interface between refractory and molten slag may slow down the process of slag infiltration into the brick [5-7]. In the current study, the effects of slag chemistry on the formation of the protective layer has been investigated through carrying out the post-mortem analysis of the used brick, measurements of as received well-quenched slag samples and isothermal laboratory finger tests samples.

Methodology of analysis and experiment

Isa smelter fresh brick and the spent one from in-contact-with-slag area were sectioned, mounted in epoxy resin, and polished for metallographic examination and microanalysis. Electron probe X-ray micro analysis (EPMA) was used to characterize microstructures and to measure the phase chemistry. An electron-probe X-ray microanalyzer, Superprobe JEOL (a trademark of Japan Electron Optics Ltd., Tokyo) 8200L EPMA equipped with five wavelength dispersive X-ray detectors was used to determine the phase compositions.

Isothermal laboratory experiment was performed using static finger test (see Figure 1). 2 kg of as-received industrial slag from Isa smelter was placed in MgO crucible using an electric furnace until a temperature of 1170 °C was reached. The preheated refractory finger was partially immersed into the liquid slag bath for 6 hours. After designated time the sample was pulled out of the bath and quenched in water. The sections were prepared similar to spent brick and then analyzed.

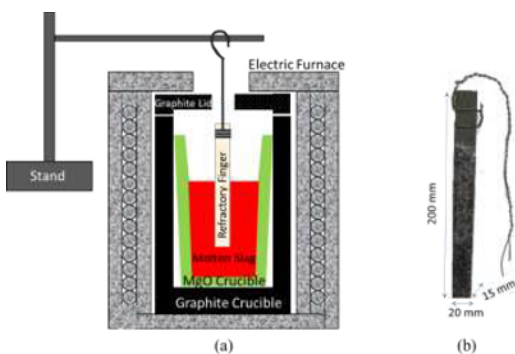


Figure 1. Apparatus of the Iso-thermal refractory test for Isa smelter and PS convertor brick at 1170 °C and immersion time: 6h, (b) refractory finger after the test

Result

Characterization of fresh Isa smelter smelting brick

The microstructure of a direct-bonded magnesia-chromite bricks (see Figure 2) is made up of large fused grains (periclase plus secondary chromite, 2-4mm), primary chromite (0.5-2mm), secondary chromite, monticellite, and pores. The bulk and the compositions of the phases are shown in Table 1. The periclase phase is highly rich in MgO (≈ 97 wt pct) and has relatively low iron content (2 wt pct). Compared to the primary chromite $[(Fe, Mg, Ca)O.(Cr, Fe, Al, As)_2O_3]$ the secondary chromite phase has higher FeO and lower Cr_2O_3 . Primary and secondary chromite phases also have different morphologies. The latter is observed either on the edge of the periclase sub-grains or inside the periclase sub-grains. The source of silica and lime in the starting materials leads to formation of forsterite and monticellite phases during the brick production process. Monticellite phase ($CaMgSiO_4$, belongs to the olivine crystal group) has a plate-shaped morphology formed around the primary chromite phase.

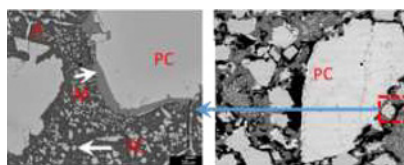


Figure 2: Back-scatter microstructures of (a) Isa smelter fresh brick (direct bond) from smelting area. Fused periclase (P), primary chromite (PC), secondary chromite (SC), monticellite (M).

Table 1: Chemical composition of phases in Isa smelter fresh brick using EPMA.

wt pct	Cu ₂ O	**FeO	S	SiO ₂	CaO	Al ₂ O ₃	MgO	Cr ₂ O ₃	As ₂ O ₃
*Bulk composition	0.0	12.8	0.0	0.9	0.8	8.1	50.9	26.4	0.0
Periclase	0.0	2.0	0.0	0.0	0.0	0.1	96.8	0.0	0.9
Primary Chromite	0.0	9.7	0.0	0.0	0.1	11.8	18.9	59.4	0.1
Secondary Chromite	0.1	28.1	0.0	0.1	0.2	10.0	20.6	40.5	0.2
Monticellite	0.0	0.9	0.0	38.5	34.5	0.2	25.5	0.4	0.2

* Bulk composition is taken from the refractory supplier datasheet.

** Iron was calculated as FeO

Used ISA Slag Brick

The back-scattered image (see Figure 3) illustrates the formation of several microstructural types starting from hot face; the reaction zone, infiltration zone and unaffected zone. The reaction zone delineates the boundary between the brick and the liquid slag phase. This layer is approximately

1mm thick starting from the hot face towards the slag/brick interface. The main phases formed in the slag/refractory reaction zone are the spinel phase, entrapped liquid and metallic copper. In addition, entrapped primary chromite from the brick (0.6 mm away from the hot face) is observed in this section.

The infiltration zone consists of original brick phases, infiltrated slag and newly formed solid phases. The infiltration depth seems to be relatively shallow (3 mm). The liquid slag infiltrated into the brick through the pores and cracks and the new phases such as spinel, and forsterite formed within the zone. Newly formed forsterite is a solid solution phase $[2(\text{Fe}, \text{Mg})\text{O} \cdot \text{SiO}_2]$ crystallized due to the chemical reaction between the slag phase (Iron oxide and silica) and MgO from the periclase matrix. The microstructure of the brick in the unaffected zone is very similar to the fresh brick; no liquid slag or newly formed phases were observed on this zone.

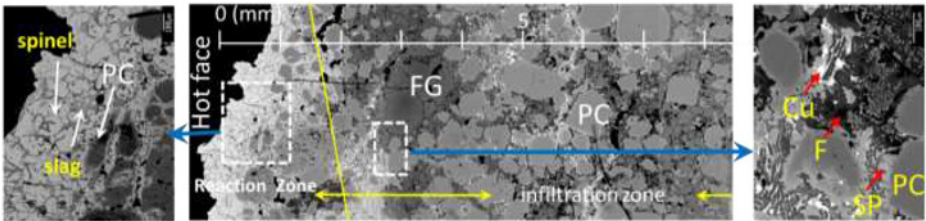


Figure 3. Back-scatter microstructures of Isa smelter-used brick taken from slag/matte area. Fused grain (FG), primary chromite (PC), spinel (Sp), and forsterite (F).

Isothermal laboratory experiment brick

Similar to the Isa spent brick microstructure, protective layer of spinel in the reaction zone, infiltration zone (newly formed forsterite and spinel) and unreacted (or unaffected) zone were observed (see Figure 4).

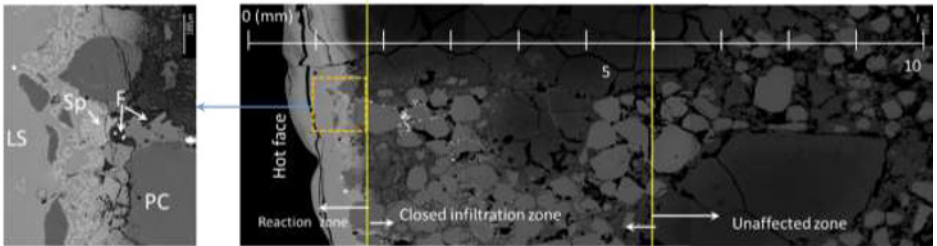


Figure 4: Back-scatter microstructure of (a) laboratory experiments with Isa slag and brick at 1170 °C, and 6h immersion. Primary chromite (PC), forsterite (F), liquid slag (LS), fused grain (FG), and spinel (Sp)

Discussions

In spent brick and also laboratory test brick, the spinel phase was formed on the slag/refractory interface as a result of the interaction between refractory components (primary chromite and periclase) and slag phase. The spinel phase seems to separate molten slag from refractory phases

slowing down further reaction (degradation) between brick and aggressive slag. Formation of forsterite in the infiltrated area seems to block open liquid channels, thus decreasing the dissolution rates and the infiltration rates of the slag phase into the brick.

Figure 5 shows the Fe/SiO₂ as a function of MgO in well-quenched bulk slag phases from the Isa smelter, the bulk samples from before and after the laboratory experiment, as well as thermodynamic model prediction with FactSage [8] for the given conditions. Fe/SiO₂ in bulk slag samples indicates that the slag phase is located on the spinel side as a primary phase crystals with MgO concentration between 1 to 1.5 wt pct in the bulk liquid slag. This is consistent with the formation of spinel in the reactive layer of Isa spent brick (see Figure 3).

For laboratory tests, the slag composition moved to the olivine and spinel sides since the bulk liquid phase was saturated with MgO (2.7 wt pct) due to carrying out the isothermal experiment in the MgO crucible. This is also consistent with the microstructural observations (see Figure 4).

The results from post-mortem analysis and the laboratory test indicate the significant effect of slag chemistry on refractory degradation. To increase the service life of the reactor it seems that fluxing recipe should be set in a way to encourage formation of spinel on the hot face of the refractory. This may slow down the dissolution of the refractory into the aggressive slag.

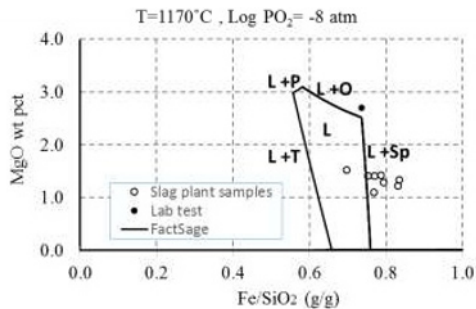


Figure 5: Fe/SiO₂ as a function of MgO in bulk slag phases of laboratory experiment, plant samples and thermodynamics calculation by FactSage [8]. Liquid (L), spinel (Sp), olivine (O), pyroxene (P) and tridymite (T).

Summary

Post-mortem analysis of the spent brick, isothermal laboratory tests along with analysis of the well-quenched slag samples from smelter were undertaken to characterize the effects of slag composition and process temperature on slag-refractory interactions. The results were related to the slag-refractory phase chemistry.

Phase analysis of used refractory and refractory after laboratory test indicated that spinel, and forsterite phases are formed due to the interaction between slag and refractory material. These solid phases block the pores in refractory leading to slowing down the refractory dissolution. This is indirect dissolution process; desired type of the refractory/slag interactions. It seems that service life of the reactor may be longer if the slag composition is moved into the primary phase field that can be formed from the refractory and slag material into spinel, or olivine phase fields.

References

1. W.G. Davenport, et al., *Extractive Metallurgy of Copper*, Elsevier Science Ltd. (2002)
2. A. Fallah-Mehrjardi, P.C. Hayes, and E. Jak, "Investigation of freeze linings in copper containing slag systems: Part II. mechanism of the deposit stabilisation," *Metall. Mater. Trans.B.*", 44B (2013), 549-560.
3. L. Scheunis, et al., "The effect of in-situ phase formation on the chemical corrosion of magnesia-chromite refractories in contact with a non-ferrous PbO-SiO₂ based slag," *Journal of the European Ceramic Society*", 34 (2014), 1599-1610.
4. L. Scheunis, et al., "The effect of a temperature gradient on the phase formation inside a magnesia-chromite refractory in contact with a non-ferrous PbO-SiO₂-MgO slag," *Journal of the European Ceramic Society*", Volume 35 (2015), 2933-2942.
5. S. Zhang, et al., "Penetration and corrosion of magnesia grain by silicate slags," *British Ceramic Transactions*", 99 (2000), 248-255.
6. W.E. Lee, B.B. Argent, and S.W. Zhang, "Complex phase equilibria in refractories design and use," *Journal of the American Ceramic Society*", 85 (2002), 2911-2918.
7. W.E. Lee, D.D. Jayaseelan, and S. Zhang, "Solid-liquid interactions: The key to microstructural evolution in ceramics," *Journal of the European Ceramic Society*", 27 (2008), 1517-1525.
8. FactSage v.6.2. 2010, CRCT - ThermFact Inc. & GTT-Technologies.

THE STUDY OF MOLTEN LIQUID - REFRACTORY INTERACTIONS – IT IS ALL ABOUT THE PHASE(S)

Andrie Garbers-Craig¹

¹Centre for Pyrometallurgy, Department of Materials Science and Metallurgical Engineering,
University of Pretoria, Lynnwood Road, Hatfield, Pretoria, 0002, South Africa

Keywords: Chemical interaction; Wear mechanisms; Slag; Metal; Matte; Refractory material

Abstract

The study of chemical interactions between slag / metal / matte and refractory materials has been an ongoing theme from the time when the first metals and alloys were produced. Over the years the refractory industry has seen extraordinary technological progress such as the development of the magnesia-carbon bricks and self-flowing castables. The advances that take place in high temperature processes, specifically the iron and steel industry, drive innovations in the refractories industry. Since these pyrometallurgical processes are dynamic, continuously improving and changing to process inter alia lower grade ores in energy more efficient and environmentally more friendly ways, the refractories industry has to keep current. This paper discusses the important role that the study of molten liquid – refractory interactions plays in understanding wear mechanisms and directing the development of refractory materials. It also gives relevant examples from refractories used in the production of different commodities.

Introduction

The refractory materials industry has been called the ‘hidden industry’ [1] and the ‘enabler of civilization’ [2]. The origin of this industry can be traced back to the ability of humans to produce and contain fire [1]. During preindustrial times, furnaces were small, reaction temperatures low (1100 to 1250°C) and times at maximum temperature short [3]. Metallurgical processes were such that the development of exotic refractory materials was not necessary. Innovation in refractory materials therefore only started with changes and developments in pyrometallurgical practices, which started to occur in the 15th century [3]. Today the refractories industry is highly sophisticated, with 38.6 Mt of refractory materials produced in 2013 [4]. In 2013, 73% of the produced refractory materials were used by the iron and steel industry, followed by the cement and lime industry (13%) and the non-ferrous metals industry (4.5%) (Figure 1) [4]. Developments in iron and steel production technology remain one of the main drivers of innovation in the refractories industry, and are likely to continue to do so for the foreseeable future.

Nearly 95 years ago Francis Pyne listed the requirements for refractories used in the copper industry as having “(1) resistance to temperatures, (2) resistance to chemical action, (3) the ability to withstand sudden temperature changes, (4) minimum absorption of slag and metal, and (5) the absence of manufacturing defects” [5]. These requirements still hold today, but with the added demands of higher productivity via longer campaign lives, emphasis on vessel

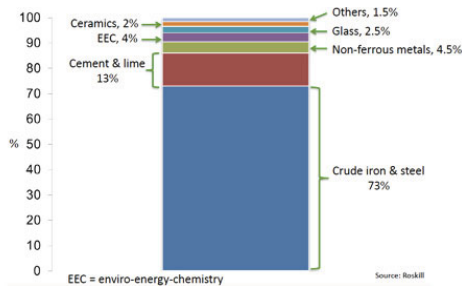


Figure 1. Global refractory market by end-user industries, 2013 [4]

availability, more efficient use of energy, reduction in greenhouse emissions and a ‘greener’ approach through recycling of refractories and sustainable use of materials [2, 6]. In addition, raw materials suppliers and refractory companies are required to adapt to a long-term decline in commodity prices as illustrated in Figure 2 [7].

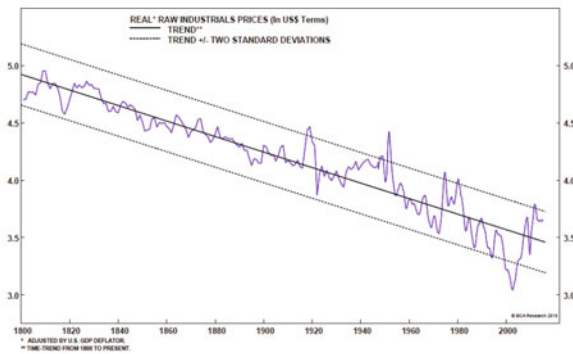


Figure 2. Trend in ‘raw industrials’ prices, 1800 - 2000 [7]

The refractories industry has developed from initially following a trial-and-error approach to an industry that innovates through a fundamental understanding of how the phase composition and microstructures of these materials are interrelated with their properties, performances and processing methods. Technological developments have been driven by studies on how chemical and physical interactions between slag / metal / matte and refractory materials impact on wear mechanisms, and also on how the refractory materials impact on product quality in the industries where they are used. This paper describes the fundamental theory on and interpretation of refractory wear through penetration and corrosion by molten liquids. It also includes a

discussion on how investigations on charge – refractory interactions have guided refractory choices and developments in the steel and platinum group metal (PGM) industries.

The study of molten liquid - refractory interactions

Fundamentals

Excellent explanations of how thermodynamic and kinetic factors impact on wear through liquid penetration, corrosion, erosion and thermal shock are available in the literature [8-12]. Equations described below are used in the design of refractory materials and slag compositions to limit refractory wear.

Penetration can be purely physical, which is then a capillary force driven flow of liquid into the refractory material, or it can be a chemical penetration, which includes chemical interaction that can lead to densification and chemical or structural spalling of the material [8]. The rate of physical penetration of a liquid into a refractory material is conventionally described by Poiseuille's law, which is dependent on the radius r of the capillary (open pore or microcrack), the capillary suction pressure ΔP , the dynamic viscosity of the liquid η , the penetration depth l of the liquid into the refractory and the time t [10]:

$$d/dt = r^2 \Delta P / (8 \eta l) \quad (1)$$

The ΔP term in equation (1) can be expressed in terms of the properties of the penetrating liquid, where γ is the surface tension of the liquid and θ is the wetting or contact angle:

$$\Delta P = 2\gamma \cos\theta / r \quad (2)$$

Substitution of Equation (2) into Equation (1), followed by integration, then gives:

$$l^2 = [r\gamma \cos\theta / (2\eta)] t \quad (3)$$

Decreasing the capillary radius and surface tension, and increasing the contact angle and viscosity of the liquid can therefore reduce penetration of a liquid into a refractory material.

Corrosion is the chemical attack of refractory, mostly by molten liquid (slag, metal and matte), but also by gas. When liquid chemically reacts with the refractory material the reaction product(s) can directly dissolve into the liquid (direct dissolution) or a solid reaction product can form at the refractory – liquid interface, which is then dissolved into the liquid (indirect dissolution) [10]. In 'direct dissolution', when the diffusivity of the reaction product(s) is faster than the rate of the chemical reaction at the interface, the initial dissolution rate can be described by:

$$J = K(A_c/A_o)C_m \quad (4)$$

where J is the dissolution rate, K the first order rate constant, A_c the actual area of refractory, A_o the apparent area of the refractory and C_m the concentration of the reactant in the melt. In the case of 'indirect dissolution', the corrosion rate can be expressed by the Nernst equation [10]:

$$J = D(C_s - C_m)/\delta \quad (5)$$

where D is the diffusion coefficient, C_s is the concentration of the component at which it is saturated in the liquid, C_m is the concentration of the component in the liquid and δ is the effective boundary layer thickness.

Corrosion is also predicted and explained through thermodynamic considerations. These include assessing phase stabilities before melting (e.g. quartz, zircon, andalusite), predicting possible chemical reactions that can take place between the charge and refractory material (whereby a reaction product interlayer could form at the hot face), the onset of melt formation in the refractory, compatibility between the slag / metal / matte and the main refractory component (oxide / carbon based), reactions between different types of refractory materials, the concept of 'local thermodynamic equilibrium' (where the penetrating and reacting liquid changes its composition as it reacts deeper into the refractory) and oxidation-reduction reactions [8, 12].

Post mortem and laboratory scale analyses on refractory materials

Analysis of wear mechanisms associated with refractory materials usually include post mortem analyses of refractory samples removed from production as well as samples from laboratory scale test work. Laboratory scale tests typically include static tests (the dipping / finger test; slag pot test; induction furnace slag test) and dynamic tests (slag drip test; rotating finger test; rotary kiln slag test). Refractory samples are then analysed using mostly chemical analysis (XRF or ICP), XRD, reflected light microscopy and SEM-EDS analyses.

Wear mechanisms are then examined and explained through the use of phase diagrams and thermodynamic calculations, using software such as FactSage and Thermocalc. It should however always be kept in mind that the observed phase relations at room temperature reflect the thermal history of the sample, and do not reveal phase relations at operating temperatures. Phase relations at room temperature should therefore always be extrapolated back to operating temperatures before corrosion mechanisms are interpreted [13].

More recent developments include in-situ analysis methods in which phase relations and corrosion mechanisms are related to dimensional changes of the refractory materials as well as their thermomechanical properties.

Refractory Development in the Steel and PGM Industries

Refractory evolution in the steel and PGM industries, which was guided through studies on charge – refractory interactions, is discussed in this section.

Steelmaking: In 1957 silica brick was still the number one steel plant refractory, even though it was meeting severe competition from basic refractories, which have far higher melting points [14]. The main reason for the successful use of silica brick was the high temperatures at which it could be used in contact with iron oxide (close to the liquidus temperature in the two-liquid region, which is in excess of 1600°C, Figure 3) and its high load-bearing capacity at these high temperatures [15, 16]. However, silica brick had the drawback of cracking and spalling when

they were rapidly heated or cooled over low temperature ranges [1], due to dimensional changes associated with the conversion of one polymorphic form of SiO₂ to the other.

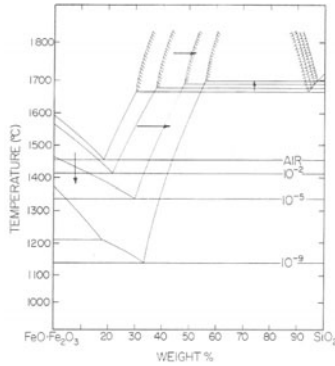
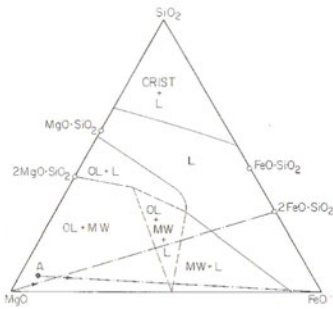
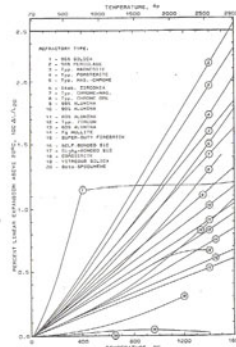


Figure 3. Pseudo binary iron oxide – SiO₂ system, indicating the variation in size and liquids temperature of the miscibility gap with changing Po₂ [15]

The rise of the LD (Linz-Donawitz) or BOF (Basic Oxygen Furnace) process resulted in the replacement of silica bricks by basic refractories [14]. The success of one such basic refractory, magnesia bricks, lies in its high melting point (2800°C) as well as its excellent resistance to attack by iron oxide, whereby the (Mg,Fe)O, (Mg,Fe)₂SiO₄ solid solution phases form under reducing conditions (Figure 4a) [15]. Its principal limitation is however, its high thermal expansion (Figure 4b), which makes the production of MgO bricks with high thermal shock resistance difficult.



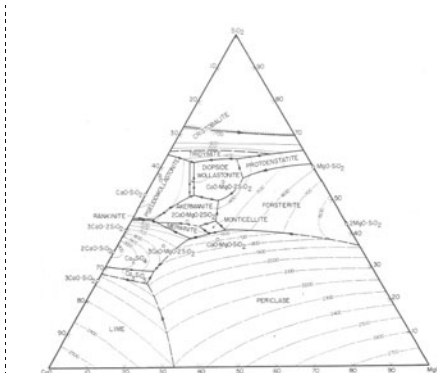
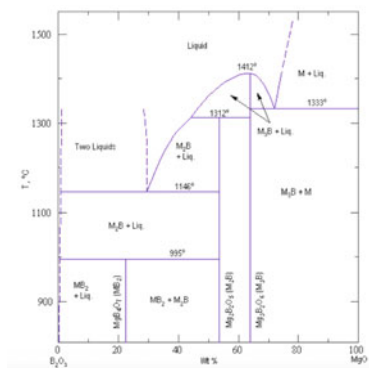
(a) 1650°C isothermal section of the MgO-FeO-SiO₂ system in contact with metallic iron [15]



(b) Percentage linear expansion of different types of refractory materials as a function of temperature [17]

Figure 4. Benefits and limitations of magnesia bricks

The earliest reference to chemically bonded basic refractory was made in 1905, referring to sodium silicate and calcium chloride as binders, while direct-bonded basic brick with low impurity content has been manufactured since the late 1950s [18]. During the early 1960s it became clear that magnesia bricks of higher purity and density were required, as impurities (which have lower melting points than MgO) cause a loss in strength of the material and provide pathways along which liquid penetration and slag attack can take place [19]. One such impurity is B_2O_3 , as it combines with MgO (and other impurities such as CaO) to form a low melting liquid, which easily wets the MgO grains and prevents direct bonding (Figure 5a [20]) [19]. Since the mid-1980s the trend has been to obtain the highest MgO content possible when manufacturing MgO brick. The importance of the CaO/SiO₂ impurity ratio in MgO bricks was also understood, as this ratio determines the temperature of initial melt formation in the brick (Figure 5b) [19].



(a) The MgO – B₂O₃ phase diagram [20] ; (b) The MgO-SiO₂-CaO phase diagram [15].

Figure 5. Influence of impurities on the refractoriness of MgO-based materials

The next step was to further densify magnesia bricks in order to improve their corrosion resistance. Penetration and corrosion resistance of a MgO refractory material can be improved by reducing its porosity, i.e. increasing its density [21]. However, when the porosity becomes too low, the thermal shock resistance of the refractory deteriorates. The design of a MgO refractory material that has a high thermal shock resistance as well as excellent corrosion resistance was therefore a matter of a delicate balance. Adding carbon in the form of pitch addressed this problem to some extent when high-strength pitch-impregnated burned magnesia bricks were developed for the high wear areas of BOF linings in the late 1960s, with MgO contents in the order of 95% [19]. Since carbon has low thermal expansion and high thermal conductivity, a material was produced with improved thermal shock resistance as well as corrosion resistance. However, since the steel industry moved from ingot to continuous casting by the late 1970s, the maximum temperature in the converter increased from 1650 to 1700°C, which necessitated the production of higher quality refractories [22]. Between 1975 and 1980 resin-bonded magnesia-carbon refractories were introduced in Japan, first for electric arc furnace hot spots and shortly

thereafter for BOFs [19, 22]. Shortly thereafter graphite became the principal carbon source. Since high carbon contents in the MgO brick introduced the severe disadvantage of oxidation and subsequent increase in porosity of the brick, the addition of antioxidants to oxide-carbon bricks followed. These bricks were the first truly composite refractory materials with a ‘self-repairing’ function when coming in contact with oxygen. The ‘self-repairing’ function includes a decrease in carbon loss by reduction of CO(g) to C(s) with an accompanying decrease in porosity, crystallization of amorphous carbon from the binder and the formation of a protective surface layer (Figure 6) [21].

Magnesia-carbon bricks are nowadays successfully used due to their excellent slag corrosion resistance and thermal shock resistance. The benefits of MgO-C bricks include low thermal expansion and high thermal conductivity (i.e. good thermal shock resistance), improved penetration resistance (due to the non-wettability of graphite by slag; the generation of CO and/or Mg vapour inside the brick which resists liquid infiltration; and the formation of a dense MgO layer at the slag/brick interface, physically preventing slag infiltration), and the reduction of iron oxide in the slag to Fe by carbon, thereby avoiding attack of the MgO by iron oxide [21, 23, 24].

However, the high carbon content in the oxide-carbon brick implied higher release of carbon dioxide during tempering and preheating, which increased pollution and carbon footprint of the brick, together with high energy losses [25]. The challenge that then followed was the reduction of the fixed carbon content of the MgO-C brick without decreasing its thermal conductivity or downgrading its corrosion resistance. Research has shown that the addition of high surface area carbon sources (such as nano-carbon) to the matrix of the brick, can reduce the fixed carbon content of the brick without decreasing its corrosion resistance and decreasing its thermal conductivity [25].

The success of oxide-carbon bricks has initiated research into the development of castables that contain graphite. However, incorporating graphite into castables is technically very difficult as graphite has a low aqueous wettability and is therefore difficult to disperse, while aluminium-based antioxidants has a tendency to hydrate [26]. Current research includes investigations into coating of the graphite and antioxidants.

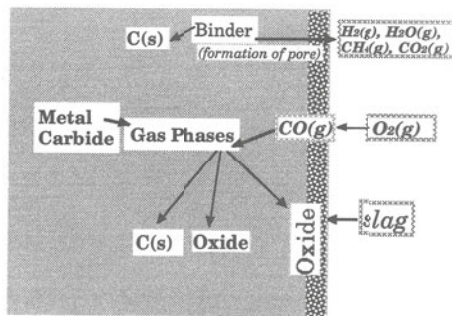


Figure 6. Illustration of the ‘self-repairing’ function of oxide-carbon materials [21]

It is also important to touch on the developments that took place in the manufacture of castable

materials, from when they were first introduced into the refractories market in the early 1900s with the industrial production of calcium alumina cement (CAC) [27]. Although the Lafarge Company in France started the commercial production of calcium alumina cement in 1918, it was only in the 1950s that high purity CACs, developed specifically for the refractories industry, came on the market [28]. By 1960 conventional castables based on high purity CAC (up to 30 wt%) and tabular alumina were in common use. Disadvantages associated with the conventional castables proved to be low strength (due to their high water content required for placement, which increased porosity), loss in strength during dehydration (in the 538 - 982°C temperature range, as the hydraulic bond was broken down and sintering was still too sluggish to allow the development of a ceramic bond) and deteriorated high temperature properties (as high concentrations of CaO favours the formation of CaO – Al₂O₃ – SiO₂ - based liquid phases on firing, Figure 7) [28].

By the end of 1960 it was clear that the cement content in castables should be reduced, i.e. to reduce the water content for placement but maintain the strength [28]. This led to the development of low (LCC) and ultra-low (ULCC) cement castables whereby flow was achieved through more efficient particle packing, together with submicron size matrix additions and the use of dispersants. These castables consist of the aggregate and a binding system, where the aggregate phases have pronounced effects on the microstructural evolution on heating, and therefore also the corrosion mechanisms in these materials. In the development of the LCCs and ULCCs the composition of the material was moved from the SiO₂-CaO-Al₂O₃ - based system of the CC to either the SiO₂-Al₂O₃ or the Al₂O₃-CaO systems [29]. In the SiO₂-Al₂O₃ system, when CaO concentrations are very low, the high melting point mullite phase is readily formed, while the Al₂O₃-CaO system aims to form the high temperature bonding phase CA₆ (Figure 7).

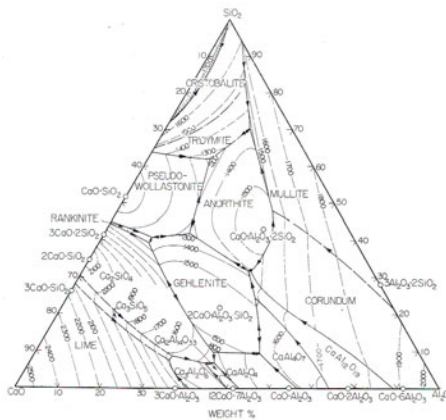


Figure 7. SiO₂-CaO-Al₂O₃ phase diagram, which describes the compositions of CCs (which contains the low melting phases CAS₂ and C₂AS) and the LCC and ULCCs, which contain either A₃S₂ or CA₆ [15]

The concern with steel cleanliness and efficiency of steel desulphurization in secondary steelmaking has sparked the development of castables based on the alumina-spinel and alumina-

magnesia systems [28, 30]. Refractories with preformed MA spinel were developed in Japan in the late 1980s, while in the 1990s in-situ spinel-forming compositions were developed [31]. The advantage of using spinel-containing alumina-based castables in contact with steelmaking slag, is that the MA spinel traps FeO and MnO from the steelmaking slag in the spinel lattice. The further infiltration of the slag is then inhibited as its liquidus temperature and viscosity are increased [32]. The pre-formed spinel alumina-based castables have in general high volumetric stability and improved chemical resistance to steelmaking slag, compared to alumina castables, while in-situ spinel forming castables have a significant lower volumetric stability, but higher corrosion resistance when compare to added MA-containing castables. The in-situ spinel castables have however the added challenge of magnesia hydration [32]. Resin-bonded AMC (alumina-magnesia-carbon) bricks for steel ladles combine the advantages of the alumina and spinel phases with those of carbon-containing refractories [33].

Through time the refractory castables have undergone major developments as a result of available raw materials of improved quality, optimisation of particle size distributions and packing design (to achieve higher density materials) and control of particle dispersion and therefore flowability [31].

Current trends in steelmaking include a focus on high quality steel grades with very low limits of residual elements and steel cleanliness, as required by end users [34, 35]. This implies that extended processing of liquid steel in secondary metallurgy can take place and increasingly complex production routes can be followed to achieve metallurgical targets. More emphasis is also placed on reduced energy consumption and increasing resource efficiency [35]. In order to achieve these aims the refractory materials that are used in specifically secondary steelmaking must continuously be re-evaluated and improved as they directly impact on steel quality and cleanliness. The steel ladle has become a “metallurgical reactor” where refractory requirements include corrosion resistance against metallurgical reactive slag, thermodynamic stability of refractory oxides to avoid re-oxidation of steel, and lower carbon content to avoid or limit C-pick up [35]. Higher purity refractories are therefore required for clean steel making. Synthetic materials such as tabular alumina or corundum have replaced natural ones such as andalusite (which has a high SiO₂ content and therefore has a low lining life against basic slags) and bauxite (which also contains significant amounts of silica and impurities such as TiO₂ and Fe₂O₃) in high alumina refractories. Significant developments have also taken place regarding energy efficiency, with for example the development of new insulating alternatives.

PGM (platinum group metal) smelting: The PGM smelting process involves the smelting of spray dried flotation concentrate to produce a Fe-Ni-Cu-based furnace matte. The matte is then converted to a Ni-Cu-based matte, which contains the PGMs. This converter matte is then treated in the base metals refinery to extract the Cu and Ni, upon which the leach residue is sent to the precious metals refinery for final separation of the PGMs.

PGM-bearing nickel-copper concentrate smelted in South Africa are mostly derived from the Merensky Reef (which has high concentrations of base metals and sulphur) and the UG2 Reef (which is rich in chromite and contains low quantities of base metal sulphides). PGM smelting has some distinct challenges as compared to copper and nickel sulphide smelting (Figure 8) [36]: Typical operating temperatures of primary copper smelting furnaces are in the 1180 – 1380°C temperature range, with matte liquidus temperatures in the range of 940 to 1125°C, while in the nickel sulphide industry slag operating temperatures vary between 1240 and 1400°C, with matte

temperatures ranging from 1150 to 1360°C [37]. Average PGM slag liquidus temperatures in primary furnaces range from 1460 to 1700°C [37], with exceptionally high matte superheats of up to 690°C [36]. The two main components in the primary PGM slags that are responsible for these high liquidus temperatures are MgO and Cr₂O₃. High concentrations of Cr₂O₃ in the slag also increase the potential for precipitation of spinel at the matte-slag interface or as build-up in the hearth [38]. Dwindling supplies of high base metals and sulphur containing Merensky concentrate have forced PGM producers to mainly use UG2 concentrate [39, 40]. The main challenge in smelting PGM concentrates from the Bushveld Complex, South Africa, is therefore the increasing chromium content of the charge [39]. Solutions to this problem include the dilution of the high chromium-containing concentrate with Mogalakwena concentrate, which originate from the Platreef ore (which is metallurgical similar to the Merensky ore [40]) and operation at deep electrode immersion and high hearth power densities [38, 41, 42].

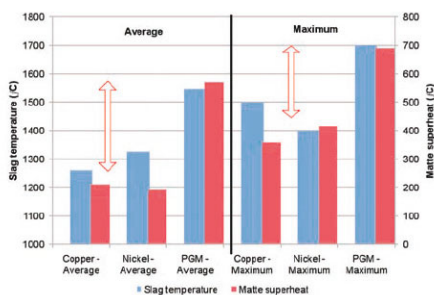


Figure 8. Comparison of operating temperatures and matte superheats across the copper, nickel, and PGM smelting industries [36]

Electric smelting of platinum concentrate started in 1969 at the Rustenburg Platinum Mines Ltd, in Rustenburg, South Africa with the commissioning of a 19.5 MVA Elkem rectangular electric furnace [43]. The sidewalls were externally water cooled, while pelletised concentrate was fed to the furnace. The furnace (27.2 m long, 8.0 m wide, 6.0 m high) was lined with magnesia bricks, while superduty fireclay bricks were used in the wall above the slag level and in the roof. Lonmin commissioned its first furnace in 1971, which was a 12.5 MW Merensky six-in-line furnace, followed by their first two 2.3 MW circular furnaces in 1982 to smelt UG2 concentrate [42].

High purity, direct bonded magnesia and magnesia-chrome bricks are typically used in the primary PGM smelter and the converter. The primary smelter slag is SiO₂ – MgO – FeO – based, but also contains some CaO, Al₂O₃ and Cr₂O₃, while a fayalitic-type slag, which contains some nickel and copper oxides, forms in the converter. The presence of high levels of FeO, and nickel and copper oxides in the converter, necessitate the presence of MgO, since MgO-based refractory can absorb substantial amounts of these oxides, without losing refractoriness. Mag-chrome and chrome-mag bricks are in general more resistant to fayalitic slags than magnesia bricks, while the chromite grains are in turn more resistant than the periclase.

Currently the largest capacity six-in-line submerged-arc furnace is the Polokwane smelter of Anglo American, which is rated at 68MW (168 MVA) and designed to treat 650 000t/a of concentrate [44]. Furnaces with such high hearth power densities, with a concentrate layer that is heat-insulating, have high sidewall heat fluxes. This necessitated the practice of using furnace sidewall cooling whereby a slag freeze lining is formed [38]. However, the use of copper coolers brings its own unique problems: Sulphur vapour, sulphur dioxide, water vapour and chlorine gas are given off during smelting [45, 46]. Sulphur vapour originates from sulphides and labile sulphur contained in the feed [45], chlorine gas from the dissociation of halides such as $KClMg(SO_4)$ and $KMgCl_3$ which can potentially be present in the feed [46], and water vapour from the moisture and chemically bound water in the feed material [47, 48]. Water vapour dissociates at high temperatures, which can then also lead to the formation hydrogen sulphide and hydrogen chloride gas [49]. High temperatures associated with the smelting process drive these gases towards a cooler place, which is in front of the copper coolers [46]. This then leads to corrosion and possible catastrophic failure of the copper coolers [44, 50]. This mechanism was confirmed by a post mortem study on the slag freeze lining and magnesia-chrome bricks removed from the concentrate-slag interface and bottom section of the slag layer. The slag freeze lining was highly porous, thereby allowing base metal sulphides and sulphur and chlorine containing gases to move through the freeze lining to the copper cooler where it sulphidised the copper, forming a non-adherent copper sulphide layer (Figure 9) [51, 52]. This corrosion mechanism has been named ‘chloride accelerated sulphidation’. Great benefits have subsequently been obtained from replacing the magnesia-chrome bricks with graphite blocks in current smelter designs. A post-mortem analysis of a graphite block, which was removed from the same PGM smelter, confirmed that graphite plays a significant role in reducing the extent of penetration and reaction of corrosive gases and base metal sulphides with the copper cooler [51, 53].

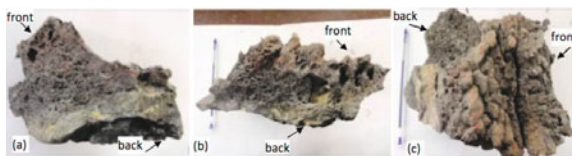


Figure 9. Freeze lining from a primary PGM smelter: (a, b) Side views; (c) Front view [52]

Magnesia-chrome and alumina-chrome bricks have been used in the matte tap hole – another area of high wear. Thermodynamic modeling [54] predicted that as the matte temperature increases the matte – tap-hole brick wear mechanism changes from solely matte penetration to penetration with accompanying chemical reaction with the brick. Laboratory-scale experiments at 1500 - 1700°C confirmed that at matte temperatures above 1500°C wear of the magnesia-chrome refractory bricks are due to extensive matte penetration, with subsequent chemical interaction between the matte and brick that caused chromium pick-up in the matte [55]. Wear of alumina-chrome brick was also characterized by extensive matte penetration. Chemical

interaction between the matte and brick occurred at temperatures above 1550°C, forming the FeCr₂O₄ spinel phase at the matte – brick interface [56].

Conclusions

Very little was known about raw materials and how their phase compositions impacted on brick-making and brick quality in the early years of refractory material production. Harbison wrote in 1866: ‘...the manufacture of brick up to this time had been purely chance work.... frequently whole kilns of brick would be...found so defective that it was unsafe to put them on the market’ [1]. Today, 150 years after Harbison’s ‘confession’, the refractories industry can pride itself on being a mature and innovative industry, with the knowledge and expertise to engineer and manufacture microstructures for specific applications with a specific set of target properties. Challenges in R&D include the development of standard in-situ refractory test methods, whereby refractory performance in service can more accurately be predicted. Exciting current research topics also include the development of bendable, flexible and self-healing refractories. These developments are all dependent on comprehensive studies on liquid – refractory interactions. - It is indeed all about the phase!

References

1. C.A. Krause, *Refractories: The Hidden Industry* (American Ceramic Society, 1987).
2. W.L. Headrick, “Toward a “Greener” Future with Advanced Refractories,” *American Ceramic Society Bulletin*, 92(7) (2013), 28-31.
3. I.C. Freestone and M.S. Tite, “Refractories in the ancient and preindustrial world,” (Proceedings of the Society Symposium on ceramic history and archeology at the 88th Annual Meeting of the American Ceramic Society, 29-30 April 1986, Chicago, Illinois), 35-63.
4. Roskill 2014, EEC environment/energy/chemicals.
5. F.R. Pyne, “Metallurgical Requirements of Refractories in Copper Smelting and Refining,” *J Amer Ceram Soc*, 6(11) (1923), 1188-1190.
6. J.G. Hemrick, “Improved refractories = energy savings,” *American Ceramic Society Bulletin*, 92(7) (2013), 32-36.
7. Caroline Miller, “*The 2015 Outlook: A Matter of Life and Debt*,” (BCA Research, 8 January 2015), page 14, http://blog.bcaresearch.com/wp-content/uploads/2015/01/Caroline_Webcast_Jan_08_2015.pdf.
8. J.P. Bennett and J.D. Smith, eds., *Fundamentals of Refractory Technology*, ed. (The American Ceramic Society, USA, 2001), 135-154.
9. C.A. Schacht, ed., *Refractories Handbook* (CRC Press, Taylor & Francis Group, Boca Raton, FL, USA, 2004), 39-77.
10. W.E. Lee and S. Zhang, “Melt Corrosion of Oxide and Oxide-Carbon refractories.” *International Materials Reviews*, 44 (3) (1999), 77-104.
11. S. Zhang and W.E. Lee, “Use of Phase Diagrams in Studies of Refractories Corrosion,” *International Materials Reviews*, 45(2) (2000), 41-58.
12. W.E. Lee, “Theory, Experiment and Practice of Slag Attack on Refractories,” *Tehran International Conference on Refractories*, 4-6 May 2004, 13-27.
13. J. Poirier et al., “Analysis and Interpretation of Refractory Microstructures in Studies of

- Corrosion Mechanisms by Liquid Oxides,” *Journal of the European Ceramic Society*, 28 (2008), 1557-1568.
14. F.H. Norton, *Refractories, 4th edition* (McGraw-Hill, New York, 1968).
 15. A. Muan and E.F. Osborn, *Phase Equilibrium among Oxides in Steelmaking* (Addison-Wesley, Reading, Massachusetts, 1965).
 16. W.D. Kingery, H.K. Bowen and D.R. Uhlman, *Introduction to Ceramics, 2nd edition* (Wiley-Interscience, New York, 1960).
 17. S.C. Carniglia and G.L. Barna, *Handbook of Industrial Refractories Technology, Principles, Types, Properties and Applications* (Noyes Publications, New York, 1992).
 18. A.M. Alper, ed., *High Temperature Oxides Part I Magnesia, Lime and Chrome Refractories*, (Academic Press, New York, 1970), 143–189.
 19. C.A. Schacht, ed., *Refractories Handbook*, (CRC Press, Taylor & Francis Group, Boca Raton, 2004), 109–149.
 20. AcerS NIST Phase Equilibria Diagrams, The American Ceramic Society.
 21. A. Yamaguchi, “Self-repairing function in the carbon-containing refractory,” *Int J Applied Ceramic Technology*, 4(6) (2007), 490–495.
 22. R. Engel, “Magnesia-Carbon Brick: a Retrospective,” *The Refractories Engineer*, (7/2013), 20-23.
 23. T. Hayashi, “Recent trends in Japanese Refractories Technology,” *Trans ISIJ*, 21 (1981), 607–617.
 24. S. Behera and R. Sarkar, “Low-Carbon Magnesia-Carbon Refractory: Use of N220 Nanocarbon Black,” *Int J Appl Ceram Technol*, 11(6) (2014), 968-976.
 25. M. Sathiyakumar et al., “Low Carbon MgO-C Refractories for Clean Steel Making in Steel Ladles,” (METEC & 2nd ESTAD 2015, Düsseldorf, 15-19 June 2015).
 26. S. Zhang and W.E. Lee, “Carbon Containing Castables: Current Status and Future Prospects,” *British Ceram Trans*, 10(1) (2002), 1-8.
 27. P. Pilate, J. Tirloq and F. Cambier, “Refractory Castables: an Overview,” *Process Engineering DKG*, 84(6) (2007), 43-49.
 28. W.E. Lee et al., “Castable refractory concretes,” *International Materials Reviews*, 46(3) (2001), 145–167.
 29. C. Parr and T.A. Bier, “The Design Fundamentals of High Technology Castables – An Understanding for Steelmakers,” (International Iron Steel Conference, Chicago, USA, 1999).
 30. C. Wöhrmeyer et al., “New Spinel Containing Calcium Aluminate Cement for Corrosion Resistant Castables,” (UNITECR2011, 30 October – 2 November 2011, Kyoto, Japan).
 31. A.P. Da Luz, M.A.L. Braulio and V.C. Pandolfelli, *Refractory Castable Engineering* (FIRE Compendium Series, Götter Verlag GmbH, Baden-Baden, Germany, 2015).
 32. M.A.L. Braulio, M. Rigaud, A. Buhr, C. Parr and V.C. Pandolfelli, “Spinel-containing alumina-based refractory castables,” *Ceramics International*, 37 (2011), 1705-1724.
 33. A. Buhr, “Refractories for Secondary Steelmaking Metallurgy,” *CN-Refractories* 6(3) (1999), 19-30.
 34. J. Poirier, “A Review: Influence of Refractories on Steel Quality,” *Metall Res Technol*, 112(4) (2015), Article 410.
 35. A. Buhr, “Trends in Clean Steel Technology and Refractories Engineering”, (UNITECR2015, 15-18 Sept, 2015, Vienna, Austria).
 36. A. Shaw et al., “Challenges and Solutions in PGM Furnace Operation: High Matte

- Temperature and Copper Cooler Corrosion,” *Journal for the Southern African Institute of Mining and Metallurgy*, 113 (2013), 251-261.
37. A.E.M. Warner et al., “JOM World Nonferrous Smelter Survey Part IV: Nickel: Sulfide,” *JOM*, April 2007, 58-72.
 38. L.R. Nelson et al., “Role of Technical Innovation on Production Delivery at the Polokwane Smelter,” (Nickel and Cobalt 2005: Challenges in Extraction and Production, Proceedings of the International Symposium on Nickel and Cobalt, Jeff Donald and Ron Shoneville, eds., 21-24 August 2005), 91-116.
 39. J. Nell, “Melting of Platinum Group Metal Concentrates in South Africa,” *Journal of the Southern African Institute of Mining and Metallurgy*, 8 (2004), 423-428.
 40. R.T. Jones, “An Overview of Southern African PGM Smelting,” (Nickel and Cobalt 2005: Challenges in Extraction and Production, Proceedings of the International Symposium on Nickel and Cobalt, Eds Jeff Donald and Ron Shoneville, 21-24 August 2005), 147-178.
 41. R.J. Hundermark et al., “The Smelting Operations of Anglo American’s Platinum Business: An Update,” (R.T. Jones and P. den Hoed, eds., Southern African Pyrometallurgy, 6-9 March 2011), 295-307.
 42. J.J. Eksteen, B. Van Beek and G.A. Bezuidenhout, “Cracking a Hard Nut: An Overview of Lonmin’s Operations Directed at Smelting of UG2-rich Concentrate Blends,” *Journal of the Southern African Institute of Mining and Metallurgy*, 111 (2011), 681-690.
 43. J.C. Mostert and P.N. Roberts, “Electric smelting at Rustenburg Platinum Mines Limited of nickel – copper concentrates containing platinum-group metals,” *JSAIMM*, 73(9) (1973), 290-299.
 44. R. Hundermark, B. de Villiers, J. Ndlovu, “Process description and short history of Polokwane smelter,” (RT Jones (Ed.), Southern African Pyrometallurgy, The Southern African Institute of Mining and Metallurgy, Johannesburg, 2006), 35-42.
 45. L. Andrews, “Base metal losses to furnace slag during processing of platinum bearing concentrates,” (Masters Thesis, University of Pretoria, South Africa, 2008).
 46. M. Hopt, E. Rossouw, “New opportunities – exhaustive monitored copper coolers for submerged arc furnaces,” *Journal of the Southern African Institute of Mining and Metallurgy*, 106 (2006) 373-378.
 47. L. Mabiza, “An overview of PGM smelting in Zimbabwe-Zimplats Operations,” (RT Jones (Ed.), Southern African Pyrometallurgy, The Southern African Institute of Mining and Metallurgy, Johannesburg, 2006), 63-75.
 48. L.C. Woollacott, R.H. Eric, “Mineral and Metal Extraction an Overview,” (The Southern African Institute of Mining and Metallurgy, Johannesburg, 1994).
 49. P. Patnik, “Handbook of Inorganic Chemicals,” (McGraw-Hill, 2003).
 50. B.M. Thethwayo and A.M. Garbers-Craig, “Laboratory Scale Investigation Into The Corrosion of Copper in a Sulphur-Containing Environment,” *Corrosion Science*, 53 (2011), 3068-3074.
 51. B.M. Thethwayo and A.M. Garbers-Craig, “Corrosion of copper coolers in PGM smelters,” (The 4th International Platinum Conference, Platinum in transition ‘Boom or Bust’, The Southern African Institute of Mining and Metallurgy, 11-14 October 2010), 187-193.
 52. B.M. Thethwayo, “Sulphidation of Copper Coolers in PGM Smelters” (MSc thesis, University of Pretoria, 2010), 21.
 53. B.M. Thethwayo and A.M. Garbers-Craig, “Interaction of Graphite with Synthetic Matte,”

(The 5th International Platinum Conference: 'A Catalyst for Change', Sun City, South Africa, 17 - 21 September 2012), 261-274.

54. J.J. Eksteen, "A Mechanistic Model to Predict Matte Temperatures During the Smelting of UG2-rich Blends of Platinum Group Metal Concentrates," *Minerals Engineering* 24 (2011), 676-687.
55. M. Lange, R. Cromarty and A.M. Garbers-Craig, "Wear of Magnesia Chrome Refractory Bricks as a Function of Matte Temperature," *Journal of the Southern African Institute of Mining and Metallurgy*, 114(4) (2014), 341-346.
56. K.K. Moalusi, "Wear of Alumina Chrome bricks as a Function of Primary PGM Matte Temperature" (BEng(Metallurgy), final year research report, University of Pretoria, 2015).

EFFECT OF SLAG IMPREGNATION ON MACROSCOPIC DEFORMATION OF BAUXITE-BASED MATERIAL

Antoine COULON¹, Emmanuel DE BILBAO¹, Rudy MICHEL¹, Marie-Laure BOUCHETOU¹,
S  verine BRASSAMIN¹, Camille GAZEAU¹, Didier ZANGHI¹, Jacques POIRIER¹

1 CNRS, CEMHTI UPR3079, Univ.Orl  ans, F-45071 Orl  ans, France

Keywords: reactive impregnation, corrosion, deformation, refractory, slag

Abstract

This work aims at studying the volume change of bauxite corroded by a molten slag. Cylindrical samples were prepared by mixing ground bauxite with slag. Optical measurement at high temperature (1450   C) of deformation with a high-resolution camera has been developed. Image processing allowed for determining the change in diameter of the sample. We showed that the deformation was induced by the precipitation of new expansive crystallised phases observed by SEM-EDS analyses. Adding pellets of the same slag upon the samples allowed to emphasize the effect of the slag amount on the size change. The change in diameter significantly increased in the impregnated area.

Introduction

Bauxite mining and industrial transformation generate wastes and by-product. A common strategy for managing the bauxite wastes and by-products is its disposal into long-term storage, despite its cost and its environmental impact. In the context of the growing scarcity of the raw material, bauxite by-products can be an important secondary mineral resource providing to know its behaviour, especially at high temperature. This motivated us to study the interaction between the bauxite and molten oxides. Corrosion mechanisms of bauxite by molten slag are well described in the literature [1-2]. The corrosion of bauxite-based [1-2] and alumina [3-5] leads to precipitation of expansive lime-alumina interlayers. The precipitation of these phases induces local strains, which can cause an inhomogeneous macroscopic change in volume of the sample. Usual dilatometers are not adapted to measure such changes in volume at high temperature because of the heterogeneity of the materials of interest and because it is not possible to add molten slag. A method consisting in measuring at room temperature the change in volume of a refractory material in contact with molten slag before and after corrosion test has already developed using a 3D coordinate measurement machine [6]. However, this methodology did not allow for characterizing in situ, namely during the test, the change in volume depending on the temperature and on the slag impregnation.

The current work deals with the first attempt to measure in situ the deformation of samples in contact with a molten slag and to relate the deformation with the thermo-chemical

transformations. In situ optical measurement of deformation has been developed to follow at high temperature the change in diameter. The experiments were performed on a sample made of bauxite aggregates mixed with reactive powder of slag. SEM-EDS analyses were carried out in order to relate the phase changes to the macroscopic deformation. In addition, pellets of slag were put on the sample to see how the slag amount could impact the size change.

Materials and methods

Sample characteristics

Bauxite aggregates were mixed with reactive slag to form cylindrical samples of 35 mm in high and 28 mm in diameter. The chemical composition of the bauxite blocks and the slag are presented in table 1. The samples were compacted under an uniaxial pressure of 16 MPa with and fired at 500 °C. Testing these samples allowed for characterizing the change in volume induced by the corrosion independently of the impregnation kinetics. Indeed the samples were assumed to be homogeneously impregnated. A second series of experiments was performed by putting slag pellets with same composition on the samples in order to highlight the effect of the amount of impregnated slag on the change in volume. In the tests performed with pellets of slag putting on the sample, the pellets weight was 3.5 % of the sample. Pellets of slag were prepared at room temperature by compacting initial powder mixture without any heat-treatment.

Table 1: Chemical composition of bauxite aggregates and reactive slag (+/- 1 wt.%)

	SiO ₂	Al ₂ O ₃	Fe ₂ O ₃	CaO	TiO ₂
Bauxite	9	60	23	5	3
Slag	6	40	14	38	2

Experimental procedure

In situ optical measurement of macroscopic deformation consists in determining the change in diameter of a cylindrical sample during a heat treatment by image post-processing. The device is composed of a furnace with a window associated with a high-resolution camera (Figure 1, a). The sample was heated up to 1450 °C during 4 h under air. The heating and cooling rates were 300 °C/h. As explained above, the tests were performed without or with pellets of slag put on the cylinder before the heating treatment. Finally, post-processing was applied to measure the evolution of the sample diameter over the time and therefore over the temperature. The sample diameter was measured throughout the height from uniformly distributed lines, represented on Figure 1.b. Relative variation of the diameter was calculated from the initial picture taken at room temperature before the heat treatment.

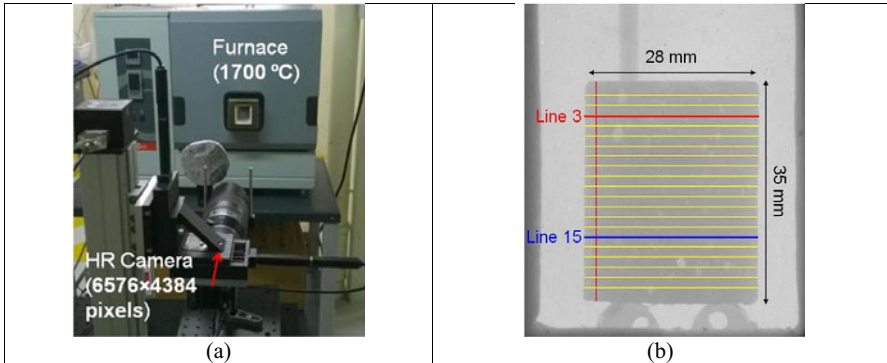


Figure 1 : Pictures of the bench test (a) and of the sample at 1450 °C (b)

Results

In situ deformation of sample alone

First, macroscopic deformation of the samples alone was measured (Figure 2).

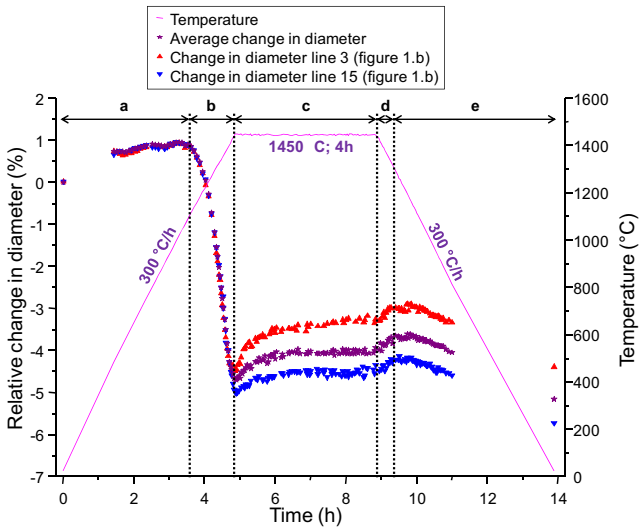


Figure 2: macroscopic deformation in time of the sample

The average change in volume of the sample was divided into 5 steps:

- $T < 1150$ °C during the heating (Figure 2, stage a): thermal expansion.

- b. $1150\text{ }^{\circ}\text{C} < T < 1445\text{ }^{\circ}\text{C}$ during the heating (Figure 2, stage b): shrinkage caused by reaction of the bauxite aggregates with the slag formerly mixed with the bauxite. The solidus and liquidus temperatures of the slag are $1140\text{ }^{\circ}\text{C}$ and $1385\text{ }^{\circ}\text{C}$ respectively determined by DSC. The change in diameter on this temperature range was equal to $- 5.7\text{ } \% \pm 0.3$.
- c. $T > 1445\text{ }^{\circ}\text{C}$ during the heating and during three first hours of the dwell (Figure 2, stage c): expansion induced by the precipitation of new expanding phases. The change in diameter on this temperature range was $+ 0.7\text{ } \% \pm 0.3$.
- d. $1250\text{ }^{\circ}\text{C} < T < 1450\text{ }^{\circ}\text{C}$ during the cooling (Figure 2, stage d): expansion due to solidification of the liquid phase. The diameter change was $+ 0.4\text{ } \% \pm 0.3$ on this temperature range.
- e. $T < 1250\text{ }^{\circ}\text{C}$ during the cooling (Figure 2, stage e): shrinkage caused by thermal expansion.

The change in diameter of the sample was varied over the height during the chemical expansion from about $+ 0.3\text{ } \% \pm 0.3$ (line 15 in the figure 2) to about $+ 1.2\text{ } \% \pm 0.3$ (line 3 in the figure 2). These differences can be explained by local heterogeneity of the sample.

In situ of sample in contact with slag

Pellets of slag was put on the sample and heated up to $1450\text{ }^{\circ}\text{C}$ for 4 hours. The slag melted completely at $1380\text{ }^{\circ}\text{C}$ and it impregnated the sample in 12 minutes (Figure 3).

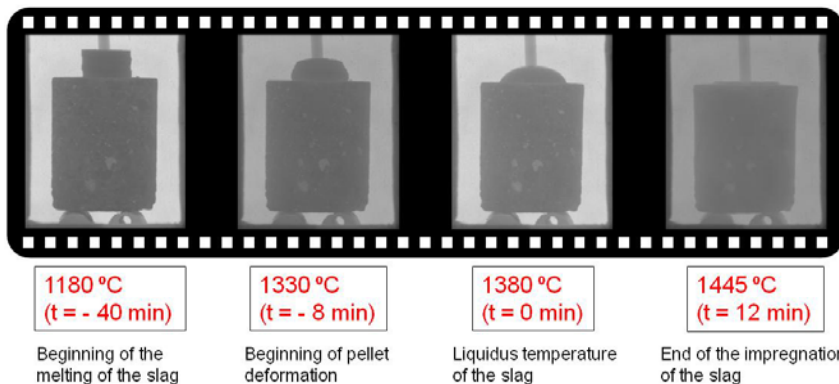


Figure 3: evolution of the sample and pellet of slag during the heat

The change in diameter of the sample with slag pellets (Figure 4) is similar to that observed on the sample alone excepted that adding slag pellets limited the sintering due to the reaction between the bauxite aggregates and the initial slag formerly mixed with the bauxite. It also led to a higher mean macroscopic expansion induced by corrosion. The average chemical expansion with the slag pellets was $1.3\text{ } \% \pm 0.3$ in diameter instead of $0.7\text{ } \% \pm 0.3$ for the sample without pellet.

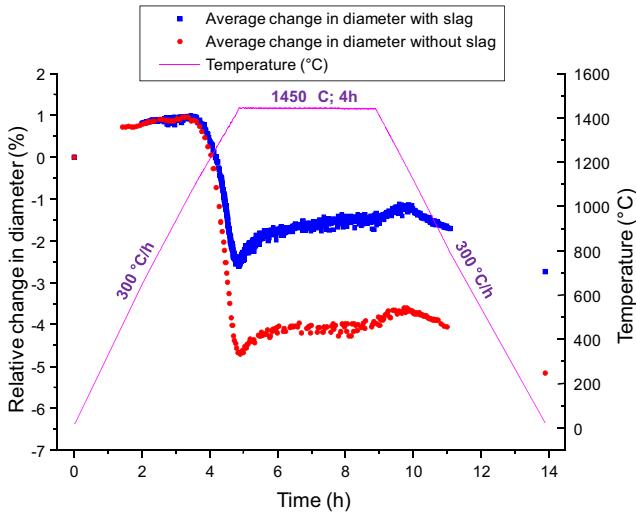


Figure 4: comparison of macroscopic deformation in time of the sample with and without liquid slag addition

In addition, measuring in situ the diameter over the high of the sample allowed for highlighting the effect of the impregnation. Indeed, it can be observed on Figure 5 that the change in diameter depends on the high. The change in diameter is less than 1.0 % in the main part of the sample up to 9 mm of its top. In the zone of the first 5 mm from the top, the material expanded more than 2.5 % in diameter. As a conclusion, the change in volume along the vertical axis of the sample and the temperature of the beginning of the chemical expansion seem to be linked to the depth of impregnation, namely to the amount of molten slag.

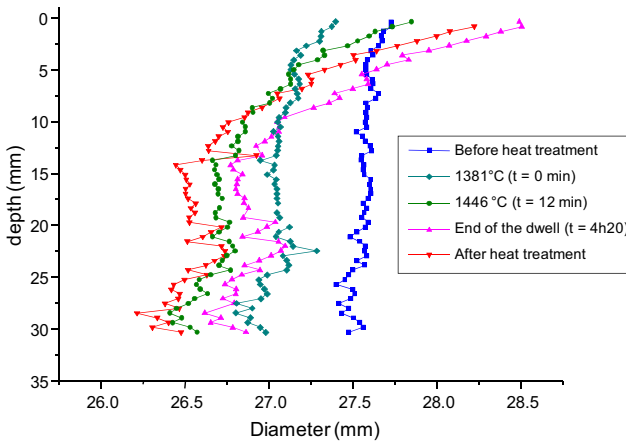


Figure 5: Diameter of the sample over the height (depth) at different temperatures

Relation between macroscopic deformation and chemical transformation

X-ray diffraction analyses and SEM-EDX were performed after heat treatment. After heat treatment, $C(A;F)_6$ [$CaO-6(Al_2O_3-Fe_2O_3)$] was the main new precipitated phase determined by X-ray diffraction. Presence of alumina, C_2AS [$2CaO-Al_2O_3-SiO_2$], CAS_2 [$CaO-Al_2O_3-2SiO_2$] and $C(A;F)_2$ [$CaO-2(Al_2O_3-Fe_2O_3)$] were also identified as minor phases.

Figure 6 shows a representative macrostructure of the sample after heat treatment. EDX performed every 30 μm following a line gave results in agreement with literature [3-5] and thermodynamic calculation using Factsage v6.4 software with FToxid database [7]. The macrostructure can be divided in 4 areas:

- The slag area whose chemical composition is closed to CAS_2 .
- The precipitation area that is composed of 2 lime-alumina solid interlayers ($C(A;F)_2$ and $C(A;F)_6$), resulting from reaction between alumina grains and molten bounding phases.
- The penetration area that constituted the border between the precipitation area and the unaffected area. This area was composed of a non reactive liquid phase poor in lime whose chemical composition is closed to CAS_2 , and two solid phases [$C(A;F)_6$ and Al_2O_3]
- The unaffected area

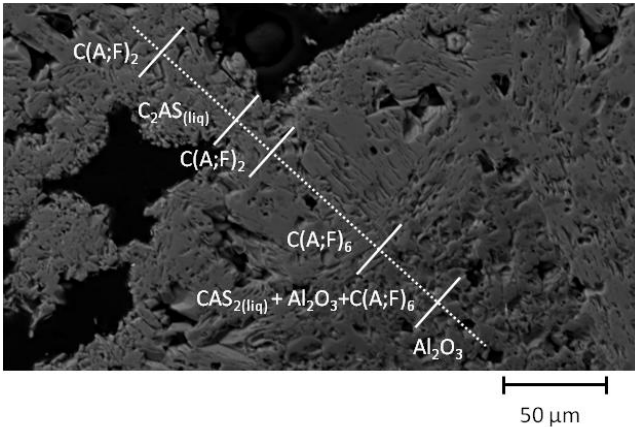


Figure 6: SEM micrograph of sample made of bauxite aggregates mixed with reactive powder of slag after heat treatment

The two new crystalline phases ($C(A;F)_2$ and $C(A;F)_6$) are expansive phases and cause the macroscopic expansion. Precipitation of $C(A;F)_6$ leads to a macroscopic expansion of 3 % and precipitation of $C(A;F)_2$ expands the volume about 24 %.

Conclusion and outlook

The change in diameter throughout a heat treatment of bauxite-based agglomerate is made by in situ optical measurement. The chemical expansion brings about a heterogeneous expansion that induces the change of the agglomerate shape. The chemical expansion is caused by reaction between a molten slag and solid phases that leads to expansive lime/alumina containing iron phases ($C(A;F)_2$ and $C(A;F)_6$). The change of the agglomerate shape is explained by the heterogeneity of the sample.

The molten slag impregnation induces an increase of the change in volume due to chemical expansion. Impregnation of the molten slag changes the chemical composition of the system that modifies the phase equilibrium. This modification promotes the precipitation of $C(A;F)_2$ phase, which is a more expansive phase than $C(A;F)_6$.

The next step will be to determine a chemical expansion coefficient by relating the deformation induced by reaction to the reaction rate.

References

- [1] J. Poirier, F. Qafssaoui, J.P. Ildefonse and M.L. Bouchetou, "Analysis and interpretation of refractory microstructures in studies of corrosion mechanisms by liquid oxides," *Journal of the European Ceramic Society*, 28 (2008), 1557-1568
- [2] E. Blond, N. Schmitt and F. Hild, "Effect of Slag Impregnation on Thermal Degradations in Refractories", *Journal of the American Ceramic Society*, 90 (2007), 154-162
- [3] E. De Bilbao, J. Poirier and M. Dombrowski, "Corrosion of high alumina refractories by Al_2O_3 -CaO slag: thermodynamic and kinetic approaches", *Metallurgical Research & Technology*, 112 (2015), 607
- [4] M. Dombrowski, "Cinétique de corrosion d'un refractaire d'alumine par les oxides liquides Al_2O_3 -CaO et Al_2O_3 -CaO- SiO_2 ," (Ph.D Thesis, Orléans University, 2015)
- [5] J.P. Guha, "Reaction chemistry in dissolution of polycrystalline alumina in lime-alumina-silica slag", *British Ceramic Transactions*, 96 (1997), 231-236
- [6] E. de Bilbao, P. Prigent, C. Mehdi-Souzani, M.-L. Bouchetou, N. Schmitt, J. Poirier and E. Blond, "Measurement of the Volume Expansion of SiC Refractories Induced by Molten Salt Corrosion". *Journal of Ceramic Science and Technology*, 4 (2013), 207-212.
- [7] C.W. Bale, E. Béliste, P. Chartrand, S.A. Decterov, G. Eriksson, K. Hack, I.H. Jung, Y.B. Kang, J. Melançon A.D. Pelton, C. Robelin, S. Petersen, "FactSage thermochemical software and databases — recent developments," *Calphad*, 33 (2009), 295-311

CORROSION RESISTANCES OF Cr-FREE REFRACTORIES TO COPPER SMELTING SLAGS

Mao Chen¹, Junhong Chen² and Baojun Zhao¹

¹The University of Queensland, Brisbane, Australia

²University of Science and Technology Beijing, Beijing, China

Keywords: Cr-free refractory, microstructure, Copper smelting slags, FactSage prediction

ABSTRACT

Appropriate selection of refractories for high temperature processes is vital to the production. Magnesite-chromite refractory has been widely used in copper making industry. However, the risk of generating high poisonous Cr⁶⁺ drives the researchers to find Cr-free refractories for copper industry.

Different materials were synthesized as raw materials of refractory in Cr-free chemical systems that are based on the MgO-Al₂O₃ system with additions of other SiO₂, TiO₂ and CaO. SEM and EPMA analyses were performed to investigate their morphologies and the homogeneities after sintering process. These refractory materials were also tested by reactions with industrial copper smelting slag under the same conditions. The corrosion resistances of different refractory materials to the slag and changes of the morphologies after the high temperature experiments were analysed and compared. The present studies will lead to the development and applications of Cr-free refractories in copper industry and reduce the potential hazards to the environment and cost of the copper production.

Introduction

Refractories play significant roles in all high temperature processes, in which refractories resist to the thermal stress, physical wear and chemical corrosions. In copper smelting process, refractories are particularly important as they experience intensive physical erosions from the strong washouts of melts (slag and matte), and extreme chemical corrosions from matte and slag penetrations and corrosive gases with high SO₂. Magnesite-chrome type bricks have been used for copper furnace linings for long time because of their good resistance to copper slag corrosions at different compositions. However, Cr³⁺ may oxidize to Cr⁶⁺ during the smelting and converting processes causing potential serious environmental problems. In addition, the fabrication of magnesite-chrome ore based refractory requires heat treatments at temperatures in excess of 1750 °C, which results in high energy consumption and greenhouse gas emissions during the manufacturing process.

Synthetics of MgO-Al₂O₃ [1], MgO-Al₂O₃-TiO₂ [2-3] and MgO-Al₂O₃-ZrO₂ [4] system materials as Cr-free refractory materials have been performed by researchers. However, limited studies were focusing on the microstructure analysis of the Cr-free refractory materials reacting with copper slags. From thermodynamic calculations [5], SiO₂, CaO and TiO₂ substantially

decrease the liquidus temperature of MgO*Al₂O₃. With the formation of the liquid phase, the sintering temperature may be decreased and the material may be denser with fewer holes. In the present study, MgO-Al₂O₃ base system with additions of SiO₂, CaO and TiO₂ respectively were chosen to investigate that: 1) whether the sintering temperature can be lowered; 2) different corrosion mechanisms through microstructure analysis. Four materials were synthesized from pure chemicals and tested with industrial copper smelting slag. The microstructures of the samples before and after the reactions with copper smelting slag were carefully analysed.

Experimental

Analytical pure chemicals were carefully weighted according to the plans (as shown in Table 1) and thoroughly mixed with water by ball mill. The mixed powders were filtrated, dried and shaped in mould. The samples were then calcined in muffle furnace. The temperatures were increased from room temperature to 1200 °C at 5 °C/min, followed by 2.5 °C/min for the temperature range between 1200 and 1580 °C, and then held at 1580 °C for 4 hours. The firing temperature was chosen at 1580 °C to have suitable amount of liquid phase formed as bonding phase in the MgO-Al₂O₃-SiO₂ and MgO-Al₂O₃-CaO systems.

Table 1. Designed compositions for synthetic materials

Sample number	Chemical system	Compositions (wt%)		
		MgO	Al ₂ O ₃	Additives
RF1	MgO-Al ₂ O ₃	28.33	71.67	0
RF2	MgO-Al ₂ O ₃ -SiO ₂	27.98	71.02	1 (SiO ₂)
RF3	MgO-Al ₂ O ₃ -CaO	27.98	71.02	1 (CaO)
RF4	MgO-Al ₂ O ₃ -TiO ₂	30.53	64.47	5 (TiO ₂)

The refractory samples were cut into 5 mm-thick pieces (ϕ 20 mm), placed in an Al₂O₃ crucible and completely surrounded by industrial copper smelting slag. The samples were heated to 1300 °C in tube furnaces and held for 2 hours in argon gas atmosphere. Detailed experimental apparatus and procedures can be found in the publications from the present authors [6]. The samples before and after reactions were sectioned, mounted and polished for examinations using Electron Probe X-Ray Microanalysis (EPMA). Typical microstructures of the samples and compositions of the phases present were measured using a JEOL JXA-8200 electron probe X-ray microanalyser with wavelength dispersive detectors. (JEOL is a trademark of Japan Electron Optics Ltd., Tokyo). An accelerating voltage of 15 KV and a probe current of 15 nA were used. The Standard used for analysis were Fe₂O₃ for Fe, CaSiO₃ for Si and Ca, CuFeS₂ for Cu and S, Al₂O₃ for Al, MgO for Mg, ZnO for Zn, PbS for Pb and TiO₂ for Ti. The Duncumb-Philibert ZAF correction procedure supplied with JEOL-8200 was applied. The average accuracy of the EPMA measurements was estimated to be within 1 weight percent.

Table 2. Composition of copper slag used in the present study

XRF	FeO	SiO ₂	Cu ₂ O	CaO	Al ₂ O ₃	MgO	S	PbO	ZnO
Copper slag	61.7	24	3.1	1	3	0.6	1.7	0.5	3.1

Results

RF1: MgO-Al₂O₃ system

It can be seen from the backscattered SEM images in Figure 1 that generally the MgO-Al₂O₃ material was well sintered, and no large crack was found in the sample. However, a large number of linked pores are still present in the sample. The compositional analyses from 20 points show that the compositions of the sample are relatively homogeneous and close to the designed one. FactSage [5] calculation predicts that the liquidus temperature and solidus temperature are 2124 °C and 1987 °C, respectively. The calcining temperature 1580 °C is lower than the solidus temperature and indicates that no liquid was formed during the sintering.

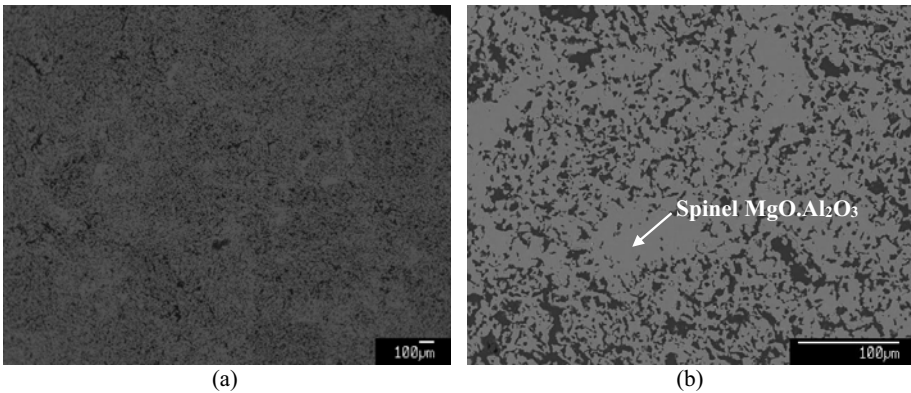


Figure 1. Backscattered SEM images of synthetic MgO-Al₂O₃ material: (a) low magnification; (b) high magnification

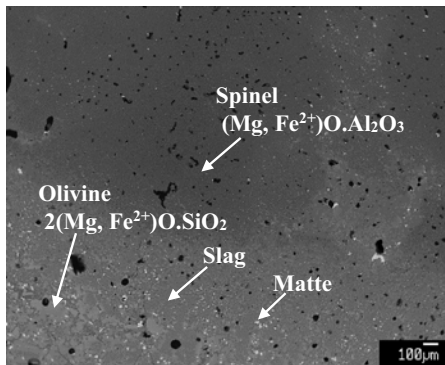


Figure 2. Backscattered SEM image of MgO-Al₂O₃ material after reacted with copper slag

The sample after reacted with copper slag is also shown in Figure 2. As it can be seen from the figure, there is no clear boundary between the synthetic material and the copper slag. The careful EPMA analysis shows that FeO has penetrated into the sample, even in the centre of the

synthetic material, and form spinel solid solution $(\text{Mg, Fe}^{2+})\text{O} \cdot (\text{Al, Fe}^{3+})_2\text{O}_3$. Matte droplets were also observed inside the refractory. EPMA measurements show that up to 13 wt% FeO can replace MgO in $\text{MgO} \cdot \text{Al}_2\text{O}_3$ spinel to form new spinel in 2 hours. The original $\text{MgO} \cdot \text{Al}_2\text{O}_3$ spinel structure was modified by copper slag, and no dense phase was formed to stop the reaction with copper slags. The $\text{MgO} \cdot \text{Al}_2\text{O}_3$ cannot be directly used as a raw material for the refractory.

RF2: $\text{MgO} \cdot \text{Al}_2\text{O}_3 \cdot \text{SiO}_2$ system

With the aim of decreasing the liquid formation temperature and testing of liquid phase as a bonding material, the $\text{MgO} \cdot \text{Al}_2\text{O}_3 \cdot \text{SiO}_2$ material was prepared. The liquid formation temperature of the $\text{MgO} \cdot \text{Al}_2\text{O}_3 \cdot \text{SiO}_2$ material with 1 wt% SiO_2 is predicted by FactSage [5] to be 1384 °C, which is 600 degrees lower than the SiO_2 -free material, and the liquidus temperature is slightly decreased to 2113 °C [5]. However, the SEM analysis of the synthesized $\text{MgO} \cdot \text{Al}_2\text{O}_3 \cdot \text{SiO}_2$ material shows that cracks were formed during the sintering process (Figure 3a). It can be seen from Figure 3b that two phases are present in the sample including $\text{MgO} \cdot \text{Al}_2\text{O}_3$ spinel and liquid phase which has ~20 wt% SiO_2 . Moreover, pores are almost isolated stopping the penetration of gas and liquid.

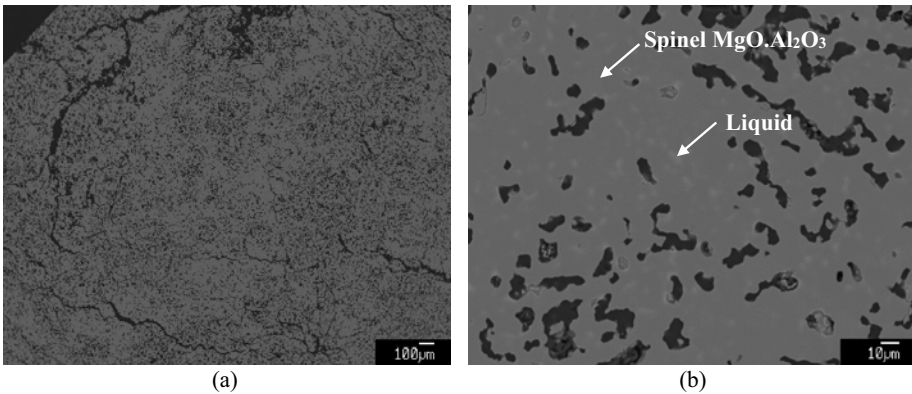


Figure 3. Backscattered SEM images of synthesized $\text{MgO} \cdot \text{Al}_2\text{O}_3 \cdot \text{SiO}_2$ material: (a) small magnification; (b) large magnification

The SEM image of $\text{MgO} \cdot \text{Al}_2\text{O}_3 \cdot \text{SiO}_2$ material after reacted with copper slag is shown in Figure 4. It can be seen that the synthetic material and copper slag do not have clear boundary indicating the copper slag has penetrated into the sample. Matte droplets can also be found to be distributed inside the synthetic material.

Figures 3 and 4 show that although the addition of SiO_2 can significantly decrease the liquid formation temperature and produce dense refractory material, no dense layer can be formed at the interface between the refractory and copper slag.

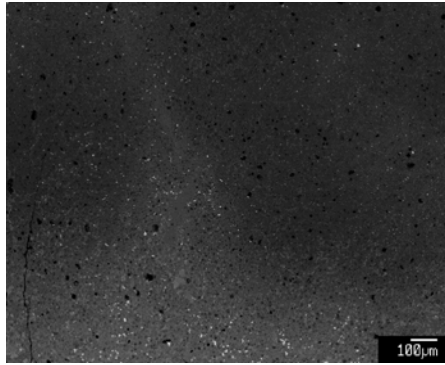


Figure 4. Backscattered SEM images of MgO-Al₂O₃-SiO₂ material after reacted with copper slag

RF3: MgO-Al₂O₃-CaO system

Similar to SiO₂, CaO was added in to MgO-Al₂O₃ system to form liquid phase at a relative lower temperature. The liquid formation temperature and liquidus temperature were predicted to be 1349 °C and 2111 °C [5] with addition of 1 wt% CaO to the MgO-Al₂O₃ system. At 1580 °C, it was predicted that approximately 3 wt% liquid was formed. Figure 5 shows the micro-structures of the sample heated at 1580 °C. No crack was formed and pore fraction seems to be much lower than that in MgO-Al₂O₃-SiO₂ material in Figure 5(a). More liquid (light areas in Figure 5(b)) can be seen in the microstructure of the sample. It can be concluded that CaO can produce more liquid phase as a binding material than SiO₂ and the sample is more densified compared to SiO₂-containing material.

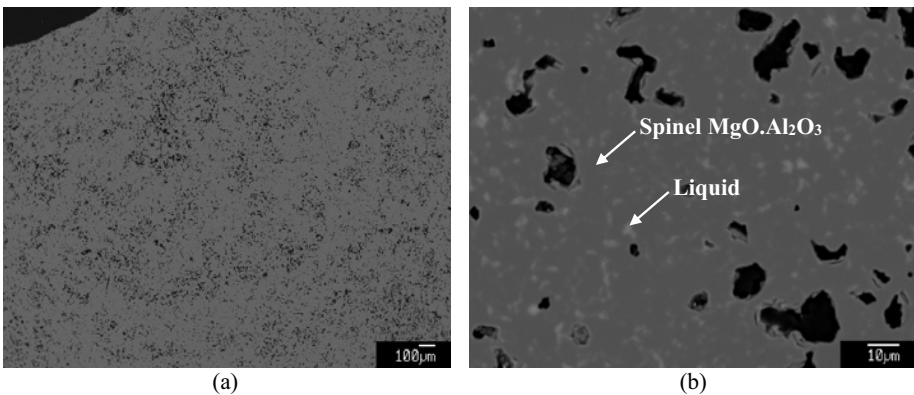


Figure 5. Backscattered SEM images of synthesized MgO-Al₂O₃-CaO material: (a) low magnification; (b) high magnification.

The microstructure of the MgO-Al₂O₃-CaO material after reacted with copper slags is shown in Figure 6 (a). Copper slag and matte droplets did not penetrate into the refractory after two hours'

reaction. Line analysis by EPMA was carried out in the sample near the interface as shown in Figure 6(a). The step of the line analysis was 30 μm and the results are shown in Figure 6(b). It can be seen that after 60 – 90 μm from the surface, the concentration of FeO sharply decreases to 0, the concentrations of Al_2O_3 and MgO remain relatively stable after 90 μm and their concentrations are closed to the original ones before reaction.

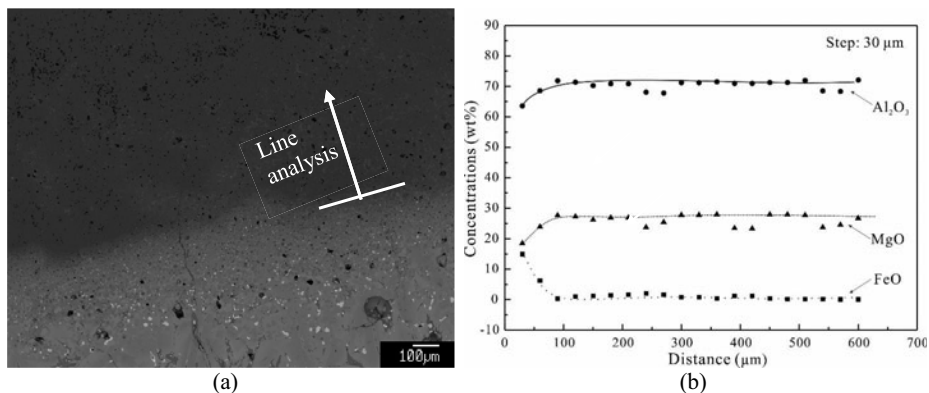


Figure 6. Backscattered SEM image of MgO- Al_2O_3 -CaO material after reacted with copper slag (a) and EPMA line analysis (b)

It seems that MgO- Al_2O_3 -CaO material may be potentially used as a refractory where the penetration of copper slag and matte is not significant. Only a thin layer of the material in contact with copper slags were reacted and the bulk remains to be compact.

RF4: MgO- Al_2O_3 -TiO₂ system

The previous test with copper slags shows that the MgO- Al_2O_3 -TiO₂ refractory has a good slag corrosion resistance and may be a potential substitution of magnesia chromite refractory [2]. Figure 7(a) shows the SEM image of the synthesized MgO- Al_2O_3 -TiO₂ material in low magnification. Holes have been developed to cracks, which can be found all over the samples. EPMA analysis shows that 1.5 wt% TiO₂ was dissolved in MgO. Al_2O_3 spinel, and the rest of TiO₂ formed MgO. \cdot 2TiO₂ in the sample. FactSage [5] predicts that with 5 wt% addition of TiO₂, the liquid formation temperature is decreased to 1591 °C and the liquidus temperature is 2094 °C. The MgO. \cdot 2TiO₂ crystals hinders the sintering process and separate the MgO. Al_2O_3 crystals as seen in Figure 7(b), which agrees with the microstructures reported by Naghizadeh *et al.* [7].

A clear boundary layer can be seen in the microstructure of MgO- Al_2O_3 -TiO₂ material reacted with copper slags as shown in Figure 8(a). The dense layer fully covers the synthetic material to prevent further penetration of the slag. Detailed EPMA analysis shows that the boundary layer is mainly formed by the (Mg,Fe²⁺)O.(Al₂O₃,TiO₂) spinel crystals with the untransformed MgO. Al_2O_3 crystals randomly distributed. SiO₂ was not detected in boundary layer. The compositions inside the refractory are close to the original compositions and no FeO was found in the MgO- Al_2O_3 spinel.

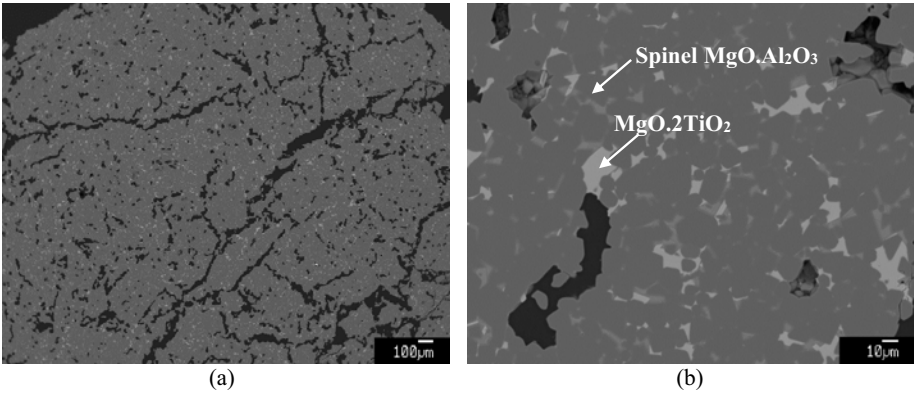


Figure 7. Backscattered SEM images of synthesized $\text{MgO-Al}_2\text{O}_3\text{-TiO}_2$ material: (a) small magnification; (b) large magnification.

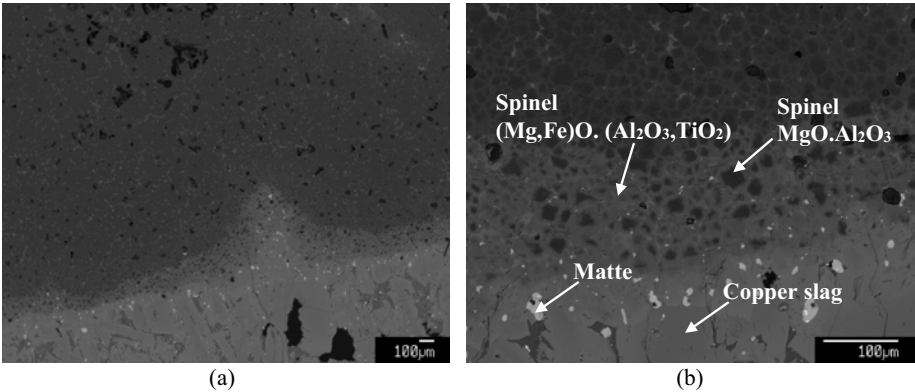


Figure 8. Backscattered SEM images of synthetic $\text{MgO-Al}_2\text{O}_3\text{-TiO}_2$ material after reacted with copper slag: (a) low magnification; (b) high magnification.

The EPMA analysis demonstrates that the dense boundary layer well stops the copper slag from further reacting with the refractory. Less pores in the synthetic materials were observed in the areas close to the copper slags compared to the area inside the sample, and no obvious crack can be seen from the microstructure shown in Figure 8(a). TiO_2 and FeO were reacted with the refractory and formed spinel composite crystals, which enlarge the spinel crystal and block the tunnel for transporting copper slag into the sample. The present investigations show that $\text{MgO-Al}_2\text{O}_3\text{-TiO}_2$ system material may be used as a potential refractory material, and the optimum TiO_2 concentration and sintering temperature should be investigated to have a better refractory material for copper smelting slags.

Conclusions

The investigations of refractory materials in MgO-Al₂O₃, MgO-Al₂O₃-SiO₂, MgO-Al₂O₃-CaO, and MgO-Al₂O₃-TiO₂ systems show that the additions of SiO₂ and CaO can significantly reduce the liquid formation temperatures. Liquid phase was found in the systems MgO-Al₂O₃-SiO₂ and MgO-Al₂O₃-CaO compared to the original synthetic MgO-Al₂O₃ material. A dense layer forms between the refractory and copper slag can stop the copper slag penetration into the refractory and protect the refractory. Such layer was not formed in the reactions with MgO-Al₂O₃ and MgO-Al₂O₃-SiO₂ materials. Although there is no clear boundary formed in the MgO-Al₂O₃-CaO material after reacting with copper slag, the addition of CaO indeed slows down the reactions and penetrations of copper slags and matte within 2 hours' reaction. The addition of 5 wt% TiO₂ can form a dense (Mg,Fe)O.(Al₂O₃,TiO₂) spinel composite layer when the refractory reacts with copper smelting slag.

The present studies of different synthetic refractory materials from pure chemicals are the first stage research within a comprehensive program to develop novel Cr-free refractory. The microstructure analysis of the refractory materials before and after reacting with copper slags helps to get more insight into the mechanism of refractory failure and corrosion. More experimental work will be carried out for the development of Cr-free refractory at reduced energy consumptions.

Acknowledgements

The authors would like to thanks Ms Jie Yu for high temperature experiments and Zibo City Luzhong Refractory Co Ltd for providing the refractory materials.

References

1. C. Aksel, B. Rand, F.L. Riley, and P.D. Warren, "Mechanical Properties of Magnesia-spinel Composites," *Journal of the European Ceramic Society*, 22(2002), 747-754.
2. M. Zou, M. Jiang, and Y. Li, "Effect of TiO₂ addition on sintering and microstructure of magnesia-alumina-tinania refractories," *Refractories*, 41(2007), 409-412.
3. L. Xu, C. Wang, W. Zhu, X. Ren, F. Gao, Y. Wang, Y. Ye, and L. Yuan, "Research on magnesia alumina titania brick for copper smelting furnace," *Refractories*, 46(2012), 347-349.
4. R. Ceylantekin and C. Aksel, "Improvements on the Mechanical Properties and Thermal Shock Behaviours of MgO-spinel Composite Refractories by ZrO₂ Incorporation," *Ceramics International*, 38 (2012), 995-1002.
5. C. Bale, E. Bélisle, P. Chartrand, S. Degterov, G. Eriksson, K. Hack, I. H. Jung, Y. B. Kang, J. Melançon, and A. Pelton, "FactSage thermochemical software and databases--recent developments," *Calphad*, 33(2009), 295-311.
6. M. Chen and B. Zhao, Phase Equilibrium Studies of "Cu₂O"-SiO₂-Al₂O₃ system in Equilibrium with Metallic Copper," *Journal of American Ceramic Society*, 96(2013), 3631-3636.
7. R. Naghizadeh, H.R. Razaie, and F. Golestani-Fard, "Effect of TiO₂ on phase evolution and microstructure of MgAl₂O₄ spinel in different atmospheres," *Ceramics International*, 37(2011), 349-354.

GASIFICATION SLAG AND THE MECHANISMS BY WHICH PHOSPHOROUS ADDITIONS REDUCE SLAG WEAR AND CORROSION IN HIGH Cr₂O₃ REFRACTORIES

James Bennett¹, Anna Nakano¹, Jinichiro Nakano^{1,2}, and Hugh Thomas¹

¹ US Department of Energy National Energy Technology Laboratory, 1450 Queen Ave., Albany, OR 97321 USA

²AECOM, P.O. Box 1959, Albany, OR 97321 USA

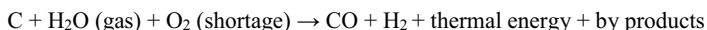
Keywords: Gasification, Refractory Wear, High Chrome Oxide

Abstract

Gasification is a high-temperature/high-pressure process that converts carbonaceous materials such as coal and/or petcoke into CO and H₂, feedstock materials used in power generation and chemical production. Gasification is considered an important technology because of its high process efficiency and the ability to capture environmental pollutants such as CO₂, SO₃ and Hg. Ash impurities in the carbon feedstock materials melt and coalesce during gasification (1325-1575°C), becoming slag that attaches to and flows down the gasifier sidewall, corroding and eroding the high Cr₂O₃ refractory liner used to protect the gasification chamber. Phosphate additions to high Cr₂O₃ refractory have been found to alter slag/refractory interactions and dramatically reduce refractory wear by the following mechanisms: a) spinel formation, b) slag chemistry changes, c) two phase liquid formation, and d) oxidation state changes. The mechanisms and how they work together to impact material wear/corrosion will be discussed.

Introduction

Gasification is a non-equilibrium process used commercially to convert high carbon materials (typically coal and/or petcoke) and water under a shortage of oxygen at high temperature and pressure into hydrogen and carbon monoxide gas (called synthesis gas or the shortened version, syngas) according to the simplified reaction:



By-products generated during gasification include hydrocarbons (primarily CH₄), minority gases (such as H₂S + CO₂), excess C as char, and ash/slag generated from minerals and organo-metallic impurities in the carbon feedstock. Air cooled entrained bed slagging gasifiers operate at temperatures between about 1325-1575°C and pressures between 2.1-6.1 MPa; consuming as much as 100 or more tons/hour of carbon feedstock. Coal and petcoke used as carbon feedstock have varying quantities of impurities depending on their sources, with coal averaging about 10 wt pct ash and petcoke about 1 wt pct. These impurities oxidize, melt, and/or coalesce to form molten slag during gasification. Slag chemistry is dependent on the carbon source, as previously described [1] and shown in Table I. When slag particles encounter the gasifier sidewall used to contain the gasification process, they typically adhere and flow down it, causing wear by

corrosion, spalling, and sometimes abrasion; as shown in Figure 1. Several types of refractory wear have been observed in gasifiers, which is shown in Figure 2. Three types are predominate; spalling, chemical dissolution, and abrasion. Abrasive wear is caused by carbon feedstock, additives, char (from carbon feedstock gasification) and/or slag particulates impacting the gasifier sidewall. It is a function of their velocity, and varies from location to location in the gasifier. Slag/refractory interactions are responsible for the two remaining types of wear - spalling and chemical dissolution of the refractory (examples shown in Figure 1). The impact of spalling and chemical dissolution wear on refractory materials is different, with a slow and predictable wear caused by chemical dissolution, and a sudden and unpredictable wear caused by structural spalling. Structural spalling is initiated by slag wetting and penetrating the high-porosity refractory, and is exacerbated by thermal cycling. The impact of refractory wear by chemical dissolution and spalling was illustrated by Bakker [2], who showed that chemical dissolution was a slow and steady wear, while spalling removed large portions of refractory at irregular intervals. A hypothetical example of these wear mechanisms is shown in Figure 3.

Table I. The average chemistry of major impurities found in Eastern U.S. coal and petcoke compiled by NETL from various sources [1]. Listings are as wt pct oxides.

Compound	Avg Coal Chemistry [1] (wt pct +/- std dev)	Avg. Petcoke Chemistry [1] (wt pct +/- std dev)
SiO ₂	43.6 +/- 16.4	14.1 +/- 8.7
Al ₂ O ₃	25.2 +/- 10.2	4.8 +/- 2.8
Fe ₂ O ₃	17.0 +/- 11.2	7.2 +/- 9.3
CaO	5.8 +/- 6.6	5.4 +/- 3.8
MgO	1.2 +/- 1.1	1.0 +/- 1.6
K ₂ O	1.4 +/- 0.7	0.5 +/- 0.4
Na ₂ O	0.9 +/- 0.6	0.8 +/- 0.8
TiO ₂	1.4 +/- 0.8	0.3 +/- 0.2
NiO	ND	8.4 +/- 3.2
V ₂ O ₅	ND	57.0 +/- 19.5

ND = Not Determined

The refractory materials used to line a gasification reaction chamber (Figure 1) can be divided into the four general classes of high chrome oxide compositions listed in Table II. Patented or proprietary additives are often made to the refractory compositions with the goal of reducing wear by limiting refractory dissolution in slag or by limiting slag penetration into the refractory.

Table II. Chemical and physical properties of the major types of refractories used in gasifiers (data from manufacturers' product data sheets)

Property		Refractory Type			
		A	B	C	D
Chemistry (wt pct)	Cr ₂ O ₃	90.1	87.0	81.0	92.0
	Al ₂ O ₃	9.3	3.0	0.4	4.7
	ZrO ₂	NL	6.5	NL	NL
	MgO	NL	NL	17.0	NL
	P ₂ O ₅	NL	NL	NL	3.3
Porosity (pct)		14.8	16.5	12.0	15.0

NL = Not Listed

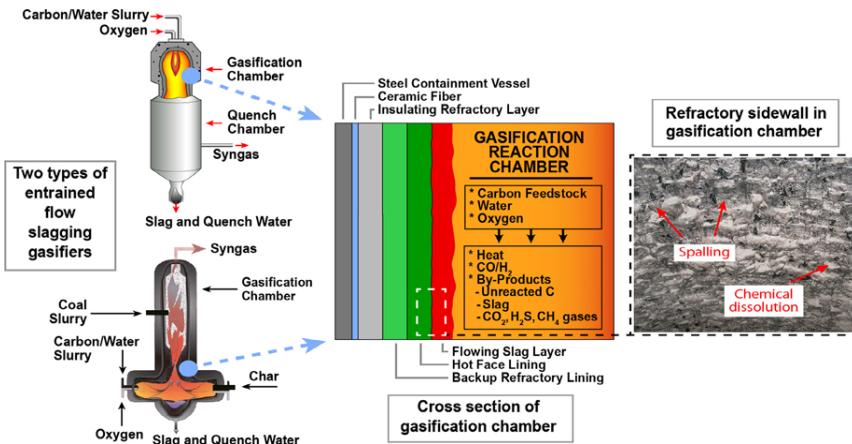


Figure 1. Two types of entrained flow slagging gasifiers with typical sidewall construction and wear patterns occurring on the refractory liner.

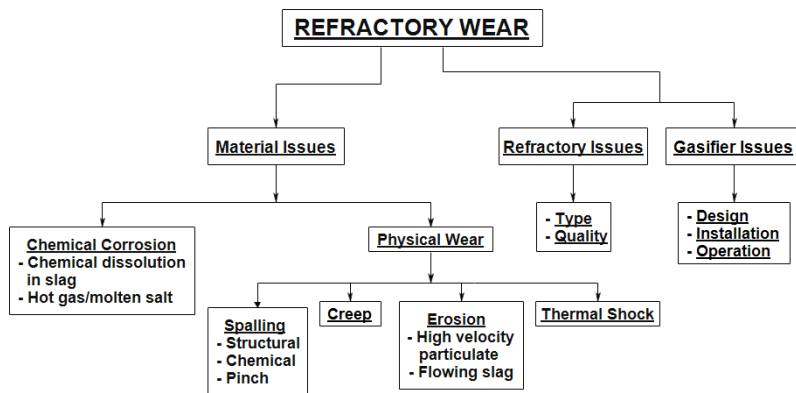


Figure 2. Types of refractory wear occurring in entrained flow slagging gasifiers.

A number of wear mechanisms have been proposed in high chrome oxide refractories to explain their superior performance over other liner materials in slagging gasifiers, with over 70 wt pct Cr_2O_3 proposed as a minimum amount necessary for adequate lining life [2]. In commercial service, it has been noted that phosphate additions to high chrome oxide refractories provide additional wear resistance, with improvements in service life of 50 pct or more observed in some commercial applications. The wear mechanisms occurring in high chrome oxide refractories with/without phosphate additions will be discussed in this paper, and include the following: a) spinel formation, b) slag chemistry changes, c) two phase liquid formation, and d) oxidation state

changes. Of those listed, spinel formation and slag chemistry changes occur in traditional refractory liners, while all four are thought to occur in materials with phosphate additions.

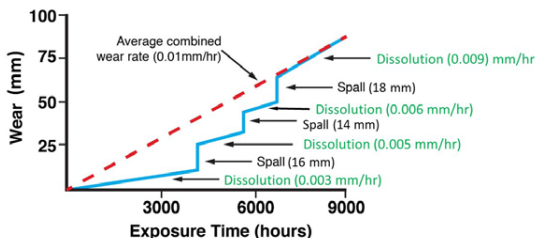


Figure 3. Hypothetical slag wear caused by spalling and dissolution of the refractory sidewall. Note spalling wear occurs as isolated incidents, while chemical dissolution occurs gradually over time [2].

Mechanisms Reducing Refractory Wear

As illustrated in Figure 2, a number of wear types are known to occur in gasifiers. The two mechanisms accounting for the greatest amount of wear, structural spalling and chemical dissolution, are shown in Figure 4. Refractory wear is influenced by the type of liner material and gasification variables including: slag composition and quantity, gasification temperature, oxygen partial pressure, carbon feedstock throughput, and gasification system cycling. The types of refractories used in gasification are listed in Table II. All are high in chrome oxide, and are based on research indicating high chrome oxide content in a refractory was necessary for sustained service life in a gasifier environment [2]. The different mechanisms thought to improve refractory performance (spinel formation, slag chemistry changes, two phase liquid formation, and oxidation state changes) are discussed individually.

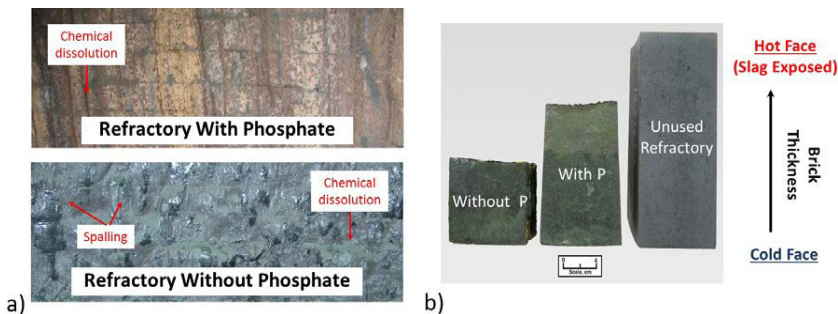


Figure 4. Spalling and chemical dissolution wear occurring in traditional refractory materials after gasifier service. a) High chrome oxide gasifier liner with/without phosphorous additions after 3 years of service, and b) side profile of refractory brick from a test panel with/without phosphorous additions after 237 days commercial service exposed to a coal slag.

a) Spinel formation

The high chrome oxide grains in gasifier refractories interact with oxides in the gasifier slag to form a complex layer structure at the refractory/slag interface, as shown in Figure 5. The $(Cr,Al)_2O_3$ refractory grain (pt 4) interacts with surface slag (pt 1) to form a solid solution zone of $(Fe,Mg)(Al,Cr)_2O_4$ as illustrated by pt 2 (composition tends toward $FeAl_2O_4$). This zone forms at the outer surface of the refractory, which is thermodynamically caused by the underlying zone of $(Fe,Mg)(Cr,Al)_2O_4$ solid solution formed at the refractory/slag interface (pt 3 – composition tends towards $FeCr_2O_4$). In general, slag oxides of Al, Fe, and/or Mg interact with $(Cr,Al)_2O_3$ grains, resulting in the two thermodynamically stable solid solution zones (pts 2 and 3) known to reduce refractory wear by chemical dissolution [3]. Note that the refractory/slag interactions alter the chemistry of slag penetrating the refractory pores, as shown in chemistry differences between pt 5 (pore slag) vs pt 1 (surface slag). It is thought that if zone 3 reaches some maximum thickness, thought to be between 20 and 50 microns, expansion differences with the underlying refractory grain and the newly created spinel result in chemical spalling, limiting the spinel layer thickness.

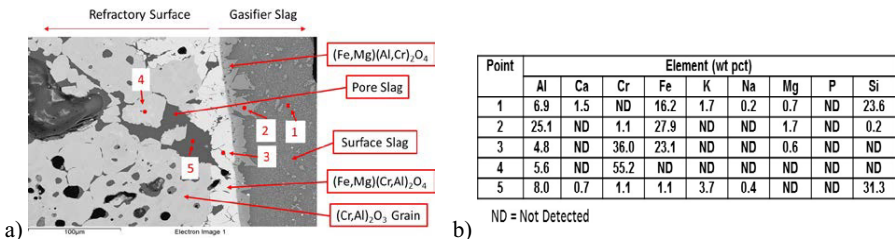


Figure 5. Surface microstructure and chemistry at the slag/refractory interface of a high chrome containing refractory with no phosphate additions determined using the SEM (in backscatter mode) and WDX. a) is the refractory/slag interface, and b) is WDX chemistry of different points indicated in image “a)”. Note that oxygen and minor elements present in low quantities are not listed and that the data has not been normalized.

b) Slag chemistry changes

As noted in the “spinel formation” discussion, changes in the slag chemistry occur as it penetrates pores of the refractory and interactions occur at the slag/refractory interface. Those changes, shown in Figure 5, result from $(Cr,Al)_2O_3$ refractory grain/surface slag interactions, causing a reduction in slag Fe and an increase in Si content in pores (pt. 5). Continual interactions occur between slag iron oxide and chrome oxide in the refractory grain leading to the formation of a $(Fe,Mg)(Cr,Al)_2O_4$ solid solution (tending towards $FeCr_2O_4$). The depletion of Fe from the slag increases Si content in it. The surface and pore slag chemistry changes are illustrated in the WDX chemistry of pts 1 and 5 of Figure 5, where relative Si increased from 23.6 to 31.3 wt pct in pores vs the surface slag, while Fe decreased from 16.2 to 1.1 wt pct.

Slag chemistry changes impact slag viscosity and its ability to flow within refractory pores. Version 7.0 of FactSageTM, a thermodynamic modelling program, and the database “Melts” were used to predict slag viscosity at 1500°C for pore and surface slags for the different Fe oxidation states and the different slag chemistries listed in Figure 5. Those calculations, presented in Table III, are for slag chemistries with Fe valence states of +2 and +3. In reality, the majority of slag in

a commercial gasifier using traditions high chrome oxide refractories (i.e. non-phosphorus containing) would contain Fe in the +2 state. For the Fe in the +2 state, a theoretical viscosity of 7.6 Pa.s was predicted for the surface slag, while a value of 2570 Pa.s was predicted for the pore slag. Differences may exist in the slag viscosities if slag Fe in the +3 state is present (as Fe₂O₃), a condition that may be caused by phosphate additions to the refractory, which will be discussed later.

Table III. Viscosities at 1500°C of pore and surface slag chemistries listed in Figure 5 b as predicted by version 7.0 of FactSage™ (version 7.0, database “Melts”) if all Fe is present as FeO or as Fe₂O₃.

Slag Location	Viscosity (Pa.s) - Fe as FeO	Viscosity (Pa.s) - Fe as Fe ₂ O ₃
Surface	7.6	14
Pore	2,570	2,510

Note that the temperature going from the hot face to the cold face within a given refractory material, along with the refractory chemistry, also impact slag penetration depth. The temperature drop, depending on the thickness of the brick, can range between 20 to 5°C/cm, with thinner linings having a greater temperature drop per unit distance, but also having a higher cold face temperature than thicker linings.

c) Two phase liquid formation

Pore slag in refractories without phosphate additions exist primarily as a single liquid phase versus a complex multiphase structure that exists within refractory pores containing phosphorous additions. Figure 6 shows pore slag adjacent to a chrome oxide grain about 0.5 mm from the slag/refractory interface in a phosphorous containing high chrome oxide refractory. This sample, also shown in Figure 4 b, had 237 days of coal slag exposure in a commercial gasifier. Microstructure, chemical, and crystalline phase analysis of the sample was conducted using TEM. Note the fine size (less than 50 nm) and the wide distribution of a spherical particles rich in P, Al, Fe, Ca, and Mg in the pore slag. Only two crystalline phases were identified using electron diffraction in the spherical particles, AlPO₄ and hexagonal FeS. The presence of the spherical phases and the change in bulk pore slag chemistry caused by a reduction in Al, Fe, Ca, and Mg would cause overall pore slag viscosity to increase (thicken), further limiting its penetration into the refractory versus slag chemistry changes alone.

d) Oxidation state changes

The temperature, oxygen partial pressure, and melt chemistry in a gasification chamber impact the oxidation state of some phases. Two elements common in coal and petcoke carbon feedstock, V and Fe, are most sensitive to environmental changes, and can exist in multiple valance states depending on the gasification environment. Iron can be present as FeO, Fe₂O₃, and/or Fe₃O₄; while V can exist as VO₂, V₂O₃, V₂O₅, or other possible states. Usually the oxidation state is determined by reduction reactions in the gasification chamber, but in phosphate-containing high chrome oxide refractories, a different oxidation state can exist in the infiltrated refractory than in the gasifier. Oxygen can be released and maintained under the slag covering in the gasifier, changing (increasing) the partial pressure in refractory material at that location. The O₂ release occurs according to the following reaction: 4AlPO₄(s) ↔ 2Al₂O₃(s) + 2O₂(g) + (P₂O₃)₂(g); creating a stable higher oxygen content locally. This reaction has been

described previously [4], and is being studied to understand its impact on slag phase valance and viscosity, and on refractory wear.

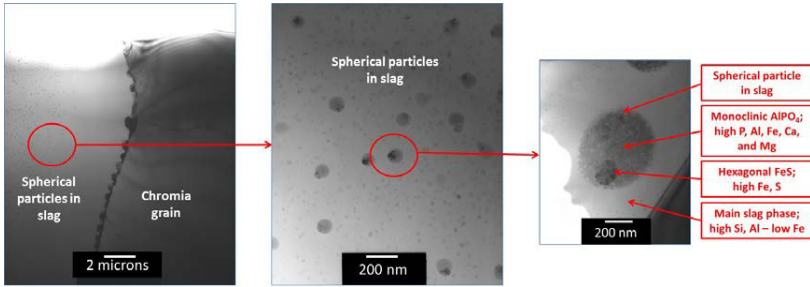


Figure 6. TEM images indicating a complex phase microstructure present in high chrome oxide pore slag with phosphate additions. The sample was exposed to slag in a commercial gasifier, and are shown in Figure 4 b. The spherical slag particles are high in Al, Fe, Ca, and Mg; while the bulk slag has become higher in Si and Al, and lower in Fe.

The impact of the multiple wear mechanisms (spinel formation, slag chemistry changes, two phase liquid formation, and oxidation state changes) is to reduce refractory wear; which have shown the greatest reductions in the high chrome oxide refractory wear when refractories contain phosphate additions (Figure 4 b). Even though sample exposures were the same for the refractories with/without phosphate additions, refractory material with phosphate additions had about 100 mm in thickness remaining on removal from the gasifier, while the refractory without phosphate additions was estimated to be about 60 mm in thickness. Slag penetration into samples shown in Fig 4 was measured by Si migration from the refractory/slag interface using SEM-WDX, and is shown in Figure 7. Phosphate additions resulted in significantly less penetration in Figure 7 b (phosphate additions) versus no phosphate additions (Figure 7 a), resulting in additional wear improvements. It is thought that two phase liquid formation and oxidation state changes caused by phosphates play a role in those additional wear improvements.

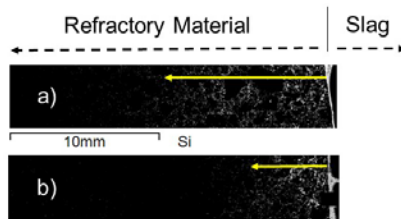


Figure 7 – Penetration of coal slag into a high chrome oxide refractory test panel of brick with/without phosphorous additions after 237 days of commercial service as measured by WDX using the SEM (samples also shown in Figure 4 b). The arrow indicates the maximum depth of Si penetration going from the exposed hot face (gasification chamber slag exposure) to the cold face on: a) refractory composition without phosphate additions, and b) refractory composition with phosphate additions.

Conclusions

Gasification is a high-temperature/high-pressure/reducing reaction converting high carbon materials such as coal and/or petcoke into CO and H₂ used in power generation and chemical production. Impurities in the carbon feedstock become ash that melt at the high temperatures of entrained bed slagging gasification (1325-1575°C), causing wear of the high chrome oxide gasifier lining protecting the gasification chamber. Refractory wear originates from many causes, with chemical dissolution and spalling being the primary ones. The following are mechanisms that reduce wear in the high chrome oxide refractories with/without phosphate additions: spinel formation, slag chemistry changes, two phase liquid formation, and oxidation state changes. A complex relationship exists between temperature, oxygen partial pressure, slag composition, and refractory composition in high chrome oxide refractories with/without phosphate additions impacting wear.

Acknowledgement

This technical effort was performed in support of the National Energy Technology Laboratory's ongoing research under the RES contract DE-FE0004000. This research was supported in part by an appointment to the National Energy Technology Laboratory Research Participation Program, sponsored by the U.S. Department of Energy and administered by the Oak Ridge Institute for Science and Education.

References

1. J.P. Bennett et al, "Microstructure and Corrosion of Phosphate Containing Cr₂O₃ Gasifier Refractories", proceedings of Corrosion 2015, Dallas, TX, Mar. 15-19, 2015.
2. W.T. Bakker, "Refractories for Present and Future Electric Power Plants," Key Engineering Materials, Trans Tech Publications, (1993), Vol. 88, pp. 41-70.
3. J.P. Bennett and K-S. Kwong, "Failure Mechanisms in High Chrome Oxide Gasifier Refractories", Met. and Mat. Trans. A, V. 42 (2011), no. 4; p. 888-914.
4. J.P. Bennett et al, "Impact of Temperature and Oxygen Partial Pressure on Aluminum Phosphate in High Chrome Oxide Refractories," proceedings of CIMTEC 2014, Montecatini Terme, Italy, June 8-13, 2014.

DISCLAIMER: "This report was prepared as an account of work sponsored by an agency of the United States Government. Neither the United States Government nor any agency thereof, nor any of their employees, makes any warranty, express or implied, or assumes any legal liability or responsibility for the accuracy, completeness, or usefulness of any information, apparatus, product, or process disclosed, or represents that its use would not infringe privately owned rights. Reference herein to any specific commercial product, process, or service by trade name, trademark, manufacturer, or otherwise does not necessarily constitute or imply its endorsement, recommendation, or favoring by the United States Government or any agency thereof. The views and opinions of authors expressed herein do not necessarily state or reflect those of the United States Government or any agency thereof."

**ADVANCES IN MOLTEN
SLAGS, FLUXES, AND SALTS:**

Proceedings of



**Additional Technical
Papers**

A HIGH TEMPERATURE DOUBLE KNUDSEN CELL MASS SPECTROMETRY STUDY OF GAS SPECIES EVOLVED FROM COAL-PETCOKE MIXED FEEDSTOCK SLAGS

Jinichiro Nakano^{1,2}, Takashi Nagai³, James Bennett¹, Anna Nakano¹, and Kazuki Morita⁴

¹ U.S. Department of Energy National Energy Technology Laboratory, 1450 Queen Ave., Albany, OR 97321 USA

² AECOM, P.O. Box 1959, Albany, OR 97321 USA

³ Department of Mechanical Science and Engineering, Chiba Institute of Technology, 2-17-1 Tsudanuma, Narashino, Chiba, 275-0016, Japan

⁴ Department of Materials Engineering, The University of Tokyo, 7-3-1 Hongo, Bunkyo-Ku, Tokyo 113-8656 Japan

Keywords: Gasification, Slag, Vanadium, Coal, Petcoke, Vapor pressure

Abstract

In this work, ion currents of gaseous species from synthetic slag mixtures mimicking those from coal-petcoke feedstock were measured by double Knudsen cell mass spectrometry at a temperature range of 1000 °C to 1300 °C and an oxygen partial pressure of approximately 10^{-10} atm. The majority of gaseous vanadium was found to be present in the form of V_2O_3 , whose vapor pressure rapidly increased with increasing petcoke slag addition to coal slag. Effects of temperature, vanadium content in slags, and coal/petcoke ratios, with an emphasis on vanadium and alkali vapor species, are discussed.

Introduction

An increased use of petcoke with/without coal as carbon feedstock in gasification has introduced vanadium oxide to the slag system, leading to unknown chemical and physical slag properties in the gasifier environment. Appreciable quantities of vapors from volatile components (including vanadium oxide) of the feedstock slag can interact with gasifier construction materials (such as the refractory liner), the radiant or convective syngas coolers, and/or thermocouple sensor; causing increased refractory wear, system fouling, or component failure.

Thermodynamic databases for vanadium-containing slags are not commercially available, which has been in part limiting optimization of gasification operation to a trial and error basis. In order to enable predictions of the thermodynamic nature of vanadium slags existing during gasification, a long-term study of experimental vanadium-bearing gasifier slags was initiated by NETL [1-5]. With an emphasis placed on phase equilibria of coal-petcoke mixed slags in the past [2, 5], a study involving thermochemical properties was needed to aid in the creation of thermodynamic databases for vanadium containing slag systems.

In this work, vapor pressures of gaseous species evolved from synthetic coal-petcoke slag mixtures were determined using ion currents measured by double Knudsen cell mass spectrometry. Effects

of temperature, vanadium oxide content, and coal slag/petcoke slag ratios on the evolution of gas species from synthetic coal/petcoke slag mixtures are discussed.

Experimental

Synthetic slag samples used in this study were prepared from reagent grade oxide powders (Alfa Aesar, 99.5%+). Coal slag and petcoke slag compositions were determined based on literature data [6-8]. The mixtures were heated at 1450 °C for 1 hour in a 64 at.% CO-36 at.% CO₂ gas mixture (an oxygen partial pressure of 3×10^{-9} atm) at 30 ml/min, then furnace cooled to room temperature in the same atmosphere. After cooling, the samples were ground to powders using a WC shutter box and stored in Ar sealed glass vials prior to designated analysis. The sample chemistry of the premelted slags was conducted using an inductively coupled plasma with optical emission spectrometry (ICP-OES) technique, with results listed in Table I. The synthetic slag compositions were varied from 0 to 100 wt.% petcoke slag, the balance being coal slag.

Table I. Chemistry of synthetic coal-petcoke slag mixtures used in this study (normalized on an oxide basis)

Sample ID	Petcoke slag in coal slag (wt.%)	Sample composition (wt.%)								
		Al ₂ O ₃	CaO	FeO	K ₂ O	MgO	Na ₂ O	SiO ₂	V ₂ O ₃	total
0PC	0 (100% Coal slag)	24.1	5.2	13.9	1.7	1.0	0.6	53.4	0.0	100.0
20PC	20	20.9	5.1	12.4	1.8	1.1	0.6	47.1	11.0	100.0
40PC	40	17.5	5.1	11.4	1.5	1.0	0.5	39.9	23.0	100.0
60PC	60	13.9	5.1	9.9	1.5	1.0	0.6	34.0	34.0	100.0
80PC	80	9.7	5.2	8.3	1.3	1.0	0.5	27.3	46.6	100.0
100PC	100 (100% Petcoke slag)	6.5	5.2	6.7	1.1	1.0	0.4	19.7	59.4	100.0

A schematic image of the high temperature double Knudsen cell mass spectrometer is shown in Figure 1. Details of the equipment are described elsewhere [9]. A sample chamber was kept in an oxygen partial pressure of approximately 10^{-10} atm by evacuating the chamber during measurements. A sample and a reference substance (V₂O₃, 99.7%, Alfa Aesar) were placed in separate Knudsen cells (Mo) which were heated by Ta resistance heating elements. Temperatures of the samples and cells were measured by three thermocouples located in holes at the bottom of the cell. An atomic beam of evaporated species from the Knudsen cells was detected by a quadrupole mass spectrometer. For each sample, ion currents of the evolved gas species were measured three times at each temperature (1000 °C through 1300 °C at 50 °C increments. This procedure was repeated three times using different portions of the samples at each temperature for reproducibility.

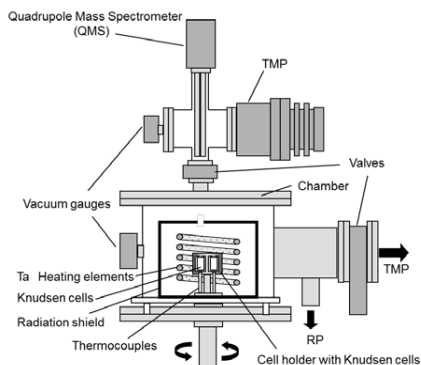


Figure 1. A schematic of the high temperature double Knudsen cell mass spectrometer used in this work

A vapor pressure of species i , P_i , was converted from ion current, I_i , measured from the mass spectrometer, using the following relationship [10]:

$$P_i = \frac{I_i}{S_i} T \quad (1)$$

where S_i is the device dependent constant including ionization cross-section and efficiency of the ion detector and T the absolute temperature of a sample.

Results and Discussion

During the ion current measurements from 1000 to 1300 °C, only Na, K, and V_2O_3 were detected as vapor species evolving from the synthetic slag samples. Wang et al. reported the presence of vanadium based gas species V, VO, and VO_2 when testing vanadium-containing slags (Al_2O_3 -CaO-MgO-SiO₂- V_2O_3) at elevated temperatures [11]. The difference may be attributed to a combination of experimental parameters; including higher temperatures (1550 – 1650 °C), lower vanadium concentrations (0.01 – 0.10 at.% V_2O_3), and higher CaO/SiO₂ basicity (0.8 – 2.0).

Vapor pressures of the species found in this study are presented in Figure 2. Absent points represent no vapor pressure, i.e., essentially zero pressure detected. In general, the vapor pressures tend to increase with increasing petcoke slag/coal slag ratios for the slag compositions studied. Note that the vanadium concentration increases as the quantity of petcoke added as carbon feedstock increases. Vanadium oxide seems to promote increases in the vapor pressure of Na and K evolved from the slags. No Na vapor was detected for 0 wt.% vanadium oxide in the slag at 1000 °C and 1050 °C. A slag composition based on at least 80 wt.% petcoke slag was required for a K vapor pressure to become detectable at 1000 °C, while it was detected in a 60 wt.% petcoke slag at 1050 °C and a 40 wt.% petcoke slag at 1100 °C.

Depressions of the Na and K vapor pressures occurred toward the mid petcoke slag concentrations, as seen in Figure 2 (b), which becomes more apparent at lower temperatures. Nakano et al. reported the presence of calcium aluminosilicate and spinel in vanadium-bearing gasifier slags [1]. In the report, the formation of calcium aluminosilicate was only noted at 1200 °C (not at or above 1350 °C). With more vanadium in the slag, the stability of calcium aluminosilicate shifted toward calcium-richer, possibly by vanadium atoms replacing aluminum atoms in the crystal structure. Calcium deficiency in slag also influences slag basicity (C/S ratio), which would affect the immiscibility of slag at lower temperatures. The decrease in the Na and K vapors with increasing vanadium oxide at a low range of the petcoke slag concentrations could be attributed to the spinel phase ($\text{Fe}(\text{Al}, \text{V}_2\text{O}_4)$) accepting more vanadium over aluminum [1], releasing aluminum into the molten slag forming an amorphous aluminosilicate which incorporate alkali metals.

Vapor pressures of V_2O_3 were not detected (or detectable) below 1250 °C in any of the slag samples. A petcoke slag concentration of at least 60 wt.% was needed to release a sufficient quantity of V_2O_3 vapor at 1300 °C, and at least 80 wt.% petcoke was needed to evolve V_2O_3 vapor at 1250 °C. The vapor pressure of V_2O_3 is likely related to the stability of the crystalline V_2O_3 phase and the saturation of V_2O_3 in slags.

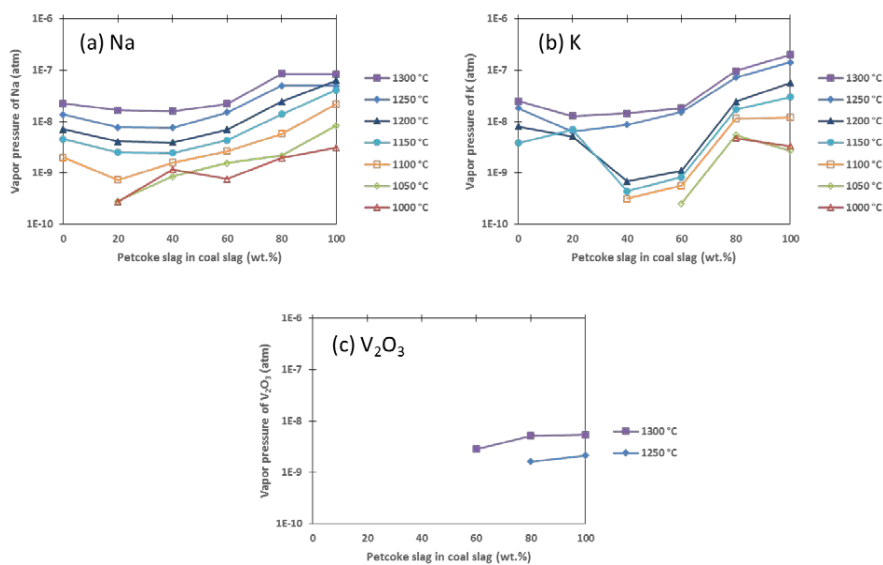


Figure 2. Partial pressures of (a) Na, (b) K, and (c) V_2O_3 evolved from synthetic coal-petcoke mixed slags with respect to petcoke slag concentration

The effect of temperature on the partial pressures of gas species evolved from the slag samples is presented in Figure 3. The vapor pressures of all gas species observed (K, Na, and V_2O_3) tend to increase with increasing temperature. The Na and K curve depressions found in Figures 2 (a) and (b) are clearly reflected in Figure 3. The presence of vanadium oxide in slags at certain

concentrations (estimated between 23 – 34 wt.%) lowered the vapor pressures of alkali metals (Na and K) while increased that of V_2O_3 . The vanadium effect on lowering the Na and K vapor evolution from molten slags is, however, minimized at temperatures higher than 1200 °C (as previously noted, 1250 °C is the temperature where V_2O_3 starts to have a measurable vapor pressure). In order to reduce the vapor pressure of V_2O_3 , crystal phases that incorporate vanadium into them may be considered. If a linear regression is assumed, an approximation of vapor pressures at higher temperature would generate useful information for the gasification industry.

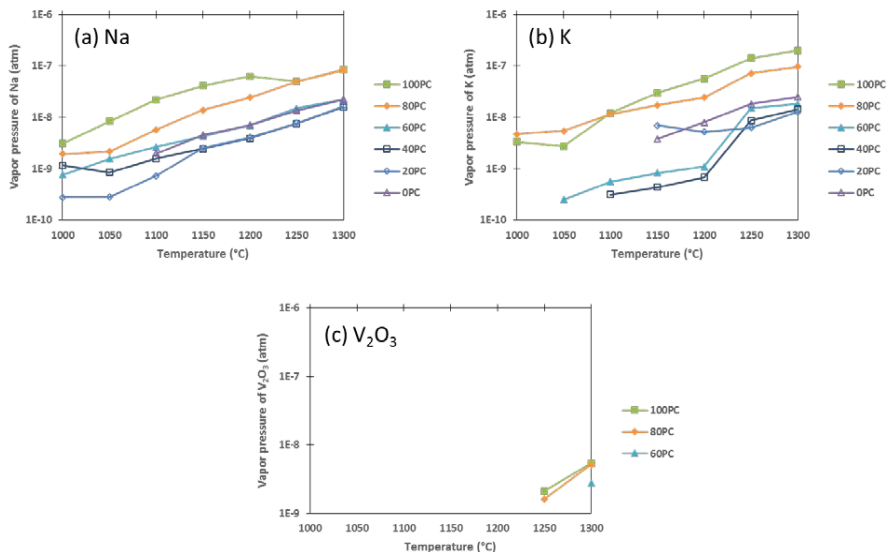


Figure 3. Partial pressures of (a) Na, (b) K, and (c) V_2O_3 evolved from synthetic coal-petcoke mixed slags with respect to temperature

Conclusions

Evolution of vapor species from synthetic slags simulating mixtures of coal slag and petcoke slag in gasifiers was investigated using a high temperature double Knudsen cell mass spectrometry technique. Na, K, and V_2O_3 species were detected at temperatures between 1000 and 1300 °C in an oxygen partial pressure of approximately 10^{-10} atm. Vapor pressures of the vapor species generally increased with increasing petcoke slag concentrations and temperature. Vapor pressures of Na and K were lowered at approximately 40 – 60 wt.% petcoke slag especially below 1250 °C, which was likely caused by a combination of thermodynamic parameters. Vapor pressure information, as thermochemical data, will contribute to the thermodynamic database development.

Acknowledgement

This technical effort was performed in support of the National Energy Technology Laboratory's ongoing research under the RES contract DE-FE0004000. This research was supported in part by an appointment to the National Energy Technology Laboratory Research Participation Program, sponsored by the U.S. Department of Energy and administered by the Oak Ridge Institute for Science and Education.

Disclaimer: "This project was funded by the Department of Energy, National Energy Technology Laboratory, an agency of the United States Government, through a support contract with URS Energy & Construction, Inc. Neither the United States Government nor any agency thereof, nor any of their employees, nor URS Energy & Construction, Inc., nor any of their employees, makes any warranty, expressed or implied, or assumes any legal liability or responsibility for the accuracy, completeness, or usefulness of any information, apparatus, product, or process disclosed, or represents that its use would not infringe privately owned rights. Reference herein to any specific commercial product, process, or service by trade name, trademark, manufacturer, or otherwise, does not necessarily constitute or imply its endorsement, recommendation, or favoring by the United States Government or any agency thereof. The views and opinions of authors expressed herein do not necessarily state or reflect those of the United States Government or any agency thereof".

References

1. J. Nakano, et al., "Crystallization of Synthetic Coal-Petcoke Slag Mixtures Simulating Those Encountered in Entrained Bed Slagging Gasifiers," *Energ Fuel*, 23 (2009), 4723-4733.
2. J. Nakano, et al., "Phase Equilibria in Synthetic Coal-Petcoke Slags (SiO₂-Al₂O₃-FeO-CaO-V₂O₃) under Simulated Gasification Conditions," *Energ Fuel*, 25(7) (2011), 3298-3306.
3. J. Nakano, et al., "Interactions of refractory materials with molten gasifier slags," *Int J Hydrogen Energ*, 36(7) (2011), 4595-4604.
4. J.P. Bennett, et al. *Causes of Phosphate Migration in High Cr₂O₃ Gasifier Refractories and the Impact on Slag Wear and Spalling*. in *UNITECR 2015*. 2015. Vienna, Austria.
5. J. Nakano, et al., "Thermodynamic effects of calcium and iron oxides on crystal phase formation in synthetic gasifier slags containing from 0 to 27 wt.% V₂O₃," *Fuel*, 161 (2015), 364-375.
6. W.A. Selvig and F.H. Gibson, *Analyses of Ash from United States Coals*. Bureau of Mines Bulletin. Vol. 567. 1956, Washington, USA: United States Government Printing Office.
7. R.W. Bryers, "Utilization of Petroleum Coke and Petroleum Coke/Coal Blends as a Means of Steam Raising," *Fuel Process Technol*, 44(1-3) (1995), 121-141.
8. M.L. Swanson and D.R. Hajicek. *Advanced High-Temperature, High-Pressure Transport Reactor Gasification*. in *International Conference on Fluidized Bed Combustions*. May 31, 2001. Reno, NV.
9. T. Nagai, et al., "Mass spectrometric study on phosphorus in molten carbonsaturated iron," *Isij Int*, 47(2) (2007), 207-210.
10. M. Heyrman, et al., "Improvements and new capabilities for the multiple Knudsen cell device used in high-temperature mass spectrometry," *Rapid Commun Mass Sp*, 18(2) (2004), 163-174.

11. H. Wang, et al., "High-temperature mass spectrometric study of the vaporization processes of V₂O₃ and vanadium-containing slags," *Rapid Commun Mass Sp*, 24(16) (2010), 2420-2430.

AN ASSESSMENT OF SLAG EYE FORMATION USING MATHEMATICAL AND PHYSICAL MODELING

Augusto Pereira de Sá¹ Filipe de Menezes Torres¹ Carlos Antonio da Silva¹ Itavahn Alves da Silva¹ Varadarajan Seshadri²

¹ Department of Metallurgical Engineering and Materials, Federal University of Minas Gerais, 6627, Av. Antonio Carlos, 31.270-901 Belo Horizonte, Brazil,

² Department of Metallurgical Engineering and Materials, Federal University of Ouro Preto, 35400-000, Ouro Preto, MG, Brazil

Abstract

Results from experiments in a physical model of a steel ladle in respect of slag eye formation during inert gas bubbling have been compared with those obtained by simulation with mathematical model, solved with Ansys Fluent software. The influence of gas flow rate, liquid metal level, thickness of slag layer, gas distribution between plugs and density difference between the two liquids on plume eye area have been studied. On the basis of experimental results regression equations for evaluating slag eye area have been developed.

Keywords: ladle, secondary refining; argon blowing; spout

Introduction

The practice of bubbling inert gas through the bottom or side of the steel plant ladle has the objective of attaining thermal and compositional uniformity of steel, acceleration of the dissolution of alloy elements and capture as well as flotation of non-metallic inclusions. However, the flow of bubbles of inert gas bursts through the slag layer, exposing molten steel to the atmosphere, which results in contamination of steel due to absorption of oxygen, nitrogen and hydrogen from the environment. The instability generated by the plume causes emulsification and entrainment of top slag in the liquid steel. The intensity of thermal losses and chemical interactions between the steel and the atmosphere depends on the size of the plume eye area. Hence the eye opening of the plume is a relevant issue in these operations. Expressions for eye opening in ladles as a function of gas flow rate, slag layer thickness, fluid properties can be found in literature (1-5). Disagreement between these studies is apparent. Also, for application of these and other relationships to industrial systems, estimation of properties of the slag, its thickness and other parameters, is required. There are difficulties in estimating the contour of the eye opening in actual practice as well as the values of physical parameters. This work deals with the comparison between measurements of eye opening as determined from physical modeling and CFD modelling.

Methodology

Parameters of a 1:5 scale physical model of a 150 ton ladle are given in Table I.

Table I. Physical model parameters.

Parameters	(cm)	Parameters	(cm)
Model height	55	Solution height	46 (1/2 ladle 75t)
Bottom diameter	47.2	Silicon oil layer height	1; 3; 5
Top diameter	51.2	Number of plugs	1; 2
Plug diameter	2.36	Gas flow rate	10l/min; 15l/min

To assess the influence of metal height two sets of experiments have been considered: a half full ladle(75 tons) and a full ladle (150 tons). In order to keep similarity gas flow rate was calculated according to :

$$Q_{model} = \lambda^{2.5} Q_{prototype} \quad (1)$$

Silicone oil with a viscosity of 100cSt or 500cSt and a thicknesses of 1, 3 or 5 cm were used for simulating the slag. ZnCl₂ water solution (density of 1300kg / m³) with higher density was chosen for simulating the steel melt in addition to water. A comparison of the behavior of silicon oil/water and silicon oil / ZnCl₂ solution should enable to assess the influence of slag/metal density ratio on eye opening. Figure 1 outlines the experimental apparatus. Particle image velocimetry (PIV) was used to capture details regarding the flow field and water-oil interaction. A camera was installed at the top to monitor the eye movement of the plume. Ten images, randomly selected, were used to determine the opening area in the case of each geometry of the injection system, the ladle geometry and varying properties of the supernatant layer.

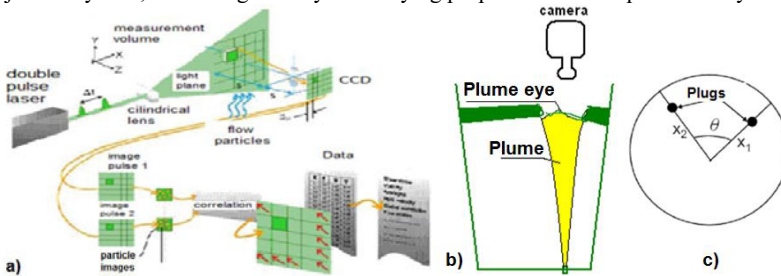


Figure 1 . a) PIV setup for mapping the velocity b) camera setup for measurements involving the plume c) positioning of the 2 plugs for gas injection.

The recirculating metal flow interacts with the slag layer and then a braking effect at their interface can be of influence as far as eye opening is concerned. For simulating the dry slag, a wooden checkered grid was used (to enable gas passing through, while keeping the braking effect). The mapping of velocity distribution was done using PIV technique in a region 4 cm below the bath level in the ladle with the help of Dynamics Studio Software – DANTEC which is capable of analysing 280 images in intervals of 3000µs and 10Hz capture frequency. The vector map generated in the square area considered, enabled determination of the velocity profile of the vertical distance from the top of the liquid steel layer toward the inside. Table II lists the physical properties of the fluids used for the simulation of steel melt and slag during argon bubbling in the ladle and in the physical modeling.

Table II. Fluid properties of the physical model and the prototype

Properties	Fluids (physical model)			Fluids(industry)		
	Air	Oil	ZnCl ₂	Argon	Slag	Steel
Density, kg.m ⁻³	1.225	950	1425	1.225	3000	7000
Dynamic viscosity, Pa.s	1.7894 x 10 ⁻⁵	0.482	0.00303	1.7894 x 10 ⁻⁵	0.4	0.005
	ZnCl ₂ /Air	ZnCl ₂ /Oil	Oil/Air			
Interfacial tension, N/m	0.055	0.030	0.018			

A mathematical model based on equations of continuity; volume conservation; conservation of momentum and k-ε model and some auxiliary equations have been considered for evaluating the velocity vectors in the ladle and the fluid dynamic behavior of the plume region.

$$\text{Continuity: } \frac{\partial \rho}{\partial t} + \nabla \cdot (\rho U) = 0 \quad (2)$$

$$\text{Sum of volume fractions: } \sum_{\alpha=1}^{N_p} r_{\alpha} = 1 \quad (3)$$

$$\text{Momentum equation: } \frac{\partial \rho U}{\partial t} + \nabla \cdot (\rho U \otimes U) - \nabla \cdot (\mu_{eff} \nabla U) = -\nabla p + \nabla \cdot (\mu_{eff} \nabla U)^T + B \quad (4)$$

$$\text{Effective viscosity: } \mu_{eff} = \mu + \mu_t \quad (5)$$

$$\text{Turbulent viscosity: } \mu_t = C_{\mu} \rho k^2 / \varepsilon \quad (6)$$

$$\text{Auxiliary equations: } \frac{\partial \rho k}{\partial t} + \nabla \cdot (\rho U k) = \nabla \cdot \left[\left(\mu + \frac{\mu_t}{\sigma_k} \right) \nabla k \right] + P_k - \rho \varepsilon \quad (7)$$

$$\frac{\partial \rho \varepsilon}{\partial t} + \nabla \cdot (\rho U \varepsilon) = \nabla \cdot \left[\left(\mu + \frac{\mu_t}{\sigma_k} \right) \nabla \varepsilon \right] + \frac{\varepsilon}{k} (C_{\varepsilon 1} P_k - C_{\varepsilon 2} \rho \varepsilon) \quad (8)$$

Where: ρ : fluid density (kg/m^3) ; t : time (s); ∇ : gradient operator; U : velocity (m/s) ; r_{α} : volumetric fraction of phase α ; N_p : number of phases ; μ_{eff} : effective viscosity (Pa.s); B : body forces, gravity; μ : dynamic viscosity (Pa.s); μ_t : turbulent viscosity (Pa.s); C_{μ} : a constant; k : turbulence kinetic energy (m^2/s^2); σ_k : a constant; P_k : rate of production of kinetic energy due to buoyancy and viscosity effects; ε : rate of dissipation of turbulent kinetic energy (m^2/s^3); $C_{\varepsilon 1}$: constant; $C_{\varepsilon 2}$: constant.

A mesh of 215,000 hexaedral elements was used in mathematical modeling . The simulation time was 20s in transient regime, which was sufficient to observe a stationary pattern. The time step was variable throughout the simulation in order to keep the Courant number close to five. This number reflects the portion of the cell that is crossed by the fluid in a time step. Thus, each time step, five cells were traversed by the fluid. Nonslipping conditions were applied to ladle walls. The top surface was taken as pressure outlet. Volume of fluid technique was used to describe the multi-phase flow.

Results and Discussion

The fluid dynamic behavior of the plume eye region was investigated by varying the gas flow, thickness of oil layer , and number of plugs for injection of air , height of the liquid column and density differences between oil layer and liquid layer according to Table 1. Figure 2a and 2b show the velocity vector map in the same area of 10cmx10cm, selected for experiments with PIV. In the zone of observation 1, for the case of absence of silicone oil (absence of slag), velocities in the surface and subsurface regions at the top of the liquid column are in general higher as indicated by red color. The decreasing velocity regions are indicated by red to yellow and then to green etc. In comparison, the presence of dry slag (presence of slag) causes damping of the velocity field in the interfacial region and those below that, modifying the velocity profile in the decreasing order as denoted by the color change in the regions. Figure 2 (right) shows a reduction of high velocity zones at the subsurface region highlighting the braking effects of the slag. The resistance to eye opening is due to the weight of the slag layer and interfacial friction. Although these results are significant, it is important to remember that there are differences between the experimental conditions in the laboratory simulation and the industrial conditions. The main difference lies in the ratio of densities between liquid steel and slag in the industrial ladle ($\rho_{slag}/\rho_{steel} = 0.43$) as against the ratio of densities of liquids namely water and silicone oil used in the laboratory ($\rho_{oil}/\rho_{water} = 0.95$). This

difference can be minimized by using (as in these experiments, a water $ZnCl_2$ solution with density of 1.3 g.cm^{-3}) a higher density liquid to simulate the steel melt.

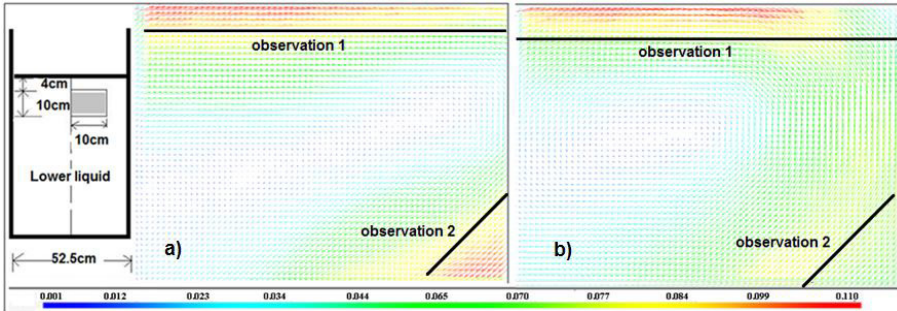


Figure 2 . Velocity profile at subsurface region (bath height = 46cm; flow rate of gas = 15 l/min) a) in the absence of slag b) in the presence of slag

The experimental data of 1445 experiments (6) were submitted to a regression analysis resulting in the following equation for eye opening (%O) : ($R^2 = 0.96$)

$$\% O = 60.04 + 0.0039 \mu - 3.56 H + 0.281 h + 2.239 Q - 5.52 N - 143.73 \Delta \rho \quad (9)$$

In the above equation, μ is the oil viscosity (100 and 500cSt); H is the oil thickness(1, 3 and 5 cm); h is the bath liquid level (46 and 71cm); Q is the gas flow rate (l/min); N is the number of plugs (1 and 2); $\Delta \rho$ is the difference between densities of lower and top fluids (g/cm^3).

Table III shows the results of influence of the change in various parameters of the regression equation given above on the percentage of eye opening area. For 10% increase in the oil thickness and density difference between the fluids, the eye opening area diminishes and for others, the gain is positive.

Table III. Relative influence of operational parameters on % eye opening.

μ	H	h	N	Q	$\Delta \rho$	% O	Parameters in regression equation (P)
300 cSt	3cm	60cm	1	15lpm	0.45	30.77	Reference value of parameters (P)
0.38	-3.47	5.48	1	10.91	-21.02		% gain of %O /10% increase in the value of P

The effects of the investigated parameters on the plume or slag eye behavior are consistent with those available in the literature (1-6). The opening of the eye of the plume was simulated in transient state using Ansys Fluent software and these were compared with the measurements made on silicone oil - $ZnCl_2$ system. It was observed that there was a small variation until a stable pattern was achieved, indicating that the steady state has been reached. The images in Figure 3 (a) were made at 20s of the beginning of mathematical simulation. One can see that in cases with higher flow rates (cases 3 and 4) slightly smaller openings result . This is probably due to the fact that the process of eye opening is still in the transient stage and has not yet reached the steady state. Figure 3 (b) shows results of cases 5 to 8 (two plugs). In this case, the thickness of the slag layer appears to be the most influential variable in the opening of the plume eye. The number of plugs also influence (one eye opening for each plug; higher eye opening for two plugs) the plume eye opening. The presence of an extra plug causes vortex agitation and hence they may have their intensity decreased by mutual cancellation. It can be observed that eye

opening area for each plug, was slightly lower in the case with two plugs compared to the results of simulation with only one plug (keeping the same flow rate per plug). Since the total flow increases, although distributed between 2 plugs, the eye opening area ratio decreases with increasing number of plugs.

To make a comparison between results from this work and those from the literature, the data analysis must be unified. From dimensional analysis and physical reasoning, it is reasonable to assume that the eye opening is a function of dimensionless parameters such as Froude number, Reynolds number and other geometric dimensionless characters. Due to the nature of the process of spout formation, the proper velocity considered for the analysis should be the plume velocity (U_p). However the plume velocity is not exactly known but can be calculated from the equation developed using experimental data from physical modeling (5). Gas superficial velocity and hence gas flow rate has been used in this equation for calculating plume velocity (5).

A comparison of data regarding percentage eye opening calculated using the relation developed in this work and other relations from literature is given in Table IV. As can be seen, there is a large discrepancy in the values computed in respect of some of the relations. It is also difficult to make a comparison between these values and industrial ones since in this case of the latter, parameters are not clearly defined (3). However the results of % opening calculated from the relation presented in this work lies in between those calculated using relations developed in references (2) and (3)

Table IV. Comparison of eye opening expressions from this work and literature (evaluated for the following data) R(ladle radius) = 1.37m ; h =3.60m; H=0.05; Q=5x10⁻³(STP)m³/s ; $\mu = 0.07 Pa.s$; $\rho = 3000 kg/m^3$; $\rho_{steel} = 7000kg/m^3$; $U_p = 4.5 Q^{1/3}h^{1/4}/R^{1/4}$ (5)).

Correlation	%Opening	Ref
$\frac{A_{eye}}{(h+H)^2} = 0.02 \left[\frac{Q^2}{gH^5} \right]^{0.375}$	9.92	2
$\log \frac{A_{eye}}{h.H} = -0.45593 + 0.83275 \log Fr - 0.14732 \{\log Fr\}^2 + 0.1789 \{\log Fr\}^3$	4.77	3
$\frac{A_{eye}}{hH} = 3.25 \left[\frac{U_p^2}{gH} \right]^{1.28} \left[\frac{\rho_{steel}}{\Delta\rho} \right]^{0.55} \left[\frac{\mu}{\rho H U_p} \right]^{-0.05}$	46.94	4
$\frac{A_{eye}}{H^2} = -0.76 \left[\frac{Q}{g^{0.5} H^{2.5}} \right]^{0.4} + 7.15 \left(\frac{\Delta\rho}{\rho_{steel}} \right)^{-0.5} \left[\frac{Q}{g^{0.5} H^{2.5}} \right]^{0.73} \left[\frac{h}{H} \right]^{-0.5}$	0.052	1
$\ln \frac{A_{eye}}{hH} = 0.635 + 0.28 \ln \frac{Q^2}{gH^5} - 0.876 \ln \frac{\Delta\rho}{\rho_{steel}} - 0.0626 \ln \frac{Q\rho}{H\eta} - 0.071 \ln(\text{number of Plugs}) - 0.356 \ln \frac{h}{R}$	7.11	This work

Figure 4 shows the comparison of experimental results of determination of the plume eye for two gas bubbling plugs and flow rates of 10 l/min and 15 l/min, thickness of slag layer (silicone oil) of 1cm and 5cm, with the mathematical simulations. Table V gives the comparison of measured and predicted eye opening for one plug after 15s for cases 1-4 in the case of physical modeling and CFD simulations. Considering the transient nature of both simulations, it can be seen that there is significant agreement between them. For this reason, the results of the model can be extended to cover industrial operations, where it is difficult to make measurements varying the parameters. In the case of ladle of 75 tons of steel and gas flow rate of 0.014 m³/s, the results of

simulation of the transient period of 20s, indicate that a larger amount of slag (2250kg) decreases the opening of the eye compared with the ladle with 900kg of slag (Figure 5). It can be seen that the results of numerical simulation have not shown a strong influence of the flow rate of gas on the area of the eye opening. This is probably due to the fact that the change in flow rate has not been significant. However, the physical model experiments support this slight influence of flow rate as seen in Figure 6.

TableV. Comparison of measured and predicted eye openings in % for one plug after 15s, cases 1-4

Case	#1	#2	#3	#4
Physical modelling	8.6%	34.4%	7%	29.6%
CFD simulation	7.1%	22.6%	6.8%	25.2%

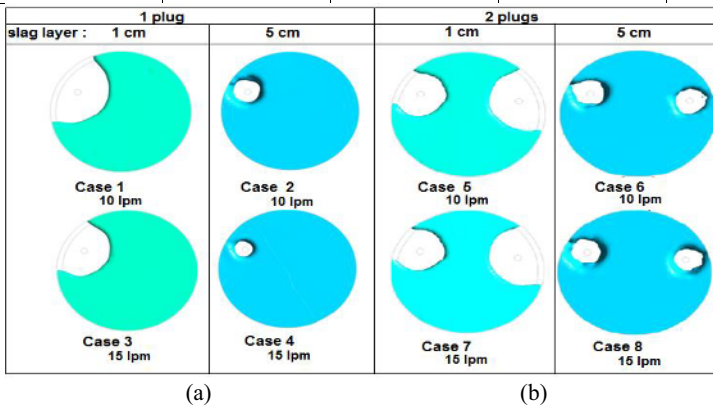


Figure 3 . (a) Top view of the eye opening cases 1-4 (1 plug); (b): Top view of the opening of the plume eye for cases 5-8 (2 plugs); 46 cm of liquid bath, flow rates are per plug

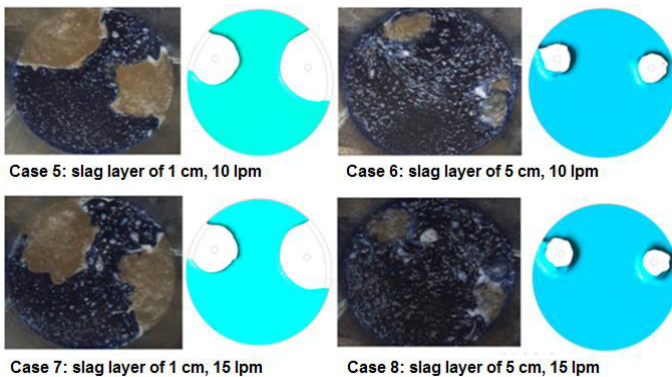


Figure 4 .Top view of the eye opening cases 5-8 (2 plugs); flow rates are per plug

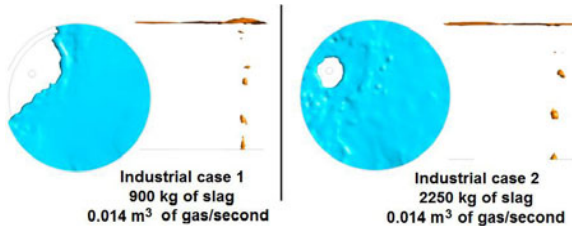


Figure 5. Views the eye and bubble plume column for industrial cases 1 and 2

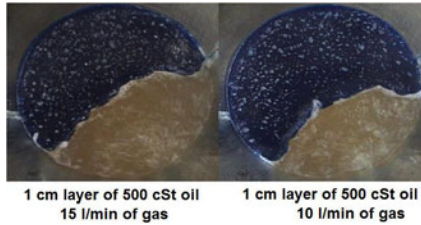


Figure 6 . Plume area comparison for variation of flow rate of air (1 cm layer of 500 cSt oil)

Figure 7 shows the velocity profile in the region close to the zinc chloride-oil interface, the final moment simulation being 20s. The velocity profiles close to the slag interface are indicative of an increase in the magnitude of the velocity of the gas plume region (near to + 0.1m in the x-axis). Outside the plume the system is relatively quieter.

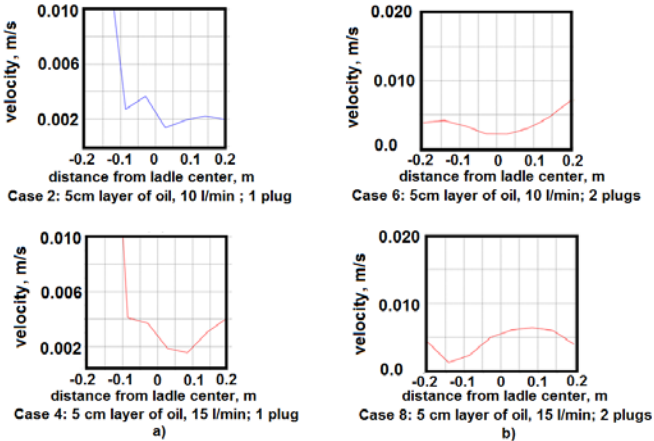


Figure 7. Velocity profile near the slag interface a) one plug; symmetry plane cutting through the plug; b) two plugs; symmetry plane between plugs.

Velocity values at the surface level are related to the mass transfer rate between metal and slag and also between metal and atmosphere. For example assuming validity of the assumptions leading to Higbie equation (7), transport coefficient at the interface (K) can be estimated from:

$$K = 2 \sqrt{D V_s / \pi R} \quad (10)$$

where D is the diffusion coefficient of the species, V_s is the superficial velocity and R the radius of the ladle. Thus a strong heterogeneity at interface is expected confirming the spout as a area of contamination (strong mass transfer). The same behavior is expected for the industrial system as seen from Figure 8.

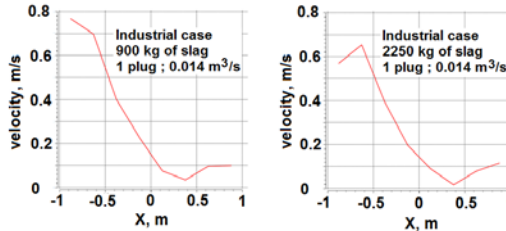


Figure 8. Expected velocity profile 5cm from metal slag interface, 1 plug; cutting from symmetry plane through the plug.

Conclusions

The opening of the plume eye is strongly influenced by the flow rate of inert gas, its distribution among plugs, heights and layers of slag and metal and density difference between the liquids. These effects were quantified. The mathematical simulation is in a position to verify the experimental results and also is in a position to predict parameters important through simulation with industrial data of steel ladle. An expression for eye opening based on dimensional analysis has been developed and the eye opening predicted is compared with the results of other relations from the literature. Models such as the one developed in this work are useful to the industry, since actual data regarding physical properties and operational parameters (slag layer thickness) are mostly unknown. This work stresses the importance of these factors

Acknowledgements

The authors wish to thank CNPq and FAPEMIG, Brazil for financial support.

References

1. K. Krishnapisharody, G. Irons, "An extended model for slag eye size in ladle metallurgy", *ISIJ International*, vol. 48, no. 12, 2008, . 1807–1809.
2. Subagyo, G.A. Brooks, G.A. Irons, "Spout Eyes Area Correlation in Ladle Metallurgy", *ISIJ International*, Vol. 43, No. 2, 2003, 262–263
3. K. Yonezawa, K. Schwerdtfeger, "Correlation for Area of Spout Eyes in Ladle Metallurgy", *ISIJ International*, Vol. 44 (2004), No. 1, . 217–219.
4. M. Peranandhanthan, D. Mazumdar, "Modeling of Slag Eye Area in Argon Stirred Ladles", *ISIJ International*, Vol. 50 (2010), No. 11, . 1622–1631;
5. D. Mazumdar, J.W. Evans, "Macroscopic Models for Gas Stirred Ladles"; *ISIJ International*, Vol. 44 (2004), No. 3, . 447–461
6. J.D. Arruda, A.L. Pereira, C.A. Silva, I.A. Silva, V. Seshadri, "Assesment of gas- metal-slag interaction in steel making ladle through mathematical and physical modeling" : *Proceedings of 6th international symposium on High Temperature Metallurgical Processing TMS 2015, Orlando, March 15th-19th*, 397-404
7. J.J. Carberry, *Chemical and Catalytical Reaction Engineering*, Dover Publications, 2001.

AN EFFECT OF PHOSPHOROUS GAS GENERATED IN SLAGGING GASIFIERS ON Pt-Rh SENSOR DEGRADATION

Anna Nakano¹, Jinichiro Nakano^{1,2}, and James Bennett¹

¹ U.S. Department of Energy National Energy Technology Laboratory; 1450 Queen Ave.;
Albany, OR 97321, USA

² AECOM; P.O. Box 1959; Albany, OR 97321, USA

Keywords: Gasification, Pt-Rh alloy, Thermocouple, Phosphorous

Abstract

Entrained flow slagging gasifiers are used to covert coal, petcoke and other carbon feedstock to syngas (CO and H₂), which is used as a fuel in power generation or is converted into chemical products. During the gasification process, gasifier components such as refractory liners, syngas coolers, and thermocouples are aggressively attacked by corrosive slags and gases originating from the carbon feedstock, materials that contain arsenic, sulfur, phosphorous and other impurities;— all of which are in a mixed equilibrium condition during gasification. This research evaluated the effect of phosphorous gas generated during gasification on the corrosion degradation of Pt-Rh thermocouple sensor materials. Phosphorous interactions with Pt-Rh_x (x = 0 – 30 wt.%) alloys have been analyzed isothermally at 1012 °C. Phosphorous diffusion into the alloy is discussed.

Introduction

Platinum (Pt) – rhodium (Rh) alloys are commonly used in high temperature thermocouple sensors for slagging gasification systems. The Rh concentration in a Pt-Rh alloy is typically varied between 0 and 30 wt.% in order to induce a voltage difference corresponding to the temperature being measured. For example, a type S thermocouple consists of pure Pt and Pt – 10 wt.% Rh; a type R thermocouple is pure Pt and Pt – 13 wt.% Rh; and a type B thermocouple has Pt – 6 wt.% Rh with Pt – 30 wt.% Rh [1]. While Pt is considered to be relatively inert, Pt based thermocouples often suffer failure in severe industrial environments. For example, thermocouples used in Integrated Gasification Combined Cycle power generation systems have to withstand high temperature (up to 1575 °C), high pressure (20-60 atm), corrosive and reducing gases, and molten slags. U.S. coal used for gasification typically contains up to 20 wt.% ash [2] that may contain volatile K₂O, Na₂O, P₂O₅, and SO₃ [3]. Some of these corrosive species are known to cause hot corrosion in downstream parts of the gasifier and can poison Pt based sensors and catalysts, leading to materials failure [4,5].

In earlier work by the present authors, the type B thermocouple failure induced by phosphorous (P) rich gas was analyzed by a non-isothermal technique [6]. Two distinct failure mechanisms driven by the P-diffusion into the Pt-Rh alloys and dependent on Rh content were found: 1) intergranular diffusion in Pt – 6 wt.% Rh; and 2) intragranular diffusion in Pt – 30 wt.% Rh. The sensor failure occurred as grains were consumed through interactions with incoming P while grain boundaries liquify due to the P-enrichment in the Pt matrix. The thermocouple failures were found

to occur in the temperature range of 929 – 979 °C. The current study focuses on the isothermal aspect of the P-rich gas interactions with Pt-Rh_x (x = 0 – 30 wt.%) alloys. Effects of Rh contents on P diffusion into the alloys and failure kinetics are discussed.

Experimental

The experimental procedure was similar to that used in previous research [6] except, in this work, the isothermal exposure was conducted by a switch gas technique. Reagent grade aluminum phosphate powder of < 5 μm (Alfa Aesar, USA) was used as the source of gaseous P. X-ray diffraction (XRD) analysis of the powder indicated 92.4 wt.% AlPO₄, 7.2 wt.% AlP₃O₉, and 0.4 wt.% Al₂O₃. The Pt – 6 wt.% Rh and Pt – 30 wt.% Rh wires of 0.38 mm diameter studied were manufactured by Engelhard (USA) and were oxyacetylene welded at the point where the two wires were joined to build a type B thermocouple.

The experimental setup employed in this work is schematically shown in Figure 1. The type B test thermocouple was placed into protection alumina tubing (3 mm ID) with the welded tip exposed to a P-bearing gas above the aluminum phosphate powder. Two grams of aluminum phosphate powder was placed in a high density alumina crucible (26 mm H × 22 mm OD × 18 mm ID) with two openings (4 mm × 4 mm each) on the gas inlet and outlet sides of the crucible for gas moving through the crucible. A high density alumina lid was used to cover the crucible. The type B test thermocouple and the crucible with the aluminum phosphate powder were set on an alumina boat within the hot zone of a horizontal CM Rapid Temp 1800 Furnace (USA). The type B process thermocouple (reference) was in a closed alumina protection tube placed next to the alumina boat.

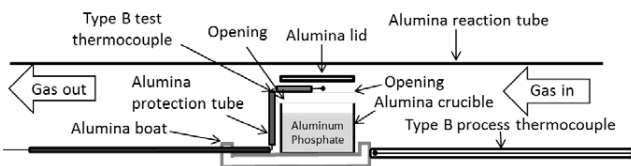


Figure 1. Schematic experimental set-up.

A heating rate during experiment was controlled using a programmable temperature controller. Sample temperature changes were continuously recorded by the process (reference) thermocouple and test thermocouple in-situ via its electromotive force (EMF). The furnace was initially purged with 5 vol.% O₂ – 95 vol.% N₂ at 100 ml/min during heating to the target temperature to prevent aluminum phosphate decomposition by maintaining its thermodynamic stability. After ensuring temperature was stabilized (60 min hold), the purge gas was switch to CO at the same rate to promote aluminum phosphate decomposition and release phosphorous vapors into the reaction zone. The test thermocouple was quenched in water at room temperature when failure was noted (i.e., EMF output from the sensor assembly discontinued). Immediately after thermocouple failure and prior to quenching, the reaction tube was purged with He at 400 ml/min for 10 min. All the gases used in the experiment were high purity and supplied by Matheson (USA).

The experimental procedure was repeated with individual (independent) Pt wires with varying Rh content (100 wt.% Pt, Pt – 6 wt.% Rh, Pt – 10 wt.% Rh, and Pt – 30 wt.% Rh). These wires were quenched after 0 min, 1 min, 3 min, and 5 min of exposure in CO at the desired test temperature. Sample exposure time to P-enriched CO gas was counted from the time when the CO valve was opened in the furnace system. All wires after the test were analyzed for phase changes using scanning electron microscopy with energy dispersive X-ray spectroscopy (SEM-EDS, FEI Inspect F and an Oxford INCA WAVE spectrometer).

Results and Discussion

Type B test thermocouple temperature readings during high temperature are shown in Figure 2. Time 0 on the graph corresponds to the time when temperature in the hot zone of the reaction tube reached 1012 °C (the type B process thermocouple reported 1013 °C at that time. The deviation was assumed to be constant throughout the current isothermal tests.) During the 60 min thermal hold (before the CO gas valve was opened), the type B test thermocouple remained intact and consistent in the constant temperature readings. Test thermocouple readings showed dramatic temperature fluctuation (± 200 °C) approximately 22 min after the CO gas was introduced into the system. After about 38 min, test thermocouple readings presented discontinuity indicating complete failure of the alloy (the two thermocouple alloys were no longer in contact). The result implies 22 min of exposure to a P-rich environment was long enough to cause failure of the type B Pt-Rh based thermocouple alloys at 1012 °C. Although not tested, the corrosion rate (and system failure) would be expected to be faster at higher temperatures and in P-richer environments.

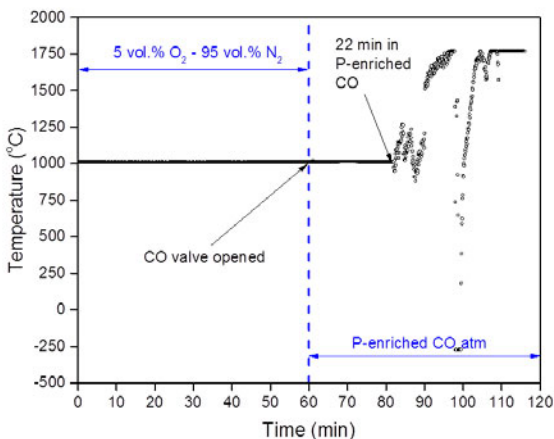


Figure 2. Type B thermocouple temperature readings.

To investigate interactions between Pt-Rh_x and P-containing gas during high temperature exposure, individual Pt-Rh_x wires were independently exposed to the same CO environment at 1012 °C for 0, 1, 3, and 5 min, followed by water quenching. Temperature was controlled by the type B process thermocouple (set to 1013 °C for the samples to be at 1012 °C). The SEM images of the quenched Pt samples with varied Rh contents are presented in Figures 3-6.

Figure 3 represents SEM secondary electron images of the cross-sectioned Pt – 30 wt.% Rh alloy. A reference alloy without any P exposure (marked as ‘0 min in P-enriched CO’) exhibits a smooth outer surface and no apparent damage. With 1 min of isothermal exposure to CO, phosphorous diffused into the grains and interacted with the Pt and Rh, forming the Rh₂P phase at the gas/ Pt – 30 wt.% Rh interface. The Pt-Rh matrix was melted due to P enrichment. The averaged EDS point analysis of the Rh₂P phase indicated 33.66 at.% P – 57.21 at.% Rh – 9.13 at.% Pt (hereafter, atomic percent is used for phase compositions to facilitate identification). Rh and Pt are expected to share the same crystallographic sites in the Rh₂P structure [6]. After 3 min of exposure, the phosphorous diffusion progressed deeper into the alloy, thickening the affected zone with larger Rh₂P precipitates. More Rh from the bulk Pt/Rh wire composition is consumed into the affected layer. After 5 min of exposure, the Rh₂P precipitates in the outer layer grew larger, with some reaching 30 μm in size.

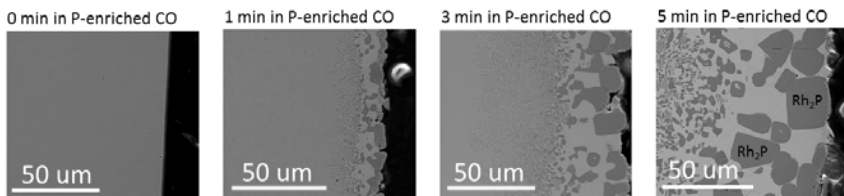


Figure 3. SEM secondary electron images of the cross-sectioned Pt – 30 wt.% Rh alloy quenched after 0 min, 1 min, 3 min, and 5 min of isothermal exposure to P-enriched CO environment at 1012 °C. The formation of the Rh₂P phase was noted in the melted outer layer of the alloy (gas/metal interface).

The SEM secondary electron images of the cross-sectioned Pt – 10 wt.% Rh alloy are shown in Figure 4. Similar to the Pt – 30 wt.% Rh alloy, the Pt – 10 wt.% Rh alloy showed no obvious damage unless the sample was exposed to CO gas in the presence of aluminum phosphate, which releases P-rich gas. After 1 min in the P-enriched CO atmosphere, phosphorous diffused along the Pt – 10 wt.% Rh grain boundaries, leading to grain boundary melting. The formation of Pt-bearing Rh₂P in grains was noted, which was likely caused by interdiffusion of P and Rh from and to the grain boundaries, respectively. With longer exposures (3 min and 5 min), the grain boundaries were further widened, and the presence of the Rh₂P phase became more apparent. The Rh₂P phase formed in the grain boundaries were determined to be on average 33.71 at.% P – 57.19 at.% Rh – 9.10 at.% Pt by EDS, which is equivalent to that found in the Pt – 30 wt.% Rh alloy.

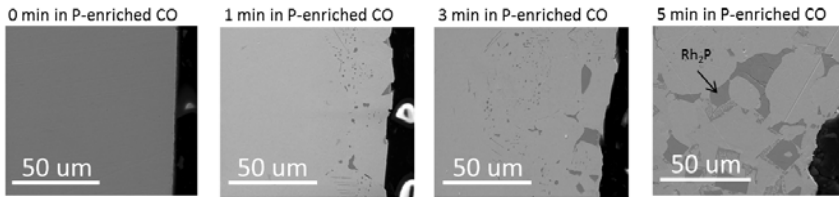


Figure 4. The SEM secondary electron images of the cross-sectioned Pt – 10 wt.% Rh alloy quenched after 0 min, 1min, 3min, and 5 min of isothermal exposure to P-enriched CO environment at 1012 °C.

The intergranular diffusion of phosphorous into the Pt-Rh_x matrix was noted in the Pt – 6 wt.% Rh alloy (Figure 5), which agrees with previous results reported [6]. Rapid P-enrichment in Pt of the grain boundaries facilitated grain boundary melting. One min of exposure to the P-rich atmosphere was long enough to promote the formation of Rh₂P in the grain boundaries. With longer exposures, more Rh was consumed from the grains, contributing to Rh₂P growth. EDS analysis indicated the Rh₂P phase composition to be on average 32.97 at.% P – 56.70 at.% Rh – 10.32 at.% Pt. The remaining Rh-poor Pt (due to the formation of Rh₂P) in the grain boundaries was enriched with P, further contributing to melting.

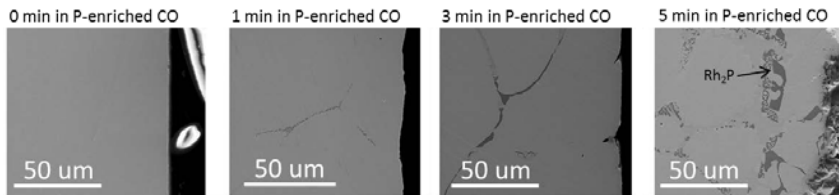


Figure 5. The SEM secondary electron images of the cross-sectioned Pt – 6 wt.% Rh alloy quenched after 0 min, 1min, 3min, and 5 min of isothermal exposure to P-enriched CO environment at 1012 °C.

Figure 6 shows SEM secondary electron images of the cross-sectioned Pt – 0 wt.% Rh alloy. Phosphorous diffused into the Pt wire along the grains (intergranular diffusion), lowering the melting point of Pt and leading to grain boundary melting. A much more rapid widening of the grain boundaries was noted in the Pt alloy without Rh. After 5 min of P-rich CO gas exposure, structural spalling of the surface grains, or complete melting and flow from the surface would be possible, causing catastrophic damage of the alloy.

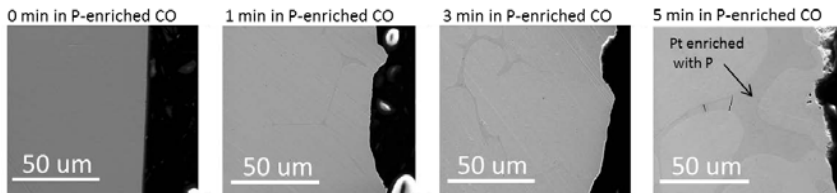


Figure 6. The SEM secondary electron images of the cross-sectioned Pt – 0 wt.% Rh alloy quenched after 0 min, 1min, 3min, and 5 min of isothermal exposure to P-enriched CO environment at 1012 °C.

The reagent grade aluminum phosphate used in the study contained approximately 7 wt.% AlP_3O_9 (s), which is expected to decompose forming AlPO_4 (s) and P_2O_5 (g) in a reducing environment such as CO [6]. FactSage 6.4 thermodynamic calculations (with the FactPS database) indicate a partial pressure of oxygen in CO at 1000 °C would be 10^{-19} atm, which allows the presence of $(\text{P}_2\text{O}_3)_2$ in the gas environment along with P_2O_5 . These P-rich gas species are expected to interact with Pt-Rh_x alloys in the current experimental configuration, acting as sources of P in the alloys.

Binary P-Rh phase diagram available in literature (Figure 7) indicates possible formation of several Rh/P phases under the experimental conditions evaluated. Those phase; Rh_2P , Rh_3P_2 , Rh_4P_3 , RhP_2 and RhP_3 ; may form in the P-Rh system at 1012 °C, depending on P concentrations. EDS analysis of the alloys exposed to P-enriched CO gas indicated the presence of the Rh_2P phase (≈ 33 at.% P) with about 10 at.% of Pt in it. Similar data was reported in [6] where the Rh_2P phase was confirmed by XRD and contained ≈ 33 at.% P and 10 to 14 at.% Pt. The Pt and Rh atoms were assumed to be substitutional and share the same crystallographic sites in PRh_2 , as implied by the (Pt + Rh)/P atomic ratio, which is close to that of the Rh_2P . According to [6], PtP_2 would form in the Pt-P system only if a sufficient P (67 at.%) is present in Pt. PtP_2 was not observed in the present alloys under the studied conditions.

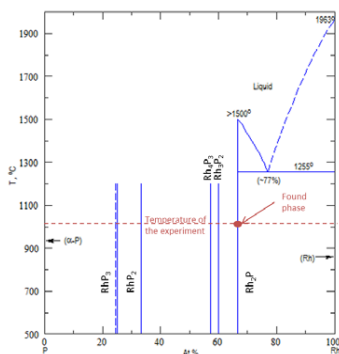


Figure 7. Binary phase diagrams of P-Rh [7].

Conclusion

An effect of phosphorous gas generated in slagging gasifier on Pt-Rh_x thermocouple sensor degradation has been investigated at 1012 °C in P-enriched CO atmosphere. The phosphorous interactions with the Pt-Rh_x alloys depended on Rh content. In the Pt – 0 wt.% Rh, Pt – 6 wt.% Rh and Pt – 10 wt.% Rh alloys, intergranular diffusion was dominant, while intragranular diffusion was governing the P transport into the Pt – 30 wt.% Rh alloys. The Rh₂P phase formed in all wires containing Rh, causing the wire shape distortion and degradation. The pure Pt wire melted due to phosphorous enrichment. Overall, the Pt-Rh_x wires suffered extreme degradation by phosphorous, which led to thermocouple failure.

Acknowledgement

Authors acknowledge Richard Chinn (NETL) for the metallographic work. This technical effort was performed in support of the National Energy Technology Laboratory's ongoing research under the RES contract DE-FE0004000. This research was supported in part by an appointment to the National Energy Technology Laboratory Research Participation Program, sponsored by the U.S. Department of Energy and administered by the Oak Ridge Institute for Science and Education.

Disclaimer: "This report was prepared as an account of work sponsored by an agency of the United States Government. Neither the United States Government nor any agency thereof, nor any of their employees, makes any warranty, express or implied, or assumes any legal liability or responsibility for the accuracy, completeness, or usefulness of any information, apparatus, product, or process disclosed, or represents that its use would not infringe privately owned rights. Reference herein to any specific commercial product, process, or service by trade name, trademark, manufacturer, or otherwise does not necessarily constitute or imply its endorsement, recommendation, or favoring by the United States Government or any agency thereof. The views and opinions of authors expressed herein do not necessarily state or reflect those of the United States Government or any agency thereof."

References

1. R. M. Park, *Manual on the Use of Thermocouples in Temperature Measurement/ sponsored by ASTM Committee E20 on Temperature Measurement*, Fourth ed., MI, 1993.
2. K. S. Vorres, "The Argonne Premium Coal Sample Program," *Energ Fuel*, 4 (1990) 420-426.
3. Argonne Premium Coal Sample. Analytical Data, <http://web.anl.gov/PCS/report/part2.html>.
4. M. Bläsing, M. Müller, "Investigations on the influence of steam on the release of sodium, potassium, chlorine, and sulphur species during high temperature gasification of coal," *Fuel*, 94 (2012) 137-143.
5. W. Heegemann, K.H. Meister, E. Bechtold, K. Hayek, "Adsorption of Sulfur on (100) and (111) Faces of Platinum - Leed and Aes Study," *Surf Sci*, 49 (1975) 161-180.
6. A. Nakano, J. Bennett, J. Nakano, "Failure mechanisms in Pt-Rh_x thermocouple sensors caused by gaseous phosphorous species," *Corrosion Science* 103 (2016) 30-41
7. H. Okamoto, "P-Rh (Phosphorus-Rhodium) System," *ASM International Bulletin. Alloy Phase Diagrams*, 11 (1990) 415-417.

AN EXPERIMENTAL STUDY OF VISCOSITY IN FeO-SiO₂-V₂O₃-TiO₂ SYSTEM

Shiyuan Liu^{a,b,c}, Lijun Wang^{a,b,c}, Kuo-chih Chou^{a,b,c}

^aCollaborative Innovation Center of Steel Technology, University of Science and Technology Beijing, China

^bState Key Laboratory of Advanced Metallurgy, University of Science and Technology Beijing 100083, China

^cSchool of Metallurgical and Ecological Engineering, University of Science and Technology Beijing, 100083, China

Keywords : vanadium slag , viscosity , Newtonian fluid , Non-Newtonian fluid

Abstract

The viscosity was the main reason that converter smelting process of slag containing vanadium caused bonding converter mouth. The study on viscosity of FeO-SiO₂-V₂O₃-TiO₂ quaternary slag system with V₂O₃ level varied from 5 to 15 mass % , TiO₂ contents in the range from 5 to 15 mass % and three different FeO/SiO₂ mass ratio in the range from 1.4 to 2.2 is important for steelmaking. The rotation cylinder method was used for the determinations of the viscosity. The influence of V₂O₃, TiO₂, FeO/SiO₂ ratio and temperature on viscosity were investigated. It was found that the viscosity of compositions with temperature shift from Newtonian fluid to non-Newtonian fluid and obey the Arrhenius law. The slag viscosity increased with increasing V₂O₃ level, and decreased with increasing temperature and FeO/SiO₂ ratio. In the Newtonian fluid, the viscosity of slag decreased with increasing TiO₂ content. In the Non-Newtonian, viscosity of slag increased remarkably with increasing TiO₂ from 5 to 10 mass % and decreased with increasing TiO₂ from 10 to 15 mass%. Viscosity η_0 in the Non-Newtonian fluid could be obtained by extrapolating viscosity of Newtonian fluid, viscosity η for Non-Newtonian fluid could be measured by the Einstein-Roscoe type equations. The measured viscosity fit with the experimental data in the Non-Newtonian fluid.

1. Introduction

Vanadium is an important metal used extensively and largely in manufacturing micro-alloyed steels etc.^[1] Iron and steel making industries consume about 85% of total vanadium production annually.^[1,2] Vanadium slag from some pyrometallurgical process is the world's principal raw material for vanadium production. The main pyrometallurgical processes for production of vanadium slag include shaking ladle process in South Africa, hot metal ladle process in New Zealand, and converter process in China and Russia.^[1]

Previous studies on vanadium containing slag systems were focused on determination of vanadium oxidation states, thermodynamic activity of vanadium oxide and phase equilibria. LiJun Wang^[3] studied determination of vanadium valence state by high-temperature mass spectrometry. Yang Yang^[4] studied effect of basicity, temperature and oxygen partial pressures for phase equilibria in CaO-SiO₂-MgO-Al₂O₃-V₂O₃ slags. Jinichiro Nakano^[5] reported phase equilibria of synthetic coal-petcoke slag and results an isothermal phase diagram

Viscosity is one of the important properties of iron and steel making industries slag and is very sensitive to compositional and temperature changes. Viscosity data with regard to slags containing vanadium oxide were rare and scattered. Zeng^[6] investigated viscosity of FeO-SiO₂-V₂O₃-TiO₂-MnO with V₂O₃ level varied from 15 to 35 mass %, and three different FeO/SiO₂ mass ratio in the range from 1.5 to 2.5. but didn't care about the effect of TiO₂ effect and was short of viscosity of high temperature. Moreover zeng didn't report effect of spinel crystallization behavior on viscosity at Non-Newtonian fluid. Study of the solid-liquid two-phase viscosity was important for industries slag. Anne-Marie studied that rheology of crystal-bearing silicate melts is primarily determined by the crystal fraction,^[7] Liushun Wu^[8] studied that that Einstein-Roscoe model could even be employed for particles having irregular shapes. Alex kondratiev employed the thermodynamic computer packing $F * A * C * T$ to model viscosities of the partly crystallized slags.^[9] The traditional research methods of viscosity containing solid particle were to add high-melting solid particle to pure liquid fluid, therefore, volume fraction of solid particle and viscosity of solid-free particle were known. the slag containing vanadium viscosity study of crystallization process has not been reported. The systematic study on viscosity of containing slag is necessary. The main chemical compositions of vanadium slag were FeO, SiO₂, V₂O₃, TiO₂. The study on viscosity of FeO-SiO₂-V₂O₃-TiO₂ quaternary slag system is important for steelmaking. The rotation cylinder method was used the determinations of the viscosity.

2. Experimental

2.1. Materials and sample preparation

The starting materials in this study, viz. SiO₂, V₂O₃, TiO₂ were Analytical-grade powder, with SiO₂ and TiO₂ calcined for 12h at 1273K in a muffle furnace to decompose any carbonate and hydroxide before use while V₂O₃ were dried at 378K for 4h to remove any moisture and kept in a desiccator. Mixed powder of analytical pure Fe and Fe₃O₄ were contained in steel dies and compacted under a pressure of 12MPa, pellets were placed in an iron crucible and heated at 1373 K for 12h to form FeO. The similar way was reported by Wang et al^[10]. The composition of slag sample for viscosity measurement were listed in

table I .Slag sample were weighed and mixed in an agate mortar ,and then compacted into pellets under a pressure of 12MPa, pellets obtained was placed in a Mo crucible .

2.2. Viscosity measurement

Rotating cylinder method was used to the viscosity measurement. The Mo crucible ,filled with 160g of the prepared slag sample, was placed in the viscometer, heated to 1793K and held for 120min under high pure grade argon gas flowrate of 3L·min⁻¹. The height of molten slag was about 40mm, then the spindle was immersed into the slag and kept at a distance of 10 mm above the crucible bottom. The crucible and the spindle must be properly aligned along the axis of the viscometer, because a slight deviation from the axis can cause large experimental errors.

The viscosity measurements were carried out at every 20K interval on cooling and held for 30 min for the next measurement to guarantee the melt uniform. At each temperature ,the different rotating speeds range from 100 to 200 rpm, distinguishing the molten was Newtonian fluid or not. The average measurement value was adopted as the viscosity value. After completing the viscosity measurement , the Mo crucible containing vanadium slag was quickly withdrawn and then quenched in water .

Table I slag composition for viscosity measurement /wt-%

Slag	FeO	SiO ₂	V ₂ O ₃	TiO ₂	FeO/SiO ₂
A1	54.64	30.36	10	5	1.8
A2	51.43	28.57	10	10	1.8
A3	48.21	26.79	10	15	1.8
B1	54.64	30.36	5	10	1.8
B2	51.43	28.57	10	10	1.8
B3	48.21	26.79	15	10	1.8
C1	46.67	33.33	10	10	1.4
C2	51.43	28.57	10	10	1.8
C3	55.00	25.00	10	10	2.2

3. Result

3.1 Effect of TiO₂

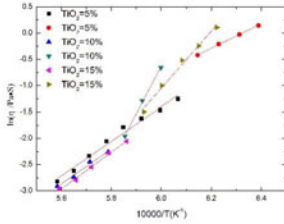


Figure 1. Viscosity variation of composition A1,A2,A3 with temperature and the rotation speed of 200rpm

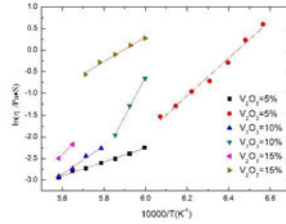


Figure 2. viscosity variation of composition B1,B2,B3 with temperature and the rotation speed of 200rpm

The effect of TiO₂ on the viscosity of the FeO-SiO₂-V₂O₃-TiO₂ slags were presented at figure 1, from which it can be seen that the Arrhenius law is obeyed and the viscosity decreases as increasing the TiO₂ level. In the Newtonian fluid, the viscosity of slag decreased with increasing TiO₂ content from 5 to 15 mass%. In the Non-Newtonian, viscosity of slag increased remarkably with increasing TiO₂ from 5 to 10 mass % and decreased with increasing TiO₂ from 10 to 15 mass%. Guanhua Wen reported that the viscosity increased with the TiO₂ content increasing from 6 to 10 mass-%^[11]. Zhen Wang also reported when the viscosity increased with the TiO₂ content increasing from 5 to 10 mass-%.^[12] X.J.Dong reported that viscosity at high temperature decrease with increasing TiO₂ from 23 to 42 mass-% and viscosity at low temperature increased with increasing TiO₂. The ionic radius of Ti⁴⁺, Si⁴⁺ were 0.68×10^{-10} m, 0.41×10^{-10} m respectively. The electrostatic potential of Ti⁴⁺, Si⁴⁺ were 1.85I, 2.51I, respectively, so the bond between Ti⁴⁺ and oxygen is weaker than that between Si⁴⁺ and oxygen, leading to the depolymerisation of the oxygen ion.^[13] the viscosity decreased as increasing the TiO₂ content in Newtonian fluid. In Non-Newtonian fluid, the viscosity increased as increasing the TiO₂ content, which is mainly due to high crystallization temperature.

3.2 Effect of V₂O₃

The effect of V₂O₃ on the viscosity of the FeO-SiO₂-V₂O₃-TiO₂ slags were presented at figure 2, from which it can be seen that the Arrhenius law is obeyed and the viscosity

increases as increasing the V_2O_5 level. The crystallization temperatures increased with the increasing V_2O_5 concentration, which is mainly due to high melting point of V_2O_5 .

3.3 Effect of FeO/SiO₂ ratio

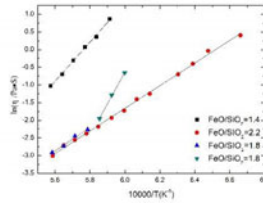


Figure 3. Viscosity variation of composition A1,A2,A3 with temperature and the rotation speed of 200rpm

The effect of FeO/SiO₂ ratio on the viscosity of the FeO-SiO₂-V₂O₃-TiO₂ slags were presented at figure 3, from which it can be seen that the Arrhenius law was obeyed and the viscosity decreased as increasing the FeO/SiO₂ ratio.

3.4 Effect of temperature

The effect of temperature on the viscosity of the FeO-SiO₂-V₂O₃-TiO₂ slag were presented at figure 1,2,3, and it shows that viscosity of the slags decreases with temperature increasing. Activation energy of different slags were listed in table II, In Newtonian fluid, the activation energy increase as increasing the TiO₂, V₂O₃ and decrease as increasing the FeO/SiO₂ ratio. There was no obvious difference of activation energies for different compositions with or without solid particle.^[14]

Table II Activation energy of different slags in Newtonian fluid

sample	A1	A2	A3	B1	B2	B3	C1	C2	C3
Activation energy/KJ • min ⁻¹ (200rpm, in Newtonian fluid)	271.50	276.93	290.72	134.84	276.93	405.46	-	276.93	266.22

4. Discussion

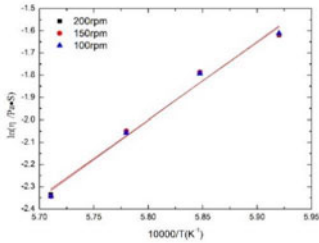


Figure 4. Viscosity variation of composition A1 with temperature and the rotation speed

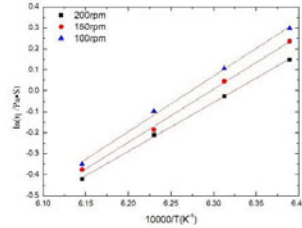


Figure 5. Viscosity variation of composition A1 with temperature and the rotation speed

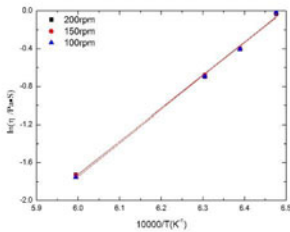


Figure 6. Viscosity variation of composition C3 with temperature and the rotation speed

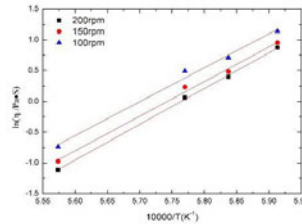


Figure 7. Viscosity variation of composition C1 with temperature and the rotation speed

There is general consensus that viscosity of Newtonian fluid do not change as different rotation speeds. Figure 5,7 indicated that viscosity decreases as the rotation speed increases and deviate from Newtonian fluid on account of solid melt suspension rather than to experimental error, which shows the viscosity of composition A1 with temperature shift from Newtonian fluid to non-Newtonian fluid and obey the Arrhenius law. [15] It is indicated from Figure 4, 6 that viscosities are in good agreement with the Arrhenius law at different temperatures for C3 and C1 melts. In Newtonian fluid, The activation energies of viscosity is almost not affected by the rotation speed. Figure 8, 9 were the scanning micrograph of the quenched samples A1 and B3 in the middle position along the central axis of crucible, from which it can be concluded that solid particle formed during the viscosity measurement.

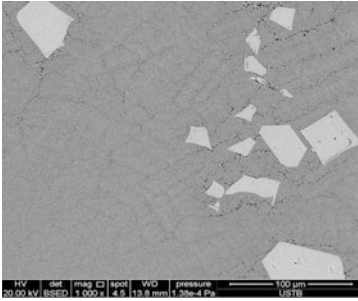


Figure 8. Micrograph of the quenched slag for A1

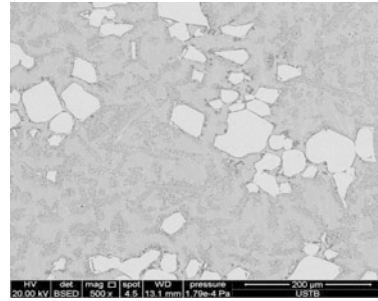


Figure 9. Micrograph of the quenched slag for B3

The general consensus is that the Einstein-Roscoe type equations were used to describing the viscosity of two-phase systems adequately, that is

$$\eta = \eta_0(1 - af)^{-n} \quad (1)$$

where η and η_0 were the viscosity of the solid containing and the solid-free melts respectively ; f is the volume fraction of solid particles in the melt ; a and n were 1.35 and 2.5 for spherical particles of a uniform size ,respectively .

According to the experimental results , the viscosities are in good accord with the Arrhenius law for A1 and B3 in Newtonian fluid . the viscosity of A1 and B3 deviate Newtonian fluid at lower temperature . If the rheology of A1 and B3 are fully liquid slags and obey the Arrhenius law at measured temperature range , viscosity η_0 in the Non-Newtonian fluid could obtain by extrapolating viscosity of Newtonian fluid. the volume fraction of solid particles was determined by micrographic analysis.^[15] therefore , viscosity η for Non-Newtonian fluid could be measured by the the Einstein-Roscoe type equations . Meanwhile , The NPL model relates the viscosity of slags to structure though the OB of the melt and were used to calculated viscosity of A1 and B3 .^[16] The Figure 11, 12 showed that viscosity predicted by Einstein-Roscoe type equations better than NPL model .

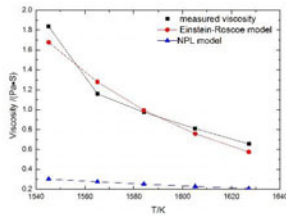


Figure 10. Measured and modeled values of viscosity η for A1

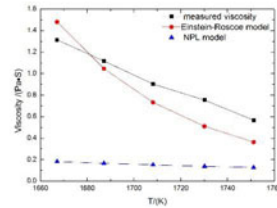


Figure 11. Measured and modeled values of viscosity η for B3

5. Conclusions

1. The viscosity of the FeO-SiO₂-TiO₂-V₂O₃ system with TiO₂ between 5 and 15 – mass %, V₂O₃ between 5 and 15-mass%, and FeO/SiO₂ mass ratio between 1.4 and 2.2 was measurement at temperature 1527K to 1791 K. the slag viscosity increased with increasing V₂O₃ level ,and decreased with increasing temperature and FeO/SiO₂ ratio. In the Newtonian fluid ,the viscosity of slag decreased with increasing TiO₂ content . In the Non-Newtonian , viscosity of slag increased remarkably with increasing TiO₂ from 5 to 10 mass % and decreased with increasing TiO₂ from 10 to 15 mass%.
2. In Newtonian fluid ,the activation energy increase as increasing the TiO₂ ,V₂O₃ and decrease as increasing the FeO/SiO₂ mass ratio.
3. In Non-Newtonian fluid , viscosity predicted by Einstein-Roscoe type equations better than NPL model .

Acknowledgment

The authors are grateful for the financial support for this work from National Nature Science Foundation of China (No.51474141), China Postdoctoral Science Foundation (2014M560046), and Beijing Higher Education Young Elite Teacher Project (YETP0349), as well as the Fundamental Research Funds for the Central Universities (FRF-TP-15-052A3).

References

1. R.R. Moskaly and A.M. Alfantazi, "Processing of Vanadium: A Review," *Minerals Engineering*, 16(2003), 793–805.
2. B. Liu et al., "A Novel Method to Extract Vanadium and Chromium from Vanadium Slag using Molten NaOH-NaNO₃ Binary System," *AIChE J.*, 59(2013), 541-552.
3. L.J. Wang et al., "Determination of Vanadium Valence State in CaO-MgO-Al₂O₃-SiO₂ System by High-temperature Mass Spectrometry," *Metallurgical and Materials Transactions B*, 44B(2013), 948–953
4. Y. Yang, L.D. Teng and S. Seetharaman, "Experimental Study of Phase Equilibria in CaO-SiO₂-MgO-Al₂O₃-V₂O₃ Slags," *Steel Research International*, 85(12) (2014), 1588-1596
5. J. Nakano et al., "Phase Equilibria in Synthetic Coal-Petcoke Slags (Al₂O₃-CaO-FeO-SiO₂-V₂O₃) under Simulated Gasification Conditions," *Energy Fuels*, 25(2011), 3298-3306.
6. X.L. Zeng, "Research on Physicochemical Properties and Phase Diagram of Vanadium" (M.S. thesis, Chongqing University, 2012), 27-49.
7. A.M. Lejeune and Pascal Richet, "Rheology of Crystal-Bearing Silicate Melts," *Journal of Geophysical Research*, 100(B3)(1995), 4215-4229.
8. L.S. Wu et al., "The Effect of Solid Particles on Liquid Viscosity," *Steel Research International*, 82(4)(2011), 388-397.
9. A. Kondratiev and E. Jak, "Modeling of Viscosities of the Partly Crystallized Slags in the Al₂O₃-CaO-FeO-SiO₂ System," *Metallurgical and Materials Transactions B*, 32B(2001), 1027-1032.
10. Y. Wang, L.J. Wang, and K.C. Chou, "Effects of CaO, MgO, Al₂O₃ and SiO₂ on the Carbothermic Reduction of Synthetic FeCr₂O₄," *Journal of Mining and Metallurgy, Section B: Metallurgy*, 51(1)(2015), 17-24.
11. G.H. Wen et al., "Development of Fluoride-Free Mold Powders for Peritectic Steel Slab Casting," *ISIJ International*, 47(8)(2007), 1117-1125
12. Z. Wang et al., "Effect of Substituting SiO₂ with TiO₂ on Viscosity and Crystallization of Mould Flux for Casting Titanium Stabilized Stainless Steel," *Ironmaking and Steelmaking*, 39(3)(2012), 210-215
13. X.J. Dong et al., "Viscosity and Viscosity Estimation Model of Fully Liquid Slags in TiO₂-Al₂O₃-CaO-SiO₂ and TiO₂-Al₂O₃-CaO-SiO₂-MgO Systems with High TiO₂ Concentration and Low Mass Ratio of CaO to SiO₂," *Ironmaking and Steelmaking*, 41(2)(2014), 99-106].
14. G.H. Zhang, Y.L. Zhen and K.C. Chou, "Influence of TiC on the Viscosity of CaO-MgO-Al₂O₃-SiO₂-TiC Suspension System," *ISIJ International*, 55(5)(2015), 922-927.
15. S. Wright et al., "Viscosity of Calcium Ferrite Slags and Calcium Alumino-Silicate Slags"

Containing Spinel Particles,” *Journal of Non-Crystalline solids*, 282(2001),15-23
16.K. C.Mills , “The Influence of Structure on the Physic-Chemical Properties of Slags ,”*ISIJ International*, 33(1)(1993), 148-155.

CAPTURING AND CONDENSATION OF SiO GAS FROM INDUSTRIAL Si FURNACE

Ksiazek Michal¹, Grådahl Svend¹, Rotevant, Eirik Andersen ², Wittgens Bernd¹

¹SINTEF Materials and Chemistry; Richard Brikelands Vei 2B, 7465 Trondheim, Norway

²Wacker Chemicals Norway AS, 7200 Kyrksaeterora, Hemne, Norway

Keywords: SiO gas, condensation, Silicon furnace

Abstract

In industrial submerged arc furnaces, SiO in the off-gas from the furnace leads to Si losses that reduces Si yield and thereby increases specific energy consumption. An understanding of formation of SiO gas and condensation of this gas to form solid / liquid SiO₂ in industrial furnace is important for improving Si yield and reduce formation of dense layers in a charge that generate operational challenges. Understanding of these mechanisms is also vital for an enhanced energy recovery from smelters. Two main goals of this research was to:

- a) verify a system designed to extract gaseous samples from the charge of a SFA,
- b) capture and analyze industrial SiO gas condensates.

This paper presents the industrial trial on capturing SiO gas and initial analysis of the samples taken from a 33 MW Si furnace.

Introduction

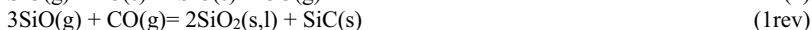
The production process for silicon has constantly improved with respect to health, safety and environmental aspects because of improved process understanding, process design, operation and quality control. The notion of a closed furnace has often been discussed as it may provide several advantages, such as improved Si recovery, reduction of electrode consumption and carbon requirements [1],[2]. Additionally, it may enable a more efficient recovery of the energy from the flue gas. A comprehensive recovery of energy requires a safe and effective way of transferring the flue gas from a furnace to a heat recovery unit. Such a concept entails mitigation strategies for clogging and fouling by dust and SiO condensates. This, in turn, calls for increased understanding of conditions and mechanisms for condensation of SiO-gas in industrial conditions. The SCORE research program (NFR 226210), performed by The Norwegian Ferroalloys Research Association (FFF), SINTEF and The Research Council of Norway (RCN) is focusing on the recovery of energy from metallurgical furnace particularly handling of unburned off-gases, containing CO, SiO, tar components and other effluents, from a submerged arc furnace.

The most common metallurgical route for Si-production involves carbothermic reduction of SiO₂ in a Submerged Arc Furnaces (SAF). The Si-reduction process requires temperature above 1800 °C hence electrical energy consumption in the order of 11-13 MWh per ton of produced metal [3]. Three submerged electrodes provide electric energy to the charge mix. Si-production

reaction (Equations 3) occurs close to the electrode tip, in the so called crater zone. Close to the crater zone reactions (Equations 1 and 2) characterizing SiO- and CO-production take place:



The produced gases travel upwards in the permeable charge towards the charge surface. Within the charge SiO is recovered either by reaction with carbon materials (equation 4) or by condensation reactions (Equations 1rev and 2rev):



CO and some of either converted or condensed SiO gas will reach the charge surface, enter the furnace hood and react with the O₂ from the surrounding air.

Comprehensive work during the recent years consider SiO gas condensation mechanisms. Tangstad et al. [4] simulated the interior of SAF by heating SiC and SiO₂ in graphite crucible. Usage of an induction furnace allowed creating the temperature gradient inside the crucible (1400 °C on the top of the charge and 1900 °C on the bottom) which corresponds to real temperatures inside a commercial reactor. The same experimental set up was used by Vangskåsen [5] [6] [7] and Ksiazek [8] to investigate the SiO gas condensation reaction mechanism and cavity formation in a silicon production process. Based on previous work, condensation occur between approximately 1435 °C and 1700 °C two types of condensates are observed: brown and white condensates [9]. The brown deposit consists of a SiO₂ matrix with Si droplets, which can constitute of 5 to 15 % of the total silicon production inside the furnace [10]. White condensates are a mixture of SiO₂, Si and SiC and occur either as a white, dens layer or as deposition of whiskers [8]. All previously mentioned studies focused on capturing the SiO inside the charge mix in an open crucible where remaining gas burned off on the charge surface. Ksiazek et al. [10] investigated the deposition of SiO gas condensates in a closed reactor in an inert atmosphere, which simulates conditions in a closed Si furnace. Both white and brown condensate deposited at temperatures above 1300 °C, which is the temperature on the top of the charge in industrial furnace.

The current paper presents results from three industrial test where off gas containing SiO was extracted through a metal lance from the silicon furnace.

Experimental

Equipment

The measuring lance consisted of a five meter long Kanthal APM (FeCrAl alloy) tube with ID 35mm for the high temperature part joined together with a 3 meter long steel pipe for the low temperature zone. In figure 1 the schematic drawing of the experimental set up is presented. At the front of the lance, a graphite crucible at that the tip of the lance duct was directed 90 degrees down towards charge surface. For evacuation of the process gas an ejector pump was used, and compressed air was connected via a control valve to control the amount of air through the lance. At the end of the lance a CO/CO₂ analyser was installed before the flue gas was mixed with air for suction; finally a 142 mm diameter large filter (Millipore) was applied to collect particles extracted from the furnace. Temperature was measured in three different areas of the lance. For

measuring the gas temperatures three K type thermocouples were set on the front of the lance with distance 30cm from each other (T1, T1, T3). Temperature was also measured in the ejector before (T4) and after (T5) the injection of air to the furnace gas. Additionally, the temperature on the surface of the charge was monitored by thermocamera (FLIR ThermoCAM SC640) In order to limit the problems related to strong electromagnetic field near the electrodes that causes temperature measurement problems the thermocouples had an Inconel sheath surrounding wires with insulated hot junction. Additionally shielded compensation cable (for high-frequency noise) with twisted leaders (against low-frequency noise) was used. A filter, made of steel wire mesh (1mm) was mounted at the end of ejector for particle/condensate collection. Separate data loggers were used for temperature measurement and gas analysis because the risk of large potential differences between the individual measuring points that can affect the measurements.

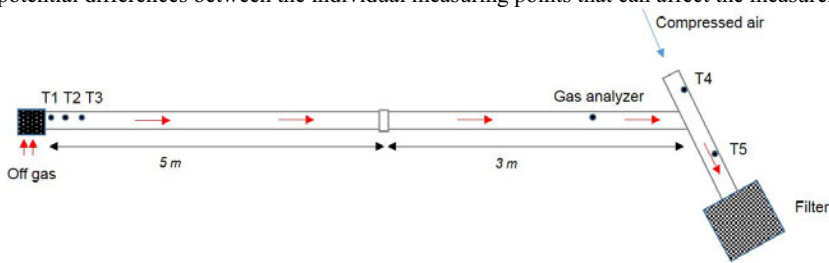


Figure 1. Experimental set up.

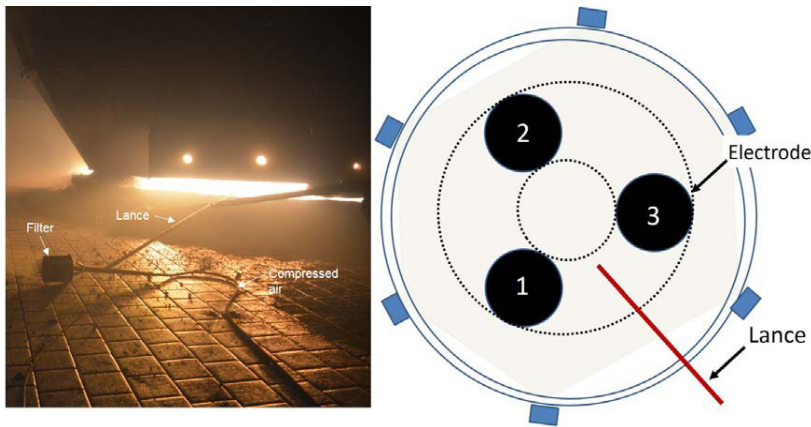


Figure 2. Test number 1. Lance inserted to the furnace.

Procedure

Three tests were performed by inserting the lance into the furnace hood through the stacking doors. Lances were placed in area an between electrode 1 and 3. Three different lance arrangement were applied: 1) lance placed on the charge surface, 2) lance submerged in the charge, 3) lance directed into a SiO gas blow. Additionally, different velocity of compressed air and duration time of test were used. During the experiment 3 the initial gas velocity was 7 m/s,

however due to a large amount of CO gas released to the working area, velocity was reduced to 5 l/m. Experimental conditions are listed in Table 1. After the experiments the lances were filled with epoxy for preservation. Then lances were cut along for visual observation of deposited material. Representative samples were collected from each lance and investigated with Electron Probe Micro Analyzer (EPMA).

Table 1. Experiment conditions.* Parameters were change during the test.

Test	Lance location	Duration	Gas velocity
1	On the charge	30min	5m/s
2	Under the charge	60min	2.5 m/s
3	SiO gas blow	30min	7-5 m/s*

Results and Discussion

Deposition of SiO condensates

Aim of this work was to verify the experimental design for capturing the SiO gas from industrial Si furnace with temperature on the top of the charge of around 1300 °C and higher. The smelting point of the lance was above 1500 °C, and maximum working temperature for the thermocouples located at the front is 1370 °C. Thus based on data from thermocouples the duration of the experiment was determined. Signal loss indicated that the lance met the SiO gas jet and smelt completely. Graphs presented on Figure 3 shows the temperatures measured at front of the lance and CO/CO₂ concentration of the extracted gas for Experiment 1 to 3. During Test 1, the lance was positioned on top of the charge; initially the temperature reaches around 1350 °C and then slowly decreases. It is worth to mention that the furnace was fed during the test, thus after some time some charge material covered the lance which could cause the temperature drop. Similar situation are observed during Test 2 where the experiment lasted approximately one hour. In this case the lance was actively submerged inside the charge mixture, because of natural sinking of charge downwards the crater zone the lance was positioned around 1 m below charge. During Test 3, where the aim was to meet the SiO gas blow, the signal from thermocouples were lost just after insertion of the lance into the furnace. In Test 1 and 2, CO₂ concentration decreased as the lance sinks with the charge downwards. However CO concentration changes during the experiments probably due to uneven gas distribution inside the charge. Nerveless, towards the end of Experiment 2 the lance was deep in the charge and the gas almost consist entirely of CO. The last picture in figure 3 shows a thermal picture of the temperatures inside the furnace before the probe reaches blowing zone.

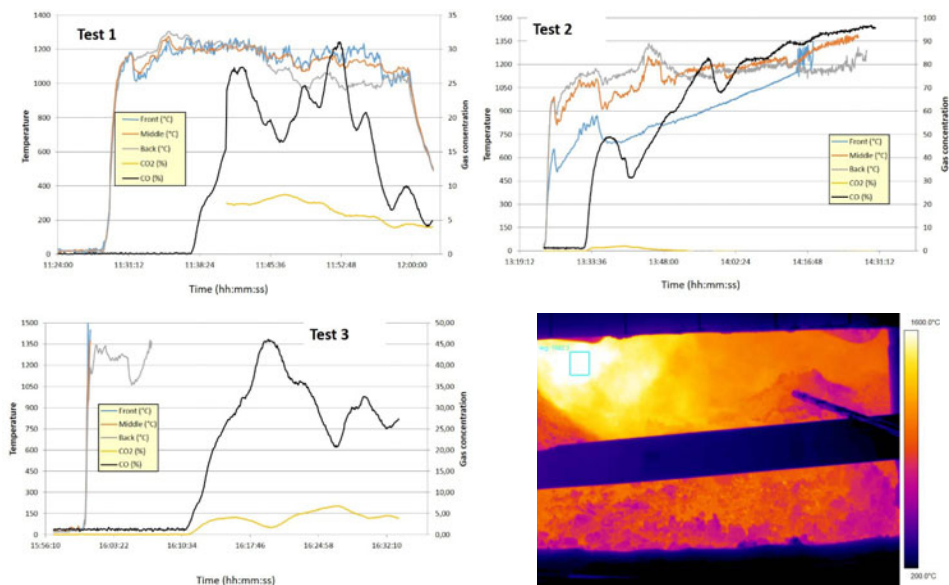


Figure 3. Measured temperature and CO/CO₂ concentration during the tests

As shown in Figure 4, lances 2 and 3 were smelted during the experiments. Deposition of black dust-like material was observed inside all of the lances, some quantity of dust was captured on the wire filters (top Figure 5) and plane filters of the gas analyser (bottom Figure 5). Samples from the front (a), middle part (b) and the end (c) of each lance was tested with EPMA and are presented in Figure 6-8.



Figure 4. Lances after experiments

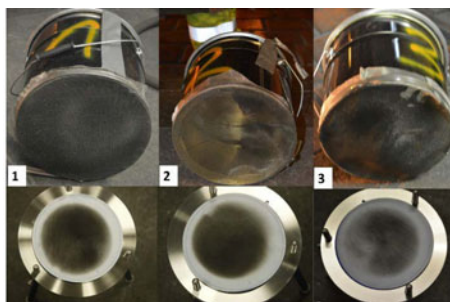


Figure 5. Dust deposited on the lance filters (top) and of gas measurement filters (below).

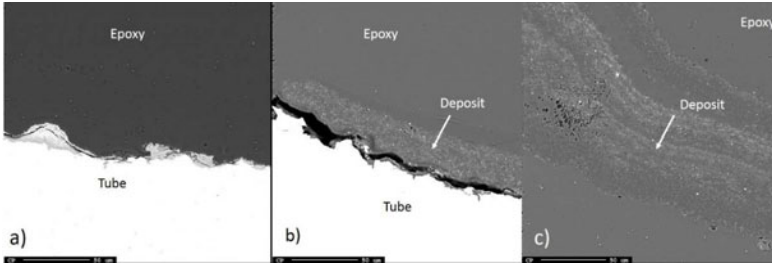


Figure 6. EPMA image of deposition found inside the lance after the experiment 1. a)-front, b) middle, c) end of lance.

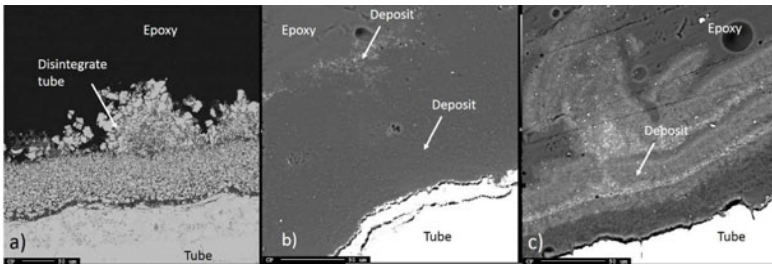


Figure 7. EPMA image of deposition found inside the lance after the experiment 2. a)-front, b) middle, c) end of lance.

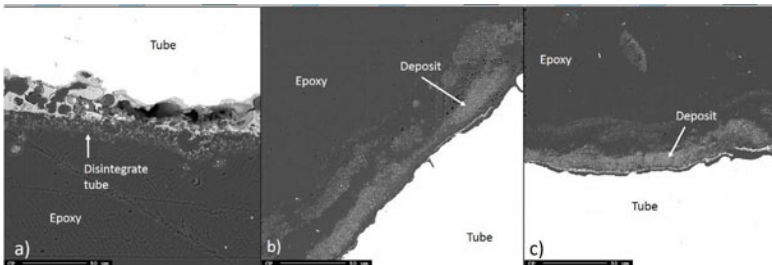


Figure 8. EPMA image of deposition found inside the lance after the experiment 3. a)-front, b) middle, c) end of lance.

Depositions were observed inside the lance for all experiments. Depositions seem to have a layered structure and its thickness varies considerably between experiments. No deposition was observed in the front part of any of the lances. Even during Experiment 1 where the temperature in the front of the lance was not higher than 1370°C , it was postulated that where SiO gas should condense in this location. Deposition starts to occur around 1.5 m from the beginning of the lance. Lances during Test 2 and 3 were smelted, indicating that the temperature was higher than 1550°C . Layers become thicker towards the end of the lance where the temperature was lower in comparison to the front. Please note, as presented on figure 2, the end (ca. 1m) of the lance was outside of the furnace, while the rest was located on the charge surface. Thus, thermocouples located inside the lance more likely show the local charge temperature than the gas temperature.

That will explain that the temperature measured by the front thermocouple (T1) is lower than those measured by thermocouple T3 located 60 cm from the tip of the lance.

Depositions are quite porous and easily penetrated by epoxy. Depositions consists of carbon, oxygen and silicon. Figure 9 presents a mapping image with concentrations of each element inside a layer. It shows that the deposition is a mixture of carbon and SiO₂ is present in the whitish areas. No particles from the charge such as small pieces of quartz or coke were found inside the lance. SiC can also be present but due to high carbon content of the cured epoxy resin, it is difficult to distinguish these two components by using the EPMA. The white droplets presented in Figure 10 are most likely Si droplets produced during the SiO gas condensation reaction (2rev). The accurate point analyze by using energy dispersive spectrometry (EDS) was also difficult to carry out, due to its small size. However, similar formation of Si droplets was reported previously by various authors [4, 10]

Figure 9. EPMA mapping image of sample from lance 2.

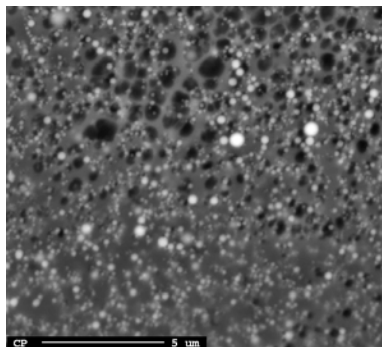
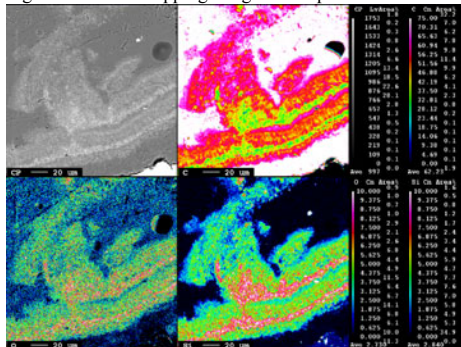


Figure 9. Image taken from sample from lance 3. Round circles are most likely Si droplets produced during SiO gas condensation.

Conclusion

The verification of an experimental set-up for capturing SiO gas from Si furnace was successfully carried out. The principle of using an ejector pump to extract the gas from the charge is a safe and efficient solution. Application of temperature and gas measurements gave indication about temperature distribution and gas composition on the surface of charge and approximately 1m below the top of the charge. Extraction of gas from a SiO blow was performed too, but the life-time of the lance is rather limited.

Porous layer containing carbon, SiO-gas condensates and Si-droplets are deposited on the internal walls of the lances approximately 1.5m from the front of the lance in all experiments, However, more extensive characterisation of the deposits must be performed to identify deposition mechanics and condensation reactions.

Lances were located in the area between electrodes 1 and 3. Temperature of the charge, but more over the local gas distribution (SiO gas blowing) caused smelting of the tip of the lances. That

shows how temperature distribution vary locally on the surface of the charge. Temperature record of Test 1 can indicate that the temperature below the charge is lower than temperature just above, where most of the heat comes from combustion of process gases.

Acknowledgements

The authors are grateful to the Norwegian Ferroalloys Research Association and the Norwegian Research Council for the funding (Project 226210 SCORE: Staged COmbustion for energy Recovery in Ferroalloy industry). Thanks are also owed to Wacker Chemical Norway for great help during the tests.

References

1. Dosaj, V. Brumels, M.D, Haines, C.M. and May, J.B.: *Proceedings of Electric Furnace Conf.* Silicon smelting in a closed furnace, 44 (1991), 265-268.
2. Arnesen, A.G. and Bjørdal, J. *Proceedings of Electric Furnace Conf.* Development and achievements with a closed 8500kW Elkem furnace producing 75% ferrosilicon. (1981) Vol 38, 191-196.
3. Schei A., Tuset J. Kr., and Tveit H., *Production of High Silicon Alloys*, Tapir, Trondheim, Norway, 1998, 89-91.
4. Tangstad M., Ksiazek M., Andersen V., Ringdalen E. *Proceedings of INFACON 12 (6-9. 06.2010) Helsinki -Finland*, Small scale laboratory experiments simulating an industrial silicon process, 661-669.
5. Vangskåsen J., *Investigation of the cavity formation in the silicon process*, NTNU internal report, 2011.
6. Vangskåsen J., Tangstad M., *Proceedings of INFACON 13(9-13. 06.2013) Almaty Kazakhstan*, Condensate in the metallurgical silicon process-reaction mechanisms, 283-289.
7. Vangskåsen J., *Metal-producing Mechnism in the carbothermic silicon process*, Master thesis, NTNU, Norway, 2012, 20-27.
8. Ksiazek M., Tangstad M., Ringdalen E. *Proceedings of Admet 2015 (4-5.06.2015) Kiev-Ukraine*, Silicon production in laboratory scale induction furnace.
9. Mølnås H., *Investigation of SiO-condensate formation in the silicon process*, NTNU internal report, 2010.
10. Ksiazek M, Kero I, Wittgens B., *Challenges in transporting the off-gasses from the silicon process*, Proceedings of Sustainable industrial processing summit, Antalya, Turkey, 2015.

CORROSION TESTING OF ZIRCONIA, BERYLLIA AND MAGNESIA CERAMICS IN MOLTEN ALKALI METAL CARBONATES AT 900°C

Valery Kaplan, Igor Lubomirsky

Department of Materials and Interfaces,
Weizmann Institute of Science,
Rehovot 76100, Israel.

Keywords: CO₂ electrolysis, molten carbonates, magnesia, zirconia, beryllia.

Abstract

An electrochemical cell containing molten Li₂CO₃-Li₂O has been proposed for the conversion of the greenhouse gas CO₂ to CO, which can then either be used to power gas turbines or converted to methanol. Since efficient electrolysis takes place at 900°C, the materials which can be used in such a cell must satisfy stringent requirements. In the current work, we have examined the static corrosion resistance of zirconia, beryllia and magnesia ceramics at 900 °C in the Li₂CO₃-Li₂O mixture and in a Li-Na-K carbonate eutectic mixture with the ultimate objective of identifying suitable electrically insulating materials. Conclusions regarding material stability were based on elemental analysis of the melt, primarily *via* X-ray photoelectron spectroscopy, a particularly sensitive technique. It was found that magnesia is completely stable for at least 33 hrs in a Li₂CO₃-Li₂O melt, while a combined lithium titanate/lithium zirconate layer forms on the zirconia ceramic as detected by XRD. Under the same melt conditions, beryllia shows considerable leaching into solution. In a Li-Na-K carbonate eutectic mixture containing 10.2 mol% oxide at 900°C under standard atmospheric conditions, magnesia showed no signs of degradation. Stabilization of the zirconia content of the eutectic mixture at 0.01-0.02 at% after 2 hrs is again explained by the formation of a lithium titanate/ lithium zirconate coating. On the basis of these results, we conclude that only magnesia can be satisfactorily used as an insulating material in electrolysis cells containing Li₂CO₃-Li₂O melts.

Introduction

Electrochemical reduction of CO₂ to CO is one of the very attractive routes for converting electrical energy from renewable sources into fuel which may be stored for later use [1-4]. CO can be used in any standard gas turbine to generate electricity, or it can be converted into methanol *via* a well-established chemical pathway. The technique for CO₂ to CO conversion that we recently described is based on the electrolysis of molten Li₂CO₃ at 900 °C using a Ti cathode and a graphite or Ti/TiC anode [5-7]. Upon melting, Li₂CO₃ converts to a Li₂CO₃/Li₂O mixture, in which the content of Li₂O (up to 18 at %) is controlled by the pressure of CO₂ in the environment [7]. Electrode reactions in carbonates are in general complex and multi-stage [8-

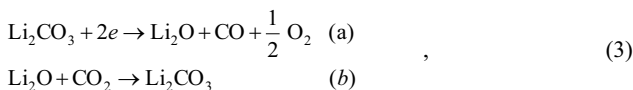
12]. The material-charge balance of the cathode reaction during the electrolysis of molten Li_2CO_3 at 900 °C with a Ti cathode is [6]:



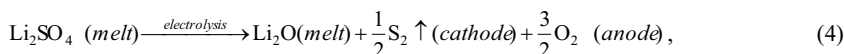
The mechanism of the anode reaction has not yet been identified: neither anode material, graphite or Ti\TiC\C, degrades during electrolysis and the overpotential does not exceed a few tens of mV even for very large current densities ($>1.5 \text{ A/cm}^2$) [5]. The material-charge balance of the anode reaction is:



The reaction $\text{CO}_3^{2-} - 2e \rightarrow \text{CO}_2 \uparrow + \frac{1}{2}\text{O}_2$ apparently does not take place because no CO_2 was found in the anode gases even when the concentration of Li_2O is only ~2at% [6]. Thus, a Li_2CO_3 electrolysis cell operates *via* the self-replenishing cycle:



The electrochemical conversion of CO_2 to CO *via* electrolysis of molten Li_2CO_3 has a number of advantages compared to alternative CO_2 reduction pathways [6,7]: **(i)** High thermodynamic efficiency (the ratio of the energy supplied with respect to the energy used to drive the reaction) is not uncommon for electrolysis with gaseous products. The entropy term $T\Delta S$ is positive, thereby reducing the decomposition potential below that of the isothermal point: the decomposition potential of Li_2CO_3 is 0.87 V at 900 °C, which is approximately 30% lower than the isothermal voltage (1.28 V at 900 °C) ($\Delta G = 246 \text{ kJ/mol}$). This implies that a significant fraction of the heat of reaction can be converted to chemical energy, thereby compensating for ohmic losses. Thermodynamic efficiency close to 100% may result. **(ii)** Since the $\text{Li}_2\text{CO}_3/\text{Li}_2\text{O}$ melt is free of precipitate at 900 °C in the presence of ~ 2 at% CO_2 [7], dilute sources of CO_2 can be used. **(iii)** The CO_2 to CO conversion is not affected by the presence of water in the incoming gas. **(iv)** Noble metals and solid electrolytes are not required, only welded Ti; therefore, process scale-up is more economically achieved than with a number of other technologies. **(v)** The electrolysis products are physically separated from each other, both within the cell and upon outflow. **(vi)** The method is tolerant to the presence of sulfur in the incoming gas: any sulfur entering the system is eventually converted into sulfate and then removed by electrolysis [13]:



Consequently, sulfur-containing flue gas from power stations can be used as the source of CO_2 . However, despite all these advantages, the CO_2 to CO conversion by electrolysis of molten Li_2CO_3 faces problems of material compatibility. Electrolysis proceeds efficiently only between 850-900 °C, and at these temperatures, the $\text{Li}_2\text{CO}_3/\text{Li}_2\text{O}$ melt is very corrosive (e.g., it dissolves alumina, Pt and Au) [6,14]. Although the melt is readily contained in a welded Ti container [13],

practical application requires construction of multi-cell devices in which insulating materials would play a dual role: (i) for the construction of high-temperature, feed-through electrical connectors and (ii) for the construction of bipolar electrodes (one surface anodic, the other surface, cathodic). Bipolar electrodes are the most common solution for connecting cells in series in order to reach the required voltage. In this way, improved matching to power sources may be accomplished. High melting point ceramics are obvious candidates and in the present study, we report the results of static corrosion testing of zirconia, beryllia, and magnesia ceramics in molten $\text{Li}_2\text{CO}_3/\text{Li}_2\text{O}$.

Experimental

Ceramics were obtained from the following sources: partially yttria-stabilized zirconia (YSZ) from Retsch GmbH (5.2% Y_2O_3 , other oxides < 0.3%, ~1at% Hf); beryllia (99.5 at%) and magnesia (>99.9 at%) both from The Institute of High Temperature Electrochemistry of the Ural Branch of the Russian Academy of Science. Of these, beryllia is the most costly and zirconia, the least costly. Beryllia and magnesia were in the form of thin, ceramic plates with a total surface area of 100-120 mm^2 while the partially yttria-stabilized zirconia sample had the approximate shape of a short sphero-cylinder with diameter ~ 12 mm, length ~ 9 mm and surface area 550-600 mm^2 . The crystal structure of the pristine zirconia sample is tetragonal; following immersion in the melt, a phase transition to monoclinic takes place. The cooled sample displays bi-phasic behavior, characteristic of weakly doped ZrO_2 . The ceramic samples were immersed in 100 ($\pm 5\%$) cm^3 of the Li_2CO_3 melt (Acros Organics), or of a Li-K-Na carbonate eutectic, in a titanium container for 2 to 33 hrs at 900 °C. For preparation of the eutectic, Na_2CO_3 and K_2CO_3 were obtained from Alfa Aesar. Prior to the immersion of the ceramics, it was verified that the melt did not contain detectable amounts of Mg, Zr or Be. Mg may pose a particularly serious problem as some commercially available sources of Li_2CO_3 contain 0.5-100 mg/kg of Mg (depending on the purity [15]). Upon heating, Li_2CO_3 converts to a $\text{Li}_2\text{CO}_3/\text{Li}_2\text{O}$ mixture releasing CO_2 . In 1 atm CO_2 the concentration of Li_2O in the $\text{Li}_2\text{CO}_3/\text{Li}_2\text{O}$ mixture is ≈ 0.2 mol% [7]; in air, the concentration of Li_2O reaches ≈ 18 mol%. Probes (0.1-0.4 cm^3) of the melt were taken using a cold rod and their content analyzed by energy-dispersive X-ray spectroscopy (EDS, qualitative analysis) and X-ray photoelectron spectroscopy (XPS, quantitative analysis) to determine the elemental composition (Table 1).

We found experimentally that this approach is far more sensitive than measuring weight loss after separating the ceramics from the solidified melt. EDS measurements were made on a Leo-Supra scanning electron microscope (SEM). XPS measurements of the Li(1s), C(1s), O(1s), Na(1s), K(2p), Mg(1s), Be(1s) and Zr(3d) core levels were carried out with the Kratos AXIS ULTRA XPS system using a monochromatic Al K_α X-ray source ($h\nu = 1486.6$ eV) at 75W and detection pass energies ranging between 20 and 80 eV. A low-energy electron flood gun (eFG) was applied for charge neutralization. Depending on the shape of the background, either a linear or Shirley background [16] was used to extract the surface concentrations of the different elements. Curve fitting analysis was based on background subtraction and use of mixed Gaussian-Lorentzian line shapes [17,18]. Powder X-ray diffraction (XRD) patterns were measured on a Rigaku TTRAXIII theta-theta diffractometer at grazing incidence (fixed angle 4.5°) with Cu K_α radiation. Phase identification and quantitative analysis was performed with Jade 9 (MDI, CA) with reference to the Powder Diffraction File (PDF-ICDD). X-ray fluorescence (XRF) was measured on a benchtop XRF ED instrument (model EX-Calibur, Xenometrix, Migdal Haemek, Israel).

Table 1. Ceramic stability in $\text{Li}_2\text{CO}_3 + \text{Li}_2\text{O}$ and $(\text{Li}, \text{Na}, \text{K})_2\text{CO}_3$ - eutectic melts at 900°C

Material	Melt content (at% metal)	Melt	Atmosphere (pressure 1 atm)	Duration (hours)	Detection Method
YSZ	n.d.*	$\text{Li}_2\text{CO}_3 + \text{Li}_2\text{O}$ (0.2 mol%)	CO_2	3,5,9,29,33	EDS, XPS
YSZ	n.d.	$\text{Li}_2\text{CO}_3 + \text{Li}_2\text{O}$ (up to 18 mol%)	Air	5,9,29,31,33	EDS, XPS
YSZ	<0.02	$(\text{Li}, \text{Na}, \text{K})_2\text{CO}_3$ - eutectic with $(\text{Li}, \text{Na}, \text{K})$ oxides (10.2 mol%)	Air	2,6	EDS, XPS
MgO	n.d.	$\text{Li}_2\text{CO}_3 + \text{Li}_2\text{O}$ (0.2 mol%)	CO_2	2,6	EDS, XPS
MgO	n.d.	$\text{Li}_2\text{CO}_3 + \text{Li}_2\text{O}$ (up to 18 mol%)	Air	31	EDS, XPS
MgO	n.d.	$(\text{Li}, \text{Na}, \text{K})_2\text{CO}_3$ - eutectic with $(\text{Li}, \text{Na}, \text{K})$ oxides (10.2 mol%)	Air	6	EDS, XPS
BeO	0.47	$\text{Li}_2\text{CO}_3 + \text{Li}_2\text{O}$ (0.2 mol%)	CO_2	3	XPS
BeO	0.42	$\text{Li}_2\text{CO}_3 + \text{Li}_2\text{O}$ (0.2 mol%)	CO_2	5	XPS
BeO	1.44	$\text{Li}_2\text{CO}_3 + \text{Li}_2\text{O}$ (0.2 mol%)	CO_2	9	XPS

* n.d. = not detectable by either EDS or XPS

Results and discussion

Ceramic stability in molten $\text{Li}_2\text{CO}_3/\text{Li}_2\text{O}$.

Figure 1a (red (lower) trace) shows the X-ray photoelectron spectroscopy (XPS) measurement of a cold rod probe of the $\text{Li}_2\text{CO}_3 + 0.2 \text{ mol}\% \text{ Li}_2\text{O}$ melt taken after a YSZ ($T_{\text{mp}} = 2715^\circ\text{C}$) ceramic spherocylinder had been immersed for 9 hrs at 900°C under 1 atm of CO_2 . The 3d photoelectron peaks of Zr, if present, would appear at 182.5 eV (5/2) and 184.9 eV (3/2). It is clear that the spectrum shows no evidence of transfer to the melt of any detectable amount of Zr. Similar negative results were obtained when the YSZ sample had been in the melt for up to 33 hrs (data not shown).

We have also immersed YSZ cylinders in the $\text{Li}_2\text{CO}_3 - \text{Li}_2\text{O}$ melt at 900°C in air for up to 33 hrs. Under these conditions, the concentration of Li_2O reaches $\approx 18 \text{ mol}\%$ and Li_2O begins to precipitate. Also in this case XPS did not reveal any Zr in a cold rod probe of the melt (data not shown). This implies that lithium zirconates either do not form at all or that they do form but are not soluble in the melt and remain on the surface of zirconia. In order to verify which possibility is the correct one, grazing incidence XRD measurements (4.5°) were made on zirconia samples which had been in the melt for 6-48 hrs (under either 1 atm air or CO_2). A thin grey colored material shell was observed to either fully or partially cover the light yellow core. After washing for 24 hrs to remove the melt residue, the diffraction patterns were shown to contain characteristic peaks of Li_2ZrO_3 (Figure 1b).

A reaction likely taking place on the surface of the zirconia ceramic:



has in fact been shown to proceed at temperatures above 700°C [19,20]. Following sample immersion for times longer than 6 hrs, the grazing incidence XRD patterns also showed evidence for the presence of LiTiO_2 on the ceramic surface. Although XPS detected only 0.3 at% Ti in the

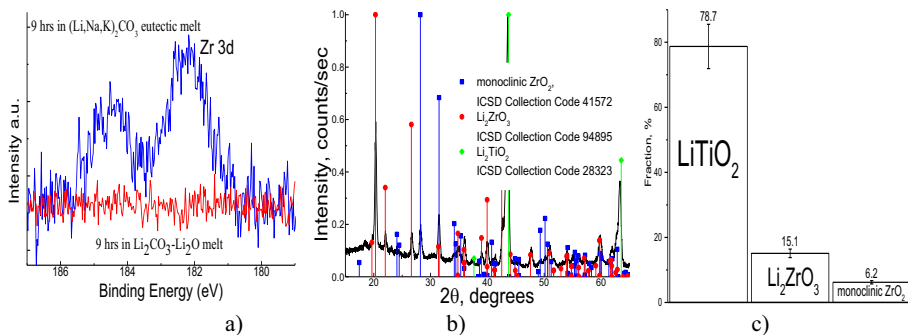


Figure 1. **a)** XPS spectra of cold rod probes taken from a $\text{Li}_2\text{CO}_3/\text{Li}_2\text{O}$ melt (under CO_2 , red trace) and from a $(\text{Li, Na, K})_2\text{CO}_3$ -eutectic melt (in air, blue trace) following 9 hrs exposure of an yttria stabilized- ZrO_2 sphero-cylinder in the former and 2-6 hrs in the latter. **b)** Grazing incidence (4.5°) XRD pattern of a washed YSZ spherocylinder after 31 hours of exposure to the $\text{Li}_2\text{CO}_3/\text{Li}_2\text{O}$ melt at 900°C in air. XRD peak positions and intensities of Li_2ZrO_3 (ICSD 94895), LiTiO_2 (ICSD 28323) and monoclinic ZrO_2 (ICSD 41572) are shown. **c)** Quantitative analysis of the XRD pattern from the grey colored coating of the YSZ spherocylinder after 31 hours of exposure to the $\text{Li}_2\text{CO}_3/\text{Li}_2\text{O}$ melt at 900°C in air.

melt (data not shown), quantitative analysis (Figure 1c) of the XRD pattern in Figure 1b showed five times as much lithium titanate as lithium zirconate. XRF spectroscopy gave definite evidence for the presence of Ti on the surface of YSZ samples, the amounts of which scaled with the intensity of the relevant XRD peaks. Interestingly, for the longer immersion times, diffraction from the YSZ core is weakened, indicating that the thickness of the lithium zirconate/lithiumtitanate layer increases with sample immersion time in the melt, thereby reducing the penetration of the grazing incidence X-ray beam. We tentatively attribute the presence of lithium titanate to the fact that the ceramic samples rest on the bottom surface of the titanium container, where it is known that both TiO_2 and LiTiO_2 layers are present [6]. Ti doping of lithium zirconate has been reported to take place upon mixing TiO_2 , Li_2CO_3 and ZrO_2 under conditions similar to those which exist in the carbonate melt [21]. In the case of MgO ($T_{\text{mp}} = 2852^\circ\text{C}$), cold rod probe XPS spectra were measured in the region of the $\text{Mg}(1s)$ core level (1303 eV) following exposure of the MgO plate to the Li_2CO_3 - Li_2O melt under 1 atm CO_2 for 6 hrs and in air for 31 hrs. No detectable amount of Mg leaching into the melt is observed for either sample (Figure 2a). Indeed, MgO is not known to form compounds with Li [22]. On the basis of these results, we were able to conclude that MgO ceramics are stable in the Li_2CO_3 - Li_2O melt at 900°C . By contrast, the exposure of a BeO ($T_{\text{mp}} = 2507^\circ\text{C}$) plate to the $\text{Li}_2\text{CO}_3+0.2 \text{ mol}\% \text{ Li}_2\text{O}$ melt under 1 atm CO_2 reveals a readily detectable amount of beryllium in the XPS spectrum (Figure 2b). The intensity of the peak due to the 1s core level increases with time of exposure up to 9 hrs. By normalizing to the XPS integrated peak intensities for the total probe elemental content, this increase is found to correspond to an increase in Be content of the melt from 0.47 at% at 3 hours to 1.44 at% at 9 hours, attesting to continuing BeO degradation. BeO is a highly amphoteric oxide with strong acidic tendencies, while Li_2CO_3 - Li_2O is strongly basic. Therefore, the reaction between BeO and Li_2O is not particularly surprising, although no relevant

thermodynamic data are available. In view of the clear signs of degradation, beryllia was excluded from further measurement.

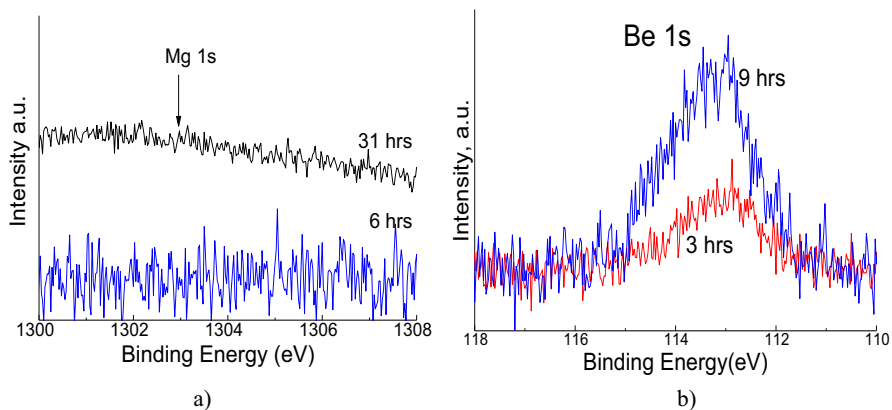


Figure 2. **a)** XPS spectra of cold rod probes taken from a Li_2CO_3 - Li_2O melt after immersion of a MgO plate: 6 hrs under 1 atm CO_2 ; and 31 hrs in air. A similar featureless spectrum is obtained for a cold rod probe taken from the alkali metal carbonate eutectic/oxide melt in air after 6 hrs exposure of the MgO plate (data not shown). **b)** XPS spectra of cold rod probes taken from a Li_2CO_3 - Li_2O (0.2 mol%) melt at 900°C after 3 (red trace) and 9 hrs (blue trace) of exposure of a BeO plate. The atmosphere was CO_2 .

Ceramic stability in molten Li-Na-K carbonate eutectic.

The flue gas from power stations often contains a few at% each of Na and K in the form of dust of various compositions, primarily silicates [23]. As an approximation to the long-term exposure of a ceramic insulator to such a dilute system, we have tested the stability of YSZ and MgO ceramics with respect to the eutectic mixture of $(\text{Li}, \text{Na}, \text{K})_2\text{CO}_3$ for 2-6 hrs at 900°C in air. Under these conditions, the eutectic mixture also contains Li, Na and K oxides which form at 900°C due to the partial loss of CO_2 . To estimate the degree of conversion of the eutectic mixture of $(\text{Li}, \text{Na}, \text{K})_2\text{CO}_3$ into a mixture of carbonates and oxides, we prepared a mixture of Li_2CO_3 , Na_2CO_3 and K_2CO_3 from nominally anhydrous powders with the proportions of Li, Na, K corresponding to the eutectic. This mixture was heated to 500°C to remove all traces of water, cooled and then weighed. The mixture was subsequently heated to 900°C for 4 hrs and then cooled and weighed; followed by heating for 24 hrs, cooling, and weighing. A weight loss of $0.7\pm 0.5\%$ was detected after 4 hours heating; after 24 hrs heating, the weight loss had stabilized at $4.5\pm 0.1\%$. This corresponds to chemical decomposition of the carbonates to oxides of 1.6 ± 1.1 mol% and 10.2 ± 0.2 mol% respectively. Actually, if during industrial operation of the cell, the contents of Na and K were to increase beyond a few at%, both cations would precipitate in the form of silicates [23], recalling (as noted above) that silicates are introduced into the melt along with the flue gas particles.

XPS measurement of a cold rod probe of the eutectic carbonate-oxide melt at 900°C after a MgO ceramic had been immersed for up to 6 hours revealed a featureless spectrum in the energy

region of the 1s photoelectron peak (data not shown). This is consistent with the earlier finding that MgO is completely stable in molten K_2CO_3 at 980 °C [24]. On the other hand, XPS does detect leaching of a small but detectable amount (0.01-0.02 at%) of Zr from YSZ into the eutectic carbonate-oxide melt after 2 hours exposure. However, the amount of Zr in the melt does not further increase with exposure for up to 6 hrs (Figure 1a blue trace). This implies that between 2-6 hrs, interaction of YSZ with the melt has ceased. Although zirconia is known to be stable in a molten Li-K carbonate eutectic to at least 560 °C [25], it does react with Na_2O -containing melts to form zirconates [26]. In order to determine the origin of this time-dependent stability, we studied the surface of the samples exposed to the melt using the EDS capability of the SEM as well as grazing incidence XRD. As described above, the YSZ samples extracted from the eutectic melt were washed, rinsed and dried. EDS found that the surface of the YSZ samples contained no statistically significant amounts of K or Na ($<0.2 \pm 0.15$ wt%, confidence level 98%). Grazing incidence XRD patterns of the ceramics exposed to the carbonate eutectic melt for 6 hrs were also measured. Of the several diffraction patterns measured from different locations on the sample surface, a subset did contain evidence for the presence of Li_2ZrO_3 (data not shown). As above, the presence of lithium zirconate can provide a plausible explanation for the stability of ZrO_2 with respect to long-term corrosion.

Conclusions

The results of XPS and EDS measurements of cold rod probes of the alkali metal carbonate/oxide melts following extended immersion of ceramic samples are summarized in Table 1. On the basis of these measurements, we conclude that MgO ceramics are suitable for use as a dielectric material in the electrochemical cell designed for reduction of CO_2 to CO by electrolysis of a $Li_2CO_3+Li_2O$ melt at 900 °C. Yttria stabilized ZrO_2 ceramics develop a Li zirconate/Li titanate surface coating, the increasing thickness of which may compromise long term structural stability, while BeO undergoes serious corrosion under melt conditions.

References

- 1.C. Graves et al., "Sustainable hydrocarbon fuels by recycling CO_2 and H_2O with renewable or nuclear energy". *Renewable & Sustainable Energy Reviews* 2011, 15, 1-23.
- 2.S. H. Jensen, P. H. Larsen, and M. Mogensen, "Hydrogen and synthetic fuel production from renewable energy sources", *International Journal of Hydrogen Energy* 2007, 32, 3253-3257.
- 3.S. D. Ebbesen and M. Mogensen, "Electrolysis of carbon dioxide in Solid Oxide Electrolysis Cells" *Journal of Power Sources* 2009, 193, 349-358.
- 4.D. S. Mallapragada et al., "Sun-to-fuel assessment of routes for fixing CO_2 as liquid fuel", *Industrial & Engineering Chemistry Research* 2013, 52, 5136-5144.
- 5.V. Kaplan, E. Wachtel, and I. Lubomirsky, "Titanium Carbide Coating of Titanium by Cathodic Deposition from a Carbonate Melt", *Journal of Electrochemical Society*, 2012, 159, E159-E161.
- 6 V. Kaplan et al., "Conversion of CO_2 to CO by Electrolysis of Molten Lithium Carbonate", *Journal of Electrochemical Society*, 2010, 157, B552-B556.
- 7.V. Kaplan, E. Wachtel, and I. Lubomirsky, "Conditions of stability for ($Li_2CO_3 + Li_2O$) melts in air", *Journal Chemical Thermodynamics*, 2011, 43, 1623-1627.

8.M. Cassir, S. J. McPhail, and A. Moreno, "Strategies and new developments in the field of molten carbonates and high-temperature fuel cells in the carbon cycle", *International Journal of Hydrogen Energy* 2012, 37, 19345-19350.

9.P. Tomczyk and M. Mosialek," Investigation of the oxygen electrode reaction in basic molten carbonates using electrochemical impedance spectroscopy", *Electrochimica Acta* 2001, 46, 3023-3032.

10.R. Wartena, J. Winnick, and P. H. Pfromm," Recycling wood pulping chemicals by molten salt electrolysis: cyclic voltammetry of mixtures containing Na_2CO_3 and Na_2SO_4 " *Journal of Applied Electrochemistry* 2002, 32, 415-424.

11.P. K. Lorenz and G. J. Janz, "Determination of the CO_2 dissociation pressures of molten carbonates by an EMF technique" *Electrochimica Acta* 1970, 15, 12, 2001-2005.

12.P. K. Lorenz and G. J. Janz, "Electrolysis of molten carbonates: anodic and cathodic gas-evolving reactions" *Electrochimica Acta* 1970, 15, 6,1025-1035.

13.V. Kaplan, E. Wachtel, and I. Lubomirsky," CO_2 to CO Electrochemical Conversion in Molten Li_2CO_3 is Stable with Respect to Sulfur Contamination", *Journal of Electrochemical Society*, 2014, 161, F54-F57.

14 T. I. Manuhina, V.I.Sannikov, O.P.Peniakova. *Interaction of metals and alloys with molten alkali metal carbonates*, (UrO RAN, Ekaterinburg 1999) 168. (in Russian).

15. See, for instance, Sigma-Aldrich products 62470, 62472, 13010 for 2N purity and 62462 for 5N purity

16.P. Van Der Heide, *X-ray Photoelectron Spectroscopy: An introduction to Principles and Practices*, (Wiley, 2011) 264.

17.J. F. Moulder et al., *Handbook of X-ray Photoelectron Spectroscopy: A Reference Book of Standard Spectra for Identification and Interpretation of XPS Data*, (Physical Electronics Division, Perkin-Elmer Corporation, 1992) 261.

18.D. Briggs and M. P. Seah, *Practical Surface Analysis, Auger and X-ray Photoelectron Spectroscopy Vol.1*, (Wiley 1990) 674.

19.J. Ida, R. T. Xiong, and Y. S. Lin,"Synthesis and CO_2 sorption properties of pure and modified lithium zirconate", *Separation and Purification Technology* 2004,36,1,41-51.

20.J. Ida and Y. S. Lin, "Mechanism of high-temperature CO_2 sorption on lithium zirconate" *Environmental science & technology* 2003, 37 (9), 1999-2004.

21.G. A. M. Dalhoeven and G. Blasse, "On the luminescence of titanium-doped lithium zirconate (Li_2ZrO_3)" *Journal of Solid State Chemistry* 1981, 39, 35-38.

22.International Crystallographic Data Base, ICSD. http://www2.fiz-karlsruhe.de/icsd_web.html;

23.V. Kaplan, E. Wachtel, and I. Lubomirsky, "Carbonate melt regeneration for efficient capture of SO_2 from coal combustion", *RSC Advances*, 2013, 3, 15842-15849.

24.M. Mizuhata et al.," Physicochemical Properties of Molten Alkali Metal Carbonates Coexisting with Inorganic Powder" *Journal of Electrochemical Society* 2004, 151, 5, E179-E185.

25.M. Mizuhata et al., "Anomalous properties of LiKCO_3 melts coexisting with porous inorganic powder" *Electrochemistry* 2005, 73, 680-685.

26.H. Nafe and R. Subasri, "Revision of the data on the standard Gibbs energy of formation of Sodium Zirconate" *Journal of Chemical Thermodynamics* 2007, 39, 22-27.

DENSITY, VISCOSITY, VAPOR PRESSURE AND THERMAL CONDUCTIVITY OF $MgCl_2 + Mg$ SALTS

Yuxiang Peng and Ramana G. Reddy

Department of Metallurgical and Materials Engineering,
The University of Alabama, Tuscaloosa, AL 35487, U.S.A

Keywords: Mg inhibitor, $MgCl_2$, density, viscosity, vapor pressure, and thermal conductivity

Abstract

The $MgCl_2$ -contained salt is considered as one of the candidates for the solar thermal energy storage applications. To protect the structural alloy from corrosion, the addition of Mg as corrosion inhibitor was investigated. Several physical properties such as density, viscosity, vapor pressure and thermal conductivity of $MgCl_2$ with different amount of Mg additions are studied in this paper. A slight variation of density and viscosity while the increase in vapor pressure and large increase of thermal conductivity were observed with the addition of Mg to $MgCl_2$ salt mixtures.

Introduction

Molten salts have unusual thermal properties which have led to their use in primary reactor coolants and heat transfer media for high-temperature applications in nuclear reactors to hydrogen production facilities [1]. They also have provided an increase of thermal energy storage media for solar energy applications. Because they could serve at high temperature [2]. One potential energy storage media of considerable technological interest is $MgCl_2$ -containing salt due to its lightweight, specific heat capacity and high energy storage properties [3]. However, the widespread applicability of $MgCl_2$ salt is limited mainly because of its ability to corrode the contact materials. Therefore, a growing interest in the application of $MgCl_2$ salt [4] has further emphasized to investigate the reliable method of protecting contacted materials in molten $MgCl_2$ salt. Among numerical methods in retarding or preventing corrosion, the use of inhibitors for the control of materials which are in contact with molten salt is an established practice [5]. Inhibitor should be more reactive than the elements in contacted alloys during corrosion in $MgCl_2$ molten salt. Thus, corrosion of alloys can be minimized by inhibitors acting as the sacrificial anode instead of elements in alloys. As the more reactive element Mg is selected as one of the proper inhibitors for numerous alloys corrosion in the severe environment [6], it also might protect or retard alloys corrosion in $MgCl_2$ molten salt. Reaction (1) is taken place as Mg added into the $MgCl_2$, showing the efficiency of Mg in protecting alloys, which exerts a continuous interest in the investigation of Mg as an inhibitor in the molten salt.



There are many studies on the corrosion behavior of inhibitor in molten salts at high temperature. However, the effect on the thermal properties of Mg added to $MgCl_2$ salt is ignored. Nowadays, besides the efficiency of the inhibitor, the effect on molten salt has to be taken into account to

choose the proper inhibitor [7]. A large change in the thermal properties will result in failure of MgCl_2 being a candidate as thermal storage media. Therefore, the investigation of change in the thermal properties of MgCl_2 molten salt with the addition of Mg inhibitor is of not only practical but also theoretical interest. The present work attempts to establish the suitability of Mg as an inhibitor for the alloys corrosion in MgCl_2 molten salt. From this point of view, density, viscosity, thermal conductivity and vapor pressure after adding different amounts of Mg in MgCl_2 molten salt are studied in this paper.

1. Calculations

The solubility of Mg in MgCl_2 is very slight, which is about 0.2 mole% [8]. Therefore, the mixture can be assumed as two individual compounds. Thus, by using mixing rule (2) to predict density, viscosity, thermal conductivity and vapor pressure, the consistently calculated result could be obtained.

$$P_{mix}^n = P_1^n * x_1 + P_2^n * x_2 \quad (2)$$

where P is thermal properties of materials and x is mole fraction for each compound, and n is taken as 1 for most properties calculation except viscosity, which is 1/3 as shown in the literature [9].

The density data for the MgCl_2 and Mg are available in the literature [10 & 11], Equations (3 and 4) give the formula for the density of liquid MgCl_2 and Mg, which shows a proportional decrease in density with the change in temperature ($T - T_m$). The temperature range for the calculation is 298.15 - 1273.15 K.

$$\rho_{Mg}: 1.584 - 0.000234 * (T - T_m) \quad (3)$$

$$\rho_{MgCl_2}: 1.68 - 0.000271 * (T - T_m) \quad (4)$$

From the mixing rule of equation (2), the viscosity of the mixture is calculated from the viscosity data of Mg and MgCl_2 obtained from literature at different temperatures and by considering the coefficients of n as 1/3 [9 & 11]. However, the viscosity of Mg at 987.15K is derived from the trend line.

The vapor pressure of the mixture is calculated from individual data of MgCl_2 and Mg in the literature [11 & 12]. Similar to the calculation of viscosity, some lacked data is predicted from trend line to calculate the vapor pressure of the mixture. However, coefficient n is chosen as 1.

The thermal conductivity is also calculated by using mixing rule (2) with n as 1. As the sample is heated to its melting point, the thermal conductivity tends to remain constant at higher temperatures [13]. The thermal conductivity is only calculated at melting point from the literature data [9 & 14].

2. Results and discussion

As the solubility of Mg is low in the MgCl_2 salt, there is no significant change in the volume of the mixture for different amounts of Mg added to the MgCl_2 salt at high temperatures. Therefore, the density calculations are accurate even at a higher concentration of Mg in the salt. From the mixing rule, the density of the mixture is calculated, and the coefficient n is considered as 1 for all the mixtures. As shown in Figure 1, the density is plotted as a function of the temperature for the various MgCl_2 -Mg mixtures.

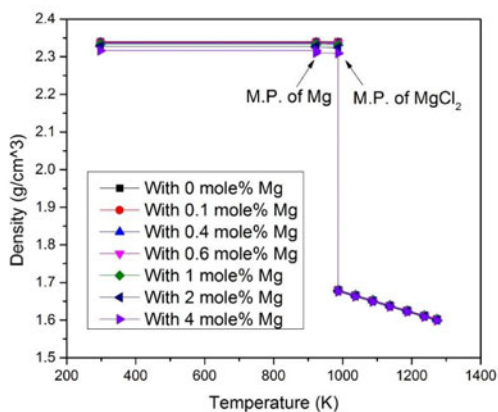


Figure 1 Density of MgCl_2 without and with different amount of Mg

The small initial decline in density of the mixture is mainly because of the conversion of solid Mg into liquid Mg. As shown in Figure 1, with the further increase in the temperature, a sudden decrease in the density was observed for all the mixtures. That is due to the conversion of the mixture into the liquid phase. However, no significant change in density of liquid mixture was observed even at 4 mole% of Mg solute. That is probably due to the similar density of MgCl_2 and Mg in the temperature range of 987.15 - 1273.15 K.

The viscosity of the mixtures are calculated only at 987.15 K (melting point of MgCl_2) and the results are illustrated in Figure 2.

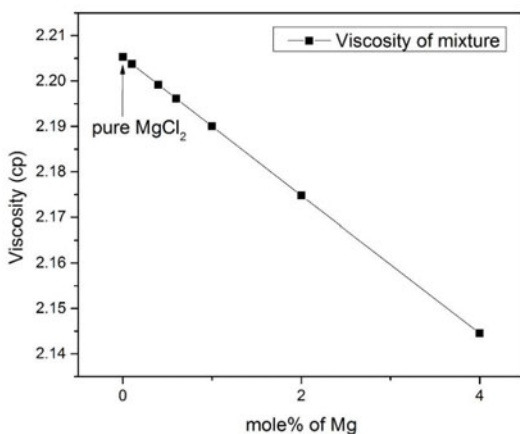


Figure 2 Viscosity of MgCl_2 without and with different amount of Mg at 987.15K

The viscosity of the mixture decreases linearly with the mole fraction of Mg at 987.15 K. Because there is no viscosity data available in the literature for the Mg, no calculations were performed at higher temperatures. The addition of Mg into MgCl₂ molten salt will decrease the viscosity, and it will be greater as more Mg added into the salt. However, about 0.06 cp decreasing can be neglected because temperature shows more significant influence on the decreasing of the viscosity [9 & 11].

Figure 3 shows the plot of thermal conductivity as a function of mole% of Mg.

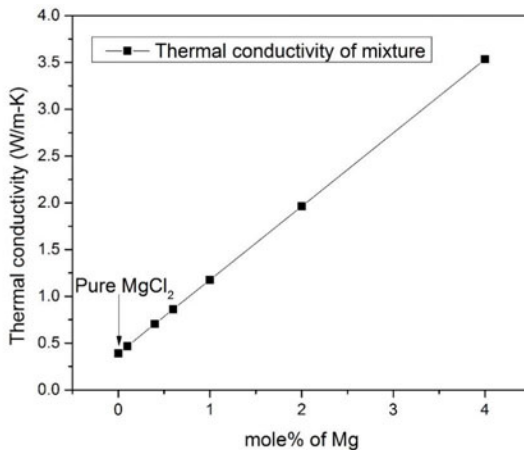


Figure 3 Thermal conductivity of MgCl₂ without and with different amount of Mg

Because the thermal conductivity of Mg inhibitor is much greater than that of MgCl₂, a significant increase in the thermal conductivity of the mixture is observed. Since, greater thermal conductivity indicates more possibility for application as heat storage media, the addition of Mg solute in MgCl₂ salt supports the thermal conductivity of the media.

The data is predicted for higher temperatures from the trend line to calculate the vapor pressure of the mixture. As the boiling point of Mg is 1364.15 K, the temperature range in the calculation is from 1051.15 to 1364.15 K, and the calculation results are shown in Figure 4.

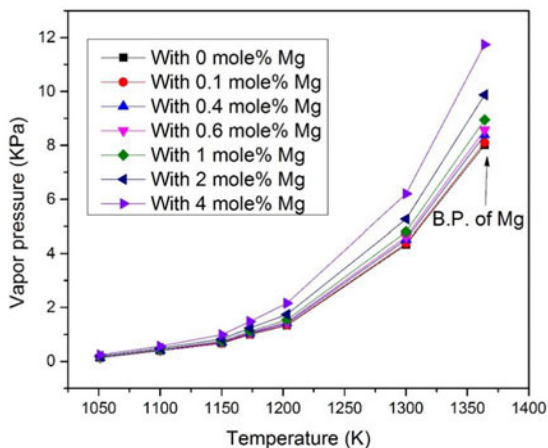


Figure 4 Vapor pressure of $MgCl_2$ without and with different amount of Mg

The vapor pressure of the mixture is increased as more Mg inhibitor is added to the salt and also with the increase in the temperature. Some of the vapor pressure contribution by Mg solute addition is slight, but considering a small amount of Mg added to the salt, amount of weight loss of Mg into the atmosphere cannot be ignored. Thus to obtain 1 mole% of Mg in the $MgCl_2$ salt, the respected initial amount of Mg should be more than 1 mole%.

Figure 5 and 6 show the effect of Mg on the thermal properties of $MgCl_2$ salt.

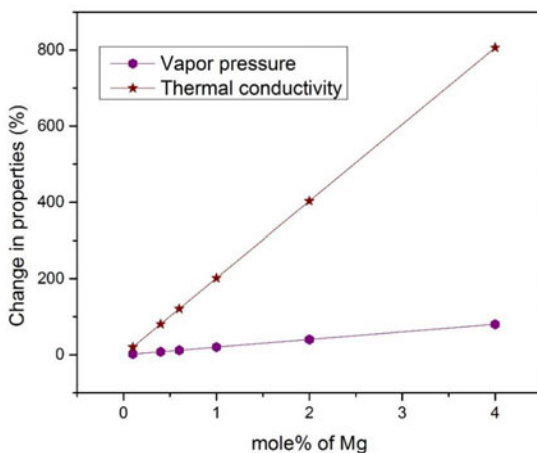


Figure 5 Change in vapor pressure at 1051.5K and thermal conductivity at 987.15K after adding different amount of Mg into $MgCl_2$ molten salt

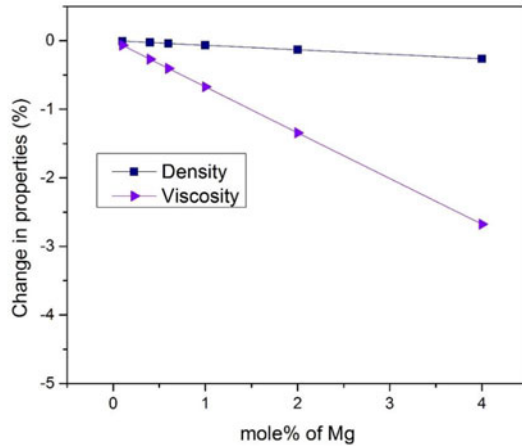


Figure 6 Change in density and viscosity at 987.15K after adding different amount of Mg into MgCl_2 molten salt

The change in thermal properties of the mixture was calculated after the addition of different amounts of Mg at 987.15 K. However, the change in the vapor pressure is calculated at the temperature of 1051.15 K. Because vapor pressure at that temperature is available for both Mg and MgCl_2 in the literature [11 & 12]. A slight change of viscosity and density after adding Mg inhibitor will not affect the application of MgCl_2 as heat storage media while large improve of thermal conductivity may increase the possibility of MgCl_2 being the proper candidate as the heat storage media.

3. Conclusions

Less than 4% change of density and viscosity after even adding 4 mol% of Mg into MgCl_2 molten salt has no significant effect on the application as heat storage media. While the considerable increase of thermal conductivity, which is over 800%, gives more potential of MgCl_2 as the media in heat transferring. However, the large vapor pressure of Mg may result in considerable weight loss, losing the ability as a corrosion inhibitor in MgCl_2 molten salt. Therefore, more Mg should be added into MgCl_2 before applying this mixture molten salt as the heat storage media.

A significant increase in the thermal conductivity will promise this mixture as a heat storage media. Although there is little change in density, viscosity and vapor pressure, which could be ignored for the application of heat storage media.

References

- [1] Williams, D. F., Assessment of candidate molten salt coolants for the NGNP/NHI Heat-Transfer Loop, ORNL/TM-2006/69, 2006. pp.1–44.
- [2] Reddy, R. G., Wang, T., and Mantha, D., Thermodynamic properties of potassium nitrate–magnesium nitrate compound [$2\text{KNO}_3 \cdot \text{Mg}(\text{NO}_3)_2$], *Thermochim. Acta*, Vol. 531, 2012. pp. 6–11, 2012.

- [3] Gomez, J. C., Change Materials (PCM) Candidates for Thermal Energy Storage (TES) Applications, Contract, Vol. 303, 2011. pp. 275-3000.
- [4] Neil, D. E., H. M. Clark, and R. H. Wiswall Jr. Thermodynamic Properties of Molten Solutions of $MgCl_2$ -KCl, $MgCl_2$ -NaCl, and $MgCl_2$ -KCl-NaCl. Journal of Chemical and Engineering Data Vol. 10.1, 1965. pp. 21-24.
- [5] Raja, Pandian Bothi, and Mathur Gopalakrishnan Sethuraman. Natural products as corrosion inhibitor for metals in corrosive media—a review. Materials letters Vol. 62.1, 2008. pp. 113-116.
- [6] J.A. Lane, H.G. MacPherson, F. Moslan (Eds.), Fluid Fuel Reactors, Addison-Wesley, 1958
- [7] Arenas, M. A., A. Conde, and J. J. De Damborenea. "Cerium: a suitable green corrosion inhibitor for tinplate." Corrosion Science Vol. 44.3, 2002. pp. 511-520.
- [8] Bredig, M. A. Mixtures of metals with molten salts. No. ORNL-3391. Oak Ridge National Lab., Tenn., 1963.
- [9] Williams, D. F. Assessment of candidate molten salt coolants for the NGNP/NHI Heat-Transfer Loop. ORNL/TM-2006/69, Oak Ridge National Laboratory, Oak Ridge, Tennessee, 2006.
- [10] Haynes, William M., ed. CRC handbook of chemistry and physics. CRC press, 2012.
- [11] International Magnesium Association, Magnesium Basics, 2015.
- [12] Stull, Daniel. Inorganic compounds. Industrial & Engineering Chemistry Vol. 39.4, 1947. pp. 540-550.
- [13] Tao Wang, Divakar Mntha, Ramana G. Reddy, Novel high thermal stability LiF-Na₂CO₃-K₂CO₃ eutectic ternary system for thermal energy storage applications, Solar Energy Materials & Solar Cells Vol. 140, 2015. pp. 366-375.
- [14] Chase, Malcolm W., et al. JANAF thermochemical tables, 1975 supplement. Journal of physical and chemical reference data Vol. 4.1, 1975. pp. 1-176.

DEVELOPMENT OF “SLAG-REMAINING+DOUBLE-SLAG” BOF STEELMAKING TECHNOLOGY IN SHOUGANG CO.

Haibo Li¹, Yanchun Lu¹, Guosen Zhu¹, Xinhua Wang²

¹Shougang Research Institute of Technology; Shijingshan District, Beijing, 100041, China

²University of Science and Technology Beijing; 30 Xueyuan Road, Beijing, 100083, China

Keywords: BOF Steelmaking, Less Slag, Lime Consumption, Dephosphorization, Slag

Abstract

The “Slag-Remaining+Double-Slag” BOF steelmaking process has been developed and applied in Shougang Corporation, Ltd., by which consumption of lime and volume of slag in BOF steelmaking are remarkably decreased. In this paper, three important technologies taken in application of the new steelmaking process are introduced: 1. To solve the two most serious problems, i.e. difficult to make fast and enough amount of deslagging and decrease the metallic Fe droplets in the slag, low basicity slag is used in the dephosphorization stage. 2. Hard blow pattern is adopted to utilize the top blown O₂ jet to strengthen agitation of the bath in the dephosphorization stage, through which good dephosphorization has been obtained. (3) By speeding up the steelmaking operations and particularly better matching the BOF, secondary refining and continuous casting productions, productivity has not been reduced though the BOF tap to tap time has been increased by about 4min after using the new process.

1. Introduction

The Chinese steel industry which has developed rapidly in the past two decades is facing serious challenges in saving natural resources, energy conservation and reducing the solid wastes generated in steel production. Taking the BOF steelmaking in China for instance, it produced about 700 million tons of steels last year and consumed about 35 million tons of burnt limes, 10 million tons of dolomites and generated about 70 million tons of slags.

In 2001, Nippon Steel Corporation [1] reported the idea of “Slag-Remaining+Double-Slag” steelmaking process and the experiment result using an 8t converter. The new steelmaking process was named as MURC, in which, the blowing is divided into two stages, i.e. the dephosphorization stage and decarburization stage. When the blowing has been completed, the slag is kept in the furnace after tapping the steel and reused in the dephosphorization stage of the next heat. It was reported [2-6] that MURC has been applied in Oita, Yawata, Muroran and Kimitsu Steelworks of Nippon Steel Corporation.

In 2009, Shougang Corporation started the investigation on developing the “Slag-Remaining +Double-Slag” steelmaking process. Now, the new steelmaking process has been applied on a large scale in its Qianan Steelworks which has five 210t combined blowing converters and Shouqin Steelworks which has three 100t combined blowing converters. After using the new process, consumptions of the burnt lime and dolomites have been decreased by more than 47%

and 55% and, the volume of slag generated in BOF steelmaking has been decreased by 30%, respectively.

2. The “Slag-Remaining+Double-Slag” Steelmaking Process developed in Shougang Co.

As illustrated in Figure 1, the “Slag-Remaining+Double-Slag” steelmaking process developed mainly consists of the following operations: (1) keeping the molten slag in the furnace after tapping of steel, (2) blowing in N₂ with the top lance to splash part of the molten slag on the lining wall, (3) adding in some lime and dolomite to fully solidify the slag, (4) charging scrapes and hot metal, (5) dephosphorization stage blowing, (6) deslagging off 50-60% slag from the furnace, (7) decarburization stage blowing, and (8) tapping while remaining the slag for next heat.

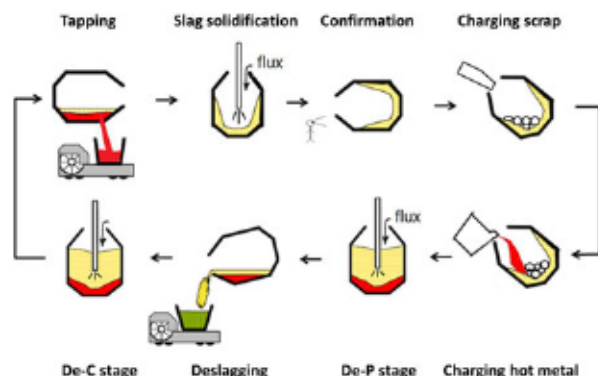


Figure 1. Illustration of the “Slag-Remaining+Double-Slag” process applied in Shougang Co

The dephosphorization stage lasts about 3.5-4 minutes, in which about 27% of the total O₂ is blown and 35% of the total lime is added. The temperature of the metal bath at end of the dephosphorization stage is between 1320-1370 °C. In decarburization blowing stage, O₂ is blown for 9.5-10 minutes and rest of flux is added in. The total lime consumed is about 22kg/t in Qianan Steelworks and 35kg/t in Shouqin Steelworks.

Taking use of the influence of the temperature change on dephosphorization is the main principle of the new steelmaking process. Taking the equilibrium constant of the dephosphorization reaction expressed by Equation (1) for instance, the equilibrium constant (K_p) calculated with the thermodynamic data given by Equation (2) and (3) [7,8] is about 1.68×10^{-11} at the temperature around 1680 °C. However, at the temperature around 1350 °C, K_p is about 5.59×10^{-7} , more than 30,000 times larger than the K_p at 1680 °C.



$$\Delta G^0 = -832384 + 632.65T \quad (2)$$

$$\log K_p = \log (a_{P_2O_5}/a_P^2/a_{[O]}^5) = 43443/T - 33.02 \quad (3)$$

In “Slag-Remaining+Double-Slag” steelmaking, the slag at the blowing end has almost no dephosphorization ability due to the high temperature. However, if the slag is used in the early blowing period of the next heat, i.e. the dephosphorization stage, it can regain the dephosphorization power because of the temperature decrease. But, the intermediate deslagging operation must be made to pour off most of the reused slag between the dephosphorization stage and the decarburization stage. Otherwise, rephosphorization from the slag will occur owing to the temperature increase in later blowing period.

Since the slag of the previous heat can be reused, consumptions of the burnt lime and dolomite and volume of the slag can be remarkably decreased. Yield of steel has also increased due to the decrease of the exhausted slag which contains 14-25 mass% Fe_2O_3 . In addition, as most of the exhausted slag in the new steelmaking process is the low basicity slag formed in the dephosphorization stage, treatment of the exhausted slag can be simplified.

3. Key Technologies of the New Steelmaking Process

3.1 Fast and Enough Deslagging after Dephosphorization Stage

In the “Slag-Remaining+Double-Slag” steelmaking process, whether or not fast and enough amount of deslagging can be made after the dephosphorization stage is of great importance. If the deslagging amount is not enough, the slag in the furnace will accumulate heat by heat. The basicity of the slag will increase and it makes more difficult to pour off the slag. Consequently, the normal circulation of the process will be stopped. Furthermore, if enough deslagging cannot be made, large amount of iron droplets will be wrapped in the slag and be poured off the furnace during deslagging. In addition, the process control can also be affected because of the variation of the slag volume in the furnace.

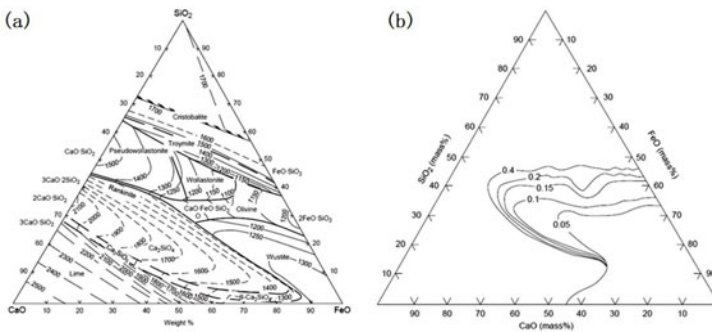


Figure 2. The phase diagram and iso-viscosity curve of the $\text{CaO-SiO}_2\text{-FeO}$ system

To make the slag with good fluidity for fast and enough deslagging, the slag should be fully melted, i.e. no undissolved lime, MgO , $2\text{CaO}\cdot\text{SiO}_2$, etc. in the slag. It can be seen in Figure 2(a) [8] which shows the phase diagram of the $\text{CaO-SiO}_2\text{-FeO}$ system that, for making fully melted slag at the end of the dephosphorization stage, the basicity of the slag $(\text{mass}\% \text{CaO})/(\text{mass}\%$

SiO₂) should be less than 1.3. As the slag also contains some Al₂O₃, MnO, etc. which enlarges the liquid phase region, the slag basicity should not be more than 1.5.

Figure 2(b) [8] shows the iso-viscosity curves of the CaO-SiO₂-FeO system at 1400 °C. It can be seen that lower viscosity slag (0.2-0.4 N·s/m²) can be obtained when the slag basicity is between 0.8-1.3. In case the basicity is above 1.3, the iso-viscosity curves become denser, i.e. the viscosity of the slag increases quickly with increasing the basicity and the fluidity of the slag will be worsen.

The relationships between the deslagging amount and the slag basicity and MgO content after the dephosphorization stage are shown Figure 3(a) and 3(b), respectively. It is seen that the deslagging amount increases with decreasing the basicity. By controlling the slag basicity within the range of 1.3-1.5, the deslagging amount each heat can be increased to more than 8.0t in Qianan Steelworks and 5.0t in Shouqin Steelworks, respectively.

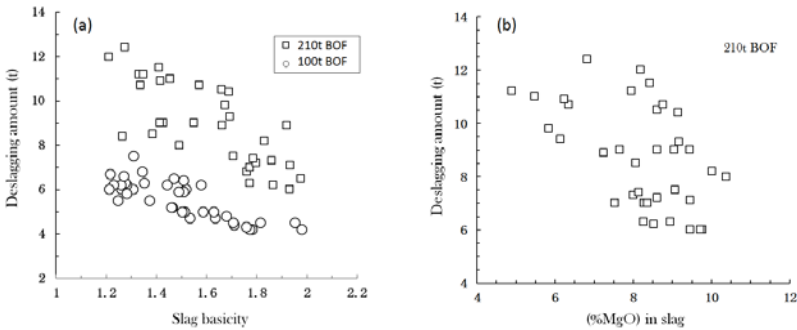


Figure 3. Relationship between deslagging amount with (a) slag basicity and (b) MgO content

As can be seen in Figure 3(b), the deslagging amount increases with decreasing the MgO content of the slag. For making fast and enough deslagging, MgO in the slag should be controlled no more than 7 mass%. This MgO control limit is less than that in conventional BOF steelmaking. But, no influence has been found on the lining life of the furnace after the new steelmaking process was applied.

By adopting the new slag basicity and MgO control strategy, the two most serious problems, i.e. difficult to make fast and enough amount of deslagging and large amount metallic iron droplets in the slag, are solved have been solved. Now, the deslagging amount each heat is 6.5~12.5t in Qianan Steelworks and 4.0~8.0t in Shouqin Steelworks, respectively, varied mainly due to the Si contents of the hot metal. The deslagging time has been decreased to 4-5min in Qianan Steelworks and 3-4.5min in Shouqin Steelworks, respectively.

3.2 High Efficient Dephosphorization in Dephosphorization Stage

Compared with conventional BOF steelmaking, dephosphorization in the “Slag-Remaining+ Double-Slag” process is more difficult because the reused slag of the previous heat already

contained about 1.5 mass% P_2O_5 and, as above mentioned, the slag basicity in the dephosphorization stage must be low to meet the demand of enough deslagging. If good dephosphorization cannot be made in the dephosphorization stage, dephosphorization burden in decarburization stage will be increased, which may result in re-blow or after-blow at the end of blowing.

In BOF steelmaking, the dephosphorization reaction may take place inside the metal bath, at the slag-metal interface and inside the foaming slag. In dephosphorization stage of the "Slag-Remaining+Double-Slag" steelmaking process, activity of the oxygen dissolved in the metal bath is governed mainly by the dissolved carbon which is usually between 3.2 mass% to 4.5 mass%. With the standard free energy change (ΔG°) of the decarburization reaction and the activity interaction coefficient given by Equation (5) and (6) [8], the activity of the dissolved oxygen ($a_{[O]}$) is between 0.00010 to 0.00018 at the temperature around 1350 °C.



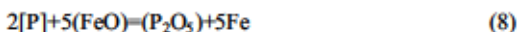
$$\Delta G^\circ = -21244 - 38.91T \quad (5)$$

$$\log f_{[C]} = 0.14[\%C] \quad (6)$$

$$\log f_{[P]} = (105.1/T + 0.0723)[\%C] \quad (7)$$

There is no basic slag inside the hot metal bath. If dephosphorization could take place inside the metal bath, the activity of the reaction product P_2O_5 would be one. With the data of the standard free energy change (ΔG°) of the dephosphorization reaction given by Equation (2) and the activity coefficient $f_{[P]}$ in high carbon molten iron given by Equation (7) [9], the free energy change (ΔG) of the dephosphorization reaction inside the metal bath in the dephosphorization stage at the temperature around 1350 °C is between 820 kJ/mol to 865 kJ/mol. It indicates that it is almost impossible that the dephosphorization takes place inside the metal bath.

However, as top blowing O_2 is used, the FeO content in the slag can be controlled at a relatively higher level. The dephosphorization reaction taking place at the slag-metal interface or inside the foaming slag between the metal droplets and the slag may occur as expressed by Equation (8). With the data of $\gamma_{P_2O_5}$ in slag [7], $f_{[P]}$ in high carbon molten iron [9] and using the usual composition of the slag in the dephosphorization stage ((CaO): 40 mass%, (MgO): 7 mass%, (FeO): 10 mass%, (P_2O_5): 3 mass%), the free energy change (ΔG) of the dephosphorization reaction expressed by Equation (8) is between -27.0 kJ/mol to -38.0 kJ/mol. In the calculation, a_{FeO} in slag is 0.2 referring to the iso-activity curve of FeO in CaO-SiO₂-FeO system [8]. This calculation result indicates that dephosphorization can take place at the slag-metal interface or inside the foaming slag.



$$\Delta G^\circ = -283634 + 403.0T \quad (9)$$

$$\log \gamma_{P_2O_5} = -9.84 - 0.142((\%CaO) + 0.3(\%MgO)) \quad (10)$$

It is known from the above discussion that, for making good dephosphorization in the dephosphorization stage, strong agitation of the metal bath is of great importance to accelerate the transfer of [P] to the slag-metal interface where dephosphorization can take place. However, most BOF steelmaking plants in China use relatively milder bottom blowing for prolonging lives of the bottom blowing units. For instance, the bottom blowing rates in Qianan Steelworks and Shouqin Steelworks of Shougang Co. are only 0.03-0.06 Nm³/min/t, which cannot provide strong enough agitation for making good dephosphorization.

So, in the new steelmaking process, hard blow pattern is adopted so as to utilize the top blown O₂ jet to strengthen the agitation of the bath in the dephosphorization stage. The oxygen lance position is 100-200mm lower than the position used in conventional BOF steelmaking and the O₂ flowrate is higher than 3.0Nm³/min/t. In addition, iron ore addition is also increased in the dephosphorization stage to compensate the FeO decrease in the slag because of the hard blowing.

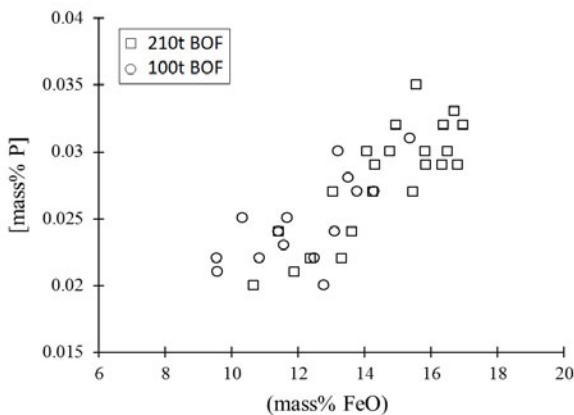


Figure 4. Relation between the phosphorus contents of the metal and slag FeO contents at end of dephosphorization stage

Figure 4 shows the relation between [P] contents after the dephosphorization stage blowing and the slag FeO contents. It can be seen that better dephosphorization has been achieved after the hard blow pattern has been applied, in spite of that the slag FeO contents are decreased. With the above mentioned techniques, phosphorus content at the end of dephosphorization stage is lowered to 0.029 mass% on average and, the [P] contents at the end of decarburization stage lowered to 0.0096 mass% on average, which can meet the specifications of most steel grades produced in Qianan Steelworks and Shouqin Steelworks.

3.3 Solidification of the Remained Molten Slag

In the “Slag-Remaining+Double-Slag” steelmaking process, the molten slag of the previous heat remained in the furnace must be fully solidified before charging hot metal so as to avoid hot

metal eruption during the charging. In Qianan Steelworks and Shouqin Steelworks, slag splashing technology is adopted to solidify the remained slag.

In the new steelmaking process, after tapping of the liquid steel of the previous heat, the top lance is lowered into the furnace to blow N_2 for 4-5 minutes to splash part of the remained slag on the lining wall of the furnace. In addition, owing to the cooling effect of the N_2 jet, temperature of the un-solidified slag pool decreases rapidly and some high melting temperature solid phases such as $2CaO \cdot SiO_2$, $3CaO \cdot SiO_2$, MgO , etc. precipitate from the molten slag.

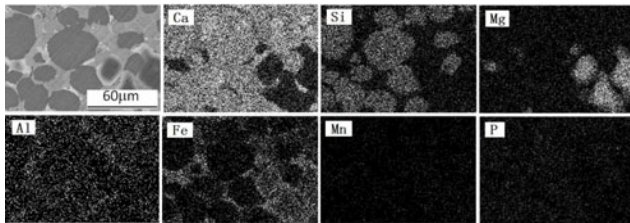


Figure 5. EDS mapping analysis result of the slag sample taken after slag splashing

As can be seen in Figure 5, after slag splashing, the un-solidified slag pool at bottom of the furnace changes to two-phase mixtures, i.e. the solidified phase of high melting temperature precipitates and the liquid “RO” phase constituted by FeO , MnO , CaO , etc. In order to fully solidify the slag, certain amount of lime and dolomite are added in. Then, the furnace is rotated forward and backward to mix the added lime, dolomite and the slag. With the above mentioned techniques, the time for slag solidification has been decreased to less than 5.5 minutes and no hot metal eruption has occurred after the new steelmaking process has been adopted in Shougang Corporation.

3.4 Fast Production Technology

The tap to tap time in the “Slag-Remaining+Double-Slag” steelmaking process is longer than the conventional BOF steelmaking due to the added operations of intermediate deslagging, solidification of the remained slag, etc. In order to minimize the influence on the productivity and particularly on the synchronization of the BOF steelmaking, secondary refining and continuous casting, production speed in the new steelmaking process must be raised.

Some measures are taken to speed up the production, which includes (1) higher oxygen blowing rate in dephosphorization stage, (2) low basicity slag to shorten the deslagging time, (3) using flux of SiO_2-C system to suppress the emulsification of the slag in slag pot during the deslagging, (4) better synchronizing the BOF steelmaking, secondary refining and continuous casting with the computer added production scheduling system, etc.

There are both three converters in the No.1 Steelmaking Plant of Qianan Steelworks and Shouqin Steelworks, which supply liquid steels to two secondary refining units and two slab casters.

Since the production rate of the three BOF converters is higher than the secondary refining and continuous casting, the productivity has not been decreased after adopting the new process.

In No.2 Steelmaking Plant of Qianan Steelworks, there are two BOF converters which supply liquid steels to two secondary units and two slab casters. As the No.2 Steelmaking Plant mainly produces narrower slabs for grades of electric steels, cold rolled sheet of LCAK steels, etc., the BOF steelmaking still can meet the demand of the two casters, although the BOF operation time is prolonged after adopting the new steelmaking process.

4. Conclusions

The “Slag-Remaining+Double-Slag” BOF steelmaking technology has been developed and applied on a large scale in Qianan Steelworks and Shouqin Steelworks of Shougang Corporation, by which consumptions of lime and dolomite and volume of slag generated in BOF steelmaking have been decreased by more than 47%, 55% and 30%, respectively.

Low basicity slag (CaO/SiO_2 : 1.3~1.5) is used in the dephosphorization stage, by which the two most serious problems in the new steelmaking process, i.e. difficult to make fast and enough amount of deslagging and large amount metallic iron droplets in the slag, are solved.

Hard blow pattern is adopted to utilize the top blown O_2 jet to strengthen agitation of the bath in the dephosphorization stage, through which good dephosphorization has been obtained.

By speeding up the steelmaking operations and better matching the BOF, secondary refining and continuous casting productions, productivities of the steelworks have not been reduced though the BOF tap to tap time has been increased after using the new technology.

References

1. Y. Ogawa, et al., “Development of the Continuous Dephosphorization and Decarburization Process Using BOF,” *Tetsu-to-Hagane*, 87(2001), 21-28.
2. M. Iwasaki and M. Matsuo, “Change and Development of Steelmaking Technology,” *Nippon Steel Technical Report*, 391(2011), 88-93.
3. M. Kumakura, “Advances in the Refining Technology and the Future Prospects,” *Nippon Steel Technical Report*, 394(2012), 4-11.
4. N. Sasaki, et al., “Improvement of Hot Metal Dephosphorization Technique,” *Nippon Steel Technical Report*, 394(2012), 26-32.
5. T. Hashimoto, et al., “Improvement in Production Capacity at Oita Works,” *Nippon Steel Technical Report*, 394(2012), 84-90.
6. M. Kobayashi, et al., “Technical Progress in Steelmaking and Casting for Special Bar and Wire Steel at Muroran Work,” *Nippon Steel Technical Report*, 394(2012), 119-124.
7. E.T. Turkdogan, “Assessment of P_2O_5 Activity Coefficients in Molten Slags,” *ISIJ International*, 40(2000), 964-970.
8. E.T. Turkdogan, *Fundamentals of Steelmaking* (London: Carlton House Terrace, 1996).
9. F. Tsukihashi, et al., “Thermodynamics of Phosphorus for the $\text{CaO-BaO-CaF}_2\text{-SiO}_2$ and $\text{CaO-Al}_2\text{O}_3$ Systems,” *Tetsu-to-Hagane*, 76(1990), 1664-1671.

EFFECT OF BASICITY ON BASIC OXYGEN FURNACE (BOF) SLAG SOLIDIFICATION MICROSTRUCTURE AND MINERALOGY

Chunwei Liu¹, Muxing Guo¹, Lieven Pandelaers¹, Bart Blanpain¹, Shuigen Huang¹

¹ KU Leuven, Department of Materials Engineering, Kasteelpark Arenberg 44 bus 2450, 3001, Belgium

Keywords: BOF slag; Valorization; Basicity; Solidification

Abstract

Slag valorization in added value construction applications can contribute substantially to the sustainability of steel industry. The present work aims to investigate the crystallization behavior of a typical industrial Basic Oxygen Furnace (BOF) slag (CaO-FeO_x-SiO₂-based slag) by varying the basicity through hot stage engineering. A sample of industry Basic Oxygen Slag (BOF) was mixed with different quantities of silica (SiO₂) to modify basicity. The effect of basicity on solidification microstructure and mineralogy was studied. The results suggest that the mineralogy of the solidified slag can be manipulated to enhance its suitability as raw material for construction applications.

1. Introduction

In steelmaking industry, steel slags are a main by-product produced during the steelmaking process, accounting for 10-15wt% of crude steel production, depending on the steel quality and the production process [1]. Recycling of slags into added value applications is therefore of great importance for the sustainability of the steel industry. In recent years, the effect of different additions and cooling methods [2-5] has been studied with respect to crystallization behavior and phase modification, aiming to use steel slags in various fields, such as landfill liner [6], hydraulic binder [7, 8] and fertilizer used in agriculture [9].

Compared to the treatment of other steelmaking slags, such as EAF (electric arc furnace) slag, AOD (argon oxygen decarburization) slag, and LM (ladle metallurgy) slag, BOF (Basic Oxygen Furnace) slag is more difficult to treat due to its higher basicity. Yet, because BOF slags make up almost half of all steelmaking slags, their valorization is key, both from an environmental and economic perspective [10]. In the past decades, utilization of BOF slag was limited due to the volume expansion occurring upon natural aging. This dimensional instability is believed to be induced by hydration and carbonation of free lime and magnesia existing inside the slag [11]. During the chemical reaction, free lime and magnesia exhibit around 10% swelling [12], leading to the disintegration of the bulk slag. Recent research stressed that 4 wt% free lime is the suggested tolerance for incorporating BOF slag in construction materials [13].

In the present work, slags with different basicities were prepared and equilibrated at 1600°C under argon atmosphere, then cooled down slowly in the furnace. X-ray diffraction (XRD) and electron probe micro-analysis (EPMA) were used for slag sample characterization. The results indicate that it is possible to optimize the slag mineralogy for subsequent use in construction materials by controlling the basicity during hot stage engineering.

2. Experimental

2.1. Materials preparation

A typical BOF slag produced from a steelmaking company was used as the master slag in this work. The slag was ground and milled to powder below 200 μm . The typical range of chemical [9] and mineral compositions of the master slag is given in Table I and Table II, respectively. The basicity R (mass ratio of CaO/SiO_2) of the master slag used in our study was measured by X-ray fluorescence (XRF, Panalytical PW2400) to be 4.39.

Table I. Chemical composition of the master slag, wt%

CaO	*T.Fe	SiO ₂	MnO	MgO	Al ₂ O ₃	P ₂ O ₅
42-55	14-20	12-18	0-8	0-5	0-3	0-2

*Fe is reported as the total iron in the oxides. Measured by X-ray fluorescence (XRF, Panalytical PW2400).

Table II. Mineral composition of the master slag

Mineral phase	Free lime	Monoxide	Aluminateferrite	Beta dicalcium silicate	Magnetite
Chemical formula	CaO	RO (FeO-MgO-MnO)	2CaO·(Al, Fe) ₂ O ₃	β -C ₂ S (Ca ₂ SiO ₄)	Fe ₃ O ₄
wt%	18.0	5.0	32.3	29.4	15.3

In order to investigate the effect of basicity on the solidification microstructure and mineralogy, sub-samples of 100g of slag was wet-mixed with 5.0 g, 10.0 g, and 15.0 g of SiO₂ (>99.90%) in ethanol utilizing a multidirectional mixer (Turbula type) to prepare three adjusted slag mixtures. After 24-hour mixing, the mixture was dried in a rotating evaporator at 65°C. The resulting mixtures have a basicity of 2.94, 2.21 and 1.77, respectively.

2.2. Experimental procedure and characterization of slag samples

10 g of sub-samples of were placed in MgO crucibles (inner diameter 15 mm, height 40 mm) and melted in a graphite heating furnace (W100/150-2200-50 LAX, FCT Systeme, Rauenstein, Germany) in argon at 1600°C for 1 h to reach equilibrium, after which each sample was cooled to room temperature in the furnace at 5°C/min.

The cooled samples were polished and characterized using electron probe micro-analysis (FE-EPMA, JXA-8530F, JEOL Ltd, Japan) that allows fully quantitative chemical analysis. During analysis, the beam current and accelerating voltage were set at 15 nA and 15 kV, respectively. Phase identification was determined by X-ray diffraction (XRD, 3003-TT, Seifert, Ahrensburg, Germany) using Cu K α radiation at 40 kV and 40 mA. Quantitative analysis of the XRD pattern was achieved with the aid of the Rietveld refinement method.

3. Results and discussion

3.1 Microstructures of slags with different basicities

Figure 1 shows typical microstructures of slags with different basicities produced through furnace cooling under Ar atmosphere. The microstructure of the master slag, without additional SiO₂ addition, is shown in Figure 1(a). This master slag contains approximately 60 μm sized free lime. With SiO₂ addition and therefore decreasing basicity, the amount of free lime is decreased. In all cases, dicalcium silicate (C₂S) and aluminatoferrite (C₂AF) are observed as the major phases except for a basicity of 1.77. Chemical analysis indicates that C₂S typically contains P₂O₅ (>2 wt%), which agrees with Rubio's study [14]. According to previous studies, 0.5 wt% P₂O₅ is enough to stabilize β-C₂S which plays an important role for cement production [15]. Another major phase is monoxide solid solution (RO). The RO phase is a FeO-based monoxide containing MgO, MnO and CaO. There are two typical morphologies of RO: one has tiny crystals (<10 μm), dispersed in C₂S and free lime; the other one has larger (>20 μm) separate grains. At a basicity of 1.77, C₂AF phase disappears and also the C₂S phase can be hardly found. Instead, a substantial amount of bredigite is formed. The chemical composition of bredigite (Ca_{1.75}Mg_{0.25}SiO₄) is very close to C₂S (Ca₂SiO₄) in which some CaO is substituted by MgO.

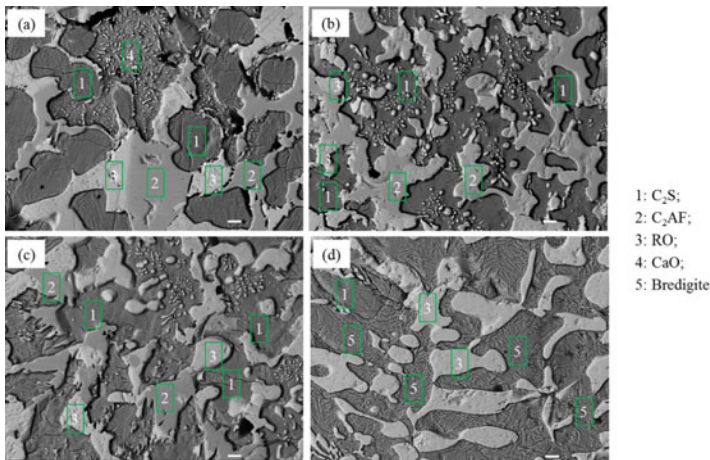


Figure 1. Microstructures of slags with different basicities R produced through furnace cooling in Ar. (a) $R=4.39$ (master slag); (b) $R=2.94$; (c) $R=2.21$; (d) $R=1.77$. Scale bar is 10 μm.

The elemental distribution of the slag at a basicity of 4.39 and 1.77 is shown in Figure 2. In the case of $R=4.39$, Ca exists in free lime and C₂S, while for $R=1.77$, Ca is present in both C₂S and bredigite, with the concentration of Ca being slightly higher in the former, as expected from the stoichiometric formulas for C₂S (Ca₂SiO₄) and bredigite (Ca_{1.75}Mg_{0.25}SiO₄). In terms of Mg distribution, in the case of $R=4.39$, it is present in RO and C₂S. In the case of $R=1.77$, most Mg combines with Fe and Mn and forms the monoxide (RO) phase, whereas some Mg is present in bredigite and the rest stays in the C₂S phase. It is interesting that no free MgO exists in the slag. WDS analysis reveals that in the RO phase the content of MgO in the case of $R=4.39$ is 26.91 wt%, but decreases to 21.28 wt% for $R=1.77$, because bredigite also combines MgO in the latter case. Whatever the basicity, most P dissolves in C₂S. Some P is in bredigite when $R=1.77$. For P₂O₅ bearing slag, [PO₄]³⁻ substitutes for [SiO₄]⁴⁻ during solidification, yielding a modified

formula $\text{Ca}_2\text{SiO}_4 \cdot \text{Ca}_3\text{PiO}_4$ [16, 17], in brief $\text{C}_2\text{S} \cdot \text{C}_3\text{P}$. According to the composition, it can be concluded that only CaO contributes to the consumption of P. The lower concentration of P in bredigite compared to C_2S may be due to the lower CaO/SiO₂ ratio in bredigite. Because in bredigite it is possible that the CaO content is insufficient to consume P after it combines with SiO₂. Therefore, the phosphorus is less concentrated in bredigite than that in C_2S phase.

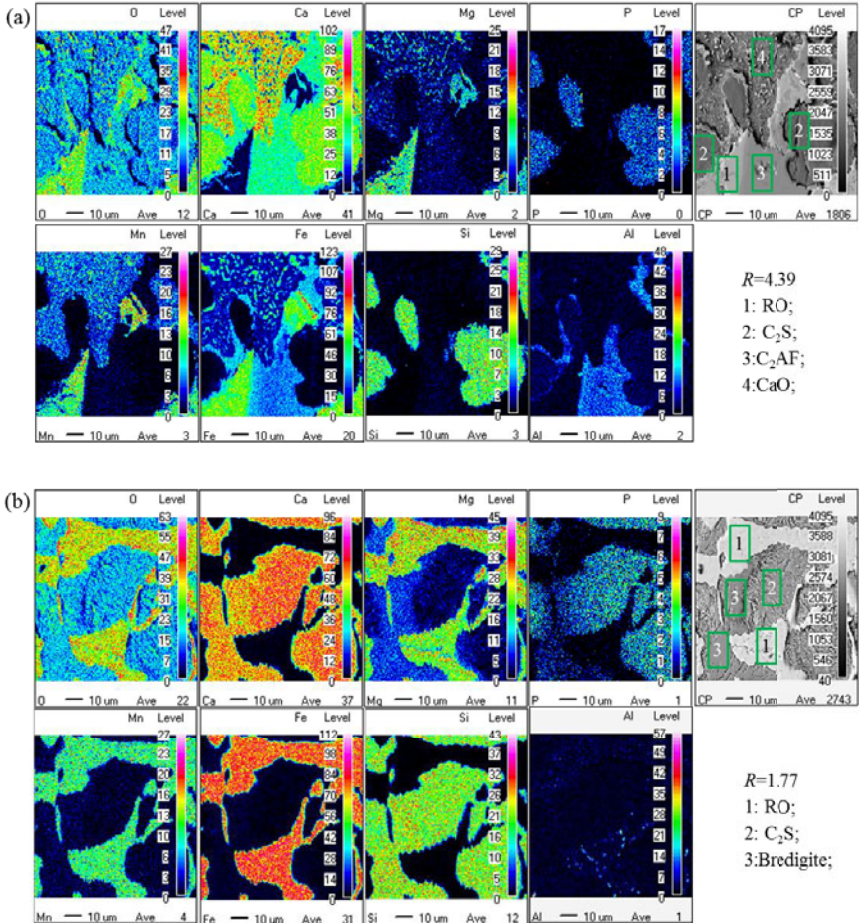


Figure 2. Elemental distribution in the slag (a) without SiO₂ addition ($R=4.39$); with 15 wt% SiO₂ addition ($R=1.77$)

3.2 Quantitative estimation of minerals content in the slag

The results of the quantitative analysis of the XRD patterns are presented in Figure 3. The high basicity industrial slag has 20 wt% free lime. With the aid of SiO₂ addition, the free lime content can be significantly decreased, as indicated by the solid line. When 10 and 15 wt% SiO₂ were added to the slag (corresponding to $R=2.21$ and $R=1.77$ respectively), free lime is completely eliminated. At the same time, the amount of RO and β -C₂S is increased. In contrast, C₂AF is decreased by increasing SiO₂, probably because SiO₂ combines with more CaO forming more β -C₂S. For the case of 15 wt% SiO₂ addition ($R=1.77$), bredigite becomes a major phase and accordingly the amount of β -C₂S is significantly decreased. This trend shows good agreement with our microstructural analysis. In the current study, the amount of β -C₂S increases to a maximum of 44.4 wt% for 10 wt% SiO₂ addition ($R=2.21$). At this basicity there is also 15.7 wt% of C₂AF. The stabilized β -C₂S and C₂AF phases play an important role in preparing cement products, implying a potential valorization direction [18]. The bredigite phase, however, makes little contribution for the cement properties due to its poor hydration behavior and should be avoided for preparing cement [2].

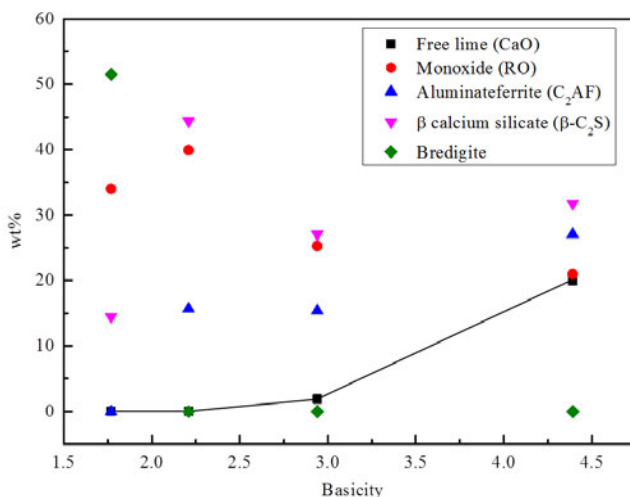


Figure 3. Quantitative XRD analysis of slags with different basicities (R), synthesized through furnace cooling in Ar. The solid line indicates the free lime content.

4. Conclusions

The effect of basicity on BOF slag solidification was studied by lab scale experiments. Stabilization of free lime was demonstrated by lowering the slag basicity with SiO₂ additions to high basicity BOF slag ($R > 4$). Meanwhile, the content of the β -C₂S was increased by decreasing the basicity to an appropriate range. When the basicity is too low ($R=1.77$ for current case), a large amount of bredigite phase is formed, incorporating some MgO. In the present study, the total amount of β -C₂S and C₂AF phases reaches 60.1 wt% when reducing the basicity to 2.21, showing a potential application in cement production.

Acknowledgement

The authors acknowledge the support from IWT grant 140514. Chunwei Liu acknowledges the support of China Scholarship Council (CSC).

References

1. Proctor, D. M. *et al.* Physical and chemical characteristics of blast furnace, basic oxygen furnace, and electric arc furnace steel industry slags. *Environ. Sci. Technol.* **34**, 1576–1582 (2000).
2. Kriskova, L. *et al.* Effect of High Cooling Rates on the Mineralogy and Hydraulic Properties of Stainless Steel Slags. *Metall. Mater. Trans. B* **44**, 1173–1184 (2013).
3. Pandelaers, L., Alfonso, A. D., Jones, P. T. & Blanpain, B. A Quantitative Model for Slag Yard Cooling. **53**, 1106–1111 (2013).
4. Wang, D. *et al.* Enrichment of Fe-Containing Phases and Recovery of Iron and Its Oxides by Magnetic Separation from BOF Slags. *Steel Res. Int.* **83**, 189–196 (2012).
5. Deo, B., Halder, J., Snoeijer, B., Overbosch, A. & Boom, R. Effect of MgO and Al₂O₃ variations in oxygen steelmaking (BOF) slag on slag morphology and phosphorus distribution. *Ironmak. Steelmak.* **32**, 54–60 (2005).
6. Andreas, L., Diener, S. & Lagerkvist, A. Steel slags in a landfill top cover – Experiences from a full-scale experiment. *Waste Manag.* **34**, 692–701 (2014).
7. Reddy, A. S., Pradhan, R. K. & Chandra, S. Utilization of Basic Oxygen Furnace (BOF) slag in the production of a hydraulic cement binder. *Int. J. Miner. Process.* **79**, 98–105 (2006).
8. Lietaert, K. & Blanpain, P. B. Production of hydraulic binder from stainless steel slag. (2010).
9. Motz, H. & Geiseler, J. Products of steel slags an opportunity to save natural resources. *Waste Manag.* **21**, 285–293 (2001).
10. Morone, M., Costa, G., Polettoni, A., Pomi, R. & Baciocchi, R. Valorization of steel slag by a combined carbonation and granulation treatment. *Miner. Eng.* **59**, 82–90 (2014).
11. Santos, R. M. *et al.* Stabilization of basic oxygen furnace slag by hot-stage carbonation treatment. *Chem. Eng. J.* **203**, 239–250 (2012).
12. Mikhail, S. A. & Turcotte, A. M. Thermal behaviour of basic oxygen furnace waste slag. *Thermochim. Acta* **263**, 87–94 (1995).
13. Wang, G., Wang, Y. & Gao, Z. Use of steel slag as a granular material: volume expansion prediction and usability criteria. *J. Hazard. Mater.* **184**, 555–60 (2010).
14. Rubio, V., de la Casa-Lillo, M. A., Aza, S. & Aza, P. N. The System Ca₃(PO₄)₂-Ca₂SiO₄: The Sub-System Ca₂SiO₄-7CaOP₂O₅SiO₂. *J. Am. Ceram. Soc.* **94**, 4459–4462 (2011).
15. Ghosh, S. N., Rao, P. B., Paul, A. K. & Raina, K. The chemistry of dicalcium silicate mineral. *J. Mater. Sci.* **14**, 1554–1566 (1979).
16. Duée, C. *et al.* Phosphorus speciation in dicalcium silicate phases: Application to the basic oxygen furnace (BOF) slag. *Cem. Concr. Res.* **73**, 207–214 (2015).
17. Nurse, R. W., Welch, J. H. & Gutt, W. High- temperature Phase Equilibria in the System Dicalcium Silicate-Tricalcium Phosphate. *J. Chem. Soc.* 1077–1083 (1956).
18. Zach, J., Kminova, H., Horky, O. & Brozovsky, J. Determination of intensity of hydration heat development of silicate binders. in *8th Int. Conf. Slov. Soc. Non-Destructive Testing, Conf. Proc.* 375–382 (2005).

EFFECT OF SLAG PREPARED WITH DIFFERENT COOLING METHODS ON CLEANLINESS OF BEARING STEEL GCr15

Dong-ping Zhan¹, Yang-peng Zhang¹, Lei Tang¹, Kun Fan¹, Zhou-hua Jiang¹, Hui-shu Zhang²

¹School of Materials and Metallurgy, Northeastern University, Shenyang 110004, China;

²School of Metallurgical Engineering, Liaoning Institute of Science and Technology, Benxi, 117004

Keywords: Bearing Steel, Different Cooling Methods Slag, Cleanliness

Abstract

Bearing steel required high cleanliness. During LF refining, the type of slag has obvious effect on its cleanliness. Two kinds of refining slags have been prepared with different cooling methods after pre-melting. Another slag was used by only mixing the raw materials. Then six heats steelmaking experiments were carried out in the MoSi₂ electric resistance furnace to study their effect on the cleanliness of bearing steel GCr15. The results show that: The water-cooled slag is full of glass phase or microcrystal phase inside, and it has the lowest melting point, the shortest melting time, the fastest desulfurization velocity and the smallest average size of inclusions. Those effects of the air-cooled slag are better than the mixed-slag's. Under the same process, the inclusion numbers and area in the steel refined by the slag with CaO/Al₂O₃=1.65 are smaller than those of the slag with CaO/Al₂O₃=0.94.

Introduction

With the development of modern industrial, excellent abrasive resistance, higher fatigue resistance of bearing steel are required. To meet the requirements, on the one hand, the content of inclusions and mass fraction of harmful elements like oxygen and sulfur must be decreased very low, on the other hand, the composition and morphology of inclusions should be controlled to ensure the good ability of plastic deformation [1-10]. In order to achieve the purpose, the refining slag could melt in a short time and achieve the purpose of desulfurization and adsorbing inclusions [11,12].

Metallurgical workers have done a lot of research works on the refining slag system. Wang Deyong [11] found that the refining slag with active Al₂O₃ and aluminum ash can significantly improve the desulfurization rate and reduce the average time of LF process. A composite slag with CaO, Al₂O₃ and CaF₂ has a low melting point and good desulfurization rate, what's more, the ability of adsorbing inclusions is also very good [12,13]. The *DaiDo steel* did some experiments [14,15], and the results showed that the mass fraction ratio of slag and metal between 1% and 3%, the basicity of slag is in 4.0 - 4.5, and the total weight of FeO and MnO in the slag is less than 1% is the suitable desulfurization condition. The study on the optimizing of refining slag composition is very mature, but the purpose of better adsorbing ability and melting speed has not been satisfied, this needs us in other ways to improve the effect of the refining slag. At present the research about preparation methods are not much, therefore, to study this topic in this aspect, different refining with different cooling method were prepared. The metallurgical properties (melting speed and desulfurization) was studied. At the same time, different

composition refining slag were prepared to study the influence on the adsorbing ability and properties of inclusions, that caused by the basicity and ratio of calcium and aluminum of the refining slag. The results in this paper shows a new way to control the cleanliness and inclusions in the GCr15 steel, even all the bearing steel, and has the obvious significance.

Experimental

The slag system used for our experimental is $\text{CaO-SiO}_2\text{-Al}_2\text{O}_3$. In the fact, the refractory material could reveal and to meet the flowing property, some MgO and CaF_2 were added in the system. But because the mass fraction of MgO and CaF_2 is very little and stable, so the slag can be treated as $\text{CaO-SiO}_2\text{-Al}_2\text{O}_3$ slag system during our study. Fig. 1 shows the $\text{CaO-SiO}_2\text{-Al}_2\text{O}_3$ phase diagram.

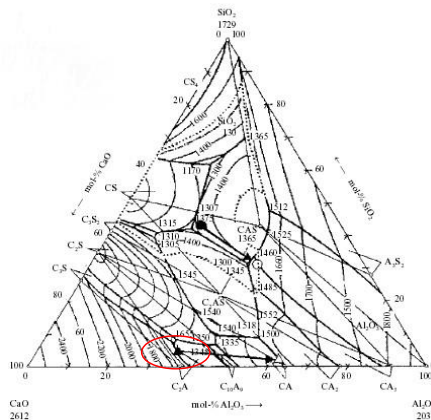


Fig. 1 Ternary phase diagram of $\text{CaO-SiO}_2\text{-Al}_2\text{O}_3$

As shown in Fig. 1, the composition range of elliptic area is 40%~60%CaO, 0%~10%SiO₂, 30%~60%Al₂O₃, which is the low melting point area. In order to control the inclusions in bearing steel in 12CaO·7Al₂O₃ and 3CaO·Al₂O₃'s low melting point area, and desulfurization conditions of high basicity and low oxygen potential. With CaO/Al₂O₃ ratio of variable, we design two experiences that the ratio of CaO/Al₂O₃ are 0.94 and 1.65 respectively. One slag is mechanical mixed by the raw materials, CaO, SiO₂, MgO, Al₂O₃, CaF₂ and so on. The other slags are water-cooled or air-cooled after smelted in a MoSi₂ electric-resistance furnace at 1873 K respectively.

Table 1 Scheme of tests on the refining slag of bearing steel

Number	Compositions /%					Basicity	CaO /Al ₂ O ₃	Process
	CaO	SiO ₂	Al ₂ O ₃	MgO	CaF ₂			
S1	40.7	8	43.3	5	3	5.09	0.94	Water-cooled
S2	40.7	8	43.3	5	3	5.09	0.94	Air-cooled
S3	40.7	8	43.3	5	3	5.09	0.94	mechanical mixed
S4	52.3	8	31.7	5	3	6.54	1.65	Water-cooled
S5	52.3	8	31.7	5	3	6.54	1.65	Air-cooled
S6	52.3	8	31.7	5	3	6.54	1.65	mechanical mixed

The difference between water-cooled slag and air-cooled slag is the cooling method. Both water-cooled slag and air-cooled slag were melted by the MoSi_2 furnace first, and the only difference between them is the cooling methods. The water-cooled slag was cooled by water and the other one was cooled by air. When the different type slags were prepared, we analysis the crystallization ratio by XRD and determinate the melting point and melting speed. To study the effect of different slags on the smelting process of Gr15 bearing steel, these six type slags were used for a slag-metal equilibrium experiment respectively. The raw material used for these six experiment is shown in table 2

Table 2 Composition of Bearing steel (GCr15) (mass fraction /%)

Element	C	Si	Mn	P	S	Cr
Content	0.95	0.25	0.33	0.010	0.004	1.50

Results and Discussion

3.1 XRD analysis

Fig. 2 shows the XRD results of the water-cooled slag and air-cooled slag. Table 3 shows the slag crystallinity analyzed by Mdi Jade 6 software. Air-cooled slag presents obviously sharp diffraction peak. However, water-cooled slag has no obvious diffraction peak, and it present a big steamed bread peak in the range of $20^\circ\sim 50^\circ$. A large percentage of air cooled slag has been crystallized. The refining slag made by water-cooled process is mainly composed of glass phase or microcrystalline phase and the phase in the slag can be ignored.

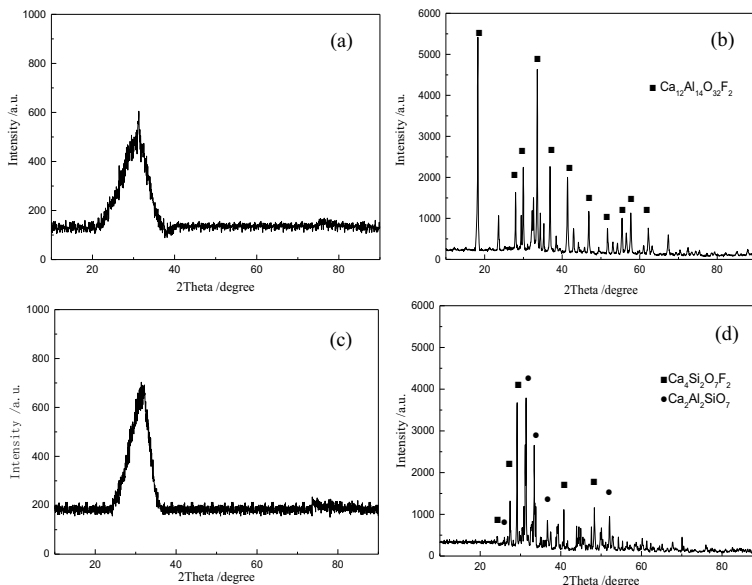


Fig. 2 XRD results of different slag.

(a) water cooled, $\text{CaO}/\text{Al}_2\text{O}_3=0.94$; (b) air cooled slag with $\text{CaO}/\text{Al}_2\text{O}_3=0.94$; (c) water cooled slag with $\text{CaO}/\text{Al}_2\text{O}_3=1.65$; (d) air cooled slag with $\text{CaO}/\text{Al}_2\text{O}_3=1.65$;

Table 3 Crystallinity of different refining slags

Number	Crystallization ratio /%
S1	0.5
S2	98.36
S4	0.2
S5	95.29

3.2 Melting Property

Melting temperature changes of different bearing steel refining slag are shown in Fig. 3.

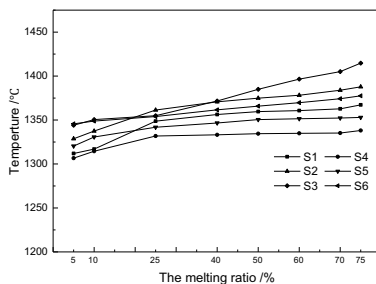


Fig. 3 Melting temperatures of different refining slags

It can be seen from the data that the melting points of S1, S2 and S3 slag successively increases, and the melting points of S4, S5 and S6 slag have the same trend. Slags with the same composition have the order of the melting point of water-cooled slag, air-cooled slag and mechanical-mixed slag. The melting point of the slag with $\text{CaO}/\text{Al}_2\text{O}_3=0.94$ is higher than that of $\text{CaO}/\text{Al}_2\text{O}_3=1.65$ when they are made by the same process. Variations of slag melting time at 1773K are shown in Fig. 4.

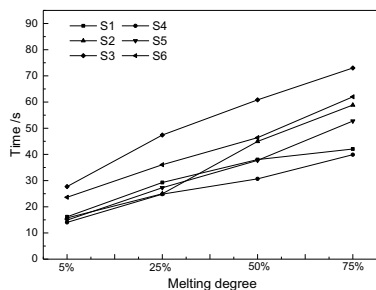


Fig. 4 Melting times of different refining slags

3.3 Deoxidation and Desulfuration

Steel samples of the steelmaking process are detected by oxygen and nitrogen analyzer. The variation of total oxygen content are shown in Fig. 5.

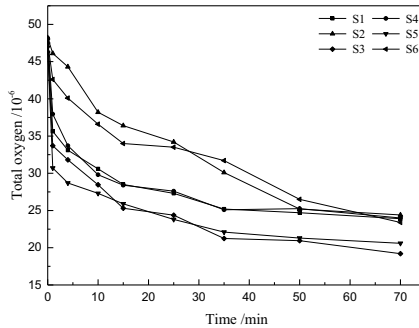


Fig. 5 Tendency of the mass fraction of total oxygen content

As can be seen from Fig. 5, the total oxygen content shows a slow decline and eventually reaching equilibrium value. Under the same preparation technology, the slag with $\text{CaO}/\text{Al}_2\text{O}_3=1.65$ has faster deoxidation rate, and lower final balanced oxygen content. This is due to the less Al_2O_3 content in this slag, which promotes the combination of $[\text{Al}]$ and $[\text{O}]$.

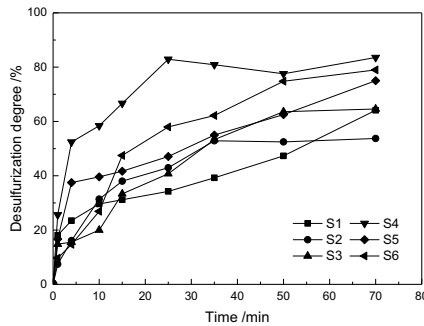


Fig. 6 Variation of desulfurization rate with time for different slags

The variations of the desulfurization rate are shown in Fig. 6. The slag with $\text{CaO}/\text{Al}_2\text{O}_3=1.65$ has the higher desulfurization rate, and the highest one reaches 79.18%. For the same composition slag made by different processes, the order of the desulfurization rate from high to low is water-cooled slag, air-cooled slag and then mechanical mixed.

3.4 Effect of refining slag on inclusions

The size distribution of inclusion in the bearing steels is shown in Fig. 7.

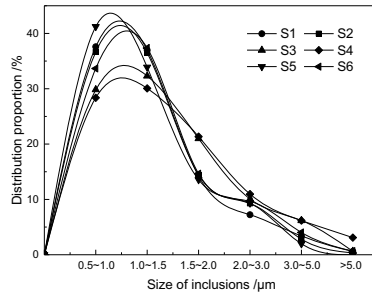
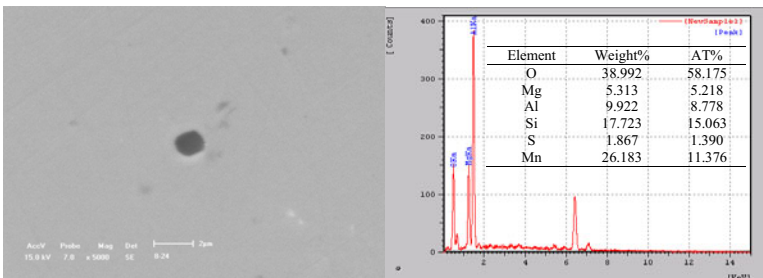


Fig. 7 Size distribution of inclusion in the bearing steels

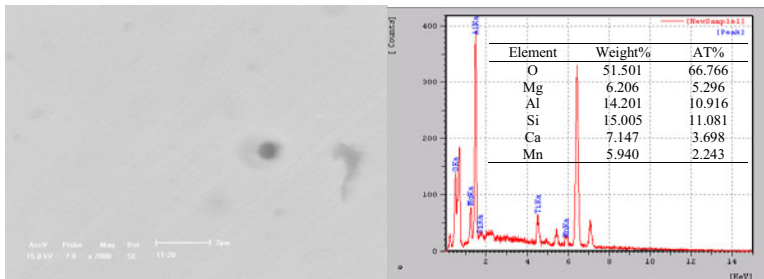
It can be seen from Fig. 7 that the amount of small inclusions in the steel with slag blended by machine is smaller than those of water-cooled slag and air-cooled slag. On the contrary, the amount of big inclusion in the steel smelted by mechanical mixed slag is the largest, and thus the average size of the inclusions in it is the biggest.

The inclusion in the steel treated by water-cooled slag has the smallest mean size. The analysis of the steel with the same preparation process and different slag composition shows that the number of large inclusions in the steel whose $\text{CaO}/\text{Al}_2\text{O}_3$ is 1.65 is smaller than that in the steel whose $\text{CaO}/\text{Al}_2\text{O}_3$ is 0.94 and the mean size is smaller. Among the slags with same treatment, the mean size of inclusions in the steel with water-cooled slag is smaller, and the inclusions distribute more uniform, and the percentage of the area of inclusion is also minimal. Under same preparation process, the number of inclusion in steel with the refining slag whose number of $\text{CaO}/\text{Al}_2\text{O}_3$ is 1.65 is smaller when number of $\text{CaO}/\text{Al}_2\text{O}_3$ is 0.94, and the area percentage is smaller.

Through analysis, the crystalline refining slags, which is same to amorphous refining slags on composition, the inclusions has little difference in their composition. But the difference between two kinds of $\text{CaO}/\text{Al}_2\text{O}_3$ inclusions and those in the bearing steel is large. In the bearing steel used the refining slag whose number of $\text{CaO}/\text{Al}_2\text{O}_3$ is 1.65, inclusions of spinel compared with those of number of $\text{CaO}/\text{Al}_2\text{O}_3$ is 0.94 decreased, while the inclusions of $\text{Al}_2\text{O}_3 \cdot \text{MgO} \cdot \text{SiO}_2 \cdot \text{CaO}$ increased. There was hardly any SiO_2 and MnS . Fig. 8 is picture of some typical inclusions.



(a) $\text{Al}_2\text{O}_3 \cdot \text{MgO}$



(b) $\text{Al}_2\text{O}_3\cdot\text{MgO}\cdot\text{SiO}_2\cdot\text{TiO}_x\cdot\text{MnS}$
 Fig. 8 Typical morphology of inclusion

Conclusions

- (1) Different cooling methods have significant effect on the physical and chemical properties of refining slag and crystal structures. The water-cooled slag is composed of glass phase or microcrystal phase, while the air-cooled slag crystallizes absolutely. The melting point of the water-cooled slag is the lowest and their melting speed is the highest. Among the slags with the same treatment, the refining slag whose $\text{CaO}/\text{Al}_2\text{O}_3$ is 0.94 has the higher melting point and lower melting speed.
- (2) Under the same preparation process, the slag with $\text{CaO}/\text{Al}_2\text{O}_3$ is 1.65 has better the dioxidization and desulphurization effect, and has more lower oxygen content.
- (3) The heat smelted by water-cooled slag with $\text{CaO}/\text{Al}_2\text{O}_3$ is 1.65 gets the best inclusions. The total number of inclusions is the lowest and the mean size is smallest. Most of the inclusions are $\text{Al}_2\text{O}_3\cdot\text{MgO}\cdot\text{SiO}_2\cdot\text{CaO}$.

Acknowledgements

The authors would like to appreciate National Natural Science Foundation of China [51574063] and National High Technology Research and Development Program [2015BAF03B01] and PhD Research Startup Foundation of Liaoning Institute of Science and Technology[1406B06] and Program for Liaoning Excellent Talents in University [LJQ2015056] for providing funding for this research.

Corresponding author: Dong-ping Zhan, Tel: +86-024-83687723; E-mail: zhandp1906@163.com

References

1. M.Q. Yu, "The Development Status of Bearing Steel and Its Grades Series," *Shanghai Metals*, 30(3) (2008), 49-54.
2. Y.D. Li et al., "Correlations Between Very High Cycle Fatigue Properties and Inclusions of GCr15 Bearing Steel," *Acta Metallurgica Sinica*, 44(8) (2008), 968-972.
3. J. Chakraborty, D. Bhattacharjee, I. Manna, "Austempering of Bearing Steel for Improved Mechanical Properties," *Scripta Materialia*, 59(2) (2008), 247-250
4. K.F. Hille, F.R. Papay, N. Genma, "Slag Control Techniques for High Quality Steel" (Paper Presented at 74th Steelmaking Conference Proceedings, Warrendale 1991), 419-422.

5. X. Yuan, M.L. Qi, "Prediction of Bearing Steel Deformation Resistance Based on RBF Neural Network," *Journal of Iron & Steel Research*, 23(2) (2011), 48-52
6. Tardy P, Tolnay L, Karoly G, et al., "Bearing Steels: Cleanliness or Inclusion Modification" (Paper Presented at The Sixth International Iron and Steel Congress Meeting. Nagoya, Japan,1990), 629-636.
7. B.H. Yoon, K.H. Heo J.S. Kim, "Improvement of Steel Cleanliness by Controlling Slag Composition," *Ironmaking and Steelmaking*, 30(2) (2003), 51-59.
8. L. Liu, "Development of Process and Equipment of RH Vacuum Refinery Technology RH," *Iron&Steel*, 41(8) (2006), 1-11.
9. Y. Kato et al., "Development of Rapid Decarburization Technology by Combined Process of Converter and RH Degasser for Ultra Low Carbon Steel," *Zairyo to Purosesu (Current Advances in Materials and Processes)*, 3(1) (1990), 160-163.
10. J. Poirier, B. Thillou, M. Guiban, "Mechanisms and Counter Measures of Alumina Clogging in Submerged Nozzles" (Paper Presented at the 78th Steelmaking Conference Proceedings, Nashville Meeting, April 2-5 1995), 451-456.
11. D.Y. Wang et al., "Effect of Al Ash on Desulphurization of Pipe-line Steel," *China Metallurgy*, 17(2) (2007), 14-16.
12. S.H. Wang et al., "Research on Physical Properties and Desulfurization Ability of 12CaO·7Al₂O₃ Refining Slag," *Journal of Hebei Institute of Technology*, 21(8) (2001), 9-12.
13. G.H. LI, R. Zhu, T.C. Lin, "Study on High Efficient Desulfurization of New Type Synthetic Refining Slag," *Journal of University of Science and Technology Beijing*, 31(12) (2009), 76-79.
14. G. Yuasa et al., "Refining Practice and Application of the Ladle Furnace (LF) Process in Japan," *Transactions of the Iron and Steel Institute of Japan*, 24(5) (1984): 412-418.
15. Kishida T, Yajima T, Ukai A. "Recent Developments of Ladle Furnace (LF) Process in Japan" (Report on the Seventh International Conference on Vacuum Metallurgy: Special Meltings and Metallurgical Coatings, Keidanren Kaikan, Japan, November 26-30 1982), 1148-1162.

EFFECT OF Zr INHIBITOR ON CORROSION OF HAYNES 230 AND NS-163 ALLOYS IN FLiNAK

Yuxiang Peng, and Ramana G. Reddy

Department of Metallurgical and Materials Engineering,
The University of Alabama, Tuscaloosa, AL 35487, U.S.A

Keywords: FLiNaK, Corrosion, Haynes 230, Haynes NS-163, Zr inhibitor

Abstract

The intrinsic corrosion behavior of Haynes 230 and NS-163 alloys after adding corrosion inhibitor Zr to LiF-NaF-KF (FLiNaK) salts was evaluated. Thermodynamic modeling studies were performed to investigate the compatibility of Haynes alloys for solar thermal energy storage applications in the molten salts. Equilibrium conditions were considered for predicting the corrosion products and weight loss of salts at higher temperatures (700 - 1000°C). Weight loss of FLiNaK salt after corrosion with or without inhibitor is less than 5%, indicating no significant change in compositions of FLiNaK even with Zr inhibitor. Furthermore, to compare with experimental data, modeling calculation with known amount of trace impurities (Ni^{2+} , Fe^{3+} and so on) added to the molten salts, shows similar trend and corrosion product with and without Zr inhibitor.

Introduction

From the reports of Oak Ridge National Lab (ORNL), early molten salts consist of fluoride salts, which are performed in the nuclear energy applications. These fuel salts always contain UF_4 as uranium is dissolved from reactor fuel. Moreover, several experiments performed by ORNL indicate UF_4 is corrosive to the structural materials [1]. Nowadays, molten fluoride salts without UF_4 have been considered as a candidate for thermal energy storage media in solar energy applications [2]. Although LiF-BeF₂ (FLiBe) has been used as the primary coolant in nuclear energy applications [3], chemical toxicity of beryllium compound has limited the development of this salt [4]. However, LiF-NaF-KF (FLiNaK) salt includes lots of good thermal properties, such as lightweight, low eutectic melting point, high heat capacity and large thermal conductivity, indicating it has more potential to be used in solar power industry [5]. However, the widespread applicability of this molten salt is limited mainly because of their ability to corrode the structural materials, and it is reported to be more corrosive than FLiBe [6]. Moreover, therefore, it is important to categorize alloys that are corrosion resistant to this molten salt [7].

Considering the structural material should be economical, alloys are chosen to be the proper candidate, although ZrO_2 -8 mol % Y_2O_3 is very stable in the FLiNaK salt [8]. A research study from National Aeronautic and Space Administration (NASA) indicates that Ni is difficult to be corroded in fluoride salts [9], and thus lots of Ni-based alloys have been tested in the FLiNaK salt to justify the corrosion resistance. Mo and Ta have also been indicated to be stable in FLiNaK [10&11]. However, more initial Cr in the alloy, faster corrosion rate will be [12]. Alloy with a high content of Mo and low content of Cr will be preferred to be the proper structural material due to the high corrosion resistance. However, at least, 6% (atomic) of Cr is needed in the alloy to prevent oxidation in the air [13]. Thus, Hastelloy (Ni-Mo-Cr) have been tested in the FLiNaK by Luke, but the strength of these alloys at high temperature are not good [14]. In fact,

considering the structural property, Haynes-230 shows more creep rupture times than Hastelloy in the same condition [15], indicating Haynes alloys have more potential to be the structural alloy even it includes lots of Cr (more than 20 mol%). Several methods have been provided to reduce the dissolution of constituent alloy elements, especially for Cr, into the FLiNaK molten salts, Ni-plating is one of the proper ways because Ni on the surface will prevent salt contacting with the alloy directly. Moreover, the result shows Ni-plated 800H alloy has the lower corrosion rate than which without Ni-plating [16]. Another plating like tantalum [17] and SiC [18] also increase the corrosion resistance of the alloys. Another method is adding more active elements into the FLiNaK molten salt, and these elements will act as a sacrificial anode to protect the alloys. Moreover, Sellers [19] has reported the addition zirconium, the active metal into FLiNaK salt will form an inter-metallic layer on the surface of the Ni-based alloy, preventing the salt contacting with the alloy directly. Moreover, adding the appropriate amount of yttrium has the similar result that Y-rich layer on the surface of the alloy may inhibit the diffusion of susceptible elements [20]. Recently, Savannah River National Laboratory (SRNL) did several corrosion experiments to study the influence of adding Zr inhibitor in FLiNaK salt because ZrF_4 shows more negative Gibbs energy of formation than several other corrosion products at 850°C. Moreover, in the current study, the effect of Zr addition to molten FLiNaK salt on the corrosion behavior of Haynes 230 (H230) and Haynes NS-163 (H163) alloys at different temperatures was evaluated using thermodynamic calculations. Sohal [3] has reported there are four corrosion mechanism of alloys corrosion in molten salt: intrinsic corrosion, corrosion by oxidizing contaminations, different solubility, and galvanic corrosion. For simplification, there is only intrinsic corrosion because salt is assumed to be pure and the temperature is assumed to be constant. Crucible is not considered; thus galvanic corrosion is ignored in the current study. The intrinsic corrosion mechanism is driven by Gibbs energy of formation of salts and metals [3]. Thus, Gibbs energy minimization method was used to predict the corrosion products of H230 and H163 alloys and weight loss of salts under the equilibrium conditions at higher temperatures (700 - 1000°C, this temperature range is the proper service temperature for FLiNaK).

1. Calculations

Thermodynamic modeling of the corrosion products and weight loss of salts was performed using thermodynamic modelling software. The calculations were based on Gibbs energy minimization method for simulating the chemical reaction equilibrium and processes.

1.1. Decomposition of molten salt with and without inhibitor

Decomposition of FLiNaK was taken as weight loss of FLiNaK salt during corrosion to determine the thermal stability of molten salt contacting with alloys at higher temperature (700-1000°C), especially with inhibitors. Weight loss of salt is calculated from weight of element transferred from salt to corrosion product. A lot of weight loss is contributed by negative ion F⁻. However, a little Potassium element will also transfer to product due to the K_3AlF_6 complex. The mole of each corrosion product was obtained at equilibrium condition by thermodynamic modelling. Thus, weight loss of element from molten salt is obtained from equation (1):

$$F = \frac{\sum n_i \cdot M_i}{m} * 100\% \quad (1)$$

Where n_i is mole of each element transferred to corrosion product from molten salt, M_i is atomic weight of each element, m is weight of initial molten salt.

1.2. Corrosion product prediction in molten salts with impurities

The corrosion behavior of H230 and H163 alloys were different in pure and impure FLiNaK salt. Due to the impurities like metal ions may take the replacement reaction or oxidizing reaction with alloys. However, activity coefficient which is less than unity and insufficient reacting time cause lots of impurities are still left in 210g FLiNaK after corrosion. Moreover, the concentration of impurities before and after alloys corrosion is shown in Table 1.

Table 1 Amount of trace metal impurities before and after H163 and H230 corrosion in experimental FLiNaK salt detected by SRNL

Fluoride Salt(ppm)	Cr	Fe	Ni	Mn	Mo	Al	Cu	Co	Ag	Ba	Ca	Cd	Ce	Nb	Nd	Pb	Re	Sn	Sr	Ti	V	Zn	Zr
Before Corrosion	< 5.27	< 65.9	< 13.4	< 2.11	< 61.4	< 119	< 15.6	< 64.2	< 79.5	< 28	44.9	28.2	81.9	79	113	396	393	123	115	11.9	138	48.7	7.63
H163	< 11.3	< 58.9	< 12	< 4.05	< 54.9	< 106	< 19.8	< 57.5	< 7.69	< 25.1	31.6	25.3	73.3	34.3	101	355	352	110	103	21	123	43.6	6.83
H230	< 55.7	< 56.3	< 11.5	< 17.2	< 52.5	< 101	< 29.4	< 54.9	< 7.34	< 24	25.2	24.1	70.1	32.8	96.5	339	336	105	98.6	10.2	118	41.7	6.53

Thus, the decreased amount of impurities have taken the replacement reaction with the alloy, and it is reasonable to consider these reacted impurities in the thermodynamic modeling. As it is in the fluoride salt, impurities are assumed to be the stable fluorides, and thus impurity fluorides sublimed or decomposed at 850°C, like NbF₅, SnF₄ and few fluoride impurities at high oxidation state are ignored. Moreover, ignoring the impurity which will not react with alloys like CaF₂, BaF₂ and so on. The amount of reacted impurities is listed in Table 2.

Table 2 Amount of reacted impurities in FLiNaK at 850°C for 100hrs

Fluoride salt (mole)	CrF ₃	FeF ₂	CoF ₂	AgF	CeF ₃	PbF ₂	ReF ₃	ZnF ₂
H163	2.13	2.63	3.07	1.40	1.29	4.16	4.62	1.64
	E-05	E-05	E-05	E-04	E-05	E-05	E-05	E-05
H230	2.13	3.15	2.21	1.40	1.77	5.77	6.54	2.25
	E-05	E-05	E-05	E-04	E-05	E-05	E-05	E-05

The amounts of the H230 and H163 alloys and the inhibitor Zr added to FLiNaK salt are listed in Table 3.

Table 3 Initial amount of alloy and inhibitors in experiment performed by SRNL

Molten salts	Amount of compound in salts (mole)		
	H230	H163	Zr
LiF-NaF-KF (210 g)	0.06	0.06	0.06

The experiment was performed in the salt at 850 °C and 1 atm. for 100hrs under Ar atmosphere. And the corroded depth measured from Scanning Electron Microscopy (SEM) of alloys after corrosion, is listed in Table 4.

Table 4 Corrosion depth of H230 and H163 after corrosion in MgCl₂-KCl for 100hrs at 850°C

	H230	H163
Corrosion depth (mm)	0.046	0.015

As Table 5 gives the dimensions of both samples, the amount which is contacted with salt can be calculated by means of measuring corroded volume fraction, which is shown in details in equation 6.

$$n = 0.06 * [1 - (W - 2d) * (L - 2d) * (T - 2d)/(W * L * D)] \quad (6)$$

Where n is the amount is contacted with salt. W, L and T is width, length and thickness of sample used in the experiments, d is corroded depth.

Table 5 Dimensions of H230 and H163 samples in experiment

Metal Coupon	Weight (g)	Dimensions			
		Length (mm)	Width (mm)	Thickness (mm)	Area (cm ²)
NS-163 (C6)	3.4273	29.98	11.72	1.26	7.99
230 (D4)	3.6879	29.95	11.95	1.23	8.09

The exact amount of H230 and H163 contacting with salt during corrosion is 0.00770 mole and 0.00434 mole from the calculation. Thus the initial input conditions of the thermodynamic modeling, i.e. pressure, temperature, and amount of salts, alloys contacting with salt, and impurities were kept same as the experimental data.

2. Results and discussion

2.1. Decomposition of FLiNaK salt with and without inhibitors

The change in the composition of the molten salt was calculated using Gibbs energy minimization method at temperatures above 700 °C. The criterion for thermal stability of the salts is their % weight loss ($\leq 5\%$) due to corrosion tests. The effect of the inhibitor on the decomposition of FLiNaK molten salts for H230 and H163 alloys were studied from 700 to 1000°C.

Figure 2 shows a comparison of the weight loss for Haynes 230 and Haynes NS-163 alloys at different temperatures with and without Zr inhibitor added to the fluoride salts.

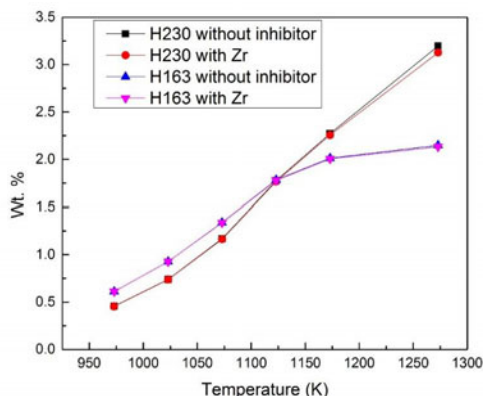


Figure 1 Weight loss of fluoride salts at different temperatures with and without Zr

Because Zr shows insignificant ability in preventing Al from dissolving into salt and Al is the main element dissolved in the salts, no significant change is observed in weight loss of fluoride salts for both the alloys. The weight loss of the FLiNaK salt with Zr inhibitor is below 5%. The Zr inhibitor has not increased the decomposition of FLiNaK salt significantly. Therefore, FLiNaK salt has not lost the candidate for the heat transferred fluid.

2.2. Experimental vs. modeling of major corroded metals

Table 6 shows a comparison of the experimental ICP-OES data with the thermodynamic modeling results for the change in mass percent of major metals (Cr and Mn) in FLiNaK salts containing Haynes alloys and inhibitor Zr at 850 °C.

Table 6 percentage Mass change of major elements in impure FLiNaK salt after corrosion of H230 and H163 at 850°C with and without addition of Zr inhibitor (E refers experimental data and M refers to model calculation)

Elements		Mass change of major elements in FLiNaK (%)	
		FLiNaK	FLiNaK with Zr
Cr in H230	E	956.93	-1.71
	M	944.11	-99.97
Mn in H230	E	715.17	175.83
	M	715.40	-99.95
Cr in H163	E	114.42	-15.18
	M	746.81	-99.97
Mn in H163	E	91.94	83.41
	M	92.99	-99.98

With no inhibitor added to the FLiNaK salt, both the experimental and modeling results confirm an increase in the mass % of Cr and Mn in salt due to corrosion of alloys at 850°C. For H230, the increased amount is comparable to both experiment and modeling. However, the amount of Cr for H163 is larger in modeling even amount of Mn is comparable. That may due to (a) reaction

time (of 100 h) is not sufficient for the complete corrosion of alloys in the corroded-depth range, (b) only the surface but not interior components of the alloys are in contact with the molten salts. Thus, the amount of reacted Cr in the experiment is less than which in the modeling calculation. Therefore, considering the appropriate amount of reactants and adjusting the equilibrium conditions of corrosion reactions could minimize the differences between experimental and modeling results. In addition, both experimental and modeling results show that the corrosion amount of Cr and Mn in H230 and H163 alloys decreases with the addition Zr inhibitor to the FLiNaK salts. However, the decreased amount is not comparable. As discussed above, the only surface contacting of Zr leads very less amount acting as sacrificial anode thus poorer ability to inhibit the corrosion, and insufficient reaction time results there is still some Cr^{2+} and Mn^{2+} cations left in the salt. While in the modeling, all the Zr acting as sacrificial anode and sufficient time to react with FLiNaK molten salt result Cr^{2+} and Mn^{2+} cations are disappeared in the salt.

It is interesting that Sellers [19] and SEM provided by SRNL both prove Zr will deposit on the samples during corrosion. Therefore, there is not only intrinsic corrosion, but galvanic corrosion takes place. And the driving force is the Gibbs energy of formation of Zr-Ni and Zr-Co intermetallic phase.

3. Conclusions

Prediction of decomposition of salts is to investigate if molten salt will lose its properties as media of heat transferred fluid. In both cases, with or without the Zr inhibitor, less than 5% is decomposed for FLiNaK salt with Haynes alloys. Therefore, it can be inferred that the corrosion of Haynes 230 and Haynes NS-163 will not affect much on the properties of molten salt even with Zr inhibitor.

Both experimental data and thermodynamic calculations show an increasing trend in the corrosion amounts of Cr and Mn from Haynes 230 and Haynes NS-163 alloys in the FLiNaK molten salts. And the corrosion amount (Table 5) is almost comparable. The corroded amount of Cr and Mn from Haynes 230 and Haynes NS-163 alloys was controlled with the addition of Zr inhibitor to the FLiNaK salts. The difference in the corroded amount in experiment is due to less amount of sacrificial Zr inhibitor and insufficient time.

References

- [1] Williams, D. F., Assessment of candidate molten salt coolants for the NGNP/NHI Heat-Transfer Loop, ORNL/TM-2006/69, 2006. pp. 1–44.
- [2] Forsberg, Charles W., Per F. Peterson, and Haihua Zhao. "High-temperature liquid-fluoride-salt closed-Brayton-cycle solar power towers." *Journal of Solar Energy Engineering* Vol. 129.2, 2007. pp: 141-146.
- [3] Sohal, Manohar S., et al. "Engineering database of liquid salt thermophysical and thermochemical properties." Idaho National Laboratory, Idaho Falls, 2010.
- [4] Cadwallader, Lee Charles, and Glen Reed Longhurst. "Flibe use in fusion reactors: an initial safety assessment." Idaho National Engineering and Environmental Laboratory, INEEL/EXT-99-00331, 1999.

- [5] Whittenberger, J. D., and Misra, A. K., Identification of salt—Alloy combinations for thermal energy storage applications in advanced solar dynamic power systems, *J. Mater. Eng.*, Vol. 9(3), 1987. pp. 293-302.
- [6] Kondo, Masatoshi, et al. "Corrosion characteristics of reduced activation ferritic steel, JLF-1 (8.92 Cr–2W) in molten salts Flibe and Flinak." *Fusion Engineering and Design* Vol. 84 (7), 2009. pp.1081-1085.
- [7] Ambrosek, J., Anderson, M., Sridharan, K., and Allen, T., Current Status of Knowledge of the Fluoride Salt (FLiNaK) Heat Transfer, *Nucl. Technol.*, Vol. 165(2), 2009. pp. 166-173.
- [8] Stourmaras, C. J., et al. "Corrosion of yttria-fully stabilized zirconias in molten fluorides." *Journal of materials science* Vol. 30, 1995. pp. 4375-4379.
- [9] Misra, A.K., and Whittenberger, J.D., in: *Proceedings of the 22nd Intersociety Energy Conversion Engineering Conference* cosponsored by the AIAA ANS ASME SAE IEEE ACS and AIChE Philadelphia, PA, AIAA-87-9226, 1987. pp. 10–14.
- [10] Liu, Min, et al. "Investigation on corrosion behavior of Ni-based alloys in molten fluoride salt using synchrotron radiation techniques." *Journal of Nuclear Materials* Vol. 440.1, 2013. pp. 124-128.
- [11] El-Dasher, Bassem, et al. "Corrosion of oxide dispersion strengthened iron–chromium steels and tantalum in fluoride salt coolant: An in situ compatibility study for fusion and fusion–fission hybrid reactor concepts." *Journal of Nuclear Materials* Vol. 419.1, 2011. pp. 15-23.
- [12] Olson, Luke, et al. "Intergranular corrosion of high temperature alloys in molten fluoride salts." *Materials at High Temperatures* Vol. 27 (2), 2010. pp. 145-149.
- [13] Alexander Lehrman, Edward Adler, Jacob Freidus, and Max Neimand. The liquidus curve and surface of the systems lithium and calcium nitrates and calcium, lithium and potassium nitrates. *Journal of the American Chemical Society*, Vol. 59, 1937. pp.179–181.
- [14] Olson, Luke C. "Materials corrosion in molten LiF–NaF–KF salt." *Journal of Fluorine Chemistry* Vol. 130 (1), 2009. pp. 67-73.
- [15] Sadananda, K., and P. Shahinian. "Creep crack growth behavior of several structural alloys." *Metallurgical Transactions A* Vol. 14 (7), 1983. pp. 1467-1480.
- [16] Olson, Luke, et al. "Nickel-plating for active metal dissolution resistance in molten fluoride salts." *Journal of Nuclear Materials* Vol. 411 (1), 2011. pp. 51-59.
- [17] Taxil, P., and J. Mahenc. "The preparation of corrosion-resistant layers by the electrolytic deposition of tantalum on nickel and stainless steel." *Corrosion Science* Vol. 21 (1), 1981. pp. 31-40.
- [18] He, Xiujie, et al. "SiC coating: An alternative for the protection of nuclear graphite from liquid fluoride salt." *Journal of Nuclear Materials* Vol. 448 (1), 2014. pp. 1-3.
- [19] Sellers, R. S., et al. "Materials corrosion in molten LiF–NaF–KF eutectic salt under different reduction-oxidation conditions." *Proc. Int. Conf. Advances in Nuclear Power Plants (ICAPP'12)*. 2012.
- [20] Li, Xiao-li, et al. "High-temperature corrosion behavior of Ni-16Mo-7Cr-4Fe superalloy containing yttrium in molten LiF–NaF–KF salt." *Journal of Nuclear Materials*, Vol. 494, 2015. pp. 342-345.

EXPERIMENTAL STUDY OF GAS/SLAG/MATTE/SPINEL EQUILIBRIA AND MINOR ELEMENTS PARTITIONING IN THE Cu-Fe-O-S-Si SYSTEM

Taufiq Hidayat, Ata F Mehrjardi, Peter C Hayes, Evgueni Jak

PYROSEARCH, School of Chemical Engineering, The University of Queensland, Brisbane,
Queensland, 4072, Australia.

Keywords: Matte-slag equilibrium, copper making process, spinel liquidus

Abstract

New data on gas/slag/matte/spinel equilibrium in the Cu-Fe-O-S-Si system at $T=1200\text{ }^{\circ}\text{C}$ and $P(\text{SO}_2)=0.25\text{ atm}$ covering a wide range of matte grades for copper smelting and converting are presented. High temperature equilibration and rapid quenching technique, followed by Electron Probe X-ray Microanalysis are used. The use of substrate made of solid spinel ensures equilibration strictly within the Cu-Fe-O-S-Si system and avoiding contaminants from crucible. The research is extended to measure partitioning of minor elements between slag and matte phases using this technique based on microanalysis. The system selected closely resembles the equilibrium condition of the actual copper smelting process. The information provided is essential for the evaluation of effect of fluxing towards the amount of chemically dissolved copper and quantity of solid in the slag. Present study is part of a larger integrated experimental and thermodynamic modelling research program on copper-making high-temperature systems.

1. Introduction

Fundamental information on slag-matte equilibria in the Cu-Fe-O-S-Si system is essential for understanding and improving the existing copper smelting and converting processes. Most of the previous investigations on the slag-matte equilibria at controlled $P(\text{SO}_2)$ have been carried out at tridymite saturation [1-6]. Analysis on the industrial sample however showed that spinel is common solid found in equilibrium with matte and slag phases [7]. Few studies available dealing with the equilibria between matte and spinel at fixed $P(\text{SO}_2)$ [8-11]. Not many attempts have been made to investigate the equilibria in the slag/matte/spinel at controlled gas atmosphere. This is due to difficulty in performing experiment since the system contains aggressive slag and matte liquids and there is no crucible that can suspend the sample without introducing contamination. Equilibration experiment using substrate techniques has been developed in PYROSEARCH to tackle this issue. In this technique, a thin film of liquid phase is equilibrated on a substrate made of the spinel primary phase. This technique gives advantages compared to the conventional bulk refractory crucible experimentation since it improves direct exposure to gas, the quenching process of the sample, as well as avoids contamination of unwanted elements into the sample. The application of this method enables the measurement of gas/slag/matte/spinel system.

2. Development of Experimental and Measurement Techniques

2.1. High temperature equilibration technique

Experimental technique used to study the complex multi-component gas/slag/matte/spinel equilibria in the Cu-Fe-S-O-Si system involves high temperature equilibration in controlled gas atmospheres, rapid quenching and direct measurement of equilibrium phases with electron probe X-ray microanalysis (EPMA), which is similar to the technique previously used to investigate gas/slag/matte/tridymite system [7, 12].

First, an artificial oxide mixture was prepared from the analytically pure powders or pre-sintered solids or pre-melted master matte/slag to obtain after equilibration a predetermined bulk composition. The starting materials thoroughly mixed using an agate mortar and pestle, and then pelletised in a die using a press. The starting composition was selected to obtain two or more phases in the final sample after equilibration. Spinel (Fe_3O_4) substrate was used for holding slag and matte sample. The spinel was prepared from 99.5 wt pct pure iron foil folded into required shape and then oxidized at 1200 °C at $P(\text{O}_2)$ corresponding to condition where spinel is stable. The furnace temperature was controlled within ± 1 K by an alumina-shielded B-type thermocouple placed immediately adjacent to the sample, and was periodically calibrated against a standard thermocouple. The overall temperature accuracy is estimated to be within 5 K or better. The gas atmosphere was maintained by mixture of 20%CO in Argon, CO_2 and SO_2 gases added in proportions calculated using reliable thermodynamic information (e.g. FactSage thermodynamic software). The required gas flow-rates were maintained with calibrated U-tube capillary flow-meters. The calibrations of 20%CO-Ar and CO gases were checked by an oxygen probe made of a yttria-stabilized zirconia solid electrolyte cell (SIRO₂®, DS-type oxygen probe; supplied by Australian Oxytrol Systems, Victoria, Australia). After equilibration for predetermined time the samples were quenched into cold water or brine solution so that the phases present at high temperature and their compositions are retained at room temperature.

The samples were mounted, polished and then examined using optical microscopy and Scanning Electron Microscopy (SEM) with Energy Dispersive Detector (EDS). The compositions of the phases were measured using a JEOL JXA 8200L (trademark of Japan Electron Optics Ltd., Tokyo) electron probe X-ray microanalyzer (EPMA) with Wavelength Dispersive Detectors (WDD). An acceleration voltage of 15 kV and a probe current of 15 nA were selected. The Duncumb-Philibert ZAF correction procedure supplied with the probe was applied. The appropriate standards were selected to the oxide or sulphide phases. The phase compositions were measured with EPMA with accuracy within 1 wt % or better. EPMA was used to measure the element concentrations; no information on the proportions of the same element having different oxidation states were acquired. For slag and solid phases, all element concentrations were recalculated to selected oxidation state for convenience of presentation and to unambiguously report the compositions of phases.

Experimental study in gas/slag/matte/spinel equilibria in the Cu-Fe-S-O-Si system has been extended to study distribution of Ag as minor elements. In this work, Ag was introduced into the initial mixture in small quantity corresponding to a total of less than 1wt% Ag in the matte phase. Two techniques were used to measure Ag composition in different phases: (i) EPMA for

elements in matte phase; and (ii) LAICPMS (Laser Ablation Inductively Coupled Plasma Mass Spectrometry) for elements in slag phase with concentration below the detection limit of EPMA.

2.2. Development of spinel substrate

Several different shapes of spinel substrate were tested. The final adopted type of substrate was the envelope shape with open ends shown in Figure 1. The bottom end of the substrate is open ensuring pathway for gas to get into contact with condensed phases and also ensuring direct contact of sample with quenching medium. Although, the envelope type substrate used in the present study is structurally stronger than that used in previous study [13], special attention on planning of the initial mixture was still needed to ensure no excessive reaction takes place between liquid slag and spinel.

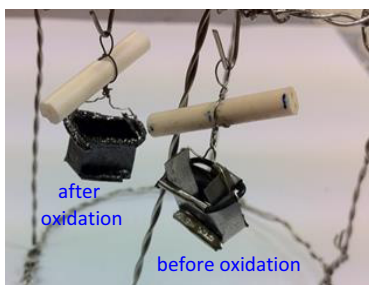


Figure 1. Shape of spinel substrate for gas/slag/matte/spinel experiment.

2.3. Confirming the achievement of equilibrium

The achievement of equilibrium in the gas/slag/matte/spinel system was confirmed by a 4-points test which covers [14]:

- i) Equilibration time variation
- ii) Phases homogeneity analysis
- iii) Equilibrium achievement from different directions
- iv) Analysis of possible reactions specific to the system.

This 4-points test approach with particular attention to the kinetics of the reactions taking place during achievement of equilibria was applied to the gas/slag/matte/spinel system in addition to continuous application and development of a number of other common measures to minimise the uncertainties. Alternative approaches or techniques and independent confirmations by different researchers were also introduced to ensure the reliability of the experimental results.

2.4. Analysis of possible reactions taking place during equilibration

Various elementary reactions take place simultaneously throughout the equilibration process. Analysis of their effects on equilibration process is important to avoid any barrier in the equilibrium process, thus ensuring that the final equilibrium point is approached from the right

direction within the required time. Several possible reactions in the gas/slag/matte/spinel equilibration process are listed below:

- (i) Reactions in a single phase, such as within gas, slag, matte and spinel.
For example: $\text{CO}_2(\text{gas}) = \frac{1}{2}\text{O}_2(\text{gas}) + \text{CO}(\text{gas})$
 $\text{SO}_2(\text{gas}) = \text{O}_2(\text{gas}) + \frac{1}{2}\text{S}_2(\text{gas})$
- (ii) Reactions between two phases, such as between gas-slag, gas-matte, gas-spinel, slag-matte, slag-spinel, and matte-spinel.
For example: $\text{Fe}_2\text{O}_3(\text{slag}) + \text{CO}(\text{gas}) = 2\text{FeO}(\text{slag}) + \text{CO}_2(\text{gas})$
 $\text{CO}_2(\text{gas}) = \text{O}(\text{matte}) + \text{CO}(\text{gas})$
 $\text{FeS}(\text{matte}) + \text{Cu}_2\text{O}(\text{slag}) = \text{FeO}(\text{slag}) + \text{Cu}_2\text{S}(\text{matte})$
- (iii) Reactions between three phases, such as between gas-slag-matte, gas-slag-spinel, gas-matte-spinel, and slag-matte-spinel.
For example: $\text{FeS}(\text{matte}) + 3\text{CO}_2(\text{gas}) = \text{FeO}(\text{slag}) + 3\text{CO}(\text{gas}) + \text{SO}_2(\text{gas})$
 $3\text{FeO}(\text{slag}) + \text{CO}_2(\text{gas}) = \text{Fe}_3\text{O}_4(\text{spinel}) + \text{CO}(\text{gas})$
 $3\text{FeS}(\text{matte}) + 10\text{CO}_2(\text{gas}) = \text{Fe}_3\text{O}_4(\text{spinel}) + 10\text{CO}(\text{gas}) + 3\text{SO}_2(\text{gas})$

Different combinations of these elementary reactions will result in different overall process kinetics.

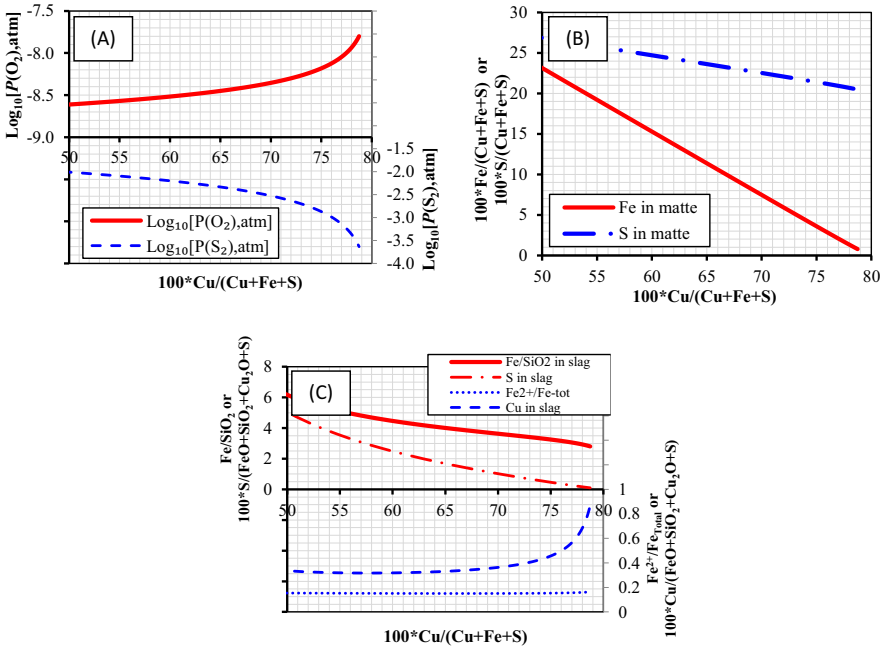


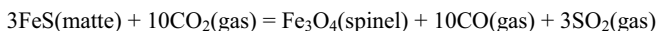
Figure 2. FactSage prediction of equilibria in the Cu-Fe-O-S-Si system between gas-slag-matte-spinel at T=1200°C and P(SO₂) = 0.25 atm: a. Partial pressure of gases vs matte grade; b. Composition of matte vs matte grade; and c. Composition of slag vs matte grade.

Figure 2 provides the predicted compositions of phases as function of copper in matte/matte grade from gas/slag/matte/spinel equilibration at 1200 °C and at $P(\text{SO}_2)=0.25$ atm from calculation using FactSage public database [15]. From this set of figures, it can be observed that approaching equilibrium point from low- to high-copper in matte leads to:

- a. An increase in effective equilibrium oxygen partial pressure and a decrease in sulphur partial pressure in the system as reaction progresses – Figure 2(a);
- b. A decrease in concentrations of Fe and S in matte – Figure 2(b); and
- c. A decrease in Fe/SiO₂ and S in slag and a slight increase in Fe²⁺/Fe total – Figure 2(c).

Approaching equilibrium point from high- to low-copper in matte will give composition changes in opposite direction.

Investigation on gas/slag/matte/tridymite equilibrium [16] showed that precipitation of solid can take place on the surface of sample and may block further reactions with gas phase. In the gas/slag/matte/spinel systems, the solid (spinel) will precipitate when approaching equilibrium point from low- to high-Cu in matte (high- to low-Fe in matte) as shown by this simplified reaction:



It may be reasonable to approach the final equilibrium point from high- to low-Cu in matte to avoid the precipitation of solid on the surface of sample that may block further reactions with gas phase. However, it is worth to note that this approach will result in a significant dissolution of spinel (Fe/SiO₂ of the liquidus increases drastically, see Figure 2(c)). Since spinel substrate is fragile and easily reacts/dissolves in slag, it is practically more convenient to approach the equilibrium point from lower Cu in matte/lower matte grade (precipitating spinel) so that the integrity of the substrate can be maintained. Several trials were carried where the final equilibrium points were achieved from lower matte grade. No blockage of sample surface by the spinel precipitation was detected. The spinel most likely precipitated in the liquid or on the existing spinel substrate. To avoid excessive precipitation of spinel, the initial mixture in the final experiments was planned as close as possible to the expected equilibrium point.

2.5. Microanalysis approach to obtain representative equilibrium phases compositions

A complete equilibrium may not be achieved across the whole sample if starting composition is far from final equilibrium point. Inhomogeneities at micro and macro scale may appear in the sample. Analysis of these compositional gradients is important to identify reactions taking place during equilibrium process. Eventually the analysis result can be used in the experiment to confirm the achievement of the final equilibrium point, for example by modifying experimental methodology, adjusting starting composition, or varying the equilibration time.

As part of the analysis of the inhomogeneity in the sample, a classification of different phases and locations has been proposed during the investigation of gas/slag/matte/tridymite equilibrium [16]. Similar classification was used in the present study on the gas/slag/matte/spinel equilibrium. Figure 3 shows modified micrograph from the gas/slag/matte/spinel to demonstrate schematically different type of phases and locations within sample. Definitions of symbols used in Figure 3 are given in Table 1 and Table 2.

Some local areas (pockets) in the sample may achieve the final equilibrium point locally. For example, location in Figure 3 at which there is contact point between gas-matte-slag (matte = b' or b , slag = B) may reach equilibrium readily. At these locations, matte and slag may have sufficient exposure to the gas atmosphere and may have shorter path for diffusion and exchange of elements between phases compared to other locations. As a result, the compositions at this location may be taken as a final result. This approach requires a careful analysis of the sample since each sample/system may be exposed to the experiment condition / may behave differently.

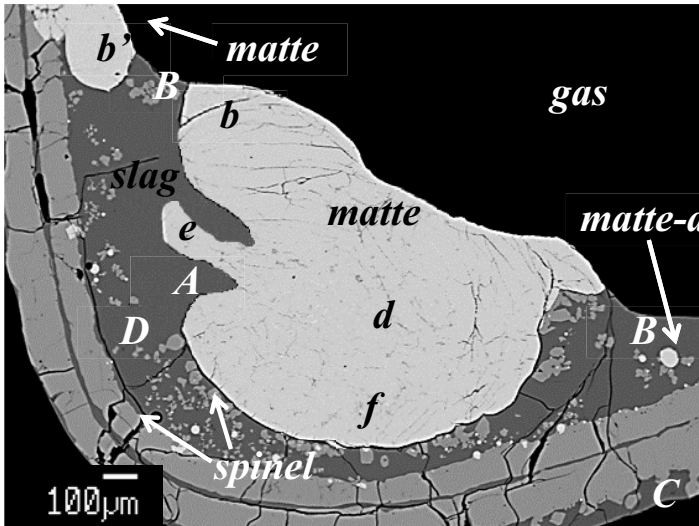


Figure 3. Schematic of different phases and locations within sample from the gas/slag/matte/spinel equilibrium.

Table 1. Definition of various types of matte related to proposed classification in Figure 3 [16].

Matte Terminology	Abbreviation
Entrapped matte, droplet	a
matte-Gas exposure close to slag, Chunky shape	b
matte-Gas exposure close to slag-small particles	b'
matte-Gas exposure far from slag	c
matte far from gas far from slag	d
matte far from gas close to slag, channel-shaped	e
matte far from gas close to slag, chunky-shaped	f

Table 2. Definition of various types of slag phase related to proposed classification in Figure 3 [16].

Slag Terminology	Abbreviation
slag-matte far from gas	A
slag-matte close to gas	B
slag far from matte close to gas	C
slag far from matte far from gas	D

3. Experimental Results

The equilibrium result in the gas/slag/matte/spinel system is represented in selected graphs which is minimum in number but sufficient to completely describe the equilibrium phases, i.e. gas, slag, and matte. A set of graphs has been developed and include the following:

i) For matte phase:

- $\text{Log}_{10}[P(\text{O}_2), \text{atm}]$ versus matte grade (matte grade = $\% \text{Cu}/[\text{Cu} + \text{Fe} + \text{S}]$)
- Sulphur in matte versus matte grade

ii) For slag phase:

- $\text{FeO}/(\text{FeO} + \text{SiO}_2 + \text{Cu}_2\text{O} + \text{S})$ in slag versus matte grade
- Sulphur in slag versus matte grade
- Cu_2O in slag versus matte grade

All expressed as a function of matte grade. Oxygen concentration in matte and $\text{Fe}^{2+}/\text{Fe}^{3+}$ in slag were not measured in this study.

Each of the graph contains experimentally measured values, values predicted with FactSage using the existing public database, and current “believed-to-be-true” equilibrium values. The “believed-to-be-true” equilibrium line is generated based on the preceding experimental results, it is continuously corrected using validated equilibrium points from on-going experimental work so that the equilibrium values are obtained systematically through iterative experiments.

3.1. Typical appearance of phases

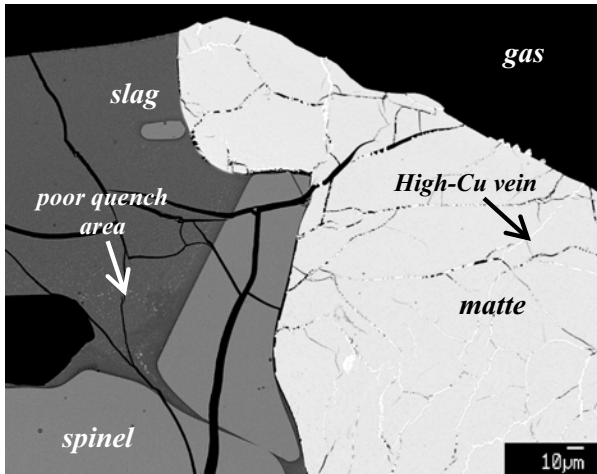


Figure 4. Micrograph of sample from gas/slag/matte/spinel experiment at $T=1200^\circ\text{C}$, $P(\text{SO}_2) = 0.25 \text{ atm}$, $\text{Log}_{10}[P(\text{O}_2), \text{atm}] = -8.5$, and equilibration time=24h.

Typical “well-quenched” sample image taken using scanning electron microscope with backscattered electron detector (SEM-BSE) is shown in Figure 4. Copper veins, most of the time associated with cracks, were observed within the matte phase. Based on numerous test, it was

decided to perform EPMA measurement using large probe diameter and across the Cu veins to obtain representative composition of the matte phase. Well crystallized spinel solids (light grey phase) were observed. It can also be seen in Figure 4 that slag phase (dark grey phase) close to the surface are relatively homogeneous, the slag phase near the spinel on the other hand was found to have few bright spots possibly due to poor quenching. Careful selection of measurement area is required to obtain true/representative compositions of phases.

3.2. Experiments with extended time

Experiments of gas/slag/matte/spinel system at extended time up to 48 hours have been carried out to ensure that 24 hours equilibration time is sufficient for the achievement of equilibrium. One condition was selected for this test at $T=1200^{\circ}\text{C}$, $P(\text{SO}_2)=0.25$ atm, $\text{Log}_{10}[P(\text{O}_2),\text{atm}]=-8.2$ with matte in the initial mixture estimated to have 70 wt % Cu. The experiment results are represented in set of graphs compiled in Figure 6. The matte compositions measured in samples after 24h and 48h equilibrations were between 73.8 and 75.1 wt% Cu. There was no clear trend or significant increase in matte grade with extending time (Figure 6(a)); the observed variation was within the experimental uncertainty. The measured slag compositions from normal equilibration time and extended time are plotted in Figure 6(c) until Figure 6(e). The figures indicate that there were no systematic changes in Cu, “FeO” and S concentrations in the slag with extending equilibration time. It can be concluded that 24 hours provides sufficient equilibration time for the gas/slag/matte/spinel system to reach equilibrium.

3.3. Independent confirmation by different researcher

Independent confirmation has also been carried out by different researcher (Dr Mehrjardi) to confirm the present experimental result. Spinel substrate with spiral shape (Figure 5) was adopted to improve equilibration process and enhance the quenching result. The experimental results for equilibrations at 1200°C , $P(\text{SO}_2)=0.25$ atm, and $\text{Log}_{10}[P(\text{O}_2),\text{atm}]=-8.5$ using two different substrates (envelope with open ends and spiral substrates) are plotted in Figure 6. There was no significant difference in matte and slag compositions between the two trials.



Figure 5. Spinel substrate with spiral shape made by oxidizing iron wire.

3.4. Ag distribution between slag and matte

The experimental results for the gas/slag/matte/spinel system containing Ag as minor elements from 24 hours equilibration at 1200°C, $P(\text{SO}_2)=0.25$ atm and $\text{Log}_{10}[P(\text{O}_2),\text{atm}]=-8.1$ are plotted in Figure 6 and Figure 7. The major elements compositions in matte and slag phases were found to be in agreement with those from experiments without Ag minor elements (Figure 6). The Ag concentration in matte of different particles was uniform around 0.15 wt%, while the Ag concentration in slag of different locations had high variation between 2 and 8 ppm. Distribution coefficient of Ag ($L_{Ag}^{s/m}$) expressed as logarithmic value of ratio between Ag concentration in slag and Ag concentration in matte was approximately -2.51. The distribution coefficient of Ag from equilibration in gas/slag/matte/spinel system is compared to those from equilibration in gas/slag/matte/tridymite system in Figure 7.

4. Discussion

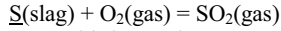
The results from equilibration experiments in the gas/slag/matte/spinel systems without and with Ag as minor element are compiled in Figure 6 together with previous results in gas/matte/spinel system and FactSage prediction calculated using public database [15].

Figure 6(a) gives relationship between matte grade and oxygen partial pressure. Only results by Kaiser & Elliot [9] are included in the figure since their investigation in the gas/matte/spinel system was carried out at the same range of $P(\text{SO}_2)$ as the present study. Kaiser & Elliot [9] carried out experiment using mixture with known Cu/Fe ratio. The matte was equilibrated in alumina crucible at 1195 °C for 24 hours under CO/CO₂/SO₂ gas stream. The oxygen partial pressure in the gas stream was adjusted to the point where spinel started to precipitate from matte, this was confirmed using optical microscope. Using scanning electron microscopy equipped with energy dispersive X-ray analysis (SEM-EDAX), it was found that the spinel contained less than 0.5 wt% Al. The present results in the gas/slag/matte/spinel system show a clear relationship between matte grade and oxygen partial pressure. The experimental results show that with increasing $P(\text{O}_2)$ from $10^{-8.5}$ to $10^{-8.2}$ atm increased the matte grade from around 63 wt% to 75 wt%. Data reported by Kaiser & Elliot [9] seems to be an extension of the present data at lower matte grade. FactSage prediction using public database reproduce the current and previous results [9].

Figure 6(b) shows that the sulphur in matte from present measurements increases with decreasing matte grade. Similar trend is shown by FactSage prediction, the prediction however cannot reproduce the trend at lower matte grade suggested by Kaiser & Elliot [9]. The discrepancy is most likely due to the matte solution in the public database was modelled as sulphide solution without oxygen component. In reality, matte at high-Fe content is an oxy-sulphide solution.

“FeO” concentration in spinel liquidus as function of matte grade is plotted in Figure 6(c). The present results suggest lower “FeO” concentration than that given by FactSage prediction. The “FeO” concentration in the liquidus indicates that the spinel solid becomes more stable with increasing matte grade.

Sulphur solubility in slag as a function of matte grade is reported in Figure 6(d). Both the present measurement and FactSage prediction show that the sulphur in slag decreases with increasing matte grade. The sulphur solubility in slag can be represented by the simplified reaction below:



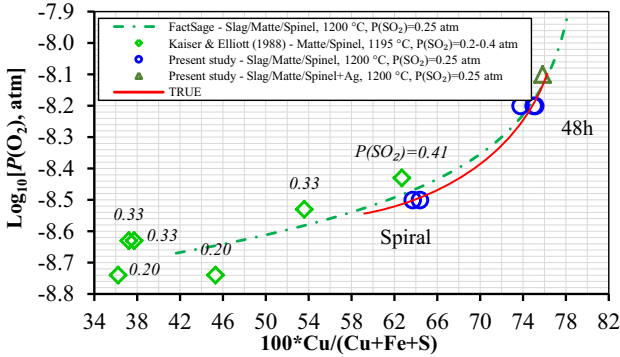
The oxygen partial pressure increases with increasing matte grade. Consequently at fixed SO_2 and assuming the activity coefficient of sulphur in slag remains constant, the sulphur in slag is expected to decrease with increasing oxygen partial pressure (or increasing matte grade).

Copper concentration in slag as function of matte grade is shown in Figure 6(e). The current experimental results give significantly higher copper in slag than that from FactSage prediction. Present result shows that at matte grade between 63 – 76 the copper concentration in slag is between 0.8 – 1.1 wt%.

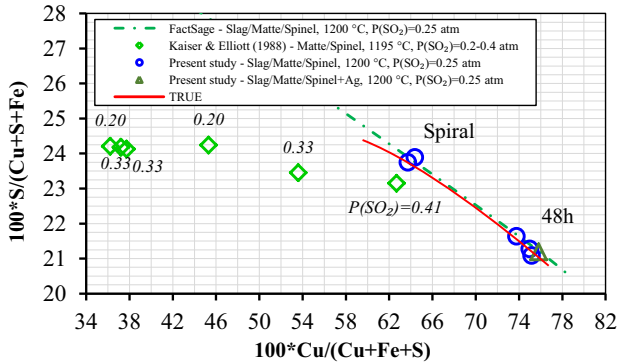
Distributions coefficient of the Ag ($L_{Ag}^{s/m}$) is presented in Figure 7. $L_{Ag}^{s/m}$ from other researchers [17, 18] from gas/slag/matte/tridymite equilibration are also compiled in the figure. In general, most of the Ag is contained within the matte phase. Previous investigations show that $L_{Ag}^{s/m}$ decreases with increasing matte grade up to ± 72 wt% above which the $L_{Ag}^{s/m}$ increases with increasing matte grade. It appears that the $L_{Ag}^{s/m}$ from the gas/slag/matte/spinel experiment is lower than those from gas/slag/matte/tridymite experiments. Experimental confirmation is required to verify this observation.

The fundamental information in the gas/slag/matte/spinel system is significantly important for understanding and improving the copper smelting and converting processes. The information provided can be used to analyse the effect of SiO_2 fluxing towards the quantity of solid (magnetite/spinel) and the amount of chemically dissolved copper in the slag. The present work demonstrates the possibility for the investigation of the intricate gas/slag/matte system. Further investigation will be directed toward the investigation of the distribution coefficients of various minor elements in the system, as well as the investigation of the effects of temperature, $P(\text{SO}_2)$ and $P(\text{O}_2)$ on the matte and slag compositions. Effect of slagging components, such Al, Ca, Mg, Cr, and Ti, on the equilibrium in the system is also a possible extension of the research program since these components are commonly found in the actual industrial sample. The present work also shows the necessity for re-optimization of the existing FactSage database. The present work is part of a larger integrated experimental and thermodynamic modelling research program on copper-making high-temperature systems.

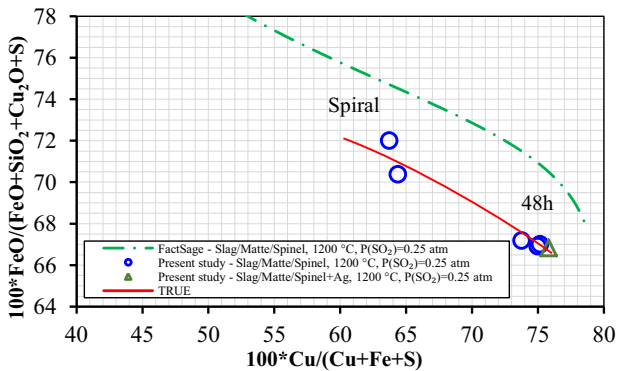
Figure 6. Set of graphs describing equilibria in the Cu-Fe-O-S-Si system between gas/slag/matte/spinel from 24 hours experiments at $T=1200^{\circ}\text{C}$ and $P(\text{SO}_2)=0.25$ atm using envelope shape substrate with open ends (48 hours experiment and experiment with spiral substrate are indicated with label).



a. Oxygen partial pressure $P(\text{O}_2)$ vs matte grade $\% \text{Cu} / [\text{Cu} + \text{Fe} + \text{S}]$



b. Concentration of sulfur in matte vs matte grade $\% \text{Cu} / [\text{Cu} + \text{Fe} + \text{S}]$



c. Concentration of iron oxide in slag vs matte grade $\% \text{Cu} / [\text{Cu} + \text{Fe} + \text{S}]$

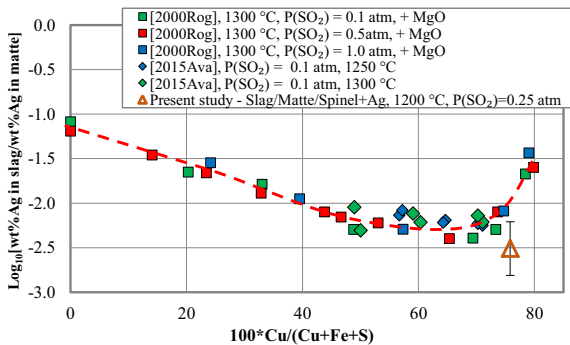
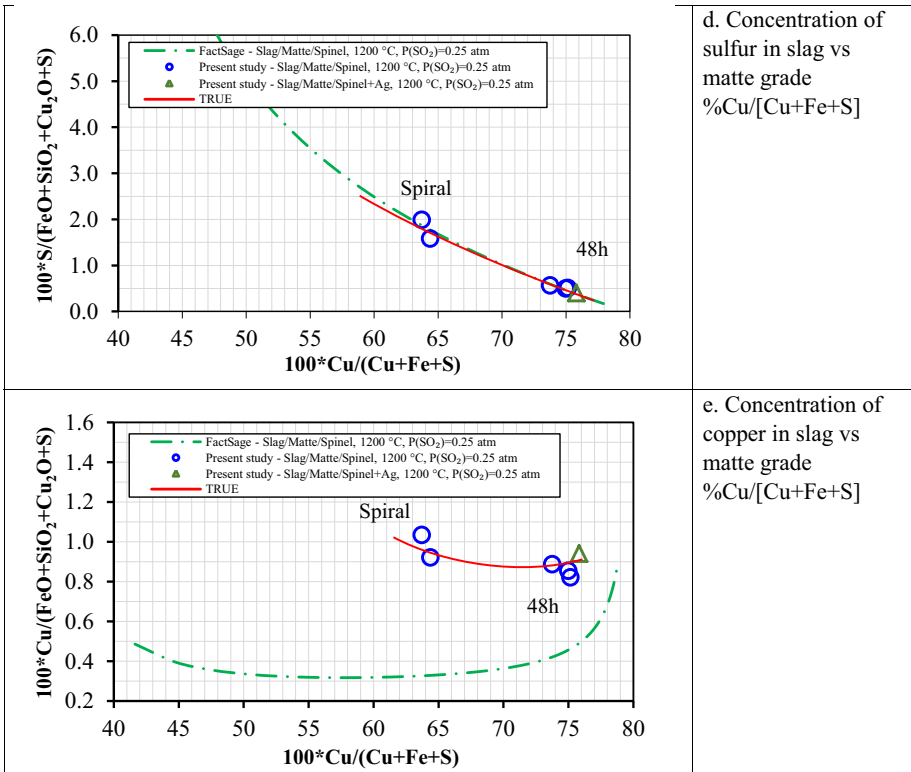


Figure 7. Distribution of Ag as minor element between slag and matte as function of matte grade in the Cu-Fe-O-S-Si system at spinel saturation from equilibration at $T=1200^{\circ}\text{C}$ and $P(\text{SO}_2)=0.25 \text{ atm}$.

5. Summary

Experimental technique has been developed to study the gas/slag/matte/spinel equilibrium in the Cu-Fe-O-S-Si system at controlled gas atmosphere. Several measures have been taken into account to ensure/confirm the achievement of equilibrium. New data on the gas/slag/matte/spinel system and the distribution of Ag in the phases within the system at $T=1200\text{ }^{\circ}\text{C}$ and $P(\text{SO}_2)=0.25\text{ atm}$ have been obtained. It was found that matte grade 63 and 75 wt% correspond to $P(\text{O}_2)$ from $10^{-8.5}$ to $10^{-8.2}$ atm, respectively. It was observed that an increase in matte grade lead to a decrease in sulphur in matte, a decrease in “FeO” in slag, and a decrease of sulphur in slag. The chemically dissolved copper in the range of matte grade under investigation was found to be around 0.8 and 1.1 wt%. The distribution coefficient of Ag between slag and matte at spinel saturation from 24 hours equilibration at $T=1200\text{ }^{\circ}\text{C}$, $P(\text{SO}_2)=0.25\text{ atm}$, and $P(\text{O}_2)=10^{-8.1}$ atm was found to be approximately -2.51. This indicates that majority of Ag was accumulated in the matte phase.

6. Acknowledgment

The authors would like to thank Australian Research Council Linkage program, Altonorte Glencore, Atlantic Copper, Aurubis, BHP Billiton Olympic Dam Operation, Kazzinc Glencore, PASAR Glencore, Outotec Oy (Espoo), Anglo American Platinum, and Umicore for the financial and technical support. The authors also thank Dr Jeff Chen for performing measurement on the sample using Laser Ablation Inductively Coupled Plasma Mass Spectrum (LAICPMS).

7. References

1. Takeda, Y, “Oxygen potential measurement of iron silicate slag-copper-matte system” (Paper presented at the International Conference of Molten Slags, Fluxes and Salts, 1997).
2. Korakas, N., “Etude thermodynamique de l'équilibre entre scories ferro-siliceuses et mattes de cuivre. Application aux problèmes posés par la formation de magnetite lors du traitement des minerais sulfurés de cuivre” (Univirsité de Liège, 1964).
3. Kuxmann, U. and F.Y. Bor, “Studies on the Solubility of Oxygen in Copper Mattes under Ferric Oxide Slags Saturated with Silica,” *Erzmetall.*, 18 (1965), 441-450.
4. Tavera, F.J. and W.G. Davenport, “Equilibrations of Copper Matte and Fayalite Slag under Controlled Partial Pressures of Sulfur Dioxide,” *Metall. Trans. B*, 10B (2) (1979), 237-241.
5. Font, J.M., et al., “Solubility of copper or nickel in iron-silicate base slag equilibrated with $\text{Cu}_2\text{S-FeS}$ or $\text{Ni}_3\text{S}_2\text{-FeS}$ matte under high partial pressures of SO_2 ,” *Metall. Rev. MMLJ*, 15 (1) (1998), 75-86.
6. Henao, H.M. and E. Jak, “Experimental study of slag-matte equilibria in the Ca-Cu-Fe-O-S-Si system at fixed $P(\text{SO}_2)$ and $P(\text{O}_2)$ ” (Unpublished work, Pyrosearch, the University of Queensland, 2013).
7. Henao, H.M., L.A. Ushkov, and E. Jak, “Thermodynamic predictions and experimental investigation of slag liquidus and minor element partitioning between slag and matte in support of the copper Isasmelt smelting process commissioning and optimisation at Kazzinc” (Paper presented at the 9th International Conference on Molten Slags, Fluxes and Salts, Beijing,2012).

8. Rosenqvist, T. and T. Hartvig, "The Thermodynamics of Fe-Cu Mattes, and Their Equilibrium with Magnetite," *Norges Tek.-Naturvitenskapelige Forskiningsrud Met. Kom. Meddel*, 12 (1958), 21-52.
9. Kaiser, D.L. and J.F. Elliott, "Saturation of copper-iron mattes with solid magnetite," *Metall. Trans. B*, 19B (6) (1988), 935-941.
10. Johannsen, F. and H. Knahl, "Solubility of Oxygen in Copper Matte," *Z. Erzbergbau Metallhuettenwes.*, 16 (1963), 611-621.
11. Lander, H.N., (S.D. thesis, Mass. Inst. Technol, 1954).
12. Sun, Z., et al. "Liquidus temperatures, major and minor elements equilibrium partitioning in copper smelting slag/matte/gas systems" (Paper presented at the Copper International Conference, Santiago, 2013).
13. Nikolic, S., P.C. Hayes, and E. Jak, "Experimental Techniques for Investigating Calcium Ferrite Slags at Metallic Copper Saturation and Application to the Systems " Cu_2O "-" Fe_2O_3 " and " Cu_2O "-CaO at Metallic Copper Saturation," *Metall. Mater. Trans. B*, 40B (6) (2009), 892-899.
14. Jak, E, "Integrated experimental and thermodynamic modelling research methodology for metallurgical slags with examples in the copper production field" (Paper presented at The Ninth International Conference of Molten Slags, Fluxes and Salts, Beijing, 2012).
15. FactSage v.6.2. 2010, CRCT - ThermFact Inc. & GTT-Technologies.
16. Mehrjardi, A.F., et al., "Experimental study of slag-matte-tridymite equilibria in the Cu-Fe-O-S-Si system at controlled $\text{P}(\text{SO}_2)$: Part 1. Development of experimental technique" (Unpublished work, Pyrosearch, the University of Queensland, 2015).
17. Roghani, G., Y. Takeda, and K. Itagaki, "Phase Equilibrium and Minor Element Distribution between FeOx-SiO₂-MgO-Based Slag and Cu₂S-FeS Matte at 1573 K under High Partial Pressures of SO₂," *Metall. Mater. Trans. B*, 31B (4) (2000), 705-712.
18. Avarmaa, K., et al., "Equilibrium distribution of precious metals between slag and copper matte at 1250-1350°C," *J. Sust. Metall.*, 1 (2015), 216-228.

EXPERIMENTAL STUDY OF LIQUIDUS OF THE “FeO”-SiO₂-PbO SLAGS IN EQUILIBRIUM WITH AIR AND WITH METALLIC LEAD

Maksym Shevchenko, Taufiq Hidayat, Peter C Hayes, Evgueni Jak

PYROSEARCH, Pyrometallurgy Research Laboratory, School of Chemical Engineering,
The University of Queensland, Brisbane 4072, Queensland, Australia

Keywords: Lead slags, Phase equilibria, Liquidus.

Abstract

Limited data are available on phase equilibria of the “FeO”-SiO₂-PbO slag system at conditions used in the lead smelting due to difficulties from lead vaporization and interactions with metal and ceramic crucibles. Recently experimental procedures have been developed and successfully applied to complex industrial slag-metal-matte systems involving high temperature equilibration on a primary phase substrate and rapid quenching followed by the electron probe X-ray microanalysis. The liquidus isotherms and invariant lines in the “FeO”-SiO₂-PbO slag system in equilibrium with air and with metallic lead have been constructed. Preliminary data compared to the FactSage package predictions demonstrate differences in some aspects, indicating the possibility for further improvement of the thermodynamic database. The present work is a part of the integrated experimental and thermodynamic modelling research program on multi-phase lead systems in support of the optimization and development of complex lead smelting, refining and recycling technologies.

Introduction

Improvement of the industrial lead production and recycling can be made through an informed decision on the selections of slag compositions, fluxing strategies, and operating conditions (temperature and oxygen blow) for given feed and product requirement. This can be facilitated through thermodynamic modeling in which phase equilibria, partitioning of major and minor elements between phases, activities, vapor pressure, and other thermodynamic properties of the relevant systems can be predicted/calculated rapidly and accurately over a wide range of process conditions in lead smelting, converting, and slag cleaning processes.

The thermodynamic information on the slags with lead as a primary component is rather scarce, in particular for the reducing conditions, involving equilibria with metallic lead, that is the most important range for smelting operations. Integrated experimental and thermodynamic modelling research program has therefore been initiated to support the optimization and development of complex lead smelting, refining and recycling. The specific focus of the present research program is to provide accurate phase equilibria and thermodynamic information for the lead oxide and sulfide high temperature multicomponent multiphase systems including slag, matte, metal, speiss and all relevant solid phases through the integrated fundamental experimental and thermodynamic modelling study.

Most of the low order PbO-containing systems have been experimentally well characterized in air previously, in nineties [1-6], and most of those systems have oxides with fixed oxidation state so that changing P_{O_2} would not affect results. The intermediate oxygen partial pressure conditions affect the equilibria in the systems with transition metals, in particular – iron-oxide-containing systems where Fe^{2+} and Fe^{3+} are always present. Present research program therefore is focused on the iron-oxide-containing systems starting from low order PbO- FeO_x and PbO- FeO_x - SiO_2 systems.

Experimental methodology

The experimental technique used to study the complex multi-component multi-phase systems involves high temperature equilibration in controlled gas atmospheres, rapid quenching and direct measurement of equilibrium phases with electron probe X-ray microanalysis (EPMA). This approach developed by the Pyrometallurgy Research Centre at the University of Queensland [7] forms the basis for the present study and is briefly outlined below.

An artificial oxide mixture is prepared from the analytically pure powders or pre-sintered solids or pre-melted master matte/metal and master slag to obtain after equilibration a predetermined bulk composition X (**Fig. 1**). The starting materials are thoroughly mixed using an agate mortar and pestle, and then pelletized in a die using a press. The starting composition is selected to obtain two or more phases in the final sample after equilibration.

Experiments are performed on substrates usually made of primary phase. This is essential for the lead metal containing system, preventing from interactions with crucible and support material and actually enables this experimental program to be performed.

Gas atmosphere during experiments is controlled. Two types of high temperature equilibration are usually performed:

1. An open-system equilibration in controlled gas atmospheres when excess of gas imposes equilibria on the condensed phases, and
2. A closed-system equilibration – when condensed system establishes the gas atmosphere in terms of oxygen partial pressure and sulphur potential – can be carried out in neutral gas atmosphere such as Ar or in sealed silica ampoules.

Both types of the experiments are performed in a vertical impervious ceramic tube in a resistance furnace (**Fig. 2**). The substrate is suspended on a wire and placed in the hot-zone of the furnace. The furnace temperature is monitored by using an alumina-shielded Pt/Pt-Rh 13% thermocouple with uncertainty within 5 K.

After equilibration for predetermined time the samples are quenched into water with ice ($T=0^\circ C$) or $CaCl_2$ solution with ice ($T=-18^\circ C$), so the phases present at high temperature and their compositions are retained at room temperature. The final microstructure and phases (**Fig. 1**) therefore represent equilibria existed at the temperature.

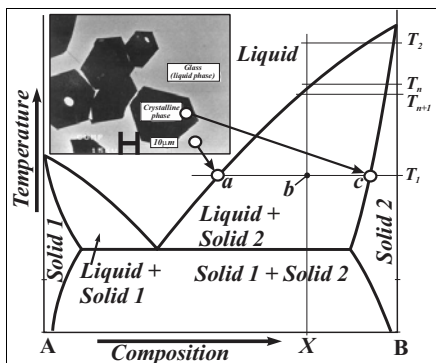


Figure 1. Hypothetical diagram to illustrate experimental technique for determination of phase equilibria.

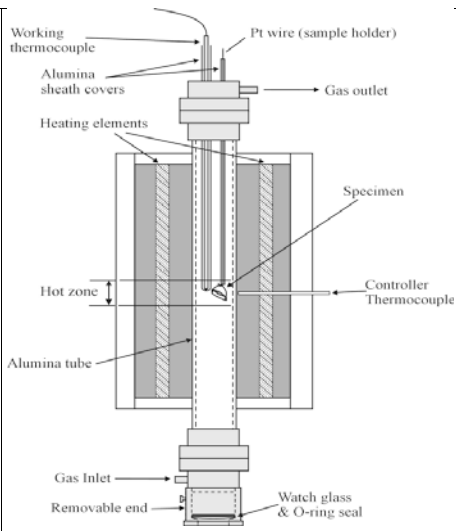


Figure 2. Experimental setup.

The samples are mounted, polished and then examined initially using optical microscopy, and then Scanning Electron Microscopy (SEM) with Energy Dispersive Detector (EDS). The compositions of the phases (glass and solids) are then measured using a JEOL JXA 8200L electron probe X-ray microanalyzer (EPMA) with Wavelength Dispersive Detectors (WDD). An acceleration voltage of 15 kV and a probe current of 15 nA are usually used. The appropriate standards are selected to the oxide, sulphide or metal phases. The phase compositions are measured with EPMA with accuracy within 1 wt % or better. EPMA is used to measure the total metal cation concentrations; no information on different oxidation states are acquired in the present study, all metal concentrations are recalculated to selected oxidation states for convenience of presentation.

Preliminary experiments and development of the experimental methodology

Quenching technique brings the advantages of static phase equilibrium determination, in particular, a possibility of accurate control and verification of achievement of equilibrium. Achievement of equilibrium is by far the most important and common uncertainty in the equilibria studies, however, is not always obvious and not always given sufficient attention to eliminate errors. The overall approach to confirm achievement of equilibrium developed and used at PYROSEARCH is summarized as a four-points test and include [7]:

1. **Equilibration time:** Confirming the equilibrium achievement by changing the equilibration time variation to confirm that no further changes take place with time.
2. **Phases homogeneity:** Confirming the chemical homogeneity of phases and samples.
3. **Approaching equilibrium from different directions,** for example by using different starting materials and compositions, temperature variation, by pre-melting of samples to ensure complete dissolution of solids and to confirm crystallization of solids; gas flow variation, by approaching the equilibrium from initially more oxidizing or reducing conditions.

4. **Analysing possible reactions specific to the system** taking place during equilibration, looking for possible signs of incomplete reaction pathways during equilibration. SEM imaging and EPMA analysis of the compositional gradients in a phase on the micro- and macro-scales are particularly effective in this analysis.

The list of some elementary reactions specific to this system identified in preliminary series of experiments is listed in Table 1. The examples of microstructures from experiments having some of these reactions with corresponding comments are given in **Fig. 3-4**. Reactions (4) and (7) change Fe^{3+}/Fe^{2+} in slag and after diffusion result in change of PbO concentration in slag through reaction (6).

Table 1. Some elementary reactions during equilibration of samples in the Pb-Fe-Si-O system

Phases	Location	Description
A. Single	Slag	a) Diffusion of Pb, Fe^{2+} , Fe^{3+} , Si, and O within liquid slag (1)
B. Two phases	Gas-Slag	a) Oxidation / reduction of slag: $2FeO (sl) + 0.5O_2 (g) \leftrightarrow Fe_2O_3 (sl)$ (2)
		b) Vaporization of lead species: $PbO (sl) = PbO (g)$ (3)
		$2FeO (sl) + PbO (sl) = Pb (g) + Fe_2O_3 (sl)$ (4)
		$Pb (met) = Pb (g)$ (5)
	Metal-Slag	Metal / slag oxidation / reduction: $Pb (met) + Fe_2O_3 (sl) \leftrightarrow PbO (sl) + 2FeO$ (6)
	Slag-solid	Precipitation / dissolution of solids (e.g. SiO_2 or iron oxides) due to slow cooling or change in composition: $FeO_{1+x} (solid) \leftrightarrow (1-2x) FeO + x Fe_2O_3 (sl)$ (7)
C. Three phases	Gas-Metal-Slag	Oxidation of metal component by gas and dissolution of oxidation product into slag: $Pb (met) + 0.5O_2 (g) = PbO (sl)$ (8)

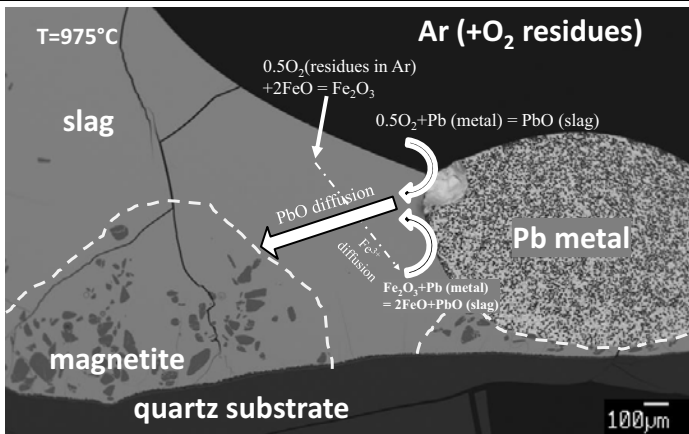


Figure 3. Example of inhomogeneity in the non-equilibrium sample from preliminary experiment at 975°C on silica substrate, probably caused by gradual oxidation of Pb (metal) to PbO (slag), enhanced by a Fe^{2+}/Fe^{3+} couple in the slag. Increased PbO concentration lowers liquidus temperature and leads to dissolution of magnetite crystals remaining only in the areas far from main places of PbO formation.

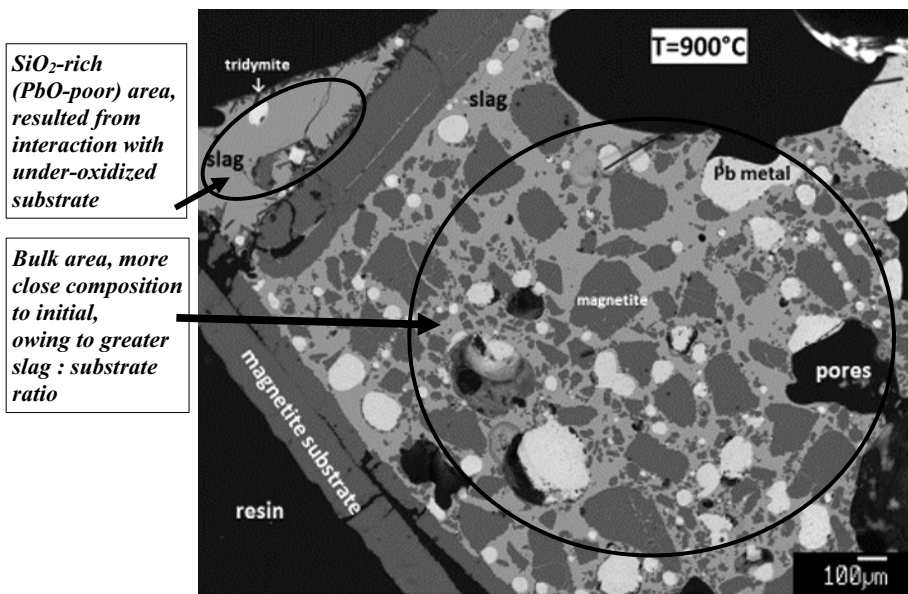


Figure 4. Non-equilibrium sample from series of preliminary experiments, affected by composition change due to the overall reaction $2\text{FeO}(\text{sol}) + \text{PbO}(\text{sl}) = \text{Fe}_2\text{O}_3(\text{sol}) + \text{Pb}(\text{met})$ with wustite-containing substrate. The extents of the composition change were different extents depending on the slag to substrate ratio in the local areas. Careful treatment of substrates has been introduced in later experiments to avoid this issue.

EPMA control of compositional gradients is essential to identify key reactions taking place in samples during equilibration. Therefore, it helps to introduce required modifications to experimental methodology; some of the modifications added in this study on the PbO-"FeO"-SiO₂-Pb system are as follows. Master-slags were introduced to facilitate formation of liquid at lower temperatures with lower PbO activity thus minimizing vaporization of Pb and PbO and speeding up dissolution of other high-melting-temperature components (Fe, Fe₂O₃, SiO₂). Preliminary sintering of wustite (FeO_{1+x}) and magnetite (Fe₃O₄) powders from pure iron foil in gas mixtures with appropriate CO/CO₂ ratios was introduced to enhance their incorporation into liquid and homogenization. The geometries of the silica substrates and the preparation methodology of the wustite (FeO_{1+x}) and magnetite (Fe₃O₄) substrates were carefully controlled to minimize corresponding uncertainties. Metallic iridium can be used as support for the PbO-"FeO"-SiO₂-Pb system, and platinum – for the oxidized system in air. Addition of CaCl₂ into quenching liquid not only decreases freezing temperature, but also increases boiling temperature of the solution (the eutectic at $-50\dots-55^{\circ}\text{C}$, 29.6 wt. %, $\rho=1.29\text{ g/cm}^3$, $T_{\text{boil}}=111^{\circ}\text{C}$) [8]. Polishing method was selected from various possible options [9] for the samples containing very soft Pb, moderately hard slag glass, magnetite and other compounds, and very hard quartz crucible. Appropriate standards were selected for accurate EPMA quantitative elemental analysis, including K-456 glass (certified $65.67\pm 0.26\%$ Pb, $13.37\pm 0.24\%$ Si by mass) standard from NIST [10] for Pb; pure SiO₂ for Si and Fe₂O₃ for Fe.

Results

Examples of typical microstructures obtained on silica and magnetite substrates are shown in **Fig. 5**.

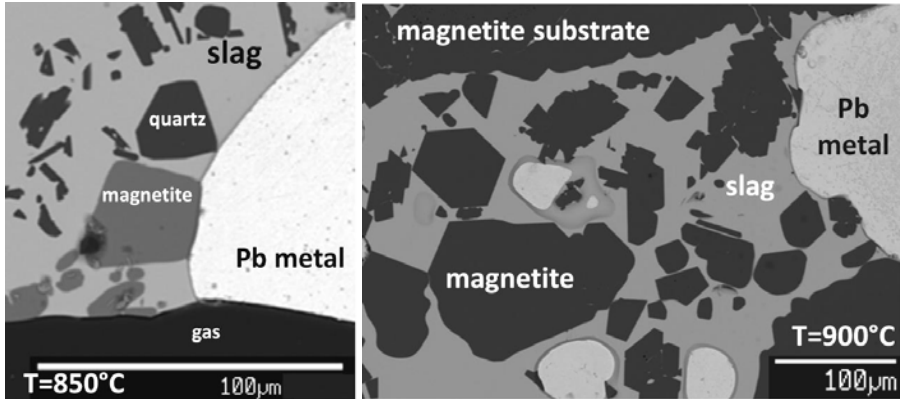


Figure 5. Examples of micrographs for samples in various areas of the PbO-"FeO"-SiO₂-Pb system.

Liquidus surface in the PbO-"FeO"-SiO₂-Pb system predicted with the current FactSage database [11] is shown in **Figure 6a**. **Figure 6b** presents preliminary estimate of the liquidus derived from experimental results obtained to date.

Comparison of **Fig. 6a** and **6b** shows that the qualitative arrangement of primary phase fields was predicted by FactSage well. Thermodynamic database for the Pb-Zn-O-containing slag developed nearly two decades ago [12] used data and models available at that time. Limited experimental information for the oxide systems only in air and in equilibrium with metallic iron was available then. Many improvements in modelling techniques have been made since that time. This explains the differences between calculated and experimental liquidus temperatures that include: 1) predicted liquidus temperatures are 100-200°C higher in the tridymite primary phase field; 2) the predicted fayalite primary phase field is about twice larger; 3) the predicted tridymite-spinel boundary line is at ~ 5% lower SiO₂ concentration; 4) the predicted spinel primary phase field is significantly smaller compared to experimental results.

Currently, the work is in progress, and further experiments are being conducted throughout all the PbO-"FeO"-SiO₂ system, both in air and in equilibrium with Pb metal.

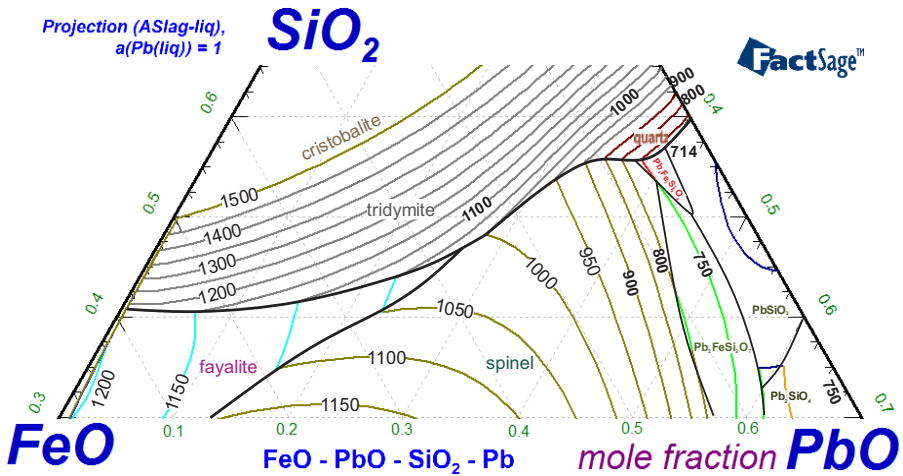


Figure 6(a). The liquidus surface of the phase diagram of the PbO-"FeO"-SiO₂-Pb system between 30-65 mol.% SiO₂, predicted with FactSage software.

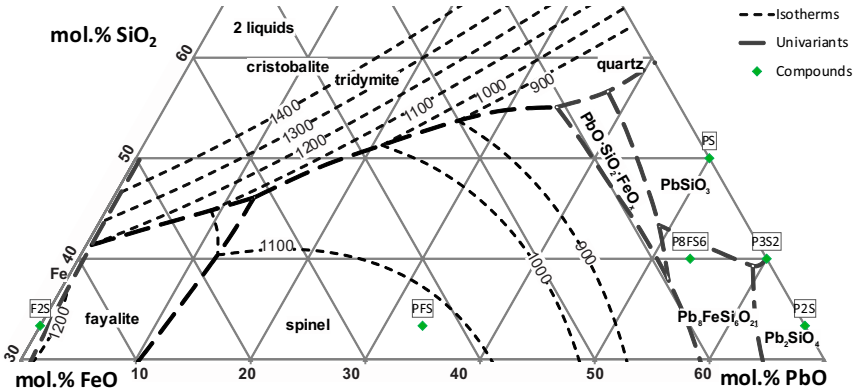


Figure 6(b). The liquidus surface of the phase diagram of the PbO-"FeO"-SiO₂-Pb system between 30-65 mol.% SiO₂, according to preliminary experimental results.

Summary

Methodology was developed for the system in equilibrium with Pb and several modifications specific to this system have been introduced to improve the reliability of results. The liquidus in the PbO-"FeO"-SiO₂ system in equilibrium with metallic lead has been systematically investigated for the first time with focus on the tridymite, magnetite and hematite primary phase fields at 800-1300°C. Further experiments are under way to refine the present results and to investigate other

conditions of interest to the lead production process. Present results are essential for further revision and improvement of the FactSage thermodynamic database.

Acknowledgements

The authors would like to thank Australian Research Council Linkage program, Aurubis, Kazzinc, Glencore, Nyrstar, Outotec Pty Ltd (Melbourne), and Umicore for the financial and technical support.

References

1. Chen S. et al., "Experimental study of phase equilibria in the PbO-Al₂O₃-SiO₂ system", *Metal.Trans.*, 2001, vol. 32B, pp 997 - 1005.
2. Chen S. et al., "Experimental study of phase equilibria in the PbO-MgO-SiO₂ system", *Metal.Trans.*, 2001, vol. 32B, pp 11-16.
3. Jak E. et al., "Experimental study of phase equilibria in the system PbO-ZnO-SiO₂", *Metal.Trans.*, 1999, vol. 30B, pp. 21-27.
4. Jak E., Liu N., Hayes P.C., "Experimental study of phase equilibria in the systems CaO-Pb-O and PbO-CaO-SiO₂", *Metal.Trans.*, 1998, vol.29B(3),pp.541-553.
5. Jak E. et al., "Thermodynamic optimisation of the systems CaO-Pb-O and PbO-CaO-SiO₂", *Can. Metal. Quart.*, 1998, vol. 37 (1), pp. 41-47.
6. Jak E. et al., "Thermodynamic optimisation of the systems PbO-SiO₂, PbO-ZnO, ZnO-SiO₂ and PbO-ZnO-SiO₂", *Metal.Trans.*, 1997, vol. 28B, pp. 1011-1018.
7. E. Jak, "Integrated experimental and thermodynamic modelling research methodology for copper and other metallurgical slags", Keynote Invited Lecture, MOLTEN 12, The 9th int. conf. on molten slags, fluxes and salts, Beijing, China, May 2012, paper w77.
8. "Calcium chloride handbook, A guide to properties, forms, storage and handling", The Dow Chemical Company, August 2003, www.dowcalciumchloride.com
9. <http://www.struers.com/>
10. <http://www.nist.gov/srm/upload/SP260-112.PDF>
11. FactSage v.6.2. 2010, CRCT - ThermFact Inc. & GTT-Technologies.
12. Jak E., Degterov S., Hayes P.C., Pelton A.D., "Thermodynamic modelling of the system PbO-ZnO-FeO-Fe₂O₃-CaO-SiO₂ for zinc/lead smelting", *Proceedings of the Fifth International Symposium on Metallurgical Slags and Fluxes*, Iron and Steel Society, AIME, Sydney, publ. Iron and Steel Society, Warrendale, PA, 1997, pp. 621-628.

FORMATION OF COPPER SULFIDE PRECIPITATE IN SOLID IRON

Kentaro Urata¹ and Yoshinao Kobayashi¹

Tokyo Institute of Technology; S8-311 2-12-1, Ookayama, Meguro-ku, Tokyo, 152-8550, Japan

Keywords: Copper sulfide, Precipitation, Growth rate, The Ostwald growth model

Abstract

The growth rate of copper sulfide precipitates has been measured in low carbon steel samples such as Fe-0.3mass%Cu-0.03mass%S-0.1mass%C and Fe-0.1mass%Cu-0.01mass%S-0.1mass%C. Heat-treatment of the samples was conducted at 1273, 1423 and 1573 K for 100 s – 14.4 ks for precipitation of copper sulfides and then the samples were observed by a scanning electron microscope and a transmission electron microscope to measure the diameter of copper sulfides precipitated in the samples. The growth rate of copper sulfide has been found to be well described by the Ostwald growth model, as follows:

$$R_t^3 - R_0^3 = (k_0/T)t$$

where R_t and R_0 are the radii of copper sulfide precipitates, respectively, at $t = t$ and $t = 0$ where t is time, k_0 is the rate constant in this model and T is thermodynamic temperature. The values of k_0 produced diffusion coefficient and activation energy, which values are close to those of copper in austenite iron. In addition, the existence of copper sulfide has been confirmed in samples of Fe-0.1mass%Cu-0.01mass%S-0.1mass%C, without and with annealing for the homogenization after melting and solidification process. The annealed sample did not show any copper sulfide precipitates in SEM images. The long homogenization treatment confirms that copper sulfide precipitation is meta stable phase caused micro-segregation by rapid solidification.

Introduction

Growing attention has been paid to the steel production from steel scrap in the respect that it yields less energy consumption and lower environmental impact compared with the ironmaking process by blast furnace. However, steel scrap usually contains a considerable amount of impurities such as copper; furthermore, repeated recycling of steel scrap gradually increases the concentrations of impurities. In particular, copper impurity has harmful effects remarkably on recycled steel. The copper in steel is enriched as copper-concentrated liquid between iron oxide called “scale” and iron matrix by selective oxidation of iron. The copper-condensed liquid penetrates into grain boundaries of the iron matrix; resultantly, this penetration of liquid copper deteriorates toughness of the iron matrix and, much worse, develops cracks around the steel surface during the rolling process. This phenomenon is termed ‘surface hot shortness’ by copper¹⁻³⁾.

This problem due to copper is very difficult to be solved because copper is nobler than iron and cannot be eliminated from molten iron by common steel refinement. Thus, another measure is required and, for instance, it has been proposed to add nickel, which can prevent surface hot shortness inasmuch as nickel helps copper to be occluded into the scale⁴⁾ and also raises the melting point of the copper-condensed phase. However, this process costs more since nickel is

expensive, moreover, nickel behaves as tramp element and is accumulated in steel as well as copper⁵). Silicon and boron have also been found to be effective to suppress surface hot shortness probably due to their effects on morphology and/or physical property of the copper-condensed phase^{6, 7}) although the effects have not been well clarified up to now.

Apart from additions of elements, rapid solidification and cooling processes such as strip casting can be one of the approaches to solve the copper problem. Rapid solidification can suppress the formation of liquid copper and then prevent surface hot shortness⁸). In addition, copper reacts with sulfur dissolved in scrap steel and precipitates in the form of copper sulfide in the casting process⁹). This formation is favorable to suppress copper surface hot shortness by reducing copper concentration in solid iron.

There have been three findings reported regarding the precipitation of copper sulfides. First, this precipitation inevitably occurs even if the concentration of copper in steel is lower than 0.01 mass% which level is almost the same as that for impurity copper in common steel¹⁰). Second, copper sulfides are classified mainly into three types¹¹) as follows:

1. Plate-like copper sulfide (PS)
2. Shell-like copper sulfide (SS)
3. Nano-scale copper sulfide (NS)

Third, the morphology strongly affects the mechanical property of steel. In particular, NS copper sulfide is known to increase yield strength by precipitation hardening rather than grain refinement^{12, 13}). As-cast strips have higher work hardening ability than heat-treated strips in case steel contains a little amount of copper and sulfur¹³). The reason has been reported as follows: nano-size copper sulfide is precipitated in as-cast strip and, by heat-treatment, the precipitate grows to have the mean size ten times larger than that in as-cast strip. This difference in precipitate size would dominate work hardenability. Although these researches reported the utility of fine copper sulfide precipitation, practical recycling steel process does not employ the precipitation as a solution for copper surface hot shortness because the stability and growth rate of copper sulfide precipitates has not been researched during heat-treatment.

The stability and growth rate of copper sulfides should be better understood to evaluate the capacity of copper for recycling steel scrap by this process because heat-treatment causes increase or decrease in size of NS precipitates, which leads to the change in the mechanical properties and copper concentration of as-casted steel after heat-treatment. The present work aims to investigate the growth rate and stability of copper sulfide precipitates in steel by two approaches: measurement of change in the size of copper sulfide after various heat-treatments and confirmation of copper sulfides formation in as cast steel and in annealed one by homogenization heat-treatment to propose a suitable heat-treatment condition to keep good mechanical property and low copper concentration of as-casted steel.

Experimental

2. 1 Sample preparation

Table 1 shows the chemical compositions of two steel samples used in the present work: it is noted that sample 1 contains higher concentrations of copper and sulfur than sample 2 and that these concentrations of copper and sulfur do not exceed the respective solubilities^{14, 15}) in each sample. These samples were prepared from electrolytic iron plates (99.99 mass% purity), copper

granules (99.5 mass% purity), FeS powders (99 mass% purity) and carbon-saturated iron lumps (Fe-3.36mass%C), the last being prepared by pre-melting the iron plates and graphite powders (99.7 mass% purity) in an alumina crucible. Sample 1 was employed for easier identification of copper sulfide precipitates, while sample 2 was for simulating copper sulfide growth in the practical operation condition. Mixtures of starting materials as above were placed in alumina crucibles and heated up to 1873 K for 1 h in a flow of argon. After melting, the samples were water-quenched and cut into small pieces. For precipitation of copper sulfides, sample 1 was heated up again to 1273 K for 100 s, 900 s, 3.6 ks and 14.4 ks in an alumina crucible; in the same manner, sample 2 was also heated up again to 1273, 1423 and 1573 K. For confirmation of copper sulfide existing, another sample 2 was melted at 1873 K, and subsequently furnace-cooled to 1673 K for 1 h and held for 24 h, followed by water-quenching compare with copper sulfide formation in as-casted sample 2.

Table 1. Chemical compositions of steel samples. (mass%)

	Fe	Cu	S	C
Sample 1	99.57	0.3	0.03	0.1
Sample 2	99.79	0.1	0.01	0.1

2. 2 Microscope observation

2. 2. 1 SEM analysis

The size and existence of copper sulfide precipitates were determined using a scanning electron microscope (SEM) for sample 2. Specimens for SEM observation were cut and embedded in polyester resin and then were polished with alumina abrasives having particle sizes from 0.1 to 3 μm . The SEM used was coupled to a back scattered-electron detector and operated at the accelerating voltage of 10 ~ 15 kV to obtain high resolution performance.

2. 2. 2 TEM analysis

The chemical compositions of precipitates were determined by a transmission electron microscope (TEM) for sample 1. Specimens for TEM observation were cut into pieces about 3 mm thick. These specimens were abraded sequentially using 200, 400, 600, 900, 1200, 2400 and 4000 grit SiC papers with a motor driven disc polisher and were further polished sequentially using 9 and 1 μm grade diamond pastes. Subsequently, the specimens were etched by 10vol%acetylacetone-1vol%tetramethylammonium chloride methyl alcohol (AA electrolyte solution). Carbon extraction replicas were also prepared through the standard procedure. Finally, specimens were etched again by AA electrolyte solution. The replicas were floated on nickel grids and a molybdenum double tilt specimen holder was used. The TEM was operated at 200 kV and was coupled to an energy dispersion spectrometer (EDS). EDS analysis was performed with high-resolution and high-speed regarding the four elements, namely, Fe, Cu, S and O, and mapping images were obtained within 5 min.

Results

3. 1 Morphology and chemical compositions of copper sulfide and oxide phase

There exist precipitates having different shapes and sizes in the SEM images of samples 1 heat-treated at 1273 K for 0 – 14.4 ks. These precipitates can be classified into three types: iron oxide, shell-like copper sulfide covering inclusions (SS) and nano-scale copper sulfide (NS). **Figures 1** shows morphology and chemical compositions of SS and NS precipitates observed by TEM, respectively. Precipitate SS is copper sulfide covering iron oxide having about 1 μm

diameter. The chemical compositions of iron oxide is approximately Fe-30at%O, which is probably a reflection of the presence of both iron and $Fe_{1-x}O$, while copper sulfide precipitate seems $Cu_{1.6}S$ or $Cu_{1.8}S$ according to the concentration ratio of copper to sulfur from EDS analysis. This composition of copper sulfide is similar to those previously reported by other researchers¹⁶⁻¹⁸. On the other hand, there are also NS precipitates observed in the sub-micron meter size. Precipitate NS seems different from SS in size and morphology but their chemical compositions are close to each other. According to the previous reports^{17, 18}, NS is considered to be $Cu_{1.8}S$.

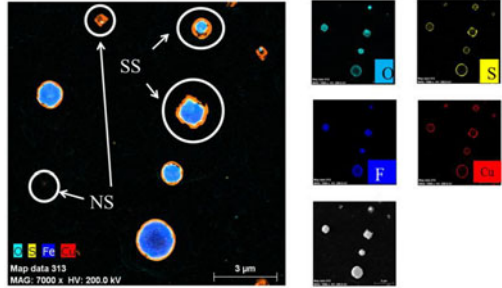


Figure 1 . TEM-EDS images of SS and NS copper sulfide precipitates in samples 1 heat-treated at 1273 K for 900 s.

3. 2 Growth rate of copper sulfide at 1273 - 1573 K

Figures 2 and 3 show SEM images of samples 2 heat-treated for 0 – 14.4 ks at 1273 and 1573 K, respectively. These samples contain almost the same types of precipitate: iron oxide, SS copper sulfide and NS copper sulfide as observed in Fig. 1. **Figure 4** shows a relationship between holding time and weighed average radius of NS precipitates with the standard deviation as the error bars. These data have been obtained from 20 of the largest precipitates in the SEM image of some photographs having the area from 4.26 to 17.04 μm^2 . The size of NS precipitates increases with holding time. In addition, as the heat-treatment temperature is higher, the size is

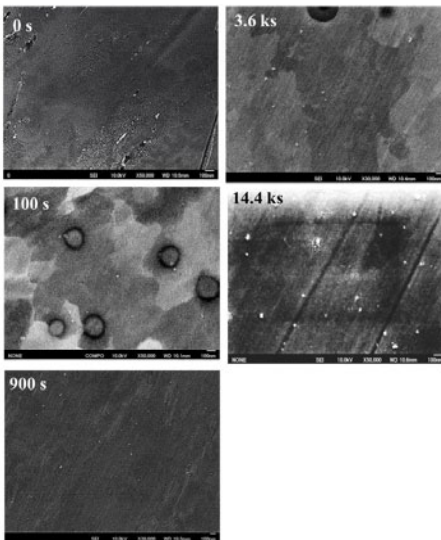


Figure 2. SEM images of samples 2 heat-treated at 1273 K for (a) 0 s, (b) 100 s, (c) 900 s, (d) 3.6 ks and (e) 14.4 ks.

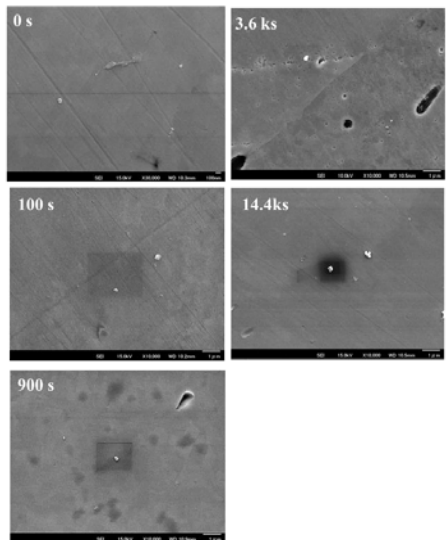


Figure 3. SEM images of samples 2 heat-treated at 1573 K for (a) 0 s, (b) 100 s, (c) 900 s, (d) 3.6 ks and (e) 14.4 ks.

larger and the number of precipitates is smaller compared with Figs. 2 and 3. In the present experimental conditions investigated, the number of precipitates is the largest in case of heat-treatment for 14.4 ks at 1273 K, and the size of precipitates is the largest in case of heat-treatment for 14.4 ks at 1573 K. Precipitate NS obtained by heat-treatment for 14.4 ks at 1573 K is comparable to those produced by Liu *et al*¹². In their report, the size of copper sulfide precipitates provided by heat-treatment for 10.8 ks at 1473 K ranged from 100 to 800 nm and the mean size was about 200 nm. The mean size of NS precipitates in the present work is about 140 nm.

3.3 Confirmation of copper sulfide formation in as-cast and annealed samples

Figure 5 shows the SEM image of samples (a) without and (b) with annealing for the homogenization. The sample (a) without heat-treatment contains some fine precipitates in the SEM image. In contrast, the SEM image of sample (b) does not show any copper sulfide precipitates. These results indicate that copper sulfide precipitation requires rapid cooling from molten iron to solid iron without annealing. In the rapid cooling process, the micro segregation of copper and/or sulfur occurs and freezes, which segregation provides super-saturated region of copper and sulfur to induce copper sulfide formation as a meta stable precipitate. On the other hand, in the sample (b), slow solidification and long annealing probably provides the chance to the homogeneous distribution of copper and sulfur; therefore, copper sulfide may not form.

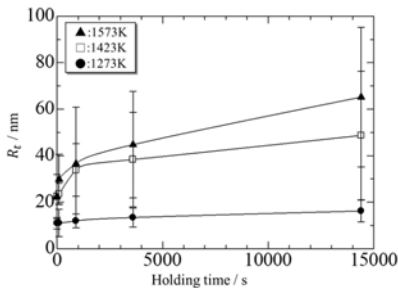


Figure 4. Radius of NS copper sulfide precipitates vs holding time.

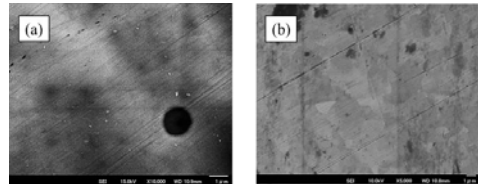


Figure 5. Microstructure of samples (a) without and (b) with homogeneous heat-treatment at 1673 K for 24 hours.

Discussion

4.1 Application of Ostwald growth model to copper sulfide precipitation

The Ostwald growth model has widely been employed to describe the growth rate of precipitates in a solid matrix. Liu *et al*¹⁹ have also applied this model to the growth of NS precipitates in iron to predict their size distribution. According to the Ostwald growth model, radius R_t of precipitates can be expressed by the following equation²⁰:

$$R_t^3 - R_0^3 = (k_0/T)t \quad (1)$$

where k_0 (m^3/s) $\equiv 8\sigma D[M]V_m/9R$, which represents the rate constant in this model, σ is the interfacial energy between copper sulfide and iron, $[M]$ is the mole fraction of copper in iron and V_m is the molar volume of copper sulfide. Figure 6 shows the relationship between holding time and values of the left-hand side of Eq. (1). The value of $(R_t^3 - R_0^3)$ is also in linear proportion to holding time. Rate constants k_0 derived from the slope of the linearity are $2.8 \times 10^4 \text{ nm}^3\text{K/s}$ at 1573 K, $9.6 \times 10^3 \text{ nm}^3\text{K/s}$ at 1423 K and $2.5 \times 10^2 \text{ nm}^3\text{K/s}$ at 1273 K. The Arrhenius relation is

applied to the values of k_0 , resulting in **Figure 7** showing the relationship between reciprocal of temperature and logarithm of k_0 in the temperature range from 1273 to 1573 K, in comparison with a value of k_0 derived from data reported by Liu *et al*¹²). These data are also in consistent with each other. The activation energy has been derived as 264 kJ/mol from the slope of the straight line, which value is in very good agreement with the activation energy reported for copper diffusion in austenitic iron, 272 kJ/mol¹⁹). The diffusion coefficient is also calculated from the relationship $k_0 = 8\sigma D[M]V_m/9R$ according to a previous work¹⁹). The interfacial tension between copper sulfide and γ -Fe is taken as 0.83 N/m. This value was basically measured for 1073 K; however, it is now assumed to be constant because the temperature coefficient of interfacial tension between Fe and Cu₂S is small, ranging from 0.61×10^{-3} N/mK²¹) to 0.09×10^{-3} N/mK²²). The molar volume of copper sulfide is 2.75×10^{-5} m³/mol¹⁹) at 1073 K and the mole fraction of copper in the matrix is 8.79×10^{-4} from the chemical composition. **Table 2** gives values of diffusion coefficient derived from values of k_0 . The diffusion coefficients from the Ostwald growth model are in very good agreement with those of copper in austenitic iron, indicating that the growth rate of copper sulfide precipitates is dominated by copper diffusion. These agreements in the activation energy and diffusion coefficient conclude that the Ostwald growth model can well describe the growth of copper sulfide precipitates in iron. This would be because the Ostwald growth of copper sulfide precipitates occurs by driving force as small as decrease in interfacial energy of the copper sulfide precipitate though the copper sulfide precipitate is not stable in the solid iron having Fe-0.1mass%Cu-0.01mass%S-0.1mass%C.

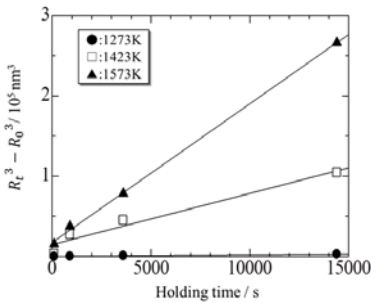


Figure 6. $(R_t^3 - R_0^3)$ of NS copper sulfide precipitates vs holding time.

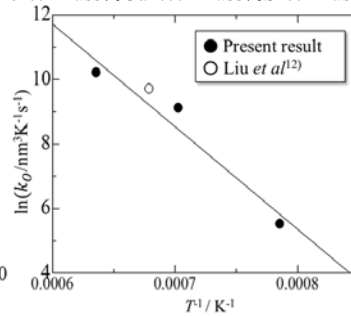


Figure 7. Arrhenius plot based on Ostwald ripening model

Table 2. Diffusion coefficients of copper in austenitic iron (m² s⁻¹)

	Ostwald growth model	Reported data
1573 K	1.27×10^{-14}	1.72×10^{-14}
1423 K	4.24×10^{-15}	1.92×10^{-15}
1273 K	1.16×10^{-16}	1.27×10^{-16}

4. 2 Suggestion to heat-treatment conditions after strip casting

On the basis of the growth rate and stability of NS precipitates, it is proposed that the heat-treatment should be conducted around 1273 K to give the good mechanical property and low copper concentration to as-casted steel because copper sulfide precipitates grow as small as 20 - 30 nm in several tens of minutes and maintain almost the number. Control of the size of copper

sulfides leads to formation of many copper sulfides precipitates at around 1273 K, as can be seen from Figs 2. **Figure 8** shows the time-temperature-precipitation curves of copper sulfides and manganese sulfides¹⁸⁾ reported by Sakai *et al*, who have investigated these sulfides by analyzing their amounts in samples of Fe-0.06mass%Mn-0.17mass%Cu-0.027mass%S heat-treated after solution treatment. This figure indicates that the nose of copper sulfide precipitation exists around 1273 K, where copper reacts with sulfur in iron to produce more nano-scale copper sulfides than at any other temperatures, and supports Fig. 5 in the present work. On the other hand, heat-treatment of higher temperature than 1423 K for long holding time gradually does not keep the size and number of the NS precipitates since the copper sulfide precipitates are not stable and then decomposed.

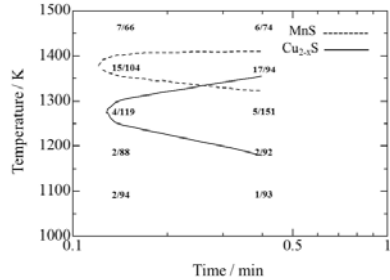


Figure 8. Time-temperature-precipitate curves of Cu_2S and MnS ($a/b = [\text{S in MnS (ppm)}] / [\text{S in Cu}_2\text{S (ppm)}]$)¹⁸⁾

Conclusion

The growth rate and stability of copper sulfide precipitates in solid low carbon steel has been investigated at temperatures of 1273, 1423 and 1573 K. Findings are summarized as follows:

- The growth rate of the precipitates can well be described by the Ostwald growth model and expressed by the mathematical form

$$R_t^3 - R_i^3 = (k_0/T)t$$

The rate constants k_0 are $2.8 \times 10^4 \text{ nm}^3\text{K/s}$ at 1573 K, $9.6 \times 10^3 \text{ nm}^3 \text{K/s}$ at 1423 K and $2.5 \times 10^2 \text{ nm}^3\text{K/s}$ at 1273 K.

- Long homogenization treatment confirms that copper sulfide precipitation requires the micro-segregation for super-saturated region caused by solidification process, which indicates that copper sulfide precipitates are meta stable in solid iron having Fe-0.1mass%Cu-0.01mass%S-0.1mass%C.
- Applying the Arrhenius relation to the rate constants has given the activation energy of copper diffusion as 264 kJ/mol. The diffusion coefficients have also been calculated from the rate constants, as given in Table 2. Both the diffusion coefficients and the activation energy are in good agreement with those for copper diffusion in austenitic iron.
- On the basis of the growth rate and stability of copper sulfide precipitates, it has been proposed that the heat-treatment for as-cast strip steel be conducted at around 1273 K, at which copper sulfide precipitates grow as small as 20 - 30 nm in several tens of minutes, possibly leading to good mechanical property and low copper concentration of solid iron.

References

- 1) D. A. Melford: *Phil Trans. R. Soc. London*, **A295**, (1980) 89

- 2) K. Born: *Stahl Eisen*, **73**, (1953) 1268
- 3) A. Nicholson and J. D. Murray: *J. Iron Steel Inst*, **203**, (1965), 1007.
- 4) T. Fukagawa and H. Fujikawa: *Oxidation of Metals*, **52**, (1999), 177
- 5) J. D. Lee, *ISIJ Int*: **43** (2003), 54
- 6) C. Nagasaki, M. Kaga, K. Shibata, K. Asakura and M. Hatano: *ISIJ Int*, **42** (2002), S57
- 7) S. J. Seo, K. Asakura and K. Shibata: *ISIJ Int*, **37** (1997), 240
- 8) T. Matsushita, K. Nakayama, H. Fukase and S. Nagata: *Journal of IHI Technologies*, **48** (2008) 77
- 9) Y. Ishiguro, K. Sato and T. Maruyama: *Material transaction*, **4**, (2005), 769
- 10) A. Guillet, E. Es-sadiqi, G. Lesperance and F. G. Hamel: *ISIJ Int*, **36**, (1996) 1190
- 11) Z. Liu, Y. Kobayashi, K. Nagai, J. Yang and M. Kuwabara: *ISIJ Int*, **46**, (2006), 744
- 12) Z. Liu, Y. Kobayashi and K. Nagai: *Materials Transactions*, **45**, (2004) 479
- 13) Z. Liu, Y. Kobayashi, J. Yang, K. Nagi and M. Kuwabara: *Materials Transactions*, **47**, (2006), 2312
- 14) Phase diagrams of iron alloys (ISBN 978-4-900041-94-3 C3057): O. A. Bannykh, K. Enami, S. Nagasaki, A. Nishiwaki, AGNE Gijutsu Center, Tōkyō, (2001), 24
- 15) Phase diagrams of iron alloys (ISBN 978-4-900041-94-3 C3057): O. A. Bannykh, K. Enami, S. Nagasaki, A. Nishiwaki, AGNE Gijutsu Center, Tōkyō, (2001), 69
- 16) K. Ishiguro, H. Murakami, K. Sato and K. Araki: *CAMP-ISIJ*, **10**, (1997), 703
- 17) Y. Ishiguro, K. Kuroda: *CAMP-ISIJ*, **22**, (2009), 516.
- 18) T. Sakai, T. Shimazu, K. Chikuma, M. Tanino and M. Matsuo: *Tetsu-to-Hagané*, **70**, (1984) 259
- 19) Z. Liu, Y. Kobayashi and K. Nagai: *ISIJ Int*, **44** (2004), 1560
- 20) The physical Metallurgy of Microalloyed Steels, T. Gladman: London, Institute of Materials; (2002), 204
- 21) K. Nogi, K. Ogino, A. Mclean and W. A. Miller: *Metall. Trans.*, **17B**, (1986) 163
- 22) V. Ya. Zaites, A. V. Vanyukov and V. S. Kolosova: *Izv. Akad. Nauk SSSR Met.*, (1968), No. 5, 39.

INTEGRATED HEAT RECOVERY AND MATERIAL RECYCLING FROM HOT SLAGS: TOWARD ENERGY SAVING AND EMISSION REDUCTION

Yongqi Sun¹, Zuotai Zhang^{1,2}, Seetharaman Sridhar³

¹Department of Energy and Resources Engineering, College of Engineering, Peking University, Beijing 100871, P.R. China

²School of Environmental Science and Engineering, South University of Science and Technology of China, Shenzhen, P.R. China

³WMG, International Digital Laboratory, University of Warwick, Coventry CV4 7AL, UK

Keywords: Heat recovery; Hot steel slags; Coal gasification; Syngas production; Kinetic mechanism

Abstract

Steel slags, untapped at 1450-1650 °C, represent a large potential of energy saving and material recycling in metallurgical industry. Conventionally, the methods used for the heat recovery could be categorized into two types and the chemical methods offered the advantage of combination of multiple industrial sectors and production of the high value syngas. Herein, a novel chemical method was investigated, i.e., gasification reaction in the atmosphere of CO₂ where both raw coal and raw char from coal pyrolysis were employed. Not only the thermodynamics of the gasification process in terms of syngas yields but also the kinetic mechanisms of the char gasification process were analyzed. It was clarified that the slag additions showed a great catalytic effect of the char gasification. Furthermore, the transformation of the iron valence state during the gasification was clarified and the potential of energy saving and emission reduction were estimated.

Introduction

Nowadays with the continuous urbanization and industrialization in China, the emission reduction and resource shortage gradually become severe issues to be addressed in modern society. To deal with these problems, improving the energy efficiency in the traditional energy-intensive industries such as the iron and steel industry contributes to a significant strategy. In the past decades numerous advanced technologies have been introduced into the steel industry such as the continuous casting [1] and it is generally believed that heat recovery from the hot slags represents one of the greatest potentials of energy efficiency improvement in the steel industry [2-3]. In 2014, the output of crude steel in China was ~823 million Mt [4], accounting for half of the global production, and consequently, ~123 Mt steel slags were discharged in the steel industry. These high temperature slags, untapped at 1450-1650 °C, carried substantial amounts of high-grade thermal energy, accounting for an important energy resource and material resource; while the recovery ratio of this energy was quite limited, i.e., less than 2% [5].

To recover the waste heat from the hot slags, numerous methods have been developed in the past decades, which could be generally divided into physical granulation methods and chemical methods [2-3,6]. The physical methods were mainly focused on the granulation of the hot slags into small particles and then the improvement of the heat transfer between the hot slags and the working medium. Thus lots of granulation methods have been exploited including rotary cup

atomizer (RCA) [7], rotary cylinder atomizer (RCLA) [8] and spinning disk atomizer (SDA) [9] methods. Compared to physical methods, chemical methods have been more extensively investigated recently because of the apparent advantages such as the production of high-value syngas and the integration of multiple sectors [6]. Meanwhile coal gasification is a clean and highly efficient route utilizing the coal resource and conventionally the heat required for coal gasification is supplied by the part combustion of the coal materials. In this case, the thermal energy in the steel slags could be a potential energy carrier supplying the heat for coal gasification, which was investigated in this study.

Experimental and methods

Sample preparations

In this study, a low-rank coal sample was first collected from Pingshuo power generation plant in Shanxi Province, China. The proximate analysis results show that the primary coal was mainly composed of 3.8% moisture, 31.6% volatile, 21.5% coal ash and 45.9% fixed carbon (wt. %). Meanwhile, an industrial steel slag was collected from Shougang Corporation in Beijing, China. The X-ray fluorescence (XRF) results show that the chemical compositions of this steel slag mainly comprised 41.9% CaO, 22.6% SiO₂, 7.3% MgO, 4.1% Al₂O₃ and 22.6% Fe₂O₃ with the Fe²⁺/TFe of 0.63.

It should be pointed out that there were two ways to treat the primary coal for the further gasification. One is to heat the raw coal in a fixed tube furnace before gasification in the N₂ agent to obtain the coal char. The compositions of the coal char prepared were 0.4% moisture, 11.7% volatile, 18.0% coal ash and 70.3% fixed carbon (wt. %). Then the coal char obtained was thoroughly mixed with the steel slags with the mass ratio of 1:1 for the sequent gasification reactions. Another strategy was that the raw coal was thoroughly mixed with the steel slags before gasification and then the pyrolysis process was proceeding in advance during the heating process from the room temperature to the coal char gasification temperature designed. These two treatment approaches would not influence the final gasification results and thus herein only the coal char gasification integrated with heat recovery from steel slags was analyzed. In addition, before gasification all the materials used were dried for 10 hours and ground into small particles less than 200 meshes for the full contact of these materials.

Apparatus and Procedure

In the present study, a series of isothermal experiments were carried out to clarify the coal char gasification mechanism and the role of the steel slags. A gasification system was used to perform these tests, as displayed in **Figure 1**, which was mainly composed of two parts, i.e., a TG analyzer part (S60/58341, Setaram) to perform the gasification experiments and a syngas analysis part (Testo pro350, Testo) to measure the contents of the syngas especially the transient CO content. From the viewpoint of carbon emission reduction, pure CO₂ was chosen as the gasifying agent with a flow rate of 100 ml/min. In order to confirm the complete gasification of the coal char, the gasification temperatures were selected as 1000 °C, 1100 °C, and 1200 °C.

The whole gasification process was mainly composed of several steps. The raw materials prepared were first placed into a corundum crucible with the height of 5 mm and diameter of 8 mm and then put into the TG heating area. Then the materials were heated from room temperature to the set gasification temperature with a heating rate of 10 K/min in the agent of 100 ml/min N₂ gas. After reaching the gasification temperature, it would be held for 10 minutes to stabilize the temperature and atmosphere. Then the N₂ agent was replaced by the 100 ml/min

CO₂ gas and the char/CO₂ gasification took place. Meanwhile mass evolutions during the gasification was detected and recorded by the TG system and the syngas released was simultaneously measured by the syngas analysis system.

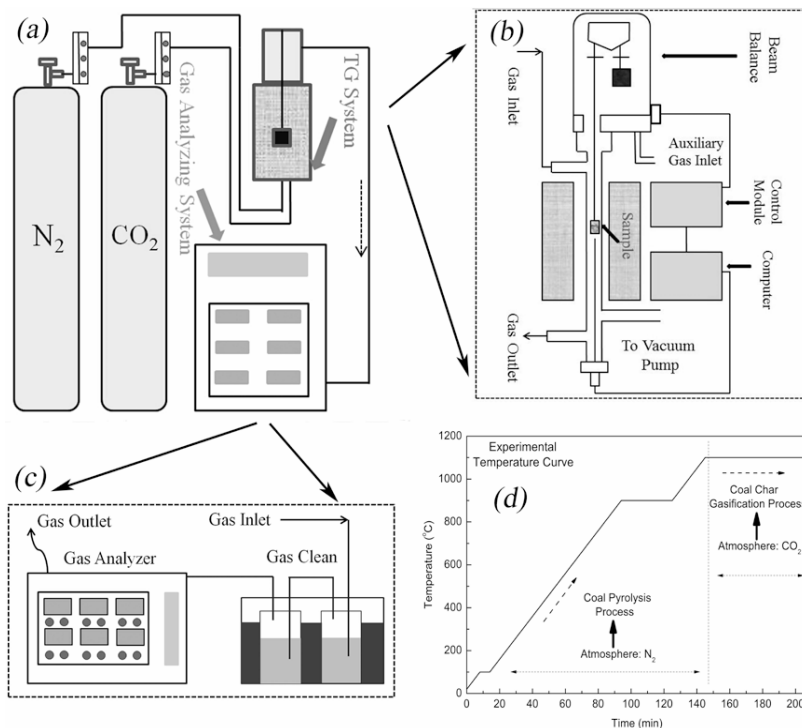


Figure 1. Schematic diagram of coal gasification system (a). This system could be mainly divided into two parts, i.e., (b) a part of gasification reaction and (c) a part of syngas measurement; (d) temperature file of the experiments

Results and discussions

General process of coal gasification

As aforementioned, generally the whole coal gasification process could be divided into two stages, i.e., a coal pyrolysis stage at low temperatures and a coal char/CO₂ gasification stage at high temperatures. As an example, the mass evolutions of the samples during gasification at 1000 °C are displayed in **Figure 2** in detail. As can be observed, the whole experimental process could be obviously divided into two steps. First, during the non-isothermal heating process, the raw coal samples were primarily pyrolyzed into coal char in the agent of N₂, during which the chemical bonds in the organics were cracked and part of the syngas was thus released. After that the gasifying agent was transferred from N₂ to CO₂ during the isothermal reactions at high temperatures, the coal char prepared would react with the CO₂ agent through the Boudouard reaction and the sample mass was further decreased.



From **Figure 2(a)**, it can also be noted that during the second stage of coal char gasification, the slope of the TG curves was remarkably increased and the reaction rate was enhanced in presence of steel slags, which could indicate a catalytic effect. In order to further clarify this point, the DTG curves of the samples during the second stage of coal char gasification was further calculated, as displayed in **Figure 2(b)** in detail. As can be observed clearly, in presence of steel slags, the reaction rate was improved and the reaction time was greatly shortened, which undoubtedly proved that the steel slags could act as not only a good heat carrier but also an effective catalyst for the coal gasification reactions.

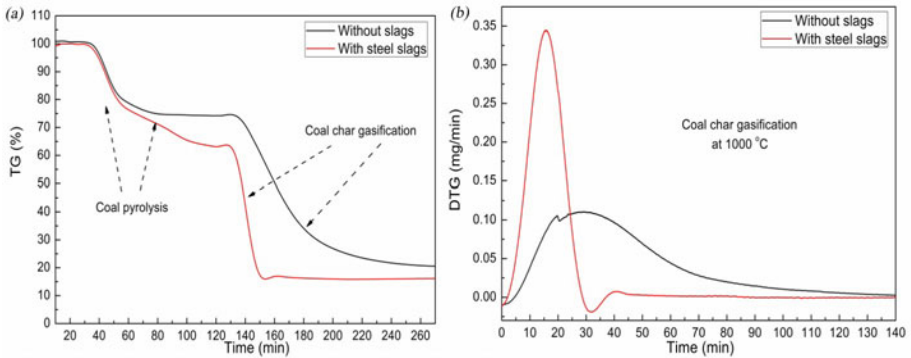


Figure 2. Mass evolutions of the samples during coal gasification at 1000 °C. (a) TG curves of raw coal gasification process and (b) DTG curves of coal char/CO₂ gasification process.

Kinetic mechanism of the coal char gasification

As aforementioned, the general process of coal gasification in presence of steel slags could be first clarified based on the TG and DTG curves. More importantly, the kinetic mechanism of the coal gasification could be identified using the TG data and in this study the mechanism of second stage of coal gasification, namely coal char/CO₂ gasification, was mainly analyzed. The analysis of the kinetic mechanism of the char gasification could be mainly divided into several steps. First, the conversion degree of the char gasification process x could be calculated based on the TG curves. Second the relationship between the conversion degree x and the time t could be described using the following equation:

$$F(x) = \int_0^x \frac{dx}{f(x)} = k(T)t \quad (2)$$

where x , t , $k(T)$, T , $f(x)$ and $F(x)$ are the conversion degree of coal gasification, time, apparent gasification rate constant, absolute temperature, differential and integral mechanism function, respectively. Then the linear relations of the integral mechanism function $F(x)$ versus time t could be analyzed using various mechanism models of gas-solid reactions developed in previous studies including Avrami-Erofeev models, shrinking core models and diffusion models [10-13].

It should be pointed out here that the analysis of the kinetic mechanism of coal char gasification was performed mainly based on three principles, i.e., the general understanding (physical meanings) of the individual kinetic models, the results demonstrated by the previous studies and the correlation coefficients (R^2) of all plots. Actually, a good linear kinetic model

could suggest none effective physical-chemical meanings despite of a good mathematic relationship [10]. All the plots were calculated and analyzed and the results for the gasification at 1000 °C are displayed in **Figure 3** in detail. It can be observed that the char/CO₂ gasification could be interpreted by an A2 model (Avrami-Erofeev) without slags; while in presence of steel slags, the mechanism model changed from an A2 model to an A4 model. This model variation was first in agreement with a previous study [11]. Furthermore, an Avrami-Erofeev was reasonable to describe the coal char gasification because the porosity of the samples gradually varied with the reaction proceeding with time [10-13].

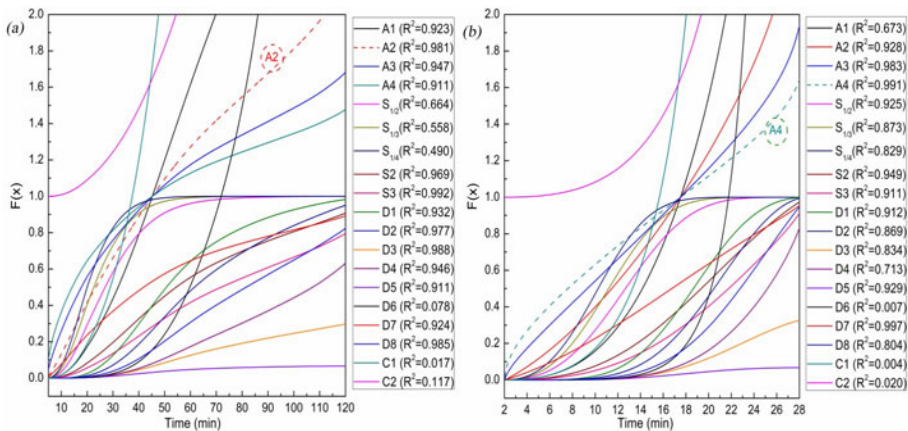


Figure 3. Kinetic mechanisms of the coal char gasification at 1000 °C. (a) Coal char without steel slags and (b) coal char with steel slags.

After determining the kinetic mechanism of the char gasification process, the apparent gasification rate could be calculated by means of **Eq. (2)**. The using these rate constants, the apparent activation energy for gasification could be further deduced using the Arrhenius equation. As a result, it was found that the activation energy remarkably decreased from ~90 kJ/mol to ~15 kJ/mol due to the addition of steel slags. This indicated that the steel slags showed a great catalytic effect on the coal char gasification process. On the other hand, this visibly decreasing activation energy also indicated that the gasification would be greatly influenced by the mass diffusion step, which should be considered during an actual gasification process.

Syngas productions and the role of steel slags

As aforementioned, during the gasification process, not only the mass evolutions of the samples were detected but also the concentrations of the syngas was simultaneously measured, especially the transient CO content. Based on the transient curves of the CO content, the total CO yield during the gasification could be calculated, which was actually one of the main objectives in this study. Analyzing the CO yields during gasification reactions, it was found that the CO yield in presence of steel slags was higher than that without steel slags. The possible reason could be that the FeO in the slags was oxidized by the CO₂ agent and thus part of CO was produced. In fact, there was high content of FeO in the steel slags, which could be oxidized by the pure CO₂ gas. In order to confirm this point, the raw steel slags were heated in the pure CO₂ agent at 1100 °C and the content of the syngas produced was measured. The CO content in the

syngas is shown in **Figure 4**. It can be proved that the raw steel slags could be oxidized, which enhanced the CO production during the char gasification process. In order to further clarify the reaction occurring, the slags after gasification were characterized by X Ray Diffraction (XRD) technique and it was found that the Fe_3O_4 phase in the slags remarkably increased. This indicated the existence of the following reaction during the coal gasification process:

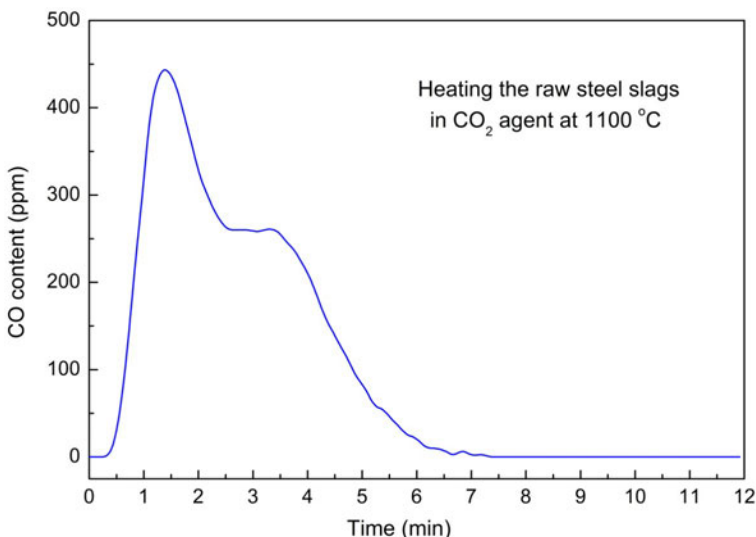
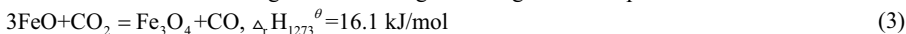


Figure 4. Industrial concept integrated of sludge gasification and heat recovery from high temperature slags

Conceptual model summarized in the present study

In the end, a conceptual composed of multiple industrial sectors could be summarized herein including the steel industry, the coal industry and the chemical engineering industry, as displayed in **Figure 5** in detail. The whole route of this strategy mainly consisted of several steps. First, the high temperature steel slags were produced during the steel making process in the steel industry. Meanwhile the primary coal was produced in the coal industry and pyrolyzed into raw coal char. Then there were two pathways to perform the char/ CO_2 gasification reactions in presence of steel slags. One was that the steel slags directly contacted with the coal char and the char gasification occurred; during this process, the full contact between these two materials was a significant factor to be controlled. The other was that the steel slags were first granulated and broken into small particles to increase the surface area through different granulation methods [7-9,14]. Consequently, the hot slags particles obtained were mixed with the coal char, the char gasification took place and then the syngas including CO , H_2 and CH_4 was produced. It should be pointed out that the syngas produced could indirectly be used in the chemical engineering industry for chemical product preparations or directly used in the steel industry after necessary gas separations.

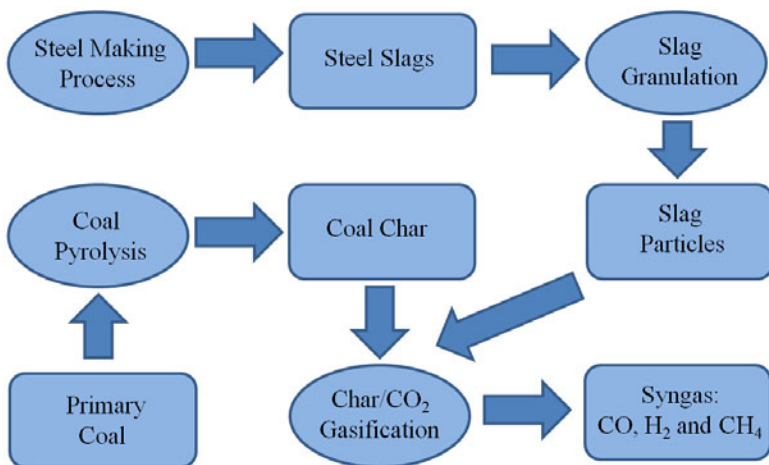


Figure 5. Conceptual model of the integration of heat recovery from high temperature steel slags and coal gasification

Conclusions

In this study, an emerging chemical method, i.e., coal gasification was investigated for the purpose of recovering the waste heat from high temperature steel slags in the steel industry. A series of isothermal experiments were performed in the temperature range of 1000-1200 °C under the CO₂ agent. The results proved that the coal gasification process could be overall divided into two stages, i.e., a low temperature pyrolysis stage and a high temperature char gasification stage. Furthermore, the steel slags greatly changed the kinetic mechanism of the coal gasification, i.e., the kinetic model of char gasification changed from an A2 model to an A4 model and the activation energy was greatly decreased indicating a catalytic effect of the steel slags. Moreover, from the thermodynamic respect, the CO yield was increased by the steel slags because of the reaction between the FeO in the steel slags and the CO₂ agent.

Acknowledgement

Supports by the National High Technology Research and Development Program of China (863 Program, 2012AA06A114) and Key Projects in the National Science & Technology Pillar Program (2013BAC14B07) are acknowledged. The authors also acknowledge financial support by the Common Development Fund of Beijing and the National Natural Science Foundation of China (51472006, 51272005 and 51172001).

References

1. M.R. Aboutalebi, M. Hasan, and R.I.L. Guthrie, "Coupled turbulent flow, heat, and solute transport in continuous casting processes," *Metallurgical and materials transactions b*, 26 (1995), 731-744.

2. M. Barati, S. Esfahani, and T.A. Utigard, "Energy recovery from high temperature slags," *Energy*, 36 (2011), 5440-5449.
3. H. Zhang, et al., "A review of waste heat recovery technologies towards molten slag in steel industry," *Applied Energy*, 112 (2013), 956-966.
4. World steel association. See also: <https://www.worldsteel.org/statistics/statistics-archive.html>.
5. J.J. Cai, et al., "Recovery of residual heat integrated steelworks," *Iron and Steel*, 42 (2007), 1-6.
6. Y.Q. Sun, et al., "Heat recovery from high temperature slags: a review of chemical methods," *Energies*, 8 (2015), 1917-1935.
7. T. Mizuochi, et al., "Feasibility of rotary cup atomizer for slag granulation," *ISIJ International*, 41 (2001), 1423-1428.
8. Y. Kashiwaya, Y. In-Nami, and T. Akiyama, "Development of a rotary cylinder atomizing method of slag for the production of amorphous slag particles," *ISIJ International*, 50 (2010), 1245-1251.
9. T. Mizuochi, and T. Akiyama, "Cold experiments of rotary vaned-disks and wheels for slag atomization," *ISIJ International*, 43 (2003), 1469-1471.
10. H. Tanaka, "Thermal analysis and kinetics of solid state reactions," *Thermochimica acta*, 267 (1995), 29-44.
11. P. Li, et al., "Adaptability of coal gasification in molten blast furnace slag on coal samples and granularities," *Energy & Fuels*, 25 (2011), 5678-5682.
12. Y.Q. Sun, et al., "Characteristics of low temperature biomass gasification and syngas release behavior using hot slags," *RSC Advances*, 4 (2014), 62105-62114.
13. Y.Q. Sun, et al., "Integration of coal gasification and waste heat recovery from high temperature steel slags: an emerging strategy to emission reduction," *Scientific reports*, 5 (2015), 16591.
14. H. Tobo, et al., "Development of continuous steelmaking slag solidification process suitable for sensible heat recovery," *ISIJ International*, 55 (2015), 894-903.

Interfacial Phenomena and Thermophysical Properties of Molten Steel and Oxides

Masahito Watanabe¹, Kenta Onodera¹, Shoya Ueno², Takao Tsukada², Toshihiro Tanaka³,
Haruka Tamaru⁴ and Takehiko Ishikawa⁴

¹Department of Physics, Gakushuin University
1-5-1 Mejiro, Toshima, Tokyo, 171-8588, Japan
²Graduate School of Engineering, Tohoku University
6-6-07 Aoba, Sendai, 980-8579, Japan
³Graduate School of Engineering, Osaka University
2-1 Yamadaoka, Suita, Osaka 565-0871, Japan
⁴Japan Astronautical Exploration Agency (JAXA)
2-1-1 Sengen, Tsukuba, 305-8505, Japan

Keywords: Slag, Flux, Interfacial tension, Levitation, Microgravity

Abstract

At present, interfacial phenomena between molten steel and oxides, usually called slag or mold flux, play an important role in steel processing for material design. Therefore, understanding interfacial tension is important for process control. From this, we propose an interfacial tension measurement technique between molten steel and oxides using a modified oscillating drop method with levitation techniques. The interfacial tension data using traditional techniques based on the sessile drop method have been obtained only at temperatures around the melting point of iron due to dissolution of containers and the substrate into molten steel and oxides in higher temperature regions. Our proposed technique to obtain the temperature dependence of interfacial tension between molten iron and oxides is to use a core-shell form droplet including an interface between two liquids using electrostatic levitation, which negates the use for containers. The experiment was performed on the International Space Station using the electrostatic levitation furnace (ELF) in the KIBO module.

Introduction

Interfacial tension measurements are required in steel industries, which include smelting, continuous casting and welding. In the continuous casting process, mold flux made of molten oxides covers steel melt in the casting pool. Here, the interfacial tension prevents the oxide from being pulled down into the steel melt. In the welding process, the welding flux, made of an oxide, encloses the steel melt in order to prevent the melt from oxidizing and to control the shape of the welded part. For this control, the interfacial tension between the welding flux and the steel melt plays an important role. The interfacial tension in these processes is changed empirically by changes in the oxide composition. Therefore, in order to systematically be able to control the interfacial tension between molten oxide and the steel melt, we need to obtain the values of this tension for many kinds of these media¹⁾. However, oxide compositions were limited by temperature in previous measurements using a sessile drop with an x-ray radiograph²⁾ due to the

difficulty in raising the temperature above the melting point of iron with conventional methods using a container. Therefore, a container-less technique must be used to measure the temperature dependence of interfacial tension between molten oxides and steel melts. As such, we planned to measure this interfacial tension using core-shell droplets with an oscillating drop technique in microgravity³. Under these conditions, two immiscible liquids form a core-shell droplet which is dominated by the surface and interfacial free energies. Then the interfacial tension, which is the interfacial free energy per unit area, can be found. The surface tension is measured using the surface oscillation technique from the surface oscillation frequencies of levitated liquid droplets. To execute the measurement of interfacial tension between molten oxide and steel melts forming a core-shell droplet, we selected the electrostatic levitation method to achieve the requirements needed for the measurement. We were able to use the electrostatic levitation furnace (ELF)⁴ installed on September 2015 in the KIBO module of the International Space Station (ISS). In this report, we review our research using the ELF for finding the interfacial tension between molten oxides and steel melts.

Basis of oscillating drop technique using core-shell droplet

a. Normal mode analysis of core-shell droplet

Under microgravity conditions, immiscible liquids form a core-shell droplet. The surface oscillation of the core-shell droplet is analyzed from the equations of motion⁵. When dealing with core-shell droplets comprising incompressible and non-viscous fluids, the equations of motion for the core-shell droplet are described by the following equations using velocity potential in spherical coordinates shown in Figure 1;

$$\omega_{\pm}^2 = K_{\pm} (W/J) \quad (1)$$

$$K_{\pm} = \frac{1}{2} \left(\frac{\sigma m_1}{\tau^3} + \frac{m_2 \tau^3}{\sigma} \right) \pm \sqrt{\frac{1}{4} \left(\frac{\sigma m_1}{\tau^3} - \frac{m_2 \tau^3}{\sigma} \right)^2 + 1} \quad (2)$$

$$\frac{W}{J} = \frac{\omega_0^2 \tau^8}{\sigma} \frac{1}{(1 + \Delta\rho)\tau^{10} + (2/3)\Delta\rho} \quad (3)$$

Equations (2) and (3) have the following parameters:

$$\tau = \sqrt{\frac{R_2}{R_1}}, \quad \sigma = \sqrt{\frac{\sigma_2}{\sigma_{12}}}, \quad \Delta\rho = \frac{3\rho_1 - \rho_2}{5\rho_2} \quad (4)$$

$$m_1 = (1 + \Delta\rho)\tau^5 - \Delta\rho\tau^{-5}, \quad m_2 = \frac{3}{5}\tau^5 + \frac{2}{5}\tau^{-5} \quad (5)$$

where R_1, R_2 are core and shell radii and ρ_1, ρ_2 are the density of the core and shell liquids, respectively. σ_2 is the surface tension of the shell liquid. In equation (3), $\omega_0 = 8\sigma_2/\rho_2 R_2^2$ is the normal mode frequency of a single droplet as derived by Rayleigh⁶ and two frequencies, ω_+ and ω_- , must exist. From these equations, interfacial tension σ_{12} is obtained from the two frequencies, ω_+ and ω_- , of surface oscillations of the levitated core-shell droplet.

Also, important parameters required for determining the values of interfacial tension are the ratio of core and shell radii and the difference in density between core and shell liquids described in eqs. (4) and (5).

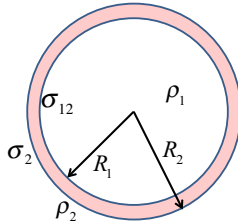


Figure 1 Schematic diagram of core-shell droplet configurations.

b. Numerical simulation of core-shell droplet

In analytical studies of the surface oscillations of a core-shell droplet, since core and shell liquids are assumed to be non-viscous fluids, we cannot know how the viscosity affects the surface oscillations. Since molten oxides are very viscous and the viscosity changes with composition, we performed numerical simulations to understand how the surface oscillations vary with changes in the viscosity of molten oxides and also the ratio of shell and core liquids⁷⁾. For the numerical simulations, we solved the Navier-Stokes equations without external forces, and a Volume of Fluid (VOF) function was used for the interface motions. Input parameters are listed in Table 1. Physical parameters of core part are used for pure iron values obtained by our experiments using electromagnetic levitation. That of shell part of oxides values are not experimental values. We use the average of values found in the literature for SiO₂-CaO-Al₂O₃, smelting slag. Figure 2 shows how the radius changes with time for core and shell liquids with different radii ratios. In these results, the viscosity ratio of shell to core liquids is fixed at 3.9. Figure 3 shows the power spectra of surface oscillations shown in Fig.2. From these power spectra, we can see two peaks and find that their intensity depends on the ratio of the radii. Through numerical simulations with different conditions of viscosity and radii ratios, we found that optimal conditions to observe precisely two peaks in the surface oscillation of core-shell droplets is a viscosity ratio below 40 and a radii ratio of 1.3.⁷⁾

Table1 Physical properties and geometrical parameters used in numerical simulations ⁷⁾

Physical properties	Iron melt	Molten slag
Density [kg/m ³]	7.03x10 ³	2.85x10 ³
Viscosity [mPa.s]	5.5	21.4, 107, 214
Surface tension [N/m]	1.76	0.450
Interfacial tension [N/m]	1.30	
Geometrical parameters		
Equilibrium radius [mm]	0.549, 0.618, 0.706, 0.823	0.988

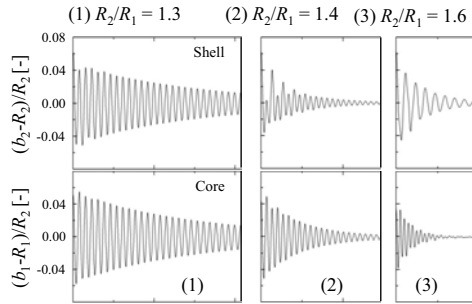


Figure 2 Effects of the ratio of shell to core liquid radii on oscillation behaviors of compound droplets for a viscosity ratio of 3.9^7 .

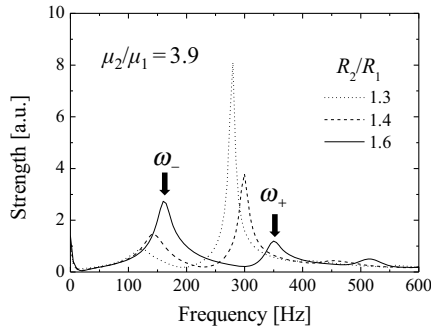


Figure 3 Effect of shell to core liquid radii ratios on frequency spectra of a compound droplet for the case of viscosity ratios of 3.9^7 .

Short duration microgravity experiments by parabolic flight to make core-shell droplets of molten oxide and iron melt

We must confirm that core-shell droplets are formed by molten oxides and steel melts under microgravity conditions before orbital experiments on the ISS are implemented. To do this, we observed the formation of core-shell droplets in microgravity experiments on a parabolic flight using a Gulfstream-II airplane operated by Diamond Air Service (DAS). On the parabolic flight experiments, we could not use the ELF due to the difficulty in maintaining the sample position during parabolic flight due to rapid variations of gravitational forces. Therefore, we used electromagnetic levitation to observe the formation of core-shell droplets of molten oxide and

steel melts. A compact electromagnetic levitation facility, specialized for use in parabolic flight experiments on the G-II airplane was developed and a schematic is shown in Figure 4⁸⁾. Using this equipment, we were able to observe the formation of core-shell droplets of molten oxides and iron melts. Figure 5 shows time-series images of the formation of core-shell droplets of molten oxide and metal liquids taken by high-speed camera in microgravity during the parabolic flights⁸⁾. The molten oxides in Figure 5 are commercially used ilmenite welding flux, which comprises mainly Al_2O_3 , CaO and Fe_2O_3 . In the case of molten oxides and ilmenite welding flux, the iron melt was fully covered and formed a core-shell droplet.

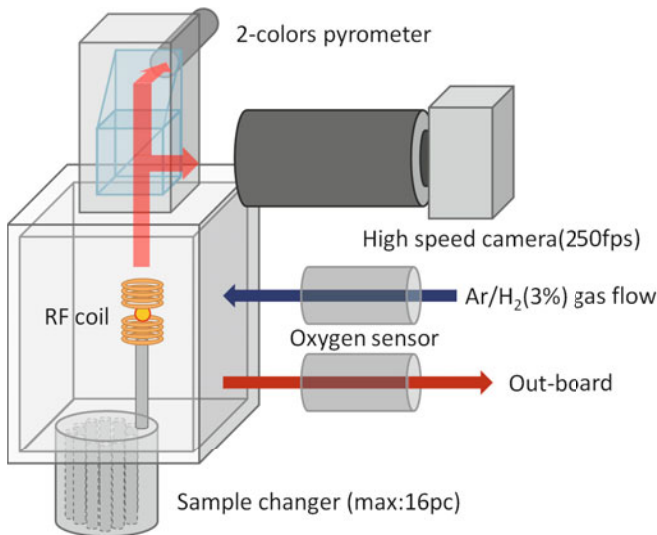


Figure 4 Schematic diagram of electromagnetic levitation facility for parabolic flight experiments.

We succeeded to make a core-shell droplet of molten oxide and iron melt, from which we were able to obtain its surface oscillation frequencies. Surface oscillation frequencies were obtained by the same procedure as the surface tension measurements using the oscillating drop technique. An outline of the levitated droplet was extracted from the time-series images taken by the high-speed camera, and then the change of radius and cross-sectional areas with time were obtained. Surface oscillation frequencies were derived from the time dependent changes using a Fast Fourier Transform (FFT) algorithm. Figure 6 shows the result of surface oscillations of the core-shell droplets in Figure 5. The power spectrum is the result from the FFT of the surface oscillations after completely covering the iron melt with molten oxides. The results show two peaks in the power spectrum of Area and R . From this we inferred that the droplet oscillated with two individual periods due to the interface between the molten oxide and the iron melt. The results confirmed that it was possible to form core-shell droplets from molten oxides and iron melt. According to the analytical solutions we can obtain the interfacial tension values from the frequencies of the two peaks, but in this parabolic flight experiment we could not capture the sample and hence could not obtain the radius ratio of core and shell described in equation (4).

Therefore, we were not able to obtain a correct interfacial tension value, however we were able to estimate an interfacial tension value of 0.7-0.8N/m using the droplet radius from the images shown in Figure 5(d) and a molten oxide density of 3600kg/m^3 . The value is reasonable considering previously reported data. From the parabolic flight experiments, we obtained important information of core-shell droplets in preparation of the samples for the orbital experiments on the ISS. On the basis of the results of this core-shell droplet phenomena, we selected 15 sample for the orbital experiments of interfacial tension measurements. Our experiment on the ISS will be conducted through 2 series before obtaining final results of interfacial tension between molten oxide and steel melts. The first series of experiments will measure the density, viscosity and surface tension of molten oxides in order to predict the interfacial tension before the orbital experiments. Molten-oxide samples are selected by refining slag based on $\text{Al}_2\text{O}_3\text{-CaO}$ with a small amount of SiO_2 . Since the selected slag's viscosity is relatively low, the viscosity ratio will be kept below 40. From the numerical simulations and the parabolic flight experiments, we were able to decide the volume ratio of oxide to iron for the core-shell droplet. For the first series samples of core-shell droplet using an oxide based on ilmenite welding flux and iron, we prepared a radius ratio of 1.3. The oxide based on ilmenite welding flux are predicted to have a relatively low viscosity and interfacial tension, thus the radius ratio were decided mainly from the viscosity effect predicted from the numerical simulations. We prepared 3 cartridges, each containing 15 samples, for the first series of experiments in order to check the reproducibility of the measurements. Our three cartridges containing oxide and core-shell droplet samples were launching successfully on December 6, 2015 onboard a Cygnus CRS OA-4 cargo from Cape Canaveral Air Force Station. The orbital experiments on the ISS of the interfacial tension measurements will start from March, 2016. The measurements made on the ISS under ideal microgravity conditions will allow us to obtain correct interfacial tension using the proposed technique.

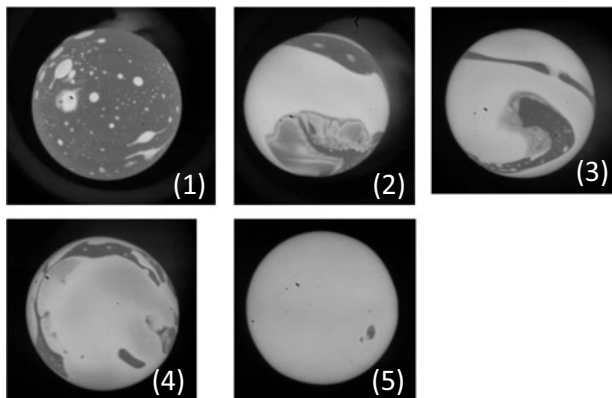


Figure 5 Time-series images of formation of core-shell droplet by the oxides used as welding flux and iron melts under microgravity conditions during a parabolic airplane flight. The droplet radius is about 5mm.

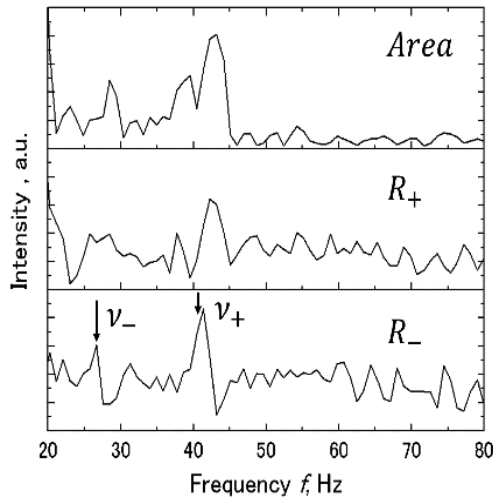


Figure 6 Power spectrum of surface oscillation of core-shell droplet by molten oxides and iron melts obtained under short duration microgravity conditions. *Area*, R_+ and R_- are cross-sectional area, sum of x-axis radius and y-axis radius and difference between x-axis radius and y-axis radius, respectively.

Conclusion

Our research project of interfacial tension measurements using core-shell droplets under electrostatic levitation and long-term microgravity conditions on the ISS had begun. These measurements of interfacial tension between molten oxides and steel melts are required for applications in the steel industry. The measurement of interfacial tension between molten oxide and steel-melts uses the modified oscillating drop method on a core-shell droplet levitated in the electrostatic levitation furnace onboard the ISS. Since measuring the interfacial tension using this modified oscillating drop method is challenging and unprecedented, we must be rigorous in order to obtain precise data of interfacial tensions. In preparation for the orbital experiments on the ISS, numerical simulations and short-duration microgravity experiments by parabolic flight have been performed in order to understand the surface oscillation phenomena of core-shell droplet. Through these preparations, the samples for the first series of orbital experiments were launched on December 6, 2015. We are refining the analysis of the surface oscillation of the core-shell droplet combined with numerical simulations in order to obtain precise values for the interfacial tension between molten oxide and steel melts from the first series of experiments in March, 2016.

Acknowledgment

This work is supported by JAXA. The Parabolic Flight experiment was supported by Diamond Air Service Inc. and Assoc. Prof. Shumpei Ozawa, Mr. Yu Kudo and Mr. Masaru Nishimira of Chiba Institute of Technology. We appreciate their support.

References

- ¹⁾ K. Ogino: *Tetsu-to-Hagane*, 61 (1975) 2118 (in Japanese).
- ²⁾ P.V. Riboud and L.D. Lucas: *Can. Metall. Quart.*, 20 (1981) 199.
- ³⁾ M. Watanabe, T. Tanaka, T. Tsukada, T. Ishikawa, H.Tamaru and A. Mizuno: *Int. J. Microgravity Sci. Appl.*, 32(2015) 320102 (in Japanese).
- ⁴⁾ H. Tamaru, T. Ishikawa, J. T. Okada, Y. Nakamura, H. Ohkuma, S. Yukizono, Y. Sakai and T. Takada, *Int. J. Microgravity Sci. Appl.*, 32(2015) 320104 (in Japanese).
- ⁵⁾ M. Saffren, D.D. Ellmann and W.K. Rhim, *Proc. 2nd International colloquium on drops and bubbles*, Monterey, USA, 1981, 7.
- ⁶⁾ Lord Rayleigh: *Proc. R. Soc. London* 29(1879) 71.
- ⁷⁾ S. Ueno, M. Kubo, T. Tsukada, K. Sugioka and M. Watanabe, *Int. J. Microgravity Sci. Appl.*, 32(2015) 320408 (in Japanese).
- ⁸⁾ K. Onodera, K. Tanaka, Y. Ishii, Y. Yamada, S. Nishikoori, H. Goto, M. Watanabe, A. Mizuno and T. Tanaka: *Int. J. Microgravity Appl.*, 33 (2016) (in printing).

Investigation of Molten Salt Phase Formation during Alkali Roasting of Titaniferous Minerals with Sodium and Potassium Hydroxide

S. Parirenyatwa, L. Escudero-Castejon, S. Sanchez-Segado, Y. Hara, A. Jha

Institute of Materials Research, University of Leeds
Houldsworth building, Leeds, LS2 9JT, United Kingdom

Keywords: Titaniferous, Alkali roasting, Liquid phase, Ternary system

Abstract

Current processes for beneficiation of titaniferous minerals are energy-intensive and produce significant waste. The benefit of alkali roasting over existing process is that it minimises waste. Previous studies on liquid phase formation during alkali roasting of titaniferous minerals were based on the use of Na_2CO_3 , whereas this study focuses on oxidative roasting of titaniferous minerals with either NaOH or KOH, using different alkali to mineral ratios. Phase equilibria of the Na/K-Fe-Ti-O system are calculated the results compared to observed results. This work attempts to characterise the alkali-rich liquid phase formed during roasting and determine its impact on alkali titanate and alkali ferrite separation, as it has been found that Ti-K-Fe-O and Ti-Na-Fe-O ternary phases can be present. The presence of the liquid phase at the reaction interface adversely affects the oxygen diffusion during roasting, which has consequences on the products formed.

Introduction

The primary natural feedstocks that used for the production of titanium chemicals are: ilmenite; rutile, anatase and leucocoxene. These titanium bearing minerals are largely used to produce pigment grade TiO_2 , with a smaller amount dedicated towards the production of Ti metal. Pigment grade TiO_2 is largely used for paper, plastics, paints and coatings industries. The two primary routes for TiO_2 pigment production are the sulphate and chloride process, with the chloride process increasingly favoured due to it being more environmentally and economically favourable[1]. However, the chloride process requires high-grade titaniferous feedstock but decreasing supplies of high quality feedstock has led to the investigation of beneficiation of these minerals. This has led to increasing production of synthetic rutile and titanium slag for use as feedstock. However, existing methods such as the Becher and Benelite process and ilmenite are limited in their ability to treat low-grade titaniferous minerals. As a result, other processes such as alkali roasting have been investigated

Previous studies focused on the alkali roasting of ilmenite include work by Foley and Mackinnon, where they roasted ilmenite with alkali carbonates at 860°C in air [2]. The resulting residues were then leached with hydrochloric acid (HCl). Lahiri and Jha investigated the kinetics and reaction mechanism of roasting ilmenite with Na_2CO_3 , in the 600°C-900°C temperature range [3]. To selectively remove the rare earth elements present in ilmenite Lahiri and Jha used KOH when carrying out oxidative roasting [4]. Ilmenite was roasted with NaOH at temperatures ranging from 550°C – 900°C, by Manhique et al, where they observed the formation of Na-Ti-Fe-O ternary

phases [5]. A study on the effects of KOH and NaOH when roasting Bomar ilmenite was reported by Sanchez Segago et al, where roasting was followed by acid leaching in order to upgrade the TiO₂ content [6]. Parirenyatwa et al performed a comparative study of the oxidative roasting of ilmenite with either KOH or NaOH, where the formation of ternary phases was also observed [7].

A key step to the commercialisation of alkali roasting is understanding the role of the liquid phase during roasting. As it is often found to limit oxygen diffusion but also creates operational problems like ring formation in the rotary kilns. Previous studies on liquid phase formation during alkali roasting of titaniferous minerals were based on the use of Na₂CO₃, where it was found that the alkali liquid played a role in the ilmenite decomposition [8]. This study focuses on oxidative roasting of titaniferous minerals with either NaOH or KOH at different alkali ratios and study the segregation of alkali titanates and alkali ferrites.

Experimental

Ilmenite mineral was used for this investigation, with the composition given in table I. The ilmenite mineral was roasted in air at 1000°C for 2 hours. For the roasting experiments, either KOH or NaOH was used in different ratios based on the stoichiometric amount needed to produce alkali titanate and alkali ferrite. The reaction mixture of alkali and ilmenite mineral was ground and well mixed before being placed in an alumina crucible. The alumina crucible was placed in a resistance furnace at 1000°C for 2 hours in air. After roasting samples were leached in hot water (90°C) for 1 hour with the solution being stirred by a magnetic stirrer throughout the leaching process. Following leaching the samples were filtered using Whatman filter paper and then dried in an oven at 90°C. The dried residues were analysed using Scanning electron microscopy – energy dispersive X-ray spectroscopy (SEM-EDX) technique. The dried residues had to be heated at 800°C for one hour in order to make them crystalline and allow them to be analysed by X-ray powder diffraction.

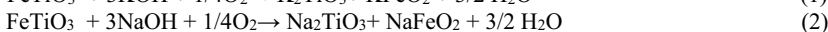
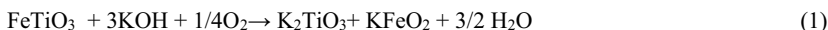
Table I. Chemical composition of ilmenite mineral used for roasting experiments, as analysed by X-ray fluorescence.

Wt. %	TiO ₂	Fe ₂ O ₃	MnO	V ₂ O ₅	Al ₂ O ₃	SiO ₂
	51.2	44.5	1.48	0.34	0.91	0.59

Results and Discussion

Thermodynamic evaluation

The roasting of ilmenite with alkali in air results in the oxidation of iron from the 2+ state to the 3+ state. The reactions performed proceed according to equations (1) and (2), which represent the stoichiometric ratios



Although the plots for the Gibbs free energy vs temperature aren't presented here the calculations were performed using HSC 5.1 software. This showed that reaction 1 is more thermodynamically

favourable than reaction 2 at 1000°C, with free energy values of -824.86 kJ and -153.83 kJ and, respectively [9].

Figure 1a and 1b are the ternary phase diagrams for $K_2O-Fe_2O_3-TiO_2$ and $Na_2O-Fe_2O_3-TiO_2$, respectively, calculated using the FACTSage software [10]. It can be observed from figure 1a that as the alkali content increases the liquid phase is present in the form of $K_4TiO_4(l)$ and $K_2O(l)$ in the K-Ti-Fe-O system. However, there are no liquid phases that form in the Na-Fe-Ti-O system (figure 1b). The alkali ferrite phase is not present in figure 1a where as it can be observed in figure 1b, which is because the thermodynamic data for the $KFeO_2$ phase is not available in the FACTSage database. No ternary phases are predicted and this can also be explained by the lack of thermodynamic data in the FACTSage database.

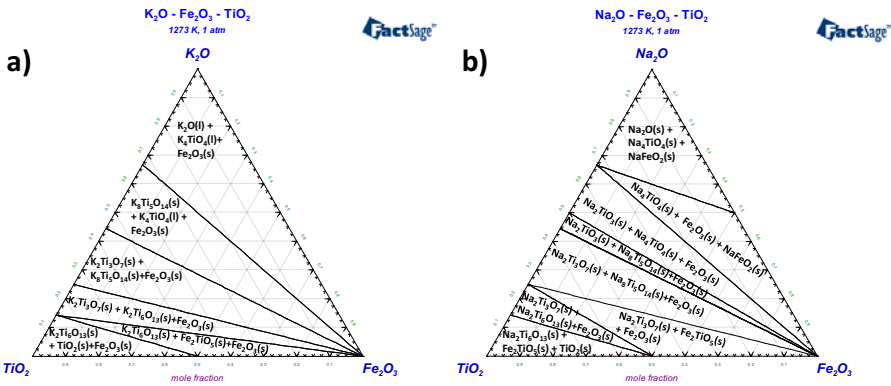


Figure 1. The ternary phase diagram of a) $K_2O-Fe_2O_3-TiO_2$ b) $Na_2O-Fe_2O_3-TiO_2$, computed at 1000 °C using FACTSage software [10].

In order to predict the phases formed when roasting with different ratios of alkali, phase equilibria calculations were performed using the Gibbs energy minimisation technique, using the FACTSage software [10]. The results from the calculation are presented in Table II. It can be seen that when the stoichiometric amount of KOH is used it is expected that $K_4TiO_4(l)$ is the dominant phase present with some hematite and $K_8Ti_5O_{14}$ present. As the KOH increases above the stoichiometric amount then it is expected that $K_4TiO_4(l)$, hematite and $KOH(l)$ will be present. The presence of this liquid potassium titanate would inhibit the diffusion of oxygen.

The phase equilibria calculations performed for the ilmenite roasting with NaOH predicted the formation Na_4TiO_4 , Na_2TiO_3 and Fe_2O_3 when using a stoichiometric amount of alkali salt. As the alkali ratio increases the presence of $NaFeO_2$ is predicted, with the Na_2TiO_3 phase disappearing. At twice the stoichiometric amount of NaOH, the hematite phase is predicted to be completely replaced with $NaFeO_2$.

The phase equilibria results for the two reaction systems differ in that it is predicted that there will be a molten titanate present when using KOH but not when using NaOH. This broadly agrees with the observation made from the phase diagrams presented in figure 1a and 1b. Also, when using NaOH it is predicted that the alkali ferrite would form but not when using KOH. This can be

explained by the fact that the thermodynamic data for KFeO_2 is not available in the FACTSage database.

Table II. Composition of roasting charge and equilibrium phase composition calculated using FACTSage software for roasting of ilmenite with either KOH or NaOH, with different ratios

	KOH				NaOH		
Stoichiometry	1x	1.5x	2x	Stoichiometry	1x	1.5x	2x
Species	Moles			Species	Moles		
FeTiO_3	0.033	0.033	0.033	FeTiO_3	0.033	0.033	0.033
KOH	0.099	0.148	0.198	NaOH	0.099	0.148	0.198
$\text{O}_2(\text{g})$	0.008	0.008	0.008	$\text{O}_2(\text{gas})$	0.008	0.008	0.008
Equilibrium phase composition (mole fraction)							
Species				Species			
$\text{K}_4\text{TiO}_4(\text{l})$	0.019	0.033	0.033	$\text{Na}_4\text{TiO}_4(\text{s})$	0.016	0.033	0.033
$\text{Fe}_2\text{O}_3(\text{s})$	0.016	0.016	0.016	$\text{Fe}_2\text{O}_3(\text{s})$	0.016	0.008	
$\text{K}_8\text{Ti}_5\text{O}_{14}(\text{s})$	0.003			$\text{Na}_2\text{TiO}_3(\text{s})$	0.016		
KOH(l)		0.012	0.061	$\text{NaFeO}_2(\text{s})$		0.016	0.033
				NaOH(l)			0.032
$\text{H}_2\text{O}(\text{g})$	0.998	0.939	0.939	$\text{H}_2\text{O}(\text{gas})$	1.000	1.000	0.994

Effect of roasting on phases formed

The X-ray powder diffraction pattern (XRPD) patterns for the water leached residues after roasting of the ilmenite and KOH mixture with different stoichiometric ratios are presented in figure 2a-c. Figure 2a shows that the stoichiometric amount of alkali led to the formation of two different ternary potassium iron titanate phases, with $\text{K}_{0.4}\text{Ti}_{0.6}\text{Fe}_{0.4}\text{O}_2$ being the more dominant phase and $\text{K}_{0.85}\text{Fe}_{0.85}\text{Ti}_{0.15}\text{O}_2$ being a minor phase. Figures 2b and 2c show that as the alkali added increases it can be seen that the intensity of peaks representing the ternary phase containing an increased amount of potassium and iron, $\text{K}_{0.85}\text{Fe}_{0.85}\text{Ti}_{0.15}\text{O}_2$, grows stronger. These results observed in the XRPD patterns differ with phase equilibria calculations displayed in table II. This is because the thermodynamic data for the K-Fe-Ti-O phase is not present in the FACTSage software database.

Figure 2d-f, the XRPD patterns for water leached residue for ilmenite samples roasted with different ratios of NaOH. It can be seen that these rather complex patterns indicate the presence of complex Na-Fe-Ti-O ternary phases and hematite. These results partially agree with phase equilibria calculations as it predicted the formation of Fe_2O_3 and NaFeO_2 , but the formation of the ternary phase was not predicted as the thermodynamic data is not available in the FACTSage database. The sodium ferrite undergoes the hydrolysis reaction described in equation (3). This was confirmed by the pH increase observed during the water leaching stage. Heating of the residues converted the $\text{Fe}(\text{OH})_3$ phase to the Fe_2O_3 phase which was observed in the XRPD patterns.



The clear differences between the XRPD patterns for the residues from KOH roasting and those the residues from NaOH roasting are that KOH patterns are less complex and show that only K-

Fe-Ti-O ternary phases formed, whereas the NaOH patterns have hematite and the Na-Fe-Ti-O ternary phases. This means that when using NaOH some of the alkali ferrite was able to segregate from the Na-Fe-Ti-O ternary phase but the alkali ferrite was unable to segregate from the K-Fe-Ti-O ternary phase. The presence of the molten salt phase may inhibit this segregation and suggests that there is less liquid present in the Na-Fe-Ti-O system than in the K-Fe-Ti-O system, as demonstrated by the phase diagrams in figure 1. For both alkali salts the roasted samples fused to the crucible because of the formation of the liquid phase.

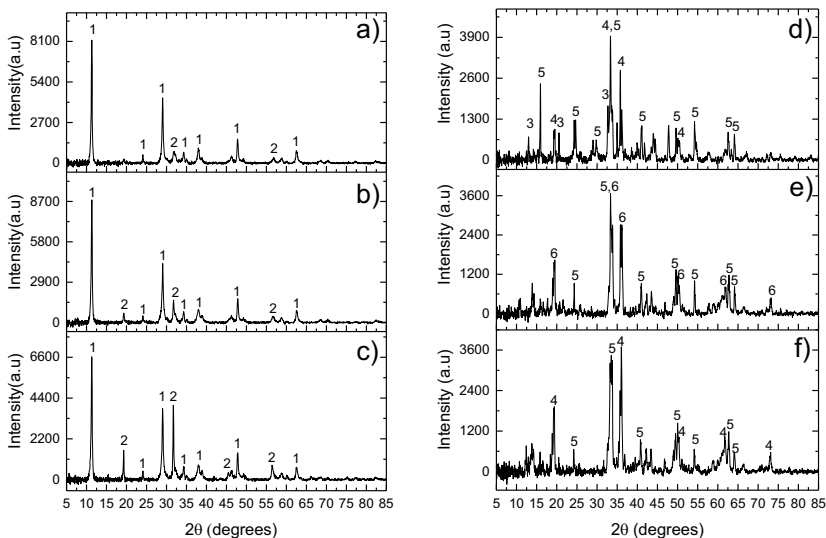


Figure 2. XRPD pattern of water leach residue after roasting ilmenite roasted with a) stoichiometric KOH b) 1.5 x stoichiometric KOH c) 2x stoichiometric KOH d) stoichiometric NaOH e) 1.5 x stoichiometric NaOH f) 2x stoichiometric NaOH. 1- $K_{0.4}Ti_{0.6}Fe_{0.4}O_2$ (04-010-9012), 2- $K_{0.85}Fe_{0.85}Ti_{0.15}O_2$ (00-062-0213), 3- $Na_2Ti_4O_9$ (04-011-2997), 4- $NaTiFeO_4$ (04-007-8937) 5- Fe_2O_3 (04-011-9586), 6- $Na_{2.65}Ti_{3.35}Fe_{0.65}O_9$ (04-014-6583)

Effect of roasting with KOH ilmenite particle microstructure

Figure 3 is the backscattered SEM image of the water leach residue after roasting of ilmenite with 2 times the stoichiometric amount of KOH. Transgranular cracks can be seen throughout the microstructure of the particle. From the elemental mapping it can be seen that there is no significant segregation of the iron. This agrees with the XRPD results (figure 2a-c), where it was seen that the K-Ti-Fe-O ternary phase was the only product formed.

Analysis of the edges of the transgranular cracks (Areas **A** and **C** in table III) shows that the iron content at these points is greater than the titanium content. Compositions of Areas **B** and **D** (in table III) agree with the compositions expected from the dominant phase, $K_{0.4}Ti_{0.6}Fe_{0.4}O_2$, observed in the XRPD patterns (Figure 2c). Point **E** is an area with significantly more titanium

than iron. Observing all the SEM-EDX results are presented in table III shows that the composition of potassium is fairly consistent at all the points analysed.

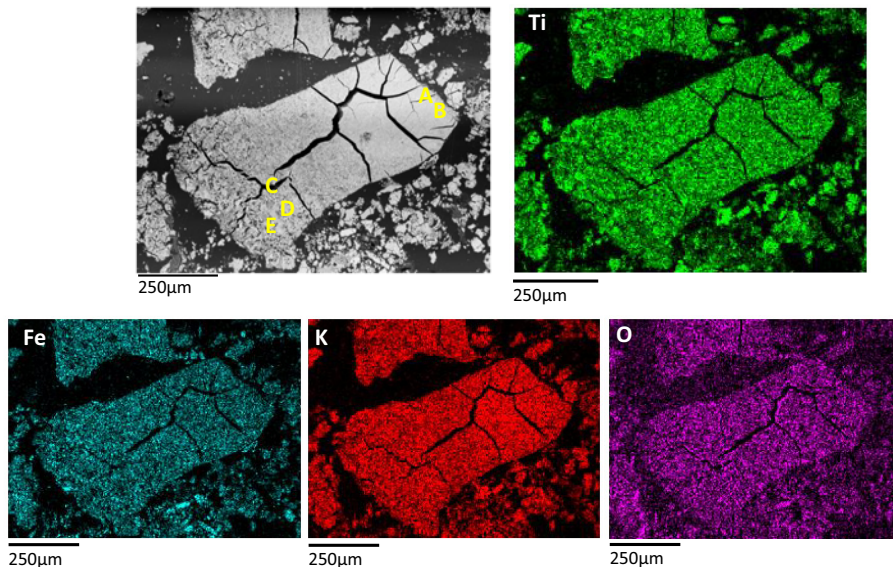


Figure 3. Backscattered SEM image and elemental mapping of water leached residue after roasting of ilmenite with 2 x stoichiometric ratio of KOH.

Table III. Elemental composition of areas A to E in Figure 3 analysed by SEM-EDX.

%Wt	Ti	Fe	O	K	Mn	V
A	21.7	29.8	34.2	14.0	-	0.3
B	30.0	19.6	34.8	15.2	-	0.1
C	22.8	26.4	36.7	13.4	0.3	0.3
D	30.0	21.8	32.6	15.3	-	0.4
E	41.4	5.7	35.9	16.7	-	0.4

Effect of roasting with NaOH ilmenite particle microstructure

Backscattered SEM image of ilmenite roasted with 2 times stoichiometric amount of NaOH and then water leached is presented in figure 4. Similarly to the particle observed when roasting with KOH, it can be seen that there are transgranular cracks within the microstructure of the particle. However, these appear to be less extensive than when using KOH and this may be because of the larger atomic size of K⁺ ions when compared to Na⁺ ions - as both diffuse through the ilmenite lattice [6]. It can also be seen that there are light grey and dark grey phases present within the

particle. Elemental mapping shows that this is due to segregation of an iron-rich phase and a titanium rich phase. Removal of iron is necessary to upgrade the TiO₂ content of ilmenite. The SEM-EDX results, presented in table IV, clearly show that the dark grey phase (Areas A, C and E in Table IV) contains more titanium and a limited amount of iron. Whereas the light grey phase (Area D in Table IV) contains more iron with less titanium present. This agrees with the XRPD patterns which showed segregation of alkali ferrite but also indicated the presence of Na-Fe-Ti-O ternary phases. Analysis of the edge of the transgranular crack (Area B on table IV) shows that there is significantly more iron present than titanium.

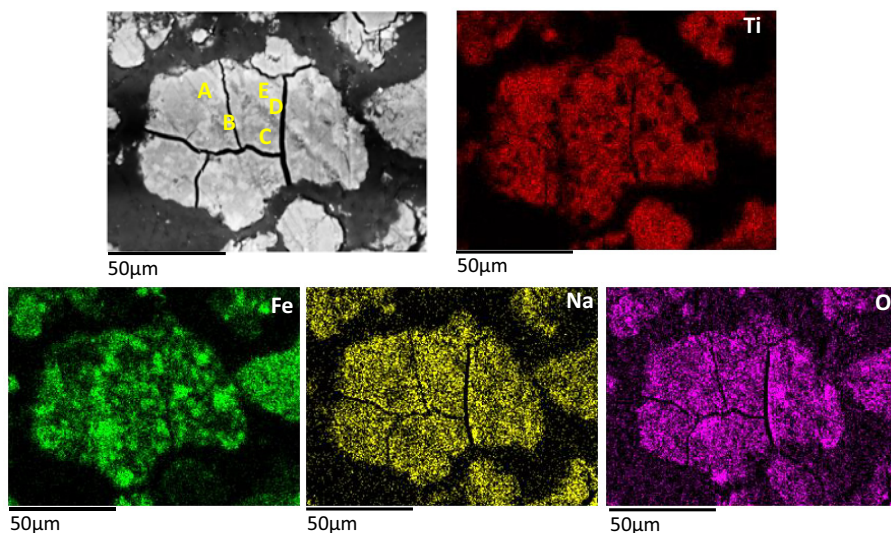


Figure 4. Backscattered SEM image and elemental mapping of water leached residue after roasting of ilmenite with 2 x stoichiometric ratio of NaOH.

Table IV. Elemental composition of areas A to E in Figure 4 analysed by SEM-EDX.

%Wt	Ti	Fe	O	Na	Mn	V	Al
A	42.4	9.4	37.5	10.8	-	-	-
B	13.8	50.5	26.6	8.3	0.2	-	0.6
C	40.3	15.4	34.0	9.8	-	0.3	-
D	4.5	63.2	23.5	8.6	-	0.2	-
E	46.2	8.2	34.1	10.9	-	0.5	0.2

Conclusion

Oxidative roasting of ilmenite with NaOH or KOH lead to the formation of a liquid phase as demonstrated by the fusion of the roasted sample to the crucible. The XRPD patterns for the residues obtained from NaOH roasting showed that the phase equilibria calculations performed

using FACTSage were partially accurate in predicting experimental results. The microstructure analysis for the water leached residues after roasting with either KOH or NaOH showed that the both alkali salts resulted in the formation of transgranular cracks, with KOH causing more cracks. There was segregation of the iron when roasting ilmenite with NaOH but this was not the case when using KOH.

Acknowledgements

The authors acknowledge the financial support from the EPSRC standard grants ([GR/T08074/01](#) and [GR/L95977/01](#)) and PhD studentships for research which were initiated in 1997 at the University of Leeds. AJ also acknowledges the support from the European Union's Marie Curie Fellowship grant number [331385](#) for Dr. Sanchez-Segado and from the NERC's Catalyst Grant reference [NE/L002280/1](#).

References

1. Auer, G., et al. (2000). Pigments, Inorganic, 2. White Pigments. Ullmann's Encyclopedia of Industrial Chemistry, Wiley-VCH Verlag GmbH & Co. KGaA.
2. Foley, E. and K. P. MacKinnon (1970). "Alkaline roasting of ilmenite." *Journal of Solid State Chemistry* 1(3–4): 566-575.
3. Lahiri, A. and A. Jha (2007). "Kinetics and Reaction Mechanism of Soda Ash Roasting of Ilmenite Ore for the Extraction of Titanium Dioxide." *Metallurgical and Materials Transactions B* 38(6): 939-948.
4. Lahiri, A. and A. Jha (2009). "Selective separation of rare earths and impurities from ilmenite ore by addition of K⁺ and Al³⁺ ions." *Hydrometallurgy* 95(3–4): 254-261.
5. Manhique, A. J., et al. (2011). "Titania recovery from low-grade titaniferous minerals." *Hydrometallurgy* 109(3–4): 230-236.
6. Sanchez-Segado, S., et al. (2015). "Alkali roasting of bomar ilmenite: rare earths recovery and physico-chemical changes." *Open Chemistry* 13(1).
7. Parirenyatwa, S., et al. "Comparative study of alkali roasting and leaching of chromite ores and titaniferous minerals." *Hydrometallurgy*.
8. Tathavadkar, V. and A. Jha (2004). The effect of molten sodium titanate and carbonate salt mixture on the alkali roasting of ilmenite and rutile minerals. VII International Conference on Molten Slags Fluxes and Salts.
9. Roine, A. and H. Outokumpu (2002). "Chemistry for Windows: Chemical Reaction and Equilibrium Software with Extensive Thermodynamical Database, Version 5.1, User's Guide." Outokumpu Research Oy, Finland.
10. Bale, C., et al. (2002). "FactSage thermochemical software and databases." *Calphad* 26(2): 189-228.

PRECIPITATION BEHAVIOR OF TITANIUM BEARING BLAST FURNACE SLAG

HU Meilong^{1*}, QU Zhengfeng¹, LV Xuewei¹, GAN Yunhua^{2*}

1. College of Materials Science and Engineering, Chongqing University, Chongqing 400044, China

2. School of Electric Power, South China University of Technology, Guangzhou, 510640, China;

Keywords: Titania, Basicity, Precipitation behavior, Titanium bearing BF slag

Abstract

Effect of titania content and the basicity on precipitation behavior of bearing titanium blast furnace slag have been investigated with confocal scanning laser microscope. The results show that $\text{Ca}_2\text{MgSi}_2\text{O}_7$ and $\text{Ca}_2\text{Al}_2\text{SiO}_7$ are the main phases CaTiO_3 crystallized from the molten slag with 10 mass percent TiO_2 . While there is only one phase crystallized when the mass percent of TiO_2 reaches 30%. On the other hand, $\text{CaMg}_{0.39}\text{Al}_{0.87}\text{Ti}_{0.48}\text{Si}_{1.26}\text{O}_6$, CaTiSiO_5 , $\text{CaMgSi}_2\text{O}_6$ are the main crystallization phases when the basicity is 0.8, which differs from the thermodynamics calculation. It is suggested that such a difference is due to the complicated crystallization of the multiple slag under large cooling rate. When the slag basicity is 1.1, which equals to industry basicity, the crystallization phase is CaTiO_3 due to the crystallization temperature of CaTiO_3 is higher than other phases.

Introduction

Panzhuhua-Xichang area has abundant vanadium-titanium magnetite ores, which accounts for more than 90% titanium resource in China. However, the current production process results in more than 50% titanium finally gathers in the blast furnace (BF) slag in which the titanium content in terms of TiO_2 in slag can be up to 23%. The high titanium content has a big influence on the utilization of the slag, especially due to its high melting point phase. The rich-titanium phase (perovskite) effects on the slag property and thus causing difficulty for extraction of titanium [1,2]. On one hand, CaO mostly exists as perovskite with TiO_2 in high titanium-bearing BF slag, which in turn makes the slag unsuitable to be used as cement like the normal BF slag. On the other hand, it has been challenging for the extraction of valuable secondary titanium resource from the slag. Historically, it was considered to be a promising technology by gathering titanium into perovskite. However, the perovskite yield is rather low owing to the adverse effects of the fine and uneven perovskite grains on the mineral separation. Therefore, it is necessary to study the crystallization behavior of perovskite in high titanium-bearing blast furnace slag.

Confocal laser scanning microscope (CLSM) has been successfully used to study the high-temperature behavior of slag system. Jung *et al.* observed the crystallization behavior of a calcium-aluminate system with various MgO content, $\text{CaO}/\text{Al}_2\text{O}_3$ ratio and cooling rates using CLSM [3]. The results indicates a change in primary phase and crystal morphology from dendrites

* Corresponding author: HU Meilong, hml@cqu.edu.cn; GAN Yunhua, ganyh@scut.edu.cn;

to faceted crystals to columnar crystals in the composition range. Jung *et al.* also investigated the effect of FeO concentration on the crystallization of high-temperature CaO–Al₂O₃–MgO–FeO melts^[4]. Continuous cooling transformation (CCT) and time–temperature transformation (TTT) diagrams were plotted for different phases crystallized during the solidification, and the morphology of the primary crystals was determined. Orrling *et al.* studied the role of alumina particle in SiO₂–CaO–Al₂O₃–MgO slag by CLSM^[5]. Semykina *et al.* observed the crystal growth of liquid FeO–CaO–SiO₂ slag during oxidation by using CLSM^[6]. Sridhar and Cramb described the kinetics of Al₂O₃ dissolution in the CaO–MgO–SiO₂–Al₂O₃ slag with CLSM. Study about of the precipitation behavior of the titanium bearing BF slag using CLSM remains few^[7].

The main aim of current study is to clear the effect of titania content and basicity on the precipitation behavior of the high titanium bearing BF slag (TiO₂>10 mass %).

Materials and Sample Preparation

To simplify the crystallization process and eliminate the impact of minor phases in industry slag such as TiC, the synthesized slag was used. The slag was prepared by pre-melting of 100g of powder mixture of chemical reagent with grade of CaO (98 pct), MgO (98 pct), SiO₂ (99 pct), TiO₂ (99 pct) and Al₂O₃ (98 pct), respectively. The aimed compositions refer to the industrial slag composition are shown in Table I. The slag was also analyzed by X-Ray fluoroscopy, and the results given in Table I shows that there is small deviation with the designed composition. The chemical reagent powder was mixed after drying at 373K (100 °C) for 6h. Then the mixed powder was put into a molybdenum crucible (50mm in inner diameter and 80mm in height) and melted with protective argon atmosphere at 1723K for 1h in MoSi₂ furnace to ensure the slag was homogenized. After melting, the slag was cooled against a copper plate. Subsequently, the slag was broken, incised and polished into small slag samples in a wafer shape of 7mm in diameter and 3mm in height. the slag sample was cleaned in ultrasonic cleaning apparatus for 10 min before running the CLSM study.

Apparatus and Procedure

The crystallization of synthesized titanium-bearing BF slag was observed in-situ by CLSM equipped with an infrared furnace (Lasertec, VL2000DX) which enables real-time in-situ observation at high temperature (up to 1973 K) of transient phenomena. The melting and solidification of the slag sample took place in a platinum crucible (inner diameter of 8mm and height of 5mm) under an argon atmosphere in the CLSM (Ar>99.999%). The platinum crucible was put on a platinum holder equipped with an R-type thermocouple in the infrared furnace. The halogen lamp irradiates light toward the golden cladding layer on of the reaction furnace chamber that reflects the energy towards the focal plane of the crucible to rapidly heat the slag sample. Prior to heating, the infrared furnace was evacuated and back-filled with argon alternatively thrice to remove the air from the furnace. The moisture and oxygen content in the argon were removed by using the purifier provided with the CLSM. After the sample reached thermal equilibrium, the melt was cooled at a controlled rate, and video images of the slag surface were collected (25 frame per second, 1920×1080). The temperature and time were recorded on the images, and this information was later used to analyze the results. The temperature accuracy was confirmed by melting experiments of pure copper (melting point: 1356

K) and pure nickel (melting point: 1726 K). In order to get the nucleation and growth of dendrite, a small undercooling based on the theoretical calculation was set to get close to the isothermal crystallization condition. Furthermore, the cooled sample were examined using X-ray diffraction (XRD: D/max 2500PC).

Thermaldynamics calculation

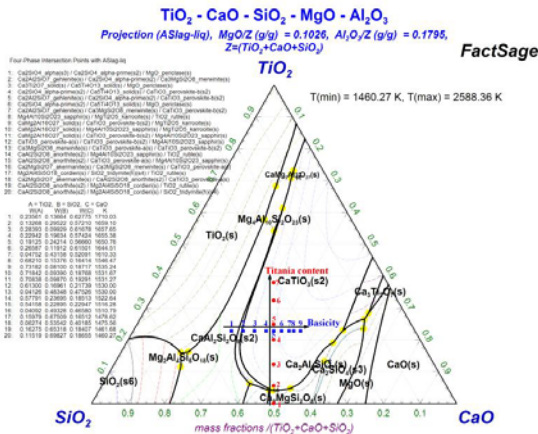


Fig.1 Diagram calculated by FactSage of titanium bearing BF slag with different titania content and basicity

In Fig 1, number 1 to 9 on the horizontal line represents different basicity from 0.5 to 1.3 shown as in table 1. From the diagram it can be seen that when the TiO_2 content in the slag keeps a certain value about 23%, $CaAl_2Si_2O_8$ would firstly crystallized. Namely, when the basicity smaller than 0.7, CaO combines with Al_2O_3 and SiO_2 to form $CaAl_2Si_2O_8$ rather than form $CaTiO_3$ with TiO_2 . It can be predicted that the activity of CaO in this titanium bearing BF slag decreases with decreasing of the basicity of the slag. When the CaO content increases and the basicity is more than 0.7, $CaTiO_3$ is able to form. It can be concluded that it is beneficial to have higher basicity in order to form $CaTiO_3$. It is almost similar with the experiment results at lower basicity due to the experiment were carried out under super cooling condition. Namely, when the cooling rate is much higher the mixed phases crystallizes, such as $CaTiSiO_5$, $CaMgSi_2O_6$, $CaMg_{0.39}Al_{0.87}Ti_{0.48}Si_{1.26}O_6$, from the molten slag at low basicity rather than single phase rutile. With basicity of the slag increasing $CaTiO_3$ gradually becomes the main phase crystallized from the molten slag when the basicity is higher than 0.7.)

Number 1 to 7 in vertical line in the phase diagram shown in Fig.1 indicates different TiO_2 content from 0 to 30%, which were chosen for experimental study and the compositions are shown in Table 2. It can be observed that $CaAl_2Si_2O_8$ firstly crystallizes when basicity in the slag keeps constant value of 1.0. Obviously, CaO reacts with SiO_2 and Al_2O_3 to form $CaAl_2Si_2O_8$

easily instead of when TiO_2 content (mass fraction) smaller than 0.4. It can be supposed that the activity of CaO in such slag become smaller with the increase of TiO_2 content. Until CaO content decreased and TiO_2 content more than 0.4, CaTiO_3 (CaTiO_3) starts to form. It can be interpreted as the higher TiO_2 content is beneficial to the reaction of CaO with Al_2O_3 and SiO_2 and higher TiO_2 content is for the formation of CaTiO_3 . As the experiment were conducted under super cooling condition, the results of the phase diagram calculation is similar with the experiment results at lower TiO_2 content. Namely, when the cooling rate is much higher the mixed phases crystallizes, such as $\text{CaMgSi}_2\text{O}_6$, $\text{Ca}(\text{Ti},\text{Mg},\text{Al})(\text{Si},\text{Al})_2\text{O}_7$, from the molten slag at lower TiO_2 content. With TiO_2 increasing CaTiO_3 gradually becomes the main phase crystallized from the molten slag when TiO_2 content is higher than 0.4.

Table I . The chemical composition of slag with different basicity

Composition (wt.%)						
No.	CaO	SiO ₂	MgO	Al ₂ O ₃	TiO ₂	C/S
1	18.3	36.7	8.0	14.0	23.0	0.5
2	20.6	34.4	8.0	14.0	23.0	0.6
3	22.6	32.4	8.0	14.0	23.0	0.7
4	24.4	30.6	8.0	14.0	23.0	0.8
5	26.0	29.0	8.0	14.0	23.0	0.9
6	27.5	27.5	8.0	14.0	23.0	1.0
7	28.8	26.2	8.0	14.0	23.0	1.1
8	30.0	25.0	8.0	14.0	23.0	1.2
9	31.0	24.0	8.0	14.0	23.0	1.3

Table II. The chemical composition of slag with different amount of TiO₂

Compositions (wt.%)						
No.	CaO	SiO ₂	MgO	Al ₂ O ₃	TiO ₂	C/S
1	39.0	39.0	8.0	14.0	0	1.0
2	36.5	36.5	8.0	14.0	5.0	1.0
3	34.0	34.0	8.0	14.0	10.0	1.0
4	31.5	31.5	8.0	14.0	15.0	1.0
5	29.0	29.0	8.0	14.0	20.0	1.0
6	26.5	26.5	8.0	14.0	25.0	1.0
7	24.0	24.0	8.0	14.0	30.0	1.0

Results and discussion

Effect of titania content

Fig.2 shows the isothermal crystallization process of the pentabasic titanium bearing BF slag with 10% TiO_2 (number 3 in table II) by CLSM at 1100°C. The initial crystalline phase is equal-axis crystal, and then the crystal grows and liquid phase decreases with increasing of the cooling time. The integrated crystallization and the crystal growth process have not been observed due to uncertainty of the initial crystallization location.

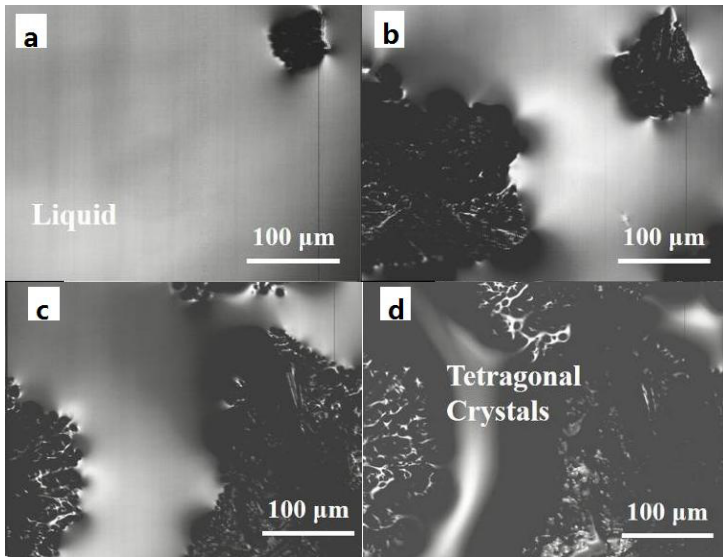


Fig. 2. The crystallization process of the slag with 10% TiO_2 .

Fig.3 shows the isothermal crystallization process of the pentabasic titanium bearing BF slag with 20% TiO_2 at 1100°C . As shown in Fig.3(a), white spot crystals appear at the beginning of the crystallization. When the isothermal crystallization time increases, white spot crystals grow up gradually and then become irregular snow spots, as shown from Fig.3(b) to Fig.3 (c). Then the dendritic crystals appear in Fig.3(d). The white rhombus crystal can be observed in Fig.3(d) during precipitation, which may be the crystallization morphology of the faceted crystal sown in upper-right corner of Fig.2(b). According to the crystallization morphology of quarternary BF slag without titanium, it can be inferred that this crystal is melilite. From Fig.3(e) to Fig.3 (f), it can be seen that the dendrite grows slowly and the dendrite size has not changed obviously, but the thickness of the dendrite increases. Two phenomena can be observed from the crystallization process, one is white spot crystal coalesces, which may be caused by spontaneous gathered and squeezed out by dendrite do not understand, the coalescence is rather natural, fig3 does not show the case when dendrite squeeze the liquid, it could be the case if those small crystal forms in between two large dendrites such that the liquid will shrink, but in that case segregation should be considered which will influence the driving force and thus the number of nuclei. The other seems a transition process, needle-shaped crystal is peeled off from dendrite constantly, finally, it attached to the white spot crystal. The needle-shaped crystal may be the small dendrite peeled off from dendrite during the dendrite growth, and white spot crystal may be grains just precipitate but not grow up. They are the same phase so that the transition for small needle-shaped has happened. According to the aforementioned speculation, all these three crystals are CaTiO_3 . With the further increase of the cooling time, the faceted crystal begin to crystallization shown as Fig.4(e)

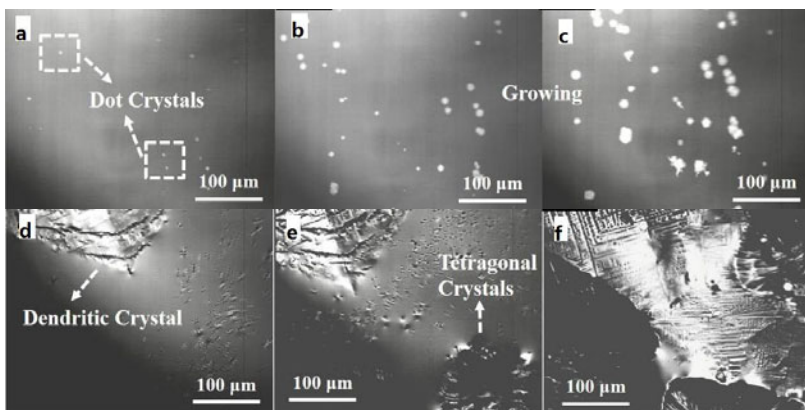


Fig. 3. The crystallization process of the slag with 20%TiO₂

Fig.4 shows the isothermal crystallization process of the pentabasic titanium bearing BF slag with 30% TiO₂ by CLSM at 1100°C. White spot crystals emerges during the crystallization process of the BF slag, which crystalline morphology is identical to the initial crystalline morphology of the isothermal crystallization process of the slag with 20% TiO₂. When the crystallization process reached to a certain time, the slag coagulated completely, shown in Fig.4.(c).

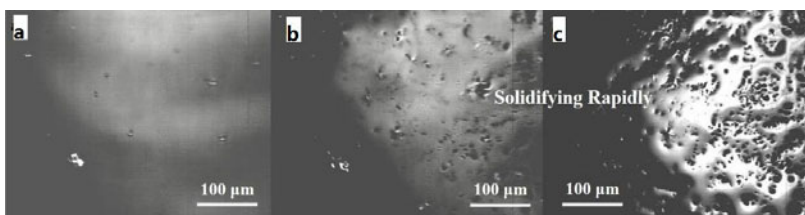


Fig. 4.The crystallization process of the slag with 30%TiO₂

Fig.5 shows the XRD results of the BF slag isothermally crystallized at the different TiO₂ content including akermanite (Ca₂MgSi₂O₇) and gehlenite(Ca₂Al₂SiO₇), which are both belong to melilite. However, it is inconsistent with the calculation results by FactSage software. Based on the aforementioned investigation, the crystal which belongs to tetragonal system, looks like equal-axis plate, is identical to the morphology observed with CLSM, so the equal-axis crystal observed in the microscope should be melilite.

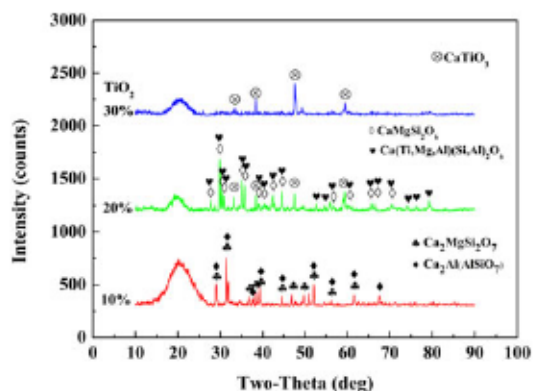


Fig. 5 XRD patterns of slag isothermally crystallized at different TiO_2 content

Three phases have formed during the isothermal crystallization process of the pentabasic titanium bearing BF slag with 20% TiO_2 at 1100°C , among which two phases are both clinopyroxene, $\text{CaMgSi}_2\text{O}_6$ and $\text{Ca}(\text{Ti},\text{Mg},\text{Al})(\text{Si},\text{Al})_2\text{O}_7$, and the third phase is CaTiO_3 . According to the XRD results shown in Fig.5, CaTiO_3 is the unique phase in isothermal crystallization process of the pentabasic titanium bearing BF slag with 30% TiO_2 with isothermally solidified at 1100°C .

Effect of basicity

Fig.6 shows the crystallization process from molten titanium bearing BF slag when the basicity is 0.6. When the temperature decreases to 1100°C crystals appear on the surface of the molten slag. The number of the crystals increase with increasing of the holding time until the molten slag solidify totally. There is no well defined morphology of solid phaseduring the crystallization. The XRD results show that the crystallization phase is CaTi_2O_3 , shown as Fig.7.

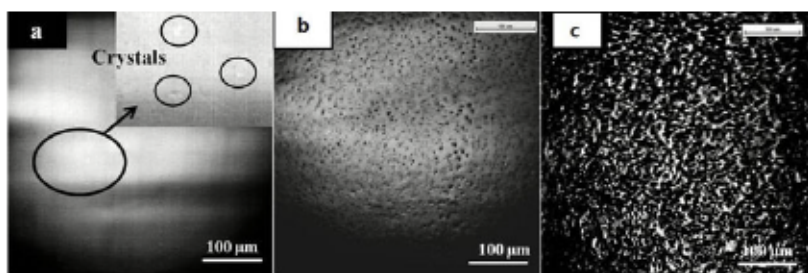


Fig. 6 The crystallization process of slag with basicity of 0.6

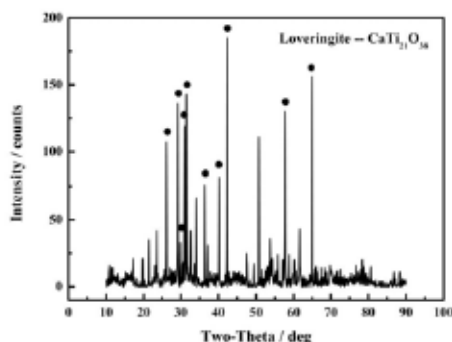


Fig.7 The XRD pattern of slag sample with basicity of 0.6 after CLSM experiment.

Fig.8 shows the crystallization process from molten titanium bearing BF slag when the basicity is 0.8. The crystallization process is more observable than that of the slag basicity is 0.6. When the temperature decreases to 1100°C, small crystals appear and the amount of the small white crystallites increases with increasing of the holding time. These small crystals finally combine with each other reforming the big crystals. With the increase of the holding time another phase appears from the molten slag and their morphology are diamond. The diamond crystallites grow and the small white crystallites gather together. Finally, the small white crystallites disappear. The XRD results shows that the crystallization phases is complicated including $\text{CaMg}_{0.39}\text{Al}_{0.87}\text{Ti}_{0.48}\text{Si}_{1.26}\text{O}_6$, CaTiSiO_5 , $\text{CaMgSi}_2\text{O}_6$, shown as Fig.9. CaTiSiO_5 belongs to silicate, monoclinic system ; and its cross section is diamond. So the crystals observed in situ probably are CaTiSiO_5 .

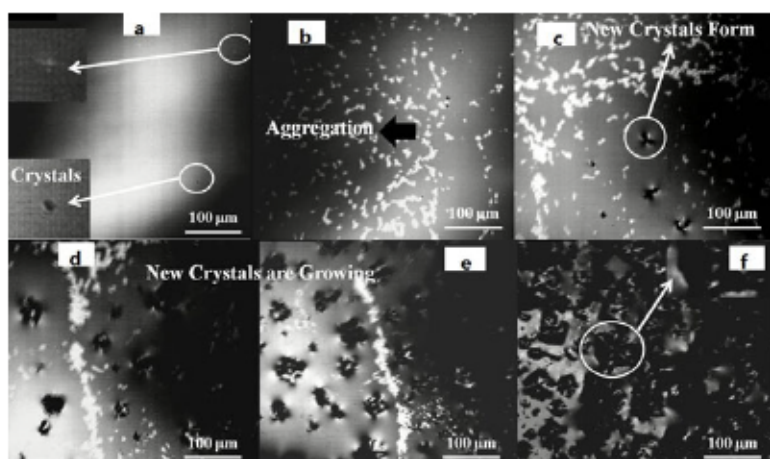


Fig.8 The crystallization process of slag with basicity of 0.8.

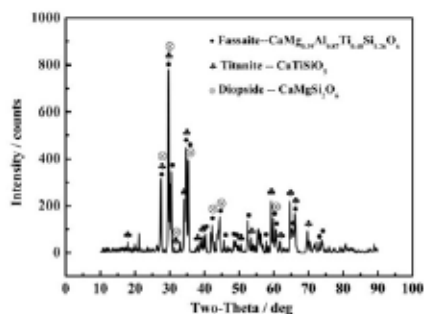


Fig.9 The XRD pattern of slag sample with basicity of 0.8 after CLSM experiment

Fig.10 shows the crystallization process from molten titanium bearing BF slag when the basicity is 1.1. When the temperature of the molten slag decreases to 1325 °C and held at the target temperature. After 3 seconds some dendrites appear and the dendrites grow mainly along certain direction until the impingement happens. The XRD results show that crystallization phase is perovskite, shown as Fig.11.

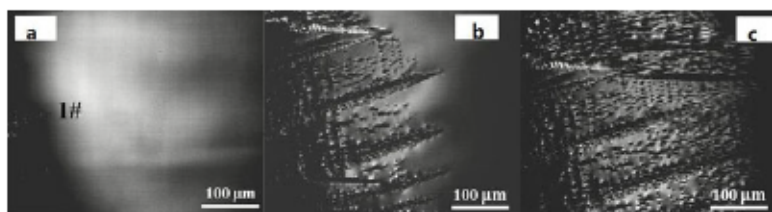


Fig.10 The crystallization process of slag with basicity of 1.1

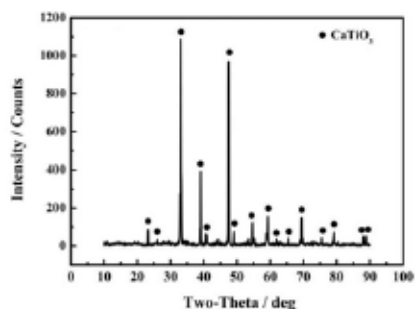


Fig. 11 The XRD pattern of slag sample isothermally crystallized with basicity of 1.1.

Conclusions

When the basicity of titanium bearing BF slag is lower than 0.5, CaO prefers to combine with SiO₂ in the presence of Al₂O₃ and MgO, rather than with TiO₂ in the slag. With the increase of basicity, CaO starts reacts with TiO₂ and forms CaTiSiO₅, CaMg_{0.39}Al_{0.48}Si_{1.26}O₆ and so on. Specially, CaTiO₃ is the single phase crystallized from titanium bearing BF slag when the basicity reaches 1.1 due to its much higher crystallization temperature. When the TiO₂ content increases from 0 to 30%, the primary solidified phase of the BF slag transits from faceted melilite to dendritic CaTiO₃ crystals. Melilite is the primary phase during crystallization process of the BF slag when the TiO₂ content ranges between 0 and 10%. On the other hand, CaTiO₃ is the unique crystalline phase for a TiO₂ content of 30%. Thus, TiO₂ content in BF slag has significant influence on the crystalline phase, crystal morphology and other solidification behaviors.

ACKNOWLEDGEMENTS

The authors are especially grateful to the project 51404044 supported by National Natural Science Foundation of China and project No. 0211002103014 supported by doctoral fund project.

References

1. Z.Z. Guo, T.P. Lou, L. Zhang, L.N. Zhang, and Z.T. Sui: *Acta Metall. Sin.*, 2007, vol. 20 (1), pp. 9–14.
2. L. Yuhai, L. Taiping, X. Yuhu, and S. Zhitong: *J. Mater. Sci.*, 2000, vol. 35 (22), pp. 5635–37.
3. S.S. Jung and I.L. Sohn: *Metall. Mater. Trans. B*, 2012, vol. 43B, pp. 1530–40.
4. S.S. Jung and I.L. Sohn: *J. Am. Ceram. Soc.*, 2012, vol. 96 (4), pp. 1309–16.
5. C. Orrling, S. Sridhar, and A.W. Cramb: *ISIJ Int.*, 2000, vol. 40 (9), pp. 877–85.
6. A. Semykina, J. Nakano, S. Sridhar, V. Shatokha, and S. Seetharaman: *Metall. Mater. Trans. B*, 2011, vol. 42B, pp. 471–6.
7. S. Sridhar and A.W. Cramb: *Metall. Mater. Trans. B*, 2000, vol. 31B, pp. 406–10.

Production of Ceramic Balls by High Temperature Atomization of Mine Wastes

Hyunsik PARK¹, Minchul HA¹, Dong-hyo YANG¹, Jeong-soo SOHN¹ and Joohyun PARK²

¹Urban Mine Department, Korea Institute of Geoscience and Mineral Resources (KIGAM), 124, Gwahak-ro Yuseong-gu, Daejeon, 34132, South Korea

²Department of Materials Engineering, Hanyang University, Ansan, 15588, South Korea,

Keywords: gold tailing, fluxes, melting and atomizing, viscosity

Abstract

Gold tailing, red mud and waste limestones are industrial wastes that are mostly landfilled near the process plants. These increase the environmental risks as well as the necessity of waste management. Recycling of materials has been limited due to the fine particle sizes, heavy metals and unique oxide compositions. The authors investigated the potential utilization of these industrial wastes by melting and granulation technique. As quartz, hematite, alumina and lime consist more than 90wt% of mine wastes, CaO-Fe₂O-Al₂O₃-SiO₂ quaternary oxide system was applied to the thermodynamic calculations. Compositions of molten oxides were designed considering the lowest melting temperature and the adequate viscosity for atomization. Samples were melted by high frequency induction furnace then the atomization was carried out by air blowing technique. Viscosities of the melts were measured to quantify the optimum melting and atomization condition. Size distribution of the produced ceramic balls was investigated to estimate potential of the product to be used as abrasive materials.

Introduction

Mine wastes such as waste rock and tailings have the potential risk to environment due to the elution of heavy metals and scattering of dusts. Tailings are usually discharges as slurry that can be hardly recycled for construction materials. Fine particle size under 100µm and high quartz contents limits the direct usage of tailings. Red mud is a byproduct from alumina refining process from bauxite. Concentrated radioactive elements and heavy metals in red mud increase concerns on general utilization. Waste limestone is commonly produced from limestone mine that has low calcite content below 40wt%. As individual materials, these components cannot be utilized for higher value added products, but optimal combination of these mining wastes using pyro-metallurgical methods may provide a solution for simultaneous consumption of these materials and additional economic benefits as products. The major components of gold tailing, red mud and waste limestone are quartz, hematite, alumina and lime. These four oxides constitute most of the iron and steelmaking slags produced from the ferrous industry.[1-2] Since the thermo-physical properties and refining capabilities of the ferrous slag systems have been extensively studied for the past century[3], existing thermodynamic data available in literature

can facilitate the study of similar oxide systems to estimate possible combinations of selected oxides and its optimal recycling conditions.

This study investigates ceramic ball production from gold tailing by using red mud and waste limestone as fluxes. Raw materials were quantitatively analyzed using XRF (x-ray fluorescence) spectroscopy. Optimal composition for melting and atomization was determined from thermodynamic calculations obtained from phase diagrams. Considering the main components of the mining wastes, the CaO-Fe₂O₃-Al₂O₃-SiO₂ quaternary oxide system was used to identify optimal mixing regions. Different ratios of gold tailing, red mud and waste limestone were tested to find adequate composition for ceramic ball production. High temperature melting was conducted at 1673K then atomization by air blowing was followed. Size distribution was evaluated by sieving to estimate potential of the product to be used as abrasive materials.

Experimental

Industrial wastes obtained were used as raw materials for the experiments. Tailing was supplied by local gold mine that has a beneficiation process. Red mud obtained from domestic alumina plant operated by Bayer process and waste limestones from local cement industry were used as fluxes. Quantitative compositional analysis was conducted by X-Ray fluorescence (XRF) spectrometry as shown in **Table I**. Gold tailing is mostly comprised by silica while alumina and hematite constitute red mud. Calcium oxide was dominant in waste limestone, but calcite is accurate form considering 35wt% of ignition loss due to calcination.

Table I. Quantitative compositional analysis of raw materials by XRF analyzer

	SiO ₂	Al ₂ O ₃	CaO	Fe ₂ O ₃	Na ₂ O	TiO ₂	MgO	K ₂ O	Ig.loss
GT	87.7	5.97	0.09	1.06	0.28	0.2	0.14	1.29	3.21
RM	12.4	24.8	4.26	30.8	8.57	6.72	-	-	12.37
WL	12.4	2.18	42.6	0.92	0.01	0.1	2.59	0.91	35.35

Moisture in the powder was removed by drying gold tailing, red mud and waste limestone at 473K for 24 hours. Fine particles sized under 100µm were sieved and used for the pelletizing. Raw materials were mixed in a rotating drum for 24 hours to obtain homogeneity. Mixed powders were agitated in a stirring mixer with addition of purified water to supply adequate moisture to paste. Samples were pelletized by hand rolling to make spherical shape with 100mm diameter. Pellets were dried at 473K for 7 days to eliminate the residual moistures.

Oxide melts corresponding to the major components of the mining waste was carefully designed based on the CaO-Fe₂O₃-Al₂O₃-SiO₂ quaternary system.[3] Lower melting temperatures of the melts were selected for the lower energy consumption process.

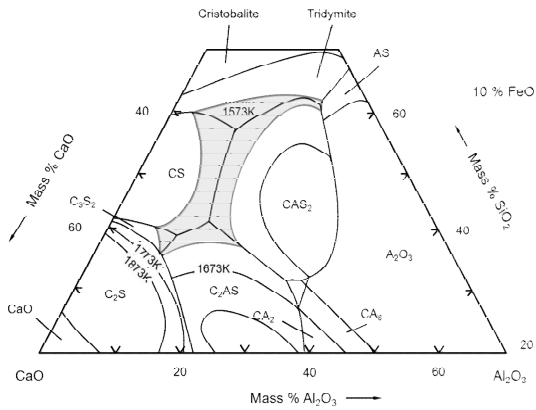


Figure 1. CaO-10Fe_tO-Al₂O₃-SiO₂ pseudo-ternary oxide system by FactSage[®]

Figure 1 shows the liquidus line of 1573K in the CaO-10Fe_tO-Al₂O₃-SiO₂ pseudo-ternary phase diagram. For the present sample preparation condition, the redox-equilibrium reaction of iron oxide in the CaO-10Fe_tO-Al₂O₃-SiO₂ pseudo-ternary system redistributes the Fe²⁺ / Fe³⁺ ratio of the Fe₂O₃ contained mainly in the red mud. Wüstite based compounds can appear depending on the basicity (CaO/SiO₂ mass ratio) in the partially liquid phase.

Compositions of samples mixed by ratio of gold tailing, red mud and waste limestone are shown in **Table II**. Mixing ratio of 2:1:1, 1:1:1 and 1:1:2 were selected to simplify raw materials preparations. Basicity that stands for the physical properties of the melts was described as ratio between CaO and SiO₂. Amphoteric oxides such as Al₂O₃, Fe₂O₃ were assumed to behave as neutral on slag basicity.

Table II. Compositions of samples mixed by ratio of GT : RM : WL

GT : RM : WL	SiO ₂	CaO	Al ₂ O ₃	Fe ₂ O ₃	Na ₂ O	TiO ₂	MgO	C/S
Sample #1 (2 : 1 : 1)	55.6	18.95	11.2	8.8	2.45	1.93	1.1	0.34
Sample #2 (1 : 1 : 1)	42.93	25.27	12.8	11.73	3.27	2.57	1.43	0.6
Sample #3 (1 : 1 : 2)	37.45	36.7	10.53	8.8	2.15	1.92	2.45	1

Dried pellets 100mm in diameter were introduced into the pure grade graphite crucible. 12 pieces of pellets weighing 70 to 80 g were used for single trial of the experiment. High frequency induction furnace with 3000 Hz and output capacity of 50 Kw was used for high temperature melting. Temperature was increased to 1673K in 30 minutes and the duration time was fixed as 30 minutes to confirm molten state. The furnace system is manufactured for tilting and pouring of the melts and the compressed air is designed to blow from the bottom of the runner. Viscosities of the molten oxides were measured by concentric cylinder rotation method [4] in the temperature ranges of 1473K and 1773K.

Results and Discussion

Three samples containing different ratio of gold tailing, red mud and waste limestone were tested to optimize the conditions for melting and atomizing. Molten state was confirmed by stirring with graphite stick when the temperature reached at 1673K. Physical property of the melts was qualitatively estimated by sampling. Sample 1 containing the highest amount of silica showed glassy and sticky behavior that was elongated on graphite stick's surface. While the other samples were sloppy liquids that flowed easily on the stick in molten state.

Video recording was conducted during the overall melting and atomization procedure. Tilting and pouring of the furnace were carried out followed by air blowing at the bottom of the tapping nozzle. Still images of atomizing experiments are showed in **Figure 2**. The images show the spray of the melt particles indicating different atomizing behavior dependent on the composition.

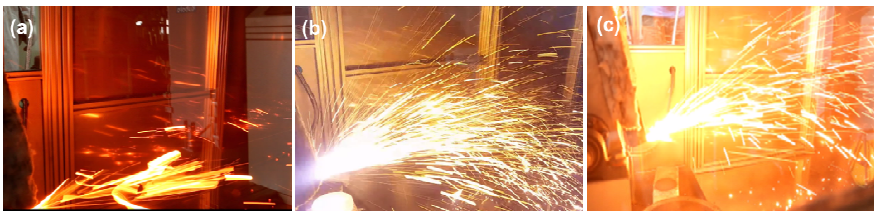


Figure 2. Still images of atomizing experiments (a) 2:1:1, (b) 1:1:1, (c) 1:1:2 at 1673K

When tilting and pouring, melt from sample 1 did not easily flow on the runner. Highly viscous melt was tapped irregularly as bulk phases. As shown in **Figure 2(a)**, stretched lines are observed due to the elongated melts. After atomizing, quenched bulks and glass fibers were seen at the bottom of the cage that indicated poor granulation performance. However, samples containing lower quantity of silica showed better atomizing behavior. In **Figure 2(b)** and **2(c)**, ceramic balls are seen as showers of spray. Molten oxides are easily poured in cases of sample 2 and 3 due to the low viscosity. When the melts encounters blowing air, they rapidly transforms into particles that spread widely at atmosphere.

Viscosity of the oxide melt is the key factor that determines atomizing behavior in air blowing. Concentric cylinder rotation method by using platinum rod was employed for viscosity

measurement. **Figure 3** shows the change of the viscosities dependent on temperatures.[4] Viscosity of sample 1 with silica rich composition rapidly increases as the temperature is lowered below 1773K. Highly viscous behavior is observed in sample 1 that explains poor atomization in **Figure 2**. In contrast, viscosity of sample 2 with GT:RM:WL ratio of 1:1:1 increases slowly until the melt reaches at 1473K. Sample 3 containing the largest amount of CaO shows the lowest viscosity until 1673K that is the indication of smooth atomization. Minimum viscosity required for atomization at current experimental setup is considered to be 15poise. Smooth atomization is possible under 15 poise of viscosity that is available above 1673K.

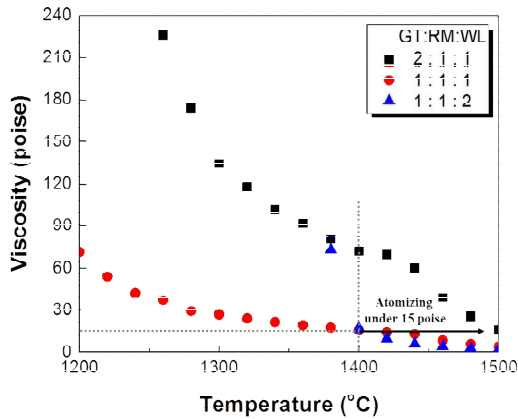


Figure 3. Viscosity of molten oxides made by mixture of GT, RM and WL

Produced ceramic balls were sieved and classified into various sizes as shown in **Figure 4**. Particle sizes from 0.5 to 5.6mm are known to have the highest economical value. Ceramic balls obtained from mine wastes have similar features as commercial products. Granulated copper slag is a typical product used for abrasives, aggregates and water treatment.[5]

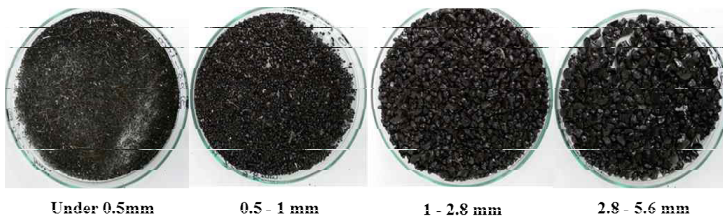


Figure 4. Digital micrograph of ceramic balls (GT:RM:WL = 1:1:1) atomized at 1673K

Size distributions of atomized ceramic balls are shown in **Table III**. Sample 1 shows the largest amount of oversized products that is hard to be utilized. High viscosity of sample 1 decreased the capability of atomization that resulted low process efficiency. However, ceramic balls of sample 2 and sample 3 have the highest proportion in the range of 2.8 - 5.6 mm and size under 5.6mm exceed 70wt% of the total products. Ball sized from 1.0mm to 5.6mm constitute the largest amount of the product that has the versatile usage such as abrasives, concrete mixture, aggregates and water treatment media.

Table III. Size distribution of ceramic balls atomized at 1673K

GT : RM : WL	under 0.5 (mm)	0.5 - 1 (mm)	1 - 2.8 (mm)	2.8 - 5.6 (mm)	over 5.6 (mm)	Size under 5.6 mm
2 : 1 : 1	3.82	2.62	16.21	28.14	49.21	50.79
1 : 1 : 1	2.23	4.27	20.22	47.98	25.32	74.68
1 : 1 : 2	1.46	4.59	23.42	48.62	21.90	78.10

Conclusions

Production of ceramic ball by utilizing gold tailing was investigated by pyrometallurgical approach. Red mud and waste limestone were used as fluxes to facilitate melting and atomization. Mixing ratio of gold tailing, red mud and waste limestone were selected as 2:1:1, 1:1:1 and 1:1:2 considering low melting temperature in CaO-Fe₂O-Al₂O₃-SiO₂ quaternary system. Sample with silica rich composition showed a poor atomization, while other samples containing higher amount of lime had smooth atomizing behavior. Viscosities of the melts were investigated to confirm optimal condition. Molten oxide's viscosity need to be maintained lower than 15poise to obtain valuable ceramic balls. Mixing ratios of 1:1:1 and 1:1:2 show fine atomization results with 70wt% of production yield. Ball sized of 2.8 - 5.6mm was the largest proportion which has the highest economic value. The present study provides a solution for simultaneous consumption of industrial wastes and additional economic benefits as products.

References

1. A.K. Biswas: *Principles of Blast Furnace Ironmaking: Theory and Practice*. (Cootha, 1981).
2. E.T. Turkdogan: *Fundamentals of steelmaking*. (Institute of Materials, 1996).
3. Verlag Stahleisen and Verein Deutscher Eisenhüttenleute: *Slag Atlas*. (Verlag Stahleisen, 1995).
4. Hyun-Shik Park, SuSang Park and Il Sohn, *Metallurgical and Materials Transactions B* 2011, vol. 42, pp. 692-699.
5. A. K. Biswas and W.g. Davenport: *Extractive Metallurgy of Copper*. (1994).

PROPERTIES OF BAYER RED MUD BASED FLUX AND ITS APPLICATION IN THE STEELMAKING PROCESS

Yanling Zhang, Fengshan Li, Ruimin Wang

State Key Laboratory of Advanced Metallurgy, University of Science and Technology
Beijing, Xueyuan Road 30, Haidian District, Beijing 100083, China

Keywords: Bayer red mud, thermodynamic properties, dephosphorization, steelmaking

Abstract

Bayer red mud is characterized as highly oxidizing (high Fe_2O_3 content) and highly alkaline (high Na_2O content), which tends to act as a flux and strong dephosphorizer in the steelmaking process. In this study, firstly, the thermodynamical properties of Bayer red mud based flux were predicted including the melting temperature and phosphorus capacity. Further, laboratory experiments on application of Bayer red mud-based flux in hot metal dephosphorization. The effects of influencing factors such as flux composition and basicity were discussed. The results gave necessary basic knowledge for promoting the application of Bayer red mud in the steelmaking process.

Introduction

With the rapid development of alumina industries in China, a large amount of red mud has been produced. Due to the high Na_2O content, red mud has been classified as a hazardous waste. The red mud from Bayer process is rich in Fe_2O_3 , Al_2O_3 , and Na_2O , during which as high as 30%-53% of Fe_2O_3 concentrated and much larger content could be obtained after usual magnetic or gravity separation. Accordingly, Bayer red mud tends to be a kind of ideal iron resource of ferrous metallurgy. Several previous studies^[1-3] have been carried out on extracting Fe element from red mud through direct reduction or indirectly using that as parts of raw materials in ironmaking such as sinter or blast furnace. However, due to the serious lining erosion and nodulation caused by strong vaporization of Na, the actual application of red mud in the above process is extremely limited.

As can be seen, Bayer red mud can be characterized as highly oxidizing (high content of Fe_2O_3) and highly alkaline (high content of Na_2O), which is exactly necessary in the steelmaking process. High content of Fe_2O_3 in Bayer red mud can work as a good slagging flux in addition to provide plentiful iron elements, and Na_2O is a well-known strong dephosphorization/desulfurization agent. Obviously, the possible corrosion of

Na₂O on the lining furnace of BOF is an important consideration. While, due to the special shape of converter: a larger ratio of diameter to height, the erosion caused by vaporization of Na₂O tends to be much less compared with that happened in Blast Furnace, which has a much smaller ratio of diameter to height and gives a much longer way to reduce vaporizing-condensing-nodules of Na₂O. However, besides Fe₂O₃ and Na₂O, some Al₂O₃ and a small amount of TiO₂ are also brought into slag when adding Bayer red mud in steelmaking process. While the research data about the comprehensive and interacting effects of Al₂O₃, Na₂O, and TiO₂ on properties of CaO-FeO-SiO₂ based steelmaking slag available is extremely limited. Therefore, in this study, in order to promote the application of Bayer red mud in steelmaking process, the thermodynamic analysis of the effects of Al₂O₃, Na₂O, TiO₂, and their interactions on the properties of CaO-FeO-SiO₂-based slag was performed. Further, the laboratory experiments on application of Bayer red mud-based flux in hot metal dephosphorization were carried out.

1. Thermodynamics prediction on liquid areas of CaO-SiO₂-FeO (-Al₂O₃-Na₂O-TiO₂) slag system

The phase diagram module of FactSage software was used to simulate the liquid areas of CaO-SiO₂-FeO (-Al₂O₃-Na₂O-TiO₂) slag system at different temperatures. The liquid areas between 1200 °C and 1600 °C in CaO-SiO₂-FeO slag are shown in Fig. 1(a). This suggests that the melting point of the CaO-SiO₂-FeO system decreases with increasing FeO content, shown by the arrows. This supports that the fluidity of the slag as well as the dissolution of lime is usually improved with increasing FeO content in slag.

The composition of initial slag is mostly around point “B” in Figure 1(a). With the progress in steelmaking, the slag composition gradually moves to near point “C”. As shown, that is in the area with melting temperature higher than 1600°C. CaF₂ is often added to improve the fluidity of slag and thus obtain a good separation of steel from slag. However, utilization of CaF₂ has been extremely limited due to its potential environment pollution, and alternative fluxes have to be pursued. The effects of Al₂O₃ and Na₂O on the liquid areas of CaO-SiO₂-FeO system at 1400 °C are shown in Fig. 1(b) and Fig. 1(c), respectively. Fig. 1(d) shows the effect of the mixture of Al₂O₃, Na₂O, and TiO₂ (denoted as “A” in the figure) with a mass ratio of Al₂O₃:Na₂O:TiO₂ = 1:0.25:0.15 (which is roughly estimated based on the typical composition of Bayer red mud in China after accounting for the possible evaporation loss of Na₂O) on the 1400 °C liquid areas of the CaO-SiO₂-FeO system. As shown, with the addition of Al₂O₃, Na₂O, and A, the liquid areas of the CaO-SiO₂-FeO system at 1400 °C is obviously enlarged. Upon adding 10% Al₂O₃ (Fig. 1(b)), 5% Na₂O (Fig. 1(c)), and 10% A (Fig. 1(d)), the liquid areas below 1400 °C (over the range of %CaO/%SiO₂ = 0.8–1.5) is nearly independent of the FeO content. This tends to indicate that it is possible to acquire good fluidity of slag with much lower FeO content, which is of great importance for decreasing iron loss. Furthermore, Fig. 1 shows that with increasing Al₂O₃ (Fig. 1(b)) or A content (Fig. 1(d)),

the 1400 °C liquid areas of the CaO-SiO₂-FeO system obviously moves towards the lower left corner, in the direction of increasing basicity. This indicates that the presence of Al₂O₃ or A can greatly decrease the melting temperature of the CaO-SiO₂-FeO slag with higher %CaO/%SiO₂ value, or it can promote the dissolution of lime in the slag. As known, the removal of phosphorus from steel to slag is an important operation in steelmaking, which thermodynamically needs a slag with higher basicity but kinetically needs a slag with lower melting temperature (good fluidity). This means that the addition of Al₂O₃ as well as Bayer red mud benefits the dephosphorization performance, and it can be expected to effectively prohibit rephosphorization because of the excellent slag situation (higher basicity and good fluidity). Diao's experiments suggested that dephosphorization ratio increased with the addition of some amount of Al₂O₃ and Na₂O into CaO-FeO-SiO₂ slag, and their kinetic models showed that both Al₂O₃ and Na₂O obviously promoted the growth of overall mass transfer coefficient [4]. It agrees reasonably well with this research data.

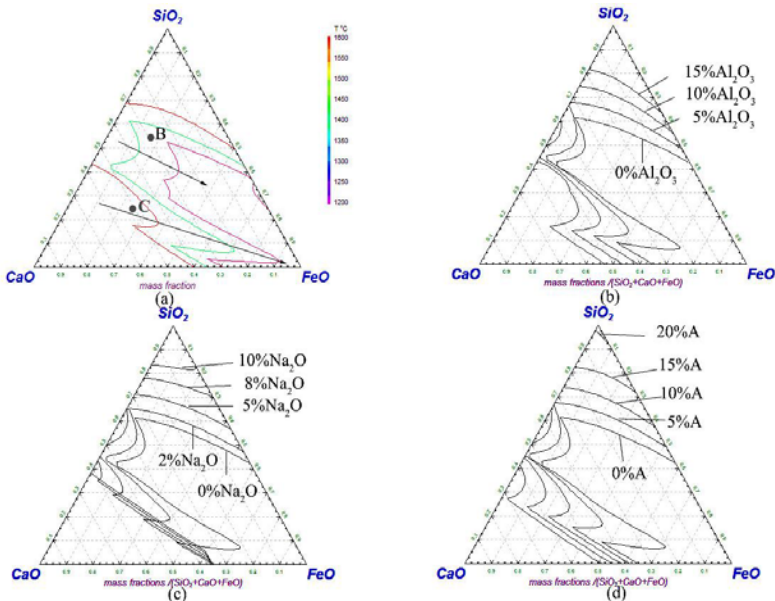


Fig.1. Phase diagram and liquid areas of the CaO-SiO₂-FeO.slag system: (a) phase diagram of CaO-SiO₂-FeO, (b) effect of Al₂O₃ on liquid areas at 1400 °C , (c) effect of Na₂O on the 1400 °C liquid areas, (d) effect of A on the 1400 °C liquid areas.

2. Experiments on hot metal dephosphorization by using Bayer red mud based flux

2.1 Materials

The high-iron red mud used in this study was sampled from Shandong Weiqiao aluminum plant, and its chemical composition determined by XRF is shown in Table 1.

Table1. Main compositions of Bayer red mud, wt%

Compositions	Fe ₂ O ₃	Al ₂ O ₃	SiO ₂	Na ₂ O	TiO ₂	CaO	Others
%	59.09	16.18	10.59	7.59	4.13	0.67	1.75

Some of the experiments were performed in a silicon molybdenum furnace. In this case the main materials used were chemically pure reagents. Saturated molten iron samples with saturated carbon and different P/Si contents were prepared by using reduced iron (AR, Fe \geq 99%), graphite powder (CP, C \geq 99.95%), ferrophosphorus (P=27.50%) and ferrosilicon (Si=98.95%). The dephosphorizer in experiments was mainly made up of Bayer red mud and CaO. Another two runs of experiments were carried out in an induction furnace, during which the industrial pig iron was chosen as main iron material, whose components are listed in Table 2.

Table2. Compositions of industrial pig iron, wt%

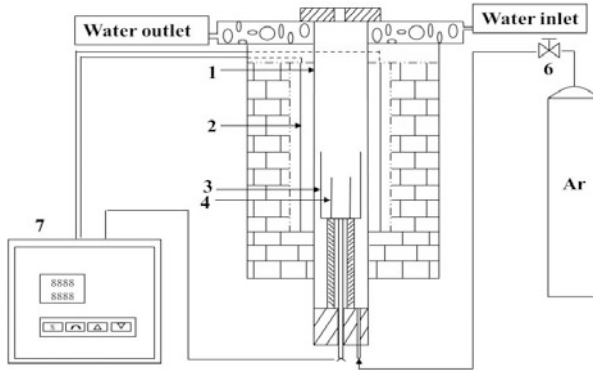
C	Si	Mn	Al	P	S	Ca	Cr
4.4	0.12	0.27	0.07	0.03	0.03	0.02	0.02

2.2 Apparatus and experimental procedure

The structure diagram of silicon molybdenum furnace used for dephosphorization experiments of hot metal pretreatment was shown in Figure 2. Raw materials were firstly thoroughly mixed in a mortar according to the requirements of the initial iron sample (C=4.5%, P=0.12%, Si=0-0.5%). 250 g of the iron sample was placed in an alumina or magnesia crucible (Φ 50 \times 140) and the amount of dephosphorization reagent (mixture of Bayer red mud and CaO) was set as 50 g or 25 g. The experiment was started when the iron sample melted completely. The initial iron sample was taken in a Φ 6 mm tube and the dephosphorizer was added into the sample crucible in three batches. The iron and slag samples were taken out in the end of the experiment and were analyzed after crushing. Another two runs of experiments were performed in a 10 kg induction furnace. The amount of pig iron was about 5 kg each time, and the mass ratio of dephosphorizer (mixture of Bayer red mud and CaO) to iron was about 10%. Firstly, the pig iron was pre-melted in the crucible, after pig iron melted completely the initial iron sample was taken out from the crucible with a Φ 6mm tube. All of the slag was added into the crucible. 25 min later, the iron and slag samples were taken out and analyzed after crushing.

Table 3 shows the specific experimental arrangements. It should be noted that the dephosphorizers of No.1 and No.2 were prepared by using pure oxides while the other ones consisted of Bayer red mud and CaO. The experiments of Nos.1-8 were conducted

in a silicon molybdenum furnace, and those of Nos.9-10 were performed in an induction furnace.



1. Al_2O_3 tube; 2. Heating element; 3. Al_2O_3 Protective crucible; 4. Experimental crucible; 5. Thermocouple; 6. Flowmeter; 7. Temperature control box

Fig. 2 The diagram of silicon molybdenum furnace

Table 3 The experimental scheme of dephosphorization

Experiments	Group	Red mud: $\text{CaO}:(\text{Fe}_2\text{O}_3)$	$[\%P]_0$	$[\%Si]_0$	Slag ratio	Temperature / °C	$[\%P]_f$	η_P
Hot metal pretreatment	1	2:1	0.12	0	0.2	1350	0.075	37.5%
	2	1:1	0.12	0.5	0.2	1400	0.099	17.5%
	3	2:1	0.12	0	0.1/0.2	1350	0.043 /0.022	64.0% /81.93%
	4	1:1	0.12	0.5	0.2	1400	0.098	18.33%
	5	2:1	0.12	0.2	0.1/0.2	1350	0.060 /0.028	49.0% /76.5%
	6	2:1	0.12	0.5	0.1/0.2	1350	0.109 /0.074	8.71% /38.06%
	7	1:1	0.12	0	0.2	1350	0.018	85.0%
	8	4:1	0.12	0	0.2	1350	0.070	41.2%
	9	1:1:0.7	0.099	0.12	0.2	1350	0.011	90.8%
	10	2:1	0.11	0.088	0.1	1350	0.070	36.4%

2.3 Analysis method

The contents of C, Si and P elements were obtained by chemical analysis method. The slag compositions of the samples were obtained by XRF analysis method. The

dephosphorization efficiency was mainly described by the dephosphorization rate, which can be calculated by Eq. (1).

$$\eta_P = \frac{[\%P]_0 - [\%P]_f}{[\%P]_0} \quad (1)$$

Here, $[\%P]_0$ is the percentage of initial phosphorus; $[\%P]_f$ is the percentage of final phosphorus in steel; η_P is the dephosphorization rate.

2.4 Results and discussion

2.4.1 Separating conditions of slag and metal phase

A complete separation between slag and metal phase is necessary for promoting the dephosphorization reaction. In the dephosphorization process, CaO-FeO-SiO₂ is generally the basic slag system. In order to investigate the fluxing action of Bayer red mud, the following comparative experiments were carried out. Based on the same mass ratio of CaO:SiO₂:Fe₂O₃, one type of dephosphorizer was prepared using pure oxides of CaO, SiO₂, and Fe₂O₃ (No. 1 and No. 2 in Table 3); and the other ones consisted of Bayer red mud and CaO (No. 3 and No. 4 in Table 3). After experiments, the separating conditions of iron and slag under different situations were shown as the follows. Fig. 3(a) and (c) showed those of using Bayer red mud-based dephosphorizer (corresponding to No. 4 and No. 3 in Table 3, respectively), and Fig.3(b) and (d) showed the separating conditions of iron and slag when using pure compounds (corresponding to No. 2 and No. 1 in Table 3, respectively). Obviously, a much better separation between the slag and the iron phases was obtained when Bayer red mud-based fluxes were used (Fig. 3(a) and (c)). In the cases where pure oxides were used, a clear interface between the slag and the iron phases could not be obtained, suggesting that because of its low fluidity, the CaO-FeO-SiO₂ based slag cannot be completely separated from the iron phase. These observations clearly show that the presence of components such as Al₂O₃ and Na₂O in Bayer red mud can act as a kind of flux to decrease the melting point of the CaO-FeO-SiO₂ based slag.

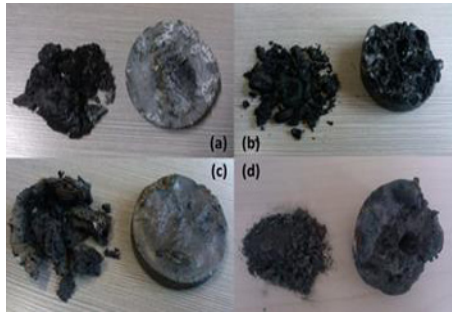


Fig. 3 Separating conditions between slag and metal phase ((a)(c) red mud based dephosphorizer were utilized, (b)(d) pure oxide were utilized).

2.4.2 Effect of components in dephosphorizer and initial silicon content of hot metal on dephosphorization ratio

The effect of composition of Bayer red mud based dephosphorizer and the initial silicon content in hot metal on the dephosphorization rate was shown in Fig. 4.

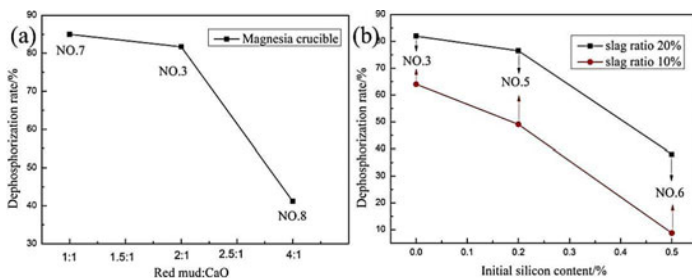


Fig. 4 The influence of different ratio of Red mud:CaO, slag ratio and initial silicon content on dephosphorization rate.

As shown in Fig. 4(a), the dephosphorization ratio decreased with increasing the mass ratio of red mud to CaO at 1350°C. When the mass ratio of red mud to CaO was changed from 1:1 to 2:1, the dephosphorization ratio changed a little, but remained > 80% and the final [P] was less than 0.018%. However, it decreased sharply to be less than 40% for red mud:CaO = 4:1. This is because the addition of excessive amounts of red mud reduced the basicity of the slag and weakened the phosphorus capacity of the dephosphorizer. As shown in Fig. 4(b), the initial [Si] in the hot metal also had a big influence on the dephosphorization rate. The higher the initial [Si], the lower was the dephosphorization rate; but for initial [Si] values less than 0.2%, this parameter had little effect on the dephosphorization rate especially when slag ratio was high (20%). This result demonstrates that the Bayer red mud-based flux can remove phosphorus and silica simultaneously if the initial [Si] is less than 0.2%. The dephosphorization ratio decreased sharply when the initial [Si] was as high as 0.5% and under these conditions, dephosphorization cannot effectively be carried out.

2.4.3 Effect of final slag basicity on dephosphorization ratio

Fig. 5(a) and 5(b) show the relation of the dephosphorization rate to the binary basicity and the optical basicity of the final slag, respectively. As can be seen, the dephosphorization rate increased with increasing basicity. Especially, when the binary basicity was as high as 12, the dephosphorization rate was 91% and the final [P] was 0.011% (see Table 3). In addition, good slag fluidity and an excellent separation between the slag and iron phase was observed even under strong alkaline conditions. This fact further proved that Al_2O_3 and Na_2O in the Bayer red mud can act as flux materials to decrease the melting point of CaO-FeO-SiO₂ slag system. And there was a more clearly linear relationship between dephosphorization rate and optical basicity (Fig. 5(b)), which illustrated that it is more accurate to use the optical basicity to describe the alkaline nature of the multiple dephosphorizer slag system used in this study.

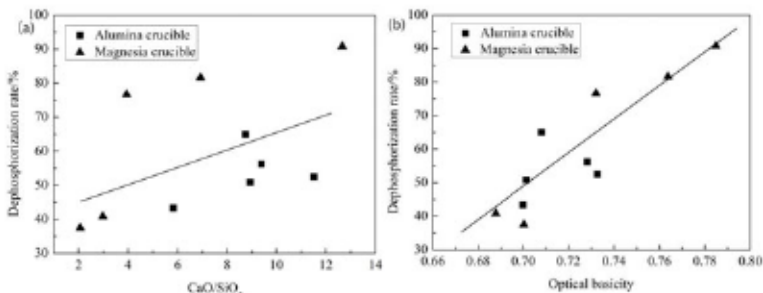


Fig. 5 The influence of (a) (%CaO/%SiO₂), and (b) optical basicity on dephosphorization

3. Conclusions

1. The liquid areas of CaO-SiO₂-FeO system are obviously enlarged with the addition of Al₂O₃, Na₂O, and mixture A; In the cases of adding 10% Al₂O₃, or 5% Na₂O, or 10% A, the liquid areas below 1400°C are nearly independent of FeO content.

2. During the hot metal dephosphorization experiments, a much better slag-iron separating result was observed in the case of that Bayer red mud was used. That suggested that Al₂O₃ and Na₂O in Bayer red mud can improve the fluidity of CaO-FeO-SiO₂ based slag.

3. In this study, when the mass ratio of Bayer red mud : CaO was between 1:1 to 2:1, a good dephosphorization effect was obtained, whose dephosphorization ratio can be reach more than 80%, and the final [P] was lower than 0.018%.

Acknowledgement

The authors are grateful to the financial support from the National Natural Science Foundation of China (No. 51474021).

References

- [1] Z.C. Huang et al., "Reduction of iron oxides of red mud reinforced by Na₂CO₃ and CaF₂," *Journal of Central South University*, 41 (3) (2010), 838-843.
- [2] V.M. Sglavo et al., "Bauxite red mud in the ceramic industry Part 1: thermal behavior," *Journal of the European Ceramic Society*, 20 (3) (2000), 235-244.
- [3] V.M. Sglavo et al., "Bauxite red mud in the ceramic industry Part2: production of clay-based ceramics," *Journal of the European Ceramic Society*, 20 (3) (2000), 245-252.
- [4] J. Diao et al., "Recovery of Phosphorus from Dephosphorization Slag Produced by Duplex High Phosphorus Hot Metal Refining," *ISIJ Int.*, 52 (6) (2012), 955-959.

REDUCTION BEHAVIOR OF ASSMANG AND COMILOG ORE IN THE SiMn PROCESS

Pyunghwa Peace Kim¹, Joakim Holtan¹, Merete Tangstad¹

¹Department of Materials Science and Engineering, Norwegian University of Science and Technology; N-7491 Trondheim, Norway

Keywords: Assmang, Comilog, SiMn, Reduction

Abstract

The reduction behavior of raw materials from Assmang and Comilog based charges were experimentally investigated with CO gas up to 1600 °C. Quartz, HC FeMn slag or limestone were added to Assmang or Comilog according to the SiMn production charge, and mass loss results were obtained by using a TGA furnace. The results showed that particle size, type of manganese ore and mixture have close relationship to the reduction behavior of raw materials during MnO and SiO₂ reduction. The influence of particle size to mass loss was apparent when Assmang or Comilog was mixed with only coke (FeMn) while it became insignificant when quartz and HC FeMn slag (SiMn) were added. This implied that quartz and HC FeMn slag had favored the incipient slag formation regardless of particle size. This explained the similar mass loss tendencies of SiMn charge samples between 1200-1500 °C, contrary to FeMn charge samples where different particle sizes showed significant difference in mass loss. Also, while FeMn charge samples showed progressive mass loss, SiMn charge samples showed diminutive mass loss until 1500 °C. However, rapid mass losses were observed with SiMn charge samples in this study above 1500 °C, and they have occurred at different temperatures. This implied rapid reduction of MnO and SiO₂ and the type of ore and addition of HC FeMn slag have significant influence determining these temperatures. The temperatures observed for the rapid mass loss were approximately 1503 °C (Quartz and HC FeMn slag addition in Assmang), 1543 °C (Quartz addition in Assmang) and 1580-1587 °C (Quartz and limestone addition in Comilog), respectively. These temperatures also showed indications of possible SiMn production at process temperatures lower than 1550 °C.

Introduction

Manganese ferroalloys, such as ferromanganese (FeMn) and silicomanganese (SiMn), are commonly consumed in steel industries as additives to achieve various grades of steels with high quality [1, 4]. As an alloying unit, the addition of FeMn or SiMn will influence the strength, toughness and hardness of steel products. They also serve as excellent desulfurizers and deoxidizers to prevent brittle and porous steel products [1-11].

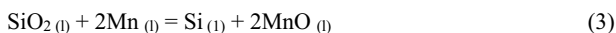
The more use of SiMn as additives in steel industries is expected to advance at a faster rate than FeMn consumption [1, 2, 12]. As deoxidizers, SiMn is more effective than FeMn. Deoxidation of steel with SiMn have given cleaner results than individual addition of ferrosilicon (FeSi) and FeMn [2]. Also, the use of SiMn is more advantageous because it contains less carbon, phosphorus, sulphur, aluminium and nitrogen compared to a mixture of FeMn and FeSi

[2]. These features of SiMn addition in steel industries makes the production of high quality SiMn an important task. However, the choice of using FeMn or SiMn in the end will always be a question of cost, and thus dependent on the global market.

Considering the process reactions for SiMn, a temperature of 1600-1650 °C is necessary to obtain SiMn with sufficiently high content of silicon and discard slag with low MnO. At this temperature, the final reduction of MnO and SiO₂ can take place as shown in the following reactions:



Also, the reduction of MnO and SiO₂ are considered to occur simultaneously in the SiMn process. Thus, the slag/metal exchange reaction of Mn and Si, which is the combination of reactions 1 and 2, has to be taken into account:



Current studies showing excavation of industrial and pilot scale furnaces provide information that reduction of MnO and SiO₂ occurs mainly at the top part of the coke bed [13, 14]. This implies that most of the raw materials are priority melted into a slag phase, and the reduction of MnO and SiO₂ occurs on the top part of the coke bed where the slag is in contact with carbon reductants. Thus, different charge materials are likely to exhibit different reduction behavior during the process because of their different melting properties such as temperature. Various types of manganese ores and high-carbon ferromanganese (HC FeMn) slag have been previously reported to have different “melting temperatures” [14, 15]. The “melting temperature” was considered as the temperature when the ore starts to form liquid slag and behaves as a liquid. Assmang, Gabonese, CVRD ore, CVRD sinter and HC FeMn slag were measured by a sessile drop furnace experiment, which gave the “melting temperatures” of approximately 1446, 1485, 1461, 1395 and 1220 °C, respectively. These different temperatures are assumed to give significant influence during the SiMn process.

While the process mechanism of FeMn have been extensively studied during the last 20 years, less effort was use to ascertain the process mechanism of SiMn. Although the process reactions of SiMn has previously been studied [2, 16], only few studies considering the reduction behavior between raw materials have been reported. Therefore, the present study focuses on an experimental investigation of the reduction behavior of raw materials in the SiMn process. In this case, two different manganese ores, Assmang and Comilog, were used to compare the reduction behavior during the SiMn process. Quartz, HC FeMn slag or limestone were added into Assmang or Comilog according to a SiMn charge, and the reduction behavior of each different charge sample was observed.

Experimental

The objective of this study was to conduct an experimental investigation to ascertain the reduction behavior of raw materials in the SiMn process. The characterization and preparation of raw materials, the TGA furnace and the experimental conditions are described in the next subsections.

A. Raw Materials and TGA Furnace

Assmang and Comilog ores were used as the main manganese source in this experiment. The chemical compositions of Assmang, Comilog, coke, quartz, HC FeMn slag and limestone used in this experiment are shown in Table I.

Table I. Chemical Composition of Raw Materials for SiMn Process [dry mass %]

Raw Materials	MnO	MnO ₂	SiO ₂	Fe ₂ O ₃	CaO	MgO	Al ₂ O ₃	CO ₂	C	Total
Assmang	32.69	33.22	5.77	15.06	6.26	1.10	0.26	3.52	0.27	98.15
Comilog	3.91	69.40	6.50	6.47	0.29	0.13	6.90	0.10	-	93.70
Coke	0.04	-	5.60	0.86	0.42	0.22	2.79	-	87.68	97.61
Quartz	0.14	-	93.85	-	0.09	0.05	1.19	-	-	95.32
HC FeMn Slag	35.23	-	25.45	-	18.45	7.53	12.30	-	0.40	99.36
Limestone	-	-	0.96	-	51.98	0.96	0.26	45.72	-	99.88

Considering the amount of oxides (CaO, MgO and Al₂O₃) for the two types of ore, Assmang contained a relatively high amount of CaO (6.34 mass %) and was considered as a basic ore. On the other hand, Comilog contained a relatively high amount of Al₂O₃ (6.70 mass %) and was considered as an acidic ore. Basic ores are known to have a relatively high melting temperature compared to acidic ores, which are considered to have a lower melting temperature [13-15]. Polish coke was used as the carbon reductant. Each of the raw material was prepared in two different size groups, 0.6-1.6 and 4.0-6.3 mm, to observe the influence of particle size during the reduction process.

The schematic of the TGA furnace is shown in Figure 1. The furnace can endure temperatures up to 1700 °C and the maximum heating rate is up to 25 °C/min. A mass balance is installed at the top and a Molybdenum (Mo)-wire was used to suspend the crucible inside the furnace. Graphite crucibles (36 mm outer diameter, 30 mm inner diameter, 70 mm height and 61 mm deep) were used to contain each charge sample in this experiment.

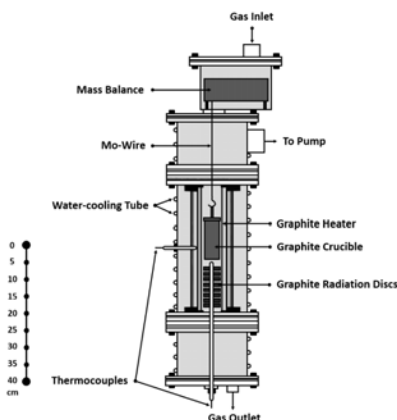


Figure 1. Experimental setup: schematic of thermo-weight furnace.

B. Procedure

Profiles for each charge sample were prepared according to Table II. Raw materials for each charge were measured and mixed into a graphite crucible. Then the graphite crucible was suspended by hooking it to the Mo-wire inside the furnace chamber.

Table II. Profile for Each Charge Sample [g]

Charge No.	Size [mm]	Assmang	Comilog	Coke	Quartz	HC FeMn Slag	Limestone	Total
As. 1A	0.6-1.6	23	-	7	-	-	-	30
As. 1B	4.0-6.3							
As. 2A	0.6-1.6	23	-	7	10	-	-	40
As. 2B	4.0-6.3							
As. 3A	0.6-1.6	13	-	7	7	13	-	40
As. 3B	4.0-6.3							
Com. 1A	0.6-1.6	-	23	7	-	-	-	30
Com. 1B	4.0-6.3							
Com. 2A	0.6-1.6	-	23	7	6	-	-	36
Com. 2B	4.0-6.3							
Com. 3A	0.6-1.6	-	18	6	7	-	5	36
Com. 3B	4.0-6.3							

The furnace was then sealed and the chamber was initially cleaned with pure Ar gas (99.9999 %). Next, heat was applied to the furnace according to temperature profile in Figure 2.

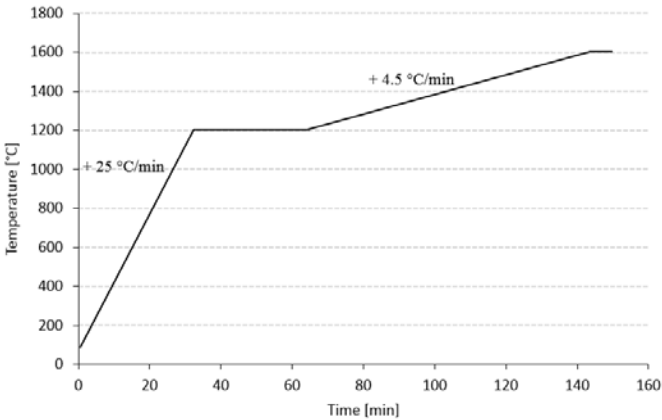


Figure 2. Temperature profile.

Initially, the furnace was heated up to 1200 °C (+ 25 °C/min): 0.5 l/min of Ar gas was supplied until the crucible temperature was approximately 500 °C and the Ar gas was converted to 0.5 l/min of CO gas above 500 °C. Each charge sample was held for 30 minutes at 1200 °C and it was assumed complete pre-reduction during this step [2, 13]. Then, further heating was done until 1600 °C (+ 4.5 °C/min). Finally, each charge sample was held for 5 minutes at 1600 °C and cooled down to room temperature. During the cooling, CO gas was supplied until the crucible temperature dropped down to approximately 500 °C and was converted to Ar gas until complete cooling. The weight loss (% mass loss) of each charge sample was recorded and data

were logged every 5 seconds during the experiment. Lastly, each charge sample was prepared by mounting in epoxy to be further analyzed. The JEOL JXA-8500, an EPMA (Electron Probe Micro-Analysis) type, was used to analyze slag compositions.

Results and Discussion

The results from the TGA furnace and EPMA analysis are presented in this section. Mass loss with time of each charge sample is described between 1200 and 1600 °C. The comparison of all charge samples is shown to see the difference of reduction behavior regarding particles size, type of manganese ore and mixture. Also, the comparison of the primary slag (calculated) and final slag (measured) of each charge samples is discussed.

The mass loss and reduction behavior of each charge sample during the reduction of MnO and SiO₂ at different temperatures between 1200 to 1600 °C is described in Figure 3. The results showed that the reduction behavior during the MnO and SiO₂ reduction are differed using different particle size, type of manganese ore and mixture.

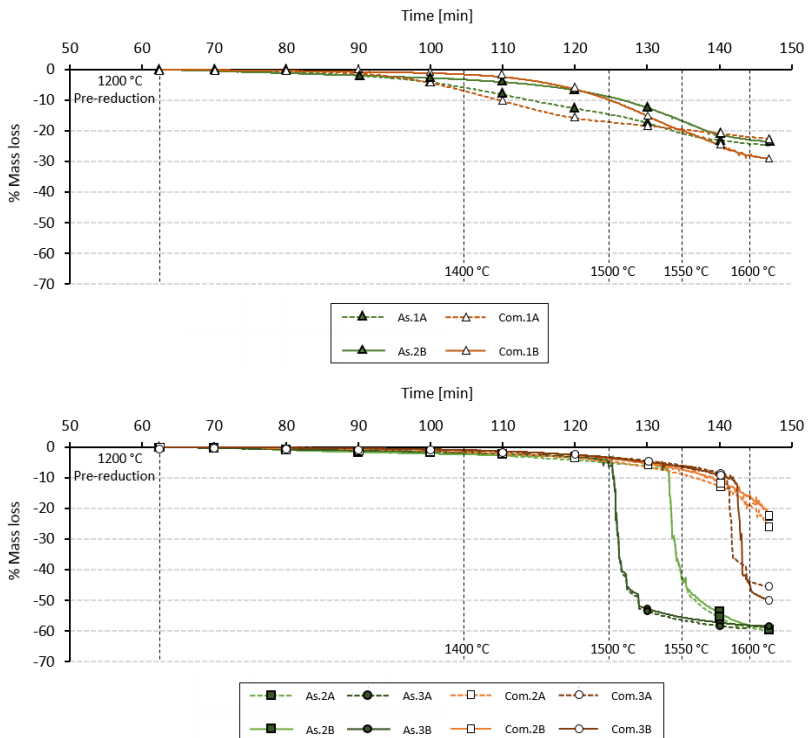


Figure 3. MnO and SiO₂ reduction results of FeMn charge samples (top) and SiMn charge samples (bottom) described in percent mass loss with time.

The influence of particle sizes showed different results for FeMn and SiMn charge samples. The mass loss difference between particle sizes was mainly observed with Assmang or Comilog mixed with only coke (As.1 and Com.1) which were representatives of FeMn charge samples. FeMn charge samples with particle sizes between 0.6-1.6 mm showed more mass loss than with particles sizes between 4.0-6.3 mm. However, when Assmang or Comilog was mixed with quartz and HC FeMn slag, which were representatives of SiMn charge samples, the mass loss difference between two different size groups were insignificant compared to FeMn charge samples during the reduction. This comparison between FeMn and SiMn charge samples shows indication that particle size might not be an evaluating variable during the reduction of MnO and SiO₂ for SiMn process. If manganese ore and quartz particles are completely dissolved into a slag phase shortly after pre-reduction, particle size will no longer be a variable influencing the mass loss and further the reduction of MnO and SiO₂. While solid MnO is present until the liquidus temperature in the FeMn process [2, 17], considerable amount of molten slag phase seems to generate during the early stages in SiMn charges.

The type of manganese ore and mixture also showed different reduction behavior during the experiment condition. For SiMn charge samples, the percent mass losses from 1200 to 1500 °C were relatively low, which were between 0 to 5 %, and similar regardless of particle size, type of manganese ore and mixture. The similar mass losses can be explained by the dominating incipient slag phase, which is generated at early process temperature for SiMn charges. Besides coke, all particles are melted into a slag phase. However, the low mass loss of SiMn charges until elevated temperatures (before rapid mass loss) indicates insignificant reduction of MnO and SiO₂. The slag composition for primary (calculated) and after 1600 °C, (measured) is shown in Table III, and the comparison of a_{MnO} shows why the MnO reduction is not occurring until a higher temperature is reached. Note that all iron oxides are assumed to be completely reduced during pre-reduction and the main slag components are MnO, SiO₂, CaO, MgO and Al₂O₃ in all charge samples.

Table III. Comparison of Primary and Final Slag Composition [mass %], and calculated activities of MnO and SiO₂ by using FACTSage

Charge No.	Primary Slag Composition (Calculated): 1200 °C							a_{MnO}	a_{SiO_2}
	MnO	SiO ₂	CaO	MgO	Al ₂ O ₃	Total			
As. 1	81.70	7.88	8.55	1.50	0.36	99.99	0.810	0.002	
As. 2	51.40	41.55	5.41	0.96	0.69	100.01	0.095	0.448	
As. 3	42.17	37.30	10.90	3.80	5.81	99.98	0.128	0.168	
Com. 1	81.45	8.72	0.39	0.18	9.27	100.01	0.655	0.004	
Com. 2	61.33	30.92	0.31	0.15	7.29	100.00	0.215	0.152	
Com. 3	48.52	34.11	11.1	0.32	5.94	99.99	0.166	0.140	
Charge No.	Final Slag Composition (Measured by EPMA): 1600 °C							a_{MnO}	a_{SiO_2}
	MnO	SiO ₂	CaO	MgO	Al ₂ O ₃	Total			
As. 1A	16.27	40.55	35.79	5.93	1.46	100.00	0.103	0.080	
As. 1B	20.77	40.47	33.71	3.69	1.36	100.00	0.112	0.093	
As. 2A	- Not observed -								
As. 2B	3.91	57.15	30.53	4.51	3.89	99.99	0.002	0.646	
As. 3A	9.59	49.35	23.67	5.49	11.89	99.99	0.011	0.344	
As. 3B	6.80	48.83	25.95	6.29	12.13	100.00	0.009	0.300	
Com. 1A	- Not available -								
Com. 1B	11.22	10.36	3.68	0.20	64.75	95.18	0.049	0.006	
Com. 2A	- Not available -								
Com. 2B	12.30	43.20	2.60	0.01	33.00	95.30	0.008	0.412	
Com. 3A	- Not available -								
Com. 3B	3.80	40.30	38.00	0.40	13.8	96.40	0.014	0.127	

The change of a_{MnO} from 1200 to 1600 °C for FeMn and SiMn charges shows good accordance with the mass losses between 1200 to 1500 °C. The difference of a_{MnO} of FeMn charges, As.1 and Com.1, from 1200 and 1600 °C is relatively significant compared to SiMn charges. This indicates the entity of the driving force for MnO reduction is in existence, and the progressive mass loss of As.1 and Com.1 shows good accordance. The low activity of MnO in SiMn charges also explain the insignificant reduction of MnO at lower temperatures.

The rapid mass losses, which were also observed with SiMn charges above 1500 °C, showed close relationship with the type of manganese ore and mixture. The starting temperature of the rapid mass loss of As.2 and As.3 was approximately 1543 and 1503 °C, and had a_{MnO} of 0.095 and 0.128, respectively. As.3 will thus have a higher driving force which explains the lower reduction temperature. The similar rapid mass loss was also observed with Comilog but only with Com.3 and at higher temperature of 1580-1587 °C. Com.2 and Com.3 has a_{MnO} of 0.215 and 0.116. Hence, the difference in reduction temperature cannot be explained by the driving force, as Com.2 has a higher driving force. The palpable reduction behavior SiMn charges is that rapid reduction of MnO and SiO₂ occurs at lower temperature with Assmang than Comilog. The amount of iron oxides in the ore can give some implication considering the different reduction behavior in SiMn charges. As Assmang has a higher iron content than Comilog, the amount of initial iron after pre-reduction can impact the reduction of MnO. Previous studies have shown that the formation of initial iron leads to MnO reduction by the dissolved carbon in the metal [18]. The activity of Mn is lower when iron is at the slag/carbon interface, thus increasing the driving force for MnO reduction.

However, the information for the reduction path of MnO and SiO₂ is insufficient and further studies are necessary.

Conclusion

The reduction behavior showed close relationship with raw materials regarding particle size, type of manganese ore and mixture. The results showed that the relationship between particle size and mass loss becomes insignificant when quartz and HC FeMn slag are added into Assmang or Comilog ore. It was thought that considerable amount of incipient slag phase have generated during the early stages of MnO and SiO₂ reduction, which likely diminished the influence of particle size in case of SiMn charges. The mixture type also showed that the reduction behavior becomes similar regardless of ore type when quartz and HC FeMn slag were added into Assmang or Comilog ore during the reduction of MnO and SiO₂. Similar mass losses, which were all relatively very low, were observed with charges samples of As.2, 3 and Com.2, 3 in this study. The already very low a_{MnO} of SiMn charges at 1200 °C shows good accordance of the lower mass losses until rapid reduction. However, the temperatures when the rapid mass loss, which indicates rapid reduction of MnO and SiO₂, begins differed with type of manganese ore and mixture. Comilog seems to have higher rapid reduction temperature than Assmang, and HC FeMn slag and limestone contributes towards lower temperature. However, the reduction path of MnO and SiO₂ needs further investigation. The temperature difference of the rapid reduction was approximately 80 °C when comparing As.3 (1503 °C) and Com.3 (1580-1587 °C). This difference shows indication of possible SiMn production at process temperatures lower than 1550 °C.

Acknowledgements

The authors acknowledge the project funds provided by the Norwegian Research Council through the SFI: Metal Production projects.

References

1. International Manganese Institute (www.manganese.org). 2014.
2. S. E. Olsen, M. Tangstad and T. Lindstad. *Production of Manganese Ferroalloys*. Tapir Academic Press, Trondheim (Norway) 2007.11-18.
3. V. Witusiewicz, F. Sommer and E. Mittemeijer. "Reevaluation of the Fe-Mn Phase Diagram". *Journal of Phase Equilibria & Diffusion*, 25(4) 2004. 346-354.
4. H. Okamoto. *Iron Binary Alloy Phase Diagrams (Alloy Phase Diagrams in ASM Handbook)*. ASM International: Materials Park, 1992.
5. Y. Tomota, M. Strum and J. Morris Jr.. "The Relationship Between Toughness and Microstructure in Fe-high Mn Binary Alloys". *Metall. Trans., A*, 1987. 18(6).
6. D. K. Subramanyam, A. E. Swansiger and H. S. Avery. *Austenitic Manganese Steels in Properties and Selection: Irons, Steels and High-Performance Alloys*. ASM International, 1990. 822-840.
7. G. F. Deev, V. V. Popovich and V. N. Palash. "Role of Iron Sulfide in the Formation of Cracks in Weld Joints". *Materials Science*, vol 18 No. 3, May-June 1982. 109-112.
8. J. R. Cain. "Influence of Sulphur, Oxygen, Copper and Manganese on the Red-Shortness of Iron". *Technological Papers of The Bureau of Standards* No. 261 (Department of Commerce, USA), Jul. 30, 1924. 327-335.
9. S. I. Gubenko and A. M. Galkin. "Nature of the Red-Shortness of Steel". *Metal Science & Heat Treatment*, vol. 26 Issue 10, Oct. 1984. 732-737.
10. R. Abushosha, S. Ayyad and B. Mintz. "Influence of Cooling Rate and MnS Inclusions on Hot Ductility of Steels". *Materials Science & Technology*, Vol. 14, Mar. 1998. 227-235.
11. O. Grong, T. A. Siewert, G. P. Martins and D. L. Olson. "A Model for the Silicomanganese Deoxidation of Steel Weld Metals". *Metallurgical Transactions*, Vol. 17A, Oct. 1986. 1797-1807.
12. W. Ding and S. E. Olsen. "Manganese and Silicon Distribution between Slag and Metal in Silicomanganese Reduction". *ISIJ International*, Vol. 40(No. 9) 2000. 850-856.
13. E. Ringdalen and M. Tangstad. "Study of SiMn Production in Pilot Scale Experiments – Comparing Carajas and Assmang Ore" *13th International Ferroalloy Congress (INFACON)*, 2013, 195-206.
14. E. Ringdalen, S. Gaal, M. Tangstad and O. Ostrovski. "Ore Melting and Reduction in Silicomanganese Production". *Metallurgical and Materials Transactions B*, Vol. 41B, Dec. 2010.1220-1229.
15. T. Brynjulfen and M. Tangstad. "Melting and Reduction of Manganese Sinter with Fluxes". *The Minerals, Metals & Materials Society (TMS)*, 2012. 147-154.
16. S.E. Olsen and M. Tangstad. "Silicomanganese Production – Process Understanding". *10th International Ferroalloy Congress (INFACON)*, 2004. 231-238.
17. T. Brynjulfen. "Reduction of Manganese Ore Agglomerates". Ph.D thesis, Department of Materials Science and Engineering (DMSE), Norwegian University of Science & Tecnology (NTNU), 2013. 15-18.
18. J. Safarian and M. Tangstad. "Slag-Carbon Reactivity". *12th International Ferroalloy Congress (INFACON)*, 2010. 327-338.

REGENERATION OF WC-Co NANOPOWDERS VIA SODIOTHERMIC REDUCTION IN MOLTEN SALTS

Na Wang^{1*}, Xue-Mei Liu¹, Li-Hua Chai¹, Jinyu Wu², Xuyang Shen¹

1. School of Materials Science and Engineering, Beijing University of Technology, Beijing, 100024, P. R. China

2. School of Metallurgical and Ecological Engineering, University of Science and Technology Beijing, Beijing 100083, P. R. China

e-mail: wnawjnw@126.com

Abstract

WC-Co nanoparticles were directly recycled via sodiothermic reduction in NaCl-52mol%CaCl₂ molten salts using oxidized hard metal scrap as the raw materials. The as-prepared samples were characterized by X-ray diffraction (XRD) and scanning electron microscopy (SEM). It was found that a series of cemented carbide, such as W, W-Co, WC and WC-Co nanoparticles, were successfully recycled using the molten salt systems. The results show that WC/WC-Co nanoparticles can be recycled from oxidized hard metal scrap via sodiothermic reduction in the NaCl-52mol%CaCl₂ molten salts.

Keywords Sodiothermic reduction; WC-Co nanoparticles; Regeneration; Hard metal scrap;

1 Introduction

Tungsten carbide is drawn much attention as one of anti-wear materials for various cutting tools application. Due to its high hardness and good wear resistance, it is widely used in the production of cemented carbides and made of cutting tools and parts [1]. WC-Co hard metals consist of hard phase tungsten carbide dispersed in ductile metal cobalt and which are processed usually via liquid-phase sintering [2, 3]. In early studies, it was found that the hardness and toughness of the manufactured parts increase as the particles size of tungsten carbide phase decreases was enough [4, 5]. And it is an issue of crucial importance to obtain the homogeneous microstructure and high densification of the production, which ensures the material with higher mechanical properties and a longer tool life [6, 7]. Thus, some recent researches have shown that the ultrafine carbide particles size (<1 μm) was used for increasing the toughness and hardness of WC-Co alloy [8, 9].

Recently, tungsten powders, a nano-metallic material for preparing of synthetic WC powder, its application was limited by increasingly serious lacking of tungsten resource and increasing gradually carbide materials demanded with the high development of society. Thus, the large amount piled up abolished cemented carbide scrapes are considered as the secondary tungsten resource, and some methods for tungsten and cobalt were put forward to recycle, such as niter-casting process[10], zinc melt and cold stream process[11], leaching method [12], aqueous-electrolysis process [13], oxidation-reduction process [14] and so on [15-18]. The present process for reprocessing cemented carbide requires a set of complicated equipment, has high production cost and time consuming, such as niter-casting process [10] and leaching method [12].

In our previous works, a new direct synthesized process for Nb-Al intermetallic nanoparticles was developed [19]. In this process, Nb-Al intermetallic nanoparticles were synthesized via the sodiothermic reduction process in molten salts, with oxide or chloride mixtures as raw materials [20-23]. So that, the purpose of this work is to present the simple, economic and direct recycling tungsten carbide powders

utilizing a sodiothermic reduction from oxidation of hard metal scrap dispersed into molten salts. In the paper W, W-Co, WC and WC-Co nanoparticles were directly recycled in NaCl-52mol%CaCl₂ molten salts by sodiothermic reduction method with oxidized hard metal scrap as the raw materials, and the as-prepared powders were examined by X-ray diffraction (XRD) and scanning electron microscopy (SEM).

2 Experimental

The raw materials used in this paper were the WC or WC-Co scrap powders and pure sodium carbonate (Na₂CO₃, purity > 99.39%). The reductant was pure sodium metal (Na, purity > 98.50%). The low eutectic point of molten salt system such as the NaCl-52mol%CaCl₂ molten salts was chosen [19-23].

In order to prepare the homogeneous reactions system, the WC or WC-Co scrap powders must be oxidized forming tungsten trioxide (WO₃) or tungsten cobalt oxide powders, which were used as raw material for preparation of hard alloys nanoparticles by sodiothermic reduction process in the molten salts. The oxidized hard metal scrap was obtained by oxidation of WC or WC-Co scrap powders in the air at 600 °C for three hours.

These raw oxidized materials with NaCl-52mol%CaCl₂ salts were mixed and then put into a corundum crucible. The reactor was dehydrated at 300 °C for 8 h in the resistance furnace under argon atmosphere, and the resistance furnace would continue to heat up to 750 °C for chemical reaction. To synthesize hard metal powders, sodium was incised to pellets and stored in an air tight test tube. Sodium particles were subsequently carried into the salt bath by argon gas to reduce tungsten trioxide or tungsten cobalt oxide and sodium carbonate. After sufficient time for reaction, the reactor was cooled down to ambient temperature. The product powders were obtained by washing, filtering and drying. X-ray diffraction (XRD) and scanning electron microscopy were used to determine the product phases, shape and particle sizes.

3 Results and discussion

3.1 Oxidation of hard metal scrap powder

The XRD patterns of the reactants and as-prepared products via the redox reaction of WC or WC-Co scrap powders at 600 °C for three hours are presented in **Fig.1** or **Fig.2**, respectively. As shown in **Fig. 1(a)**, the WC scrap powders as raw material can be indexed to well crystallized WC structure (PDF NO. 73-471). The pure WO₃ (PDF NO. 72-1465) powders were obtained by oxidizing WC scrap powders in the air, as shown in **Fig. 1(b)**. Also, **Fig. 2(a)** and **Fig. 2(b)** show the phase composition of the reactants and products before and after the oxidizing WC-Co scrap powders in the air, respectively. It was found that the main phase in the reactants is WC (PDF NO. 73-471), and some other phase is Co (PDF NO. 5-727), as shown in **Fig. 1(a)**. **Fig. 2(b)** shows the XRD pattern of the as-prepared products after oxidizing WC-Co scrap powders, certainly, the WO₃ (PDF NO. 72-1465) powders with CoWO₄ (PDF NO. 15-867) are observed in the products indicating that WC-Co scrap could be oxidized in the process.

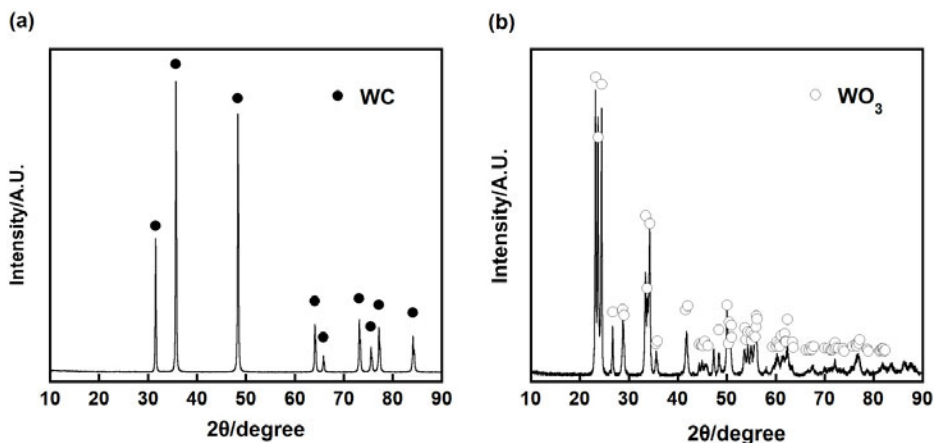


Fig. 1. XRD patterns of the WC scrap powders (a) and the oxidized products of WC scrap powders (b)

According to the experimental results in the air, the chemical reactions between WC/WC-Co scrap with O₂ were occurred. By the enthalpy (H), entropy (S) and heat capacity (C) chemistry (referred to as HSC) thermodynamics calculation, the redox reaction WC/WC-Co scrap may occur according to the following Reactions (1) and (2) in the air.

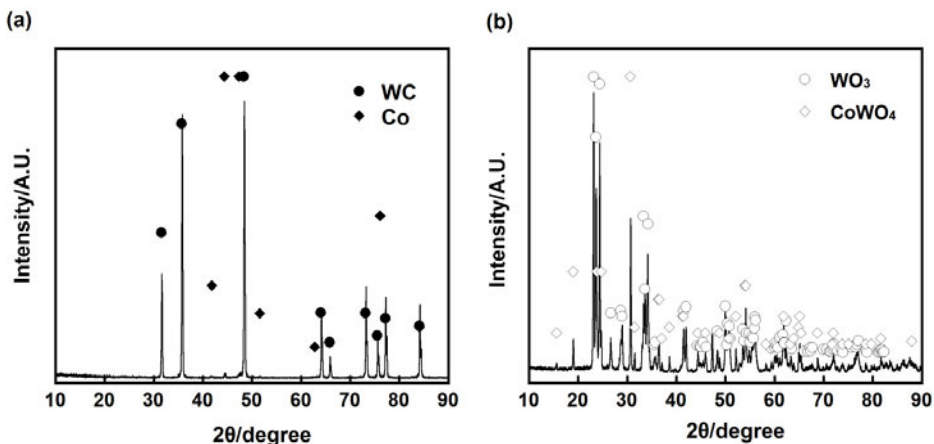
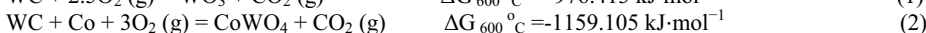


Fig. 2. XRD patterns of the WC-Co scrap powders (a) and the oxidized products of WC-Co scrap powders (b)

Therefore, for the oxidized reaction of WC scrap powders at 600 °C, there can only be one chemical

reaction with O_2 took place according to Reactions (1) in the air. For the oxidized reaction of WC-Co scrap powders, there are two chemical reactions occurred according to the following Reactions (1) and (2) in the air at 600 °C. The $CoWO_4$ would be come into being only when the Co phase is present in the hard metal scrap.

3.2 Preparation of W or W-Co powder

The XRD patterns and FESEM images of the as-prepared products by sodiothermic reduction of WO_3 or $CoWO_4$ - WO_3 in $NaCl$ -52mol% $CaCl_2$ molten salts at 750 °C are presented in **Fig. 3**. As shown in **Fig. 3(a)**, the pure W (PDF NO. 89-3012) powders were obtained via sodiothermic reduction of oxidation of WC scrap powders at 750 °C in the NC molten salts. Also, the as-prepared products using the oxidized WC-Co scrap powders as raw material can be indexed to well crystallized W (PDF NO. 89-3012) and Co (PDF NO. 5-727) structure, as shown in **Fig. 3(b)**. That is, the W-Co alloy powders were obtained by sodiothermic reduction of oxidation of WC-Co scrap powders at 750 °C in the NC molten salts, as shown in **Fig. 3(c)**. Moreover, it can be observed from **Fig. 3(c)** that the particle size of W nanopowders is about 20~120 nm while the as-prepared W-Co nanoparticles are obtained with the particle size range of 50-200 nm, as shown in **Fig. 3(d)**.

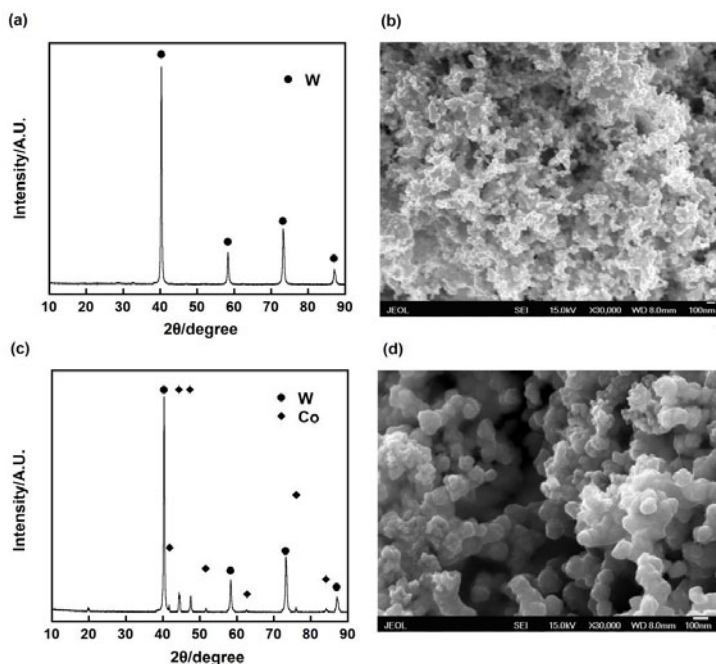


Fig. 3. XRD patterns (a), (c) and FESEM images (b), (c) of the as-prepared products via sodiothermic reduction of oxidized powders of WC or WC-Co scrap powders, respectively.

3.3 Preparation of WC or WC-Co powder

Fig. 4 shows the XRD patterns and FESEM images of the as-prepared products by sodiothermic reduction of WO_3 and Na_2CO_3 or $CoWO_4$ - WO_3 and Na_2CO_3 in NC molten salts at 750 °C. According to the theoretical binary phase diagram of W-C system, the stoichiometric molar ratios of WO_3 to Na_2CO_3

as raw materials should be 1:1, with the aim to prepare WC. It can be seen from Fig. 4(a) that the pure WC products using WO₃ and Na₂CO₃ as raw materials with a molar ratio of 1:1 can be characterized clearly as such by a standard card of WC (PDF NO. 73-471). Also, well the major WC (PDF NO. 73-471) phase with Co (PDF NO. 5-727) phase of the WC-Co products nanopowders are synthesized as shown in Fig. 4(c). In addition, as shown in Fig. 4(b) and Fig. 4(d), the obtained WC and WC-Co are nanosized particles in the range of 100-250 nm and 40-250 nm, respectively.

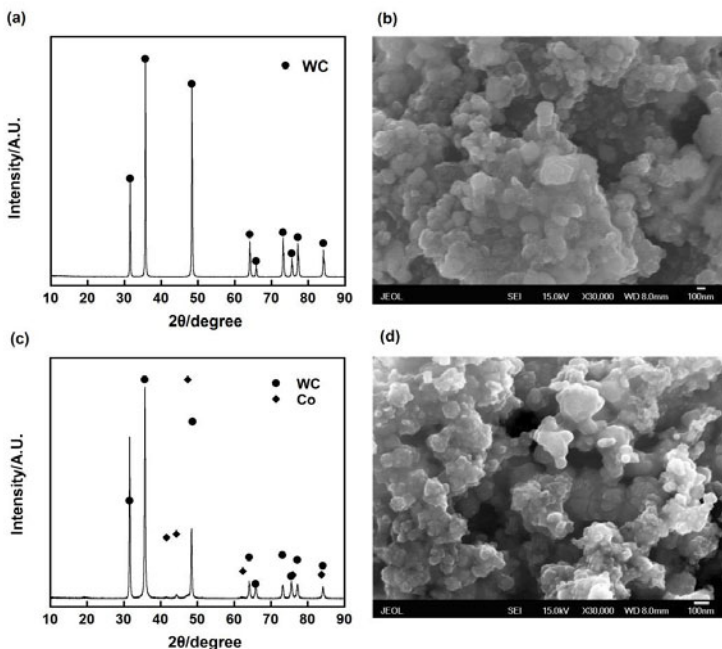
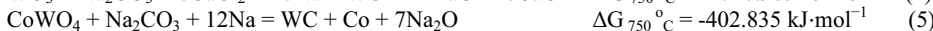


Fig. 4. XRD patterns (a), (c) and FESEM images (b), (c) of the as-prepared products by sodiothermic reduction of oxidized WC or WC-Co scrap powders with Na₂CO₃, respectively.

According to the experimental results in NC molten salt systems, the chemical synthesis reaction between the redox reactions of WC or WC-Co scrap powders with Na₂CO₃ by the sodiothermic reduction method took place at 750 °C. By the enthalpy (H), entropy (S) and heat capacity (C) chemistry (referred to as HSC) thermodynamics calculation, the sodiothermic reduction WO₃ and Na₂CO₃ or CoWO₄-WO₃ and Na₂CO₃ may happen according to the following Reactions (3) - (6) in molten salts. Because of the negative ΔG_{750}° , WC or WC-Co alloy particles were easier to synthesize from WO₃ and Na₂CO₃ or CoWO₄-WO₃ and Na₂CO₃ with CaCl₂ by sodiothermic reduction process. However, WC or WC-Co powders can be prepared from the oxidized WC/WC-Co scrap powders and Na₂CO₃ with CaCl₂ according to the Reactions (3) and (6).



Besides, CaO has certain solubility in the molten salt with CaCl₂ as solvent, for instance, the

solubility of CaO is about 21 mol% in the CaCl₂ molten salts at 1000 °C [24–26]; when the temperature increasing from 650 to 850 °C, the CaO solubility ranges were about 5.92 mol%~8.14 mol% in the NaCl-50mol%CaCl₂ molten salts. Thus, the CaO solubility is estimated to 7.31 mol% at 750 °C in the NaCl-52 mol% CaCl₂ molten salts based on the findings in S. L. Wang's paper [27]. Therefore, the optimum CaCl₂ content in molten salts plays not only the role of reactants but also porter in the formation of pure Nb powders in molten salts [22].

4 Conclusions

WC-Co tungsten carbide nanoparticles were directly recycled via sodiothermic reduction process in molten salts using oxidized hard metal scrap as powders the raw materials. The as-prepared samples were characterized by X-ray diffraction and scanning electron microscopy. The WC/WC-Co scrap powders are oxidized and WO₃ or CoWO₄ were formed in the air, and these oxides with Na₂CO₃ were dissolved in NaCl-CaCl₂ molten salts forming a homogeneous system. It was found that a series of tungsten and its alloy nanoparticles, such as W, W-Co, WC and WC-Co, were successfully recycled to synthesize at 750 °C using the homogeneous molten salts systems. Furthermore, the particle size of the as-prepared products is about 20~300 nm.

Acknowledgments

This work was financially supported by the National Natural Science Foundation of China (Nos. 51401004 and 51301005).

References

- [1]. G. S. Upadhyaya. Cemented tungsten carbides [J]. Mater. Des. 2001, 22: 411-412.
- [2]. G. S. Upadhyaya. Materials science of cemented carbides-an overview [J]. Mater. Des. 2001, 22: 483-489.
- [3]. J. Guo, P. Fan, X. Wang, et al. Formation of Co-capping during sintering of straight WC-10 wt.% Co [J]. Int. J. Refract. Met. Hard Mater. 2010, 28: 317-323.
- [4]. K. Friedrichs, K. Moertl. Development of new types of carbides with ultrafine and even finer tungsten carbide powders [C]. in: Proceedings of Powder Metallurgy World Congress, Orlando, U.S.A., 2002.
- [5]. V. I. Stanciu, V. Vitry, F. Delaunois. Tungsten carbide powder obtained by direct carburization of tungsten trioxide using mechanical alloying method [J]. J. Alloys Compd. 2016, 659: 302-308.
- [6]. W. Su, Y. X. Sun, J. Feng, et al. Influences of the preparation methods of WC-Co powders on the sintering and microstructure of coarse grained WC-8Co hard metals [J]. Int. J. Refract. Met. Hard Mater. 2015, 48: 369-375.
- [7]. S. H. Chang, P. Y. Chang. Investigation into the sintered behavior and properties of nanostructured WC-Co-Ni-Fe hard metal alloys [J]. Mater. Sci. Eng. 2014, 606 (A): 150-156.
- [8]. L. Prakash. Applications of fine grained tungsten carbide based cemented carbides [J]. Int. J. Refract. Metals Hard Mater. 2005, 13: 257-264.
- [9]. R. Porat, S. Berger, A. Rosen. Synthesis and Processing of Nanocrystalline WC/Co Powders [C]. in: 14th Plansee Seminar 97, Plansee Proceedings, v.2, Cemented Carbides and Hard Materials, 1997, 582-595.
- [10]. J. P. Deloume, P. Marote, C. Sigala, et al. Study of the reaction of tungsten carbide in molten alkali metal nitrates, Syntheses of divalent (s and d blocks) metal tungstates [J]. Int. J. Refract. Metals Hard Mater. 2003, 174: 1-10.
- [11]. C. S. Freemantle, N. Sacks, M. Topic, et al. Impurity characterization of zinc-recycled WC-6 wt.% Co [J]. Int. J. Refract. Metals Hard Mater. 2014, 44: 94-102.
- [12]. T. Indrek, T. Thomas, K. S. Kontturi, et al. Nanostructured carbide-derived carbon synthesized by chlorination of tungsten carbide [J]. Carbon. 2011, 49: 4427-4433.

- [13]. S. Hairunnisha, G. K. Sendil, J. P. Rethinaraj, et al. Studies on the preparation of pure ammonium para tungstate from tungsten alloy scrap [J]. *Hydrometallurgy*. 2007, 85: 67-71.
- [14]. W. G. Jung. Recovery of tungsten carbide from hard material sludge by oxidation and carbothermal reduction process [J]. *Int. J. Refract. Metals Hard Mater*. 2014, 20(4): 2384-2388.
- [15]. A. Sampath, T. S. Sudarshan. Recycling of WC-Co from scrap materials [J]. *Powder Metall*. 2002, 45: 21-25.
- [16]. S. Venkateswaran, W. D. Schubert, B. Lux. W-scrap recycling by the melt bath technique [J]. *Int. J. Refract. Met. Hard Mater*. 1996, 14: 263-267.
- [17]. J. C. Lee, E. Y. Kim, J. H. Kim, et al. Recycling of WC-Co hardmetal sludge by a new hydrometallurgical route [J]. *Int J Refract Met Hard Mater*. 2011, 29: 365-371.
- [18]. P. K. Mehrotra. Strategies to reduce environmental impact of hardmetal production [J]. *Int J Refract Met Hard Mater*. 2015, 49: 95-98.
- [19]. N. Wang, C. Du, J. G. Hou, et al. Preparation of Nb-Al nanoparticles by sodiothermic homogeneous reduction at low temperature in molten salts [J]. *Intermetallics*, 2013, 43: 45-52.
- [20]. C. Du, N. Wang, J. G. Hou, et al. Facile synthesis of Nb-Al alloy powders via sodiothermic reduction in molten salts [J]. *J. Alloys Compd*. 2013, 555: 405-411.
- [21]. C. Du, N. Wang, J. Zhu, et al. Production of intermetallic compound powders through sodium and hydrogen reduction [J]. *Mineral Process. Extra. Metall. Review*. 2013, 122: 219-222.
- [22]. N. Wang, K. Huang, J. G. Hou, et al. Preparation of niobium powder by sodiothermic reduction of Nb₂O₅ in molten salts [J]. *Rare Metals*, 2012, 31(6): 621-626.
- [23]. N. Wang, C. Y. Huang, Y. Zhang, et al. Preparation of Nb₃Al powder by chemical reaction in molten salts [J]. *Rare Metals*, 2015, 06, 17.
- [24]. E. B. Freidina and D. J. Fray, Study of the ternary system CaCl₂-NaCl-CaO by DSC [J]. *Thermochimica Acta*. 2000, 356 (1-2): 97-100.
- [25]. E. B. Freidina and D. J. Fray. Study of the ternary system CaCl₂-NaCl-CaO by DSC [J]. *Thermochimica Acta*. 2000, 354: 59-62.
- [26]. R. O. Suzuki. Calciothermic reduction of TiO₂ and in situ electrolysis of CaO in the molten CaCl₂ [J]. *J. Phys. Chem. Solids*. 2005, 66 (2-4): 461-465.
- [27]. S. L. Wang and F. S. Zhang. Dissolution thermodynamics of CaO in CaCl₂-CaO and equimolar CaCl₂-NaCl-CaO [J]. *J. Northeastern University (Natural Science)*. 2010, 31 (01): 92-95.

RHEOLOGICAL BEHAVIOR OF FAYALITE BASED SECONDARY COPPER SMELTER SLAG IN IRON SATURATION

Huayue Shi¹, Liugang Chen¹, Annelies Malfliet, Tom Peter Jones¹, Bart Blanpain¹, Muxing Guo¹

¹Department of Materials Engineering, KU Leuven

Kasteelpark Arenberg 44 bus 2450, 3001 Leuven, Belgium

Keywords: rheology, shear thinning, fayalite slag, slag polymerization

Abstract

A fayalite based slag is formed during the smelting process of secondary copper containing resources. Of particular importance is the slag viscosity which quantifies the flow properties of the slag and affects the reaction kinetics, the refractory corrosion in the smelter and operational practice. In the present work, a high temperature rheometer system has been employed to study the rheological behavior of the industrial slag system FeO-ZnO-SiO₂-Al₂O₃-CaO (FeO/SiO₂ = 1-1.5, ZnO = 6-8 wt %, CaO = 1.5 wt % and Al₂O₃ = 4.5 wt %) at 1150 °C with iron saturation. The slag behaves as a shear thinning fluid. The degree of shear thinning was quantified by fitting the flow curve with the Oswald-De Waele power law model. The relation between the slag composition and the flow behavior index has been discussed.

Introduction

A fayalite based slag is formed during copper smelting processes of secondary resources. Besides FeO and SiO₂, this slag also contains a considerable amount of ZnO, Al₂O₃ and traces of CaO, Na₂O and Cr₂O₃. As a key property of the slag, viscosity influences the performance of this metallurgical process in both kinetic and thermodynamic ways.

Due to its particular importance in many metallurgical slags, the viscosity of the FeO-SiO₂ system has been studied for many decades. However, among all the reported data, large scatter exists. Some researchers found that the viscosity of FeO-SiO₂ exhibits a peak near the fayalite composition (2FeO-SiO₂), while others denied the existence of the viscosity peak [1-3]. Moreover, most of the reported viscosity of fayalite slag was measured at relatively high temperature (>1250 °C). Viscosity data in the temperature range of secondary copper smelting (1130 °C-1150 °C) is rare. Hence, the study of the rheological behavior of the secondary copper smelter slag not only offers guidelines for the industrial, but also contributes to the deeper understanding of the fayalite based slag system.

In this research, an Anton Paar FRS-1600 high temperature rheometer system was employed. By measuring the viscosity at various shear rates, the rheological behaviour of the industrial slag system FeO-ZnO-SiO₂-Al₂O₃-CaO (FeO/SiO₂ = 1-1.5, ZnO = 6-8 wt %, CaO = 1.5 wt % and Al₂O₃ = 4.5 wt %) at 1150 °C was studied. In order to mimic the reducing atmosphere of the industrial process, the measurements were conducted under iron saturation.

Experimental Procedure

The samples were prepared from fayalite slag which was produced in a secondary copper smelting process. The slag had been tapped at around 1150 °C and instantly quenched in water. The slag granules were then dried and ground into powders. SiO₂ or ZnO were added into the slag to achieve the desired composition (Table 1). According to the previously studied phase relation of the same slag system, the composition of the sample was chosen within the fully liquid range to ensure that no solid precipitation will occur at 1150 °C [4].

Table1: Chemical composition of the slag samples for viscosity measurement

sample	Composition (wt %)						
	FeO	SiO ₂	ZnO	CaO	Al ₂ O ₃	Na ₂ O	FeO/SiO ₂
A1	49.45	33.96	8.34	1.76	4.06	2.41	1.46
A2	47.58	36.46	8.02	1.69	3.91	2.32	1.31
A3	45.69	41.44	6.07	1.22	4.54	1.04	1.10
A4	43.67	44.03	5.80	1.16	4.34	0.99	0.99

The rheological properties of the slag samples were measured using a rheometer system (Anton Paar FRS 1600), as shown in Fig. 1. The system consists of a DSR 502 air bearing rheometer head and a tube furnace (Carbolite STF 16/180) which enables the rheological measurement up to 1600 °C. The rheometer was water- and air- cooled to prevent overheating of the electronic units.

In order to ensure the reducing atmosphere, an iron crucible and spindle were employed. The inner diameter and depth of the crucible were 30 mm and 80 mm, respectively. The cylinder spindle has a height of 41 mm and the diameter was 27.6 mm. The tip of the cylinder was cone shaped. The spindle was connected to the rheometer with a concentric alumina shaft. A similar alumina shaft supported the crucible on the pneumatic lift. During the measurement, argon was used to protect spindle and crucible from oxidation, the flow rate was 200 L/h.

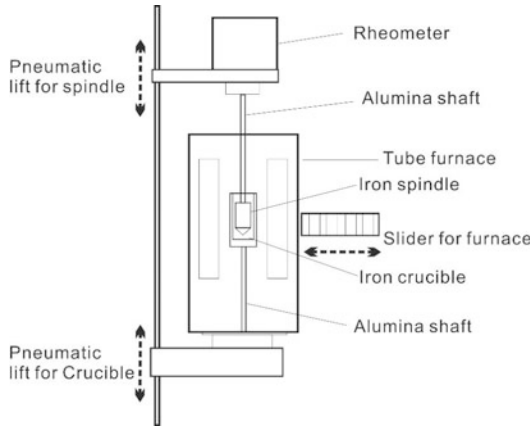


Figure 1. Schematic of FRS-1600 high temperature rheometer

In order to eliminate possible errors caused by the end effect, the measuring position of spindle in the crucible was fixed at 13.5 mm from the bottom. In the viscosity measurement, 60 gram of powder was required to ensure the complete immersion of spindle. The furnace was heated up to 1170 °C with an average heating rate of 28 °C/min, and was held at this temperature for 20 minutes to melt the powder. Then the furnace temperature was lowered to 1150 °C where it was maintained for another 30 minutes to allow the slag to equilibrate. The spindle was slowly lowered into the melt. After reaching the measuring position, the spindle was kept still for another 10 minutes to make sure both the spindle and slag sample are at the correct temperature before starting the rotation.

The spindle was first rotating at a shear rate of 1 s⁻¹ and gradually the rotation speed was increased to the final shear rate of 100 s⁻¹. The rheometer measured the torque and normal force applied on the spindle during the process. Five data points were recorded in each decade (1-10 s⁻¹, 10-100 s⁻¹) to characterize the slag viscosity at different shear rates. The first 2 data points were neglected due to the unstable flow at the beginning of the measurement. The measurement were repeated for 3-5 times for each sample to obtain average value.

Results and Discussion

The viscosity as a function of the shear rate in the range 1-100 s⁻¹ is shown in Fig. 2. For all the slag samples, different shear rates yield different viscosity. More specifically, all the slag samples exhibit a typical shear thinning behavior, i.e. the viscosity decreases with increasing shear rate. It is also noteworthy that in the present case, the shear thinning effect did not continue consistently over the entire shear rate range. As shown in Fig. 2, for all the samples the viscosity

decreases sharply in the low shear rate range ($<10 \text{ s}^{-1}$) and tends to be gradually stabilized with further increasing the shear rate. As the shear rate approaches 100 s^{-1} , the influence of increasing shear rate on the slag viscosity is decreased.

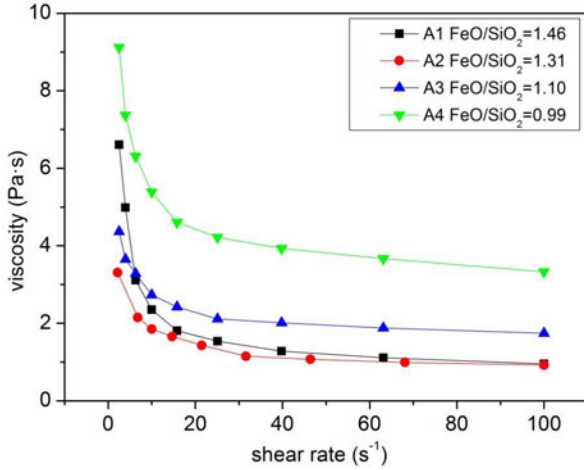


Figure 2. Relation between the viscosity and the shear rate, $1150 \text{ }^{\circ}\text{C}$

The Oswald-De Waele power law model was used to quantify the degree of shear thinning:

$$\eta = K \dot{\gamma}^{n-1} \quad (1)$$

$$\log \eta = \log K + (n-1) \log \dot{\gamma} \quad (2)$$

In Eq. (1), the power law model characterizes the viscosity (η) as a function of shear rate ($\dot{\gamma}$), flow consistency index (K) and flow behavior index (n). The flow behavior index (n) indicates the degree of shear thinning/thickening. In the case of Newtonian fluids, n takes the value of 1. For a shear thickening fluid, n is higher than 1 while for a shear thinning fluid, n takes a value between 0 and 1. As n approaches 0, the degree of shear thinning increases. By applying logarithm on Eq. (1), as shown in Eq. (2), the logarithm of the viscosity is linearly correlated with the logarithm of the shear rate, with a slope of $(n-1)$.

In Fig. 3, the viscosity-shear rate relation is shown in a double logarithmic plot. The flow behavior index n can be obtained by fitting the data points with Eq. (2). As mentioned before, the shear thinning trend of the slag does not continue consistently over the entire shear rate range. Hence the flow behavior index was evaluated by stage, in which n_1 , n_2 and n_0 were used to

denote the flow behavior index in the shear rate of 1-10 s^{-1} , 10-100 s^{-1} , and the entire range, respectively.

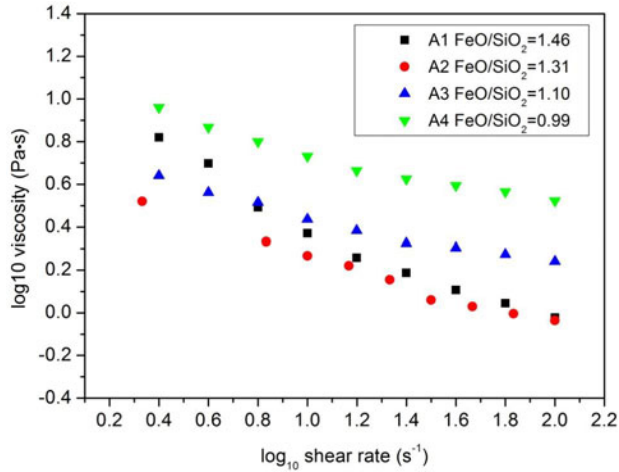


Figure 3. Viscosity-shear rate relation at 1150 °C in logarithm scale

In Fig. 4, the average values of the three indexes for the slag samples are shown. For all the measured samples, a lower shear rate yields a smaller flow behavior index compared with the higher shear rate range, which means stronger shear thinning in the low shear rate range.

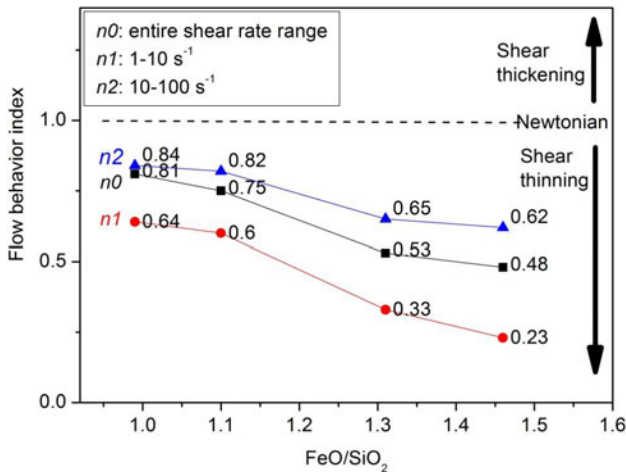


Figure 4. In-step flow behavior index of the slag system as a function of FeO/SiO₂ at 1150 °C

Similar shear-thinning behavior was reported by Shin in the case of calcium-silicate based mold flux at 1350 °C [5, 6]. It was also found that the shear-thinning was weakened by applying higher shear rate ($> 35 \text{ s}^{-1}$). The shear thinning effect of the silicate melt was explained by the concept of temporary viscosity loss. The molecular bonds of the molten mold flux, which were randomly oriented before applying any shear stress, started to align in a single direction in the rotation process. This gives rise to the viscosity decrease in the early stage of the measurement. Once the bonds were completely aligned in the same direction, the viscosity was stabilized. The amount of molecule bond was found closely related with the degree of polymerization. In the mold flux with higher degree of polymerization, stronger shear thinning was found.

Fig. 4 shows the relation between the slag composition and the flow behavior index. FeO is often considered as a network modifier in the silicate melt and has a disruptive effect on the network. However, this is not the case for the present slag. As can be seen in Fig. 4, the increase of FeO/SiO₂ ratio gives rise to a lower value of the flow behavior index, which corresponds to a stronger shear thinning. This implies that with increasing FeO content in the slag system, the degree of polymerization is increased.

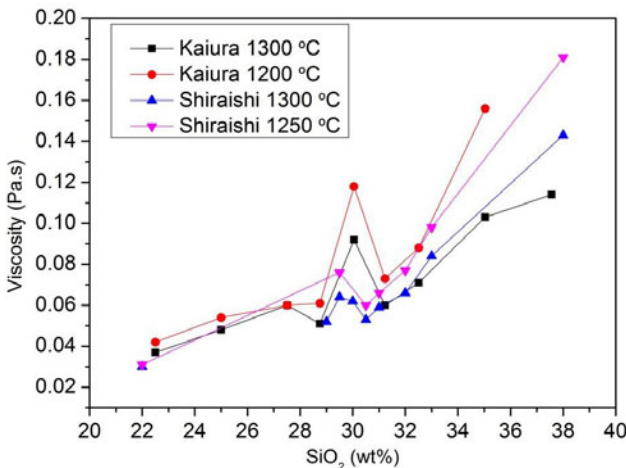


Figure 5. Published viscosity measurement data of FeO-SiO₂ system at 1200 °C -1300 °C

The viscosity of FeO-SiO₂ system has been studied for decades. Many researchers reported that at the composition corresponding with fayalite (Fe₂SiO₄), the viscosity exhibits a local maximum value, as shown in Fig. 5. Kaiura reported that the local viscosity maximum can be identified in the temperature range of 1200 °C - 1350 °C. A theory was proposed that molecular clusters were formed at this temperature range, which was accountable for the viscosity increase[1]. It was estimated by Shiraishi that the average molecule cluster consists of 11-12 molecules and takes

around 15% in volume at the melting point of fayalite and gradually vanished by increasing temperature[2].

As in the present case, by increasing the FeO content, the composition of the slag moves towards the fayalite composition (corresponding weight ratio $\text{FeO}/\text{SiO}_2 = 2.5$), where there is a tendency for the molecular units to aggregate to form clusters. The formation of clusters increases the degree of polymerization of the slag system and yields a shear thinning effect. This hypothesis also explains the divergence in the reported viscosity data of fayalite based slag. In Fig.3, the viscosity of A1 (with lowest SiO_2 content among the four samples) is higher than A2 and A3 which contains more SiO_2 . As the shear rate increases, the viscosity of A1 decreases dramatically and finally became the lowest among the 4 samples. Similarly, an obvious local maximum of viscosity can be detected if the slag system was measured with low shear. By increasing shear rate, the local maximum turns to be less evident and even vanished.

Conclusion

The rheological behavior of the industrial slag system $\text{FeO-ZnO-SiO}_2\text{-Al}_2\text{O}_3\text{-CaO}$ ($\text{FeO}/\text{SiO}_2 = 1\text{-}1.5$, $\text{ZnO} = 6\text{-}8$ wt %, $\text{CaO} = 1.5$ wt % and $\text{Al}_2\text{O}_3 = 4.5$ wt %) was studied with a high temperature rheometer system at 1150 °C in a condition of iron saturation.

It was found that the slag behaves as a shear thinning fluid. The Oswald-De Waele power law model was used to quantify the rheological behavior of the slag samples. The slag yields a stronger shear thinning in the low shear rate range (< 10 s^{-1}) than in the high shear rate range (> 10 s^{-1}). This was explained by the alignment of molecule bonds at the early stage of rotation.

The slag with high FeO was found to have smaller flow behavior index, e.g. higher degree of shear thinning. This phenomenon was explained by the theory of slag polymerization. Molecule clusters are formed at the composition of fayalite (Fe_2SiO_4) and this increases the degree of polymerization in the slag melt. The closer the composition of the slag towards fayalite, the higher degree of polymerization is expected, which leads to more pronounce shear thinning.

References

1. G. H. Kaiura, J.M.Toguri. and G. Marchant, *Viscosity of the fayalite-based slag*. The Metallurgical Society of CIM, 1977. **Annual Volume**: p. 156-160.
2. Y. Shiraishi, K.Ikeda., A. Tamura, and T. Sairo, *On the viscosity and density of the molten FeO-SiO₂ system*. Transactions of the Japan Institute of Metals and Materials, 1978. **19**: p. 264-274.
3. M. Chen, S. Raghunath, and B. Zhao, *Viscosity Measurements of “FeO”-SiO₂ Slag in Equilibrium with Metallic Fe*. Metallurgical and Materials Transactions B, 2013. **44**(3): p. 506-515.
4. H. Shi, L. Chen, P.T. Jones, B. Blanpain, M. Guo, *Composition modification of the ZnO containing fayalite slag from secondary source copper smelting*, TMS 2016, Nashville , U.S
5. S. Shin, J. Cho, S. Kim, *Shear Thinning Behavior of Calcium Silicate-Based Mold Fluxes at 1623 K*. Journal of the American Ceramic Society 2014. **97**(10): p. 3263-3269.
6. S. Shin, D. Yoon, J. Cho, S. Kim, *Controlling shear thinning property of lime silica based mold flux system with borate additive at 1623K*. Journal of Non-Crystalline Solids, 2015. **425**: p. 83-90.

SILICON AND MANGANESE PARTITION BETWEEN SLAG AND METAL PHASES AND THEIR ACTIVITIES PERTINENT TO FERROMANGANESE AND SILICOMANGANESE PRODUCTION

Hakan Cengizler¹ and R Hurman Eric²

¹TMYO, Celal Bayar University, Turgutlu, Turkey

² Metallurgy and Materials Engineering, University of the Witwatersrand, Johannesburg, South Africa
Rauf.Eric@wits.ac.za, phone: +27117177537

Keywords: Ferromanganese, silicomanganese, slag, metal, equilibrium

Abstract

Equilibrium between MnO-CaO-MgO-SiO₂-Al₂O₃ slags and carbon saturated Mn-Si-Fe-C alloys was investigated under CO at 1500°C. Manganese and silicon activities were obtained by using the present data and the previously determined MnO and SiO₂ activities of the slag. Quadratic multi-coefficient regression equations were developed for activity coefficients of manganese and silicon. The conclusions of this work are: (i) increase in the basicity and the CaO/Al₂O₃ ratios decreases the Mn distribution ratio, (ii) increase in the silica concentration and the MgO/CaO ratio increases the Mn distribution ratio, (iii) carbon and manganese as well as carbon and silicon of the metal phase are inversely proportional, (iv) as Mn/Fe and Mn/Si ratio increases in the metal the carbon solubility increases, (v) decrease in the basicity increases the silicon content of the metal and (vi) increase in the silica content of the slag increases the silicon content of the metal and this effect is more pronounced at the higher Mn/Fe and Mn/Si ratios.

Introduction

High-carbon ferromanganese is the most common alloy used as an additive in the steel industry to control deoxidation of steel and to produce manganese-bearing alloys. Two processes are employed in the manufacture of high carbon ferromanganese referred to as the low- (discard) and high- (enriched) slag practice. The low slag practice is the least economical in terms of production costs per ton of ferromanganese and it produces the normal grades of high-carbon ferromanganese with secondary slags ranging from 8 to 15 per cent contained MnO. This practice is employed when the manufacturer does not produce silicomanganese for which a slag of higher manganese content can be used as a raw material or has no sale for the higher MnO containing slag. In high slag practice, the slags produced during manufacture of high-carbon ferromanganese contain between 25 and 40 per cent MnO. These manganese-rich slags are used for the production of silicomanganese by carbothermic reduction due to their extremely high Mn-to Fe ratio, high silica content and low phosphorus content. In manufacturing high-carbon ferromanganese and silicomanganese in the smelting furnace, the factor which determines the quality of the product, the efficiency of the process and the final recovery rate of manganese is the distribution of the valuable manganese between the alloy, slag and gas phases and the phase equilibria among them. In other words, the efficiency is governed, to a large extent, by the thermodynamic activities of MnO in the slag^{1,2} and that of Mn in the alloy phase. An extensive experimental data and information on the thermodynamic activity of MnO in MnO-CaO-MgO-SiO₂-Al₂O₃ synthetic ferromanganese slags

were gathered and was reported¹⁻³ elsewhere. Some noteworthy relationships from literature pertinent to this work are the following. Firstly, the inverse relationship between the silicon and carbon in the metal phase and the increase in carbon solubility of the melt with a decrease in Fe/Mn ratio can be mentioned^{4, 5-10}. Although, the reported data⁵⁻¹⁰ are not in good agreement with each other, a general tendency is that the increasing carbon and silicon additions lower the manganese activity leading to large negative deviations from ideality in liquid manganese. Although it appears that a substantial amount of information has been available on manganese containing liquid alloy systems, the majority of these are related to conditions in iron and/or steelmaking where manganese is in low concentrations. Furthermore, there are few studies on thermodynamics and slag-metal equilibria pertinent to high-carbon ferromanganese and silicomanganese smelting at typical process temperature of 1500°C. The present research work is directed to fill in some of these gaps.

Experimental procedure

A gas-tight vertical molybdenum resistance furnace has been assembled and employed for the study of slag-metal equilibrium. The reaction tube was continuously purged with chemically pure CO gas which was introduced from the bottom end of the alumina furnace work tube and was vented to the fume hood through the gas outlet on the top of the work tube. Actual sample temperatures in the furnace were measured with a Pt-6 %Rh/Pt-30%Rh (B-type) thermocouple. In the slag-metal distribution experiments, graphite crucibles were used. The slag was prepared as a homogenous mixture made from its pure components. In total, 55 slag samples of different compositions containing MnO, CaO, MgO, SiO₂ and Al₂O₃ were prepared from analytical-reagent grade oxide powders. However, prior to use, all the oxides except MnO were first calcined in an electrical resistance-heated muffle furnace for about 24 hours at 1200°C. After cooling, the required amount of CaO, MgO, SiO₂ and Al₂O₃ were carefully weighed and thoroughly mixed in the desired proportions to give slags of the designed compositions in an agate mortar under a liquid blanket of acetone until all the acetone had vaporized. The dried mixtures were then pressed into disks. These disks were re-calcined for 12 hours at about 1200°C in order to promote sintering, and thereby homogenization of the samples. On cooling, the homogenized disks were crushed and ground in an agate mortar and mixed with required quantities of reagent-grade MnO in an agate mortar as described above before every individual run. The slag basicity ranged from about 0.4 to 1.2 and MnO contents ranged from 5 to 30 mass per cent. The initial Al₂O₃ content of slags were kept at 5 mass per cent level. CaO content varied in the range 20 to 35 mass percent, MgO in the 5 to 17.5 mass percent and SiO₂ in the 27 to 58 mass percent range. The metal charge which consisted of Mn, Si, C and Fe was prepared from electrolytic manganese, iron, high-purity silicon and spectrographic-grade graphite powders. From these, a number of master alloys were prepared by melting the elements under an argon atmosphere in graphite crucibles. The composition of the alloys for the experimental runs was adjusted by adding the necessary pure elements in powder form to these master alloys. The ranges of initial alloy compositions as determined by chemical analysis are shown in Table 1. It was found that a minimum of 10 hours was necessary for equilibration¹. In the slag-metal equilibrium distribution experiments, the charge consisted of about 6 g of metal and 4 g of slag of selected compositions and was contained in graphite crucibles. The reaction tube of the furnace was flushed for about 15 minutes with spectrographically pure argon before the CO atmosphere was employed. The flow rate of CO was kept at 600 cm³/min. After equilibration at 1500°C the CO gas was turned off and the argon was allowed to pass through the reaction tube and the crucibles were lowered to the bottom water-cooled end of the furnace quickly. The apparatus was opened from the bottom, and the graphite crucibles with their contents were immediately quenched in water. The crucible was broken and the slag and metal phases were removed from the crucible and separated. Both phases were crushed, ground, pulverized and were

Table 1. The initial metal-phase compositions.

Phase	Mn, %	Fe, %	Si, %	C, %
Ferromanganese	82.19	9.34	1.50	7
	79.77	11.73	1.50	7
	74.56	16.94	1.50	7
Silicomanganese	66.64	19.30	12.34	1.7
	62.55	19.30	16.46	1.7
	57.04	19.30	21.94	1.7

kept in sealed bottles in desiccators until their contents were analysed. The analysis of alloys was done for Mn, Si, Fe and C. The whole composition of slag was analysed and the total composition amounted to within 98 and 101 mass per cent.

Results and Discussions

Manganese distribution

The effect of basicity ratio on the logarithm of the distribution ratio of manganese is seen in Figure 1. The distribution ratio of a species “i” is defined as per cent of “i” in the slag divided by per cent of “i” in the metal phase. In all the figures, round and square brackets indicate the slag and metal phases respectively. Figure 1 shows that an increase in the basicity ratio causes an increase in the manganese content of the metal phase relative to that of the slag. It is well known¹¹⁻¹⁴ that the interaction of Ca^{2+} ions with SiO_2 is stronger than those of mixed Ca^{2+} and Mg^{2+} ions and Mg^{2+} . Thus, one can conclude that an increase in the amount of CaO can lead to an increase in the formation of Ca_2SiO_4 orthosilicate, leading to higher a_{MnO} values in the slags. The increase in the a_{MnO} values favours the transfer of manganese into the metal phase.

Figure 2 shows the relation between CaO-to- Al_2O_3 ratio and the Mn distribution between slag and metal phases. The Si-to-Fe ratio is 0.23 in the metal phase. As it is seen in the figure, when CaO replaces Al_2O_3 in the slag, the Mn transfer to the metal phase increases. This can also be explained by referring to increased MnO activities by an increase in the concentration of CaO in the slag.

In the metal phase, the carbon and manganese concentrations are directly proportional to each other as seen in Figure 3. An increase in manganese concentration increases the saturation limit of carbon in Mn-Fe-Si-C ferroalloys. Linear regression equation was derived to predict the carbon concentration (in mass per cent) and very high correlation coefficient ($r^2=0.930$) was obtained. At 1500°C, the regression equation is: $\text{C}\% = 30.6952 + 5.4453 \text{ Mn}\%$.

Silicon distribution

The relationship between the equilibrium solubility of carbon (at saturation) and silicon in Mn-Fe-Si-C alloys is illustrated in Figure 4 which is applicable for ferromanganese alloys where three different data groups with different Mn-to-Fe ratios (3.7, 6.7, and 7.4) are plotted. It can be seen that, at constant silicon contents, as the Mn-to-Fe ratio increases, the carbon solubility in the metal phase increases. The carbon and silicon concentrations in the metal phase are inversely related as expected and this behaviour can be explained in terms of the stability of carbides. As silicon lowers the solubility of carbon, the conditions becomes less favourable for carbide formation. Thermodynamically, this is an indication that silicon lowers the activity of carbon.

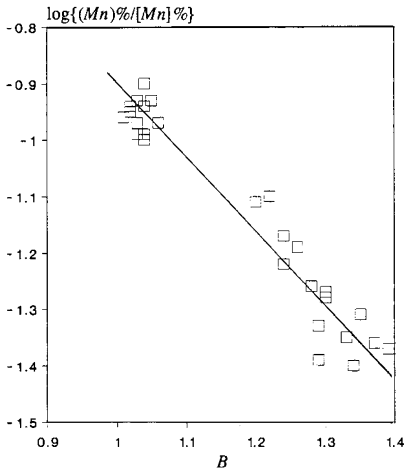


Figure 1. The effect of basicity ratio on manganese distribution at 1500°C under CO atmosphere.

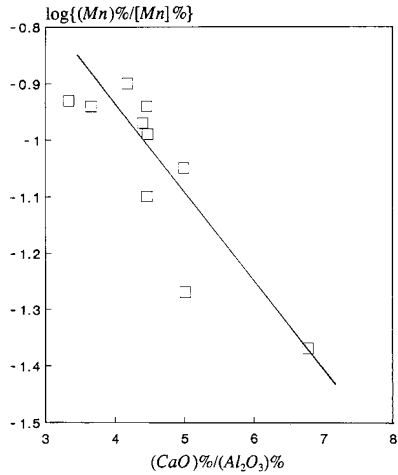


Figure 2. The effect of CaO/Al₂O₃ ratio on manganese distribution at 1500°C under CO atmosphere. Si/Mn=0.23

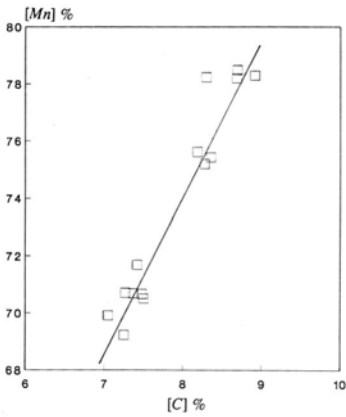


Figure 3. The effect of the Mn content on the C content of the metal phase (Si:Fe \cong 0.18) at 1500°C under CO atmosphere.

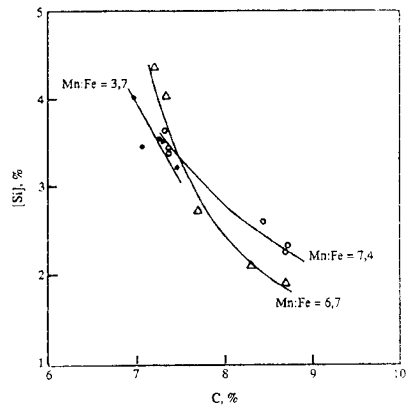


Figure 4. The effect of the Si content on the C content of the metal phase with different Mn-to-Fe ratios at 1500°C under CO atmosphere.

The silicon content of the metal phase in ferromanganese and silicomanganese compositions are to a great extent affected by the silica content of the slag with which they are in equilibrium. Figure 5 show the effect of the Mn-to-Fe ratios of the metal phase on the relationship between the silicon content of the metal and silica content of the slag in ferromanganese compositions. In Figure 5, three data groups with different Mn-to-Fe ratios (3.7, 5.5, and 6.7) are superimposed. The increase in the silica activity in the slag with increasing silica concentration results in the transfer of silicon from the slag to the metal.

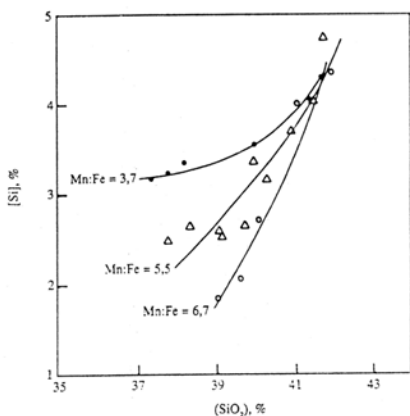


Figure 5. The effect of silica content of the slag on the Si content of the metal at 1500°C under CO.

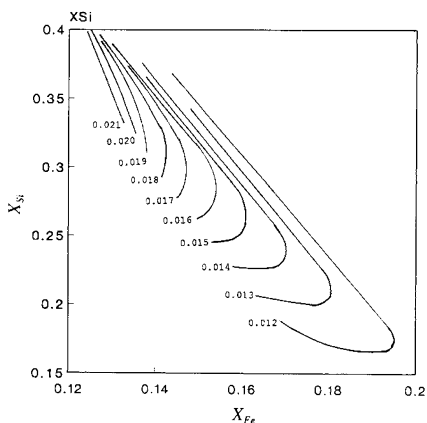
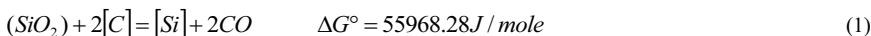


Figure 6. Iso-activity curves of Si in silicomanganese melts saturated with C at 1500°C.

It is also established that as the CaO-to-Al₂O₃ ratio increases (at more or less constant Al₂O₃ content) the silicon content of the metal decreases. As the Mn-to-Fe and Mn-to-Si ratio increases, the effect of increasing CaO-to-Al₂O₃ ratio on the silicon content of metal is even greater. This indicates that the activity of silica in the slag is decreased by the substitution of CaO in accordance with the network modification power of CaO.

Manganese and silicon activities in Mn-Si-Fe-C melts

The results of the previous investigation by the present authors on MnO activities¹ in manganese slags were in excellent agreement with those predicted from the slag model developed by Gaye¹⁵. Therefore, SiO₂ activities in the slag were predicted through the same slag model¹⁵ in order to calculate the Si activities in Mn-Si-Fe-C metal phase and the compositional information of the slag and metal phases were provided from the results of slag-metal equilibrium experiments making use of the following reaction at the experimental temperature of 1500°C.



The equilibrium constant of this reaction can be written as:

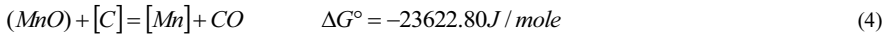
$$K = \frac{a_{Si} \times (p_{CO})^2}{a_{SiO_2} \times (a_C)^2} \quad (2)$$

In equation (2), $a_C = 1$ and $p_{CO} = 1$ atm. Thus, the equation (2) reduces to:

$$K = \frac{a_{Si}}{a_{SiO_2}} \quad (3)$$

Where $K = 0.02244$.

The Mn activities were also calculated similarly using known activities of MnO in the slag^{1,2} through the equation



The equilibrium constant of this reaction can be written as:

$$K = \frac{a_{Mn} \times p_{CO}}{a_C \times a_{MnO}} \quad (5)$$

In equation (5), $a_C = 1$ and $p_{CO} = 1$ atm, therefore, the equation (5) reduces to:

$$K = \frac{a_{Mn}}{a_{MnO}} \quad (6)$$

Where $K = 4.953$.

The activities of Si and Mn can be easily calculated through the equations (3) and (6).

The model equations for activity coefficients of Si and Mn for silicomanganese compositions are:

$$\ln \gamma_{Si} = 8.2237 - 13.4747X_{Si} - 123.5X_{Fe} - 28.5236X_{Mn}^2 + 199.7X_{Mn}X_{Fe} + 79.5894X_{Si}X_{Fe} \dots \dots \dots (7)$$

$$\ln \gamma_{Mn} = 74.4176 - 300.1X_{Mn} + 320.5X_{Mn}^2 - 122.8X_{Si}^2 - 143.8X_{Mn}X_{Fe} + 332.3X_{Si}X_{Fe} \dots \dots \dots (9)$$

and the model equations for activity coefficients for ferromanganese compositions are:

$$\ln \gamma_{Si} = 9.6390 - 14.4553X_{Mn} - 108.7X_{Si} - 247.9X_{Fe} + 352.9X_{Mn}X_{Fe} + 1106.0X_{Si}X_{Fe} \dots \dots \dots (8)$$

$$\ln \gamma_{Mn} = -6.8048 + 8.0995X_{Mn} + 30.2975X_{Si} - 1427.3X_{Si}^2 - 303.9X_{Fe}^2 + 1263.2X_{Si}X_{Fe} \dots \dots \dots (10)$$

Activities of manganese and silicon display strong negative deviations from ideality in both silicomanganese and ferromanganese compositions. The iso-activity contours of silicon for silicomanganese and ferromanganese compositions were derived through the model equations (7) and (9) at 1500°C and are shown in Figures 6 and 7.

As it was mentioned before, the figures represent a carbon-saturated system and if atomic fraction of silicon (X_{Si}) increases, then, atomic fraction of carbon (X_C) decreases. Namely, the carbon concentration

decreases as it goes up to the top part of the figure. In this system, X_C takes a certain value if the atomic fraction of iron; X_{Fe} and X_{Si} are given, and therefore, the compositions of all carbon-saturated alloy melts of the Mn-Si-Fe-C system can be represented on a plane with X_{Fe} and X_{Si} on both axis as shown in Figures 6 and 7.

In silicomanganese composition (Figure 6), the predicted iso-activity contour values vary between 0.012 and 0.021. However, in ferromanganese composition (Figure 7), the silicon activities are even smaller (between 5×10^{-4} and 3×10^{-3}). The difference between the silicon activities in these two compositions can to a certain extent, be explained according to the difference in silicon concentrations (being higher in silicomanganese composition) in these compositions. Concerning the carbon saturated system Mn-Si-Fe-C; the related thermodynamic data is very scarce. Therefore, it is difficult to explain the order of magnitude change in iso-activity curves.

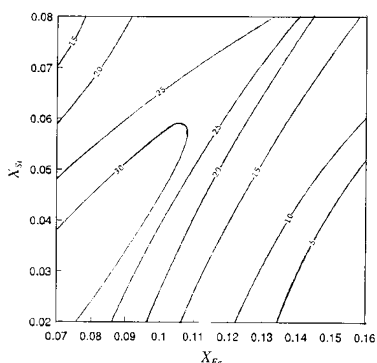


Figure 7. Iso-activity curves of Si in ferromanganese melts saturated with C at 1500°C ($\times 10^{-4}$).

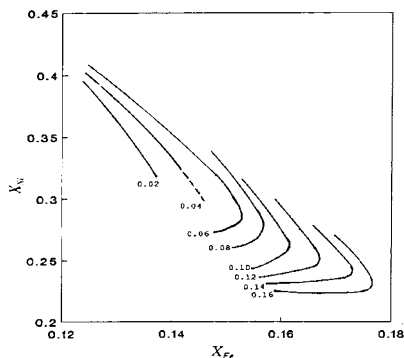


Figure 8. Iso-activity curves of manganese in silicomanganese melts saturated with C at 1500°C.

Figures 8 and 9 show the iso-activity contours of manganese which are derived through the model equations (8) and (10) for silicomanganese and ferromanganese compositions respectively. In Figure 8, in silicomanganese composition, an increase in X_{Fe} decreases a_{Mn} values. A decrease in X_{Fe} will increase X_{Mn} and X_{Si} in carbon-saturated system and this will lead to higher a_{Mn} values. In Figure 9, a decrease in X_{Si} at constant X_{Fe} first increases and then decreases the a_{Mn} values in ferromanganese composition. The increase in a_{Mn} is clear due to increase in X_{Mn} at fixed X_{Fe} and X_C values. However, even a further decrease in X_{Si} causes a_{Mn} to start decreasing which may be due to the fact that at very low silicon concentrations, the saturation solubility limit of carbon increases substantially favouring stronger Mn-C interactions and a tendency for Mn_5C_2 formation which will tend to decrease a_{Mn} values. When the results of the present study, are compared to the results of Tanaka^{16,17} who studied the same system, it is seen that the iso-activity contours of silicon and manganese have very similar patterns and there is reasonable agreement between the actual activity values.

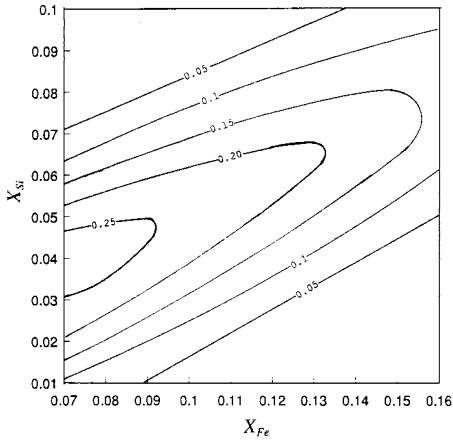


Figure 9. Iso-activity curves of manganese in ferromanganese melts saturated with C at 1500°C.

Conclusions

This research work was carried out to study the equilibrium distribution of Mn and Si between carbon-saturated Mn-Si-Fe-C alloys and MnO-CaO-MgO-SiO₂-Al₂O₃ slags that are typical of the production of ferromanganese in submerged arc electric furnaces in South Africa. Furthermore, an attempt was made to determine the activities of Mn and Si in the metal phase. The conclusions are outlined as follows:

- An increase in basicity ratio of the slag decreases the Mn distribution ratio,
- An increase in silica concentration of the slag increases the Mn distribution ratio,
- An increase in CaO-to-Al₂O₃ ratio of the slag decreases the Mn distribution ratio,
- An increase in MgO-to-CaO ratio of the slag increases the Mn distribution ratio,
- The carbon and manganese contents of the metal phase are directly proportional,
- The carbon and silicon concentrations in the metal phase are inversely related and, as the Mn-to-Fe or Mn-to-Si ratio increases, the carbon solubility in the metal phase decreases,
- An increase in the silica content of the slag phase increases the silicon content of the metal phase and this effect is even more pronounced at the higher Mn-to-Fe or Mn-to-Si ratios,
- The activities of Mn were computed by making use of slag-metal equilibrium data and MnO activity data gathered in earlier part of the present work^{1,2}.
- The activities of Si were computed by making use of slag-metal equilibrium data and the SiO₂ activities predicted through the slag model¹⁵
- Statistical model equations which represent $\ln \gamma_{Mn}$ and $\ln \gamma_{Si}$ data successfully were developed in order to use to predict the activity coefficients of Mn and Si in the compositional range of the present work.
- The iso-activity contours of Si and Mn in silicomanganese and ferromanganese compositions were derived.

References

1. Cengizler, H. (1993): Thermodynamic activity of MnO in manganese slags and slag- metal equilibria. Ph.D. Thesis”, University of the Witwatersrand, Faculty of Engineering, Johannesburg, South Africa.
2. Cengizler, H., Eric, R.H. Thermodynamic activity of manganese oxide in ferromanganese slags and the distribution of manganese between metal and slag phases, “Proceedings of the 6th International Ferroalloys Congress”, Cape Town, South Africa, 1992, Vol. 1, pp. 167- 174.
3. Cengizler,H., Eric, R.H. and Reuter, M. Modelling of Activity of MnO in Ferromanganese and Silicomanganese slags by Neural Nets, Proceedings of the 5th International Conference on Molten Slags, fluxes and salts, January, 1997, Sydney, Australia, ISS, Warrendale-PA, pp. 75-90.
4. Tuset, J.Kr., Sandvik, J., and Venås, K. SINTEF Research Report No. 340420, Trondheim, Norway, 1970.
5. Esin, O.A. and Vatolin, N.A. Application of the electro-force method to the study of the liquid manganese alloys, Zhur Priklad Khim, vol. 27, 1954, pp. 1252-1256.
6. Turkdogan, E.T., Hancock, R.A. and Herlitz, S.I. The solubility of graphite in manganese, cobalt and nickel, Journal of Iron and Steel Institute, vol. 182, 1956, pp. 274-277.
7. Petrushevskii, M.S. and Gel'd P.V. Equilibrium of carbon with liquid alloys of Fe, Mn, Si and C, Journal of Applied Chemistry of USSR, vol. 32, 1959, pp. 86-94.
8. Skiredj, O. and Elliot, J.F. carbon content of graphite-saturated Fe-Si-Mn alloys, 1400° to 1650 °C, Transactions of the Metallurgical Society of AIME, vol. 227, 1963, pp. 536- 538.
9. Tanaka, A. Activities of manganese in Mn-Fe-C, Mn-Si-C and Mn-Fe-Si-C melts at 1673 °K, Transactions of the Japan Institute of Metals, vol. 21, Oct. 1980, pp. 27-33.
10. Ni, R., Ma, Z., and Wei, S. Thermodynamic of Mn-Fe-C and Mn-Si-C system, Steel Research, vol. 61, no. 3, 1990, pp. 113-116.
11. Kubachevski, O., Evans, E.U., and Alcock, C.B. Metallurgical Thermochemistry, 5th ed. Oxford: Pergamon Press, 1979, pp. 114-178.
12. Barin, I. Thermochemical Data of Pure Substances, VCH Verlagsgesellschaft mbH, D-6940 Weinheim (Federal Republic of Germany), 1989, Part 2.
13. Pankratz, L.B., Stuve, J.M. and Gokcen, N.A. Thermodynamic data for Mineral Technology, Bulletin 677, U.S. Bureau of Mines, (1978).
14. Robie, R.A., Hemingway, B.S., and Fisher, J.R. Thermodynamic Properties of Minerals and Related Substances at 298,17K and 1 Bar (105 pascals) Pressure and at Higher temperatures. Bulletin 1452, Washington, U.S.A., Geological Survey, (1978), p. 456.
15. Gaye, H. A model for the representation of the thermodynamic properties of multicomponent slags, Centenary of Metallurgy Teaching in Glasgow, June, 1984, pp. 1-14.
16. Tanaka, A. Activities of manganese in Mn-Fe-C, Mn-Si-C and Mn-Fe-Si-C melts at 1673 °K, Transactions of the Japan Institute of Metals, vol. 21, Oct. 1980, pp. 27-33.
17. Tanaka, A. Equilibria between Mn alloy melts saturated with C and various kinds of molten slags and calculation of the activities, Tetsu-to-Hagane, vol. 66, 1980, pp. 1474-1483.

STABILITY OF FLUORINE-FREE MOULD FLUXES $\text{SiO}_2\text{-CaO-Al}_2\text{O}_3\text{-B}_2\text{O}_3\text{-Na}_2\text{O}$ FOR STEEL CONTINUOUS CASTING

Lin Wang¹, Jianqiang Zhang¹, Yasushi Sasaki¹, Oleg Ostrovski¹, Chen Zhang², Dexiang Cai²

¹School of Materials Science and Engineering, UNSW Australia, Sydney, 2052, Australia

²Steelmaking Research Department, Baosteel Group Corporation Research Institute, Shanghai, 201900, China

Keywords: mould flux, B_2O_3 , Na_2O , thermogravimetric analysis, evaporation

Abstract

B_2O_3 and Na_2O are key components of fluorine-free mould fluxes for continuous casting, but both are highly volatile which affects the flux stability. This paper investigates evaporation of the $\text{SiO}_2\text{-CaO-Al}_2\text{O}_3\text{-B}_2\text{O}_3\text{-Na}_2\text{O}$ fluxes (Na_2O : 6-10 wt%, CaO/SiO_2 ratio: 0.8-1.5) in the temperature range 1573 to 1673K using a thermogravimetric analysis method. The weight loss as a result of the flux evaporation increased with increasing temperature. The rate of evaporation increased significantly with the increase in the Na_2O content. The effect of the CaO/SiO_2 ratio in the range 0.8-1.3 on the evaporation rate was marginal. However, the increase of this ratio to 1.5 slowed down evaporation after approximately 1000 s. When 6.2 wt% Na_2O was added to the $\text{SiO}_2\text{-CaO-Al}_2\text{O}_3\text{-B}_2\text{O}_3$ flux, the apparent activation energy E_a for the evaporation reaction decreased from 365 to 193 kJ/mol, while a further increase in the Na_2O content to 9.1 wt% had a minor effect on E_a . The high evaporation rate of boracic fluxes in the presence of B_2O_3 and Na_2O was attributed to the formation of highly volatile NaBO_2 .

1. Introduction

Conventional commercial mould fluxes usually contain 4-10 wt% of fluoride to maintain heat transfer, melting temperature, and viscosity appropriate for the steel continuous casting [1]. However, the emission of fluorine causes water pollution, equipment corrosion, and health hazards [2]. Therefore, development of the fluorine-free mould fluxes is important to decrease environmental impact of metallurgical industry and equipment corrosion [2, 3, 4]. Na_2O is added to the fluorine-free mould fluxes to accelerate the crystallisation of mould fluxes and to decrease their melting temperature [5]. It was also suggested that the combination of B_2O_3 and Na_2O leads to the formation of boracic phase which might replace cuspidine, which is a key crystal phase in the fluorine-containing fluxes [2, 6].

However, high volatility of sodium containing compounds is a limitation in the industrial use of the Na_2O -containing boracic fluxes [7]. Besides, B_2O_3 itself might also evaporate at high temperatures. High volatility of Na_2O and B_2O_3 can change the chemical compositions of mould fluxes, and therefore their physicochemical properties. It was also reported that CaO/SiO_2 ratio could affect the flux evaporation rate because of the alternation of flux physicochemical properties, e.g. viscosity [8]. Thus, knowledge of kinetics and mechanism of evaporation of mould fluxes containing both B_2O_3 and Na_2O is important for the development of the F-free mould fluxes. Research in this area has been quite limited [8, 9, 10]. The purpose of this work was to investigate the evaporation of $\text{CaO-SiO}_2\text{-Al}_2\text{O}_3\text{-B}_2\text{O}_3\text{-Na}_2\text{O}$ fluxes, focussing on effects of the Na_2O content and CaO/SiO_2 ratio.

2. Experimental procedure

2.1 Sample preparation

In this study, slag samples were prepared using chemical reagents of CaCO_3 , Na_2CO_3 , SiO_2 , Al_2O_3 , and B_2O_3 powders, with several carbonates being substituted for oxides due to their stability in air. The mixture of components was ground in an agate mortar for 20 min, and placed to the furnace in a high-purity graphite crucible. After heating and melting at 1400°C , and holding at this temperature for 20 min, the slag was poured onto a steel plate and cooled to the room temperature. Subsequently, the slag sample was crushed and ground, forming homogenized fine powder. Compositions of fluxes analysed by X-ray fluorescence are listed in Table I. Fluxes No. 1, 4, 5 and 6 have varied Na_2O contents from 0 to 9.1 wt% at a fixed CaO/SiO_2 ratio of 1.3, while Fluxes No. 2, 3, 5 and 7 have varied CaO/SiO_2 ratios from 0.8 to 1.5 at Na_2O contents in the narrow range 7.8-8.4 wt%.

Table I. Chemical compositions (wt%) of test fluxes

Flux No.	CaO/SiO ₂ ratio	CaO	SiO ₂	Al ₂ O ₃	B ₂ O ₃	Na ₂ O
1	1.3	51.1	39.2	3.2	6.4	0
2	0.8	36.8	44.9	3.5	6.6	8.2
3	1.0	40.5	40.8	3.6	6.7	8.4
4	1.3	47.2	36.4	3.6	6.6	6.2
5	1.3	46.2	35.7	3.5	6.7	7.9
6	1.3	45.3	35.3	3.8	6.5	9.1
7	1.5	49.5	32.8	3.4	6.5	7.8

2.2 Thermogravimetric measurement

The evaporation experiments were conducted using STA449-F1 calorimeter (NETZSCH Instruments, Germany) in the isothermal mode at 1300, 1350 and 1400°C in Ar atmosphere. Pt/Ph crucibles with 6 mm inside diameter and a volume of 84 μL were employed as the containers for the slag samples. The crucibles were cleaned after each use, using the solution of 25 wt% HCl.

Before the furnace was heated, the chamber was evacuated and purged with argon gas for 300 s to ensure a steady gas flow. The sample was then heated to a pre-determined temperature with a heating rate of 50 K/min, the maximum heating rate for the apparatus. The gas flow rate was kept constant at 70 ml/min for the duration of the experiment, which was reported to be above the starvation rate[11]. Therefore, evaporated species at the interface are expected to be immediately swept away from the liquid/gas interface. The sample was kept at the experimental temperature for 60 min. During the

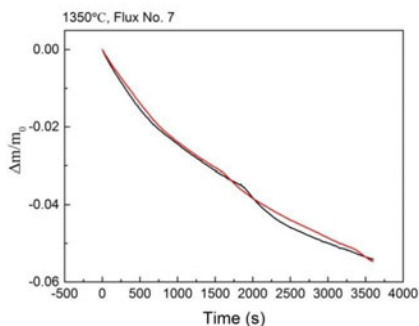


Figure 1. Weight loss of Flux No.7 in parallel experiments at 1350°C .

experiment, the weight change and the temperature of the sample were recorded every 0.1 s. Parallel experiments for some selected fluxes demonstrated a good reproducibility of the experimental results (Figure 1).

3. Results and discussion

3.1 Weight loss of fluxes

The measured weight loss of fluxes (represented as $\Delta m/m_0$, where Δm is the weight change and m_0 is the original sample weight) over time during isothermal conditions (1300-1400°C) is shown in Figure 2. Figures 2a, c and e show the weight loss of fluxes with a fixed CaO/SiO₂ ratio at 1.3 but varied Na₂O contents at different temperatures. In general, the weight loss increased with the increasing temperature. For Flux No.1 containing 6.4 wt% B₂O₃ and no Na₂O, the weight loss was less than 0.002% at all temperatures for 1 h. The addition of 6.2 wt% Na₂O produced a significant weight loss (Figures 2a and c). With further increase of the Na₂O content, the increase in the evaporation slowed down. No change in the evaporation rate was observed at 1300°C when Na₂O increased from 7.9 to 9.1 wt% (Figure 2a).

Figures 2b and d show the evaporation rates of fluxes with a fixed Na₂O content at approximately 8 wt% but varied CaO/SiO₂ ratios at 1300 and 1350°C, respectively. Increase in the CaO/SiO₂ ratio from 0.8 to 1.3 had no significant influence on the weight loss at 1300°C (Figure 2b). However, when the CaO/SiO₂ ratio increased further to 1.5, the sample weight changed slowly after around 1000s, although there was no difference in the evaporation rate before this time (Figures 2b and d).

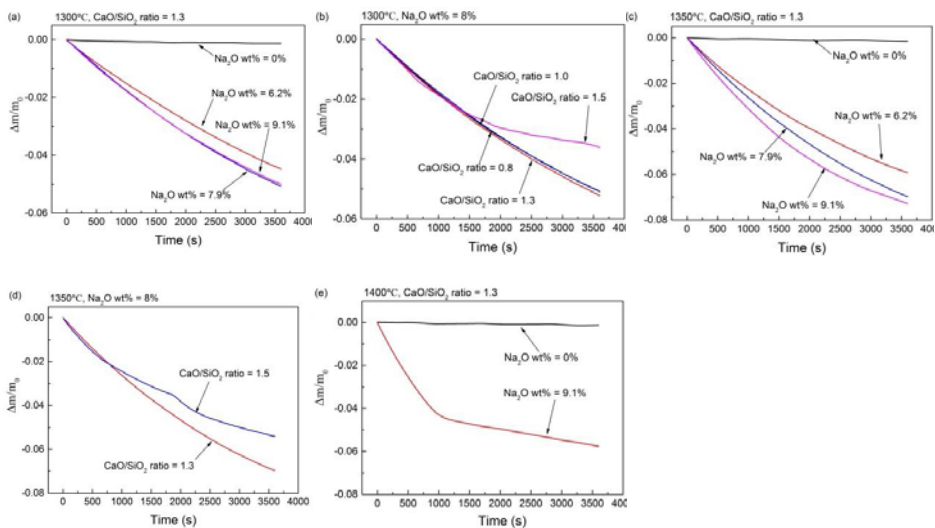


Figure 2. Weight loss as a function of time at (a,b)1300°C, (c,d)1350°C, and (e)1400°C with (a,c,e) a fixed CaO/SiO₂ but varied Na₂O content, and (b,d) a fixed Na₂O but varied CaO/SiO₂.

3.2 Evaporation rate and activation energy

The evaporation rates were analysed during first 10 min of the weight measurements. To take this short time only is by considering the flux chemistry change because of evaporation which would alter the original flux evaporation rate. Evaporation rate k , s^{-1} , was expressed as:

$$k = \frac{\Delta m/m_0}{t_i} \quad (1)$$

$$\Delta m = m_i - m_0 \quad (2)$$

where $\Delta m/m_0$ is the flux mass change, and m_i , g, is the flux mass at time t_i , s. Table II shows the calculated evaporation rates of different fluxes. The evaporation rate increased with the increase of the Na_2O content at the fixed CaO/SiO_2 ratio of 1.3, while the CaO/SiO_2 ratio at the constant Na_2O content had almost no effect on k .

Table II. Evaporation rate k (s^{-1}) of fluxes

Flux No.	1300°C	1350°C	1400°C
1	-3.08×10^{-7}	-8.21×10^{-7}	-1.90×10^{-6}
2	-1.93×10^{-5}	--	--
3	-1.93×10^{-5}	--	--
4	-1.54×10^{-5}	-2.43×10^{-5}	--
5	-1.81×10^{-5}	-2.89×10^{-5}	--
6	-1.87×10^{-5}	-3.34×10^{-5}	-4.91×10^{-5}
7	-2.03×10^{-5}	-2.89×10^{-5}	--

*-- Evaporation rates were not measured under these conditions

The apparent activation energies for the evaporation process were estimated from the Arrhenius plots using data on k obtained at different temperatures:

$$\ln k = \ln A + \frac{E_a}{RT} \quad (3)$$

where A is the pre-exponential factor, E_a is the apparent activation energy, kJ/mol, R is the gas constant, 8.314 J/(mol.K), and T is the absolute temperature, K. Values of E_a were obtained from the slope of $\ln k$ vs $1/T$ (shown in Figure 3) and listed in Table III. Addition of 6.2 wt% Na_2O to the $CaO-SiO_2-Al_2O_3-B_2O_3$ system significantly decreased E_a . A further increase in the Na_2O content from 6.2 to 9.1 wt% had a minor effect on E_a . Experimental data for fluxes containing 7.9 and 9.1 wt% Na_2O were available only at 1300 and 1350°C, what is not sufficient for the accurate estimation of the apparent activation energy.

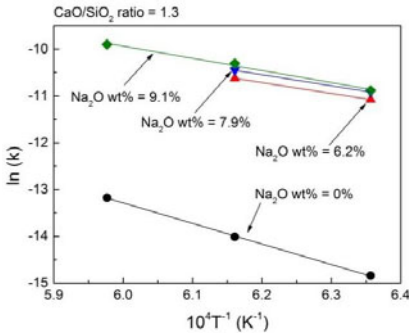


Figure 3. Arrhenius plots for fluxes with varying Na_2O contents.

Table III. Calculated E_a as a function of Na₂O content

Flux No.	Na ₂ O, wt%	E_a , kJ/mol	R ²
1	0	365	0.99
4	6.2	193	--
5	7.9	203	--
6	9.1	211	0.98

3.3 Estimation of vapour pressures of Na, O₂, B₂O₃ and NaBO₂

The evaporation of B₂O₃ at high temperatures from the B₂O₃ containing fluxes was observed in works [10, 12]. However, the vaporisation of fluxes containing Na₂O, which is a common component in the mould fluxes, has significant differences as the vaporization species include Na₂O and also other compounds. Generally, vaporisation of Na₂O and B₂O₃ can be described by the following reactions [8, 9]:



In these reactions (Na₂O) and (B₂O₃) are oxides dissolved in the flux. The weight loss of Flux No.1 (Figures 2a, c and e) was very low, indicating evaporation of B₂O₃ can be neglected. Therefore, Na, O₂ and NaBO₂ are considered as the major evaporative species. Once the evaporation starts, gaseous species evaporate from the interface and leave the system with the carrier Ar gas. After a certain time, a steady-state is established in which the concentrations of gaseous species in argon gas become constant [13].

The flux of each gaseous component J_A , mol/s, is defined as:

$$J_A = \frac{\Delta m_A}{t M_A} \quad (7)$$

where M_A is molecular weight, g/mol, and Δm_A is the mass loss of component A (A : B₂O₃, Na, O₂, NaBO₂).

In order to simplify the problem, it is assumed that there is no convection occurring inside the crucible[9]:

$$\frac{J_A}{S} = \frac{(P_A^i - P_A^b) D_{A-Ar}}{LRT} \quad (8)$$

where i and b represent the interface and bulk, respectively. S is the area of the interface, and L is boundary layer thickness which is assumed to be the distance between the surface of liquid slag and the crucible top, cm. P_A^i and P_A^b are the partial pressures at the interface and in the bulk gas, respectively. P_A^b is assumed to be zero since the gas flow rate is not starved under the experimental conditions. D_{A-Ar} is the diffusion coefficient of gaseous species through Ar gas, cm²/s, which can be calculated by Chapman-Enskog equation[14]:

$$D_{A-Ar} = 0.0018583 \times \frac{T^{3/2}}{P \cdot \sigma_{A-Ar}^2 \cdot \Omega_{A-Ar}} \times \left(\frac{1}{M_A} + \frac{1}{M_{Ar}} \right)^{1/2} \quad (9)$$

where P is the pressure, atm, M_A and M_{Ar} are molecular weights of gaseous species and Ar, and Ω_{A-Ar} is the collision integral for diffusion, which is a function of the dimensionless temperature kT/ε_{A-Ar} [14].

Parameters σ_{A-Ar} , \AA and ε_{A-Ar} , J, are parameters of the Lennard-Jones potential which can be estimated from the following equations [14]:

$$\sigma_{A-Ar} = \frac{1}{2}(\sigma_A + \sigma_{Ar}) \quad (10)$$

$$\varepsilon_{A-Ar} = (\varepsilon_A \varepsilon_{Ar})^{1/2} \quad (11)$$

In the present study, the values $\frac{\varepsilon_{Ar}}{k}$ and σ_{Ar} taken from [15] are 122.4K and 3.432 \AA , respectively. The values of ε_A and σ_A can be estimated by the following empirical equations [16]:

$$\frac{\varepsilon_A}{k} = 1.92T_{m,A} \quad (12)$$

$$\sigma_A = 1.222V_{m,A}^{\frac{1}{3}} \quad (13)$$

where k is Boltzmann constant, 1.38×10^{-23} J/K, T_m is the melting temperature, K, and $V_{m,A}$ is the molar volume at melting temperature, cm^3/mol . Table IV shows the calculated $\frac{\varepsilon_A}{k}$ and σ_A using Equations 12 and 13.

Table IV. Parameters $\frac{\varepsilon_A}{k}$ and σ_A for different gaseous species

Gaseous species	M_A , g/mol	ρ_{liq} , g/cm ³	V_m , cm ³ /mol	T_m , K	$\frac{\varepsilon_A}{k}$, K	σ_A , \AA
B ₂ O ₃ (g)	69.62	2.46	28.30	723	1388.16	3.724
Na(g)	22.99	0.93	24.80	371	712.32	3.560
O ₂ (g)	32.00	--	--	--	113[15]	3.433[15]
NaBO ₂ (g)	65.80	2.46	26.75	1239	2378.88	3.655

Calculated kT/ε_{A-Ar} are shown in Table V. Using collision integrals together with the Lennard-Jones potential for the prediction of transport properties of gases at low densities [15], values of Ω_{A-Ar} for different species are presented in Table V. Estimated D_{A-Ar} values using Equation 9 are also shown in Table V.

Table V. Estimated diffusion coefficients of gaseous species in Ar gas (10^{-4} m²/s)

Parameter	1300°C	1350°C	1400°C
$kT/\varepsilon_{B_2O_3-Ar}$	3.79	3.91	4.03
$\Omega_{B_2O_3-Ar}$	0.8952	0.8897	0.8845
$D_{B_2O_3-Ar}$	2.02	2.13	2.24
kT/ε_{Na-Ar}	5.29	5.46	5.63
Ω_{Na-Ar}	0.8428	0.8428	0.8129
D_{Na-Ar}	2.96	3.1	3.36
kT/ε_{O_2-Ar}	13.29	13.71	14.13
Ω_{O_2-Ar}	0.7025	0.7025	0.7025
D_{O_2-Ar}	2.29	3.28	3.43
$kT/\varepsilon_{Na_2BO_2-Ar}$	2.90	2.99	3.08
$\Omega_{Na_2BO_2-Ar}$	0.9588	0.9500	0.9418
$D_{Na_2BO_2-Ar}$	1.94	2.05	2.17

The rate of total weight loss of the molten flux can be calculated using the following equation:

$$\frac{\Delta m}{t} = \sum M_A J_A \quad (14)$$

Table VI shows the estimated vapour pressures of major gaseous species for Flux No.5 using thermochemical software Factsage 7.0. Clearly, the vapour pressure of NaBO₂ is the highest, indicating it is a dominant volatile species.

Table VI. Estimated vapour pressure P_A^i (Pa) for major gaseous species for Flux No.5

P_A	1300°C	1350°C	1400°C
B ₂ O ₃ (g)	4.72×10^{-4}	1.31×10^{-3}	3.35×10^{-3}
Na(g)	1.38	2.84	5.60
O ₂ (g)	0.34	0.71	1.39
NaBO ₂ (g)	58.37	104.16	177.96

By combining Equations 8 and 14, total weight loss can be estimated from the following equation:

$$\frac{\Delta m_{RTL}}{tS} = \sum M_A D_{A-Ar} P_A^i \quad (15)$$

The calculated weight loss for Flux No.5, compared with the experimental measurement, is shown in Table VII. In general, the measured values are slightly lower than the calculated ones, but both are in reasonable agreement.

Table VII. A comparison of measured and estimated weight loss $\frac{\Delta m}{t}$ (10^{-9} g/s) for Flux No.5

Temperature	1300°C	1350°C
Measured	513.83	900.56
Calculated	611.05	1141.82

4. Conclusions

In the present study, stability of the fluorine-free mould flux SiO₂-CaO-Al₂O₃-B₂O₃-Na₂O for the steel continuous casting was investigated, and the following results were obtained:

- (1) The weight loss as a result of the flux evaporation increased with the increasing temperature. The rate of evaporation increased with the increasing Na₂O content, while the effect of the CaO/SiO₂ ratio on the flux evaporation rate was marginal.
- (2) The apparent activation energy E_a for the evaporation reaction decreased from 365 to 193 kJ/mol when 6.2 wt% Na₂O was added to the SiO₂-CaO-Al₂O₃-B₂O₃ flux. A further increase in the Na₂O content to 9.1 wt% had a minor effect on E_a .
- (3) The high rate of evaporation of the SiO₂-CaO-Al₂O₃-B₂O₃-Na₂O system was attributed to the formation of highly volatile NaBO₂.

Acknowledgements

This project was financially supported by Baosteel through BAJC, Abel Metal, and Australian Research Council (ARC LP130100773).

References

1. E. Brandaleze et al., *Mould Fluxes in the Steel Continuous Casting Process*, in *Science and Technology of Casting Processes*. 2012.205-233.
2. A.B. Fox et al., *Development of Fluoride-free Fluxes for Billet Casting*. ISIJ International, 2005. 45(7), 1051-1058.
3. G.H. Wen et al., *Development of Fluoride-free Mold Powders for Peritectic Steel Slab Casting*. ISIJ International, 2007. 47(8), 1117-1125.
4. J.L. Klug et al., Fluorine-Free Mould Powders for Slab Casting: *Crystallization Control in the CaO-SiO₂-TiO₂-Na₂O-Al₂O₃ System*. Steel Research International, 2012. 83(12), 1186-1193.
5. C.-B. Shi et al., *Crystallization Characteristics of CaO-Al₂O₃-Based Mold Flux and Their Effects on In-Mold Performance during High-Aluminum TRIP Steels Continuous Casting*. Metallurgical and Materials Transactions B, 2014. 45(3), 1081-1097.
6. S.Y. Choi et al., *Properties of F-free Glass System as a Mold Flux: Viscosity, Thermal Conductivity and Crystallization Behavior*. Journal of Non-Crystalline Solids, 2004. 345, 157-160.
7. R.G.C. Beerkens, *Modeling the kinetics of volatilization from glass melts*. Journal of the American Ceramic Society, 2001. 84(9), 1952-1960.
8. Z.T. Zhang, S. Sridhar, and J.W. Cho, *An Investigation of the Evaporation of B₂O₃ and Na₂O in F-Free Mold Slags*. Isij International, 2011. 51(1), 80-87.
9. M. Li, T. Utigard, and M. Barati, *Kinetics of Na₂O and B₂O₃ Loss From CaO-SiO₂-Al₂O₃ Slags*. Metallurgical and Materials Transactions B-Process Metallurgy and Materials Processing Science, 2015. 46(1), 74-82.
10. V.L. Stolyarova, G.G. Ivanov, and S.V. Stolyar, *Vaporization and thermodynamic properties of melts in the Na₂O-B₂O₃-SiO₂ system*. Glass Physics and Chemistry, 2002. 28(2), 112-116.
11. M. Persson, S. Seetharaman, and S. Seetharaman, *Kinetic Studies of Fluoride evaporation from slags*. ISIJ international, 2007. 47(12), 1711-1717.
12. V.L. Stolyarova et al., *Thermodynamic properties of silicate glasses and melts: VII. System MgO-B₂O₃-SiO₂*. Russian Journal of General Chemistry, 2010. 80(12), 2405-2413.
13. J. Szekely and N.J. Themelis, *Rate phenomena in process metallurgy* (New York, NY: Wiley-Interscience, 1971), 439.
14. R.B. Bird, W.E. Stewart, and E.N. Lightfoot, *Transport phenomena* (New York, NY: John Wiley & Sons, 2007), 525-542.
15. R.B. Bird, W.E. Stewart, and E.N. Lightfoot, *Transport phenomena* (New York, NY: John Wiley & Sons, 2007), 864-866.
16. R.B. Bird, W.E. Stewart, and E.N. Lightfoot, *Transport phenomena* (New York, NY: John Wiley & Sons, 2007), 22.

Study of MnO Activity in CaO-SiO₂-MnO-Al₂O₃-MgO Slags

Jun Tao¹, Dongdong Guo¹, Baijun Yan¹, Longmei Wang²

¹ School of Metallurgical and Ecological Engineering, University of Science and Technology
Beijing

Beijing 100083, P.R. China

² Central Iron & Steel Research Institute, Beijing 100081, P.R. China

Keywords: High MnO slags, Activity, Regular solution model

Abstract

Liquid copper was used as reference metal phase to equilibrate with CaO-SiO₂-MgO and CaO-SiO₂-MnO-Al₂O₃-MgO slags under a controlled oxygen partial pressure ($p_{O_2} = 1.76 \times 10^{-6}$ Pa) at 1873K. Based on the activity of Mn in Cu-Mn melts, the activities of MnO in slags were determined. The activities of MnO in the two kinds of slags increase gradually with the increasing of MnO content. For the slags with the same MnO content, the activity of MnO in the ternary slags is smaller than that in the five components slags. Furthermore, according to the measured activities of MnO in slags, the conversion factor in the quadratic formalism based on regular solution model was corrected. And an expression was obtained; it can estimate the activities of MnO in the both slags satisfactorily.

Introduction

Twinning induced plasticity (TWIP) steels are one of the best choices for next generation automotive high strength steels due to its excellent mechanical properties. As the major alloying element, the concentration of manganese in TWIP steels is as high as 15wt. %-30wt. %^[1-2]. From the perspective of economical producing of high manganese TWIP steels, the maximum use of manganese ore in the steelmaking process is more economic and reasonable. Consequently, it is of fundamental and practical importance to understand the thermodynamic behavior of MnO in the steelmaking slags, especially in the high MnO slags.

Concerning the thermodynamic activity of MnO in high MnO slags, some investigations can be found in the literatures^[3-10], but the data in CaO-SiO₂-MnO-Al₂O₃-MgO system are scarce. Therefore, in the present study, activities of MnO over a wide compositional range in the CaO-SiO₂-MnO and CaO-SiO₂-MnO-Al₂O₃-MgO system at 1873K were determined experimentally. Furthermore, the applicability of the regular-solution model in these two systems was examined.

Experimental and Principle

The experimental setup is schematically shown in **Figure 1**. A resistance furnace with MoSi₂ heating element was used. An alumina tube was employed as the reaction chamber. A water-

cooled quenching chamber was internally connected on the top of the reaction tube. The temperature of the sample was followed by a W-5%Re/W-26%Re thermocouple placed beneath the bottom of the crucible. Molybdenum crucible containing the sample was hung by molybdenum wire on the steel rod connected to a lifting system. The lifting unit could lift the sample very fast to the quenching chamber with 1-2 seconds.

To start the experiment, 3g slag was placed above 5g copper in a molybdenum crucible (16.4mm ID, 18mm OD and 32mm height). After the whole system was carefully sealed, the reaction tube was evacuated using a vacuum pump and then filled with Ar. This procedure was repeated at least three times. Thereafter, the CO/CO₂ gas mixture with volume ratio of 99 (oxygen partial pressure 1.76×10^{-6} Pa at 1873K) was introduced, the flow rate was maintained 40 ml/min until the experiment was finished. The furnace was heated up at a rate of 5K/min to the 1873K, and the slag equilibrated with liquid copper at 1873K for 20h before quenching.

The quenched sample was taken out, and the slag was carefully separated from the solid copper. Then, the content of Mn in copper was analyzed by ICP-AES. The morphology of the quenched slag was examined by SEM and its composition was determined by EPMA.

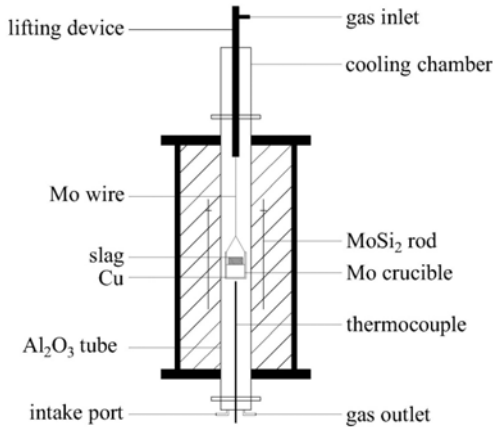
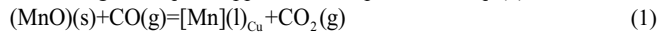


Figure 1 Schematic diagram of the experimental apparatus

The reaction took place between slag and liquid copper can be expressed as Eq. (1).



$$\Delta G_1^\theta = -120\,000 - 0.96T \text{ (J/mol)} \quad (2)$$

$$\Delta_r G_1^\theta = -RT \ln \frac{a_{[\text{Mn}]} \cdot (p_{\text{CO}_2} / p^\theta)}{a_{(\text{MnO})} \cdot (p_{\text{CO}} / p^\theta)} \quad (3)$$

Where, parentheses and square bracket denote the component in slags and liquid copper, respectively. From Eq. (3), the activity of MnO in slags can be determined from Eq. (4)

$$a_{(\text{MnO})} = x_{[\text{Mn}]} \cdot \gamma_{[\text{Mn}]} \cdot (p_{\text{CO}_2} / p_{\text{CO}}) \cdot \exp(\Delta_r G_1^\theta / RT) \quad (4)$$

The activity coefficient of Mn in liquid copper, $\gamma_{[\text{Mn}]}$, have been reported in our previous paper [12]. And the relationship between $\gamma_{[\text{Mn}]}$ and $x_{[\text{Mn}]}$ at 1873K can be expressed as Eq. (5).

$$\ln \gamma_{[\text{Mn}]} = -10.052(1 - x_{[\text{Mn}]})^2 + 9.112 \quad (5)$$

Combining Eq. (4) and Eq. (5), the activity of MnO in slag can be determined by using the concentration of Mn in the liquid copper equilibrated with slag.

Results and discussion

1. MnO activity in slags

In **Figure 2**, the typical microphotographs of slags of two different systems are presented. It can be seen that the slags investigated in the present study are single liquid phase at 1873K, which agrees well with the phase diagram. The compositions of the slags measured by EPMA are listed in **Table I**, the measured compositions are very close to the weighed-in compositions.

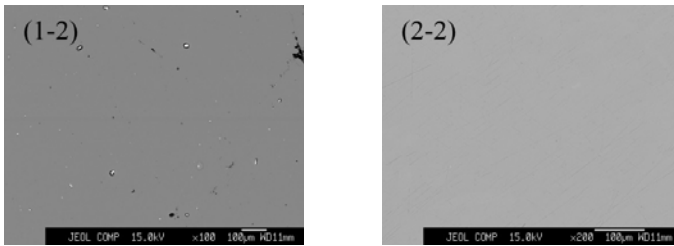


Figure 2 SEM microphotography of slag samples quenched from 1873K
CaO-SiO₂-MnO (1-2), CaO-SiO₂-MnO-Al₂O₃-MgO (2-2)

The concentrations of Mn in the Cu-Mn melts equilibrated with various slags, as well as the activities of MnO in slags calculated using Eq. (4) and Eq. (5), are listed together in **Table I**.

Table I. Experimental Results and Activities of MnO in Slags

Slag System	Sample No.	Compositions of slags and the Cu-Mn melts						a_{MnO}
		Slags					Mn in Cu (mass %)	
		CaO	SiO ₂	MnO	Al ₂ O ₃	MgO		
MnO-CaO-SiO ₂	1-1	38.22	50.36	11.42	-	-	0.398	0.009
	1-2	32.52	46.82	20.66	-	-	0.408	0.022
	1-3	27.11	41.55	31.34	-	-	0.424	0.043
	1-4	21.96	37.22	40.82	-	-	0.446	0.074
	1-5	16.79	33.31	49.90	-	-	0.487	0.135
	1-6	12.24	30.39	57.37	-	-	0.523	0.193

Table I continued. Experimental Results and Activities of MnO in Slags

Slag System	Sample No.	Compositions of slags and the Cu-Mn melts						a_{MnO}
		Slags					Mn in Cu (mass %)	
		CaO	SiO ₂	MnO	Al ₂ O ₃	MgO		
MnO-CaO-SiO ₂ -Al ₂ O ₃ -MgO	2-1	31.91	38.82	6.48	17.74	5.05	0.088	0.010
	2-2	29.69	36.76	10.69	18.16	4.70	0.174	0.021
	2-3	23.81	30.45	21.36	19.77	4.61	0.340	0.042
	2-4	17.77	27.63	34.36	15.94	4.30	0.798	0.109
	2-5	11.89	23.42	43.85	16.60	4.24	1.253	0.190
	2-6	6.56	19.44	52.08	17.67	4.25	1.547	0.250

From the activity data of MnO in slags shown in **Table I**, it can be seen obviously that the activity of MnO in both systems increase gradually with the increasing of MnO content in slags. Comparing the activities of MnO in the ternary system with that in the five components system, it can be found that the activities of MnO in CaO-SiO₂-MnO-Al₂O₃-MgO slags are larger than those in CaO-SiO₂-MnO slags. This indicates that the addition of Al₂O₃ and MgO to the CaO-SiO₂-MgO slags is beneficial to the increasing of MnO activity.

2. Thermodynamic model of MnO activity in slags

For the silicate melts that is not strictly regular solution, the activity coefficient of components can be approximately expressed with the Eq. (6):

$$RT \ln \gamma_i = \sum_j \alpha_{ij} x_j^2 + \sum_j \sum_k (\alpha_{ij} + \alpha_{ik} - \alpha_{jk}) x_j x_k + I' \quad (6)$$

where α_{ij} denote the interaction energy between the cation, *i.e.* (*i* cation)-O-(*j* cation), I' is the conversion factor of activity coefficient between hypothetical regular solution and the real solution. And all the parameters of the interaction energy and the conversion factor can be found in the literature [13]. Then, the expression shown as Eq. (7) can be obtained to predict the activity coefficient of MnO in silicate melts.

$$\begin{aligned} RT \ln \gamma_{\text{MnO}} = & -92050x_{\text{CaO}}^2 - 75310x_{\text{SiO}_2}^2 - 83680x_{\text{AlO}_{1.5}}^2 + 61920x_{\text{MgO}}^2 \\ & - 33470x_{\text{CaO}}x_{\text{SiO}_2} - 20920x_{\text{CaO}}x_{\text{AlO}_{1.5}} + 70290x_{\text{CaO}}x_{\text{MgO}} \\ & - 31380x_{\text{SiO}_2}x_{\text{AlO}_{1.5}} + 53550x_{\text{SiO}_2}x_{\text{MgO}} + 49370x_{\text{AlO}_{1.5}}x_{\text{MgO}} \\ & + 16496 \end{aligned} \quad (7)$$

Using Eq. (7), the activities of MnO in the slags were calculated, and the calculated values were compared with the experimental results. It can be seen from **Figure 3** that the calculated activities of MnO in the slags are larger than the experimental measured values. However, a good linear relationship exists between the calculated values and the experimental values. This implies that the quadratic formalism based on the regular solution model can predict the trend of activity coefficient of MnO in slags perfectly.

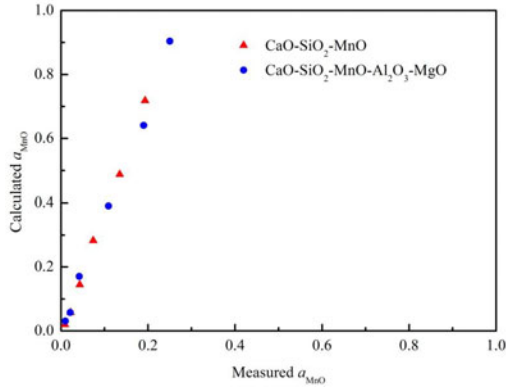


Figure 3 Comparison of MnO activities calculated by RS model ([Eq. 7]) with the measured values in CaO-SiO₂-MgO and CaO-SiO₂-MnO-Al₂O₃-MgO slags at 1873K

In order to make the quadratic formalism shown as Eq. (7) can estimate the activity of MnO in slags satisfactorily, the conversion factor, I' , was corrected based on the measured activities of MnO in slags. Then, the expression shown as Eq. (8) was obtained.

$$\begin{aligned}
 RT \ln \gamma_{\text{MnO}} = & -92050x_{\text{CaO}}^2 - 75310x_{\text{SiO}_2}^2 - 83680x_{\text{AlO}_{1.5}}^2 + 61920x_{\text{MgO}}^2 \\
 & - 33470x_{\text{CaO}}x_{\text{SiO}_2} - 20920x_{\text{CaO}}x_{\text{AlO}_{1.5}} + 70290x_{\text{CaO}}x_{\text{MgO}} \\
 & - 31380x_{\text{SiO}_2}x_{\text{AlO}_{1.5}} + 53550x_{\text{SiO}_2}x_{\text{MgO}} + 49370x_{\text{AlO}_{1.5}}x_{\text{MgO}} \\
 & - 3406
 \end{aligned} \tag{8}$$

By using the Eq. (8), the activities of MnO were calculated again and compared with the measured values. The new comparing result is present in **Figure 4**. In **Figure 4**, it can be seen clearly that the calculated values show good agreement with the measured values.

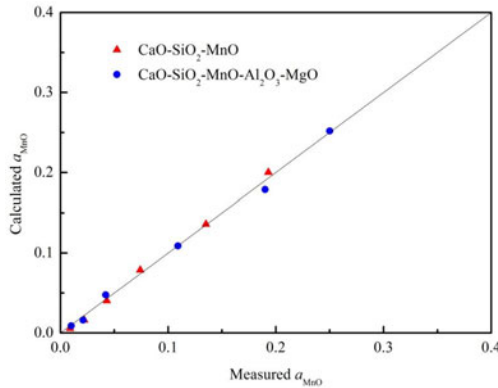


Figure 4 Comparison of MnO activity calculated by modified RS model ([Eq. 8]) with measured data in CaO-SiO₂-MgO and CaO-SiO₂-MnO-Al₂O₃-MgO slags at 1873K

Conclusions

The activities of MnO in the liquid CaO-SiO₂-MnO-Al₂O₃-MgO and CaO-SiO₂-MgO slags were measured at 1873K by equilibrating the slags with Cu-Mn melts. The oxygen partial pressure of the reaction system was controlled using CO/CO₂ gas mixture. The obtained results could be summarized as follows:

1. The activity coefficients of manganese in Cu-Mn melts at 1873K could be expressed as:

$$\ln \gamma_{[\text{Mn}]} = -10.052(1 - x_{[\text{Mn}]})^2 + 9.112$$

2. For the CaO-SiO₂-MnO-Al₂O₃-MgO and CaO-SiO₂-MnO slags with the same MnO contents, the activity of MnO in the ternary system is smaller than that in the five components system. Therefore, the addition of Al₂O₃ and MgO to the CaO-SiO₂-MgO slags is believed to increase the activity of MnO.
3. The corrected quadratic formalism based on the regular solution model can estimate the activity of MnO in the slags satisfactorily.

References

- [1] K. Sugimoto et al, "Retained Austenite Characteristics and Tensile Properties in a TRIP Type Bainitic Sheet Steel," *ISIJ International*, 40(9)(2000), 902-908.
- [2] Y. Wu et al, "Texture and Microstructure Evolution During Tensile Testing of TWIP Steels with Diverse Stacking Fault Energy," *Acta Metallurgica Sinica (English Letters)*, 26(6)(2013), 713-720.
- [3] A. Sobandi, H.G. Katayama, and T. Momono, "Thermodynamics of Mn-O Interactions in Liquid Copper Alloys and Activities of MnO in MnO-SiO₂ Slag," *ISIJ International*, 37(6)(1997), 552-556.
- [4] H. Suito and R. Inoue, "Thermodynamic Considerations on Manganese Equilibria between Liquid Iron and Fe_xO-MnO-MO_x (MO_x= PO_{2.5}, SiO₂, AlO_{1.5}, MgO, CaO) Slags," *Transactions of the Iron and Steel Institute of Japan*, 24(4)(1984), 301-307.
- [5] D.H. Woo, Y.B.Kang, and H.G. Lee, "Thermodynamic Study of MnO-SiO₂-Al₂O₃ Slag System: Liquidus Lines and Activities of MnO at 1823 K," *Metallurgical and Materials Transactions B*, 33(6)(2002), 915-920.
- [6] H. Ohta, and Suito H, "Activities of MnO in CaO-SiO₂-Al₂O₃-MnO (<10 Pct)-Fe_xO(<3 pct) Slags Saturated with Liquid Iron," *Metallurgical and Materials Transactions B*, 26(2)(1995), 295-303.
- [7] M.A. Van et al, "Manganese and Chromium Distribution Between CaO-SiO₂-MgO_{sat}-CrO_{1.5}-MnO Slags and Fe-Cr-Mn Stainless Steel," *ISIJ International*, 48(10)(2008), 1331-1338.
- [8] S.M. Jung et al, "Thermodynamic Study on MnO Behavior in MgO-Saturated Slag Containing FeO," *ISIJ International*, 33(10)(1993), 1049-1054.

- [9] S.M. Jung, C.H. Rhee, and D.J. Min, "Thermodynamic Properties of Manganese Oxide in BOF Slags," *ISIJ International*, 42(1)(2002), 63-70.
- [10] A.T. Morales, and R.J. Fruehan, "Thermodynamics of MnO, FeO and Phosphorus in Steelmaking Slags with High MnO Contents," *Metallurgical and Materials Transactions B*, 28(6)(1997), 1111-1118.
- [11] E.T. Turkdogan, *Physical chemistry of high temperature technology* (New York, NY: Academic Press, 1980).
- [12] B.J. Yan, D.D. Guo, and Z.Z. Zhao, "Thermodynamics of Mn in Cu-Mn Melts," *Metallurgical and Materials Transactions B*, 45(4)(2014), 1175-1180.
- [13] S. Ban-Ya, "Mathematical Expression of Slag-Metal Reactions in Steelmaking Process by Quadratic Formalism Based on the Regular Solution Model," *ISIJ International*, 33(1)(1993), 2-11.

STUDY ON ELECTRICAL CONDUCTIVITY OF CaO-SiO₂-Al₂O₃-FeO_x SLAGS

Guo-Hua ZHANG^{*}, Jun-Hao LIU and Kuo-Chih CHOU

State Key Laboratory of Advanced Metallurgy, University of Science and Technology Beijing, China

Keywords: Ionic conductivity, Electronic conductivity, Arrhenius law, Charge compensation

Abstract

As a fundamental study on properties of the Fe_xO-bearing slags, the total electrical conductivity and electronic/ionic properties of Fe_xO-SiO₂-CaO-Al₂O₃ slags were measured at different oxygen potentials (controlled by CO-CO₂ mixture gas) and temperatures by using four-electrode method. From experiments results, it can be seen that the total conductivity changes little as increasing the ratio of CO to CO₂ (decreasing the oxygen potential), while the electronic and ionic conductivities of all slags decreases and increases monotonously, respectively. The temperature dependences of the total electrical conductivity, electronic, and ionic conductivities follow the Arrhenius law. It was also found that with increasing CaO/Al₂O₃ ratio, the total electrical conductivity and ionic conductivity firstly decrease and then increase, while electronic conductivity firstly almost keeps constant but then increases from CaO/Al₂O₃=1. The minimum values of the total electrical conductivity and ionic conductivity occurs near the ratio of CaO/Al₂O₃ = 1, which is mainly resulted from the charge compensation effect of Al³⁺ ions.

Introduction

The electrical conductivity of molten slag is not only an important physical property that plays a prominent role in modeling and operating the electric smelting furnace and optimizing the metallurgical process, but also important for understanding the structure of molten slags¹⁻⁴. Indeed, many studies have been conducted on investigating the electrical conductivity of molten slags. For instance, the electrical conductivities of Fe_xO-CaO-SiO₂⁵⁻⁷, Fe_xO-CaO-MgO-SiO₂⁸, Fe_xO-CaO-SiO₂-Al₂O₃⁹, Ni_xO-CaO-SiO₂¹⁰, and Ni_xO-CaO-MgO-SiO₂¹⁰ slags had been measured and reported in published literatures. Because for slag systems containing the transition metal oxides, the electrical conductivity includes two parts, ionic conductance and electronic conductance, both of which are very complicated functions of temperature and composition. Consequently, the estimations for both of them will be difficult. The FeO_x containing slags are widely used and play significant roles in many pyrometallurgical processes, so more experimental studies should be done about them. The objective of this work was to study the electrical and electronic conductivity of Fe_xO-CaO-SiO₂-Al₂O₃ slags at various temperature and oxygen potentials which controlled by the ratio of CO₂/CO, which will be beneficial for modeling and operating the electric smelting furnace.

Experimental Procedure

Table 1 shows the chemical composition for each sample. Three different categories of samples were prepared. In group A, contents of FeO and SiO₂ were kept constant, while CaO

^{*}Corresponding author. Email: ghzhang_ustb@163.com

was gradually increased. It should be pointed out that C/A is defined as the mole fraction ratio of CaO to that of Al₂O₃. For groups B and C, SiO₂ content was kept constant, while CaO content was gradually increased. Slag samples were prepared using reagent grade SiO₂, Al₂O₃, CaCO₃ and Fe₂O₃ powder (all reagent are analytically pure, Sinopharm Chemical Reagent Co., Ltd, China), all of which were calcined at 1273 K for 10 h in a muffle furnace to decompose any carbonate and hydroxide before use. Pure FeO was obtained by calcining Fe and Fe₂O₃ powder in CO/CO₂ atmosphere at 1373 K for 24 hours. Then about 12 g mixtures were precisely weighted according to the compositions shown in Table 1, and mixed in an agate mortar thoroughly.

Table 1. Composition of slag sample (mole percent).

	FeO	SiO ₂	CaO	Al ₂ O ₃	C/A
Group A	20	44	24	12	2
			20	16	1.25
			16	20	0.8
			12	40	0.5
Group B		55	40	5	8
			35	10	3.5
			30	15	2
			25	20	1.25
			20	25	0.8
Group C		65	30	5	6
			25	10	2.5
			20	15	4/3
			15	20	0.75

A four terminal method, which had already successfully used to measure the electrical conductivity of molten slags, was employed to accomplish the electrical conductivity measurements in this study. The descriptions of experimental principle and device have already been mentioned in our previous study¹¹. During the whole heating process and the first two hours holding at the target temperature (1823K), the slag was exposed to CO₂, and the flow rate of gas was controlled by a mass flowmeter. The input gas was varied from pure CO₂ to CO₂-CO mixed gas to control the oxygen partial pressure. For group A, the experimental measurements were carried out at every 50 K interval on cooling from 1823 K, and for group B and C, the resistance measurement was carried out at every 25 K interval on cooling from 1873 K. At each temperature, the slag was kept for 2 hours before measurement for the purpose of equilibrium and uniformity of slag.

All the measurements were recorded using a CHI 660a electrochemical workstation (Shanghai Chenhua Instrument Co., Ltd.). The resistance was found to be independent of the frequency, over the range 0.5 kHz to 100 kHz. All of the measurements were carried out at 20 kHz.

Results and Discussion

1. Influence of temperature on electrical conductivity

It is widely accepted that the temperature dependence of electrical conductivity can be expressed by the Arrhenius law as:

$$\sigma = A \exp(-E/RT) \quad (1)$$

where σ is electrical conductivity, $\Omega^{-1}\text{cm}^{-1}$; A is pre-exponent factor; E is activation energy, $\text{J}/(\text{mol}\cdot\text{K})$; R is the gas constant, $8.314 \text{ J}/(\text{mol}\cdot\text{K})$; T is the absolute temperature, K . Figures 1 to 3 show the change of electrical conductivity as a function of temperature for group A slags, at $\text{CO}/\text{CO}_2 = 0.2$. It can be seen from these figures, that the electrical conductivity increases by increasing the temperature, furthermore, the temperature dependence of electrical conductivity obeyed the Arrhenius law very well.

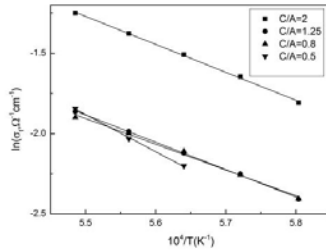


Figure 1. Arrhenius plot of total electrical conductivity for group A slags when $\text{CO}/\text{CO}_2 = 0.2$.

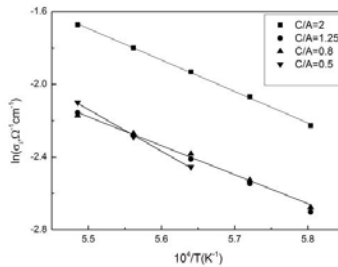


Figure 2. Arrhenius plot of the ionic conductivity for group A slags when $\text{CO}/\text{CO}_2 = 0.2$.

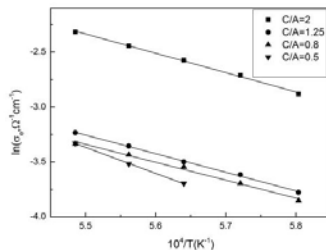


Figure 3. Arrhenius plot of the electronic conductivity for group A slags when $\text{CO}/\text{CO}_2 = 0.2$.

2. Influence of equilibrium oxygen potential on electrical conductivity

The total electrical conductivity for group A slags at 1823 K as a function of CO/CO₂ ratio is shown in Figure 4. As can be noted, the total conductivity changes little in the oxygen potential range of the present study.

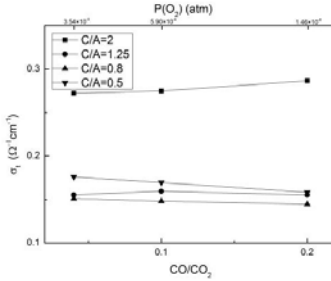


Figure 4. The total electrical conductivity of group A slags for different CO/CO₂ ratio at 1823 K.

The ionic conductivity for group A slags at 1823 K as a function of equilibrium CO/CO₂ is shown in Figure 5. It is evident from figure 5 that the ionic conductivity of all group A slags increases with increasing the ratio of CO/CO₂. From Eq. (2), it can be known that more and more ferric ion will replace ferrous ion with decreasing the CO/CO₂ ratio (or increasing the oxygen potential). According to conclusions of Fontana et al.¹², ferrous ion is the only iron ion that significantly contributes to the ionic conduction in iron-oxide-containing melts. The tendency of the ferric ion toward covalent binding with oxygen is strong enough to stimulate the formation of highly covalent anions (FeO₄⁵⁻ or Fe₂O₅⁴⁻) instead of an isolated Fe³⁺ cation, which will lead to greatly reduced mobility compared with ferrous ion. Therefore, the ionic conductivity of all slags increases with increasing the ratio of CO/CO₂.

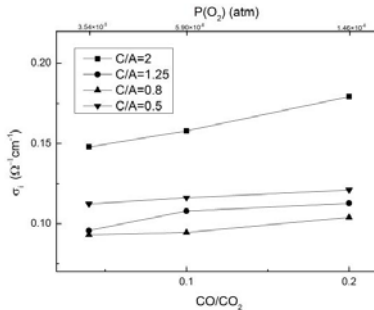


Figure 5. The ionic conductivity of group A slags for different CO/CO₂ ratio at 1823 K.

The effect of the CO/CO₂ ratio on electronic conductivity for group A slags at 1823 K is shown in Figure 6. As can be noted, the electronic conductivity decreases with increasing the ratio of CO to CO₂. According to the above results, it can be known that the ionic conductivity of all slags increases with increasing the ratio of CO to CO₂, which leads to the little change of total conductivity as shown in Figure 7

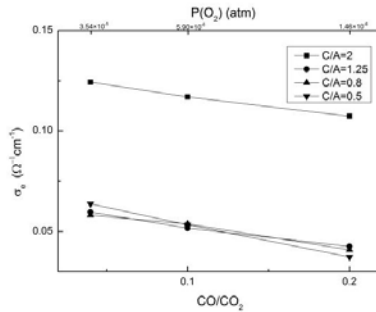


Figure 6. The electronic conductivity of group A slags for different CO/CO₂ ratio at 1823 K.

3. Influence of the ratio of CaO/Al₂O₃ on electrical conductivity

The total electrical conductivity and electronic/ionic conductivity for group A slags with different ratios of CaO/Al₂O₃ at fixed FeO and SiO₂ contents under the atmosphere of CO/CO₂=0.2 at 1823 K are shown in Figure 7. As can be noted, by increasing CaO/Al₂O₃ ratio, the total electrical conductivity and ionic conductivity firstly decrease and then increase, while electronic conductivity firstly almost keeps constant but then increases from CaO/Al₂O₃=1. The minimum values of the total electrical conductivity and ionic conductivity occurs near the ratio of CaO/Al₂O₃ = 1. The electrical conductivity for group B and C slags with different ratios of CaO/Al₂O₃ at fixed SiO₂ content at 1873 K are shown in Figure 8 and Figure 9, respectively. As the CaO/Al₂O₃ ratio increases, the electrical conductivity will decrease firstly and then increase. In other words, the electrical conductivity exhibits a minimum value with the change of CaO/Al₂O₃ ratio, which occurs near the ratio of CaO/Al₂O₃ equal to 1.

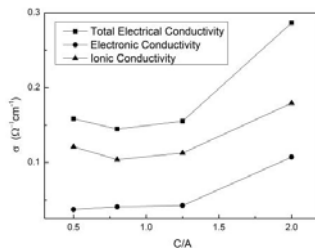


Figure 7. The total electrical, electronic and ionic conductivities of group A slags for different CaO/Al₂O₃ ratio at 1823 K when CO/CO₂ = 0.2.

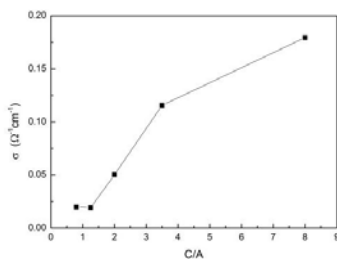


Figure 8. The electrical conductivity of group B slags for the different CaO/Al₂O₃ ratio at 1873 K.

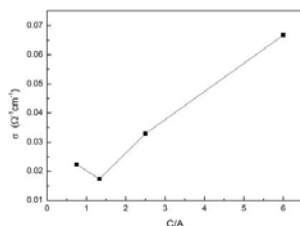


Figure 9. The electrical conductivity of group C slags for the different CaO/Al₂O₃ ratio at 1873 K.

For the Al₂O₃ bearing molten slag, when there are several basic oxides, there is a strict order for cations when charge compensating the Al³⁺ ions. In the present system, there are two basic oxides. The priority order for charge-compensation of Al³⁺ ions fulfills Ca²⁺ > Fe²⁺.¹³ In other words, when there is enough Ca²⁺, Fe²⁺ with a lower priority will not be used to charge compensate the Al³⁺ ion. Intuitively, Ca²⁺ mainly contributes ionic conductivity, while Fe²⁺/Fe³⁺ influence both electronic and ionic conductivities. In FeO-CaO-Al₂O₃-SiO₂ system, there are two types of Ca²⁺ cations: One compensates Al³⁺ ion and the other forms nonbridging oxygen. Figure 10 shows the schematic diagrams. The transport ability of the former type of cation is much weaker than that of the latter type of cation. In the case of x(CaO) < x(Al₂O₃), as increasing CaO content the degree of polymerization is enhanced which decreases ionic conductivity. Whereas, the increase of concentration of metal cations will have little influence on ionic/electrical conductivity because in this case most of the new added Ca²⁺ ion are used for charge compensators of Al³⁺ and have little mobile ability. In the case of x(CaO) > x(Al₂O₃), with the addition of CaO content, the degree of polymerization decreases and the concentration of metal cations increases, both of which will enhance the ionic conductivity.^{14,15} Therefore, there should be a minimum value for ionic conductivity near the ratio of CaO/Al₂O₃ = 1.

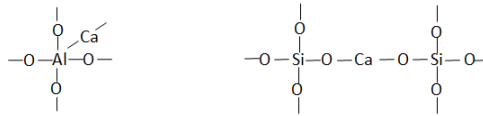


Figure 10. The schematic diagrams of tow type of Ca^{2+} ions.

However, it has been pointed out that the electronic conductivity is determined by the concentration product of Fe^{2+} and Fe^{3+} ions.⁷ Therefore, the electronic conductivity will increase when the concentration of Fe^{3+} ion increases. It is known to us that the ratio of Fe^{3+} ion to total Fe ion is affected by temperature, oxygen potential and the basicity of the slag. When temperature and oxygen potential are kept constant, the proportion of Fe^{3+} ion increases as increasing the basicity, which can be seen easily from Eq. (3). In Eq. (3), O^{2-} expresses the free oxygen ion. In the case of $x(\text{CaO}) < x(\text{Al}_2\text{O}_3)$, almost all the CaO all used for charge compensation, the concentration of free oxygen ion O^{2-} doesn't have an equivalent increase as increasing $\text{CaO}/\text{Al}_2\text{O}_3$ ratio. Consequently, there is little change of Fe^{3+} ion concentration, so the electronic conductivity almost keeps constant. However, when $x(\text{CaO}) > x(\text{Al}_2\text{O}_3)$, all the Al^{3+} ions are get compensation, so there will be an large increase of free oxygen ion as increasing $\text{CaO}/\text{Al}_2\text{O}_3$ ratio. Based on Eq. (3), the concentration of Fe^{3+} ion (highly covalent anion such as FeO_4^{5-} is always formed instead of an isolated Fe^{3+} cation) will also increase which enhances the electronic conductivity.

According to the above analyses, as increasing $\text{CaO}/\text{Al}_2\text{O}_3$ ratio, the ionic conductivity first decreases and then increases, while the electronic conductivity firstly almost keeps constant and then increases from $\text{CaO}/\text{Al}_2\text{O}_3 = 1$. Therefore, the total electrical conductivity also firstly decreases and then increases with the change of $\text{CaO}/\text{Al}_2\text{O}_3$ ratio, with the minimum value occurring near $\text{CaO}/\text{Al}_2\text{O}_3 = 1$. For $\text{CaO}-\text{SiO}_2-\text{Al}_2\text{O}_3$ slags, the minimum value of electrical conductivity near $\text{CaO}/\text{Al}_2\text{O}_3 = 1$ is also resulted from the charge compensation effect of Al^{3+} ions.

Conclusions

The electrical conductivity of $\text{Fe}_x\text{O}-\text{SiO}_2-\text{CaO}-\text{Al}_2\text{O}_3$ slags was measured by a four-terminal technique. The results show that the temperature dependences of ionic, electronic and total conductivity for different compositions obey the Arrhenius law. The experimental results show that the total conductivity changes little as increasing the ratio of CO to CO_2 , while the electronic and ionic conductivities of all slags decreases and increases monotonously, respectively. With increasing $\text{CaO}/\text{Al}_2\text{O}_3$ ratio, the total electrical conductivity and ionic conductivity firstly decrease and then increase, while electronic conductivity firstly almost keeps constant but then increases from $\text{CaO}/\text{Al}_2\text{O}_3=1$. The minimum values of the total electrical conductivity and ionic conductivity occurs near the ratio of $\text{CaO}/\text{Al}_2\text{O}_3 = 1$, which is resulted from the charge compensation effect of Al^{3+} ion.

Acknowledgements

Thanks are given to the financial supports from the National Natural Science Foundation of China (51304018).

References

1. S.C. Britten, U.B. Pal: "Solid-state amperometric sensor for the *In-situ* monitoring of slag composition and transport properties", *Metallurgical and Materials Transactions B*, 31 (2000), 733-752.
2. C.Y. Sun and X.M. Guo: "Electrical conductivity of MO(MO=FeO, NiO)-containing CaO-MgO-SiO₂-Al₂O₃ slag with low basicity", *Transactions of Nonferrous Metals Society of China*, 21 (2011), 1648-1654.
3. S. Jahanshahi, S. Sun and L. Zhang: "Recent Developments in Physicochemical Characterization and Modelling of Ferroalloy Slag Systems", *Journal of the Southern African Institute of Mining and Metallurgy*, 2004, 316-332.
4. Y. Li and I.P. Ratchev: "Rate of interfacial reaction between molten CaO-SiO₂-Al₂O₃-Fe_xO and CO-CO₂", *Metallurgical and Materials Transactions B*, 33B (2002), 651-660.
5. K. Narita, T. Onoye, T. Ishii and K. Uemura: "Electric conductivity of CaO-SiO₂-Fe_tO slag", *ISIJ International*, 61 (1975), 2943.
6. T. Hoster and J.P. Essen: "The electric conductivity of FeO-containing CaO-Al₂O₃-SiO₂ slags with basicities ≤ 1.5 at 1450 to 1650°C" *Archiv Eisenhüttenwes*, 54 (1983), 389-394.
7. M. Barati and K.S. Coley: "Electrical and electronic conductivity of CaO-SiO₂-FeO_x slags at various oxygen potentials: Part I. Experimental results" *Metallurgical and Materials Transactions B*, 37 (2006), 41-49.
8. L. Bobok, L. Bodnar and J. Schmiedl: "Specific electric conductivity of FeO-SiO₂-X slag systems" , *Hutnicke Listy*, 37 (1982), 419-425.
9. S.N. Shin, S.A. Lyamkin, R.I. Gulyaeva and V.M. Chumarev: "Electrical conductivity of melts FeO_x-Al₂O₃-CaO-SiO₂ system" , *Rasplavy*, 5 (1998), 20-24.
10. M. Kawahara, K.J. Morinaga and T. Yanagase: "Behavior of MgO and NiO in Molten Slags", *Canadian Metallurgical Quarterly*, 22 (1983), 143-147.
11. J.H. Liu, G.H. Zhang, and K.C. Chou: "Study on Electrical Conductivity of CaO-SiO₂-Al₂O₃ slags", *Canadian Metallurgical Quarterly*, 54 (2015), 170-176.
12. A. Fontana, K. Segers, K. Twite and R. Winand: "Electrical conductivity of ferrous silicate melts from slag cleaning operations", *The Metallurgical Society/AIME*, 1984, 84-93.
13. G.H. Zhang, K.C. Chou and K. Mills: "A Structurally Based Viscosity Model for Oxide Melts", *Metallurgical and Materials Transactions B*, 45B (2014), 698-706.
14. G.H. Zhang and K.C. Chou: "Measuring and Modeling Viscosity of CaO-Al₂O₃-SiO₂(-K₂O) Melt", *Metallurgical and Materials Transactions B*, 43 (2012), 841-848.
15. G.H. Zhang, B.J. Yan, K.C. Chou and F.S. Li: "Relation Between Viscosity and Electrical Conductivity of Silicate Melts", *Metallurgical and Materials Transactions B*, 42 (2011), 261-264.

THE DISTRIBUTION RULES OF ELEMENT AND COMPOUND OF COBALT/IRON/COPPER IN THE CONVERTER SLAG OF COPPER SMELTING PROCESS

Hongxu Li^{1,2}, Ke Du^{1,2}, Shi Sun^{1,2}, Jiaqi Fan^{1,2}, Chao Li^{1,2}

¹ School of metallurgical and ecological engineering, University of science and technology, 30# Xueyuan Road, Beijing, 100083, China

²The Beijing Key Laboratory of Recycling and Extraction of Metals (REM), University of science and technology, 30# Xueyuan Road, 100083, Beijing China

Keywords: converter slag, distribution rule, isomorphism, mineralogy

Abstract

In ISA copper smelting process, recovery Co from the converter slag usually through reduction and vulcanization method. While Co usually exists in fayalite and iron oxide, in the form of isomorphism-phase by replace of Fe. By analyses different micro areas of the converter slag using SEM and EDS, the distribution trends of Fe and Co, Cu and Co were acquired. The results indicate that the percentage of compositions of Fe and Co present positive correlation, while those of Cu and Co present negative correlation. According to the distribution trends, the distribution curves of Fe ~ Co and Cu ~ Co are fitted, and the mechanism has been studied based on the oxidation order of the three metal sulfide as $FeS > CoS > Cu_2S$, and the similarity of the element property of Cu and Co such as atom outer shell electron distribution and ionic radius, which will provide necessary theoretical reference for effective recovery of cobalt by reduction smelting process.

Introduction

The ISA smelting has become a very widely applied process in copper smelters in the world these years. The content of cobalt in the burden of ISA furnace is 0.1~0.4%, and based on the calculation during ISA smelting, about 60% cobalt comes into matte, and goes to converting process with matte; in converting process, about 50% cobalt comes into converter slag, whose content of cobalt reaches 0.8~2.5%. In converting process, almost all the iron, cobalt and several amount of copper is oxidized coming into the converter slag, and generates compounds with gangue which have complex composition and structure, while the distribution rules of Fe~Co and Cu~Co appeal to be different. Commonly, the recovery of Co from converter slag is through reduction and vulcanization method, based on which moderate vulcanizing agent is added with the reducing agent to guarantee the reduced metal Fe, Cu and Co can easily dissolved in matte forming Fe-Cu-Co alloy; and next, the system cooling process is choose to guarantee the nucleation and growth of the alloy crystal; at last, the matte is crushed and Co is separated and recovered by magnetic separation and hydrometallurgy method. Through the reduction and vulcanization method, the recovery rate of Co is able to reach 95%.

Cobalt is a kind of significant strategic metal, which has excellent physical and chemical performance and mechanical property, and whose minerals and compounds have a wide range of applications in material field such as ceramics, glass, and enamel etc. In the late 20th century,

cobalt and its alloy began to be widely used in areas of machine, chemical industry, aeronautics and astronautics etc., the consumption of which rises every year. Therefore the high amount of cobalt in the converter slag has a high recovery value [1-3], and grasping the distribution rules among iron, copper and cobalt will definitely contribute to the recovery of cobalt.

Composition and distribution rules of Fe/Cu/Co in the converter slag

The elements composition of the converter slag sample

The result of the chemical analysis of the converter slag samples provided by Chambishi Copper Smelter LTD (CCS) is shown in Table I.

Table I. The content of the main elements in the converter slag samples /%

	Si	S	Cu	Co	Fe
Converter slag sample 1	8.54	0.65	8.56	2.84	48.55
Converter slag sample 2	10.03	0.58	8.76	1.97	48.97
Average	9.29	0.62	8.66	2.41	48.76

From Table I we know that the converter slag samples have very high content of cobalt which can reach 2.41%, besides, iron and copper also have relatively high contents, which are 48.76% and 8.66%. The result of the XRD analysis of the converter slag sample is shown in Figure 1.

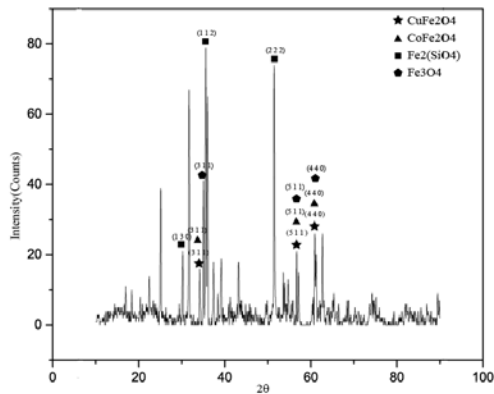


Figure 1. The XRD spectrum diagram of the converter slag sample

As shown in Figure 1, in the converter slag, iron, copper and cobalt can combine with each other generating complex compounds. As for iron, it is not only able to generate iron oxide and fayalite, but also to generate CuFe_2O_4 and CoFe_2O_4 with copper and cobalt; while copper has not generated compound with cobalt.

The correlation of iron, copper and cobalt in the slag

The SEM energy spectrum analysis is conducted upon the converter slag sample to analyze the composition of the 38 selected micro areas, the images and data obtained from the test are shown in Figure 2 and Table II respectively.

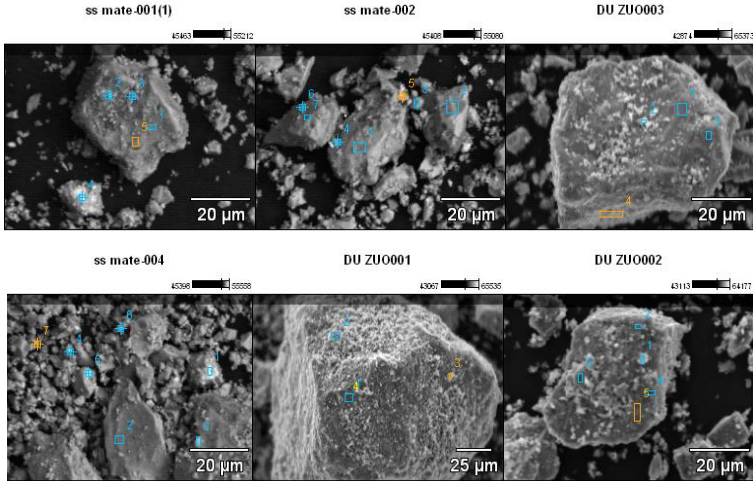


Figure 2. The SEM image of the converter slag sample

Table II. The composition of the 38 selected micro areas of the converter slag sample /%

	Fe	Cu	Co	Si	O	S
1	75.53	1.06	5.3	0.87	19.93	0.35
2	54.44	6.05	2.31	10.67	23.01	2.9
3	43.9	8.87	1.58	12.24	27.34	4.22
4	21.61	49.62	0.65	3.37	8.74	15.56
5	60.38	1.19	2.59	10.73	24.01	0.66
6	52.89	4.93	2.81	10.92	24.62	3.5
7	69.66	3.03	3.98	1.26	21.95	1.12
8	56.61	2.51	2.57	11.71	24.7	1.37
9	83.69	6	5.05	1.47	2.89	0
10	76.6	8.31	6.01	3.85	6.39	1.81
11	45.6	9.9	1.08	8.76	20.75	12.59
12	49.27	0.74	1.35	15.69	31.79	0.16
13	12.75	59.12	0.45	2.28	8.47	16.5
14	15.07	52.67	0.91	3.24	6.79	10.24
15	7.95	61.04	0.4	2.36	9.11	17.05
16	58.11	1.19	2.28	13.63	24.17	0.31

Continued from Table II

	Fe	Cu	Co	Si	O	S
17	50.98	0.94	1.85	14.14	30.3	0.36
18	55.33	1.29	3.56	13.8	25.21	0.55
19	49.21	2.1	1.66	13.72	30.77	1.26
20	12.8	62.25	0.33	2.32	7.93	13.65
21	69.72	0.69	3.64	0.83	25.63	0
22	53.45	2.41	3.66	13.7	25.6	0.97
23	29.83	31.22	1.5	8.08	19.92	8.71
24	33.01	44.13	1.17	2.02	6.44	6.97
25	24.45	39.65	1.04	6.5	18.29	9.68
26	60.07	3.43	1.59	6.15	25.8	1.2
27	61.37	2.96	2.36	10.82	19.92	1.65
28	51.85	8.71	1.24	9.78	23.65	3.62
29	66.41	7.4	3.45	8.8	10.99	1.42
30	49.11	2.49	1.02	14.64	30.27	1.22
31	51.26	2.57	2.64	14.64	27.19	1.41
32	53.02	0	2.02	15.67	28.53	0
33	47.52	2.1	1.01	18.62	24.17	1.14
34	51.1	1.72	1.11	15.39	28.44	0.65
35	52.53	1.25	1.25	14.14	29.28	0.29
36	52.11	1.9	3.9	10.93	28.65	1.54
37	74.8	1.01	7.01	1.27	20.3	0.3
38	71.59	6.6	6.6	4.24	12.56	1.22
Average	50.147	13.291	2.393	8.770	20.645	3.846

As shown in Figure 2 and Table II, the main compositions of the slag are iron oxide and fayalite which distributed widely appearing masses and plates; the distribution of Co is dispersive and the independent cobalt phase has not been observed, and in the areas such as 13, 14, 20, which has high content of Cu, the content of Co is low relatively. In the areas of 18, 22, 24, 29, 36 and 38, the contents of Fe, Co and O are relatively high, while that of Si is low, which indicates that the cobalt exists in the iron oxide phase in above areas; in the areas of 17, 18, 22 and 31, the contents of Fe, Co and Si are relatively high, and that of O is moderate, which indicates that the cobalt exists in the fayalite phase in above areas. The tendency of the distribution correlation of Fe~Co and Cu~Co are shown in Figure 3.

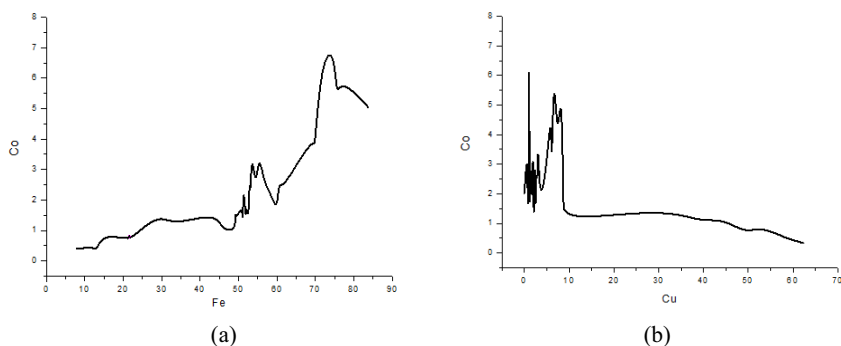


Figure 3. The distribution correlation of Fe~Co (a) and Cu~Co (b) in the slag

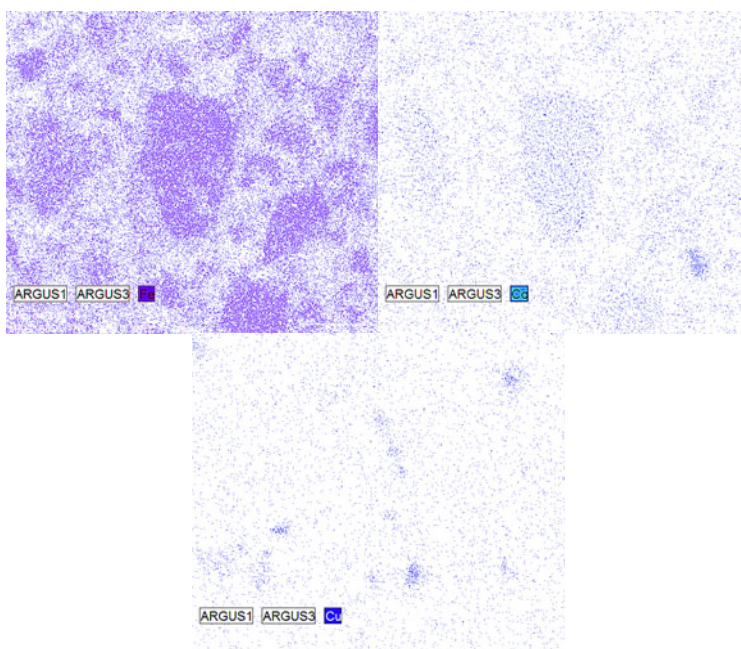


Figure 4. The surface distributions of Fe, Co and Cu in the converter slag sample

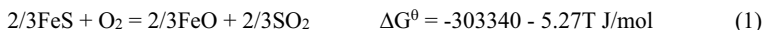
The Figure3 (a) and (b) clearly show that the distributions of iron and cobalt present positive correlation, the content of cobalt rises as that of iron rises, which indicates cobalt is liable to gather with iron in iron oxide and fayalite; while the distributions of copper and cobalt present negative correlation: after the point of 10% content of Cu, the content of cobalt falls with that of copper rises, which is because the gradually reducing iron reduces the content of cobalt gathering

with iron. The result of the SEM Surface scanning of the converter slag sample is shown in Figure 4, which further confirms the similarity of the distribution of iron and cobalt and the difference between that of copper and cobalt.

The mechanism of Fe/Cu/Co mineralogy formation during converting

The oxidation order of the sulfide of iron, copper and cobalt in converting process

There are two stages in the converting of matte, which are slag making stage and copper making stage. In the stage of slag making, almost all the iron and a part amount of sulfur in the matte are oxidized, and the iron oxide comes into the slag combining with SiO₂ from gangue and flux; In the stage of copper making, part amount of the Cu⁺ is oxidized to Cu²⁺, and the following cross reaction of them occurs, which generates Cu. In the converting process, almost all the FeS, CoS and a little amount of Cu₂S are oxidized to oxide coming into the converter slag, the related reactions are shown below [4-6].



The reactions above are all based on 1mol O₂, from which the trends of the reactions can be compared. The relationship of ΔG^θ-T of reaction (1) is minimum, (3) is moderate, and (2) is maximum, which indicates FeS is the most liable to be oxidized, and the next is CoS and Cu₂S. In fact, even if the Cu₂S and CoS are oxidized to Cu₂O and CoO, their oxide will also be reduced by FeS if there is FeS remaining; at the same time, the reaction of Cu₂O and CoS can occur which generate CoO and Cu₂S. The reactions related are shown below [7-8].



As the reactions show, in the stage of slag making, iron is firstly oxidized, cobalt is oxidized gradually with the rise of oxidation potential and almost all the cobalt comes into the slag when close to the end-point of converting process. And when in the stage of copper making, only a little amount of copper oxide enters the slag. The metal oxides combine and generate complex compounds with gangue and flux in the slag. In fact, the slag loss of copper also includes physical loss, namely some matte particles mixed in the slag which have little sizes, and are not liable to gather and settle. The amount of physical loss is roughly equal to that of the chemical loss.

The mechanism of isomorphism in the gathering of iron and cobalt

In nature, cobalt exists in forms of compounds and isomorphism which have different crystal chemical properties in cobalt minerals. The compounds mainly exist in sulfide, arsenide, selenide and etc., such as linnaeite and smaltite. And the isomorphous cobalt optionally enters the lattice of oxide and saline material as the accessory constituent of carrier mineral [9-10]. For instance, cobalt usually replaces the iron existing in fayalite and iron oxide as isomorphism in the converter slag. Cobalt belongs to the first transitional element, and has similar properties with

iron which both have the transitivity of oxyphile and sulfophile. Some element parameters of iron and cobalt are shown in Table III.

Table III. Element parameters of iron and cobalt

	Fe	Co
Atomic weight	55.85	58.93
Atomic volume($\text{cm}^3 \cdot \text{mol}^{-1}$)	7.1	7.1
Atomic number	26	27
Element period	4	3
Element group	VIII	VIII
Outer shell electron distribution	$3d^64S^2$	$3d^74S^2$
Crystal texture	face-centered cubic, body-centered cubic	face-centered cubic
Valence	+6、+3、+2	+3、+2
High spin radius of divalent ion	0.76	0.75
Low spin radius of divalent ion	0.64	0.65

The Table III shows the very similar element parameters of iron and cobalt which necessarily have very similar properties. Especially, the outer shell electron distribution of iron is $3d^64S^2$, and that of cobalt is $3d^74S^2$ which are exactly similar and based on which they are both liable to lose their two outermost electrons to generate divalent ion; in addition, $(R_2 - R_1) / R_2 = 0\% \sim 6.6\% < 10\% \sim 15\%$ (the R_2 is the bigger radius, R_1 is the smaller radius), which indicates the two ions have nearly equal radiuses. Therefore, the similarity of element properties determines cobalt is liable to replace the iron as isomorphism which exists in different kinds of iron oxide and iron silicate, and their compositions have infinite solubility [11-13]. In fact, the content of cobalt existing in the form of compounds in different minerals is just a few percent of the total content of cobalt on earth, and most of cobalt exists freely as isomorphism in different kinds of dark iron silicate (pyroxene, hornblende, and biotite etc.) and magnetite. Moreover, cobalt is also able to enter in the ores of sulfide, arsenide, selenide and telluride containing iron as isomorphism, such as pyrite (FeS_2), chalcopyrite (CuFeS_2), arsenopyrite (FeAsS), symplectite (FeAs_2), achavalite (FeSe_2) and durdenite (FeTe_2) etc., whose contents of cobalt are all in the scope of $0.n \sim 1$, and which can be exploited as the main cobalt deposits[14]. The above distribution rules and their mechanism will provide necessary theoretical reference for the effective recovery of cobalt. For instance, cobalt replaces iron as isomorphism, therefore in the reduction smelting process, the system temperature must be high enough which is above 1623K to break the Fe-O and Co-O bond and release Co as much as possible; the reduction order is $\text{Cu} > \text{Co} > \text{Fe}$, therefore the amount of reducing agent must be enough to guarantee the total recovery of Cu and the very low content of Fe in the slag, which will insure the high reduction rate of Co.

Conclusion

The converter slag samples provided by CCS have very high content of cobalt which can reach 2.41%. In the samples, iron is not only able to generate iron oxide and fayalite, but also to generate CuFe_2O_4 and CoFe_2O_4 with copper and cobalt; while copper cannot generate compound with cobalt. The distribution rules are acquired by the analysis of the composition of the 38 selected micro areas of the slag, which is that the distributions of iron and cobalt present positive

correlation, and that of copper and cobalt present negative correlation, and which indicates cobalt is liable to gather with iron in iron oxide and fayalite. In the converting process, almost all the FeS, CoS and a little amount of Cu₂S are oxidized coming into the slag, and the oxidation order is FeS > CoS > Cu₂S; the slag loss of copper also includes physical loss, whose amount is roughly equal to that of the chemical loss. The similarity of element properties such as outer shell electron distribution and ionic radius determines cobalt is liable to replace the iron as isomorphism which exists in different kinds of iron oxide and iron silicate. For the effective recovery of cobalt, the system temperature must high enough which is above 1623K, and amount of reducing agent must be enough to guarantee the high reduction rate of Co.

Acknowledgments

The authors gratefully acknowledge the financial support of the National Science Foundation of key funds PRC for the research project (No.51234008), also the financial support of Beijing technical development project (No. 00012132) and the development of science and technology fund supported by CCS.

References

1. X.G. Sun, "The distribution and application of cobalt resource in the world," *World Nonferrous Metals*, 1 (2000), 38-41.
2. W.Z. Zhao, "Attach importance to the strategic function of cobalt resources," *World Nonferrous Metals*, 10 (2007), 6-9.
3. Y.S. Cao, "Situation and prospect of the world cobalt industry," *China Metal Bulletin*, 42 (2007), 30-34.
4. H.H. He and Q.F. Cai, *China nickel and cobalt metallurgy*. (Beijing: Metallurgical Industry Press, 2009), 169-180.
5. X.J. Zhai, *Heavy metal metallurgy*. (Beijing: Metallurgical Industry Press, 2011), 133-139.
6. A. Yazawa, "Thermodynamic considerations of copper smelting," *Canadian Metallurgical Quarterly*, 13 (3) (1974), 443-453.
7. K.S. Yoshiki-Gravelsins and J.M. Toguri, "Oxygen and sulfur solubilities in Ni-Fe-SO melts," *Metallurgical Transactions B*, 24 (5) (1993), 847-856.
8. M.L. Sorokin et al., "Thermodynamic of Nickel Matte Converting," *Converting, Fire Refining and Casting*, (1994), 59-68.
9. R. Sridhar, J.M. Toguri and S. Simeonov, "Copper losses and thermodynamic considerations in copper smelting," *Metallurgical and Materials transactions B*, 28 (2) (1997), 191-200.
10. Y.J. Liu, *Introduction to elemental geochemistry*. (Beijing: Geological Publishing House, 1987), 220-222.
11. B. Chen and C.M. Qi, "The occurrence state of cobalt and its significance in prospecting and resource assessment," *Journal of Changchun university of science and technology*, 31 (3) (2001), 217-218.
12. T.G. Dai and Y.Z. Long, "Preliminary study on occurrence status and synthesis utilizing of Co associated with iron ore in Yushiwa," *Hunan Geology*, 19 (1) (2000), 54-57.
13. I. Komazawa, T. Otake and I. Hattori, "Separation of cobalt and nickel using solvent extraction with acidic organophosphorus compounds," *Journal of chemical engineering of Japan*, 16 (5) (1983), 384-388.

THE MANAGEMENT OF LEAD CONCENTRATE ACQUISITION IN “TREPÇA”

Ahmet Haxhiaj¹, Maoming Fan², Bajram Haxhiaj³

¹ Fakulteti i Gjeoshkencave; Universiteti i Mitrovices “Isa Boletini”, Rr. Parku Industrial, 40000 Mitrovicë, Kosovo

² EFD, Eriez Manufacturing Co.; 2200 Asbury Road, Erie, PA 16506, USA

³ Fakulteti I Arkitektures; Universiteti Prishtines “Hasan Prishtina”, 10 000 Prishtinë, Kosovo
ahmet.haxhiaj@umib.net; ahaxhiaj52@yahoo.com

Keywords: Mineral, Reagents, Grinding, Flotation, Pb Concentrate, Pirotine, Sterile

Abstract

Based on the placement of lead and its consumption in industry branches, the paper deals with the composition of lead in the ores of Kopaonik, grinding and flotation recovery of galena. In the flotation process, the flotation machine, the flotation reagents, chemical composition of the flotation concentrates and tailings were discussed in this paper. Verification of the chemical composition of Pb concentrates with Pb, Zn, and Ag, etc. was conducted in this study. It is special that the ratio of Pb to Zn in Kopaonik massive composition is 1.4:1.0. During the flotation, lead tends to float with concentrate more than allowed. In this investigation, effects have been made to minimize the loss of Pb to concentrates. This paper as such gave the first effects in optimizing of these parameters with positive effects in the flotation process in Trepça.

1. Introduction

The management of lead concentrates grade, quantity of lead in Pb and Zn concentrates, and Pb recovery in the flotation process in "Stan Terg", is especially important. The process is necessary in recovering lead in technological processes though it is complicated. This paper discusses the flotation setup, flotation reagents and the operation parameters. In flotation process, the chemical composition of the sulfide mineral is: $3.17\% \leq \text{Pb} \leq 3.85\%$, $2.26\% \leq \text{Zn} \leq 2.54\%$, and $51.6\text{g/t} \leq \text{Ag} \leq 59.2\text{g/t}$. As such the use of selective flotation process is preferred for enrichment. Lead composition in tailing and tailing losses is complex and depends on many factors. Managing of Pb concentrate quantity and tailings of lead is subject of study in this paper, which refers to technological parameters of flotation process. The parameters that influence the lead losses to tailing are: load balance, temperature, grinding and chemical composition of flotation feed. Industrial process of flotation analyses, chemical analyses of flotation products during beneficiation of lead concentrates to achieve technological and economical benefits.

2. Fundamentals

2.1 Froth Flotation

Froth flotation has become the dominant process to concentrate valuable minerals from low grade and complex ores, which would be worthless without flotation. Mineral particle froth flotation is based on differences in the ability of air bubbles to selectively attach to specific hydrophobic mineral surfaces in the slurry (as schematically shown in Figure 1). The particles with attached air bubbles are then carried to the pulp surface and removed, while the particles with hydrophilic surface won't attach to bubbles and stay in the liquid phase. In Figure 1, the rotor draws slurry through the stator and expels it to the sides, creating a suction that draws air down the shaft of the stator. The air is then dispersed as bubbles through the slurry, and comes in contact with particles in the slurry.

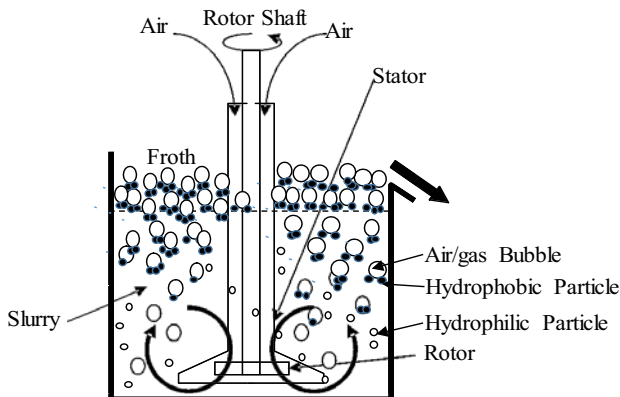


Figure 1. Schematic of a conventional cell flotation.

Froth flotation can be adapted to a broad range of mineral separations, as it is possible to use chemical treatments to selectively alter mineral surfaces so that they have the necessary properties for the separation. It is particularly useful for processing fine-grained ores that are not amenable to conventional gravity concentration.

2.2 Reagents

Collectors and frothers are generally needed to adjust the relative hydrophobicities of the mineral particles, and to maintain the proper froth characteristics, respectively. Although there are many individual collectors for sulfide minerals, the most common collectors are the sulfhydryl collectors, such as the various xanthates and dithiophosphates. Xanthates are most commonly used. Xanthates are highly selective collectors for sulfide minerals, as they chemically react with the sulfide surfaces and do not have any affinity for the common non-sulfide gangue minerals. Figure 2 shows the structure of a typical xanthate collector (ethyl xanthate). The OCSS- group attaches irreversibly to the sulfide mineral surface. Using xanthates with longer hydrocarbon chains tends to increase the degree of hydrophobicity when they adsorb onto the surface.

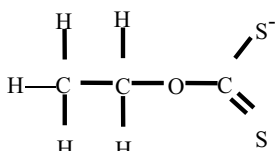


Figure 2. Structure of a typical xanthate collector (ethyl xanthate).

Other highly-selective collectors for use with sulfide minerals, such as dithiophosphates, have somewhat different adsorption behavior and so can be used for some separations that are difficult using xanthates. The first choice of frother is alcohol type frother.

3. The Management of Lead Mineral Resources

Table 1 shows the chemical composition of six lead ores in Kopaunik Massif's place resources. It can be seen from Table I that the composite lead ore resources contain Pb and a significant quantity of Zn. These ores also contain Ag, Au, Cu, and Bi, etc.

Table I. Chemical Composition of Lead Ores in Kopaunik Massif.

Type of Ores	Pb(%)	Zn(%)	Ag(g/t)	Fe(%)	Cu(%)	S(%)	SiO ₂ (%)
1	5.5	13.0	-	9.4	-	-	18.0
2	8.5	13.8	-	1.8	1.0	-	20.0
3	6.0	13.1	-	-	-	16.0	19.0
4	4.0	2.8	60	-	-	-	-
5	2.8	2.1	51	-	-	-	-
6	3.7	2.4	52	-	-	-	-

Trepca's mine has the ore capacity of from 500,000 up to 650,000 tons a year. This mine has three wells developed in 12 horizons with modern infrastructure based on contemporary underground mining model, as well as with modern methods of filling,

3.1 Galena Reserves

Table II presents the quantity of lead and ore in metallurgical belt of Trepca. Place resources of lead in Kosovo lie in the so-called metallurgical belt of Trepca, which is situated in the northeast of Kosovo starting from Leposavic to Gjilan. Length of the belt is over 80km and average width of it is 30km.

Table II Galena Ore Reserves

Resource Locations	Ores(ton)	Pb(%)	Pb metal(ton)
Stan Terg	35,081,000	3.85	1,349,579
Cernac BBGom	7,544,227	6.85	516,645
ArtanesCB complex	16,837,227	4.67	749,354
Total	58,662,569	4.46	2,615,578

3.2 Flotation Process

The ore from Stan Terg mine is carried by train to flotation plant. The following three processing stages are included before flotation process: 1) grinding; 2) classification of sizes, and 3) conditioning. Flotation process of minerals is based on physical-chemical attributes of each mineral phase and their interaction laws. The basic goal of the flotation process is selective separation of useful compounds from the others. Bubbles/aggregate of bubbles and mineral particles has a smaller density than slurry, rise to the surface of pulp and form the floated product. Air bubbles are possible to interact with the mineral particles with hydrophobic surface which is created by reagents used in flotation process. Table III shows the reagents with dosages used in the flotation process.

Table III. Reagents Used in Flotation of Lead Ore

Reagents	Dosage (g/t)
Frother	12-120
Collectors	20-1,200
Carbohydrate Oil	500-2,500
pH Regulators	550-5,000
Activators	250-1,000
Depressants	250-500
Deactivators	25-250

Base and controlling flotation is done in pneumatic machines with "Denver" impeller type. In series are established 12 cells, each cell has a volume $V=2.83\text{m}^3$. Scavenger flotation is done in mechanical machines with impeller and air. The machine has 14 cells, each cell has a volume $V=1.1\text{m}^3$. Dense mass $0.074 \mu\text{m}$ as digestion is dosed in base flotation in the machine with 12 cells, and floated product is carried to machine number 8 of digestion flotation. While the flotation tailing is carried to entrance of controlling flotation for reflation. The controlling flotation product is managed as follows: Quantity of first 6 cells is carried in cell number 4 of digestion flotation as final product (concentrate), while the product of 6 other cells of controlling flotation is returned in conditioner. Whereas the low mass of 6 cells of controlling flotation, goes as sterile.

4. Experimentals and Results

4.1 Mathematical Models for Evaluating Flotation Performances

There is no universal method for expressing the effectiveness of a separation, but there are several methods that are useful for examining froth flotation processes:

(a) Ratio of Concentration: the weight of the feed relative to the weight of the concentrate. The ratio of concentration is F/C , where F is the total weight of the feed and C is the total weight of concentrate. While this data is available in laboratory experiments, in the plant it is likely that the ore is not weighed and only assays will be available. However, it is possible to express the ratio of concentration in terms of ore assays. Starting with the mass balance equations, and the definition of the ratio of concentration:

$$F = C + T \quad (1)$$

$$Ff = Cc + Tt \quad (2)$$

where F, C, and T are the % weights of the feed, concentrate, and tailings, respectively; and f, c, and t are the assays of the feed, concentrate, and tailings. After eliminating T from these equations, the ratio of concentration(F/C) can be obtained:

$$F/C = (c - t)/(f - t) \quad (3)$$

(b) Metal Recovery (%): percentage of the metal in the original feed that is recovered in the concentrate. This can be calculated using weights and assays. The % metal recovery can be calculated from assays alone using:

$$\text{Metal Recovery (\%)} = 100(c/f)(f - t)/(c - t) \quad (4)$$

(c) Metal Loss (%): the opposite of the % metal recovery, and represents the material lost to the tailings. It can be calculated simply by subtracting the % metal recovery from 100%:

$$\text{Metal Loss (\%)} = 100\% - \text{Metal Recovery (\%)} \quad (5)$$

(d) Mass(Weight) Recovery (%): essentially the inverse of the ratio of concentration, and equals:

$$\text{Mass Recovery (\%)} = 100 \cdot C/F = 100 \cdot (f - t)/(c - t) \quad (6)$$

(e) Enrichment Ratio: calculated directly from assays as c/f.

4.2 Main Parameters and Flotation Performances Evaluation Results

Table IV shows the main parameters of lead flotation in “Trepca” Company. Using the models described above, the flotation performances evaluation results are shown in Tables V-VI and Figures 3 and 4.

Table IV. Main Parameters of Lead Flotation in "Trepca" company

Parameters	Unit	Alt. I Sampling Date: 06/18/2013	Alt. II Sampling Date: 06/19/2013	Alt. III Sampling (Artanes Ore) Date: 06/20/2013
Flotation Feed Rate	t/h	150	150	150
Feed Pb Grade	%	3.17	3.17	4.67
Concentrate Pb Grade	%	75.3	73.6	74.4
Tailing Pb Grade	%	0.29	0.14	0.29

Table V. Flotation Performances Evaluation Results

Tests	Quantity of Pb in mineral t h ⁻¹	Quantity of Pb concentrate t h ⁻¹	Quantity of Pb, in Pb concentrate t h ⁻¹	Quantity of Pb in losses t h ⁻¹
Alt.I	4.753	5.7993	4.366	0.389
Alt.II	4.753	6.207	4.568	0.167
Alt.III	7.005	8.865	6.595	0.47

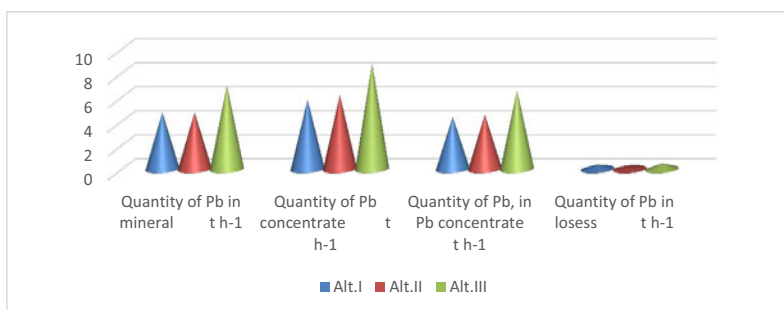


Figure 3. Quantity of Pb in mineral, Pb concentrate, Pb in concentrate and Pb quantity in losses.

Table VI. Pb and Mineral Enrichment.

Tests	Mineral enrichment %	Pb enrichment %
Alt. I	23.753	23.752
Alt. II	23.217	23.217
Alt. III	15.931	15.931

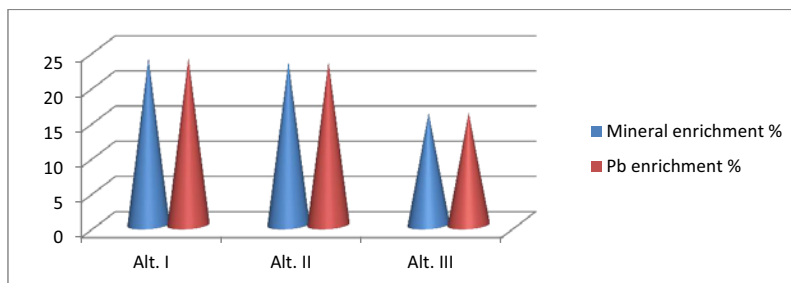


Figure 4. Pb and mineral enrichment.

5. Ag Quantity in Lead Minerals.

“Trepca” sulfur minerals(Pb-Zn) are rich with precious metals. Table VII shows the chemical analysis results of some samples in the laboratory of Trepca's company(Date: 06/19/2014).

Table VII. Ag Quantity in Lead Minerals

Sample	Shift	Quantity g t ⁻¹
1	1	11.38
2	2	38.50
3	3	16.67

Ag quantity in mineral can be calculated with mathematical expression.

$$C_{Ag} = F \times g \text{ t}^{-1} \text{ Ag}^{\text{mineral}} \quad (8)$$

Ag quantity for the first sample is:

$$C_{Ag} = 150 \text{ t h}^{-1} \times 11.38 \text{ g t}^{-1} = 1.707 \text{ kg h}^{-1}$$

Ag quantity for the second sample is:

$$C_{Ag} = 150 \text{ t h}^{-1} \times 38.50 \text{ g t}^{-1} = 57.750 \text{ kg h}^{-1}$$

Ag quantity for the third sample is:

$$C_{Ag} = 150 \text{ t h}^{-1} \times 16.67 \text{ g t}^{-1} = 25.005 \text{ kg h}^{-1}$$

6. Results Discussion

The main flotation process parameters have been investigated in the industrial scale flotation tests in "Trepca". It can be seen from the tests of Alt. I and II with the treated Pb mineral of 3.17%Pb that:

- Quantity of Pb in mineral is 4.755 t/h.
- Quantity of Pb concentrate and quantity of Pb in Pb concentrate for Alt. II has an increase with value $C = 0.4053 \text{ t/h}$, while Pb quantity in Pb concentrate has an increase with value $C_{Pb} = 0.202 \text{ t/h}$.
- Quantity of Pb losses for Alt. II has a decrease with value of 0.222 t/h.
- Mineral enrichment for Alt. II has a decrease with value of 0.536 t/h.
- Loses weight for Alt. II has a decrease with value 0.407 t/h.
- Pb enrichment during the flotation process in Alt. II has a decrease with value 0.535%.

In flotation test of Alt. III, the flotation feed from Artana contained 4.67 % Pb. The industrial scale flotation test results in "Trepca" and laboratory analysis showed that:

- Pb enrichment during the flotation process in Alt. II has a decrease with value 0.535%.
- Quantity of Pb concentrate and quantity of Pb in Pb concentrate increases with average value $C = 2.961 \text{ t/h}$ and $CPb = 2.192 \text{ t/h}$.
- Quantity of Pb in losses increases with average value $C_{losses} = 0.8455 \text{ t h}^{-1}$

- d) Enrichment of Pb during flotation test Alt. III has a decrease with average value of enrichment Pb = 7.5315 %. These parameters of technological flotation process identify a good management and a not good management of flotation process of Pb mineral in "Trepca".

7. Conclusions

Based in industrial process tests of flotation and in calculation results, it can be concluded that all the balance positions of lead concentrate are variable. To minimize the loss of lead to tailings, the flotation parameters should be optimized.

The flotation process in the test of Alt. II has a decrease of Pb quantity that lost to tailings. In Test of Alt. III, the flotation feed contained 4.67%Pb. Quantity of mineral and main parameters of flotation process as grinding, conditioning, pH and drying are the same as in Alt. I, and II. Pb quantity dosed in flotation process with mineral is 7.005 t/h which is higher than those in Alt. I, II for 2.25 t/h. Quantity of Pb concentrate has an increase with average value 2.851 t/h toward Alt. I, and II. Quantity of Pb in losses as an increase with average value 0.192 t/h, a quantity that has a bad impact on economical sustainability in flotation processes in Trepca.

Based on laboratory assays and graphic analysis, the losses of lead in tailings with the values from 0.167 t/h to 0.471 t/h is a crucial parameter for managerial quality of flotation process in Trepca.

7. References

1. S.K. Kawatra and T.C. Eisele, (1992) "Recovery of Pyrite in Coal Flotation: Entrainment or Hydrophobicity?" *Minerals and Metallurgical Processing*, 9(2) (1992), 57-61.
2. A. HAXHIAJ, D. ELEZI, S. SHKOLOLLI, "Mjedisi dhe menaxhimi i gazrave termike në zonën e parangrohjes të furrave Vatergjakete në Trepçë". Simpozium VI, Materials and their use, 2006, Tiranë.
3. A. HAXHIAJ, "Materialna i toplotna bilansa PORTPIRI pec", magistarski rad, Sveučilište u Zagrebu, 1989, MF u Sisku.
4. A. Haxhij, M. Rizaj, D. Elezi, "The management of coke and the optimum percentage of lead in agglomerate in Port-Piri furnace". 10TH National conference of Metallurgy, 2007, Bullgari.
5. A. HAXHIAJ, "Intensifikimi dhe optimizimi i procesit të shkrirjes reduktuese të aglomeratit të plumbit në furrat shahte", punim i doktoratës, 2003, UP FXM, Mitrovicë.
6. M. RIZAJ, A. TERZIQI, E. BEQIRI, N. KAMBERAJ, "Concentration and Distribution Characteristics of Trepça Shaft Furnace Slag", *World of Metallurgy-Erzmetall* 61(2) (2008), 109-114, Clausthal-Zellerfeld, Germany.
7. A. Haxhij and E. Haxhij, "The Optimization of the Coke and Agglomerate Quantity in Lead Production in "Water-Jacket" Furnace", (Paper presented at TMS Annual Meeting & Exhibition, Seattle Washington, 14-18 February 2010), 249-257.

THE MINERAL CONSTITUTION AND LEACHABILITY CHARACTERISTICS OF DUSTS FROM DIFFERENT LEAD SMELTING FURNACE

Hongxu Li^{1,2}, Yang Xie^{1,2}, Chao Li^{1,2}, Zhaobo Liu^{1,2}, Mengmeng Huang^{1,2}

¹ School of metallurgical and ecological engineering, University of science and technology, 30# Xueyuan Road, Beijing, 100083, China

²The Beijing Key Laboratory of Recycling and Extraction of Metals (REM), University of science and technology, 30# Xueyuan Road, 100083, Beijing China

Keywords: Metallurgical waste, Lead smelting dusts, Characterization, Leachability

Abstract

The lead smelting dusts contain complex composition such as Pb, Zn, Cd, S and As, which pose serious environment problem. This research used several physical and chemical methods to study the basic properties of different lead smelting dusts including blast furnace dust, reduction furnace dust, reverberatory furnace dust and bottom blowing furnace dust. The results of characterization showed that these dusts have different phases, element composition and surface morphology. In addition, the distribution of elements and compounds presented a certain trend, which will impact the leachability of their major elements. At the same time, leaching experiments were carried out on the four types lead smelting dusts to provide leachability information for metal recovery.

Introduction

The world lead production in 2012 was 10.56 million tons, among which China contributed 43 % of the total lead production. Being the largest lead producer and consumer in the world [1], China produced 4.54 million tons of lead concentrates in 2013 according to the data released by the China nonferrous metals industry association [2,3]. While more than 80% of lead is produced by traditional sintering, roasting, and reduction smelting process, which is a continuous oxidation and reduction process. In this process lead sulfide concentrate, flux, return dusts and dolomite or calcite lime are granulated first and then sintered at the temperature of 800°C in oxygen sufficient condition, followed by adding coke and return slag in reduction process to produce crude lead [4, 5]. There are obvious differences among the lead smelting dusts derived from different smelting process. Blast furnace dusts is produced from raw material sintering process in which galena is oxidized, which is collected after being treated in fuming furnace [6]. Reducing furnace dust is derived from reducing process of sinter slag, and metal oxide in slag is reduced into metal by carbon oxide and part of materials go into flue gas with rising airstream during the process. At the same time, part of lead stream would be secondary oxidized in the process of rising [7].

A reverberatory furnace smelting method has been carried out for reusing the low concentration SO₂ gas. A series of tasks including galena roasting, mutual reaction, melting slagging and refining containing liquation and impurities removal are completed in the same reverberatory

furnace. The process produces material containing 99% of Pb and a small amount of matte [8]. Besides, another method named bottom blowing oxidation process (SKS lead smelting method) aiming at solving SO₂ pollution problem was operated in the year of 2002 for the first time in China[9, 10]. The amount of bottom blowing furnace dust produced from the strong oxidation phase is huge due to inlet of oxygen-enriched air.

According to national list of hazardous waste, the lead smelting dusts are classified as dangerous pollutant because they contain lead, cadmium, arsenic and chloride compounds which are considered as primary or secondary pollutants[11, 12]. Besides, the production and storage amount of lead smelting dusts are huge, so these dusts cannot be recycled in the process because of contaminating the primary materials. These lead smelting dusts can lead to environment problem if discharged directly without adequate treatment.

Therefore, it is necessary to determine how to separate and recover these valuable elements from the dusts before discharge. Many comprehensive recovery methods have been developed by researchers in recent years. Fu et al [13] used a selective chlorination roasting method to remove fluoride and chloride from lead fuming furnace; Tang [14] et al investigated the zinc extraction experiments using ammonium sulfate solution at high temperatures; Turan et al [15] applied the method of concentrated sulfuric acid roasting followed with water to recover huge acid insoluble metals; Ruiz et al[16] prepared zinc oxide after dust being leached with ammonia. However, most objects of those researches were electric arc furnace dust [17-21], which has different chemical composition and mineralogical structure with lead smelting dusts, and there is few report about the characterization of lead smelting dusts. Therefore, it is necessary to study the chemical and mineralogical characterization of different kinds of lead smelting dusts for selecting the most suitable methods to recovery them.

Materials and Experiments

Dust characterization

The experimental samples were derived from four types of lead smelting dusts named blast furnace dust(D1), reducing furnace dust(D2), reverberatory furnace dust(D3)and bottom blowing furnace dust(D4)produced in JINLI lead smelting industry of Henan province. Before analysis, the samples were dispersed by ethanol. Blend samples evenly before sampling to ensure representativeness of samples. The chemical composition of dust samples were analyzed by X-ray fluorescence (XRF), which was focused on determination of specific elements such as lead, zinc, cadmium, sulfate, chloride, arsenic. Chemical titration analysis, atomic absorption spectrometry (AAS) and emission spectrometry by inductively coupled plasma (ICP) and ion exchange chromatography are also used to check the chemical compositions of dusts.

The structural characterizations of lead smelting dusts were performed through X-ray diffraction analysis in a Siemens appliance model D500. X-ray patterns of samples powdered to 400 mesh were obtained with monochromatic Cu K α radiation in the 2 θ -range from 10 $^{\circ}$ ~90 $^{\circ}$ at a scan rate of 1 $^{\circ}$ ·min $^{-1}$, and fixed counting time of 1s for each step. X-ray diffraction patterns were analyzed both visually and by the comparison technique using the Joint Committee of Powder Diffraction Standard (JCPDS) data. Use Jade 5.0 software to analyze detection results.

FTIR spectra were collected on a Model Nicolet iS5 FTIR. For each spectrum, 32 scans with a resolution of 2 cm $^{-1}$ between 4000 and 400 cm $^{-1}$ were used in transmission mode on KBr pellets made with 2mg sample and 200 mg KBr. It is aimed at analyzing surface adsorption group.

Scanning electron microscopy (SEM) with X-ray energy dispersive spectrometry (EDS) was performed to gain further knowledge of the lead smelting dust particles structure, morphology and their chemical composition..

Leaching Test

Leaching tests were carried out in a beaker immersed in a thermostatic water bath under mechanic agitation to keep solid particle suspended evenly. The water solubility and acid solubility of main elements in four dust samples were taken into account. Sulfuric acid was selected as leaching agent because it could separate lead from most acid-soluble ions. The effects of acid concentration (0-70 g/L), solid/liquid ratio (5:1-30:1), leaching temperature (25-80°C) and leaching time (5-30 min) on the elements content in leached residue were investigated. The major elements were analyzed for Pb, Zn, Cd, As, S and Cl in residue.

Results and Discussion

The elemental composition of dusts

Table I shows the chemical composition results of lead smelting dusts determined by X-ray fluorescence method. The elements presented in four dust samples were similar and the majority elements were lead, zinc, cadmium, sulfur, arsenic, and chlorine. The minor elements were iron, copper, aluminum, silicon, sodium and potassium. The amount of elements was different in four dust samples. The lead content in blast furnace dusts was relatively high because D1 was derived from the first step of raw materials treatment so that partial of materials would volatilization. Major metals in reduction furnace dusts were lead, zinc and cadmium. Chlorine content was relatively high due to the volatilization of chloride under high temperature and reducing atmosphere. The major elements of reverberatory furnace dust were lead, zinc, cadmium, iron, copper and sodium, because they were produced from a continuous process of raw material treatment to remove impurities. Owing to lead and cadmium sulfide or sulphate were served as bottom blowing furnace raw materials, the major elements in D4 were lead, cadmium and sulfur, and zinc content was relatively lower than the other three dust samples.

The results of individual metal content analysis in four dusts point to the need of examining its physical and chemical properties since it is considered to be a type of industrial waste. Moreover, special attention will be given to the content of major elements in water or acid leachates in order to find a proper solution for their recovery. As seen from Table 1, it is better to recycle lead, zinc and cadmium from D1 and D2; and there is more economical advantage to recycle lead and cadmium from D4; besides, it is more difficult to comprehensively recycle elements from D3 due to its complexity.

Table I. The chemical composition of lead smelting dust (%)

Element	Pb	Zn	Cd	S	As	Cl	Fe	Cu	Si	Al	Na	K
D ₁	61.84	12.21	9.67	7.91	1.85	2.16	0.40	0.12	0.13	0.05	1.05	2.74
D ₂	37.75	26.38	14.04	5.36	2.56	8.79	0.19	0.14	0.14	0.07	<0.01	2.74
D ₃	49.87	3.38	6.71	7.58	0.03	1.05	2.13	2.13	0.64	0.03	12.03	<0.01
D ₄	39.92	0.27	34.49	18.79	<0.01	3.68	0.07	0.26	0.01	0.04	0.27	<0.01

derived from the strong oxidation process of raw materials, so the lead sulfide or lead arsenic could not be found from Fig.2. The diffraction peaks of zinc compounds were covered by other strong peaks because of minor zinc content. Cadmium oxide was confirmed to be the major phase in D4. Besides, cadmium sulfide and sulphate could not be ruled out because they had those major phases like XRD pattern.

Table II. Results of phase analysis of lead smelting dusts samples

sample	Identified phase										
	1	2	3	4	5	6	7	8	9	10	11
	PbS	Pb ₂ O ₃	Pb ₃ (AsO ₄) ₃ Cl	PbSO ₄	Pb ₃ O ₈ Cl ₂	PbAs ₂ S ₄	PbO	Pb ₃ O ₄	Pb ₃ O(SO ₄)	PbO ₂	ZnS
D ₁	●	○	○	○	○	○	○	×	×	×	○
D ₂	○	○	○	×	×	×	○	○	×	×	×
D ₃	○	○	×	●	×	×	×	×	○	×	○
D ₄	×	×	×	●	×	×	○	○	×	○	○
sample	Identified phase										
	12	13	14	15	16	17	18	19	20	21	
	ZnO	Zn ₃ (AsO ₄) ₂	ZnAs	Zn ₃ As ₂	CdO	CdS	CdAs	Cd ₂ As ₂ Cl ₂	CdSO ₄	Cd ₃ (AsO ₄) ₂	
D ₁	○	×	×	○	×	○	●	×	○	×	
D ₂	●	○	○	×	×	●	○	×	○	×	
D ₃	×	×	×	×	×	○	○	×	○	○	
D ₄	○	×	×	×	●	○	×	×	○	×	

* (●) Identified phases in major peak (○) Identified phases in minor peak (×) Phases undetected

In general, the lead smelting dusts were composed of metal oxide, sulfide, sulphate, arsenic, arsenate and chlorine-containing compounds. Not all the identified phases in minor peaks displayed in TableII were confirmed in the diffractogram due to the superimposition of their diffraction peaks with those of the more abundant phases.

The infrared spectra of D1~D4 samples can be seen in Fig.3. All the spectra presented a broad band around 3460cm⁻¹ due to O-H stretch of hydrogen bonded water. D4 displayed the strongest O-H stretch vibration [17, 22]. All the four spectra displayed a band around 1640 cm⁻¹ assigned to a vibration of the water molecule [22], which were surface absorbed or entrapped in cavities. It could be found water molecule content in D4 was the highest, but few could be identified in D2. A weak absorption peak near 779 cm⁻¹ was attributed to SiO₂[23], which is an impurity phase of quartz. The vibration degrees of SiO₂ were related to the silicon content in dusts, so the vibration of D₃ was the strongest. Seen from the spectrum of four dusts, it could be presumed that the band located around 1120 cm⁻¹ is due to a sulfate (SO₄²⁻) vibration, being the other strong sulfate vibration, expected around 617 cm⁻¹[18]. It could be found that sulfate content in four dusts was in the order of D₄ > D₃ > D₂ > D₁. The bands around 500 cm⁻¹ were assigned to vibrations of simple oxides[24] such as lead oxide, zinc oxide and cadmium oxide. The vibration in D₂ was most obvious, which could be speculated to be caused by ZnO and PbO according to TableII. Although no sulfur was expected in the spectra, sulfide could not be ruled out in dusts.

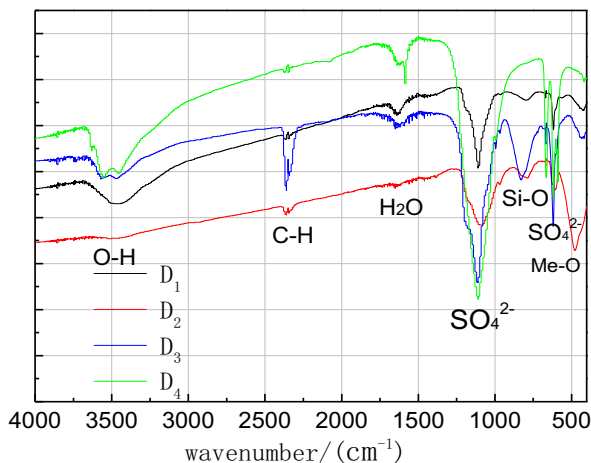


Figure 3. FTIR spectra curves of lead smelting dusts samples prepared as KBr

Microstructure of the dusts

SEM micrographs of D1, D2, D3 and D4 samples can be seen in Fig.4. The grains in four samples have displayed various different morphology such as spherical, block, cubic crystalline structure and some irregular non-crystalline state. It is reported that the formation of dusts undergoes two steps: first, the emission of dust “precursors” (vapors, metal droplets, and solid particles) inside the furnace; second, the conversion of those precursors into dusts through agglomeration and physico-chemical transformations [17].

As seen from Fig.4 D1a~b, the particle size of D1 was between 0.1~1 μ m, which was smaller than the data detected in granular analyses. It can be seen from D1a~b that particles distribution of D1 was even and most of them displayed spherical structure, which indicated that they have been formed from the liquid state after evaporation condensation or volatilization of fine particle. The white substance in Fig.4 D1c whose EDS elemental analysis pointed to zinc oxide was wrapped by black fine particle aggregates assigned to lead compounds and next to grey substance assigned to cadmium sulfide. The microstructure of D2 observed in Fig.4 D2a~c indicated that the size distribution range was wide and particle forms were various. The spherical shapes of granules with Pb and O as major elements were assigned to lead oxide phase. The cubic particle whose EDS analysis pointed to lead sulfide was derived from the unreacted raw material. As shown from D2b, particles were wrapped or agglomerated. The fine particles being wrapped were mainly composed of zinc oxide and cadmium sulfide through EDS analysis. The spherical shapes were the main microstructure of D3 seen in Fig.4 D3a~c. The granules were mixture of zinc, cadmium, copper, iron and sodium compounds identified by EDS analysis. The distribution of phase was relatively homogeneous in D3c, because reflecting smelting process was continuous so that dust component was diverse and mixed. The microstructure of D4 observed in Fig.4 D4a-c was irregular sintering phase, indicating the granules have undergone sinterization during fly off from the molten metal to the bag filter. The amorphous phase identified as sulfate was formed by reaction of metal oxide and rapidly released SO₂.

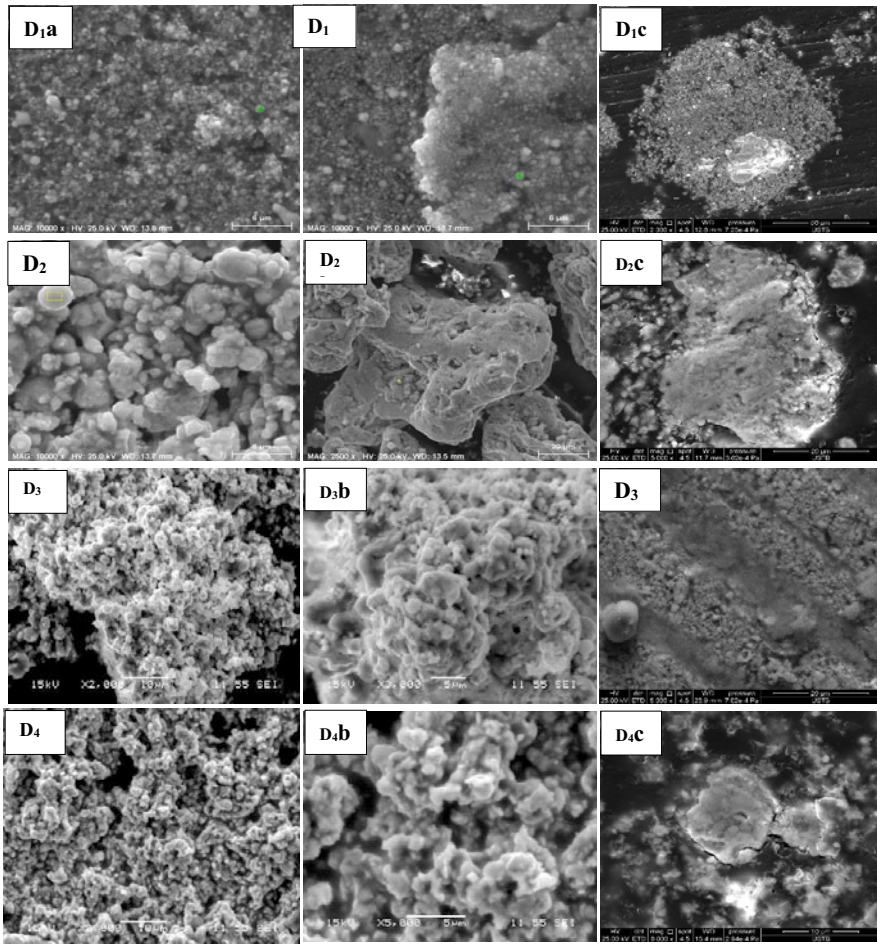


Figure 4. Microstructure photos of four lead smelting dusts

The leachability of the different dusts

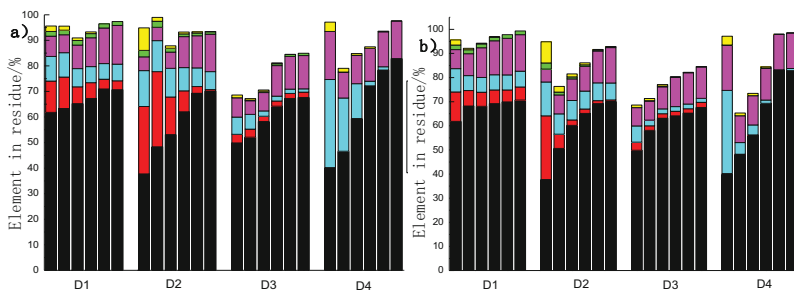
Considering sulfuric acid can easily dissolve a large part of elements from dusts, the experiment of ions leachability of dusts was carried out in sulfuric acid solution. As seen from Fig.5a~d, the first column of each dust presents the elements content in dust before leaching.

Fig 5a indicates the effect of sulfuric acid concentration on elements content in the residues. With acid concentration increasing, zinc content in D1 and D2 were significantly decreased. When acid concentration reached 70 g/L, zinc in D2 was totally leached, while zinc in D1 and D3

were just leached 54.8% and 42.9% respectively. The leached amount of cadmium in D₄ was affected by acid concentration obviously, and cadmium was totally leached as acid concentration reached 70 g/L, besides, the cadmium in D₁, D₂, D₃ were reduced about 38.2%, 40.5% and 80.4% respectively at the same concentration. As partial particles of D₂ were wrapped shown in Fig.4 D₂b, the wrapped arsenate (Zn₃ (AsO₄)₂) would be released with dissolution of zinc and cadmium. The arsenic has dissolved 17.3% in D₁ and 63.7% in D₂ at the concentration of 70 g/L. The effect of leaching time on elements content in the residues is shown in Fig 5b. The chloride ions were totally removed from four dusts between 5 and 10 min. The ions leaching rate of D₁ was relatively fast due to a considerable part of compounds were insoluble sulfide and the leached amount of zinc, cadmium and arsenic reached 54.6%, 38.1%, 14.6% in 5 min. It took 30 min to leach whole zinc from D₂, while just 51.25% of cadmium and 87.5% of arsenic were removed at most. On the other hand, it just needed 10 min to obtain the largest removed amount of zinc and cadmium from D₃, but increasing time to 30 min was beneficial to increase the lead content in residue due to the complexity of elements. It only took 20 min to totally leach cadmium from D₄.

Fig. 5c shows the effect of leaching temperature on the elements content in residue. Increasing temperature was beneficial to remove cadmium, zinc, arsenic and chloride from four dusts at different extent. It can be seen from Fig. 5c that 60°C was considered as optimum leaching temperature, and higher temperature did adversely affect the leaching result because of water evaporation. As seen from Fig.5d, liquid solid ratio of 20:1 could be selected as proper parameter for leaching D₁, D₂ and D₄, because soluble compounds were relatively less in D₁ and particle sizes of D₃ and D₄ were relatively small. However, increasing liquid solid ratio to 30:1 was better to reach the optimal ions leaching amount of D₂.

Above all, combined with characterization results of dusts, all the chloride ions could be removed from dusts. Besides, 17.3% and 63.7% of arsenic identified as arsenate could be removed from D₁ and D₂ respectively. About 54.5% of leached zinc from D₁ was contributed to dissolution of zinc oxide, and about 38.2% of cadmium from D₁ was derived from cadmium sulphate and cadmium oxide. As to ions leachability of D₂, all zinc could be totally leached, which was identified as soluble zinc oxide, and 40.5% of leached cadmium was contributed to cadmium sulphate. About 42.9% of zinc came from arsenate could be leached from D₃, and 80.4% of cadmium derived from sulphate and arsenate could be also removed from D₃. The cadmium existed as cadmium oxide and cadmium sulphate in D₄ could be totally leached at optimal conditions.



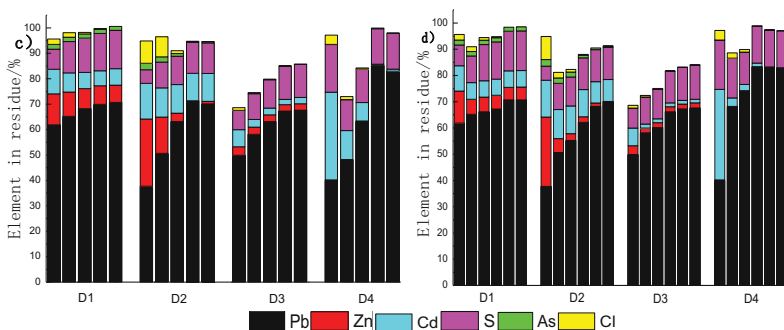


Figure 5. The effects of different leaching conditions on the elements content in leached residue: a) acid concentration (from left to right: elements content in dusts, treated with water, 10g/L acid, 30g/L acid, 50g/L acid, 70g/L acid); b) leaching time (from left to right : elements content in dusts, 5min, 10min, 15min, 20min, 30min); c) leaching temperature (from left to right : elements content in dusts, 25 °C, 40 °C, 60 °C, 80 °C); d) liquid to solid ratio (from left to right : elements content in dusts, 5:1, 10:1, 15:1, 20:1, 30:1).

Conclusions

The characterization results of four lead smelting dust samples show that there are obvious differences in chemical composition, particle size distribution, phase composition and microstructure among four studied samples. D₁ contains high amount of lead and unoxidized sulfides and arsenides because it was obtained from the first step of treating raw materials. Most of lead and zinc compounds in D₂ were oxides for sintering slag as the material. It is more difficult to recycle elements from D₃ due to its chemical complexity. As for D₄, cadmium content was relatively high and almost all cadmium compounds were oxides and sulphates. In order to obtain the highest leaching efficiency when using sulfuric acid as reactant, the appropriate leaching conditions were determined as follows: acid concentration of 70g/L (for four dusts), leaching temperature of 60°C (for four dusts), leaching time of 5 min (for D₁), or 30min (for D₂, D₃), or 20min (for D₄), liquid to solid ratio of 20:1 (for D₁, D₃, D₄) or 30:1 (for D₂).

Acknowledgments

The authors gratefully acknowledge the financial support of the National Science Foundation of key funds PRC for the research project (No.51234008), also the financial support of Beijing technical development project (No. 00012132) and the development of science and technology fund supported by CCS

References

1. B.H. Jia, "The lead market review and outlook in July 2013," *Nonferrous Metals Engineering*, 3 (4) (2013), 9-10.
2. W. Ye, "The lead market review and outlook in March 2013," *Nonferrous Metals Engineering*, 3 (2) (2013), 9-10.

3. H.Y. Sohn and M.O.Martinez, "Chapter 2.3 – Lead and Zinc Production, *Treatise on Process Metallurgy*," (Beijing: Metallurgical Industry Press, 2014), 29-31.
4. C.Y. Wang, W. Gao and F. Yin, "Present situation of lead smelting technology and the performance of trial production of the first lead flash smelting furnace in China," *Nonferrous Metal:Smelting*, 1 (2010), 9-13.
5. W.F. Li, X.G. Zhang and X.Y. Guo, "Status and progress of lead smelting technology in China," *China Nonferrous Metallurgy*, 2 (2010), 29-33.
6. Z.D. Wang, T. Lei and Z. Shi, "Experimentation on treatment of slag from lead smelting furnace by fuming process," *Yunnan Metallurgy*, 6 (1) (2007), 45-47.
7. J.B. Wang, J. Wang and X.M. Wand, "Renovation of ESP in the process of rich oxygen under-gate blast reduction," *Industrial Safety and Environmental Protection*, 29 (7) (2003), 8-9.
8. L.M. Liu, "A new indium extration process from lead dross reverberatory furnace dust," *Rare Metal*, 27 (1) (2003), 112-115.
9. A.H. Jiang, S.H. Yand and C. Mei, "Exergy analysis of oxygen bottom blown furnace in SKS lead smelting system," *Journal of Central South University (Science and Technology)*, 41 (3) (2010), 1191-1193.
10. M. Guo, "Technical analysis and energy-saving and emission reduction effects of lead metallurgy by advanced oxygen bottom-blowing process," *Nonferrous Metallurgy and Energy Saving*, 5 (2008), 15-19.
11. Mushak, "Chapter3-Lead in the Human Environment: Production, Uses, Trends," *Trace Metals and other Contaminants in the Environment*, 10 (25) (2011), 31.
12. M.F. Gomes, T.F. Mendes, and K. Wada, "Reduction in toxicity and generation of slag in secondary lead process," *Journal of Cleaner Production*, 19 (9) (2011), 1096-1103.
13. L. Jiang, G.F. Fu and D.Q. Wang, "Removal off and Cl from zinc oxide dust using selective chlorination roasting process," *Nonferrous Metals*, 53 (3) (2001), 28-31.
14. M.T. Tang, P. Zhang and J. He, "Leaching zinc dust in system of Zn (II)-(NH₄)₂SO₄-H₂O," *J. Cent. South Univ. (Science and Technology)*, 38 (5) (2007), 867-872.
15. M.D. Turan, H.S. Altundoğan and F. Tümen, "Recovery of zinc and lead from zinc plant residue," *Hydrometallurgy*, 2004 (75), 169-176.
16. O. Alguacil, "Recycling of an electric arc furnace flue dust to obtain high grade ZnO," *Journal of Hazardous Material*, 2007 (141), 33-36.
17. F.M. Martins, J.M. Neto and C.J. Cunha, "Mineral phases of weathered and recent electric arc furnace dust," *Journal of hazardous materials*, 2008 (154), 417-425.
18. C.L. Zhang, "Mineralogical characteristics of unusual black talc ores in Guangfeng County," *Jiangxi Province, China, Applied Clay Science*, 2013 (74), 37-46.
19. T. Sofilić et al., "Characterization of steel mill electric-arc furnace dust," *Journal of hazardous materials*, 2004 (109), 59-70.
20. J.G. Machado et al., "Chemical, physical, structural and morphological characterization of the electric arc furnace dust," *Journal of hazardous materials*, 2006 (136), 953-960.
21. S. Kelebek, S. Yörük and B. Davis, "Characterization of basic oxygen furnace dust and zinc removal by acid leaching," *Minerals Engineering*, 2004 (17), 285-291.
22. K. Nakamoto, "Infrared and Raman Spectra of Inorganic and Coordination Compounds, Chapter[], third ed." *Wiley Interscience*, New York, 1978, 132-148.
23. Patrick N L et ai., "Influence of the chemical and mineralogical composition on the reactivity of volcanic ashes during alkali activation," *Ceramics International*, 2014 (40), 811-820.

24. M. Paul and G.C. Allen, "Chemical characterization of transition metal spinel type oxides by infrared spectroscopy," *Appl. Spectrosc*, 1995 (49), 451-458.
25. Medina A et al., "Fly ash from a Mexican mineral coal I: Mineralogical and chemical characterization," *Journal of hazardous materials*, 2010 (181), 82-90.
26. D. Zingg and D.M. Hercules, "Electron spectroscopy for chemical analysis studies of lead sulfide oxidation," *The Journal of Physical Chemistry*, 1978 (82), 1992-1995.
27. A.P. Davis and C. Huang, "The removal of substituted phenols by a photocatalytic oxidation process with cadmium sulfide," *Water Research*, 1990 (24), 543-550.

The Wetting Behavior of CrMnNi Steel on Mg-PSZ as a Function of Phosphorous, Sulphur and Titanium Content

Tobias Dubberstein¹, Hans-Peter Heller¹, Claudia Wenzel², Christos G. Aneziris²

¹Institute of Iron and Steel Technology, TU Bergakademie Freiberg, Leipziger Straße 34, 09599, Freiberg, Germany

²Institute of Ceramic, Glass and Construction Materials, TU Bergakademie Freiberg, Agricolastraße 17, 09596, Freiberg, Germany

Keywords: Wetting, Interfacial Reaction, Cr-Mn-Ni Steel, SNMS, Mg-PSZ ceramic

Abstract

The effect of temperature and elemental concentrations of phosphorous, sulphur and titanium in high alloyed Cr-Mn-Ni TRIP/TWIP steels (16 %Cr, 7 %Mn, 6 % Ni) on the wettability of MgO partially stabilized zirconia (Mg-PSZ) substrates was studied. The investigation of the wetting behavior is of a major importance of the infiltration of steel into open foam ceramics and in interfacial contact of steel & ceramic powder in the spark plasma sintering. The interfacial reaction was characterized using X-ray and secondary neutral mass spectrometry analysis. The contact angle was investigated between 1500 °C and 1600 °C in argon (99.999 vol% Ar) atmosphere and was found to decrease with increasing temperature. At 1600 °C sulphur decreased the contact angle from 103 ° (100 ppm S) to 92 ° (1000 ppm S) in Fe-Cr-Mn-Ni. Increasing phosphorous content was found to increase the interfacial oxygen content in samples and the contact angle decreased to ca. 97 °. For titanium alloyed Cr-Mn-Ni sample, a Ti_xO_y interfacial layer was found after experiments and the contact angle was ca. 87 ° at maximum Ti content of 0.232 %.

Introduction

Thermophysical properties such as viscosity, surface tension and density are major material properties of high temperature liquid phases [1]. Although their role in metallurgical processing such as casting has been widely known theoretically for a long time, their precise measurement or modeling remains complex [2]. According to the Young Equation, wetting by a liquid metal of solid substrate is described by Equation (1) [3]

$$\sigma_{sv} - \sigma_{sl} - \sigma_{lv} \cdot \cos\theta = 0 \quad (1)$$

here: σ_{sv} is the interfacial energy of solid/vapour (N m^{-1}), σ_{sl} is the interfacial energy of solid/liquid in (N m^{-1}), σ_{lv} is the interfacial energy or surface tension of the liquid (N m^{-1}) and θ is the contact angle in (°).

Recently, austenitic stainless steels with high manganese (≤ 10 % Mn) and phosphorous (≤ 0.2 % P) contents have been developed for the macro infiltration of open-cell MgO-partially stabilized ZrO₂ ceramic foams. It was observed that with increasing phosphorous content in Fe-Cr-Mn-Ni-P alloys the penetration of ZrO₂ open foam ceramics increased, and the pore volumes were most filled at highest phosphorous content [4,5]. During the infiltration of a porous body, the wetting

by the liquid phase of the porous solid is of importance. Karasangabo et al. [6] had investigated the contact angle of Fe-P binary alloys on alumina substrates. In that research, the contact angle was reported to decrease with increasing phosphorous content. Moreover, Krause et al. [7] had investigated the surface tension of iron alloyed with 0.49 % P using the maximum bubble pressure method. It was found, that the effect of a finer cast structure with increasing P-content was not explained by an effect of surface tension. The findings were in agreement to that of Jahn et al. [4] where phosphorous was not surface active and did not significantly change surface tension in high manganese austenitic as-cast steel. Previous studies on the interfacial reaction of iron base alloys and α -polycrystalline Al_2O_3 substrate indicated an influence of phosphor on the contact angle [8].

In the present paper, the contact angle of Cr-Mn-Ni steel on Mg-PSZ substrates were studied. Experiments were carried out in order to obtain information about the influence of the temperature and the elemental concentrations of phosphorous, sulphur and titanium on the contact angle.

Materials and Methods

Within the present investigation Cr-Mn-Ni steel on Mg-PSZ ceramics were used to analyze the interfacial wetting and interfacial reaction between liquid steel and solid ceramic ZrO_2 substrate. The steel was manufactured using a vacuum induction furnace with argon atmosphere (< 2 ppm O_2). Samples were analyzed using optical emission spectrometry (OES), combustion technique for carbon and sulphur. The total oxygen and nitrogen were analyzed using hot gas extraction technique. The phosphorous content was varied from 0.0097 % to 0.2320 % P, the sulphur content was varied from 0.0114 % to 0.0696 % S, and the titanium content was varied from 0.0312 % to 0.2160 % Ti in high alloyed Cr-Mn-Ni steels. The chemical composition is given in **Table 1**.

Table 1. Chemical composition of Cr-Mn-Ni steel with P, S, and Ti content in mass percent and ppm

Sample	Fe	C	Si	Mn	Cr	Ni	Mo	Al	Ti	N	O _{tot}	S	P
P200	bal.	0.028	0.91	6.97	15.7	6.23	0.078	0.004	0.001	245	321	67	97
P500	bal.	0.028	0.89	7.09	15.7	6.25	0.081	0.005	0.001	240	14	72	427
P1000	bal.	0.025	0.97	6.94	15.7	5.87	0.083	0.014	0.001	230	15	143	1340
P1500	bal.	0.026	0.89	6.91	15.2	5.80	0.077	0.008	0.001	236	65	117	1550
P2000	bal.	0.029	0.90	7.06	15.8	5.87	0.084	0.011	0.001	280	15	140	2320
S1	bal.	0.030	0.995	7.15	15.9	5.95	0.090	0.004	0.001	211	38	114	137
S2	bal.	0.034	1.04	7.07	16.0	5.98	0.089	0.005	0.001	322	19	155	129
S3	bal.	0.027	0.85	7.07	16.0	6.11	0.096	0.006	0.001	255	38	296	118
S5	bal.	0.035	0.99	6.82	16.1	6.06	0.088	0.005	0.001	271	17	420	122
S10	bal.	0.024	0.82	7.17	16.1	5.96	0.089	0.006	0.001	244	25	696	98
Ti5	bal.	0.034	0.10	7.00	16.2	5.97	0.080	0.016	0.031	25	34	136	277
Ti10	bal.	0.043	0.96	6.80	16.2	6.00	0.073	0.012	0.098	218	9	133	248
Ti20	bal.	0.041	0.98	6.90	15.9	5.80	0.071	0.018	0.216	295	12	84	176

The hot stage microscope used for sessile drop measurements is shown in **Figure 1**. The main setup is located inside a vacuum chamber. In order to remove impurities from the ambient gasses, it is evacuated $\leq 10^{-3}$ mbar. For the experiment, the vacuum vessel is flushed with argon (5.0). The sample is heated using an RF of 10 kW and 100 kHz and a graphite tube. The specimen is placed into the furnace using a precise linear guiding. A high temperature zirconia

oxygen probe is installed for the analysis of the oxygen partial pressure p_{O_2} in the gas outlet stream of the vessel at a cell reference temperature of about 750 °C. The sample temperature was controlled via a type-B thermocouple (Pt30Rh-Pt6Rh). A CCD-camera (resolution 640x480 pixels) continuously recorded the drop profile [19]. The contact angle was calculated by a mathematical approximation of the drop contour and the tangents of the contact area between the liquid drop and the substrate.

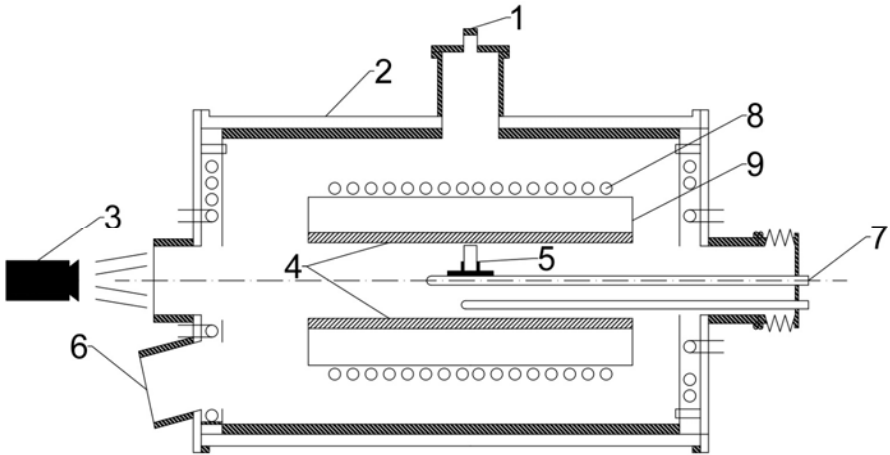


Figure 1. Hot stage microscope for sessile drop method (1: gas inlet, 2: vacuum vessel, 3: CCD-Camera, 4: graphite tube, 5: sample, 6: gas outlet and high temperature sensor, 7: thermocouple, 8: rf-heating, 9: Al_2O_3 tube)

Within the contact angle measurements, the argon gas was provided by a liquid gas tank ($V = 3.4 \text{ m}^3$, $p = 32 \text{ bar}$) with a vaporizer unit. In order to obtain material properties relevant for metallurgical processes, namely casting and metal spraying, no further gas purification was installed. The cold furnace revealed an oxygen content below 1 ppm. Furthermore, the interfacial reaction was characterized using a secondary neutral mass spectrometry recently reported in reference [8,9]. The sputtering rate of the metal surface within the framework of the present investigation was approximately $1 \text{ nm}\cdot\text{s}^{-1}$. The surface roughness of the Mg-PSZ substrates was controlled by similar grinding and polishing procedures before experiments. Confocal laser microscope surface profiling did not show any variation within the surface profile after preparation procedure.

Experimental Results

Phosphor alloyed Cr-Mn-Ni steel

The experimental results of contact angle measurements of phosphorous-alloyed Cr-Mn-Ni steel is presented in **Figure 2**. In all alloys (P200 to P2000) the contact angle was decreased steadily with higher temperatures. The isothermal curve of the contact angle in **Figure 3** for Fe-Cr-Mn-P at 1600 °C indicated, that the wetting of the Mg-PSZ substrate was improved from ca. 102° for

97 ppm P (P200) to ca. 98 ° for 2320 ppm P (P2000). A previous study of Fe-Cr-Mn-Ni on Al₂O₃ substrates revealed a similar influence of phosphorous on the wetting characteristic [4]. After the experiments, there was no visible reaction layer on the metal neither on the ceramic interface. The work of adhesion was calculated from the present wetting results and previous surface tension measurements using sessile drop and the maximum bubble pressure method. The work of adhesion increased from 1.082 J·m⁻² for P200 to 1.166 J·m⁻² for P2000 at 1600 °C.

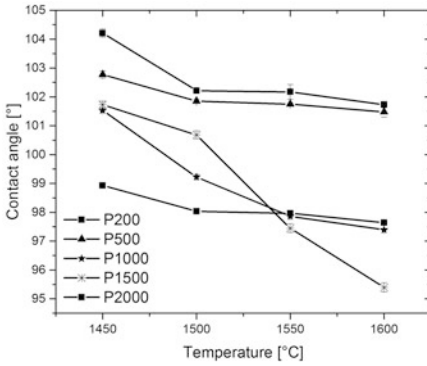


Figure 2. Contact angle for Fe-Cr-Mn-Ni-P alloys (P200-P2000) as a function of temperature

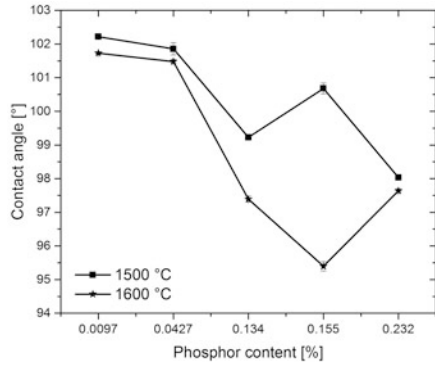


Figure 3. Contact angle as a function of phosphor content in Fe-Cr-Mn-Ni-P for 1500 °C and 1600 °C

The secondary neutral mass spectrometry (SNMS) for P200 sample is shown in **Figure 4**. At the interface at 0 s an enrichment of the oxygen was observed from the intensity signals. Furthermore, some zirconium cation diffused into the metal sample. The oxygen diffusion layer was slightly increased with higher phosphorous content, see **Figure 5**. Phosphor can increase the oxygen activity at the interface, which was earlier reported by Vogel [10]. The increase of the oxygen activity at the interface is assumed to have decreased the contact angle with increasing P content in the investigated samples.

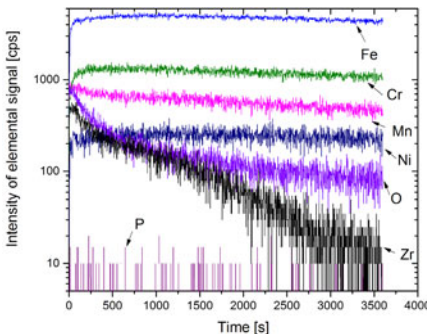


Figure 4. Elemental intensity as a function of sputter time for P200 (ca. 100 ppm P)

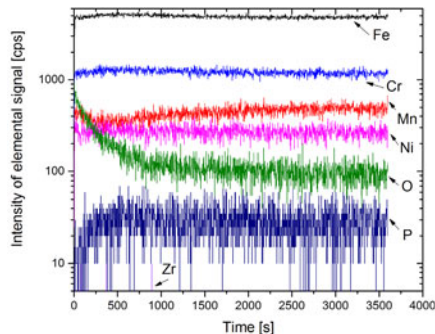


Figure 5. Elemental intensity as a function of sputter time for P1000 (ca. 1340 ppm P)

Sulphur alloyed Cr-Mn-Ni steel

For all Fe-Cr-Mn-Ni-S specimen the contact angle decreased slightly in the considered temperature range from 1450 °C to 1600 °C, refer to **Figure 6**. The contact angle decreased from ca. 102 ° for S1 (137 ppm S) to ca. 92 ° for S10 (696 ppm S) at 1600 °C. The interfacial work of adhesion was 0.880 J·m⁻² for S1 and 0.907 J·m⁻² for S10 at 1600 °C.

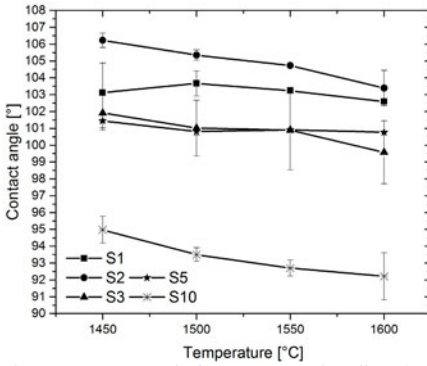


Figure 6. Contact angle for Fe-Cr-Mn-Ni-S alloys (S1-S10) as a function of temperature

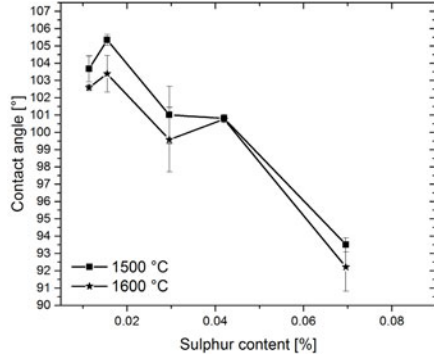


Figure 7. Contact angle as a function of sulphur content in Fe-Cr-Mn-Ni-S for 1500 °C and 1600 °C

The analysis of the interface by SNMS for S1 is presented in **Figure 8**. At the metal interface no sulphur enrichment could be analyzed. The oxygen activity was not significantly increased in the vicinity of the metal / ceramic interfacial layer. The spectrometer analysis of intensity signals for S10 alloy (**Figure 9**) showed, that the sulphur signal significantly increased at the vicinity of the metal interface. As known from Fe-S and AISI 304 sulphur is a strongly surface active element, which was also found for high manganese TRIP/TWIP steels in a previous investigation [11,12].

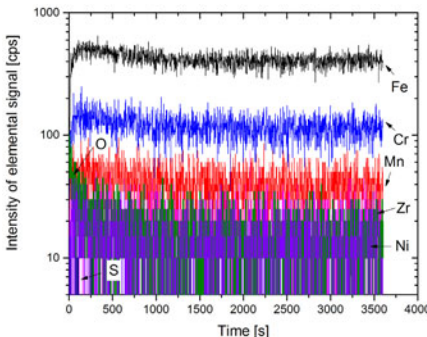


Figure 8. Elemental intensity as a function of sputter time for S1 (ca. 100 ppm S)

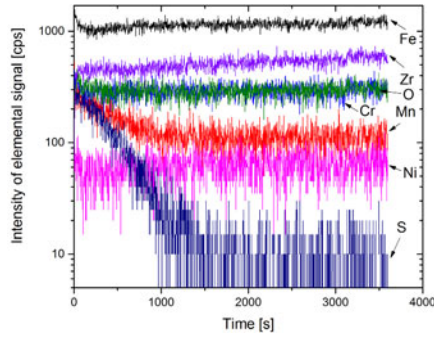


Figure 9. Elemental intensity as a function of sputter time for S10 (ca. 700 ppm S)

Titanium alloyed Cr-Mn-Ni steel

For titanium alloyed Cr-Mn-Ni steel, the contact angle was decreased with temperature as shown in **Figure 10**. From Ti5 with 0,031 % Ti to Ti20 with 0,216 % Ti the wetting was improved from 99 ° to 87 ° at 1600 °C. According the Young-Dupré equation the work of adhesion was increased from 1.027 J·m⁻² (Ti5) to 1.252 J·m⁻² (Ti20) at 1600 °C which is comparable to results for Fe-ZrO₂ interfaces [13]. There is a stronger influence at the metal interface of titanium than of sulphur or phosphorous in Cr-Mn-Ni steel.

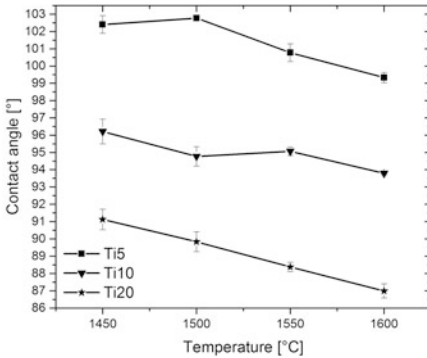


Figure 10. Contact angle for Fe-Cr-Mn-Ni-Ti alloys (Ti5-Ti20) as a function of temperature

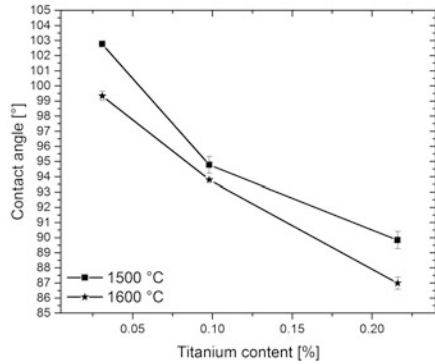


Figure 11. Contact angle as a function of titanium content in Fe-Cr-Mn-Ni-Ti for 1500 °C and 1600 °C

Within the Ti5 sample with very low titanium, no titanium activity was found at the interface (**Figure 12**). However, for Ti20 alloy a thick reaction layer (Zr, O, Ti) of several microns was formed at the metal interface. Fe, Cr, Mn, Ni signals were in the vicinity of the background scattering of the SNMS apparatus. According to the work of Mukai et al. [14] the contact angle was slightly decreased with titanium in low alloyed carbon steel.

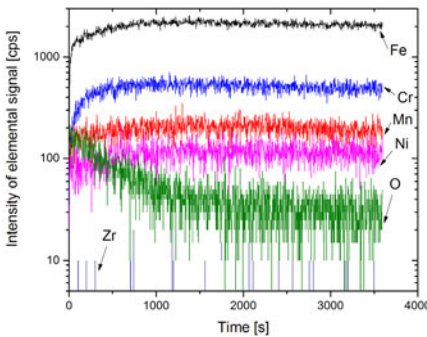


Figure 12. Elemental intensity as a function of sputter time for Ti5 (ca. 300 ppm Ti)

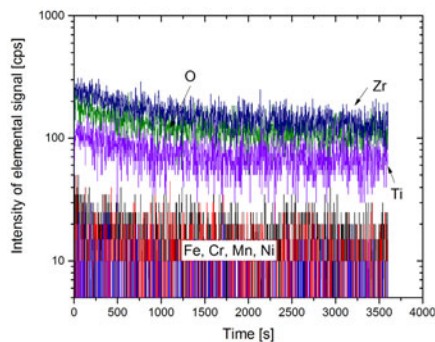


Figure 13. Elemental intensity as a function of sputter time for Ti20 (ca. 2000 ppm Ti)

Conclusions

In the present investigation, the contact angle and the interfacial reaction were analyzed for high-alloyed Cr-Mn-Ni steel with varying P, S, and Ti content and as a function of temperature (1450 °C to 1600 °C). The main results are the following:

- The contact angle decreased with temperature in Fe-Cr-Mn-Ni-(P, S, Ti).
- For phosphor and sulphur alloyed Cr-Mn-Ni steel the contact angle was slightly influenced.
- Sulphur was found as a surface-active element at the steel / ceramic interface.
- Titanium showed a strong interaction at the steel interface, a Ti-O-Zr layer was found with the application of the secondary neutral mass spectrometry.
- The wetting of Cr-Mn-Ni steel was improved with higher titanium content.
- Furthermore, the work of adhesion for all stainless steel alloys was only slightly influenced by a variation in the trace elements.

The improvement of wetting along with the interfacial layer formation via use of titanium are of major importance for the metallurgical manufacturing by a liquid steel infiltration of open foam ceramics for a TRIP-matrix Composite.

Acknowledgement

The present research was financially supported by the German Research Foundation (DFG) within the framework of the subproject A2 “liquid steel design” of the Collaborative Research Centre SFB 799 (TRIP-Matrix-Composite) at the Institute of Iron and Steel Technology IEST, Technical University Bergakademie Freiberg, which is hereby gratefully acknowledged. Dipl.-Ing. O. Krivtsova is acknowledged measuring the contact angles.

References

1. T. Iida, R.I.L. Guthrie, *The physical properties of liquid metals*, (Oxford, GB: Clarendon Press, 1993), v-vii.
2. E.W. Washburn, “The dynamics of capillary flow,” *Phys. Rev.*, 17 (1921), 273–283.
3. T. Young, “An Essay on the Cohesion of Fluids,” *Philos. Trans. R. Soc. Lond.*, 95 (1805), 65–87.
4. A. Jahn, K.-P. Steinhoff, T. Dubberstein, P. Franke, M. Weider, S. Wolf, et al., “Phosphor Alloyed Cr-Mn-Ni Austenitic As-cast Stainless Steel with TRIP/TWIP Effect,” *Steel Res. Int.*, 85 (2014), 477–485.
5. M. Weider, K. Eigenfeld, “Manufacturing of austenitic stainless steel-zirconia composites by infiltration,” *Steel Res. Int.*, 82 (2011), 1064–1069.
6. A. Karasangabo, C. Bernhard, “Investigation of alumina wetting by Fe-Ti, Fe-P and Fe-Ti-P alloys,” *J. Adhes. Sci. Technol.*, 26 (2012), 1141–1156.
7. W. Krause, F. Sauerwald, M. Michalke, “Die Oberflächenspannung geschmolzener Metalle und Legierungen Die Oberflächenspannung von Gold, Zink, Gold-Kupfer-, Silber-Kupfer- und Eisenlegierungen,” *Z. Für Anorg. Allg. Chem.* 181 (1929), 353–371.

8. T. Dubberstein, A. Jahn, M. Lange, H.-P. Heller, P.R. Scheller, "Interfacial Reaction between Iron-Based Alloys and Polycrystalline α -Al₂O₃," *Steel Res. Int.*, 85 (2014), 1220–1228.
9. H. Oechsner, W. Bock, M. Kopnarski, M. Müller, "INA-X: An advanced instrument for electron-Gas SNMS," *Mikrochim. Acta.*, 133 (2000) 69–73.
10. M.E. Vogel, *Messung und Modellierung der Sauerstoffaktivität in Schmelzen aus hochlegiertem Stahlguss* (Freiberg, GER: Universitätsbibliothek der TU BAF, 2002), 1-126.
11. T. Dubberstein, H.-P. Heller, J. Klostermann, R. Schwarze, J. Brillo, "Surface tension and density data for Fe–Cr–Mo, Fe–Cr–Ni, and Fe–Cr–Mn–Ni steels," *J. Mater. Sci.*, 50 (2015), 7227–7237.
12. T. Dubberstein, H.-P. Heller, "Effect of Surface Tension on Gas Atomization of a CrMnNi Steel Alloy," *Steel Res. Int.*, 84 (2013), 845–851.
13. D. Sotiropoulou, P. Nikolopoulos, "Work of adhesion in ZrO₂-liquid metal systems," *J. Mater. Sci.*, 28 (1993), 356–360.
14. K. Mukai, L. Zhong, M. Zeze, "Interfacial properties of molten low carbon steel containing Ti, Nb or B in relation to the behavior of fine particles in continuous casting process," *ISIJ Int.*, 46 (2006), 1810–1816.

Thermodynamic modelling of liquid slag-matte-metal equilibria applied to the simulation of the Peirce-Smith converter

Denis Shishin¹, Taufiq Hidayat¹, Sergei Dectero², Evgueni Jak¹

¹PYROSEARCH, Pyrometallurgy Research Center, School of Chemical Engineering, The University of Queensland, Brisbane, Queensland, 4072, Australia.

²Centre for Research in Computational Thermochemistry (CRCT), École Polytechnique, Montréal, Québec, Canada

Keywords: copper production, slag, matte, liquid copper, thermodynamic modelling, Peirce-Smith converter, liquidus, distribution of elements

Abstract

Computer simulation plays an increasingly important role in improving the environmental and economic performance of pyrometallurgical extraction processes. The thermodynamic description of the chemical systems involved is at the core of such advanced simulation software. A thermodynamic database has been developed to describe the phase relations and chemical reactions in the Al–Ca–Cu–Fe–Mg–O–S–Si chemical system with support from the leading copper producers. The database contains model parameters for gas, liquid slag, liquid matte and metal, spinel and numerous solid phases. Models based on the Modified Quasichemical Formalism were used for the slag, matte and liquid metal. The internal consistency of the database provides accurate and reliable predictions outside of the usual operating conditions. The development of the database was closely integrated with the experimental studies of this chemical system. The database works in the environment of FactSage software. The application of thermodynamic modelling is illustrated by the example of the Peirce-Smith converter.

Introduction

The overall economic efficiency and environmental performance of the copper plant depend on numerous factors. The examples of variable process parameters are temperature, oxygen enrichment of the blow, amount of fuel, internal recycle of slags and dusts, target slag composition (Fe/SiO₂), final matte grade during smelting and converting and many others. The optimization of the process can be achieved by the implementation of the computer models of the process, which, in turn, require deep understanding of chemistry involved. The development of large thermodynamic databases helps to collect and systematically evaluate the experimental information on the chemical systems, important for the industry. In copper industry, the core chemical system is Al–Ca–Cu–Fe–Mg–O–S–Si, plus major impurities Pb, Ni, plus minor elements As, Sb, Bi, Zn, Sn, Au, Ag. The most important phases are gas, liquid matte, metal and slag, spinel solid solution, and numerous solid silicates, oxides and sulfides. The recent experimental and modelling project aimed at addition of Cu and S to the core chemical system has been undertaken by Pyrosearch (The University of Queensland) in collaboration with CRCT (Ecole Polytechnique de Montreal). The introduction of Pb and minor elements to the copper database is currently in progress. The thermodynamic databases are developed within the environment of FactSage software [1].

In the thermodynamic modelling, all available thermodynamic and phase diagram data are evaluated simultaneously in order to obtain one set of model equations for the Gibbs energies of

all phases as functions of temperature and composition. Recent advances in thermodynamic modeling of the subsystems of the core system are: Cu–O and Cu–O–S [2], Fe–O [3], Fe–O–S [4], Cu–Fe–O [5], Cu–Fe–O–S [6], Al–Fe–O [7], Ca–Fe–O [8], Fe–Si–O [9], Cu–Si–O, Cu–Ca–O, Cu–Ca–O–Si [10], Ca–Fe–Si–O [11]. The results of project on the core chemical system are summarized in two PhD theses [12, 13].

In the present article the application of the database is demonstrated on the example of the simulation of Peirce-Smith converter.

1. Thermodynamic database

The following section contains brief descriptions of the thermodynamic models used for matte/metal, slag and spinel phases. More details on the model parameters are available elsewhere [12]. The gas phase is modeled as an ideal solution. The properties of the gaseous species were taken from the standard FactSage database [1].

1.1. Matte

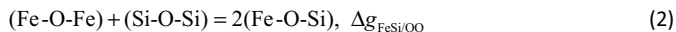
Liquid matte and metal are modeled as one solution:



In this model, species are not charged and placed on one sublattice, so no condition of electroneutrality is imposed. This allows the model for the liquid phase to cover the whole compositional range inside the Cu–Fe–O–S system from metals to oxides (in absence of SiO₂), to sulfides, to non-metals. This way, the deviation of Cu₂S–FeS stoichiometry of mattes is taken into account. The very strong interaction between metals and nonmetals creates short range ordering (SRO) between first nearest neighbors (FNN), which affects the entropy of mixing. This effect is modeled using the Modified Quasichemical Formalism in pair approximation [14, 15]. The meaning of numbers I, II and III is close to the concept of valence. They reflect the fact that in the MQM species have different coordination numbers. The ratio of coordination numbers determines the composition of maximum short range ordering (SRO) between a pair of species: Cu^I:O^{II} = 2:1, Fe^{II}:S^{II} = 1:1, Fe^{III}:O^{II} = 2:3, etc. The absolute values of coordination numbers have minor effect, compared to their ratio. Fe^{III} and Cu^{II} appear only at high oxygen partial pressure, in the order of 10⁻⁷ atm and 0.21 atm at 1200 °C, respectively. Under conditions of pyrometallurgical copper production, Cu and Fe in matte and in metal exist almost exclusively as Cu^I and Fe^{II}.

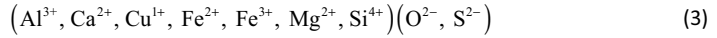
1.2. Slag

Compared to mattes, slags have more distinct ionic characteristics. With the introduction of silica into metal oxide melt, the structure of the liquid solution becomes more complicated. Metals surround themselves by oxygen, but at the same time there is a strong tendency to get Si⁴⁺ cations second next to basic cations (Fe²⁺, Ca²⁺ etc.):



In other words, slags exhibit a significant second nearest neighbor (SNN) short-range ordering (SRO) between basic cations and acidic Si⁴⁺ cations. The existing thermodynamic models are not able to model simultaneously FNN and SNN SRO for species in one sublattice. However, in case of slags it is not necessary, because the range of nonstoichiometry towards metal and toward

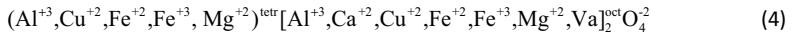
nonmetal is usually very small. Sulfur is soluble in slags, but to a relatively small extent. Thus, slag is modeled using separate solution from matte, where cations and anions species are placed on separate sublattices:



In this way, the magnitude of FNN SRO is represented by the Gibbs energies of the slag solution end-members: oxides CaO, FeO, SiO₂ and sulfides CaS, Cu₂S, FeS, etc. These Gibbs energies are the most important model parameters. To take into account the effect of SNN SRO on the thermodynamic properties of slag liquid, the Modified Quasichemical Formalism in quadruplet approximation was used [16].

1.3. Spinel

The spinel solution, extended during the recent project, is represented by the formula



The model is developed within the Compound Energy Formalism (CEF) [17, 18]. According to CEF, 35 Gibbs energy expressions (G_{ij}) are required for the pseudo components of this spinel. They are related to those of real spinels, but they should not be confused. The procedure, developed by Decterov et al. [19] uses linear combinations of G_{ij} to minimize the number adjustable of model parameters. The reader is referred to Shishin (2013) [12] for the detailed description of the spinel model.

2. Slag-matte equilibrium

The following section contains the description of the slag-matte equilibrium which is of primary importance for the copper smelting and converting. For the sake of simplicity, all calculations are performed within the Cu–Fe–O–S–Si system. The thermodynamic database can be used for the prediction of the effect of Al, Ca and Mg on the slag-matte equilibrium. In the Cu–Fe–O–S–Si system, 5 + 2 = 7 degrees of freedom must be fixed to set the equilibrium. The conventional selection of the degrees of freedom is 1) temperature 2) total pressure (usually 1 atm) 3) presence of slag phase 4) presence of matte phase 5) saturation with SiO₂, or with spinel, or Fe/SiO₂ in slag; first two are limiting cases 6) presence of metal phase (as in the direct-to-blister process) or fixed $P(\text{SO}_2)$ 7) final wt% Cu in matte, or wt%Fe in matte, or $P(\text{O}_2)$. The last degree of freedom serves as an X-axis in Figure 1, while other 6 are fixed. They demonstrate the model predictions of the slag-matte equilibrium at total pressure of 1 atm, 1200 °C, SiO₂ or spinel saturation, $P(\text{SO}_2) = 0.16$ atm as a function of matte grade. These conditions are close to those during the slag blow stage in the Peirce-Smith copper converter. The model calculations are in agreement with the available experimental data as shown in Shishin (2013) [12].

Copper industry is particularly interested in the equilibrium copper content of slag (Figure 1a), because it gives the lower limit of copper losses. In practice, copper content of slag is always higher than equilibrium value due to the physical entrainment of matte into the slag. Nevertheless, the absence/existence of the maximum on the wt%Cu in slag vs wt% Cu in matte curve remains the object of debate among metallurgists. Previous FactSage model by Decterov and Pelton (1999) [20] and MPE model by Chen and Jahanshahi (2013) [21] give the monotonous rise of wt% Cu in slag vs matte grade. The group of Yazawa in Tohoku University

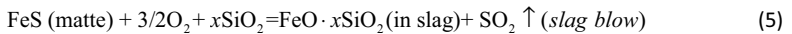
long believed in the existence of the maximum and explained it using the concept of sulfidic solubility of copper in slag [22]. This was supported by several authors [23, 24]. Some researchers did not observe the maximum [25].

In the updated database, sulfur in slag behaves as anion and forms quadruplets with Fe^{2+} and Cu^+ cations and O^{2-} . Thus, the sulfur content in slag and copper content in slag are correlated, and related to the Fe/SiO_2 in slag. The quadruplet model makes it possible to describe the maximum, reported for equilibrium with liquid copper [26, 27]. The experimental work is currently under way in Pyrosearch to confirm the presence of the maximum at higher $P(\text{SO}_2)$.

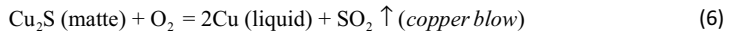
3. Peirce-Smith process simulation

3.1. Simulation formulation

Peirce-Smith is the batch process [28], which mostly consists of reaction of between matte and oxygen aided by fluxing. The reactions may be represented as:



And



The connection between thermodynamics and time is reached through division of the process into equilibrium steps. At each step, the portion of the blow participates in the reaction with condensed phases. The gas phase is removed from the reaction zone and condensed phases proceed to the next iteration. In this sense the procedure is similar to that of Pengfu (2007) [29]. Advanced thermodynamic database allows to take into account mass and energy balance at each iteration simultaneously using the Gibbs energy minimization software based on FactSage. Two external factors: the rate of heat loss to the environment and furnace heat capacity are treated as process parameters. To the first approximation, they are considered to be independent from temperature. The third process parameter is oxygen efficiency. Due to kinetic reasons, only a portion of oxygen participates in chemical reactions. At the same time, “inert” oxygen is assumed to participate in heat balance: some heat is required to raise its temperature. The last process parameter is matte entrainment in slag. It shows the mass of matte that should be tapped together with each 100 g of slag during the skimming. The level of entrainment depends on many factors, such as viscosity of slag, settling time and skimming procedure. In the present study it was assumed to be constant. The list of the process parameters is given in Table 1.

3.2. Results of the simulation

The process starts when a large amount of matte together with reverts is charged in the converter and blowing starts. The high copper slag from anode furnace or from over oxidized blister copper is often charged at some point during the slag blow. At this stage, it is acceptable to add reverts with significant iron content. The amount of input flux can be roughly calculated from the knowledge of starting matte grade, desirable final matte grade and mass of matte. The target Fe/SiO_2 ratio in the slag is 1.5 – 2.0 depending on the final matte grade. Figure 2 shows slag liquidus in equilibrium with matte of different grades. It is evident from Figure 2 that higher matte grades require higher temperature in order to keep the slag liquid. The amounts of phases are plotted in Figure 3.

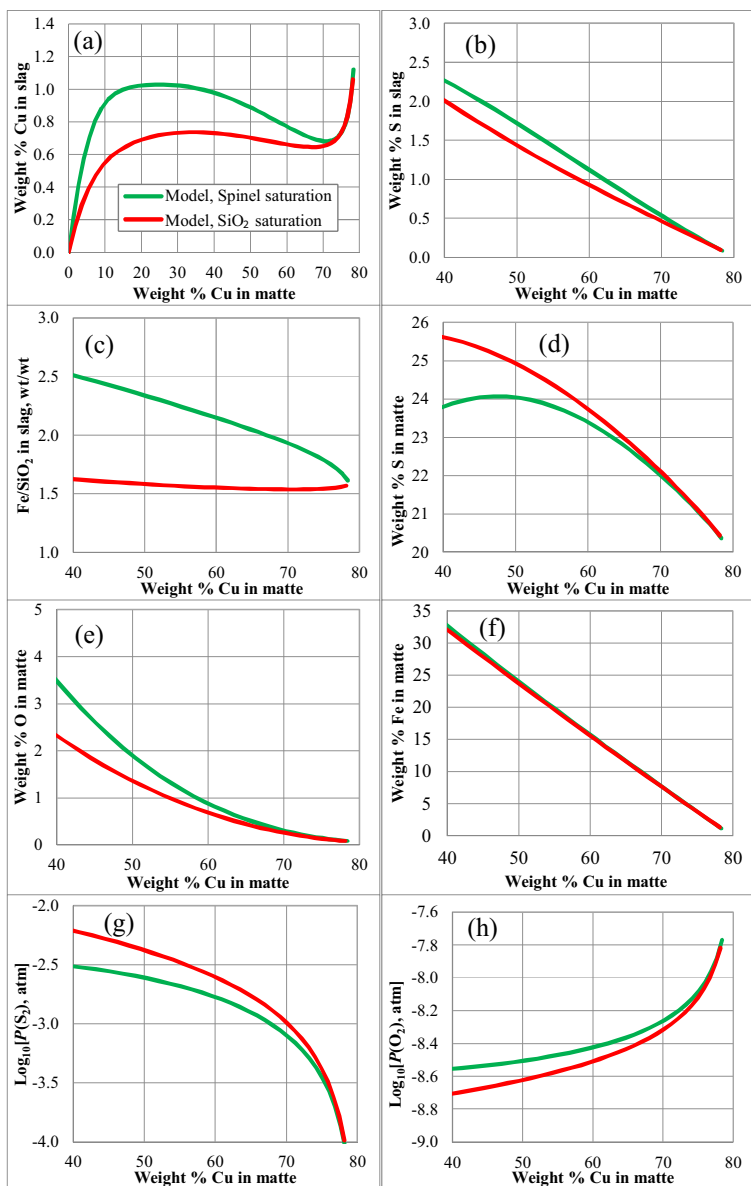


Figure 1. Cu–Fe–O–S–Si system: Slag, matte, spinel or SiO₂ equilibrium at $P(\text{SO}_2) = 0.16$ atm and 1200 °C.

The starting temperature of the furnace is assumed to be 1100 °C, but the charge of high-temperature matte (see Table 2) from the smelting furnace causes the rise in temperature. Reverts and fluxes cool down the furnace (see Table 2). The cumulative effect is calculated by the model (Figure 4) with furnace heat capacity taken into the account.

When the blow starts, iron sulfide from matte reacts with oxygen to form spinel. Spinel is shown by purple patch in Figure 3. This exothermic reaction causes the rise of the temperature (Figure 4). The steepness of the rise is negatively correlated with the rate of heat loss to the environment and the heat capacity of the furnace. When temperature rises to the certain level, determined by solidus in Figure 2, spinel starts to react with silica flux to form liquid slag. Silica is shown by light blue patch and liquid slag is shown by red patch in Figure 3.

After a significant amount of slag is accumulated, it is skimmed and replaced by the new portion of matte and flux (Table 2). The level of acceptable slag accumulation is determined by the geometry of the furnace. Large amounts of slag cause splashing. The ladle which collects the slag was assumed have 30 tons maximum capacity.

According to the model, the equilibrium concentration of chemically dissolved copper is always below 2%. (Figure 5). Due to the matte entrainment, it is substantially higher, 4.0-5.5% (see Table 2).

The procedure of accumulation and skimming of slag is repeated several times, while the overall matte grade increases (Figure 6). The goal is to remove iron from matte as much as possible during the slag blow, because during the copper blow all iron will convert to solid spinel causing problematic deposits. In the simulation, it is assumed that all the remaining slag is removed at Skim slag 4.

The oxygen partial pressure rises and sulfur partial pressure falls during the process (Figure 7). Partial pressure of SO₂ was calculated to be 0.15-0.20 atm for the chosen oxygen enrichment of the blow (25 vol% O₂).

During the copper blow, it is not desirable to load any reverts containing iron. The temperature is kept lower than in the end of slag blow to prevent the excessive wear of refractory and tuyeres [28]. The cooling is achieved by the addition of high-copper reverts. The simulation shows that, once all iron is removed from matte and oxygen starts oxidize Cu₂S, the reaction becomes much less exothermic. The converting continues until no matte is left. It is not desirable to further oxidize copper and form a high-copper slag due to its high corrosiveness and decrease in copper yield. Figure 10 shows the overblow and the disappearance of spinel and formation of high-copper slag after 424 minutes. This slag is to be collected and recycled.

Table 1. The list of process parameters used in the simulation of the Peirce-Smith copper converter.

Process parameters	Slag blow 1-4	Copper blow
Blow rate, kNm ³ ·hr ⁻¹ [28]	37	40
Oxygen enrichment, vol% O ₂ [28]	25	25
Matte entrainment, %	5	Not applicable
Oxygen efficiency, %	90	80
Rate of heat loss, MW	2.0	2.0
Furnace heat capacity, MJ·K ⁻¹	370	370

Table 2. The list of input and output of the Peirce-Smith copper converter. Output temperatures and compositions are the result of the simulation.

Time, min	Temperature, °C	Charge	Mass, tonne	wt%Cu	wt%Fe	wt%S	wt%O	wt%SiO ₂
0	25	Silica flux	9.0	0.0	1.0	0.0	0.4	94.6
0	1200	Anode slag	30.0	42.0	26.0	0.0	15.0	17.0
0	1200	Matte	200.0	62.0	12.9	24.8	0.2	0.1
0	25	High Fe reverts	15.0	50.0	20.0	15.0	5.0	10.0
0	25	Reverts	5.0	100.0	0.0	0.0	0.0	0.0
44	1171	Skim slag 1	-30.0	4.0	49.2	1.4	15.0	30.4
49	1210	Matte	30.0	62.0	14.0	23.8	0.1	0.1
49	25	Silica flux	5.0	1.0	0.5	0.0	0.4	94.6
84	1209	Skim slag 2	-30.0	4.3	48.5	1.3	14.8	31.1
87	1200	Matte	30.0	62.0	14.0	23.8	0.1	0.1
87	25	Silica flux	4.0	0.0	0.5	0.0	0.2	94.6
114	1232	Skim slag 3	-15.0	4.5	47.2	1.2	14.4	32.7
115	25	Silica flux	4.0	0.0	1.0	0.0	0.4	94.6
148	1263	Skim slag 4	-14.2	5.5	47.3	1.1	14.8	31.3
154	25	Solid blister	30.0	100.0	0.0	0.0	0.0	0.0
170	25	Anode scrap	10.0	100.0	0.0	0.0	0.0	0.0
178	25	White metal	10.0	78.0	1.0	19.5	0.5	1.0
220	25	Anode scrap	10.0	100.0	0.0	0.0	0.0	0.0
330	25	Solid blister	10.0	98.0	1.0	0.5	0.5	0.0
390	25	Solid blister	10.0	98.0	1.0	0.5	0.5	0.0
432	1191	Skim High-Cu slag	-10.7	58.7	23.3	0.0	17.0	0.9
432	1191	Skim blister Cu	-258.6	99.2	0.0	0.0	0.8	0.0

4. Conclusion and further development

The multicomponent thermodynamic database has been developed for applications in pyrometallurgy of copper. It covers the core chemical system that is necessary to predict phase equilibria, chemical reactions, energy balance and the distribution of elements in copper making processes. This is illustrated by the example of simulation of the Peirce-Smith converter. Thermodynamic models used in the present study are flexible and can be used to extend the database further. In particular, lead and minor elements can be added to the database. These projects are currently under way in Pyrosearch.

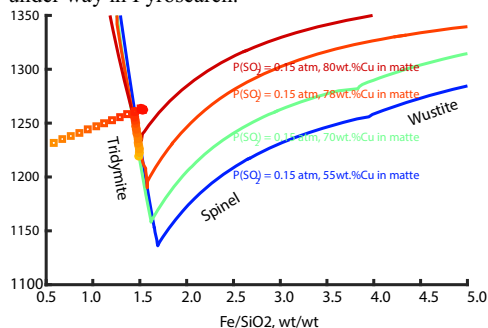


Figure 2. Calculated liquidus of the slag in equilibrium with matte of different grades (55, 70, 78 and 80). Symbols show the conditions at Slag blow 4 (115 – 148 min): squares are bulk composition of slag+solids, circles are compositions of liquid slag. The color of symbols correspond to matte grade.

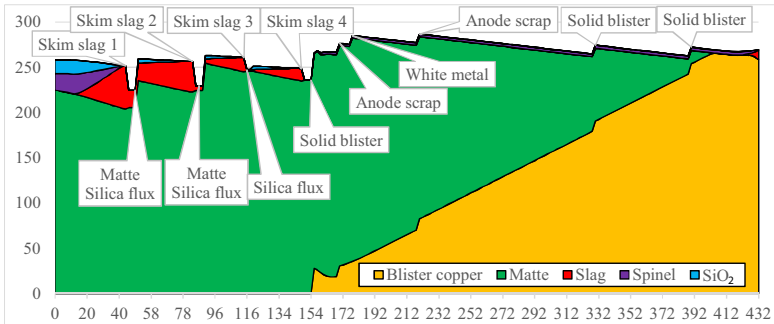


Figure 3. The amounts of condensed phases in the Peirce-Smith copper converter as a function of time. Results of the simulation.

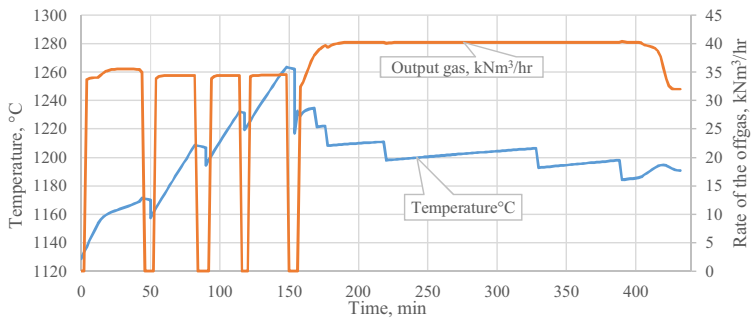


Figure 4. Temperature and flow rate of off gas in the Peirce-Smith copper converter as a function of time. Results of the simulation.

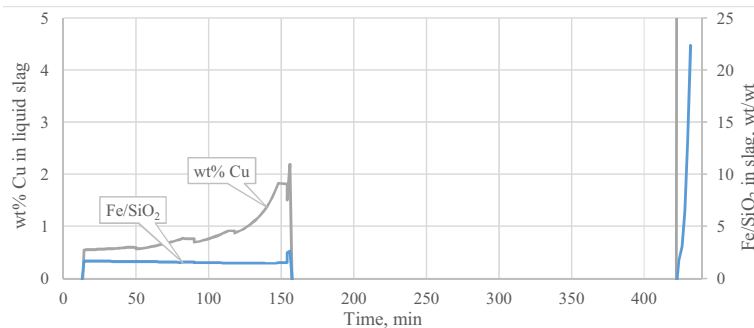


Figure 5. Composition of liquid slag in the Peirce-Smith copper converter as a function of time. Results of the simulation . Matte entrainment, solid SiO₂ and spinel are not included.

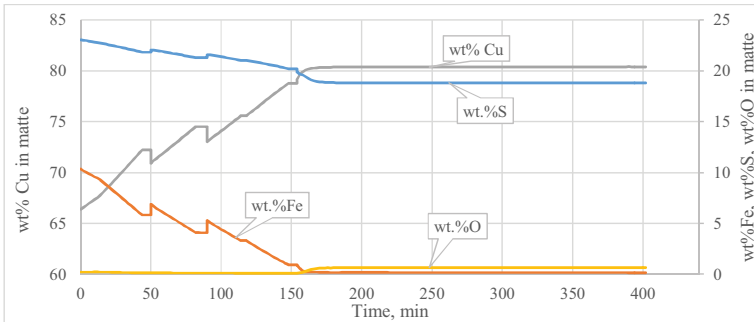


Figure 6. Composition of the matte phase in the Peirce-Smith copper converter as a function of time. Results of the simulation.

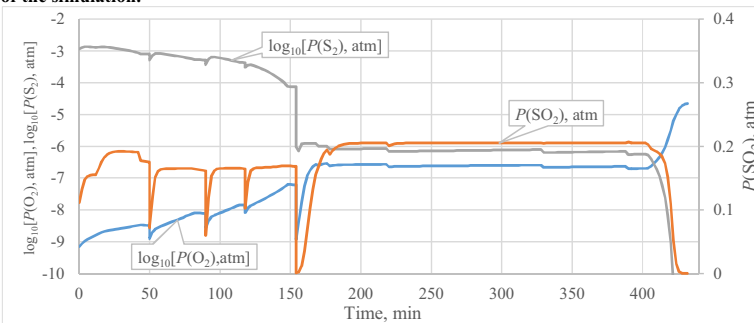


Figure 7. Equilibrium partial pressures of O₂, S₂ and SO₂ in the Peirce-Smith copper converter as a function of time. Results of the simulation. Please, note that the volume fraction of O₂ in the offgas is much higher than equilibrium value when oxygen efficiency is less than 100%.

References

1. C.W. Bale, E. Belisle, P. Chartrand, S.A. Deckerov, G. Eriksson, K. Hack, I.-H. Jung, Y.-B. Kang, J. Melancon, A.D. Pelton, C. Robelin, and S. Petersen: "FactSage thermochemical software and databases - recent developments", *Calphad*, 2009, 33(2), p. 295-311.
2. D. Shishin and S.A. Deckerov: "Critical assessment and thermodynamic modeling of Cu-O and Cu-O-S systems", *Calphad*, 2012, 38, p. 59-70.
3. T. Hidayat, D. Shishin, E. Jak, and S. Deckerov: "Thermodynamic Reevaluation of the Fe-O System", *Calphad*, 2015, 48, p. 131-144.
4. D. Shishin, E. Jak, and S.A. Deckerov: "Critical assessment and thermodynamic modeling of Fe-O and Fe-O-S systems", *J. Phase Equilib. Diff.*, 2015.
5. D. Shishin, T. Hidayat, E. Jak, and S. Deckerov: "Critical assessment and thermodynamic modeling of Cu-Fe-O system", *Calphad*, 2013, 41, p. 160-179.
6. D. Shishin, E. Jak, and S.A. Deckerov: "Thermodynamic assessment and database for the Cu-Fe-O-S system", *Calphad*, 2015, 50, p. 144-160.
7. D. Shishin, V. Proshakova, E. Jak, and S. Deckerov: "Critical assessment and thermodynamic modeling of the Al-Fe-O system", *Metall. Mater. Trans. B*, 2015.

8. T. Hidayat, D. Shishin, S.A. Decterov, and E. Jak: "*Thermodynamic optimization of the Ca-Fe-O system*", *Metall. Trans. B, Ahead of Print*, 2015.
9. T. Hidayat, D. Shishin, S.A. Decterov, and E. Jak: "*Experimental Study and Thermodynamic Re-evaluation of the FeO-Fe₂O₃-SiO₂ System*", submitted to *Metall. Trans. B*, 2012.
10. T. Hidayat and E. Jak: "*Thermodynamic modelling of the "Cu₂O"-SiO₂, "Cu₂O"-CaO, and "Cu₂O"-CaO-SiO₂ systems in equilibrium with metallic copper*", *International Journal of Materials Research*, 2014, 105(3), p. 249-257.
11. T. Hidayat, D. Shishin, S.A. Decterov, and E. Jak: "*Critical thermodynamic evaluation and optimization of the CaO-FeO-Fe₂O₃-SiO₂ system*", submitted to *Metall. Trans. B*, 2012.
12. D. Shishin: "Development of a thermodynamic database for copper smelting and converting", Ph. D. thesis, Ecole Polytechnique of Montreal, 2013.
13. T. Hidayat: "Equilibria Study of Complex Silicate-based Slag in the Copper Production", Ph.D. thesis, The University of Queensland, 2013.
14. A.D. Pelton, S.A. Decterov, G. Eriksson, C. Robelin, and Y. Dessureault: "*The Modified Quasichemical Model. I - Binary Solutions*", *Metall. Mater. Trans. B*, 2000, 31(4), p. 651-659.
15. A.D. Pelton and P. Chartrand: "*The Modified Quasichemical Model. II - Multicomponent Solutions*", *Metall. Mater. Trans. A*, 2001, 32(6), p. 1355-1360.
16. A.D. Pelton, P. Chartrand, and G. Eriksson: "*The modified Quasichemical Model. IV - Two Sublattice Quadruplet Approximation*", *Metall. Mater. Trans. A*, 2001, 32A(6), p. 1409-1415.
17. M. Hillert and L.-I. Staffansson: "*The Regular Solution Model for Stoichiometric Phases and Ionic Melts*", *Acta Chem. Scand.*, 1970, 24, p. 3618-3626.
18. M. Hillert, B. Jansson, and B. Sundman: "*Application of the Compound-Energy Model to Oxide Systems*", *Z. Metallkd.*, 1988, 79(2), p. 81-87.
19. S.A. Decterov, E. Jak, P.C. Hayes, and A.D. Pelton: "*Experimental Study and Thermodynamic Optimization of the Fe-Zn-O System*", *Metall. Mater. Trans. B*, 2001, 32(4), p. 643-657.
20. S.A. Decterov and A.D. Pelton: "*A Thermodynamic Database for Copper Smelting and Converting*", *Metall. Mater. Trans. B*, 1999, 30B(4), p. 661-669.
21. C. Chen, L. Zhang, and S. Jahanshahi: "*Application of MPE model to direct-to-blister flash smelting and department of minor elements*". in *Proceeding of Copper*. 2013: Santiago, Chile.
22. A. Yazawa and S. Nakazawa: "*Dissolution of metals in slag with special reference to phase separation thermodynamics*". in *Proc. Int. Conf. Molten Slags, Fluxes Salts '97, 5th*. 1997: Iron and Steel Society Warrendale, PA.
23. M. Nagamori: "*Metal Loss to Slag: Part I. Sulfidic and Oxidic Dissolution of Copper in Fayalite Slag from Low Grade Matte*", *Metall. Trans. B*, 1974, 5B(3), p. 531-538.
24. Y. Takeda: "*Oxidic and Sulfidic Dissolution of Copper in Matte Smelting Slag*". in *Proc. 4th Int. Conf. of Molten Slags and Fluxes, ISIJ*. 1992.
25. R. Sridhar, J.M. Toguri, and S. Simeonov: "*Copper Losses and Thermodynamic Considerations in Copper Smelting*", *Metall. Mater. Trans. B*, 1997, 28B(2), p. 191-200.
26. A. Yazawa, S. Nakazawa, and Y. Takeda: "*Distribution behavior of various elements in copper smelting systems*". 1983: Metall. Soc. AIME.
27. R. Shimpo, S. Goto, O. Ogawa, and I. Asakura: "*A Study on the Equilibrium between Copper Matte and Slag*", *Can. Metall. Q.*, 1986, 25(2), p. 113-121.
28. W.G.I. Davenport, M. King, M. Schlesinger, and A.K. Biswas, *Extractive metallurgy of copper, 4th edition*. 2002: Pergamon Press, Oxford, United Kingdom. 155-171.
29. P. Tan: "*Applications of thermodynamic modeling in copper converting operations*", *Int. J. Mater. Res.*, 2007, 98(10), p. 995-1003.

THERMODYNAMICS OF THE $2\text{CaO}\cdot\text{SiO}_2\text{-}3\text{CaO}\cdot\text{P}_2\text{O}_5$ SOLID SOLUTION AT STEELMAKING TEMPERATURE

Hiroyuki Matsuura¹, Ming Zhong^{1,2}, Xu Gao^{1,3}, Fumitaka Tsukihashi¹

1 Graduate School of Frontier Sciences, The University of Tokyo;

5-1-5 Kashiwanoha, Kashiwa, Chiba 277-8561, Japan

2 Institute of Advanced Energy, Kyoto University;

Gokasho, Uji, Kyoto 611-0011, Japan

3 Institute of Multidisciplinary Research for Advanced Materials, Tohoku University;

2-1-1 Katahira, Aoba, Sendai, Miyagi 980-8577, Japan

Keywords: Thermodynamics, Steelmaking, Dephosphorization, Multi-Phase Flux

Abstract

Recently the application of CaO-based multi-phase flux has received much attention and thus various physicochemical properties of the CaO-FeO-SiO₂ slags have been investigated. In the present paper, the thermodynamic properties of the 2CaO·SiO₂-3CaO·P₂O₅ solid solution which is the main solid phase constituting the multi-phase flux were studied. The activity of P₂O₅ was measured by the chemical equilibration method between molten iron and the solid solution, the solid solution and CaO mixture, or the solid solution and MgO mixture at 1823 and 1873 K with low oxygen partial pressure. The activities of P₂O₅, 3CaO·P₂O₅ and 3MgO·P₂O₅ were calculated by analyzed compositions and reported thermodynamic data. The activity of P₂O₅, 3CaO·P₂O₅ or 3MgO·P₂O₅ increased with the increase of 3CaO·P₂O₅ content in the solid solution.

Introduction

Since phosphorus segregates in the grain boundary of austenite which increases the fracture appearance transition temperature to cause the cold embrittlement of steel, it should be removed from molten iron and steel during the dephosphorization process as much as possible. Usually CaO is used as a flux to form highly basic CaO-FeO_x-SiO₂ slag and in most cases extra CaO is added to achieve high dephosphorization efficiency, while the CaO consumption and the slag amount significantly increase. Meanwhile, the generated slag after the dephosphorization process is hard to recycle since unreacted CaO remains in slag or CaO-based compounds precipitate during solidification.

It is well known that CaO reacts with SiO₂ to form 2CaO·SiO₂ on the surface of CaO in the CaO-FeO-SiO₂-P₂O₅ system during the dephosphorization process and then 2CaO·SiO₂ reacts with P₂O₅ to form the 2CaO·SiO₂-3CaO·P₂O₅ solid solution[1-3]. Besides, 2CaO·SiO₂ and 3CaO·P₂O₅ form a pseudo-binary solid solution over a wide composition range at steelmaking temperature[4]. Based on the large partition ratio of P₂O₅ between the solid solution and liquid slag[5-7], the multi-phase flux has been considered to be utilized for the dephosphorization process.

In order to understand the multi-phase flux better, the reaction mechanisms between solid CaO or 2CaO·SiO₂ and molten CaO-FeO_x-SiO₂-P₂O₅ slag have been intensively studied[8-14]. The

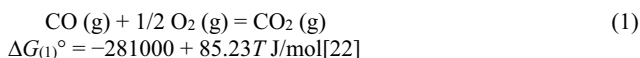
phase relationship for the $\text{CaO-FeO}_x\text{-SiO}_2\text{-P}_2\text{O}_5\text{-(-Al}_2\text{O}_3)$ system has been also studied[15-17]. The activity of P_2O_5 in the $2\text{CaO}\cdot\text{SiO}_2\text{-3CaO}\cdot\text{P}_2\text{O}_5$ solid solution has been measured by the chemical equilibration method at 1573 K[18].

In the present study, thermodynamic properties of the $2\text{CaO}\cdot\text{SiO}_2\text{-3CaO}\cdot\text{P}_2\text{O}_5$ solid solution have been studied by the chemical equilibration method between the solid solution and molten iron at 1823 or 1873 K and summarized in this paper[19-21].

Experimental

The solid tablet of the $2\text{CaO}\cdot\text{SiO}_2\text{-3CaO}\cdot\text{P}_2\text{O}_5$ solid solution, or the mixture of solid solution and CaO or MgO was equilibrated with molten iron at 1823 or 1873 K. The mixture of SiO_2 , $\text{CaHPO}_4\cdot 2\text{H}_2\text{O}$, MgO and CaO was sintered to prepare the oxide powder. The mixture was heated in air at 1873 K in a platinum crucible for 48 hours and then the sintered material was ground into fine powder before sintering for the next 48 hours. After the second sintering, the mixture was ground into fine powder again and about 1.5 g powder was charged in a steel dies to be pressed into a cylindrical tablet (diameter: 18 mm, thickness: 3 mm) at 50 MPa. The formation of desired phases was confirmed by XRD.

About 10 g of electrolytic iron with the initial concentration of P less than 0.0003 mass% was equilibrated with the prepared tablet in an MgO crucible (outer diameter: 25 mm, inner diameter: 20 mm, height: 60 mm) in an Al_2O_3 reaction tube (outer diameter: 60 mm, inner diameter: 50 mm, length: 1000 mm). The equilibrium duration was 24 hours which was enough to reach the equilibrium confirmed by preliminary experiments. The oxygen partial pressure was controlled by the mixture of CO and CO_2 gases with the total flow rate around 350 mL/min according to reaction (1). The oxygen partial pressure was 5.22×10^{-12} atm (CO:CO₂=110:1) at 1823 K, and 1.41×10^{-11} atm (CO:CO₂=110:1) or 4.25×10^{-10} atm (CO:CO₂=20:1) at 1873 K.



After the equilibrium was established, the sample was quenched by Ar stream at the outside of the furnace. Concentrations of P in iron and P_2O_5 in tablet were analyzed by spectrophotometry. Compositions of CaO, FeO and MgO in tablet were determined by ICP-OES and that of SiO_2 in tablet was determined by gravimetry.

Results and Discussion

Figure 1 shows concentration of phosphorus in molten iron after equilibrium with $2\text{CaO}\cdot\text{SiO}_2\text{-3CaO}\cdot\text{P}_2\text{O}_5$ solid solution, mixture of the solid solution and CaO, or mixture of the solid solution and MgO. In all cases, the phosphorus concentration increased with the increase of the $3\text{CaO}\cdot\text{P}_2\text{O}_5$ content in the solid solution and equilibrium temperature.

Figure 2 shows the phosphorus partition ratio between molten iron and solid solution, solid solution saturated with CaO, or solid solution saturated with MgO. Phosphorus partition ratio decreased with increasing $3\text{CaO}\cdot\text{P}_2\text{O}_5$ content in the solid solution. Comparing three conditions, the partition ratio was largest when the solid solution was saturated by CaO.

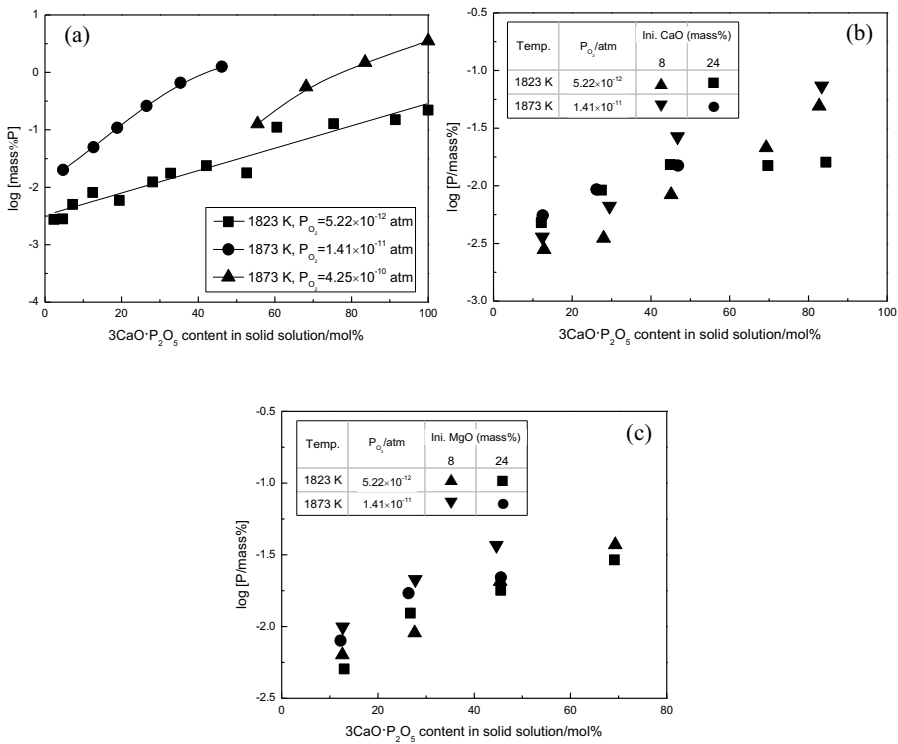


Figure 1. Phosphorus concentration in molten iron after equilibrium with (a) 2CaO-SiO₂-3CaO·P₂O₅ solid solution, (b) mixture of solid solution and CaO, and (c) mixture of solid solution and MgO.

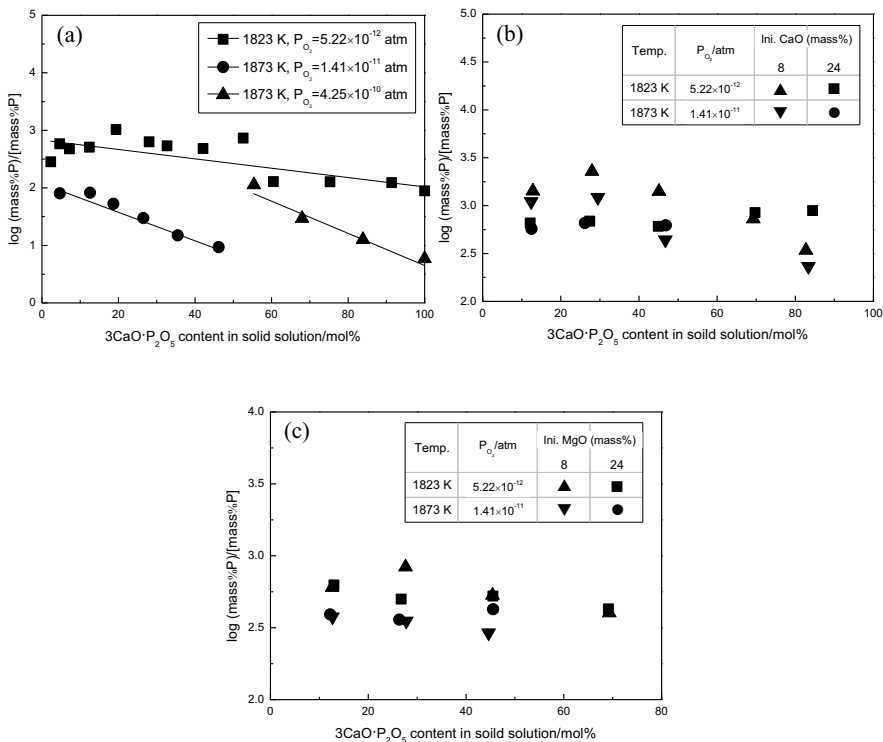
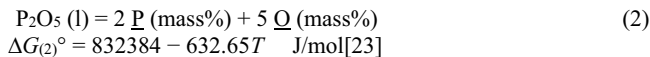
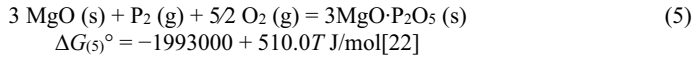
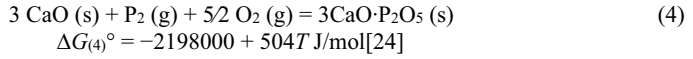
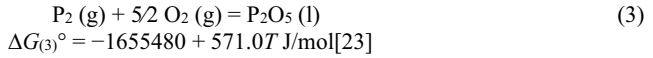


Figure 2. Phosphorus partition ratio between molten iron and (a) $2\text{CaO}\cdot\text{SiO}_2\text{-}3\text{CaO}\cdot\text{P}_2\text{O}_5$ solid solution, (b) mixture of solid solution and CaO, and (c) mixture of solid solution and MgO.

The activity of P_2O_5 relative to the hypothetical liquid P_2O_5 were determined from phosphorus concentration by the following reaction and reported interaction coefficients as shown in Fig. 3.



In the case of pure $2\text{CaO}\cdot\text{SiO}_2\text{-}3\text{CaO}\cdot\text{P}_2\text{O}_5$ solid solution, the activity of P_2O_5 in the solid solution was in the range from $10^{-24.6}$ to $10^{-20.7}$ at 1823 K and from $10^{-22.8}$ to $10^{-13.1}$ at 1873 K, respectively. On the contrary that in the solid solution saturated by CaO largely decreased. When the solid solution is saturated by CaO or MgO, the activities of $3\text{CaO}\cdot\text{P}_2\text{O}_5$ or $3\text{MgO}\cdot\text{P}_2\text{O}_5$ relative to these pure solids can be estimated from following thermodynamic data.



The estimated activities are shown in Fig. 4 as a function of 3CaO·P₂O₅ content in the solid solution. They also increased with the increase of 3CaO·P₂O₅ content.

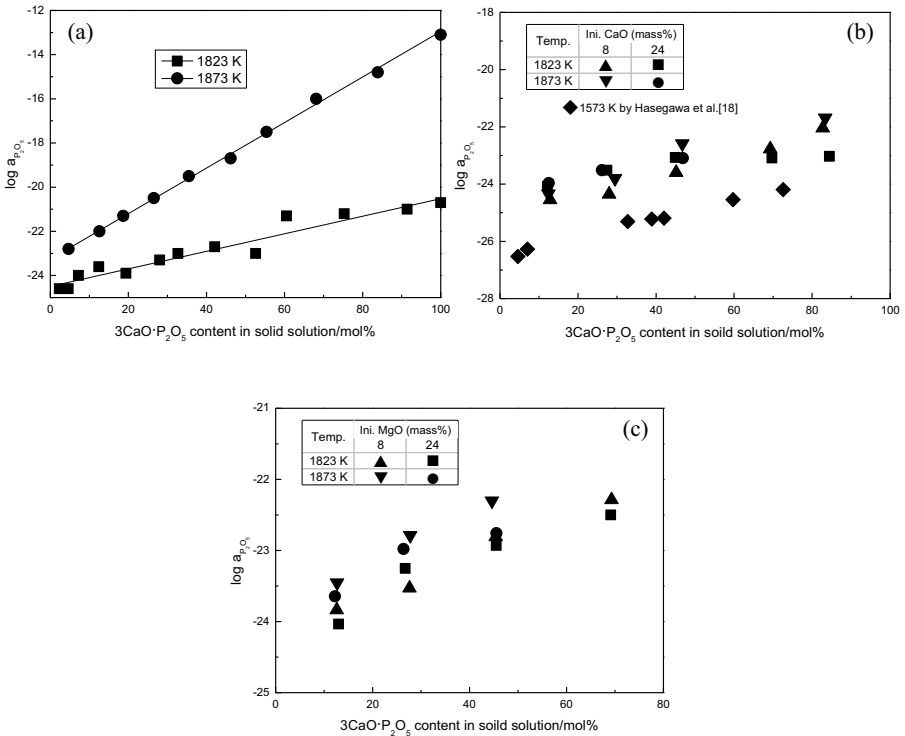


Figure 3. Activity of P₂O₅ relative to the hypothetical liquid P₂O₅ in (a) 2CaO·SiO₂-3CaO·P₂O₅ solid solution, (b) mixture of solid solution and CaO, and (c) mixture of solid solution and MgO.

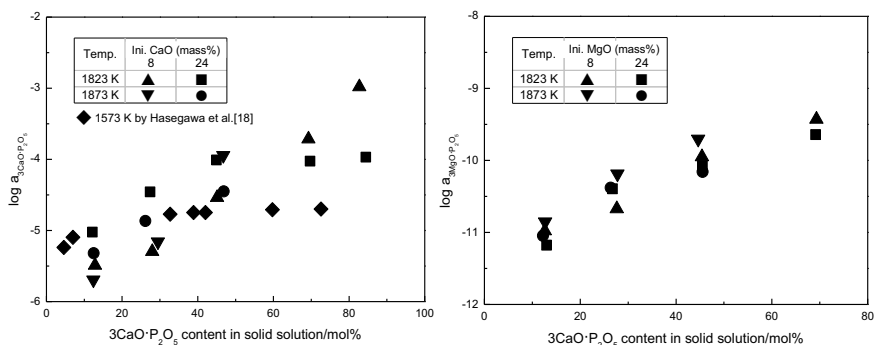


Figure 4. Estimated activities of 3CaO·P₂O₅ or 3MgO·P₂O₅ relative to each pure solid as a function of 3CaO·P₂O₅ content in the solid solution.

Conclusions

By applying the chemical equilibration method, the equilibrium between molten iron and the 2CaO·SiO₂-3CaO·P₂O₅ solid solution, mixture of solid solution and CaO, or mixture of solid solution and MgO was observed at 1823 K with the oxygen partial pressure of 5.22×10^{-12} atm and at 1873 K with the oxygen partial pressure of 1.41×10^{-11} atm or 4.25×10^{-10} atm.

The activity of P₂O₅ relative to the hypothetical pure liquid P₂O₅ in the 2CaO·SiO₂-3CaO·P₂O₅ solid solution increased with the increase of the 3CaO·P₂O₅ content in the solid solution.

The activity of P₂O₅ in the solid solution saturated by CaO was significantly smaller than that in pure solid solution.

The activity of 3CaO·P₂O₅ or 3MgO·P₂O₅ relative to their pure solids was also estimated in CaO or MgO saturation condition, respectively.

References

1. R. Inoue and H. Suito, "Phosphorous Partition between 2CaO·SiO₂ Particles and CaO-SiO₂-Fe₂O Slags," *ISIJ Int.*, 46 (2) (2006), 174-179.
2. H. Suito and R. Inoue, "Behavior of Phosphorous Transfer from CaO-Fe₂O-P₂O₅(-SiO₂) Slag to CaO Particles," *ISIJ Int.*, 46 (2) (2006), 180-187.
3. R. Inoue and H. Suito, "Mechanism of Dephosphorization with CaO-SiO₂-Fe₂O Slags containing Mesoscopic Scale 2CaO·SiO₂ Particles," *ISIJ Int.*, 46 (2) (2006), 188-194.
4. W. Fix, H. Heymann and R. S. Heinke, "Subsolidus Relations in the System 2CaO·SiO₂-3CaO·P₂O₅," *J. Am. Ceram. Soc.*, 52 (6) (1969), 346-347.
5. F. Pahlevani et al., "Distribution of P₂O₅ between Solid Solution of 2CaO·SiO₂-3CaO·P₂O₅ and Liquid Phase," *ISIJ Int.*, 50 (6) (2010), 822-829.

6. K. Shimauchi, S. Kitamura and H. Shibata, "Distribution of P₂O₅ between Solid Dicalcium Silicate and Liquid Phases in CaO-SiO₂-Fe₂O₃ System," *ISIJ Int.*, 49 (4) (2009), 505-511.
7. K. Ito, M. Yanagisawa and N. Sano, "Phosphorus Distribution between Solid 2CaO-SiO₂ and Molten CaO-SiO₂-FeO-Fe₂O₃ Slags," *Tetsu-to-Hagané*, 68 (2) (1982), 342-344.
8. S. Kitamura et al., "Mass Transfer of P₂O₅ between Liquid Slag and Solid Solution of 2CaO-SiO₂ and 3CaO-P₂O₅," *ISIJ Int.*, 49 (4) (2009), 1838-1844.
9. T. Hamano, S. Fukagai and F. Tsukihashi, "Reaction Mechanism between Solid CaO and FeO_x-CaO-SiO₂-P₂O₅ Slag at 1573 K," *ISIJ Int.*, 46 (4) (2006), 490-495.
10. S. Fukagai, T. Hamano and F. Tsukihashi, "Formation Reaction of Phosphate Compound in Multi Phase Flux at 1573 K," *ISIJ Int.*, 47 (1) (2007), 187-189.
11. X. Yang, H. Matsuura and F. Tsukihashi, "Condensation of P₂O₅ at the Interface between 2CaO-SiO₂ and CaO-SiO₂-FeO_x-P₂O₅ Slag," *ISIJ Int.*, 49 (9) (2009), 1298-1307.
12. X. Yang, H. Matsuura and F. Tsukihashi, "Formation Behavior of Phosphorous Compounds at the Interface between Solid 2CaO-SiO₂ and FeO_x-CaO-SiO₂-P₂O₅ Slag at 1673 K," *Tetsu-to-Hagané*, 95 (3) (2009), 268-274.
13. X. Yang, H. Matsuura and F. Tsukihashi, "Reaction Behavior of P₂O₅ at the Interface between Solid 2CaO-SiO₂ and Liquid CaO-SiO₂-FeO_x-P₂O₅ Slags saturated with Solid 5CaO-SiO₂-P₂O₅ at 1573 K," *ISIJ Int.*, 50 (5) (2010), 702-711.
14. X. Yang, H. Matsuura and F. Tsukihashi, "Dissolution Behavior of Solid 5CaO-SiO₂-P₂O₅ in CaO-SiO₂-FeO_x Slag," *Mater. Trans.*, 51 (6) (2010), 1094-1101.
15. X. Gao et al., "Phase Relationship of CaO-SiO₂-FeO-5 Mass Pct P₂O₅ System with Low Oxygen Partial Pressure at 1673 K (1400 °C)," *Metall. Mater. Trans. B*, 43B (4) (2012), 694-702.
16. X. Gao et al., "Phase Relationship for the CaO-SiO₂-FeO-5 Mass Pct P₂O₅ System with Oxygen Partial Pressure of 10⁻⁸ atm at 1673 and 1623 K," *Mater. Trans.*, 54 (4) (2013), 544-552.
17. X. Gao et al., "Phase Equilibrium for the CaO-SiO₂-FeO-5mass%P₂O₅-5mass%Al₂O₃ System for Dephosphorization of Hot Metal Pretreatment," *ISIJ Int.*, 53 (8) (2013), 1381-1385.
18. M. Hasegawa, Y. Kashiwaya and M. Iwase, "Thermodynamic Properties of Solid Solutions between Di-Calcium Silicate and Tri-Calcium Phosphate," *High Temp. Mater. Proc.*, 31 (4-5) (2012), 421-430.
19. M. Zhong, H. Matsuura and F. Tsukihashi, "Activity of P₂O₅ in Solid Solution between Di-Calcium Silicate and Tri-Calcium Phosphate at 1823 and 1873 K," *ISIJ Int.*, 55 (11) (2015), 2283-2288.
20. M. Zhong, H. Matsuura and F. Tsukihashi, "Activity of Phosphorus Pent-Oxide and Tri-Calcium Phosphate in 2CaO-SiO₂-3CaO-P₂O₅ Solid Solution saturated with CaO," *Mater. Trans.*, 56 (8) (2015), 1192-1198.
21. M. Zhong, H. Matsuura and F. Tsukihashi, "Thermodynamic Properties of Phosphorus Oxide in the 2CaO-SiO₂-3CaO-P₂O₅ Solid Solution saturated with MgO," *Metall. Mater. Trans. B*, under review.
22. E. T. Turkdogan, *Physical Chemistry of High Temperature Technology* (New York, NY: Academic Press, 1980), 7 and 14.
23. E. T. Turkdogan, "Assessment of P₂O₅ Activity Coefficients in Molten Slags," *ISIJ Int.*, 40 (10) (2000), 964-970.
24. A. Tagaya et al., "Determination of the Standard Gibbs Energies of the Formation of 3CaO-P₂O₅, 4CaO-P₂O₅ and 3(3CaO-P₂O₅)-CaF₂," *Trans. ISS*, 11 (July) (1991), 63-69.

UNDERSTANDING PHASE EQUILIBRIA IN SLAGS CONTAINING VANADIUM

Jinichiro Nakano^{1,2}, Marc Duchesne³, James Bennett¹, Anna Nakano¹, Robin Hughes³, In-Ho Jung⁴

¹U.S. Department of Energy National Energy Technology Laboratory, 1450 Queen Avenue, Albany, OR 97321 USA

²AECOM, P.O. Box 1959, Albany, OR 97321 USA

³Natural Resources Canada, CanmetENERGY, 1 Haanel Drive, Ottawa, ON K1A 1M1 Canada

⁴Department of Mining and Materials Engineering, McGill University, 3610 University Street, Montreal, QC H3A 0C5, Canada

Keywords: Gasification, Thermodynamics, Coal, Petcoke

Abstract

In modern high temperature entrained flow gasifiers, the extensive use of petroleum coke (petcoke) as a replacement for or an addition to coal as a carbon feedstock introduces an appreciable amount of vanadium in the molten slag, resulting in unknown chemical and physical slag properties. A long-term research effort to understand phase equilibria of Al_2O_3 -CaO-FeO-SiO₂-V₂O₃ slag system representative of that commonly found in coal/petcoke carbon feedstock mixtures was initiated by the U.S.-DOE NETL. In collaboration with CanmetENERGY and McGill University, synthetic vanadium bearing slag was investigated for phases formed under controlled temperature, partial pressure of oxygen, and composition. The slag compositions representing U.S. and Canadian coal and petcoke ashes are considered in this work. Equilibrium phase diagrams of the vanadium slag systems are reported.

Introduction

Entrained flow slagging gasifiers typically run at temperatures from 1325 to 1575 °C in an oxygen partial pressure around 10^{-8} atm [1, 2]. Increasing quantities of petroleum coke (petcoke) have been added to or replaced traditional coal feedstock as an economical alternative. The resulting slag is dramatically different in composition from traditional coal gasifier slags due to the high vanadium content in petcoke ashes, which contributes to uncertainty in gasifier performance. Understanding the thermodynamic nature of the vanadium-bearing slags is required to improve gasifier modeling and operation; however, no thermodynamic database for vanadium-containing slags is commercially available.

Thermodynamic equilibrium knowledge of a gasifier slag would aid in predicting its crystallization behavior, information needed to control and optimize the gasification process. Crystallization kinetics in vanadium-bearing slags is influenced by chemistry and temperature under a constant oxygen partial pressure [3]. Slag viscosity, affected in part by crystallization, is one of the key properties controlling slag flow from a gasifier and penetration of the slag into refractory pores and grain boundaries [4]. The viscosity generally decreases with increasing

temperature and increases with higher crystallinity [5, 6]. Solid layers may protect from refractory corrosion or slow down its process [7].

In this work, thermodynamic phase equilibrium was evaluated using synthetic slags containing from 0 to 27 wt.% vanadium oxide and gasifier conditions of 1500 °C and $P_{O_2} \approx 10^{-8}$ atm. Building upon a previous report [8], the present work varied concentrations of calcium oxide and iron oxide (additives used by industry) during the course of the thermodynamic phase investigation. The effects of these additives on slag homogeneity and crystal formation in vanadium-bearing slags were analyzed.

Experimental procedure

Compositions of slag constituents studied in this work simulate those found in industrial coal ash and coal-petcoke ash mixtures of the U.S. and Canada. Reagent grade powders (Alfa Aesar) of Al_2O_3 (99.5%, < 37 μm), CaO (99.95%, < 10 μm), Fe_2O_3 (99.945%, < 5 μm), SiO_2 (99.5%, < 44 μm), and V_2O_3 (99.6%, < 100 μm) were used to make synthetic mixes of target compositions. Compositions using oxide powders were dry-mixed to produce 3 groups of compositions where CaO was fixed at 6, 13, and 20 wt.% and where the $SiO_2/Al_2O_3 = 2.23$ (average) to simplify dimensions of the thermodynamic study.

Equilibration tests were conducted by placing synthetic slag mixtures (approximately 340 mg each) in Pt crucibles (99.99%) and firing the mixtures in a closed horizontal tube resistance furnace (CM Rapid Temp 1800). Throughout the firing process, an oxygen partial pressure of approximately 10^{-8} atm at 1500 °C was maintained by flowing a mixture of 64 mol.% CO-36 mol.% CO_2 at 30 ml/min. The samples were equilibrated at a sample temperature of 1500 °C \pm 0.8 °C for 72 hours, followed by purging with Ar (99.999 %) at 400 ml/min for 3 minutes, then quenching samples in a bucket of water at 20°C. The total time required for quenching a sample (from opening of the end cap to sample-water contact) was less than 30 seconds, with approximately 1 second needed to remove the sample from the furnace and place it in water. Quenched slag samples were analyzed for crystal phase identification by powder X-ray diffractometry (XRD), by inductively coupled plasma with optical emission spectrometry (ICP-OES) for chemical analysis, and by scanning electron microscopy with wavelength dispersive spectroscopy (SEM-WDX) for phase compositions. Chemical analysis was performed after equilibration tests and is listed in Table I. FeO and V_2O_3 were assumed to be the dominant forms of iron and vanadium oxides in this work. Detailed experimental procedures are explained elsewhere [1].

Results and Discussion

From XRD and SEM-WDX analyses, four distinct phase fields were identified in the samples that included slag, $Al_6Si_2O_{13(s)}$ (orthorhombic mullite), and/or $V_2O_3(s)$ (rhombohedral karelianite). No crystal was found with low V_2O_3 and high FeO content. Mullite crystals were present below 9 wt.% FeO in slags at 6 wt.% CaO, while they were not present at 13 and 20 wt.% CaO at any FeO contents evaluated. The $V_2O_3(s)$ crystal phase was found in all slag mixtures containing CaO and FeO, and containing more than 2 wt.% V_2O_3 . At 6 wt.% CaO and < 8 wt.% FeO, $V_2O_3(s)$ tended to coexist with mullite in slags for V_2O_3 contents higher than 2 wt.%.

Table I. Synthetic sample compositions studied (determined after exposure at 1500 °C in a 10^{-8} O₂ pp for 72 hours) (wt.%). S = slag, M = mullite, V = V₂O_{3(solid)}.

Samples	Al ₂ O ₃	CaO	FeO	SiO ₂	V ₂ O ₃	Total	Equilibria
Ca6-1	28.7	5.3	4.9	59.3	1.9	100.0	S + M
Ca6-2	27.6	5.3	8.1	58.9	0.0	100.0	S + M
Ca6-3	25.4	5.4	4.7	48.0	16.6	100.0	S + V + M
Ca6-4	25.8	5.7	2.2	60.9	5.4	100.0	S + V + M
Ca6-5	22.2	5.8	6.7	46.3	19.1	100.0	S + V
Ca6-6	26.5	6.0	6.9	55.1	5.6	100.0	S + V + M
Ca6-7	22.9	6.2	6.8	50.0	14.1	100.0	S + V
Ca6-8	25.2	6.2	9.3	59.2	0.0	100.0	S
Ca6-9	20.6	6.4	5.9	42.9	24.3	100.0	S + V
Ca6-10	21.1	6.4	10.5	44.7	17.2	100.0	S + V
Ca6-11	17.8	6.5	12.5	38.3	24.9	100.0	S + V
Ca6-12	23.0	6.6	9.3	49.9	11.2	100.0	S + V
Ca6-13	24.1	6.6	9.8	55.2	4.3	100.0	S + V
Ca6-14	24.3	6.7	1.5	59.2	8.2	100.0	S + V + M

Samples	Al ₂ O ₃	CaO	FeO	SiO ₂	V ₂ O ₃	Total	Equilibria
Ca13-1	22.2	11.5	1.5	52.8	12.2	100.0	S + V
Ca13-2	24.3	11.5	2.2	62.0	0.0	100.0	S
Ca13-3	16.7	11.9	8.4	35.8	27.2	100.0	S + V
Ca13-4	17.7	11.9	2.4	41.6	26.4	100.0	S + V
Ca13-5	21.9	12.2	5.0	49.6	11.3	100.0	S + V
Ca13-6	20.3	12.3	3.5	41.8	22.0	100.0	S + V
Ca13-7	16.5	12.5	13.4	38.8	18.8	100.0	S + V
Ca13-8	23.4	12.6	1.8	58.2	4.0	100.0	S + V
Ca13-9	24.9	12.8	3.5	54.3	4.5	100.0	S + V
Ca13-10	18.9	12.9	12.2	41.8	14.3	100.0	S + V
Ca13-11	27.7	13.1	3.9	55.3	0.0	100.0	S
Ca13-12	20.9	13.2	1.8	52.3	11.9	100.0	S + V
Ca13-13	23.0	13.3	6.7	56.9	0.0	100.0	S
Ca13-14	16.1	13.3	14.1	36.1	20.3	100.0	S + V
Ca13-15	25.2	13.7	4.3	50.9	5.9	100.0	S + V

Samples	Al ₂ O ₃	CaO	FeO	SiO ₂	V ₂ O ₃	Total	Equilibria
Ca20-1	23.7	17.9	1.5	57.0	0.0	100.0	S
Ca20-2	17.4	18.3	5.1	35.4	23.8	100.0	S + V
Ca20-3	24.9	18.7	2.7	53.7	0.0	100.0	S
Ca20-4	22.3	19.1	1.6	53.1	3.8	100.0	S
Ca20-5	20.5	19.6	1.5	50.6	7.9	100.0	S + V
Ca20-6	21.7	19.7	3.1	43.7	11.8	100.0	S + V
Ca20-7	19.2	20.2	2.2	43.1	15.3	100.0	S + V
Ca20-8	22.7	20.9	6.2	50.1	0.0	100.0	S
Ca20-9	18.0	21.3	8.1	43.0	9.6	100.0	S + V
Ca20-10	23.0	21.4	4.7	45.2	5.8	100.0	S
Ca20-11	16.8	21.7	9.5	33.3	18.7	100.0	S + V
Ca20-12	20.9	22.5	3.6	48.8	4.2	100.0	S
Ca20-13	14.4	22.5	10.0	30.5	22.5	100.0	S + V

Boundaries existing between these phase fields enable borders to be drawn estimating realms of common thermodynamic phase equilibria. The sensitivity of the border locations was determined using relative characteristics from XRD and SEM analyses; *i.e.*, relative XRD peak intensities were assumed to correspond to crystal fractions and SEM area fractions were assumed to indicate phase fractions. Isothermal cuts at 1500 °C in $P_{O_2} = 10^{-8}$ atm corresponding to fixed CaO contents (6, 13, and 20 wt.%) were constructed. Figure 1 shows the proposed phase diagram at 6 wt.% CaO on axes normalized only to Al₂O₃, FeO, SiO₂, and V₂O₃ (*i.e.*, pseudo-quaternary system of Al₂O₃-FeO-SiO₂-V₂O₃). The secondary axes represent approximate bulk (whole system) compositions including CaO (± 0.1 wt.%). Phase morphology representing the four phase fields is also shown in Figure 1.

In Figure 1, directions of the boundary between the ‘Slag_(l) + V₂O_{3(s)}’ and the ‘Slag_(l) + Mullite_(s) + V₂O_{3(s)}’ regions, and the location of the boundary between the ‘Slag_(l)’ and the ‘Slag_(l) + Mullite_(s)’ regions were determined strictly using experimental values. It is indicated a metastable extension from the boundary separating the ‘Slag_(l)’ region and the ‘Slag_(l) + mullite_(s)’ region exists within the ‘Slag_(l) + V₂O_{3(s)}’ region. Schreinemaker’s metastable extensions rule [9] then fixes the directions of the phase boundaries. A metastable extension of the boundary between the ‘liquid slag’ and the ‘Slag_(l) + V₂O_{3(s)}’ regions then falls within the ‘Slag_(l) + mullite’ region, implying the liquid slag stability increases with FeO content.

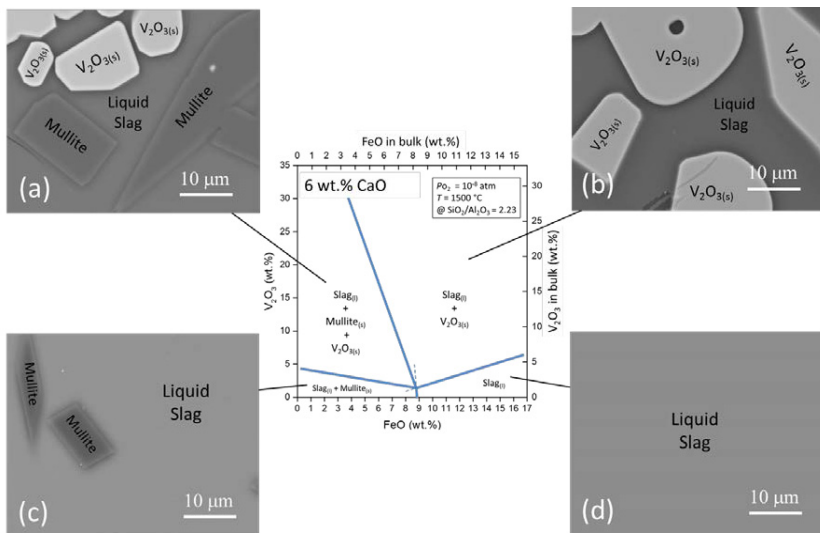


Figure 1. Proposed isothermal section of the Al₂O₃-CaO-FeO-SiO₂-V₂O₅ slag system at 1500 °C in $P_{O_2} \approx 10^{-8}$ atm at 6 wt.% CaO. Secondary axes represent approximate respective concentrations in bulk slag. SEM backscatter micrographs present phase regions of (a) ‘liquid slag + karelianite + mullite’ in 6CaO-3, (b) ‘liquid slag + karelianite’ in 6CaO-11, (c) ‘liquid slag + mullite’ in 6CaO-2, and (d) ‘liquid slag’ in 6CaO-8.

Crystal-free slags, for which higher fluidity would be expected, tend to exist at low V₂O₃ (0 to about 2 wt.%) and high FeO (greater than about 8 wt.%) in the bulk slag. The slag homogeneity region expands with higher CaO and/or FeO content; i.e., more V₂O₃ solubility can be obtained by adding CaO and FeO (Figure 2 (a)). In order to minimize the crystal formation in gasifier slags, more than 8 wt.% FeO is needed at 6 wt.% CaO, or any FeO contents at or above 13 wt.% CaO. Viscosity of liquid slag is reported to decrease at higher V₂O₃ content, but excessive amounts would cause karelianite crystals to precipitate, causing an increase in viscosity of the slag mixture [7,10].

As vanadium oxide is the key component to form karelianite crystal and its formation may cause flow and clogging issues in gasifiers, fluxes such as calcium oxide-based and iron oxide-based additives are frequently used to control (increase) V_2O_3 solubility in liquid slag [10, 11]. The slags studied in this work showed that V_2O_3 solubility in liquid slag increased with increasing basicity as defined as CaO/SiO_2 . The solubility of V_2O_3 in liquid slag increased from 5 wt.% to 35 wt.% by increasing the basicity from 0.4 to 0.8 at 20 wt% CaO. Similar rates were noted at 6 and 13 wt.% CaO. Plots shown for different CaO concentrations in Figure 2 (b) indicate the effect of basicity on the slopes of V_2O_3 solubility is not influenced by the CaO concentrations studied. If the CaO/SiO_2 ratio is maintained, the higher V_2O_3 solubility can be achieved with lower CaO concentrations. The result should be interpreted with care in the presence of the V_2O_3 crystal in molten slag.

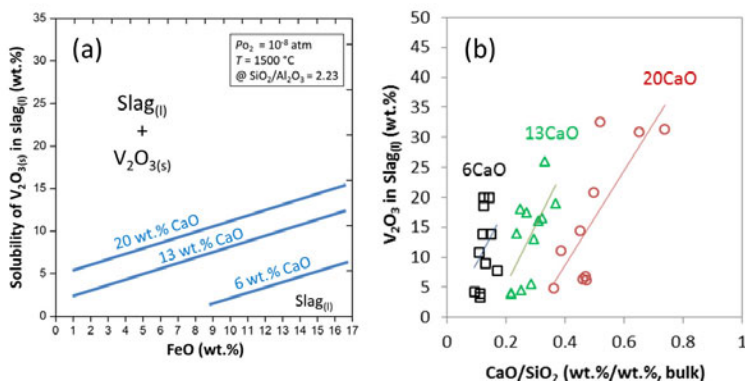


Figure 2. Solubility of V_2O_3 in liquid slag (a) as liquidus for 6, 13, and 20 wt.% CaO, and (b) with respect to basicity and three CaO levels. Fitted regression lines in (b) are only to show general trends in experimental data points.

Conclusions

Equilibria in synthetic slags (Al_2O_3 - CaO - FeO - SiO_2 - V_2O_3) with 0 – 27 wt.% vanadium oxide was evaluated in a simulated gasifier environment at 1500 °C with an oxygen partial pressure of approximately 10^{-8} atm. Based on experimental results, isothermal phase diagrams were constructed. Increasing CaO content, FeO content, or both contents expanded the homogeneous slag region and reduced composition ranges exhibiting crystals. Mullite ($Al_6Si_2O_{13}$) was not present in the slags containing more than 8.1 wt.% FeO (bulk), while karelianite (V_2O_3) always existed if a sufficient amount of vanadium was present in the slag.

Acknowledgement

This technical effort was performed in support of the National Energy Technology Laboratory's ongoing research under the RES contract DE-FE0004000. Part of this research has been funded by the Natural Sciences and Engineering Research Council of Canada and by Natural Resources Canada through the Program of Energy Research and Development. Funding was also provided

by the Clean Energy Dialogue to promote U.S.-Canada collaboration in energy technology development. Anna Nakano acknowledges the support of a postdoctoral fellowship at the U.S. Department of Energy, administered by Oak Ridge Institute for Science and Education.

Disclaimer: "This project was funded by the Department of Energy, National Energy Technology Laboratory, an agency of the United States Government, through a support contract with URS Energy & Construction, Inc. Neither the United States Government nor any agency thereof, nor any of their employees, nor URS Energy & Construction, Inc., nor any of their employees, makes any warranty, expressed or implied, or assumes any legal liability or responsibility for the accuracy, completeness, or usefulness of any information, apparatus, product, or process disclosed, or represents that its use would not infringe privately owned rights. Reference herein to any specific commercial product, process, or service by trade name, trademark, manufacturer, or otherwise, does not necessarily constitute or imply its endorsement, recommendation, or favoring by the United States Government or any agency thereof. The views and opinions of authors expressed herein do not necessarily state or reflect those of the United States Government or any agency thereof".

References

1. J. Nakano, et al., "Thermodynamic effects of calcium and iron oxides on crystal phase formation in synthetic gasifier slags containing from 0 to 27 wt.% V_2O_5 ," *Fuel*, 161 (2015), 364-375.
2. *U.S. Department of Energy National Energy Technology Laboratory. Gasifipedia*. 2015.
3. J. Nakano, et al., "Crystallization of Synthetic Coal-Petcoke Slag Mixtures Simulating Those Encountered in Entrained Bed Slagging Gasifiers," *Energ Fuel*, 23 (2009), 4723-4733.
4. H. Soll-Morris, et al., "The interaction of spherical Al_2O_3 particles with molten Al_2O_3 -CaO- FeO_x - SiO_2 slags," *Fuel*, 88(4) (2009), 670-682.
5. M.A. Duchesne, et al., "Flow behaviour of slags from coal and petroleum coke blends," *Fuel*, 97 (2012), 321-328.
6. J.X. Zhu, et al., "Viscosity Determination of Molten Ash from Low-Grade US Coals," *High Temp Mat Pr-Isr*, 31(4-5) (2012), 569-580.
7. J. Nakano, et al., "Interactions of refractory materials with molten gasifier slags," *Int J Hydrogen Energy*, 36(7) (2011), 4595-4604.
8. J. Nakano, et al., "Phase Equilibria in Synthetic Coal-Petcoke Slags (SiO_2 - Al_2O_3 - FeO - CaO - V_2O_5) under Simulated Gasification Conditions," *Energ Fuel*, 25(7) (2011), 3298-3306.
9. F.A.H. Schreinemakers, *In-, mono-, and di-variant equilibria*, in *Papers by F. A. H. Schreinemakers*. 1965, The Pennsylvania University: University Park, Pennsylvania. p. 116-126.
10. M.S. Najjar, *Partial oxidation process*. 1987, Texaco Inc., White Plains, NY.: U.S.
11. M.S. Najjar and R.J. Corbeels, *Partial oxidation process*. 1990, Texaco Inc., White Plains, NY.: U.S.

This Article was produced under collaboration between the United States Department of Energy's National Energy Technology Laboratory and CanmetENERGY at Natural Resources Canada, Government of Canada. Canadian law provides for the Crown to retain copyright to

materials produced by employees of the Government of Canada - © Her Majesty the Queen in Right of Canada as represented by the Minister of Natural Resources, 2016.

VANADIUM OXIDATION STATE DETERMINATION BY X-RAY ABSORPTION SPECTROSCOPY

Marc A. Duchesne¹, Jinichiro Nakano^{2,3}, Yongfeng Hu⁴, Aimee MacLennan⁴,
Robin W. Hughes¹, James Bennett² and Anna Nakano²

¹Natural Resources Canada, CanmetENERGY; 1 Haanel Drive; Ottawa, ON K1A 1M1 Canada

²U.S. Department of Energy National Energy Technology Laboratory; 1450 Queen Ave.;
Albany, OR 97321 USA

³AECOM; P.O. Box 1959; Albany, OR 97321 USA

⁴Canadian Light Source; 44 Innovation Boulevard; Saskatoon, SK S7N 5A9 Canada

Keywords: Slag, Vanadium, Oxidation, Valence, X-ray absorption

Abstract

Vanadium is found in slags produced during metal refinement and fossil fuel combustion/gasification. The oxidation state of vanadium in slag has technological and environmental implications. For example, it may affect slag flow and refractory wear inside reactors, as well as leachability and toxicity of industrial by-products. Determination of vanadium's oxidation state in crystalline phases can be achieved via the widely adopted X-ray diffraction (XRD) technique. However, this technique does not provide information on vanadium in amorphous phases. The objective of this research is to determine the oxidation state of vanadium in petroleum coke gasification samples and laboratory samples using X-ray absorption spectroscopy (XAS) with Canadian Light Source's soft X-ray micro-characterization beamline (SXRMB). Linear combination fitting of XAS spectra with reference samples allowed quantitative determination of vanadium speciation.

Introduction

Understanding vanadium redox speciation is important for several reasons. For instance, vanadium speciation in by-products from metal refinement, fossil fuel combustion and fossil fuel gasification has technological and environmental implications. It may affect slag flow and refractory wear inside reactors [1], as well as leachability and toxicity from industrial by-products [2].

Determination of vanadium's oxidation state in crystalline phases can be achieved via the widely adopted X-ray diffraction (XRD) technique. However, this technique does not provide detailed information on vanadium in amorphous phases. Several techniques to study both amorphous and crystalline vanadium phases may be found in the literature: wet chemistry [3], electron paramagnetic resonance (EPR) [4–6], X-ray photoelectron spectroscopy (XPS) [7], high temperature mass spectrometry (MS) [8], electron energy loss spectroscopy (EELS) [9,10], inductively coupled plasma mass spectrometry (ICP-MS) [2], and X-ray absorption spectroscopy (XAS) [11,12].

The objective of this study is to determine the oxidation state of vanadium in petroleum coke gasification samples and laboratory samples using X-ray absorption spectroscopy (XAS) with Canadian Light Source's soft X-ray micro-characterization beamline (SXRMB).

Materials and Methods

Vanadium reference samples were selected to match common vanadium oxidation states and symmetries (Table I). All reference samples, except Ref4 and Ref5, were purchased as powder from Alfa Aesar and are 99%+ pure. Ref4 and Ref5 were purchased as rock samples from Weinrich Minerals and ground to below 60 mesh (250 μm). With the exception of Ref1, the composition of all reference samples was verified by X-ray diffraction. Ref3 contained 52.5 wt.% vanadium oxide (V_6O_{13}) and 47.5 wt.% vanadium (IV) oxide (VO_2). The average valence of Ref3 is therefore 4.2. For all other reference samples, only the expected vanadium compound was detected. Ref4 and Ref5 also included expected non-vanadium compounds.

Table I. Reference samples

Name	Description	Formula	Valence	Symmetry
Ref1	Vanadium (II) oxide	VO	2	Octahedral
Ref2	Vanadium (III) oxide	V_2O_3	3	Octahedral
Ref3	Vanadium (IV) oxide	$\text{VO}_2/\text{V}_6\text{O}_{13}$	4.2	Octahedral
Ref4	Cavansite	$\text{Ca}(\text{VO})(\text{Si}_4\text{O}_{10})\cdot 4(\text{H}_2\text{O})$	4	Square pyramidal
Ref5	Pascoite	$\text{Ca}_3(\text{V}_{10}\text{O}_{28})\cdot 17(\text{H}_2\text{O})$	5	Octahedral
Ref6	Vanadium (V) oxide	V_2O_5	5	Square pyramidal

From 2007 to 2011, Pratt & Whitney Rocketdyne (PWR) designed, constructed and operated a 16 tonne per day gasification system at the Gas Technology Institute in Des Plaines, United States [13,14]. Samples collected from petroleum coke gasification with that system are used in this study and listed in Table II as Gas1-Gas5. They are further described in [15] under *Test ID DAP 44*. Synthetic samples used in this study are mixtures of V_2O_3 powder with CaO or MgO powder. They are listed in Table II as Syn1-Syn10 with the weight percentage of CaO or MgO indicated, where the balance is V_2O_3 . Details of synthetic sample preparation procedures are described in [16], with the oxygen partial pressure controlled by a gas supply of air or a CO/ CO_2 mixture. During the sample preparation, Syn1-Syn10 were equilibrated for 48 hours at designated temperatures and oxygen partial pressures, followed by water quenching.

Table II. Gasifier and synthetic samples

Name	Description	Temperature (°C)	log <p>O₂ in atm]</p>
Gas1	gasifier feed	N/A	N/A
Gas2	gasifier cyclone fines	N/A	N/A
Gas3	gasifier filter fines	N/A	N/A
Gas4	gasifier char	N/A	N/A
Gas5	gasifier slag	N/A	N/A
Syn1	53 wt.% CaO	1500	-0.68
Syn2	27 wt.% CaO	1500	-0.68
Syn3	46 wt.% MgO	1500	-0.68
Syn4	21 wt.% MgO	1500	-0.68
Syn5	53 wt.% CaO	1500	-4
Syn6	80 wt.% CaO	1500	-8
Syn7	53 wt.% CaO	1500	-8
Syn8	10 wt.% CaO	1500	-8
Syn9	53 wt.% CaO	1200	-12
Syn10	20 wt.% CaO	1200	-12

X-ray absorption spectroscopy (XAS) was performed at the Canadian Light Source (CLS) using its soft X-ray micro-characterization beamline (SXRMB). A Si(1 1 1) double crystal monochromator was used, giving an energy resolving power of 10,000 eV. The sample was mounted using double-sided conducting carbon tape and loaded into a vacuum chamber (base pressure of 1×10^{-8} Torr). Vanadium K-edge XAS spectra were recorded in the total electron yield (TEY) mode by monitoring the drain sample current. The accuracy of energies reported here is 0.1 eV. The collected XAS spectra were processed with Athena software, version 0.9.21 [17]. Analysis was performed with averaged spectra resulting from 2 or more scans. All samples were normalized by fitting two parallel lines in the pre-edge and post-edge regions, then setting these regions to absorption levels of 0 and 1, respectively. A typical XAS spectrum is shown in Figure 1. It is characterized by different regions which are affected by the electronic configuration of the atoms bombarded by X-rays. Different atoms produce peaks in different energy ranges. By focusing on the energy range specific to vanadium K-edge absorption, it is possible to differentiate vanadium species by their oxidation state and coordination symmetry. For this differentiation, the X-ray absorption near-edge structures within ~40 eV of the main edge (XANES) are of particular interest. The extended X-ray absorption fine structures (EXAFS) region provides information on coordination, bonding lengths and molecular environment.

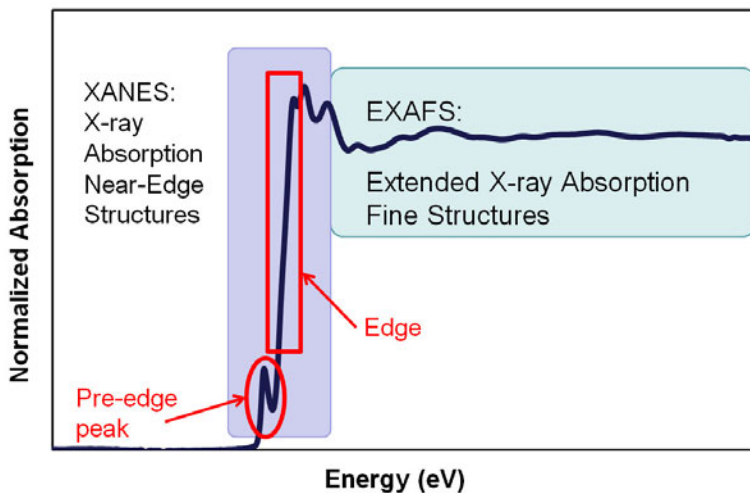


Figure 1. Typical XAS spectrum.

Results and Discussion

There are several methods to determine the vanadium oxidation state and symmetry from XANES features [12]. The two methods used in this study are: (1) comparison of the main edge energies; and (2) linear combination fitting. The energy of the absorption edge is usually defined as the energy of the first point of inflection of the principal absorption edge, or as the energy measured half way up the normalized-edge step (*i.e.*, at a normalized absorption of 0.5). In this study, the latter definition is used. An increase in absorption edge energy is generally associated with an increase in oxidation state. To compare values from different sources, the edge energy values are often expressed as energy values relative to the first peak in the derivative spectrum of metallic vanadium. Metallic vanadium foil was scanned at CLS. The first peak in the derivative spectrum was at 5463.5 eV. Figure 2 compares experimental relative absorption edge energies found in literature for various vanadium oxidation states [12,18,19] to reference samples, gasifier samples and synthetic samples. The reference samples used in this study fall within or near the ranges of literature values for their corresponding vanadium oxidation state. As can be seen in Figure 2, the relative energy may not always be used to differentiate the oxidation state of vanadium as there is some overlap in the oxidation state ranges. The gasifier feed (Gas1) is near the V^{4+} and V^{5+} ranges. The other gasifier samples are near the V^{3+} and V^{4+} ranges. The lower oxidation state of samples exiting the gasifier (Gas2-Gas4) than entering (Gas1) is expected due to the reducing conditions present in the gasifier. Of the synthetic samples prepared in air, two (Syn1 and Syn2) are near the V^{5+} range, while the other two (Syn3 and Syn4) are near the V^{4+} and V^{5+} ranges. Other synthetic samples are near the V^{5+} range (Syn5, Syn6, Syn7 and Syn9), while some (Syn8 and Syn10) are near the V^{3+} and V^{4+} ranges. Higher oxidation states are expected for the synthetic samples prepared in air, compared to those prepared in reducing gases.

A drawback of the main edge energy comparison method is that it does not distinguish components in mixtures of vanadium oxidation states.

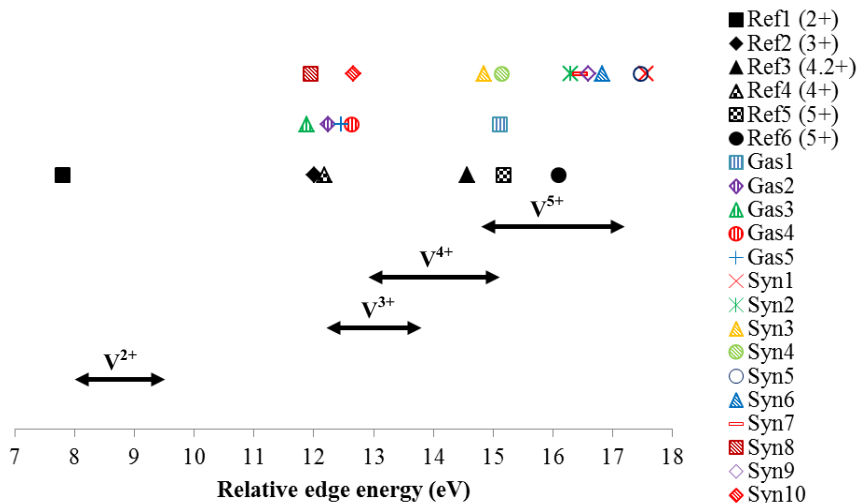


Figure 2. Comparison of relative edge energies (double arrow lines indicate value ranges in literature [12,18,19]).

By curve fitting the spectra of gasifier and synthetic samples with spectra from reference samples, it is possible to get an indication of relative quantities of vanadium species found in the gasifier and synthetic samples. A similar approach was previously taken for the speciation of sulfur in coals and chars [20]. Linear curve fitting (LCF) was performed using Athena software, version 0.9.21 [17]. The energy range used to perform fitting started at the inflection point at the start of the pre-edge peak, and ended at the energy where the main edge reached a value of 1. This range intentionally includes the pre-edge peak and edge as the shapes and locations of these two features are known to correlate with the oxidation state and symmetry of vanadium atoms [11,12]. Post-edge features can be affected by other factors. For example, Wasiucionek *et al.* reported fewer modulations in the EXAFS region of spectra from amorphous vanadium compared to crystalline vanadium [21]. LCF was conducted with the objective of minimizing the R-factor, which is used to assess the deviation between the measured and the fitted spectrum [17], by considering combinations of up to four different reference samples. Results with negative weights associated with reference samples were ignored. The best fitting combinations for the gasifier and synthetic samples are reported in Table III, along with the associated R-factors. The results indicate that the gasifier feed (Gas1) contains V⁴⁺ and V⁵⁺, while the by-products (Gas2-Gas5) contain mainly V³⁺ and V⁴⁺. The lower oxidation state in the by-products is expected due to the reducing conditions in the gasifier, and agrees with the relative edge energy comparison. The synthetic samples prepared in air (Syn1-Syn4) or with a pO₂ of 10⁻⁴ atm (Syn5) contain 74% or more V⁵⁺. This agrees with the relative edge energy comparison. Unexpectedly, the LCF results indicate three of the samples (Syn6, Syn7 and Syn9) prepared with a pO₂ of 10⁻⁸ atm or lower, contain 94% or more V³⁺. This may be due to poor fitting with

the references samples, as the R factors range 0.13-0.16. However, the relative edge energy comparison also indicates V^{5+} is predominant. The high content of CaO in these samples (53-80 wt.%) could be promoting a higher vanadium oxidation state, in part due to the formation of calcium vanadate in these binary mixtures [22]. Syn8 and Syn10 were also prepared with pO_2 of 10^{-8} atm or lower, but contain less CaO (10-20 wt.%). LCF results indicate V^{2+} , V^{3+} and V^{4+} are predominant in these samples.

Table III. Linear combination fitting results for gasifier and synthetic samples

	V^{2+}	V^{3+}	V^{4+}	V^{4+}	V^{5+}	V^{5+}	
Sample	Ref1	Ref2	Ref3	Ref4	Ref5	Ref6	R factor
Gas1			0.45			0.55	0.05
Gas2	0.03	0.84	0.13				0.00
Gas3		1.00					0.03
Gas4	0.06	0.58	0.36				0.01
Gas5		0.79	0.21				0.00
Syn1				0.20		0.80	0.06
Syn2	0.08			0.12	0.36	0.44	0.02
Syn3	0.20			0.07	0.15	0.59	0.05
Syn4	0.23				0.03	0.74	0.03
Syn5				0.21		0.79	0.06
Syn6						1.00	0.16
Syn7	0.06					0.94	0.14
Syn8	0.27	0.33	0.40				0.01
Syn9	0.04					0.96	0.13
Syn10	0.27	0.08	0.58	0.07			0.04

Conclusion

Vanadium K-edge X-ray absorption spectroscopy was applied to determine the oxidation state of vanadium in gasifier and synthetic samples by comparing with various reference samples. The petroleum coke feed to a gasification system contains mainly V^{4+} and V^{5+} , while the by-products contain mainly V^{3+} and V^{4+} . A decrease in oxidation state from feed to by-products was expected due to the reducing gas environment in the gasification system. The synthetic samples prepared in air or with a pO_2 of 10^{-4} atm contain mainly V^{3+} . Synthetic samples with a high CaO content (≥ 53 wt.%) and prepared with a pO_2 of 10^{-8} atm or lower, contain mainly V^{5+} . Synthetic samples with a low CaO content (≥ 20 wt.%) and prepared with a pO_2 of 10^{-8} atm or lower, contain mainly V^{2+} , V^{3+} and V^{4+} .

Acknowledgements

This work was supported by the Government of Canada's Program of Energy Research and Development, ecoENERGY Innovation Initiative, and Natural Sciences and Engineering

Research Council of Canada. Funding was also provided by the Clean Energy Dialogue to promote U.S.-Canada collaboration in energy technology development. Anna Nakano acknowledges the support of a postdoctoral fellowship at the U.S. Department of Energy, administered by Oak Ridge Institute for Science and Education. Samantha Bryson and Lawrence Cheung supported data processing activities during co-op work terms with Natural Resources Canada. This technical effort was performed in support of the National Energy Technology Laboratory's ongoing research under the RES contract DE-FE0004000. The Gas Technology Institute gasifier samples were provided by Steve Fusselman. Testing of the gasifier was funded in part by Alberta Innovates Energy and Environment Solutions.

Disclaimer: "This project was funded by the Department of Energy, National Energy Technology Laboratory, an agency of the United States Government, through a support contract with URS Energy & Construction, Inc. Neither the United States Government nor any agency thereof, nor any of their employees, nor URS Energy & Construction, Inc., nor any of their employees, makes any warranty, expressed or implied, or assumes any legal liability or responsibility for the accuracy, completeness, or usefulness of any information, apparatus, product, or process disclosed, or represents that its use would not infringe privately owned rights. Reference herein to any specific commercial product, process, or service by trade name, trademark, manufacturer, or otherwise, does not necessarily constitute or imply its endorsement, recommendation, or favoring by the United States Government or any agency thereof. The views and opinions of authors expressed herein do not necessarily state or reflect those of the United States Government or any agency thereof".

References

- [1] Nakano J, Sridhar S, Moss T, Bennett J, Kwong K-S. Crystallization of Synthetic Coal-Petcoke Slag Mixtures Simulating Those Encountered in Entrained Bed Slagging Gasifiers [†]. *Energy Fuels* 2009;23:4723–33. doi:10.1021/ef801064y.
- [2] Larsson MA, Baken S, Smolders E, Cubadda F, Gustafsson JP. Vanadium bioavailability in soils amended with blast furnace slag. *J Hazard Mater* 2015;296:158–65. doi:10.1016/j.jhazmat.2015.04.034.
- [3] Wang H, Li F, Sichen D. Development of an Analytical Technique to Determine the Fractions of Vanadium Cations with Different Valences in Slag. *Metall Mater Trans B* 2010;42:9–12. doi:10.1007/s11663-010-9448-3.
- [4] Farah H, Brungs M. Oxidation-reduction equilibria of vanadium in CaO-SiO₂, CaO-Al₂O₃-SiO₂ and CaO-MgO-SiO₂ melts. *J Mater Sci* 2003;38:1885–94.
- [5] Farah H. V⁴⁺ in quenched calcium silicates: An electron spin resonance spectroscopic investigation. *J Mater Sci* 2003;38:727–37.
- [6] Wei Q, Zhang PX, Zhang DY, Zhou JH. Investigations of the electron paramagnetic resonance spectra of VO₂⁺ in CaO-Al₂O₃-SiO₂ system. *Pramana* 2009;73:1087–94.
- [7] Silversmit G, Depla D, Poelman H, Marin GB, De Gryse R. Determination of the V2p XPS binding energies for different vanadium oxidation states (V⁵⁺ to V⁰⁺). *J Electron Spectrosc Relat Phenom* 2004;135:167–75. doi:10.1016/j.elspec.2004.03.004.
- [8] Wang L, Teng L, Chou K-C, Seetharaman S. Determination of Vanadium Valence State in CaO-MgO-Al₂O₃-SiO₂ System By High-Temperature Mass Spectrometry. *Metall Mater Trans B* 2013;44:948–53. doi:10.1007/s11663-013-9836-6.

- [9] Fitting Kourkoutis L, Hotta Y, Susaki T, Hwang HY, Muller DA. Nanometer Scale Electronic Reconstruction at the Interface between LaVO₃ and LaVO₄. *Phys Rev Lett* 2006;97. doi:10.1103/PhysRevLett.97.256803.
- [10] Tan H, Verbeeck J, Abakumov A, Van Tendeloo G. Oxidation state and chemical shift investigation in transition metal oxides by EELS. *Ultramicroscopy* 2012;116:24–33. doi:10.1016/j.ultramicro.2012.03.002.
- [11] Sutton SR, Karner J, Papike J, Delaney JS, Shearer C, Newville M, et al. Vanadium K edge XANES of synthetic and natural basaltic glasses and application to microscale oxygen barometry. *Geochim Cosmochim Acta* 2005;69:2333–48. doi:10.1016/j.gca.2004.10.013.
- [12] Chaurand P, Rose J, Briois V, Salome M, Proux O, Nassif V, et al. New Methodological Approach for the Vanadium K-Edge X-ray Absorption Near-Edge Structure Interpretation: Application to the Speciation of Vanadium in Oxide Phases from Steel Slag. *J Phys Chem B* 2007;111:5101–10. doi:10.1021/jp063186i.
- [13] Pratt & Whitney Rocketdyne. Hydrocarbon upgrading gasification program final test report. Alberta Innovates Energy and Environment Solutions; 2011.
- [14] Higan C, van der Burgt M. *Gasification*. 2. ed. Amsterdam: Elsevier/GPP, Gulf Professional Publ; 2008.
- [15] Duchesne MA, Hughes RW. Partitioning of inorganic elements in pilot-scale and demonstration-scale entrained-flow gasifiers. *Fuel* 2014;127:219–27. doi:10.1016/j.fuel.2013.08.051.
- [16] Nakano J, Duchesne M, Bennett J, Kwong K-S, Nakano A, Hughes R. Thermodynamic effects of calcium and iron oxides on crystal phase formation in synthetic gasifier slags containing from 0 to 27 wt.% V₂O₃. *Fuel* 2015;161:364–75. doi:10.1016/j.fuel.2014.11.008.
- [17] Ravel B, Newville M. ATHENA, ARTEMIS, HEPHAESTUS: data analysis for X-ray absorption spectroscopy using IFEFFIT. *J Synchrotron Radiat* 2005;12:537–41. doi:10.1107/S0909049505012719.
- [18] Wong J, Lytle FW, Messmer RP, Maylotte DH. K-edge absorption spectra of selected vanadium compounds. *Phys Rev B* 1984;30:5596–610. doi:10.1103/PhysRevB.30.5596.
- [19] McKeown DA, Muller I, Matlack K, Pegg I. X-ray absorption studies of vanadium valence and local environment in borosilicate waste glasses using vanadium sulfide, silicate, and oxide standards. *J Non-Cryst Solids* 2002.
- [20] Wang M, Liu L, Wang J, Chang L, Wang H, Hu Y. Sulfur K-edge XANES study of sulfur transformation during pyrolysis of four coals with different ranks. *Fuel Process Technol* 2015;131:262–9. doi:10.1016/j.fuproc.2014.10.038.
- [21] Wasiucionek M, Garbarczyk J, Bacewicz P, Józwiak J, Nowiński JL. EXAFS/XANES studies of the local structure of amorphous ionic and electronic-ionic conductors. *Mater Sci Pol* 2006;24:181–6.
- [22] Muan A, Najjar MS. Patent: Compositions involving V₂O₃-CaO. US5077260 A, 1991.

This Article was produced under collaboration between Canadian Light Source, the United States Department of Energy's National Energy Technology Laboratory and CanmetENERGY at Natural Resources Canada, Government of Canada. Canadian law provides for the Crown to retain copyright to materials produced by employees of the Government of Canada - © Her Majesty the Queen in Right of Canada as represented by the Minister of Natural Resources, 2016.

AUTHOR INDEX

Advances in Molten Slags, Fluxes, and Salts: Proceedings of the 10th International Conference on Molten Slags, Fluxes and Salts

A

Abdeyazdan, H.	135
Ahmad, Shahreer	1031
Aketagawa, Mayu	221
Allen, Charlotte	961
Amini, Shahriar	493
Andersen, Eirik	1153
Aneziris, Christos G.	1371
Assis, Karina Lara Santos	307
Avarmaa, Katri	193
Azekenov, Turarbek	1071

B

Bai, Chenguang	405
Barati, Mansoor	237, 279
Basu, Somnath	677
Behera, Narottam	1031
Bello, Sandra Díaz	79
Bennett, James P.	619, 1109, 1119
.....	1135, 1397, 1405
Bernd, Wittgens	1153
Bessada, Catherine	799
Beyers, Lesley J.	511
Bhattacharya, Diptak	255
Bing, Pan	211
Binz, Florian	899
Blanpain, Bart	221, 245, 439
.....	511, 1185, 1301
Bouchetou, Marie-Laure	1093
Brassamin, Séverine	1093
Brooks, Geoffrey A.	511
Burbano, Mario	799

C

Cadars, Sylvian	799
Cai, Dexiang	335, 1319
Cao, Qing	1009
Castillo, G. Alan	1053
Cengizler, Hakan	1309
Chai, Li-Hua	1293
Chambers, E.E.	771
Chapman, M.W.	135
Chen, Chunlin	667
Chen, Jeff (Jiang)	961
Chen, Jiang	707, 947
Chen, Junhong	1101
Chen, Liugang	245, 1301
Chen, Mao	175, 1101
Chen, Min	455

Chen, Weiqing	279
Cho, Jung-Wook	447, 485
Chotoli, Fabiano F.	847
Chou, Kuo-chih	155, 167, 1143, 1335
Chung, Yongsug	573
Coley, Kenneth S.	989
Coulon, Antoine	1093

D

da Silva, Carlos Antonio	1043, 1127
da Silva, Itavahn Alves	1043, 1127
Davis, Boyd	657
De Bilbao, Emmanuel	1093
de Sá, Augusto Pereira	1127
Decterov, Sergei	947, 1379
Deev, Alex	547
Desai, Bhavin	677
Dogan, Neslihan	135, 989
Dou, Zuoyong	357
Du, Chuan-ming	909
Du, Ke	1343
Duan, Peining	423
Dubberstein, Tobias	1371
Duchesne, Marc A.	557, 1397, 1405

E

Eilbeigi, Shahnavaaz	837
Endo, Rie	327, 357, 477
Eriç, Rauf Hürman	919, 999, 1309
Escudero-Castejon, L.	71, 1253
Esfahani, Shaghayegh	237

F

F., Gerardo R.F. Alvear	667
Fabritius, Timo	999
Fan, Jiaqi	1343
Fan, Kun	1191
Fan, Maoming	1351
Fan, Yong	687
Fan, Youqi	203
Faria, João O.G.	847
Fatollahi-Fard, Farzin	761
Fenggang, Wang	211
Fontana, Andrea	3
Frazeo, Michael	317
Fredericci, Catia	847
Friedmann, David	97
Friedrich, Bernd	97, 899, 1063
Fruehan, Richard J.	127

Fujii, Yusuke63

G

Gan, Yunhua1261
Gao, Jinxing291
Gao, Xu909, 1389
Garbers-Craig, Andrie87, 855, 1077
Gazeau, Camille1093
Glaser, Björn431, 565
Goso, Xolisa105
Grogan, Joseph879
Gu, Kezhuan989
Gu, Yaowu203
Guan, Xiaofei781
Guo, Dongdong1327
Guo, Muxing221, 245, 439, 1185, 1301
Guo, Zhancheng731
Guoxing, Ren211
Guzmán, A.M.1053

H

Ha, Minchul1271
Haarberg, Geir Martin817
Haas, Tim999
Hack, Klaus397
Hakamada, Shinya929
Hamuyuni, Joseph937
Han, Chen175
Han, Yong-Uk501
Hara, Y.1253
Harmuth, Harald299
Haxhijaj, Ahmet1351
Haxhijaj, Bajram1351
Hayashi, Miyuki183
Hayes, Peter C.707, 947, 961
.....1071, 1207, 1221
He, Meile455
Heller, Hans-Peter1371
Hessling, Oscar565
Hidayat, Taufiq947, 1207, 1221, 1379
Hino, Mitsutaka29
Holappa, Lauri1017
Holtan, Joakim1285
Hosseini, Seyed Vahid837
Hu, Meilong1261
Hu, Yongfeng1405
Huang, Mengmeng1359
Huang, Shuigen245, 1185
Huang, Ting291
Huang, Weijun455
Hughes, Robin W.557, 1397, 1405
Hunt, Adam349

I

Ibarra, L. Tadeo1053
Iizuka, Atsushi687
Inoue, Ryo865
Ishikawa, Takehiko1245
Isohookana, Erik999

J

Jahanshahi, Sharif493
Jak, Evgueni707, 947, 961
.....1071, 1207, 1221, 1379
Jha, A.71, 1253
Jia, Xinlei731
Jiang, Fatian203
Jiang, Tao423
Jiang, Zhou-hua1191
Jin, Yongli229
Jin, Zheshi3
Jones, Peter Tom245, 439, 1301
Jung, In-Ho1397
Jung, Sung Mo17, 1025

K

Kaçar, Yilmaz1017
Kang, Youn-Bae271
Kaplan, Valery1161
Kargl, Florian929
Kärnä, Aki999
Kashiwaya, Yoshiaki335
Katabe, Fuminori829
Kaußen, Frank1063
Kawashima, Hidenori519
Kikuchi, Naoki63
Kikuchi, Tatsuya589
Kim, Min-Su271
Kim, Pyunghwa Peace1285
Kim, Seon-Hyo447, 485
Kim, Sun-joong909
Kim, Wan-Yi369
Kitamura, Shin-ya909
Kitano, Ryo723
Kobayashi, Yoshinao327, 357, 1229
Kono, Yuta327
Kumar, Avinash255
Kumar, Deepoo145
Kuroda, Yoshitaka519
Kwong, Kyei-Sing619

L

Lai, Pingsheng405
Lavoie, Pascal791
Le, Thu Hoai221
Leão, Paula Maria Gomes Cunha1043

Lebel, Trevor	657
Lee, Jaewoo	565
Lee, Kyuyong	573
Lehmann, Jean	697
Li, Baowei	229
Li, Chao	1343, 1359
Li, Fengshan	1277
Li, Haibo	1177
Li, Hongxu	1343, 1359
Li, Min	807
Li, Mu	477
Li, Qiuhuan	731
Li, Shengping	405
Li, Yongzhi	229
Liu, Chunwei	1185
Liu, Jun-Hao	1335
Liu, Shiyuan	1143
Liu, Xue-Mei	1293
Liu, Zhaobo	1359
Liu, Zhihong	971
Liu, Zhuangzhuang	439
Longbottom, R.J.	135
Lotto, Andre A.	847
Lu, Boxun	263
Lu, Yanchun	1177
Lubomirsky, Igor	1161
Luidold, Stefan	53
Lv, Xuewei	405, 415, 1261

M

Ma, Guojun	889
Ma, Zhuang	229
Machado, Kelly	799
MacLennan, Aimee	1405
Mahashabde, Vinay V.	255
Malfliet, Annelies	221, 245, 1301
Malynowskyj, António	847
Mandal, A.K.	873
Mansuri, Irshad	3
Maroufi, Samane	3, 493
Marschall, Irmtraud	299
Martinez, D.I.	1053
Martinsson, Johan	431
Matsuura, Hiroyuki	829, 1389
McLean, Alexander	279
Mehrjardi, Ata Fallah	947, 1071, 1207
Meiqiu, Xie	211
Michal, Ksiazek	1153
Michel, Rudy	1093
Miki, Takahiro	29
Miki, Yuji	63
Min, Dong Joon	17, 501, 607
Misra, Siddhartha	255
Monaghan, B.J.	135
Morita, Kazuki	723, 1119

Mu, Haoyuan	127
Muhmood, Luckman	547, 581
Müller, Michael	397
Murase, Hironori	29

N

Nagai, Takashi	1119
Nakai, Yoshie	63
Nakamura, Airi	929
Nakamura, Takashi	687
Nakano, Anna	627, 1109, 1119
.....	1135, 1397, 1405
Nakano, Jinichiro	627, 1109, 1119
.....	1135, 1397, 1405
Nashimoto, Ryota	589
Nastac, Laurentiu	1009
Natsui, Shungo	589
Nell, Johannes	105
Neto, João B. Ferreira	847
Nikolic, Stanko	667
Nilfroushan, Mohammad Reza	837
Nishi, Tsuyoshi	519
Nolte, Elizabeth	317

O

O'Brien, Hugh	193
O'Kane, Paul	3
O'Malley, Ronald J.	317
Ohta, Hiromichi	519
Ojima, Junpei	519
Okabe, Toru H.	751
Onodera, Kenta	929, 1245
Ostrowski, Oleg	335, 493, 1319

P

P, Álvaro H. Forero	79
Pal, Uday	465, 597, 781
Pandelaers, Lieven	439, 1185
Parada, Roberto	657
Parienyatwa, S.	71, 1253
Park, Hyunsik	1271
Park, Ji-Ook	1025
Park, Joo Hyun	715, 745, 1271
Park, Min-Seok	343
Park, Youngjoo	607
Parra, Roberto	657
Patterson, M.N.	771
Peng, Yuxiang	525, 1169, 1199
Petersen, Jochen	105
Pfeifer, Herbert	999
Pistorius, Petrus Christiaan	117, 145
.....	307, 761
Pitts, April	1009
Piva, Stephano P.T.	117

Poirer, Jacques1093
 Powell, Adam465
 Price, J.C.771
 Prince, Sarfo889

Q

Qiu, Guibao405
 Qu, Zhengfeng1261
 Quarcioni, Valdecir A.847

R

Raddadi, Ahmad1031
 Rasch, Ron175
 Reddy, Ramana G. 525, 807, 1169, 1199
 Restrepo, Oscar J.79
 Rhamdhani, M.A.135
 Ribeiro, Tiago R.847
 Ringdalen, Eli43
 Rodrigues, Eliana Ferreira1043
 Rotevant1153

S

Sagadin, Christoph53
 Sahajwalla, Veena3
 Salanne, Mathieu799
 Sanchez-Segado, S. 71, 1253
 Santoso, Imam979
 Sarou-Kanian, Vincent799
 Sasaki, Yasushi 29, 335, 1319
 Sato, Yoshiya865
 Schriner, Doug879
 Seebold, Sören397
 Seetharaman, Seshadri581
 Seshadri, Varadarajan 1043, 1127
 Shan, Chen405
 Shan, Yu455
 Shen, Xiang455
 Shen, Xuyang1293
 Shevchenko, Maksym1221
 Shi, Huayue1301
 Shi, Qiyong203
 Shi, Zhongning807
 Shibata, Etsuro687
 Shibata, Hiroyuki519
 Shibayama, Atsushi865
 Shin, Seung-Ho447
 Shishin, Denis 947, 1379
 Sichen, Du431, 535
 Silva, Andre N.L.847
 Sinha, O.P.873
 Skidmore, Catherine3
 Smith, Jeffrey D.317
 Sohn, Jeong-soo1271
 Somerville, Michael667

Song, Shengqiang855
 Songwen, Xiao211
 Sridhar, Seetharaman1237
 Stewart, Bridget349
 Su, Shizhao 465, 597, 781
 Sukenaga, Sohei519
 Sulasalmi, Petri999
 Sun, Shi1343
 Sun, Shouyi547
 Sun, Yongqi1237
 Susa, Masahiro 327, 357, 477
 Sutcliffe, Neil317
 Suzuki, Ryosuke O.589
 Svend, Grådahl1153

T

Takasaki, Yasushi865
 Tamaru, Haruka1245
 Tanaka, Toshihiro1245
 Tang, Lei1191
 Tang, Ping291
 Tangstad, Merete 43, 1285
 Taninouchi, Yu-ki751
 Tao, Jun1327
 Taskinen, Pekka Antero .. 193, 937, 971, 979
 Tathavadkar, Vilas677
 Taylor, Mark P.791
 Taylor, Patrick879
 Tewari, Neeraj1031
 Thomas, Hugh1109
 Torres, Filipe de Menezes1127
 Tsukada, Takao1245
 Tsukihashi, Fumitaka 829, 1389

U

Uchida, Yu-ichi63
 Ueda, Shigeru909
 Ueno, Shoya1245
 Urata, Kentaro1229
 Ushkov, Leonid1071

V

Vakil, Kaushik677
 Van Long, Tran29
 Verhaeghe, Frederik511
 Villalón Jr., Thomas 465, 597
 Visuri, Ville-Valtteri999
 Viswanathan, Nurni N.581

W

Wagner, Christoph53
 Wang, Li Ju477
 Wang, Lijun 155, 167, 1143

Wang, Lin	1319
Wang, Longmei	1327
Wang, Min	357
Wang, Na	1293
Wang, Nan	455
Wang, Qi	155
Wang, Ruimin	1277
Wang, Wanlin	263
Wang, Xinhua	1177
Wang, Zhaowen	807
Watanabe, Masahito	929, 1245
Webler, Bryan A.	127
Wegener, Mirco	547
Weitz, Heine	87
Wen, Guanghua	291
Wenzel, Claudia	1371
Wenzl, Christine	53
Westphal, B.R.	771
White, Jesse F.	535, 565
Williams, Robert	1009
Wright, Steven	369
Wu, Guixuan	397
Wu, Jinyu	1293
Wu, Tuo	731

X

Xia, Longgong	971
Xiao, Dan	263
Xiao, Songwen	203
Xie, Yang	1359
Xing, Xia	211
Xu, Jian	415
Xue, Xiangxin	423

Y

Yan, Baijun	1327
Yan, Wei	279
Yan, Zhiming	405, 415
Yang, Dong-hyo	1271
Yang, Jian	335
Yang, Jun-Gil	745
Yang, Xiao	299
Yang, Yindong	279
Yoo, Shin	343
Yoon, Dae-Woo	485
Yoon, Tae Hee	573
Young, Courtney	889
Young, Jamie	889
Youqi, Fan	211
Yu, Ying	175
Yücel, Onuralp	647
Yue, Hongrui	423

Z

Zaharia, Magdalena	3
Zang, Likun	829
Zanghi, Didier	799, 1093
Zayhenskikh, Elena	397
Zeghaibi, Othman	1031
Zhan, Dong-ping	1191
Zhang, Chen	335, 1319
Zhang, Daojie	1009
Zhang, Fushun	229
Zhang, Guo-Hua	829, 1335
Zhang, Hui-shu	1191
Zhang, Jianqiang	335, 1319
Zhang, Jie	415
Zhang, Xinwang	263
Zhang, Xuefeng	229
Zhang, Yang-peng	1191
Zhang, Yanling	731, 1277
Zhang, Zuotai	1237
Zhao, Baojun	175, 1101
Zhao, Zengwu	229
Zhong, Ming	1389
Zhou, Qian	829
Zhu, Guosen	1177
Zietsman, Johannes H.	635

SUBJECT INDEX

Advances in Molten Slags, Fluxes, and Salts: Proceedings of the 10th International Conference on Molten Slags, Fluxes and Salts

3

3D CFD Modeling1009

A

Activation Energy237
Activity723, 1327
Al₂O₃9 37
Alkali Roasting1253
Alumina135, 145, 791
Alumina Solubility465
Aluminium791
Aluminium Electrolysis817
Aluminium Recovery873
Aluminosilicate Melts715
Aluminum Oxide723
Aluminum Production781
Amphoteric Slags1063
Anionic Species799
Antimony899
Antimony White899
AOD999
Apparent Viscosity431
Arc Furnace647
Argon Blowing1127
Arrhenius Law1335
Assmang1285
Avrami237

B

B₂O₃1319
Basic Oxygen Furnace1043
Basicity1185, 1261
Bayer Red Mud1277
Bearing Steel1191
Beryllia1161
BF Slag405
Bingham369
Blast Furnace879
Blister Copper667
BOF431, 989, 1017
BOF Slag439, 837, 1185
BOF Steelmaking1177
Borosilicate Melt519

C

C₂S-C₃P Solid Solution909
Ca₄Al₆CrO₁₆855
Ca₆Al₄Cr₂O₁₅855

Calcium Alumina Cement855
Calcium Aluminate135
Calcium Aluminate Flux1031
Calcium Fluoride327
Calcium Oxide723
Calcium Silicide357
Calcium Transfer145
CaO79, 937
CaO-“Fe₂O₃”-SiO₂7 07
CaO-Al₂O₃-Based2 79
Carbon Composite Agglomerate1025
Carbon Pickup343
Carbothermal889
Cathodoluminescence317
Cement837
Cement Slag847
Cerium Oxide723
Characterization889, 1359
Charge Compensation1335
Chemical Interaction1077
Chemical Shifts799
Chromite Ore71
Chromium731, 919
Chromium Recovery71
Chromium-Bearing Slag167
Clean Steel117
Cleanliness1191
CO627
CO₂627
CO₂ Electrolysis1 161
Coal1119, 1397
Coal Gasification1237
Coal Slag Viscosity619
Cobalt647
Cold Finger307
Combustion Ash29
Comilog1285
Complex Deoxidation723
Concentrates667
Concentration791
Condensation1153
Conductivity465
Constrained Sessile Drop557
Continuous Casting271, 307, 317
.....327, 349, 447
Converter Slag1343
Copper647, 971, 1071
Copper and Lead Smelting947
Copper Making Process1207
Copper Production1379
Copper Slag647, 687

Copper Slags	657
Copper Smelting	193, 937
Copper Smelting Slags	1101
Copper Sulfide	1229
Corrosion	53, 1093, 1199
Cr(Vi)	855
Cr ₂ O ₃ -Containing Castables	855
Cr-Free Refractory	1101
Cr-Mn-Ni Steel	1371
Crystallisation Behaviour	335
Crystallization	229, 279, 299
Crystallization Behavior	291
Crystallization Kinetics	237
Cu ₂ O	937
Current Efficiency	817

D

Deformation	1093
Degree of Polymerization	175
Density	557, 929, 1169
Deoxidation	751
Dephosphorization	989, 1025
.....	1177, 1277, 1389
Desulfurization	1025
Desulfurization Kinetics	1009
DHTT	335
Different Cooling Methods Slag	1191
Dimensional Analysis	607
Direct Slag Reduction	97
Distribution	193
Distribution of Elements	1379
Distribution Ratio	731
Distribution Rule	1343
Dynamic Viscosity Measurement	447
Dynamic Wetting	565

E

EAF Slag System	607
EAF-Slag	837
Electrical Conductivity	501
Electrode	745
Electrolysis	791
Electronic Conductivity	1335
Electrorheology	423
Elution	865
Emulsion	431
Entrapped Matte	677
Environment Rehabilitation	829
EPMA	193, 971
Equilibrium	1309
E-Scrap	193
ESR (Electro-Slag Remelting)Process	745
Evaporation	1319
Extinction Coefficient	485

F

Factsage	105
Factsage Prediction	1101
Fayalite Slag	245, 1301
Fe-Ni-V-C Quo-Ternary Phase Diagram	29
Ferroalloys Production	53
Ferromanganese	1309
Ferronickel	79
FLiNaK	1199
Flotation	1351
Fluid Flow Characteristics	1009
Fluid Type	423
Fluidity	369
Fluoride Free Mould Powder	349
Fluoride Free	279, 299
Fluorine-free Mould Fluxes	335
Flux	1245
Fluxes	1017, 1271
Foaming Index	607
Foaming Slag	431
Freeze-Lining	245
Front-heating Front-detecting Laser	
Flash Method	519
Fuming	899
Functional Theory of Density (DFT)	799
Funnel Mold	255
Furnace Method	87

G

Gas/Slag Equilibrium	167
Gasification	619, 627, 1109
.....	1119, 1135, 1397
Gas-Liquid-Liquid System	589
GBF-Slag	837
Gibbs Energy	535
Gold Tailing	1271
Graphite	565
Grinding	1351
Growth	237
Growth Rate	1229

H

H ₂	627
H ₂ O	627
Hard Metal Scrap	1293
Haynes 230	1199
Haynes NS-163	1199
Heat Capacity	525
Heat Flux	255
Heat Recovery	1237
Heat Transfer	263, 307, 335, 349
Heterogeneous Reaction	535
Hexavalent Chromium	865

High Al Steel	271, 291
High Chrome Oxide	1109
High MnO Slags	1327
High Temperature NMR	799
High TiO ₂	405
High-Aluminum Steel	279
Homogeneous	369
Hot Face	1071
Hot Stage Slag Engineering	439
Hot Steel Slags	1237

I

Ilmenite	761
Immobilization	865
Impurities	817
Inclusion	145
Inclusion Formation	127
Inclusion Modification	117
Inclusions	697
Industrial Waste	29
Industrial Wastes	873
Infiltration	565
Infrared Emitter Technique	485
Ingot	745
<i>In-situ</i> CLSM Observation	229
In-Situ Observation	221
Interface	535
Interfacial Oxygen Potential	989
Interfacial Phenomena	535
Interfacial Reaction	1371
Interfacial Tension	1245
Interpolate	635
Ionic Conductivity	1335
Iron and Steelmaking	627
Iron Oxide	357
Iron Oxide Melts	511
Isomorphism	1343

K

Kinetic Mechanism	1237
Kinetics	117, 1017
KOH	71

L

Ladle	1127
Ladle Metallurgical Furnace	1009
Ladle Slag	1031
LA-ICP-MS	193
Leachability	1359
Leaching	909
Lead Recycling	879
Lead Slags	1221
Lead Smelting Dusts	1369
Less Slag	1177

Levitation	929, 1245
LF	1017
Lime Consumption	1177
Liquid Copper	1379
Liquid Phase	1253
Liquidus	707, 947, 1221, 1379
Liquidus Surface	105
Liquidus Zone	415
Longitudinal Cracks	255
Low Carbon Ferrochrome	87

M

Magnesia	1161
Magnesium Salts	525
Magnetite Precipitation	687
Manganese Ore	63
Mass Transfer	127, 989
Mathematical Modeling	1043
Matte	919, 1077, 1379
Matte-Slag Equilibrium	1207
Maximum Bubble Pressure	597
Mechanisms	1017
Melting	263
Melting and Atomizing	1271
Melting Point	63, 525, 979
Metal	697, 1077, 1309
Metal Droplets	989
Metal Melt	731
Metallurgical Waste	1359
Metal-Slag Separation	1025
Mg + MgCl ₂ Salts	525
Mg Inhibitor	1169
MgCl ₂	1169
Mg-PSZ Ceramic	1371
Microgravity	1245
Microstructure	245, 1101
Mineral	1351
Mineralogy	1343
Minor Elements Distribution	947
Mixing Time	999
MnO-SiO ₂ -Al ₃ Slag	211
Model	397
Modelling	899
Mold Flux	279, 291, 307, 317, 447
Mold Powder	299
Molecular Dynamic	799
Molten Alkali Silicates	183
Molten Carbonates	1161
Molten Fluoride Salts	597
Molten Metal-Slag	589
Molten Oxidation	687
Molten Salt	761
Molten Salt Phase	71
Molten Silica	43
Molten Slag	397, 929

Molybdenum	29
Mortar	837
Mould Flux	327, 357, 477, 1319
MPE	667
MTDATA	971
MTOX	971
Multi-component Kinetic Model	271
Multi-phase Flow	589
Multi-phase Flux	1389
Multiphysics Model	635

N

Na ₂ O	335, 1319
Na ₂ SiO ₃ Modification	909
NaF-AlF ₃	799
NaOH	71
Newtonian	369
Newtonian Fluid	1143
Ni-Base Alloys	745
Nickeliferous Laterites	79
NMR Spectroscopy	715
Non-Metallic Inclusions	117, 155
Non-Newtonian Fluid	1143
Nucleation	237

O

Orinoco Tar	29
Oxidation	1405
Oxidation Thermodynamics	511
Oxidative Roasting	71
Oxy-Fluoride Molten Salt	465
Oxygen Removal	751

P

Partition/Distribution	919
Paste	837
Pb Concentrate	1351
PCBs	203
Peirce-Smith Converter	1379
Petcoke	1119, 1397
Phase Chemistry	1071
Phase Diagram	635, 937, 971
Phase Equilibria	105, 707, 947, 961, 1221
Phase Precipitation	221
Phase Relations	723
Phase Transformation	237
Phosphorous	1135
Phosphorus	697
Phosphorus Recovery	909
Pirotine	1351
Polarizable Ion Model (PIM)	799
Polymerization Degree	455
Polymetallic Deep-Sea Nodules	97
Precious Metal	193

Precipitation	1229
Precipitation Behavior	1261
Pt-Rh Alloy	1135
Pyrolusite	211
Pyrometallurgy	847
Pyroprocessing	771

Q

Quantitative Microanalysis	961
Quartz	43
Quasi-steady State Hot Plate Method	475

R

Radiative Heat Transfer	327, 485
Raman	715
Raman Spectroscopy	455
Raman Spectrum	175
Rare and Precious Metals	203
Rare Earth	229
Rare Earths	221
Rare-Earth Element	723
Reaction Kinetics	989
Reactive Impregnation	1093
Reactive Wetting	573
Reagents	1351
Recovery	889
Recovery of Metals	873
Recycling	751, 829, 947
Reduction	357, 657, 791, 889, 1285
Reference	369
Refined Slag	155
Refractories	53
Refractory	1071, 1093
Refractory Ceramics	573
Refractory Corrosion	1063
Refractory Material	1077
Refractory Wear	1109
Regeneration	1293
Regular Solution Model	1327
Rheology	1301

S

Scattering	485
Sea Desertification	829
Secondary Refining	1127
Selenium Dioxide	677
Sessile Drop	597
Shear Thinning	447, 1301
Silica Glass	477
Silicate	369
Silicomanganese	1309
Silicon	43
Silicon Furnace	1153
Silicothermic Reduction	87

SiMn	1285
Single Hot Thermocouple Technique (SHTT)	237
Single-Stage Copper Making	667
SiO	565
Sio Gas	1153
SiO ₂ -CaO Slag	1 75
Slag	53, 145, 369, 557, 573, 677, 697 731, 889, 919, 947, 979, 999, 1071, 1077 1093, 1119, 1177, 1245, 1309, 1379, 1405
Slag Attack	53
Slag Chemistry	879
Slag Cleaning	657
Slag Design	97
Slag Designing	17
Slag Fluidity	1031
Slag Formation	1017
Slag Management	619
Slag Melting	565
Slag Polymerization	1301
Slag Pool Thickness	343
Slag Reduction	127
Slag Rim	343
Slag Solidification	229
Slag Splashing	1043
Slag Structure	501
Slag Utilization	627
Slag Wetting	135
Slag/Steel Reaction	263
Slags	707
Slurry	837
Smelting	203
Smelting Process	79
Smelting Reduction	211, 873
SNMS	1371
Sodiothermic Reduction	1293
Solid Oxide Membrane	781
Solid Particles	439
Solidification	1185
Solubility	979
Spent Lithium-Ions Battery	211
Spent Lubricant	29
SPH	589
Spinel	135, 145
Spinel Liquidus	1207
Spout	1127
Spreading Rate	573
Stability	501
Stainless Steel	155
Stainless Steelmaking Slag	865
Steel	723
Steel Slag	847
Steelmaking	117, 1277, 1389
Steelmaking Slag	829, 909
Steel-Slag Reactions	117
Sterile	1351

Structural Relaxation	183
Structural Species	511
Structure	17, 291, 397, 455, 715
Submerged Arc Furnace	97
Sulfide Capacity	715
Sulfur	697
Sulphide Capacity	167
Surface Tension	557, 597, 607
Syngas Production	1237
Synthetic Rutile	761

T

Tellurium	979
Ternary System	1253
TG-DTA	63
The Ostwald Growth Model	1229
Thermal Conductivity	477, 519, 1169
Thermal Effusivity	519
Thermo-Chemical Modelling	97
Thermocouple	1135
Thermodynamic	79
Thermodynamic Calculation	1063
Thermodynamic Modelling	397, 947, 1379
Thermodynamic Properties	1277
Thermodynamics	979, 1017, 1389, 1397
Thermogravimetric Analysis	1319
Thermo-Physical-Chemical Properties	405
Ti-Bearing Slag	423
TiC	423
Titania	1261
Titaniferous	1253
Titanium	415, 731, 761
Titanium Bearing BF Slag	1261
Titanium Scrap	751
Titanomagnetite Slag	105
Top-Blowing	999
Trace Elements	961
TSL Smelting	667

U

Ultra-low Carbon Steel	343
Ultrasonic Waves	183
Uranium Recycle	771

V

Valence	1405
Valorization	1185
Vanadium	29, 1119, 1405
Vanadium Slag	455, 1143
Vapor Pressure	1119, 1169
Viscosities	697
Viscosity	17, 279, 369, 397, 415, 439, 455 501, 511, 607, 929, 1143, 1169, 1271

Viscosity Calculation1063

W

Waste Smartphone203

WC-Co Nanoparticles1293

Wear Mechanisms1077

Welding Flux929

Wettability573

Wetting1371

X

X-ray Absorption1405

X-ray Diffraction63

Y

Yttria Stabilized Zirconia781

Z

Zirconia145, 1161

Zirconia Solubility465

Zr Inhibitor1199